Further Studies on the Anodic Corrosion of Lead in H_2SO_4 Solutions

J. J. LANDER

Naval Research Laboratory, Washington, D. C.

ABSTRACT

Anodic corrosion of lead in sulfuric acid was studied in detail at potentials near the reversible $PbO_2/PbSO_4$ potential. Results indicate that the first step in the corrosion process was reaction of lead with water to form lead dioxide. The solid-phase reaction $Pb + PbO_2 = 2PbO$ probably occurred below a certain potential, and this reaction plus two electrochemical reactions rendered lead dioxide unstable at lower potentials. A potential was found at which the corrosion rate reached a sharp peak. Above this peak lead dioxide was found in the reaction product.

Kinetic treatment was only partially successful. In 30% acid, at potentials just below the reversible $PbO_2/PbSO_4$ potential, conversion of lead dioxide film to lead sulfate took place, and the rate of corrosion appeared to be controlled by diffusion of the electrolyte into the film. Above the reversible $PbO_2/PbSO_4$ potential, a protective lead dioxide film was formed, and a linear rate of corrosion was found which increased with increasing temperature and decreasing acid concentration.

INTRODUCTION

A previous paper showed results of corrosion of lead in sulfuric acid using constant potential techniques (1). The potential range of about 0.1–1.0 volt less noble than the reversible $PbO_2/PbSO_4$ potential was studied. More recently, corrosion was studied in detail at potentials near the positive plate potential, because at these potentials corrosion rates are more directly related to conditions of battery service. The primary aim of this work is to elucidate the thermodynamics and kinetics of the corrosion process, in the hope that results might indicate methods of preventing or slowing down corrosion, thus allowing longer positive grid life.

THEORY

Thermodynamics

Standard electrode potentials for some reactions concerned in the electrochemistry of lead are given in Table I. The discussion to follow will tell what reactions are to be expected in the several potential ranges involved in the work.

The electrochemical couples H_2/H^+ and Hg/Hg_2SO_4 are included for reference. The oxidation of water to oxygen is theoretically reversible at 1.23 v, but actually it is subject to such a large overvoltage that oxygen production is not observed except at potentials several tenths of a volt more noble than the reversible potential for the $PbO_2/PbSO_4$ couple.

The potential limit of the reaction $Pb + PbO_2 = 2PbO$, which has been shown to take place in the solid phase (2), is placed at +1.58 v. It is believed that the occurrence of the reaction during anodization of lead and the potential at which it is limited may be inferred from the data of this paper. For purposes of discussion, it will be assumed here that the reaction does, in fact, occur below the potential given. Unlike electrochemical reactions, this potential is not a reversible one; it does not represent a point at which a net forward or reverse reaction begins. Rather, it may be rationalized that for the reaction to go, lead dioxide must take electrons away from the lead metal; if so, the possibility exists that lead can be polarized to some positive potential beyond which lead dioxide can no longer pull away electrons, effectively stopping the reaction. It is to be expected that this potential will not depend on the electrolyte concentration as do the reversible potentials for the other reactions.

The reaction $Pb + H_2SO_4 = PbSO_4 + 2H^+ + 2e$ occurs at the negative plate of the lead-acid cell. It has nothing to do with the corrosion process occurring at the positive plate of a battery, and it is given in the table for orientation purposes only. In a constant-current anodization process it would be the first reaction to occur.

The oxidation of lead to lead monoxide has been shown to occur at potentials more noble than +0.252 (1, 3), and lead monoxide (tetragonal) was found to be the principal reaction product up to potentials approaching the open-circuit value for the positive plate (1). Evidently, the lead sulfate coating formed on the outside protects the lead oxide film from rapid attack by the acid. At more noble potentials, the next reaction which can occur is the direct oxidation of lead to lead dioxide by water, $E_0 = +0.666$ v; and if the film is porous, the reaction would be expected to occur. It is to be noted that lead dioxide formation is possible a full volt below the reversible positive-plate potential. However, it is not stable below that potential, tending to react at the solution interface with sulfuric acid and hydrogen ion to give lead sulfate and lead monoxide, and at the metal interface to give lead monoxide by the solid-phase reaction. Above potential +1.100, corresponding to the reaction $PbO + H_2O = PbO_2 + 2H^+ + 2e$, lead dioxide would no longer be unstable due to reaction with hydrogen ion, but it would still be unstable on both the other counts. The fact that above this voltage

TABLE I. *Standard electrode potentials for various reactions*

Reaction	E_0
$Pb + H_2SO_4 = PbSO_4 + 2H^+ + 2e$	−0.355
$H_2 = 2H^+ + 2e$	0
$Pb + 2H_2O = Pb(OH)_2 + 2H^+ + 2e$	+0.242
$Pb + H_2O = PbO + 2H^+ + 2e$	+0.252
$2Hg + H_2SO_4 = Hg_2SO_4 + 2H^+ + 2e$	+0.616
$Pb + 2H_2O = PbO_2 + 4H^+ + 4e$	+0.666
$PbO + H_2O = PbO_2 + 2H^+ + 2e$	+1.100
$2H_2O = O_2 + 4H^+ + 4e$	+1.230
$Pb + PbO_2 = 2PbO$ (Solid phase, voltage limit of)	+1.58
$PbSO_4 + 2H_2O = PbO_2 + H_2SO_4 + 2H^+ + 2e$	+1.684

lead monoxide is found to be the chief product (1) shows that the corrosion process goes by direct oxidation to lead monoxide or by oxidation to lead dioxide followed by the solid-phase reaction. The possible reaction $PbO + H_2O = PbO_2 + 2H^+ + 2e$ does not go to any appreciable extent; otherwise, either lead dioxide would be found in the reaction product or lead sulfate would be the chief product. X-ray analysis indicates only lead monoxide and lead sulfate, and the reaction corresponds to Faraday's Law for $Pb = Pb^{++} + 2e$ (1).

At more noble potentials, if the primary reaction is oxidation of lead to lead dioxide, then lead dioxide should become evident in the reaction product as the potential passes the value +1.58. It should occur along with lead sulfate, lead oxide no longer being present. Finally, above the reversible $PbO_2/PbSO_4$ potential, PbO_2 should be the sole solid product.

Kinetics

When a nonporous film is formed, either a linear or a parabolic rate law may apply, depending on whether the rate is limited by reaction at one of the interfaces (4) or by migration of ions through the film (5).

Evans (6) considered mechanical breakdown of films growing in gaseous media and showed that if breakdown of a continuous film produces cracks too fine to allow the oxidizing medium to reach the metal surface, then migration of ions along the cracks should take place at an enhanced rate, the parabolic law being retained. If breakdown results because of blister formation, and the blister walls are impervious to the oxidant, then the flat cavities resulting constitute barriers to migration, and a logarithmic relationship between film weight and time is exhibited. In this case, it may be noted that breakdown results in a lower rate than a continuous film would provide. Analogous rate-controlling factors can be envisioned for electrochemical film-forming processes.

If the film is porous, the situation is by no means clear-cut, and rate laws are difficult to derive because they depend on the modes of crystallization and growth of the film substance. However, if the pore area becomes constant after a time, then the mathematical treatment is simplified, and linear or parabolic equations for the rate may be derived. A linear relation would be expected if the intrinsic rate of the reaction at the metal surface is controlling. In this case, the rate constant would be small enough that rates would not be limited by diffusion. Parabolic equations result if the rate is diffusion-controlled or if the film growth is limited by resistance of the electrolyte in the pores of the film.

Evidently, there are several mechanisms that can each lead to parabolic and linear w vs. t relationships; for data which fit either form, the form would not be sufficient to characterize the mechanism. Choice among mechanisms would have to be made on the basis of constants of the equations. This could be difficult because of lack of knowledge of the values of some of the constants concerned, e.g., pore area.

Experimental

Samples of lead were corroded at various constant potentials near the reversible $PbO_2/PbSO_4$ potential. The method, apparatus, and techniques employed have been described previously (1). Single samples were used for voltages below the $PbO_2/PbSO_4$ potential, and these were corroded for times up to 72 hr. Corrosion current was recorded, the films were stripped, and weight losses were determined. The weight-loss results were checked against values calculated from Faraday's Law and the current-time trace.

For rate determinations above the $PbO_2/PbSO_4$ potential, longer times were necessary to enable an estimate of the rate; furthermore, some of the current went to oxygen evolution so current could not be used to measure rates. Consequently, four or five samples were used. These were removed from the corrosion cell one at a time over a week or so, stripped in an alkali-hydrazine-mannitol bath, and weight losses were determined. Results were plotted against time, and slopes of the curves were measured to get rates.

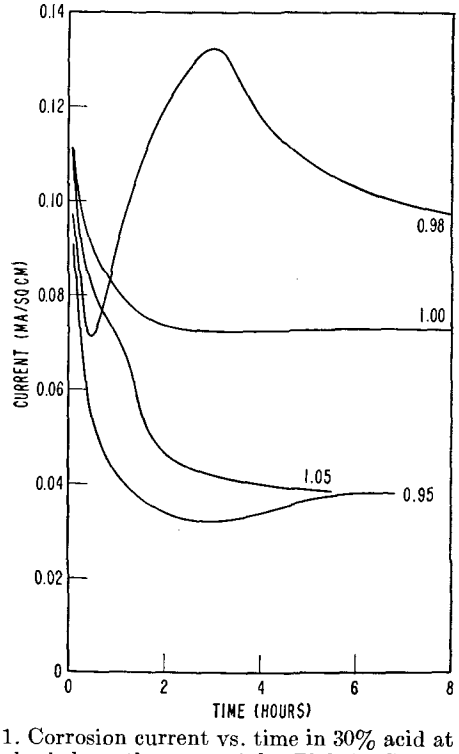

FIG. 1. Corrosion current vs. time in 30% acid at several potentials below the reversible $PbO_2/PbSO_4$ potential (1.100 volt).

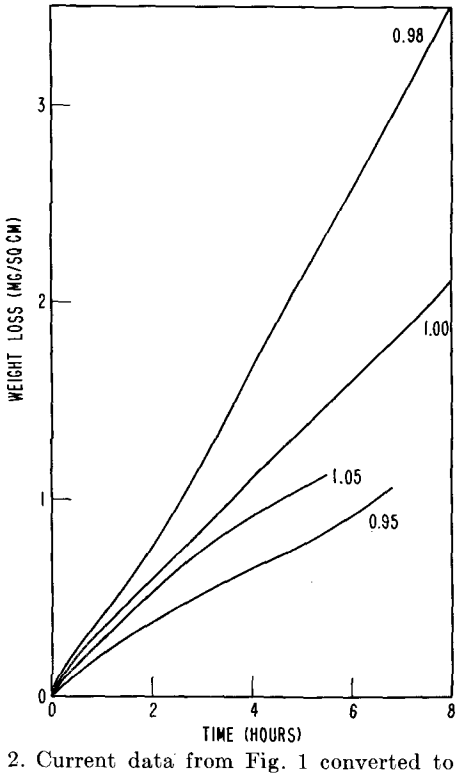

FIG. 2. Current data from Fig. 1 converted to weight loss.

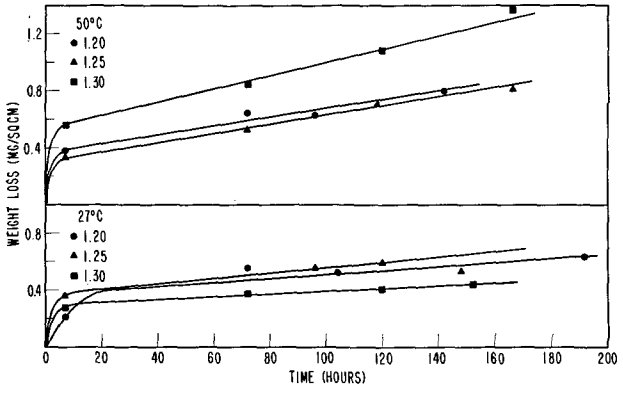

FIG. 3. Corrosion above the $PbO_2/PbSO_4$ reversible potential in 30% acid.

All potentials were measured against an Hg/Hg_2SO_4 reference electrode in the electrolyte of the anodizing cell.

RESULTS

Corrosion current data at room temperature were obtained at potentials ranging from about 0.2 v below the $PbO_2/PbSO_4$ reversible potential to as high as 0.20 v above, in acid strengths of 1%, 10%, 30%, and 40% by weight. Weight losses were obtained for these samples by stripping to check against those calculated from Faraday's Law. Fig. 1 shows a typical set of current curves at various potentials[1] for the 30% acid. At some potentials both divalent and tetravalent corrosion products were formed, in which case the weight loss measurement

[1] To save space, the data for each concentration of acid are not given. Complete data can be found in NRL Report 4475.

TABLE II. *Corrison rates above the* $PbO_2/PbSO_4$ *potential*

% Acid	Voltage	Penetration rate (cm/yr)	
		30°C	50°C
10	1.15	3.0×10^{-3}	3.5×10^{-3}
	1.20	4.2	4.3
	1.25	3.0	7.7
30	1.125	1.5	—
	1.20	1.2	2.1
	1.25	1.3	2.4
	1.30	0.9	3.9
40	1.25	0.4	1.5
	1.30	—	2.8
	1.35	0.9	3.3

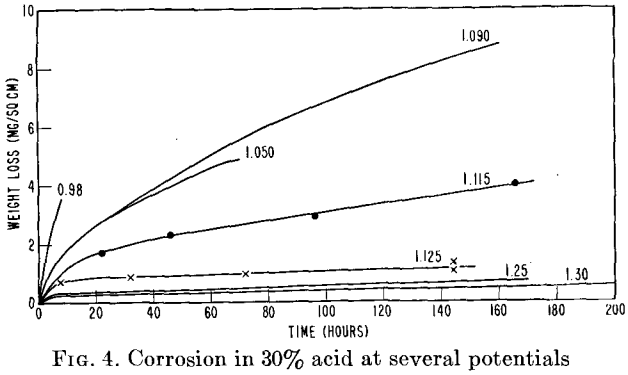

FIG. 4. Corrosion in 30% acid at several potentials

enabled estimation of current distribution between the two kinds of products. Weight loss curves calculated for Fig. 1 data are shown in Fig. 2. When lead dioxide is present only the final weight loss is exact, because the fraction of current going to each valence state was not constant with time, as was assumed in calculating the curves. This will be shown in subsequent data. Nevertheless, the weight-loss curves do give a good idea of the effect of potential.

A typical set of curves for corrosion above the $PbO_2/PbSO_4$ potential is shown in Fig. 3. Data were also obtained for 10% and 40% at both temperatures. The penetration rates calculated from slopes of the linear portions of the curves are given in Table II.

To obtain the corrosion rate vs. voltage relationship in still finer detail just above the $PbO_2/PbSO_4$ potential, additional runs were made in 30% acid at 1.115 and 1.125 v. Data are shown in Fig. 4, which includes data from Fig. 2 and 3 for comparison. This set of curves suggested the possibility of an inflection in the rate vs. potential curve just below the $PbO_2/PbSO_4$ potential, so this range was studied in greater detail for 30% acid.

In this case, several single samples were run for various times at a given constant potential and stripped to obtain weight loss. Current was measured vs. time to enable determination of the effect of time on the distribution of products between di- and tetravalent compounds. Fig. 5 shows a typical set of data for 1.100 and 1.108 v. Data were also obtained at potentials of 1.050, 1.075, and 1.090.

DISCUSSION

The data of this paper and the previous paper (1) may be combined to give a plot of corrosion rate vs. potential

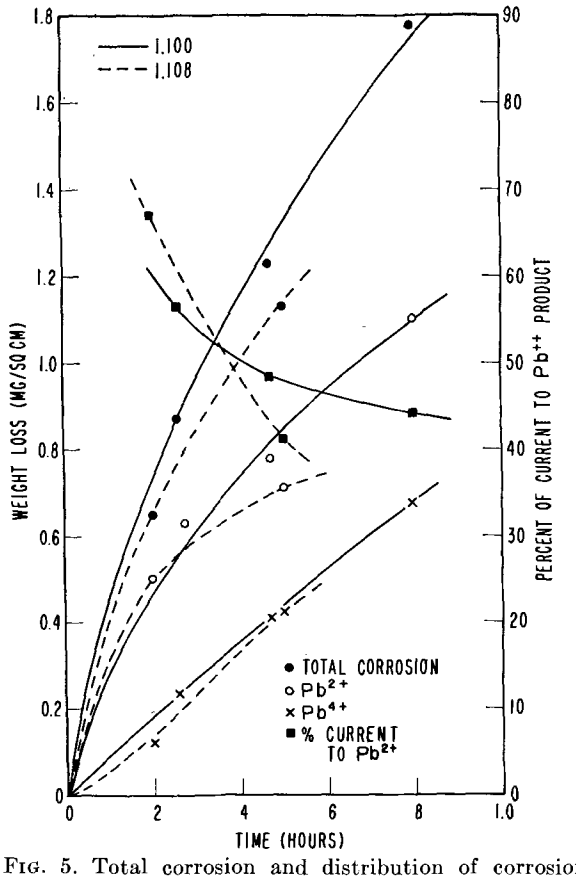

FIG. 5. Total corrosion and distribution of corrosion products in 30% acid at two potentials.

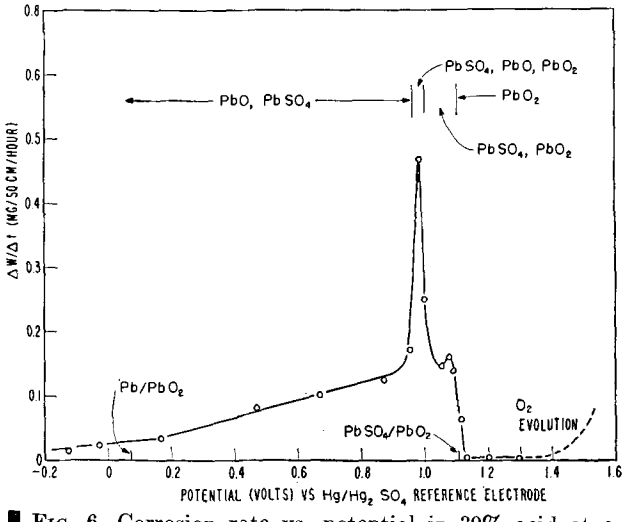

■ FIG. 6. Corrosion rate vs. potential in 30% acid at a constant weight loss of 1.18 mg/cm² (~10,000 Å).

over the range −0.134 to +1.30 v. This is shown for 30% acid at room temperature and a constant weight loss of 1.18 mg/cm² in Fig. 6. The reaction products found over the various potential ranges are also shown.

It was previously suggested (1) that corrosion below the peak of the curve was governed by an activated process and that the reaction involved was $Pb + H_2O = PbO + 2H^+ + 2e$. A different treatment of the data (7) indicated that the primary reaction is formation of lead dioxide above the potential +0.666 (on the hydrogen

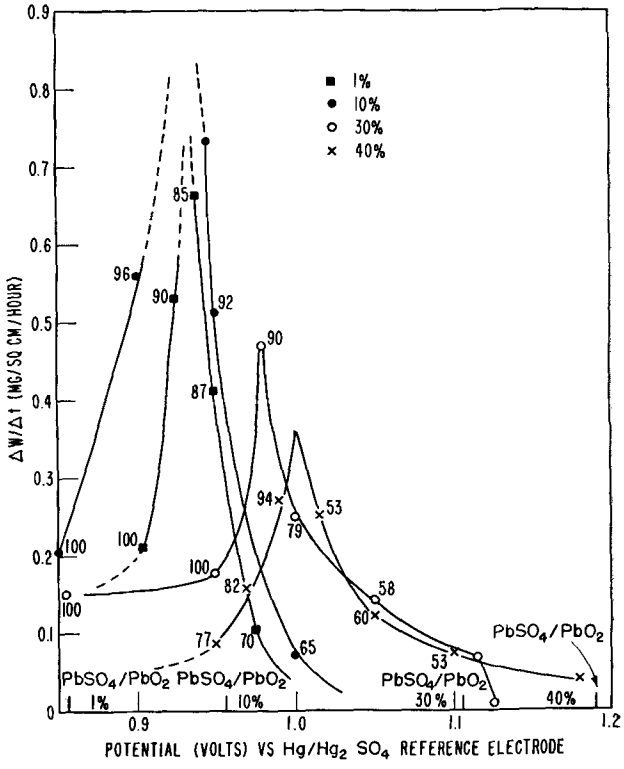

FIG. 7. Rate of corrosion vs. potential for several acid strengths at a constant weight loss of 1.18 mg/cm².

scale), and that polarization in the linear range above that point corresponds to *IR* drop through a porous lead monoxide film. Lead monoxide was formed because the lead dioxide is unstable on the several counts discussed in the theoretical section of this paper.

Actually, for a cell in any kind of service, the voltage range below some potential in the neighborhood of the peak of the curve is not of interest in the practical corrosion problem inasmuch as rates are not controlled by the same mechanism on either side of the peak. Positive-plate voltages, even in a cycling cell, do not drop below the voltage of the peak, except perhaps for short times only on a deep discharge or a high-rate discharge.

Data taken for the 1%, 10%, 30%, and 40% electrolytes, such as shown in Fig. 1 and 2, cover the voltage range of the peak of the corrosion curve. From that data, curves shown in Fig. 7 were obtained by plotting the slopes of the weight-loss curves at a constant value of weight loss against potential. The estimated per cent of current going to form divalent product is given by the number at each point. The reversible potential values for $PbO_2/PbSO_4$ couples are shown on the potential axis.

As voltage increased, a steep rise in the rate took place when lead dioxide became evident in the reaction product. It was not found in quantity, however, until the peak was passed and rates fell off sharply.

Attention may be directed to several features of these curves. First, the positions of the peaks have nothing to do with the location of the reversible $PbO_2/PbSO_4$ potentials, being found below by varying amounts in the stronger acids, but above in the 1% electrolyte. Second, the chief products of reaction on the low voltage side of

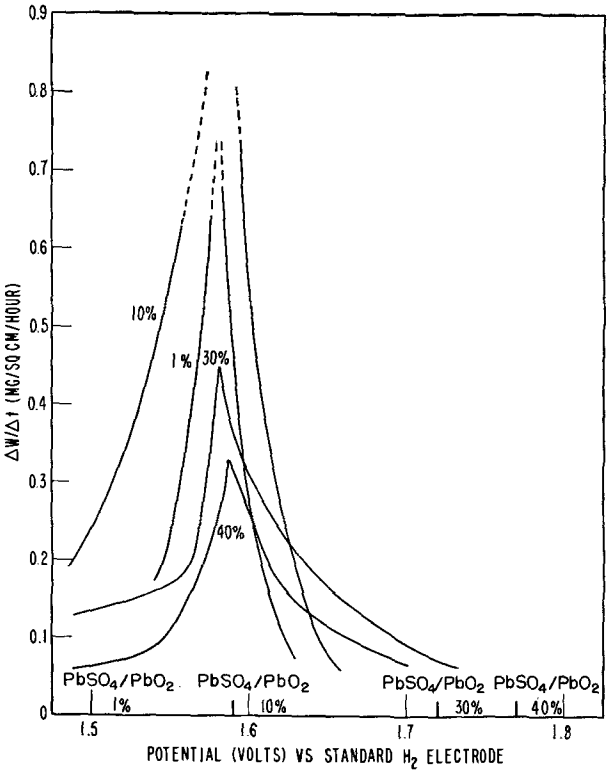

FIG. 8. Data of Fig. 7 vs. potential referred to the standard hydrogen electrode.

the peaks were lead monoxide and lead sulfate. Third, in the case of the 1% electrolyte, the chief reaction product was lead monoxide even at 0.1 v higher than the reversible $PbO_2/PbSO_4$ potential. Fourth, as shown in Fig. 8, positions of all the peaks fall at the same potential, regardless of acid concentration, when rate is plotted vs. potential referred to the standard hydrogen electrode; in other words, the position of the peaks does not vary with voltage.

It was shown in earlier work (2) that lead dioxide undergoes a solid-phase reaction with lead to form lead monoxide. It was suggested then that on discharge the lead dioxide formed during the previous charge might give this reaction with the grid metal and so contribute to corrosion in a cycling cell. It is now suggested that the maximum in the rate curves, illustrated in Fig. 8, corresponds very nearly to the potential above which the solid-phase reaction won't go, as discussed in the theory. Although no direct evidence is available to prove this, it seems to fit in with the experimental data,[2] especially the two facts that the potential of the peak does not vary with concentration, and that lead monoxide is the chief reaction product in 1% acid at voltages beyond the reversible $PbO_2/PbSO_4$ potential.

The picture now seems clear: lead dioxide is formed in the initial corrosion reaction at the metal surface at voltages well below the $PbO_2/PbSO_4$ reversible potential; being unstable, it goes to lead monoxide and lead sulfate at voltages below the peak, and to lead sulfate at voltages above the peak but below the $PbO_2/PbSO_4$ voltage, where the solid-phase reaction cannot go. Just below the peak the highly resistant lead monoxide film ceases to be the dominant rate-controlling factor, as lead dioxide begins to appear, breaking up the lead monoxide film.

It is now evident from Fig. 7, that the suggestion offered before (2), i.e., on discharge the solid-phase reaction contributes to the corrosion process, must be modified because polarization to the extent of 0.15–0.25 v is required. This does not occur except on high-rate discharges or discharges beyond the knee of the curve. Consequently, it is to be expected that, for cells in ordinary operation, lead dioxide will always be found next to the metal surface, and that the characteristics of this PbO_2 film will be important in determining corrosion rates.

The most important characteristic of the lead dioxide film is obvious from the thermodynamic and the corrosion rate vs. potential data: on discharge the lead dioxide film, which forms an effective barrier to corrosion during the previous charge, is converted to lead sulfate, and corrosion by the reaction $Pb + 2H_2O = PbO_2 + 4H^+ + 4e$ proceeds.

The factors which control rates at discharge potentials can be determined from data exemplified by Fig. 5, for the 30% acid. In Fig. 9, all the data taken at the several

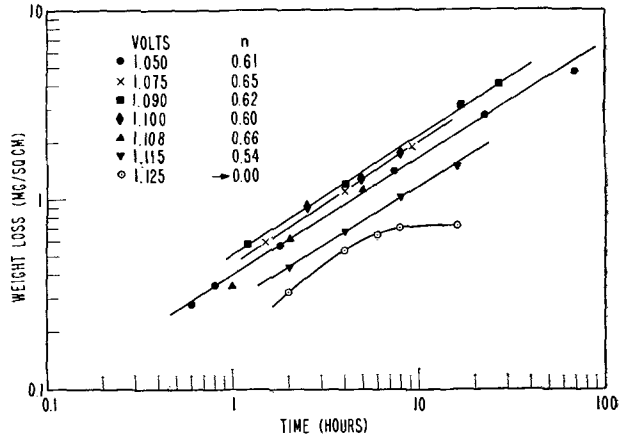

FIG. 9. Total weight loss vs. time at various potentials in 30% acid.

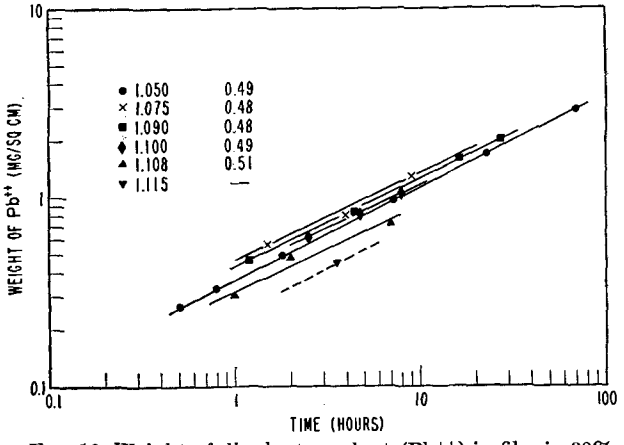

FIG. 10. Weight of divalent product (Pb^{++}) in film in 30% acid at the same potentials as Fig. 9.

[2] Additional evidence is given by our unpublished data which show that a 4½% tin alloy of lead does not exhibit the peak in the rate curve. This alloy does not undergo the solid-phase reaction to any appreciable extent.

potentials are plotted as total weight loss vs. time on a log log scale. Slopes of these curves all lie close to 0.6. Data for the formation of divalent product are plotted on a log log scale in Fig. 10. Slopes of these curves all lie close to 0.5, and the experimental equation for the formation of $PbSO_4$ is $w = kt^{1/2}$ and the data are accurately parabolic. This suggests that the rate of conversion of the underlying lead dioxide is diffusion-controlled. It has been shown (7) that a diffusion-controlled process fits the constants of the parabolic equation. It can be shown that control by a solid film or by the electrical resistance of a porous film results in unreasonable values for the constants in either case.

The conversion reaction tends to keep the lead dioxide from building up to thicknesses at which it becomes protective. At the same time, total corrosion proceeds somewhat faster than the conversion reaction because the latter actually undercuts some lead dioxide and isolates it electrically (Fig. 11), so it can not go to lead sulfate. This process allows quantities of lead dioxide larger than necessary for a protective film to be present in the reaction product, as can be seen by comparing Fig. 3 and 5. Therefore, it is not quite the rate of conversion of the lead dioxide film which limits the over-all rate, but, more exactly, it is the rate of penetration of the conversion process into the underlying film.

If the rate of corrosion at constant weight loss is plotted vs. potential, the curve shown in Fig. 12 is obtained. Numbers at the points show per cent of current going to divalent product. Ordinarily, the curve would be expected to follow the course of the dotted line as the concentration gradient of sulfate ion approaches the maximum value allowed by the concentration in the body of the solution. The rapid rise in the rates below about 1.025 v is indicative of a new reaction, i.e., the solid-phase reaction. The rate goes up because the underlying lead dioxide film is attacked from the metal side as well as the solution side, rendering the film more porous. The reason for the minimum at 1.050 v is not understood.

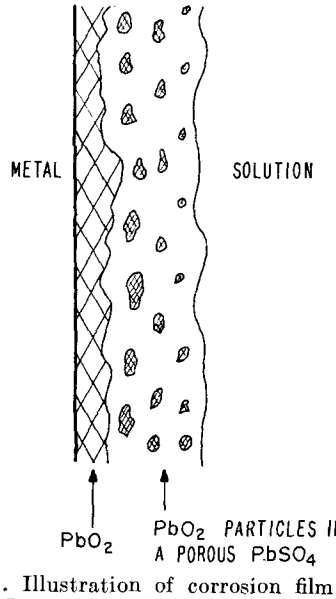

FIG. 11. Illustration of corrosion film just below the reversible $PbO_2/PbSO_4$ potential.

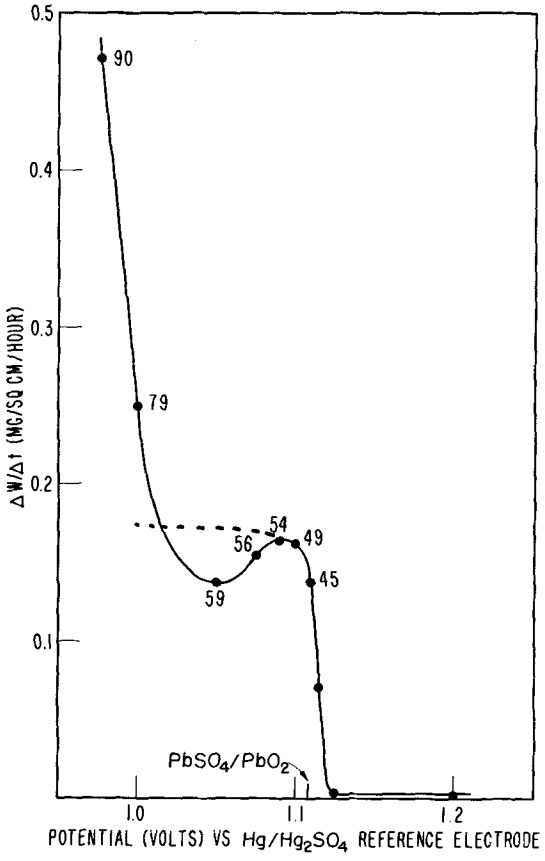

FIG. 12. Corrosion rate vs. potential at constant weight loss (1.18 mg/cm²) just below the $PbO_2/PbSO_4$ potential.

It seems that, above the $PbO_2/PbSO_4$ reversible potential, data are insufficient during the time of rapid film formation to characterize the mechanism definitely. Table II and Fig. 3 show the rates, determined from the linear portions of the curves, as a function of potential, acid strength, and temperature. There seems to be a trend toward higher rates at higher temperatures and lower acid concentrations. The effect of potential is uncertain, but must be small, from the data for 30% acid at 30°C.

Data of Fig. 3 show that something occurs in the lead dioxide film which slows down the rate quite sharply after an initial period of rapid film growth. This might be a case of blistering such as proposed by Evans (6). At any rate, the linear w vs. t curve and the very low rate for the thin films concerned imply ionic diffusion through a continuous film.

Discussion in Terms of Battery Service

Corrosion in cells on float may proceed at the very low rates of 1–3 × 10^{-3} cm penetration/year for pure lead. The data of Table II indicate that some life might be gained for batteries on float by changing to acids stronger than are usually employed (~30%). It is also indicated that the positive plate can be maintained over a rather wide range of potential (e.g., 1.125–1.30 for 30% acid at 30°C) without much effect on corrosion rate, so rigid voltage control might not be necessary. If these tests were extended to considerably longer times, however, small differences in rate might become apparent. These

could be appreciable in their effect on the life of a cell which is measured in terms of years.

In the past, antimonial alloys were used for grids of cells in float service, as for other types of service. Recently, it has been indicated that a binary alloy of calcium and lead might be more suitable for float service (8). With the antimonial alloys, float voltages were governed by the necessity for supplying enough current to the negative plates to keep them in good condition. With the calcium alloy the negative plate is no longer a problem, and, at the same float voltages, much smaller currents [of the order of $\frac{1}{10}$–$\frac{1}{70}$ (9)] will suffice for the negative plate. With lower currents, there may be danger that the positive-plate voltage will fall below the protective range. In such an event, higher float voltages than were used for the antimonial cells would be necessary to obtain the life increase expected of this alloy. Long-term tests should be run to determine whether a corrosion-rate minimum exists in the protective potential range.

Dropping down on the voltage scale, the next potential range for consideration is one in which the automobile battery operates. That is to say, it alternates between a stand condition and float, with short high-rate charge and discharge periods. The times on charge and discharge are relatively short and probably may be neglected in considering life.

It appears from Fig. 12 that the life of positive grids of automobile batteries should approach that of the same batteries on float, the life being shortened somewhat by the time spent on stand, during which time the positive-plate potential will be located somewhere on the steep portion of the curve at the reversible $PbO_2/PbSO_4$ potential. If most of the stand time were spent at the bottom of this steep curve, then the reduction in life should be small—a likely condition for batteries of cars that are run daily, because it takes an appreciable time for the positive-plate voltage to fall to the open-circuit value after a charge.

A peculiarity of automobile-battery service may be expected to become important as the end of life approaches, i.e., the constant-voltage charge. As the cell gets older, the hydrogen overvoltage at the negative plate falls off for batteries with antimonial grids, which means that the positive-plate voltage increases proportionately; when this voltage gets in the gassing range, faster corrosion during the time the car is running will ensue, hastening the end of life. Furthermore, the time spent at these higher voltages will be longer because the negative-plate voltage come-up will be sluggish, with the same effect.

Batteries which operate under a cycling program, such as industrial truck and submarine batteries, spend an appreciable part of their life on discharge; and during discharge, positive-plate potentials will be well up on the steep portion of the curve. This is unquestionably the reason why batteries in cycling service have relatively short lives in comparison with batteries in other types of service.

Because corrosion during discharge is limited by the rate of diffusion of acid into the corrosion film, it is to be expected that, as the film builds up in thickness, the rate at which acid can diffuse to the corroding surface will slow down, until eventually it becomes less than the linear rate observed for stand conditions. Then the rate of corrosion under cycling conditions should become the same as that for the linear rate on float, which does not depend on film thickness. This has been observed (10).

The theory presents two obvious methods of attack on the problem; the diffusion coefficient can be made smaller by increasing the viscosity, and possibly the diffusion path could be made tortuous or the pore area smaller. Lowering the diffusion coefficient is not a solution, because it would result in lower rates and energies which could be drawn from the cell, inasmuch as the active material discharge depends on this factor. The viscosity of the electrolyte could be increased by increasing the acid strength, and lower initial corrosion rates are actually found in the stronger electrolytes (2, 10). However, such an expedient can be utilized to a limited extent only, before the negative plate begins to show decreased capacity (11). In addition, although initial corrosion rates are higher in low-gravity acids, they slow down much faster, and after a time the corrosion rate in the high-gravity acid becomes larger (10, 12). On the whole, it is concluded that not much is to be gained in this way. Methods of affecting pore area and path length are not immediately evident. Apparently, what must be found is some method or trick of selectively preventing the normal discharge reaction from taking place at the lead dioxide coating on the grid.

Summary

Anodic corrosion of lead in sulfuric acid was studied in detail near the positive-plate reversible potential using constant-potential techniques. In general, it is indicated that the electrochemical reactions expected on the basis of thermodynamic data occur at their proper potentials. There are several of these reactions, and in addition chemical reactions also occur.

Mechanisms governing rates have not been determined in all the potential ranges concerned; indeed, the whole picture is rather complicated because of the number of reactions occurring.

Data for the several voltage ranges may be interpreted more specifically to show:

1. Formation of lead dioxide by the reaction $Pb + 2H_2O = PbO_2 + 4H^+ + 2e$ is the first step in the corrosion process above the reversible potential for that reaction. It is unstable both on chemical and electrochemical grounds at the lower potentials and goes to lead monoxide and lead sulfate.

2. A voltage limit above which the solid-phase reaction $Pb + PbO_2 = 2PbO$ cannot go has been shown to be about +1.58 v to the standard hydrogen electrode. This voltage marks the appearance of lead dioxide in the corrosion product and is characterized by a peak in the corrosion-rate vs. potential curve which separates the kinetic behavior of the corrosion processes. At more noble potentials, just below the reversible positive-plate potential, corrosion rates are limited by penetration of the positive plate discharge reaction into an underlying lead dioxide

film. This penetration is controlled by diffusion of $SO_4^{=}$ through a porous film of mixed lead dioxide and lead sulfate. At slightly less noble potentials, diffusion control gives way to a relatively rapid process because the solid-phase reaction begins to take place and the lead dioxide film is attacked from both sides.

3. Above the reversible $PbO_2/PbSO_4$ potential, corrosion rates fall off very rapidly to extremely low values, because a protective lead dioxide film is built up. Rates in this potential range do not vary with potential at room temperature within experimental error, but they do increase with increasing temperature and decreasing acid concentration.

Gains in knowledge of the corrosion process resulting from this work do not appear to indicate definite means of slowing down corrosion for cells in cycling service. The possibility of slowing corrosion in floating cells by increasing the electrolyte concentration is indicated.

Manuscript received May 20, 1955. Most of the data in this paper was presented at the Boston Meeting, October 3 to 7, 1954.

Any discussion of this paper will appear in a Discussion Section to be published in the December 1956 JOURNAL.

REFERENCES

1. J. J. LANDER, *This Journal*, **98**, 213 (1951).
2. J. J. LANDER, *ibid.*, **98**, 220 (1951).
3. E. F. WOLF AND C. F. BONILLA, *Trans. Electrochem. Soc.*, **79**, 307 (1941).
4. N. E. MOTT AND R. W. GURNEY, "Electronic Processes in Ionic Crystals," p. 250, Clarendon Press, Oxford (1940).
5. C. WAGNER, *Z. Physik. Chem.*, **B32**, 447 (1936); T. P. HOARE AND L. E. PRICE, *Trans. Faraday Soc.*, **34**, 867 (1938).
6. U. R. EVANS, "An Introduction to Metallic Corrosion," Edward Arnold, London (1948). *See also* U. R. EVANS, *Trans. Electrochem. Soc.*, **91**, 547 (1947).
7. J. J. LANDER, NRL Report 4475, Jan. 31, 1955.
8. U. B. THOMAS, F. T. FOSTER, AND H. E. HARING, *Trans. Electrochem. Soc.*, **92**, 313 (1947).
9. J. F. RITTENHOUSE AND H. E. JENSEN, "The Lead-Calcium Battery," C. and D. Batteries, Inc., Conshohocken, Pa. (1953).
10. J. J. LANDER, *This Journal*, **99**, 467 (1952).
11. G. W. VINAL, "Storage Batteries," 3rd ed., p. 217, John Wiley & Sons, Inc., New York (1940).
12. J. J. LANDER, Unpublished data.

Theoretical Electromotive Forces for Cells Containing a Single Solid or Molten Chloride Electrolyte

WALTER J. HAMER, MARJORIE S. MALMBERG AND BERNARD RUBIN

National Bureau of Standards, Washington, D. C.

ABSTRACT

From thermodynamic data, electromotive forces have been calculated for reversible galvanic cells of the type $M/MCl_n/Cl_2(z)$ where M is a metallic element in the solid, liquid, or gaseous state and MCl_n is the corresponding chloride in the solid or liquid state. Results are given for temperatures from 25° to 1500°C.

The chlorides are listed in a series and compared with the electromotive force series of the elements in aqueous solutions. Comparisons are given with results obtained from galvanic cells with fused chlorides or from measurements of decomposition voltages.

INTRODUCTION

Standard oxidation-reduction potentials are available for numerous electrochemical reactions in aqueous systems at 25°C (1). These potentials refer to the potentials when all solid or dissolved substances taking part in the oxidation-reduction processes are at unit activity and all gases are at a fugacity of one atmosphere. When the potentials of the elements alone are arranged in series in decreasing or increasing order of magnitude, relative to the conventional hydrogen electrode as reference, the series is generally referred to as "the electromotive force series of the elements."

A similar series for molten or fused systems is unavailable at present. Such a series would differ fundamentally from a series for aqueous systems in that a different standard state is involved for each electrolyte since the molten phase is a pure ionic fluid of one component. Potentials for half-cell reactions are, therefore, within present knowledge not feasible. However, a series may be established based on the free energies of formation of the electrolytic phase, these phases being of like type, such as chlorides, bromides, oxides, etc. These values would correspond to the decomposition voltages of fused salts, assuming the decomposition voltages as determined experimentally contain no ohmic voltages and are free of effects of polarization.

The theoretical decomposition voltages of fused electrolytes would correspond to the reversible electromotive force (emf) of galvanic cells composed of the electrolyte and two electrodes, one of which is reversible to the anion and the other to the cation of the fused electrolyte, the

fused electrolyte and the two electrodes being in their standard states of unit activity or unit fugacity. This reversible electromotive force is also related to the free energy of formation of the fused electrolyte through the relation

$$E^0 = -\Delta F_f^0/n\mathbf{F} \qquad [1]$$

where ΔF^0 is the standard free energy of formation of the electrolyte, E^0 is the standard emf, $\mathbf{F}$ the faraday constant, and n the number of faradays involved in the electrochemical reaction.

Although experimental measurements of decomposition voltages usually do not agree with theoretical values, owing to several factors, including the chemical interaction of the electrodes with the electrolyte, the production of electrodes in a nonstandard state, deviations from isothermal conditions, and electrode polarization, it is nonetheless important to know the theoretical values for the systems under study. These values aid in elucidating mechanisms and in interpretations of experimental observations on fused electrolytes.

It is the purpose of this paper to present the theoretical standard electromotive forces of cells containing a single solid or molten (fused) chloride electrolyte for which the necessary thermodynamic data are available. Data used were obtained from Kelley (2), from Brewer (3), and from the National Bureau of Standards (4). When estimates of heat capacity were required, the rule of Kelley (5) was used, namely, 7.0 cal/°/mean gram-atom for solid compounds, 8.0 for liquid compounds, 7.3 for solid metals, and 7.5 for liquid metals, or the method of Shomate (6) using values of heat content and heat capacity given by National Bureau of Standards (4) was employed. For this paper no attempt was made to review critically or include thermodynamic data other than those contained in the above references. Delimarski (7) conducted a somewhat similar investigation. He determined the potential of 21 metals in their respective chlorides relative to sodium, assigning to the latter a potential of zero, and formulated an electrochemical series on this basis at 500°, 700°C, and the fusion temperature of each chloride. Within the experimental uncertainties his series agrees, as to order, with that presented herein.

No attempt is made to evaluate the accuracy of the quantities used. This phase is discussed in each of the above references; in Table I are listed the uncertainties in emf at 25°C corresponding to the uncertainties in the heat of formation of the chlorides at 298.16°K quoted by Brewer (3), which uncertainties were assumed to apply also to the data in the National Bureau of Standards Circular (4) since the values listed agree closely and their sources are the same. The uncertainties in entropy values are, in general, small compared to those in heats of formation; thus, the uncertainties in emf here listed are based on uncertainties in heats rather than on free energies of formation. Furthermore, the authors are concerned more with the relative values (or order of the chlorides) than with actual values, and in all probability the order (*see* Table I) will remain the same whether the uncertainties are based on heats or free energies of formation.

Method of Evaluation of Standard EMF's

The method of evaluating the standard reversible emf of cells composed of a solid or molten chloride and two electrodes, one of which is reversible to the anion and the other to the cation of the fused chloride, follows well-known thermodynamic relations, considered most elementary by the thermodynamicist. The emf of such cells, namely,

metal/metallic chloride/chlorine gas[1] [A]

is related to the free energy change for the chemical reaction:

metal + chlorine gas → metallic chloride [B]

According to convention this free energy change is the free energy of formation, ΔF_f^0, of the chloride when the chloride, metal, and gas are in their standard states, and is related to the heat of formation, ΔH_f^0, by the equation

$$\Delta F_f^0 = \Delta H_f^0 - T\Delta S^0 \qquad [2]$$

where ΔS^0 is the difference in the entropy of the products and the reactants of the chemical reaction. Tables of thermodynamic data give ΔF_f^0 and/or ΔH_f^0 for 298.16°K.

To obtain ΔF_f^0 at temperatures above 298.16°K use is made of the equation

$$\frac{d\left(\frac{\Delta F_f^0}{T}\right)}{dT} = -\frac{\Delta H_f^0}{T^2} \qquad [3]$$

However, ΔH_f^0 is a function of temperature, and depends on the difference between the heat capacities of the products and reactants, as expressed by

$$\Delta H_f^0 = \Delta H_0^0 + \int_{T_1}^{T_2} \Delta C_P \, dT \qquad [4]$$

where ΔH_0^0 is evaluated from the heat of formation at 298.16°K as shown below, and ΔC_P represents the sum of the heat capacities of the products of a reaction less the sum of the heat capacities of the reactants and is usually expressed as a function of temperature by an equation of the empirical form:

$$\Delta C_P = \Delta a + (\Delta b)T + \frac{\Delta c}{T^2} \qquad [5]$$

[1] It is assumed that chlorine gas is adsorbed on an inert electronic conductor.

TABLE I. *Standard electromotive forces for single solid or molten metallic chlorides**

Order 25°C	Metal ion	E^0														
		25°C (aqueous)	25°C (solid)	Uncertainty (25°C)	100°C	200°C	300°C	350°C	400°C	450°C	500°C	550°C	600°C	800°C	1000°C	1500°C
		volts	*volts*	*volts*	*volts*	*volts*	*volts*	*volts*	*volts*	*volts*	*volts*	*volts*	*volts*	*volts*	*volts*	*volts*
1	Ra^{+2}	4.28	4.336	±0.07	4.272	4.189	4.108	4.068	4.029	3.990	3.952	3.913	3.876	3.723	3.569	3.098
2	K^{+1}	4.285	4.232	±0.01	4.158	4.056	3.954	3.904	3.854	3.805	3.755	3.707	3.658	3.441	3.155	2.598
3	Sm^{+2}	<4.52	4.206	±0.15	4.147	4.071	3.998	3.962	3.926	3.891	3.856	3.822	3.787	3.661	3.559	3.317
4	Ba^{+2}	4.26	4.202	±0.01	4.139	4.056	3.975	3.935	3.888	3.848	3.808	3.768	3.728	3.568	3.412	3.079
5	Cs^{+1}	4.283	4.189	±0.01	4.109	4.002	3.896	3.843	3.791	3.739	3.692	3.645	3.599	3.362	3.078	2.667 (1300V)
6	Rb^{+1}	4.285	4.177	±0.04	4.101	3.998	3.897	3.846	3.795	3.745	3.695	3.645	3.595	3.314	3.001	2.428 (1381V)
7	Sr^{+2}	4.25	4.048	±0.01	3.987	3.909	3.832	3.794	3.757	3.720	3.684	3.648	3.612	3.469	3.333	2.977
8	Li^{+1}	4.405	4.011	±0.09	3.955	3.881	3.800	3.761	3.722	3.684	3.646	3.608	3.571	3.457	3.352	3.122 (1382V)
9	Na^{+1}	4.074	3.980	±0.004	3.910	3.810	3.712	3.663	3.615	3.566	3.519	3.471	3.424	3.240	3.019	2.366 (1465V)
10	Ca^{+2}	4.230	3.888	±0.02	3.830	3.754	3.680	3.643	3.607	3.570	3.534	3.498	3.462	3.323	3.208	2.926
11	La^{+3}	3.88	3.565	±0.03	3.504	3.426	3.350	3.313	3.277	3.241	3.205	3.170	3.134	2.997	2.876	2.607
12	Ce^{+3}	3.84	3.517	±0.03	3.456	3.378	3.303	3.266	3.229	3.193	3.157	3.121	3.086	2.945	2.821	2.540
13	Pr^{+3}	3.83	3.481	±0.01	3.420	3.342	3.266	3.229	3.192	3.156	3.120	3.085	3.049	2.911	2.795	2.523
14	Nd^{+3}	3.80	3.430	±0.01	3.369	3.291	3.215	3.177	3.140	3.103	3.067	3.030	2.994	2.856	2.736	2.455
15	Pm^{+3}	3.78	3.410	±0.03	3.353	3.279	3.208	3.173	3.139	3.105	3.072	3.038	3.006	2.884	2.784	2.554
16	Sm^{+3}	3.77	3.380	±0.10	3.322	3.249	3.178	3.143	3.109	3.075	3.041	3.008	2.975	2.861	2.763	2.712 (1107D)
17	Eu^{+3}	3.77	3.340	±0.10	3.283	3.210	3.139	3.104	3.070	3.036	3.002	2.969	2.936	2.828	2.815 (>827D)	—
18	Gd^{+3}	3.76	3.317	±0.01	3.260	3.187	3.116	3.081	3.047	3.013	2.979	2.946	2.913	2.807	2.709	2.483
19	Tb^{+3}	3.75	3.261	±0.03	3.204	3.130	3.059	3.025	2.990	2.956	2.923	2.890	2.858	2.754	2.657	2.433
20	Dy^{+3}	3.71	3.206	±0.03	3.149	3.075	3.004	2.970	2.935	2.901	2.868	2.835	2.802	2.690	2.599	2.359
21	Y^{+3}	3.73	3.163	±0.04	3.106	3.032	2.961	2.926	2.892	2.858	2.824	2.791	2.758	2.643	2.548	2.329
22	Ho^{+3}	3.68	3.134	±0.01	3.077	3.003	2.932	2.897	2.863	2.829	2.796	2.762	2.729	2.610	2.511	2.283
23	Er^{+3}	3.66	3.119	±0.01	3.062	2.989	2.918	2.883	2.849	2.815	2.781	2.748	2.715	2.589	2.488	2.257 (1497V)
24	Tm^{+3}	3.64	3.086	±0.01	3.029	2.956	2.884	2.850	2.815	2.781	2.748	2.715	2.682	2.553	2.447	2.221 (1487V)
25	Yb^{+3}	3.63	3.075	±0.10	3.017	2.944	2.873	2.838	2.804	2.770	2.736	2.703	2.670	2.542	2.434	2.449 (1027D)
26	Mg^{+2}	3.73	3.070	±0.004	3.006	2.922	2.840	2.800	2.760	2.720	2.680	2.641	2.602	2.460	2.346	1.974 (1418V)
27	Lu^{+3}	3.61	3.049	±0.01	2.988	2.909	2.834	2.796	2.760	2.723	2.687	2.652	2.616	2.478	2.356	2.108 (1477V)
28	Sc^{+3}	3.44	2.946	±0.01	2.885	2.807	2.731	2.694	2.657	2.621	2.585	2.549	2.514	2.375	2.264 (967V)	—
29	Zr^{+2}	—	2.905	±0.43	2.847	2.772	2.699	2.664	2.629	2.594	2.560	2.526	2.508 (577D)	—	—	—
30	U^{+3}	3.16	2.846	—	2.788	2.713	2.639	2.602	2.566	2.530	2.494	2.458	2.423	2.280	2.162	1.886
31	Th^{+4}	3.26	2.840	±0.05	2.779	2.699	2.622	2.584	2.546	2.509	2.472	2.435	2.399	2.264	2.208 (921V)	—
32	Zr^{+3}	—	2.790	±0.29	2.736	2.668	2.603	2.571	2.540	2.509	2.492 (477D)	—	—	—	—	—
33	Hf^{+4}	3.06	2.537	±0.32	2.481	2.409	2.340	2.328 (317S)	—	—	—	—	—	—	—	—
34	U^{+4}	2.86	2.493	—	2.436	2.362	2.289	2.252	2.217	2.181	2.146	2.111	2.078	1.974	1.953 (827V)	—
35	Be^{+2}	3.21	2.435	±0.11	2.382	2.315	2.252	2.222	2.192	2.167	2.144	2.122 (547V)	—	—	—	—
36	Mn^{+2}	2.54	2.287	±0.02	2.235	2.166	2.098	2.065	2.032	1.999	1.967	1.935	1.902	1.807	1.725	1.649 (1190V)

37	Zr^{+4}	2.89	2.266	±0.22	2.209	2.135	2.063	2.041 (331S)	—	—	—	—	—	—	—	—
38	Ti^{+2}	2.99	2.255	±0.22	2.202	2.134	2.069	2.037	2.006	1.975	1.945	1.914	1.885D	—	—	—
39	$(Al^{+3})_2$	3.02	2.200	±0.01	2.150	2.097 (180S)	—	—	—	—	—	—	—	—	—	—
40	Ti^{+3}	ca 2.57	2.154	±0.14	2.097	2.024	1.954	1.919	1.886	1.852	1.836 (475D)	—	—	—	—	—
41	V^{+2}	ca 2.54	2.103	±0.43	2.044	1.970	1.898	1.863	1.828	1.794	1.761	1.727	1.695	1.566	1.441	1.269 (1377V)
42	Tl^{+1}	1.696	1.916	±0.02	1.865	1.798	1.732	1.696	1.660	1.629	1.606	1.583	1.561	1.473	1.470 (806V)	—
43	Zn^{+2}	2.123	1.914	±0.01	1.854	1.776	1.706	1.680	1.655	1.629	1.603	1.577	1.552	1.476 (756V)	—	—
44	Cr^{+2}	2.27	1.846	±0.06	1.795	1.729	1.664	1.632	1.600	1.568	1.537	1.505	1.474	1.352	1.262	1.137 (1302V)
45	$(Si^{+3})_2$	—	1.778	±0.07	1.736	1.713 (145V)	—	—	—	—	—	—	—	—	—	—
46	Cd^{+2}	1.763	1.775	±0.01	1.715	1.637	1.560	1.521	1.481	1.442	1.403	1.364	1.331	1.193	1.002 (980V)	—
47	Ti^{+4}	—	1.748	±0.11	1.700	1.678 (136V)	—	—	—	—	—	—	—	—	—	—
48	V^{+3}	ca 2.23	1.735	±0.43	1.674	1.596	1.576 (227D)	—	—	—	—	—	—	—	—	—
49	Ga^{+2}	ca 1.81	1.713	±0.22	1.659	(200D)	—	—	—	—	—	—	—	—	—	—
50	In^{+1}	ca 1.61	1.709	±0.22	1.654	1.581	1.520	1.492	1.465	1.439	1.414	1.389	1.364	1.360 (609V)	—	—
51	Cr^{+3}	2.10	1.706	±0.07	1.646	1.567	1.489	1.451	1.412	1.374	1.336	1.299	1.261	1.113	1.006 (947S)	—
52	In^{+2}	ca 1.66	1.657	±0.06	1.601	1.528	1.464	1.435	1.407	1.380	1.361 (485V)	—	—	—	—	—
53	In^{+3}	1.702	1.641	±0.04	1.588	1.519	1.451	1.417	1.384	1.352	1.321 (498S)	—	—	—	—	—
54	Pb^{+2}	1.486	1.627	±0.01	1.569	1.493	1.420	1.383	1.345	1.307	1.271	1.243	1.215	1.112	1.039 (954V)	—
55	Ga^{+3}	1.89	1.619	±0.01	1.572	1.528 (200V)	—	—	—	—	—	—	—	—	—	—
56	Sn^{+2}	1.496	1.607	±0.02	1.556	1.490	1.428	1.400	1.373	1.346	1.320	1.295	1.270	1.259 (623V)	—	—
57	Fe^{+2}	1.80	1.565	±0.02	1.516	1.451	1.388	1.357	1.327	1.297	1.267	1.237	1.207	1.118	1.050	1.041 (1026V)
58	Si^{+4}	—	1.484	±0.005	1.466 (57V)	—	—	—	—	—	—	—	—	—	—	—
59	Co^{+2}	1.637	1.464	±0.02	1.408	1.337	1.269	1.236	1.203	1.171	1.140	1.109	1.079	0.977	0.900	0.881 (1050V)
60	Ni^{+2}	1.610	1.412	±0.04	1.355	1.282	1.210	1.174	1.139	1.104	1.070	1.036	1.003	0.875	0.763 (987V)	—
61	V^{+4}	—	1.323	±0.32	1.281	1.253 (152V)	—	—	—	—	—	—	—	—	—	—
62	Cu^{+1}	0.839	1.232	±0.02	1.191	1.140	1.093	1.071	1.050	1.035	1.024	1.013	1.003	0.970	0.943	0.862
63	Sn^{+4}	1.35	1.228	±0.01	1.184	1.176 (113V)	—	—	—	—	—	—	—	—	—	—
64	Ge^{+4}	—	1.225	±0.16	1.190 (83V)	—	—	—	—	—	—	—	—	—	—	—
65	Fe^{+3}	1.396	1.197	±0.06	1.147	1.084	1.023	1.016 (319V)	—	—	—	—	—	—	—	—
66	Ag^{+1}	0.560	1.137	±0.01	1.093	1.037	0.984	0.959	0.935	0.911	0.896	0.883	0.870	0.826	0.784	0.665
67	Sb^{+3}	—	1.122	—	1.077	1.028	1.019 (221V)	—	—	—	—	—	—	—	—	—
68	Bi^{+3}	—	1.102	—	1.051	0.986	0.926	0.896	0.867	0.844 (441V)	—	—	—	—	—	—
69	$(Hg^{+1})_2$	0.571	1.092	±0.01	1.022	0.930	0.840	0.800	0.730	0.663	0.597	0.540 (543D)	—	—	—	—
70	As^{+3}	—	1.019	—	0.986	0.973 (130V)	—	—	—	—	—	—	—	—	—	—

TABLE 1.—*Continued*

Order 25°C	Metal ion	E^0														
		25°C (aqueous)	25°C (solid)	Uncertainty (25°C)	100°C	200°C	300°C	350°C	400°C	450°C	500°C	550°C	600°C	800°C	1000°C	1500°C
		volts	*volts*	*volts*	*volts*	*volts*	*volts*	*volts*	*volts*	*volts*	*volts*	*volts*	*volts*	*volts*	*volts*	*volts*
71	Hg^{+2}	0.506	0.952	±0.02	0.892	0.814	0.743	0.741 (304V)	—	—	—	—	—	—	—	—
72	Cu^{+2}	1.023	0.846	±0.11	0.791	0.721	0.654	0.621	0.589	0.558	0.528	0.506 (537D)	—	—	—	—
73	Ir^{+1}	—	0.794	±0.13	0.751	0.699	0.650	0.626	0.603	0.580	0.558	0.536	0.515	0.433 (799D)	—	—
74	Pd^{+2}	0.373	0.768	±0.06	0.714	0.646	0.581	0.549	0.518	0.487	0.457	0.427	0.397	0.331 (737D)	—	—
75	Mo^{+2}	—	0.759	±0.06	0.711	0.651	0.593	0.566	0.538	0.511	0.485	0.471 (527D)	—	—	—	—
76	Sb^{+5}	—	0.742	—	0.701	0.665 (172V)	—	—	—	—	—	—	—	—	—	—
77	Ir^{+2}	<0.26	0.733	±0.06	0.685	0.625	0.567	0.539	0.512	0.485	0.458	0.432	0.406	0.320 (771D)	—	—
78	Mo^{+3}	1.56	0.723	±0.07	0.669	0.602	0.536	0.519 (327D)	—	—	—	—	—	—	—	—
79	Ir^{+3}	ca 0.21	0.665	±0.04	0.610	0.539	0.472	0.439	0.406	0.374	0.342	0.311	0.280	0.180 (765D)	—	—
80	Mo^{+4}	—	0.650	±0.05	0.600	0.582 (127D)	—	—	—	—	—	—	—	—	—	—
81	W^{+2}	—	0.629	±0.11	0.581	0.521	0.463	0.435	0.408	0.393 (427D)	—	—	—	—	—	—
82	Mo^{+5}	—	0.597	±0.02	0.550	0.491	0.463 (268V)	—	—	—	—	—	—	—	—	—
83	Rh^{+3}	ca 0.56	0.593	±0.04	0.539	0.471	0.406	0.374	0.343	0.312	0.281	0.251	0.221	0.104	0.020 (948D)	—
84	Rh^{+2}	ca 0.76	0.575	±0.06	0.524	0.460	0.398	0.368	0.339	0.310	0.281	0.253	0.225	0.142	0.093 (958D)	—
85	Pt^{+1}	—	0.572	±0.13	0.525	0.465	0.407	0.380	0.353	0.326	0.300	0.274	0.257 (583D)	—	—	—
86	Pt^{+2}	ca 0.16	0.564	±0.06	0.513	0.449	0.387	0.357	0.328	0.299	0.270	0.242	0.225 (581D)	—	—	—
87	W^{+4}	—	0.564	±0.03	0.513	0.449	0.432 (227D)	—	—	—	—	—	—	—	—	—
88	Ru^{+3}	—	0.546	±0.04	0.494	0.428	0.364	0.333	0.303	0.273	0.243	0.214	0.185	0.170 (627D)	—	—
89	W^{+5}	—	0.538	±0.03	0.491	0.431	0.392 (276V)	—	—	—	—	—	—	—	—	—
90	Rh^{+1}	ca 0.76	0.520	±0.13	0.478	0.425	0.376	0.352	0.328	0.305	0.282	0.260	0.238	0.153	0.084 (965D)	—
91	W^{+6}	—	0.513	±0.03	0.464	0.401	0.343	0.325 (337V)	—	—	—	—	—	—	—	—
92	Pt^{+3}	—	0.484	±0.07	0.426	0.351	0.279	0.243	0.209	0.185 (435D)	—	—	—	—	—	—
93	Pt^{+4}	—	0.465	±0.03	0.412	0.344	0.278	0.261 (327D)	—	—	—	—	—	—	—	—
94	Au^{+3}	−0.140	0.211	±0.03	0.162	0.101	0.043	0.021	−0.001	—	—	—	—	—	—	—
95	Au^{+1}	ca −0.320	0.182	±0.04	0.138	0.082	0.037 (287D)	—	—	—	—	—	—	—	—	—
96	C^{+4}	—	0.178	±0.005	0.147 (77V)	—	—	—	—	—	—	—	—	—	—	—

S = sublimation; V = vaporization; D = decomposition.

* Values listed at the sublimation, vaporization, or decomposition temperatures obviously apply to cells with the solid or molten electrolyte, that is, slightly below the sublimation, vaporization, or decomposition temperatures.

where a, b, and c are known numerical values. Substitution of equation [5] in equation [4] and integration gives

$$\Delta H_0^0 = \Delta H_f^0 - (\Delta a)T - \frac{(\Delta b)T^2}{2} + \frac{\Delta c}{T} \qquad [6]$$

Substitution then of equation [6] in equation [3] and integration gives

$$\Delta F_f^0 = \Delta H_0^0 - (\Delta a)T \ln T - \frac{(\Delta b)T^2}{2} - \frac{\Delta c}{2T} + IT \qquad [7]$$

which gives ΔF_f^0 as a function of temperature. If ΔF_f^0 and ΔH_f^0 (or ΔH_0^0) are known at some temperature, usually 298.16°K, the integration constant I may be evaluated. Equation [7] is then valid for the calculation of values of ΔF_f^0 from 25°C up to temperatures for the first change in state for the chloride or metal, i.e., for the first transition, fusion, or vaporization of the products (metallic chloride) or reactants (metal and chlorine gas). At this point, the heat change for the transition, fusion, or vaporization must be added for products, subtracted for reactants, to the ΔH_f^0 at the temperature in question. Then, from this revised ΔH_f^0 and the new ΔC_P values resulting from the change in state, a new ΔH_0^0 and a new integration constant, I', must be calculated. This procedure is followed for each change in state of the products or reactants.

Values of ΔF_f^0 are then calculated for selected temperatures by equation [7] and values of the reversible emf are calculated from these ΔF_f^0 by equation [1]. The temperatures selected for the purpose of this paper were 25°, 100°, 200°, 300°, 350°, 400°, 450°, 500°, 550°, 600°, 800°, 1000°, and 1500°C. In these calculations 23060.5 cal/abs. volt g-equiv. was used for **F** and t°C + 273.16 for T [4].

The complete evaluation of 96 chlorides was done with the aid of the Standard Eastern Automatic Computer (SEAC) of the National Bureau of Standards, maximum operating time being 30 sec. The necessary data on the metals (or nonmetals) and chlorides used in these computations are not listed here since they are readily available in references (2), (3), and (4). Chlorine gas is common to all the systems and its heat capacity as a function of temperature is given by equation [8], namely (8):

$$\Delta C_P(\mathrm{Cl_2, gas}) = 8.79 + 0.00022\ T - 66{,}000/T^2 \qquad [8]$$

Results

The electromotive forces thus calculated when the chloride is solid or molten are given in decreasing order in Table I. A vertical line in the table indicates that the values to the left of the line are for solid chlorides and those to the right for molten or fused chlorides. The higher the emf value, the greater is the reducing power of the metal in a chloride system. For example, if magnesium were placed in fused zinc chloride it would displace zinc with the formation of magnesium chloride (i.e., zinc ions are reduced) thus

$$\mathrm{Mg + ZnCl_2 \rightarrow Zn + MgCl_2} \qquad [C]$$

This follows from the most elementary fact that the free energies of formation may be added or subtracted, hence at 400°C, for example:

$$\mathrm{Mg + Cl_2 \rightarrow MgCl_2} \qquad \Delta F_1 = -127{,}300 \text{ cal}, \quad E_1 = 2.76 \text{ v} \qquad [9]$$

$$\mathrm{Zn + Cl_2 \rightarrow ZnCl_2} \qquad \Delta F_2 = -76{,}300 \text{ cal}, \quad E_2 = 1.66 \text{ v} \qquad [10]$$

Then, subtracting [10] from [9] one has reaction [C] for which E = 1.10 v and ΔF^0 = −51,000 cal, and reaction [C] would be a spontaneous one.

The question next arises as to whether or not reaction [C] goes to completion, or proceeds only part way to an equilibrium state. From thermodynamic relations it is known that

$$-n\mathbf{F}E^0 = \Delta F^0 = -RT \ln K \qquad [11]$$

where K is the equilibrium constant of a chemical reaction under study, and for reactions [9] and [10] is, respectively:

$$K_{\mathrm{MgCl_2}} = \frac{a_{\mathrm{MgCl_2}}}{a_{\mathrm{Mg}}\, a_{\mathrm{Cl_2}}} \qquad [12]$$

and

$$K_{\mathrm{ZnCl_2}} = \frac{a_{\mathrm{ZnCl_2}}}{a_{\mathrm{Zn}}\, a_{\mathrm{Cl_2}}} \qquad [13]$$

where a represents the activity in the equilibrium mixture (not the standard state) of the species denoted by subscripts. For reaction [C] the equilibrium constant is

$$K_C = \frac{a_{\mathrm{MgCl_2}}\, a_{\mathrm{Zn}}}{a_{\mathrm{Mg}}\, a_{\mathrm{ZnCl_2}}} = \frac{K_{\mathrm{MgCl_2}}}{K_{\mathrm{ZnCl_2}}} \qquad [14]$$

Using the ΔF^0 values given above in equations [9] and [10], $K_{\mathrm{MgCl_2}}$ and $K_{\mathrm{ZnCl_2}}$ are, respectively, 2.133×10^{41} and 5.903×10^{24}. Then $K_C = 3.6 \times 10^{16}$ which means for all intents and purposes reaction [C] goes to completion.

For free energy changes when the reactants and products are not in their standard states, thermodynamics gives:

$$\Delta F_{\mathrm{MgCl_2}} = \Delta F^0_{\mathrm{MgCl_2}} + RT \ln \frac{a_{\mathrm{MgCl_2}}}{a_{\mathrm{Mg}}\, a_{\mathrm{Cl_2}}} \qquad [15]$$

$$\Delta F_{\mathrm{ZnCl_2}} = \Delta F^0_{\mathrm{ZnCl_2}} + RT \ln \frac{a_{\mathrm{ZnCl_2}}}{a_{\mathrm{Zn}}\, a_{\mathrm{ZnCl_2}}} \qquad [16]$$

and $\Delta F = \Delta F^0$ only when the a's are unity (the standard state). When one is dealing with the pure fused salt and the pure electrode phases, the activities are all unity and the last terms in equations [16] and [17] are zero. However, when reaction [C] proceeds, the zinc chloride originally present as a pure phase becomes diluted with magnesium chloride as it forms during the chemical reaction, and the

fused electrolyte and each electrode may or may not be mutually soluble in each other, and the activities of the fused phases (or phase) can no longer be taken as unity. When the system [*C*] attained equilibrium, each phase (electrode and electrolyte) could be analyzed. The activity of each component in each phase would be given by

$$a_{Zn} = N_{Zn}f_{Zn};\ a_{Mg} = N_{Mg}f_{Mg};\qquad a_{ZnCl_2} = N_{ZnCl_2}f_{ZnCl_2}$$

and $a_{MgCl_2} = N_{MgCl_2}f_{MgCl_2}$ where N represents mole fraction and f the activity coefficient. Analysis will give N but not f, but the latter is obtained from the expression

$$\frac{f_{Zn}f_{MgCl_2}}{f_{Mg}f_{ZnCl_2}} = \frac{K_{MgCl_2}N_{Mg}N_{ZnCl_2}}{K_{ZnCl_2}N_{Zn}N_{MgCl_2}} \qquad [17]$$

which follows from the substitution in equation [14] of the relations $a = Nf$ with the appropriate subscripts. To obtain values of each activity coefficient separately would be extremely involved and would entail information on each phase separately. If magnesium and zinc did not dissolve in the fused phase or the fused phase dissolve in them, their activities would be unity and equation [17] would reduce to

$$\frac{f_{MgCl_2}}{f_{ZnCl_2}} = \frac{K_{MgCl_2}N_{ZnCl_2}}{K_{ZnCl_2}N_{MgCl_2}} \qquad [18]$$

involving only the fused phase. Since the term on the right side of this equation is known, the ratio of the activity coefficients could be evaluated. However, for the present case we are concerned only with the relative position of the solid elements in a series (i.e., the values of K, the equilibrium constant) and the added refinement of determining the activity coefficients is unnecessary.

In this connection it should also be stressed that many cells, when constructed, would not give the theoretical electromotive forces as listed in Table I. For example, a cell made with a sodium electrode and a chlorine electrode in molten sodium chloride would not give the theoretical values because of the solubility of sodium in molten sodium chloride and of sodium chloride in molten sodium [*see* reference (9)], and the activities of sodium and molten sodium chloride would not be unity, and ΔF rather than ΔF^0 applies (*see* equations [15] and [16]).

Discussion

Solid and Aqueous States

Reference to Table I shows that the relative position of the elements is nearly the same whether the electrolyte phase is solid or molten. Values of aqueous systems at 25°C are also listed in Table I. The values obtained for the solid electrolyte, providing the solid phase is anhydrous, and aqueous systems differ in the free energy associated with the process of dilution of the saturated solution of the electrolyte to a solution of unit mean activity, $a_{\pm}$. The difference in free energy between a solid phase and a solution saturated with the solid phase is zero. Thus,

$$\Delta F^0_{aqueous} - \Delta F^0_{solid} = -RT \ln a^r_{\pm} \text{ (in sat. sol.)} \qquad [19]$$

or

$$\Delta F^0_{aqueous} - \Delta F^0_{solid} = -rRT \ln [(r^r_+ r^r_-)]^{1/r} \gamma m \qquad [20]$$

where m and y are, respectively, the molality and activity coefficient of the saturated aqueous solution, and r = the sum of the number, r_+ ions and the number, r_- ions into which the electrolyte dissociates. Therefore, since $\Delta F^0 = -nE\mathbf{F}$ one has

$$E^0_{aqueous} - E^0_{solid} = \frac{2.303RT}{n\mathbf{F}} \log a^r_{\pm} \qquad [21]$$

or

$$E^0_{aqueous} - E^0_{solid} = \frac{2.303RTr}{n\mathbf{F}} \log[(r^r_+ r^r_-)]^{1/r} \gamma m \qquad [22]$$

Thus, E^0_{aq} is higher than E^0_s for most highly soluble salts. For example, Owen (10) from potentiometric measurements and Gledhill and Malan (11) from conductometric measurements obtained 1.334×10^{-5} g-equiv/liter and 1.337×10^{-5} g-equiv/liter, respectively, for the solubility of silver chloride in water at 25°C, or an average value of 1.778×10^{-10} for the solubility product. When this value is substituted for $a_{\pm}$ in equation [21] and 0.05916 is used for 2.303 $RT/n\mathbf{F}$ one finds that $E^0_{aq} - E^0_s$ is -0.577 volt. The data of Table I give -0.577 volt in excellent agreement. Scatchard, Hamer, and Wood (12) give an activity of 6.1870 and 2.8248 for the saturated solutions of sodium chloride and potassium chloride, respectively. When these values are substituted in equation [21] one obtains, respectively, 0.0936 volt and 0.0533 volt between E^0_{aq} and E^0_s for sodium chloride and potassium chloride, whereas the data of Table I give 0.094 volt and 0.053 volt, in excellent agreement. In other cases, the agreement is not so good; however, the disagreements are in general well within the uncertainties listed in column 5 of Table I.

Molten State

Comparison of the data of Table I with data reported in the literature for those cases where the electrolyte is in the molten state could be most extensive. As an illustration, we shall compare the data with those reported in the literature for $PbCl_2$ and $ZnCl_2$, only, and for which a number of investigations have been made. These comparisons will suffice for the purpose of this paper.

Data for fused lead chloride have been obtained over a considerable range of temperature by Wachter and Hildebrand (13), Weber (14), Hildebrand and Rule (15), Czepinski (16), and Lorenz and Velde (17). These experimenters made observations on cells of the type, $Pb/PbCl_2/Cl_2$, C and all except Czepinski took special care to remove air

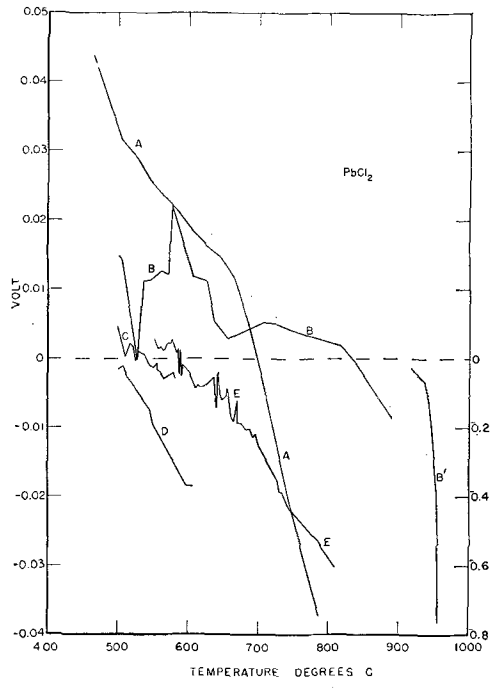

FIG. 1. Deviations of observed emf values for lead chloride from those calculated from thermodynamic quantities: curve A—Czepinski + 0.06 v; curve B—Weber (ordinate scale at left); curve B'—Weber (ordinate scale at right); curve C—Wachter and Hildebrand; curve D—Hildebrand and Rule; curve E—Lorenz and Velde.

and moisture from their cells; Weber removed air only, and all except Wachter and Hildebrand subjected their electrodes to polarization prior to the measurements of emf. For the temperature range 771°–1227°K, the data of this paper give

$$E^0 = 1.9049 + (5.796 \times 10^{-4})T \log T - (2.3950 \times 10^{-9})T^2 + 0.71551/T - (2.4934 \times 10^{-3})T \quad [23]$$

for the emf as a function of temperature. For the range 772.26°–855.26°K Wachter and Hildebrand, for the range 825.66° and 1082.56°K Lorenz and Velde, and for the range 779.16°–1063.16°K Weber gave, respectively,

$$E^0 = 1.2730 - 0.000625(t - 500°C) \quad [24]$$

$$E^0 = 1.2467 - 0.00065(t - 550°C) \quad [25]$$

and

$$E^0 = 1.2818 - 0.000584(t - 506°C) \quad [26]$$

Hildebrand and Rule, and Czepinski did not give equations for the emf as a function of temperature, nor did Weber for his data above 890°C. In Fig. 1, deviations of results of the various authors from the theoretical values, i.e., those calculated from thermodynamic data, are shown as a function of temperature. The data of Wachter and Hildebrand agree quite well with the theoretical values, within a few millivolts, over the temperature range studied. Data of Hildebrand and Rule agree well with the theoretical values from 500° to 545°C, but become increasingly lower than the theoretical values at the higher temperatures. Data of Lorenz and Velde show similar increasingly lower values at the higher temperatures. This falling off of the observed emf data at the higher temperatures is probably due to increased polarization or electrode-electrolyte interaction at the higher temperatures. Czepinski's values are lower than the theoretical values by 0.019 v at 466°C and by 0.097 v at 786°C; his values were undoubtedly affected by polarization and show the effects of the presence of air and moisture on the emf's.

Data for fused zinc chloride have been obtained by Wachter and Hildebrand (13), Lorenz and Velde (17), Czepinski (16), and Kirk and Bradt (18). Kirk and Bradt obtained their results at 400°C only and by means of measurements of decomposition voltages using platinum cathodes and graphite anodes. Their value of 1.96 v is much higher than the theoretical value of 1.655 v (*see* Table I); their results apparently indicate that electrode phenomena, other than the primary ones, occurred at either or both of their electrodes, or that the techniques involved in measuring decomposition voltages lead to incorrect values. The other experimenters made their observations on cells of the type $Zn/ZnCl_2/Cl_2(g)$, C and with the exception of Czepinski took special care to eliminate water and air from the cell system and only Wachter and Hildebrand worked with unpolarized electrodes. For the temperature range 692.7°–1029°K, the data of this

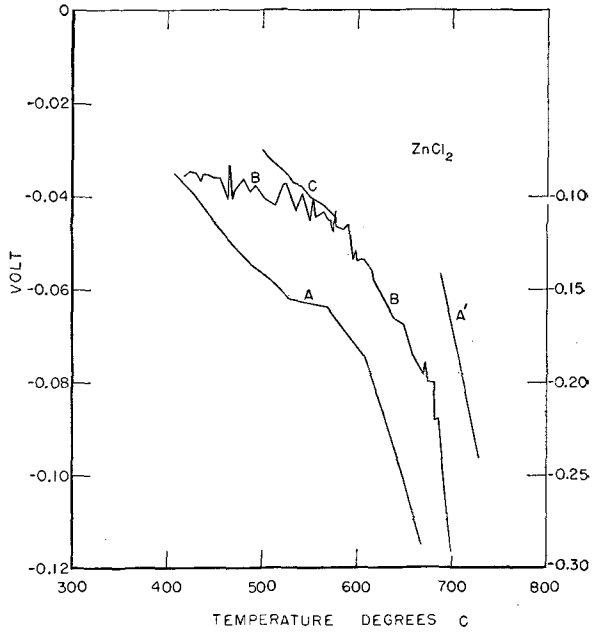

FIG. 2. Deviations of observed emf values for zinc chloride from those calculated from thermodynamic quantities: curve A—Czepinski (ordinate scale at left); curve A'—Czepinski (ordinate scale at right); curve B—Lorenz and Velde; curve C—Wachter and Hildebrand.

paper give

$$E^0 = 2.1310 + (3.8492 \times 10^{-4})T \log T - (2.385 \times 10^{-9})T^2 + 0.71551/T - (1.7941 \times 10^{-3})T \quad [27]$$

for the emf as a function of temperature. In Fig. 2 the deviations of the results of the various authors from the thermodynamic values are shown as a function of temperature. The observed data of Wachter and Hildebrand and of Lorenz and Velde lie approximately 0.03–0.04 v below the thermodynamic values at moderate temperatures; deviations become successively more marked at the higher temperatures. The reason for the differences between the observed emf and the thermodynamic value is not apparent. The fact that the observed emf values are low suggests that the galvanic cell $Zn/ZnCl_2/Cl_2(g)$, C is subject to polarization or electrode-electrolyte interactions.

The above two examples illustrate the agreement that may be expected between the theoretical values (Table I) of cells of the type (A) and those obtained either with galvanic cells or from measurements of decomposition voltages.

Acknowledgments

Acknowledgment is gratefully given to Miss Genevie Hawkins, Mrs. Ethel Marden, and Milton Abramowitz of the Computation Laboratory, Applied Mathematics Division, National Bureau of Standards for their assistance and the use of the Standard Eastern Automatic Computer (SEAC) during the course of this investigation.

Manuscript received July 11, 1955. This paper was prepared for delivery at the Boston Meeting, October 3 to 7, 1954.

Any discussion of this paper will appear in a Discussion Section to be published in the December 1956 JOURNAL.

REFERENCES

1. W. M. LATIMER, "The Oxidation States of the Elements and Their Potentials in Aqueous Solutions," 2nd ed., Prentice-Hall, Inc., New York (1952).
2. K. K. KELLEY, Bulletin 476, U. S. Dept. of the Interior, (1949); *also* Bulletins 383 (1935) and 393 (1936).
3. L. BREWER, "The Chemistry and Metallurgy of Miscellaneous Materials, Thermodynamics," L. L. Quill, Editor, McGraw-Hill Book Co., Inc., New York (1950).
4. "Selected Values of Chemical Thermodynamic Properties," National Bureau of Standards Circular 500 (1952); *also* Series III (1948–53).
5. Reference (2), p. 206.
6. C. H. SHOMATE, *J. Am. Chem. Soc.*, **66,** 928 (1944).
7. Y. K. DELIMARSKII, *Ukranian Khim. Zhur.*, **16,** 414 (1950).
8. D. D. WAGMAN, Private communication; equation given is better representation than that of K. K. Kelley, reference (2).
9. M. A. BREDIG, J. W. JOHNSON, AND W. T. SMITH, JR., *J. Am. Chem. Soc.*, **77,** 307 (1955).
10. B. B. OWEN, *ibid.*, **60,** 2229 (1938).
11. J. A. GLEDHILL AND G. McP. MALAN, *Trans. Faraday Soc.*, **48,** 258 (1952).
12. G. SCATCHARD, W. J. HAMER, AND S. E. WOOD, *J. Am. Chem. Soc.*, **60,** 3061 (1938).
13. A. WACHTER AND J. H. HILDEBRAND, *ibid.*, **51,** 4655 (1930).
14. O. H. WEBER, *Z. anorg. Chem.*, **21,** 305 (1899).
15. J. H. HILDEBRAND AND G. C. RULE, *J. Am. Chem. Soc.*, **49,** 722 (1927).
16. V. CZEPINSKI, *Z. anorg. Chem.*, **19,** 208 (1899).
17. R. LORENZ AND H. VELDE, *ibid.*, **183,** 81 (1929).
18. R. C. KIRK AND W. E. BRADT, *Trans. Electrochem. Soc.*, **70,** 231 (1936).

Lead- and Manganese-Activated Cadmium Fluorophosphate Phosphors

ROBERT W. WOLLENTIN

Lamp Division, Westinghouse Electric Corporation, Bloomfield, New Jersey

ABSTRACT

The characteristics of lead- and manganese-activated cadmium fluorophosphates and homologous materials containing aluminum, barium, calcium, strontium, magnesium, zinc, sodium, and potassium as partial replacements for cadmium are described. With low activator concentrations in cadmium fluorophosphate, a double band emission is obtained with peaks at 4500 Å and 5900 Å. At high activator concentrations the blue peak is suppressed.

The luminous output and spectral emission of the mixed phosphors are dependent upon activator concentration, the amount of halide relative to the cadmium phosphate portion of the phosphor, the amount of phosphorus relative to cadmium, and the cation which replaces cadmium. Substitutions of sodium, potassium, and zinc for cadmium shift the emission and excitation spectra toward longer wave lengths. The x-ray patterns of these phosphors are quite complex and vary from sample to sample. However, they are all similar to an apatite configuration with the exception of the alkali modified phosphors which display quite different and unidentified patterns. In the case of the double band emission of the unmodified phosphor, the yellow band is suppressed at low temperatures and phosphorescence is enhanced. Above room temperature the fluorescence and phosphorescence of all the phosphors are decreased almost to extinction at 150°C.

INTRODUCTION

Manganese-activated cadmium phosphate phosphors have been described by several investigators. McKeag (1) and McKeag and Ranby (2, 3) described the influence of small amounts of lead and fluorine and various proportions of sodium fluoride on the fluorescence and phosphorescence of manganese-activated cadmium phosphate. Prener (4) described the influence of zinc fluoride on the emission spectrum of manganese-activated cadmium phosphate and found that 5–20% of zinc fluoride incorporated in the phosphor caused a substantial shift of the emission wave lengths toward the red end of the spectrum.

In the course of an investigation of the cadmium phosphate phosphors for consideration in fluorescent lamp applications, it was found that lead and manganese combinations, in proper proportions, acted as double activators for cadmium phosphate containing a substantial amount of fluorine. These materials were characterized by a double-band emission, with both peaks in the visible under 2537Å ultraviolet excitation. The relative heights of the two peaks, one in the blue and one in the orange-red, were dependent upon the concentration of activators.

This paper presents some of the luminescence and structural properties of a group of phosphors herein referred to as lead- and manganese-activated cadmium fluorophosphates and homologous materials where portions of the cadmium constituent are replaced by a variety of other cations. The experimental results are grouped into five sections as follows: (*a*) cadmium fluorophosphate, (*b*) mixed fluorophosphates, (*c*) excitation spectra, (*d*) structure studies, and (*e*) some observations on the temperature dependence of the luminescence. The implications of some of these results are given in a later section.

EXPERIMENTAL PROCEDURES

The chemical reagents used as raw materials in the preparation of cadmium fluorophosphates consisted o reagent grades of cadmium oxide, diammonium phos phate, manganous chloride or manganous carbonate, lead nitrate, and luminescent grades of cadmium fluoride and other fluorides. The powdered raw materials were mixed in about 40 g quantities in an acetone slurry, dried at 100°C, and ground thoroughly in a mortar. Firing of the mixes was performed in covered silica crucibles in an air atmosphere in an electric wire-wound furnace. The firing temperature was selected to provide maximum reaction of the raw materials without excessive sintering according to the composition of the phosphor.

Relative luminous output measurements were made on powdered samples under 2537Å ultraviolet excitation. A photronic cell corrected to eye sensitivity by suitable filters, a bridge circuit, and a sensitive galvanometer were used to compare the brightness relative to a standard 3500° white calcium halophosphate set at a value of 87 on an arbitrary scale.

Spectral emission measurements were obtained on powdered samples employing an automatic recording G.E. Spectroradiometer and a filtered 2537Å ultraviolet source for excitation. The curves so obtained were normalized to a peak height of 100.

Excitation measurements were obtained by means of a recording spectroradiometer employing a Beckman Model DU monochromator and a hydrogen discharge lamp as the exciting source. The luminescence of the sample was

detected by a photomultiplier circuit and automatically plotted against wave length of exciting energy. The curves were adjusted to correct for the energy distribution of the hydrogen source and the dispersion of the monochromator according to data supplied by the manufacturer. No correction was applied for the scattering of light in the instrument. Curves were finally normalized to a peak value of 100.

Structural studies were made employing a recording North American Philips Geiger Counter x-ray diffractometer.

Qualitative examination of the influence of temperature on luminescence was obtained by observation of the emission characteristics of the phosphor under filtered 2537Å ultraviolet excitation at −196°C, +21°C (room temperature), +100°C, and higher temperatures by means of a laboratory hot plate.

Experimental Results

Cadmium fluorophosphate.—When lead is introduced into a base material of cadmium fluorophosphate, which may be represented by the hypothetical formula: $3Cd_3(PO_4)_{2.5}\cdot 2.5CdF_2$,[1] a weak but detectable blue emission composed of a single band peaked at about 4500Å is obtained. The position of the peak is relatively independent of the lead concentration. An optimum amount of lead for maximum luminous output occurs at about 1.0%.[2] In the case of activation by manganese alone, a weak emission occurs which is characterized by a prominent peak at about 6000Å and a smaller secondary peak at about 4000Å. The relative height of the latter is decreased with respect to the 6000Å peak on increasing the manganese concentration.

The simultaneous addition of lead and manganese results in phosphors displaying a plurality of emission spectra dependent upon activator concentration. In the series of curves presented in Fig. 1, manganese was held constant at about 0.035% and the lead was varied from 0.5 to 10.0%. When increasing amounts of lead are added, the 4500Å peak is reduced relative to the longer wavelength peak near 5900Å, the 4500Å peak shifts to a new position at 4600Å, and the manganese peak is also shifted slightly toward longer wave lengths. In the case of higher manganese concentrations, the same influence on the relative peak height occurs; however, in this case the relative height of the blue peak is less than for the corresponding case with lower manganese concentration. With still higher manganese concentration, 0.35% and greater, the emission spectrum is relatively independent of the lead concentration as shown in Fig. 2.

The luminous output of the doubly activated cadmium fluorophosphate is dependent upon the activator, fluoride, and phosphate concentrations. In order to demonstrate the influence of the activator concentrations on the powder brightness of the phosphor, the concentration of

[1] All compositions are stated in terms of the number of moles present in the unfired mix. An explanation of the phosphate proportion follows later in this same section.

[2] All activator concentrations are expressed in per cent by weight of the cadmium orthophosphate portion of the phosphor.

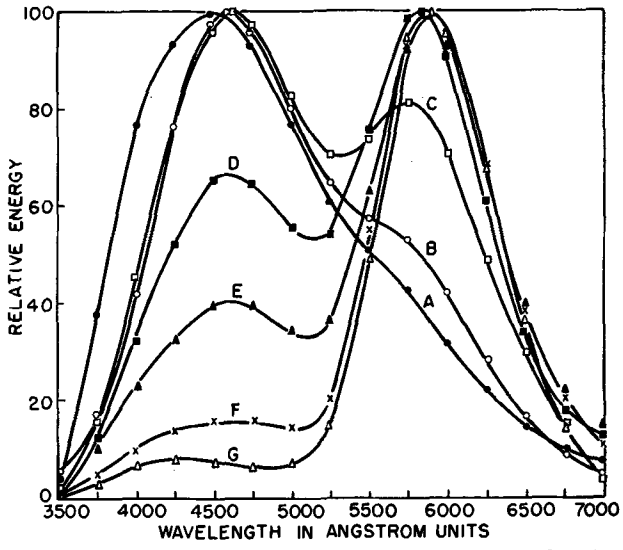

Fig. 1. Influence of lead concentration on spectral emission of $3Cd_3(PO_4)_{2.5}\cdot 2.5CdF_2$:0.035% Mn, xPb; firing temp, 750°C. Curve A, 0.5% Pb; curve B, 1.0% Pb; curve C, 2.0% Pb; curve D, 4.0% Pb; curve E, 6.0% Pb; curve F, 8.0% Pb; curve G, 10.0% Pb.

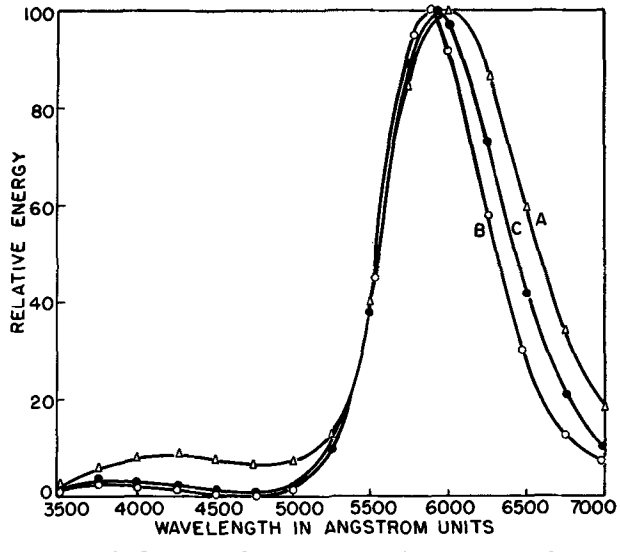

Fig. 2. Influence of lead concentration on spectral emission of $3Cd_3(PO_4)_{2.5}\cdot 2.5CdF_2$:0.35% Mn, xPb. Curve A, 0.1% Pb; curve B, 4.0% Pb; curve C, 10.0% Pb.

lead was varied from 0.05 to 10.0% and manganese from 0.035 to 1.40%. Experimental results indicate that the optimum manganese concentration is 0.70% while the concentration of lead is not critical above 2.0% and should amount to between 4.0 and 6.0%. The brightness value for the optimum formulation is of the same order of magnitude as for a well-made 3500° white halophosphate (87 on the scale used), but there is a considerable difference, of course, between the spectral distributions of the two phosphors.

The dependence of brightness upon the fluoride concentration is shown in Fig. 3, curve A, for the case where the cadmium fluoride of the raw mix was introduced in amounts up to 5.0 moles per 3.0 moles of cadmium orthophosphate. A clearly defined optimum occurs at 3.0

moles of cadmium fluoride. The spectral emission of the phosphor is shifted about 100Å toward shorter wave lengths on increasing the amount of cadmium fluoride from 1 to 5 moles per 3.0 moles of $Cd_3(PO_4)_{2.5}$.

The brightness of the phosphor is also dependent on the amount of phosphate relative to cadmium. When the phosphate is increased from the proportion of exact stoichiometry of the orthophosphate, a broad maximum occurs at a mixture of about 7.5 atoms of phosphorus to 9.0 atoms of cadmium in the brightness curve, Fig. 4. This amounts to a 25.0 mole % excess of phosphate over that required to form cadmium orthophosphate. Because of the benefit on brightness derived therefrom, all

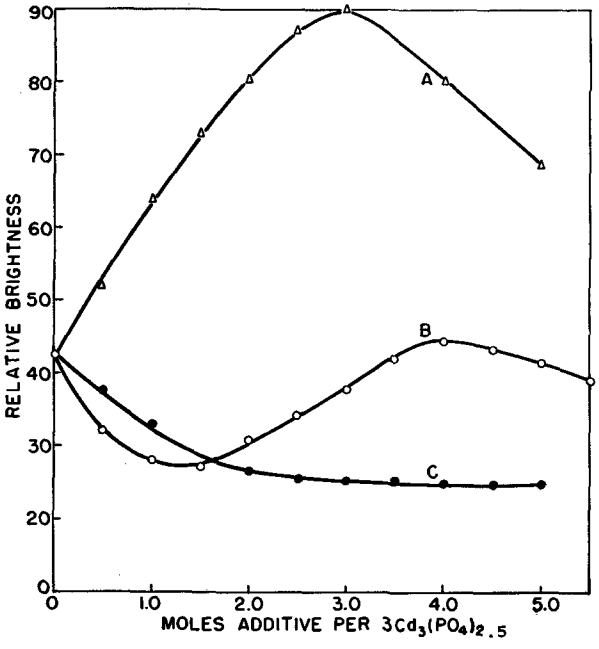

FIG. 3. Brightness of cadmium fluorophosphate phosphors

Curve	Composition	Firing Temp, °C
A	CdF_2 in $3Cd_3(PO_4)_{2.5}\cdot x CdF_2$:1.0% Mn, 4.0% Pb	750
B	NaF in $3Cd_3(PO_4)_{2.5}\cdot x NaF$:0.70% Mn, 6.0% Pb	650
C	KF in $3Cd_3(PO_4)_{2.5}\cdot x KF$:1.0% Mn, 4.0% Pb	600

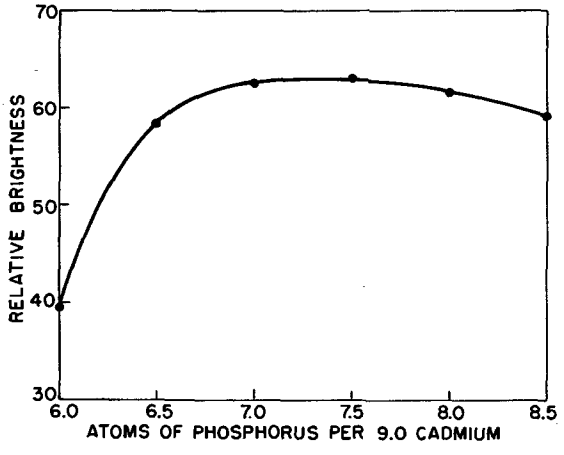

FIG. 4. Dependence of brightness on mole ratio of phosphorus to cadmium in $3Cd_3(PO_4)_x\cdot 2.5CdF_2$:1.0% Mn, 4.0% Pb prepared at 750°C.

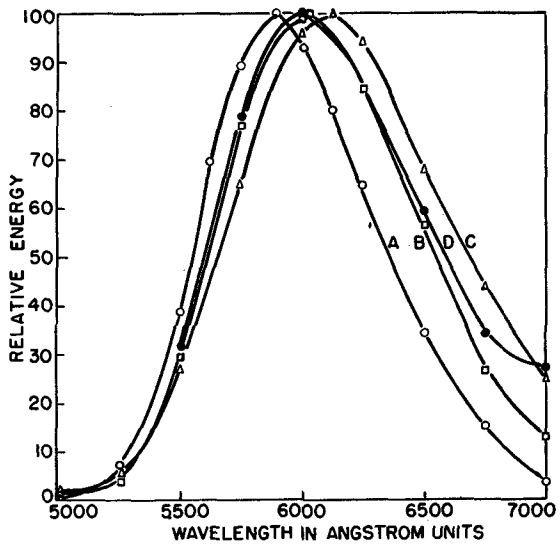

FIG. 5. Influence of partial cation substitution on spectral distribution of $3Cd_3(PO_4)_{2.5}\cdot 1.3CdF_2\cdot 1.2xF_2$:0.7% Mn, 6.0% Pb.

Curve	Substituent	Firing Temp, °C
A	AlF_3	800
	BaF_2	800
	SrF_2	800
	CaF_2	750
B	NaF	650
	MgF_2	750
C	KF	600
D	ZnF_2	800

compositions reported here contain a 25.0% excess of phosphate in the prefired mixture.

Mixed fluorophosphates.—Fluorides of the elements aluminum, calcium, strontium, barium, zinc, magnesium, potassium, and sodium influence the luminescence characteristics of the doubly activated cadmium fluorophosphate. Partial replacement of the cadmium fluoride in the formulation $3Cd_3(PO_4)_{2.5}\cdot 2.5CdF_2$:0.70% Mn, 6.0% Pb by the fluorides mentioned above resulted in decreased brightness in all instances. In this respect, substitutions of the monovalent cations were most detrimental in that small amounts caused a large loss in luminous efficiency and 2.5 moles resulted in a drop of 70.0%, while the same amounts of the divalent substituents caused losses between 30.0 and 45% and the same concentration of trivalent aluminum resulted in only an 18.0% loss.

The effect of these partial substitutions on the spectral emission of the phosphor is shown graphically in Fig. 5 where 1.2 moles of cadmium fluoride in the formulation: $3Cd_3(PO_4)_{2.5}\cdot 2.5CdF_2$:0.70% Mn, 6.0% Pb are replaced by the fluorides of the cations previously mentioned. In the cases of aluminum, strontium, barium, and calcium, the emission spectrum remains unaltered with the peak wave length at about 5900Å. Sodium, magnesium, and zinc cause the peak wave length to shift to about 6000Å, while potassium causes the peak to shift to about 6130Å.

When the above-mentioned fluorides are added to the phosphor in various amounts in the absence of cadmium fluoride, the brightness vs. additive concentration curves, Fig. 6 and 3, display maxima at different concentrations, dependent upon the substituent cation. The optimum

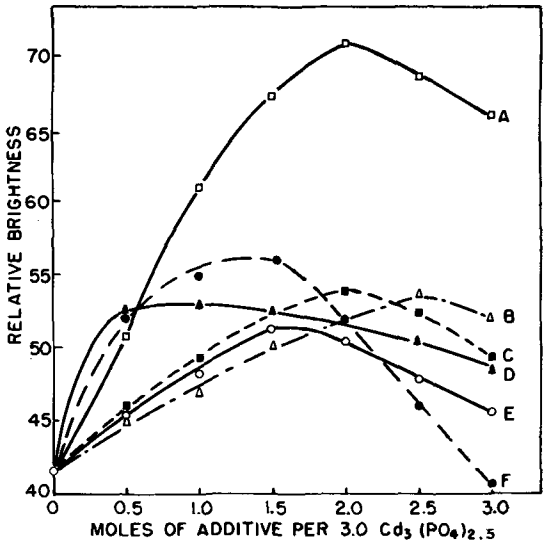

FIG. 6. Influence of foreign cation concentration on brightness of $3Cd_3(PO_4)_{2.5}\cdot nxF_2$:0.7% Mn, 6.0% Pb.

Curve	Substituent	Firing Temp, °C
A	AlF_3	800
B	SrF_2	800
C	MgF_2	750
D	ZnF_2	800
E	CaF_2	750
F	BaF_2	800

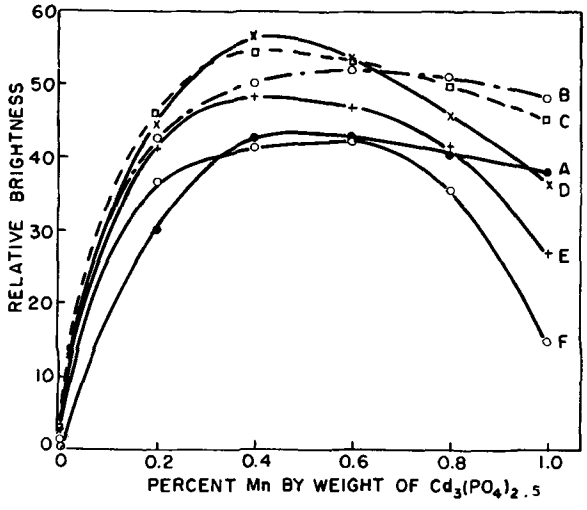

FIG. 7. Influence of activator concentration on the brightness of $3Cd_3(PO_4)_{2.5}\cdot 4.0NaF:x$Mn, yPb, firing temp, 650°C. Curve A, 0% Pb; curve B, 0.5% Pb; curve C, 2.0% Pb; curve D, 4.0% Pb; curve E, 6.0% Pb; curve F, 8.0% Pb.

molar contents, for 3.0 moles of $Cd_3(PO_4)_{2.5}$, are as follows: aluminum and magnesium fluorides, 2.0 moles; strontium fluoride, 2.5 moles; calcium and barium fluorides, 1.5 moles; zinc fluoride, about 1.0 mole; sodium fluoride, 4.0 moles; and potassium fluoride, no apparent optimum.

Spectral distribution measurements of phosphors containing 2.0 moles of the various fluorides per 3.0 moles of cadmium orthophosphate showed the same pattern of emission shift as for the case where cadmium fluoride was present, except that without the cadmium fluoride the influence is more pronounced. Aluminum, calcium, barium, and strontium still show very little effect. The presence of sodium causes the peak to shift 200Å and potassium 300Å toward the red, while magnesium causes only a slight shift toward the red. Zinc not only shifts the emission peak 200Å toward longer wave lengths, but also increases the red tail of the emission.

The orange-red emitting cadmium-sodium fluorophosphate was examined more closely, since red or near-red emitting materials are of considerable interest with respect to fluorescent lamp applications. The brightness of the phosphor is strongly dependent on the activator concentration. The optimum activator concentrations for maximum luminous output in $3Cd_3(PO_4)_{2.5}\cdot 4NaF$ are 4.0% lead and 0.40% manganese as shown in Fig. 7, curve D. The spectral emission of the phosphor is dependent upon the activator concentration and the sodium fluoride content relative to cadmium orthophosphate. With regard to activator concentration, the emission consists of a single peak which shifts toward longer wave lengths with increasing activator contents as shown in Table I. The influence of the sodium fluoride content on spectral emission is illustrated graphically in Fig. 8, where the sodium fluoride was introduced into a base composition of $3Cd_3(PO_4)_{2.5}$:0.70% Mn, 4.0% Pb in amounts up to 5.0 moles. The shift toward longer wave lengths is gradual with increasing amounts of sodium fluoride up to 4.0 moles, curve C, above which no further shift occurs.

The phosphor system consisting of cadmium-potassium fluorophosphate is somewhat similar to the system containing sodium. However, in the case of the potassium-containing phosphor, the luminous output of the phosphor is continually decreased with increasing amounts of potassium fluoride (see Fig. 3, curve C).

The influence of potassium fluoride content on the spectral distribution of $3Cd_3(PO_4)_{2.5}\cdot n$KF:1.0% Mn, 4.0% Pb is shown in Fig. 9. The emission peak is shifted continuously toward longer wave lengths to about 6280Å with amounts up to 2.0 moles potassium fluoride. Greater amounts do not influence the emission spectrum.

Variation of activator concentration in two formulations containing 2.0 and 4.0 moles potassium fluoride per 3.0 moles cadmium orthophosphate, Fig. 10, shows an optimum concentration of 2.0–4.0% lead, but does not indicate that an optimum concentration of manganese was reached. The body color of the phosphor becomes more pink with increasing amounts of manganese, which

TABLE I. *Influence of activator concentration on spectral emission peak of* $3Cd_3(PO_4)_{2.5}\cdot 4.0NaF:x$Mn,$y$Pb

% Lead	% Manganese				
	0.2	0.4	0.6	0.8	1.0
	Å	Å	Å	Å	Å
0	6140	6180	6200	6200	6200
0.5	6160	6180	—	6200	—
2.0	6160	—	—	6200	—
4.0	6160	6200	6220	6250	6230
6.0	6190	—	—	6250	—
8.0	6190	6200	6220	6250	6250

indicates an absorption band extending into the visible region of the spectrum. The emission spectrum is also dependent upon activator concentration. Increasing amounts of activators cause a gradual shift toward longer wave lengths, as shown in Table II.

Excitation spectra.—The normalized excitation spectra for some of the mixed cadmium fluorophosphates are shown in Fig. 11. All of the phosphors for these curves contained 0.70% manganese and 6.0% lead except for the sodium- and potassium-containing phosphors, which contained 1.0% manganese and 4.0% lead.

The excitation spectrum of unmodified cadmium fluorophosphate (Fig. 11, curve E) is characterized by two maxima, one at 2350Å and a secondary one at about

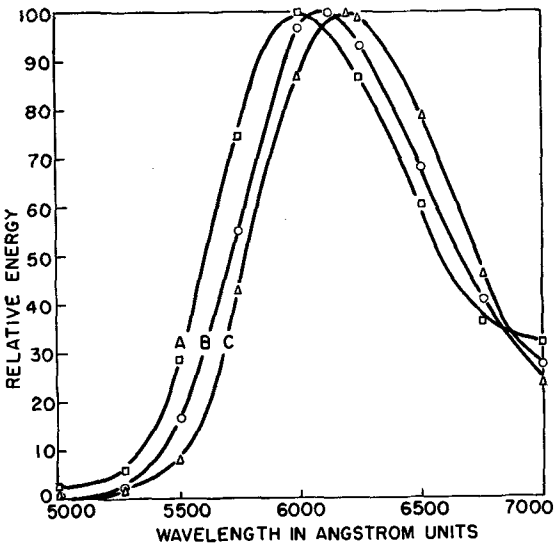

FIG. 8. Influence of sodium fluoride concentration on the spectral emission of $3Cd_3(PO_4)_{2.5}\cdot n$NaF:0.70% Mn, 4.0% Pb; firing temp, 650°C. Curve A, 0.5 mole NaF; curve B, 2.0 moles NaF; curve C, 4.0; 5.0 moles NaF.

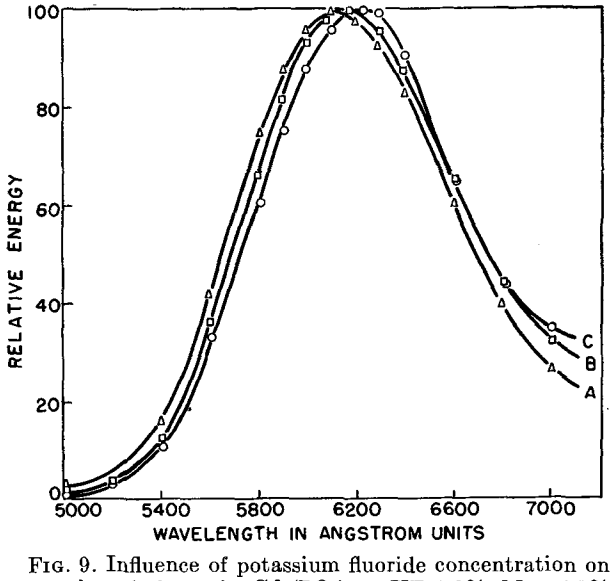

FIG. 9. Influence of potassium fluoride concentration on spectral emission of $3Cd_3(PO_4)_{2.5}\cdot n$KF:1.0% Mn, 4.0% Pb; firing temp, 600°C. Curve A, 0.5 mole KF; curve B, 1.0 mole KF; curve C, 2.0; 3.0; 5.0 moles KF.

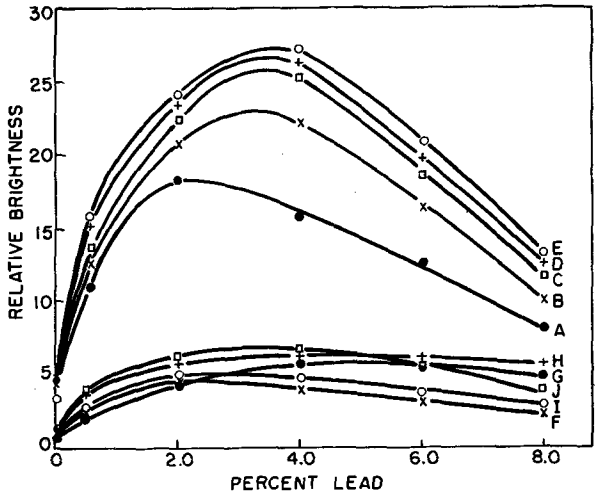

FIG. 10. Influence of activator concentration on brightness of lead- and manganese-activated cadmium-potassium fluorophosphates, firing temp, 600°C.

% Mn	2.0 KF	4.0 KF
0.2	A	F
0.4	B	G
0.6	C	H
0.8	D	I
1.0	E	J

2500Å, and a rather rapid fall-off on the long wave-length edge. When strontium or aluminum fluorides (Fig. 11, curves B and C, respectively) replace cadmium fluoride, the 2350Å peak is shifted to 2300Å and the 2500Å peak is decreased. The substitution of sodium fluoride (Fig. 11, curve D) causes a similar shift of the 2350Å peak, a lowering of the 2500Å peak, and also extends the long wavelength edge to longer wave lengths. Zinc fluoride (Fig. 11, curve F) increases the relative sensitivity to longer wave lengths without influencing the position of the maxima. Potassium fluoride (Fig. 11, curve G) increases the 2500Å peak and also increases the sensitivity to longer wave lengths without influencing the 2350Å peak. Barium fluoride (Fig. 11, curve A) shifts the 2500Å peak to about 2700Å and the 2350Å peak to 2300Å.

X-ray diffraction studies.—The x-ray diffraction pat-

TABLE II. *Influence of activator concentration on the emission peak of* $3Cd_3(PO_4)_{2.5}\cdot n$KF:x%Mn, y%Pb

(A) 2.0 KF

% Lead	% Mn			
	0.2	0.4	0.6	1.0
	Å	Å	Å	Å
0	6120	6150	6180	6200
0.5	6120	6160	6180	6230
2.0	6150	6160	6190	6250
4.0	6150	6180	6200	6260
8.0	6150	6180	6200	6280
(B) 4.0 KF				
0	6200	6210	6240	6260
0.5	6200	6210	6240	6260
2.0	6200	6220	6260	6280
4.0	6210	6220	6260	6280
8.0	6210	6240	6280	6300

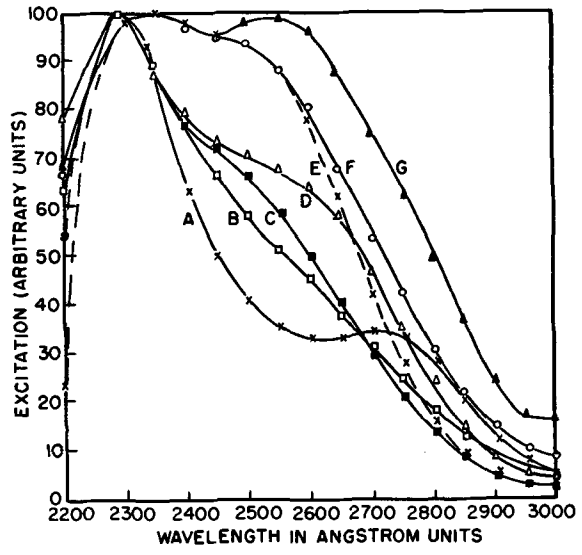

FIG. 11. Excitation spectra of mixed cadmium fluorophosphates

Curve	Composition	Firing Temp, °C
A	$3Cd_3(PO_4)_{2.5}$·2.0 BaF_2:0.70% Mn, 6.0% Pb	800
B	$3Cd_3(PO_4)_{2.5}$·2.0 SrF_2 :0.70% Mn, 6.0% Pb	800
C	$3Cd_3(PO_4)_{2.5}$·2.0 AlF_3 :0.70% Mn, 6.0% Pb	800
D	$3Cd_3(PO_4)_{2.5}$·2.0 NaF :1.0% Mn, 4.0% Pb	650
E	$3Cd_3(PO_4)_{2.5}$·2.0 CdF_2:0.70% Mn, 6.0% Pb	750
F	$3Cd_3(PO_4)_{2.5}$·2.0 ZnF_2:0.70% Mn, 6.0% Pb	800
G	$3Cd_3(PO_4)_{2.5}$·2.0 KF :1.0% Mn, 4.0% Pb	600

terns of a number of these phosphors show a number of variations. In some instances, the patterns contain more than forty lines, which vary in order of line intensity from sample to sample. In general, however, the patterns may be roughly classified into four groups as shown in Table III. One of these groups, designated A in the table, agrees closely with the apatite structure reported by Rooksby and McKeag (5). Another of these groups (A_1) is quite similar with respect to line position but differs slightly in line intensities. The third group (B) departs radically in the order of line intensities from the apatite pattern, and the fourth group (D) consists of a miscellaneous group of patterns all differing from one another and from an apatite pattern.

Some observations on the temperature dependence of the luminescence.—A qualitative examination showed the fluorescence and phosphorescence to be influenced by temperature. Unmodified cadmium fluorophosphate, with low activator concentration and hence having a double-band emission, is most noticeably influenced. At −196°C the orange band is considerably suppressed while the blue band is relatively unaffected. Above room temperature the orange emission appears to shift toward the yellow, and practically all emission is suppressed at +150°C. The phosphorescence is yellow at all temperatures and is more persistent at low temperatures. In the case of higher activator concentrations in the unmodified cadmium fluorophosphate and also in the mixed fluorophosphates, where the emission spectra consist of single bands, lowering the temperature enhances phosphorescence and causes a slight shift of the emission toward the yellow. Above room temperature, phosphorescence and fluorescence are decreased to extinction at about 150°C.

TABLE III. *X-ray diffraction patterns of cadmium fluorophosphates*

Moles halide per $3Cd_3(PO_4)_{2.5}$	% Mn	% Pb	Pattern type*
1.0 CdF_2	0.70	6.0	B
3.0 CdF_2 (opt.)	0.70	6.0	A_1
5.0 CdF_2	0.70	6.0	A_1
2.5 CdF_2	0.35	6.0	A
2.5 CdF_2	0.70	6.0	A
2.5 CdF_2	1.40	6.0	A
2.5 CdF_2	0.035	0.1	B
2.5 CdF_2	0.035	4.0	B
2.5 CdF_2	0.035	10.0	A
1.0 AlF_3	0.70	6.0	B
2.0 AlF_3 (opt.)	0.70	6.0	A
3.0 AlF_3	0.70	6.0	A_1
0.5 BaF_2	0.70	6.0	B
1.5 BaF_2 (opt.)	0.70	6.0	A
3.0 BaF_2	0.70	6.0	D_1
0.5 NaF	0.70	6.0	D_2
1.5 NaF	0.70	6.0	D_3
4.0 NaF (opt.)	0.70	6.0	D_4
5.5 NaF	0.70	6.0	D_5
0.5 KF	0.70	6.0	B
1.5 KF	0.70	6.0	B
3.0 KF	0.70	6.0	B
3.0 ZnF_2	0.70	6.0	D_6

* A, apatite structure; A_1, similar to apatite structure, but differing in order of intensities; B, pattern different from A and A_1; D, miscellaneous patterns different from B and A and each other.

DISCUSSION AND CONCLUSIONS

The double activation of cadmium fluorophosphate by lead and manganese is another addition to the growing list of sensitized phosphors. The cadmium fluorophosphate matrix is inefficiently activated by either activator alone, but in combination these activators provide a phosphor of high efficiency. While the more efficient phosphors of the system lack the double-band emission necessary to produce white, they possess other worthy characteristics which make them of use in blends and in theoretical considerations on the mechanism of luminescence.

Data on the influence of the concentration of activators on spectral emission, Fig. 1, are of particular interest at low activator concentrations. On the introduction of small amounts of lead, emission is predominantly blue. This indicates preferential excitation of blue-emitting lead centers which are sufficiently removed from manganese centers to prevent efficient transfer of energy between the two kinds of centers and, hence, gives rise to the blue lead emission. An increase of either lead or manganese concentration places some of the manganese centers within sufficient proximity to lead centers to permit some transfer of energy from the lead to the manganese, and thus gives rise to excitation and emission of both centers. Higher activator concentrations, therefore, provide the necessary proximity of both centers to allow efficient transfer of energy from the lead to the manganese to give rise to the preferred manganese emission.

In the mixed phosphors and the unmodified cadmium fluorophosphate, the structure studies (Table III) throw some light on the appearance of optima in the brightness vs. concentration curves of Fig. 3 and 6. In the case of cadmium fluorophosphate, there appear to be three

separate patterns dependent upon the halide content. Here, and also for the other fluorides studied, with the exception of sodium and potassium fluorides, maximum brightness occurs when the basic structure is most similar to the apatite configuration. The second pattern (B) which is also common to all but the sodium fluoride modification is present at concentrations of the fluoride below optimum. This pattern probably represents a mixture of cadmium phosphates and halides. Positive identification of this phase and others is complicated by the lack of published data and standard x-ray patterns on cadmium phosphates and related compounds. However, further consideration of this problem is being given and will be reported at a later date. The pattern group (A_1) in the unmodified cadmium fluorophosphate occurs for higher than optimum concentrations of cadmium fluoride and also in the case of aluminum fluoride, and closely resembles the apatite pattern. The difference in line intensities between this and the apatite pattern may be caused by further substitutional solid solution by the fluorine ion into sites which differ from the lattice position normally occupied by the fluorine in forming the apatite configuration. The sodium-containing phosphors seem to involve a slightly different structure which is not definable in the light of presently available data.

In those phosphors where the emission spectrum is located further in the red portion of the spectrum than the unmodified cadmium fluorophosphate, excitation spectra peaks show either a shift toward wave lengths longer than 2537Å or an increase in the relative height of the long wave-length tail of the excitation spectrum. The cadmium-barium fluorophosphate (Fig. 11, curve A) is peculiar in that the excitation spectrum contains a secondary peak at 2750Å, but the emission spectrum does not differ materially from the unmodified cadmium fluorophosphate.

Summary

A system of phosphors composed of lead- and manganese-activated cadmium fluorophosphates and homologous materials formed by the substitution of aluminum, barium, strontium, calcium, magnesium, zinc, sodium, and potassium for portions of the cadmium have been described.

The luminous output and spectral distribution of the phosphors under 2537Å ultraviolet excitation were shown to be dependent on concentration of activators, fluoride content, the specific cation selected to replace cadmium, and the amount of phosphorus relative to cadmium.

The spectral emission of the unmodified cadmium fluorophosphate consists of one band at high concentration, and two bands at low concentrations of lead and manganese. The two bands are peaked at about 4500Å and 5900Å.

Substitutions of aluminum, barium, strontium, and calcium fluorides for the cadmium fluoride portion of the phosphor result in products of lowered luminous output, essentially the same emission spectrum, and different excitation spectra dependent on the cation present. Replacements of cadmium fluoride by sodium and potassium fluorides cause the emission peak to shift to about 6200Å. Replacements of cadmium fluoride by magnesium and zinc fluorides cause the emission peak to shift to 5950Å and 6000Å, respectively.

X-ray diffraction studies established a direct correlation between the apatite configuration and optimum proportions of halide for maximum luminous output, except for the case of sodium and potassium fluoride modifications. Besides the apatite pattern, a number of other patterns occur dependent on the concentration of the particular cations present. Identification of the various patterns obtained on these fluorophosphates is in progress and will be reported at a later date.

The fluorescence and phosphorescence of the cadmium fluorophosphates are dependent on temperature. At −196°C the yellow or red emission is greatly suppressed and the phosphorescence increased. Above room temperature, phosphorescence and fluorescence are decreased to extinction at about 150°C.

Manuscript received May 16, 1955. This paper was prepared for delivery before the Cincinnati Meeting, May 1 to 5, 1955.

Any discussion of this paper will appear in a Discussion Section to be published in the December 1956 JOURNAL.

REFERENCES

1. A. H. McKEAG, (To General Electric Co.) U. S. Pat. 2,214,643, Sept. 10, 1940.
2. A. H. McKEAG AND P. W. RANBY, (To General Electric Co. Ltd.) Brit. Pat. 581,778, Oct. 24, 1946.
3. A. H. McKEAG AND P. W. RANBY, (To General Electric Co.) U. S. Pat. 2,476,676, July 19, 1949.
4. J. S. PRENER, (To General Electric Co.) U. S. Pat. 2,636,010, April 21, 1953.
5. H. P. ROOKSBY AND A. H. McKEAG, *General Electric Co. Journal, England*, **17**, 89 (1950).

Dielectric Behavior of Electroluminescent Zinc Sulfides

WILLI LEHMANN

Lamp Division, Westinghouse Electric Corporation, Bloomfield, New Jersey

ABSTRACT

The complex dielectric factor of electroluminescent zinc sulfides was measured as a function of the voltage and frequency applied to the electroluminescent cell. Both the real and the imaginary part of the dielectric factor obey the law: $k = k_0 +$ function of (L/f), where L is the time average of the electroluminescent emission and f is the frequency. For low and moderate voltages, this expression becomes $k = k_0 + c(L/f)^{1/2}$, where k_0 may depend on frequency f, but c is a constant independent of voltage and frequency.

INTRODUCTION

During measurements concerning the efficiency (lumens per watt) of several electroluminescent phosphors it was necessary to determine the complex dielectric factor of the phosphors as accurately as possible. These measurements produced several unexpected results which may help in understanding the mechanism of electroluminescence. It should be mentioned that it is somewhat misleading to speak about a "dielectric constant" in the present case. The designation "dielectric factor" is preferred here since this factor is, at least in electroluminescent phosphors, not constant but dependent on field strength and frequency.

The results given in this report are mainly related to a zinc sulfide phosphor activated with 0.3 mole % copper and 0.05 mole % lead (amounts added before firing). This phosphor emits green light for applied frequencies up to about 500 cps and turns blue for higher frequencies. The phosphor is mainly cubic and has an average particle size of about 4 μ. This phosphor is given here as a typical example. Other zinc sulfides gave similar results, however.

Measurements of the complex dielectric factor of an electroluminescent zinc sulfoselenide have been made by Roberts (1). However, his results are quite different from those reported here. Roberts found that the dielectric factor first decreased then increased with increasing field strength, while the results given here show only an increase of the dielectric factor with the field strength. The reasons for these differences are not clear.

EXPERIMENTAL ARRANGEMENT AND PROCEDURE

The phosphor was mixed with castor oil and placed in a cell consisting of an aluminum back electrode and a front electrode of conducting glass (Fig. 1). The distance between the two electrodes was about 60 μ, and the area of the cell was 11 cm^2. The sinusoidal voltage applied to this cell could be varied between 0 and 600 rms volts and the frequency between 20 and more than 20,000 cps. It must be noted that the electrical and optical properties of the cell are somewhat variable, since the phosphor particles can move in the viscous liquid dielectric (the castor oil). However, after applying a high voltage to the cell for several minutes the phosphor reaches a geometrical arrangement which is stable for some time; therefore, if the measurements are made carefully and not too long after the "stable" condition is reached, it is possible to obtain reproducible results. Three types of measurements were made, the electroluminescent brightness, the electrical capacity of the cell, and the phase angle of the cell, all as a function of voltage and frequency. All measurements were made only at room temperature.

The light emitted from the cell was detected by a photomultiplier. The voltage drop produced by the photocurrent across a resistor was measured by a vacuum tube electrometer (Keithley Model 200). Precautions were taken to avoid the photocurrent becoming too high with increasing cell brightness and also to avoid any effect of the stray electric field from the electroluminescent cell upon the photomultiplier. With this arrangement it was possible to measure the electroluminescent brightness over a range of more than seven orders of magnitude with an accuracy of better than $\pm 10\%$.

The capacity $\vec{C}$ of the cell is complex. The real part C' of the capacity gives a current which is 90° out of phase with the applied voltage; the imaginary part C'' of the capacity gives a current in phase with the voltage. The magnitude, $C = [(C')^2 + (C'')^2]^{1/2}$, of the capacity is directly measured by comparison with a standard capacitor (General Radio Type 505) of about the same capacity by measuring the currents through both (Fig. 2a). Thus C can be obtained with an accuracy better than $\pm 1\%$.

The phase angle, $\varphi = \tan^{-1}(C''/C')$, of the cell has been measured in a bridge with four standard capacitors as shown in Fig. 2b. Here the capacity of C_a is about the same as that of the cell, while C_b is about 100 times larger, so that about 99% of the voltage from the power supply appears across C_a and only about 1% across C_b. Since the phase angle of the cell is not very dependent on voltage, this deviation of 1% is unimportant. The electronic phase angle meter (Advance Electronics Model 405) used in connection with the bridge permits readings of phase angle differences with an accuracy of about $\pm 0.2°$. A calculation of the electrical behavior of the bridge shows that the phase angle meter does not measure the true phase angle φ of the cell, but a slightly smaller angle ψ, where

$$\tan \varphi = (1 + C/C_b) \cdot \tan \psi \qquad \text{(I)}$$

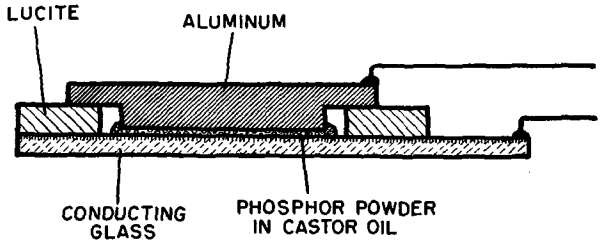

FIG. 1. Electroluminescent cell used for measurements

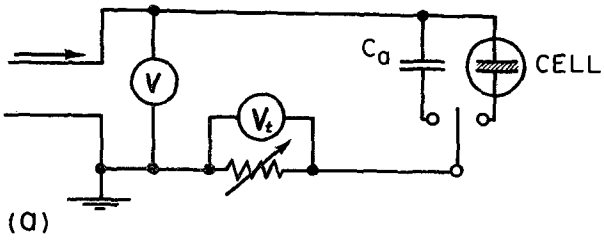

FIG. 2a. Circuit for measurements of cell capacitance. C_a = standard capacitor, V_t = vacuum tube voltmeter.

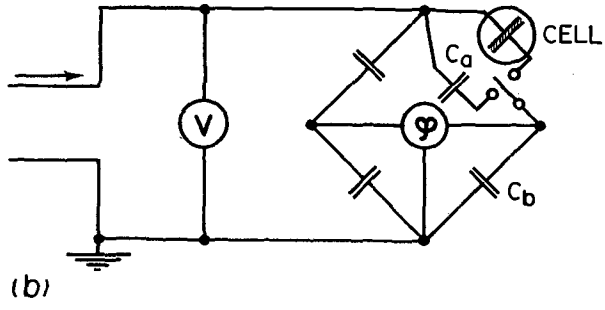

FIG. 2b. Circuit for measurement of phase angle of the cell.

Since C_b is about 100 times greater than C, this correction, in general, can be neglected.

The following results are indicated with the index 0 relating to air, with 1 relating to the castor oil, with 12 relating to the mixture of oil and phosphor, and with 2 relating to the phosphor itself. For example, C'_{12} means the real part of the capacity of the whole cell containing oil and phosphor.

RESULTS OF MEASUREMENTS

The electroluminescent cell filled only with castor oil (without phosphor) has a very small phase angle φ_1, so that practically here $C_1 = C'_1$. By dividing this real capacity C'_1 by the real capacity C'_0 (here $C_0 = C'_0 = 154$ $\mu\mu f$) of the cell containing only air, the real dielectric factor k'_1 of the castor oil is obtained. The value of k'_1 varies between 3.78 for 20 cps and 3.70 for 40,000 cps and is practically independent of voltage. The phase angle φ_1 of the castor oil was found to be roughly $45/f$ where f = the applied frequency, e.g., f = 20 cps, $\varphi_1 = 2.2°$. This phase angle is practically independent of voltage and is always much smaller than the phase angle φ_{12} of the mixture of phosphor and oil. The imaginary part, k''_1, of the dielectric factor of the castor oil is

$$k''_1 = k'_1 \tan \varphi_1 \qquad \text{(II)}$$

or approximately

$$k''_1 = 2.95/f \qquad \text{(III)}$$

The same cell is next filled with a mixture of 80% by volume of castor oil and 20% of phosphor. Now the magnitude C_{12} of the cell capacity and the phase angle φ_{12} of the whole cell are greatly dependent on voltage and frequency. Both C_{12} and φ_{12} increase with increasing voltage and with decreasing frequency. Maxima or minima for certain voltages or frequencies are not observed, and in general the behavior agrees with that reported by Jerome and Gungle (2). Some typical values are given in Table I below.

TABLE I

V (volts rms)	f (cps)	C_{12} ($\mu\mu f$)	φ_{12} (degrees)
50	20	1270	9.5
300	20	3140	53
50	1000	960	6.5
300	1000	1205	15.4

From these measured data of C_{12} and φ_{12} the real dielectric factor of the phosphor-oil mixture can be found from the equation

$$k'_{12} = (C_{12}/C_0) \cos \varphi_{12} \qquad \text{(IV)}$$

and the imaginary dielectric factor from the equation

$$k''_{12} = (C_{12}/C_0) \sin \varphi_{12} \qquad \text{(V)}$$

The emission intensity L of the phosphor used here is shown graphically in Fig. 3. These intensity values are not those measured directly, but they have been corrected for the influence of the change in color of the emission when the frequency is varied and for the spectral response of the

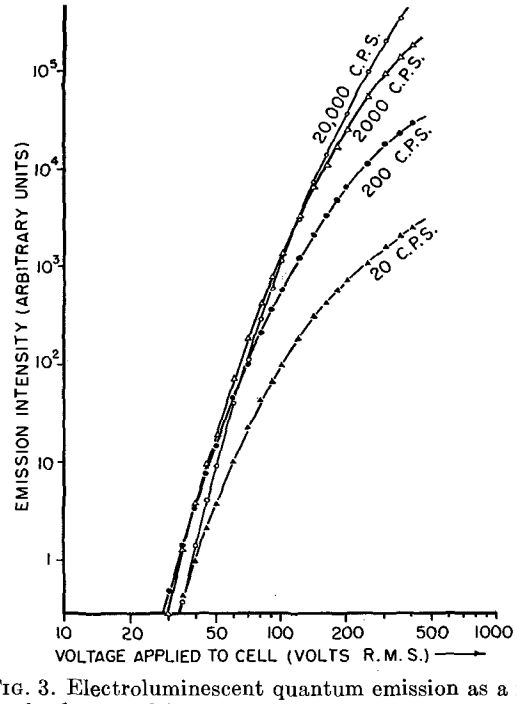

FIG. 3. Electroluminescent quantum emission as a function of voltage and frequency.

photocell. Values given in Fig. 3 are thus proportional to the number of emitted light quanta for all voltages and frequencies.

Methods of Determining the Dielectric Factor of the Phosphor

From the measured data for the dielectric factor of the oil and of the mixture of phosphor and oil it should be possible to determine the dielectric factor of the phosphor itself. This determination is possible, however, only under the assumption that the phosphor particles are essentially uniform as regards dielectric properties and, furthermore, it depends greatly on the geometrical arrangement of the phosphor in the cell. Three different geometrical arrangements are possible.

1. The phosphor has settled down on the surface of one electrode and is there essentially separated from the castor oil.
2. The phosphor is uniformly distributed throughout the insulating oil.
3. Under the influence of the strong electric field the phosphor particles form bridges between the electrodes

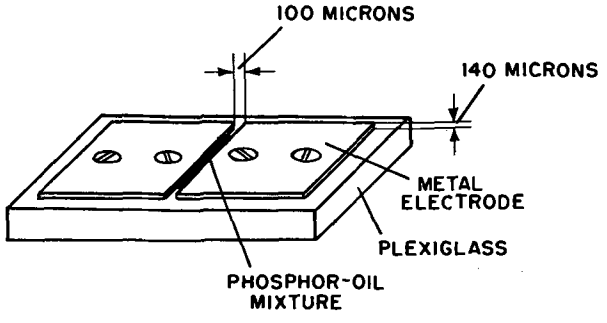

Fig. 4. Experimental cell to show phosphor bridges between electrodes.

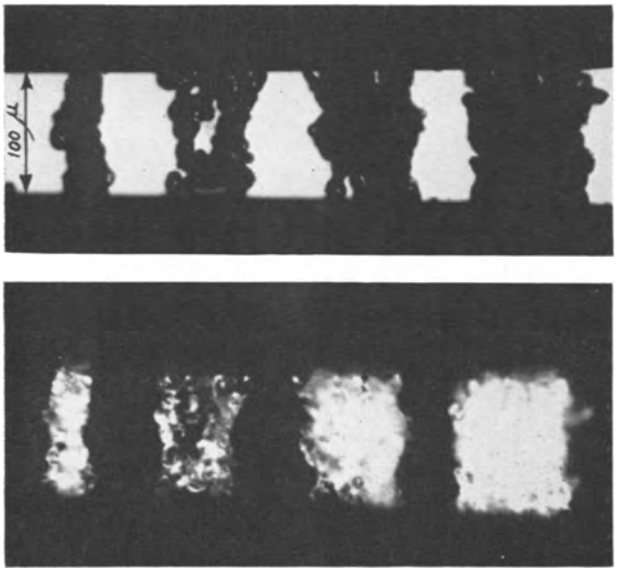

Fig. 5. (*Above*) Phosphor bridges between electrodes, illuminated with white light; (*below*) phosphor bridges in their own electroluminescent light.

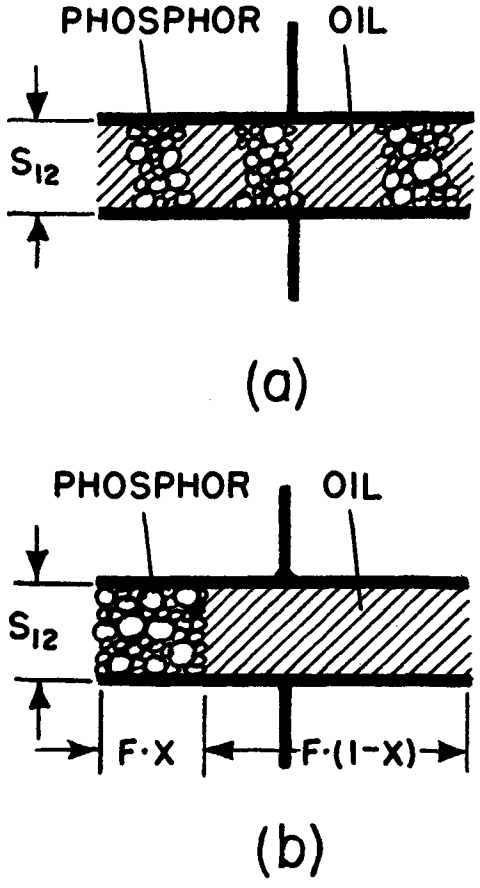

Fig. 6a. Electroluminescent cell with phosphor bridges between the electrodes; b, the equivalent capacitor.

like iron powder between the poles of a magnet. This effect is well known and has been reported in a similar case by Pearce (3).

Actually, it is observed that case 3 most nearly describes the situation in the castor oil cells used. The effect is so distinct that it can be seen even with the unaided eye.

A separate experiment was made in order to show the phosphor bridges as clearly as possible. Two pieces of metal of about 140 μ thickness were mounted with a separation of about 100 μ on a piece of plexiglass, as shown in Fig. 4. The space between the two metal electrodes was filled with the usual mixture of an electroluminescent phosphor in castor oil, and this mixture was observed microscopically. Before a voltage was applied, the phosphor particles were randomly distributed as might be expected. After application of 600 volts rms (of any frequency) the phosphor particles form close bridges between the two metal electrodes. These bridges are shown in two photomicrographs, in Fig. 5a illuminated with white light, and in Fig. 5b in their own electroluminescent light.

Considering the electrical behavior of an electroluminescent cell with bridges between the electrodes, the actual particle distribution, as shown in Fig. 6a, can be simplified to that of Fig. 6b. This system can be considered as two parallel connected capacitors, C_1 and C_2, which have the same thickness S_{12}, but different areas, $(1 - x) \cdot F$ and xF, and different dielectric factors, k_1 and

k_2. Then simply $C_{12} = C_1 + C_2$ with

$$C_{12} = \frac{Fk_{12}}{4\pi S_{12}}; \quad C_1 = \frac{(1-x)Fk_1}{4\pi S_{12}}; \quad C_2 = \frac{xFk_2}{4\pi S_{12}} \qquad \text{(VI)}$$

Combining these formulas and separating k_2 gives the result

$$k_2 = \frac{k_{12} - (1-x)k_1}{x} \qquad \text{(VII)}$$

Of course, this equation can be only an approximation, since the particle bridges in Fig. 6a are still different from the close packed solid phosphor, as assumed in Fig. 6b. But the particles in the bridges between the electrodes are packed very closely; therefore, the approximation seems to be good. Equation (VII) is valid for both the real and the imaginary part of the dielectric factor.

The observed phenomenon of phosphor bridges between the electrodes provides a convenient method of determining the average electric field strength across the phosphor particles. Normally this determination is dependent on the dielectric constant of the phosphor and of the embedding oil, and, therefore, is dependent in a complicated way on the voltage and frequency applied to the cell. But in the case of the phosphor bridges shown in Fig. 5 and 6 there is, in effect, only phosphor between the electrodes; therefore, the average electric field strength E across the phosphor particles is simply given by

$$E = V/S_{12} \qquad \text{(VIII)}$$

where S_{12} is the electrode separation and V the voltage applied to the cell. Equation (VIII) is independent of all changes in the dielectric factors of the phosphor and of the oil. In practice, however, equation (VIII) is only an approximation.

The Imaginary Dielectric Factor of the Phosphor

By use of equation (VII), the imaginary part of the dielectric factor of the phosphor itself can easily be determined. The result for a typical electroluminescent zinc sulfide activated with copper (as described above) is shown graphically in Fig. 7.

It is obvious that there must be some connection between the appearance of electroluminescent emission and the increase of the imaginary part of the dielectric factor (which is responsible for the power absorbed) with increasing voltage. A quantitative correlation between the measured output, L, and the measured increase of the imaginary dielectric factor should then be expected. To consider only this increase of k_2'', it is split into two parts:

$$k_2'' = k_{20}'' + \Delta k_2'' \qquad \text{(IX)}$$

Here the constant k_{20}'' has nothing to do with electroluminescence and may be due to other losses of energy in the phosphor. k_{20}'' can be determined for each frequency by graphical extrapolation to zero voltages as shown in Fig. 7. The other part, $\Delta k_2''$, may be plotted as a function of the emission intensity, L, in a diagram with logarithmically calibrated axes. It is found empirically that the curves obtained in this way are identical within the accuracy of the measurements if $\Delta k_2''$ is plotted not simply as a function of L but as a function of L/f. This is shown in Fig. 8 for the phosphor considered here. Similar diagrams have been obtained also for other electroluminescent phosphors of the type ZnS:Cu. It may be seen in Fig. 8 that all points of measurements approach a straight line with the slope 1:2, except the points for high values of $\Delta k_2''$ (i.e., for high applied voltages). Therefore, within the accuracy of the measurements, the dependence of $\Delta k_2''$ on L/f can be described by

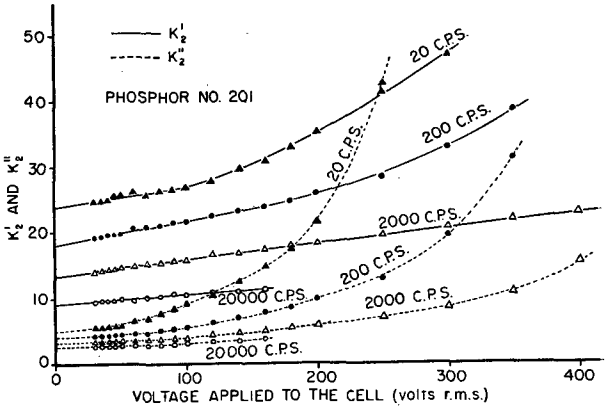

FIG. 7. Variation of the real and imaginary parts of the dielectric factor with voltage and frequency.

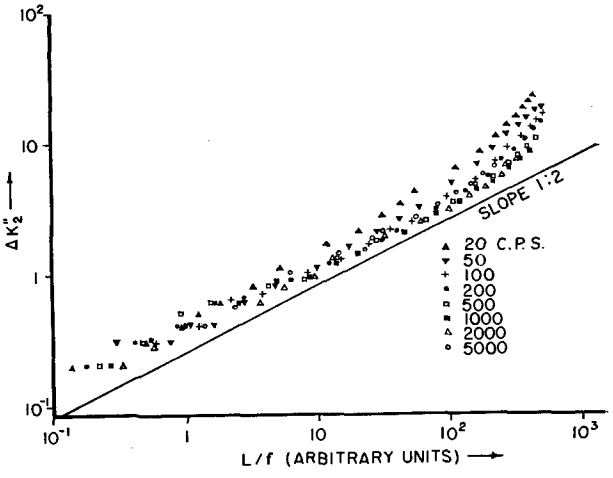

FIG. 8. $\Delta k_2''$ plotted as function of L/f

$$\Delta k_2'' \propto (L/f)^{1/2} \qquad \text{(X)}$$

It is possible to interpret this result by the assumption that the concentration of free carriers in the phosphor is responsible for both the electroluminescent emission and the increasing imaginary dielectric factor. Considering a constant applied frequency, this increase in k_2'' is proportional to the conductivity and, therefore, proportional to the carrier concentration, n, and the average mobility of the carriers, μ:

$$\Delta k_2'' \propto n\mu \qquad \text{(XI)}$$

Introducing (XI) into (X) for the case f = const. gives

$$n^2\mu^2 \propto L \qquad \text{(XII)}$$

The emission mechanism of photoluminescence in these

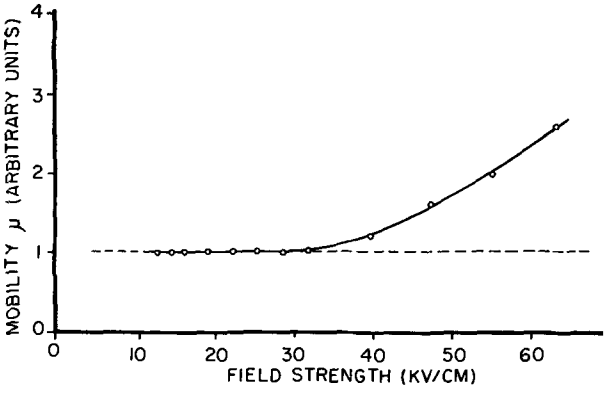

FIG. 9. Possible dependence of the effective mobility on the electric field strength.

phosphors can be described roughly by a bimolecular law (4) (this is a simplification, however; the real mechanism is more complicated). Equation (XII) now shows directly that, within the accuracy of the measurements, the emission mechanism of electroluminescence obeys a bimolecular law, at least for not too high voltages. This result confirms the assumption, made already in practically all theories of electroluminescence, that the electroluminescence is different from the photoluminescence in its excitation mechanism, but not in its emission mechanism. The influence of the frequency in relations such as equation (X) is not yet rigorously understood, however. This influence of the frequency exists without any doubt and has been observed in all other electroluminescent phosphors examined in this laboratory.

A distinct deviation from the straight line with the slope 1:2 in Fig. 8 is to be observed, however, for high values of $\Delta k_2''$ (i.e., for high applied voltages). Several explanations of this deviation have been attempted. It might be assumed that the deviation results from an inaccurate determination of k_2'' caused by the fact that the bridges of phosphor particles in the cell (Fig. 5 and 6a) are not identical with the solid phosphor (Fig. 6b). This assumption cannot be true as shown by the following consideration: equation (VII) is linear in k_2'' and in k_{12}''. Further, the imaginary dielectric factor k_1'' of the castor oil is relatively small compared to that of the phosphor. Therefore, $\Delta k_{12}''$ should be dependent upon L in the same way as $\Delta k_2''$ is. This is indeed the case. A plot of $\Delta k_{12}''$ as a function of L gives a diagram similar to that of Fig. 8 for $\Delta k_2''$. Since the imaginary part of the dielectric factor of the whole cell, k_{12}'', can be directly measured without any calculations, the conclusion must be drawn that the values of k_2'' determined with equation (VII) are relatively accurate.

A further proof that Fig. 6b describes the geometrical situation in the castor oil cell used can be found in the fact that the values of k_2'' determined with equation (VII) are independent (within the limit of error) over a wide range of the ratio phosphor:oil in the cell. This has been checked by measurements. Table II gives some data for a particular phosphor, at a constant voltage of 400 volts rms and a constant frequency of 500 cps, but for various phosphor concentrations x in the cell.

TABLE II. *Variation of the dielectric factor, k_2'', with phosphor concentration, x*

x	0.02	0.03	0.04	0.06	0.10	0.15	0.20	0.30
k_2''	1.4	1.3	1.4	1.3	1.4	1.6	1.4	1.2

Also other possibilities of error have been considered, such as a mechanical deformation of the cell under the influence of electrostatic forces, or the influence of selective polarization of the phosphor particles, but they cannot explain the observed deviation for very high field strengths. One possibility has been found by considering equations (X) and (XI), with the conclusion that the mobility μ in the region of very high field strengths is no longer constant. If so, then the mobility is constant for an average field strength up to about 30 kv/cm and increases strongly for higher field strengths. An example of this possible behavior of the mobility as a function of the average alternating field strength across the cell is given in Fig. 9. It cannot be decided by these experiments whether this assumed increase is due to the mobility of free electrons in the conduction band, or to holes in the valence band, or to both. Furthermore, this dependence of the mobility on the field strength is only a possibility and not a rigorous conclusion.

THE REAL DIELECTRIC FACTOR OF THE PHOSPHOR

The real part of the dielectric factor of the phosphor itself can also be determined by means of equation (VII). Results are given in Fig. 7. As in the case of the imaginary part, the real part k_2' also increases with increasing voltage and decreasing frequency, but these variations, in general, are relatively less than those of the imaginary part. The behavior of the real part of the dielectric factor has also been examined as a function of L/f and found to agree with that of the imaginary part as shown in Fig. 10. The reason for this agreement may be found in an electrical polarization of the phosphor particles due to free carriers, so that the same carrier concentration plays the major role as in the case of the imaginary part. This assumption agrees with results on nonelectroluminescent phosphors obtained by Dropkin (5) who showed that the dielectric dispersion at lower frequencies is due to grain conductivities.

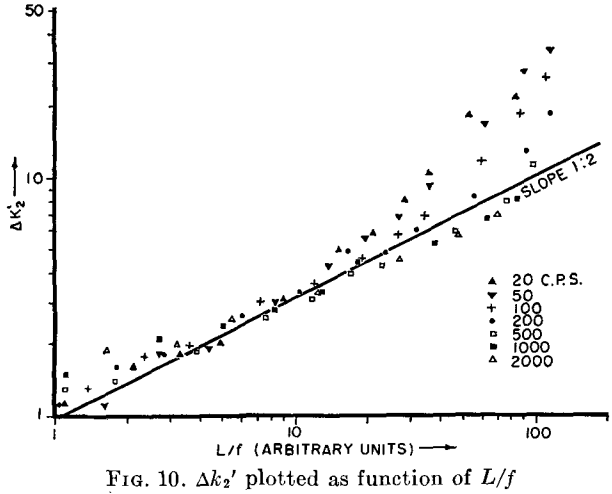

FIG. 10. $\Delta k_2'$ plotted as function of L/f

However, independent of any theoretical explanation, the behavior of the dielectric factor of the phosphor can now be described with two similar equations:

The real part:

$$k_2' = k_{20}' + a(L/f)^{1/2} \quad \text{(XIII)}$$

The imaginary part:

$$k_2'' = k_{20}'' + b(L/f)^{1/2} \quad \text{(XIV)}$$

Here k_{20}' and k_{20}'' may be dependent on frequency, but they are independent of the voltage, while a and b are two constants, both independent of frequency and voltage. These two equations (XIII) and (XIV) are valid only in the region of low and moderate electric field strengths. For higher field strengths, $(L/f)^{1/2}$ has to be replaced by a more complicated expression, but it seems that this new expression is dependent only on the ratio L/f, as can be seen in Fig. 8 and 10.

A dielectric behavior similar to that described here is observed also on many other electroluminescent zinc sulfides. The assumption is made, therefore, that equations (XIII) and (XIV) hold for all electroluminescent phosphors of this type.

ACKNOWLEDGMENT

The author is indebted to Dr. H. F. Ivey for discussion and for aid in instrumentation.

Manuscript received May 16, 1955. This paper was prepared for delivery before the Cincinnati Meeting, May 1 to 5, 1955.

Any discussion of this paper will appear in a Discussion Section to be published in the December 1956 JOURNAL.

REFERENCES

1. S. ROBERTS, *J. Opt. Soc. Amer.*, **42**, 850 (1952).
2. C. W. JEROME AND W. C. GUNGLE, *This Journal*, **100**, 34, (1953).
3. C. A. R. PEARCE, *Brit. J. Appl. Phys.*, **5**, 136 (1954).
4. G. F. J. GARLICK, "Luminescent Materials," p. 15 ff, Clarendon Press, Oxford (1949).
5. J. J. DROPKIN, "Photoconduction in Phosphors," Final Report, Contract N6onr-26313, Polytechnic Institute of Brooklyn, June 30, 1954.

The System Cadmium Oxide-Boric Oxide

I. Phase Equilibria

E. C. SUBBARAO AND F. A. HUMMEL

Department of Ceramic Technology, College of Mineral Industries, The Pennsylvania State University, University Park, Pennsylvania

ABSTRACT

Phase relationships in the system CdO-B_2O_3 were investigated by the quench method and by differential thermal analyses. A large region of liquid immiscibility extends from practically 100% B_2O_3 to about 46% B_2O_3. The compounds $2CdO \cdot 3B_2O_3$ (44.86% B_2O_3), and $3CdO \cdot 2B_2O_3$ (26.55% B_2O_3) both melt congruently near 1000°C and form a simple eutectic system. The compound $2CdO \cdot B_2O_3$ (21.33% B_2O_3) undergoes a rapid, reversible inversion near 900°C and melts congruently at 980°C. A large volume change attends a polymorphic transition in the compound $3CdO \cdot B_2O_3$ (15.31% B_2O_3) at 875°C and it melts at 1020°C. The compounds and polymorphs were characterized by x-ray diffraction, optical and thermal data. Some experiments on the solid solubility of MnO in the C_2B_3, C_3B_2, and C_2B [1] compounds are described.

INTRODUCTION AND LITERATURE SURVEY

Many investigators (1–4) have reported on the luminescence of manganese-activated cadmium borate compositions, but very little documented information has accumulated on the number or thermal behavior of compounds which exist in the system CdO-B_2O_3. Likewise, the phase diagram (Fig. 1) of Mazetti and deCarli (5a) appears to be incomplete in view of more recent work on binary borate systems such as CaO-B_2O_3, ZnO-B_2O_3, BaO-B_2O_3, etc.

The present work was undertaken to clarify the phase relationships in the system and to provide a substantial background for further work on the luminescent behavior of the cadmium borates.

[1] C = CdO, B = B_2O_3.

EXPERIMENTAL PROCEDURE

Raw Materials and Methods

The chemically pure raw materials boric acid, cadmium carbonate, and manganous carbonate were used in the preparations. The quench method (6) was used to investigate that part of the system from 44–100 mole % B_2O_3 (30–100 wt % B_2O_3). When using the quench method it is customary to melt each composition and use the glass as a starting material for the determination of liquidus and solidus temperatures. In this system homo-

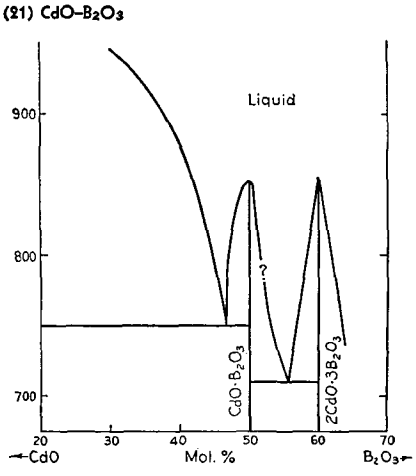

FIG. 1. The system CdO-B_2O_3 (from Hall & Insley, "Phase Diagrams for Ceramists," p. 25, Fig. 49, drawn from the data of Mazetti and deCarli, reference 5b).

geneous glasses can be obtained only in the range 44–51 mole % B_2O_3 (30–46 wt % B_2O_3). Compositions richer in B_2O_3 develop immiscible liquids, while those richer in CdO than the 1:1 mole ratio crystallize so rapidly from the fused condition that glasses cannot be obtained.

At least two previous investigators examined the range of glass formation in the system CdO-B_2O_3 and the present results are in good agreement with both sources. Kordes (9) melted binary cadmium borate glasses with the following results:

Wt % B_2O_3	Density	N_D *
44.2	3.842	1.672
38.3	4.159	1.705
33.8	4.434	1.732
29.4	4.696	1.750

* Refractive index.

More recently Dale and Stanworth (10) claimed a region of glass formation between 31 and 33 wt % B_2O_3, but these compositions seem to be very near to the low B_2O_3 limit of the glass-forming range according to the present work.

In the CdO-rich portion of the system it is necessary to use the method of Differential Thermal Analysis (D.T.A.) and high temperature x-ray diffraction data to determine the phase relationships. These two techniques have been described in previous papers (7, 8). Copper Kα radiation from a wide angle Norelco Geiger counter unit or from a G.E. XRD-3 unit was used in all diffraction work. Platinum ware was used throughout the investigation for fusions, calcinations, D.T.A., and high temperature x-ray work.

Compositions

Table I shows the analyzed compositions which were investigated and the refractive indices of those compositions which could be obtained as glasses. Many supplemental compositions were prepared during the course of the work, but they were not analyzed. The molecular

TABLE I. *Analyzed compositions and refractive indices of glasses*

No.	% B_2O_3	Refractive index of glass (±0.003)
1	46.09	1.670
$2CdO \cdot 3B_2O_3$	44.86	—
2	44.13	1.676
3	43.73	1.677
4	37.82	1.715
5	34.93	1.726
6	33.34	1.736
7	29.15	1.765
8	27.32	—
$3CdO \cdot 2B_2O_3$	26.55	—
9	26.38	—
10	22.49	—
11	21.44	—
$2CdO \cdot B_2O_3$	21.33	—
12	20.16	—
13	19.00	—
$3CdO \cdot B_2O_3$	15.31	—

compositions C_2B_3, C_3B_2, C_2B, and C_3B are included in the table as reference points, since they were found to be true compounds. In preparing glasses for the quench work, ten-gram batches were mixed with ethyl alcohol, dried at 110°C, and fused at 1100°C. For solid-state reactions, thermal expansion, and D.T.A. measurements, 60-gram batches were prepared.

RESULTS

The system divides rather naturally into three regions, (*a*) the immiscible liquid region, (*b*) the region between the C_2B_3 and C_3B_2 compounds, and (*c*) the cadmium oxide-rich region ranging from the compound C_3B_2 to the end member, CdO.

In the following discussion, reference should be made to Fig. 2 which shows the entire binary system including the two-liquid region, and Fig. 3 which shows an enlargement of the region lying between the compound C_2B_3 and CdO. The latter diagram contains the compositions o greatest interest with respect to luminescent properties The interval in which homogeneous glass can be obtained is also indicated on this diagram.

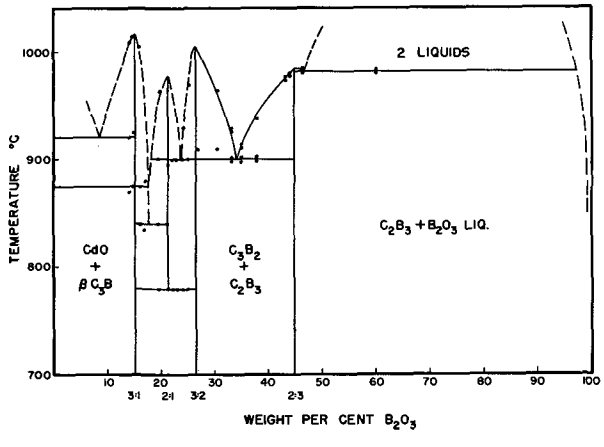

FIG. 2. The system CdO-B_2O_3—C = CdO, B = B_2O_3

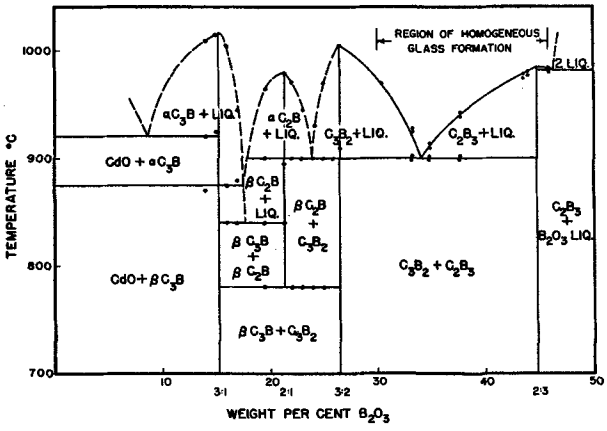

FIG. 3. The system CdO-2CdO·$3B_2O_3$—C = CdO, B = B_2O_3.

The Immiscible Liquid Region

A very extensive region of liquid immiscibility was established which ranges from 46.4% B_2O_3 to nearly 100% B_2O_3, in agreement with that found in other RO-B_2O_3 systems such as MgO-, CaO-, and BaO-B_2O_3. The liquid separation took place readily in platinum crucible melts giving a light layer with a refractive index of 1.455, very close to that of pure B_2O_3 glass. The refractive index of the heavy layer was about 1.67 (Table I).

All preparations under the immiscibility gap when heated in the range 600°–980°C, gave only the C_2B_3 phase when examined petrographically and by x-rays. The second phase which should be present in compositions in this area is B_2O_3 glass, but its detection is difficult or impossible when present in small quantities or as thin films surrounding the C_2B_3 crystals. Since manganese-activated phosphor compositions of a 1:2 and 1:3 ratio have been mentioned in the literature, it was thought that the presence of manganese might promote the formation of compounds of these molecular ratios. Extensive investigation of manganese-containing compositions lying between the 2:3 compound and 100% B_2O_3 proved that only 2CdO·$3B_2O_3$ existed below 980° in this region.

It is interesting to compare the extent of experimentally determined liquid immiscibility in the system CdO-B_2O_3 with that in the systems discussed recently by Shartsis and Capps (11). These authors related the ionic potential (z/R) to the mole per cent of monovalent or divalent oxide present in the heavy liquid in nine borate systems shown in Table II. It is obvious that the data obtained in the present work allow CdO to fall into the anticipated position in the series as indicated.

TABLE II. *Ionic potential and immiscibility in simple borate systems (after Shartsis and Capps)*

Ionic radius R(a.u.)	Valence (Z)	Ionic potential (Z/R)	Immiscibility gap mole % of oxide
K 1.33	1	0.75	0
Na 0.98	1	1.02	0
Li 0.78	1	1.28	0
Ba 1.43	2	1.40	16
Pb 1.32	2	1.51	19
Sr 1.27	2	1.57	21
Ca 1.06	2	1.89	27
Cd 1.03*	2	1.94	39
Zn 0.83	2	2.41	49
Mg 0.78	2	2.56	50

* Data from this paper.

The Region Between the Compounds C_2B_3 *and* C_3B_2

Compounds C_2B_3 *and* C_3B_2.—The compound 2CdO·$3B_2O_3$ has been shown to melt congruently at 980° ± 5° by both quench and D.T.A. data. The crystals are highly birefringent with N_{max} = 1.630 and N_{min} = 1.617. A

TABLE III. *X-ray data on cadmium borates*

2:3		3:2		2:1		β3:1		α3:1	
d	R.I.	d	R.I.	d	R.I.	d	R.I.	d	R.I.
5.53	65	6.15	7	6.14	10	4.33	7	4.95	22
5.38	75	5.98	7	5.98	10	4.23	40	4.33	20
4.57	12	5.15	6	4.64	50	3.74	18	4.21	20
4.16	30	4.64	50	4.41	10	3.53	6	4.13	20
4.12	30								
3.73	85	4.41	6	4.33	27	3.41	10	4.03	45
3.67	65	4.19	6	4.05	30	3.36	7	3.60	20
3.56	55	3.50	5	3.62	15	3.24	6	3.57	20
3.21	100	3.37	5	3.42	30	2.99	43	3.49	12
3.00	30	3.21	20	3.24	60	2.87	100	3.41	55
2.93	70	3.07	30	3.22	60	2.81	8	3.27	15
2.75	30	3.02	13	3.14	5	2.68	50	3.23	55
2.69	20	2.97	44	3.07	25	2.56	8	2.98	100
2.56	85	2.84	100	3.00	90	2.44	47	2.90	60
2.46	18	2.77	25	2.97	50	2.39	15	2.86	30
2.38	25	2.72	25	2.92	60	2.25	4	2.79	45
2.34	8	2.58	10	2.82	100	2.11	4	2.75	10
2.29	80	2.40	10	2.80	15	1.936	7	2.72	30
2.20	7	2.29	4	2.77	60	1.868	30	2.57	25
2.18	40	2.24	6	2.71	30	1.843	5	2.56	20
2.06	13	2.22	6	2.58	35	1.786	35	2.46	10
2.02	50	2.09	35	2.47	5	1.703	20	2.44	10
1.971	75	1.961	10	2.40	30	1.688	10	2.41	25
1.920	18	1.886	7	2.33	30	1.660	15	2.38	40
1.856	18	1.847	8	2.23	20	1.641	5	2.35	40
1.847	5	1.789	7	2.16	15	1.493	7	2.32	45
1.834	40	1.776	9	2.09	50	1.468	11	2.31	10
1.797	25	1.732	20	2.02	5	1.458	11	2.11	20
1.792	35	1.723	20	2.00	8	1.416	36	2.07	14
1.781	45	1.703	5	1.886	5	1.407	10	1.996	30
1.757	6	1.694	5	1.850	17	1.388	6	1.955	15
1.732	40	1.682	5	1.806	3	1.363	9	1.870	25
1.691	8	1.641	20	1.776	10	1.341	6	1.847	30
1.676	8	1.617	4	1.729	16	1.267	6	1.812	10
1.660	18	1.592	12	1.705	10	1.199	6	1.799	10
1.604	14	1.534	4	1.657	5	1.195	4	1.773	20
1.571	12	1.509	6	1.641	10	1.123	4	1.760	15
1.524	16	1.474	5	1.611	5	1.117	5	1.744	20
1.520	15	1.430	6	1.594	17	1.110	8	1.703	25
1.461	19	1.416	4	1.431	7	1.094	5	1.688	40
1.422	10	1.407	5	1.394	10			1.657	40
1.403	12	1.358	50	1.352	5			1.609	10
1.370	10	1.348	5	1.344	8			1.591	30
1.353	13	1.241	10	1.232	6				
1.303	10	1.185	5						
1.277	8								
1.265	9								
1.168	6								
1.161	6								
1.157	6								
1.148	6								
1.131	8								
1.128	8								

few of the crystals develop sharp hexagonal outlines. The compound can be formed by solid-state reaction at any temperature ranging from 600°C up to its melting point or by recrystallization of a quenched glass between 600° and 980°C. The x-ray pattern is given in Table III.

The compound $3CdO \cdot 2B_2O_3$ has been shown to melt congruently at 1005° ± 5° by D.T.A. data only. Well-grown crystals are elongated and highly birefringent with $N_{max} > 1.790$ and $N_{min} = 1.745$, but the crystals generally do not show any characteristic shape or cleavage under the microscope. The compound can be prepared by solid-state reaction between 600°–1000°C or by recrystallization from fusions. The x-ray pattern is given in Table III.

Solid-state reactions.—All compositions lying between the C_3B_2 and C_2B_3 compounds reacted to give these two phases when heated between 600° and 900°. Both compounds could be distinguished in these intermediate mixtures by optical and x-ray methods.

The liquidus region.—The range of glass formation in this area did not extend beyond compositions containing less than 30% B_2O_3 if the following criterion was used: A 10-gram batch fused in a 20 cc platinum crucible at 1100°C for 10–15 min must yield a clear, homogeneous glass when the outside of the crucible is water-quenched. Using this criterion, the part of the system lying between the C_3B_2 compound (26.55% B_2O_3) and a composition containing about 30% B_2O_3 is not a glass-forming region. However, small batches (ca. 0.2 gram) will yield glasses in this compositional range when quenched rapidly, but they cannot be used to obtain dependable liquidus data (*see* section on Compounds C_2B_3 and C_3B_2).

Data for quenched samples upon which the liquidus curve in Fig. 2 and 3 is based are shown in Table IV.

TABLE IV. *Quench data for cadmium borates*

Composition No.	% B_2O_3	Temp, °C	Time, min	Phases present
0	60.00	982	20	2 Liquids
		980	20	C_2B_3 + B_2O_3 liquid
1	46.09	982	20	Glass
		980	15	Glass + C_2B_3
2 (2:3)	44.13	980	25	Glass
		978	15	Glass + C_2B_3
3	43.73	977	15	Glass
		975	15	Glass + C_2B_3
4	37.82	942	15	Glass
		940	15	Glass + C_2B_3
		902	20	Trace glass
		898	15	No glass
5	34.93	914	25	Glass
		910	20	Glass + C_2B_3
		901	20	Trace glass
		899	20	No glass
6	33.34	927	25	Glass
		923	15	Glass + trace C_3B_2
		901	20	Trace glass
		899	15	No glass

Since Botden and Kroger (1) and Mazetti and deCarli (5b) claimed the existence of the compound $CdO \cdot B_2O_3$, special care was taken in the examination of compositions in this neighborhood. Both solid-state and quench work failed to reveal a compound of this composition, so additional work was done with a high temperature x-ray diffraction furnace to test for a possible limited existence

TABLE V. *D.T.A. data for cadmium borates*

Composition No.	% B_2O_3	Previous heat treatment, temp, °C	hr	Temp of differential thermal peaks, °C			
14(2:3)	44.8	760	20	900	990		
15	30.4	700	3	910	970		
16(3:2)	26.5	780	12	910	1005		
17	25.0	700	1	780	903	970	
18	24.0	700	1	780	900	930	
19	23.0	700	1	775	900	945	
20	22.0	700	1	780	900	970	
21(2:1)	21.5	700	1	780	840	895	980
22	19.5	830	20	780	840	900	965
23	17.0	800	18	835	880	945	
24	16.0	700	1	835	880	1005	
25(3:1)	15.0	700	1	875	925	1015	
26	14.0	630	4	870	920	1010	

TABLE VI. *Thermal expansion data for cadmium borates*

Composition	Temp range, °C	Coefficient of linear thermal expansion $\times 10^7$
C_2B_3	25–700	53.6
C_3B_2	25–700	66.7
βC_2B	25–700	57.2
βC_3B	25–700	92.3
C_2B_3 glass	25–500	63.7 (interferometer)

TABLE VII. *Solid solubility of* MnO *in cadmium borates*

	Sintered			Fusion (1100°C)	
	Concentration of MnO, %	Temp, °C	Result	Temp of recrystallization, °C	Result
C_2B_3	5	800	No color		
	8	800	No color		
	10	800	Very slight brown color	620	No color
	12			650	Considerable brown color
C_3B_2	1	800	No color	600	Practically no color
	3	800	No color	600	Slight brown color on crystals
	5	800	Thin brown coating on crystals		
C_2B	0.015			550	No color
	0.0286			700	No color
	0.06			710	Brown color on crystals
	0.5	800	No color		
	2	800	Very slight brown color on crystals		

near the liquidus. However, diffraction data obtained in the temperature range 750°–860°C gave no evidence for a CB compound.

On the basis of both quench and D.T.A. data the eutectic between the C_2B_3 and C_3B_2 compounds has been placed at 900°C and approximately 34 wt % B_2O_3.

The Cadmium Oxide-rich Region

This portion of the system was the most difficult to investigate experimentally since glasses could not be obtained and the deduction of all high temperature events had to be based on D.T.A. and high temperature x-ray data. In addition, volatility problems arose when compositions were held near the liquidus for more than 10–30 min. Hence this portion of the system is drawn in dashed lines in Fig. 2 and 3, indicating some uncertainty in the relationships. X-ray data for the low form of C_2B compound and the low and high forms of the C_3B compound are shown in Table III.

The C_2B *compound.*—This compound appears to have a lower temperature limit of stability at 780°C. When the composition is held at 700°, only the βC_3B and C_3B_2 compounds appear. At 780°C the composition gives an intense nonreversible D.T.A. peak which signals the formation of the βC_2B compound. Further heating then yields a reversible D.T.A. peak at 900° (β-α inversion), and final melting takes place at 980°. Although the formation of the βC_2B compound from βC_3B and C_3B_2 is very rapid on heating to 780°, the reverse dissociation does not occur on cooling. Samples which have been heated between 780° and 980° (or samples which have been fused) cool to room temperature as the βC_2B phase. If the compound is held at 725° for 20 hr, it begins to show the dissociation products in the x-ray pattern. The αC_2B phase was detected by D.T.A. and by a high temperature x-ray pattern taken at 930°.

The absence of x-ray lines at d values of 4.05 and 2.00Å is characteristic of the α form of C_2B. On the other hand, the α form has prominent lines at d values of 2.45 and 2.35 which do not appear in the pattern of the β form.

It is very difficult to distinguish the βC_2B and C_3B_2 compounds by x-ray patterns. Likewise, it is difficult to differentiate between the compounds optically, since the βC_2B crystals are highly birefringent with $N_{max} > 1.790$ and $N_{min} = 1.775$.

The C_3B *compound.*—The C_3B compound melts congruently at 1020°C, and exists in two polymorphic forms. The reversible inversion occurs at 870°C. The high temperature form on cooling from fusion reverts to the low temperature form with a very large change in volume, causing the sample to fall to dust, reminiscent of the well-known β to γ "dusting" of dicalcium silicate, one of the constituents of cement clinker. Table V gives the principal D.T.A. data upon which the CdO-rich portion of the diagram was constructed.

Thermal Expansion Data

The linear thermal expansions of the four compounds and the C_2B_3 glass were measured with the results shown in Table VI.

The four crystalline compounds had been sintered at 800°–830° for 20 hr prior to the dilatometric thermal expansion determination.

Solid Solubility of MnO *in Cadmium Borates*

The solid solubility of MnO in the three compounds C_2B_3, C_3B_2, and βC_2B was estimated by adding varying amounts of MnO and heating in the solid state or by fusing the sample and then observing the crystals under the microscope. The appearance of brown specks or surface discolorations on the crystals would indicate the presence of oxidized manganese and the limit of the solid solubility. This method can only give a rough approximation of the solubility, but some interesting observations were made as summarized in Table VII.

It appears from these data that the solid solubility of MnO in the sintered βC_2B and C_3B_2 compounds is relatively low (approx. 1–3%). In contrast, the C_2B_3 compound can probably take about 5–8% MnO into solid solution. The fused samples are in general agreement with the solubility data for sintered samples, but in this case it is very unlikely that only divalent manganese is present, since the fusions always yield purple crystalline masses or pink to purple glasses.

The luminescent properties of the compounds $2CdO \cdot B_2O_3$, $3CdO \cdot 2B_2O_3$, and $2CdO \cdot 3B_2O_3$ are being investigated and will be reported at a later date.

Manuscript received June 6, 1955. This paper was prepared for delivery before the Cincinnati Meeting, May 1 to 5, 1955. Contribution #54–58 from the Dept. of Ceramic Technology, College of Mineral Industries, Pennsylvania State University, University Park, Pa.

Any discussion of this paper will appear in a Discussion Section to be published in the December 1956 JOURNAL.

REFERENCES

1. TH. P. J. BOTDEN AND F. A. KROGER, *Physica*, **13**, 216 (1947).
2. R. NAGY AND C. K. LUI, *J. Opt. Soc. Amer.*, **37**, 37 (1947).
3. F. A. KROGER, "Some Aspects of the Luminescence of Solids," p. 60, Elsevier Publishing Co., New York (1948).
4. H. W. LEVERENZ, "An Introduction to Luminescence of Solids," pp. 175 and 234, John Wiley & Sons, Inc., New York (1950).
5a. F. P. HALL AND H. INSLEY, *J. Am. Ceram. Soc.*, **30**, 25 (Fig. 49) (1947).
5b. C. MAZETTI AND F. DECARLI, *Gazz. chim. ital.*, **56**, 19 (1926).
6. E. S. SHEPHERD, G. A. RANKIN, AND F. E. WRIGHT, *Am. J. Sci.* (4th series), **28** (4), 293 (1909).
7. R. M. GRUVER, *J. Am. Ceram. Soc.*, **31** (12), 323 (1948).
8. R. ROY, E. T. MIDDLESWARTH, AND F. A. HUMMEL, *Am. Mineralogist*, **33**, 458 (1948).
9. E. KORDES, *Z. anorg. u. allgem. Chem.*, **241**, 1 (1939); *Glastech. Ber.*, **17**, 67 (1939).
10. A. E. DALE AND J. E. STANWORTH, *J. Soc. Glass Technol.*, **33**, 167 (1949).
11. L. SHARTSIS AND W. CAPPS, *J. Am. Ceram. Soc.*, **35**, 169 (1952).

Time-Average Electroluminescence Output of Some Zinc Sulfide Phosphors

SOL NUDELMAN

U. S. Naval Ordnance Laboratory, White Oak, Maryland, and University of Maryland, College Park, Maryland

AND

FRANK MATOSSI

U. S. Ordnance Laboratory, White Oak, Maryland

ABSTRACT

Dependence of time-average electroluminescence output on field strength and frequency is observed for frequencies up to 20 kcps for green and blue emission. The field dependence can be described either by a power law or by an exponential law. The frequency dependence is discussed in terms of theoretical relations connecting the light output to recombination characteristics or to polarization effects. The polarization effects are of minor importance. Light outputs from sinusoidal and square wave excitation are compared.

INTRODUCTION

Dependence of time-average light output on field strength and frequency is one of the fundamental properties of electroluminescent phosphors. In several papers (1–3), the general increase of light output with field strength and frequency has been reported. In some cases, a saturation at high frequencies was observed. Furthermore, it was established that these properties are different in different spectral regions. Most of this work was restricted to frequencies up to about 3 kcps and to phosphors used in the Sylvania Panelescent Lamp.

The purpose of this paper is to extend the experimental material to higher frequencies as well as to other phosphors, and to compare the output of sinusoidally excited electroluminescence to that excited by square wave fields. The results will be discussed, as far as possible, in the light of several theoretical expressions (4).

EXPERIMENTAL PROCEDURE

Phosphors were embedded in Parlodiun[1] and used in cells of about 5 cm^2 area and about 0.2 mm thickness, as described previously (5). Sylvania lamps were used as delivered. Resistance of the conducting glass electrode of the cells was constant in the frequency range 10 cps-100 kcps. For typical cells it was about 600 ohms. The capacitance of the cells was of the order of 100 $\mu\mu f$, varying slightly for different cells because of different phosphor materials and different thicknesses of the phosphor-plastic layer. Cell impedance at 1000 cps was of the order of 5×10^5 ohms. Phosphors were of the zinc sulfide type and were copper-activated. Some of them were commercial products;[2] some were made in the laboratory according to the methods of Homer and co-workers (6). These include phosphors No. 23, ZnS(Cu, Pb), cubic, and No. 11, ZnS(Cu, Pb, Mn), cubic. Phosphor No. 23 was of the same type as that used in the Green Sylvania Lamp, giving results very similar to those obtained with the panel. Phosphor No. 11 is similar to a Sylvania yellow phosphor.

The light output passed through a Wratten filter No. 21 (transmitting above 5300 Å) or through a Wratten filter No. 3 and a Corning filter 5850 (transmitting from 4300 to 4800 Å) in order to separate the green and blue regions of the emission spectrum. Thus, the central part of the emission spectrum was excluded so that overlapping of the two bands found in the green Sylvania type phosphors (2) was minimized.

The luminescence output was received by a 1P21 photomultiplier. The output of the photomultiplier consisted of a periodic ripple superimposed on a steady background. Its time-average was measured with a vacuum tube voltmeter in an appropriate averaging circuit.

A sinusoidal signal generator and power amplifier produced the fields, which could be varied from 0 to 500 v in the frequency range of 100–10,000 cps. For higher frequencies, the output voltage dropped so that at 20 kcps only 200 v were available. For a few measurements, the frequency range could be extended down to 10 cps, with a voltage of only 100 v. All voltages refer to rms values, if not stated otherwise.

The cells were operated well below breakdown voltages and showed no signs of heating. In addition, since the impedance of the cell is so much greater than the resistance of the conducting film on the glass surface, any voltage drop across the phosphor plastic layer will be large compared to that across the film. Thus, in the investigation of the frequency dependence of the phosphor light output, constant voltage applied to the cell is es-

[1] A highly purified form of nonexplosive cellulose nitrate manufactured by Mallinckrodt Chemical Works.

[2] No. 3-310, General Electric Co., ZnS, Se(Cu), cubic; No. Q 62-2666, E. I. du Pont de Nemours and Co., ZnS (Cu), hexagonal; Sylvania Green Panelescent Lamp, Sylvania Electric Products Inc., ZnS(Cu, Pb), cubic.

sentially equivalent to constant voltage applied to the phosphor plastic layer.

Because of appreciable fatigue of the cells in the first 24 hr of use, all cells were aged before usage by applying a potential difference of 300 v at 5000 cps for at least 24 hr before measurements were started. If necessary, measurements could be corrected for changes occurring after that time. Blue emission seemed to fatigue faster than green. Decay during fatigue could be described by power laws (intensity proportional to t^{-n}), with n ranging from 0.1 to 0.2.

Results and Discussion

Frequency Dependence

Fig. 1 shows typical results for the frequency dependence of the time-average light output B. Most phosphors follow the behavior shown for phosphors 3–310. Qualitatively, different curves were obtained only for phosphor No. 23, where the green emission reaches an intermediate quasi-saturation after going through a small maximum. The width of this plateau decreases with increasing applied voltage, and its beginning shifts to higher frequencies. This plateau cannot be associated with any electrical

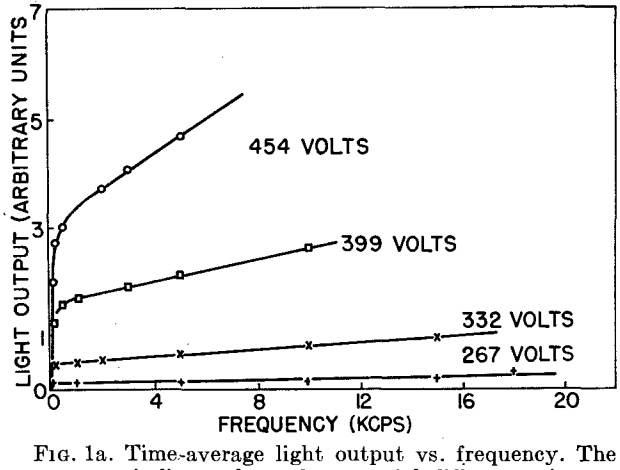

Fig. 1a. Time-average light output vs. frequency. The parameters indicate electrode potential differences in rms values. Phosphor 3–310, green emission.

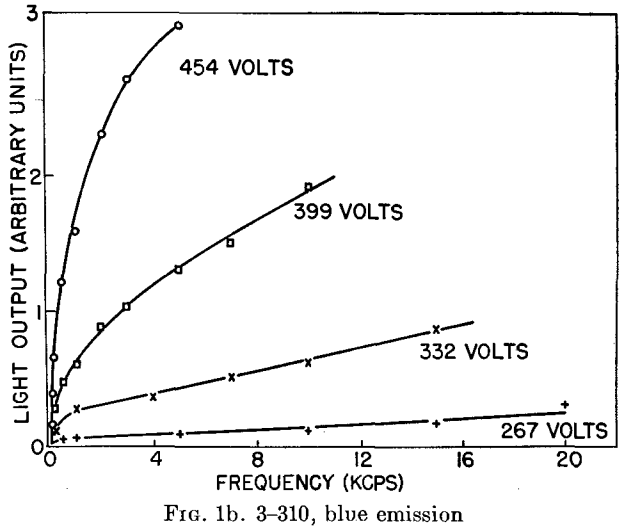

Fig. 1b. 3–310, blue emission

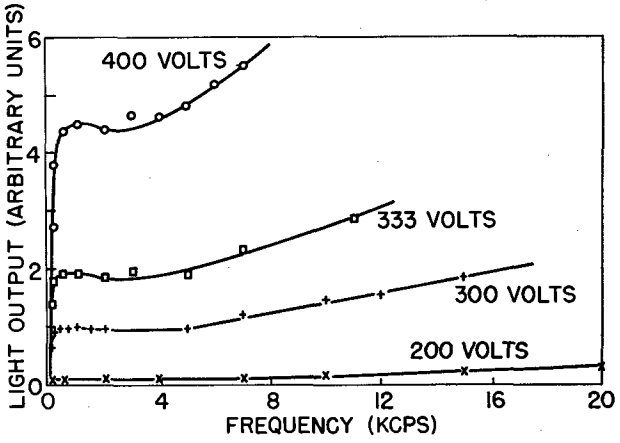

Fig. 1c. 23, green emission

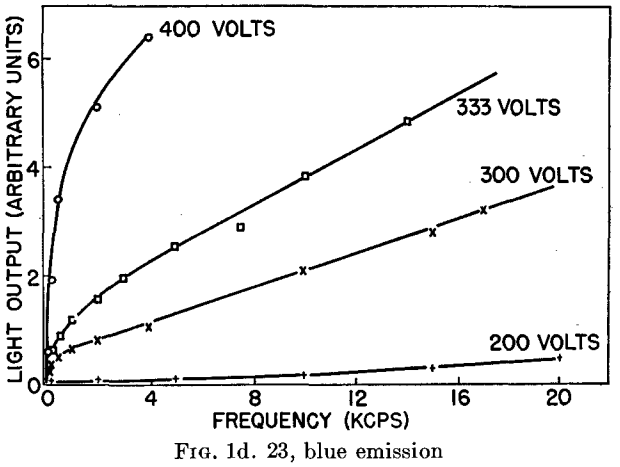

Fig. 1d. 23, blue emission

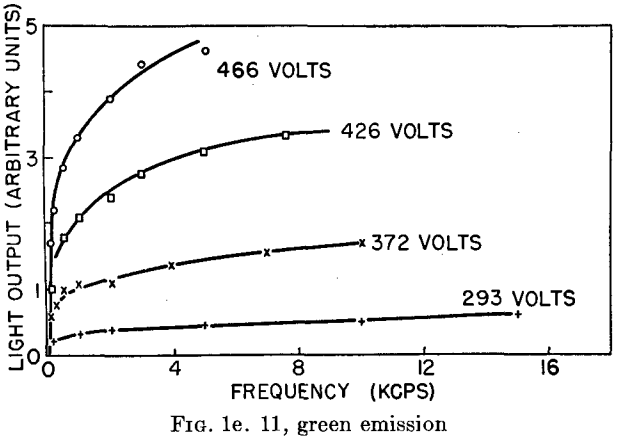

Fig. 1e. 11, green emission

property of the cell, since it would then also appear in the blue emission. Phosphor No. 23 is similar to that in the Green Sylvania Lamp, so the saturation in the green luminescence reported for that phosphor (1) may in reality be only such a plateau. Unfortunately, this lamp was too great a load for the equipment, so it was not possible to obtain the frequencies and voltages necessary to investigate the lamps for such a plateau.

If the data are plotted as in Fig. 2, i.e., as $1/B$ vs. $1/f$ (f = frequency), there is for all phosphors an extended linear region ranging from 100 cps (the low-frequency limit

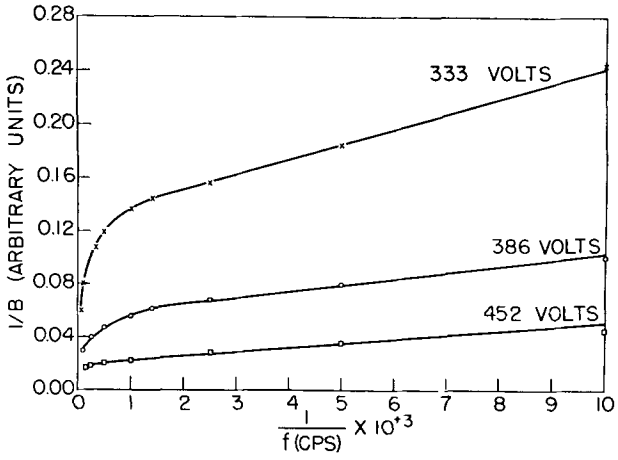

FIG. 2a. $1/B$ vs. $1/f$. Electrode potential differences in rms values. Q 62–2666, green emission.

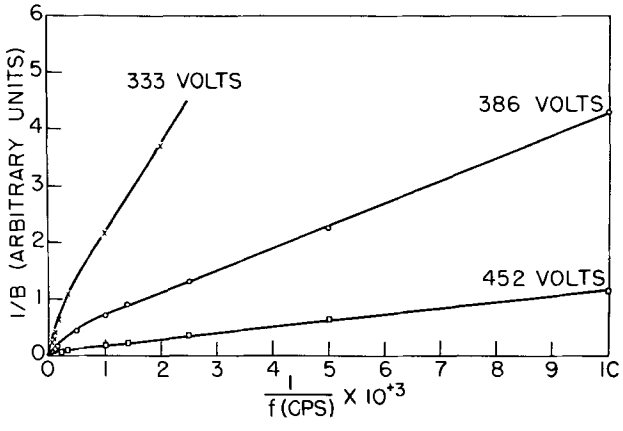

FIG. 2b. Q 62–2666, blue emission

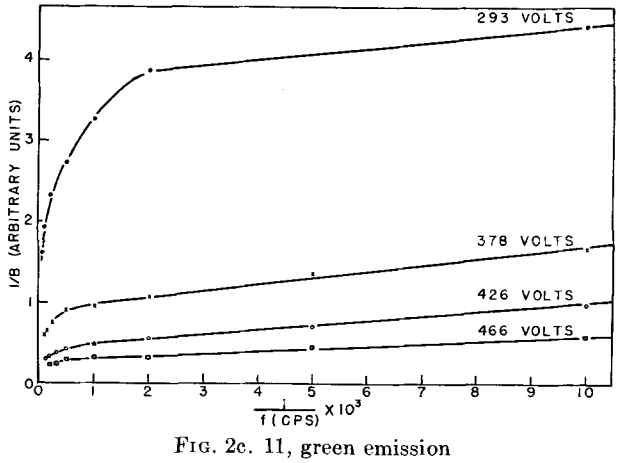

FIG. 2c. 11, green emission

of most of the measurements) to about 1000 cps, except for the green band of the green Sylvania phosphors, according to the irregular shape of the curves of Fig. 1c. The linear region was, in general, larger at higher fields.

For the linear regions of the curves of Fig. 2, Curie (4) derived an approximate formula, according to which

$$1/B = (1/Cn_0^2\alpha)(1 + n_0\alpha/2f) \qquad \text{(I)}$$

where C is a constant and α describes the decrease of the number of electrons in the conduction band from its maximum n_0 at the beginning of the decay. Equation (I) thus describes the light output in terms of recombination characteristics, for which Curie assumed, as an approximation, the equation $dn/dt = -\alpha n^2$ with n being the number of conduction electrons. Equation (I) is presumably valid for frequencies for which polarization effects may be neglected. At high frequencies, the observed curves deviate from the linear relation of $1/B$ vs. $1/f$. This is to be expected since n_0 was assumed to be independent of frequency, which may not be true at higher frequencies, as Curie points out.

From the slopes and the intercepts at $1/f = 0$ of the linear parts of the $1/B$ vs. $1/f$ relations, numerical values for $n_0\alpha$ can be obtained. These are smallest for the green band of phosphor No. 23, where they vary from about 10 sec^{-1} at 100 v to about 200 sec^{-1} at 400 v. This is consistent with the existence of the quasi-saturation plateau, since equation (I) reduces to $B = constant$ for $n_0\alpha \ll 2f$. The higher values of $n_0\alpha$ at higher fields are also consistent with the shift of the quasi-saturation plateau at such fields.

For α and n_0 separately, only relative values can be obtained because of the unknown constant C. For the blue luminescence of phosphor No. 23, α turns out to be constant within 2% between 300–400 v, for which the most accurate measurements are available, while n_0 increases with field strength. ($n_0\alpha$ = 415 sec^{-1} at 293 v, 600 sec^{-1} at 333 v, 1260 sec^{-1} at 400 v; α = 56, 54, and 55, respectively, in arbitrary units.) This behavior would be expected, and similar qualitative results are also obtained with other phosphors with one exception: the blue emission of the 2666-phosphor yields α-values that definitely decrease with increasing field while n_0 still increases.

Although equation (I) describes well the qualitative aspects of the time-average light output as evidenced by the linearity of the curves of Fig. 2, it should be kept in mind that it is of approximate character only, and that it may be oversimplified because of the law for dn/dt which actually is more complicated than has been assumed. Therefore, it cannot be expected to yield exact numerical values for the parameters n_0 and α.

For low frequencies, where polarization effects are assumed to be important, Curie (4) has suggested another relation, which considers the influence of polarization charges on the effective field. For very low frequencies, Curie obtains

$$B = \text{const}\, f \exp(-b'/Ef) \qquad \text{(II)}$$

where E is the applied field and b' a constant. Equation (II) would require that $dB/df = 0$ for $f = 0$. This contradicts the observations. Measurements with the Sylvania Lamp at frequencies below 100 cps down to 10 cps ruled out any possibility of a horizontal tangent to the frequency axis. On the contrary, equation (I) describes the green as well as the blue light output adequately even at these low frequencies. Another discrepancy between observations and equation (II) is the fact that $b'/f = b$ is nearly independent of frequency (*see* next section), while it should be inversely proportional to f if equation (II) is valid.

This analysis, in connection with the discussion of the previous paragraphs, indicates that polarization effects are of minor importance for the frequency dependence of the time-average light output. The principal factor governing this output is, rather, the number of electrons in the conduction band. However, the specific equation accounting for this effect, viz., equation (I), needs refinement. Observations with nonsinusoidal fields (7) have also shown that the polarization field alone cannot account for the frequency dependence of luminescence intensity, but that the decay characteristics of the phosphor are essential even at low frequencies, although polarization charges play an important role in other respects.

Field Dependence

The measurements were not primarily intended to test different laws of the field dependence of the brightness, but, as a by-product of the measurements of frequency dependence at different field strengths, some data on field dependence were obtained. Within the restricted range of voltages covered, both a power law, $B = aE^n$, with n ranging from 4 to 8, and an exponential law, $B = aE^2 \exp(-b/E)$, with b ranging from 500 to 900 v, agree well with the observations. The constants n and b vary, if at all, only very little with frequency. Only one phosphor (No. 11) showed appreciable deviations from the exponential law at low fields, but the output of this phosphor could well be described by $B = aE \exp[-b''/(E + E_0)]$, where $E_0 = 11$ v and $b'' = 700$ v at 1000 cps, while b had the value 550 v. A law of this kind was recently proposed (8) on an empirical basis, and generally offers better agreement at lower voltages. A definite decision among the different laws proposed cannot be made. The authors' observations disagree, however, with exponential laws of the form (9) $B = aE \exp(-b/E^{1/2})$.

Sinusoidal and Square Wave Output

Fig. 3a and 3b give characteristic examples of the dependence of the time-average light output excited by square wave and sinusoidal fields on frequency. At low frequencies, the light output excited by square wave fields rises faster than that excited by sinusoidal fields. Similar results have been reported by Schwertz (10), but the quantitative details are somewhat different. The maximum of the Sylvania Lamp square wave light output at about 3000 cps agrees well with the expectation derived from the measurements of peak heights and the continuous background of square wave excited brightness waves (7). The maximum for the sinusoidal light output in the vicinity of 6000 cps is consistent with the work of Schwertz (10) in that he found at low field strengths similar maxima below 20 kcps for a variety of phosphors. At higher field strengths, such maxima do not appear (*see* Fig. 1a–1e). They apparently shift to higher frequencies with increasing voltage.

Another characteristic feature of Fig. 3 is the crossing of corresponding curves for sinusoidal and square wave excitation at some characteristic frequency. This frequency shifts with the "rise time" of the square wave field, which actually should be described as an "exponential" field. For rise times of 25 μsec and 100 μsec (time to

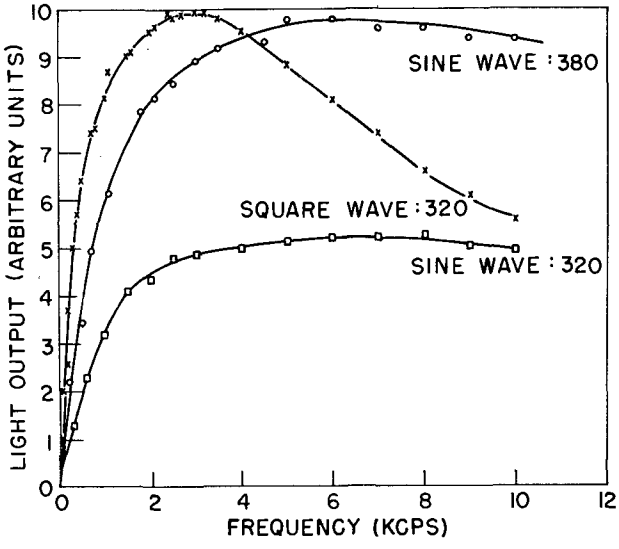

FIG. 3a. Time-average output vs. frequency. The parameters give peak voltage of electrode potential difference. Blue emission of Green Sylvania Lamp, rise time of square wave field 25 μ sec.

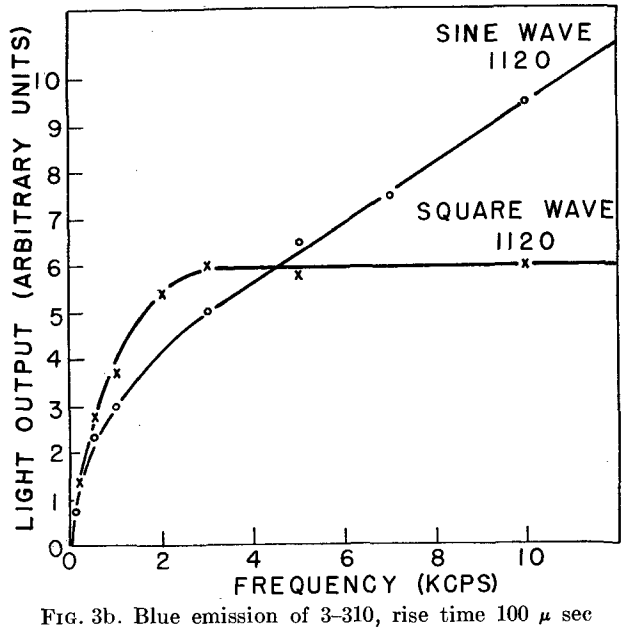

FIG. 3b. Blue emission of 3-310, rise time 100 μ sec

obtain 95% of maximum field strength), this frequency was observed at about 15 kcps and about 4.5 kcps, respectively. The crossing occurs, therefore, when the half period is of the order of the rise time.

The larger output with square wave fields at low frequencies is probably due to the fact that the amplitudes of the brightness waves generally increase with decreasing field rise times, since the influence of polarization charges that weaken the effective field needs time to develop. The crossover point and its dependence on rise time can be related to the relative rate of field change from square wave and sinusoidal fields as the frequency is increased. Exponential fields with rise times much shorter than the half period rise faster than sinusoidal fields of the same frequency. However, for half periods much smaller than

the rise time, the sinusoidal field becomes steeper, since the exponential waves assume the shape of triangular waves with increasing frequency. Therefore, corresponding to the change in slope of the sinusoidal wave relative to that of the square wave, the intensity ratio of the outputs is expected to reverse at some frequency related to the rise time. An exact definition of the characteristic frequency in terms of rise time is, however, difficult.

The frequency of the crossing point was dependent only on the rise time and not on the kind of phosphor, the spectral region, or other details of the luminescence. However, in accordance with the interpretation of the amplitude maximum of square-wave-induced light emission as being related to decay characteristics and polarization effects (7), the position of the output maximum was not appreciably influenced by the rise time of the field.

Acknowledgment

The authors wish to thank Dr. J. F. Waymouth, Sylvania Electric Products, for information about the Sylvania panel and Dr. Meschter, du Pont Company, for providing wo electroluminescent phosphors. They also wish to hank Dr. D. R. Frankl, Sylvania Electric Products, and Dr. F. A. Schwertz, Mellon Institute, for kindly sending reports on unpublished results.

Manuscript received June 6, 1955. This paper is based on a dissertation submitted by Sol Nudelman to the University of Maryland in partial fulfillment of the requirements for the Ph.D. degree.

Any discussion of this paper will appear in a Discussion Section to be published in the December 1956 JOURNAL.

REFERENCES

1. C. JEROME AND W. GUNGLE, *This Journal*, **100**, 34 (1953).
2. J. F. WAYMOUTH, *ibid.*, **100**, 81 (1953).
3. P. ZALM, G. DIEMER, AND H. A. KLASENS, *Philips Research Repts.*, **9**, 81 (1954).
4. D. CURIE, *J. Phys. Radium*, **14**, 672 (1953).
5. F. MATOSSI AND S. NUDELMAN, *Phys. Rev.*, **89**, 660 (1953).
6. H. H. HOMER, R. M. RULON, AND K. H. BUTLER, *This Journal*, **100**, 566 (1953).
7. S. NUDELMAN AND F. MATOSSI, *ibid.*, **101**, 546 (1954).
8. B. T. HOWARD, H. F. IVEY, AND W. LEHMANN, *Phys. Rev.*, **96**, 799 (1954).
9. F. A. SCHWERTZ, J. J. MAZENKO, AND E. R. MICHALIK, *ibid.*, **98**, 1133 (1955).
10. F. A. SCHWERTZ, Private communication.

Reactions of Refractory Silicides with Carbon and Nitrogen

LEO BREWER AND OSCAR KRIKORIAN

Department of Chemistry and Chemical Engineering and Radiation Laboratory, University of California, Berkeley, California

ABSTRACT

Silicides of Ti, Zr, Ce, and Nb were investigated to determine the phases present at temperatures around 2000°K. Ce-C and Nb-C systems were also investigated to a limited extent. Reactions of silicides of Ti, Zr, Ce, Nb, Ta, Mo, and W with carbon were studied at these temperatures. Also, a limited amount of work was done on the reactions of some silicides with nitrogen. The data have been used to establish ternary phase diagrams for the systems and to obtain upper and lower limits for heats of formation of the silicides.

INTRODUCTION

Silicides of titanium, zirconium, cerium, niobium, tantalum, molybdenum, and tungsten were investigated to fix their thermodynamic stabilities and thus determine their importance as refractories. These metals are expected to form the most stable silicides from a comparison with the carbide stability region in the periodic table.

Combustion calorimetry and solution calorimetry are not easily applicable in determining heats of formation of silicides due to their inertness toward oxidation and solvents. Dissociation pressure measurements would probable be the most applicable in determining their stabilities. Searcy and McNees (1) determined the stabilities of rhenium silicides by studies of this type. In order to undertake such studies on other refractory silicides, information on the phases present, their approximate stabilities, and suitable containers are of great importance.

In this work high temperature equilibrium studies involving silicides are used to obtain useful information about their stabilities. Equilibrium studies involved the systems M-Si, M-Si-C, M-Si-N_2, and M_1-M_2-Si. By comparing the stabilities of the silicides with the corresponding carbides and nitrides it was possible to set upper and lower limits to the stabilities of many of the silicides. The M_1-M_2-Si equilibria gave information about the relative stabilities of the silicides.

EXPERIMENTAL PROCEDURE

M-Si, M-Si-C, and M_1-M_2-Si reactions were carried out by mixing together 140–400 mesh powders of the reactants and heating them to about 2100°K for 15–60 min in the inductively heated equipment already described (2). Argon, at 0.75 atm, was used to suppress volatilization of the silicon. Molybdenum crucibles were found to be satisfactory containers since molybdenum silicides were less stable than most of the other silicides studied. When

sample silicides were less stable than the molybdenum silicides, crucible attack still did not occur, providing the samples did not fuse. A protective silicide layer on the surface of the molybdenum evidently prevented further attack. Graphite crucibles were used when samples contained excess graphite. Usually, equilibrium was rapidly established between the reactants which then sintered and drew away from the container.

M-Si-N_2 systems were studied by allowing metal and silicon powder mixtures to come into equilibrium with N_2 at about ¾ atm pressure and at various temperatures. Molybdenum containers were again used for most of the heatings, although they were not satisfactory with titanium and zirconium systems because of crucible attack. ZrO_2 containers were also used for these systems.

Samples were quenched by turning off the induction heater and cooling with the gas in the system. About 3 min were required to cool from 2100° to 1200°K.

Temperatures were measured with an optical pyrometer. X-ray powder diffraction patterns were taken of the resulting samples. The new phases found and x-ray data for the various phases will be given in a forthcoming paper (3). All compositions of samples are given in atomic per cent and all temperatures are expressed in °K unless otherwise indicated.

Starting materials.—Silicon metal[1] was ground to finer than 140 mesh with a steel mortar and pestle. Spectroanalysis showed the main impurities to be: titanium less than 1%, chromium 0.1–1%, and aluminum and iron approximately 0.1%. X-ray analysis showed a very weak unidentified second phase.

Zirconium metal was obtained in the form of high purity, hafnium-free sponge from K. K. Kelley of the U. S. Bureau of Mines at Berkeley. X-ray analysis of the titanium metal powder ($a = 2.950 \pm 0.003$ *A*, $c = 4.692 \pm 0.005$ *A*) indicated that it contained roughly 4.5 at. % oxygen (4). Cerium metal obtained in the form of rods contained 4.5 at. % carbon as the main impurity. All other metals were of 99.9% or greater purity.

Binary Systems

The Ta-Si, Mo-Si, and W-Si systems at the temperatures of interest here have already been studied (5). The following phases were found: $TaSi_2$, $TaSi_{0.6}$, $TaSi_{0.4}$, $TaSi_{0.2}$; $MoSi_2$, $MoSi_{0.65}$, Mo_3Si; WSi_2, $WSi_{0.7}$. The $MoSi_{0.65}$ and $WSi_{0.7}$ phases were recently shown to be isomorphous with the tetragonal Cr_5Si_3 phase (52).

In an x-ray investigation of Ta-Si system (6), structures were assigned to phases $Ta_{4.5}Si$, Ta_2Si, and Ta_5Si_3. The x-ray pattern found for $Ta_{4.5}Si$ was different than that for the $TaSi_{0.2}$ reported by Brewer and co-workers (2). These two phases may be high and low temperature forms of the same compound. Ta_2Si corresponds to the $TaSi_{0.4}$ of Brewer and co-workers. The Ta_5Si_3 pattern, however, is different from the $TaSi_{0.6}$ phase reported by them. The two phases may again be high and low temperature modifications or, as is discussed later, the Ta_5Si_3 phase may have been stabilized by carbon impurity.

In this work the systems Ti-Si, Zr-Si, Ce-Si, and Nb-Si were investigated for the phases present at high temperatures. The results of the Ti and Zr heatings are presented in Tables I and II. The cerium and niobium results are discussed in the text. The detailed tabulated data are given by Krikorian (45). The symbols s. (strong), m. s. (moderately strong), m. (moderate), m.w. (moderately weak), w. (weak), and v.w. (very weak) refer to observed x-ray intensities. Maximum temperature attained is given in the tables. Molybdenum containers were used for all heatings unless otherwise indicated. Any evidence of melting of the sample has also been indicated. In all cases where the samples fused, they had a silvery-gray metallic luster.

TABLE I. Ti-Si *system*

Atomic % Si	Temp (°K)	Description of sample	Phases observed
17.8	2105	Fused Cruc. attack	Mo (m.s.) + Ti_5Si_3 (m.w.)
20.2	1691	Fused	Ti_5Si_3 (s.) + Ti (v.w.)
30.0	2105	Fused	Ti_5Si_3 (s.) + Mo (v.w.)
33.5	2105	Sintered Porous	Ti_5Si_3 (s.)
37.5	2105	Partially fused	Ti_5Si_3 (s.)
50.5	1933	Partially fused	Ti_5Si_3 (m.) + TiSi (w.) + ? (v.w.)
50.5	2105	Fused	Ti_5Si_3 (s.) + TiSi (w.)
60.0	2141	Fused	Ti_5Si_3 (s.) + ? (v.w.)
60.2	2190	Fused Al_2O_3 cruc. Crystals above melt	$TiSi_2$ (s.) + Ti_5Si_3 (w.)
67.1	2105	Fused	$MoSi_2$ (s.) + Ti_5Si_3 (w.)
71.9	1618	Partially fused	$TiSi_2$ (m.) + Si (w.)

Ti-Si *system.*—In addition to $TiSi_2$, the Ti_5Si_3 phase already reported (7) was found. The Ti_5Si_3 lattice constants were found to vary with the silicon content of the sample from 20 to 60 at. % Si. Such an effect is not necessarily indicative of a wide homogeneity range in the binary system, but may be due to presence of oxygen in the sample from the titanium starting material, as well as possible solubility of the molybdenum container material in the Ti_5Si_3 lattice.

The reported TiSi phase (8) was not observed in pure

[1] Supplied by the J. T. Baker Chemical Co., Phillipsburg, N. J.

TABLE II. Zr-Si *system*

Atomic % Si	Temp (°K)	Description of sample	Phases observed
22.4	1952	Fused Condensate on walls	A phase (m.)
35.0	1952	Partially fused	Zr_2Si (m.) + Zr_5Si_3 (w.)
40.4	1952	Sintered	Zr_2Si (m.s.) + ? (v.w.)
40.4*	2156	Well-sintered Brown color on surface	Zr_5Si_3 (m.s.)
42.6	1952	Sintered	Zr_2Si (m.s.) + Zr_5Si_3 (w.) + ? (w.)
42.6*	2156	Slightly sintered Brown color on surface	Zr_5Si_3 (m.s.) + Zr_3Si_2 (w.)
45.4	1952	Sintered	Zr_2Si (m.s.) + ? (w.)
45.4*	2156	Not sintered	Zr_5Si_3 (m.) + Zr_6Si_5 (m.) + Zr_3Si_2 (w.)
45.4*	2156	Sintered	Zr_5Si_3 (m.) + Zr_6Si_5 (m.) + Zr_3Si_2 (w.) + ? (w.)
49.8	1952	Sintered	ZrSi (m.s.) + Zr_2Si (m.w.)
49.8*	2156	Not sintered Brown color on surface	ZrSi (m.) + Zr_6Si_5 (m.)

* Preceding sample reheated.

phase. Many weak lines appeared in the TiSi region along with Ti_5Si_3. $TiSi_2$ and Ti_5Si_3 were found together in a sample heated in an alumina crucible, indicating that the Ti_5Si_3 phase is sufficiently stabilized by oxygen to cause disproportionation of TiSi. The presence of oxygen in the starting Ti metal is undoubtedly responsible for the difficulty of the production of the TiSi phase even when molybdenum containers are used.

Attack of the crucible by a sample containing 67% silicon showed that molybdenum is capable of reducing $TiSi_2$ to Ti_5Si_3. Also its presence in fused samples of Ti_5Si_3 indicates that Ti_5Si_3 is stable in the presence of molybdenum.

Zr-Si *system.*—For the preparation of compounds of silicon with pure zirconium, small pieces of sponge zirconium were heated with silicon for an hour at 1952°K. Some samples were then powdered to 140 mesh or finer and reheated. Results of the x-ray analyses are given in Table II.

Samples of zirconium silicides have been prepared by others (9–11); the phases ZrSi, Zr_6Si_5, Zr_4Si_3, Zr_3Si_2, Zr_2Si, and Zr_4Si, in addition to the previously known $ZrSi_2$, were reported (9). Their identifications were based largely upon metallographic analysis. The phase Zr_5Si_3, with the Mn_5Si_3 structure, was said to be the only phase between Zr_2Si and ZrSi (10). McPherson (43) and Pietrokowsky (11) kindly supplied samples of all their phases for comparison with present samples.

X-ray examination of the samples received from McPherson showed characteristic x-ray patterns for each of the five lower silicides. Except for Zr_4Si, all of these phases appeared in the authors' samples. A sample containing 22.4 at. % Si fused at 1952°K without apparent crucible attack and appeared to contain a single phase different from the Zr_4Si of McPherson. Pietrokowsky obtained yet another diffraction pattern for Zr_4Si. The structure of none of these phases has been worked out. Pietrokowsky (11) determined the structure of Zr_2Si. In the present work Zr_2Si was obtained as a practically pure phase near 35 at. % Si. It appeared in small amounts in samples containing up to 50 at. % Si apparently due to incomplete attainment of equilibrium since the Zr_2Si disappeared upon powdering and reheating the samples.

The sample designated as Zr_3Si_2 by McPherson was found to have the Mn_5Si_3 structure and is designated here as the Zr_5Si_3 phase. This composition is consistent with the data reported in reference (9). Pietrokowsky prepared a single crystal of the phase designated as Zr_4Si_3 by Mc-

Pherson and found it to have the tetragonal U_3Si_2 structure reported by Zachariasen (12). This phase is designated here as Zr_3Si_2. The structures of the Zr_6Si_5 and ZrSi phases have not yet been determined. ZrSi does not index well on the hexagonal lattice reported by Lundin and co-workers (9).

Zr_5Si_3 shows a varying lattice constant depending upon the preparation, which may indicate a wide homogeneity range. Since the ternary diagram studies show that this phase takes up elements like carbon, nitrogen, and oxygen, the variation may be due to impurities.

To check the effect of impure zirconium, preparations were made using zirconium powder. Ignition of the zirconium powder indicated 21.4 at. % oxygen, assuming all the impurity was oxygen. X-ray analysis showed the presence of a pure zirconium phase plus a zirconium phase with a lattice constant corresponding to 22 at. % oxygen, assuming all the impurity to be oxygen (13). The preparations gave single-phase samples of ZrSi and Zr_5Si_3, but patterns of the Zr_3Si_2 and Zr_6Si_5 phases could not be positively identified. These results indicate that the absence of these phases in the work of Schachner and co-workers (10) may be due to the presence of oxygen, carbon, or nitrogen dissolving in and stabilizing the Zr_5Si_3 phase, thus causing the disporportionation of the Zr_3Si_2 and Zr_6Si_5 phases. The results presented below for the Zr-Si-C system confirm this. Heatings with 15–18 at. % oxygen and with less than 30 at. % silicon at temperatures above 1900°K yield only the phases Zr and Zr_5Si_3. The Zr lattice was expanded, indicating dissolved oxygen. Lowering of the zirconium activity by oxygen apparently causes the disproportionation of the Zr_4Si and Zr_2Si phases. Above 1900°K the impurity reduces the number of silicide phases to Zr_5Si_3, ZrSi, and $ZrSi_2$. As the temperature is lowered, reduction of the zirconium activity is not so great and it is possible to prepare Zr_2Si. The oxygen impurity also raises the eutectic temperature for the Zr-Zr_5Si_3 region. Samples were well sintered at 2000°K and were probably close to the eutectic temperature.

To check the effect of oxygen on the Zr-Si system, the composition triangles of the Zr-Si-O system were determined. A join was found between ZrO_2 and $ZrSi_2$. Thus, none of the other zirconium silicides can exist in equilibrium with zircon or any silicon oxide. There is also a join between $ZrSi_2$ and SiO_2. Thus, silicon reacts with ZrO_2. Most of the binary silicide phases below $ZrSi_2$ are of no importance in the ternary Zr-Si-O diagram because of the stabilization of the Zr_5Si_3 phase, and no phases are found between Zr and Zr_5Si_3 at 2000°K within the ternary diagram. Also, it appears that no phases are stable between Zr_5Si_3 and ZrSi at 2000°K within the ternary diagram. A ternary diagram is given in Fig. 1 to represent the probable behavior at 1950°K. At lower temperatures, where the solubility of oxygen in the Zr_5Si_3 phase decreases thus increasing its activity, the other binary phases appear to become important and joins should be drawn between the binary zirconium silicides and ZrO_2.

Ce-Si *system.*—Ce-Si samples were prepared by reacting small pieces of Ce rod with Si powder at about 1700°K. They all had the appearance of being fused or partially fused. It was not possible to determine visually the extent of the fusion. There was no evidence of crucible attack.

The samples were prepared for x-ray analysis by grinding them to 200 mesh in a dry box under argon and sealing the specimens in capillary tubes.

The x-ray patterns were rather poor and the samples were inhomogeneous mixtures; however, it was established that several lower silicides exist. These are provisionally assigned the formulas $CeSi_{0.35}$, $CeSi_{0.5}$, and $CeSi_{0.75}$.

The $CeSi_{0.35}$ phase appeared along with CeO_2 in all of its samples. In spite of precautions, the CeO_2 probably came from oxidation of Ce metal during preparation of the specimens for x-ray study. Therefore, it is believed that $CeSi_{0.35}$ is the lowest silicide.

The $CeSi_{0.5}$ appeared in samples containing 33–37 at. % Si, and $CeSi_{0.75}$ appeared in samples containing 40–50% Si. $CeSi_2$ was obtained in single phase and its lattice constants were measured: $a = 4.175 \pm 0.002$ *A*, $c = 13.848 \pm 0.006$ *A*. It is reported to have the tetragonal $\alpha ThSi_2$ type structure with the lattice constants $a = 4.16 \pm 0.03$ *A*, $c = 13.90 \pm 0.07$ *A* (12).

Nb-Si *system.*—The Nb-Si system showed the two lower silicides $NbSi_{0.55\pm0.1}$ and Nb_5Si_3. $NbSi_{0.55}$ is isostructural with the $TaSi_{0.6}$ phase reported earlier (5). It was obtained in equilibrium with niobium metal up to 36 at. % Si. Nb_5Si_3 has Mn_5Si_3 type structure. $NbSi_{0.55}$ and Nb_5Si_3 were not obtained together in equilibrium and the region should be more fully investigated.

It has been possible to set the Nb-$NbSi_{0.55}$ eutectic, or peritectic, temperature as greater than 2095°K and the Nb_5Si_3-$NbSi_2$ eutectic, or peritectic, at 2110° ± 30°K.

M-Si-C Systems

From heats of formation of the carbides in these systems it is possible to obtain limits on heats of formation of silicides. To make these calculations, use is made of the approximate relation:

$$\Delta F^0_T = \Delta H^0_{298} - T\Delta S^0_{298}$$

Assuming that ΔS^0_{298} is zero when all reactants and products are solids, the heats of formation of the carbides directly

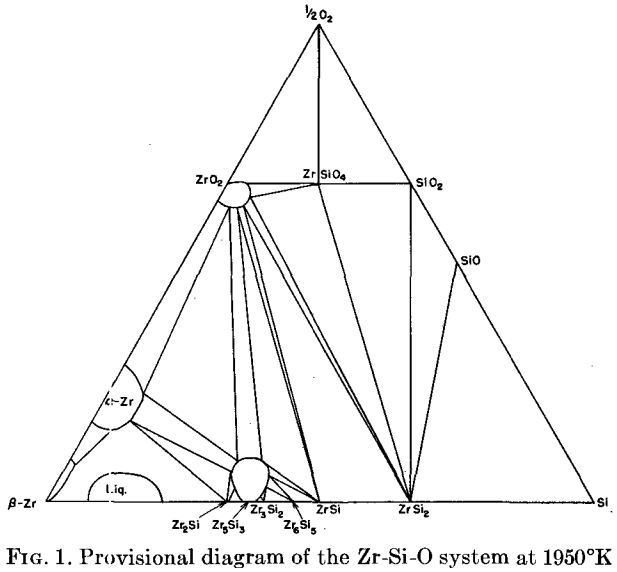

FIG. 1. Provisional diagram of the Zr-Si-O system at 1950°K

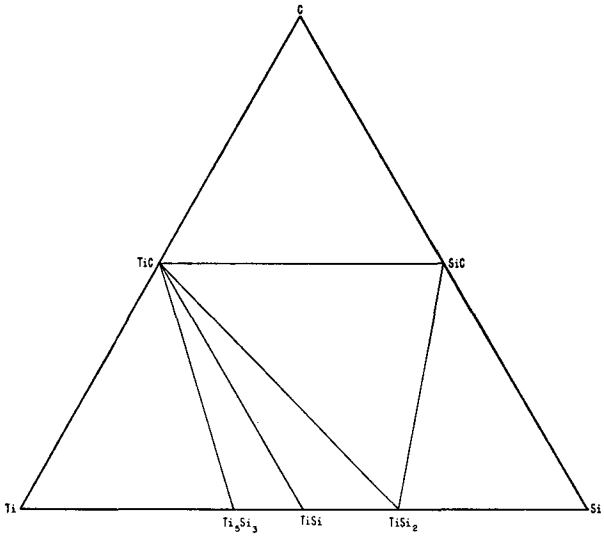

FIG. 2. Ti-Si-C system

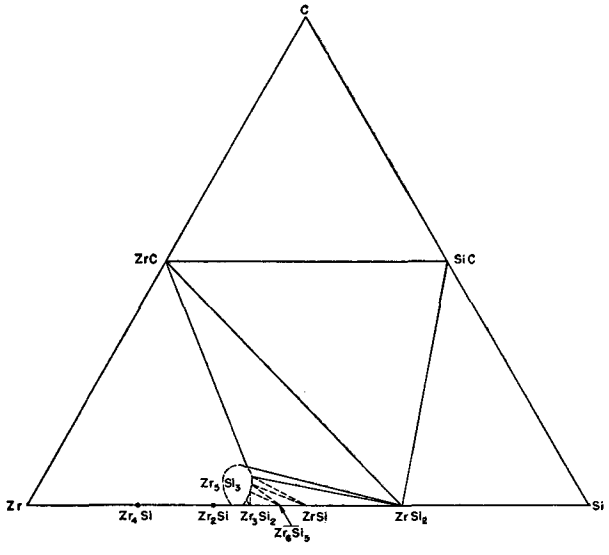

FIG. 3. Zr-Si-C system

set limits for heats of formation of the silicides. As an example:

$$\tfrac{1}{2}\ MSi_2 + \tfrac{3}{2}\ C \rightarrow \tfrac{1}{2}\ MC + SiC$$

$$\tfrac{1}{2}\ MC + \tfrac{3}{2}\ Si \rightarrow \tfrac{1}{2}\ MSi_2 + \tfrac{1}{2}\ SiC$$

If the ΔH^0_{298} of formation of SiC is -13.0 kcal (14) and that of MC is A, then ΔH^0_{298} of formation for MSi_2 must be greater than $(A - 26.0)$ kcal and less than $(A + 13.0)$ kcal for the reactions to go as written.

The calculations may be improved somewhat if the entropies of the silicides become available. Third law entropy values are available for SiC, TiC, and TaC (15). Entropies for the other carbides may be estimated by Latimer's method (16). One may assign an entropy contribution for carbon in a solid compound by subtracting the contribution of the metal from the known entropies of carbides (15). It is found that about -4.1 e.u. may be assigned to carbon for its contribution in a carbide of one to one metal to carbon ratio, about -7.2 e.u. in a carbide of two to one or three to one metal to carbon ratio and about -14 e.u. in a carbide of four to one metal to carbon ratio.

The absolute entropy of WC, for example, is estimated as $S^0_{298} = S^0_M + S^0_C = 15.0 - 4.1 = 10.9$ e.u. Using values of 8.04 and 1.36 e.u. (15) for the absolute entropies of W and C, respectively, ΔS^0_{298} of formation for WC is estimated as 1.5 ± 1 e.u.

The heat of formation of SiC is available (14), as are those for TiC and TaC (17, 18) and for WC (19). For NbC, $\Delta H^0_{298} = -33.7$ kcal was obtained from Kelley (51).

Heats of formation of Mo_2C and MoC were calculated from equilibrium constant data of Browning and Emmett (20) for the reactions $2Mo + CH_4 = Mo_2C + 2H_2$ and $Mo_2C + CH_4 = 2MoC + 2H_2$. In making these calculations the S^0_{298} for Mo_2C and MoC were estimated by the method described above. The heat capacity of MoC was estimated to be $\frac{2}{5}$ the heat capacity of Cr_3C_2 (21), that for Mo_2C was assumed to be $\frac{3}{10}$ the heat capacity of Cr_7C_3 (21). Estimated values were combined with thermodynamic data for the other substances (21, 15) involved in the reaction to tabulate $(\Delta F^0_T - \Delta H^0_{298})/T$ functions for the reactions. ΔH^0_{298} was found to be 13.67 ± 1.09 kcal for the first reaction and 18.11 ± 0.20 kcal for the second reaction. With the value of -17.89 kcal/mole for ΔH^0_{298} of formation for methane (22), ΔH^0_{298} of formation is -4.22 ± 1.09 kcal for Mo_2C and -2.00 ± 0.65 kcal for MoC. The respective ΔS^0_{298} values were estimated to be 2.4 ± 1 and 0.0 ± 1 e.u.

The ternary diagrams of Fig. 2 to 7 have been used to show phases resulting from M-Si-C heatings. Several of the diagrams were not completed, but the joins that were established are indicated. Other joins, boundaries, or homogeneity ranges that were inferred are indicated by dotted lines. For simplicity, homogeneity ranges for carbide phases have been omitted. In the Mo-Si-C system, an attempt was made to give the general form of the melting region along with several ternary eutectic temperatures. The melting diagram of the molybdenum-silicon system was given by Kieffer and Cerwenka (23) and also by Ham and Herzig (24). Results have been re-interpreted to obtain better agreement with the data. The Mo-Mo_2C eutectic temperature is given by Sykes, Van Horn, and Tucker (25) and the Mo_2C melting temperature by Agte and Alterthum (26).

After this work had been completed, word was received that the Mo-Si-C system had been determined in more detail (27). Results are in essential agreement with the authors except for an MoC phase in their samples. This phase is unstable at low temperatures and may have been retained by a faster quenching.

In the Mo-Si-C system a ternary compound was observed at about the composition Mo_4CSi_3. Considerable variation of lattice parameters with composition was observed for ternary compound. Evidently carbon replaces Mo in a Mo_5Si_3 lattice until the composition Mo_4CSi_3 is obtained on the high carbon side. Lattice constants for the composition Mo_4CSi_3 are $a = 7.285 \pm 0.007$ A and $c = 5.242 \pm 0.007$ A.

Using the lattice constants for Mo_4CSi_3 the calculated x-ray density is 6.62 g/cm³ for Mo_4CSi_3 and 7.94 g/cm³

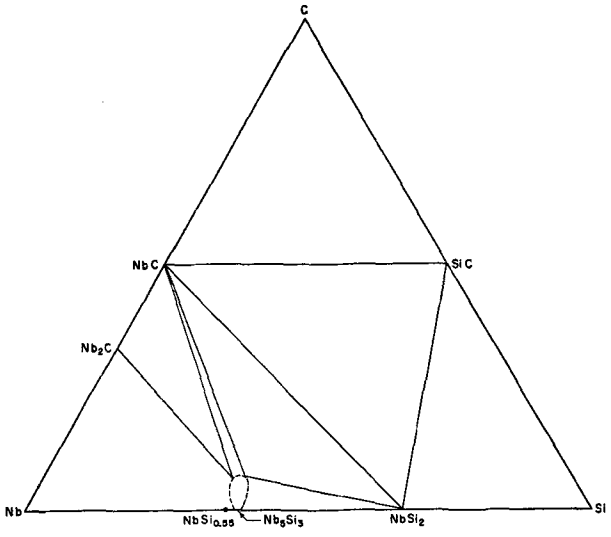

FIG. 4. Nb-Si-C system

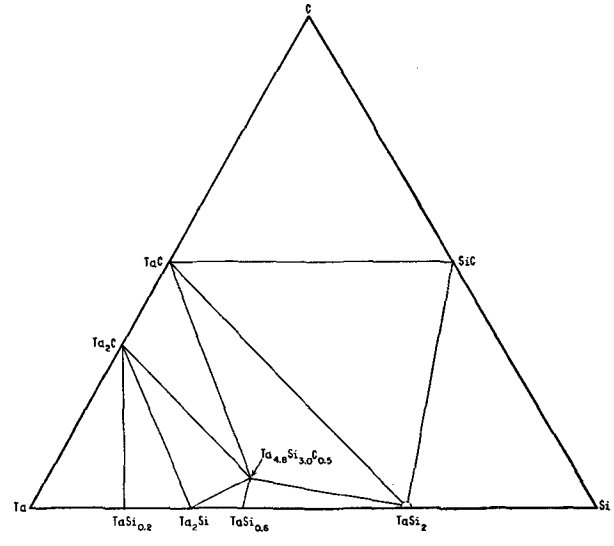

FIG. 5. Ta-Si-C system

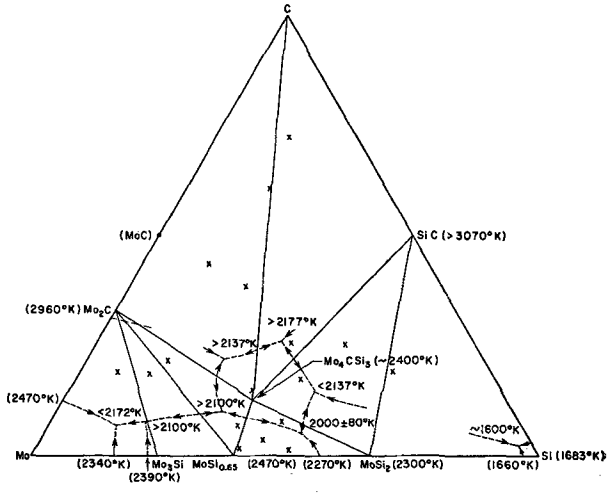

FIG. 6. Mo-Si-C system

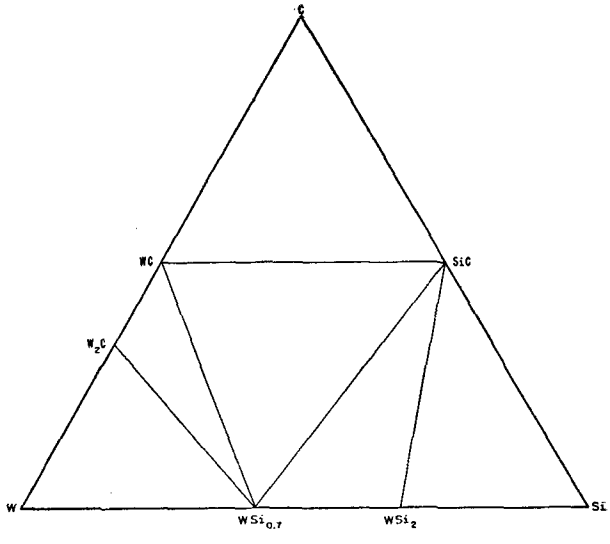

FIG. 7. W-Si-C system

for Mo_5Si_3. The measured density for a single-phase sample of Mo_4CSi_3 was found to be 6.9 g/cm³ which gives fair agreement with its composition. The homogeneity range for the compound is believed to extend to lower carbon contents but does not reach the binary Mo-Si region. Mo_4CSi_3 is the only molybdenum silicide phase found that is stable in the presence of graphite.

In the Ta-Si-C system a ternary compound appeared in single phase with the Mn_5Si_3 structure in a sample of composition $Ta_{4.8}Si_3C_{0.5}$ with parameters $a = 7.494 \pm 0.007$ *A* and $c = 5.242 \pm 0.007$ *A*. No variation in lattice constants was observed in the x-ray patterns, so that there is no evidence for an extended homogeneity range.

The Mn_5Si_3 structure has two molecules per unit cell. Assuming that the carbons in $Ta_{4.8}Si_3C_{0.5}$ are interstitial and the departure of the number of Ta's from 5 is due to vacancies in the lattice, the calculated x-ray density is 12.48 g/cm³ for $Ta_{4.8}Si_3C_{0.5}$. The density of the powder measured with a pycnometer using the volume displacement of CCl_4 gave 12.4 g/cm³.

A phase Ta_5Si_3, of the Mn_5Si_3 structure, has been reported (6) with lattice constants $a = 7.474$ *A* and $c = 5.225$ *A*. These values are close to those which obtained here for $Ta_{4.8}Si_3C_{0.5}$. In the work on the Ta-Si system (5), Ta_5Si_3 with the Mn_5Si_3 structure was not found, although a phase of composition $TaSi_{0.6}$ was found which did not have the Mn_5Si_3 structure. Nowotny and co-workers (6) also report that Ta_5Si_3 transforms to a new phase somewhere between 1600° and 1800°K. This high temperature phase may be the $TaSi_{0.6}$ reported by Brewer and co-workers. If $TaSi_{0.6}$ is stable only at high temperatures, it is easily quenched since the Ta_5Si_3 phase has not been observed in this work in binary Ta-Si samples. The Mn_5Si_3 type structure is stabilized by oxygen, carbon, and nitrogen impurities and was obtained with added nitrogen or carbon in the present ternary diagram studies. Thus, it is likely that the Ta_5Si_3 phase is unstable at all temperatures in the binary system and requires a third component for its existence. A variation of lattice constants was observed for $TaSi_2$ from the $TaSi_2$-SiC-Si region to the $TaSi_2$-SiC-TaC region, indicating solubility of carbon in $TaSi_2$.

Both Zr_5Si_3 and Nb_5Si_3 showed large homogeneity ranges in the presence of carbon. Other than this there was

TABLE III. ΔH°_{298} *of formation in kcal/gram atom* Si

$\frac{1}{2}TiSi_2$	−15.4 to −34.9	$\frac{5}{3}$ $TaSi_{0.6}$	−20 to −77.2
TiSi	−15.4 to −65.8	Ta_2Si	−20 to −90.1
$\frac{1}{3}Ti_5Si_3$	−20 to −86.1	$5TaSi_{0.2}$	<−20
$\frac{1}{2}ZrSi_2$	−30.5 ± 5	$\frac{1}{3}Ta_{4.8}Si_3C_{0.5}$	−20 to −74.7
ZrSi	−58 ± 10	$\frac{1}{2}MoSi_2$	−5.8 to −15.5
$\frac{1}{6}Zr_6Si_5$	−66 ± 10	$10/6.5MoSi_{0.65}$	−18.4 ± 1.6
$\frac{1}{2}Zr_3Si_2$	−70 ± 10	Mo_3Si	−20
$\frac{1}{3}Zr_5Si_3$	−72 ± 10	$\frac{1}{3}Mo_4CSi_3$	−19.6 ± 2
Zr_2Si	−74 ± 10	$\frac{1}{2}WSi_2$	−1.6 to −17.2
Zr_4Si	−76 ± 10	$10/7WSi_{0.7}$	−4.6 to −20
$\frac{1}{2}CeSi_2$	−16.6 to −34.4	$\frac{1}{2}ReSi_2$	−12.5*
$1/xCeSi_x$	<−16.6	ReSi	−11.6*
$\frac{1}{2}NbSi_2$	−8.5 to −28	Re_3Si	−6.2*
$\frac{1}{3}Nb_5Si_3$	−8.5 to −63		
$20/11NbSi_{0.55}$	−8.5 to −68		
$\frac{1}{2}TaSi_2$	−12.8 to −32.3		

* Values for the Re silicides (1) have been recalculated using ΔH°_{298} = 105 kcal for the heat of sublimation of Si (41, 42).

no indication of ternary compound formation in the systems. A hexagonal phase (a = 3.117 ± 0.003 A, c = 4.969 ± 0.005 A) isomorphous with Ta_2C was observed in the Nb-Si-C system, indicating the presence of an Nb_2C phase (28, 29, 30). To confirm this, a powder mixture of 67% Nb and 33% carbon was held at 2130°K for 38 min in a Mo crucible under vacuum. The phases Nb_2C and NbC were obtained. Similar treatment of a mixture of 75% Nb and 25% carbon at 1920°K yielded Nb_2C as the principle phase with a very small amount of NbC present.

In the Ce-Si-C system a sample containing 25% Ce, 50% Si, and 25% carbon was held at 1605°K for 44 min. X-ray analysis showed $CeSi_2$, plus an unidentified phase. The sample was gray-brown and gave off an acetylene odor. An investigation of the Ce-C system in the range between 50% and 67% carbon showed the phases CeC, Ce_2C_3, and CeC_2, plus several unidentified phases. None of these could be identified in the Ce-Si-C sample. The Ce_2C_3 (body-centered cubic Pu_2C_3 type) lattice constant was a = 8.455 ± 0.008 A (31); the CeC (NaCl type) lattice constant was a = 5.130 ± 0.002 A (31); the Ce-C samples were golden brown.

Details of calculations of the stabilities of silicides of Mo and Zr from data of the M-Si-C systems follow. Calculations for the other systems are similar. Pertinent results are summarized in Table III. The numbers below each species are the values for ΔH^{0}_{298} of formation expressed in kilocalories.

Mo-Si-C *system.*—Recent studies (32) on the vapor pressure of Si over Mo + Mo_3Si give a preliminary value of −20 kcal for ΔH^{0}_{298} of Mo_3Si.

$$0.71\,Mo_3Si + 0.29\,SiC \rightarrow \frac{10}{6.5}\,MoSi_{0.65} + 0.29\,Mo_2C$$

$$-14.2 \qquad -3.8 \qquad <-16.8 \qquad -1.2$$

$$\frac{10}{6.5}\,MoSi_{0.65} + \frac{19}{13}\,Mo \rightarrow Mo_3Si$$

$$>-20 \qquad -20$$

Therefore, ΔH^{0}_{298} for $10/6.5\ MoSi_{0.65}$ = −18.4 ± 1.6 kcal.

$$\frac{10}{6.5}\,MoSi_{0.65} + \frac{17}{39}C \rightarrow \frac{1}{3}\,Mo_4CSi_3 + \frac{4}{39}\,Mo_2C$$

$$-18.4 \qquad <-18.0 \qquad -0.4$$

$$\frac{1}{3}\,Mo_4CSi_3 + \frac{7}{3}\,Mo \rightarrow Mo_3Si + \frac{1}{3}\,Mo_2C$$

$$>-21.4 \qquad -20 \qquad -1.4$$

Therefore, ΔH^{0}_{298} for Mo_4CSi_3 = −19.7 ± 2 kcal.

$$\frac{1}{2}\,MoSi_2 + \frac{3}{4}\,C \rightarrow \frac{1}{8}\,Mo_4CSi_3 + \frac{5}{8}\,SiC$$

$$>-15.5 \qquad -7.4 \qquad -8.1$$

$$\frac{1}{8}\,Mo_4CSi_3 + \frac{3}{4}\,Si \rightarrow \frac{1}{2}\,MoSi_2 + \frac{1}{8}\,SiC$$

$$-7.4 \qquad <-5.8 \qquad -1.6$$

Zr-Si-C *system.*—From the Zr-Si-O system, using oxide heats of formation (33)

$$\frac{1}{2}\,ZrO_2 + \frac{3}{2}\,Si \rightarrow \frac{1}{2}\,ZrSi_2 + \frac{1}{2}\,SiO_2$$

$$-130.9 \qquad <-25.8 \qquad -105.1$$

The carbide ternary diagram yields

$$\frac{1}{2}\,ZrSi_2 + \frac{3}{2}\,C \rightarrow \frac{1}{2}\,ZrC + SiC$$

$$>-35.2 \qquad -22.2 \qquad -13.0$$

Therefore, ΔH^{0}_{298} for $\frac{1}{2}$ $ZrSi_2$ = −30.5 ± 5 kcal. The Zr-Si phase diagram established by Lundin and co-workers (9) shows that all of the zirconium silicides except Zr_6Si_5 have incongruent melting points. Thus, at the $ZrSi_2$ peritectic there are $ZrSi_2$, ZrSi, and a Si rich melt in equilibrium; at the ZrSi eutectic ZrSi, Zr_6Si_5, and a Si rich melt in equilibrium; and so on to Zr_2Si, Zr_4Si, and a Zr rich melt in equilibrium.

If the activity of Si or of Zr in the melt at the peritectic points can be estimated, then heats of formation of all of the other zirconium silicides can be calculated from the heat of formation of $ZrSi_2$. The activity of Si in the melt is estimated to be roughly equal to the mole fraction of Si between the stable solid compound and pure Si, when working on the Si rich side of the diagram. The free energy of solution of Si from its standard state can then be calculated.

$$Si\ (s) \rightarrow Si\ (l);\ \Delta F^{0}_{T} = \Delta H^{0}_{f} - T\Delta S^{0}_{f}$$

$$Si\ (l) \rightarrow Si\ (sol'n);\ \overline{\Delta F}_{T} = RT \ln a_{Si}$$

$$Si\ (s) \rightarrow Si\ (sol'n);\ \overline{\Delta F}_{T} = \Delta H^{0}_{f} - T\Delta S^{0}_{f} + RT \ln a_{Si}$$

On the Zr rich side of the diagram a similar calculation is made referring to the activity of Zr rather than Si. For the fusion process ΔS_f^0 is taken as 6.6 e.u. for Si (34) and 2.3 e.u. for Zr (34), ΔH_f^0 is taken as 11.1 kcal for Si (34) and calculated as 4.9 kcal for Zr from the melting point of Zr given by Lundin and co-workers (9). In the calculations that follow, the numbers below the Si and Zr solutions represent the $\overline{\Delta F}_T$ of solution.

$ZrSi_2 = ZrSi + Si(sol'n, a_{Si} = 0.47); \quad T = 1790$

$-61 \quad -57.6 \quad -3.4$

$6ZrSi = Zr_6Si_5 + Si(sol'n, a_{Si} = 0.108); \quad T = 2370$

$-345.6 \quad -330.6 \quad -15.0$

$5Zr_3Si_2 = 2Zr_6Si_5 + 3Zr(sol'n, a_{Zr} = 0.084);$

$-700.5 \quad -661.2 \quad -39.3 \quad T = 2500$

$2Zr_5Si_3 = 3Zr_3Si_2 + Zr(sol'n, a_{Zr} = 0.147);$

$-430.5 \quad -420.3 \quad -10.2 \quad T = 2480$

$3Zr_2Si = Zr_5Si_3 + Zr(sol'n, a_{Zr} = 0.352); \quad T = 2380$

$-220.8 \quad -215.3 \quad -5.5$

$Zr_4Si = Zr_2Si + 2Zr(sol'n, a_{Zr} = 0.601); \quad T = 1900$

$-76.4 \quad -73.6 \quad -2.8$

M-Si-N_2 Systems

The M-Si-N_2 systems can yield information about the stabilities of silicides of Ti, Zr, Ce, Nb, and Ta since these elements form stable nitrides at high temperatures. The nitrides of these metals are more stable than the silicides at lower temperatures, but at high temperatures the nitrides become less stable due to their negative entropy of formation. Determination of the temperature at which this reversal of stabilities occurs would be very valuable in fixing the stabilities of the silicides.

ΔH_{298}^0 values for Si_3N_4 and CeN are available (35) as is ΔS_{298}^0 of formation of Si_3N_4 (15). The other entropies have been estimated.

From the observations of Schönberg on the Ta-N system (36) the phases prepared and investigated by earlier workers can be identified. Neumann, Kröger, and Kunz (37) have determined the heat of combustion of tantalum nitride. Their method of preparation indicates the compounds are $TaN_{0.846}O_x$ and $TaN_{0.955}O_y$. In order to interpret the results, x is assumed to be 0.060. $TaN_{0.846}O_{0.060}$ is treated as being a solid solution of 0.012 Ta_2O_5 in 0.976 $TaN_{0.867}$ with zero heat of solution. Thus -199.3 kcal is obtained as the ΔH_{298}^0 of combustion for $TaN_{0.867}$. Combining this value with the heat of formation of Ta_2O_5 (33) the ΔH_{298}^0 of formation is -59.2 ± 2 kcal per equivalent of N for $TaN_{0.867}$.

Slade and Higson (38) have studied the dissociation pressure of a tantalum nitride. From their method of preparation, they were probably studying the equilibrium $2\ TaN_{0.8} = Ta_2N + \frac{3}{10}\ N_2$. The dissociation pressure leads to $\Delta H_{298}^0 = 29.6 \pm 2$ kcal for this reaction. Combining this with the above value for $TaN_{0.8-0.9}$ yields a ΔH_{298}^0 of -65.2 ± 5 kcal for Ta_2N.

An experimental difficulty was encountered in attaining equilibrium in the M-Si-N_2 systems. As some of the samples nitrided, they sintered and formed a crust on the surface so that the samples were not homogeneous in nitrogen throughout. More useful results would be obtained by introducing nitrogen into the system in the form of a metal nitride. Preparation of Si_3N_4 and Ta_2N was investigated for this purpose.

To prepare Si_3N_4, Si metal powder was heated in a Mo crucible under about $\frac{3}{4}$ atm of N_2. The rate of the nitriding reaction was very slow below 1600°K while, above 1900°K, Si_3N_4 showed considerable decomposition. The sample was first heated to 1660°K. The temperature was then gradually increased to 1800°K over a period of an hour. Sintered portions of the resulting sample were crushed and the sample was reheated. The final product was grayish white. X-ray analysis showed a strong Si_3N_4 pattern plus weak Si.

Ta_2N was prepared by heating Ta powder contained in a Mo crucible to 2100°K for 33 min under $\frac{3}{4}$ atm of N_2. From the weight gain the composition was calculated to be $Ta_{1.96}N$. The x-ray diffraction pattern showed Ta_2N as a single phase.

Work on the M-Si-N_2 systems was concentrated on the Ta-Si-N_2 system with only a few reactions in the other systems being studied. A summary of the reactions studied is presented in Table IV. Heatings at 1600°K in the Ta-Si-N_2 system show that $TaSi_2$ is unstable in the presence of N_2 and reacts to give $Ta_{5-x}Si_{3-y}N_z$. Si_3N_4 would also be expected to form, however it was not picked up by x-ray analysis. When samples of Si content 38% and lower were heated in N_2 at 1600°K they showed a considerable gain in weight. The phase Ta_2N appeared in equilibrium with $Ta_{5-x}Si_{3-y}N_z$. Some weak unidentified lines were also present. These lines may be due to $TaN_{0.8\ 0.9}$ and TaN. From these data a provisional form of the Ta-Si-N_2 diagram has been constructed at 1600°K (*see* Fig. 8).

At 2109°K $TaSi_2$ was found to be stable in the presence of N_2. This means that the following reaction can proceed as written:

$$\frac{1}{4}\ Ta_2N + \frac{1}{3}\ Si_3N_4 = \frac{1}{2}\ TaSi_2 + 1\frac{9}{24}\ N_2(g)$$
$$-5.6 \qquad -2.4 \qquad -8.0$$

The ΔF_T^0 of formation of Ta_2N and Si_3N_4 have been indicated in the equation. Thus, ΔH_{298}^0 of formation for $TaSi_2$ is less than -8.0 kcal. This does not improve the limits set by the carbide equilibria; however, a study of the equilibrium at a lower temperature would give additional data.

The Nb-Si-N_2 system appears to be similar to the Ta-Si-N_2 system. Joins were established between $Nb_{5-x}Si_{3-y}N_z$ and N_2 and between $Nb_{5-x}Si_{3-y}N_z$ and $NbSi_2$.

From the gain in weight and physical appearance of a sample of Ce + 2Si heated in N_2, it is evident that $CeSi_2$ is unstable in the presence of N_2. The x-ray pattern was too poor to reveal anything. Providing no ternary compounds are formed in the Ce-Si-N_2 system, the following reaction can proceed at 1610°K. From a calculation of ΔF_T^0 for CeN and Si_3N_4, ΔH_{298}^0 of formation of $CeSi_2$ is greater than -34.4 kcal/equivalent of Si

$$\frac{1}{2}\ CeSi_2 + 1\frac{1}{12}\ N_2 = \frac{1}{2}\ CeN + \frac{1}{3}\ Si_3N_4$$
$$> -34.4 \qquad -18.4 \qquad -16.0$$

TABLE IV. M-Si-N_2 *systems*

Reactants	Cruc.	Temp (°K)	Weight change	Description of sample	Phases observed
Ti + 0.61 Si + N_2	ZrO_2	2109	−4.0%	Not sintered Gold color	TiN (s.)
Ti + 2.18 Si + N_2	Mo	2146	Unknown	Partially fused Gold color Crucible attack	? (m.s.) + TiN (m.s.)
Zr + 2.04 Si + N_2	Mo	2146	Unknown	Partially fused Gold color Crucible attack	$MoSi_2$ (v.s.) + ZrN (s.) + $ZrSi_2$ (w.) + ? (v.w.)
Zr + 13.1 Si_3N_4 + N_2	ZrO_2	2109	−54%	Not sintered	? (s.) + Si (m.s.)
Ce + 2.23 Si + N_2	Mo	1610	13.5%	Black brittle solid. Strong odor of NH_3	? (v.w.)
Nb + 0.60 Si + N_2	ZrO_2	2109	−0.2%		$Nb_5Si_3N_z$ (m.s.)
Nb + 1.17 Si + 0.28 Si_3N_4 + N_2	Ta	2365	Unknown	Fused Crucible attack	(Ta, Nb)Si_2 (m.s.) + (Ta, Nb)$_5Si_3N_z$ (m.s.) + (Ta, Nb)$Si_{0.6}$ (w.)
Nb + 2.01 Si + N_2	Mo	2146	Unknown	Partially fused Crucible attack	$NbSi_2$ (m.) + $Nb_5Si_3N_z$ (m.) + ? (w.)
Ta + 0.20 Si + N_2	Mo	1602	+4.2%	Sintered	$Ta_5Si_3N_z$ (m.) + ? (m.w.)
Ta + 0.40 Si + N_2	Mo	1602	+3.7%	Sintered	$Ta_5Si_3N_z$ (m.s.) + Ta_2N (m.w.) + ? (v.w.)
Ta + 0.61 Si + N_2	Mo	1602	+4.3%	Sintered	$Ta_5Si_3N_z$ (m.s.) + $TaSi_2$ (m.) + ? (w.)
Ta + 1.07 Si + 0.30 Si_3N_4 + N_2	Ta	2365	Unknown	Fused Crucible attack	$TaSi_2$ (m.) + $Ta_5Si_3N_z$ (m.) + $TaSi_{0.6}$ (v.w.)
Ta + 1.13 Si + 1.72 Si_3N_4 + N_2	Mo	1651	+5.5%	Not sintered	$TaSi_2$ (m.) + $Ta_5Si_3N_z$ (m.) + Ta_2N (w.)
Ta + 2.20 Si + N_2	Mo	2146	Unknown	Partially fused	$TaSi_2$ (v.s.)
Ta + 2.30 Si + N_2	Mo	1602	+7.1%	Not sintered Top of sample	$TaSi_2$ (s.) + Si (m.) + ? (v.w.)
Ta + 2.30 Si + N_2	Mo	1602	+7.1%	Not sintered Bottom of sample	$TaSi_2$ (s.) + $Ta_5Si_3N_z$ (m.)
$TaSi_{2.30}N_{1.24}$ + N_2	Mo	1651	+3.0%	Not sintered Previous sample	$TaSi_2$ (s.) + $Ta_5Si_3N_z$ (m.s.) + Ta_2N (w.)
Ta_2N + 0.81 Si_3N_4 + N_2	Mo	2109	−14.1%	Sintered	$TaSi_2$ (s.) + $Ta_5Si_3N_z$ (m.s.)

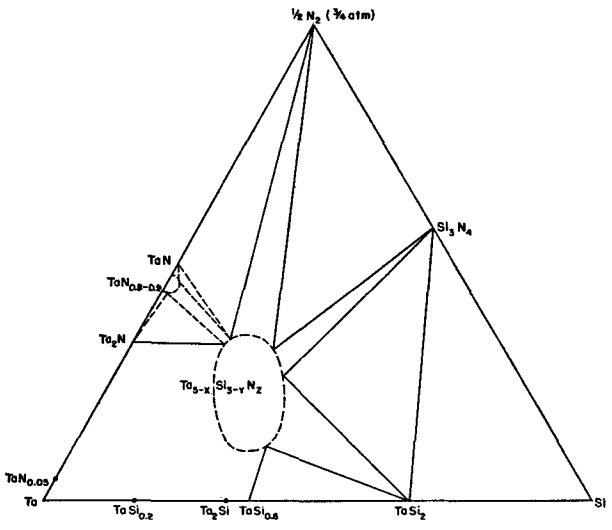

FIG. 8. Ta-Si-N system at 1600°K

Since there was no attack of the container by Si, it is assumed that a join exists between $CeSi_2$ and Si_3N_4, so that the reaction

$$\underset{-39.0}{\tfrac{1}{2}\ CeN} + \underset{}{1\tfrac{1}{8}\ Si} = \underset{<-16.6}{\tfrac{1}{2}\ CeSi_2} + \underset{-22.4}{\tfrac{1}{8}\ Si_3N_4}$$

can go as written. Assuming $\Delta S^0_{298} = 0$ for this reaction, ΔH^0_{298} of formation of $CeSi_2$ is less than -16.6 kcal/equivalent of Si. These calculations are, of course, provisional.

In the Ti-Si-N_2 system a sample containing 62% Ti and 38% Si reacted with N_2 to give TiN. No other phases were found, indicating a wide homogeneity range for TiN in the ternary system. A sample initially containing 69% Si showed considerable attack of the Mo container yielding TiN plus an unidentified phase.

When a sample containing 33% Zr and 67% Si was heated in N_2 in a Mo crucible it yielded $MoSi_2$, ZrN, $ZrSi_2$, plus weak unidentified lines. Crucible attack would be expected since $ZrSi_2$ was previously found to be unstable in the presence of Mo. When Zr metal was heated with excess Si_3N_4 in a ZrO_2 container in the presence of N_2 at 2100°K, an unidentified hexagonal ($a = 7.603 \pm 0.008$ A, $c = 2.906 \pm 0.003$ A) phase of strong intensity appeared along with Si metal.

M_1-M_2-Si Systems

In the M_1-M_2-Si systems it is difficult to obtain thermodynamic data from the phases observed because of extended solid solubilities in these systems. Nevertheless some useful data were obtained. The main region studied was that of low Si content. A summary of the heatings is given in Table V.

$TaSi_{0.6}$ and Ta_2Si were found to be stable in the presence of Mo, as was Ta_2Si in the presence of W.

A join was found to exist between Ta_2Si and Ti_5Si_3. The lattice constants of Ti_5Si_3 were expanded, indicating a solubility of Ta in Ti_5Si_3.

Mo reduces $TiSi_2$ to Ti_5Si_3 which is believed to be stable in the presence of Mo. It is believed that a join exists between Ti_5Si_3 and $MoSi_2$.

Mo_3Si was found to be stable in the presence of W with no apparent change in lattice constants of either phase.

A join exists between Zr_5Si_3 and Nb. Nb_5Si_3 and Zr_5Si_3 appear to be completely soluble in each other. X-ray analysis of the region showed a phase of the Mn_5Si_3 structure with lattice constants intermediate between Nb_5Si_3 and Zr_5Si_3.

The relative stabilities of the silicides may be summarized as follows: Ti_5Si_3, $TaSi_{0.6}$, Ta_2Si, $TaSi_{0.2}$ > Mo_3Si > $WSi_{0.7}$; Zr_5Si_3, Zr_2Si, Zr_4Si > $NbSi_{0.55}$.

Discussion of Results

The results of this investigation have been combined with available data in the literature and summarized as ternary phase diagrams given in Fig. 1 to 8, and summarized in terms of heats of formation of the various phases studied in Table III. These heats are consistent with the observations and, through thermodynamic calculations, may be used to reproduce the observations of this work as well as to predict the behavior of these materials under conditions not yet studied. Except for the Mo-Si-C diagram, the positions of the liquidus surfaces are not indicated and only the composition triangles are presented to indicate the phases at equilibrium with one another.

It is of interest to note that in the ternary systems involving carbon, no binary metal silicides were found to be stable in the presence of carbon, although one ternary compound Mo_4CSi_3 was stable in the presence of carbon. This is in contrast to the results presented by Brewer and Haraldsen (44) for the metal-carbon-boron systems where many borides are stable in the presence of carbon. Fig. 8 represents the Ta-Si-N system at 1600°K and shows that none of the silicides of tantalum is stable in the presence of nitrogen at this temperature, but a ternary Ta-Si-N compound is stable. However, at high temperatures, $TaSi_2$ does become stable in the presence of nitrogen and the solid solution range of the ternary compound becomes greatly reduced and might even disproportionate completely.

One of the purposes of this investigation, as well as that of the corresponding study of borides (44), was to obtain enough data to compare the bond strengths of these compounds with those of the carbides, nitrides, etc., of the transition metals. It was hoped that these data would yield some insight into the nature of the bonding and allow prediction of the stability of compounds for which no data exist. Bonding energies of the refractory compounds were calculated in the following way. The heats of formation (45) of the compounds from the elements at 298°K were combined with the heats of sublimation or dissociation to the gaseous atoms at 298°K to obtain the heats for the reaction MX(s) = M(g) + X(g). This heat which is needed to produce two gram-atoms of monatomic gaseous products from a mole of the solid MX compound is a measure of the bonding strengths and is referred to as the bonding energy. Evaluation of this quantity for borides, carbides, silicides, nitrides, oxides, sulfides, and halides was carried out for the MX compounds of the transition metals of the fourth row or period of the periodic table from calcium through the iron group metals and for the transition metals of the fifth and sixth rows from stron-

TABLE V. M_1-M_2-Si *systems*

Atomic % M_1	Atomic % M_2	Atomic % Si	Atomic % O	Temp (°K)	Description of sample	Phases observed
40.3-Ti	39.1-Zr	7.1	12.5	2071	Partially fused	? (m.)
34.0-Ti	32.7-Zr	22.8	10.5	1995	Partially fused	$(Ti, Zr)_5Si_3$ (m.) + ? (v.w.)
51.0-Ti	15.5-Ta	31.1	2.4	2142	Partially fused	$(Ti, Ta)_5Si_3$ (s.)
30.6-Ti	30.9-Ta	37.0	1.5	2071	Partially fused	Ti_5Si_3 (s.) + Ta_2Si (m.) + ? (v.w.)
29.4-Ti	53.5-Mo	15.6	1.5	1920	Sintered	Mo_3Si (s.) + Mo (s.) + ? (v.w.)
27.4-Ti	18.9-Mo	52.3	1.4	1920	Sintered	Ti_5Si_3 (m.s.) + $(Ti, Mo)Si_2$ (m.)
33.9-Zr	35.3-Nb	21.5	9.3	1995	Sintered	Zr_5Si_3 (m.) + Nb (w.)
29.7-Zr	31.1-Nb	31.2	8.0	2071	Partially fused	$(Nb, Zr)_5Si_3$ (m.) + Nb (m.)
26.4-Zr	27.7-Nb	38.9	7.0	2071	Sintered	ZrSi (m.s.) + ? (m.)
26.0-Zr	27.9-Ta	39.0	7.1	2071	Partially fused	Ta_2Si (m.s.) + Ta (m.) + ? (m.)
37.5-Zr	39.2-Mo	13.2	10.1	1995	Sintered	(Mo, Zr) (m.) + ? (w.)
33.5-Zr	34.6-Mo	23.0	8.9	2142	Sintered	(Mo, Zr) (s.) + ? (m.)
7.7-Ce	77.0-Ta	15.3		1920	Sintered	Ta_2Si (m.) + CeO_2 (w.) + ? (v.w.)
37.8-Nb	39.7-Mo	22.5		1995	Sintered	Mo_3Si (s.) + Mo_3Si_2 (w.)
29.2-Nb	29.4-Mo	41.4		2071	Sintered	(Mo, Nb) (s.) + ? (m.)
38.2-Nb	38.6-W	23.2		1995	Sintered	W (s.) + $WSi_{0.7}$ (m.)
45.0-Ta	45.9-Mo	9.1		1983	Sintered	(Mo, Ta) (m.s.) + Ta_2Si (m.)
41.1-Ta	41.2-Mo	17.7		2142	Well-sintered	Ta_2Si (m.s.) + (Mo, Ta) (m.) + ? (v.w.)
38.4-Ta	38.4-Mo	23.2		2142	Well-sintered	(Mo, Ta) (s.) + $(Mo, Ta)Si_{0.6}$ (m.s.)
44.25-Ta	46.75-W	9.0		1983	Sintered	W (m.s.) + Ta_2Si (w.) + ? (v.w.)
41.2-Ta	42.1-W	16.7		2142	Slightly sintered	W (s.) + (W, Ta) (s.) + Ta_2Si (m.s.)
33.2-Ta	33.2-W	33.6		2071	Well-sintered	W (s.) + $WSi_{0.7}$ (m.) + Ta_2Si (w.)
41.7-Mo	43.7-W	14.6		1983	Sintered	Mo_3Si (s.) + W (m.)

tium and barium through the platinum group metals. Where the MX compounds were thermodynamically unstable with respect to disproportionation or decomposition to other compounds, an upper limit was set to the stability of the MX compound. The conclusions that can be drawn from the examination of the bonding energies of the refractory compounds will be briefly reviewed.

Data were incomplete for some of the rows, but sufficient data were available to show that the bonding energy varies greatly with the metal within a row. For every type of compound a sharp maximum in bonding energy is found in the middle of the row with the bonding energy falling off rapidly to either side. To illustrate the behavior, curves are shown in Fig. 9 for the bonding energies of the carbides of the fourth row together with the bonding energies of the corresponding pure metals phase for comparison and for the bonding energies of the nitrides of the sixth row together with the energies for the metals of the same row. Complete data and other plots are given by Krikorian (45). To put the bonding energies of the refractory compounds and of the metals on the same basis, bonding energies of the metals are given as twice the heats of sublimation; so that two gram-atoms of gaseous products are formed in all cases.

Plots of bonding energy for the various refractory compounds were remarkably similar. For the oxides and nitrides, a maximum was found in the compounds of the fourth group of the periodic table in all three rows. Thus the compounds of Ti, Zr, and Hf have higher bonding energies than compounds of any other metals in the corresponding rows. When the compounds of maximum bonding energies are compared, the nitrides are found to be about 10 kcal higher than the oxides and the carbides about 20 kcal higher than the nitrides. Although TiC has a higher bonding energy than any other carbide of the fourth row, the maximum for the bonding energies of the carbides of the fifth and sixth rows occurs in the fifth group with Nb and Ta. Silicide bonding energies are about 50 kcal lower than those of the corresponding carbides, with the borides intermediate between the carbides and silicides.

There are several striking characteristics of the plots of bonding energies. One thing is that the bonding energies of these refractory compounds are close to and even greater than the values for the metals. Although the maximum bonding energy is found in the fourth group with nonmetals containing many valence electrons, the maximum shifts to the fifth group as the number of valence electrons of the nonmetal decreases and, finally, for the pure metals the maximum shifts over more to the right reaching the sixth group metal tungsten in the sixth row of the periodic table. It is striking that the maxima for the metals occur in that region of the periodic table where the maximum number of unpaired d electrons is found. The shift of the maximum to the left in the periodic table as nonmetals with increasing numbers of valence electrons are added seems to indicate that the nonmetals contribute electrons to the metallic bonding. Thus the optimum number of unpaired electrons occurs in a group with less valence electrons when nonmetals are added. An especially striking observation is that the bonding energies of the metals and refractory compounds all increase as the size

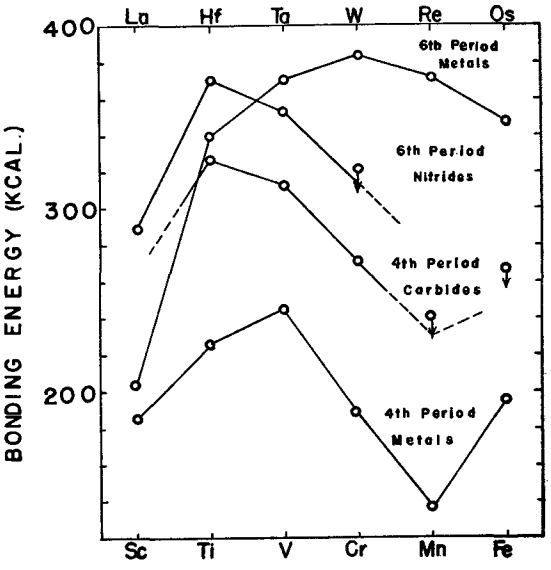

FIG. 9. Typical curves of bonding energies of metals and metallic type compounds in the fourth and sixth periods of the Periodic Table.

of the elements is increased from the fourth row to the sixth row. This is unusual, since bonding energies usually decrease in any series where the sizes of the bonding elements are increased. The close similarity of the bonding energy curves indicates that the type of bonding is similar in all the MX compounds from borides to oxides as well as in the pure metals for the transition elements. Similar calculations of bonding energies were carried out for some compounds of formula MX_2. Oxides show a maximum in bonding energy at the fourth group with a rapid drop as one moves to the right in the periodic table.

All of the plots of bonding energy for the compounds and pure metals of the fourth row showed a maximum at titanium or vanadium and a minimum at manganese. This is very suggestive as the bonding energies of the halides (46) of the dipositive oxidation state of these elements as well as the hydration energies (47–49) of the dipositive ions of these elements show a similar behavior and this has been attributed to stabilization of the ions in the electric field of the crystal by splitting the degeneracy of the free ion electron levels (46–48, 50). Thus, in the presence of the electric field of a crystal, dipositive manganese ion with a half-filled d electron shell retains spherical symmetry; whereas, other transition metal dipositive ions of the fourth row become asymmetric and highly polarized in the field and accommodate themselves to a lattice with a higher bonding energy than obtainable with the spherical ion. Splitting of d electron levels may occur for the divalent ions on either side of Mn^{+2} in the periodic table, and leads to stabilization due to lowering of the ground state energy of the ion. Mn^{+2} cannot partake in this stabilization due to nondegeneracy of its ground state.

The observation of a minimum in the bonding energies of the metals and refractory compounds at manganese suggests that a bonding model involving positive ions, i.e., metal atoms with d electron configurations the same as those of the dipositive ions, might be fruitful for further investigation. The possibility of accounting for the varia-

tion of the bonding energies of the refractory compounds of the transition elements by an ionic model was considered. A simple ionic model with only simple coulombic interactions that does not take into account polarizability is a good approximation for compounds like the alkali halides and the alkaline earth oxides. Such a model is quite unsatisfactory for the refractory compounds of the transition elements, since the effect of the strong force fields upon the *d* electron orbitals and other polarizability effects should be very large for these compounds. At present, these effects cannot be estimated, but it is hoped that absorption spectra and other similar measurements will be carried out for these compounds in an effort to gain further insight into the nature of their bonding.

From the practical point of view, immediate application of the plots of bonding energies can be made. From the rather similar behavior of the plots for the various compounds, it is possible to fill in missing values. In this way, one can estimate heats of formation of compounds for which values are not yet available. These estimated values are, of course, rather uncertain, but they can be of value. The following ΔH^0_{298} of formation values were estimated: ½ $TiSi_2$, -28 ± 5; TiSi, -48 ± 10; ⅓ Ti_5Si_3, -75 ± 20; ⅓ Nb_5Si_3, -52 ± 20; ½ $TaSi_2$, -25 ± 8; ⅝ $TaSi_{0.6}$, -53 ± 20; ½ WSi_2, -13 ± 5; and 1⅐ $WSi_{0.7}$, -18 ± 5 kcal.

Acknowledgment

The x-ray diffraction films were prepared by Mrs. Helena Ruben and interpreted by Mrs. Carol Dauben. The authors would like to express their appreciation for this help which was essential for this work. The authors would also like to thank Dr. John Conway for spectroanalyses.

This work was performed under the auspices of the U. S. Atomic Energy Commission.

Manuscript received January 31, 1955. This paper was prepared for delivery before the Wrightsville Beach Meeting, September 13 to 16, 1953, and was abstracted from the thesis of Oscar Krikorian in partial fulfillment of the Ph.D. degree in chemistry at the University of California.

Any discussion of this paper will appear in a Discussion Section to be published in the December 1956 JOURNAL.

REFERENCES

1. A. W. Searcy and R. A. McNees, Jr., *J. Am. Chem. Soc.*, **75**, 1578 (1953).
2. L. Brewer, L. A. Bromley, P. W. Gilles, and N. L. Lofgren, Declassified Atomic Energy Commission Report MDDC-367, August 4, 1945.
3. D. H. Templeton and C. H. Dauben, paper in preparation.
4. E. S. Bumps, H. D. Kessler, and M. Hansen, *Trans. Am. Soc. Metals*, **45**, 1008 (1953).
5. L. Brewer, A. W. Searcy, D. H. Templeton, and C. H. Dauben, *J. Am. Ceram. Soc.*, **33**, 291 (1950).
6. H. Nowotny, H. Schachner, R. Kieffer, and F. Benesovsky, *Monatsh. Chem.*, **84**, 1 (1953).
7. P. Pietrokowsky and P. Duwez, *J. Metals*, **3**, No. 9, 772 (1951).
8. M. Hansen, H. D. Kessler, and D. J. McPherson, *Trans. Am. Soc. Metals*, **44**, 518 (1951).
9. C. E. Lundin, D. J. McPherson, and M. Hansen, *ibid.*, Preprint No. 41 (1952).
10. H. Schachner, H. Nowotny, and R. Machenschalk, *Monatsh. Chem.*, **84**, 677 (1953); *see* also, R. Kieffer, F. Benesovsky, and R. Machenschalk, *Z. Metallkunde*, **45**, 493 (1954).
11. P. Pietrokowsky, Private communication.
12. W. H. Zachariasen, *Acta Cryst.*, **2**, 94 (1949).
13. R. F. Domagala, D. J. McPherson, and M. Hansen, "The Zirconium-Oxygen System," Armour Research Foundation of Illinois Institute of Technology, Report No. 4, Summary (COO-181), March 31, 1953.
14. G. L. Humphrey, S. S. Todd, J. P. Coughlin, and E. G. King, U. S. Bureau of Mines Report of Investigations 4888, July 1952.
15. K. K. Kelley, U. S. Bur. Mines Bull. No. 477 (1950).
16. W. M. Latimer, "The Oxidation States of the Elements and Their Potentials in Aqueous Solutions," 2nd ed., Prentice-Hall Inc., New York (1952).
17. G. L. Humphrey, *J. Am. Chem. Soc.*, **73**, 2261 (1951).
18. G. L. Humphrey, *ibid.*, **76**, 978 (1954).
19. G. Huff, E. Squitieri, and P. Snyder, *J. Am. Chem. Soc.*, **70**, 3380 (1948).
20. L. C. Browning and P. H. Emmett, *ibid.*, **74**, 4773 (1952).
21. K. K. Kelley, U. S. Bur. Mines Bull. No. 476 (1949).
22. F. D. Rossini, D. D. Wagman, W. H. Evans, S. Levine, and I. Jaffe, U. S. Bureau of Standards Circular 500 (1952).
23. R. Kieffer and E. Cerwenka, *Z. Metallkunde*, **43**, 101 (1952).
24. J. L. Ham and A. J. Herzig, Second Annual Report to Office of Naval Research, Misc-1951-132 (Climax Molybdenum Company of Michigan, 1951).
25. W. P. Sykes, K. R. Van Horn, and C. M. Tucker, *Am. Inst. Mining Met. Engr.*, Techn. Publ. No. 647 (1935).
26. C. Agte and H. Alterthum, *Z. Techn. Physik*, **11**, 182 (1930).
27. H. Nowotny, E. Parthé, R. Kieffer, and F. Benesovsky, *Monatsh. Chem.*, **85**, 255 (1954).
28. G. Brauer, H. Renner, and J. Weinet, *Z. anorg. u. allgem. Chem.*, **277**, 249 (1955).
29. J. S. Umanski, *Zhur. Fiz. Chim.*, **14**, 332 (1940).
30. G. F. Hardy and J. K. Hulm, *Phys. Rev.*, **93**, 1004 (1954).
31. C. H. Dauben, Private communication.
32. A. W. Searcy and A. G. Tharp, Private communications.
33. L. Brewer, *Chem. Rev.*, **52**, 1 (1953).
34. L. Brewer, National Nuclear Energy Series, Vol. 19B, Paper 3, L. L. Quill, Editor, McGraw-Hill Book Co., New York (1950).
35. L. Brewer, L. A. Bromley, P. W. Gilles, and N. L. Lofgren, *ibid.*, Paper 4.
36. N. Schönberg, *Acta Chem. Scand.*, **8** [No. 2], 199 (1954).
37. B. Neumann, C. Kröger, and H. Kunz, *Z. anorg. u. allgem. Chem.*, **218**, 379 (1934).
38. R. E. Slade and G. I. Higson, *Chem. News*, **108**, 166 (1913).
39. R. Kieffer, F. Benesovsky, H. Nowotny, and H. Schachner, *Z. Metallkunde*, **44**, 242 (1953).
40. R. Kieffer, F. Benesovsky, and E. Gallistl, *Z. Metallkunde*, **43**, 284 (1952).
41. R. E. Honig, *J. Chem. Phys.*, **22**, 1610 (1954).
42. R. F. Barrow and H. C. Rowlinson, *Proc. Roy. Soc. A*, **224**, 374 (1954).
43. D. J. McPherson, Private communication.
44. L. Brewer and H. Haraldsen, *This Journal*, **102**, 399 (1955).
45. O. Krikorian, Ph.D. Thesis, University of California (1955).
46. Z. Z. Hugus, Jr., Unpublished work.
47. O. Holmes, Ph.D. Thesis, University of California (1955).
48. L. E. Orgel, *J. Chem. Soc.*, **1952**, 4756.
49. D. S. McClure and R. E. Connick, Private communications.

50. J. H. VAN SANTEN AND J. S. VAN WIERINGEN, *Rec. Trav. Chim.*, **71**, 420 (1952).
51. K. K. KELLEY, Unpublished work.
52. C. H. DAUBEN, C. E. MEYERS, D. H. TEMPLETON, AND A. W. SEARCY, paper presented at the Amer. Cryst. Assoc. Meeting, Pasadena, Calif., June 27, 1955.

The Fracture of Brittle Chromium by Acid Etching

W. H. SMITH

Research Laboratory, General Electric Company, Schenectady, New York

ABSTRACT

A mechanism is presented to explain the formation of transcrystalline cleavage cracks during the etching of brittle annealed chromium. The mechanism proposed is the formation of a face-centered-cubic chromium hydride on the surface which, due to its larger volume, initiates cracks in the brittle material beneath. These cracks may then propagate by a stress corrosion mechanism. Room temperature ductile material appears to be capable of taking up this volume expansion without cracks being initiated. X-ray data confirm the existence of the face-centered-cubic hydride.

INTRODUCTION

For many metals it has been found that embrittlement occurs because of hydrogen pick-up during etching (1). Two types of embrittlement are observed, one associated with the formation of a brittle hydride, and the other occurring as a result of solution of hydrogen in the metal, as in iron. In the first case, the formation of the hydride results in a lattice expansion which ruptures the brittle hydride. The source of brittleness in the second case is not completely understood. A number of theories have been proposed to explain the hydrogen embrittlement of iron and related materials, but none is entirely satisfactory.

Little information is available regarding the changes in mechanical properties brought about by hydrogen in chromium. The solubility of hydrogen in solid chromium is very small (2, 3), appreciably less than the solubility of hydrogen in iron or nickel. This small amount of hydrogen in solution appears to have very little effect on the mechanical properties of the metal; however, no detailed study has been made over a wide temperature range. Snavely in 1947 (4) confirmed the existence of face-centered-cubic and hexagonal-close-packed hydrides of chromium and described their properties, stabilities, and lattice structures.

Within the past few years it has also been established that room temperature brittle cold-worked chromium can often be made ductile by etching away the surface, either anodically in a bath consisting of 64% orthophosphoric acid, 15% sulfuric acid, balance water, or chemically in a hydrochloric acid solution (5–7). Experiments confirming this behavior have been performed here. No embrittling effect due to hydrogen occlusion in cold-worked chromium during acid etching has been observed. The most detailed analysis of this phenomenon has been made by Wain and Henderson (6). Their results showed conclusively that the etching process removed the badly nitrided surface layers formed during fabrication.

Room temperature brittleness of chromium has been shown to be due to the presence of nitrogen and possibly carbon as impurities (6, 8). It has been fairly well established that about 0.005 wt % nitrogen renders annealed chromium brittle at room temperature, while a nitrogen content above 0.02 wt % will render wrought chromium brittle. The critical limit for carbon is believed to be around 0.01%.

No information has been presented on the effects observed when annealed chromium of low and high nitrogen contents is etched in acid. Marked physical and mechanical changes have been found to occur when high-nitrogen-content, annealed chromium is etched in hydrochloric acid. This paper presents a description of the changes observed, along with evidence supporting the belief that they are brought about by the formation of face-centered-cubic chromium hydride.

OBSERVATIONS

In marked contrast to the behavior of cold-worked chromium, very severe transcrystalline cracking occurs when brittle annealed chromium (nitrogen content > 0.005%) is etched in hydrochloric acid (Fig. 1). Chromium which is ductile as annealed (nitrogen content < 0.005%) does not exhibit any tendency toward crack formation on etching (Fig. 2). If the etching of brittle annealed chromium is done anodically, and hence with no hydrogen evolution at the surface of the specimen, cracks are not observed (Fig. 3). In Fig. 4, a micrograph of the brittle annealed chromium before etching is presented. It can be seen that cracks are not present. Dye check of the specimen also failed to reveal any cracks.

Since etching cracks were formed in material which had been given a very thorough anneal, 24 hr at 1300°C in a dry hydrogen atmosphere and furnace cooled, it appeared unlikely that residual stresses in the material could account for the behavior. From these observations it

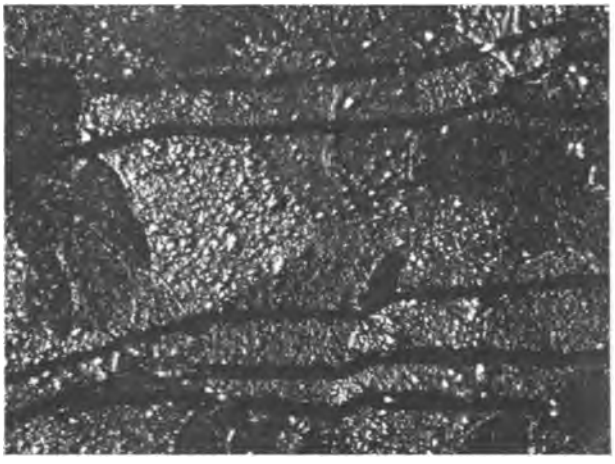

FIG. 1. Annealed chromium containing 0.022 wt % nitrogen, etched in HCl, showing transcrystalline cracks. ×22.

FIG. 2. Annealed chromium containing <0.005 wt % nitrogen, etched in HCl. No cracks are developed. ×22.

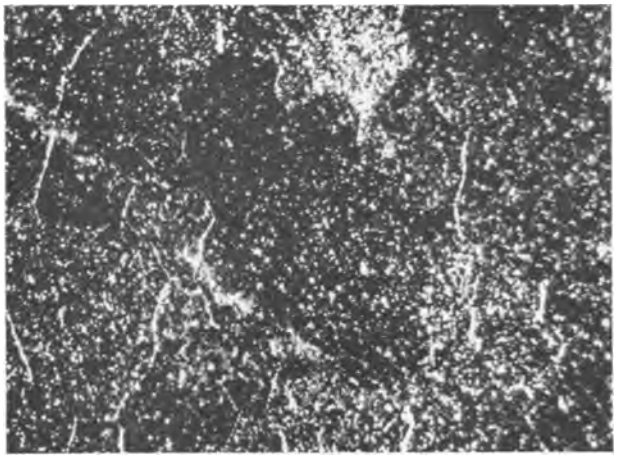

FIG. 3. Annealed chromium containing 0.022 wt % nitrogen, etched anodically. No cracks are developed. ×22.

seemed probable that cracks developed during etching were related to the liberation of hydrogen at the surface of the specimen. To establish the role of hydrogen more firmly, an annealed specimen containing 0.022% nitrogen

FIG. 4. Annealed chromium containing 0.022 wt % nitrogen, unetched. ×22.

FIG. 5. Annealed chromium containing 0.022 wt % nitrogen made the cathode in an H_2SO_4 solution. Transcrystalline cracks developed. ×22.

was made the cathode in a sulfuric acid solution and a voltage applied to the cell, using a platinum anode. Rapid evolution of hydrogen was allowed to occur, and in a relatively short time transcrystalline cracks were developed (Fig. 5).

MECHANISM OF CRACK FORMATION

From the foregoing it appears that the following facts must be accounted for in any proposed mechanism of crack formation:

1. Evolution of hydrogen must occur at the chromium surface.
2. The chromium must be brittle, i.e., high in nitrogen (or possibly carbon) and in the annealed condition.
3. Annealing in a hydrogen atmosphere does not produce cracks.

Since the mechanism sought was one of initiating cracks in brittle material, it appeared that the idea of a hydride formation might account for the observed phenomena. Snavely (4) was able to show that both face-centered-cubic and hexagonal-close-packed chromium hydrides are formed during the electrodeposition of chromium from chromic

acid solutions. Chromium-hydrogen combinations in the formular range of from CrH to CrH_2 gave face-centered-cubic structures with the chromium atoms at the normal corner and face-centered-cubic positions. Hydrogen atoms occupy from one-half to all of the second-largest interstitial openings, the former giving a zinc-blend type of structure, the latter a fluorite structure. Metal-hydrogen ratios in the range Cr_2H to CrH crystallize in the hexagonal-close-packed arrangement. Hydrogen atoms again occupy the second-largest interstices, giving a lattice similar to an incomplete or complete wurtzite structure. Unfortunately, the hydrogen atoms do not produce x-ray diffraction lines and their positions can only be determined by deduction. It is now possible by neutron diffraction methods to check these proposed positions. Prior to the work of Snavely, it was generally believed that the face-centered-cubic and hexagonal-close-packed structures were allotropic modifications of chromium.

The lattice dimensions of the hexagonal-close-packed hydride of chromium are given as a = 2.71(7) Å and c = 4.41(8) Å; the face-centered-cubic hydride has an a_o = 3.85 Å. Snavely also demonstrated that these hydrides are relatively unstable at room temperature and revert quickly to normal body-centered-cubic structure by the evolution of hydrogen. He also showed that a volume expansion of about 16.4% could be expected in converting the metal to the face-centered-cubic hydride and a 15.6% expansion in going to the hexagonal-close-packed hydride. This would give linear expansions of about 5.5%.

To determine whether or not hydrides were being formed during acid etching, the following experiments were performed. A specimen of brittle annealed chromium containing 0.022% nitrogen and 0.0002% hydrogen was obtained. Dye check failed to reveal any surface cracks and x-ray diffraction patterns showed only normal body-centered-cubic chromium lines with an a_o = 2.886 Å (Handbook value 2.885 Å). Cracks were developed in this material by etching in (1:1) hydrochloric acid. Following the etch the specimen was immediately quenched in liquid nitrogen. An x-ray diffraction pattern obtained on this sample revealed body-centered-cubic lines with an a_o = 2.885 Å and a face-centered-cubic structure with an a_o = 3.86 Å. Comparison of the face-centered-cubic values with Snavely's pattern for face-centered-cubic chromium hydride showed excellent agreement. Nitrogen gas cooled by passing through liquid nitrogen was blown across the specimen while the x-ray diffraction pattern was being obtained. It is estimated that the specimen temperature never exceeded −100°C. On allowing this sample to stand at room temperature for eight hours and rerunning the diffraction pattern, it was found that only chromium lines were obtained. This confirms Snavely's remarks regarding the instability of the hydride. These particular experiments were repeated several times with the same results. No evidence for the formation of hexagonal hydride was obtained.

Patterns of face-centered-cubic chromium hydride were found in all cases in which the samples were etched in acid with the evolution of hydrogen or when the piece was made the cathode in an acid cell. A pattern for Cr_2O_3 was obtained when chromium was made anodic.

With identification of the hydride, it was possible to propose a mechanism for crack development in brittle annealed chromium. Since a volume expansion accompanies the formation of the hydride, it would be expected that brittle material might be stressed to the point where the fracture stress is exceeded and cracks could be initiated. The propagation of the cracks could then occur by a stress corrosion mechanism. Room temperature ductile material would be able to take up the linear expansion plastically, or crack propagation by a stress corrosion mechanism might not occur.

X-ray analysis of the crack orientation revealed that fracture was occurring on the (100) cleavage planes.

Acknowledgment

The author is indebted to Mrs. A. Cooper, who obtained the x-ray data presented. Helpful discussions with Dr. J. R. Low, Jr., H. C. Rogers, and Dr. A. U. Seybolt and many other members of the Metallurgy and Ceramics Research Department are also acknowledged.

Manuscript received July 28, 1955.
Any discussion of this paper will appear in a Discussion Section to be published in the December 1956 JOURNAL.

REFERENCES

1. D. P. SMITH, "Hydrogen in Metals," University of Chicago Press, Chicago (1948).
2. A. SIEVERTS AND A. GOTTA, *Z. anorg. u. allgem. Chem.*, **172,** 1 (1928).
3. L. LUCKEMEYER-HASSE AND H. SCHENAK, *Arch. Eisenhüttenw.*, **6,** 209 (1932).
4. C. A. SNAVELY, *Trans. Electrochem. Soc.*, **92,** 537 (1947).
5. W. J. KROLL, *Metal Ind.*, **85,** 345 (1954).
6. H. L. WAIN, F. HENDERSON, AND S. T. M. JOHNSTONE, *J. Inst. Metals,* **83,** 133 (1954).
7. H. JOHANSEN AND G. ASAI, *This Journal*, **101,** 604 (1954).
8. W. H. SMITH AND A. U. SEYBOLT, Unpublished research.

Temperature Dependence of Hardness of the Equi-Atomic Iron Group Aluminides

J. H. WESTBROOK

Research Laboratory, General Electric Company, Schenectady, New York

ABSTRACT

A series of iron group aluminides, a typical group of intermetallic compounds, were prepared by arc melting and their hardness studied as a function of temperature and composition using a modified Bergh instrument. FeAl-, CoAl-, and NiAl-based materials were studied up to 800°C and over the entire homogeneity range of each compound. The results appear to be related to the defect structure in such materials.

INTRODUCTION

As a part of a general investigation of the strength of solids as a function of temperature, it was decided to study the temperature dependence of hardness of a group of intermetallic compounds. The literature on the mechanical properties of intermetallic compounds has been reviewed recently in some detail (1), and it will suffice here to state only the principal conclusions. While most compounds are hard and brittle at ordinary temperatures, all become at least somewhat ductile if the temperature is raised sufficiently. The homologous temperature[1] at which ductility becomes apparent is about the same for many compounds in a given test, but may vary widely with the type of test used. Few satisfying correlations have been established between fundamental parameters and the mechanical properties of intermetallic compounds or the temperature dependence thereof. The melting point, crystal structure, interatomic bond type, ionic charge, polarization parameters, atom size, and presence of ordering have been indicated to be important factors, but the details of their effects and possible interactions are not yet understood.

In selecting a particular group of compounds for study, it was thought wise to choose a group in which at least some of the above factors could be held constant. It was also considered helpful for this group to have a fairly rich literature covering the pertinent phase diagrams, physical properties, etc. Further, it was desirable that the group comprise compounds in which there is some practical interest. Such considerations led to the selection of the equi-atomic iron group aluminides—FeAl, CoAl, and NiAl.

The nickel aluminide has been of interest as a deleterious second phase in certain high temperature alloys and cermets (2–4), as a binder for a TiC base cermet (5), and recently has even been proposed as a base for high temperature materials (6–9). All three compounds, CoAl, FeAl, and NiAl, and certain of their binary and ternary combinations are important constituents in the class of permanent magnet alloys known as "alnico's" (10).

Probably as a result of these manifold practical interests, the literature on this triad of compounds is unusually rich. Their phase diagrams have been determined, crystal structures are known, diffusion rates and certain chemical properties measured, bond type established, atomic arrangements studied in exquisite detail by Bradley's group in England, and many other physical properties measured—electrical resistance, magnetic properties, thermal expansion, etc. Specific references to this literature are made later in connection with the results of the present investigation.

The triad of aluminides have in common a number of those factors which have been thought to be important in controlling the mechanical properties of intermetallic compounds. They are all Hume-Rothery phases or electron compounds and hence have essentially the same type of interatomic bonds. All have the ordered BCC or CsCl structure and are supposed to maintain this structure from room temperature up to the melting point.[2] NiAl and CoAl both form congruently from their melts at about 1650°C and thus have melting points in excess of those of both the component elements. FeAl has a considerably lower melting point than the other compounds, about 1270°C. The phase diagrams (11) for the three systems are shown in Fig. 1. Those for the nickel and cobalt systems are very similar. The current phase diagram for the Fe-Al system is somewhat different and shows FeAl as forming continuously from the alpha solid solution. It should be noted, however, that considerable uncertainty exists in the portion of the diagram near FeAl; the diagram as drawn is not compatible with modern views on the order-disorder transformation (12). All three compounds exist over rather wide ranges of composition which include the stoichiometric value. Finally, as shown in Table I, the the atomic parameters of all three transition elements are very similar but in distinct contrast to those of aluminum. Thus, the equi-atomic iron group aluminides appeared to be an excellent base for the proposed study.

EXPERIMENT

Preparation of Samples

Because of the refractory nature of the compounds, conventional melting methods were not convenient for the preparation of the alloys to be tested. Therefore, resort was made to arc melting. For this purpose a small multiple

[1] The homologous temperature is the ratio of the test temperature to the melting point when expressed in absolute degrees, $T_h = T/T^{mp}$ (°K).

[2] Recent work indicates that FeAl may disorder below its melting point. See further discussion in a later section of this paper.

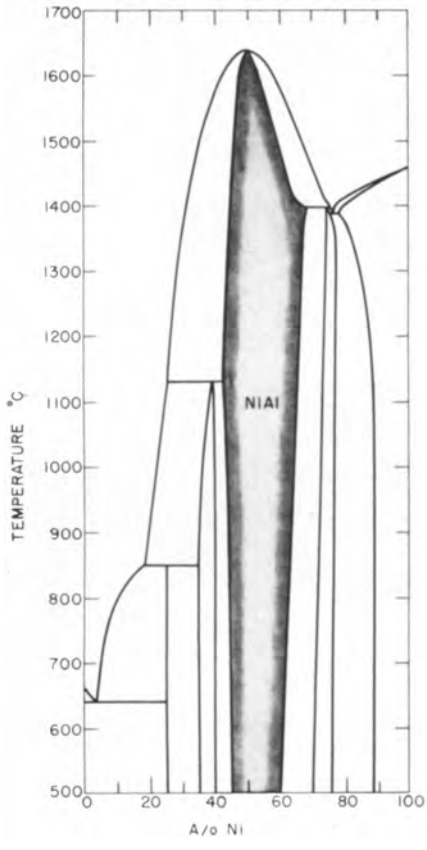

FIG. 1a. Phase diagram of the Ni-Al system

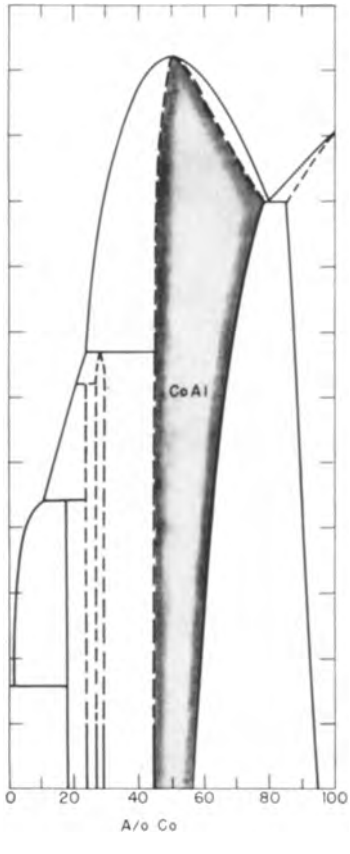

FIG. 1b. Phase diagram of Co-Al system

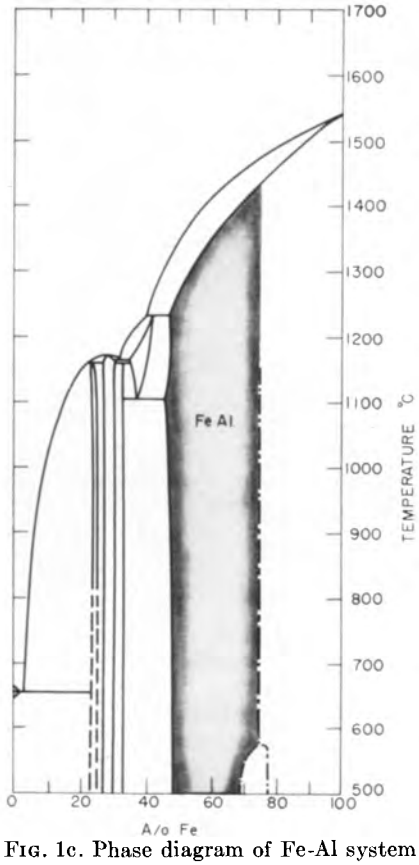

FIG. 1c. Phase diagram of Fe-Al system

TABLE I. *Some physical and chemical properties of iron, cobalt, nickel, and aluminum**

Element	Electron structure				Atomic radii *A*	Standard electrode potential E_0 volts	Work of cohesion kcal/mole	Compressibility x × 10^7 kg/cm	Sat. Mom. β at 0°K
	3s	*3p*	*3d*	*4s*					
Iron	2	6	6	2	1.24	0.441	94	5.9	2.22
Cobalt	2	6	7	2	1.25	0.278	85	5.3	1.71
Nickel	2	6	8	2	1.24	0.231	85	5.4	0.61
Aluminum	2	1	0	0	1.43	1.70	55	13.7	—

* Except for aluminum, data were taken from a similar table published by Zackay (13).

hearth button furnace previously developed in this laboratory (14) was found to be quite suitable. This furnace utilized a water-cooled copper crucible and an argon atmosphere. Provision is made for electromagnetic rotation of the arc to ensure uniform melting.

The metals used for making up the alloys were as follows:

	Form	Source	Nominal purity %
Nickel	Pellets	Whitehead Metal Products	99.8
Cobalt	Rondelles	African Metals Corp.	99.4
Iron	Electrolytic plast iron	National Radiator Co.	99.95
Aluminum	Pig, swaged to ⅛-in. rod and cut up	Aluminum Co. of America	99.99

TABLE II. *Nominal or intended composition*

Alloy No.	Atomic %				Weight %				Remarks
	Ni	Fe	Co	Al	Ni	Fe	Co	Al	
5815-9-25	45	—	—	55	64.0	—	—	36.0	Two phase
5815-22-1	45.4	—	—	54.6	64.7	—	—	35.3	
5815-22-37	46	—	—	54	65.0	—	—	35.0	
5815-21-34	47	—	—	53	65.8	—	—	34.2	
5815-22-38	48	—	—	52	66.8	—	—	33.2	
5815-7-2	49	—	—	51	67.6	—	—	32.4	
1459A	50	—	—	50	68.6	—	—	31.4	
1629C	50	—	—	50	68.6	—	—	31.4	Single phase
5815-16-6	51	—	—	49	69.4	—	—	30.6	
1702B	52	—	—	48	70.2	—	—	29.8	
5815-7-15	54	—	—	46	71.9	—	—	28.1	
5815-7-14	56	—	—	44	73.4	—	—	26.6	
1703B	58	—	—	42	75.1	—	—	24.9	
5815-16-4	61	—	—	39	77.3	—	—	22.7	
1843B	—	48	—	52	—	65.5	—	34.5	Two phase
5815-7-1	—	49	—	51	—	66.4	—	33.6	At phase boundary
1457A	—	50	—	50	—	67.4	—	32.6	
1844B	—	53	—	47	—	70.0	—	30.0	Single phase
5815-16-5	—	58	—	42	—	74.1	—	25.9	
1845B	—	63	—	37	—	78.0	—	22.0	
1922B	—	—	48	52	—	—	67.0	33.0	At phase boundary
5815-21-35	—	—	49	51	—	—	67.7	32.3	
1759B	—	—	50	50	—	—	68.6	31.4	Single phase
1852C	—	—	52	48	—	—	70.6	29.4	
1851C	—	—	54	46	—	—	72.6	27.4	
1860B	16.6	16.7	16.7	50	23.1	21.9	23.2	31.8	
1861B	—	25.0	25.0	50	—	33.1	34.9	32.0	Single phase
1862B	25.0	—	25.0	50	34.2	—	34.4	31.4	
1863B	25.0	25.0	—	50	34.9	33.1	—	32.0	

Table II lists all of the compositions melted. Previous experience had indicated that little loss would be experienced on melting, so the weighed amounts charged into the furnace corresponded exactly to the intended compositions. Checks were made of the resulting composition of several representative arc-melted buttons by wet analysis. Results are compared with the intended compositions in Table III. The differences are seen to be negligible, as had been expected; intended compositions are therefore used throughout the balance of this report. Little difficulty was experienced in the melting operation itself except for the susceptibility of the buttons of some compositions, particularly the alloys containing cobalt, to crack badly because of the unavoidably high thermal stresses induced on cooling.

TABLE III. *Intended composition*

Alloy No.	Atomic %	Weight %	Analyzed composition weight %
1457A	50.0 Fe	67.4	67.0
	50.0 Al	32.6	33.1
1759B	50.0 Co	68.6	68.8
	50.0 Al	31.4	31.1
1629C	50.0 Ni	68.6	67.8
	50.0 Al	31.4	31.4
1459A	50.0 Ni	68.6	68.4
	50.0 Al	31.4	31.5
1702B	52.0 Ni	70.2	70.4
	48.0 Al	29.8	29.3
1703B	58.0 Ni	75.1	74.8
	42.0 Al	24.9	24.8

Many of the buttons after arc melting were found by metallographic examination to be homogenous, single-phase, rather coarse grained materials. Any specimens not showing good homogeneity in either macro or micro examination were given a subsequent homogenization anneal at a temperature about 250°C below their melting points. Such treatment was usually successful, but, as indicated in Table II, certain of the compositions near the published phase boundaries apparently are two-phase in the equilibrium condition. This result is a consequence of the poor definition of phase boundaries in the existing literature. General dispersion of the second phase was found to raise hardness values significantly. On the other hand, if the second phase were restricted to grain boundaries, hardness values obtained for indentations falling within the grains apparently could be taken as truly representative of the saturated phase.

After the homogeneity of a particular button had been established, it was prepared as a hardness specimen. In some cases it was possible to grind the requisite disk-shaped samples (approximately $\frac{3}{8}$-in. thick by $\frac{3}{4}$ in. in diameter) directly from the buttons. In many other cases, however, where the thermal stress cracking mentioned above was severe, it was impossible to obtain pieces of sufficient size to yield the disk-shaped samples. In these instances it was found convenient to mount irregularly shaped fragments in copper by melting the copper in situ about the fragment held in an iron tube. Times at temperature were kept very short, and careful metallographic examination showed no significant amount of diffusion between the mounting

metal and the sample. Specimens so mounted were then surface ground on the faces on the disk.

All samples were given a metallographic polish prior to hardness testing. Metallographic preparation of these samples presented a curious anomaly. Despite their rather high hardness, which necessitated the use of diamond polishing techniques, the surface of the specimens flowed quite easily. This unfortunate situation has been noted previously in the literature in another connection (7, 15). It was necessary, therefore, to polish and etch repeatedly in order to secure an apparently undisturbed surface. Some experiments were done with electropolishing to avoid this tedious method of preparation, but only limited success was obtained and the technique was abandoned.

Experimental Procedure

Hardness values were obtained on the samples over the temperature range from room temperature to 800°C using a micro hot hardness tester of modified Bergh design (16, 17). Load is applied hydraulically by moving the specimen on an anvil against a fixed indenter; specimen and indenter are heated by a resistance furnace, and all components of the tester are enclosed within a large evacuated chamber. The sample was heated continuously during a test run and hardness impressions and thermocouple readings made at desired intervals. Preliminary experiments disclosed that the hardness of the aluminide specimens was independent of load from about 50 to 1000 grams. Most of the data herein reported were obtained at 200-grams load; a Vickers diamond indenter and a 15-sec load duration were used throughout the study. Measurement of the size of indentations was made at room temperature and the data expressed in the conventional Vickers fashion in terms of the impressed load divided by the contact area of the indentation in units of kilograms per square millimeter. The various precautions usual in microhardness testing were observed.

A portion of a typical hardness run is illustrated in Fig. 2. The small loads used and the coarse grain size of the specimens resulted in effect in a single crystal measurements. No significant effects of anisotropy were observed, however. Preliminary experiments established the reproducibility of duplicate runs on the same sample as well as on duplicate samples. Annealing following polishing was

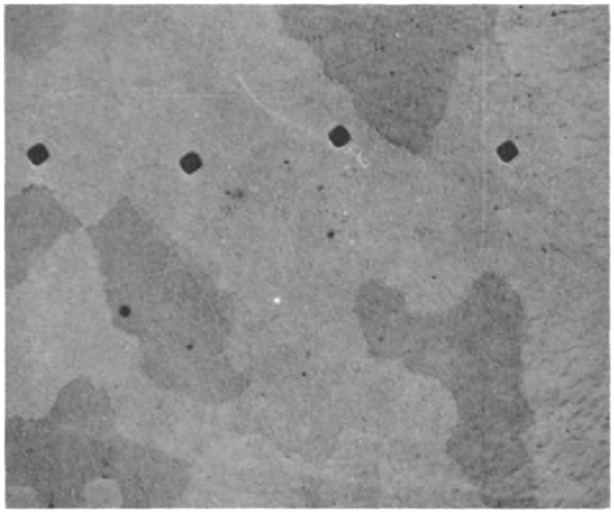

FIG. 2. Portion of a typical hardness-temperature run. 50×

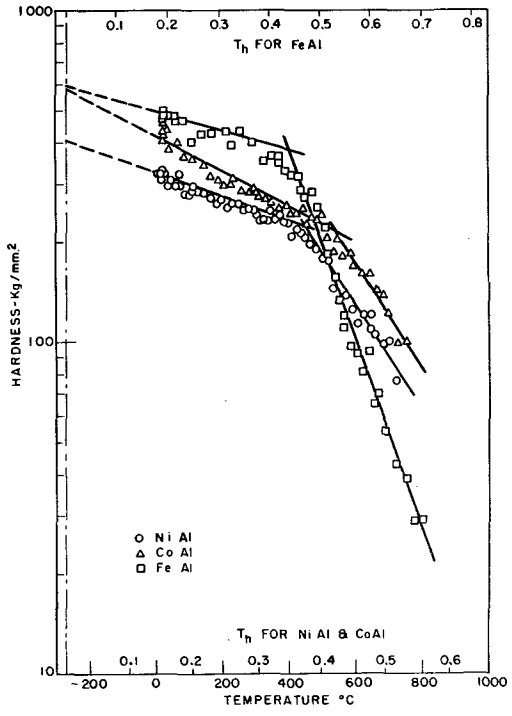

FIG. 3. Temperature dependence of hardness of the three equi-atomic iron group aluminides at the stoichiometric composition.

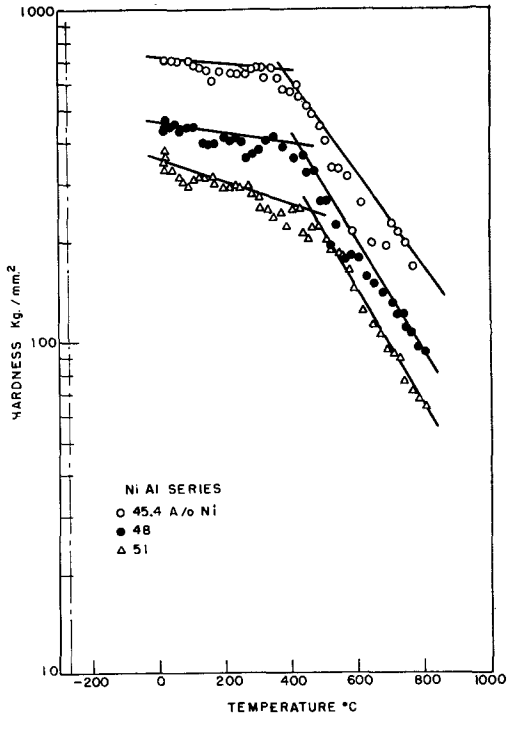

FIG. 4. Temperature dependence of hardness of some NiAl compositions.

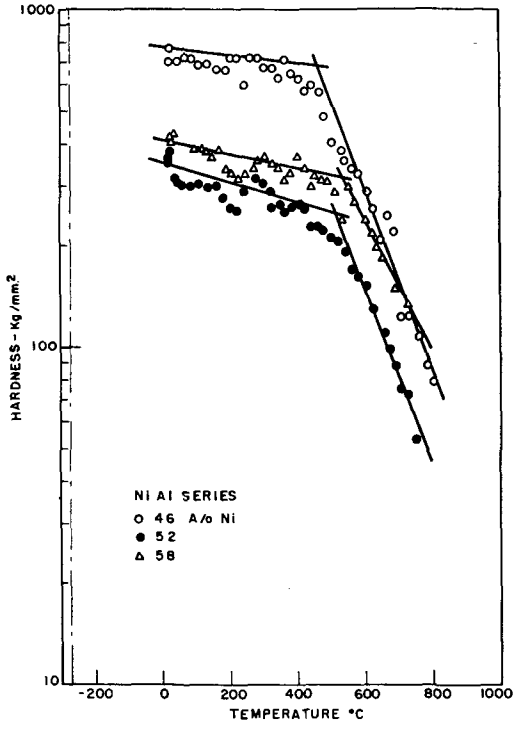

FIG. 5. Temperature dependence of hardness of some NiAl compositions.

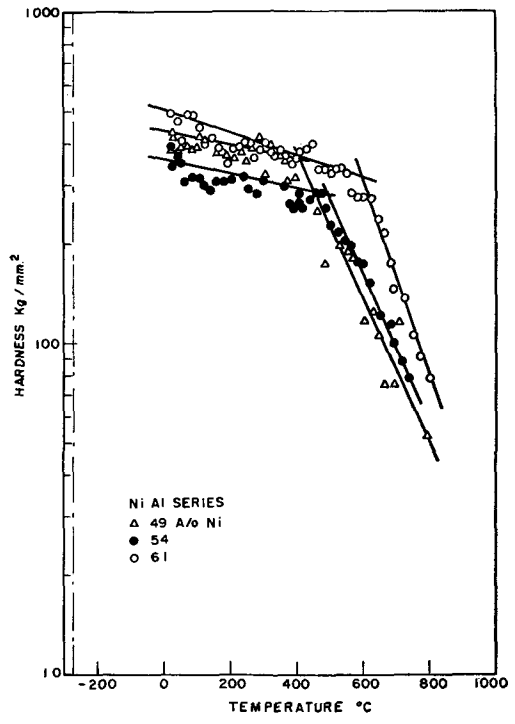

FIG. 7. Temperature dependence of hardness of some NiAl compositions.

frequently required to eliminate surface work hardening from the polishing operation.

Treatment of Data

Assessment of the possible scatter as well as subsequent detailed analyses of the data were facilitated by the use of a semilogarithmic method of plot. This procedure, in which the logarithm of hardness is plotted against temperature, has been demonstrated (17, 18) to yield a two-segmented linear plot for a wide variety of materials. This result implies a hardness-temperature relation of the sort $H = Ae^{-BT}$, where A and B have one set of values at low temperatures and another set at high temperatures.

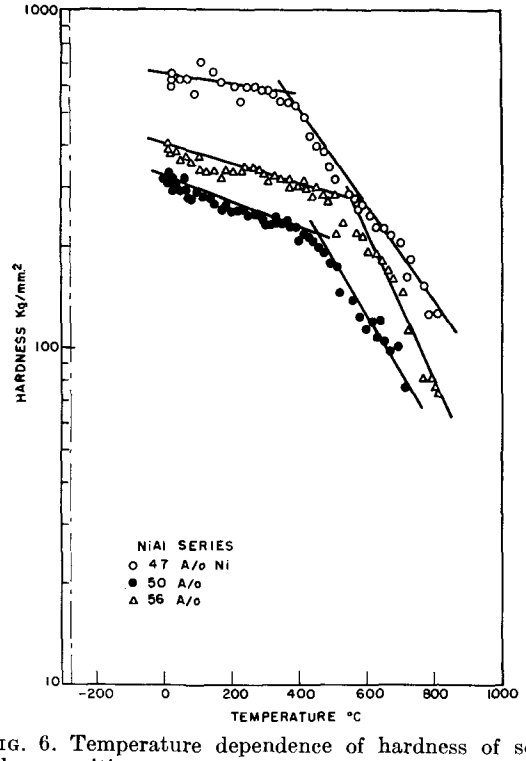

FIG. 6. Temperature dependence of hardness of some NiAl compositions.

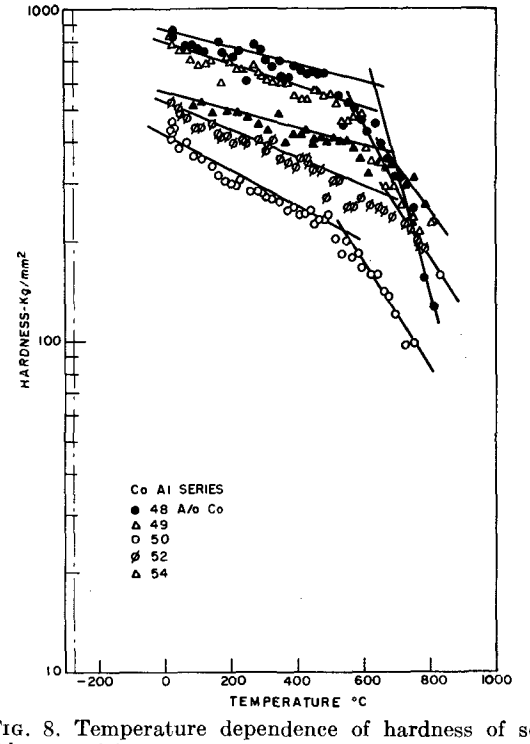

FIG. 8. Temperature dependence of hardness of some CoAl compositions.

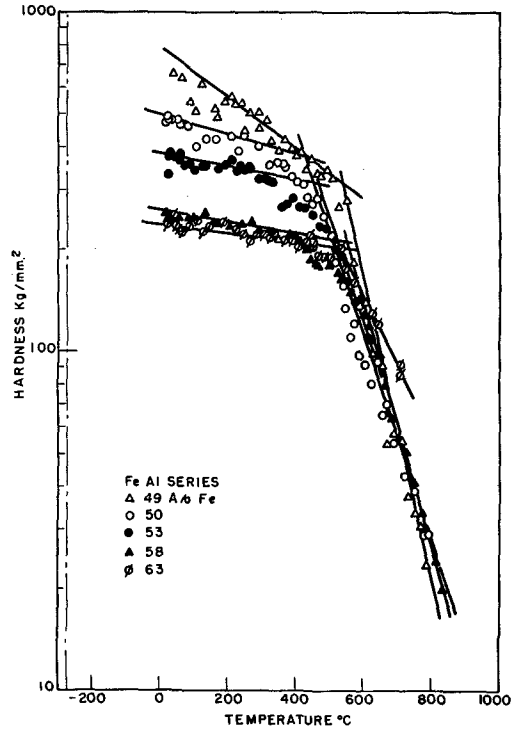

FIG. 9. Temperature dependence of hardness of some FeAl compositions.

Occasional points were found in hot hardness runs on the aluminides which deviated considerably from the normal scatter band. In almost every case these deviations could be associated with excessive cracking or with the presence of an inclusion, grain boundary, or other incidental defect in the material. Therefore, such points were not considered valid and have been eliminated from the plots shown in the figures. The usual procedure was to take 30 to 50 points over the 800°C temperature range, to plot all points for which visually acceptable impressions were obtained, and to represent the data by the best linear plot approximating the upper envelope of the scatter band. This procedure is in accord with the view of Winchell (19) in analyzing the results of room temperature microhardness tests on brittle materials.

The principal experimental results are shown in Fig. 3 through 9. Fig. 3 compares the three equi-atomic aluminides at the stoichiometric composition, i.e., 50 at. % aluminum. Fig. 4 to 7 show data for various compositions within the phase limits of the NiAl structure, while Fig. 8 and 9 represent similar studies on CoAl- and FeAl-based alloys, respectively.

DISCUSSION

Stoichiometric Compounds

As indicated above, a convenient method of analyzing hardness-temperature data is in terms of the constants describing the straight line segments of the semilogarithmic plot of the data. Table IV presents a comparison of such data for the low temperature branch of the stoichiometric aluminide curves with similar data for hypothetical pure metals of equivalent melting point derived from curves

TABLE IV

	A (kg/mm²)	$B \times 10^3$(°C⁻¹)	$T_b(T_h)$	T_{mp}(°C)
NiAl	410	0.863	0.38	1640*
CoAl	580	1.209	0.44	1625*
FeAl	600	0.663	0.46	1270*
Hypothetical pure metal	140	0.60	0.55	1630†
Hypothetical pure metal	100	1.00	0.55	1270†

* This study.
† Interpolation from (18).

of a previous study (18). Data are also listed for T_b, the break temperature or the temperature at which the change in slope occurs expressed as a homologous temperature.

Several important differences can be noted relative to the behavior of pure metals. First, the intrinsic hardness as given by the constant A is several times that for typical pure metals. This is not too surprising, however, considering the greater complexity of the cesium chloride structure as compared to those for the common metals. The slope or temperature coefficient B appears to be about the same as for the metals. On the other hand, break temperature data are rather unusual. Not only are all of the aluminide break temperatures significantly lower on the homologous scale than for the pure metals, but also the value for NiAl is even lower than those for FeAl and CoAl. It is also apparent from the tabulation that no correlation exists between A and B values and the melting points of the compounds, in contrast to the case of the isomorphous pure metals (18). Several other types of correlation were attempted without success. Therefore, it is already obvious that the behavior of these materials is both considerably different and more complex than for the pure metals.

The rather low hardness of NiAl at high temperatures is also worthy of note, particularly since this compound has been considered as a base for high temperature materials. Stern (6) and later his associate, Wachtell (7), reported good high temperature strengths for NiAl, but the hardness data of the present study as well as tensile experiments by McMullin (20) at this laboratory and by Maxwell and Grala (9) at NACA fail to confirm these results. It appears that the major reason for the difference in the behavior of the material produced by Stern and Wachtell at the American Electro Metallurgical Co. and that produced at this laboratory and at NACA lies in the fact that the former was hot pressed from powder, whereas the NiAl in the latter studies was prepared by melting. Oxide or other impurities introduced in powder processing have been known in other instances to result in substantial strengthening particularly at high temperatures (21, 22).

Effects of Composition

Effects of composition variation on the hardness of the single-phase aluminides observed in this study can be demonstrated in two ways, either through study of hardness-composition isotherms or by analysis of the effects of composition on the parameters A, B, and T_b. The first of these approaches was applied to the NiAl based compositions by cross plotting the data of Fig. 4 through 7. Results

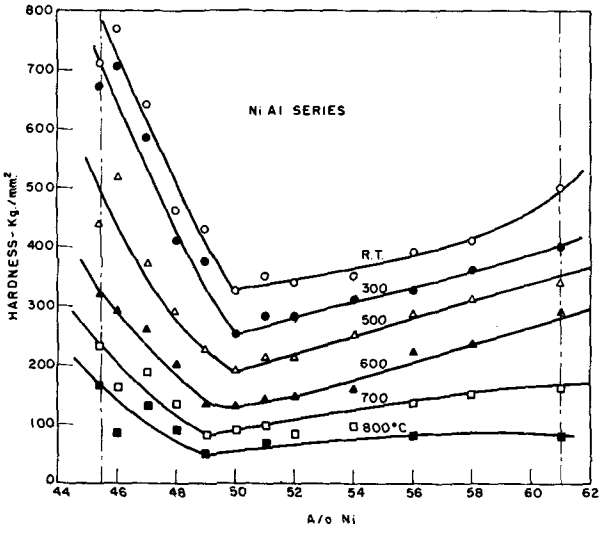

FIG. 10. Hardness-composition isotherms in the NiAl series.

of this cross-plot are shown in Fig. 10 and may be compared with atomic structure data derived from the work of Bradley and Taylor (23) in Fig. 11. The hardness minima exhibited at the stoichiometric composition are the most striking feature of the plot and correspond to the minimum density of defects as shown in Fig. 11.

Minima such as shown in Fig. 10 have been noted many times before for intermetallic compounds having a range of homogeneity, principally by the Russian group at the Leningrad Polytechnic Institute (24), but in only a few instances (25, 26) have temperatures other than room temperature been investigated. Furthermore, in these previous cases, only a very limited number of compositions was studied, and structural data for corresponding alloys were not available. In the cases cited, the Russians also observed the flattening of the minimum as the temperature is increased. The hardness increase on both sides of stoichiometry is of particular interest in the case of the nickel-aluminum system since it indicates that vacancies can be at least as potent a strengthening element as the substitution of solute atoms. Minima in the electrical resistivity (27) and in the diffusion of Co^{60} (28) at stoichiometry have also been noted. Both of these latter effects are not unexpected since the most perfectly ordered structure obviously exists at the stoichiometric composition. Diffusion data show that the deformation process is not diffusion-controlled within the temperature range studied (maximum homologous temperature $\sim$ 0.55). However, the flattening of the hardness minima with increasing temperature may be indicative of a trend in this direction. Possibly at some higher temperature or longer time the hardness-composition curves might invert to show maxima at stoichiometry as suggested by Kornilov (26).

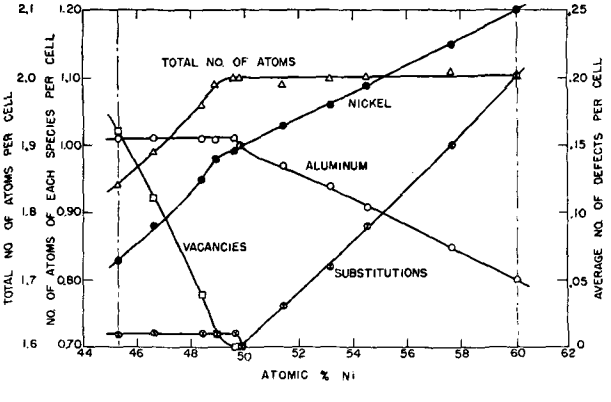

FIG. 11. Defect structure as a function of composition in NiAl (from Bradley and Taylor).

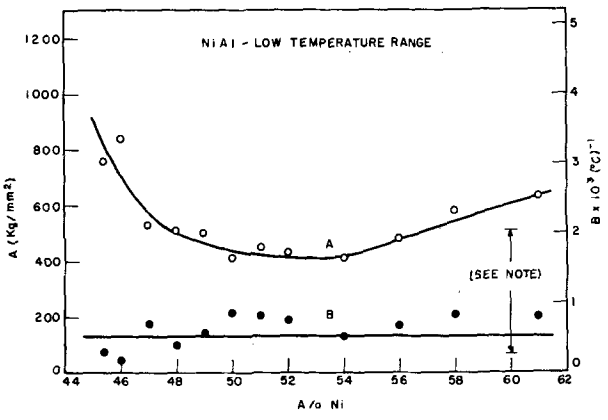

FIG. 12. Variation of the hardness parameters A and B for the low-temperature region as a function of composition in NiAl. (The arrow denotes the breadth of the scatter band for the B values for pure metals of corresponding melting point as previously determined.) (18)

Analysis of the constants A and B describing the linear segments of hardness-temperature curves was also made for the NiAl based compositions. The effect of composition on these constants for the low temperature segment is shown in Fig. 12. It is apparent that the primary effect of composition is on A, the intrinsic hardness of the materials; variations observed in the temperature dependence or B values are thought to be within the scatter of the data. Similar results were obtained for the high temperature segment except that the scatter was considerably greater.

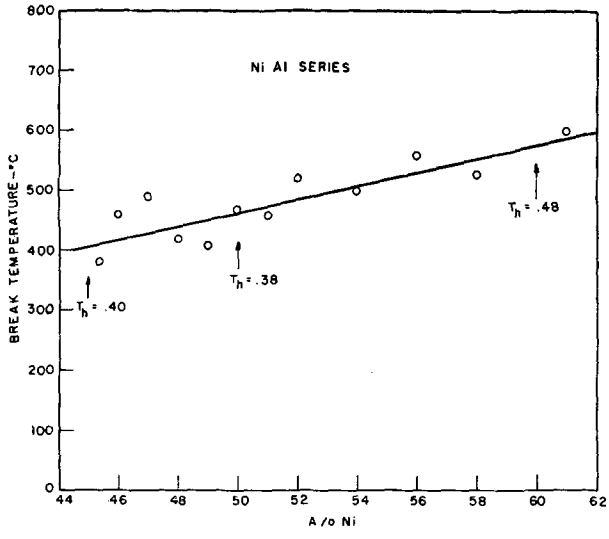

FIG. 13. Variation of break temperature with composition in the NiAl series.

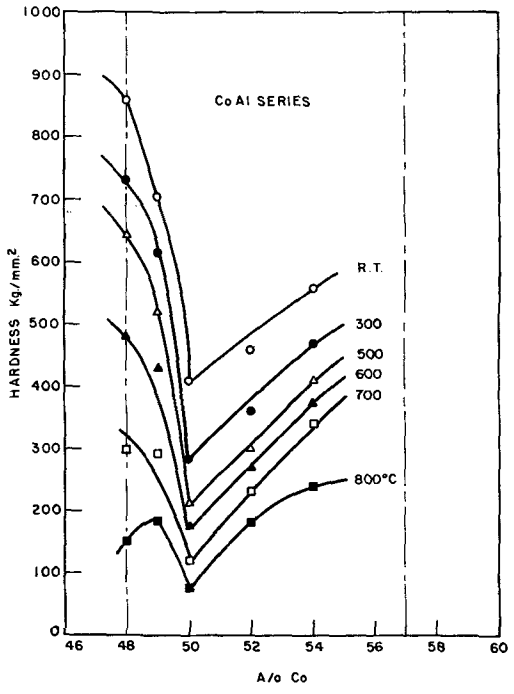

FIG. 14. Hardness-composition isotherms in the CoAl series.

Another, and perhaps more interesting, aspect of these results is presented in Fig. 13, which shows that there is a progressive increase in the break temperature with increasing nickel content over the whole composition range. This is rather surprising in view of the facts that the melting point, resistivity, lattice spacing, and diffusion constants show either maxima or minima at the stoichiometric composition. A possible interpretation of the behavior shown in Fig. 13 is that the compound becomes increasingly metallic with increasing nickel content.

The first few experiments on the cobalt aluminides gave results very similar to those for the nickel aluminides and consequently the CoAl-based compositions were not studied in great detail. A cross plot of the hardness isotherms is shown in Fig. 14. The similarity of the CoAl series with the NiAl group was perhaps to be expected in view of the marked similarity in the phase diagrams.

TABLE V

Property	NiAl	CoAl	FeAl
T^{mp} °C	1640 (13)	1625 (13)	1270 (13)
a_o A	2.887 (23)	2.862 (29)	2.910 (30)
kx	2.881 (23)	2.856 (29)	2.903 (30)
% Contraction in atomic vol	15.3 (31)	15.8 (32)	13 (33)
ΔHf $\frac{\text{kcal}}{\text{g atom}}$	17.0 (34)	13.2 (34) 16 (35)	6.1 (34)
δ g/cc	5.92 (23)	6.08 (29)	5.59 (30)
D_{Co^*} cm²/sec	0.2×10^{10} at 1150°C (36)	2.8×10^{10} at 1250°C (37)	
ρ $\mu\Omega$ cm	14.9 (27) 20-30 (7)		
$\frac{\partial \rho}{\partial T}$ $\mu\Omega$ cm/°C	0.0023 (27)		
α in./in./°C	15.1×10^{-6} (7)		

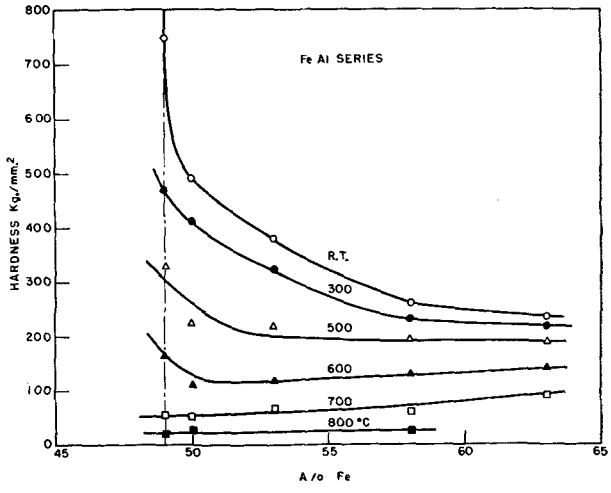

FIG. 15. Hardness-composition isotherms in the FeAl series.

Furthermore, x-ray studies by Bradley and Seager (29) show the defect structure to be of the vacancy type on the high aluminum side and substitutional on the high cobalt side, as in the case of NiAl. Further evidence of the close similarity of the NiAl and CoAl compounds is given by the comparison of property data in Table V. In view of the limited number of hardness data obtained and the close similarity with the nickel aluminides, no further analyses were carried out.

Iron-aluminides gave results which contrast sharply with those on the CoAl- and NiAl-based compositions. The cross plot of the hardness isotherms is given in Fig. 15. No sharp minimum is present at any temperature. At low temperatures hardness seems to decrease monotonically with increasing iron content. At the highest temperature used in the experiments there is no clear-cut effect of composition. These results may be compared with those of the x-ray structure studies by Bradley and Jay (30) replotted in Fig. 16. In contrast to the situation with NiAl and CoAl, no vacancy formation occurs on the high aluminum side; defects are substitutional on both sides of stoichiometry. Unlike the other two members of the triad, however, substitution of the iron group atoms at normal aluminum sites in FeAl lowers the hardness. This result is

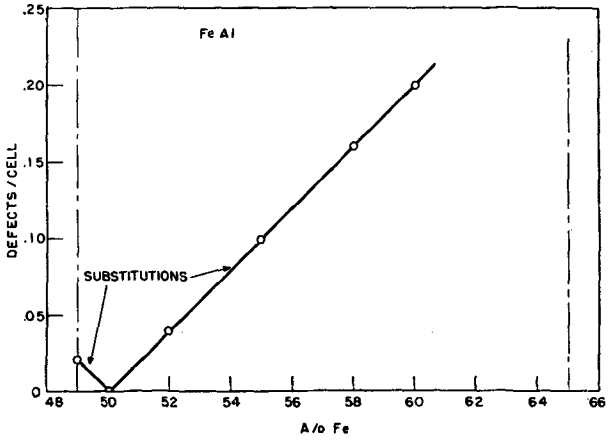

FIG. 16. Defect structure as a function of composition in FeAl (from Bradley and Jay).

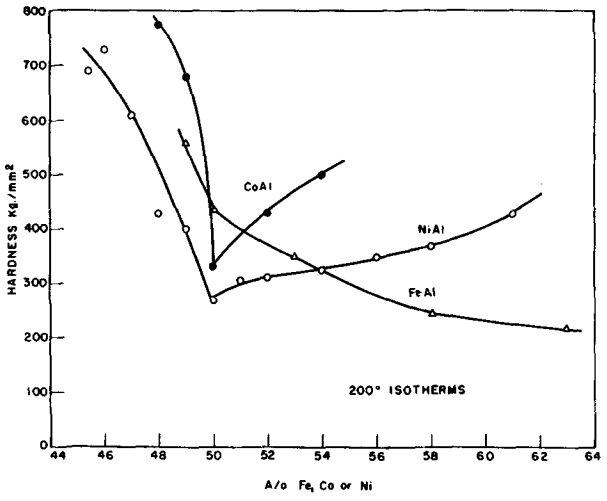

FIG. 17. Comparative hardness-composition isotherms for the three equi-atomic iron group aluminides.

most clearly illustrated in Fig. 17, which compares the 200°C isotherms for all three series. In addition, certain regular but not reproducible anomalies were sometimes encountered in the log hardness-temperature curves for FeAl compositions above about 700°C. No ready explanation for either of these effects is apparent. It is clear, however, from the phase diagram and the property data of Table V that the compound is considerably different from the other two, although it is isomorphous with them. It has been noted that the high temperature portion of the Fe-Al phase diagram as shown in Fig. 1 is rather uncertain in the vicinity of the compound FeAl. It is quite possible that a redetermination of this portion of the diagram might show a situation which would render the present hardness results more explicable (see further below).

Effects of Temperature on Degree of Order

It was thought at one time that perhaps some of the anomalies observed in the hardness data might result from a considerable decrease in the degree of order at a temperature within the range studied, although the phase diagrams represent all the aluminides as essentially completely ordered up to the melting point.

The literature shows several x-ray studies on NiAl conducted both at temperature and on quenched specimens. Results are contradictory. Isaichev and Mirekskii (38) claim that significant disordering and vacancy formation occur at temperatures as low as 900°C, although the ordering reaction is virtually insuppressible by quenching. Guseva (27) on the other hand finds no change in ordering at 900°C and only a negligible difference in the lattice parameter between quenched and annealed samples. In view of these contradictions, it was decided to test for disordering tendencies by an alternative method—electrical resistivity. A flat horseshoe-shaped strip specimen was ground from part of an annealed button of NiAl and its resistivity measured in the conventional manner to above 1200°C. The resistivity of the material was found to increase smoothly and not excessively over the entire temperature range. It is therefore unlikely that significant disordering takes place in NiAl within this temperature range, although the possibility cannot be dismissed that a resistance change below the sensitivity of the experiment occurs with disordering.

As indicated above, the published phase diagram as well as the present experimental results render the Fe-Al high temperature equilibria particularly suspect. In particular, in view of the shape of the solidus and liquidus curves it seems quite possible that the compound disorders before melting. Unfortunately, no further studies of this portion of the diagram have been made since the work of Bradley and Jay (30) over twenty years ago, and this extended to only 700°C. However, some results recently obtained by Bradley (39) on a section of the Fe-Ni-Al ternary led him to suspect that a different and more complex situation exists in the Fe-Al binary than had been indicated by his previous work. As a consequence of the anomalies encountered in the present study, some survey experiments have been initiated to re-examine this suspect portion of the binary diagram. Of these, only the resistance-temperature studies are complete as yet. Inconclusive results, similar to those for NiAl, were obtained. Other studies are in progress.

SUMMARY

This investigation has established that the temperature dependence of hardness of the equi-atomic iron group aluminides does not follow the empirical rules found previously to hold for the pure metals. The intrinsic hardness of the aluminides is considerably higher than would be expected for a pure metal of equivalent melting point, although the slope of the log hardness temperature curve is of the same order for both types of material. In addition, the change in slope of the log hardness temperature plot occurs at a lower homologous temperature for the aluminides than for the pure metals. Within the homogeneity range of any particular compound, hardness is controlled by the defect structure. For NiAl and CoAl, hardness minima are observed at the stoichiometric composition which flatten with increasing temperature. Knowledge of the details of the defect structure permits the further conclusion that either vacancies or substitutional defects can harden the material. Within the temperature range studied ($<0.55\ T_{mp}$) short-time hardness is not diffusion-controlled. The FeAl compounds are anomalous in that hardness at constant temperature decreases with increasing iron content on both sides of stoichiometry. This anomaly and the failure to obtain a satisfactory correlation for the relative hardness of the three stoichiometric aluminides indicates that factors other than those now known—melting point, crystal structure, and defect structure—are significant in the control of strength of pure intermetallic compounds. The possibility of significant disordering with increasing temperature was considered for certain compounds. No evidence was found for this in stoichiometric NiAl up to above 1250°C; it appears likely, however, that stoichiometric FeAl disorders between 700° and 1250°C.

ACKNOWLEDGMENTS

The assistance and advice of many members of the Metallurgy Research Department of the General Electric Research Laboratory aided materially in this research.

Mr. Arthur Peat contributed in a major way to all of the experimental phases of the work. The chemical analyses were made by Ledoux and Co., and the resistivity determinations on NiAl and FeAl by T. S. Jones. J. E. Burke, R. W. Guard, and W. R. Hibbard read and criticized the manuscript.

Manuscript received August 1, 1955. This paper was prepared for delivery before the Chicago Meeting, May 2 to 6, 1954.

Any discussion of this paper will appear in a Discussion Section to be published in the December 1956 JOURNAL.

REFERENCES

1. J. H. WESTBROOK, Report in preparation.
2. H. V. KINSEY AND M. T. STEWART, *Trans. Am. Soc. Metals*, **43**, 193 (1951).
3. H. V. KINSEY AND M. T. STEWART, *Can. J. Research*, **27**, No. 2-F (1949).
4. E. D. SAYRE, General Electric Report No. R54AGT115, March 1954.
5. C. C. MCBRIDE, H. M. GREENHOUSE, AND T. S. SHEVLIN, *J. Am. Ceram. Soc.*, **35**, 28 (1953).
6. G. STERN, Reported at the 1952 Air Force Conference on Cermets, Wright-Patterson Air Force Base, Oct. 6-8, 1952.
7. R. L. WACHTELL, Wright Air Development Center Report No. 52-291, Sept. 1953.
8. J. G. MCMULLIN, Unpublished research.
9. W. A. MAXWELL AND E. M. GRALA, NACA Tech. Note No. 3259, August 1954.
10. R. M. BOZORTH, "Ferromagnetism," Van Nostrand Co. Inc., New York (1951).
11. ASM Metals Handbook, 1948 Edition.
12. F. N. RHINES AND J. B. NEWKIRK, *Trans. Am. Soc. Metals*, **45**, 1029 (1953).
13. V. F. ZACKAY AND T. H. HAZLETT, *Acta Met.*, **1**, 624 (1953).
14. P. C. ROSSIN, *General Electric Research Lab. Memo*, **7**, 2 (1953).
15. H. V. KINSEY AND M. T. STEWART, Discussion of Ref. (2) p. 225.
16. P. S. BERGH, Tech. Rept. No. M-5, Silver Springs Lab., The Kellex Corp., December 1948.
17. J. H. WESTBROOK, GE Research Lab. Rept. No. RL-1029, February 1954.
18. J. H. WESTBROOK, *Trans. Am. Soc. Metals*, **45**, 221 (1953).
19. H. WINCHELL, *Ann. Mineralogist*, **30**, 583 (1945).
20. J. G. MCMULLIN, Unpublished research.
21. R. IRMANN, "Sintered Aluminum of High Resistance to Heat," *Rev. aluminum*, **28**, 269, 311 (1951).
22. R. IRMANN, *Metallurgia*, **46**, 125 (1953).
23. A. J. BRADLEY AND A. TAYLOR, *Proc. Roy. Soc.*, **A159**, 56 (1937).
24. N. KURNAKOW, S. ZEMCZUZNY, AND M. ZASEDATELEV, *J. Inst. Metals*, **40**, 305 (1916).
25. V. P. SHISHOKIN AND V. A. AGEEVA, *Tsvetnye Metal.*, **2**, 119 (1932).
26. I. I. KORNILOV, *Doklady Akad. Nauk. S. S. S. R.*, **86**, 721 (1952).
27. L. N. GUSEVA, *ibid.*, **77**, 415 (1951).
28. A. E. BERKOWITZ, F. E. JAUMOT, AND F. C. NIX, "Diffusion of Co^{60} in some NiAl Alloys Containing Excess Vacancies," paper presented at Am. Phys. Soc. meeting, March 1954.
29. A. J. BRADLEY AND G. D. SEAGER, *J. Inst. Metals*, **64**, 81 (1939).
30. A. J. BRADLEY AND A. H. JAY, *Proc. Roy. Soc. London*, **A136**, 210 (1937).
31. A. WESTGREN AND A. ALMIN, *Z. phys. Chem.*, **B5**, 14 (1929).
32. E. ZINTL AND G. BRAUER, *Z. physik. Chem.*, **B20**, 245 (1933).
33. W. EKMAN, *ibid.*, **B12**, 57 (1931).
34. W. OELSEN AND H. MIDDEL, *Mitt. Kaiser Wilhelm. Inst. Eisenforsch. Düsseldorf*, **19**, 101 (1937).
35. W. BILTZ, *et al.*, *Z. anorg. u. allgem. Chem.*, **134**, 25 (1924).
36. R. SMOLUCHOWSKI AND H. BURGESS, *Phys. Rev.*, **76**, 309 (1949).
37. F. C. NIX AND F. E. JAUMOT, *ibid.*, **33**, 1275 (1951).
38. I. ISAICHEV AND V. MIREKSKII, *J. Tech. Phys. USSR*, **10**, 316 (1940).
39. A. J. BRADLEY, *J. Iron Steel Inst.*, **163**, 19 (1949).

Mathematical Studies on Galvanic Corrosion

IV. Influence of Electrolyte Thickness on the Potential and Current Distributions over Coplanar Electrodes Using Polarization Parameters

JAMES T. WABER AND BERTHA FAGAN

University of California, Los Alamos Scientific Laboratory, Los Alamos, New Mexico

ABSTRACT

Extensive numerical evaluation was performed on a Fourier series derived for the potential distribution in an electrolyte lying above a plane containing infinitely long, narrow electrodes juxtaposed and arranged in an infinitely alternating array with even symmetry. In contrast to the previous studies in this series, the limitation that the electrolyte has finite depth was imposed. Four perspective drawings of the reduced potential function were made to scale to illustrate the potential variation throughout the solution. From this study a practical rule was established for deciding from the behavior of the electrochemical system what effectively is an "infinite thickness" of the electrolyte. Current density variation over the anode was evaluated for several different combinations of relative thickness b/c and of relative polarization parameter $\mathfrak{P}/c$. When b/c is small, the major part of the corrosion current is concentrated in the vicinity of the anode-cathode junction, provided that the electrical resistance of corrodent is not too high or the polarization too strong, i.e., provided that $\mathfrak{P}$ is relatively small in comparison with c. Several graphs of $C_a^*(x)$ were included to illustrate the effects of the dimensionless groups (a/c), (b/c), and $(\mathfrak{P}/c)$. Comparison with published experimental data was made, and the agreement is reasonably good. Detailed discussion of the influence of several factors is also presented.

INTRODUCTION

In any practical study of galvanic corrosion and of pertinent potential distributions, it is not possible to cover the electrodes with an infinitely thick layer of corrodent. The necessary condition of a finite liquid thickness requires modification of the mathematical analysis. In the cases discussed so far (1–3), it is assumed that a perpendicular erected on the plane of the electrodes lies entirely in the region of consideration and does not intersect a boundary, i.e., the electrolyte depth was assumed to be infinitely larger than the characteristic repeat distance of the alternating array of electrodes.

Experimentally, this condition can be realized only if the galvanic cell behaves "microscopically." As explained earlier (1–3), the absolute dimensions of a galvanic cell have no physical significance, but they must be compared with the size of the polarization parameter. A given electrochemical system behaves as though it were composed of microscopic elements if the critical dimension λ of the system is smaller than the polarization parameter. Such a system is called "microscopic." An important characteristic of such a microscopic system is that the distribution of corrosion attack is relatively uniform over the electrode surface.

In treating the general behavior of corroding metals, it is necessary to consider the dimensionless group $(b/\mathfrak{P}_i)$ where b is the perpendicular thickness or depth of the liquid and $\mathfrak{P}_i$ is the smaller of the two polarization parameters. That is, one should identify b in many cases as λ, as it very strongly affects current distribution over the electrodes.

Whenever $\mathfrak{P}$ is large in relation to the critical dimension, the potential distribution becomes uniform. Given $\mathfrak{P}$, if the width of the anodes, $2a$, is small enough in comparison with b, the depth of the corroding liquid has little if any influence on the potential value measured in the liquid. However, in treating thin or shallow electrolyte layers, b may be smaller than a or $\mathfrak{P}$, and b in these instances is correctly λ. The greatest corrosion attack occurs within a distance a few times larger than b of the anode-cathode junction. There is significantly less attack on the anodes, and less hydrogen evolution on the cathodes elsewhere.

The effect of "truncating" the infinite column of corrodent lying above the electrode plane is the subject of this report. In general, the liquid layer thickness will be similar to or less than the electrode widths. As a qualitative rule useful in designing experiments, the liquid is essentially "infinitely deep" if it is deeper than the sum of anode and cathode widths. Further increase in the depth contributes only 2 or 3% at most to the local corrosion current density.

The effect of very thin liquid films on corrosion is also amenable to the analysis presented here. On the basis of physical reasoning, one might expect that, as the thickness of the liquid becomes smaller than the polarization parameter, the corrosion current, i.e., the attack, would concentrate more toward the anode-cathode junction. Meanwhile, much of the liquid remote from the junction would approach a uniform potential value. This phenomenon would limit the total corrosion current. Decreas-

ing the liquid thickness has a similar effect on the total corrosion (4).

Boundary Conditions

The physical arrangement of electrodes is identical to that employed before (1–3). Coplanar, parallel, juxtaposed electrodes of finite width and great length are alternately arranged in an infinite array of even symmetry. The choice of even symmetry is equivalent to locating insulators at the edges of the cathodes away from the anode-cathode junction, thus limiting attention to one period. Location of the origin is indicated in Fig. 1. The important change in the boundary conditions is the assumption that an insulating plane is located parallel to the plane of the electrodes at a distance b units above. The specific boundary conditions are:

$$\lim_{y \to b} \frac{\partial P^*}{\partial y} = 0 \qquad \text{(I)}$$

$$\left.\frac{\partial P^*}{\partial x}\right|_{x=0} = \left.\frac{\partial P^*}{\partial x}\right|_{x=c} = 0 \qquad \text{(II)}$$

$$P^*(x, 0) - \mathfrak{L} \left.\frac{\partial P^*}{\partial y}\right|_{y=0} = E_a S_a(x) \qquad \text{(III)}$$

where $S_a(x)$ is the step function used previously (1–4), and E_a is the difference in potentials between the anode and cathode extrapolated to zero current flow. A more explicit definition of E_a has been given by Wagner (5). The definition and significance of $\mathfrak{L}$ has been discussed elsewhere (2–5). Since there are no sources or sinks for ions in the liquid phase, the polarized potential $P^*(x, y)$ satisfies Laplace's equation in two dimensions and in general must be real, finite, and continuous except on the boundaries of the liquid. The region under consideration is an infinite slab lying between the planes $x = c$, $x = -c$, $y = 0$ and $y = b$. Boundary values of the normal gradient, namely $\partial P^*/\partial y$, are obtained by approaching the boundary along paths lying wholly within the region. Because of the assumed even symmetry, boundary conditions (II) apply to either right or left handed derivatives. In contrast, at $x = a$ the limit approached by $\partial P^*/\partial y$ from the left applies to the anodic section and that approached from the right, to the cathodic section of the boundary. It is important to realize that these two limits differ in sign.

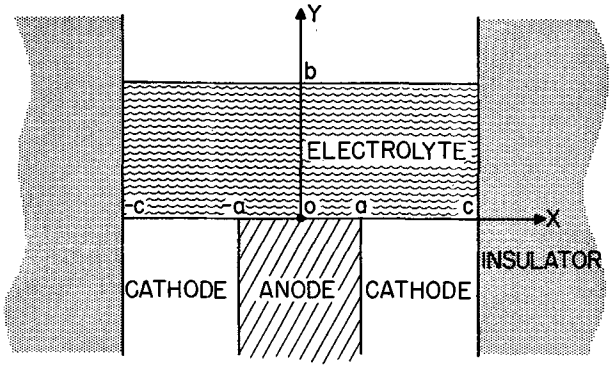

Fig. 1. Geometric relation of the electrodes and the location chosen for the origin.

Inasmuch as the interfacial potential $P^*(x, 0)$ is a periodic function of x, the potential at the interface and in the liquid is expressed by a Fourier series. It has been shown elsewhere (6), that

$$P^*(x,y) = \frac{E_a a}{c} + \frac{2E_a}{\pi} \sum_{n=1}^{\infty} \frac{\sin\left(\frac{n\pi a}{c}\right) \cos\left(\frac{n\pi x}{c}\right) \cosh\left[\frac{n\pi}{c}(b - y)\right]}{n\left[\cosh\left(\frac{n\pi b}{c}\right) + \left(\frac{n\pi \mathfrak{L}}{c}\right) \sinh\left(\frac{n\pi b}{c}\right)\right]} \qquad \text{(IV)}$$

and that P^* satisfies the several conditions imposed on it.

Interfacial Potential

The expression for the potential within the solution can be simplified in the event that $y = 0$:

$$P^*(x, 0) = \frac{E_a a}{c} + \frac{2E_a}{\pi} \sum_{n=1}^{\infty} \frac{\sin\left(\frac{n\pi a}{c}\right) \cos\left(\frac{n\pi x}{c}\right)}{n\left[1 + \left(\frac{n\pi \mathfrak{L}}{c}\right) \tanh\left(\frac{n\pi b}{c}\right)\right]} \qquad \text{(V)}$$

This equation was used to obtain the variation of the interfacial potential over the electrodes, and the variation in current density was obtained therefrom.

Equation (V) involves three adjustable parameters, and complete exploration of their effects would require evaluating this expression 50–100 times over the range of x. To minimize the time taken for computation, only two values of a/c were employed to analyze the effect of liquid thickness.

The values of the interfacial potential are tabulated elsewhere (7) and are graphically summarized for two cases in Fig. 2 and 3. When b/c is small, the curve of the interfacial potential approaches the ideal step function $S_a(x)$ despite the relatively large polarization parameter. As the ratio (b/c) becomes equal to the ratio (a/c), the full effect of polarization takes force.

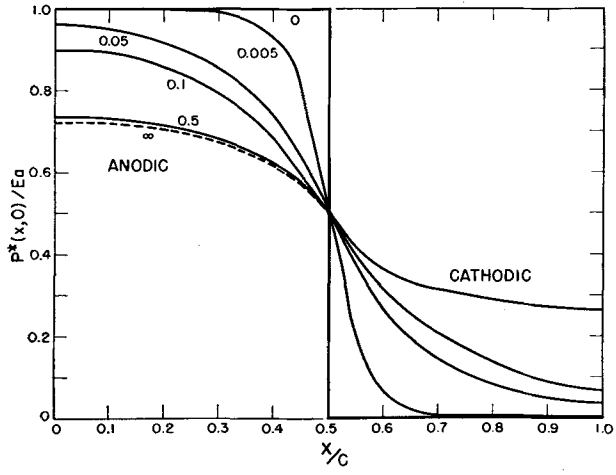

Fig. 2. Interfacial potential evaluated for $a/c = \frac{1}{2}$, $a/\mathfrak{L} = 1$, and for the b/c ratios 0.005, 0.05, 0.1, 0.5, and ∞.

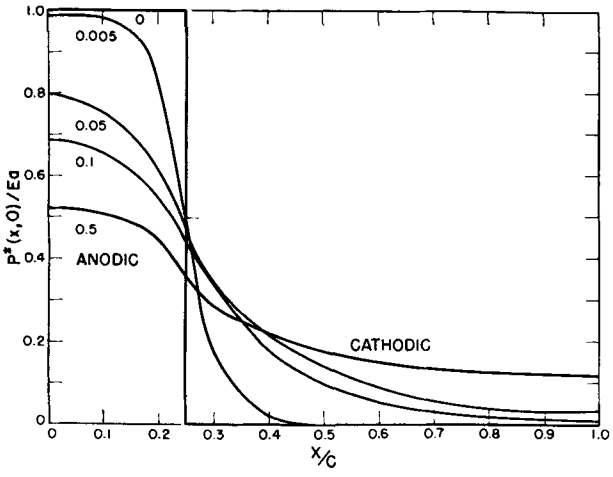

FIG. 3. Interfacial potential evaluated for $a/c = \frac{1}{4}$, $a/\mathfrak{L} = 1$, and for the b/c ratios 0.005, 0.05, 0.1, and 0.5.

Potential at the Outer Liquid Boundary

The expression used for series evaluation of the potential at the outer boundary of liquid was

$$P^*(x, b) = \frac{E_a\, a}{c} + \frac{2E_a}{\pi} \sum_{n=1}^{\infty} \frac{\sin\left(\frac{n\pi a}{c}\right) \cos\left(\frac{n\pi x}{c}\right)}{n\left[\cosh\left(\frac{n\pi b}{c}\right) + \left(\frac{n\pi \mathfrak{L}}{c}\right) \sinh\left(\frac{n\pi b}{c}\right)\right]} \qquad \text{(VI)}$$

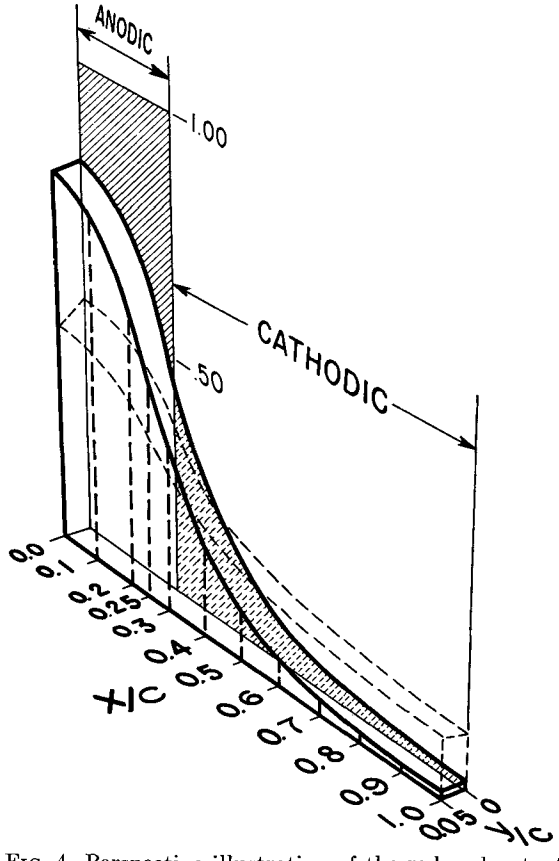

FIG. 4. Perspective illustration of the reduced potential function $P^*(x, y)/E_a$. Drawn for the relative liquid thickness of $b/c = \frac{1}{20}$ and for the ratio of anode to cathode widths of $\frac{1}{3}$.

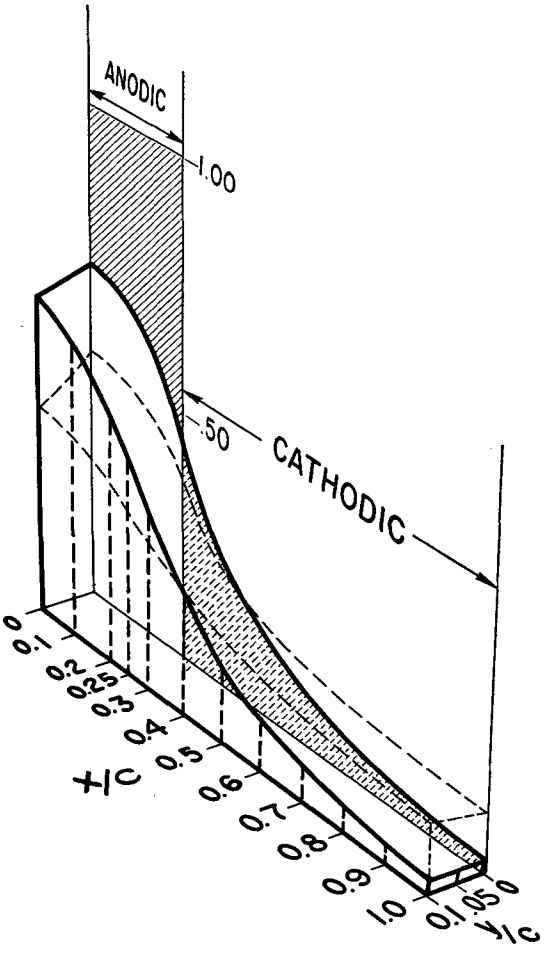

FIG. 5. Perspective illustration of the reduced potential function $P^*(x, y)/E_a$. Drawn for the relative liquid thickness of $b/c = \frac{1}{10}$ and for the ratio of anode to cathode widths of $\frac{1}{3}$.

From results tabulated elsewhere (7) it was seen that the potential does not have a constant value along this boundary.

A graphical summary of these potential evaluations was made in the form of four perspective illustrations drawn to scale. For reference, the potential distribution over the electrodes was evaluated for an infinite liquid depth at two y values, 0 and b, and is plotted as dotted lines on each perspective graph. As (b/c) approaches 1 there are only tiny differences between the curves for larger finite and for infinite (b/c) values. Fig. 4, 5, and 6 show the anodic fraction (a/c) of $\frac{1}{4}$. The curves are included for finite and infinite liquid thickness on each drawing.

To illustrate the effect of a small polarization parameter, Fig. 7 was prepared for $a/\mathfrak{L} = 500$ and for the special case $a/c = b/c = \frac{1}{2}$. When $a/\mathfrak{L}$ is very small, the potential is approximately $E_a(a/c)$ everywhere in the liquid, so perspective graphs were not prepared for this case.

CORROSION CURRENT

Corrosion current density can be calculated from interfacial potentials (2, 3). The dimensionless $C^*(x)$ group[1]

[1] This quantity is frequently written without subscripts. When a distinction between the cathodic $C_c^*(x)$ and the anodic $C_a^*(x)$ values is desirable, the appropriate subscripts are used.

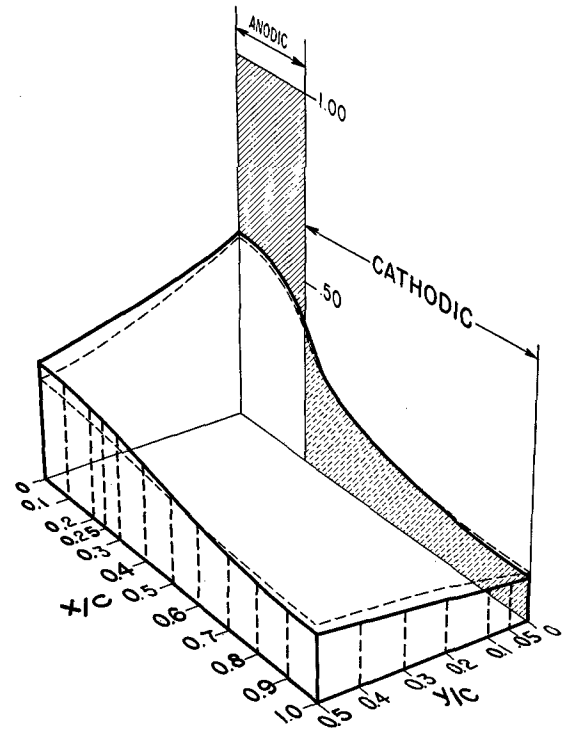

FIG. 6. Perspective illustration of the reduced potential function $P^*(x, y)/E_a$. Drawn for the reduced liquid thickness of $b/c = \frac{1}{2}$ and for the ratio of anode to cathode widths of $\frac{1}{3}$.

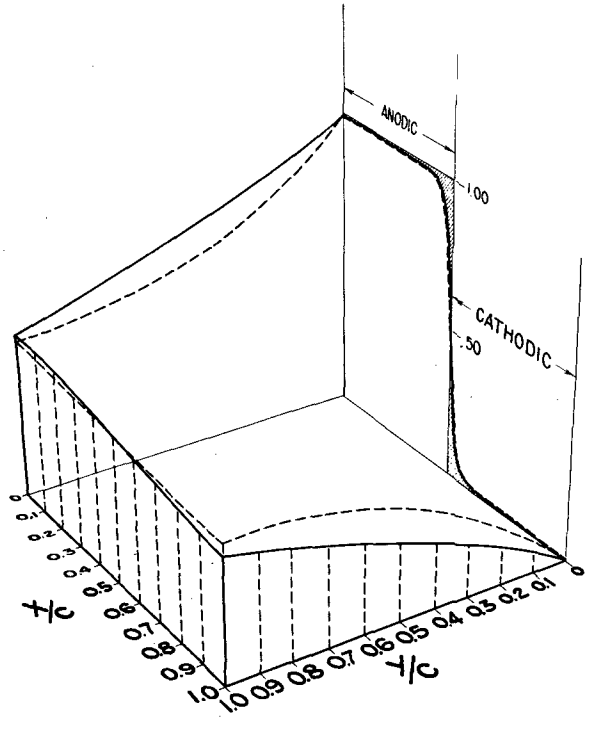

FIG. 7. Perspective illustration of the reduced potential function $P^*(x, y)/E_a$. Almost negligible polarization has been assumed. Drawn for the relative liquid thickness of $b/c = 1$, for equal anode and cathode widths and for $a/\mathfrak{L} = 500$. The dotted curve, appropriate to the interfacial potential for an infinite liquid thickness, has been separated from the curve for the finite liquid to facilitate illustration.

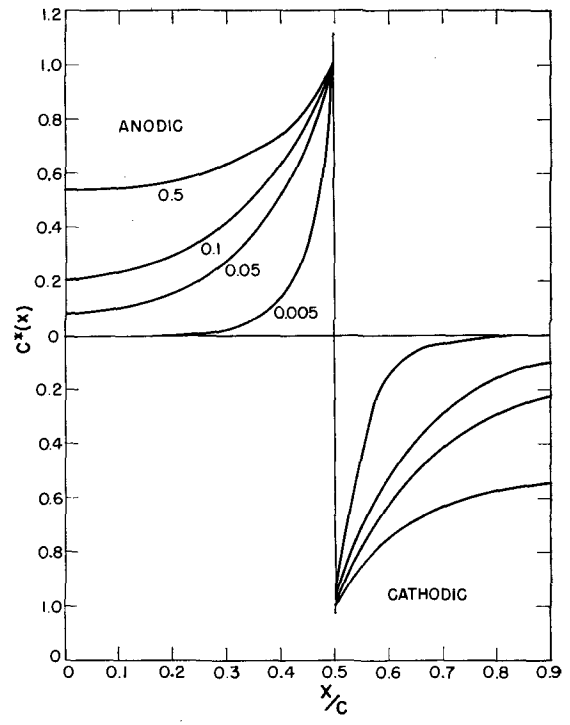

FIG. 8. Relative corrosion current parameter $C^*(x)$ evaluated for equal anode and cathode widths. Illustrates the effect of the various relative liquid thicknesses, $(b/c) = 0.005, 0.05, 0.1$, and 0.5.

representing current is defined as

$$C^*(x) \equiv \left(-\frac{2a}{E_a}\right)\frac{\partial P^*}{\partial y}\bigg|_{y=0} \qquad \text{(VII)}$$

It can be shown from boundary condition (III) that

$$C^*(x) = \frac{2a}{\mathfrak{L}}\left[S_a(x) - \frac{P^*(x, 0)}{E_a}\right] \qquad \text{(VIII)}$$

The $C^*(x)$ values computed for 4 values each of the (b/c) ratio and for $(a/c) = \frac{1}{2}$ and $\frac{1}{4}$ are graphically summarized in Fig. 8 and 9. A single value of $\mathfrak{L}$ was employed so that $a/\mathfrak{L}$ was 1 for $a/c = \frac{1}{2}$ and $a/\mathfrak{L}$ was $\frac{1}{2}$ for $a/c = \frac{1}{4}$.

Fig. 10 illustrates the combined effects of polarization and electrolyte thickness on $C_a^*(x)$ for three $\mathfrak{L}/c$ values and for the respective relative thickness of $\frac{1}{10}$. Equal anode and cathode widths were assumed. Study elsewhere (7) shows that a reduction in thickness concentrates the current into the vicinity of the anode-cathode junction. When b/c and $\mathfrak{L}/c$ are small, the concentration is quite effective, and for a given b/c value of the order of $\frac{1}{10}$ or less, a maximum in $C_a^*(x)$ occurs as $\mathfrak{L}/c$ is increased. This phenomenon is discussed more fully later.

EXPERIMENTAL STUDIES

The principal value of this paper lies not in demonstrating the inadequacy of experimental studies or the large gap between theory and practice but in guiding an experimenter in selection of his experimental conditions. Particularly, it indicates that an "infinite depth" of liquid in any probable experiment is effectively equal to the sum of anode and cathode widths.

Qualitative results of Akimov and Golubev.—Akimov and

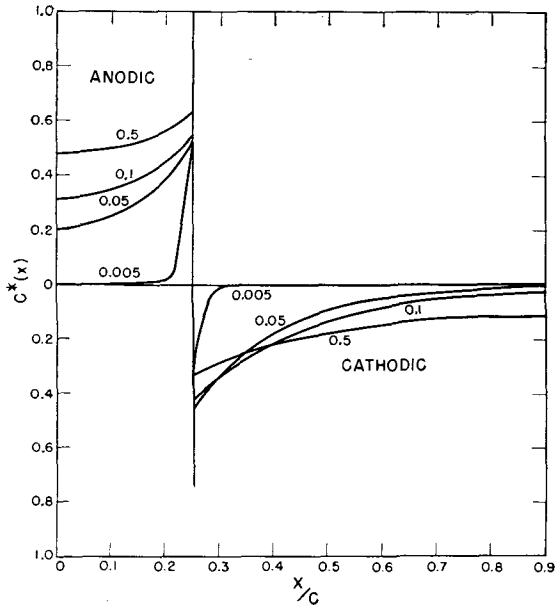

FIG. 9. Relative corrosion current parameter $C^*(x)$ evaluated for the ratio of anode to cathode widths of $\frac{1}{3}$. Illustrates the effect of various relative liquid thicknesses. Drawn for b/c = 0.005, 0.05, 0.1, and 0.5.

Golubev considered the question of potential distribution in the corrodent (9) and the distribution of corrosion attack (10) over the anode. They pointed out that in many earlier researches into the behavior of model local cells, e.g., (11–13), the experimenters employed models

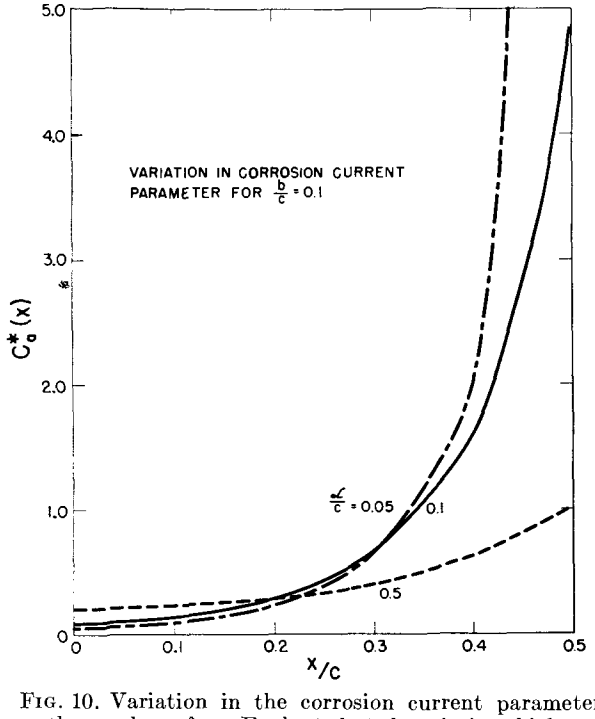

FIG. 10. Variation in the corrosion current parameter over the anode surface. Evaluated at the relative thickness $b/c = \frac{1}{10}$ and at various ℓ/c values. Illustrates the combined effects of these parameters in concentrating the current into the vicinity of the anode-cathode junction. Note that $C_a^*(x/c = 0.25)$ passes through a maximum as ℓ/c increases.

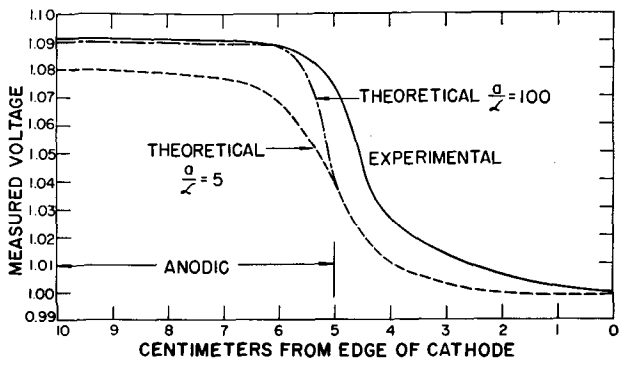

FIG. 11. Comparison between the experimental data of Akimov and Golubev for the Interfacial potential and the theoretically derived results.

with the electrodes physically separated and located in different planes. They emphasized the use and importance of short-circuited coplanar electrodes in trying to elucidate phenomena attending galvanic corrosion. Specifically, they employed rectangular and circular forms for both electrodes arranged to give several anode-cathode ratios. Further, they examined the influence of different thicknesses of electrolyte.

Their electrodes were copper and zinc immersed in a solution containing 3% sodium chloride, 0.06*N* hydrochloric acid and 0.24% hydrogen peroxide. They measured the anodic polarization curve of zinc in this solution as well as the cathodic polarization curve of copper. From these curves it is possible to estimate that $\ell_a \simeq 0.01\ \ell_c$. Thus the primary assumption in the present paper, that ℓ_a equals ℓ_c, does not apply.

Nevertheless these experimental results can be compared with the theoretical results to obtain some idea of the influence of widely differing polarization parameters. In Fig. 11, the experimental variation of the interfacial potential (estimated from their Fig. 1) is plotted together with the theoretical curve which was evaluated for $a/\ell = 5$. The abscissa that Akimov and Golubev used has been reversed so that the anodic portion of the electrode surface is on the left. This brings their graph into agreement with the location of electrodes employed here.

The differential form of Tafel's equation (5)

$$\left|\frac{\partial \Delta E_c}{\partial J_c}\right| = \frac{\mathbf{b}}{J_c} \qquad \text{(IX)}$$

where ΔE_c and J_c are the cathodic overvoltage and current density, respectively, and where **b** is the coefficient of the logarithmic term of Tafel's equation, may be used to estimate ℓ_c. From their data, it was probably in the range 0.4–2.5 cm. For convenience, the geometric mean value of 1 cm was employed in the theoretical calculations.

As defined by Wagner (5), E_a is not the open cell voltage but must be obtained by extrapolating tangents drawn to the polarization curves at appropriate current densities back to zero current density. The second paper by Akimov and Golubev (10) provides sufficient data for this procedure. The cathodic current density was found to be 6 ma/cm² from their Fig. 3. The value of E_a would be very large if the tangent were drawn at 6 ma/cm², since a new cathodic process sets in at approximately this value.

Note that as the current density is raised from 5 to 6 ma/cm², the overvoltage is raised from 0.4 to 1.2 v. By drawing a tangent to the final rising portion of the curve in their Fig. 1, and by drawing a tangent to the anodic polarization curve in their Fig. 2, a reasonable value of 100 mv was obtained. This voltage is compatible with the potential obtained from the curve appearing in their Fig. 6, after allowance is made for the polarization of the anode and cathode. It was somewhat arbitrarily assumed that the extrapolated value of the cathodic voltage $E_{c(0)}$ is 0.99 v on their scale.

Returning now to Fig. 11, the cathodic portion of their experimental curve approaches the present theoretical curve near the edge of the electrode. Near the junction ($x = 5$), the experimental curve is higher than the computed curve. This is not surprising since the slightly polarized anode is contributing significantly more current to the polarization of the cathode near the junction than would be possible if $\mathfrak{R}_a$ were equal to $\mathfrak{R}_c$ as assumed in the theoretical computation. In support of this argument, $C_a^*(x)$ for $a/\mathfrak{R} = 100$ is 3.27 at $x = 4$ cm and 74.2 at $x = 4.99$ cm, whereas $C_a^*(x)$ evaluated for $a/\mathfrak{R} = 5$ is 2.03 and 4.85 respectively (8). Since b/c is 0.6 in the Akimov and Golubev paper (9, 10), and $\mathfrak{R}$ only moderately large, use of the data calculated for an infinite thickness (8) is justified, and the data are approximately correct.

In the anodic portion of the experimental curve the behavior is not surprising. The anodic portion of the theoretical curve computed for $a/\mathfrak{R} = 100$ has been included. Thus, the potential on this surface remains essentially constant (to within 1 mv on the present voltage scale) up to within a centimeter of the anode-cathode junction. Substantial current can be tolerated on the anode without a large degree of polarization, so the change in potential at the junction is not large.

In Fig. 12, experimental variation of the potential at the outer boundary was plotted for two liquid thicknesses. These data were estimated from their Fig. 1. Two equivalent theoretical curves based on $b/c = \frac{1}{2}$ were computed for $a/\mathfrak{R} = 5$ and $a/\mathfrak{R} = 500$. These curves were included on Fig. 12 for comparison. It is somewhat surprising that the measured potential above the cathode approaches the values characteristic of the anodic region. The entire curve lies significantly above the theoretical curve. No simple explanation for this observation can be offered.

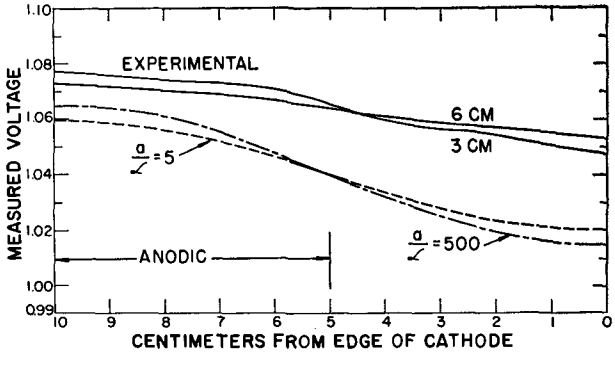

FIG. 12. Comparison between the experimental data of Akimov and Golubev for the potential at the outer liquid boundary and the theoretically derived results.

However, assumptions of the theoretical analysis differ from the experimental conditions in one further way. In the derivation, an array of galvanic cells was assumed so that edge effects could be ignored. In the case under discussion, a single pair of electrodes were immersed in a wider bath of corrodent. As a result, current flow lines were not as crowded as assumed in the theory, and the total current on both electrodes was larger than computed. Although this increased *IR* drop would have the effect of lowering the potential at the outer boundary above the anodic portion of the electrode surface and increasing it over the cathodic portion, it is not apparent that the effect should be as large as indicated by Fig. 12.

The general qualitative behavior is well illustrated by these two graphs, and it is gratifying that the agreement between theory and practice is this good, considering that experimental polarization parameters are not equal and that the liquid extends farther to each side than the electrodes.

Comparison with the Jaenicke and Bonhoeffer data.— An experimental variation in the relative current was estimated from Fig. 10 of Jaenicke and Bonhoeffer (14), and this is plotted as $J(x)/J(x = 1.6)$ in Fig. 13. Using equation (IX) to compute $\mathfrak{R}_c$, it was found to lie in the range 0.0225–0.2 cm. Thus, calculations of the theoretical curves were made for $\mathfrak{R}/c = 0.005$, 0.01, and 0.1, since the experimental range $\mathfrak{R}_c/c$ of values was covered by the latter two $\mathfrak{R}/c$ ratios. From their Fig. 9, $a = 2.05$ cm and $c = 2.30$ cm. Three theoretical curves, evaluated for $b = 2.5$ cm, are presented in Fig. 13. The fourth theoretical

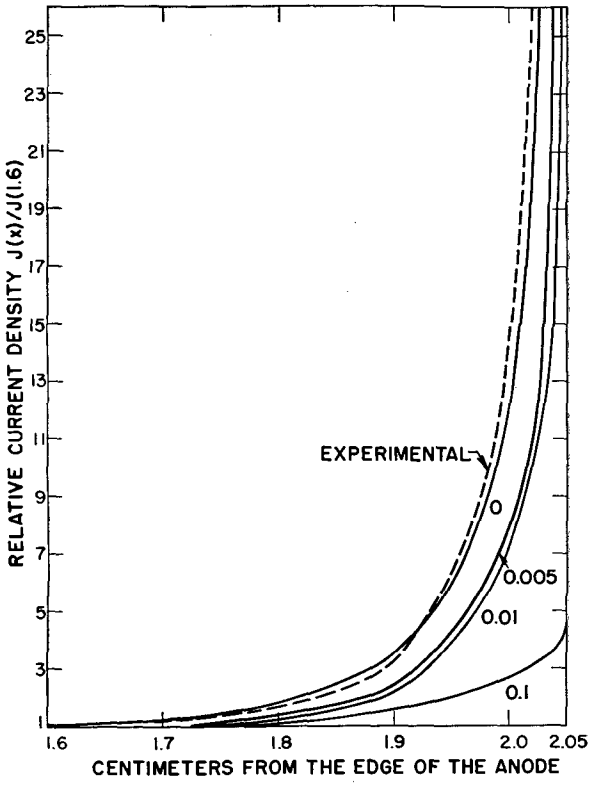

FIG. 13. Comparison between the experimental variation in the relative current density based on Jaenicke and Bonhoeffer's data and the theoretically derived variations for several $\mathfrak{R}/c$ values.

curve, for $\mathfrak{L} = 0$, was calculated from equation [4] of reference (1). Note that in equation (V) of the present paper when $\mathfrak{L} = 0$, the dependence on b drops out, and the equation reverts to equation [9] of (1) evaluated for $y = 0$. Thus the corrosion current parameter can be computed from the analytic expression [4] of (1).

As in the previous case, the experimental curve is not in agreement with the best theoretical estimates. Here the estimated curve lies above the curve computed for $\mathfrak{L} = 0$, i.e., for no polarization. Part of the difficulty could be removed by making the experimental $J_a(x = 1.6)$ somewhat larger or the x values slightly smaller. It is difficult to work accurately with their Fig. 10. However, it is possible that the actual current density is higher than computed because the liquid was not confined in width to the dimensions of the electrodes as required by the present analysis. This might be expected to contribute more to the remote portions of the electrodes than to the vicinity of the anode-cathode junction.

An important point is that Jaenicke and Bonhoeffer (14) used cylindrical, not plane, specimens. Thus, the present theoretical analysis cannot be expected to apply exactly. The boundary conditions and preliminary analysis for the RZ plane of the cylindrical coordinates (i.e., θ constant) is similar to that in the XY plane of the Cartesian coordinates employed in the present analysis. The physical separation between the RZ planes increases for two θ values as R increases. As a result, the current flow lines are not as crowded at appreciable distances above the electrodes in the cylindrical case. Thus, it would be expected that the current densities at the electrodes would be higher than if planar specimens were used.

For these reasons, agreement between the computed and the experimentally measured current densities is good. Further improvement can be made by modifying the experimental curve in either or both of the ways indicated. This would be arbitrary and would accomplish little.

Discussion

It is clear from the results presented that with increased ratios of a to $\mathfrak{L}$, local current densities as reflected by values of $C^*(x)$ become less uniform, and that the relative current density $C^*(x)/C^*(x = 0)$ becomes higher as x approaches the anode-cathode junction. That is, the galvanic system behaves more "macroscopically" as $a/\mathfrak{L}$ or $c/\mathfrak{L}$ is increased. This effect has been established earlier (1, 2). The novel and more interesting effect of the liquid layer thickness has been thoroughly examined for the first time, and it has been found that when b is small enough, the potential distribution over the electrodes at the metal-electrolyte interface approaches the limiting distribution found for negligible polarization in (1). Variation of current density over the electrode surface becomes increasingly sharp as the liquid layer becomes shallower. In compatability with the influence of the polarization parameter, the system behaves "macroscopically" when c/b is large. In certain instances, behavior of the galvanic system must be regarded as "macroscopic" even though there is sufficient polarization, because the liquid film is thin. In such instances the critical dimension λ is b, not a or c as it most frequently is.

When b is identified as the critical dimension λ and therefore is relatively small in comparison to the electrode size or the polarization parameter, the current density (dimensionless) parameter $C^*(x)$ is smaller in magnitude for a given set of a, c, $\mathfrak{L}$, and x values than it is when b is large. Thus, although the system appears to behave "macroscopically," which frequently connotes high current densities, the local current densities are limited and reduced by the corrodent thickness. In this sense, too, b may be regarded properly as the critical dimension.

Another interesting feature of this work is the determination of potential variation at the outer boundary of the corrodent as well as at the electrode boundary of the corrodent. Fig. 4 to 7 show that the potential variation is influenced by both c/b and $c/\mathfrak{L}$. When $c/\mathfrak{L} = 2$, the potential distribution approaches that obtained for an infinitely thick liquid when c/b becomes smaller than 2. However, when the polarization is slight or liquid conductivity high (for instance when $c/\mathfrak{L} = 1000$), and when $c/b = 2$, then the potential is significantly less uniform parallel to the electrode surface than in the case just mentioned. The relative thickness b/c must be further increased before the potential distribution can approximate that found for an infinite thickness of liquid. This combined effect of polarization and liquid thickness is of importance in designing a proper corrosion experiment. The liquid depth should be at least equal to the sum of the anode and cathode dimensions. This "rule" is supported by Fig. 6, 7, and 10.

Most of the statements made for potential distribution at the outer boundary apply equally well to potential distribution at the inner liquid boundary, i.e., to the interfacial potential. The influence of small b on increasing the variation of the interfacial potential is demonstrated by Fig. 2 and 3. The contrary influence of large $\mathfrak{L}$ on decreasing the variation for a given b can be shown.

The analytic results for corrosion current can be examined for limiting values. It is clear that the minimum current density should be found at $x = 0$ for any given set of a, c, $\mathfrak{L}$, and b values, and that the maximum current will be found adjacent to the junction, namely at $x = a - 0$. A simple expression for the limiting value of the maximum current density can be obtained from equation (VIII) for any nonzero value of $\mathfrak{L}$. Note that

$$\lim_{x \to a-0} P^*(x, 0) = \tfrac{1}{2} E_a \qquad \text{(X)}$$

if $a/c = \frac{1}{2}$. This can be seen from equation (V) since the numerator of the summand vanishes for both odd and even values of n. Therefore, since in the anodic region $S_a(a - 0) = 1$,

$$\lim_{x \to a-0} C_a^*(x) = \max C_z^* = \frac{a}{\mathfrak{L}} \qquad \text{(XI)}$$

If then a/c is less than $\frac{1}{2}$, the value of $P^*(a, 0)/E_a$ lies between (a/c) and $\frac{1}{2}$ as seen in Fig. 3. Thus

$$\frac{a}{\mathfrak{L}} \leq \max C_a^* \leq \frac{2a}{\mathfrak{L}} \left(1 - \frac{a}{c}\right) \qquad \text{(XII)}$$

Similarly, if a/c is greater than $\frac{1}{2}$, it can be shown that

the value of $P^*(a, 0)/E_a$ lies between ½ and a/c. Thus

$$\frac{a}{\mathfrak{L}} \geq \max C_a^* \geq \frac{2a}{\mathfrak{L}}\left(1 - \frac{a}{c}\right) \qquad \text{(XIII)}$$

These limits are independent of the relative thickness b/c if the latter is not zero. In the event that one has $b/c = 0$, then the dependence on polarization drops out as both equation (V) and equation (VI) show, and the interfacial function behaves like the step function. This would be expected if there were no liquid. Thus, the limit in equation [X] becomes E_a independent of a/c just as though $\mathfrak{L} = 0$. However, if the ratio b/c remains constant or greater than zero as c goes to infinity, the absolute upper limit on the current parameter for a finite width of anode is $2a/\mathfrak{L}$ as seen from equation (XII). This result agrees with that deduced in a different manner in equation [41] of (2). It has been pointed out previously (2, 3) that $P^*(x, 0)$ approaches $(a/c)E_a$ as $\mathfrak{L}$ becomes very large. This can be seen from equation (V).

The minimum current density is not well behaved in comparison to the maximum current density. The value of the minimum corrosion current parameter $C_a^*(0)$ is plotted in Fig. 14 as a function of both $\mathfrak{L}/2a$ and b/c for $(a/c) = ½$. The reason for the maximum in this quantity as $\mathfrak{L}/2a$ increases can be understood on the basis of physical considerations. When $\mathfrak{L}$ is small, i.e., in a high resistance solution where little polarization occurs, the bulk of the reaction can occur only in the vicinity of the anode-cathode junction, or the resistance of the bath will be prohibitively high. The concentration of current lines into this region is increased when (b/c) is small, i.e., when a thin film is present. This statement is borne out by Fig. 8 and 9. The thinner the liquid film, the closer together the current lines, with an accompanying increase in total resistance. As conductivity of the corrodent increases or polarization increases, the current speads laterally from the anode-cathode junction, mainly over the cathode (when it is the larger electrode and vice versa). Thus, a higher current density occurs at the center of the anode, i.e., at $x = 0$.

However, when $\mathfrak{L}$ is large, i.e., when the system is behaving "microscopically" (since $a/\mathfrak{L}$ is small), the corrosion current parameter decreases, and it approaches the line $a/\mathfrak{L}$ on the right side of Fig. 14 whenever $\mathfrak{L}/a$ is greater than about one. As previously (2) current density becomes more uniform when $\mathfrak{L}$ is large, that is when the electrochemical system can be considered "microscopic." The minimum value of $C_a^*(x)$ converges toward the value $a/\mathfrak{L}$ and the maximum toward $(2a/\mathfrak{L})(1 - a/c)$ as the parameter $a/\mathfrak{L}$ becomes small.

In contrast, the minimum and maximum current density differ by several orders of magnitude on the left hand of Fig. 14, when b/c is large. The system is "macroscopic." However, if the relative thickness is small, the value of $C_a^*(x)$ over most of the electrode surface is approximately that of the minimum. The system would be regarded as completely "microscopic" if it were not for the fact that the current density in the immediate vicinity of the anode-cathode junction remains high and relatively independent of the electrolyte thickness. The difference between maximum and minimum is increased when b/c is small since the minimum is reduced. In the sense that the current density is uniform over most of the electrode surface when the thickness is small, the dimension b may be regarded as λ. When $b/\mathfrak{L}$ is small, the system can be regarded as "microscopic."

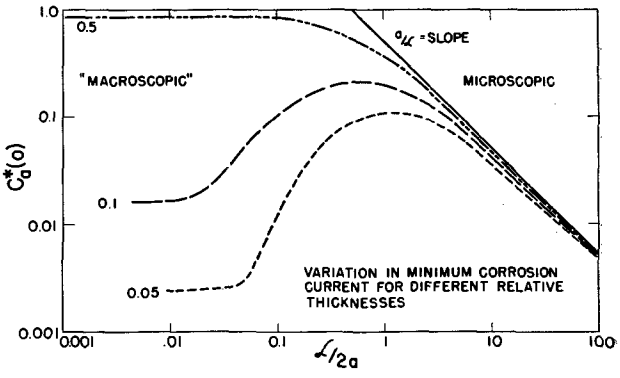

FIG. 14. Variation in the minimum corrosion current density parameter for several relative thicknesses of electrolyte.

Evidence for the a maximum current density, at a given location on the electrode, when b/c and $a/\mathfrak{L}$ take on certain values can be seen in Fig. 14. It can also be seen on the cathodic side of Fig. 9. At $x/c \simeq 0.35$ the parameter $C^*(x)$ increases as b/c is increased from 0.005 to approximately 0.1, and then decreases. $C^*(x)$ is still increasing at $x/c = 0.9$ for increasing values of b/c up to ½. The phenomenon illustrated by Fig. 13 is not a special case, as it has been established with other a/c ratios. There is evidence in Fig. 10 to illustrate the fact that the current density parameter $C_a^*(x)$ passes through a maximum as $\mathfrak{L}/c$ increases. This phenomenon of a maximum holds for a range of x/c values as in Fig. 9 and 10. However, when b/c is as large as ½, the minimum current remains fairly constant over a range of $\mathfrak{L}/c$ values, then decreases rapidly as $\mathfrak{L}/c$ exceeds one. This general phenomenon of concentration is more conclusively demonstrated by a detailed examination of the tables of $C_a^*(x)$ presented elsewhere (7).

Akimov and Golubev (10) concluded that the height of the field of forces is equal to about one-half the sum of lengths of the anode and cathode. This working rule is adequate if $a/\mathfrak{L}$ is one or smaller. However, the perspective drawings show that when $a/\mathfrak{L}$ is large, for instance in the absence of strong polarization, the potential at the outer boundary of a liquid with the relative thickness $b/c = ½$ is significantly different from the potential at $y/c = ½$ (i.e., at the same distance from the plane of the electrodes) in an infinitely thick electrolyte. Therefore, the rule suggested here that liquids in which b is greater than c can be considered "infinitely" thick would appear to be more reliable than that stated by Akimov and Golubev.

CONCLUSION

Many and detailed numerical evaluations of Fourier series (V) and (VI) have permitted elucidation of the opposing influences of the liquid depth and the polarization parameter. In relatively thin liquid films, the interfacial potential is forced toward the values expected with slightly

polarized electrodes, despite the fact that conductivity of the corrodent and its capacity for polarizing the electrodes would be high enough to polarize the electrodes strongly if the liquid layer were infinitely thick. One common effect of both parameters is that in general small b/c and large ℓ/c values reduce the local current density.

These numerical evaluations made it possible to show that in thin films corrosion attack is confined largely to the immediate vicinity of the anode-cathode boundaries, and that this region enlarges as ℓ/c increases.

It has been possible to establish as a "working rule" that a film of liquid is effectively "infinitely thick" if its depth is greater than the sum of the characteristic anode and cathode dimensions.

Acknowledgments

The authors are indebted to Andrew Dravnieks for the translation of the papers by Akimov and Golubev. John Morrissey contributed significantly to the success of this report by performing many numerical calculations. The authors would like to thank John Ruth for many helpful discussions and for checking the mathematics contained herein. The continuing interest and helpful guidance of Professor Carl Wagner was greatly appreciated.

Manuscript received December 27, 1954. This paper was prepared for delivery before the Cincinnati Meeting, May 1 to 5, 1955. Work done under the auspices of the Atomic Energy Commission.

Any discussion of this paper will appear in a Discussion Section to be published in the December 1956 JOURNAL.

REFERENCES

1. J. T. WABER, *This Journal*, **101**, 271 (1954).
2. J. T. WABER AND M. ROSENBLUTH, *This Journal*, **102**, 344 (1955).
3. J. T. WABER, *This Journal*, **102**, 420 (1955).
4. J. T. WABER, "Mathematical Analysis of Galvanic Corrosion. Part IV. Effect of Polarization and Liquid Thickness on the Total Corrosion Current," Los Alamos Scientific Laboratory Report LA-1686, June 1954.
5. C. WAGNER, *This Journal*, **99**, 1 (1951).
6. J. T. WABER, Report No. LA-1386, Los Alamos Scientific Laboratory, March 1952.
7. J. T. WABER, Unpublished report.
8. J. T. WABER, Report No. LA-1656, Los Alamos Scientific Laboratory, June 1954.
9. G. V. AKIMOV AND A. I. GOLUBEV, *Zhur. Fiz. Khim.*, **20**, 303 (1946).
10. A. I. GOLUBEV AND G. V. AKIMOV, *Zhur. Fiz. Khim.*, **20**, 309 (1946).
11. A. THIEL AND J. ECKELL, *Z. Elektrochem.*, **33**, 370 (1927).
12. M. STRAUMANIS AND M. CENTNERSWER, *Z. phys. Chem.*, **128**, 369 (1927).
13. G. V. AKIMOV, G. BRUSHEN, AND G. B. CLARK, *Zhur. Fiz. Khim.*, **6**, 1151 (1935).
14. W. JAENICKE AND K. F. BONHOEFFER, *Z. phys. Chem.*, **193**, 301 (1944).

Technical Feature

Electrochemical Corrosion in Nearly Neutral Liquids[1]

U. R. Evans

Department of Metallurgy, Cambridge University, Cambridge, England

Introduction

Two feelings are uppermost in your Lecturer's mind: first, appreciation of the honour which is being done him; second, the hopelessness of presenting in an hour any complete or convincing account of his subject. The best that can be hoped is that the lecture may arouse sufficient interest to encourage the reading, in the original journals, of papers about corrosion, and a habit of calm thinking on what has been read. If this is achieved, it will be something worth while, since reading and thought, once regarded as essential features of education and research, tend to be neglected today. It is impossible to open a scientific journal without feeling that some authors do not consult in the original the papers cited in their reference lists, nor even satisfy themselves that these represent the latest pronouncements of the scientists quoted. There is no need to take the situation too tragically, but it is certain that closer reading and clearer thinking would be in the interests of research. After this brief introduction—which combines gratitude, humility, and exhortation—it is time to approach the subject of the lecture.

Modes of Oxidation

A reaction can only occur spontaneously if it represents the passage from a less stable to a more stable state. The combination of a metal with oxygen frequently fulfills this condition, the stability of the final state being connected with two facts:

1. The capture of two electrons by an oxygen atom converts it to an anion possessing a stable structure comparable to that of an inert-gas atom.

2. The oxide formed consists of oxygen anions and metal cations with the particles of opposite charge placed closer together than those of like charge.

However, electron transfer from metal to oxygen can occur in two ways: the oxygen can gain electrons and the metal lose them at points separated by distances measurable in Angstrom units; or the gain and loss can occur at points separated, perhaps, by some millimeters. The first mechanism, which generally produces an oxide film, is commonly known as "simple oxidation," and the second, which generally requires the surface to be wetted with an aqueous solution (and often produces not an anhydrous oxide but a hydroxide), is called "electrochemical corrosion." The naming is imperfect; it is becoming evident that even the first mechanism is far from "simple," and, since it involves movement of electrons and ions through the film, it possesses some claim to be called "electrochemical." Nevertheless, it is convenient to retain the nomenclature, reserving the name "electrochemical corrosion" for cases involving the movement of ions over a liquid path. The length of that path is generally great compared to the thickness of an ordinary film, so that we may call the phenomenon "oxidation from a distance," perhaps even "tele-oxidation."

Simple Oxidation

This lecture is not concerned with the first mechanism, but it may be mentioned that simple oxidation has been studied lately in my Laboratory by Davies (1) using iron, Mills (2) using copper, and Hart (3) using aluminium; also that I have published, in response to an invitation from Australia (4), a simplified mathematical statement of the various oxidation-time laws. Moreover, if reminiscence is permissible, it may be recalled that my first American paper was devoted to film growth. It appeared, by invitation, in your Journal in 1924 (6)—the year following the appearance, in an English journal, of the classical work of the American investigators, Pilling and Bedworth (5); thus, two examples of transatlantic publication on the subject were provided within two years. It will be recalled that Pilling and Bedworth divided the metals into two classes: (*a*) the light metals, forming porous, nonprotective films which were believed to thicken (given constancy of temperature, a condition difficult to observe) by the rectilinear law with a velocity defined by the boundary reactions; and (*b*) the heavy metals forming compact relatively protective films, thickening by the parabolic law at a rate controlled by transport through the film. I ventured to propose (6), on theoretical grounds, a more general equation (now known as the "mixed parabolic equation") to cover cases where boundary reaction and transport both play their parts in controlling the oxidation rate; the rectilinear and simple parabolic equations became limiting cases of this more general equation. Afterwards Fischbeck (7) provided what I now regard as a more satisfactory derivation of the mixed parabolic equation and demonstrated that it was obeyed for the action of steam on iron; still later, Wagner and Grünewald (8) verified it for the oxidation of copper at low pressures.

Differences between Simple Oxidation and Electrochemical Corrosion

Disregarding very light metals, with their porous, nonprotective oxide films (5), it may be said that the rate of simple oxidation generally falls off as the oxide film thickens. In contrast, electrochemical corrosion in a salt solu-

[1] Palladium Medal Lecture delivered at the Pittsburgh Meeting, October 9 to 13, 1955.

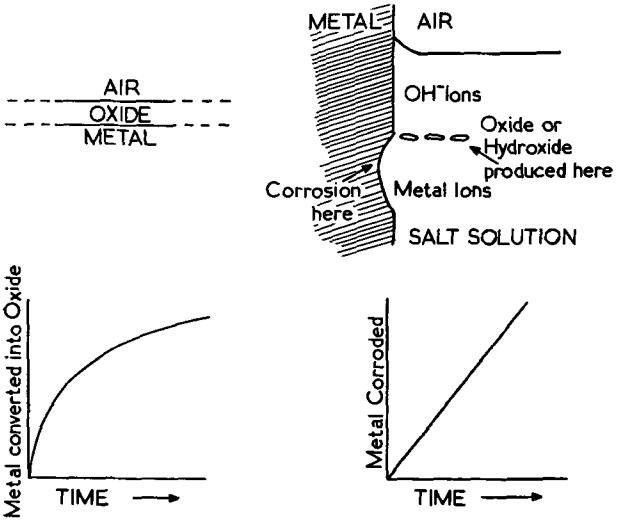

FIG. 1. Contrast between simple oxidation (*left*) and "electrochemical corrosion" ("oxidation from a distance") (*right*).

tion can, in absence of complicating factors, continue at an undiminished rate, provided that the immediate products are freely soluble (Fig. 1). Thus, on zinc partly immersed in sodium or potassium chloride solution, oxygen is readily renewed near the water line and captures electrons, becoming converted, not to O^{--} ions (which would be unstable in solution) but to OH^- ions; since this keeps removing electrons from the metal, cations (atoms short of electrons) can continuously enter the liquid without any accumulation of electric charge. The "anodic reaction"

$$Zn = Zn^{++} + 2e$$

occurs mainly on the lower part of the specimen, and the "cathodic reaction"—which is in effect—

$$O + H_2O + 2e = 2OH^-$$

at the water line. (In that region, a film is soon formed, ultimately thickening to produce interference tints, so that in the water line zone, there is no appreciable passage of cations into the liquid, at least in the early stage.) The Zn^{++} and OH^- ions, meeting near the junction of the cathodic and anodic areas, produce zinc hydroxide at a place where it cannot obstruct further attack;[2] thus the corrosion-time curves may be straight.

How straight the corrosion-time curves can be, if disturbances are avoided, is shown by curves (Fig. 2) produced in my laboratory by Borgmann (10), now President of Vermont University, and published in the Society's JOURNAL. Small amounts of copper or iron in the zinc caused a slight increase in the corrosion rate, while aluminium had the opposite effect; very pure zinc, kindly provided by American friends, gave rates appreciably slower than that of ordinary zinc, but in all cases the curves were straight.

[2] Oxide or basic salts may be formed under some conditions; corrosion products have been examined in detail in Feitknecht's laboratory at Berne (9).

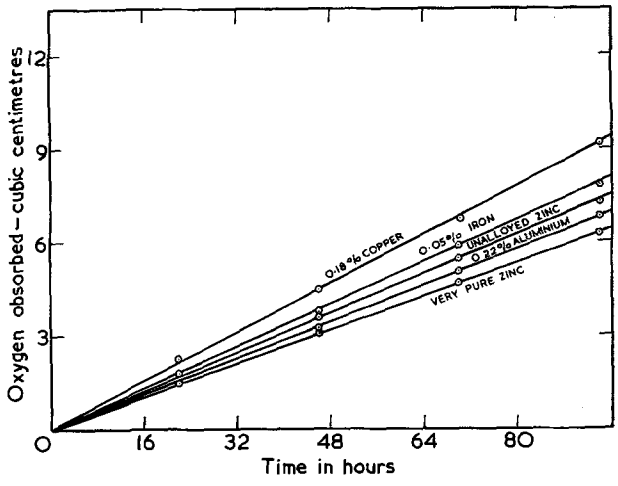

FIG. 2. Corrosion of zinc and its alloys in $N/10$ potassium chloride (C. W. Borgmann and U. R. Evans).

MEASUREMENT OF CORROSION CURRENT

That an electric current was really passing through the liquid between the anodic and cathodic regions on partly immersed zinc had been shown qualitatively in my early work (11). Just before the war stopped pure-science work in 1939, Agar (12) succeeded in measuring that current, and found that it corresponded to the corrosion rate in the sense of Faraday's law. He used (Fig. 3) zinc plates in sodium chloride (or sulphate) with two calomel (or mercurous sulphate) electrodes connected by tubuli, one (B) being fixed at an "infinite distance" from the zinc (a few inches sufficed), while the other (A) could be moved by racking in any of three directions; the three coordinates defining the position of the tubulus-tip were read off on three scales. In that way, equipotential surfaces in the liquid could be traced (Fig. 4), and, the conductivity of the liquid being known, the current flowing could easily be calculated on the basis of Ohm's law.

The corrosion of iron partially immersed in, say, sodium chloride solution is slightly more complicated, because the

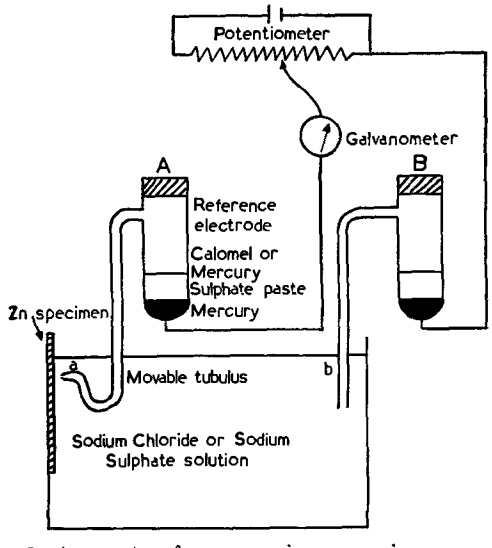

FIG. 3. Apparatus for measuring corrosion currents on zinc (J. N. Agar and U. R. Evans).

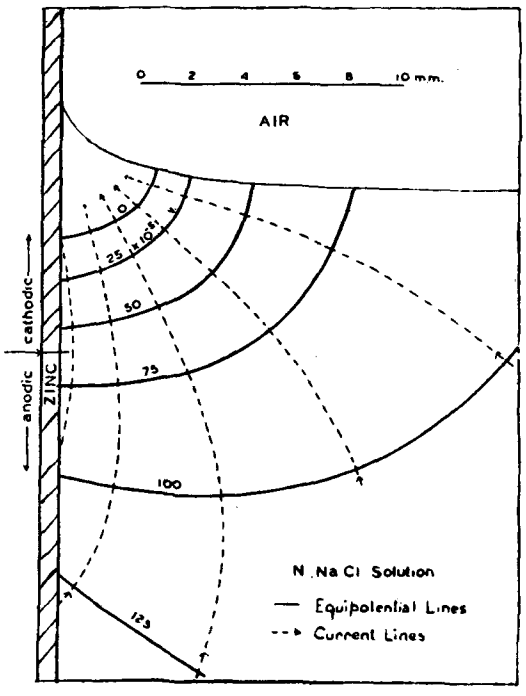

FIG. 4. Equipotential curves around zinc in N sodium chloride (J. N. Agar and U. R. Evans).

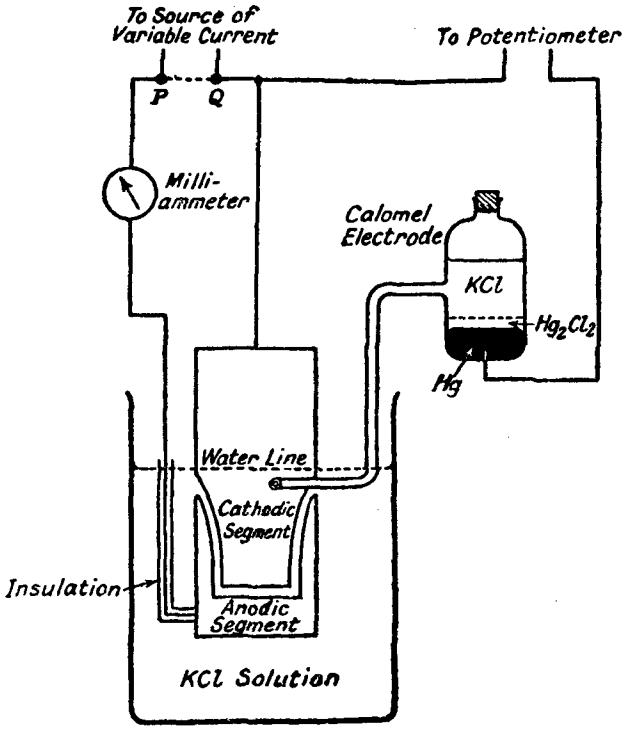

FIG. 5. Apparatus for measuring corrosion currents on iron (T. P. Hoar and U. R. Evans).

valency of iron is variable. Ferrous hydroxide is not precipitated as such, and the solid product obtained is, according to the oxygen-supply, red-brown FeO(OH), black magnetite, or sometimes green ferrous-ferric compounds. However, the accurate measurement of the corrosion currents was carried out earlier on iron than on zinc, being accomplished by Hoar (13) in 1932. Success was made possible by steel of special quality, provided by the late W. H. Hatfield, so uniform in composition that in concentrated salt solution the distribution of corrosion was always the same. Thus, specimens could be cut along the line separating what would be the corroded and uncorroded areas and the two parts mounted almost in their natural relative positions, but just out of contact. At some concentrations it was possible to measure the current directly by joining the two segments through a low-resistance milliammeter, but this procedure, although simple in principle, was not very accurate; nor could it be employed except within a limited range of concentration. A more satisfactory method was to join the segments to an external source of microcurrent (Fig. 5) and measure, by means of a tubulus opening close to the cathodic area and joined to a calomel electrode and potentiometer, the relation between cathodic potential and curent flowing; the curve obtained (Fig. 6) made it possible, by measuring the cathode potential on an uncut specimen, to read off the current flowing. Thus the corrosion rate obtained by application of Faraday's law could be compared with that measured directly from loss of weight; the agreement (Fig. 7) was surprisingly good.

On vertical specimens partly immersed in potassium or sodium chloride, the cathodic area is the zone lying just below the water line where oxygen needed for the cathodic reaction can readily be replenished; the anodic area, where attack occurs, is further down. On a horizontal, fully immersed surface, no part is specially favoured as regards oxygen supply (except that at the edges replenishment is somewhat better than elsewhere); the anodic and cathodic areas move about, so that in the end the whole area may become corroded, each point having been anodic at some time or other. The current here is much smaller than on partly immersed specimens, but Noordhof (14), by means of a tubulus consisting of two concentric tubes leading, respectively, to two silver chloride electrodes, succeeded in measuring it, after suitable amplification, and found that the electrically calculated corrosion rate was in reasonable accord with that observed directly. In the early stages, when only certain regions of the specimen were showing

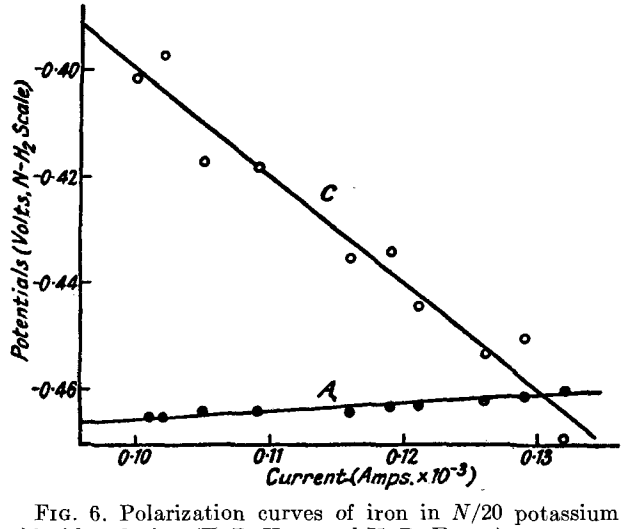

FIG. 6. Polarization curves of iron in $N/20$ potassium chloride solution (T. P. Hoar and U. R. Evans).

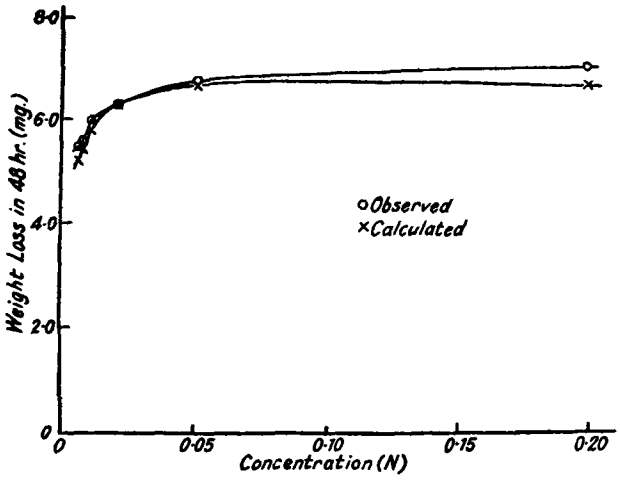

FIG. 7. Comparison between observed and electrically calculated values of corrosion (T. P. Hoar and U. R. Evans).

visible corrosion, it was found that these were identical with the regions shown by the electrical instrument to be anodic. It is believed that, in such cases, anodic polarity is generally dependent on physical looseness of structure rather than chemical differences. Groups of atoms, which can detach themselves most easily, pass into the liquid by an anodic reaction; when the loosened portion is exhausted, anodic attack shifts to another region.

In certain cases, however, the anodic regions seem to be connected with damage to an invisible oxide film. This is true of aluminium, which builds a very protective film. Brown and Mears (15), tracing scratch lines on aluminium, found that these were anodic to the rest, and that the current flowing corresponded to the corrosion rate. Unintentional blemishes, such as can be seen often on commercial aluminium sheet, were sometimes noticed to form the seats of anodic attack. Brown and Mears cut a piece of aluminium into two pieces, blocking out all the blemishes on one piece with a wax-resin mixture and applying the mixture to the whole surface of the other except for the blemishes. On joining the two pieces, immersed in liquid, through a milliammeter, the current flowing was found to be equivalent to the corrosion rate.

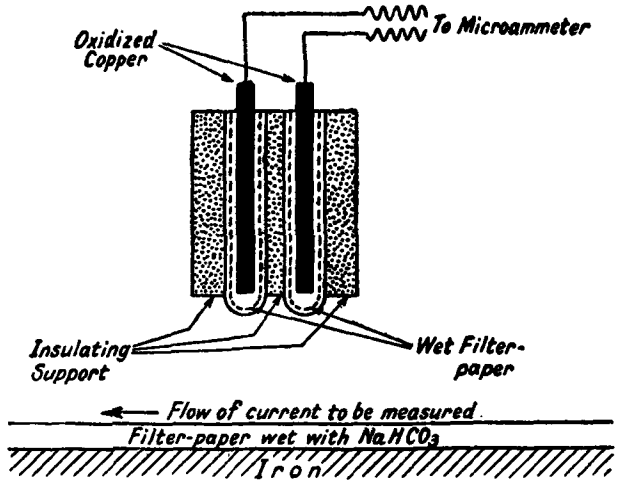

FIG. 8. Dielectrode (U. R. Evans)

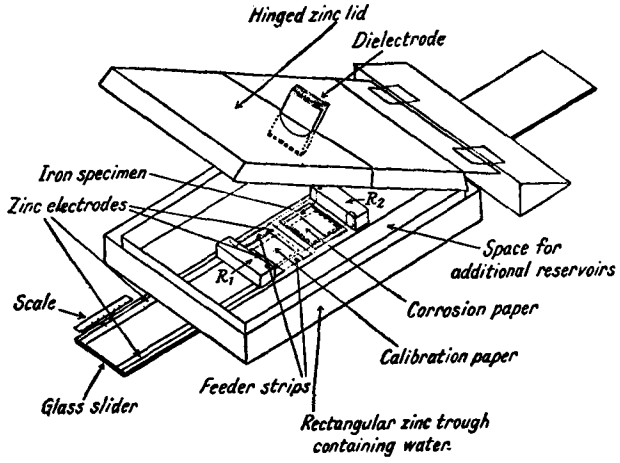

FIG. 9. Improved dielectrode apparatus with calibration circuit (R. S. Thornhill and U. R. Evans).

On iron, corrosion only occurs selectively at a scratch line if the liquid is made just sufficiently "inhibitive" to keep the main part of the film in repair (as explained later). If we engrave a scratch line on iron which has been exposed for some days to dry air after being cleaned by abrasion and then place upon it filter paper soaked in sodium bicarbonate solution of a concentration chosen as standing between the higher range (which produces passivity) and the lowest range (which produces corrosion), rust will generally appear along the scratch line, but not, on good specimens, elsewhere. In 1935 I proved (16) that current was really passing through the wet filter paper between the scratch line (as anode) and the uncorroding region on both sides (as cathodes) by bringing down the "dielectrode" shown in Fig. 8 into contact with the filter paper at some measured distance from the scratch line; the two Cu/Cu_2O electrodes were virtually nonpolarizing and a very small fraction of the current flowing horizontally along the filter paper was diverted through a central-zero microammeter. There was clearly a relation between the readings of that instrument and the current flowing through the filter paper. Thornhill (17), who evolved a greatly improved apparatus (Fig. 9), calibrated the dielectrode on a strip of wet filter paper through which known currents from an outside source were made to flow.

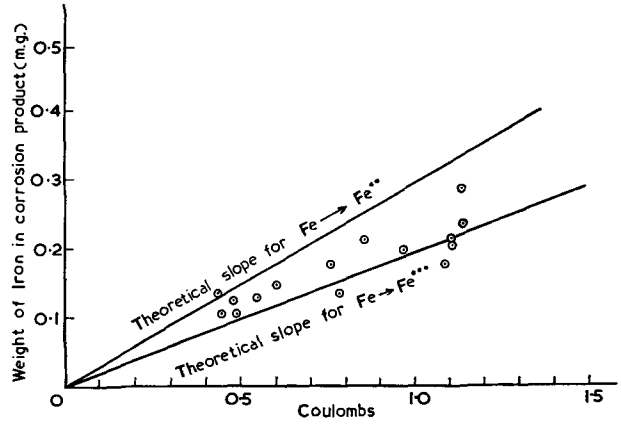

FIG. 10. Comparison between corrosion and coulomb measurements (R. S. Thornhill and U. R. Evans).

In that way the curves of Fig. 10 were obtained. The correlation between the total coulombs generated and the weight of iron corroded show that the former is greater than would be expected if the iron passed into solution merely in the ferrous state; the measurements indicate that not only the reaction

$$Fe = Fe^{++} + 2e$$

but also $$Fe^{++} = Fe^{+++} + e$$

can take an electrochemical course. It had hitherto been assumed that the anodic corrosion of iron to form ferrous products was electrochemical, but that the subsequent oxidation to the ferric state occurred "chemically" out of contact with the metal; probably the assumption was correct for iron immersed in liquid, but the stagnant conditions existing in sodden filter paper are favourable for the electrochemical oxidation of Fe^{++} to Fe^{+++}—explaining Thornhill's results.

Importance has been attached at Cambridge (England) to the measurement of the currents flowing over "naturally corroding" metal, since the comparison between calculated and observed values of the corrosion provide convincing quantitative evidence for the electrochemical mechanism. Not all of this work, however, was carried out in my laboratory; that of Brown and Mears was conducted at New Kensington after Dr. Mears had left Cambridge, and may perhaps be regarded as yet another friendly link between the American and British laboratories.

Influence of the Solubility of Primary Products

The rapid and persistent corrosion of zinc or iron in sodium or potassium chloride solution is clearly connected with the high solubility of the products formed at the anodes and cathodes; a solid corrosion product is ultimately formed, but, being precipitated well away from the site of corrosion, does not interfere with attack. Where the primary anodic product is sparingly soluble, corrosion is usually slow; the remarkable resistance of lead toward sulphate solutions, of silver toward chloride solutions, and of magnesium toward fluoride solutions is usually ascribed to the limited solubilities of lead sulphate, silver chloride, and magnesium fluoride.

Some measurements which I carried out (18) in 1924 with drops placed on a horizontal steel surface exposed to air at 29°C may serve to illustrate the influence of solubility. The corrosion, measured by a simple colorimetric method with thiocyanate, is shown in Table I. It may be remarked that the reproducibility was usually better in the short experiments than the long ones, especially with the potassium salt solutions, where during the longer periods the potassium hydroxide formed as cathodic product round the drop margin (where oxygen is best renewed) crept outward over the surface to an extent which varied from one drop to another.

Some apology is needed for putting forward measurements made thirty years ago, but even today they serve to illustrate certain features of the situation. With all those potassium salts which form a freely soluble cathodic product (potassium hydroxide) and a freely soluble anodic product (the appropriate ferrous salt), the corrosion rate is considerably greater than that produced by the distilled water used for making the solution (which probably contained traces of tin). The phosphate normally gave negligible corrosion, evidently due to the sparingly soluble anodic product, iron phosphate, but one exceptional specimen (probably carrying some abnormally weak point) suffered much attack. Zinc sulphate produced less corrosion than distilled water alone, evidently due to the sparingly soluble cathodic product, zinc hydroxide. [The fact that zinc sulphate retards the cathodic reaction was afterwards shown at Cambridge by Chyżewski (19) and has been confirmed by Cross and Hackerman (20).] Nickel sulphate caused considerable corrosion, and here the cathodic product may well have been metallic nickel, which would certainly not hinder the cathodic reaction; that explanation was not offered in the 1924 paper.

Two Cambridge researches of 1928 and 1929 on the corrosion of partially immersed steel plates provide a further example of the same principle. Magnesium sulphate solution (giving magnesium hydroxide as cathodic product,

TABLE I. *Corrosion on steel by single drops at 29°C, expressed in mg*

Time (hr)	5.5	18.5	24.0	48.7
Distilled water	0.26 0.30 0.25 0.25	0.73 0.77 0.75 0.70	1.0 1.05 0.95 0.95	0.95 1.47 1.47 1.40
N/10 KCl	0.65 0.65 0.66 0.66	1.91 2.10 2.00 1.94		3.50 2.57 3.25 5.12
N/10 K_2SO_4	0.71 0.73 0.77 0.77	2.22 2.07 2.15 1.97		3.25 3.27 4.35 3.05
N/10 KNO_3	0.80 0.75 0.82 0.77	2.08 2.64 2.32 2.35		3.00 3.02 3.57 3.07
N/10 (*M*/30) Na_2HPO_4			0.000 0.005 0.65 (Sic) 0.005* 0.006* 0.007*	
N/10 $ZnSO_4$			0.17 0.12 0.17 0.30 0.16	
N/10 $NiSO_4$			0.75 0.55 0.48 0.55 0.90 0.82	

* Temperature varied from 27° to 29°C in these three experiments.

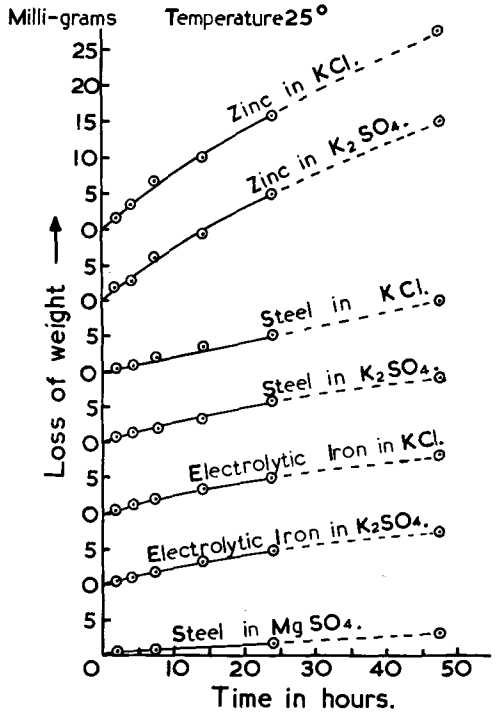

FIG. 11. Some early time-corrosion curves (U. R. Evans)

which afterwards undergoes transformation by interaction with anodic products) caused less attack than the distilled water employed to make it (21, 22). The curves of Fig. 11 show corrosion of partly immersed plates at 25.0°C. The zero points are off-set (otherwise many of the curves would fall on the top of each other), but the gradient of the curves provides a basis of comparison. Magnesium sulphate produces far less rapid corrosion than potassium sulphate, but there is little difference between potassium sulphate and chloride or between electrolytic iron and the steel then used [it was afterwards found by Hoar (13) that different steels corroded at significantly different rates]; the corrosion rate of zinc was much higher.

STARTING PLACES OF ATTACK

The 1929 observations on partly immersed plates brought out the fact that attack started locally on all the metals studied, but spread out on zinc, iron, and copper, while tending to remain localized on aluminium; later work suggested that the spreading was particularly rapid on iron.

The corrosion pattern on steel was rather similar to that on pure iron; actually there were more points of initiation of attack on the purer material which was attributed to greater frequency of rolling defects; however some of the initial attack on pure iron failed to develop. A sand-blasted steel behaved differently from the same steel with an abraded surface, developing a systematic distribution of corrosion spots each marked by a little tuft of rust.

In 1929, I devoted a second research (23) to the discovery of the nature of the starting points. In order to avoid complications due to local oxygen-exhaustion and to the interaction of cathodic and anodic products formed at contiguous points, the specimen was made entirely anodic in an oxygen-free solution of potassium chloride, by means of an external emf. Oxygen was removed by the passage of current between two auxiliary iron electrodes, giving a precipitate which was at first brown, then green, and finally white, indicating a satisfactory removal of oxygen. Passage of current between the auxiliary electrodes was then discontinued, and the experimental specimen was made the anode toward a 4th electrode as cathode. Experiments on pure iron, steel, zinc, and aluminium in different conditions always led to attack starting locally at points which were most numerous near the edges, where the metal had been stressed in cutting. On abraded specimens, the points lay on the major abrasion lines. On rolled specimens, they fell on lines following the rolling direction, even though the rolling had taken place some years earlier. It was suggested in 1929 that the sites of local corrosion represented weak spots where the protective film broke down, but that they could not in all cases be pre-existing gaps; they might be places of surface irregularity or regions where intense internal stresses left in the metal kept the oxide skin in a distended condition. In some instance, it was stated, weak spots undoubtedly coincided with cavities in the metal itself; but the existence of pores in the metal (as such) did not seem to be a necessary condition for localized corrosion. Weak places could be produced artificially in the laboratory, but the uniform groove left by a diamond point was less effective than the irregular scratch made by a steel file. Modern views on oxidation would suggest that, where groups of disarrayed atoms exist below an oxide film, they will possess sufficient energy to pass outward through a film sufficiently thick to resist passage by atoms from parts which are not disarrayed.

IMPORTANCE OF PHYSICAL AND CHEMICAL PECULIARITIES IN DECIDING CORROSION PATTERNS

All this seems to suggest that the starting points of attack are spots which are *physically*—rather than *chemically*—different from the rest of the surface. Traces of impurity in the metal, in the liquid, may, however, be important in deciding whether or not the starting places develop into pits. Aziz and Godard (24) find that the addition of iron to superpure aluminium increases the probability of pitting, although it has no effect on aluminium of commercial purity. Sometimes the pitting may be due to metal deposited from the water; Porter and Hadden (25) find that 0.02 ppm copper in water can cause trouble. Homer (26), studying localized attack on smooth iron surfaces in chloride-carbonate solutions, found it to take place at the sites of sulphide inclusions; on roughened surfaces, however, the effect of the roughening was more important than the effect of the inclusions. On the smooth specimens the hydrogen sulphide, formed by action of the anodically formed acidity on the sulphides, probably promoted anodic attack (by decreasing polarization), as suggested by statistical work of Hoar and his colleagues (27), as well as by that of Mears (28). On the other hand,

Davies (29) found that the pitting of pure zinc in very pure water followed the same general pattern as that of less pure zinc.

In potassium sulphate solution, I found (30) that two sides of the *same* piece of rolled zinc behaved differently, the duller sides showing *fewer* starting places than the brighter side; starting points were often connected with tiny scratches or rolling defects—where microscopic cavities probably existed; it was found that if the specimens were placed in a closed vessel, which was evacuated before the solution was introduced—a procedure which would facilitate entry of liquid into cavities—the starting of point-corrosion occurred much more quickly. Earlier Seligman and Williams (31) had produced pitting on aluminium by forming small depressions, closing them up with a hammer and placing the aluminium in hard water; they ascribed the pitting and blistering of certain aluminium vessels in hard water to the presence of microscopic cavities, closed over in the rolling process. Recently, Forsyth (32) has found that an aluminium surface, electropolished and then deformed sufficiently to produce gliding, suffers pitting in acid preferentially along the microledges produced where a gliding plane cuts the surface.

Two recent papers on tin suggest that physical and mechanical factors are all-important in deciding the starting points of corrosion. Britton and Michael (33) subjected three varieties of tin to cathodic cleaning and after minimal air exposure (about 25 sec) immersed them in N ammonia; all suffered rapid attack. Other specimens were exposed to air for 2 hr before they entered the ammonia; in two cases the corrosion rate was reduced to $\frac{1}{60}$th of its original value, but the third variety, which carried rolling defects, corroded at the same rate as before, suggesting that it is difficult to produce and maintain a protective oxide film on a defective surface.

Ross (34) transferred the invisible film from air-exposed tin to a sintered glass plate, connected to a manometer, by sticking the tin to the glass with shellac, leaving a central area (1 mm in diameter) free from shellac; the metal was then removed by ferric chloride or fusion in vacuo, leaving the film on the sintered glass. Such a film would normally withstand a small water pressure applied on the outside for 48 hr; but if sodium alkyl sulphate was added to the water, the film began to leak within about 5 min. Now metallic tin suffers pitting when placed in water containing sodium alkyl sulphate. More than one interpretation of Ross' results is possible, but the facts suggest that the oxide film, although normally able to withstand its internal strains, collapses under them in presence of the sodium alkyl sulphate. The criterion for any spontaneous collapse is that the decrease in strain energy brought about by fracture must exceed the increase in interfacial energy involved in the newly formed surface. That the sodium alkyl sulphate does decrease interfacial energy is shown by experiments on tin spheres (oxide-coated, it is presumed); the force needed to separate them in sodium alkyl sulphate is less than half that needed in water or sodium sulphate. The real existence of internal strains in oxide films has frequently been established, notably by the tendency to wrinkle or curl when transferrred to a soft basis such as vaselined glass (34). Thus the argument seems complete.

"Crack-heal"

In 1946 a research (36) on iron suggested that weak points keep appearing spontaneously in the invisible oxide film formed at ordinary temperatures. Heat-tinted steel specimens were inscribed with scratch lines, exposed to air for 5 min, and then immersed in a sodium carbonate-bicarbonate buffer solution, sufficiently inhibitive to confine attack to a few exceptional points situated on these scratch lines. At intervals the specimens were withdrawn in such a way that they came into contact with filter paper soaked in the same solution at the moment of emergence, and remained covered with the wet filter paper for 5 min in air; stains of rust were produced at places where the iron was corroding, and when the specimen was returned to the vessel containing the liquid, the filter paper was preserved as a permanent record of the pattern of rust spots. Five minutes later a fresh pattern was obtained and the specimen again returned to the liquid. This procedure was continued many times. So long as there was no direct exposure to air other than through the wet filter paper, the rusting always continued at the same points; the pattern of rust spots, produced on successive filter papers, remained practically unchanged (Fig. 12). If, however, the specimen was washed, dried, exposed to air for 5 min, and then put back, the same sequence of operations being followed, it was found that attack had ceased at most of the original spots; however, after further immersion in the liquid, new spots started at new points.

The best interpretation of these results is that weak places are developing spontaneously and sporadically in the film. If corrosion is already proceeding at several places along the lines, the new spots receive "cathodic protection," since the metal is being denuded of electrons owing to the corrosion already proceeding, and no fresh corrosion starts at the new points. If, however, most of the corroding points have disappeared because of direct exposure to air, new corrosion starts at some of the spontaneously forming weak points.

We thus get a picture of a process which is conveniently called "crack-heal," although it seems likely that the

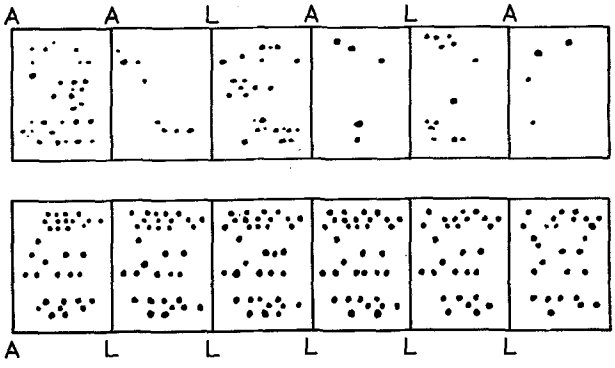

Fig. 12. Position of rust spots during successive 5-min periods, separated by 5 min in the liquid (L) or in air (A) (U. R. Evans).

spontaneous production of weak points is not due to mechanical stresses but to the vagaries of atomic movements which on rare occasions and for short periods leave a chain of structural defects sufficiently continuous to provide an outward path for the iron ions. If the iron is exposed unwetted to dry air, crack-heal will cause local and intermittent thickening of the film on an atomic scale; possibly the very slow increase of weight noted by Vernon (37) on iron even after 50 days' exposure to air (relative humidity, 10%) may be attributed to a crack-heal mechanism.

Although it is probable that crack-heal goes on even in the absence of liquid, contact with water or aqueous solution will modify the results. In presence of certain anions (e.g., Cl^-), metal cations can enter the liquid, and the film, far from being healed, will be undermined, and attack will accelerate. Even if film-forming substances (oxidizing agents or anions forming sparingly soluble salts) are present, some corrosion may occur before repair is definitely established, since in general the liquid near the metal must first become supersaturated and must then produce nuclei before repair takes place. If the liquid contains an organic substance carrying a polar group, the local electrical fields set up where the molecules are adsorbed will probably either aid or retard movement of cations through the film. This may perhaps explain the results of Holness and Ross (38), who found that such substances sometimes accelerate corrosion and sometimes retard it.

It has sometimes been argued that, if the exact nature of the weak places where corrosion starts could be established, so that these points could be eliminated, corrosion would be avoided altogether; unfortunately, this is not always true; elimination of the most sensitive set of points generally causes attack to start at the second most sensitive set which would otherwise be immune. Britton (39) found that plates of a certain iron, finely ground and baked in air for 30 min at 150°C, and then placed vertically in $N/10$ potassium chloride, corroded only along the edges and bottom; but when these edges and bottom had been protected with baking enamel, attack then started at central points, which had been immune on specimens with unprotected edges owing to the cathodic protection afforded by the anodic attack at those edges.

Oxygen as Inhibitor or Corrodent

Consider a number of drops of water placed on an iron surface and surrounded by air. Where a major weak point occurs on the area covered by the drop, corrosion is likely to occur; where there is only a minor weak point, there will be none. Thus, some of the drops develop much rust, others absolutely none. If we surround the drops with oxygen instead of air, only the drops with exceptionally weak spots will develop rust, but these particular ones will rust quicker than in air, since oxygen arriving at the cathodic areas around the points of anodic corrosion accelerates attack at those points. Mears (40) made a statistical study of drops of water on iron below different oxygen-nitrogen mixtures, and found that the proportion of drops developing rust diminished steadily as the oxygen content increased, but that the rate of corrosion attained by those which corroded at all became higher with increasing oxygen content.

Specimens of iron and zinc placed in distilled water under stagnant conditions usually corrode, but this can be avoided by violent relative movement, which will help the renewal of oxygen. An early paper (41), which I contributed by invitation to an American symposium, described how the whirling of pure iron in distilled water containing oxygen prevented almost entirely the rusting which occurred under stagnant conditions.. Davies (29) obtained similar results with zinc in extremely pure water. Here corrosion was completely prevented by whirling, but under stagnant conditions small white dots appeared on the surface with pronounced pits below them. Where a polythene thread was stretched over the surface, so as to shield a thin line of metal from oxygen, there were far more pits on the shielded line than on the surrounding area. Evidently those points which were insufficiently weak to develop corrosion with the slow rate of oxygen supply which occurs under ordinary stagnant conditions were able to start corrosion when there was additional shielding from oxygen by the polythene thread. On a vertical zinc surface, particles of corrosion product falling from a pit which had already developed on the upper part of the surface, and lodging at points below it, themselves caused shielding and started pitting where otherwise it would not have occurred. This explained the curious arrangement of the pits on zinc in vertical lines, a phenomenon noted in 1919 by Bengough and Hudson (42).

Even under stagnant conditions, Davies (29) was able to avoid corrosion of zinc by distilled water if oxygen was applied under a pressure of some atmospheres, so that oxygen solubility was increased. He introduced oxygen under pressure into the vessel while the zinc was still dry; afterwards, when water was introduced, pitting was avoided. This plan followed the method of Bengough and Wormwell (43) who had shown in 1934 that on iron high oxygen pressures tend to oppose corrosion.

Presumably if an oxidizing agent much more soluble than oxygen itself could be used, inhibition of corrosion under stagnant conditions would be easily obtained. This is probably the main cause of inhibition of potassium chromate solution, which, as Mayne and Pryor (44) have shown, produces a film which is mainly iron oxide, even when the specimens were free from oxide on immersion in the chromate solution. Chromium compounds are sometimes present in the film, as shown chemically by Hoar (45); also by Brasher and Stove (46) and by Simnad (47), using radioactive tracer methods. It is not certain whether they contribute to the protection; King, Goldschmidt, and Mayer (48) consider that they detract from it.

Salt Solutions

Let us now consider the case where the water contains chloride. If the supply of oxygen is ample, we may still succeed in arresting any metal ions which start to pass outward through some at least of the weak places in the film, so that the oxide film will merely thicken at such points. If the supply of oxygen is insufficient to prevent emergence into liquid at the weakest points, then corro-

sion will set in (provided that the chloride is soluble). If so, the relatively slow arrival of oxygen at the area around the weak point will stimulate the attack, by using up electrons in the cathodic reaction, so that the emergence of metallic ions at the weak point can proceed continuously without accumulation of electric charge. The higher the concentration of chloride, the greater the effect, since points at a greater distance from the weak point can act as cathodes, owing to the greater conductivity of the liquid. On the other hand, at very high chloride concentrations, the oxygen solubility declines, and this usually depresses the corrosion velocity. Provided the oxygen supply has not reached the level at which it prevents corrosion at weak places, the attack becomes more rapid as the oxygen supply increases. Replenishment of oxygen at the area around the weak point will also have the effect of causing trains of chlorine ions to move toward the weak point, thus favouring corrosion.

This will happen even if the distribution of oxygen to all parts of the surface is uniform. The danger of unequal distribution (differential aeration) is that it tends to intensify corrosion if the shielded (anodic) area is small compared to the exposed (cathodic) area. No one has ever claimed that differential aeration is a necessary condition for corrosion in salt solution. The paper (11) in which differential aeration was first discussed makes this quite clear. Comparative experiments were described on (*a*) zinc specimens with virtually the whole area exposed to the liquid, and (*b*) others with part of the area shielded from oxygen; the total corrosion measured was actually *greater* in the first case but it was more intense in the second case, being largely concentrated on the shielded region.

Now consider that sodium phosphate instead of sodium chloride is the chief salt present. The cathodic reduction of oxygen over the main area will cause phosphate ions, instead of chloride ions, to migrate toward the points where, in chloride solution, corrosion would develop. Now, however, solid iron phosphate will be formed at this point, and the leakage will be repaired. At points somewhat less weak, the oxygen supply may be sufficient to carry out the repairs. This doubtless explains the results of Mayne and Menter (49) who found that the film produced on iron which had remained in a solution of disodium phosphate (Na_2HPO_4) containing oxygen, and had escaped visible attack, consisted largely of gamma ferric oxide, but there were inclusions of hydrated ferric phosphate at certain places. It also explains the results of Pryor and Cohen (50) who found that oxygen is required for inhibition by sodium phosphate although, in the absence of oxygen, corrosion, being of the hydrogen evolution type, is commonly slow in almost any slightly alkaline solution.

If, to a chloride solution, sodium phosphate is added with the intention of inhibiting the corrosion of iron, but in insufficient amount, a protective film may be produced over the greater part of the surface, but at the weakest spots, particularly those situated in shielded places where the inhibitor is not readily replenished, corrosion may start; the iron salts there produced may precipitate the phosphate in membraneous form at a slight distance from the points of attack, so that the inhibitor will subsequently fail to reach those places where it is most needed if attack is to be halted. The combination of large cathode and small anode leads to intense attack (for the same reason that attack is intense at a small bare area on steel elsewhere plated with copper). This intensified attack is met with in chloride-phosphate mixtures where contact of, say, a glass rod with the steel provides a shielded area, and also at the meniscus zone of partly immersed specimens. Recent work by Peers (51) has indicated that the intense water line attack in chloride-phosphate solutions, often leading to perforation of steel sheets which elsewhere remain immune, is due to exhaustion of inhibitor at the meniscus crevice.

Alkali as an Inhibitor

Another way of inhibiting the corrosion of iron is by alkali addition. In this case the conversion of oxygen into OH^- ions over the main part of the surface permits the opposite reaction to occur at the weak points, so that instead of metal ions entering the solution, oxide is formed; thus the oxygen arriving over the large area around the weak point can act, as it were, by proxy, at the weak point in question, which is, therefore repaired; evidently a small supply of oxygen per unit area represents a large total if the cathodic area is large, and oxygen can produce inhibition in alkaline solutions where it would cause corrosion in neutral or weakly acid solutions.

This explains some interesting results obtained at the U. S. Bureau of Standards by Groesbeck and Waldron (52). Increase of the amount of oxygen in water brought to a definite *p*H by means of sodium hydroxide and/or carbon dioxide, was found first to increase corrosion, and then to diminish it, the oxygen becoming an inhibitor at high concentrations. The maximum occurred at a smaller oxygen concentration when the *p*H was high than when it was low. The fact that corrosion first increases and then decreases with increasing oxygen concentration is clearly shown in recent work by Uhlig, Triadis, and Stern (53).

Pitting in Water Containing Salts

Since corrosion usually starts locally, there are three possibilities at each point of attack: (*a*) it may heal up; (*b*) attack may remain localized, producing a pit; and (*c*) attack may spread out, giving general corrosion. If the total attack is even partly controlled by the cathodic reaction, pitting must lead to intensified attack, and it is important to know when it will occur.

Corrosion in a salt solution which is nearly neutral at the outset will produce a strongly alkaline reaction at the cathodic area, since reduction of oxygen provides OH^- ions, while liberation of hydrogen uses up H^+ ions. To a lesser extent it may produce acid at points where anodic attack is starting, although not all anodic reactions produce acidity. On zinc, for instance, of the three anodic reactions:

$$Zn = Zn^{++} + 2e$$

$$Zn + H_2O = ZnOH^+ + H^+ + 2e$$

$$Zn + 2H_2O = Zn(OH)_2 + 2H^+ + 2e$$

only the second and third produce acidity. If corrosion is proceeding slowly, so that the amounts of the three products formed correspond roughly to the equilibria

$$Zn^{++} + 2H_2O \rightleftharpoons Zn(OH)^+ + H^+ + H_2O$$
$$\rightleftharpoons Zn(OH)_2 + 2H^+$$

it would be expected that, starting from a neutral solution, the acid-forming reactions will predominate at first; later, when the liquid has become slightly acid, the first should predominate, and the fall in the *p*H should become very slow. An important question is whether the zinc hydroxide concentration formed by the last reaction will ever become high enough to cause the deposition of solid hydroxide; probably this will not be the case, since the *p*H will start to fall at once, so that the third reaction will soon cease to be important, although the second one, which also produces acidity, may continue. If so, the liquid produced at the anodic points should be capable of dissolving the zinc oxide film present on the face of the specimen, since zinc oxide is slightly more soluble than the γ-hydroxide and much more soluble than the ϵ-hydroxide (29).

On metals like aluminium or tin, forming salts very prone to hydrolysis, the acid-forming reactions are likely to predominate until the liquid has become distinctly acid. In both cases, the formation of solid products at the anodic points may be expected. On aluminium, for instance, we have the following possibilities

$$Al = Al^{+++} + 3e$$
$$Al + H_2O = AlOH^{++} + H^+ + 3e$$
$$Al + 2H_2O = Al(OH)_2^+ + 2H^+ + 3e$$
$$Al + 3H_2O = Al(OH)_3 + 3H^+ + 3e$$

The last reaction may be expected to predominate at about *p*H 7, while the first will probably only become important below *p*H 6. The liquid produced at the anode is likely to become supersaturated with respect to the hydroxide and oxide (both very sparingly soluble substances) and is unlikely to be capable of dissolving the oxide film present on the metal; even if it should become theoretically capable of dissolving the film, the rate of dissolution will be very slow, as explained below.

The gradual development of acidity around an aluminium anode (with current supplied from an outside battery) has been followed quantitatively by Edeleanu (54). He reached the conclusion that, on an aluminium specimen immersed in a neutral salt solution (without any current from an external source), those weak points which start to corrode will develop acidity, and the *p*H will sink from 7 to some lower value (perhaps about 5), beyond which it will sink no further, since most of the change will then follow the first (nonacid-forming) reaction; any small amount of acidity still produced will be used up in secondary reactions, such as a local attack of the hydrogen-evolution type. This establishment of acid conditions at the original weak spot will ensure that corrosion, once fairly started, will continue there, in preference to other places, since the first reaction will produce no film and will undermine and remove the film present already.

It may be urged that the anodic reaction should heal the weak point by building up a film of hydroxide. However, Edeleanu has calculated, that, provided the acidity is allowed to accumulate, the *p*H will have sunk to a range at which the first reaction begins to predominate before enough hydroxide has been produced to cover the entire surface. Sometimes, of course, accumulation of acid may be prevented, and then the weak points will heal up. For instance, Wright and Godard (55) showed that rapid movement of water prevents pitting of aluminium; probably it sweeps away the acid. Even under stagnant conditions, the alkali from the cathodic regions may interfere with the accumulation of acid in incipient pits, for instance, if OH^- ions migrate toward the anodic points. Thus it is not surprising that buffer substances promote pitting, since they prevent any large concentrations of OH^- and thus render small the proportion of current carried by OH^- ions. Porter and Hadden (25) found that waters containing calcium bicarbonate often produce pitting, especially if traces of copper are present; doubtless the reaction with alkali helps to keep low the OH^- concentration outside the pits; mounds (largely aluminium hydroxide formed by interaction between anolyte and catholyte) are formed over the pits, and probably prevent the buffer from entering and destroying the acidity within. Farmery's observation (56) that the addition of small amounts of sodium bicarbonate to sodium chloride solution greatly promote the stress corrosion cracking of certain aluminium alloys—another type of localized attack—has probably a similar explanation. Conversely, the prevention of the pitting of stainless steel in chloride solution by means of sodium hydroxide is attributed by Matthews and Uhlig (57) to the neutralization of acid products formed by anodic action.

Eighteen years ago, Hoar (58) studied the corrosion of tin; he reached the conclusion that the first change was a reinforcement of the natural film at certain weak points, along with the accumulation of acid; when the local conditions had become sufficiently acid, the production of soluble tin salts became the main anodic reaction, leading to intense corrosion. He thus explained the "black spots," an old-standing trouble in dairies where tinned equipment was used.

On iron and zinc, the anodic production of acid may not be necessary to prevent healing (their salts hydrolyze less readily, and the production of Fe^{++} or Zn^{++} ions may become important at *p*H values close to neutrality). However, some acidity is undoubtedly formed, and may have another important effect, namely, a dissolution of the oxide film. It is known that zinc oxide, even in the massive form which mineralogists call zincite, is readily attacked by acids, in contrast to aluminium oxide (corundum) which suffers only an extremely slow attack. The direct attack on ferric oxide, which forms the natural film on iron, is very slow, but in contact with the metal, a ferric oxide film suffers rapid reductive dissolution (59, 60). Thus if plates of iron or zinc are partly immersed in sodium or potassium chloride solution in a vertical or nearly vertical position (22), the corrosion which starts at weak points on the face produces a heavy product (an acid solution of ferrous or zinc chloride) which sinks downward and spreads sideways covering an arch-shaped area;

the acid reaction destroys the film, and soon the whole of the arch-shaped area is suffering anodic attack (Fig. 13). Later similar arch-shaped areas develop from other points higher up and in the end nearly the whole immersed area is suffering corrosion, which, being well distributed, is not intense. Mantles of membranous hydroxide are formed along the borders of the arch-shaped areas where anolyte and catholyte interact, and on some types of iron two or three mantles (1, 2, and 3 in Fig. 13) may be produced at successive stages. The corrosion pattern varies with structure and surface condition, but a rather rapid passage from local to general attack is typical of iron and zinc in salt solutions.[3]

The fact that the anodic product does really destroy the oxide film on iron has been demonstrated by special experiments on heat-tinted iron. Each of the specimens used consisted of two rectangular segments mounted in a single plane so that one formed a continuation of the other, the two segments being out of electrical contact and separated by a 1 mm gap; the compound specimen was placed in a sloping position in $N/10$ sodium chloride solution, so that the upper segment passed through the water line. Vertical scratch lines had been traced through the oxide film on the upper segment, exposing the metal, but not on the lower specimen. In general, corrosion started at the scratch lines, and the colours disappeared over arch-shaped areas, around the scratch lines, as would be expected; but the colours also disappeared on the lower segment over streaky areas forming the prolongation of the scratch lines, the oxide film being here destroyed by the heavy anodic products descending from the upper segment.

On aluminium, the spreading of corrosion over arch-shaped areas has not been observed; it would hardly be expected, since the liquid formed at the anodic points will probably be supersaturated with respect to Al_2O_3, and in any case the direct dissolution of alumina by acid is a very slow process. However, there may be some attack at areas originally immune for other reasons. Thus Schikorr (63), studying aluminium in sodium chloride solution, observed that both the primary products, aluminium chloride and sodium hydroxide, can attack the metal with evolution of hydrogen. The attack by alkali would prevent corrosion being confined to the pits; calcium bicarbonate will remove alkali and help pitting. If the liquid contains a trace of copper (either as an original constituent or through the presence of copper in an aluminium alloy) the cathodic deposition of metallic copper may favour pitting, first, by preventing attack at the areas where alkali is formed, and, second, by providing a surface on which the cathodic reaction proceeds efficiently, increasing anodic attack in the pits. Acid liquids behave differently. Bryan and Morris (64), studying solutions containing both citric acid (0.5%) and sodium chloride (0.2 or 2%), noted

[3] Reference should here be made to two early papers which express similar but perhaps not identical ideas. Atkins (61) showed that ferrous salt solutions become acid on standing with precipitation of ferric hydroxide; the *p*H value may sink to 2.6. Bengough and Wormwell (62), discussing the spreading of corrosion producing from a susceptible spot downward and sideways over an arch-shaped area, emphasize the fact that alkali cannot exist in regions covered by iron salts.

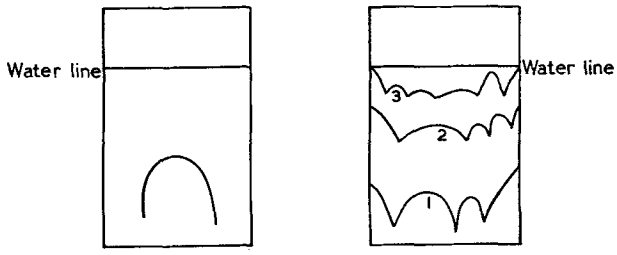

FIG. 13. Arch-shaped extensions of corrosion from a single point (*left*); successive positions of membranes (*right*).

that the attack was most general at the higher chloride concentration and on impure aluminium; the danger of pitting was greatest when the chloride was low and the aluminium "pure" (99.992%).

Other metallic impurities in water may favour pitting. Bird (65) found that small amounts of iron salts reduced the total attack, but tended to localize it as pits; possibly the iron was plated out as a very thin film by simple replacement, which was largely protective, but at discontinuities the combination of large cathode and small anode produced intense attack. Wilkins (66), on theoretical grounds, thinks that all metals more noble than hydrogen will promote pitting, while those less noble than chromium will not do so; the action of intermediate metals is variable.

Pitting in Pure Water

Zinc and iron do not require the anodic production of acid to prevent healing, and since the effect of such acid is to spread out the attack, corrosion is most localized in distilled water. Davies (29) produced very marked pitting of zinc in water of high purity where the formation of acid by traces of foreign anions is extremely unlikely. It might be expected that zinc in distilled water would cover itself with a hydroxide film and suffer no attack. In fact, the attack does tend to stifle itself in time; Bengough, Stuart, and Lee (70) showed that the corrosion-time curve of zinc in distilled water, or even in very dilute potassium chloride, was asymptotic, the corrosion rate ultimately becoming very slow, in contrast to the curves in more concentrated chloride, which were straight. However, the stifling of corrosion only becomes reasonably complete after a lengthy period and meanwhile the attack, becoming increasingly localized, bores down into the metal, producing deep pits. Much of the zinc compound appears, not as a surface film, but as colloidal particles in the liquid; in Davies' work the water acquired the power to produce a good Tyndall cone, and the particles showed cataphoresis in an electric field. The failure to build a protective film rapidly is probably connected with the high nucleation energy of the zinc hydroxides; this is well shown by the fact that the ϵ-hydroxide, which, being the least soluble, should be the most stable, is, under ordinary circumstances, never produced at all (68).

Corrosion of iron seems to show more tendency to spread than that of zinc, although an exact study under comparable conditions of purity seems to be lacking. The author's observations (41) refer to steel in distilled water containing small amounts of carbon dioxide; there seems to have

been some tendency for corrosion to extend, but certainly less than in salt solution. The extension may have been due to reductive dissolution of the film.

The behaviour of aluminium in carefully prepared distilled water has recently been studied at Cambridge by Hart (69). The essential result is film formation; pitting is rare, but intergranular attack, another form of relatively localized corrosion, is met with. Pitting produced on aluminium in hot chromic-phosphoric acid has been examined by Pearson, Huff, and Hay (70) whose electromicrograms suggest that the attack is controlled by crystallographic factors, since the surfaces exposed by it are cube faces; the attack tunnels into the metal along passages which from time to time turn sharply at right angles. Extensive tunnelling of this nature was photographed with the electron microscope in 1951 by Harris and Tull in thin aluminium foil treated anodically in a hot dilute solution of hydrochloric acid and sodium chloride (71).

Final Remarks

The fact that pitting is a form of corrosion having more serious results than general attack has produced the belief that it is an extreme form, and due to some adverse factor not operative in well-distributed corrosion. In fact, however, pitting is an intermediate form standing between general corrosion and immunity; it is essentially a type of "oxidation from a distance" where the collecting area for oxygen is large, the areas where cations leave the metal are small, and where the oxide (hydroxide or basic salt) collects as nodules over the rapidly forming pits. In almost all cases, corrosion starts locally, and if the conditions are such that there is neither healing nor spreading, it remains localized, producing pits which extend inward and/or sideways. The factors deciding the geometry of the advance being essentially crystallographic, are mainly physical, but in some cases the segregation of noble impurities or sulphide inclusions in certain regions may increase the probability of pit-development, while the cathodic deposition of noble metals from the water can increase the severity of pitting and prevent spreading. Thus the situation is often complicated. Nevertheless, pitting is not something mysterious and peculiar, and it is believed that the mechanism of corrosion presented above is capable of explaining the three phenomena—general corrosion, pitting, and immunity.

I commenced my lecture with an appeal for clear thinking; I would end by saying that it should also be broad thinking, not confined to phenomena which happen to be catastrophic, sensational, or financially remunerative. The key to a better understanding of corrosion science may be found in the study of cases of corrosion possessing minor industrial importance. If, for that reason, the experimenter, lacking financial support on a grand scale, has to make do with inexpensive equipment and simple methods, his results may be none the worse on that account. Indeed, simple methods may often give more value than the showy ones, provided always that full use is made of the human brain—a far finer instrument than any produced by stringing together valves or transistors.

Any discussion of this paper will appear in a Discussion Section to be published in the December 1956 JOURNAL.

REFERENCES

1. D. EUROF DAVIES, U. R. EVANS, AND J. N. AGAR, *Proc. Roy. Soc. London*, **A225,** 443 (1954).
2. T. MILLS, Unpublished work.
3. R. K. HART, Unpublished work.
4. U. R. EVANS, *Rev. Pure and Appl. Chem. (Australia)* **5,** No. 1, 1 (1955).
5. N. B. PILLING AND R. E. BEDWORTH, *J. Inst. Metals*, **29,** 529 (1923).
6. U. R. EVANS, *Trans. Am. Electrochem. Soc.*, **46,** 247 (especially p. 269) (1924).
7. K. FISCHBECK (with L. NEUNDEUBEL AND F. SALZER), *Z. Elektrochem.*, **39,** 316 (1933); **40,** 517 (1934).
8. C. WAGNER AND K. GRÜNEWALD, *Z. physik. Chem.*, **B40,** 455 (1938).
9. K. FEITKNECHT (with H. WEIDMANN AND E. HÄBERLI), *Helv. Chim. Acta*, **26,** 1911 (1943); **32,** 2294 (1949); **33,** 922 (1950); R. PETERMANN, Dissertation, Berne (1945); F. M. AEBI, Dissertation, Berne (1946).
10. C. W. BORGMANN AND U. R. EVANS, *Trans. Electrochem. Soc.*, **65,** 249 (1934).
11. U. R. EVANS, *J. Inst. Metals*, **30,** 239 (1923).
12. J. N. AGAR, quoted by U. R. Evans, *J. Iron Steel Inst.*, **141,** 220P (1940).
13. U. R. EVANS AND T. P. HOAR, *Proc. Roy. Soc. London*, **A137,** 343 (1932).
14. G. S. NOORDHOF, quoted by U. R. Evans, *Proc. International Congress Pure and App. Chem. (London)*, **5,** 743 (1947).
15. R. H. BROWN AND R. B. MEARS, *Trans. Electrochem. Soc.*, **74,** 495 (1938); **81,** 455 (1942).
16. U. R. EVANS, *Nature*, **136,** 792 (1935).
17. R. S. THORNHILL AND U. R. EVANS, *J. Chem. Soc.*, **1938,** 614.
18. U. R. EVANS, *J. Soc. Chem. Ind.*, **43,** 315 T (1924).
19. E. CHYŻEWSKI AND U. R. EVANS, *Trans. Electrochem. Soc.*, **76,** 215 (1939).
20. B. L. CROSS AND N. HACKERMAN, *Corrosion*, **10,** 407 (1954).
21. U. R. EVANS, *J. Soc. Chem. Ind.*, **47,** 55T (1928).
22. U. R. EVANS, *J. Chem. Soc.*, **1929,** 111.
23. U. R. EVANS, *ibid.*, **1929,** 92.
24. P. M. AZIZ AND H. P. GODARD, *Corrosion*, **10,** 269 (1954).
25. F. C. PORTER AND S. E. HADDEN, *J. Appl. Chem.*, **3,** 385 (1953).
26. C. E. HOMER, *Iron Steel Inst. London, Carnegie Schol. Mem.*, **21,** 35 (1932); *Rep. Corr. Com. Iron Steel Inst.*, **2,** 225 (1934).
27. T. P. HOAR, D. HAVENHAND, T. N. MORRIS, AND W. B. ADAM, *J. Iron Steel Inst.*, **133,** 239P (1936); **140,** 55P (1939); **144,** 133P (1941).
28. R. B. MEARS, *Iron Steel Inst. Carnegie Schol. Mem.*, **24,** 69 (1935).
29. U. R. EVANS AND D. EUROF DAVIES, *J. Chem. Soc.*, **1951,** 2607.
30. U. R. EVANS, *J. Soc. Chem. Ind.*, **45,** 37T (1926).
31. R. SELIGMAN AND P. WILLIAMS, *J. Inst. Metals*, **23,** 159 (1920).
32. P. J. E. FORSYTH, *Phil. Mag.*, **45,** 344 (1954).
33. S. C. BRITTON AND D. G. MICHAEL, *J. Appl. Chem.*, **5,** 1 (1955).
34. T. K. ROSS, *J. Appl. Chem.*, **5,** 10 (1955).
35. U. R. EVANS, "Symposium on Internal Stresses on Metals and Alloys" (Inst. Met.) p. 291 (1948).
36. U. R. EVANS, *Nature*, **157,** 732 (1946).
37. W. H. J. VERNON, *Trans. Faraday Soc.*, **31,** 1668, esp. p. 1671 (1935).
38. H. HOLNESS AND T. K. ROSS, *J. Appl. Chem.*, **1,** 158 (1951); **2,** 520, 526 (1952).
39. S. C. BRITTON AND U. R. EVANS, *Trans Electrochem. Soc.*, **61,** 441, esp. p. 454 (1932).
40. R. B. MEARS AND U. R. EVANS, *Trans. Faraday Soc.*, **31,** 527, esp. p. 530 (1935).
41. U. R. EVANS, *Ind. Eng. Chem.*, **17,** 363 (1925).

42. G. D. Bengough and O. F. Hudson, *J. Inst. Metals*, **21**, 37, esp. p. 59 (1919).
43. G. D. Bengough and F. Wormwell, *Report Chem. Res. Board 1935–37* (H.M.S.O.) p. 17 (1938).
44. J. E. O. Mayne and M. J. Pryor, *J. Chem. Soc.*, **1949**, 1831.
45. T. P. Hoar and U. R. Evans, *ibid.*, **1932**, 2476.
46. D. M. Brasher and E. R. Stove, *Chem. Ind.*, **1952**, 171.
47. M. T. Simnad, "Properties of Metallic Surfaces," Inst. Met. p. 23 (1953).
48. C. V. King, E. Goldschmidt, and N. Mayer, *This Journal*, **99**, 423 (1952).
49. J. E. O. Mayne and J. W. Menter, *J. Chem. Soc.*, **1954**, 103.
50. M. J. Pryor and M. Cohen, *This Journal*, **98**, 263 (1951); **99**, 542 (1952); M. J. Pryor, *Corrosion*, **9**, 467 (1953).
51. A. M. Peers and U. R. Evans, *J. Chem. Soc.*, **1953**, 1093.
52. E. C. Groesbeck and L. J. Waldron, *Proc. Am. Soc. Testing Materials*, **31**, II, 286 (1931).
53. H. H. Uhlig, D. N. Triadis, and M. Stern, *This Journal*, **102**, 59 (1955).
54. C. Edeleanu and U. R. Evans, *Trans. Faraday Soc.*, **47**, 1121 (1951); C. Edeleanu, *J. Inst. Metals*, **80**, 187 (1951–52); *also* C. Edeleanu, Private communications.
55. T. E. Wright and H. P. Godard, *Corrosion*, **10**, 195 (1954).
56. H. K. Farmery, Dissertation, Cambridge (1955).
57. J. W. Matthews and H. H. Uhlig, *Corrosion*, **7**, 419 (1951).
58. T. P. Hoar, *Trans. Faraday Soc.*, **33**, 1152 (1937).
59. U. R. Evans, *J. Chem. Soc.*, **1930**, 478.
60. M. J. Pryor and U. R. Evans, *J. Chem. Soc.*, **1949**, p. 3330; **1950**, 1259 (4 papers).
61. W. R. G. Atkins, *Trans. Faraday Soc.*, **18**, 310 (1922–23).
62. G. D. Bengough and F. Wormwell, *Proc. Roy. Soc.* **A140**, 399 (esp. p. 405) (1933).
63. G. Schikorr, *Mitt. Mat. Prüfungs-anstalten, Sonderheft*, **22**, 22 (1933).
64. J. M. Bryan and T. N. Morris, *J. Soc. Chem. Ind.*, **59**, 159 (1940).
65. C. E. Bird, Dissertation, Cambridge (1955).
66. N. J. M. Wilkins, Atomic Energy Research Establishment M/R 1296, (Nov. 1953). Abstract in Bulletin of British Non-ferrous Metals Research Association, p. 156, April 1955.
67. G. D. Bengough, J. M. Stuart, and A. R. Lee, *Proc. Roy. Soc.*, **A116**, 425 (1927); **121**, 88 (1928); **127**, 42 (1930).
68. F. M. Aebi, Dissertation, Berne (1946); W. Feitknecht and E. Häberli, *Helv. Chim. Acta*, **33**, 922 (1950).
69. R. K. Hart, Unpublished work.
70. E. C. Pearson, H. J. Huff, and R. H. Hay, *Can. J. Tech.*, **30**, 11 (1952).
71. A. L. Williams, Private communication.

Anodization of Lead in Sulfuric Acid

JEANNE BURBANK

U. S. Naval Research Laboratory, Washington, D. C.

ABSTRACT

The anodic corrosion product formed on lead in sulfuric acid solutions depends on the potential of the metal surface.

In the potential range between lead-lead sulfate and lead sulfate-lead dioxide, the following compounds were identified by electron diffraction: monobasic lead sulfate, lead hydroxide, and lead monoxide. In addition, the diffraction pattern for an unidentified material was observed. Coordinated potential-time curves show arrests corresponding to the appearance of these compounds. The physical nature of these corrosion films is discussed.

INTRODUCTION

A study of positive grid corrosion in the lead acid storage battery led to a detailed investigation of the electrochemical and physical processes associated with anodizing lead in sulfuric acid solutions (1–3). Rate of attack and composition of the corrosion product vary with potential.

Pseudomorphic, epitaxial, and oriented overgrowths have been postulated for many systems where oxide films are formed electrochemically. Lead monoxide and lead dioxide were identified as products of anodic attack on lead. Lead monoxide was shown by Lander (1) to be the tetragonal form which is a layered structure parallel to the (001) planes described by other workers (4, 5). Wyckoff (6) gave a description of lead dioxide. Their structures indicate that these compounds may grow epitaxially on the lead lattice.

In addition to a diffraction study of the anodic products formed on lead in sulfuric acid, this investigation was concerned with discharge curves of a lead electrode coated with lead dioxide. In the discharge of such a surface, the potential remains constant under a given set of conditions, and, when a new process becomes dominant, the surface potential will change and level off again at some new value characteristic of the new set of conditions. These "plateaus" may represent distinct electrode processes, each producing characteristic compounds as corrosion products. This study was undertaken (*a*) to determine where such arrests occur on the discharge of a lead dioxide electrode in sulfuric acid, and (*b*) to identify and characterize by electron diffraction the anodic products formed at various potentials.

EXPERIMENTAL

Although most of the pure lead used for this study was manufactured by the National Lead Company, a few castings made of very pure (99.9998%) lead were used in checking runs to eliminate the possibility that some electrochemical effects were caused by impurities.

The cast specimens were milled flat, polished, and etched. The etch was followed by a rinse in saturated ammonium acetate solution and a thorough rinsing in city water, then in distilled water. For polarization studies, the specimen was inserted in the cell while still wet from the final rinse. For electron diffraction study, the specimen was cleaned in the same way, but it was also rinsed in boiling distilled water, blown dry, then mounted in the camera. In this process, less than 2 min elapsed between the final rinse and attainment of essentially full vacuum. About one out of five preparations resulted in a film-free surface despite the short time exposed to the air.

Single grains cut from polycrystalline castings were used in orientation studies. Grains having the desired orientations were selected with an optical goniometer.

After anodizing, the electrodes to be examined by electron diffraction were usually rinsed in boiled distilled water; however, in some instances no water rinse was used, and the electrodes were blotted dry with tissue or rinsed in acetone and blown dry.

The electrolyte, 1.210 specific gravity sulfuric acid, was prepared from Baker's C.P. acid and distilled water. Etchants were made from Baker's C.P. acetic and nitric acids, Merck's C.P. ammonium acetate, and Superoxol.[1]

Polarization studies were carried out in a methyl methacrylate cylinder that was threaded to receive the specimen mount described earlier (3). Specimens for electron diffraction examination were anodized by submerging a cleaned lead surface in the electrolyte in a glass beaker. By rapid manipulation of the specimens, formation of chemical reaction products could be minimized in the rinsing and drying process. Diffraction specimens were held at the desired potentials for various periods of time in order to develop coatings suitable for electron diffraction study. The time varied from 10 min to 24 hr. A sheet of pure lead was used as a cathode; its area was ten or more times the area of the anode.

Potential of the anodizing specimen was measured with a mercury, mercurous sulfate reference electrode, a high impedance bridge, and recording potentiometer. In this paper, potentials are given in reference to the electrode that is 0.68 volt positive to the normal hydrogen electrode in 1.210 specific gravity sulfuric acid. Several potentials of interest are given by Lander (1).

Polarization studies were made by applying the potential to the cell before introduction of the electrolyte or before insertion of the electrode into the solution. In this

[1] 30% H_2O_2 manufactured by Merck and Co., Inc., Rahway, N. J.

way only a short time is required for the specimen to reach the potential selected for anodization. The discharge of lead dioxide films was studied by time potential records. To obtain reproducible curves, the clean specimen, still wet with the final rinse, was polarized above the lead dioxide, lead sulfate potential as rapidly as possible, and this potential was held for specific periods of time. Potential changes and arrests displayed by lead surfaces were followed with the reference electrode (*a*) during anodization, (*b*) on open circuit stand or "self discharge," (*c*) on closed circuit discharge through a resistance, and (*d*) with discharging current applied.

In one instance the specimen was made by withdrawing an iron wire loop from molten lead to form a thin foil that could be totally anodized. The foil was anodized to translucency at a potential of −0.60 v. It was blotted dry and the diffraction pattern recorded by transmission. Other foils made by rolling or etching were anodized above the lead dioxide, lead sulfate potential.

Electron diffraction patterns were recorded with the diffraction attachment of an RCA EMU electron microscope. Patterns were taken mostly by reflection, but a few were made by transmission, and several patterns of scrapings from anodic coatings were obtained with an extended field attachment. Many attempts were made to strip the oxide films, but none proved wholly satisfactory. The usual mercury treatment (7) was not successful, but several sulfate films were stripped in glacial acetic acid. Film fragments were washed in distilled water and studied by transmission diffraction.

Several x-ray diffraction patterns were recorded with a North American Phillips geiger counter spectrometer from lead sheet specimens that were anodized in 0.0005 and 0.1M sulfuric acid.

Results and Discussion

Reproducibility of the electrochemical measurements was affected by preparation and pretreatment of the metal surface. After drying, a polished and etched lead surface became covered with an air-formed film. This deposit resulted in an open-circuit potential of approximately −0.6 v with respect to the mercury, mercurous sulfate electrode when the specimen was first introduced into the electrolyte. This film was identified as lead hydroxide by electron diffraction (8). When allowed to stand in acid, a lead surface with such a coating gradually assumed the lead, lead sulfate potential of −0.93 v if the air-formed film was thin enough. Such films present on the surface prior to anodizing interfered with prompt development of a uniform lead dioxide coating.

When first introduced into the electrolyte, a lead surface free of oxide or hydroxide films displayed an open-circuit potential of −1.1 v to the reference. After a while this potential rose to the lead, lead sulfate potential. A specimen prepared as described and introduced into the electrolyte while still wet from the final rinse consistently showed the −1.1 v potential that is attributable to the low concentration of lead ion in the acid.

Because the amount and nature of the material present on the metal surface affected electrochemical results in short term experiments such as the present ones, specimens were kept wet with distilled water after preparation and anodized immediately.

The commonly used acetic acid-Superoxol and nitric acid etches (9) formed an oriented film of $3PbO \cdot 2Pb(OH)_2$ on the surface of pure lead (10), as shown by electron diffraction examination of the etched surface. This coating could be removed by rinsing the specimen in saturated ammonium acetate solution or in nonoxidizing acids such as acetic or hydrochloric.

Satisfactory electron diffraction patterns of lead could be obtained from specimens that were dried after final rinsing if these were used within a reasonable time after preparation. In no instance was it possible to obtain the open-circuit potential of lead, Pb^{++}, or lead, lead sulfate from specimens that were dried before use. This indicated that the electrochemical measurements were sensitive to films less than 10 Å thick, which is the approximate limit registered by electron diffraction (11).

In using an optical goniometer for orientation determinations, it was found that the faces developed by the acetic acid-Superoxol etchant depended on concentration of the solution. Barrett and Levensen (12) gave the etch mixture for developing the cube planes, i.e., 2 volumes water, 2 volumes acetic acid, and 3 volumes hydrogen peroxide. The concentration of hydrogen peroxide was not stated. The relation between the etch composition and the planes developed on specimens of pure lead was determined by optical goniometer measurements (Table I).

The discharge of lead dioxide coatings formed on pure lead were recorded in time-potential curves, and the one shown in Fig. 1 is typical. For pure lead, the length of each

TABLE I. *Etch composition and planes developed on pure lead*

Volume of water	Volume of glacial acetic acid	Volume of Superoxol	Planes developed
0	95-99	5-1	(111) Octahedral
2	2	3	(100) (110) Decahedral
20	20	3	(100) Cubic

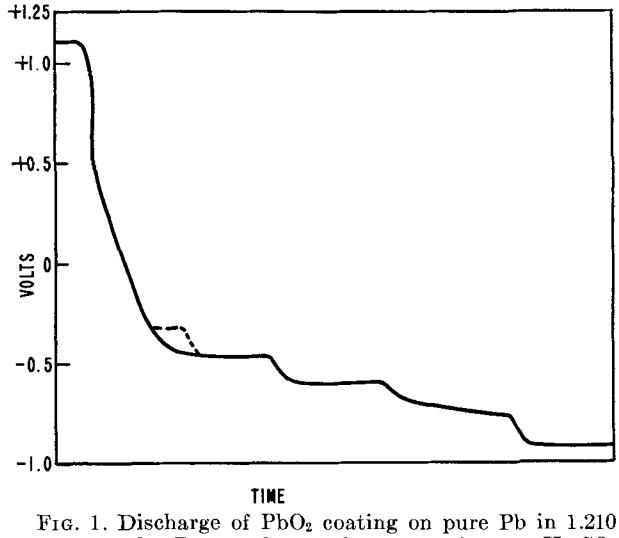

FIG. 1. Discharge of PbO_2 coating on pure Pb in 1.210 sp. gr. H_2SO_4. Potentials are shown vs. the Hg, Hg_2SO_4 electrode.

plateau varied with pretreatment of the specimen. Thus, a slow polarization up to the lead dioxide, lead sulfate potential resulted in a short arrest at this potential upon discharge, and in prolonged arrests at the intermediate plateaus. The most reproducible results were obtained by polarizing to lead dioxide as rapidly as possible. With the exception of the short arrest at −0.32 v, the discharge curves were similar in form whether taken on open circuit self-discharge, with current drain, or with discharging current applied.

As indicated in Fig. 1, arrests occurred at −0.93, −0.73, −0.61, −0.48, −0.32, and 1.1 v vs. the mercury, mercurous sulfate electrode. Compounds appearing on the surface at −0.93, −0.48, and 1.1 v were reported earlier (1) and verified in the present work as lead sulfate, lead monoxide (tetragonal), and lead dioxide, respectively.

The arrest at −0.32 v was not identified as being associated with the appearance of a particular compound. This arrest was consistently of short duration on open-circuit discharge and did not appear on closed-circuit discharge. Tetragonal lead monoxide was found on specimens anodized between a potential of −0.4 and +0.9 v. It is possible that the −0.32 arrest is a polarized lead monoxide potential.

At no time in this work was a lead dioxide film observed to discharge directly to the lead, lead sulfate potential, although thin films apparently by-passed the intermediate plateaus and discharged directly to −0.73 v.

The compound identified by diffraction on the surface of specimens that were anodized at −0.73 v was monobasic lead sulfate (13, 14). Extra lines and bands appeared in many of the electron diffraction patterns of specimens that were anodized near this potential, and this plateau had a slope. It is possible that a series of basic sulfates was actually formed during anodization.

The −0.73 v arrest was stable and frequently held for several days of soaking in the acid. If a specimen showing this potential was cut or scratched, or if a sheet electrode was further lowered into the electrolyte, the potential dropped to −0.93 v but rose again to −0.73 v, presumably as the "break" in this film "healed" by sulfation. The persistence of this plateau suggested that in aqueous solutions the basic sulfate rather than the normal sulfate was the more characteristic coating at the metal-coating interface.

The plateau at −0.64 v was associated with the formation of lead hydroxide identified on the surface of specimens that were anodized at this potential. A thin foil was totally anodized at −0.6 v, and the electron diffraction pattern showed primarily lead hydroxide with a few strong lines from lead sulfate (Table II).

The occurrence of lead monoxide and lead hydroxide in sulfuric acid solution was somewhat anomalous; however, these two compounds were readily identified by their diffraction patterns. Lander (1) suggested that the water molecule is the attacking species in sulfuric acid, and identification of the monoxide and hydroxide supports this view. The sulfate film apparently acts as a barrier to sulfate ions while permitting access of water molecules to the metal surface. Displacement of the observed potentials from the thermodynamically calculated values (Table III) is caused by the fact that the surface is not at thermodynamic equilibrium. The arrest at 1.1 v corresponded to the electrode lead dioxide, lead sulfate in sulfuric acid. An electron diffraction examination of the surface of a specimen anodized at this potential showed a clear strong pattern for lead dioxide. If a single crystal of lead was anodized for 10 min above the lead dioxide, lead sulfate potential, the film was extremely thin, oriented, and showed interference colors. The (100) plane of the lead dioxide lattice was parallel to the (110) plane of the base lead, and the [001] direction was parallel to the [100] direction in lead. Fig. 2 is a drawing of the space lattices of the two crystals. The tetragonal cell in the lead lattice (Fig. 2A), which is bounded by four (110) and two (100) planes, has the dimensions: 4.94 x 3.5 x 3.5 Å. The distances between lead atoms in the oxide structure (6) are 4.97 x 3.4 x 4.97 Å. As shown in Fig. 2B, this is an exceptionally good fit in two crystallographic dimensions; the third, however, is larger by more than 21%. Since 15% is generally accepted as the maximum difference tolerated for lattice continuity, the coating would be expected to fracture away from the base after a limited number of layers form. This was substantiated by the fact that lead dioxide of random orientation was observed on surfaces of single crystals of lead after anodization. There appeared to be a thin layer of oriented lead dioxide immediately adjacent to the metal surface. The patterns showed

TABLE II. *Electron diffraction pattern of lead hydroxide*

Electron diffraction pattern from anodized* lead		Electron diffraction pattern of $Pb(OH)_2$	
d	*I*	*d*	*I*
3.62	s	3.68	ms
3.30	vs	3.33	ms
3.01†	w	—	—
2.64	vs	2.65	s
2.39	vs	—	—
2.33	s	2.27	s
2.13	s	2.16	fm
1.92	vvw	1.91	m
1.77	vvs	1.73	fm
1.69	s	—	—
1.60	w	—	—
1.52	s	1.53	f
1.42	vs	—	—
1.37	w	—	—
1.33	w	1.33	f
1.29	w‡	1.28	f

* Anodized at −0.6 v vs. the mercury, mercurous sulfate electrode in H_2SO_4.

† The extra lines in this pattern may be accounted for from the diffraction pattern of lead sulfate.

‡ There follow many more lines in the patterns for which there are no comparison data.

TABLE III. *Standard and observed electrode potentials*

Electrode	Standard in 28% H_2SO_4 (v)	Observed (v)
PbO_2, $PbSO_4$	1.097	1.1
Hg, Hg_2SO_4	0.00	0.0
Pb, PbO	−0.344	−0.48
Pb, $Pb(OH)_2$	−0.35	−0.64
Pb, $PbSO_4$	−0.971	−0.93
Pb, $PbO \cdot PbSO_4$	−0.81	−0.73
Pb, Pb^{++}, (10^{-10}M)	−1.1	−1.1

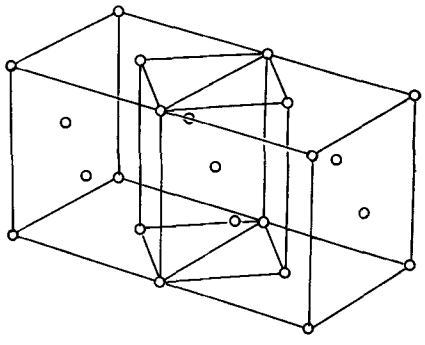

(A)

FIG. 2A. Space lattice of two face-centered cubes of Pb with the body-centered tetragonal cell indicated. (For clarity the relative atomic and ionic sizes, and the crystal structure of PbO_2 have not been indicated in these drawings. The parameters, given in Angstrom units, indicate the distances between lead atom or ion centers.)

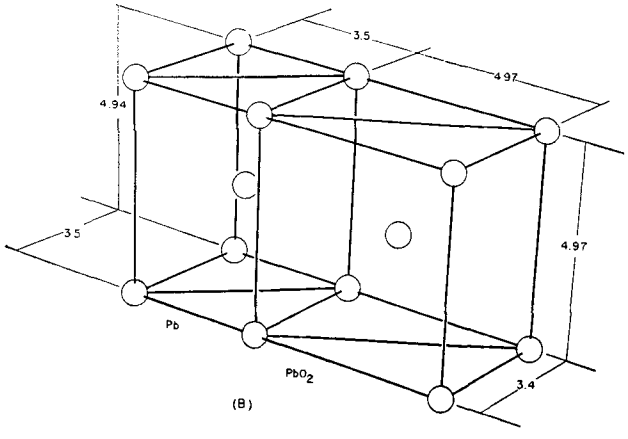

FIG. 2B. Space lattices of Pb and PbO_2 indicating the two-dimensional fit between the body-centered tetragonal cells of metallic Pb and PbO_2.

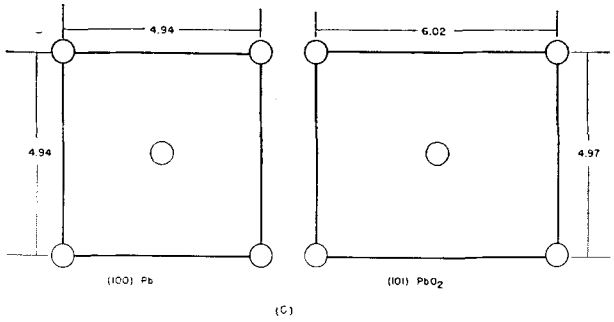

FIG. 2C. The dimensions of (100) Pb and (101) PbO_2 lattice planes.

that many small crystals developed across the surface of a single crystal of lead. The orientation was of high degree, but the spots show a divergence of 7–12°. According to the orientation shown in Fig. 2B, the (101) plane of the oxide would be expected to fall within 10° of the (100) plane of lead. Lead atoms in the (101) planes of lead dioxide have a face-centered configuration (Fig. 2C). The strain produced by such an oxide growing on a metal surface would be expected to result in distortion and possibly cause or contribute to the buckling and growth of pure lead when anodized in sulfuric acid.

TABLE IV. *Diffraction patterns of unidentified material*

Electron diffraction pattern		X-ray diffraction pattern		Calculated diffraction pattern assuming a body centered tetragonal lattice of $a_0 = 3.54$ $c_0 = 5.86$ kx	
d	*I**	*d*	*I*†	*d*	hkl
—	—	5.89	14	5.86	001
—	—	5.00	1	5.00	110
—	—	—	—	3.03	101
2.95	vs	2.93	100	2.93	002
2.53	s	2.50	14	2.50	220
—	—	1.95	13	1.95	003
—	—	—	—	1.90	112
—	—	1.83	1	—	—
1.77	m	—	—	1.77	200
—	—	1.71	8	1.71	103
—	—	1.53	1	1.53	121
1.51	m	1.52	1	1.52	202
1.45	s	1.46	20	1.46	004
—	—	1.35	1	—	—
—	—	1.29	1	—	—
1.24	w	1.24	1	1.25	440
1.16	m	1.17	2	1.17	005
1.13	w	—	—	1.13	204
1.02	vw	—	—	1.05	132
0.972	vw	—	—	0.976	303, 006
0.870	mb	—	—	0.885	400

* Intensities estimated visually.
† Intensities relative to the strongest line.

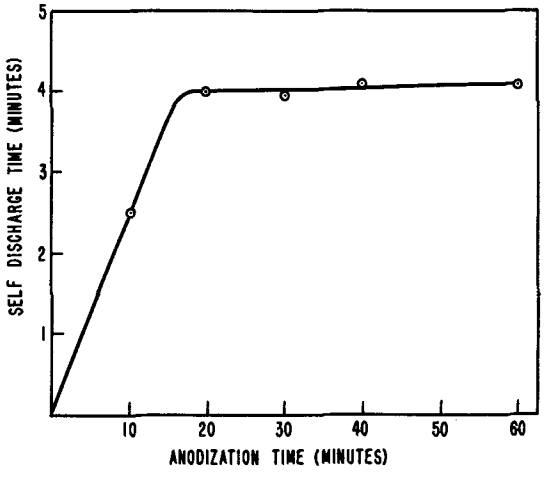

FIG. 3. Relationship of the length of the PbO_2, $PbSO_4$ plateau observed on self-discharge and the time of anodization.

This electron diffraction work showed that polycrystalline coatings of lead dioxide were not always completely converted to sulfate after discharge to the lead, lead sulfate potential. Such remaining lead dioxide was electrically isolated from the surface and contributed nothing to the discharge process.

An unidentified material believed to be a form of lead oxide was also present in some anodic coatings, and the electron diffraction pattern observed for this material is presented in Table IV. Anodized pure lead foil was examined by electron diffraction, and patterns were obtained in which the arcs of the pure lead pattern were doubled. One of the sets of spots was attributed to lead and the other to

the unidentified material. The strong orientation exhibited by this material indicated that it was formed epitaxially on the base lead. This material might have been a cause of the growth and buckling of pure lead, and it also might have contributed to the disparity in the standard and observed electrode potentials in the middle range. Unpublished work with the several lead monoxides indicates that this may be a form of lead monoxide rather than a higher oxide. Complete identification of this material and clarification of its importance to the storage battery corrosion problem rests with future investigation.

A plot of the length of the lead dioxide plateau vs. the length of anodizing time (Fig. 3) shows that anodizing above 20 min contributed little to the self-discharge time. In the first portion of the curve the relationship is essentially linear, i.e., the length of discharge time is directly proportional to the length of anodization. But, beyond 20 min, little additional discharge time is observed. The corrosion rate determined by Lander (1) showed this same configuration with time. The point of slope change in the two cases is different because of differences in experimental details. Direct proportionality at the beginning of the curves, however, suggests that this range corresponds to the lateral growth of coatings across the surface of the specimen. The leveling off may correspond to a much slower rate of film thickening. The slow rate may be even lower than indicated by the corrosion curve, since it represents an over-all corrosion process that included the increase in thickness of the coating plus the "healing" of fissures caused by discontinuities in the metal itself and fractures in the coating.

It is also notable that the leveling off of the curve occurred at about the same time that randomly oriented polycrystalline lead dioxide became the only pattern observed on the surface by electron diffraction.

Conclusions

This study showed that during discharge of a lead dioxide coating on lead, the electrode assumed a series of stable arrests believed to represent several distinct processes. The following compounds were formed upon anodizing lead in sulfuric acid: lead dioxide, lead monoxide (tetragonal), lead hydroxide, $PbO \cdot PbSO_4$, and lead sulfate. These appeared at characteristic potentials that corresponded to the arrests in the discharge process. In addition, an unidentified material believed to be a form of lead monoxide was observed.

The lead dioxide coating was oriented to a limited depth with respect to the underlying lead from which it formed. The orientation may be described:

(100) PbO_2 || (110) Pb
[001] PbO_2 || [001] Pb

The unidentified material was tentatively described as having a body-centered tetragonal space lattice of $a = 3.54$ and $c = 5.86$ kX units. If the suggested lattice is assumed, its orientation may be described:

(100) unknown || (110) Pb
[001] unknown || [001] Pb

Manuscript received July 7, 1955. This paper was prepared for delivery before the Boston Meeting, October 3 to 7, 1954.

Any discussion of this paper will appear in a Discussion Section to be published in the December 1956 Journal.

References

1. J. J. Lander, *This Journal*, **98**, 213 (1951).
2. J. J. Lander, *ibid.*, **98**, 220 (1951).
3. J. Burbank and A. C. Simon, *ibid.*, **100**, 11 (1952).
4. R. G. Dickinson and J. B. Friauf, *J. Am. Chem. Soc.*, **46**, 2457 (1924).
5. W. J. Moore, Jr., and L. Pauling, *ibid.*, **63**, 1392 (1941).
6. R. W. G. Wyckoff, "Crystal Structures," Chap. IV, Interscience Publishers, Inc., New York (1951).
7. S. Wernick, *J. Electrodepositors' Tech. Soc.*, **9**, 163 (1933/34).
8. S. Fordham and J. T. Tyson, *J. Chem. Soc.*, **1937**, 483.
9. J. R. Vilella, "Metals Handbook," p. 1558, American Society for Metals, Cleveland (1939).
10. G. L. Clark and W. P. Tyler, *J. Am. Chem. Soc.*, **61**, 58 (1939).
11. G. P. Thomson and W. Cochrane, "Theory and Practice of Electron Diffraction," p. 153, Macmillan & Co., Ltd., London (1939).
12. C. S. Barrett and L. H. Levenson, *Trans. Am. Inst. Min. and Met. Engrs.*, **137**, 76 (1940).
13. J. J. Lander, *This Journal*, **95**, 174 (1949).
14. Shell Petroleum Company, "X-Ray Diffraction Patterns of Lead Compounds," p. 48, Shell Petroleum Company, Chester, England (1954).

A Self-Discharge Reaction of Cells with Manganese Dioxide and Metal Electrodes

W. C. Vosburgh, D. R. Allenson, and Stanley Hills

Duke University, Durham, North Carolina

Introduction

Metals in water or solutions of electrolytes have been shown to reduce oxygen to hydrogen peroxide (1, 2). It has also been shown that, in ammonium chloride electrolyte, hydrogen peroxide reduces manganese dioxide instead of being entirely decomposed catalytically by it (3). It follows that a cell with manganese dioxide and metal electrodes might undergo self-discharge by this reaction in the presence of oxygen. A decrease in potential of a manganese dioxide electrode in ammonium chloride electrolyte

with a piece of zinc close to it has been observed (4). Further study has shown that this reaction is a possible source of error in experimental work, especially with silver electrodes in chloride electrolytes, if suitable precautions are not taken. It may be one of the self-discharge processes of the Leclanché cell.

Experimental

Manganese dioxide electrodes were made by electrodeposition on graphite rods (3, 4). Total manganese content was 0.2 millimole and the composition $MnO_{1.9}$. The electrodes were kept for a day after preparation in a solution 1M in ammonia and either 2M in ammonium chloride or 1M in ammonium sulfate, depending on the electrolyte in which they were to be used, or in the electrolyte itself if it was not an ammonium salt. They were then stored in water.

For use the electrodes were mounted by means of a rubber stopper in the middle of a glass vessel of about 200 ml capacity. Sheet metal electrodes of silver, zinc, or lead could be inserted into the vessels so as to line the inside wall and encircle the manganese dioxide electrode. Five different electrolytes were used: (*a*) 2M ammonium chloride with enough ammonia to give *p*H 7.3, (*b*) a similar 1M ammonium sulfate solution, (*c*) 2M ammonium chloride and 0.2M zinc chloride, *p*H 5, (*d*) like (*c*), but with enough ammonia to give *p*H 7.2, (*e*) 0.2M potassium chloride in an equimolal (0.025M) phosphate buffer, *p*H 6.7. Measurements of open-circuit potentials of the dioxide electrodes against a saturated calomel electrode were made by a recording potentiometer. The electrolytes were stirred during measurements by a magnetic stirrer.

Fig. 1, redrawn from the recorder curves, shows the behavior of manganese dioxide electrodes with and without metal electrodes present. Fig. 1A represents duplicate control experiments with ammonium chloride electrolyte and with no metal present at any time. The potential was measured for 3-hr periods on each of three successive days. The changes in potential were increases and not more than 3 mv in 3 hr. Fig. 1B shows the effect of clean silver electrodes in ammonium chloride electrolyte. The manganese dioxide electrodes in duplicate cells were affected by the silver electrodes. In a 3-hr preliminary test without the silver electrodes, one varied only a little, and the other was constant. The vertical dashed line at 3 hr indicates introduction of the silver electrode and a 24-hr period thereafter. During this time the manganese dioxide electrodes decreased in potential. The decrease continued fairly rapidly on the second day, with stirring (3–6 hr in Fig. 1) becoming slower with time. The second dashed line indicates a second 24-hr period, but without the silver electrode. A significant increase in potential took place. In the subsequent measuring period (6–9 hr without the silver electrode) one electrode was constant while the other decreased for a time and became constant. At the third dashed line the silver electrode was again inserted with only a few minutes' interruption of the measurement which continued for another 3 hr. After a period of constancy the potential decreased significantly, but less than when the electrodes had stood overnight.

The decrease in potential indicates reduction of the manganese dioxide. It may be postulated that a reducing agent formed by the metal electrode can be carried to the cathode by convection or stirring and react there. Since metals can reduce oxygen to hydrogen peroxide (1, 2), and since atmospheric oxygen was present in the above experiments, hydrogen peroxide might be the reducing agent. Samples of an ammonium chloride solution that have been in contact with a silver electrode and air reduce permanganate and oxidize iodide ion, indicating hydrogen peroxide.

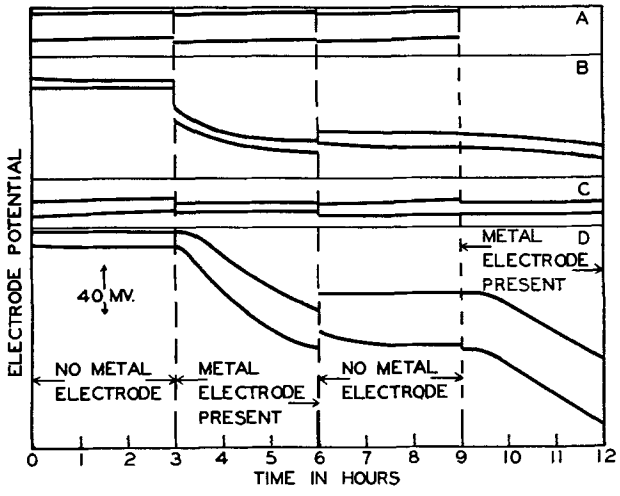

Fig. 1. Effect of a metal electrode on the manganese dioxide electrode potential. A, controls, no metal electrode at any time, ammonium chloride electrolyte; B, silver electrodes in chloride electrolyte; C, silver electrodes in sulfate electrolyte; D, zinc electrodes in potassium chloride electrolyte with phosphate buffer. Dashed line at 3 hr indicates introduction of metal electrode and 12-hr rest period; at 6 hr, removal of metal electrode and 12-hr rest period; at 9 hr, introduction of metal electrode with no rest period.

When an ammonium chloride electrolyte was freed from oxygen by a current of nitrogen before silver and manganese dioxide electrodes were introduced, and a current of nitrogen passed through the cell, the potential of the manganese dioxide electrode was much more nearly constant than when air was present.

Fig. 1C represents a similar experiment with a silver electrode and an ammonium sulfate electrolyte of *p*H 7. The behavior is not enough different from the controls (Fig. 1A) to indicate any effect of the presence of the silver. Appreciable *p*H changes accounted for part of the small potential changes. The test for hydrogen peroxide in the electrolyte was negative.

Zinc in a potassium chloride electrolyte with a phosphate buffer at *p*H 7 was found by Delahay (2) to reduce oxygen to hydrogen peroxide. A cell constructed with this electrolyte showed the most pronounced decrease observed, as shown in Fig. 1D. The procedure was the same as for the cells of Fig. 1B, and the curves are similar, except that no decrease took place during the first night. After standing overnight the zinc electrodes were covered with a loosely adherent gray film. Also, the test for hydrogen peroxide was negative when the cell had stood overnight with the zinc electrode in place. However, it became positive the next day when the solution was stirred.

When a clean zinc electrode was tried in the same way

in an ammonium chloride electrolyte containing zinc chloride and ammonia, *p*H 7, the manganese dioxide electrode showed no change during the 3-day period. A similar electrolyte of *p*H 5 gave indeterminate results, changes little larger than the experimental error. In agreement, the test for hydrogen peroxide in these solutions was negative.

The result for zinc at *p*H 5 does not disagree with Jennings and Vosburgh (5). Their observation of a decrease in potential of a manganese dioxide electrode in the presence of zinc was made over a period of several weeks, and the change per day was small. However, the manganese dioxide was probably reduced by hydrogen peroxide rather than undergoing loss of oxygen as assumed by them.

A clean lead electrode in ammonium sulfate electrolyte of *p*H 7 also caused no observable reduction of the manganese dioxide electrode. Clean lead on which lead sulfate had been deposited electrolytically formed too little hydrogen peroxide for a positive test on standing overnight in ammonium sulfate electrolyte. However, electrodes made of uncleaned sheet lead that had acquired a surface coating of oxide during storage acted like silver in chloride solutions and zinc in phosphate solutions. Such an electrode caused reduction of a manganese dioxide electrode in a cell with an ammonium sulfate electrolyte. Also, ammonium sulfate solutions that had stood overnight with the uncleaned lead electrodes gave positive tests for hydrogen peroxide. In this case the test with titanium(IV) sulfate was positive; it is not sufficiently sensitive in chloride solutions.

Observable amounts of peroxide were formed by the three electrodes that either had a surface coating or formed one as the result of oxygen attack. These were silver in chloride solutions, zinc in phosphate solutions, and uncleaned lead. Clean metals that stayed clean evidently caused catalytic decomposition of the peroxide as fast as formed. A suitable surface film must retard the decomposition more than the formation.

To see whether the self-discharge reaction would go on indefinitely, a cell with silver and manganese dioxide electrodes was allowed to stand for a month during which time the manganese dioxide electrode potential decreased continuously from an initial value of 0.453 to 0.237 v.

Rough measurement of the concentration of peroxide in solutions that had stood two or three days with metal electrodes gave $10^{-4}N$ for both chloride electrolyte with silver and sulfate electrolyte with uncleaned lead.

Errors can be avoided in experiments with manganese dioxide (and perhaps other) electrodes and silver, lead, or zinc electrodes by the use of clean metal and conditions not leading to film formation. Exclusion of oxygen is also effective. If silver electrodes must be used in chloride solutions, a layer of silver chloride thick enough to retard peroxide formation will prevent trouble. Two silver electrodes coated with silver chloride electrolytically with a current of 0.25 ma/cm² for 50 hr and kept in boiling water for 3 hr to insure absence of peroxide caused no significant change in a manganese dioxide electrode when tested as above. Such electrodes seem to be able to acquire some peroxide on standing in water and also from the electrolyte in which they are coated with chloride. Freshly coated silver electrodes not given the boiling water treatment, and electrodes that had stood for some time caused decreases of the order of 10 mv on standing overnight in chloride electrolytes with manganese dioxide electrodes.

Acknowledgments

Part of this work was carried out under Contract Nonr-1016(00) with the Office of Naval Research and part with the help of a fellowship supported by E. I. du Pont de Nemours and Company.

Manuscript received July 11, 1955.

Any discussion of this paper will appear in a Discussion Section to be published in the December 1956 Journal.

References

1. J. W. Mellor, "A Comprehensive Treatise on Inorganic and Theoretical Chemistry," Vol. 1, p. 925, Longmans Green & Co., London (1922).
2. P. Delahay, *This Journal*, **97**, 205 (1950).
3. A. M. Chreitzberg, Jr., D. R. Allenson, and W. C. Vosburgh, *ibid.*, **102**, 557 (1955).
4. D. T. Ferrell, Jr., and W. C. Vosburgh, *ibid.*, **98**, 334 (1951).
5. C. W. Jennings and W. C. Vosburgh, *ibid.*, **99**, 309 (1952).

A Technique for Evaluating Various Cathode Materials

C. K. Morehouse and R. Glicksman

RCA Laboratories, Radio Corporation of America, Princeton, New Jersey

ABSTRACT

An apparatus and technique are described which enables a quick preliminary evaluation to be made of various manganese dioxides and other cathode materials in various electrolytes. Data are presented which show that the capacity of the manganese dioxide electrode exceeds that calculated for its reduction to $Mn_2O_3 \cdot H_2O$ when discharged at low current drains or with a flow of electrolyte over the electrode. It is also shown that the structure of the manganese dioxide material is an important property which determines the performance that is obtained when the electrode is discharged, not only in a NH_4Cl-$ZnCl_2$ type of electrolyte, but also in a basic electrolyte.

Introduction

It is well known that the manganese dioxide cathode is the limiting electrode of the Leclanché dry cell. Manganese dioxide is not a simple compound of constant properties and its value for battery use does not depend merely on its purity (1, 2). The x-ray spectrometer, the electron microscope, differential thermal analysis, and magnetic susceptibility have all thrown new light on its characteristics. In spite of the recent advances, no satisfactory single physical or chemical method of evaluating cathode materials has been developed, and actual trials in operating cells have been necessary to establish their battery quality.

Cahoon (3) suggests the use of the following two electrochemical tests as a means of evaluating a manganese dioxide: (*a*) determination of the *p*H-potential relation in zinc and ammonium chloride electrolyte; and (*b*) determination of the "utilization factor," i.e., the extent of cathodic reduction in a continuous stream of fresh electrolyte.

In this paper a technique for evaluating various cathode materials is presented. The apparatus which was designed for this work is similar to that described by Cahoon (3) for his "utilization test;" however, the procedure and methods of measurement have been considerably modified.

Equipment and Procedure

The apparatus used is shown in Fig. 1, and the procedure used in making cathode polarization studies is as follows.

A piece of filter paper supported by cotton gauze is fastened to a glass cylinder, 1⅝ in. I.D. and 1¾ in. in length, by means of a rubber band. A layer of Acheson No. 615 graphite wet with electrolyte is laid on the filter paper inside the glass cylinder. On top of this is placed 0.5 g of cathode material previously ground with 10% by weight of Shawinigan acetylene black. The cathode material is then covered with a layer of graphite and a perforated graphite disk. A graphite rod, on top of which is placed a 2 kg weight, makes contact with the perforated graphite disk and acts as a terminal electrode for the cathode. A zinc sheet placed outside the reservoir at a controlled distance from the cathode material acts as the anode.

After the cell is assembled, electrolyte is flushed through the cathode chamber to wet completely the cathode material. The cell is then discharged by withdrawing a constant current from the cell, either with electrolyte flowing over the cathode material at a controlled rate or with no flow of electrolyte. In this work measurements were made with no flow of electrolyte, i.e., under static conditions. The inner chamber, containing the cathode material, holds 15–20 ml of electrolyte and the outer chamber approximately 60 ml of electrolyte.

The potential of the cathode or anode is measured by means of a saturated calomel reference electrode which is contained in the outer chamber close to the cathode in a fixed position. Measurements are made at definite time intervals with a L&N type K potentiometer.

The procedure differed from that of Cahoon's in the following ways: (*a*) the cathode material was discharged under static conditions with a fixed quantity of electrolyte; (*b*) measurements were made while the cathode material was discharging.

The results presented are lower than the true polarization values since they include a small constant *IR* drop which is characteristic of the electrolyte, apparatus, and procedure. If necessary, this *IR* drop can be eliminated by using various known procedures (4), or it can be measured by an oscillographic technique (5).

The purpose of this study was to evaluate the performance of various cathode materials, and, since the manner in which the voltage of the electrode changed with time is the most important factor, measurements were made by the simpler technique. In these experiments, a current drain of 0.050 amp was used, which corresponds to a discharge rate of 0.100 amp/g for the 0.5-g sample of cathode material.

Evaluation of Technique

A number of manganese dioxides which are now being used in batteries were tested. It was found that differences in the polarization behavior of the various manganese dioxides were comparable with test results reported for cells containing these oxides. In order to be positive about the method, several samples of manganese dioxide were obtained as unknowns from the Signal Corps Engineering Laboratories. Information about source, structure, and performance in actual cells was withheld until after dis-

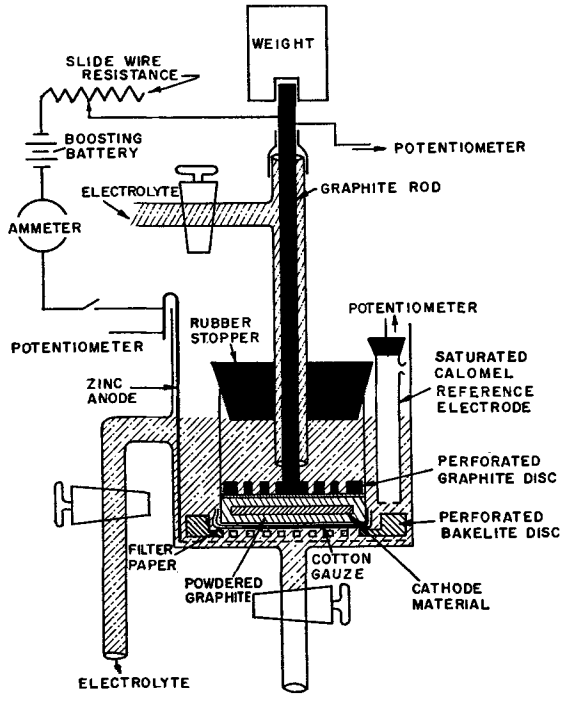

FIG. 1. Apparatus for evaluating cathode materials.

charge data on the above equipment had been gathered and the samples rated according to these data. The various types of manganese dioxides are characterized by the chemical and physical data shown in Table I. Fig. 2 shows the capacity in ampere-minutes per cubic inch for these manganese dioxides. On the basis of the data in Fig. 2 taking a cut-off voltage of +0.5 v for the manganese dioxide, samples were rated for expected performance in dry cells on high current drain applications. Taking a +0.10 v cut-off, samples were also rated for expected performances in batteries on low drain applications. A complete tabulation of the discharge data and rating for high drain applications along with the cell performance data and rating is shown in Table II. Comparative data and rating for low drain applications are given in Table III.

The discharge data presented in these tables are on the basis of ampere-minutes per gram and ampere-minutes per cubic inch of the manganese dioxide materials. Cell discharge data presented were gathered by the Signal Corps Engineering Laboratories.

It should be pointed out that the rating of the manganese dioxide materials based on discharge data expressed in ampere-minutes per cubic inch more closely approaches the rating based on actual cell discharge data than that based on discharge data expressed in ampere minutes per gram since the density factor of the sample is taken into account. This is important because only a certain volume of manganese dioxide can be introduced into a specific cell size.

TABLE I. *Various properties of manganese dioxide materials*

Classification	Electro ore #1 (F)		Electro ore #2 (B)		Electro ore #3 (D)		Chem ore #1 (E)		Chem ore #4 (A)		Chem ore #3 (G)		Chem ore #2 (C)		African ore (J)		Mexican ore (I)	
Method of preparation	Anodic deposition on graphite electrodes from aqueous solution of H_2SO_4 and $MnSO_4$						Reduced African MnO_2, treated with H_2SO_4 solution. The MnO_2 which settles out is filtered and washed free of acid.						Thermal decomp. of $Mn(NO_3)_2$		Naturally occurring			
Available oxygen as % MnO_2	89.2		85.0		65.6		79.9		68.6		85.0		84.6		84–85		70.3	
% Total Mn	57.7		59.0		61.5		55.3		45.8		59.0		58.1		58.0		49.0	
	d	I/I_1	*d*	I/I_1	*d*	I/I_1	*d*	I/I_1	*d*	I/I_1	*d*	I/I_1	*d*	I/I_1	*d*	I/I_1	*d*	I/I_1
Electron diffraction data	4.10	100	2.41	100	4.68		3.53		4.0	37	2.41	100	4.18		4.37	12	3.11	
	3.70	59	2.12	43	3.96		3.11	69	3.68	100	7.14	75	2.39	100	3.11		2.43	100
	2.955	6	1.83		3.16		2.43	100	2.45	5	1.65	50	2.115	83	2.57	100	2.16	72
	2.467	2	1.64	28	2.74	24	2.16	70	1.39	25	1.55		1.63	52	2.43	61	1.83	39
	2.410	1.7	1.495	18	2.43	100	1.83	20			1.44	50	1.415	55	2.16	18	1.70	39
	2.207	10	1.222	9	2.15	65	1.65	51			1.31	25	1.345	50	1.84	35	1.54	
	2.117	1.2	1.165	11	2.04	13	1.54								1.62		1.44	60
	2.052	6	1.065	11	1.84	17	1.42	91							1.54	47	1.37	70
	1.850	2.5	0.85		1.64	53	1.37	32							1.44	23		
	1.743	2.5	0.84		1.54		1.29	12							1.37			
	1.606	1.7			1.44	66	1.05								1.29			
	1.501				1.41	52									1.24			
	1.477				1.31	17												
	1.417																	
	1.389				1.17													
	1.268				1.06													
	1.228																	
	1.116				0.99													
	1.099																	
	1.005																	

These results show that the method is of value in making preliminary evaluations of cathode materials. Large differences should be easily recognized. The method does have limitations in that it tells nothing about the concen-

TABLE II. *Discharge data and ratings of various manganese dioxide materials for use in batteries designed for high drain applications compared with Signal Corps battery data and rating*

Source	Classification	Apparent density g/in.³	Discharge data: 0.5 g MnO_2 material discharged at 0.100 amp constant current per gram to +0.50 v in 20% NH_4Cl-33% $ZnCl_2$-47% H_2O electrolyte				Signal Corps Battery data	
			Weight basis		Volume basis			
			Wt basis amp min/g	Rating	Vol. basis amp min/in.³	Rating	Capacity hr*	Rating
Electro ore #1	F	19.4	5.8–5.4	2	112–105	2	7.9	1
Electro ore #2	B	21.0	5.3	3	111	1	6.5–7.5	2
Chem ore #1	E	16.1	4.9–4.3	4	77–69	4	6.8	3
Chem ore #2	C	11.5	8.8–6.6	1	101–76	3	6.4	4
Chem ore #3	G	18.5	3.0–2.6	5	56–48	5	4.5–5.0	5
Electro ore #3	D	21.8	2.3–2.0	6	50–44	6	4.5	6
African ore (natural)	J	22.5	1.9–1.1	7	43–25	7	4	7
Mexican ore (natural)	I	23.3	0.6	8	14–2.3	8	2.1	8
Chem ore #4	A	13.1	0.3–0.2	9	3.9–2.6	9	Very low	9

* "A" size Leclanché cells discharged continuously through a 16⅔ ohm resistance to 1.00 v/cell.

TABLE III. *Discharge data and ratings of various manganese dioxide materials for use in batteries designed for low drain applications compared with Signal Corps battery data and rating*

Source	Classification	Apparent density g/in.³	Discharge data: 0.5 g of MnO_2 material discharged at 0.100 amp/g to +0.10 v in 20% NH_4Cl-33% $ZnCl_2$-47% H_2O electrolyte				Signal Corps battery data	
			Weight basis		Volume basis			
			Wt. basis amp min/g	Rating	Vol. basis amp min/in.³	Rating	Capacity hr*	Rating
Electro ore #1	F	19.4	12.4–11.3	2	241–219	2	140.9	1
Electro ore #2	B	22.5	11.4–11.1	3	257–250	1	130–135	2
Chem ore #1	E	16.1	11.5–10.7	4	185–172	4	101.3	3
Chem ore #2	C	11.5	18.6–17.5	1	214–201	3	96.8	4
Chem ore #3	G	18.5	7.9–6.8	5	146–126	5	85.9	5
African ore (natural)	J	21.0	6.8–5.8	6	143–122	6	80	6
Electro ore #3	D	21.8	5.2–4.8	8	113–105	7	61.8	7
Chem ore #4	A	13.1	4.7–4.6	9	62–60	9	50	8
Mexican ore (natural)	I	23.3	5.3–2.9	7	123–68	8	36.0	9

* "A" size Leclanché cells discharged through a 116⅔ ohm resistance to 1.13 v/cell.

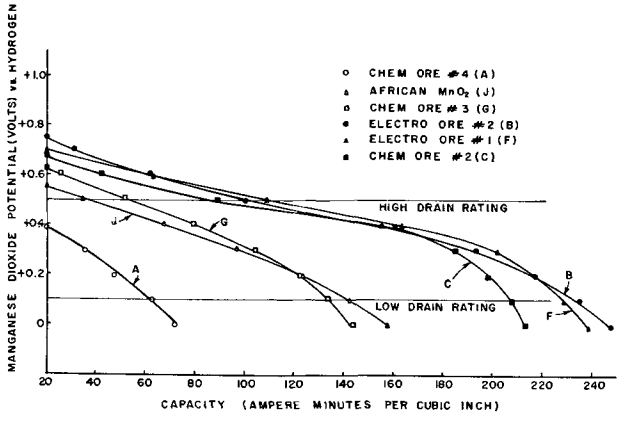

FIG. 2. Capacity in ampere-minutes per cubic inch of various manganese dioxides discharged at 0.100 amp/g in 20% NH_4Cl-33% $ZnCl_2$-47% H_2O electrolyte.

tration of impurities, stability, or solubility of a particular material, such properties being important in designing a cell with a good shelf life. Data of this type will have to be obtained from other measurements or from experimental cells.

CAPACITY STUDIES

The apparatus can also be used to study the effect of various factors on the efficiency of a manganese dioxide electrode. For example, attempts to obtain maximum efficiency from a manganese dioxide electrode were made by reducing the discharge rate, allowing greater chance for ions to diffuse away or to the electrode. Results of these experiments are shown in Fig. 3. In accordance with cell test data, as the current drain is reduced, the ampere-minutes capacity per gram of manganese dioxide to any cut-off voltage is increased. Data also show that if the current drain is low enough, it appears possible to reduce the manganese below its oxidation state in $Mn_2O_3 \cdot H_2O$.

It was reasoned that, by flowing the electrolyte over the manganese dioxide, diffusion effects would be minimized, and in addition the hydrogen ion concentration at the electrode would be kept more constant. Data obtained on an electrode (Electro MnO_2 #2) discharged at a current drain rate of 0.100 amp/g with electrolyte flowing through the cathode chamber at a rate of 6–9 ml/min are shown in Fig. 4. As expected, the capacity of the manganese dioxide is much greater than if it were discharged under static conditions with a constant volume of electrolyte. It should

be noted that the capacity exceeds the theoretical capacity calculated on the basis of reduction to $Mn_2O_3 \cdot H_2O$, but not below Mn_3O_4. An examination of the effluent showed the presence of Mn^{II}, which verifies the findings of other workers (3).

Since the discharge products were not analyzed, the exact reaction mechanism cannot be determined. However, a review of the literature, along with other experimental data, indicates that the following possible reactions could occur which might explain the increased capacity beyond the $Mn_2O_3 \cdot H_2O$ theoretical limit:

$$MnO_2 + 4H^+ + 2e^- \rightarrow Mn^{++} + 2H_2O$$

$$Mn_2O_3 + 2H^+ \rightarrow Mn^{++} + MnO_2 + H_2O$$

$$3Mn_2O_3 + 2H^+ + 2e^- \rightarrow 2Mn_3O_4 + H_2O$$

$$3MnO_2 + 4H^+ + 4e^- \rightarrow Mn_3O_4 + 2H_2O$$

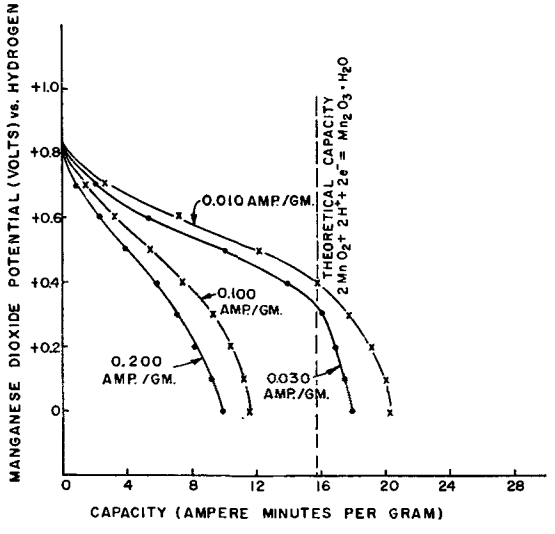

FIG. 3. Capacity in ampere-minutes per gram of Electro Ore #2 (B) discharged at various current drains in 20% NH_4Cl-33% $ZnCl_2$-47% H_2O electrolyte.

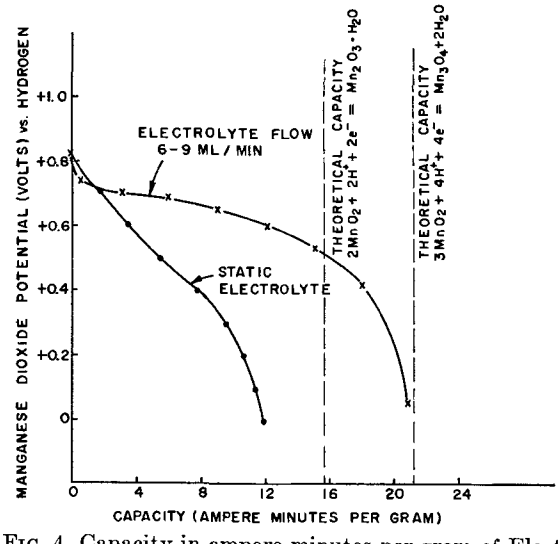

FIG. 4. Capacity in ampere-minutes per gram of Electro Ore #2 (B) discharged at 0.100 amp/g in 20% NH_4Cl-33% $ZnCl_2$-47% H_2O electrolyte, under static conditions and with a continuous flow of electrolyte.

The possibility of the last two reactions occurring is supported by the work of Copeland and Griffith (6).

The technique described in this paper can also be used to study the performance of various cathode materials in different electrolytes. Fig. 5 shows the relative performance of two types of manganese dioxides discharged in acid and basic electrolytes. The manganese dioxide prepared electrolytically gives a greater capacity in both basic and acid electrolytes than the naturally occurring African manganese dioxide. The importance of the structure of manganese dioxide on its performance in Leclanché cells containing an NH_4Cl—$ZnCl_2$ electrolyte has been shown

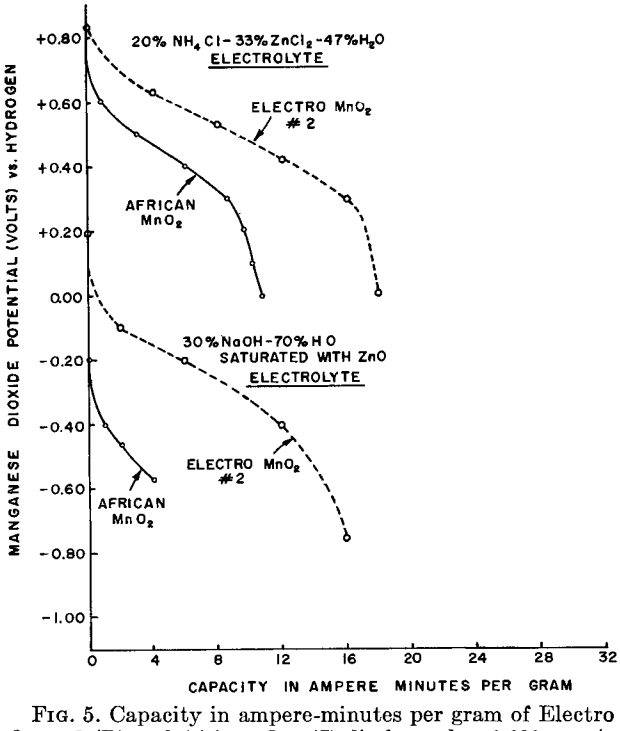

FIG. 5. Capacity in ampere-minutes per gram of Electro Ore #2 (B) and African Ore (J) discharged at 0.030 amp/g in acid and base electrolytes.

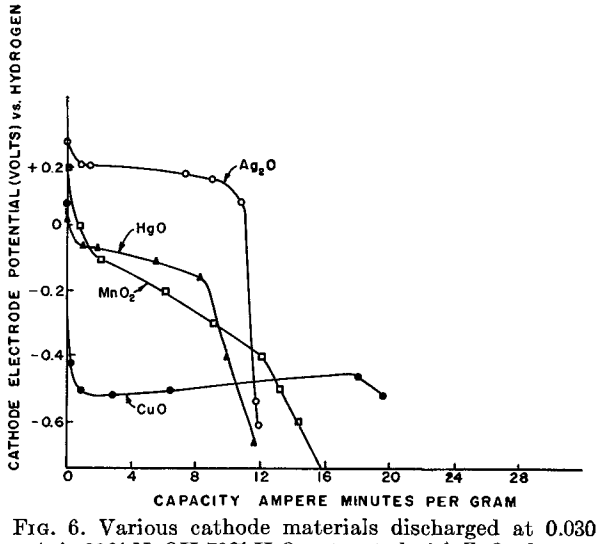

FIG. 6. Various cathode materials discharged at 0.030 amp/g in 30% NaOH-70% H_2O, saturated with ZnO, electrolyte.

previously. It is evident from these data that structure is also an important property with respect to the performance of manganese dioxide in strongly basic electrolytes.

Studies of Other Cathode Materials

Discharge data obtained on other cathode materials which have been used in primary batteries are shown in Fig. 6. It should be noted that the discharge curves and voltage levels of these materials simulate the type and level of discharge curves found in actual cells made with these materials. The cathode potentials are all lower than found in actual cells due to an *IR* drop which is included in the potential measurements. Since the measurements were all made using an electrolyte of the same composition and with the same electrode spacings, this *IR* drop becomes a constant for all measurements enabling comparisons to be made between different materials.

Summary

A convenient method has been devised which enables a quick evaluation to be made of different manganese dioxides and other cathode materials in various electrolytes. Like all methods proposed to date, this method has limitations in that it tells nothing about the concentration of harmful impurities, solubility, or stability of a particular cathode material in the electrolyte. Such data, which are important for the design of a practical cell with a long shelf life, have to be determined by other chemical methods or by experimental cells.

The apparatus and technique can also be of value in obtaining a better understanding of reaction rates and conditions under which maximum cathode efficiency can be obtained.

Acknowledgment

The authors wish to thank the Power Sources Branch of the Signal Corps Engineering Laboratories for making available the dry cell capacity and chemical analysis data of the various manganese dioxides, as well as Dr. J. A. Amick of the RCA Research Laboratories for gathering the electron diffraction data.

Manuscript received June 15, 1955. This paper was prepared for delivery before the Pittsburgh Meeting, October 9 to 13, 1955.

Any discussion of this paper will appear in a Discussion Section to be published in the December 1956 Journal.

REFERENCES

1. G. Leclanché, *Les Mondes*, **16**, 532 (1868).
2. G. W. Vinal, "Primary Batteries," John Wiley & Sons, Inc., New York (1951).
3. N. C. Cahoon, *This Journal*, **99**, 343 (1952).
4. G. Kortum and J. O'M. Bockris, "Textbook of Electrochemistry," Vol. II, Elsevier Publishing Co., New York (1951).
5. R. Glicksman and C. K. Morehouse, *This Journal*, **102**, 273 (1955).
6. L. C. Copeland and F. S. Griffith, *Trans. Electrochem. Soc.*, **89**, 495 (1946).

The Influence of Nitrogen-Containing Organic Inhibitors on the Electrode Potential of Steel in Sulfuric Acid

R. N. Ride

Department of Supply, Commonwealth of Australia, Victoria, Australia

ABSTRACT

Corrosion inhibition of mild steel in 1*N* sulfuric acid has been studied by observing electrode potentials and corrosion rates for thirteen compounds. The mechanism of inhibition is discussed with special reference to the nature of the adsorption interphase and a revised theory of inhibition is proposed.

From hydrogen overvoltage and other considerations, it is postulated that the inhibitor is mainly physically adsorbed as a second phase on the chemisorbed hydrogen film already present on the metal. Inhibition is due primarily to increased hindrance to the anodic dissolution process, accompanied at higher inhibitor concentrations by a rise in hydrogen overvoltage.

The measurable quantities, electrode potential, inhibitive efficiency, and inhibitor concentration are related in an adsorption equation which can be applied to compounds adsorbed in a single and fixed mode of molecular orientation.

Introduction

Extensive investigations have been made of the corrosion inhibition of steel in acid solutions, due to the presence of small quantities of organic compounds containing nitrogen, oxygen, or sulfur. There are several comprehensive reviews of the literature on earlier work, notably those by Hackerman and his co-workers (1, 2).

Most investigators agree that inhibition occurs as a result of adsorption of the organic compounds on the metal surface. The presence of an adsorbed inhibitor

layer, generally assumed to be monomolecular, has been shown by Rhodes and Kuhn (3) by analytical methods and by Hackerman and Glenn (4) using electron diffraction techniques. Existing theories on inhibition differ principally on the question of whether inhibition is due to adsorption of the inhibitor only at cathodic areas on the metal or to general nonspecific adsorption.

The several investigations of Mann and his co-workers (5–7) and others (8–10) led to the theory of specific adsorption of positively charged inhibitor ions at cathodic sites on the surface. Inhibition was attributed to hindrance of the discharge of hydrogen ions. The compounds examined by Mann, mainly aliphatic and aromatic amines, were supposed to be attached with the chain or ring essentially vertical to the metal surface through forces acting on the positively charged nitrogen atom in the molecule. Inhibition efficiency was claimed to be related to the vertically projected area of the molecules on cathodic sites. Nonsymmetrical substitution of alkyl groups on the benzene ring was found to increase the inhibiting efficiency of the compounds. This was interpreted in terms of the tilting of these molecules, due to attractive forces between the positive alkyl groups and the negative benzene ring, with a resulting increase in projected area of the molecule.

Later investigators (11, 12) have criticized this "cathode screening" theory on the following grounds: (*a*) not all organic compounds showing inhibitive properties are positively charged; (*b*) the difference in electrode potential between anodic and cathodic sites on a freely corroding steel surface in sulfuric acid is likely to be very small; there is, therefore, little reason for assuming preferential and specific attraction to cathodic sites; and (*c*) the degree of electrolytic migration of large charged ions to cathodic points must be negligible in a solution containing a high concentration of hydrogen ions.

The "cathodic screening" theory has been based mainly on results derived from external cathodic polarization experiments on specimens in inhibited acid solutions; proponents of this theory do not appear to have investigated the anodic process by anodically polarizing the specimens. Several investigators (2, 3, 7) have apparently misinterpreted the work of Chappell, Roetheli, and McCarthy (9) in this respect, as showing that no appreciable change in potential occurred on anodic polarization in the presence of the inhibitor. It is quite clear from their report that Chappell and his co-workers did not anodically polarize their specimens, their "anode potential" being simply the normal corrosion potential of a specimen with no externally applied current. This anode potential was found to be slightly more cathodic in the presence of their inhibitor, a certain indication that the inhibitor affects the anodic process.

The experimental basis for the cathodic screening theory is also open to question on several grounds. Even if external cathodic polarization at current densities up to some fifty times greater than the normal local action current density could be justified as a valid basis for interpretation, the apparent increase in hydrogen overvoltage does not exclude the possibility of considerable anodic polarization. As pointed out by Hoar (11), Mann's (7) correlation of relative efficiencies of inhibitors from cathodic polarization and weight loss data merely indicated that the fraction of the surface covered with inhibitor molecules is the same as when no current is applied.

Recent work supports the view that inhibition is the result of general adsorption of inhibitor molecules on the metal surface, whereby both the anodic and cathodic reactions are affected. Hoar (11) and Hackerman and Sudbury (1) showed that, for a large number of compounds in sulfuric acid, steady-state potentials invariably moved in the cathodic direction relative to specimens in uninhibited acid, which indicates a greater degree of anodic than cathodic self-polarization (11). Hackerman and Sudbury (1), externally polarizing specimens both cathodically and anodically, and Cavallaro (13) in galvanic tests with copper-iron and iron-zinc couples, concluded that both anodic and cathodic sites are involved in the inhibition mechanism.

The present work on nitrogen-containing organic inhibitors was undertaken to investigate: (*a*) the individual contribution of each of the two electrode processes to the inhibited state; (*b*) the relationship between the concentration and efficiency of the dissolved inhibitor; (*c*) the significance of the difference in the steady-state potentials between specimens in inhibited and noninhibited solutions.

Experimental

Method of investigation.—The behavior of steel in inhibited 1*N* H_2SO_4 solutions was studied by observing average corrosion rates and changes in steady-state electrode potentials. The measurement of electrode potentials under steady-state conditions ($(\Delta e/\Delta t) < 1$ mv/hr), as discussed by Gatty and Spooner (14), is of considerable importance in systems of this type in which $\Delta e/\Delta t$ is initially large. It was found that the electrode potential of the specimen reached a steady-state condition after about 2.5 hr; all experiments in inhibited solutions were conducted on specimens which had been allowed to corrode freely for this period in a noninhibited 1*N* H_2SO_4 solution.

This pretreatment followed Hoar's recommendation (11) in removing the original abraded surface, but was found to give more reproducible electrode potentials (±1 mv) after the 2.5 hr period than his HNO_3 treatment.

Materials and equipment.—Mild steel rod (C 0.10%, Mn 0.65%, Si 0.02%, S 0.03%, P 0.03%) of 0.24 in. diameter was used as the test material. Specimens 5½ in. long were rotated in a chuck at 1400 rpm and abraded with "Hydrodurexsil" 280 C and 400 grade emery paper. They were then swabbed with acetone and distilled water, dried with a clean cloth, and stored for approximately 20 hr in a desiccator over potassium hydroxide.

Electrode potential measurements were made against a saturated calomel reference electrode. Electrical connection was made from the calomel electrode via a saturated KCl-agar bridge to an isolating tube containing 1*N* H_2SO_4 and thence by filter paper strips moistened with 1*N* H_2SO_4 to seven specimen tubes. All specimen tubes and the reference electrode assembly were maintained at 25° ± 0.25°C throughout the test.

A four-stage double-channel d-c amplifier with a high

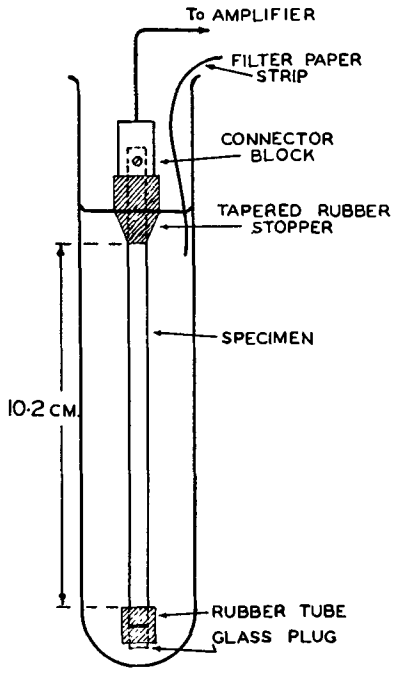

FIG. 1. Test assembly

input impedance [modified from a design by Shepard (15)] was used to measure electrode potentials. The amplifier input connection was made via a selector switch to brass connector blocks from which the specimens were suspended in the solution (Fig. 1). A voltage-backing network in the amplifier permitted an arbitrary zero to be fixed at a convenient reference level. This was maintained at a constant value throughout of −0.405 v with respect to the reference electrode; potentials quoted in the text are negative with respect to this level. As the tests were concerned only with potential differences, no corrections were made for liquid junction potentials; individual differences in liquid junction potentials between each of the seven tubes and the reference electrode were less than 1 mv.

All inhibitors were either of Analytical Reagent grade or were fractionally redistilled. The quinoline and quinaldine were synthesized and redistilled. Inhibitors were dissolved in 1*N* H_2SO_4 (A.R.) at the highest concentrations required; this solution was then diluted with 1*N* H_2SO_4 to give the appropriate lower concentrations.

Procedure.—For each inhibitor, seven concurrent tests covered a range of concentrations. Specimens were weighed and assembled as in Fig. 1.

A short length (approximately ½ in.) of close-fitting rubber tubing containing a short glass plug in one end was placed over the bottom end of the specimen. A rubber stopper, ground as shown in Fig. 1, was then placed on the rod so that a length of exactly 4 in. was exposed between the adjacent edges of the rubber tube and stopper. The taper prevented hydrogen bubbles collecting on the underside. The specimen was suspended in a test tube (8 in. long, 1½ in. diameter) containing 110 ml of the test solution so that the liquid level covered the tapered edge of the stopper. This method of assembly restricted the specimen under test to a cylindrical surface with an area of 3.01 in.² (19.4 cm²).

Specimens were inserted in the tubes containing uninhibited 1*N* H_2SO_4 at 5-min intervals. After exactly 2.5 hr, during which the specimens corroded freely, an electrode potential reading was taken. The uninhibited acid in each tube was sucked into separate flasks, together with 50 ml of 1*N* H_2SO_4 added to the tubes for rinsing, and the tubes were refilled immediately with 1*N* H_2SO_4 containing the dissolved inhibitor. One tube, acting as a control, was refilled with noninhibited 1*N* H_2SO_4. This changeover operation occupied less than 1 min. The electrode potential was read within 2 min of changing the solutions and at intervals of 20–30 min thereafter.

After a second 2.5-hr period, each specimen was removed in turn from its solution, washed thoroughly, dried, and weighed.

If w_i = weight of iron dissolved during the period in the inhibited solution, this is given by $w_i = W - w_0$, where W = total loss of weight (in 5 hr), and w_0 = weight dissolved in the first 2.5 hr (determined volumetrically with 0.02*N* potassium dichromate on the extracted solution in the flasks).

The apparent efficiency of the inhibitor is determined from the usual equation,

$$\text{efficiency} = 100 \cdot \frac{w_b - w_i}{w_b} \%$$

where w_b = weight of iron dissolved in the control (noninhibited) solution during the second 2.5-hr period.

A test period of 2.5 hr in the inhibited solution was chosen because the corrosion rate of the control specimen was found to be almost constant during this time. Tests over longer periods showed that the average corrosion rate changed from about 0.3 mg/min after 2.5 hr, to about 0.5 mg/min after 23 hr, probably due to the increase in surface area. The short test period resulted in a proportionately lower weight loss on the control specimen and, hence, lower efficiency values for a given inhibitor than have been reported by other investigators using much longer times.

RESULTS

The following nitrogen-containing organic compounds were investigated: aniline, ethylaniline, dimethylaniline, diethylaniline, pyridine, quinoline, quinaldine (2-methylquinoline), β-naphthoquinoline, diethylamine, di-*n*-butylamine, piperazine, tetramethyldiamino-diphenyl methane, and brucine.

The various relationships between efficiency, concentration, and electrode potential are given in Fig. 2 to 10.

Reproducibility of results was satisfactory as is shown in duplicate tests on β-naphthoquinoline, diethylamine, and tetramethyldiamino-diphenyl methane.

DISCUSSION

Introductory Comments on Inhibitor Efficiency, Concentration, and Potential Curves

Fig. 2–7 show curves typical of those found by other investigators. Several attempts have been made to relate either inhibitor efficiency (6, 7, 11) or electrode potential (1) with inhibitor concentration through adsorption isotherms of the Langmuir or Freundlich type. The usual

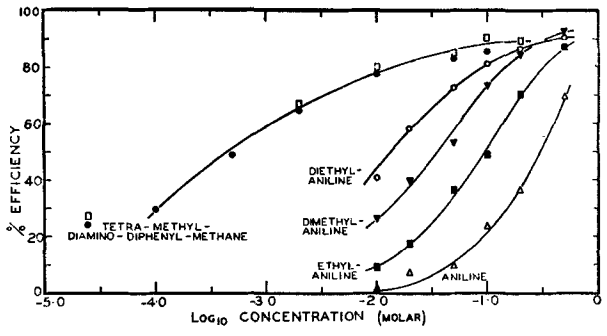

FIG. 2. Relationship between inhibitor efficiency and concentration.

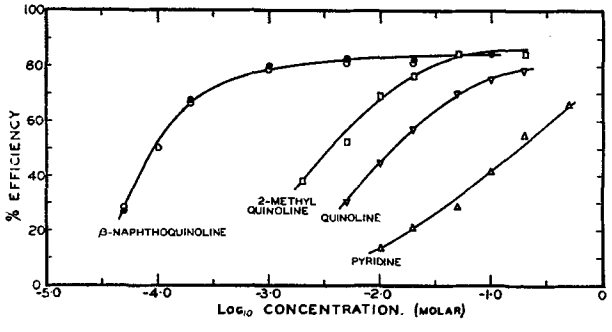

FIG. 3. Relationship between inhibitor efficiency and concentration.

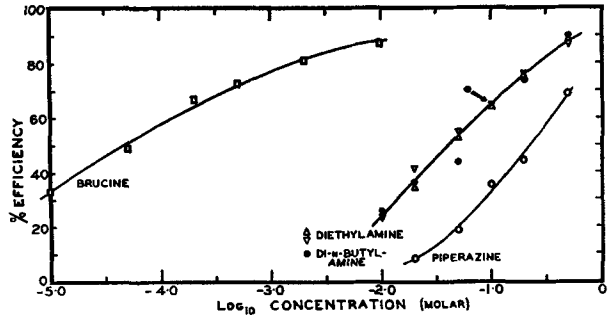

FIG. 4. Relationship between inhibitor efficiency and concentration.

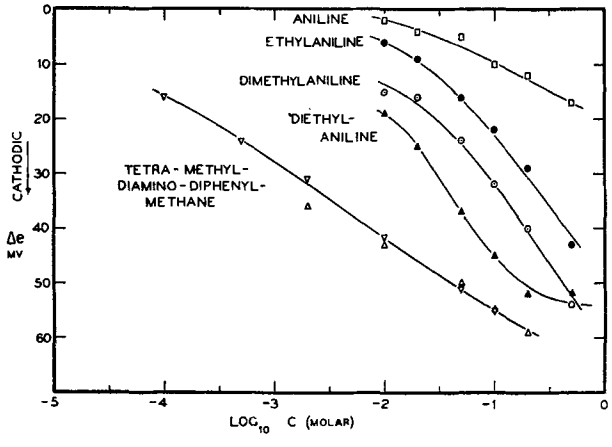

FIG. 5. Change in electrode potential as a function of inhibitor concentration.

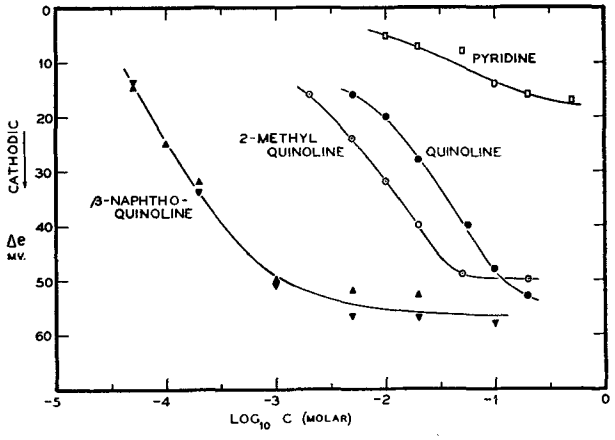

FIG. 6. Change in electrode potential as a function of inhibitor concentration.

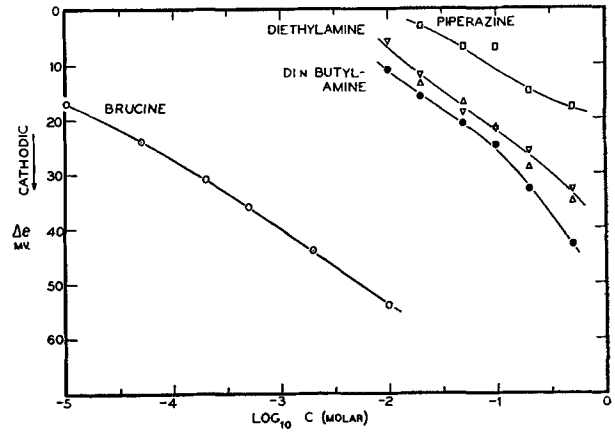

FIG. 7. Change in electrode potential as a function of inhibitor concentration.

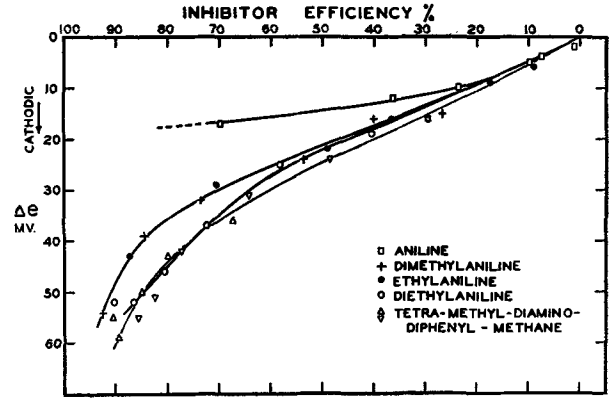

FIG. 8. Change in electrode potential related to inhibitor efficiency.

assumptions made in these calculations are that inhibitor efficiency or change in electrode potential is proportional to the fraction of the surface covered by the inhibitor. In later discussion, it will become evident that these assumptions are oversimplified.

Fig. 8–10 have been drawn so as to show the relation between the change in electrode potential and inhibitor efficiency in terms of the conventional potential vs. corrosion current-type curves. (Plotting inhibitor efficiency in a

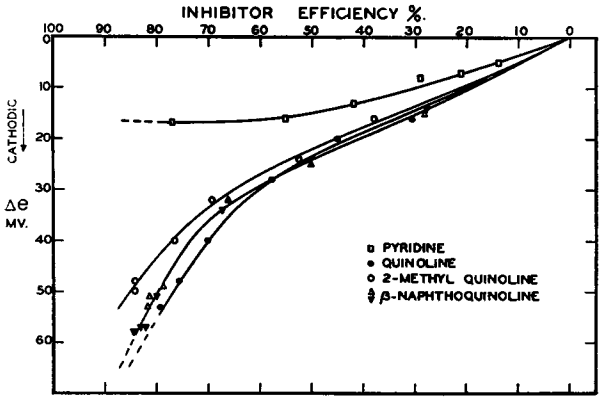

FIG. 9. Change in electrode potential related to inhibitor efficiency.

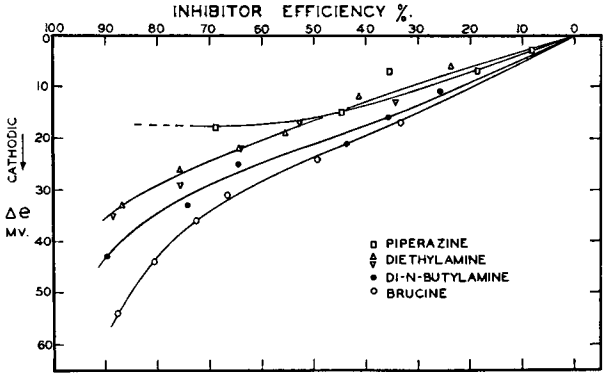

FIG. 10. Change in electrode potential related to inhibitor efficiency.

negative sense is equivalent to plotting percentage weight loss and, hence, corrosion current in the positive sense.)

The change in electrode potential, Δe, is

$$\Delta e = E_p - E_i$$

where E_p = corrosion (steady-state) potential of the specimen in noninhibited acid, and E_i = average potential (integrated and averaged over the "inhibition" period of the test)[1] for the specimen in a solution containing an inhibitor at a specified concentration.

The curves show that (*a*) the over-all movement in potential for each inhibitor is in the cathodic direction, indicating predominantly anodic hindrance to the corrosion process; and (*b*) the value of electrode potential *for a given efficiency* (*current*) differs for each compound. If all inhibitors acted in a purely anodic manner, the observed potentials for all compounds would be identical and would correspond to a point on the cathodic polarization (hydrogen overvoltage) curve. The present observation can only mean that each compound produces a characteristic degree of cathodic polarization.

Taking both observations, it is evident that the inhibitor is adsorbed generally or, at least, in a manner which affects both electrode reactions, rather than specifically at cathodic areas, as Mann and others have suggested.

[1] At higher concentrations of a few inhibitors, a slow drift in potential of a few millivolts occurred during the test period; for this reason, all potentials were integrated on a time basis and averaged. It was assumed that a corresponding slow change occurred in the corrosion rate which would, however, be included in the term weight-loss, itself an integrated quantity.

Nature of the Electrode Surface

Before proceeding to a detailed interpretation of the results, it is necessary to summarize the existing theory on the probable nature of the electrode surface at which adsorption occurs. Except for Hoar and Holliday's paper (16), little consideration appears to have been given to this important aspect.

Most modern theories on hydrogen overvoltage agree that an electrode evolving hydrogen is almost completely covered with a chemisorbed monolayer of atomic hydrogen (17–19). Hickling and Salt (17) state that any electrode at which hydrogen is present is to be regarded simply as an atomic hydrogen electrode, the pressure of atomic hydrogen determining the electrode potential according to the electrode material and the experimental conditions.

Gatty and Spooner (20), in their comprehensive studies of corroding systems, consider the nature of the electrode surfaces in detail. They have produced substantial evidence (on grounds other than overvoltage) from which they infer that, in air-free acid solutions, the surface of many metals (including iron) undergoing corrosion is almost completely covered with an adsorbed atomic hydrogen film. Anodic dissolution takes place only through pores in this film; the continuous change in location and magnitude of these pores accounts for the uniform etching of the whole surface. The total instantaneous area of the anodic sites comprises only a very small fraction of the total surface and, certainly for iron, anodic polarization is very high, even in noninhibited solutions (20, 21).

According to the theory of overvoltage, the hydrogen discharge process, essentially

$$M—H + H_3O^+ + e \rightarrow M + H_2 + H_2O$$

takes place on the adsorbed hydrogen film. From Gatty and Spooner's conclusions, it follows that, where hydrogen is being evolved as a result of corrosion in acid solution, the cathodic current density will be very small compared with that at the anodic pores, because of the very large difference in cathode and anode areas.

The following experimental evidence indirectly supports this view of the conditions at the electrode surface. Kuznetzov and Iofa (22) concluded from their inhibitor studies that hydrogen evolution occurred from the whole surface, whereas dissolution of iron occurred only at the edges of grains. Hoar and Havenhand (23), investigating 36 steels in noninhibited citric acid, found that all materials under a wide variety of test conditions had approximately equivalent cathodes and that the different rates of corrosion were due to widely differing anodes. Further, Frumkin (24) quotes experimental work indicating that the factors governing hydrogen overvoltage (including the constants in the Tafel equation) are not necessarily altered by the simultaneous existence of a metal dissolution process.

The probable nature of the surface of an iron electrode

undergoing corrosion in air-free[2] acid solutions may therefore be summarized as follows: (*a*) the cathodic field consists of a chemisorbed atomic hydrogen film which almost completely covers the electrode surface; (*b*) anodic dissolution occurs at pores in the cathodic field. These pores occupy a very small fraction of the total surface and the anodic reaction is highly polarized.

Adsorption of the Inhibitor and Mechanism of Inhibition

Most of the evidence available favors the view that adsorption of nitrogen-containing inhibitors from acid media is mainly physical rather than chemical. The following typical adsorption characteristics, taken together, indicate the probability of van der Waal's forces being involved: (*a*) asymptotic increase in adsorption (judged on inhibitor efficiency) with increasing concentration; (*b*) adsorption is rapid (in the present work, it was observed that on adding the inhibitor, the change in electrode potential to a fairly steady value was almost instantaneous); (*c*) reversibility [although not always complete (1)]; (*d*) low heats of adsorption (16); and (*e*) decreasing adsorption with increasing temperature (1, 16).

On the other hand, there is little doubt from the theory of overvoltage that the hydrogen film is chemically adsorbed. For a chemisorbed hydrogen film on iron at −96° to −78°C, Emmett and Harkness (25) found the heat of adsorption to be about 10,400 cal/g mole. At 25°C, the value should be rather larger. While heat of adsorption data for organic inhibitors is meager, Hoar and Holliday (16) quote values of approximately 3,000–8,500 cal/g mole for several quinoline compounds.

It is important to note that, hitherto, adsorption of the inhibitor has been either directly or implicitly assumed to occur on the bare metal surface. Since, however, the chemisorbed hydrogen film will not be displaced by a process involving physical adsorption especially if, as is likely, the heat of adsorption is less, it is necessary to consider the possibility that the inhibitor is physically adsorbed on top of the hydrogen film.

As already mentioned, the rapid movement in electrode potential on first adding the inhibitor indicates that it evidently experiences no difficulty in becoming adsorbed. Benton and White (26) and Insley (27) have shown that, for iron and other metals, hydrogen can be physically adsorbed on a pre-existing chemisorbed hydrogen monolayer. The possibility of inhibitor adsorption in an analogous manner does not appear to have been considered previously. While further experimental evidence is required, this inference appears a necessary and logical outcome from preceding considerations.

It is visualized, therefore, that the inhibitor is physically adsorbed on the cathodic hydrogen field and covers, at the same time, the small anodic pores possibly by "bridging." The possibility of direct physical or chemical adsorption of the inhibitor on the bare metal at sufficiently large anodic pores is not excluded. This may, in fact, account for the small residual of undesorbed inhibitor observed by Hackerman and Sudbury (1).

The effect of the inhibitor film on the separate electrode reactions is now examined.

Anodic polarization.—The presence of the inhibitor film, even at very low concentrations, markedly hinders the outward migration of ferrous ions from the anodic pores. Whether this is due to concentration polarization or increased diffusion resistance is not yet clear. Machu's resistance measurements (28) appear to support the latter view. This further hindrance, added to the already existing high state of polarization at anodic sites, will determine almost exclusively the magnitude of the local action current. On the other hand, at these low inhibitor concentrations, very little increase in polarization of the large cathodic field occurs.

The predominantly anodic behavior of the inhibitor is shown in Fig. 11. Here, the change in electrode potential, Δe, is plotted against the logarithm of the corrosion rate (in relative units). For a purely anodic inhibitor, the movement in electrode potential with decreasing corrosion rate would follow the cathodic polarization (hydrogen overvoltage) curve, represented by the usual Tafel expression

$$\eta = a + b \log_{10} (\text{current density})$$

where η = overvoltage and a, b are constants. In Fig. 11, b has been assigned the usual value for iron = 0.12 (29). (In earlier experiments in this series, using applied current, approximate values of b between 0.12 and 0.16 were obtained.) The proximity of the inhibitor curves, in the early stages of inhibition, to the overvoltage curve is indicative of substantially increased anodic polarization.

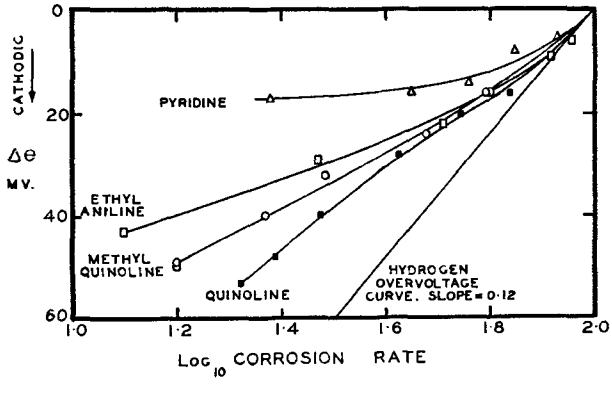

FIG. 11. Change in electrode potential vs. log corrosion rate for several inhibitors in relation to the hydrogen overvoltage curve for iron.

[2] Though probably not air-free in the strict sense, it is unlikely that the present solutions contained more than very small amounts of dissolved oxygen. Hydrogen was continuously evolved from almost all specimens and the solutions were quiet with an air-liquid interphase of less than 1 cm². It is also interesting to note that, within certain limits, conditions at the metal surface controlling hydrogen evolution are not materially affected by appreciable amounts of dissolved oxygen. Thus, saturation of the solution with oxygen does not affect hydrogen overvoltage values (on copper amalgam) at current densities greater than about 10^{-4} amp/cm² (33). In the present low oxygen solutions, current densities were of the order of 10^{-3} amp/cm². Uhlig (34) observed a difference of only 1 mv in the electrode potential shift due to the addition of an inhibitor to acid solutions bubbled with either oxygen or nitrogen. Also, in low *p*H solutions, where hydrogen evolution is the main cathodic reaction, small amounts of oxygen have a negligible effect on corrosion rate (35).

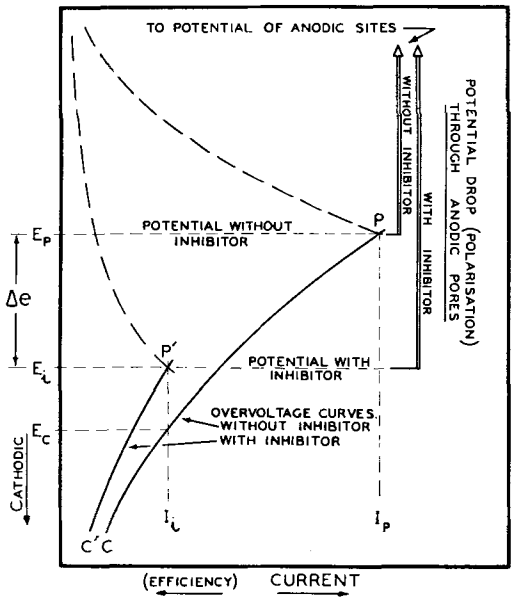

FIG. 12. Schematic potential-current relationship for inhibited and noninhibited surfaces.

The gradual divergence of the curves with increasing efficiency points to an increasing effect of the inhibitor on the kinetics of the cathodic process.

Cathodic polarization and the significance of the change in electrode potential.—It is recognized that the observed electrode potential of a corroding surface is influenced by the relative areas of the anodic and cathodic zones (30). Where, as in the present study, the cathodic field covers almost all the metal surface, the observed potential will be approximately that of the cathodic film (20). The observed potential, in either inhibited or noninhibited solutions, is therefore virtually independent of the potential of the anodic sites and approximately equal to that of an iron electrode evolving hydrogen at a rate depending on its normal overvoltage characteristics and the current. The latter is essentially determined by the degree of anodic polarization. The relationship is shown diagrammatically in Fig. 12. *PC* and *P'C'* are the hydrogen overvoltage curves for noninhibited and inhibited solutions, respectively.

The significance of the change in cathodic polarization potential, E_c to E_i, on adding the inhibitor to the system can now be examined. E_c and E_i are the potentials of noninhibited and inhibited surfaces, respectively, at which hydrogen is being discharged at a rate corresponding to a current I_i in each case.

Adsorption of the inhibitor on to the chemisorbed hydrogen film may conceivably increase cathodic polarization by increasing (*a*) the diffusion resistance; (*b*) the activation energy required for the overvoltage process; (*c*) the current density.

(*a*) From their overvoltage measurements by the direct and indirect methods, Bockris and Conway (31) found no appreciable increase in film resistance in the presence of inhibitors. Also calculations in connection with the present work show that, for the idealized case of a complete monolayer of plane circular molecules, disposed in an ordered manner to give greatest packing density, the proportion of free space (area not covered by inhibitor) is about 5%. The diffusion resistivity through such a monolayer would need to be improbably high to account for changes in potential observed. It is most unlikely in any case that the proportion of free space would ever approach such a small value in view of the irregular shape of most molecules and the dynamic nature of the adsorption process.

(*b*) Except for Bockris and Conway's conclusions, there is no evidence to date in favor of increased activation energy causing the change in potential. It is interesting to note that, for magnesium in acid solution, Hurst and Jermyn (32) showed that the activation energy was of the same order in either inhibited or noninhibited acid. They concluded that while a proportion of the surface was isolated by the inhibitor, the residual reaction was the same as in noninhibited acid.

(*c*) The view that increased cathodic polarization may be due simply to reduction in the total area available for hydrogen discharge, with a corresponding rise in the current density on the free area, was proposed by Mann and his school to explain the "specific cathodic adsorption" theory. Machu (28) has also admitted the feasibility of this mechanism. This approach has been applied to the "general adsorption" argument developed here and leads to an adsorption isotherm expression which is substantially supported by present experimental data.

Derivation of Equation Relating Electrode Potential, Inhibitor Efficiency, and Concentration

It is assumed that the rise in overvoltage from E_c to E_i is due solely to an increase in current density (the inhibitor film having reduced the available cathode area) and that no change in activation energy is involved. The usual Tafel equation then still applies with its constants unchanged. In Fig. 12, this means that for a given current I_i, $E_i - E_c$ corresponds to the difference between two values of the Tafel equation containing only different current density terms.

For a noninhibited surface

$$E_c = a + b \log_{10} \frac{I_i}{A_p}$$

where A_p = the cathode area.

For an inhibited surface

$$E_i = a + b \log_{10} \frac{I_i}{A_i}$$

where A_i = the uncovered area (free space) of the cathode surface corresponding to the current I_i

$$A_i = A_p(1 - \theta)$$

where θ = the fraction of the surface covered by the inhibitor.

Taking A_p as unit area, and $E_i > E_c$, and since the current is the same in each case

$$E_i - E_c = b \log_{10} \frac{1}{A_i}$$

$$= b \log_{10} \frac{1}{1 - \theta}$$

from which

$$\frac{\theta}{1-\theta} = \text{antilog}\,\frac{(E_i - E_c)}{b} - 1$$

From Fig. 12,

$$\frac{E_i - E_c}{b} = \frac{(E_p - E_c) - \Delta e}{b}$$

where Δe is the observed difference in potential between noninhibited and inhibited surfaces for current I_i.

Thus

$$\frac{E_i - E_c}{b} = \frac{1}{b}\left[\left(a + b\log_{10}\frac{I_p}{A_p}\right) - \left(a + b\log_{10}\frac{I_i}{A_p}\right)\right] - \frac{\Delta e}{b}$$

$$= \log_{10}\frac{I_p}{I_i} - \frac{\Delta e}{b}$$

Hence

$$\frac{\theta}{1-\theta} = \text{antilog}\left(\log_{10}\frac{I_p}{I_i} - \frac{\Delta e}{b}\right) - 1$$

$$= \frac{I_p}{I_i}\,\text{antilog}\left(-\frac{\Delta e}{b}\right) - 1$$

Following the form of the Langmuir isotherm used by Hoar (11, 16) in which

$$\log_{10}\frac{\theta}{1-\theta} = \log_{10} K + \log_{10} c - \frac{Q}{2.3\,RT}$$

where c = bulk concentration of the inhibitor, Q = heat of adsorption, and K = constant, one may write

$$\log_{10} c = \log_{10}\left[\frac{I_p}{I_i}\,\text{antilog}\left(-\frac{\Delta e}{b}\right) - 1\right] - \log_{10} K + \frac{Q}{2.3\,RT}$$

Now we have an isothermal equation relating electrode potential, concentration, and inhibitor efficiency, which depends primarily on the two assumptions: (*a*) that increased overvoltage is due to increased current density; and (*b*) that inhibitor adsorption follows the Langmuir theory.

Application of Equation to Present Data

In Fig. 13 to 15, $\log_{10} c$ has been plotted[3] against $\log_{10}[I_p/I_i\ \text{antilog}\,(-\Delta e/b) - 1]$ (denoted by $\log_{10} F$) for the inhibitors studied. For the nine compounds, aniline, ethylaniline, dimethyl- and diethylanilines (except for the points of lowest concentration), diethyl- and dibutylamines, pyridine, piperazine, and 2-methyl quinoline, data are in good linear agreement with the equation. For pyridine, dibutylamine, and dimethylaniline, the slopes of the curves are close to unity, as is required by the equation. While the slopes for the other six compounds are generally of the right order, it is evident that adsorption is also influenced by an additional unknown factor characteristic of each compound.

[3] Least squares lines have been drawn to all data, except for the point of lowest concentration for each of the anilines which was not included in the calculations. The value of the Tafel constant b was taken as 0.12. The linearity of the expression is independent of b and the slope of the curves is only slightly affected by adopting an approximate value.

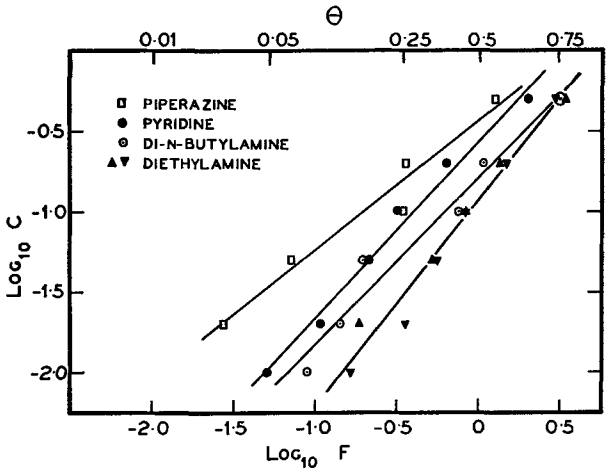

FIG. 13. Adsorption isotherms relating inhibitor concentration (log C) with electrode potential and corrosion current (log F).

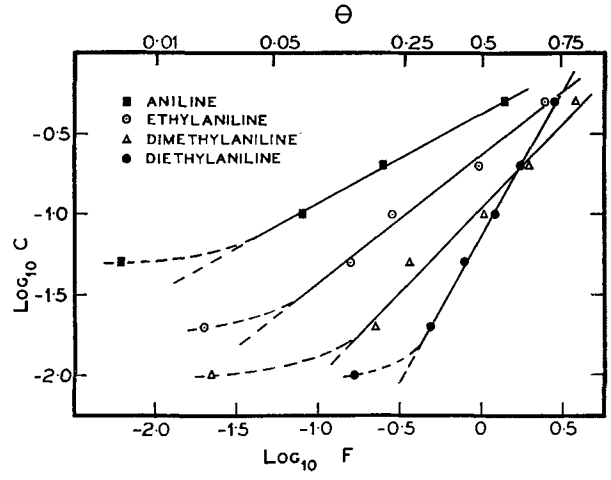

FIG. 14. Adsorption isotherms relating inhibitor concentration (log C) with electrode potential and corrosion current (log F).

The case of the lowest concentration points of the anilines is of special interest. While the position of these points is less certain because of the relatively large effect of small experimental errors in measuring Δe, the fact that all points fall on the same side of the linear curve is probably significant. The present theory assumes that, as the inhibitor concentration increases, the current density at the cathodic field also rises. If, however, at low inhibitor concentrations, the fractional decrease in corrosion current due to anodic polarization very nearly equals the fractional decrease in cathode film area, the current density over this range of concentration will be nearly constant. The equation, which relates changing current density with concentration, will then not apply and calculated data will fall to the left of the equation line as occurs for the anilines. This reasoning implies that, at low concentrations, anilines have a slightly stronger anodic influence than other compounds of this group, although the cause of this behavior is not yet clear.

Molecular orientation.—Except for pyridine, the compounds showing substantial agreement with the equa-

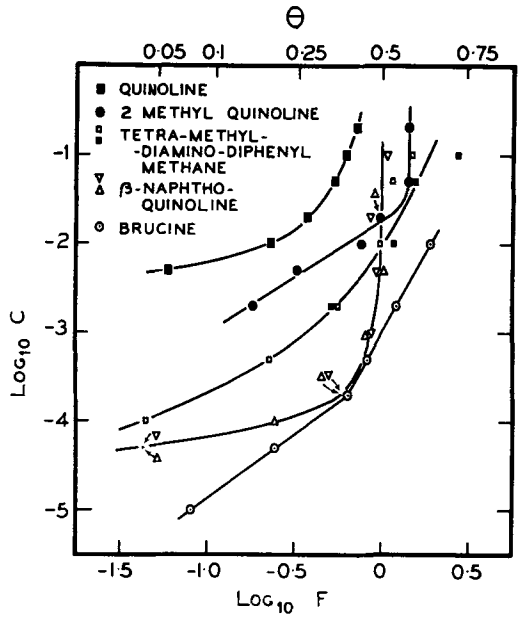

FIG. 15. Adsorption isotherms relating inhibitor concentration (log C) with electrode potential and corrosion current (log F).

tion contain the nitrogen atom "within" the structure of the molecule. If, as is generally agreed, the adsorption forces are directed mainly to this atom, these molecules, on adsorption, should exhibit only a single mode of orientation. Ring compounds, like ethylaniline, for example, should only be oriented "flat" or parallel to the adsorbent surface.

Pyridine, quinoline and β-naphthoquinoline have the nitrogen atom located on the outside of the ring structure. In this position it is always accessible to the adsorption forces so that these molecules are capable of adsorption in either the "flat," "inclined," or "vertical" modes of orientation, depending on surface concentration.[4] It is not surprising, therefore, that quinoline and β-naphthoquinoline do not conform to the equation, since the fraction of the surface covered depends not only on the bulk concentration but also on the molecular orientation which will vary with surface concentration. This behavior was not observed for pyridine which is a relatively weak inhibitor and evidently exhibits a single (possibly preferred) orientation at the comparatively lower surface concentrations existing.

For 2-methyl quinoline, the position of the methyl group (adjacent to the nitrogen atom) should permit adsorption of the molecule only in the flat orientation. Closer observance of the data to the equation for this material compared to the parent compound quinoline supports this view. The vertical section of the 2-methyl quinoline curve suggests that a state of maximum adsorption has been reached.

Brucine may be adsorbed through either of its two nitrogen atoms, although not through both at the one time. The two linear sections of the brucine curve appear to indicate two distinct modes of orientation.

The nonconformity of tetra-methyl-diamino-diphenyl methane with the equation is not unexpected as adsorption is possible through either or both of its nitrogen atoms. As the surface concentration increases, the 'single atom' mode of orientation should predominate, since it requires a smaller area for adsorption.

Revised Theory on the Mechanism of Inhibition[5]

It has been suggested that the true picture of the mechanism of inhibition probably involves aspects of both the "cathodic screening" theory typified by Mann and the "general adsorption—mainly anodic inhibition" theory of Hoar, Hackerman, and others. The present argument embraces the main features of both these theories and, with the additional evidence, presents a more complete account of the probable inhibition mechanism than has been available previously.

The theory is also consistent with modern views on hydrogen overvoltage.

It can be summarized as follows:

1. A steel surface corroding in an acid solution is covered with a chemisorbed atomic hydrogen film which comprises the cathode area of the corrosion process. Anodic dissolution takes place only at pores in this film.

2. The inhibitor is physically adsorbed on to the hydrogen film. Anodic pores are also covered, probably by bridging, although at sufficiently large pores, some direct adsorption, either physical or chemical, may occur.

3. Reduction in the local action current is primarily due to increased polarization at the anodic pores.

4. Reduction of the available cathode area by the adsorbed inhibitor causes a rise in hydrogen overvoltage due to increased current density.

5 For adsorbed nitrogen-bearing inhibitors having only one mode of orientation, the relation between bulk concentration, corrosion current, and electrode potential can be expressed quantitatively for the most part by the derived equation

$$\log_{10} c = K' \log_{10}\left[\frac{I_p}{I_i}\,\text{antilog}\left(-\frac{\Delta e}{b}\right) - 1\right] - \log_{10} K + \frac{Q}{2.3\,RT}$$

where c = molar concentration, I_i and I_p = current (corrosion rate) with and without the inhibitor, respectively, Δe = difference in electrode potentials of inhibited and uninhibited surfaces for current I_i, b = Tafel overvoltage constant, Q = heat of adsorption, and K and K' = constants; ideally K' should equal unity.

The over-all picture of the mechanism of inhibition is still incomplete in many respects. The kinetics of anodic polarization of iron with and without inhibitors require

[4] Hackerman and Glenn's (4) electron diffraction studies on an alkyl pyrrolidine-dione, which has a similarly placed nitrogen atom, obtained evidence indicating that the orientation of the adsorbed molecules changed from the flat to inclined mode as the surface concentration increased.

[5] The theory is, for the moment, restricted to compounds containing only nitrogen as the active atom for adsorption. Sulfur-bearing compounds like the thioureas not only exhibit a different electrode potential behavior but stimulate corrosion at very low concentrations. See also Hoar and Holliday (16).

further elucidation as does the effect of molecular structure and adsorbed orientation on inhibition. The collection of additional experimental data to confirm or modify the present views on the nature of the adsorbent interphase and the manner of adsorption appears to be the next step toward interpreting other complex aspects of inhibition.

ACKNOWLEDGMENT

This paper is published with the permission of the Chief Scientist, Department of Supply, Australia.

Manuscript received July 23, 1954.
Any discussion of this paper will appear in a Discussion Section to be published in the December 1956 JOURNAL.

REFERENCES

1. N. HACKERMAN AND J. D. SUDBURY, *This Journal*, **97**, 109 (1950).
2. N. HACKERMAN AND H. R. SCHMIDT, *Corrosion*, **5**, 237 (1949).
3. F. H. RHODES AND W. E. KUHN, *Ind. Eng. Chem.*, **21**, 1066 (1929).
4. N. HACKERMAN AND E. E. GLENN, *J. Phys. Chem.*, **54**, 497 (1950).
5. C. A. MANN, B. P. LAUER, AND C. T. HULTIN, *Ind. Eng. Chem.*, **28**, 1048 (1936).
6. C. A. MANN, *Trans. Electrochem. Soc.*, **69**, 115 (1936).
7. S. J. CH'IAO AND C. A. MANN, *Ind. Eng. Chem.*, **39**, 910 (1947).
8. E. JIMINO, I. GRIFOLL, AND F. R. MORRAL, *Trans. Electrochem. Soc.*, **69**, 105 (1936).
9. E. L. CHAPPELL, B. E. ROETHELI, AND B. Y. MCCARTHY, *Ind. Eng. Chem.*, **20**, 582 (1928).
10. L. E. SWEARINGEN AND A. F. SCHRAM, *J. Phys. Chem.*, **55**, 180 (1951).
11. T. P. HOAR, "Pittsburgh International Conference on Surface Reactions," p. 127, Corrosion Publishing Co., Pittsburgh (1948).
12. N. HACKERMAN, *Corrosion*, **8**, 143 (1952).
13. L. CAVALLARO, *Métaux & corrosion*, **23**, 184 (1948).
14. O. GATTY AND E. C. R. SPOONER, "The Electrode Potential Behaviour of Corroding Metals in Aqueous Solutions," Chap. 1, Clarendon Press, Oxford (1938).
15. W. G. SHEPARD, *Electronics*, **20**, (10), 174 (1947).
16. T. P. HOAR AND R. D. HOLLIDAY, *J. Appl. Chem. London*, **3**, 502 (1953).
17. A. HICKLING AND F. W. SALT, *Trans. Faraday Soc.*, **38**, 474 (1942).
18. P. J. HILLSON AND E. K. RIDEAL, *Proc. Roy. Soc. London*, **A199**, 295 (1949).
19. N. K. ADAM, "The Physics and Chemistry of Surfaces," pp. 326 and 330, Oxford University Press, London (1941).
20. O. GATTY AND E. C. R. SPOONER, *op. cit.*, pp. 314–5 and Chap. 1.
21. S. GLASSTONE, "An Introduction to Electrochemistry," p. 462, D. Van Nostrand Co., Inc., New York (1942).
22. V. A. KUZNETZOV AND Z. A. IOFA, *J. Phys. Chem. U.S.S.R.*, **21**, 201, (1947); *C. A.*, **41**, 6115c (1947).
23. T. P. HOAR AND D. HAVENHAND, *J. Iron Steel Inst. London*, **133**, 239 (1936).
24. A. FRUMKIN, Discussions of the Faraday Society No. 1, "Electrode Processes," p. 57 (1947).
25. P. H. EMMETT AND R. W. HARKNESS, *J. Am. Chem. Soc.*, **57**, 1631 (1935).
26. A. F. BENTON AND T. A. WHITE, *ibid.*, **54**, 1373, 1820 (1932).
27. E. G. INSLEY, *J. Phys. Chem.*, **39**, 623 (1935).
28. W. MACHU, *Trans. Electrochem. Soc.*, **72**, 333 (1937).
29. A. HICKLING AND F. W. SALT, *Trans. Faraday Soc.*, **36**, 1226 (1940).
30. W. J. MULLER, *Trans. Electrochem. Soc.*, **76**, 167 (1939).
31. J. O'M. BOCKRIS AND B. E. CONWAY, *J. Phys. Chem.*, **53**, 527 (1949).
32. R. HURST AND M. A. JERMYN, *J. Chem. Soc.*, **1950**, 158.
33. A. HICKLING AND F. W. SALT, *Trans. Faraday Soc.*, **37**, 319 (1941).
34. H. H. UHLIG, *Ind. Eng. Chem.*, **32**, 1490 (1940).
35. O. GATTY AND E. C. R. SPOONER, *op. cit.*, pp. 276–7

Oxidation of Tungsten

WATT W. WEBB,[1] JOHN T. NORTON, AND CARL WAGNER

Department of Metallurgy, Massachusetts Institute of Technology, Cambridge, Massachusetts

ABSTRACT

Two oxide layers form during the oxidation of tungsten between 700° and 1000°C. The outer layer is porous, powdery, yellow tungstic oxide, WO_3, and the inner layer is a dense, thin, dark-blue, tightly adherent oxide of uncertain composition. The oxidation reaction follows initially the parabolic rate law, but eventually there is a transition to the linear rate law. The rate of formation of the inner oxide is presumably inversely proportional to its thickness. The inner oxide seems to transform to the outer oxide at a constant rate. Upon combining the rate laws of the two individual processes, an overall rate equation covering the whole range is obtained. The thickness of the inner layer tends to a limiting value when the rate of its formation is equal to the rate of transformation to the outer layer.

INTRODUCTION

The oxidation of tungsten has been investigated by several authors. Gulbransen and Wysong (1) found the parabolic rate law applicable under most conditions up to 550°C. Likewise Dunn (2) found the parabolic rate law to hold between 700° and 1000°C. In contrast, Scheil (3) reports a linear rate law between 500° and 900°C. Results obtained by Nachtigall (4) and Kieffer and Kölbl (5) suggest an intermediate rate law. To clarify, the oxidation

[1] Allegheny Ludlum Steel Co. Fellow, 1953–1955; present address: Metals Research Lab., Electro Metallurgical Co., Union Carbide and Carbon Corp., Niagara Falls, N. Y.

of tungsten has been re-investigated between 700° and 1000°C. Seemingly conflicting observations have been resolved by covering a wide span of time ranging from several minutes up to more than one day.

Gulbransen and Wysong (1) noted appreciable volatility of tungsten oxides only under good vacuum above 800°C. Millner and Neugebauer (6) reported that tungsten trioxide is not volatile at 1000°C in oxygen, argon, or in a vacuum of 1 μ mercury. However, they found that tungsten trioxide volatilized in the presence of water vapor in excess of 30 volume per cent. The present investigation confirms that volatilization of tungsten oxides in dry oxygen up to 1000°C is insignificant, and, therefore, oxidation can be followed by measuring the weight gain of specimens.

Hickman and Gulbransen (7) have studied the crystal structures of the oxides formed on tungsten up to 700°C. Below 700°C they found only WO_3, but at 700°C both WO_2 and WO_3 were reported. According to studies of phase relations in the system tungsten-oxygen, especially x-ray investigations. the occurrence of other phases may also be expected. The following stable phases have been reported (8–15):

αWO_3 triclinic pseudo-orthorhombic (stable below 720°C),

$\alpha' WO_3$ tetragonal (stable above 720°C),

$\beta W_{20}O_{58} = WO_{2.90}$ monoclinic,

$\gamma W_{18}O_{49} = WO_{2.72}$ monoclinic,

δWO_2 monoclinic.

Each of these phases is supposed to exist in a finite homogeneity range, the limits of which are temperature dependent.

In addition, there is a cubic phase, W_3O (15), which however does not seem to be stable above 700°C.

The available thermodynamic data on the tungsten oxides have been summarized by Coughlin (16).

Experimental

The weight of tungsten specimens suspended in a tube furnace by quartz filaments from a standard analytical balance was read periodically as the oxidation proceeded. Since all the oxide remained on the surface of the specimens, the amount of oxide formed was thus obtained. Specimens of 0.05-cm thick tungsten sheet weighing from

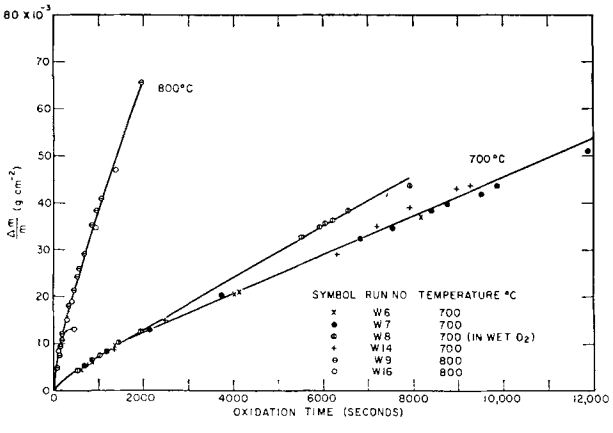

Fig. 1. Oxidation of tungsten at 700° and 800°C

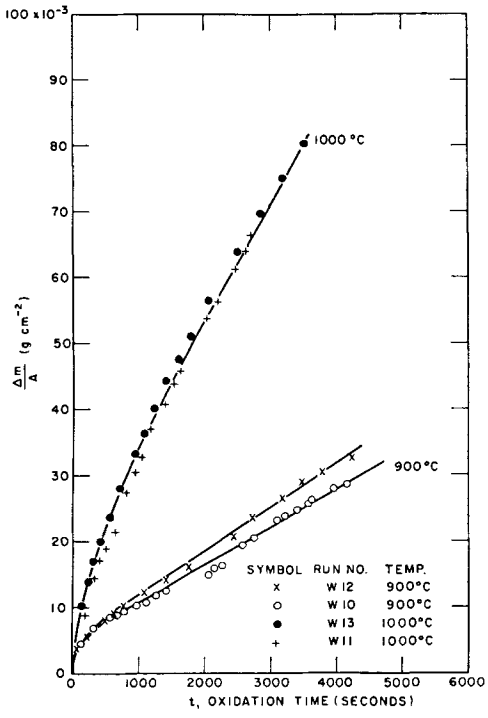

Fig. 2. Oxidation of tungsten at 900° and 1000°C

2 to 10 g with surface areas from 4 to 10 cm² were polished on 120-mesh Alundum abrasive paper and washed with C.P. acetone. U.S.P. tank oxygen was passed over "Ascarite," $CaSO_4$, and "Anhydrone" for purification before being admitted to the furnace at flow rates of 2–5 liter/hr.

To start a run, the specimen was raised from a cold zone below the bottom of the furnace into the oxygen-filled hot zone maintained at the desired temperature within ±5°C. About 1 min was required for the specimens to reach the desired temperature. The alternative method of initiating runs by introducing oxygen into the furnace with the specimen already at reaction temperature in an inert atmosphere was rejected since calculations indicated that, in this case, initial evolution of the heat of formation of the oxide would produce significant overheating of the specimen and hence give spurious results.

Tungsten sheet from the A. D. McKay Company was reported to be 99.9% pure. An analysis revealed the following impurities: 0.002% Fe, 0.005% Si, 0.01% Al, 0.033% C, and 0.004% sulfur.

Experimental data are presented in Fig. 1 and 2. No allowance is made for the time required to reach the reaction temperature. Deviations between duplicate runs had about the same magnitude as the scatter of points during an individual run. Points at short oxidation times have been omitted for clarity.

The weight gain curves start out with a steep slope which gradually decreases and tends to a limiting value corresponding to a virtually constant rate. This suggests that a parabolic rate law may represent the data for a short time at the beginning of the experiments. Subsequently, transition to a linear law seems to occur. On this basis, limiting rate constants k_2 and k_1 have been evaluated

TABLE I. *Rate constants for the oxidation of tungsten*

Temp, °C	Run No.	k_2	k_1	y_{max}	d_{max}	$t_{0.5}$
		g^2/cm^4sec	g/cm^2sec	g/cm^2	cm	sec
700	6	2.5×10^{-9}	3.9×10^{-7}			
700	7	‡	3.9×10^{-7}			
700	8*	2.5×10^{-9}	5.6×10^{-7}			
700	14†	‡	4.3×10^{-7}			
700	best values	2.5×10^{-9}	4.0×10^{-7}	3.1×10^{-3}	2.0×10^{-3}	1490
800	9	3.0×10^{-8}	3.2×10^{-6}			
800	16	3.0×10^{-8}	3.0×10^{-6}			
800	best values	3.0×10^{-8}	3.2×10^{-6}	4.7×10^{-3}	3.1×10^{-3}	280
900	10	1.0×10^{-7}	5.8×10^{-6}			
900	12†	1.3×10^{-7}	7.5×10^{-6}			
900	best values	1.0×10^{-7}	6.0×10^{-6}	8.4×10^{-3}	5.5×10^{-3}	264
1000	11	7.3×10^{-7}	1.8×10^{-5}			
1000	13	7.3×10^{-7}	1.8×10^{-5}			
1000	best values	7.3×10^{-7}	1.8×10^{-5}	2.0×10^{-2}	1.35×10^{-2}	214

* Oxidized in O_2 saturated with H_2O at 23°C.
† Large edge-to-area ratio.
‡ No value of k_2 has been obtained in view of irregularities at small oxidation times.

and are tabulated in the third and the fourth column of Table I. The parabolic rate constants k_2 are in general agreement with those of Dunn (2) whose runs did not exceed 3 hr. Scheil (3) found that the linear rate law applied when specimens were oxidized up to 90 hr at 700°C. This is also in agreement with the results of the present investigation because for such long oxidation times the transition from the parabolic to the linear rate law is virtually complete.

Two experiments were made in order to determine the effect of variations in the experimental conditions which may be expected to be critical.

In view of the reported volatility of WO_3 in water vapor (6), one run was made in oxygen saturated with H_2O at 23°C. The only significant difference was a slight increase in the constant oxidation rate approached after long times. No deposit of oxide appeared at the exit of the furnace.

Since preferred oxidation at edges and corners was noticed, specimens with an exceptionally large ratio of edge length to surface area were oxidized. They showed some small irregularities in rate, but, as a whole, results did not differ widely from results for standard samples.

On the outer surface of the specimens a thick, powdery, porous layer of the yellow tungstic oxide, WO_3, appeared. The oxide appeared to have grown outward perpendicular to the flat surfaces of the specimens as has previously been observed by Scheil (3). After the yellow oxide had reached a thickness of the order of 1 mm, preferred oxidation near the edges was quite evident, particularly at the higher temperatures where eventually the yellow oxide layer projected from the edges like petals. Weight gain data were not taken after the preferred oxidation became evident since, by that time, the effective area of the specimens had changed excessively. The porosity of this layer was clearly evidenced by rapid absorption of ink from a fountain pen point touched to the oxide surface, and by microscopic examination (see Fig. 3). Pycnometric density measurements indicated about 30% porosity. Absorption of water or glycerin during density determinations was slight, apparently due to poor wetting of the oxide. X-ray diffraction powder patterns taken with a Geiger counter spectrometer revealed only WO_3. Presumably, the α' structure was formed above 710°C but transformed on cooling.

On scraping the yellow oxide from the surface, a hard, dark-blue substrate was found which yielded an x-ray diffraction pattern different from tungsten and different from that for any of the known tungsten oxides. The observed diffraction lines coincided with some of the lines observed for WO_3 and with some of those reported for the blue tungsten oxide listed as W_4O_{11} in the ASTM x-ray diffraction data cards. The five lines that appeared were

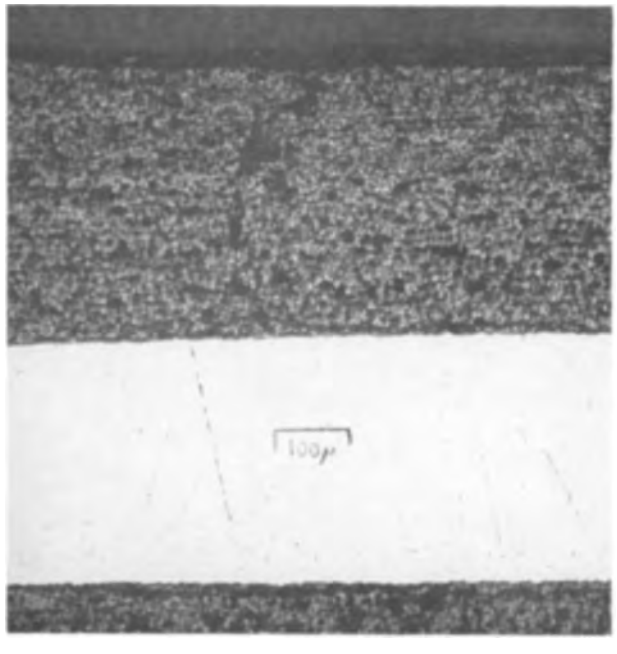

FIG. 3. Tungsten oxidized at 700°C showing porosity in the yellow oxide (no etch). The light area is unoxidized metal.

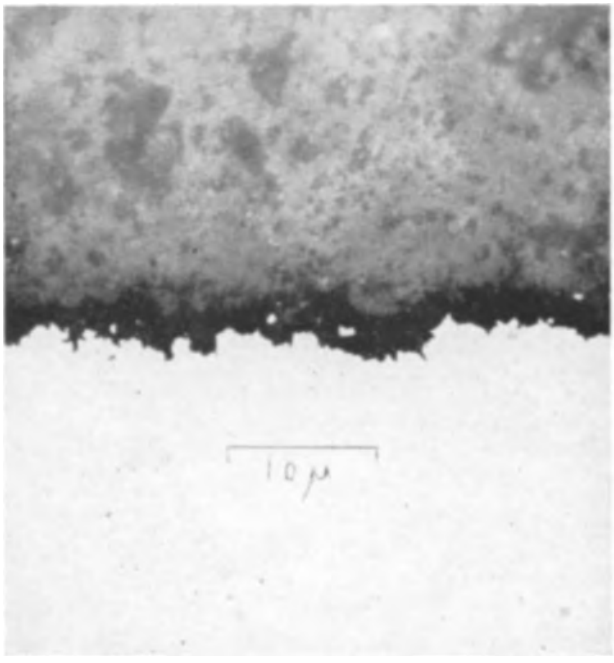

FIG. 4. Tungsten oxidized at 700°C for 4 hr observed with oil-immersion objective (no etch). The dark, irregular band in the middle is the 4- to 15-μ thick "blue oxide" layer between yellow WO_3 at the top and metal at the bottom. The distinct identity of the blue oxide is emphasized by examination with a polarizing microscope or with a sensitive tint plate.

all sharp and could be indexed on the assumption of a cubic lattice with a parameter of 3.77 Å. The composition and structure were not definitely determined, but it may be surmised that this oxide is a metastable modification of one of the intermediate oxide phases.

The thickness of the blue oxide formed by protracted oxidation at several temperatures was estimated roughly from the relative integrated intensities of diffraction lines from the blue oxide layer and from the underlying tungsten. At 700°C, the estimated thickness was of the order of 15 μ. At 900°C, the thickness was roughly two times greater. The thickness found at 700°C is close to an estimate of 10 μ obtained by microscopic observation of a cross section, part of which is shown in Fig. 4.

Specimens oxidized for about 5 min at 700°C were found to have almost the same thickness of the blue oxide as those oxidized for extended periods but only a very thin, powdery layer of yellow oxide. This indicates that the blue oxide forms quite rapidly during the early stages of oxidation but later ceases growing.

DISCUSSION

According to Loriers (17) the transition from the parabolic to a linear rate law occurs when the primary oxidation product is a nonporous oxide which transforms to another porous oxide by take-up of additional oxygen. The formation rate of the primary oxide is assumed to be inversely proportional to its thickness, whereas the rate of transformation to the porous oxide is assumed to be constant. Then one has the rate equations

$$dy/dt = a/y - b \quad \text{(I)}$$

$$dz/dt = fb \quad \text{(II)}$$

where y is the mass of oxygen in the barrier layer per unit area at time t, z is the mass of oxygen in the outer porous oxide layer, f is the ratio of the oxygen content per gram-atom metal in the outer layer to that in the inner layer, and a and b are constants.

The total amount of oxygen per unit area, equal to the increase in mass per unit area, is

$$\Delta m/A = y + z \quad \text{(III)}$$

For short times, when the barrier layer is thin and thus y is relatively small, the first term on the right-hand side of equation (I) predominates. Consquently, the constant a may be calculated as

$$a = \lim_{t=0}\left\{\frac{1}{2}\frac{d}{dt}\left[\left(\frac{\Delta m}{A}\right)^2\right]\right\} = \frac{1}{2}k_2 \quad \text{(IV)}$$

Hence a is one-half the rate constant, k_2, of the parabolic rate law of Pilling and Bedworth (18). At longer times, the amount of oxygen in the barrier layer tends to a limiting value y_{max} when the rate of formation of this layer is equal to the rate of transformation to the nonporous oxide. From equation (I), it follows that

$$y_{max} = a/b \quad \text{(V)}$$

If $y = y_{max}$, the rate of change in mass per unit area is essentially equal to dz/dt. Hence, in view of equation (II),

$$bf = \lim_{t=\infty}\left[\frac{d(\Delta m/A)}{dt}\right] = k_1 \quad \text{(VI)}$$

where k_1 is the rate constant of the linear rate law valid for long oxidation times.

On this basis, Loriers has explained qualitatively the gradual transition from a parabolic to a linear rate law observed for cerium (17). Subsequent measurements by Cubicciotti (19) are in accord herewith. The same behavior has been found for the oxidation of uranium (20).

In the case of tungsten, it is also possible to represent the experimental data with the help of equations (I) and (II) at intermediate times when neither limiting rate law applies.

Integration of equations (I) and (II) yields

$$\ln(1 - by/a)^{-1} - by/a = b^2t/a \quad \text{(VII)}$$

$$z = bft \quad \text{(VIII)}$$

whereby the values of y and z in equation (III) as functions of time are determined.

Introducing the auxiliary values

$$X = \ln(1 - by/a)^{-1} \quad \text{(IX)}$$

$$Y = b^2t/a \quad \text{(X)}$$

we may rewrite equation (VII) as

$$X - (1 - e^{-X}) = Y \quad \text{(XI)}$$

and plot log Y calculated from equation (XI) vs. log X. With the help of this plot, one may obtain the value of X for a given value of $Y = b^2t/a$.

Substitution of equations (VII) and (VIII) in equation (III) yields

$$\Delta m/A = (a/b) \ln (1 - by/a)^{-1} + b(f - 1)t = (a/b)[X + Y(f - 1)] \quad \text{(XII)}$$

In this way, one may calculate $\Delta m/A$ for any time t for a comparison with observed values in order to check the applicability of the rate laws assumed in equations (I) and (II). If the inner oxide had the approximate composition $WO_{2.75}$, the value of f would be 1.09. Since the actual composition of the inner oxide is uncertain, however, f has been taken as unity for the sake of simplicity. Hence, a is equal $\frac{1}{2}k_2$ and b is taken as equal to k_1 according to equations (IV) and (VI). Values of k_1 and k_2 are listed in Table I.

Fig. 5 shows that the observed oxidation curves generally agree with the calculated curves within the limits of uncertainty. Deviations at short times which are emphasized by the logarithmic scale are due to an uncertainty of about 30 sec in fixing the effective starting time of the experiments and to an uncertainty in the calculation of the limiting parabolic rate constant.

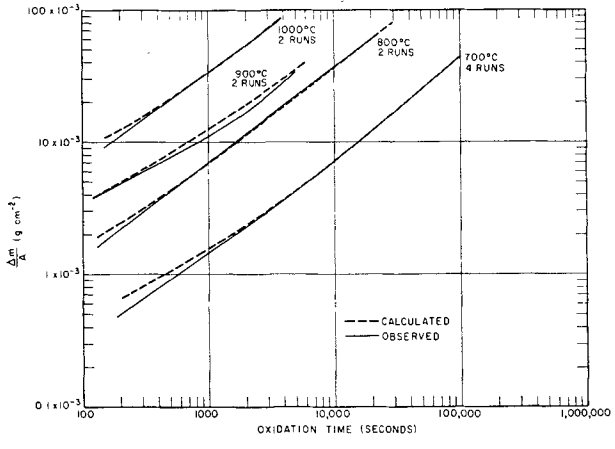

FIG. 5. Comparison of calculated and observed values of $\Delta m/A$ for the oxidation of tungsten.

In addition, the value of y_{max} calculated from equation (V) may be used in order to obtain the maximum thickness of the inner oxide film,

$$d_{max} = y_{max} M/16x\rho \quad \text{(XIII)}$$

where M is the formula weight of the inner oxide involving one atom of tungsten, x is the number of oxygen atoms per tungsten atom, and ρ is the density of the inner oxide. The evaluation of equation (XIII) has been based on the formula WO_3, although the actual value of x is smaller than 3. Calculated values of d_{max} agree with the observed values within a factor of two which is about the magnitude of the experimental uncertainty. The observed trend of d_{max} with temperature is in accord with the calculations.

From equations (V) and (VII), one may also calculate the time $t_{0.5}$ required for $y = 0.5\, y_{max}$ when half the limiting thickness of the protective oxide layer has been reached,

$$t_{0.5} = (a/b^2)(\ln 2 - 0.5) = 0.19(a/b^2) \quad \text{(XIV)}$$

Values of $t_{0.5}$ listed in Table I show that most of the inner oxide layer is built up in a rather short time, especially at higher temperatures. This shows the difficulties of obtaining an adequate value of k_2.

Manuscript received August 25, 1955. This paper was prepared for delivery before the Pittsburgh Meeting, October 9 to 13, 1955, and is based in part on a thesis submitted by W. W. Webb in partial fulfillment of the requirements for the D.Sc. degree from Massachusetts Institute of Technology.

Any discussion of this paper will appear in a Discussion Section to be published in the December 1956 JOURNAL.

REFERENCES

1. E. A. GULBRANSEN AND W. S. WYSONG, *Trans. Am. Inst. Mining Met. Engrs.*, **175**, 611 (1948).
2. J. S. DUNN, *J. Chem. Soc. (London)*, **1929**, 1149.
3. E. SCHEIL, *Z. Metallkunde*, **29**, 209 (1937).
4. E. NACHTIGALL, *ibid.*, **43**, 23 (1952).
5. R. KIEFFER AND F. KÖLBL, *Z. anorg. u. allgem. Chem.*, **262**, 229 (1950).
6. T. MILLNER AND J. NEUGEBAUER, *Nature*, **163**, 601 (1949).
7. J. W. HICKMAN AND E. A. GULBRANSEN, *Trans. Am. Inst. Mining Met. Engrs.*, **171**, 371 (1947).
8. H. BRAKKEN, *Z. Krist*, **78**, 484 (1931).
9. O. GLEMSER AND H. SAUER, *Z. anorg. u. allgem. Chem.*, **252**, 144 (1943).
10. G. HÄGG AND A. MAGNELI, *Arkiv Kemi, Mineral. Geol.*, **19A**, No. 2, (1944).
11. A. MAGNELI, *ibid.*, **24A**, No. 2, (1946).
12. A. MAGNELI, *Arkiv Kemi*, **1**, 223, 513 (1949).
13. R. UEDA AND T. ICHINOKAWA, *Phys. Rev.*, **80**, 1106 (1950); **82**, 563 (1951).
14. W. L. KEHL, R. G. MAY, AND D. WAHL, *J. Appl. Phys.*, **23**, 212 (1952).
15. N. SCHÖNBERG AND G. HÄGG, *Acta Cryst.*, **7**, 351 (1954).
16. J. P. COUGHLIN, *U. S. Bur. Mines Bull. 542* (1954).
17. J. LORIERS, *Compt. rend.*, **231**, 522 (1950).
18. N. B. PILLING AND R. E. BEDWORTH, *J. Inst. Metals*, **29**, 529 (1923).
19. D. CUBICCIOTTI, *J. Am. Chem. Soc.*, **74**, 1200 (1952).
20. J. LORIERS, *Compt. rend.*, **234**, 91 (1952).

Oxidation Studies in Metal-Carbon Systems

WATT W. WEBB,[1] JOHN T. NORTON, AND CARL WAGNER

Department of Metallurgy, Massachusetts Institute of Technology, Cambridge, Massachusetts

ABSTRACT

A general analysis of the characteristics of the oxidation of alloys containing carbon or carbides is given. Evolution of gaseous CO and CO_2 may rupture oxide films which, in the absence of carbon, are highly protective. On the other hand, if the base metal has a high affinity for oxygen, carbon may be retained in the alloy, or carbon may diffuse across the oxide layer. Experimental data are reported for the systems Ni—C, W—C, Mn—C, and Ti—C.

INTRODUCTION

A determining factor for the oxidation resistance of hard metals based on metal carbides and of carbon-bearing alloys may be the presence of carbon which may yield gaseous reaction products, CO and CO_2. Some carbon-bearing materials are of industrial interest due to their high strength at elevated temperatures, but, for widest applicability, their oxidation resistance must also be sufficiently high (1). In general, oxidation resistance of a metal is due to the formation of a solid protective metal oxide film which acts as a diffusion barrier and limits the rate of oxidation (2), but the formation of gaseous reaction products such as CO and CO_2 may disrupt the protective oxide film. Therefore, the oxidation of various metal-carbon systems has been investigated to clarify this situation.

Oxidation of a metal such as nickel or manganese at elevated temperatures yields an oxide layer virtually without pores, and the rate is controlled by diffusion of ions and electrons across the oxide film. If carbon is present as an alloying element, the formation of CO or CO_2 at the alloy-oxide interface may rupture the oxide layer and, therefore, change the kinetics of the oxidation process.

If the metal oxide adjacent to the alloy has the formula MeO_y, evolution of CO and CO_2 may be due to the reactions

$$C(\text{alloy}) + 1/y\ MeO_y = CO(g) + 1/y\ Me(\text{alloy}) \quad (I)$$

$$C(\text{alloy}) + 2/y\ MeO_y = CO_2(g) + 2/y\ Me(\text{alloy}) \quad (II)$$

The corresponding equilibrium partial pressures of CO and CO_2 are

$$p_{CO} = K_1 a_C/(a_{Me})^{1/y} \quad (III)$$

$$p_{CO_2} = K_2 a_C/(a_{Me})^{2/y} \quad (IV)$$

where K_1 and K_2 are the equilibrium constants of reactions (I) and (II), respectively, and where a_{Me} and a_C are the activities of metal and carbon, respectively, at the alloy-oxide interface.

The following two principal cases are to be considered.

Case I.—If metal Me has a relatively low affinity for oxygen and, accordingly, the sum $p_{CO} + p_{CO_2}$ [calculated from equations (III) and (IV) with the carbon activity of the original alloy] is much greater than the surrounding pressure P, outburst of CO and CO_2 is likely to rupture the oxide film. Then molecular oxygen may diffuse through the resulting cracks toward the alloy-oxide interface so that the oxidation of the metal may proceed much more rapidly than in the absence of carbon unless the oxide layer shows a very good "healing tendency."

Under these conditions, the activity of carbon at the alloy-oxide interface will be much lower than in the bulk alloy. In view of the porosity of the oxide, the sum of p_{CO} and p_{CO_2} may be assumed to be virtually equal to the surrounding pressure P,

$$p_{CO} + p_{CO_2} = P \quad (V)$$

The CO_2/CO ratio is given by the reaction

$$1/y\ MeO_y + CO = 1/y\ Me + CO_2 \quad (VI)$$

with the equilibrium condition

$$p_{CO_2}/p_{CO} = K_3/(a_{Me})^{1/y} \quad (VII)$$

Upon combining equations (V) and (VII), one may calculate the values of p_{CO} and p_{CO_2} and finally, on using equations (III) or (IV), the activity of carbon at the alloy-oxide interface.

The following possibilities under Case I are to be considered.

(*A*) A much lower carbon activity at the alloy-oxide interface than in the bulk alloy may result in diffusion of carbon toward the oxide-alloy interface and, therefore, in preferential oxidation of carbon. This has been found in the system Ni—C.

(*B*) In spite of depletion of carbon at the metal-oxide interface, diffusion of carbon may be negligible. By and large, the rate of diffusion in a single phase is determined by the product of a diffusion constant and a concentration gradient which, in turn, is essentially proportional to the homogeneity range of the phase. Therefore, if the homogeneity ranges of the phases of the Me—C system which are involved are very small and the rate of oxide formation is high, diffusion of carbon will be insignificant as can be shown by calculations omitted in this paper. Thus, non-preferential oxidation of carbon is expected as has been found in the system W—C.

Case II.—In systems involving a high absolute value of the standard free energy of formation of metal oxide per gram-atom of oxygen, the sum $p_{CO} + p_{CO_2}$ calculated

[1] Allegheny Ludlum Steel Co. Fellow, 1953–1955; present address: Metals Research Lab., Electro Metallurgical Co., Union Carbide and Carbon Corp., Niagara Falls, N. Y.

from equations (III) and (IV) with the carbon activity of the original alloy is less than the surrounding pressure unless the temperature is very high. Under these conditions, carbon may be retained in the alloy underneath a dense oxide film, but it is also possible that carbon is oxidized as is shown below. The following possibilities under Case II are to be considered.

(*A*) Carbon rejected at the alloy-oxide interface may diffuse backward into the bulk alloy as has been found in the system Mn—C. Possibly, phases richer in carbon than that in the original alloy may form. If the sum $p_{CO} + p_{CO_2}$ calculated from equations (III) and (IV) with the carbon activity prevailing at the alloy-oxide interface does not exceed substantially the surrounding pressure, no rupture of the oxide film is to be expected and the oxidation rate is supposed to be essentially the same as in the absence of carbon except for a small effect due to the lower activity of the metal.

Enrichment of carbon at the alloy-oxide interface, however, may in some systems result in a large increase in the activity of carbon and a pressure $p_{CO} + p_{CO_2}$ which is substantially greater than the surrounding pressure. Thus, after a certain amount of carbon-rich alloy or, eventually, graphite has been formed, rupture of the oxide film may occur. Access of oxygen will decrease the carbon activity with following healing of the ruptured oxide film and accumulation of carbon until once more the critical activity of carbon for rupture of the oxide film has been reached. Thus, periodic changes of the oxidation rate would occur. So far, no experimental evidence for this type of oxidation is available.

(*B*) Backward diffusion of carbon will not occur if the alloy is saturated with graphite and, accordingly, there is no activity gradient of carbon. In this case, more graphite may be formed at the alloy-oxide interface. If graphite appears in disperse form, the cross section of oxide available for migration of ions and electrons is changed only to a minor extent and so the oxidation rate may not differ widely from that for a system free of carbon. No example can be quoted at the present.

(*C*) In special cases, outward migration of carbon across an "oxide layer" may occur if carbon is sufficiently soluble therein. The presence of carbon in the oxide may increase or decrease the concentration of lattice defects which are decisive for the rate of migration of ions and electrons in the oxide and, therefore, may increase or decrease the rate of oxidation of the metal. Dissolution of carbon in oxide may be considered as an important factor when TiC is oxidized because TiC and TiO are known to be mutually soluble, and there may be some carbon solubility in TiO_2. So far, however, no direct experimental proof has been obtained.

The foregoing discussion is based on the assumption of attainment of thermodynamic equilibrium at the various phase boundaries. It is possible, however, that the breakup of metal-carbon bonds in a carbide phase requires a high activation energy and thus becomes the rate-determining step. Under these conditions, oxidation of a carbide may follow a linear rather than a parabolic rate law and is substantially slower than the oxidation of the corresponding metal under comparable conditions during a certain span of time. Although there is no direct evidence, this may be an important possibility to account for the oxidation resistance of some carbides and other constituents in hard metals such as borides and nitrides.

These general principles for the oxidation of metal-carbon systems are illustrated by investigations on the systems Ni—C, W—C, Mn—C, and Ti—C.

Experimental Procedure

The weight change of specimens heated in dry oxygen of atmospheric pressure was measured in the same manner as for the oxidation of tungsten (3). In view of the loss of carbon, however, the weight change is not a direct measure of the oxidation rate. Therefore, the amount of carbon being oxidized was determined separately in parallel runs. The gas passed over the specimen was led into an auxiliary furnace with cupric oxide as a catalyst, where CO was converted into CO_2 which was finally collected in weighing bottles containing Ascarite and Anhydrone. The oxygen take-up per unit surface area $\Delta m_{ox}/A$ may then be calculated as

$$\Delta m_{ox}/A = \Delta m/A + (12/44)(\Delta m_{CO_2}/A) \quad \text{(VIII)}$$

where $\Delta m/A$ is the observed change in mass of the sample per unit area and $\Delta m_{CO_2}/A$ is the amount of CO_2 per unit area collected during the same time.

If metal and carbon are oxidized nonpreferentially, we have the equation

$$(1 - x)\text{Me} + x\text{C} + \left[\frac{1}{2}(1 - x)y + x\right]\text{O}_2 = (1 - x)\text{MeO}_y + x\text{CO}_2 \quad \text{(IX)}$$

where x is the mole fraction of carbon in the original alloy or carbide, and y is the average number of oxygen atoms per metal atom in the oxide layer.

From equation (IX) it follows that

$$\frac{\Delta m_{CO_2}/A}{\Delta m/A} = \frac{44x}{16(1 - x)y - 12x} \quad \text{(X)}$$

if neither metal nor carbon is oxidized preferentially.

If equation (X) holds, the oxygen take-up per unit area may be calculated directly from the weight change of the sample. Upon substitution of equation (X) in equation (VIII), it follows that

$$\frac{\Delta m_{ox}}{A} = \frac{16(1 - x)y}{16(1 - x)y - 12x}\frac{\Delta m}{A} \quad \text{(XI)}$$

Conversely, $\Delta m_{ox}/A$ may also be calculated from the amount of CO_2. Substitution of equation (X) in equation (XI) yields

$$\frac{\Delta m_{ox}}{A} = \frac{16(1 - x)y}{44x}\frac{\Delta m_{CO_2}}{A} \quad \text{(XII)}$$

Values calculated from equations (VIII), (XI), or (XII) have been used in order to calculate the parabolic rate constant as $(\Delta m_{ox}/A)^2/t$ in g^2cm^{-4} sec^{-1} as far as the parabolic rate law applies.

Equations (VIII) and (X) involve data from parallel runs since the weight change of a sample and the amount

of CO_2 were not determined simultaneously. The applicability of equations (VIII) and (X) requires, therefore, a sufficient reproducibility. Checks showed that deviations between different runs were of the same order of magnitude as the weighing errors in an individual run (about ± 0.001 g corresponding to an error of 0.0002 g/cm^2 in $\Delta m/A$ or $\Delta m_{CO_2}/A$ for a sample of 5 cm^2 area).

The System Ni—C

When pure nickel is oxidized at 1000°C, the parabolic rate law is obeyed, i.e., a protective layer of NiO is formed. For nickel saturated with graphite and coexisting with nickel oxide, NiO, the sum $p_{CO} + p_{CO_2}$ calculated from equations (III) and (IV) and data compiled by Coughlin (4) is of the order of 10^6 atm at 1000°C. This suggests that CO and CO_2 formed by reactions (I) and (II) will rupture a nickel oxide film. This is confirmed by a comparison of the oxidation rates of pure nickel and a Ni-C alloy containing 2.3% carbon at 1000°C. Data are presented in Fig. 1.

Virtually pure nickel was obtained from Vacuum Metals Corporation, Cambridge, Massachusetts. A nominal analysis indicates the presence of the following impurities: 0.004% C, 0.002% O, 0.0045% S, 0.003% Co, 0.003% Si.

In accordance with previous investigations (5, 6, 7), pure nickel was found to oxidize very slowly. The parabolic rate constant was found to be 4×10^{-10} g^{2}cm^{-4} sec^{-1} at 1000°C.

A Ni-C alloy with 2.3% C was prepared by melting pure nickel with carbon in an induction furnace and sucking the liquid alloy into a Vycor tube. Thus, rods with a diameter of 0.4 cm were obtained. Since the solubility of graphite in nickel amounts to only 0.27% at 1000°C (8), the alloy consisted of nickel saturated with graphite and excess graphite in nodular and flake form as was found by microscopical examination. In oxidation tests, samples showed a weight decrease rather than a weight increase because the mass of carbon being oxidized exceeded the oxygen take-up due to formation of nickel oxide. Analogous observations have been made by Gulbransen and Hickman (9) when carbon-containing alloys were exposed to much lower oxygen pressures of the order of 1 μ.

The amount of CO_2 collected during the first few hours, which is shown as the uppermost curve in Fig. 1, clearly indicates preferential oxidation of carbon. Only after longer exposure when the CO_2 evolution had ceased, a weight increase of the Ni-C alloy was observed.

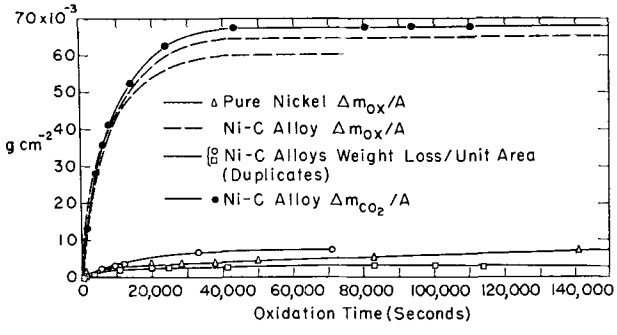

FIG. 1. Oxidation of nickel and a nickel-carbon alloy at 1000°C.

From equations (III), (V), and (VII) it follows that the carbon concentration at the alloy-oxide interface is virtually zero. Thus there is formed a one-phase alloy with a variable carbon content, ranging from zero to 0.27% C, between the alloy-oxide interface and the core of the original two-phase alloy. In view of the concentration gradient in the one-phase region, carbon diffuses outward, and the boundary between the one-phase and the two-phase region is shifted inward because excess graphite dissolves. A similar situation occurs during the decarburization of Fe-C alloys in a H_2O-H_2 atmosphere according to Pennington (10). A mathematical analysis for a plane sample has been given by Jost (11). The decarburization rate observed in the present experiments is somewhat higher than the value estimated from the diffusion constant of carbon in nickel, which has been reported to be 3×10^{-7} cm^2/sec at 1000°C (8).

A photomicrograph of a sample after oxidation for 17 hr confirmed virtually complete decarburization in accordance with the end of the CO_2 evolution. Voids were found instead of the original graphite inclusions.

The rate of formation of nickel oxide on the alloy depends on the damage done to the protective layer by gas evolution. No detailed mechanism can be suggested. Thus the observed oxidation rate cannot be related to other data. The fact that the rate of nickel oxide formation after complete decarburization drops to values lower than those observed for pure nickel after equal times indicates that the damage to the oxide caused by gas evolution later disappears by some kind of "healing process." Microscopical examination of oxidized samples showed an inner oxide layer consisting of a porous aggregate of fine grains whereas the outer layer was more coherent. It is probable that the porous part of the oxide was formed during the early stages of oxidation while gas was evolved rapidly and that the less porous outer part was formed later when gas evolution was slow or had ceased.

To summarize, the oxidation of a Ni-C alloy containing 2.3% carbon is an example for Case I(A) considered above.

The System W—C

In the system W—C, two carbides, W_2C and WC, of nearly invariable composition are found. The solubility of carbon in tungsten is very low. Thus virtually no diffusion of carbon and no preferential oxidation of carbon can be expected. From previous investigations (12), it is already known that W_2C and WC are oxidized at a high rate, but no quantitative evaluation is possible since only the weight change of samples was determined but not the loss of carbon.

In view of the general program outlined above, the rate of oxidation of the compound WC was investigated for a comparison with the rate of oxidation of pure tungsten. Outburst of CO and CO_2 is likely to occur at 1000°C but thermodynamic calculations for lower temperatures are not conclusive in view of uncertainties of the free energies of formation of WC and the various oxides.

Specimens of WC were prepared by hot-pressing pure WC powder obtained from A. D. McKay Company. The resulting material had a relative density of about 90%.

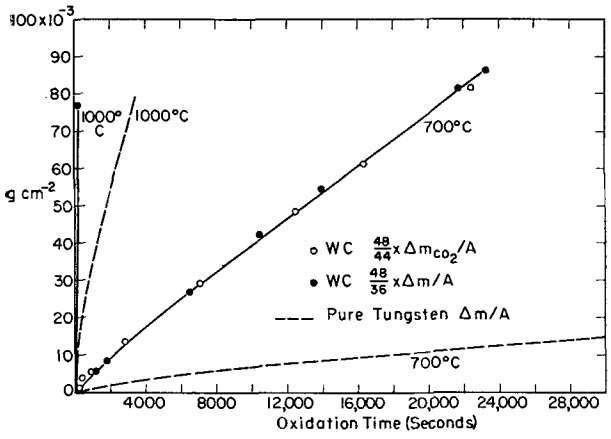

FIG. 2. Oxidation of tungsten and tungsten carbide

Data for the oxidation of WC are shown in Fig. 2 and are compared with data concurrently obtained for tungsten (3). At 700°C, the oxidation of WC follows the linear rate law. The rate constant is 4×10^{-6} g cm^{-2}sec^{-1}. Results for 1000°C are rather of a qualitative nature in view of the exceedingly high rate. The amount of CO_2 collected indicates nonpreferential oxidation of carbon corresponding to the over-all reaction

$$WC + 2.5\ O_2 = WO_3 + CO_2$$

The higher rate for the oxidation of WC in comparison to that of tungsten suggests rupture of the oxide film due to formation of CO and CO_2. Thus the oxidation of WC follows the pattern for Case I(*B*) considered above.

An examination of the oxide film formed on WC at 700°C revealed only the presence of yellow WO_3, but no blue oxide was found in contrast to the finding with pure tungsten (3).

The System Mn—C

Manganese has a high affinity for oxygen. Therefore, it is expected that during the oxidation of Mn-C alloys no CO or CO_2 is formed, but carbon is retained in the alloy.

The oxidation of pure manganese has been studied by Gurnick and Baldwin (13), who overcame the tendency of manganese samples to disintegrate on heating by electroplating manganese on a strong base material. The parabolic law was followed during oxidation in air between 400° and 1100°C. The parabolic rate constant was found to be 5×10^{-8} g^{2}cm^{-4}sec^{-1} at 1000°C. About 10% MnO and 90% Mn_3O_4 were formed.

The manganese-carbon phase diagram has been studied by Isobe (14) and by Vogel and Döring (15) who have shown that there is a high temperature γ phase, similar to γ iron, which dissolves carbon up to about 2 wt % at 1000°C. At higher carbon contents, there seems to be a carbide with a homogeneity range from about 3 to 4 wt % carbon at 1000°C. The available information on the manganese carbides has been summarized by Kuo and Persson (16).

A sample of manganese obtained from Electro Metallurgical Company, New York, New York, contained 0.92% Fe, 0.21% Si, and 0.21% C. A Mn-C alloy containing 1.33% C was prepared by melting manganese and chips of spectroscopically pure carbon in an alumina crucible

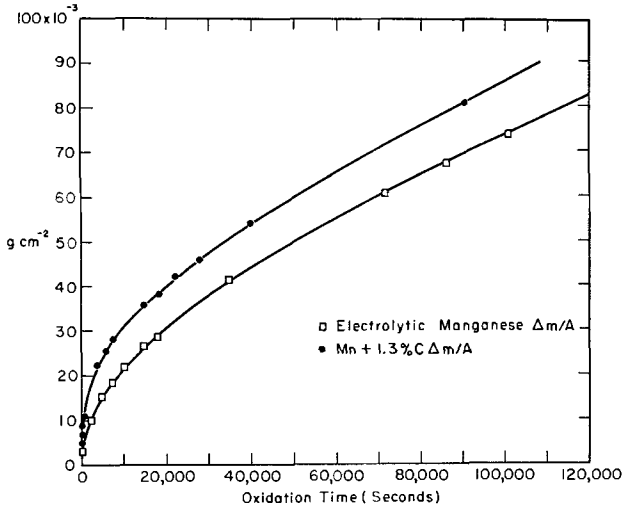

FIG. 3. Oxidation of manganese and a manganese-carbon alloy.

under a purified argon atmosphere. Rods were obtained by sucking the liquid metal into Vycor tubes. Oxide-free surfaces resulted, but specimens of both manganese and the manganese-carbon alloy invariably cracked during cooling. However, it was possible to select suitable pieces, cut them to size, abrade their surfaces, and reheat them for oxidation experiments without disintegration.

Data for 1000°C are presented in Fig. 3. Unalloyed manganese was found to oxidize according to the parabolic rate law with a constant of 5×10^{-8} g^{2}cm^{-4}sec^{-1} in agreement with Gurnick and Baldwin (13). The Mn-C alloy oxidized at a somewhat higher rate.

Only small amounts of CO_2 were collected. A stoichiometric calculation indicates that 0.17 g CO_2/1 g O take-up should be collected if neither manganese nor carbon were oxidized preferentially. After 90,000 sec, a weight increase of 0.08 g/cm^2 was found, whereas the amount of CO_2 collected amounted to only 0.00027 g/cm^2 which is 2% of the amount expected for nonpreferential oxidation. In another run of 44 hr (160,000 sec), the amount of CO_2 was $\frac{1}{20}$ the amount expected for nonpreferential oxidation.

That nearly all the carbon does remain in the manganese during oxidation was confirmed by a carbon analysis of a representative sample of the metallic core from another test after 25 hr (90,000 sec) of oxidation. The analysis showed 2.15 wt % carbon in exact agreement with the amount expected, assuming that all carbon remains in the specimen. Metallographic examination revealed the presence of a distinct layer, about 100 μ thick at the surface of the metallic core. Presumably, there was a carbide phase stable at 1000°C which transformed on cooling to other phases stable at lower temperatures. In the oxide layer, no pores were visible.

To summarize, the oxidation of a Mn-C alloy containing 1.33% carbon is an example for Case II(*A*) considered above.

The System Ti—C

Titanium also has a high affinity for oxygen and accordingly the sum $p_{CO} + p_{CO_2}$ at the alloy-oxide interface is expected to be low so that rupture of the oxide film on Ti-C alloys should not and did not occur. Nevertheless,

nonpreferential oxidation similar to that of WC was found.

The titanium-carbon system has a narrow, terminal solid solution and a very stable carbide, TiC, with a substantial homogeneity range (17).

The titanium-oxygen system is characterized by a large terminal solid solubility of oxygen in titanium and by at least three oxides: TiO, Ti_2O_3, and TiO_2 (18, 19)

Oxidation of pure titanium has been studied by several authors and the references through 1954 are given by Simnad, Spilners, and Katz (20). The parabolic rate law is obeyed fairly well. There are essentially two simultaneous processes, namely, solution of oxygen in titanium, and formation of a layer of titanium oxides, mainly TiO_2. Simnad, Spilners, and Katz have separated the rates of these processes.

In what follows, comparative values for the oxidation of pure titanium, TiC, and carbon-deficient TiC are reported.

Titanium metal specimens were cut from swaged rods of vacuum-melted iodide titanium. Commercially pure titanium carbide powder was hot-pressed into specimens having apparent densities in excess of 97%. Carbon deficient titanium carbide containing 15.8 wt % carbon was made by reacting stoichiometric TiC with titanium powder reported to be 99.9% pure (A. D. McKay Company) at 1600°C in vacuo for 1 hr. This material was crushed in order to obtain a uniform powder. The carbon content corresponded to the formula $TiC_{0.63}$. Hot-pressed specimens were rather porous and contaminated by carbon from the graphite die at their outer surfaces. Contamination was removed by grinding.

Upon comparing weight change and CO_2 evolution during oxidation, it was found that essentially equation (X) holds, i.e., titanium and carbon are oxidized nonpreferentially. Therefore, the oxygen take-up was calculated from weight gain measurements and from the amount of CO_2 with the aid of equations (XI) and (XII), respectively. Results are shown in Fig. 4.

At 1000°C, the oxygen take-up corresponding to the formation of TiO_2 is about the same for titanium metal and $TiC_{0.63}$ but is somewhat lower for TiC. The parabolic law does not apply strictly. The rate found for pure titanium is somewhat greater than that found by Simnad, Spillners, and Katz (20) for both pure titanium and oxygen-saturated titanium.

Oxidized $TiC_{0.63}$ samples showed no internal oxidation in spite of the porosity of the original sample.

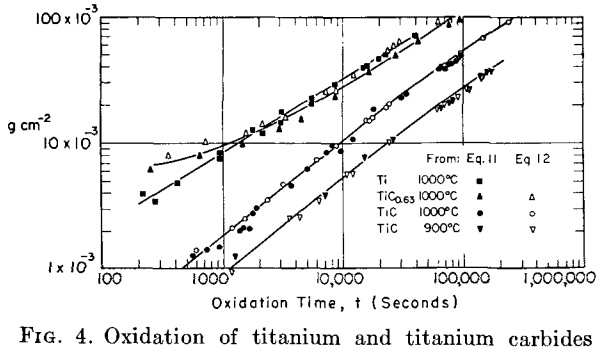

FIG. 4. Oxidation of titanium and titanium carbides

The structure of the scale on both titanium and titanium carbide was investigated by metallographic techniques and x-ray diffraction.

The only oxidation product was TiO_2, with the exception of one experiment in which pure titanium was oxidized for about one week and an intermediate layer of TiO was found. The TiO structure was ascertained by x-ray diffraction.

On titanium carbide oxidized for 24 hr at 1000°C, two conjugate layers were found microscopically. Both layers had the rutile structure. Using the polarizing microscope, it was seen that the outer layer was composed of large grains most of which extended all the way through it, whereas the inner layer consisted of much smaller grains and many pores. The layer structure was similar to that described by McDonald and Dravnieks (21) in their discussion of the "Zone of Metal Phase Consumption." The occurrence of a porous zone is not consistent with diffusion of oxygen ions only via vacancies in TiO_2. Chemical analysis of a portion of the outer layer without any visible TiC gave a value of 0.05% carbon. This is an indication that carbon may dissolve in TiO_2 and diffuse outward.

In an attempt to establish whether carbon escapes from the sample by solution in and diffusion through titanium dioxide, slices from a single crystal of rutile were packed in titanium carbide powder and heated in helium at 900° and 1000°C for two days and then were cleaned and analyzed for carbon. The crystals were reduced as was indicated by the change in color. The analysis did not reveal the presence of carbon in excess of that in a blank (0.005% carbon).

The mechanism of carbon transport across the oxide layer, therefore, remains open to question because diffusion in the form of CO or CO_2 is unlikely, nor has diffusion of carbon atoms been ascertained.

Oxidation of Some Hard Metals

Oxidation of a commercial hard metal consisting of titanium carbide bonded with 20% nickel gave results similar to those obtained for pure titanium carbide. Titanium and carbon are oxidized nonpreferentially, whereas nickel is left over in metallic form near the alloy-oxide interface. This indicates that the chemical potential of oxygen at the alloy-oxide interface is very low and the TiO_2 layer is essentially nonporous.

A commercial hard metal in which tantalum and niobium had been added to the carbide in order to improve the oxidation resistance also showed nonpreferential oxidation of titanium and carbon. After oxidation for 10,000 sec at 1000°C, the oxygen take-up per unit area was found to be four times less than that found for TiC. An alloy containing about the same amounts of the metallic elements without carbon showed a similar improvement of the oxidation resistance in comparison to pure titanium, presumably because of a lower concentration of oxygen ion vacancies in the TiO_2 layer due to the presence of Nb_2O_5 and Ta_2O_5.

As a whole, the presence of carbon seems to have a relatively minor effect on the oxidation characteristics of hard metals based on titanium carbide.

Conclusions

In this paper, an attempt has been made to show the large variety of possibilities which may occur when alloys containing carbon or carbides are oxidized, but detailed investigations have been deferred. In particular, further investigations are desirable in order to determine the effect of carbon concentration on the oxidation rate of alloys in which evolution of CO and CO_2 ruptures an oxide layer. Moreover, the mechanism of carbon migration through a TiO_2 layer needs clarification.

Note added in proof: The curves in Fig. 1 labeled $\Delta m_{ox}/A$ actually show the weight of nickel oxide formed per unit area, i.e., $4.67 \times \Delta m_{ox}/A$.

Manuscript received August 25, 1955. This paper was prepared for delivery before the Pittsburgh Meeting, October 9 to 13, 1955, and is based in part on a thesis submitted by W. W. Webb in partial fulfillment of the requirements for the D.Sc. degree from Massachusetts Institute of Technology.

Any discussion of this paper will appear in a Discussion Section to be published in the December 1956 Journal.

References

1. P. Schwarzkopf and R. Kieffer, "Refractory Hard Metals," Macmillan Co., New York (1953).
2. O. Kubaschewski and B. E. Hopkins, "Oxidation of Metals and Alloys," Academic Press, New York (1953).
3. W. W. Webb, J. T. Norton, and C. Wagner, *This Journal*, **103**, 107 (1956).
4. J. P. Coughlin, *U. S. Bur. Mines Bull.* 542 (1954).
5. O. Kubaschewski and O. von Goldbeck, *Z. Metallkunde*, **39**, 158 (1948);
   O. Kubaschewski and B. E. Hopkins, *loc. cit.*, p. 177.
6. W. J. Moore and J. K. Lee, *Trans. Faraday Soc.*, **48**, 916 (1952).
7. E. A. Gulbransen and K. F. Andrew, *This Journal*, **101**, 128 (1954).
8. J. J. Lander and A. L. Besch, *J. Appl. Phys.*, **23**, 1305 (1952).
9. E. A. Gulbransen and W. Hickman, *Pittsburgh Intern. Conf. Surface Reactions*, p. 222 Corrosion Publishing Co., Pittsburgh (1948).
10. W. A. Pennington, *Trans. Am. Soc. Metals*, **37**, 48 (1946).
11. W. Jost, "Diffusion in Solids, Liquids, Gases," pp. 69 ff., Academic Press, New York (1952).
12. R. Kieffer and F. Kölbl, *Z. anorg. u. allgem. Chem.*, **252**, 229 (1950).
13. R. S. Gurnick and W. M. Baldwin, Jr., *Trans. Am. Soc. Metals*, **42**, 308 (1950).
14. M. Isobe, *Sci. Repts. Res. Inst. Tohoku Univ.*, **3A**, 468 (1951).
15. R. Vogel and W. Döring, *Arch. Eisenhüttenw.*, **9**, 247 (1935).
16. K. Kuo and L. E. Persson, *J. Iron Steel Inst.*, **178**, 39 (1954).
17. P. Schwarzkopf and R. Kieffer, *loc. cit.*, p. 83.
18. P. Ehrlich, *Z. Elektrochem.*, **45**, 362 (1939).
19. E. S. Bumps, H. D. Kessler, and M. Hansen, *Trans. Am. Soc. Metals*, **45**, 1008 (1953).
20. M. Simnad, A. Spillners, and O. Katz, *J. Metals*, **7**, 645 (1955).
21. H. J. McDonald and J. Dravnieks, *This Journal*, **94**, 139 (1948).

Spectral Energy Distribution Curves of ZnS:Ag and ZnCdS:Ag after Thermal Vacuum Treatment

C. H. Bachman, M. L. Sawner, and Wm. Allen

Physics Department, Syracuse University, Syracuse, New York

Abstract

Liquid settled screens of ZnS:Ag and of ZnCdS:Ag of thickness comparable to those of cathode ray tubes were subjected to various temperatures in vacuum. The temperatures ranged from 300° to 800°C and exposure times from 5 to 30 min. Spectral energy distribution curves were then obtained for these phosphors under electron bombardment. Intensity changes, color shifts, and the appearance of new emission bands are noted. These seem to be related to the diffusion and evaporation rates of the phosphor components and the effects depend upon screen thickness as well as time and temperature of exposure.

Introduction

A major problem in the development of cathode ray tubes has been the appearance of blemishes on the luminescent screens due to the bombardment of the screens by ions in the supposedly pure electron beam. These "ion burns" were especially detrimental in obtaining lasting picture quality in television tubes and therefore much attention has been directed to the study of the nature and origin of ions in cathode ray tubes. This phase of the problem has been most recently discussed by Bachman, Hall, and Silberg (1). As a result of such studies, various means have been devised for trapping negative ions before they can strike the screens, and modern cathode ray tubes incorporate some device of this sort. Thus, most of the objectionable blemishes have been removed, although continued electron bombardment can also produce deterioration of the screens.

Although the cause of screen blemishes has been determined and at least partially removed, the actual mechanism for destruction of luminescent efficiency by the ions is unknown. Observations on ion burned screens indicate that the destruction is due to energy transferred from the

fast moving particles to the phosphor screen. Both positive and negative ions will produce a burn, and the degree of burn is roughly proportional to the beam intensity. The burns are usually neutral in color, or exhibit the same color as unburned phosphor but with reduced intensity; however, some have been observed to be violet or green. No correlation between such colors and the ions of any particular element is apparent. The amount of destruction of luminescence seems to be controlled in part also by the penetrating power of the particles, since electrons produce burns at a much slower rate than the more massive ions. Also, aluminum backed screens are less susceptible to ion burning, with burns due to heavier ions diminished more effectively than those due to the lighter ones. Such considerations lead to the hypothesis that ion burns might be due to a localized heating at the point of bombardment. Since phosphors are in general poor heat conductors, dissipated energy would be largely confined to the region near the point of bombardment. Thus it might be that high local "temperatures" are produced on or near the surfaces of the screens. As well as being dependent on the beam intensity, such local temperatures would also depend on the penetrating power of the particles, as determined by their energy and size.

Actual ion burns are difficult to analyze since only the surface portions of the thin screen are affected, and any tests are masked by the predominance of unburned phosphor. A new approach seemed necessary and, following the assumption that local temperatures at the point of ion bombardment could be duplicated on bulk material, the possibility of using thermal vacuum treatment as means of simulating ion burns has been investigated. Such treated materials can be obtained in sufficient quantity for analysis, and studies of their luminescent characteristics can be compared to actual ion burned samples to establish the validity of the approach. Early experiments of this sort showed that thermal vacuum treatment does produce permanent changes in both the color and intensity of luminescence not unlike those observed on ion burned screens. These experiments also established that the changes could not be due to contamination such as by copper. For example, effects were produced on the surface of a phosphor layer which was heated in vacuum by infrared focused on the surface through an infrared transmitting window. In other studies of nearly enclosed pellets of phosphor there occurred gradations in color of luminescence through the pellet, pointing to the importance of the diffusion and evaporation of the phosphor components as factors in thermal destruction. These preliminary experiments which will not be detailed here established that the phosphors could be changed by thermal vacuum treatment and the purpose of this paper is to present data describing such changes.

To gain more quantitative information about this thermal destruction, apparatus was constructed to measure the spectral energy distributions of treated phosphors under cathode ray excitation. Screens of about the standard cathode ray tube thickness were studied. Preliminary experiments of this sort, as well as the pellet study mentioned above, indicated that the screen thickness was an important factor, and must be considered as one of the variables.

On these typical screens the effect was predominantly surface only, as a result of the diffusion and evaporation. It is the authors' intent to look for any correlation between such screens and ion burned screens, but as yet no such correlation has been proven. The data presented are of interest in themselves since the conditions are to some extent encountered in commercial phosphor applications.

The following is then an account of the effects of thermal vacuum treatment on the luminescence of ZnS:Ag and ZnCdS:Ag as controlled by the time and temperature of the heat treatment and the thickness of the screen.

Experimental Procedure

Phosphor screens were prepared on Vycor slides, heated in a vacuum furnace, and finally spectral energy distributions were measured relative to untreated samples under cathode ray excitation. In all handling of phosphors great care was taken to insure that any changes in color or intensity depended only on the thermal treatment, and not on such external factors as contamination, nonuniform screens, or varying properties of the cathode ray tube during measurements.

The phosphors were settled in water on Vycor slides, each of which had an area of about 3 cm^2. These slides were placed on glass rod platforms in the bottom of glass beakers. From a stock suspension of 1 gram of phosphor in 100 ml of water, 10, 20, and 40 ml were added to three 100 ml beakers containing the slides, together with enough water to fill the beakers completely. After allowing the particles to settle for about 30 min, the water was drained off with a capillary tube siphon. Two screens were prepared

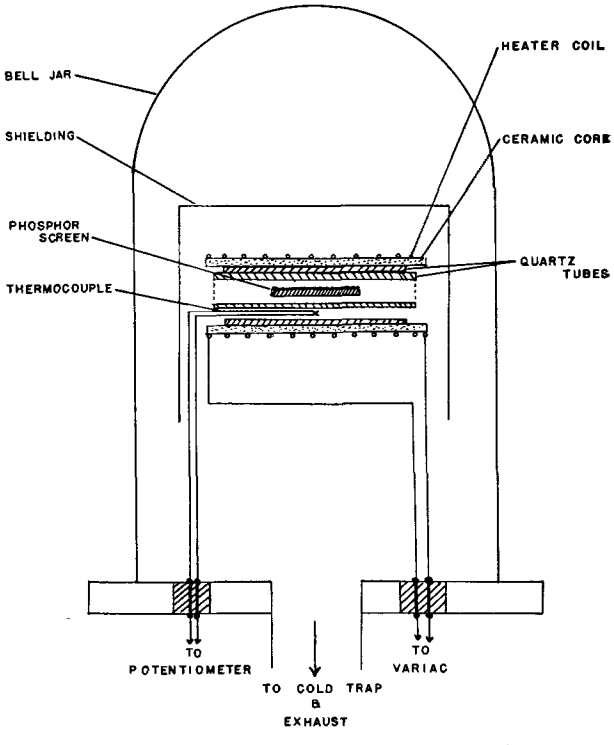

Fig. 1. Thermal vacuum treating apparatus

in each settling so that every treated screen could have an identical untreated standard for comparison. Samples prepared in this way had uniform screen densities of about 2.5 mg/cm², 4.5 mg/cm², and 9 mg/cm². (These will be denoted by I, II, and III in later parts of this paper.)

Thermal treatments were carried out in a bell jar vacuum system evacuated with a metal oil diffusion pump provided with a cold trap (see Fig. 1). Dry ice and acetone were used as the refrigerant. The furnace consisted of a nichrome heater coil surrounded by stainless steel shielding. To guard against any material being ejected from the walls of the furnace onto the sample, the sample was held in a quartz tube within the heater coil. An iron-constantan thermocouple was used for measuring the temperature within the coil. As it required from one to five minutes for the furnace to come to the desired temperature, time measurements were started when the sample reached this temperature. With only manual control the temperature could be maintained to within 10°C. At the end of the heating period, the system was allowed to cool to below 100°C before admitting air to the system. Some uncertainty is introduced here, since some changes in the phosphor constitution affecting luminescence might occur during the heating and cooling periods, which required different times for different temperatures.

The arrangement for measuring the spectral energy distribution of the treated samples is shown in Fig. 2. In brief, the system consisted of a demountable cathode ray tube in which any one of several samples could be viewed at will under irradiation by a diffuse, ion-free, electron beam accelerated to about 1000 v. Our preparation of the phosphor screens results in a surface effect. The ion burn is also a surface effect and the use of this low voltage accentuates the phenomenon by giving greater contrast.

At any time the treated sample could be replaced by its companion standard without varying the exciting electron beam. Thus it was possible to compare the intensity of a treated sample with a standard at any wave length under equivalent conditions of electron beam voltage and current density. The emitted light was analyzed by a prism spectrometer provided with a photo cell. Photocurrents were read with an RCA microammeter and corrections were made for the nonlinear response of the phototube. Such corrections were obtained by making observations

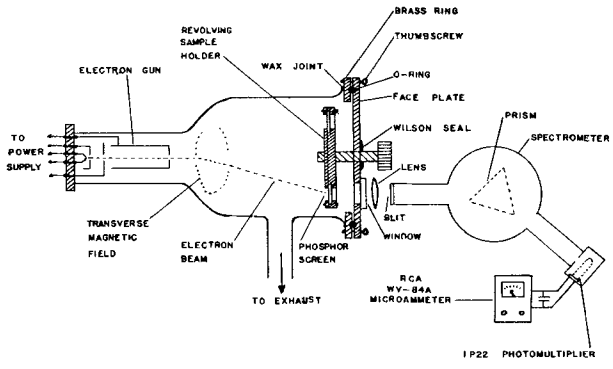

FIG. 2. Arrangement of apparatus for obtaining spectral energy data under electron bombardment.

on a ribbon tungsten filament of known temperature, and determining multiplying factors to fit the photocurrent vs. wave-length curve to the black body curve corrected for the emissivity of tungsten.

In running an energy curve, repeated reference to the intensity of some particular wave length was necessary to detect any small changes which might occur in the cathode ray tube or phototube circuits. Such repeated references at the peak intensity seldom showed variations of more than 3 or 4%. Photocurrent data were then corrected by assuming that these small changes in intensity varied linearly during the short time between references. The intensity standardization was made by observing the photocurrent at the peak wave length for an untreated sample, then immediately rotating the treated sample into view for a similar measurement. Several ratios of intensity of the treated screen to that of the standard at this wave length were averaged. Except at very low intensities (ratios less than 0.2) these ratios showed variations about the average of less than +5%. Calling the peak intensity of the standard unity, this average was then the relative intensity of the treated sample at this wave length. The rest of the distribution was then adjusted to be proportional to this relative intensity at the standardizing wave length. All intensity measurements are therefore relative to a similar untreated sample.

RESULTS

Spectral energy distribution (S.E.D.) curves from treated phosphors are shown in the accompanying illustrations. The intensity relative to the peak intensity of an untreated screen of like thickness is plotted vs. wave length, for screens of three different thicknesses for each temperature and time interval. The phosphors used in this study were furnished by the General Electric Company. The yellow component was 53% CdS and 47% ZnS. Both phosphors contained 0.05% Ag by weight and also 0.015% Cl, 0.05% Na, and 0.04% ZnO. Average particle size was 9 microns. The ZnCdS was, of course, hexagonal, and the ZnS was cubic with a trace of hexagonal form as determined by x-ray diffraction studies.

The effects of the heat treatment on the S.E.D. of ZnS:Ag is shown in the curves of Fig. 3. As can be seen from these the most prominent effect observed is the appearance of two new emission bands, one (5380 Å) appearing at 600°C, the other (5140 Å) appearing at 700°C. Treatments below 500°C have little effect on the intensity or color of luminescence. Samples run at 400°C (not shown in the figure) showed less than a 20% drop in intensity for all three screens. Also, higher temperatures do not cause as large a decrease in the intensity of the blue emission band. There was a slight indication of a more complex structure of the blue emission band, or a possible shift to a slightly longer wave length. This is not shown in the curves but, while points near the peaks usually did not deviate from a smooth rounded curve, slight deviations were noted in the peaks of the samples treated above 600°C.

The results for ZnCdS:Ag are shown in Fig. 4. This phosphor is more sensitive to the treatments, temperatures as low as 300°C lowering the intensity by as much as 50%.

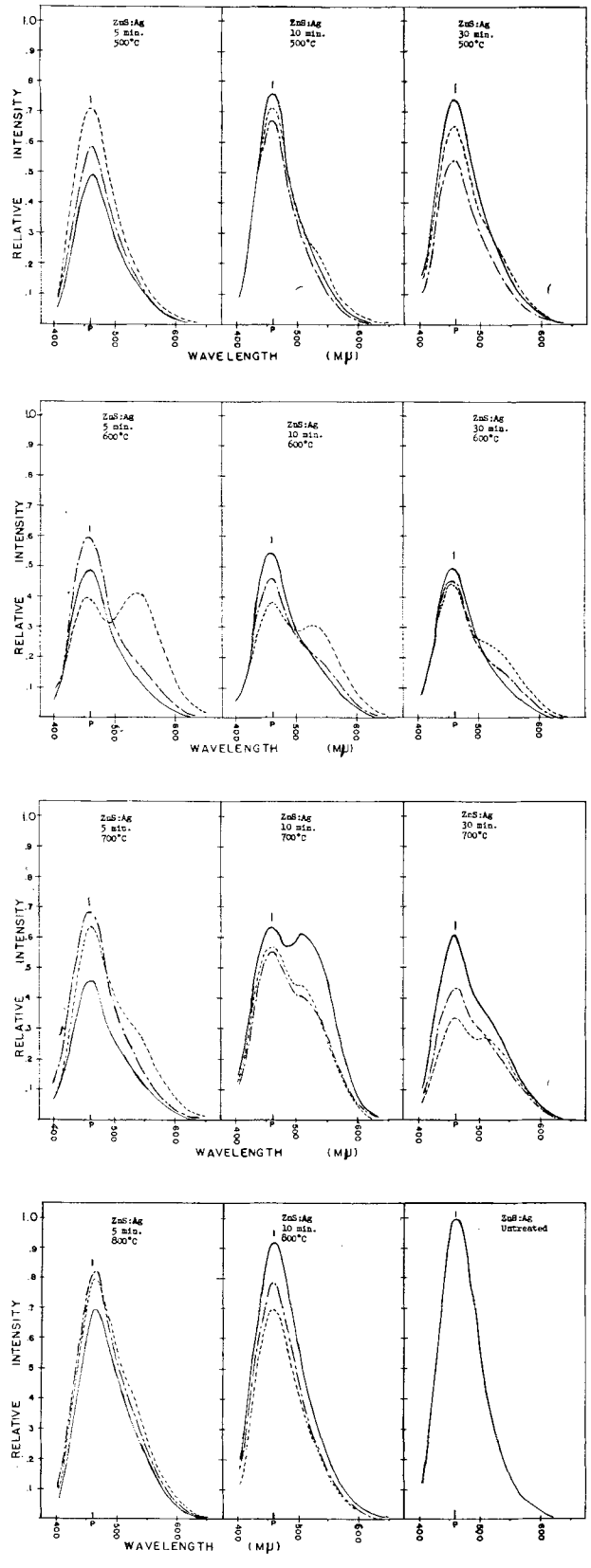

FIG. 3. Spectral energy distribution curves for ZnS:Ag after various thermal vacuum treatments. Dotted lines are for thin screens, broken lines for medium screens, and solid lines for thick screens (see text). "P" indicates peak wave length.

This is of practical interest since such temperatures are used in the industrial processing of cathode ray tubes. There is a tendency for the emission band to shift to shorter wave lengths. Visually, screens treated for 30 min at 700°C fluoresced grayish-blue with a very low intensity. Note that at 300° and 400°C, and also for the longer treatments at 500° and 600°C, the thin screens have a higher intensity than the medium. This might be an indication of a new emission band similar to those observed in treated ZnS:Ag. The long wave-length side of the emission band is broadened for these screens, and a minor emission band appears in the red portion for one of these samples. For both phosphors, material was observed deposited on the inner sur-

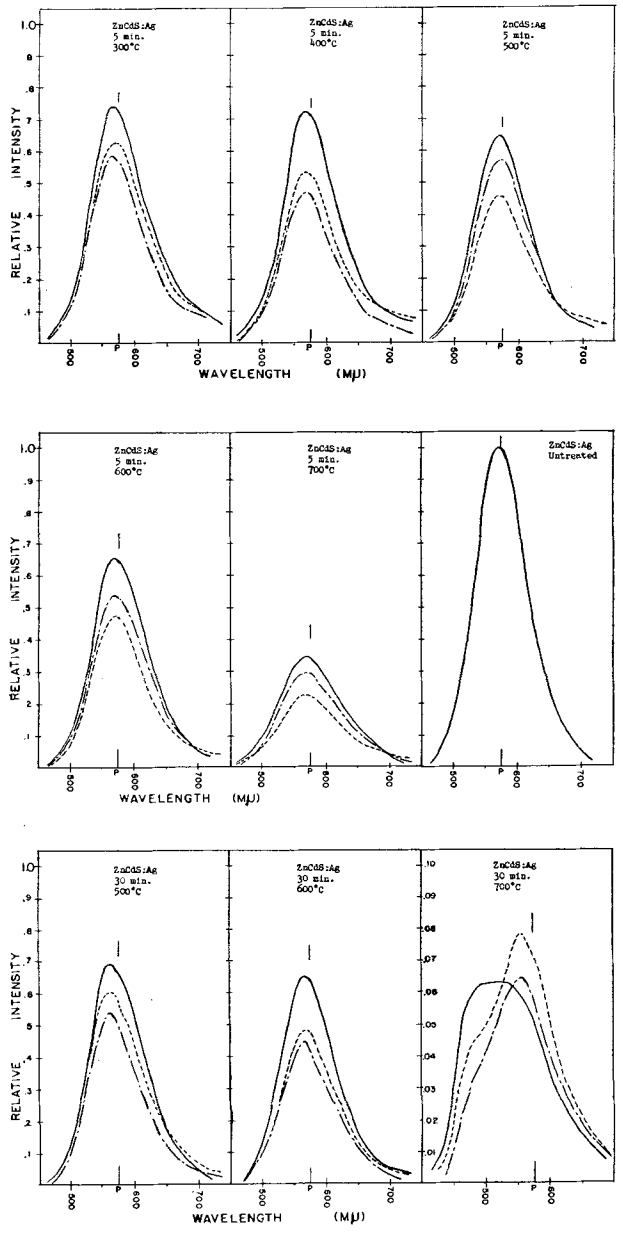

FIG. 4. Spectral energy distribution curves for ZnCdS:Ag after various thermal vacuum treatments. Dotted lines are for thin screens, broken lines for medium screens, and solid lines for thick screens (see text). "P" indicates peak wave length.

face of the quartz tube in which samples were treated, but the amount was insufficient for analysis.

Discussion

Various tests were conducted on treated ZnS:Ag phosphors in an effort to account for the appearance of the two green emission bands. To determine whether they were due to the formation of ZnO, treated samples were washed in acetic acid to dissolve any traces of a surface oxide layer. This affected neither of the bands. X-ray diffraction studies failed to show any observable changes in the crystal structure.

Recent work by Smit and Kroger (2) indicates that a green band peaking at 5140 Å may be produced by heating ZnS in a reducing atmosphere. This band is evidently due to an excess of zinc over the exact stoichiometric composition. It seems quite probable that the 5140 Å band observed in the authors' samples treated at 700°C is due to such an excess produced by evaporation of sulfur. However, a longer wave-length green band (5380 Å) was also observed, most prominent on thin screens treated at 600°C. This might indicate that excess zinc atoms can produce two slightly different emission bands depending on their position in the lattice. At the lower temperatures sulfur may be removed, leaving the zinc atoms more or less in their original positions. At the higher temperatures, zinc may volatilize appreciably, and upon cooling recrystallization might force any extra zinc atoms into interstitial positions. Therefore, one might attribute the longer wave-length green band to excess zinc at normal lattice sites with sulfur vacancies, and the other band to excess zinc atoms in interstitial positions.

Since the longer wave-length green band is attributed to defects in the normal crystal lattice, this emission might be expected to resemble that produced by a substitutional impurity, in contrast to the shorter band, which would be similar to foreign interstitial activation. Leverenz (3) points out that there is evidence indicating a rather clear distinction between the luminescences associated with substitutional and interstitial activation, and has listed the characteristics of phosphors usually associated with the two types of impurity center. Observations on the treated phosphors here seem to be in agreement with this distinction, on two accounts at least. The treated phosphor having the 5140 Å band was observed to have a rather long persistence, usually associated with interstitial activation. The optimum concentration for a substitutional activator is generally much greater than that of an interstitial one. As can be seen in the curves, the 5380 Å band was most prominent on thin screens, appearing on the thicker screens only after long treatment. At higher temperatures zinc may volatilize, thus lowering the effective concentration of the excess zinc activator. Any interstitial zinc produced upon cooling would have a low concentration, lowest on thick screens, where this band is most prominent.

Kroger's theory of self-activated ZnS attributes the blue emission band to zinc vacancies. The presence of silver stimulates the formation of these vacancies, and shifts the emission band to a slightly shorter wave length. Vaporization of sulfur would account for any lowering in the intensity of the blue emission band but, at higher temperatures where sulfur evaporation would be greater, this blue emission is less affected, indicating that a constructive process is also taking place. Assuming the correctness of Kroger's theory, and the above hypothesis concerning the green band, the various emission bands which might occur in a thermally treated ZnS:Ag phosphor are:

(*A*) The original Ag-activated band (4550 Å);

(*B*) A green band due to sulfur vacancies (5380 Å);

(*C*) A green band due to interstitial zinc (5140 Å);

(*D*) The blue emission of self-activated ZnS due to the zinc vacancies not influenced by association with Ag (4700 Å).

The results indicate that each of these emission bands may be produced. The formation of the green bands, and the lowering of intensity of the blue emission band may both be attributed to sulfur evaporation. At the higher temperatures, appreciable zinc evaporation will occur, and zinc vacancies may be produced in certain parts of the crystals. Such vacancies may be produced in the neighborhood of a Ag atom, and hence add to the original emission band, or they may be independently formed, having an emission band of a slightly longer wave length. Such occurrences would account for the apparently enhanced blue emission, and the complex structure of this band noted in the samples treated at the higher temperatures. The dependence of the formation or destruction of the various emission bands on time, temperature, and screen thickness must finally be accounted for by the different rates of evaporation and diffusion of the phosphor components.

The lowering of intensity of the yellow emission of ZnCdS:Ag must presumably be of the same character. However, since there is no apparent reinforcement of intensity at higher temperatures, evidently the rates of diffusion and evaporation are such that there is no tendency for cation vacancies to form. There is only a slight indication that anion vacancies, or interstitial Zn or Cd may produce a new luminescent band. Perhaps certain temperatures and times intermediate to those tested here might bring out these more distinctly. The general tendency for the emission band to shift to shorter wave lengths is due to the higher rate of evaporation of cadmium, this tending to revert the emission band to that of pure ZnS. The odd shaped S.E.D. curve for samples treated at 700°C for 30 min could be due to the presence of regions of the screens which have been predominantly freed of cadmium.

Several interesting observations were noted on treated screens. One of the samples having the 5140 Å band showed signs of deterioration under the short exposure to electrons during measurement. Grotheer has shown (4) that electron burning is most noticeable on phosphors having long persistence, and this is considered an indication that deterioration is enhanced when the luminescent centers are excited. Untreated ZnS:Ag is not electroluminescent, but treated samples with and without the green bands were found to exhibit a weak luminescence excited by an electric field. Samples having the 5140 Å band flashed brightly for a brief instant upon application of the field, indicating the presence of an effective electron trapping mechanism in this phosphor.

Conclusion

The original reason for studying thermal vacuum treatments of phosphors was an attempt to gain further insight into the destruction of luminescence by ion bombardment. Although the validity of the hypothesis that ion burns are due to high local "temperatures" at the point of ion impact has not been firmly established, these studies do indicate that the destruction produced thermally is caused by the ejection of material from the phosphor, such as might be expected to occur with ionic impact.

However, there seems to be one clear distinction between thermally induced destruction and ion burns, especially with the ZnS:Ag. With this phosphor, a constructive process appears at high temperatures, and thus the intensity of the samples was not lowered to less than 70%. Visual observations on ion burned samples of ZnS:Ag seem to indicate a much more pronounced lowering of intensity. If ion burns were completely like thermal burns, one would expect that under some conditions of ion bombardment this constructive process might take place and give rise to a permanent enhancement of luminescence. This has not been noted, and here the analogy between the two types of destruction may fail. The ion burn is an extremely localized affair, and the diffusion and evaporation picture must appear quite different from the case of the more evenly distributed thermal energy of heat treatments. Therefore, the chance of forming zinc vacancies without accompanying anion vacancies would be less, since the formation of these vacancies under thermal treatment is apparently closely connected with the rate of diffusion of zinc through the samples. The chance occurrence of zinc being ejected by the ions may, however, account for the occasional temporary increase of light output sometimes noted on ion bombarded screens.

In addition to possibly furthering the understanding of ion burn phenomena, thermal vacuum treatments such as described here might also be useful in studying the self-activation of other phosphors, and might also lead to the appearance of new emission bands and other luminescent properties such as the green bands and the electroluminescent effects noted here.

Manuscript received June 17, 1955. Portions of this work were sponsored by the office of Ordnance Research, U. S. Army.

Any discussion of this paper will appear in a Discussion Section to be published in the December 1956 Journal.

References

1. C. H. Bachman, G. L. Hall, and P. A. Silberg, *J. Appl. Phys.*, **24**, 427 (1953).
2. N. W. Smit and F. A. Kröger, *J. Opt. Soc. Amer.*, **39**, 661 (1949).
3. H. W. Leverenz, "Excitation and Emission Phenomena in Phosphors," Preparation and Characteristics of Solid Luminescent Materials, Cornell Symposium of Am. Phys. Soc., John Wiley & Sons, Inc., New York (1948).
4. W. Grotheer, *Z. Phys.*, **112**, 541 (1939).

Electrophotoluminescence Effects

Frank Matossi

U. S. Naval Ordnance Laboratory, White Oak, Maryland

and

Sol Nudelman

U. S. Naval Ordnance Laboratory, White Oak, Maryland and University of Maryland, College Park, Maryland

Abstract

Various electrophotoluminescence effects of phosphors continuously excited by ultraviolet radiation were studied for their dependence on field strength and frequency. These effects include luminescence stimulations at application and removal of alternating electric fields, quenching, and a periodic fluctuation of luminescence (ripple) during the field application. For some electroluminescent phosphors, the gradual transition from the quenching ripple to the electroluminescence brightness wave was observed, indicating that the brightness waves and the ripple patterns are produced by independent processes. The observations are discussed in the light of previous theoretical considerations.

Introduction

If electroluminescent or nonelectroluminescent phosphors of the zinc-sulfide type are excited to luminescence by ultraviolet radiation (or by x-rays), the application of an alternating electric field modifies the luminescence. This modification, either during continuous excitation by radiation or during phosphorescence afterglow, is called, according to Destriau (1) "electrophotoluminescence." It is a complex phenomenon consisting of several partial effects (2–4), which are indicated in Fig. 1. During "field on," the intensity varies periodically with twice the frequency of the field. This "ripple" is superimposed on a stimulation

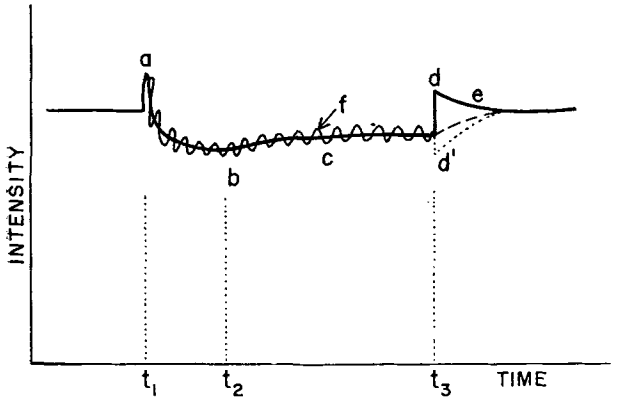

FIG. 1. Electrophotoluminescence, schematical. t_1, field on; t_3, field off; a, electric or first stimulation; b (at t_2), maximum quenching; c, intermediate recovery to steady quenching; d, cut-off or second stimulation (———), sometimes missing (-------) or replaced by d', cut-off quenching (·····); e, final recovery; f, ripple. Time scale distorted: $t_3 - t_2 \gg t_2 - t_1$.

at the instance of field application and on a quenching that exists during field application. The quenching is particularly strong just after the field is applied. The maximum of the first stimulation occurs after a few periods of the field; maximum quenching is reached after about $\frac{1}{10}$ sec; the intermediate recovery takes many seconds; the final recovery, a few seconds.

This paper is mainly concerned with a study of the frequency and field strength dependence of the stimulations, the quenching effect, and the ripple amplitudes of electrophotoluminescence. In addition, for electroluminescent phosphors, the transition from ripple pattern to brightness wave with increasing field strength will be described. It will be shown that the ripple pattern and the brightness wave have independent origins.

Experimental Procedure

Twenty-eight ZnS-phosphors of cubic or hexagonal structure, made with or without flux, and with a variety of activators were examined in this investigation. For detailed quantitative work, only about half of this number was used. These include commercial products such as the electroluminescent phosphors Q62-2666 (du Pont de Nemours & Co., Wilmington, Del.), 3-310 (General Electric Co., Cleveland, Ohio), and Sylvania Panelescent Lamps (Sylvania Electric Products Inc., Salem, Mass.), and the nonelectroluminescent phosphors 1402 (du Pont), 2301 (New Jersey Zinc Co., Palmerton, Pa.), and MB-19 (Stroblite Co., New York, N. Y.). Among the noncommercial phosphors, the most extensively used corresponded to electroluminescent Sylvania type of phosphors. They were prepared in this Laboratory according to the methods of Homer and co-workers (5) and include a green phosphor (No. 23), a blue-green (No. 22), and a yellow phosphor (No. 11).

All phosphors were embedded in parlodium (except the Sylvania Lamps, which were used as delivered) and investigated in cells of the usual construction (3), with about 5 cm² area and about 0.2 mm thickness of the phosphor layer. A d-c-operated argon lamp with a Wratten filter No. 18A transmitting from 2900 to 3900 Å served as the ultraviolet source. Other filters between the cell and the 1P21 photomultiplier separated the green and blue luminescence emission (Wratten No. 21, transmitting above 5300 Å, or Wratten No. 3 and Corning 5850, transmitting from 4300 to 4800 Å).

The output of the photomultiplier was observed either with an oscilloscope or with a vacuum tube voltmeter in an averaging circuit. The last method was used in particular for the measurements of the steady-state quenching, while oscilloscopic observations served for the measurement of the phenomena of short duration. Photographic records or direct readings on the screen were utilized for the oscilloscopic measurements.

The electric field was applied after the ultraviolet excited luminescence had reached its equilibrium value. Ultraviolet excitation was maintained continuously during field application. The applied field was obtained from sinusoidal generators together with power amplifiers. The output of these systems could be varied from zero to 500 v (rms) in the frequency range from 100 cps up to 10 kcps. At higher and lower frequencies the output voltage decreased appreciably. In a few instances, square wave fields from an appropriate generator were used. Except for the square wave fields, all potential differences refer to rms-values.

The measurements of the first stimulation were difficult at low frequencies. Below about 50 cps, they become very sensitive to the phase at which the field is applied to the phosphor. Since this was not regulated, measurements varied sometimes by as much as 25%. Other measurements were reproducible to better than 3%. At frequencies below a few kilocycles per second, the large ripple amplitude during the application of the field also interferes with accurate measurements of stimulation effects.

Results

All phosphors exhibit the two stimulations, the quenching, and the ripple. Frequency and field strength dependence of these effects, however, show notable quantitative differences for the various phosphors. These differences, however, did not show any systematic dependence on the method of preparation (kind of activator or flux) or on other luminescence properties such as time of afterglow or whether electroluminescent or not.

Stimulation.—The first stimulation always decreases with increasing frequency up to about 10 kcps, then either slowly increases or remains nearly constant. The typical behavior is shown in Fig. 2. The values at frequencies below 2 kcps are too high because the large ripple amplitude could not be separated, in these measurements, from the stimulation effect proper.

The cut-off stimulation consists of two components. A very sharp peak, not illustrated in Fig. 1, is followed by a tail ("final recovery") of long duration (Fig. 3). The tail has the shape of the solid or dashed curves at e in Fig. 1. The dashed curve is normally observed only at frequencies below several hundred cps. But for two phosphors, No. 11 and MB-19, this behavior was found at all frequencies. In these cases (Fig. 3B), the peaks were observable down to about 1000 cps, while usually (Fig. 3A) the peaks

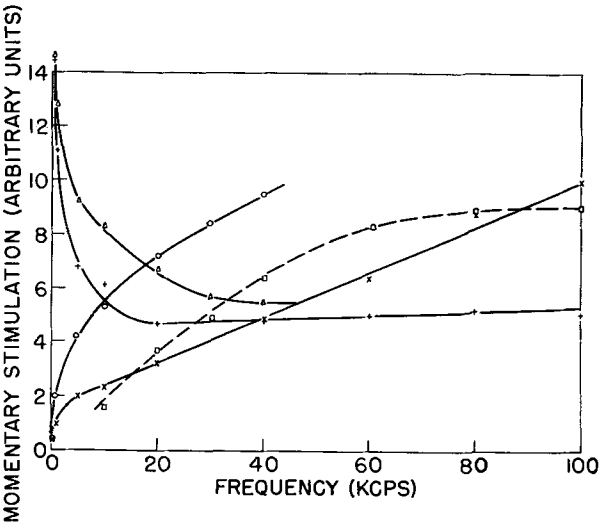

FIG. 2. Stimulation vs. frequency.

△ —— △ 1st stimulation, 105 v
+ —— + 1st stimulation, 53 v } phosphor
○ —— ○ 2nd stimulation, 105 v } 3-310
× —— × 2nd stimulation, 53 v
□ - - - □ 2nd stimulation, 40 v Green Sylvania Lamp

The experimental points for frequency zero correspond to 60 cps.

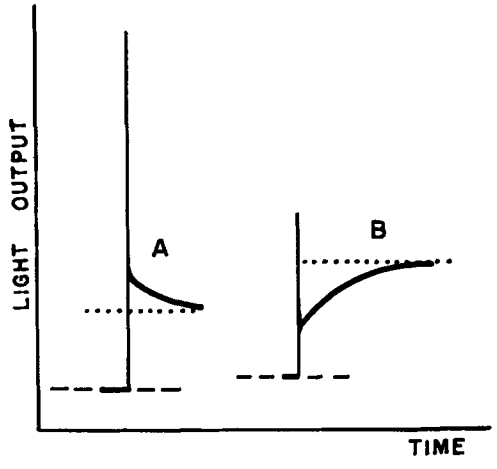

FIG. 3. Cut-off stimulation. A, Green Sylvania Lamp, 4 kcps; B, Phosphor MB-19, 9 kcps; - - - steady-state quenching; ··· output without field.

appeared only above 5 to 10 kcps. The peak intensity increases with frequency and for some phosphors (in particular for the Sylvania Lamps) reaches a saturation value. This saturation occurs sooner with higher applied voltage. The "tail intensity" also increases with frequency at the low frequencies but does not vary appreciably after the peaks can be observed. The curves shown in Fig. 2 for the second stimulation refer to the maximum peak height above the reference level (output without field). The large ripple amplitude at low frequencies prevented the use of the steady quenching level as reference level for the cut-off effects.

All phosphors showed the stimulation. In one case, the cut-off stimulation was reversed into a cut-off quenching (*d'* in Fig. 1). This happened with phosphor No. 22 at low frequencies. At other frequencies, this phosphor behaved like all others. Stimulation effects become stronger at higher field strengths, but the increase with field strength is not very pronounced.

Quenching.—The typical frequency dependence of the maximum quenching and of the steady-state quenching is illustrated in Fig. 4. The curves for phosphor 2301 represent the most generally observed type. A minimum of the quenching at a frequency of the order of 5 to 10 kcps, as shown for MB-19, is observed only for a few other phosphors, notably for No. 11 and 3-310. All these are cubic phosphors, although other cubic phosphors did not show this behavior. The electroluminescent green Sylvania phosphors produced even more complicated curves. It may be pointed out that Destriau (6) recently observed quenching in some fast-decaying phosphors even with d-c fields.

Larger fields increase the quenching with an almost linear dependence on field strength in most nonelectroluminescent phosphors. In electroluminescent phosphors, however, quenching begins to diminish at some field strength, since high fields will produce electroluminescence in these phosphors. The transition from quenching to electroluminescence will be described below.

For many phosphors, the quenching effect appears only in the green emission, although stimulation effects can be observed also in the blue. Phosphors with predominantly blue emission, however, showed quenching also in the blue region.

Ripple amplitude.—In Fig. 5, the frequency dependence of the amplitude of the ripple during the steady-state quenching and of the electroluminescence brightness waves are shown. The maximum of the ripple near 100 cps

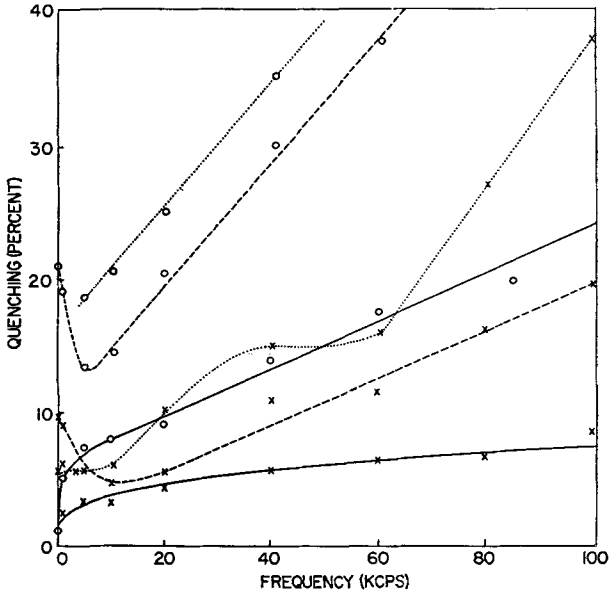

FIG. 4. Quenching vs. frequency (per cent of output without field). XXX Steady-state quenching; OOO maximum quenching; —— Phosphor 2301, green emission; - - - Phosphor MB-19, blue emission; ···· Green Sylvania Lamp, green emission. Frequency zero corresponds to 20 cps.

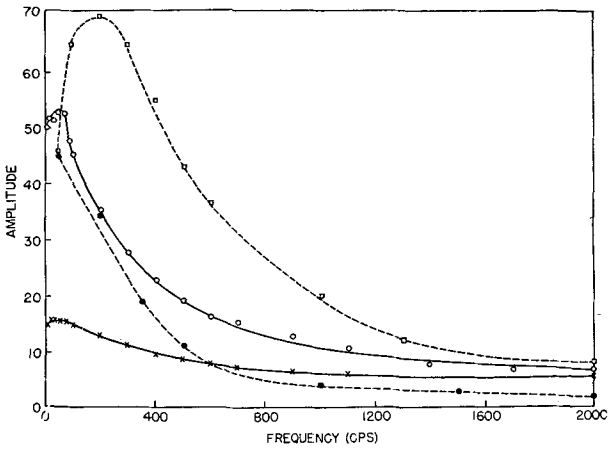

FIG. 5. Ripple and brightness wave amplitude vs. frequency.

——— Ripple amplitudes (per cent of output without field)
OOO green band } of Sylvania Lamp
XXX blue band }
– – – Brightness wave amplitude in arbitrary units (units different for green and blue band)
●●● green band } of phosphor 22
□□□ blue band }

occurs also in other phosphors. This behavior is quite different from that of the brightness wave amplitudes, where maxima occur above or below this frequency in the blue and green bands, respectively. Immediately after the field is applied, i.e., during the first stimulation and the decline to maximum quenching, the amplitudes of the ripple are, in general, much larger than in the steady state.

Transition from quenching to electroluminescence.— Fig. 6 presents a series of oscillograms obtained for increasing potential difference. They show two periods of the ripple during steady-state quenching. It can be seen that the quenching occurs actually only during part of the period and that the two peaks per period are of very unequal height. Increasing the voltage will at first increase the net quenching. Then, at a potential difference that would be just sufficient to produce electroluminescence in the same cell in the absence of ultraviolet radiation, a new peak begins to develop (marked by arrows in Fig. 6). This peak grows with increasing potential difference and finally takes over entirely. At the same time, the total light output increases until the quenching effect has disappeared and an electroluminescence brightness wave is obtained. It shows the usual phase shift of brightness waves, since it slightly precedes the field, whereas the ripple peaks during pure quenching have a phase shift in the opposite direction. The phase change from ripple to brightness wave is not a gradual shift, but it is the result of different relative intensities of two independent peaks whose individual phases remain constant.

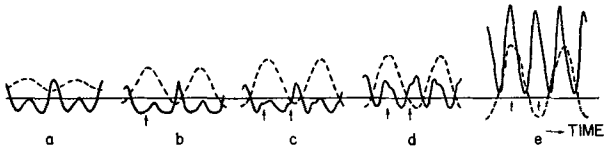

FIG. 6. Oscillograms for Green Sylvania Lamp excited by 60 cps field and ultraviolet. --- field; —— ripple pattern. *a*, 26; *b*, 90; *c*, 110; *d*, 125; *e*, 160 volts rms. The continuous solid line: intensity without field. Arrows: brightness wave peaks.

There is, however, an important difference between the brightness waves of Fig. 6*e* and those obtained without any ultraviolet radiation. Only one peak per half-period appears in Fig. 6*e*, while in a brightness wave very often two are observed. Actually, an additional small peak appears slowly if the ultraviolet radiation is cut off. The shape of this normal brightness wave (without ultraviolet) is seen in Fig. 7, where the peaks are named B and C peaks (in phase and out of phase with the field, respectively) in accordance with the designation of similar peaks observed with nonsinusoidal fields (7). The time required for the C peaks to attain a constant height varies from several minutes to a quarter of an hour after removal of the radiation. By applying ultraviolet again, the additional peaks disappear at once. These effects have been observed for various other electroluminescent phosphors.

The ultraviolet radiation tends, for some electroluminescent phosphors, to unbalance markedly the light output for successive half-periods of the field. This was most pronounced in phosphor 3-310 (Fig. 8), a phosphor that did not exhibit C peaks with sinusoidal fields.

Fig. 9 shows a series of oscillograms similar to Fig. 6 but for square wave fields. Again there are marked quali-

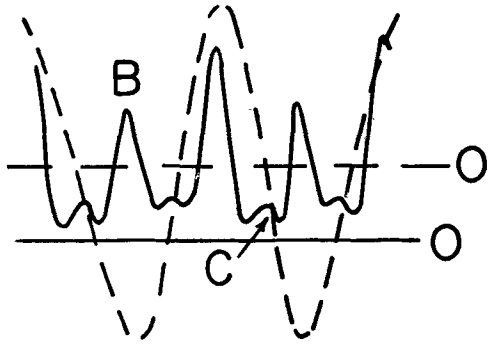

FIG. 7. Brightness wave without u.v., 60 cps, Green Sylvania Lamp. --- Field; —— brightness wave.

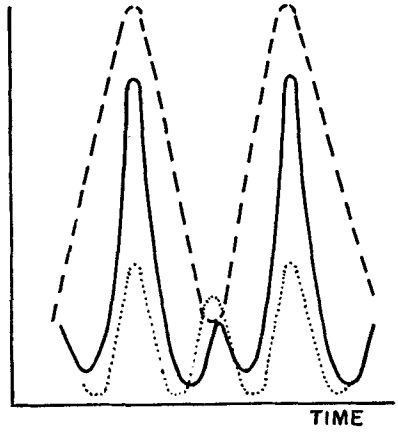

FIG. 8. Dissymmetry of brightness waves, 60 cps, phosphor 3-310. --- Field; —— light output with u.v.; ···· light output without u.v.

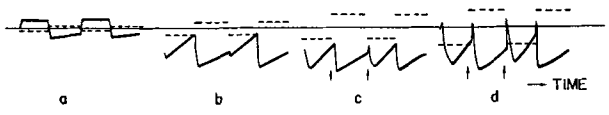

FIG. 9. Oscillograms for Green Sylvania Lamp excited by 60 cps square wave field and ultraviolet. --- Field; —— ripple pattern. *a*, 5; *b*, 35; *c*, 53; *d*, 80 volts. Continuous solid line: intensity without field. Arrows: brightness wave peaks.

tative differences between the two half-periods. At low voltages, the one half-period does not seem to be affected at all, while in the other a maximum quenching is followed by a partial recovery. At a certain critical potential difference (again the voltage for which electroluminescence would begin to appear), spikes begin to develop. These spikes grow gradually with increasing field, and the ripple pattern transforms to the brightness wave of square wave excited electroluminescence (7).

DISCUSSION

Several theoretical aspects of electrophotoluminescence effects in a continuously ultraviolet-excited phosphor have been discussed previously (8). This treatment leaves sufficient freedom to accommodate the variety of behavior found for the different phosphors. The basic assumptions and conclusions may be briefly reviewed:

(*A*) The field may empty the traps; this is the main contribution to the first stimulation.

(*B*) The field induces radiationless transitions of conduction electrons; this is the main contribution to quenching.

(*C*) These two processes describe the behavior between t_1 and t_2 of Fig. 1. After this time, the induced radiationless transitions become relatively ineffective, the centers available to them becoming filled. These centers may be assumed to be near the surface, to which the electrons are drawn by the field. Continuous excitation by ultraviolet of the phosphor in this state of intermediate equilibrium, at the time of maximum quenching, yields a growth curve that reaches a final equilibrium different from that without field, equivalent to steady quenching. It is not necessary to assume actual recombinations for the quenching mechanism. If electrons are trapped at the surface, they may attract holes so that these holes cannot be trapped in activator levels, thus diminishing the possibility of radiative transitions of conduction electrons with empty activator levels. This process is mathematically equivalent to the field-induced radiationless transitions assumed above.

(*D*) Excess charges accumulate in the conduction band during field application; their release at field removal produces the cut-off stimulation. These excess charges may in part be due to polarization charges trapped near the surface and released only after final removal of the field. Evidence for such quasi-permanent polarization has recently been offered from quite different experiments (9). The observations shall be discussed in the light of these assumptions and conclusions.

As mentioned above, the intermediate recovery was interpreted (8) as a growth curve. But there is another possibility, viz., the existence of two quenching processes, a fast one with high efficiency and a slow one with low efficiency. The fast process is assumed to be the same as that described above, radiationless transitions of conduction electrons to empty centers or deflection of holes from centers by surface-trapped electrons. This process ceases to be effective after a certain time, i.e., after all surface traps have been filled, equivalent to maximum quenching. The slow process remains and is the only process acting in the steady-state quenching. The intermediate recovery then is the gradual transition to this state. This slow process might be the one assumed by Zalm and co-workers (10), i.e., emptying of hole traps with subsequent radiationless recombinations of the released holes with electrons in traps. It can be shown, by considerations similar to those used in (8), that the ratio of the time constants of the two processes is equal to the ratio of the number of conduction electrons to the number of empty centers, which was assumed to be small.

The slow component of the second stimulation (the final recovery) can readily be ascribed to the slow release of trapped polarization charges as mentioned above. The sharp overshoot, however, requires another source of excess electrons. Curie (11) has pointed out that the lifetime of the cloud of free electrons created by excitation of electroluminescence effects may be several 10^{-4} sec. (In Curie's paper, this time is referred to as the lifetime of an electron in the conduction band, but its real significance is with respect to the cloud and not to an individual electron.) This estimate may be assumed to be valid also for electrophotoluminescence effects. Therefore, at frequencies higher than a few kcps, some free electrons will be retained in the conduction band at every period of the field, with the result that, over many periods, an excess charge is accumulated that increases with frequency for a fixed time of observation. The dumping of these free excess electrons at "field off" should give the observed sharp peak. At frequencies much higher than the reciprocal of the lifetime of the cloud, which is also a measure for the build-up time, saturation may be expected, since the cloud will not be regenerated sufficiently fast.

The disappearance of the quenching and of the slow component of the cut-off stimulation at low frequencies is attributed (8) to the possible existence of currents. This would compensate any loss of electrons and also drain off any excess electrons, maintaining a constant charge density. The individual differences in the quenching behavior at low frequencies (Fig. 4) are, however, difficult to understand from a general viewpoint. Probably, individual surface properties come into play.

It should not be necessary to discuss the frequency dependence of the first stimulation independently since it is intimately connected with that of the quenching (8). If quenching increases with frequency, the first stimulation should decrease if the number of traps emptied per period is considered to be independent of frequency. But this last condition need not hold in all cases and, therefore, no rigorous correspondence between first stimulation and quenching can be expected.

The appearance of certain peaks in electroluminescent phosphors only in the absence of ultraviolet excitation can be ascribed to polarization and diffusion processes

(12). These C peaks, which begin to grow whenever the applied field decreases, were interpreted (7) as being due to polarization charges periodically accumulated by the field and released when the field diminishes. It is plausible that the ultraviolet radiation creates so many free electrons in the bulk of the phosphor particle that the released polarization charges cannot easily diffuse back to empty centers because the charge density gradient has become smaller. Thus, the additional peaks would not appear.

The frequency dependence of the ripple amplitude and of the brightness wave amplitude is due to different processes. While the brightness wave amplitudes are governed mainly by the excitation efficiency and the decay times of the luminescence processes (7), the ripple amplitude depends mainly on the ratio of the transition probabilities from the conduction band to either empty centers or traps. Theory predicts (8) a maximum of the ripple amplitudes at some critical frequency. But since it is doubtful whether the observed maximum (Fig. 5) is actually due to this effect rather than to polarization and possible barrier effects, no numerical evaluation of the probability ratio shall be tried.

Observations on the transition from quenching to electroluminescence also indicate the independent origin of ripple pattern and brightness wave. Both patterns superpose additively. The forward phase shift of the brightness wave is generally assumed to be due to the action of polarization charges (13), although the detailed mechanism of this effect is not yet completely understood since different methods of computing the polarization field lead to different results. The quenching effect is assumed to be due to a loss of free electrons available for luminescence transitions. This loss yields a phase shift in the direction opposite to that caused by polarization effects, as was pointed out by Curie (11) in a simplified consideration of the particle balance.

The assumptions about the cause of the quenching are also supported by the fact that quenching is observed, for many phosphors, in the green emission only. This is true in particular for the green Sylvania phosphor, where two separate emission bands with different excitation mechanisms are established (7, 14) and where only the green band involves conduction electrons. This argument is valid also for the quenching process proposed by Zalm (10) since the trapped electrons come from the conduction band.

No interpretation can yet be given of the unbalancing effect of the ultraviolet radiation. It may be connected with the experimental circumstance that only one side of the cell is exposed to radiation and that the cell is not symmetric with respect to the electrodes.

After submission of this paper for publication, similar work became known (15) in which unbalancing effects were observed under various circumstances. The authors want to point out that such effects do not contradict the model used here (8) since the shape of the ripple pattern is not derived from the model, but is put into the mathematical formalism.

Conclusion

The properties described and discussed in the previous sections, although demonstrated only in a few examples, are typical for all phosphors investigated quantitatively or tested qualitatively. In particular, the qualitative features of the frequency dependence of the electrophotoluminescence effects and the transition to electroluminescence are common to many phosphors, and they agree well with the general picture derived for these effects from other observations and from theoretical considerations. On the other hand, there is a wide spread in the quantitative aspects. Any speculation about the individual differences would be premature. The general properties and their interpretation seem, however, to be well established.

Acknowledgment

The authors thank Dr. J. F. Waymouth, Sylvania Electric Products Inc., for information about the Sylvania panels and Dr. E. Meschter, du Pont de Nemours and Co., for providing two electroluminescent phosphors.

Manuscript received June 30, 1955. This paper was delivered before the Cincinnati Meeting, May 1 to 5, 1955, and is based in part on a dissertation submitted by one of the authors (S. N.) to the University of Maryland in partial fulfillment of the requirements for the Ph.D. degree.

Any discussion of this paper will appear in a Discussion Section to be published in the December 1956 Journal.

REFERENCES

1. G. Destriau, *Phil. Mag.*, **38**, 700, 880 (1947).
2. G. Destriau and J. Mattler, *J. Phys. radium*, **11**, 529 (1950).
3. F. Matossi and S. Nudelman, *Phys. Rev.*, **89**, 660 (1953).
4. K. W. Olson, *ibid.*, **92**, 1323 (1953).
5. H. H. Homer, R. H. Rulon, and K. H. Butler, *This Journal*, **100**, 566 (1953).
6. G. Destriau, *J. Appl. Phys.*, **25**, 67 (1954).
7. S. Nudelman and F. Matossi, *This Journal*, **101**, 546 (1954).
8. F. Matossi, *Phys. Rev.*, **94**, 1151 (1954).
9. J. F. Waymouth and F. Bitter, *ibid.*, **95**, 941 (1954).
10. P. Zalm, G. Diemer, and H. A. Klasens, *Philips Res. Rpts.*, **9**, 181 (1954).
11. D. Curie, *J. Phys. radium*, **14**, 672 (1953).
12. F. Matossi, *Phys. Rev.*, **98**, 434 (1955).
13. D. Curie, *J. Phys. radium*, **14**, 510 (1953).
14. L. Burns, *This Journal*, **100**, 572 (1953).
15. W. Low, I. T. Steinberger, and E. Alexander, *also*, R. E. Halsted, Unpublished papers presented at Symposium on Electroluminescence and Photoconduction in Inorganic Phosphors, Brooklyn Polytechnic Institute, Sept. 9, 1955.

Effect of Zone-Refining Variables on the Segregation of Impurities in Indium-Antimonide

T. C. HARMAN

Battelle Memorial Institute, Columbus, Ohio

ABSTRACT

Upon zone-refining indium-antimonide, ultimate concentrations of two slowly segregating impurities are approached. The most slowly segregating impurity, identified as tellurium, was found to be n-type which lowers the melting point of indium-antimonide. The second most slowly segregating impurity, identified as zinc, was shown to be p-type which raises the melting point of indium-antimonide. Both impurities originated in the indium. Electrorefining is an effective technique for removal of zinc from indium. Zone-refining is an effective technique for removal of tellurium from indium. There are no indications that deviations from stoichiometry prevent the attainment of extrinsic carrier concentrations below $10^{14}/cm^3$ in indium-antimonide.

INTRODUCTION

At the present time, there is considerable interest in the semiconducting compound, indium antimonide. This interest may be grouped broadly under the categories constituting practical applications and those involving basic advances in present knowledge of solid-state phenomena.

Both the fabrication of devices and the carrying out of fundamental studies requires ultra-high purity material with impurity contents of the order of one part per hundred million or less. It is the purpose of this paper to discuss the nature of the problems involved in the preparation of high-purity InSb and to give an account of the solution of such problems.

EXPERIMENTAL

Preparation and Purification of the Compound

Indium-antimonide ingots were prepared by direct reaction of the elements in a Vycor container under a reduced pressure of pure, dry hydrogen. The compound was purified by the zone-melting technique (1). Initially, the ratio of zone length to ingot length was ½ and the rate of travel of the molten zone was 30 cm/hr. These quantities were gradually decreased until the zone length was 2.0–2.5 cm with a 20 cm ingot, and the rate of pass was 1 cm/hr. The final 10–15 zone-melt passes were made under these conditions.

During the course of the zone-refining passes, 1-cm lengths were cut from the impure ends and discarded. Also, specimens were removed from various portions of the ingot for electrical measurements. In addition, the ingot was probed periodically to determine the sign of the thermal emf at room temperature and at 80°K, to ascertain whether p- or n-type conduction predominated. The electrical measurements indicated that, initially, the entire ingot was p-type. However, upon subsequent zone passing, the region at the end of the ingot which was last to freeze became n-type. Subsequent passes increased the length of this n-type region as determined by electrical measurement at 80°K. After 30 passes, it extended over half the length of the ingot. After a total of 30 or more zone passes, thin slices cut perpendicular to the direction of travel of the molten zone were removed from the ingot. Hall coefficient and resistivity measurements at 80°K were carried out on specimens prepared from these slices. Carrier concentrations, type of conduction, and mobilities were determined from the electrical data. Analyses of the electrical properties as a function of distance along the ingot after a large number of zone passes, as well as information obtained during the course of zone-refining passes, indicated that the most slowly segregating impurity is n-type, and that it lowers the melting point of indium-antimonide. The second most slowly segregating impurity is p-type; it raises the melting point. Early in the investigation it was found that the final concentration of these two slowly segregating impurities in indium-antimonide depended on the purity of the indium used in the preparation of the compound. In the experiments to be described in this paper, the antimony was zone melted prior to use in preparations of indium-antimonide. However, recent measurements show that concentration of these troublesome impurities is much lower in high-purity antimony than it is in the indium.

Zinc Impurity in InSb

Fig. 1 shows how the purity of indium-antimonide, after 17 zone-melt passes, is affected by the purity of the indium. As indicated in the figure, indium-antimonide was prepared from as-received indium and indium further purified by zone refining and by electrorefining. Both electrorefining and zone refining of the indium are effective in removing the p-type impurity. The p-type impurity concentrates at the front of the InSb ingot during zone refining. Spectrographic analyses on the ends of an indium-antimonide ingot after five and nine zone passes showed that zinc segregates to the portion of the ingot first to crystallize, while copper, lead, tin, and nickel segregate to the portion of the ingot last to freeze. These results suggest that the unknown p-type impurity is zinc.

Confirmatory evidence was obtained by a zinc-doping experiment. An ingot of pure indium-antimonide (total impurity concentration less than 10^{16} at./cm^3) was doped with 2.6×10^{18} zinc at./cm^3. After five zone-leveling passes,

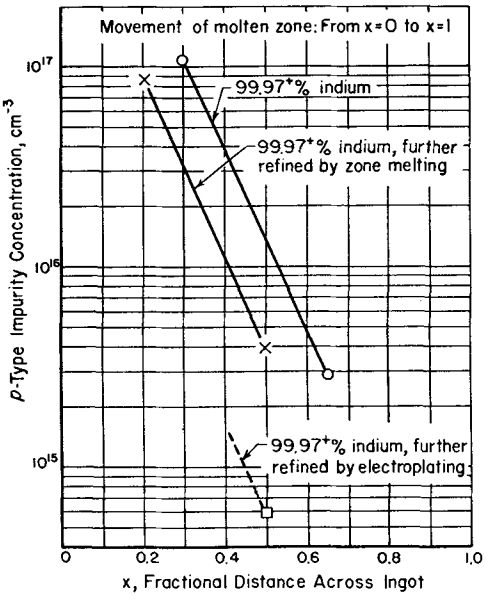

FIG. 1. Effect of indium purification on the concentration of the second most slowly segregating impurity found in InSb after 17 zone-melt passes.

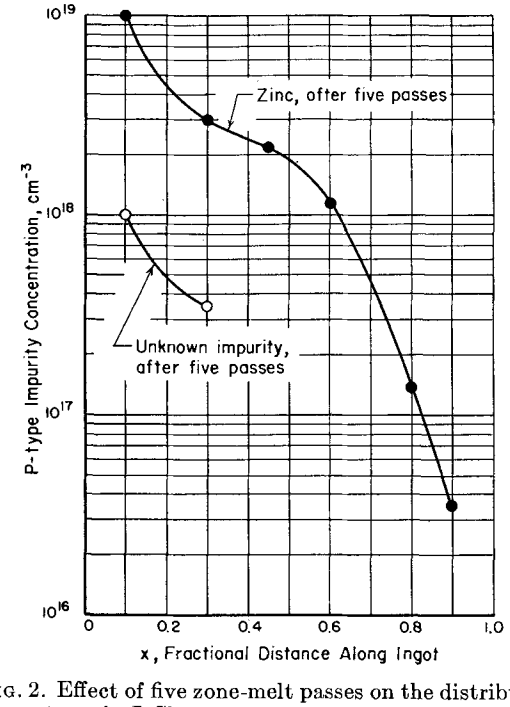

FIG. 2. Effect of five zone-melt passes on the distribution of zinc atoms in InSb.

the carrier concentration varied from 1.7×10^{18} cm^{-3} to 3.1×10^{18} cm^{-3}, indicating that each zinc atom had contributed one hole.

The distribution after five zone-melt passes is shown in Fig. 2. The lower curve gives the distribution of the slowly segregating p-type impurity found in indium-antimonide after five zone-melt passes. Thus, it is further verified that zinc is the slowly segregating p-type impurity in indium-antimonide and has a segregation coefficient greater than one.

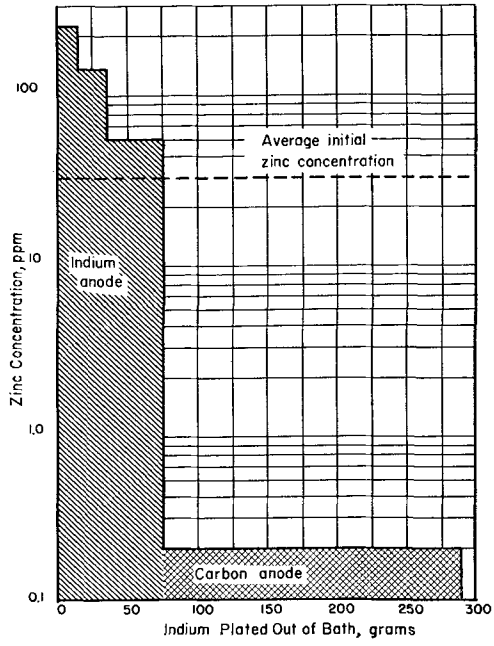

FIG. 3. Segregation of zinc from indium by electroplating.

Another important consequence of this experiment is that the information obtained can be used to determine the concentration of zinc in indium. This is done in the following manner. An indium-antimonide ingot prepared from indium with an unknown concentration of zinc and pure antimony is given five zone-melt passes. From a comparison of the concentration of the p-type impurity in this ingot with the concentration measured in the zinc-doped ingot, the zinc concentration in the indium can be calculated. Using this technique, it was found that the 99.97+ % purity indium obtained from the Indium Corporation of America has a zinc concentration of 20–30 ppm.

Results of studies of electrorefining processes for the reduction of the zinc impurity in the indium are shown in Fig. 3. The zinc concentration, as determined by the technique just described, is plotted as a function of the amount of material plated out of the bath. The electroplating cell consists of an indium anode, an indium fluoborate electrolyte, and a steel cathode upon which the indium is plated. For the first 75 g, additional indium is being dissolved in the electrolyte and zinc-rich indium is plated out of the bath. Then, the indium anode is replaced by a carbon anode and the pure indium remaining in the electrolyte is plated out.

n-Type Impurities in Insb

The most slowly segregating impurity found in indium-antimonide also was investigated. As discussed previously, it is n-type and segregates to the rear of the indium-antimonide ingot during zone melting. Fig. 4 shows the effect of the further purification of indium on the concentration of the n-type impurity in indium-antimonide. To minimize compensation effects caused by the p-type impurity, a large number of zone passes were given to move the zinc to the front of the ingot. The mobilities at 80°K of speci-

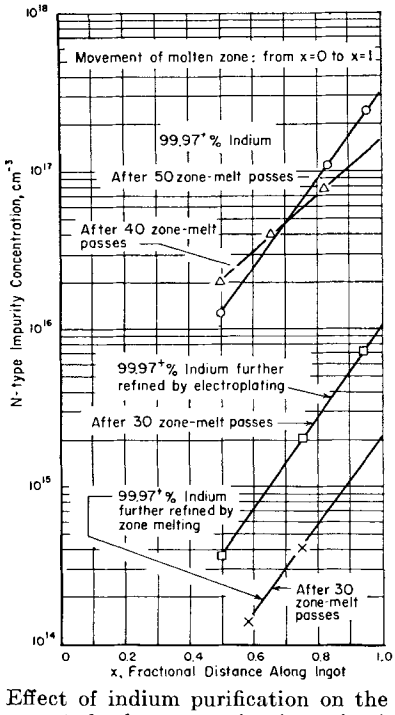

FIG. 4. Effect of indium purification on the concentration of the most slowly segregating impurity in InSb.

mens whose impurity concentrations are given in Fig. 4 varied from 500,000 cm²/volt-sec to 40,000 cm²/volt-sec in a manner consistent with increasing impurity concentration. This behavior is consistent with a negligible amount of compensation. Further evidence that the material is uncompensated is afforded by extrapolating to this region the *p*-type concentration gradient at the front of the ingot. It is then found that the concentration of zinc is at least an order of magnitude lower than the *n*-type impurity. In general, uncompensated *n*-type specimens of best purity are cut approximately 5 cm from the *p-n* junction in extensively zone-refined ingots of 20 cm length.

As shown by the upper curves, distribution of the *n*-type impurity after 40 zone-melt passes does not differ greatly from the distribution after 50 zone-melt passes. The larger number of zone passes continues to purify the compound, but the process becomes inefficient. Purification efficiency is greatly enhanced by removing the slowly segregating impurity from the indium before the compound is formed. An effective method for removing this impurity was found to be zone melting of the indium. The techniques used in this process are as follows. Approximately 1 lb indium was placed in a high-purity graphite boat 30 cm long. The boat was placed in a sealed Vycor tube under a reduced pressure of hydrogen. Zone lengths of 2.5–5 cm were maintained by means of a resistance heater. Five zone-melt passes were made at 7.5 cm/hr and five additional passes were made at 1 cm/hr. The front and rear sections of this ingot were used to prepare indium-antimonide ingots for extensive zone refining. Analysis of the measurements made on the extensively zone-refined indium-antimonide showed that the front section of the indium ingot contained approximately two orders of magnitude less of the slowly segregating *n*-type impurity than had been present in the rear section. In an effort to identify the unknown impurity, spectrographic analyses were carried out. Even though electrical data indicated the presence of 8 ppm of the unknown impurity, no impurity was detected. Therefore, the impurity is one whose spectrographic detection limit is at a rather high concentration. A possibility which was considered is selenium, since this element has a relatively high detection limit and is known to be an *n*-type impurity in InSb. However, activation analyses for selenium, which were obtained, did not confirm selenium to be the impurity in question.

The rates of segregation of various impurities in a material upon zone melting are usually widely different. Hence, by comparing the distribution of the unknown impurity found in indium-antimonide ingots after five zone passes with the distribution of various known impurities, it should be possible to identify the unknown material. It is known that the Group VI elements are *n*-type impurities in indium-antimonide and that they have high spectrographic detection limits. Work on the segregation coefficients (2) of various impurities in germanium has shown that the smaller atoms usually segregate the more slowly. Since sulfur is a small atom and a Group VI element, it was studied first. Fig. 5 compares the distribution of the sulfur impurity with the unknown impurity after five zone passes as a function of fractional distance along the ingot.

The information about the segregation of the unknown impurity was obtained by zone leveling rear sections of extensively zone-refined indium-antimonide ingots. The impurity concentrations of all other impurities except the unknown are estimated to be below 10^{15}/cm³. After zone leveling, a zone of 2.5 cm was passed along the 20-cm ingot a total of five times. The impurity distribution was then determined by Hall effect measurements at 80°K.

A similar technique was used for determining the distribution of the sulfur atoms. Indium-antimonide of 10^{15}/cm³ purity was doped with 1.2×10^{18}/cm³ sulfur atoms. After zone-leveling, the impurity concentration was

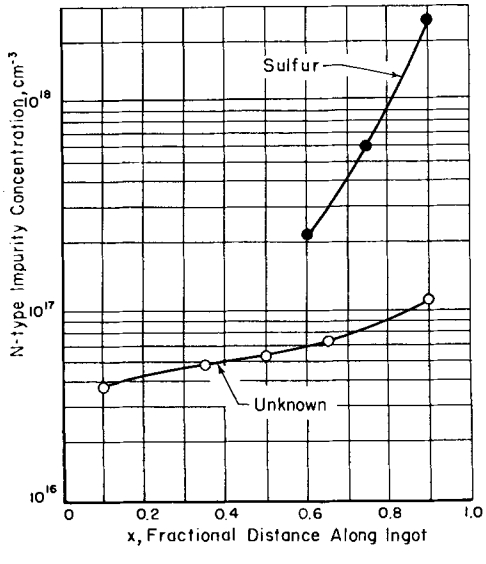

FIG. 5. Behavior of sulfur contrasted with that of the unknown *n*-type impurity in InSb after five zone-melt passes.

relatively uniform, varying from $7 \times 10^{17}/cm^3$ to $1.25 \times 10^{18}/cm^3$. Rate of pass, zone lengths, and ingot lengths were kept constant for the various dopings. By comparing the behavior of the two impurities, one can readily see that sulfur segregates much faster than does the unknown.

Fig. 6 shows the behavior of selenium contrasted to that of the unknown after five zone-melt passes. These results

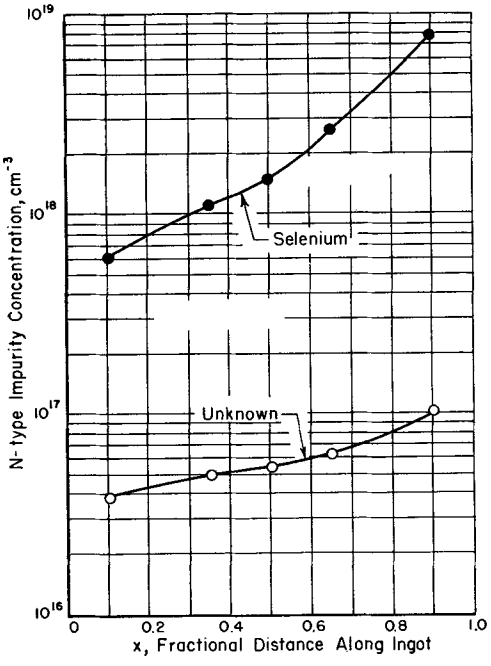

FIG. 6. Behavior of selenium contrasted with that of the unknown n-type impurity in InSb after five zone-melt passes.

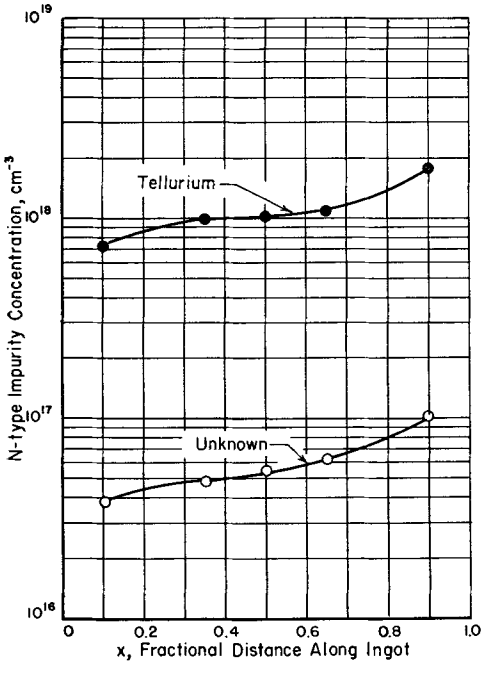

FIG. 7. Behavior of tellurium contrasted with that of the unknown n-type impurity in InSb after five zone-melt passes.

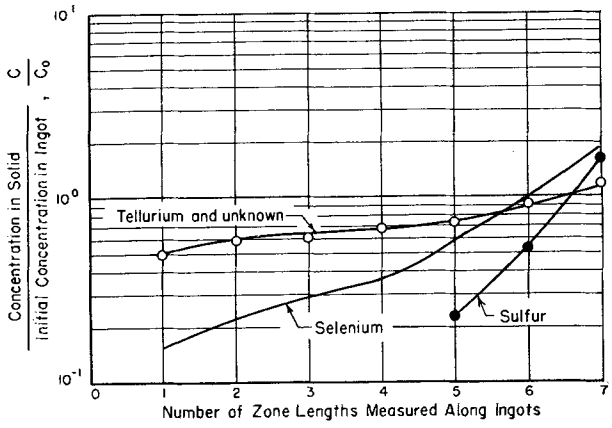

FIG. 8. Normalized values of the concentration along the ingot of some group VI impurities in InSb after five zone-melt passes.

indicate that selenium segregates more slowly than does sulfur but not so slowly as the unknown. This is rather surprising since, in germanium, the segregation coefficients deviate further from unity with increasing atomic number of impurities from Groups III and V of the periodic table (2). Confirmatory evidence that the situation is reversed for some Group VI impurities in indium-antimonide is shown in Fig. 7. Here it is seen that tellurium segregates more slowly than does selenium and that its rate of segregation is, in fact, identical to that of the unknown.

Fig. 8 summarizes the distributions of the principal Group VI impurities in indium-antimonide after five zone passes. Recently, Reiss (3) has developed equations for the redistribution of solute after zone passing. His equations for the case of a finite bar with a segregation coefficient close to unity describe fairly well the distribution of tellurium after five passes when a segregation coefficient of 0.8 is used. Since equations for the case of a finite bar with a segregation coefficient differing appreciably from unity have not been developed, effective segregation coefficients of the other impurities studied can only be roughly estimated. They are 10 for zinc, 0.5 for selenium, and 0.1 for sulfur.

Summary and Conclusions

The information obtained on the most slowly segregating p-type impurity found in indium-antimonide is summarized as follows:

1. The impurity is zinc.
2. It has a segregation coefficient greater than 1 in indium-antimonide.
3. It originates in the indium. The concentration in Indium Corporation of America's 99.97+ % purity is 20-30 ppm.
4. It has a segregation coefficient less than 1 in indium.
5. Electrorefining is an effective technique for removal of zinc from the indium.

The information obtained on the most slowly segregating n-type impurity found in InSb is summarized as follows:

1. The impurity is tellurium.

2. It has a segregation coefficient slightly less than 1 in indium-antimonide.

3. It originates in the indium. The concentration in 99.97+ % purity indium is about 1 ppm.

4. It has a segregation coefficient considerably less than 1 in indium.

5. Zone refining of the indium is an effective technique for removal from the indium.

In conclusion, the preceding work has shown that by purifying the elements as well as zone-refining the compound, it is possible to achieve uncompensated extrinsic carrier concentrations of below $10^{14}/cm^3$ in indium-antimonide. For purities in this range, there are no indications that deviations from stoichiometry offer a barrier to the attainment of this low extrinsic carrier concentration.

ACKNOWLEDGMENTS

The author is indebted to H. L. Goering, R. K. Willardson, and A. C. Beer for many valuable discussions, and to W. G. Hespenheide for carrying out the electroplating.

Manuscript received July 21, 1955. This paper was prepared for delivery before the Cincinnati Meeting, May 1 to 5, 1955. The work was supported in part by Wright Air Development Center, Air Research and Development Command, U. S. Air Force.

Any discussion of this paper will appear in a Discussion Section to be published in the December 1956 JOURNAL.

REFERENCES

1. W. G. PFANN, *J. Metals*, **4**, 747 (1952).
2. J. A. BURTON, E. D. KOLB, W. P. SLICHTER, AND J. D. STRUTHERS, *J. Chem. Phys.*, **21**, 1991 (1953).
3. H. REISS, *J. Metals*, **6**, 1053 (1954).

Electrolytic Stream Etching of Germaniun

MILES V. SULLIVAN AND JOHN H. EIGLER

Bell Telephone Laboratories, Inc., Murray Hill, New Jersey

ABSTRACT

A technique has been developed for the electrolytic etching of germanium in a controlled stream of 0.1% potassium hydroxide. By means of a special jig, the etching is restricted to the junction area without the aid of the usual masking waxes.

INTRODUCTION

In the processing of semiconductor materials for use in transistor devices, it is necessary to etch the surface in order to remove all the mechanical debris formed in cutting and shaping operations. This etching also removes any chemical contamination introduced during processing.

In the past, this etching has been done with very corrosive chemicals such as hydrofluoric acid, nitric acid, acetic acid, bromine, and hydrogen peroxide. Because these materials are so very corrosive, it has been necessary to protect solder joints, lead wires, and other portions of the device by masking them with an inert material. The application of this masking material is done under a microscope by a skilled operator and is both difficult and time consuming. The desire to eliminate this masking and the subsequent unmasking operation led the authors to develop a technique of stream electroetching which does not require masking. It will be seen, however, that other advantages have also accrued.

Electroetching of germanium which is submerged in an electrolyte has been previously described (1), but this method requires masking to protect the surfaces which are not to be etched. Jet electroetching of germanium was introduced by Tiley and Williams (2) and has been successfully applied to the fabrication of certain types of transistors, but has not been adapted for use on grown junctions. The technique to be described in this paper is another modification of electroetching in which a stream of electrolyte is allowed to flow over certain portions of the sample to be etched but is restrained from wetting other portions by surface tension between the stream and a special etching jig.

APPARATUS AND PROCESS

Four principles in the process restrict the etching current to the desired areas of the device. First, the use of an electrolyte whose conductivity is lower than that of the material being etched assures one that the most intense etching takes place on those portions of the germanium which are the nearest to the cathode. And since the cathode can be positioned close to the *p-n* junction, one is then able to give the junctions the most intense etching. Second, the use of a close electrode spacing along with the low-conductivity electrolyte results in a rapid etching rate for those areas directly opposite the cathode. Third, the use of a shaped cathode aids considerably in giving a relatively uniform etch to that area of the germanium which is directly opposite the cathode. Fourth, the use of a restricted stream of etchant very definitely limits the etching to those areas which are wetted by the electrolyte.

These restrictions to the etching current permit one to control the etching pattern precisely enough to make it unnecessary to resort to masking in any of the applications of this technique. A convenient jig for maintaining a restricted stream of electrolyte around a typical junction bar is a hairpin-shaped piece of platinum wire (see Fig. 1). The electrolyte which is gravity fed from a nozzle above the hairpin is constrained by surface tension to flow between

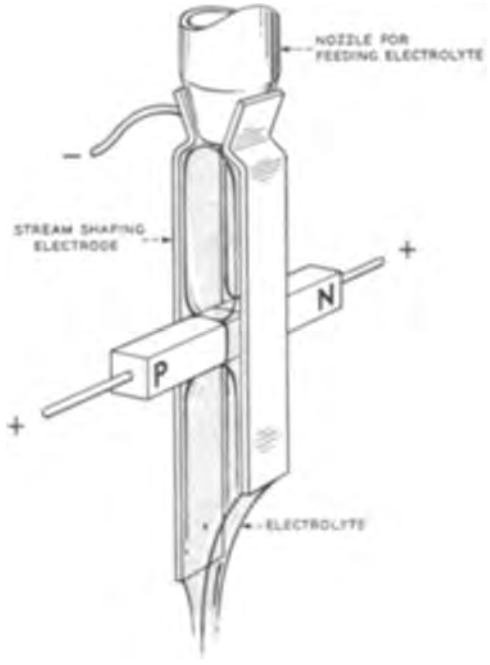

FIG. 1. Stream electrolytic etching a p-n junction

the legs of the hairpin. The germanium bar is brought up from below and placed between and at right angles to the legs of the hairpin. The rate of flow of electrolyte is adjusted to maintain a flow over only that portion of the germanium bar which lies between the hairpin legs but not for any appreciable distance beyond. In this manner the leads which are connected to the ends of the germanium bar are not wetted.

Etching times and currents vary with the material being etched and its past history. With 0.1% potassium hydroxide as the electrolyte, the first etch after the usual mechanical shaping operation requires 1–2 min, whereas a cleanup etch after waxing and dewaxing requires only a few seconds. Etching current densities up to 15 amp/cm² have been employed although most of this work has been carried on at 1.5 amp/cm².

RESULTS

Starting with a p-n junction diode whose surface has been lapped with 600 carborundum, Fig. 2 shows that about 25 μ (0.025 mm) of damaged material[1] must be removed before a low saturation current is obtained on the diode. The subsequent decrease in current as more material is removed is the result of reducing the cross-sectional area. (Original cross section was 0.63 x 1.27 mm.)

Fig. 3 shows the appearance of the original surface of the diode (frame 0) and the effect of successive 1-min applications of electroetching. Note that the extremities of the bar are not etched.

In the processing of n-p-n grown junction triodes, the introduction of this technique in place of chemical etching

[1] This figure is in agreement with the depth of damage due to various mechanical surfacing treatments on germanium reported by T. M. Buck and F. S. McKim at the Semiconductor Symposium of The Electrochemical Society in May 1955.

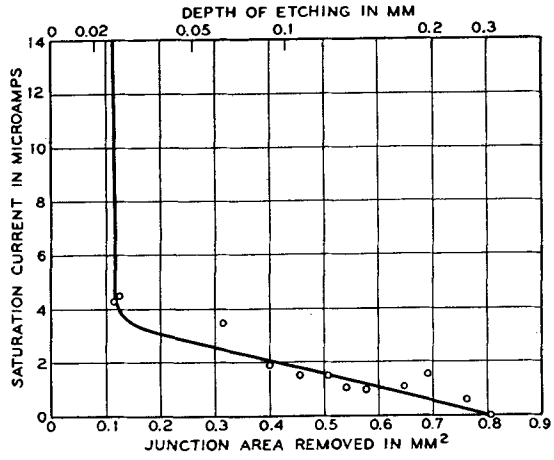

FIG. 2. Effect of electroetching on the saturation current of a p-n junction.

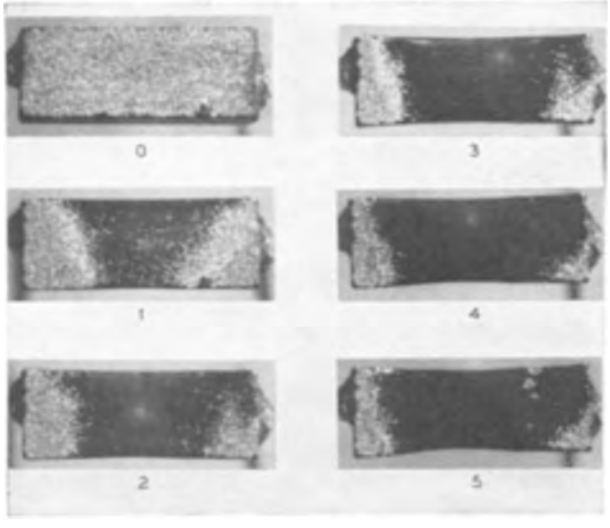

FIG. 3. P-n junction after successive 1-min electroetches.

has resulted in a considerable simplification of the fabrication. This includes the elimination of long-lifetime treatments[2] and their associated washes and masking operations and their subsequent removal with the appropriate organic solvents. This has resulted in an over-all savings of about 20% on the man hours required in the processing of such devices. In addition to the rather obvious economic advantage gained by cutting down the number of steps required, it has been found that a number of other advantages have accrued.

1. *Rate of etching can be controlled.* It is quite evident that the electroetching rate is under far better control than is realized in simple chemical etching. There is the further implication, however, that the process may be speeded up considerably. Although it is possible to perform the entire etching in a few seconds, from practical considerations, times of the order of one minute are usually employed.

2. *Contamination is minimized.* Since a continuously

[2] An anodic treatment in a suspension of hydrolyzed antimony trichloride.

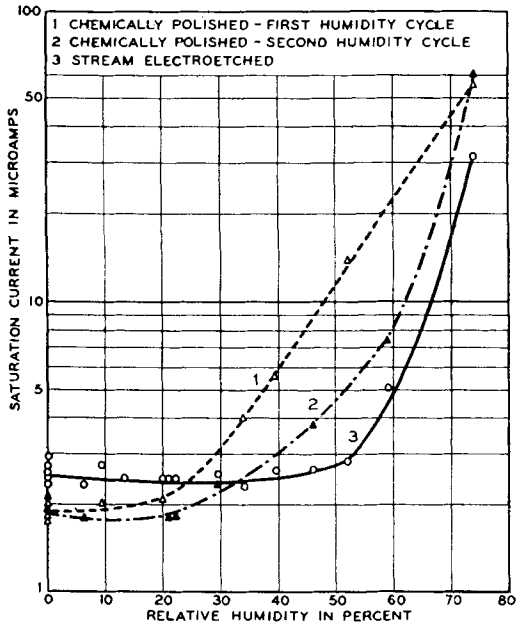

FIG. 4. Humidity stability of electroetched junctions. Curve 3 contains points from both the first and the second humidity cycle.

flowing system is used, contamination from previous etchings will be minimized. Further, since there is no masking, there will be no contamination by the masking material itself or by etchant which may be trapped or adsorbed by the masking.

3. *Etchant is inexpensive.* It is less than one-tenth the cost of chemical etchants usually employed. It should be pointed out that this cost differential will be even greater in large-scale production since it will then be necessary to neutralize the chemical etchants before disposing of them.

4. *Etchant is nonhazardous.* This appears as a pleasant change from the very hazardous chemical etches, the handling and disposal of which posed a considerable problem for very large-scale commercial usage.

5. *Etching can be done after the germanium has been mounted on its header.* When chemical etches were employed, it was customary to mask and etch at an early stage in the fabrication process since masking becomes more difficult and is more extensive as the device is further assembled. Now that the necessity for masking has been eliminated, the etching may be postponed to a later stage of fabrication, thus decreasing the chances for contamination and simplifying the precautions necessary during the early processing.

6. *A more stable surface is formed.* A number of recent tests have shown that a germanium surface which has been anodically etched in potassium hydroxide is more desirable than the chemically etched surface. For example, the electroetched grown junctions maintain their low reverse current even when exposed to a relative humidity of 50% (see Fig. 4). Under these same conditions, chemically etched junctions show over a 100% change in reverse current. Each point in Fig. 4 is the average of six junctions and the data were taken after at least 24 hr in the indicated humidity. Also, electroetched surfaces have low surface recombination rates, in fact, lower than has been reported for many of the other usual chemical etches (3, 4). And last, the spread in electrical characteristics has been noticeably less on electrolytically etched surfaces than on chemically etched surfaces.

Because of the very interesting properties displayed by these surfaces, they have been examined (5) by electron diffraction techniques. These studies have shown that some of the germanium dioxide which is formed during the electrolysis remains on the surface of the germanium as a thin film. It is believed that this oxide film is responsible for some of the unusual properties of electroetched germanium. In fact, the different reaction of the chemically etched surface after the first humidity cycle in Fig. 4 may be attributed to the slow building of an oxide film on the surface.

Microscopic examination of the electroetched surface shows various types of etch pits, including those found at lattice dislocation centers (6). Although a certain degree of control over the appearance of these pits may be achieved in the etching process, the exercising of this type of control has very little influence on the electrical characteristics of the etched device.

A technique has been developed for the electrolytic etching of germanium in a controlled stream of electrolyte. The three main advantages of the process as compared to chemical etching are: (*a*) the product has been improved, presumably by virtue of the oxide film formed during the etching; (*b*) handling and treatment operations are simplified by eliminating the masking and unmasking operations; and (*c*) the safety conditions have been improved by eliminating hazardous chemicals.

Manuscript received August 15, 1955. This paper was prepared for delivery before the Chicago Meeting, May 2 to 6, 1954.

Any discussion of this paper will appear in a Discussion Section to be published in the December 1956 JOURNAL.

REFERENCES

1. F. JIRSA, *Z. anorg. u. allgem. Chem.*, **268**, 84 (1952).
2. J. W. TILEY AND R. A. WILLIAMS. *Proc. I.R.E.*, **41**, 1706 (1953).
3. T. M. BUCK AND W. H. BRATTAIN, *This Journal*, **102**, 636 (1955).
4. J. P. MCKELVEY AND R. L. LONGINI. *J. Appl. Phys.*, **25**, 634 (1954).
5. Electron Diffraction Studies Performed at B.T.L. by Mrs. M. H. Read.
6. F. L. VOGEL, W. G. PFANN, H. E. COREY, AND E. E. THOMAS, *Phys. Rev.*, **90**, No. 3, 489 (1952).

Thermodynamics of the Oxidation of Chromium

J. N. Ramsey,[1] D. Caplan, and A. A. Burr

Department of Metallurgical Engineering, Rensselaer Polytechnic Institute, Troy, New York

ABSTRACT

By a microbalance technique in which oxidized chromium sheet is heated in prepared H_2-H_2O atmospheres the dissociation pressure of Cr_2O_3 is determined over the temperature range 598°–1154°C. From these data are calculated the free energy and enthalpy of formation of Cr_2O_3.

Introduction

Excellent oxidation resistance and strength at elevated temperatures make chromium an attractive base metal for heat-resistant alloys. Unfortunately, poor formability and extreme brittleness at room temperature have thus far hindered commercial development. Investigations now in progress at several laboratories and some recent publications (1–4) indicate that ductile chromium-base alloys can be produced provided that the impurity level is reduced to a sufficiently low value. Oxygen is known to embrittle the other body-centered cubic, high-melting metals, iron, molybdenum, and tungsten, and it is believed that it may also raise the ductile-to-brittle transition temperature of chromium. For this reason an investigation of the chromium-oxygen system was undertaken. A survey of the literature on the dissociation pressure of Cr_2O_3 revealed a considerable spread between the data of the various investigators. With the availability of high grade chromium sheet, experimental work was undertaken to check existing data. This paper describes the simple and direct experimental technique which was used.

The thermodynamics of the chromium-oxygen system may be arrived at either by determining experimentally the atmosphere which is in equilibrium with metal and oxide at various temperatures, or by calculating from tabulated entropy and heat capacity data (5, 6, 7) for oxygen, chromium, and chromium oxide along with the heat or free energy of formation of the oxide at one temperature. Results of such calculations are usually expressed by an equation having the form

$$\Delta F^\circ_T = \Delta Ho + aT \ln T + bT^2 + cT^{-1} + IT \qquad (I)$$

which expresses the standard state free energy change for the oxidation reaction as a function of temperature and constants related to entropy and heat content data. This free energy change is related to the equilibrium constant, K, by the expression

$$\Delta F^\circ_T = -RT \ln K \qquad (II)$$

Hence, for the reaction

$$2Cr + \tfrac{3}{2} O_2 = Cr_2O_3 \qquad (III)$$

$$\Delta F^\circ_T = -RT \ln \frac{1}{P^{\frac{3}{2}}_{O_2}} = RT \ln P^{\frac{3}{2}}_{O_2} \qquad (IV)$$

which by combination with equation (I) allows the calculation at any temperature of P_{O_2}, the equilibrium dissociation pressure of the oxide.

Such treatments have been described, notably by Maier (8), Thompson (9), Ellingham (10), Lustman (11), Richardson and Jeffes (12), Ward, Ray, and Herres (13), Smithells (14), Brewer (15), and Coughlin (16). The calculated curves of four of these investigators are drawn in on Fig. 1 and show a considerable variation. The most recent (16) is considered to embody the most accurate thermodynamic data, including a new determination of the heat of formation of Cr_2O_3 (17).

There have been several experimental determinations of the dissociation pressure of chromium oxide (18–23). Wartenberg and Aoyama (18) heated polished chromium at 600°–1400°C in a stream of hydrogen containing known small amounts of water vapor and estimated the equilibrium temperature for dissociation by the appearance and disappearance of temper colors on the specimen. Granat (20) passed dry hydrogen slowly through hot Cr_2O_3 at 1000°–1500°C and determined the H_2O content of the emerging gas. Grube and Flad (21, 22) passed hydrogen of known moisture content over Cr_2O_3 powder, part of which had previously been reduced to metal. Over the range 780°–1300°C equilibrium temperatures were obtained by detecting the temperature at which the powder

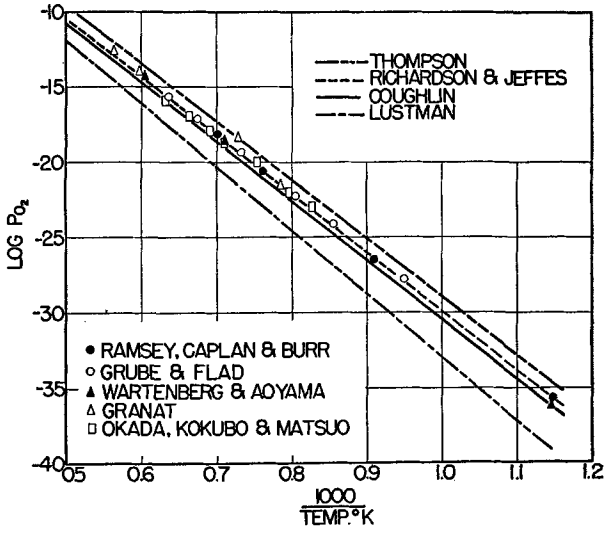

Fig. 1. Calculated and experimental data for the equilibrium dissociation pressure of Cr_2O_3.

[1] Present address: Massachusetts Institute of Technology, Cambridge, Mass.

neither gained nor lost weight while in a particular atmosphere. Okada, Kokubo, and Matsuo (23) used a similar constant weight technique to determine the equilibrium temperatures from 939° to 1310°C.

In the present work the equilibrium temperature is determined by detecting with a microbalance the point at which oxide-coated specimens begin to lose weight.

Experimental

The chromium used for the experiments was in the form of sheet which had been prepared by sheath rolling and finished by a pass or two in air at about 500°C. The following impurity contents were determined by semi-quantitative spectrographic analysis: Al 0.005, Mg 0.005, Ti 0.01, Zr < 0.001, Si 0.001, Fe 0.005, Ni 0.001, Mo < 0.001, Mn 0.001, Pb 0.005, Cu 0.005%. The specimen measured 0.012 x 0.6 x 1.2 in. and weighed approximately 1.0 g. Before each run it was heated in oxygen to form a surface layer of chromium oxide.

Fig. 2 is a schematic diagram of the apparatus used in the determination of the dissociation pressure. The oxidized sample of chromium sheet was attached to the beam of a quartz microbalance by a fine tungsten wire and hung in the vertical tube furnace. A plastic housing around the microbalance protected it from air currents. Changes in weight were detected by observing with a microscope sighted on a reference point on the tungsten suspension wire.

Hydrogen of a constant and known moisture content was prepared by passing cylinder hydrogen over platinized asbestos at 425°C to convert oxygen to water, adding an excess of water vapor with a humidifier, and condensing out the excess in a constant temperature cold trap consisting of 25 ft of copper tubing coiled in a thermoregulated bath of refrigerant. Any desired H_2-H_2O ratio could be obtained by suitable adjustment of the cold trap temperature. To avoid pick-up of moisture or oxygen only glass, copper, and porcelain was used in the gas train.

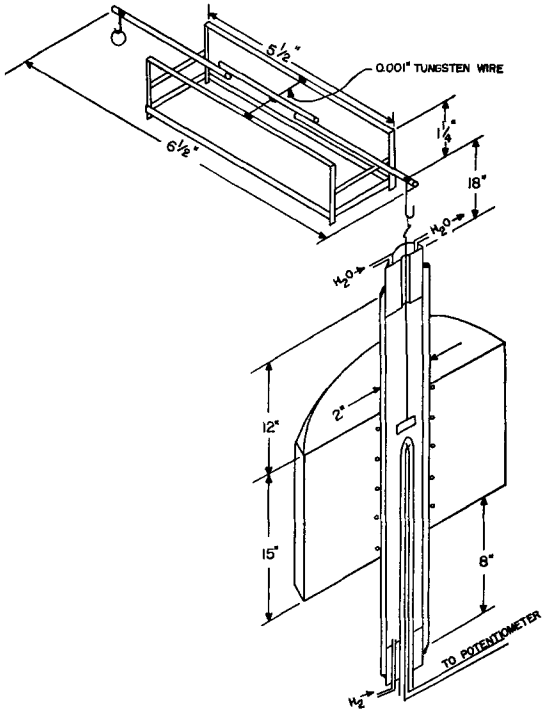

FIG. 2. Schematic diagram of microbalance and vertical tube furnace.

With the prepared atmosphere entering the vertical furnace tube at the bottom and the specimen hung just above the thermocouple used for measuring the temperature, the furnace was slowly heated and the temperature recorded at which the specimen first began to lose weight. Near the equilibrium temperature a heating rate of 2°C/min was used.

Results

The equilibrium temperatures for different settings of the cold trap temperature are shown in the first two columns of Table I. Using the following relationships, these data are converted to dissociation pressures or to standard free energies of formation: From the equation for the formation of water vapor

$$H_{2(g)} + \tfrac{1}{2}\,O_{2(g)} = H_2O_{(g)} \qquad (V)$$

one can write

$$2 \log K_{H_2O} = \frac{-2\Delta F^\circ_T}{4.576T}$$

From this relation, values of $2 \log K_{H_2O}$ at the equilibrium dissociation temperatures are obtained by substituting the corresponding known values of ΔF°_T [e.g. reference (12)]. Since the P_{H_2} of the experiments is essentially one atmosphere, the term $2 \log P_{H_2O}/P_{H_2}$ can be evaluated from the known vapor pressure of ice at the various cold trap temperatures (24). In this way the dissociation pressure is calculated and, through equation (IV), the standard state free energy change. Values so obtained are shown in the last two columns of Table I.

By combining these experimentally determined values of ΔF°_T with heat capacity and entropy data in the literature (5, 6), the standard heat of formation of Cr_2O_3 at the reference temperature 298°K can be calculated. One such procedure is that outlined by Darken and Gurry (25).

Thus for the reaction

$$\tfrac{2}{3}\,Cr + H_2O = \tfrac{1}{3}\,Cr_2O_3 + H_2 \qquad (VI)$$

values of the function $(F^\circ_T - H^\circ_{298})/T$ are calculated at even temperatures for the species Cr and Cr_2O_3 by expressing the function in the form $(H^\circ_T - H^\circ_{298})/T - (S_T - S_{298}) - S_{298}$. Values for these three terms are taken from Kelley's tables (5, 6). For the species H_2 and H_2O the function $(F^\circ_T - H^\circ_0)/T$ has already been tabulated (26). It is readily converted to the function above by the relationship $(F^\circ_T - H^\circ_{298})/T = (F^\circ_T - H^\circ_0)/T - (H^\circ_{298} - H^\circ_0)/T$.

By combining the $(F^\circ_T - H^\circ_{298})/T$ functions for the four reactants at even temperatures, values of $(\Delta F^\circ_T - \Delta H^\circ_{298})/T$ are obtained.[2] When this is done, interpolation to the

[2] These same values can be more simply obtained in another way since ΔF°_T data for H_2O and Cr_2O_3 are included in the tabulations of Coughlin (16). After subtracting ΔH°_{298} from the tabulated ΔF°_T values and dividing by T, combination of the resulting functions yields the $(\Delta F^\circ_T - \Delta H^\circ_{298})/T$ for the reaction.

TABLE I. *Experimental values for the oxidation of chromium to Cr_2O_3*

Cold trap temperature (°C)	Dissociation temperature (°C)	$\frac{P_{H_2O}}{P_{H_2}}$	P_{O_2} (atm)	$\Delta F°$ (kcal)
−74	598	1.38×10^{-6}	2.1×10^{-36}	−213.2
−49.5	826	4.41×10^{-5}	3.1×10^{-27}	−200.0
−28	1039	4.61×10^{-4}	2.4×10^{-21}	−185.7
−18	1154	1.23×10^{-3}	6.8×10^{-19}	−178.0

TABLE II. *Thermodynamics of the reaction* $\frac{2}{3}$ Cr + H_2O = $\frac{1}{3}$ Cr_2O_3 + H_2

Temp (°K)	$\frac{\Delta F°_T - \Delta H°_{298}}{T}$ (e.u.)	$K = \frac{P_{H_2}}{P_{H_2O}}$	$\frac{\Delta F°_T}{T}$ (cal/deg)	$\Delta H°_{298}$ (cal)
871	9.71	7.25×10^5	−26.82	−31820
1099	9.20	2.27×10^4	−19.93	−32010
1312	8.82	2.17×10^3	−15.27	−31600
1427	8.64	8.13×10^2	−13.32	−31340

four experimental temperatures gives the values for $(\Delta F°_T - \Delta H°_{298})/T$ seen in the second column of Table II.

The equilibrium constant for reaction (VI), $K = P_{H_2}/P_{H_2O}$, which has been determined in the four experiments, permits the calculation of $\Delta F°_T/T = -4.576 \log K$. This may now be combined with the values determined for the function $(\Delta F°_T - \Delta H_{298})/T$ to give values for $\Delta H°_{298}$. That is, $\Delta H_{298}/T = \Delta F°_T/T - (\Delta F°_T - \Delta H_{298})/T$. Table II shows the four values of ΔH_{298} obtained. The average value is $\Delta H_{298} = -31690$ cal.

Since the standard heat of formation at 298°K of $H_2O_{(g)}$ is −57,798 cal (16), addition of equations (V) and (VI) gives

$$\tfrac{2}{3}\,Cr + \tfrac{1}{2}\,O_2 = \tfrac{1}{3}\,Cr_2O_3 \qquad \Delta H°_{298} = -89490 \text{ cal}$$

That is, the standard heat of formation of Cr_2O_3 at 298°K [equation (III)] is −268,500 cal.

Discussion

As can be seen from Fig. 1 the results of this research and of most of the prior work when plotted on the coordinates logarithm of the dissociation pressure and reciprocal of the absolute temperature lie nicely along a straight line nearly coincident with the calculated curve of Richardson and Jeffes (12). This curve is based on the equation

$$2Cr + \tfrac{3}{2}\,O_2 = Cr_2O_3;\ \Delta F°_{298-1868} = -267{,}750 + 62.10T$$

which embodies the Roth and Wolf (27) determination of $\Delta H°_{298} = -268.9$ kcal. It might have been expected that the theoretical curve of Coughlin (16) would most closely describe the experimentally determined values but, as the graph shows, values of the dissociation pressure read from the Coughlin curve would be slightly different from the experimental data and, from the Lustman or Thompson curve, more different still. The Coughlin curve, for the same reaction as above, is based on the equation

$$\Delta F°_{298-1823} = -274{,}670 - 14.07T \log T + 2.01 \times 10^{-3} T^2 + 0.69 \times 10^5 T^{-1} + 105.65T$$

which incorporates a recent determination by Mah (17) of $\Delta H°_{298} = -272.7$ kcal.

Coughlin (16) has combined this experimentally determined $\Delta H°_{298}$ with heat capacity and entropy data to calculate $\Delta F°_T$ and $\Delta H°_T$. In the present investigation, an experimental determination of K and hence of $\Delta F°_T$ has been combined with the same heat capacity and entropy data to yield $\Delta H°_{298}$. This value (−268.5 kcal) is slightly less negative than that given by Mah (−272.7 kcal). The difference probably lies within the combined experimental uncertainty of both values. A possible source of error in the present measurements is thermal separation in the H_2-H_2O atmosphere, although it is believed this has been minimized by arranging to have the uniform hot zone in the vertical tube furnace long relative to the length of the specimen. In this way a steady state should become established such that the gas composition around the specimen is that dictated by the cold trap temperature. The fact that the presently determined value for $\Delta H°_{298}$ checks the Roth and Wolf (27) value within 0.5 kcal probably does not lend support to either of these relative to the Mah value of −272.7 kcal.

Conclusions

1. The dissociation pressure of Cr_2O_3 is obtained as a function of temperature in the range 598°–1154°C from which is calculated the standard free energy change for the reaction

$$2Cr + \tfrac{3}{2}\,O_2 = Cr_2O_3$$

2. The average value for the standard state heat of formation at 298°K of Cr_2O_3 calculated from the above is $\Delta H_{298} = -268.5$ kcal.

3. Of several calculated equations in the literature for the free energy of formation of Cr_2O_3 as a function of temperature, the one which best fits the experimentally determined data both of the present research and of much of the prior work over the temperature range 600°–1500°C is that due to Richardson and Jeffes:

$$\Delta F°_T = -267{,}750 + 62.10T$$

Acknowledgment

The authors wish to express their appreciation to Mr. R. W. Loofbourow of Utica Drop Forge and Tool Corporation for furnishing the spectrographic analysis, and to the United States Bureau of Mines, Albany, Oregon, for supplying the chromium sheet.

The work was done under Ordnance Contract No. DA-30-115-ORD-324. The authors are grateful to Watertown Arsenal and the Ordnance Corps for permission to publish.

Manuscript received March 31, 1955. This paper was prepared for delivery before the Cincinnati Meeting, May 1 to 5, 1955.

Any discussion of this paper will appear in a Discussion Section to be published in the December 1956 Journal.

References

1. A. H. Sully, E. A. Brandes, and K. W. Mitchell, *J. Inst. Metals*, **81**, 585 (1953).
2. H. L. Wain, F. Henderson, and S. T. M. Johnstone, *ibid.*, **83**, 133 (1954).

3. H. JOHANSEN AND G. ASAI, *This Journal*, **101**, 604 (1954).
4. H. B. GOODWIN, R. A. GILBERT, C. M. SCHWARTZ, AND C. T. GREENIDGE, *ibid.*, **100**, 152 (1953).
5. K. K. KELLEY, *Bur. Mines Bull. 476*, 241 pp (1949).
6. K. K. KELLEY, *Bur. Mines Bull. 477*, 147 pp (1950).
7. F. D. ROSSINI, D. D. WAGMAN, W. H. EVANS, S. LEVINE, AND I. JAFFE, *Natl. Bur. Standards Circ. 500* (1952).
8. C. G. MAIER, *Bur. Mines Bull. 436*, 109 pp (1942).
9. M. DEK. THOMPSON, "The Total and Free Energies of Formation of the Oxides of Thirty-Two Metals," Electrochem. Soc. 89 pp (1942).
10. H. J. T. ELLINGHAM, *J. Soc. Chem. Ind.*, **63**, 125 (1944).
11. B. LUSTMAN, *Metal Progr.*, **50**, 850 (Nov. 1946).
12. F. D. RICHARDSON AND J. H. E. JEFFES, *J. Iron Steel Inst.*, **160**, 261 (1948).
13. J. J. WARD, J. P. RAY, AND S. A. HERRES, Douglas Aircraft Co., Report R-108, 97 pp (1948).
14. C. J. SMITHELLS, "Metals Reference Book," Interscience Publishers, New York (1949).
15. L. BREWER, *Chem. Revs.*, **52**, 1 (1953).
16. J. P. COUGHLIN, *Bur. Mines Bull. 542*, 80 pp. (1954).
17. A. D. MAH, *J. Am. Chem. Soc.*, **76**, 3363 (1954).
18. H. v. WARTENBERG AND S. AOYAMA, *Z. Elektrochem.*, **33**, 144 (1927).
19. S. AOYAMA AND E. KANDA, *J. Chem. Soc. Japan*, **55**, 1174 (1934).
20. I. Y. GRANAT, *Metallurg*, **11**, No. 10, 34 (1936).
21. G. GRUBE AND M. FLAD, *Z. Elektrochem.*, **45**, 835 (1939).
22. G. GRUBE AND M. FLAD, *ibid.*, **48**, 377 (1942).
23. S. OKADA, S. KOKUBO, AND K. MATSUO, *J. Soc. Chem. Ind. Japan*, **46**, 324 (1943).
24. International Critical Tables, Vol. III, p. 210, McGraw-Hill Book Co., New York (1928).
25. L. S. DARKEN AND R. W. GURRY, "Physical Chemistry of Metals," p. 231, McGraw-Hill Book Co., New York (1953).
26. National Bureau of Standards, Selected Values of Chemical Thermodynamic Properties. Series III.
27. W. A. ROTH AND W. WOLF, *Z. Elektrochem.*, **46**, 45 (1940)

Mathematical Studies on Galvanic Corrosion

V. Calculation of the Average Value of the Corrosion Current Parameter

J. T. WABER, JOHN MORRISSEY, AND JOHN RUTH

University of California, Los Alamos Scientific Laboratory, Los Alamos, New Mexico

ABSTRACT

Mathematical analysis for the mean current density has been completed for one general and two limiting ratios of electrode and corrodent dimensions with the same coplanar, juxtaposed arrangement of long, narrow electrodes as used previously. The resulting mathematical expressions were reduced to numerical evaluations, and many of these results have been graphically summarized in perspective illustrations.

The characteristic ratio ($\lambda/\mathfrak{L}$) was used to explain the behavior of all similar electrode systems and to emphasize that relative, not absolute, dimensions of the system establish its behavior. The theory and two experimental studies were in good agreement.

INTRODUCTION

Mixtures of phases are frequently present in commercial metals, and much of the gross corrosion behavior of such metals results from the action of local galvanic cells formed between constituents. Aside from the presence of impurity phases, certain commercial metals consist of two or more phases, and the percentage of the minor constituent in the matrix may approach 50%. Therefore, it is important to describe analytically the effect of increasing the percentage of one constituent on the average corrosion rate. In a two component phase diagram total corrosion should increase to a maximum with increase of the less noble phase, A, then decline as the fraction of B decreases so far that there are insufficient sites for cathodic reactions to occur without substantial polarization. Experience is in accord with this qualitative argument.

In many cases, interest does not lie in the detailed distribution of corrosion attack over the anodes, as described in previous papers (1–4), but in the average corrosion rate of one phase. For this reason attention was turned to the problem of calculating total and average values of the corrosion current parameter $C_a^*(x)$. This general problem can be investigated quantitatively assuming (*a*) the anodic and cathodic polarization parameters $\mathfrak{L}_a$ and $\mathfrak{L}_c$ are equal, and (*b*) the electrodes consist of long strips which are arranged alternately in a common plane. Avoidance of these limitations would introduce serious mathematical difficulties and would not contribute significantly more to an understanding of corrosion phenomena than does the present analysis.

The over-all behavior of the galvanic system can be characterized in terms of three parameters, each involving the ratio of lengths: a/c, $\mathfrak{L}/c$, and b/c (4). For purposes of describing commercial metals, a may be defined as the average radius of particles of the anodic phase, and c as half the average distance between centers of the anodic inclusions. However, the specific definitions of a and c which apply to the present analysis are: a is the half-width of the anodic strips, and c is half the distance between the repeated anodes. The quantity b is the thickness of the liquid electrolyte layer above the plane of the electrodes. In this paper both finite and infinite thicknesses are considered.

Mathematical Results

Boundary conditions.—The case of a finite thickness of the corrodent is physically equivalent to placing an insulator at the outer boundary of the liquid. This condition at the boundary can be expressed mathematically as

$$\left.\frac{\partial P^*}{\partial y}\right|_{y=b} = 0 \qquad [1]$$

An even, symmetrical, infinite, alternating array of electrodes juxtaposed and lying in a common plane is considered, as this arrangement is most pertinent to the practical case of local galvanic cells. At the center of the anode and cathode, the corrosion current must be continuous and have continuous derivatives. Thus, in terms of the geometrical relation of electrodes used before (1–4),

$$\left.\frac{\partial P^*}{\partial x}\right|_{x=0} = \left.\frac{\partial P^*}{\partial x}\right|_{x=c} = 0 \qquad [2]$$

The origin is taken at the center of one of the anodes. For polarized electrodes the following boundary condition (5) is used:

$$P^*(x, 0) - \mathfrak{L}\left.\frac{\partial P^*}{\partial y}\right|_{y=0} = E_a S_a(x) \qquad [3]$$

The definition of the anodic corrosion current parameter can be employed:

$$C_a^*(x) = \left(-\frac{2a}{E_a}\right)\left.\frac{\partial P^*}{\partial y}\right|_{y=0} \qquad (0 \le x < a) \quad [4]$$

This quantity is a dimensionless parameter since a and y are distances and E_a and P are voltages. Thus, equation [3] for the anodic side can be written:

$$P^*(x, 0) + \left(\frac{\mathfrak{L}E_a}{2a}\right) C_a^*(x) = E_a \qquad [5]$$

since the value for the step function $S_a(x)$ is unity in the anodic region.

Series solution of the problem.—A Fourier series which satisfies Laplace's equation and these several boundary conditions has been shown elsewhere (4) to be

$$P^*(x, y) = A_0^* + \sum_{n=1}^{\infty} A_n^* \cosh\left[\frac{n\pi}{c}(b - y)\right] \cos\left(\frac{n\pi x}{c}\right) \qquad [6]$$

where the coefficients are

$$A_0^* = E_a(a/c)$$

$$A_n^* = \frac{2E_a}{\pi n}\left[\frac{\sin\left(\frac{n\pi a}{c}\right)}{\cosh\left(\frac{n\pi b}{c}\right) + \left(\frac{n\pi\mathfrak{L}}{c}\right)\sinh\left(\frac{n\pi b}{c}\right)}\right] \qquad [7]$$

Derivation of mean parameter.—The mean value of the corrosion current parameter on the anode is obtained by integrating $C_a^*(x)$ over the interval

$$\overline{C_a^*} \equiv \frac{1}{a}\int_0^{a-0} C_a^*(x)\, dx \qquad [8]$$

Substituting $C_a^*(x)$ from either equation [4] or [5] gives the correct expression, but for practical reasons it is imperative to use [5]. The series obtained by differentiating P^* as in [4] depends on the denominator $[1 + (n\pi\mathfrak{L}/c) \tanh (n\pi b/c)]$ for convergence, whereas P^* is employed directly in [5] and the resulting series converges as $n[1 + (n\pi\mathfrak{L}/c) \tanh (n\pi b/c)]$, hence more rapidly. The integration step [8] raises the power of n in either denominator by one. Consequently, the series converges to a given accuracy with fewer terms if [5] is employed. Note that from equation [5]

$$C_a^*(x) = \frac{2a}{\mathfrak{L}}[1 - P^*(x, 0)/E_a] \qquad (0 \le x < a) \quad [9]$$

since $S_a(x)$ is unity in the anodic interval. By substitution, it is simple to show that

$$\overline{C_a^*} = \frac{2a}{\mathfrak{L}}\left(1 - \frac{a}{c}\right) - \frac{2c}{\mathfrak{L}\pi}\sum_{n=1}^{\infty} A_n^*\left(\frac{1}{n}\right) \cdot\cosh\left(\frac{n\pi b}{c}\right)\sin\left(\frac{n\pi a}{c}\right) \qquad [10]$$

The integration can be done termwise since the potential function has sufficient continuity to permit interchange of the order of summation and integration. Substitution from equation [7] leads to the series

$$\overline{C_a^*} = \frac{2a}{\mathfrak{L}}\left(1 - \frac{a}{c}\right) - \frac{4c}{\pi^2\mathfrak{L}}\sum_{n=1}^{\infty} \frac{\sin^2\left(\frac{n\pi a}{c}\right)}{n^2\left[1 + \left(\frac{n\pi\mathfrak{L}}{c}\right)\tanh\left(\frac{n\pi b}{c}\right)\right]} \qquad [11]$$

after dividing numerator and denominator of each term by the appropriate hyperbolic cosine.

An equivalent expression can be derived for an infinite liquid depth by replacing equations [6] and [7] with the appropriate Fourier series. The same expression can be obtained from [11] by noting that the hyperbolic tangent of an infinite argument is unity. Thus

$$\lim_{b\to\infty} \overline{C_a^*} = \frac{2a}{\mathfrak{L}}\left(1 - \frac{a}{c}\right) - \frac{4c}{\pi^2\mathfrak{L}}\sum_{n=1}^{\infty} \cdot\left[\frac{\sin\left(\frac{n\pi a}{c}\right)}{n}\right]^2\left(1 + \frac{n\pi\mathfrak{L}}{c}\right)^{-1} \qquad [12]$$

Definition of the average parameter.—Expressions [11] and [12] are developed for the mean current distributed over the anode. In practice, this quantity is less useful than the average of the anodic current distributed over the entire electrode surface. That is, it is more common to employ the latter average when calculating polarization curves, etc. This is done since it is not always convenient to obtain independently the percentage of anodic phase.

Thus, Γ_a^* has been identified as the total or integrated corrosion current parameter,

$$\Gamma_a^* \equiv \int_0^{a-0} C_a^*(x)\, dx \qquad [13]$$

and the distinction between the mean and the average as Γ_a^*/a and Γ_a^*/c, respectively, has been made. It is clear then that

$$\frac{1}{c}\Gamma_a^* = \left(\frac{a}{c}\right)\overline{C_a^*} \qquad [14]$$

and the values of the more conventional and convenient average can be obtained easily from [11] and [12]. In the absence of external sources of current, $\Gamma_a^* = -\Gamma_c^*$, which is the total cathodic current.

Mean parameter for infinite cathode and infinite electrolyte.—When the electrodes are polarized, the coupling of an infinite cathode with a finite anode increases the current flowing, but the current remains finite. Because of the practical importance of this problem it seemed desirable to investigate it on its own merits. Further, previous results obtained by means of Fourier integrals (2) permit investigation of the limiting value of the mean corrosion current parameter as the anodic fraction (a/c) goes to zero. It should be emphasized that the ensuing derivation relates only to an infinite liquid layer thickness. A finite case is discussed below.

It was established elsewhere (2) that $C_a^*(x)$ for infinite c is

$$C_a^*(x) = \frac{2a}{\mathfrak{L}}\left\{\left[\frac{\pi}{2} - Si(\lambda)\right]\cos\lambda + Ci(\lambda)\sin\lambda + \left[\frac{\pi}{2} - Si(\lambda')\right]\cos\lambda' + Ci(\lambda')\sin\lambda'\right\} \qquad [15]$$

where the auxiliary dimensionless variables λ and λ' were defined as

$$\lambda = (a + x)/\mathfrak{L}$$
$$\lambda' = (a - x)/\mathfrak{L} \qquad [16]$$

and where x, a, and $\mathfrak{L}$ have the same meanings as employed before (1–4). The $Si(\lambda)$ and $Ci(\lambda)$ functions are the sine and cosine integrals.

From [13], [15], and [16],

$$\Gamma_a^* = \frac{2a}{\mathfrak{L}}\left\{\int_{a/\mathfrak{L}}^{2a/\mathfrak{L}}\left(\left[\frac{\pi}{2} - Si(\lambda)\cos\lambda + Ci(\lambda)\sin\lambda\right)d\lambda + \int_0^{a/\mathfrak{L}}\left(\left[\frac{\pi}{2} - Si(\lambda')\cos\lambda' + Ci(\lambda')\sin\lambda'\right)d\lambda'\right\}\right. \qquad [17]$$

Since λ' is the variable of integration (the dummy index) in the second definite integral, it may be replaced by the symbol λ.

$$\Gamma_a^* = \frac{2a}{\mathfrak{L}}\int_0^{2a/\mathfrak{L}}\left\{\left[\frac{\pi}{2} - Si(\lambda)\right]\cos\lambda + Ci(\lambda)\sin\lambda\right\}d\lambda \qquad [18]$$

This may be solved by integrating by parts. The sine and cosine integrals $Si(\lambda)$ and $Ci(\lambda)$ must be differentiated with respect to their upper limits. Recalling that

$$\frac{d}{da}\int_b^a f(x)\,dx = f(a) \qquad [19]$$

substitution of this expression into the results obtained by partially integrating [18] yields

$$\Gamma_a^* = a\sin\left(\frac{2a}{\mathfrak{L}}\right) - \frac{2a}{\pi}\{Si(\lambda)\sin\lambda + Ci(\lambda)\cos\lambda\}\Big|_0^{2a/\mathfrak{L}} + \frac{2a}{\pi}\int_0^{2a/\mathfrak{L}}\sin\lambda\left(\frac{\sin\lambda}{\lambda}\right)d\lambda - \frac{2a}{\pi}\int_0^{2a/\mathfrak{L}}(-\cos\lambda)\left(\frac{\cos\lambda}{\lambda}\right)d\lambda \qquad [20]$$

After combining the sine squared and cosine squared terms in the integrand, it can be shown that

$$\Gamma_a^* = a\sin\left(\frac{2a}{\mathfrak{L}}\right) + \frac{2a}{\pi}\{\ln\lambda - Si(\lambda)\sin\lambda - Ci(\lambda)\cos\lambda\}\Big|_0^{2a/\mathfrak{L}} \qquad [21]$$

This expression cannot be evaluated directly since both the logarithm and the cosine integral become infinite as λ approaches zero.

One of the definitions of the cosine integral is

$$Ci(\lambda) = \ln\lambda\gamma - \int_0^{\lambda}\frac{1 - \cos t}{t}\,dt \qquad [22]$$

where $\ln\gamma = 0.577216$. After substituting [22] into the previous equation, regrouping terms gives

$$\Gamma_a^* = a\sin\left(\frac{2a}{\mathfrak{L}}\right) + \frac{2a}{\pi}\left\{(1 - \cos\lambda)\ln\lambda - \ln\gamma\cos\lambda - Si(\lambda)\sin\lambda + (\cos\lambda)\int_0^{\lambda}\frac{1 - \cos t}{t}\,dt\right\}\Big|_0^{2a/\mathfrak{L}} \qquad [23]$$

By applying l'Hôpital's rule,

$$\lim_{\lambda\to 0}(1 - \cos\lambda)\ln\lambda = 0 \qquad [24]$$

Using the trigonometric identity

$$(1 - \cos\lambda) = 2\sin^2(\lambda/2) \qquad [25]$$

equation [23] reduces to

$$\Gamma_a^* = a\sin\left(\frac{2a}{\mathfrak{L}}\right) + \frac{2a}{\pi}\left\{2\sin^2\left(\frac{a}{\mathfrak{L}}\right)\ln\left(\frac{2a\gamma}{\mathfrak{L}}\right) - Si\left(\frac{2a}{\mathfrak{L}}\right)\sin\left(\frac{2a}{\mathfrak{L}}\right) + \cos\left(\frac{2a}{\mathfrak{L}}\right)\int_0^{2a/\mathfrak{L}}(1 - \cos t)\,d\ln t\right. \qquad [26]$$

after applying the limits of integration. Γ_a^*/a is a dimensionless quantity.

Mean parameter for infinite cathode but finite electrolyte.—The potential can be represented by the Fourier integral

$$P^*(x, y) = \int_0^{\infty} A^*(n)\cos(xhn)\cosh[(b - y)hn]\,dn \qquad [27]$$

where h is a quantity (to be chosen later) having the dimensions of reciprocal length needed to render the quantities in the arguments of the hyperbolic and circular cosine functions dimensionless. The quantity $A^*(n)$ must be chosen so that $P^*(x, y)$ converges to prescribed boundary conditions. Utilizing the boundary condition similar to [3],

$$P^*(x, 0) - \mathfrak{L}\left.\frac{\partial P^*}{\partial y}\right|_{y=0} = E_a S_a'(x) \qquad [28]$$

but with $S_a'(x)$ being the infinite step function defined earlier (2), it can be shown that

$$\int_0^\infty A^*(n)[\cosh(bhn) + (\mathfrak{L}hn)\sinh(bhn)]\cos(xhn)\,dn = E_a S_a'(x) \quad [29]$$

In order to obtain the coefficient $A^*(n)$ in this integral, both sides are multiplied by cos (xhm) and integrated with respect to x.

$$\int_0^\infty \cos(mhx)\left\{\int_0^\infty A^*(n)[\cosh(bhn) + (\mathfrak{L}hn)\sinh(bhn)]\cos(nhx)\,dn\right\}dx = \int_0^\infty E_a S_a'(x)\cos(mhx)\,dx \quad [30]$$

Substituting the value of $S_a'(x)$ into the right-hand side and rearranging the order of integration on the left,

$$\frac{1}{h}\int_0^\infty A^*(n)[\cosh(bhn) + (\mathfrak{L}hn)\sinh(bhn)]\cdot\left[\int_0^\infty \cos(mhx)\cos(nhx)\,d(hx)\right]dn = E_a\frac{\sin(mha)}{mh} \quad [31]$$

The inner integral on the left-hand side is equivalent to the Dirac function $\delta(n - m)$. Utilizing the properties of this function, the left-hand side reduces to

$$\frac{1}{h}\left(\frac{\pi}{2}\right)A^*(m)[\cosh(bhm) + (\mathfrak{L}hm)\sinh(bhm)] = \frac{E_a\sin(ahm)}{mh} \quad [32]$$

In this manner the coefficient $A^*(m)$ can be found and substituted into [27]. Thus the polarized potential function consistent with the imposed boundary conditions is

$$P^*(x, y) = \frac{2E_a}{\pi}\int_0^\infty \frac{\sin(ahn)\cosh[(b-y)hn]\cos(xhn)\,dn}{n[\cosh(bhn) + (\mathfrak{L}hn)\sinh(bhn)]} \quad [33]$$

Evaluation of this definite integral in terms of tabulated functions appears to be difficult. However, a simpler expression for the interfacial potential may be used (6),

$$P^*(x, 0) = \frac{2E_a}{\pi}\int_0^\infty \frac{\sin(ahn)\cos(xhn)\,dn}{n[1 + (\mathfrak{L}hn)\tanh(bhn)]} \quad [34]$$

This relation can be utilized to compute the anodic corrosion current parameter $C_a^*(x)$ from equation [5].

The mean value of the parameter $C_a^*(x)$ may then be computed. Thus the total anodic current is

$$\Gamma_a^* = \frac{2a}{\mathfrak{L}}\int_0^a\left[1 - \frac{P^*(x,0)}{E_a}\right]dx \quad [35]$$

For convenience there can be substituted into [35] an even simpler expression for the interfacial potential,

$$P^*(x, 0) \equiv E_a\int_0^\infty P(n)\cos(xhn)\,dn \quad [36]$$

where the symbol $P(n)$ is the appropriate function of n, a, $\mathfrak{L}$, and b, but not of x, defined so that [34] and [36] are identical.

Then the mean value for anodic current parameter is

$$\frac{\Gamma_a^*}{a} = \frac{2}{\mathfrak{L}}\int_0^{a-0}\left[1 - \int_0^\infty P(n)\cos(xhn)\,dn\right]dx \quad [37]$$

Changing the order of integration,

$$\frac{\Gamma_a^*}{a} = \frac{2a}{\mathfrak{L}} - \frac{2}{\mathfrak{L}h}\int_0^\infty P(n)\left(\frac{\sin han}{n}\right)dn \quad [38]$$

or finally, after inserting the definition of $P(n)$,

$$\frac{\Gamma_a^*}{a} = \frac{2a}{\mathfrak{L}}\left\{1 - \frac{2}{ah\pi}\int_0^\infty \frac{\sin^2(ahn)\,dn}{n^2[1 + (\mathfrak{L}hn)\tanh(bhn)]}\right\} \quad [39]$$

Into this general expression, there is inserted the choice of h, $(2/\mathfrak{L})$, to bring equations [26] and [39] into more formal agreement.

Symmetry of the mean corrosion current.—The mean corrosion current parameter $\overline{C}_a^*$ is symmetrical about the value of $a/c = \frac{1}{2}$ when the polarization parameter $\mathfrak{L}$ is held constant. However, that point is considered again below.

For convenience, the three dimensionless ratios

$$\alpha = a/c; \quad \beta = c/\mathfrak{L}; \quad \eta = b/c \quad [40]$$

are introduced. On substitution into [11],

$$\frac{\Gamma_a^*}{a} = 2\alpha\beta(1-\alpha) - \frac{4\beta}{\pi^2}\sum_{n=1}^\infty \frac{\sin^2(n\pi\alpha)}{n^2[1 + (n\pi\beta^{-1})\tanh(n\pi\eta)]} \quad [41]$$

To show that this parameter is symmetrical about $\frac{1}{2}$, it is assumed that

$$\alpha = \tfrac{1}{2} \pm \delta \quad [42]$$

where δ is some positive real number lying between zero and one half. On substitution,

$$\frac{\Gamma_a^*}{a} = \left(\frac{\beta}{2}\right) - 2\beta\delta^2 - \frac{4\beta}{\pi^2}\sum_{n=1}^\infty \frac{\sin^2 n\pi(\tfrac{1}{2} \pm \delta)}{n^2[1 + n\pi\beta^{-1}\tanh(n\pi\eta)]} \quad [43]$$

First, it is necessary to show that the numerator of the summand in [43] is symmetrical. After expressing the sine of a sum of two angles and squaring it,

$$\sin^2\left(\frac{n\pi}{2} \pm n\pi\delta\right) = \sin^2\left(\frac{n\pi}{2}\right)\cos^2(n\pi\delta) + \cos^2\left(\frac{n\pi}{2}\right)\sin^2(n\pi\delta) \pm 2\sin\left(\frac{n\pi}{2}\right)\cos\left(\frac{n\pi}{2}\right)\sin(n\pi\delta)\cos(n\pi\delta) \quad [44]$$

Note that

$$2\sin\left(\frac{n\pi}{2}\right)\cos\left(\frac{n\pi}{2}\right) = \sin(n\pi) = 0 \quad [45]$$

Thus, the numerator of the summand in equation [43] is independent of the choice of the sign accompanying δ, since [45] causes the cross product term on the right side of [44] to drop out, and only this term is affected by the choice. The term $\alpha(1 - \alpha)$ in [41] is symmetrical about ½. Therefore, the expression for either the mean or the average value of the corrosion current parameter is symmetrical about one half.

This statement is correct as long as β or η are independent of changes in α. Specifically, $\overline{C_a}^*$ is calculated in a later section subject to the condition that $a/\mathfrak{L}$ or $\alpha\beta$ is constant. In this case, Γ_a^*/a increases rapidly as α approaches zero. Graphical examples demonstrating the important difference between the two conditions were prepared.

The symmetrical behavior of the integrated anodic current parameter Γ_a^* is similar to that of Γ_a^*/c. It is clear that the parameter Γ_a^* can be related to total current flowing in a galvanic system by substituting the values of a, E_a, and the specific conductivity σ which are pertinent to the system.

Numerical Evaluation

Summation of the series.—Details of coding these problems for calculation on the MANIAC computer need not be presented here. Convergence of the series was so rapid that serious errors were not introduced by truncation of the series at $n = 100$.

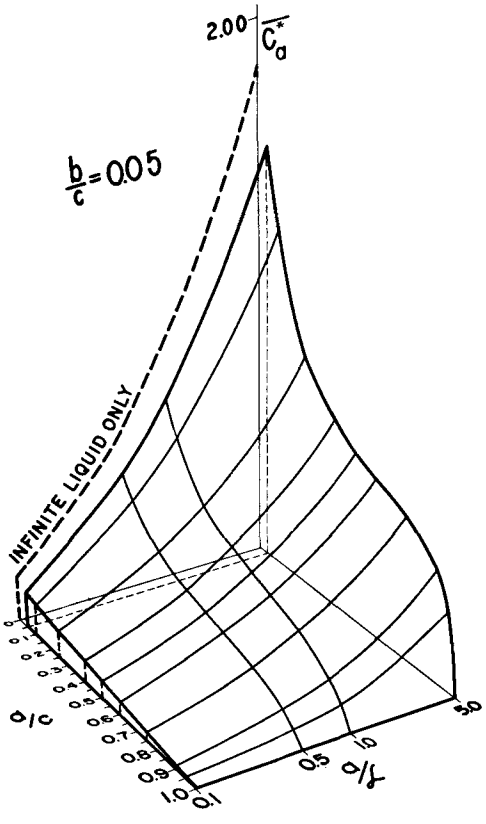

FIG. 1. Dependence of the mean value of the anodic current density parameter $\bar{C}_a^*$ on the characterizing ratio $(a/\mathfrak{L})$ and the anodic fraction (a/c). Computed for a relative thickness (b/c) of the electrolyte equal to 0.05.

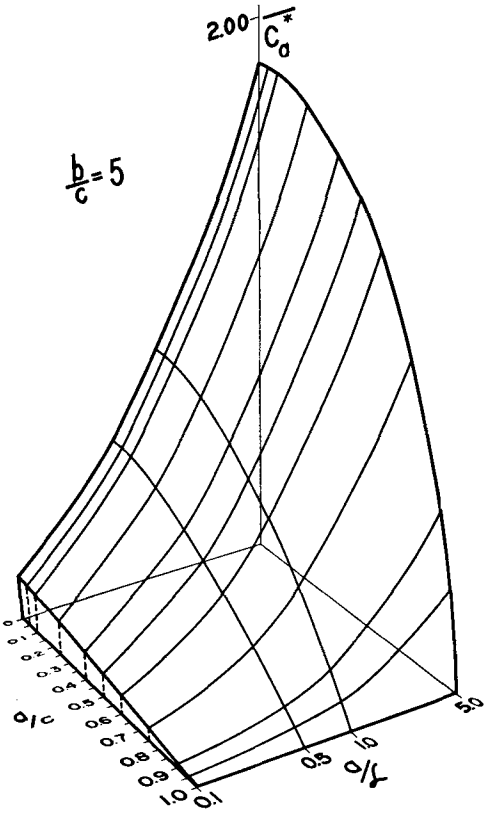

FIG. 2. Dependence of the mean value of the anodic current parameter $\bar{C}_a^*$ on the characterizing ratio $(a/\mathfrak{L})$ and the anodic fraction (a/c). Computed for a relative thickness of 5.

To facilitate computation of each term in the series, it was noted that the hyperbolic tangent did not differ significantly from one when its argument exceeded five. This substitution of unity eliminated the separate series evaluation of hyperbolic tangent for each term after the N_0-th which was dependent on b/c.

Values of the quantities chosen.—In the detailed evaluation, c was fixed at 10, as has been done in many of the calculations to date, and the dependence on (a/c) was investigated by letting a vary in the range 0–10. Five relative thicknesses of liquid layer, namely b/c = 0.005, 0.05, 0.5, 1.0, and 5.0, were employed. Two choices were available for using the polarization parameter. In most of the evaluations, constant values of the dimensionless ratio $(a/\mathfrak{L})$ were chosen rather than constant $\mathfrak{L}$ values. This choice, of course, affects the values of $\mathfrak{L}/c$ which appear in the denominator of equations [11] and [12]. This ratio was found from the product $(a/c)(\mathfrak{L}/a)$ without the intervening computation of $\mathfrak{L}$.

Values of the mean anodic current parameter.—Values of the mean anodic corrosion current parameter were computed for over 400 combinations (7) of the ratios $(a/\mathfrak{L})$, (a/c), and (b/c). In these calculations the polarization parameter was not fixed but was permitted to vary in such a way that the ratio $(a/\mathfrak{L})$ characterizing the behavior of the galvanic system was kept constant. Some of the values have been assembled into graphical summaries. Two perspective drawings made to scale are presented in Fig. 1 and 2. In the former, b/c was chosen as 1/20 and, in the latter,

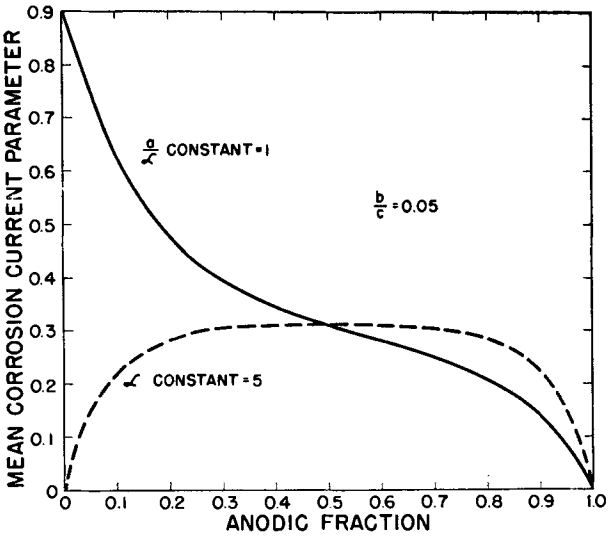

FIG. 3. Comparison of the mean anodic current density for constant ℓ and for constant (a/ℓ) values. Curves computed for a relative thickness of 0.05.

as 5. It was shown (4) that the electrolyte layer is effectively "infinitely thick" whenever the relative thickness (b/c) exceeds unity, in all practical problems. Thus the two graphs pertain to a small finite and an "infinite" liquid layer thickness, respectively.

Note that in these perspective drawings the characterizing ratio (a/ℓ) is plotted on a logarithmic scale with large values of ℓ in the front and with a increasing in relative size on the receding "picture planes." This choice of logarithmic scale permits combining a large amount of data into a form which can be easily assimilated and giving equal weight to very small and to very large (a/ℓ) values.

In many practical problems, one might regard ℓ as essentially fixed and wish to know how the mean current density would vary with the (a/c) ratio. For this reason, additional values of the mean, namely (Γ_a^*/a), have been computed with ℓ constant and a varying in the (a/c) ratio. Fig. 3 compares the values of $\overline{C_a}^*$ obtained when (a/ℓ) or ℓ are fixed. The dotted line is for the constant ℓ data. As would be expected, the curve for constant ℓ is symmetrical about the line $a/c = \frac{1}{2}$. In the case of the constant ratio curves, the increasing polarization parameter (as a/c is increased above $\frac{1}{2}$) reduces the corrosion current density over the entire anode and thus reduces Γ_a^*. However, when a/c is small, the ℓ values in the constant ratio curves are also small. The corrosion current density rises rapidly.

Average corrosion current parameter.—There is no important difference between the *average* value of the corrosion current parameter on the anode and on the cathode, since Γ_a^* is equal in magnitude to Γ_c^* but has the opposite sign and, in either case, c is the divisor. This is not true of the mean values; thus the distinction between the two quantities in this section.

Values of Γ_a^*/c were obtained from the mean values by equation [14]. A graphical summary of the important results is presented in Fig. 4 and 5. The same values of the three parameters were employed in these graphs as in

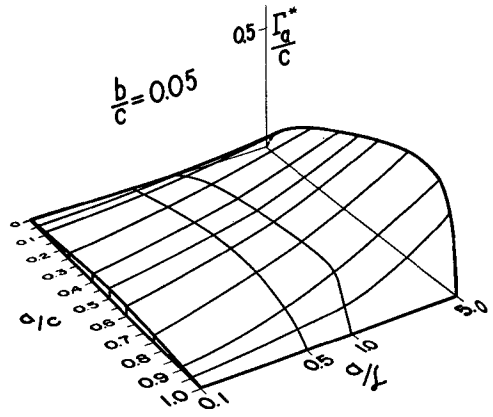

FIG. 4. Dependence of the average value of the current density parameter upon the ratios (a/ℓ) and (a/c). Computed for a (b/c) value of 0.05. This illustration supplements Fig. 1.

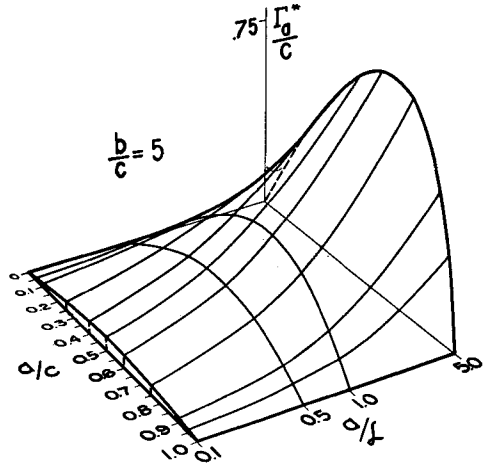

FIG. 5. Dependence of the average value of the current density parameter upon the ratios (a/ℓ) and (a/c). Computed for a (b/c) value of 5. This illustration supplements Fig. 2.

Fig. 1 and 2, respectively. These four drawings are complementary.

Effect of relative thickness.—The previous illustrations have shown the effect of two limiting relative thicknesses of the corrodent layer. However, it seemed desirable to present in one or two graphs a summary of the effects to be expected with intermediate thicknesses.

Fig. 6 was constructed for a constant value of the characterizing ratio (a/ℓ). Examination indicates that, when sections of the surface are taken at constant small (b/c) values, the curves are similar in shape to those presented in Fig. 1, and that, as the relative thickness is increased, there is a smooth transition toward a curve which is concave downward as the surface is in Fig. 2. Note that here, as in several other perspective drawings, the surface is not extended to intersect the plane corresponding to a zero anodic fraction. Such an extension could be made by computing the values from the integral derived above in connection with the second limiting case. When the anode is greater than about one-ninth the size of the cathode $(a/c > 1/10)$, the current is less for relatively shallow cor-

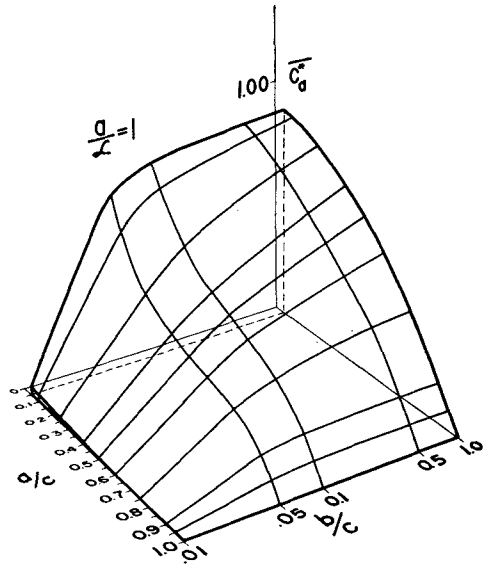

FIG. 6. Dependence of the mean current density on the relative thickness (b/c) and the anodic fraction (a/c). Computed for $(a/\mathfrak{L}) = 1$.

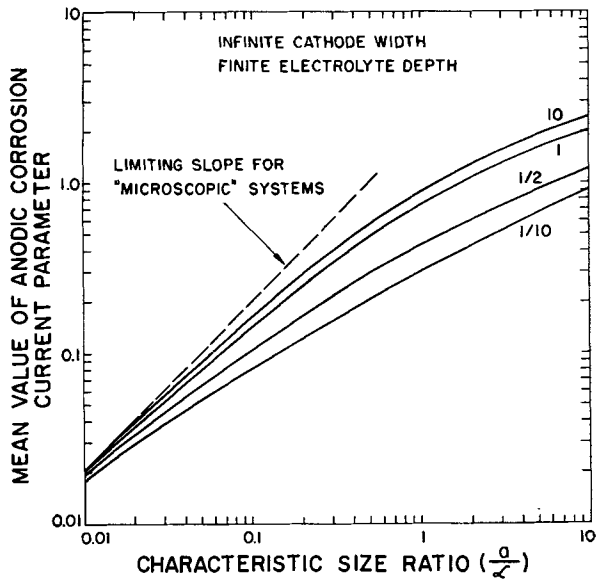

FIG. 7. Variation of the mean value of the anodic corrosion current parameter $\bar{C}_a^*$ with the characterizing ratio $(a/\mathfrak{L})$. Computed for $(b/a) = 0.1$, 0.5, 1, and 10 as a parameter.

rodents than for deep ones. This apparently results from concentration of the corrosion current into the vicinity of the anode-cathode junction (4). This concentration is greater when (b/c) is smaller than (a/c). In Fig. 6, the mean value of the corrosion current parameter, $\bar{C}_a^*$, decreases very rapidly as (b/c) approaches 0.01 at which time the latter becomes significantly smaller than any of the (a/c) values employed. However, as (a/c) approaches zero, and (a/c) becomes smaller than the intermediate values of (b/c) which have been used to construct Fig. 6, the values of $\bar{C}_a^*$ rise rapidly.

When the value of $\mathfrak{L}$ is, relatively speaking, ten times as large as in Fig. 6, an upswing of the $\bar{C}_a^*$ values as (a/c) approaches zero also occurs for small (b/c) values. Similarly, a curve drawn for $(b/c) = 1$ is concave downward.

Further discussion in terms of small (a/c) is presented in the next section, where the numerical results pertinent to the two limiting cases are discussed.

Evaluation of the mean current parameter for the limiting cases.—Equation [26] was numerically evaluated by hand as the integral in it converges rapidly after the first ten terms. The sine and cosine terms had been evaluated previously for large arguments (2). Tabulated values of the sine and cosine integrals were used.

The reduction of the integral in [39] to tabulated functions did not appear to be simple. Therefore, numerical integration was used, since convergence should be rapid. The maximum error is less than 1% and decreases rapidly as $(a/\mathfrak{L})$ increases.

By far the more important limiting case is the second, which involves finite liquid depths, since it is more pertinent to the material already presented. The case of an infinite liquid depth can be regarded as a limit to the case under discussion. The finite liquid case is discussed in more detail for this reason.

A graphical summary of the mean values of $\bar{C}_a^*$ computed for various $(a/\mathfrak{L})$ and (b/a) values from equation [39] is presented in Fig. 7. The curve for $(b/a) = 10$ is

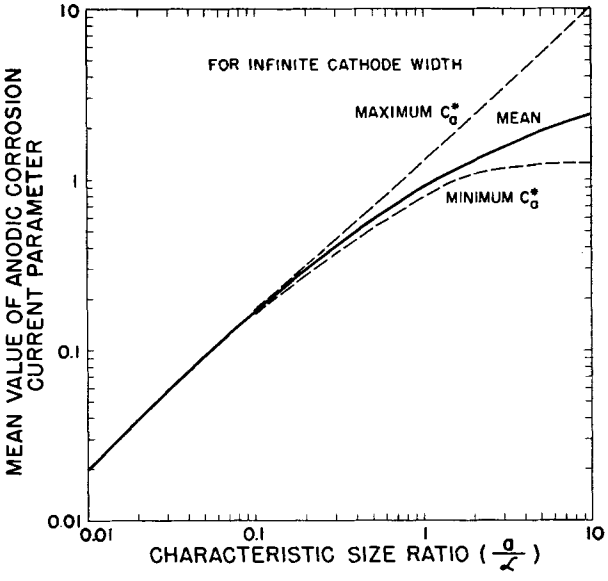

FIG. 8. The spread between the maximum, mean, and minimum values of $\bar{C}_a^*(x)$ for different fixed values of the characterizing ratio $(a/\mathfrak{L})$.

indistinguishable from that drawn for $(b/a) = \infty$. However, when b is much smaller than a, say for $(b/a) = 1/10$, the current density is small. Thus, in this sense b is the critical dimension λ.

The limiting value of $(2a/\mathfrak{L})$ for $\bar{C}_a^*$ which results for small values of the characterizing ratio $(a/\mathfrak{L})$ was added as a tangent to this figure. It can be deduced from earlier equations (2). Inspection of Table I of (2) indicates that for small $a/\mathfrak{L}$ values, the maximum value of C_a^* is approximately $2a/\mathfrak{L}$.

Using equation [15], it can be shown that

$$\lim_{(a/\mathfrak{L})\to 0} \max C_a^* = \lim_{(a/\mathfrak{L})\to 0} C_a^*(0) = \frac{2a}{\pi\mathfrak{L}}\left\{\frac{\pi}{2}+\frac{\pi}{2}\right\} = \frac{2a}{\mathfrak{L}} \quad [46]$$

since all of the quantities within the brace can be approximated by either 1, λ, or λ'. Therefore, those which would be second order in $(a/\mathfrak{L})$ in the total expression can be neglected. Only the two terms containing $(\pi/2 \cdot \cos 0)$ remain. The manner in which the mean value $\overline{C}_a^*$ is bounded between the maximum and minimum values of $C_a^*(x)$ is indicated in Fig. 8, which has been plotted from Table I of (2) and the data computed from equation [26].

Comparison with Experimental Results

Jaenicke and Bonhoeffer (8) employed a galvanic assembly in which thin cathodic cylinders of platinum were bolted between two anodic cylinders of zinc. The platinum cylinders were varied in length to give different anode-cathode ratios. The assembly was immersed in acid solution contained in a shallow dish, and the quantity of zinc dissolved in a given time was used to compute the dissolution rate and thus the average cathodic current. The dissolution rate of the zinc, under the same conditions but while not coupled to the platinum, was subtracted from the latter rate to obtain the correct rate due to galvanic action. Their data are tabulated as mean cathodic current densities.

The quantity $\mathfrak{L}_c$ can be obtained from their data by the formula Wagner (5) used,

$$\mathfrak{L}_c = \sigma\beta/J_c \qquad [47]$$

where σ is the specific conductivity in $ohm^{-1}cm^{-1}$, β, the coefficient in Tafel's equation for hydrogen overvoltage, is 0.050, and J_c is current density in amp/cm^2. Employing the data given for J_c in their Table 4, the value of $\mathfrak{L}_c$ for 0.05N hydrochloric acid lies in the range 0.0225–0.069 cm, whereas the calculated values for 0.05N hydrochloric acid plus 1M potassium chloride range from 0.145 to 0.252 cm. The equivalent limiting values of $a/\mathfrak{L}$ are 133, 44, and 21, 12 respectively in the two media.

The average current density over the cathode, J_c, was computed from the mean anodic corrosion current parameter $\overline{C}_a^*$ by the expression

$$\overline{J}_c = \left(\frac{E_a}{2a}\right)\sigma\left(\frac{a}{c-a}\right)\overline{C_a^*} \qquad [48]$$

In this equation, the a in the numerator and denominator has not been cancelled to facilitate rapid recognition of the source of each factor. $\overline{C}_a^*$ was computed for $b = 2.5$ cm, for several values of the parameter $a/\mathfrak{L}$, (15, 30, 60, 120), and for each cathode breadth which Jaenicke and Bonhoeffer employed. The appropriate values of σ and E_a were estimated from their data. The resulting $\overline{J}_c$ data are tabulated in Fig. 9. The agreement is surprisingly good in the case of the more concentrated solution. However, the data for 0.05N hydrochloric acid are smaller by a factor of three or four than would have been expected from the low $\overline{J}_c$ values. In the more poorly conducting solution, the voltage difference between the two materials was higher, otherwise the current density would have been significantly smaller. Comparison of the two curves for $a/\mathfrak{L} = 30$ shows that the product $(E_a\sigma)$ appearing in [48] was approximately constant for the two solutions. Thus the data for hydrochloric acid are low for some reason.

Robertson and Uhlig (9) prepared alloy mixtures of magnesium and tin which contained the intermetallic compound Mg_2Sn. The composition of six alloys used was adjusted so that a different percentage of the compound would be mixed with either parent metal. Samples of these alloys were immersed in a 1N sodium chloride solution. The hydrogen that evolved during the corrosion was collected and served as a measure of the average corrosion rate. The authors did not study polarization characteristics of Mg_2Sn, magnesium, or tin present in their alloys, and the self-corrosion rates of magnesium and Mg_2Sn were not obtained separately. Thus, accurate values of $\mathfrak{L}_a$ and $\mathfrak{L}_c$ cannot be obtained. Equation [47] may be employed to estimate $\mathfrak{L}_c$ from the rate of hydrogen evolution shown in their Fig. 10. The rate for 70% free magnesium gives $\mathfrak{L}_c \simeq 0.8$ cm, which is consistent with values noted in other experimental studies (2-4). Robertson and Uhlig employed powdered samples, and the size of the particle ranged from 0.015 to 0.065 cm. Thus, if virtually the entire particle was free magnesium, the maximum value of $a/\mathfrak{L}$ was 0.04, since a is chosen as one half of the anode size. The average cathodic current at 30 and 80% compound was compared with data computed for a constant $a/\mathfrak{L} = 0.05$ and for $b/c = 0.1$. The experimental ratio is 1.49, whereas the theoretical ratio was 1.48. This suggests good agreement.

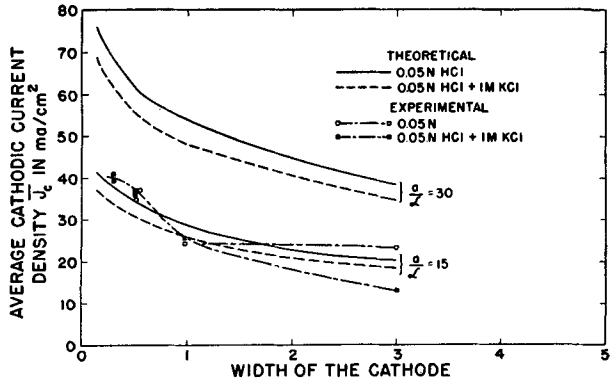

FIG. 9. Comparison between the computed and experimental values of $\bar{J}_c$, based on the data of Jaenicke and Bonhoeffer.

Discussion

When the characterizing ratio $(a/\mathfrak{L})$ is kept constant as in Fig. 1, and (a/c) approaches zero, then in the limit either $\mathfrak{L}$ must go to zero to maintain $(a/\mathfrak{L})$ constant or c must go to infinity. The former case has been discussed. The rapid increase in the average current near the origin of Fig. 1 is due to the forced, simultaneous decrease in $\mathfrak{L}$. Fig. 2 reveals that the same increase is, however, small when (b/c) is large.

A constant $(a/\mathfrak{L})$ section was made through the surfaces in Fig. 1 and 2, and these sections were combined in constructing Fig. 10. The two curves with the largest and smallest (b/c) values become equal when the anodic function (a/c) approaches either one of its limiting values, zero or unity, i.e., when either the anode or the cathode, respectively, becomes vanishingly small. However, near the middle range of (a/c), the mean corrosion current is less for shallow electrolyte "films" than deep liquid layers.

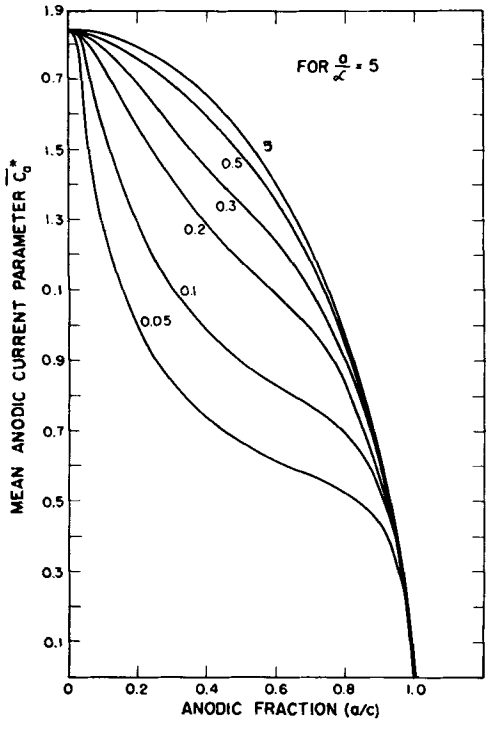

FIG. 10. Variation with the anodic fraction of the mean values of the anodic corrosion current parameter. Computed for $(b/c) = 0.05, 0.1, 0.2, 0.3, 0.5$, and 5. Curves for the smallest and largest relative thicknesses were obtained from Fig. 1 and 2, respectively.

Thus, one may conclude that the current is concentrated into the vicinity of the junction and limited in magnitude when the relative thickness (b/c) is small in comparison to unity. This behavior was convincingly displayed earlier (4).

As might be expected for larger values of (b/c), the significant departure from equality does not occur until the anodic fraction is substantially farther away from the limits, one or zero. That is, when (b/c) is large, the electrolyte appears to be "infinitely deep" for most electrode widths. It is important to look at the relative size of b and of the smaller electrode width, a or $(c - a)$. For clarity, four additional curves were added to Fig. 10; these were computed for $(b/c) = 0.1, 0.2, 0.3$, and 0.5.

Similar slopes of the family of curves near $\alpha = 0$ can be deduced qualitatively. When a becomes very small in comparison to some finite c, b will become larger than a as long as the relative thickness (b/c) is fixed. Earlier (4) it was concluded that the corroding liquid was essentially "infinitely deep," if its dimension were a few times larger than the anode dimension. This means that the various values of $\overline{C}_a^*$ become essentially equal to the single value obtained for infinite b when α is very small. However, this is based on the assumption that the sum of the anode and cathode widths c is finite.

The argument also applies when c is infinite. Then, of course, both α and η are zero. The ratio (b/a) may take on any value and still satisfy the condition that α and η are zero. For any given (a/ℓ) value in Fig. 7, the values of $\overline{C}_a^*$ approach a limit, set by the infinite electrolyte depth, as b/a increases. That is, b is essentially "infinite," if it is several-fold larger than a. Thus one may arrive at the conclusion that the curves will asymptotically approach the limiting curve in Fig. 10 in the region of $\alpha = 0$, even though c is finite but very much larger than a.

The discussion of these two limiting cases has increased the understanding of the over-all behavior of similar electrochemical systems. When ℓ is large, the $\overline{C}_a^*$ values are small and are approximately equal, independent of the relative sizes of the dimensions a and b, i.e., when the galvanic system is behaving "microscopically." However, in certain instances, either a (or b) may be larger than ℓ, and the other one, (b or a) may limit the local distribution of the current density. In such cases, the system will be "microscopic" if that dimension, say b, is much smaller than ℓ.

When c is very large, the really significant ratio becomes (b/a), and the direct dependence upon c is eliminated. A variation of this statement is that either a or b may become the critical dimension λ, i.e., that dimension which most strongly affects the distribution of current density. For a fixed (b/c) ratio, a becomes λ as the anodic fraction α goes to zero, since b appears to be "infinite." The curves for $\alpha = 0$ in Fig. 1 and 2 can be derived from the limiting cases of finite and infinite electrolytes, respectively.

If (b/c) is large but c finite, then, as the anode becomes vanishingly small, the current approaches a uniform value over the anode, and the electrochemical systems appear to behave microscopically. A similar result is obtained when the cathode width $(c - a)$ becomes infinitely small in comparison with the size of the anode a. The limiting case just discussed of an infinite cathode and electrolyte also adequately describes this feature of the over-all behavior.

The second limiting case of a thin finite electrolyte layer pertains to Fig. 1 where it is assumed that in most cases the anode and cathode are larger than the liquid depth. The smallest value of the anodic fraction (a/c) employed in the calculation is 0.05 which is equal to the specific value of the relative thickness used for constructing that figure. That is, the smallest (a/b) used was unity.

When the anode is very tiny in comparison to b or c, because of a fixed (b/c) ratio, a is the critical dimension, and the liquid depth appears to be "infinite" despite the smallness of b, because the ratio (b/a) is large. A similar argument applies to vanishingly small cathodes as well.

When (b/a) is smaller than approximately one, the current will be concentrated into the vicinity of the anode-cathode junction, and the curve of the mean value of C_a^* as a function of α in Fig. 4 reflects this fact. That is, the $\overline{C}_a^*$ curve for small b/c lies below that for infinite relative thickness. When b/c is small, the significant ratio (b/a) can be greater than one for very small values of a/c. Analysis of the second limiting case shows that mean value of $\overline{C}_a^*$ rapidly approaches a certain maximum value as a becomes infinitely small and that this maximum value is that obtained for an infinite electrolyte in the other limiting case.

Qualitatively this result can be deduced by noting that for any b/c value greater than zero, there will be some values of a/c such that a/b will be smaller than one half. Thus, for any thin film of electrolyte, there will be some small size of either the anode or the cathode for which this

film will effectively be "infinitely deep." Thus, the equality of the $\overline{C}_a^*$ curves at $\alpha = 0$ or 1 in Fig. 11, independent of the (b/c) values, is explained, and the general behavior of any similar electrochemical system which is consistent with the basic premise of equal polarization parameters is elucidated.

Summary

On the basis of the detailed theoretical analysis it can be concluded that the mean current density over the anodes is a maximum when the anodic fraction $(a/c) = \frac{1}{2}$ and becomes zero as either the anode or cathode becomes vanishingly small, provided the polarization parameter $\mathfrak{P}$ is constant. This maximum value is dependent on the relative liquid depth. In the event that the characterizing ratio $(a/\mathfrak{P})$ is kept constant, the same mean current density increases to a large value which is independent of the relative electrolyte depth, as the anodic fraction approaches zero. These phenomena can be explained in terms of the characteristic ratio $(\lambda/\mathfrak{P})$. For a given anodic fraction, other than zero or unity, as the relative electrolyte thickness (b/c) is reduced, the mean current density decreases from some maximum value. The qualitative agreement between these theoretical deductions and two previously published experimental studies was discussed.

Acknowledgment

The authors are deeply indebted to Professor Carl Wagner who checked the integration of the Fourier series and who has offered considerable guidance and inspiration during the course of this work.

Calculations for Fig. 8 were performed by Max Goldstein and Clifford Moss. The authors are grateful to them for this important assistance. Miss Elizabeth Scott constructed the perspective illustrations for this report.

Manuscript received March 10, 1955. Work on this paper was done under the auspices of the Atomic Energy Commission.

Any discussion of this paper will appear in a Discussion Section to be published in the December 1956 JOURNAL.

REFERENCES

1. J. T. WABER, *This Journal*, **101**, 271 (1954).
2. J. T. WABER AND M. ROSENBLUTH, *ibid.*, **102**, 341 (1955).
3. J. T. WABER, *ibid.*, **102**, 420 (1955).
4. J. T. WABER AND B. FAGAN, *This Journal*, **103**, 64 (1956).
5. C. WAGNER, *ibid.*, **98**, 116 (1951).
6. J. T. WABER AND J. MORRISSEY, Unpublished work.
7. J. T. WABER AND J. MORRISSEY, Unpublished work.
8. W. JAENICKE AND K. F. BONHOEFFER, *Z. phy. Chem.*, **193**, 301 (1944).
9. W. D. ROBERTSON AND H. UHLIG, *Trans. Electrochem. Soc.*, **96**, 27 (1949).

Resistivity Studies of Various Leclanché Cathode Materials

RICHARD GLICKSMAN AND C. K. MOREHOUSE

RCA Laboratories, Radio Corporation of America, Princeton, New Jersey

ABSTRACT

It has been suggested that there is a correlation between dry cell performance and resistivity of various manganese dioxides. Resistivity data obtained on four types of manganese dioxides over a range of applied pressures up to 100,000 lb/in.^{2} (7.03×10^6 g/cm^2) show quite different resistivity vs. applied pressure relationships. These differences, however, are minimized by blending high resistivity manganese dioxide with low resistivity acetylene black and electrolyte, and it is concluded that resistivity of manganese dioxide cannot have an appreciable effect on the performance of a dry cell.

INTRODUCTION

The importance of the manganese dioxide electrode of the Leclanché-type dry cell and the variation in performance between cells containing manganese dioxide materials of different crystallographic forms has prompted a number of questions as to the electrical properties of manganese dioxide.

In this paper, resistivity data at various applied pressures and apparent densities of dry cell components, including acetylene black, various types of manganese dioxides, and mixtures of each, are presented. This study was made to determine whether a correlation in cell performance with resistivity of cathode materials could be made.

EXPERIMENTAL APPARATUS

The apparatus used for measuring resistivities is shown in Fig. 1. It consists essentially of a pair of steel electrodes (approximately 1½ in. diameter and 1 in. long) with arms $1\frac{1}{32}$ in. long and ¼ in. diameter. These arms fit closely into a plastic liner (natural paper base tubing,[1] ¼ in. I.D.) which was placed in a steel cylinder for support. A small sample (0.1–0.5 g) of the material to be measured was placed between the ends of the electrodes inside the plastic tubing and compressed successively from 1,250 to 100,000 lb/in.^{2} (8.79×10^4 to 7.03×10^6 g/cm^2) by applying pressure to the ends of the electrode by means of a hydraulic press.

Resistance and volume measurements were made at various applied pressures. The resistance of the powder was measured with a Leeds & Northrup Type S-2 portable Wheatstone bridge (0.1% accuracy). All measurements were corrected for the resistance of the steel electrodes and connecting wires (0.033 ohm). The volume occupied by the sample at various pressures was determined from a knowledge of the cross-sectional area which is defined by the I.D. of the tubing, and by the difference between the known length of the electrodes and the measured length with the sample between the electrodes. Resistivity (ohm-cm) and apparent density (g/cc) were calculated for each pressure.

[1] Obtained from the Synthane Corp., Oaks, Pa.

ELECTRICAL RESISTIVITY DATA FOR ACETYLENE BLACK[2]

Acetylene black is an important constituent of dry cells and is blended with the highly resistant manganese dioxide cathode to provide an electrode of low resistance. Benson, Gluck, and Kaufmann (1) measured the resistivity of acetylene black over a pressure range of 100–2000 lb/in.^{2} ($7.0 \times 10^3 - 1.4 \times 10^5$ g/cm^2). Extending this work, resistivity data obtained on 0.1 g samples of acetylene black, 50% compressed, over a pressure range of 1,250–100,000 lb/in.^{2} ($8.79 \times 10^4 - 7.03 \times 10^6$ g/cm^2) are presented in this paper.

The measured resistivity values for acetylene black, plotted against apparent density and applied pressure are shown in Fig. 2 and 3. Each point on the curves represents the average of three different samples, with the individual measurements deviating from the mean no more than 5%. Also shown are results for an acetylene black, 100% compressed, reported by Benson and co-workers as sample B in Table II of their paper. Their results reported in ohm-in.[3] were converted to ohm-cm.

Benson, Gluck, and Kaufmann (1) and Sweitzer and Goodrich (3) found that in comparing the resistivity of carbon blacks of widely different properties, standard pressure could not be used as the only basis, and that values at equal apparent densities gave more comparable results, which is in accord with the findings of this work.

It is possible to compare the two sets of data over only a limited range of apparent densities, since much higher pressures were applied in the present study. For an apparent density of 0.70 g/cc, Benson and co-workers measured a resistivity of 0.086 ohm-cm as compared with the value of 0.061 ohm-cm found by the present authors. Benson (4) reported a resistivity of 0.076 ohm-cm at a density of 0.70 g/cc for both 50 and 100% compressed acetylene black. Thus, there is a reasonable agreement between the two sets of data.

In Fig. 2 and 3 it is seen that the resistivity approaches a constant value of 0.010 ohm-cm at pressures of approximately 30,000–40,000 lb/in.^{2} ($2.1–2.8 \times 10^6$ g/cm^2) and

[2] Material obtained from Shawinigan Chemicals Ltd., Shawinigan Falls, Que., Canada.

[3] In the original publication the results were erroneously printed as ohm/in. instead of ohm-in. (2).

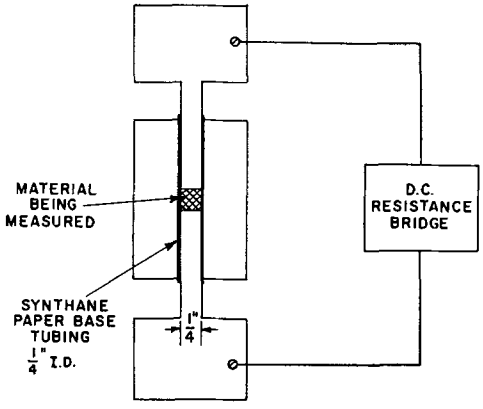

FIG. 1. Apparatus for measuring resistivity of powdered materials.

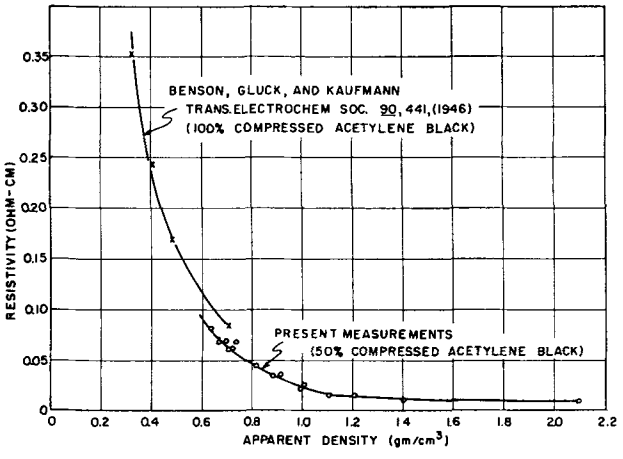

FIG. 2. Resistivity measurements of acetylene black at various apparent densities.

at an apparent density of approximately 1.2 g/cc. Thus contact resistance between particles ceases to become a variable at pressures and apparent densities above these values.

ELECTRICAL RESISTIVITY DATA FOR VARIOUS MANGANESE DIOXIDES

A survey of the literature shows that resistivity values of manganese dioxide ranging from 100 to 10^6 ohm-cm have been reported (5–7); however, these values have not been carefully identified with respect to the physical and chemical properties of the material. Fox (8) more recently investigated the effects of hot pressing various manganese dioxides, and prepared materials with a density of 2.0–2.7 g/cc which have a resistivity of less than 100 ohm-cm.[4]

Resistivity data were gathered on four different types of manganese dioxides which are characterized by the chemical and physical data shown in Table I and Fig. 4. Manganese dioxide, type A, was made by the thermal decomposition of manganese nitrate. Type B was prepared by anodic deposition on graphite from a hot sulfuric acid solution of manganous sulfate. Type C manganese dioxide was prepared by treating a reduced African manganese dioxide material with sulfuric acid. The manganese dioxide which settled out was filtered and washed free of acid.

[4] These results were reported as ohms/cc.

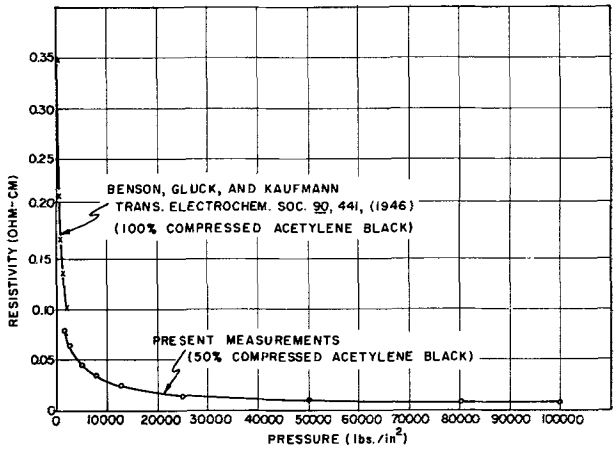

FIG. 3. Resistivity measurements of acetylene black at various applied pressures.

Type D was naturally occurring African Gold Coast manganese dioxide. Data presented in Fig. 5 and 6 represent the average of two different 0.5 g samples, with the individual measurements deviating from the mean by less than 10%. These results were obtained by the same technique as described for measuring the resistivities of acetylene black.

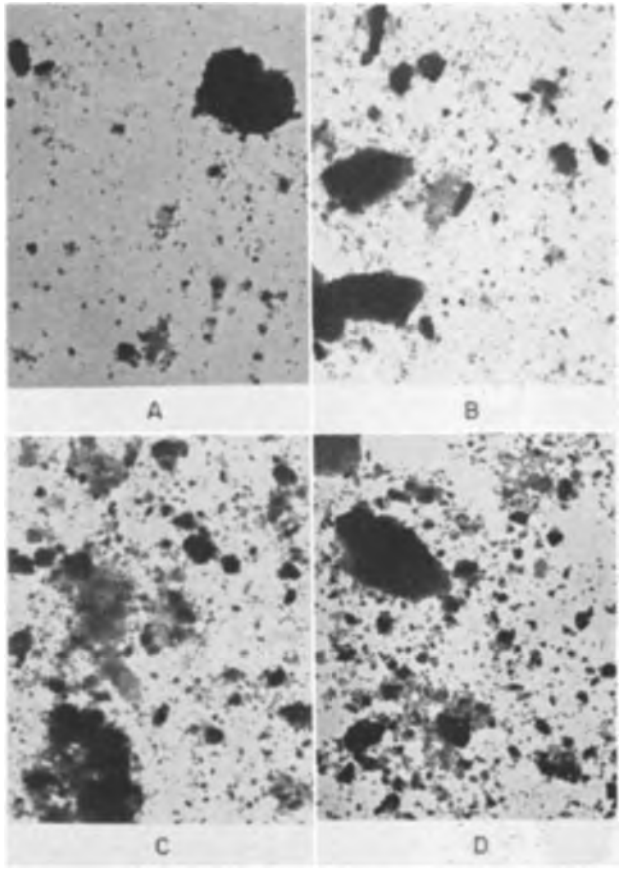

FIG. 4. Electron micrographs of various types of manganese dioxide: (*A*) from thermal decomposition of $Mn(NO_3)_2$; (*B*) produced electrolytically; (*C*) produced by chemical treatment of African ore; (*D*) naturally occurring African ore. (10,000× before reduction for publication.)

TABLE I. *Various properties of manganese dioxide materials*

Classification	A		B		C		D	
Method of preparation	Thermal decomposition of $Mn(NO_3)_2$		Anodic deposition on graphite electrodes from aqueous solution of H_2SO_4 and $MnSO_4$		Chemically treated African ore		Naturally occurring African Gold Coast	
% MnO_2	84.6		85.0		85.0		84–85	
% Total Mn	58.1		59.0		59.0		58.0	
Apparent density	0.70 g/cc (11.5 g/in.^{3})		1.28 g/cc (21.0 g/in.^{3})		1.12 g/cc (18.5 g/in.^{3})		1.37 g/cc (22.5 g/in.^{3})	
	X-ray diffraction patterns							
	d	I/I_1	*d*	I/I_1	*d*	I/I_1	*d*	I/I_1
	7.312	12	7.107	16	5.046	11.4	4.045	35.4
	5.842	15.7	4.085	23.2	4.005	14	3.376	13.6
	3.890	26.2	2.433	28.9	3.376	22	3.142	24.7
	3.491	19.1	2.337	100	3.142	40	2.587	12.6
	3.142	10.4	2.131	14.9	2.419	100	2.419	63
	2.742	11.8	2.036	18.9	2.337	93.5	2.337	100
	2.405	63.5	1.635	33.3	2.153	29.4	2.153	28.4
	2.350	100	1.438	7.1	2.109	29.4	2.036	25
	2.142	2	1.395	11.9	2.036	22.3	1.896	13.5
	2.036	57	1.221	3.9	1.845	17.9	1.829	13.6
	1.914	7.2	1.174	4.9	1.628	79.2	1.635	59
	1.628	4	1.061	4.2	1.561	22.3	1.567	8.4
	1.521	12			1.544	28	1.428	17.4
	1.468	8.5			1.428	46.4	1.363	19.4
	1.428	18.7			1.385	22.7	1.304	14.4
	1.395	4.3			1.304	22.3	1.221	8.4
	1.346	18.2			1.223	15.3	1.168	5
	1.304	8.5			1.058	5	1.069	9.1
	1.218	8.5			0.9996	8.9		
	1.063	6.7						
	0.9121	8.5						

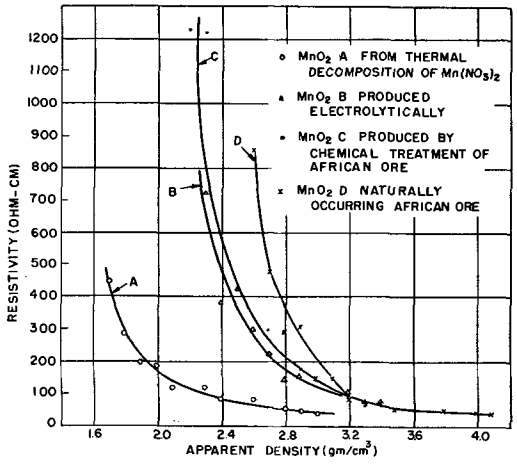

FIG. 5. Resistivity measurements of different manganese dioxides at various apparent densities.

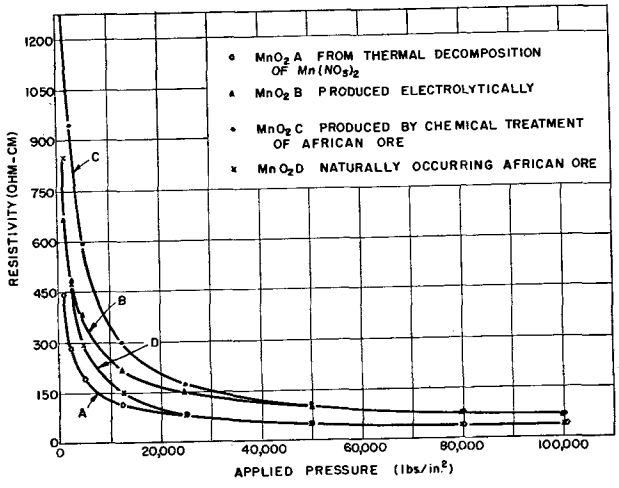

FIG. 6. Resistivity measurements of different manganese dioxides at various applied pressures.

The data show that as the pressure on the sample or the apparent density is increased, all four samples approached resistivity values between 37–77 ohm-cm at about 100,000 lb/in.^{2} (7.03×10^6 g/cm^2) or at 3.0–3.4 g/cc. Thus it appears that at these high pressures and densities, the contact resistance between the particles is practically eliminated, and the specific electrical resistivity of the material is approached.

At equal apparent densities, before the materials reached their lowest resistivity, material A had lower resistivity value than the other three manganese dioxides. It might be thus surmised that the contact resistance between particles of material A was lower than that between particles of the other three materials. From x-ray diffraction and electron micrograph data, it is seen that the structure and particle size distribution is different in all four of these materials. Material A appears to have a larger number of smaller particles than the others, and it is believed that the difference in resistivity of the four

manganese dioxides is due to differences in particle size and structure of the materials. Since manganese dioxide is a semiconductor, variation in impurities might also account for these differences.

Since there is an obvious difference between the resistivity curves of the four materials as the applied pressure is varied, an attempt was made to correlate the resistivity data with manganese dioxide performance, both in polarization studies and in actual cells.

If the manganese dioxides are rated on the basis of lowest resistivity at a given apparent density, it is found that the lower the resistivity of the sample, the greater is the capacity in amp-min/g (9). The results are reported in Table II, where the rating of four manganese dioxides is given both on a weight and volume basis, along with other data.

TABLE II. *Rating of various types of manganese dioxides**

Classification of manganese dioxide	Method of preparation	Scotts density (g/in.^{3})	Polarization studies		Signal Corps data** capacity (hr)
			Capacity (amp-min/g)	(amp-min/in.^{3})	
A	Thermal decomposition of $Mn(NO_3)_2$	11.5	6.6–8.8	76–101	6.4
B	Electrolytic deposition	21.0	5.3	111	6.5–7.5
C	Chemically treated African ore	18.5	2.6–3.0	48–56	4.5–5.0
D	Naturally occurring African ore	22.5	1.1–1.9	25–43	4

* Ref. (9).

** "A" size Leclanché cells discharged continuously through a 16⅔ ohm resistance to 1.00 v per cell. Data supplied by Power Sources Branch of the Signal Corps Engineering Laboratories.

TABLE III. *Resistivities in ohm-cm of various materials, both pure and when mixed with acetylene black, at various pressures*

Material	Pressure (lb/in.^{2})			
	40,000 (2.8×10^6)*	60,000 (4.2×10^6)*	80,000 (5.6×10^6)*	100,000 (7.0×10^6)*
MnO_2 C	120	96.0	81.0	67.7
10–1 MnO_2 C —black mix	0.87	0.67	0.60	0.54
MnO_2 D	60.0	50.0	47.8	40.0
10–1 MnO_2 D —black mix	0.70	0.61	0.52	0.48
Sulfur	$>10^9$	$>10^9$	$>10^9$	$>10^9$
10:1 sulfur —black mix	2.11	1.81	1.69	1.59
Acetylene black	0.012	0.009	0.009	0.008

* Values in parenthesis are in g/cm^2.

Making the same comparison of resistivity with capacity in amp-min/in.^{3}, and in actual cells, the ratings of the two best manganese dioxides are (materials A and B) reversed. This would be expected in view of the low density of material A compared with that of B, as found by Scotts density method (10). Material A would therefore give less capacity in an actual dry cell than material B, since the capacity of a dry cell is dependent on the amount of material in the cell, as well as its activity per unit weight.

From the above data it might be inferred that a correlation between resistivity and the capacity of manganese dioxides in dry cells exists. However, before any conclusions can be drawn from the data, it is necessary to clear up two important points: first, the effect of blending the manganese dioxides with acetylene black on the resistivity of the mixture, since such a mixture constitutes the cathode of a dry cell; second, the over-all effect of the internal resistance on cell performance.

Resistivity measurements of mixtures of ten parts manganese dioxide to one part acetylene black are shown in Table III for materials C and D. Additional measurements were made of similar sulfur-acetylene black mixtures for comparison. The results are reported at the higher pressures in order to minimize resistivity differences resulting from contact resistance. At these high pressures, the uncertainty involved in measuring small changes in apparent density is large, so resistivities are given at equal applied pressures.

As shown in Table III, the bulk resistivity of manganese dioxide is about 10^4 times that of acetylene black. Conduction through mixtures containing one part acetylene black and ten parts manganese dioxide, therefore, is predominantly through chains of the very low resistivity acetylene black particles. Resistivities of such mixtures are little affected by substituting manganese dioxides with different resistivities. Even when sulfur, with a resistivity greater than 10^9 ohm-cm, is substituted for manganese dioxide, with a resistivity of approximately 100 ohm-cm, the resistivity of the mixture is increased by a factor of only three. The small effect of resistivity differences of various manganese dioxides is further decreased in conventional dry cells, wherein the cathode material has been mixed not only with acetylene black, but also with a highly conducting electrolyte. It is concluded that the resistivity of the manganese dioxide is of little importance in determining the internal resistance of a dry cell. Furthermore, the internal resistance of a dry cell is initially low and changes very little during discharge (11) so the resistivity of manganese dioxide is not an important factor in eventual cell failure.

In view of the above, no correlation can be made between the resistivity of a manganese dioxide and its performance in a cell. That there does appear to be a correlation stems from the fact that the differences in resistivity values of the manganese dioxides can be accounted for by differences in particle size and structure. These differences can also influence cell performance, as has been shown by other investigators.

ACKNOWLEDGMENT

The authors wish to thank the Power Sources Branch of the Signal Corps Engineering Laboratories for making

available the dry cell capacity and chemical analysis data of the various manganese dioxides. They also wish to thank Dr. J. A. Amick of the RCA Laboratories for the x-ray diffraction data and electron micrographs.

Manuscript received June 15, 1955. This paper was prepared for delivery before the Pittsburgh Meeting, October 9 to 13, 1955.

Any discussion of this paper will appear in a Discussion Section to be published in the December 1956 JOURNAL.

REFERENCES

1. G. BENSON, J. GLUCK, AND C. KAUFMANN, *Trans. Electrochem. Soc.*, **90**, 441 (1946).
2. B. P. BUCKLEY, Private Communication.
3. C. W. SWEITZER AND W. C. GOODRICH, *Rubber Age*, **55**, 469 (1944).
4. G. BENSON, *ibid.*, **58**, 461 (1946).
5. A. A. SOMERVILLE, *Met. Chem. Eng.*, **10**, 422 (1912).
6. P. FISCHER, *Z. Elektrochem.*, **32**, 538 (1926).
7. M. LEBLANC AND H. SACHSE, *Physik. Z.*, **32**, 887 (1931)
8. A. L. FOX, U. S. Pat. 2,631,116, March 10, 1953.
9. C. K. MOREHOUSE AND R. GLICKSMAN, *This Journal*, **103**, 94 (1956).
10. Specification for Battery-Grade Electrolytic Manganese Dioxide by Power Sources Branch, Components Division, Signal Corps Engineering Laboratories, Fort Monmouth, N. J., dated March 23, 1955, p. 22.
11. R. GLICKSMAN AND C. K. MOREHOUSE, *J. Electrochem. Soc.*, **102**, 273 (1955).

Anodic Film Growth on Hafnium in Nitric Acid

R. D. MISCH AND E. S. FISHER

Metallurgy Division, Argonne National Laboratory, Lemont, Illinois

ABSTRACT

In 70% nitric acid at room temperature, an anodic film developed uniformly over single hafnium crystals with a thickness dependent upon the metal crystal orientation. At 0.025 ma/cm² the cell voltage did not exceed 1.5 v. At 1.5 ma/cm² the cell voltage rose to 185 v and the film was broken down by sparking. In each case, the anodizing produced more oxide on metal crystal planes which had shown greater oxide growth on zirconium under similar conditions. At 90°C and 0.025 ma/cm², the oxide developed discontinuously over single hafnium crystals with the formation of wedge-like patches. The degree to which these patches covered the grains was not related to the metal crystal face in the same way as the thickness of the room temperature film. The discontinuous growth was attributed to nucleation at metal surface imperfections. An orientation effect in the electropolishing of hafnium was also noted.

INTRODUCTION

Many metals which can be anodized develop a film whose thickness is proportional to the cell voltage (1). This behavior has been shown to apply to zirconium (2) and was indicated for hafnium (3). Also, in the case of zirconium, a steady growth of oxide occurs at a low and steady cell voltage (3). This was designated as "low-resistance" oxide to distinguish it from the oxide whose thickness was proportional to cell voltage (designated "high-resistance"). The rate of formation of the low-resistance oxide was found to be dependent on the orientation of the underlying metal crystal (4) as well as on current density and on concentration of nitric acid.

In the case of hafnium, a high-resistance film, similar to the film on tantalum (3), occurred at 1 ma/cm². Evidence for the low-resistance type of oxide has now been obtained and is presented here. Both high- and low-resistance films were found to be influenced by the metal orientation. Nucleation effects were indicated in the latter case.

EXPERIMENTAL

A large-grained hafnium specimen was cleaned by polishing and etching. It was then anodized in 70% nitric acid at 0.025 and at 1.5 ma/cm², room temperature, and at 0.025 ma/cm², 90°C. The specimen consisted of a cross section of hafnium crystal bar which was machined to a disk 0.45 cm thick × 3.0 cm diameter. The original wire used in production could be seen in the center of the disk. The specimen was chosen because of its large grains (containing marked substructure). Spectrographic analysis of the turnings showed the following composition in weight per cent: Zr, 3; Ti, 0.3; As, Ba, Ca, Mo, P, V, Zn, less than 0.1; Ag, Al, B, Be, Bi, Co, Cr, Cu, Fe, K, Li, Mg, Mn, Na, Ni, Pb, Sb, Si, Sn, less than 0.01. A tantalum rod was screwed to the rim of the disk when anodizing. The tantalum was insulated from the electrolyte by anodizing to 240 v direct current in dilute KOH before insertion into the hafnium. Wet grinding consisted of polishing to 400 grit paper on a wheel with flowing water. A solution of HF and HNO_3 [1] was used for etching, followed by an immediate hot tap water rinse. Electropolishing was done in a mixture of acetic and perchloric acids[2] cooled with tap water. All photomicrographs were taken with bright field illumination. Orientations of the underlying metal grains were determined after anodizing by the back-reflection Laue technique.

[1] 8 ml conc. hydrofluoric acid (48%), 50 ml conc. nitric acid (70%), 50 ml hot tap water.

[2] 100 ml conc. perchloric acid (70%), 1000 ml glacial acetic acid.

FIG. 1. Appearance of a section of hafnium crystal bar after anodizing at 1 ma/cm² in 70% nitric acid 3 hr at room temperature.

FIG. 2. Hafnium crystal bar after etching in HF-HNO_3. 500× before reduction for publication.

RESULTS

Anodizing with High Film Resistance

The specimen was first studied under conditions which produce a high-resistance film. These were 1.5 ma/cm² and room temperature. At this current density, the surface developed interference colors which varied from grain to grain. At 170 v a play of sparks began on the surface and the clear interference colors began to disappear until a dull gray surface resulted. Each of the extremely fine sparks caused a localized destruction of the oxide layer.

TABLE I. *Orientation and appearance of 8 grains on hafnium crystal bar after various surface treatments*

Degrees from (001)	Appearance after anodizing 0.025 ma/cm²		Nature of furrow-like structure after electropolishing
	Room temperature	90°C	
34	Dark*	Solid to nearly solid black	Random
50	Dark*	Variable, from no black to scattered black areas	Random
50	Dark*	Solid black	Random
68	Dark*	Very light brown, no black oxide	Oriented†
68	Dark*	Very fine scattered black areas distributed in a parallel reticulated pattern	Oriented†
83	Light	No black	None
87	Light	Nearly solid black	None
88	Light	Scattered to solid black	None

* Color differences were not sufficiently distinctive to be useful.

† These grains showed an interference grating effect.

The sparks were short-lived at first but persisted longer as the anodizing continued and became fewer in number. They were also observed to spread out in a circle of increasing diameter until a grain boundary or previously sparked area was encountered. As the line of sparks advanced, the surface was observed to change sharply from a clear blue or green color to dull gray.

The sparking produced more oxide on some grains than on others. When anodizing was prolonged beyond the voltage maximum (185 v) for a total of 3 hr at 1.5 ma/cm² (room temperature), the result shown in Fig. 1 was obtained. In this photograph the white areas consist of a relatively thick friable layer of HfO_2 [3] and the other areas are dull gray. A quantitative estimate of the amount of oxide produced was not made. The grains in the foreground show a difference in oxide thickness in orthogonal directions.

Laue back-reflection patterns were obtained from two of the hafnium metal grains, one of which had a gray surface and the other a white surface. For this purpose, the friable oxide was removed by scraping.

The plane of anodizing of the hafnium grain which had a white surface was close to $(11\bar{2}6)$, 27° from the basal plane. The plane of anodizing of the grain with a gray surface was close to (3123), 60° from the basal plane. The former plane was also preferentially anodized in the case of zirconium (4), suggesting a similarity in anodic mechanism.

Anodizing with Low Film Resistance

The specimen was next studied under two conditions selected to produce a low-resistance film. These were: 0.025 ma/cm², 25°C and 0.025 ma/cm², 90°C. The results of these treatments are described below. In consideration of the surface changes which occurred, an area of particular interest on the specimen is shown in Fig. 2 (as etched).

[3] Monoclinic HfO_2 as determined by x-ray powder pattern.

The anodizing characteristics of the three contacting grains were very different as indicated in successive figures. These particular grains were too small for convenient determination of their orientation.

Anodizing at 0.025 ma/cm², 25°C.—Preliminary anodizing of the hafnium disk overnight at 0.025 ma/cm² produced a film with thicknesses dependent on the underlying metal grain. The cell voltage did not rise above 1.5 v. The formation of an equivalent thickness of high-resistance film would require 10–15 v. The existence of a film was verified by electropolishing and etching. The film on certain metal grains dissolved first, leaving the other grains in relief.

The specimen was cleaned and anodized again for 3 hr at the same current density and temperature. Upon removal, the specimen had a variegated color pattern which seemed to vary with grain structure. The colors were not distinct enough to characterize the films in terms of interference thicknesses. In diffuse light the anodizing differences were most noticeable in terms of shades of gray, while the colors were most pronounced in reflected light. As before, the light-film areas were etched to bare metal before the dark-film areas.

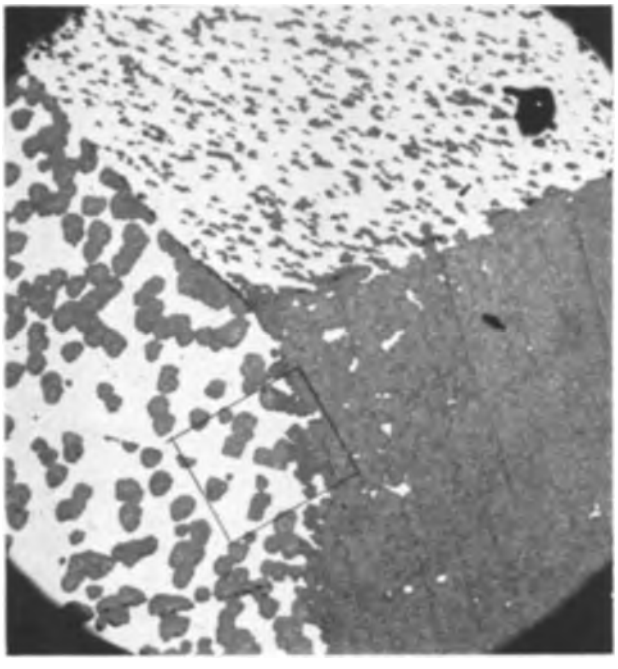

FIG. 3. Anodized pattern on hafnium crystal bar after 4 hr 10 min at 0.025 ma/cm², 70% nitric acid at 90°C. 100× before reduction for publication.

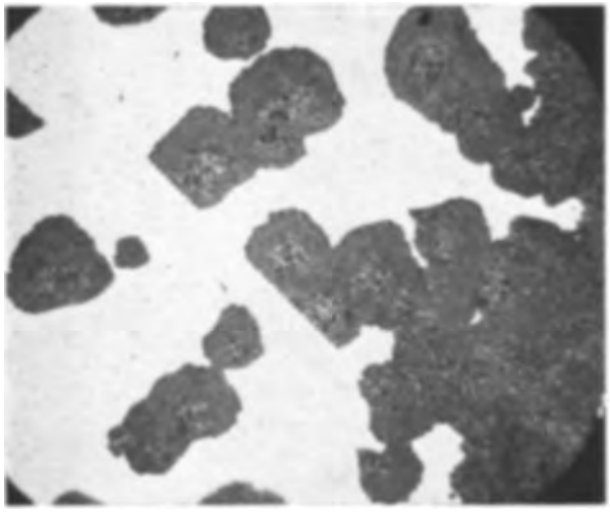

FIG. 4. Enlargement of part of the area in Fig. 3. 500× before reduction for publication.

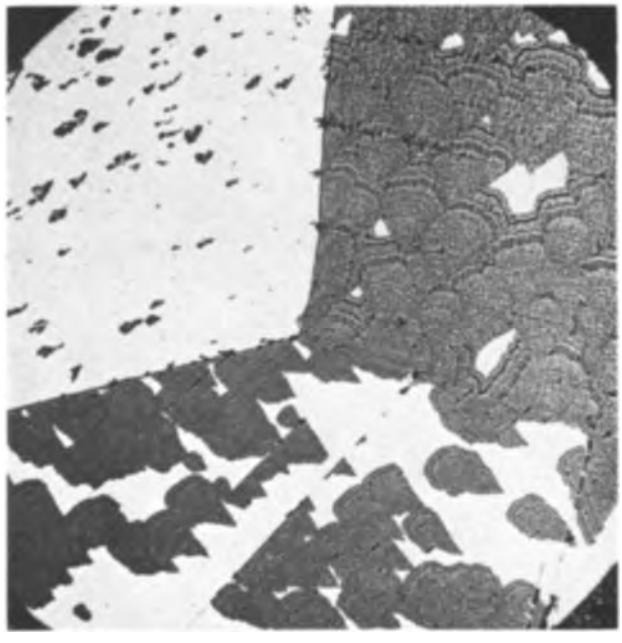

FIG. 5. Anodized pattern on hafnium crystal bar after 7 hr 30 min at 0.025 ma/cm². Pretreatment differed from that which produced Fig. 3 (same area). 100× before reduction for publication.

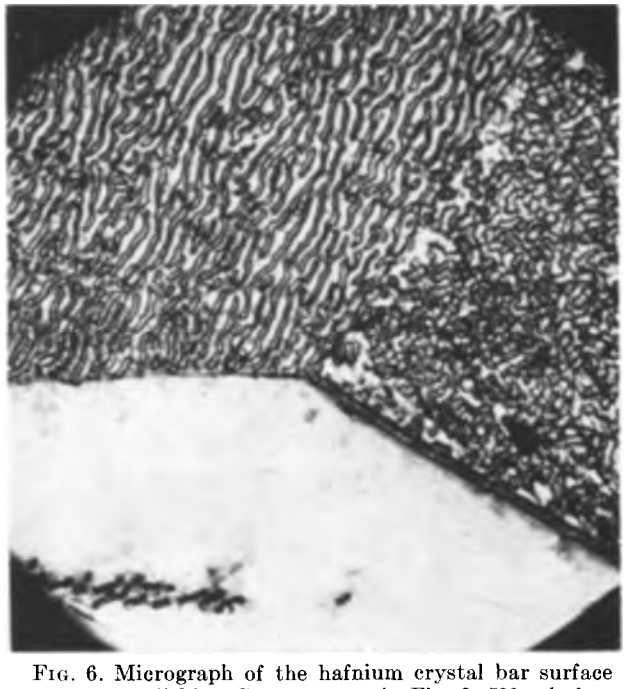

FIG. 6. Micrograph of the hafnium crystal bar surface after electropolishing. Same area as in Fig. 2. 500× before reduction for publication.

With the specimen in the anodized condition, the orientations of 8 metal grains were determined by the Laue back-reflection method. The grains were selected for large size and variation in shape from metallic to a bluish-black. The data are given in Table I. A more complete survey would require a quantitative measure of film thickness. The correlation between film thickness and the angular distance of the underlying crystal plane from the basal plane is similar to that observed on zirconium after the same type of treatment.

Anodizing at 0.025 ma/cm², 90°C.—The disk was anodized for 4 hr 10 min. The cell voltage rose slowly to a maximum of about 1.5 v. Selective darkening could be seen after 14 min. Upon removal, the specimen was rinsed and the surface examined.

The black oxide was concentrated chiefly in the outer area of the disk. It was observed that areas on single grains which had etched preferentially after 25°C anodizing (indicating a thinner film) were not darkened. Thus, it appeared that the initial oxide growth at 25° and 90°C may have been similar, but that the anodized areas at 90°C remained more localized. At least 20 well-defined grains were only partially darkened after the 90°C treatment. One of these grains had developed black oxide on approximately half of its area. To determine whether this difference was due to orientation differences within the grain, both areas were checked by the Laue technique. The orientation was the same. Seven other grains were then examined for surface appearance and orientation. The observations are presented in Table I. The distribution of the black oxide was not systematically dependent on orientation as in the room temperature case.

The same area as in Fig. 2 was photographed again at 100× (Fig. 3). The pattern of the oxide was distinctive. The black oxide appeared to nucleate at points and spread out over the surface. As shown in Fig. 4, the growth of black oxide stopped at a twin except at one end where the twin encountered a grain boundary. Inclusions in the surface also appeared to serve as nuclei.

The above procedure was repeated with some modification. The specimen, after repolishing mechanically and etching, was kept overnight under distilled water which was being stirred. The object was to extract any etchant which might have been trapped in crevices. The specimen was then anodized for 7 hr 30 min instead of 4 hr 10 min. The time was extended because at 4 hr 10 min only one small area on a circular face was completely black. As before, the edge of the disk darkened faster than the circular face.

The distinctive anodizing pattern is shown in Fig. 5 for the same area as presented in Fig. 2, 3, and 4. The oxide grew in the form of wedges which all pointed in the same direction within any one grain.

Effect of Electropolishing

Electropolishing was considered as a surface preparation, but was not used because of the nature of the surface that was produced. The conditions are detailed here because of an orientation effect. The disk was first wet-polished to 6 micron cloth on both faces and along the edge. It was then electropolished for eight 5-sec intervals at 100 v direct current in the acetic-perchloric electropolish. Approximately 30 sec was allowed for cooling after each polishing period. The bath was kept at about 15°C. After treatment, some grains were mirrorbright while others were slightly dull. Some of the latter exhibited faint interference colors which changed with the angle of viewing. Upon metallographic examination, the bright areas were seen to be flat while the dull areas had a furrow-like structure. The dull or matte areas exhibiting interference colors were found to have a parallel distribution of the furrows. The resultant grating would account for the interference pattern.

A micrograph of the three-grain area is shown in Fig. 6. The furrow pattern is similar to that produced on aluminum (5). The dependence on orientation is summarized in Table I.

Conclusions

The growth of oxide was influenced by orientation in two cases at room temperature: 0.025 ma/cm² and 1.5 ma/cm². In the former case, the cell voltage did not rise beyond 1.5 v and the film was evidently of lower resistance than in the latter case where the cell voltage rose to 185 v. In each case, a systematic dependence of film thickness upon metal orientation was observed.

Metal orientation also played a role in the growth of anodic oxide at 0.025 ma/cm² and 90°C, but the effect was secondary to nucleation. Comparison of the photomicrographs in this paper with those of Vermilyea (6) suggests that the oxide grew laterally in the shape of wedges. Vermilyea found that the anodic oxide on tantalum recrystallized in the form of segments which grew outward from a point. Preferred growth directions were not noted. The anisotropic growth on hafnium may have resulted from the hexagonal close-packed structure. Tantalum is body-centered cubic.

Nucleation as a factor in film growth thus appears to be associated with higher temperature. For some reason the transition to a low-resistance layer is localized. Possibly, a thicker high-resistance film may be responsible. Further work on hafnium must take account of these complexities.

Manuscript received July 27, 1955.

Any discussion of this paper will appear in a Discussion Section to be published in the December 1956 Journal.

REFERENCES

1. A. Gunterschulze and H. Betz, "Elektrolyt-Kondensatoren," M. Krayn, Berlin (1937); Edwards Brothers Lithoprint, Ann Arbor, Mich. (1944).
2. A. Charlesby, *Acta Metallurgica*, **1**, 340 (1953).
3. R. D. Misch and W. E. Ruther, *This Journal*, **100**, 531 (1953).
4. "The Metallurgy of Zirconium," p. 674, B. Lustman and F. Kerze, Jr., Editors, McGraw-Hill Book Co., New York (1955).
5. G. L. Bucknell, G. A. Geach, and N. C. Welsh, *Research*, **5**, 289 (1952).
6. D. A. Vermilyea, *This Journal*, **102**, 207 (1955).

Plating Thickness by the Attenuation of Characteristic X-Rays

PAUL D. ZEMANY AND HERMAN A. LIEBHAFSKY

Research Laboratory, General Electric Company, Schenectady, New York

ABSTRACT

When an x-ray beam of sufficient energy and intensity strikes a plated metal, it will excite a characteristic line of the substrate metal. Of the quanta excited, those properly oriented will pass through, or be absorbed by, the plating. As a consequence of the absorption, x-rays will be emitted from the plated metal at intensities less than those correspondingly obtained from the unplated. This attenuation of x-rays can be used to measure plating thickness, as has been demonstrated for tin plate and an *unresolved* x-ray beam.

In the present investigation, the attenuation by iron foil of a characteristic line from either silver or zirconium as substrate has been measured in a spectrograph provided with a good collimator and with an analyzing crystal. The results, when corrected for background, show that the exponential absorption law is followed closely. Furthermore, these results are in accord with the known mass absorption coefficients of iron, which increases confidence in the method.

Comparison of this with other x-ray methods of determining film thickness indicates that its inherent advantages are great enough to warrant its extended application.

INTRODUCTION

During the last decade, the use of x-rays to measure the thickness of thin films on thick substrates has made rapid progress.

Shortly after Clark, Pish, and Weeg (1) had obtained diffraction patterns from coatings as thin as $5(10^{-6})$ cm, three successful laboratory methods were developed for estimating thickness by use of diffraction techniques. Birks and Friedman (2, 3) used a Geiger counter to measure attenuation by a coating of a suitable x-ray line diffracted by the substrate. Gray (4) and Eisenstein (5) independently developed a photographic method in which thickness was determined by comparing the integrated intensity of a line diffracted by the coating with that of another line diffracted by the substrate.

The application of x-ray emission (x-ray fluorescence) to this important problem was begun before 1950, the year in which Beeghly (6) published results obtained in this way on tin plate. He showed that the thickness of the tin coating could be determined practically and satisfactorily by using a Geiger counter to measure the radiant energy from a sample in which the characteristic K lines of iron had been excited by a filtered polychromatic beam. In this method (Method I), the beam emerging from the substrate (iron) is attenuated by the coating (tin) and then proceeds directly to the detector through a slit. Two years later, Pellissier and Wicker (7) revealed that a similar method had been under investigation in the United States Steel Company since 1946. Also in 1952, Koh and Caugherty (8) showed that the thickness of very thin coatings could be estimated by measuring the intensity of a characteristic line of the coating (Method II). The authors used a spectrograph provided with a good collimator and with a reflecting crystal (lithium fluoride) as analyzer to measure the attenuation of a characteristic line from the substrate as a means of determining film thickness (Method III).

EXPERIMENTAL

Method III was tested on silver and on zirconium as substrate metal covered with a "plating" built up of iron foil 0.6 mil (0.00152 cm) thick. The substrate metals were chosen because their K_α lines, although differing considerably in wave length, can yet excite the K lines of iron. The use of foil made it easy to obtain "plating" thicknesses of high precision.

Under the conditions of Table I, the times for 2^{14} counts were measured for each substrate bare and covered with different thicknesses of iron foil. One background count was determined for iron near the wave length of each substrate K_α line, and the corrected counting rate for each experiment was obtained by subtracting the background counting rate from the observed. The growing importance of the background at increasing thicknesses of iron foil is clear from Fig. 1, where average counting rates, observed and corrected, are plotted as logarithmic ordinates against "plating" thickness.

DISCUSSION

In Fig. 1, virtually all the corrected average counting rates lie close to a straight line for each substrate, which means that the exponential absorption law is obeyed in each case over almost the entire thickness range. With zirconium, where the corrected counting rate varies through five powers of ten, the concordance of the results is especially impressive even though it is fortuitous at the two greatest thicknesses.

Statistical considerations show why the concordance of these last two points is fortuitous. Owing to random

TABLE I. *Experimental data for iron on silver or zirconium*
Tungsten target 50 kv and 50 ma

Thickness of iron (mils)	Silver (K_α)			Zirconium (K_α)		
	Time to 2^{14} counts (sec)	$\overline{CPS}$ (observed) (counts/sec)	$\overline{CPS}$ (corrected) (counts/sec)	Time to 2^{14} counts (sec)	$\overline{CPS}$ (observed) (counts/sec)	$\overline{CPS}$ (corrected) (counts/sec)
0	2.12	7730	7660	0.533*	30740	30700
0.6	3.00	5460	5395	1.98*	8270	8230
1.2	4.55	3600	3535	9.72	1686	1645
1.8	7.95	2060	1995	25.28	648.1	607
2.4	12.50	1310	1245	77.88	210.4	169
3.0	19.88	824	758	188.12	87.1	45.9
3.6	29.80	550	484	302.90	54.1	12.9
4.2	41.12	398	332	360.95	45.4	4.2
4.8	62.30	263	197	390.05	42.0	0.84
5.4	85.50	192	125	394.85	41.5	0.33
6.0	104.70	156	90	395.28	41.4	0.28
Background†	247.00	66	—	398.00	41.2	—

* Measured at 5 ma and listed for 50.

† Measured for iron near the wave length of the proper characteristic line.

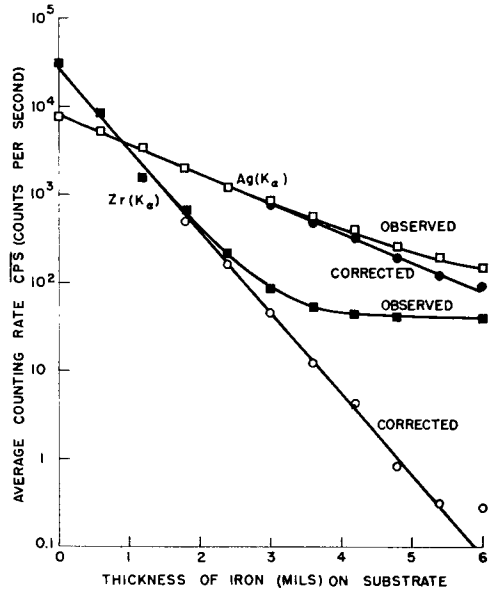

FIG. 1. Experimental results, observed and corrected for background, to test Method III in the case of iron on silver or zirconium.

fluctuations, the minimum uncertainty as measured by the "predictable standard deviation" (10) is

$$s_C = \sqrt{N_T + N_B} \qquad \text{(I)}$$

where N_T is the total and N_B the background count at the wave length of the characteristic line involved; N_B is computed for the counting interval of N_T. For Table I,

$s_C \sim \sqrt{2^{14}}$, or 2^7, at low thickness (background negligible) (II)

$s_C \sim \sqrt{2^{15}}$, or $\sqrt{2}$ (2^7), at high thickness (N_T and N_B comparable) (III)

It is easy to tell from Table I when s_C is significant relative to the number of counts used in establishing thickness. For example, at 6 mils of iron on zirconium, this number of counts is 0.28 counts/sec for 395 sec, or approximately 110 counts; and s_C is approximately 180 counts. It would not be surprising, therefore, if the corresponding point in Fig. 1 were even further from the line.

Inasmuch as the thickness measurement depends on the absorption of x-rays by iron, the results of Fig. 1 ought to be in accord with the known mass absorption coefficients of that element. Whether such accord exists can be determined by using the exponential absorption law in the form

$$\ln [I_0/I] = [\mu_1/\sin\theta_1 + \mu_2/\sin\theta_2]\rho d \qquad \text{(IV)}$$

In equation (IV), I_0/I, usually an intensity ratio, is the quotient of the corrected average counting rate for the exposed substrate by that for the substrate covered with d cm of iron foil. The mass absorption coefficients of iron are μ_1, a mean value for the incident (polychromatic) beam; and μ_2, for the characteristic line being counted. The angles θ_1 and θ_2 are those made with the sample by the incident beam (30°) and by the emergent beam (60°), the beams being regarded as rays and the surface as plane.

For present purposes, it is convenient to replace μ_1 and μ_2 by μ_{avg}, an over-all average for incident and emergent beams. From equation (IV),

$$\mu_{avg} = 2.303(S)/3.155\ (7.86)\ (0.00254) = 36.56(S) \qquad \text{(V)}$$

where

$$S = \log [I_0/I]/d \text{ (in mils)} = \text{Slope in Fig. 1} \qquad \text{(VI)}$$

and the numbers taken in order [1] convert the logarithms, [2] take path length (θ_1 and θ_2) into account, [3] introduce the density of iron, [4] convert from mils to centimeters.

The concordance of the results in Fig. 1 with the known mass absorption coefficients of iron may be judged from Table II.

The wave length at the K edge is the longest that can excite the coresponding K_α line, and it will therefore be somewhat greater than λ_1, the effective wave length of the incident beam. The wave length of the emergent beam λ_2 is that of the K_α line. The over-all average mass absorption coefficient should correspond to a wave length somewhere between λ_1 and λ_2. Comparison of μ_{avg} with the known values shows that this is true, especially when allowance is made for the way in which absorption coefficients are known to decrease with wave length (9). There fore, the conclusion is that the experimental results of Fig. 1 could have been satisfactorily predicted from known data.

Equations (V) and (VI) show that the thickness range over which the present method can be relied upon is determined largely by the value of μ_{avg}; the larger this coefficient, the smaller this thickness range. It was found in

TABLE II*. *Test of experimental data in Fig. 1*

Substrate	S [eq. (III)]	μ_{avg}	K_α (substrate)	K edge (substrate)	Known μ(iron)
Zr	0.944	34.7	0.78Å	0.69Å	38.5 at 0.71Å
Ag	0.333	12.2	0.56Å	0.48Å	14.0 at 0.50Å

* Known data in last three columns from Compton and Allison (9).

this connection that a single layer of 0.6-mil iron foil on a nickel substrate absorbed the K_α line of nickel so effectively that the present method was useless at this thickness. The mass absorption coefficient involved was near 400, whence S in equation (VI) exceeds 10. As is clear in Fig. 1, these considerations also help fix the thickness range over which the correction for background may be ignored. This range is near 2 mils of iron for zirconium as substrate, and about twice as great for silver.

In comparing published results for Method I (6, 7) with those given herein, it is important to remember that Method I was developed primarily for industrial control, and that equipment now available for x-ray emission spectrography was not on the market when this development began. The most important difference between the two methods is this. In Method III, improved collimation and the use of an analyzing crystal effectively eliminate interference by the characteristic lines of the coating (and by diffracted lines whatever their source). Consequently the potential difference across the x-ray tube does not have to be kept below that capable of exciting characteristic lines in the coating, as it does in Method I.

This restriction was not serious in the work on tin plate. The excitation potential of tin K_α is about 29 kv, far above that of copper K_α (about 8 kv), the line used for excitation (6). The L lines of tin, although emitted by the coating (excitation potential, 4 kv), did not interfere because they were sufficiently attenuated by air so as not to affect the detector significantly. Circumstances are quite different in the present investigation. Owing to the fact that iron K_α has a much lower excitation potential than the corresponding line of either silver or zirconium, it is not possible here to excite the substrate K_α without exciting iron K_α as well. Following are estimated K_α counting rates (counts per second) for the massive metals under the experimental conditions employed: Fe, 200,000; Zr, 32,000; Ag, 8100. Clearly Method I would fail here if K_α lines were used.

The increased potential difference available (50 kv for Table I) in Method III tends to compensate the loss of intensity that is the price of high resolution. For laboratory purposes at least, the advantages of Method III would seem to justify the additional equipment required relative to Method I.

Method III has advantages over the diffraction methods (2–5). Because the latter depend upon crystal structure, crystal orientation, and crystal size, they would seem to be more subject to uncontrolled factors than is Method III. Also, the intensity of the diffracted rays at the counter will often be less than that of the emitted.

Finally, Method III seems to complement Method II, which is restricted to very thin coatings (8, 11).

Manuscript received May 31, 1955.
Any discussion of this paper will appear in a Discussion Section to be published in the December 1956 JOURNAL.

REFERENCES

1. G. L. CLARK, G. PISH, AND L. E. WEEG, *J. Appl. Phys.*, **15,** 193 (1944).
2. L. S. BIRKS AND H. FRIEDMAN, *Phys. Rev.*, **69,** 49 (1946).
3. H. FRIEDMAN AND L. S. BIRKS, *Rev. Sci. Instruments*, **17,** 99 (1946).
4. R. B. GRAY, *Phys. Rev.*, **69,** 49 (1946).
5. A. EISENSTEIN, *J. Appl. Phys.*, **17,** 874 (1946).
6. H. F. BEEGHLY, *This Journal*, **97,** 152 (1950).
7. G. E. PELLISSIER AND E. W. WICKER, *Elec. Mfg.*, **49,** 124 (1952).
8. P. K. KOH AND B. CAUGHERTY, *J. Appl. Phys.*, **23,** No. 4, 427 (1952).
9. A. H. COMPTON AND S. K. ALLISON, "X-rays in Theory and Experiment," 2nd ed., D. Van Nostrand Co., Inc., New York (1935).
10. H. A. LIEBHAFSKY, H. G. PFEIFFER, AND P. D. ZEMANY, *Anal. Chem.*, **27,** 1257 (1955).
11. R. M. BRISSEY, H. A. LIEBHAFSKY, AND H. G. PFEIFFER, "Examination of Metallic Materials by X-ray Emission Spectrography," ASTM Special Tech. Publication No. 157.

Contribution to the Problem of Nonstoichiometry in Oxygen-Dominated Phosphors

J. L. Ouweltjes and W. L. Wanmaker

N. V. Philips' Gloeilampenfabrieken, Eindhoven, Holland

ABSTRACT

Oxygen-dominated phosphors of highest efficiencies are generally obtained with nonstoichiometrical compositions. This has been explained with the hypothesis that crystal defects are essential to obtain luminescence. In this paper it is postulated that the ideal, and therefore stoichiometric crystal should have maximum efficiency. The fact that an excess of one of the ingredients in general results in higher efficiency is explained with certain factors arising from the mechanism of the solid-state reactions, such as the difficulty of reaching equilibrium conditions.

The incorporation of the activator, the presence of u.v. absorbing separate phases, the problem of homogeneity of the phosphors, and the reactivity of the ingredients used for the synthesis are discussed, mainly on the basis of experimental evidence gathered in the study of the phosphors used in fluorescent lamps.

Introduction

One of the most important characteristics of phosphors used in fluorescent lamps and electronic devices is their efficiency. A great deal of work has been done, mainly in industrial laboratories, in an effort to produce phosphors of highest possible efficiency, but little has been published on the general principles involved in their synthesis.

From the beginning, phosphor chemists have recognized that very high chemical purity of the raw materials is a matter of primary importance in the preparation of highly efficient phosphors. This purity requirement is especially important with sulfide phosphors where the activator concentration is very low, such that heavy metal contamination must not exceed 10^{-5}%. With this type of phosphor, the purity of the ingredients is undoubtedly the most critical requirement in their preparation. In many cases it alone will determine the efficiency of the phosphor.

In many other phosphors, however, the activator concentration is far greater than in the sulfides, and, in consequence, the tolerance for heavy metal impurities will likewise be greater. In common phosphors such as the halophosphates and silicates, the activator concentration is of the order of 1% and the impurity limit will be of the order of 10^{-3}%. This purity is relatively easy to realize and offers no major problem to the phosphor chemist.

With these phosphors other problems arise. Even with chemicals having a purity far beyond that actually required, it may prove very difficult to prepare a silicate or a halophosphate of high efficiency. Various lots of raw materials may behave quite differently in phosphor preparation, even if the chemical analysis reveals no significant differences.

Another problem unknown in sulfide chemistry is that of the relative proportion of the basic and acidic components forming the luminescent compound. The composition of the sulfides is always practically stoichiometric, and the introduction of an excess of zinc or sulfur, for example, must be compensated for in one way or another. In oxide systems the situation is entirely different. Many patents have been granted for the attainment of unusually high efficiencies with special phosphor compositions, and various authors have correlated maximum efficiency at nonstoichiometrical compositions with the fundamentals of luminescence.

Strange (1) suggests that luminescence should not arise in perfect crystal forms, but should be associated with imperfections and dislocations. Indeed, the present theory of the luminescent centers in sulfide phosphors relates the emission to electronic transitions in lattice ions, near lattice vacancies or near foreign ions having a different valency. It does not seem probable, however, that the same applies to oxygen-dominated phosphors. The luminescence of the activated oxidic systems is of the characteristic type: the electronic transitions involved in luminescence are supposed to occur in the activating ions. It may be argued that even in this case the presence of neighboring lattice vacancies or dislocations is essential for luminescence, but then a specific influence of the activator might be expected, and the effect can hardly be considered to offer a general explanation of the principle of nonstoichiometry.

In this paper an opposite line of thought is followed. It is assumed that luminescence in oxygen-dominated phosphors, in principle, shows its maximum efficiency in perfect stoichiometrical crystals, and that various effects may tend to blur the picture, effects that are due to the history and details of the phosphor synthesis. Oxidic phosphors are generally prepared by a solid-state reaction from the oxides, or materials yielding the oxides during the firing process. The fact that these reactions seldom lead to equilibrium conditions may affect the efficiency and make it desirable to add an excess of one of the components. In this paper the following points are discussed in more detail: (*a*) incorporation of the activator; (*b*) presence of foreign materials in the fired phosphor; (*c*) fluctuations in composition from particle to particle; and (*d*) reactivity of the ingredients.

Incorporation of the Activator

One well-known phosphor system in which an excess of one of the components is required for high efficiency, is that of the halophosphates. It is reported that an excess of phosphate is necessary to obtain a good phosphor. Moreover, it is very probable that this excess of phosphate is incorporated in the crystal lattice.

Arnold (2) has shown that in precipitates of calcium phosphate an apatite structure is maintained even when the molar Ca/P ratio is 1.33 instead of the theoretical value of 1.67. The same holds for halophosphate phosphors. The authors prepared phosphors with (Ca + Mn + Sr)/phosphate ratios ranging from 1.33 to 1.75. All showed the apatite structure, and no indications of foreign substances were found, except for the presence of calcium antimonate in the materials with the highest (Ca + Mn + Sr)/P ratios. Halophosphates, therefore, might be an example of phosphors requiring an excess of one of the components within the crystal lattice for highest efficiency.

Two series of experiments were made. In the first series the composition was varied over a broad range and the efficiency of the phosphors was compared by measurements on 40-w fluorescent lamps coated with these phosphors. The phosphors were prepared by mixing $CaHPO_4$, Sb_2O_3, $MnCO_3$, CaF_2, and $SrCl_2$ in constant proportions with varying amounts of $CaCO_3$. The results are shown in Table I and Fig. 1.

In the second series of experiments the (Ca + Sr + Mn)/PO_4 ratio was varied from 1.56 to 1.67, and the efficiency of the phosphors was compared by measuring their brightness. In these samples the state of the antimony was followed by determination of its amount present in the form of trivalent antimony and the acid-insoluble rest. A similar series of samples had been prepared by Kröger (3). Trivalent antimony was determined by titration with potassium bromate and brilliant-ponceau as indicator. The acid-insoluble rest consists mainly of calcium antimonate. The results are given in Table II.

Although the antimony content was the same for all the firing mixtures it will be noted from Table II that the total antimony in the fired products is not constant. In all firings a considerable loss of antimony was found. These losses of antimony depend on the (Ca + Sr + Mn)/P ratio, and on the reactivity of the various components (*see* below).

The maximum of the efficiency curve (Fig. 1) is not very sharp. Moreover, in further experiments, its position appeared to depend entirely on the reactivity of the ingredients used and the firing conditions. This will be discussed later.

TABLE I. *Relation between the* Ca + Mn + Sr/P *ratio of halophosphates and their efficiency*

(Ca + Mn + Sr)/P ratio	Efficiency in lpw
1.33	58.0
1.42	60.6
1.50	61.1
1.56	62.0
1.65	58.3
1.75	ca. 5

However, there is a sharp drop in efficiency beyond the stoichiometric composition. This is not related to a change in the crystal lattice, since the material with a 1.75 ratio still shows the apatite structure. As Kröger pointed out the luminescence is due to trivalent antimony, and with increasing (Ca + Sr + Mn)/P ratio an increasing amount of the antimony is transformed into calcium antimonate, especially if the firing temperature is somewhat low. It is assumed that antimony substitutes for calcium. Therefore, a (Ca + Sr + Mn)/P ratio of 1.65 is the highest to allow the incorporation of sufficient antimony to obtain a good phosphor. With (Ca + Sr + Mn)/P ratios exceeding 1.67 all of the antimony in the fired phosphor is present in the form of calcium antimonate. As a consequence there is no trivalent antimony available and the substance becomes nonluminescent. This is clearly shown in Table II and Fig. 2.

The case in which an excess of the base constituent of the host crystal prevents the activator from being incorporated is not restricted to the halophosphates. The activator is a foreign constituent, and the free energy of the combination (host crystal + free activator oxide) should, in general, be smaller than the free energy of the combination (activated host crystal + free oxide of the host metal). It is a general experience that manganese-activated materials have a brownish appearance due to Mn^{3+} or Mn^{4+} provided an excess of metal is present, due to the fact that the manganese is not incorporated in the lattice. This makes it desirable to work with an excess of the acid radical in all those cases where a metallic activator is used. In this case, therefore, the nonstoichiometry has nothing to do with the necessity to create imperfections in the host crystal, but is simply a necessary requirement for the incorporation of the activator.

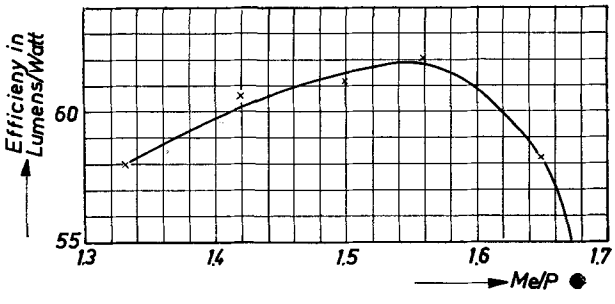

FIG. 1. Relation between the Me/P ratio of a halophosphate and its efficiency.

TABLE II. *State of the antimony and brightness of halophosphates with varying* (Ca + Mn + Sr)/P *ratios*

(Ca + Mn + Sr)/P	Weight % Sb^{3+}	Weight % insoluble residue	Rel. brightness
1.56	0.65	0.06	106
1.57	0.72	0.02	105
1.58	0.90	0.02	103
1.60	0.92	0.08	105
1.63	1.07	0.22	102
1.65	0.93	0.50	104
1.67	0.09	1.16	45

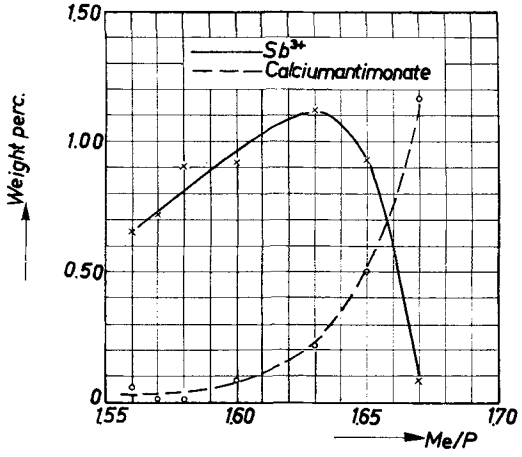

FIG. 2. Weight per cent Sb^{3+}, resp. Ca-antimonate in fired halophosphates as a function of the Me/P ratio.

TABLE III. *Effect of u.v. absorbing (antimony trioxide) and low absorbing material (unactivated halophosphate) on the brightness and luminous efficiency of a halophosphate*

% Sb_2O_3 added	Brightness of powder mixture	LPW test lamp	% Unact. haloph. added	Brightness of powder mixture	LPW test lamps
0	100	63.5	0	105	60.5
0.3	83	59.5	—	—	—
0.5	74	57.6	—	—	—
1.0	64	54.8	1	104	—
1.5	55	52.8	—	—	—
2	52	—	2	105	61.5
3	44	—	—	—	—
5	39	—	5	104	61.1
			7.5	107	59.3
			10	107	59.9
			15	101	58.8
			20	98	58.5

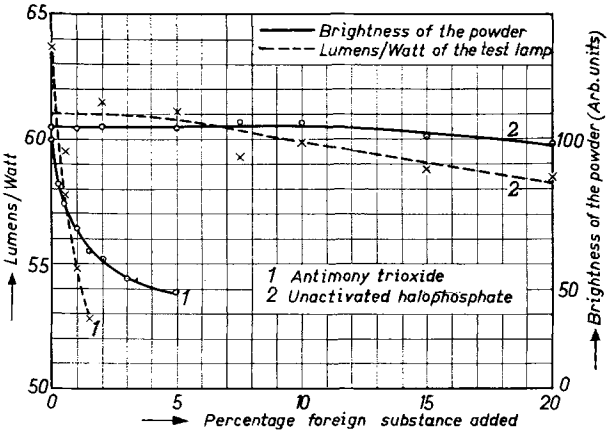

FIG. 3. Effect of u.v. absorbing (calcium antimonate) and nonabsorbing material (unactivated halophosphate) on the efficiency of halophosphate.

PRESENCE OF FOREIGN MATERIALS IN THE FIRED PHOSPHOR

As already mentioned, phosphors are generally made by means of solid-state reactions from suitable primary materials. These reactions seldom lead to entirely homogeneous products, especially in the case of phosphors, where excessive firing is preferably avoided in order to prevent the material from sintering. Therefore, it must be considered very likely that under phosphor firing conditions small amounts of the unreacted raw materials may be left in the fired phosphor. The effect of these remnants depends mainly on their ability to absorb ultraviolet radiation. If a substance is present which has a strong absorption for a certain exciting radiation, the efficiency of the phosphor will be reduced considerably, while a nonabsorbent material may have almost no deleterious effect at all.

In cathode ray excitation all foreign materials will tend to reduce the efficiency, since some or all of the energy of electrons striking the foreign materials will be lost for the purpose of excitation.

The ideas just mentioned will be demonstrated on three phosphors.

Halophosphates

To show the effect of strongly absorbing and low-absorbing foreign materials on efficiency, halophosphate phosphor was mixed with various amounts of antimony trioxide and unactivated but fired halophosphate, respectively. The u.v. absorption of the unactivated halophosphate and Sb_2O_3 is 94 and 58%, respectively.[1] The brightness data of the powder mixtures are given in Table III and Fig. 3.

To demonstrate that, under given conditions, free antimony oxide may remain as a separate phase in halophosphates the following example may be quoted. It was thought that by firing in nitrogen the formation of pentavalent antimony might be avoided and an increase of the trivalent antimony content might be obtained. An experiment was made in which varying amounts of antimony trioxide were added to the firing mixture and the firing was performed in a covered crucible placed in a stream of nitrogen. One of the fired samples showed a trivalent antimony content of 2.4%, and a brightness of 70% compared with the laboratory standard. After washing with 5*N* NaOH solution and water to dissolve the antimony trioxide not incorporated in the halophosphate lattice, the antimony content was reduced to 1.3%, while the brightness increased to 100% of the standard. This shows how strongly the presence of as little as 1% of an absorbing material may affect the efficiency of a phosphor.

Magnesium Tungstate

If a solid AB is formed by solid phase reaction from A and B, the reaction will, in general, proceed by the formation of a thin film of AB at the grain boundaries, followed by diffusion of either A or B through this layer AB. Several examples may be cited in which the u.v. absorbing component diffuses into the nonabsorbing material, and in all these cases an excess of the absorbing substance has proved to be extremely harmful to the efficiency of the phosphor. In these cases, a large excess of the nonabsorbent component is generally employed, thereby reducing the thickness of the compound layer formed and speeding up the removal of the last traces of the absorbing constituent.

[1] These figures are based on a reflectance of 77% for magnesium oxide.

An example of a reaction of this kind is the formation of magnesium tungstate from magnesium oxide and tungstic oxide. According to Jander (4), in the reaction between zinc oxide and magnesium tungstate, tungstic oxide is the diffusing agent. Therefore, one may expect that in the reaction between magnesium oxide and tungstic oxide the latter will also be the diffusing agent. This was confirmed by recent experiments by Kressin (5) in which pellets of magnesium oxide and tungstic oxide were placed on top of each other and then fired. Luminescent magnesium tungstate was formed on the surface of the magnesium oxide. The reaction between MgO and WO_3 starts with the formation of a thin layer of magnesium tungstate on the surface of the MgO and proceeds with the diffusion of WO_3 through this layer.

In the last stages of the reaction the product may be visualized as consisting of magnesium tungstate particles, with an excess of magnesium oxide in the core (either in solid solution or as a separate phase), and residues of unreacted tungstic oxide at the surface. As tungstic oxide strongly absorbs 2537 Å radiation, it will greatly reduce the luminescence efficiency of the magnesium tungstate. It has been proposed to add 100% MgO in excess of the stoichiometric composition $MgWO_4$. As a consequence, the magnesium tungstate is often referred to as Mg_2WO_5 (6). With sufficiently reactive ingredients, however, it is possible to prepare magnesium tungstate of nearly stoichiometric composition and with an efficiency comparable with that of products fired with a large excess of MgO.

This may be illustrated by the following series of values obtained on phosphors that had been prepared by making a wet paste of magnesium oxide and ammonium paratungstate, drying, and firing at 1050°C (Table IV).

Calcium tungstate.—An interesting case is furnished by calcium tungstate, where an excess of any of the components leads to the formation of ultraviolet-absorbing separate phases. As already mentioned, tungstic acid strongly absorbs 2537 Å, whereas an excess of calcium yields nonluminescent Ca_3WO_6, which also absorbs 2537 Å strongly and, therefore, also causes a drop in efficiency. In this case the only possibility of making a good phosphor is to maintain the stoichiometric formula. It is true that the addition of sulfuric acid (7) allows the use of an excess of calcium, but the function of the sulfuric acid is to neutralize any free calcium oxide that might react to form Ca_3WO_6 (8). Thus the ultimate purpose of the sulfuric acid is to maintain the stoichiometric composition of the luminescent phase itself.

Fluctuations in Composition from Particle to Particle

The idea that the core of a phosphor is different from the surface is a very common one among phosphor chemists. As a recent example Butler and co-workers (9) gave evidence that the surface of halophosphate particles must be considered to be of a different composition than the core. The question arises whether these fluctuations in composition should also extend to the different particles of a phosphor. Cohn (10) has pointed out that in a solid-phase reaction only adjacent particles may react with each other. Even in a perfect mixture only a statistical distribution may be obtained, and a situation in which every nondiffusing particle is in contact with exactly the number of diffusing particles required for obtaining the average composition will never occur in practice. This must imply that fluctuations in the composition of the individual particles of the phosphor are to be expected, and this may affect the efficiency. If, in a halophosphate, the over-all composition is exactly stoichiometric, then some of the particles might contain an excess of phosphate, while in others calcium would be in excess This excess of calcium will expel the trivalent antimony and, as already pointed out, render the particles nonluminescent.

However, it is very likely that there exists a certain interchange of ions between the particles, and this will tend to neutralize these fluctuations. The following experiments were designed to test this effect.

A normal halophosphate having a (Ca + Sr + Mn)/P ratio of 1.56 was mixed in a 1:1 ratio with an unactivated but fired halophosphate (no Sb, no Mn) having a (Ca + Sr)/P ratio of 1.68. This mixture was fired at different temperatures for 3 hr. Properties of the fired products are given in Table V.

Further details are found in a recent publication (11).

As might be expected from similar results already presented in Table III, the brightness of the unfired mixture (73%) is considerably higher than the 50% value expected from the brightness of the components (100% and 0%, respectively) and the mixing ratio alone.

The u.v. absorption has been calculated on the basis of a value of 100 for the activated material (with 0.82% Sb^{3+}). The real absorption is about 90%.

From column 3, Table V, it may be seen that the u.v. absorption increases as the firing temperature is raised. This cannot be due to the formation of calcium antimonate as practically no antimonate was analytically found in the products with the highest u.v. absorption.

The relation between the u.v. absorption and the Sb^{3+} content of halophosphates (free of calcium antimonate)

TABLE IV. *Brightness of magnesium tungstates with varying* MgO/WO_3 *ratios*

MgO/WO_3 ratio	Brightness in % of standard
0.95	61
0.98	90
1.00	93
1.01	94
1.04	90
1.10	95
1.48	99
1.98	97

TABLE V

Firing temp, °C	Brightness	U. V. abs.	$\frac{\text{Red}}{\text{Blue}}$ ratio	% Sb^{3+}	% Insoluble residue
Unfired mixture	73	75	108	0.40	Absent
1000	70	83	50	0.34	Ca. 0.1
1050	70	89	47	0.35	Ca. 0.1
1100	72	95	48	0.42	Trace
1160	67	98	43	0.40	Trace

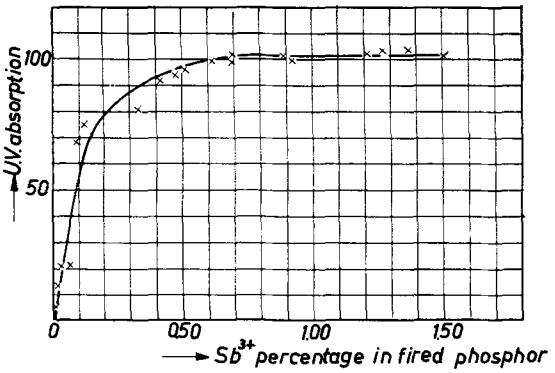

FIG. 4. Relation between the u.v. absorption of halophosphate and the Sb^{3+} content.

is given in Fig. 4. It is apparent that the u.v. absorption remains constant from about 0.60% Sb^{3+} on. Therefore, a considerable decrease of the antimony content of the above-mentioned halophosphate with 0.82% Sb^{3+} does not result in a perceptible decrease of its u.v. absorption. When Sb^{3+} is transported by a diffusion process to the unactivated halophosphate, the u.v. absorption of the latter increases. The consequence will be an increase in the u.v. absorption of the fired mixture as compared with the unfired mixture. The increase in the u.v. absorption actually found, therefore, leads to the conclusion that the Sb^{3+} ions are mobile at the firing temperatures employed.

It can be concluded further from these experiments that the Ca^{2+} ions are also mobile. The unactivated halophosphate has the high (Ca + Sr)/P ratio of 1.68. We have seen that such a halophosphate can contain only a very small amount of Sb^{3+}. Firing a halophosphate with this composition in air results in a nearly complete transformation of Sb_2O_3 into the calcium antimonate. From the u.v. absorption it follows that the unactivated halophosphate has taken up Sb^{3+}. This can only be possible if the (Ca + Sr)/P ratio has decreased by transfer of Ca^{2+} ions (and Sr ions) from the unactivated to the activated halophosphate.

The simultaneous distribution of the Mn^{2+} ion between the particles of the two samples of halophosphates can be inferred from the decrease of the red/blue ratio, because the intensity of the Mn-band (peak wave length of 5800 Å) decreases in a halophosphate at decreasing Mn^{2+} content. At a higher firing temperature the red/blue ratio decreases as compared with a lower firing temperature. This is due to the increase of the mobility of the Mn^{2+} ions at higher temperatures.

The possibility that the fired mixture might consist of an Sb-activated and, therefore, blue luminescent phosphor as a separate phase next to the original Sb-Mn-activated phosphor, was ruled out by microscopic examination which showed that a homogeneously colored material was obtained.

Summarizing, it is concluded that from a temperature of about 1000°C on Ca^{2+}, Mn^{2+}, and Sb^{3+} ions in halophosphates are interchangeable between halophosphate particles of different compositions. Thus, local deviations from the average composition, caused by incomplete mixing, will tend to be equalized in the firing process by transport of Ca^{2+} ions from particles with higher, to particles with lower (Ca + Sr + Mn)/P ratio. However, a small excess of phosphate should help considerably to avoid a local excess of calcium, and this might be another reason for its practical use.

Reactivity of the Ingredients

As mentioned in the introduction, the study of the chemistry of phosphor preparation has been concentrated largely on the purity of the ingredients, whereas considerations regarding their reactivity, which depends on properties such as particle size and surface activity, have been restricted to the desirability of maximum reactivity. Sufficiently high reactivity is, of course, very important. In order to obtain a good phosphor, it may prove advantageous, however, to employ one or more ingredients deliberately in a less reactive condition. This may be illustrated by means of two examples.

To prepare zinc beryllium silicate, zinc oxide, silica, beryllium oxide, and manganous carbonate are usually mixed and fired at 1150° – 1250°C. As Froelich has pointed out (12), it is most important that the zinc oxide should be sufficiently reactive toward the silica, otherwise the growth of zinc oxide particles interferes with this reaction. The authors found that beryllium oxide behaves quite differently. It proved very difficult to incorporate the manganese if the beryllium oxide was too reactive; the phosphors had a brownish tinge after firing and the efficiency remained low. Prefiring this reactive beryllium oxide in order to make it less reactive caused a definite improvement. The method of mixing also had an effect. Ball milling the dry ingredients yielded a better phosphor than ball milling in alcohol, followed by drying (13).

Beryllium oxide that is too coarse will also produce inferior phosphors. It must be concluded that a well balanced combination of reactivities is required in order to obtain maximum efficiency of the phosphor.

Another example of the fact that a too highly reactive component may cause trouble was encountered in the preparation of halophosphates from calcium hydrogen phosphate, calcium carbonate, calcium fluoride, strontium chloride, antimony oxide, and manganous carbonate. Here the use of a very reactive calcium fluoride resulted in a shift of the emission color toward the green and a very rapid deterioration of the quartz vessels in which the firing was carried out (14). With coarser calcium fluoride, the other ingredients and the firing conditions remaining the same, it was found that some calcium fluoride may be left unreacted (11). This may explain the shift of the color toward green, when a more reactive CaF_2 is used. Another possibility is that an early incorporation of the fluorine during the firing process makes it more difficult for the chlorine to enter the lattice.

The simplest way of correcting for a lack of reactivity of a component is to increase its relative amount in the firing mixture. Froelich has already pointed out (12) that, in the batch composition of a phosphor, the surface area of the ingredients should be considered rather than the absolute quantities. The question whether this really holds will depend on the firing process. If a phosphor is underfired, then indeed the surface area of the raw ma-

terials must be the factor determining the completeness of the reaction, whereas firing at a higher temperature or increasing the firing time will tend to reduce the influence of the surface area and the relative quantities will be more important instead.

As an example to show how the reactivity of one of the components may influence the chemical properties of the fired phosphor reference may again be made to the halophosphates. As the calcium hydrogen phosphate used for its synthesis gets coarser, the reaction between the excess phosphate and the calcium antimonate formed during the firing becomes increasingly more difficult. As a consequence, more of the antimony will be found in the form of antimonate, and less antimony will be incorporated in the trivalent state. Increasing the firing time and/or the firing temperature will favor the reaction and result in an increased Sb^{3+} content. On the other hand, the volatilization of the antimony as the chloride is found to be stronger with a more reactive calcium hydrogen phosphate, or with a larger excess of phosphate. The latter effect is demonstrated in Table II. A more detailed account of the other effects will be given in a paper to be published in the future.

The examples given here will suffice to show that there is a close connection between the reactivity of the ingredients and their relative amounts as used in the synthesis of a phosphor. The reactivities of the components will therefore be reflected in the formula finally adopted for the large-scale production of a phosphor. This formula may also be expected to offer some protection against inevitable variations in reactivity of the ingredients from batch to batch and, therefore, in general, will deviate more or less from the stoichiometric composition.

Conclusion

Summarizing, it may be stated that, for the phosphors discussed in this paper, there is no reason to postulate that an excess of one of the components is an essential point in order to obtain a luminescent material with a high efficiency. An excess of one of the components often helps to facilitate the incorporation of the activator, or to avoid the presence of u.v. absorbing materials in the fired phosphor. Therefore, in practice, using an excess of one constituent will generally be preferred over a procedure relying on exact stoichiometric formulation. No indications have been found in the authors' work on phosphors which are commonly employed in fluorescent lamps that nonstoichiometry has a fundamental meaning in these phosphors.

Manuscript received April 13, 1955. This paper was prepared for delivery before the Cincinnati Meeting, May 1 to 5, 1955.

Any discussion of this paper will appear in a Discussion Section to be published in the December 1956 Journal.

References

1. J. W. Strange, Symposium on Luminescence, Cambridge, 1954, British Journal of Applied Physics, Supplement 4, p. 4.
2. P. W. Arnold, *Trans. Faraday Soc.*, **46**, 1061 (1950).
3. F. A. Kröger, Unpublished work.
4. W. Jander, *Z. anorg. Chem.*, **190**, 397 (1930).
5. G. Kressin, Techn. Wiss. Abhandl. Osram Ges., **6**, 89 (1953).
6. H. W. Leverenz, "An Introduction to Luminescence of Solids," John Wiley & Sons, Inc., New York (1950).
7. W. A. Roberts, U. S. Pat. 2,312,267.
8. F. A. Kröger, "Some Aspects of the Luminescence of Solids," p. 111, Elsevier Publishing Co., Inc., New York (1948).
9. K. H. Butler, Paper presented at ECS Cincinnati Meeting, 1955.
10. G. Cohn, *Chem. Revs.*, **42**, 527 (1948).
11. W. L. Wanmaker, A. H. Hoekstra, and M. G. A. Tak, *Philips Res. Repts.*, **10**, 11 (1954).
12. H. C. Froelich, "Preparation and Characteristics of Solid Luminescent Materials," p. 44, Cornell Symposium, John Wiley & Sons, Inc., New York (1948).
13. J. Broos, Private communication.
14. L. J. Nijssen, Private communication.

Studies on the Mechanism of the Electrolytic Formation of Perchlorate

Kiichiro Sugino and Shigeru Aoyagi

Laboratory of Organic Electrochemistry, Department of Chemical Engineering, Tokyo Institute of Technology, Tokyo, Japan

ABSTRACT

Current-potential curves of the electrolytic oxidation of chlorate were determined polarographically using a platinum microanode. The nature of the polarogram thus obtained was quite different from that of the usual oxidation-reduction process. Two potential stages were found; the lower one is believed to be the potential of oxygen evolution and the higher one the potential of perchlorate formation. Probably the limiting current for the oxidation of water could also be seen in the polarogram.

Electrolysis of chlorate solution at definite anodic potentials corresponding to the higher stage of the polarogram was carried out in order to confirm the results of the polarographic study. From these experiments, it was clear that the first step of perchlorate formation was probably the discharge of chlorate ion at higher potential than that of oxygen evolution.

Introduction

Production of perchlorate is the typical electroprocess which cannot be carried out successfully by any other method.

The anodic potential of the formation of perchlorate has been considered to be very high, and this electrolytic preparation has been successfully accomplished only by use of a smooth platinum anode which has the highest oxygen overvoltage. A new electrolytic process for this product was developed, using a lead peroxide anode instead of platinum (1). In this case, a small amount of sodium fluoride must be added to the electrolyte to increase the oxygen overvoltage on the lead peroxide anode. The reason for this device is that the potential for anodic formation of perchlorate is very high, but it may still occur at a potential lower than that of oxygen evolution. However, it has not yet been accurately determined, and its variation with chlorate concentration is also unknown. Therefore, the present study seeks to measure accurately the anodic potential of perchlorate formation and, at the same time, to present the most probable mechanism of this process.

Anodic Polarogram of the Electrolysis of Chlorate by a Platinum Microanode

The electrolytic reduction potentials of organic compounds, which are lower than those of hydrogen evolution at the dropping mercury cathode, and the variation of these potentials with concentration of the depolarizer can be measured polarographically. The same principle was applied to the anodic process of perchlorate formation. If the anodic potential of perchlorate formation is lower than that of oxygen evolution at a platinum anode, a typical anodic polarogram will be obtained by a platinum microanode. A hypothetical polarogram is shown in Fig. 1.

Variation of anodic potential with chlorate concentration is represented approximately by the following formula:

$$E = \frac{RT}{2F} \ln \frac{K}{C_{ClO_3^-} a^2_{OH^-}} \qquad (I)$$

where $C_{ClO_3^-}$ is the concentration of chlorate, K is a constant, and the other symbols have their usual significance. If these assumptions are verified by experiments, the formation of perchlorate must be expressed by the following mechanism (2):

$$2\,OH^- - 2e \rightarrow 2\,OH \rightarrow O + H_2O \qquad (II)$$

$$ClO_3^- + O \rightarrow ClO_4^- \qquad (III)$$

On this basis, current-potential curves of the electrolytic oxidation of chlorate were determined polarographically under various conditions.

Measurement of Current-potential Curves

A micro rotating platinum electrode and a smooth platinum plate of large area were used as anode and cathode, respectively. Details of cell design and measuring circuit are shown in Fig. 2*a* and 2*b*.

Electrolytic cell.—A section of 0.3 mm diameter platinum wire sealed in a glass tube was used as the anode and gave an area of 10^{-3}–10^{-4} cm². The cathode was a 10 mm² platinum plate. Throughout the electrolysis, the current was less than 7×10^{-4} amp. The stem of the anode—a glass tube—was rotated at 1000 rpm, which prevented accumulation of oxygen gas on the anode surface and maintained constant thickness of the anodic diffusion layer during the measurement. Better reproducibility in the measured current-potential curves may therefore be expected.

Polarograph.—Sensitivity of the galvanometer used was 3.5×10^{-6} amp/mm/m.

Apparatus for the cathodic potential measurement.—When the cathode has a large area and the current is very small, it is generally expected that polarization at the cathode is very small. In this case, however, it amounted to about 500 mv at 3.5×10^{-3} amp/cm². Thus, the cathodic potential had to be measured continually throughout the current-potential curve determination. For this purpose, the simple apparatus illustrated in Fig. 2*b* was

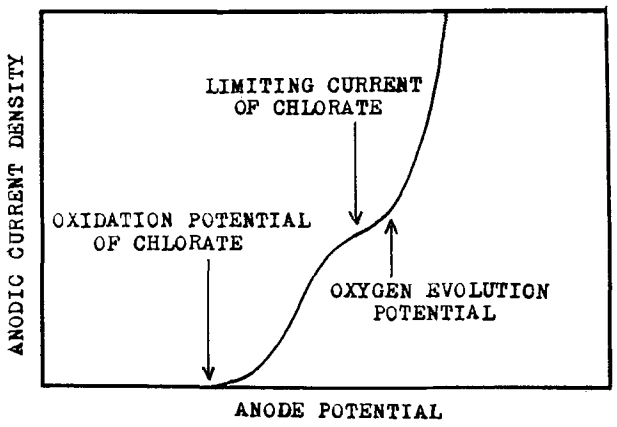

FIG. 1. An assumed polarogram in which the potential of perchlorate formation is lower than that of oxygen evolution.

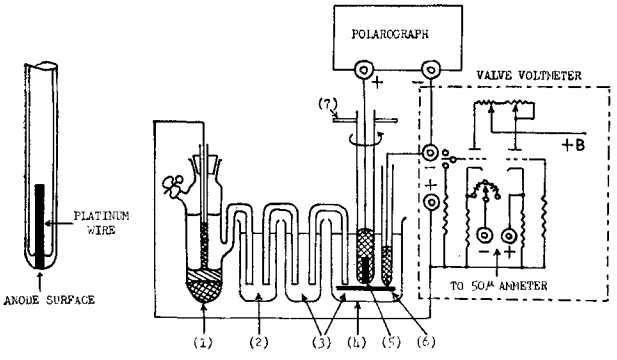

FIG. 2*a* and 2*b*. (*Left*) Details of the anode (2*a*); (*right*) the electrolytic cell, also the apparatus of the cathodic potential measurement (2*b*) for the polarographical measurement, 1—saturated calomel electrode, 2—KCl saturated solution, 3—electrolytic solution, 4—electrolytic cell, 5—anode, 6—cathode, 7—stroboscope.

satisfactory. It had a sensitivity of 3 mv and a range of −450 to +450 mv.

Temperature.—The electrolytic cell and the calomel electrode were immersed in a thermostat regulated at 17° ± 0.02°C.

Electrolyte.—Aqueous solutions of sodium chlorate (1–6M) were used. Such high concentration of the electrolyte, together with the relatively large anodic current density described above, makes the condition of the present current-potential curve measurement quite different from that of the ideal polarographic method. But well-known anodic processes of lower potential than that of oxygen evolution were carried out in the same apparatus and under the same conditions; they gave their normal polarograms.

Results and Discussion

Anodic polarograms[1] are shown in Fig. 3. The abscissa corresponds to the anodic potential on the hydrogen scale, the numerical values of which were obtained by subtracting the cathodic potential from the cell voltage. The ordinate corresponds to the apparent anodic current density in amperes per square decimeter. Its value, however, was not so reliable in view of the unknown true area of the anode.

Some characteristics of the polarograms are:

1. In a moderately concentrated solution of chlorate, two stages of potential were definitely observed.

2. In the first, or lower stage, the potential is between 1.7 and 1.9 v; in the second, or higher stage, it is higher than 2.3 v.

3. Contrary to the usual polarogram, the height of the wave of the first potential stage was seen to be inversely proportional to the concentration of chlorate.

4. For a sufficiently dilute solution, this wave height grew so high that it reached beyond the range of the measurement, a simple exponential curve being observed.

If an analogous interpretation were made for these polarograms compared to the usual cathodic ones, the first stage would be the potential of the chlorate oxidation and the second one would be for oxygen evolution. This, however, is denied by the fact that the height of the wave corresponding to the first stage is inversely proportional to the chlorate concentration. In addition, the value of the potential of the first stage corresponds to that of oxygen evolution. The reversible oxygen potential is about 0.8 v for any solution of *p*H 7. Estimating about 1 v for oxygen overvoltage on smooth platinum at 1 amp/dm², the actual oxygen evolution potential for any solution concerned amounts to about 1.8 v.

If the lower potential corresponds to the electrolysis of water and is the potential of oxygen evolution, the higher one is that of the chlorate oxidation. Thus, these polarograms should be classified as another type of the current-potential curve, different from those of the ordinary oxidation reduction process. It is certain that the oxidation of chlorate occurs at a potential higher than

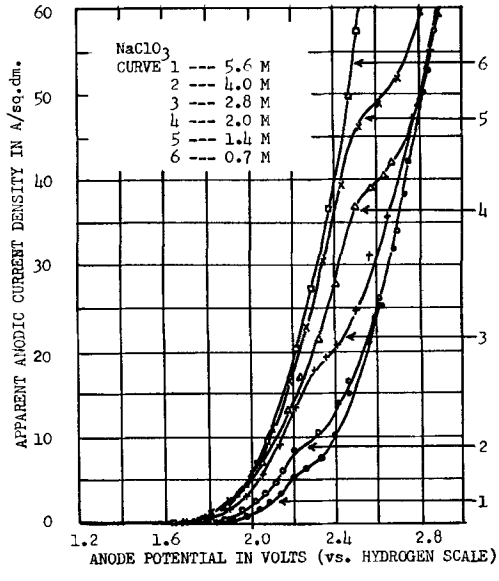

FIG. 3. Anodic polarograms of $NaClO_3$. The potentials of the second stage are about: 2.3 v for 5.6M solution, 2.3 v for 4.0M solution, 2.5 v for 2.8M solution, 2.6 v for 2.0M solution, 2.7 v for 1.4M solution.

[1] The polarograms shown in this paper (Fig. 3, 4, 5, and 10) are not a common photograph, but a plotting curve of current against applied voltage.

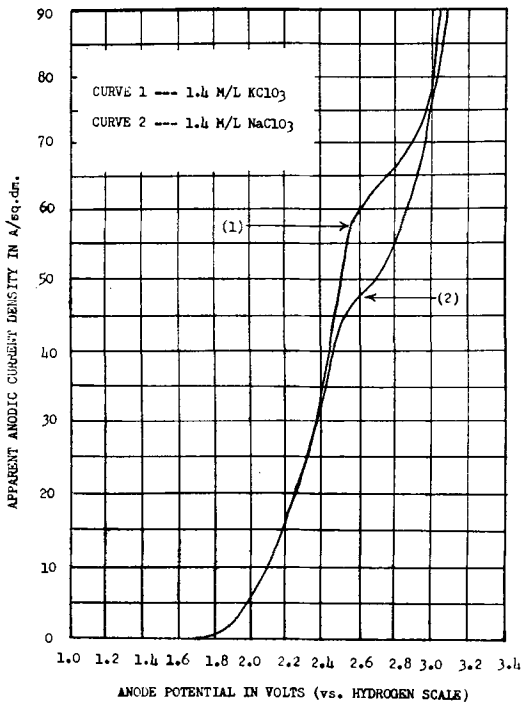

FIG. 4. Anodic polarograms of 1.4M $NaClO_3$ and 1.4M $KClO_3$.

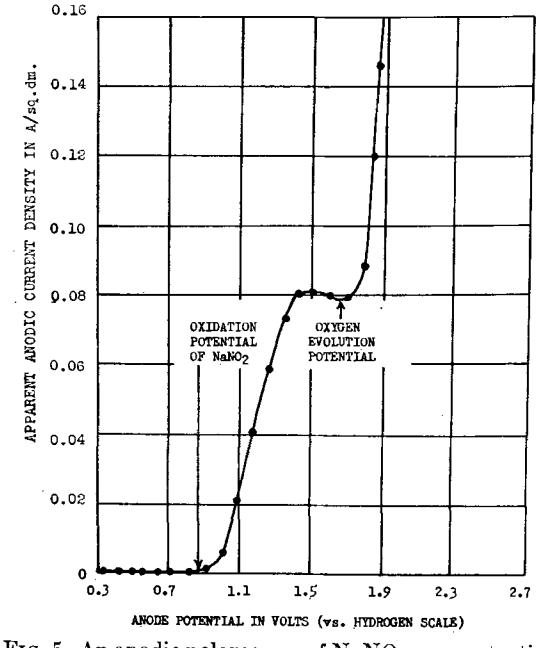

FIG. 5. An anodic polarogram of $NaNO_2$, concentration—0.013M.

that of oxygen evolution. These facts are not explainable by the mechanism of equations (II) and (III).

An alternative mechanism was adopted by the authors in which discharge of chlorate ion was assumed. This may be formulated as follows:

$$2ClO_3^- - 2e \rightarrow 2ClO_3 \text{ (or } O_3Cl\cdot ClO_3) \quad \text{(IV)}$$

$$2ClO_3 + H_2O \rightarrow HClO_3 + HClO_4 \quad \text{(V)}$$

or

$$ClO_3^- - e \rightarrow ClO_3 \quad \text{(VI)}$$

$$OH^- - e \rightarrow OH \quad \text{(VII)}$$

$$ClO_3 + OH \rightarrow HClO_4 \quad \text{(VIII)}$$

This mechanism (IV, V) has been proposed by others (3, 4), but experimental verification has been lacking.

The reason for the possibility of chlorate ion discharge at a higher potential than that of oxygen evolution is based on a decrease of the activity of water in the neighborhood of the anode surface. This can be ascribed to the extraordinarily high concentration of the electrolyte and to the hydration power of existing ions.

In order to throw some light on the latter assumption, the polarograms of 1.4M solutions of $NaClO_3$ and of $KClO_3$ were made (Fig. 4).

In Fig. 4 the wave height of the first potential stage of

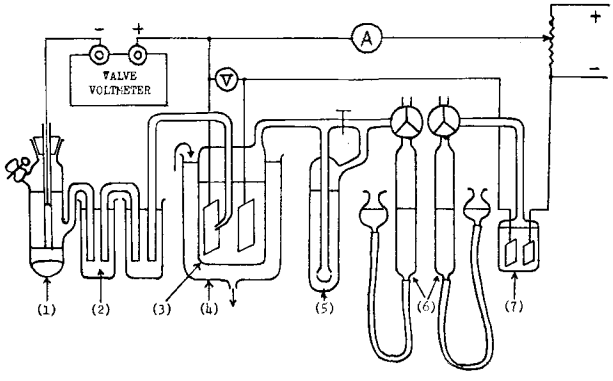

FIG. 6a. Equipment for the electrolysis of $NaClO_3$ at definite anodic potential, 1—saturated calomel electrode, 2—KCl saturated solution, 3—electrolytic cell, 4—water bath (cooling water), 5—2*N* KI solution (acidified), 6—gas buret, 7—detonating gas coulometer.

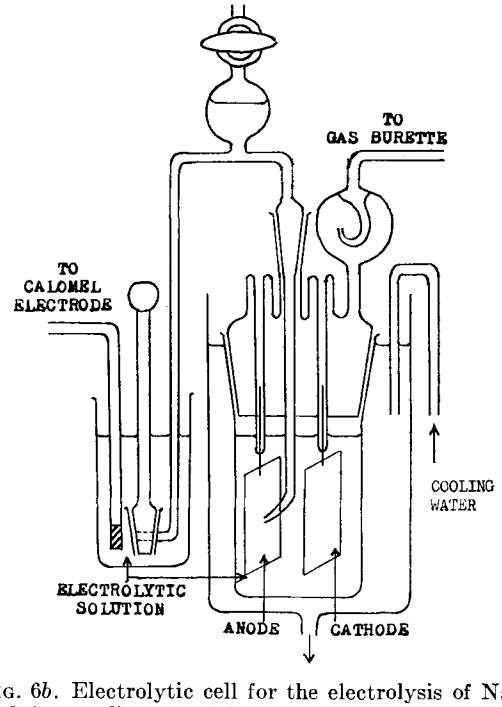

FIG. 6b. Electrolytic cell for the electrolysis of $NaClO_3$ at definite anodic potential.

$NaClO_3$ was found to be lower than that of $KClO_3$. This is taken as being related to the difference in hydration powers of Na^+ and K^+, which may be the reason for the difference in current efficiency of perchlorate formation from various chlorates (5).

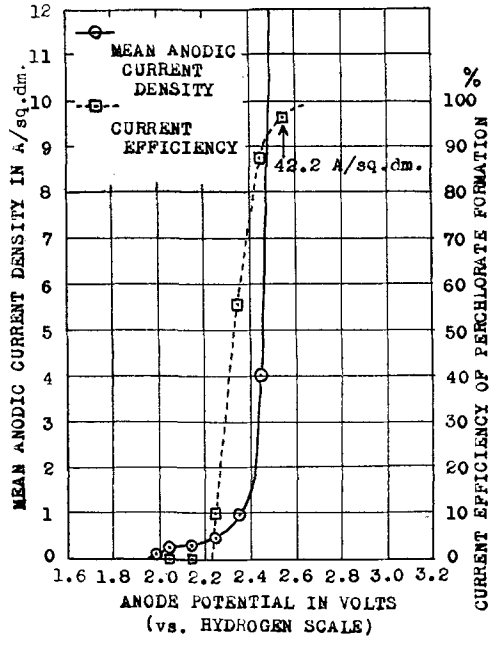

FIG. 7. Electrolysis of 5.58M $NaClO_3$ at constant anodic potential. Effect of applied anodic potential (also of anodic current density) on the current efficiency of perchlorate formation.

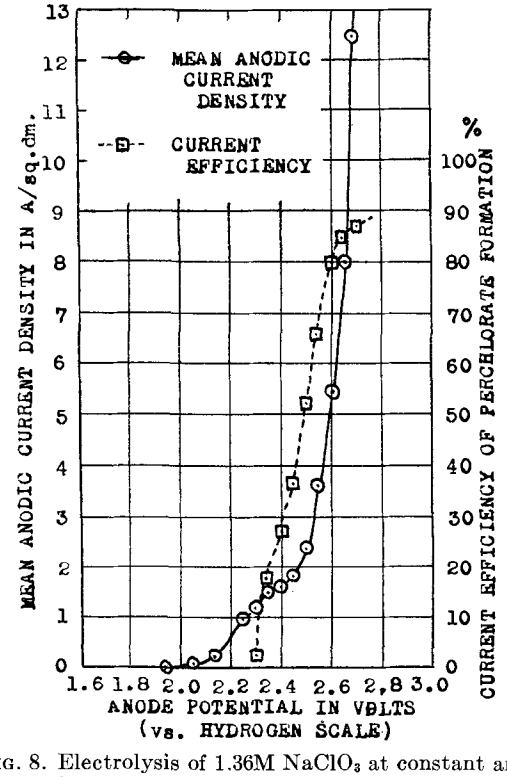

FIG. 8. Electrolysis of 1.36M $NaClO_3$ at constant anodic potential. Effect of applied anodic potential (also of anodic current density) on the current efficiency of perchlorate formation.

In order to confirm the accuracy of the polarographic method, current-potential curves were made for several typical anodic reactions (electrolysis of KCl, KBr, KI, $NaNO_2$, $Na_2S_2O_3$, Na_2SO_3, etc.) which seemed to occur at a lower potential than that of oxygen evolution. In the polarograms thus obtained, the potential stage corresponding to each anodic reaction was observed definitely

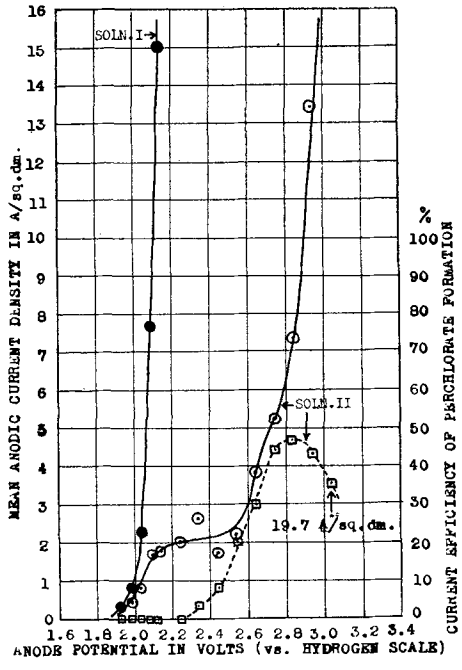

FIG. 9. Electrolysis of 0.11M $NaClO_3$ (solution I) and 0.11M $NaClO_3$ plus 1.25M $NaClO_4$ (solution II) at constant anodic potential. Effect of applied anodic potential (also of anodic current density) on the current efficiency of perchlorate formation.

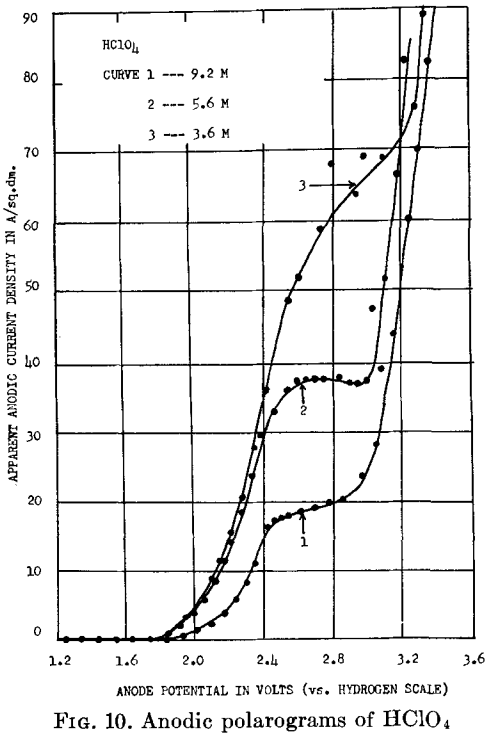

FIG. 10. Anodic polarograms of $HClO_4$

at lower potential than that of oxygen evolution (Fig. 5).

These results showed that the polarogram of the electrolytic oxidation of chlorate described above and the proposed mechanism based on the polarogram were both probably correct.

Electrolysis of Chlorate Solution at Definite Anodic Potentials

In view of the prospective discussion on the relationship between chlorate ion discharge and perchlorate formation, it is necessary to confirm the formation of perchlorate at the potential of the second stage of the polarogram in Fig. 3. For this purpose the electrolysis of chlorate solution was carried out under various conditions at a definite anodic potential corresponding to the second stage in Fig. 3.

Experimental Procedures

An aqueous solution of sodium chlorate and a mixture of it with sodium perchlorate were electrolyzed under a series of constant anodic potentials. The current efficiency of perchlorate formation was determined mainly by comparing the volume of gases generated from the electrolytic cell and from a gas coulometer in series. The circuit and gas measuring apparatus are shown in Fig. 6*a*. Details of the electrolytic cell are shown in Fig. 6*b*.

The anode and cathode were both of smooth platinum plate; the apparent areas were about 10 cm^2. The anode potential was measured directly by means of a valve voltmeter. Cell temperature was maintained at 17°–20°C during electrolysis.

For each electrolysis, 200 cc of the solution were employed. Each run was carried out to obtain a single point of the curves in Fig. 7–9. Throughout each electrolysis, $\frac{1}{6}$ amp-hr of electricity was passed, and the average anodic current density was calculated by dividing the amount of current by the duration of electrolysis.

Results and Discussion

At first, 5.58 m/l and 1.36 m/l sodium chlorate solution were subjected to electrolysis under constant anodic potential, and the anodic current density and the current efficiency of perchlorate formation at that current density were plotted against the applied anodic potential. A current-potential curve was obtained from these experiments. Examples are shown in Fig. 7 and 8.

The character of the current-potential curve was similar to that of the curves obtained by the polarographic method. The current efficiency of perchlorate formation increased with increasing current density due to the increase of applied anodic potential. In the case of 5.58 m/l solution, it reached above 90% at a potential of nearly 2.55 v (C. D. 42.2 amp/dm^2). Oxygen evolution began at a potential lower than that of perchlorate formation and continued to evolve together with perchlorate formation with a very poor efficiency.

Next, a similar experiment was carried out using 0.11 m/l chlorate solution and a mixed solution of 0.11 m/l chlorate and 1.25 m/l perchlorate. The current-potential curves obtained are shown in Fig. 9.

In the case of 0.11 m/l chlorate solution, the current-potential curve was quite simple and became exponential at 1.95–2.15 v. This showed that oxygen evolution was the only reaction which occurred. When the same amount of chlorate in 1.25 m/l perchlorate solution was electrolyzed, a curve having two potential stages similar to Fig. 8 was obtained. This showed clearly the occurrence of perchlorate formation with a fair current efficiency. This seems to be the reason for the almost perfect conversion of chlorate to perchlorate by the electrolysis on a commercial scale.

In this experiment, if a potential higher than 2.85 v was applied (current being increased with the applied potential), the current efficiency of perchlorate formation was again decreased, and oxygen evolved vigorously. This phenomenon may be due to the discharge of perchlorate ion. In this connection, the polarograms of perchloric acid obtained in the same apparatus are shown in Fig. 10.

In these polarograms,[2] two potential stages were observed, just as in the case of the polarograms of Fig. 3. As described above, the first stage corresponds to the potential of oxygen evolution and the second stage to the potential of the discharge of ClO_4^- ion. This gives[3]

$$ClO_4^- - e \rightarrow ClO_4 \qquad \text{(IX)}$$

$$ClO_4 \rightarrow ClO_2 + O_2, O_3, \text{etc.} \qquad \text{(X)}$$

Conclusion

1. It was proved that the first step of perchlorate formation was the discharge of chlorate ion at a higher potential than that of oxygen evolution.
2. It is suggested that the discharge of chlorate ion is possible not only because of the high oxygen overvoltage on special anodic materials, but also the decrease of the activity of water in the neighborhood of the electrode surface. The latter follows because of the extraordinarily high salt concentration of the electrolyte and because of the strong hydration power of existing ions.
3. High anodic current density is one of the necessary conditions for maintaining the anodic potential at higher values suitable to the discharge of ClO_3^- ion.
4. The complete conversion of chlorate to perchlorate is due to the co-existence of a large amount of perchlorate in the same solution.

Acknowledgment

The aid of a grant for fundamental scientific research from the Ministry of Education of Japan is gratefully acknowledged.

[2] The effect of temperature upon the wave height of the first potential stage was exactly measured for 9.2M solution of perchloric acid. The increase of the limiting current due to the increment of temperature was definitely observed. The result may be reported later.

[3] The occurrence of these reactions has already been reported by other investigators (6). The authors also confirmed it by the electrolysis.

Manuscript received Feb. 27, 1953. This paper was prepared for delivery before the New York Meeting, April 12 to 16, 1953.

Any discussion of this paper will appear in a Discussion Section, to be published in the June 1956 JOURNAL.

REFERENCES

1. K. SUGINO, *Bull. Chem. Soc. Japan*, **23**, 115 (1950).
2. C. W. BENNETT AND E. L. MACK, *Trans. Am. Electrochem. Soc.*, **29**, 323 (1916).
3. W. OECHSLI, *Z. Elektrochem.*, **9**, 807 (1903).
4. N. V. S. KNIBBS AND H. PALFREEMAN, *Trans. Faraday Soc.*, **16**, 402 (1920).
5. A. IZGARYSHEV AND M. G. KHACHATURYAN, *Doklady Akad. Nauk. S. S. S. R.*, **59**, 1125 (1948); S. AOYAGI, Unpublished work.
6. G. GRUBE AND K. H. MAYER, *Z. Elektrochem.*, **43**, 859 (1937); G. L. PUTNAM, R. W. MOULTON, W. W. FILLMORE, AND L. H. CLARK, *J. (and Trans.) Electrochem. Soc.*, **93**, 211 (1948).

Fusion Electrolysis of Bismuth Trichloride

PAUL M. GRUZENSKY

Northwest Electrodevelopment Laboratory, U. S. Bureau of Mines, Albany, Oregon

ABSTRACT

Bismuth has been deposited from a fused electrolyte containing 33 wt % bismuth trichloride in a lithium chloride-potassium chloride eutectic mixture as carrier salt at approximately 400°C. The electrolyte was maintained at the desired temperature by the electrolyzing current, requiring 1.27 kwhr of power per pound of bismuth deposited. The cathode current efficiency was nearly 100% and the average yield was 88.8%. The process readily lends itself to continuous operation.

INTRODUCTION

Although the use of aqueous solutions for electrodeposition and electrorefining of bismuth has attracted considerable attention, very little has been reported in the literature concerning fused electrolytes. Early attempts to prepare bismuth by fusion electrolysis of bismuth trichloride were discouraged by the high solubility of the metal in the molten salt. In 1900 Helfenstein (1) reported that no metal regulus was obtained upon electrolysis of molten bismuth trichloride. The electrolyte became dark colored during electrolysis and the solidified melt was permeated with bismuth, giving the salt a metallic luster. Drossbach (2) electrolyzed bismuth trichloride at 340°C for 16 hr, using a 2-amp current, and obtained a 49.3% yield of bismuth. He pointed out that the phase diagram for the system bismuth-bismuth trichloride indicated that prolonged electrolysis was necessary before bismuth metal was obtained. Cleary and Cubicciotti (3) determined the solubility of bismuth in bismuth trichloride to be 47.5 mole % at 450°C. They investigated the effect which addition of other chlorides had on this solubility and reported that the larger the anion to cation ratio of the added salt, the less effective the salt in reducing the solubility, and the more electropositive the cation of the added salt, the more effective the salt in reducing the solubility. Recently Morris, Douglass, and Vaughn (4) reported successful deposition of bismuth from fused electrolytes containing 10 or 25% bismuth trioxide in a calcium chloride-sodium chloride eutectic mixture or in the individual salts at temperatures of 600°–900°C.

The present work was undertaken in an effort to determine if the solubility of bismuth in bismuth trichloride could be reduced sufficiently by the presence of other salts to permit a feasible electrolysis to be carried out. A lithium chloride–potassium chloride eutectic mixture was chosen as the carrier salt because it has a low melting point (352°C) and because it meets the recommended qualifications (3) for reducing effectively the solubility of bismuth in bismuth trichloride. Although a lithium chloride-sodium chloride mixture would have provided the most electropositive cations, the higher melting point of the eutectic (552°C) would have been a disadvantage.

Since no ores in this country are mined chiefly for their bismuth content, no work with ores was carried out; however it is of interest to note that chlorine metallurgy has been employed in the treatment of bismuth ores in Romania (5). Pulverized ore containing 37.5% bismuth was chlorinated at 500°C, and distilled bismuth chlorides were collected in glass condensers. Wet chemistry was then employed for purification and preparation of bismuth subnitrate or, alternatively, bismuth metal was recovered by cementation on iron bars.

Rogers and Campbell (6) have recently reported the preparation of high-purity bismuth trichloride by chlorination of crude bismuth metal.

EXPERIMENTAL

Apparatus and Materials

The electrolytic cell used in the experimental work is shown in Fig. 1.

Direct current was supplied by a 25 v, 50 amp selenium rectifier and alternating current by a 3 kw welding transformer. An ampere-hour meter was included in the d-c circuit.

All of the chemicals used were Baker "Analyzed Reagent" grade. The eutectic mixture was prepared in 1 kg lots by mixing 59 mole % lithium chloride with 41 mole % potassium chloride and melting the mixture under vacuum at 450°C. The solidified salts were broken up and stored in a tightly stoppered bottle.

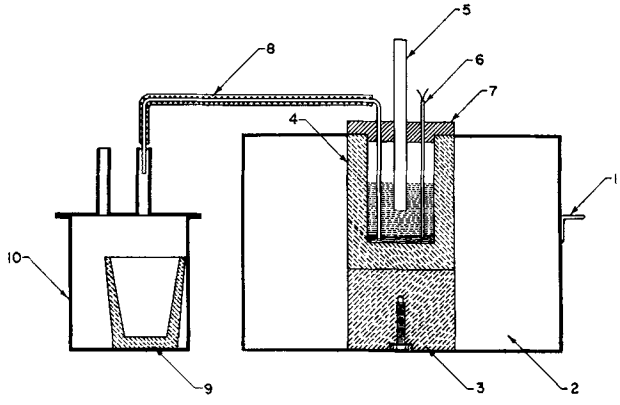

FIG. 1. Schematic diagram of electrolysis cell and auxiliary equipment. The various components are: 1, cathode connection welded to steel shell; 2, insulation; 3, graphite block bolted to steel shell; 4, graphite crucible; 5, graphite rod anode; 6, Vycor thermocouple well; 7, asbestos-cement board cover; 8, Vycor siphon tube wrapped with heating tape; 9, clay crucible; 10, steel container attached to vacuum line.

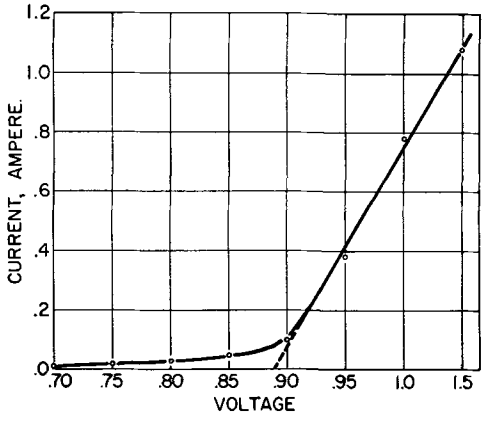

FIG. 2. Decomposition potential curve for $BiCl_3$ in LiCl-KCl eutectic at 420°C.

Procedure

At the start of each run, 200 g of eutectic salt mixture were melted in the cell with alternating current from the welding transformer, using a ¼ in. diameter graphite rod electrode. When the molten salts were at the desired temperature, the alternating current was disconnected, 100 g of bismuth trichloride were added, the cover replaced, and the direct current was connected. The current was somewhat erratic for a minute or two while the bismuth trichloride was melting, but could soon be adjusted to a constant value. In all the experiments the graphite crucible was made cathodic and the central graphite rod was made anodic. Bismuth depositing at the sidewalls of the crucible dropped to the bottom and accumulated there. Every 15 min additional bismuth trichloride was added, the amount depending on the magnitude of the current employed, assuming the depletion of bismuth trichloride from the electrolyte to be taking place at 100% current efficiency. Addition of bismuth trichloride to the cell was always accompanied by fuming, so an effort was made to minimize volatilization losses by adding the bismuth trichloride as rapidly as possible and replacing the cover immediately.

To recover the deposited metal, the heated siphon tube was placed in the crucible and the molten bismuth was siphoned over by applying a vacuum to the receiving container. Molten bismuth was removed from the cell when 65–70 ml of metal had accumulated.

The anode was raised periodically to prevent short-circuiting as bismuth accumulated at the bottom of the cell. As the surface level of the electrolyte was raised, more salts deposited on the cover from spray produced by chlorine evolution at the anode. From this standpoint, it was advantageous to keep the surface level as low as possible by periodically removing the deposited metal.

Decomposition potential

To determine the decomposition potential of the electrolyte, a cell similar to the one shown in Fig. 1, was used; nichrome heating elements maintained the temperature constant. The electrolyte contained 33% bismuth trichloride by weight in a lithium chloride-potassium chloride eutectic carrier salt mixture at 420°C. Fig. 2 shows current values plotted as a function of voltage. Extrapolation of

TABLE I.—*Data for bismuth deposition*

Experiment No.	Duration, hr	Cell voltage	Current, amp	Temp, °C	Cathode current density amp/dm²	Wt $BiCl_3$ consumed, g	Wt Bi recovered, g	Cathode current efficiency, %	Yield, %	Kwhr/lb Bi
1	6	6.4	38.5	394	26.4	949	585	97.5	93.0	1.15
2	6	7.2	46.2	426	31.6	1,230	703	97.8	86.2	1.29
3	6	6.7	44.5	409	30.5	1,135	676	97.3	89.9	1.20
4	7	7.7	34.3	402	23.5	1,080	583	93.2	81.5	1.44
5	7	6.9	39.4	406	27.0	1,210	706	98.5	88.0	1.22
6	16	6.9	38.4	403	26.3	2,480	1,452	90.9	88.3	1.33
7	7	6.9	39.7	400	27.2	1,160	708	98.0	92.1	1.23
8	6	7.6	38.8	404	26.6	980	597	98.5	92.0	1.35
9	7	6.8	44.7	385	30.6	1,340	758	93.2	85.4	1.27
10	10	6.7	39.3	392	26.9	1,580	961	94.2	91.8	1.24

the steep portion of the curve to zero current gave a value of 0.89 volt for the decomposition potential.

From the data of Villa (7) the free energy of the reaction

$$\tfrac{1}{3}Bi\ (1) + \tfrac{1}{2}\ Cl_2\ (g) = \tfrac{1}{3}\ BiCl_3\ (1)$$

is -20.1 ± 1.5 kcal at 420°C. To obtain the free energy of the reaction occurring in the electrolysis cell:

$$\tfrac{1}{3}\ Bi\ (1) + \tfrac{1}{2}\ Cl_2\ (g) = \tfrac{1}{3}\ BiCl_3\ (1, M\% = 0.081)$$

$\frac{1}{3}\ RT$ ln (0.081) must be added to the -20.1 the result being -21.2 ± 1.5 kcal or 0.92 ± 0.06 volt. This value is in good agreement with the decomposition potential determined experimentally, indicating that the cell reaction was essentially that postulated.

Discussion of Results

Data pertaining to the electrolysis tests are shown in Table I. In all cases the molten electrolyte remained clear enough that bismuth metal was visible at the bottom of the cell.

Calculation of the percentage yield was based on the grams of bismuth produced and on the grams of bismuth trichloride consumed in each run. Higher yield values undoubtedly would be realized on a larger scale with continuous operation since no efforts were made to account for the bismuth trichloride remaining in the cell at the end of each run. Loss of bismuth trichloride by volatilization, especially at the time of addition to the cell, was probably the major factor in reducing the percentage yield. Only a small amount of fuming was noted during electrolysis as long as the cell was covered; however, considerable fuming occurred when the molten bath was exposed to the atmosphere during the bismuth trichloride additions.

The power required for deposition of bismuth averaged 1.27 kwhr/lb of metal for the combined operations of electrolysis and bath temperature maintenance at approximately 400°C.

Since the anode was raised periodically to prevent short-circuiting, no effort was made to determine the anode current density precisely; however, approximate anode current densities were of the order of 200–300 amp/dm^2. At no time was the "anode effect" observed.

During the course of the experimental work the question of carbon content of the deposit was raised, since a graphite crucible was being used. No carbon analyses were obtained on the deposits; however, Griffith and Mallett (8) have shown that the solubility of carbon in bismuth varies with the temperature according to the equation $\log_{10}$wt % $C = -(360/T) - 3.17$. Taking 400°C as the temperature of operation, the deposited bismuth should have contained approximately 1 ppm of carbon.

Mathers (9) reported that bismuth deposits obtained from acidified aqueous bismuth trichloride solutions were contaminated with 0.3% chlorine. This contamination was explained on the basis of inclusion in the cathode deposit by adsorption, by precipitation as the basic salt, or by being discharged along with the metal from a complex cation, with some preference given to the latter view. Analysis of the bismuth obtained by fusion electrolysis of bismuth trichloride indicated the presence of 0.05% chlorine. Melting of the deposited bismuth with a sodium hydroxide flux, which is common practice in pyrometallurgical refining, reduced the chlorine content to 0.006%.

Spectrographic analysis of the deposits revealed only trace quantities of metallic impurities such as iron and copper. In view of the choice of electrolyte, special efforts were made to determine if any lithium had been codeposited with the bismuth. No lithium was detected spectrographically.

Conclusions

It has been shown that the solubility of bismuth in fused bismuth trichloride is reduced sufficiently by the use of a lithium chloride-potassium chloride eutectic mixture as a carrier salt to permit a feasible electrolysis to be carried out. Bismuth metal was deposited at an average current efficiency of 96% with an average yield of 88.8%. The power required for electrolysis and for maintaining the electrolyte molten was 1.27 kwhr/lb of bismuth. By plotting current values as a function of voltage, the decomposition potential of the electrolyte was determined to be 0.89 volt, at 420°C. The deposit was found to contain 0.05% chlorine, but this contamination was reduced to 0.006% by remelting the bismuth with a sodium hydroxide flux. Since bismuth is deposited in the liquid state, its removal from the cell can be accomplished by siphoning, and thus the process readily lends itself to continuous operation.

Acknowledgment

The author is indebted to Mr. A. R. Borgersen and Mr. C. E. Martin for their assistance with portions of the experimental work.

Manuscript received July 21, 1955. This paper was prepared for the Pittsburgh Meeting, October 9 to 13, 1955.

Any discussion of this paper will appear in a Discussion Section to be published in the December 1956 Journal.

REFERENCES

1. A. Helfenstein, Z. *anorg. Chem.*, **23**, 296 (1900).
2. P. Drossbach, *Z. Elektrochem.*, **44**, 124 (1938).
3. G. Cleary and D. Cubicciotti, *J. Am. Chem. Soc.*, **74**, 557 (1952).
4. K. B. Morris, D. Z. Douglass, and C. B. Vaughn, *This Journal*, **101**, 343 (1954).
5. R. Ripan and C. Liteanu, *Acad. Rep. Populare Romane, Bul. Stiint, Ser. Mat., Fiz., Chem.*, **2**, 257 (1950).
6. R. R. Rogers and R. A. Campbell, *Can. Mining Met. Bull.*, **48**, 121 (1955).
7. H. Villa, *J. Soc. Chem. Ind.*, **69**, 9-18, (1950).
8. C. B. Griffith and M. W. Mallett, *J. Am. Chem. Soc.*, **75**, 1832 (1953).
9. F. C. Mathers, *Proc. Am. Electroplaters' Soc.*, **26**, 134 (1939).

Polarization in an Aluminum Reduction Cell

WARREN E. HAUPIN

Aluminum Research Laboratories, Aluminum Company of America, New Kensington, Pennsylvania

ABSTRACT

A new method, which combines the technique of current reversal with the use of an a-c bridge, is presented for determining polarization in an aluminum reduction cell. Polarization was found to be composed of two parts. One part had a very short time constant and the other, a very long time constant.

Increasing the alumina concentration of the bath caused a large decrease in polarization. Vigorous agitation had the same effect. An increase in the NaF/AlF_3 ratio produced a moderate decrease in polarization, while an increase in the baking temperature of the anode produced a moderate increase in polarization. Additions of MgF_2, CaF_2, or SrF_2 had no noticeable effect on polarization. Polarization was found to increase with increasing current density, but the increase did not follow Tafel's law.

INTRODUCTION

Aluminum smelters are interested in electrolytic polarization of an aluminum reduction cell because polarization increases the cell voltage and thereby increases the power required to produce aluminum. Polarization is important also from a theoretical standpoint because an understanding of polarization may help in understanding the processes occurring in the cell. From the theoretical aspect, it would be desirable to separate anodic and cathodic polarization. This would require a stable reference electrode.

Both carbon and graphite were found to be unsatisfactory as reference electrodes since they did not give reproducible results. Piontelli and Montanelli (1) and Rempel and Khodak (2) used molten aluminum held in a corundum container as a reference electrode. This arrangement required the bath to be saturated with alumina. Since an important part of the present investigation was to be a study of the effect of alumina concentration in the bath, a corundum container could not be used. A study of the literature revealed no electrically insulating material that would not be attacked by molten cryolite. The container problem ruled out the silver-molten silver chloride reference electrode described by Senderoff and Brenner (3).

This lack of a suitable reference electrode eliminated the possibility of direct measurement of polarization, as well as making it impossible to separate anode and cathode polarization. However, there remained indirect methods that would allow the total cell polarization to be determined. The most common indirect methods of measuring polarization make use of current interruption, current reversal, or the superimposition of alternating current on direct current.

EXPERIMENTAL

Preliminary tests.—The method of current interruption was investigated first. A special circuit breaker permitted the breaking of up to 75 amp in less than 1/1000 sec. The circuit simultaneously triggered the sweep of a DuMont Model 304-A cathode ray oscillograph an instant before the current was interrupted and the voltage vs. time trace was photographed from the face of the oscillograph. These discharge curves were then analyzed by the method described by Busing and Kauzmann (4).

Two types of polarization with two very different time constants were found to be present simultaneously. The first type disappeared in much less than 1/1000 sec. The second type took several minutes to decay. Unfortunately, this method lacked the desired precision, largely because the inductance of the cell made the measurements of the part of polarization with the short time constant inaccurate.

Wohr (5) described a method of measuring cell resistance by superimposing, sequentially, alternating currents of two frequencies on the direct current and measuring the alternating currents and voltages through the cell. There will be considerable error in this method unless the direct current source is of high impedance since it represents a parallel path for the alternating current. At the frequencies recommended, the cell resistance obtained includes any short time constant polarization. If the measurements could be made at much higher frequencies, probably all polarization could be eliminated.

A combination of the bridge method, using superimposed alternating current and current reversal, was found more satisfactory. The modified method is easier to understand if the equivalent electrical circuit of the reduction cell derived from the preliminary tests is examined first.

Equivalent circuit.—Fig. 1 shows the equivalent circuit. Starting from left to right, E_d represents the decomposition potential, or the minimum voltage at which the overall cell reaction can take place. The voltage discharge curves indicated that E_d was about 1.2 v. However, rather large deviations from this value frequently occurred which could not be correlated with electrode condition, bath temperature, or bath composition. Nevertheless, 1.2 v agrees surprisingly well with the equilibrium reaction potential, 1.17 v, calculated from the free energy of the reaction $2Al_2O_3 + 3C = 4Al + 3CO_2$ at 980°C.

Next in Fig. 1 are two circuits, each composed of a variable resistor and variable capacitor in parallel. These represent polarization. One part of the polarization had a very short time constant and probably was caused by a gas

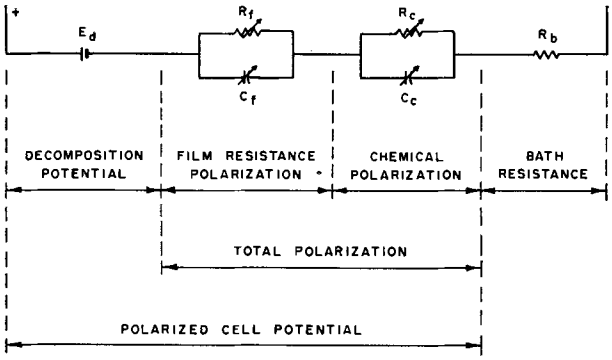

FIG. 1. Electrical equivalent circuit of aluminum reduction cell.

film on the anode, but might represent any adsorbed double layer. The resistance and capacitance associated with this polarization are referred to as R_f and C_f, respectively. The value of C_f was not determined, but was very small. The other part of the polarization had a very long time constant and is associated with R_c and C_c on the diagram. It was probably caused by the slowness of some step in the chemical reaction, but could be caused by any diffuse double layer or concentration gradient. The capacitance, C_c, increased with increasing current density, being about 0.05 farad at 50 amp. For simplicity, R_f will be referred to as film resistance and IR_c as chemical polarization.

Since the determination of E_d was inaccurate and some authorities question the reversibility of the reaction, the sum of E_d plus polarization will be referred to as the polarized cell potential. The polarized cell potential then equals $E_d + IR_f + IR_c$. While the equivalent circuit would indicate that there are only two factors involved in polarization, actually several factors having a long time constant may have been lumped together and several factors having a short time constant may have been lumped together.

The true ohmic resistance of the bath exclusive of electrode reactions is represented by R_b. For a constant temperature, bath composition and electrode composition, E_d and R_b are constant for a given cell. R_f, C_f, R_c and C_c are functions of current density.

Apparatus and procedure.—Electrolytic tests were conducted in graphite crucibles, 3 in. ID by 4¼ in. deep. An overflow hole was drilled at the 3.1 in. level. The crucibles were protected from oxidation by aluminum coated steel containers. Three hundred grams of the desired bath were added to the crucible. After the bath melted, 490 g of 99.95% aluminum (1095 grade) was added, providing a metal depth of 2.3 in. at the center, 1.3 in. at the edge, and an average depth of 1.85 in. The aluminum caused a small amount of bath to overflow, and in this way maintained a constant bath level. Actual bath compositions were determined by chemical analysis of a bath sample taken at the end of each test. The compositions stated are average values for each group. Individual analysis ranged ±1% from the average.

The anode immersion was controlled by lowering the anode by means of a screw adjustment until electrical contact was made, then lowering it 0.26 in. further. This gave a nominal anode area of 3 in.². Both the anode and cathode were provided with separate current and potential contacts. The current contact to the cathode was made through the bottom of the graphite crucible, while the cathode potential contact was made at the top edge of the crucible.

The anodes were made from a standard prebake anode mix, pressed into 1½ in. diameter electrodes, 1½ in. high, and baked at 1000°C (except when stated otherwise) for 24 hr at temperature. The cell was externally heated in an electric furnace, automatically controlled at 980°C. However, owing to the flow of current through the cell, the actual bath temperature fluctuated between 980° and 995°C. Temperatures were measured with Chromel-Alumel thermocouples with ±0.75% guaranteed accuracy.

The electrical circuit used is shown schematically in Fig. 2. It will be seen that the cell was in one leg of a Kelvin bridge circuit. A sine wave alternating current of 0.04 v rms was superimposed on the direct current to the cell. By turning the superimposed AC on and off and noting that no change in d-c voltage or current accompanied the change in AC, it was determined that the AC was not changing the cell characteristics. Use of 1020-cycle filters at the input to the oscillograph made the bridge sensitive to 1020 cycle AC only. Before each run, a preliminary adjustment of the Y axis phase control was made with a pure resistance substituted for the reduction cell. The oscillograph's X and Y inputs were made to agree in phase. When the cell was put in the circuit, balance was then indicated by a horizontal line. Resistive out of balance caused the line to slope up or down, while reactive out of balance caused the line to open into an ellipse.

Referring to Fig. 1, the bridge measures $R_b + R_f$ because, at 1020 cycles, C_c shunts R_c. Unfortunately, this bridge would not operate at frequencies high enough for C_f effectively to shunt R_f and allow determination of R_b. Therefore, the bath resistance was obtained by applying 6 amp of reversed polarity direct current to depolarize the cell. The a-c resistance measured on the bridge would fall with the application of reversed direct current. In a few seconds, a steady value was reached. This value was recorded as the bath resistance. After thus stabilizing, the value was independent of the reverse current from 0 to

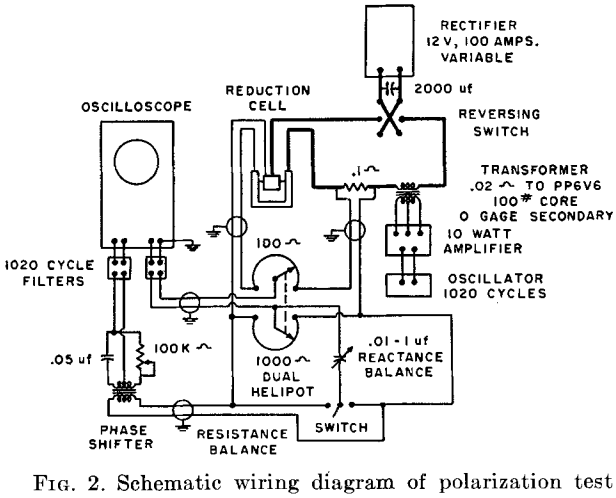

FIG. 2. Schematic wiring diagram of polarization test setup.

24 amp and increased only about 1% at 75 amp, indicating negligible reverse current polarization with a time constant less than 0.001 sec. A new anode was used for each determination to avoid the possibility that the reversed current had changed the anode permanently.

These measurements determined R_b, $R_b + R_f$, and the total cell voltage for each value of current. Subtracting IR_b from the total cell voltage gave the polarized cell potential. Subtracting R_b from $R_b + R_f$ gave the film resistance. Multiplying the film resistance by the current gave IR_f, the film resistance polarization. The mean values were reproducible to about ±0.1 v.

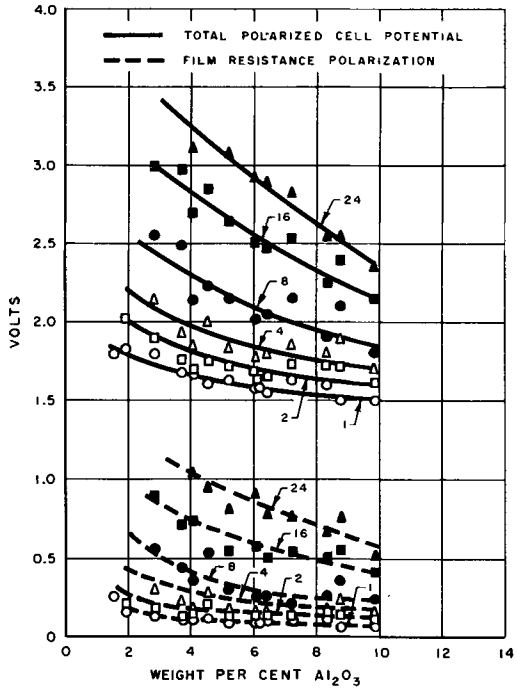

FIG. 3. Effect of Al_2O_3 concentration on polarization in Hall bath having a NaF/AlF_3 weight ratio = 1.47. Curve numbers indicate amp/in.² anode current density.

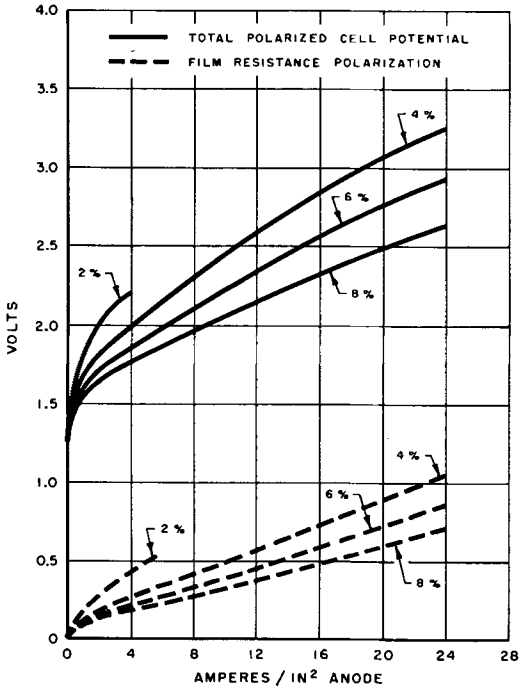

FIG. 4. Effect of current density on polarization in Hall bath having a NaF/AlF_3 weight ratio = 1.47. Curve numbers indicate % Al_2O_3 by weight in the bath.

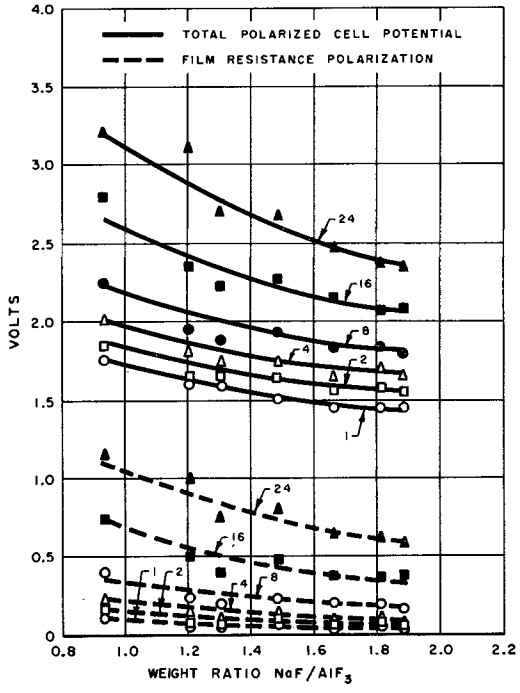

FIG. 5. Effect of bath ratio (NaF/AlF_3) on polarization in Hall bath containing 5.8% Al_2O_3. Curve numbers indicate amp/in.² anode current density.

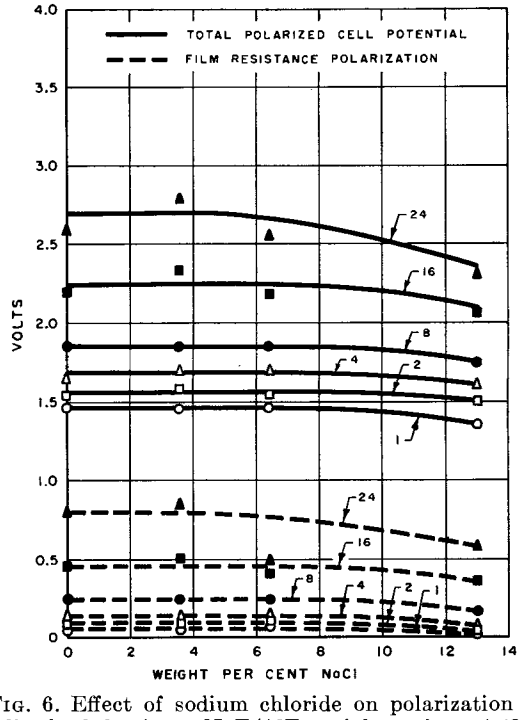

FIG. 6. Effect of sodium chloride on polarization in a cryolite bath having a NaF/AlF_3 weight ratio = 1.43 and containing 7.7% Al_2O_3. Curve numbers indicate amp/in.² anode current density.

Discussion of Results

These tests indicated that the largest factors affecting polarization were the alumina content of the bath and the current density. Fig. 3 presents the polarized cell potential as a family of curves at various anode current densities plotted against the alumina content of the bath. In all tests, the anode current density was about four times as great as the cathode current density. Unfortunately, this is a much greater ratio of anode to cathode current density than exists in a commercial cell. However, there seemed to be no way to avoid this discrepancy, for, if the anode were made larger, the current to the side walls would become excessive.

The current distribution over both the cathode and the anode must have been nonuniform because of the complex shape of the cathode. No means was found to avoid this difficulty. Nonuniform current distribution would cause the polarization to appear higher for a given nominal current density than it would be with a uniform current distribution. However, the effect could not have been very severe, for some of the results were checked in a large commercial cell having a quite uniform current distribution and were found to agree well.

The lower family of curves represents the part of polarization with a short time constant. A large decrease in both types of polarization with increasing alumina concentration is apparent. The effect is more marked at high current densities than at low current densities. The electrolytic baths in these tests contained cryolite plus 10% CaF_2, and had an average NaF/AlF_3 weight ratio of 1.47.

The data of Fig. 3 are replotted in Fig. 4 as a function of anode current density to show how polarization varies with current density. There is considerable deviation from Tafel's law (6) which states that the relationship between polarization voltage and current density is $E = a + b \log I$, where E is the polarization voltage, a and b are constants, and I is the current. Both the polarized cell potential and the film resistance polarization increased less with increasing currents than would be predicted by Tafel's law at low currents and more than would be predicted at high currents. Only above 4 amp/in.^{2} chemical polarization appeared to follow Tafel's law.

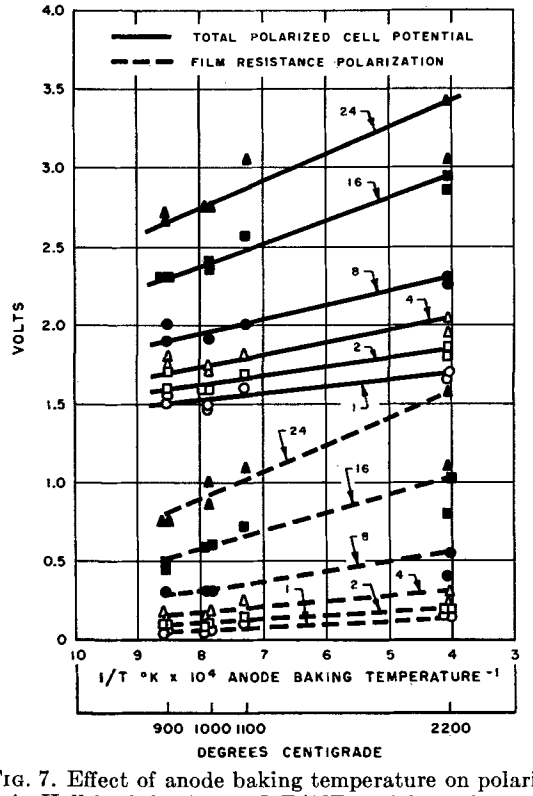

Fig. 7. Effect of anode baking temperature on polarization in Hall bath having a NaF/AlF_3 weight ratio = 1.48 and containing 6.7% Al_2O_3. Curve numbers indicate amp/in.^{2} anode current density.

Fig. 5 shows that there was a moderate decrease in polarization with increasing NaF/AlF_3 ratios. These baths contained 10% CaF_2, 5.8% Al_2O_3, and Na_3AlF_6 plus NaF or AlF_3 to give the NaF/AlF_3 weight ratio indicated.

Sodium chloride had little effect on polarization at practical current densities. There was a moderate decrease in polarization with increasing NaCl concentration at very high current densities, as shown in Fig. 6. The bath was composed of cryolite, 7.7% alumina, and additions of NaCl. The NaF/AlF_3 ratio was 1.43. Other bath additions, namely KF up to 12%, MgF_2 up to 11%, CaF_2 up to 18%, and SrF_2 up to 10%, produced no significant effect on polarization.

Increasing the baking temperature of the anode over the normal range of practice caused a very slight increase in polarization. However, as shown in Fig. 7, use of graphite produced a fairly large increase in polarization. The bath used in these tests contained 6.7% Al_2O_3, 10% CaF_2, and cryolite, giving a NaF/AlF_3 ratio of 1.48.

Bath temperature was found to have an insignificant effect on polarization over the temperature range of 970°–1010°C, except at the highest current densities where there

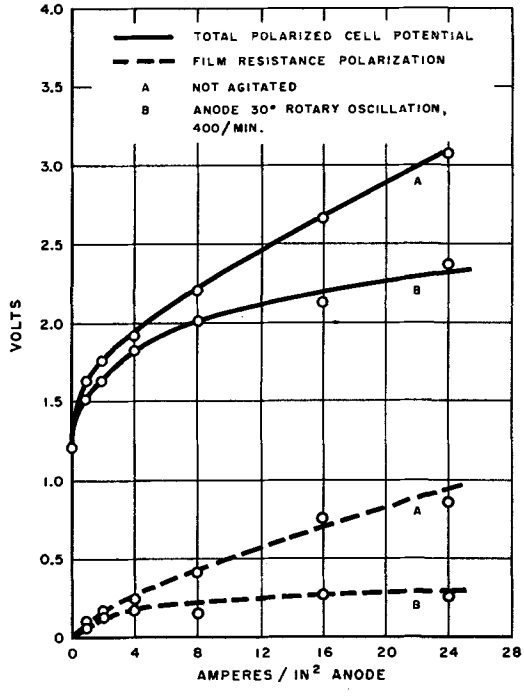

Fig. 8. Effect of agitation on polarization in Hall bath having a NaF/AlF_3 weight ratio = 1.48 and containing 5.2% Al_2O_3.

was a slight decrease in polarization with increasing temperature.

Polarization was reduced markedly by agitation. The most effective type of agitation investigated was a simple harmonic rotary oscillation of the anode through 30° at 400/min. The effect of rotary oscillation is shown in Fig. 8, for bath containing 10% CaF_2, 5.2% Al_2O_3, and cryolite, giving a NaF/AlF_3 ratio of 1.48.

There appears to be a close relationship between the ability of bath to wet carbon and polarization. Those additions which reduced polarization were observed also to improve the wetting of the carbon by the bath.

The author's measurements of polarized cell potential agree with measurements of Nozaki and Miyanchi (7) and Boner (8) who measured the average polarization on lines of commercial cells by the method of current interruption. Nozaki found the average polarized cell potential to be 1.72 v and Boner found 1.8 v for normal pot lines. Both values are within the range of the author's data which would compare with normal cell operation.

Probably the major portion of the polarization occurs at the anode. Rempel and Khodak (2) found extremely little polarization at the cathode. However, Piontelli and Montanelli (1) observed several tenths of a volt cathode polarization depending on bath composition. The total polarized cell potential calculated from data reported by Rempel and Khodak at 1.6 amp/in.^{2} in bath containing 4% excess AlF_3 and saturated with Al_2O_3 was 1.5 v. This agrees with the author's value of $E_d + IR_c$ under similar conditions. Apparently Rempel and Khodak did not include film resistance polarization. Piontelli and Montanelli reported only cathode polarization, so their results cannot be compared with this author's.

Manuscript received June 24, 1955.
Any discussion of this paper will appear in a Discussion Section to be published in the December 1956 JOURNAL.

REFERENCES

1. R. PIONTELLI AND F. MONTANELLI, *Alluminio*, **22**, 672 (1953).
2. S. I. REMPEL AND L. P. KHODAK, *Zhur. Priklad. Khim.*, **26**, 857 (1953).
3. S. SENDEROFF AND A. BRENNER, *This Journal*, **101**, 31 (1954).
4. W. R. BUSING AND W. KAUZMANN, *J. Chem. Phys.*, **20**, 1129 (1952).
5. D. F. WOHR, *Z. Elektrochem.*, **39**, 756 (1933).
6. J. TAFEL, *Z. physik. Chem.* **54**, 641 (1905).
7. H. NOZAKI AND K. MIYANCHI, *J. Chem. Soc. Jap., Ind. Chem. Sect.*, **51**, 5 (1948).
8. J. E. BONER, *J. four élec.*, **60**, 143 (1951).

Mechanisms of Hydrogen Producing Reactions on Palladium

II. Diffusion of Electrolytic Hydrogen through Palladium

SIGMUND SCHULDINER AND JAMES P. HOARE

Naval Research Laboratory, Washington, D. C.

ABSTRACT

The rate of diffusion of hydrogen through several thicknesses of palladium for varying current densities was measured. The relationship between the diffusion current and the total polarizing current was established.

INTRODUCTION

It has been shown (1) that, under steady-state current flow, atomic hydrogen formed at a β-palladium cathode can produce molecular hydrogen both by the so-called catalytic and electrochemical mechanisms. If the palladium cathode is in the form of a diaphragm which separates two isolated bodies of solution, then the atomic hydrogen formed on the polarization side of the diaphragm may either be removed from this surface by the catalytic or electrochemical mechanism or it may diffuse through the metal and be removed from the back (diffusion) surface by catalytic combination. For such a diaphragm, production of molecular hydrogen may take place simultaneously on both surfaces or may favor either surface, depending on the relative rates of each hydrogen producing mechanism.

In this paper a study of the rates of diffusion of hydrogen through a palladium cathode-diaphragm is reported. Lewis and Ubbelohde (2) showed that they could get quantitative removal of hydrogen from palladium-hydrogen alloys by oxidation with ceric ion. In the present investigation, the rate of reduction of ceric ion on the dif-

fusion side of the diaphragm was used as a means of measuring the rate of flow of hydrogen through palladium. An application of these diffusion data in the investigation of the mechanisms of hydrogen producing reactions on palladium is given in Part III (3) of this series.

Experimental Method

The cell used in this study is shown in Fig. 1. It was constructed of Teflon; the solution capacity of each compartment was about 8 ml. The pre-electrolysis cathodes were platinum wires (0.05 in. diameter) which were pulled out of the solution (while the current was still passing) after pre-electrolysis was completed. The platinum electrodes were made of gauze; the reference electrodes were about 2 cm² in area and the electrodes used as anodes were about 18 cm². The palladium diaphragm (99.7%, annealed and hole-free) was mounted between two polyethylene washers and had an exposed area of 0.1413 cm². The cell compartment in which current passed between the Pt anode and the Pd cathode-diaphragm is referred to as the polarization compartment. The other compartment, in which there was no current flow, is called the diffusion compartment. The temperature was 37 ± 1°C.

Solution preparation (2*N* sulfuric acid) pre-electrolysis, and activation of the palladium cathode on the polarization side of the cell were done as previously reported (1). The diffusion side of the cell was filled with triply distilled water until preparation of the polarization side was completed. At that time the water in the diffusion compartment was replaced with a measured amount of a 0.12*N* ceric sulfate solution in 2*N* sulfuric acid. A rapid flow of purified hydrogen was passed through the polarization compartment. The diffusion side was stirred with a moderate flow of highly purified helium. Current was allowed to flow in the polarization compartment. After a ten-minute interval (in order to remove completely the dissolved oxygen in the diffusion compartment), a 0.600 ± 0.002 ml sample of ceric sulfate solution was removed from the diffusion compartment with a hypodermic syringe through the opening provided for the pre-electrolysis electrode. This sample was analyzed with standard ferrous ammonium sulfate using diphenylamine as an indicator. The titration was done with a Gilmont microburette which could be read to 0.001 ml.

For a particular run the current flow through the polarization side of the cell was set at a given value. The hydrogen overvoltage on the polarization side was determined. At the end of a 1000-sec interval a sample was removed from the diffusion compartment and analyzed for ceric ion. From six to eight successive 1000-sec determinations were made for each run. The remaining volume of the ceric sulfate solution was noted for each determination and the ceric ion concentration changes with time were converted to gram-equivalents of atomic hydrogen per second. Check runs were made for each current density value. Although the precision of the individual 1000-sec determinations of the rate of hydrogen flow through the diaphragm in any particular run was low (±35% of the mean value), the precision over the check runs was within 5%. This was because the successive determinations of hydrogen diffusion rates were self-compensating. Palladium diaphragms 0.001, 0.002, and 0.004 in. thick were used. At the end of a run the diaphragms were examined for holes by holding them against an intense light source in a dark room. Checks were made on several specimens by means of x-ray microradiographs. In only one case (0.0005 in. Pd) was the diaphragm punctured during a run. This run gave erratic results and the diaphragm was replaced.

The possibility of loss of hydrogen by diffusion from the edges of the palladium diaphragm was checked. This was done by carefully covering the edges of several specimens with molten polyethylene. These gave the same experimental results as diaphragms with uncovered edges. Examination of the covered edges at the end of a run showed no evidence of significant hydrogen loss from this source.

Results and Discussion

Fig. 2 shows the relationship between the per cent of hydrogen transmitted through palladium diaphragms of various thickness against the polarization current density. All of the current was used in the production of atomic hydrogen, part of which may have been removed as molecular hydrogen from the polarization side of the diaphragm and the remainder reacted with ceric ion on the diffusion side. The hydrogen transmitted through the diaphragm was calculated as a diffusion current density, j. This can be expressed by the equation:

$$i = i_p + j$$

where, i is the current density flowing to the palladium cathode, i_p is the equivalent current density representing

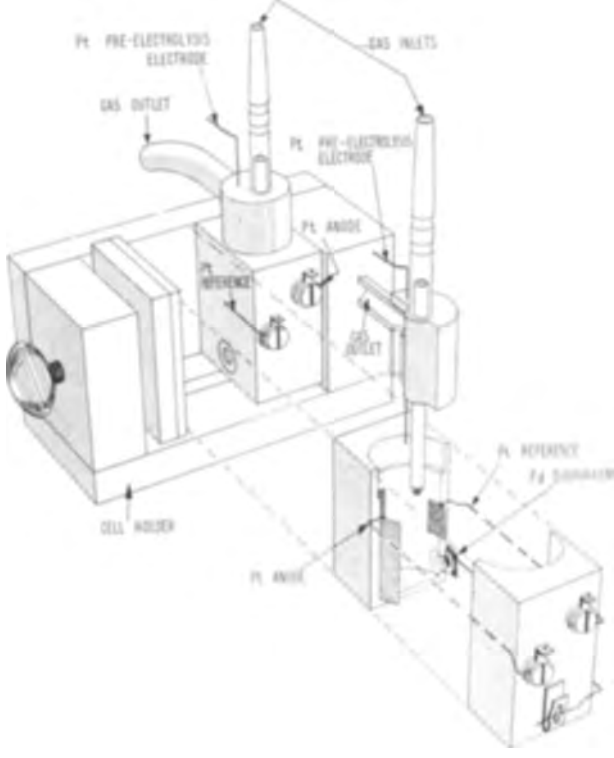

Fig. 1. Electrolytic cell

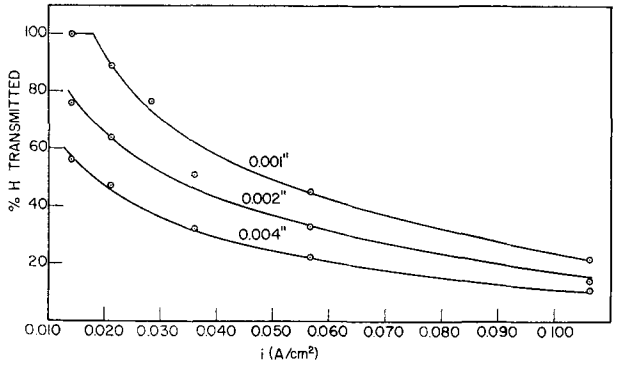

FIG. 2. Effect of current density on per cent hydrogen transmitted through palladium diaphragms of various thicknesses. The best possible fit of the points for the 0.001 in. curve indicated that 100% of the hydrogen was transmitted up to a current density of about 0.018 amp/cm².

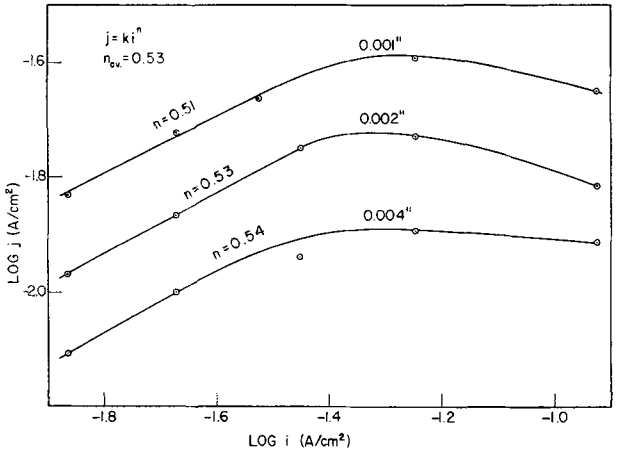

FIG. 3. Relationship between log i vs. log j

TABLE I. *Diffusion rates*

δ cm $< 10^3$	j_{max} g-eq. cm^{-2} sec^{-1} $\times 10^8$
2.54	13.26
5.08	9.70
10.16	6.64

molecular hydrogen evolution from the polarization surface, and j is the equivalent diffusion current density.

When log j is plotted against log i, the curves shown in Fig. 3 are obtained. These curves at the lower current densities show a linear portion which give the relationship:

$$j = Ki^{0.53}$$

Bodenstein (4) showed a $i^{\frac{1}{2}}$ relationship for the rate of diffusion of electrolytic hydrogen through iron. Barrer (5) and Heath (6), under certain conditions, show an $i^{\frac{1}{2}}$ relationship for palladium. At higher current densities j reaches a maximum and then declines slightly at the highest values of i. This j_{max} occurs at the current density at which the polarization side of the palladium approaches saturation with hydrogen (atomic ratio H/Pd $\sim$ 1). The phenomenon of saturation of palladium with hydrogen has been noted in the overvoltage studies of the authors (1, 3) and when this ratio of H/Pd is reached the overvoltage, η_p, of the polarization side becomes virtually independent of the current density. Thus, when the H/Pd ratio approaches unity, the hydrogen concentration of the palladium just under the surface layer of the polarization side reaches its maximum value. When this condition is reached, it has been shown (1) that a new electrode system sets in for which the catalytic properties are increased for the molecular-hydrogen-producing reaction. At current densities above this transition value, the removal of hydrogen by combination from the polarization surface of the palladium is so rapid that there appears to be a small decrease in the hydrogen concentration near this surface which results in a lowering of j. Barrer (5) at high current densities showed a transmission rate of electrolytic hydrogen through active palladium which was essentially independent of current density. However, a close examination of his data [(5) Fig. 4] indicates a small falling off of transmission rate with current density after the maximum j is reached.

The data shown in Table I indicate that the diffusion current, j_{max}, is inversely proportional to $\delta^{\frac{1}{2}}$ (where δ is the thickness of the Pd diaphragm) rather than to δ as required by Fick's first law. This means either that a surface reaction is an important factor in the rate-controlling process or that if the primary rate-determining step is diffusion of hydrogen through the palladium, then for this system the diffusion coefficient, D, is not a constant. The conclusion reached is that the latter condition prevails.

The reasons why the possibility of a retarded surface reaction determining the rate of j_{max} was eliminated are:

(*A*) Since at j_{max} the overvoltage on the polarization side of the palladium diaphragm is independent of current density, it was concluded (1) that the reactions on this side of the electrode are virtually at equilibrium and the activation energy required for the surface reactions is nearly equal to zero. Thus, the possibility of a retarded surface reaction on the polarization side is unlikely.

(*B*) Considering the surface reactions of the diffusion side of the palladium diaphragm, it is apparent that the reaction between the powerful reducing agent, adsorbed atomic hydrogen, and the strong oxidizing agent, ceric ion, would be extremely rapid and experimental observations by Lewis and Ubbelohde (2) and the authors have indicated that this is true. There would also be the possibility that a limiting diffusion current of ceric ions to the interface has been reached at j_{max}. But this possibility can be ruled out because j_{max} would not be an inverse function of the thickness of the palladium diaphragm; also, it would be fortuitous that j_{max} should occur at the point at which the overvoltage on the polarization side becomes independent of current density.

Experimental evidence indicates that hydrogen up to a H/Pd atomic ratio of 0.6 is dissolved as protons and above this it is dissolved differently (7, 9, 10). It is suggested that a possible explanation for the two solution mechanisms of hydrogen in palladium is as follows.

There are about 0.6 holes per atom in the d band of palladium. It was deduced (7), by magnetic susceptibility measurements, that up to an atomic ratio H/Pd $\sim$ 0.6 the dissolved hydrogen was completely ionized by giving up its electrons to the d bands. Additional evidence has

been given by nuclear magnetic resonance measurements (8). It is proposed that this amount of hydrogen is more or less strongly bound in the interior of the palladium electrode.

These measurements have also indicated that when H/Pd exceeds 0.6, the additional hydrogen is dissolved by a different mechanism. It is further proposed that hydrogen above the atomic ratio of 0.6 is dissolved as atomic hydrogen in the octahedral holes of the face-centered cubic lattice of the beta palladium.[1] The protons could be accommodated in either the tetrahedral or octahedral holes because of their very small size. Beta-palladium represents a closely packed system and, therefore, the hydrogen in the octahedral holes will be in relatively unstable positions. It is believed that this less firmly bound hydrogen is the hydrogen that diffuses through palladium and, because of the concentration gradient across the palladium, these hydrogen atoms will diffuse through the octahedral holes. This is in accord with the fact that it is impossible to prepare stable dried samples of palladium with more than 0.6 atomic ratio of dissolved hydrogen, and with the fact that the lattice constant increases linearly with the concentration of dissolved hydrogen (9) above this ratio.

[1] The effective radius of a tetrahedral hole is equal to $(a/2)\ [(3^{1/2}/2) - 2^{-1/2}]$; that of an octahedral hole is $(a/2)\ (1 - 2^{-1/2})$. Assuming a lattice constant, a, of 4.06Å, the effective radius of a tetrahedral hole is 0.322Å; that of an octahedral hole is 0.595Å. Since the effective radius of a hydrogen atom is 0.37Å, hydrogen atoms would most likely be accommodated in the octahedral holes.

ACKNOWLEDGMENT

The authors are indebted to Dr. J. C. White for many helpful discussions concerning this work. They are also grateful to Dr. C. Wagner for his assistance in the revision of the manuscript for publication.

Manuscript received March 21, 1955.

Any discussion of this paper will appear in a Discussion Section to be published in the December 1956 JOURNAL.

REFERENCES

1. J. P. HOARE AND S. SCHULDINER, *This Journal*, **102,** 485 (1955).
2. F. A. LEWIS AND A. R. UBBELOHDE, *J. Chem. Soc. London*, **1954,** 1710.
3. J. P. HOARE AND S. SCHULDINER, *This Journal*, to be published.
4. M. BODENSTEIN, *Z. Elektrochem.*, **28,** 517 (1922).
5. R. M. BARRER, *Trans. Faraday Soc.*, **36,** 1235 (1940).
6. H. R. HEATH, *Brit. J. Appl. Phys.*, **3,** 13 (1952).
7. N. F. MOTT AND H. JONES, "Theory of the Properties of Metals and Alloys," p. 200, Clarendon Press, Oxford (1936); J. R. LACHER, *Proc. Roy. Soc. London*, **A161,** 525 (1937).
8. R. E. NORBERG, *Phys. Rev.*, **86,** 745 (1952).
9. D. P. SMITH, "Hydrogen in Metals," pp. 104–107, University of Chicago Press, Chicago (1948).
10. B. SVENSSON, *Ann. Physik*, (5), **18,** 299 (1933); C. WAGNER, *Z. Physik. Chem.*, **193,** 407 (1944); Z. L. VERT AND I. P. TVERDOVSKI, *Zhur. Fiz. Khim.*, **28,** 317 (1954).

Mechanism of Hydrogen Evolution at Tellurium Cathodes in Hydrochloric Acid

I. A. Ammar and S. A. Awad

Faculty of Science, University of Cairo, Cairo, Egypt

ABSTRACT

Hydrogen overpotential at tellurium cathodes was studied in the concentration range 0.005*N*–5*N* aqueous hydrochloric acid at 30°C. The results indicated absence of specific adsorption. In dilute solutions a simple electrochemical mechanism, with two Tafel line slopes of 0.04 v and 0.12 v at 30°C, was established as the rate-determining mechanism. In concentrated solutions, a rate-determining dual electrochemical catalytic mechanism, with a slope of 0.06 v at 30°C, was suggested to explain the results in the low current density range. This dual mechanism changed to a simple one at high cathodic polarization.

Theoretical calculations of the Tafel line slopes for various dual mechanisms were also carried out. It was found that, for a dual slow discharge electrochemical mechanism or a dual slow discharge catalytic mechanism, the slope was exactly the same as that for the simple slow discharge, i.e., 0.12 v at 30°C.

The effect of neutral salts on hydrogen overpotential, η, at constant *p*H was studied. Addition of lanthanum chloride increased the numerical value of η at constant *p*H and current density. From the salt effect on η in 0.05*N* hydrochloric acid, the zeta potential was calculated and was found to have a value of *ca.* 0.05 v.

Introduction

Numerous researches have been carried out on the overpotential of metals (1), but overpotential studies on metalloids and nonmetals are very limited. Thus, Bowden and Rideal (2) studied the hydrogen overpotential on carbon cathodes and obtained a value of 0.84 v for the Tafel line slope.

The aim of the present investigation was to apply the experimental techniques of Bockris and co-workers (3), in order to calculate the parameters of the cathodic hydrogen evolution reaction on the metalloid tellurium.

Experimental

The electrolytic cell (Fig. 1*a*) was essentially similar to that of Bockris and Potter (4). However, it was necessary to separate the anode compartment *A* from the cathode compartment *B* by a third compartment *C*, in order to minimize the diffusion of gaseous anodic products toward the cathode. A sintered glass disk *D* was inserted between *C* and *B* for the same purpose. Compartment *C* was also used for the electrolytic purification of the solution. Water-sealed taps and ground glass joints were used to retard the diffusion of atmospheric oxygen into the cell.

The electrode[1] was in the form of a spectroscopically pure tellurium rod (7 mm diameter) with an apparent surface area of 4 cm². Since tellurium does not make a tight seal to glass, sublimes easily under heat, and its vapor combines with hydrogen to form tellurium hydride, the method involving heat treatment of the electrode in hydrogen (5) could not be used. The electrode was, however, fixed to glass in a manner shown by Fig. 1*b*. A thin tungsten wire, *a*, was tightly wrapped around one end of the tellurium rod, *b*. This end was squeezed inside a clean glass tubing, *c*, and the glass was sealed over the tungsten wire at *d*. The glass tubing was then sealed to the piston of a hypodermic syringe, whose barrel *E* (Fig. 1*a*) was fixed to the top of the cathode compartment of the electrolytic cell. The glass used for the electrode preparation was first cleaned with a mixture of A.R. nitric acid and A.R. sulfuric acid, followed by washing with conductance water ($K = 1 \times 10^{-6}$ mhos), and then dried in the flame. After being fixed into glass, the electrode was washed with conductance water and fixed in its position in the previously cleaned cell. Each electrode was used to trace one Tafel line only.

Appropriate conditions for the electrolytic purification of the solution were determined by successive increases in the amounts of pre-electrolysis until the overpotential remained constant (within ±10 mv) upon further increase (2–3 times) of the extent of pre-electrolysis (3, 6). Preliminary experiments with a tellurium pre-electrolysis electrode had shown that this electrode disintegrated into black colloidal tellurium in solutions containing traces of oxygen. For this reason tellurium could not be used as a pre-electrolysis electrode, so a platinum electrode was used instead. Pre-electrolysis was carried out on the auxiliary platinum electrode (apparent surface area of 1 cm²) for about 20 hr using a current of 30–40 ma. These conditions were satisfactory to obtain reproducible results (within ±10 mv) in all solutions studied in the present investigation.

Hydrogen was purified from oxygen, carbon dioxide, and carbon monoxide in an all-glass apparatus (3). Hydrochloric acid solutions were prepared from the constant boiling acid. All glass parts of the apparatus were made of

[1] Prepared by Johnson and Matthey, Ltd., London, England.

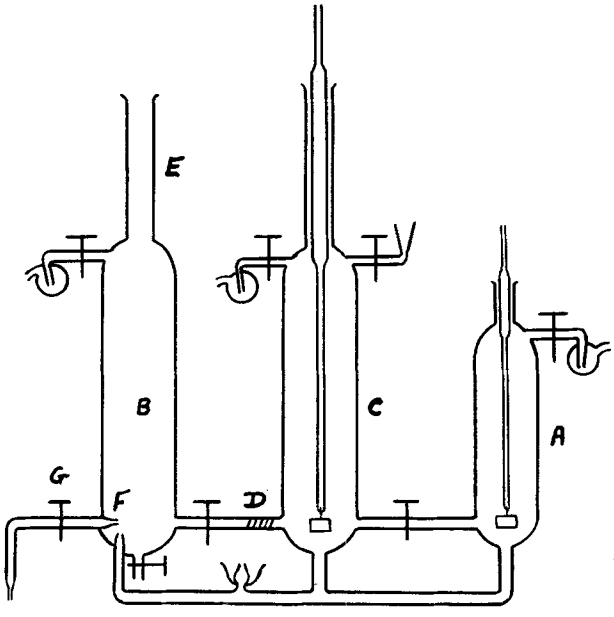

FIG. 1a. Electrode

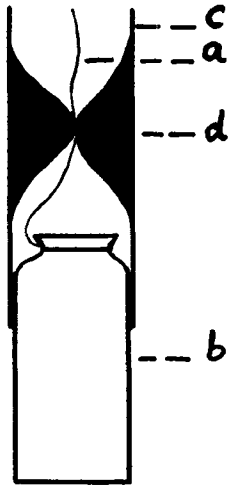

FIG. 1b. Electrolytic cell

hard borosilicate arsenic-free glass technically known as hysil.[2]

Before each run, the cell was cleaned with a mixture of A.R. nitric acid and A.R. sulfuric acid. This was followed by a thorough washing with conductance water. The cell was then fixed in its position, the electrode suspended in the cathode compartment, the cell filled with conductance water, the water displaced by pure hydrogen, the solution introduced and divided between the compartment A and C (Fig. 1a), and pre-electrolysis was begun by lowering the pre-electrolysis electrode, with a current of 30–40 ma imposed on it, into the solution in compartment C. After 20 hr, the pre-electrolysis electrode was drawn out of the solution, with the current still on, and part of the pre-electrolyzed solution in C was introduced into compartment B with a stream of hydrogen. The test tellurium electrode, with a current of 40 ma imposed on it, was then lowered into the solution and was adjusted to touch the tip of the Luggin capillary F.

A saturated calomel electrode, with a saturated KCl bridge (potential 238 mv at 30°C) was used as a reference electrode.

Diffusion of impurities from the salt bridge to the cathode compartment was hindered by keeping the level of the cathode compartment higher than the level of the salt bridge, and also by inserting a tap, G, between the Luggin, F, and the salt bridge (cf. Fig. 1a).

The direct method and the rapid technique (3) were employed, and the Tafel line was rapidly traced down to 10^{-6} amp/cm^2. The current was measured with a multirange millimicroammeter and the potential by a valve potentiometer. Temperature was kept constant with the aid of an air thermostat.

RESULTS

All results included in this section are the mean of six individual results which are reproducible among themselves to within ± 10 mv.

Fig. 2, 3, and 4 show the mean Tafel lines for tellurium cathodes in 5, 2, 1, 0.5, 0.3, and 0.1N aqueous hydrochloric acid between 10^{-6}–10^{-2} amp/cm^2 at 30°C. It is clear from these figures that Tafel lines obtained for tellurium cathodes in concentrations above 1N hydrochloric acid show a linear logarithmic section with one slope. However, Tafel lines in 1N hydrochloric acid and lower con-

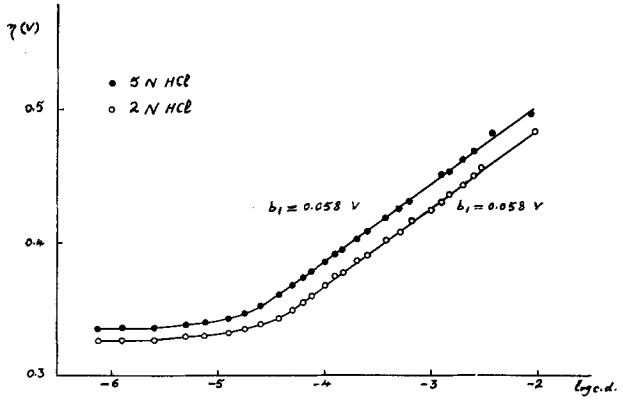

FIG. 2. Hydrogen overpotential on tellurium in 5N and 2N hydrochloric acid.

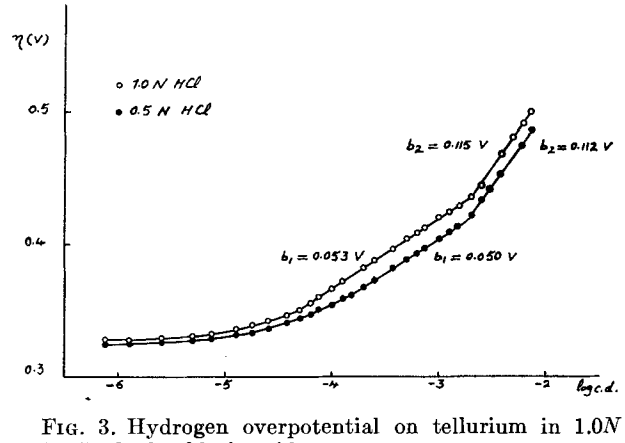

FIG. 3. Hydrogen overpotential on tellurium in 1.0N and 0.5N hydrochloric acid.

[2] Made by Chance Bros., Ltd., Birmingham, England.

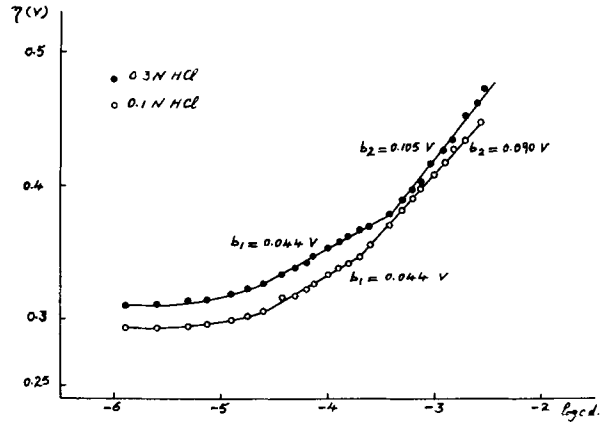

FIG. 4. Hydrogen overpotential on tellurium in 0.3N and 0.1N hydrochloric acid.

TABLE I

Conc.	b_1	b_2	η at 10^{-4}	Conc.	b_1	b_2	η at 10^{-4}
5.0N	58	—	386	0.1N	44	90	333
3.0N	51	—	380	0.05N	40	90	334
2.0N	58	—	368	0.03N	44	90	332
1.0N	53	115	365	0.02N	44	90	329
0.5N	50	112	354	0.01N	40	115	333
0.3N	44	105	352	0.005N	40	93	332

centrations clearly indicate the occurrence of two slopes in the linear logarithmic section. At comparatively low current densities, a region of stationary potential is obtained in all concentrations.

Table I contains the mean values of the slopes b_1 (at the low current density range) and b_2 (at the high current density range), together with the values of η at 10^{-4} amp/cm^2, for the various hydrochloric acid concentrations at 30°C.

Values of η (referred to the reversible hydrogen electrode), b_1, and b_2 are in millivolts.

It is clear from Table I that the overpotential is almost independent of pH, below 0.1N hydrochloric acid.

Fig. 5 shows the effect of adding an excess of lanthanum chloride (100 g/l HCl solution) on the Tafel line in 0.05N hydrochloric acid. It is clear from this figure that the neutral salt numerically increases η on tellurium cathodes in dilute solutions.

DISCUSSION

The pH effect observed above 0.1N hydrochloric acid (cf. Table I) indicates a slight numerical increase of η with increase of concentration. Bockris and Conway (6) also observed a numerical increase of η with increase of concentration above 1N hydrochloric acid on silver cathodes, but the work of Jofa (7) on mercury clearly indicates a numerical decrease of η with increase of hydrochloric acid concentration.

The pH effect observed by Jofa (7) in high acid concentrations was attributed to the specific adsorption of anions as well as to the change of the activity coefficient of hydrogen ions in the double layer as compared with the bulk activity coefficient. Specific adsorption of anions resulted in the decrease of the overpotential values at low current densities. This caused an increase in the Tafel line slope at low current densities as compared with the slope at high current densities (7). Since this phenomenon was not observed in the present investigation on tellurium, it is possible to assume that specific adsorption of chloride ions does not occur on tellurium. The pH effect (cf. Table I) observed on tellurium in concentrated hydrochloric acid may thus be attributed to the change in the activity coefficient of hydrogen ions in the double layer as compared to the bulk value.

The occurrence of two slopes for the Tafel lines on silver in hydrochloric acid has been attributed by Bockris and Conway (6) to the specific adsorption of hydrogen ions. This causes the inflection of the Tafel lines to occur at increasingly low current densities, with increase of hydrochloric acid concentration (6). Since this is not the case with the results on tellurium (cf. Fig. 3 and 4), specific adsorption of cations cannot be the cause of change in slope for Tafel lines on tellurium.

From Table I it is clear that in dilute solutions (below 0.3N) the values of b_1 lie between 0.040 v and 0.044 v while those of b_2 lie between 0.090 v and 0.115 v. The occurrence of two slopes of b_1 = 0.040 v and b_2 = 0.120 v at 30°C indicates a simple electrochemical mechanism (8). This mechanism rquires that η be independent of pH, in absence of specific adsorption and under the conditions where Stern's theory applies (in dilute solutions). It can, therefore, be concluded that in solutions below 0.3N HCl the rate-determining step for hydrogen evolution on tellurium is the simple electrochemical mechanism, since η is independent of pH (cf. Table I).

Levina and Zarinskii (9) studied the effect of lanthanum chloride on hydrogen overpotential. Excess lanthanum ions compress the diffuse double layer and result in a value of zeta potential, ζ, very near to zero. The salt effect, at a constant current density and pH, for the simple electrochemical mechanism, in the region of the Tafel line with a slope of 0.040 v, is given by (8):

$$\eta = \text{constant} - \zeta/3 \qquad \text{(I)}$$

It is possible to use the above equation to evaluate ζ from hydrogen overpotential data. From Fig. 5, the value of η at 10^{-4} amp/cm^2 in presence of excess lanthanum chloride is −0.350 v in 0.05N hydrochloric acid. In absence of

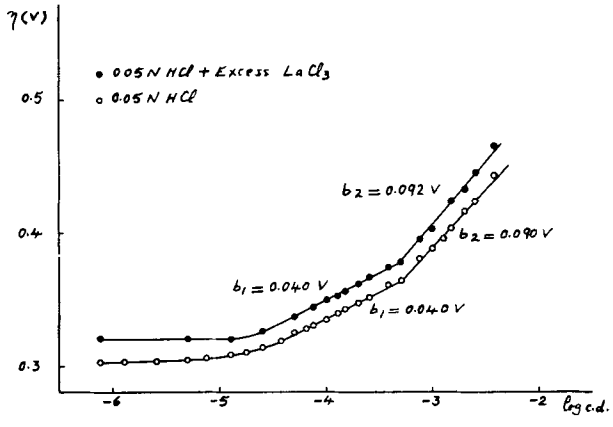

FIG. 5. Effect of excess lanthanum chloride on the hydrogen overpotential of tellurium in 0.05N hydrochloric acid.

lanthanum chloride, η at 10^{-4} amp/cm^2 is -0.335 v in the same hydrochloric acid concentration. Since in excess lanthanum chloride $\zeta = 0$, the constant in equation (I) is -0.350 v. Therefore, ζ is approximately 0.05 v. This result lies within the range of values for zeta potentials calculated by Frumkin (10) from hydrogen overpotential data on mercury.

Although results of the present investigation on tellurium in dilute (below 0.3N) hydrochloric acid are accounted for by the simple electrochemical mechanism, results in high acid concentrations cannot be explained by any of the simple mechanisms. Complex mechanisms were suggested by Kobozev and Nekrasov (11), by Lukovzew (12), and by Parsons (13) to explain the change of the slope of Tafel lines with cathodic polarization.

In the following discussion, the term "dual mechanism" is employed to cover the case when the rate of the over-all hydrogen evolution reaction is governed by two steps with nearly equal rates. The rates of the slow discharge step, V_1, of the electrochemical step V_2, and of the catalytic step, V_3, are given by (8):

$$V_1 = k_1 (1 - x)\, a_{H+} \exp\left(-\frac{\Delta\phi F}{2RT}\right) \qquad \text{(II)}$$

$$V_2 = k_2(x \cdot 10^{-9}) a_{H+} \exp\left(-\frac{\Delta\phi F}{2RT}\right) \qquad \text{(III)}$$

$$V_3 = k_3(x^2 \cdot 10^{-18}) \qquad \text{(IV)}$$

where k_1, k_2, and k_3 are rate constants, x is the coverage of the surface with adsorbed hydrogen atoms, a_{H+} is the activity of hydrogen ions in the double layer, and $\Delta\phi$ is the galvanic potential difference between the Helmholtz double layer and the metal. Consider the following dual mechanisms.

1. A rate-determining dual slow discharge electrochemical mechanism, under the following condition:

$$V_1 \simeq V_2 \gg V_3 \qquad \text{(V)}$$

Substituting in (V) for V_1 and V_2 by their values as given by (II) and (III), the surface coverage, x, becomes:

$$x = k_1/(k_1 + k_2 \cdot 10^{-9}) \qquad \text{(VI)}$$

From equations (II) and (VI) or (III) and (VI), the net cathodic current at constant pH is given by:

$$i_c = \text{constant} \times \exp\left(-\frac{\Delta\phi F}{2RT}\right) \qquad \text{(VII)}$$

From (VII), it is clear that the slope of the Tafel line is equal to 0.120 v at 30°C, similar to that of the simple slow discharge mechanism and to that of the simple electrochemical mechanism at high cathodic polarization (8).

2. A rate-determining dual electrochemical catalytic mechanism (14), under the following condition:

$$V_1 \gg V_2 \simeq V_3 \qquad \text{(VIII)}$$

Substituting in (VIII) the values of V_2 and V_3 given by (III) and (IV), the surface coverage, x, becomes:

$$x = [k_2/(k_3 \cdot 10^{-9})] a_{H+} \exp\left(-\frac{\Delta\phi F}{2RT}\right) \qquad \text{(IX)}$$

From (III) and (IX) or (IV) and (IX), the net cathodic current, at constant pH, is given by:

$$i_c = \text{constant} \times \exp\left(-\frac{\Delta\phi F}{RT}\right) \qquad \text{(X)}$$

Equation (X) clearly indicates that the Tafel line slope is 0.060 v at 30°C.

3. A rate-determining dual slow discharge catalytic mechanism, under the following conditions:

$$V_1 \simeq V_3 \gg V_2 \qquad \text{(XI)}$$

$$a_1(1 - x) = a_3 x^2 \qquad \text{(XII)}$$

where a_1 and a_3 [cf. ref. (8)] are given by:

$$a_1 = k_1(a_{H+}) \exp\left(-\frac{\Delta\phi F}{2RT}\right) \qquad \text{(XIII)}$$

$$a_3 = k_3 \cdot 10^{-18} \qquad \text{(XIV)}$$

From (XII):

$$x = \frac{-a_1 + \sqrt{a_1(a_1 + 4a_3)}}{2a_3} \qquad \text{(XV)}$$

The solution of the above equation for x depends on the relative values of a_1 and a_3. Consider the following possibilities:

(i) $a_1 \gg a_3$. From (XV), the coverage becomes $x \simeq 0$.

(ii) $a_3 \gg a_1$. From (XIII), (XIV), and (XV), at constant pH, the surface coverage is given by:

$$x = \sqrt{\frac{a_1}{a_3}} = \text{constant} \cdot \exp\left(-\frac{\Delta\phi F}{4RT}\right) \qquad \text{(XVI)}$$

From (IV) and (XVI), the net cathodic current at constant pH becomes:

$$i_c = \text{constant} \cdot \exp\left(-\frac{\Delta\phi F}{2RT}\right) \qquad \text{(XVII)}$$

indicating a slope of 0.120 v at 30°C.

(iii) $a_1 \simeq a_3$. From (XII): $(1 - x) \simeq x^2$ and $x \simeq 0.62$. Substituting this value of x in equation (II), the net cathodic current is given by an equation similar to (XVII), and the slope of the Tafel line is 0.120 at 30°C.

Table II gives the possible values of the slope for the various rate-determining dual mechanisms at 30°C.

From the above discussion, it is clear that the results of hydrogen overpotential measurements on tellurium in concentrated (above 0.3N) hydrochloric acid, are best explained on the basis of a dual electrochemical catalytic mechanism, at the low current density range, probably changing to a simple electrochemical mechanism or a slow discharge mechanism at higher current densities (cf. Tables I and II). The fact that Tafel lines with only one slope are obtained in concentrations above 1N hydrochloric

TABLE II

Rate-determining mechanism	Slope (volt)
Dual slow discharge electrochemical	0.120
Dual electrochemical catalytic	0.060
Dual slow discharge catalytic	0.120

acid (cf. Table I and Fig. 2) might be explained by the assumption that the change of mechanism in such concentrations takes place at current densities higher than those used in this investigation.

At low current densities, the Tafel lines become parallel to the log current density axis at potentials negative with respect to the reversible hydrogen potential. This behavior is similar to that of nickel in acid solutions (15) at low current densities, and is similarly attributed to the dissolution of the cathode.

ACKNOWLEDGMENT

The authors wish to express their thanks to Professor A. R. Tourky for helpful discussions.

Manuscript received February 11, 1955.

Any discussion of this paper will appear in a Discussion Section to be published in the December 1956 JOURNAL.

REFERENCES

1. J. O'M. BOCKRIS, *Chem. Rev.*, **43**, 525 (1948).
2. F. P. BOWDEN AND E. RIDEAL, *Proc. Roy. Soc. London*, **A120**, 59 (1928).
3. A. AZZAM, J. O'M. BOCKRIS, B. CONWAY, AND H. ROSENBERG, *Trans. Faraday Soc.*, **46**, 918 (1950).
4. J. O'M. BOCKRIS AND E. C. POTTER, *J. Chem. Phys.*, **20**, 614 (1952).
5. J. O'M. BOCKRIS AND B. CONWAY, *J. Sci. Inst.*, **25**, 8 (1948).
6. J. O'M. BOCKRIS AND B. CONWAY, *Trans. Faraday Soc.*, **48**, 724 (1952).
7. S. A. JOFA, *Acta Physicochim., U. R. S. S.*, **10**, 903 (1939).
8. J. O'M. BOCKRIS AND E. C. POTTER, *This Journal*, **99**, 169 (1952).
9. S. LEVINA AND W. ZARINSKII, *Acta Physicochim., U. R. S. S.*, **7**, 485 (1937).
10. A. FRUMKIN, *Trans. Faraday Soc.*, **36**, 117 (1940).
11. N. KOBOZEV AND N. I. NEKRASOV, *Z. Elektrochem.*, **36**, 529 (1930).
12. P. LUKOVZEW, *J. Phys. Chem., U. S. S. R.*, **21**, 589 (1947).
13. R. PARSONS, *J. Chim. Phys.*, **49**, 83 (1952).
14. I. A. AMMAR, Ph.D. Thesis, London, (1953).
15. A. FRUMKIN AND J. KOLOTYRKIN, *Compt. rend. Acad. Sci., U. R. S. S.*, **33**, 445 (1941).

Effect of the Walls of Electrolytic Cells on Current Distribution

FUMIO HINE, SHIRO YOSHIZAWA, AND SHINZO OKADA

Department of Industrial Chemistry, Kyoto University, Kyoto, Japan

ABSTRACT

The field in the rectangular cell with two parallel and flat plates as electrodes has been analyzed. In this paper, no consideration is given to polarization phenomena for mathematical convenience.

As a numerical example, current distribution at the surface of the electrode has been calculated in detail for the special case where distance between electrodes equals cell width. Moreover, diagrams are given to show numerical relations such as the ratio of current on inner and outer surfaces, total current distribution over the electrodes, etc., for the general case.

INTRODUCTION

Lately much attention has been given to the design of electrolytic cells in the field of chemical engineering; one of the most important problems is the distribution of potential or current in such cells. No basic solution has yet been attained in spite of many efforts, e.g., Kasper (1), Wagner (2), and others, partly because of difficulties due to polarization phenomena near the surface of electrodes.

Analysis of the electric field is one of the fundamental problems involved, and special attention must be paid eventually to polarization phenomena. For mathematical simplicity, the effect of polarization is neglected in the present paper. This approximation is made regretfully, but it is believed that the results will nevertheless be suggestive in many respects.

Another difficulty is the fact that the domain of the electric field under consideration is limited by the electrolytic cell. If the field were unrestricted in all directions, analysis would be much simpler; but in the case of parallel-plate electrodes in a rectangular electrolyzer, which is the usual type of bath in electrochemistry and in the electrochemical industry, the mathematical treatment becomes very difficult.

In the following, the problem is treated as a two-dimensional one, and the Schwarz-Christoffel transformation is used. If the effects of four walls in a rectangular cell are considered, a hyper-elliptic integral appears, and the analysis is beyond possibility. Therefore, another model must be employed.

It is known from experience that the walls facing the back of electrodes have relatively small influence on the distribution of potential and current, especially when the electrodes extend close to the side walls. Accordingly, the present treatment considers only the effect of the side

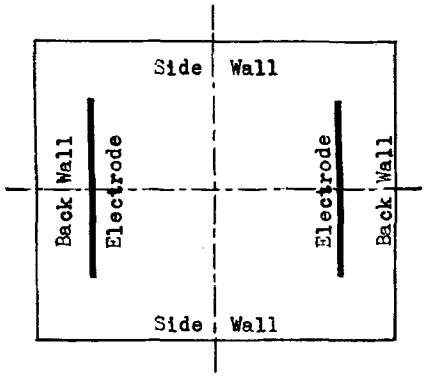

FIG. 1. Profile of the rectangular bath

walls on the current distribution and assumes that the back walls are far removed from the electrodes.

MATHEMATICAL METHOD

Applying the above-mentioned assumptions, the model in Fig. 1 can be represented by the z-plane of Fig. 2. Applying the methods of conformal mapping, the interior of the polygon (OA'B'C'H'RHCBAO) formed at the upper half of this z-plane can be transformed on the upper half of the t-plane. Here, 2α, 2β, and 2γ are the distances between the electrodes, the width of the electrodes and of the cell, respectively.

The transformation from the z-plane to the t-plane can be made by the equation

$$\frac{dz}{dt} = M \frac{t^2 - b^2}{\sqrt{t^2 - a^2}\sqrt{t^2 - c^2}\,(t^2 - h^2)} \qquad [1]$$

where M is a constant and a, b, c, and h are also constants corresponding to the positions of the points A, B, C, and H on the t-plane, respectively.

Using the equation (6)

$$t^2 = \wp(s) - e_3 \qquad [2]$$

the t-plane is transformed within the rectangle of the s-plane with $2\omega_1$ and ω_3/i as the lengths of its adjacent sides. If, of the two periods $2\omega_1$ and $2\omega_3$ of the Weierstrass $\wp$-function, $\wp(s)$, the former is a real number, then the latter is purely imaginary, and $\omega_1 > 0$, $\omega_3/i > 0$. Therefore, from equations [1] and [2] and the use of the relation

$$\wp'(s) = -2\sqrt{\wp(s) - e_1}\sqrt{\wp(s) - e_2}\sqrt{\wp(s) - e_3}$$

one obtains

$$\frac{dz}{ds} = M \frac{-\{\wp(s) - \wp(\mu)\}\wp'(s)}{2\sqrt{\wp(s) - e_1}\sqrt{\wp(s) - e_2}\sqrt{\wp(s) - e_3}\,\{\wp(s) - \wp(\nu)\}} \qquad [3]$$

$$= M \frac{\wp(s) - \wp(\mu)}{\wp(s) - \wp(\nu)}$$

Here, μ and ν are the coordinates of the points B and H on the s-plane, respectively; e_j stands for $\wp(\omega_j)$, with $j = 1, 2, 3$.

This result coincides with the relation derived by Sasaki and others in their research on the lift of an aerofoil placed near a plane wall (3–5).

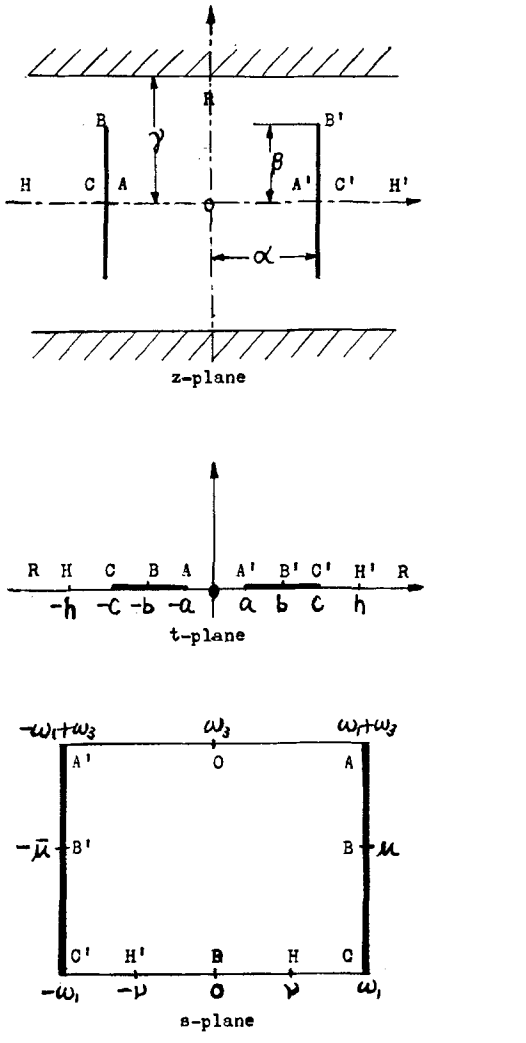

FIG. 2. Conformal mappings between the original, the parametric, and the potential planes.

Employing the addition formula of the Weierstrass ζ-function

$$\frac{\wp'(u)}{\wp(u) - \wp(v)} = \zeta(u - v) + \zeta(u + v) - 2\zeta(u)$$

one finds from equation [3]:

$$\frac{dz}{ds} = M \frac{\wp(\nu) - \wp(\mu)}{\wp'(\nu)}[\zeta(\mu + \nu) - \zeta(\mu - \nu) - \zeta(s + \nu) + \zeta(s - \nu)] \qquad [4]$$

Considering the relation

$$\zeta(u) = \frac{d}{du}\log\sigma(u) \qquad [5]$$

there is obtained:

$$z = M \frac{\wp(\nu) - \wp(\mu)}{\wp'(\nu)} \cdot \left[\{\zeta(\mu + \nu) - \zeta(\mu - \nu)\}s - \log\frac{\sigma(s + \nu)}{\sigma(s - \nu)}\right] + C \qquad [6]$$

To determine the integration constant C, make $z = 0$ and $s = \omega_3$:

$$0 = M\frac{\mathcal{P}(\nu) - \mathcal{P}(\mu)}{\mathcal{P}'(\nu)} \cdot \left[\{\zeta(\mu+\nu) - \zeta(\mu-\nu)\}\omega_3 - \log\frac{\sigma(\omega_3+\nu)}{\sigma(\omega_3-\nu)}\right] + C \quad [7]$$

Substituting equation [7] into equation [6]

$$z = M\frac{\mathcal{P}(\nu) - \mathcal{P}(\mu)}{\mathcal{P}'(\nu)}\left[\{\zeta(\mu+\nu) - \zeta(\mu-\nu)\}(s-\omega_3) - \log\frac{\sigma(s+\nu)\sigma(\omega_3-\nu)}{\sigma(s-\nu)\sigma(\omega_3+\nu)}\right] \quad [8]$$

The constant M can now be obtained. The following relations concerning the σ-functions are available (6)

$$\sigma(u \pm \omega_j) = \pm e^{\pm\eta_j u}\sigma(\omega_j)\sigma_j(u), \qquad j = 1, 2, 3 \quad [9]$$

and

$$\log\frac{\sigma(\omega_1+\omega_3+\nu)\sigma(\omega_3-\nu)}{\sigma(\omega_1+\omega_3-\nu)\sigma(\omega_3+\nu)} = \log\frac{\sigma(\nu-\omega_2)\sigma(\nu-\omega_3)}{\sigma(\nu+\omega_2)\sigma(\nu+\omega_3)} = -2\nu(\eta_2+\eta_3) = 2\nu\eta_1 \quad [10]$$

where

$$\eta_j = \zeta(\omega_j)$$

Substituting the coordinates of the point $A(z = -\alpha, s = \omega_1 + \omega_3)$ into equation [8], and considering the above relations, one has

$$-\alpha = M\frac{\mathcal{P}(\nu) - \mathcal{P}(\mu)}{\mathcal{P}'(\nu)} \cdot [\{\zeta(\mu+\nu) - \zeta(\mu-\nu)\}\omega_1 - 2\nu\eta_1] \quad [11]$$

On the other hand, as $z = -\alpha$ and $s = \omega_1$ at the point C, equation [8] becomes

$$-\alpha = M\frac{\mathcal{P}(\nu) - \mathcal{P}(\mu)}{\mathcal{P}'(\nu)} \cdot [\{\zeta(\mu+\nu) - \zeta(\mu-\nu)\}(\omega_1-\omega_3) - 2\nu(\eta_1-\eta_3)] \quad [12]$$

because from equations [9] and [10],

$$\log\frac{\sigma(\omega_1+\nu)\sigma(\omega_3-\nu)}{\sigma(\omega_1-\nu)\sigma(\omega_3+\nu)} = \log\frac{\sigma(\nu+\omega_1)\sigma(\nu-\omega_3)}{\sigma(\nu-\omega_1)\sigma(\nu+\omega_3)} = 2\nu(\eta_1-\eta_3) \quad [13]$$

Consequently, from equations [11] and [12], one obtains

$$M\frac{\mathcal{P}(\nu) - \mathcal{P}(\mu)}{\mathcal{P}'(\nu)}[\{\zeta(\mu+\nu) - \zeta(\mu-\nu)\}\omega_3 - 2\nu\eta_3] = 0 \quad [14]$$

As it is clear that

$$M\frac{\mathcal{P}(\nu) - \mathcal{P}(\mu)}{\mathcal{P}'(\nu)} \neq 0$$

it follows from equation [14] that,

$$\zeta(\mu+\nu) - \zeta(\mu-\nu) = \frac{2\nu\eta_3}{\omega_3} \quad [15]$$

Next, the sign of $M[\mathcal{P}(\nu) - \mathcal{P}(\mu)/\mathcal{P}'(\nu)]$ must be considered.

If one considers the domain, $c < t < h$, in equation [1], it will be clear that $dz/dt > 0$, $t^2 - b^2 > 0$, $\sqrt{t^2-a^2} > 0$, $\sqrt{t^2-c^2} > 0$ and $t^2 - h^2 < 0$, and accordingly, $M < 0$. Consequently from the relation

$$\mathcal{P}'(\nu) = -z\sqrt{\mathcal{P}(\nu)-e_1}\sqrt{\mathcal{P}(\nu)-e_2}\sqrt{\mathcal{P}(\nu)-e_3} \quad [16]$$

it can be concluded that $\mathcal{P}'(\nu) < 0$ if $0 < \nu < \omega_1$.

The $\mathcal{P}$-function can be represented by ϑ-functions that is,

$$\mathcal{P}(u) = e_j + \frac{1}{4\omega_1^2}\left[\frac{\vartheta_1'(0)}{\vartheta_{j+1}(0)}\right]^2\left[\frac{\vartheta_{j+1}(v)}{\vartheta_1(v)}\right]^2, \quad j = 1, 2, 3 \quad [17]$$

where ϑ_j represents the families of the ϑ-function, and $v = u/2\omega_1$. Putting

$$\nu_1 = \frac{\nu}{2\omega_1} \quad [18]$$

$$\mu_1 = \frac{\mu}{2\omega_1} \quad [19]$$

and

$$\mu = \omega_1 + i\mu'' \quad [20]$$

equation [17] yields

$$\mathcal{P}(\nu) - \mathcal{P}(\mu) = \frac{1}{4\omega_1^2}\left[\frac{\vartheta_1'(0)}{\vartheta_{j+1}(0)}\right]^2 \cdot \left\{\left[\frac{\vartheta_{j+1}(\xi_1)}{\vartheta_1(\nu_1)}\right]^2 - \left[\frac{\vartheta_{j+1}(\mu_1)}{\vartheta_1(\mu_1)}\right]^2\right\} \quad [21]$$

In equation [21] it is known that

$$\frac{1}{4\omega_1^2}\left[\frac{\vartheta_1'(0)}{\vartheta_{j+1}(0)}\right]^2 > 0$$

so, the sign of the left hand side of equation [21] is the same as that of the bracket $\{\}$. For instance, if $j = 1$, one has

$$\left[\frac{\vartheta_2(\nu_1)}{\vartheta_1(\nu_1)}\right]^2 - \left[\frac{\vartheta_2(\mu_1)}{\vartheta_1(\mu_1)}\right]^2 = \left[\frac{\vartheta_2(\nu_1)}{\vartheta_1(\nu_1)}\right]^2 + \left[\frac{\vartheta_1\left(\frac{i\mu_1''}{\tau}\middle|-\frac{1}{\tau}\right)}{\vartheta_4\left(\frac{i\mu_1''}{\tau}\middle|-\frac{1}{\tau}\right)}\right]^2 > 0 \quad [22]$$

If it is considered that (7)

$$\vartheta(iv + \tfrac{1}{2}\pi) = \vartheta_2(iv) \quad [23]$$

$$\vartheta_2(iv + \tfrac{1}{2}\pi) = -\vartheta_1(iv) \quad [24]$$

then

$$\vartheta_1(iv\,|\,\tau) = i\sqrt{\frac{i}{\tau}}\,e^{v^2\pi i/\tau}\vartheta_1\left(\frac{iv}{\tau}\middle|-\frac{1}{\tau}\right) \quad [25]$$

and

$$\vartheta_2(iv\,|\,\tau) = i\sqrt{\frac{i}{\tau}}\,e^{v^2\pi i/\tau}\vartheta_4\left(\frac{iv}{\tau}\middle|-\frac{1}{\tau}\right) \quad [26]$$

Therefore,

$$\mathcal{P}(\nu) - \mathcal{P}(\mu) > 0 \qquad [27]$$

and

$$M \frac{\mathcal{P}(\nu) - \mathcal{P}(\mu)}{\mathcal{P}'(\nu)} > 0 \qquad [28]$$

Consequently, equation [8] can be expressed as

$$z = M \frac{\mathcal{P}(\nu) - \mathcal{P}(\mu)}{\mathcal{P}'(\nu)} \cdot \left[\frac{2\nu\eta_3}{\omega_3}(s - \omega_3) + \log \frac{\sigma(s - \nu)}{\sigma(s + \nu)} \frac{\sigma(\omega_3 + \nu)}{\sigma(\omega_3 - \nu)}\right] \qquad [29]$$

in which the first term has been rewritten by substituting the relation stated in equation [15]. Moreover, at the point R, $z = i\gamma$, $s = 0$, and

$$\log \frac{\sigma(-\nu)}{\sigma(\nu)} \frac{\sigma(\omega_3 + \nu)}{\sigma(\omega_3 - \nu)} = \log \frac{\sigma(\nu + \omega_3)}{\sigma(\nu - \omega_3)} = i\pi + 2\nu\eta_3$$

Consequently, from equation [29]

$$M \frac{\mathcal{P}(\nu) - \mathcal{P}(\mu)}{\mathcal{P}'(\nu)} = \frac{\gamma}{\pi} \qquad [30]$$

By substituting this into equation [29], one has,

$$z = \frac{\gamma}{\pi}\left[\frac{2\nu\eta_3}{\omega_3}(s - \omega_3) + \log \frac{\sigma(s - \nu)}{\sigma(s + \nu)} \frac{\sigma(\omega_3 + \nu)}{\sigma(\omega_3 - \nu)}\right] \qquad [31]$$

while substitution of equation [30] into equation [11] yields

$$-\alpha = \frac{\gamma}{\pi}\left[2\frac{\nu\eta_3}{\omega_3}\omega_1 - 2\nu\eta_1\right] = -\frac{\gamma}{\pi}\frac{2\nu}{\omega_1}[\eta_1\omega_3 - \eta_3\omega_1]$$

If the Legendre relation

$$\eta_1\omega_3 - \eta_3\omega_1 = \pi/2$$

is applied, one obtains

$$\nu = \frac{\alpha}{\gamma}\frac{\omega_3}{i} \qquad [32]$$

Next the value of μ must be determined. Employing the relations $z = -\alpha + i\beta$ and $s = \mu$ at the point B, the following equation is derived from equation [31]

$$-\alpha + i\beta = \frac{\gamma}{\pi}\left[\frac{2\nu\eta_3}{\omega_3}(\mu - \omega_3) + \log \frac{\sigma(\mu - \nu)}{\sigma(\mu + \nu)} \frac{\sigma(\omega_3 + \nu)}{\sigma(\omega_3 - \nu)}\right] \qquad [33]$$

Thus, equations [15], [32], and [33] yield the constants ω_3, ν, and η. Because of the uniform distribution of potential, as is clear from the nature of the s-plane in Fig. 2, equation [31] indicates directly the relation between the original plane and the potential plane. It gives the potential function, $s = f(z)$, of the electric field, which is depicted in the z-plane and may be obtained by solving equation [31]. The next step is to expand these equations into the theta function $\vartheta(v)$, for the sake of convenience in numerical calculations.

Expression by the Theta Functions

In the first place, the addition theorem of the ζ-function, applied to equation [15], leads to

$$2\zeta(\nu) + \frac{\mathcal{P}'(\nu)}{\mathcal{P}(\nu) - \mathcal{P}(\mu)} = \frac{2\nu\eta_3}{\omega_3} \qquad [34]$$

On combining the following relation (8)

$$\zeta(u) = \frac{\eta_1 u}{\omega_1} + \frac{1}{2\omega_1}\frac{\vartheta_1'(v)}{\vartheta_1(v)} \qquad [35]$$

with the Legendre relation, $\eta_1\omega_3 - \eta_3\omega_1 = \pi/2$, one obtains

$$2\zeta(\nu) - \frac{2\nu\eta_3}{\omega_3} = \frac{\pi}{\omega_1}\left\{\frac{\alpha}{\gamma} + \frac{1}{\pi}\frac{\vartheta_1'(\nu_1)}{\vartheta_1(\nu_1)}\right\} \qquad [36]$$

On the other hand, from the relation (9)

$$\mathcal{P}'(\nu) = -\frac{\pi}{4\omega_1^3}[\vartheta_1'(0)]^2 \frac{\vartheta_2(\nu_1)\cdot\vartheta_3(\nu_1)\cdot\vartheta_4(\nu_1)}{[\vartheta_1(\nu_1)]^3} \qquad [37]$$

and equation [21], one gets

$$\frac{\mathcal{P}'(\nu)}{\mathcal{P}(\nu) - \mathcal{P}(\mu)} = -\frac{\pi}{\omega_1}[\vartheta_1'(0)]^2 \frac{\vartheta_2(\nu_1)\cdot\vartheta_3(\nu_1)\cdot\vartheta_4(\nu_1)}{[\vartheta_1(\nu_1)]^3} \frac{1}{\left[\frac{\vartheta_2(\nu_1)}{\vartheta_1(\nu_1)}\right]^2 + \left[\frac{\frac{1}{i}\vartheta_1(i\mu_1'')}{\vartheta_2(i\mu_1'')}\right]^2} \qquad [38]$$

Substituting equations [36] and [38] into equation [34], and solving for the term $[1/i\vartheta_1(i\mu_1'')/\vartheta_2(i\mu_1'')]^2$:

$$\left[\frac{1/i\vartheta_1(i\mu_1'')}{\vartheta_2(i\mu_1'')}\right]^2 = \frac{\vartheta_2(\nu_1)}{[\vartheta_1(\nu_1)]^3} \frac{1}{\alpha/\gamma + \frac{1}{\pi}\frac{\vartheta_1'(\nu_1)}{\vartheta_1(\nu_1)}} \left\{[\vartheta_2(0)]^2\cdot\vartheta_3(\nu_1)\cdot\vartheta_4(\nu_1) - \vartheta_1(\nu_1)\cdot\vartheta_2(\nu_1)\cdot\left[\frac{\alpha}{\gamma} + \frac{1}{\pi}\frac{\vartheta_1'(\nu_1)}{\vartheta_1(\nu_1)}\right]\right\} \qquad [39]$$

In the next place, consider the expansion of equation [33]. Introducing the well-known relation

$$\sigma(u \pm \omega_j) = \pm e^{\pm\eta_j u}\sigma(\omega_j)\cdot\sigma_j(u), \quad j = 1, 2, 3 \qquad [40]$$

one obtains

$$\frac{\sigma(\mu - \nu)}{\sigma(\mu + \nu)} = \frac{\sigma(\nu - i\mu'' - \omega_1)}{\sigma(\nu + i\mu'' + \omega_1)} \frac{\sigma(\nu + \omega_3)}{\sigma(\nu - \omega_3)} = e^{-2\nu(\eta_1 - \eta_3)} \frac{\sigma_1(\nu - i\mu'')}{\sigma_1(\nu + i\mu'')} \qquad [41]$$

Furthermore, since (10)

$$\sigma_1(u) = \frac{\vartheta_2(v)}{\vartheta_2(0)} e^{2\eta_1\omega_1 v^2} = \frac{\vartheta_2(v)}{\vartheta_2(0)} e^{\eta_1 u^2/2\omega_1} \qquad [42]$$

it is found that

$$\frac{\sigma_1(\nu - i\mu'')}{\sigma_1(\nu + i\mu'')} = e^{-i2\eta_1\nu\mu''/\omega_1} \frac{\vartheta_2(\nu_1 - i\mu_1'')}{\vartheta_2(\nu_1 + i\mu_1'')} \qquad [43]$$

Moreover, the ϑ-function may be represented by infinite products as follows (11)

$$\frac{\vartheta_2(\nu_1 - i\mu_1'')}{\vartheta_2(\nu_1 + i\mu_1'')} = \frac{\cos\pi(\nu_1 - i\mu_1'')}{\cos\pi(\nu_1 + i\mu_1'')} \frac{\prod_{n=1}^{\infty}\{1 + 2q^{2n}\cos 2\pi(\nu_1 - i\mu_1'') + q^{4n}\}}{\prod_{n=1}^{\infty}\{1 + 2q^{2n}\cos 2\pi(\nu_1 + i\mu_1'') + q^{4n}\}} \qquad [44]$$

Considering the relation

$$\log \frac{a+ib}{a-ib} = i\cdot 2\tan^{-1}\frac{b}{a} \qquad [45]$$

the logarithm of equation [44] becomes

$$\log \frac{\vartheta_2(\nu_1 - i\mu_1'')}{\vartheta_2(\nu_1 + i\mu_1'')} = i\cdot 2\tan^{-1}\left(\tan\frac{\pi\nu}{2\omega_1}\cdot\tanh\frac{\pi\mu''}{2\omega_1}\right)$$
$$+i\cdot 2\sum_{n=1}^{\infty}\tan^{-1}\left(\frac{2q^{2n}\sin\frac{\pi\nu}{\omega_1}\cdot\sinh\frac{\pi\mu''}{\omega_1}}{1+2q^{2n}\cos\frac{\pi\nu}{\omega_1}\cdot\cosh\frac{\pi\mu''}{\omega_1}+q^{4n}}\right) \qquad [46]$$

Substituting this equation into equation [43], one has

$$\log\frac{\sigma_1(\nu-i\mu'')}{\sigma_1(\nu+i\mu'')} = -i\frac{2\eta_1\nu\mu''}{\omega_1}$$
$$+i\cdot 2\tan^{-1}\left(\tan\frac{\pi\nu}{2\omega_1}\cdot\tanh\frac{\pi\mu''}{2\omega_1}\right) \qquad [47]$$
$$+i\cdot 2\sum_{n=1}^{\infty}\tan^{-1}\left(\frac{2q^{2n}\sin\frac{\pi\nu}{\omega_1}\cdot\sinh\frac{\pi\mu''}{\omega_1}}{1+2q^{2n}\cos\frac{\pi\nu}{\omega_1}\cdot\cosh\frac{\pi\mu''}{\omega_1}+q^{4n}}\right)$$

Also, the substitution of equation [47] into equation [33] yields

$$-\alpha+i\beta = \frac{\gamma}{\pi}\left[-\frac{i}{\omega_3}\pi\nu - i\frac{i}{\omega_3}\frac{\pi\nu\mu''}{\omega_1}\right.$$
$$+i\cdot 2\tan^{-1}\left(\tan\frac{\pi\nu}{2\omega_1}\cdot\tanh\frac{\pi\mu''}{2\omega_1}\right) \qquad [48]$$
$$\left.+i\cdot 2\sum_{n=1}^{\infty}\tan^{-1}\left(\frac{2q^{2n}\sin\frac{\pi\nu}{\omega_1}\cdot\sinh\frac{\pi\mu''}{\omega_1}}{1+2q^{2n}\cos\frac{\pi\nu}{\omega_1}\cdot\cosh\frac{\pi\mu''}{\omega_1}+q^{4n}}\right)\right]$$

From the imaginary part of equation [48] the following result is obtained:

$$\frac{\beta}{\alpha} = -\frac{\mu''}{\omega_1}+\frac{\gamma}{\alpha}\frac{2}{\pi}\left[\tan^{-1}\left(\tan\frac{\pi\nu}{2\omega_1}\cdot\tanh\frac{\pi\mu''}{2\omega_1}\right)\right.$$
$$\left.+\sum_{n=1}^{\infty}\tan^{-1}\left(\frac{2q^{2n}\sin\frac{\pi\nu}{\omega_1}\sinh\frac{\pi\mu''}{\omega_1}}{1+2q^{2n}\cos\frac{\pi\nu}{\omega_1}\cdot\cosh\frac{\pi\mu''}{\omega_1}+q^{4n}}\right)\right] \qquad [49]$$

On the other hand, at the surface of the electrode, it is clear that $s = \omega_1 + is''$ and $x = \alpha$. Substituting these coordinates into equation [31], one obtains

$$\frac{\gamma}{\alpha} = -\frac{s''}{\omega_1}+\frac{\gamma}{\alpha}\frac{2}{\pi}\left[\tan^{-1}\left(\tan\frac{\pi\nu}{2\omega_1}\cdot\tanh\frac{\pi s''}{2\omega_1}\right)\right.$$
$$\left.+\sum_{n=1}^{\infty}\tan^{-1}\left(\frac{2q^{2n}\sin\frac{\pi\nu}{\omega_1}\cdot\sinh\frac{\pi s''}{\omega_1}}{1+2q^{2n}\cos\frac{\pi\nu}{\omega_1}\cdot\cosh\frac{\pi s''}{\omega_1}+q^{4n}}\right)\right] \qquad [50]$$

Intensity of the Electric Field at the Electrode Surface

If the conjugate complex is denoted by $\mathfrak{K}$, the intensity of the electric field $\mathfrak{E}_s$ can be represented as

$$\mathfrak{E}_s = \mathfrak{K}\left[i\frac{ds}{dz}\right]_s \qquad [51]$$

where the suffix s means the electrode surface. Equations [3] and [30] yield

$$\frac{ds}{dz} = \frac{\pi}{\gamma}\frac{\wp(\nu)-\wp(\mu)}{\wp'(\nu)}\frac{\wp(s)-\wp(\nu)}{\wp(s)-\wp(\mu)} \qquad [52]$$

where $(ds/dz)_s$ proves to be a real number, because both $\wp(i\mu''+\omega_1)$ and $\wp(is''+\omega_1)$ are necessarily real when both $i\mu''$ and is'' are imaginaries, as is known from the nature of the $\wp$-function. Therefore:

$$\mathfrak{E}_s = -i\frac{\pi}{\gamma}\frac{\wp(\nu)-\wp(\mu)}{\wp'(\nu)}\frac{\wp(s)-\wp(\nu)}{\wp(s)-\wp(\mu)} \qquad [53]$$

Furthermore, this may be expressed in terms of the ϑ-function for the convenience of numerical calculation:

$$\mathfrak{E}_s = i\frac{\omega_1}{\gamma}\frac{1}{\frac{\alpha}{\gamma}+\frac{1}{\pi}\frac{\vartheta_1'(\nu_1)}{\vartheta_1(\nu_1)}\left[\frac{\frac{1}{i}\vartheta_1(is_1'')}{\vartheta_2(is_1'')}\right]^2-\left[\frac{\frac{1}{i}\vartheta_1(i\mu_1'')}{\vartheta_2(i\mu_1'')}\right]^2}\left[\frac{\frac{1}{i}\vartheta_1(is_1'')}{\vartheta_2(is_1'')}\right]^2+\left[\frac{\vartheta_2(\nu_1)}{\vartheta_1(\nu_1)}\right]^2 \qquad [54]$$

in which equations [17], [34], and [36] are taken together into account.

Fig. 3 to 7 show some examples of a tentative numerical calculation of the electrical field intensity on the electrode surfaces in an electrolytic cell whose width (2γ) is equal to the distance between the electrodes (2α). Although it is easily understood that the larger the electrodes and the nearer they are to the walls, the more uniform the electrical field intensity and the current distribution, this is shown in concrete and quantitative form in the figures. The per cent of current allotted to the inner and the outer surface of the electrode is given; total current in per cent is referred to over-all current when the electrodes touch the side walls, i.e., when $\beta = \gamma$.

The calculations shown in Fig. 3–7 were made for the

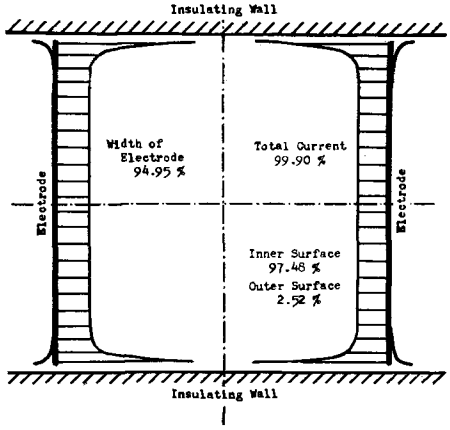

Fig. 3. Current distribution when the electrode width is 94.95% of the bath width.

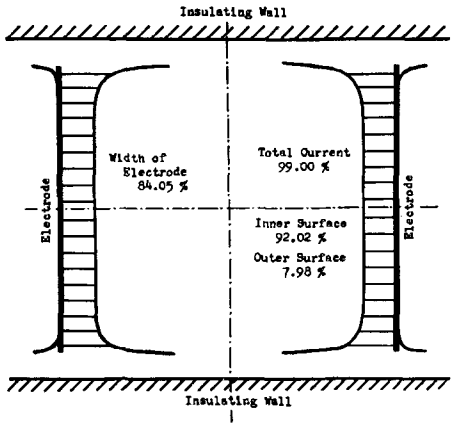

FIG. 4. Current distribution when the electrode width is 84.05% of the bath width.

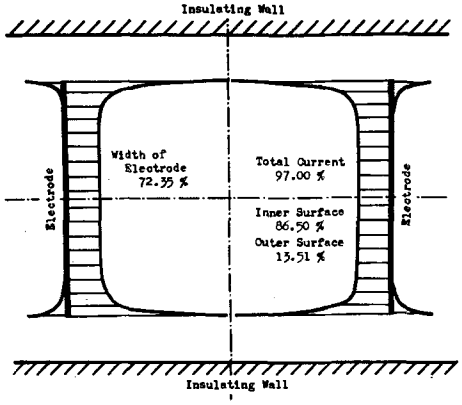

FIG. 5. Current distribution when the electrode width is 72.35% of the bath width.

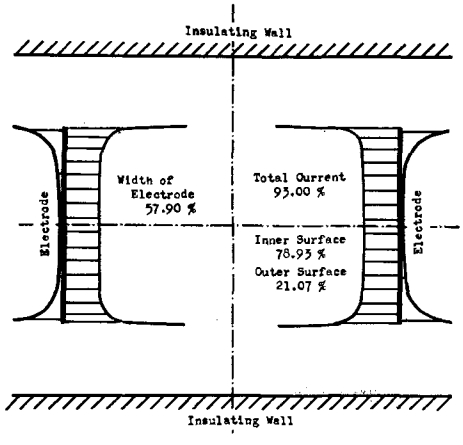

FIG. 6. Current distribution when the electrode width is 57.90% of the bath width.

special case where $\gamma/\alpha = 1$. Each new cell design requires an independent set of calculations, which are laborious and time-consuming. For this reason Fig. 8 has been prepared, as a more or less satisfactory approximation for practical use. The meaning and use of this figure are discusssed below.

Diagram of Current Distribution in the Electrolytic Cell

On the abscissa of Fig. 8 is scaled, from left to right, the percentage of the width of the electrode to that of the cell ($\beta/\gamma \times 100\%$), so that the scale from right to left shows

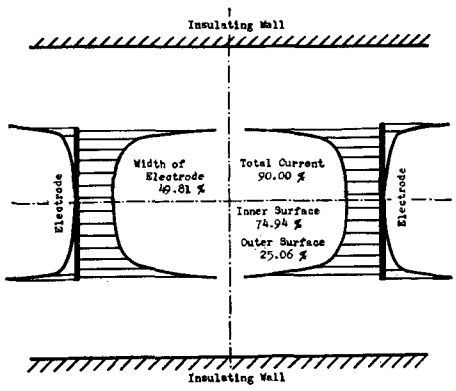

FIG. 7. Current distribution when the electrode width is 49.81% of the bath width.

the percentage of the gap between the edge of the electrode and the insulating wall [$(\gamma - \beta)/\gamma \times 100\%$]. The ordinate indicates the percentage of the electric current at the inner surface to the total current when read upward and that at the outer surface when read downward. The inner surface must carry 100% of the current when the electrode is as wide as the cell; the shares of both surfaces are equal in the extreme case of a point electrode. The current distribution is shown by the S-shaped lines, each of which represents a constant value of γ/α as labelled, from 1 to 100.

The finer lines numbered from 10 to 90 are the lines of equipercentage of the total current referred to the current when the electrodes touch the side walls. This percentage shows a characteristic decrement as the gap between electrode and wall grows larger.

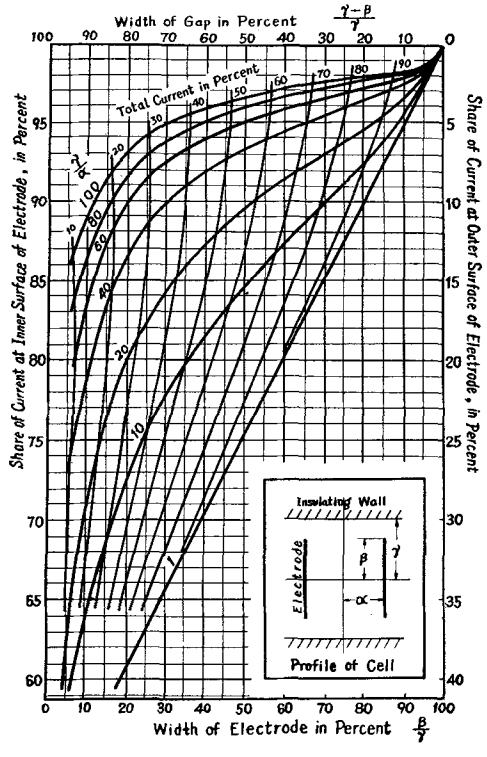

FIG. 8. Diagram of the current distribution at the suface of the electrode.

Explanation of Usage by a Numerical Example

The use of Fig. 8 can be clarified by consideration of a practical example. Assume electrodes 40 cm in width, 2 cm apart, immersed in a cell 50 cm wide. Then

$$\beta/\gamma \times 100 = (40/50) \times 100 = 80\%$$

$$\gamma/\alpha = 50/2 = 25$$

Although the diagram lacks a line at $\gamma/\alpha = 25$, one estimates the values: share of the inner surface, 95.5%; share of the outer surface, 4.5%. The current is about 85% of its value for the widest electrodes, since the point located above lies between the finer lines for 80% and 90%.

Discussion

In the analysis of the electric field shown in Fig. 2, the Weierstrass $\wp$-function was used for the Schwarz-Christoffel transformation. It is also possible to use Jacobi's function to arrive at the same conclusion, as Kiyono actually has done to confirm this method.

Although this investigation was confined to the effect of the side walls as stated earlier, similar analysis is possible in cases when side walls are sufficiently distant and back walls approach the electrodes. Such cases, however, are of small importance to industrial electrolytic cells.

As shown in Fig. 3 to 7, one may conclude that when cells of the same size and form are in question, larger electrodes cause better uniformity in the current distribution at the electrode surface, as far as the inner surface is concerned. This is not inconsistent with what experience has taught, but present results make the conclusion exact and concrete.

Electrodes which fit closely in the cell would seem at first glance to be ideal, since the current distribution is best, total current is highest for a given applied voltage, and power efficiency is greatest. But in actual practice technical difficulties arise, such as insufficient agitation of solution around the electrodes. When gases are evolved and must be expelled rapidly, as in the horizontal mercury

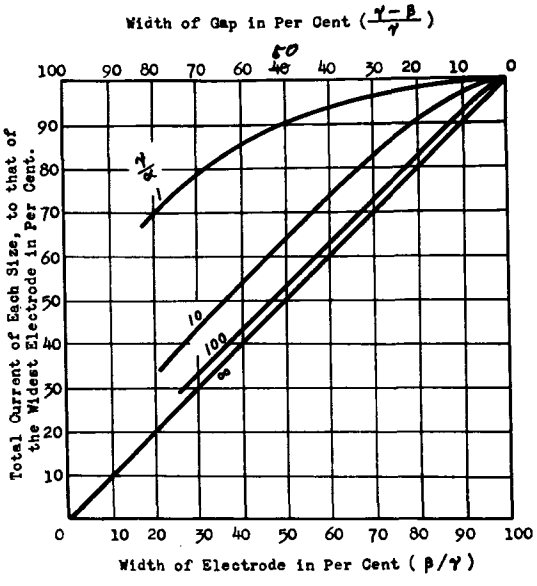

FIG. 9. Total current referred to the widest electrode

cathode chlorine cell, it is advisable to have wider gaps than otherwise necessary, between electrodes and cell walls. Such dilemmas are often encountered, and other viewpoints are necessary to find the most economical cell design.

In combination with this question, the S-curves in Fig. 8 may be considered. The ratio γ/α becomes nearly 100 in an electrolyzer 40 to 50 cm wide with the electrodes as close to each other as 0.5 cm, as is exemplified in the horizontal mercury cathode chlorine electrolyzer. This type of horizontal cell requires special consideration, since the mercury cathode covers the entire cell profile, and β and γ may be nearly equal. In this case, neither the total current nor the distribution at inner and outer anode surfaces change much for the ratios of γ/α between 50 and 100, as seen in Fig. 8. If β/γ becomes smaller than 95%, however, the ratio γ/α has more importance. Ordinary cells for redox and oxidation electrolysis have γ/α equal to 10 to 30, and there are scarcely any industrial cells with γ/α as low as 1. Examples might be found in cells for electroplating, but these will not be discussed here, because the shapes of the cathodes are variable and accessory anodes are often used, making the geometric form of the cell quite different from the present model. It is not rare in laboratories to encounter a case where γ/α is 0.1, as in the Haring cell used to test throwing power in electroplating, or when electrodes are simply inserted in a beaker. Although such a case is not shown in Fig. 8, it is almost identical with the line for $\gamma/\alpha = 1$.

Examination of the curves in Fig. 8 for high values of γ/α shows that, after a small abrupt access of current to the outer electrode surface as the gap between wall and electrode is opened, the distribution changes only a few per cent until the gap width becomes very large. In this case, when the gap width is small, most of the current to the outer surface is concentrated at the edges.

On the other hand the larger the value of γ/α, the more rapidly the total current (at constant applied voltage) diminishes with decreasing electrode area (relative to cell width). This is illustrated more clearly in Fig. 9, where the ordinates represent total current, relative to maximum current with no gap. When $\gamma/\alpha = \infty$, indicating an infinitely wide electric field, the total current is simply proportional to electrode area. This is nearly true where $\gamma/\alpha = 100$; but when $\gamma/\alpha = 1$, the total current remains near its maximum value while the electrode area is reduced as much as 50%. This factor should not be overlooked in cell design, especially for large cells.

Summary

The electric field in an electrolytic cell has been analyzed as a function of electrode width and distance between electrodes, both relative to cell width, by the method of conformal transformation. The results obtained have been illustrated with various examples. The current distribution between inner and outer electrode surfaces, and the total current at constant applied voltage, as a function of relative electrode size, have been plotted in a comprehensive diagram as an aid in the design of new cells. For mathematical simplicity, the effects of the back walls and of electrode polarization have been neglected, but it is believed

that this will not detract from the usefulness of the diagram for industrial cell design.

ACKNOWLEDGMENTS

The author's thanks are due to Professor T. Kiyono and Professor G. Araki for their useful suggestions and kindly advice.

Manuscript received March 23, 1953.

Any discussion of this paper will appear in a Discussion Section to be published in the December 1956 JOURNAL.

REFERENCES

1. C. KASPER, *Trans. Electrochem. Soc.*, **77**, 353, 365 (1940); *ibid.*, **78**, 131, 147 (1940).
2. C. WAGNER, *This Journal*, **98**, 116 (1951).
3. T. SASAKI, *J. Aero. Res. Inst. Tokyo Imp. Univ.*, **4**, 149 (1928).
4. L. ROSENHEAD, *Proc. Roy. Soc. London*, **132**, 127 (1931).
5. S. TOMOTIKA, *J. Aero. Res. Inst. Tokyo Imp. Univ.*, **8**, 157 (1934).
6. E. T. WHITTAKER AND G. N. WATSON, "A Course of Modern Analysis," 4th Ed., p. 448, Cambridge Univ., Cambridge, (1927).
7. S. TOMOTIKA, "Daen Kansu-ron" (Theory of the Elliptic Functions), 2nd ed., pp. 139 & 170, Kawade & Co., Tokyo (1943). In Japanese.
8. S. TOMOTIKA, *ibid.*, p. 152.
9. S. TOMOTIKA, *ibid.*, p. 156.
10. S. TOMOTIKA, *ibid.*, p. 151.
11. S. TOMOTIKA, *ibid.*, p. 148.

Technical Review

Electrochemical Techniques in the Thermodynamics of Metallic Systems

R. A. Oriani

Research Laboratory, General Electric Company, Schenectady, New York

ABSTRACT

The use of galvanic cells employing nonaqueous electrolytes and operating at elevated temperatures is a relatively little known technique. Some of the details for the successful operation of such cells are described both for liquid and for solid alloys. The kind and the accuracy of the information obtained are discussed. Applications to the determination of phase diagrams are outlined, and the possibilities of obtaining surface free energies are discussed. A comprehensive bibliography of galvanic cell studies of metallic systems is presented.

Introduction

This paper is concerned only with the electrochemical techniques of use in studying the thermodynamics of metallurgical systems. In practice, the only such technique is that of the galvanic cell, which can be used to study both thermodynamic magnitudes and phase relationships. The first section of the paper is devoted to a brief account of the basic relations. The second section discusses the experimental procedures in some detail, and a subsequent section presents some examples of experimental results. The physical significance of these results is beyond the scope of this paper.

General Relations

The type of galvanic cell useful in alloy studies can be symbolized by

$$A(\mathrm{l, s})\,|\,A^{z+}, \text{ ionic electrolyte }|\,A_xB_y(\mathrm{l, s})$$

The more electropositive metal, A, and the metallic solution of that metal, may be in the solid or in the liquid state, but the physical set-up of the cell will be different for the different possibilities. At each electrode there is an equilibrium between the A^{z+} in the ionic electrolyte and the metallic state of A, so that the open-circuit emf reflects the difference in activity of species A in the two electrodes. Since one gram atom of metal A is transferred from pure A electrode to the alloy electrode by a current of $z\mathbf{F}$ coulombs ($\mathbf{F}$ = the Faraday equivalent = 23,066 cal/volt), the amount of work required is

$$-z\mathbf{F}E = \overline{\Delta G_A} \equiv \overline{G} - G_A^0 \qquad \text{(I)}$$

where E is the emf, $\overline{G}$ is the partial molar Gibbs free energy of A in the metallic solution, and G_A^0 is the molar Gibbs free energy of pure A in the state of aggregation of the electrode A. If one selects pure A at the existing state of aggregation of the A-electrode at temperature T as the reference state, equation (I) becomes (R = gas constant = 1.987 cal/deg. g-atom)

$$-z\mathbf{F}E = RT \ln a_A - RT \ln 1 = RT \ln a_A \qquad \text{(II)}$$

It is generally preferable to use as reference state the pure metal of the same state of aggregation as that of the metallic solution at the temperature in question. A change of reference state with respect to state of aggregation may readily be made by remembering that the free energy difference between pure liquid and pure solid is given by

$$G_{\mathrm{liq}}^0 - G_{\mathrm{sol}}^0 = \Delta S^0(T_0 - T) \qquad \text{(III)}$$

in which ΔS^0 is the entropy of fusion of the pure reference substance, assumed independent of the temperature, and T_0 is the melting temperature of the pure reference substance. For example, suppose that the measured E is that developed by a solid solution against a pure liquid electrode. Then, the activity calculated by (II), $\ln a_A' = -z\mathbf{F}E/(RT)$, will refer the activity of A in the solid solution to the pure liquid A. In order to refer the activity to pure solid, the following scheme is useful:

$$\text{Add} \begin{cases} A_{(l)} = A(B)_{(s)},\ \overline{\Delta G_{A'}} = RT \ln a_A' \\ A_{(s)} = A_{(l)},\ \Delta S_A^0(T_0 - T) \end{cases}$$

$$\overline{A_{(s)} = A(B)_{(s)},\ \overline{\Delta G'} + \Delta S_A^0(T_0 - T)}$$

$$= \overline{\Delta G_A} = RT \ln a_A$$

Measuring the emf as a function of temperature, as long as each electrode is single-phased, yields the partial molar entropy of solution, $\overline{\Delta S_A}$, since $(\partial E/\partial T)_x = (\partial/\partial T)\,(-\overline{\Delta G_A}/z\mathbf{F}) = \overline{\Delta S_A}/(z\mathbf{F})$. The reference state for this quantity is again the state of aggregation of the pure electrode actually employed, and changes in reference state may be carried out by a scheme analogous to that given above for the free energy. The partial molar enthalpy of solution, $\overline{\Delta H_A}$, may be calculated from the relation $\overline{\Delta G_A} = \overline{\Delta H_A} - T\overline{\Delta S_A}$, and the same remarks apply to this quantity.

After measurements of the partial molar properties of component A have been carried out as a function of concentration, the partial molar properties of the second constituent in the binary system may be obtained by

graphical integrations of the Gibbs-Duhem equation. The most convenient form for graphical integration is

$$\overline{\Delta A_B}^E(x) = \int_0^X \frac{\overline{\Delta A_A}^E}{(1-x)^2}\,dx - \frac{\overline{x\Delta A_A}^E}{1-x} \qquad \text{(IV)}$$

where $\overline{\Delta A_i}^E$ represents the excess partial molar property (the free energy, entropy, or enthalpy) of component i, and x is the mole fraction of component A. The excess partial molar property is defined relative to the value of that property for an ideal solution, i.e.,

$$\overline{\Delta A_i}^E = \overline{\Delta A_i} - \overline{\Delta A_i}\,(\text{ideal}) \qquad \text{(V)}$$

The excess integral molar properties may be formed by combining the excess partial molar properties of the two components:

$$\Delta A^E = \overline{x\Delta A_A}^E + \overline{y\Delta A_B}^E \qquad \text{(VI)}$$

Darken (1) and Wagner (2) have presented computational methods for ternary systems.

Experimental Details

General Considerations (3)

Implicitly behind the above calculations is the assumption that the galvanic cell has behaved reversibly in order that the data be thermodynamically meaningful. From an empirical point of view, the criteria of reversibility are the time-independence of an emf at constant temperature, the reproducibility of a value of emf irrespective of whether it is approached from the high temperature or from the low temperature side, and recoverability of a value of emf after passage of a small amount of current through the galvanic cell in either direction. In order to achieve reversibility, the experimental conditions must be adjusted in the light of the following considerations. First, the electrolyte must exhibit only ionic conductivity, and the valence of the ion of the more electropositive metal as it exists in the electrolyte must be definite and known. These conditions follow from the necessity that the partial molar free energy be described by equation (I).

Second, only one reaction should occur at the electrode interface: $A \rightleftharpoons A^{z+} + ze$. This implies that oxidizing and reducing agents must be avoided in the electrolyte, in the gaseous atmosphere above the electrolyte, and in the vessel material. It also means that the extent of the analogous reaction, $B \rightleftharpoons B^{p+} + pe$, for the less electropositive component must be negligible. One can estimate the extent of this reaction by calculating the free energy of the reaction

$$zB + pACl_z \rightleftharpoons zBCl_p + pA \qquad \text{(VII)}$$

if, for example, chloride is the anion of the electrolyte. If the equilibrium point for the above reaction is not sufficiently far toward the left, it may be possible that changing to some other anion would increase the disparity between the metals A and B.

Third, it is necessary that the temperature of operation be high enough to enable diffusion to equalize activity gradients between the interior and the surface of the electrode. Such gradients will come about because of the finite value of the equilibrium constant of reaction (VII), and because small flows of current such as inevitably accompany the balancing of the potentiometer circuit used for measurement of the emf will change the concentration of electropositive metal at the electrode-electrolyte interface. Experience has shown that operating temperatures not lower than 0.3 or 0.4 of the absolute melting temperature of the alloy are suitable.

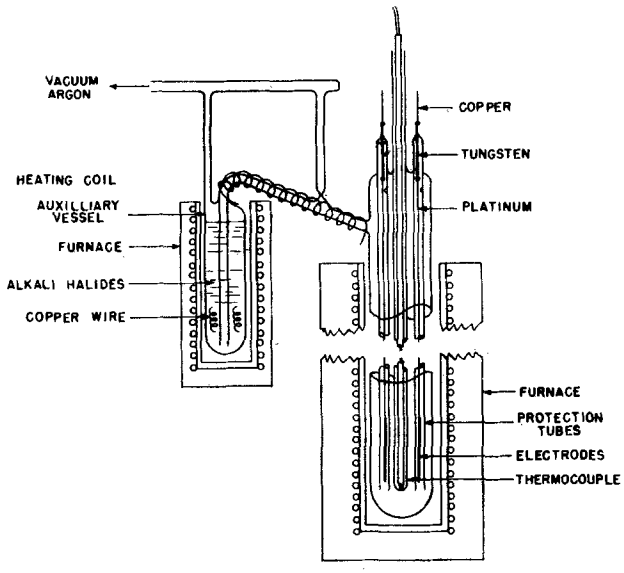

FIG. 1. Galvanic cell employed for solid electrodes at high temperatures.

In addition to considering the reversibility of the cell, attention must be paid to minimizing the thermoelectric emf developed by the cell, which adds algebraically to the purely galvanic emf. The furnace gradient should be as small as possible, and the thermoelectric effect should be measured in separate experiments in which all experimental conditions of the main experiment are reproduced except that the electrolyte is omitted, and the alloy and reference electrodes are interconnected within the cell.

Constructional Details (4)

The construction of a galvanic cell that has been found useful for the study of solid alloys with a solid reference electrode is shown in Fig. 1. The electrodes are spot-welded to the lead wires made of tungsten or of platinum; the lead wires are spot-welded to tungsten-Pyrex seals at the top, and connection to the potentiometer circuit is made by copper clips. This cell is designed to be used up to about 1100°C with mixtures of alkali metal chlorides as the electrolyte. Silica is an excellent construction material for use with fused chlorides as long as the latter are free of water. The cell shown in Fig. 1 has silica tubes surrounding each electrode in order to avoid accidental contact among the electrodes, and in order to reduce diffusive and convective transport of material through the electrolyte. This latter purpose is important because the finite magnitude of the equilibrium constant for the reaction

$$zB + pA^{z+} \rightleftharpoons zB^{p+} + pA \qquad \text{(VIII)}$$

furnishes a mechanism for the transport of metal from one electrode to another, with a consequent change in composition.

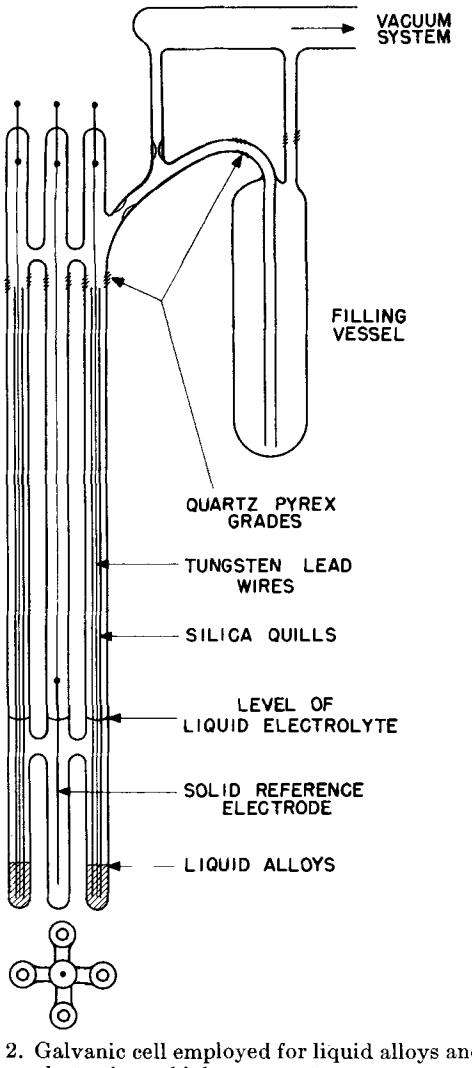

FIG. 2. Galvanic cell employed for liquid alloys and solid reference electrode at high temperatures.

Other electrolytes may be found useful as long as they are ionic conductors, have rather low vapor pressures, are stable at the temperatures involved, and a construction material can be found that is inert toward them. These requirements restrict the possibilities markedly. Hauffe and Vierk (5), Vierk (6), Kubaschewski and Huchler (7), Frauenschill and Halla (8), and Croatto and Bruno (9) have employed solid glasses as electrolytes. Molten metaborates may be used. Vatolin and Esin (10) have used a molten mixture of oxides and sodium sulfide, and Sanbongi and Ohtani (11) employed a "carbide slag" dissolved in high melting oxides for the measurements of the activity of sulfur and of carbon, respectively, in molten iron. Sometimes the charge carried by the relevant ion in the electrolyte may be in doubt and accessory experiments may be necessary to determine it. The ceramic known as Mullite is a useful construction material for holding some liquid oxides; its utility is enhanced by the fact that it can be joined to Nonex glass. The electrolyte most commonly used in high temperature galvanic cells is the eutectic mixture of KCl and LiCl, which melts at 360°C. Lower melting temperatures may be obtained by adding RbCl to the eutectic mixture.

Fig. 2 shows a cell designed for use at about 1100°C for the combination of liquid alloys and solid reference electrode. The tungsten or platinum lead wires are enclosed in thin-walled silica quills which are kept in position by being spotted near their upper ends to the silica vessel. This cell design provides a long diffusion path between electrodes through the electrolyte.

Operational Details

Once the galvanic cell has been constructed and well-homogenized alloys of known composition have been sealed in place, there remains the pretreatment of the electrolyte and of the cell. The objective of the pretreatment is to rid the electrolyte and cell walls of all deleterious material, generally moisture, oxidizing agents, and material decomposable at the temperatures of cell operation. The method to be used depends on the nature of the electrolyte. The procedure used by the writer for the KCl-LiCl mixture is described as illustrative of the necessary precautions.

The salt mixture is introduced into a filling vessel, such as shown in Fig. 2. An amount of the lower chloride of the more electropositive metal is added; in general, the amount of ACl_z to be added should be quite small, 0.5% or less, in order to restrain the formation of B^{z+} ions according to equation (VIII). However, there is indication in the literature that in some cases, too small an amount of ACl_z will lead to irreversible behavior of the cell, so that the optimum amount must be determined by trial. In the filling vessel is placed a clean strip or wire of the pure metal B which serves to reduce any higher chlorides of B that may be present.

After the filling vessel and cell are interconnected and attached to a vacuum system, both the filling vessel and cell are heated under vacuum in separately controlled furnaces. The salt mixture is maintained liquid at 500°C for about one week in order to destroy any chlorates present, and to desiccate the salts thoroughly. The cell is maintained at as high a temperature consistent with the vapor pressure of the metals involved in order to desiccate the walls of the cell thoroughly. After this treatment, the electrolyte is transferred to the cell by first sealing off the vertical connecting tube between cell and vacuum system, then admitting pure helium over the liquid in the filling vessel to force the liquid up and over into the cell. The auxiliary heating coil shown in Fig. 1 is not necessary if gas flames are used to preheat the connecting tube. After all the electrolyte has been transferred, more helium is admitted until the pressure is about half an atmosphere, whereupon the cell is sealed off. The helium serves to repress volatilization of the fused salts. Using this method of preparation, the writer has been able to operate a galvanic cell for nine months after which the silica did not show any attack at all. Unfortunately, this electrolyte wets silica so well that if the salts are allowed to freeze the cell invariably breaks.

After filling the cell, it is usually found necessary to wait from some hours to days before the electrode emf's become stable at constant temperature. The reason for this aging period is not clear, though it may be associated with the establishment of the equilibrium (VIII). Since

this equilibrium cannot be satisfied simultaneously for various electrodes of different compositions, it seems best to use electrodes of similar compositions when data of highest accuracy are required. After the electrode emf's become stable, data can be taken at a speed that depends on the furnace constant, whether the alloys are liquid or solid, and whether or not the alloys are undergoing a metallurgical transformation. With liquid alloys, data points can be obtained as rapidly as the furnace permits a change of temperature. With solid alloys, the waiting times at constant temperature should be such that no further changes are observed, the magnitude of the permissible change in the emf being regulated by the accuracy desired. In any case, reproducibility of measurements taken with decreasing and with increasing temperatures is the final criterion of the adequacy of the procedure. Any one emf reading should be done by a potentiometer the key of which should be depressed only momentarily since the galvanic cell is easily polarized.

Experimental Information

The primary result of galvanic cell investigations of the type here described is information relating to the thermodynamics of solutions. This includes numbers for the thermodynamic activities of the constituents and, therefore, the free energy of solution, i.e., of formation, the partial and integral enthalpies of solution, and the partial and integral entropies of solution. In principle, it is also possible to measure the deviation of the heat capacity of the alloy from the Kopp-Neumann rule of additivity by measuring the variation of the enthalpy of solution with temperature, but in practice the accuracy of the measurements is almost never great enough. Useful tabulations of results of galvanic cell studies are given by Wagner (3), Kubaschewski and Evans (4), and by Chipman and Elliott (12) for liquid alloys.

It is difficult to assess the accuracy of emf studies. The limiting factor is certainly not the accuracy with which a voltage may be measured, but usually is associated with the extent to which ions of the more noble metal are produced. Less subtle are the errors associated with temperature measurement, chemical analysis of the alloys, and failure to correct for thermoelectric effects. It sometimes happens also that investigators fail to wait long enough for metallurgical changes, such as changes of phase, or of degree of order, so that equilibrium is not achieved in the time allotted.

Measurement of entropies of solution, depending as they do on the temperature variation of an emf, may have a relative error of five to ten times that in the value of the free energy itself. The computation of the partial molar property of component B from the measured values of A also introduces error, not only because of the errors inherent in a graphical integration, but also because of the necessary extrapolation to $x = 0$ of the integrand. It is in this connection that the use of excess partial molar quantities in equation (IV) is advantageous, because then the integrand extrapolates to a finite value as $x \rightarrow 0$ rather than to negative infinity as occurs when partial molar $\overline{\Delta G_A}$ and $\overline{\Delta S_A}$ are used. The calculation of the enthalpy from the free energy and the product of temperature and entropy depends on the difference of two numbers, so that the errors of each accumulate in the difference. Therefore, it is very worth while to carry out independent calorimetric determinations of the enthalpy of solution.

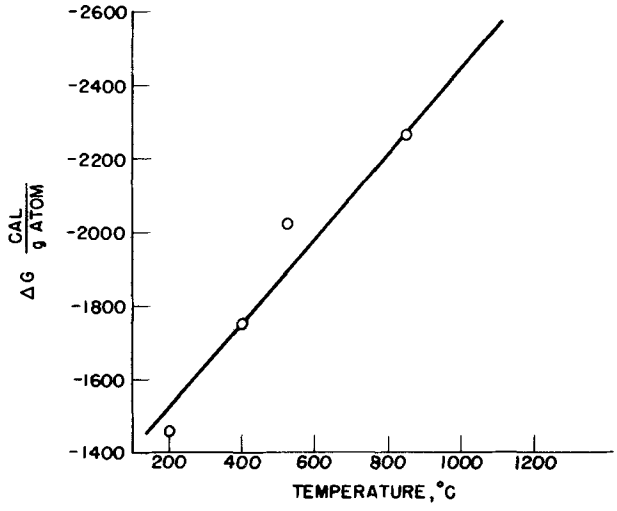

Fig. 3. Galvanic cell results for the integral molar free energy of formation of solid $Ag_{1/2}Au_{1/2}$: 200°C, solid AgCl as electrolyte (17); 400°C, solid glass as electrolyte (7); 527°C, liquid KCl + AgCl as electrolyte (16); 850°C, liquid KCl + LiCl + AgCl as electrolyte (18).

Empirically, there are two ways of estimating[1] the accuracy of galvanic cell measurements of thermodynamic properties. The first is to compare the results of galvanic cell work of various investigators of the same alloy system, particularly when different electrolytes are used. The second way is to compare galvanic cell results with those from other techniques. As an example of the use of different electrolytes, although by the same investigators (13), there are the galvanic cell studies on liquid Pb-Bi solutions using both LiCl-KCl and sodium acetate as electrolytes, between which excellent agreement exists. The liquid Cd-Sb system has been investigated by the emf technique both by Seltz and DeWitt (14), and by Chipman and Elliott (15), again with excellent agreement. Fig. 3 shows the results of four galvanic cell investigations (7, 16–18), at different temperatures and with four types of electrolytes, of solid Ag-Au alloys. Table I presents the enthalpy of formation derived from the same measurements; the agreement among the ΔH values is not so good as that shown by the ΔG-T results. Table II shows the excellent agreement obtained by two galvanic cell investigations (19, 20) using the same electrolyte with solid, disordered $Au_{1/2}Cu_{1/2}$ both for the ΔH and the ΔS of solution. These examples are merely illustrative, and certainly do not exhaust the available cases where good agreement exists among various galvanic cell studies.

A comparison of the results of galvanic cell studies with those of other thermodynamic techniques is more pertinent. Hildebrand and Eastman's (21) vapor pressure measurements on thallium amalgams agree within a few per cent with the emf measurements of Richards and Daniels (22). Schmahl's (23) measurements of the activity of Ag in solid Ag-Au alloys at 550° by a chemical equilibration technique agree very well with the galvanic

TABLE I. *Heat of formation of solid* $Ag_{1/2}Au_{1/2}$ *from galvanic cell studies*

ΔH, cal/gram atom	Reference
−1300	(16)
−947	(17)
−950	(7)
−970	(18)

TABLE II. *Heat and entropy of formation of disordered* $Au_{1/2}Cu_{1/2}$ *from galvanic cell studies*

ΔH, cal/gram atom	ΔS, cal/deg.-g.atom	Reference
−1230	1.26	(19)
−1200	1.31	.20)

cell results at 525°C of Wagner and Engelhardt (24). Gonser's (25) determination of the activities in liquid Pb-Bi alloys agree very well with the emf results of Strickler and Seltz (13). The ΔH of solution of solid $Cu_{3/4}Au_{1/4}$ from emf measurements (20) was found to be −1080 cal/gram atom at 427°C, which compares favorably with the calorimetrically determined value (26) of −1124 ± 55 cal/gram atom at 0°C. Similarly, the emf value (18) for the ΔH of solution for solid $Ag_{0.42}Au_{0.58}$ is −940 cal/gram atom at 850°, to be compared with a calorimetric value (27) of −1010 ± 25 cal/gram atom at 0°C.

The galvanic cell can be used to yield information not only on the thermodynamic properties of the solution referred to its constituents, but also on the phase relations within the alloy system. Such information is obtained from the principle that across a two-phase region an isothermal line is also an isoactivity line; it is implied that the identical reference state is used for any one component in all the phases concerned. Dunkerley and Mills (28) give a valuable review of the use of emf data in establishing phase boundaries; in this connection the monograph by Lumsden (29) should also be consulted. There is space here to refer only to a case where the galvanic cell technique proved particularly apt in establishing phase boundaries (20). Fig. 4 shows the phase relationships about the superlattices in CuAu. The solid points were obtained directly from the temperatures at which the emf-temperature curves showed inflections; the open points were obtained from the measurements of activity and the condition of isoactivity across a two-phase field. The results show that the superlattices in this system are Gibbsian phases, a question which has been the topic for much debate.

Applications to Interfaces

The galvanic cells under consideration in this paper depend for their success, among other factors, on diffusive interchange between the interior of the electrode and the electrode-electrolyte interface. A galvanic cell, $Cu\,|\,Cu^{++}$ aq $|$ calomel electrode, operating at room temperature can respond only to the atoms of copper directly in contact with the aqueous electrolyte. Tragert and Robertson (30) used such a cell, and, by amalgamating the surface of single crystals of copper to provide a mechanism for surface mobility, have been able to show qualitatively that the oxidation potential of the copper is dependent on the crystallographic configuration of the atoms on the surface, and that the (111) plane has the lowest oxidation potential, and hence presumably the lowest activity.

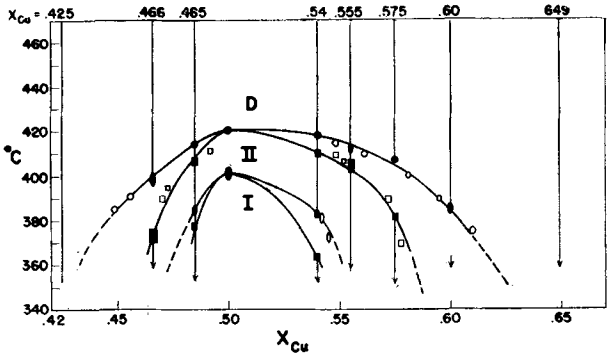

FIG. 4. Phase relationships about the composition $Cu_{1/2}Au_{1/2}$ as established by the galvanic cell technique. *D* represents the f.c.c. disordered solid solution, II represents the orthorhombic superlattice, and I the tetragonal superlattice.

However, a galvanic cell may in principle be used to obtain quantitative, equilibrium information on interfacial free energy. The following experiment is proposed as a method for obtaining the surface tension of a solid and its temperature variation, that is, the surface entropy. Set up the cell, $Ag_{(s)}|\ Ag^+$, KCl, LiCl $|Ag_{(s)}$, where silver is used as an example. One electrode is a pure silver bar of normal diameter, 1/16 in. or larger; the other electrode is a very fine wire of uniform diameter, say 0.0005 in., of the same silver. The emf between these electrodes, after correction for any thermoelectric emf, will depend on the diameter, d, of the narrow wire and the interfacial free energy of silver, σ, according to the relation

$$E = -\frac{2\sigma V_m}{z\mathbf{F}d} \qquad \text{(IX)}$$

where V_m is the molar volume of the metal. Using 1000 ergs/cm² as an estimate for the interfacial energy of silver, the observed emf would be about 20 μv, a magnitude within experimental accessibility. This experiment would yield the interfacial free energy of the metal-fused salt interface, a quantity of lesser immediate theoretical significance than the interfacial free energy of the metal-vacuum interface.

Acknowledgment

This work was supported by AEC Contract No. W-31-109-Eng-52.

Manuscript received July 26, 1955. This paper was prepared for delivery before the Cincinnati Meeting, May 1 to 5, 1955.

Any discussion of this paper will appear in a Discussion Section to be published in the December 1956 JOURNAL.

REFERENCES

1. L. S. Darken, *J. Am. Chem. Soc.*, **72**, 2909 (1950).
2. C. Wagner, "Thermodynamics of Alloys," Chap. 1, Addison-Wesley Press, Cambridge, Mass. (1952).
3. Ref. 2, Chap. 6.
4. For other designs, *see* O. Kubaschewski and E. L. Evans, "Metallurgical Thermochemistry," Chap. 2, Academic Press, New York (1951).
5. K. Hauffe and A. L. Vierk, *Z. Elektrochem.*, **53**, 151 (1949).
6. A. L. Vierk, *ibid.*, **54**, 436 (1950).
7. O. Kubaschewski and O. Huchler, *ibid.*, **52**, 170 (1948).
8. H. Frauenschill and F. Halla, *ibid.*, **53**, 144 (1949).
9. U. Croatto and M. Bruno, *Gazz. chim. Ital.*, **79**, 379 (1949).
10. N. A. Vatolin and O. A. Esin, *Zhur. Obshchei Khim.*, **24**, 795 (1954).
11. K. Sanbongi and M. Ohtani, *Sci. Rep. Res. Insts. Tohoku Univ., Ser. A*, **4**, 59 (1952).
12. J. Chipman and J. F. Elliott, in "Thermodynamics in Physical Metallurgy," American Society for Metals monograph (1950).
13. H. S. Strickler and H. Seltz, *J. Am. Chem. Soc.*, **58**, 2084 (1936).
14. H. Seltz and B. J. DeWitt, *ibid.*, **60**, 1305 (1938).
15. J. F. Elliott and J. Chipman, *Trans. Faraday Soc.*, **47**, 138 (1951).
16. A. Olander, *J. Am. Chem. Soc.*, **53**, 3577 (1931).
17. A. Wachter, *ibid.*, **54**, 4609 (1932).
18. R. A. Oriani, *Acta Metallurgica, to be published.*
19. F. Weibke and U. von Quadt, *Z. Elektrochem.*, **45**, 715 (1939).
20. R. A. Oriani, *Acta Met.*, **2**, 608 (1954).
21. J. H. Hildebrand and E. D. Eastman, *J. Am. Chem. Soc.*, **37**, 2452 (1915).
22. T. W. Richards and F. Daniels, *ibid.*, **41**, 1732 (1919).
23. N. G. Schmahl, *Z. anorg. u. allgem. Chem.*, **266**, 1 (1951).
24. C. Wagner and G. Engelhardt, *Z. physik. Chem.*, **A159**, 241 (1932).
25. U. Gonser, *Z. physik. Chem. N.F.*, **1**, 1 (1954).
26. L. R. Rubin, J. S. L. Leach, and M. B. Bever, *J. Metals*, **7**, 421, (1955).
27. L. B. Ticknor and M. B. Bever, *ibid.*, **4**, 941 (1952).
28. F. J. Dunkerley and G. J. Mills, in "Thermodynamics in Physical Metallurgy," American Society for Metals monograph (1950).
29. J. Lumsden, "Thermodynamics of Alloys," The Institute of Metals, London (1952).
30. W. E. Tragert and W. D. Robertson, *This Journal*, **102**, 86 (1955).

Bibliography of Galvanic Cell Studies of Metallic Systems

The numbers in brackets following the temperature range and the composition range indicate the number of temperatures and of compositions studied in the cases where it is convenient so to indicate. The state of aggregation of the alloy electrodes is signified in the fourth column by S for solid and L for liquid. This compilation is intended to be as comprehensive as possible up to June 1955, and is based on a preliminary list prepared by Leslie Seigle and David Turnbull, General Electric Research Laboratory Report 108. The aid of W. K. Murphy in checking the references is gratefully acknowledged.

System	Temp. range, °C	Comp. range, mole % of 1	State	Reference
1 *2*				
Ag-Al	370–550 [3]	5–95 [14]	S	(1)
Ag-Au	1085	26–85 [5]	L	(2)
	1030–1140	11–73 [11]	L	(3)
	413–774	8–80 [7]	S	(2)
	850	11–73 [8]	S	(3)
	200–430	15–86 [7]	S	(4)
	720–890	25–94	S	(5)
	300–630	4–73	S	(6)
Ag-Cd	410–450 [5]	0.5–5.2 [6]	L	(7)
	400–500 [2]	20–60	S	(8)
Ag-Cd-Hg	16	[11]	L	(61)
Ag-Hg-Pb	17	[9]	L	(61)
Ag-Hg-Zn	16	[8]	L	(61)
Ag-Sb	430–470 [2]	68–98	S	(9)
Ag-Sn	627	0–70 [9]	L	(10)
	333–412 [5]	0.6–14 [10]	L	(11)
Au-Bi	600–800 [3]	5–79 [22]	L	(12)
Au-Cd	250–730	2–84 [62]	S	(17)
Au-Cd-Hg	16	[8]	L	(61)
Au-Cu	390–605	14–93 [8]	S	(2)
	400–850 [6]	10–93 [9]	S	(13)
	345–490	23–57 [12]	S	(14)
	930–1040	15–85 [8]	L	(3)
	250–700	5–85 [22]	S	(15)
Au-Hg-Pb	17	[9]	L	(61)
Au-Hg-Zn	16	[13]	L	(61)
Au-Ni	700–900	5–95	S	(16)
Au-Pb	450–800	4–79 [18]	L	(18)
Au-Sb	315–355	50–75	S	(19)
Au-Sn	269–370 [3]	0.2–5.5 [10]	L	(11)
	500–600	25–90 [13]	L	(20)
Au-Tl	600–800 [3]	10–82 [17]	L	(12)
Ba-Hg	25	0.16×10^{-3}–3.8×10^{-3}	L	(60)
Bi-Cd	420–580 [4]	14–89 [16]	L	(21)
	400–600	5–90 [10]	L	(22)
	400–650	10–89	L	(33)
Bi-Cd-Pb	380–600	[11–94] Cd; Pb/Bi = 0.5–1.9	L	(23)
Bi-Cd-Sn	410–475 [5]	[5–90] Cd; [0–75] Sn [9]	L	(24)
Bi-Ce-Hg	18	[10]	L	(61)
Bi-Pb	124–213	5–33	S	(25)
	360–480 [7]	15–89 [8]	L	(25)
	475–665 [2]	28–92 [7]	L	(2)
Bi-Sn	330	23–92 [9]	L	(2)
	412–500 [6]	16–90 [9]	L	(26)
Bi-Tl	120–295	3–84	S	(27)
	270–480 [2]	17–80 [6]	L	(2)
	495	5.5–87.5 [8]	L	(62)
Bi-Zn	600	3–94 [19]	L	(28)
C-Fe	1440–1540	0.1–4.4 [13]	L	(29)
Cd-Cu	410–550 [5]	91.5–99.6 [7]	L	(7)
Cd-Cu-Hg	16	[8]	L	(61)
Cd-Hg	25–75 [3]	1–100 [32]	L	(30)
	25	10^{-6}–3.8 [9]	L	(61)
Cd-Hg-Na	300–400 [14]	[10–90] Na; [25–75] Cd	L	(58)
Cd-Mg	270–300	3–99.5	S	(31)
Cd-Na	395	10–85 [9]	L	(32)
Cd-Ni	410–556 [5]	94.4–99.5 [7]	L	(7)
Cd-Pb	427–572 [4]	12–79	L	(21)
	400–600	10–95 [10]	L	(22)
Cd-Pb-Sb	380–600	[8–95] Cd; Pb/Sb = 0.5–2	L	(23)
Cd-Pb-Sn	380–600	[11–95] Cd; Pb/Sn = 0.5–2	L	(23)

System	Temp. range, °C	Comp. range, mole % of 1	State	Reference
1 2				
Cd-Sb	240–290	26–86 [8]	S	(34)
	395–435	37–43 [3]	S	(35)
	400–600	14–95 [9]	L	(22)
Cd-Sn	400–600	10–95 [9]	L	(22)
	432–585 [4]	8–82 [8]	L	(21)
	430–550	[7]	L	(59)
Cd-Te	355–440	5–15 [4]	S	(36)
Cd-Zn	435–540 [3]	15–85 [12]	L	(21)
Ce-Hg-Sn	18	[10]	L	(61)
Co-Pt	700–900	32–73 [8]	S	(37)
Cu-Hg-Zn	16	[6]	L	(61)
Cu-Pt	400–650	14–98 [14]	S	(38)
Cu-Zn	333–626	5–58	S	(39)
Fe-S-C	1250	(0.05-33) S; C sat'd.	L	(40)
Fe-Si	1450–1540	0–99.9 [27]	L	(41)
Hg-K	0–50 [5]	98–99.98 [8]	L	(42)
Hg-Mg-Sn	18	[12]	L	(61)
Hg-Na	−40–320	15–95	S	(43)
	5–25 [3]	95–99.6 [7]	L	(44)
	21–45 [20]	20–45	L	(45)
	15–35 [3]	45–98 [17]	L	(46)
	299–375 [2]	10–61 [15]	L	(32)
Hg-Na-Pb	350–400	(10–90) Na; Hg/Pb = 1–4 [9]	L	(47)
Hg-Pb	17	[11]	L	(61)
	95–155	[1]	L	(63)
Hg-Tl	−74–−8	70–78	S	(48)
	20–40	57–99.7 [12]	L	(49)
Hg-Zn	12–50 [4]	0.6–93 [15]	L	(50)
	16	[13]	L	(61)
	18–30 [3]	[18]	L	(64)
In-Zn	362–517 [4]	10–100 [13]	L	(51)
Na-Pb	425–475 [2]	34–94 [14]	L	(65)
Na-Sn	480	27–95 [19]	L	(65)
Na-Tl	352–375 [2]	25–96 [18]	L	(65)
Pb-Sb	370–630	11–87 [9]	L	(52)
	450–750		L	(53)
Pb-Sn	410–550 [5]	1–9.2	L	(7)
Pb-Te	355–408	16–40	S	(36)
Pb-Tl	352–478	21–90 [16]	L	(54)
	245–295	4–84	S	(55)
Pb-Zn	653	1–96 [16]	L	(28)
Sb-Sn	333–412 [5]	0.6–14 [45]	L	(11)
	632	10–90 [9]	L	(56)
Sb-Zn	560–700	15–68 [16]	L	(57)
Sn-Te	270–395	5–15	S	(36)
Sn-Tl	414–478 [3]	10–79 [16]	L	(54)
	462	7.2–94.5 [7]	L	(62)
Sn-Zn	430–570 [4]	15–86 [12]	L	(21)
Te-Zn	355–418	86–96	S	(36)

References for Bibliography

1. M. Hillert, B. L. Averbach, and M. Cohen, Tech. Report. No. 20, Massachusetts Institute of Technology, May 31, 1955.
2. C. Wagner and G. Engelhardt, *Z. physik. Chem.*, **159A,** 241 (1932).
3. R. A. Oriani, *Acta Met.*, in press.
4. A. Wachter, *J. Am. Chem. Soc.*, **54,** 4609 (1932).
5. A. Olander, *ibid.*, **53,** 3577 (1931).
6. O. Kubaschewski and O. Huchler, *Z. Elektrochem.*, **52,** 171 (1948).
7. R. A. Schaeffer and F. Hovorka, *Trans. Electrochem. Soc.*, **87,** 479 (1945).
8. A. Olander, *Z. physik. Chem.*, **163A,** 107 (1933).
9. F. Weibke and I. Efinger, *Z. Elektrochem.*, **46,** 61 (1940).
10. R. O. Frantik and H. J. McDonald, *Trans. Electrochem. Soc.*, **88,** 253 (1945).
11. J. A. Yanko, A. E. Drake, F. Hovorka, *ibid.*, **89,** 357 (1946).
12. O. J. Kleppa, *J. Am. Chem. Soc.*, **73,** 385 (1951).
13. P. Chiche, *Compt. rend.*, **234,** 830 (1952).
14. R. A. Oriani, *Acta Met.*, **2,** 608 (1954).
15. F. Weibke and U. F. von Quadt, *Z. Elektrochem.*, **45,** 715 (1939).
16. L. L. Seigle, M. Cohen, and B. L. Averbach, *J. Metals*, **4,** 1320 (1952).
17. A. Olander, *J. Am. Chem. Soc.*, **54,** 3819 (1932).
18. O. J. Kleppa, *ibid.*, **71,** 3275 (1949).
19. F. Weibke and G. Schrag, *Z. Elektrochem.*, **46,** 658 (1940).
20. O. J. Kleppa, *J. Am. Chem. Soc.*, **72,** 3346 (1950).
21. N. W. Taylor, *ibid.*, **45,** 2865 (1923).
22. J. F. Elliott and J. Chipman, *Trans. Faraday Soc.*, **47,** 138 (1951).
23. J. F. Elliott and J. Chipman, *J. Am. Chem. Soc.*, **73,** 2683 (1951).
24. S. Mellgren, *ibid.*, **74,** 5037 (1952).
25. H. S. Strickler and H. Seltz, *ibid.*, **58,** 2084 (1936).
26. H. Seltz and F. J. Dunkerley, *ibid.*, **64,** 1392 (1942).
27. A. Olander, *Z. physik. Chem.*, **169A,** 260 (1934).
28. O. J. Kleppa, *J. Am. Chem. Soc.*, **74,** 6052 (1952).
29. K. Sanbongi and M. Ohtani, *Sci. Repts. Res. Insts. Tohoku Univ. A*, **5,** 263 (1953).
30. H. C. Bijl, *Z. physik. Chem.*, **41,** 641 (1902).
31. F. A. Trumbore, W. E. Wallace, and R. S. Craig, *J. Am. Chem. Soc.*, **74,** 132 (1952).
32. K. Hauffe, *Z. Elektrochem.*, **46,** 348 (1940).
33. A. V. Nikol'skaya and Ya. I. Gerasimov, *Zhur. Fiz. Khim.*, **28,** 713 (1954); *Chem. Abs.*, **48,** 11159h.
34. A. Olander, *Z. physik. Chem.*, **173A,** 284 (1935).
35. H. Seltz and J. C. DeHaven, *Trans. Am. Inst. Mining Met. Engrs.*, **117,** 218 (1935).
36. J. H. McAteer and H. Seltz, *J. Am. Chem. Soc.*, **58,** 2081 (1936).
37. R. A. Oriani, *Acta Met.*, **1,** 144 (1953).
38. F. Weibke and H. Matthes, *Z. Elektrochem.*, **47,** 421 (1941).
39. A. Olander, *Z. physik. Chem.*, **164A,** 428 (1933).
40. N. A. Vatolin and O. A. Esin, *Zhur. Obschei. Khim.*, **24,** 795 (1954); *Chem. Abs.*, **48,** 13578d (1954).
41. K. Sanbongi and M. Ohtani, *Sci. Repts. Res. Insts. Tohoku Univ. A*, **5,** 350 (1953).
42. H. E. Bent and E. S. Gilfillan, *J. Am. Chem. Soc.*, **55,** 3989 (1933).
43. H. E. Bent and A. F. Forziati, *ibid.*, **58,** 2220 (1936).
44. H. E. Bent and E. J. Swift, *ibid.*, **58,** 2216 (1936).
45. E. S. Gilfillan and H. E. Bent, *ibid.*, **56,** 1505 (1934).
46. T. W. Richards and J. B. Conant, *ibid.*, **44,** 601 (1922).
47. F. Halla and R. Herdy, *Z. Elektrochem.*, **56,** 213 (1952).
48. A. Olander, *Z. physik. Chem.*, **171A,** 425 (1934).
49. T. W. Richards and F. J. Daniels, *J. Am. Chem. Soc.*, **41,** 1732 (1919).
50. E. Cohen and P. H. von Ginneken, *Z. physik. Chem.*, **75,** 437 (1911).
51. W. J. Svirbely and S. M. Selis, *J. Am. Chem. Soc.*, **75,** 1532 (1953).
52. H. Seltz and B. J. DeWitt, *ibid.*, **61,** 2594 (1939).
53. V. N. Eremenko and O. M. Eremenko, *Ukrain. Khim. Zhur.*, **18,** 232 (1952); *Chem. Abs.*, **48,** 3115e (1954).
54. J. H. Hildebrand and J. N. Sharma, *J. Am. Chem. Soc.*, **51,** 462 (1929).
55. A. Olander, *Z. physik. Chem.*, **168A,** 274 (1934).

56. R. O. FRANTIK AND H. J. MCDONALD, *Trans. Electrochem. Soc.*, **88,** 243 (1945).
57. H. SELTZ, *ibid.*, **57,** 233 (1940).
58. H. FRAUENSCHILL AND F. HALLA, *Z. Elektrochem.*, **53,** 144 (1949).
59. K. SANO AND K. OKAJIMA, *Mem. Fac. Eng. Nagoya Univ.*, **5,** 88 (1952); *Bull. Research Inst. Mineral Dressing and Met. Japan*, **8,** 149 (1952); *Chem. Abs.*, **48,** 13394h (1954).
60. P. A. ANDERSON, *J. Am. Chem. Soc.*, **48,** 2285 (1926).
61. G. TAMMANN AND W. JANDER, *Z. anorg. Chem.*, **124,** 105 (1922).
62. A. L. VIERK, *Z. Elektrochem.*, **54,** 436 (1950).
63. M. KATAYAMA, *Z. physik. Chem.*, **61,** 566 (1908).
64. J. N. PEARCE AND J. F. EVERSOLE, *J. Phys. Chem.*, **32,** 209 (1928).
65. K. HAUFFE AND A. L. VIERK, *Z. Elektrochem.*, **53,** 151. (1949).

MANUSCRIPTS AND ABSTRACTS FOR FALL MEETING

Papers are now being solicited for the Fall Meeting of the Society, to be held at the Statler Hotel in Cleveland, September 30, October 1, 2, 3, and 4, 1956. Technical sessions will be scheduled on Batteries, Corrosion, Electrodeposition, Electrothermics and Metallurgy, and Theoretical Electrochemistry (joint symposium with Electrodeposition).

To be considered for this meeting, triplicate copies of abstracts (not to exceed 75 words in length) must be received at Society Headquarters, 216 West 102nd St., New York 25, N. Y., *not later than June 15, 1956. Please indicate on abstract for which Division's symposium the paper is to be scheduled.* Complete manuscripts should be sent in triplicate to the Managing Editor of the JOURNAL at the same address.

***

The Spring 1957 Meeting will be held in Washington D. C., May 12, 13, 14, 15, and 16, at the Statler Hotel. Sessions will be announced in a later issue.

The Kinetics of the Corrosion of Copper in Acid Solutions

JOHN RANDEL WEEKS[1] AND GEORGE RICHARD HILL

Institute for the Study of Rate Processes, Metallurgy and Fuel Technology Departments, University of Utah, Salt Lake City, Utah

ABSTRACT

The mechanism of the initial corrosion of copper in hydrochloric acid solutions has been investigated, using a radioactive tracer technique. Kinetic data have been obtained showing the effect of *p*H, dissolved oxygen, chloride ion, and temperature on the corrosion rate. Surface areas were measured using a modified electrolytic method. On the basis of these data (reproducible to ±20%), a mechanism for the initial corrosion process is proposed and discussed. Specific rate constants, heats, and entropies of activation for the slow step in the corrosion process were determined.

INTRODUCTION

The initial rate of corrosion of copper by neutral chloride solutions has been determined recently (1). Under conditions where the chemical reaction at the metal surface itself is the rate-determining factor, a corrosion rate corresponding to 1600 mdd was measured in a neutral, normal potassium chloride solution. From kinetic data obtained by experimental measurement of the amount of electricity necessary to electroreduce the cuprous oxide produced by the initial reaction, the following rate-determining step of the initial process was proposed:

$$2Cu + H^+ + O_2 \rightarrow 2Cu^+ + HO_2^-$$

In acid chloride solutions in which the Cu_2O produced is soluble, the earlier experimental method is no longer applicable. The initial corrosion mechanism might, however, be expected to proceed for some time in these solutions, provided diffusion of the reacting species to the metal surface does not become rate-determining. The purpose of the present investigation was to examine the kinetics of the initial reaction of copper with acid chloride solutions in order to investigate the corrosion mechanism.

The dissolution of copper in hydrochloric acid over extended periods of time has been investigated recently by Katz (2, 3). He reported that the corrosion rate gradually increases over periods of several days, and postulated that the cupric ions that build up in the solution accelerate corrosion by reacting according to the equation,

$$Cu^{++} + Cu^0 \rightarrow 2Cu^+$$

Such a reaction, however, clearly cannot represent an initial corrosion process.

Recent polarographic investigations by Delahay (4, 5) on the reduction of oxygen on various metals indicated that in many cases hydrogen peroxide is produced as an intermediate product in solution corrosion processes. Possible subsequent reactions of this hydrogen peroxide have been considered by van Rysselberghe and co-workers (6–8) to play an important role in the understanding of corrosion behavior.

EXPERIMENTAL

Corrosion rates were measured by a radioactive tracer method. Because there are no suitable isotopes of copper, the pure metal, to which approximately 0.01% radioactive cobalt had been added, was used in this investigation. In addition to its availability, long half-life, and high specific activity, cobalt 60 was selected because it is considerably electropositive with respect to copper and forms a solid solution alloy with it to a sufficient extent. A homogeneous alloy of this type would be expected to corrode at approximately the same rate as pure copper; as the cobalt atoms appear on the metal surface, they, being electropositive to the copper atoms, should dissolve preferentially by a simple galvanic mechanism. The rate of appearance of activity in the solution would therefore indicate the rate of corrosion of the copper.

Samples were prepared by electroplating approximately 0.001 g of radioactive cobalt on a small strip of pure copper. This coated strip, with sufficient additional copper to bring the total sample weight to 10 g, was vacuum sealed in a short length of ¼ in. fused silica tubing. The sample was melted and held in the liquid state for one hour, after which it was quenched in an oil bath. Preliminary investigations using nonradioactive cobalt showed that this treatment produced a uniform, fine-grained alloy in samples containing 0.10% cobalt in copper. The sample thus produced was roughly cylindrical with tapered ends and showed several surface pit-like indentations. No internal porosity was noted in six samples.

All corrosion rates were measured from the same sample, which was stored in a small glass vial of acetone between experiments. All water used in the experiments was redistilled from an alkaline solution of potassium permanganate into a Vycor condenser. Fresh corrosion solutions were made frequently using this purified water. All glassware was cleaned in dichromic acid, and rinsed thoroughly with tap, distilled, and redistilled water. Extreme laboratory cleanliness was found necessary to obtain reproducible results. Reproducibility also re-

[1] Present address: Brookhaven National Laboratory, Upton, N. Y.

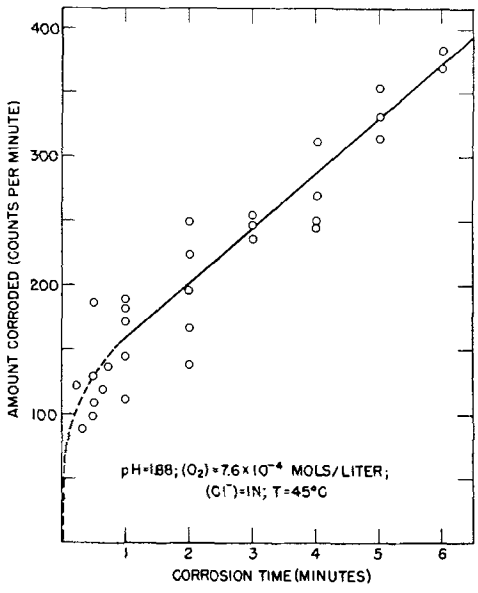

FIG. 1. Effect of time on the corrosion of copper in acid chloride solution.

quired that a series of experiments using a given corrosion solution be performed within 24 hr after the solution was made.

At the beginning of an experiment, the sample was transferred directly from the glass vial into a Pyrex holder, rinsed in fresh acetone, and cleaned 1 min in a 10% solution of ammonium persulfate. This treatment was known from previous experience (1) to yield a clean, oxide-free surface. The cleaned sample was transferred quickly into two successive beakers of re-distilled water, and then placed in the beaker of corrosion solution. After a measured corrosion time, the sample was removed from the solution, rinsed, and returned to a vial of fresh acetone until again needed. Thirty-five ml of corrosion solution was placed in a 50 ml beaker for each experiment. The beaker was suspended 30 min in a constant temperature water bath before the corrosion sample was admitted. Solutions were covered and stirred by passing a stream of gas of known composition through a sintered glass orifice immersed into them through a hole in the cover glass. After the metal sample was removed, the cover glass and gas orifice were rinsed into the sample solution. The solution was then diluted to bring its level to a known height in the beaker, and was placed directly beneath the end-window of a G-M counting tube. Thus, all samples were counted under as nearly identical geometry as practicable. Conversions to absolute units were made by measuring the sample weight loss in 15 and 30 min attack by the persulfate cleaning solution, and measuring the activity of the resultant solution as before. The corrosion rate in mdd was found to be equal to the measured rate in counts per minute for 10-min corrosion time multiplied by 44.7 and divided by the surface roughness factor.

The surface area of a similar, nonradioactive sample was estimated using a modified Bowden-Rideal electrolytic method (9). The charge placed on the metal surface during a known increment of its cathodic polarization in a dilute acid solution was recorded using a calibrated electrolytic capacitor placed in series with the metal-solution interface. By comparing the amount of this charge with that measured on a mercury surface of known area, the surface area of the unknown sample could be calculated. This method (10) is somewhat similar to that proposed by Wagner (11). The surface area of the sample as cast was approximately 80 times the apparent area. After being treated by three cleaning-corroding cycles like the one discussed, the true area had decreased to 35 times the apparent area. This roughness factor decreased steadily to a value of 9.2 after prolonged etching in ammonium persulfate (equivalent to the dissolution effect of nearly 100 cycles). After 6 hr in the etching solution, the roughness factor was still nearly five. Nearly 60 corrosion cycles were performed before reproducible data were obtained. At this time, the surface roughness factor was probably nearly 20; it dropped gradually to a value of about 5 after 300 samples had been run. A surface area change of this magnitude was found to agree with the corrosion rate data.

RESULTS

The rate of corrosion of copper in dilute hydrochloric acid solutions was measured as a function of time, *p*H, concentration of dissolved oxygen, and temperature, in order to determine the corrosion mechanism. All solutions were maintained 1*N* in chloride ion concentration by mixing HCl and KCl to give a solution of the desired acidity. All rate data, except for the temperature effect measurements, were obtained at 45°C in order for the rate to be large enough for convenient measurement. All solutions, except those for determining the oxygen concentration effect, were stirred with a stream of oxygen. All solutions were of *p*H range 0.8 to 2.8; in this range of acidity no evidence of surface oxide was noted even after extended corrosion times. Because of an appreciable scatter in experimental data, measurements had to be repeated several times in order to evaluate the results obtained. This scatter can perhaps be attributed to possible segregation of the cobalt tracer atoms in the alloy, oxide inclusions in the alloy, and fluctuations in the surface area of the sample during cleaning. With sufficient data, however, mean average rates were definite, reproducible, and probably accurate within ±20%.

Effect of Time: After a rapid corrosion during the first few seconds, the amount of corrosion products obtained varied linearly with time, as seen in Fig. 1. This linear relationship continued at least to 40 min corrosion time. The reaction rate, or slope of the linear portion of the curve, is 400 counts per minute per 10 min corrosion time. Assuming the surface roughness factor on these first experiments to be 20, this value corresponds to 90 mdd. The intercept obtained from extrapolating time curves to zero time proved to be nearly independent of the variables investigated, except the surface area; it thus served as a useful indication of the change of surface roughness of the sample. The interpretation given the very rapid initial corrosion rate will be discussed later.

*Effect of p*H: The variation of the corrosion rate with *p*H is shown in Fig. 2. The rate of dependence on the

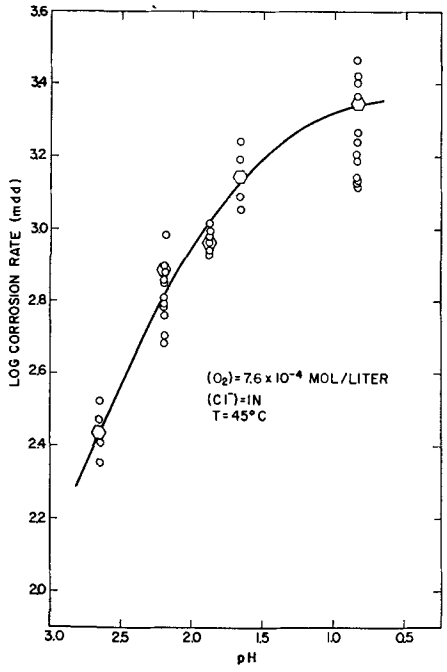

FIG. 2. Effect of pH on the corrosion rate

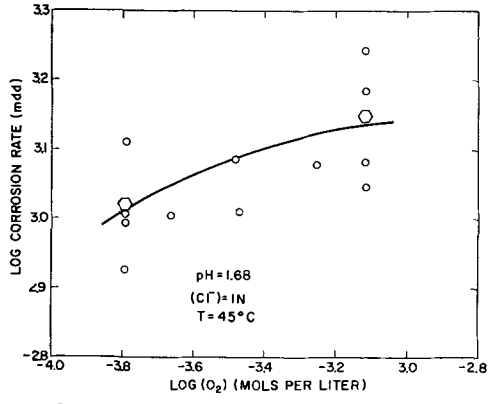

FIG. 3. Effect of dissolved oxygen concentration on the corrosion rate.

acid concentration is seen to be somewhat less than first order, and to decrease with increasing acidity. In this figure, the measured rates have been converted to mdd. The smooth curve is a plot of the rate equation derived in the next section. Other results, using very acid solutions, under somewhat different conditions, indicated that there is very little increase in corrosion rate due to increasing the acidity above 0.1N. Low corrosion rates in solutions less acid than 0.001N made reproducible data difficult to obtain by the method used.

Effect of Oxygen Concentration: A typical variation of the corrosion rate with oxygen concentration is shown in Fig. 3. Here again the smooth curve is that of the rate equation derived in the next section. Oxygen, compressed air, and known mixtures of oxygen and nitrogen were used to stir the solutions. The concentration of dissolved oxygen in the solution was considered from Henry's law to be equal to the fractional pressure of oxygen in the gas mixture times the solubility of pure oxygen in water at

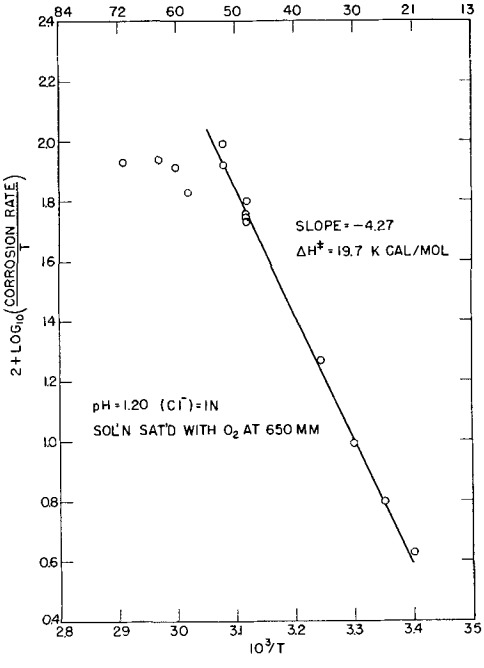

FIG. 4. Effect of temperature on the corrosion rate

the prevailing conditions of temperature and pressure. The solution was assumed to have been aspirated at a sufficient rate to maintain oxygen saturation. Many similar curves were obtained, each using a solution of slightly different pH. The rate dependence on oxygen concentration is seen to be somewhat less than half-order; with increasing acidity this dependence decreases. Many curves at a pH of 0.8 to 1.0 showed little distinguishable effect of oxygen pressure.

Effect of Stirring Rate: No appreciable effect on the corrosion rate was observed when the rate of aspirating the solution was either increased or decreased by a factor of five from the rate normally used in these experiments. This suggests that transfer of reactants to the metal surface is not controlling the process.

Effect of Temperature: The corrosion rate was measured over a temperature range from 20° to 70°C. In Fig. 4, the data obtained are plotted as log rate/T vs. $1/T$, according to the theory of absolute reaction rates:

$$\text{Rate} = C\,\frac{kT}{h}\,e^{-\frac{\Delta H^\ddagger}{RT}}\,e^{\frac{\Delta S^\ddagger}{R}}$$

when the reactants are in constant concentration. At temperatures from 21° to 52°C, the measured rates are seen to lie on a straight line, when corrected for variations in oxygen solubility, assuming ½ order dependence (these corrections were quite small). From the slope of this line, the heat of activation, $\Delta H^\ddagger$, for the reaction was found to be 19.7 kcal/mole. This value clearly indicates that the rate of the process studied was controlled by chemical reaction rather than by diffusion of the reactants, according to King's criteria (12). The marked decrease in the temperature coefficient above 52°C was possibly due to a shift in the control of the reaction rate to diffusion of dissolved oxygen to the metal surface. This shift is thought to be due to a combination of the

TABLE I. *Corrosion in the "absence" of oxygen*

Solution	Measured rate c/m/10 min corrosion
$HClO_4$ + $KClO_4$ (Sat)	72
$HClO_4$ + $KClO_4$ (Sat)	74
HCl + KCl (1*N*)	66
HCl + KCl (1*N*)	75

*p*H = 0.96, T = 45.5°C, solution aspirated with pure nitrogen.

decreasing solubility of oxygen and the rapidly increasing reaction rate at these high temperatures. Other data obtained in the higher temperature region at a slightly different *p*H show an activation energy of about 5 kcal/mole and a temperature rate coefficient of 1.3; these values comply with King's criteria for diffusion-controlled reaction (12).

The shift in mechanism was never found to occur at a temperature lower than 52°C in four experiments using solutions of different *p*H. Thus, it is felt that the temperature selected for the investigation of concentration effects, 45°C, was within the range of chemical rather than diffusion control.

Corrosion in the Absence of Oxygen: Copper has been reported (13) to be attacked by HCl in the absence of oxygen according to the reaction,

$$2Cu + 4HCl = 2HCuCl_2 + H_2$$

Since it was not possible to exclude oxygen entirely from the solution with the apparatus used, the effect of this reaction was investigated indirectly by comparing the rates of solution of copper in hydrochloric and perchloric acid solutions of the same *p*H which were stirred with a stream of nitrogen. The measured rates from the two solutions were identical within the limits of experimental error, as seen in Table I. Therefore, it was considered that the amount of copper dissolved according to the above equation was negligible under the conditions of the experiments.

Mechanism of the Reaction

In order to explain the measured dependence of the corrosion rate on the reactants investigated, the following sequence of reactions is proposed:

$$2Cu + O_2 \rightleftharpoons Cu_2 \cdot O_2 \text{ (adsorbed)} \quad \text{(I)}$$

$$Cu_2 \cdot O_2 \text{ (ads.)} + H^+ + Cl^- \rightleftharpoons Cu_2 \cdot O_2 \cdot HCl \text{ (adsorbed)} \quad \text{(II)}$$

$$Cu_2 \cdot O_2 \text{ (ads.)} + H^+ \rightarrow 2Cu^+ + HO_2^- \quad \text{(III)}$$

The first stage of oxidation is the reversible adsorption of a dissolved oxygen molecule from the solution on a pair of copper atoms on the metal surface, forming an "oxidized site." This is followed either by adsorption of H^+ and Cl^- ions in pairs[2] from the solution on the oxidized site, as shown by equation (II), or by discharge of the oxidized site due to collision with a hydrogen ion from the solution, as shown by equation (III). The net reaction for this rate-determining portion of the reaction sequence is

$$2Cu + H^+ + O_2 \rightarrow 2Cu^+ + HO_2^- \quad \text{(IV)}$$

which is identical with that proposed by Hill (1) for the slow step in copper corrosion in neutral or basic solutions, and is similar to that discussed by Delahay, Pourbaix, and van Rysselberghe (14) for the first stage of the anodic reduction of oxygen. The concept of adsorption of oxygen as $(O_2^=)$ in the initial stage of anodic reduction, followed by production of (HO_2^-) by reaction with hydrogen ions is due in part to Berl (15), who also established that the biperoxide ion is frequently an intermediate product in the reaction mechanism.

Before examining the above reactions in terms of the experimental data, first consider possible subsequent reactions in the solution phase. Experimentally, the copper was found in solution as Cu^{++}; tests for hydrogen peroxide in the bulk solution were negative. Copper ions have been observed to decompose H_2O_2 catalytically (16). The mechanism for this type of decomposition was first discussed by Haber and Wilstatter (17), Haber and Weiss (18), and more recently by Evans, Baxendale, and Park (19). A catalytic decomposition similar to that described by these last authors predicts a net reaction for the solution phase of

$$HO_2^- + 2Cu^+ + 3H^+ \rightarrow 2Cu^{++} + 2H_2O \quad \text{(V)}$$

The net reaction for the over-all corrosion process then becomes

$$2Cu + O_2 + 4H^+ \rightarrow 2Cu^{++} + 2H_2O \quad \text{(VI)}$$

Derivation of the rate equation.—Since it was the rate at which the copper atoms leave the metal surface that was measured experimentally, an expression for the reaction rate derived from a steady-state consideration of reactions (I), (II), and (III) must satisfy the experimental data. Letting x represent the fraction of the metal surface covered with "oxidized sites," y the fraction of the surface taken up by "oxidized sites" upon which acid adsorption has taken place, and s the fraction of unoccupied sites on the metal surface, the steady-state equations for the reaction sequence become

$$\frac{dx}{dt} = 0 = \vec{k}_1 s(O_2) - \overleftarrow{k}_1 x - \vec{k}_2 x(H^+)(Cl^-) + \overleftarrow{k}_2 y - k_3 x(H^+) \quad \text{(VII)}$$

$$\frac{dy}{dt} = 0 = \vec{k}_2 x(H^+)(Cl^-) - \overleftarrow{k}_2 y \quad \text{(VIII)}$$

$$s + x + y = 1 \quad \text{(IX)}$$

where $\vec{k}_1$ and $\overleftarrow{k}_1$ are the specific reaction rate constants for the adsorption and desorption, respectively, of oxygen on the metal surface (I); $\vec{k}_2$ and $\overleftarrow{k}_2$ are the specific reaction rate constants for the adsorption and desorption, respectively, of HCl on the "oxidized sites" (II); and k_3 is the specific reaction rate constant for reaction (III).

From these equations can be readily derived the useful relationships

[2] Or a neutral HCl molecule.

$$x = \frac{\vec{k}_1 s(O_2)}{\overleftarrow{k}_1 + k_3(H^+)} = \frac{K_1 s(O_2)}{1 + (k_3/\overleftarrow{k}_1)(H^+)} \quad (X)$$

where

$$K_1 = \frac{\vec{k}_1}{\overleftarrow{k}_1} \quad (Xa)$$

$$y = \frac{\vec{k}_2 x(H^+)(Cl^-)}{\overleftarrow{k}_2} = K_2 x(H^+)(\overline{Cl^-}) \quad (XI)$$

where

$$K_2 = \frac{\vec{k}_2}{\overleftarrow{k}_2} \quad (XIa)$$

and

$$s = \frac{1 + (k_3/\overleftarrow{k}_1)(H^+)}{1 + (k_3/\overleftarrow{k}_1)(H^+) + K_1(O_2)\{1 + K_2(H^+)(Cl^-)\}} \quad (XII)$$

The rate of appearance of copper ions in solution from reaction (III) is

$$\frac{d(Cu^+)}{dt} = k_3 x(H^+) \quad (XIII)$$

Combining (XIII) with (X) and (XII), one has an expression for the reaction rate:

$$\frac{d(Cu^+)}{dt} = \frac{k_3 K_1(H^+)(O_2)}{1 + (k_3/\overleftarrow{k}_1)(H^+) + K_1(O_2)\{1 + K_2(H^+)(Cl^-)\}} \quad (XIV)$$

Evaluation of constants.—The constants appearing in the rate expression (XIV) were evaluated from the reaction rate dependence on the hydrogen ion and oxygen concentrations. The average experimental data used, shown by hexagons in Fig. 2 and 3, are given in Table II. These were substituted into equation (XIV), and numerical values of the constants obtained by solving simultaneously all combinations of five of the seven resultant equations. Average values obtained were (at 45°C)

$$k_3 = 1.51 \times 10^5 \text{ (mdd)(1/mole)}$$

$$K_1 = 1.64 \times 10^4 \text{ 1/mole}$$

$$K_2 = 54.9 \text{ 1/mole}$$

$$\vec{k}_1 = 3.28 \times 10^7 \text{ (mdd)(1/mole)}$$

$$\overleftarrow{k}_1 = 2 \times 10^3 \text{ mdd}$$

From the value for k_3 and the intercept of the straight line of Fig. 4, the entropy and free energy of activation for the process were calculated to be

$$\Delta S^* = 19.7 \text{ cal/deg mole}$$

$$\Delta F^{\ddagger} = 13.4 \text{ kcal/mole}$$

Effect of chloride ion concentration.—As a check on the final term in the denominator of the reaction rate expression (XIV), a qualitative chloride ion dependence was determined. The results obtained are shown in Fig. 5.

TABLE II. *Average rate data used in evaluation of rate equation*

Solution pH	H^+ (mole/liter)	O_2 (mole/liter)	Measured rate	
			c/m/dm² / 10′ corrosion	mg/dm² / day
2.66	0.00219	7.6×10^{-4}	87	272
2.19	0.00645	7.6×10^{-4}	245	767
		1.6×10^{-4}	162	507
1.88	0.0132	7.6×10^{-4}	294	921
1.66	0.0219	7.6×10^{-4}	450	1410
		1.6×10^{-4}	332	1040
0.84	0.145	7.6×10^{-4}	705	2210

Temperature 45°C, rates are per dm² true surface area, measured electrolytically.

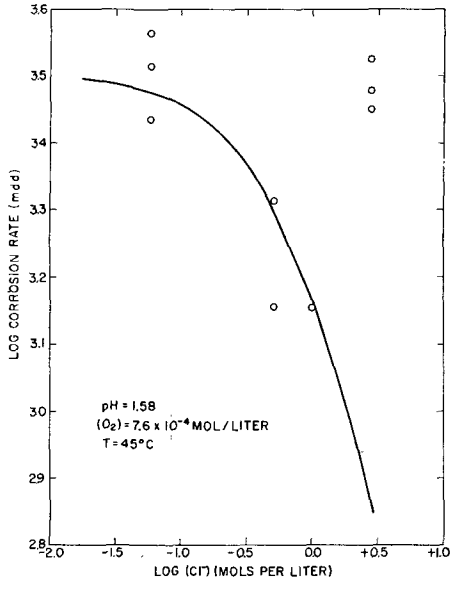

FIG. 5. Effect of chloride ion concentration on the corrosion rate.

It can be seen that the general behavior of the corrosion rate is as predicted over a range of concentrations $0.05N$–$1N$. The previously discussed corrosion in the absence of oxygen would, *a priori*, be second order with respect to the chloride ion concentration; perhaps this process contributes appreciably to the reaction rate in the solutions $3N$ in chloride ion, and causes the observed rate increase.

DISCUSSION

In evaluating the kinetic data, many surface reaction sequences were considered. However, only a double adsorption mechanism of the type described herein yields a reaction rate equation consistent with all of the experimental results.

A typical corrosion rate from this investigation, for comparison with earlier published results, is 190 mdd at 25°C in N KCl solution at a pH of 1.20, the solution saturated with oxygen at 650 mm Hg pressure, and a surface roughness of 5. This corresponds to about 900 mdd when the rate/dm² of geometric area is considered. This is the rate at steady-state conditions, and does not take into account the very much faster rate during the first few seconds.

Part of the large amount of corrosion products that appeared during the first few seconds might be considered in terms of the proposed mechanism to represent corrosion during establishment of the steady state. During the first few seconds, the metal surface rapidly becomes covered with adsorbed oxygen. Thus, initially, there are a large number of oxidized sites uncovered by any adsorbed acid. These could then readily be discharged according to reaction step (III). The electroreduction curves obtained by Hill (1) on copper cathodes cleaned in an identical manner suggest that the surface was initially oxide-free. However, were it not, a rapid dissolution of surface oxide might be expected upon dipping the sample into the acid solution. Part of the rapid initial solution rate may thus be attributable to the surface oxide.

The value of the free energy for hydrogen ion adsorption as calculated from the experimentally determined equilibrium constant K_2 is 2.5 kcal/mole. This is much too small a potential to represent any appreciable bonding between the ion and the "oxidized site." Since the chloride ion is suspected also to adsorb on the oxidized sites jointly with the hydrogen ion, ion pair adsorption is indicated. However, all solutions were 1*N* in chloride ion concentration; therefore, the value of K_2 and, thus, of the adsorption energy is not changed by this consideration. Recently, Hackerman and Stephens (21) have reported that sulfate ions chemisorb from solution on metallic iron in the presence of oxygen. They also found that the presence of chloride ions decreases the amount of sulfate adsorption from solutions of equal concentrations. Thus the chloride ion, or some derivative of it, apparently chemisorbs also on clean iron surfaces. Very possibly it also chemisorbs on clean copper surfaces. The equilibrium reaction K_2 possibly represents a true adsorption equilibrium since the adsorbed product is not removed by subsequent steps (as are the oxidized sites). A possible explanation of the low magnitude of the calculated adsorption potential, in view of the suggested chemisorption, is that the hydrogen and chloride ions do not adsorb as ion pairs but rather as the free hydrochloric acid molecule. In this case the reaction becomes

$$Cu_2 \cdot O_2 \text{ (ads.)} + HCl \rightleftharpoons Cu_2 \cdot O_2 \cdot HCl \qquad (IIa)$$

The concentration of the neutral hydrochloric acid molecules in solution is less than that of hydrogen ions by a factor of 10^7. Thus, the adsorption energy becomes 12 kcal/mole, a much more reasonable value for explaining the observed effects.

The concept of adsorption of neutral acid or base molecules has been successfully used by Cook and coworkers (22–26) to explain other experimental results. It may possibly be applicable also in this system.

Acknowledgment

This research was supported in part by a grant from the Atomic Energy Commission. The assistance of Dr. M. E. Wadsworth in interpreting the adsorption effects is gratefully acknowledged.

This paper represents part of the work submitted by J. R. Weeks to the University of Utah in partial fulfillment of the requirements for the Ph.D. degree in metallurgy.

Manuscript received April 18, 1955. This paper was prepared for delivery before the Boston Meeting, October 3 to 7, 1954.

Any discussion of this paper will appear in a Discussion Section to be published in the December 1956 JOURNAL.

REFERENCES

1. G. R. HILL, *This Journal*, **100,** 345 (1953); *also*, Tech. Rpts. I and V, Research Contract N7 onr 45103, Dec. 1949, and Feb. 1951.
2. W. KATZ, *Werkstoffe u. Korrosion*, **1,** 393 (1950).
3. W. KATZ, *Metalloberfläche*, **4A,** 101 (1950).
4. P. DELAHAY, *This Journal*, **97,** 198 (1950).
5. P. DELAHAY, *ibid.*, **97,** 205 (1950).
6. P. VAN RYSSELBERGHE, "Polarographic Study of Corrosion Phenomena," Tech. Rept. to the Office of Naval Research (1947).
7. P. VAN RYSSELBERGHE, J. M. MCGHEE, A. H. GROPP, R. D. WILLIAMS, AND P. DELAHAY, *Corrosion and Material Protection*, **5,** 11 (1948).
8. P. VAN RYSSELBERGHE, P. DELAHAY, A. H. GROPP, J. M. MCGHEE, AND R. D. WILLIAMS, *Corrosion*, **6,** 105 (1950).
9. F. P. BOWDEN AND E. K. RIDEAL, *Proc. Roy. Soc.*, **A120,** 59, 80 (1928).
10. G. R. HILL AND J. R. WEEKS, USAEC Document No. AECU-1776.
11. C. WAGNER, *This Journal*, **97,** 71 (1950).
12. C. V. KING, *Trans. N. Y. Acad. Sci.*, Series II, **10,** [7], 262 (1948).
13. J. W. MELLOR, "A Comprehensive Treatise on Inorganic and Theoretical Chemistry," Vol. III, p. 81, Longmans, Green and Co., London (1928).
14. P. DELAHAY, M. POURBAIX, AND P. VAN RYSSELBERGHE, *Comité intern. thermodynam. et cinét. electrochim.*, Compt. rend. de la II Reunion, Milan (1950).
15. W. G. BERL, *Trans. Electrochem. Soc.*, **83,** 253 (1943).
16. W. MACHU, "Das Wasserstoffperoxyd und die Perverbindungen," p. 62, J. Springer, Vienna (1937); [original not available for examination; referred to in Ref. (5)].
17. F. HABER AND R. WILSTATTER, *Ber.*, **64,** 2844 (1931).
18. F. HABER AND J. WEISS, *Proc. Roy. Soc.*, **A147,** 332 (1934).
19. M. G. EVANS, J. T. BAXENDALE, AND G. S. PARK, *Trans. Faraday Soc.*, **42,** 155 (1946).
20. T. MOELLER, "Inorganic Chemistry," p. 314, J. Wiley & Sons, Inc., New York (1952).
21. N. HACKERMAN AND S. J. STEPHENS, *J. Phys. Chem.*, **58,** 904 (1954).
22. M. A. COOK, *Eng. Min. J.*, **150,** [2], 110 (1949); *Chem. Eng. News*, **27,** [9] 489 (1949).
23. M. A. COOK AND J. C. NIXON, *J. Phys. Colloid Chem.*, **54,** 445 (1950).
24. G. A. LAST AND M. A. COOK, *ibid.*, **56,** 637 (1952); *ibid.*, **56,** 643 (1952).
25. M. E. WADSWORTH, R. G. CONRADY, AND M. A. COOK, *ibid.*, **55,** 1219 (1951).
26. M. E. WADSWORTH AND M. A. COOK, "Acid-Base Adsorption Processes," Utah Eng. Expt. Sta. Bull. No. 51, July 1951.

Oxidation of Aluminum in the Temperature Range 400°–600°C

W. W. Smeltzer

Aluminium Laboratories Limited, Kingston, Ontario, Canada

ABSTRACT

The surface oxidation kinetics of metallographically polished high purity aluminum were studied in the temperature range 400°–600°C using a vacuum microbalance technique. The oxidation rate of aluminum decreased to a low value after a formative stage of film growth which was governed by a parabolic law. Values of the activation energies of reaction were determined from the temperature coefficient of the parabolic law constants and were compared with other values reported in the literature. By attaching equal significance to gaseous and anodic oxidation results, a value of 37.2 kcal/mole (1.6 ev) was determined for the potential energy barrier against ion diffusion at the metal/oxide interface.

Introduction

Most workers in the field of surface oxidation of aluminum hold the view that this metal forms a thin oxide film. Film thicknesses of 10–30Å at room temperature have been measured (1–6). Measurements by Cabrera and Hamon (3), Hass (4), and Treadwell and Obrist (7) have shown that the film thickness does not exceed 200Å at temperatures up to 300°C. In the temperature range 500°–600°C oxidation virtually ceased at a film thickness of approximately 2000Å (8, 9).

Reaction kinetics have been treated quantitatively by Gulbransen and Wysong (10) who found that the oxidation rates of aluminum obeyed a parabolic law in the temperature range 350°–475°C, with an activation energy and entropy of reaction of 22.8 kcal/mole and of −25.4 to −28 eu, respectively. Above 475°C, the reaction deviated from the parabolic rate law. Although these oxidation tests were carried out for only 2 hr, general conclusions have been drawn concerning the reaction kinetics. Many authors have not conceded the virtual cessation of oxidation at elevated temperatures, and believe that aluminum exhibits a parabolic or paralinear law of oxidation. Also, the value of 22.8 kcal/mole for the activation energy of reaction is inconsistent with a value of 37–42 kcal/mole determined by Charlesby (11) from anodic oxidation results. Hence, in this investigation the studies of Gulbransen and Wysong (10) have been extended to elucidate the reaction kinetics; this was accomplished by completing oxidation tests for exposures of 24 hr in the temperature range 400°–600°C.

Experimental

Apparatus

A vacuum microbalance assembly similar to that described by Gulbransen (12) was employed for the kinetic measurements. The quartz microbalance was used for following weight changes; this was done by observing pointers on the balance beam and frame with a sliding microscope. The balance sensitivity was 1 division (0.001 cm) of the micrometer slide per 3.4 μg for a sample and counterweight of 0.6800 g. The micrometer readings were estimated to one-fourth of a division which represented 5Å of film thickness for the 5 × 2 cm specimens taken. This is valid on the assumption that the oxide film density is 3.4 for gamma-alumina and the surface roughness ratio is unity.

The vacuum system was of conventional design and consisted of pressure gauges, oxygen purification train and storage, microbalance container, triple stage oil diffusion pump, and other standard accessories. All openings in the vacuum manifold to the microbalance were larger than 12 mm diameter in order that specimens could be degassed rapidly in a vacuum of 10^{-6} mm. A liquid air trap was placed between the balance container and the vacuum manifold to protect the metal specimens from reaction with mercury vapor.

The furnace, which was positioned about the quartz microbalance tube by a counterweight, consisted of a 12 in. × 1 in. diameter McDanel combustion tube wound with a monel heating element and insulated by vermiculite in an aluminum container. Two iron-constantan thermocouples were set in the lower end of the combustion tube, one of which was connected to a Minneapolis Honeywell temperature indicating controller with electropulse duration control; the other one was connected to a potentiometer for setting and checking temperatures. The temperature in the region for metal specimens was determined by attaching a calibrated iron-constantan thermocouple to a metal specimen suspended in position in the quartz reaction tube. Temperatures were controlled to ±1°C.

Materials and Their Preparation

Specimens were prepared from a 4 in. × 1¼ in. cylinder machined from super purity aluminum of impurity contents: iron, 0.002%; copper, magnesium, 0.001%; boron, beryllium, bismuth, calcium, chromium, gallium, man-

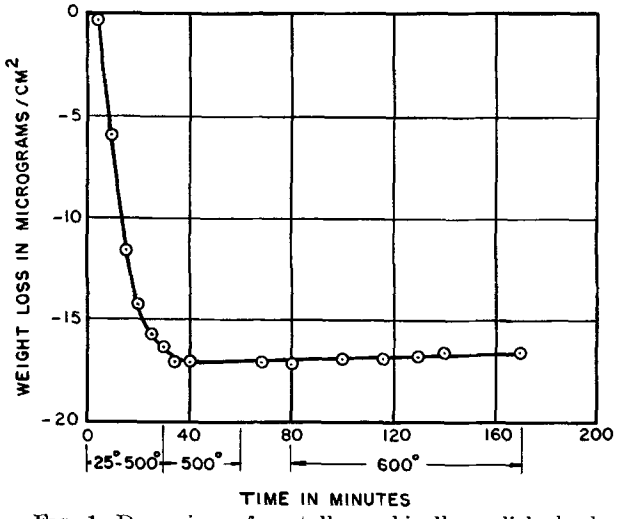

FIG. 1. Degassing of metallographically polished aluminum.

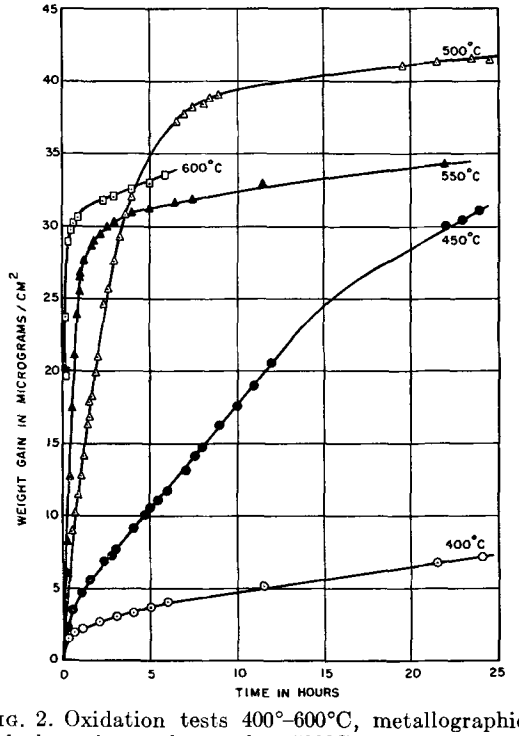

FIG. 2. Oxidation tests 400°–600°C, metallographically polished specimens degassed at 500°C.

ganese, nickel, silicon, sodium, titanium, tin, lead, vanadium, zirconium less than 0.001%. This cylinder was melted, degassed, and solidified in a vacuum of 10^{-6} mm after which the surface was scalped. The slug was then cold rolled to a thickness of 0.12 in., annealed for 30 min at 550°C and given a final cold reduction of 0.01 in. thickness. This sheet was stored in a desiccator.

Specimens were cut from the sheet and polished metallographically with emery papers 0, 00, and 000, respectively, with the last polish completed under a solution of paraffin in kerosene. Specimens were given a final polish with a dry Selvyt cloth to remove polishing material embedded in the metal surface, cut into 5½ × 2 cm strips, and stored in a desiccator. For oxidation tests, specimens were trimmed to a weight of 0.6800 g.

Oxygen was purified by passing commerical cylinder oxygen through a train consisting of Ascarite for removal of carbon dioxide, heated platinum for oxidation of hydrogen and carbon monoxide, phosphorous pentoxide for removal of water, and a liquid air trap for removal of residual condensable vapors.

Procedure

A specimen was degassed carefully before oxidation by subjecting the specimen to a vacuum of 10^{-6} mm at room temperature for 5 hr and at 500°C for a further 30 min. The furnace was set then at a temperature for an oxidation test or for a further vacuum anneal at 500° or 600°C.

Oxide film formation on aluminum was studied as a function of time and temperature at 7.6 cm oxygen pressure. This pressure was chosen for experimental convenience since the rate of oxidation of aluminum is largely independent of pressure (10). In the first group of oxidation tests, the specimens were vacuum annealed for 30 min at 500°C and exposed in the temperature range 400°–600°C. In the second group of oxidation tests, the specimens were vacuum annealed 1 hr at 600°C and exposed in the temperature range 400°–600°C.

RESULTS AND DISCUSSION

Vacuum degassing.—A typical degassing curve is illustrated in Fig. 1. Evolution of gas was slow below 200°C but with higher temperatures, gas evolved rapidly with complete degassing of the specimen taking place after heating for 30 min at 500°C. The weight loss of 17 $\mu g/cm^2$ represented a gas content of 500 ppm. The degassing curve showed that under a vacuum of 10^{-6} mm the specimen exhibited a slow weight increase due to the gettering property of aluminum at elevated temperatures.

Oxidation tests.—Fig. 2 shows oxidation curves at various temperatures in the range 400°–600°C for specimens vacuum annealed 30 min at 500°C. The manner in which the oxide film grew on the aluminum specimens was similar at all elevated temperatures, i.e., there was an initial rapid rate of oxidation which was followed by an approximately constant rate of film growth for a period which was dependent on the temperature. After this formative stage, the rate of oxidation fell off to a low value. Consideration of the curves in Fig. 1 for the 400°–500°C range suggests that there is some justification for a prevalent view that the oxidation rates of aluminum obey a parabolic law in the temperature range 350°–475°C and a linear law at higher temperatures. The curves are parabolic in form for the two lower temperatures and approximately linear in form at 500°C. However, the oxidation curves at the higher temperatures of 550° and 600°C limit this view of paralinear oxidation to specific regions of film thickness. This is also borne out by data presented in a previous publication (13).

Annealing the specimen in vacuum at elevated temperatures altered its oxidation characteristics (13). It was found that the oxidation rate of metallographically polished aluminum at 500° was dependent on the temperature and time of vacuum annealing of the specimens. Specimens annealed at 600°C oxidized less rapidly than

those annealed at 500°C. The specimen which had undergone a longer vacuum anneal at 500°C had a lower rate of oxidation. Also, specimens vacuum annealed at 600° for 1 and 2 hr oxidized less rapidly than did a specimen annealed for 30 min at 600°C. These decreases in oxidation rates due to vacuum annealing may be caused by alteration of the initial surface oxide film present on the aluminum from amorphous to crystalline oxide or by a change in defect and dislocation concentration. This conclusion is borne out by the work of De Brouckère (14) who showed by electron diffraction that after 6 hr of heating at 400°C and after 1 hr of heating at 500°C, gamma-alumina forms in the oxide film on metallographically polished aluminum, and it forms after 1 min on the surface of molten aluminum.

The final film thicknesses illustrated in Fig. 2 for 550° and 600°C were less than the film thickness at 500°C. This anomaly may be due to the formation of crystalline oxide at these higher temperatures during the degassing stage since adjustment of the temperature at 550° or 600°C required 30 min after the vacuum anneal at 500°C.

In view of this influence of vacuum annealing, oxidation tests, illustrated in Fig. 3, were carried out using specimens vacuum annealed 1 hr at 600°C. These curves are similar in form to those of Fig. 2. Oxidation rates of samples annealed at 600°C, however, were less at 400°, 450°, and 500°C due probably to the formation of a more crystalline film. At 550° and 600°C, initial oxidation rates were identical, but the rate of film growth decreased more slowly for specimens annealed at 600°C. The fact that initial oxidation rates at these latter temperatures are equal indicates that the film structure is essentially the same at these temperatures in spite of variations in the vacuum anneals. The final thickness of the film may be greater for specimens annealed at 600°C due to an increase in concentration of such surface impurities as copper and iron which have a detrimental effect on the protective properties of the oxide film (9, 15).

Experimental precision.—Individual oxidation curves for specimens removed from a small section of the sheet and vacuum annealed at 500°C were reproducible within 10%. In the case of specimens vacuum annealed at 600°C for 1 hr, the oxidation tests at 500°C exhibited a greater deviation. An explanation of this effect is not possible unless extensive diffraction studies are undertaken of film structures in situ and the effects of impurities on oxidation rates determined.

Oxidation Mechanism

No oxidation rate law satisfies the experimental results over all ranges of film thickness. Although deviations exist, the concept of diffusion-controlled parabolic oxidation is probably the best approach and is therefore employed in this analysis. That this is the most reasonable choice is borne out first by Cabrera, Mott, and their coworkers (2, 3, 16–22) who postulate that the surface film on aluminum consists of a "metal-excess" oxide and that film growth occurs by diffusion of metallic ions through lattice interstitial positions; and second by Charlesby (11, 23) who has demonstrated that this theory is applicable to the anodic oxidation of aluminum. According to their views, the kinetics of gaseous oxidation of aluminum should be governed by a parabolic law in the temperature range 400°–600°C.

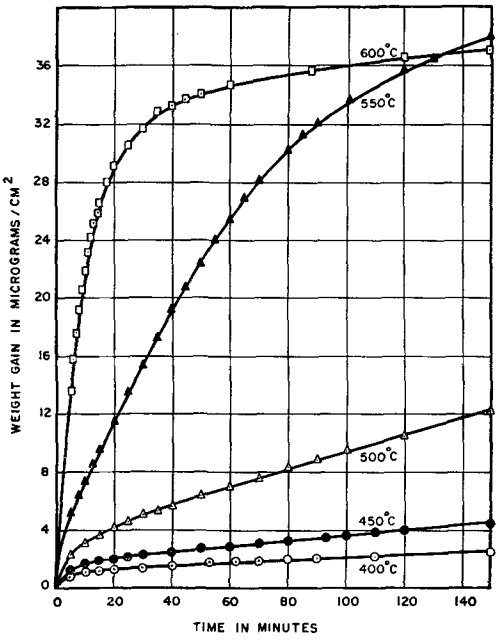

FIG. 3. Oxidation tests 400°–600°C, metallographically polished specimens degassed at 600°C.

The equation for the parabolic law of oxidation is:

$$x^2 = Kt + C \tag{I}$$

where x is the film thickness, t is the time, K is the parabolic rate constant, and C is a constant representing the initial film thickness.

Cabrera and Mott (2) showed that this law is applicable to the growth of both thin and thick films. The parabolic rate constant for a thin film is:

$$K = \frac{V\Omega q_i}{a_i}\frac{\gamma}{kT}\exp - W/kT \tag{II}$$

and for a thick film:

$$K = 2\Omega(N_iN_e)^{1/2}a_i^2\gamma \exp - \tfrac{1}{2}(W_i + \phi) - U/kT \tag{III}$$

Here W and ϕ are the potential energy barriers at the metal/oxide interface against ion and electron diffusion, respectively, W_i and U are the potential energy barriers between ion diffusion states from metal to oxide and between interstitial positions in the oxide, respectively, N_i and N_e are the concentrations of interstitial positions in the oxide and electrons in the metal, respectively, V is the potential across the oxide film, Ω is the volume of oxide per metal ion, q_i is the electrical charge of the metallic ion, γ is the frequency of vibration of the oxide lattice, a_i is the half-width of the potential barrier against ion diffusion, k is Boltzmann's constant, and T is the absolute temperature.

Gulbransen (24) has applied transition state theory to express the parabolic rate constant by the equation:

$$K = \frac{2kT\lambda^2}{h}\exp\frac{\Delta S^*}{R}\exp - E/RT \tag{IV}$$

where E and ΔS^* are the activation energy and entropy

of reaction, respectively, k is Boltzmann's constant, R is the gas constant, h is Planck's constant, and λ is the interatomic distance between diffusion sites.

Fig. 4 shows the experimental results at 550°C plotted on a parabolic scale, i.e., $(g/cm^2)^2$ vs. time. This curve shows an initial linear section which undergoes transition to a second linear section of greater slope and this, in turn, gives way as exposure time increases to a section with lower slope. This type of curve is obtained at all temperatures in the region 400°–600°C with the duration of each linear section dependent on the temperature. It is arbitrarily assumed that these linear sections of the curves yield the values of the parabolic rate constants for the thin and thick film ranges. These constants are recorded in Tables I and II.

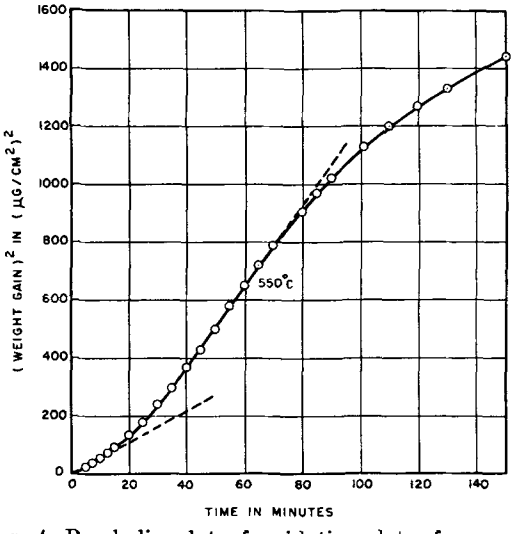

FIG. 4. Parabolic plot of oxidation data for specimen degassed at 550°C.

Parabolic oxidation rate constants are expressed in Arrhenius form:

$$K = Ae - E/RT \qquad (V)$$

where A is the frequency factor and E is the energy of activation.

Fig. 5 shows plots of log K vs. $1/T$ for specimens vacuum annealed at 500°C; a similar linear plot was obtained for specimens vacuum annealed at 600°C. The frequency factors and energies of activation with a

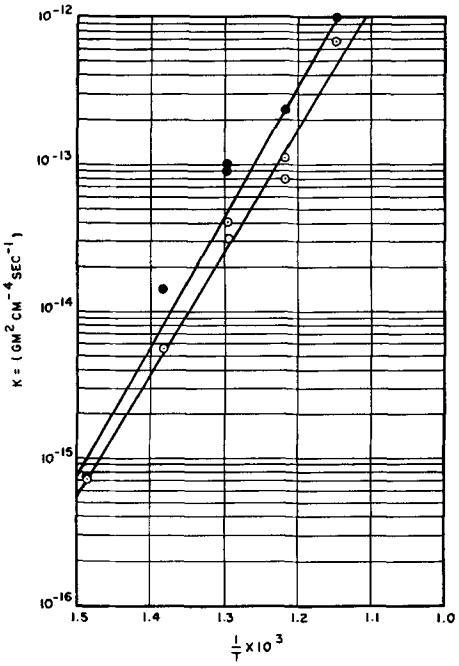

FIG. 5. Arrhenius plots of parabolic rate constants for specimens degassed at 500°C. ⊙—Thin film; ●—thick film.

TABLE I. *Parabolic rate constants, energies, and entropies of activation for the oxidation of metallographically polished aluminum degassed for 30 min at 500°C*

	1st Section of parabolic plot				2nd Section of parabolic plot			
Temp, °C	K $(g/cm^2)^2/sec$	A $g^2cm^{-4}sec^{-1}$	E cal/mole	ΔS^* cal/degree mole	K $(g/cm^2)^2/sec$	A $g^2cm^{-4}sec^{-1}$	E cal/mole	ΔS^* cal/degree mole
400	7.2×10^{-16}	1.6×10^{-3}	37,900	−7.1	7.5×10^{-16}	1.7×10^{-2}	40,500	−3.2
450	5.5×10^{-15}		37,900	−7.2	1.4×10^{-14}		40,500	−1.7
500	3.3×10^{-14}		37,900	−7.1	1.0×10^{-13}		40,500	−1.5
	4.0×10^{-14}		37,900	−6.7	8.9×10^{-14}		40,500	−1.8
550	7.9×10^{-14}		37,900	−8.4	2.4×10^{-13}		40,500	−3.1
	1.1×10^{-13}		37,900	−7.7	2.3×10^{-13}		40,500	−3.2
600	6.8×10^{-13}		37,900	−7.0	1.1×10^{-12}		40,500	−3.2

TABLE II. *Parabolic rate constants, energies, and entropies of activation for the oxidation of metallographically polished aluminum degassed for 1 hr at 600°C*

	1st Section of parabolic plot				2nd Section of parabolic plot			
Temp, °C	K $g^2cm^{-4}sec^{-1}$	A $g^2cm^{-4}sec^{-1}$	E cal/mole	ΔS^* cal/degree mole	K $g^2cm^{-4}sec^{-1}$	A $g^2cm^{-4}sec^{-1}$	E cal/mole	ΔS^* cal/degree mole
400	6.7×10^{-16}	8.0×10^{-3}	41,000	−2.7		6.0		
450	1.9×10^{-15}		41,000	−5.0	2.4×10^{-15}		50,700	8.9
500	1.3×10^{-14}		41,000	−5.0	2.6×10^{-14}		50,700	9.0
550	1.2×10^{-13}		41,000	−3.8	2.3×10^{-13}		50,700	9.3
600	6.0×10^{-13}		41,000	−3.7	9.6×10^{-13}		50,700	8.4

precision of ±5000 cal/mole are tabulated in Tables I and II. Energies of activation of 37.9 and 41.0 kcal/mole for the first linear section of the parabolic plots represent $W_i + U$ [equation (II)], and energies of activation of 40.5 and 50.7 kcal/mole for the second linear section represent $\frac{1}{2}(W_i + \phi) + U$ [equation (III)], if the considerations of Mott and Cabrera are valid. These values of the activation energies, which are larger in the thick film range, do not substantiate their suggestion that the increase in the parabolic rate constant is caused by a decrease in the activation energy by assuming that $W_i > \phi$.

Equation (IV) was used to calculate, arbitrarily, values of the entropy of activation for the two linear sections of the parabolic plots with the assumption that the interatomic jump distance for diffusion was 3.74Å. Values of this term are recorded in Tables I and II. Two conclusions are apparent: the entropy of activation is negative and becomes of smaller negative value with increasing film thickness and this value is more positive for specimens vacuum annealed at the higher temperature of 600°C. Gulbransen (25) suggested that large negative values indicate the presence of short-circuiting diffusion paths around the grain boundaries. This view has been questioned by Moore (26) for aluminum because the crystalline size in the amorphous oxide is so small that no electron diffraction pattern has been observed. Since Wilsdorf (27) has interpreted the diffraction photographs of the amorphous oxide film as consisting of totally disordered Al_4O_6 molecular groups, diffusion may occur at elevated temperatures by paths around and through aggregates of these molecular groups. The fact that the entropy of activation becomes more positive for longer exposure times and for specimens vacuum annealed at the higher temperature of 600°C indicates that those molecular groups, within themselves bound by ionic forces, become larger by crystallization and remove short-circuiting paths. Support for these views on the effect of crystallization is found in a reduction of oxidation rates of aluminum vacuum annealed for relatively longer times and higher temperatures.

Kinetic measurements, alone, do not aid substantially in elucidating the mechanism of the high temperature oxidation of aluminum. The concept of diffusion-controlled parabolic oxidation has stringent limitations because no account is taken of variations in crystalline structure of the oxide film. In an attempt to place the experimental data within this theoretical framework, two arbitrary assumptions have been made, namely, that oxidation rate constants can be determined from finite linear sections of the parabolic law plots and that these constants obey the Arrhenius relation, although crystallization of oxide is occurring simultaneously with film growth.

Literature Assessment

The activation energy of reaction in the thin film range represents, according to the Mott and Cabrera theory, the potential energy barrier against ion diffusion at the metal/oxide interface. Values for this barrier of 37.9 and 41.0 kcal/mole (1.6 and 1.8 ev) from this investigation are in excellent agreement with values of 1.6 and 1.8 ev determined by Charlesby (11) from results on the anodic oxidation of aluminum. These values are inconsistent with a determination of 22.8 kcal/mole by Gulbransen and Wysong (10) from high temperature gaseous oxidation studies. These investigators found large variations in oxidation rates for two samples of high purity aluminum and interpreted the data separately for each sample. Plots of log K vs. $1/T$ for parabolic rate constants of their investigation and those for the initial stage of parabolic oxidation of this study are shown in Fig. 6. Because of the broad scatter of experimental values the root mean square value of the activation energy may be most appropriate for determination of the barrier against ion diffusion. Accordingly, the value of the parabolic rate constant for the high temperature oxidation of aluminum in the thin film range is:

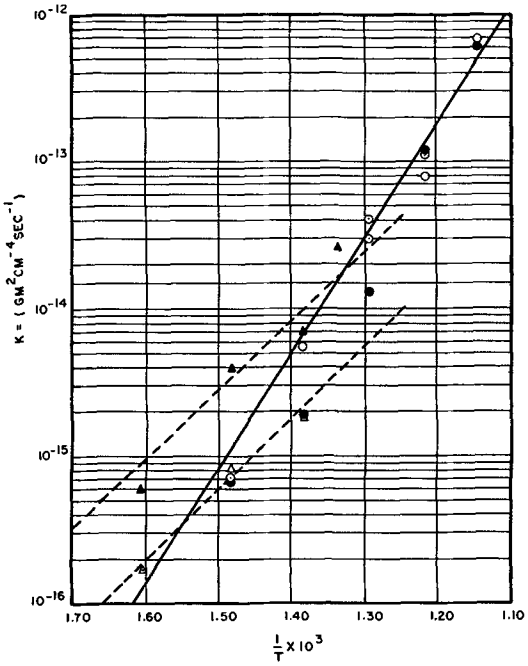

FIG. 6. Arrhenius plots of parabolic rate constants for thin oxide film. ▲ △—Determinations by Gulbransen and Wysong; ● ⊙—determinations of this investigation; ----------—Gulbransen and Wysong plot; ————root mean square plot.

$$K(g^2\,\mathrm{cm}^{-4}\,\mathrm{sec}^{-1}) = 6.33 \times 10^{-5} \exp - 33{,}100/RT$$

A mean value of 37.2 kcal/mole (1.6 ev) is obtained for the potential barrier against ion diffusion at the metal/oxide interface if the same significance is attached to the two determinations from anodic oxidation data and this root mean square value of the energy of activation.

SUMMARY

Reactions of aluminum with oxygen have been studied, using a vacuum microbalance technique, over the temperature range 400°–600°C. At all temperatures there was an initial rapid rate of oxidation which was followed by an approximately constant rate of film growth for a period dependent on temperature. After this formative

stage, the rate of oxidation decreased to a negligible value. Vacuum annealing metallographically polished aluminum in the temperature range 500°–600°C caused formation of an oxide film which was more resistant to oxidation.

Reaction rate results were interpreted according to a parabolic law of oxidation. Values of 37.9 and 41.0 kcal/mole were determined for the activation energy of reaction in the thin film range for specimens vacuum annealed at 500° and 600°C, respectively. A mean value of 37.2 kcal/mole was obtained for the energy barrier against ion diffusion at the metal/oxide interface by attaching equal significance to results from gaseous and anodic oxidation. An increase in the magnitude of the energy of activation at larger film thickness and the cessation of oxidation have emphasized the limited applicability of present theories in explaining the high temperature oxidation mechanism of aluminum.

Acknowledgments

The author is indebted to Mr. G. Ensell and Dr. E. J. Caule and Dr. M. Cohen, National Research Council Laboratories, Ottawa, Canada, for construction of the vacuum microbalance and information on their experimental techniques for metal oxidation studies. Special thanks are due to Dr. H. H. Podgurski, Engineering Research Laboratory, E. I. du Pont de Nemours and Co., Wilmington, Del., for helpful discussion.

Manuscript received July 7, 1955.
Any discussion of this paper will appear in a Discussion Section to be published in the December 1956 Journal.

References

1. N. K. Andrushenko and P. D. Dankov, *Compt. rend. acad. Sci. U.R.S.S.*, **62**, 353 (1948).
2. N. Cabrera and N. F. Mott, *Repts. Progr. Phys.*, **12**, 163 (1949).
3. N. Cabrera and J. Hamon, *Compt. rend.*, **224**, 1713 (1947).
4. G. Hass, *Optik*, **1**, 134 (1946).
5. F. Keller and J. D. Edwards, *Metal Progr.*, **54**, 35 (1948).
6. G. Tolley, "Properties of Metallic Surfaces," p. 327, Institute of Metals, London (1953).
7. W. D. Treadwell and A. Obrist, *Helv. Chim. Acta*, **26**, 1816 (1943).
8. N. B. Pilling and R. E. Bedworth, *J. Inst. Metals London*, **29**, 429 (1923).
9. J. Herenguel and J. Boghen, *Rev. Met.*, **51**, 265 (1954).
10. E. A. Gulbransen and W. S. Wysong, *J. Phys. & Colloid Chem.*, **51**, 1087 (1947).
11. A. Charlesby, *Proc. Phys. Soc. London*, **66**, 317 (1953).
12. E. A. Gulbransen, *Rev. Sci. Instr.*, **15**, 201 (1944).
13. W. W. Smeltzer, *Corrosion*, **11**, 366 (1955).
14. L. De. Brouckère, *J. Inst. Metals London*, **71**, 131 (1945).
15. T. P. Hoar and U. R. Evans, *This Journal*, **99**, 212 (1952).
16. N. Cabrera, *Phil. Mag. London*, **40**, 175 (1949).
17. N. Cabrera, *Rev. Met.*, **45**, 86 (1948).
18. N. Cabrera, J. Terrien, and J. Hamon, *Compt. rend.*, **224**, 1558 (1947).
19. N. Cabrera and J. Hamon, *ibid.*, **225**, 59 (1947).
20. N. Cabrera, *ibid.*, **220**, 111 (1945).
21. N. F. Mott, *Trans. Faraday Soc.*, **35**, 1175 (1939).
22. N. F. Mott, *ibid.*, **36**, 472 (1940).
23. A. Charlesby, *Proc. Phys. Soc. London*, **66**, 533 (1953).
24. E. A. Gulbransen, *Trans. Electrochem. Soc.*, **83**, 301 (1943).
25. E. A. Gulbransen, *Ann. N. Y. Acad. Sci.*, **58**, 830 (1954).
26. W. J. Moore, *This Journal*, **100**, 302 (1953).
27. H. G. F. Wilsdorf, *Nature*, **168**, 600 (1951).

The Voltage Drop Through Phosphor Screens and Its Bearing on Performance of Cathodoluminescent Lamps

L. R. Koller

Research Laboratory, General Electric Company, Schenectady, New York

ABSTRACT

Measurements have been made of the voltage drop when an electron beam passes through a fluorescent screen. This varies from a few volts to several hundred volts depending on the nature of the phosphor. By choosing phosphors with high conductivity, the major part of the voltage drop across an electron tube is made available for excitation of the phosphor. This principle is applied to the construction of 120-volt cathodoluminescent lamps.

Introduction

The efficiency of light production in many cathode ray and television tubes, although of less importance than the brightness of the cathode spot, may be fairly high. Values of 24% radiation efficiency at 20 kv have been reported by Bril and Klasens (1) and a luminous efficiency of 98 lpw has been obtained with phosphors such as ZnCdS:Ag where the emission band is in the middle of the visible spectrum. These values are sufficiently high to make cathode ray excitation attractive as a source of illumination. The disadvantages of lamps operating in the kv range are obvious. Accordingly, it

seemed worthwhile to investigate the possibilities of cathode ray excitation at ordinary commercial voltages, say 120 v.

When the voltage for cathode ray excitation is lowered from several kilovolts to some tens of volts, three limitations which are of little importance at the higher voltage must be considered. These are: (*a*) the "dead voltage;" (*b*) the first "crossover" for secondary emission; (*c*) the voltage drop through the phosphor screen.

The relation between voltage and brightness for phosphors is of the form $L = Af(i)(V - V_o)^n$, where L = luminescence emission, i = current density, V = applied anode voltage, V_o = "dead layer voltage," n = a constant, usually in the range from 1 to 3. V_o, the dead voltage is interpreted as the voltage required to penetrate an inert nonluminescent layer on the surface of the phosphor grains. It is usually of the order of a few tens to a few hundreds of volts. It is just in this range that it would be desirable to operate cathode ray lamps. Accordingly, the dead voltage results in a considerable decrease in efficiency as anode potential is reduced to the low voltage (120 v) region. Attempts have been made to remove the dead layer by chemical treatment (2), but no study has been made of the effectiveness of this treatment at low voltage.

The second effect which limits the excitation of phosphors at low voltages is the secondary electron emission from the phosphor. In most cathode ray tubes the phosphor is prevented from charging up by the emission of secondary electrons. Unless the number of secondary electrons emitted is equal to the number of incident electrons the phosphor rapidly charges up to cathode potential. The number of secondaries emitted per incident primary is a function of the primary voltage. Below a critical voltage known as the "first crossover" the number of secondaries per primary becomes less than unity and a tube with a phosphor on an insulating surface becomes inoperative. For many phosphors the first crossover is between 50 and 200 v which again is just in or above the range in which we wish to operate lamps.

An alternative method of discharging the phosphor is to apply it to a conducting anode so that the charge can leak off the phosphor to the anode. This results in a voltage drop through the screen. It was the purpose of this investigation to measure the voltage drop through phosphor screens and to find out what bearing this had on the operation of cathode ray lamps.

Some measurements were made to select phosphors of various resistances for these tests. The measurements were made on 0.5 g cylindrical pellets of the various phosphors pressed in a hand press using a die, 0.3 in. in diameter. Contact was made with brass electrodes by dusting a little metallic zinc powder on the bottom of the die and on top of the powder, before pressing. The height of the pellets was 2 mm or more depending on the density of the powder. Materials such as ZnO and Zn_2SiO_4 made compact durable pellets, while those of ZnCdS were very fragile. Values of resistance were measured in vacuo with a megohmmeter which impressed 10–20 v across the sample. The phosphors tested and the measured resistances of the pellets are listed in Table I. In spite of the variation in compactness of the powder in the various pellets, it was evident that zinc oxide phosphor had a conductivity higher by at least three orders of magnitude than 12 other common phosphors tested.

TABLE I. *Resistance measured in vacuo with megohmmeter and 10–20 v impressed across sample*

Resistance of phosphor pellets Phosphor	Resistance of 0.5 g pellet in vacuo
ZnO:Zn (N.J. Zinc Co. No. 2100)	$0.4 \times 10^6\ \Omega$
ZnO:Zn (N.J. Zinc Co. No. 2100)	$60 \times 10^6\ \Omega$
ZnO:Zn (N.J. Zinc Co. No. 2100)	$20 \times 10^6\ \Omega$
ZnO:Zn (N.J. Zinc Co. No. CE4107)	$55 \times 10^6\ \Omega$
Zn_2SiO_4:Mn (GE Co.)	$>5 \times 10^{10}\ \Omega$
ZnS:Ag (Patterson No. 1410)	$>5 \times 10^{10}\ \Omega$
$CaMg(SiO_3)_2$:Ti (Sylvania No. 270)	$>5 \times 10^{10}\ \Omega$
$Ca_3(PO_4)_2$:Ce	$>5 \times 10^{10}\ \Omega$
CaO:Pb (Fonda)	$>5 \times 10^{10}\ \Omega$
ZnS:Zn (Prener)	$>5 \times 10^{10}\ \Omega$
ZnCdS:Ag (90% Cd)	$>5 \times 10^{10}\ \Omega$
ZnS·Se:Cu (GE Co. 3-310)	$>5 \times 10^{10}\ \Omega$
ZnO·MgO (N.J. Zinc Co. No. 2115)	$>5 \times 10^{10}\ \Omega$
Mg Titanate (N.J. Zinc Co. No. 2125)	$>5 \times 10^{10}\ \Omega$
CdS:Ag (Fonda)	$>5 \times 10^{10}\ \Omega$

The zinc oxide phosphor used was much finer grained than the other phosphors. It showed the well-known increase in resistance due to adsorption of O_2 which has been studied by Morrison (3). One sample dropped from $10^9\ \Omega$ at one atmosphere to $4 \times 10^5\ \Omega$ in vacuo in about 3 hours' time. This effect was completely reversible.

Screen Voltage Drop Measurements

With this information as a guide, the voltage drop through a number of different phosphor screens was studied in a special form of cathode ray tube. Some of these screens consisted essentially of monolayers of grains and had no binder (4). The average coating weight for screens of this kind is less than 2 mg/cm². Several screens, settled by the conventional liquid settling process, using Kasil binder, were also tested, as well as one deposited by the Studer and Cusano (5) vapor reaction process. The phosphors and the coating weights are listed in Table II.

The tube contained a simple electron gun which focused a beam of electrons on the phosphor screen, a coarse mesh grid to collect secondaries, and a phosphor screen deposited on a surface of conducting glass with which contact was made by a wire sealed through the glass. A moveable shutter over the end of the anode prevented barium from depositing on the screen during activation of the cathode. The tube construction is shown schematically in Fig. 1. A fixed potential of 200 v was applied to the first anode and to the grid. This gave a beam current of approximately 1 ma to the anode (screen) and a spot about 1 cm in diameter.

The relation between anode current and anode voltage for a tube with a conducting glass anode (and no phosphor coating) is shown in Fig. 2, curve *a*. The current saturates at about 10 v. At higher voltages the anode current decreases, as shown by the dotted line, because of secondary emission from the anode. However, we are not concerned with this part of the curve. The volt ampere curve up to saturation shows the relation for this geometry

TABLE II. *Voltage drop through phosphor screens*

Phosphor	Screening procedure	Estimated thickness	Voltage drop at 1 μa/cm²	Voltage drop at 100 μa/cm²
		μ		
ZnO:Zn (N.J. Zinc Co. No. 2100)	Monoparticle layer	4	<1	<1
ZnS:Zn (Prener)	Monoparticle layer	5	10	130
ZnCdS:Ag (65% Zn, 35% Cd)	Monoparticle layer	5	4	27
Zn_2SiO_4:Mn (GE)	Monoparticle layer	5	34	220
ZnS:Ag (Patterson No. 1410)	Monoparticle layer	5	2	27
ZnS:Mn	Vapor reaction film	8.5	—	30
ZnO:Zn (N.J. Zinc Co. No. 2100)	Liquid settled 5 mg/cm²	9	—	65
Zn_2SiO_4:Mn (GE)	Liquid settled 5 mg/cm²	13	33	240
Zn_2SiO_4:Mn (GE)	Liquid settled 10 mg/cm²	26	75	420

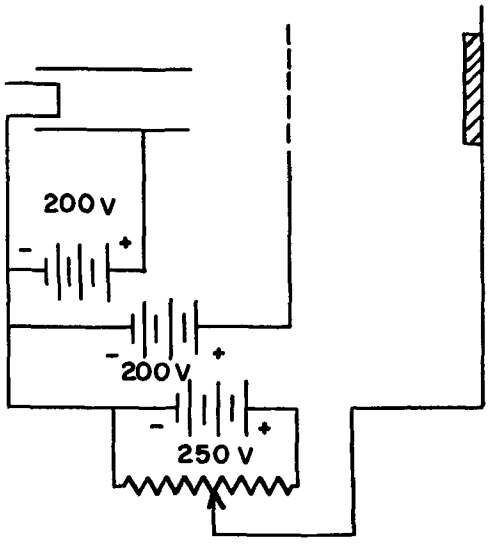

FIG. 1. Schematic diagram of tube for measurement of screen characteristics.

between beam current and the potential of the surface of the anode. Fig. 2, curve *b* shows the anode volt ampere relation for a tube of identical construction, differing from the first only in that the anode has a phosphor coating. Curve *b* is displaced to the high voltage side of curve *a* by an amount corresponding to the voltage drop through the phosphor, the voltage drop through the space being given the abscissas of curve *a*.

From data such as these, curves of current through the screen vs. voltage drop across the screen for various phosphors can be constructed. These curves are all of the same general form shown in Fig. 3, indicating a very high impedance for small currents which drops to a much smaller value with increasing current. The latter part of the curve fits an exponential of the form

$$i = Ke^{V/a}$$

where i = beam current, V = beam voltage, and K, a = constants. This part of the curve corresponds to average field strengths across the phosphor of 10^5–10^6 v/cm.

Table II shows the voltage drop measured by this method at two different values of current density. The higher current density approximates the value used in some low voltage cathode ray lamps to be described later. The table shows that the voltage drop at 100 μa/cm² through monolayer phosphor screens is less than 1 v for the zinc oxide phosphor and from 27 to 220 v for the other four phosphors deposited in this way. The Zn_2SiO_4 shows the highest voltage drop. For thicker screens, the voltage drop increases roughly in proportion to screen thickness as is shown by the data on liquid settled Zn_2SiO_4:Mn. The drop through a 10 mg/cm² liquid settled Zn_2SiO_4:Mn screen at 100 μa/cm² is 420 v.

Cathode Ray Lamp Characteristics

With information about the phosphor voltage drop, it is possible to predict the characteristics of cathode ray lamps. Consider a lamp consisting of a hot cathode at the center of a spherical bulb, the inside of the bulb having a transparent conducting coating on which the phosphor is

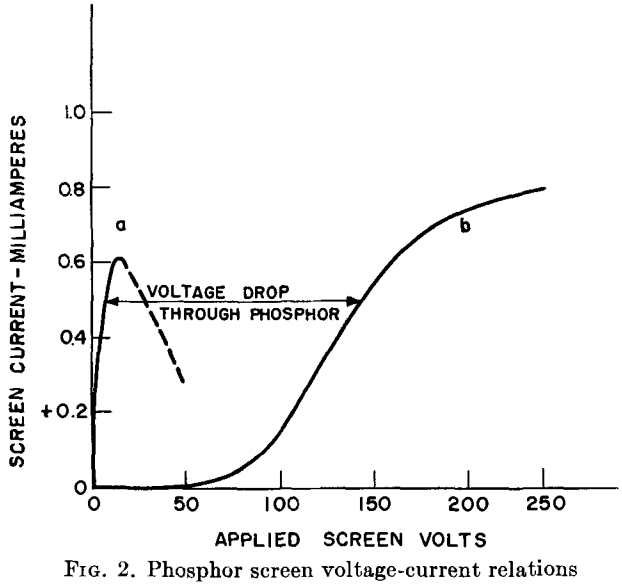

FIG. 2. Phosphor screen voltage-current relations

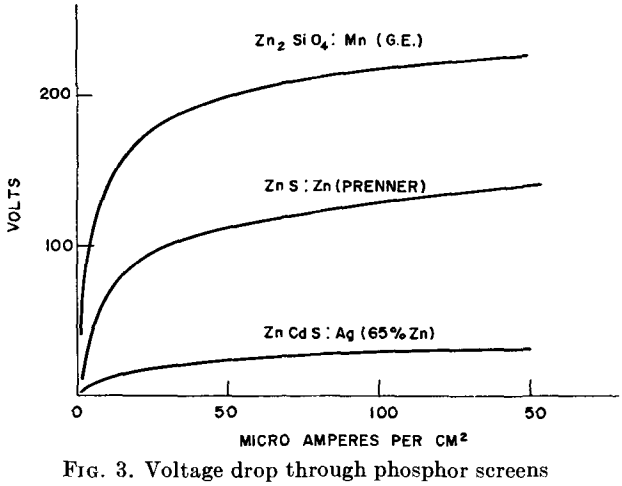

FIG. 3. Voltage drop through phosphor screens

deposited. Fig. 4 shows, on the left, the voltage current relation for this device as it would be if limited by the 3/2 power space charge law only, that is, with no phosphor on the anode. On the right is shown the phosphor voltage current relation. The lamp will operate at a current determined by the intersection of these two curves. The applied voltage will be divided between the space and the phosphor in the ratio V_s to V_p. V_s is useful in accelerating electrons across the space and exciting luminescence. V_p is the voltage drop necessary for the passage of current through the phosphor and does not contribute to the luminescence.

Fig. 5 shows calculated lamp characteristics for three different phosphors. The phosphor voltage current relations were determined by the cathode ray tube method already described. The relation for the lamp without the phosphor was calculated from the 3/2 power law. The heavy curve shows the characteristic for a 250-v lamp and the dashed curve shows it for a 120-v lamp.

From the figure it is evident that for a given lamp construction a high-resistance phosphor can only operate at a small current density with a relatively small fraction of the applied voltage available for excitation. With a low-resistance phosphor, on the other hand, the current is limited practically only by space charge and most of the applied voltage is available for excitation.

The applied voltage can be a very misleading criterion of phosphor brightness because the drop through the phosphor accounts for such a large fraction of the voltage. For instance, Fig. 5 shows that with 120 v applied to a lamp with a willemite screen, the drop through the screen accounts for 110 v, leaving only 10 v for acceleration of the electrons. Thus, the luminescence observed is due to 10-v electrons and not 120-v electrons.

A number of low voltage cathode ray lamps were constructed with various phosphors. These consisted of 3 in. Pyrex glass bulbs with SnO_x conducting coatings on the inside walls and centrally located indirectly heated oxide coated cathodes. The cathodes were capable of supplying ample emission so that they were not a limiting factor in the operation of the lamps. The bulbs were coated on the inside wall with a nitrocellulose suspension of the phosphor. The nitrocellulose was burned out by baking in a stream of oxygen and the bulbs were then evacuated. Lamps with zinc oxide coatings were found to operate over any desired voltage range. Luminescence was uniform over the entire bulb and increased steadily in brightness from a threshold of a few volts. [Shrader and Kaisel (6) have shown a threshold for excitation of luminescence in zinc oxide of less than 3 v.] The volt ampere characteristic of the lamp with the phosphor coating was almost the same as for the lamp with the conducting tin oxide coating only, showing that the voltage drop through the phosphor is negligibly small.

With Zn_2SiO_4:Mn coatings, no luminescence was observed up to about 200 v where the lamp current was only a few microamperes. At this voltage a few small luminescent spots appeared. These shifted and grew in extent and brightness in a rather erratic manner with increasing voltage. This behavior is probably due to inhomogeneities or variations in thickness of different parts of the coating.

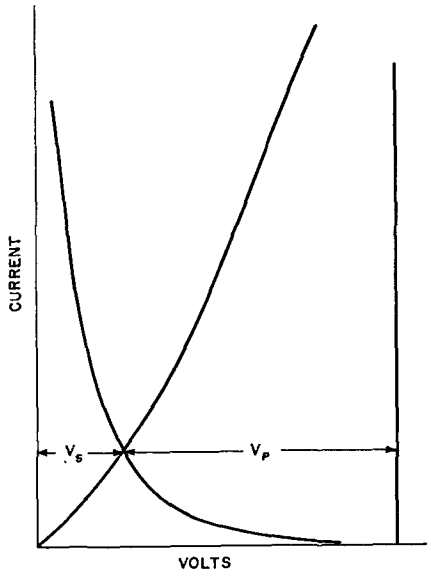

FIG. 4. Potential distribution in cathode ray lamp

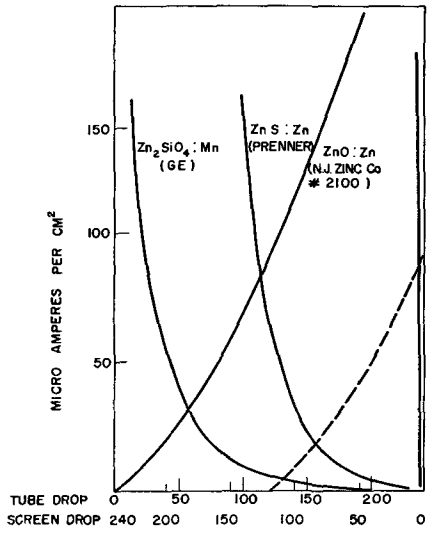

FIG. 5. Potential distribution in cathode ray lamps with various phosphors.

ZnS:Ag coatings gave considerably larger currents than Zn_2SiO_4:Mn and above 100 v the lamps showed uniform luminescence over most of the bulb. Currents were about 1/10 as large as for zinc oxide coatings. Thus, the characteristics of the lamps are in qualitative agreement with the characteristics predicted from measurements of the voltage drop through phosphor screens.

Since the screens studied in the cathode ray tube and those in the lamps were deposited by such different methods, quantitative agreement could not be expected.

From these experiments it was concluded that one of the most desirable properties in a phosphor to be used in low voltage cathode ray lamps is a high conductivity. The only available phosphor which meets this requirement [with the possible exception of ZnF_2:Mn (7)] is ZnO:Zn.

Manuscript received June 7, 1955. This paper was prepared for delivery before the Cincinnati Meeting, May 1 to 5, 1955.

Any discussion of this paper will appear in a Discussion Section to be published in the December 1956 JOURNAL.

REFERENCES

1. A. BRIL AND H. A. KLASENS, *Philips Tech. Rev.*, **15**, 67 (1953).
2. H. W. LEVERENZ, U. S. Pat. 2,164,533, July 4, 1939.
3. S. R. MORRISON, Contract N6-ONR-24914, Aug. 7, 1952.
4. L. R. KOLLER, *J. Opt. Soc. Amer.*, **43**, 7 (1953).
5. F. J. STUDER AND D. A. CUSANO, *ibid.*, **45**, 495 (1955).
6. R. E. SHRADER AND S. F. KAISEL, *ibid.*, **44**, 135 (1954).
7. H. J. CRAWFORD AND F. E. WILLIAMS, *J. Chem. Phys.*, **18**, 775 (1950).

Five Metal Hydrides as Alloying Agents on Silicon

MILES V. SULLIVAN AND JOHN H. EIGLER

Bell Telephone Laboratories, Incorporated, Murray Hill, New Jersey

ABSTRACT

The use of certain metal hydrides to promote alloying to silicon is described. Good ohmic contacts to both *n*- and *p*-type silicon have been made. The electrical resistance of a typical 1 cm² contact is less than 0.001 ohm. The depth of alloying may be controlled from 0.025 mm to 0.0025 mm depending on the alloy and the alloying temperature. Completed contacts exhibit tensile strengths in excess of 4500 psi.

INTRODUCTION

The use of silicon as a semiconductor involves the application of two or more electrical contacts to the silicon. These contacts may be rectifying or nonrectifying depending on what is used for the contact material and how the contact is made. Quite often a particular kind of contact can be made rectifying or nonrectifying by the addition of small amounts of donor or acceptor impurities to the contact material.

Alloying is the most satisfactory method of obtaining an intimate and permanent contact between any two materials. Tin-lead solder, one of the most commonly used contact materials in the field of electronics, depends on alloying to attain the very desirable electrical and mechanical properties usually associated with it. It is a rather common experience, however, to find that a flux is necessary in order to obtain good uniform wetting of most surfaces by solder.

In the case of silicon, the stable oxide film on the surface requires the employment of a more active flux for soldering than is used on common metals. Most of the conventional fluxes that are active enough to promote good soldering also leave corrosive residues. However, certain metal hydrides can be successfully employed as fluxes or alloying agents for silicon without producing corrosive residues. With such hydrides one product of their decomposition is hydrogen and the remainder is a metal which then forms part of the soldering alloy. In certain applications it may be necessary to add a small amount of impurity to the solder in order to obtain the desirable electrical properties.

This hydride method resembles a technique patented by Kelly (1) for making metal-ceramic seals. In such seals titanium hydride was used to obtain good wetting of a ceramic surface by a metal such as silver or copper. Heating in that case was done in a vacuum furnace. Other workers, including Cleveland (2), have extended this technique to include other hydrides, some of which are more convenient to use than the titanium hydride.

Briefly, the hydride process as applied to silicon consists of coating the silicon with a thin film of the hydride and bringing this coated silicon surface into contact with the solder at an elevated temperature in an inert atmosphere. For convenience of application the powdered hydride may be suspended in an organic binder such as an amyl acetate solution of cellulose nitrate. The time in the furnace is of the order of 1–10 min; the atmosphere is nonoxidizing (nitrogen or hydrogen); and the temperature of the furnace may be 600°–900°C, depending on which hydride is employed.

Since the solder melts before the alloying temperature is reached, some provision must be made to hold the liquid solder in place while the assembly is being brought up to temperature. One method of accomplishing this is to dip the silicon specimen into the molten solder. Another method illustrated in Fig. 1 is the use of a pretinned metal cap. In this case the solder wets the cap and is held in place by surface forces. The choice between these two methods depends on the ultimate use of the contact. In many applications the retaining cap may be a structural part of the finished device, and the cap method would then be preferred. On the other hand, it may be impractical to submit certain portions of the device to the rather high temperature required for alloying and, in this case, the dipping technique plus a subsequent low temperature soldering operation is most convenient. The cap technique with the caps being made of Kovar was used for all of the data reported here.

HYDRIDES

A series of tests were made in which contacts were placed on opposite faces of thin slices of silicon, as shown in Fig. 1. The total resistance (d-c voltage/d-c current) of the structure was then measured and plotted against

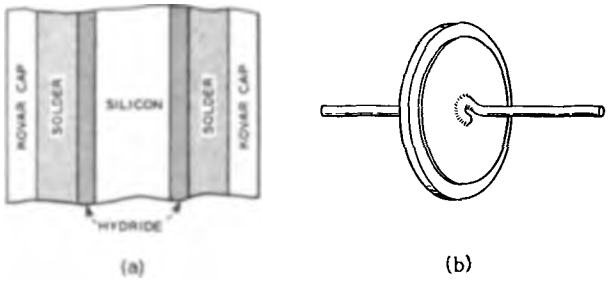

FIG. 1. (*a*) Section of assembly, not to scale; (*b*) completed test structure with leads attached for resistance measurements.

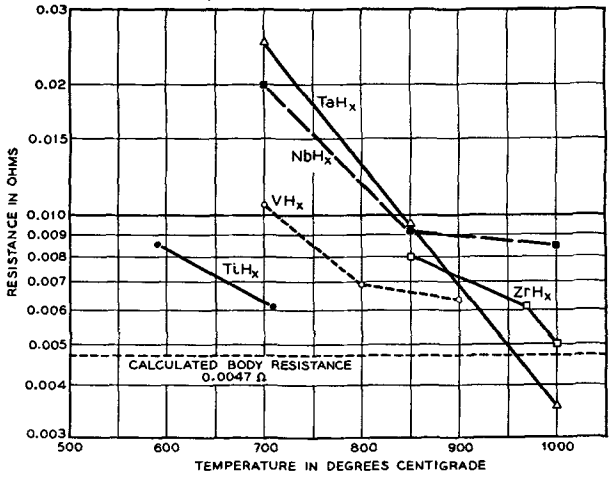

FIG. 2. Resistance as a function of alloying agent and temperature of alloying. Contact area is 1 cm².

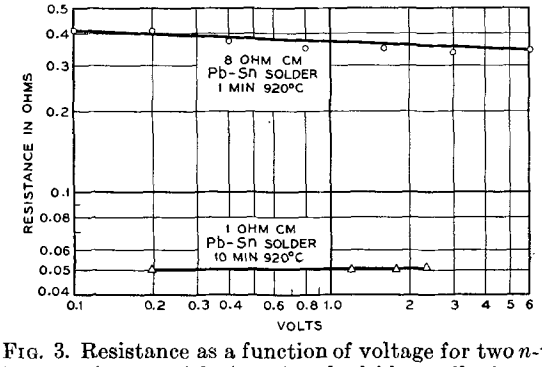

FIG. 3. Resistance as a function of voltage for two *n*-type silicon specimens, with zirconium hydride as alloying agent and a contact area of 1 cm².

the temperature of alloying for each of the five metal hydrides,[1] as shown in Fig. 2. The calculated body resistance is indicated by the dotted line. A minimum temperature of 600°–700°C must be employed before any alloying is obtained. At higher temperatures the contact is improved and the total resistance measured approaches the calculated body resistance. An examination of all six of the specimens which had been made with zirconium hydride indicated that the variation of resistance was due mainly to the fact that the surface was only partially wet at the lower temperatures of alloying. Even when only partial wetting occurred, however, the contacts were nonrectifying.

[1] Hydrides were obtained from Metal Hydrides Inc., Beverly, Mass.

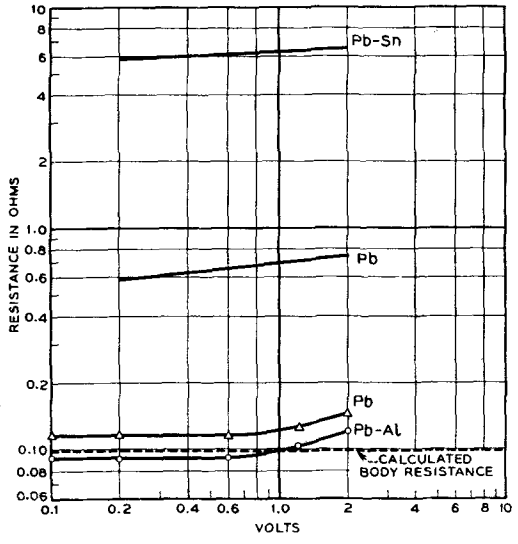

FIG. 4. Resistance as a function of voltage for 1 ohm-cm *p*-type silicon specimens, with zirconium hydride as alloying agent and a contact area of 1 cm².

TABLE I. *Depth of penetration as a function of alloy and alloying agent. Heating time is 1 min*

Solder alloy	Zirconium hydride at 900°C	Titanium hydride at 700°C
Pb	<0.0025 mm	<0.0025 mm
Pb-Sn (55:45)	0.01 to 0.015 mm	<0.0025 mm
Pb-Ga (98:2)	0.012 to 0.025 mm	<0.0025 mm

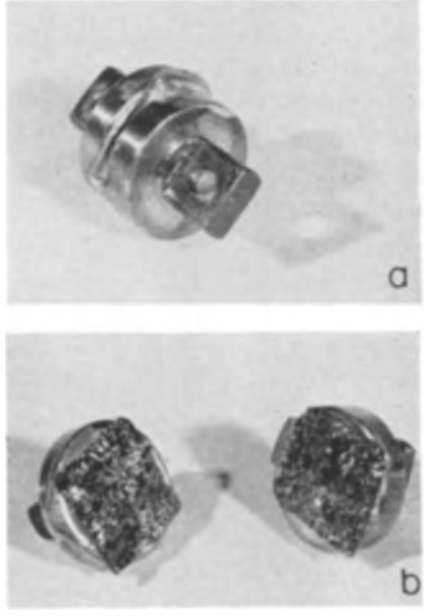

FIG. 5(*a*). Sample with heavy caps ready for tensile strength tests; FIG. 5(*b*). Sample after test showing the fractured silicon surface.

CONTACT TO *N*-TYPE SILICON

Contacts to *n*-type silicon are ohmic, as is indicated in Fig. 3. Here there are plotted the d-c resistances of two

test diodes as a function of voltage with silicon resistivity as the parameter. In both cases the observed resistance was so close to the calculated body resistance that no significant value could be assigned to the contact.

Contact to *P*-Type Silicon

In the evaluation of the various hydrides previously described, low resistivity (0.038 ohm-cm) *p*-type silicon was used. From these data it would appear that good contacts may be easily made on low-resistivity *p*-type material.

With *p*-type silicon in the 1 ohm-cm range, however, appreciable contact resistance was observed as indicated in Fig. 4. The calculated body resistance of the diode is about 0.1 ohm but the measured resistance of a typical specimen is about 6 ohms when tin-lead solder is used, or about 0.6 ohm when pure lead (99.99+%) is used. The contact resistance in this case would be about 6 ohms for the solder and 0.5 ohm for lead. The contact resistance is easily brought down to a negligible value, however, by doping the lead with about 1% aluminum as indicated by the circles, or by first providing a more heavily doped layer on the surface and then making a contact with pure lead as indicated by the triangles.

The necessity for doping the solder when used on *p*-type material but not when used on *n*-type suggests that a donor-type impurity may be present in the solder. An analysis of the alloy formed in the contact when tin-lead solder was used indicates the presence of antimony which is normally found in commercial solder. The antimony content can be reduced considerably by using a high purity lead in the tin-lead solder. In addition to the antimony there were appreciable percentages of iron, nickel, and cobalt. These presumably come from Kovar cap and may be eliminated if desired by the choice of another cap material, for example, molybdenum, or of no cap at all, in which case one may use the dipping technique mentioned previously.

Depth of Penetration

For certain uses the depth of alloying may be important. The depth of penetration of the contact as a function of alloy composition and of alloying agent is given in Table I. Heating time in each case was 1 min. Penetration measurements were made by an optical examination of the sectioned contacts at a magnification of 500. The accuracy of the measurements was about ±0.0025 mm. Penetration appears to be less than 0.0025 mm whenever lead is used as the solder or whenever the temperature is kept down to 700°C. On the other hand, for lead alloys at 900°C the penetration appears to be between 0.01 mm and 0.025 mm. Several of the other hydrides and other common flux materials were employed at the same temperature. The depth of penetration did not appear to be a function of the nature of the flux.

Mechanical Properties

Plated or soldered contacts are often tested by measuring the force required to strip the bond at the interface between the two phases. Tensile strength tests were made on several specimens 1 cm^2 and 1.25 mm thick and provided with specially designed heavy caps. In Fig. 5(*a*) a sample is shown ready for test and in Fig. 5(*b*) the sample has been tested and shows the fractured silicon surfaces. The silicon broke in every case at a stress between 20 and 35 kg/cm^2 (3000 and 5000 $lb/in.^2$). The break was always in the silicon about midway between the two contacts. In the sample shown, polycrystalline silicon was used. When monocrystalline material is used fewer cleavage planes appear.

Manuscript received September 15, 1955. This paper was prepared for delivery before the Cincinnati Meeting, May 1 to 5, 1955.

Any discussion of this paper will appear in a Discussion Section to be published in the December 1956 Journal.

REFERENCES

1. U. S. Pat. No. 2,570,248.
2. Private communication.

The Effect of Electron Traps on Electroluminescence

P. D. Johnson, W. W. Piper, and F. E. Williams

Research Laboratory, General Electric Company, Schenectady, New York

ABSTRACT

Measurements of the temperature dependence of electroluminescent brightness and thermoluminescence of phosphor powder suspensions in Lucite and of single crystals demonstrate that electroluminescent brightness can be affected by electron traps. At low temperatures traps may, by field ionization, supply electrons in the region of high field. At higher temperatures they are thermally emptied, enhancing the field in the barrier region. Decreases in electroluminescent brightness occur in the temperature range where the role of traps is changing.

Introduction

In electroluminescent zinc sulfide phosphors shallow occupied electron traps or donors generate a region of high field by emptying to form an exhaustion layer. Deeper donors are field ionized to provide conduction electrons which are accelerated, in the region of high electric field, to velocities sufficient for impact excitation of activators (1). Comparison of the temperature dependence of electroluminescent brightness and of thermoluminescence suggests that in some temperature ranges traps have pronounced effects on electroluminescent brightness.

In order to determine the mechanism of the effect of traps on electroluminescent brightness, both powdered phosphors suspended in Lucite and single crystals have been studied in this work. Thermoluminescence and temperature dependence of brightness have been measured with photoluminescent and with electroluminescent excitation. The effect of frequency of the applied voltage on the brightness-temperature characteristics has also been determined.

Experimental

Measurements were made on powder samples of ZnS:Cu,Al suspended in Lucite, referred to hereafter as powder cells, and on single crystals of ZnS:Cu. Powdered phosphors were made by firing 60 g of ZnS with 0.7075 g of $CuSO_4 \cdot 5H_2O$ and 1.954 g of $Al_2(SO_4)_3 \cdot 18H_2O$ at 1100°C for ½ hr in an atmosphere of 55 parts by volume of H_2S to 20 parts CO_2, a moderately oxidizing condition.

Plastic suspensions were made by milling together the phosphor and Lucite in the volume ratio of 0.288 with a small amount of ethylene dichloride and then pressing this material out to a thickness of about 100 μ in a steam-heated press. The pressing operation was repeated several times to make electroluminescent sheets of uniform thickness and composition.

Activated single crystals were grown by sublimation in a small sealed-off quartz tube (2). The charge consisted of approximately 5 g of ZnS mixed with 5 mg of CuS which had been precipitated from a $CuSO_4$ solution.

Thermoluminescence and temperature dependence of brightness measurements on powdered samples were made with a previously described apparatus (3). The heating rate for thermoluminescence was 5°C/min. Temperature dependence of brightness was determined point by point, allowing several minutes at each temperature before recording the brightness, in order to ensure steady-state conditions. A glass plate with conducting tin oxide coating held the electroluminescent layer against a metal disk which was in good thermal and electrical contact with the temperature-controlled block. A small amount of silicone oil was used on each side of the sample to eliminate air gaps at the electrodes. Electrical connections for electroluminescent excitation and dielectric constant and loss measurement were made to the temperature-controlled block and through an insulated thimble to the conducting glass coating. Most of the electroluminescent brightness measurements were made with 150 v rms applied to the sample.

For single crystals, a vacuum apparatus previously used for temperature dependence of conductivity (4) was provided with a window for excitation or observation. The crystal was pinched between platinum electrodes which were contained within a heavy-walled copper well. Electroluminescent brightness vs. temperature was determined with excitation by 200 v rms. The electrode separation was approximately 0.5 mm.

Results and Discussion

Glow curves obtained on the phosphor powder before incorporation into the dielectric matrix are the same as that shown in Fig. 1 for a powder cell. The procedure of excitation with the G.E. B-H4 lamp (mainly 3650 Å radiation) substantially saturated the traps. With electroluminescent excitation at 400 v and 1000 cps, the glow curves were the same as for ultraviolet excitation except that the intensities were lower by factors ranging from 100 to 1000. As shown in Fig. 2, only the principal glow peak at 123°K is observable in the single crystals, and this only with 3650 Å excitation. Both from theory and from microscopic observations (5–7) of electroluminescent phosphors, it is believed that electroluminescent excitation is localized, thus accounting for the small number of traps filled during electroluminescent excitation.

In Fig. 3 are shown the photoluminescent and electroluminescent brightness of the powder cell, on which the data of Fig. 1 were obtained, as a function of temperature at several different frequencies of excitation. It is apparent

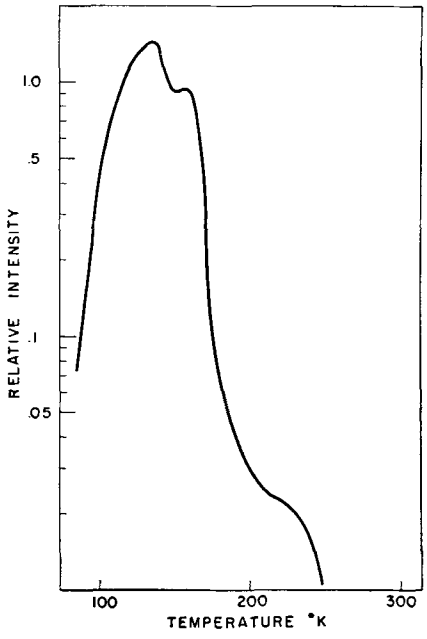

FIG. 1. Thermoluminescence of ZnS:Cu,Al powder

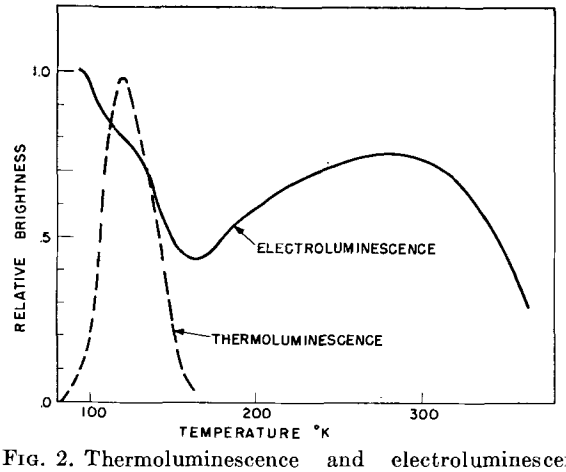

FIG. 2. Thermoluminescence and electroluminescent brightness of ZnS:Cu single crystal.

that the variations of electroluminescent brightness with temperature are peculiar to electroluminescent excitation rather than to the activator itself. The fact that similar behavior is observed in single crystals indicates that variations in brightness are not due to the characteristics of the dielectric. This view is substantiated by measurements of dielectric constant and loss of the phosphor suspensions and of pure Lucite. Pure Lucite shows a monotonic increase of dielectric constant and dielectric loss in going from 80° to 375°K, as do unexcited phosphor suspensions. However, there are pronounced maxima of dielectric loss near the temperatures of the glow peaks during thermoluminescence or at the temperature of the minimum in brightness during electroluminescent excitation of the powder cells.

It will be noted that the minimum in electroluminescent brightness occurs at a temperature a few degrees above the temperature of the principal glow peak. The structure in the temperature dependence of brightness shifts to

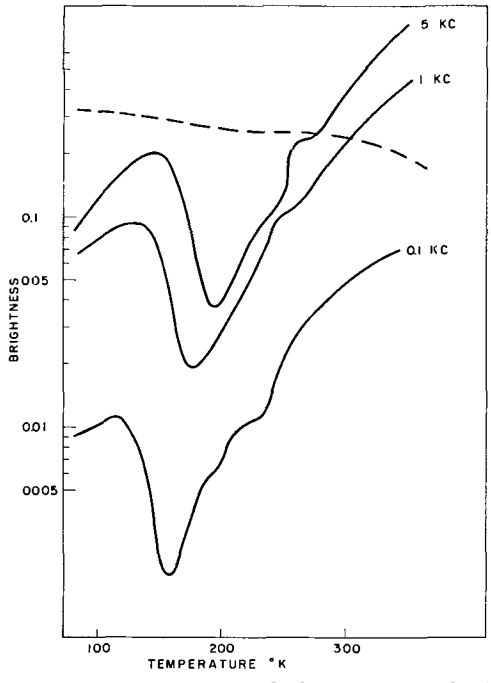

FIG. 3. Photoluminescent (dashed line) and electroluminescent brightness (solid lines) vs. temperature of ZnS:Cu,Al in Lucite.

higher temperatures with higher frequency of excitation. Changing the voltage of excitation over the range 120–300 v only shifts the characteristic temperature-brightness curve in brightness, not in temperature. The data are independent of the direction of temperature change and of the excitation history of the sample in contrast to the results of Gobrecht and co-workers (8) and of Neumark (9). In this work the sample attains a steady-state condition at the temperature of each measurement.

In this and other investigations (10) powder suspensions have been found in which the brightness drops off as the temperature is decreased and does not again rise at the lowest temperature measured, in contrast to the behavior of the samples reported here. The mechanism responsible for the temperature dependence of brightness should explain both types of behavior.

Electroluminescence is a field-dominated phenomenon. Large variations in brightness with temperature, therefore, may be expected if the electron traps responsible for thermoluminescence can in certain temperature ranges alter significantly the formation of the high-field region. The magnitude of the field, E, in the exhaustion layer increases with the number of shallow donors which can become thermally ionized during the half-voltage cycle. The localized states may be neutral when occupied, or may have a negative charge which is compensated by a nearby positive center, such as an ionized activator. In either case there will be an increase in the field in the exhaustion layer when an electron from the trapping state is removed from the barrier region. The density, N, of traps which ionize during the half-voltage cycle, τ, is

$$N = N_T(1 - e^{-k_1\tau}) \qquad (I)$$

where N_T is the number of trapped electrons per unit volume and k_1 is the rate constant for thermal emptying

of traps and is given by $k_1 = s_1 e^{-\epsilon_1/kT}$. The quantities s_1 and ϵ_1 are the frequency factors for untrapping and trap depth, respectively. The average field $\bar{E}$ resulting from the formation of an exhaustion barrier region with a concentration N of empty traps and N_d of empty donors is

$$\bar{E} = \left[\frac{2\pi e V_o}{\kappa}\right]^{1/2} (N + N_d)^{1/2} \qquad \text{(II)}$$

where V_o is the magnitude of the applied voltage and κ is the dielectric constant of the phosphor. The exact expression for brightness depends on a detailed knowledge of all localized levels in the phosphor system. However, the following equation should describe to good approximation the dependence of the brightness on average field (1).

$$B_1 = Ae^{-C/\bar{E}} \qquad \text{(III)}$$

where A is a proportionality constant, and C is a constant characteristic of the material which depends on the efficiency of the excitation process and varies inversely with this efficiency. Substituting equation (I) and equation (II) in (III) the expression for the dependence of brightness on temperature resulting from the contribution of traps to the brightness by means of the exhaustion process is

$$B_1 = B_{10} \exp[-\beta e^{-k_1 \tau}] \qquad \text{(IV)}$$

The constants B_{10} and β result from combining constant terms of equations (I), (II), and (III). In order to obtain (IV) the approximation $N < N_d$ has been made. This approximate expression deviates from the more cumbersome, exact one only in the temperature range where the contribution of this term to the total brightness is quite small.

At low temperatures the traps may contribute to the electroluminescent output by being field ionized in the region of high field, thereby producing the electrons which are accelerated to impact excitation. The traps may provide the charge carriers for acceleration to the extent that they are not thermally ionized during the half-voltage cycle. This contribution to the brightness is given by

$$B_2 = B_{20} e^{-k_1 \tau} \qquad \text{(V)}$$

where B_{20} is temperature independent and is proportional to N and is also a function of the local field configuration. The total contribution to electroluminescent brightness from electron traps characterized by rate constant k_1 is

$$B = B_{10} \exp[-\beta e^{-k_1 \tau}] + B_{20} e^{-k_1 \tau} \qquad \text{(VI)}$$

Differentiating (VI) with respect to temperature gives the following expression for the temperature, T_m, of the minimum

$$T_m = \frac{\epsilon_1}{k \ln(s_1 \tau/\alpha)} \qquad \text{(VII)}$$

where α is a constant given by

$$\alpha = \ln\left(\beta \ln \beta \frac{B_{20}}{B_{10}}\right)$$

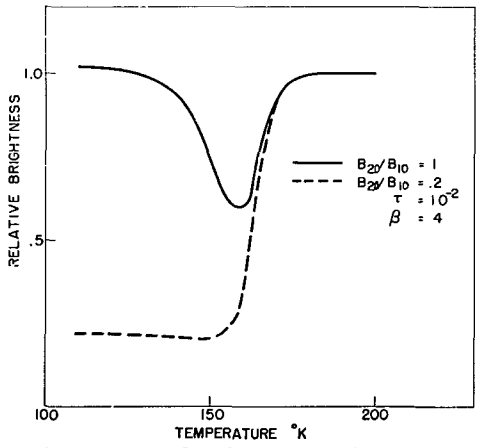

FIG. 4. Typical calculated electroluminescent brightness vs. temperature characteristics.

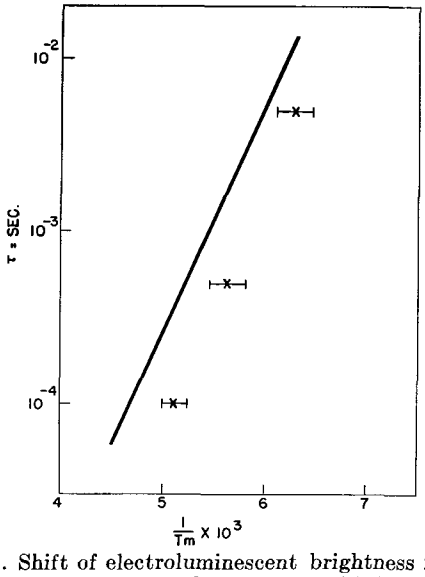

FIG. 5. Shift of electroluminescent brightness minimum with excitation frequency. Calculated: solid line; observed: points ($\beta = 4$ $B_{20}/B_{10} = 1$).

As seen on comparing Fig. 2 and 3 with Fig. 4, equation (VI) gives a temperature dependence of brightness in good agreement with experiment using values of $s_1 = 10^{10}$ sec^{-1} and $\epsilon_1 = 0.25$ ev which are in accord with the thermoluminescence data. In addition, in Fig. 5, it is seen that by employing these same values in equation (VII) the position of the minimum agrees within 10% and its shift with frequency of excitation is in quantitative accord with the theory. There is evidence in the half-widths of both the thermoluminescence peak and the electroluminescent brightness minimum and in the temperature of the minimum for a considerable amount of retrapping and for the presence of more than a single trap depth. The small displacement of the calculated curve for the brightness minimum from the experimental points may be accounted for by the reduction of trap depth in regions of moderate field or by the uncertainty in frequency factor resulting from retrapping. Data of the type of Alfrey and Taylor are in accord with a low value of B_{20} as compared with B_{10}, Fig. 4, lower curve.

An alternative mechanism for the effect of electron traps on electroluminescent brightness requires a thermally

activated process governed by trapping for removal of electrons from ionized activators from the region of excitation. Removal from activators is followed by trapping in the bulk of the crystal. At low temperatures electrons cannot return to the activators, which results in a lower effective activator concentration and, therefore, lower efficiency. This mechanism results in the expression for brightness

$$B = B_0 \frac{[1 - e^{-k_1 \tau}]}{[1 - e^{-(k_1+k_2)\tau}]} \qquad \text{(VIII)}$$

where k_2 and k_1 are the rates for removal from and return to the activators, respectively. Equation (VIII) is in accord with the data of Alfrey and Taylor. The return to high brightness at low temperature, characteristic of the authors' data, cannot be accounted for by equation (VIII) unless the system is permitted to relax completely during each cycle; such a relaxation process does not appear appropriate for the model. A similar difficulty arises when the effect of traps on mobility of conduction electrons is considered. A thermal contribution to the emptying of the deep donors responsible for electroluminescent excitation, suggested by Alfrey and Taylor (8), cannot result in a return of electroluminescent brightness to high values at low temperature and, thus, cannot account for the minimum in brightness reported here.

It is concluded that the effect of electron traps on electroluminescent brightness is largely the result of traps contributing to the exhaustion mechanism for high-field production at high temperatures and as sources of electrons for acceleration to impact excitation at low temperatures.

ACKNOWLEDGMENTS

The authors are indebted to Dr. J. S. Prener for supplying the powder phosphors, to Dr. S. Roberts for preparation of the phosphor dielectric suspensions and for many helpful discussions, and to F. R. Petersen, R. D. Smith, and F. L. Hughes for assistance in the experimental work.

Manuscript received August 10, 1955. This paper was prepared for delivery before the Cincinnati Meeting, May 1 to 5, 1955.

Any discussion of this paper will appear in a Discussion Section to be published in the December 1956 JOURNAL.

REFERENCES

1. W. W. PIPER AND F. E. WILLIAMS, *Phys. Rev.*, **87**, 151 (1952); *Brit. J. Appl. Phys.*, **54**, 539 (1955); *Phys. Rev.*, **98**, 1809 (1955)
2. W. W. PIPER, *J. Chem. Phys.*, **20**, 1343 (1952).
3. P. D. JOHNSON AND F. E. WILLIAMS, *ibid.*, **21**, 125 (1953).
4. W. W. PIPER, *Phys. Rev.*, **92**, 23 (1953).
5. S. ROBERTS, *Bull. Am. Phys. Soc.*, **28**, Paper N5 (Jan. 1953).
6. E. E. LOEBNER AND H. FREUND, *ibid.*, **30**, Paper L4 (Mar. 1955).
7. J. F. WAYMOUTH AND F. BITTER, *Phys. Rev.*, **95**, 941 (1954).
8. H. GOBRECHT, D. HAHN, AND H. GUMLICH, *Z. Physik.*, **136 S**, 623 (1954).
9. G. NEUMARK, *Bull. Am. Phys. Soc.*, **30** [2] Paper L10, (March 1955).
10. G. ALFREY AND J. B. TAYLOR, Discussion on Paper 7 (Piper and Williams) *Brit. J. Appl. Phys.*, Suppl. No. 4, p. S44 (1955).

Erosion of Steel by Hot Gases

M. J. FRASER AND A. A. BURR

Department of Metallurgical Engineering, Rensselaer Polytechnic Institute, Troy, N. Y.

ABSTRACT

A vent-plug device for producing eroded surfaces on steel and other metals is described. Surfaces so treated have been shown by metallographic and x-ray analysis to duplicate structures encountered in many service applications. During the erosion of steel, as many as five distinct surface layers are produced. Retention of austenite in these eroded surfaces is an indication of the chemical alteration of the surface layers during erosion. The major portion of the investigation is concerned with a modified SAE 4330 steel. However, comparison experiments were made on Armco iron, and SAE 1015, 1040, and 1070 steels. The effect of carbon content on erosion behavior is illustrated by x-ray analysis.

INTRODUCTION

The interaction of a metal with high temperature, high pressure, and high velocity gases usually results in a significant deterioration of the surface, leading to a loss of material. This erosion is limited to surface deterioration by chemical alteration, which generally is the fundamental process. However, a complete description of erosion includes such possible simultaneous processes as mechanical abrasion, progressive stress damage, and surface fusion. In some applications, these processes may mask the effects of chemical alteration and control the erosion.

Erosion is a serious limitation in many applications where metals are exposed to gases at high temperatures. The bulk of prior observations (e.g., ordnance research) have been made on service-eroded material where an adequate knowledge of the conditions existing during

erosion is rare (1). To investigate the problem systematically it is necessary to simulate service-erosion conditions on a laboratory scale. One of the best ways to accomplish this is with a suitable vent-plug device. The various types of vent-plug devices which have been employed in previous research have two common features, namely: (*a*) an explosion source and chamber producing the high temperature, high pressure gases, and (*b*) a sample vent through which the explosion gases escape at high velocity.

In most of the previous vent-plug experiments, little or no attempt was made to insure actual service conditions in the vent-plug device. Consequently in general, erosion conditions were too severe to study adequately the effect of chemical alteration of the surface, i.e., surface fusion predominated (1). In addition, relatively few metallographic studies of vent-plug erosion have been made. However, concurrently with this research Dieter and Rink (2) studied the metallurgical aspects of vent-plug erosion of steel. Their results are pertinent to this report and will be discussed later. In addition to vent-plug experiments, considerable effort has been devoted to the study of service-eroded surfaces such as those of gun bores (3–11).

In the present work, conditions of erosion have been so adjusted that chemical alteration could be studied. By comparison of the surface layers of the vent-plug specimens with actual service-eroded material, it has been demonstrated that the surface structures are essentially identical.

Experimental

Vent-plug device.—Fig. 1 illustrates the vent-plug device which consists of a rifle receiver and action (A) coupled to an explosion block (B) by a section of rifle barrel. The explosion block is fitted for a knock-out plug (C) and a specimen and rupture-disk assembly (D). For comparison, a 30-06 caliber cartridge case (E) (length, 2.5 in.) is included. The important component of this device is the relatively long "L"-shaped gas path from the explosion source to the vent. In addition to baffling and cooling the gases, the "L" path provides a wad-catcher which prevents the rather heavy charge wadding from interfering with the gas passage through the vent. The total internal volume of the assembled device is about 15 cm^3.

The specimen and rupture-disk assembly, based on a design by Evans, Horn, Shapiro, and Wagner (12) is shown

Fig. 1. Erosion vent plug device. A—Rifle receiver and action; B—explosion block; C—knock-out plug; D—specimen and rupture-disk assembly; E—30-06 caliber cartridge case (length—2.5 in.).

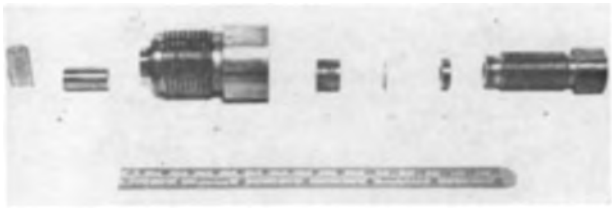

Fig. 2. Specimen and rupture-disk assembly. A—Vent-plug specimen; B—assembly body; C—choke; D—disk; E—retaining ring; F—retainer plug.

TABLE I. *Nominal analysis of I.M.R. powder types 4064, 4320, and 4350 products of combustion*

Component	% by Volume at room temperature	% by Volume at temperature of explosion
CO_2	18.8	10.09
CO	46.4	45.35
H_2	20.9	13.21
CH_4	0.6	—
N_2	13.3	11.00
H_2O	—	20.19
Metals as gas	—	0.16

in Fig. 2. The components are: assembly body (*B*), choke (*C*), disk (*D*), retaining ring (*E*), and retainer plug (*F*). A vent-plug specimen (*A*) is also included. One feature of this design is the location of the rupture disk on the exit side of the specimen vent. This insures maximum pressure build-up over the vent surface prior to the exhaust of the explosion gases. Rupture disks, with a circular unsupported area (0.25 in. in diameter) can be used to vary the bursting pressure over a wide range. In these experiments, 70-30 brass disks were employed. They were 0.020 in. thick and limited the bursting pressure to 16,000–18,000 psi. Pressures were determined by auxiliary crusher-gauge experiments. The choke diameter was fixed at 0.08 in. during these experiments, but it may be varied up to a diameter of 0.25 in.

The explosion charge was contained in a 30-06 cartridge case and was maintained in place with Duco cement. The entire charge of a Western "Super X" cartridge, loaded for a 220 grain projectile, was used. The powder in this commercial loading is single-base with a cylindrical grain. The average charge weight was 2.9106 g with a maximum weight difference between cartridges of about 0.04 g. This charge burns with an adiabatic flame temperature of about 2660°C and a maximum pressure potential of about 55,000 psi. Gas components produced during the explosion and their approximate proportions are listed in Table I (13).

Specimen materials and geometry.—Most of the vent plugs used in this investigation were machined from a modified SAE 4330 steel of the following composition: 0.34% C, 0.56% Mn, 0.21% Si, 0.017% P, 0.015% S, 2.6% Ni, 0.98% Cr, 0.15% V, and 0.24% Mo. Neither metallographic nor x-ray analysis showed the formation of an altered surface structure as a result of machining. The vents were rectangular in cross section and split longitudinally to give two specimens from each vent plug. The width and length of the vent were standardized at

0.30 and 0.75 in., respectively, while the thickness was varied to yield different surface areas. Unless otherwise specified, each sample was fired once.

The eroded surfaces were examined metallographically on a section cut at a fifteen degree taper to the surface. X-ray analysis was accomplished on a Norelco high-angle goniometer spectrometer with a chromium-target tube. Thermal treatments in purified hydrogen were also employed, in conjunction with metallographic and x-ray analysis, to investigate the specific character of individual layers. Weight-loss measurements were made on an analytical balance after the surface was carefully cleaned according to the following standardized procedure. Each half of a specimen was washed with water and soap. A nylon-bristle brush was used to insure complete removal of combustion products. Washing was continued for a period of 1 min. The specimen was then immersed in acetone, and finally blown dry in a filtered air blast.

In addition to the SAE 4330 vent plugs, 0.30 x 0.025 x 0.75 in.^{3} vent plugs were machined from Armco iron, and SAE 1015, 1040, and 1070 steels. To illustrate the effect of carbon content on erosion behavior, these specimens were eroded and the surfaces studied by x-ray and metallographic analysis.

Results and Discussion

With a given set of explosion conditions in the vent-plug device (constant charge) and a specific material, the surface temperature of the specimen is a function of its vent surface area. Since erosion is sensitive to thermal input, i.e., cal/in.^{2}/sec, it can be expected to vary with the vent surface area, which was conveniently altered by changing the vent thickness. The various layers produced during erosion generally have been described as chemically altered and thermally altered. The chemically altered layers, lying closest to the surface, undergo a significant compositional change as a result of chemical and thermal interaction with the explosion gases. However, the deeper thermally altered layers are not chemically changed except in the region closest to the overlying chemically altered layers. The thermally altered layers are differentiated from the base metal by microstructural changes.

A satisfactory nomenclature for the erosion layers is difficult to formulate. Because not all possible layers are always present in a given steel surface and because early erosion work generally did not detect chemically altered layers, some confusion exists in the literature. The fact that the metallographic appearance of the outer surface layers is radically altered leads to the inevitable conclusion that definite chemical changes have taken place. These layers are herein described (from the surface inward) as the outer white layer, the inner white layer, and the austenite-bearing layer. The designation of the "white" layers simply reflects their resistance to etching, which leaves them essentially as-polished in cross-section metallographic examination. The average total thickness of these layers ranges from 2×10^{-4} to 6×10^{-4} cm, and varies with the thermal input to the surface (vent surface area), the outer white layer being particularly sensitive in this respect. The thermally altered layers (commonly called "the white layer" by the early investigators) are heated above the lower-critical temperature. They therefore undergo a structural alteration which leads to their delineation by differential etching. They consist of a thick layer heated above the upper-critical temperature and a relatively thin layer heated above the lower-critical temperature. These layers range in total thickness from 3.5×10^{-3} to 11.0×10^{-3} cm, being thicker the smaller the vent surface area. Under the conditions imposed, the thickness increased approximately linearly with decreasing vent surface area at a rate of about 0.0878 cm/in.^{2} of surface area. Dieter and Rink (2) found that, with a fixed vent surface area, the depth of the thermally altered layers increased approximately linearly with adiabatic flame temperature of the charge. Both results reflect an increasing thickness with increasing thermal input to the surface (increasing severity of erosion conditions).

An interesting observation concerning the thermally altered layers is that almost complete structural homogenization is achieved during the first exposure. Only where segregation is pronounced, as in an annealed structure, is there any residual inhomogeneity after one exposure. Even in this extreme case, the remaining segregation is well toward the interior of the thermally altered layers. Thus, it appears that, after the initial exposure, there should be no effect of original microstructure on the chemical erosion behavior of the steel since the structure in the pertinent volume, close to the surface, is always the same. This qualitative observation is in agreement with the results of Dieter and Rink (2) who found no dependence of erosion weight loss on the original microstructure of a given steel.

Fig. 3 shows the layer configuration in the eroded surface of a 0.30 x 0.050 x 0.75 in.^{3} vent plug (surface area = 0.525 in.^{2}). Two apparently chemically altered layers are noted—the outer and the inner white layers. A portion of the upper-critical, thermally altered layer is also shown. The x-ray spectrometer trace (Fig. 4*A*) indicates, in addition to the ferrite (110) peak, a weak austenite (111)

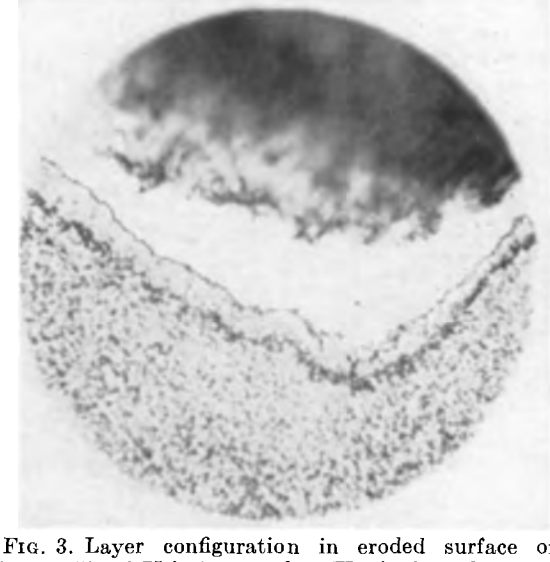

Fig. 3. Layer configuration in eroded surface of a 0.30 x 0.050 x 0.75 in.^{3} vent plug (Kalling's etch—1500 ×) (15° taper section).

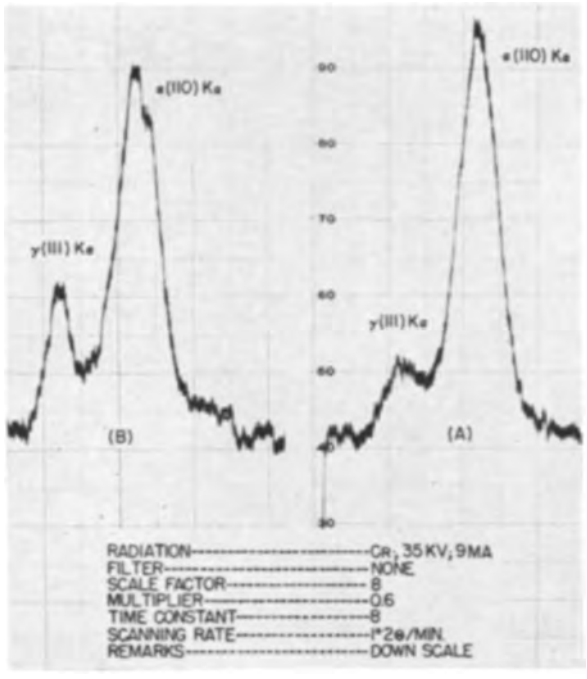

FIG. 4. X-ray spectrometer traces of eroded surfaces. A—0.030 x 0.050 x 0.75 in.³ vent plug; B—0.30 x 0.040 x 0.75 in.³ vent plug.

peak. The ferrite (110) peak intensity is considerably lower than that from the as-machined surface. This may mean that this diffraction is coming from the thermally altered layers. Some of the reduction in intensity may be attributed to residual stress and some to the absorption effect of the overlying chemically altered layers. Heat treatments in purified hydrogen, designed to decompose the retained austenite, produced no simultaneous metallographic alteration of the outer or inner white layers. Therefore, it was concluded that these layers did not contain the retained austenite. The relatively small amount revealed by x-ray analysis is apparently not sufficient to produce a recognizable indication of the austenite-bearing layer in a metallographic cross section of this narrow region.

Fig. 5 is the metallographic section of a 0.30 x 0.040 x 0.75 in.³ vent plug (surface area = 0.510 in.²). In addition to the outer and inner white layers, a third chemically altered layer is present in this specimen. Fig. 4*B* shows the x-ray spectrometer trace from the surface of this specimen. Note the increase in the austenite (111) peak intensity and the decrease in the ferrite (110) peak intensity in comparison to Fig. 4*A*. The specific character of the additional layer in this specimen was indicated by the heat treatments described above, in which the thermal decomposition of the retained austenite (verified by x-ray analysis) led to the metallographic change illustrated in Fig. 6 (14). This layer is, therefore, designated as the austenite-bearing layer.

As the vent surface area was further reduced to 0.472 in.² by reducing the vent cross section, there was no appreciable change in the layer configuration. The only change noted was in layer thicknesses. The x-ray data indicate an increasing proportion of austenite in the

FIG. 5. Layer configuration in eroded surface of a 0.30 x 0.040 x 0.75 in.³ vent plug (Kalling's etch—1500 ×) (15° taper section).

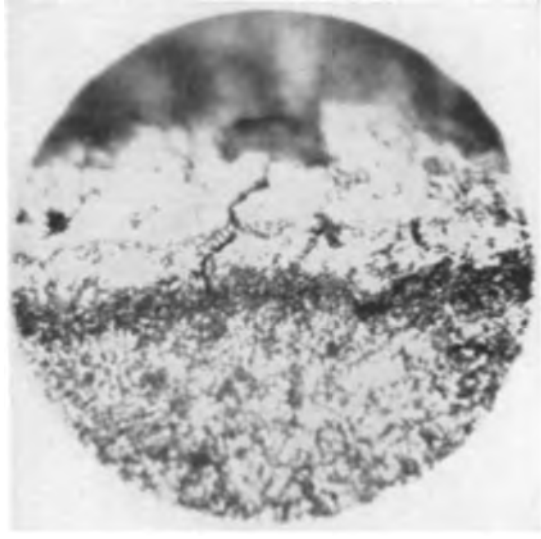

FIG. 6. Layer configuration in eroded surface of a 0.30 x 0.025 x 0.75 in.³ vent plug after thermal treatment at 1200°F for 2 min (Kalling's etch—1500 ×) (15° taper section).

irradiated volume with decreasing vent surface area. To illustrate this tendency, the ratio of the integrated intensity of the austenite (111) line to that of the ferrite (110) line ($I\gamma/I\alpha$), as a function of vent surface area, is shown in Fig. 7. Integrated instead of peak intensities were used to take into account the effect of residual stress on the peak intensity of the ferrite (110) line.

Table II lists observed x-ray parameter data for various materials in vent-plug surfaces. The lattice parameter of the retained austenite was quite constant even after several exposures of a given vent plug. The maximum variation in parameter was about $\pm 3 \times 10^{-3}$Å in repeated experiments up to twelve exposures. This indicates that the austenitizing element, which could be carbon or nitrogen, singly or in combination, is absorbed to saturation in the retained phase. Although quantitative figures are impossible on the basis of this research (since the

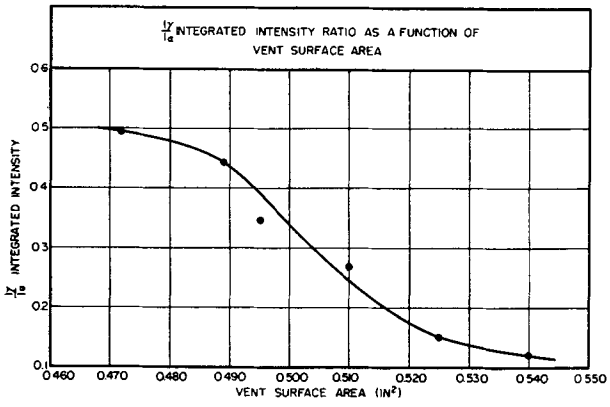

FIG. 7. Variation of the integrated-intensity ratio $I\gamma(111)/I\alpha(110)$ as a function of vent surface area.

TABLE II. *Lattice constants of materials in vent-plug surfaces*

Peak identification	Bragg angle (Degrees 2θ)	"d" (Å)	Lattice parameter (Å)	Remarks
Ferrite (110)	68.40	2.038	2.882	Ferrite in the as-machined surface
Ferrite (110)	68.24	2.042	2.888	Ferrite in the eroded surface
Austenite (111)	66.00	2.103	3.643	In eroded surface
Martensite (110)	68.45	2.037	$A_0 = 2.880$	
Martensite (101)	68.10	2.046	$C_0 = 2.906$ ($C/A = 1.009$)	In eroded surface after a number of exposures

exact effect of the alloy elements and possibly oxygen from the explosion gases is unknown), it is probable that the observed parameter involves a concentration of about 1.7 wt % carbon or about 2.0 wt % nitrogen (15, 16). These estimates are based on an oversimplified picture of single-element interaction. Speculating further, a consideration of the Fe-C (17) and Fe-N (16) phase diagrams indicates that carbon may be the major austenitizing element under the imposed conditions. If the hypothesis that the active austenitizing element is absorbed to saturation is correct, the low temperature (about 775°C) associated with saturated nitrogen-austenite at 2.0 wt % nitrogen eliminates it as the active element. This follows from the fact that the relatively thick thermally altered layers (heated above about 720°C) preclude this low temperature in the austenite-bearing layer which is much closer to the surface. Following Feurstein and Smith (18), and Dieter and Rink (2), it is clearly meaningless to discuss thermal levels in eroded surfaces on the basis of equilibrium diagrams. Dieter and Rink (2) show that the rate of heating which obtains in eroded vent-plug surfaces (10^5°F/sec) can cause an increase in the lower critical temperature of at least 500°F. However, this should not affect the general conclusions derived from observations of the equilibrium diagrams.

FIG. 8. Surface of as-machined vent plug (unetched—1500 ×).

Dieter and Rink (2) also investigated the relative amounts of retained austenite formed by various explosion gases. Explosions of N_2O-H_2 and of CO-O_2 gas mixtures gave about the same relative amounts of retained austenite. Explosions of H_2-O_2 gas mixtures, although free of carbon and nitrogen, produced smaller but significant amounts of retained austenite. This last result apparently indicates that the enrichment of the retained austenite zone is not entirely due to interaction with the explosion gases. Therefore, internal segregation due to the steep thermal gradient from the surface inward may generally account for a small part of the retained austenite.

After a number of exposures of a given vent, the ferrite (110) line tends to dissociate into a doublet, indicating tetragonal martensite in the thermally altered layers. The doublet is resolvable after two or three exposures with a 0.30 x 0.025 x 0.75 in.^{3} vent plug. The lattice constants for this martensite are given in Table II. On the basis of the above discussion, carbon is assumed to be the major contributor to the tetragonality, and the martensite probably contains approximately 0.43 wt %. The fact that the solute content required for the martensite observation is less than that required for the austenite observation is consistent with the position of the retained austenite closer to the vent surface than the martensite.

The precise nature of the outer and inner white layers was not determined in this investigation. Deep etching failed to develop any structure in either of the layers, and both appeared to be generally unattacked by standard etching reagents. The inner white layer seems less resistant to erosion than either the outer white layer or the austenite-bearing layer. This is illustrated in Fig. 5 where pocket-type erosion at the base of cracks extending through the outer white layer is evident.

That chemical interaction occurs without appreciable surface fusion is indicated by Fig. 8, 9, and 10. Fig. 8 shows the as-machined surface, while Fig. 9 is a photomicrograph of the surface of a 0.30 x 0.050 x 0.75 in.^{3} vent plug which was fired once. A comparison with Fig. 3 shows that chemical interaction took place even though

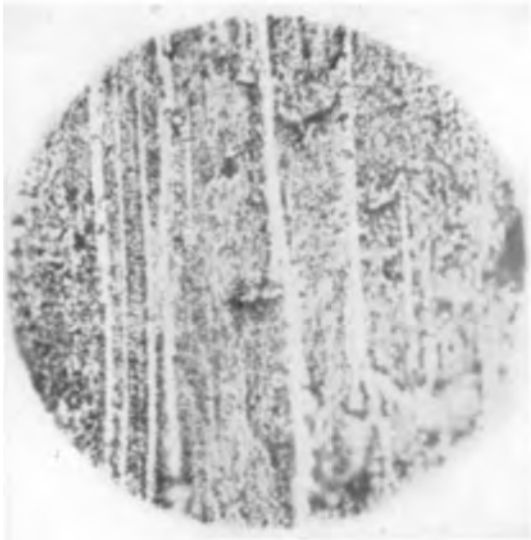

FIG. 9. Surface of eroded, 0.30 x 0.050 x 0.75 in.³ vent plug (unetched—1500 ×).

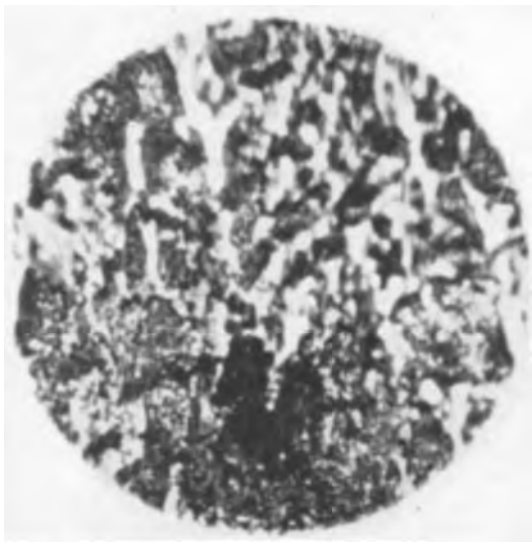

FIG. 11. Surface of heavily-eroded 0.30 x 0.025 x 0.75 in.³ vent plug—after 12 exposures (unetched—1500 ×).

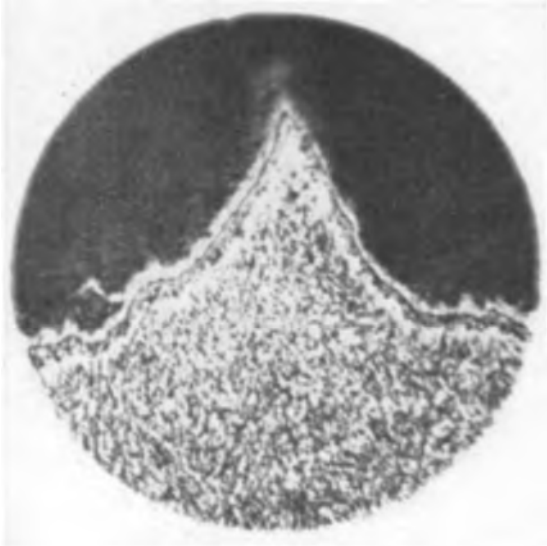

FIG. 10. Layer configuration in eroded surface of a 0.30 x 0.040 x 0.75 in.³ vent plug—near exit end (Kalling's etch—1500 ×) (15° taper section).

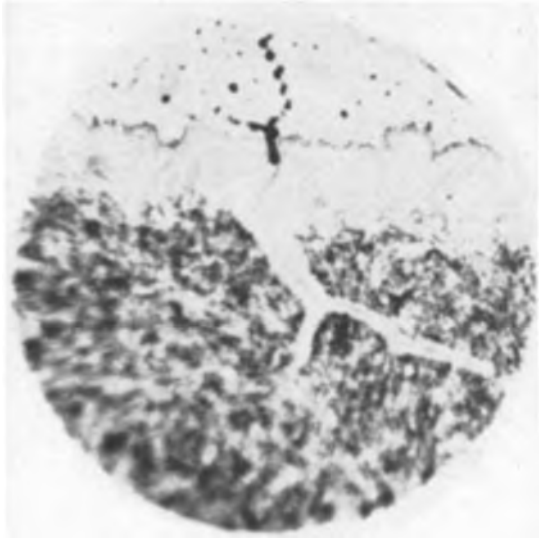

FIG. 12. Layer configuration in heavily eroded 0.30 x 0.025 x 0.75 in.³ vent plug showing chemical alteration penetrating along crack (Kalling's etch—1500 ×) (15° taper section).

the surface appears essentially unchanged by firing. Actually the rather sharp machining marks which are out of focus in the photomicrographs did not suffer resolvable change as a result of this exposure. It is expected that fusion would be most evident at these projections and would result in pronounced smoothing. Fig. 10 illustrates the appearance of such a projection on taper section. Further evidence against appreciable surface fusion, i.e., fusion of outer white layer material, is given in Fig. 5. The existence of pocket-type erosion at the base of cracks in the outer white layer indicates the rigidity of this material during erosion. As the vent surface area was reduced, the machining marks were gradually leveled by erosion. Complete leveling occurred first near the entrance end of the vent. However, no obvious signs of general surface fusion were noted after one exposure, although it is entirely possible that fusion did occur at the immediate entrance end. Fig. 11 shows the surface of a 0.30 x 0.025 x 0.75 in.³ vent plug which was fired twelve times. The obvious wash pattern indicates general fusion.

Microcracking was often seen in the vent-plug surfaces after erosion. Cracks had their origin either in the outer white layer or appeared to radiate from inclusions in the thermally altered layer. These cracks result from thermal shock and volume changes during transformation which are experienced by the hot surface layers as they are quenched by the surrounding mass of the vent-plug device. Unlike many examples of service erosion, cracking does not appear to play an important role in this vent-plug erosion. Penetration of the chemically altered layers into the first thermally altered layer was, however, noted to occur along cracks which were open to the explosion gases. Fig. 12 illustrates this process in a 0.30 x 0.025 x 0.75 in.³ vent plug fired six times.

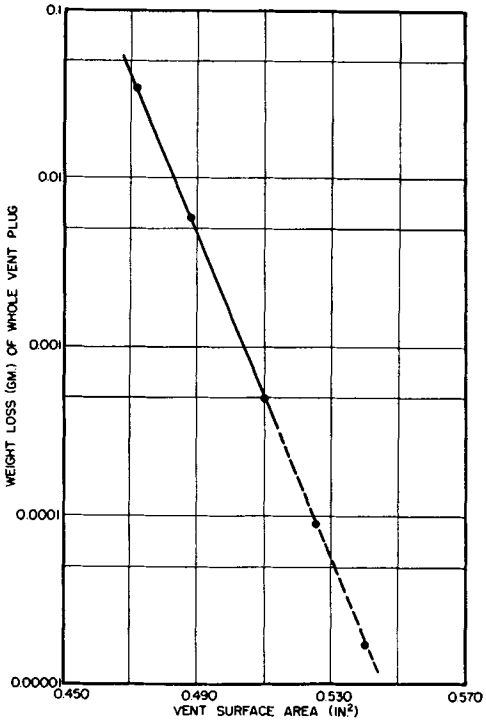

FIG. 13. Weight loss due to erosion as a function of the vent surface area.

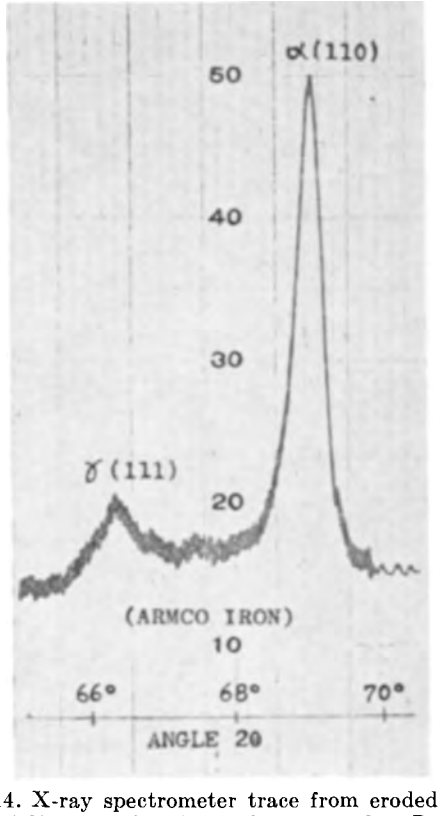

FIG. 14. X-ray spectrometer trace from eroded surface of 0.30 x 0.020 x 0.75 in.³ Armco-iron vent plug. Radiation, Cr, 35 kv, 9 ma; filter, none; scale factor, 16; multiplier, 0.6; time constant, 8; scanning rate, 1° 2θ/min; remarks, downscale.

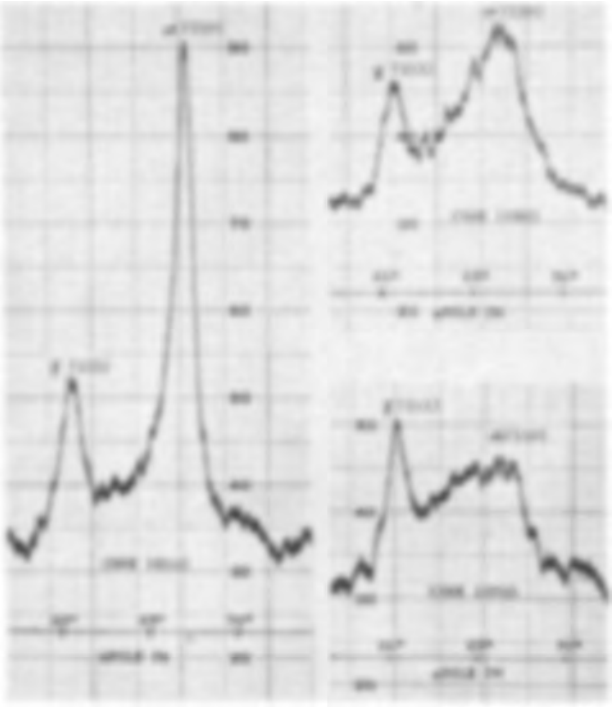

FIG. 15. X-ray spectrometer traces from eroded surfaces of 0.30 x 0.025 x 0.75 in.³ vent plugs made from S.A.E. 1015, 1040, and 1070 steels. Radiation, Cr, 35 kv, 9 ma; filter, none; scale factor, 8; multiplier, 0.6; time constant, 8; scanning rate, 1° 2θ/min; remarks, downscale.

As was mentioned previously, the effects of erosion under a given set of conditions can be expected to vary with the vent surface area. Therefore, the loss of surface material due to erosion should vary with the vent surface area. The smaller the area the greater should be the weight loss. Fig. 13 illustrates this behavior. The logarithm of the weight loss under the imposed conditions is seen to be a linear function of the vent surface area.

As a comparison experiment, Armco iron, and SAE 1015, 1040, and 1070 steels were eroded. All specimens were 0.30 x 0.025 x 0.75 in.³ vent plugs and were fired once. X-ray spectrometer traces of the eroded surfaces are shown in Fig. 14 and 15. It is evident that as the carbon content of the base steel increases, the greater is the quantity of retained austenite and the more strained is the ferrite or martensite, as the situation may be. Note that even in Armco iron some retained austenite is produced in the eroded surface by this short exposure. Layered surface structures similar to those developed on SAE 4330 vent plugs also appeared on these specimens.

CONCLUSIONS

1. The process of chemical erosion may be conveniently studied with a vent-plug device in which suitable cooling of the explosion gases prevents surface fusion.

2. It appears that significant erosion can occur by the interaction of high temperature, high pressure, and high velocity gases without the expedients of appreciable surface fusion and mechanical factors.

3. The eroded surfaces produced under these conditions consist of various chemically and thermally altered layers.

4. Austenite, retained in the surface (neglecting small amount apparently due to internal segregation), is a product of erosion and indicative of chemical alteration. The relative amount of retained austenite varies with the exposure, being greater the more severe the conditions, in this case, the smaller the vent surface area.

5. Both nitrogen and carbon derived from the explosion gases could cause the retention of austenite. On the basis of lattice parameter measurements, it appears that carbon is probably more active than nitrogen in this respect.

6. The original carbon content of the steel has a pronounced effect on the character of the eroded surface as studied by x-ray analysis. The greater the original carbon content, the greater the quantity of retained austenite in the surface and the more strained is the ferrite or martensite in the thermally altered layers.

7. Metallographic observations of the thermally altered layers indicate that there should be virtually no dependence of erosion behavior on the original microstructure of the steel.

ACKNOWLEDGMENT

The authors wish to acknowledge the helpful discussions and criticisms extended by Dr. P. R. Kosting of the Watertown Arsenal Laboratory. This work was done as part of Ordnance Contract DA-30-115-ORD-380. The authors are grateful to Watertown Arsenal and the Ordnance Corps for permission to publish.

Manuscript received August 4, 1955. This paper was prepared for delivery before the Cincinnati Meeting, May 1 to 5, 1955.

Any discussion of this paper will appear in a Discussion Section to be published in the December 1956 JOURNAL.

REFERENCES

1. J. H. WIEGAND, *J. Franklin Inst.*, **244,** 291 (1947).
2. G. E. DIETER AND J. R. RINK, Ballistics Research Lab. Report No. 941 (July 1955).
3. H. FAY, *Trans. Am. Inst. Mining Met. Engrs.*, **56,** 468 (1917).
4. H. M. HOWE, *ibid.*, **58,** 542 (1918).
5. W. W. SVESHNIKOFF, U. S. Bur. Mines, Technologic Paper No. 191 (1921).
6. H. E. WHEELER, *Trans. Am. Inst. Mining Met. Engrs.*, **67,** 257 (1922).
7. H. E. WHEELER, *Army Ordnance*, **5,** 800 (1925).
8. W. W. SVESHNIKOFF, *ibid.*, **5,** 794 (1925).
9. W. H. SNAIR AND W. P. WOOD, *Trans. Am. Soc. Metals*, **27,** [3], 608 (1939).
10. H. H. LESTER, *Trans. Am. Soc. Steel Treating*, **16,** [5], 1 (1929).
11. R. H. GREAVES, H. H. ABRAM, AND S. H. REES, *J. Iron Steel Inst.*, **119,** [1], 113 (1929).
12. R. C. EVANS, F. H. HORN, Z. M. SHAPIRO, AND R. L. WAGNER, *J. Phys. & Colloid Chem.*, **51,** 1404 (1947).
13. J. E. HEINLEN, Private communication.
14. R. D. LUPI AND A. A. BURR, Third Interim Report Watertown Arsenal Laboratory File, No. W.A.L. 731/385-18(1954).
15. C. S. ROBERTS, *Trans. Am. Inst. Mining Met. Engrs.*, **197,** 203 (1953).
16. K. H. JACK, *Proc. Royal Soc.*, **208,** 200 (1951).
17. "Metals Handbook," American Society for Metals, Cleveland (1948).
18. W. J. FEURSTEIN AND W. K. SMITH, *Trans. Am. Soc. Metals*, **46,** 1270 (1954).

Sodium-Aluminum Equilibria in Cryolite-Alumina Melts

MORRIS FEINLEIB AND BERNARD PORTER

Chemical Research Department, Kaiser Aluminum and Chemical Corporation, Permanente, California

ABSTRACT

A qualitative and quantitative study of sodium-aluminum equilibria in cryolite-alumina melts was undertaken to shed more light on the cathode reactions in the aluminum cell. Measurements were made in alumina crucibles from 940° to 1010°C. Lead was used as an auxiliary sodium "sink." Results show that, while aluminum is more noble than sodium, their deposition potentials are not far apart (of the order of 0.1–0.2 v), and that, under the nonequilibrium conditions existing in an industrial cell, some sodium may be codeposited with aluminum at the cathode.

INTRODUCTION

Although aluminum has been produced commercially by electrolysis for over sixty years, much basic knowledge of the reduction process is still missing. This lack of information is largely due to such experimental difficulties as:

1. The lack of materials of construction which are completely resistant to the action of molten cryolite and aluminum around 950°–1000°C. Even carbon or graphite is not inert in the presence of aluminum and fused fluorides. Practically all metals alloy with molten aluminum, and most nonmetallic refractories dissolve in fused fluorides to some extent.

2. Room temperature studies of solidified melts are often meaningless; major changes in melt structure may take place on going from the liquid to the solid state. Furthermore, certain chemical states which exist at high temperatures are unstable at room temperature and vice versa.

In view of these problems and others, it is not surprising

that several theories have been proposed to explain the cathodic processes in the aluminum cell.

Present Status of Aluminum Reduction Theories

Various theories pertaining to the electrolytic production of aluminum have been summarized recently (1, 2).

Most investigators attribute the Faraday inefficiency at the cathode of aluminum cells to the formation of metallic sodium. There are three main groups:

(*A*). The "primary sodium" school of thought, which maintains that sodium is produced at the cathode by direct electrochemical reduction and then displaces aluminum from the melt chemically (3–6).

(*B*). The Grünert group (7), which states that sodium is more noble than aluminum and that kinetic factors account for the fact that the major cathodic product is aluminum.

(*C*). The "primary aluminum" school, which believes that aluminum metal comes from the direct electrochemical reduction of an aluminum donor from the melt (1, 2, 8–12).

In recent years, it has been recognized that monovalent aluminum compounds may constitute another important source of current inefficiency in aluminum cells (9, 11). Such monovalent aluminum compounds can result from incomplete cathodic reduction or from chemical interaction between aluminum metal and trivalent aluminum compounds; they can then be reoxidized at the anode.

There is also a possibility that carbide formation at the carbon cathode may account for some current inefficiency. Aluminum carbide Al_4C_3 is commonly observed in the lining of cells which have been removed from service. It has been shown (13) that this compound can be formed electrochemically. It is also possible that sodium carbide Na_2C_2 may play a part in cathode reactions. This compound has been reported on several occasions (14–16). From the meager data available, Na_2C_2 appears to be a gas at cell temperatures. Its sublimation temperature is lower than the boiling point of sodium and its stability range is not definite. Altogether, Piontelli (10) feels that carbide reactions are important only during the early stages of operation of a cell.

The object of the present work is to provide additional data for evaluation of the various theories of cathode reactions in the aluminum cell.

Preliminary Experiments

It was decided to study first the spontaneous reactions of aluminum and sodium with cryolite melts. If a reaction between sodium or aluminum and a melt can take place spontaneously, then it can certainly occur when these elements are produced by electrolysis from this same melt, physical conditions being identical. Therefore, a study of the spontaneous reactions between aluminum or sodium and cryolite-alumina baths should shed some light on the phenomena taking place during electrolysis.

Grjotheim (9) passed sodium vapors through powdered cryolite at 900°C and detected aluminum globules after the experiments. Therefore, under these conditions, sodium is less noble than aluminum.

Unfortunately, Grjotheim's conditions differ from those existing in a reduction cell in several important respects:

1. Cell operating temperatures are of the order of 970°C, or well above the boiling point of sodium. Consequently, if any sodium exists in a cell, it cannot be present at a partial pressure much above 1 atm. Accordingly, the activity of sodium in an industrial cell may be widely different from that in Grjotheim's experiments. This point is amplified further below.
2. The equilibrium constant may change between 900° and 970°C.
3. Reactions in solid baths may differ from those in molten salts.

Grube and Hantelmann (17) also reacted pure sodium with cryolite-base melts at 1000°–1020°C. They found that aluminum was displaced by sodium from $NaF \cdot AlF_3$ melts. Although sodium is above its boiling point at 1000°C and vaporizes rapidly, the contact time between liquid Na and melt appeared to be sufficiently long to displace aluminum.

To come closer to industrial cell conditions, a series of reactions between cryolite-base melts and sodium were run at usual cell temperatures and above. Since pure liquid sodium cannot exist at these temperatures at atmospheric pressure, sodium-lead alloys were used to supply the necessary Na at a partial pressure of 1 atm. This was achieved by heating, at atmospheric pressure, Na-Pb alloys containing excess Na to the temperature at which the reaction between sodium and melt was to be carried out. Aluminum is only slightly soluble in molten lead and sodium is almost insoluble in aluminum; as a result, any appreciable amount of aluminum formed by reaction between Na-Pb alloys and cryolite-base melts comes out as a distinct phase of nearly pure aluminum.

Na-Pb alloy was reacted in graphite crucibles with the following melts: (*a*) pure cryolite at 1010°C; (*b*) 92% cryolite, 8% calcium fluoride at 975°C; (*c*) 88% cryolite, 4% alumina, 8% calcium fluoride at 975°C.

In all cases the charge was melted first, then the alloy was dropped into the melt. Reaction times were of the order of 15–30 min, after which the melts were cooled. In all cases a number of small globules of aluminum were found floating on top of the lead alloy layer as a distinct phase.

These experiments prove that, in pure cryolite as well as in reduction baths, sodium at 1 atm partial pressure displaces aluminum spontaneously. They show that sodium is less noble than aluminum under reduction pot operating conditions, and thus disprove Grünert's theory (7). They do not necessarily eliminate the possibility that, during electrolysis, a certain amount of sodium may be codeposited at the cathode with aluminum.

To obtain additional information on the latter point, a quantitative study of sodium-aluminum equilibria was undertaken.

Theoretical Considerations

Experience and previous work (18) indicate that some sodium is always present when aluminum is in contact with cryolite-base melts. The equilibrium amount of sodium in such a system is very small for the following reasons.

1. The solubility of sodium in aluminum is very low

(0.01–0.1 at. %). Since the reactions take place above the boiling point of sodium, no separate liquid sodium phase exists in the reaction mixture.

2. Sodium at 1 atm partial pressure produces aluminum in the presence of cryolite-base melts. Therefore, the equilibrium vapor pressure of sodium must be less than 1 atm, and its concentration in molten aluminum must be below its solubility limit.

The concentration of sodium in aluminum metal is so low that usual analytical methods are not sufficiently accurate. To overcome this difficulty lead was used as an auxiliary sodium "sink," and the concentration of sodium was determined in the lead phase rather than in the aluminum phase. From this, the sodium activity can be obtained (19).

As stated above, the mutual solubilities of lead and aluminum are small [Pb in Al, 1.8 at. %; Al in Pb, 10 or less at. % at 970°C (20)] and the solubility of sodium in lead is high. Therefore, at 940°–1010°C there are two phases, i.e., a phase rich in aluminum containing small amounts of lead and sodium, and a lead-rich phase containing most of the sodium and a little aluminum. Accordingly, it was assumed that the activity of aluminum in the aluminum-rich layer is essentially unity, and that neither the activity nor the concentration of sodium in the lead layer is significantly altered by the amount of aluminum in that layer.

An aluminum cell, under normal conditions, does not operate reversibly. The cathode polarization can cause a build-up of sodium in aluminum in excess of the equilibrium activity a_e. As the overvoltage gradually increases, the sodium at the cathode eventually reaches a level corresponding to a partial pressure of 1 atm and, from that point on, sodium will be evolved continuously.

The activity of sodium in aluminum or lead corresponds, at any temperature, to a definite sodium fugacity and approximately to the sodium vapor pressure p. If p^0 is the vapor pressure of pure sodium at that temperature, the relation is $a \approx p/p^0$.

The sodium activity at 1 atm partial pressure, a_L, becomes

$$a_L = 1/p^0 \qquad \text{(I)}$$

if p^0 is in atmospheres.

Any further increase in the cathode potential only increases the rate of evolution of sodium gas, but cannot raise the activity above a_L.

At the cathode potential required to deposit aluminum reversibly, the sodium activity has its equilibrium value a_e. To calculate the extra voltage required to evolve sodium at 1 atm.

$$E_L = \frac{RT}{n\mathbf{F}} \ln \frac{a_L}{a_e} \qquad \text{(II)}$$

or, in the case of sodium,

$$E_L = 1.984 \times 10^{-4} T \log \frac{a_L}{a_e} \qquad \text{(III)}$$

E_L is the difference between the reversible deposition potential of aluminum and that of sodium at 1 atm partial pressure of sodium vapor.

Previous Work

The sodium-aluminum equilibrium in fluoride melts has been studied by Jander and Hermann (18). They reacted aluminum with NaF-AlF_3 melts at 1090°C and determined the concentration of sodium in the aluminum metal and of total aluminum compounds in the melt. Alumina containers were used to run the reactions. No attempt was made to correct for the difference between concentrations and activities, and equilibrium constants were calculated on the basis of concentrations. Accuracy of the results was further limited by the small concentrations of sodium which had to be analyzed.

Grube and Hantelmann (17) determined the melt composition at which aluminum is in equilibrium with sodium at 1000°–1020°C as being about 6% AlF_3–94% NaF, whether or not alumina was present. Since elemental sodium was introduced into the reaction mixture and was vaporizing rapidly, there is some question as to whether true equilibrium was attained.

The use of lead as an auxiliary sodium "sink" has been mentioned by several workers in the field of aluminum research. Pearson and Waddington (21) tried to extract "metal fogs" with lead, and found evidence of sodium in the lead. Andrieux and Bonnier (22) ran short-term laboratory electrolyses with lead cathodes. Fischer (23) ran an industrial aluminum cell with a lead cathode for many months. It is important to note that none of these experiments represents reversible equilibrium conditions.

Experimental

The determination of the equilibrium activity of sodium in lead, in the presence of aluminum and cryolite melts, consisted of: (*a*) determination of the equilibrium concentration of sodium in lead after reaction; and (*b*) measurement of the activity of sodium in lead at various concentrations and temperatures in a separate study (19).

The general procedure consisted of reacting a cryolite melt, aluminum, and lead or a sodium-lead alloy in a covered container for varying periods of time. The reaction furnace was open to air and the container was not wholly airtight. At the end of each run, the container was chilled and samples taken for analysis.

The choice of container material was critical. Graphite crucibles were used at first, but were unsuitable for quantitative studies. Both sodium and aluminum react with carbon at the temperatures at which the experiments were performed. As a result, sodium is removed at the crucible walls, so that a true equilibrium can never be attained; instead, a steady state is reached where sodium is removed by the graphite at the same rate as it is driven into the lead layer. This steady state is dependent upon container geometry and, consequently, has no thermodynamic significance.

Grube and Hantelmann (17) also found that graphite crucibles were not suitable and used BeO crucibles instead. Since the solubility of BeO in cryolite is 8% by weight (24), some of this material dissolves; also, since the rate of dissolution is slow, the amount of BeO in the cryolite melt varies with the reaction time. This introduces a component into the melt whose effect is unknown.

Alumina was the only other available material that would not introduce a new component into the reaction mixture. However, use of this material automatically restricted these experiments to melts saturated with alumina. When carrying out experiments in alumina containers, powdered Al_2O_3 was added to cryolite in a quantity sufficient to attain saturation.

Vitrified alumina crucibles (Remmey 99AV) were used, with cover plates cut from Monofrax MH fused-cast alumina (Carborundum Co.). The cover was drilled to allow insertion of a stirrer. Since carbon could not be tolerated, the stirrer was fabricated by inserting a sealed piece of inconel tubing part way into a piece of dense alumina tube, so that inconel was in contact with melt but not with any liquid metal. A thermocouple was inserted inside the inconel tubing for temperature measurement. The maximum life of these stirrers was 4–5 hr. No absolutely leakproof all-alumina thermocouple protection tubes were available for the above use.

Equilibrium was approached from the low-sodium side, by using sodium-free lead plus aluminum, and from the high-sodium side by using sodium-rich lead plus aluminum. In the latter case the extra aluminum was added solely to maintain a homogeneous system, by providing an aluminum reservoir for side reactions.

Raw materials were natural cryolite (commercial), alumina (Kaiser, reduction grade), AlF_3 (Alcoa X-2A), NaF (reagent), lead (C.P.), aluminum (99.99%), and sodium (reagent).

TABLE I. *Sodium-aluminum equilibria*

Equilibrium concentration of Na in Pb, in the presence of Al metal and cryolite melt saturated with Al_2O_3. No carbon present.

Initial metal phases	Temp, °C	Na in Pb % by wt	NaF:AlF_3 final wt ratio
Al + Na-Pb	1010	5.78	1.50
Al + Na-Pb	1010	5.87	1.42
Al + Na-Pb	1010	6.05	1.89
		5.90avg	
Al + Na-Pb	970	5.63	1.67
Al + Na-Pb	970	5.06	1.60
Al + Na-Pb	970	6.46	1.71
Al + Na-Pb	970	5.02	1.66
		5.54avg	
Al + Pb	970	3.80	1.54
Al + Pb	970	3.89	1.58
Al + Pb	970	4.26	1.60
Al + Pb	970	3.98	1.60
		3.98avg	
Al + Na-Pb	940*	5.08	1.65
Al + Na-Pb	940	5.81	1.54
		5.44avg	

* Phillips, Singleton, and Hollingshead (25) report that the freezing point of the cryolite-alumina eutectic is 962°C. The fact that the melt was still liquid at 940°C in the present equilibrium investigations may have been due to supercooling, or excess NaF, or both.

Reaction time was varied from about 30 min to 6 hr. Jander and Hermann (18) state that 1 hr appears to be sufficient for reaching equilibrium. However, in the present work, attainment of equilibrium appeared to require a somewhat longer period of time (approx. 2 hr) because of the additional lead phase in the system. In order to help reach equilibrium as quickly as possible, intermittent stirring was used.

Temperature varied from 940° to 1010°C. At the end of each run, the container was removed from the furnace and placed on a graphite plate for rapid chilling, to avoid possible composition changes during cooling.

Once cold, the container was cracked. The metal slug was cleaned to remove any melt, and the aluminum part was separated from the lead layer. The latter was then sampled for sodium analysis, which was carried out with a Beckman DU spectrophotometer with flame photometer attachment.

The NaF:AlF_3 ratio of the melt after reaction was checked by pyrotitration.[1]

During the course of an experiment, the NaF:AlF_3 ratio changed. When starting with a sodium-rich lead alloy, aluminum is displaced from the melt and replaced by sodium ions so that the ratio increases. Conversely, when starting with sodium-free lead and aluminum the ratio decreases. It was generally attempted to achieve a final ratio of 1.50 by adjusting the initial melt composition. However, because of the empirical nature of this correction, some variation in final NaF:AlF_3 ratio occurred, as shown in Table I.

Results

The results of sodium-aluminum equilibrium determinations are presented in Table I.

At 970°C, the final Na content of the lead in an initially Na-free Pb is consistently lower than in an initially Na-rich Pb alloy. This gives a range within which the true equilibrium value must lie, and also shows the experimental limitations of the method used. Better reproducibility and better definition of the limits within which the equilibrium lies probably could be achieved by working in an inert atmosphere.

The data from Table I were used to calculate E_L [equation (II)]. The equilibrium activities of sodium in lead were determined from the corresponding concentrations (19). Values of p^0 for sodium used to calculate a_L were obtained from the following expression

$$\log P_{(mm)} = -5567/T - 0.5 \log T + 9.235 \quad (26) \qquad (IV)$$

These results are given in Table II.

Discussion

Table II shows that the values of E_L are quite small. It requires only 0.1 to 0.2 v above the thermodynamic deposition potential of aluminum to start producing the

[1] Cryolite corresponding to a balanced formula Na_3AlF_6 has a NaF:AlF_3 weight ratio of 1.50 and is neutral to phenolphthalein, while for NaF:AlF_3 > 1.50 it is alkaline. Pyrotitration consists in adjusting an unknown melt composition with known amounts of reagents until the neutral point is reached and then calculating the unknown composition.

TABLE II. *Results*

Temp, °C	1010	970	970	940
Initial metal phases in equilibrium runs	Al + Na-Pb	Al + Na-Pb	Al + Pb	Al + Na-Pb
Equilibrium % Na in Pb by wt (avg)	5.90	5.54	3.98	5.44
Equilibrium mole fraction N (Na in Pb)	0.360	0.345	0.272	0.342
Equilibrium activity of Na in Pb (a_e)	0.17	0.12	0.068	0.10
a_L	0.347	0.461	0.461	0.582
E_L (in mv)	79	143	205	184

first traces of sodium at 1 atm pressure, under which conditions it can be given off continuously from the cathode. This small difference in deposition potentials explains why, until recently, the controversy between the proponents of primary aluminum deposition and primary sodium deposition has remained unresolved.

From a quantitative standpoint the results are valid only in melts saturated with Al_2O_3. Qualitatively, however, it was shown earlier that aluminum is more noble than sodium in melts ranging from pure cryolite to cryolite saturated with alumina, i.e., E_L must have the same sign in all these melts. From mass-action considerations, it would be expected that Al_2O_3 would shift the reaction

$$3Na + Al^{+3} \rightleftharpoons Al + 3Na^{+}$$

to the right (in this equation Al^{+3} represents any aluminum donor, not necessarily Al^{+++} ions). Consequently, it is reasonable to believe that, at lower alumina concentrations, sodium activity would be somewhat higher and the value of E_L somewhat smaller than in cryolite melts saturated with alumina. However, since E_L is already small in Al_2O_3-saturated melts, it cannot be much smaller in ordinary reduction bath. In this connection the studies of Grube and Hantelmann (17) showed that the presence of alumina did not affect the reactions between sodium or aluminum and AlF_3-NaF melts. Experimental verification of this point must await the development of an inert container material.

Mass-action considerations would also predict that, when the NaF:AlF_3 ratio increases, the Na activity in lead or aluminum increases likewise. The present work was not intended to investigate the ratio effect and, within the narrow limits of NaF:AlF_3 ratio covered by these data, no significant trend is apparent. Again, the necessity of working in saturated alumina solutions limits the possibility of investigating the effect of ratio, since, at a fixed temperature, the alumina solubility varies as the ratio changes; thus, the effect of more than one variable would come into play.

Table II brings out the effect of temperature on E_L. Even though the equilibrium concentration of sodium may not greatly change between 940° and 1010°C, the equilibrium activity increases at higher temperatures, while the limiting activity decreases at the same time. As a result, E_L decreases by almost 100 mv between 940° and 1010°C.

The data show a small but definite range of cathode potential in which aluminum can be produced electrolytically, but in which sodium cannot be evolved at a partial pressure of 1 atm. The lower limit of this range is the reversible deposition potential of aluminum, and its span is E_L. In this range, the sodium activity at the cathode must lie between a_e and a_L. If the cathode potential is raised to the upper limit of this range, the aluminum reduction continues, but, in addition, sodium begins to come off the cathode. A further increase in current density and cathode potential should increase the total production of both aluminum and sodium.

It does not appear reasonable that the mechanism of aluminum production at the cathode should change abruptly as the cathode potential becomes sufficiently high to start liberating sodium. Therefore, the theory which holds that aluminum is produced by direct cathodic reduction of an aluminum donor and that any sodium evolved from the cathode is the result of a parallel or parasitic reduction appears to be correct (10, 2). The assumption of primary sodium deposition at the cathode is no more justified in the present case than in the case of electrolysis of aqueous sodium salt solutions.

In industrial cells, sodium has been often observed. This would mean that such cells are operated at a cathodic overvoltage in excess of E_L. The only available data are those of Piontelli and Montanelli (11); they indicate that, at normal cathode current densities, aluminum cells operate at cathodic overvoltages of 0.4–0.5 v.[2] This is well above the values of E_L shown in Table II. Therefore, there is good reason to believe that some sodium is actually liberated at cathodes of aluminum cells.

Along the same lines, it is interesting to examine Fischer's data on running an industrial cell with an auxiliary lead cathode (23). This cell was operated at 930°–958°C, and the sodium content of the lead layer built up to 11–12%. This corresponds to a sodium activity of 0.55 (19), which is equal to the value of a_L at 945°–950°C. Sodium activity at the cathode cannot exceed a_L and any sodium produced beyond this point is free to escape. Since Fischer's pot was run under conditions representative of industrial operation, his data indicate that his pot as well as normal industrial pots liberate some sodium at the cathode.

It is reasonable to assume that evolution of sodium on a liquid aluminum cathode is governed by an overvoltage. Since sodium is a gas at cell temperatures, it is likely that its overvoltage is different from that of aluminum deposition on the same cathode. No data on sodium overvoltages in an aluminum cell are available, and therefore there is no way of predicting the amount of sodium that is produced

[2] In a private communication, Piontelli indicates that the above overvoltage values represent a maximum and are probably on the high side. On the basis of more recent results with improved techniques (still to be published), he estimates that, at 1000°C and 1 amp/cm², the cathodic overvoltage is of the order of 0.20 v.

as a function of current density. The effect of temperature, however, can be seen from Table II; other conditions being constant, an increase in temperature reduces the value of E_L and consequently increases the relative amount of sodium evolved. This deduction is substantiated by observations which have been made many times in aluminum reduction plants.

It is important to emphasize that the cathodic production of sodium may not be the only cause of current inefficiency in industrial aluminum cells; it may not even be the most important factor. As previously indicated, the formation of carbides, and especially monovalent aluminum compounds, may contribute substantially to loss of current efficiency. At the present time, insufficient data are available to evaluate the relative importance of each side reaction.

Summary and Conclusions

A study of sodium-aluminum equilibria in cryolite-alumina melts indicates the following:

1. Aluminum is more noble than sodium in pure cryolite or cryolite-alumina melts in the temperature range of 940°–1010°C.

2. In cryolite-base melts, the reversible deposition potential of aluminum and that of sodium at 1 atm partial pressure are close to each other. In cryolite saturated with alumina, the difference between these potentials is of the order of 0.1–0.2 v; it decreases with increasing temperature.

3. From the experimental data, it appears that, in the aluminum cell, aluminum is formed at the cathode by direct electrochemical reduction from an aluminum donor. Any sodium liberated at the cathode is the result of a parallel reduction.

4. There are indications that, in an industrial cell, the cathode overvoltage is sufficiently high to liberate some sodium.

Acknowledgment

The authors wish to acknowledge the help of J. I. Davis, who carried out much of the laboratory work on which this material is based. The analytical determinations were carried out by K. Lincoln, C. Lynd, J. Winkler, and E. W. Yim.

Manuscript received September 15, 1955. This paper was prepared for delivery before the Chicago Meeting, May 2 to 6, 1954, and the Cincinnati Meeting, May 1 to 5, 1955.

Any discussion of this paper will appear in a Discussion Section to be published in the December 1956 Journal.

References

1. A. Vajna, *Proc. Intern. Aluminum Congress*, Paris, p. 123, June 14–19, 1954.
2. T. G. Pearson, "The Chemical Background of the Aluminum Industry," Royal Institute of Chemistry, Monograph No. 3, London (1955).
3. E. Bonnier, *Bull. soc. chim. France*, **1950,** D131.
4. P. Drossbach, "Electrochemistry of Fused Salts," p. 119–128, Springer, Berlin (1938).
5. M. M. Fréjacques, *Bull. soc. franç. elec.*, **9,** 684 (1949).
6. R. Gadeau, *ibid.*, **74,** 540 (1947).
7. E. Grünert, *Z. Elektrochem.*, **48,** 393 (1942).
8. A. I. Belyaev, *Tsvetnaya Met.*, **13,** [7], 87 (1938).
9. K. Grjotheim, *Alluminio*, **22,** [6], 679 (1953).
10. R. Piontelli, *Chimica e industria, Milan*, **22,** [11], 501 (1940).
11. R. Piontelli and G. Montanelli, *Alluminio*, **22,** [6], 672 (1953).
12. M. Rolin, *Bull. soc. franç. elec.*, (7th series), **13,** 35 (1952).
13. U. V. Baimakov, V. P. Mashovetz, and I. G. Kil, *Legkie Metal.*, **6,** 22 (1937).
14. U. V. Baimakov, *Tsvetnaya Met.*, **14,** [7], 84 (1939).
15. H. N. Gilbert (to E. I. du Pont de Nemours and Co.), U. S. Pat. 2,642,347, June 16, 1953.
16. E. W. Guernsey and M. S. Sherman, *J. Am. Chem. Soc.*, **48,** 141 (1926).
17. G. Grube and P. Hantelmann, "The Reactions of Al and Na with Melts of the System NaF-AlF_3 and NaF-AlF_3-Al_2O_3," Institut für Physikalische Chemie der Metalle am Kaiser Wilhelm-Institut für Metallforschung, February 1945.
18. W. Jander and H. Hermann, *Z. anorg. u. allgem. Chem.*, **239,** 65 (1938).
19. B. Porter and M. Feinleib, *This Journal*, to be published.
20. "Metals Handbook," p. 1165, American Society for Metals, Cleveland (1948).
21. T. G. Pearson and J. Waddington, *Disc. Faraday Soc.*, **1,** 307 (1947).
22. J. L. Andrieux and E. Bonnier, "Sur l'Electrolyse des Sels Fondus," Colloque International Sur l'Electrolyse, p. C15–C17, CNRS, Paris, May 23–27, 1952.
23. J. W. Fischer, *Angew. Chem.*, **20,** 17 (1948).
24. "Cryolite, Properties and Industrial Applications," p. 8, Pennsylvania Salt Mfg. Co., Philadelphia (1950).
25. N. W. F. Phillips, R. H. Singleton, and E. A. Hollingshead, *This Journal*, **102,** 649 (1955).
26. R. N. Lyon (Editor), "Liquid Metals Handbook," p. 53, Atomic Energy Commission, Washington (1952).

Mechanisms of Hydrogen Producing Reactions on Palladium

III. Hydrogen Overvoltage on the Polarization and Diffusion Sides of a Cathode-Diaphragm

JAMES P. HOARE AND SIGMUND SCHULDINER

Naval Research Laboratory, Washington, D. C.

ABSTRACT

Overvoltage-log current density relationships on both the polarization and diffusion sides of palladium cathode-diaphragms were measured. Effect of diaphragm thickness, cold working, and poisons were determined. It was shown that on the diffusion side, η_d is a function of the atomic hydrogen concentration, and the rate of the hydrogen producing mechanism is diffusion controlled.

INTRODUCTION

As before (1), the palladium cathode was in the form of a diaphragm separating two isolated bodies of solution. In this investigation, the current density-overvoltage relationships of the polarization and diffusion sides were determined.

Earlier (2) it was shown that the hydrogen overvoltage mechanism on the polarization side was controlled either by the combination, electrochemical, or slow discharge step depending on the *p*H and current density.

In addition to reporting further work on the overvoltage on the polarization side, it is the purpose of this paper to investigate the overvoltage on the diffusion side and determine its mechanism.

EXPERIMENTAL METHOD

The experimental technique used was essentially the same as that already reported (2). The electrolytic cell was the same as used in Part II (1). A rapid flow of purified hydrogen was passed through each compartment both of which contained the same solution (either $2N$ H_2SO_4 or approximately $0.5N$ H_2SO_4 + $0.5N$ Na_2SO_4). In the polarization compartment, current was passed between the platinum anode and the palladium cathode. The overvoltage on both the polarization and diffusion sides of the palladium diaphragm was measured against the Pt/H_2 electrodes in each compartment.

As the palladium was electrolyzed, bubbles of hydrogen, which formed on the surface, coalesced and were held by the rim of the teflon opening until a critical bubble size was reached, at which time the entire bubble left the surface. At this point the overvoltage on the polarization side was measured and the solution *IR* component determined by use of a current interrupter. Under steady-state current conditions these measurements gave consistent results over a reasonable period of time. Since there was no current flow in the diffusion compartment there was no solution *IR* drop and direct overvoltage measurements could be taken. Under constant current conditions the overvoltage measurements on both sides of the diaphragm were independent of time.

Temperature was maintained at 37 ± 1°C. The *p*H of each of the sulfuric acid-sodium sulfate solutions was determined at the end of the run. The exposed area of the palladium electrode was about 0.14 cm². Palladium diaphragms 0.0005 in., 0.002 in., 0.003 in., and 0.004 in. were used. All the diaphragms were made of annealed, hole-free palladium, except that the 0.003 in. specimen was made by cold rolling a 0.004 in. piece of foil.

RESULTS

The overvoltage-log current density relationships for both the polarization and diffusion sides of palladium diaphragms are given in Fig. 1 and 2. For the same current density, the overvoltage measured on the polarization side

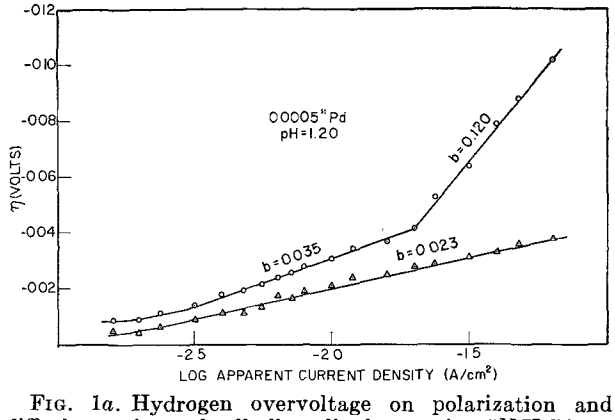

FIG. 1*a*. Hydrogen overvoltage on polarization and diffusion surfaces of palladium diaphragms in $0.5N$ H_2SO_4 + $0.5N$ Na_2SO_4. ⊙ = η_p; △ = η_d.

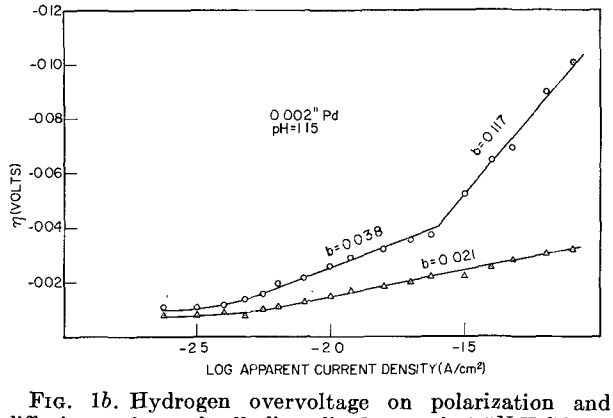

FIG. 1*b*. Hydrogen overvoltage on polarization and diffusion surfaces of palladium diaphragms in $0.5N$ H_2SO_4 + $0.5N$ Na_2SO_4. ⊙ = η_p; △ = η_d.

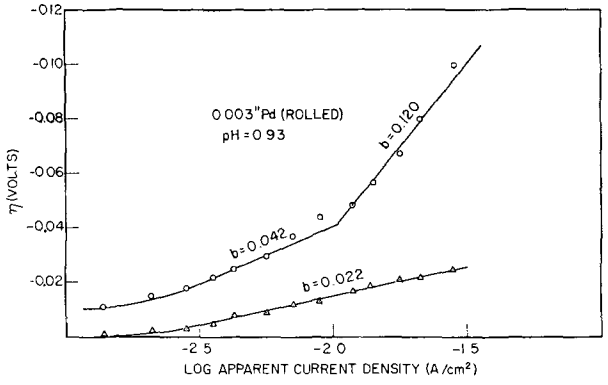

FIG. 1*c*. Hydrogen overvoltage on polarization and diffusion surfaces of palladium diaphragms in 0.5*N* H_2SO_4 + 0.5*N* Na_2SO_4. ⊙ = η_p; △ = η_d.

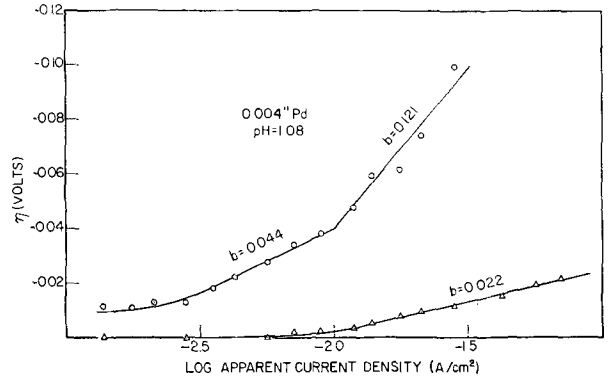

FIG. 1*d*. Hydrogen overvoltage on polarization and diffusion surfaces of palladium diaphragms in 0.5*N* H_2SO_4 + 0.5*N* Na_2SO_4. ⊙ = η_p; △ = η_d.

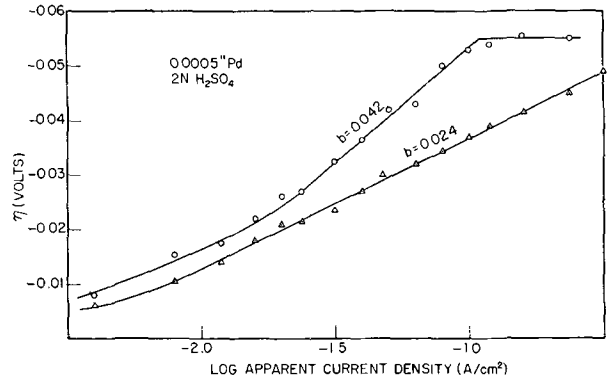

FIG. 2*a*. Hydrogen overvoltage on polarization and diffusion surfaces of palladium diaphragms in 2*N* H_2SO_4. ⊙ = η_p; △ = η_d.

(η_p) of a palladium diaphragm was essentially the same as the η_p determined in Part II where the diffusion compartment contained ceric sulfate solution. These results confirm in general the data found for a palladium bead which was reported in Part I.

There was also a linear relationship between the overvoltage on the diffusion side (η_d) and the log of the current density with a Tafel *b* slope of 0.021–0.024. This slope was independent of solution and thickness of the diaphragm. Frumkin and Aladjalova (3) obtained similar results.

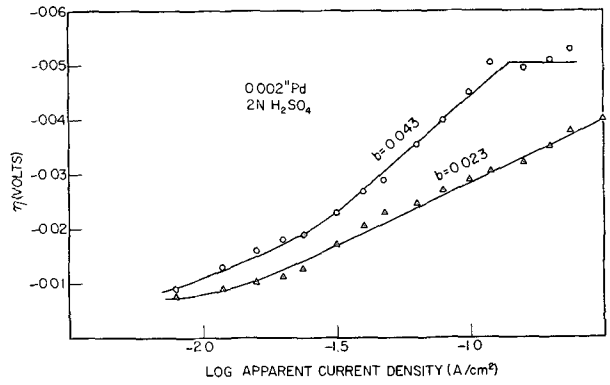

FIG. 2*b*. Hydrogen overvoltage on polarization and diffusion surfaces of palladium diaphragms in 2*N* H_2SO_4. ⊙ = η_p; △ = η_d.

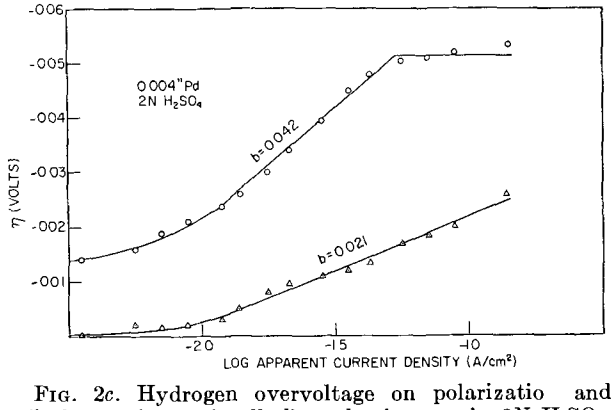

FIG. 2*c*. Hydrogen overvoltage on polarizatio and diffusion surfaces of palladium d phragms in 2*N* H_2SO ⊙ = η_p; △ = η_d.

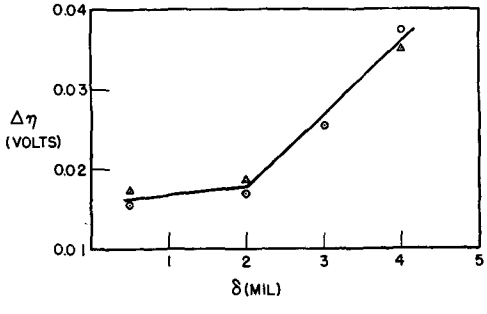

FIG. 3. Effect of diaphragm thickness on $\eta_p - \eta_d$

The separation between the polarization and diffusion overvoltage

$$\Delta\eta = \eta_p - \eta_d$$

at the point where the mechanism of hydrogen production on the polarization side changes (the *b* slope changes from 0.04 to 0.12 or ~0) has been plotted against diaphragm thickness and is shown in Fig. 3.

On opening the circuit, the decay in η_p with time was followed for cases where the diffusion compartment either did or did not contain a strong oxidizing agent. When the solution in the diffusion compartment was 2*N* H_2SO_4 saturated with hydrogen, η_p reached a value of +0.046 v at the end of 19 hr. Even after this time, however, the po-

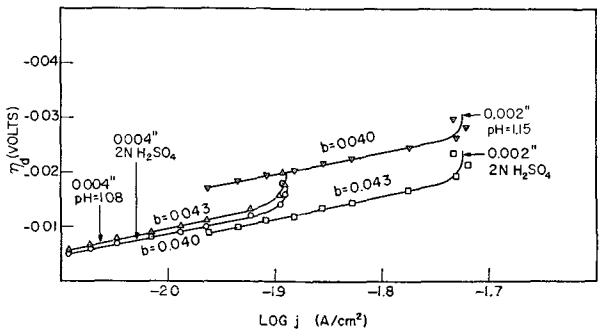

FIG. 4. Relationship between η_d and log j

tential was still very slowly changing in a positive direction. When 0.12N ceric sulfate in 2N sulfuric acid solution was put in the diffusion compartment, η_p reached a steady decay value of +0.050 v at the end of 2 hr. This shows that, when a strong oxidizing agent is present, β-palladium reverts to the α-form much more readily than in the absence of such an oxidant.

DISCUSSION

All the mechanisms of hydrogen overvoltage for the polarization side of the diaphragm have been discussed (2). Also, it was shown (1) that concentration of hydrogen in the palladium diaphragm up to a H/Pd atomic ratio of 0.6 is bound in the lattice. Additional hydrogen is not so firmly bound and may diffuse relatively freely through the lattice. If it is assumed that the slow step for the hydrogen producing mechanism on the diffusion side is the combination of hydrogen atoms to molecules, a Tafel slope of 0.031 should be obtained. This can be seen from the following:

Case (I). Combination controlled mechanism for η_d.

$$i \rightarrow \mathrm{H}\begin{cases} (p) \xrightarrow[\text{slow}]{+\,\mathrm{H^+} + e} \mathrm{H_2}(b = 0.04) \\ (d) \xrightarrow[\text{slow}]{+\,\mathrm{H^+}} \mathrm{H_2}(b = 0.03) \end{cases}$$

where p represents sites on the polarization side and d sites on the diffusion side.

Case (II). Diffusion-controlled mechanism for η_d.

$$i \rightarrow \mathrm{H}\begin{cases} (p) \xrightarrow[\text{slow}]{+\,\mathrm{H^+} + e} \mathrm{H_2}(b = 0.04) \\ (d) \xrightarrow[\text{slow}]{\text{diffusion}} \mathrm{H_{dif}} \xrightarrow{+\,\mathrm{H}} \mathrm{H_2}(b \neq 0.03) \end{cases}$$

Experimental results consistently show a b slope on the diffusion side lower than 0.031. This indicates that case (II) is the mechanism that applies for this system.

Fig. 3 also indicates that the rate-controlling step may be the diffusion of hydrogen through the palladium. In Part II the relationship ($j = ki^n$) between the rate of diffusion of hydrogen through palladium and the applied current density was determined. Since a diffusion-controlled mechanism is indicated here, this relationship can be applied. From this, the diffusion overvoltage, η_d, can be plotted against log j, where j is the diffusion current density (rate of hydrogen diffusion through palladium). These data are given in Fig. 4.

Fig. 4 shows a linear relationship between η_d and log j with a b slope of 0.040–0.043 until a limiting current density, j_{lim}, is reached. This limiting current density is a function only of diaphragm thickness.

It will be observed in Fig. 4, that at a given j, η_d is lower for the more acid solutions. The reason for this is as follows. On the polarization side for a given η_p, the current density is higher for the more acid solutions (2) and, therefore, the diffusion current, j, is greater. For a given η_p there is only a small variation of η_d with acid concentration (Fig. 1 and 2). Therefore, the curve for the more acid solution will lie below that for the less acid solution. Since at a given η_d the j's for the thinner diaphragms are greater than those for the thicker ones, the separation of the curves should be greater for the thinner diaphragms. Also the limiting current for the thinner diaphragms should be greater.

It was shown in Part II (1) that, when the atomic ratio of H/Pd < 1, the relationship between the polarization current i and the diffusion current j was:

$$j = ki^{0.53}$$

Since,

$$\eta_d = a - 0.0415 \log j$$

$$\eta_d = a' - 0.0415 \times 0.53 \log i = a' - 0.022 \log i$$

This shows that the mean b slope for the diffusion overvoltage against log i should be equal to 0.022. This is exactly the mean slope obtained from Fig. 1 and 2. From the above relationships, the a' and b' values for

$$\eta_d = a' - b' \log i$$

have been calculated from the data in Fig. 4 and compared with the experimental values of these constants obtained from Fig. 1 and 2. These results are shown in Table I.

TABLE I. *Comparison of calculated a' and b' values with experimental results*

Diaphragm thickness (in.)	Composition of solution	$\eta_d = a - b \log j$		$j = ki^n$ [see (1)]		$\eta_d = a' - b' \log i$			
						b'		a'	
		b	a	n	k	calc ($b' = nb$)	exp	calc	exp
0.002	2N H_2SO_4	0.040	−0.0888	0.53	0.109	0.021	0.023	−0.051	−0.051
0.002	0.5N H_2SO_4 0.5N Na_2SO_4	0.043	−0.0958	0.53	0.109	0.023	0.021	−0.054	−0.055
0.004	2N H_2SO_4	0.043	−0.0932	0.54	0.080	0.023	0.022	−0.046	−0.043
0.004	0.5N H_2SO_4 0.5N Na_2SO_4	0.040	−0.0958	0.54	0.080	0.022	0.022	−0.052	−0.046

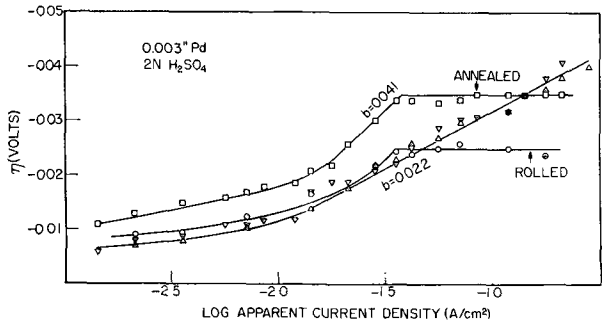

FIG. 5. Effect of cold working on hydrogen overvoltage. ⊡ = η_p, annealed; ⊙ = η_r, rolled; ▽ = η_d, annealed; △ = η_d, rolled.

These observations present strong evidence that on the back side of the palladium diaphragm the hydrogen producing mechanism is diffusion controlled. In principle, further evidence to support this contention could be found by decreasing the thickness of the palladium diaphragm to a point where the rate of diffusion through the metal would approach a value where the rate of the combination reaction on the diffusion surface is controlling. As this critical thickness is approached the *b* slope should increase to 0.031 which would be the value expected if the combination reaction were rate-determining. Some evidence for just such an effect can be obtained from the *b* values for the 0.0005 in. compared to the thicker diaphragms. Fig. 1*a* and 2*a* show that in both cases the *b* value for the 0.0005 in. palladium is 0.024. Fig. 1 and 2 show also that in all cases, except one, the *b* value for the 0.002–0.004 in. diaphragms is either 0.021 or 0.022. If one extrapolates this apparent trend, then, at a diaphragm thickness of about 0.000005 in., the rate of diffusion should be fast enough so that the combination reaction is controlling and the *b* slope should be 0.031. Unfortunately, additional experimental evidence for this would be difficult to obtain since a 0.0005 in. diaphragm is about the minimum practicable thickness.

ACKNOWLEDGMENT

The authors are indebted to Dr. J. C. White for many helpful discussions.

Manuscript received March 21, 1955. This paper was prepared for delivery before the San Francisco Meeting, April 29 to May 3, 1956.

Any discussion of this paper will appear in a Discussion Section to be published in the December 1956 JOURNAL.

REFERENCES

1. S. SCHULDINER AND J. P. HOARE, *This Journal*, **103**, 178 (1956).
2. J. P. HOARE AND S. SCHULDINER, *ibid.*, **102**, 485 (1955).
3. A. FRUMKIN AND N. ALADJALOVA, *Acta Physicochim., URSS*, **19**, 1 (1944).
4. G. TAMMANN AND J. SCHNEIDER, *Z. anorg. u. allgem. Chem.*, **172**, 43 (1928); D. P. SMITH, "Hydrogen in Metals," University of Chicago Press, Chicago, p. 21 (1948); F. A. LEWIS, G. E. ROBERTS, AND A. R. UBBELOHDE, *Proc. Roy. Soc.*, **A220**, 279 (1953); T. SUGENO AND M. KOWAKA, *J. Appl. Phys.*, **25**, 1063 (1954).

APPENDIX I

EFFECT OF COLD WORKING ON HYDROGEN OVERVOLTAGE

A 0.004 in. thick specimen of palladium foil was cold rolled to 0.003 in. Fig. 5 shows that, in 2*N* H_2SO_4 solution, cold working substantially lowers the potential at which the overvoltage becomes independent of current density on the polarization side of the electrode. The electrode was then vacuum annealed at 1200°C for 3 hr. This annealing raised the levelling off point by 10 mv. The diffusion overvoltage for both the rolled and annealed specimens was the same.

Fig. 1*c* shows the overvoltage-log current density relationships for both front and back sides of the cold rolled palladium electrode in sulfuric acid-sodium sulfate solution. Here there is no apparent deviation from the annealed specimens shown in Fig. 1 and Fig. 3. Evidently the only major effect of cold working is to lower the potential at which the overvoltage becomes independent of current density (point at which the palladium is completely saturated with hydrogen).

More experimental work on the effect of cold working on the electrolytic properties of pallidium is obviously needed before a general understanding of this system can be reached. Several investigators (4) have reported on this problem.

APPENDIX II

EFFECT OF POISONING THE POLARIZATION SURFACE ON η_p AND η_d

The polarization surface of both a platinum (0.005 in. annealed) and a palladium (0.003 in. annealed) diaphragm was poisoned with arsenic and η_p and η_d were measured. Results are shown in Table II. The clean platinum surface showed no evidence of hydrogen diffusion through the diaphragm even after polarization times as long as 5 hr. When the polarization side was poisoned, however, there was evi-

TABLE II. *Effect of poisoned polarization surface on polarization and diffusion overvoltages*

Current density (amp/cm²)	Platinum (0.005 in.) in 1*N* H_2SO_4				Palladium (0.003 in.) in 2*N* H_2SO_4			
	$-\eta_p$(v)		$-\eta_d$(v)		$-\eta_p$(v)		$-\eta_d$(v)	
	Clean surfaces	Poisoned* polarization surface	Clean surfaces	Poisoned* polarization surface	Clean surfaces	Poisoned† polarization surface	Clean surfaces	Poisoned† polarization surface
0.00175	0.027	0.6	0	0	—	—	—	—
0.0035	0.038	0.65	0	0.001	0.015	0.15	0.0095	0.018
0.0053	0.048	0.7	0	0.002	0.016	0.17	0.010	0.019
0.025	—	—	—	—	0.028	0.25	0.020	0.023
0.050	—	—	—	—	0.035	0.27	0.027	0.028
0.100	—	—	—	—	0.035	0.29	0.033	0.030

* Added 1 ml of 0.01M As_2O_3 (area of electrode = 0.57 cm²).
† Added 0.1 ml of 0.01M As_2O_3 (area of electrode = 0.1413 cm²).

dence of a small amount of hydrogen diffusion to the back side.

Since the rate of diffusion of hydrogen through platinum is evidently very low, for a clean surface, none of the hydrogen will diffuse through the metal. However, if the rate of the combination reaction on the polarization side of the platinum is greatly lowered, as it is by poisoning, then some of the hydrogen may diffuse through the metal because the relative rates of the diffusion and combination reaction (on the polarization side) will more nearly approach one another.

The effect of poisoning the polarization side of the palladium was to raise effectively the overvoltage on the diffusion side at low current densities. However, as the current density was increased, there was little difference between the diffusion overvoltages for clean and poisoned polarization surfaces.

Arsenic effectively destroys the catalytic activity of the molecular hydrogen-producing reactions on the palladium polarization surface. This in turn increases the atomic hydrogen concentration in the metal near the front side, hence, the diffusion gradient through the metal is greater, and the rate of flow of hydrogen through the metal is increased. For the palladium diaphragm at the higher current densities, the polarization side of the metal is completely saturated with hydrogen even on the clean surface; therefore, there is no effective increase in the diffusion gradient on poisoning.

Measurement of the Acidity of Aqueous Solutions at High Temperatures and Pressures

RATHINDRA N. ROYCHOUDHURY AND CHARLES F. BONILLA

Chemical Engineering Laboratories, Engineering Center, Columbia University, New York, New York

ABSTRACT

The potential of a platinized platinum-hydrogen electrode in two dilute hydrochloric acid solutions was measured with respect to a silver-silver chloride electrode from room temperature to 250°C at a total pressure from atmospheric to 600 psig.

A fused quartz cell was employed inside a steel bomb which contained the vapor pressure of the electrolyte plus the added hydrogen pressure.

The silver-silver chloride electrode was a silver plated and chloridized platinum gauze at the bottom of the cell. The hydrogen electrode was half immersed in the solution at the top.

The results were reasonably reproducible and permit estimating the acidity of the solution within approximately 0.1 to 0.2 *p*H units. The results agree reasonably well with theoretical calculations from the Debye-Hückel theory by Lietzke.

INTRODUCTION

Most of the electrode systems used for *p*H measurement are satisfactory only near room temperature, and none of them seems to have been applied or tested above 100°C.

However, control of aqueous reactions, such as hydrolyses and esterifications in chemical industry, and maintenance of aqueous solutions, such as boiler waters and nuclear reactor solutions, make continuous and rapid *p*H measurement at high temperatures and pressures desirable. The range of interest reaches to the critical point, but room temperature to about 250°C and up to a pressure of 600 psia covers most cases. An electrode system suitable for rapid and continuous measurement of *p*H over wide ranges of temperatures and pressures would evidently be of considerable interest.

The effect of high pressure on electrode potential has received little attention. No appreciable effect on electrodes involving only solids and liquids would be expected at the usual commercial process pressures. When a gas is involved in the electrode reaction, a definite effect on the fugacity, and thus on the electrode potential, is predicted by the Nernst equation. The most pertinent experimental work is that of Hainsworth, Rowley, and MacInnes (1), who found that up to 9000 psia a cell at 25°C containing a hydrogen electrode and a HgCl electrode obeys the usual Nernst equation very closely. Above that pressure increasing deviations occur.

The effect of high temperature has also been investigated very little, although three studies are pertinent. The antimony electrode is the only one that has been used for *p*H measurements well above room temperature. It is used for measuring the *p*H of cane juices from 80° to 100°C and covers the range of *p*H 2 to 12 (2).

Myers (3) studied the antimony electrode against a silver-silver chloride electrode and found an irreversible effect from 30° to 50°C, but obtained fairly reproducible emf measurements from 60° to 100° C. He applied nitrogen to obtain a total pressure of 2000 psi and carried the electrode system up to 300°C. These results were reproducible, but yielded the irregularities shown in Fig. 1. The breaks in the curve may be due to the formation of different hydrates with differing solubilities as the temperature is raised. This would seem to be an undesirable effect, and antimony electrodes cannot be expected to be serviceable above 100°C.

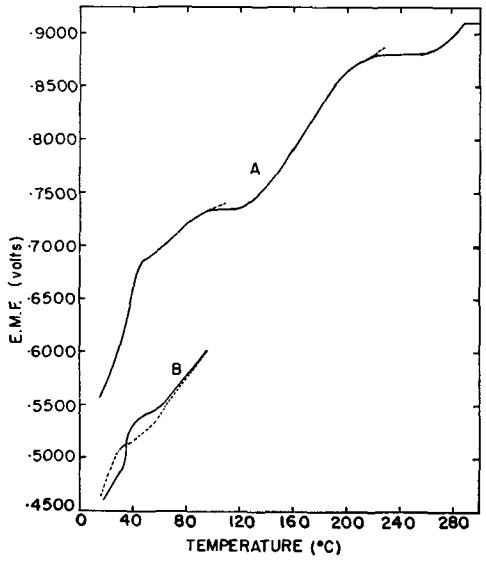

FIG. 1. EMF-temperature relationship (3) for the antimony-silver chloride cell in a buffered solution, pressurized with nitrogen. Curve A, *p*H = 7.0 at 25°C; total pressure = 2000 psia; curve B, pH = 4.0 at 25°C; total pressure = 14.7 psia.

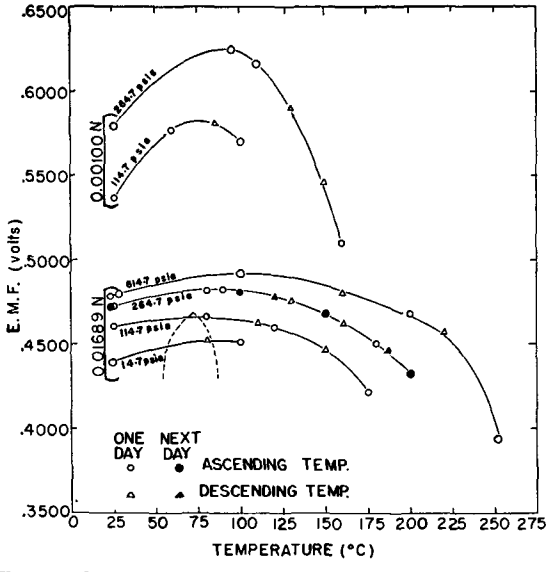

FIG. 2. EMF of the hydrogen-silver chloride cell in dilute aqueous hydrochloric acid as a function of temperature, pressure, and concentration. Dashed line is observed emf for the silver chloride thermogalvanic cell vs. temperature in °C, with 0.1*N* HCl and one electrode at 25°C (4).

Levin and Bonilla (4) set up a thermogalvanic cell with one AgCl electrode at room temperature (25°C) and another at temperatures up to 90°C, measuring the temperature coefficient in several different electrolytes. In hydrochloric acid solution these were found to increase at first with increase of temperature, pass through a maximum at about 72°C, and then decrease (Fig. 2).

Bonnemey (5) studied the H_2 electrode at a total pressure of 14.7 atm abs and found the electrode voltage to be linear with temperature over a range of 35°C.

The present study was aimed at determining the suitability of a hydrogen electrode and a silver-silver chloride electrode for acidity determinations in a single compartment cell at temperatures up to 250°C and total pressures up to 600 psig.

APPARATUS

The apparatus is shown in Fig. 3. The cell was of fused quartz. A platinum lead-in wire sealed through the bottom connected to a gauze in the lower compartment. The cell was open at the top, so inner and outer pressures were equal.

A steel bomb with $\frac{3}{8}$ in. walls to withstand the high temperature and pressure served as container for the cell. A 27 in. length of nominal $\frac{1}{8}$ in. iron pipe was screwed into the top of the bomb and a fitting with four tapped connections was mounted on its top. A spark plug at the top served as lead-in and support for the hydrogen electrode. A hole on one side of the top fitting connected to a hydrogen cylinder, and one on the other side to a vacuum pump and a manometer. The long stem on the cell and bomb was cooled at the middle so as to prevent evaporation from the electrolyte and condensation on the insulation at the top.

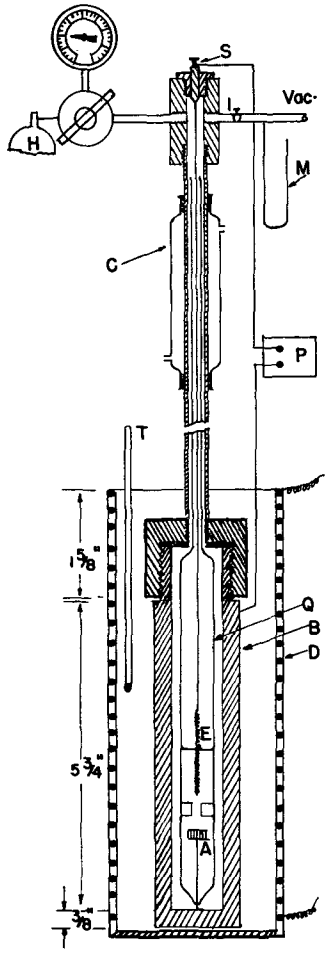

FIG. 3. Cell and bomb used in high pressure tests with the hydrogen-silver chloride electrode system. A—AgCl electrode; B—steel bomb; C—condenser; D—heating jacket; E—platinized platinum electrode; H—hydrogen cylinder; I—gas outlet valve; M—manometer; P—potentiometer; Q—quartz cell; S—spark plug; T—thermometer.

The bomb and quartz cell were brought to and maintained at the desired temperature by an external electrical resistance wire heater.

The platinum gauze, ½ in. on a side, was plated and chloridized to provide an Ag, AgCl electrode. The short platinum lead from the Ag/AgCl electrode was connected to a pure thermocouple-iron wire attached to the inside wall of the bomb. The hydrogen electrode was a spiral of platinized platinum half-immersed in the electrolyte. It hung by another iron wire from the central terminal of the spark plug. Other iron wires led from the outside of the bomb and from the spark plug terminal to a potentiometer. All connections were silver-soldered.

The platinum-iron junctions at the hydrogen electrode and the silver electrode nullify each other's thermoelectric effect, and no difference from platinum or silver leads is obtained.

Experimental Procedure

Solutions of hydrochloric acid were prepared by diluting reagent-quality acid. The *p*H of each solution was measured with a Beckman *p*H meter at room temperature. Normality of each solution was determined by titrating with standard alkali.

The platinum gauze in the cell was cleaned by washing several times with boiling nitric acid and then rinsing thoroughly with distilled water.

The compositions of the strike solution and the plating solution for the silver plating were taken from Promisel and Wood (6). The platinum gauze was silver plated for ½ min in the strike solution and then for 15 hr in the plating bath, using a silver anode and a current of 8 ma. After removal from the plating bath, it was washed frequently with distilled water for one week to remove adsorbed contamination (7).

After the washing it was chloridized anodically in molar hydrochloric acid at 5 ma for 1 hr (8). It was then washed repeatedly with distilled water and kept in very dilute hydrochloric acid for a week to complete the aging (8). Eight silver foils of the same size were simultaneously chloridized in the same way. Five of the eight silver electrodes were found to agree with each other within 0.1 mv in dilute HCl, the other 3 not being much farther off. This agreement showed that the chloridizing conditions were correct. More accuracy (0.02 mv), as claimed by Smith and Taylor, might have been achieved with more precaution and with improvements in the methods of measurements, but for the present purpose it was considered unnecessary.

Two pieces of 0.025 in. platinum wire one inch long were wound in the form of a narrow spiral and cleaned by repeated heating in a Bunsen flame and dipping in concentrated hydrochloric acid. The platinization was carried out by electrolysis at room temperature of a solution containing 3% chloroplatinic acid, using the two platinum spirals alternately as cathode and anode with a 2-v storage battery as an energy source.

When the two spirals were covered with a fairly thick, black velvety deposit, they were removed and washed with water. To remove adsorbed oxygen, the electrodes were reduced cathodically for 15 min in very dilute sulfuric acid, using a platinum anode and the 2-v battery. The process was repeated with distilled water and then the electrodes were stored in distilled water.

A L&N type K-2 potentiometer and wall galvanometer were used to measure the emf.

The desired total pressure was maintained by supplying hydrogen from a cylinder through a Hoke high pressure gas regulator. A standard rubberized asbestos high temperature gasket was used at the top of the bomb. The threaded pipe joints were made tight with pipe dope. The whole assembly was sufficiently leak proof that pressure could be maintained sensibly constant for 48 hr with valve I and the hydrogen cylinder shut off.

The pressure was always kept well above the vapor pressure of water to prevent boiling of the solution. Decreases in temperature or pressure were always made very slowly to prevent any possible foaming of the electrolyte up the tube. An hour was allowed at each new temperature and pressure change to ensure equalization of the temperature and concentrations throughout the cell.

Results and Discussion

The potential of the cell was measured at several high temperatures and pressures with solutions of hydrochloric acid that were 0.00100 and 0.01689*N* at room temperature. The emf values with ascending and descending temperatures are seen to agree closely in Fig. 2, demonstrating the good reversibility of the electrode system.

The electrode system also yielded excellent reproducibility over longer intervals as shown by the solid points in Fig. 2, which were obtained one day later.

Accuracy of the experimental set-up was shown by the fact that cell potentials at atmospheric pressure and room temperature for the two concentrations here studied fall on the same smooth curve of emf vs. concentration given by Harned and Ehler's measurements (9) at the same conditions.

The Nernst equation should apply to all ionic cells under any conditions. For this cell:

$$\text{Cell reaction: } \tfrac{1}{2}H_2 + AgCl = Ag + H^+ + Cl^-$$

$$\text{Cell potential: } E = E^\circ - \frac{RT}{F} \ln \frac{(m\gamma_\pm)^2}{\sqrt{P'}} \qquad \text{(I)}$$

where m = molality of the HCl solution, $\gamma_\pm$ = average activity coefficient of H^+ and Cl^- ions, and P' = fugacity of the hydrogen.

Lietzke (10) calculated and plotted the potentials given by equation (I) for 0.01689*N* HCl and these same experimental conditions. E° was obtained by extrapolating Harned and Ehler's values vs. temperature. The activity coefficient of HCl at high temperatures was calculated by two methods.

(*a*) The thermodynamic relation

$$\left(\frac{\delta \ln \gamma_\pm}{\delta T}\right) = \frac{\bar{L}_2}{\nu R T^2}$$

was integrated with the required temperature correction over the interval from 0° to 250°C to yield $\gamma_\pm$ in 25°C steps. $\bar{L}_2$ is the relative partial molal heat content of the HCl in the solution.

(*b*) The Debye-Hückel equation was used (9) in the form

$$-\log \gamma_{\pm} = \frac{1.8123 \times 10^6 \sqrt{C}}{(DT)^{3/2}} \cdot \frac{1}{1 + 50.288 \times 10^8 (DT)^{-1/2} a_i \sqrt{C}} \quad \text{(II)}$$

D is the dielectric constant, C is the hydrogen ion concentration in moles per liter, and the distance a_i of closest approach of the ions was taken as 5×10^{-8} cm.

The activity coefficients calculated by the two methods differed by a maximum of 0.6%, corresponding to a maximum variation in the calculated potentials of 0.4 mv.

The hydrogen partial pressures were converted to fugacities by using the data of Deming and Shupe (11) and by assuming that the water vapor does not affect the fugacity of the hydrogen. At the highest hydrogen partial pressures the correction amounted to about 3%.

Lietzke's values are plotted in Fig. 4 for comparison with the experimental data. Calculated and experimental potentials are seen, in general, to agree within a few millivolts.

Hydrogen was found to have considerable effect on the potential of AgCl electrodes. To measure its effect two AgCl electrodes were set up in the same 100 ml beaker and another in a different beaker. The beakers were connected by a bridge containing the same solution but not permitting appreciable hydrogen diffusion between the vessels. The potential between any two of the Ag/AgCl electrodes was under 0.1 mv. Hydrogen was then bubbled, at atmospheric pressure and temperature, past one of the two electrodes in the same beaker. This electrode became 2.3 mv more negative than the other electrode in the same beaker, and 7.6 mv more negative than the third electrode, in the other beaker. This diminution by hydrogen of the potential of an AgCl electrode toward that of a hydrogen electrode may be due to the coexistence of simultaneous hydrogen and AgCl electrodes at the hydrogenated AgCl electrode, yielding an intermediate potential which depends on the resistance and overvoltage characteristics of each electrode reaction. The effect seemed to be reversible, since a good potentiometer balance was readily obtained. It is presumably reproducible, since interchanging any two AgCl electrodes yielded the same result. This effect would be more pronounced at the higher temperatures, due to higher solubility and higher diffusion rate of hydrogen gas, and also at a higher hydrogen pressure at a given temperature.

Lietzke points out that hydrogen reduction of part of the AgCl in an AgCl electrode would increase the acid concentration in the AgCl coating and, hence, would lower the potential of the system. This is another possible explanation.

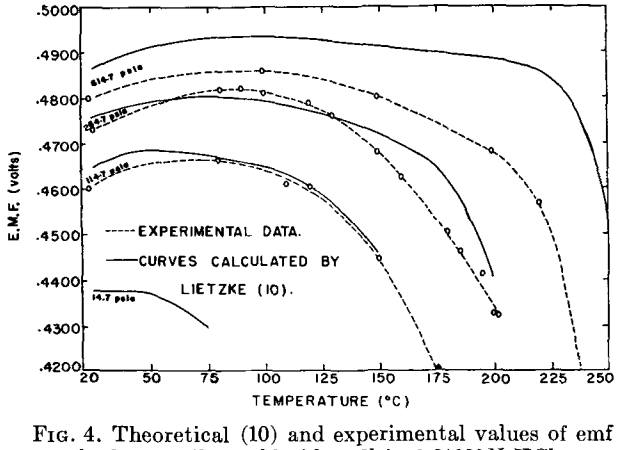

FIG. 4. Theoretical (10) and experimental values of emf of the hydrogen-silver chloride cell in 0.01689*N* HCl.

EFFECT OF HYDROGEN PRESSURE ON OVER-ALL CELL POTENTIAL

The curves of Fig. 2 have been crossplotted in Fig. 5 to show the effect of hydrogen pressure on the over-all cell potential at constant temperature. The lower limit of the curves at the boiling point of the electrolyte is shown dotted, for orientation purposes.

Neglecting the effect of H_2 on the AgCl electrode and considering the over-all reaction as involving gaseous hydrogen in an ideal state, the difference in emf values of the over-all cell at constant temperature and two different hydrogen partial pressures may be represented as follows:

$$E_{P_2} - E_{P_1} = \frac{RT}{2F} \ln \frac{P_2}{P_1} \quad \text{(III)}$$

Fig. 6 has been plotted for P_2 constant at 614.7 psia. With the coordinates employed, equation (III) is a straight line through the origin with a slope of unity. While the present 25°C curve agrees somewhat with equation (III), it is evident that, at the higher temperatures, agreement is quite poor. From Hainsworth's work it is evident that the deviation from equation (III) does not occur at the hydrogen electrode. Abnormalities in solubility or crystalline form of the AgCl would not show up as deviations unless they were functions of hydrogen pressure, which seems unlikely. The only remaining possibility seems to be a reproducible, nonequilibrium condition in which hydrogen electrode sites are established in the Ag electrode itself, as previously suggested. At constant pressure this

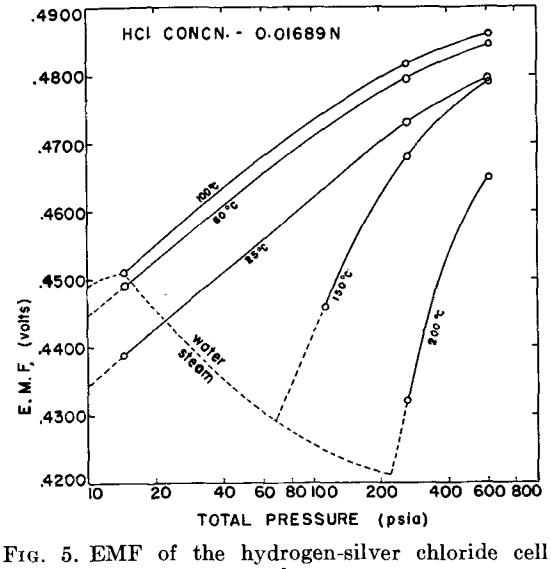

FIG. 5. EMF of the hydrogen-silver chloride cell in 0.01689*N* HCl vs. pressure and temperature.

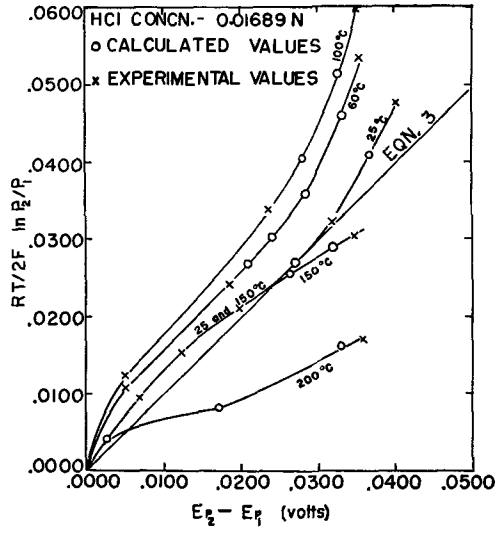

FIG. 6. Effect of hydrogen on the hydrogen-silver chloride cell voltage, in terms of pressure. P_2 = 614.7 psia.

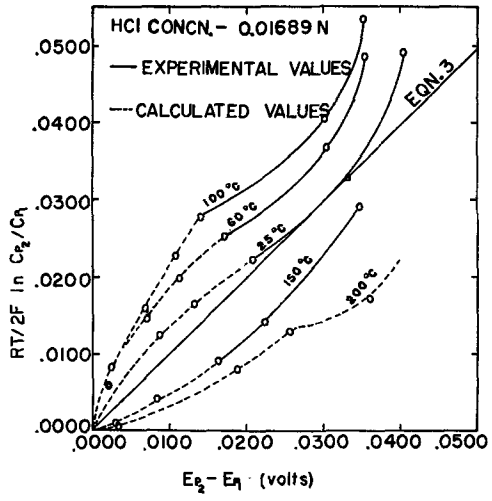

FIG. 7. Effect of hydrogen on the hydrogen-silver chloride cell voltage, in terms of concentration. P_2 = 614.7 psia.

would be expected to decrease the cell potential more the higher the temperature (witness the trend to the left from 25° to 100°C). At constant temperature it should decrease the potential more the higher the pressure (see the upward curvature at the end of the 25° to 100°C isotherms). No explanation is evident for the voltage increase at 150° and 200°C.

Mercury is noted for high hydrogen overvoltage, which may be the reason for the apparent lack of effect of hydrogen on Hainsworth's calomel electrode. In addition, the calomel bed was evidently deep, while these electrodes had only the usual thin AgCl coating and were probably less effective in preventing diffusion of dissolved hydrogen to the silver.

Assuming that γ_{H_2}, a_{H^+}, and a_{Ag^+} remain constant at a given temperature over the range of hydrogen partial pressures from P_1 to P_2, correction for variation in hydrogen pressure may be made by writing

$$E_{P_2} - E_{P_1} = \frac{RT}{2F} \ln \frac{C_{P_2}}{C_{P_1}} \qquad \text{(IV)}$$

where C_P = solubility of hydrogen at the specified pressure. Fig. 7 is a check of equation (IV). No improvement in correlation is evident. This plot is of additional interest in view of Rideal and Bowden's finding (12) that overvoltage (ΔE_0) is a linear function of the logarithm of the polarizing current, equivalent to the rate of hydrogen diffusion through the AgCl coating. Thus

$$\Delta E_0 = a + b \log I = c + d \log (C_{H_2}) \qquad \text{(V)}$$

and one might expect isotherms on Fig. 7 to be straight, assuming constancy of the AgCl coating, even when they did not agree with equation (IV). It is seen that equation (V) does not bring these data into agreement.

Practical Correlation of Cell Voltage against Acidity

In the cell $Pt(H_2)/HCl, AgCl/Ag$ there are four variables, viz., concentration of HCl, temperature, pressure, and emf, of which one (generally considered the emf) is dependent on the other three. In a graphical correlation, or calibration curve, two independent variables and one dependent variable, at the most, can be conveniently represented. It has already been shown that a correlation eliminating the effect of pressure could not be obtained, and none would be expected that corrects for temperature, on account of the complicated effect of temperature on the over-all cell. Therefore, it is desirable to attempt to include the effect of acid concentration on the cell voltage as a theoretical correction to the observed voltage.

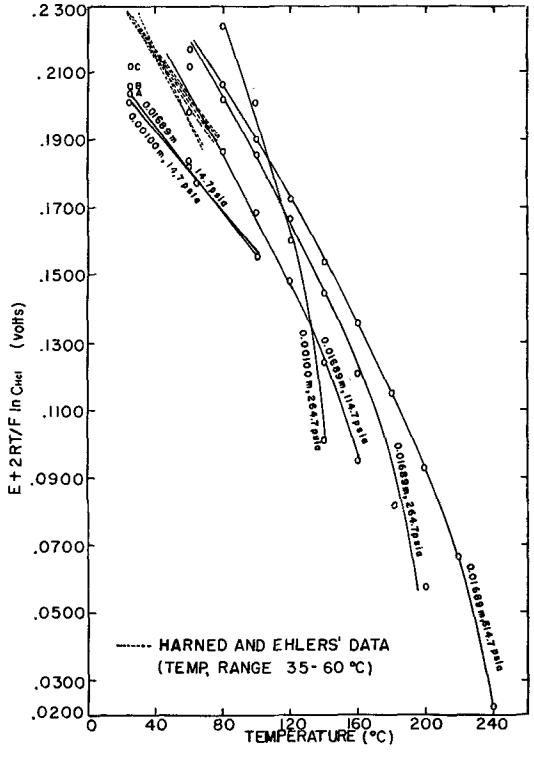

FIG. 8. Effect of HCl concentration on cell voltage—calibration curves for hydrogen-silver chloride cell for pH determination in dilute aqueous HCl solution. Dashed lines show data calculated from Harned and Ehler.

In this cell the effect ΔE_c on the cell potential due to a change from ionic activities of unity may be represented by

$$\Delta E_c = -\frac{RT}{\mathbf{F}} \ln (C_{H^+}\gamma_{H^+} \cdot C_{Cl^-}\gamma_{Cl^-})$$

$$= -\frac{2RT}{\mathbf{F}} \ln (C_{HCl}\,\gamma_{\pm})$$

Taking the right-hand side as the concentration correction and subtracting it from the cell emf, the effect of concentration should vanish. If this correction is valid, plotting $(E + 2RT/\mathbf{F} \ln C_{HCl}\,\gamma_{\pm})$ vs. temperature should yield the same curve for different concentrations at the same pressure.

Compared to an activity coefficient of unity, predicted values of $\gamma_{\pm}$ would only change ΔE_c by a maximum of 6 to 7 mv in the case of the 0.01689*N* HCl solution and less in the more dilute solution. As this difference in ΔE_c is less than the apparent experimental uncertainty, $\gamma_{\pm}$ was assumed unity for simplicity (Fig. 8).

The dashed lines on the top of Fig. 8 are calculated from the data of Harned and Ehler at 35°–60°C (9). The rest of the curves represent the present data. The concentrations of HCl in Harned and Ehler's work lie between the two concentrations used in the present experiments. The present two lines at atmospheric pressure agree with each other, as do the lines of Harned and Ehler, but the average discrepancy between the two sets of lines is about 20 mv. This discrepancy must be due to the effect of hydrogen on the AgCl electrode, as described before. To show in Fig. 8 the magnitude of this effect as here observed, points *A*, *B*, and *C* have been plotted. The distance *AB* is the potential difference between the electrode in the stream of H_2 bubbles and the other one in the same beaker, and *AC* is the potential difference between the electrode in the H_2 stream and the one in the separate container. Although these potential differences are well under the 20 mv discrepancy, it is quite possible that the AgCl electrode in the quartz cell had a thinner AgCl deposit and a larger hydrogen correction than the ones prepared and tested externally.

The lines at 264.7 psia cross, but do not coincide as might have been desired. However, except for the 264.7 psia line for the dilute solution, the lines constitute a reasonably smooth family. Accordingly, a plot of the form of Fig. 8 seems to constitute a satisfactory calibration curve for a given hydrogen/AgCl cell.

In conclusion, the one-compartment hydrogen/AgCl cell is not ideal for *p*H measurement at high temperatures and pressures, due apparently to a slight polarization of the AgCl electrode by the hydrogen. However, when directly calibrated or reproducibly manufactured it is apparently suitable, at least up to 250°C, for *p*H determination to within better than 0.2 *p*H units. Its sensitivity is yet greater, so that still smaller variations in acidity in a process stream could be detected. Fig. 8 should be fairly reliable for electrodes made as herein described. Probably a two-compartment cell which prevents hydrogen from reaching the AgCl electrode would be slightly more accurate.

Manuscript received June 15, 1955. This paper is Contribution No. 61 from the Chemical Engineering Labs., Engineering Center, Columbia University, New York, N. Y.

Any discussion of this paper will appear in a Discussion Section to be published in the December 1956 JOURNAL.

REFERENCES

1. W. R. HAINSWORTH, H. J. ROWLEY, AND D. A. MACINNES, *J. Am. Chem. Soc.*, **46**, 1437 (1924).
2. W. N. GREER, *Trans. Electrochem. Soc.*, **72**, 153 (1937).
3. C. M. MYERS WITH C. F. BONILLA, Senior Research Thesis in Chem. Engineering, Johns Hopkins University (1947).
4. H. LEVIN AND C. F. BONILLA, *This Journal*, **98**, 388 (1951).
5. M. BONNEMEY, *J. Chim. Phys.*, **46**, 176 (1949).
6. N. E. PROMISEL AND D. WOOD, "Modern Electroplating," pp. 205–313, John Wiley & Sons, Inc., New York (1942).
7. W. R. CARMODY, *J. Am. Chem. Soc.*, **51**, 2901 (1929).
8. S. R. SMITH AND J. K. TAYLOR, *J. Research Natl. Bur. Science*, **20**, 839 (1938).
9. D. A. MACINNES, "The Principles of Electrochemistry," p. 187, 143, Reinhold Publishing Co., New York (1939).
10. M. H. LIETZKE, Atomic Energy Commission Report, ORNL 1741 (July 14, 1954) from Oak Ridge National Laboratory; Paper #223, American Chemical Society paper before the Engineers' Joint Council Nuclear Engineering Congress (December, 1955).
11. W. E. DEMING AND L. E. SHUPE, *Phys. Rev.*, **40**, 848 (1932).
12. E. K. RIDEAL AND F. P. BOWDEN, *Proc. Roy. Soc.*, **120A**, 59 (1928).

Oxygen Overvoltage in Concentrated Acid Solutions

I. Perchloric Acid

T. R. Beck[1] and R. W. Moulton

University of Washington, Seattle, Washington

ABSTRACT

Oxygen overvoltage was measured on platinum electrodes in 5M perchloric acid from −45° to +40°C and in 0.005-9M perchloric acid at 0°C. A limiting current density that was found is due to activation overvoltage at the anode surface. This limiting current density decreased at lower temperatures and in higher perchloric acid concentrations. It also marked the beginning of ozone formation. Adsorption of perchlorate ions is believed to be the cause of the limiting current density.

Introduction

Although most commercial electrolysis reactions are carried out in concentrated electrolytes, little work on anodic overvoltage has been done in concentrated electrolytes. To fill this gap partly, anodic overvoltage was studied in concentrated perchloric acid solutions in connection with prior work (1) on electrolytic ozone. Platinum and platinum-iridium alloy were chosen for anodes because they give the highest yields of ozone.

In general, overvoltage at an electrode may be resolved into three components (2): (*a*) an ohmic *IR* drop, η_o, through a film on the electrode surface or through the electrolyte adjacent to the surface; (*b*) concentration polarization, η_c, caused by difference in concentration of electrolyte between the bulk solution and the electrode surface; and (*c*) an activation overvoltage, η_a, associated with the rate-controlling step at the electrode surface. The total overvoltage, η, is the sum of these three terms:

$$\eta = \eta_o + \eta_c + \eta_a$$

The relation of activation overvoltage to ozone formation will be shown.

Considerable controversy is evident in the literature regarding the mechanism of electrolytic oxidations (3). There are two general mechanisms postulated to explain electrolytic oxidation reactions in aqueous media: (*a*) formation from discharge of OH^- ions or water molecules of an intermediate oxidizing agent common to all reactions which accomplishes the reaction chemically; and (*b*) direct discharge of the reacting ions. The intermediate oxidizing agent has been attributed by various investigators to be oxygen (4), atomic oxygen (5), hydrogen peroxide (6), and hydroxyl radical (7). Experiments of Butler (8, 9) and Hickling (10) indicate that a layer of adsorbed oxygen or platinum oxide is formed on platinum anodes prior to oxygen evolution. The direct discharge theory has become more plausible since the chemistry of free radicals has become better known (11).

[1] Present address: Kaiser Aluminum and Chemical Corp., Permanente, Calif.

Experimental Apparatus and Procedure

Electrodes.—Pure platinum and 95% platinum-5% iridium alloy were used as anode materials in all the experimental work. Platinum anodes have been found to give the highest yield of ozone (1) which has been believed to be the result of the high oxygen overvoltage associated with them. The platinum-iridium alloy which behaves similarly is used extensively in the electrochemical industry because of its better corrosion resistance (12). Several anodes were used in the form of wire, tube, and sheets. Inert cathodes of platinum, platinum-iridium, or palladium-gold were used.

Cells.—The two cells used in most of this work are shown on Fig. 1 and 2.

Cell A was a tall 200-ml beaker fitted with a rubber stopper supporting the electrodes and Luggin capillary. An annular palladium-gold alloy cathode surrounded the anode to give a uniform anode current density. Several different anodes were used. The first was a 0.30 cm OD 95% platinum-5% iridium tube with 3.08 cm^2 exposed area. It was sealed to a glass tube and plugged with a glass bead at the lower end. All electrical contacts to the glass sealed platinum electrodes were made with mercury. The temperature of this hollow anode was measured by means of a thermocouple within it. The second anode was a 0.71 mm platinum wire with 0.38 cm^2 exposed area, also sealed to a glass tube. The third anode was a 0.14 cm platinum wire with 0.12 cm^2 exposed area. It was fastened in a paraffin insulated steel shaft which was rotated by an electric stirring motor.

Cell B was designed for simultaneously measuring ozone concentration and overvoltage. The electrolyte volume was 21.0 ml and there was a minimum volume for gas. The anode was a 0.30 cm OD 95% platinum-5% iridium tube with an exposed area of 6.10 cm^2. Teflon gaskets held under compression by brass stay bolts exterior to the cell formed a liquid-tight seal at each end of the cell. A tube was provided for filling the cell and sampling electrolyte. The cathode, a length of 0.71 mm platinum wire, entered through a Teflon sealed capillary tube and traversed the length of the cell on each side of the cell parallel to the anode to give a uniform anode current density.

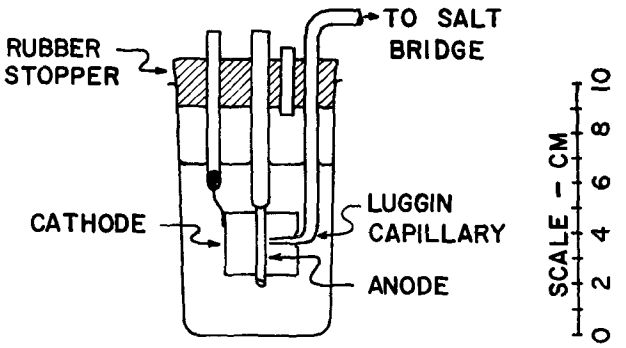

FIG. 1. Cell A, for measurement of anodic overvoltage

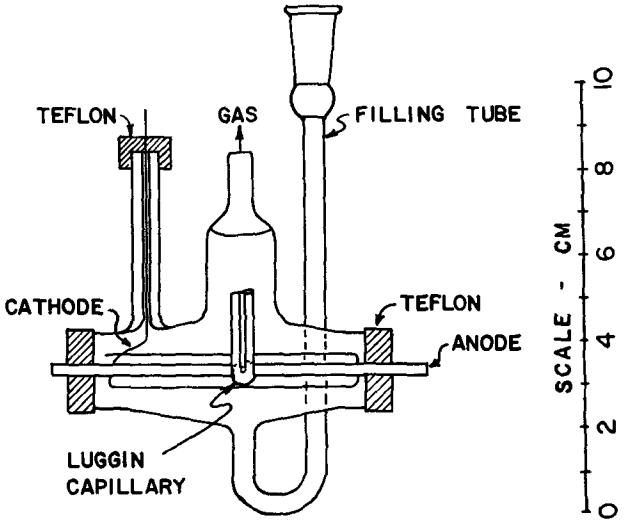

FIG. 2. Cell B, for simultaneous measurement of ozone concentration and overvoltage.

Electrical circuit.—The power supply for the cells was a 50 v lead acid storage battery. Current was measured with a Weston Model 785 industrial circuit tester which had 50 microamp, 1, 10, and 100 milliamp, and 1 and 10 amp scales. Potentials were measured with a Leeds and Northrup student type potentiometer. A vernier decade resistance box was constructed to vary the current from 0.000001 to 10 amp continuously without breaking the circuit. Anode potential was measured on each of the cells by means of a Luggin capillary connected through salt bridges to a saturated potassium chloride calomel electrode.

Salt bridge and calomel cell.—A saturated potassium chloride calomel electrode was used as reference electrode because of its reliability and simplicity. Hydrochloric acid was used as intermediate connecting solution to the perchloric acid electrolytes in order to avoid formation of insoluble potassium perchlorate at a perchloric acid-potassium chloride junction. The bridge was a 1 mm ID glass tube filled with sintered glass to minimize liquid flow through it.

The calomel cell and liquid-liquid junctions were calibrated against an hydrogen electrode in the electrolytes studied because there is no exact method of calculating junction potentials. The temperature of the calomel electrode and liquid junctions was held at 25°C, while the temperature of the electrolyte and hydrogen electrode was varied over the full range of temperatures under which overvoltage was studied.

The reversible oxygen potential for various temperatures was calculated from an expression for the free energy of water decomposition (13). The reversible potential was not corrected for the small deviation due to the change in the activity of water in the concentrated electrolyte solutions. The deviation of the water activity from unity in 5M perchloric acid at 25°C (14) causes an error of only 0.006 v.

Ultraviolet photometer for ozone determination.—An ultraviolet photometer similar to the instrument described by Klotz (15) was constructed to measure ozone concentration. The instrument calibration was based on the Lambert-Beer law and the known extinction coefficient of ozone at a wave length of 253 mμ (16) and was checked by idometric titration. The 1-cm thick sample cell allowed rapid and accurate measurement of ozone from 0.1 to 3 wt % concentration.

EXPERIMENTAL RESULTS

This study followed an observation of a limiting current density shown on Fig. 3 for a cell used to prepare electrolytic ozone. The cell [shown in Fig. 1 in prior work (1)] had a 2.8 x 1.0 cm sheet platinum anode. The relation shown in Fig. 3 was obtained with 5M perchloric acid

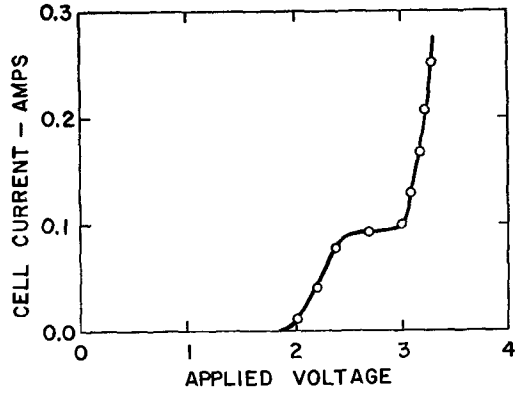

FIG. 3. Current-voltage curve for ozone cell

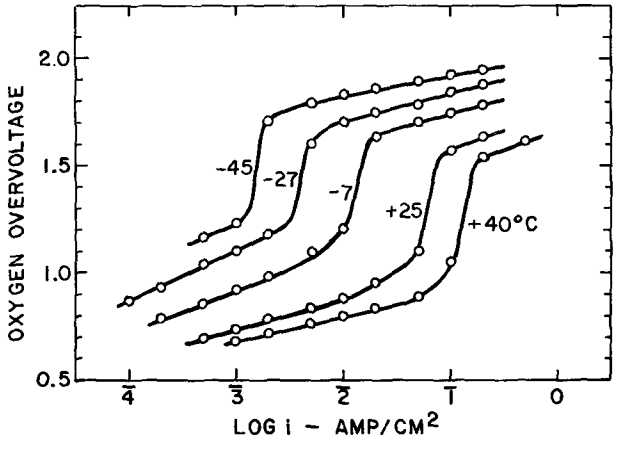

FIG. 4. Oxygen overvoltage in 5M perchloric acid. Effect of temperature.

TABLE I. *Values of b in Tafel equation, 5M $HClO_4$ electrolyte*

Temp, °C	−45	−25	−7	+25	+40
b, lower line	—	0.26	0.22	0.14	0.11
b, upper line	0.11	0.15	0.14	—	—

at 0°C. The apparent limiting current density was most unexpected because there was no ionic specie present which would be expected to give rise to concentration polarization, the usual cause of a limiting current density.

Overvoltage in 5M perchloric acid—temperature effect.—The limiting current density was found to be an effect occurring entirely at the anode. Fig. 4 shows oxygen overvoltage determined in 5M perchloric acid at several temperatures with cell A, using the 3.08 cm^2 platinum-iridium alloy anode. Temperature was controlled by a methanol-solid carbon dioxide bath below 0°C and a water bath at higher temperatures. The oxygen overvoltage at a given temperature was correlated by the Tafel equation, $\eta = a + b \log i$, above and below the limiting current density.

Slopes of the upper and lower Tafel lines are shown on Table I. The lower lines below 0°C have unusually large slopes. It may be noted on Fig. 4 that there is about a one hundredfold variation in the limiting current density between −45° and +40°C.

The experimental procedure followed in obtaining the curves on Fig. 4 was to pre-electrolize for 1 hr or more at a current density of 0.1–1.0 amp/cm^2 to reach a steady-state potential. The potential was then recorded and the current was reduced by a small increment, taking care not to break the circuit. The potential was again recorded when it became "approximately constant." This was repeated for each of the points. "Approximately constant" was defined as it was by Hickling and Hill (17) to be a potential change of less than 0.01 v in 30 min, or 0.0003 v/min. The procedure of descending current density was used because of the much shorter time required for the potential to become approximately constant. Essentially the same steady-state values were obtained with ascending current density, but only after a longer period of time. Above and below the region of the limiting current density a steady-state condition was reached within 5 or 10 min, while in the transition region 1 hr or more was required for the potential to become approximately constant.

The limiting current density is displaced to a higher value upon either increasing or decreasing the current in rapid successive steps. The overvoltage tends to follow the lower line past the limiting current density if the current is rapidly increased. If the current is then held constant, the potential rises slowly to the upper line. When the limiting current density is approached from above on the upper line by rapidly decreasing the current, the potential will drop to the lower line at a current greater than the limiting current density. Again, if the current is held constant here, the potential will rise slowly back to the upper line.

Effect of electrolyte concentration.—The effect of perchloric acid concentration at a temperature of 0°C is shown on Fig. 5. These data were obtained with cell A and the

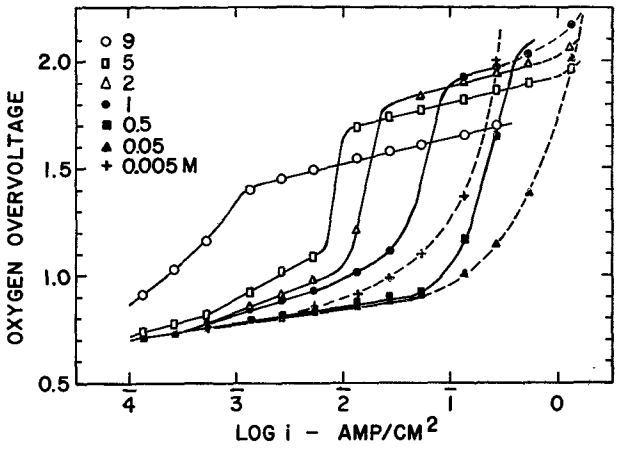

FIG. 5. Oxygen overvoltage at 0°C. Effect of perchloric acid concentration.

0.38 cm^2 wire anode. The following may be observed on Fig. 5:

1. The limiting current density decreases in higher perchloric acid concentration.
2. At low current density, overvoltage for all concentrations approaches the same limiting curve.
3. The slope of the upper curves is independent of concentration. The slopes of the upper and lower Tafel lines are presented in Table II.
4. The overvoltage of the upper curves decreases with increased perchloric acid concentration at a given current density.
5. At concentration less than 0.5M, ohmic overvoltage becomes appreciable before the limiting current density is reached due to increased electrolyte resistance. This was demonstrated by plotting the difference between the observed overvoltage and the extrapolated lower Tafel line against current density for the 0.05 and 0.005M solutions. A linear relation was obtained that was not found at higher concentration. It is noted on Fig. 5 that there is a deviation from the upper Tafel lines at about 1 amp/cm^2 for higher concentrations which can be traced to ohmic overvoltage. Therefore, the limiting current density reported here at concentrations above 0.5M is not due to ohmic overvoltage.

Overvoltage with rotating electrode.—The limiting current density was shown not to be due to concentration polarization by use of a rotating anode. Exactly the same curve was produced in 5M perchloric acid at 25°C with the 0.12 cm^2 electrode stationary as with a rotation of 500 rpm. Rotation of the anode would reduce the film thickness and hence increase the limiting current density. The identical values indicate that the limiting current density is not diffusion controlled.

Since the limiting current density is due neither to ohmic nor to concentration overvoltage, it must be an

TABLE II. *Values of b in Tafel equation, perchloric acid at 0°C*

Conc. M	0.005	0.05	0.5	1	2	5	9
b, lower line	0.07	0.07	0.075	0.15	0.20	0.27	—
b, upper line	—	—	—	—	0.12	0.12	0.12

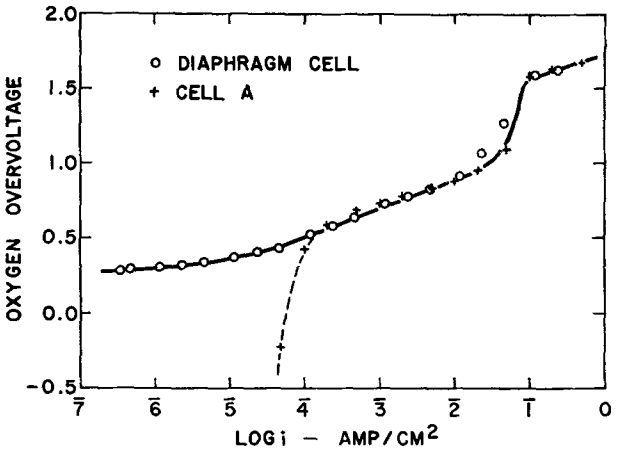

FIG. 6. Oxygen overvoltage extended to low current densities with cell A and with diaphragm cell.

activation overvoltage due to a change in the electrode surface reaction.

Overvoltage with diaphragm cell.—An experiment with a diaphragm cell showed that the limiting current density is not due to depolarization of the anode by diffusion of hydrogen from the cathode. Fig. 6 shows the oxygen overvoltage over an extended range of current density in 5M perchloric acid obtained with cell A without a diaphragm and a second cell (not shown) with diaphragm to restrict mixing of catholyte and anolyte. Below 0.0001 amp/cm² with cell A the overvoltage fell to negative values due to depolarization by hydrogen formed at the cathode. This agrees with the results of Hickling (18), who showed experimentally in 1M hydrochloric acid and analytically from diffusion theory, that the limiting current density for diffusion of oxygen dissolved at 1 atm was about 0.0001 amp/cm². The same order of magnitude of this limiting current density would be expected for both hydrogen and oxygen diffusion. Above 0.001 amp/cm² in unstirred solutions Hickling found that the dissolved oxygen had no effect on hydrogen overvoltage. Similarly in this work the curve for cell A and for the diaphragm cell coincided above 0.001 amp/cm². The limiting current density due to the electrode surface reaction occurred at the same point in both cells. The leveling of the nondepolarized curve at low current density at a potential above the reversible oxygen potential is in accord with data of Hickling and Hill (17).

Electrode reactions.—Anodic products under various conditions of temperature and current density were investigated to clarify the chemistry of the anode reactions.

Ozone formation.—A study was made in the region of the limiting current density using cell B, designed for simultaneous measurement of ozone concentration and overvoltage. Prior work on electrolytic ozone (1) was done at low temperatures and at current densities well above the limiting current density and gave no indication of behavior in this region.

Fig. 7 shows the relationship of ozone formation to the overvoltage curve. Ozone, it is seen, is first detected at the point where the slope of the lower overvoltage line deviates from the Tafel correlation. The current efficiency for ozone formation (equivalent to the weight per cent ozone in the anode gas) goes through a maximum of about 4% at the point of inflection of the overvoltage curve. This can be seen by comparison to the plot of the slope of the overvoltage curve. The ozone current efficiency goes through a minimum as the current density is further increased. A still further increase in current density will raise the current efficiency to better than 30% as has been reported previously (1).

The same relation of ozone production to the limiting current density was found to hold for other perchloric acid concentrations. The height of the current efficiency maximum appeared to increase in higher concentration electrolytes and lower temperatures. These curves were reproducible with ascending or descending current density if the current was changed slowly without interruption and a sufficient time was allowed to reach steady state. Rapidly increasing the current density caused the initial point of ozone detection to be displaced, corresponding to the increase in the limiting current density. The maximum of the transient ozone concentration curve was also higher than the steady-state curve.

Chlorine dioxide formation.—Chlorine dioxide was detected by its yellow color in the electrolyte and anode gas in the electrolysis of 9M perchloric acid above the limiting current density. This is in agreement with the work of Grube and Mayer (19) who showed that electrolysis of 11.4M perchloric acid at 0.22–0.75 amp/cm² with platinum electrodes at 0°C produced chlorine dioxide and chloric acid at current efficiencies up to 10%. More oxygen was obtained than could be accounted for by the electrolysis of water. They explained this by the following reactions

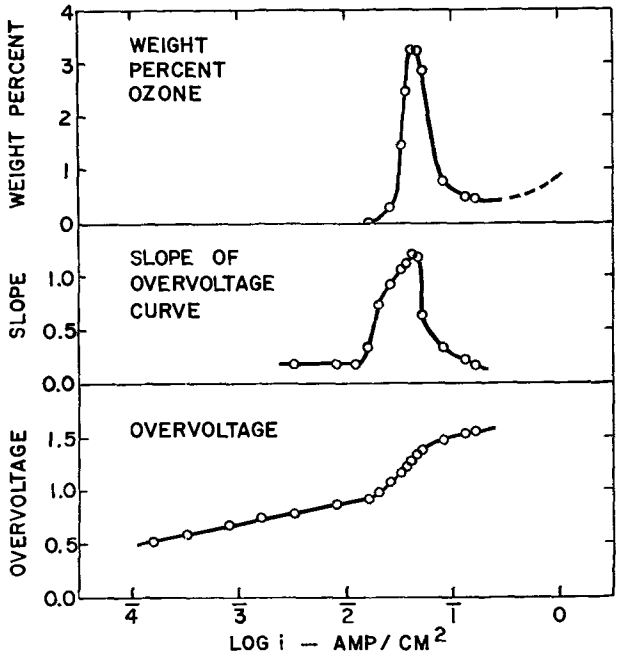

FIG. 7. Relationship of initial ozone concentration to the overvoltage curve.

involving direct discharge of perchlorate ion to form perchlorate free radicals:

$$ClO_4^- \rightarrow ClO_4\cdot + e$$

$$ClO_4\cdot \rightarrow ClO_2 + O_2$$

$$2ClO_2 + 2OH^- \rightarrow 2\,HClO_3 + 2e$$

Their excess oxygen was closely accounted for quantitatively by measuring the chlorine dioxide and chloric acid and calculating the excess oxygen from the above equations. Their ozone current efficiency was small at this high acid concentration.

Boelter (20) showed that chlorine dioxide is also formed in detectable amounts in 2M perchloric acid at 10 amp/cm². He detected chlorine dioxide as did Grube and Mayer by absorbing the anode gas in ferrous ion solution and titrating the chloride ion formed with silver nitrate. His points of initial detection of chlorine dioxide occurred at currents greater than ten times the limiting current density in 2–11M perchloric acid at 0°C. No change is observed in the slope of the overvoltage curve at the point where chlorine dioxide is first detected.

Oxygen formation.—Ozone and chlorine dioxide were not detected below the region of the limiting current density. In fact, no substance was present in the electrolyte below the region of the limiting current density in any concentrated perchloric acid that could be detected idometrically with a sample of the electrolyte after electrolysis. Therefore, it is concluded that oxygen is the only anode product liberated.

Hickling (21) has suggested the following mechanism for oxygen formation in basic solution:

$$OH^- \rightarrow \cdot OH + e$$

$$\cdot OH + \cdot OH \rightarrow H_2O_2$$

$$H_2O_2 + \cdot OH \rightarrow H_2O + HO_2^-$$

$$HO_2^- + \cdot OH \rightarrow H_2O + O_2$$

In acid solution the first step would be

$$H_2O \rightarrow \cdot OH + H^+ + e$$

This is the only step for which a lower activity of water would reduce the reaction rate.

Discussion

The limiting current density and overvoltage rise can best be explained by adsorption of perchlorate ions. The following mechanism is postulated:

1. Perchlorate ions are adsorbed on the anode due to a combination of adsorption forces and coulombic attraction to the positively charged anode. They either displace or adsorb on the already existing monolayer of oxygen.

2. Oxygen formation reactions are crowded onto sites unoccupied by perchlorate ions. Therefore, the actual current density at a given apparent current density increases and this increases the overvoltage.

3. Overvoltage increases until perchlorate ions discharge. Discharge of perchlorate ions results in the upper Tafel line.

Decrease in the limiting current density in increased perchloric acid concentration is to be expected for an adsorption mechanism. A plot of the logarithm of the limiting current density from Fig. 5 vs. the logarithm of perchloric acid activity yields a straight line. For convenience the limiting current density was arbitrarily taken as the midpoint of the curve connecting the upper and lower Tafel lines. Perchloric acid activity was calculated from the data of Robinson and Baker (14). There is no such relation of the limiting current density to the activity of water. The limiting current density continues to increase with dilution, but the water activity reaches a limiting value of unity. It appears then that interaction of perchlorate ion rather than a slow reaction involving water is the cause of the limiting current density.

The decrease in the limiting current density at low temperatures is also in accord with the adsorption mechanism. Lower temperature favors physical adsorption in general, and the increase in oxygen overvoltage at low temperature favors coulombic attraction. The slow approach to steady-state potentials in the region of the limiting current density is also in accord with the general slow attainment of adsorption equilibrium.

The point of inflection of the curve connecting the upper and lower Tafel lines is assumed to represent the point where perchlorate ion discharge begins. This is in accord with the detection of chlorine dioxide on the upper Tafel line where there is no further change in slope. The first perchlorate ions to discharge are evidently reacted to form $HClO_3$ and oxygen by a mechanism similar to that postulated by Grube and Mayer (19), but, as the current density is increased, chlorine dioxide is formed at a sufficient rate to escape from the solution.

The ozone produced in the region of the limiting current density and the ozone produced in high concentration at high current density can be explained by two different mechanisms. The first is probably produced by discharge of water by a similar mechanism to oxygen formation and the formation of ozone by electrolysis of concentrated potassium hydroxide solutions at low temperature (22). The initial increase in overvoltage provides the energy for this reaction. The rate of ozone formation becomes constant or decreases when perchlorate ion discharge begins, thus resulting in a maximum in concentration. The high concentration ozone at high current density could be explained by a reaction involving perchlorate free radicals. This is analogous to the formation of ozone by heating persulfates in sulfuric acid reported by Ulrich (23).

The above theory explains qualitatively all of the experimental facts. Data for other electrolyte systems will be presented in another paper.

Acknowledgment

The writers wish to express their appreciation to Dr. G. L. Putnam who recommended the problem and offered many helpful suggestions, to Dr. E. D. Boelter for his valuable contributions, and to I. J. Groce and P. K. Schoening who did a portion of the experimental work. The program was carried out under fellowships awarded

by the University of Washington Engineering Experiment Station and Standard Oil Company of California.

Manuscript received August 16, 1955.
Any discussion of this paper will appear in a Discussion Section to be published in the December 1956 JOURNAL.

REFERENCES

1. G. L. PUTNAM, R. W. MOULTON, W. W. FILLMORE, AND L. H. CLARK, *J. (and Trans.) Electrochem. Soc.*, **93**, 211 (1948).
2. G. KORTUM AND J. O'M. BOCKRIS, "Textbook of Electrochemistry," Vol. II, p. 398, Elsevier Press, Inc., New York (1951).
3. A. HICKLING, *Disc. Faraday Soc.*, **1**, 225 (1947).
4. C. J. THATCHER, *Z. Physik. Chem.*, **47**, 641 (1904).
5. F. FOERSTER, "Electrochemie Wasseriger Losungen," p. 806, (1922).
6. S. GLASSTONE AND A. HICKLING, *Chem. Rev.*, **25**, 407 (1939).
7. A. KLEMENK, *Z. Physik. Chem.*, **185**, 1 (1939).
8. J. A. V. BUTLER, *Proc. Roy. Soc.*, **A137**, 604 (1932).
9. J. A. V. BUTLER, *ibid.*, **A143**, 89 (1933).
10. A. HICKLING, *Trans. Faraday Soc.*, **41**, 333 (1945).
11. W. A. WATERS, "Chemistry of Free Radicals," p. 142, Oxford Press, Oxford (1946).
12. R. F. VINES, "The Platinum Metals and their Alloys," p. 74, International Nickel Co., Inc., New York (1941).
13. S. GLASSTONE, "Introduction to Electrochemistry," p. 241, D. Van Nostrand and Co., New York (1949).
14. R. A. ROBINSON AND O. J. BAKER, *Trans. Proc. Royal Soc., (New Zealand)*, **76**, 250 (1946).
15. I. M. KLOTZ, *Ind. Eng. Chem., Anal. Ed.*, **15**, 277 (1943).
16. A. LAUCHLI, *Z. Physik.*, **53**, 92 (1929).
17. A. HICKLING AND S. HILL, *Disc. Faraday Soc.*, **1**, 236 (1947).
18. A. HICKLING, *Trans. Faraday Soc.*, **37**, 319 (1941).
19. G. GRUBE AND K. H. MAYER, *Z. Elektrochem.*, **43**, 859 (1937).
20. E. D. BOELTER, Thesis, Ph.D., University of Washington (1952).
21. A. HICKLING, *Quarterly Rev. Chem. Soc.*, **3**, 95 (1949).
22. E. BRINER, H. HAEFELI, AND H. PAILLARD, *Helv. Chim. Acta*, **20**, 1510 (1937).
23. F. J. ULRICH, *Prakt. Chem.*, **153**, 91 (1939).

The Anode Behavior of Germanium in Aqueous Solutions

D. R. TURNER

Bell Telephone Laboratories, Inc., Murray Hill, New Jersey

ABSTRACT

The anode characteristics of n- and p-type germanium are different. A large voltage barrier is observed at about 0.8 ma/cm^2 current density at room temperature on n-type but not on p-type electrodes. The voltage barrier on 3 ohm-cm n-type germanium anodes breaks down at about 9 volts in many electrolytes. During anodic dissolution the germanium surface appears to be covered with about a monolayer of oxide or hydroxide. This suggests that germanium goes into solution as a complex ion with the hydroxyl or oxide radicals attached. A mechanism is proposed for the over-all anode dissolution process involving two holes and two electrons for each germanium atom dissolving.

INTRODUCTION

The relatively small number of current carriers in semiconductors such as germanium make them poor conductors of electricity as compared to most metals. This low carrier density and the fact that current may be carried by both electrons and holes has an effect on the electrolytic behavior of germanium in electrolytes since it is possible to produce appreciable carrier concentration gradients inside the semiconductor at moderate current densities.

The semiconductor physics of n- and p-type germanium as anode and cathode in electrolytes has been investigated by Brattain and Garrett (1, 2). By changing the relative concentration of holes and electrons in the germanium surface with light, they have shown that the rate of the anodic dissolution process is controlled by the supply of holes at the germanium-electrolyte interface. The observed potential of a germanium anode therefore may be composed of three parts: (*a*) the reversible potential of germanium in the electrolyte; (*b*) the polarization potential which is given by the Tafel equation; and (*c*) an internal space charge potential due to a concentration gradient of holes just under the germanium surface. The latter is significant only when holes are the minority carrier, i.e., when the germanium is n-type.

The anodic solution of germanium has been studied by Jirsa in acid and alkaline solutions (3). He reports that germanates are formed in alkaline solutions while the corresponding germanium salts are formed in acid electrolytes. There is good evidence, however, which indicates that the stable form of germanium in acid solutions is metagermanic acid, H_2GeO_3 (4).

The purpose of this investigation was to learn something of the nature of the electrode reactions occurring at a germanium anode in aqueous solutions.

EXPERIMENTAL

Two methods were used to study the anode behavior of germanium: (*a*) the electrode potential was measured relative to a saturated calomel reference electrode at various current densities; and (*b*) electrode potential

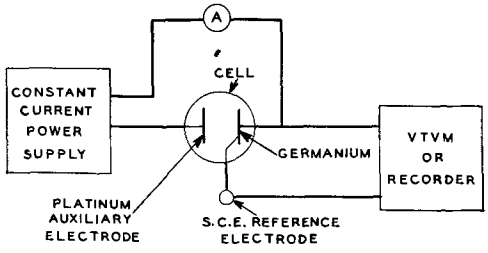

FIG. 1. Experimental arrangement for dynamic potential studies.

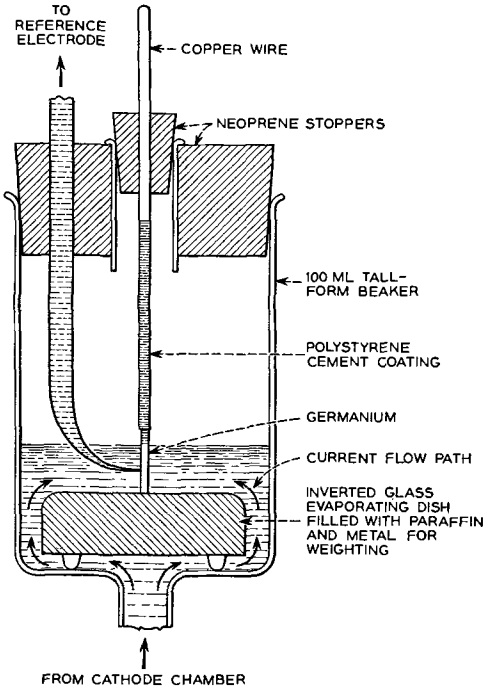

FIG. 2. Cross-section view of the anode chamber designed for uniform current distribution.

changes with time were recorded while a constant current was started, stopped, or reversed through the electrolytic cell.

The experimental arrangement is shown schematically in Fig. 1. Voltages up to 1.4 v were measured with a Leeds and Northrup *p*H indicator meter. A General Radio Type 728-A d-c vacuum tube voltmeter was used for higher voltage measurements. Potential-time curves were recorded on a Model 127 Sanborn recorder. The electrolytic cell was designed so that current distribution over the germanium electrode was uniform, see Fig. 2. The tip of the Luggin capillary was positioned so that only one corner touched the germanium electrode. This arrangement produces a negligible amount of masking by the capillary tip and yet insures sufficient proximity to avoid including an appreciable solution *IR* drop in the potential measurement. A constant current power source consisted of 180 v (large dry cell batteries) in series with a large resistance. A platinum electrode 1 cm² area was used as the auxiliary electrode. Single-crystal germanium bars 2 mm x 1 mm in cross section and lengths of about 1 cm for *p*-type and 2 cm for *n*-type were used as electrodes. These were soldered with appropriately doped lead-tin solder to 50 mil diameter copper wires for support and an ohmic electrical connection. The solder joint and an area above and below were coated with polystyrene cement. Electrodes usually were immersed up to the edge of the polystyrene coating. The resistivity of both types of germanium was about 3 ohm-cm.

Solutions of 0.1*N* sulfuric acid and 1*N* potassium hydroxide either initially free of germanium or saturated with germanium dioxide were used for most of the experiments. The most reproducible data were obtained with electrolytes saturated with germanium dioxide.

Electrode Potential-Current Characteristics

The primary anode reaction at a germanium electrode in aqueous solutions is germanium dissolution. At low current densities, anodes of both *n*- and *p*-type germanium obey the Tafel equation: $E = a + b \log i$, where E is the anode polarization potential, i is the current density, and a and b are constants. In 0.1*N* sulfuric acid, the slope b is 0.12 which is about the value usually observed. Deviations from the Tafel relation occur with both germanium types, but the greatest change takes place with *n*-type electrodes as shown in Fig. 3. The large rise in potential in the vicinity of 0.8 ma/cm² current density is similar to the current block obtained with solid-state rectifiers. The value of 0.8 ma/cm² cannot be considered too significant, since the saturation current density is a function of the resistivity and the minority carrier lifetime of the germanium used as anode. Uhlir (5) has found that the temperature variation of the saturation current of the barrier between *n*-type germanium and potassium hydroxide solution is quite like that of a *p-n* junction. About a tenfold increase in the saturation current is obtained for each 30°C rise in temperature. The anode potential in the saturation current region is also photosensitive (6). Light furnishes hole-electron pairs at the surface which tend to destroy the voltage barrier. All electrode potential-current measurements were made with the germanium electrode under study in the dark. The saturation current observed on *n*-type germanium anodes has been shown by Garrett and Brattain (2) to be due to a depletion of holes at the anode surface. Since holes are the minority carrier in *n*-type germanium, the saturation current repre-

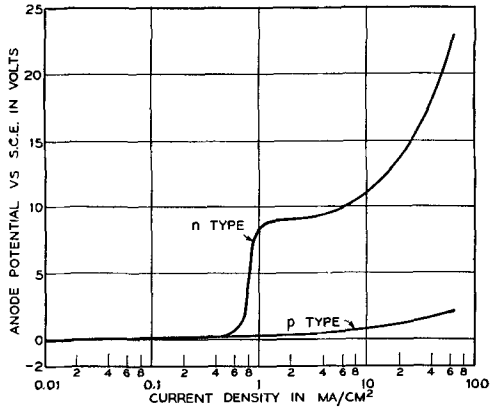

FIG. 3. Typical anode potential-current density curves for *n*- and *p*-type germanium in 0.1*N* H_2SO_4 saturated with GeO_2. Temp. ≃25°C; electrode in dark.

sents the point at which holes are used up in the anode process as fast as they are able to diffuse in the germanium from the bulk to the surface.

The anode voltage barrier on *n*-type germanium breaks down at about 9 v in 0.1*N* sulfuric acid as shown in Fig. 3. The breakdown potential should be a function of the resistivity of the germanium (7). The higher the resistivity the greater the breakdown voltage. There is a tendency for the anode potential to continue up without a breakdown under some conditions. This always occurs in concentrated salt solutions of sodium dichromate or sodium nitrate. When breakdown does occur even in these electrolytes, however, the anode potential never falls below about 9 v. The breakdown in the voltage barrier is assumed to be an avalanche type of breakdown (7). Hole-electron pairs are produced in the breakdown process and the anode current is no longer controlled entirely by the diffusion of holes from the germanium bulk. *n*-Type germanium electrodes were always pitted after being made anode above the breakdown potential. It is believed that breakdown only occurs at these points of pitting and the reason breakdown may not take place in concentrated electrolytes is that any pits which form become filled with anodic products which are not readily soluble in the electrolyte. This may also explain the rapid rise in potential at high current densities in 0.1*N* sulfuric acid as shown in Fig. 3.

The anode efficiency of germanium dissolution was measured in a 1*N* potassium hydroxide electrolyte at current densities ranging from 3.5 to 50 ma/cm² using a copper coulometer. Assuming a germanium valence of four, the anode efficiencies were remarkably uniform at about 95%.

The relatively small deviation in the anode potential of *p*-type germanium from the Tafel equation at high current densities can be attributed to two *IR* drops, one in the germanium and the other in an anode film of germanium dioxide which forms faster than it can be dissolved by the electrolyte. The *IR* drop in the germanium electrode at the highest current was less than 0.2 v which accounts for only a portion of the deviation.

Oscillographic Studies of Germanium Surfaces

The nature of the surface of germanium after a chemical or electrochemical treatment may be studied by either reducing or oxidizing the surface layer electrochemically. The technique involves starting, stopping, or reversing a constant current through the cell while the electrode potential against a saturated calomel reference electrode is recorded on an oscillograph. These potential-time records may be used to determine the number of coulombs required to carry out a particular electrochemical reaction and thus the amount of material involved in the process. The potentials themselves are characteristic of the materials taking part in a particular electrode process. This technique has been used in the study of tarnish films (8).

A typical oscillograph record with germanium electrodes made anode and cathode in 0.1*N* sulfuric acid is shown in Fig. 4. The record begins with the open circuit (zero current) electrode potential and then successively the germanium is made anode, cathode, and anode again.

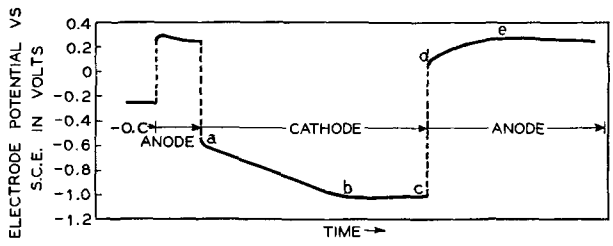

FIG. 4. Typical oscillograph record of germanium made anode and cathode in 0.1*N* H_2SO_4; current density ≃0.3 ma/cm².

When germanium is made anode in solutions there always is some "overshoot" in potential. The term "overshoot" is applied to the initial maximum observed in potential-time curves and is often observed for other metals. In oxidizing solutions such as chromic acid this can be a very large effect on germanium amounting to several volts. The actual amount of overshoot voltage obtained appears to be a logarithmic function of the constant current applied to the cell. Oxidizing solutions appear to form a protective oxide layer on germanium which inhibits the anodic dissolution process. This causes the electrode potential to rise above the normal dissolution potential for the applied current. As the protective film is removed by being physically displaced or undermined, the anode potential drops to the stable value. The steady-state anode reaction is germanium dissolution. A discussion of this process will be given later.

When the electrode is switched from anode to cathode (by reversing the cell current) in Fig. 4, the potential changes abruptly to *a*. The potential at *a* is about −0.65 v vs. S.C.E. or −0.4 v on the hydrogen scale. The standard electrochemical potential of germanium is believed to be about the same value. This is followed by a relatively slow linear increase in the cathode potential with time along *ab*. At *b* the electrode potential reaches a stable value. The cathode reduction process *ab* always requires about 4×10^{-4} coulomb/cm² regardless of the cathode current density or the anodic pretreatment time or current. This is significant since it means that in the continuous anode dissolution process the germanium surface layer always contains a definite amount of reducible material. These results will be considered in discussing the anode and cathode processes. The final cathode reaction *bc* is the discharge of hydrogen ions and evolution of visible hydrogen gas. The cathode potential at *b* increases in proportion to the log of the current density. This also results in a slight increase in the length of section *ab* and is attributed to the coulombs required to charge the electrical double layer capacity (about 20 μF/cm²) to the higher cathode potential. The anode curve obtained when the germanium electrode is switched from cathode to anode has an approximately linear section *de* which involves about 2×10^{-4} coulombs/cm² or half of that used in the cathode process *ab*.

DISCUSSION

The voltage barrier observed when *n*-type germanium is made anode at a critical current density has been at-

tributed to a p-n junction at the surface (2, 9). A layer of negative charges attracted to the surface by the anode bias induces in the surface of the germanium a thin layer which is changed from n- to p-type. This p-type surface layer next to the n-type bulk germanium makes a p-n junction and the voltage bias is in the blocking direction. No anode voltage barrier is found with p-type germanium since the anodic surface condition described only tends to make the germanium surface layer more p-type than the bulk.

The critical current at which blocking begins on n-type germanium when made anode in an electrolyte is determined by the rate at which electrons are extracted from the solution into the germanium and/or holes diffuse from the germanium bulk to the surface. Electrons can be extracted from solutions only by anion discharge. Hydroxyl ions are the most easily discharged anions in the solution studied. No oxygen gas bubbles were visible at the anode, however, to indicate hydroxyl ion discharge. Furthermore, anode efficiency measurements show that the sole anode process at the point of current saturation is germanium dissolution. Thus, saturation current appears to be controlled only by the rate of hole diffusion. In order to put a germanium ion into solution from a site on the surface of a crystal lattice, chemical bonds to underlying germanium atoms must be broken. The process requiring the least amount of energy to break these bonds is the migration of holes from the germanium bulk to the surface. Below the breakdown potential these holes come largely from the bulk. Above breakdown, the migrating holes multiply in the high field of the space charge region at the surface to increase germanium dissolution and the flow of current through the electrolysis cell.

A breakdown in the voltage barrier would also occur if the potential at the germanium-solution interface were to exceed that required for the continual discharge of anions (10). As previously stated, however, no anion discharge was observed.

The electrochemistry of the steady-state anode reaction at germanium electrodes in sulfuric acid below the saturation current for n-type was studied with the aid of cathodic reduction experiments. The observed linear change in cathode potential with time at a constant current after an anodic pretreatment is the type of curve expected where the material being reduced is present initially as a monolayer or less. The cathode potential increases as the surface area covered with the material being reduced decreases. As the concentration of the reducible material approaches zero, the cathode potential becomes relatively constant and corresponds to the polarization voltage of hydrogen ion discharge on germanium.

A mechanism of germanium dissolution was suggested by the results of the anode-cathode curves in 0.1N sulfuric acid. The 4×10^{-4} coulombs/cm^2 required in the cathode reduction process turns out to be about 4 electrons per surface germanium atom, assuming that the true area of a chemically polished surface is about 1.4 times the apparent area (11) and the surface atoms are arranged according to a ⟨100⟩ crystal orientation. Since the same amount of material is cathodically reduced regardless of the anodic pretreatment time or current density, the germanium surface layer must contain a fixed amount of reducible substance continuously during the anode process. This result can be explained if it is assumed that the surface layer always contains about a monolayer of hydroxide or oxide during germanium dissolution. Since free Ge^{+4} germanium ions do not exist in aqueous solutions to any extent, it is likely that germanium ions go into solution as complex ions with the hydroxide or oxide radicals attached. This anode process may be shown schematically as follows:

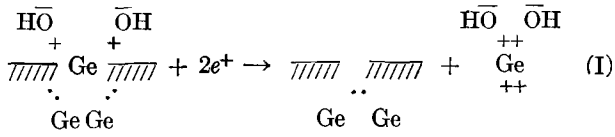

(I)

(The dots represent covalent bonding electrons and e^+ represents a hole.)

The electrochemical reaction written suggests that in the anodic process the covalent bonds between a surface germanium and underlying atoms are broken by the arrival of two holes. It has been shown that holes are required to carry out the primary anode process on germanium (2). As the germanium ion enters the solution, it reacts chemically with hydroxyl ions. In neutral or acid solutions, metagermanic acid is formed:

$$Ge(OH)_2^{++} + 2OH^- \rightarrow H_2GeO_3 + H_2O \qquad (II)$$

It was stated previously that hydroxyl ions did not discharge to form visible oxygen gas on germanium anodes in the electrolytes used. It is believed, however, that hydroxyl ions react with clean surface germanium atoms to the extent that a monolayer of hydroxide or oxide is maintained, as follows:

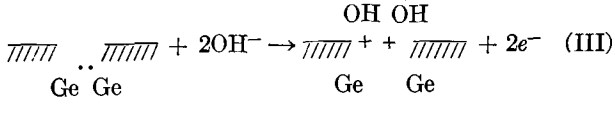

(III)

The over-all germanium anode reaction in aqueous solutions is, therefore:

$$Ge + 2e^+ + 2OH^- \rightarrow Ge(OH)_2^{++} + 2e^- \qquad (IV)$$

The four electronic charges required to dissolve one germanium atom are conducted away from the surface as two holes and two electrons. This is consistent with the results of Garrett and Brattain (2) who found that when holes were injected into an n-type germanium anode, the anode current changed about twice that of the injected hole current.

Above the breakdown potential, about 9 v in 0.1N sulfuric acid, it is assumed that holes also become available at the surface as the result of the creation of hole-electron pairs in the space charge region by the avalanche process, and the kinetics of the germanium dissolution process is no longer limited by hole diffusion from the bulk.

At very high current densities germanium may go into solution so rapidly that the electrolyte cannot dissolve it all and white GeO_2 forms on the surface. Occasionally an orange colored deposit is observed on germanium after being anodized at high current densities. This has been

identified as the germanium monoxide (3). The effective valence for germanium dissolution under these conditions is two. The primary reaction may be as follows:

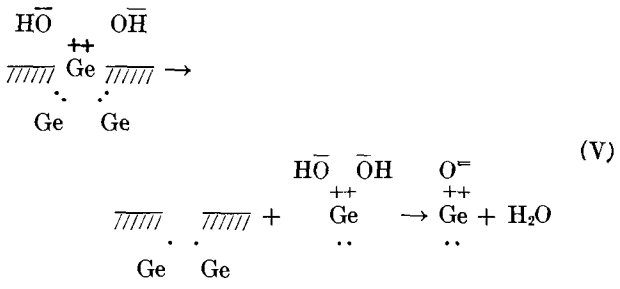

(V)

The two electrons are obtained in returning the monolayer of hydroxide to the surface, equation (III).

The initial reaction proposed when a germanium electrode is switched from anode to cathode, i.e., when the current is reversed in the electrolytic cell, is the reduction of the hydroxide or oxide surface layer and the formation of a hydride layer as follows:

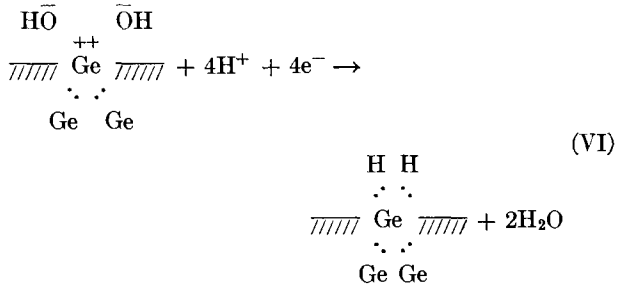

(VI)

This is the electrochemical process which was observed experimentally and required about 4×10^{-4} coulomb/cm^2 or four electrons for each surface germanium atom. The initial assumption about the nature of the germanium anode surface is based on these results.

When germanium is made anode immediately after being cathode, only two electrons per surface germanium atom were required in the initial oxidation process. This result can be explained if it is assumed that the hydrogen atoms of the surface hydride prefer to combine chemically as molecular hydrogen rather than be oxidized back to hydrogen ions when the current is reversed:

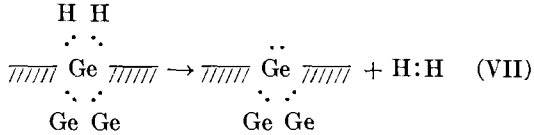

(VII)

This chemical process may then be followed by the electrochemical reaction:

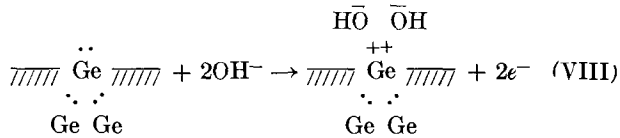

(VIII)

where two electrons are required for each surface germanium atom to return it to the condition of anode dissolution.

Summary and Conclusions

1. The primary anode reaction at a germanium electrode is germanium dissolution. The *E-I* curve obtained for a germanium anode in aqueous solutions is different for *n*- and *p*-type germanium. A surface barrier is observed with 3 ohm-cm *n*-type germanium electrodes at room temperature at about 0.8 ma/cm^2 current density. The voltage barrier which is attributed to a limiting rate of hole diffusion to the surface breaks down at about 9 v. The breakdown is presumed to be similar to the avalanche type of breakdown which occurs in solid-state *p-n* junctions.

Deviations from the Tafel equation with *p*-type germanium at high anode current densities are attributed to *IR* drops in the bulk of the electrode and an anode film of germanium dioxide.

2. When germanium is made anode in aqueous solutions, the anode potential-time curve passes through an initial maximum which signifies that germanium has some difficulty in dissolving at first. This is attributed to a protective oxide layer on the surface which inhibits dissolution until it is removed by some displacement process. The effect is very large in strongly oxidizing solutions such as chromic acid where the oxide layer is more protective against anodic dissolution.

3. The results of the anode-cathode potential-time curves indicate that during anodic dissolution the germanium surface is always covered with a monolayer of hydroxide or oxide. It is suggested that germanium goes into solution as a complex ion with the hydroxide or oxide radicals attached. The mechanism proposed for germanium anode dissolution is a two stage process: (*a*) the germanium complex ion goes into solution when two holes arrive at the surface, and (*b*) two hydroxyl ions react with the surface giving up to conducting electrons to the germanium and renewing the surface monolayer of hydroxide or oxide.

Acknowledgments

The author wishes to acknowledge the many helpful comments and criticisms received from H. E. Haring, U. B. Thomas, and J. F. Dewald during the course of the work and the preparation of this paper.

Manuscript received August 29, 1955. This paper was prepared for delivery before the San Francisco Meeting, April 29 to May 3, 1956.

Any discussion of this paper will appear in a Discussion Section to be published in the December 1956 JOURNAL.

REFERENCES

1. W. H. Brattain and C. G. B. Garrett, *Phys. Rev.*, **94**, 750 (1954).
2. C. G. B. Garrett and W. H. Brattain, *Bell System Tech. J.*, **34**, 129 (1955).
3. F. Jirsa, *Z. anorg. u. allgem. Chem.*, **268**, 84 (1952).
4. O. H. Johnson, *Chem. Rev.*, **51**, 431 (1952).
5. A. Uhlir, Work to be published.
6. O. Loosme, Private communication.
7. K. G. McKay and K. B. McAfee, *Phys. Rev.*, **91**, 1079 (1953).
8. W. E. Campbell and U. B. Thomas, *Trans. Electrochem. Soc.*, **76**, 303 (1939).
9. R. B. Gibney, U. S. Pat. 2,560,792 (1951).
10. H. E. Haring, *This Journal*, **99**, 30 (1952).
11. J. T. Law, *J. Phys. Chem.*, **23**, 543 (1955).

Technical Note

Etching Silver with Chromium Trioxide-Sulfuric Acid Solution

PHILIP F. KURZ

Battelle Memorial Institute, Columbus, Ohio

The purpose of the etching process described in this paper is to clean and alter the surface of silver to provide a substrate suitable for subsequent surface treatment. A comparable conditioning procedure, for example, is the etching of aluminum foil for electrolytic capacitors to clean and roughen its surface in order to increase the capacitance per unit of superficial area. The process for surface-conditioning silver can be made essentially continuous and is carried out at room temperature with a dilute aqueous solution of chromium trioxide and sulfuric acid.

Neither of these substances alone in dilute aqueous solution attacks silver at room temperature. Boiling 2% aqueous sulfuric acid solution shows virtually no attack on a silver surface and boiling 2% aqueous chromium trioxide produces only a slight etch on a silver surface immersed for 2 min in the solution.

However, if the two substances are present simultaneously in one solution, their combined action on silver is evident at once. For example, if a strip of silver foil 0.5 mil to 1 mil in thickness is suspended in a boiling solution containing 2% by weight CrO_3 and 1% by volume of H_2SO_4, sp gr 1.84, the solution attacks the silver so rapidly that the foil is completely dissolved in about 5–10 sec.

At room temperature the attack of the chromium trioxide-sulfuric acid solution on silver is much more moderate than at about 100°C where rapid dissolution of the foil occurs. Exposure of the silver to the etching solution at room temperature for 15 or 30 sec produced fairly well-etched surfaces. A 1-min immersion of the foil gave a good etch, and a 2-min exposure an excellent etch. A 4-min immersion caused slightly more loss of thickness than was desirable. Eight-minute and 12-min immersions caused further loss in thickness but no noticeable erosion or cavitation at the edges of 1-mil foil. A 16-min immersion reduced 1-mil foil to less than one-half its original thickness and showed evidence of preferential erosion at the edges of the specimen.

A 1- to 2-min immersion was estimated to be sufficient to produce an etched surface of the type desired without sacrificing too much of the original thickness of the material.

About 125 ft² of silver surface in the form of 1-mil foil, 3 in. wide could be etched satisfactorily with the following solution:

Chromium trioxide	40 g
Sulfuric acid (sp gr 1.84)	20 cc
Water	2000 cc

A coating of red-brown material, presumably silver dichromate, remains on the silver as it is drawn from the etching bath. However, this coating is not very adherent and is rinsed off readily with water sprays directed against both sides of the strip of foil.

Manuscript received November 23, 1955.

Any discussion of this paper will appear in a Discussion Section to be published in the December 1956 JOURNAL.

Technical Feature

Energy Losses from Furnaces and the Concept of Efficiency

Implications for Furnace Design and Operation

VICTOR PASCHKIS

Heat and Mass Flow Analyzer Laboratory, Columbia University, New York, New York

INTRODUCTION

To succeed in any line of human endeavor it is necessary to have reliable criteria of success to apply to the intermediate operations that lead to the final result. In particular, furnaces are normally operated for eventual profit, and reliable criteria are needed to determine when operations are economical. The criterion most commonly used for this purpose is efficiency. The following text exposes some weaknesses of this usage, and suggests a systematic procedure by which these weaknesses can be eliminated.

The terms "energy balance" and "heat balance" are also used as criteria of performance, and it is shown here that they frequently lead to very much the same difficulties as the concept of efficiency.

Both efficiency and energy balance can be defined simply. However, these concepts are tools, and frequently these tools are not flexible enough to do the job at hand. The basic relationships that underlie the definitions merit serious consideration. Such consideration will lead to better design and more economical operation of equipment.

This paper points out the limitations of the usual concepts, and shows how to classify in a concrete and useful way the various mechanisms by which energy is either used profitably or lost.

CONCEPT OF EFFICIENCY

The term "efficiency" is widely used in technical literature. Sometimes it means "yield" as in the useful expression "kwhr/lb of product." However, this use of the word is misleading, especially in furnace operation where it is easily confused with "energy efficiency." A better term would be "specific yield." In the following text the word efficiency will be used only in the sense of the following definition:—

Efficiency = useful energy/total energy consumption

This is a simple expression and in many cases it is a useful one. However, it has limitations when used in real situations, as will be shown.

The concept of efficiency is used to compare the economic utility of two or more furnace operations. This comparison may involve different furnaces of the same type, furnaces of different types, or the same furnace at different times. The various combinations are obvious. For example, two arc furnaces may be compared for a given smelting operation, or an arc furnace can be compared with an induction furnace.

The engineer must make these comparisons by the best means at hand. The concept of efficiency was used in analyzing mechanical apparatus, motors, and power generating equipment long before it was applied to furnaces. It has been used in furnace work, but examples to follow will show that the disarming simplicity of the original idea has been carried over to furnace practice without sufficiently critical examination and with resulting difficulties.

Note, for example, that it is meaningless to say that a given furnace has a certain specified efficiency unless it is also specified (*a*) whether or not the furnace is fully loaded, (*b*) what process is being carried out, (*c*) the operating schedule, and (*d*) the functioning of any auxiliary equipment. More specific examples follow.

Consider a simple resistance-type furnace used for heat treating, and assume that the wall losses are constant at 20 kw. The maximum available power is 200 kw, but the power input is adjusted to the size of the load to maintain a constant heating rate. When the furnace is fully loaded, the full power of 200 kw can be applied, and all but the 20 kw wall losses is useful energy. The efficiency is then 180/200 = 0 90. Assume an extreme case in which the furnace is operated at one-tenth of its full-load value, or 18 kw. However, the wall losses remain at 20 kw, so the total input must become 38 kw, an efficiency of 0.47. The efficiency is, therefore, a function of furnace load.

Consider an arc furnace for steel production. Since constant temperature is maintained during the refining period, no useful heat is consumed in this period. Depending on end requirements, the refining period may vary from one to three hours, showing a large variation in efficiency. The efficiency in this case is a function of the operating schedule.

The experienced furnace man will realize without further examples that an efficiency figure becomes meaningful only when hedged in by a number of restrictions that make it quite unwieldy. The result is that the true efficiency of a furnace can be recorded and studied only by compiling a large volume of data that can be grasped in entirety only by considerable effort.

HEAT BALANCES

Heat balances avoid some of the objections raised against the use of "efficiency." This comes about because it is not necessary to label heat "useful" or "lost." The competent engineer will know at once which portions of the energy consumed are useful for his particular purpose,

TABLE I. *Energy balance of arc furnace in per cent*

Input	
Electrical energy	84
Heat of reaction	9
Heat produced by oxidation of electrodes	7
	100
Energy expenditures	
Temperature increase of steel	42
Temperature increase of slag	8
Wall losses by surface radiation	17
Wall losses by water cooling	13
Losses from escaping gases	4
Electrical losses	16
	100

TABLE II. *Energy balance of arc funace in kwhr*

Input	
Electrical energy	5460
Heat of reaction	585
Heat produced by oxidation of electrodes	455
	6500
Energy expenditures	
Temperature increase of steel	2730
Temperature increase of slag	520
Wall losses by surface radiation	1105
Wall losses by water cooling	845
Losses from escaping gases	260
Electrical losses	1040
	6500

and he avoids having to use troublesome and largely unnecessary labels. As long as he knows where the energy is going he has all the necessary information. However, the following example will show that heat balances also can prove to be pitfalls for the unwary.

Consider an arc furnace used for melting steel. Table I gives an energy balance in percentages of the total. However, this tabulation is quite inflexible. Note that if any item, such as load or electrode diameter, is changed, all the percentages will have to be changed to make the totals come out to 100%.

The above situation can be improved somewhat by writing a new balance in kilowatt hours, assuming that the total energy required for a heat is 6500 kwhr. This is done in Table II.

However, the simplicity of this tabulation can be misleading. Consider what happens if the load is increased somewhat and the heat required by the steel and slag increase by 10%, to 3003 and 572 kwhr, respectively. If these increased figures are merely written in the place of the old ones in Table II, the assumption is being made that the other energy expenditures remain unchanged. This assumption is not true. Power input and/or time of heating must be increased. Either one increases electrical losses, and longer time of heating results in increased wall losses. The conclusion is that a 10% change in load makes an entirely new heat balance necessary. This is essentially the same difficulty encountered in the use of "efficiency" as a criterion of effectiveness.

The foregoing text has shown that the traditional ways of analyzing furnace operations frequently lead to undesirable complexities. The remainder of this paper explores a new method of classifying energy expenditures with a view to making the analysis simpler and less ambiguous.

Gross Useful Heat

Before developing the proposed new method of classifying energy expenditures, a definition is necessary. First, the total energy input to the furnace will be considered to comprise two components: (*a*) gross useful heat, and (*b*) losses. Gross useful heat then consists of any energy increase, as expressed in temperature rise and increased latent heat content, of material not permanently in the furnace. Thus, it includes energy stored in containers and in means of conveyance in heat treating furnaces, heat stored in metal as well as in slag in melting furnaces, etc. Note that this definition is unambiguous, since the permanent parts of the furnace are clearly and easily distinguishable from the materials and equipment that pass in and out of the furnace in operation.

Losses are defined as the difference between total energy input and gross useful heat.

Classification of Losses

The classification of energy losses is the essential feature of the point of view described in this paper. Note that any specified loss may or may not be proportional to gross useful heat. It also may or may not depend on other losses. Losses are, therefore, divided into the following four classifications:

(*a*) Proportional dependent
(*b*) Proportional independent
(*c*) Nonproportional dependent
(*d*) Nonproportional independent

This system of classification involves one slight complication that must be faced at the outset. An example will make it clear. Consider the sum of the ohmic losses in electrodes, bus bars, transformer, and reactor of an electric furnace. This ohmic loss is generally proportional to total power input into the furnace proper, which input depends both on gross useful heat and on other losses, e.g., wall losses from the furnace shell. These electric losses therefore comprise two parts, one proportional independent and the other nonproportional dependent.

Such losses will be classified as "proportional dependent." In general they will not be simultaneously proportional and dependent, as perhaps implied by the literal meaning of the words. In this context, the term will be used to denote such losses as comprise two parts, one proportional to gross useful heat and the other dependent on other losses.

To render the above classification more concrete, a number of examples of losses will be given. At this point it is convenient to start with the simplest classification, nonproportional independent.

The most important examples of nonproportional independent losses are wall losses in furnaces and core losses in transformers.

An interesting example of proportional independent losses occurs in heat treating a stack of bars where part of the stack protrudes from the furnace. Heating of the

protruding ends, while unavoidable, is not necessary, and constitutes a loss that is proportional to gross useful heat and independent of other losses.

Other examples of proportional independent losses are part of the ohmic losses in electrodes, busses, etc., as already noted, and part of the coil losses in induction furnaces.

Nonproportional dependent losses are widespread. For example, the losses mentioned in the preceding paragraph have a component in this category.

Some of the advantages obtained by analyzing energy expenditures in this way are illustrated by the following examples.

Furnaces that are expected to undergo extended periods of operation at reduced output call for extreme care in reducing nonproportional losses, even, if necessary, at the expense of proportional ones. This procedure may in some cases even result in higher power consumption at full load, but will reduce power consumption during the periods of limited output.

The electrical efficiency of induction heating equipment is frequently only 50%. Only 50% of the electrical input to the generator finds its way into the charge as heat. Part of this heat is lost by radiation from the crucible. This energy lost by radiation has first to be transferred (in the form of electrical energy) from the coil to the charge. Assume a specific case in which thermal insulation would reduce the radiation by 2 kw or 6800 BTU/hr. To get this 2 kw, which can be saved, into the work requires the expenditure of 4 kw of electrical energy at the input of the generator. The cost of the insulation should then be compared with the saving, not of 2 kw, but of 4 kw.

Consider a furnace for which conditions have been well established and assume that the operating schedule has to be changed. If the operator has analyzed the past operation of the furnace in the way recommended in this paper, he will immediately know whether the operating data being obtained under the newly established conditions are normal or indicate a need for further adjustment of the operating parameters. These considerations are especially true when furnaces must be run at reduced output, since the danger of uneconomical operation is usually increased at such times.

In general, a close analysis of losses and the relationships between them will enable the operator to make maximum use of the data already recorded in predicting the results to be expected under changed conditions.

Algebraic Analysis

It would be highly advantageous to reduce the recommended procedures to a series of algebraic operations that would yield the desired information almost automatically. While this objective can probably be attained in some cases, it is not attainable in general. However, a start has been made in this direction and is outlined below.

Consider the total energy q required for a process. The gross useful heat is u and the sum of the nonproportional independent losses is NI. These figures represent energy per batch or cycle for a cyclic operation or per hour for a continuous operation. Then,

$$q = \frac{u(1 + P) + NI}{D} \qquad \text{(I)}$$

where P and D are defined as follows: P is defined by the postulate that Pu is the sum of all proportional independent losses. P is then the sum of P_1, P_2, P_3, etc. Each P_1 represents for one kind of proportional independent loss the ratio "loss/gross useful heat." The value of P is not limited, and it will exceed one if proportional losses are larger than gross useful heat.

D is defined by equation (I) above, which can be rewritten as follows:

$$D = \frac{u(1 + P) + NI}{q} \qquad \text{(II)}$$

Note the resemblance to the equation defining the "thermal efficiency" E,

$$E = \frac{u}{q} \qquad \text{(III)}$$

D therefore bears a family resemblance to E, but permits the proportional independent losses Pu and the nonproportional independent losses NI to appear explicitly in equation (I).

In combustion furnaces, D might conveniently be called "efficiency of combustion" and defined as:

$$\frac{\text{Heat content of fuel} - (\text{stack losses} + \text{losses from incomplete combustion})}{\text{Heat content of fuel}}$$

In induction heating, D might be called electrical efficiency and defined as:

$$\frac{\text{Power input} - \text{ohmic losses in the coil}}{\text{Power input}}$$

Conclusion

The classification of losses by the method outlined in this paper is recommended to the designer and operator of furnaces as a new analytical tool. In general, these procedures will be less simple than older methods, but the effort required will be rewarded by more economical furnace design and operation.

Acknowledgment

G. H. Fetterley, to whom the author is very grateful, engaged in a thorough discussion of a number of points raised in this paper.

Manuscript received April 7, 1955. This paper was prepared for delivery before the New York Meeting, April 12 to 16, 1953.

Any discussion of this paper will appear in a Discussion Section to be published in the December 1956 Journal.

Dissolution of Cadmium in Chromic Chloride Solutions

CECIL V. KING AND EDWARD HILLNER

Department of Chemistry, New York University, New York, New York

ABSTRACT

The dissolution rate of cadmium has been determined in dilute chromic chloride solutions containing hydrochloric acid up to 4M as functions of concentration, stirring speed, and temperature. A small amount of hydrogen is produced, but the main reaction is the reduction of chromic to chromous ion. Reaction with the violet hexaaquo chromic ion is slow and under chemical or electrochemical control; with the green dichlorotetraaquo ion it is much faster and transport- or diffusion-controlled. In each case, the driving force is only a few millivolts. The potential of the metal in these solutions is essentially that of the cadmium-cadmium ion couple, and there is little if any anodic polarization.

INTRODUCTION

The research described below follows a general plan to study the corrosive dissolution of metals in such solutions that insoluble films are not formed, and that the driving force of the reaction is small. If cadmium is immersed in dilute, unacidified chromic chloride, oxide or hydroxide films are deposited, but this does not occu with 0.5–4M hydrochloric acid present.

The following standard reduction or electrode potentials are found in the literature:

$$Cd^{++} + 2e \rightarrow Cd \qquad E^0 = -0.402 \text{ v}$$

$$Cr^{+++} + e \rightarrow Cr^{++} \qquad E^0 = -0.40 \text{ or } -0.41 \text{ v}$$

The chromic-chromous potential cannot be measured on platinum, which catalyzes the chromous-hydrogen ion reaction, but has been measured on mercury (1). It is sensitive to traces of oxygen, and the standard potential E^0 is uncertain to ±5 mv or more. Exact potentials for the solutions employed in the present research are even less certain, but it is evident that the reaction

$$Cd + 2Cr^{+++} \rightarrow Cd^{++} + 2Cr^{++} \qquad (I)$$

has little driving force, or only a small free energy change. The fact that cadmium ion forms stable chloride complexes helps the forward reaction, but even in 4M HCl it does not go to completion.

EXPERIMENTAL

Cylinders of best commercial cadmium (99.9%) were used, each approximately 2.5 cm long and 1.5 to 2 cm in diameter. They were mounted on a motor shaft with the ends protected. The rotational speed was established with a stroboscope (calibrated with the aid of a synchronous motor), and was adjusted to obtain the desired peripheral speed of the cylinder.

The reaction vessel was a 4-oz square bottle, fitted with a nitrogen inlet tube, and mounted in a 400 ml beaker. The square bottle allowed use of a small solution volume, preventing cavitation at the stirring speeds employed without introduction of baffle plates or sealing the cell. The vessel was kept at constant temperature (±0.3°C) by circulating water from a thermostat through the beaker. All solutions were deaerated as well as possible by bubbling nitrogen through them for 30 min prior to, and during, each run. Nitrogen was passed over copper turnings at 450°C, then through water. A small space between the Bakelite sleeve of the motor shaft and the bottle neck allowed the nitrogen to escape.

Stock solutions of violet chromic chloride were prepared by dissolving the green crystals (Analytical or Reagent grade) in water and allowing to stand at least a week; as shown below, about 98% of the ion was then in the hexaaquo form $Cr(H_2O)_6^{+++}$. Green solutions were prepared by dissolving the salt in at least 2M hydrochloric acid, which makes hydrolysis of the green ion $CrCl_2(H_2O)_4^+$ to the violet very slow, since this rate is inversely proportional to hydrogen ion concentration (2). Fresh green stock solution was prepared every 7–10 days since lower rates were found with older solutions. Stock solutions were analyzed by oxidizing samples with sodium peroxide to chromate, then following a standard volumetric procedure.

Reaction solutions were made up by mixing the proper amounts of stock solution with standardized hydrochloric acid and water, with a final volume of 70 ml in all cases. The amount of dissolution in suitable time intervals was determined by weight loss of the cylinders and was corrected for weight loss in the acid alone to obtain the amount of chromic ion reduction. In several runs this was checked by analysis for chromous ion; excess deaerated dichromate was added to the solution, which was then titrated with ferrous sulfate.

Violet Solutions

The dissolution rate in violet solutions was small, a few mg/hr from a cylinder 15 cm² in area. The cylinders were polished with #600 silicon carbide paper, immersed at the proper rotational speed, and taken out each hour for weighing, without repolishing until a new solution was used. Dissolution was much greater in the first hour or two than in subsequent hours because of the small amount of green ion present. The latter reacts at a transport-controlled rate, and is essentially all used up in an hour or two with the solution volume and stirring speeds employed.

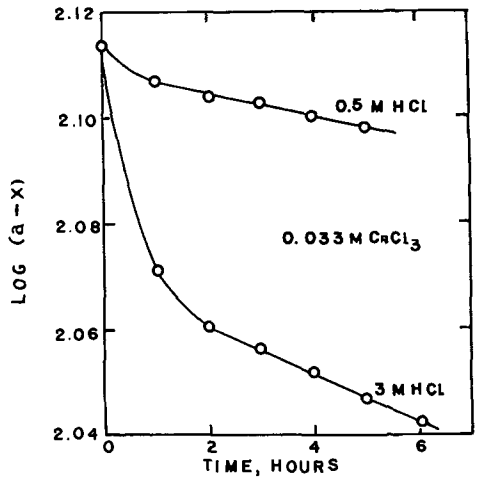

FIG. 1. Evaluation of first order rate constants in violet chromic chloride; 25°C, peripheral speed 15,000 cm/min.

TABLE I. *Rate constants k_c in cm/hr in violet chromic chloride, 25°C and 15,000 cm/min*

C_{HCl}, M	Concentration $CrCl_3$, M				Avg k_c
	0.033	0.066	0.10	0.133	
0.5	0.015	0.011	0.012	0.014	0.013
1.0	0.016	0.020	0.016	0.014	0.016
2.0	0.022	0.024	0.023	0.017	0.022 0.021*
					0.021†
3.0	0.055	0.133	0.092	0.175	0.114
					0.096*
					0.102†
4.0	0.304	0.244	—	—	0.274

* At 7500 cm/min.
† N_2 bubbling only.

During the first-hour runs a gray deposit appeared on the cylinders, in a spiral pattern related to the paths of solution flow. The film could be wiped off with moist filter paper, and microanalysis of the resulting smudge showed no metal other than cadmium. In all other experiments the metal surface remained bright or at least had no loose deposit.

First order rate constants were obtained in accordance with the equation

$$k_c = \frac{2.3V}{At} \log \frac{a}{a - x} \qquad \text{(II)}$$

with V in cm^3, A the measured area in cm^2, t in hours. The dissolving capacity of the solution a was calculated from the composition, since it was not practical to determine the extent of reaction at equilibrium. A comparatively small fraction of the reaction was followed, and thus k_c is a measure of the forward rate of reaction (I). As shown in Fig. 1, a plot of log $(a - x)$ vs. time becomes linear after an hour or two, and k_c is found from the slope. All weight losses were corrected for the amount dissolving in the acid alone, before making the plots.

Values of k_c for 25°C and a peripheral speed of 15000 cm/min are given in Table I. Most of these runs were repeated at 7500 cm/min, and with no stirring except nitrogen bubbling. Examples are included in the table.

TABLE II. *Activation energy in violet solutions*

C_{HCl}, M	0.5	1.0	2.0	3.0	4.0
E, cal/mole...	8900	10,500	12,800	14,300	15,400

While the experimental error is large in some cases, it is evident from Table I that there is no consistent trend in k_c with chromium chloride concentration or with stirring speed. Several qualitative experiments were done with no stirring at all; a cadmium cylinder was immersed in deaerated solution contained in a narrow tube about 25 cm long. The tube was sealed and allowed to stand. Within 24 hr the solution around the metal became light blue, and above the cylinder there was a sharp boundary between blue and violet solutions. With no stirring the dissolution is then diffusion-controlled.

Experiments were carried out at 15° and 35° with stirring at 7500 cm/min only. Results are similar to those at 25°, including the large effect of hydrochloric acid above 2M. Plots of log k_c vs. reciprocal of absolute temperature were linear within experimental error for each acid concentration. Activation energies are given in Table II.

Green Solutions

Dissolution is so much faster in green solutions that the runs took a few minutes rather than several hours. For example, in 0.033M $CrCl_3$, 1.0 M HCl, 35°C, same area and peripheral speed, the following weight losses were found: violet solution, 10.1 mg in 5 hr; green solution, 33.6 mg in 3 min. Because of the high rate, the weight loss was followed over a large per cent of the total reaction. Since in only a few of the solutions used does the reaction go nearly to completion, plots of log $(a - x)$ are not linear with time. Equation (II) must be modified as follows:

$$k_f + k_b = \frac{2.3V}{At} \log \frac{x_e}{x_e - x} \qquad \text{(III)}$$

where k_f is the rate constant for the forward reaction, k_b for the reverse reaction, and x_e is the amount of chromic ion reduction at equilibrium.

Values of x_e were determined by shaking cadmium cylinders with solution until equilibrium was attained, then measuring the weight loss. This was done in thermostatted flasks which were evacuated to deaerate the solutions, and which were attached to manometers through flexible glass capillary tubes. The pressure rise, calibrated with cadmium in acid alone, was used to make corrections for hydrogen evolution. At least two, generally three runs were made at each concentration, for example, of 6-, 7-, and 9-hr duration, to be sure that equilibrium had been reached. While determinations were made at 15°, 25°, and 35°C, most of the values were within a range of 15 mg and showed no trend with temperature. Therefore, average values are given in Table III.

Plots of log $(x_e - x)$ vs. time were linear from zero time as shown in Fig. 2, and rate constants $k_T (= k_f + k_b)$ were calculated from the slopes. Reproducibility was of the order of 5% and average deviation from the mean for the four concentrations was seldom greater. Average values

TABLE III. *Values of x_e, mg cadmium dissolved at equilibrium in 70 ml solution (corrected for hydrogen evolution)*
Average for 15°, 25°, 35°C

C_{HCl}, M	Concentration $CrCl_3$, M			
	0.033	0.066	0.10	0.133
0.5	100	208	318	435
1.0	104	227	342	462
2.0	119	243	366	481
4.0	123	248	374	492
Theory.....	130	257	393	523

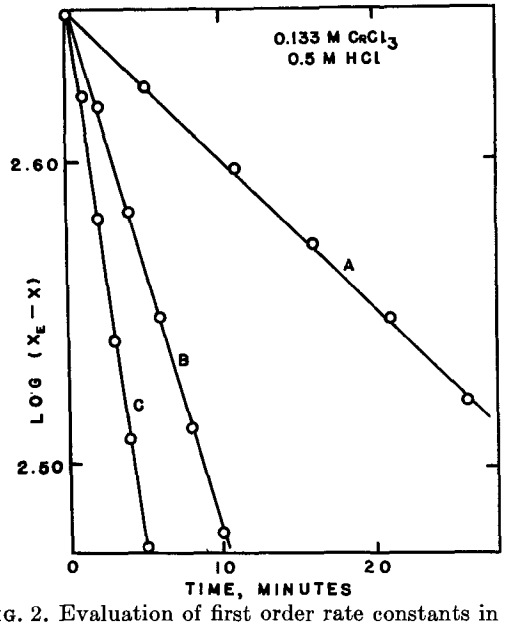

FIG. 2. Evaluation of first order rate constants in green chromic chloride; 25°C. Curve A, nitrogen stirring only; curve B, 7500 cm/min; curve C, 15,000 cm/min.

TABLE IV. *Values of k_T, cm/min, in green chromic chloride*

Temp.	C_{HCl}, M	N_2 bubbles	7500 cm/min	15000 cm/min
°C				
15	0.5	0.047	0.24	0.41
	1.0	—	0.23	—
	2.0	0.048	0.19	0.31
	4.0	0.041	0.21	0.31
25	0.5	0.057	0.30	0.49
	1.0	—	0.31	—
	2.0	0.055	0.25	0.40
	4.0	0.058	0.23	0.35
35	0.5	0.076	0.29	0.49
	1.0	0.068	0.32	0.55
	2.0	0.064	0.31	0.49
	4.0	0.071	0.36	0.52

of k_T are given in Table IV. The rate appears to be independent of acid concentration as well, greatest deviations being at the highest speed.

Plots of log k_T vs. $1/T$ are linear; activation energies are given in Table V.

Unacidified solutions.—A few runs were made in green solutions with no added acid. The dissolution rate decreased rapidly with time, and after 20 min the solution was violet rather than green. While hydrogen evolution is not rapid, the *p*H at the metal surface evidently rises to a value at which attainment of the green-violet equilibrium occurs quickly.

TABLE V. *Activation energy in green solutions*

Stirring.....	N_2	7500 cm/min	15000 cm/min
E, cal/mole.....	3700	3400	3300

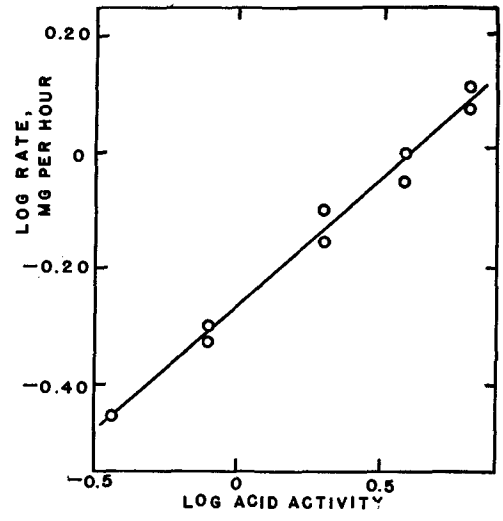

FIG. 3. Dissolution of cadmium in hydrochloric acid alone.

Dissolution in Acid Alone

The dissolution rate of the cadmium cylinders in deaerated hydrochloric acid is very small. The amount dissolved in the first hour is somewhat larger than in the following hours, when a "steady-state" value is attained. For example, 3M HCl dissolved 1.6 mg in the first hour, 1.0 mg in each subsequent hour (from 15 cm^2 surface area). The rate is independent of stirring speed, and while only a few runs were made at 15° and 35°C, the temperature coefficient appears to be small.

In Fig. 3, the log of the steady-state rate at 25°C is plotted vs. log of the mean ion activity of the hydrochloric acid (3). The slope of the straight line is 0.45, and therefore the equation

$$\text{rate} = ka_{\pm}^{0.45} \qquad \text{(IV)}$$

represents the rates at least empirically.

Potentials

The potential of the rotating cadmium cylinder vs. the saturated calomel electrode was measured first in deaerated hydrochloric acid, then with violet and green chromic chloride added, and with other salts for comparison. All measurements were at room temperature, 24°–28°C. Potentials became linear with time after a few minutes, as shown in Fig. 4. The straight lines were extrapolated to zero time to obtain representative values,[1] which

[1] Possibly the cadmium surface is not quickly cleaned in the more dilute acid (Fig. 4); the potential should drift slowly in a less negative direction as metal dissolves, after the initial clean-up.

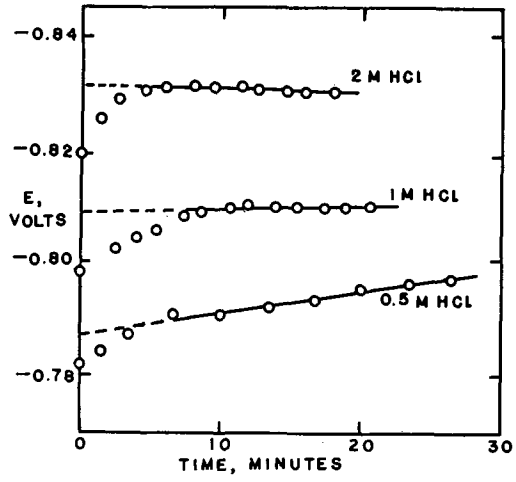

FIG. 4 Change in potential of cadmium with time in hydrochloric acid (vs. saturated calomel cell).

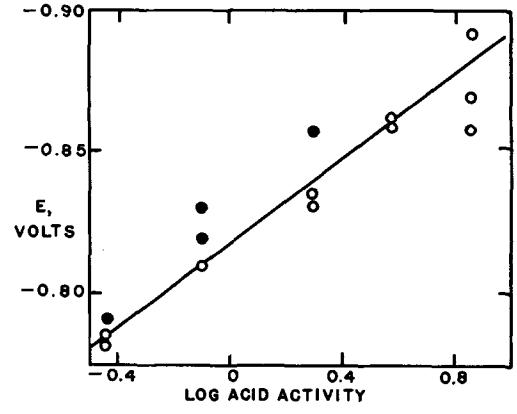

FIG. 5. Extrapolated potential as function of mean ion activity of acid. Black circles are for polished cylinders.

are plotted in Fig. 5 vs. log $a_{\pm}$ (HCl). The straight line shown has the slope, −0.070 v/log unit.

Mixtures such as 2M HCl, 2M NaCl give potentials in the same range as 4M HCl, showing the importance of the cadmium-chloride ion complex. Addition of 0.1M $CdCl_2$ shifts the potential in the cathodic (less negative) direction, to be expected with more free Cd^{++} present. Green chromic chloride does the same, since it dissolves considerable cadmium in a few minutes. The violet form has little effect and the same is true of sodium and aluminum chlorides at a concentration of 0.1M.

Potentials were measured with cadmium rotating in perchloric acid up to 4M to avoid the chloride complex. Values were erratic with time and about the same at each acid concentration. The average was −0.66 ± 0.01 v.

DISCUSSION

It became obvious in this investigation that cadmium does not catalyze the reoxidation of chromous ion by hydrogen ion, nor is hydrogen evolution hastened in any other manner. Experiments in the evacuated flasks with attached manometers showed hydrogen evolution to be somewhat slower in the chromic chloride solutions, both green and violet, than in the acid alone. Zinc reacts quite differently in these solutions. There is always copious hydrogen evolution in the violet solutions, and whether chromous ion or hydrogen is formed in green solutions seems a matter of chance (4).

The low rates, lack of effect of stirring speed, and comparatively high temperature coefficients in the violet solutions show that the surface process is rate-controlling. There are no permanent anodic and cathodic areas on the cadmium; the cylinder may become roughened and eroded if run many hours without repolishing, but not pitted. The measured potentials do not indicate whether polarization of the cathodic reaction, reduction of chromic to chromous ion, accompanies its rate-determining role. The hydrogen evolution potential is of course highly polarized.

The gray film formed initially in violet solutions may have been cadmium deposited by the reverse reaction. When starting with far higher concentrations of the green ion, such redeposited metal should probably not be expected to show up in this way until the reaction was near the equilibrium point.

In the green solutions the magnitude of the rate constants indicate that convective-diffusive transport is the controlling step, and the effect of stirring speed and low temperature coefficients substantiate this. Using an estimated 4.5×10^{-4} cm^2/min for the diffusion coefficient of chromic ion, the "effective" diffusion layer thickness is calculated to be similar to values found in other transport-controlled systems (5). Over the limited range of stirring employed, k_T is approximately proportional to the 0.7 power of stirring speed, which agrees with the relations found by other authors in unbaffled systems (6). At higher speeds we should expect a power near unity in a well-baffled system (5). In employing equation (III) it was assumed that the reverse reaction is first order, and the results seem to agree with this. It takes place only on the surface of the cylinder, i.e., cadmium never precipitates in the solution or on the vessel walls. The rate constant for the forward reaction can be calculated if desired, since $k_f a/x_e = k_T$, where a is the amount which would be dissolved with complete reaction (7). However, the important thing is that the constants for the chemical process (k_c) in the green solutions are larger than any values of k_f, and much larger than k_c for the violet solutions.

The obvious reasons for the different reactivities of the two ions lie in (*a*) the different charge types of the two chromium ions, and (*b*) the different compositions and polarizabilities (the structures being similar). The charge type is important in homogeneous reactions, for instance in anion catalysis of the nitramide reaction (8), and in the reaction of thiosulfate ion $S_2O_3^=$ with a bromo-ester or the corresponding bromo-anion (9).

Silver dissolves 15 or 20 times as fast in ferric sulfate solutions as in ferric perchlorate (10), reflecting the difference between the ions $FeSO_4^+$ and (hydrated) Fe^{+++} or $Fe(OH)^{++}$. However, it is believed that the silver surface is positively charged due to preferential adsorption of silver ions. In the present case one expects the cadmium surface to be negatively charged, and electrostatic effects would favor reaction with the triply charged violet ion.

The very great increase in rate in violet solutions above 2M HCl suggests that two reaction mechanisms are involved. This is supported by the increase in activation energy at high acidity. The kinetics must eventually be referred to the rate of formation and decay of one or more

activated states, which in chemical reactions are assumed to involve "critical complexes." The following mechanisms are postulated:

1. In violet solutions with low HCl concentration, the critical complex consists mostly of one or two adsorbed chromic ions associated with a cadmium atom or ion; decomposition results in Cd^{++} in solution, which then forms the chloride complex.

2. At high HCl concentration, Cl^- ions are found in the critical complex, which results in direct formation of cadmium-chloride ions in solution.

3. The green ion which already contains chloride should form chloride-containing critical complexes most rapidly.

The problem here is similar to that found in the electrodeposition of chromium from aqueous Cr(III) ion, which involves reduction to Cr(II) as the first step. Lyons (11) has pointed out that, in general, halo-aquo ions require less activation energy than aquo-ions for electroreduction.

Study of the dissolution in perchloric acid alone and with the violet ion, with chlorides and other salts, would be helpful.

Potential and rate.—In hydrochloric acid alone the following equation represents the cadmium potential (Fig. 5):

$$E = E' - 0.070 \log a_{\pm} \qquad (V)$$

At first sight, the slope may seem anomalous since other metals, especially iron, give a smaller slope of opposite sign (12, 13). However, this is a cadmium-cadmium ion potential, not a hydrogen or atomic hydrogen potential.

In these hydrochloric acid solutions most of the cadmium is present as $CdCl_3^-$ (14). The activity of the free cadmium ion is given by

$$a_{Cd^{++}} = K a_{CdCl_3^-}/a^3_{Cl^-} \quad \text{or} \quad K a_{CdCl_3^-}/a^3_{\pm} \qquad (VI)$$

At comparable stages of the dissolution it may be assumed from equation (IV) that

$$a_{CdCl_3^-} = k' a_{\pm}^{0.45} \qquad (VII)$$

Combining (VI) and (VII)

$$a_{Cd^{++}} = K k' a_{\pm}^{-2.55} \qquad (VIII)$$

The cadmium potential is given by

$$E = E^{0'} + 0.0295 \log a_{Cd^{++}} \qquad (IX)$$

From (VIII) and (IX), combining constants,

$$E = E'' - 0.075 \log a_{\pm} \qquad (X)$$

In view of the approximations made and neglect of other complexes than $CdCl_3^-$, agreement with the experimental slope is satisfactory. It would be difficult to calculate E'', but if 10^{-6} is assumed as a reasonable value for $a_{Cd^{++}}$ when $a_{\pm} = 1$,

$$E = -0.402 - 0.246 - 0.177 = -0.825$$

vs. the calomel cell (cf. Fig. 5).

Potentials of cadmium in perchloric acid are erratic but more cathodic, indicating that more free Cd^{++} is present; the buffering and stabilizing effect of the chloride ion is missing.

Spectrophotometry of Chromic Chloride Solutions

When the more rapid initial rates in violet solutions were found, a search was made for the cause. Preelectrolysis and experiments with small additions of Cu^{++} and Pb^{++} indicated that heavy metal impurities were not responsible. Addition of small amounts of green ion, either initially or after one or two hours, showed the reason. Extrapolation of log $(a - x)$ vs. t plots to zero time would most likely serve to analyze the mixtures.

The absorption spectra of violet and green solutions were determined in the range 300–750 mμ with a Beckman DU instrument, and the molar extinction coefficients were plotted vs. wave length. There are two absorption bands with peaks at 407 and 575 mμ for the violet form; the bands for the green form are very similar with the peaks displaced about 15 mμ toward longer wave lengths. The curves are not reproduced here, since they are almost identical with absorption curves found by Marks for violet and green chromic sulfates (15). Marks showed that by working somewhat off the absorption maxima, where the extinction coefficients differ most, a rather good analysis of mixtures of the two ions can be made. The method did not look promising in the present case, and exact analysis proved to be unnecessary.

Manuscript received August 30, 1955. This paper was prepared for delivery before the Pittsburgh Meeting, October 9 to 13, 1955. It was taken from the Ph.D. thesis submitted by Edward Hillner to the Graduate School Faculty of New York University. Work done under Contract No. DA-30-069-ORD-1113 of the Office of Ordnance Research.

Any discussion of this paper will appear in a Discussion Section to be published in the December 1956 JOURNAL.

REFERENCES

1. G. S. FORBES AND H. W. RICHTER, *J. Am. Chem. Soc.*, **39**, 1140 (1917).
2. A. B. LAMB, *ibid.*, **28**, 1710 (1906); A. B. LAMB AND G. R. FONDA, *ibid.*, **43**, 1154 (1921); R. E. HAMM AND C. M. SHULL, *ibid.*, **73**, 1240 (1951).
3. H. S. HARNED AND B. B. OWEN, "The Physical Chemistry of Electrolytic Solutions," p. 547, Reinhold Publishing Corp., New York (1943).
4. C. V. KING AND N. MAYER, *This Journal*, **100**, 473 (1953).
5. C. V. KING AND M. SCHACK, *J. Am. Chem. Soc.*, **57**, 1212 (1935).
6. M. EISENBERG, C. W. TOBIAS, AND C. R. WILKE, *This Journal*, **101**, 306 (1954).
7. S. GLASSTONE, "Textbook of Physical Chemistry," p. 1070, D. Van Nostrand Co., New York (1946).
8. R. P. BELL, "Acid-Base Catalysis," Oxford Press (1941).
9. E. S. AMIS AND W. J. BROACH, *J. Chem. Phys.*, **22**, 952 (1954).
10. H. SALZBERG AND C. V. KING, *This Journal*, **97**, 290 (1950); C. V. KING AND F. S. LANG, *ibid.*, **99**, 295 (1952).
11. E. H. LYONS, JR., *ibid.*, **101**, 363 (1954).
12. J. D'ANS AND W. BRECKHEIMER, *Z. Elektrochem.*, **56**, 585 (1952).
13. A. C. MAKRIDES, N. M. KOMODROMOS, AND N. HACKERMAN, *This Journal*, **102**, 363 (1955).
14. C. E. VANDERZEE AND H. J. DAWSON, *J. Am. Chem. Soc.*, **75**, 5659 (1953).
15. G. W. MARKS, *U. S. Bur. Mines Rept. Invest.* No. 4779, March 1951.

High Pressure Oxidation of Metals—Tungsten in Oxygen

J. P. Baur, D. W. Bridges, and W. M. Fassell, Jr.[1]

Department of Metallurgical Engineering, University of Utah, Salt Lake City, Utah

ABSTRACT

Tungsten rod and sheet were found to oxidize linearly in oxygen from 600° to 850°C at oxygen pressures ranging from 20 to 500 psia. Oxidation rate increased with increased oxygen pressure at temperatures 750°–850°C. Theoretical considerations indicate that an equilibrium adsorption process occurs prior to the rate-determining step. The assumption of a linear change of adsorption energy with increase of surface coverage allowed observed oxidation rates to be corrected for pressure effect. The activation energy was 48 kcal. Tungsten sheet volatilization losses were appreciable above 800°C. Only tungsten rod data were free from volatilization losses at 850°C. Photographs are included showing the effect of shearing samples at room temperature prior to oxidation on the final physical appearance of the oxide. Cold shearing produces exfoliated tungsten oxide.

Introduction

Tungsten has been the subject of many theoretical papers dealing with the adsorption of oxygen upon the metal surface (1). Langmuir's original work in the field of chemisorption dealt with tungsten-oxygen systems at extremely low pressures (2–4).

Gulbransen and Wysong (5) employed the microbalance technique in a study of the oxidation behavior of tungsten in the temperature range 25°–550°C (7.6 cm-Hg). The metal was reported to oxidize according to the parabolic rate law. Dunn (6) reported the parabolic rate law is obeyed in air from 700° to 900°C with an anomaly occurring at 850°–950°C, attributed to a phase change from alpha WO_3 to beta WO_3. The parabolic law was also reported by McAdam and Geil (7). Nachtigall (8) published some oxidation data for tungsten (500°–800°C). Published curves are neither ideally linear nor parabolic. Almost linear relationships were obtained by Scheil (9), and by Kieffer and Kolbl (10) between 500° and 900°C.

There is no recorded study of the effect of oxygen pressure variation upon the oxidation rate of tungsten. Also no information is available on the oxidation behavior of tungsten in oxygen at pressures in excess of 1 atm. The present work is an investigation of the oxidation behavior of tungsten over the temperature range 600°–850°C and oxygen pressures from 20 to 500 psia.

Experimental Procedure

Four different types of tungsten were employed: General Electric Co. sheet of approximately 20 mil thickness, Fansteel Metallurgical Corp. and Westinghouse Electric Manufacturing Co. sheet of approximately 5 mil thickness, and tungsten rod, $\frac{1}{10}$ in. diameter, of unknown manufacture.

Tungsten sheet sheared at room temperature exhibited markedly undesirable properties; it was necessary to resort to special sample preparation. The tungsten sheet was heated to about 800°C in an oxygen-natural gas burner. The samples were then hot sheared to the desired size (recorded in Table I) by means of a DI-ARCO precision shear. A $\frac{3}{32}$ in. diameter hole was hot punched at one end of each small sample The resulting oxide scale was removed by immersion in a boiling solution of potassium ferrocyanide and potassium hydroxide (11). Following washing in distilled water and drying, the sample was abraded with 6/0 garnet paper and the geometrical surface area was determined.

The high temperature-high pressure furnaces and the experimental techniques used to follow the reaction have been discussed in detail in a previous paper (12). Data are recorded in the form of curves showing weight gained as a function of time.

Experimental Results

Tungsten metal was oxidized from 600° to 850°C over an oxygen pressure range of 20–500 psia. Under the imposed conditions it was found that the oxidation rate is governed by the linear law. Deviations from the linear rate of oxidation for the first few minutes were observed at 600° and 650°C; however, subsequent long periods of observation show no deviation from linearity for 3 hr.

It was found that tungsten oxide, formed on tungsten sheet, sublimed at temperatures in excess of 850°C. This sublimation resulted in deviations from linear rate and caused the rate to change but slightly with temperature increase. Comparison with observed rates using tungsten rod seemed to indicate that the total surface area exposed is the most important factor in the influence of volatilization on the oxidation rate. Changes in surface roughness as well as accelerated attack of active centers during the initial phases of oxidation could also account for the high temperature deviations. However, it is felt that volatilization is probably the largest factor. It should be stressed that the experimental technique used is a static method; volatilization losses should be much greater in an oxygen flow system.

Table I is a compilation of tungsten oxidation data which represents selection of data in the respect that, although

[1] Present address: Howe Sound Co., Salt Lake City, Utah.

TABLE I. *Observed oxidation rates of tungsten in oxygen*

Temp	Type of tungsten	Oxygen pressure	Oxidation rate	Value of θ calculated by equation (XII)
°C		*psia*	$mg \cdot cm^{-2}\ hr^{-1}$	
600	A	50	0.2	
		100	0.2	
650	A	50	0.9	
		100	0.9	
700	B	20	3.1	
		30	2.9	
		50	3.4	
		100	3.3	
		150	3.2	
		200	3.4	
750	C	20	6.9	0.55
		50	8.1	0.64
		200	9.5	0.77
		300	9.9	0.81
		500	11.2	0.86
	B	30	8.7	
		100	9.2	
		200	12.4	
800	C	20	22.5	0.58
		50	27.6	0.69
		100	31.1	0.77
		150	29.9	0.81
		200	33.8	0.85
		300	34.7	0.89
		400	34.3	0.93
		500	33.5	0.95
850	C	20	40.2	0.32
		30	47.3	0.36
		50	54.1	0.53
		100	76.1	0.69
		200	85.2	0.84
		300	86.7	0.94

A—Westinghouse sheet (rolled by H. Cross Co., N. Y., N. Y.) $1\frac{1}{4}$ in. x $\frac{3}{8}$ in. x 0.005 in.; surface area: 6.25 cm².

B—Fansteel Metallurgical Corp. sheet, 2 in. x 0.4 in. x 0.005 in.; surface area: 8.2 cm².

C—Tungsten rod (unknown manufacturer) $\frac{3}{4}$ in. lengths x 0.1 in. dia. Surface area: 1.6 cm².

some 200 samples were oxidized; high temperature data on the sheet tungsten are not tabled since the material suffered from volatilization losses. Oxidation rates for the tabled metal in the region reported are quite satisfactorily reproducible. Low temperature tungsten rod data are lacking since the surface area of the rod was insufficient to allow a measureable rate to be obtained. It should be borne in mind that the specific gravity of tungsten is 19.3 and thus a sample of sufficient surface area and mass not exceeding two grams (the latter restriction is imposed by the use of the quartz spring technique) is difficult to obtain.

Originally the tungsten samples were sheared to size from the manufacturer's larger sheets at room temperature. This "cold shearing" disrupted the grain structure of the sheet in the vicinity of the sheared edge. This ruptured area permitted rapid oxidation to take place along these edges producing the exfoliated condition shown in Fig. 1. The samples, after oxidation for 20 min at 600°–850°C, consisted of a large number of plates. Each platelet contained unreacted tungsten embedded in the oxide. This sandwich effect resulted in an irregular increase in the mass change per unit time since the surface area increases as the plates form. Volatilization losses were markedly greater with the "cold sheared" tungsten occurring at lower temperatures. In order to eliminate this difficulty the later samples were "hot sheared" as described above. Fig. 2 shows the final appearance of hot sheared samples oxidized in the temperature and pressure range of Table I. The oxidation rates of these samples were highly reproducible. In spite of the hot shearing, preferential oxidation at higher temperatures occurred along the edges and around the hole, as shown in Fig. 3.

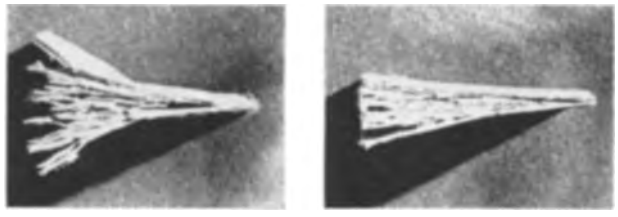

FIG. 1. Photographs showing effect of cold shearing on final appearance of oxidized tungsten sheet. *Left*, 800°C, 100 psia; oxidized 18 min; *right*, 750°C, 100 psia; oxidized 21 min.

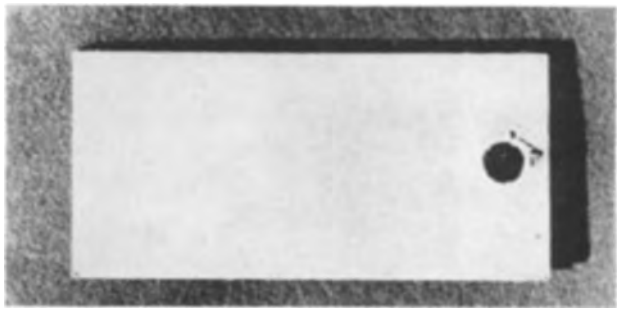

FIG. 2. Final appearance of hot sheared tungsten sheet in the temperature range of Table I. Hot sheared; oxidized 21 min, 700°C, 100 psia.

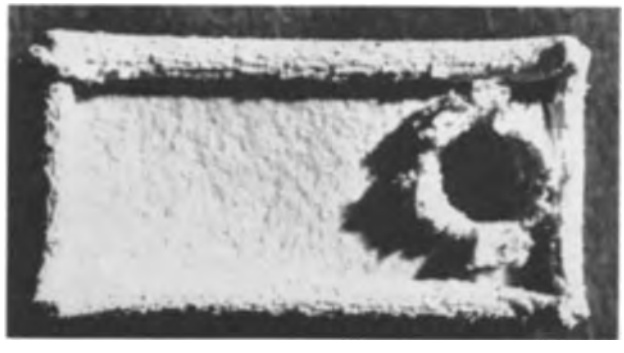

FIG. 3. Hot sheared tungsten sheet oxidized in excess of 850°C. Hot sheared; oxidized 25 min, 1000°C, 100 psia.

It was reported by Dunn (6) that the color of the oxide formed at ordinary temperatures (presumably below

850°C) was deep orange. Smithells (11) states that "tungstic oxide, WO_3, is yellow, the exact shade depending very much on particle size. On heating to about 500°C the color changes to an orange brown but reverts to yellow again on cooling" . . . (p. 47, *op cit*). All samples at all temperatures and pressures investigated in this study were yellow in color when removed from the furnace. One sample was purposely oxidized in air at 900°C to determine whether or not the other gases present affected the color. This sample was similar in color to the others.

Discussion of Experimental Results

Previous articles from this laboratory have discussed and developed a general treatment of the effect of oxygen concentration upon the rate of oxidation (12, 13). Briefly this development combines the Eyring rate equation (14) and the explicit surface oxygen concentration factor resulting from surface site saturation considerations. This results in the general pressure sensitive linear oxidation rate equation:

$$\text{Rate} = k_0 \cdot f(\theta) \cdot \frac{kT}{h} \cdot \exp[-\Delta F^*/RT] \qquad \text{(I)}$$

where k_0 is a proportionality constant with the dimensions of ML^{-2} and includes the correction factors for the true surface area involved in the oxidation reaction, i.e., the surface roughness factor, as well as the number of active sites per square centimeter. The other terms retain their customary significance as in the Eyring absolute reaction rate theory with the transmission coefficient assumed equal to unity (14). The concentration factor, $f(\theta)$, represents a function of θ, the fraction of the surface covered with oxygen molecules or atoms. The exact nature of this term depends on the type of adsorption mechanism postulated.

Molecular adsorption is assumed. Following Langmuir, one can write:

$$S + O_2 = S \cdots O_2 \qquad \text{(II)}$$

where S represents an active site at the zone of reaction; O_2, an oxygen molecule; and $S \cdots O_2$, the adsorbed oxygen molecule. If θ is the fraction of the corrected surface area covered with oxygen molecules, the vacant sites, S, are then $[1 - \theta]$.

The mechanism depicted is that of an oxygen molecule adsorbing upon an active site in molecular form. Decomposition of the adsorbed oxygen molecule or some subsequent phase boundary step is the slow rate-determining step. Hence, the surface sites are always in equilibrium with the external gas phase and the adsorption process may be treated as an equilibrium process.

Expression for $f(\theta)$ results from a consideration of the equilibrium expression for the appropriate surface mass balance equation, equation (II). The activity of the surface concentration of the adsorbed oxygen or oxygen phase immediately adjacent to the zone of reaction is assumed to be proportional to the fugacity of the external oxygen phase, $f(O_2)$, which leads to the expression:

$$f(O_2) = [O_2] = n/V = P/RT \qquad \text{(III)}$$

where R, the molar gas constant, is used as 0.08206 ltr-atmo/mole-degree Kelvin. If K_1 represents the molar equilibrium constant of equation (II), $f(\theta)$ can be derived as follows:

$$K_1 = \frac{\theta}{[1-\theta]\cdot[O_2]} = \exp\left[\frac{-(\Delta H - T\cdot\Delta S)}{RT}\right] \qquad \text{(IV)}$$

$$\theta = \frac{K_1\cdot[O_2]}{1 + K_1\cdot[O_2]} \qquad \text{(V)}$$

$$\text{Rate} = K_0 \frac{K_1[O_2]}{1 + K_1[O_2]} \qquad \text{(VI)}$$

where K_0 represents the Eyring absolute reaction rate constant, $kT/h \cdot \exp[-\Delta F^*/RT]$.

In order to satisfy equation (VI) the following conditions must be satisfied:

1. Values of K_0 must be greater than any observed oxidation rate at the temperature in question. This would be expected as,

$$\lim_{[\theta \to 1]} dm/dt = K_0$$

2. Slope of plot, $\log_{10}K_0$ vs. 1/°K, must be negative in order that the energy of activation for the oxidation process be positive.

3. Slope of plot, $\log_{10}K_1$ vs. 1/°K, must be positive, since the heat of chemisorption of oxygen must be exothermic.

4. Values of K_1, equilibrium constant for chemisorption of oxygen, must be greater than unity since it is necessary that

$$\Delta F_{ads} \leq 0 \text{ and } K_1 = \exp[-\Delta F/RT]$$

Where the effect of interaction between the adsorbed molecules on the energy of adsorption cannot be neglected, the classic Langmuir type derivation for θ, the fraction of the surface covered, equation (IV), must be amended. Langmuir recognized this and wrote an alternate expression for the fraction of the surface covered applicable for a varying energy of adsorption (15, 16):

$$\theta = \sum_i K_i P/(1 + K_i P) \qquad \text{(VII)}$$

K_i is no longer a constant but varies according to the extent and nature of the interaction energy. Most often the assumption is made that the enthalpy of adsorption is a linear function of surface coverage:

$$\Delta H_{ads} = \Delta H^0_{ads} + \theta z V \qquad \text{(VIII)}$$

where ΔH^0_{ads} is the enthalpy of adsorption for $\theta = 0$. Since V is defined as the positive molar energy of interaction, the enthalpy becomes less and less negative as the surface coverage approaches its equilibrium limit. The coordination number, z, of the monolayer ($0 \leq z \leq 6$) is dependent on the nature of the monolayer and the degree of completeness of coverage. Thus it is seen that under the above scheme the first adsorbed molecules are more strongly adsorbed than the last.

The assumption of equation (VIII) is not as artificial as may be thought at first glance. It results from consideration of the distribution of adsorbed molecules as completely random (14, 17) and has been experimentally observed in the case of hydrogen on tungsten (18–20).

Modification of the Langmuir derivation under the condition of equation (VIII) has been published by

Brunauer and co-workers (21). Their derivation (with slight alteration in definitive terminology) will be outlined briefly. Let an equilibrium constant for changeable adsorption enthalpy be defined as:

$$\begin{aligned} K_1 &= \exp[-(\Delta F^0_{ads} + \theta z V)/RT] \\ &= K_1^0 \cdot \exp[-\theta z V/RT] \end{aligned} \quad \text{(IX)}$$

where $K_1^0 = \exp[-(\Delta H^0 - T \cdot \Delta S^0)/RT]$, the value of the equilibrium constant for $\theta = 0$.

The expression for the surface coverage, θ, is now the summation of small differential units of coverage, θ_s, each involving a different enthalpy and valid over a small element of area, ds. Equation (V), with K_1 defined as in equation (IX), expresses θ_s. Then the fraction of the entire area covered with adsorbed molecules is:

$$\begin{aligned} \theta = \Sigma \theta_s \cdot ds &= \int_0^\theta \theta_s \cdot ds \\ &= \int_0^\theta \frac{K_1^0 \cdot [O_2] \cdot \exp[-s \cdot zV/RT]}{1 + K_1^0 \cdot [O_2] \cdot \exp[-s \cdot zV/RT]} \cdot ds \end{aligned} \quad \text{(X)}$$

This integral is of the form $\int dU/U$, where U is the denominator above. Integrating equation (X), one obtains:

$$\theta = 2.3RT/zV \log_{10}\left\{\frac{1 + K_1^0 \cdot [O_2]}{1 + K_1^0 \cdot [O_2] \cdot \exp[-\theta \cdot zV/RT]}\right\} \quad \text{(XI)}$$

where $K_1^0[O_2] \gg 1 \gg K_1^0[O_2] \cdot \exp[-z\theta V/RT]$

$$\begin{aligned} \theta &\approx 4.6T/zV\{\log_{10}[O_2] + \log_{10} K_1^0\} \\ &= 4.6T/zV\left\{\log_{10}[P_{O_2}] + \log_{10}\left(\frac{K_1^0}{RT}\right)\right\} \end{aligned} \quad \text{(XII)}$$

Equation (XII) is a result first derived semi-empirically by Frumkin and Slygin (22). These workers and also

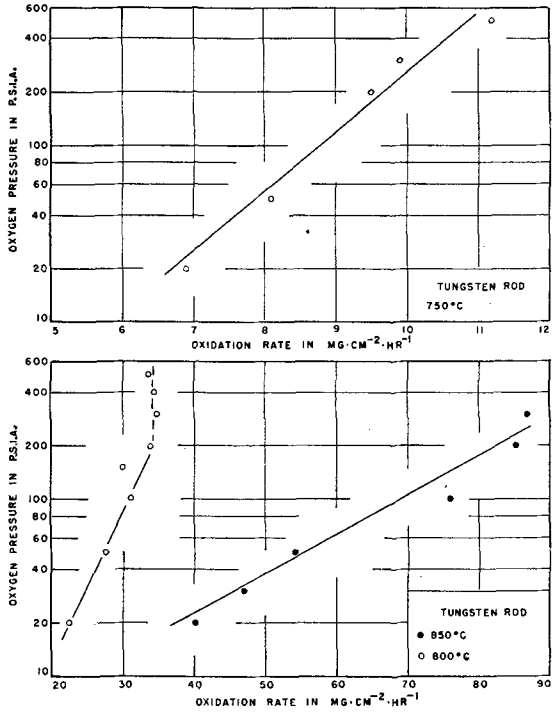

FIG. 4. Data of Table I plotted according to equation (XIII)

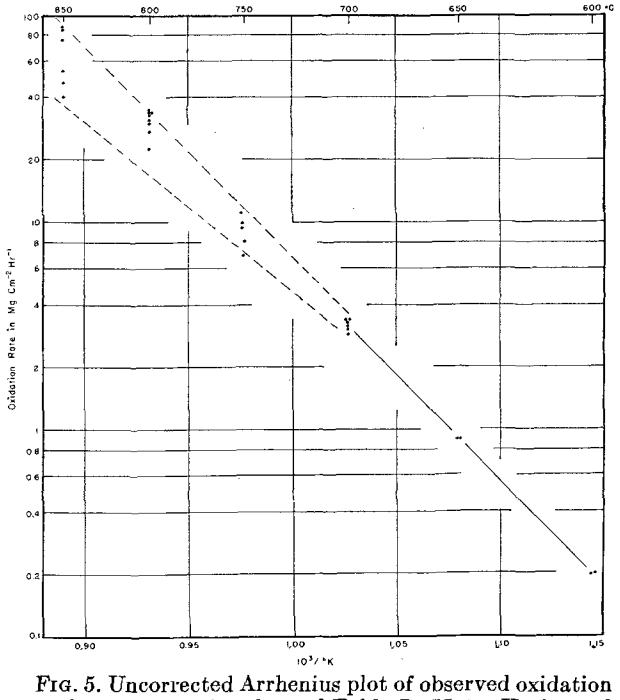

FIG. 5. Uncorrected Arrhenius plot of observed oxidation rate of tungsten, using data of Table I. (Note: Horizontal arrays of points indicate the same oxidation rate at the particular temperature.)

TABLE II. *Estimate of interaction energy and adsorption equilibrium constant*

Temp	Assumed K_0	zV in calories	K_1^0
°C			
750	11.5	21,285	3.24×10^4
800	35.0	18,874	1.82×10^4
850	89.0	9,850	4.57×10^2

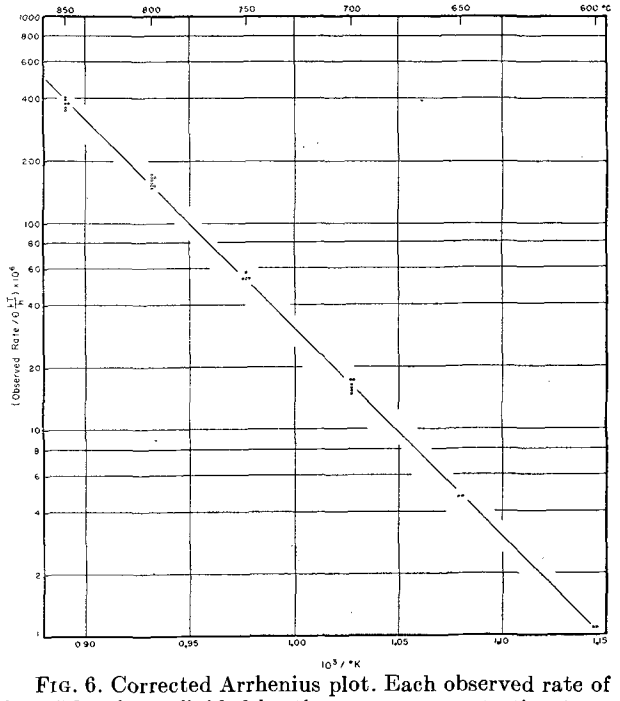

FIG. 6. Corrected Arrhenius plot. Each observed rate of Fig. 5 has been divided by the proper concentration term (θ). (Note: Horizontal arrays of points indicate the same oxidation rate at a particular temperature.)

TABLE III. *Tabulation of the experimentally determined interplanar spacings of oxidized tungsten with listing of the ASTM cards for comparison*

600°C 100 psia	650°C 100 psia	700°C 100 psia	750°C 100 psia	800°C 125 psia	850°C 100 psia	900°C 100 psia	900°C 100 psia Ground	Tungstite mineral	WO_3 5-0363,4	WO_2 5-0431	W_4O_{11}	$W_{20}O_{58}$ 5-0386,7
4.321	4.353	4.210	4.332							4.78		4.28
3.95	3.942		3.917	3.934							3.92	
3.883							3.867					3.89
	3.850		3.850					3.84	3.835			
3.770		3.818	3.770	3.825	3.786	3.818	3.786	3.76	3.762		3.78	3.77
	3.739	3.723		3.723	3.738	3.723	3.678					3.70
		3.633	3.648		3.663	3.619		3.63	3.642		3.63	3.64
3.414	3.414	3.414	3.414	3.479	3.562		3.376		3.411	3.45		
		3.314	3.351	3.401	3.225	3.314			3.342			
3.164	3.159	3.079	3.089	3.132	3.028	3.079	3.153	3.07	3.109			
							3.110		3.076	2.828		3.821
2.734	2.722			2.698			2.722		2.684		2.74	2.729
2.683	2.683	2.675	2.659	2.659		2.667	2.675	2.66	2.661			2.707
						2.644	2.644					2.640
2.564	2.556	2.629	2.622		2.621	2.600		2.62	2.617		2.62	2.620
				2.536	2.592		2.528		2.528			
		2.508	2.501		2.481	2.501			2.509	2.446		
	2.436			2.429						2.436	2.44	
										2.428		
2.392		2.404	2.398							2.418		
			2.287	2.321	2.265	2.254				2.393		
2.188	2.191		2.206	2.233	2.227		2.206				2.22	2.211
				2.176	2.181	2.171	2.161		2.172	2.181		
		2.151	2.151			2.146		2.15	2.149	2.150		
2.122	2.122	2.089		2.058	2.127				2.098			
	2.040	2.032	2.036	2.036		2.036			2.038			
		2.010	2.010	2.014	2.014	2.014	2.010		2.020			
									2.011			
	2.002			1.994	1.994	1.994			1.991		1.98	
		1.969	1.969		1.965	1.969	1.977	1.97	1.966			1.963
1.949	1.941			1.937	1.953		1.926					
1.914		1.914	1.918			1.914		1.92	1.917			1.898
	1.895	1.873	1.877	1.895	1.899	1.877	1.884	1.88	1.879			1.884
1.845	1.841				1.859					1.847	1.85	
1.828	1.824	1.817	1.824	1.838		1.821	1.828	1.82	1.820	1.827		
		1.798	1.797	1.811	1.784	1.807	1.804	1.79	1.807			
1.773							1.755		1.793		1.75	1.741
1.728	1.727			1.722			1.728			1.724		1.720
	1.704	1.705	1.713	1.703		1.707			1.707	1.709		1.700
			1.691		1.692		1.698	1.69		1.698	1.70	1.695
	1.684	1.684				1.687			1.687			1.680
1.664		1.664	1.669		1.675	1.670			1.670		1.67	1.674
	1.656			1.653			1.661	1.65	1.654			1.666
									1.646			
		1.639	1.642		1.626	1.639	1.642	1.64	1.638			
1.599									1.593	1.593		
	1.566	1.578		1.563			1.578		1.580			1.562
	1.554	1.554	1.554	1.551		1.553			1.554	1.545	1.55	1.550
1.542					1.542	1.537	1.534	1.53	1.538	1.537	1.53	1.537
		1.540	1.540						1.527			1.524
				1.510	1.528	1.514	1.508		1.514			
1.502	1.499		1.501			1.497		1.50	1.499			
1.486		1.486	1.488	1.475	1.490	1.484	1.484	1.48	1.486			
		1.467	1.467		1.478	1.463		1.47	1.464	1.464	1.46	
					1.457							
1.406	1.408						1.414		1.411	1.412		
									1.406	1.406		
1.388	1.393	1.400	1.399	1.400					1.399			
						1.388	1.386		1.390	1.391		
	1.384				1.379				1.381	1.387		1.365
							1.359		1.358			1.359
1.351	1.352			1.351					1.347	1.354		
		1.342	1.342	1.342		1.336	1.336		1.342		1.34	1.337
	1.331		1.336		1.334			1.33	1.331			
		1.310	1.312	1.318			1.316		1.322			
									1.317			
						1.307		1.31	1.308			
1.299					1.302				1.297	1.297		1.282
	1.287	1.280	1.281	1.287	1.274	1.281	1.287	1.28	1.283	1.284	1.29	1.275

TABLE III—*Continued*

600°C 100 psia	650°C 100 psia	700°C 100 psia	750°C 100 psia	800°C 125 psia	850°C 100 psia	900°C 100 psia	900°C 100 psia Ground	Tungstite mineral	WO_3 5-0363,4	WO_2 5-0431	W_4O_{11}	$W_{20}O_{58}$ 5-0386,7
1.268		1.258							1.264		1.26	1.269
	1.251			1.248			1.252		1.254			1.262
		1.242	1.242		1.237	1.237	1.242	1.24	1.245			1.255
									1.242			1.248
									1.238			
									1.235			
	1.222			1.220			1.218	1.22			1.21	
		1.215	1.217							1.215		
						1.212			1.213	1.212		
1.204					1.209					1.209		
										1.207		
1.196				1.197			1.197		1.201	1.195		1.207
1.183	1.181	1.175	1.176	1.181	1.172	1.175	1.168		1.191	1.184		1.196
	1.161	1.157	1.157	1.161	1.151	1.157	1.157					1.189
	1.145	1.139	1.141	1.144			1.143					1.147
1.131	1.131	1.125	1.128	1.130			1.130					1.141
1.122	1.124				1.123	1.126	1.120					1.133
	1.095	1.114	1.115	1.118	1.109	1.114	1.109					
	1.090	1.085	1.105	1.107	1.100	1.105						
	1.074	1.068	1.085	1.086	1.065	1.068						1.105
	1.041	1.037	1.068	1.071			1.050					
	1.031	1.028	1.046	1.050	1.045	1.037	1.031					
			1.037	1.041	1.034	1.026						
			1.028	1.029	1.025							
	0.9976	0.9934	0.9955		0.9934	0.9962						
				0.9871	0.9816		0.9864					
	0.9783											
	0.9684	0.9621		0.9646	0.9621	0.9609	0.9653					
0.9483	0.9469	0.9451	0.9457	0.9469	0.9434	0.9446	0.9469					
0.9354	0.9354				0.9321	0.9326	0.9337					
0.9166	0.9140	0.9135										
	0.9090	0.9066	0.9066	0.9070	0.9056	0.9080						

Temkin and Pyzkov (23) used it in connection with the explanation of the adsorption of NH_3 on iron catalyst. It is applied to NH_3 on a double promoted iron catalyst 931 by Love and Emmett (24). It should be noted that equation (XII) is not good at either limit of the allowed values for θ, the fraction of the surface covered. K^0 will only be a true measure of the adsorption potential where the change of adsorption enthalpy with surface coverage is linear over the entire range of θ values as $\theta \rightarrow 0$; this may not be universally applied at all temperatures.

Subsitution of equation (XII) into the general rate expression, equation (I), yields:

$$\text{Rate} = \frac{4.6T}{zV} \cdot K_0 \cdot \{\log_{10}[P_{O_2}] + \log_{10}(K_1^0/RT)\} \quad \text{(XIII)}$$

where $K_0 = k_0 \cdot (kT/h) \exp[-\Delta F^*/RT]$, the absolute reaction rate constant.

Plots of observed rate vs. the logarithm of oxygen pressure for 750°, 800°, and 850°C data of Table I are shown in Fig. 4. Correlation of the data seems to indicate that the adsorption of oxygen on tungsten in the observed range of this investigation is in accordance with equation (XIII). Assuming the limiting observed rate as an approximate value for K_0, the quantity zV may be estimated for the slopes of plots of Fig. 4. Results are tabulated in Table II.

The adsorption equilibrium constant descends with increasing temperature as is to be expected in accordance with energy considerations (see third condition stated above). However, it can be readily judged that a plot of $\log_{10}K_1^0$ vs. 1/°K would not be linear attesting to the fact that the approximation of completely random interaction is not valid over the entire range of surface coverage.

Fig. 5 is the uncorrected Arrhenius plot ($\log_{10}$ rate vs. 1/°K). Fig. 6 is the corrected Arrhenius plot for the oxidation of tungsten. Within the pressure sensitive range the observed rate has been divided by $\theta \cdot kT/h$, where θ is the fraction of the surface covered with oxygen. The activation energy (calculated from the slope of Fig. 6) is 48 kcal.

X-ray Diffraction Studies

Gulbransen and Hickman (25) state that WO_3 is the stable oxide below approximately 600°C, while WO_2 first forms at 700°C. Magneli (26) showed molybdenum and tungsten oxides existed as homologous series of the form Me_nO_{3n-1} and Me_nO_{3n-2}. No data exist on the oxides present on tungsten in the pressure range studied in this report. X-ray diagrams were made of the *in situ* oxide coatings and the interplanar spacings are shown on Table III. Difficulty arose in measuring the exact positions of the lines because of the diffuse broad peaks caused by the small particle size. Also, a certain amount of lattice strain may be present due to the rapid growth of the oxide. This strain effect is shown by a comparison of columns 7 and 8. Column 8 shows the interplanar spacings of the oxide coating formed at 900°C and 100 psia after the oxide had been scraped from the sheet and ground. The agreement between the values of column 8 and those

of the mineral tungstite (column 9) and the data on WO_3 of Magneli is quite satisfactory There appears to be no general shift in the "*d*" values, indicating no change in lattice parameter with temperature or no formation of a solid solution series. The presence of "*d*" values at about 3.4Å and 2.4Å suggests the presence of WO_2 in small amounts, but the similarity of the patterns of the various oxides and the large number of lines present make it almost impossible to state exactly which oxides are present unless a detailed analysis is made. The presence of lines at about 4.3Å and 3.93Å is difficult to explain unless the oxides present are W_4O_{11} and $W_{20}O_{58}$. There is some question as to the existence of W_4O_{11}.

Conclusions

The summary of the oxidation behavior of tungsten in oxygen from 600° to 850°C at pressures ranging from 20 to 500 psia (total oxygen pressure) is as follows:

1. Tungsten oxidizes linearly at all temperatures and pressures investigated.
2. The oxidation rate increases with increasing oxygen pressure at temperatures above 750°C.
3. Theoretical considerations indicate that an equilibrium adsorption process occurs prior to the rate-determining step. Interaction between adsorbed molecules is sufficient to require modification of the Langmuir idealized adsorption mechanism.
4. The ultimate end product is almost wholly WO_3, although some indication of the presence of WO_2 was detected.
5. The enthalpy of activation for the oxidation of tungsten (600°–850°C) is 48,000 cal.
6. Oxidation of tungsten is accompanied by subsequent volatilization of the oxide above 800°C.

Acknowledgments

The authors wish especially to thank Mrs. Gretta Scott Baur who performed the x-ray diffraction analysis summarized in Table III. The authors acknowledge the interest shown in this project by Dr. John R. Lewis, Head, Department of Metallurgy, and express their appreciation to the Office of Ordnance Research, U. S. Army and the Watertown Arsenal Laboratory for the funds that made the work possible.

Manuscript received August 22, 1955.

Any discussion of this paper will appear in a Discussion Section to be published in the December 1956 Journal.

References

1. The reader is referred to the following three references as representative: E. K. Rideal, and B. M. W. Trapnell, *Proc. Roy. Soc.*, **A205,** 409 (1951); J. K. Roberts, *Proc. Cambridge Phil. Soc.*, **36,** 53–68 (1940); R. C. L. Bosworth, *Proc. Roy. Soc., N. S. Wales,* **83,** 31–38 (1949).
2. I. Langmuir, *J. Am. Chem. Soc.*, **38,** 2269 (1916).
3. I. Langmuir, *Ind. Eng. Chem.*, **22,** 393 (1930).
4. I. Langmuir, *Chem. Rev.*, **13,** 150 (1933).
5. E. A. Gulbransen, and W. S. Wysong, *Metals Technol.*, **14,** 1 (1947).
6. J. S. Dunn, *J. Chem. Soc.*, **132,** 1149, (1929).
7. G. McAdams and G. Geil, J. Research Nat. Bur. Standards, **28,** 593–635, (1942).
8. E. Nachtigall, *Z. Metallkunde,* **43,** 23 (1952).
9. E. Scheil, *ibid.*, **29,** 209 (1937).
10. R. Kieffer and F. Kolbl, *Z. anorg. Chem.*, **262,** 229 (1950).
11. C. J. Smithells, "Tungsten," p. 122, 3rd ed., Chapman and Hall Ltd., London (1952).
12. R. C. Peterson, W. M. Fassell, Jr., and M. E. Wadsworth, *J. Metals,* **6,** 1038 (1954).
13. J. P. Baur, D. W. Bridges, and W. M. Fassell, Jr., *This Journal,* **102,** 490 (1955).
14. S. Glasstone, K. Laidler, and H. J. Eyring, "Theory of Rate Processes," McGraw-Hill Book Co., New York (1941).
15. I. Langmuir, *J. Am. Chem. Soc.*, **40,** 1361 (1918).
16. I. Langmuir, *Trans. Faraday Soc.*, **17,** 607 (1922).
17. R. Fowler and E. A. Guggenheim, "Statistical Thermodynamics," p. 429, Cambridge University Press, Cambridge (1949).
18. J. K. Roberts, *Proc. Roy. Soc., London,* **A152,** 445 (1935).
19. B. M. W. Trapnell, *ibid.*, **A206,** 39 (1951).
20. E. K. Rideal and B. M. W. Trapnell, *Chim Phys.*, **47,** 126 (1950).
21. S. Branauer, K. S. Love, and R. G. Keenan, *J. Am. Chem. Soc.*, **64,** 751 (1942).
22. A. Frumkin and A. Slygin, *Acta physiocochim., U.R.S.S.*, **3,** 791 (1935).
23. M. Temkin and V. Pyshev, *ibid.*, **12,** 327 (1940).
24. K. Love and P. Emmett, *J. Am. Chem. Soc.*, **63,** 3297 (1941).
25. J. W. Hickman and E. A. Gulbransen, *Metals Technol.*, **14,** T. P. 2144 (1947).
26. A. Magneli, *Acta cryst.*, **6,** 495 (1953).

Oxidation of Oxygen-Free High Conductivity Copper to Cu_2O

J. P. Baur, D. W. Bridges and W. M. Fassell, Jr.[1]

Department of Metallurgical Engineering, University of Utah, Salt Lake City, Utah

ABSTRACT

The effect of oxygen upon the oxidation behavior of OFHC copper was studied under conditions that assured that the involved system is $Cu/Cu_2O/O_2$. Oxidation rate was correlated through use of two parallel reaction rates: (*a*) a diffusion step (resulting in a pressure sensitive parabolic constant, k_p), and (*b*) a phase boundary reaction (pressure insensitive). Application of the equation: k_p = const. $(P_{O_2})^{1/n}$ led to values for n: 950°C, n = 2.0; and 1000°C, n = 3.4. Theoretical considerations are outlined to emphasize that surface site saturation will lead to a cessation of the increase in k_p with increased oxygen pressure when the oxygen concentration and adsorption potential are sufficient to accommodate oxygen on all available sites. Photomicrographs of the growth of CuO on Cu_2O are included.

Introduction

Oxidation of copper has been studied extensively (1). Study and interpretation of results are complicated by the fact that the system, $Cu/Cu_2O/CuO/O_2$, is stable at oxygen pressures in excess of 160 mm-Hg (the oxygen partial pressure of atmospheric air) over the entire temperature range below 1050°C. However, at reduced oxygen pressures, CuO becomes unstable and oxidation is possible involving the system $Cu/Cu_2O/O_2$. The dissociation pressure of CuO as a function of temperature has been reported (2, 3).

The classical theory of parabolic oxidation due to Wagner (4–6, 1) dealt with the systems $Cu/Cu_2O/O_2$ and $Ni/NiO/O_2$. He reported that the oxidation of copper to Cu_2O from 0.23 to 60 mm-Hg oxygen pressure and 1000°C was not ideally parabolic. Diffusion alone was not rate-determining, but a phase bounday reaction at the Cu/Cu_2O interface also effected the reaction rate. Jost (6) states, "If both processes, viz., reaction at an interface and diffusion, proceed with comparable speed, the 'reaction resistivities' might be expected to be additive (7)". The foregoing considerations yield an expression:

$$\Delta m/k_1 + \Delta m^2/k_p = t \qquad \text{(I)}$$

where Δm is the weight increase per unit surface area, k_1 and k_p are the linear and parabolic reaction rate constants, respectively, and t is the time. A more complete derivation of equation (I) can be found on page 44, reference (1).

Wagner plotted $t/\Delta m$ as a function of Δm from which k_1 could be determined from the reciprocal of the $t/\Delta m$ intercept ($\Delta m \rightarrow 0$) and k_p from the reciprocal of the slope. Values of k_1 found by Wagner were relatively pressure insensitive, thus leading him to the conclusion that the interface in question was the Cu/Cu_2O interface. K_p was found to be proportional to the seventh root of the oxygen pressure. These findings were in good agreement with theoretical considerations yielding a $\frac{1}{8}$ power dependency and the electrical conductivity measurements of Wagner and Dunwald (8) on the system Cu_2O-O_2 which yielded a seventh root dependency of oxygen pressure.

Wagner and Hammen (9) reported an oxygen pressure dependency of 1/5 root found by determining the concentration of cupric ions (lattice vacancies). This was justified by assuming the defect activity was not ideal. The assignment of an activity coefficient of $\frac{1}{2}$ yielded a theoretical oxygen dependency of the 1/5.2 root.

The present paper deals with the oxidation behavior of high purity Oxygen Free High Conductivity (OFHC) copper at temperatures of 900°, 950°, and 1000°C at oxygen pressures which permit the formation of Cu_2O alone. The purpose is to criticize the universal use of a limited approximation, equation (III*a*), for the explanation of the effect of oxygen pressure on the magnitude of the parabolic oxidation rate constant.

Experimental Procedure

The vacuum furnace employed is shown schematically in Fig. 1. It was patterned after the standard high temperature-high pressure furnaces designed in this laboratory (10). It consists of a central glass-zirconia vacuum chamber surrounded by a steel outer chamber, both of which can be evacuated or pressurized independently. This construction was necessary in order to maintain the same oxygen pressure on both sides of the central tube, thereby equalizing the heat conduction. Kanthal A-1 furnace windings are wound, not on the zirconia tube, but on a concentric alundum tube. This was to prevent the recurrence of an earlier implosion due to the slagging of the zirconia tube by the winding at 1000°C. A platinum, platinum-rhodium thermocouple is mounted within the zirconia tube less than an inch from the sample.

A helical quartz spring, on which the sample to be oxidized is suspended by means of a platinum chain, is mounted concentrically within a 4-ft vertical glass extension above the zirconia tube. The spring system can be raised and lowered by means of a small glass winch made from a standard glass tapered joint and located at the top of the vertical glass extension.

The copper samples, 1 in. x $\frac{3}{8}$ in. x 0.019 in., are etched

[1] Present address: Howe Sound Co., Salt Lake City, Utah.

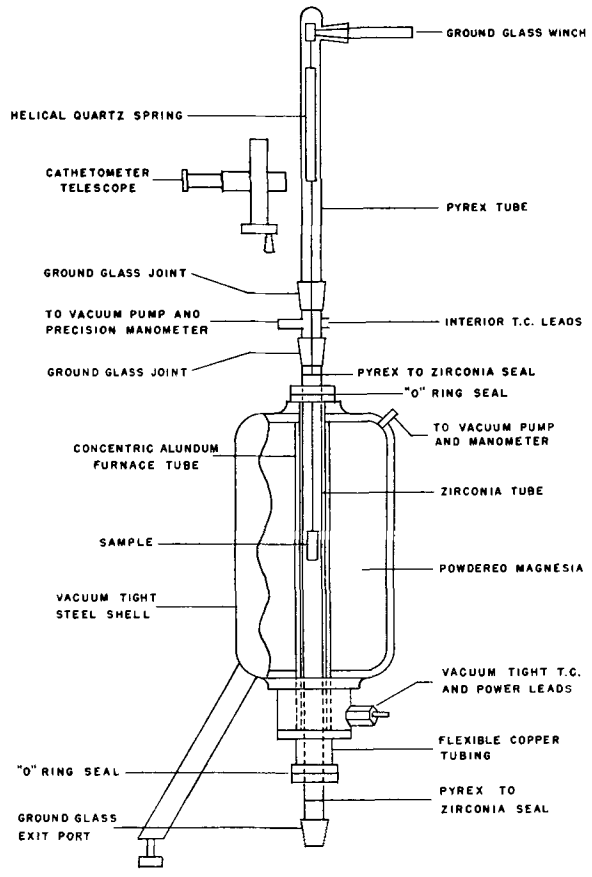

FIG. 1. Schematic drawing of vacuum furnace

for 15 min in 3–5% ammonium persulfate solution, washed in distilled water, rinsed in acetone, and dried. The sample is raised into the hot zone of the vacuum chamber following the obtainment of thermal equilibrium. The gain in weight is measured by following the deflection of the quartz spring by means of a cathetometer telescope.

The oxygen pressure is read on a precision dial manometer. Constant oxygen pressure is maintained through the use of a microleak valve connecting the system to the oxygen supply.

The results of spectrographic analysis of the copper revealed the following elements present: boron, 0.002%; silicon, 0.0015%. No other elements were detected.

EXPERIMENTAL RESULTS

At all temperatures and oxygen pressures investigated, the samples were found to oxidize in a "nonideal" parabolic manner. The oxidation behavior could not be expressed by the relationship (11):

$$(\Delta m)^2 = k \cdot t + C \qquad \text{(II)}$$

where k and C are constants, Δm is the weight gained per unit area, and t is the time. Fig. 2 shows a typical family of oxidation rate plots of (weight gained)^2 vs. time.

If one follows Wagner (4) and assumes that an interface reaction (Cu/Cu_2O interface) influences the reaction rate, the data could best be represented by equation (I). The parabolic rate constant k_p can then be found from the reciprocal of the slope and the linear constant k_l from the

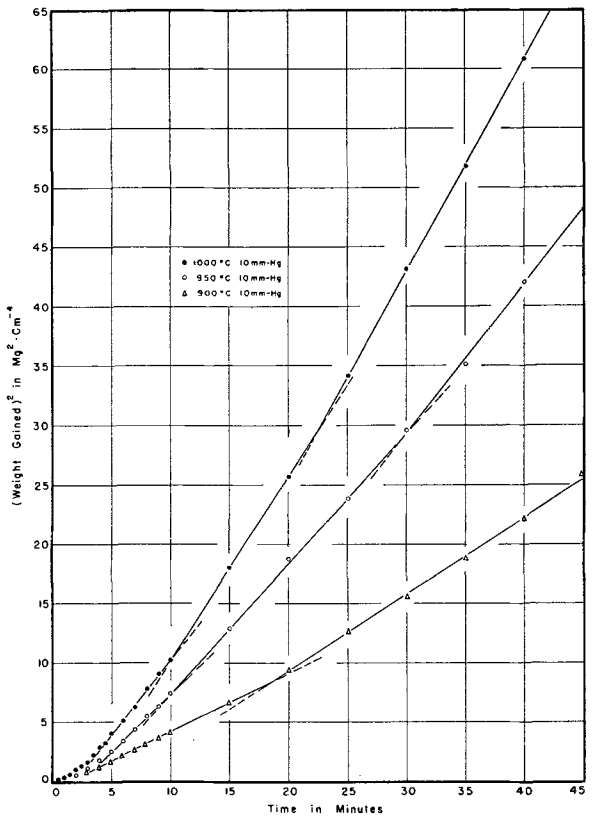

FIG. 2. Oxidation rate curves for OFHC copper in oxygen

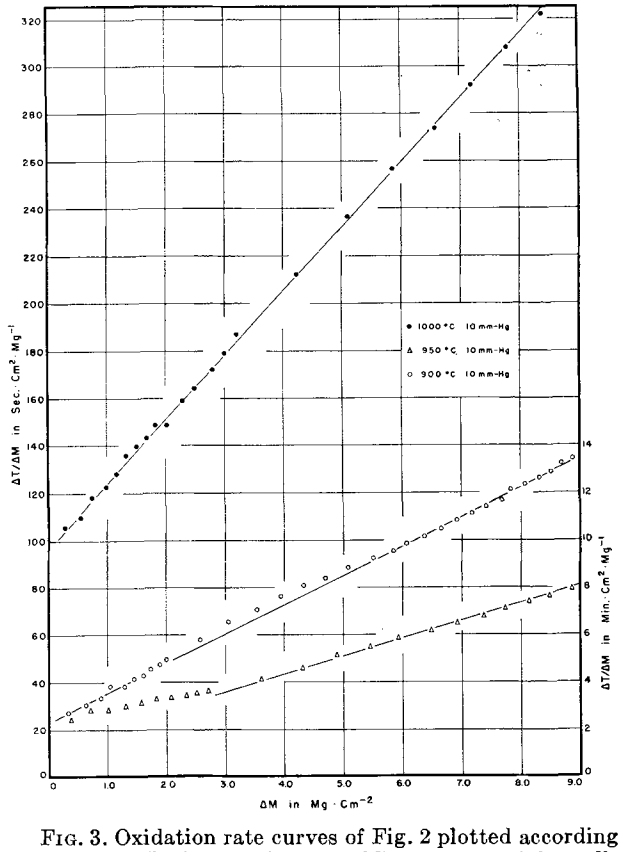

FIG. 3. Oxidation rate curves of Fig. 2 plotted according to equation (I). (For 900° and 950°C curves use right ordinate.)

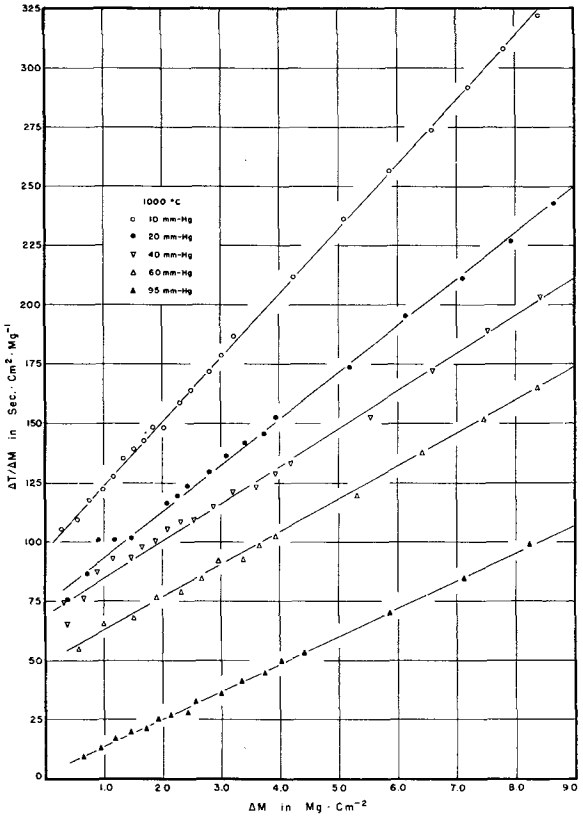

FIG. 4. Oxidation rate curves for OFHC copper, 1000°C at various pressures. (*Note*: add 10, 50, and 84 sec·cm²·mg⁻¹ to the ordinates of the 40, 60, and 95 mm Hg curves, respectively.)

TABLE I. *Summary of oxidation rate constants for high purity oxygen free high conductivity copper at 900°, 950°, 1000° C*

Temp	Oxygen pressure	Parabolic constant	Linear rate constant
°C	*mm Hg*	$mg^2cm^{-4}hr^{-1}$	$mg\ cm^{-2}hr^{-1}$
900	5	43.2	78.2
	10	48.2	26.0
950	10	81.5	40.4
	20	122.6	29.4
	30	136.0	33.2
	35	149.7	29.0
1000	5	126.7	49.3
	10	133.2	37.0
		152.3	42.7
	20	173.5	40.3
		190.8	41.6
	30	220.0	49.5
		225.4	40.4
	40	232.9	44.5
		239.0	34.1
	50	250.2	49.7
		249.1	39.5
	60	254.4	37.4
		236.5	48.6
	70	247.3	60.0
		256.7	52.3
	80	252.4	51.5
		268.2	51.9
	95	287.8	42.6

TABLE II. *Comparison of the parabolic rate constants obtained in this survey and those available in the literature for 1000° C for oxygen pressures of 10 mm-Hg to 95 mm-Hg**

Oxygen pressure	Parabolic constant in g·eq·cm·⁻¹ $sec^{-1} \times 10^9$ (12)		
	This project	Wagner (4)	Feitknecht (13)
mm-Hg			
10	3.37	4.5 (11 mm)	
	3.85		
20	4.39		
	4.82		
30	5.56		
	5.70		
40	5.89		
	6.04		
50	6.30		
	6.32		
60	5.98	6.2 (63 mm)	
	6.43		
70	6.25		
	6.49		
80	6.38		
	6.78		
95	7.27		7.29 (100 mm)

* Three experimental determinations of Moore and Lee (14) are within the temperature-pressure range of this investigation. The number following the investigators' initials are in the same units as Table II above. 1000°C, 5 mm-Hg: ML, 8.6×10^{-9}; BBF, 3.2×10^{-9}; 950°C, 5 mm-Hg: ML, 5.6×10^{-9}; BBF, (10 mm-Hg) 2.1×10^{-9}; 900°C, 5 mm-Hg: ML, 1.9×10^{-9}; BBF, 1.1×10^{-9}.

reciprocal of the intercept. Fig. 3 shows the family of curves of Fig. 2 plotted in accordance with equation (I). A series of 1000°C curves is plotted according to equation (I) on Fig. 4. The values of k_p and k_1 determined as above are listed in Table I.

The relative constancy of k_1 indicates that the phase boundary reaction is pressure independent. The pressure dependence of k_p can be estimated from a plot of log k_p vs. log P_{O_2} according to the equation:

$$k_p = K[P_{O_2}]^{1/n} \qquad \text{(IIIa)}$$

or,

$$\log k_p = 1/n \cdot \log P_{O_2} + \log K \qquad \text{(IIIb)}$$

Values of n for 950° and 1000°C are 2.0 and 3.4, respectively. A comparison of the values of k_p with those of other workers is shown by Table II.

Discussion of Experimental Results

Effect of Surface Concentration of Oxygen

Theoretical considerations of the effect of oxygen concentration on the oxidation rate of copper to Cu_2O are discussed in detail elsewhere (1, 4, 6, 15, 16). It is universally agreed that the migration of copper through the Cu_2O lattice occurs by diffusion of copper ions through cation vacancies (17). Wagner (4, 5, 8) expresses the production of vacancies by the equilibrium consideration:

$$4\,Cu^+ + 4e + O_2(gas) = 4h(Cu^+) + 4h(e) + 2\,Cu_2O \qquad \text{(IV)}$$

where Cu^+ is a cuprous ion, e is an electron, and $h(\ )$ terms represent vacancies (holes). The equilibrium con-

stant, K', for the above equation can then be written:

$$K' = \frac{[h(Cu^+)]^4 \cdot [h(e)]^4 \cdot [a_{Cu_2O}]^2}{[a_{Cu^+}]^4 \cdot [e]^4 \cdot [P_{O_2}]} \quad (V)$$

Assuming the activities of cuprous ions, electrons, and cuprous oxide to be essentially constant (this is equivalent to assuming a small density of vacancies), the concentration of vacancies, $[h(Cu^+)]$, is expressed as:

$$[h(Cu^+)] = \{K'' \cdot P_{O_2}\}^{1/8} \quad (VI)$$

since electroneutrality considerations lead to, $[h(Cu^+)] = [h(e)]$. Acceptance of equation (VI) as an expression of vacancies led Wagner to his parabolic oxidation equation, pressure dependency of which for constant temperature is of the form of equation (III*a*).

This equation is applicable only for the region of small surface coverage where the approximation of linear change of surface coverage with oxygen pressure can be made. Returning to equation (IV), one notes that for general discussion the term, O_2(gas), should not be used. The correct expression should read O_2(surface). This is correctly formulated elsewhere by Wagner (18) and also by Mott and Gurney (15).

Expression for the surface activity, or surface concentration, of oxygen must include consideration of the fact that there can be only a definite finite number of available sites for the accommodation of oxygen per unit surface area of the oxide-oxygen interface. Statistically Fermi-Dirac statistics would apply (19). Less formal formulation can be accomplished in the manner attributed to Langmuir (20, 21). One writes the expression:

$$S + O_2 = S \cdots O_2 \quad (VII)$$

where S represents an available site; O_2, an oxygen molecule; $S \cdots O_2$, an adsorbed molecule. An equilibrium expression for this equation can be written in terms of θ, the fraction of the total sites covered with adsorbed oxygen ($S \cdots O_2$ units). The equilibrium constant for this adsorption process is:

$$K_a = \frac{\theta}{[1-\theta] \cdot [O_2]_{gas}} \quad (VIII)$$

Expression for the concentration of the external oxygen phase, $[O_2]_{gas}$, can be formulated by assumption of the perfect gas law, $[O_2]_{gas} = n/V = P/RT$. It is noted that at constant temperature the only variable is the oxygen partial pressure. If the adsorption of oxygen is assumed much faster than the rate-determining steps [both this survey and Wagners' (4) indicate that the slow phase boundary reaction is at the Cu/Cu_2O interface], the fraction of the surface sites covered, θ, can then be used as an expression for the surface oxygen concentration, $[O_2]_{surface}$:

$$[O_2]_{surface} = \theta = \frac{K_a \cdot [O_2]_{gas}}{1 + K_a \cdot [O_2]_{gas}} \quad (IX)$$

It is seen that the approximate solution, equation (VI), can apply only where $K_a[O_2]_{gas} \ll 1$. Thus, eventually an oxygen pressure will be reached for any constant temperature above which the surface oxygen concentration will not be proportional to the external oxygen pressure. Moreover, a pressure will be reached above which the surface concentration of oxygen will not change at all, i.e., $\theta \approx 1$. Thus, regardless of whether the internal structure of the oxide were that of an "ideal dilute solution" (5) or not, the concentration of lattice vacancies will not continue indefinitely to increase with increase of oxygen pressure.

Using equation (VI) (with P replaced by θ) and equation (IX), the expression for the concentration of vacancies assuming molecular adsorption with no interaction between adsorbed molecules is:

$$[h(Cu^+)] = \{K'' \cdot \theta\}^{1/8} = \left\{K'' \cdot \frac{K_a \cdot [O_2]_{gas}}{1 + K_a \cdot [O_2]_{gas}}\right\}^{1/8} \quad (X)$$

If the assumption of constant adsorption equilibrium constant, K_a (i.e., K_a assumed invariant with change of surface coverage) is not valid, an alternate expression for the concentration of vacancies can be formulated:

$$[h(Cu^+)] = \{K''\theta\}^{1/8} \approx \left[K'' \cdot (4.6T/zV) \cdot \log_{10}\left(\frac{1 + K_a^0[O_2]}{1 + K_a^0[O_2] \cdot \exp(-\theta zV/RT)}\right)\right]^{1/8} \quad (XI)$$

Complete derivation of the equation is included in the Appendix to this paper and elsewhere (22–24). Although the above equality is exact it must be understood that the logarithmic approximation that follows is not proposed for universal application. The extent of its suitability is brought out in the Appendix. Considerations of the type presented by Wagner and Hammen (9) would cause K'' to be no longer a function of temperature alone [see equation (XIV)].

A General Reaction Rate Expression

A general rate equation for pressure sensitive oxidation processes which are diffusion controlled was recently proposed (15):

$$m \cdot \frac{dm}{dt} = k_p = C_0 \cdot f(\theta) \cdot kT/h \cdot \exp\left[\frac{-\Delta F^*}{RT}\right] \quad (XII)$$

Equation (XII) is applicable only if the gain of weight is directly proportional to the gain in the rate-controlling oxide thickness. Thus, for the case of two or more thermodynamically stable oxides variation in percentage composition of the oxides with temperature would result in the necessity for the inclusion of a temperature sensitive function for the conversion of weight increase to increase in thickness. Even for constant temperature the ratio of the two oxides must not change with time and oxygen concentration (pressure). For the oxidation of copper to cuprous oxide, $C_0 = 2\lambda^2 \cdot (-\Omega) \cdot k_0$, where λ is the vacancy jump distance of diffusing cuprous ions, Ω is the ratio of the metal oxide volume to an equivalent volume of metal, k_0 is a proportionality constant with dimensions of ML^{-2} and includes the correction factor for the true surface area (surface roughness and number of active sites per unit surface area) involved in the oxidation reaction. $kT/h \cdot \exp[-\Delta F^*/RT]$ results from the temperature dependence of the diffusion constant according to the Eyring theory

(25). ΔF^* is the activation free energy for vacancy migration and kT/h is the traditional Eyring frequency factor. The resulting function of surface coverage, $f(\theta)$, for the process is:

$$f(\theta) = [h(Cu^+)] = (K'' \cdot \theta)^{1/8} \quad \text{(XIII)}$$

where K'', the equilibrium constant for the production of vacancies, is:

$$K'' = \exp(-\Delta F_1/RT) \quad \text{(XIV)}$$

where ΔF_1 is the free energy involved in vacancy formation. The formulation of this factor has been discussed already (26–28).

Thus, for the oxidation of copper to cuprous oxide, the parabolic rate constant as a function of surface oxygen concentration and temperature is:

$$k_p = \theta^{1/8} \cdot C_0 \cdot kT/h \cdot \exp[-(\Delta F^* + \Delta F_1/8)/RT] \quad \text{(XV)}$$

For constant temperature and adsorption phenomena departing from ideal Langmuir behavior, the parabolic constant would be expressed by

$$k_p = \theta^{1/8} \cdot K_0 \approx K_0' \cdot \sqrt[8]{\log_{10}(1 + K_a^0[O_2])} \quad \text{(XVI)}$$

where $K_0 = C_0 \cdot kT/h \cdot \exp[-(\Delta F^* + \Delta F_1/8)/RT]$

$$K_0' = (4.6T/zV)^{1/8} \cdot K_0$$

and assuming in equation (XI) that,

$$K_a^0[O_2] \cdot \exp[-\theta \cdot zV/RT] \ll 1$$

The data of Table I plotted in accordance with equation (XVI) is shown in Fig. 5. Correlation is good enough to warrant the assumptions made, i.e., the adsorption potential varies linearly with surface coverage, or expressed more precisely, postulation of a random distribution of surface sites occupied by oxygen molecules with interaction between the pairs of nearest neighbors. K_a^0, the adsorption equilibrium constant for 950° and 1000°C, respectively, are 83,900 and 79,390. These values yield a mean adsorption free energy, ΔF^0, of approximately −12,000 calories per mole oxygen.

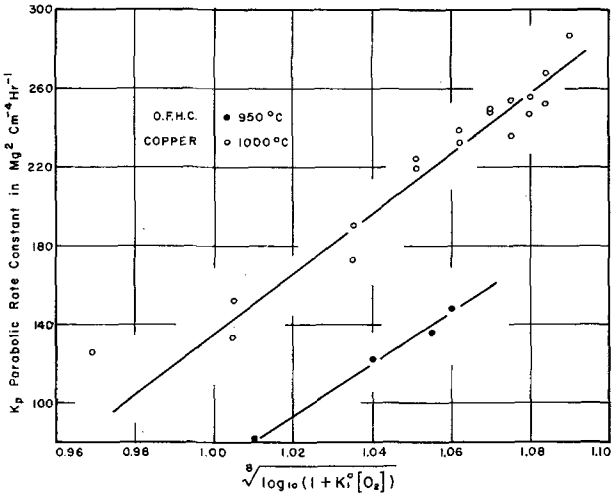

FIG. 5. Data of Table I plotted according to equation (XVI).

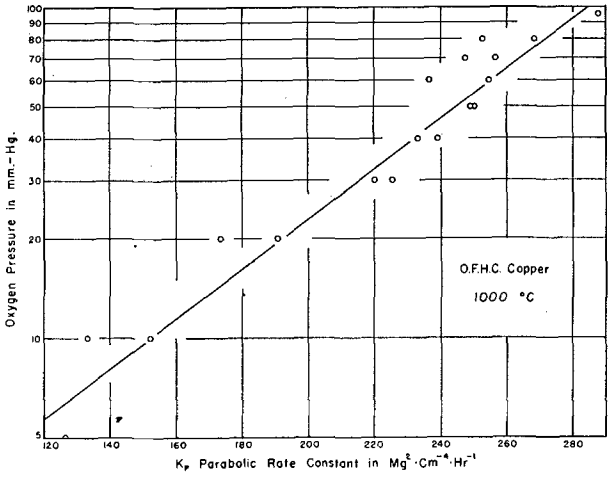

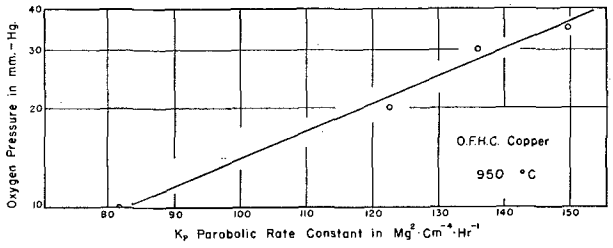

FIG. 6. Data of Table I plotted according to equation (XVII).

According to the boundary exhaustion layer theory of Hauffe and Engell (29, 30), the data of Table I could also be represented by an equation of the form

$$k_p \approx \text{const } \{\log_{10}(P_{O_2}) + \text{const}'\} \quad \text{(XVII)}$$

This correlation is shown in Fig. 6. Equation (XVII) assumes small surface coverage and a migration velocity controlled by an electrical field. This electric field strength is a function of the concentration of adsorbed oxygen ions.

PHOTOMICROGRAPHIC STUDY

In spite of the fact that the copper samples were oxidized under conditions of temperature and oxygen pressure such that Cu_2O was the only stable oxide present, x-ray diffraction patterns of the oxide coatings formed showed that a small amount of CuO was present in all samples formed during the period the sample was lowered from the hot zone (30 sec). It was felt that a photomicrographic study of the formation and growth of CuO on the surface of the Cu_2O layer would be of interest. Fig. 7 shows these photomicrographs under the experimental conditions of temperature and oxygen pressures wherein only Cu_2O can be formed in the hot zone. In all cases these surfaces are as formed and have not been etched or polished in any manner. The micrograph at 900°C and 5 mm-Hg oxygen pressure is typical of the oxide surface formed under conditions wherein only Cu_2O can exist. Several interesting features are apparent:

1. Sharp, well-defined crystals of a variety of sizes.
2. Deep angular recesses between the crystals possibly extending to the base metal.

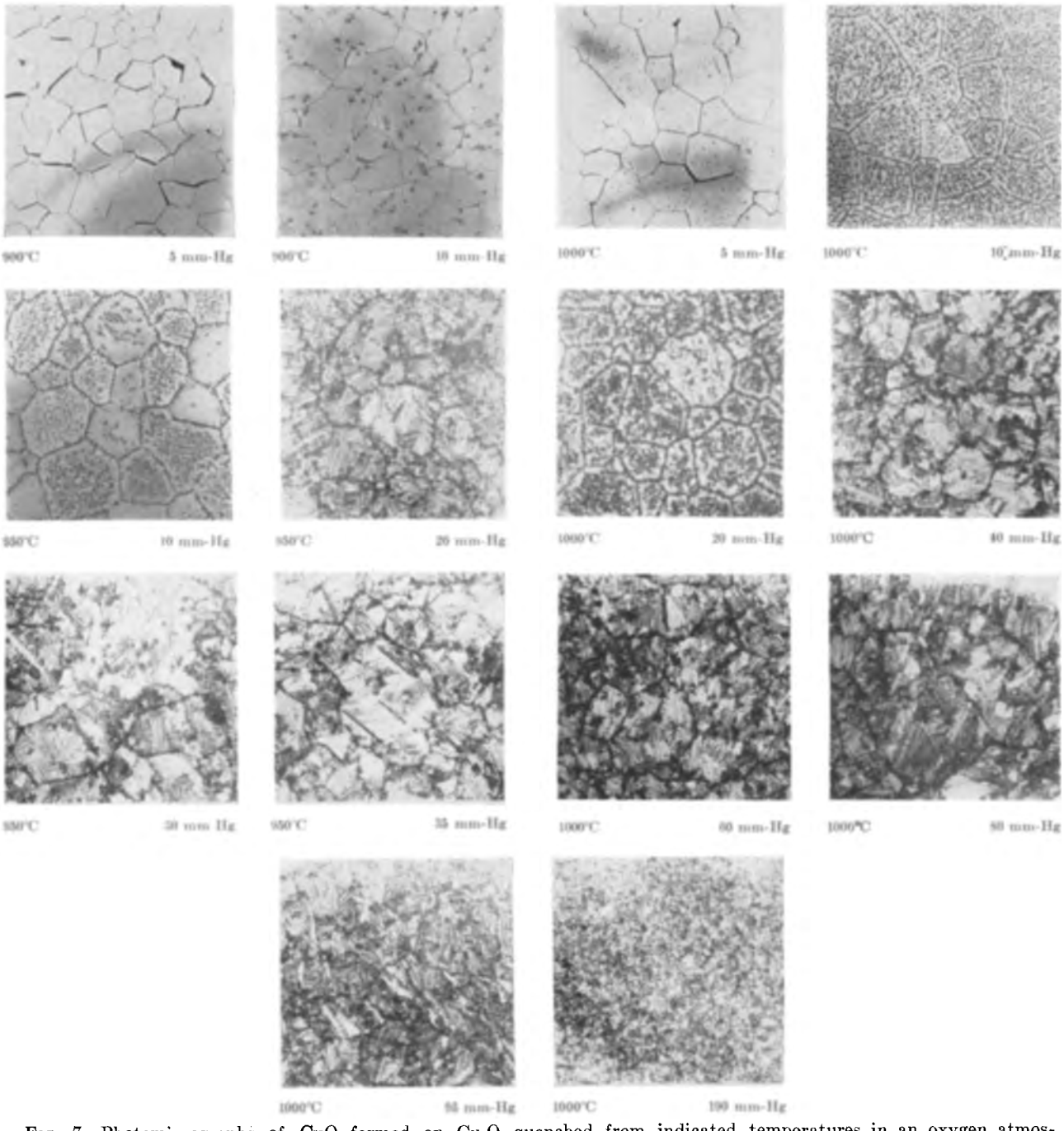

FIG. 7. Photomicrographs of CuO formed on Cu_2O quenched from indicated temperatures in an oxygen atmosphere of indicated partial pressure. 169× before reduction for publication.

3. Predominant appearance of one type of crystal face.

4. All flat faces are the same height above the base metal lying within the focal plane of the microscope objective.

This specimen had a hard mirror-like surface ruby red in color. The x-ray diffraction pattern of this surface showed no CuO to be present, and that the surface was oriented.

As the temperature and pressure increase, the amount of CuO increases from a few scattered dendrite-like formations at 950°C and 10 mm-Hg oxygen pressure through the fern leaf-like structures at the intermediate pressures to the fine grained structures shown in the photomicrograph at 1000°C and 190 mm-Hg which is characteristic of those surfaces formed above the dissociation pressure of CuO and at higher pressures, i.e., greater than 1 atm.

Fig. 8 shows successively higher magnifications of the CuO formed at 1000°C and 80 mm-Hg. The beautiful leaf-like patterns are clearly in evidence.

The oxide surface formed at 900°C and 5 mm-Hg was observed under crossed nicol prisms. Photomicrograph A of Fig. 9 in which the microscope is focused on the surface shows the bright and dark patches of ruby red under the surface grains whose boundaries are visible. Photograph B of Fig. 9 represents the same area except the focal plane is now on the oxide-metal interface. Closer inspection

FIG. 8. Higher magnifications of 1000°C, 80 mm-Hg oxidized surface. *Left*, 500×, *right*, 800× before reduction for publication.

shows the grain boundaries of the annealed copper visible in the bright patches. Photograph C of Fig. 9 is a superposition of the negatives of micrographs A and B.

In order to demonstrate that the CuO was formed as a result of the lowering of the sample from the hot zone, a simple experiment was performed. The sample was oxidized in the usual fashion at 1000°C and 80 mm-Hg. Before the sample was lowered from the hot zone, the system was evacuated, thereby preventing the rapid formation of CuO. Fig. 10*a* which shows a comparison of the surfaces formed under both methods definitely establishes the fact that only one oxide Cu_2O exists in the hot zone. X-ray analysis of this surface again showed only Cu_2O

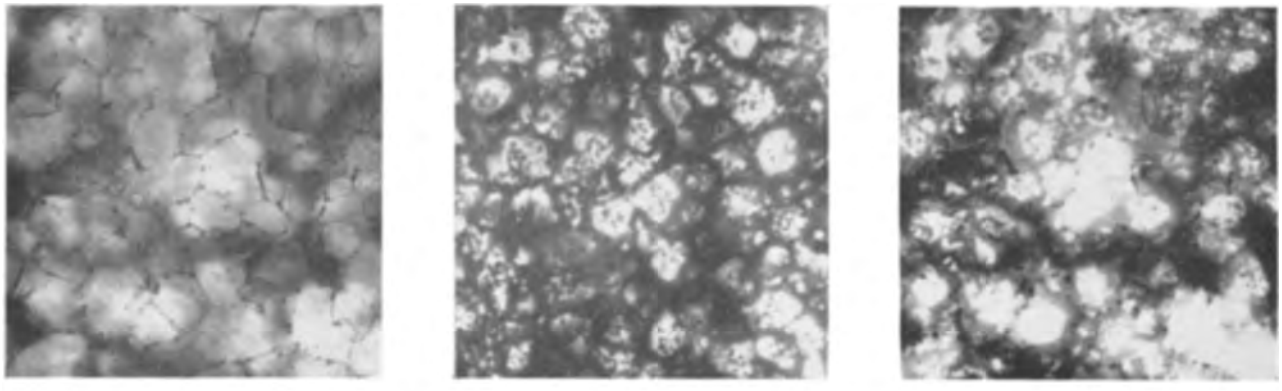

FIG. 9. Observation of cuprous oxide, Cu_2O, formed at 900°C, 5 mm-Hg under crossed nicol prisms. A—Focal plane on oxide surface; B—focal plane on oxide-metal interface; C—photographs A and B superimposed. 169× before reduction for publication.

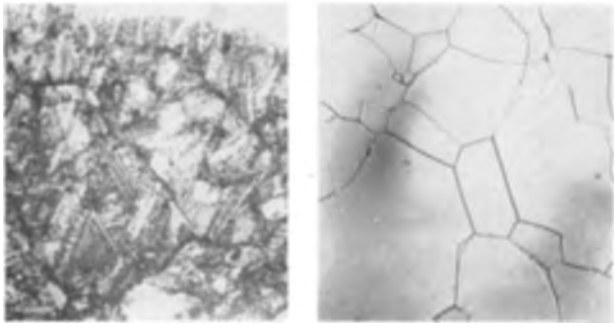

FIG. 10*a*. Sample oxidized at 1000°C, 80 mm-Hg for 45 min. *Left*, quenched in 80 mm-Hg; *right*, quenched in vacuum. 169× before reduction for publication.

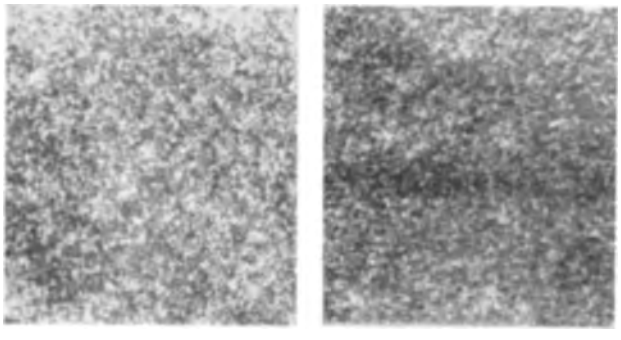

FIG. 10*b*. Sample oxidized at 1000°C, 190 mm-Hg for 45 min. *Left*, quenched in 190 mm-Hg; *right*, quenched in vacuum. 169× before reduction for publication.

to be present in a similarly oriented manner as the 900°C −5 mm-Hg surface. To establish the existence of both oxides, CuO and Cu_2O, above 98 mm-Hg at 1000°C, a sample was lowered after evacuation of the system as before. A comparison of the photomicrographs of Fig. 10*b* shows the same structure in both cases. X-ray diffraction patterns of both samples show the presence of both Cu_2O and CuO.

Fig. 11 is an example of the structure of the boundaries

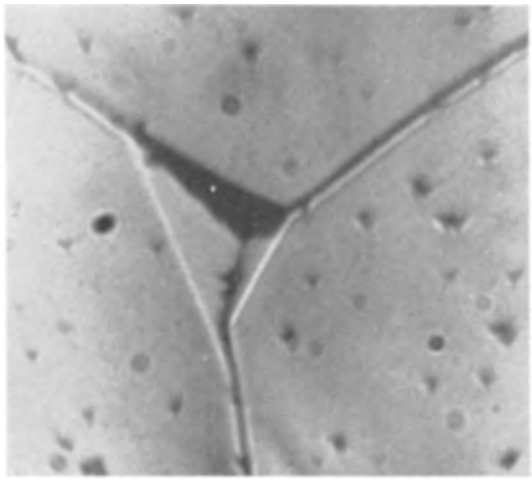

FIG. 11. An example of the structure of the boundaries between the oxide grains. Sample oxidized at 1000°C and 5 mm-Hg. 1250×.

between the oxide grains formed at 1000°C, 5 mm-Hg oxygen pressure.

The inclusion of this photomicrographic study showing the growth of CuO on the Cu_2O substrate as a layer is not intended to indicate that such growth is the case under conditions of temperature and pressure wherein both oxides are stable. The phenomena illustrated in Fig. 7 to 11 occurred under nonisothermal conditions.

Concluding Remarks

The explanation of Wagner (5, 9) of the deviation from ideality cannot be disregarded. The departure from the predicted eighth root dependency has sometimes been attributed to association of the defects (17, 31). Complete association results in the limit of one-fourth power dependency. Correlation of data obtained in the present investigation by use of equation (III*a*) led to values for the parameter n of less than four for both the 950° and 1000°C isotherms. Clearly it is not a case of deviation from ideal solution behavior alone. The effect of surface saturation of oxygen must be included in any general discussion of pressure sensitive oxidation. This will become even more apparent when the results of the high pressure oxidation study of nickel performed by two of the authors is reported (32).

The adsorption equilibrium step is not essential to the argument. A form identical to equation (IX) results from the so-called "steady-state" method employed by other workers (33, 34).

A reviewer brought out a well-founded objection to the authors' conclusions of the origin of the departure from true parabolic behavior. He suggested that the nonideality could arise from the fact that the surface is obviously not plane. Photomicrographs displaying the same phenomenon as Fig. 11 have been recorded on nickel oxide surfaces (32) and on cobalt oxide surfaces (35). Nickel oxidation data requires the use of equation (I). Cobalt seems to obey equation (II) quite rigorously.

Acknowledgments

The authors especially thank H. M. Schleicher, Metallurgical Department, American Metal Co., Limited, who graciously supplied the OFHC Copper used in this study.

They thank Dr. J. R. Lewis, Head, Department of Metallurgy, University of Utah, for his support of this project. Thanks are due to the Watertown Arsenal Laboratory, Department of Ordnance Research, who supplied the funds which made this work possible.

Manuscript received August 29, 1955. This paper was presented at the Pittsburgh Meeting, October 9 to 13, 1955.

Any discussion of this paper will appear in a Discussion Section to be published in the December 1956 Journal.

REFERENCES

1. O. Kubaschewski and B. E. Hopkins, "Oxidation of Metals and Alloys," Academic Press Inc., New York (1953).
2. F. Hastings Smith and H. R. Robert, *J. Am. Chem. Soc.*, **42**, 2582 (1920).
3. F. Becker, Physikalisch-chemische Tabellen 3. Erganzungsband, 3. Teil. Berlin, Springer (1935).
4. C. Wagner and K. Grunewald, *Z. Physik Chem.*, **B40**, 455 (1938).
5. C. Wagner, "Diffusion and High Temperature Oxidation of Metals" in the American Society of Metals publication, "Atom Movements," ASM, Cleveland (1951).
6. W. Jost, "Diffusion in Solids, Liquids, and Gases," Academic Press Inc., New York (1952).
7. K. Fishbeck, L. Neundeubel, and F. Salzer, *Z. Elektrochem.*, **40**, 517, (1934).
8. H. Dunwald and C. Wagner, *Z. physik Chem.*, **B22**, 212 (1933).
9. C. Wagner and H. Hammen, *ibid.*, **B40**, 197 (1938).
10. R. C. Peterson, W. M. Fassell, Jr., and M. E. Wadsworth, *J. Metals*, **6**, 1038 (1954).
11. O. Kubaschewski and B. E. Hopkins, *op cit*, p. 37.
12. *Ibid.*, p. 122. This reference outlines the method of conversion from direct mass increase units to gram-equivalent type units.
13. W. Feitknecht, *Z. Elektrochem.*, **35**, 142 (1929).
14. W. J. Moore and B. Selikson, *J. Chem. Phys.*, **19**, 1539 (1951). The conversion to units of Table II is: const. in gram-equivalents of copper times ($cm^{-1}sec^{-1}$) equals $(\frac{1}{2}V_{eq})^{-1}$ times Moore's constant (cm^2sec^{-1}). V_{eq} is the volume of Cu_2O containing an equivalent. The factor $\frac{1}{2}$ occurs as Cu_2O contains two equivalents of copper per gram-equivalent of Cu_2O.
15. N. F. Mott and R. W. Gurney, "Electronic Processes in Ionic Crystals," 2nd ed., Oxford Press, London, (1948).
16. J. P. Baur, D. W. Bridges, and W. M. Fassell, Jr., *This Journal*, **102**, 490 (1955).
17. J. Bardeen, W. H. Brattain, and W. Shockley, *J. Chem. Phys.*, **14**, 714 (1946).
18. H. Dunwald and C. Wagner, *op cit*, p. 224, section 8, second paragraph.
19. R. Fowler and E. Guggenheim, "Statistical Thermodynamics," chap. 10, Cambridge (1949).
20. I. Langmuir, *Ind. Eng. Chem.*, **22**, 393 (1930).
21. P. H. Emmett, Editor, "Catalysis," Vol. I, chapter by K. Laidler entitled 'Chemisorption,' chap. 3, Reinhold Publishing Corp., New York (1954).
22. D. W. Bridges and W. M. Fassell, Jr., "Niobium in Oxygen," Interim-Technical Report 9, Army Ordnance Contract DA-04-495-ORD-237.
23. J. P. Baur, D. W. Bridges, and W. M. Fassell, Jr., "Tungsten in Oxygen," Interim Technical Report 8, Army Ordnance Contract DA-04-495-ORD-237.
24. S. Brunauer, K. S. Love, and R. G. Keenan, *J. Am. Chem. Soc.*, **64**, 751 (1942).
25. S. Glasstone, K. Laidler, and H. Eyring, "The Theory of Rate Processes," McGraw-Hill Book Co., New York (1950).
26. N. F. Mott, *Trans. Faraday Soc.*, **36**, 472 (1940).
27. E. A. Gulbransen, *Trans. Electrochem. Soc.*, **83**, 391 (1943).
28. E. A. Gulbransen, Proceedings of the International Symposium on the Reactivity of Solids, Gothenburg 1952, Part II, 899, Goteborg, Elanders Boktryckeri Aktiebolag (1954).
29. B. Chalmers, Editor, "Progress in Metal Physics," Vol. 4, Chap. 2 by K. Hauffe entitled "Mechanism of Oxidation of Metals and Alloys," p. 101, Equation 71, Interscience Publishers Inc., New York (1953).
30. K. Hauffe, Proceedings of the International Symposium on the Reactivity of Solids, Gothenburg 1952, Part II, p. 842, Equation 46, (This article is in German), Goteborg, Elanders Boktryckeri Aktiebolag (1954).
31. N. F. Mott, *Nature*, **145**, 996 (1940).
32. J. P. Baur and W. M. Fassell, Jr., Work begun under an International Nickel Co. fellowship and continued under the Office of Ordnance Research Project DA-04-495-ORD-237. The system $Ni/NiO/O_2$ is stable over the entire oxygen pressure range. Over the majority of the pressure range (10 mm-Hg to 300 psia O_2) there is relatively little change in the magnitude

of the parabolic constant for 1100°, 1150°, and 1200°C, respectively.

33. W. J. Moore and J. K. Lee, *Trans. Faraday Soc.*, **47**, 501, (1951).
34. K. Hauffe and H. Pfeiffer, *Z. Elektrochem.*, **56**, 390 (1952).
35. Unpublished data.

APPENDIX

Where the effect of interaction between the adsorbed molecules on the energy of adsorption cannot be neglected, the original Langmuir derivation for θ (1), the fraction of the surface covered, equation (IX) of the text, must be amended. Langmuir recognized this and wrote an alternate expression (2) for the fraction of the surface covered applicable for a varying energy of adsorption (1, 2)

$$\theta = \sum_i K_i/(1 + K_i \cdot P) \qquad \text{(I)}$$

K_i is no longer a constant, but varies according to the extent and nature of the interaction energy. Most often the assumption is made that the enthalpy of adsorption is a linear function of surface coverage:

$$\Delta H_{ads} = \Delta H^0_{ads} + \theta z V \qquad \text{(II)}$$

where ΔH^0_{ads} is the enthalpy of adsorption for $\theta = 0$. As V is defined as the positive molar energy of interaction, the enthalpy becomes less and less negative as the surface coverage approaches its equilibrium limit. The coordination number, z, of the monolayer ($0 \leq z \leq 6$) is dependent on the nature of the monolayer and the degree of completeness of coverage. Thus, it is seen that under the above scheme the first adsorbed molecules are more strongly adsorbed than the last.

The assumption of equation (II) is not as artificial as may be thought at first glance. It results from consideration of the distribution of sites with adsorbed molecules as completely random (3, 4) and has been experimentally observed in the case of hydrogen on tungsten (5–7).

Modification of the Langmuir derivation under the conditions of equation (I) has been published by Brunauer (8). Their derivation (with slight alteration in definitive terminology) is outlined briefly. Let an equilibrium constant for changeable adsorption enthalpy be defined as:

$$K_a = \exp\left[-(\Delta F^0_{ads} + \theta \cdot zV)/RT\right] = K^0_a \exp\left[-\theta \cdot zV/RT\right] \qquad \text{(III)}$$

where $K^\theta_a = \exp\left[(-\Delta H^0 - T \cdot \Delta S^0)/RT\right]$, the value of the equilibrium constant for $\theta = 0$.

The expression for the surface coverage, θ, is now the summation of small differential units of coverage θ_s, each involving a different enthalpy and valid over a small element of area, ds. Equation (IX) of the text, with K_a defined as in equation (III) expresses θ_s. Then the fraction of the entire area covered with adsorbed molecules is:

$$\theta = \Sigma\, \theta_s \cdot ds = \int_0^\theta \theta_s \cdot ds = \int_0^\theta \frac{K^0_a \cdot [O_2] \cdot \exp\left[-s \cdot zV/RT\right]}{1 + K^0_a \cdot [O_2] \cdot \exp\left[-s \cdot zV/RT\right]} \cdot ds \qquad \text{(IV)}$$

This integral is of the form $\int dU/U$, where U is the denominator. Integrating equation (IV), one obtains:

$$\theta = \frac{RT}{zV} \cdot 2.3 \log_{10} \left\{ \frac{1 + K^0_a \cdot [O_2]}{1 + K^0_a \cdot [O_2] \cdot \exp\left[-\theta \cdot zV/RT\right]} \right\} \qquad \text{(V)}$$

where

$$K^0_a[O_2] \gg 1 \gg K^0_a[O_2] \exp\left[-z\theta V/RT\right]$$

$$\theta \approx 4.6\, T/zV \{\log_{10}[O_2] + \log_{10} K^0_a\} = 4.6\, T/zV \left\{\log_{10}[P_{O_2}] + \log_{10}\left(\frac{K^0_a}{RT}\right)\right\} \qquad \text{(VI)}$$

Equation (VI) is a result first derived semi-empirically by Frumkin and Slygin (9). These workers and also Temkin and Pyzkev (10) used it in connection with the explanation of the adsorption of NH_3 on iron catalyst. Love and Emmett (11) applied it to a similar system. It should be noted that equation (VI) is not good at either limit of the allowed values for θ, the fraction of the surface covered. A completely different derivation of equation (VI) accredited to Roginski (12) arises from considerations of surface nonuniformity.

REFERENCES TO APPENDIX

1. I. Langmuir, *J. Am. Chem. Soc.*, **40**, 1361 (1918).
2. I. Langmuir, *Trans. Faraday Soc.*, **17**, 607 (1922).
3. R. Fowler and E. A. Guggenheim, "Statistical Thermodynamics," p. 429, Cambridge (1949).
4. S. Glasstone, K. Laidler, and H. Eyring, "Theory of Rate Processes," p. 364, McGraw Hill Book Co., New York (1941).
5. J. K. Roberts, *Proc. Roy. Soc. London*, **A152**, 445 (1935).
6. B. M. W. Trapnell, *ibid.*, **A206**, 39 (1951).
7. E. K. Rideal and B. M. W. Trapnell, *J. chim. phys.*, **47**, 126 (1950).
8. S. Brunauer, K. S. Love, and R. G. Keenan, *J. Am. Chem. Soc.*, **64**, 751 (1942).
9. A. Frumkin and A. Slygin, *Acta physicochim., U.R.S.S.*, **3**, 791 (1935).
10. M. Temkin and V. Pyskev, *ibid.*, **12**, 327 (1940).
11. K. Love and P. Emmett, *J. Am. Chem. Soc.*, **63**, 3297 (1941).
12. "Advances in Catalysis, V", Chapter by J. G. Tolpin and coauthors entitled 'Contributions of Russian Scientists to Catalysis,' pp. 240, Academic Press, Inc., New York (1953).

Corrosion of Copper-Gold Alloys by Oxygen-Containing Solutions of Ammonia and Ammonium Salts

J. I. FISHER[1] AND J. HALPERN

Department of Mining and Metallurgy, University of British Columbia, Vancouver, B.C., Canada

ABSTRACT

Copper-gold alloys, ranging in gold content from zero to 15 at. %, were exposed to stirred aqueous solutions of ammonia and ammonium salts under oxygen partial pressures of up to 6.8 at. Only copper dissolved under these conditions, a gold-rich film being left behind on the surface of the alloy. As the gold content of the alloys was increased, the rate of solution of copper generally fell off and the rate law shifted from linear, usually to parabolic. Alloys containing 15 at. % gold corroded slowly in solutions containing ammonia only, but were passive in the presence of ammonium sulfate. The effect on the kinetics of solution composition, oxygen pressure, and temperature are described, and some of the factors which limit the rate of corrosion are discussed. It is concluded that, under certain conditions, copper oxides are formed which contribute to the film structure and to limiting the corrosion rate.

INTRODUCTION

A kinetic study of the solution of copper in oxygen-containing aqueous solutions of ammonia and ammonium salts was described in an earlier paper (1). The over-all reaction in ammonia solutions is:

$$Cu + 4NH_3 + \tfrac{1}{2}O_2 + H_2O \rightarrow Cu(NH_3)_4^{++} + 2OH^- \quad (I)$$

and in solutions containing, also, ammonium salts,

$$Cu + 2NH_3 + 2NH_4^+ + \tfrac{1}{2}O_2 \rightarrow Cu(NH_3)_4^{++} + H_2O \quad (II)$$

It was shown that the rate-determining step is the chemical attack of a NH_3 molecule or NH_4^+ ion on the oxygen-covered copper surface. The observed rate is thus comprised of two independent contributions, of first order with respect to the concentrations of NH_3 and NH_4^+, respectively. Both rates are independent of the concentration of dissolved oxygen, provided that the latter is present in excess, so that its transport to the metal surface does not become rate-limiting. Where such limitation occurs, the kinetics are altered so as to obscure the mechanism of the chemical reaction (1, 2).

The object of the present study was to determine the effect on this reaction of alloying copper with another metal which is itself thermodynamically immune to attack by the corroding solutions. Gold, which fulfills this condition, was selected as the alloying element, since copper forms with it a continuous solid solution of well-known structural properties. There have been several earlier studies of the corrosion of copper-gold alloys in other media (3–5), but these have been concerned mainly with the determination of practical parting limits.

EXPERIMENTAL

Specimen ingots of pure copper and of four copper alloys, containing 2.0, 5.0, 10.0, and 15.1 at. % gold (designated as alloys 2, 5, 10, and 15, respectively), were prepared by induction melting in carbon crucibles under purified argon. Spectroscopic analysis of the final alloy specimens indicated a total foreign metal impurity content of less than 0.01%.

Ingots were homogenized in an argon atmosphere at 850°C for 70 hr, furnace cooled to 500°C, and finally quenched in water to ensure a disordered structure. Machined cylindrical specimens were then mounted in Bakelite so as to leave exposed a circular cross section of accurately measured geometrical area. Prior to re-use, each specimen was refaced in a lathe to remove the surface effects resulting from the previous experiment, and the freshly exposed surface was polished by standard metallographic techniques. This procedure was found to give reproducible results.

Corroding solutions were prepared from C. P. reagents and distilled water.

The stainless steel autoclave used for the experiments has been described earlier (1). The Bakelite mount containing the electrically insulated metal specimen was positioned, face downward, in the solution with the exposed surface about 5 mm above the impeller. The latter was 10.9 cm in diameter and rotated at 720 rpm, throwing the solution upward against the specimen face. The temperature of the solution and the partial pressure of oxygen were held constant at desired values. Most of the experiments were made at 25°C and O_2 partial pressure of 6.8 at.

The reaction was followed by withdrawing samples of the solution periodically for analysis. The concentration of dissolved copper was measured with a Beckman DU spectrophotometer using the carbamate method (6). A colorimetric procedure, involving the addition of rhodanine (7), was used to test the solutions for gold, concentrations of less than 1 mg/l being readily detectable. NH_3 concentrations were determined by potentiometric titration with standard HCl.

Following completion of the experiment the specimen was removed and subjected to visual and microscopic in-

[1] Present address: Physical Metallurgy Div., Mines Branch, Department of Mines and Technical Surveys, Ottawa, Ont., Canada.

spection. In some cases surface film scrapings were taken for chemical and x-ray diffraction analysis.

Results

In general, the copper and alloy specimens were found to undergo corrosion when exposed to solutions containing ammonia and oxygen, either in the absence or presence of added ammonium sulfate. An exception was alloy 15 which did not corrode in the presence of ammonium sulfate. The corrosion reaction comprised, essentially, dissolution of copper in accordance with equations (I) and (II). At no time could any gold be detected in the solution.

Some typical rate plots for solutions containing NH_3 only are shown in Fig. 1 and for those containing both NH_3 and $(NH_4)_2SO_4$ in Fig. 2. For pure copper the rate plots were always linear and solution rates were usually in agreement with those reported earlier (1). On the other hand, solution rates of copper from the copper-gold alloys generally fell off with time, the rate plots sometimes assuming complex shapes. This made it impossible to compare corrosion rates for different experiments in terms of a uniform rate constant. Instead, the amount of Cu dissolved in the first 3 hr of each experiment was arbitrarily adopted as a measure of the corrosion rate for comparative purposes, the relatively long reaction time being chosen in order to minimize spurious initial effects.

Corrosion in solutions containing NH_3 only.—Rate plots for the solution of copper from the various alloys in solutions containing NH_3 but no added ammonium salts are shown in Fig. 1. The curves for the alloys are of complex shape and cannot be fitted by either a linear or parabolic relation. Some of them are characterized by two apparent regions, an initial period of relatively rapid corrosion during which the rate falls off with time, and a final slower stage during which the rate remains essentially constant.

The results are summarized in Fig. 3 where the corrosion rates are plotted as functions of the gold content of the alloy and of the NH_3 concentration of the solution. It is seen that alloying the copper with gold even in concentrations as low as 2 at. % drastically reduces its rate of solution. Increasing the gold content between 2 and 15 at. % has relatively little further effect.

Increasing the NH_3 concentration of the solution between zero and 2 mole/l results in an increased corrosion rate for pure copper and for each of the alloys. The apparent levelling off of the rate at high NH_3 concentrations in the case of pure copper has been attributed to the influence of limitation by oxygen transport (1). With the alloys whose corrosion rates and hence oxygen requirements are much lower, this effect is less pronounced.

Corrosion in solutions containing NH_3 and $(NH_4)_2SO_4$.—No corrosion, either of pure copper or of the alloys, could be detected when they were exposed to solutions containing only $(NH_4)_2SO_4$ and no free NH_3. Apparently, some free NH_3 is required to form the soluble cuprammine salt, as suggested by equations (I) and (II). However, in the presence of NH_3, addition of small amounts of $(NH_4)_2SO_4$ was found to have a profound effect both on the corrosion rates and on the shapes of the rate plots.

The rate plots shown in Fig. 2 are typical of those obtained for the alloys in solutions containing both NH_3 and $(NH_4)_2SO_4$ and are seen to conform to a parabolic relation. As shown in Fig. 4, the rate for each alloy increases with increasing NH_4^+ concentration and finally levels off at a value which depends inversely on the gold content.

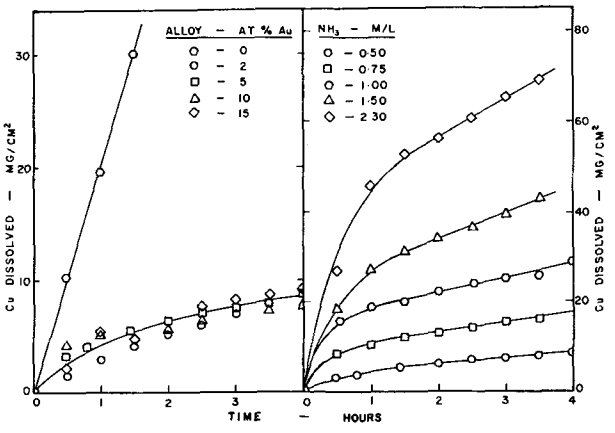

FIG. 1. Rate plots for the corrosion of copper and alloys in NH_3 solutions containing no NH_4^+ salts; 25°C, 6.8 at. O_2. (*a*) Corrosion of different alloys in 0.5M NH_3 solution; (*b*) corrosion of alloy 5 in solutions of different NH_3 concentration.

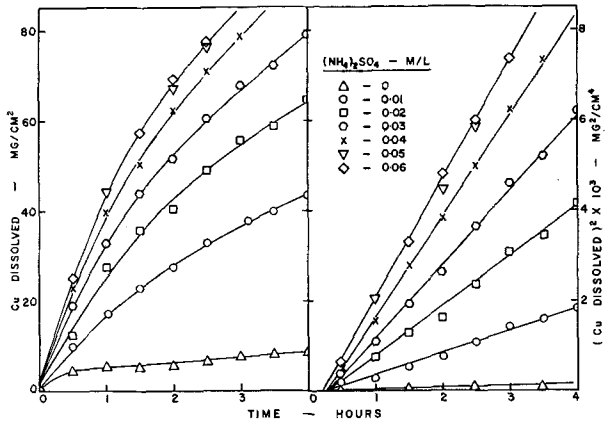

FIG. 2. Corrosion of alloy 10 in 0.5M NH_3 solutions containing various amounts of $(NH_4)_2SO_4$, 25°C, 6.8 at. O_2.

For a specified solution the rate falls off as the gold content of the alloy increases until the latter reaches about

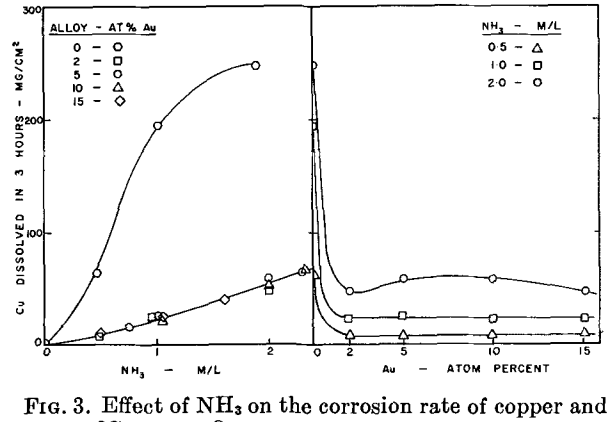

FIG. 3. Effect of NH_3 on the corrosion rate of copper and alloys, 25°C, 6.8 at. O_2.

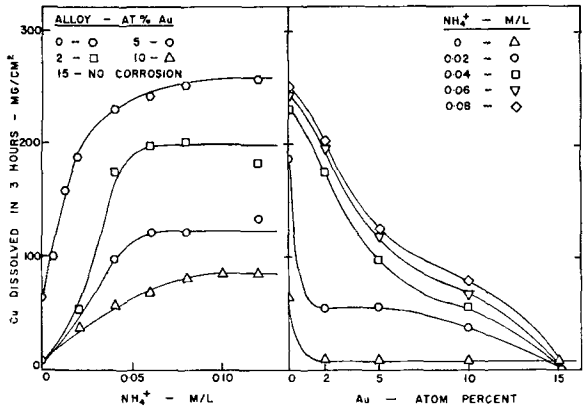

FIG. 4. Effect of NH_4^+ on corrosion of copper and alloys in solutions containing 0.5M NH_3, 25°C, 6.8 at. O_2.

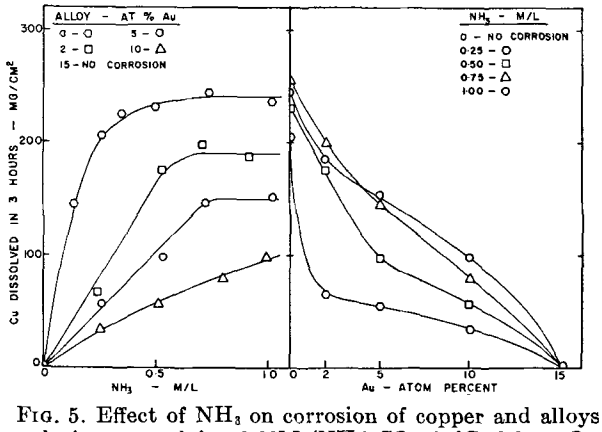

FIG. 5. Effect of NH_3 on corrosion of copper and alloys in solutions containing 0.02M $(NH_4)_2SO_4$, 25°C, 6.8 at. O_2.

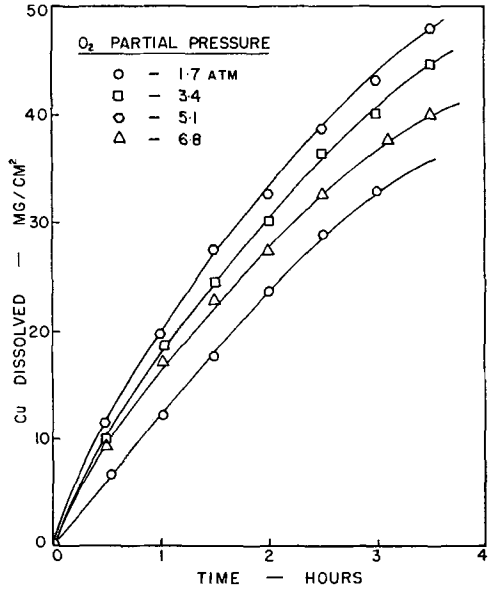

FIG. 6. Effect of varying O_2 pressure on corrosion of alloy 10 in solutions containing 0.5M NH_3, 0.01M $(NH_4)_2SO_4$, 25°C.

15 at. %. In no case, where solutions containing both NH_3 and $(NH_4)_2SO_4$ were used, could any corrosion of alloy 15 be detected either by examination of the specimen surface or by analysis of the solution.

Fig. 4 reveals that the effect of $(NH_4)_2SO_4$ addition is particularly marked for the alloys of low gold content, i.e., alloy 2, and diminishes as the gold content increases. Surprisingly, with alloy 15, addition of $(NH_4)_2SO_4$ appears to have a reverse effect since it inhibits completely the corrosion observed in its absence, i.e., in solutions containing NH_3 only. As shown in Fig. 5, the effect of varying the NH_3 concentration in solutions containing a constant amount of $(NH_4)_2SO_4$ parallels that obtained on varying the NH_4^+ concentration, except that the sensitivity of the rate to NH_3 is considerably lower. Thus about 10 times as much NH_3 is required to produce an effect of comparable magnitude. The limiting rate reached by increasing the NH_3 concentration approximates, for each alloy, that attained with NH_4^+. Inspection of Fig. 5 reveals that, as with NH_4^+, the effect of NH_3 is particularly pronounced for alloys of low gold content.

Effect of oxygen partial pressure.—With each alloy, measurements were made at several O_2 partial pressures ranging from zero to 6.8 at. No corrosion was observed in the absence of O_2. For pure copper the rate increases with the O_2 pressure until about 5 at., above which it remains substantially constant. It has been shown earlier (1) that in this region the transport of O_2 is sufficiently rapid so that the corrosion rate is chemically determined.

Typical of the results which were obtained for the alloys are the rate plots shown in Fig. 6. The rate increased slightly as the O_2 partial pressure was raised from 1.7 to 5.1 at., passed through a maximum, and then fell again as the O_2 pressure was further increased.

Effect of temperature.—The rate of solution of pure copper increases systematically with the temperature corresponding to an apparent activation energy of 5540 cal/mole (1). With the alloys, however, it was found that, while the initial rates followed a similar trend, corrosion rates were soon attained in each experiment which showed an inverse dependence on temperature. This is illustrated in Fig. 7 where rate plots for alloy 2, typical of those obtained for all the alloys, are shown for several temperatures ranging from 15° to 50°C.

Examination of corroded surfaces.—Apart from etching,

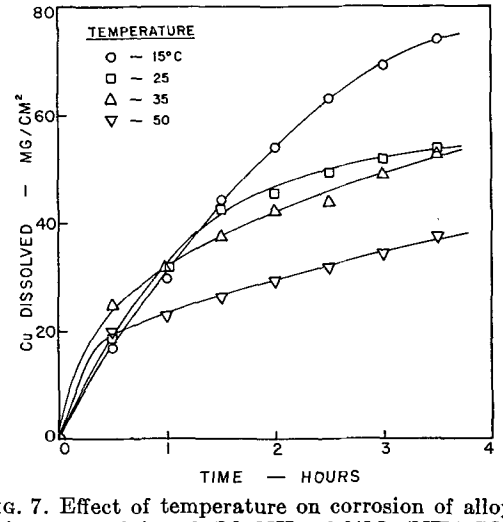

FIG. 7. Effect of temperature on corrosion of alloy 2 in solutions containing 0.5M NH_3, 0.01M $(NH_4)_2SO_4$, 6.8 at. O_2.

no surface changes, i.e., no film formation, could be observed following corrosion of the pure copper specimens. Examination of the alloy specimens generally revealed that corrosion had been accompanied by the formation of a surface film, presumably containing the gold which was left behind as the copper dissolved. In many cases, particularly with the gold-rich alloys, the appearance of the surface left little doubt that a phase rich in metallic gold had been formed.

Microscopic examination of the surface usually revealed complicated film structures which varied considerably with alloy composition and with the conditions of the experiment, but which could not be interpreted or correlated in any conclusive manner. In general, it was noted that the films on alloy 2 were rather more porous than those on alloys of higher gold content and that they tended to become denser and more compact as the corrosion temperature was increased. Often inclusions of very fine black particles were observed in the film. A sufficient quantity of this material could not be isolated for identification, but its appearance suggested that it was an oxide, i.e., CuO or Cu_2O, rather than a metal.

Attempts were made to characterize the film by x-ray diffraction analysis of powdered surface scrapings. However, excessive broadening of the lines precluded any positive identification. Qualitatively, the pattern appeared to resemble that for Cu_2O.

Discussion

With pure copper the reaction has been shown (1) to proceed by essentially chemical attack of NH_3 and NH_4^+ on the metal surface, following rapid chemisorption of oxygen, and resulting in solution of copper as the cuprammine ion. The surface of the corroding metal remains substantially unchanged with no indication of any film formation. Hence, the rate plots are consistently linear.

Judging from the continuity and over-all similarity of the results, it would appear that, initially at least, solution of copper from the alloys proceeds by a similar mechanism. It is clear, however, that as corrosion of the alloy proceeds, a surface film is formed and that, as the film thickens, it impedes to an increasing extent the transport of reactants and products between the reacting metal and solution, thus limiting the rate. In the first instance, at least, this film appears to be associated with the gold or gold-rich metal phase which is left behind as the copper dissolves. These considerations are supported by the observations that corrosion rates of the alloy specimens usually decrease with time and with increasing gold content. The parabolic rate relation which was observed in many of the experiments is characteristic of other corrosion systems in which the rate is determined by transport through a surface film of reaction products which thickens as the reaction proceeds (8).

There is a further strong suggestion both from the kinetic results and from the physical characteristics of the surface films that, in addition to the gold which is left behind, an oxide, probably Cu_2O and/or CuO, may form on the surface of the corroding alloy and that this deposit may also contribute to the film structure and to the slowing of the reaction. Such a deposit might be expected to accompany or result from the formation of the initial gold-rich film skeleton, since the latter would give rise to stagnant solution regions, i.e., in the film pores, protected from the bulk of the solution, which would be deficient in NH_3 and NH_4^+ and in which corrosion products, i.e., Cu^{++}, Cu^+, and OH^-, would tend to accumulate. Such a condition would favor the precipitation of CuO and Cu_2O. This picture is particularly helpful in explaining the results of experiments at very low NH_3 and NH_4^+ concentrations where unusually low corrosion rates were observed for the alloys of low gold content, i.e., alloy 2, despite the fact that the gold films formed were apparently very porous. The very marked effect of increasing the NH_3 and, particularly, the NH_4^+ concentrations on the corrosion rate of these alloys suggests that passivation is largely due to deposited oxides.

Oxide formation is apparently of greatest importance in solutions low in NH_4^+, i.e., those to which no $(NH_4)_2SO_4$ was added. This is understandable in terms of the buffering effect of NH_4^+ in whose presence solution of copper oxides is facilitated by the following reactions:

$$CuO + 2NH_3 + 2NH_4^+ \rightarrow Cu(NH_3)_4^{++} + H_2O \qquad (III)$$

$$Cu_2O + 2NH_3 + 2NH_4^+ \rightarrow 2Cu(NH_3)_2^+ + H_2O \qquad (IV)$$

This may explain the insensitiveness of the corrosion rate in such solutions to the gold content of the alloy (*see* Fig. 1 and 2), i.e., the readily formed copper oxide inhibits corrosion even of the low-gold alloys whose porous gold films are not, themselves, protecting. Increasing the gold content of the alloy has little effect since the copper oxide deposit continues to be controlling and may even act physically to prevent the formation of a coherent gold film. The oxide film itself cannot be completely protecting since it dissolves slowly in the ammonia solutions. Hence even the gold-rich alloys, i.e., alloy 15, continue to corrode in solutions containing NH_3 only. The linear regions of the rate plots (*see* Fig. 1) corresponding to the later stages of corrosion of the alloys in such solutions are consistent with a steady-state condition in which a copper oxide film dissolves at the same rate at which it is being restored.

The generally observed increase in corrosion rates of most of the alloys with increasing NH_3 and NH_4^+ concentration, to limiting values, may be due to higher rates of transport of these reactants through the film to the underlying dissolving copper, coupled with a reduced tendency for the precipitation of copper oxides, as suggested earlier. However, ultimately, at high NH_3 and NH_4^+ concentrations, the rate must become controlled by the transport of oxygen or corrosion products through the gold film whose formation is favored under these conditions and whose thickness and permeability should depend inversely on the gold content of the alloy. This corresponds to the region in which a limiting rate, characteristic of the alloy composition, is reached and further increases in the NH_3 and NH_4^+ concentrations are without effect. In this region, transport of oxygen through the film, from the solution to the underlying copper-rich metal, or transport of copper in the opposite direction is presumably rate-controlling. The existence of an analagous region for the corrosion of pure copper, where it has been

shown that transport of oxygen to the metal surface is rate-limiting (1), favors the former alternative.

The fact that the rate passes through a maximum with increasing oxygen pressure and then falls off again can also be explained in these terms. At low oxygen pressures, transport of O_2 either through the film or the solution may be, in whole or part, rate-limiting and, hence, the corrosion rate increases with the O_2 pressure. At the same time depletion of NH_3 and NH_4^+ and accumulation of Cu^{++} and OH^- are enhanced with the resulting formation of a protective copper oxide film. A point thus exists beyond which an increase in oxygen pressure impedes the reaction. This is somewhat analagous to the well-known behavior of iron exposed to neutral or alkaline solutions, where increasing the oxygen concentration may first accelerate corrosion, while a still higher oxygen concentration inhibits it by favoring the formation of a passivating oxide film (9).

The inverse dependence of corrosion rates of the alloys on temperature may be similarly understood. At higher temperatures the precipitation of copper oxides and the formation of denser film structures are both favored. The appearance of the films supports this explanation.

ACKNOWLEDGMENT

Support of this work through a research grant from the National Research Council of Canada is gratefully acknowledged.

Manuscript received September 13, 1955.
Any discussion of this paper will appear in a Discussion Section to be published in the December 1956 JOURNAL.

REFERENCES

1. J. HALPERN, *This Journal*, **100**, 421 (1953).
2. G. A. DEITZ AND J. HALPERN, *J. Metals*, **5**, 1109 (1953).
3. G. TAMMANN, *Z. anorg. u. allgem. Chem.*, **142**, 61 (1925).
4. W. J. MULLER, H. FREISSLER, AND E. PLETTINGER, *Z. Elektrochem.*, **42**, 366 (1936).
5. R. LANDAU AND C. S. OLDACH, *Trans. Electrochem. Soc.*, **81**, 521 (1942).
6. E. B. SANDELL, "Colorimetric Determination of Traces of Metals," p. 204, Interscience Publishers Inc., New York (1950).
7. Reference (6), p. 306.
8. U. R. EVANS, "Metallic Corrosion, Passivity and Protection," pp. 134–147, Edward Arnold & Co., London (1946).
9. E. C. GROESBECK AND L. J. WALDRON, *Proc. Am. Soc. Testing Materials*, **31** Part II, 279 (1931).

Acceleration of the Dissolution of Iron in Sulfuric Acid by Ferric Ions

HARRY C. GATOS[1]

Engineering Research Laboratory, Engineering Department, E. I. du Pont de Nemours and Company, Inc., Wilmington, Delaware

ABSTRACT

The dissolution of iron in H_2SO_4 solutions was studied as a function of Fe^{+++} concentration. In 1*N* H_2SO_4 the dissolution rate (5-hr period) increased at first with Fe^{+++} concentration and then decreased beyond 0.47 Fe^{+++} g ion/l until at 4.00 Fe^{+++} g ions/l, it became approximately equal to the rate in 1*N* H_2SO_4 containing no Fe^{+++}. The hydrogen evolution rate decreased with time and with Fe^{+++} concentration. For a given Fe^{+++} concentration, the dissolution rate decreased, and the hydrogen evolution rate increased with increasing H^+ concentration.

The accelerating effect of Fe^{+++} is due to the direct reduction of the Fe^{+++} to Fe^{++}. Consumption of Fe^{+++} was related to iron dissolution according to Faraday's law. Decrease in hydrogen evolved was considered the result of unfavorable electrode conditions for the reduction of H^+, created by the reduction of Fe^{+++} to Fe^{++}.

INTRODUCTION

In nonoxidizing acids, like dilute H_2SO_4, the dissolution of iron can be described:[2]

$$\text{anodic reaction: } Fe \rightarrow Fe^{++} + 2e^- \qquad [1]$$

$$\text{cathodic reaction: } 2H^+ + 2e^- \rightarrow \underset{\text{nascent}}{2[H]} \rightarrow H_2 \qquad [2]$$

Ferric ions in acid media are spontaneously reduced to Fe^{++}, which in turn are quite stable. The thermodynamic stability of the Fe^{+++} and Fe^{++} in acids can be appreciated by the following potential diagram (1):

$$Fe \xrightarrow{E_o = -0.440\ v} Fe^{++} \xrightarrow{E_o = 0.771} Fe^{+++} \xrightarrow{E_o > 1.9} FeO_4^=$$

Because of their oxidizing properties, ferric ions accelerate the dissolution of iron in acids. This acceleration constitutes a problem during acid-cleaning operations of ordinary steel equipment bearing ferric oxide scale. In the presence of Fe^{+++}, a number of corrosion inhibitors become ineffective (2).

The accelerating action may be brought about either

[1] Present address: Lincoln Laboratory, Massachusetts Institute of Technology, Lexington, Mass.

[2] All ionic symbols in this paper omit specific reference to solvation.

by the acceleration of reaction [2] as a result of the following reaction:

$$Fe^{+++} + [H] \rightarrow Fe^{++} + H^{+} \quad [3]$$

or by the direct reduction of Fe^{+++}:

$$Fe^{+++} + e^{-} \rightarrow Fe^{++} \quad [4]$$

By combining the anodic reaction [1] and cathodic reaction [4], the following over-all reaction is obtained:

$$Fe + 2\,Fe^{+++} \rightarrow 3\,Fe^{++} \quad [5]$$

Van Name and Hill (3), in studying the dissolution of iron in Fe^{+++} solutions, considered the kinetics of reaction [5] without reference to the electrochemical aspects of the dissolution process.

Alquist, Wasco, and Robinson (2) concluded that in HCl solutions, reactions [3] and [5] take place simultaneously. According to these authors, the fact that the hydrogen evolved during the dissolution of iron is decreased in the presence of Fe^{+++} indicates that reaction [3] takes place; the fact that the presence of Fe^{+++} increases the amount of iron attacked indicates that reaction [5] takes place. Cardwell (4) stated that in Fe-HCl systems reaction [3] prevails.

However, it is quite possible that reaction [4] becomes the main cathodic reaction, and reaction [2] is partially or completely suppressed. In fact, experimental results reported in the present paper show that reaction [4] is primarily responsible for the acceleration of the dissolution of iron in nonoxidizing acid by Fe^{+++}.

Because of the importance of the Fe^{+++} action both from the theoretical and practical points of view, it was felt worth while to investigate quantitatively the role of Fe^{+++} on the dissolution of iron in acids. The present work also concerns the changes in hydrogen evolution which result from the presence of Fe^{+++}.

Experimental

Weight-loss and hydrogen-evolution tests.—The metal was SAE 1030 steel: 0.29% C, 0.37% Mn, 0.04% S, 0.01% P, 0.002% Si, 0.09% Cu, and the balance Fe. Test metal specimens measured 1 x 1.5 x $\frac{1}{8}$ in. Prior to testing, they were abraded with 120-grit paper, scrubbed with liquid soap, degreased in benzene, and desiccated.

The weight-loss and hydrogen evolution tests were performed in an apparatus consisting of an Erlenmeyer flask and a gas buret with a mercury leveling bulb. One specimen at a time was suspended by a glass rod and was totally immersed in the solution contained in the flask. The solution was 600 ml of 1*N* H_2SO_4, containing the desired amount of Fe^{+++}. Ferric sulfate served as the source of Fe^{+++}. The H_2SO_4 solution was saturated with hydrogen in the apparatus at the test temperature, and the whole apparatus was flushed with hydrogen before immersing the steel specimens. All dissolution experiments were performed at 25°C. The hydrogen evolved was collected in the gas buret. Its volume was corrected to S.T.P. No correction was made for hydrogen entering the steel specimens since it was considered insignificant for the present study.

Determination of Fe^{+++} and Fe^{++}.—The original concentration of the Fe^{+++} was determined volumetrically. Ferric ions were reduced to Fe^{++} in a Jones reductor and then titrated with standard $KMnO_4$. Upon completion of each test, a portion of the 1*N* H_2SO_4 was titrated directly with $KMnO_4$ to determine the total amount of Fe^{++} present. Another aliquot was passed through the Jones reductor, and then titrated with $KMnO_4$. This titration yielded the total amount of Fe^{++} and Fe^{+++} in the acid after the test. The amount of unreduced ferric ions was obtained by subtracting the amount of Fe^{++} from the total amount of iron ions.

Potential measurements.—The potential-measuring apparatus could accommodate six specimens at a time. Each specimen was partially immersed in 250 ml of solution. Both sides of a one-half inch square of the immersed part of the specimen were exposed to the solution. The remaining immersed part of the specimen was electrically insulated with a transparent cement. In order to minimize motion during measurements, specimens were suspended by rigid copper rods mounted on a Lucite plate. Electrical contact between test solutions and the reference electrode was established with agar gel bridges containing small amounts of KNO_3. These led to a saturated KCl solution, in which the capillary tip of a saturated KCl calomel reference electrode was also immersed. All agar bridges were renewed with every run. A *p*H meter with an impedance of 10^{10} to 10^{12} ohms was connected in series with the potentiometer and served as null current indicator. This arrangement yielded very reproducible results.

All electrode potential data have been converted to the standard hydrogen electrode scale.

Dissolution of Iron as a Function of Time in the Presence of Fe^{+++}

Before determining the effect of Fe^{+++} concentration on the dissolution rate of iron in 1*N* H_2SO_4 it was considered necessary to establish the dissolution of iron as a function of time at specific Fe^{+++} concentrations. In the absence of Fe^{+++} the dissolution rate of iron remains constant for at least 45 hr and is equal to 0.33 mg/cm²/hr. Dissolution of iron in Fe^{+++} – H_2SO_4 has been reported as a first-order reaction [3]. This was confirmed for 1*N* H_2SO_4 containing 0.042 and 0.416 g ions/l. Reaction constant K_1 is approximately 0.03 cm/sec. It was determined from the following equation describing a first-order reaction involving the dissolution of a metal:

$$K_1 = \frac{2.3\,V}{At} \log \frac{a}{a-n} \quad (I)$$

where V = volume of solution in ml, A = area of metal in cm², t = time in seconds, a = initial amount of Fe^{+++} in oxidation equivalents, and n = amount of Fe^{+++} in oxidation-equivalents reacting in time t. The dissolution rate in the 0.042 and 0.416 g ions/l solutions did not change detectably within 20 and 6 hr, respectively. Results for one concentration are shown in Fig. 1. The presence of moderate amounts of Fe^{++} does not affect the dissolution of iron in acids (5).

Dependence of dissolution rate on time was also reflected in the electrode potential of iron (Fig. 1).

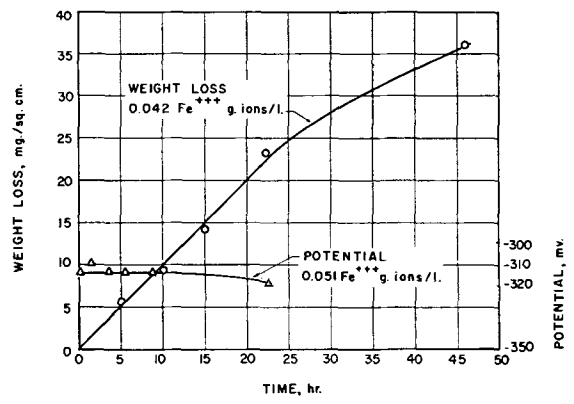

FIG. 1. Dissolution of iron in 1N H_2SO_4 containing Fe^{+++}

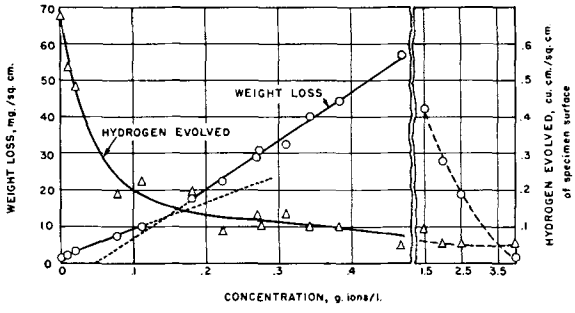

FIG. 2. Dissolution of iron in 1N H_2SO_4 containing Fe^{+++}; dissolution time, 5 hr.

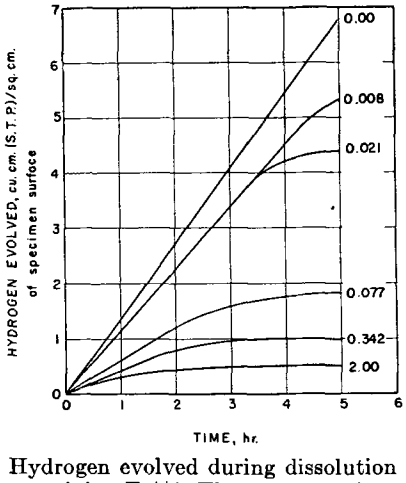

FIG. 3. Hydrogen evolved during dissolution of iron in 1N H_2SO_4 containing Fe^{+++}. The concentration of Fe^{+++} is indicated for each curve in g ions/l.

Effect of Fe^{+++} *Concentration on Dissolution of Iron and Evolution of Hydrogen*

On the basis of the results described above, a 5-hr period was chosen for studying this effect. During this period, the dissolution rate remained constant for Fe^{+++} concentrations up to about 0.47 g ions/l and was characteristic of the original concentration of Fe^{+++}. Above 1.5 Fe^{+++} g ions/l, the dissolution rate changed somewhat abnormally with time and approached zero within a few hours. For comparison purposes, however, all dissolution data are expressed in terms of weight loss of iron in mg/cm² of specimen surface/5 hr.

Fig. 2 illustrates the effect of Fe^{+++} concentration on the dissolution of iron at 25°C and on the amount of hydrogen evolved during dissolution. A concentration range up to 4 Fe^{+++} g ions/l was covered. The amount of hydrogen evolved is expressed in cubic centimeters per square centimeter of specimen surface. In this way, errors due to small variations in the size of the specimens are eliminated.

Fig. 2 shows that the weight loss of iron increases with Fe^{+++} concentration up to about 0.47 Fe^{+++} g ions/l in 1N H_2SO_4. At this concentration, the weight loss is about 35 times as great as in the absence of Fe^{+++}. Beyond 0.47 Fe^{+++} g ions/l, the weight loss gradually decreases and eventually approaches the weight loss value of iron in 1N H_2SO_4 containing no Fe^{+++}.

The hydrogen evolved during the dissolution of iron decreases rapidly at first, and then slowly, with increasing Fe^{+++} concentration (Fig. 2). This represents a twelvefold decrease in the amount of hydrogen at the highest Fe^{+++} concentration employed.

Hydrogen was not evolved at a constant rate during the 5-hr tests, except at zero Fe^{+++} concentration. The amount of hydrogen evolved as a function of time for various Fe^{+++} concentrations is shown in Fig. 3. For any given time, within the 5-hr period, the amount of hydrogen evolved decreases as the Fe^{+++} concentration increases. For a given Fe^{+++} concentration, the amount of hydrogen evolved increases linearly at first with time; then its rate of evolution decreases, and eventually becomes zero. The higher the Fe^{+++} concentration, the sooner the rate of evolution becomes zero. At concentrations higher than those indicated in Fig. 3, the hydrogen evolution stops within a few minutes.

These experiments, plus the fact that the iron dissolution continues even after the hydrogen evolution stops, indicate that reactions [2] and [4] proceed simultaneously at first; reaction [2], however, is gradually suppressed until reaction [4] becomes the principle cathodic reaction.

Reaction [3] most likely does not enter into the dissolution process. If the consumption of Fe^{+++} were due to their reduction by hydrogen, this reduction should proceed with 100% efficiency, while no hydrogen was being evolved. Such efficiency is unlikely under the present experimental conditions. Furthermore, on the basis of the reduction of Fe^{+++} by hydrogen it is difficult to explain why a minimum amount of time is required before the hydrogen is completely consumed as fast as it is generated.

Effect of Fe^{+++} *as a Function of* H^+ *Concentration*

A series of experiments was performed by means of which the effect of a specific concentration of Fe^{+++} was determined in various H_2SO_4 concentrations. The Fe^{+++} concentration chosen was 0.135 g ions/l, with a H_2SO_4 concentration range from 0.25 to 2.0N. Both weight-loss and hydrogen-evolution measurements were made. The weight loss of iron decreases slowly with increasing normality of H_2SO_4 (Fig. 4). The effect of H_2SO_4 concentration is in contrast to that observed in the absence of Fe^{+++}; in this case, the weight loss of iron (W, mg/cm²/5 hr)

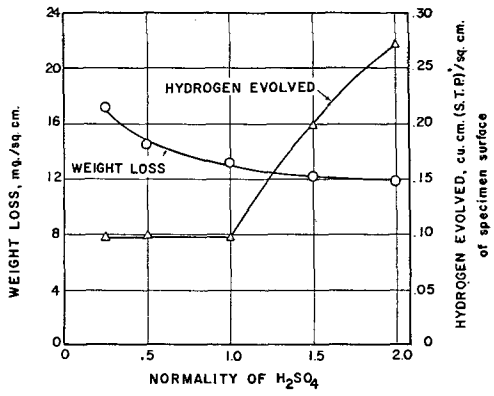

FIG. 4. Dissolution of iron in H_2SO_4-solutions containing 0.135 Fe^{+++} g ions/l. Dissolution time, 5 hr.

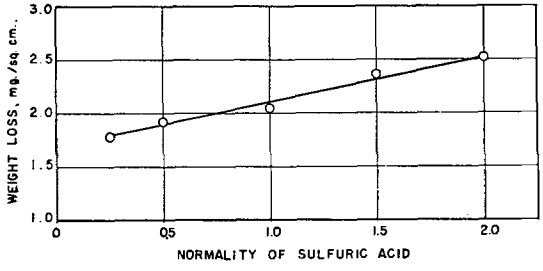

FIG. 5. Dissolution of iron as a function of H_2SO_4 concentration; dissolution time, 5 hr.

increases with the normality of H_2SO_4 (N), as described by equation:

$$W = 2.1\ N^{0.25} \qquad \text{(II)}$$

(*See* Fig. 5).[3] Hydrogen evolved in the presence of Fe^{+++} increases with increasing normality of H_2SO_4, particularly above the value of 1N. The fact that acceleration of Fe^{+++} decreases with hydrogen ion concentration, whereas the amount of hydrogen evolved increases, suggests that the direct reduction of Fe^{+++} (reaction [4]) is gradually suppressed in favor of the direct reduction of H^+ (reaction [2]), which becomes the principle cathodic reaction at about 1N H_2SO_4. These results are consistent with the ones described above, which showed that for a constant hydrogen ion concentration, reaction [2] is gradually suppressed by reaction [4], as the Fe^{+++} concentration increases.

Consumption of Fe^{+++}

By employing the analytical procedures described earlier in this paper, it was possible to determine the consumption of Fe^{+++}, and at the same time confirm the mass balance among the various quantities of Fe^{++} and Fe^{+++} ions involved during the 5-hr dissolution tests.

The results obtained for the tests reported in Fig. 2 up to a concentration of 0.47 Fe^{+++} g ions/l are shown in Table I.

The consumption of Fe^{+++} is plotted in Fig. 6 as a function of Fe^{+++} concentration. It is apparent that this consumption as a function of Fe^{+++} concentration resembles very closely the weight loss of iron as a function of Fe^{+++} concentration, shown in Fig. 4.

[3] The curve must go through the origin.

By calculating the weight loss of iron from the Fe^{+++} consumed on the basis of equation [5], and the weight loss corresponding to the hydrogen evolution (Fig. 2), it was found that the sum of the two weight losses is equal, within experimental error, to the actual weight loss determined gravimetrically, as shown in Table II. The weight loss corresponding to the amount of hydrogen represents a very small fraction of the total weight loss, except at low Fe^{+++} concentrations. Apparently no catalytic effects or side reactions are caused by the presence of Fe^{+++}.

Potential Measurements

The data reported above were supplemented by potential measurements of iron in 1N H_2SO_4, containing 0–2.5 Fe^{+++} g ions/l. Results are shown in Fig. 7. The potentials are the values obtained after the iron was immersed for 2 hr. As a general rule, in all Fe^{+++} concentrations, the potential reached a steady state in less than 2 hr and remained constant for several hours thereafter

TABLE I. *Experimental values for the various quantities of* Fe^{++} *and* Fe^{+++} *involved in dissolution tests*

$(Fe^{+++})_{original}$†	$(Fe^{++})_{total}$†	$(Fe^{++})_{dissolution}$‡	$(Fe^{++})_{Fe^{+++}}$§	$(Fe^{+++})_{unreduced}$§	(Fe ions)$_{solution}$†
10*	3	2	2	7	—
21	5	2	2	19	24
77	19	7	13	100	120
113	21	8	14	99	117
180	36	13	23	157	188
221	54	19	35	186	240
269	57	19	37	232	288
274	64	22	42	232	293
311	65	22	43	269	328
342	89	30	59	283	376
383	92	32	61	322	412
467	105	36	69	398	—

* All quantities in this table are expressed in mg ions/l.
† Values obtained directly by titration.
‡ Values obtained from weight loss measurements.
§ Values calculated from first and second columns.

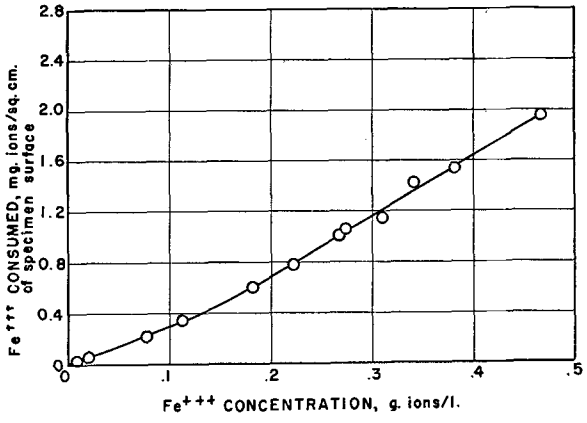

FIG. 6. Consumption of Fe^{+++} by iron in 1N H_2SO_4; time, 5 hr.

TABLE II. *Weight loss of iron in 1N H_2SO_4 containing Fe^{+++}; dissolution time 5 hr*

$(Fe^{+++})_{original}$	$(Fe)_{H_2}$	$(Fe)_{Fe^{+++}}$	$(Fe)_{H_2} + (Fe)_{Fe^{+++}}$	Actual weight loss
g ions/l				
0.010	1.3	1.0	2.3	2.1
0.021	1.2	1.7	2.9	3.2
0.077	0.4	9.6	10.0	7.8
0.113	0.7	9.9	10.6	10.8
0.180	0.5	17.0	17.5	17.7
0.221	0.3	22.6	22.9	23.9
0.270	0.4	28.6	30.0	29.3
0.274	0.3	29.7	30.0	31.1
0.311	0.4	32.0	32.4	32.4
0.342	0.2	40.0	40.2	40.2
0.383	0.2	42.7	42.9	44.3
0.467	0.1	55.0	55.1	57.0

$(Fe)_{H_2}$ = wt loss corresponding to the hydrogen evolved.
$(Fe)_{Fe^{+++}}$ = wt loss due to Fe^{+++} on the basis of equation [5].
Weight loss is expressed in mg/cm² of iron surface.

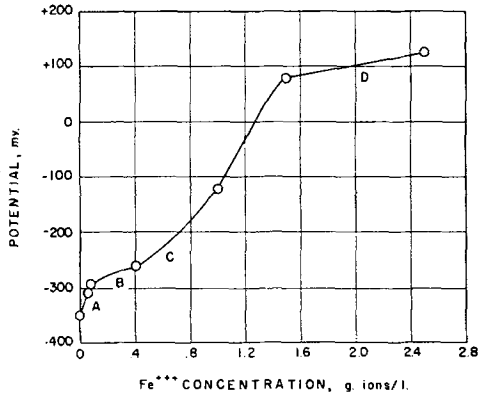

FIG. 7. Potential of iron after 2 hr in 1N H_2SO_4 containing Fe^{+++}.

(Fig. 1). Eventually, it drifted toward the potential of iron in 1N H_2SO_4, containing no Fe^{+++}.

As shown in Fig. 7, the potential of iron shifts toward more cathodic values with increasing Fe^{+++} concentration. At first this shift is rapid (Part A of the curve), then it becomes slow (Part B), then rapid again (Part C), and finally slow (Part D). It is of interest to note that the weight loss of iron and the hydrogen evolution plotted as a function of Fe^{+++} concentration, (Fig. 2) are reflected somewhat in the potential of iron as a function of Fe^{+++} concentration. Thus, Part A of the curve in Fig. 7 corresponds to the rapid decrease in hydrogen evolution; Part B corresponds to the slow decrease in hydrogen evolution; Part C corresponds to the change of the weight-loss function from increasing to decreasing with increasing Fe^{+++} concentration; and Part D corresponds to the relatively sharp decrease of the weight loss of iron with increasing Fe^{+++} concentrations.

Discussion

Nernst (6) suggested that on the boundary surface of two phases the chemical potential varies considerably between neighboring points. As a result, at such surfaces chemical reactions take place at extremely high rates. Thus, the diffusion rate of the reactants to the surface becomes the reaction rate-determining step. According to these views, the reaction rate dm/dt is given by the following equation

$$dm/dt = K(C - C_s) \qquad \text{(III)}$$

where K is the reaction constant, C is the concentration of the reactants in the bulk of the solution, and C_s the concentration in the solution at the boundary surface of the two phases.

These views were supported by Van Name and Hill (3), who stated that metal dissolution processes in many cases are diffusion-controlled, including the dissolution of iron in Fe^{+++} solutions. The latter case was studied by the above authors with Fe^{+++} concentrations below 0.1 g ions/l. They found that the dissolution rate increased linearly with concentration, according to equation (III), which is in agreement with the diffusion control theory. Similar results were recently obtained in HCl containing Fe^{+++} and other depolarizers by Makrides, Komodromos, and Hackerman (7).

The results of the present investigation are in agreement with those of the above authors, i.e., the dissolution rate of iron increases linearly with Fe^{+++} concentration below 0.1 Fe^{+++} g ions/l and in the range of approximately 0.15–0.47 g ions/l (Fig. 2). The slope, however, in the two ranges of concentration is 70 and 130, respectively, in units of Fig. 2. Any stirring effects caused by hydrogen evolution at low Fe^{+++} concentrations should, if anything, increase the slope in this range. Thus, the diffusion control theory alone appears inadequate to explain the dissolution of iron in the presence of Fe^{+++}, particularly when considering concentrations higher than the ranges mentioned above and the hydrogen evolution associated with the dissolution process.

It is believed that the electron transfer from the metal to the H^+ or its hydrated form is preceded by adsorption of these ions on the metal surface. In the presence of Fe^{+++},

TABLE III. *Potential of iron in H_2SO_4 containing 0.135 Fe^{+++} g ions/l*

Normality of H_2SO_4	Potential in v
0.25	−0.266
0.50	−0.268
1.00	−0.272
1.50	−0.272
2.00	−0.276

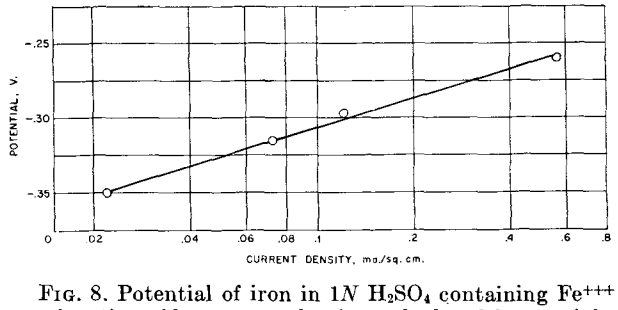

FIG. 8. Potential of iron in 1N H_2SO_4 containing Fe^{+++} as a function of log current density, calculated from weight loss.

both ions compete for the available sites, which are not necessarily restricted to specific areas on the surface. At low Fe^{+++} concentration, both H^+ and Fe^{+++} are adsorbed and subsequently reduced simultaneously (Fig. 2). In this case hydrogen ion reduction contributes appreciably to the dissolution process (Table II) and undoubtedly interferes with the reduction of Fe^{+++}. Hydrogen ions and hydrogen atoms on the surface limit the number of sites available for the reduction of Fe^{+++}. As the concentration of Fe^{+++} increases, the potential shifts toward more positive values (Fig. 7), resulting in a decrease of the hydrogen reduction rate (8). Thus, the interference of the reduction of Fe^{+++} by the hydrogen evolution process decreases as the concentration of Fe^{+++} increases. Above approximately 0.15 g ions/l the reduction of hydrogen is suppressed considerably (Fig. 3), and its contribution to the dissolution process becomes negligible (Table II). Thus, in the range 0.15–0.47 g ions/l the reduction of Fe^{+++} becomes the principal cathodic reaction which is under diffusion control. Below this concentration range it is difficult to define the rate-determining step of the dissolution process, although phenomenologically the dissolution process appears to be under Fe^{+++} diffusion control. The fact that a certain amount of H_2 is evolved in the beginning of the dissolution process, even at high Fe^{+++} concentration, is probably due to the finite time necessary for the cathodic potential shift.

The above views are further supported by the results of Fig. 4, where the interference of the Fe^{+++} reaction by hydrogen ions is demonstrated unambiguously. For a given Fe^{+++} concentration by increasing the hydrogen ion concentration the dissolution rate decreases slowly. In the absence of Fe^{+++}, by increasing the hydrogen ion concentration the dissolution rate increases (Fig. 5). Thus, in Fig. 4 the Fe^{+++} reduction is being suppressed by the increasing hydrogen ion reduction rate. This is consistent with the observed slow shift of the potential toward more anodic values as the hydrogen ion concentration was increased (Table III). The increase of the dissolution rate expected from the increase in the hydrogen reduction rate is masked by the corresponding relatively large decrease due to decrease of the Fe^{+++} reduction rate.

By plotting the potential obtained as described earlier against the logarithm of the current density for Fe^{+++} concentrations up to 0.4 g ions/l, a linear relationship is observed (Fig. 8). Current density was calculated from weight loss and by assuming a roughness factor of 4.0 (7). The equation describing this relationship is:

$$\text{Potential} = -0.3 + 0.06 \log i \qquad \text{(IV)}$$

where i is the current density in ma/cm^2. The same type of relationship was first observed by Makrides, Komodromos, and Hackerman (7) in the dissolution of iron in hydrochloric acid solutions containing Fe^{+++} and other depolarizers. This plot could be considered as an approximate polarization curve for the anodic reaction (7). The limitations of this approximation are pointed out by the above authors.

Above 0.47 Fe^{+++} g ions/l the dissolution rate (or current density) decreases with increasing Fe^{+++} concentration (Fig. 2) while the potential shifts rapidly toward more cathodic values. In this range the dissolution process obviously ceases to be under diffusion control. If the shift of potential is still indicative of the polarization of the anodic reaction, then in the above Fe^{+++} concentration range there is a rapid polarization of the anodic reaction. No clear explanation can be given for this at present, other than that the potential of iron becomes so noble in these Fe^{+++} concentrations that the anodic reaction becomes the rate-determining step with a high activation energy.

Conclusions

1. The dissolution of iron in H_2SO_4 solutions is greatly accelerated by Fe^{+++} as a result of adsorption and subsequent cathodic reduction of Fe^{+++} to Fe^{++}. It is diffusion controlled only within limited ranges of Fe^{+++} concentration.

2. The accelerating effect of Fe^{+++} follows Faraday's law and is quantitatively expressed by the over-all equation [5].

3. In 1N H_2SO_4, the accelerating effect increases with Fe^{+++} concentration up to 0.47 Fe^{+++} g ions/l. It decreases at higher concentration. For a given Fe^{+++} concentration, the accelerating effect decreases slowly with increasing H^+ concentration.

4. The rate of the hydrogen evolution associated with the iron dissolution process decreases with increasing Fe^{+++} concentration, and for a given Fe^{+++} concentration decreases with time.

5. For a given Fe^{+++} concentration, the hydrogen evolution rate increases with increasing H^+ concentration particularly above 1N.

6. At high Fe^{+++} concentrations (greater than 0.47 g ions/l), the accelerating effect becomes less pronounced, probably due to polarization of the anodic reaction.

Acknowledgment

The author wishes to express his appreciation to A. M. Madarassy for his skillful assistance and many suggestions during the course of this investigation.

Manuscript received July 27, 1955. This paper was prepared for delivery before the Pittsburgh Meeting, October 9 to 13, 1955.

Any discussion of this paper will appear in a Discussion Section to be published in the December 1956 Journal.

REFERENCES

1. W. M. Latimer, "Oxidation Potentials," 2nd ed., p. 228, Prentice-Hall, Inc., New York (1952).
2. F. N. Alquist, J. L. Wasco, and H. A. Robinson, *Corrosion*, **3**, 482 (1947).
3. R. G. Van Name and D. U. Hill, *Am. J. Sci.*, (4), **42**, 307 (1916).
4. P. H. Cardwell, *Trans. Am. Soc. Mech. Engrs.*, **76**, 47 (1954).
5. H. C. Gatos, *Corrosion*, in press.
6. W. Nernst, *Z. physik. Chem.*, **47**, 52 (1904).
7. A. C. Makrides, N. M. Komodromos, and N. Hackerman, *This Journal*, **102**, 363 (1955).
8. G. Kortüm and J. O'M. Bockris, "Textbook of Electrochemistry," Vol. II, p. 425, Elsevier Publishing Co., New York (1951).

Polymer Synthesis by Gamma Radiation

T. D. CALLINAN

U. S. Naval Research Laboratory, Washington, D. C.

ABSTRACT

Monomers have been polymerized successfully by the action of gamma rays to high molecular weight solids without the employment of elevated temperatures or catalysts. Among the monomers polymerized were ethylene, styrene, methylstyrene, acrylonitrile, and methyl methacrylate. Low molecular weight polyester syrups have been solidified into hard transparent solids without the use of the usual catalysts and accelerators. Some chemical and physical properties of these polymers have been determined. Observed values are compared with the properties of polymers obtained by thermal and catalytic activation. Radiation energies required for causing polymerization have been determined.

INTRODUCTION

The widespread demand for nonpolar, lossless dielectrics presents problems in synthesis which are frequently uneconomical. For example (1), while polyethylene in theory is both nonpolar and almost lossless, the economical production of this item entails the addition of judicious quantities of oxygen to the ethylene, without which low yields and exorbitant temperatures and pressures are encountered. The commercial product, while exceptional electrically and used extensively in pulse cables, possesses a slight but measurable permanent polarity and a moderate molecular weight. The temperature at which this material undergoes fairly sharp softening is 110°C. The molecular weight varies, depending on the conditions of synthesis, from 3000 to 50,000.

The use of catalysts in the polymerization of monomers is widespread, frequently consisting of the addition of benzoyl peroxide or lauryl peroxide, both sources of free radical initiators. It follows that these materials tend to produce polymers having permanent electric moments also. Since not all of the catalyst is used completely, it is often found that with time the reaction continues and changes in the physical, mechanical, and electrical properties occur.

Gamma radiation offers a tool for synthesizing high-melting, cross-linked dielectric solids from simple reagents without the use of adulterants (2). Through this technique the contaminating effect of catalysts is avoided. Where cost is not a factor, it offers a means of producing truly tailor-made dielectrics. Where the use of gamma radiation is economically feasible, it offers still other advantages. For these two reasons this study on polymer synthesis was undertaken.

Monomers have been polymerized successfully by the action of gamma rays to high molecular weight solids without the employment of elevated temperatures or catalysts. In these studies three distinct classes of compounds have been investigated, viz., (*a*) vinyl derivatives, (*b*) polyesters, and (*c*) polysiloxanes.

EXPERIMENTAL

The 2,300-curie source of Cobalt 60 located at the Naval Research Laboratory was employed in these tests. The radiation which emanates from the radioactive cobalt arises from the radiative decay of the metal to a stable isotope of nickel (3). The radioactive cobalt is located at the bottom of the well, under 12 ft of water, to protect personnel against the rays. In the case of reactions induced by the radiation, which happen to be exothermic, the water also acts as a cooling medium; the amount of heat liberated by the source itself is insignificant. The procedure for irradiating materials consists in placing an ampoule or glass container in one or two cells which can be lowered into the radiation field. Mechanisms by which gamma rays transform organic compounds have been described elsewhere in detail (3). Samples of liquids in glass containers were placed in the gamma field and the time required for solidification noted. Dosages were calculated from known field constants (4). No effort was made to exclude air (except in the case of ethylene) from the sample, nor to remove stabilizers incorporated by the producer, nor to control the temperature, since one of the purposes of the work was to determine the immediate feasibility of using gamma radiation under the fewest limitations. The significance of such variables as oxygen content, temperature, and volume is being investigated. Suffice it to say, lower dosages have been found necessary in solidifying large volumes than in converting small quantities of similar reagents. More of the radiationally generated free radicals are quenched at the container walls when small volumes are used. Similarly, lower dosages are needed when lower radiation rates are employed for solidifying equal volumes. This is because the reaction mixture has time, when irradiated slowly, to solidify by conventional means as well as by radiational means. In establishing the constant describing the amount of energy required to solidify a given amount of sample a necessary distinction is between compounds which become increasingly viscous and those which yield precipitates. Thus Type I may be described as polymers which are soluble in the mother liquor and which have as a general effect the increase in viscosity of the liquid being irradiated. Type II polymerizations yield solids which are insoluble in the reagent and, hence, appear as precipitates almost immediately on being introduced into the field. No particular increase in the viscosity of the reagent is noticed.

Calculations of the energy required for solidification involve simply determining the amount of precipitate formed through a unit of dose. In the case of Type I polymerizations the energy required is determined when the entire sample has solidified. Styrene, methyl styrene, methyl acrylate, methyl methacrylate, and 1-vinyl-2-pyrrollidone are typical Type I polymerizations, while ethylene and acrylonitrile form insoluble precipitates and are Type II polymerizations. Each of these syntheses is described and some of the characteristics which have been determined are presented.

Ethylene

A steel cylinder (2 in. in diameter, 14 in. high) containing 112 g of ethylene gas (molecular weight 28.03; melting point −169.4°C; boiling point −104°C; density, 1.245 g/l; purity, 99.94%) at an initial pressure of 1200 psi was placed in gamma fields having an intensity of 5×10^5 r/hr for a period of 72 hr. On removing and opening the cylinder, 14 g (12.5% yield) of a white semifibrous solid was obtained, having the following properties: softening point, 129°C, specific gravity, 0.88; Shore "A" durometer hardness, 45; water absorption after immersion for 24 hr, 0.005%; soluble in chlorinated aliphatic and aromatic compounds at elevated temperatures. The sharpness of the softening point is qualitative evidence for uniformity of molecular weight and freedom from cross-linking. The solid was found to be readily moldable in standard plastic forming equipment at a temperature of 125°C and a pressure of 5000 psi. Under these conditions the material discolored to a deep brown. Pressing at lower temperatures and higher pressures yielded white soap-like products similar in appearance to commercial polyethylene.

Additional syntheses of polyethylene from compressed ethylene gas resulted in yields presented graphically in Fig. 1. It would appear that there is an induction period after which the polymerization proceeds at a satisfactory rate. The reaction is a Type II polymerization.

Methyl Methacrylate

Five grams of commercial methyl methacrylate (mobile, colorless liquid, molecular weight, 100; melting point, −48°C; boiling point, 101°C; specific gravity, 0.940) containing 0.1% benzophenone as a stabilizer were sealed under air in a glass tube (15 × 100 mm) and found to have solidified after being subjected to a total dose of 10×10^6 r gamma.

The product was a clear transparent solid which could be molded at 187°C and 6000 psi, but suffered distortion under mechanical stress at 146°–153°C. This latter is apparently a phase transition similar to that suffered by electron cross-linked polyethylene at 120°C. The solid was found to have the following properties: specific gravity 1.20; Shore "D" durometer hardness, 90; water absorption after immersion for 24 hr, 0.21; solubility, affected by ketones.

Properties of this radiationally prepared polymer are similar to conventional polymethyl methacrylate except that the former has a heat distortion temperature from 16°–23° higher. It is thought that this process might offer a solution to the problem of aircraft canopies distorting at the temperatures arising from aerodynamic heating at high velocities.

Methyl Acrylate

Five grams of commercial methyl acrylate (colorless, mobile liquid, molecular weight 86.05, specific gravity 0.956; boiling point 80.5°C; melting point −75°C) were sealed under air in a glass ampoule (15 × 100 mm) and subjected to 40×10^6 r, whereupon it was removed from the field. The polymerization was Type I, the sample becoming increasingly viscous with time; obviously the sample could have been removed sooner, but the plastic product would have had a lower heat distortion temperature. The particular product obtained was a clear, transparent, colorless elastomer, which became brittle at 10°–20°C but which did not distort without pressure even at 195°C. The material had the following properties: specific gravity, 1.19; Shore "D" durometer hardness, 5; water absorption after immersion for 24 hr, 0.4%; soluble in ketones and chlorinated compounds. This sample was 25% denser than conventional polymethyl acrylate; its mechanical stability at elevated temperatures indicated a high degree of cross-linking.

The properties obtained indicate the versatility and usefulness of radiationally polymerized methyl acrylate both *per se* and in copolymerizations. These latter possibilities are reported under another heading.

Styrene

Ten grams of commercial styrene (colorless liquid, molecular weight 104.06; melting point −31°C; boiling point 146°C; specific gravity, 0.9074) were irradiated under air in a sealed glass ampoule (15 × 100 mm) and removed from the field after receiving 31×10^6 r. The orange-brown clear, transparent solid had a specific gravity of 1.04, distorted at 102°C, possessed a Shore "D" durometer hardness of 85, and absorbed 0.005% water after being immersed for 24 hr. This substance had density and hardness characteristics similar to conventional polystyrene, but differed appreciably in distortion temperature (14°–20°C higher than conventional), absorbed less water, and, on being removed from the gamma field, was colored. On standing at room temperature for 2 months or on being heated to 90°C, the radiationally prepared sample "bleached" appreciably.

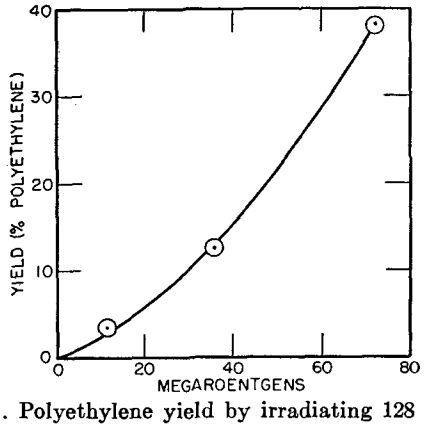

FIG. 1. Polyethylene yield by irradiating 128 g of ethylene gas.

Methyl Styrene

A sample consisting of 146 g of commercial methyl styrene (colorless, liquid; melting point, −131; boiling point, 164; specific gravity 0.88) was irradiated in the presence of air until solid. It had been subjected to 38 × 10^6 r, and the solid product was orange colored, had a specific gravity of 1.30, a heat distortion temperature of 187°C, Shore "D" durometer hardness of 91, and absorbed 0.14% water on being immersed 24 hr. This product was 20% denser than conventional polymethyl styrene and its heat distortion temperature was 40°C higher. On being heated the color of the radiationally prepared polymer "bleached" and approached that of the conventionally colorless polymethyl styrene.

1-Vinyl-2-Pyrrolidone

One hundred and fifty grams of commercial 1-vinyl-2-pyrrolidone were sealed in glass under air and were subjected to 2.2 × 10^6 r of gamma radiation and transformed into a hard, water-dispersible red solid. Considerable heat was evolved during the Type I polymerization. The monomer (colorless liquid, molecular weight 111, boiling point 96_{14} mm°C; specific gravity, 1.07) was transformed into a solid which swells in water, has a specific gravity of 1.51, and a Shore "D" durometer hardness of 75. The density of the material was 20% greater than conventional polyvinylpyrrolidone. The red color faded after 2 months at room temperature or after 2 hr at 135°C, or on being dispersed in water, and a slightly yellow solid was obtained.

TABLE I. *Dosages* for 50–50 copolymers*

	Acrylonitrile	Methyl methacrylate	Styrene	Methyl acrylate
Acrylonitrile	1.2	3.6	6.0	8.0
Methyl methacrylate	3.6	6.0	8.2	9.2
Styrene	6.0	8.2	11.0	19.0
Methyl acrylate	8.0	9.2	19.0	24.0

Relative dosages for 50–50 copolymers*

Acrylonitrile	1	3	5	7
Methyl methacrylate	3	5	7	8
Styrene	5	7	10	16
Methyl acrylate	7	8	16	20

* Megaroentgens at 0.5 mg/hr using 3-g sample.

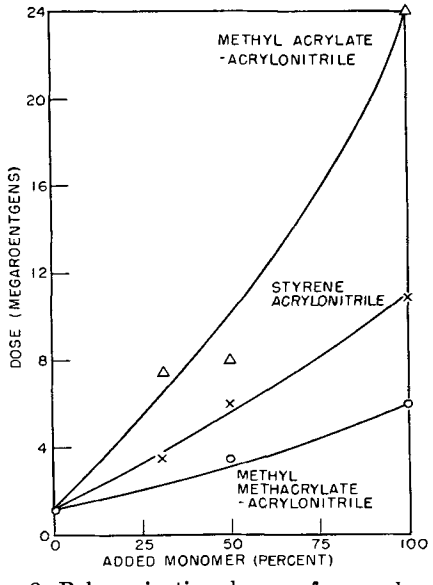

FIG. 2. Polymerization dosages for copolymers

Acrylonitrile

Eight grams of acrylonitrile (straw yellow, mobile water soluble liquid; molecular weight 53.03; melting point −84; boiling point, 77.3; specific gravity 0.80) were converted totally into a white powder on being subjected to 3.1 × 10^6 r of gamma radiation. Considerable heat was evolved during the Type II polymerization and care must be exercised to prevent an explosion occurring. The solid polyacrylonitrile obtained decomposed without melting and was found to be insoluble in common organic solvents. It was very slightly soluble in butyl lactone.

Copolymers

Of the myriad of copolymers conceivable from the monomers studied 50–50 pairs of the following four monomers were prepared and subjected to irradiation, viz., acrylonitrile, methyl methacrylate, styrene, and methyl acrylate. In every case, 3-g samples of each of the mixtures in the presence of air were irradiated at the rate of 5 × 10^5 r/hr and removed on becoming solid. In Table I the dosages in megaroentgens are listed and the relative dosages calculated. In general, it would appear that a Maxwell-type law of mixtures governs the dosages required, the dosages for a 50–50 mixture being intermediate between the dosages required for either of the components

TABLE II. *Copolymers of acrylonitrile*

% Acrylonitrile	% Styrene	Dose	Appearance	Sp gr	Hardness
100	0	1.2	White powder	0.99	90
67	33	4.0	Gray transparent solid	1.13	86
50	50	6.0	Brown transparent plastic	1.25	83
33	67	7.0	Green transparent plastic	1.18	86
0	100	11.0	Straw-colored transparent plastic	1.04	85

% Acrylonitrile	% Methyl methacrylate	Dose	Appearance	Sp gr	Hardness
100	0	1.2	White powder	0.99	90
50	50	3.6	Dark transparent solid	1.37	90
0	100	6.0	Clear transparent plastic	1.20	90

% Acrylonitrile	% Methyl methacrylate	Dose	Appearance	Sp gr	Hardness
100	0	1.02	White powder	0.99	90
70	30	7.5	Two-phase solid; *top:* crepe elastomer, *bottom:* straw-colored transparent plastic	1.25	10/85
30	70	9.5	Green transparent solid	1.39	83
0	100	24.0	Clear transparent solid	1.19	0–10

according to some simple logarithmic relation. This is shown in Fig. 2 where the effect of blending various quantities of more slowly polymerizing monomers on the dosages required for solidifying acrylonitrile is shown. Table II lists some physical qualities of acrylonitrile copolymers showing the variety of characteristics available. In Table III characteristics and dosage requirements of methyl acrylate, styrene, and methyl methacrylate copolymers are listed for those who require transparent plastics.

Casting and Potting Compounds

Samples of commercial polyesters liquids (Paraplex P-43, Laminac 4116, Laminac 4128) were subjected to irradiation and found to be readily convertible into clear hard transparent solids. Such liquids require conversion dosages of 2–4 $\times$ 10^5 r for equal quantities of the monomers previously reported (except vinyl pyrrolidone). The radiationally solidified polyester differs from the conventionally prepared solids in the following ways: they are 10–12% denser, usually have color (yellow-pink), shrink more on curing, and frequently absorb less water on being immersed for 24 hr. Continued irradiation of the polymer after initial solidification has the effect of increasing the hardness, coloration, and heat distortion temperature of the plastic. Thus, 10 g of Paraplex P-43 were solidified after absorbing 3 $\times$ 10^5 r and found to have a heat distortion temperature of 135°C; further irradiation resulting in the polymer receiving a total dose of 10 $\times$ 10^5 r produced a solid having a heat distortion temperature of 146°C, while continued irradiation up to 270 $\times$ 10^5 r gave a final heat distortion temperature of 154°C. The hardness of samples increased slightly during irradiation.

Elastomers

Silicone oils on being subjected to gamma radiation are converted into solid elastomers and products resembling rubber. For this reason the cross-linking and polymerization of polysiloxanes by gamma rays is sometimes referred to as vulcanization. Dosages required to vulcanize some Dow-Corning 200 silicone fluids of different viscosities are shown in Fig. 3. Silicone oils of low molecular weight 300–20,000 on being irradiated have been found to yield clear transparent solids by Type I polymerization. These crumble into soft gels on handling. On the other hand, irradiation of 10 g of silicone oil having an initial molecular weight of 400,000 yields a clear transparent elastomer having a tensile strength of 110 psi, a density of 0.932, a heat distortion temperature of −68°C, and a water absorption value of 0.2% after 24 hr of immersion. By judiciously blending silica (40%) into 10 g of the original oil, and irradiating the sample with 4 $\times$ 10^6 r a semitransparent elastomer having a tensile strength of 1100 psi was obtained.

Another series of elastomers have been prepared by the irradiation of acrylic acid dispersions. Five grams of a commercial 60% solution of acrylic acid in water stabilized with 0.1% beta-naphthol (I) were irradiated and found to solidify after being subjected to 1.1 $\times$ 10^6 r of gamma rays. A known solid elastomer was obtained. It was found that

TABLE III. *Copolymers of methyl acrylate*

% Methyl acrylate	% Styrene	Dose	Appearance	Sp gr	Hardness
100	0	24	Clear transparent elastomer	1.19	0–5
67	33	22	Light-brown semitransparent solid	1.12	90
50	50	19	Light-brown transparent solid	1.06	65
33	67	16	Light-brown transparent solid	1.30	90
0	100	11	Straw-colored transparent solid	1.04	85
% Methyl acrylate	% Methyl methacrylate	Dose	Appearance	Sp gr	Hardness
100	0	24	Clear transparent elastomer	1.19	0–5
50	50	9.2	Straw-colored transparent plastic	1.31	90
0	100	6	Clear transparent plastic	1.20	90

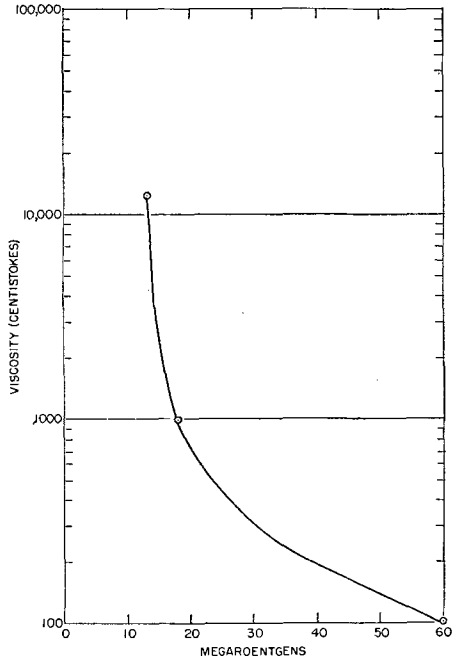

FIG. 3. Polymerization dosages for silicone oils of different viscosities.

dosages of this order 1–4 $\times$ 10^6 r could convert 50–50 mixture of (I) and styrene, acrylonitrile, methyl methacrylate, and methyl acrylate, respectively, into elastomeric bodies.

CONCLUSIONS

It would appear from the results obtained that the irradiation of monomers with gamma rays yields products differing from polymers made by conventional means. In the cases where increased density, heat distortion, or resistance to solvents is desirable, the employment of

gamma rays may be warranted. Where freedom from adulterants and additives is required, gamma radiation techniques are recommended.

Manuscript received September 6, 1955.
Any discussion of this paper will appear in a Discussion Section to be published in the December 1956 JOURNAL.

REFERENCES

1. R. L. WAKEMAN, "The Chemistry of Commercial Plastics," p. 575, Reinhold Publishing Corp., New York (1947).
2. K. H. SUN, *Modern Plastics*, **32**, 141 (1954).
3. T. D. CALLINAN, *Elec. Eng.*, **74**, 510 (1955).
4. H. RABIN AND W. E. PRICE, *Nucleonics*, **13**, 33 (1955).

Preparation of Pure Nickel by Electrolysis of a Chloride Solution

W. A. WESLEY

Research Laboratory, The International Nickel Company, Inc., Bayonne, New Jersey

ABSTRACT

Pure nickel was prepared in the form of malleable electrodeposited sheets as thick as 6 mm from purified nickel chloride-boric acid solution using iridium-platinum alloy anodes. The over-all reaction is

$$NiCl_2 = Ni(metal) + Cl_2(gas)$$

As electrolysis proceeded, purified chloride solution was added automatically to maintain the metal content of the electrolyte. The total of spectrographically detectable impurities is estimated to be about 34 ppm. Carbon content of 26 ppm was reduced to 9 ppm by heating the metal in tank hydrogen and it is believed that any hydrogen, oxygen, and chlorine in the nickel were also substantially reduced by this treatment.

INTRODUCTION

For many research purposes and for spectrographic reference standards, nickel of the highest purity is required in a massive form. The term "high purity" signifies a widely different level of total impurity content when it is applied to different metals. In the present state of the art nickel is considered of high purity if it contains less than about 100 ppm of spectroscopically detectable contaminants. Little information is available on preparations reported to date regarding their content of nonmetallic elements.

A summary of the literature to 1938 on preparation of pure nickel is available (1). No descriptions of preparation of spectrographically pure nickel have been found in the literature since that date. It seems probable that the purest massive metal was prepared by Fink and Rohrman (2) who electrolyzed an impure solution of nickel chloride with a stationary insoluble anode and a cathode rotating at high velocity. First, copper was selectively deposited at a low cathode current density, then iron was removed chemically by oxidation and precipitation with ammonium hydroxide. The electrolyte thus purified was then electrolyzed at a higher current density to give a deposit of nickel on the rotating aluminum cathode from which it was finally stripped mechanically. Purity of the product was assessed only spectrographically because "chemical analytical methods were found inadequate to detect and determine any traces of impurities remaining."

Nickel prepared in this laboratory by the procedure described below has been used as a reference standard and for a wide variety of research purposes over the past fifteen years by more than one hundred research workers in universities, industrial laboratories, and other institutions. No question has been raised by the recipients which would throw doubt on the assumed purity of the metal, namely, a total content of 34 ppm of metallic impurities.

CHOICE OF METHOD

The object was to produce a malleable nickel 6 mm thick and in pieces weighing 1–5 kg each. By analogy with attempts to prepare pure iron it seemed unlikely that any pyrometallurgical or sintering process could be devised which would produce nickel of better than 99.85% purity (1500 ppm impurities) (3). Regardless of how pure the metal could be made in some particulate form it was not believed possible to melt it or otherwise consolidate it to a massive form without contamination, since nickel has a melting point of 1455°C. Such recent developments as levitation melting and drip melting may alter this picture and permit wider choice of methods in the future.

The distillation of nickel chloride in a stream of hydrogen chloride gas, a procedure used in purifying nickel chloride for atomic weight determination, would be cumbersome and hazardous to operate on a larger scale. A nickel carbonyl process would suffer from the same disadvantages. It was concluded that the following procedure was best suited in principle for operation on the desired scale to produce directly a pure malleable nickel.

Commercial nickel refined by the carbonyl process, hence low in cobalt, is dissolved in hydrochloric acid to

form a concentrated solution of nickel chloride. Copper is removed by a hydrogen sulfide treatment. Cobalt, iron, and zinc are removed by treatment with an excess of nickel peroxide. The purified, concentrated nickel chloride solution then serves as the stock to feed an electrolysis cell in which the electrolyte is a more dilute, hot solution of the pure nickel chloride containing boric acid. The latter is added as a buffer to improve physical properties of the deposit. Insoluble iridium-platinum anodes are used with a flat, nonreactive cathode sheet but without a diaphragm of any kind. As electrolysis proceeds the electrolyte becomes depleted in nickel and chlorine in nearly equivalent amounts. These are replaced by addition of the stock purified nickel chloride solution. The *p*H reaches a steady-state value determined by the boric acid content and the fact that the electrolyte is maintained saturated with chlorine by the anode reaction. The net cell reaction is

$$NiCl_2 = Ni(metal) + Cl_2(gas)$$

Hydrated nickel peroxide was selected as the oxidizing reagent to be used for purification because it combines four necessary properties, namely, it is a noncontaminating reagent which can safely be added to the electrolyte in excess to oxidize iron and cobalt (4), its reduction products are harmless in a nickel plating solution, it raises the *p*H of the solution to assist in removal of iron and zinc, and it is a colloid which can adsorb impurity cations.

Details of Preparations

Preparation of the high purity nickel was carried out three times, first in 1932 when a batch of about 3 kg was prepared, then in 1940 with about 6 kg, and finally in 1952 with 32 kg. Details of only the most recent preparation are given.

Dissolving Mond pellets.—For the 1952 preparation it was necessary to dissolve a large quantity of the impure material, namely, about 50 kg. This was obtained from the Mond Nickel Co., Ltd., in the form of pellets made by the carbonyl process. This metal is the best starting material because it is substantially free from cobalt which is a most difficult impurity to remove. The principal impurities are iron, carbon, copper, and silicon.

It is not as easy to dissolve 50 kg of nickel in a large tank as to dissolve a few kilos in laboratory glassware. The process was accelerated by anodic dissolution in contact with an iridium-platinum electrode, the electrolyte being initially 35 liters of 4.7*N* chemically pure hydrochloric acid. Eventually all the desired nickel was dissolved and 375 liters of nickel chloride solution obtained with the following composition: nickel, 127 g/l; copper, 5.3 mg/l; iron, 37.8 mg/l; cobalt, 1.2 mg/l; manganese, <0.1 mg/l; lead, 0.6 mg/l; zinc, $\ll$5 mg/l; *p*H, 0.3.

Chemical purification.—Sufficient hydrogen sulfide was introduced to precipitate the copper. Copper sulfide was removed by filtration and the excess hydrogen sulfide blown out by a stream of clean air.

A batch of nickel peroxide sufficient to neutralize the acid of the chloride solution was prepared by chilling a solution of 14 kg of C.P. caustic soda in 150 liters of water, chilling this solution to −8°C, dissolving 5.1 kg chlorine gas in it, chilling 46 liters of the nickel chloride solution to 5°C and mixing the two solutions by pumping the hypochlorite solution into the nickel solution with rapid agitation. The black nickel peroxide slime thus formed was filtered, washed, and added to the main tank of nickel chloride solution. The *p*H of the latter rose to 4.5 but, since most of the peroxide had dissolved, a fresh small batch of the black slime was prepared, quickly added to the solution, and then the solution was filtered. This was stored in clean glass carboys. Plant-type equipment was used throughout.

The nickel chloride solution was analyzed spectrographically in direct comparison with a sample of nickel chloride made from the 1940 high purity nickel. The results indicated that the new solution could yield nickel as pure as the earlier laboratory preparation, the only difference in the spectrographic results being the presence of a small amount of sodium and a trace of calcium and magnesium in the large new nickel chloride solution.

Electrodeposition of massive nickel.—A 39-liter Koroseal-lined steel tank was selected to serve as a plating cell in the first run. In later runs a 10-liter Pyrex battery jar of rectangular cross section was used to permit observation of the growing cathode and to correct early any tendency for warping due to unequal current distribution on the cathode surface. The cathode was cut from Inconel or stainless steel (type 316) sheet, 0.8 mm thick, in a rectangular shape which substantially filled the central vertical cross section of the cell. Two anodes of 10% iridium-platinum alloy sheet were suspended at opposite sides of the cell in such a way that any condensed or spattered liquid reaching the outside metal connector or supports could not drip back into the cell. The submerged areas of the anodes gave an effective anode area of 877 cm^2. Sheets of glass were mounted over the cell to reduce danger of contamination of the solution by falling or wind-blown particles. The cell was set up within a chemical hood to exhaust the chlorine gas evolved at the anodes.

In a typical run the plating cell was filled with the purified nickel chloride solution, diluted to about 2*N*, and sufficient chemically pure boric acid was dissolved in it to provide a concentration of 30 g/l. With the electrolyte at 50°C the cathode was first coated all over, including those portions later to extend above the solution to serve as connectors, with pure nickel to a thickness of one or two hundred microns. The cathode was then mounted exactly midway between the anodes and parallel to them. Separate ammeters were connected to the anodes so that exactly equal currents could be supplied to each side of the cathode and thus prevent warping.

Since 5 or 10 days of uninterrupted electrolysis were required to grow the cathode deposits, automatic control of conditions in the plating cell was desirable. This was made easy by the nature of the over-all cell reaction, namely, the production of almost equivalent quantities of nickel and chlorine at the cathode and anode, respectively. Even though the cathode efficiency was less than 100% the excess anode efficiency simply caused evolution of a little more chlorine from the already saturated electrolyte and the *p*H did not fluctuate much. By arranging a constant-level jar device and filling it with pure nickel chloride solution the latter entered the plating cell at a rate equal to the

TABLE I. *Electrodeposition data*

Run	5-29-52	6-27-52	11-20-52	12-5-52	12-18-52
Plating cell	Koroseal	Koroseal	Pyrex	Pyrex	Pyrex
Capacity, liters	39	39	10	10	10
Cathode area, dm^2	23.4	20.0	12.1	12.1	12.1
Electrolyte					
$NiCl_2$ g/l†	280–140	280–100	100–120	130–80	90–110
H_3BO_3 g/l	30	26–30	34	36	37
*p*H	2.5–3.3	2.4–2.8	2.6–2.7	2.3–2.9	1.7–3.8
Cath. cur. density, amp/dm^2	2.6–3.4	2.5–4.2	3.0	2.6	2.6
Duration, hr	51	220	41	244	242
Approx. cathode efficiency, %	90			80	87
Pure nickel					
No. of pieces	2	2	2	2	2
Weight,* kg	2.7	10.5	1.1	5.4	6.0
Thickness, mm	1.4	6.6	1.0	5.6	6.3
Condition	Warped	Good	Warped	Excellent	Excellent

* Estimated weight after shearing edges and removing starting sheet.
† Roughly estimated from sp gr readings at bath temperatures.

rate of evaporation of water from the electrolyte. Evaporation rate was controlled automatically by regulating the temperature and the rate of deposition of nickel by controlling the electrolysis current. It was thus necessary only to balance temperature and current flow so that nickel chloride was decomposed at exactly the same rate as that at which fresh chloride feed entered the cell.

Quantitative data relating to the several runs are presented in Table I. The total amount of usable metal prepared was about 32 kg. This included an estimated 6 kg of edge scrap which is not in the desired form but is useful for many research purposes.

Purity of Product

The accurate analysis of metals of high purity poses difficulties which require intensive research to overcome.

TABLE II. *Spectrographic examination of high purity nickels*

Element	Amounts in nickel prepared in		
	1932	1940	1952
Al	NF	NF	2–11 ppm
Sb, Ba, Bi, Cr, Co, Ge, Au, In, Ir, Mn, Hg, Mo, Os, Pt, K, Rh, Ru, Sc, Sr, Ta, W, Y	NF	NF	NF
As, B, Pd, Na	NF	VST	VST
Cd, P	NF	NF	
Cs, Ga, La, Li, Nb, Rb, Te, Tl		NF	NF
Fe, Ag	Trace	Trace	Trace
Ca	NF	<1 ppm	<1 ppm
Cu	Present	≪4 ppm	≪4 ppm
Pb	NF	4 ppm	4 ppm
Mg	NF	1 ppm	1 ppm
Re	NF		
Si	NF	NF	2 ppm
Sn	NF	3 ppm	3 ppm
Ti	NF	NF	<1 ppm
V	NF	VST	<1 ppm
Zn	NF	≪1 ppm	≪1 ppm
Zr		<1 ppm	<1 ppm

NF = None found. VST = Very slight trace.

TABLE III. *Results of wet chemical analysis of pure nickels*

Element	Results in 1952		1952 Accuracy	In 1932	In 1940
	12-5-52	12-18-52			
	ppm	*ppm*		*ppm*	*ppm*
Cobalt	5	3	±0.8	3	4
Copper	4	4	±2	8	2
Iron	10	10	±5	5	11

There has not been sufficient need thus far for exact knowledge of the composition of the nickel made here to justify such research. The spectrographic data recorded in Table II represent results obtained in three different decades by different spectrographers. It can be seen that there is little doubt of the absence of metallic impurities except aluminum, cobalt, copper, iron, lead, silicon, and tin. Repeated analyses by standard colorimetric methods in 1932, 1940, and 1953 yielded the data of Table III. Procedures were similar to those approved by the A.S.T.M. (5) and commonly known as the thiocyanate method for iron, the hydrobromic acid method for copper, and the nitroso-R salt method for cobalt. A large sample of 10 or 20 g was taken for each determination. Blanks for aluminum, lead, gold, silicon, and tin were too large in comparison with the amounts of these elements present to permit their determination by standard wet methods.

Nonmetallic impurities.—Of the nonmetallic impurities whose presence might be suspected, other than those included in Table II, there remain carbon, sulfur, oxygen, hydrogen, nitrogen, and chlorine to be considered.

Sulfur could not be detected.

For carbon determinations the greatest care must be exercised to avoid contamination of the sample by particles of steel in the cutting tools and by contact with the fingers or even with wax on the cap of a sample bottle. In addition, the carbon level is low enough that low precision was inevitable with conventional methods. The data of Table IV indicate a carbon level of 20–30 ppm in the nickel in its as-deposited condition. A conductometric method was employed in making these carbon determinations.

TABLE IV. *Removal of carbon from pure nickel by annealing in hydrogen*

Time of heating	Avg carbon content* in ppm ±2	
	12-18-52 nickel	12-5-52 nickel
None	28	24
24 hr	26	15
48	25	15
72	20	15
96	10	8

* As determined by the Laboratory Equipment Co. in their conductometric apparatus for determination of very low carbon values.

It is known that the carbon, oxygen, and hydrogen contents of pure iron can be reduced greatly by merely heating it in undried hydrogen at 400°–500°C to remove surface carbon and then in dry hydrogen at 1100°C to remove oxygen (3). With nickel it should be unnecessary to use dry hydrogen. Accordingly, small pieces of the 12-5-52 nickel and millings of the 12-18-52 nickel were placed on trays of pure nickel and heated in tank hydrogen at 540°C. Each day a portion of the nickel was removed from the furnace and retained for analysis. The data of Table IV show that the carbon content was indeed lowered by the heating treatment.

At present this laboratory is not equipped for vacuum fusion gas analysis and no information is available on the gas content of the pure nickel. By analogy with results published by the National Bureau of Standards for commercial nickel deposited at *p*H 3 from a nickel chloride plating bath (6) there might be as much as 150 ppm oxygen, 10 ppm hydrogen, and 15 ppm chloride in such nickel. It is reasonable to assume that the long treatment of the pure nickel in hot hydrogen reduced its content of these gases below 10 ppm at the same time that the carbon was eliminated. The solubility of hydrogen in nickel at 540°C is probably less than 5 ppm (7).

Probable purity.—Weighing all the evidence in Tables II, III, and IV it can be concluded that nickel can be prepared by the electrolysis of purified nickel chloride on a rather large scale with the following purity:

Metallic impurities		Nonmetallic impurities		
			As-deposited	Annealed
	ppm		*ppm*	*ppm*
Al	6			
Co	4	C	26	9
Cu	4			
Fe	10	H*	(10)	(<10)
Pb	4	O*	(150)	(10)
Mg	1	Cl*	(15)	(<10)
Si	2			
Sn	3			
	34			

* Not determined, see text.

Properties of Pure Nickel

As deposited from the chloride solution the nickel was very smooth of surface even at the relatively great thickness of 6 mm. The metal retains high residual internal stresses and these should be reduced by annealing before proceeding with cold forming operations in using it. In some of the individual deposits a lamellar structure occurred which could be detected by the growth of blisters within the metal upon heating. These faults are believed to have been due to occasional accidental interruption in the direct current supply during deposition.

Specimens of the 1932 batch of pure nickel have been employed by workers in a number of laboratories for research purposes. Many of these data were included in a paper by Wise and Schaefer (8). Table V lists significant values for interesting properties of the 1932 nickel.

Acknowledgment

The author wishes to express his thanks to N. B. Pilling for guidance in the earlier preparations, to E. G. Mohling and E. J. Roehl for assistance in the earlier preparations, and to R. G. Lomell, H. B. Canada, and N. E. Gordon for analytical data.

TABLE V. *Properties of the 1932 pure nickel*

	Value communicated	Reference
Lattice constant	3.5168 A.U. at 24.8°C	(9)
Density	8.908 computed from lattice constant	(8)
Avg. coef. of thermal expansion	10.22×10^{-6}/°C at −180 to 0°C	(8)
	13.3×10^{-6} 0 to 100	
	14.63×10^{-6} 0 to 300	
	15.45×10^{-6} 0 to 500	
Thermal diffusivity	0.15885 ± .00009 cm²/sec at 25°C	(10)
Thermal conductivity	0.618 watt/cm °C at 25°C	(10)
Electrical resistivity	6.141 microhm cm at 0°C	(8)
	6.844 microhm cm at 20°C	
Temp. coef. of electrical resistivity	0.00682/°C at 0 to 100°C	(8)
	0.00692 (vacuum annealed)	
Coercive force	2.73 oersteds	(8)
Tensile strength	Annealed: 46,000 psi	(8)
Yield strength	0.2% offset; annealed 8,500 psi	(8)
Recrystallization temperature	After cold rolling 50%: 370°C	(8)

Manuscript received September 30, 1955. This paper was prepared for delivery before the Pittsburgh Meeting, October 9 to 13, 1955.

Any discussion of this paper will appear in a Discussion Section to be published in the December 1956 JOURNAL.

REFERENCES

1. A. E. VAN ARKEL, "Reine Metalle," p. 349, Julius Springer, Berlin (1939).
2. C. G. FINK AND F. A. ROHRMAN, *Trans. Am. Electrochem. Soc.*, **58**, 403 (1930); **59**, 359 (1931).
3. G. A. MOORE, *Trans. Am. Inst. Mining Met. Engrs.*, **197**, 1443 (1953).
4. R. L. SUHL, J. W. SANDS, AND O. B. J. FRASER, Canadian Pat. 264,172, Sept. 7, 1926.
5. "A.S.T.M. Methods of Chemical Analysis," American Society for Testing Materials, Philadelphia (1950).
6. V. ZENTNER, A. BRENNER, AND C. W. JENNINGS, *Plating*, **39**, 865 (1952).
7. C. J. SMITHELLS, "Metals Reference Book," Vol. 2, p. 535, New York (1955).
8. E. M. WISE AND R. H. SCHAEFER, *Metals & Alloys*, **16**, 424 (1942).
9. E. R. JETTE AND F. J. FOOTE, *J. Chem. Phys.*, **3**, 605 (1935).
10. C. STARR, *Rev. Sci. Inst.*, **8**, 61 (1937).

Determination of the Activity of Sodium in Sodium-Lead Alloys at High Temperatures

BERNARD PORTER AND MORRIS FEINLEIB

Chemical Research Department, Kaiser Aluminum & Chemical Corporation, Permanente, California

ABSTRACT

The activity of sodium in sodium-lead alloys was determined by the concentration cell method. The emf of cells

Na (pure)/Na^+/Na in Pb

was directly measured up to 820°C, using alumina containers impregnated with Na_2CO_3 in an argon atmosphere. Results were converted to activities and extrapolated to 1010°C. To check the extrapolation, emf's of cells of the type

Na(a_1) in Pb/Na^+/Na(a_2) in Pb

were measured up to 1010°C The a_2/a_1 ratios calculated from the measurements were compared with those obtained by extrapolation. Fair agreement was found.

INTRODUCTION

In connection with a study of sodium-aluminum equilibria (1) it was necessary to determine the activity of sodium in various sodium-lead alloys at temperatures up to 1010°C. Few published data are available on the activity of sodium in sodium-lead alloys at elevated temperatures. Hauffe and Vierk (2) determined these activities at temperatures ranging from 425° to 475°C. They measured the emf of cells consisting of pure sodium on one hand and various sodium-lead alloys on the other.

The activity of sodium in the alloy was obtained from the Nernst equation:

$$E = \frac{RT}{n\mathbf{F}} \ln \frac{a_{\mathrm{Na(Pb)}}}{a_{\mathrm{Na(pure)}}} = 1.984 \times 10^{-4} T \log a_{\mathrm{Na(Pb)}} \qquad \text{(I)}$$

since the activity of pure sodium is unity at any temperature. E is expressed in volts and T in °K. Wide departures from ideal solutions were observed.

In Hauffe and Vierk's studies, the pure sodium and the alloys were contained in sodium glass, which also furnished the electrolytic path between the two half-cells. At higher temperatures, glass is not suitable, as it was necessary to find a material that would not react with sodium or lead, yet would provide an electrolytic path for sodium ions.

EXPERIMENTAL

The cell material selected was fused-cast alumina Monofrax MH (Carborundum Co.). It is 99+% alumina, and contains sodium aluminate. In order to insure a good electrolytic path for Na^+ and to reduce the possibility of Na^+ concentration gradients, the cells were impregnated by fusing anhydrous Na_2CO_3 in the cell cavities for several hours at 1000°C.

Cells (Fig. 1) were fabricated from Monofrax MH bricks as follows: a block of the desired size was cut with a diamond saw and was carefully examined to make sure that no large blowholes were present. Block dimensions were approximately 3 in. high x 2⅛ in. long x 1⅛ in. wide, but were not critical. A slot was next cut down the center of the block, to within about ¾ in. to 1 in. of the bottom. Two ½ in. D. cavities were then drilled with a diamond core drill to a depth of about 1½ in.; a 3/16 in. D. thermocouple hole was also drilled in one side. The blocks were oven-dried, then impregnated as mentioned above.

In order to get reliable emf data, it is necessary that the sodium concentration should remain constant throughout a run. This can only be accomplished in a sealed chamber, in which the liquid sodium or alloy is in equilibrium with sodium vapor, with no chance of vapor escape. This

becomes especially important at the elevated temperatures of these experiments, where sodium has a high vapor pressure (its boiling point is 880°–890°C).

In order to provide an electrical connection to the liquid metals and to seal the cell cavities, metal caps were used. The caps need only withstand the action of sodium vapor, and therefore were made of mild steel. Since the thermal expansion coefficient of steel is considerably higher than that of alumina, the caps had to be machined undersize, so that, at the highest temperature of a given run, they would just seal the cavity. Experience showed that sufficient Na_2O was present so that, once the cavities were sealed at a high temperature, the seal remained intact upon cooling.

The electrical lead-in wire had to withstand the action of both lead and sodium up to 1000°C; molybdenum was chosen as one of the few suitable metals. (Graphite was unsuitable because of carbide reactions with sodium.) Since molybdenum wire becomes brittle when welded, it was joined to the cap as illustrated in Fig. 1. A small hole was drilled through the cap, and the wire inserted through this hole and welded at the top of the cap, so as to completely seal the hole at the same time. Thus the cap itself furnished protection against bending of the wire. A Nichrome wire was also welded to the outside of the cap for connection to a potentiometer.

In view of the ease with which sodium is oxidized, the experiments were run in an inert atmosphere. This was most readily accomplished in a vacuum apparatus provided with electrical connections and a furnace.

A typical run was carried out as follows.

Sodium and lead were weighed out in approximately the desired proportions and placed in one cavity; pure sodium was placed inside the other cavity. The caps were inserted, and the cell positioned inside the furnace. An Inconel thermocouple protection tube was inserted into the thermocouple well in the Monofrax block, and a thermocouple put inside the tube. The fused-cast alumina is a fair conductor of heat and will reach a uniform temperature rather fast; therefore, by locating the well within the block itself, a representative measurement of cell temperature could be achieved.

Next, all thermocouple and electrical connections were completed. The vacuum apparatus was closed and pumped down to approximately 150 μ. Argon was then led into the vacuum chamber until the pressure approached atmospheric. The chamber was again evacuated to about 150 μ while the temperature was raised to approximately 200°C. The apparatus was refilled with argon to almost atmospheric pressure. The temperature was then raised to the maximum level at which measurements were to be taken. With pure sodium in one of the cell cavities, this maximum temperature usually did not exceed 820°C. After temperature equilibrium was attained, emf readings were taken every two minutes until a steady value was observed. A Beckman battery-operated pH meter with a millivolt scale was used for measuring the potentials.

After a minimum of 6 steady emf readings were obtained at the highest temperature, the temperature was dropped in a number of steps, holding it at each level until thermal and emf equilibrium was attained. After the last reading, the system was allowed to cool to room temperature in argon.

The cell was removed from the chamber and the alloy compartment opened; the seal was usually so strong that considerable force was required to break it. A ½ in. drill was first used to remove the top portion of the alloy and thus avoid possible contamination of samples with Na_2O. A smaller drill was then used to get turnings from several spots in the remaining alloy for sodium analysis. In the case of high-sodium alloys, samples had to be taken and weighed rapidly to avoid air oxidation and moisture pickup. Sodium analyses were performed with a Beckman DU spectrophotometer, using a flame photometer attachment.

It is important to point out that all of this work is based on the assumption that the alloy composition does not change from the time the first emf readings are taken at the highest temperature till the end of the run. When the cap sealing was satisfactory, there is good reason to believe that the assumption was justified. If sealing was not adequate, it was not usually possible to get steady emf readings at a given temperature, and such runs were discarded.

It was mentioned above that, with pure sodium in one of the cavities, the highest practical temperature level was 820°C. Since it was necessary to know the values of sodium activity in lead alloys at temperatures ranging from 940°C to 1040°C, an extrapolation of the measured activities to these temperatures had to be made (*see* later). As a check on the validity of this extrapolation, it was decided to run a few concentration cells at temperatures up to 1010°C, using a high-sodium-lead alloy in one compartment and a lower sodium alloy in the other. Except for the temperature range, the procedure was as already described. In the case of double-alloy cells, both compartments were analyzed for sodium.

In a double-alloy cell, the Nernst equation relating sodium activities and emf's becomes:

$$E = 1.984 \times 10^{-4} T \log \frac{a_{1\,\mathrm{Na(Pb)}}}{a_{2\,\mathrm{Na(Pb)}}} \qquad \text{(II)}$$

where a_2 is the high-sodium alloy activity and a_1 that of the lower sodium alloy. Activity ratios obtained from these direct measurements were compared with those taken from extrapolated activity-concentration curves.

Results and Discussion

Results of a typical activity determination are given in Table I and for several runs in Fig. 2. The activity of sodium vs. temperature at a given concentration is almost linear on a semi-log scale, and therefore is most readily extrapolated.

The curve of limiting activity

$$a_L = \frac{1}{p^0} \qquad \text{(III)}$$

where p^0 is the vapor pressure of pure sodium, has also been plotted (Fig. 2) to show the limits beyond which the extrapolation cannot be used when working at atmospheric pressure. Fig. 3 shows the variation of sodium activity

TABLE I. *Activity of sodium in a sodium-lead alloy**

Temp		emf† mv	a = sodium activity	γ = activity coefficient
°C	°K			
827	1100	389	16.5×10^{-3}	7.78×10^{-2}
798	1071	393	14.2×10^{-3}	6.70×10^{-2}
763	1031	398	11.6×10^{-3}	5.47×10^{-2}
730	1003	400	9.77×10^{-3}	4.61×10^{-2}
695	968	405	7.78×10^{-3}	3.67×10^{-2}
664	937	408	6.38×10^{-3}	3.01×10^{-2}
622	895	409	4.98×10^{-3}	2.35×10^{-2}
552	825	409	3.17×10^{-3}	1.50×10^{-2}
502	775	404	2.36×10^{-3}	1.11×10^{-2}

* Wt % Na in Pb = 2.90 (N_{Na} = 0.212).
† Emf of pure sodium against the above alloy.

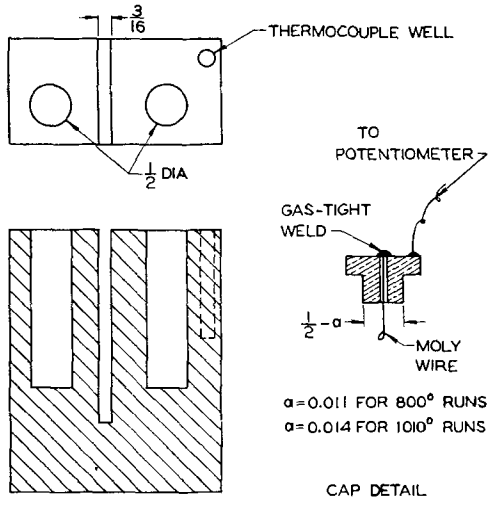

FIG. 1. Cell for the determination of sodium activity in sodium-lead alloys.

with its mole fraction in sodium-lead alloys at various temperature levels.

Fig. 2 and 3 show that the precision of the activity determinations and extrapolations is limited. In Fig. 3 there is a considerable scattering of measured activity values; this becomes even more serious for extrapolated values.

TABLE II. *Double-alloy cells; comparison of directly measured and calculated activity ratios*

Pb-Na alloy composition	Temp	a_2/a_1 from Fig. 3	a_2/a_1 from emf (meas)	% difference = $\left(\frac{\text{meas.} - \text{calc.}}{\text{meas.}} \times 100\right)$
	°C			
$N_1 = 0.171$	1008	2.80	2.97	+5.7
$N_2 = 0.301$	970	2.84	3.01	+5.7
	938	2.85	3.01	+5.3
	898	2.91	2.92	+0.5
	806	3.04	3.09	+1.6
	706	3.12	2.98	−4.7
	608	3.10	2.94	−5.5
$N_1 = 0.222$	1010	3.31	3.58	+7.5
$N_2 = 0.371$	968	3.41	3.78	+9.8
	936	3.41	3.84	+11.1
	894	3.42	3.75	+8.8
	801	3.67	3.90	+5.9
	700	3.84	3.99	+3.8
	597	3.80	4.01	+5.3

Measurement errors can account for some of the inaccuracy. The potentiometer used in the emf measurements could be read to ±1 mv, causing an uncertainty in the activity of ±1.3%. A temperature error of 1°C causes a

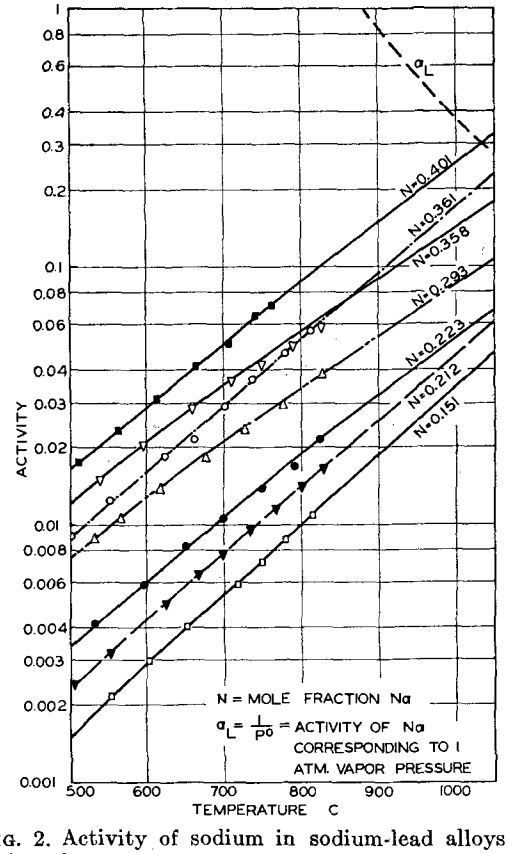

FIG. 2. Activity of sodium in sodium-lead alloys as a function of temperature.

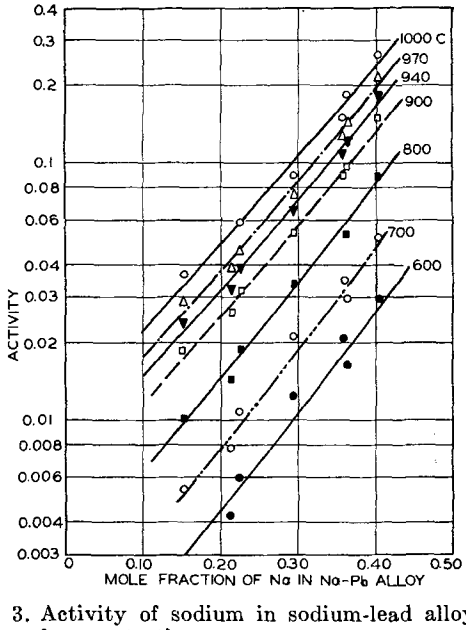

FIG. 3. Activity of sodium in sodium-lead alloys as a function of concentration.

change of 0.5% in the activity. Sodium analyses are no better than ±2% of the sodium concentration, causing a corresponding error in the mole fraction values used in Fig. 3.

A major source of error could be the establishment of metallic or electronic paths between the two cell compartments, either on top between the caps, or within the cell material itself. This was the reason for cutting the slot between the cell compartments (Fig. 1); such a slot breaks up the continuity of the top surface and at the same time lengthens the electrolytic path between the two half-cells.

Finally, whereas the assumption of constant alloy composition during a run appears to be justified, there is no way of making certain of this, other than observing the constancy of potential readings at each temperature and checking each cell at the end of the runs for cracks, etc.

To test extrapolated activity values, two double-alloy cells were run as previously described. The results of these runs were taken into account in determining the best line to draw through the extrapolated points plotted in Fig. 3.

A comparison of activity ratios calculated from double-alloy cell measurements and those taken from Fig. 3 is given in Table II.

In view of the experimental difficulties and the assumptions involved, it may be stated that the agreement between measured and extrapolated values is acceptable, and that the extrapolation of activity measurements of sodium-lead alloys against pure sodium is on the whole justified.

ACKNOWLEDGMENT

The authors wish to acknowledge the help of J. I. Davis in carrying out the laboratory work. Analytical determinations were performed by K. Lincoln and J. Winkler. The machine work was carried out by K. I. Booth and T. G. Glassey.

Manuscript received September 15, 1955. This paper was prepared for delivery before the Cincinnati Meeting, May 1 to 5, 1955.

Any discussion of this paper will appear in a Discussion Section to be published in the December 1956 JOURNAL.

REFERENCES

1. M. FEINLEIB AND B. PORTER, *This Journal*, **103**, 232 (1956).
2. K. HAUFFE AND A. L. VIERK, *Z. Elektrochem.*, **53**, 151 (1949).

Electrochemical Characteristics of Melts in the $Sb\text{-}Sb_2S_3$ System

TSUTOMU YANAGASE[1] AND GERHARD DERGE

Carnegie Institute of Technology, Pittsburgh, Pennsylvania

ABSTRACT

Liquid Sb and Sb_2S_3 were equilibrated at various temperatures and electrolyzed with the metal phase as anode and the sulfide phase as cathode. Current efficiencies varied below 60% and analysis of the data indicated that the balance of the current should be accounted for by the electronic character of the melt rather than losses or side reactions. This was confirmed by direct measurement of the conductivity of the melt as a function of its composition.

INTRODUCTION

The electrical conduction of molten copper sulfide, iron sulfide, and their mixtures has been shown to be electronic in character (1). Therefore, it was of interest to investigate in detail the electrical properties of molten antimony sulfide (Sb_2S_3) since early electrolysis experiments (2) indicated it has some ionic character even though current efficiencies were too low to be of commercial interest. The ionic character of solid Sb_2S_3 was also demonstrated by electrolysis (3).

Preliminary experiments showed measurable changes in composition of the anode and cathode compartments after electrolysis of molten Sb_2S_3 in a simple Vycor H-cell with graphite electrodes. Free sulfur was also observed at the anode. This confirmed the reported presence of ions in the melt. It was evident that a useful study of the system would require a more elaborate cell and control of the experimental variables. This is due chiefly to the mutual solubility of the liquid metal and sulfide phases as shown in Fig. 1. In order to measure the current efficiency for deposition of metal at the cathode, it would be necessary to have the sulfide electrolyte previously saturated with metal at the temperatures of electrolysis. The cell and the experiments developed for this study will now be described.

[1] Present address: Department of Metallurgy, Kyushu University, Fukuoka, Japan.

EXPERIMENTAL PROCEDURE

Molten antimony metal was used as the anode in order to prevent the formation of free sulfur (as observed at an inert graphite anode) which might in turn react with the metal deposited at the cathode. The electrolyte should be

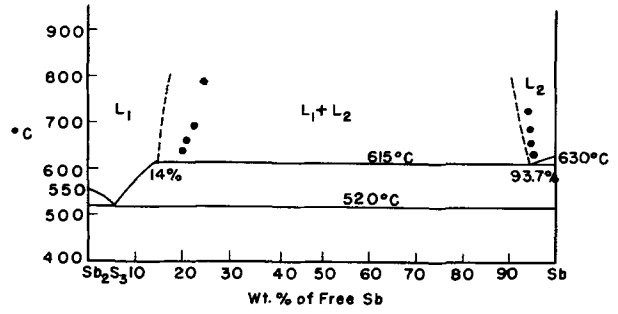

FIG. 1. Phase diagram of the Sb-Sb_2S_3 system, based on the diagram of Hansen (4) for the Sb-S system. ● = Data from this research.

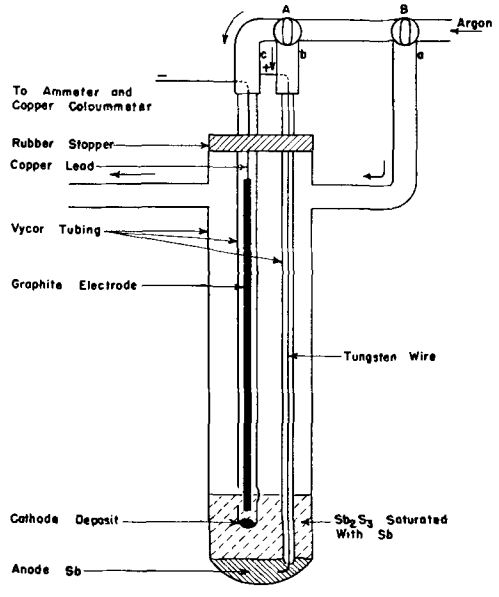

FIG. 2. Cell for the electrolysis of molten antimony sulfide.

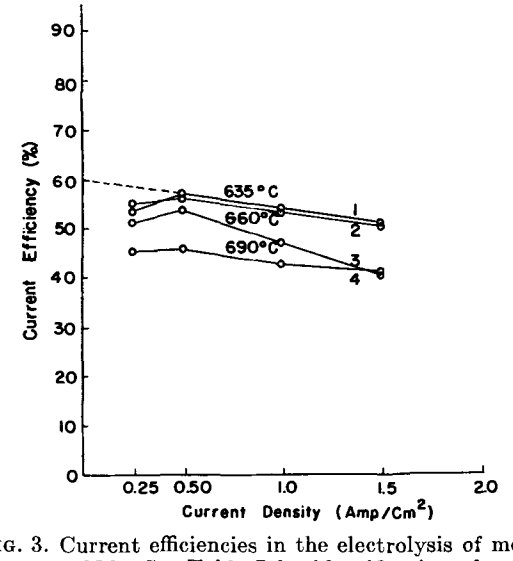

FIG. 3. Current efficiencies in the electrolysis of molten antimony sulfide. See Table I for identification of curves.

saturated with metal previously so that all antimony formed as a result of cathode reaction can be collected and weighed. These and related considerations form the basis for the cell and technique.

The cell is shown in Fig. 2. It is constructed of Vycor, connected to the Pyrex stopcock system A and B so that argon can be introduced as the cell atmosphere or bubbled through the anode holder to provide stirring. The cathode consisted of a graphite electrode in a perforated chamber which collected the liquid antimony deposit as formed. Other features become evident in the description of the procedure. The antimony metal was C.P. grade and the Sb_2S_3 was Fisher, Technical.

The liquid metal and sulfide phases were presaturated in a similar cell without electrical connections by bubbling argon for 3 hr at selected temperatures.

The Vycor cell, with electrodes elevated, was charged with 30 g of Sb_2S_3 and 15 g of Sb, previously equilibrated as above, and the charge melted under argon.

The anode tube was lowered into the melt and argon bubbled at constant temperature for 1 hr in order to insure equilibrium between phases. The bubbling was stopped for 15 min to allow Sb droplets to settle from the sulfide layer.

The cathode tube (*c*) was then lowered into the melt with argon flowing through it to maintain the neutral atmosphere. Electrolysis was started and the amount of current measured by a copper coulometer connected in series.

The cathode tube was raised out of the cell and cooled rapidly with an air blast. The metal button was separated and weighed.

The current efficiency was calculated on the assumption that all ions discharged were Sb^{+3}.

The results of such experiments in the temperature range 635°-690°C, with current densities increasing to 1.5 amp/cm², are shown in Fig. 3 and listed in Table I. They show that the current efficiency decreases with increasing current density and higher temperature. Since the melting point of antimony is 630°C, the curve for 635°C represents the limiting temperature for these experiments. The points at 0.25 amp/cm² are believed to be the least reliable because only a small amount of metal was deposited and

TABLE I. *The electrolysis of molten* Sb_2S_3

Run No. in Fig. 3	Temp.	Current density	Volt	Time	Cathode deposit	Current efficiency	Remarks
	°C	amp/cm²		min	g	%	
1	635	0.25	1.0	120	0.4075	53.3	
	635	0.5	1.7	90	0.6400	56.6	
	635	1.0	2.8	60	0.8086	53.5	
	635	1.5	3.8	40	0.7648	50.6	
2	635	0.25	1.0	120	0.4234	53.3	Bubbling
	635	0.5	2.2	90	0.6300	55.7	during
	635	1.0	2.6	60	0.7992	52.9	elec-
	635	1.45	3.5	60	1.0942	50.0	trolysis
3	660	0.25	0.6	120	0.3740	51.1	
	660	0.48	1.3	90	0.5816	53.3	
	660	1.0	2.2	60	0.7014	46.6	
	660	1.5	2.7	40	0.6050	40.0	
4	690	0.25	0.8	120	0.3530	45.1	
	690	0.5	0.9	90	0.5105	45.2	
	690	1.0	1.6	60	0.6414	42.4	
	690	1.5	2.0	40	0.6200	41.0	

all measurements involved high percentage error. If these are ignored, and the data extrapolated to zero current density it would seem that, even under optimum conditions, the maximum attainable current efficiency is only about 60%. In order to understand the reasons for this low value a number of factors have been considered.

Several possible sources of error in the experiment were considered. The data for curve 2 of Fig. 3 were obtained by bubbling argon continuously during the electrolysis. In other cases this procedure gave erratic results due to disturbance of the metal-sulfide interface and it was not generally used, but it is believed that the evidence at hand is sufficient to show that failure of the liquids to remain saturated was not a source of serious error.

The possibility of loss of antimony from the cathode by vaporization during electrolysis was checked by blanks with 1 g of metal in the cathode chamber. The maximum loss observed was 0.5% of the metal after 1 hr at 690°C. This is negligible in comparison to the changes observed during electrolysis.

Analysis of the cathode metal button showed that it contained from 2–4% Sb_2S_3, or less than 1%S, which is less than the equilibrium solubility of Fig. 1 and is too small to be important.

The presence of Sb^{+5} in the system could account for the observed low current efficiencies. However, this does not seem likely in the presence of metallic antimony for the reaction:

$$2Sb + 3Sb^{+5} \rightleftarrows 5Sb^{+3}$$

will not only prevent the formation of appreciable amounts of the pentavalent ion, but will become more effective with increase in temperature. This is contrary to the trend of current efficiency.

Since the sources of experimental error did not appear to be great, it was desirable to seek another explanation for the low observed current efficiencies by examining the electrical characteristics of the molten sulfide through direct measurement of conductivity as influenced by the dissolved metal, according to Fig. 1. It might be expected that a part of the conductance is by an electronic mechanism.

Influence of Dissolved Antimony on the Electrical Conductivity of Molten Antimony Sulfide

Conductivity measurements were made with the four terminal cell, a-c potentiometer circuit developed and described in connection with studies of other sulfide systems (1). Sulfides were prepared with varying amounts of dissolved antimony by equilibrating the sulfide and metal at various temperatures as already described for the electrolysis experiments. After equilibration the sulfide layer was separated and its conductivity measured. The analyses of both layers are shown in Table II for identification in connection with the conductivity data. These analyses are also plotted as solid points on Fig. 1 since they define the two-liquid region of this system, which has previously been uncertain, as indicated by the dashed lines of Fig. 1. Conductivity data are plotted as a function of temperature in Fig. 4 where it is evident that the conductivity of the system is very sensitive to small amounts of dissolved metal. For all compositions measured, the positive temperature coefficient of conductivity is large and the specific conductance is above 5 $\Omega^{-1}cm^{-1}$ at temperature above 800°C. These high values certainly indicate that a large part of the conductance in this system must be electronic.

TABLE II. *Analysis of sulfide and metal equilibrated at various temperatures*

Run No. in Fig. 4	Temp	Metal layer		Sulfide layer	
		%S	%Sb_2S_3 (calcd.)	%S	%Sb† (calcd.)
	°C				
1	635	1.46	5.2	22.5	21
—	660	1.52	5.4	22.4	21.5
2	690	1.65	5.9	22.0	22
3	735	1.76	6.2	21.7	23
4	790	1.27(?)	—	21.3	24
5*	—	—	—	24.6	12.8

* Prepared by fusion of C.P. grade Sb_2S_3 powder. Sulfur loss observed.

† Sb in excess of that required for Sb_2S_3.

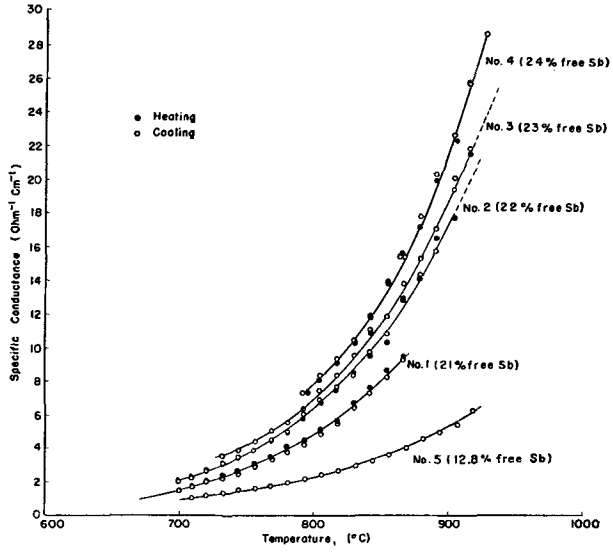

FIG. 4. Specific conductance of antimony sulfide with dissolved antimony. See Table II for complete identification of melts. Curve No. 1, 21% dissolved Sb; curve No. 2, 22% dissolved Sb; curve No. 3, 23% dissolved Sb; curve No. 4, 24% dissolved Sb; curve No. 5, 12.8% dissolved Sb.

Discussion

The electrolysis of molten antimony sulfide is characterized by low current efficiencies (never observed to exceed 60%) even when the experiment is carefully controlled to remove disturbing side reactions by the use of sulfide saturated antimony anode and antimony saturated sulfide electrolyte. This is attributed to the fact that the solution of antimony in the Sb_2S_3 causes an increasing amount of electronic conduction in the electrolyte. This is demonstrated by measurements of conductivity, showing that it increases with dissolved antimony and with temperature and exceeds the magnitude normally associated with simple ionic conduction. This explanation of the observed data is preferred by the authors as it cor-

relates with the major controlled changes in the system and the known behavior of other sulfides. It is of course possible that unknown impurities could be partially responsible, but there is no compelling reason for not accepting the more direct explanation.

Although not directly related to the electrolysis of antimony sulfide, the conductivity of the metal layer equilibrated with sulfide at 790°C was also measured. It is interesting to note that, unlike pure metal, this has a slight positive temperature coefficient, increasing from about 9200 $\Omega^{-1}cm^{-1}$ at 800°C to about 9300 $\Omega^{-1}cm^{-1}$ at 900°C.

Acknowledgments

The authors appreciate helpful discussions of this work with Drs. G. M. Pound, M. Simnad, L. Yang, and M. Bourgon and the analytical assistance of N. A. Mooney.

The work was done under Contract No. AT(30-1)-1024 with the United States Atomic Energy Commission.

Manuscript received August 1, 1955. This paper was prepared for delivery before the Cincinnati Meeting, May 1 to 5, 1955.

Any discussion of this paper will appear in a Discussion Section to be published in the December 1956 JOURNAL.

REFERENCES

1. G. M. POUND, G. DERGE, AND G. OSUCH, *Trans. Am. Inst. Mining Met. Engrs.*, **203**, 481 (1955).
2. R. E. VIVIAN, *Trans. Electrochem. Soc.*, **69**, 637 (1936).
3. G. S. SON FREY, *Arkiv. Kemi Mineral. Geol.*, **11A**, No. 4, 1 (1932).
4. M. HANSEN, "Aufbau der Zweistofflegierungen," p. 1033, Springer, Berlin (1936).

Anodic Transients of Copper in Hydrochloric Acid

RALPH S. COOPER

Physics Department, University of Illinois, Urbana, Illinois

ABSTRACT

Anodic transients for the system Cu | HCl were studied using horizontal anodes shielded to prevent convection. With the exception of the appearance of a second plateau the results are in quantitative agreement with Müller's "Bedeckungstheorie." The reaction occuring during the first plateau is

$$Cu + Cl^- \rightarrow CuCl + e^-$$

The second plateau is due to the initiation of a new reaction involving the OH^- ion. Potential measurements and visual observation indicate it to be

$$2\ Cu + 2\ OH^- \rightarrow Cu_2O + H_2O + 2e^-$$

Studies made with $0.5N$–$6N$ hydrochloric acid show the layer thickness to be given by a relation of the form $\delta = Di_I^{-m}$ with m independent of concentration and D proportional to it. These results were compared with some obtained with vertical unshielded anodes to determine the effect of convection. For rapid transients (< 3 sec) Müller's theory held with both types of anode. Otherwise results were qualitatively similar with the exception of the appearance of overshoot and a steady state with the unshielded anodes.

INTRODUCTION

An understanding of the fundamental mechanisms involved in layer formation at anodes would be of great value in such fields as corrosion, passivity, polarization, electrolytic rectification, refining, and polishing. Previous studies at this laboratory dealt with Fe | H_2SO_4 (1, 2) and Cu | 2N HCl (3) systems. Current and potential transients were investigated and in the latter system the anodic layer was identified as CuCl. The present paper is a continuation of the work on the Cu | HCl system and has four major objectives: (*a*) identification of the processes taking place; (*b*) application of Müller's theory (4, 5) to the prediction of the current transient; (*c*) a study of the effect of hydrochloric acid concentration; and (*d*) an investigation of the influence of convection.

Müller's theory is based on two types of layer growth; first, the spread of a solid layer of constant thickness (6) across the anode face until only small pores in layer remain, and, second, the increase in depth of the layer with the pore area constant. If a high current density is applied to an anode, a saturated solution of the anode salt will be formed in the neighborhood of the electrode surface and subsequently a solid film of the salt will be deposited on the anode face. For the initial process Müller (6) assumes that (*a*) the solution and diffusion of the salt is negligible, (*b*) the solid film spreads from random nuclei [as has been directly observed (3)], (*c*) this film maintains a constant thickness, (*d*) the anode potential is constant, i.e., neglecting concentration polarization, and (*e*) the conductivity of the salt is negligible, thus causing the current to flow only through the uncovered areas until they diminish in size to small pores in an otherwise complete layer. The resistance of the layer-pore system is relatively small until about 99% of the surface is covered, at which time the resistance increases sharply, becoming the controlling one in the circuit and causing the current to decrease. The current-time behavior is represented by the equation:

$$t = \tau + A\left[\frac{-1}{i_I - i} + \frac{1}{i_I}\ln\left(\frac{i_I - i}{i}\right)\right] \qquad (I)$$

where i_I is the total current during the first plateau,[1] and τ and A are constants for a given transient. τ is a measure of the duration of the current plateau, and A is inversely related to the rate at which the current decreases at the termination of the plateau. The form of this relation for several values of the parameters is shown in Fig. 1. By substituting $x = i/i_I$

$$t - \tau = +\frac{A}{i_I}\left[-\frac{1}{1-x} + \ln\left(\frac{1-x}{x}\right)\right] = +\frac{A}{i_I}f(x) \qquad (II)$$

Thus, all transients obeying this law would have the same form (Fig. 2) except for the multiplicative factor A, which in effect expands or contracts the time scale. The validity of the relation and the constants A and τ is determinable by plotting $f(x)$ vs. t for a given transient. This should result in a straight line of slope $-i_I/A$ and intercept τ on the t axis. These constants contain the thickness of the layer δ, the conductivity of the solution in the pores κ, and other physical properties of the system. Solving for δ and κ:

[1] Unfortunately there is conflicting nomenclature in the literature. i_I here represents the total current (not current density) during the first plateau in agreement with references (2) and (3), while Müller used i_o for this quantity. i_o here refers to the value of i immediately upon closing the circuit. A is a constant, while the symbol S is used to denote areas. Müller used F in place of S; C for τ and μ for t_+. The general nomenclature, especially the usage of E, V, and ϵ is consistent with references (2) and (3) as this work is a continuation of the latter.

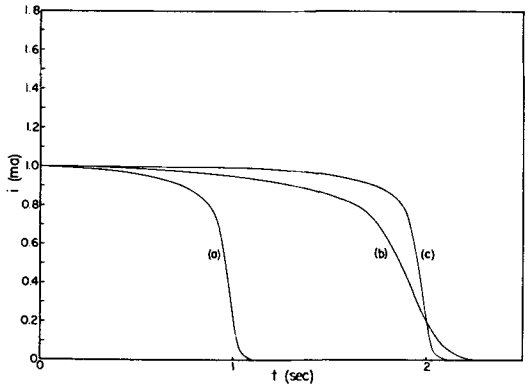

FIG. 1. The shape of current transients according to Müller. i_I = 1 ma. Curve (*a*) τ = 1 sec, A = 0.02 ma-sec; curve (*b*) τ = 2 sec, A = 0.06 ma-sec; curve (*c*) τ = 2 sec, A = 0.02 ma-sec.

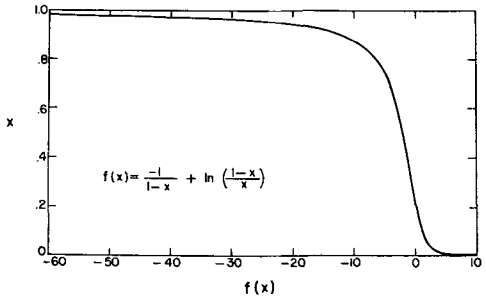

FIG. 2. The form of the current transient, according to Müller; i vs. t has the same form with t as the abscissa.

$$\delta = \frac{\tau k(1 - t_+)i_I}{\rho S} \qquad \text{(III)}$$

$$\kappa = \frac{\tau^2 i_I^2 k(1 - t_+)}{A\rho S^2(R + r_o)} \qquad \text{(IV)}$$

k is the equivalent weight of the precipitated salt divided by the Faraday constant, ρ is its density, t_+ is the transference number of the cation, and S is the apparent area of the electrode. $(R + r_o)$ is the total resistance initially present in the circuit. All quantities appearing in equations (III) and (IV) are assumed to be constant for this phase of the transient.

As the pore area becomes smaller the current density in the pores rises, and instead of the pores closing entirely, the layer grows in depth, with the pore area constant. Müller assumes the layer becomes deeper by the anodization of the metal at the base of the pores only, but no mechanism for this is given in his work. The transition from the spreading process to the growth in depth is a relatively sharp one, but no theory has been developed which predicts at what point it occurs.

On the basis of Müller's assumption, the increase in layer depth (7) is governed by the relations

$$t - t_1 = B\left(\frac{1}{i^2} - \frac{1}{i_1^2}\right) \qquad \text{(V)}$$

$$B = \frac{\kappa(E - \epsilon)s_p^2}{k(1 - t_+)} \qquad \text{(VI)}$$

where B is a constant, E is the applied voltage, ϵ the anode potential, and s_p is the total area of the pores in the solid layer. i_1 is the value of the current at any particular time t_1 during the period of growth in depth. A plot of i^{-2} vs. t results in a straight line of slope B^{-1} for the period during which this process is occurring. The pore area may be calculated from B and compared to that computed for the spreading process at the time that the transition occurs.

Müller found these relations to hold in many simple acid-metal systems. However, the Cu/HCl system has several complicating features which are interrelated. The most apparent deviation is the appearance of a second plateau. This is interpreted as the occurrence of a second electrode reaction. Next in importance is the complex ion formation of dissolved CuCl as $CuCl_2^-$ and $CuCl_3^=$. This is accompanied by a strong dependence of solubility upon Cl^- concentration (and hence on hydrochloric acid concentration), resulting in a large variation in conductivity, as CuCl is only slightly soluble in water. The electrode potential, ϵ, varies for several reasons. It is a function of the concentration and the $CuCl_2^-$ content of the acid in the immediate neighborhood of the anode, which is different than the bulk values because of the Nernst diffusion layer. The presence of a solid film also alters ϵ. Finally, the transference number of the cation may change as the H^+ is replaced by Cu^+ near the anode face. The rates of the reactions involved are believed to be too rapid to produce observable effects in these experiments.

EXPERIMENTAL

Apparatus.—The basic circuit used was that described previously (3).

For very fast interruption experiments an apparatus was devised using a pair of Westinghouse No. 275c relays (Fig. 3). A variable resistance was placed in series with one relay and both relays were powered by the same 22.5 v dry cell battery. By varying the resistance, one relay (A) could be adjusted to close from 0 to 20 msec after the other (B). The circuit was broken only for the period when only one relay was closed. The cell circuit could thus be opened conveniently for periods as short as 50 μsec to observe the electrode potential and resistance. A motor driven switch was placed in the battery circuit so

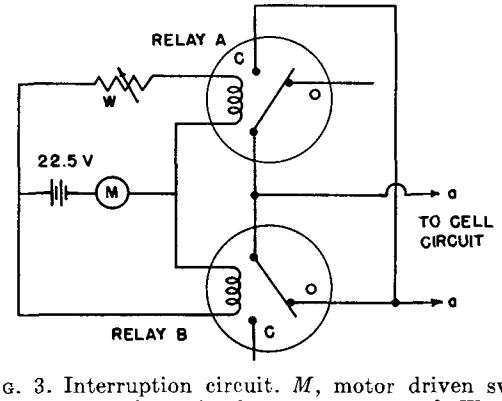

FIG. 3. Interruption circuit. M, motor driven switch. Both relays are shown in the open position, O. When the relays are energized relay B closes first, A shortly after, breaking circuit a-a momentarily.

that the interrupting mechanism could be actuated up to six times per second during the course of a transient. In addition, this device was used in conjunction with a Tektronix 512 oscilloscope and a 35 mm still camera, to obtain information of the very early stages ($<10^{-3}$ sec) of transients and of potential decays.

The cathode was of platinized platinum, 10 cm² in area, the potential of which was constant within 0.01 v. An 0.1*N* calomel electrode placed very close to the cathode was used as reference. All potentials given here are with respect to this reference unless otherwise noted. The applied voltage E is defined to include the potential of the cathode, which was nonpolarizable under currents of 50 ma or less. The open circuit anode potential was approximately −0.35 v on this scale so that applied voltages above this value, even if negative, were anodic. The internal resistance r represents the total resistance between the tip of the reference and the anode metal, and includes the resistance of the bulk of the solution and of all liquid and solid anode films. V is the potential of the anode metal with respect to the reference cell and includes the IR drop in the electrolyte and film.

In 2*N* hydrochloric acid the reference showed a liquid junction potential of 0.06 v when checked against an Ag/AgCl electrode. Thus, the platinized platinum hydrogen electrode displayed a potential of −0.40 v instead of −0.335 v. The liquid junction potential was negligible in 0.1*N* hydrochloric acid. Most of the anodes used were copper wire and rolled rod. A few measurements were made with single crystals of copper, but no significant differences were observed. Anodes of various areas were investigated but were usually of 0.176 cm² cross section. They were screwed or soldered into brass rods, with all but the face covered with some form of insulation. The most satisfactory insulation consisted of seven coats of Micro Supreme Stop Off Laquer HR-302 (Michigan Chrome Company), but even shellac and paraffin, although not as durable, produced the same results. The construction of shielded anodes is shown in Fig. 4. These showed no tendency for preferential etching at the sharp edge, even after prolonged use.

Procedure.—In the previous work anodes were polished with 4/0 emery paper before each run. In a study of the effect of varying the electrode area, it was observed that reproducibility was improved if several runs were made with the same anode before taking data. This removes the material severely cold worked by the mechanical polishing. Thus, the procedure was as follows.

An anode was ground down with 2/0 and 4/0 emery paper and up to 20 runs were made; no data were taken until the fourth run. Between each run the anode and/or solution was agitated to permit the solution of the CuCl layer, which could be detected by its effect on the open circuit potential of the electrode. In solutions 1*N* or less, the layer was more difficultly soluble, and in these cases the anode was removed and cleaned with 2*N* HCl. Air saturated solutions were made from 'Baker Analyzed' Reagent grade HCl, and were maintained at 25 ± 1°C. Each run was made with a constant applied voltage, E, and fixed external resistance, R.

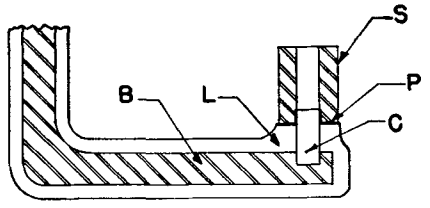

FIG. 4. Detail of shielded anode. *C*, copper specimen; *B*, brass support; *L*, 7 coats of lacquer; *S*, Lucite shield; *P*, parafin seal.

RESULTS AND DISCUSSION

Shielded Anodes in 2N HCl

General nature of transients.—The results presented in this section were obtained, unless otherwise specified, by using a shielded anode of 0.176 cm² cross section and zero external resistance. The current transients are qualitatively similar to those obtained previously (3) for unshielded anodes. Two examples are shown in Fig. 5. In Fig. 5*a* is a transient made with small applied voltage (−0.24 v), which is a low-current, slow transient with an initial decrease before the stationary current of the first plateau is reached. This is followed by a single slow decrease in current. With greater applied voltages the initial current becomes larger and the time (τ) to the current decrease shorter. At about 0.5 v a second plateau becomes clearly discernible, although it is present at applied voltages (E) as low as 0 v, and can be better observed with a larger (R = 150 Ω) external resistance. A typical transient of this type is shown in Fig. 5*b*. It has two plateaus and a region where the i^{-2} law holds. A set of characteristic curves (Fig. 6) can be drawn relating i and V (the anode potential including IR drop in the solution) for the stationary values on the first (i_I, V_I) and second (i_{II}, V_{II}) plateaus.

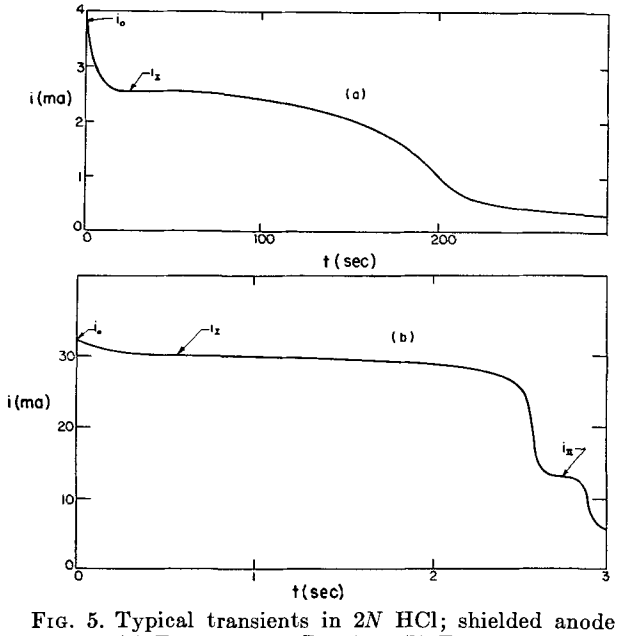

FIG. 5. Typical transients in 2*N* HCl; shielded anode 0.176 cm². (*a*) E = −0.24 v, R = 0 Ω; (*b*) E = +0.4 v, R = 150 Ω.

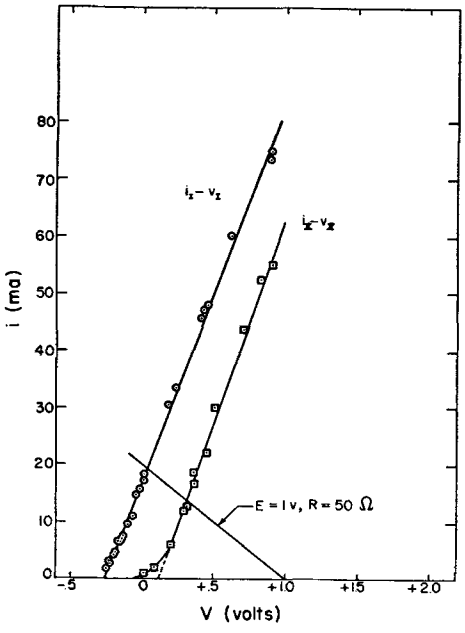

FIG. 6. Characteristic curves for shielded anode (0.176 cm²) in 2N HCl, showing locus of stationary values of current and voltage on first plateau (i_I, V_I) and second plateau (i_{II}, V_{II}). No steady state exists. A typical "load line," with E = 1 v, R = 50 Ω is shown.

Since Ohm's laws applied to the circuit results in the equation

$$V = E - iR \qquad \text{(VII)}$$

the $i - V$ relation for any given transient can be represented by a "load line" (3) of slope $-1/R$ and intercept, E. For R = 0 Ω the load line is vertical, and an example with E = 1.0 v, R = 50 Ω is shown in Fig. 6. The intersection of the load line with the characteristic curve gives the values of i and V on the plateaus. The i_I, V_I and i_{II}, V_{II} curves are straight lines, with slopes representing resistances of about 14 ohms, that of the solution in the cell. No steady state is reached within 10 min. Interruption experiments were performed to determine the electrode potential (ϵ) and resistance (r). Fig. 7 shows i, ϵ, and r, as functions of time for E = 0.2 v, R = 150 Ω. It may be noted that r is constant on the second plateau at a value larger than r_o, which is somewhat different from the previous results. The variations in ϵ and r are discussed later.

Initial current peak.—When a copper rod is placed in 2N hydrochloric acid free of Cu^+ ion, its potential cannot be determined by the Nernst equation, but is partially the result of local action cells (8). The potential is dependent upon the very small amount of Cu^+ which goes into solution and upon its rate of removal by diffusion. Thus, while the observed potential is −0.44 v for vertical unshielded electrodes, the shielded anode displays a potential of −0.35 v (which approaches −0.44 v upon vigorous stirring of the solution). These potentials may vary as much as ±0.02 v, but such variations have negligible effect upon the transients. For both types of electrodes in 2N hydrochloric acid saturated with CuCl, the observed potential is −0.27 v. This value may be calculated from the Nernst

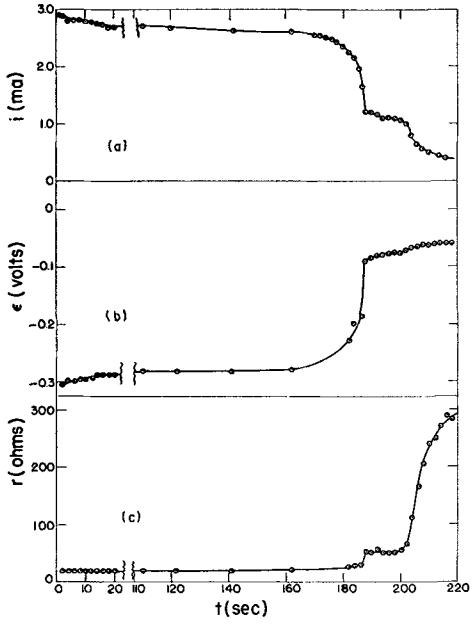

FIG. 7. Results of interruption experiments 2N HCl; E = 0.2 v; R = 150 Ω. (*a*) i vs. t; (*b*) ϵ vs. t; (*c*) r vs. t.

equation. Therefore, for a transient in pure hydrochloric acid there is initially a short period during which the acid is becoming saturated with CuCl, and ϵ is changing from −0.35 v to −0.27 v. During this time, the interruption experiments (Fig. 7) show that r is constant, and hence the initial current peak is due entirely to changes in ϵ. The current is given by Ohm's law for the circuit

$$i = \frac{E - \epsilon}{R + r} \qquad \text{(VIII)}$$

Thus, for large applied voltage (E) (and hence large i_o, i_I) the effect of an 0.08 v change in ϵ is relatively small. Also for large initial currents, the solution near the anode becomes saturated more quickly and so the transition from i_o to i_I is of shorter duration.

The first plateau.—During the first plateau the potential is steady at the value of −0.27 v; the resistance r remains as its initial value. This can be accounted for completely by the ohmic resistance of the solution. The shield contains a cylinder of acid 1.2 cm long and 1.76 cm² in cross section. If one adds the radius of the cylinder to correct roughly for the end effects, and uses the value of 0.56 $\Omega^{-1}cm^{-1}$ for the bulk electrolytic conductivity (9, 10) one obtains a value of 14 ohms. This compares well with the values obtained by interruption methods 17 ± 4 ohms (Fig. 7) and from the slope of i_I, V_I curve 14.3 ± 0.5 ohms. The large uncertainty in the value from the interruption experiment is due to the small potential drop of only 0.045 ± 0.01 v in the example given. One with a potential drop of 0.415 v gave r = 14.2 ± 0.5 Ω. As the layer nears completion, the resistance increases as expected. However, the potential ϵ also begins to change, becoming less negative. The effect of this change depends upon the amount of shift in ϵ compared to the total potential applied to cell. ϵ changes only by about 0.2 v at the maximum, while E may be chosen at will and has been

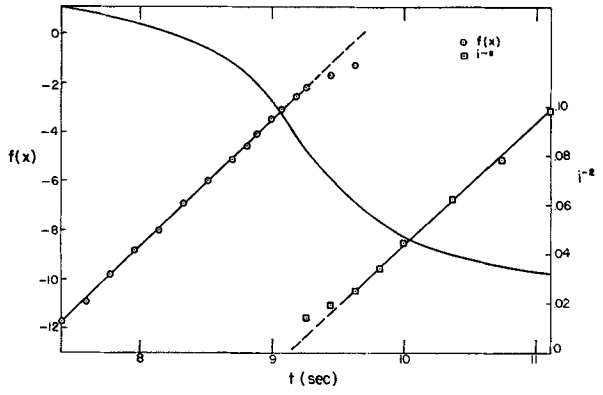

FIG. 8. The validity of Müller's laws. $f(x)$ vs. t and i^{-2} vs. t for shielded anode $E = 0$ v; $R = 0\ \Omega$.

made as high as 4.5 v in this study. Thus, the variation of ϵ may be expected to cause some deviation from the ideal behavior previously derived. Nevertheless, the linear relation between $f(x)$ and t holds well for $E = 0$ (Fig. 8) and even lower.

The solid product was identified previously as CuCl (3). The potential of the first plateau (-0.27 v) has been noted to be identical with the potential of a copper electrode in $2N$ hydrochloric acid saturated with CuCl. There are two possible net reactions:

$$Cu + 2\ Cl^- \rightarrow CuCl_2^- + e^- \qquad (IX)$$

and

$$Cu + Cl^- \rightarrow CuCl + e^- \qquad (X)$$

For saturated solutions of CuCl in HCl nearly equal potentials are calculated from the Nernst equation for the two reactions. Including liquid junction potentials the result is -0.27 v for reaction (IX) and -0.28 v for reaction (X) in $2N$ hydrochloric acid saturated with CuCl. It is to be expected that during the period when the hydrochloric acid is unsaturated, reaction (IX) alone takes place.

When the solution is saturated, the electrode should assume the $Cu/CuCl/Cl^-$ potential. To check this both a Cu and Ag/AgCl electrode were immersed in various concentrations of hydrochloric acid saturated with CuCl. The difference in standard potential of the $Ag/AgCl/Cl^-$ and $Cu/CuCl/Cl^-$ electrodes is 0.100 v and the experimental value is within ± 0.01 v of this, down to $0.05N$ hydrochloric acid. This indicates that the anode is behaving as a $Cu/CuCl/Cl^-$ electrode. During the transient, changes of composition in the diffusion layer take place, altering the concentration of the potential determining species at the anode face and introducing a small free diffusion potential.

Taking the solid product as CuCl one can compute the layer thickness δ and the conductivity (κ) in the pores for a series of transients. i_I, τ, A, δ, and κ for a wide range of transients are tabulated in Table I. First, consider τ, which is related to the length of the first plateau. A plot of $\log \tau$ vs. $\log i_I$ (Fig. 9) gives a straight line, indicating the relation,

TABLE I. *Results in 2N* HCl

E volts	R Ω	i_I ma	τ sec	$A \times 10^3$ ma-sec	$\delta \times 10^3$ cm	$\kappa \times 10^3$ $(\Omega\ cm)^{-1}$
0.10	0	21.6	5.70	1.94	0.21	5.7
0	0	15.7	9.70	3.01	0.25	5.1
−0.10	0	9.52	22.8	5.10	0.36	6.2
−0.15	0	6.60	42.5	7.09	0.48	8.0
−0.20	0	4.64	81	13.7	0.62	7.0
−0.20	0	4.52	84	13.0	0.63	7.4
−0.24	0	2.55	210	24.0	0.89	7.9
0.20	150	2.74	193	3.23	0.89	6.1
0.50	50	11.0	16.6	1.78	0.30	2.8
0	50	4.06	92	2.31	0.62	9.3

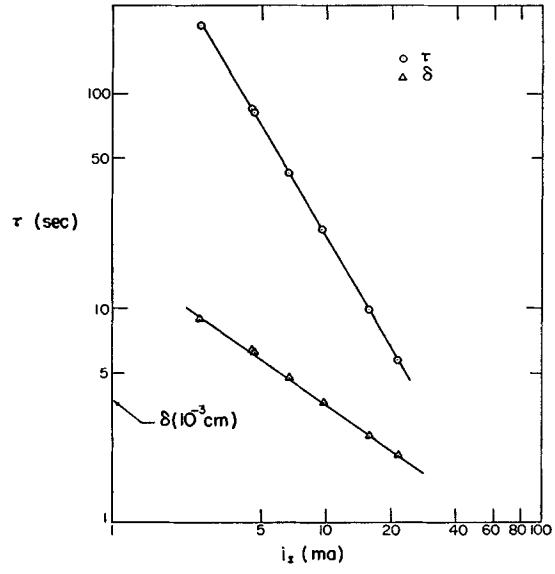

FIG. 9. The duration of the first plateau (τ) and the layer thickness (δ) as functions of i_I ($2N$ HCl).

$$\tau = 1025\ i_I^{-1.685} \qquad (XI)$$

i_I in milliamperes. δ, the layer thickness, can be computed from τ and is given by

$$\delta = 1.70 \times 10^{-3}\ i_I^{-1.685}\ \text{cm} \qquad (XII)$$

Müller found a variation of δ with i_I of this form with various exponents in many systems which he explained on the basis of crystallization of smaller particles at higher current densities, and consequently higher supersaturation at the anode face. That δ depends on the current density only, rather than total current, may be seen from Fig. 10, in which data for a shielded anode of 0.176 cm^2 cross section, taken with various values of R, are shown and compared with the results obtained from a smaller unshielded one (0.021 cm^2), adjusted to the same current density. δ ranged from 24×10^{-3} to 0.1×10^{-3} cm in this study, and was computed on the basis of $t_+ = 0$, i.e., that H^+ and Cl^- were carrying most of the current during the major portion of the current plateau. This is reasonable in view of the fact that the Cu in solution is present almost entirely as $CuCl_2^-$ and $CuCl_3^=$ complexes (11, 12).

The conductivity (κ) of the solution in the pores is found to vary between 8.0×10^{-3} and $4 \times 10^{-3}\ \Omega^{-1}cm^{-1}$. The conductivity of $2N$ hydrochloric acid is $0.56\ \Omega^{-1}cm^{-1}$

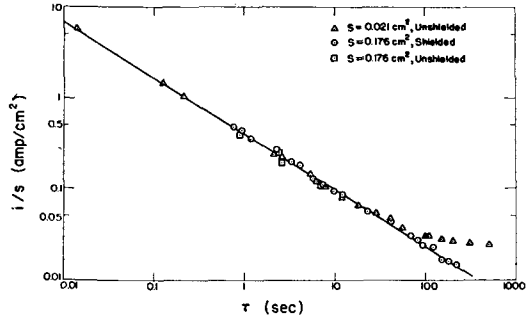

FIG. 10. τ vs. current density, showing identical results for large and small anodes and the effect of convection on unshielded anodes at low current densities (2N HCl).

and that of saturated aqueous CuCl approximately 1.5 $\times$ 10^{-4} $\Omega^{-1}cm^{-1}$, while the conductivity of the solution in the pores lies somewhere in between, at about the geometric mean of the two. A qualitative understanding of this may be based on concentration changes occurring in diffusion layer during the transient. The concentration of hydrochloric acid at the anode appears to decrease according to the Schlieren observation made earlier (3) and this is to be expected from the depletion of Cl^- ions by formation of CuCl. Thus, if the major portion of the concentration change occurs before the current drops, the conductivity in the pores may be expected to have a roughly constant low value for the relatively short duration of the current decrease at the end of the plateau.

The observed value of κ is equivalent to a hydrochloric acid concentration of 0.02N. If κ lessens during the decrease of the current, then the slope of the $f(x)$ vs. t curve should become smaller and this behavior is confirmed by observation, especially with large external resistance R. Also decreasing hydrochloric acid concentration decreases CuCl solubility, thus tending to precipitate it from solution. Despite these aberrations the theory apparently does hold quantitatively for most of the conditions studied, and qualitatively for the rest. In most cases a precise value of $A(\pm 5\%)$ can be found to fit the current transient. Since A is proportional to δ^2, a plot of log A vs. log i_I (Fig. 11) should be a straight line of slope -1.36. Actually, such a plot has a slope of -1.19, the difference being due to the variation with the external parameters (E and R) of the conductivity in the pores.

The second plateau.—For applied voltages of 0.1 v or more the decrease in current is interrupted by a second plateau. The locus of the i_{II}, V_{II} values are shown in Fig. 6. In 2N hydrochloric acid the second plateau is much shorter than the first and less reproducible in all features. At times it is only a small inflection or discontinuity in slope. Interruption experiments show that ϵ changes after the first plateau and rises to the value of -0.05 v on the second, during which it remains constant. The resistance also is constant during the plateau period. The i_{II}, V_{II} curve approaches a straight line (for large currents), with an intercept of + 0.11 v. However, potential decay and interruption experiments always give the value of ϵ to be -0.05 v during the second plateau. In earlier work (3) it was observed that the first decrease was due to the sudden change of ϵ (assumed due to the formation of a very

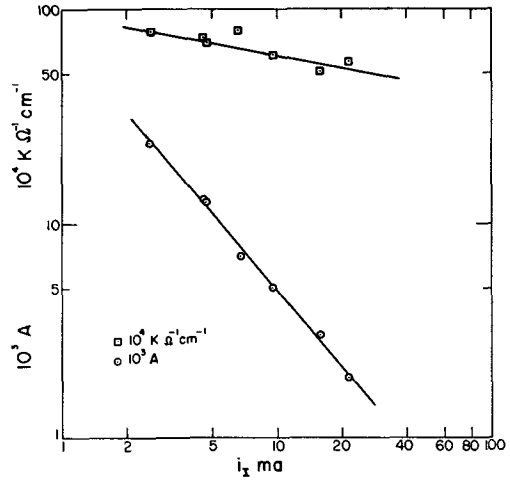

FIG. 11. κ and A vs. i_I (2N HCl)

thin complete layer of CuCl over the surface) and that there was a slight delay before r increased, thus causing a second decrease in current. The explanation of the second plateau postulated here is that a new reaction occurs on the second plateau, forming a solid layer at the base of the pores in the CuCl layer. It was observed that the second plateau became more prominent as the concentration of the acid was reduced. In 0.5N HCl the second plateau was more prominent and reproducible than at higher concentrations and lasted 4 or more times as long as the first plateau. This is a strong indication that the reaction occurring during the second plateau involves the OH^- ion. Next, consider the situation just before the second plateau begins. The conductivity of the solution in the pores has been shown to be about 6 $\times$ 10^{-3} $\Omega^{-1}cm^{-1}$ which corresponds to 1.5 $\times$ $10^{-2}N$ HCl. In addition, the composition of the solution in the pores is probably nonuniform due to diffusion caused concentration gradients which are likely to be set up, especially under such large current densities as 3 amp/cm². However, since the solid CuCl layer can act as a source of CuCl, the minimum conductivity should be that of a saturated solution of CuCl. Even if the hydrochloric acid concentration at the anode surface were as high as the average in the pores, of the order of $10^{-2}N$, it would permit the reaction:

$$2\,Cu + 2\,OH^- \rightarrow Cu_2O + H_2O + 2e^- \qquad \text{(XIII)}$$

The possibility of Cu_2O formation is also indicated by the presence of a reddish-brown powder observed on anodes upon removal from solution after electrolysis in 0.5N hydrochloric acid. The equilibrium potential of this reaction in $10^{-2}N$ HCl is +0.03 v, neglecting liquid junction and free diffusion potentials which may be of the order of ± 0.06 v. Any migration effects would cause the concentration of the HCl at the anode surface to be less than the average concentration in the pores, which would favor the above reaction at lower potentials. The major problem in comparing the experimental and theoretical electrode potential is caused by the unknown value of the concentration potential across the diffusion layer adjacent to the anode. CuOH and basic salts are the only other possibilities. Nevertheless, it appears clear that the forma-

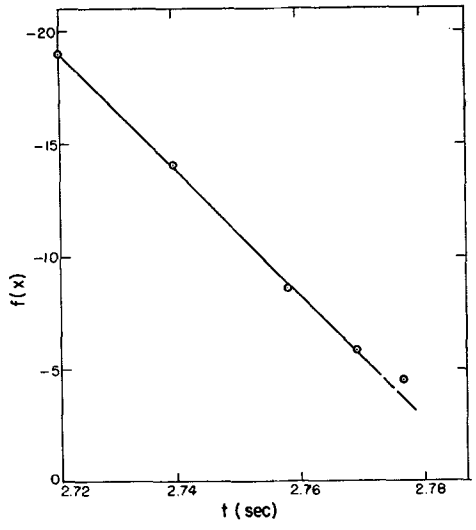

FIG. 12. The validity of Müller's law for the second plateau, 2*N* HCl, unshielded anode.

tion of Cu_2O is consistent with the observed potential for the second plateau. In addition the shape of the current-time curve during the drop after the second plateau indicates that Müller's theory holds here also. Fig. 12 shows an example, taken with a small unshielded anode in 2*N* HCl.

Layer growth in depth.—Following the last plateau, and in certain cases between the first and second plateaus, the transient is observed to follow Müller's depth increase law. An example of this is shown in Fig. 8, where i^{-2} is plotted against t for a shielded anode with only one plateau. This line represents equation (V) and from its slope the pore area, s_p, may be found. The value of κ used ($5.1 \times 10^{-3}\ \Omega^{-1}\text{cm}^{-1}$) was determined from the first plateau. t_+ was assumed to be zero and ϵ to be -0.27 v. This resulted in value for s_p of 2.5×10^{-3} cm², which is 1.4% of the total apparent area of the anode. The value of the pore area thus obtained may be compared with that computed for the sideways growth at the time of transition to the new process. For the example shown, the transition begins at about 9.3 sec, there being a period of about 0.2 sec during which the change is completed. Evaluating s_p at the middle of this period, one obtains $s_p = 2.3 \times 10^{-3}$ cm². This is rather good agreement; in view of the assumptions and uncertainties a difference of 20% is still satisfactory. This value of the pore area indicates a large actual current density of 3.3 amp/cm² in the pores.

Effect of Concentration

If the concentration of hydrochloric acid is varied, the characteristic curves are altered in a predictable way. The slope of the i_I, V_I curve is proportional to the specific conductance of the acid, and the intercept on the V axis is the value of the corresponding Cu | CuCl | Cl^- potential. This is shown in Fig. 13 and Table II. The duration of the first plateau increases with increasing acid concentration. At all concentrations investigated (0.5*N*-6*N*) the length of the plateau is given by a relation of the form $\tau = D' i_I^{-m}$, (Fig. 14). m is approximately constant and D' is

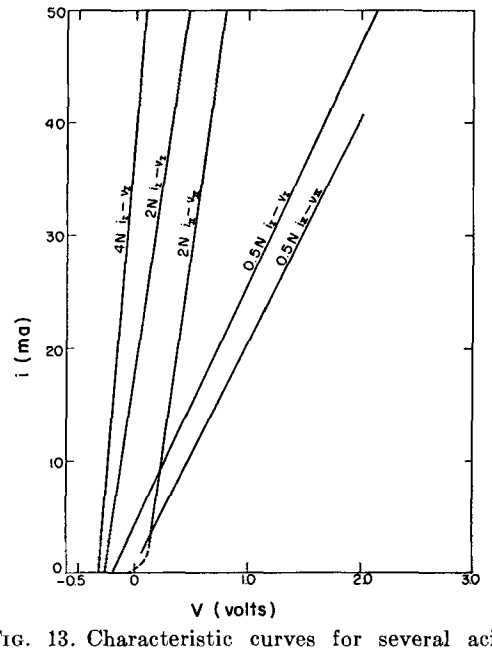

FIG. 13. Characteristic curves for several acid concentrations.

TABLE II

HCl	0.5*N*	2*N*	4*N*	Source
r_0	56	14	9.6	Characteristic curves
r_0	44	14	9.6	Conductivity calculations
ϵ_I	−0.21	−0.27	−0.32	Characteristic curves
ϵ_I	−0.22	−0.27	−0.32	Potential calculations
ϵ_I	−0.22	−0.275	−0.32	Potential of Cu | CuCl satd. HCl
ϵ_{II}	−0.05	−0.05	—	Interruption experiments
ϵ_{II}	−0.05	+0.11	—	Characteristic curves

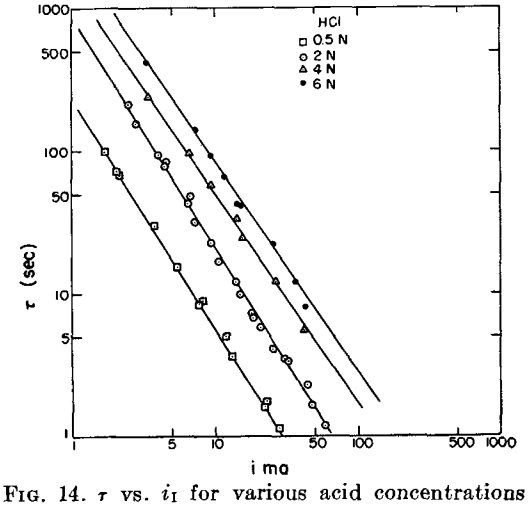

FIG. 14. τ vs. i_I for various acid concentrations

roughly proportional to the concentration. The length of the second plateau is the feature of the transient most dependent upon acid concentration. It barely appears in 4*N* and 6*N* acid, but is very prominent in 1*N* and 0.5*N* HCl. With lower acid concentrations the H^+ is depleted

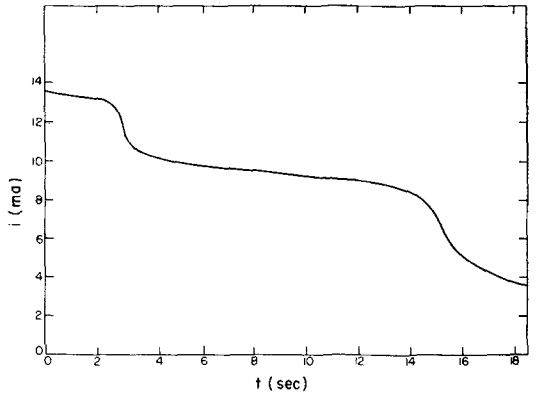

FIG. 15. i vs. t showing long second plateau in 0.5N HCl

more quickly at the anode surface, the oxide formation probably begins sooner and has a greater area upon which to form. An example in 0.5N HCl is shown in Fig. 15. Interruption experiments, performed on an exactly similar transient, resulted in a value of -0.05 v for the open circuit potential (ϵ_{II}) during the second plateau. This is the same value as that obtained by extrapolating the i_{II}, V_{II} line (Fig. 13) and the same as that obtained by interruption experiments in 2N HCl. Interruption experiments show the open-circuit potential during the first plateau, ϵ_I, to be -0.20 v in 0.5 N hydrochloric acid, in agreement with the value obtained by extrapolation of the i_I, V_I line and by potential measurements of a copper electrode in hydrochloric acid saturated with CuCl. Thus, ϵ_I varies with hydrochloric acid concentration while ϵ_{II} does not. This tends to confirm the view that the second plateau is the result of the initiation of a new electrode reaction, corresponding to the depletion of H^+ ion at the anode surface.

Unshielded Anodes

Except for steady-state behavior, the results obtained with both shielded and unshielded anodes have been found to be qualitatively, and in many cases, quantitatively, the same. The general temporal behavior is the same, both showing one or two plateaus according to the values of external parameters E and R. The chief difference between the two cell geometries is the effect of convection. Re-examining Fig. 10, it may be noted that the shielded and unshielded anodes give quantitatively identical results except at very low current densities where the plateau is very long in duration, greater than 20 sec. Only then do the unshielded electrodes show quantitatively different results. The convection current is the result of a saturated solution of cuprous ion complexes which is denser than the surrounding hydrochloric acid. Convection carries away some of the products of solution of the layer and hence retards its completion. For low currents, the layer is removed as fast as it is formed and thus is never completed. However, τ and Q, the total charge having flowed during the first plateau, are functions only of i_I for anodes of a given size and geometry as shown in Fig. 16, for vertical unshielded anodes of 0.021 cm² cross section. As was assumed by Stephenson (13) the dissolution may be considered equivalent to a removal current i_r, and so Q may be considered as a function of $(i_I - i_r)$.

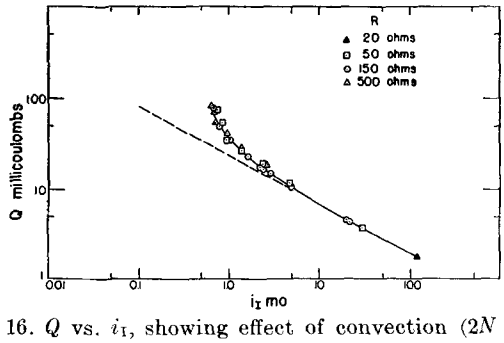

FIG. 16. Q vs. i_I, showing effect of convection (2N HCl)

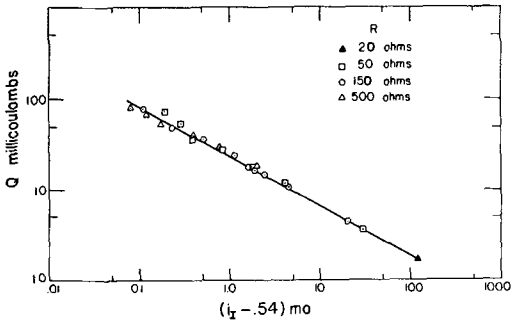

FIG. 17. Q vs. $(i_I - 0.54)$, corrected for removal current

For the geometry mentioned above, the correction is negligible for $i_I > 5$ ma and by taking i_r to be 0.54 ma, the unshielded anode (Fig. 17) displays a linear relation between log Q and log i_I over the entire range, exactly similar to the case of shielded anodes.

Two other effects of convection are the production of overshoot and of a steady state. With shielded anodes a steady state is never achieved within 10 min, the current dropping slowly to very low values instead, while, with unshielded ones of 0.02 cm² cross section, convection and diffusion are able to maintain steady-state current densities of the order of 0.1 amp/cm². Overshoot, the appearance of a current minimum after the plateaus, was absent in shielded anode transients while almost invariably present in both vertical and horizontal unshielded ones. This type of overshoot is interpreted as due to the variation of solubility of CuCl in hydrochloric acid at the anode surface brought about by convection. The minimum rarely appears before 3 sec of the transient have elapsed, at which time the effects of convection are first observed (using Schlieren methods). For a rapid transient ($\tau < 3$ sec) the Cl^- at the anode surface is quickly depleted, reducing the solubility of the layer and consequently permitting only a small current to flow. However, convection both carries away the products of solution and replenishes the solvent ion (Cl^-) at the anode surface, tending to establish a thinner, less resistant layer and, thus, the current rises to the steady-state value, completing the overshoot. Overshoot occurs with unshielded anodes also when the current decreases rapidly (e.g., because of completion of a solid layer) since the diffusion convection layer ($\sim$ 0.5 mm thick) is slow in its response to the change in the boundary condition (i). An example of this is overshoot which occurs following the current decrease after a long (30 sec) plateau. The reduced

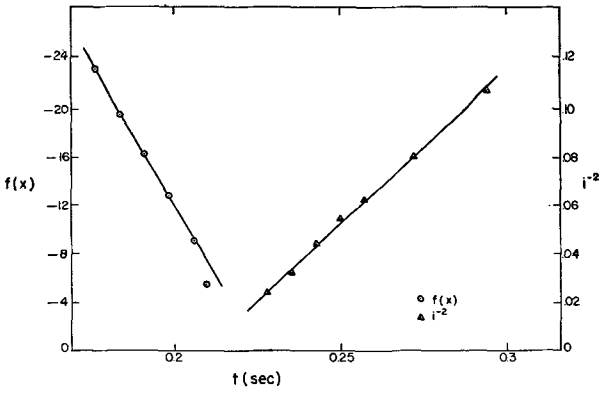

FIG. 18. The validity of Müller's laws for an unshielded anode, 2*N* HCl, E = 1.0 v, R = 50 Ω.

current is in equilibrium with a lower Cl^- concentration gradient, and hence with a higher Cl^- concentration at the surface. As before the layer resistance decreases as the system tends toward equilibrium, producing overshoot. This type of overshoot does not occur with shielded anodes because diffusion alone is not sufficient to establish equilibrium (steady-state) conditions. Transients whose significant events occur before 3 sec are identical for all cell geometries. Both of Müller's laws are found valid, as are shown by the example in Fig. 18. Thus, correct quantitative results may be expected in general for short transients independent of cell geometry.

Reproducibility

Polishing with 4/0 emery paper gave anodes which were not completely satisfactory in their reproducibility, especially for such quantities as the length of plateaus. For unshielded anodes i_I, i_∞, and i_{II} could be reproduced to 2% deviation from the mean, but τ and Q varied as much as 20%. Electrolytic polishing of the anode in 50% phosphoric acid for 5 min improved the results only slightly. An investigation of the effect of repeated use of a single anode without removing it from solution showed that the electrolytic anodization formed by dissolution of the copper produced a uniform reproducible surface. The anodization removes the cold worked surface produced by the mechanical polishing. One test was made by repeatedly using the anode with E = 0.3 v and R = 500 Ω for 11 runs. The first run (with a mechanically polished surface) had a plateau of 20-sec duration while all the runs with an anodized surface had plateaus of 27 sec to within 0.5 sec, which was the limit of precision of measurement. For all runs, i_I, i_{II}, and i_∞ had mean deviations of 1%, which also was the limit of precision. The open-circuit potential varied from −0.34 to −0.40 v without affecting the results. However, the more sensitive features of the transient, e.g., the shape of drop and the second plateau, changed during the first 3 runs. The second plateau appeared clearly for the first time in the 4th run, i.e., the anode having been etched 3 times by previous use. From the 4th run to the 11th and last, the transients were identical in all respects to within the limits of measurement. Results obtained on different days with anodized anodes agreed to within 2%.

SUMMARY

When a copper electrode, shielded to prevent convection, is made anodic in hydrochloric acid the transient current behavior is essentially as predicted by Müller, with the exception of a second plateau due to the initiation of a new reaction. The transient begins with a decreasing current as the solution near the anode becomes saturated with CuCl. There follows a period of constant current, during which a solid layer of CuCl is being deposited on the anode face. spreading sideways from random nuclei. This is terminated by a drop in the current as the layer is completed, leaving small pores in it. A second current plateau appears during which a new reaction takes place. The effect of acid concentration, the observation of a red-brown deposit, and the measured electrode potential indicate this to be the formation of Cu_2O. Finally, the layer grows in depth with constant pore area. The duration of the first plateau and thickness of the CuCl layer can be correlated with the current during the plateau. Studies with unshielded anodes give results which are qualitatively similar except for overshoot and steady-state behavior. For fast transients (<3 sec) both types of anodes show quantitatively identical behavior.

ACKNOWLEDGMENTS

This work was supported by the Office of Ordnance Research under contract DA-11-022-ORD-939. The author is greatly indebted to Professor J. H. Bartlett for his encouragement and aid and to Professor Sherlock Swann, Jr., for his careful and considerable help with the manuscript. Thanks are due also to Mr. James Briggs, who designed and built the interruption relay.

Manuscript received August 26, 1955.
Any discussion of this paper will appear in a Discussion Section to be published in the December 1956 JOURNAL.

REFERENCES

1. J. H. BARTLETT, *Trans. Electrochem. Soc.*, **87**, 521 (1945).
2. J. H. BARTLETT AND L. STEPHENSON, *This Journal*, **99**, 504 (1952).
3. J. H. BARTLETT AND L. STEPHENSON, *ibid.*, **101**, 571 (1954).
4. W. J. MÜLLER, "Die Bedeckungstheorie der Passivitat der Mettale und ihre experimentalle Begrundung," Verlag Chemie (1933).
5. W. J. MÜLLER, *Trans. Faraday Soc.*, **27**, 737 (1931).
6. W. J. MÜLLER AND K. KONOPICKY, *Monatsh. Chem.*, **48**, 711 (1927).
7. W. J. MÜLLER AND K. KONOPICKY, *ibid.*, **50**, 385 (1929).
8. O. GATTY AND E. C. R. SPOONER, "Electrode Potential Behavior of Corroding Metals in Aqueous Solution," pp. 22 and 182, Clarendon Press, Oxford (1938).
9. B. B. OWEN AND F. H. SWEETON, *J. Am. Chem. Soc.*, **63**, 2811 (1941).
10. R. A. ROBINSON AND R. H. STOKES, "Electrolyte Solutions," p. 361, Butterworths Scientific Publications, London (1955).
11. A. A. NOYES AND M. CHOW, *J. Am. Chem. Soc.*, **40**, 739 (1918).
12. K. S. CHANG AND Y. CHA, *J. Chinese Chem. Soc.*, **2**, 298 (1934).
13. L. P. STEPHENSON, Ph.D. Thesis, University of Illinois, p. 79 (1953).

Electrokinetic Potentials on Bulk Metals by Streaming Current Measurements

II. Gold, Platinum, and Silver in Dilute Aqueous Electrolytes

RAY M. HURD AND NORMAN HACKERMAN

Defense Research Laboratory and Department of Chemistry, The University of Texas, Austin, Texas

ABSTRACT

The electrokinetic (ζ) potentials of platinum, gold, and silver in contact with distilled water were found to be 60.8, 61.0, and 49.0 mv, respectively. The ζ potentials of these metals were also measured as a function of concentrations of KCl and KOH. Maxima were observed in all cases except that of gold in KCl solutions. These maxima are qualitatively related to the solubilities of the corresponding chlorides and hydroxides.

INTRODUCTION

In a previous paper (1), a method was described whereby the electrokinetic potentials of bulk metals could be obtained from streaming current measurements.[1] The method consisted essentially of using a recording milli-microammeter of low internal impedance, so that the streaming current was shunted through an external circuit rather than returning through the capillary itself. By this means the troublesome "shorting" resistance of the metal capillary was eliminated as a factor in the electrochemical circuit. For a complete description of the circuitry and a proof of the method, reference should be made to the first paper.

EXPERIMENTAL

Short lengths of platinum, gold, and silver seamless drawn tubing with nominal internal diameters of 0.005 in., 0.010 in., and 0.015 in. were furnished by the Baker and Company platinum works. Capillaries of various lengths were cut from each piece of tubing and sealed into small bore Pyrex glass tubing with Apiezon "W" hard wax. A sketch of a typical finished capillary is shown in Fig. 1*a*. The ends of the capillary were ground down to a knife edge, and the sealing wax was made to cover as much of the external wall as possible. The inside walls of the capillaries were cleaned by rinsing with warm dilute HNO_3, followed by a prolonged rinsing with distilled water. The finished capillaries were then stored in distilled water to allow the metal-water interface to reach an equilibrium state, which was found to require about 24 hr.

Since the streaming current is directly proportional to the square of the capillary radius, it was essential that accurate measurements of this value be obtained. It was calculated from Poiseuille's law from measurements of water flow rate through the capillaries at a series of applied pressure differences. The length of each capillary was measured with a traveling microscope. A summary of the pertinent data for all capillaries is given in Tables I, II, and III. The values of the critical dimensional factor (ratio of length to radius squared) are accurate to within $\pm 0.5\%$.

In order to measure the streaming current directly, it is important that the total resistance (ionic plus electronic) from one end of the capillary through the external circuit to the other end of the capillary be kept as low as possible. This places the following restrictions on electrode construction and location:

(*A*) The electrode reactions must not polarize the electrodes. Because the current is extremely low ($\sim 10^{-10}$ amp), this causes little difficulty. Smooth platinum gauze with a total area of approximately 1 cm^2 exposed to the solution is adequate, and does not introduce any contaminants into the solution.

(*B*) The electrodes must be placed as close to the ends of the capillary as possible in order to minimize the ionic resistance. This was accomplished by sealing the gauze electrodes into the 7 mm glass tubing which constituted the fluid flow circuit, and then joining the capillary to the glass tubing by means of short pieces of flexible Tygon tubing as shown in Fig. 1*b*.

The apparatus for controlling and measuring the pressure difference applied to the capillary is shown in Fig. 2. Pressure was supplied by means of tank helium, and was measured by reading the height of the water column. The dimensions of the capillaries were such that fairly low pressures (<100 cm H_2O) were necessary to avoid turbulent flow.

A conductivity cell (D, Fig. 2) was incorporated directly into the fluid flow path so that a continuous check could be maintained against possible contamination of the solution.

The water used in all determinations was obtained by twice redistilling the "stock" distilled water obtained from a Barnstead still. The final distillation was made from dilute permanganate in order to destroy organic contaminants. No special efforts were made to obtain water with the same value of specific conductivity for each run;

[1] As pointed out in the previous paper (1), this method was used first by Eversole and Boardman (2). It has been brought to the attention of the authors that subsequent work using streaming current methods has been done by Neale and Peters (3) and Buchanan and Heymann (4).

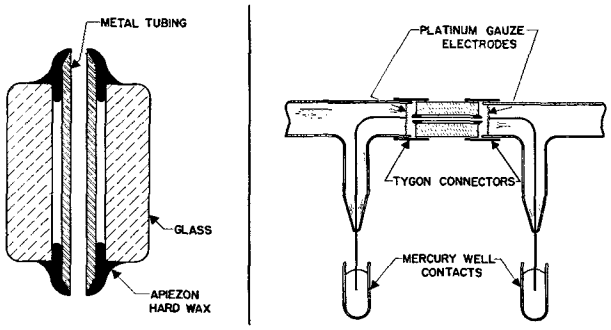

FIG. 1. Typical capillary construction and mounting. (*a*) (left), typical capillary construction; (*b*) (right), electrodes and contacts.

TABLE I. *Gold capillaries in distilled* H_2O

Dimensions	Ratio, l/r^2	t	$I/\Delta P \times 10^{12}$	ζ
		°C		mv
$r = 7.02 \times 10^{-3}$ $l = 1.521$	3.09×10^4	22.0	4.5	61.0
$r = 1.38 \times 10^{-2}$ $l = 1.724$	1.10×10^4	22.0	12.7	61.1
$r = 1.89 \times 10^{-2}$ $l = 3.251$	9.09×10^3	18.0	14.1	61.9
$r = 1.89 \times 10^{-2}$ $l = 5.50$	1.54×10^4	24.5	9.4	60.0

TABLE II. *Platinum capillaries in distilled* H_2O

Dimensions	Ratio, l/r^2	t	$I/\Delta P \times 10^{12}$	ζ
		°C		mv
$r = 6.81 \times 10^{-3}$ $l = 1.502$	3.24×10^4	18.0	3.88	60.8
$r = 1.29 \times 10^{-2}$ $l = 1.527$	9.13×10^3	17.0	13.2	60.0
$r = 1.87 \times 10^{-2}$ $l = 3.198$	9.15×10^3	21.0	15.0	61.5
$r = 1.87 \times 10^{-2}$ $l = 5.50$	1.57×10^4	21.0	8.7	61.5

TABLE III. *Silver capillaries in distilled* H_2O

Dimensions	Ratio, l/r^2	t	$I/\Delta P \times 10^{12}$	ζ
		°C		mv
$r = 6.64 \times 10^{-3}$ $l = 1.721$	3.90×10^4	25.0	2.80	44.8
$r = 1.17 \times 10^{-2}$ $l = 1.821$	1.32×10^4	19.0	8.14	50.6
$r = 1.87 \times 10^{-2}$ $l = 3.142$	9.03×10^3	16.0	10.4	48.0
$r = 1.87 \times 10^{-2}$ $l = 5.50$	1.58×10^4	20.0	7.2	52.5

however, the conductivity was less than 2.0×10^{-6} in all cases.

All runs were made at room temperature, which varied throughout the range 15°–25°C. From the data, the ζ-potential was essentially independent of temperature in this interval. It was of course necessary to measure the temperature of the solution in order to use the proper value for viscosity.

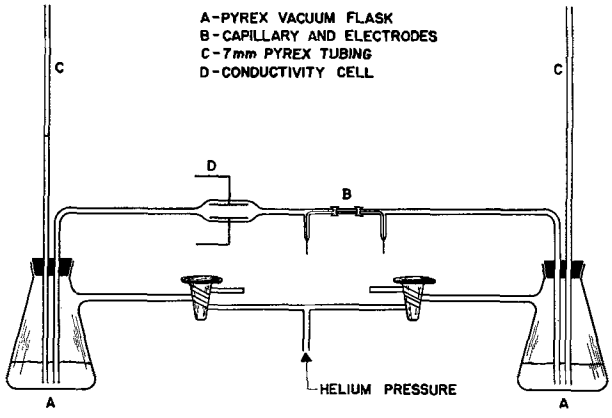

FIG. 2. Fluid flow system

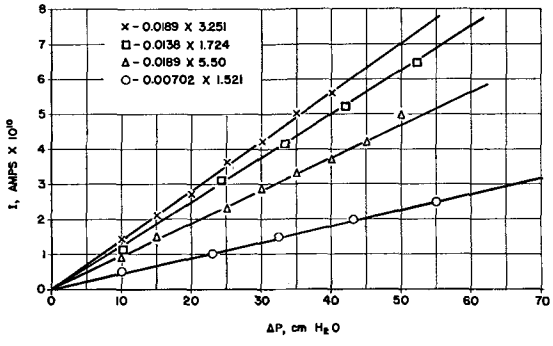

FIG. 3. Gold capillaries in distilled water

The dilute electrolyte solutions were prepared from reagent grade chemicals.

RESULTS AND DISCUSSION

ζ-Potential at the gold-water interface.—Curves of streaming current vs. pressure drop across the gold capillaries are shown in Fig. 3. In a previous paper (1) results were shown with flow in both the left-to-right and the right-to-left directions; however, after enough curves of that type were taken to show definitely that the two segments were always of the same slope, runs were made with flow in one direction only.

With these and all other capillaries tested (platinum and silver), the electrode *toward* which the fluid was flowing became more positive, which means that the excess ions traveling with the fluid flow were cations. For such a case, the ζ-potential is given a negative sign by convention.

Pertinent data and calculated ζ-potentials[2] for the gold capillaries are summarized in Table I. The mean value for the ζ-potential, 61.0 ± 1.0 mv, was obtained only after the capillaries had been in contact with the water long enough to reach an equilibrium condition. If the runs were made too soon after cleaning with dilute HNO_3, the ζ-potentials were invariably larger and inconsistent. By prolonging the time of contact with the HNO_3 solution, a ζ-potential of 134 mv was obtained for one of the capillaries; this value decreased slowly with storage in

[2] From the equation $\zeta = [4\eta/D][l/r^2][I/\Delta P]$. *See* reference (1).

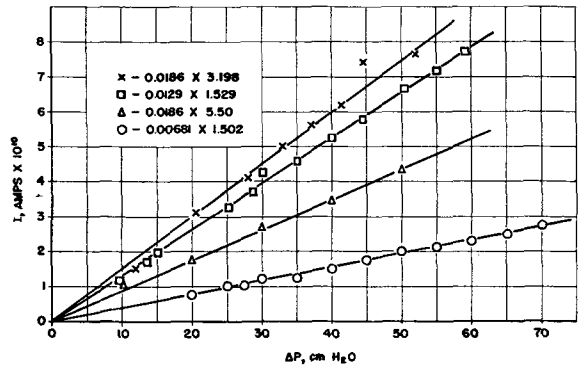

FIG. 4. Platinum capillaries in distilled water

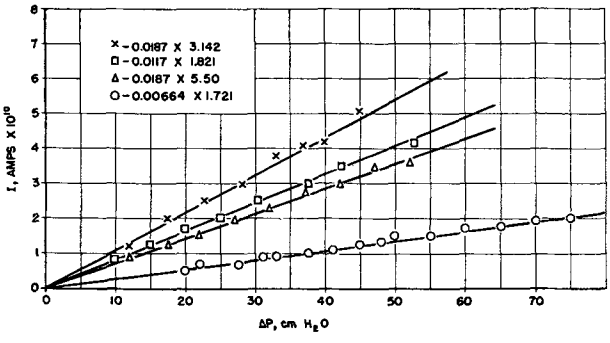

FIG. 5. Silver capillaries in distilled water

distilled water, until the equilibrium potential was reached after approximately nine days. With capillaries subjected to the usual cleaning procedure, the interface attained the equilibrium state after only one or two days, and no further changes were noted even after storing in water for as long as thirty days.

The higher ζ-potentials observed immediately after rinsing with HNO_3 were observed also with silver and platinum, and are attributed to a more highly oxidized state of the surface than is present after equilibrium is reached. This fits well with the description of the metal-solution interface given by de Boer and Verwey (5), who attribute the negative ζ-potential to a layer of oxygen chemically adsorbed on the surface. Electrophoretic measurements have shown that, by carefully excluding all oxygen during the preparation of platinum sols, it was possible to reverse the sign of the ζ-potential (6). Streaming current measurements on bulk metals to confirm these results could probably be made, and should be an object of future research.

ζ-Potential at the platinum-water interface.—The curves of streaming current vs. pressure drop for the four platinum capillaries in distilled water are shown in Fig. 4. Table II summarizes the data and gives the calculated ζ-potentials, the mean value of which is 60.8 ± 1.0 mv. It is somewhat surprising that the ζ-potentials for gold and platinum are practically identical, even though one would not expect them to be very different.

ζ-Potential at the silver-water interface.—Whereas the values of the ζ-potential for gold and platinum were remarkably consistent from one capillary to another, considerably more variation was found among the silver capillaries. The curves for the four capillaries in distilled

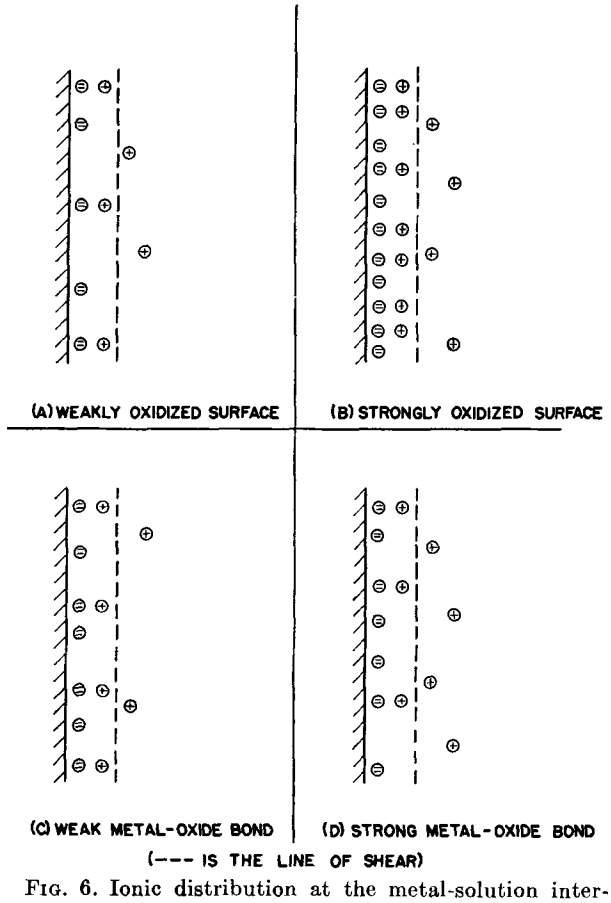

FIG. 6. Ionic distribution at the metal-solution interface.

water are shown in Fig. 5, and a summary of the data is given by Table III. The ζ-potential for silver is 49.0 ± 4.0 mv, a value significantly lower than that found for gold and platinum. An explanation of this may arise from the fact that the silver-oxygen bond in the oxide layer is somewhat weaker than the corresponding platinum and gold bonds with oxygen. Most authors are in agreement that the ionic distribution at the metal solution interface can be shown pictorially as in Fig. 6, in which the double negative charges represent the oxide layer and the positive charges the counter ions in solution. For a double layer structure of this type, one may draw the following qualitative conclusions:

(*A*) For a given metal, a more highly oxidized surface results in a higher number of positive ions per square centimeter in the movable part of the double layer (compare Fig. 6*a* and 6*b*).

(*B*) A weaker bond between the metal ion and the oxide ion results in a stronger bond between the oxide ion and the counter ion in solution, thus leaving fewer excess positive ions in the movable part of the double layer (compare Fig. 6*c* and 6*d*).

Both of these conclusions are in agreement with the results described above. That is, assuming the silver-oxygen bond to be weaker than the corresponding gold- and platinum-oxygen bonds, then the original highly oxidized surface produced by nitric acid cleaning will be dissolved to a greater extent in the case of silver. The greater ease with which the oxide is removed from the

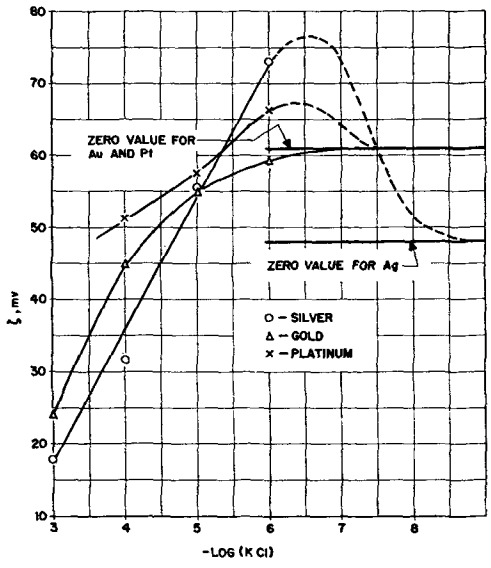

FIG. 7. Metal capillaries in dilute KCl

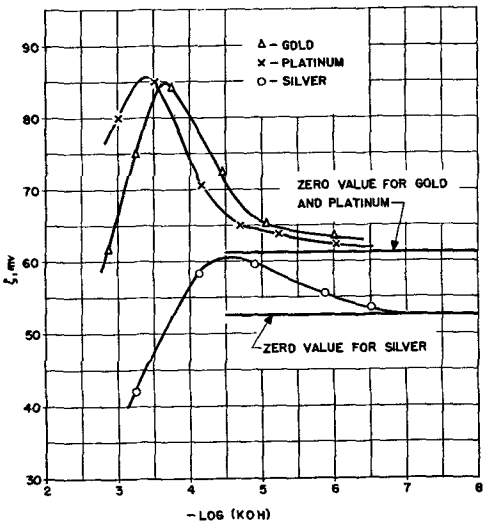

FIG. 8. Metal capillaries in dilute KOH

silver surface would also explain the greater variation in ζ-potential from capillary to capillary. Thus, either of the double-layer configurations (A) and (B) (Fig. 6) may explain the results obtained In all likelihood, both mechanisms contribute. However, in view of the fact that actual equilibrium data on the surface oxidation states are unavailable, these mechanisms can be presented only as *possible* explanations.

ζ-Potentials at the interface metal-dilute KCl.—Streaming current measurements were made on one capillary of each metal, using dilute solutions of KCl as the liquid phase. KCl concentrations of 10^{-6}, 10^{-5}, 10^{-4}, and $10^{-3}N$ were used. Results are shown in Fig. 7, in which the ζ-potentials are plotted against the negative logarithm of the KCl concentration. It is notable that the effect of KCl on the ζ-potential is at least qualitatively related to the solubility of the corresponding metal chloride. Thus, silver, which forms a very insoluble chloride, shows a marked maximum in ζ at low chloride concentrations; platinum, which forms a sparingly soluble chloride, shows a much smaller maximum; and gold, whose chlorides are very soluble, shows no increase in ζ at all. The maxima in the case of silver and platinum are ascribed to filling in, by chloride ions, of vacant spots in the oxide layer, thus yielding the same effect as a more highly oxidized surface. The tendency of these metals to form coordination complexes with chloride ions may also be of importance here, but the correlation is not as evident as the solubility relationship.

The decreasing ζ-potentials at the higher KCl concentrations is a general phenomenon encountered with almost all solid surfaces and electrolytes, and is due to the fact that solutions with high ionic strengths "compress" the entire double layer to the extent that only a small amount of the total potential drop remains in the diffuse part of the layer.

ζ-Potentials at the interface metal-dilute KOH.—ζ-potentials for the three metals in contact with dilute KOH solutions are plotted in Fig. 8 as a function of the KOH concentration. The curves for gold and platinum are almost identical in both the magnitude of the maxima and the value of KOH concentration at which they occur. For the silver capillary the maximum was less pronounced, and was also shifted approximately one *p*H unit toward the lower KOH concentrations.

These maxima very likely result from a surface change similar to that proposed for the chloride solutions, with the exception that in this case the weakest binding for the adsorbing OH^- ion is presented by silver, with the result that silver shows the least change in ζ-potential. Since platinum and gold possess almost identical ζ-potentials in distilled water, it is reasonable to conclude that the metals should behave similarly toward the OH^- ion, which, insofar as adsorption at a surface is concerned, is not essentially different from the oxygen molecule. The marked similarity of the curves for platinum and gold in Fig. 8 was therefore not unexpected.

Future work in this investigation will be directed first of all to the measurement of ζ-potentials on metal surfaces from which the oxide layers have been removed. Afterwards, a method of measuring these potentials as a function of externally applied polarizing potentials will be sought.

Manuscript received September 21, 1955. This paper was prepared for delivery before the San Francisco Meeting, April 30 to May 3, 1956.

Any discussion of this paper will appear in a Discussion Section to be published in the December 1956 JOURNAL.

REFERENCES

1. R. M. HURD AND N. HACKERMAN, *This Journal*, **102**, 571 (1955).
2. W. EVERSOLE AND W. BOARDMAN, *J. Phys. Chem.*, **46**, 914 (1942).
3. S. M. NEALE AND R. H. PETERS, *Trans. Faraday Soc.*, **42**, 478 (1946).
4. A. S. BUCHANAN AND E. HEYMANN, *J. Colloid Sci.*, **4**, 157 (1946).
5. J. DE BOER AND E. J. VERWEY, *Rec. Trav. Chim.*, **55**, 675 (1936).
6. N. BACH AND N. BALAŞCHOWA, *Acta Physicochim., U.R.S.S.*, **3**, 79 (1935).

Galvanic Potentials of Grains and Grain Boundaries in Copper Alloys

R. Bakish and W. D. Robertson

Hammond Metallurgical Laboratory, Yale University, New Haven, Connecticut

ABSTRACT

Potentials of grains and grain boundaries were measured in pure copper, Cu_3Au, and in alpha brass; the three cases represent the structural grain boundary in a pure metal, an alloy in which only one component is oxidized, and an alloy in which both components are oxidized. Potentials were measured in ferric chloride and in aqueous ammonia, the former representing an electrolyte in which only Cu_3Au is susceptible to stress cracking and the latter representing conditions in which brass is susceptible to stress cracking. In general, it was found that the measured potentials could be correlated directly with observed structural changes and susceptibility to stress corrosion cracking.

Introduction

The measurement of electrochemical potential differences between grains and grain boundaries in aluminum alloys (1) has contributed greatly to an understanding of the electrochemical mechanism of stress corrosion cracking in age-hardening systems. The corresponding problem in homogeneous solid solutions has not been extensively studied. In fact, it appears that only one measurement of grain boundary potentials in brass is available (2).

There is no evidence that precipitates or impurities are responsible for intergranular stress corrosion cracking and intergranular corrosion of brass (3). On the other hand, it has been shown that the phenomenon is associated only with alloys and does not occur in pure metals (4).

Since pure metals are structurally similar to homogeneous alloys, it is necessary to measure and compare potentials as a function of composition in order to separate the effect of the structural grain boundary from the combined structural and compositional factors. Furthermore, stress corrosion cracking of copper base alloys is dependent on the environment and, accordingly, it is also desirable to obtain boundary potentials in several environments for correlation with the corresponding corrosion cracking susceptibility.

The following measurements were made to provide information necessary for an evaluation of the effects of alloy composition, structure and electrolyte.

1. Electrochemical potentials of grains and grain boundaries of pure copper were measured in 2% ferric chloride.
2. Galvanic potentials of polycrystalline copper-gold and copper-zinc alloys were measured as a function of alloy composition, including the pure components, in 2% ferric chloride and aqueous ammonia.
3. Potentials of grains and grain boundaries of a homogeneous copper-gold alloy (Cu_3Au) and alpha brass (copper-zinc) were measured in 2% ferric chloride as examples of two alloys of which only copper-gold is susceptible to cracking in the particular environment.
4. Potentials of grains and grain boundaries in alpha brass were measured in 2% ferric chloride and aqueous ammonia.

Structural observations of boundary corrosion of the various alloy and electrolyte combinations were also made for the purpose of correlation with electrochemical measurements.

Experimental Procedure

Materials.—All metals and alloys used in this investigation, Table I, were specially prepared for the purpose from materials of at least 99.99% purity or better, indicated by spectroscopic analysis, and they were annealed at a high temperature prior to preparation as electrodes.

Fine grained polycrystalline electrodes were made by conventional rolling and recrystallization techniques. Large grained copper specimens, for grain boundary measurements, were obtained by solidification in a single crystal furnace and the one-half inch cylindrical specimens were sectioned along the axis of the cylinder. Coarse grained copper-gold alloys were obtained by annealing at a high temperature. Large grained alpha brass was obtained by slow solidification and also by recrystallization; the latter specimens were kindly supplied by D. H. Thompson of the American Brass Co. and there is reason to believe that they are from the same lot of material used by Dix (2). Grain diameters in all coarse grained specimens for boundary measurements were about one centimeter.

Surface preparation.—After annealing, all polycrystalline electrodes in the form of sheet or more massive blocks were polished with levigated alumina and, finally, electropolished immediately before introduction in the measuring cell. Exposed areas were of the order of several square centimeters, and all edges and electrical connections were masked with an organic resin (Epon 100).

Grain boundaries were isolated from the adjacent grains, as far as possible, by masking the grains with the above resin and leaving the grain boundary exposed in an area about 0.03 mm wide. This operation was accomplished under a microscope at 100× by placing a drop of resin on the grain and moving it toward the grain boundary by means of a nylon tip attached to a micromanipulator. Obviously the exposed width is much greater than that associated with a grain boundary, but it appears that the

TABLE I. *Atomic per cent*

Alloy	Copper	Gold	Zinc
Copper	99.99+	—	—
Gold	—	99.99+	—
Zinc	—	—	99.99+
Cu_3Au	75	25	—
Cu Au	50	50	—
Brass	89.8	—	10.2
Brass	79.5	—	20.5
Brass	74.4	—	25.6
Brass	69.2	—	30.8

contribution of the boundary to the galvanic potential is sufficiently large so that its polarity and change of potential with time can be measured reproducibly; the absolute values, of course, have no significance. Potential measurements of the individual crystals in a polycrystalline aggregate were obtained by masking the grain boundaries with resin.

Measuring cell and standard electrode.—All potentials were measured with respect to the normal silver-silver chloride electrode. A silver wire, anodized in 10% hydrochloric acid, was inserted into a glass tube containing 1*N* potassium chloride; the tube was closed by an agar-agar diaphragm. Potential differences between a number of standard electrodes were less than 0.01 mv.

The standard electrode and the metallic electrodes were placed in a glass cell covered with a rubber stopper through which all electrical connections were passed. The cell was immersed in a water thermostat controlled to 0.005°C. Generally, polycrystalline electrodes, grain boundary, and matrix electrodes of the same composition were placed in the cell at one time, except in the case of zinc which could not be combined with copper electrodes. Most of the grain boundary and matrix potential measurements were repeated four times with a new surface preparation between each individual run. All potentials were measured over prolonged periods of time with a precision potentiometer.

Experimental Results

Pure copper.—Fig. 1 shows the results obtained on polycrystalline copper, copper grain boundaries and grains in 2% ferric chloride. Four independent runs were made and the variation between results was greatest in the case of the isolated grains in which the potentials at the maximum, for example, varied within ±0.005 v. Grain boundary potentials, on the other hand, were surprisingly reproducible to about ±0.001 v and values for the polycrystalline electrodes were within ±0.0002 v.

Since copper is readily oxidized by ferric chloride, the effect of cupric ion in the electrolyte was investigated to determine whether the changes of potential in time were associated with electrolyte composition. After reaching stable values, the copper ion concentration of the electrolyte was increased by adding cupric chloride. No permanent effect due to cupric ion concentration was observed.

Observed potential differences between grains and grain boundaries of pure copper are in complete accord with metallographic observations on copper specimens immersed in ferric chloride for periods of many weeks. Starting with a flat surface, a groove forms at the junction of the boundary and the surface, similar to boundary grooves characteristic of thermal etching; after establishment of a stable groove, copper continues to be removed uniformly from the surface, maintaining the equilibrium boundary angle. In terms of potentials, the grain boundary is initially more active than the grain, with an increasing potential difference in time; after a period of several hours the potential difference diminishes and finally goes to zero at about 10 hr and remains at zero for the duration of the experiment, which was prolonged to 50 hr. These results are also in accord with the fact that stress corrosion cracking and intergranular corrosion, beyond superficial grain boundary grooves, are not observed in pure copper.

Composition dependence of galvanic potential in copper-gold alloys.—Galvanic potentials of polycrystalline pure copper, copper-gold alloys and pure gold in ferric chloride are shown in Fig. 2. To compare potentials in terms of composition, steady-state values at 20 hr are plotted in Fig. 3 as a function of gold content and an average curve is drawn to emphasize the change in potential as a function of composition.

Grain and grain boundary potentials in Cu_3Au.—One of four sets of potential values for grains and grain boundaries of Cu_3Au in ferric chloride is shown in Fig. 4 as a function of time. In all four independent experiments, grain boundaries were invariably more active than the grains; furthermore, the observed potential difference of 0.005–0.006 v was constant in time to 50 hr. The evidence of a continuous

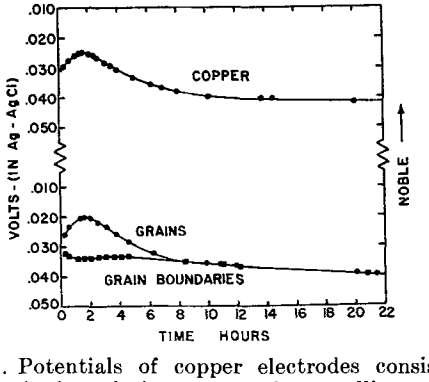

Fig. 1. Potentials of copper electrodes consisting of grains, grain boundaries, or a polycrystalline aggregate measured in ferric chloride.

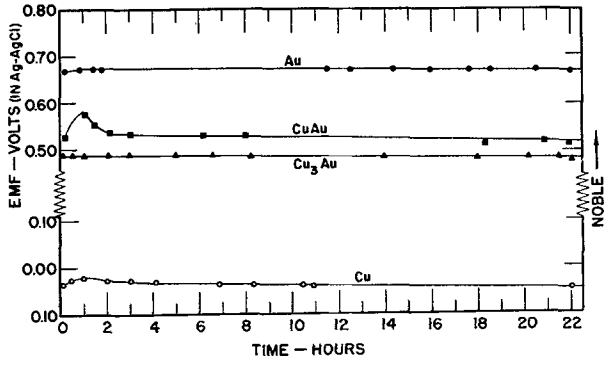

Fig. 2. Galvanic potentials of copper-gold alloys in ferric chloride as a function of time.

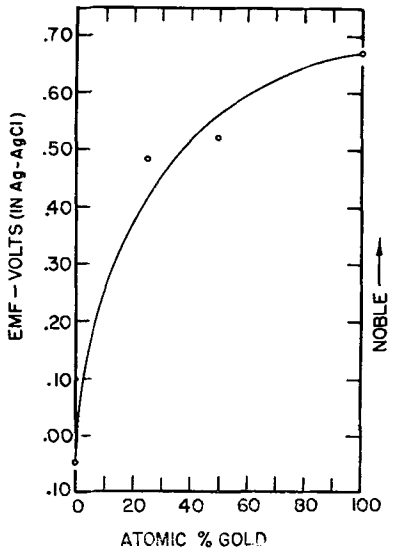

FIG. 3. Galvanic potentials of copper-gold alloys as a function of composition.

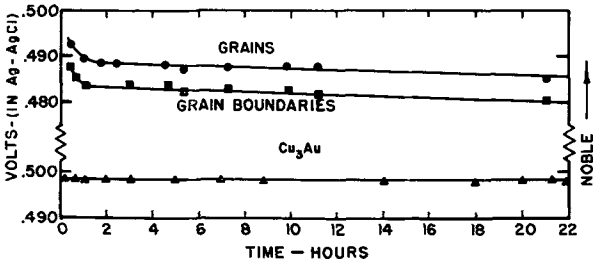

FIG. 4. Potentials of Cu_3Au electrodes consisting of grains, grain boundaries, or polycrystalline aggregates in ferric chloride.

driving force is in agreement with the observed structures and is in sharp contrast with the behavior of pure copper.

It has already been established (5) by prolonged immersion of Cu_3Au in ferric chloride that copper alone is removed from the alloy; at least, spectroscopic analysis of the solution shows no trace of gold. Furthermore, the reaction is preferentially concentrated at grain boundaries where penetration continues through the specimen, leaving a gold sponge in the vicinity of the boundary; reaction also proceeds normal to the outer surface and to the plane of the grain boundary, although at a comparatively slow rate, with the resulting structural pattern of attack shown schematically in Fig. 5. It seems that boundary activity is responsible for the nucleation of reaction at this location and, subsequently, the large potential difference between this alloy and residual gold, about 0.2 v, from Fig. 3, causes rapid and continuing penetration down the plane of the boundary.

The potential of the polycrystalline aggregate is nearly that observed for the grains. When individual grain and grain boundary electrodes are short circuited outside the cell, after reaching steady state, the potential of the combined electrodes is almost identical with that observed for the polycrystalline electrode; when the circuit between the two electrodes is opened, the individual potentials are re-established almost immediately.

Composition dependence of potentials in the copper-zinc system in $FeCl_3$.—Potentials of copper-zinc polycrystalline alloys in the alpha solid solution range, and pure zinc, were determined in ferric chloride with results shown in Fig. 6. Again, for comparative purposes, the values at 20 hr are shown in Fig. 7 as a function of composition.

In this case, a steady state evidently is not reached. Zinc becomes progressively more noble, presumably due to the formation of hydrated oxides, while the copper-zinc alloys become more active. The scale should be emphasized in Fig. 6 where the potential difference between zinc and the most active copper alloy is large, about 0.9 v at 20 hr.

Potentials of grains and grain boundaries of brass in ferric chloride.—Results of typical measurements of grain, grain boundary, and polycrystalline alpha brass (70%Cu–30%Zn) are presented in Fig. 8. Reproducibility was ade-

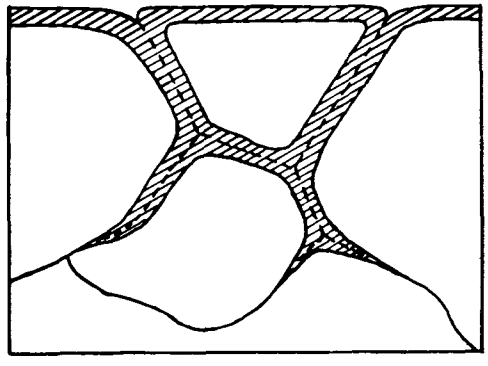

FIG. 5. Schematic drawing showing the preferential removal of copper from grain boundaries in Cu_3Au by ferric chloride and the relatively slow penetration of grains normal to the outer surface and to the boundary planes.

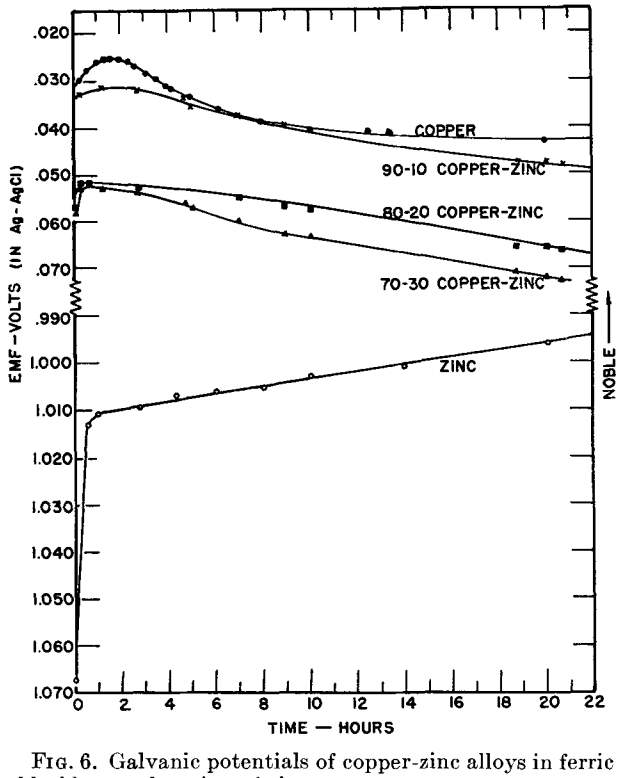

FIG. 6. Galvanic potentials of copper-zinc alloys in ferric chloride as a function of time.

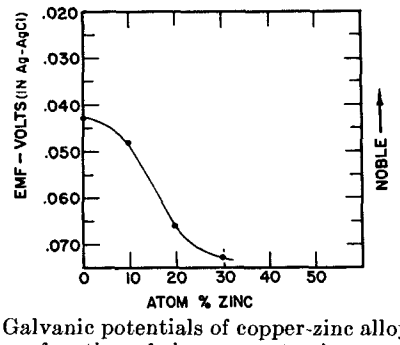

FIG. 7. Galvanic potentials of copper-zinc alloys in ferric chloride as a function of zinc concentration.

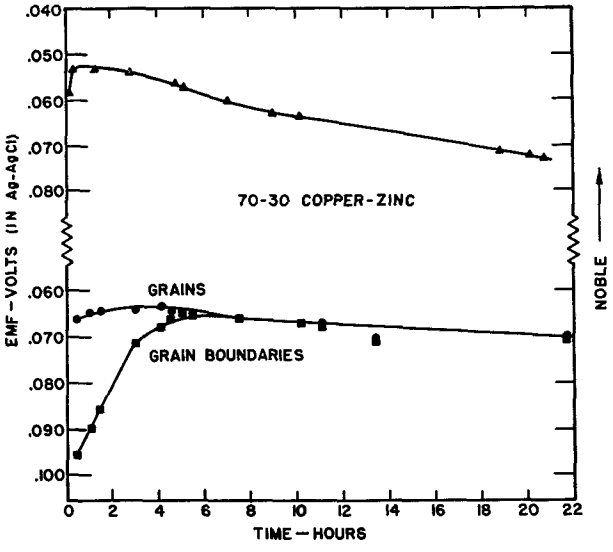

FIG. 8. Potentials of alpha brass (70% Cu–30% Zn) electrodes consisting of grains, grain boundaries, or a polycrystalline aggregate in ferric chloride.

quate for the purpose; for example, in four runs between which the specimens were completely repolished, the potential value at the maximum of the curve for the grains was -0.065 ± 0.004 v and similar deviation from the average of four was observed in polycrystalline electrodes.

Like pure copper, the potential difference between grains and grain boundaries goes to zero after about 8 hr and continues at zero thereafter. Again, this is in accord with structural observations. Immersion of annealed specimens in ferric chloride for prolonged periods results in dezincification and the formation of equilibrium grooves at the intersection of boundaries with the surface; continuous penetration of the boundary, characteristic of susceptibility to stress corrosion cracking, does not occur in conformity with the observed absence of cracking of brass in ferric chloride.

Composition dependence of potential of copper-zinc alloys in aqueous ammonia.—Present results in ammonia should be compared with corresponding results obtained in ferric chloride, the former constituting a combination in which brass is susceptible to cracking and the latter in which there exists little or no such susceptibility.

Data on copper, 70–30 copper-zinc, and pure zinc in 2% aqueous ammonia are presented in Fig. 9. It is clear that, in spite of the ammonia complex formed by copper, zinc and copper-zinc alloys remain active relative to copper in ammonia solutions. With respect to the ammonia electrolyte, however, the additional factor of oxygen concentration must be considered because, unlike ferric chloride, no oxidizing agent is present other than oxygen.

Grain and grain boundary potentials of brass in ammonia.—Except Dix (2), other investigators (6, 7) who have measured grain and grain boundary potentials of brass in ammonia have found invariably the grain boundaries to be more noble than the grains.

In the present case, six different experiments involving three runs with cast and homogenized 70/30 brass, two runs with recrystallized 70/30 brass, the latter specimens probably from the same piece as that used by Dix (2), and one run with 75/25 cast brass all confirmed the results of other investigators in that the boundary was invariably cathodic to the adjacent grains. Results for 75/25 brass are presented in Fig. 10. By comparison with previously

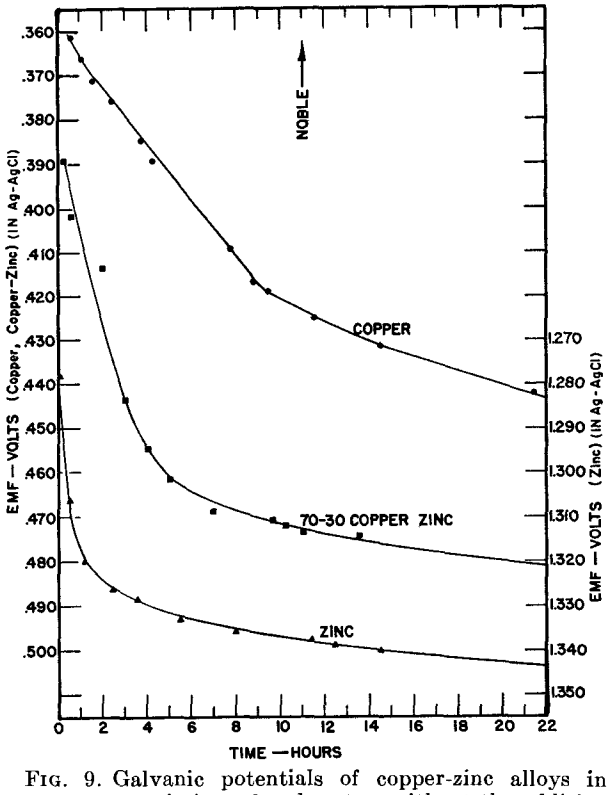

FIG. 9. Galvanic potentials of copper-zinc alloys in aqueous ammonia in a closed system without the addition of oxygen.

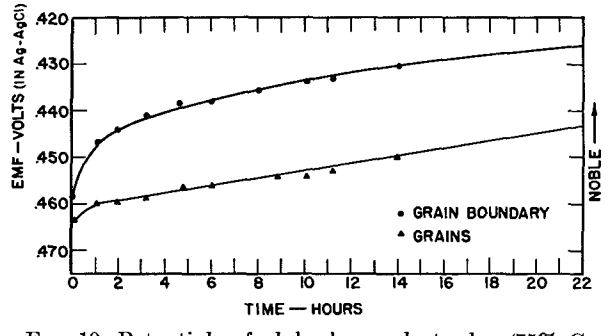

FIG. 10. Potentials of alpha brass electrodes (75% Cu–25% Zn) consisting of grains or grain boundaries in aqueous ammonia without oxygen additions.

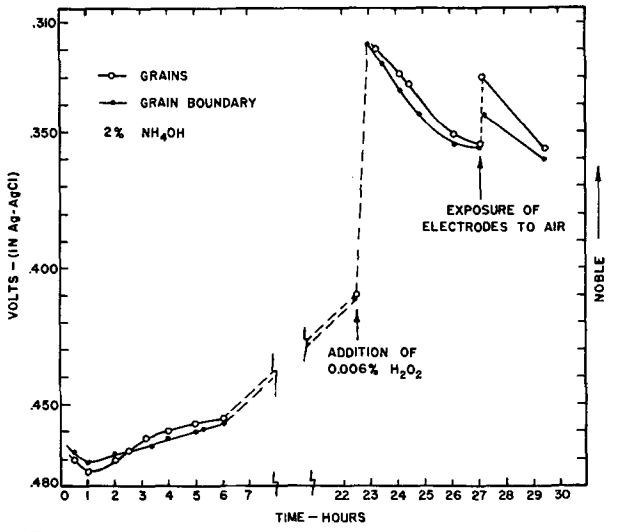

FIG. 11. Effect of oxygen on the potentials of grains and grain boundaries of alpha brass (75% Cu–25% Zn) in aqueous ammonia.

described experiments in different electrolytes, reproducibility of absolute values in ammonia was poor; however, the polarity was always that shown in Fig. 10 and exactly the inverse of what might be expected. Also, the observed difference in potential remained essentially constant in time up to 24 hr.

After considering that all measurements were conducted in a cell two-thirds filled with aqueous ammonia and closed with a rubber stopper, and that stress corrosion cracking is dependent on oxygen concentration (8), it was concluded that the above results in ammonia might be associated with a limited supply of oxygen.

Numerous trial runs in which hydrogen peroxide was added to the electrolyte generally confirmed the conclusion that previous results were associated with the relative absence of an oxidizing agent in the solution. However, the presence of hydrogen peroxide resulted in excessive gas evolution and erratic readings. Accordingly, a set of measurements was made with the cell open to the air with results shown in Fig. 11. Initially the grain boundaries were cathodic, as before, but in 2.5 hr the potential difference decreased to zero, subsequently reversed, and finally stabilized at a difference of about 1.5 mv with the grain boundaries active, a condition which was maintained for about 18 hr. At this time, a very small quantity of hydrogen peroxide was added to the cell which caused a large shift in both potentials in a noble direction; the potential difference between grains and boundaries first increased and finally decreased again while the absolute magnitude shifted back to more negative values, presumably due to the decomposition of the small quantity of hydrogen peroxide. As a further demonstration of the large effect of oxygen, the electrodes were removed from the cell and momentarily exposed to air before replacing in the same position. Again, all potentials shifted in a noble direction and, significantly, the potential difference between grains and boundaries increased to 14 mv; the potential difference subsequently diminished to about 4 mv, presumably as a result of oxygen consumption. Thus, while additional quantitative data are necessary, the general qualitative effects appear to be quite consistent and in harmony with observed stress corrosion cracking phenomena.

DISCUSSION OF RESULTS

The results indicate that there exists a direct, empirical relation between measured grain boundary potentials in copper alloys and observed structural reactions and stress corrosion cracking susceptibility. Such a correlation already exists for age hardening aluminum base alloys in which compositional changes associated with precipitation clearly account for the observed galvanic potentials between grains and their boundaries. The corresponding mechanism in homogeneous copper solid solutions is not so clear.

With respect to pure copper, it appears from the data in Fig. 1 that the initial active potential measured at the boundary is directly related to the reaction at the non-equilibrium grain corner, where the plane of a boundary meets the plane of the surface. However, when an equilibrium configuration is established, further reaction occurs without regard to structure and, in particular, continued preferential penetration at the grain boundary does not occur, as shown by metallographic examination and indicated by the subsequent equality of potentials in Fig. 1. It seems possible to conclude, therefore, that the structural boundary itself does not produce a galvanic potential, measurable with present methods.

In copper-gold alloys, crystallographically similar to pure copper, the situation is quite otherwise. Measurement of boundary potentials, Fig. 4, shows that a constant potential difference exists between grains and their boundaries, and metallographic examination shows that penetration proceeds preferentially down the boundary until a specimen is completely penetrated.

A potential difference of about 200 mv in ferric chloride exists between gold and a Cu_3Au alloy. Evidently, if a reaction removing copper is able to start at some preferred site, the large galvanic potential between the remaining gold and the copper alloy will result in further, and continuous, removal of copper. However, that both a preferred structural path and composition are involved in the mechanism is indicated by two facts: (*a*) the path of penetration down grain boundaries in Cu_3Au is enormously more rapid than through the grains, and (*b*) the characteristic penetration does not occur at all in pure copper or in a copper-gold alloy.

It appears, therefore, that the nucleating reaction is most probably the same one that occurs in pure copper at a boundary with the removal of copper at the grain edge; however, in the Cu_3Au alloy the resulting galvanic potential between the remaining gold sponge and the alloy increases greatly with the removal of copper and produces the observed continuous penetration. In the CuAu alloy, in which the potential differences are of the same magnitude and, therefore, electrochemically comparable, copper is surrounded by more gold atoms and the removal of additional copper, after the first superficial attack, apparently is limited by the remaining coherent layer of gold which renders the underlying copper inaccessible to the electrolyte (9).

Similar phenomena in copper-zinc alloys are complicated by the fact that both components of the alloy are chemically active. Since galvanic potential differences are evidently involved it is apparent that the relative activity of reactive components must be considered with regard to the electrolyte. Thus, the potential difference between grains and boundaries in copper-zinc alloys in ferric chloride goes to zero, after initial boundary activity, Fig. 8, in exactly the same manner as pure copper. Again it appears that this is primarily a structural phenomenon associated with the establishment of an equilibrium configuration at grain corners. However, it remains to explain why, in this alloy, penetration ceases after the formation of an initial groove at the boundary.

In the latter connection, it is instructive to compare Fig. 3 and 7 from which it is apparent that the change of potential with composition, measured in ferric chloride, is much greater in copper-gold alloys than in copper-zinc alloys, specifically about 22 mv/atom % gold as compared with approximately 1 mv/atom % zinc; furthermore, in zinc alloys the potential changes in the active direction with increasing zinc concentration. It seems, therefore, that the removal of zinc at boundaries by ferric chloride may result in diminishing the active potential of boundary areas with respect to adjacent grains, so that continued boundary penetration ceases.

It has been shown, qualitatively, that the polarity of grains and grain boundaries in alpha brass in ammonia is dependent on oxygen concentration, and that, in the presence of sufficient oxygen, the boundaries are active with respect to the grains. While this result is in complete accord with observations on intergranular corrosion and stress corrosion cracking, the detailed mechanism involving oxygen is not clear.

It is even more difficult to explain why the grain boundaries are reproducibly *cathodic* to the grains, Fig. 10, under conditions where oxygen is limited. Obviously, a quantitative study using various proportions of oxygen and gaseous ammonia is indicated and no general conclusions regarding the mechanism can be drawn without such data. It is also apparent that no consistent results are obtainable without quantitative control over this variable.

Conclusions

1. It has been shown that the measured potentials of grains and grain boundaries in pure copper and two different homogeneous copper alloys in two electrolytes are in complete conformity with corresponding intergranular corrosion and stress corrosion cracking observations.

2. In pure copper, the grain corners where the plane of the boundary meets the external surface is the site of a nucleating reaction. In copper and brass in ferric chloride, preferential reaction at the boundary ceases after an equilibrium configuration is established and potential differences between grains and grain boundaries go to zero; in copper-gold alloys penetration in the plane of the boundary continues, apparently as a result of the large potential difference created between the alloy and gold remaining after the oxidation of copper at the boundary.

3. The structural grain boundary, in itself, is not a source of galvanic potential measurable with the present technique after the initial reaction at the unstable corner where the plane of the boundary meets the outer surface. The boundary does, however, provide a preferential path for reaction when the necessary driving force is produced by the removal of one component of an alloy.

4. The polarity of grains and grain boundaries of brass in aqueous ammonia is dependent on oxygen concentration and, at low oxygen concentrations, boundaries are cathodic to the grains while, at higher oxygen concentrations, grain boundaries are anodic, in conformity with observed susceptibility to stress corrosion cracking and intergranular corrosion.

Acknowledgment

The authors are indebted to Handy and Harman, particularly to Mr. Ernest Chamer and Mr. John L. Christie for assistance rendered in preparation of the gold alloys. They are also indebted to the Office of Naval Research for financial support of this work and, accordingly, reproduction in whole or in part is permitted for any purpose of the United States Government.

Manuscript received November 7, 1955. This paper was prepared for delivery before the Pittsburgh Meeting, October 9 to 13, 1955, and was abstracted from a dissertation presented by R. Bakish to the School of Engineering, Yale University, in partial fulfillment of the requirements for the degree of Doctor of Engineering.

Any discussion of this paper will appear in a Discussion Section to be published in the December 1956 Journal.

References

1. R. B. Mears, R. H. Brown, and E. H. Dix, Jr., Symposium on Stress-Corrosion Cracking of Metals, A.S.T.M.—A.I.M.E., p. 323 (1944).
2. E. H. Dix, Jr., *Proc. Am. Soc. Testing Materials*, **41**, 928 (1941).
3. T. C. Wilson, G. Edmunds, E. A. Anderson, and W. M. Peirce, Symposium on Stress-Corrosion Cracking of Metals, A.S.T.M.—A.I.M.E., p. 173 (1944).
4. D. H. Thompson and A. W. Tracy, *J. Metals*, **1**, 100 (1949).
5. R. Bakish and W. D. Robertson, submitted to *J. Metals*; W. D. Robertson, "Impurities and Imperfections," p. 170, A.S.M., Cleveland (1955).
6. E. C. W. Perryman, Private communication relative to beta brass.
7. Hugh L. Logan, Private communication relative to alpha brass.
8. R. G. Johnston, *Sheet Metal Ind.*, **14**, 1197 (1940).
9. L. Graf, *Z. Metallkunde*, **40**, 275 (1949).

High Pressure Oxidation of Niobium

DONALD W. BRIDGES AND W. MARTIN FASSELL, JR.[1]

Department of Metallurgical Engineering, University of Utah, Salt Lake City, Utah

ABSTRACT

Niobium oxidizes according to the linear rate law from 400°–800°C (14.7–605 psia O_2). The oxidation rate is extremely pressure sensitive above 550°C. Theoretical considerations indicate that an equilibrium adsorption process occurs prior to the rate-determining step. It was necessary to include a term in the rate equation for the interaction between the adsorbed molecules to interpret results above 650°C. The interaction energy is influenced by the initial orientation of the metal surface. The activation energy for the oxidation process is approximately 9 to 10 kcal (500°–800°C).

INTRODUCTION

Oxidation data for niobium or columbium are not extensive. Gulbransen (1–3) found the metal to obey the parabolic rate law (200°–375°C). It has been stated (4) that the oxide formed at 200°C in air is adherent, preventing further oxidation unless the temperature is increased. McAdams and Geil (5) reported some data on relatively impure niobium. Inouye (6) published a survey of the scaling of niobium in dry air and in air containing water vapor (400°–1200°C). The metal oxidized according to the linear rate law (400°–1200°C) although irregular behavior occurred in dry air at 400°C, and in air containing moisture at temperatures below 600°C. Both black and white oxides were formed and identified as Nb_2O_5; three modifications were found.

According to Brauer (7) the following oxides exist: NbO_2, NbO, and Nb_2O_5. Nb_2O_5 has three forms: the so-called "low form," stable to 900°C; "medium form," 1000°–1100°C; and "high form," stable at temperatures above 1100°C. Recent work (6, 8) questions the transition temperatures cited by Brauer. A mixture of NbO and Nb_2O_5 has been reported at 400°C (2). Seybolt (9) investigated the solubility of oxygen in niobium (800°–1100°C). Kubaschewski and Schneider (10) studied the oxidation of several alloy systems containing niobium.

The present paper concerns the behavior of niobium in pure oxygen (14.7–605 psia) from 400° to 800°C.

EXPERIMENTAL PROCEDURE

Equipment and general technique are discussed in detail in a recent publication (11). Weight change is measured by observing the deflection of a quartz spring. Each individual experimental determination was made at constant temperature and constant pressure. The niobium used was Fansteel Metallurgical Corp. commercial sheet. Spectrographic analysis of the metal revealed traces of the following elements: aluminum, copper, gold, silver, zirconium, osmium, and rhodium. Average sample size was 1.5 in. x 0.375 in. x 0.02 in., a geometric surface area of about 1.2 in.^{2}.

[1] Present address: Howe Sound Co., Salt Lake City, Utah.

EXPERIMENTAL RESULTS

Effect of Oxygen Pressure

In all experimental determinations, the oxidation behavior of niobium was best represented by a linear rate law, i.e., $\Delta W/\Delta t = K$. K is a function of pressure and temperature and is referred to as the observed rate. Considerable time was required at 400°C to establish linearity. At 400°C and 14.7 psia oxygen, nearly six hours were required before the rate was truly linear. In dry air (one-fifth the concentration of pure oxygen) Inouye (6) required 21 hr to reach linearity at 400°C. Table I summarizes the data at 400° and 450°C. Above 500°C linear oxidation was observed from first recorded time to completion. Some samples ignited at 800°C at oxygen pressures in excess of 200 psia.

Fig. 1 shows the effect of oxygen pressure on the oxidation rate of niobium from 400° to 800°C. Niobium follows the general oxidation pattern of tantalum (11). The essentially "pressure independent" linear oxidation region terminates most abruptly at 500°C. The pressure dependent zone has its maxima at 575°C, with minima in the isobars at 650°C. A similar shaped plot has been obtained by oxidizing niobium under conditions of a linear increase in temperature (12).

Effect of Prior History of Niobium Metal

Two separate lots of niobium metal designated as "A" and "B" were used in this study. Marked differences in the oxidation behavior were observed in the two lots. Fig. 2 compares two isotherms of metal "A" with two isotherms of metal "B" in the same temperature region. Spectrographic analysis revealed no difference in composition between the two lots. Likewise metallographic work showed no marked difference; the grain size of both lots was very small. X-ray diffraction patterns showed that the orientation of the niobium surface of metal "A" differed from that of metal "B". The exact orientation of neither lot was determined.

Additional evidence that a difference existed between the corrosion behavior of the two lots was gained by following the wet corrosion of samples of metal "A" and metal "B" with periodic x-ray diffraction studies of the corroded surfaces. A hot solution of potassium hydroxide and potassium ferrocyanide [44.5 g/l KOH and 305 g/l $K_4Fe(CN)_6$]

TABLE I. *Oxidation rate of niobium "A" in oxygen for temperatures below 500°C*

Temp, °C	Oxygen pressure (psia)	Observed rate ($mg \cdot cm^{-2} \cdot hr^{-1}$)	Elapsed observed time before $\Delta W/\Delta t$ = const.	Observed period during which $\Delta W/\Delta t$ = const*
			min	*min*
400	14.7	0.18	350	200
400	30	0.27	200	200
400	400	0.13	300	100
450	100	5.8	Nil	70
450	200	3.8	Nil	70
450	300	2.8	15	40

* Run was terminated at the end of this period.

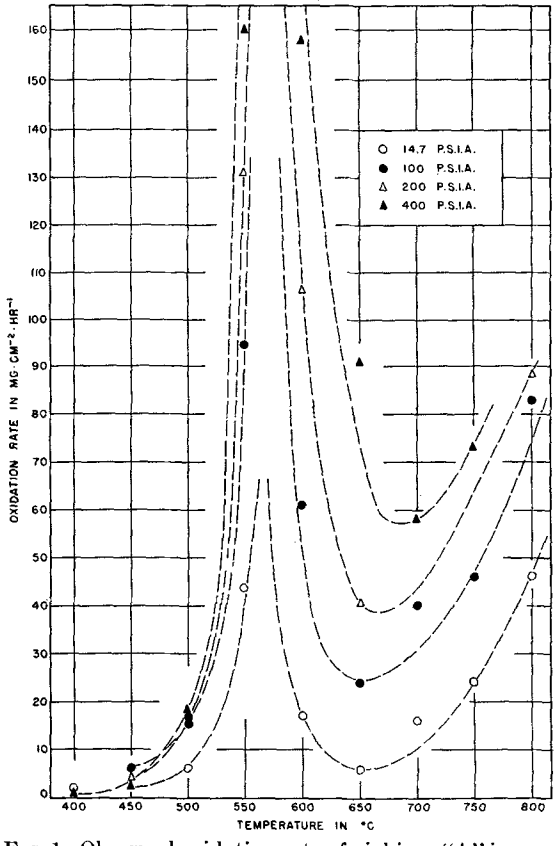

FIG. 1. Observed oxidation rate of niobium "A" in oxygen at various temperatures and pressures.

was employed as the corroding medium. Niobium samples of 20 mil thickness were corroded to an eventual thickness of 3–4 mils. A comparison of the relative intensities of the diffraction peaks as the surface was corroded revealed that corrosion occurred along different planes in the two lots.

The only data available for metal "B" are shown on Fig. 2. All other data reported are for metal "A". Repeated measurements under the same experimental conditions showed that the reproducibility of observed rates was most satisfactory.

X-ray Diffraction Results of Formed Oxides

Oxide coatings formed at various temperatures and pressures were examined by x-ray diffraction. Table II summarizes results and attempts a comparison with the available ASTM cards. Nb_2O_5 seems the most likely oxide present. Identification of the particular form of Nb_2O_5 is not attempted. The sample removed at the end of three hours' oxidation at 400°C and 14.7 psia was black in color, while the sample removed at the end of 25 hr was white. The oxides formed above 400°C were all white in color.

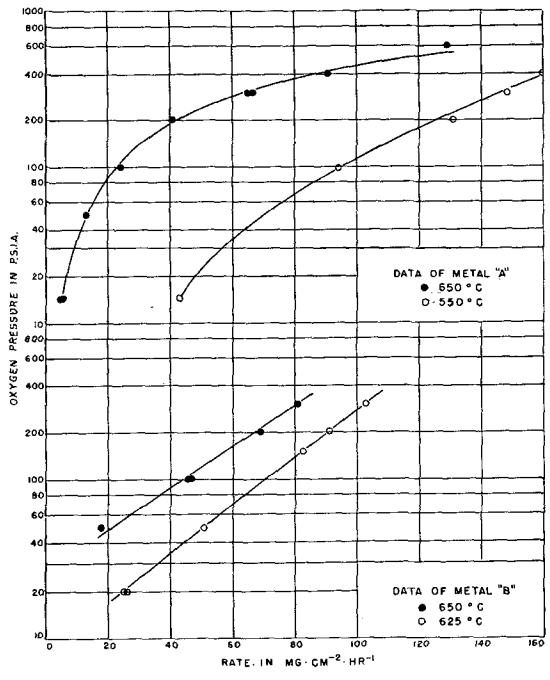

FIG. 2. Comparison of oxidation rates of metals "A" and "B" within "Dome" region (550°–650°C).

DISCUSSION OF EXPERIMENTAL RESULTS

No interpretation of the data below 500°C is attempted, as these rates were not initially linear. The observed rate of oxidation above 500°C is ideally linear, hence the rate-determining step is a phase boundary reaction (13). Recent work (14) suggests an underlying oxide as the zone of reaction in the linear oxidation of tungsten. Another possible interface for the reaction is the metal-metal oxide boundary. The basic assumption of the discussion to follow is that the adsorption of oxygen at the reaction boundary is much faster than the subsequent rate-controlling step and may be treated as an equilibrium process. A previous paper (11) develops concepts based on this assumption in detail and illustrates that application of the Theory of Absolute Reaction Rates (15) results in the following kinetic expression for an oxidation process governed by a boundary reaction,

$$\text{rate} = dm/dt = k_0 \cdot f(\theta) \cdot (kT/h) \cdot \exp(-\Delta F^*/RT) \quad \text{(I)}$$

k_0 is a proportionality constant with the dimensions of ML^{-2} and includes factors estimating the true surface area involved in the reaction. $f(\theta)$ is a function of θ, the fraction of the surface covered with adsorbed oxygen; expressions for this concentration term depend upon the nature of the adsorbed phase. $kT/h \cdot \exp(-\Delta F^*/RT)$ is the Eyring rate equation (15) with the transmission coefficient assumed to be unity.

TABLE II. *Comparison of interplanar spacings of the oxide scale formed on niobium metal*

Niobium metal		Diffraction data from this work					ASTM card information	
As determined this laboratory	ASTM Data card work of Meisel, and co-workers	400°C		575°C 100 psia (oxide surface white)	700°C 100 psia (oxide surface white)	750°C 100 psia (oxide surface white)	ASTM Card 5-03252 Niobium pentoxide ignited at 1000°C, work of Hahn, *JACS*, 73, 5091 (1951)	L.S. Iverm Westinghouse
		14.7 psia 3 hr (oxide surface black)	30 psia 25 hr (oxide surface white)					
7.369		7.248	7.248	5.242	5.181	5.211	5.241	4.04
2.336	2.336	3.966	3.914	3.931	3.931	3.931	4.329	3.17
1.652	1.65	3.151	3.140	3.463	3.463	3.463	3.931	2.48
1.348	1.35	2.378	2.434	3.162	3.151	3.151	3.484	1.97
1.168	1.17	1.679	2.120	3.097	3.097	3.097	3.140	1.81
1.166		1.362	1.959	2.736	2.728	2.728	2.855	1.67
0.044	1.04	1.182	1.819	2.460	2.460	2.453	2.728	1.65
0.041		1.059	1.652	2.116	2.434	2.421	2.590	1.57
		0.960	1.574	2.017	2.116	2.116	2.447	1.46
0.953	0.95	0.889	1.190	1.963	2.009	2.009	2.120	1.34
0.950				1.829	1.963	1.963	1.962	1.23
				1.792	1.829	1.829	1.908	1.18
0.882	0.88			1.660	1.789	1.789	1.825	1.14
				1.635	1.657	1.663	1.792	1.06
0.880				1.574	1.630	1.630	1.661	1.01
				1.460	1.572	1.572	1.571	1.00
0.825	0.83			1.336	1.541	1.541	1.543	0.94
				1.323	1.460	1.460	1.459	0.92
0.823				1.227	1.336	1.336	1.336	0.88
				1.195	1.323	1.323	1.322	0.86
				1.142	1.227	1.227	1.226	
						1.208	1.209	
						1.193	1.197	
							1.144	
							1.022	
							0.99	

Where interaction between the adsorbed molecules is negligible and the assumption of equilibrium allowable, the expression for $f(\theta)$ employed in the explanation of the linear oxidation of tantalum (11, 12) is suitable and equation (I) becomes,

$$\text{rate} = \theta \cdot K_0 = K_0 \frac{K_1[O_2]}{1 + K_1[O_2]} \qquad \text{(II)}$$

where K_0 equals $k_0(kT/h)\exp(-\Delta F^*/RT)$ and K_1 is the molar equilibrium constant for the adsorption of oxygen molecules. $[O_2] = P/RT$, and is the oxygen gas concentration provided the bulk gas phase obeys the perfect gas law (11, 12).

In order to satisfy equation (II) the following conditions must be satisfied.

Condition 1. Values of K_0 must be greater than any observed rate at the temperature in question. This would be expected as, limit $(\theta \rightarrow 1)$ $(dm/dt) = K_0$.

Condition 2. The slope of the plot, $\log_{10} K_0$ vs. 1/°K, must be negative in order that the activation energy for the process be positive.

Condition 3. The slope of the plot, $\log_{10} K_1$ vs. 1/°K, must be positive, since the heat of adsorption must be exothermic.

Condition 4. Values of K_1, the adsorption equilibrium constant, must be greater than unity since it is necessary that the adsorption free energy be negative or zero,

$$\Delta F_{ads} \leq 0, \text{ and}$$
$$K_1 = \exp(-\Delta F_{ads}/RT) = \exp(-(\Delta H_{ads} - T \cdot \Delta S_{ads})/RT) \qquad \text{(III)}$$

TABLE III. *Comparison of observed oxidation rates of niobium "A" and trial and error fit of data by equation (II)*

Temp, °C	O_2 Pressure psia	Observed rate mg-cm^{-2}-hr^{-1}	Calc. rate mg-cm^{-2}-hr^{-1}	Constants	θ
550	14.7	43.4	43.4		0.26
	100	94.4	118.7	K_1, 23.3	0.70
	200	131	139.7		0.82
	300	148.4	148.3	K_0, 169.5	0.88
	400	159.9	153.2		0.91
600	14.7	17.2	13.1		0.06
	50	40	39.2		0.17
	100	61	67	K_1, 4.25	0.28
	200	106	105		0.44
	300	124	129	K_0, 238	0.54
	400	158	146		0.61
650	14.7	5.9	4.5		0.01
	50	13.6	14.8		0.05
	100	24.2	25.9	K_1, 1.1	0.08
	200	40.2	51.6		0.16
	300	66.7	71.9	K_0, 315	0.23
	400	91	88.9		0.28
	605	129	118		0.38

Trial and error fits, using equation (II), for the 550°, 600°, and 650°C isotherms for metal "A" are tabulated in Table III.

Fig. 3 illustrates the relationships found to exist between values of K_0, the absolute reaction rate constant, and reciprocal absolute temperature; as well as the relationship between the adsorption equilibrium constant, K_1, and

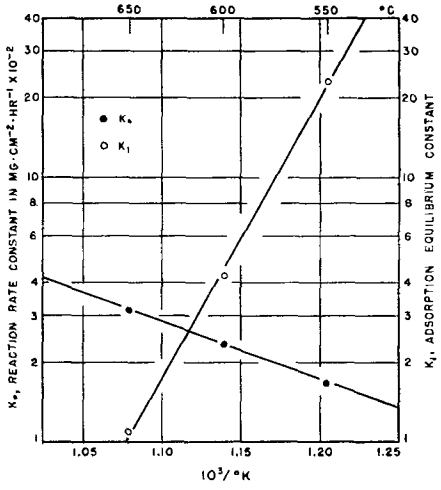

FIG. 3. Plot showing variation of the constants of Table III with temperature.

reciprocal absolute temperature. Slopes of the curves of Fig. 3 yield an activation energy, ΔH^*, of 9.9 kcal and an adsorption enthalpy, ΔH_{ads}, of −48.6 kcal/mole oxygen.

When adsorption occurs with appreciable interaction between the adsorbed molecules equation (II) is not applicable. The assumption of random distribution of the adsorbed molecules and interaction between the pairs of nearest neighbors lead to a varying adsorption enthalpy (16):

$$\Delta H_{ads} = \Delta H^0_{ads} + \theta z V, \qquad \text{(IV)}$$

where ΔH^0_{ads} is the enthalpy of adsorption for $\theta = 0$. zV is the product of the molar interaction energy, V, and the coordination number, z, i.e., the interaction energy of a pair of near neighbors multiplied by the number of such pairs. The adsorption entropy is assumed constant, thus the change in the adsorption potential, ΔF_{ads}, is identical with the change in ΔH_{ads}. Such behavior has been experimentally observed for the adsorption of hydrogen on tungsten (17).

A previous paper (18) has expanded these concepts into a suitable approximation for the rate of oxidation, viz.,

$$\text{rate} = \theta \cdot K_0 (4.6T/zV) K_0 [\log_{10} P + \log_{10} (K_1^0/RT)] \qquad \text{(V)}$$

TABLE IV. *Estimate of interaction energy, data of metal "A"*

Temp, °C	K_0	zV in cal	K_1^0
500	18	8,300	398
700	58	8,800	278
750	73	12,900	660
800	90	11,900	1470

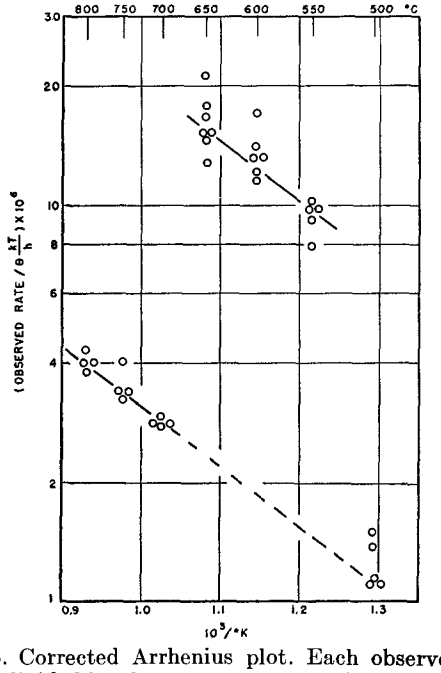

FIG. 5. Corrected Arrhenius plot. Each observed rate has been divided by the proper concentration term (θ).

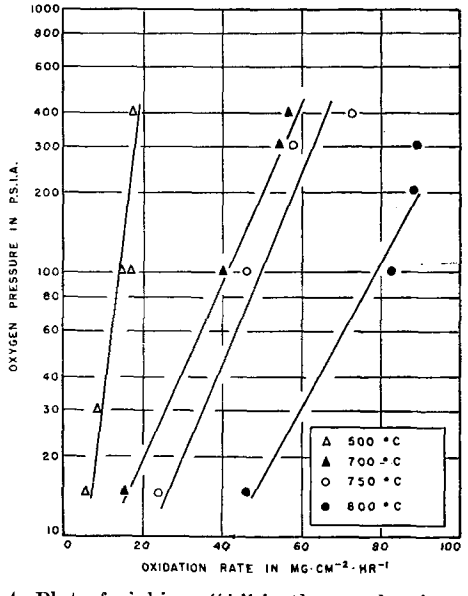

FIG. 4. Plot of niobium "A" isotherms showing correlation of data by application of equation (V).

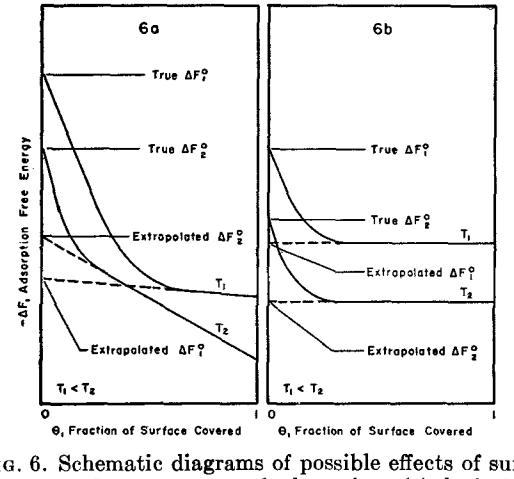

FIG. 6. Schematic diagrams of possible effects of surface coverage on the free energy of adsorption: (*a*) deviation of adsorption free energy from the linear behavior predicted by equation (IV) as $\theta \rightarrow 0$ results in extrapolated values of ΔF_{ads} differing from condition 3; (*b*) adsorption free energy, ΔF_{ads}, values result which are lower than the true values if the interaction energy is not negligible as $\theta \rightarrow 0$.

where K_0 is the absolute reaction rate constant as before and K_1^0 is the adsorption equilibrium constant for $\theta = 0$. The equilibrium constant is dependent on θ and is defined by

$$K_1 = K_1^0 \exp(-\theta z V/RT) \qquad \text{(VI}a\text{)}$$

where

$$K_1^0 = \exp(-\Delta F^0_{ads}/RT) \qquad \text{(VI}b\text{)}$$

Plots of observed rate vs. the logarithm of oxygen pressure for 500°, 700°, 750°, and 800°C are shown in Fig. 4. It is felt that the correlation of the data warrants application of equation (*V*). Estimation of zV is accomplished by selection of K_0 values in accordance with Conditions 1 and 2. These values are tabulated in Table IV. Plot of the logarithm of K_0 vs. reciprocal absolute temperature yields an enthalpy of activation, ΔH^*, of 8,750 cal.

Fig. 2 shows the 625° and 650°C isotherms for metal "B" plotted according to equation (V). It suggests that differences in surface orientation of metal "B" favor stronger interaction between the adsorbed oxygen molecules.

Fig. 5 represents the corrected Arrhenius plot. Each observed rate has been divided by the concentration term, θ, the fraction of the surface covered. The slope (and hence the activation energy) is essentially the same from 500° to 800°C, although the correlation of data by the two methods results in two parallel trends rather than a single straight line plot of absolute reaction rate constant vs. reciprocal temperature. Changes in the magnitude of the absolute reaction rate constant could be due to one or a combination of several factors: (*a*) difference in the entropy of activation, ΔS^*; (*b*) change in the number of active sites per unit area; or (*c*) change in surface roughness. A change in one of these quantities by a factor less than ten would correct the break (offset) in the plot.

The effect of surface coverage on adsorption free energy, demonstrated to apply in the investigated region of θ, may not be valid as the surface coverage, θ, approaches zero. The following evidence substantiates this conclusion: (*a*) the temperature dependence of K_1^0 (700°–800°C) is the reverse of the expected; (*b*) the adsorption free energies (550°–650°C) are extremely low. Fig. 6 shows a possible explanation. Neither the noninteraction nor linear enthalpy variation mechanism is obeyed for extremely low values of θ. The initial effect of interaction is much stronger than the variation over the investigated pressure range and causes a sharp descent in the adsorption potential in the region, $\theta \rightarrow 0$, followed by a linear dependence on θ, or, if zV is small, an essentially nonvarying enthalpy. Fig. 6*a* depicts the probable behavior of adsorption free energy as a function of surface coverage in the region of temperature 700°–800°C. Although the adsorption free energy always decreases as temperature increases, the actual nature of the deviation with respect to θ for the individual isotherms may result in an apparent violation of Condition 3, i.e., K_1^0, and hence free energy, increases with temperature. This violation would result if the initial abrupt descent in free energy places the straight line portions of Fig. 6*a* in such a position that the extrapolated lines intersect within the allowed θ values ($0 \leq \theta \leq 1$). Likewise Fig. 6*b* illustrates a case which would explain the low values of the free energy in the 550°–650°C region. It graphically expresses the belief that equation (II) results when the term θzV can be neglected in equation (IV).

Acknowledgments

The authors wish especially to thank Mrs. Gretta S. Baur who performed the diffraction analysis summarized in Table II. They also thank Mr. John P. Baur who interpreted the x-ray diffraction data gained in monitoring the wet corrosion phase of the investigation. They express their appreciation to the Office of Ordnance Research, U. S. Army, and their Watertown Arsenal Laboratory, for the funds that made the work possible, and to Dr. John R. Lewis, Head, Dept. of Metallurgy, University of Utah, for his support and interest in this work.

Manuscript received August 4, 1955. This paper was prepared for delivery before the Pittsburgh Meeting, October 9 to 13, 1955.

Any discussion of this paper will appear in a Discussion Section to be published in the December 1956 JOURNAL.

REFERENCES

1. E. A. GULBRANSEN AND K. F. ANDREWS, *J. (and Trans.) Electrochem. Soc.*, **96**, 364 (1949).
2. R. T. PHELPS, E. A. GULBRANSEN, AND J. W. HICKMAN, *Ind. Eng. Chem. Anal. Ed.*, **18**, 391 (1946).
3. E. A. GULBRANSEN AND K. F. ANDREWS, *J. Metals*, **2**, 586 (1950).
4. Technical Bulletin, Fansteel Metallurgical Corporation, Chicago (1945).
5. G. J. MCADAMS AND G. W. GEIL, *J. Research Nat. Bur. Standards*, **28**, 593 (1942).
6. H. INOUYE, ORNL-1565, Sept. 24, 1953; (Nuclear Science Abstracts, **7**, No. 22, 5933, Nov. 30, 1953).
7. G. BRAUER, *Z. anorg. u. allgem. Chem.*, **248**, 1 (1941).
8. A. V. LAPITSKII, *et al.*, *Zhur. Fiz. Khim.*, **26**, 56 (1952).
9. A. U. SEYBOLT, *J. Metals*, **6**, 774 (1954).
10. O. KUBASCHEWSKI AND A. SCHNEIDER, *J. Inst. Met.*, **75**, 403 (1949).
11. R. C. PETERSON, W. M. FASSELL, JR., AND M. E. WADSWORTH, *J. Metals*, **6**, 1038 (1954).
12. J. P. BAUR, D. W. BRIDGES, AND W. M. FASSELL, JR., *This Journal*, **102**, 490 (1955).
13. N. F. MOTT AND R. W. GURNEY, "Electronic Processes in Ionic Crystals," 2nd ed., p. 250, Oxford Press, New York (1948).
14. W. W. WEBB, J. T. NORTON, AND C. WAGNER, *This Journal*, **103**, 107 (1956).
15. S. GLASSTONE, K. LAIDLER, AND H. EYRING, "Theory of Rate Processes," McGraw Hill Book Co., New York (1941).
16. R. FOWLER AND E. A. GUGGENHEIM, "Statistical Thermodynamics," p. 429, Cambridge (1949).
17. J. K. ROBERTS, *Proc. Roy. Soc.* (London), **A152**, 445 (1935).
18. J. P. BAUR, D. W. BRIDGES, AND W. M. FASSELL, JR., *This Journal*, **103**, 266 (1956).

Inhibition of Iron Dissolution in Acid Solutions

CECIL V. KING AND ERIC RAU[1]

Department of Chemistry, New York University, New York, New York

ABSTRACT

The inhibition of iron dissolution from rotating cylinders has been studied in solutions of dilute hydrochloric or perchloric acid with excess nitrate as depolarizer. No better over-all oxidizing inhibitor than dichromate was found. Complexing and chelating agents greatly improve protection by dichromate in hydrochloric acid although they simultaneously shift the iron potential in the anodic direction. Iron is protected better by dichromate alone in perchloric acid; chelants tend to make the potential more cathodic, but shorten the time of protection.

Neocupferron, which forms insoluble chelate salts with iron ions, protects iron for many hours in these solutions. Carbon monoxide was studied as an adsorption inhibitor.

INTRODUCTION

Iron does not dissolve rapidly in dilute acids because hydrogen is not evolved freely on the pure metal. Maximum dissolution rates are attained with a suitable depolarizer; with excess nitrate present the dissolution rate can be that of convective-diffusive transport of acid to the metal surface (1). With 0.02M HCl, 0.06M KNO_3 as a representative corroding solution, addition of 0.01M $K_2Cr_2O_7$ reduces the weight loss in a 5-min run by 90% (2). Further addition of 0.01M sodium fluoride inhibits completely for 5 min, and various complexing and chelating agents aid in dichromate protection for a longer time (3). Eventually iron develops pits and corrodes rapidly in these solutions; zinc can be protected for a longer time.

The purpose of the present research was to investigate inhibition in solutions of this type (0.02M HCl, 0.06M KNO_3) in more detail. Inhibition is always due to some kind of protective film, which may be a comparatively thick layer of oxide or other insoluble compound, or a simple adsorbed film, monolayer or even less in coverage. In the solutions mentioned, any defection shows up quickly in terms of weight loss and pitting of the surface. Especial attention was given to a search for inorganic oxidizing inhibitors other than dichromate, to the role of chelating agents, to the effect of chloride ion, to weight gains as evidence of thick films, to the role of adsorption vs. insoluble compounds, and to the effect of some of the reagents on the potential of iron.

EXPERIMENTAL

Cylinders of SVEA Metal[2] 2.5 cm long and about 1.8 cm in diameter were mounted on a motor shaft with the ends protected. Rotation was adjusted with a calibrated stroboscope to give a peripheral speed of 15000 cm/min. Runs were made at room temperature, which varied from 20° to 30°C, but care was taken to run any comparable series at the same temperature ±1°C. Solution *p*H was measured, where mentioned, with a Beckman meter. Potentials were measured with a Student type potentiometer; contact to the rotating cylinder was made through the motor shaft with a carbon brush or a mercury cup. A commercial KCl-saturated calomel cell (S.C.E.) served as reference electrode. Corrosion was followed by weighing the cylinders to 0.1 mg.

The metal surface was prepared by polishing with progressively finer silicon carbide papers, ending with No. 600. The final surface was as free of flaws and pits (left from previous runs) as possible and was scanned carefully with a low-power microscope. Other polishing procedures are described later. In a series of runs in the same solution the cylinder was not repolished unless this is mentioned.

Oxidizing agents.—Several inorganic oxidizing agents were tried for comparison with dichromate, with iron and with zinc and cadmium cylinders of the same size. Table I gives results for the most effective concentrations which left the *p*H not above 2.

Permanganate left a loose film of oxide which was easily wiped off, leaving the metal stained. Arsenate and arsenite left a brown or black coating, probably elementary arsenic. Sodium fluoride did not improve inhibition except with dichromate.

Various combinations of arsenate, arsenite, and dichromate resulted in less than 1 mg weight loss in 5 min (for example, 0.004M Na_3AsO_4, 0.004M $K_2Cr_2O_7$, loss 0.5 mg). Longer runs led to rapid corrosion through pitting. The iron surface was examined under a low-power microscope and the number of pits per unit area (field of view, about 0.3 mm²) counted. Before immersion an average of 3 spots which might be incipient pits was found. After a 5-min run an average of 67 pits was found in the field; this number did not increase as corrosion continued.

Complexing agents.—Attention was now turned to the effect of complexing and chelating agents with dichromate on iron. This is an extension of previous work (3); more care was taken to keep the *p*H near 2. Results are summarized in Table II. Weight gains are indicated as negative weight losses, and were checked with several runs. When such runs were continued for a longer time, weight losses usually continued at about the same rate for a while, then turned sharply upward as pitting became evident; or weight gains reached a maximum, then decreased with

[1] Present address: Bettis Plant, Westinghouse Electric Corp., Pittsburgh 30, Pa.

[2] Iron from Swedish Iron and Steel Co., stated to contain 0.02–0.05% C, less than 0.01% each of Mn, Si, and P, and less than 0.015% S.

TABLE I. *Effect of oxidizing agents in* 0.02M HCl, 0.06M KNO_3, 250 *ml solution, peripheral speed* 15000 *cm/min*

Oxidizing agent	Weight loss, mg in 5 min		
	Fe	Zn	Cd
None	65	75	123
0.01M $K_2Cr_2O_7$	5.7	5	7
0.01M $KClO_3$	67	84	73
0.007M NH_4VO_3	8	40	90
0.02M $KMnO_4$	3.7	2.3	4.9
0.01M Na_3AsO_4	1.7	29	40
0.01M $NaAsO_2$	1.1	33	29

TABLE II. *Inhibition of iron corrosion by dichromate and complexing agents*

0.02M HCl (except as specified), 0.06M KNO_3, 0.01M $K_2Cr_2O_7$, 250 ml, 15000 cm/min

Complexing agent	*p*H	Weight loss, mg in 5 min
None	1.8	5.7
0.01M glycine	2.0	0.7
0.005M nitrilotriacetic acid	1.8	2.4
0.01M nitrilotriacetic acid	1.8	−0.7
0.011M 1,10-o-phenanthroline	2.0	−0.9
0.008M Versen-ol*, 0.04M HCl‡	2.0	2.1
0.01M Quadrol†, 0.03M HCl‡	2.1	0.7
0.013M α,α' dipyridyl, 0.03M HCl‡	2.0	−0.3

* Trisodium *N*-hydroxyethylethylenediaminetriacetate Bersworth Chemical Co. (now Versenes Incorporated).

† *N,N,N',N'*-tetrakis (2-hydroxypropyl) ethylenediamine, Wyandotte Chemicals Corp.

‡ Part of the HCl is neutralized.

obvious pitting. It was necessary to abrade the cylinder enough to remove all pits between runs; otherwise early breakdown usually occurred.

The *o*-phenanthroline developed a yellowish film on the iron surface. After longer runs, a zone of interference colors was observed at each pit, widest at the pit and trailing out to a tip behind the pit. Evidently some ferrous ion is carried within the hydrodynamic boundary layer for a short distance before precipitating on the metal surface.

Table III gives details of two longer runs with dipyridyl. After pitting became pronounced in the first run the cylinder was repolished and immersed in the same solution (2nd run). It is evident that the surface condition, not solution depletion, is responsible for inhibition breakdown.

Pitting did not occur at random, but preferentially along certain abrasion marks. It was possible to photograph the same spot before and after a run as shown in Fig. 1; the area is about 0.4 x 0.6 mm. The behavior suggested that a smoother surface might result in better protection, and various procedures were tried as shown in Table IV. A high polish was obtained with rouge on a damp cloth, leaving only traces of the abrasion marks. The chemical etch was in 0.02M HCl, 0.06M KNO_3, and removed about 3 μ of iron.

It has been reported that even light abrasion of iron may result in a surface temperature as high as 900°C (4). In an attempt to avoid the resulting air oxidation the iron was electropolished in a perchloric acid-acetic anhydride solution (5) with an aluminum beaker as cathode. After several trials most of the cylinder came out well polished. On rinsing and starting to dry, flash oxidation of the surface often took place, interference colors spreading across the

TABLE III. *Inhibition breakdown in* 0.05M HCl, 0.06M KNO_3, 0.01M $K_2Cr_2O_7$, 0.032M *dipyridyl* 250 ml, 15000 cm/min, *p*H 2.05

Time, min	Weight loss, mg	
	1st run	2nd run
5	0	−0.5
10	0.1	−0.5
20	−0.1	−0.1
30	0.2	−0.2
60	0.2	−0.2
120	1.1 pitted	1.2 pitted

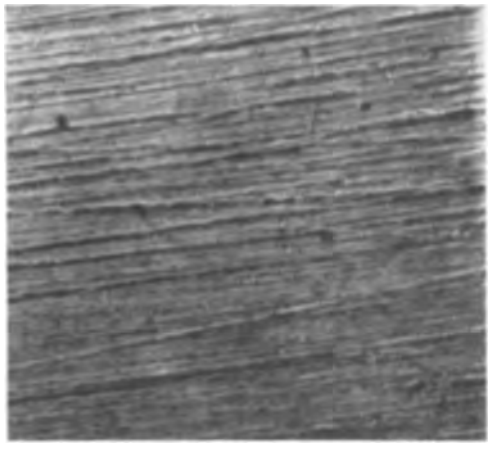

FIG. 1*a*. Abrasion marks on iron cylinder before immersion

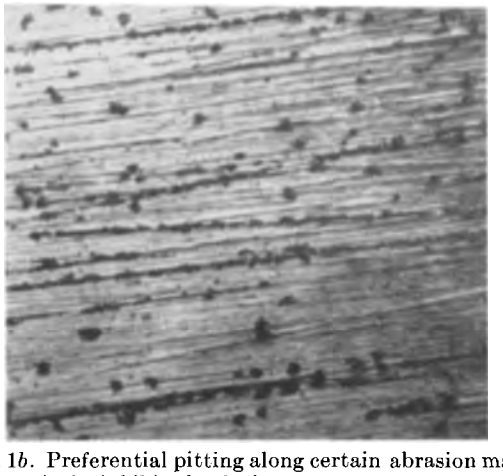

FIG. 1*b*. Preferential pitting along certain abrasion marks after 30 min in inhibited solution.

TABLE IV. *Effect of surface preparation in* 0.04M HCl, 0.06M KNO_3, 0.01M $K_2Cr_2O_7$, 0.012M *dipyridyl* 250 ml, 15000 cm/min, *p*H 2.0

Treatment	Weight loss, mg in 5 min	Time to appearance of pits, min
No. 600 SiC paper	0	240
Rouge polish	0.1	210
Chemical etch	0.1	270
Electropolish	16.7	—

TABLE V. *Effect of pH on iron inhibition* HCl, 0.06M KNO_3, 0.01M $K_2Cr_2O_7$, 0.013M dipyridyl, 250 ml, 15000 cm/min

pH	Weight loss, mg, 30 min	pH	Weight loss, mg, 30 min
5	0	2.1	−0.4
4	0.5	2.0	−0.4
2.9	1.4	1.9	9.1
2.5	2.0	1.8	11
2.2	0.5	1.5	25

TABLE VI. *Protection time with pH less than* 2, 0.06M KNO_3, 0.01M $K_2Cr_2O_7$, 15000 cm/min

Complexing agent	Breakdown time, min	
	HCl	$HClO_4$
None	Immediate	330
0.004M Versen-ol	120	210
0.01M glycine	240	240
0.013M dipyridyl	240	90

cylinder, with enough heat to produce bursts of steam. Eventually, after electropolishing, the cylinder was immersed in a Versene solution for an hour, washed, and dried without developing evident heat; no doubt this only results in a thinner oxide film. The electropolished iron was always much more active than other samples; the initial film is important in protection.

Although inhibition wih dichromate and dipyridyl does not depend on a visible compound on the iron surface, a precipitate formed throughout the solution 15–30 min after the start of each run, and was identified as the dichromate salt of the ferrous-dipyridyl complex. Neither dipyridyl nor the other complexing agents previously mentioned inhibited in the absence of dichromate. Dipyridyl was found to have a maximum effect at *p*H 2.0–2.1 as shown in Table V (the *p*H was adjusted with additions of concentrated acid).[3]

Perchloric acid.—Many experiments similar to the above were carried out with perchloric acid and potassium nitrate, with the addition of dichromate and various complexing agents. Dichromate alone proved to be the best inhibitor; there were weight gains up to 1.2 mg in the first 5 min and no weight loss for about 5 hr. The chelants all decreased the time at which pitting became pronounced and rapid corrosion set in. Table VI compares breakdown times in HCl and $HClO_4$.

Potentials.—All potential measurements were made in deaerated solutions. The rotating iron cylinder was immersed in 100 ml of solution contained in a square bottle with neck only slightly larger than the cylinder and the motor shaft sleeve. The bottle had two holes, one for a nitrogen tube, the other for a KNO_3-agar bridge. Nitrogen was passed over hot copper, through water, and through the reacting solution for 30 min before, and during, the run.

Potentials of iron vs. the S.C.E. in HCl solutions are shown in Fig. 2. In HCl-KNO_3 (curve A) the potential

[3] Actually, the effect of dipyridyl was not examined at the higher *p*H values. In the range 3–1.5, dichromate alone allows weight losses similar to those in Table I, or greater.

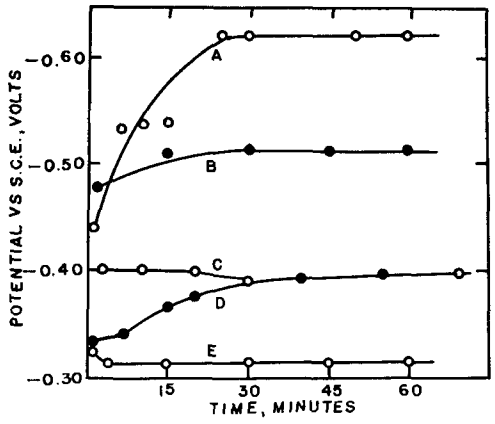

FIG. 2. Potential of iron as function of time. All solutions contain 0.02M HCl and the following additions: A, 0.06M KNO_3; B, acid alone; C, 0.06M KNO_3, 0.01M $K_2Cr_2O_7$, 0.01M dipyridyl; D, 0.06M KNO_3, 0.01M $K_2Cr_2O_7$, 0.01M glycine; E, 0.06M KNO_3, 0.01M $K_2Cr_2O_7$.

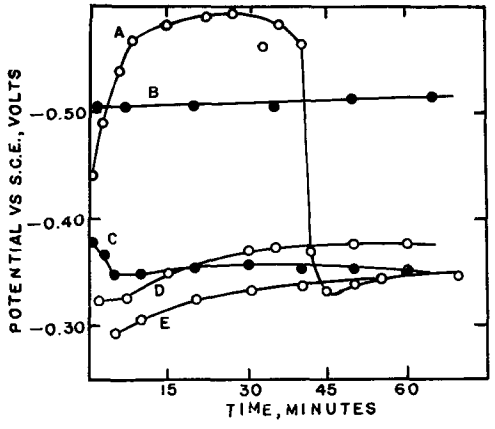

FIG. 3. Potential of iron as function of time. All solutions contain 0.02M $HClO_4$ and the following additions: A, 0.06M KNO_3; B, acid alone; C, 0.06M KNO_3, 0.01M $K_2Cr_2O_7$; D, 0.06M KNO_3, 0.01M $K_2Cr_2O_7$, 0.013M dipyridyl; E, 0.06M KNO_3, 0.01M $K_2Cr_2O_7$, 0.01M glycine.

rises rapidly in the anodic direction because of the rapid corrosion. In HCl alone (curve B) the anodic drift is slow, but when corrosion has proceeded to the same extent (after several hours) the potential is similar to that with the depolarizer. Dichromate makes the iron slightly noble with respect to a hydrogen electrode in the same solution. The chelants partly reverse this effect.

In perchloric acid (Fig. 3) there are two noteworthy features. In $HClO_4$-KNO_3 the potential changes 0.25 v in the cathodic direction when the *p*H reaches 4.5; and chelants make the initial potential more cathodic than dichromate alone, although this effect disappears in time.

In acid alone a greenish coating formed on the cylinder when the solution *p*H became 4–4.5; this was probably ferrous hydroxide since the solution gave no test for ferric ion. With nitrate present a brown coating appeared at about the same *p*H (but in much shorter time); this was no doubt hydrated ferric oxide, and the solution contained ferric ions. In HCl the coating was nonadherent and slow corrosion continued; in $HClO_4$ it was adherent and corrosion was arrested, small weight gains being noted. The

TABLE VII. *Inhibition by neocupferron in air-saturated solutions*
0.02M HCl, 0.06M KNO_3, 100 ml, 15000 cm/min

Neocup.	Time, min	Weight loss, mg	Neocup.	Time, min	Weight loss, mg
0.001M	5	36	0.01M	10	−6.6
0.001	5	−0.4		60	−7.9
	10	27		1170	−8.3
0.002	5	0		2700	−4.3
	16	−0.1		2960	4.5
	31	4.7		3000	12
	36	25	0.01*	5	−1.6
0.005	5	−1.0		100	−1.8
	15	−1.1		260	−0.7
	75	−0.7		500	1.8
	330	−0.8		555	4.4
	1170	27			

* Wiped with acetone at each weighing.

coating appeared at the same time as the large change in potential.

Neocupferron.—It was found previously (3) that cupferron (the ammonium salt of nitrosophenylhydroxylamine) protects iron with an insoluble film. The acid form of cupferron is not very stable. Neocupferron (the ammonium salt of nitrosonaphthylhydroxylamine) is more stable in acid solution and forms even less soluble chelated ferrous and ferric salts (6). Consequently it was investigated as an inhibitor.

The commercial salt was recrystallized twice by dissolving in water, filtering, and evaporating the solution to dryness under vacuum at room temperature. Solutions were made by dissolving weighed samples in potassium nitrate and adding the acid last. With 0.01M neocupferron this resulted in a small amount of white precipitate (the acid form), which soon dissolved when the run was started. The compound did not change the *p*H appreciably.

Table VII shows details of some runs. At low concentrations protection is uncertain and lasts only a short time. With 0.01M neocupferron protection was obtained up to 50 hr. Addition of glycine, dipyridyl, or fluoride had little, if any, effect. The neocupferron becomes oxidized eventually and too little is left for protection; by replacing the solution each 40 hr one run (actually with 0.01M dipyridyl, which was unnecessary) was kept going for 132 hr with a weight loss of 6 mg.

Yellow films, streaked with brown oxidation products, formed on the iron in these solutions. The films could be wiped off with acetone or benzene, leaving the iron bright and shiny. It was noted that the visible film contributed practically nothing to the weight gains, but, if dissolved off frequently, the time of protection was decreased. If a cylinder which had formed a film was run in the corroding solution without neocupferron, protection broke down in about an hour.

Since neocupferron is lost by air oxidation, further experiments were run in solutions deaerated with nitrogen. Some results are shown in Table VIII. Two observations stand out: protection was always for a shorter time than in air (10 hr compared to 50 hr), and the visible yellow film contributed most or all of the weight gain. On wiping with acetone or benzene there was usually a net weight loss, in contrast to the experiments in air, where such wiping did not decrease the weight as much as 0.1 mg.

The best protection by neocupferron required rotation of the cylinders. The following experiment is informative: a cylinder was immersed (0.01M neocupferron, air) for 30 min with no rotation. About 40% of the surface was covered with visible film, in wedges, apex up, and the cylinder had lost 5 mg. The cylinder was now rotated at 15000 cm/min for 5 min. The entire surface was covered with film, but areas previously covered were clearly visible, with more new film on the leading than on the trailing edges; the iron had gained 2 mg. On standing still in the solution for 24 hr, the trailing edges of the wedge-shaped areas were badly pitted. Net weight loss was 5 mg. Fig. 4 is a photograph of this cylinder and the lower third shows the typical appearance. The white portions are corroded; black spots are resinous oxidation products.

These experiments indicate that iron dissolves at anodic spots and the ferrous ion precipitates some distance away. As a further test an iron disk 1.8 cm in diameter was given a very smooth machine polish, and inhibited solution was forced in a fine stream onto the center of the smooth surface. Corrosion took place at the impact point and a film built up around it, getting thicker toward the edges.

Other possible inhibitors.—The ammonium salt of nitroso-

TABLE VIII. *Inhibition by neocupferron in deaerated solutions*
0.02M HCl, 0.06M KNO_3, 100 ml, 15000 cm/min

Neocup.	Time, min	Weight loss, mg	Neocup.	Time, min	Weight loss, mg
0.005M	10	−0.9	0.01M	15	−3.0
	60	−1.9		90	−5.8
	100	−2.3		290	−7.2
	300	−2.5		525	−11.6
	390	−2.3		585	−6.4
	Pitting			Pitting	

FIG. 4. Corrosion along trailing edge of initially protected area.

TABLE IX. *Inhibition of iron corrosion by carbon monoxide*
0.02M HCl, 0.06M KNO_3, 100 ml, 15000 cm/min

Time, min	Weight loss, mg				
	1	2	3	4	5
60	0.2	—	7.6	1.4	0.7
120	0.6	5.4	10.3	—	1.5
180	0.8	—	12.5	4.3	2.1
240	1.0	7.4	—	—	3.5
300	—	9.0	16	—	—
600	—	—	21	9.9	—

fluorenylhydroxylamine has been reported useful in analysis (7). A sample was prepared[4] and tested, but found ineffective, perhaps because the compound is only slightly soluble in water.

Stearato chromic chloride (8), tricresyl phosphate, heptacosafluorotributylamine, perfluorodecanoic acid (9) form water-repellent coatings on many materials. These were tried as corrosion solution additives (saturated solution with execss) and for surface treatment of iron, zinc, and cadmium cylinders before immersion. None was successful as an inhibitor.

Carbon monoxide.—It has been shown by Uhlig (10) that carbon monoxide is a good inhibitor for stainless steel, fair for mild steel, in moderately concentrated HCl with no depolarizer. Runs were now made in which carbon monoxide was bubbled through the corroding solution (0.02M HCl, 0.06M KNO_3) in which the iron cylinder was rotated. The commercial CO contained a little iron carbonyl, which was caught in a dry-ice trap. Some of the results are shown in Table IX.

No weight gains were ever noted. The exact amount of corrosion must depend on accidental factors. In run 5 the cylinder had a preliminary etch; in run 3 it was kept in CO gas 20 min before immersion. No other treatments were more effective. Pitting became evident in all runs but not at a reproducible stage of time or weight loss. The total dissolving capacity of these solutions is about 50 mg of iron, and without carbon monoxide this amount would dissolve in about 30 min, whether in air or nitrogen.

Discussion

It is evident that, in all the experiments with dichromate, protection is accompanied by the formation of comparatively thick oxide films. The electropolishing experiments emphasize the fact that iron, exposed to air, is always covered with an oxide film, formed with evolution of heat. Such air-formed films are not protective in acid solution; this has been ascribed to weak spots or flaws in the film. Most forms of Fe_2O_3 do not dissolve readily in acids, but, if in contact with iron, reductive dissolution may occur more rapidly. According to Pryor and Evans (11), ferric oxide is a sufficiently good electronic conductor to function as cathode in the cell Fe/acid/Fe_2O_3; the oxide is reduced simultaneously with iron dissolution at the anodes. For best protection the oxide film must be continuous and be replaced as fast as it dissolves. If unprotected pits are present and function as anodes, they will lead eventually to uncontrollable corrosion.

[4] Courtesy of T. Kaniecki, New York University.

The iron cylinders of 14 cm^2 area gained as much as 1.2 mg in weight in the first 5 min in $HClO_4$-KNO_3-$K_2Cr_2O_7$ solutions. This indicates a film of Fe_2O_3 about 5×10^{-5} cm thick if no ferrous or ferric ion escaped into solution. The weight gain persisted for several hours before pitting resulted in a net weight loss. Investigators of the Evans school believe that oxidizing inhibitors tend to repair flaws in the oxide film and at the same time thicken the good film as iron ions migrate through from the underlying metal. Unfortunately only a few oxidizing agents are effective. Chromate and dichromate are perhaps the best; oxygen can inhibit in neutral and alkaline solution if its concentration is high enough. Molybdate and tungstate are somewhat effective (12) but offer difficulties in acid solution (2). The reduction products of permanganate, arsenite, and arsenate offer only porous mechanical barriers.

A comparison of the experiments with hydrochloric and perchloric acids is significant. Complexing or chelating agents are essential to make dichromate an effective inhibitor with hydrochloric acid. It was suggested previously (3) that complexing agents dissolve loose precipitates or prevent their formation, allowing dichromate to reach the clean metal surface. Chloride ion apparently prevents the formation of large continuous crystals of oxide film, so that the cleaning process is necessary in its presence. The "peptizing" effect of chloride ion in such cases has been discussed by Gatty and Spooner (13).

In perchlorate solutions the dichromate can form much larger crystals or aggregates of "good" oxide film. Now complexing agents can dissolve "good" oxide as well as loose material, although at a slower rate. They limit the protective time before pits become pronounced to about the same value in both acids, by creating new weak spots or preventing really good coverage of old ones. In hydrochloric acid chelants make the iron more anodic while helping protect it (Fig. 2), which indicates more rapid ion exchange and electron flow through a film which still allows less dissolution than that formed by dichromate alone. Chelants tend to make the initial potential in perchloric acid more cathodic, which may indicate a slightly better initial film. This effect disappears as the breakdown time approaches (Fig. 3). It has been noted by Cohen (14) that in inhibited neutral or slightly alkaline solutions certain chelants make the iron potential more anodic and increase the corrosion rate.[5]

In acid alone the iron potential becomes more negative with time until ferrous hydroxide (or perhaps a ferrous-ferric mixture or compound) is formed on the surface. This occurs at a bulk *p*H of 4–4.5 and a ferrous ion concentration near 10^{-2}M. The potential is about −0.36 v on the hydrogen scale, and according to the potential-*p*H diagrams prepared by Pourbaix (15) for Fe-$Fe(OH)_2$ equilibrium at this potential the surface *p*H should be 6.5–7. It is not unlikely that a *p*H gradient exists through the film since slow corrosion continues.

With nitrate present, the potential changes sharply in the anodic direction since hydrogen evolution is eliminated

[5] Most chelants are more effective at higher *p*H; in acid solution the metal ion must compete with H^+ for the chelant K: HK (or HK^+) + $M^+ \rightleftharpoons MK + H^+$.

as the cathodic process and the local anodes are depolarized. Ferric hydroxide is formed when the bulk *p*H rises to 4 or 4.5. With chloride present there is no protective film, corrosion continues, and the potential remains far away from the Fe-$Fe(OH)_3$ equilibrium value. In perchloric acid the potential changes to a value which corresponds to this equilibrium if the surface *p*H is about 6 (15). Small weight gains were noted at this point.

Dichromate converts the potentials to slightly noble values. The potential for reversible hydrogen evolution is −0.37 v at *p*H 2 and −0.49 v at *p*H 4 (vs. the S.C.E.). The reversible iron-ferrous ion potential is about −0.75 v with a low concentration of ferrous ion; the anodic process is very highly polarized in all the inhibited systems.

Neocupferron.—It has been suggested that chelants, molecules which have two or more points of attachment to metal ions, may be especially good adsorption inhibitors (16). Neocupferron forms very insoluble chelate salts with both ferrous and ferric ions, but does not inhibit by adsorption; iron must dissolve, then form the insoluble complex. If the neocupferron concentration is high enough the solubility is exceeded very near the iron surface, and it is probable that nucleation occurs more readily on the iron than in the solution.

The film formed in air-saturated solution consists of two layers, an outer yellow one which is very thin, since it does not contribute appreciably to the weight gain, and an inner invisible film which must consist at least partly of iron oxide formed by oxygen under the protection of the yellow film. This oxide may be quite porous and plugged by neocupferron compound, since the weight gain is large for oxide alone; but the appearance is that of shiny iron. In deaerated solution such oxidation cannot take place and the yellow film is thicker. If frequently removed and the cylinder re-immersed the film forms again, but not as heavily, until the neocupferron is exhausted.

Weight gains found in the deaerated solutions are plotted in Fig. 5 against the square root of time. While the data are meager, they seem to indicate an initial parabolic film growth law (17), with later deviations due to partial disintegration of the films.

Carbon monoxide.—This compound fulfils the requirements stated by Uhlig for an adsorption inhibtior (18). It is strongly chemisorbed on iron (19, 20) but reacts only very slowly to form carbonyl, which is probably not stable in the acid solutions (21). The carbon monoxide molecule most likely has a pair of electrons strongly directed away from the carbon-oxygen bond (22), which should facilitate adsorption on a metal with unfilled electron levels. Carbon monoxide is not adsorbed on zinc and does not inhibit zinc dissolution. It should be noted that neither the rather high heat of adsorption (20) nor the "Lewis base" electrons are necessary for adsorption or inhibition. Other gases with equal or greater adsorption enthalpy are not inhibitors, while substances adsorbed by electrostatic or van der Waals forces are (16). However, other molecules with "lone-pair" electrons such as nitric oxide NO are suggested as possible inhibitors.

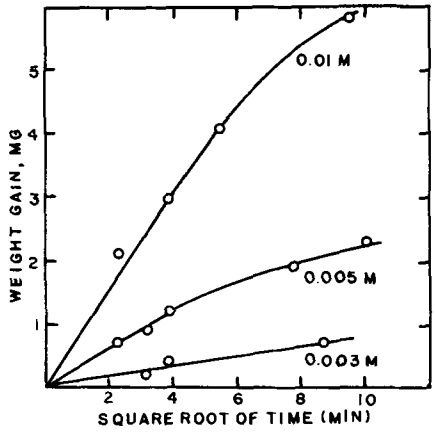

FIG. 5. Weight of film on iron with neocupferron concentrations as shown.

Carbon monoxide is not completely effective, i.e., there is no complete lack of weight loss for even short periods of time. This is generally true of pure adsorption inhibitors. It is not known whether this is due to insufficient solubility of CO at atmospheric pressure, or to inability to be adsorbed on and protect certain areas (which show up as pits and are anodic in nature). The latter is probably the correct reason.

It has been shown by Cartledge (22) that pertechnetate ion is an exceptionally good inhibitor for steel in water, as little as 5×10^{-5}M $KTcO_4$ stopping corrosion in aerated distilled water. With such low concentrations the protection has to be due to adsorption or coverage of only a few active spots, but it was shown that less than 1% of a monolayer is actually adsorbed or deposited. Probably no prediction can be made as to inhibition by the pertechnetate ion in the acid solutions of the present research.

Manuscript received October 21, 1955. This paper was prepared for delivery before the San Francisco Meeting, April 29 to May 3, 1956, and taken from a Ph.D. thesis submitted by Eric Rau to the Graduate Faculty of New York University. Work done under Office of Ordnance Research Contract No. DA-30-069-ORD-1113.

Any discussion of this paper will appear in a Discussion Section to be published in the December 1956 JOURNAL.

REFERENCES

1. M. B. ABRAMSON AND C. V. KING, *J. Am. Chem. Soc.*, **61**, 2290 (1939).
2. C. V. KING, E. GOLDSCHMIDT, AND N. MAYER, *This Journal*, **99**, 423 (1952).
3. C. V. KING AND E. HILLNER, *ibid.*, **101**, 79 (1954).
4. R. P. AGARWALA AND H. WILMAN, *Proc. Phys. Soc. (London)*, **66B**, 717 (1953).
5. G. KEHL, "The Principle of Metallographic Practice," McGraw-Hill Book Co., New York (1949).
6. G. F. SMITH, "Cupferron and Neocupferron," G. Frederick Smith Chemical Co., Columbus, Ohio (1938).
7. R. E. OESPER AND R. E. FULNER, *Anal. Chem.*, **25**, 908 (1953).
8. R. K. ILER, *Ind. Eng. Chem.*, **46**, 766 (1954).
9. F. SCHULMAN AND W. A. ZISMAN, *J. Am. Chem. Soc.*, **74**, 2123 (1952).
10. H. H. UHLIG, *Ind. Eng. Chem.*, **32**, 1490 (1940).
11. M. J. PRYOR AND U. R. EVANS, *J. Chem. Soc.*, **1950**, 1259.
12. W. D. ROBERTSON, *This Journal*, **98**, 94 (1951).
13. O. GATTY AND E. SPOONER, "Electrode Potentials of Corroding Metals," Oxford Press (1938).
14. M. COHEN, Paper presented at Pittsburgh Meeting of The Electrochemical Society, October, 1955.
15. M. J. N. POURBAIS, "Thermodynamics of Dilute

Aqueous Solutions," Edward Arnold and Co., London (1949).
16. N. Hackerman and A. C. Makrides, *Ind. Eng. Chem.*, **46**, 523 (1954).
17. H. H. Uhlig (Editor), "Corrosion Handbook," John Wiley & Sons, Inc., New York (1948).
18. H. H. Uhlig, *Ann. N. Y. Acad. Sci.*, **58**, 843 (1954).
19. P. H. Emmett and S. Brunauer, *J. Am. Chem. Soc.*, **59**, 310 (1937).
20. J. Bagg and F. C. Tompkins, *Trans. Faraday Soc.*, **51**, 1071 (1955).
21. J. R. Partington, "General and Inorganic Chemistry," p. 876, Macmillan and Co., London (1949).
22. C. A. Coulson, "Valence," Oxford Press, New York (1932).
23. G. H. Cartledge, *J. Am. Chem. Soc.*, **77**, 2659 (1955); *Corrosion*, **11**, 335t (1955); *J. Phys. Chem.*, **59**, 979 (1955).

Electrical Conductivity of Carbon Black-Reinforced Elastomers

Gerard Kraus

Research Division, Phillips Petroleum Company, Bartlesville, Oklahoma

and

J. F. Svetlik

Rubber Chemicals Division, Phillips Chemical Company, Akron, Ohio

ABSTRACT

Electrical conductivity of carbon black-reinforced elastomers at fixed loading is a function of the particle size and aggregation habit of the carbon black, its intrinsic conductivity, and the ability of the black to adsorb certain ionic impurities. These factors vary greatly in their relative importance, depending on the filler concentration. The mechanism of conduction is primarily one of carbon black chain formation. Experimental evidence suggests the existence of a small number of highly conductive paths consisting of rather large black aggregates in contact in addition to a fine network of carbon black chains formed by otherwise well-dispersed black. Electrical conductivity data supporting the above conclusions are presented for nine carbon blacks in GR-S, natural, and butyl rubbers.

Introduction

One of the many interesting characteristics of carbon black-reinforced elastomeric compounds is their unique electrical behavior which makes it possible to vary their electrical conductivity over a 10^{12}-fold range while maintaining their useful mechanical properties. This enormous change in conductivity is brought about simply by the choice of the type and volume loading of carbon black.

It is generally accepted that the electric current is carried by continuous chains of contacting carbon black particles and, indeed, all published experimental evidence is consistent with this view (1–6). There are, however, a number of effects associated with the conductivity behavior of rubber vulcanizates which are still far from being completely understood. These include a rather surprising increase in resistivity accompanying the addition of the first small amount of carbon black to the rubber compound, the existence of a well-defined threshold loading for incipient conductivity, dependence of conductivity on the dimensions of the test specimen, and the role of the intrinsic conductivity of the carbon black. The present investigation was undertaken with the objective of contributing toward a better understanding of some of these phenomena.

Experimental

The GR-S, natural rubber, and butyl rubber compounds included in this investigation were formulated according to the following basic recipes. The black level was varied while all other ingredients in each formulation were held constant:

GR-S-101	100	—	—
Hevea (No. 1 Smoked sheet)	—	100	—
GR-I-17	—	—	100
Carbon black	Variable	Variable	Variable
Zinc oxide	3	4	5
Stearic acid	—	3	1
Sulfur	1.75	2	2
Santocure[a]	1.10	0.5	—
Tuads[b]	—	—	1
Captax[c]	—	—	1

[a] *N*-cyclohexyl-2-benzothiazyl sulfenamide; [b] Tetramethylthiouram disulfide; [c] Mercaptobenzothiazole.

GR-S-101 is a 75/25 copolymer of butadiene and styrene of 48 Mooney viscosity, polymerized in a sugar-free recipe

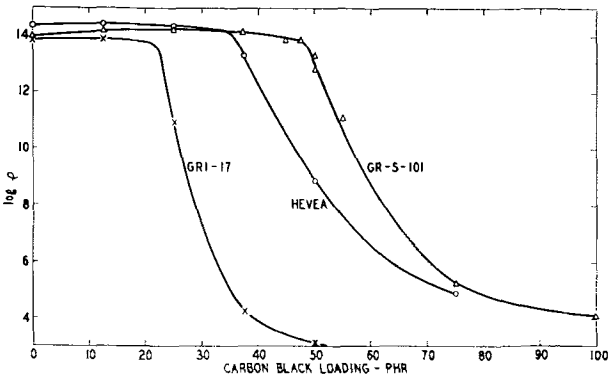

FIG. 1. Electrical resistivity as a function of filler loading FEF black (Philblack A).

at 5°C. GR-I-17 is a standard butyl rubber of 1.5% unsaturation. The carbon blacks investigated represent a fairly complete cross section of commercial rubber-grade carbons. They are identified by the standard carbon black type symbols: FT—fine thermal, SRF—semireinforcing furnace, FEF—fast extrusion furnace, HAF—high abrasion furnace, EPC—easy processing channel, SAF—super abrasion furnace. For convenience their trade names have been listed in parentheses. Graphon from Godfrey L. Cabot, Inc., is a carbon derived from graphitization of channel black by heating for 2 hrs at 2700°–3000°C; it is not a commercial rubber black. For a summary of physical and chemical properties of these blacks see reference (7).

All rubber compounds were mixed on a 6 x 12-in. roll mill with a friction ratio of 1.4 to 1. Experimental 6 x 6 x 0.075-in. slabs were vulcanized for 45 min at 153°C.

The electrical resistivities reported in this paper are all for direct current. The apparatus employed in the determination of the resistivity utilized an electrode with a guard ring of the type recommended in standard procedures for measuring dielectric constant (8). All of the highly resistant stocks were tested at an impressed voltage of 45 volts using a feedback microammeter arrangement similar to the one described by Roberts (9) to measure current flow from which the specific resistivity was calculated. The resistivity of more conductive stocks was determined with a direct reading ohmmeter (VOMAX, Model 900).

To decrease contact resistance the surfaces of the slabs were painted with a dilute graphite (Aquadag) paint. The entire surface on one side was covered; on the other side only an area corresponding to the size of the test electrode was painted with the Aquadag. Testing was conducted under a load of 1.75 psi to insure good contact between the electrode and rubber specimen. Two test electrodes were used having areas of 5 and 20 cm^2, respectively. The small electrode was used only in the experiments concerned with resistivity fluctuations over the face of a test slab.

Sections of rubber stocks for microscopic examination were prepared by embedding small slivers of rubber in an 80/20 mixture of *n*-butyl and methyl methacrylates, polymerized *in situ* using 2,4-dichlorobenzoyl peroxide as initiator. Polymerization time was usually about 8 hr to produce a hard resin suitable for cutting on a Minot Ultra Thin Sectioning microtome employing a glass knife. Sections were cut one micron thick, straightened by floating on water, and transferred to the microscope slides.

Magnetic susceptibilities of carbon blacks were determined by the Gouy method (10).

Results and Discussions

A set of typical resistivity vs. carbon black-loading curves is shown in Fig. 1. At small black loadings the resistivity is of the same order of magnitude as for the gum vulcanizates. Beyond a certain point the resistivity begins to change abruptly, falling several decades on addition of only a small increment of carbon black. This threshold loading is different for each rubber; it will be seen that it is also characteristic of the carbon black. Resistivity-loading curves eventually level out to values determined to a considerable extent by the carbon black. It is convenient to divide the conductivity curve into three distinct sections: (*a*) the range between zero loading and the threshold loading, covering all electrically insulating stocks; (*b*) a transition range extending over the large resistivity drop in the vicinity of the threshold loading; and (*c*) the conductive range.

Insulation Range

Table I shows resistivity data for several carbon black-natural rubber combinations below the threshold loading. Similar results are obtained with synthetics. It is apparent that the observed behavior is hardly that expected for a mixture of a conductor and a nonconductor. The electrical conductivity, k, of a random dispersion at low concentration of the disperse phase is given by the classical Maxwell equation:

$$k = k_1 \frac{k_2 + 2k_1 - 2v_2(k_1 - k_2)}{k_2 + 2k_1 + v_2(k_1 - k_2)} \qquad (I)$$

TABLE I. *Electrical resistivity of insulating stocks (Hevea Rubber)*

Carbon black	Specific surface area (m^2/g)		Loading	Resistivity × 10^{14}
	Nitrogen adsorption[a]	Electron microscope		
			phr[b]	*ohm-cm*
None	—	—	—	2.35
FT (P-33[c])	13.7	17	12.5	2.28
			25	2.22
			37.5	2.11
			50	2.26
SRF (Gastex[d])	27.6	35	12.5	2.55
			25	2.23
			37.5	1.98
FEF (Philblack[e] A)	45.6	65	12.5	2.65
			25	2.34
HAF (Philblack[e] O)	75.1	94	12.5	2.83
			25	2.34
EPC (Wyex[f])	114.2	89	12.5	2.50
			25	2.05
Acetylene	58.0	65	12.5	2.72
SAF (Philblack[e] E)	142.6	138	12.5	2.79

[a] Method of Brunauer, Emmett and Teller; *J. Am. Chem. Soc.*, **60**, 309 (1938).
[b] Parts (by weight) per 100 parts of rubber.
[c] From Thermatomic Carbon Co.
[d] From General Atlas Carbon Co.
[e] From Phillips Chemical Co.
[f] From J. M. Huber Corp.

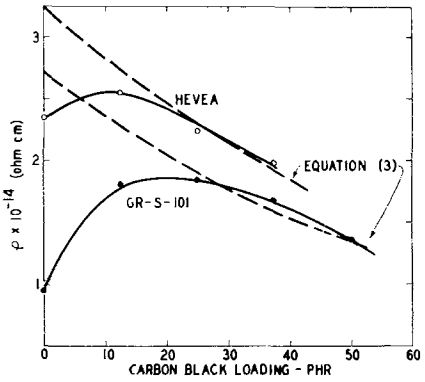

FIG. 2. Resistivity of rubber vulcanizates below the threshold loading SRF black (Gastex).

where k_1 is the conductivity of the continuous phase, k_2 that of the disperse phase, and v_2 the volume fraction of the disperse phase. A recent treatment by Baron (11) which extends the validity of Maxwell's theory to high-volume loadings gives

$$\frac{k - k_2}{k_1 - k_2} = (1 - v_2)\left(\frac{k}{k_1}\right)^{1/3}. \qquad \text{(II)}$$

When $k_2 \gg k_1$, as in the case of carbon black and rubber, equation (II) leads to

$$\rho = \rho_1(1 - v_2)^3 \qquad \text{(III)}$$

where ρ is the resistivity of the mixture and ρ_1 that of the continuous phase.

In almost every instance the resistivity increases initially and then falls (Fig. 2) at a rate roughly of the order predicted by equation (III). The only plausible explanation for such an effect appears to be that carbon black exerts an influence on the resistivity of the rubber matrix itself, possibly through immobilization of trace ionic impurities by adsorption. This view has also been advanced in a recent paper by Kickstein (12). In any event, it seems clear that there can be no continuous conductive paths *extending through the entire sample* at these loadings, for, in this instance, a far more drastic drop in resistivity than predicted by equation (III) would be expected. It also appears that those ionic impurities which are immobilized by the carbon black must be present in minute quantities so that the peak in resistivity is reached at low loadings and is relatively insensitive to the specific surface area of carbon black. Fig. 3 shows that at a loading of 12.5 phr of carbon black the rise in resistivity is related to the specific surface area of the black but levels out at 60 square meters/gram.

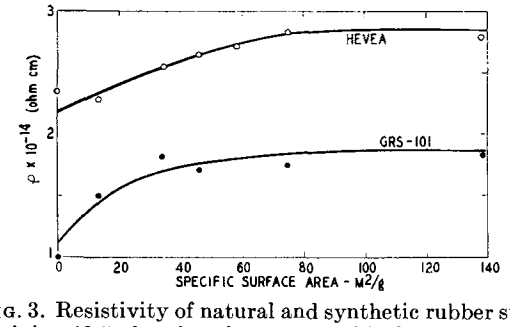

FIG. 3. Resistivity of natural and synthetic rubber stocks containing 12.5 phr of various carbon blacks as a function of specific surface area of the black.

Transition Range

The extremely sharp drop in resistivity at the threshold loading suggests that continuous conductive paths are formed suddenly in great abundance on incorporation of only a small amount of additional black. This sudden formation of a conductive network can only be visualized if the elements of the network are present even below the threshold loading as structures requiring only a relatively small quantity of black to weld them into a continuous maze of carbon chains.

Many carbon blacks show a definite tendency toward forming chain-like aggregates (13). This effect is usually referred to as "structure" (a more appropriate term would be "aggregate structure") and can be estimated by an oil absorption test. The test consists of adding linseed oil slowly to a weighed sample of black until a single ball of stiff paste is obtained. At this point the oil completely fills the space in the interstices between particles. Defining a packing factor γ such that

$$\gamma \equiv Nd^3 \qquad \text{(IV)}$$

where N is the number of particles per unit volume and d their average diameter, it can be shown that

$$\gamma = 6/\pi(1 + A\delta) \qquad \text{(V)}$$

where δ is the density of the black and A is the oil absorption in ml/g. A sort of coordination number (Z) for the black particles can be estimated by calculating γ's for several regular lattices and using the resulting curve to read off the Z-values.

Lattice	Z	γ
Face-centered cubic	12	1.41
Body-centered cubic	8	1.29
Simple cubic	6	1.00
Diamond	4	0.650

The data of Table II were compiled in this manner. Assuming that the coordination of particles is at least *qualitatively similar* in rubber and in oil, it follows that the over-all tendency for chain formation can be expressed as a function of the ratio of the specific surface area to the coordination number. This is so because the total number of particles capable of forming chains increases at a fixed

TABLE II. *Aggregation habit of carbon blacks from oil absorption test*

Carbon black	Oil absorption	γ	Z
	ml/g		
FT (P-33)	0.55	0.940	5.7
SRF (Gastex)	0.81	0.766	4.6
EPC (Wyex)	1.13	0.628	4.0
HAF (Philblack O)	1.14	0.620	3.9
FEF (Philblack A)	1.17	0.613	3.8
SAF (Philblack E)	1.28	0.585	3.6
FEF (Sterling SO)	1.38	0.546	3.4
Acetylene	2.40	0.355	2.2

TABLE III. *Threshold black loadings for incipient electrical conductivity*

Carbon black	S/Z[a]	Approximate threshold loading (phr)		
		GR-S-101	Hevea	GR-I-17
FT (P-33)	3.0	85	72	44
SRF (Gastex)	7.6	75	50	—
FEF (Philblack A)	17.1	49	35	22
FEF (Sterling SO)	19.1	47	30	20
EPC (Wyex)	22.3	30	32	17
HAF (Philblack O)	24.0	37	36	14
Acetylene black	29.6	25	18	5
SAF (Philblack E)	38.4	21	24	12

[a] S = electron microscope surface area.

loading with the specific surface area, and because the size of the aggregates increases with lower coordination number by virtue of their smaller density.

A test of these hypotheses is shown in Table III where the threshold loadings are compared with the ratio of electron microscope surface area to coordination number (S/Z). In general, the threshold loadings tend to vary inversely as the ratio S/Z. Thus, the behavior is consistent with the idea of the merging of black aggregates which are already present below the threshold loading but not in continuous paths through the sample.

Two questions arise: (*a*) can these aggregates be detected by microscopic examination; and (*b*) what is the order of magnitude of the conductivity contributed by one single path (or bundle of paths) formed on contact of these aggregates. The first of these questions may safely be answered in the affirmative. Even stocks of 10^{14} ohm-cm resistivity showed some visual evidence of flocculates under the optical microscope. The second question poses considerably more difficulty. If the average resistance of a continuous path is r and the number of paths per unit area is n, the resistivity of the slab is

$$\rho = r/n \qquad \text{(VI)}$$

as long as the resistivity of the matrix is much larger than r. If n is still relatively small near the threshold loading, one would expect to find considerable fluctuations in the conductivity of small areas tested randomly over the surface of a test slab. On the other hand, the conductivity should not vary greatly with position, both below and above the threshold loading. Table IV shows that at least qualitatively the behavior is as expected. Conductivity measured at different positions of a test slab varies most drastically near the threshold loading. However, even at 80 phr loading of FEF black the spread is appreciable, much more than can be accounted for by a random distribution of paths. Judging by the rather high conductivity at 80 phr loading the number of effective paths must be considerable, if indeed one may still speak of individual paths at all.

It may be shown that a completely random occurrence of paths would lead to the distribution (*see* Appendix)

$$p(x) = \bar{x}^x e^{-\bar{x}}/x! \qquad \text{(VII)}$$

where p is the probability of finding exactly x paths in the electrode area, and $\bar{x}$ is the mean number of paths for an area of the size of the electrode. The standard deviation of this distribution is $\bar{x}^{\frac{1}{2}}$, which means that the relative deviation is $\bar{x}^{-\frac{1}{2}}$. For an $\bar{x}$ of as little as 10 the relative deviation would be only 31.8% which would be reasonable for the spread in conductivities observed with FEF black at 80 phr, but here $\bar{x}$ is undoubtedly much larger than 10. The explanation must lie in the fact that the individual paths vary tremendously in their conductivity, which in turn implies that they must be formed by aggregates of widely different sizes, including some very large ones. In all probability only these largest flocculates are visible under the optical microscope.

It is somewhat peculiar that in the rubber reinforced with 50 phr of FEF black the conductivities deviating most from the mean value are *low*, indicating a deficiency of conductive paths at a relatively few locations. One might be tempted to interpret this as being due to flexing of the slab which might rupture the conductive chains at these points. Although mechanical deformation is known to affect resistivity (1), the effect is not nearly large enough to account for the 600-fold difference observed here (6), particularly since considerable care was taken in handling the slabs to insure freedom from flexing. Local contact resistance likewise appears to be an unlikely cause for the fluctuations in conductivity over the surface of the slab. Contact resistances necessary to account for the observed results appear prohibitively large, and there is no reason to expect extremely large contact resistance to occur locally and only at certain black loadings. It is also apparent from Table IV that in the regions of highest and lowest conductivity the fluctuations hardly exceed the experimental error as required by the theory.

TABLE IV. *Electrical conductivity as a function of position over test slab*

Loading (phr)	m	Conductivity (mho-cm^{-1}) $\times 10^m$											
		Readings at individual positions										Mean	Std. Dev.
FEF black (Philblack A) in GR-S-101; threshold loading—49 phr													
12.5	14	1.31	1.26	1.48	1.30	1.39	1.35	1.09	1.20	1.22	1.11	1.27	0.11
50	11	0.35	2.51	7.80	3.60	8.40	0.051	0.014	0.065	3.76	4.71	3.13	2.99
80	7	3.06	3.92	5.25	4.85	3.94	1.91	2.08	3.36	2.90	2.22	3.35	1.08
SAF black (Philblack E) in GR-I-17; threshold loading—12 phr													
12.5	12	4.00	12.5	0.19	1.26	1.20	3.02	—	—	—	—	3.70	4.13
50	3	1.31	1.49	1.81	1.65	1.63	1.30	1.67	1.88	1.56	—	1.59	0.19

Another point of interest is the rather systematic variation of the threshold loading with the type of rubber. In almost all instances the order of decreasing threshold loading is

GR-S-101 > Hevea > GR-I-17

This behavior suggests an increasing tendency toward chain formation of all blacks in butyl rubber as compared to Hevea and, in particular, GR-S. Evidently the coordination number Z is different for each rubber, which is hardly surprising. It must be remembered that the numerical values of Z given in this paper are for linseed oil and can therefore only serve to compare trends between blacks. They allow no comparison between different media.

Conductive Range

As the carbon black loading is raised to higher levels and the number of conductive paths becomes very large, the intrinsic conductivity of the carbon black exerts a noticeable influence on the conductivity of the rubber compound. At the same time particle size and aggregation habit are still important variables. The inability to control these last two variables completely makes it extremely difficult to demonstrate the intrinsic conductivity effect clearly. One example in which a comparison is possible is that of channel and furnace blacks. EPC and HAF blacks have nearly the same threshold loadings and S/Z ratios (Table III). Nevertheless they yield greatly different resistivities in rubber at high (and equal) loadings (Table V).

The relatively high resistivity of the EPC black stock is readily explained by the fact that channel blacks contain appreciable amounts of combined noncarbon constituents, particularly hydrogen and oxygen, the presence of which may be expected to tie up electrons and decrease the intrinsic conductivity (14, 15). Another example of the intrinsic conductivity effect is observed on graphitization of carbon black. Graphon, a carbon produced from channel black by exhaustive graphitization, yields rubber vulcanizates of extremely high conductivity.

In general, high conductivity of a rubber compound at fixed black loading may be brought about by a combination of the three factors already mentioned: small particle size (large surface area), high "structure," and high intrinsic conductivity. Of these only the estimation of intrinsic conductivity poses any real difficulty. However, it is found (16) that the diamagnetic susceptibility of a carbon black furnishes an excellent index of its intrinsic conductivity. The susceptibility increases both with the desorption of chemisorbed oxygen and hydrogen and with increasing degree of graphitization as inferred from x-ray analysis (17–19). These changes are in accord with theoretical considerations on the electronic structure of carbon blacks and graphites (20). For the examples of Table V, the magnetic susceptibilities are:

TABLE V. *Electrical resistivity at 50 phr loading*

	Resistivity, ohm-cm		
	GR-S-101	Hevea	GR-I-17
EPC (Wyex)	2.6×10^9	1.6×10^8	6.6×10^5
HAF (Philblack O)	1.2×10^7	3.7×10^4	1.2×10^3
Graphon	6.0×10^2	3.2×10^3	5.2×10^2

	Mass susceptibility
EPC (Wyex)	-0.59×10^{-6}
HAF (Philblack O)	-0.79×10^{-6}
Graphon	-2.78×10^{-6}

Conclusions

The experimental evidence indicates that electrical conductivity in carbon black-reinforced rubbers is due to conductive chains formed by carbon black particles. Below the critical threshold loading for conductivity these chains do not extend continuously throughout the rubber sample and hence do not cause conductivity, the resistivity of random dispersion being independent of particle size and shape [equation (III)]. High surface-area blacks appear to adsorb ionic impurities to produce an increase in resistivity at low loadings which is not offset by the conductivity of the carbon blacks themselves. Because high surface area blacks also contain the largest number of particles per unit volume, the very blacks which produce the most highly resistant stocks at small loadings also yield the most conductive rubbers at high black contents. Particle aggregation habit contributes strongly in determining the conductivity of rubber stocks at intermediate and high black loadings, but the intrinsic conductivity of the carbon black exerts a noticeable influence only at high black concentrations.

Manuscript received August 8, 1955. This paper was prepared for delivery before the Cincinnati Meeting, May 1 to 5, 1955.

Any discussion of this paper will appear in a Discussion Section to be published in the December 1956 JOURNAL.

REFERENCES

1. B. B. S. T. BOONSTRA AND E. M. DANNENBERG, *Ind. Eng. Chem.*, **46**, 218 (1954).
2. L. H. COHAN AND J. F. MACKEY, *ibid.*, **35**, 806 (1943).
3. P. E. WACK, R. L. ANTHONY, AND E. GUTH, *J. Appl. Phys.*, **18**, 456 (1947).
4. D. BULGIN, *Trans. Inst. Rubber Ind.*, **21**, 188 (1945).
5. B. DOGADKIN, K. PECHKOVSKAYA, AND M. DASHEVSKII, *Kolloid Zhur.*, **10**, 357 (1948).
6. L. R. SPERBERG, G. E. POPP, AND C. C. BIARD, *Rubber Age*, **67**, 561 (1950).
7. G. KRAUS, *J. Phys. Chem.*, **59**, 343 (1955).
8. A.S.T.M. Standards on Rubber Products, Test Designation D150-47T, American Society for Testing Materials, Philadelphia, Pa. (1947).
9. S. ROBERTS, *Rev. Sci. Instr.*, **10**, 181 (1939).
10. L. G. GOUY, *Compt. rend.*, **109**, 935 (1889).
11. T. BARON, unpublished work; cf. R. E. DE LA RUE AND C. W. TOBIAS, "Conductivities of Random Dispersions", paper presented at 107th meeting of The Electrochemical Society, Cincinnati, May 1 to 5, 1955.
12. G. KICKSTEIN, *Kautschuk and Gummi*, **7**, 50 (1954); *Rubber Chem. Tech.*, **27**, 940 (1954).
13. C. W. SWEITZER AND W. C. GOODRICH, *Rubber Age*, **55**, 469 (1944).
14. M. L. STUDEBAKER, *Kautschuk and Gummi*, **6**, 193 (1953).
15. M. L. STUDEBAKER, *India Rubber World*, **129**, 485 (1954).
16. G. KRAUS, to be published.
17. C. R. HOUSKA AND B. E. WARREN, *J. Appl. Phys.*, **25**, 1503 (1954).

18. J. Biscoe and B. E. Warren, *J. Appl. Phys.*, **13**, 364 (1942).
19. W. D. Schaeffer, W. R. Smith, and M. H. Polley, *Ind. Eng. Chem.*, **45**, 1721 (1953).
20. S. Mrozowski, *Phys. Rev.*, **85**, 609 (1952).

APPENDIX

Area Distribution of Conductive Paths

The problem is to calculate the probability of finding exactly x paths in the area A of the test electrode. For this purpose one may divide the area A into n subareas large enough to accommodate no more than one path. If p is the probability of finding a path in a subarea, the desired probability is

$$p(x) = \frac{n!\, p^x (1-p)^{n-x}}{x!(n-x)!} \tag{I}$$

The probability p is given by

$$p = \bar{x}/n \tag{II}$$

where $\bar{x}$ is the mean number of paths for an area the size of the electrode. Then

$$p(x) = \frac{n!\, \bar{x}^x \left(1 - \frac{\bar{x}}{n}\right)^{n-x}}{x!(n-x)!\, n^x} \tag{III}$$

and on applying Stirling's approximation to the factorials involving n (since $n \gg x$), one arrives at

$$p(x) = \frac{e^{-x}\bar{x}^x}{x!} \cdot \left(\frac{n-x}{n-\bar{x}}\right)^x \cdot \left(\frac{n-\bar{x}}{n-x}\right)^n \cdot \left(\frac{n}{n-x}\right)^{\frac{1}{2}} \tag{IV}$$

Also, because $n \gg x$, we may neglect x against n except where the result is raised to the power n, so that

$$p(x) = \frac{e^{-x}\bar{x}^x}{x!} \cdot \left(\frac{n-\bar{x}}{n-x}\right)^n \tag{V}$$

Furthermore, for large n

$$\left(\frac{n-\bar{x}}{n-x}\right)^n \cong e^{-\bar{x}}/e^{-x}$$

and

$$p(x) = \frac{e^{-\bar{x}}\,\bar{x}^x}{x!} \tag{VI}$$

The standard deviation, σ, of this distribution is obtained as follows. One has

$$\sigma^2 = \overline{x^2} - \bar{x}^2 \tag{VII}$$

so that it is only necessary to evaluate $\overline{x^2}$:

$$x^2 = e^{-\bar{x}} \sum \frac{x^2 \bar{x}^x}{x!} = e^{-\bar{x}}\,\bar{x}^2 \sum \frac{x^2 \bar{x}^{x-2}}{x!} \tag{VIII}$$

The summation yields

$$0 + \bar{x}^{-1} + 2 + 3\bar{x}/2! + 4\bar{x}^2/3! \cdots + m\bar{x}^{m-2}/(m-1)! \cdots$$

which is recognized as

$$e^{\bar{x}} + \frac{1}{\bar{x}}\, e^{\bar{x}}$$

Hence,

$$\overline{x^2} = \bar{x}^2 + \bar{x} \tag{IX}$$

and

$$\sigma = \sqrt{\bar{x}} \tag{X}$$

Activator Systems in Zinc Sulfide Phosphors

J. S. Prener and F. E. Williams

Research Laboratory, General Electric Company, Schenectady, New York

ABSTRACT

Zinc sulfide containing copper at random zinc sites was prepared by radioactive decay of Zn^{65}. Measurements indicate that the isolated copper impurities do not contribute to luminescent emission. Using a covalent model of zinc sulfide, and recognizing the acceptor-donor nature of activators and coactivators, association of these impurities is found and the luminescent center is identified as second or third nearest neighbor associated activator-coactivator pairs. The nearest neighbor pairs are transparent to 3650Å radiation and have many of the characteristics necessary to account for edge emission.

Introduction to Zinc Sulfide Phosphors

In many ways zinc sulfide phosphors form a unique class of luminescent solids. The most effective activators and coactivators, both of which are apparently necessary for luminescence, lie in columns of the periodic table on either side of zinc and sulfur. Thus, elements which have been recognized as activators are copper, silver, and gold in group I B, and phosphorus (1) and arsenic (2) in group V B; those elements most effective as coactivators are chlorine, bromine, and iodine in group VII B, and aluminum, gallium, and indium (3) in group III B. Activation by manganese has been recognized to be of quite a different nature than the activation by the elements described above (4).

Zinc sulfide is essentially a covalent crystal as indicated by the directional tetrahedral bonds in the structure and

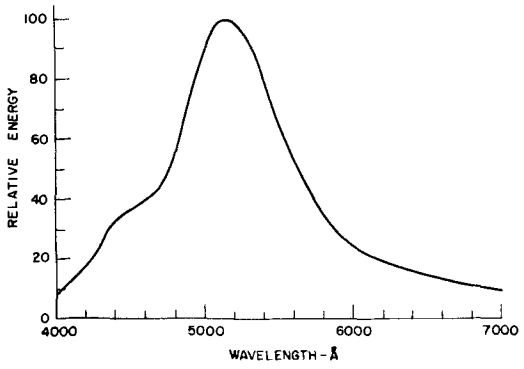

FIG. 1. Emission spectrum of $Zn^{65}S$:Cu:Cl under 3650Å excitation.

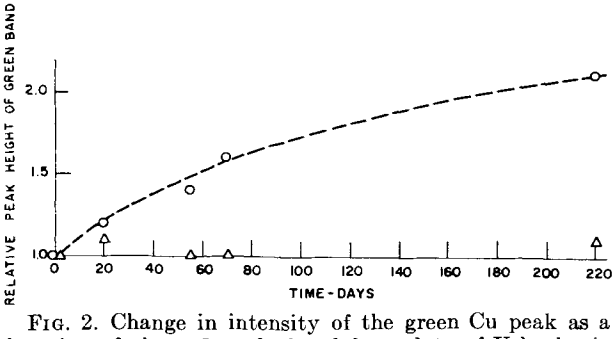

FIG. 2. Change in intensity of the green Cu peak as a function of time. O, calculated from data of Urbach; △, experimental points.

is, therefore, quite different in nature from the ionic phosphor systems on which most theoretical work has been done.

The nature of the activator and coactivator systems in zinc sulfide phosphors has been the subject of a great deal of discussion in the literature. The most recent work on this subject has been done by Klasens (5) who, using an ionic model of zinc sulfide, concluded that the activators copper, silver, and gold are present in zinc sulfide as unipositive ions at zinc sites. The localized negative charge in the neighborhood of the activator perturbs the levels of $S^=$ ions immediately surrounding it, providing a localized filled level above the valence band. It is this perturbed $S^=$ ion which constitutes the luminescent center. The local excess positive charge in the neighborhood of the coactivator is capable of acting as an electron trap. Aside from the inappropriate use of an ionic model for zinc sulfide, the activation of zinc sulfide by such elements as phosphorus or arsenic is less satisfactorily accounted for by the ionic model. If one assumes that the group V B elements substitute in zinc sulfide as trinegative ions at sulfide sites, the sulfide ions whose levels would be perturbed would be those in the next nearest neighbor positions. The effect of the excess negative charge would be expected to be smaller than if the sulfide ions were nearest neighbors as in the case of copper, silver, or gold. Yet the yellow and orange emissions in these phosphors would indicate a larger effect.

Formation of Substitutional Activator by Radioactive Decay

In order to learn more about the activator systems in zinc sulfide phosphors at low activator concentrations, a method was devised for preparing zinc sulfide containing copper impurities unambiguously located at random substitutional zinc sites. A study of the luminescent properties of this material was expected to aid in elucidating the nature of the activator systems in zinc sulfide phosphors prepared by conventional methods.

The zinc sulfide was prepared with the radioisotope Zn^{65} by first sealing 1.25 grams of Johnson, Mathey and Company high-purity zinc oxide in a quartz ampule and irradiating for twelve days in the Materials Testing Reactor at Idaho Falls. The sample was placed in a region of the reactor where the neutron flux was 1.7×10^{14} neutrons/cm²/sec. The natural isotope Zn^{64} was converted to Zn^{65} and the final activity of the sample was calculated to be 350 millicuries corresponding to a Zn^{65} concentration of 0.0034%. Zn^{65} decays to stable Cu^{65} with a half-life of 250 days by K-electron capture and the emission of a 1.12 mev gamma ray. A recoil energy of 10.3 ev is imparted to the nucleus by the emission of the gamma ray.

The radioactive zinc oxide was then converted to zinc sulfide by heating for 45 min at 900°C in a stream of dry hydrogen sulfide containing about 2% hydrogen chloride. The initial copper content due to the decay of the Zn^{65} during irradiation and in the time before the zinc sulfide was prepared amounted to 0.00025% by weight of the zinc sulfide. This copper, together with the hydrogen chloride used in the preparation, gave rise to the emission spectrum shown in Fig. 1. Under 3650Å excitation, the luminescent emission consisted of the green "copper" band at 5160Å and the blue "self-activated" band at 4500Å. Similar preparations of zinc sulfide from an unirradiated sample of the same zinc oxide had only the blue emission band. Additional emission spectra were taken over a period of 220 days during which time the copper content rose to 0.0015%, a sixfold increase. What was sought was an increase in the intensity of the green band.[1] Experimental results are given in Fig. 2, in which the height of the green band relative to its initial value is plotted as a function of time. During the period of the experiment, no change in the emission spectrum was detected. Assuming the copper impurities formed by the decay of the Zn^{65} could give rise to those centers responsible for the green emission in zinc sulfide, then the data of Urbach (6) and the control experiments in the present work could be used to indicate the expected change in the intensity of the green band with time. Urbach's data are also plotted in Fig. 2, and indicate that a change should have been observed if indeed the copper impurities could give rise to luminescent centers.

The question of the effect of the 10 ev recoil energy acquired by the copper nucleus due to the emission of the 1.12 mev gamma ray was examined. Electron bombard-

[1] The ratio of the blue to green band was used as a measure of any changes in the intensity of the green band. The sample, the exciting source, and the spectrometer were positioned in as much the same manner for each measurement of the emission spectrum as was possible considering the difficulties of handling samples having activities near 300 millicuries. As far as could be noticed, there was no change in the relative intensity of the green to blue band, in the absolute intensity of the green band itself, or in the over-all efficiency of the phosphor.

ment experiments on germanium (7), which has the same structure as cubic zinc sulfide, indicated that, in order to produce vacancies and interstitials in these solids, recoil energies of the order of 30 ev are required. An approximate calculation based on an ionic model of zinc sulfide indicated that at least one-half of the copper impurities formed by the decay process would remain at substitutional zinc sites. One would expect that the covalency would increase the fractions remaining at substitutional sites.

It is evident, therefore, that an appreciable fraction of the copper impurities remained at zinc sites. Since no detectable increase in concentration of activator systems occurs during the transmutation, the conclusion that isolated copper impurities at substitutional zinc sites do not give rise to a luminescent center in zinc sulfide is inescapable.

Covalent Model for Zinc Sulfide Phosphors

In order to account for these results and to explain in a consistent manner the unique features of the zinc sulfide class of phosphors discussed in the first part of this paper, we propose an acceptor-donor model of the activator and coactivator, respectively, together forming the luminescent center and each located at substitutional sites.

Both zinc and sulfur in zinc sulfide can be considered to have a hybrid sp^3 configuration (8). Thus, both zinc and sulfur can form the four tetrahedral bonds to neighboring atoms. The formation of zinc sulfide can then be written as

$$\mathrm{Zn}\,(\cdots 3d^{10}4s^2) + \mathrm{S}\,(\cdots 3s^23p^4) \rightarrow \mathrm{Zn}^{=}\,(\cdots 3d^{10}4s4p^3) + \mathrm{S}^{++}\,(\cdots 3s3p^3) \quad \text{(I)}$$

Incidentally, the electron distributions in the bonds will be strongly enhanced in the region of the S^{++}. This is equivalent to an ionic contribution to the electronic structure. Therefore, the ionic species $Zn^{=}$ and S^{++} are merely a convenient basis for the description of the covalent model.

The structure of zinc sulfide is shown pictorially in Fig. 3*a*. In Fig. 3*b* the corresponding energy band scheme of zinc sulfide is indicated schematically. The electronic states of the valence band are those of the least tightly bound electrons in the system, namely, the electrons in the zinc to sulfur bonds. The band gap of 3.7 ev is the minimum

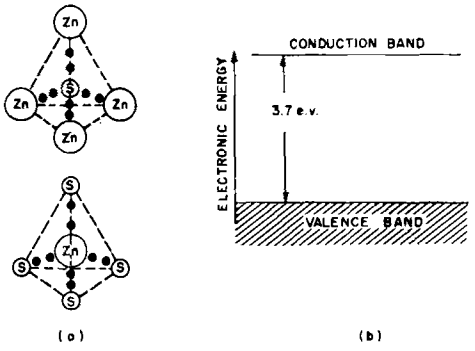

FIG. 3. (*a*) Representation of the electronic structure of zinc sulfide, indicating the four covalent bonds each containing two electrons in localized orbitals; (*b*) corresponding energy band scheme of zinc sulfide showing the separation between the highest lying filled band and empty conduction band.

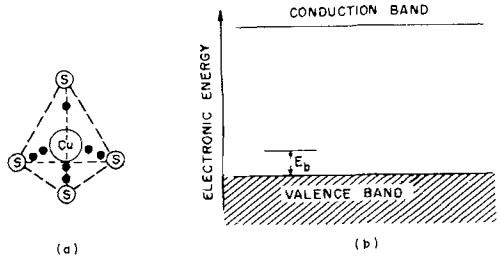

FIG. 4. (*a*) Representation of the local electronic structure around a single copper impurity in zinc sulfide indicating a missing electron in the copper-sulfur bonds; (*b*) corresponding energy band scheme. The empty localized level corresponds to a trapped hole. E_b is the energy required to remove an electron from a zinc sulfur bond and place it in the incomplete copper-sulfur bond.

energy required to remove an electron from a bond and free it in the crystal maintaining the atomic configuration of the perfect lattice. Consider the situation if an element of group I B is placed at a zinc site without making any other changes in the lattice. This is what occurs, for example, in the decay of zinc^{65} to copper^{65}. These elements have the configuration $(\cdots nd^{10}(n+1)s)$ where $n = 3$, 4, or 5 for copper, silver, or gold. The replacement reaction may be visualized as

$$\mathrm{M}[\cdots nd^{10}(n+1)s] + \mathrm{Zn}^{=}(\cdots 3d^{10}4s4p^3) \rightarrow \mathrm{M}^{=}[\cdots nd^{10}(n+1)s(n+1)p^2] + \mathrm{Zn}(\cdots 3d^{10}4s^2) \quad \text{(II)}$$

Thus, copper, silver, or gold can only form three good bonds to neighboring sulfur atoms with the fourth bond being incomplete. In other words, because Zn in group II B is replaced by an element of group I B, an electron must be missing from the system in order to maintain electrical neutrality and the missing electron will be one of the least tightly bound ones, that is, an electron in the covalent bond. Again, the situation can be illustrated as in Fig. 4*a* and give the corresponding energy band scheme in Fig. 4*b*. The incomplete bond gives rise to a localized level above the valence band. The energy E_b is the energy required to remove an electron from a zinc to sulfur bond and place it in the incomplete bond between the impurity and the four surrounding sulfurs. Thus, while copper at a substitutional zinc site gives rise to a localized level above the valence band, the level is unfilled and cannot give rise to luminescence when excited by 3650Å radiation. A similar scheme can, of course, be used to indicate the origin of a localized level when an element of group V B, such as phosphorus or arsenic, replaces sulfur.

$$X(\cdots ns^2np^3) + \mathrm{S}^{++}(\cdots 3s3p^3) \rightarrow X^{++}(nsnp^2) + \mathrm{S}(\cdots 3s^23p^4) \quad \text{(III)}$$

Again the activator can only form three good bonds, the fourth being incomplete, with this incomplete bond giving rise to an empty localized level above the valence band.

Consider now an impurity such as chlorine at a sulfur site. The elements of group VII B have the configuration $\cdots ns^2np^5$ and the replacement reaction can again be written as

$$X(\cdots ns^2np^5) + \mathrm{S}^{++}(\cdots 3s3p^3) \rightarrow X^{+++}(\cdots nsnp^3) + e^{-} + \mathrm{S}(\cdots 3s^23p^4) \quad \text{(IV)}$$

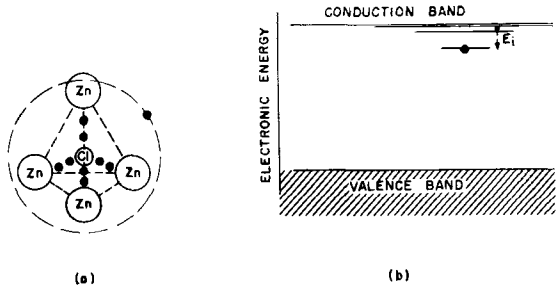

FIG. 5. (*a*) Representation of the local electronic structure around a single chlorine impurity in zinc sulfide indicating the four complete covalent bonds and the extra electron moving in a bound hydrogen-like orbit around the excess positive charge; (*b*) corresponding energy band scheme. The trapped electron lies in a localized level near the conduction band. E_i is the energy required to ionize this electron into the crystal. Some of the excited, more diffuse, coulombically bound states are also indicated.

The elements of group VII A can, therefore, form four tetrahedral bonds to neighboring zincs with the extra electron trapped in the coulomb field of the local excess positive charge. The case here is illustrated in Fig. 5*a* with the corresponding energy band scheme given in Fig. 5*b*. There is a filled localized level below the conduction band and the energy E_i is the energy required to ionize the trapped electron into the crystal. In addition, there are a series of excited hydrogen-like levels below the conduction band. E_i is of the order of the ionization energy of a hydrogen atom in a medium whose dielectric constant is that of zinc sulfide.

A similar scheme applies to coactivators of group III B at zinc sites. These have a configuration $(\cdots ns^2np)$ and the replacement reaction can be written as

$$\mathrm{M}(\cdots ns^2np) + \mathrm{Zn}^{=}(\cdots 3d^{10}4s4p^3) \rightarrow \mathrm{M}^{-}(\cdots nsnp^3) + e^{-} + \mathrm{Zn}(\cdots 3d^{10}4s^2) \quad \text{(V)}$$

In an actual phosphor the activator and coactivator are both needed to produce luminescence. At equilibrium the electron trapped in the field of the coactivator will be transferred to the low-lying empty level due to the presence of the activator. The activator and coactivator then each form four complete tetrahedral bonds. The energy of the system is thereby reduced by approximately the energy required to ionize an electron from a covalent bond. This accounts for the increased solubility of copper in zinc sulfide in the presence of aluminum coactivator as found by Froelich (9).

To summarize, the localized level above the filled valence band arises from the fact that the periodic potential of the zinc sulfide lattice in which the valence electrons move is perturbed locally in the vicinity of the activator impurity. The more negative potential in this vicinity is less binding and raises the energy of the localized states of the electrons in the vicinity of the impurity. The extent to which the localized level is raised above the filled band will depend on the electron density in the region where the perturbing potential due to the activator is largest. It has been indicated that the electron density in bonds is enhanced in the region of the sulfur sites. The localized level arising from a phosphorus or arsenic impurity at a sulfur site would be expected to lie higher above the valence band than the localized level arising from a copper, silver, or gold impurity at a zinc site. The emission at longer wave lengths of phosphors activated by group V B elements as compared to those activated by group I B elements can thus be understood qualitatively when a covalent model of the zinc sulfide phosphors is used.

Associated Activator-Coactivator System

Since an activator impurity and a coactivator impurity each forming four covalent bonds constitute locally an excess negative and positive charge, respectively, there is an electrostatic attraction between the two. At the firing temperatures of zinc sulfide phosphors where diffusion is rapid, this attraction must lead to deviations from a random distribution of the two impurities. The activator and coactivator tend to be close together and it is possible to make some estimates of the deviations from a random distribution due to electrostatic interactions, using the mass action law and free energy considerations. Defining α_i as the fraction of copper impurities having a chlorine impurity in the i^{th} shell of sulfur sites around the copper, then (10)

$$\frac{\alpha_i}{(\alpha_1 + \alpha_2 - 1)^2} = cz_i e^{-E_i/kT} \quad \text{(VI)}$$

Where z_i is the number of available sites in the i^{th} shell of sulfurs around the copper, E_i is the interaction energy between the copper and the chlorine, and c is the concentration of copper or chlorine in gram atoms per mole of zinc sulfide. The interaction energy between activator and coactivator will be taken as

$$E_i = -e^2/\kappa r_i \quad \text{(VII)}$$

where κ is the static dielectric constant of zinc sulfide and r_i is the distance between the copper and the chlorine. Using a concentration of 10^{-4} and a temperature of 1000°K, $\alpha_1 = 0.60$ and $\alpha_2 = 0.03$. Other activator-coactivator systems will also obviously be associated, although some, such as copper-aluminum, cannot form nearest neighbor pairs.

For the nearest neighbor associated activator-coactivator system, the localized states of the separated activator and coactivator vanish because of overlap. The perturbation is no longer that of a charge but that of a dipole. Based on Handler's calculation (11) of an electron interacting with a dipole, weakly bound states are found very

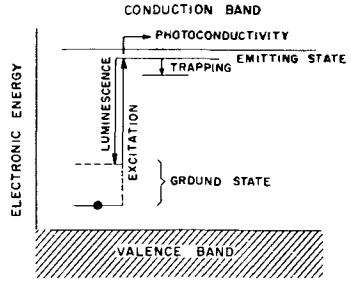

FIG. 6. The luminescent center in ZnS phosphors. The filled localized level near the valence band which constitutes the ground state of the luminescent center and the empty localized level near the conduction band which constitutes the emitting state are shown. The trapping state is also indicated.

close to the conduction and valence bands. The nearest neighbor pairs are, therefore, quite transparent to 3650Å radiation. Many characteristics of "edge emission" are, however, in accord with the nearest neighbor associated activator-coactivator system (10).

It is known from the interpretation of the nonlinear characteristics of zinc sulfide phosphors that the luminescent center excited by 3650Å has a large probability of ionization compared to emission (12). Consequently, these experimental results using radioactive Zn^{65} indicate that the copper formed by the decay of zinc must differ from copper centers in ordinary zinc sulfide phosphors in other than the occupancy of the localized state in the unexcited crystal. This difference can be explained on the basis of the above discussion of association of activators and coactivators since copper formed by the decay of Zn^{65} would have a negligible probability of having a chlorine at a second nearest neighboring sulfur site. There is other evidence to indicate association of activator and coactivator in zinc sulfide phosphors, since it has been found that the line emissions of praseodymium (3) and samarium (13) when used as group III coactivators are markedly different in the presence of different coactivators.

It is probable that the second nearest-neighbor associated coactivator provides a localized emitting state of the luminescent centers in zinc sulfide phosphors. Emission could occur by transitions between the excited hydrogen-like states associated with the coactivator and the localized state associated with the activator. These excited states have large orbits and overlap the low lying state associated with the activator thus facilitating transitions between the two. They are more nearly coulombically bound than the lowest lying state of the coactivator, which can be identified with the trapping states in these phosphors. Thus, the emission spectra will be independent of the nature of the coactivator, whereas trap depths will depend on the specific coactivator used (14).

In summary, we consider the luminescent center in zinc sulfide phosphors to consist of an activator impurity and an associated (but not nearest neighbor) coactivator impurity. Excitation by 3650Å results in a transition between the localized state associated with the activator and one of the coulombically bound states associated with the coactivator (Fig. 6). The reverse transition, after atomic rearrangement which perturbs the localized state associated with the activator upward, results in luminescence. The electron may, however, also be trapped in the lowest localized state associated with the coactivator or be thermally excited to the conduction band resulting in photoconductivity.

Manuscript received August 10, 1955. This paper was prepared for delivery before the Cincinnati Meeting, May 1 to 5, 1955.

Any discussion of this paper will appear in a Discussion Section to be published in the December 1956 JOURNAL.

REFERENCES

1. A. H. McKEAG AND P. W. RANBY, *J. (and Trans.) Electrochem. Soc.*, **96,** 85 (1949).
2. J. S. PRENER, *This Journal*, **98,** 406 (1951).
3. F. A. KRÖGER AND J. DICKHOFF, *Physica*, **16,** [3], 297 (1950).
4. F. E. WILLIAMS, *Brit. J. Appl. Phys., Supplement No.* **4,** 597 (1954).
5. H. A. KLASENS, *This Journal*, **100,** 72 (1953).
6. D. PEARLMAN, N. R. NAIL, AND F. URBACH, "Preparation and Characteristics of Solid Luminescent Materials," p. 365, John Wiley and Sons, Inc., New York (1948).
7. K. LARK-HOROVITZ, "Semi-conducting Materials," p. 64, Academic Press, Inc., New York (1951).
8. C. A. COULSON, "Valence," p. 263 Oxford University Press, London (1952).
9. H. C. FROELICH, *This Journal*, **100,** 280 (1953).
10. J. S. PRENER AND F. E. WILLIAMS, *Phys. Rev.*, **101,** 1427 (1956). J. S. PRENER AND F. E. WILLIAMS, Paris Luminescence Symposium (1956).
11. G. S. HANDLER, *J. Chem. Phys.*, **23,** 1977 (1955).
12. S. ROBERTS AND F. E. WILLIAMS, *J. Opt. Soc. Amer.*, **40,** 516 (1950).
13. Z. A. TRAPEZNIKOVA, *Zhur. Eksptl. i. Teoret. Fiz.*, **21,** 283 (1951).
14. W. HOOGENSTRAATEN, *This Journal*, **100,** 356 (1953).

Ductile Chromium

W. H. Smith and A. U. Seybolt

Research Laboratory, General Electric Company, Schenectady, New York

ABSTRACT

The effects of certain impurities on the room temperature ductility of chromium have been investigated. Results indicate that nitrogen in amounts <0.01% raises the bend transition temperature of annealed material above room temperature. No effect of oxygen on the ductility in amounts <0.3% was found. Sulfur in amounts as great as 0.1% does not appear to affect adversely the bend ductility of as-cast material. It appears that carbon in amounts greater than 0.02% cannot be tolerated. Preliminary work on the development of chromium-base alloys containing more than 90% chromium developed many unsolved problems. The beneficial effects of adding rare earths to tie up harmful impurities in chromium are discussed. Results of mechanical tests on chromium-cerium alloys are presented.

Introduction

Parke and Bens (1) in 1946 and Havekotte, Greenidge, and Cross (2) in 1950 studied the high temperature strength and creep properties of chromium-base alloys. While some of their compositions showed promise, none of their alloys showed any ductility at or near room temperature; these were all cast materials.

Blocher and associates (3) succeeded in fabricating sheet in small quantities from pure metal prepared from the iodide. While much of their material was cold bendable, it exhibited little or no tensile ductility near room temperature. They felt that carbon and sulfur could not be tolerated for cold ductility if the sum of these two were greater than 0.015 wt%. They also found that over 0.2% nickel was very detrimental. Oxygen up to 0.3% had no effect, nor did nitrogen in quantities up to about 0.03%.

Johansen and Asai (4) describe the successful preparation of room temperature ductile chromium at the Bureau of Mines Laboratory at Albany, Oregon. This procedure is essentially the purification of electrolytic chromium by an elevated temperature treatment in pure hydrogen, followed by consumable electrode arc-melting to a 2-in. diameter ingot which is then fabricated to sheet. Much of the sheet is cold bendable, and wire has also been prepared which is not only bendable, but which exhibits considerable reduction in area during a tensile test.

Wain and Henderson (5) reported on high-purity electrolytic chromium made by arc melting and hot-rolling at 900°C in mild steel, which was ultimately etched away. Even as-recrystallized, this material was cold bendable. No detectable metallic impurities could be found, and the nonmetallic impurities were 0.06% oxygen, < 0.001% nitrogen, and < 0.005% carbon. More recent work by Wain and Henderson (6, 7) is in agreement with many of the findings reported here.

Sully and co-workers (8) reported on an extensive investigation into the metallurgy of chromium, which dealt with the properties and fabrication of pure chromium and some chromium alloys. Sully's main findings were that metallic additions could not be tolerated in the sense that everything he added rapidly raised the bend transition temperature. He had no success in achieving any measure of cold ductility. Most of his specimens were prepared by powder metallurgical techniques.

To summarize the previously existing knowledge, there was evidence that sufficiently pure chromium was room temperature ductile, but aside from the information cited above there was almost none on what impurity or combination of impurities was most critical.

The immediate objectives of this work were to determine the most critical impurities, to find the level of concentration needed to cause trouble, to find means of eliminating this difficulty, and to establish a practical procedure for the preparation of room temperature ductile metal and to prepare such metal in sufficient quantity for various mechanical property tests.

Properties of Electrolytic Chromium

Electrolytic chromium appears to be the only practicable starting material for the production of chromium and chromium alloys at present.

To test the possibility that mere spheroidization of the oxide inclusions might be enough to cause some improvement in ductility, a sample of electrolytic chromium containing 0.003% nitrogen and 0.50% oxygen was heated in argon to 1400°C for 6½ hr. Although spheroidization was practically complete, the sample was brittle at room temperature and failed with the customary transgranular fracture. The hardness of this sample was 119 VHN, about as low a hardness as has been observed on any samples of chromium examined during this investigation, including samples of ductile chromium. A careful determination of the bend transition temperature, however, revealed that the temperature was lowered from >500°C for the as-deposited material to 150° to 200°C for the annealed material.

Purification of Electrolytic Chromium

The Bureau of Mines group considered oxygen the most objectionable impurity. They removed it by hydrogen reduction at 1200°C or higher, using a recirculating system with ZrH_2 as a source of hydrogen.

There is reason to believe that the reason for their success in making ductile chromium was the use of this hydrogen system, and possibly more important the fact that the furnace tube containing the chromium also contained zirconium turnings as a getter. While their 1200°C hydrogen treatment lowers the oxygen content to about 0.01%, it also appears to lower the nitrogen content even more, to the neighborhood of 0.001%.

The material thus produced showed some room temperature ductility, at least in the as-rolled or work hardened condition. When it was vacuum annealed or otherwise recrystallized, apparently without atmosphere contamination, it generally became brittle.

Hydrogen Reduction Technique

Hydrogen treatment was employed in the present work to eliminate oxygen from electrolytic chromium. However, since there was no critical temperature limitation, much higher temperatures were used to speed up oxygen removal and to reduce the oxygen content still further. At about 1400°C and with soaking times of approximately 20 hr, the oxygen content was reduced to about 0.001%. Hydrogen was first passed through a palladium catalyst and an activated alumina dryer to remove oxygen and water, respectively. From this it was passed through a tube furnace containing an iron pipe at 600°C charged with metallic calcium to pick up nitrogen, since it was noted early in the work that the chromium tended to show nitride needles in the microstructure.

Since there was evidence that, in spite of the precautions noted above, the chromium was still being contaminated with nitrogen, some turnings of a 50-50 zirconium-titanium alloy were placed at either end of the molybdenum boat containing the chromium. At the conclusion of the 20-hr 1400°C run it was noted that the turnings at the gas entrance opening had largely turned yellow, indicative of titanium or zirconium nitride. On the other hand, the turnings at the exit end were still clean and bright.

It has been observed in many cases where the zirconium-titanium alloy has been used close to the sample to be treated that the sample which previously had been brittle was now ductile. Evidently some impurity had been removed from the chromium which had caused brittleness.

While the hydrogen treatment at 1400°C was originally used only to reduce the oxygen content to very low levels, it has been shown that, properly conducted, it can also lower the nitrogen content to about 0.001% or lower. The hydrogen content is also reduced so much that it cannot be measured by vacuum fusion analysis.

Vacuum Heat Treatment

The nitrogen pressure over the chromium-nitrogen solid solution (at temperatures over 1200°C) is the order of millimeters (9), and it was clear that vacuum degassing of the chromium should be possible. Accordingly, some brittle hydrogen-treated electrolytic flake was given a 24-hr heat treatment in a vacuum furnace at 1150°C. At the conclusion of this test, the chromium could be bent cold if the rate of bending was slow. Analysis[1] showed 0.002% nitrogen, while after a similar heat treatment on some chromium which had originally a somewhat higher nitrogen content, the nitrogen content was 0.003%, but this material was brittle. These experiments and others of a similar nature suggest that (*a*) nitrogen is at least one source of brittleness, and (*b*) the critical nitrogen content may be around 0.002–0.003% or even less. This statement cannot be made unequivocally because it is known that the amount of damage done by nitrogen is a function of the cooling rate. A fast cooling rate from an elevated temperature tends to keep nitrogen in solution and to raise the transition temperature, while a very slow cooling rate allows more complete nitrogen precipitation, in which form it is not so harmful. In addition, the brittleness of any sample depends upon factors such as the amount of cold work it has had, possibly grain size, surface smoothness, and similar variables.

[1] Analytical accuracy is about 0.002%.

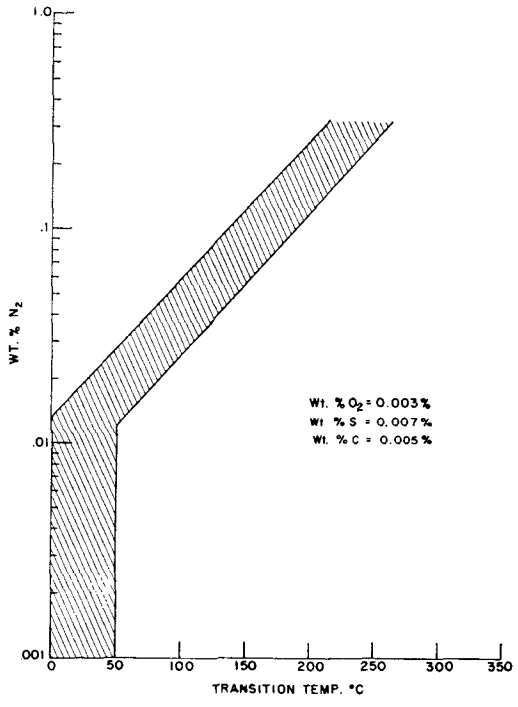

FIG. 1. Effect of N_2 content on the slow bend transition temperature of chromium.

ADDITION OF CONTROLLED IMPURITIES

Nitrogen.—In order to know how much impurity is needed to cause embrittlement, some quantitative relationship had to be established such as per cent impurity vs. transition temperature in slow bending or in impact bending. For this work, arc cast samples $\frac{1}{8}$-in. thick by $\frac{3}{8}$-in. wide by $1\frac{1}{4}$ in. long with a 1-in. gauge length, were slowly bent around a $\frac{1}{16}$-in. radius. Some rolled specimens were also tested in the form of sheet of varying dimensions and gauge length. While a few impact tests were made, the slow bend test using an Instron testing machine with a strain rate of 0.1 in./min was customary.

An attempt was made to prepare chromium samples of similar composition and structure but with varying amounts of nitrogen. This was done by heating as-cast samples of chromium containing 0.029% N_2, 0.003% O_2, 0.007% S, and 0.005% C either in vacuum to lower the

nitrogen content, or in a nitrogen atmosphere to raise the nitrogen content. Fig. 1 shows the transition temperature-percent nitrogen plot obtained on samples prepared from one lot of arc-melted chromium. These results should be regarded as preliminary, since adequate control over the nitrogen content at low levels was difficult to obtain, and similar tests on wrought material would probably show much less scatter. As mentioned earlier, the specific effect of nitrogen depends upon the mechanical and thermal history.

The experiments of Wain and co-workers (7) show conclusively that nitrogen contents of about 0.001% can cause brittleness in recrystallized chromium.

To establish the effect of cooling rate on the bend transition temperature samples of chromium containing 0.029% N_2 were heated to 1200°C in H_2, followed by either water quenching or slow cooling. The transition temperature for the water-quenched sample was 150°–200°C, while for the furnace cooled sample it was about 50°C. These results indicate that nitrogen in solution is more harmful to ductility than is precipitated chromium nitride.

Tests were made to determine if grain orientation in cast, rolled, or recrystallized material influenced the transition temperature. In none of these experiments was it found that the transition temperature changed by an amount greater than the suggested accuracy of the results ±25°C.

A great deal has been written concerning the effect of surface preparation on the ductility of chromium. It has been stated that cold-rolled material exhibits ductility only after the rolled surface is removed by polishing or etching. This effect has been attributed to such factors as oxygen, nitrogen, and notch sensitivity. In this laboratory cold-rolled sheet has been produced which exhibits room temperature ductility without any surface preparation after rolling. Samples of annealed chromium severely vacuum etched had the same transition temperature as similar samples polished through 3-0 paper. In general etching or polishing the surface helped restore ductility only when there was some indication that nitride contamination of the surface had occurred. These results are in agreement with those of Wain and co-workers (7).

Oxygen.—So far, no data have been obtained which clearly suggest that oxygen has an appreciable effect upon the ductility of chromium. Experiments can be cited which make it appear likely that the oxygen content is of no consequence.

It was found that oxygen up to 0.34% has no appreciable effect on the brittle-to-ductile transition temperature of as-cast chromium. For material in the cold-worked or recrystallized condition, chromium with oxygen contents as high as 0.04% had the same transition temperature as material with 0.001% oxygen. Higher oxygen contents were not examined for cold-worked or recrystallized material. Specimens containing 0.04% oxygen and <0.002% nitrogen had the same transition temperature regardless of whether they were rapidly or slowly cooled from the recrystallization temperature.

In another set of experiments, bend tests of the type already described were made on cast ingots containing 0.3% oxygen and 0.005% nitrogen. From Fig. 1 a transition temperature at about 30°C is expected for this much nitrogen if the oxygen content were simply ignored. The measured transition temperature was 75° ± 25°C, showing that, in this case at least, oxygen appeared to have an insignificant effect.

Finally, the results of Wain and co-workers (7) appear to indicate quite clearly that oxygen is an insignificant factor in cold ductility.

Carbon and sulfur.—Slow bend tests have been performed on as-cast chromium samples containing 0.02%, 0.08%, and 0.12% carbon. The oxygen, nitrogen, and sulfur contents were all less than 0.005%. These tests indicated that 0.02% carbon is not detrimental to room temperature ductility. Alloys of higher carbon content showed considerably higher transition temperatures, the value increasing as the carbon content increased. Attempts to prepare test bars without cracks from alloys containing more than 0.50% carbon were not successful. Examination of the fracture after bending revealed an increasing amount of intercrystalline failure as the carbon content increased. At a composition of 0.12% carbon the fracture was completely intercrystalline.

Slow bend tests on cast samples containing 0.1% sulfur indicated the transition temperature to be less than 100°C. This is in the range expected for material of the base composition used, without sulfur. The sulfur was observed to be present both by chemical analysis and by the microstructure.

Metallic additions.—The discouraging results found by Sully and co-workers (5) for all metallic additions have already been mentioned, as has the equally deleterious effect of nickel observed by Blocher and co-workers (3).

The observations made here on the effects of metallic additions have thus far been very incomplete, and have not always been under good control. Many of the observations, for example, have been made before the marked deleterious effect of nitrogen was realized. Certain additions such as copper, silver, and gold in amounts of a few per cent seem to have comparatively little effect on the hardness of chromium (and hence, presumably, upon the strength), although there appears to be some solubility of copper or silver in solid chromium.

Some elements like silicon, titanium, tantalum, nickel, beryllium, iron, tungsten, and aluminum are very potent hardeners, and make chromium even more brittle. This effect is so marked that it is often difficult to arc-cast these alloys without getting cracks in the ingot, particularly in small buttons of around 100 grams or less which cool very rapidly in the water-cooled hearth.

Addition of Scavenging Elements

The prior work of the Bureau of Mines group included the preparation of a number of alloys with the primary intention of tying up oxygen as more stable oxides such as Al_2O_3, Ta_2O_5, ZrO_2, etc. Formation of stable compounds is of course an appropriate expedient for removing effectively any undesirable element, such as carbon, oxygen, nitrogen, sulfur, etc. The Bureau of Mines' efforts to secure room temperature ductility in chromium by this means were not successful. It is not entirely clear why this method does not work better; similar experiments here have been dis-

appointing, although partial success was achieved by the addition of cerium.

Cerium was added to scavenge oxygen, nitrogen, or sulfur since it is known that very stable compounds of these three impurities and the rare earths are formed. The results of such additions on the bend transition temperature for as-cast specimens are shown in Fig. 2. It will be noted that at about 2 per cent of cerium the transition temperature reaches an approximate minimum value. Fig. 3 shows the effect of cerium on the Vickers hardness number for as-cast alloys. Here again, little is gained by adding more than about 2%. It is considered at present that the major effect of the rare earth addition is in tying up the nitrogen content as CeN.

Unfortunately, the cerium addition does not prevent or nullify further nitrogen contamination, presumably be-

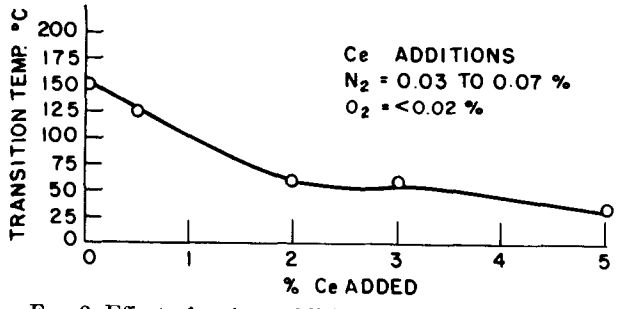

FIG. 2. Effect of cerium additions on the slow bend transition temperature of as-cast chromium containing approximately 0.03–0.07% N_2. Oxygen content < .02%.

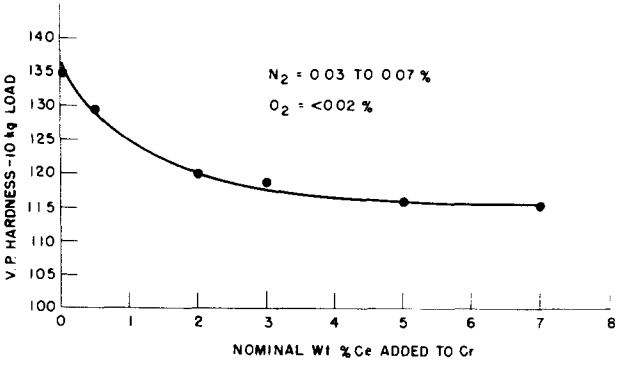

FIG. 3. Effect of Ce additions on the as-cast hardness of Cr.

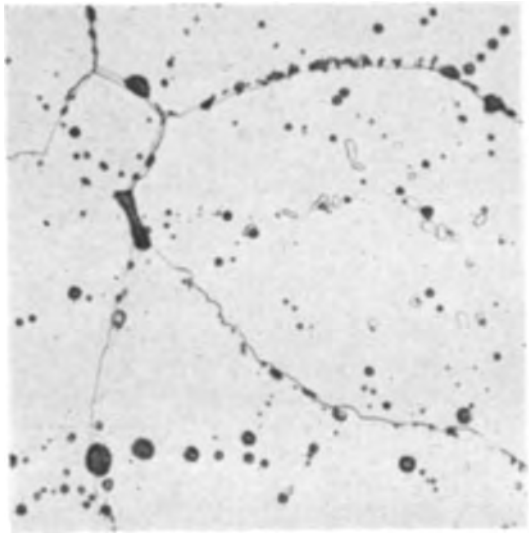

FIG. 4. 98% Cr + 2% Ce heated at 800°C in a N_2 atmosphere. Blak inclusions are Ce, light inclusions within grains andc at grain boundaries are nitrides. (500×).

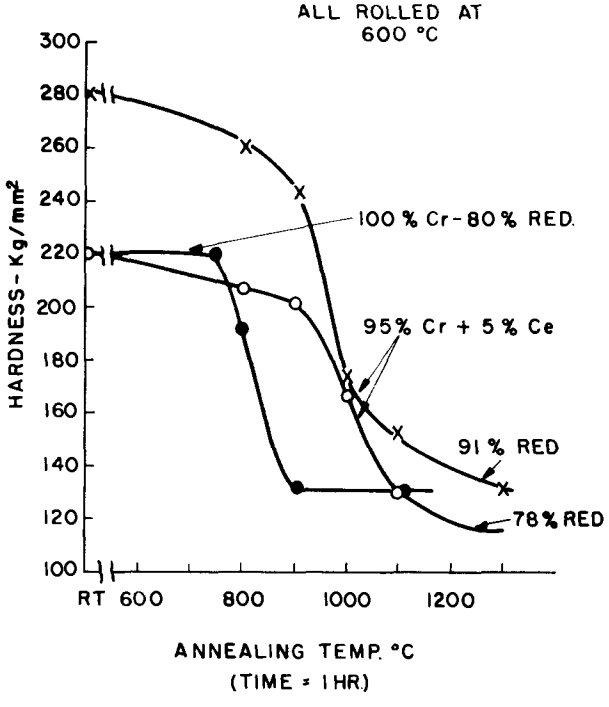

FIG. 5. Effect of annealing temperature on the hardness of rolled Cr and Cr + 5% Ce alloys.

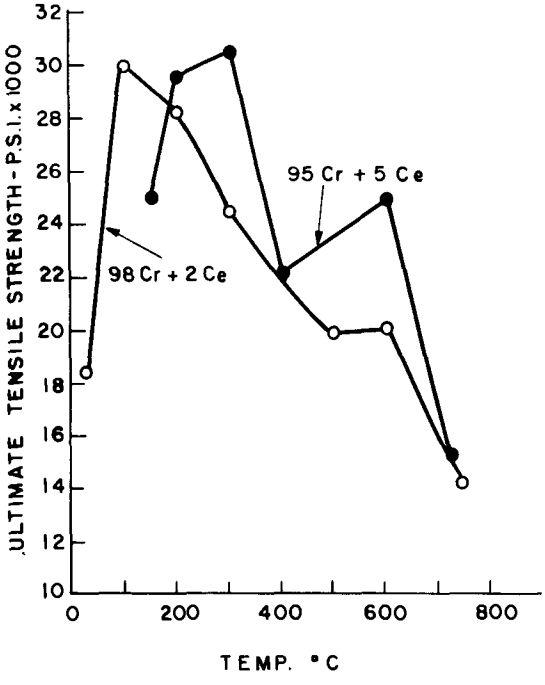

FIG. 6. Ultimate tensile strength of as-cast Cr-Ce alloys as a function of testing temperature.

cause cerium is present mainly as an insoluble second phase of very limited solubility in solid chromium. Fig. 4 shows the microstructure of a 2% cerium alloy which was heated in a nitrogen atmosphere. The dark areas are globules of cerium while the light-etching, almost white, inclusions are the nitride Cr_2N. The fact that these can coexist in this manner means that the previously existing islands of cerium are relatively ineffective in gettering the nitrogen as it diffuses into the chromium.

The recrystallization temperature behavior for a chromium-5% cerium alloy reduced 91% and 78% at 600°C is shown in Fig. 5, together with some nominally pure chromium with an 80% reduction at the same temperature. Cerium appears to exert an appreciable resistance to recrystallization.

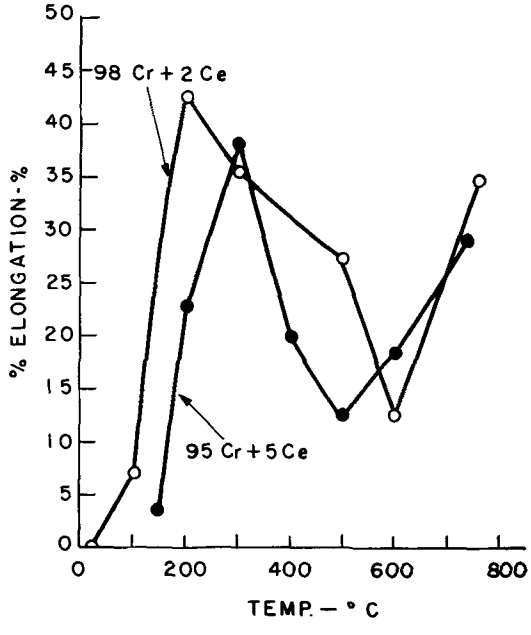

FIG. 7. Ductility of as-cast Cr + Ce alloys as a function of testing temperature.

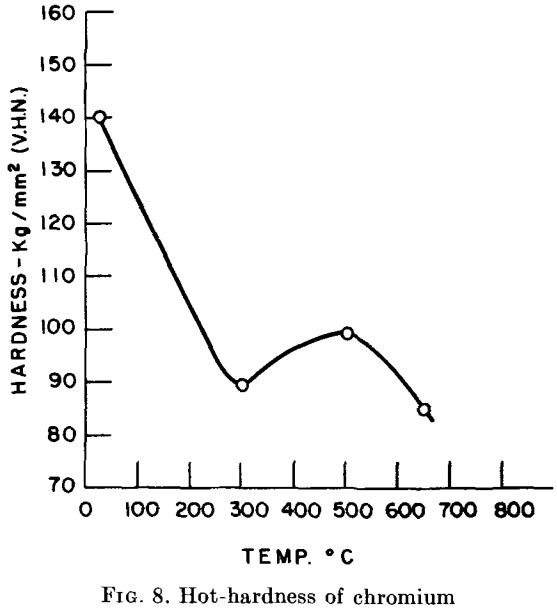

FIG. 8. Hot-hardness of chromium

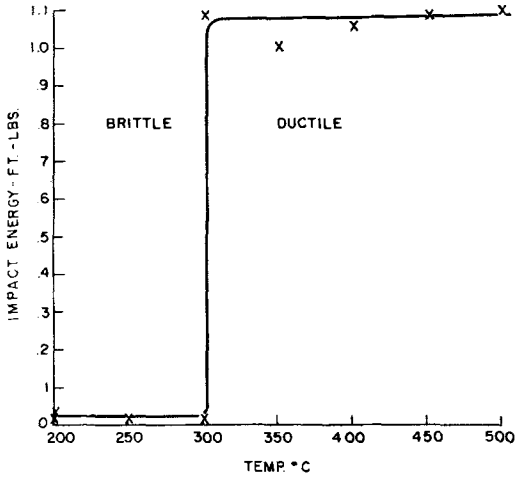

FIG. 9. The transition temperature of as-cast Cr + 2% Ce alloy as measured in impact on unnotched miniature Charpy bars.

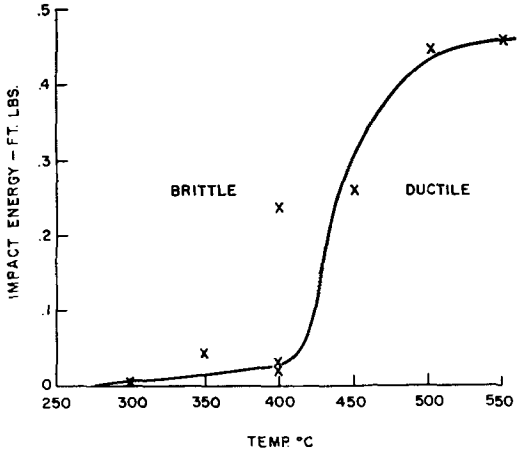

FIG. 10. Transition temperature of as-cast Cr + 2% Ce alloy as measured in impact on notched miniature Charpy bars.

MECHANICAL PROPERTIES OF CAST CHROMIUM-CERIUM ALLOYS

Results of some short-time tensile tests on cast chromium-cerium alloys are shown in Fig. 6 and 7. The pronounced minimum at 500°–600°C in per cent elongation (1-in. gauge length) may be associated with some precipitation phenomena. This might be due to the same agent which causes the maximum in hot hardness at this temperature (10) (see Fig. 8). The maximum in ductility near 200°C was unexpected. The tensile-test results in Fig. 6 and 7 require additional work for confirmation. It is expected that similar tests on cold-worked material will be performed.

Impact transition temperature data as measured on as-cast unnotched 2% cerium samples are plotted in Fig. 9. A much higher temperature, with considerably more scatter, was found for the same material tested as notched specimens (Fig. 10).

SUMMARY

While there is no question that small amounts of nitrogen impurity in the range around 0.001% to 0.005% (by

weight) has a marked deleterious effect on the ductility of annealed chromium, Wain and co-workers (7) claim that as much as 0.02% N_2 has little adverse effect upon the ductility of cold-worked chromium.

There is some rather convincing evidence that oxygen is probably not an important impurity, particularly after a nominal clean-up by a high temperature hydrogen anneal. Carbon when present in amounts greater than 0.02% forms a brittle grain boundry film which raises the transition temperature well above room temperature. Sulfur in amounts up to 0.10% does not appear to be harmful to low temperature ductility.

Much larger additions of metallic alloying metals are required to obtain embrittlement, i.e., 1% or more, as contrasted to the great sensitivity of chromium to nitrogen. The sensitivity, however, of chromium to small percentages of many alloying additions does cause some concern about the problem of chromium-rich alloy development. Fortunately, there is some evidence that chromium-base alloys containing rather large amounts of alloying metals (for example around 30–40% iron or nickel) are not as sensitive as alloys much richer in chromium. However, a 1% titanium and 5% tungsten alloy in the rolled condition showed some cold ductility (6).

It is not possible at present to explain some of the vagaries of ductility as a function of amount of cold work or of heat treatment. For example, it has been noted that chromium which has been "cold" rolled at 700°C to 0.021-in. thick had a transition temperature between room temperature and 50°C after a total reduction of 90%. The same sheet after further reduction, which brought the total to 94%, and the sheet thickness to 0.015 in., had a transition temperature of −25°C. This same sheet, if recrystallized by a vacuum anneal without apparent change in composition, has a transition temperature of 150°–200°C.

On the other hand, ductile chromium has been prepared in the as-recrystallized condition, so that a cold-worked structure is not a prerequisite for cold ductility. However, there is evidence that the chromium which exhibits ductility only in the cold-worked state is somewhat less pure than the chromium which is ductile in the recrystallized condition. These ideas are in agreement with Wain and co-workers (7).

It has also been found that by the addition of cerium it is possible to lower markedly the brittle to ductile transition temperature of chromium containing nitrogen. Evidence now available indicates this improvement in ductility is due to the removal of nitrogen from the chromium matrix by the formation of a stable insoluble nitride and to the extremely limited solid solubility of cerium in chromium.

Manuscript received July 22, 1955.
Any discussion of this paper will appear in a Discussion Section to be published in the December 1956 JOURNAL.

REFERENCES

1. R. M. PARKE AND F. B. BENS, ASTM Symposium, "Gas Turbines" (1946).
2. W. L. HAVEKOTTE, C. T. GREENIDGE, AND H. C. CROSS, *Am. Soc. Testing Materials, Proc.*, **50**, 1101 (1950).
3. J. M. BLOCHER, JR., I. E. CAMPBELL, D. J. MAYKUTH, R. I. JAFFEE, AND H. B. GOODWIN, "The Development of Chromium-Base Heat Resistant Alloys", WADC Tech. Rept. 53-470 (1954).
4. J. JOHANSEN AND G. ASAI, *This Journal*, **101**, 604 (1954).
5. H. L. WAIN AND F. HENDERSON, *Proc. Phys. Soc.*, **B66**, 515 (1953).
6. F. HENDERSON, S. T. QUAASS, AND H. L. WAIN, *J. Inst. Metals*, **83**, 126 (1954).
7. H. L. WAIN, F. HENDERSON, AND S. F. M. JOHNSTONE, *ibid.*, **83**, 133 (1954).
8. A. H. SULLY, "Metallurgy of the Rarer Metals: Chromium," Academic Press, New York (1954).
9. A. U. SEYBOLT, To be published.
10. J. WESTBROOK, Private communication.

Technical Feature

Electric Smelting Furnaces

MARVIN J. UDY

546 Portage Road, Niagara Falls, New York

ABSTRACT

Design and operation of electric smelting furnaces go hand in hand. The kilowatt per cubic foot of molten material is an important factor in operation, and constancy of the peripheral ohms factor, for slag forming or smelting operations, is another. Both factors are basically important, and must be properly coordinated with operation to get the best results. In recent work, it is shown that the peripheral ohms factor is a very useful criterion where slags of very high resistance are encountered. An even more useful factor is the kilowatt per square inch of electrode, or of electrode periphery, in contact with the slag.

INTRODUCTION

In the design of smothered arc smelting furnaces the kilowatt per cubic foot of molten material produces the highest energy efficiency. This is in accord with Stansfield's opinion.[1] However, enlarging the smelting zone by high heating rates is more a factor of operation than design. The highest efficiency would be obtained when operating at sufficiently high kilowatt per cubic foot of molten material so that continuous tapping was attained. Under such conditions a definite and constant size of smelting zone would result and there would be no corrosion of the side walls.

Most operations are of the intermittent type wherein the highest heating rate is attained directly after tapping, with a constantly lowered heating rate during the period between taps. Heating rates can be lowered too much and the material will freeze on the bottom of the furnace if the periods between taps are too long.

Thus, to meet the conditions laid down by Stansfield, tapping must be done on a regular basis, e.g., every hour, and becomes more of an operating condition than a factor of design.

Andreae (2) showed that the peripheral ohms factor[1] is a constant for any particular operation where slag is produced. This factor must be determined by experiment. The author has found the peripheral ohms factor to be very useful in the design of the electric smelting furnace. In dealing with the electric furnace, one should know the conditions necessary at the tip of the electrode to produce a given result with the lowest energy cost and greatest recovery. The conditions are temperature, nature of slag (acid or basic), resistance, and the maximum kilowatts per cubic foot that can be put through the particular type of slag. All are important to the proper design of the electric smelting furnace. Other factors of importance are electrode spacing, electrode size, and physical characteristics of the material to be smelted, as well as the time of tapping which controls the kilowatts per cubic foot of molten material. The peripheral ohms factor provides a means of determining these conditions and, thus, a way to design the proper furnace.

To obtain the right conditions of temperature in the electric furnace, full arc heating, arc bath resistance heating, and full bath resistance heating may be used. Proper use and coordination of these factors makes it possible to produce almost any temperature desired, and, when coupled with the proper rate of feed, maintain that temperature within close limits.

The usual furnace design is based on the standard commercial electrodes available, their current carrying capacity, transformer limitations, and bus. Results are not always satisfactory because of the necessary limitations.

TABLE I. *Average data for 100-kw furnace*

Kw total	110
Power factor	95
Voltage (phase)	240
Amp	460
Electrode diameter	4 in.
Resistance at tip	0.248 ohm
Peripheral ohms	3.0

In some recent work on high resistance slags predominating in silica and other acid materials, the author has found that data are needed regarding what takes place at the tip of the electrode in the area where most of the heat is developed in the full open arc, and the point where most of the heat is developed in the slag just short of full bath resistance heating.

The peripheral ohms factor is a good guide in most cases, but it is not always enough. In one operation using a small 100-kw furnace, the peripheral ohms factor was determined for the best results, both operational and economic. Operation under these particular conditions was highly successful as to metallurgical results, electrode consumption, and workability of the furnace, as well as kilowatt hour per ton of product. Results were not entirely satisfactory since a comparatively high voltage was needed for a small energy input. The voltage required was 240 for about 100 kw input with two 4-in. electrodes and an electrode spacing of approximately 12 in. between centers.

[1] Resistance between electrode tip and furnace bottom × electrode circumference.

TABLE II. *Calculated relationships for one electrode of a 3300-kw furnace*
Power factor (P.F.) = 95%

Phase, volts	Effective volts†	Tip volts*	Electrode		Amp in peri.‡	In. in peri.	Electrode		Amp in.²	Res. at tip, ohms
			kw	Amp			Dia.	Area		
200	190	110	1042	9500	36.7	260	82.5	5350	1.78	0.0116
220	208	120	1042	8700	40.0	217	66.5	3900	2.22	0.0137
240	228	132	1042	7900	44.0	179	57.0	2660	2.97	0.0167
260	246	142	1042	7350	47.5	155	49.0	1880	3.88	0.0193
280	265	153	1042	6825	51.0	134	42.5	1420	4.80	0.0224
300	286	165	1042	6320	53.2	119	38.0	1130	5.57	0.0260
320	303	175	1042	5950	57.2	104	33.0	852	6.95	0.0294
340	322	185	1042	5650	61.5	92	29.2	667	8.50	0.0328
360	341	197	1042	5300	66.7	79	25.0	492	10.75	0.0371
380	360	208	1042	5000	69.2	72	23.0	415	12.00	0.0416
400	380	220	1042	4750	73.0	65	20.6	332	14.30	0.0463
480	455	263	1042	3970	87.7	45	14.3	160	24.80	0.0660

* Effective volts ÷ $\sqrt{3}$ = tip volts.
† Phase volts × P.F. = effective volts.
‡ Amp in peri. = volts ÷ 3 (the peripheral ohms).

TABLE III. *Voltage-current relations with electrodes submerged in slag*

Volts	Electrode on surface of slag		Electrodes 1 in. submergence in slag		Electrodes 2 in. submergence in slag	
	Amp	kw	Amp	kw	Amp	kw
200	200	40	490	98	820	164
220	365	80	840	185	975	215
240	460	110	910	218	Reached limit	
260	500	130	760	198	of circuit	
280	580	160	850	238	breaker	
300	530	159				
320	520	167				

Translating these figures to a 3-phase 3300-kva furnace, and maintaining a peripheral ohms factor of 3.0, conditions shown in Table II result.

From Table II it is obvious that conditions desired, as shown in Table I, could not be met at 200–260 v. Electrodes would be excessively large and current densities extremely low for practical operation. In the range of 280–320 v, conditions could be met with a reasonable electrode size and low resistance, but current densities would still be extremely low. At 340–480 v, electrode sizes are more reasonable, but current densities are low, except at 480 v. The only possible range of operati on would be at 480 v o

TABLE IV. *Calculations for submerged electrodes*

Phase volts	4 in. Electrode, 12.57 in.² on surface of slag					4 in. Electrode, 25.50 in.²; submerged 1 in. in slag						4 in. Electrode, 38.4 in.²; submerged 2 in. in slag					
	Amp	C.D. amp/in.²	Peri. ohms	Kw/electrode	Kw/in.²	Amp	C.D. amp/in.²	Peri. ohms	Kw/electrode	Kw/in.² in peri.	Kw/in.² in electrode	Amp	C.D. amp/in.²	Peri. ohms	Kw/electrode	Kw/in.² in peri.	Kw/in.² in electrode
200	200	16	5.97	20.0	1.60	490	19	2.44	48	3.81	1.88	820	21.6	1.46	84	6.70	2.22
220	365	29	3.60	40.0	3.18	840	33	1.56	92	7.30	3.60	975	25.6	1.39	107	8.50	2.81
240	460	36	3.10	55.5	4.20	910	35	1.57	109	8.65	4.27			—			—
260	500	39	3.10	65.0	5.17	760	29	2.22	96	7.62	3.76			1.42 avg.			2.51 avg.
280	580	46	2.88	81.0	6.45	850	33	1.96	114	9.12	4.46						
300	530	42	3.47	79.5	6.30			—			—						
320	520	41	3.65	83.5	6.65			1.95 avg.			3.59 avg.						
			—		—						4.00 avg. of last 4 readings						
			3.67 avg.		4.79 avg.												

Note: Area of 4 in. electrode—12.57 in.²; circumference—12.57 in.

TABLE V. *Effect of electrode size on total power input*

Diam, in.	Area, in.²	Circumference, in.	Area 1 in. submergence	Total kw at 4 kw in.²
10	78.5	31.42	109.92	439.6
14	153.9	43.98	197.88	791.5
16	201.1	50.26	251.36	1055.4
20	314.2	62.83	377.03	1508.1

The data on a 24-hr basis averaged as shown in Table I with the tips of the electrodes just on the surface of the slag; much higher voltages were required for operation with a full arc.

TABLE VI. *3300 Kva furnace based on 4 kw/in.² effective electrode area*

Volts	P.F.	Eff. v	Tip v	Kw/elect.	Amp/elect.	Electrode 16 in. effect. area 1 in. submergence	C.D. amp/in.²	Res. at tip
200	95	195	110	1042	9500	251.3	37.8	0.0116
220	95	208	120	1042	8700	251.3	34.6	0.0137
240	95	228	132	1042	7900	251.3	31.4	0.0167
260	95	246	142	1042	7350	251.3	29.3	0.0193
280	95	265	153	1042	6825	251.3	27.0	0.0224
300	95	284	164	1042	6320	251.3	25.0	0.0260
320	95	303	175	1042	5920	251.3	23.6	0.0294

higher. At any lower voltage there would be excessive surface oxidation of the electrodes, resulting in high electrode consumption due primarily to the low current densities.

In order to get within reasonable voltages for safe operation, the region of submergence of the electrode in the slag was explored. The same 100-kw furnace was used and the same type slag. In 3-phase furnaces there is a limit to submergence of the electrodes in any particular slag, beyond which the arc-bath-resistance type of heating is lost and true bath resistance heating takes place with loss of automatic control of the electrode position in the slag. This can result in burned out furnace bottoms and generally poor operation. The results of these tests are shown in Table III, using the same two-electrode furnace and 4 in. diameter electrodes.

Using the above data, Table IV shows the results of calculating amperes per square inch of effective electrode area, peripheral ohms factor, and the kilowatts per square inch of effective electrode area. From these results the kilowatt per square inch of effective electrode area appears to be about as constant as the peripheral ohms factor, within the limits of accuracy of the readings. Power factor is taken as 95.

Calculation of Furnace Design

With these data it becomes quite easy to design a furnace with the electrodes at the surface of the slag bath or with 1 in. or 2 in. submergence that will give reasonably safe working voltages. Thus, to design a 3300 kva 3-phase furnace at 4 kw/in.^{2} of effective electrode area, 1 in. submergence, and to operate at a reasonable and safe voltage, calculations for various electrode sizes are made as shown in Table V.

Since a 3300 kva furnace at 95 P.F. requires 1042 kw/electrode, it is obvious from Table V that a 16 in. electrode is needed at 4 kw/in.^{2} effective electrode area. Calculations on this basis for a 3300 kva furnace are shown in Table VI.

Operating at 2 in. submergence with a 16 in. electrode, the current density would be 31.6 amp/ft^2 for 200 v and 29 amp/ft^2 for 220 v. The resistance would remain the same.

It is plain that a 16 in. diameter carbon electrode with 1 in. submergence of the tip in the slag gives reasonable voltages and current densities within the range of standard practice for carbon electrodes. Much smaller graphite electrodes could, of course, be used; the kilowatt per square inch of effective electrode area would be higher.

Electrode Spacing

Once having determined the voltage range and size of electrode, the next important problem is that of electrode spacing. In smelting furnaces making metal and a slag, matte and a slag, or spiess and a slag, the electrode spacing should be such that the resistance in the slag from electrode to electrode is less than the resistance through the slag to the metal, matte, or spiess in the bottom. Slag composition and characteristics become very important. In high-resistant slags and close electrode spacing, metals like antimony, which melts at 630.5°C, can be frozen on the bottom when the slag reaches much more than 7 in. Spiess, which melts in the 1200°C range, can also be frozen on the bottom when the slag reaches much more than 7 in. in depth. Likewise, pig iron, steel, and ferroalloys will freeze on the bottom if the electrode spacing and slag depth have unsuitable values.

If the electrode spacing is too large and too much of the power goes to the bottom and through the metal, the metal becomes hot and the slag freezes on top.

There is a correct electrode spacing for every type of smelting operation, but it is not always easy to meet the conditions of electrode spacing mechanically. However, in recent years much has been done to improve the design of electrode clamps so that it is now possible to get electrode spacings as low as 18 in. between faces for large 35 in. electrodes. For the most part, the electrode spacing from electrode face to electrode face should be from one-half the diameter of the electrode for very high-resistance slags to one and one-half times the diameter for the more conductive slags. In general, a spacing of one diameter between the electrode faces will satisfy most conditions.

Manuscript received December 27, 1954. This paper was prepared for delivery before the Cincinnati Meeting, May 1 to 5, 1955.

Any discussion of this paper will appear in a Discussion Section to be published in the December 1956 JOURNAL.

REFERENCES

1. A. STANSFIELD, "The Electric Furnace," 2nd ed., p. 126, McGraw Hill Book Co., New York, (1914).
2. F. V. ANDREAE, *Trans. Electrochem. Soc.*, **67**, 168 (1935).

Discussion Section

HIGH TEMPERATURE OXIDATION OF TWO ZIRCONIUM-TIN ALLOYS

M. W. Mallett and W. M. Albrecht (pp. 407–414)

DAVID A. VERMILYEA[1]: The oxygen consumed is used up in two processes: (*a*) solution in the metal, and (*b*) formation of an oxide film. Have the authors any estimate, either experimental or from diffusion calculations, of the amount used in each process?

M. W. MALLETT AND W. M. ALBRECHT: Calculations based upon diffusion data indicate that about 0.5–1.5% of the total amount of oxygen consumed by a reacted specimen was used up in the diffusion process. Normal variations in rate data are greater than this. In the proposed mechanism, solution of oxygen must occur. However, not all of the dissolved oxygen diffuses into the metal core since much of it is incorporated into the advancing oxide film by further oxidation.

APPLICATION OF BACKSIDE LUGGIN CAPILLARIES IN THE MEASUREMENT OF NONUNIFORM POLARIZATION

M. Eisenberg, C. W. Tobias, and C. R. Wilke (pp. 415–419)

ROBERTO PIONTELLI[2]: This valuable paper points out some problems of general interest. The main problem in electrochemical kinetics is actually that of the methods for measuring overvoltages at different electrodes, in the very wide range of conditions covered by: plating, refining, finishing, corrosion of metals and alloys. The fear of the systematic errors involved by the so-called "direct" methods, in which the overvoltages are measured during current flow, has given incentive to other techniques (commutator, thyratron potentiometer, alternate current, limit current, etc.).

Although these methods give useful information on some particular aspects of the problems, they are less general and exhaustive than the "direct methods," whose results are moreover exempt from the more or less explicit hypothesis involved by the other ones. For making the direct methods correspond to the requirements of precision measurements, in addition to the general precautions concerning: purity of materials, control of the surface conditions of electrodes, form of current supply, quick and complete recording of voltages (easy at present, thanks to electronics), a satisfactory solution of the problem of the choice of the electrolysis cell, and of the "tensiometric element," formed by coupling the studied electrode to a reference electrode through a probe (so-called capillary), was however urgently required.

The electrolysis cells must grant the uniformity of the current distribution on electrodes[3] and a reasonable control of the conditions of diffusion or convection.

The tensiometric element must avoid the inclusion in the measured overvoltages of parasitic ohmic drops, or, on the contrary, of shielding effects. In this respect the backside capillary[4] presents the advantage that the systematic error is in any case in the same direction, and one may evaluate it with a reasonable approximation. We are therefore in agreement with the authors in believing that this device can find satisfactory application when any interference with hydrodynamic conditions at the solution-electrolyte interface has to be avoided. However, this point is essential, in our opinion, only when conditions of nonturbulent flow are to be investigated.

In our cells[5] a perfect symmetry of geometric conditions is realized such as to permit carrying out experiments in conditions of very regular diffusion.

On the other hand it is also possible, in the aim of minimizing the concentration changes at the electrode surface, to obtain a very efficient stirring by rapid circulation of the solution, which enters and leaves the cell very near to the electrode surface.

The presence of a frontal capillary of our type [represented in Fig. 1(b) of the discussed paper] not only respects the geometric symmetry but does not lower appreciably the local efficiency of the convection due to the turbulent flow of the solution. As a matter of fact, in our cells distribution of current (controlled, for instance, by means of the distribution of the cathodic deposit or of the anodic attack) is perfectly uniform on the electrode to be investigated both in the presence and absence of stirring. These properties are not shown by the capillaries of the classic Luggin type. We succeeded in improving the backside capillary so as to eliminate the systematic error involved by this probe.[6]

For minimizing the sources of systematic errors involved by direct methods, one must in fact apply the following rule: the uniformity of distribution of the current on the electrode to be investigated must be granted by a suitable design of the electrolysis cell and not perturbed by the presence of the capillary of tensiometric element, which must incorporate only the limiting bound-

This Discussion Section includes discussion of papers appearing in the JOURNAL of The Electrochemical Society, **102,** No. 7–12 (July–December 1955). Discussion not available for this issue will appear in the Discussion Section of the December 1956 JOURNAL.

[1] Research Lab., General Electric Co., Schenectady, N. Y.

[2] Lab. of Electrochemistry, Polytechnic Institute of Milan, Milan, Italy.

[3] The experiments of Eisenberg, Tobias, and Wilke confirm once more the dependence of the values of the measured overvoltage on the position of the capillary, when the current distribution is nonuniform on the electrode. The cells sometimes used for measuring hydrogen overvoltages [J. O'M. BOCKRIS, *This Journal,* **98,** 153*C* (1951)], in which a tip electrode is utilized, are therefore, in our opinion, unsuitable also from this point of view.

[4] Perhaps utilized in a quite rough form of realization by other authors before the Piontelli-Poli experiments mentioned in the discussed paper.

[5] R. PIONTELLI, U. BERTOCCI, G. BIANCHI, C. GUERCI, AND G. POLI, *Z. Elektrochem.,* **58,** 86 (1954).

[6] R. PIONTELLI, *Gazz. chim. ital.,* **83,** 357, 370 (1953); *Z. Elektrochem.,* In press; R. PIONTELLI, G. BIANCHI, U. BERTOCCI, C. GUERCI, AND B. RIVOLTA, *ibid.,* **58,** 54 (1954).

ary layer of the electrode solution, avoiding also any current leakage in the rest of the element itself.

For making the backside capillary correspond to these requirements, it is sufficient to introduce a nearly complete obstruction of the capillary by means of a piece of insulating material, protruding in the solution for a length of the order of the capillary diameter. In this manner the current on the studied electrode is uniform, while any inlet of current lines in the probe is avoided, without hindering the convection obtainable by an efficient stirring, or a regular diffusion in absence of stirring.

We seize this opportunity for pointing out once more the advantages of the frontal capillary of the type represented in Fig. 1(b) of the discussed paper,[7] for experiments concerning: single crystals and, generally, electrodes not allowing the application of a backside capillary; conditions requiring special care for avoiding any contamination source; and some others. The application of the rule above led us also to some satisfactory solutions of the problem of the overvoltage measurements in fused salts.[8]

Recently progress has been made with the elaboration of a new type of probes called "electrode probes." As to the arrangement of these probes, they also obey the general rule mentioned above. In the new type the reference electrode may be arranged for instance in such a manner as to be in direct contact with a solution layer very near to the electrode surface. The properties and possible applications of these devices are discussed elsewhere.[9]

CHARLES W. TOBIAS AND MORRIS EISENBERG: We were very interested in the valuable comments made by Professor Piontelli. For some time we have been sharing with him, and a few other workers in this field, a serious concern about the direct methods for measurements of potentials of polarized electrodes.

It has been recognized for some time that, while achievement of uniform *primary* current distribution is possible by proper design of cell geometry, the *actual, secondary* current distribution is rarely uniform throughout the surface of the polarized electrode. Theoretically, the only cases in which the secondary current distribution is uniform are: (*a*) when a pure unidirectional (normal to electrode surface) diffusion of the potential determining species takes place, (*b*) in case of perfect homogeneous turbulence resulting in a mass transfer boundary layer of uniform thickness on the electrode surface.

It must be pointed out, however, that the realization of these two ideal conditions in laboratory practice is quite difficult. For instance, the commonly used mechanical stirring or the bubbling of a gas in the vicinity of the electrode certainly cannot be expected to produce uniform turbulence and cannot be subjected to a rigorous hydrodynamic analysis. On the other hand, the case of pure diffusion can be realized (in case of a metal deposition system) by placing the cathode at the top end of a vertical cell and eliminating possible thermal gradients. In this case, the use of a perpendicular capillary pressing against the electrode, as suggested by Piontelli, is quite acceptable and free of error. We wish to emphasize these points because very frequently one finds polarization data taken on the assumption that pure diffusion was operative and ignoring the large contribution of free convection.

In principle, it is not possible to provide a uniform boundary layer, by stirring or by flow of the electrolyte or when natural convection takes place, in the vicinity of limiting walls or protrusions on a plane surface. Although this principle has been well known to us, we performed some simple experiments, in which a Lucite (insulator) rod of 2 mm diameter was fitted into a hole of exactly the same diameter in the electrode surface. The electrode was placed in a vertical position, so that the Lucite rod was horizontal. Current distribution due to geometry was perfect, since the anode was parallel to cathode, and all edges were connected by parallel insulating planes. Copper was deposited at current densities well below the limiting, under the following conditions: (*a*) no stirring, (*b*) stirring by 2 glass propellers placed on two sides of rod, (*c*) flow of electrolyte parallel to cathode surface.

Following each experiment, the Lucite rod was removed, and the deposit adjacent to the hole observed by means of photomicrographs. In each case, the deposit thickness was appreciably smaller in the direction of flow, e.g., where the rod "shielded" the flow. In case (*a*), in which natural convection was operative, a well-defined groove formed in an exactly vertical direction above the hole.

We cannot accept the idea that proper measurements of concentration polarization can be made by a junction piece which interferes with the flow at the electrode surface. The error will be particularly large if such a capillary tube touches the surface.

However, if mass transfer is not controlling (e.g., polarization due to concentration changes in the electrolyte is negligible compared to activation polarization), frontal capillary arrangements can be used satisfactorily.

In selecting the method for coupling the polarized electrode with a reference electrode, it is necessary to choose carefully the type of capillary best justified under the existing conditions. Piontelli's work in this field is of great value and has certainly contributed to a better awareness of the errors involved in the traditional use of frontal Luggin capillaries at some distance from the electrode surface. The realization of the importance of hydrodynamic factors affecting these problems has, in recent years, added to a better understanding of the relative advantages and disadvantages of the various methods, and, since there is no one single, perfect method applicable to all cases, it is hoped that workers in this field will examine their experimental techniques in the light of the present discussion.

ROBERTO PIONTELLI: The stimulating reply of the authors makes some supplementary information opportune

[7] We regret that one of the few presentations of this device in the English language [J. O'M. BOCKRIS, "Modern Aspects of Electrochemistry," p. 265, Fig. 10, Academic Press, New York (1954)] is unfortunate insofar as the probe is represented (Fig. 10 of Bockris' work) placed at some distance from the electrode surface, while, for an efficient shielding of the covered part of the electrode surface, this probe must be pressed against the electrode.

[8] R. PIONTELLI AND G. MONTANELLI, *J. Chem. Phys.*, **22**, 1781 (1954); R. PIONTELLI AND G. STERNHEIM, *ibid.*, **23**, 1358 (1955); R. PIONTELLI, B. RIVOLTA, AND G. MONTANELLI, *Z. Elektrochem.*, **58**, 64 (1954).

[9] R. PIONTELLI, *Rend. ist. lombardo sci.*, **85**, 665 (1955).

on our technique,[10] which takes into account the difficulties pointed out by the authors.

The main goal of our experiments is that of measuring "activation overvoltages" in conditions in which concentration changes at electrodes are minimized. We are in agreement with the authors in believing that stirring obtained by means of propellers or bubbling of gases in the cells may result unsatisfactory, while a liquid flow parallel to the electrode surface may be shielded by an obstacle.

For these reasons, in our cells the active area of electrodes (in the shape of a quite narrow annulus) is uniformly swept by a rapid circular flow of solution entering from two tangential inlets.[11] The cells are designed for working with their axis either horizontal or vertical, but in our present practice this second arrangement is preferred (the electrode surface being thus horizontal), also when stirring is applied. The electrodes are, moreover, subject only to short current pulses.

These precautions, suitable for minimizing composition changes at the electrode surface, also make secondary current distribution very satisfactory, likewise in immediate proximity to the probe. Clear evidence on this point is given in a paper in preparation. Our cells are designed for working in absence of stirring too, but keeping their axis vertical; the known effects, due to natural convection on vertical electrodes in presence of obstacles, recalled by the experiments quoted in the authors' reply, are absent, because the material flow is normal to the electrode surface and unperturbed by the probe. Of course, the realization of conditions of pure diffusion control is by no means easy.

Concluding, I share with the authors of this valuable paper the hope that the problems pointed out by this discussion will find due consideration finally by workers in experimental electrochemistry.

ELECTRODEPOSITION OF MOLYBDENUM ALLOYS FROM AQUEOUS SOLUTIONS

D. W. Ernst, R. F. Amlie, and M. L. Holt (pp. 461–469)

STANLEY J. KLIMA[12]: How stressed are the nickel-molybdenum deposits?

M. L. HOLT: No measurements were made of the stress in the alloy deposits; however, I would guess that some of the deposits were rather highly stressed.

PERIODIC CURRENT REVERSAL IN PLATING COPPER-LEAD ALLOYS

Nelson W. Hovey, John L. Griffin, and Albertine Krohn (pp. 470–473)

ABNER BRENNER[13]: The method of obtaining current reversals in different ratios to the direct current developed by the authors is quite ingenious. I would like to suggest a simplification of the apparatus. Instead of using commutator segments and shorting screws, simply 2 metal disks, each of which consists of 2 insulated halves or sectors, could be used. Each sector of one disk is connected by a single flexible lead to the corresponding sector of the other disk. The two brushes for each disk are 180° apart, that is, at opposite ends of a diameter.

Two methods of obtaining reversal of the current may be used. The simplest would be to have the brushes for one disk fixed in position. The brushes for the other disk are set in a frame so that the diameter-line drawn between the brushes can be set at any desired angle to that of the first set of brushes. One set of brushes serves as the input, the other as the output. By simply changing the angle between the diameter-lines of the two sets of brushes, any ratio of direct to reverse current may be obtained. The other method would be to have all four brushes fixed in a frame and to simply rotate one disk to a fixed position relative to the other, such that the diameters along which the half circles are insulated are at an angle to each other.

ALBERTINE KROHN: The authors appreciate Dr. Brenner's evaluation of this paper and his suggestions for the simplification of the apparatus described.

FORMATION OF MANGANESE(II) ION IN THE DISCHARGE OF THE MANGANESE DIOXIDE ELECTRODE

A. M. Chreitzberg, Jr., D. R. Allenson, and W. C. Vosburgh (pp. 557–561)

J. BRENET[14]: With the assumptions put forward by the authors on the formation of Mn^{2+}, at the time of the discharge of the electrode of MnO_2, it is considered that the reduction product of MnO_2 during the discharge of the cell is, in fact, MnOOH. We have just proved with our collaborators[15, 16] that during the discharge the nature of the active dioxide used has a certain influence, as we have been able to show clearly in the discharged cathodes either the structure of manganite, MnOOH, or the one of γMn_2O_3 isostructural of Mn_3O_4. Besides, in the experimental method utilized by Vosburgh and his collaborators, the deposited dioxide on the carbon is obtained by anodic oxidation. Very certainly it would be easy to verify that γMnO_2 is thus formed. In this case we have shown[15, 16] that γMnO_2 during the discharge evolves toward γMn_2O_3 and not toward MnOOH. Of course, even in the case of γMn_2O_3 it could be considered the ion Mn^{2+} is formed in solution. It would also be interesting for the same authors to examine the case in which utilized dioxide is formed with αMnO_2, as well as with βMnO_2 (pyrolusite), although the activity for the latter one is very weak. Considered from the fundamental mechanisms viewpoint, these studies should be extremely important.

I should add that the reduction of MnO_2 during the discharge is not entirely influenced by the presence of carbon in the cathodes, as we have just shown, when effecting discharges on cathodes entirely free from carbon, therefore composed entirely of MnO_2.

All these researches are extremely important, but, in my opinion, have not yet really allowed the working out

[10] R. PIONTELLI, *Z. Elektrochem.*, **58**, 86 (1954); *ibid.*, **59**, 778 (1955).

[11] Dr. U. Bertocci has given very valuable cooperation in realizing this device in which the liquid flow is derived by argon or nitrogen.

[12] Sperry Gyroscope Co., Great Neck, N. Y.

[13] National Bureau of Standards, Washington 25, D. C.

[14] 9 Rue d'Artois, Paris, 8a, France.

[15] J. BRENET AND A. M. MOUSSARD, Proceedings of the International Symposium on the Reactivity of Solids, Gothenborg 1952, Part II, p. 593, Elanders Boktryckeri Aktiebolag, Gothenborg (1954).

[16] J. BRENET, A. M. MOUSSARD, AND A. GRUND, *Compt. rend.*, **236**, 615 (1953).

of an energetic balance in the Leclanché cells founded on purely chemical mechanisms. Furthermore, none of the theories put forward takes into account the more or less high activities of various dioxides. A complete and satisfactory theory of depolarizing, in my opinion, will have to allow at the same time an energetic balance and a factor characterizing the dioxide activity. Those are points that I have been attempting to develop for several years and which it would be desirable to have investigated further by others.

W. C. VOSBURGH: Our experiments and our conclusions are independent of the exact nature of the lower oxide formed. We have often called the reduction product merely lower oxide in order to avoid naming a particular compound that was not identified in our experiments. When writing equations it is necessary to use a definite formula and we have used MnOOH to represent reduction to the trivalent state and Mn_3O_4 to represent further reduction. It should be noted that the lower oxide is assumed to be formed on the surface, and in this state it may not have the same form as the lower oxide found in the discharged electrode.

THE NATURE OF ALUMINUM AS A CATHODE

M. J. Pryor and D. S. Keir (pp. 605–607)

H. K. FARMERY[17]: Dr. Pryor and Dr. Keir's Technical Note is extremely interesting to those studying the corrosion behavior of aluminum, although the title is perhaps a little misleading since it is the oxide that is really being considered.

When the surface film on the metal is essentially aluminum oxide, then not only will the weak spots be the most likely places for electrons to migrate through the film but also the metal cations. In other words, the anodic and cathodic regions will be in close proximity. If, however, the oxide film contains other metal ions apart from aluminum, e.g., copper or iron, it becomes more conductive and, consequently, electrons can migrate through thicker films; in this way the anodic and cathodic reactions can be spatially separated.

Such mixed oxide films are more likely to occur on clean metal surfaces exposed to the air at room temperature than at high temperatures, since the oxide will be formed from the metal atoms at the surface in the first case, whereas, at high temperatures, with greater diffusion rates, preferential oxidation can occur.

This may account partially for the greater reactivity of etched aluminum surfaces compared with those carrying a high temperature formed film although the greater thickness of the latter will obviously affect the movement of electrons and metal cations. As examples of this enhanced reactivity, the stress-corrosion lives of susceptible Al–7% Mg and Al–4% Cu sheet tensile specimens when stressed at a high proportion of their Proof Stress in 3% NaCl solution can be cited.[18]

Material	Lives with thick heat-treated film present	Lives when tested after etching
		min
Al–7% Mg	~4 days	1½–3
Al–4% Cu	>1 week	18–30

Furthermore, etched Al–7% Mg will crack in completely deaerated 3% NaCl solution. This surprising result shows that when the metal carries only the thin room temperature air-formed film, corrosion can proceed without the presence of dissolved oxygen, at least in the early stages.

With regard to the patterns of copper deposition:

(*A*) I would not say that the spots are entirely random on the cold-rolled sample and could be visualized as sitting on the boundaries of elongated grains, although in a less continuous state than on the annealed sample; perhaps knowing the grain size and shape would help here.

(*B*) Is the pattern obtained with the annealed sample independent of heat treatment? Several workers have demonstrated that high purity aluminum can suffer from intense intercrystalline corrosion in hydrochloric acid after a particular heat treatment (usually quenching from a high temperature) and this is ascribed to segregation of impurity atoms such as iron and copper to the grain boundaries. If the annealed sample is in such a condition, an alternative explanation of the copper deposition along grain boundaries could be that the mixed oxide above such regions has a better electronic conductivity than the more pure alumina over the grain interiors and will therefore be more likely to function as a cathode.

It would be interesting to know whether similar patterns are obtained with no applied current and also with higher current densities than those mentioned.

Finally, I think the authors will agree that the patterns they obtain and the conclusions they draw apply mainly to surfaces carrying only a very thin film and that, if both samples had been tested as-received, in other words, with a high temperature formed film, there would have been much less difference in behavior.

M. J. PRYOR AND D. S. KEIR: We thank Dr. Farmery for his interesting discussion and suggestions. It is, of course, implicit that one must consider the characteristics of oxide-covered aluminum in neutral solutions containing dissolved air, rather than those of the metal itself. We agree that the so-called "weak spots" in the air-formed film will probably constitute preferential sites not only for electron migration but also for anion migration. However, it is not necessarily true that impurity atoms in the metal must decrease the electronic resistance of thin oxide films. Very thin oxide films of up to about 50 Å on most metals will contain very substantial quantities of excess metal ions and therefore will show a high degree of *n* type semiconduction irrespective of whether the bulk oxide exhibits semiconduction of the *n* or the *p* types. Whether foreign atoms present in the metal will further enhance the conductivity of thin oxide films will depend among other things on whether they may be easily substituted in the oxide lattice. This may be achieved only if the cation is of similar size to that of the aluminum ion in the oxide lattice. Furthermore, the effect of small quantities of impurity atoms might well be masked by the larger quantities of excess metal ions in very thin oxide films.

It would appear more logical to attribute the greater electronic resistance of thicker thermally produced oxide film to the fact that the number of *n* type defects (due to

[17] Fulmer Research Institute, Stoke Poges, Bucks., England.

[18] H. K. FARMERY AND U. R. EVANS, In press.

excess aluminum ions in the oxide lattice) will decrease with increasing distance from the metal/oxide interface. Therefore, the outer portions of the thermal films should be much less defective in nature and should exhibit much higher electronic resistances. It is of interest to point out that in fairly thick films of Cu_2O (which exhibits p type semiconduction in the bulk oxide) there will be a fairly well defined p-n junction some 50–100 Å from the oxide/metal interface.

With regard to the patterns of copper deposition on the cold-rolled aluminum, it is possible that a case could be made out for grain boundary deposition. However, if this is assumed then it must also be considered that the deposition is much less continuous than on the annealed specimens. We believe that the pattern of copper deposition on annealed aluminum is not markedly sensitive to annealing treatment. Whereas it has been postulated that the distribution of impurity atoms in aluminum is affected by heat treatment, we believe, for the reasons stated above, that the impurity atoms have rather little effect on the conductivity of thin aluminum oxide films. Such impurity atom effects might be more logically anticipated on the thicker thermal films where the effect of metal excess defects should be smaller.

Similar copper deposition patterns may be obtained with no applied current. However, as pointed out in the article, more general conduction of electrons occurs at higher current densities of around 20 $\mu a/cm^2$.

In conclusion, the results described are specific for aluminum carrying thin air-formed films (approximately 50 Å thick). With thicker thermal films we suspect somewhat different results would be obtained and that the problem would be greatly complicated, particularly on ferrous materials by the formation of multilayer scales.

THE ELECTROCHEMICAL BEHAVIOR, INCLUDING HYDROGEN OVERVOLTAGE, OF IRON IN ACID ENVIRONMENTS

Milton Stern (pp. 609–616)

J. O'M. Bockris[19]: I am most glad to have read Dr. Stern's stimulating paper. His approach is exceedingly clear and we have waited a long time for the kind of data which he has been measuring.

The pre-electrolysis carried out in the NaCl-HCl solution was only at 15 μa for 24 hr. It is, in my experience, rather better to carry out pre-electrolysis of such solutions at a current density corresponding to the highest potential which one is going to measure during the course of the work. Capillary active substances are then given to have the best possible opportunity to deposit.

It is quite easy to develop an expression for the corrosion rate in the absence of surface films and I believe that the one expression recently developed[20] would be applicable with little modification to most of Dr. Stern's results.

I agree strongly with Dr. Stern's remarks on the importance of concentration overpotential. It is, however, possible to stay away from this troublesome interference if one calculates that the actual current densities measured are always less than about one tenth of the limiting current densities for the species involved. An upper limit for i_L can always be calculated with some approximate appropriate value of δ, the diffusion layer thickness.

Regarding the mechanism of the hydrogen discharge reaction after the limiting current for the discharge process for hydroxonium ions has been reached, it is not so much that the dissociation of water is too low (which it is) but that it is too *slow*. It would be possible to have water dissociating near to the cathode and giving rise to protons, which then, after hydration, discharge, even though the equilibrium dissociation of water is very low. This is not the case as was shown by the calculations carried out by Watson.[21]

Milton Stern: We were well aware of the careful work of Professor Bockris and his associates concerning solution purification and pre-electrolysis. However, our purpose was to study the relations which exist between hydrogen overvoltage and the corrosion behavior of iron. Thus our system, of necessity, contained corrosion products. For many of the alloys studied, the corrosion products in solution undoubtedly played a significant role in determining the overvoltage behavior. Our experiments showed that cathodic polarization did not appreciably affect the corrosion potential after the applied current was stopped. The electrode rapidly assumed its initial steady-state potential. This was interpreted as an indication that deposition of capillary active substances during cathodic polarization played an insignificant role.

It is true that one may eliminate concentration polarization interference by maintaining current densities which are less than about one tenth the limiting diffusion current density. However, this in itself does not guarantee that a real Tafel slope will be observed. For a corroding electrode, it is necessary that one apply a current density many times greater than the corrosion current density in order to observe Tafel behavior. Thus the corrosion current density must be at least one hundredth of the limiting diffusion current density to permit an experimental determination of the constants β and i_o.

The clarification by Professor Bockris of the mechanism of hydrogen discharge at high current densities is sincerely appreciated. The concepts which he has presented in his many publications stimulated the approach taken in this investigation. Application of the principles presented in his most recent book will lead undoubtedly to marked advances in the understanding of corrosion mechanisms, polarography, and electrodeposition phenomena.

A. J. deBethune[22]: Referring to the diagram, how is the corrosion current $I_{corr.}$ determined without a knowledge of the anodic polarization curve?

Milton Stern: The answer to the question by Professor deBethune is adequately presented by equation (VIII) and its associated discussion on page 613 of the original paper. However, a general discussion of the method may prove more satisfactory. When a metal corrodes electrochemically, the total rate of all the reduction reactions which occur must equal the total rate of all the oxidation

[19] John Harrison Lab. of Chemistry, University of Pennsylvania, Philadelphia 4, Pa.

[20] J. O'M. Bockris, "Modern Aspects of Electrochemistry," Chapter IV, Academic Press, New York (1954).

[21] Watson, Thesis, London (1951).

[22] Boston College, Chestnut Hill 67, Mass.

reactions. For iron corroding in an acid, two electrochemical oxidation-reduction systems are operative. The first is the hydrogen ion–hydrogen gas system, while the second is the iron (metal)–iron (ferrous) system. The possible oxidation reactions are (*A*) Fe (metal) $\rightarrow Fe^{++} + 2e$ and (*B*) $H_2 \rightarrow 2H^+ + 2e$. The possible reduction reactions are (*C*) $Fe^{++} + 2e \rightarrow$ Fe (metal) and (*D*) $2H^+ + 2e \rightarrow H_2$.

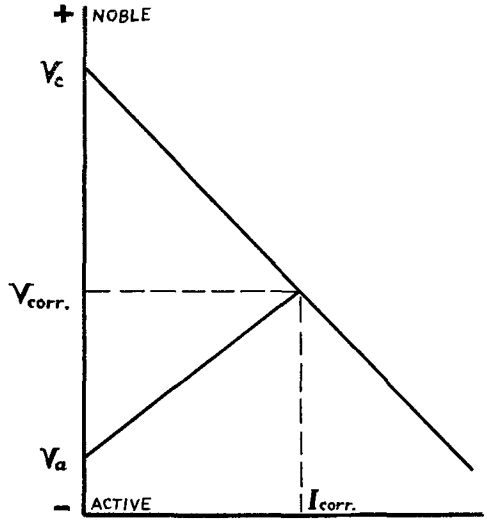

$f(I)$

At the corrosion potential, the sum of the rates *A* and *B* equals the sum of the rates of *C* and *D*. Since the corrosion potential is not close to the equilibrium potentials of either of the oxidation-reduction systems, reactions *B* and *C* proceed at negligible rates. Therefore, the total rate of reduction of hydrogen ions (reaction *D*) equals the total rate of oxidation of iron (reaction *A*). By definition, the corrosion rate is equal to the rate at which reaction *A* proceeds. Therefore, one may determine the corrosion rate by determining the rate of reduction of hydrogen ions at the corrosion potential. The Tafel constants β and i_o describe the rate of reduction of hydrogen ions at any potential in accordance with equation (VI) of the original paper.

$$\eta_a = -\beta \log \frac{i_{\text{reduction}}}{i_o}$$

If β, i_o, and $\eta_{\text{corr.}}$ are known, $i_{\text{reduction}}$ may be calculated. As stated above, this is equivalent to the corrosion rate.

ELECTRODEPOSITION OF TITANIUM ON BASE METALS

M. E. Sibert and M. A. Steinberg (pp. 641–647)

MORRIS EISENBERG[23]: 1. Did you determine the porosity of the titanium coating on steel?

2. You stated that as a result of the high temperature a TiC-layer formed between the steel base or coating. Wouldn't this cause brittleness in the substrata with a resulting poor adhesion? Was the adhesion of the coating measured?

M. E. SIBERT AND M. A. STEINBERG: 1. No absolute porosity determinations were made. Corrosion testing in HCl, H_2SO_4, HNO_3, and NaCl solution indicated that the coatings were essentially nonporous for practical purposes. Some surface porosity does exist, but in no case was this metallographically observed to be continuous through the coating to the base metal.

2. In the case of deposits applied to mild steel, a layer which is probably a Ti-C alloy is formed between base metal and the coating. Adhesion was excellent on as-deposited specimens in terms of resistance to peeling or flaking during cutting and grinding operations. Adhesion of worked coatings was not as satisfactory. This property was not measured quantitatively.

LEO GOLDENBERG[24]: The authors have presented a fine contribution to the knowledge of titanium deposition from a fused salt bath. I was particularly impressed with the description of the properties which the titanium plate was found to possess. At the same time I was somewhat disappointed that the bibliography did not include the citation of *Industrial and Engineering Chemistry*.[25] The similarity of the author's plate to what I had reported there is striking.

However, there are some features of the article about which I am curious. From a comparison of the amount of titanium plated to the number of ampere hours for each run as noted in Table I of the article under discussion, I have calculated a cathode current efficiency of less than 10%. Is this correct? How much, if any, metallic titanium is precipitated in the electrolyte as powder? At what point does the build-up of alkali metal fluorides interfere with cell operation? How stable is the K_2TiF_6 at plating temperatures in excess of 800°C? It would appear that any instability would add to the build-up of alkali metal fluorides in the electrolyte. What was the composition of the gaseous materials leaving the electrolyte during the plating operation?

M. E. SIBERT AND M. A. STEINBERG: Current efficiency based on the plate alone is only 5–15%. Over-all current efficiency including adhering titanium powder amounts to 40–60%. In this study no effort was made to avoid deposition of some powder. The powder is not precipitated in the electrolyte but deposits as an adherent mass after 0.002–0.003 in. of plate has been deposited.

The melt is operated satisfactorily with F^- contents up to 35%. At least 6–8 K_2TiF_6 charges (16 wt %) may be made before this occurs.

The K_2TiF_6 is increasingly unstable with temperature although dilution with NaCl and fluorides minimizes the loss of TiF_4. At 850°C with no current, the loss figure is <10% of initially charged Ti/hr. This figure is reduced considerably on application of a current and as fluoride concentration is built up.

Composition of the effluent gas during plating is approximately 1% CO, <0.5% CO_2, 20% Cl_2, and the balance argon.

[23] Stanford Research Institute, Stanford, Calif.

[24] 1005 Merrimac Drive, Silver Spring, Md.

[25] L. GOLDENBERG, *Ind. Eng. Chem.*, **46**, 13A (1954).

INFLUENCE OF THE K ABSORPTION EDGES OF CADMIUM AND SILVER ON THE X-RAY DIFFRACTION PATTERNS OF SOME CADMIUM COMPOUNDS

R. J. Robinson and F. Schossberger (pp. 685-686)

W. G. BURGERS[26]: In connection with the interesting results of their paper, it may be of interest to the authors that a similar "shifting-out" of a narrow spectral band due to the closeness of the K absorption edges of silver in the film emulsion and the substance matter of the specimen (in this case tin) was observed by Arlman and Kronig[27] in an investigation of diffuse x-ray reflections of a single crystal of tin.

[26] Laboratorium voor Physische Chemie, Technische Hogeschool, Julianalaan 136, Delft, Netherlands.

[27] J. J. ARLMAN AND R. KRONIG, *Physica*, **10**, 795 (1943).

FUTURE MEETINGS OF The Electrochemical Society

Cleveland, September 30, October 1, 2, 3, and 4, 1956

Headquarters at the Statler Hotel

Sessions will be scheduled on

Batteries, Corrosion, Electrodeposition, Electrothermics and Metallurgy, Theoretical Electrochemistry (joint with Electrodeposition), and Theoretical Electrochemistry

★ ★ ★

Washington, D. C, May 12, 13, 14, 15, and 16, 1957

Headquarters at the Statler Hotel

★ ★ ★

Buffalo, October 6, 7, 8, 9, and 10, 1957

Headquarters at the Statler Hotel

★ ★ ★

New York, April 27, 28, 29, 30, and May 1, 1958

Headquarters at the Statler Hotel

★ ★ ★

Ottawa, September 28, 29, 30, October 1, and 2, 1958

Headquarters at the Chateau Laurier

★ ★ ★

Papers are now being solicited for the meeting to be held in Cleveland. Triplicate copies of each abstract (*not exceeding 75 words in length*) are due at the Secretary's office, 216 West 102nd Street, New York 25, N. Y., *not later than June 15, 1956* in order to be included in the program. *Please indicate on abstract for which Division's symposium the paper is to be scheduled.* Complete manuscripts should be sent in triplicate to the Managing Editor of the JOURNAL at the same address.

The Nature of the Film Formed on Copper during Electropolishing

E. C. Williams and Marjorie A. Barrett

Metals Division Research Department, Imperial Chemical Industries Ltd., Kynoch Works, Birmingham, England

ABSTRACT

The thin film shown by Hoar and Farthing to exist on the surface of copper during electropolishing in orthophosphoric acid has been found, by electron diffraction methods, to be composed of a phosphate of copper. This evidence would appear to confirm the basic assumption of Elmore's theory of electropolishing of a limit to the solubility of copper in the boundary layer of electrolyte. Since the film is soluble in phosphoric acid in the absence of an applied potential, this limit is attributed to a decrease in hydrogen ion concentration at the anode surface during polishing.

Introduction

Elmore's theory (1) of the electropolishing of copper in aqueous solutions of orthophosphoric acid rests on the basic assumption that there is a limit to the solubility of the phosphate of the metal in this acid. The theory then develops with the argument that, because of this limit, concentration of copper ions in the electrolyte at the anode surface increases with current density up to a maximum value. Dissolution continues beyond this point only to the extent allowed by diffusion of copper ions into the bulk of the electrolyte from the boundary layer, and the rate of such diffusion is greatest at those parts of the surface where there are asperities and where the local current density is highest. Investigations by Edwards (2) have confirmed that the polishing, or smoothing action of anodic dissolution involves a diffusion control mechanism. Edwards, however, objects to Elmore's basic assumption for the reason, among others, that there is no well-defined limit to the amount of copper that can be dissolved anodically in phosphoric acid; he considers that solubility is governed by the availability of phosphate ions to accept the metal into solution in the form of an unspecified complex. According to this hypothesis the diffusion control mechanism refers to the migration of phosphate ions toward the anode rather than of copper ions in the opposite direction.

The purpose of the present communication is to report the identification by electron diffraction of a film of copper phosphate on the surface of electropolished copper, and to adduce it as evidence in favor of Elmore's theory. The existence of a thin, solid film on the surface of copper as it is being electropolished, and the subsequent disappearance of the film on switching off the current while a specimen is left immersed in the acid has been inferred by Hoar and Farthing (3) from the results of their mercury-drop experiment.

Jacquet and Jean (4) have evidence that copper surfaces after electropolishing in orthophosphoric acid are contaminated by traces of a compound containing phosphorus. Allen (5) examined electropolished copper surfaces by means of the cathodic reduction method and concluded that freshly prepared surfaces washed in distilled water and ethyl alcohol were contaminated with a substance which was not cuprous oxide and which he suggested was a phosphate. He found no evidence of contamination when specimens were washed in a 10% solution of orthophosphoric acid in water. Batashev and Nikitin (6) determined the composition of the electrolyte at different stages of electropolishing of copper in orthophosphoric acid, their results indicating the occurrence of secondary and tertiary phosphates of copper in solution.

Experimental Procedure

Small, rectangular-shaped specimens, approximately 2 cm x 3 cm and 3 mm thick, of annealed, oxygen-free, high-conductivity copper were prepared by mechanical polishing of one face, followed by preliminary electropolishing to remove the distorted and abrasive-contaminated surface layer. The apparatus for electropolishing consisted of two plates of copper approximately 3 cm^2, held horizontally and parallel to each other at a 3.5 cm distance apart and suspended by stiff copper wire from terminals in an insulating base, which rested on the rim of a 500 cc beaker containing the electrolyte. This arrangement permitted rapid withdrawal of the specimen, resting on the lower of the two plates, from the electrolyte. A 50% by-volume solution of orthophosphoric acid in water was used as electrolyte without agitation. Fresh solution was made up for each specimen and cooled to room temperature before use.

The current-voltage characteristic of the cell described above, given in Fig. 1, was determined with a previously electropolished specimen of copper as the anode by raising the voltage across the cell in steps and noting the steady value of the current at each step. Over a small range of voltage, indicated by the shaded region in Fig. 1, oscillations of current and voltage occurred. It is of interest to note that this graph was reproducible for previously electropolished specimens but not for specimens which had been abraded or mechanically polished.

Specimens were polished at various voltages for a standard time of 15 min. At the end of this period, the electrode assembly was quickly raised from the electrolyte and the specimen immediately washed by directing a jet of water from a wash-bottle on to its polished surface. The object of this immediate washing was to prevent any

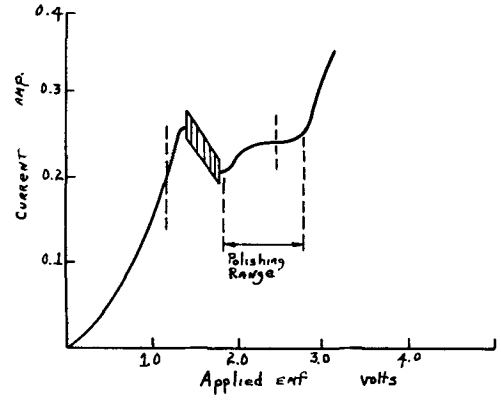

FIG. 1. Current-voltage characteristics of the cell used for electropolishing copper.

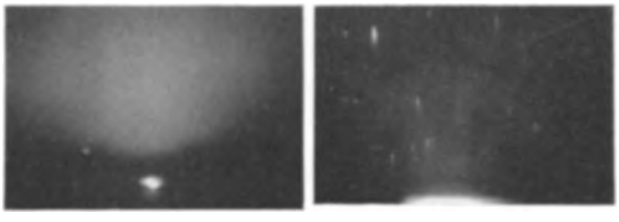

FIG. 2. (*left*) Diffuse scattering pattern from copper electropolished and immediately washed with water.

FIG. 3. (*right*) As Fig. 2, but specimen immersed in fresh solution of orthophosphoric acid after initial washing with water.

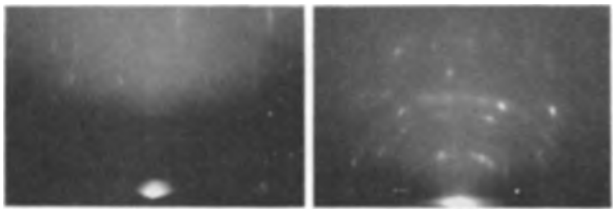

FIG. 4. (*left*) Pattern of cupric phosphate from water-washed specimen after heating to 450°C in vacuo.

FIG. 5. (*right*) Modified pattern of cupric phosphate from specimen washed with white spirits after heating to 900°C in vacuo.

change in surface condition through contact with the electrolyte in the absence of an applied voltage. In later experiments various organic liquids were tried as washing agents. All specimens were given a final washing in water and then rinsed, successively, in ethyl alcohol and acetone. Each specimen was mounted on the stage of an electron diffraction instrument while still wet with acetone, and in this way appreciable oxidation of the metal surface through exposure to the atmosphere was avoided.

RESULTS

Primary Observations

After electropolishing at all voltages in the polishing range, Fig. 1, and immediate washing with water, the surface was covered with an amorphous film as indicated by diffuse scattering of electrons, Fig. 2. Solubility of the film in phosphoric acid in the absence of an applied voltage is indicated by the pattern of Fig. 3 which refers to a specimen which was electropolished, immediately washed with water, and then immersed in a fresh solution of phosphoric acid for 1 min before final washing and drying. Reflections by individual crystals of copper are clearly visible in this pattern. In the case of diffraction by a surface on which there are numerous small and sharp asperities, such reflections appear as rounded spots, but they are elongated into vertical streaks in Fig. 3 because of the smoothness of the electropolished surface and the consequent restriction on the penetration of the diffracting crystals by the incident beam.

It is sometimes possible to crystallize amorphous substances by heating; this method was applied in the present instance in order to identify the film. A specimen which had been electropolished at point A of Fig. 1 and immediately washed with water was mounted on a hot stage so that it could be heated in the vacuum of the electron diffraction instrument. The temperature of the specimen was raised gradually, and the diffraction pattern kept under continuous observation. At 450°C a pattern of well-defined rings appeared, Fig. 4. The corresponding lattice spacings are in good agreement with those of cupric phosphate filed in the A.S.T.M. x-ray diffraction index. Lattice spacings and relative intensities are compared in Table I. The A.S.T.M. index attaches no formula to this pattern which differs in many respects from patterns for various basic and hydrated forms of cupric phosphate, e.g., $Cu_3(PO_4)_2 \cdot 3H_2O$.

In Fig. 4 there is evidence of diffraction by the underlying metal in the form of a few streaks similar to those in Fig. 3. No such streaks were observed for any specimen having an amorphous film which can be assumed, therefore, to have been of sufficient thickness to obscure the metal from the incident beam. The fact that diffraction was observed after crystallization but not before may be explained by granulation of the film, the metal being exposed in between the granules.

Since the amorphous film prevents diffraction by the metal, its thickness lies in a range with a lower limit of the order of 30Å. This figure is deduced from the glancing angle of the incident beam to the surface, which was approximately 0.5°, on the assumption that the surface is perfectly plane and smooth and that the thickness of film penetrated by a 50 kv electron beam without appreciable loss of energy through inelastic scattering is 1,000 Å. There are no means of estimating the upper limit which, however, must be below about 250 Å because, at this value, some effect on the optical reflectivity of the surface would be visible.

Further Experiments

The above results can be considered as establishing the structure and identity of a film on the surface of copper during electropolishing only if the assumption is correct that washing a specimen with water immediately on removal from the electrolyte preserves the surface condition unchanged. Doubt was cast on the validity of this assumption when it was observed that some specimens were stained with a bluish-white substance after washing and these also gave the halo diffraction pattern of Fig. 2.

TABLE I. *Comparison of diffraction data*

Cupric phosphate A.S.T.M. Card 1-0897		Water-washed specimen heated to 500°C		White spirits-washed specimen heated to 900°C		Unidentified pattern from etched specimen	
d, Å	I/I_1	*d*, Å	I/I_1	*d*, Å	I/I_1	*d*, Å	I/I_1
4.15	32	4.20	w	4.17	m		
3.76	32	3.90	vw			3.72	w
3.10	32	3.16	s	3.16	s	3.24	s
2.96	100	2.95	ms				
2.80	70						
2.69	8					2.72	s
2.58	60	2.56	ms	2.59	w		
2.42	40						
2.18	16	2.19	ms			2.29	s
2.06	32	2.09	mw				
1.98	24	1.91	mw	1.91	s	1.94	s
1.82	20	1.83	w			1.90	w
1.74	4	1.72	w			1.75	vw
1.69	8	1.67	w			1.71	m
1.65	16						
1.62	4	1.59	mw	1.62	s	1.62	mw
1.59	8	1.56	mw	1.58	m		
1.46	32	1.45	w			1.47	vw
1.44	32						
1.40	16	1.36	w	1.36	w	1.41	vw
1.31	8	1.30	w			1.30	w
1.25	4	1.24	w	1.23	m		
1.18	4	1.17	vw	1.18		1.20	vw
1.15	4	1.10	vw	1.10	m		
1.12	4	1.07	vw	1.04	w	1.09	w

Note: w = weak, m = medium, s = strong, mw = medium to weak, ms = medium to strong, vw = very weak.

Although it was found that staining could always be avoided by washing away the electrolyte adhering to the surface as rapidly as possible, the amorphous film on unstained specimens might still have been formed as a result of subsequent processes and not at all during electropolishing. In order to resolve this uncertainty ethyl alcohol, acetone, and white spirits or mineral spirits (a light petroleum distillate) were substituted for water in the initial washing.

Washing in either alcohol or acetone caused precipitation of a flocculent bluish-white substance in the liquid adhering to and running off the specimen, as well as pronounced staining of the surface. On washing with white spirits no precipitation or staining occurred, but the surface was covered with the amorphous film. This precipitate was probably copper phosphate of which the trihydrate, at least, is known to be insoluble in water and in alcohol. Precipitation on washing with alcohol or acetone is explained by the fact that these two liquids are only partially miscible with water, and on admixture with an aqueous solution have the effect of throwing out of solution any substance which they do not themselves dissolve. Washing with water can have the same effect, although in this case there is ultimately complete miscibility, because it is unlikely that the highly viscous layer of phosphoric acid with copper in solution will be uniformly and instantaneously diluted, and the condition of partial miscibility will obtain initially. White spirits is completely immiscible with water and it is therefore a justifiable assumption that its use for removing the residual electrolyte involves no danger of precipitation.

The experiment of heating on the electron diffraction hot stage in order to crystallize the amorphous film was repeated for a specimen washed with white spirits. The film did not crystallize at 750°C which was the highest temperature that could be attained on the hot stage. A similar specimen maintained for half an hour at 900°C in an evacuated silica tube gave the diffraction pattern of Fig. 5. This differs from the pattern of Fig. 4 as the comparison in Table I indicates, in that some reflections are absent, probably as a result of preferred orientation which is also manifest in the intensification of parts of some of the rings that are visible. There are also spots lying on the rings, some sharp and others diffuse, and arranged in horizontal rows in the manner of cross-grating patterns obtained with single crystals, and they are therefore probably due to one particularly large crystallite. A similar diffraction pattern was obtained by heating water-washed specimens to 900°C *in vacuo*.

These observations constitute strong evidence that the film first shown by Hoar and Farthing (3) to exist on the surface of copper during electropolishing in phosphoric acid is amorphous, and composed of a phosphate of copper. There is the possibility that the film initially consisted of some other substance, an oxide for example, which was transformed to phosphate when the specimen was removed from the solution. The experiments of Batashev and Nikiten (6) indicate, however, that the ultimate product of the anodic reaction, which they found by analysis of the solution, is copper phosphate $Cu(PO_4)_2$. The secondary phosphate $CuHPO_4$ is formed in the first 200 sec of electrolysis and is then converted to the tertiary phosphate. The appearance of this salt in solid form is therefore probable, if conditions are such that its solubility is limited. These conditions are considered later.

The difference between the temperatures of crystallization of films on specimens washed with water and white spirits remains to be explained. It is reasonable to suppose that washing with water, although not necessarily producing a visible stain on a specimen, results in slight precipitation of phosphate onto an existing amorphous film and the precipitated particles might well act as crystallization nuclei and thus lower the temperature for crystallizing the underlying amorphous material. There is possible evidence of such a microcrystalline deposit in two very faint but sharp diffraction rings superimposed on the diffuse scattering pattern of Fig. 2.

Secondary Observations

In the course of this investigation the surface condition of copper after anodic treatment in phosphoric acid at voltages below the polishing range was examined by the methods described above. The results are included here mainly as a matter of interest and for the sake of the record. At lower voltages, such as point B in Fig. 1, etching occurred and specimens gave a diffraction pattern, also recorded in Table I, which could not be identified. Diffraction rings were fairly sharp and of a width commensurate with a crystal size of at least 100 Å linear dimension, but

the substance was not considered to be in the form of a continuous film covering the surface because diffraction rings due to the metal were clearly visible for all specimens. The same diffraction pattern was obtained with specimens of copper which had been etched in a 50% by volume solution of nitric acid in water and also with specimens which had been brightened in a mixture of nitric and sulfuric acids and water in the volume ratios 6:3:1. It would appear, therefore, that the formation of this substance is not dependent on the presence of any particular anion, and it may be a hitherto unrecognized basic oxide of copper.

A common occurrence in electropolishing copper is the formation during the first few minutes of a visible, dark film which soon becomes detached and floats away leaving the surface bright. It is then slowly dissolved by the acid. In the present investigation it was observed that the film was formed on abraded or mechanically polished specimens, but never on those which had been previously electropolished. The nature of this film has never been made clear and in the practice of electropolishing it seems to be regarded as an agglomeration of oxide particles and detritus in the worked surface layer of the metal released by anodic dissolution. A transmission diffraction pattern of a piece of this film was identical with the A.S.T.M. pattern of cupric phosphate recorded in Table I, and it is suggested that the film is formed under the same conditions as are necessary to the formation of the invisible, amorphous film.

Discussion

The results of this investigation support Elmore's theory of electropolishing, since the presence of a film of phosphate on the anode under the correct conditions of current density for polishing indicates that there must be a limit to the amount of copper that can be taken into solution in the vicinity of the anode. A possible explanation of this limit is suggested by the observation that the film is soluble in phosphoric acid in the absence of an applied voltage. Edwards (2) has, in fact, mentioned that variations in the hydrogen ion concentration of the anolyte with current density may be a factor in polishing, and it can be concluded that a decrease in hydrogen ion concentration at the anode surface to a critical value corresponding to the minimum current density for polishing is responsible for limiting the solubility of copper phosphate.

Once this condition is established, the salt appears as a solid film which, however, does not continue to increase appreciably in thickness except in the case of abraded or mechanically polished specimens and then only in the initial stages, after which the bulk of it floats away leaving an invisible film. This fact suggests that a dynamic equilibrium is set up at the outer boundary of the film between the rate of diffusion of copper ions into the electrolyte, which is governed, as in Elmore's theory, by local variations in current density and the geometric form of the surface, and the rate of arrival of ions through the film from the metal. The crystalline film of phosphate formed initially on mechanically polished copper probably owes its much greater thickness to a slower rate of dissolution in the acid, but no reasons can be suggested for this difference. It may be related to the observed difference in structural state.

The acceptor hypothesis of Edwards has been adopted by Wagner (7) as the basis of a theoretical analysis of the diffusion-control mechanism. Wagner has rejected Elmore's postulate of a solubility limit to the salt of the metal because the wide variation in anode potential at constant current density is not compatible with a constant concentration of metal ions at the anode. This objection cannot be raised if, as is now apparent, the surface is covered with a layer of salt which is probably variable as regards thickness and conductivity. Wagner's analysis is, however, applicable to diffusion of copper ions away from the boundary layer of electrolyte because his particular solution to the general diffusion equation, when the sign of the entire expression is changed from + to − and when a constant is added, satisfies the boundary condition implicit in Elmore's theory equally well. The resulting expression for the concentration gradient normal to the surface is unchanged except in sign, which accords with diffusion of cations rather than of negative "acceptor" ions.

Hoar and Mowatt (8) have suggested that solid films formed on metal anodes cause dissolution of the metal to be uniform over the surface, and to be independent of variations in free energy due to anisotropy and structural discontinuities, because paths for diffusion of ions through the films are randomly distributed. Whereas it may well be true that the mobility of a cation in the film is independent of its original location in the structure of the metal, the present authors consider, in view of the weight of supporting evidence obtained by both Elmore and Edwards, that smoothing of the surface is primarily the result of a diffusion control mechanism operating in the boundary layer of electrolyte. Formation of a film, at least on copper in phosphoric acid, should be regarded as a subsidiary phenomenon which merely signifies the attainment of a solubility limit.

Manuscript received September 7, 1955.

Any discussion of this paper will appear in a Discussion Section to be published in the June 1957 Journal.

References

1. W. C. Elmore, *J. Appl. Phys.*, **10,** 724 (1939).
2. J. Edwards, *This Journal*, **100,** 189*C*, 223*C* (1953).
3. T. P. Hoar and T. W. Farthing, *Nature*, **169,** 324 (1952).
4. P. A. Jacquet and M. Jean, *Compt. rend.* **230,** 1862 (1950); *Rev. Met.*, **48,** 537 (1951).
5. J. A. Allen, *Trans. Faraday Soc.*, **48,** 273 (1952).
6. K. P. Batashev and E. N. Nikitin, *Zhur. Priklad. Khim.*, **23,** 263 (1950).
7. C. Wagner, *This Journal*, **101,** 225 (1954).
8. T. P. Hoar and J. A. S. Mowatt, *Nature*, **165,** 64 (1950).

High Temperature Scaling of Nickel-Manganese Alloys

E. B. Evans, C. A. Phalnikar, and W. M. Baldwin, Jr.

Department of Metallurgical Engineering, Case Institute of Technology, Cleveland, Ohio

ABSTRACT

Scaling rates and scale compositions of nickel-manganese alloys were determined. All the alloys scaled according to the parabolic rate law between 600° and 1000°C. At any given temperature the scaling rate increased at low manganese concentrations, then levelled off at intermediate concentrations, approaching the scaling rate of manganese as the upper limit.

Both an external scale and a subscale were found after scaling, the scale composition being a function of alloy composition and temperature. Above a critical concentration of manganese (15% at 600°C to 60% at 1000°C), the external scale consisted exclusively of manganese oxides; the subscale was MnO. Below this critical concentration, complex external scales consisting of the oxides of both nickel and manganese were found along with subscales of either NiO or a solid solution of the monoxides (MnO + NiO). The spinel oxide ($NiO \cdot Mn_2O_3$) found in most of the complex scales was not associated with improved oxidation resistance. Schematic isothermal sections of the deduced Ni-Mn-O phase diagram were applied as an aid in interpreting the scaling behavior. It is concluded that none of the current theories of scaling of alloys describes the present case.

Scaling Behavior of Nickel

A summary of the crystal structures of nickel and its oxides and nitrides is given in Table I. The nickel-oxygen phase diagram is available (1).

Nickel oxidizes according to the parabolic rate law in the temperature range 600°–1200°C. Scaling constants reported by numerous investigators have been plotted on log K vs. $1/T$ coordinates in Fig. 1. All of the data—except those of the three latest studies (18–20)—cluster along a straight line. The scatter about this line has been attributed to the effect of those impurities most frequently found in commercial nickel, i.e., manganese and iron. Wagner (2) predicts that oxidation rates of metals such as nickel which form metal-deficit oxides are increased by additions of metals of higher valencies such as manganese. The markedly lower scaling constants obtained in the three latest studies cannot be explained with any definiteness. Moore and Lee (20) used preoxidized samples which may have affected their results. Gulbransen and Andrew (18) claim their results differ because the metal was exceptionally pure; however, it seems unusual that nickel of 99.9% purity has ten times the scaling resistance of nickel of 99.8% purity (carbonyl nickel). And, in fact, this is not true if the scaling constant at 750°C determined from their data is included in Fig. 1. (This point was not included in their plot of log K vs. $1/T$.) This point differs from the older work by a factor of two at the most. It may well be that better agreement could be obtained at still higher temperatures. However, it should be noted that Frederick and Cornet (19) also obtained lower rate constants using high purity carbonyl nickel.

Excluding the data of these latest studies, there is little difference in the scaling rate in an atmosphere of pure oxygen (PO_2 = 760 mm Hg) as compared with air (PO_2 = 152 mm Hg) for comparable grades of nickel. By Wagner's theory the scaling rate would be expected to increase with the one-fifth power (approximately) of the partial pressure of oxygen, so that the scaling rate at these two pressures should stand in the ratio of 0.738:1. The pressures used in the three latest investigations (PO_2 = 76, 100, and 152 mm Hg) were also close enough so that this factor is unlikely as a possible explanation for the wide discrepancy obtained in the scaling constants.

Scaling Behavior of Manganese

The known facts summarizing the structures of manganese and its oxides and nitrides are given in Table I.

The scaling behavior of manganese in air has been studied only once to date by Gurnick and Baldwin (40). They report that manganese oxidizes parabolically with time at a given temperature and that the parabolic constant adheres to a straight line in an Arrhenius plot (Fig. 2).

The scale formed on manganese from 400° to 1100°C consisted of an outer gray-black layer with a green interleaf between this layer and the metal, appearing at 600°C. Since x-rays revealed both Mn_3O_4 and MnO in the scale it was assumed that the black layer was Mn_3O_4 and the green layer was MnO. This assumption is particularly weak and a careful x-ray and metallographic study of the nature of the scale (to be described below) proved it to be in error. (This means, too, that Gurnick and Baldwin's discussion of the application of Valensi's theory to the scaling of manganese is in error.)

To study the nature of the scales, some Bureau of Mines electrolytic manganese was polished metallographically and heated in air to temperatures of 500°–1125°C for periods of over 100 hr in most cases. The scales were composed of two major layers.

At the lower temperatures (<825°C) the inner scale was green and x-rayed as MnO; the outer scale was grayish-black and x-rayed as Mn_2O_3 with some Mn_3O_4. Above 825°C the inner layer was black with a green interleaf next to the metal; the outer layer was still gray-black, but both x-rayed as MnO! Fig. 3*a* and 3*b* are photomicrographs of these two types of scales. They show, in addition to the major features just described, some secondary but

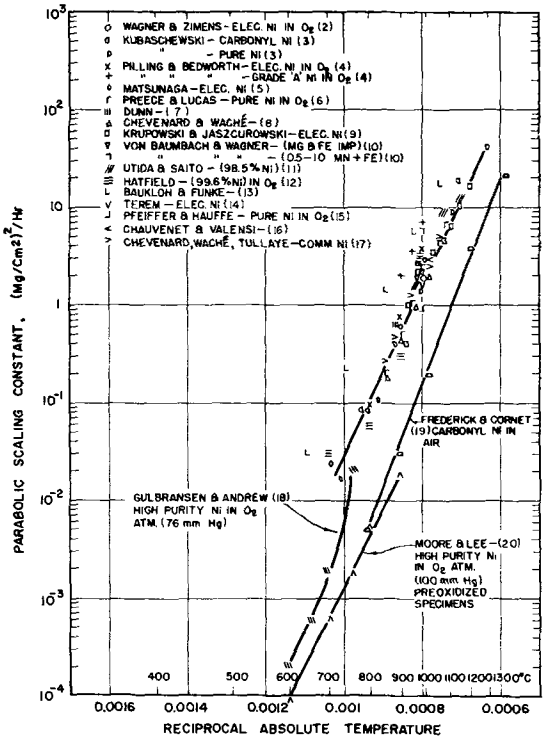

FIG. 1. Oxidation of nickel in air. Relationship between parabolic scaling constant and temperature.

important points of interest. In the outer MnO layer at 1000°C there is a dispersed precipitate that increases in quantity in moving outwardly to the exterior of the scale. It is presumed that this is Mn_3O_4 since some very weak diffraction lines of this phase were picked up in x-rays of the outer layer.[1] The photomicrograph of the scale formed at 1000°C also reveals a veneer outside of the outer MnO layer which glancing x-rays showed to be Mn_3O_4.

The outer Mn_2O_3-Mn_3O_4 layer occupied about 65% of the total scale thickness at low temperatures (600°C), but became relatively thinner as temperature went up until, at the critical temperature of about 825°C, it disappeared. As temperature was further increased, the outer layer of MnO first appeared in relatively thin layers, but increased gradually until at 1125°C it occupied over 80% of the scale thickness. These relationships are shown in Fig. 4. A point of interest is that the Mn_2O_3 layer disappears from the scale at about 825°C whereas its dissociation temperature in air is 940°C.

Since the MnO was found as a double layer above 825°C, the growth mechanism of the two layers was studied at 1000°C by scaling a specimen painted with a marker of zirconium oxide. Visual examination after scaling revealed the marker at the interface between the two MnO layers. This suggests that the outer MnO layer grows by diffusion of manganese ions outward and the inner MnO layer grows by diffusion of oxygen ions inward,[2] similar to the case of cobalt (6).[3]

Thickness measurements were also made of metal before and after scaling in the temperature range 800°–1125°C. Parabolic scaling constants calculated from the metal loss are entered in the Arrhenius plot of reaction rate in Fig. 2. (These constants were obtained by first calculating the loss in weight of metal from the metal thickness before and after scaling. It was assumed that the metal lost was combined with oxygen as oxides whose relative amounts were obtained from Fig. 4. The oxygen pickup could then be estimated and, assuming parabolic behavior, the scaling constants determined.) Fair agreement is found between these values and those obtained from the weight increase measurements of Gurnick and Baldwin, except at 1125°C where it is noted that the over-all scaling constant, K, determined by the metal loss method is greater than the extrapolated value of the weight increase method. This break in the straight line relationship of log K vs. $1/T$ cannot be ascribed to a change in scale composition since MnO is the predominate oxide above 825°C, and presumably the over-all scaling rate is determined by the growth of MnO. The transformation of manganese may be a factor since β-manganese transforms to α-manganese at 1060°–1100°C. Of equal note is the fact that no break in the Arrhenius curve is found at 825°C when the scales did change in composition.

Scaling Behavior of Nickel-Manganese Alloys

Nickel-manganese alloys form a series of solid solutions (26). The scaling behavior of a few nickel-rich alloys has been studied. These alloys oxidize according to the Pilling and Bedworth parabolic law. The scaling constant increases steadily with increasing manganese content up to 10 wt %, the maximum concentration studied (2, 42).

To study the scaling behavior of a much wider range of alloy compositions, six nickel-manganese alloys containing 3.7, 9.1, 20.4, 24.1, 34.8, and 46.6 wt % manganese were prepared. All the alloys were one-phase (alpha) with the exception of the 46.6% manganese alloy which showed a two-phase (alpha + theta) structure. The alloys were made by vacuum induction melting carbonyl nickel and electrolytic manganese in alundum crucibles. The ingots, about 1 in. in diameter and 4 in. long, were cropped and scalped to a $\frac{3}{4}$ in. square cross section, homogenized at 1750°F for 2 hr, hot rolled at 1650°F to $\frac{1}{8}$ in. thickness, scalped to $\frac{1}{16}$ in. thickness, and cold rolled to 0.040 in. strip. The ingots containing 34.8 and 46.6% manganese, respectively, were difficult to work and were processed by cropping, homogenizing at 1750°F for three days in a vacuum of 10^{-5} mm, and scalping (by grinding) to about a $\frac{3}{4}$ in. square bar. Samples approximately $\frac{1}{16}$ in. thick were obtained from the bars; 1-in. squares were cut from the cold rolled strip. Specimens were polished metallo-

[1] This Mn_3O_4 could conceivably appear either by a eutectoidal decomposition of MnO on cooling or by precipitation because of a decreasing solubility of oxygen in MnO as temperature is dropped. The latter cause seems more probable for the following reasons: (*a*) eutectoidal decomposition of MnO would give Mn_3O_4 and manganese; the latter was not detected; and (*b*) the dispersed Mn_3O_4 phase is in heaviest concentration at the exterior of the outer MnO layer where the oxygen content of the MnO is the highest.

[2] The growth mechanism at low temperatures could not be determined by this method since the scale formed was too thin.

[3] Carter and Richardson (41) report that only a single layer of CoO is formed; however, scaling studies by the authors (to be published soon) are in agreement with Preece and Lucas that a double layer of CoO is formed above 900°C.

TABLE I. *Crystal structure and stability of nickel and manganese and their respective oxides and nitrides*

Metal or compound	Crystal structure	Lattice Constant, Å a_o	c_o	Stability range, °C	Remarks
		Pure Metals (1, 21–26)			
Nickel	FCC	3.52		Up to 1455° (m.p.)	
Manganese	α BCC	8.89		Up to 680°	58 atoms to unit cell
	β BCC	6.30		680°–1100°	20 atoms to unit cell
	γ FCT	3.77	3.53	1100°–1138°	
	δ BCC	3.08		1138°–1245° (m.p.)	
		Oxides (6, 7, 10, 21, 27–38)			
NiO	NaCl-cubic	4.17		Up to 1575°	Green, gray, metal-deficit
	Rhombohedral	2.95	(α = 60°4.2′)	Unstable	
MnO	NaCl-cubic	4.43		Up to 1790° (m.p.)	Green, black, metal-deficit
Mn_3O_4	Spinel, tetr.	8.14	9.42	Up to 1580° (m.p.)	Black
Mn_2O_3	Cubic	9.41		Up to 940°	Black
MnO_2	Tetragonal	4.44	2.89	Up to 425°	Black
MnO_3	?			Unstable	Red, deliquescent
Mn_2O_7	?			Unstable at RT	Red, oily
		Nitrides (37, 39)			
Ni_3N	C.P. hexagonal			Up to 380°	
Ni_3N_2	Amorphous			Unstable	
Mn_4N	Cubic	3.80			
Mn_5N_2	Hexagonal			Up to 600°	
Mn_2N	Hexagonal				
Mn_3N_2	Tetragonal				

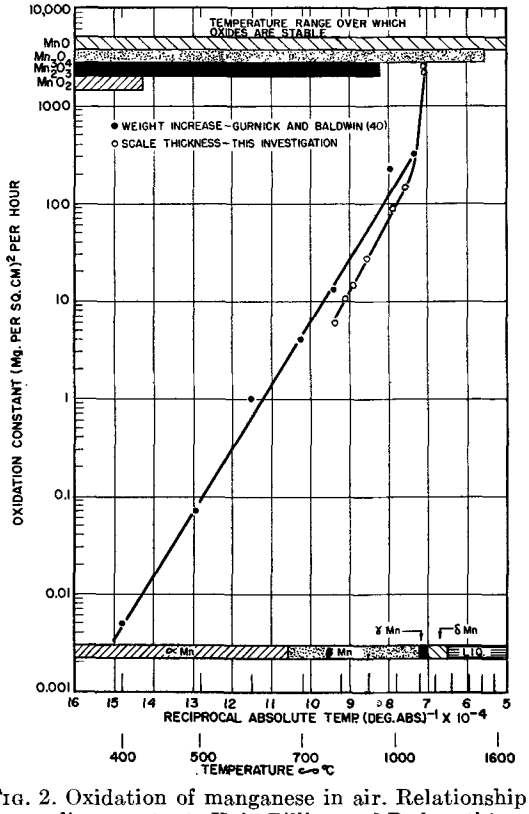

FIG. 2. Oxidation of manganese in air. Relationship between scaling constant, K, in Pilling and Bedworth's equation, $W^2 = Kt$, and temperature.

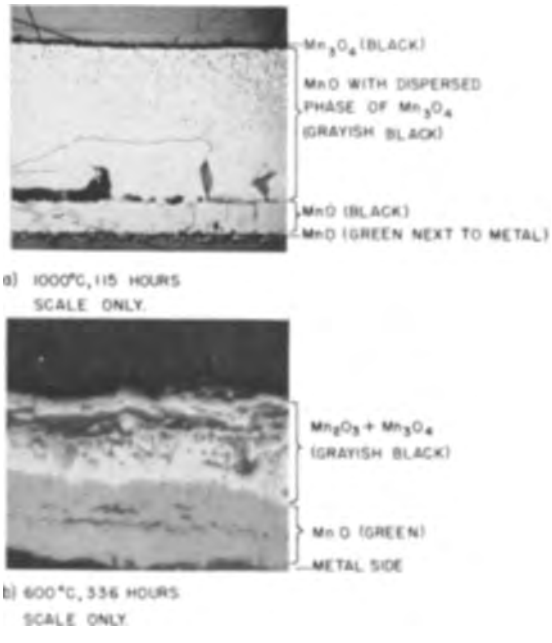

FIG. 3*a* and *b*. Microstructures of the scales formed on electrolytic manganese oxidized in air at the indicated temperatures and times. Unetched. *a*, 50× and *b*, 500× before reduction for publication.

graphically, washed in alcohol, dried, and scaled in air for various times in the temperature range 600°–1100°C. Each specimen was suspended into a resistance-wound vertical tube furnace by a fine nichrome wire from one arm of a magnetically damped chainomatic chemical balance (sensitivity 0.1 mg). Continuous weight measurements were taken from the moment the specimen was suspended and centered in the furnace.

All of the Ni-Mn alloys investigated formed a double-layered external scale. In addition, microscopic examination showed no alloy to be exempt from subscale formation. Wherever possible the external scale layers were

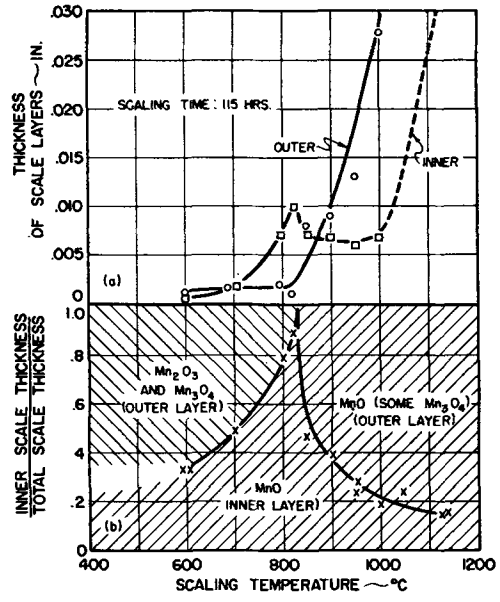

FIG. 4. Effect of temperature on the thickness and composition of the scale layers formed on manganese. The thickness of the individual layers was measured (with micrometers) directly and/or by difference of sample thickness before and after splitting off the layer in question. All scale layers individually x-rayed except those at 600°C.

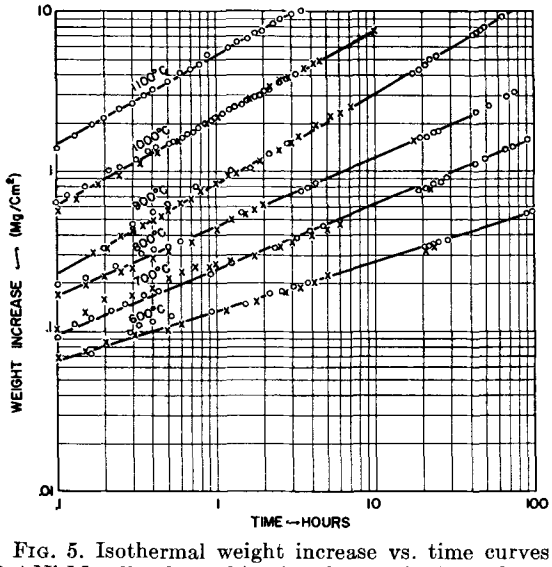

FIG. 5. Isothermal weight increase vs. time curves for 96:4 Ni-Mn alloy heated in air. (Crosses indicate duplicate runs)

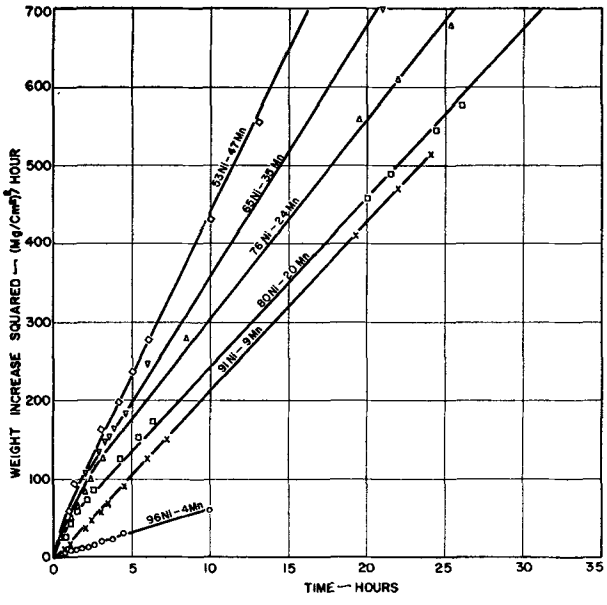

FIG. 6. Weight increase squared vs. time for Ni-Mn alloys heated in air at 1000°C.

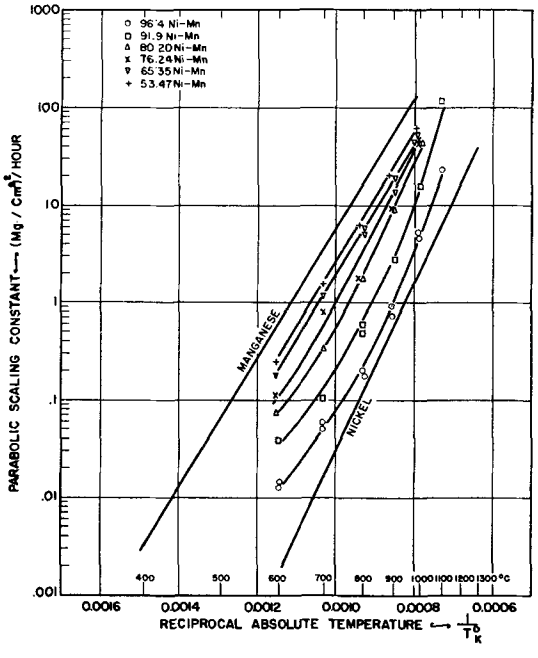

FIG. 7. Arrhenius plot of scaling rate for Ni-Mn alloys heated in air.

separated and x-rayed individually using powder samples. When the layers could not be separated, individual layers could be identified in some instances by x-raying the scale surface before and after grinding off the outer layer; otherwise, the total scale conglomerate was x-rayed using powder samples. To identify the subscale, glancing x-rays were used after the specimen was chipped and scraped clean of its external scale.

Some of the x-ray patterns contained diffuse diffraction lines of an NaCl structure whose lattice parameter was intermediate to that of MnO and NiO, indicating a variable composition of a solid solution of these oxides. Since both NiO and MnO are of the same crystal structure and since their respective cation diameters differ by only 15%, a complete series of solid solutions of these oxides is within the realm of possibility.[4] This point was checked by mixing equal proportions of the pure oxide powders, compacting a pellet, and heating the pellet at 1000°C for 50 hr in a vacuum of 10^{-5} mm mercury. X-rays of the powdered pellet revealed five sharp lines whose "*d*" values were intermediate to the five strongest lines of MnO and NiO,

[4] Rigamonte (43) reports that, when the difference in cation diameters does not exceed 13%, a continuous series of solid solutions is formed between oxides of divalent metals.

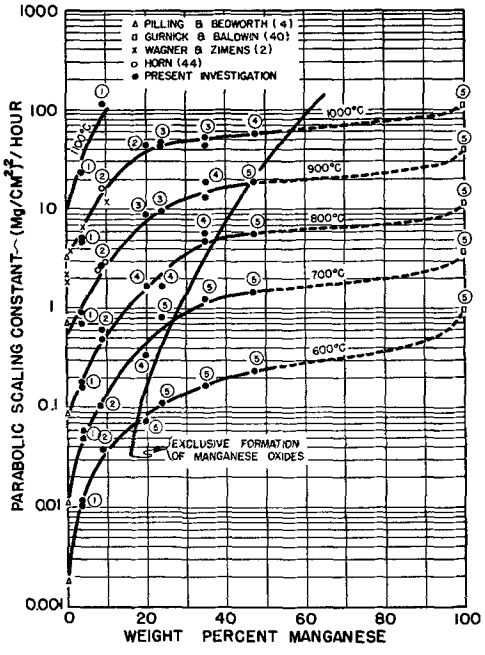

FIG. 8. Parabolic scaling constant vs. alloy composition for Ni-Mn alloys oxidized in air. Encircled numbers indicate scaling patterns (*see* text).

TABLE II. *Scaling patterns of* Ni-Mn *alloys*

Scaling pattern	Subscale	External scale	
		Inner layer	Outer layer(s)
1	NiO	NiO	Spinel
2	NiO	NiO, or A(NiO) and NiO	Spinel and Mn_2O_3[a]
3	A(NiO)	A(NiO) and spinel	Spinel and Mn_3O_4
4	A(MnO)	A(MnO)	Spinel and Mn_3O_4 and Mn_2O_3[a]
5	MnO	MnO[b]	Mn_3O_4 and Mn_2O_3[a]

[a] No Mn_2O_3 above 800°C since this oxide is not stable above this temperature.

[b] No nickel was detected in these scales by a Feigl spot test (45).

Note: Scales denoted "A" were solid solutions of the monoxides MnO and NiO. The oxide noted in parentheses was predominate. In all cases, x-rays of the metal surface after removing the external scale revealed not only the subscale oxide but also a face-centered cubic alloy phase. The composition of this phase was not determined, but from comparison with the *"d"* values of pure nickel and Ni-Mn alloys before oxidation was known to be high in nickel.

close to the MnO side. These oxides quite probably form a complete series of solid solutions.

RESULTS

Kinetics.—Weight increase vs. time data on a log-log scale for different isothermal runs (600°–1100°C) for one of the alloys are shown in Fig. 5.[5] The parabolic scaling law is essentially obeyed at all temperatures for all the alloys, although at the lower temperatures the reaction proceeded somewhat faster at the shorter times than at the

[5] Log-log plots of the data for the other alloys may be obtained from the authors.

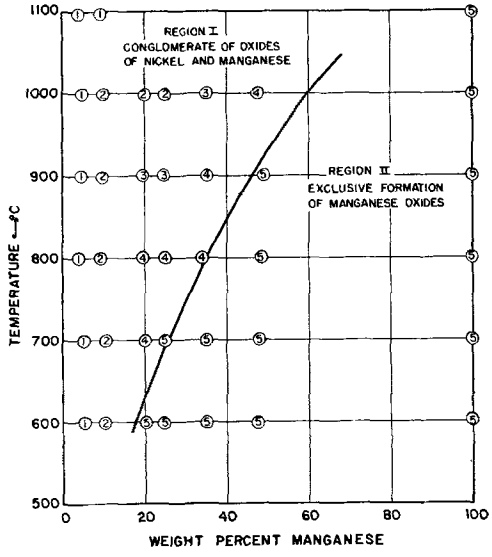

FIG. 9. Composition of scales formed on Ni-Mn alloys heated in air. Scaling patterns are given by encircled numbers.

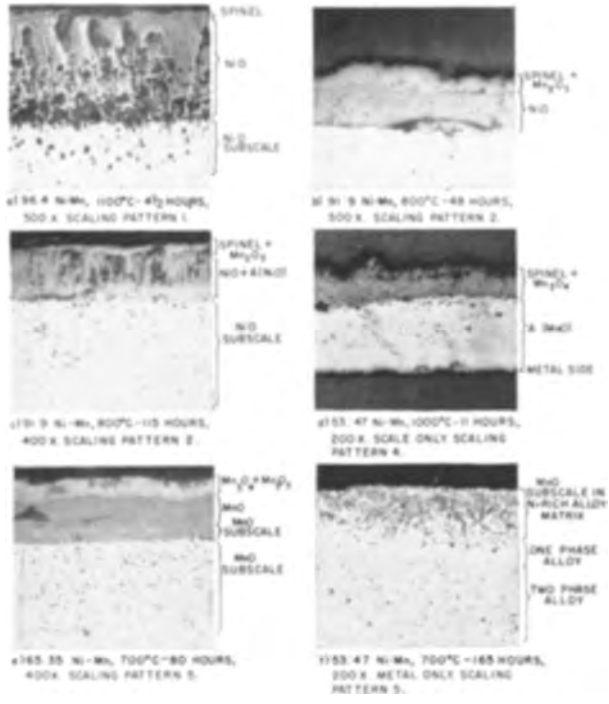

FIG. 10*a–f*. External scales and subscales on Ni-Mn alloys oxidized in air at the indicated temperatures and times. Unetched.

longer times. The parabolic scaling constants were obtained from the curves shown in Fig. 6.

An Arrhenius plot (Fig. 7) shows that the data for the 35 and 47% manganese alloys give straight lines, whereas the data for each of the other alloys follow a slight curve such that the activation energy increases with increasing temperature.

The parabolic scaling rates (log scale) are also plotted as a function of the alloying element (manganese) for constant scaling temperatures in Fig. 8. It is apparent that at each temperature the scaling rate increases con-

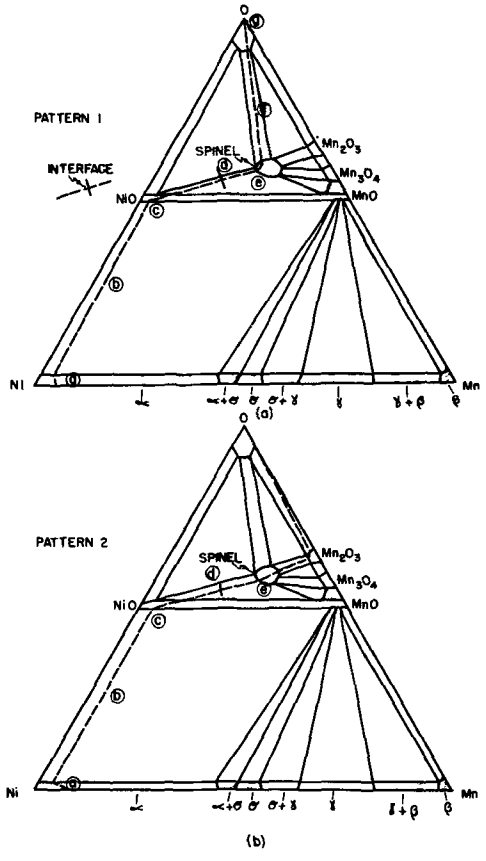

FIG. 11*a–b*. Schematic isothermal sections of the Ni-Mn-O equilibrium diagram showing the scaling patterns of Ni-Mn alloys.

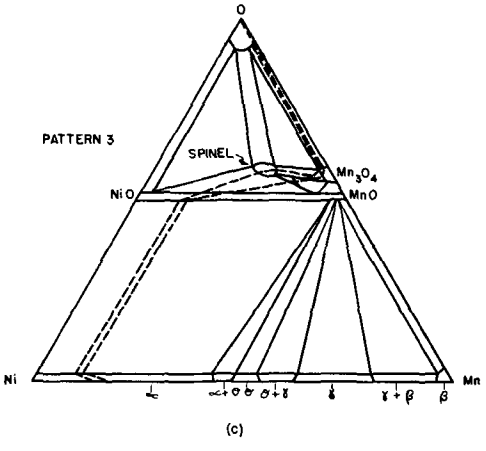

FIG. 11c. Schematic isothermal sections of the Ni-Mn-O equilibrium diagram showing the scaling patterns of Ni-Mn alloys.

tinuously with increasing additions of manganese, approaching the scaling rate of manganese as a limit.

Scale structure.—Scales were formed on the alloys in one of five different patterns listed in Table II, depending on alloy composition and temperature as shown in Fig. 9.[6]

Typical microstructures of most of these patterns are given in Fig. 10.

[6] In some cases the scaling pattern was also dependent on time at the scaling temperature; however, the patterns plotted in Fig. 14 pertain to the longer scaling times where steady state is assumed to hold. A complete record of the description and x-ray identification of the external scale and subscale formed on Ni-Mn alloys is on file at Case Institute of Technology (Doctor's Thesis by E. B. Evans).

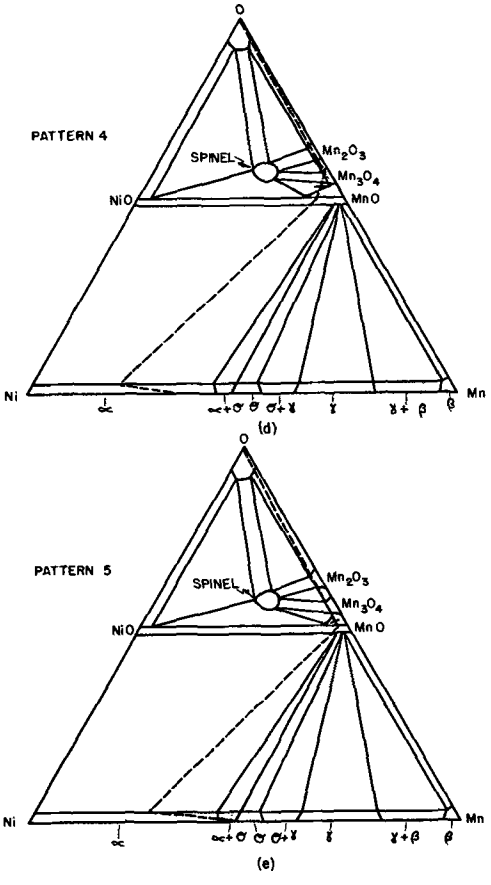

FIG. 11*d* and *e*. Schematic isothermal sections of the Ni-Mn-O equilibrium diagram showing the scaling patterns of Ni-Mn alloys.

DISCUSSION

The scaling patterns can be laid out with a fair degree of certainty in schematic isothermal sections of the ternary Ni-Mn-O phase diagram, Fig. 11, as an aid in visualizing the progressive changes in scaling behavior wrought by alloy composition. The application of phase diagrams to the rationalization of scaling behavior has been discussed in detail by Rhines (46).

The dotted paths shown in Fig. 11 were constructed as to satisfy the demands of the experimentally observed scale structures. (The path must place the compounds found in the various layers in their proper order; it must reveal a progressive oxygen gradient and still be compatible with the topology of the phase diagram.) Furthermore, as Rhines points out, one-phase and two-phase fields in the isothermal sections correspond to scale layers on the specimen, while three-phase fields in the diagrams correspond to interfaces. An exception in the case of the two-phase fields is that these areas correspond to interfaces rather than layers when the path follows a tie-line.

Pattern 1.—As Fig. 9 shows, Pattern 1 is found on relatively nickel-rich alloys only. The path thus starts on the Ni-Mn edge of the ternary diagram near the nickel corner (point *a* in Fig. 11*a*). According to Table II the inner layer

of the external scale is a NiO-rich monoxide. The path thus is drawn to this phase (point *c*) but the fact that a NiO-rich monoxide subscale is found (see Fig. 10*a*) indicates that the path crosses some tie-lines between the alpha phase and the monoxide phase (point *b*). The outer layer of the external scale according to Table II is spinel, hence the path is drawn through this one-phase region to indicate this fact (point *c*). Since the inner and outer layers have a sharp interface, the path between *c* and *e* must follow a tie-line between these two single phases (point *d*). The path then is carried out to the oxygen corner of the diagram (point *g*) along a tie-line between the spinel field and the oxygen field (point *f*) to indicate the sharp interface between the outer layer of spinel and the surrounding air. In some cases at low temperatures no subscale formation was observed although all other features of the pattern were retained.

Pattern 2.—According to Table II, Pattern 2 is similar to Pattern 1 except for the outer layer. Hence the path depicting this pattern, Fig. 11*b*, is the same as the path of Fig. 11*a* up to point *e*. The outer layer of Pattern 2 is given as Mn_2O_3 and spinel in Table II. Whether the Mn_2O_3 and spinel exist as separate layers or as a conglomerate in the outer layer could not be determined because of the thinness and brittleness of the scale layers. If the two oxides were separate layers, the path through the spinel-Mn_2O_3 field would follow a tie-line; otherwise, it would cross tie-lines in this zone. As in the case of Pattern 1, the subscale was not always observed at low temperatures. At 900°C and above, Mn_2O_3 did not appear in the outer layers (nor did it appear in the case of pure manganese) and Pattern 2 became the same as Pattern 1 except that the inner layer was much richer in manganese.

Pattern 3.—This pattern was observed only above 800°C where Mn_2O_3 was not to be found; therefore, the isothermal section was altered so as to exclude this oxide, Fig. 11*c*. Since the subscale consists of A(NiO) in a nickel-rich matrix while the inner scale contains A(NiO) and spinel, the path must cross these two-phase zones. Two choices are open for the path through the outer scale of spinel and Mn_3O_4: (*a*) the path may pass through the spinel zone, then follow a tie-line for some distance in the spinel-Mn_3O_4 zone before bending to the left in this zone, thus crossing the tie-line as shown in the upper path in Fig. 11c; or (*b*) the path may extend through the spinel-MnO-Mn_3O_4 field (which constitutes an interface), then cross the spinel-Mn_3O_4 field as shown in the lower path of Fig. 11*c*.

The latter path seems more likely in that it does not necessitate that the path first follows then diverges from a tie-line in a two-phase zone.

Pattern 3 shows a marked difference from Patterns 1 and 2 in that spinel is found in the inner as well as the outer layer. A feature common to these three patterns is that the inner layer consists of NiO or A(NiO).

Pattern 4.—The likely succession of zones traversed by the path that satisfies the requirements of this pattern is given in Fig. 11*d*. Since the subscale consists of A(MnO) in a matrix of nickel-rich alloy and the inner layer is composed of A(MnO) only, the path must cross this two-phase and one-phase area, respectively. The path through the outer layer(s) poses a problem. Since Mn_3O_4 and Mn_2O_3 with small amounts of spinel were found in the outer scale, more than one layer must be present but which could not be resolved under the microscope. The path drawn in Fig. 11*d* meets this demand in that it crosses a three-phase field denoting a sharp interface between the inner and outer layers, and it also passes through one- and two-phase fields which are compatible with the composition of the outer layers.

Pattern 5.—The only path that is compatible with this scaling pattern is shown in Fig. 11*e*. Here the 47% manganese alloy was chosen to illustrate this scaling behavior since it was the only two-phase alloy investigated and some interesting features are to be noted in the underlying metal, Fig. 10*f*. Between the two-phase alloy ($\alpha + \theta$) and the external scale, two layers were found as can be predicted from the isothermal section: (*a*) an α-layer next to the two-phase alloy matrix, and (*b*) an α-layer containing particles of MnO. Here enrichment of nickel and depletion of manganese in the alloy led to the α-layer between the two-phase MnO-α layer and the two-phase alloy matrix. Since the inner scale contains only MnO while the outer scale contains Mn_3O_4 and Mn_2O_3 (or only Mn_3O_4 above 825°C), the path must cross this one-phase and two-phase field, respectively. It must follow a tie-line between the two to indicate the sharp interface.

Scales formed on the alloys which followed this scaling pattern were similar in composition and structure to the scales formed on pure manganese at corresponding temperatures. The scaling behavior of pure manganese differs from Pattern 5 only in the absence of the subscale.

Patterns 4 and 5 have the common feature that the inner layer is a MnO-rich monoxide.

For all their differences in detail, all the patterns in Fig. 11 have a similar shape: instead of being straight lines from the original alloy composition to the oxygen corner of the ternary diagram they veer first to the nickel-rich side of a direct route and then to the manganese-rich side. This implies that the manganese ion diffuses outwardly at a much higher rate than the nickel ion. When the manganese content of the original alloy is high, the faster outward diffusion of manganese leads to the formation of manganese scales exclusively (Pattern 5). The minimum manganese content of the original alloy necessary for this to occur is drawn in as a solid line in Fig. 9. The fact that it runs as low as 15% at 600°C and as high as 60% at 1000°C indicates that the relative speed of the manganese ion over the nickel ion is greater at low temperatures.[7]

The scaling rate as a function of alloy composition has been depicted in Fig. 8 as increasing continuously with increasing manganese content. It should be pointed out, however, that horizontal breaks in the curve may possibly occur at high enough manganese concentrations where a two-phase alloy region is in equilibrium with the external scale, i.e., the two-phase alloy region immediately adjacent to the external scale. Thermodynamically, a two-phase region is a heterogeneous system at equilibrium

[7] A number of analyses have been proposed for predicting the minimum concentration of an alloy constituent necessary for the exclusive formation of its oxide (47, 48), but none of these applies here since they are based on assumptions that are not even closely approached in the present study.

wherein the activity of an element in the alloy is identical in the two phases. If the activity is a measure of the driving force of the oxidation reaction and equilibrium obtains, then the scaling rate and consequently the oxidation products should be the same over a two-phase field. It is not enough to say that this would hold true for alloys which are two-phase at the start of the scaling reaction, for as shown in the case of the 47% manganese alloy the metal surface is so depleted in manganese during the scaling reaction that a one-phase alloy and not a two-phase alloy was in equilibrium with the external scale. In any case, this behavior cannot be established with any definiteness for the case of the Ni-Mn alloys for the following reasons: (*a*) a prohibitive number of alloys would be required to describe the scaling behavior over that range of alloy compositions (say greater than 50% manganese) encompassing the one- and two-phase alloy regions, and (*b*) the expected change in scaling rate in this range is seen to be so small as to be within the realm of experimental error. However, preliminary results with Cu-Cr alloys indicate that the scaling rate is about the same for a number of different alloys lying in the broad two-phase field in this system. Further studies of the dependency of the scaling rate upon alloy composition in the one- and two-phase fields are underway for the case of Ni-Cr and Co-Cr alloys which show a very strong dependence of scaling rate upon alloy composition.

The increase in the scaling rate by small additions of manganese to nickel has also been found with small additions of chromium to nickel (or cobalt). This increase has been explained on the basis that trivalent manganese or chromium dissolves in the metal-deficit NiO (or CoO) and replaces some of the divalent nickel (or cobalt) ions (2), thus providing new cation defects for the diffusion of nickel (or cobalt) ions. Alternately, the rise in scaling constant with manganese additions may be attributed to the relatively greater mobility of the manganese ion over that of the nickel ion, since the inner layer was identified by x-rays as the bivalent monoxide, be it NiO, MnO, or a solid solution of the two. The fact that manganese effects a smaller increase in scaling constant at high temperatures than at low temperatures (see Fig. 8) may be consonant with the deduction noted above that the relative speed of the manganese ion *vis à vis* the nickel ion was not as great at high temperatures as it was at low temperatures. However, it should be pointed out that this alternate mechanism assumes that the same stoichiometry is maintained by the oxides. This assumption may not hold here. In the high temperature scaling of iron, for example, the "FeO" layer may contain as much as 30% trivalent iron ions. In any case, the present evidence is not adequate to distinguish between these two possible mechanisms.

Lastly, it is to be noted that although spinel was found in the scales at certain alloy compositions it did not effect any drop in scaling rate. This finding parallels that of Preece and Lucas (6) and Yearian (49) that spinels do not lead to low scaling rates in the Co-Cr, Fe-Cr and other analogous alloy systems.[8]

[8] The low scaling rate of nichrome has often (but erroneously) been attributed to the presence of spinel (2, 50, 51).

Conclusions

1. Nickel-manganese alloys scaled according to the Pilling and Bedworth parabolic law.

2. At a given temperature the scaling rate of Ni-Mn alloys increased with increasing additions of manganese which would seem to preclude their use as oxidation resistant components.

3. The composition of both the external and subscale found in these alloys was dependent on alloy composition and temperature. Above a critical concentration of manganese, the external scale consisted exclusively of manganese oxides and MnO subscale; below this critical composition complex external scales of the oxides of both nickel and manganese were formed along with a subscale of NiO or a solid solution of monoxides. The critical concentration of manganese was as low as 15% at 600°C, and as high as 60% at 1000°C.

4. The increase in scaling rate as manganese was added to nickel was due to (*a*) the faster mobility of the manganese ion, or (*b*) an increase in lattice defects in the monoxide introduced by manganese. The present evidence was not adequate to distinguish between these two mechanisms.

5. Spinel formation observed in most of the complex scales had no apparent beneficial effect on the scaling resistance.

Acknowledgments

The authors are especially indebted to the Office of Ordnance Research whose sponsorship made this work possible. They also wish to thank C. A. Barrett and F. Karpoff who performed some of the tests.

Manuscript received August 15, 1955.

Any discussion of this paper will appear in a Discussion Section to be published in the June 1957 JOURNAL.

REFERENCES

1. "Metals Handbook," Edited by Taylor Lyman, p. 1231, American Society for Metals, Cleveland, (1948).
2. C. WAGNER AND K. E. ZIMENS, *Acta Chem. Scand.*, **1**, 547 (1947).
3. O. KUBASCHEWSKI AND O. VON GOLDBECK, *Z. Metallkunde*, **39**, 158 (1948).
4. N. B. PILLING AND R. E. BEDWORTH, *J. Inst. Metals*, **29**, 529 (1923).
5. Y. MATSUNAGA, *Japan Nickel Rev.*, **1**, 347 (1933).
6. A. PREECE AND G. LUCAS, *J. Inst. Metals*, **81**, 219 (1952).
7. J. S. DUNN AND F. J. WILKINS, "The Oxidation of Non-Ferrous Metals," Section 4, p. 78, Review of Oxidation and Scaling of Heated Solid Metals, Dept. of Scientific and Industrial Research, London, His Majesty's Stationery Office (1935).
8. P. CHEVENARD AND X. WACHÉ, *Rev. Met.*, **45**, 121 (1948).
9. A. KRUPOWSKI AND J. JASCZUROWSKI, *ibid.*, **33**, 646 (1936).
10. H. H. VON BAUMBACH AND C. WAGNER, *Z. phys. Chem.*, **B24**, 59 (1934).
11. Y. UTIDA AND M. SAITO, *Sci. Repts., Tohoku Imp. Univ.*, **13**, 391 (1925).
12. W. H. HATFIELD, *J. Iron Steel Inst.*, **115**, 483 (1927).
13. W. BAUKLOH AND P. FUNKE, *Korrosion u. Metallschultz*, **18**, 126 (1942).
14. H. N. TEREM, *Bull. Soc. Chim.*, **6**, 664 (1939).
15. H. PFEIFFER AND K. HAUFFE, *Z. Metallkunde*, **43**, 364 (1952).
16. G. CHAUVENET AND G. VALENSI, *Compt. rend.*, **205**, 317 (1937).

17. P. Chevenard, X. Waché, and R. De la Tullaye, *Bull. Soc. Chim.*, **11**, 41 (1944).
18. E. A. Gulbransen and K. F. Andrew, *This Journal*, **101**, 128 (1954).
19. S. F. Frederick and I. Cornet, *ibid.*, **102**, 285 (1955).
20. W. J. Moore and J. K. Lee, *Trans. Faraday Soc.*, **48**, 916 (1952).
21. C. D. Hodgman, ed., "Handbook of Chemistry and Physics," p. 370, Chemical Rubber Publish Co., Cleveland (1948).
22. B. F. Naylor, *J. Chem. Phys.*, **13**, 329 (1945).
23. Z. S. Basinski and J. W. Christian, *Proc. Roy Soc.*, **223**, 554 (1954).
24. D. Schlain and J. D. Prater, *J. (and Trans.) Electrochem. Soc.*, **94**, 58 (1948).
25. E. V. Potter, H. C. Lakens, and R. W. Huber, *Trans. Am. Inst. Mining Met. Engrs.*, **185**, 399 (1949).
26. W. Koster and W. Rauscher, *Z. Metallkunde*, **39**, 178 (1948).
27. S. Miyake, *Sci. Papers Inst. Phys. Chem. Research (Tokyo)*, **31**, 161 (1937).
28. P. W. Selwood, "Valence Inductivity and Catalytic Action," Pittsburgh International Conference on Surface Reactions, Corrosion Publishing Co., Pittsburgh, p. 49 (1948).
29. Y. Shimomura and Z. Nishiyama, *Mem. Inst. Sci. Ind. Research Osaka Univ.*, **6**, 30 (1948).
30. H. P. Rooksby, *Acta Cryst.*, **1**, 226 (1948).
31. M. J. Robin, *Compt. rend.*, **235**, 1301 (1952).
32. R. W. G. Wyckoff, "Crystal Structures," p. 253, Interscience Publishers, Inc., New York (1948).
33. M. LeBlanc and H. Sachse, *Z. Elektrochem.*, **32**, 58 (1926).
34. G. Valensi, *Compt. rend.*, **201**, 523 (1935).
35. R. L. Tichenor, *J. Chem. Phys.*, **19**, 796 (1951).
36. H. W. Foote and E. K. Smith, *J. Am. Chem. Soc.*, **30**, 1344 (1908).
37. C. J. Smithells, "Metals Reference Book," Interscience Publishers, Inc., New York (1955).
38. W. J. Moore, Rept. No. 1, AEC, Contract No. At(11-1)-250, Indiana University, May 1, 1953.
39. O. Kubaschewski and B. E. Hopkins, "Oxidation of Metals and Alloys," Academic Press, Inc., New York (1953).
40. R. S. Gurnick and W. M. Baldwin, Jr., *Trans. Am. Soc. Metals*, **42**, 308 (1950).
41. R. E. Carter and F. D. Richardson, *J. Metals*, **7**, 336 (1955).
42. L. Horn, *Z. Metallkunde*, **38**, 73 (1949).
43. R. Rigamonte, *Gazz. chim. ital.*, **76**, 474 (1946) (ASTIA AD No. 13051).
44. L. Horn, *Z. Metallkunde*, **36**, 142 (1933).
45. F. Feigl, "Spot Tests," p. 141, Elsevier Publishing Co., New York (1954).
46. F. N. Rhines, *Trans. Am. Inst. Mining Met. Engrs.*, **137**, 246 (1940).
47. C. Wagner, *This Journal*, **99**, 369 (1952).
48. L. S. Darken, *Trans. Am. Inst. Mining Met. Engrs.*, **150**, 157 (1942).
49. H. J. Yearian, "Investigations of the Oxidation of Chromium and Nickel-Chromium Steels," Purdue Research Foundation, Summary Technical Report to Office of Naval Research, Contract N7 onr-39419, June 1954.
50. K. Hauffe, "The Mechanism of Oxidation of Metals and Alloys at High Temperatures," in "Progress in Metal Physics," Vol. IV, pp. 71–104, Interscience Publishers, Inc., New York (1953).
51. K. Hauffe, *Z. Metallkunde*, **42**, 34 (1951).

Pitting Corrosion of 18Cr–8Ni Stainless Steel

M. A. Streicher

Engineering Research Laboratory, Engineering Department, E. I. du Pont de Nemours and Co., Inc., Wilmington, Delaware

ABSTRACT

I. Factors controlling pitting corrosion and laboratory methods used for its study are reviewed. An electrolytically accelerated test was developed for investigation of pit initiation. A controlled direct current was passed through a cell whose anode was the stainless steel specimen and whose electrolyte was the pitting solution. The number of pits formed depended on the current density, the steel specimen (composition and surface treatment), and the solution (composition and temperature).

II. The accelerated electrolytic pitting method described in Part I was used to determine the influence of alloying elements added to 18Cr-8Ni stainless steel on pit initiation in sodium chloride and bromide solutions. Reduction in carbon content, increase in nitrogen content of these steels, and alloying additions of molybdenum and silicon increased resistance to pit initiation. Grain boundaries, rather than nonmetallic inclusions, were primary sites of pit initiation during simple immersion or in the electrolytically accelerated test.

I. Development of an Accelerated Pit Initiation Method

Introduction

Pitting may be divided into two distinct steps: (*a*) pit initiation or surface breakdown, and (*b*) pit growth in depth and volume. Although the factors determining pit initiation are largely unknown, pit growth has been described in some detail in the literature.

The intensity of localized attack which leads to growth of deep pits results from several factors. The pit is the

anode, and the unaffected area surrounding the point of penetration is the cathode of a cell whose electrolyte is the corrosive solution. On metals covered by protective films, the surface area available for cathodic reactions is very large compared with that available for the anodic reaction, which takes place at breaks in the film. As a result, the current/unit area of cathode surface remains low, and large areas may be exposed to cathodic reaction accelerators in the solution, e.g., oxidizing agents which depolarize this reaction and thereby stimulate the anodic reaction. Anodic dissolution may also be stimulated by reduction of ferric to ferrous ions at cathodic areas (1).

The anodic current density is high, and enough metal is soon removed to form a depression in the surface, unless corrosion products stifle the reaction. In some cases, oxygen combines with metal ions produced by corrosion to form protective oxide films. However, if there is insufficient oxygen available, or if the oxides formed are not protective, the pit grows. A cavity is soon formed in which oxygen is not easily replenished and is, therefore, soon exhausted. Also, the corrosion current causes any chloride ions present to migrate to the anode (2). These ions tend to destroy the protective qualities of any films which may still be present and will acidify the solution in the pit. The combination of large cathodic and small anodic areas, oxygen exhaustion, chloride accumulation, and acid conditions produces an intensely localized form of attack.

Oxygen plays a dual role by its ability (*a*) to stifle the anodic reaction through film formation, and (*b*) to accelerate the cathodic process by removal of hydrogen and by regenerating ferrous to ferric ions. Both of these effects may be operative at the same time. The over-all result on the corrosion rate depends on whether anodic retardation or cathodic stimulation is dominant (3). For example, in a study of crevice corrosion on straight chromium (17% Cr) stainless steel in sea water (4) the amount of corrosion in the crevice (pit) was directly proportional to the size of the uncorroded (cathodic) area surrounding the crevice. Thus, as long as the amount of oxygen available/unit area of cathode exposed to flowing sea water was constant, the extent of stimulation depended only on the size of the cathodic area. In another investigation (5) pitting of Type 304 stainless steel in sodium chloride solutions exposed to the atmosphere was almost completely suppressed when oxygen was removed. Oxygen was acting as a cathodic stimulant. However, when the oxygen pressure was increased to 60 atm pitting was also retarded, because at this pressure the film-forming properties of oxygen became dominant.

Some Factors Affecting Pitting of Stainless Steels

Crevice conditions are especially severe in sea-water exposures where there is a high concentration of chlorides combined with severe attachment of barnacles and other marine organisms on the metal surfaces. Of all the standard AISI-300 series grades of stainless steels, Type 316 (Table I) is the most resistant, i.e., the addition of 2–3% molybdenum increases the sea-water pitting resistance of 18 Cr-8 Ni steels (6). The beneficial effects of molybdenum additions have also been observed by Smith (7) in his ferric chloride thermal convection test (described below). In addition, Type 302B stainless steel (18Cr-8Ni + 2.5% Si) was found superior in this test to regular 18 Cr-8Ni grades. An 18Cr-8Ni steel to which both silicon and molybdenum had been added, each in amounts of 2–3%, has been described by Riedrich (9). In a comparison of this steel with nickel, Monel, and an 18Cr-8Ni-2 Mo-1 Nb steel, Riedrich's steel showed the best pitting

TABLE I. *Analyses of stainless steels used in pitting tests (per cent by weight)*

Steel, AISI type	Code	Cr	Ni	C	N	Mo	Si	Mn	P	S	Nb	Ti	Cu	Al
304	EX-1	18.22	8.97	0.061			0.58	0.56	0.025	0.011				
304	ER-1	18.23	8.59	0.070			0.56	0.69	0.012	0.003				
304	ER-2	18.45	8.90	0.063			0.58	0.66	0.015	0.008				
304L	FK-4	18.30	11.02	0.020	0.033		0.37	1.06	0.018	0.014				
304L	FK-9	19.12	10.96	0.016	0.12		0.56	1.22	0.022	0.015				
302	GF-2	18.37	8.71	0.10			0.60	0.93	0.019	0.009				
302B	302B	18.79	9.19	0.060			2.49	0.38	0.01	0.012				
302B	302BP	17.30	8.62	0.14			2.71	1.44						
321	FF-7	17.83	9.21	0.061			0.79	1.25	0.028	0.023		0.31		0.041
347	EX-2	18.58	11.27	0.058			0.58	1.76	0.026	0.020	0.87			
347L	FE-6	17.14	11.00	0.016	0.029						0.33			
316	EW-5	17.93	13.50	0.031		2.47	0.31	1.77	0.023	0.006				
316	C-1	17.78	13.22	0.056		2.32	0.71	1.70	0.021	0.009				
316	C-2	17.80	12.52	0.055		2.28	0.58	1.53	0.017	0.005				
316L	FH-3	17.71	11.17	0.020	0.032	2.44								
316L	FH-1	17.85	11.34	0.027	0.13	2.25								
316L + Nb	FN-3	18.62	14.02	0.022	0.028	2.15					0.32			
316 + Si	SP-1	18.05	9.92	0.072	0.062	2.21	2.39	0.61	0.012	0.020			0.08	
316 + Si	SP-2	18.79	9.24	0.039	0.23	2.40	2.50	0.77					0.02	
316 + Si	SP-3	18.60	8.99	0.038	0.059	3.70	2.29	0.86					0.02	

Steel, AISI type	Cr	W	Fe	C	Si	Co	Mn	Cu	V	Mo	P	S	Ni
"Hastelloy" C*	16.38	4.55	5.18	0.06	0.43	1.58	0.58	0.09	0.27	16.77	0.017	0.006	Bal.
"Hastelloy" B	0.24		6.60	0.04	0.11		0.52		0.35	28.22			Bal.

* Nominal analysis.

resistance in solutions of acidified ferric chloride, iodine-alcohol, and mercurous chloride.

Nitrogen may increase the pitting resistance of stainless steels, e.g., a 23Cr-4Ni-0.3N steel showed greater resistance in 20% ferric chloride solution than did standard 18-8 stainless steel (10). It was also found that 0.24% N in 18Cr-8Ni stainless steel increased pitting resistance in ferric chloride solution (11). Nitrogen is 25–30 times more efficient than nickel as an austenitizer. In general, a single-phase austenitic structure is preferred in the 18 Cr-8Ni stainless steels because of its superior mechanical properties and corrosion resistance (8). Thus, it is possible that beneficial effects may be obtained when nitrogen is used as an addition agent, either for its own sake or to offset the ferrite-forming tendencies of other elements, such as silicon and molybdenum which may be added to increase corrosion resistance.

Pit Initiation Studies

Immersion Methods

In laboratory investigations of pitting corrosion the most difficult problem has been that of finding a controllable and reproducible pit initiation test. One of the most successful has been the "square drop" test (12–14) in which it was found that on iron corroding in potassium chloride solutions under oxygen-nitrogen mixtures, the probability of attack diminishes and the rate of corrosion increases with oxygen concentration. Certain types of nonmetallic inclusions were found to increase the probability of corrosion of low-carbon steels.[1]

The search for a satisfactory pit initiation technique has been a particularly acute problem in the case of pitting studies on stainless steels. Extensive efforts to solve this problem are described in the literature (19). Smith (7) used an apparatus for circulating by thermal convection a solution of ferric chloride and hydrochloric acid over the surface of the metal to be pitted in such a way that edge effects and crevice corrosion were avoided. As indicated above, he found that the addition of 3% molybdenum and, to some extent, silicon to 18Cr-8Ni steel reduced its tendency toward pitting. From metallographic observations of pitted surfaces, it was concluded that finer metallographic polishes reduce pitting attack and that factors other than microscopic inclusions were of primary importance in pit initiation. These were assumed to be cracks and pores in the protective film.

Objections were raised to the pitting test accelerated by acidified ferric chloride because it could not be used as an index of resistance of an alloy to attack by any solution other than ferric chloride. It was pointed out that the insolubility of ferric ion at *p*H 3 or higher makes vulnerable any theory that pitting of stainless steel in sea water, *p*H 8, is initiated by ferric chloride which might have been generated by iron or steel corroding in the vicinity (20).

[1] Mears and Brown (14) used the square drop technique and methods of pit isolation in studies of pitting on aluminum. Other techniques used for pitting research include radioactive tracers (16), radiography (17), and electrolytic pit initiation for studies of pit growth (18).

Electrolytic Methods

Many attempts have been made to produce controlled corrosion reactions electrolytically. Thus, Donker and Dengg (21) applied an external emf to a cell consisting of an iron anode and a silver cathode in solutions of various salts. A breakdown potential was reached at which there was a large increase in the current through the cell. The increase in cell current was caused by dissolution of the iron. This technique was used by Uhlig and Wulff (22), and, in modified form, by Brennert (23, 24) and by Mahla and Nielsen (25) for a study of the passivity of stainless steels. Measurements of breakthrough potentials were made in these investigations on relatively small areas from which edge effects were excluded. Breakthrough potential data and confirmatory immersion-corrosion data showed that no passivation treatment confers lasting protection to a stainless steel immersed in media which corrode unpassivated metal (25).

Experimental

The present investigation is concerned with factors producing breakdown of the passive surface. Simple immersion of the specimen in a given corroding solution was tried, but, as in previous investigations, most of the pitting attack took place at the edges of the specimen. An attempt was made to adapt the square drop method (15) to stainless steels. Again, practically all attack was at the edges, in this case at the edges of the wax coating. The pitting attack at the edge of the coating outlines the wax grid.

Because of difficulties with these pitting tests, electrolytic methods of acceleration were investigated, and a modified potential breakdown apparatus was constructed. In previous investigations the breakdown apparatus was used to determine the electrode potential at the breakdown of a relatively small area of stainless steel surface. In the modified apparatus (Fig. 1) a 25 cm² surface area was tested, and the primary measurement was the number of points of film breakdown, i.e., the number of pits initiated, rather than the potential at the breakdown.

A stainless steel specimen is made the anode of an electrolytic cell, and a platinized wire gauze, 6 cm in diameter, is the cathode. Gauze is used rather than sheet to allow hydrogen liberated during the test to rise through the horizontal mesh instead of forming large bubbles on the surface. The cathode is immersed in a porous cup to restrict diffusion of the alkaline catholyte into the solution

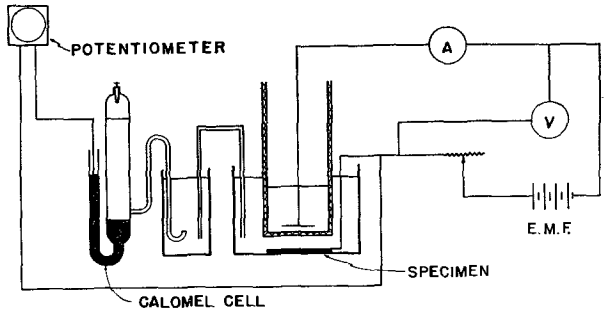

Fig. 1. Schematic diagram of electrolytic pitting apparatus

in which the steel is immersed. A crystallizing dish containing 1800 ml of electrolyte is set in a thermostated water bath.

Recording meters are used to measure the current through the cell and the voltage across the electrodes. Changes in the electrode potential between the specimen surface and the solution are measured against a calomel cell and are automatically recorded.

Characteristics of the Electrolytic Pitting Test

Preparation of specimens.—Specimens were cut from sheet stock 0.07 in. thick, in 2 in. squares. After removal of scale by grinding, stainless steel wires were spot-welded to one corner for electrical contact. Specimens were then suspended in a pickling bath containing 360 ml 65% nitric acid, 60 ml 48% hydrofluoric acid, and 60 ml 37% hydrochloric acid added to 3000 ml distilled water at 70°C (25). After about 20 min in this solution, Type 304 (18-8-S) stainless steel showed a characteristic flashing of the surface while a dark film, formed during the initial phases of pickling, dissolved, leaving a relatively uniform and bright surface. Electrode potential measurements made during this pickling process showed that no pronounced changes in potential accompanied the flashing phenomenon. There was only a gradual change in the direction of a more noble potential, probably indicating the progressive thickening of a passive film. Type 316 (18-8-S-Mo) stainless steel did not show flashing.

As soon as the surfaces were bright the specimens were removed from the pickling bath, rinsed with water, and immersed (when desired) in a passivating solution containing 180 ml 65% nitric acid and 15 g potassium dichromate in 3000 ml distilled water at 70°C for 30 min (25). On removal from this solution, specimens were rinsed and dried. When dry, the back, sides, and the wire were covered with a transparent plastic coating, Fig. 2. After the uncoated area was pitted, the coating was dissolved in acetone and the reverse side of the specimen was used for another pitting run, after a repetition of the chemical treatments and recoating.

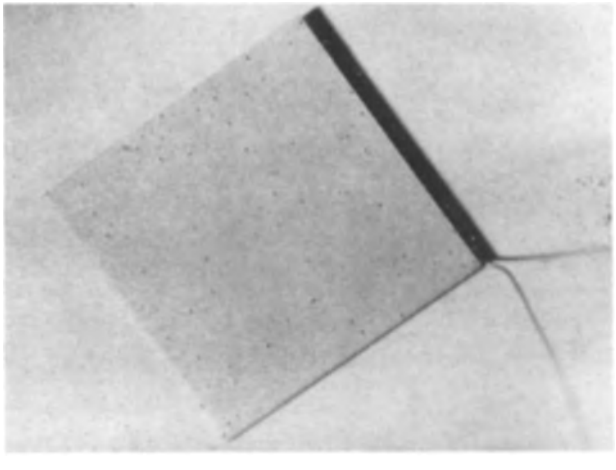

Fig. 2. Pitting test specimen. A stainless steel wire has been spot welded on the back of the specimen to make electrical contact. The wire, the edges, and the back of the specimen have been masked with a transparent insulating coating. The specimen is 5 x 5 cm and shows pits formed in the electrolytically accelerated test.

Testing procedure.—Runs to determine pitting resistance were made by placing a specimen (prepared as described in the previous section) at the bottom of a crystallizing dish containing 1800 ml of solution. The distance between the porous cup (containing the cathode) and the specimen was fixed, as well as the depth of immersion of the cup in the solution. The solution in the porous cup was of the same composition as that in the crystallizing dish, and its quantity did not affect the test as long as the cathode was covered. All solutions were renewed for every run.

By means of the slide wire, driven by a constant-speed motor, the external voltage across the specimen and the cathode was increased from zero to given voltage at the rate of about 2 v in 5 min. The electrode potential, voltage, and current were recorded on automatic instruments. As the external current was slowly increased, very faint pits appeared, which gradually increased in number and size. When the desired current density or voltage was reached, the slide wire motor was turned off and the voltage or current held constant for 5 min to enlarge any pits which may have just appeared.

Factors determining the number of pits.—As the voltage across the specimen and the cathode was gradually increased by the motor slide wire, the total number of pits increased. Since the current density was increasing at the same time, it was desirable to establish which of these elements, the potential difference across the cell or the current density, determined the pitting intensity (pits/cm^2).[2] Two series of runs were made in 0.1N sodium chloride using sets of 18Cr-8Ni (Type 304) stainless steel specimens whose areas were 4–40 cm^2. In one series of runs the external emf was allowed to increase to 2 v and was then held constant for 5 min. In this way, since the exposed area varied for each specimen, different current densities were obtained on the surface being pitted. For the second series of runs a value of 5 ma/cm^2 was chosen as the maximum current density to be applied to all specimens. By multiplying the area of each specimen (cm^2) by 5, the total current required (as registered on the milliammeter) was found. The voltage was allowed to increase in each run until the desired current was reached. Since the current is proportional to the voltage, various potential differences were produced across the cell while the maximum current density for each specimen remained constant.

At constant voltage.—If voltage across the cell is the determining factor in producing pits, then the number of pits per square centimeter will be constant, regardless of the area of the specimen, at a given potential difference across the cell. In a series of runs for which the voltage was increased from zero to a maximum of 2 v, while the area of the specimens was varied, the number of pits per square centimeter decreased with increasing specimen area. When the number of pits per square centimeter was plotted against the reciprocal of the area, a straight line

[2] The role of the single electrode potential is discussed below.

resulted. Therefore, at constant maximum voltage, the number of pits per square centimeter was inversely proportional to the area of the specimen. A plot of pits per square centimeter vs. current density (determined by dividing the maximum current at 2 v by the area of the specimen) also gave a straight line. Therefore, the number of pits formed is proportional to the current density on the specimen, and changes in cell geometry introduced by specimens of various sizes do not affect the pit initiation process.

At constant-current density.—To verify this effect of current density on pitting and to establish the effect, if any, of varying the maximum voltage across the cell, a second series of runs was made to a constant maximum current density. In Fig. 3 it is seen that the number of pits per square centimeter does not vary with voltage across the cell as long as the current density remains constant.

At constant area.—The effect of current density on the number of pits formed per square centimeter was studied on three types of 18Cr-8Ni stainless steels in both the pickled and the passivated condition. A series of specimens was exposed to 0.1*N* sodium chloride solutions at 25°C, while the current density was increased from zero to values ranging from 10 to 85 ma/25 cm². Data for a Type 304 stainless steel are given in Fig. 4. The linear relationship between current density and pits/25 cm² is apparent for both the passivated and the pickled condition. The parallel lines in Fig. 4 indicate the 68% tolerance limits. For the pickled specimens, 68% of all values fall within ±16 pits/25 cm² (or ± 0.65 pits/cm²) of the line and for the passivated, ±8.67 pits/25 cm² (0.34 pits/cm²). These values are typical. The fact that the lines do not go through the origin indicates that acceleration of pitting by chloride ions in this test is dependent on a certain minimum current density of the order of 0.4 ma/cm², below which no pitting occurs in the solutions used. From Fig. 4 it is seen that current densities of 60 ma/25 cm² or greater are desirable to bring out clearly the differences in pitting resistance between various steels and surface treatments. For this reason a maximum current density of 3 ma/cm² (75 ma/25 cm²) was chosen for all tests.

Effect of time.—To determine the effect of time and the quantity of electrical charge on the pitting intensity, two runs were made during which the same quantity of electricity was passed through the specimens at different current densities. From Fig. 4 it is seen that for pickled Type 304 stainless steel the pitting rate at 75 ma/25 cm² (specimen held for 5 min at maximum c.d.) is 140 pits/25 cm². A series of ten specimens of the same steel was run up to only 30 ma/25 cm² and held for 26 min. In this way, the total number of coulombs (current x time) was made the same in both runs. The average of the ten specimens from the 30 ma run was 77 pits/25 cm². Fig. 4 reveals that this is within 10% of the average at 30 ma for runs held only 5 min at this current density. Therefore, within the range studied, the number of pits formed is independent of the number of coulombs passing through the specimens or of the length of time for which the current density is held constant.

The assumption implicit in this check is that the average of ten pitting runs made with a certain maximum current

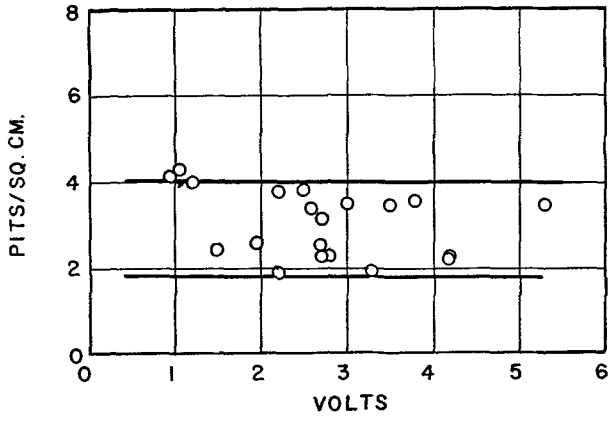

FIG. 3. Effect of voltage on the pitting intensity at constant current density (5 ma/cm²) on Type 304 stainless steel in 0.1*N* NaCl at 25°C.

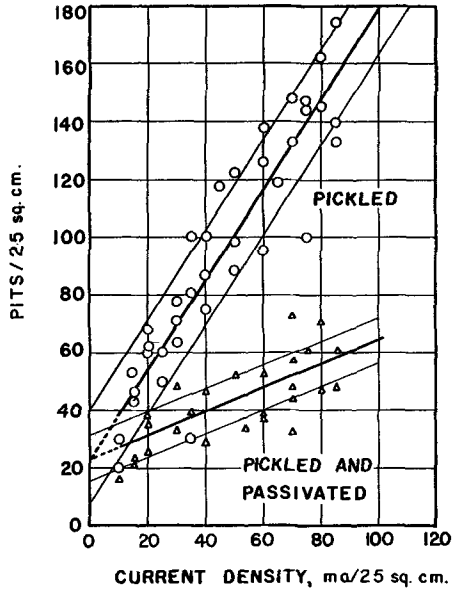

FIG. 4. Effect of current density on pitting of Type 304 stainless steel (EX-1) in 0.1*N* NaCl at 25°C.

density is comparable with the pitting intensity obtained from the lines of Fig. 4 which are based on data obtained over a range of maximum current densities. That this is a valid comparison is shown by data obtained on Type 347 stainless steel. From a plot for Type 347 steel similar to that of Fig. 3, it was found that in the passivated condition this steel may be expected to average 74 pits/25 cm² or 2.95 pits/cm² when a maximum current density of 3 ma/cm² is used. In two separate tests, run to a maximum current density of 3 ma/cm², the averages of two sets of ten specimens were 2.9 and 2.5 pits/cm². These values are in good agreement with the 2.95 pits/cm² obtained from a plot similar to Fig. 4.

In summary, the number of pits per unit of area found for a specific combination of steel and corrosive solution depends directly on the density of the current (ma/cm²) passing through the surface of the specimen and is independent of the voltage across the cell, the specimen area, the length of time of holding at constant current density, the total quantity of electricity passing through the cell,

the maximum electrode potential, or the prior appearance of pits.

The standard testing procedure derived from these experiments consists of increasing the current from zero to 3 ma/cm² and holding for 5 min at this current density to develop and reveal clearly any pits which may have just been initiated upon reaching the maximum current density. Only about 15 min is required to complete the test on one specimen, and the accelerating factor, the electrical current, is readily controlled. Thus, the modified test begins where the original Brennert test ends, i.e., when the first pit forms. In place of an electrode potential measurement, made at the initiation of the first pit, the number of pits formed on a relatively large surface area is used as a measure of resistance to pit initiation.

Reproducibility.—In order to obtain a measurement of the pitting resistance of a stainless steel, runs are made on ten specimens with the current increasing from zero to 3 ma/cm². At the completion of the runs, the total number of pits is counted and divided by the area of the specimen (usually about 25 cm²) to obtain the number of pits per square centimeter. The results of ten such runs are averaged to give a value, in pits per square centimeter, of the pitting resistance of that steel in a given corrosive solution at a controlled temperature. From a statistical study of typical data obtained on several types of steel at various temperatures in chloride solutions, it was found that 90% of the averages of ten such runs as described above will be within ±0.5 pits/cm² of the "true average," i.e., the average of an infinitely larger number of runs (confidence limits). Also, 95% of the time, 75% of the pits/cm² obtained in an individual run will be within ±1 pit/cm² of the average of ten runs (tolerance limits).

The data obtained from 70 comparable runs on Type 304 stainless steel in 0.1*N* sodium chloride solution fall on a symmetrical distribution curve. Efforts to reduce the tolerance limits by various methods of surface preparation, grinding, and pickling procedures, and by controlling the time between specimen preparation and testing were without success.

Electrode potential measurements.—As previously described, in the Brennert (23) method of electrolytic accleration of the breakdown of passive surfaces, the electrode potential was used as a measure of the passivity of the surface toward a given corrosive solution. The potential measured was that of about 1 cm² of surface just before film breakthrough of the weakest point. The data obtained with the modified test and plotted in Fig. 4 indicate that in the region of low current densities (where, presumably, the weakest points break down) there is less distinction between various surface treatments than at higher current densities. One possible interpretation of this observation is that passivation, while reducing the number of weak points in the surface, is not effective in eliminating all types of the weakest points. Electrode potential measurements were also made in the present investigation to determine their relationship, if any, to the formation of pits.

Typical electrode potential data obtained during a regular run are plotted in Fig. 5. As the voltage across the specimen anode-platinum cathode was increased continuously from zero, there was a very rapid change in electrode potential of the specimen in the cathodic direction. During this period of rapid increase in electrode potential there was no measurable flow of current. This initial phase was terminated by a sudden leveling off of the electrode potential, which occurred despite continuing increases in the voltage across the cell. At this point current began to flow through the cell, indicating that electrochemical reactions, gas evolution, or pitting were taking place at the anode, and hydrogen was being evolved at the cathode. The electrode potential at which this sudden change occurred on pickled Type 316 stainless steel varied from 0.49 v to 0.64 v in three tests, and the voltages across the cell at this point were 0.6, 0.6, and 0.7 v. Further increases in voltage increased the current through the cell. Beginning at about 2.5 v (Fig. 5) the current increased linearly with increasing voltage. The slope of this line is the same for various specimens of a given steel in both the pickled and the passivated condition. The slope depends on the solution composition (specific conductance).

After current flowed through the cell, the electrode potential gradually changed in the cathodic direction in a somewhat irregular fashion. When pits formed the potential remained constant, or even decreased slightly. Then as the current through the cell increased, the potential increased again until another group of pits appeared, causing another leveling off or slight drop in electrode potential. This influence of the pits on the electrode potential was probably the reason for the observation, based on 50 runs, that the maximum potential reached at the end of the run is independent of the number of pits formed. However, there is some correlation between the maximum potential and the milliamperes per pit at the end of the run. On Type 304 stainless steel in 0.1*N* NaCl at 25°C the maximum potential changed 0.125 v when

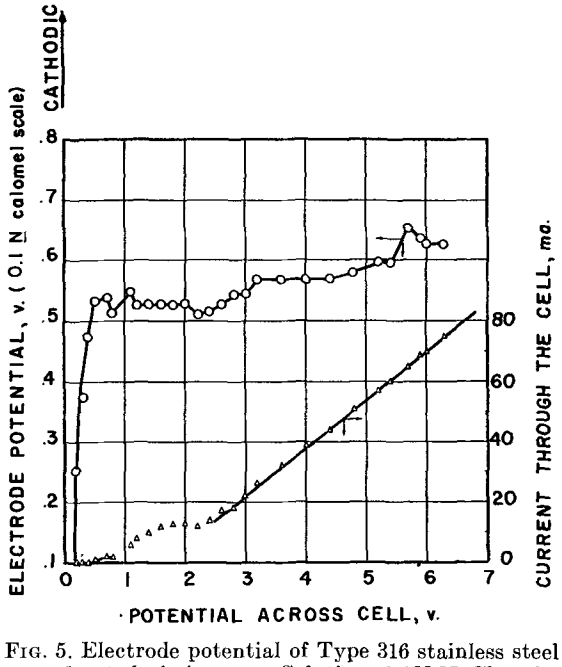

FIG. 5. Electrode potential of Type 316 stainless steel in the accelerated pitting test. Solution: 0.1*N* NaCl at 25°C; specimen: pickled only, 198 pits at end of run.

the calculated current density in the pits was increased from 0.3 to 1.8 ma/pit.

The weight loss per pit was inversely proportional to the total number of pits formed. Thus, when the total amount of electricity (coulombs = amp x sec) passing through the cell was constant (as in the case of repeat runs, given the steel and test solutions) the weight of metal dissolved was constant, and the amount removed from any one pit depended on the total number of pits. The size (depth and diameter) of pits formed during the electrolytic pitting test was essentially uniform on a given specimen when exposed to a certain solution. As the current density was increased continuously there was relatively rapid polarization of any pits that had been initiated. This increasing anodic polarization gradually resulted in complete passivity, i.e., the pits stopped growing. When this stage was reached, further increases in current density resulted in increases in electrode potential until another group of pits formed.

The electrode potential data obtained in a run using a steel which did not form any pits were similar to those of a run on a specimen which pitted readily (Fig. 5). The characteristics of the current-voltage curve were identical in both cases, and the electrode potential differed only in that, during the periods of current flow through the cell, the gradual change in the cathodic direction was more consistent and reached a maximum which was about 0.6 v higher than that given in Fig. 5. This again showed the influence of pit formation on the electrode potential. Pitting decreased the maximum potential at a given current density. At about 2.5 v across the cell the specimen surface became yellow, and soon thereafter gas bubbles appeared.

When the voltage across the cell was increased in discrete steps, rather than continuously, the electrode potential did not level off but dropped sharply in the anodic direction when current began to flow through the cell.

Electrochemistry of the pitting test.—As the potential across the specimen anode-platinum cathode is increased by application of an external emf while there is no current flow through the cell, a two-part layer forms on the specimen surface (26, 27). One layer, which is approximately a single anion in thickness, remains almost fixed to the solid surface. In this layer there is a sharp fall of potential. The second part extends some distance into the liquid phase and is diffuse. The distribution of positive and negative ions is not uniform since the electrostatic field of the anions at the surface results in preferential attraction of cations. The adsorption of anions on a (mercury) surface increases in the order $F^- < OH^- < Cl^- < Br^- < NO_3^- < I^- < ClO_4^- < CNS^-$ (Hofmeister or lyotropic series) (28). The least hydrated ions adsorb most readily on the metal surface. This double layer is electrically similar to a condenser of large specific capacity and causes a rapid change in electrode potential during the charging operation. The relation of anion adsorption on pit initiation is discussed in Part II. Increases in voltage across the cell eventually cause a flow of current and a considerably slower change in the electrode potential. The anodic processes responsible for current flow are usually assumed to take place in the order of greater oxidation potentials (26). In the case of a sodium chloride solution, oxygen (0.401 v) and chlorine (1.358 v) might be expected to be evolved in that order. However, it has been found that, on electrolysis of chloride solutions, chloride ions are discharged first and that evolution of oxygen soon follows, as the potential is changed in the more cathodic direction (26, 29). The order of anodic reactions depends on the concentrations of reactants and is probably related to the preferential adsorption of chloride ions during anodic polarization, which was found to prevent the formation of oxygen layers (30). Thus, in the electrolytic pitting test three reactions may take place on the anode: (*a*) discharge of chloride (halide), (*b*) evolution of oxygen, and (*c*) dissolution of metal, pitting.

During the current flow through the pitting cell, chloride ions migrate toward the specimen anode. This change in chloride-ion concentration in the solution surrounding the anode has been measured, confirming that the increase in concentration is proportional to the quantity of electricity (coulombs) passing through the cell (2). However, the change in chloride-ion concentration is not the controlling factor in acceleration of pit initiation in the test used in this investigation. It was shown above that pit initiation is not a function of the quantity of electricity passing through the cell, but only of the current density. Further support of this cause of pit initiation is given by the data on the effect of chloride-ion concentration (Part II) which showed that pit initiation actually decreases with increasing concentration of chloride ion in the pitting solution. Therefore, surface breakdown does not depend on the concentration of chloride ions in the solution around the specimen, but on the rate with which the chloride ions are brought to the surface. This is probably the determining factor in the adsorption, amount, and degree of surface coverage of the chloride ions on the stainless steel specimen.

II. Investigation of Variables in the Metal and in the Electrolyte Which Control Pit Initiation

Results of Pitting Tests

Pitting by various chlorides.—Nine different chloride salts were used for pitting tests on Type 304 stainless steel at 25°C. The solutions were 0.1*N* in chloride ion. All specimens were in the passivated condition and the standard testing procedure was used (*see* Part I). The chlorides tested and the results are given in Table II. Variation in pitting intensity among the various chlorides used was largely a function of the *p*H of these solutions. As the *p*H of the solution increased, the pitting intensity decreased. This was in agreement with other runs in which it was found that additions of sodium hydroxide to chloride solutions almost completely suppressed pit initiation. It was also in agreement with the results of other

TABLE II. *Effect of various chloride salts on pitting of stainless steel*

Steel, AISI-304 (ER-2) passivated; temp, 25°C; solution, 0.1*N* in chloride ion; standard test.

	*p*H	Pits/Cm²*
Chloride		
NaCl	6.22	3.4
$FeCl_3$	2.05	3.8
$CrCl_3$	3.14	4.5
$CuCl_2$	4.19	3.0
KCl	5.97	2.2
$CaCl_2$	6.90	3.2
$NiCl_2$	5.72	3.9
$MgCl_2$	6.20	2.3
LiCl	7.03	2.9
AISI-316		
NaCl	6.22	0.46
$FeCl_3$	2.05	1.3

* Average of 10 runs.

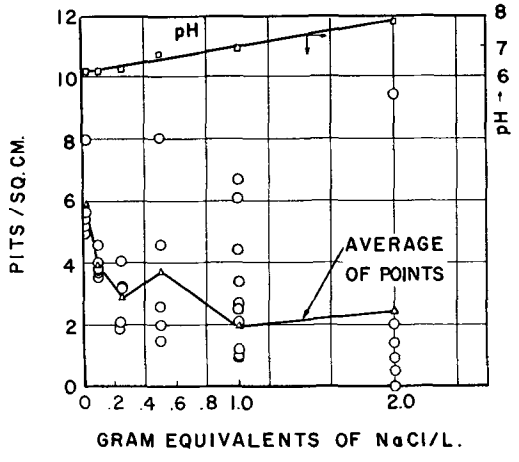

FIG. 6. Effect of concentration of NaCl on pitting of passivated AISI 304 steel (ER-2) at 25°C.

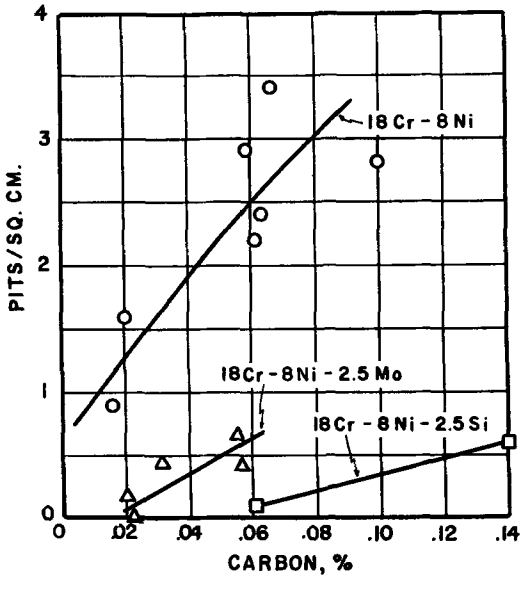

FIG. 7. Influence of carbon in stainless steels on pitting in 0.1*N* NaCl at 25°C in the standardized test. Specimens were pickled and passivated.

investigators (31–33) and with practical experience on the use of hydroxides to suppress chloride pitting of stainless steels. Thus, among the constituents of the solution, the chloride ion is the primary factor in the electrolytic pit initiation test, and the cationic member of the chloride salt plays only a minor role, if any.

Effect of chloride-ion concentration.—It was shown in Part I that the current density on the specimen rather than the quantity of electricity passing through the cell determined the number of pits formed per unit area. Since the quantity of electricity passing through the cell determined the chloride-ion concentration near the surface of the specimen, it was concluded that increasing the solution concentration would not appreciably affect pit initiation. To obtain further data on the effect of the chloride ion, tests were made in solutions 0.02–2*N* in sodium chloride. There was a tendency toward large numbers of pits in some runs, while the majority of specimens showed a definite decrease in pit initiation with increasing concentration of chloride ions (Fig. 6). On pickled Type 316 stainless steel (EW-5) the decrease was even more pronounced. The averages of ten runs were 7.3 pits/cm² at 0.1*N* sodium chloride and 0.92 pits/cm² in 1*N* sodium chloride.

The scatter in the data (Fig. 6) suggests that opposing factors are introduced as the chloride concentration is increased. Among those which contribute to a decrease in pit initiation are lower equivalent conductance and higher *p*H at higher chloride concentration. Increased adsorption of chloride ions at higher chloride concentrations may tend to increase pit initiation. These results on the effect of chloride concentrations on pit initiation are not expected to agree with studies of this effect based on weight-loss measurement, which include the results of pit initiation and growth. Uhlig (2) found an increasing weight loss with increasing concentration of chloride ions. The weight loss (total corrosion current) is a function of specific conductance, which increases rapidly with increasing concentration of sodium chloride.

Pitting of various grades of stainless steels in chloride solution.—To determine the influence on pit initiation of various alloying additions to the basic 18Cr-8Ni composition, all the more common types of the AISI-300 series steels and a number of special heats were submitted to the standardized, accelerated pitting test in 0.1*N* sodium chloride at 25°C. "Hastelloy" B and C were included for comparison.

Most alloys were tested in two conditions: pickled only, and pickled and passivated. Results are listed in Table III; some are plotted in Fig. 7.

In reference to Table III:

1. In every case the passivation treatment decreased pit initiation. The ratio (*R*) of the number of pits initiated in the pickled condition to that in the passivated condition may be used as a measure of the response of the steel to passivation. For the basic 18Cr-8Ni steels (304, 304L, 302, and 302B) this ratio is approximately 2.5.

Even though the pitting intensity of AISI-316 in the pickled condition is about the same as that of AISI-304, the response to passivation is much greater, $R = 15$. This ratio is 30 on the low-nitrogen, low-carbon, 18Cr-8Ni-Mo

(FH-3) steel. Thus, molybdenum additions do not change the basic (pickled) pitting resistance but greatly increase the response to passivation, especially on low-carbon steel.

This is in contrast to silicon additions, which considerably reduce pitting in the pickled condition but do not change the response to passivation.

2. In every case, decreasing the carbon content decreased pit initiation, Fig. 7. The basic 18Cr-8Ni curve includes AISI-302, 304, 304L, 321, 347, 347L. Addition of stabilizing elements, niobium in Type 347 and titanium in Type 321, did not affect pitting results. Since all steels were tested in the annealed condition (or in the case of Types 321 and 347 steels, the stabilized conditions), it may be concluded that carbon in solid solution (or in the form of titanium or niobium carbides) adversely affects pitting resistance. The nitrogen content of the steels used to obtain data for Fig. 7 was about 0.02%.

3. Steels containing higher amounts of nitrogen showed less pitting than those containing normal amounts of this element. The austenitic stainless steels normally contain about 0.02% nitrogen. A five to tenfold increase decreased pit initiation. This is in agreement with previously published results (10, 11) on stainless steels immersed in acidified ferric chloride.

4. These observations indicate that pitting resistance of the basic 18Cr-8Ni composition might be improved by additions of silicon, molybdenum, and nitrogen, and by keeping the carbon content as low as possible. An 18Cr-8Ni steel containing both molybdenum and silicon has already been described (9). The silicon and molybdenum contents were each limited to about 2.5% because of difficulties encountered in mechanical processing at higher percentages. Both of these elements are ferrite formers, and Riedrich's (9) steel contained 10–20% ferrite. A laboratory heat (SP-1) of this type of steel was prepared. It contained about 20% ferrite and did not pit in the accelerated laboratory test in the pickled or in the passivated condition at 25°C (Table III).

A second heat of 18Cr-8Ni-Mo-Si steel (SP-2) was made. Laboratory pitting results on low-carbon, high-nitrogen steels, described above, were considered in selecting the desired composition. The carbon content was reduced as much as possible (0.039%), and the nitrogen content was increased to 0.23%. The increase in nitrogen made the steel completely austenitic. As in the case of SP-1, there was no pitting in the accelerated laboratory test at 25°C.

Neither of these steels pitted in the accelerated test at 25°C, but under the more severe pitting conditions of sea-water exposure and immersion in ferric chloride, the high-nitrogen, low-carbon steel was definitely superior.

Effect of heat treatment on the pitting of stainless steels.— Stainless steels containing silicon were the most resistant to pit initiation in the accelerated pitting test. However, silicon in excess of about 1% increases the corrosion of annealed stainless steels in the standard, boiling 65% nitric acid test (36). In accordance with expectations, these steels (302B, SP-1, and SP-2) have nitric acid corrosion rates 2–40 times greater than the acceptable rate of 0.0015 in./mo (Table IV). The high rates were due to general corrosion, not intergranular attack. Since the object of the nitric acid tests is to detect susceptibility to intergranular corrosion, the lack of agreement between nitric acid corrosion rates and resistance to pit initiation was not surprising.

TABLE III. *Pitting of various grades of stainless steels in 0.1N NaCl at 25°C (Influence of surface treatment)*

Steel, AISI type	Code	Description	Pits/cm²*		Ratio,
			Pickled	Pickled + passivated	Pickled/passivated
304	EX-1	C = .061	5.6†	2.2†	2.5
304	ER-2	C = .063	7.4	3.4	2.2
304L	FK-4	N = .033	4.5	1.6	2.8
304L	FK-9	N = .12		0.9	
302	GF-2	C = .10	6.3	2.8	2.2
302B	302B	Si = 2.5		0.1	
302B	302BP	Si = 2.7	1.5	0.6	2.5
321	FF-7	Ti = .31		2.4	
347	EX-2	Nb = .87		2.9	
347L	FE-6	C = .016		0.9	
316	EW-5	Mo = 2.47	7.3	0.46	15.8
316	C-1		6.6*	0.42	15.6
316	C-2			0.65	
316L	FH-3	N = .032	5.0	0.17	29
316L	FH-1	N = .13		0.0	
316L + Nb	FN-3	Mo = 2.15		0.0	
316 + Si	SP-1	Si = 2.4	0.0	0.0	
316 + Si	SP-2	N = .23	0.0	0.0	
"Hastelloy" B				0.0	
"Hastelloy" C				0.0	

* Average of 10 runs.
† Obtained from Fig. 4.

High rates on austenitic stainless steels in the nitric acid test are usually due to rapid intergranular attack on steels containing intergranularly precipitated chromium carbides (or other phases). Chromium carbides are precipitated most readily at about 1250°F (677°C) and greatly increase the nitric acid corrosion rate (Table IV, AISI-304 and 321).

Five different steels were tested in the accelerated, electrolytic pitting apparatus following a heat treatment of 1 hr at 1250°F (677°C). In two of these steels (AISI-304 and 321) large amounts of chromium carbide were precipitated at the grain boundaries. In two others no carbides were precipitated, because the carbon in the steel was very low (AISI-316L) or was held in combination with a stabilizing element (AISI-347). Results of pitting tests on heat-treated steels are given in Table V. On AISI-304 in the passivated condition there was essentially no difference (3.4 vs. 3.3 pits/cm²) between pit initiation of the annealed (carbon in solution) and the sensitized [1 hr 1250°F (677°C)] steel, containing large amounts of intergranularly precipitated chromium carbides.

Since all the chemically treated specimens were exposed to a pickling treatment which preferentially attacks the grain boundaries containing intergranularly precipitated chromium carbides, other methods of surface preparation were investigated. In place of chemical treatments, grinding on a 120-grit belt was used to prepare the surfaces for pitting. Even though the grain boundaries remained

TABLE IV. *Nitric acid corrosion rates of steels used for pitting tests*

Steel, AISI type	Code	Corrosion rate, in./mo	
		As-received	1 hr 1250°F, WQ
304	ER-2	0.00084	0.0276
304L	FK-4	0.00053	
302	GF-2	0.0010	
302B	302B	0.0139	
302B	302BP	0.0705	
316	EW-5	0.00081	0.00397
316L	FH-1	0.00090	0.0063
316 + Si	SP-1	0.00384	
316 + Si	SP-2	0.00321	
321	FF-7	0.00093	0.01239
347	EX-2	0.00068	0.00093
347L	FE-6	0.00063	

TABLE V. *Effect of surface preparation and heat-treatment on pitting of stainless steels in* 0.1*N* NaCl *at 25°C*

Steel, AISI type	Code	Pits/cm²*		
		Pickled	Passivated	Ground‡
304	ER-2	7.4	3.4	3.1
304†	ER-2†		3.3	5.0
316	EW-5	7.3	0.46	0.0
316†	EW-5†		0.76	
316L	FH-3	5.0	0.17	1.2
316L†	FH-3†	3.5	1.4	1.5
321	FF-7		2.4	3.9
321†	FF-7§		1.5	0.5
347	EX-2		2.9	6.7
347†	EX-2†		2.5	6.4

* Average of 10 runs.
† Heated 1 hr at 1250°F.
‡ Ground to 120-grit finish.
§ The amount of titanium added to this steel is insufficient to tie up all carbon. Thus, after heating for 1 hr at 1250°F there is extensive precipitation of chromium carbides at grain boundaries. This may explain in part the reduction in pit initiation following the (1 hr at 1250°F) heat treatment. After this heat treatment the amount of carbon left in solid solution may be unusually low. As shown in Fig. 7 there is a reduction in the number of pits/cm² when the carbon content in solid solution is reduced.

unattacked by this procedure, they were probably affected by the flowed metal layer formed during mechanical grinding. Also, the true surface area, and, therefore, the true current density during the test were altered to an unknown extent.

On some steels grinding increased pit initiation somewhat, while on others there was either no change, or a decrease, as compared with passivated specimens. The only exception was the AISI-316L steel on which pit initiation increased considerably in the "as-received" condition. However, even this steel showed no difference between passivated and ground specimens in the heat-treated condition [1 hr at 1250°F (677°C)]. So, this heat treatment did not influence pit initiation to any great extent under the present experimental conditions.

Effect of temperature on pit initiation.—To determine the effect of temperature on pit initiation, runs were made at 50° and at 70°C in 0.1*N* NaCl solution. Average results of ten runs at each temperature are plotted in Fig. 8 and 9.

Of particular interest is the large increase in pitting on Type 316 steel. This was investigated on three different heats and all showed a greater pit initiation at 50° and 70°C than any other AISI-300 series steel. The maximum displayed by one heat (EW-5) was checked by extra runs.

The addition of silicon to Type 316 stainless steel, as in SP-1 and SP-2, eliminated the large increase in pit initiation at higher temperatures. In general, the superiority of the steels containing silicon at 25°C held at higher temperatures also. However, both SP-1 and SP-2 steels pitted at temperatures above 25°C.

The decrease in pit initiation with increasing temperature found for AISI-304 steel was also observed for Type 302 stainless steel in which the number of pits per square centimeter changed from 2.8 at 25°C to 1.4 at 70°C.

The great variety of responses to pit initiation at elevated temperatures indicated that pitting data obtained for a certain stainless steel at one temperature could not be used to predict behavior for other steels or

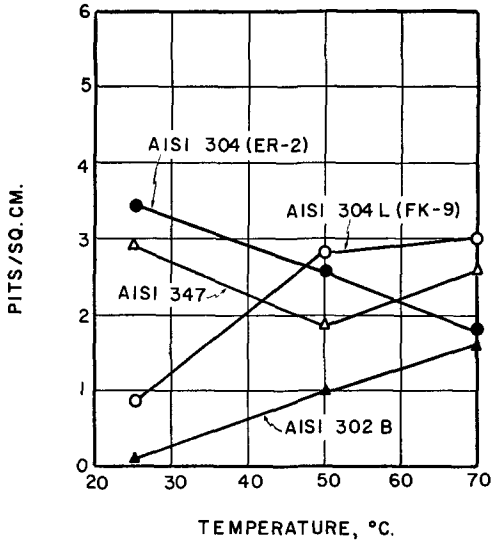

FIG. 8. Effect of temperature on pitting of 18Cr-8Ni steels in 0.1*N* NaCl.

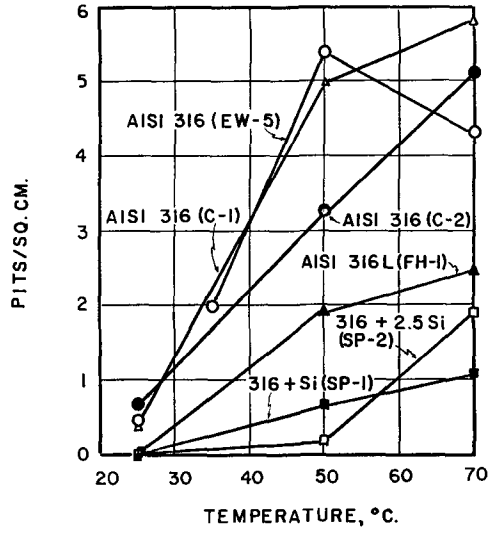

FIG. 9. Effect of temperature on pitting of 18Cr-8Ni-2.5Mo steels in 0.1*N* NaCl.

TABLE VI. *Effect of sodium nitrate on pitting of stainless steels in 0.1N NaCl at 25°C in the accelerated test*

Steel, AISI type	Condition	Pitting without inhibitor, pits/cm²	Minimum amount* of $NaNO_3$, g/l
304 (ER-2)	Pickled	7.4	0.60
304 (ER-2)	Passivated	3.4	0.40
316 (EW-5)	Pickled	7.3	0.25
316 (EW-5)	Passivated	0.46	

* Minimum amount of inhibitor required to suppress all pitting in the standard pitting test.

other temperatures. The versatility of temperature control possible in the accelerated, electrolytic test used in this study is one of its advantages over previously used accelerated tests, in which increased temperatures were used to produce accelerated corrosion. Some results on the effect of temperature on ferric chloride immersion tests are described below.

Inhibition of chloride pitting.—A number of pitting tests were made in 0.1*N* sodium chloride with sodium nitrate, a commonly used inhibitor for ferrous metals. Various amounts of sodium nitrate were added to determine the minimum amount of inhibitor required for suppression of all pitting in the standardized, electrolytic test. Results are listed in Table VI. The passivated specimens required less nitrate for inhibition than those that were pickled only. Also, the superior response of 18Cr-8Ni-2.5Mo (AISI-316 stainless steel) to passivating conditions was again evident. Even though in the pickled condition both AISI-304 and 316 pitted alike, the amount of nitrate required to suppress pitting on the pickled AISI-316 stainless steel was less than half the amount required for AISI-304 stainless steel.

The nitrate probably does not completely prevent breakdown of the surface but acts to heal rapidly and effectively all points which are beginning to break down and, thereby, prevents the formation of pits. Nitrate is consumed in the process of healing breaks in the protective film. Therefore, unless there is periodic replenishment, the initial addition of inhibitor merely delays the onset of corrosion (2, 37).

Protective film formation on corroding surfaces was observed on specimens which were scratched with a sharp instrument to produce a fresh surface. Two types of tests were made. In the first, SP-2 specimens were scratched in air before immersion in chloride solution (containing potassium ferrocyanide) for the accelerated, electrolytic test. There was no pitting or general corrosion in the scratches or on the unscratched surfaces during the test. In the second test, scratches were made while the steel was immersed in the chloride solution. Soon after the current was passed through the specimen, the scratch turned blue at about 0.3 ma/cm². However, as the current density was increased to about 1 ma/cm² the formation of blue ferri-ferro cyanide ceased, and what had formed earlier diffused away. Metallographic examination of the scratch after this test confirmed a small amount of general corrosion in the scratch.

Pit initiation by other halides.—To compare pitting properties of halogen salts, tests were made with the electrolytic apparatus in sodium fluoride, sodium bromide, and potassium iodide. Only the bromide salts pitted stainless steels so extensively that 0.01*N* solutions and a maximum current density of 2.3 rather than 3 ma/cm² were used for further tests.

TABLE VII. *Pitting of stainless steels in 0.01N NaBr at 25°C in the accelerated pitting test*

Steel, AISI type	Code	Pits/cm²*	
		0.01 *N* NaBr†	0.1 *N* NaCl
304	ER-2	6.4 (10)‡	3.4
304L	FK-9	3.4 (4)	0.9
304L	FK-4	3.2 (6)	1.6
316	EW-5	6.6 (10)	0.46
302B	302B	1.0 (9)	0.1
316 + Si	SP-1	1.8 (7)	0.0

* Passivated specimens.
† Maximum current density 2.3 ma/cm².
‡ Indicates number of specimens run.

Results of pitting tests in sodium bromide are listed in Table VII along with those obtained on the same steels in 0.1*N* sodium chloride. Even though the tests were made on passivated specimens, pit initiation on AISI-316 is the same as that on Type 304, in contrast to the behavior in 0.1*N* sodium chloride. It has been indicated that in bromide solutions the resistance to pit initiation of these two steels is identical (22). However, the weight loss on the 18Cr-8Ni-2.5Mo steel was lower than on 18Cr-8Ni steel (25) indicating that the steel containing molybdenum can heal more readily a surface breakdown. Weight-loss determinations give a measure of both pit initiation and pit growth and may, therefore, differ from pit initiation data.

As in the case of chloride solution, additions of about 2.5% silicon (302B, SP-1) to the 18Cr-8Ni and the 18Cr-8Ni-2.5Mo steels considerably increased the resistance to pit initiation in 0.01*N* bromide solution (Table VII).

Changes in pit initiation of AISI-316 steel with bromide ion concentration are shown in Fig. 10. An almost threefold increase in pit initiation was found but with practically no change in *p*H (cf. figure for chloride effect).

Pit initiation results with the various halides are generally in agreement with the Hofmeister series, i.e., the fluoride ion (no pitting) is the least readily adsorbed (most hydrated) and the bromide (greatest amount of pitting) is more readily adsorbed than the chloride. Also, nitrate ions, which inhibit pitting by chlorides, are more readily adsorbed than chloride ions. However, the iodide is even more readily adsorbed than any of the others, but does not pit in the accelerated test. It should be pointed out that adsorption of halide, while a necessary requirement for pit initiation, is only the first step in pit formation. Whether a pit forms depends on whether adsorption is followed by reaction between the surface and the halogen ion.

Correlation of results of electrolytic pitting test.—Total immersion tests of a number of stainless steels were made in 10% ferric chloride solutions for 72 hr and for 144 hr at 25°C and 50°C in order to compare with results of the accelerated pitting tests. Those steels which did not pit in the 72-hr periods also were immune to pitting after 144 hr. At 25°C, Type 316 stainless steel (passivated), "Hastelloy" C and the 316 + 2.5% Si (SP-2) steel did not

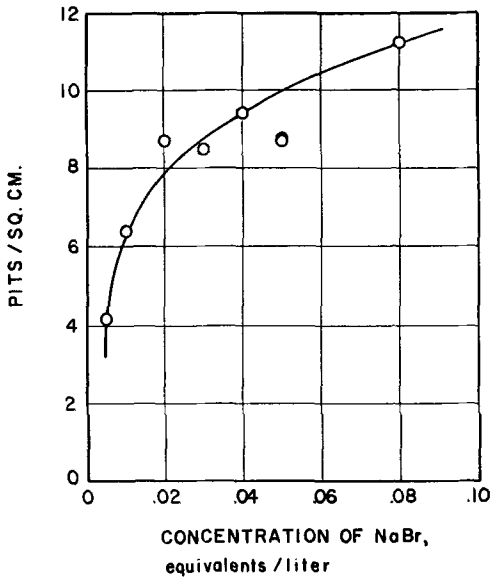

FIG. 10. Effect of concentration of NaBr on pitting of passivated AISI 316 (EW-5) steel in accelerated pitting test at 25°C. Maximum current density = 2.3 ma/cm².

pit (Cf. Table III and Fig. 8 and 9). At 50°C there was no pitting on the completely austenitic SP-2 alloy or "Hastelloy" C. Both AISI-304 and 316 steels pitted, but there were more pits on the Type 316 steel. The SP-1 steel which contained 10–20% ferrite pitted slightly at the stamped numbers.[3] These observations, even though based on a relatively brief exposure test in ferric chloride solution, nevertheless tend to confirm the results of the electrolytic test.

The 18Cr-8Ni steel containing 2.5% silicon (302B) showed relatively few pits, but these grew into enormous cavities underneath the surface. Thus, silicon, while decreasing pit initiation, could not be used alone to decrease pitting, but should be used together with molybdenum, which increased the response to passivation (film healing). The stabilized steels (AISI-321 and 347 steels) pitted more in ferric chloride than the other steels. This is in contrast to their behavior during simple immersion in sodium chloride, where they do not pit more than AISI-304 steel.

With sea-water exposure.—A set of 6 x 12 in. panels was completely immersed in sea water for 6 months.[4] During this period they were completely covered by a variety of marine organisms which produced severe crevice conditions. Only titanium, "Hastelloy" C, tantalum, and platinum are known to survive this type of exposure without attack. When the marine organisms were removed, it was found that "Hastelloy" C was unattacked, and the completely austenitic, high-nitrogen, low-carbon, silicon-modified Type 316 steel, SP-2, showed only minor edge attack on the two panels used. The samples resisted pitting in the order "Hastelloy" C, SP-2, SP-1, SP-3, AISI-316 stainless steel, AISI-304 stainless steel. These steels were then exposed for 6 more months with new nonmetallic washers mounted on them to render them more susceptible to crevice attack. The results of this second exposure confirmed those of the first 6 months. "Hastelloy" C was unattacked, and corrosion on the crevice on SP-2 was about one-half of that on AISI-316 stainless steel. Thus, the sea-water exposure tests confirm the results of the accelerated laboratory and the ferric chloride immersion tests, in that additions of silicon improve the pitting resistance of AISI-316 stainless steel and that low-carbon and high-nitrogen contents are also beneficial.

[3] A third heat of modified Type 316 steel, SP-3, containing about 50% ferrite, 3.7% Mo and 2.3% Si, was definitely less resistant to pit initiation than either SP-1 or SP-2.

[4] Exposure tests were made at the Harbor Island Marine Corrosion Test Station of the International Nickel Company.

METALLOGRAPHY OF PITTING

Previous investigators (19, 38) of the loci of pit initiation in stainless steel surfaces have come to the conclusion that depressions such as cracks, cusps, striations, and scarifications are the cause of pit initiation. Such depressions were thought to cause pitting by serving as minute reservoirs for the accumulation and stagnation of corrosive salt solution, which would result in a local electrolytic element (concentration cell). However, these depressions are not the sole cause, because steels which have been thoroughly pickled to remove depressions are still subject to pitting. Also, there is no relation between pitting and the number of nonmetallic inclusions (39). This is in agreement with the present investigation in which no correlation was found between the number of inclusions and the number of pits developed.[5]

Experimental methods.—Experiments were made in an effort to observe the loci of pit initiation. Such tests were difficult because the time required to form a pit was unpredictable and, once formed, pits grew so rapidly that it was almost impossible to observe the type of microstructure at which they originated. This was especially difficult on small-grained steels such as AISI 321 and 347. The pits had to be observed while they were smaller than one grain and on steels whose grain boundaries are readily etched. Therefore, this investigation on pit initiation was confined to AISI-304 stainless steel. In a few cases it was possible to observe pit initiation on polished surfaces during simple immersion. Other tests were made by observing portions of immersed surfaces while they were pitted electrolytically by making them anodic, as in the accelerated pitting test.

To observe the loci of electrolytic pit initiation, a stainless steel box was made with an open top and a window on one side. A polished stainless steel specimen was clamped about ¼ in. behind the window, the polished surface parallel to the window. This arrangement permitted observation of the immersed surface with a binocular microscope while the specimen was made anodic in chloride solution.

Two perpendicular lines were scratched on a polished surface to assist in the location of a specific area. Photomicrographs were then made of the polished surface in the four quadrants to locate nonmetallic inclusions. The specimen then either was immersed in chloride solution or electrolytically pitted in the box described above. As soon as pits were observed, the specimens were removed, dried, and photographed at the same magnification as before. By superimposing the two negatives, the relationship of pits to inclusions could be determined. The location of pits

[5] The free-machining, AISI-303 steel, which has numerous sulfide or selenide inclusions, is an exception.

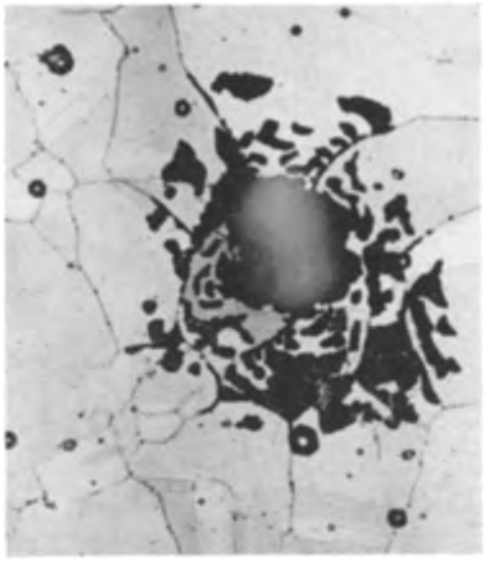

FIG. 11. Electrolytically formed pit. Mechanically polished AISI 304 steel (annealed) pitted electrolytically in 0.1*N* NaCl and then electrolytically etched in nitric acid to bring out grain boundaries. 350× before reduction for publication.

in relation to grain boundaries was obtained by lightly etching a pitted surface to reveal the grain boundaries.

Results.—A characteristic pit formed electrolytically in chloride solution in the observation box is illustrated in Fig. 11. The large pit formed when the surface was penetrated in a small area, then grew rapidly into a large cavity underneath the surface. Progressive growth of the cavity caused further penetration of the surface from below. Part of the roof of the cavity then collapsed. The pit shown in Fig. 11 was formed by making the surface anodic. However, the morphology of pits formed by simple immersion was identical with that of pits formed electrolytically at low current densities.

Results of the metallographic techniques for study of pit initiation indicated that pits were formed primarily at grain boundaries in the metal surface. In Fig. 12 two photomicrographs are shown of polished Type 304 stainless steels which were immersed in ferric chloride solution. Pits formed at grain boundaries on both the annealed and heat-treated [1 hr at 1250°F (677°C)] specimens. Although some pits may have formed at inclusions, they were not preferred sites of attack. Whether the pits were formed by anodic treatment or by immersion, the majority were nucleated at grain boundaries. Only at the higher current densities and in the more aggressive pitting solutions (NaCl solutions to which HCl had been added) were larger numbers of pits nucleated in the interior parts of the grain surfaces. Thus, pits formed more readily at grain boundaries than on interior grain surfaces and appeared to be independent of the inclusions in stainless steels, except in the case of the steel (AISI-303) which contained large numbers of sulfide inclusions.[6]

[6] Because of the difficulty of reproducing the low-contrast prints, made from superimposed negatives which show the relation of pits to inclusions, none has been included in this paper.

These observations are supported by several other experimental results.

Effect of polishing.—In agreement with other results (7), resistance to pit initiation increased with the degree of mechanical polishing. Thus, a metallographically polished surface was more resistant to pitting than a belt-ground surface. During mechanical polishing, a layer of highly deformed metal was produced on the surface, which probably covered and obscured the grain boundaries. This view was given further support by the fact, observed in this study, that electropolishing produced a surface which was the most susceptible of all to pit initiation. In this case, metal was removed selectively from the surface by electrolytic action without the formation of a flowed metal layer to obscure grain boundaries.

Effect of heat treatment.—During heat treatment of 1 hr at 1250°F (677°C) of certain stainless steels large quantities of intergranular inclusions (chromium carbides), which frequently enveloped almost all grains, were formed. These intergranular "inclusions" did not affect appreciably pit

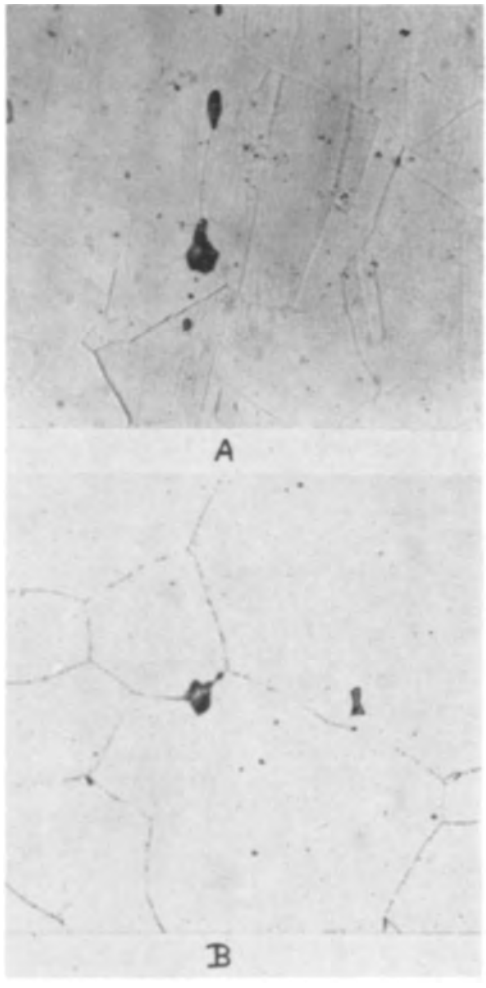

FIG. 12. Pits formed by simple immersion. Mechanically polished specimens of AISI 304 steel immersed 24 hr in 10% ferric chloride solution and etched electrolytically in oxalic acid to bring out grain boundaries. A, annealed—carbides in solid solution; B, sensitized—heated 1 hr at 1250°F to precipitate chromium carbides at grain boundaries. Note large inclusion near grain boundary which did not cause pit formation. 350× before reduction for publication.

initiation (Table V). However, in ferric chloride they accelerated pit growth along grain boundaries (40). The role of chromium carbides in pit initiation appeared no more significant than that of other nonmetallic inclusions in stainless steels, which have not been found to influence pit initiation.

Effect of grain-boundary etching.—When the grain boundaries on polished steels were electrolytically etched in nitric acid before electrolytic pitting in sodium chloride solution, pits formed almost entirely in the grain centers and only rarely at grain boundaries. Etching appeared to desensitize the grain boundaries toward pit initiation. This may explain the effect of pickling treatments by a titanium chloride, hydrochloric acid, sulfuric acid, and nitric acid on the pitting of stainless steels. The solution vigorously attacks stainless steels, but makes them more resistant to pitting in chloride solutions; Uhlig (38) stated that the steels became more resistant to pitting because mechanical depressions, adherent particles, and inhomogeneities were removed by pickling. Action of the pickling treatment on reducing pit initiation may also be assumed to involve desensitization of the main sites of pit initiation, i.e., the grain boundaries.

A further relationship between grain-boundary etching and pit initiation was shown by etching characteristics of the 18Cr-8Ni-2.5Mo-2.5Si steels. These steels (SP-1 and SP-2) were the most resistant to pit initiation and were also the most difficult to etch. The usual electrolytic etching reagents (oxalic acid and sodium cyanide) did not reveal the austenitic grain boundaries. Aqua regia solutions were required to bring out the grain structures.

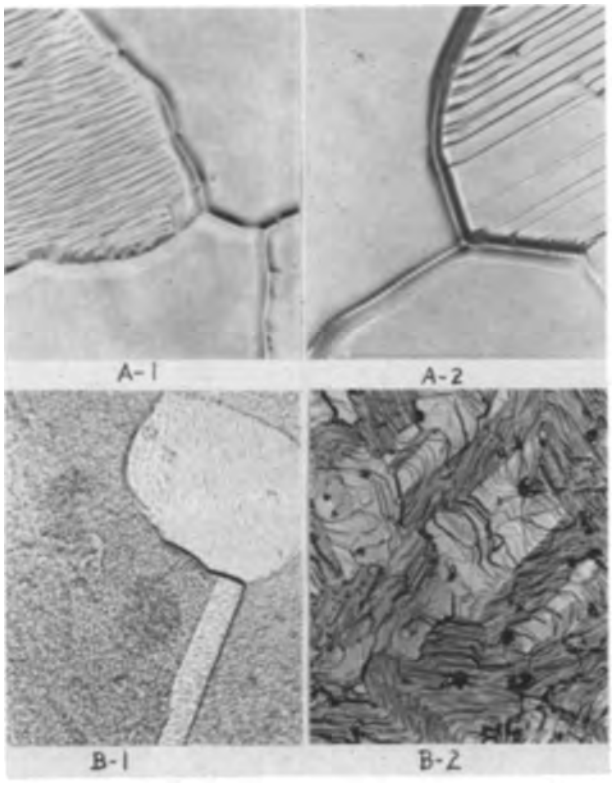

FIG. 13. Thermally etched stainless steels (etched by heating 24 hr at 2000°F in evacuated tube). A-1, AISI 304 (18Cr-8Ni); A-2, AISI 316 (18Cr-8Ni-2.5Mo); B-1, AISI 302B (18Cr-8Ni-2.5Si); B-2, SP-1 (18Cr-8Ni-2.5Mo-2.5Si). 1000× before reduction for publication.

Thermal-etch structures.—The pronounced influence of silicon on grain-boundary properties was further illustrated by the response of various stainless steels to thermal etching. Polished metal surfaces were etched by heating at high temperatures in controlled atmospheres or in vacuum. At elevated temperatures, structures were formed by surface diffusion which reflected the crystallographic characteristics of the grains and their boundaries. A relatively simple method was developed for thermally etching stainless steels. A polished stainless steel specimen was placed in a 12-in. long quartz tube which was heated to 400°C, evacuated to 5×10^{-5} mm Hg, and sealed. For thermal etching this tube was placed in a combustion tube furnace with the specimen in one end of the tube and the other end protruding 1–2 in. from the furnace to act as a condenser. The specimen was then heated at 1093°C for 24 hr and allowed to cool in the furnace. When cool, the tube was cracked open to remove the specimen.

Photomicrographs of four thermally etched stainless steels are given in Fig. 13. The 18Cr-8Ni (Type 304) and 18Cr-8Ni-Mo (Type 316) steels showed pronounced grooving at the grain boundaries. The angle at the bottom of these grooves varied with the orientation of the grains as well as the orientation of the boundary (41). The addition of about 2.5% Si, to give AISI-302B and the SP steels, completely eliminated all grooving at the grain boundaries, and in some cases produced pronounced steps between grains. Thus, there was a marked effect produced by silicon in these steels on the properties of their grain boundaries, which were the primary sites of pit initiation. It was demonstrated in a number of tests described above (Tables III and VII) that silicon additions to 18Cr-8Ni stainless steels increased the resistance to pit initiation. Thus, thermal etches provided further evidence for the primary role of grain boundaries in pit initiation.

Summary and Discussion

The present investigation showed that pitting resistance of 18Cr-8Ni stainless steels may be increased: (*a*) by increasing the basic resistance to pit initiation, and (*b*) by increasing the response to passivation, i.e., the ability to heal breaks in the protective films. Additions of silicon changed the properties of grain boundaries, which were the primary sites of pit initiation. Molybdenum additions to stainless steels did not change the grain-boundary properties, but greatly increased the ability of the steel to heal breaks in the protective film and to respond to oxidizing inhibitors. Lowering the carbon content increased the basic pitting resistance and also increased the response to passivation (Table III). The role of nitrogen in increasing pitting resistance was more difficult to determine. Nitrogen in its role as an austenitizer eliminated ferrite in the steels containing silicon and molybdenum and probably contributed to pit corrosion resistance in this way. The results on SP steels supported this conclusion. It has also been reported that 18Cr-8Ni-2.5Mo steels, containing ferrite, pit more readily than those which are completely austenitic (8). In addition, there is some evidence that increasing

the nitrogen content of completely austenitic steels improves pitting resistance (Table III).

The improvement in pitting resistance (initiation and growth) of 18Cr-8Ni stainless steels produced by individual use of silicon or nitrogen additions or removal of carbon was relatively small. However, when used in combination (molybdenum, silicon, and nitrogen additions, and removal of carbon) the resulting austenitic alloy (SP-2) was superior to the regular 18Cr-8Ni-2.5Mo (Type 316) steel, even in sea water.

The unique physical and chemical properties of grain boundaries have been revealed in a large variety of measurements (42). They are frequently preferred sites for the accumulation of impurities, for precipitation of new phases from solid solution, for adsorption, and for chemical attack. The boundary represents a transition from one crystal lattice to another. Such transition regions have a high density of lattice imperfections, i.e., dislocations, which are sites of preferential chemical attack (43, 44). These imperfections probably influence the structure and properties of any films formed on them. Thus, the portions of the protective film over the imperfections probably also contain structural imperfections, which are more susceptible to breakdown than other portions of the surface.

On exposure of a stainless steel surface to chloride solutions there probably is preferential adsorption (especially at grain boundaries) of chloride ions, which tends to exclude adsorption of film healing oxygen, as in the case of platinum surfaces (30). At certain imperfections in the protective film, occurring primarily at grain boundaries, cations from the metal can diffuse through the film more readily than at other points (45, 46).

This diffusion process may also be accelerated if chloride ions become imbedded in the lattice of the protective film; these chloride ions would then prevent the formation of protective oxides (47). Thus, chloride ions may contribute in several ways to the breakdown of protective films and may also prevent the healing of such points of breakdown by excluding oxygen and by decreasing the pH of the solution adjacent to the surface. In acid solution, solid corrosion products, which might serve to plug any points of film penetration, become soluble (48).

The enhanced self-passivating property of 18Cr-8Ni stainless steel containing molybdenum has also been demonstrated by a reverse of the breakdown method. In this technique, electrode potential measurements are made on stainless steels which have been activated by chemical pickling (35, 49, 50) or mechanical scratching (51) to determine whether or not, and the rapidity with which, passivity is reestablished in a given solution. It was found that molybdenum additions to stainless steels greatly increase the rate at which passivity is restored. In the present investigation it was concluded in agreement with others (35, 49, 51) that passivity is restored by a protective film which is a product of the reaction between the corroding metal and some constituent of the potentially corrosive solutions. The temperature of the corroding solution greatly influences the capacity for self-passivation. This is shown by the results on the influence of molybdenum on pit initiation at temperatures between 35° and 70°C. The beneficial effects of molybdenum, observed at room temperature, are lost at higher temperatures.

This dynamic view of passivity is supported by the fact that certain inhibitors are consumed, even though the metal being inhibited does not corrode appreciably. At numerous points of incipient breakdown in the surface the inhibitor reacts with the metal ions diffusing through nonprotective areas to form protective films before actual pits are formed.

ACKNOWLEDGMENT

The author wishes to thank Mr. F. L. LaQue, Vice President, and Dr. T. P. May, The International Nickel Company, New York, N. Y., for arranging the sea-water exposure tests and Mr. J. L. Sheppard and Mr. S. J. Kucharsey for their assistance with the experimental work.

Manuscript received September 14, 1955. This paper was prepared for delivery before the Pittsburgh Meeting, October 9 to 13, 1955.

Any discussion of this paper will appear in a Discussion Section to be published in the June 1957 JOURNAL.

REFERENCES

1. R. H. BROWN AND R. B. MEARS, *Trans. Faraday Soc.*, **35,** 467 (1939).
2. H. H. UHLIG, *Trans. Am. Inst. Mining Met. Engrs.*, **140,** 442 (1940).
3. R. B. MEARS AND R. H. BROWN, *This Journal*, **97,** 75 (1950).
4. O. B. ELLIS AND F. L. LAQUE, *Corrosion*, **7,** 362 (1951); *see also* E. WYCHE, L. R. VOIGHT, AND F. L. LAQUE, *Trans. Electrochem. Soc.*, **89,** 149 (1946).
5. F. G. FRESE, *Ind. Eng. Chem.*, **30,** 83 (1938).
6. International Nickel Co., "Nickel Topics," **4,** [2], 7 (1951).
7. H. A. SMITH, *Metal Progr.*, **33,** 596 (1938).
8. S. P. ODAR AND H. A. SMITH, *Trans. Am. Inst. Mining Met. Engrs.*, **135,** 526 (1939).
9. G. RIEDRICH, *Metallwirtschaft*, **21,** 407 (1942).
10. W. TOFAUTE AND H. SCHOTTKY, *Arch. Eisenhüttenw.*, **14,** 71 (1940); *see also* H. BENNEK, **15,** 515 (1942).
11. H. H. UHLIG, *Trans. Am. Soc. Metals*, **30,** 947 (1942).
12. U. R. EVANS AND R. B. MEARS, *Proc. Roy. Soc.*, **146A,** 153 (1934).
13. R. B. MEARS, *Iron Steel Inst. (London) Carnegie Schol. Mem.*, **24,** 69 (1935).
14. R. B. MEARS AND R. H. BROWN, *Ind. Eng. Chem.*, **29,** 1087 (1937); *Trans. Electrochem. Soc.*, **74,** 495 (1938).
15. R. B. MEARS AND U. R. EVANS, *Trans. Faraday Soc.*, **31,** 527 (1935).
16. P. M. AZIZ, *This Journal*, **101,** 120 (1954).
17. H. A. LIEBHAFSKY AND A. E. NEWKIRK, *Corrosion*, **9,** 432 (1953).
18. R. MAY, *J. Inst. Metals*, **32,** 65 (1953).
19. J. WULFF, H. A. SMITH, AND H. H. UHLIG, Progress Reports to the Chemical Foundation, Massachusetts Institute of Technology No. I-VI (1936-38).
20. W. A. WESLEY AND C. H. LINDSLEY, *Metals and Alloys*, **8,** 335 (1937).
21. H. J. DONKER AND R. A. DENGG, *Korrosion u. Metallschutz*, **3,** 217, 241 (1927).
22. H. H. UHLIG AND J. WULFF, *Trans. Am. Inst. Mining Met. Engrs.*, **135,** 494 (1939).
23. S. J. BRENNERT, *J. Iron Steel Inst. (London)*, **135,** 101 (1937); *also Korrosion u. Metallschutz*, **13,** 379 (1937).
24. U. R. EVANS, "Metallic Corrosion, Passivity and Protection," p. 21, Ed. Arnold & Co., London (1946).
25. E. M. MAHLA AND N. A. NIELSEN, *Trans. Electrochem. Soc.*, **89,** 167 (1946).

26. S. GLASSTONE, "Textbook of Physical Chemistry," pp. 1016, 1221, D. Van Nostrand Co., New York (1947).
27. O. STERN, *Z. Elektrochem.*, **30,** 508 (1924).
28. D. C. GRAHAME, *Chem. Rev.*, **41,** 441 (1947).
29. A. HICKLING, *Trans. Faraday Soc.*, **41,** 333 (1945).
30. B. ERSHLER, "Discussions of the Faraday Society on Electrode Processes," No. 1, p. 269, Gurney and Jackson, London (1947).
31. L. CAVALLARO AND C. BIGHI, *Metallurgia ital.*, **44,** 361 (1952).
32. J. W. MATTHEWS AND H. H. UHLIG, *Corrosion*, **7,** 419 (1951).
33. H. H. UHLIG AND M. C. MORRILL, *Ind. Eng. Chem.*, **33,** 875 (1941).
34. K. BUNGARDT, *Stahl u. Eisen*, **70,** 582, 589 (1950).
35. W. G. RENSHAW AND J. A. FERREE, *Corrosion*, **7,** 353 (1951).
36. M. H. BROWN, W. B. DELONG, AND W. R. MYERS in "Symposium on Evaluation Tests for Stainless Steels," STP-93, A.S.T.M. p. 103–120 (1949).
37. E. M. MAHLA AND N. A. NIELSEN, Unpublished results.
38. H. H. UHLIG, U. S. Pat., 2,172,421, Sept. 12, 1939.
39. E. E. THUM, "Book of Stainless Steels," p. 693, American Society for Metals, Cleveland (1935).
40. N. A. NIELSEN, Unpublished results.
41. B. CHALMERS, R. KING, AND R. SHUTTLEWORTH, *Proc. Roy. Soc.*, **A193,** 465 (1948).
42. R. KING AND B. CHALMERS, "Progress in Metal Physics I," pp. 127–62, Interscience Publishers Inc., New York (1949).
43. R. GEVERS, S. AURELINCKX, AND W. DEKEYSER, *Naturwissenschaften*, **39,** 448 (1952).
44. W. T. READ, "Dislocations in Crystals," p. 158, McGraw-Hill Book Co., New York (1953).
45. J. V. PETROCELLI, *Trans. Electrochem. Soc.*, **97,** 10 (1950).
46. T. P. HOAR AND U. R. EVANS, *This Journal*, **99,** 212 (1952).
47. E. J. W. VERWEY, *Philips Tech. Rev.*, **9,** 46 (1947); "Proceedings of the International Symposium on the Reactivity of Solids," Part II, p. 844. Elanders Boktryckeri, Gothenburg (1952).
48. T. P. HOAR, "Discussions of the Faraday Soc. on Electrode Processes," No. 1, p. 299, Gurney and Jackson, London (1947).
49. L. GUITTON, *Metal Treatment*, **14,** [53], 3 (1948).
50. H. H. UHLIG, *Trans. Am. Inst. Mining. Met. Engrs.*, **140** 387 (1940).
51. G. V. AKIMOV AND G. B. CLARK, *Compt. rend. acad. sci. U.R.S.S.*, **45,** 379 (1944).

A Study of Whisker Formation in the Electrodeposition of Copper

P. A. VAN DER MEULEN AND H. V. LINDSTROM

Ralph G. Wright Laboratory, Rutgers University, New Brunswick, New Jersey

ABSTRACT

Under certain conditions the electrolysis of acid copper sulfate between copper electrodes leads to formation of long filaments, or "whiskers," of copper on the cathode. Certain additives in the electrolyte are capable of overcoming the tendency toward abnormal growth and act to give smooth copper deposits. Possible mechanisms involved in electrolytic copper filament formation and its prevention are discussed, and a reasonable hypothesis to explain the process is suggested.

INTRODUCTION

In commercial copper electrorefining with acid copper sulfate electrolyte the current density is usually around 2.0 amp/dm^2 (18 amp/ft^2). This leads to copper deposits which tend to give nodules or trees unless smoothing agents are added. If the current density is quite low (0.05–0.10 amp/dm^2) and if the electrolyte is quite pure, a fairly smooth deposit is obtained. Under some conditions the deposits at these low current densities show abnormalities which do not occur at higher current densities and may, therefore, be considered characteristic of low current operation. These abnormalities are manifested as fine filaments or "whiskers" of copper on the cathode. Only a small part of the copper deposited electrolytically appears in the form of whiskers. In one case this amounted to about 5% of the total, the other 95% forming a fairly smooth deposit. Calculation reveals that copper deposition at the tip of the whisker takes place nearly a thousand times as fast as on the smooth part of the cathode. At higher current densities these growths appear to form nodules or spikes.

Most of the references in the literature on the subject of metal whiskers relate to filaments formed on metals in dry environments. Wakelin (1) reported the appearance of whiskers on heated copper and has given a review of the subject. Compton, Mendizza, and Arnold (2) described whisker growths on metal surfaces used in telephone communications equipment. In the field of copper electrodeposition from acid copper sulfate baths, copper whiskers were described by Gollop (3) who stated that very low current densities and absence of motion of cathode or electrolyte are needed before filaments can grow. Turnbull (4) described the appearance of copper spikes on cathodes in large electroforming baths which contain chloride and which are operated at higher currents.

This paper reports a study of the growth of fine copper filaments on copper cathodes in acid copper sulfate cells operated at low current densities. Two types of whiskers

grew under these conditions. One, grown in the presence of chlorides, is a straight needle-like filament which may have the appearance of a single crystal. The other, grown in the presence of cationic surface-active agents, appears as a polycrystalline filament which is a twisting hair of varying diameter.

Experimental

The Experimental Cell

Results of work in open beakers were not reproducible. It was suspected that whiskers could not accumulate enough copper to grow to visible size in beaker experiments because they dissolved in the oxygen-containing electrolyte. To test the dissolution tendency of copper under these conditions, copper strips were partially submerged in acid copper sulfate solution open to the air. It was noted that copper dissolved fairly rapidly at the air-electrolyte interface. However, if antioxidants (such as tertiary butyl cresol) were added to the electrolyte, the rate of loss of copper at this interface was very low.

To control all factors which might affect copper filament formation, a closed glass cell was constructed. High purity copper electrodes could be inserted and tightened to give a glass-to-copper contact. The cell volume was about 30 ml, but cells two and three times as large gave identical results. Fig. 1 shows the parts in proper relative positions before assembling.

The control electrolyte consisted of reagent grade copper sulfate pentahydrate (120 g/l), reagent grade sulfuric acid (72 g/l), and reagent grade hydroxylamine sulfate (5 g/l). The presence or absence of the hydroxylamine sulfate had no effect on whisker manifestation. However, it did give finer grain deposits and was included to insure smooth control cathodes for purposes of comparison. The electrolyte was at equilibrium with air prior to its addition to the cell. The cell was then sealed with a glass stopper so that the electrolysis was performed without further contact with air. In no instance could filaments be formed with the control electrolyte alone. When filament-generating substances were present in the electrolyte, whisker formation took place to a maximum extent if nitrogen gas was used to sweep the cell and its contents prior to electrolysis. If the cell and its contents were treated with oxygen gas to saturate the electrolyte prior to electrolysis, practically no whiskers formed. This was an indication that whiskers in their early stage probably dissolve in the electrolyte with the aid of oxygen and are prevented from growing. If the cells which had been treated with oxygen were allowed to run longer at the usual current or were run at somewhat higher currents, some whisker formation did take place. It is likely that the oxygen is depleted, then the filaments grow.

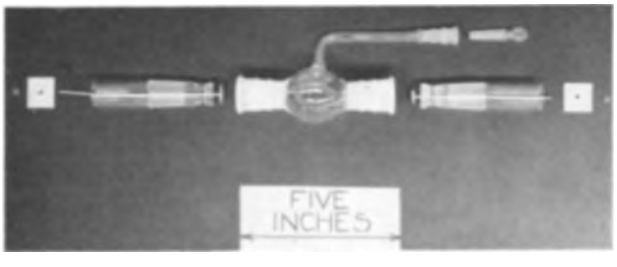

Fig. 1. Glass cell and copper electrodes used in this work to grow copper filaments electrolytically.

Filaments Generated by Chlorides

Chlorides have been used for many years as addition agents in copper electroplating baths utilizing acid copper sulfate. This halide reportedly removes silver as silver chloride and keeps the codeposition of antimony and bismuth with copper to a minimum. The concentration used in practice varies from 10 to 50 mg/l as chloride ion. A comprehensive study of the effect of chlorides on copper deposition was made by Winkler and co-workers (5, 6). They showed that chloride ions in acid copper sulfate have no effect on electrode processes below a definite minimum concentration (9 mg/l at 25°C), corresponding to the solubility of cuprous chloride in their electrolyte. Their work was concerned with electrode appearance and polarization, so they did not mention whisker formation. They operated at about 2 amp/dm², much too high for filament formation at low chloride levels, according to the present work.

Here chloride was added as the calcium and sodium salts and as hydrochloric acid; all were effective in growing filaments. Only hydrochloric acid was used after preliminary experiments had shown that chloride ion is the essential constituent. It was found that whiskers would grow at 25°C from electrolyte containing chloride in the range from 5–15 mg/l. Above this level a coating of white cuprous chloride formed on the cathode. The optimum appeared to be 10 mg/l which corresponds to the 9 mg/l mentioned above (5, 6). The most effective current densities for whisker formation, utilizing chloride at 10 mg/l, were in the range of 0.05–0.20 amp/dm². Under these conditions whiskers develop in about 48 hr. At higher values the filaments became branched, changed into trees, or collapsed into nodules. Fig. 2 is a photograph of the whisker type brought about with chloride at 10 mg/l. The filaments are straight and needle-like with a sharp point and have the appearance of single crystals.

At first the chloride experiments were not reproducible.

Fig. 2. Copper filaments grown with chloride at 10 mg/l using a current of 0.07 amp/dm².

Under apparently identical conditions, some cells might produce whiskers and others not. The cause of these variations was traced eventually to the presence of suspended particles in the electrolyte. If the electrolyte with chloride present was filtered through an ultrafine filter[1] prior to use, the variability disappeared almost completely and essentially no filaments would form. The effect of suspended particles was confirmed by adding such materials as carbon black, clay, or silica to the filtered electrolyte. Invariably such additions increased whisker formation by chloride ion and gave satisfactory reproducibility. The presence of these added particles did not bring about filament growth in the absence of chloride. It seems to be clear that dust and foreign material present in supposedly pure chemicals play an important role in the whisker formation brought about by chloride ion.

Filaments Generated by Cationic Surface-Active Agents

Copper filaments, of a type different from those grown with chloride, could be formed on the cathodes in the presence of cationic surface-active agents in the electrolyte. Except for substituting surface-active agents for chloride, all operating conditions were the same. These filaments were polycrystalline and grew in a twisting fashion. They were fine hairs elongated to a considerable extent, in contrast to the relatively short, thick needles formed in the presence of chloride. Fig. 3 is a photograph of filaments formed with cetyl trimethyl ammonium bromide as the generating substance. Similar filaments were grown with cetyl dimethyl ethyl ammonium bromide and cetyl pyridinium bromide. No whisker formation was possible with tetramethyl ammonium bromide. These surface-active agents, being cationic, may migrate to the cathode, and this fact probably may play a large role in filament formation. Various anionic and nonionic surface-active agents did not produce whiskers on the cathode. Suspended particles were shown to play a role here as well as in the case of chloride, because solutions containing cetyl trimethyl ammonium bromide filtered through an ultrafine glass filter did not produce filaments.

FIG. 3. Copper filaments grown with cetyl trimethyl ammonium bromide at 100 mg/l.

[1] Bacteria Filter Apparatus No. 68235, Emil Greiner Co.

Certain cationic polysoaps, described by Strauss and Gershfeld (7), are also capable of producing hairlike filaments. In this case, however, the whiskers are shorter and quite brittle in comparison to the wire-like and ductile filaments produced in the presence of cetyl trimethyl ammonium bromide. One of Strauss' polysoaps (polymerized vinyl pyridine partially quaternized with lauryl bromide and labeled G 147) gave reproducible results and was studied in detail. In this instance, passage through the ultrafine filter prior to electrolysis did not prevent the formation of filaments. This is very likely due to the fact that dispersed G 147 polysoap is not filtered out but still has a particle size capable of aiding whisker growth. This is in addition to its action as a cationic surface-active agent.

The cationic surface-active agents described here bring about whisker formation most readily at concentrations from 20 to 100 mg/l in electrolyte.

Cathode Potentials

The influence of various whisker-forming agents, in a concentration of 100 mg/l, on the cathode potential was studied in a glass electrolytic cell operating at 0.07 amp/dm^2. These potentials were measured by the use of a calomel half-cell dipping into an electrolyte reservoir connected to the cell by means of a glass tube of small bore, the tip of which was placed almost in contact with the cathode surface. Readings were made with a L&N Type K potentiometer. Observed increases in cathode potential are given in Table I. The whisker promoters, cetyl pyridinium bromide, cetyl trimethyl (or dimethyl ethyl) ammonium bromide, and the quaternized polysoaps give large increases and therefore may have a strong tendency to form a film on the cathode. Materials which did not promote whiskers show small increases to indicate a lesser tendency to form a cathode film. The effect of chloride at 100 mg/l was included, even though this level is too high for filament formation by chloride. It indicates that the chloride mechanism probably differs from the surface-active agent mechanism. It might be noted here that it was possible to obtain chloride whiskers at 100 mg/l by the use of higher currents (0.50 amp/dm^2). Some relationship exists between chloride level and current density as far as whisker formation is concerned. Thick spikes of copper in large electroplating baths do occur under conditions of commercial operation where the chloride level and current density are both higher than in the cells under discussion.

TABLE I. *Relation between cathode potential and filament formation*

Additive (100 mg/l)	Increase in cathode potential (mv)	Filament formation
Cetyl pyridinium bromide	225	Good
Cetyl trimethyl ammonium bromide	251	Good
Cetyl dimethyl ethyl ammonium bromide	254	Good
Tetramethyl ammonium bromide	1	None
Polysoap G146 (Strauss)	224	Good
Polysoap G147 (Strauss)	270	Good
Polysoap G254 (Strauss)	224	Fair
Polyvinyl pyridine (Strauss) (not quaternized)	23	Poor
Chloride ion (HCl)	27	Good at higher current

Influence of Various Factors on Filament Formation

It has been shown above that filaments of copper grow most readily when the proper generating agent (chloride or cationic surface-active agent) is present, when the current density is low, and when oxygen is absent. Other factors have little, if any, bearing on the formation of whiskers. Although high purity copper was used in these experiments, it was found that whiskers would grow also on impure copper cathodes. When the standard electrolyte was diluted to one-half and to one-fourth concentration with distilled water prior to use, filaments grew as readily as in the more concentrated solution. Whiskers grew regardless of the position of the electrodes. The general manifestation was the same whether the electrodes were vertical or horizontal, or whether the cathode was the upper or lower electrode. When the cells were rotated slowly and continuously during the electrolysis the whiskers gave way to nodules.

Prevention of Whisker Growth

A search was made for materials which could be added to the electrolyte to prevent formation of whiskers by polysoap G 147, which was chosen as a standard filament generator. Results are given in Table II. Cystine and thiourea prevent filament formation if added just prior to cell operation. However, they are unstable in the electrolyte and lose their effectiveness. The successful smoothing action of pure phenazine and of the phenazine dyes (Safranine T and Neutral Red) indicates a unique ability of the phenazine grouping to stop whisker growth. When the phenazine group of safranine is opened to give an indamine molecule (by the use of Toluylene Blue dye) whisker growth is unhampered. Both of the nitrogen atoms in the center of the phenazine molecule appear to be necessary for effective smoothing action. When one of these nitrogen atoms is replaced by oxygen, sulfur, or carbon (by selecting, respectively, Brilliant Cresyl Blue, Thionin, and Acridine) the smoothing action is lost.

Safranine dyes continue to prevent whisker formation after prolonged aging of the electrolyte at room temperature. Dye preparations of Safranine T (Du Pont 125%) in a concentration of 20 mg/l in electrolyte have been effective after an aging period of four months. The chromophoric nature of the dye undergoes a change, however, after such storage. The absorption spectrum of freshly prepared Safranine T in electrolyte shows a single peak at 5200Å, but on standing the 5200Å peak decreases in height and a new peak appears at 4400Å. Since the smoothing action is dependent on the phenazine group, and the phenazine group itself has no dye properties, a change of color does not necessarily indicate a loss of smoothing action.[2]

TABLE II. *Effect of additives on "whisker" formation by Polysoap G147 (100 mg/l)*

Additive	Concentration of additive (mg/l)	Smoothing action on cathode
Anionic detergent (Sodium lauryl sulfate)	100	Poor
Nonionic detergent (Polyoxyethylated nonylphenol)	100	Poor
Aniline	100	Poor
Phenylhydrazine	25	Poor
Nitrobenzene	25	Poor
Azoxybenzene	25	Poor
Cresol Indophenol	25	Poor
Chrysoidine Y	25	Poor
Ethylene Diamine	25	Poor
Malonic ester	25	Poor
Methionine	100	Poor
Cystine (freshly added)	50	Excellent
Cystine (after 30 days at 25°C in electrolyte)	50	Poor
Thiourea (freshly added)	50	Excellent
Thiourea (after 30 days at 25°C in electrolyte)	50	Poor
Bismarck brown Y	100	Poor
Zambesi black VD	100	Poor
Supranol brown RL	100	Poor
Safranine T (freshly added)	20	Excellent
Safranine T (after 4 months at 25°C in electrolyte)	20	Excellent
Neutral red	20	Excellent
Phenazine	20	Excellent
Brilliant cresyl blue	20	Poor
Thionin	20	Poor
Acridine	20	Poor
Toluylene blue	20	Poor

TABLE III. *Cathode potentials brought about by mixtures of polysoap and smoothing agents*

Electrolyte additive (G147 Polysoap 100 mg/l) (smoothing agents 20 mg/l)	Cathode potential (mv)
G147 Polysoap alone	273
Cystine alone	37
Cystine plus G147 Polysoap	250
Thiourea alone	33
Thiourea plus G147 Polysoap	276
Safranine alone	70
Safranine plus G147 Polysoap	78
Neutral Red alone	58
Neutral Red plus G147 Polysoap	85
Phenazine alone	12
Phenazine plus G147 Polysoap	82

[2] Patents have recently been issued for the use of safranine dyes to assure smooth electrolytic copper deposits from acid baths in the electroplating industry (8, 9). These came to the authors' attention after the completion of this work.

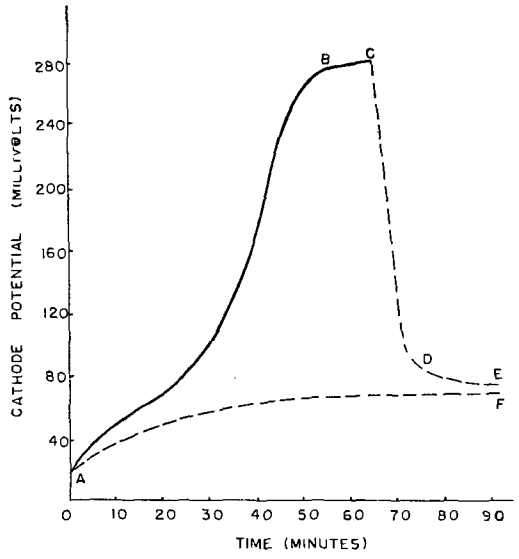

FIG. 4. Influence of additives on the copper cathode potential in a closed cell operating at 0.07 amp/dm². Curve ABCDE shows the increase in cathode potential due to the addition of polysoap, and its reduction by Safranine T. At A, 100 mg/l of polysoap G147 was added to the cell, and measurements of cathode potential were made at intervals. The potential rose to 270 mv in about 60 min (B), and remained constant. At (C), 20 mg/l of Safranine T was added. The cathode potential dropped sharply to a value of 80 mv (D), and then remained practically constant (E). Curve AF shows the effect of the addition of 20 mg/l of Safranine T to the cell when no polysoap is present. The cathode potential value rises to about 75 mv.

Under the conditions of the experiments, whisker-producing agents raise the copper cathode potential more than 200 mv (Table I). Table III gives the copper cathode potentials brought about by whisker-preventing agents and also shows the effect of these agents on the high potentials brought about by the whisker-forming agent G 147. Addition of a phenazine dye alone raises the cathode potential to a relatively moderate extent (70 mv), and reduces the rise in cathode potential brought about by whisker-producing agent G 147. Fig. 4 shows that this reduction is sufficient to bring the potential down to the level produced by the dye alone. This nullification may well be involved in the smoothing action of safranine dyes. With the smoothing agents cystine and thiourea, a reduction of the high potential does not take place.

Undoubtedly the action of fiber-generating agents begins with adsorption of the substance on the copper cathode. The large increase of the cathode potential brought about by cetyl trimethyl ammonium bromide indicates strong adsorption. The whisker-forming chloride ion is also adsorbed on copper metal as was shown when typical Freundlich adsorption isotherms were obtained utilizing finely divided copper powder[3] as adsorbent in pure water as solvent. The whisker-preventing agent Safranine T was also strongly adsorbed on copper metal. The dye probably displaces whisker-forming agents, and this results in a reduced cathode potential. Nullification of a high cathode potential does not necessarily have to enter into whisker-prevention, but when it does, there is likely to be a more effective smoothing action.

[3] Supplied by U. S. Metals Co., Carteret, N. J.

DISCUSSION

The results of the experimental work described above lead to a reasonable hypothesis to explain the whiskering process. The generating substance forms a film on the cathode and interferes with the normal deposition of the copper. In the case of chloride this film is cuprous chloride and in the case of the cationic surface-active agent this film is the oriented molecule held tightly to the copper cathode because of the surface-active grouping and because of its positive charge. During copper electrodeposition, these films are responsible for an increase in potential between the cathode and the solution. Certain areas may be bare for shorter or longer periods of time. These spots have a relatively higher current density and copper tends to deposit on them more readily than on the rest of the surface. However, the presence of these bare spots alone does not account for whisker growth. Suspended particles are also necessary. These probably adsorb copper sulfate. When such a particle with its adsorbed copper sulfate layer settles on a bare spot on the copper surface, there will be a rapid deposition at this spot and a fiber starts. The particle will be carried away from the cathode on top of the depositing copper, but will continue to furnish a convenient path for supplying copper from the solution to the growing fiber. Obviously the particle can continue most effectively in an unstirred solution. The sides of the fiber will be coated with a film in the same manner as the cathode proper. Lateral growth of the fiber is, therefore, inhibited. The tip of the fiber is free from such a film because copper is depositing selectively at this point faster than film-forming substance can get to the growing surface. In the acid solution, dissolved oxygen tends to dissolve the fine whiskers before they grow very long. If oxygen is removed, or if antioxidants are present, whisker growth is facilitated. The strong adsorption tendency of some smoothing agents on copper undoubtedly aids smoothing action. The apparently specific action of safranine dyes, as opposed to azo dyes, etc., has been shown to involve the phenazine grouping. Both of the nitrogen atoms of this phenazine appear to be necessary, since substitution of oxygen, sulfur, or carbon for one of these nitrogen atoms results in a loss of smoothing action.

ACKNOWLEDGMENTS

The authors wish to acknowledge the assistance of Dr. Y. E. Lebedeff of the Central Research Laboratory of the American Smelting and Refining Company for valuable suggestions and helpful discussions.

This investigation was sponsored by the Naval Ordnance Laboratory, Silver Spring, Maryland, and was carried out under Bureau of Ordnance Contract NOrd 14075.

Manuscript received October 24, 1955.

Any discussion of this paper will appear in a Discussion Section to be published in the June 1957 JOURNAL.

REFERENCES

1. R. J. WAKELIN, *Bull. Inst. Metals*, I (**20**), 186 (1953).
2. K. G. COMPTON, A. MENDIZZA, AND S. M. ARNOLD, *Corrosion*, **7**, 327 (1951).

3. H. Gollop, *Bull. Inst. Metals*, II (1), 7 (1953).
4. J. G. M. Turnbull, *ibid.*, II (3), 19 (1953).
5. W. H. Gauvin and C. A. Winkler, *This Journal*, **99**, 71 (1952).
6. L. Mandelcorn, W. B. McConnell, W. Gauvin, and C. A. Winkler, *ibid.*, **99**, 84 (1952).
7. U. P. Strauss and N. L. Gershfeld, *J. Phys. Chem.*, **58**, 747 (1954).
8. H. Brown, H. Woods, and R. A. Fellows (Udylite Corp., Detroit, Mich.), U. S. Pat. No. 2,707,166, April 26, 1955.
9. E. W. Hoover and H. Woods (Udylite Corp., Detroit, Mich.), U. S. Pat. No. 2,707,167, April 26, 1955.

Deposition of Titanium from Titanium-Oxygen Alloys on Copper, Iron, and Mild Steel

S. T. Shih,[1] M. E. Straumanis, and A. W. Schlechten

Department of Metallurgy, University of Missouri School of Mines and Metallurgy, Rolla, Missouri

ABSTRACT

The presence of some oxygen was found to be beneficial in coating titanium on other metals in a fused alkali chloride bath. An improved method of titanizing was developed by controlling the amount of oxygen by the use of prepared titanium-oxygen alloys or of titanium fines of known oxygen content as a source of titanium. The object to be coated with titanium was embedded in a mixture of NaCl or KCl and the alloy, and was heated in helium for several hours at about 850°C for copper objects, and about 1000° for those of iron and mild steel. The thickness of the coating depends primarily on temperature and secondarily on time, oxygen content of the alloy, and composition of the bath. The same bath can be used repeatedly. The coatings adhere well to the base metals and protect them from corrosion. Deformation within the elasticity limits of the base metal does not affect the quality of the coating.

Introduction

Previous work has shown that copper, iron, or nickel pieces can be coated with titanium, if they are embedded in titanium powder, covered with salt, and heated in air, or if the piece of metal and a piece of titanium were put adjacent to each other and heated in a salt bath in presence of air. Titanium corroded (1) while the other metal was covered with titanium (2). However, if the process was carried out in vacuum, good coatings were not obtained. This suggests that the presence of air was helpful to the production of the coating. Indeed, later work showed that one of the main corrosion products of titanium in a fused salt bath was a titanium-oxygen alloy containing 9–11% by weight of oxygen (3). As this product was formed in the vicinity of the corroded titanium (1) it seemed reasonable to believe it might play an important role in the titanizing process. Therefore, experiments were performed to study this process in a fused salt bath, using titanium-oxygen alloys as a starting material, and to study the properties of the coatings obtained.

Experimental

Preparation of Titanium-Oxygen Alloys

The alloys were prepared by heating metallic titanium powder and titanium dioxide in a vacuum furnace (4) at about 1150°C. The purity of the titanium powder[2] used was better than 99%, and the titanium dioxide was of C. P grade. Charges were calculated on the basis of the desired oxygen content, which was supplied by the titanium dioxide in the charge. For instance a titanium-oxygen alloy of the composition 90 Ti–10 O (or $TiO_{0.11}$) was made up by taking about 51 parts by weight of titanium and 5 parts by weight of titanium dioxide. Each charge was ground in a mortar, thoroughly mixed, and heated in an alundum crucible in a vacuum furnace at less than 10 μ of gas pressure at 1150°C for 4 hr.

The alloys prepared, containing approximately 5, 7, 10, 20, and 30 at. % of oxygen, had a metallic, titanium-like luster and color, those with a higher oxygen content being darker. They were brittle, could be crushed, and showed a quite homogenous crystalline structure under the microscope.

Titanium fines screened out of crushed sponge were also used. They contained more oxygen than coarse sponge. Analysis of one sample showed 97.7 at. % titanium.

Experimental Procedure

Three series of plating experiments were carried out with the titanium-oxygen alloys.

The first was of an exploratory nature, and was simply performed in air with potassium chloride mixed with 20% of different titanium-oxygen alloys.

The second series was conducted in an inert atmosphere. The furnace was so arranged that its mullite tube could be

[1] Present address: Department of Metallurgy, Montana School of Mines, Butte, Mont.

[2] From the Belmont Smelting and Refining Works, Inc., Brooklyn, N. Y.

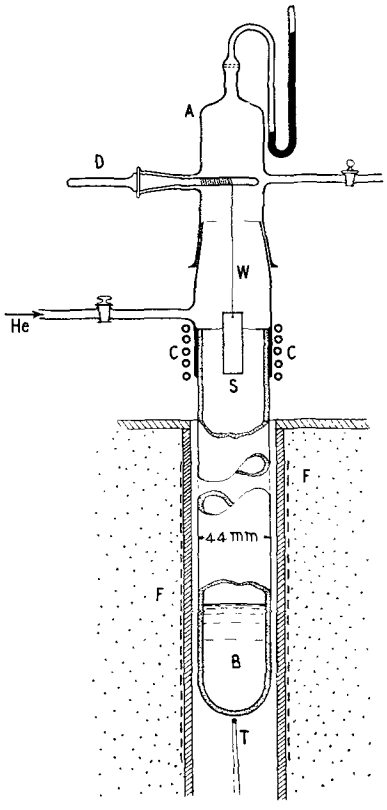

FIG. 1. Device for lowering the sample into the molten salt bath and raising the sample in an atmosphere of helium. S—sample to be titanized; B—molten salt bath containing TiO_x; W—Pt wire; D—cranking device; F—furnace; C—coil with cooling water; A—cap of Pyrex glass; T—end of the thermocouple.

connected either to the vacuum system or to a source of dry purified helium.

The ground and polished specimen, embedded in a mixture of titanium alloy and salt (KCl or NaCl in a porcelain or iron crucible) was dried in the furnace, which then was flushed with helium. During the coating experiments at 900°–1000°C the pressure in the furnace was held a few centimeters above atmospheric pressure to prevent ingress of air. Separation of the sample from salt occurred as already described (2).

This method was time consuming and somewhat wasteful because (*a*) some of the fine titanium powder was further oxidized during the leaching process, (*b*) some titanium, transformed into chloride, was hydrolyzed, and (*c*) the salt dissolved in the same process is lost if not recovered from the solution.

As a result, the third series of experiments was made to find a better way to separate the coated sample from the molten salt bath without exposing it and the sample to air. The experiments were performed on a small scale by inserting a winding device into the cap on the mullite tube which held the bath, as sketched in Fig. 1. On the spindle was wound a fine platinum wire to the end of which the sample could be hooked.

First the cap, A, was removed, the sample hooked to the end of the wire, W, the salt and titanium oxide mixture was charged into the bottom, B, of the tube, and the cap replaced so that the sample was somewhere in the middle of the tube. Then helium gas was fed into the tube and the current was turned on. At a temperature of 1000°C the sample was lowered into the bath, B, left there for 3 hr, and raised out into the water cooled zone, C, while the furnace was shut off. When the furnace was cooled below 400°C, the sample was removed, a new sample was hung in its place, and the experiment was repeated. In this way several samples could be titanized using the same bath with insignificant titanium losses.

In a modification of this series of experiments the disadvantage of heating and cooling the furnace for each separate sample was overcome as follows. When the titanized sample cooled off in zone C with the furnace still on, the helium pressure was increased and cap A was lifted; then the sample was replaced by a new one, the tube closed, and after a short time of flushing with helium the new sample was lowered into the bath, B, and so on. Thus, the penetration of air was prevented by the countercurrent of helium and by "getters" (such as pieces of titanium above the sample) in the inside of the tube. A series of runs were carried out continuously in this way without changing the temperature of the furnace. Each sample was weighed before and after the run (the thin adhering salt layer was washed off) to obtain the increase in weight due to the coating.

RESULTS

Tests in Air and Helium

Only experiments performed in air with titanium oxide alloys containing 10 at. % of oxygen or less were somewhat successful, although in all cases the inside walls of the crucibles were covered with a shining layer of titanium (2). To avoid further oxidation of titanium by air, the next coating experiments were made on copper in helium using titanium alloys containing 5, 7, and 10 at. % oxygen. Results are summarized in Table I.

The table shows that pure titanium did not produce coherent coatings, but that titanium-oxygen alloys were effective. The samples usually showed an increase in

TABLE I. *Deposition of* Ti *on* Cu *samples* (He *atmosphere*) *at 850°C*

O in TiO_x in at. %	Bath: TiO_x* in wt %	Time in hr	Cu sample	Quality of Ti coating
0	5 (x = 0)	5	Wire, spiral	Poor, only a few Ti spots.
5	15	4	Penny	Good, coated all over.
5	15	4	Wire, spiral	Good, coated all over.
5	15	2	Plate	Good, coated all over.
5	20	4	Plate	Fairly good, coated but rough.
7	15	2.5	Penny	Good, coated all over.
10	5	1.5	Plate	Coated all over, except a few spots.
10	10	1.5	Plate	Good, coated all over.
10	15	1.5	Wire	Embedded part well coated.
10	20	3	Plate	Good, coated all over.

* Balance being KCl.

weight of 10–13 mg, from the charge which usually contained 1 g of the titanium-oxygen alloy.

Thus, only about 1 or 2% of the alloy in the salt bath was used for the coating. X-ray diffraction patterns of the unused and recovered alloy showed that the latter differed from the original one only by a slight increase in oxygen content. If so, the recovered alloy should be able to produce coatings on new samples, and experiments on both copper and iron samples showed this to be true.

Deposition of Titanium on Iron and Steel in a Helium Atmosphere

Ingot iron, some iron pennies, and 1012 steel samples were used for the coating experiments. Since iron-titanium-oxygen alloys formed during the deposition process on the iron surface (5) have a higher melting point than the respective copper alloys, higher temperatures of 900°–1000°C were used. Temperatures below 900°C as well as mixtures with less than 10 wt. % of the titanium alloys were usually insufficient to produce good coatings (exception, *see* sample 9, Table II). The samples were well coated from all sides.

In Fig. 2 some of the mild steel objects of intricate shape containing about 0.15% carbon, coated all over with titanium, are shown.

This titanizing method has certain advantages as compared with the older method (2): (*a*) more uniform coatings covering all sides of the samples can be achieved, (*b*) a titanium metal of inferior grade can be used, thereby lowering the cost of raw materials, and (*c*) there is less waste of titanium through oxidation by air.

Four variables may influence the quality and the thickness of the coatings produced: temperature, time, oxygen content of the TiO_x alloys, and composition of the bath. The effects produced by each of these variables were studied, using ingot iron samples and changing the four variables in a systematic manner.

Most of the samples used were in the form of 58 x 19 x 16 mm strips of ingot iron. Ground, polished, and brushed samples were embedded vertically in the bath mixtures in crucibles made of iron pipe. The inside of the crucibles was precoated with titanium to avoid drawing titanium from the baths in the subsequent experiments. Smaller samples, (indicated with *a* in Table II) 13 x 13 x 3 mm, were embedded horizontally in porcelain crucibles filled with the bath mixture. All coatings were made under helium gas.

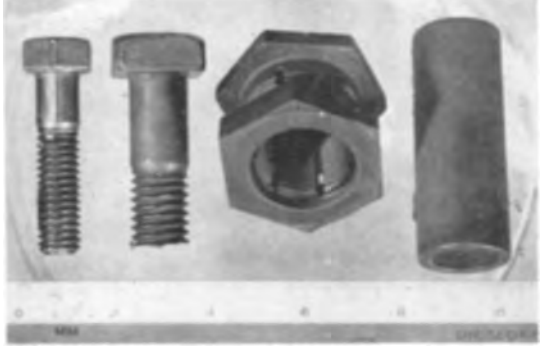

FIG. 2. Four mild steel objects coated with Ti in 3 hr, 950°C, using a TiO_x alloy with 5 at. % O, in a mixture with NaCl (10 wt % of the alloy and 90% NaCl). He atmosphere.

After coating, the samples were separated from the salt, examined, weighed, and corrosion tested. Measurements of the average increase in thickness for some samples were also made. This increase, measured with a micrometer, did not represent the thickness of the titanium coating because titanium diffused inward into the iron and iron also diffused outward into titanium. The actual thickness of the coatings was measured with a metallographic microscope on cross sections of the coated samples perpendicular to the surface. To reveal the coating microstructure the polished sections were treated by cumulative stain etching (6). The titanium coating, separated into several thin layers, appeared blue in color after etching, while the color of the diffusion layer was quite different, so that the coating and the diffusion layer could be differentiated clearly. Data are given in Table II. The following conclusions can be drawn from Table II with regard to the four variables studied:

Influence of temperature.—Samples 1, 4, and 7 clearly show the increase of weight with increasing temperature. The same trend is found when the thicknesses of the diffusion layers plus that of the coatings high in titanium content obtained at temperatures of 850°, 950°, and 1000°C are considered. The thickness of the coatings plus the diffusion layers agree well with those given previously (2), indicating that the coating process is the same regardless of whether solid titanium or titanium-oxygen alloys are used as a titanium source. The relationship between the increase in thickness of the titanium coating and the diffusion layer with temperature and time is further shown in Fig. 3. To demonstrate the difference between the coating and diffusion layer, a section through a sample is shown as Fig. 4.

Influence of time.—Time has an effect similar to that of temperature as clearly demonstrated by Fig. 3. However, growth rates of the titanium coating and of the diffusion layer are quite different: the thickness of the coating, which is of paramount importance for protection from corrosion, grows only slowly in the course of time, while the diffusion layer increases faster during the same period of time. So it may happen that with prolonged time of treatment the coating layer becomes thinner while a much thicker diffusion layer is being created. Evidence of this phenomenon can be seen in Table II, by comparing the thickness data for samples 15*a* and 16*a*.

Since temperature has a more marked effect than time on the thickness of the coating, a higher temperature and a shortened processing time should be applied for the production of thicker outer coatings. For instance, a sample prepared at 1000°C for 2 hr had a thicker coating layer than the one made at 950°C for 6 hr, although the latter had a slightly thicker diffusion layer due to longer diffusion time.

Influence of the composition of the TiO_x *alloy.*—Samples 7, 11, and 12 were coated at identical conditions except for the composition of the titanium-oxygen alloys. Thus, sample 7 (with 95 at. % Ti in the TiO_x alloy) gained 0.0065 g/cm², sample 11 (with 90 at. % Ti) gained 0.0059 g/cm², while sample 12 (with 80 at. % Ti) increased in weight by only

TABLE II. *Titanium coatings on ingot iron obtained in fused salt baths containing* TiO_x *alloys*
Helium atmosphere

Sample No.	Coating		Bath composition		Weight increase g/cm²	Avg increase in thickness,‡ mm	Thickness of	
	Temp, °C	Time, hr	Wt. % KCl†	At % Ti in TiO_x			Coating, mm	Diffusion layer, mm
1	850	4	90	95	0.0005	0.010	0.004	0.000
2	850	6	90	95	0.0008	0.013	0.006	0.000
3	950	2	90	95	0.0026	—	0.008	0.044
4	950	4	90	95	0.0045	—	0.012	0.068
5	950	6	90	95	0.0052	—	0.014	0.088
6	1000	2	90	95	0.0060	0.043	0.015	0.082
7	1000	4	90	95	0.0065	—	0.016	0.135
7*a*	1000	4	90	95	—	0.065	0.016	0.112
8	1000	4	80	95	0.0075	0.053	0.012	0.078
9	1000	4	95	95	0.0042	0.025	0.016	0.064
10	1000	4	90*	95	0.0066	0.050	0.015	0.115
11	1000	4	90	90	0.0059	0.038	0.012	0.100
12	1000	4	90	80	0.0032	0.013	0.012	0.084
13	1000	4	90	Ti fines	0.0061	0.048	0.014	0.067
14	1000	6	90	Ti fines	—	0.063	0.015	0.103
15	1000	6	90	95	0.0086	—	0.016	0.160
15*a*	1000	6	90	95	—	0.093	0.020	0.150
16*a*	1000	9	90	95	—	—	0.013	0.164
17*a*	1150	4	90*	Ti fines	—	—	0.021	0.245

* NaCl instead of KCl.
† Balance TiO_x.
‡ Measured with a micrometer.

0.0032 g/cm², all in 4 hr. Sample 13 showed results like those of sample 7. Analysis showed that the titanium fines contained 97.7% titanium as compared to 98.3% Ti for TiO_x with 95 at. % Ti. This is the optimum composition of the titanium bearing ingredient, since mixtures with less or no oxygen produce bad coatings. Titanium fines can be obtained at a lower price since it is not useful for ingot melting.

Influence of the composition of the bath.—Comparison of samples 9, 7, and 8 shows that a bath with a larger proportion of titanium gives a thicker coating. The increase in thickness measured by a micrometer followed the same trend. However, addition of the titanium compound is limited by the decreased fluidity of the resulting bath, which becomes too viscous if the TiO_x content is as high as 20 wt %.

As to the use of sodium or potassium chloride for the dispersion medium, samples 11 and 7 and also other experiments showed no appreciable difference in the quality of the coatings produced.

Influence of the metal to be titanized.—As already mentioned (2) many metals can be coated with a titanium. The quality of the coating on iron depends on its carbon content: electrolytic, ingot iron, and mild steel containing up to 0.2 wt % carbon can be titanized without difficulty by the method described. The higher the carbon content of iron, the higher the temperature required to produce good coatings. Evidently formation of titanium carbide on the surface of the steel samples hampers the diffusion inward and the accumulation of titanium on the surface of the samples.

Deposition of titanium in used baths in a continuous process.—In all of these experiments the coated sample was separated from the bath by leaching with water, and the unused titanium-oxygen alloy was recovered. However, this method wastes time and materials.

Obviously, a better way to separate the coated sample from the bath is to withdraw the sample from the molten bath into an inert atmosphere. This procedure was tested on a small scale using an arrangement sketched in Fig. 1. The bath, consisting of 70 g of 90 wt % sodium chloride and 10% titanium sponge mixture, was charged into the tube. Then the cap A was put on, the tube was evacuated, helium was admitted, and the sample was titanized at 1000°C in a manner already described. Four samples were coated successfully in this way until the platinum wire broke.

In a modification of this series of experiments, the cooling of the furnace was avoided and samples were removed in helium gas as described under the experimental procedure. This series was discontinued after the sixth run because of the breakage of the platinum wire. Nevertheless, all the samples had good titanium coatings, even those immersed in the bath for only 1.5 hr. Those immersed for 11.5 hr increased in weight about three times as much as those deposited at 2 hr. Increases in weight for the samples of the six runs were added and gave a sum of only 0.0346 g of titanium as compared with the total of 6.84 g originally present in the charge, showing that a large amount of titanium was still left unused. This titanium-oxygen alloy was recovered by filtering the leaching solution, and drying the residue in a vacuum oven at 105°C overnight. A gram of this residue was mixed with 9 g of sodium chloride to make a bath which was run at 1000°C for 4 hr. A piece of ingot iron embedded in this bath was found to be well coated with titanium. This experiment indicated that the residual titanium-oxygen alloy was still active, and that many other samples could be titanized in the same bath.

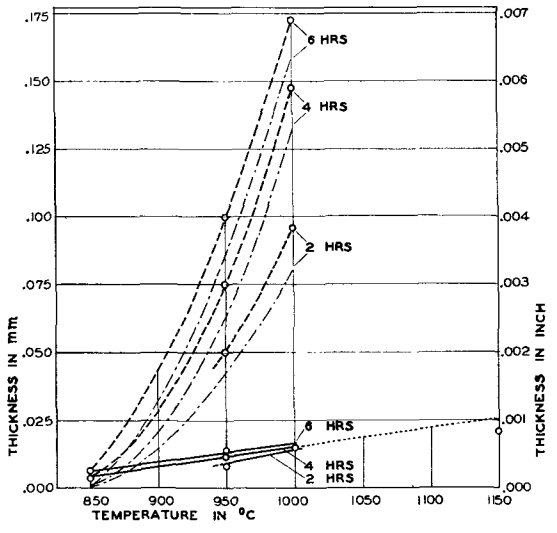

FIG. 3. Increase in thickness of titanium coatings (solid lines) and diffusion layers (dash-dot) with temperature and time. Dashed lines: total thickness of the deposit (coating plus diffusion layer). Conditions of coating, see Table II.

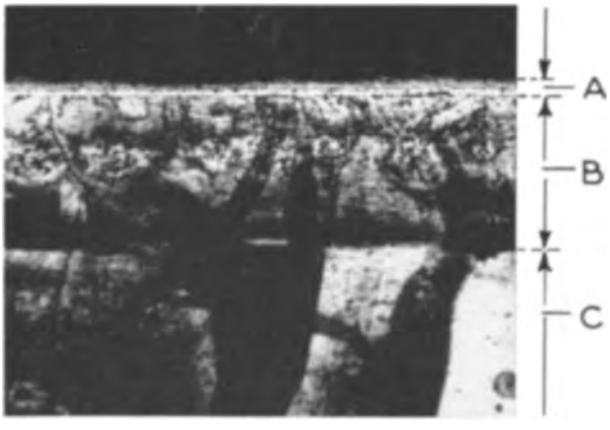

FIG. 4. Structure of a coating and diffusion layer produced on ingot iron (sample No. 14, Table II). A—Ti coating, B—diffusion layer, C—Fe core. Magnification 200×.

The success of the continuous run showed the practicability of the process and indicated the possibility of working on a larger industrial scale, provided the proper type of furnace and a suitable device for moving the specimens in and out of the bath and furnace under the protection of an inert gas were available.

Chemical and Physical Characteristics of the Coating

Samples titanized under different conditions were used for the tests. The objects were completely resistant to the action of dilute and concentrated nitric acid, and no copper was deposited on immersion in a copper sulfate solution. However, red specks or pinholes appeared if the objects were not well cleaned before titanizing. Not only the outside surface, but the deep threads of screws and the inside of the pieces of iron tubing were titanium plated. The surface of the objects was dark grey, but on polishing the typical color of titanium metal appeared (Fig. 2).

The high corrosion resistivity of the titanium coating was demonstrated with samples partially immersed in the titanizing bath and afterwards treated with nitric acid. The uncoated parts were severely attacked by the nitric acid (Fig. 5), while the coated parts were intact. Generally, the titanium coatings show the same corrosion properties (9) as solid titanium metal although corrosion rates of the coatings were not determined. Further tests included hardness measurements of the titanium coatings with a Knoop Diamond Indenter in a Tukon Hardness Tester machine, bending of the coated samples to examine the tendency of the coating to pull loose under stress, and tensile tests with a Dillon Tensile Tester to determine to what extent the base metal could be stressed before there was any separation of the coating.

The hardness tests, made chiefly on titanized Armco ingot iron samples, did not give very definite results, but several trends could be picked out: (*a*) almost without exception hardness increased with thicker coatings; (*b*) coatings were hardest when TiO_x with 95 at. % Ti, or titanium fines was used; (*c*) increasing the amount of the titanium-oxygen alloy in the bath did not have as great an influence on the hardness as did temperature or time variations; (*d*) sodium or potassium chloride baths gave practically the same results.

Samples that had a Knoop hardness traverse run across their cross sectioned surfaces (7, 8) gave results that were in agreement with the general trend, although the actual values were not the same as obtained by surface tests. In each instance the ingot iron base metal was much softer than the titanium coating which was especially hard at the line in contact with the diffusion layer (10). Qualitative abrasion tests also proved that the outermost surface of the titanium coatings is comparatively soft, and is then followed by much harder layers and finally by the soft iron core.

Bend tests showed that titanium coatings held fast to the side of the bent sample in tension, and only tore apart if the base metal, which was brittle, was ripped by the severity of the bend. On the compression side there was a tendency for some of the coatings to buckle in strips, which climbed on one another and flaked off. Nevertheless, the coatings obtained in a helium atmosphere withstood bend tests up to 30 degrees quite well.

In tensile tests the titanium coatings were all quite sound and adherent up to a load of half that required to break the sample, but after rupture it was found the coatings had cracked, checked, and flaked off.

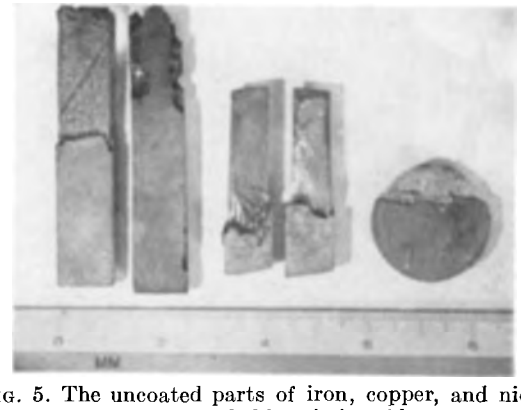

FIG. 5. The uncoated parts of iron, copper, and nickel samples are severely corroded by nitric acid.

Conclusions

Thick and corrosion resistant coatings of titanium on ingot iron, mild steels, and other metals can be obtained by treating them under an inert gas in fused salt baths containing a titanium-oxygen alloy high in titanium content, and as large an amount of such alloy as possible without sacrificing the fluidity of the bath. High temperatures and longer coating times are preferable. A typical run consists of a bath containing 90% sodium chloride, 10% TiO_x with 95 at. % Ti or titanium fines of similar oxygen content. An ingot iron sample is covered at 1000°C in 4 hr with a coating about 0.0006 in. (0.015 mm) thick. Including the diffusion layer the thickness of the whole layer is about 0.0051 in. (0.13 mm) in this case. An industrial application of the titanizing process described is possible since it can be arranged for continuous runs. There is some similarity of the coatings described with those obtained electrolytically by Sibert and Steinberg (10).

The titanium coating is harder than the core and is quite adherent under reasonable stress. Only when the base metal is deformed beyond its elastic limit is there a tendency for the coating to develop cracks, checks, and to flake off.

Acknowledgments

The authors are grateful to the Wright Air Development Center for support of this work and permission to publish the results obtained. The mechanical properties of the coatings were explored by Dr. C. B. Gill. The thickness measurements under microscope were made by Mr. P. J. Chao.

Manuscript received August 1, 1955. This paper was prepared for delivery before the San Francisco Meeting, April 29 to May 3, 1956. Based on a portion of work carried out at the Missouri School of Mines and Metallurgy for the Wright Air Development Center under Contract No. AF 33(616)-75.

Any discussion of this paper will appear in a Discussion Section to be published in the June 1957 JOURNAL.

REFERENCES

1. C. B. Gill, M. E. Straumanis, and A. W. Schlechten, *This Journal*, **102**, 42, Fig. 2 (1955).
2. A. W. Schlechten, M. E. Straumanis, and C. B. Gill, *ibid.*, **102**, 81 (1955).
3. M. E. Straumanis, K. C. Chiou, and A. W. Schlechten, in preparation for publication.
4. P. Ehrlich. *Z. anorg. Chem.*, **247**, 53 (1941).
5. R. L. Hadley and G. Derge, *J. Metals*, **7**, 55 (1955).
6. E. Ence and H. Margolin, *ibid.*, **6**, 346 (1954).
7. M. B. Bever and C. F. Floe, in "Surface Protection against Wear and Corrosion," p. 85, 87, 88, American Society of Metals, Cleveland (1954).
8. U. Zwicker, *Metalloberflache*, **6**, A81 (1952).
9. M. E. Straumanis and P. C. Chen, *Corrosion*, **7**, 229 (1951).
10. M. E. Sibert and M. A. Steinberg, *This Journal*, **102**, 641, *see* e.g. Fig. 6 (1955).

Two Arsenate Phosphors and the Significance of Their Emission

Gorton R. Fonda[1]

The General Electric Company, Schenectady, New York

ABSTRACT

Four phosphors of weak to moderate luminescence were prepared: two from zinc arsenate activated separately with lead and manganese, and two from calcium fluoroarsenate activated with antimony alone and with antimony and manganese together. Their manganese emission band was shifted to longer wave lengths than is characteristic of their phosphate homologues: from 6380Å to 6550Å in the case of the zinc compounds, and from 5680Å to 6200Å for the fluoroapatites. The effect was ascribed to depression of excitation levels of activator ions under increased field strength of oxygen ions in their environment.

Introduction

Two noteworthy phosphors of phosphate composition have been developed in recent years: zinc phosphate activated with manganese (1) and calcium halophosphate activated with antimony and manganese (2). Arsenates are closely related to phosphates; in fact, the law of isomorphism was discovered by the observation that phosphates and arsenates conform to it. Properties of their various salts are very similar, their analogous salts have the same structure, their solubility is of the same order, and they respond similarly to various reagents. Just as there is a mineral, apatite, which has the composition of calcium fluorophosphate, so there is likewise a mineral, svabite, a calcium fluoroarsenate which has a similar composition and structure.

It seemed of interest, therefore, to investigate arsenates and haloarsenates as possible bases for the emission of luminescence. As early as 1949, two pairs of phosphors were found which exhibited similar composition and activation to the phosphates mentioned above. They

[1] Present address: 1028 Parkwood Blvd., Schenectady, N. Y.

included zinc arsenate activated with manganese, which in addition could also be activated with lead, and calcium fluoroarsenate activated with antimony alone and with antimony and manganese together. Full publication of their characteristics has been delayed until the present. Some optical properties of the fluoroarsenates have already been recorded (3). Measurements of their spectral emission disclosed a greater shift to longer wave lengths than exhibited by the corresponding phosphates. Explanation for the change appears to lie in the field strength exercised on the activator ions by the oxygen ions of their environment. The same explanation can be applied to the variations in spectral emission that characterize other groups of oxygen-dominated phosphors whose composition and structure are related.

Zinc Arsenate Phosphor

At 25°C, essentially no fluorescence was obtained with the arsenates of calcium, magnesium, and cadmium under 2537Å, 3650Å, or cathode rays. Zinc arsenate responded to activation by both manganese and lead to emit fluorescence of moderate intensity, lying in the orange and whitish blue, respectively.

These phosphors were prepared by firing at 700°–1000°C, preferably in an atmosphere of nitrogen, a mixture of zinc oxide and arsenic pentoxide in a proportion to yield the orthoarsenate, $Zn_3(AsO_4)_2$. A compound of the activator was added before firing. There was only a small loss in weight, and this was due to the water content of the pentoxide; the loss remained constant whether the crucible was placed in the furnace at full temperature or brought up to temperature slowly. Maximum brightness resulted from firing at 800°C for 3 hr.

The concentration of manganese, introduced as carbonate, was about 0.5% by weight. Its fluorescence was reduced when lead was present as well. As shown by the curves of Fig. 1, its peak emission at room temperature was at 6550Å; at −193°C it was displaced to 6720Å. Under excitation by 2537Å, its quantum output at room temperature was about 10% of that of magnesium tungstate.

When a phosphor was prepared by addition of 2% lead oxide and firing at 800°C for 1 hr, the product emitted a broad band at room temperature with a peak at 4500Å but extending so strongly into the higher wave-length range, as shown in Fig. 1, that the color of its fluorescence was a bluish white. Reduction in temperature to −193°C served likewise to displace its peak luminescence to longer wave length, 4700Å. At room temperature its quantum output was somewhat higher than that of the manganese activated phosphor.

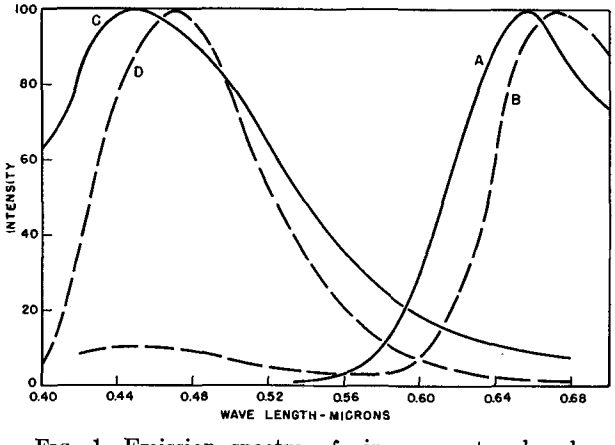

Fig. 1. Emission spectra of zinc arsenate phosphors excited by 2537Å. A—$Zn_3(AsO_4)_2$:Mn at 25°C; B—$Zn_3(AsO_4)_2$:Mn at −193°C; C—$Zn_3(AsO_4)_2$:Pb at 25°C; D—$Zn_3(AsO_4)_2$:Pb at −193°C.

Calcium Fluoroarsenate Phosphor

When the experiments were extended to the haloarsenates, calcium fluoroarsenate was the only compound which showed a notable response to excitation by 2537Å, 3650Å, or cathode rays at 25°C. It was prepared from a mixture of 9 moles calcium oxide, 3 moles arsenic pentoxide, and 1 mole calcium fluoride. Faint or weak luminescence was obtained with activation by bismuth, cerium, lead, tin, and thallium. The brightest phosphors resulted by adding antimony or manganese or both as activators and firing at 1150°C in a quartz tube closed at the end within the furnace and plugged with glass wool at the outer end. The preparation of this phosphor has been briefly described by Rothschild (4).

With antimony alone the fluorescence was a greenish yellow, with a peak at 5000Å as shown in Fig. 2. Its brightness was a maximum when 0.5–4.0% antimony as antimony oxide was added to the mixture before firing. Its quantum output under excitation by 2537Å was 15% of that of magnesium tungstate. As determined from reflection measurements (5) its absorption of 2537Å was 81%. Its quantum efficiency would therefore be 19% of magnesium tungstate (3).

With manganese alone, which had been added as the carbonate, there was a weak red emission. Its intensity was greatly increased on addition of antimony, denoting that the latter had a sensitizing action. The peak of the manganese emission was at 6200Å. With 1% manganese its brightness remained at a maximum over the range of 0.5–2.0% antimony. The spectral distribution of a product prepared with 1% manganese and 2.0% antimony is given in Fig. 2. Despite the appreciable antimony content, the

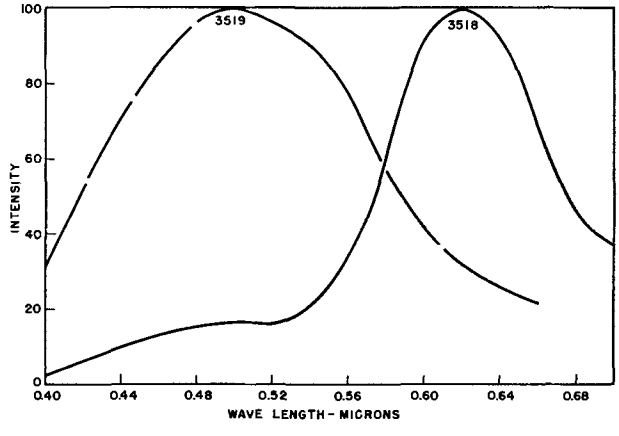

Fig. 2. Emission spectra of calcium fluoroarsenate phosphors excited by 2537Å. 3518—$3Ca_3(AsO_4)_2 \cdot CaF_2$:Sb:Mn at 25°C; 3519—$3Ca_3(AsO_4)_2 \cdot CaF_2$:Sb at 25°C.

TABLE I. *Spectral emission of arsenate and phosphate phosphors*

Phosphor	Peak Emission (Å)	
	Sb band	Mn band
$Zn_3(AsO_4)_2$:Mn	—	6550
$Zn_3(PO_4)_2$:Mn	—	6380
$3Ca_3(AsO_4)_2 \cdot CaF_2$:Sb:Mn	5000	6200
$3Ca_3(PO_4)_2 \cdot CaF_2$:Sb:Mn	4800	5680
$3Ca_3(PO_4)_2 \cdot CaCl_2$:Sb:Mn	4800	6000

antimony band is almost completely suppressed by the manganese. Under excitation by 2537Å its quantum output was 27% of that of magnesium tungstate. With an absorption of 84% for 2537Å, its quantum efficiency became about 30% of magnesium tungstate.

X-ray diffraction patterns showed these fluoroarsenates to be of apatite structure with a somewhat larger unit cell than characterizes the fluorophosphate. This result is in agreement with measurements by Rothschild on calcium apatite phosphors which he prepared (4).

Comparison of Arsenate and Phosphate Phosphors

The two arsenate phosphors just described are similar in composition and isomorphous in structure with the corresponding phosphates. Both pairs have the same activators. It is therefore reasonable to expect a relationship in spectral emission between the arsenates and phosphates of the same type. A comparison is given in Table I.

Discussion

An explanation for the differences observed can be found in the differences in field strength to which activator ions are subjected by their environment. This explanation should be applicable to any group of phosphors which have related composition and structure. It has been applied by Klasens, Zalm, and Huysman to double fluorides of perovskite structure which have the composition ABF_3, where A is a monovalent alkaline metal and B a divalent metal of the second periodic column (6). The spacing between a fluorine ion and the activator ion, manganese, depends upon the ionic size of the metals A and B. An increase in this spacing was accompanied by a corresponding shift of the peak emission to shorter wave lengths. As the authors phrase it, "the greater the space available for the manganese ion, the more the state of the free ion will be approached, hence the shift to shorter wave length."

When a manganese ion is in the field of the crystal lattice, the distances between its energy levels become smaller. The outer orbits of the ion, those occupied by excited electrons, are under the repulsive force exerted by the field of the adjacent anions and their energy levels are correspondingly depressed. The extent of the depression depends on the field exercised by the anions and this, in turn, on their proximity, the smaller the spacing, the greater is the field and the greater likewise is the depression in the energy levels of the excited electrons; consequently, the greater is the shift in emission to longer wave lengths.

The view of Klasens, Zalm, and Huysman (6) is applicable to other phosphors. Although similar quantitative data on spacings between manganese ions and anions are not generally available, the direction in which the change in spacing occurs can frequently be perceived from related characteristics, such as the relative ionic sizes of the cations in a series of related compounds, or the relative spacings of cations and anions in their oxides. Inasmuch as manganese substitutes for the cation of such compounds, the change to a larger cation carries with it an increase in the spacing between manganese and its surrounding oxygen ions. A possible illustration that is at least suggestive, is offered by the silicates of Table II activated with manganese to give a double band emission. The emission peaks cited are the currently accepted values.

Both bands are shifted to longer wave length as the spacing is reduced in the metallic oxide from which the phosphor was prepared.

The silicates are, it is true, all of different structure, and this tends to weaken the validity of the illustration because structural features may be playing a more fundamental role than the spacings in the oxides. It seems probable, however, that the coordination of a cation remains the same in a silicate as in its oxide. In the case of magnesium silicates, at least, the change from metasilicate to the orthosilicate produces only a moderate alteration in spectral emission, insufficient to affect the argument.

In a less debatable case, the same relation was found by Kreidl on partial substitution in sodium silicate glasses activated by manganese (7). Substitution of potassium, of larger ionic size, for one half of the sodium shifted the fluorescence from greenish yellow to green, a result of the enlarged spacing. Substitution of one half of the sodium by lithium, of smaller ionic size, produced the reverse effect by shifting the fluorescence to yellow.

With these examples in mind, the same viewpoint can be applied to the arsenates and phosphates of Table I. The situation is somewhat different. In the previous examples, the emission band was shifted to longer wave lengths when the cation of the compound was changed to one of smaller ionic size, thus bringing the manganese ion substituting for it closer to the oxygen ions which surrounded it. In the present example, the emission is shifted to longer wave lengths by changing the metal of the acid radical to arsenic, an element of larger ionic size than phosphorus. A brief consideration shows that the effect on the manganese ion is the same as in the previous examples.

The lower field strength of the larger arsenic ion allows an enlargement of the acid forming tetrahedron, in this case the AsO_4 group; a redistribution occurs in the field strength of the oxygen ions composing it, less is directed

TABLE II. *Effect of cation constituent on fluorescence of silicates*

Composition	Emission peaks (Å)	Cation to anion spacing in oxide (Å)
Zn_2SiO_4:Mn	5250, 6000	2.00, 3.22
$CaSiO_3$:Mn	5600, 6200	2.40
$CdSiO_3$:Mn	6000, 6240	2.35
$MgSiO_3$:Mn	6600, 7400	2.10
Mg_2SiO_4:Mn	6400, 7400	2.10

inward to the arsenic core than would be to the phosphorus core, and more becomes available for direction on the zinc or calcium ions which are dispersed around the acid tetrahedral groups. This decreases the spacing between zinc or calcium ions and oxygen ions. Whenever a manganese ion is substituted for zinc or calcium, the energy levels of its excited states are accordingly lowered as before, and the emission is shifted as before to longer wave lengths.

The antimony emission of the fluoroarsenate is also shifted to longer wave lengths, indicating that antimony ions are subjected to similar forces as manganese. This in turn denotes that antimony ions, as activators, substitute also for calcium in the lattice rather than for arsenic or phosphorus.

A similar situation arises in another pair of compounds which are related to one another, zinc germanate and silicate, both activated by manganese. The substitution of germanium, of larger ionic size than silicon, acts to shift the peak of the emission band from 5250Å to 5370Å.

In the halophosphates the substitution of chlorine for fluorine produces a similar shift. A chlorine ion is of larger ionic size than fluorine; its field strength, the quotient of its charge by its ionic radius, is therefore less. This results in a lower electrostatic attraction between it and its neighboring calcium ion so that the spacing between them is increased. The spacing between this calcium ion and its other neighboring anions, three oxygen ions, is correspondingly reduced under the stronger residual field of the calcium ion. When a manganese ion substitutes for this calcium, its energy levels are depressed as in the previous case where arsenic was substituted for phosphorus, and its emission is again shifted to the longer wave lengths cited in Table I for the chloroapatite.

ACKNOWLEDGMENT

The author is greatly indebted and very grateful to Dr. Frank J. Studer and Miss Gwen Lloyd of the Research Laboratory of the General Electric Co. for the absorption and spectral distribution measurements.

Manuscript received June 27, 1955. This paper was prepared for delivery before the Cincinnati Meeting, May 1 to 5, 1955.

Any discussion of this paper will appear in a Discussion Section to appear in the June 1957 JOURNAL.

REFERENCES

1. A. L. SMITH, *This Journal*, **98**, 363 (1951).
2. H. G. JENKINS, A. H. MCKEAG, AND P. W. RANBY, *ibid.*, **96**, 1 (1949).
3. S. JONES AND G. R. FONDA, Abstract No. 41 "Enlarged Abstracts of Papers Presented by the Electronic Division of the Electrochemical Society" (1952), page 39.
4. S. ROTHSCHILD, *Brit. J. Appl. Phys.*, Supplement No. 4, 32 (1955).
5. F. J. STUDER AND G. R. FONDA, *J. Opt. Soc. Amer.*, **39**, 658 (1949).
6. H. A. KLASENS, P. ZALM, AND F. O. HUYSMAN, *Philips Research Repts.*, **8**, 441 (1953).
7. N. J. KREIDL, *J. Opt. Soc. Amer.*, **35**, 249 (1945).

Reaction of Hydrogen with Uranium

W. M. Albrecht and M. W. Mallett

Battelle Memorial Institute, Columbus, Ohio

ABSTRACT

The reaction of hydrogen with uranium to produce uranium hydride was studied in the temperature range 96°–400°C at pressure levels of $p - p_0$ equal to 430, 150, and 70 mm of mercury (where p is system pressure and p_0 is the plateau dissociation pressure of the uranium hydride product). Reaction rates followed the linear law. At a given $p - p_0$, the linear rate increased with increasing temperature in the range 96° to about 250°C and decreased with increasing temperature from about 250° to 400°C. Variation of the linear rate with temperature and pressure in the range 96° to about 250°C is given by the equation:

$$r = 4.11 \times 10^{-3} p^{3/4} \exp(-1820/RT)$$

where r is in units of ml/cm²/sec and p is in units of mm Hg. In the range from about 250° to 400°C an empirical relationship between the reaction rate and pressure is proposed where the rate is a function of $p - p_0/p_0$. However, since none of the reaction mechanisms was determined, the significance of the pressure dependencies is not known. Two different initial reactions were obtained. One in the range 96° to about 250°C at $p - p_0$ of 70 and 150 mm Hg and 96°–400°C at $p - p_0$ of 430 mm Hg showed a gradual increase in the rate of hydrogen consumption until the rate became linear. The other initial reaction followed the parabolic rate law in the range of about 250°–400°C at $p - p_0$ of 70 and 150 mm Hg.

Introduction

Katz and Rabinowitch (1) have reviewed most of the investigations of the kinetics of the reaction of uranium with hydrogen carried out before 1944. Another study was made by Straetz and Draley.[1] Most of this work was performed in systems containing hydrogen at 1 atm pressure. It was found generally that the reaction followed a linear rate law, with a maximum reaction rate occurring at about 225°–250°C. This could be explained since the plateau dissociation pressure, p_0, that is the equilibrium hydrogen pressure of a uranium-uranium hydride-hydrogen system, increases very rapidly with temperature at about 250°C. The isothermic plateau dissociation pressure is about 4 mm Hg at 250°C and 760 mm at 433°C. Therefore, at a fixed system pressure, p, the excess pressure, $p - p_0$, over the dissociation pressure decreases with increasing temperature, and it would be expected that the reaction rate would decrease. With the system maintained at 1 atm pressure of hydrogen, there would be no reaction to produce hydride at 433°C and above.

There have been other investigations (1)[2] in which the effect of pressure on the kinetics of the reaction was studied. These investigations were carried out in a constant-volume apparatus in which the rate of decrease of pressure with time at constant temperature was determined. Data are reported which follow the equation $-(dp/dt) = K(p_t - p_0)^{5/2}$, where p_t is the residual hydrogen pressure after the reaction has proceeded for time, t. However, there is no ready explanation of the 5/2 power in the equation.

For the present study, the kinetics of the reaction of hydrogen with uranium was studied under the condition that $p - p_0$ is a constant, that is, the hydrogen pressure in excess of the plateau dissociation pressure of the uranium hydride product was constant. The temperature range of 100°–400°C was chosen.

Values of p_0 used in this study were obtained previously.[3] The variation of p_0 with temperature is given by the equation $\log p_{mm} = -4590/T + 9.39$, which is in good agreement with data presented by other investigators (1).

Experimental Procedure

Materials

The uranium used in this study was fabricated (2) into a ⅜-in. diameter rod. Test specimens were machined from these rods. Analysis of the uranium was obtained by spectrographic, chemical, and vacuum-fusion techniques. The total of all the measured impurities was less than 400 ppm, and each impurity was present in a concentration of less than 100 ppm. The following elements were detected as impurities: aluminum, carbon, chromium, cobalt, copper, iron, magnesium, manganese, nickel, nitrogen oxygen, silicon, and a few others in very low concentrations.

Pure hydrogen was obtained from the thermal decomposition of uranium hydride. The hydride was prepared by reacting dried tank hydrogen with degreased high purity uranium chips.

Method

The general method for measuring the rate of reaction between uranium and hydrogen has been described previously for other metal-gas reactions (3, 4). The apparatus is basically the same as that described in a previous paper (3), but a pressure regulator has been incorporated in the

[1] Classified information.

[2] Classified information.

[3] Classified information.

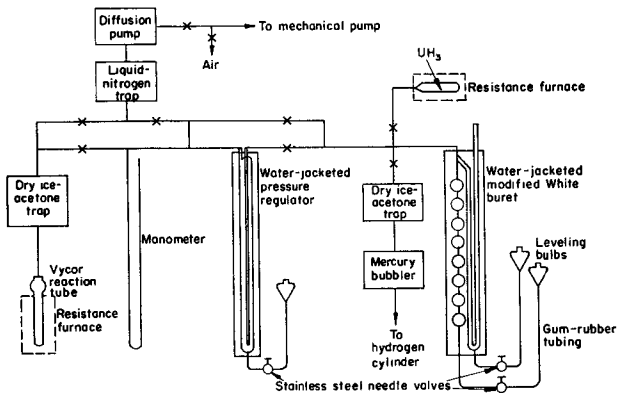

FIG. 1. Schematic diagram of modified Sieverts apparatus

design. A schematic diagram of the apparatus used is shown in Fig. 1. The system was evacuated by a two-stage mercury-diffusion pump backed by a mechanical pump.

The modified White gas buret (5) used to store the hydrogen and to measure the consumption rate consisted of eight bulbs, each of approximately 50 ml, and an open-end mercury manometer, one arm of which was a graduated 50-ml buret. The pressure regulator (see Fig. 1) consisted of an outer Pyrex tube, 40 mm in diameter and 90 cm long, which was connected to the reaction tube. An inner 2-mm Pyrex capillary tube which extended from the top to about 3 cm above the bottom of the outer tube was connected to the gas buret. The pressure, p, to be maintained in the reaction tube was set by lowering the mercury level in the pressure regulator a distance, p mm, below the mercury level when at barometric height. In operation, hydrogen was consumed by a specimen and replacement gas bubbled through the mercury from the capillary tip to maintain the desired pressure (± 1 mm of mercury) in the reaction tube. Both the buret assembly and pressure regulator were water jacketed and maintained at constant temperature (± 0.5°C during the course of a reaction rate run).

The Vycor reaction tube was sealed to the system with Apiezon W wax, and its dead volume was decreased with a solid Pyrex rod. This dead space also was used to hold a platinum platinum-10% rhodium thermocouple in contact with the top of a specimen. The thermocouple was used to measure the specimen temperature during the course of a rate experiment.

The reaction tube was heated with a resistance-wound furnace which was controlled by a Foxboro controller, using a Chromel-Alumel thermocouple placed at the resistance windings of the furnace. Temperature of a specimen was maintained to ± 3°C.

Prior to specimen preparation, machined uranium cylinders about 0.8 cm in diameter and ranging from 1 to 4 cm long were abraded with 240-grit silicon carbide paper and vacuum annealed at 600°C for 3 hr. Specimens then were abraded with 240, 400, and 600-grit silicon carbide papers. After the dimensions and weight of the specimens were determined, they were given a final polish with dry 600-grit silicon carbide paper, immediately placed in the reaction tube, and sealed into the system. The system was evacuated for 1 hr at a pressure better than 10^{-5} mm Hg. During this evacuation, the portion of the reaction tube above the specimen was flamed periodically to remove adsorbed gases from the walls of the tube. The specimen was then slowly heated to the temperature of the reaction-rate run and held at temperature for a period of about $1\frac{1}{2}$ hr. It was found necessary to take these precautions to keep the induction period of the reaction to a minimum.

While the specimen was being heated at temperature, hydrogen was generated and stored, and the pressure regulator adjusted to the pressure conditions of the run.

With the specimen at the desired temperature, hydrogen was admitted from the gas buret through the pressure regulator which maintained the desired pressure in the reaction tube. By manipulations of the buret leveling bulb and stainless steel needle valve, the buret was continuously balanced to atmospheric pressure. Readings of the buret manometer arms were made at ½- to 2-min intervals, depending on the reaction rate. The quantity of gas consumed by the specimen was the difference between the volume added from the buret and volume remaining in the gas phase in the calibrated dead space. Original geometric dimensions of specimens were used in calculating the quantity of hydrogen reacted per unit area, in units of ml STP hydrogen per cm².

Results and Discussions

Films

Visual observation of the surface of a uranium specimen during the course of a run showed that at the start of a reaction a very thin blue-black hydride film formed which was considered to be adherent to the metal since it showed no evident cracking or flaking. The same type of protective film existed throughout the reaction where the parabolic rate law was followed. No extensive investigation of the adherent films could be made since they could not be preserved upon cooling of the specimen from the temperature of the rate experiment. As soon as the furnace was removed from the reaction tube, the reaction product began dusting off the specimen. At the longer times wherever the linear rate law was followed there was a continual dusting of the hydride.

Inspection of the metal surfaces at the end of a reaction experiment showed them to be relatively smooth. The decrease in the surface areas during the experiments averaged about 3% or less, based on the decrease in the dimensions of the metal specimens. Since the change in surface area was so small, no corrections were made on the original geometric dimensions in calculating the quantity of hydrogen consumed per unit area.

Rate Data

Rates of reaction of pure hydrogen with massive uranium were determined in the range 96°–394°C at three hydrogen pressure levels of $p - p_0$: 430, 150, and 70 mm of mercury. At all pressure levels, after initial deviations, the rates followed the linear law, $w = rt$, where w is the ml STP hydrogen consumed per cm² of surface, t is time, and r is the linear reaction rate in units of ml/cm²/sec. In each case, the linear rate increased with increasing temperature at lower temperatures, but decreased with increasing temperatures above a certain temperature which depended upon the pressure.

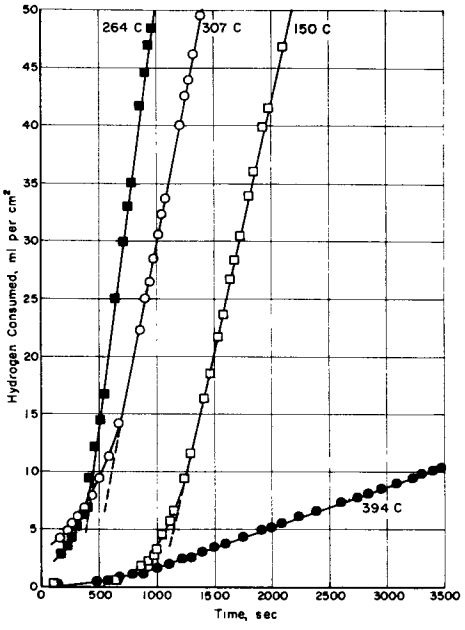

FIG. 2. Reaction of uranium with hydrogen for $p - p_0 =$ 430 mm Hg.

For $p - p_0 = 430$ mm of mercury, Fig. 2 shows typical plots of w vs. t. It is seen that after initial deviations (a gradual increase in rate) the data follow the linear law. Values of the linear rate, calculated from the various plots, are given in Table I. The rates range from 3.5×10^{-2} ml/cm²/sec at 102°C to a maximum of 7.6×10^{-2} ml/cm²/sec at 264°C, and then decrease to 3.6×10^{-3} ml/cm²/sec at 394°C.

In Fig. 3 are typical plots of w vs. t for $p - p_0 = 150$ mm of mercury pressure. In Table II are given the values of the linear rates which range from 1.2×10^{-2} ml/cm²/sec at 96°C to 2.8×10^{-2} ml/cm²/sec at 200°C, and then decrease to 1.9×10^{-3} ml/cm²/sec at 356°C. However, at this pressure level two different types of initial deviations were obtained. In the range 96°–200°C and at 356°C the reaction rate gradually increased until the rate became linear. However, in the range 254°–326°C the initial reactions followed the parabolic rate law, $w^2 = rt$, where r is the parabolic rate (ml/cm²)²/sec. The parabolic behavior can be seen in Fig. 4, where the square of w is plotted as a function of t for a number of runs, and it is seen that the data fall on straight lines. The parabolic rates which were obtained from these plots and the initial time that the

TABLE I. *Rates for the reaction of uranium with hydrogen at $p - p_0 = 430$ mm Hg*

Temp, °C	p_0, mm Hg	Linear rate, ml/cm²/sec
102	0.002	3.5×10^{-2}
150	0.035	4.3×10^{-2}
155	0.050	4.4×10^{-2}
171	0.12	4.9×10^{-2}
206	0.63	5.5×10^{-2}
264	5.5	7.6×10^{-2}
307	30	5.0×10^{-2}
308	30	2.9×10^{-2}
346	93	1.5×10^{-2}
394	316	3.6×10^{-3}

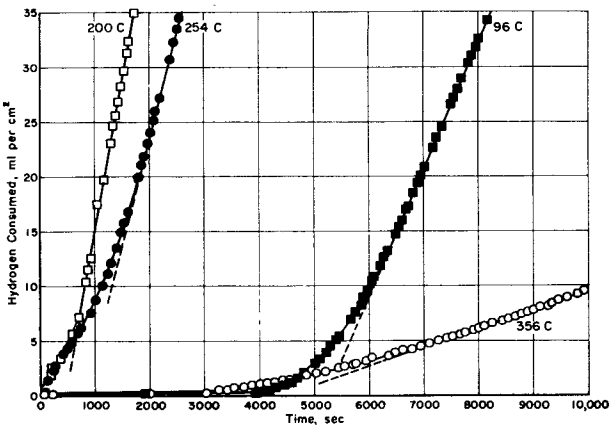

FIG. 3. Reaction of uranium with hydrogen at $p - p_0 =$ 150 mm Hg at 96°–356°C.

parabolic rate was followed are also given in Table II. The rates ranged from 3.8×10^{-2} (ml/cm²)²/sec at 254°C to 2.2×10^{-2} (ml/cm²)²/sec at 326°C.

For $p - p_0 = 70$ mm Hg, Fig. 5 shows typical plots of w vs. t. The linear rates obtained from such plots are given in Table III. Values range from 7.7×10^{-3} ml/cm²/sec at 96°C to 1.3×10^{-2} ml/cm²/sec at 206°C, and then decrease to 3.0×10^{-3} ml/cm²/sec at 253°C. In the range 96°–206°C initial deviations showed a gradually increasing rate, and in the range 206°–303°C they showed a parabolic rate. Parabolic plots are included in Fig. 4. The parabolic rates and the time that the parabolic rate was followed are given in Table III. Rates range from 2.1×10^{-2} (ml/cm²)²/sec at 206°C to 1.1×10^{-2} (ml/cm²)²/sec at 303°C.

It has been found generally that the temperature dependence of rate measurements follows the Arrhenius-type equation, $k = A \exp(-Q/RT)$, where k is the rate constant, A is the frequency factor, and Q is the energy of activation. Therefore, a plot of logarithms of the rate constants vs. the reciprocals of the absolute temperatures should yield a straight line. Such plots are given in Fig. 6 for the linear rates which are constant at a given pressure for the reaction of massive uranium with hydrogen at the three levels of $p - p_0$ equal to 430, 150, and 70 mm of Hg pressure. Equations for the best straight lines through the various sets of points were determined by the method of least squares. It can be seen that the rate constants go

TABLE II. *Rates for the reaction of uranium with hydrogen at $p - p_0 = 150$ mm Hg*

Temp, °C	p_0, mm Hg	Time of initial parabolic reaction, sec	Parabolic rate, (ml/cm²)²/sec	Linear rate, ml/cm²/sec
96	0.001	None	—	1.2×10^{-2}
110	0.003	None	—	1.6×10^{-2}
121	0.006	None	—	1.5×10^{-2}
146	0.028	None	—	1.7×10^{-2}
163	0.070	None	—	2.1×10^{-2}
200	0.60	None	—	2.8×10^{-2}
254	4.7	500	3.8×10^{-2}	2.0×10^{-2}
300	25	1200	3.2×10^{-2}	9.1×10^{-3}
326	53	600	2.2×10^{-2}	5.6×10^{-3}
356	123	None	—	1.9×10^{-3}

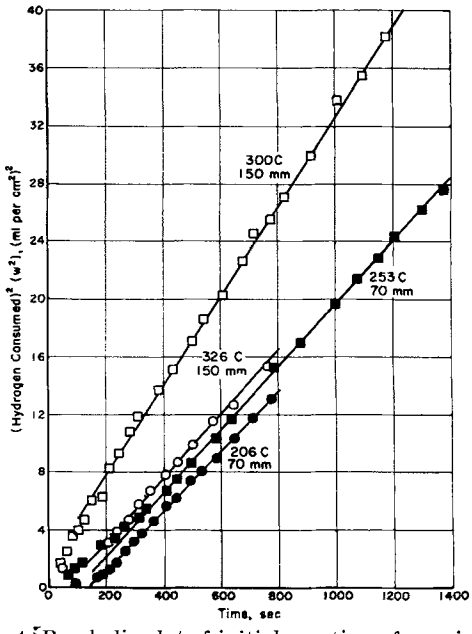

FIG. 4. Parabolic plot of initial reaction of uranium with hydrogen at $p - p_0 = 150$ and 70 mm Hg.

through a maximum at each level. The expressions for the linear rate constants are given in Table IV. At the higher temperature where the linear rate decreases with increasing temperature, an apparent negative "energy of activation" is obtained. Theoretically this is meaningless. Therefore, some other pressure dependency in addition to $p - p_0$ is necessary to define the reaction in the higher temperature range (250°–400°C).

The effect of pressure on the linear reaction rates can be seen in Fig. 6. From the equations given in Table IV, linear rates were calculated at all three $p - p_0$ levels at temperatures in the range 100°–250°C. Also in this range, p_0 is small, 1 mm of mercury or less, and the quantity $p - p_0$ is not significantly different from the system pressure, p. Therefore, pressure dependency of the reaction up to 250°C may be considered as a function of p alone. A plot of log r vs. log p gave straight lines with slopes of about 0.75, which indicates the following relationship between rate and pressure:

$$r = \frac{dw}{dt} = kp^{3/4}$$

A plot of the logarithms of the values of $r/p^{3/4}$ vs. $1/T$ is given in Fig. 7. Using these data, and applying the method of least squares the following equation for the linear rate, r, in ml/cm²/sec, was obtained,

$$r = 4.11 \times 10^{-3}\, p^{3/4} \exp - 1820/RT$$

where p is in mm of mercury for the range 96°–250°C.

Various reaction mechanisms were considered to explain the reaction in the higher temperature range (250°–400°C). Such theoretical treatments as that presented by Peterson, Fassell, and Wadsworth (6) were tried. In this, a pressure dependency based on Langmuir's adsorption isotherm Type-I was found for the linear oxidation of tantalum. However, no such dependency could be shown for the present work.

Since the hydrogen-uranium reaction is at nearly equilibrium conditions, it would appear that some function including $p - p_0$ (7) is necessary to explain the pressure dependency. Qualitatively, the reaction in the forward

TABLE III. *Rates for the reaction of uranium with hydrogen at $p - p_0 = 70$ mm Hg*

Temp, °C	p_0, mm Hg	Time of initial parabolic reaction, sec	Parabolic rate, (ml/cm²)²/sec	Linear rate, ml/cm²/sec
96	0.001	None	—	7.7×10^{-3}
145	0.026	None	—	1.1×10^{-2}
168	0.15	None	—	1.2×10^{-2}
206	0.70	800	2.1×10^{-2}	1.3×10^{-2}
220	1.2	1000	2.2×10^{-2}	8.2×10^{-3}
253	4.6	4000	2.1×10^{-2}	3.0×10^{-3}
303	26	9000	1.1×10^{-2}	None

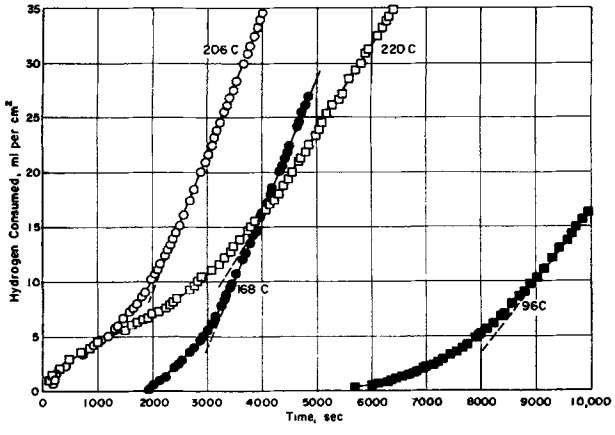

FIG. 5. Reaction of uranium with hydrogen at $p - p_0 = 70$ mm Hg at 96°–220°C.

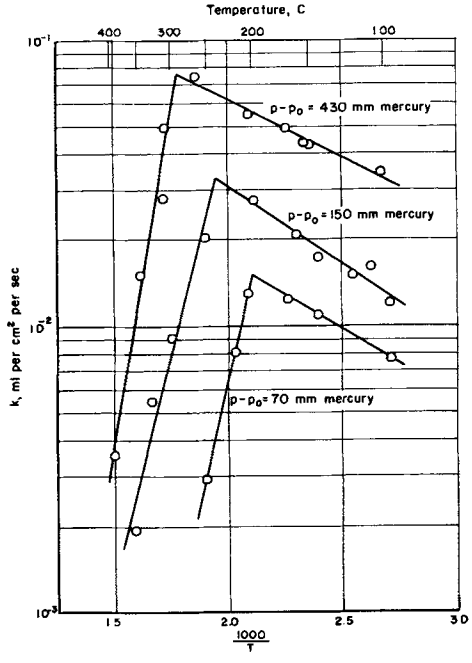

FIG. 6. Temperature dependence of linear rate constant for uranium-hydrogen reaction.

TABLE IV. *Expressions for linear rate constants for the reaction of uranium with hydrogen*

Pressure, $p - p_0$, mm Hg	Temp range, °C	Expression for linear rate constant k	Approximate error, in a calculated k, relative %
430	102–264	$0.421 \exp(-1890/RT)$*	3.5
	307–394	$6.30 \times 10^{-10} \exp(20{,}700/RT)$	20
150	96–200	$0.399 \exp(-2540/RT)$†	5.0
	254–356	$2.35 \times 10^{-8} \exp(14{,}500/RT)$	19
70	96–168	$0.118 \exp(-2160/RT)$‡	1.2
	206–253	$8.41 \times 10^{-10} \exp(15{,}700/RT)$	1.1

*, †, ‡ = Activation energies for these reactions are 1890 ± 110, 2540 ± 200, and 2160 ± 80 cal/mole, respectively.

direction (hydride produced) is dependent on the system pressure while the reaction in the reverse direction (hydride dissociated) is dependent on the dissociation pressure of the hydride. Thus, the net forward reaction to produce hydride is dependent on the quantity $p - p_0$. However, as noted in Fig. 6, the application of this dependency alone gave an apparent negative activation energy in the range 250°–400°C. After many considerations, an empirical equation was found which could be applied to the data. The equation is:

$$r = k \frac{(p - p_0)}{p_0}$$

Fig. 8 shows a plot of $\log r/(p - p_0/p_0)$ vs. reciprocal temperature for the data in the range of about 250°–400°C. The best straight line was drawn through the points using the method of least squares. The apparent activation energy was calculated to be 11,900 ± 1300 cal/mole. The scatter of data arises from the difficulty of keeping $p - p_0$ constant. Since p_0 increases rapidly with temperature in the range 250°–400°C, small variations in temperature produce large errors in the selected p_0 for an experiment.

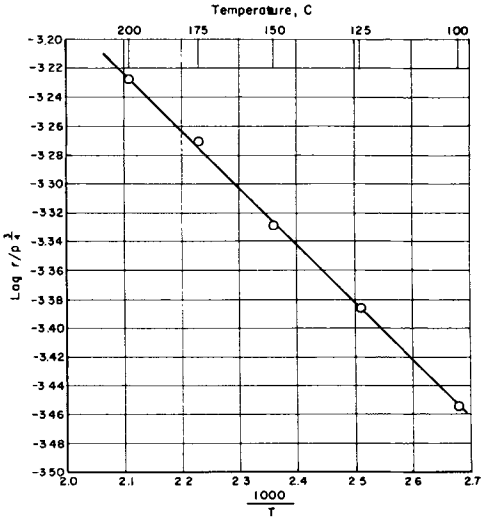

FIG. 7. Variation of rate constant with temperature for pressure dependency of $p^{3/4}$.

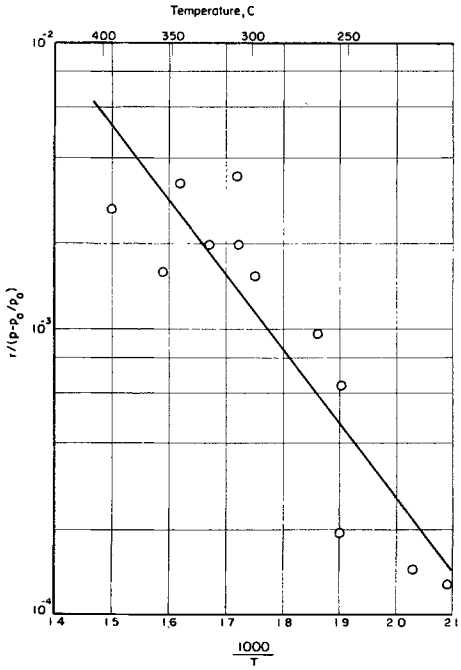

FIG. 8. Variation of rate constant with temperature for pressure dependency of $p - p_0/p_0$.

Duplicate rates obtained at $p - p_0 = 430$ mm Hg and 307°C varied from 2.0×10^{-3} to 3.5×10^{-3} ml/cm²/sec.

Upon consideration of the meager parabolic data obtained in the study, there appeared to be very little change of the parabolic rate with temperature and pressure. Therefore, no attempts were made to derive any relationships between these variables for the parabolic data.

CONCLUSIONS

The reaction of uranium with hydrogen was found to follow a linear rate law after initial deviations. Inspection of the data indicates that there are at least two different rate-controlling processes in the temperature and pressure ranges investigated. In the range 96°–250°C a pressure dependency of $p^{3/4}$ was obtained. At higher temperatures, 250°–394°C, reasonable fit of the data was obtained with a pressure dependency of $p - p_0/p_0$. However, since none of the reaction mechanisms was determined, the significance of these pressure dependencies is not known.

ACKNOWLEDGMENTS

The authors gratefully acknowledge the assistance of Mr. W. R. Hansen and Mr. B. G. Koehl in making the experimental reaction rate runs.

Manuscript received March 24, 1955. This paper was prepared for delivery before the Cincinnati Meeting, May 1 to 5, 1955. The work was performed under AEC Contract W-7405-eng-92.

Any discussion of this paper will appear in a Discussion Section to be published in the June 1957 JOURNAL.

REFERENCES

1. J. J. KATZ AND E. RABINOWITCH, "The Chemistry of Uranium," Part I, p. 193 ff, National Nuclear Energy Series, McGraw-Hill Book Co., Inc., New York (1951).

2. M. W. Mallett and A. F. Gerds, *This Journal*, **102**, 292 (1955).
3. J. Belle, B. B. Cleland, and M W. Mallett, *ibid.*, **101**, 211 (1954).
4. M. W. Mallett and W. M. Albrecht, *ibid.*, **102**, 407 (1955).
5. A. H. White, *J. Am. Chem. Soc.*, **22**, 343 (1900).
6. R. C. Peterson, W. M. Fassell, and M. E. Wadsworth, *J. Metals*, **6**, 1038 (1954).
7. L. S. Darken and R. W. Gurry, "Physical Chemistry of Metals," p. 465 ff. Metallurgy and Metallurgical Engineering Series, McGraw-Hill Book Co., Inc., New York (1953).

Allotropic Modifications of Calcium

J. F. Smith, O. N. Carlson, and R. W. Vest

Institute for Atomic Research, Iowa State College of Agriculture and Mechanic Arts, Ames, Iowa

ABSTRACT

X-ray diffraction patterns of calcium samples of different purities have shown that 99.9+% Ca exists in only two allotropic forms: face-centered cubic to 464°C and body-centered cubic from 464°C to the melting point. These results for the high temperature allotrope differ from the widely accepted structure; handbooks and tables currently list the high temperature allotrope as hexagonal closest-packed. It has been further shown that a previously reported intermediate allotrope of complex structure is due to contamination. The temperature dependence of the electrical resistivity of the 99.9+% Ca was found to be linear for both the face-centered cubic allotrope and for the body-centered cubic allotrope. Calcium was observed to be self-annealing at room temperature.

Introduction

An x-ray diffraction investigation of calcium was undertaken because calcium was reported to exist in three allotropic forms (1) and because there was some question about the lattice type of the intermediate allotrope existing between 300° and 450°C. Evidence for the existence of an intermediate allotrope in this temperature range has been reported (2–4). Further, there existed a discrepancy in the reported structure of the high temperature allotrope; Graf (5) originally reported the high temperature allotrope to be b.c.c. while Ebert, Hartman, and Peisker (6) reported h.c.p. Graf (4) extended his investigation using five different grades of calcium, one of which was obtained from Ebert. Graf found both high temperature forms; from the sample obtained from Ebert both forms were obtained on the same diffraction pattern. The intermediate allotrope was found in all five calcium samples. Graf concluded from his studies that there were three allotropes of calcium and that the structure of the high temperature form of pure calcium was h.c.p. However, Graf's estimate of purity was apparently based on method of preparation since no analytical data were given for the higher purity calcium samples. His conclusion about the high temperature phase is in disagreement with results obtained in this investigation.

Experimental and Results

Calcium Preparation

Purification studies preceded preparation of the metal used in the experimental investigation. Crude calcium metal which had been prepared by the alumino-thermic reduction of calcium oxide (7) was obtained from the New England Lime Co., Canaan, Conn. Past research by the authors has shown that this material can be separated readily from most of its impurities by a vacuum distillation. Typical results of a single vacuum distillation at 900°C are shown in Table I. Distillations on a 200-lb scale were carried out in a 310 Nb stabilized stainless steel retort at pressures of the order of 10^{-3} mm Hg, and the condensate was collected on an air-cooled condenser maintained at 300°–400°C. Analyses were run on calcium granules obtained by grinding the calcium in a Wiley Mill; fine particles were removed by screening. Data in Table I illustrate that magnesium is not readily removed by this distillation process.

For this investigation, calcium of the highest possible purity was desired and methods for the removal of the magnesium were considered. Fujita, Yokomizo, and Kurozaki (8) effected a magnesium separation by collecting the metallic vapors on a hot surface (600°–800°C), while work done by Betcherman and Pidgeon (9) on the vapor pressures and rates of sublimation of calcium and magnesium suggested that magnesium might be preferentially sublimed from calcium at a temperature below the melting point of calcium metal. Considerable experimental work was done on the latter approach to determine conditions for removal of magnesium.

Calcium of three different grades, hereafter referred to as calcium A, calcium B, and calcium C, was prepared for use in this investigation. Calcium A was prepared by four successive distillations at 900°C. The magnesium content was not noticeably reduced.

The other two specimens were prepared in the following manner. Calcium metal which had been purified by vacuum distillation and thus contained magnesium as the

TABLE I. *Analysis of major impurities in N.E.L. calcium before and after distillation at 900°C*

Impurity	Analysis before distillation in wt %	Analysis after distillation in wt %
Al	0.1–0.2	0.002
Fe	0.01	0.005
N	0.06–0.1	0.003
Mg	0.3	0.3
Mn	0.02	0.003

TABLE II. *Analysis of calcium samples used in this study*

Impurity	Calcium A analysis in wt %	Calcium B analysis in wt %	Calcium C analysis in wt %
Mg	0.300	0.110	0.010
N	0.025	0.022	0.011
Fe	0.006	0.010	0.010
Al	0.001	0.001	0.001
Mn	0.004	0.005	0.005
Net Ca.....	99.66	99.85	99.96

major impurity (0.3 wt%) was ground to a fine particle size (−20 mesh). About 500 g of this material was heated in an evacuated chamber at 600°C for 8 hr at a pressure of less than 10^{-4} mm Hg. The sublimate containing most of the magnesium was collected on a water-cooled condenser. The calcium remaining in the charge was then distilled off under vacuum by heating to 900°C. The resulting condensate appeared to divide naturally into two nearly equal portions. Calcium B was that portion which appeared to have distilled off last and still contained appreciable amounts of magnesium. Calcium C, that portion which distilled off first, contained very little magnesium. This was then redistilled for final purification. The reason for this unusual separation is not fully understood at this time. Possibly during sublimation the magnesium was depleted from the outer region of each calcium granule and on subsequent distillation the magnesium-depleted regions were the first to distill.

Aluminum, iron, magnesium, and manganese contents were determined spectrographically, and the nitrogen content was determined by the micro-Kjeldahl method. Analyses are shown in Table II. No values are reported for oxygen or carbon because of the difficulty in analyzing for these elements in calcium. However, there is no reason to expect appreciable contamination from either of these elements. The most likely source of carbon would be the diffusion pump oil, and a liquid nitrogen cold trap was used in the vacuum line to prevent oil vapors from reaching the calcium. An estimate of <0.01 wt % oxygen would seem to be a reasonable value since oxygen and nitrogen contamination both results from reaction of calcium with residual air in the vacuum system. Spectrographic analyses of the initial calcium showed trace amounts of boron, cadmium, silicon, sodium, lithium, and potassium. These may have carried through to the final product.

Contamination during Fabrication and Experimentation

Because of the high reactivity of calcium, particularly at elevated temperatures, it was found necessary to take precautions against contamination during fabrication and during the thermal changes in the experiments. Fabrication was accomplished in the following manner. Calcium was fused in a sealed iron tube at a temperature above 900°C. Subsequently, the iron was turned off in a lathe, leaving a solid calcium rod. For x-ray diffraction studies, a calcium rod $\frac{3}{8}$ in. in diameter by 1 in. long was milled into a bar with a thickness of $\frac{3}{16}$ in. An additional $\frac{1}{16}$ in. was removed by filing under a dry helium atmosphere. The resulting specimen was $\frac{1}{8}$ in. x $\frac{3}{8}$ in. x 1 in. For resistivity studies, calcium was turned in a lathe to form a rod 0.2 in. in diameter by 5 in. long.

Spectroscopic analysis showed that the pick-up of iron from the crucible was less than 50 ppm. Calculations using ambient temperature and pressure indicated that charging and sealing the crucibles in air could result in a maximum increase in nitrogen and oxygen content of 350 ppm. This contamination would be considerably less if there were any tendency toward segregation at the surface.

X-ray and resistivity studies were carried out under an inert atmosphere of helium. The high vapor pressure (10, 11) of calcium precluded a vacuum, and the high rate of reactivity at elevated temperatures made an inert atmosphere necessary. Initial experiments showed that commercial "Grade A" helium contained sufficient oxygen and water vapor to react with calcium to form a surface film which masked the x-ray reflections from the metal lattice. Thus helium was purified via a train which consisted of a series of two liquid nitrogen cold traps preceded by a getter-furnace filled with calcium turnings heated to 600°C. The specimen chamber and purification train were filled by first evacuating to a pressure of 5×10^{-6} mm Hg and then slowly introducing the helium. Evacuation and refilling were repeated several times before the sample was heated. With this helium purification a calcium sample could be kept in the x-ray camera for a week or more with daily heating and cooling without picking up a detectable oxide film. Helium purification was also used for the resistivity measurements.

X-Ray Diffraction Results

All x-ray patterns were taken with a Geiger-counter diffractometer adapted for high temperature studies as described by Chiotti (12). All diffraction peaks were confirmed with two independently prepared bar specimens. Data for calcium A were also checked with powder patterns. Interfering oxide and hydroxide peaks appeared rapidly in the powder pattern even under purified helium. Temperatures were measured with a chromel-alumel thermocouple in contact with the base of the test specimens.

Results indicate that calcium is self-annealing at room temperature. Diffraction peaks were observed to have normal shape and intensity as soon as measurement could be made after cold working by milling and filing. Minimum time between working the sample and observing the first diffraction peaks was approximately 10 min. Corroborative evidence for this self-annealing is available from past experience in the lack of hardening after extensive cold working.

Face-centered cubic phase.—There is no doubt that the room temperature phase of calcium is f.c.c. This phase was first

TABLE III. *Reflections from complex phase at 319°C*
Copper $K\alpha$ radiation*
Calcium A

2θ	d	$\sin^2\theta$
26.52	3.358	0.05244
27.50	3.241	0.05641
28.20	3.162	0.05934
30.80	2.901	0.07054
34.15	2.624	0.08644
45.60	1.988	0.1502
47.20	1.924	0.1603
52.30	1.748	0.1945
56.05	1.667	0.2209
67.00	1.396	0.3046
73.50	1.287	0.3576
75.40	1.260	0.3739
90.70	1.083	0.5062
110.15	0.9395	0.6724
118.00	0.8986	0.7348

* The 2θ values were converted to d-spacings with National Bureau of Standards tables based on the $K\alpha_1$, wave length of 1.54050Å.

pattern could not be indexed on the basis of a cubic, hexagonal, or tetragonal lattice. An attempt to index the pattern in the orthorhombic system by numerical methods (14–16) was unsuccessful. The possibility that the diffraction pattern represents a multiple phase region still exists.

This complex phase was not found initially in calcium C. After a specimen of calcium C had been in the camera for four days, with a considerable fraction of the time at high temperatures, some peaks characteristic of the complex phase appeared in addition to those of the f.c.c. phase in patterns run at 414° and 450°C. When the specimen was taken from the camera, the surface removed by filing, and the specimen remounted, the peaks from the complex phase no longer appeared. The appearance of the complex phase after prolonged heating at elevated temperatures and the elimination of this phase by removal of the surface layer were reproducible. It was concluded from this behavior that the appearance of the complex phase was due to a change in the surface layer of the calcium. In addition it was reasoned that, since the complex phase was characteristic of the lower purity calcium A and

TABLE IV. *Comparison of observed transitions in calcium*

Temp, °C	Graf*	Calcium A 99.66%	Calcium B 99.85%	Calcium C 99.96%
100	f.c.c. $a = 5.57$Å	f.c.c. $a = 5.612 \pm 0.012$Å	f.c.c.	f.c.c. $a = 5.582 \pm 0.004$Å
200				
300	300°C	300°C	300°C	
		complex 375°C		
400	complex 450°C		complex 450°C	
500		h.c.p. $c/a = 1.63$ 500°C		464°C
	h.c.p. $c/a = 1.64$			
600		b.c.c. $a = 4.474 \pm 0.004$Å	b.c.c.	b.c.c. $a = 4.477 \pm 0.007$Å
700				
800				

* Data represent Graf's best calcium.

reported by Hull (13) who gave the lattice parameter as $a = 5.57$Å. All subsequent investigators have corroborated this structure. In this investigation all of the calcium samples were f.c.c. at room temperature, and the lattice parameter at 18°C was $a = 5.612 \pm 0.012$Å for calcium A and $a = 5.582 \pm 0.004$Å for calcium C. No attempt was made to obtain high precision parameters; parameters were calculated primarily for phase identification. The f.c.c. phase was found to persist up to about 300°C in calcium A and calcium B and up to about 460°C in calcium C.

Complex phase.—A phase of complex nature was found in calcium A between 300° and 375°C and in calcium B between 300° and 450°C. Diffraction peaks for calcium A at 319°C are listed in Table III. The correspondence of the diffraction peaks indicates that this is the intermediate phase reported by Graf (4). In agreement with Graf this calcium B, this behavior must result from an increase in impurity content at the surface. Such an increase might occur in at least three possible ways. First, there might be enough residual contaminant in the helium atmosphere to react with the calcium surface at elevated temperatures. Calcium is known to react rapidly with many gases at elevated temperatures. Second, preferential sublimation of calcium at elevated temperatures could enrich the surface in nonvolatile impurities. Evidence for calcium sublimation was inferred from the embrittlement of the tantalum heating element which necessitated frequent replacement during the course of the experiments. Third, differential solubility as a function of temperature could have created a concentration gradient (17) between the surface and the bulk of the sample. A temperature gradient between the surface and the base of the calcium undoubtedly existed because of the geometry of the furnace

and sample mount. Any one of these factors, or combination of them, could account for the observed behavior of calcium C.

Hexagonal closest-packed phase.—The high temperature allotrope of calcium is widely quoted in handbooks and tables as being h.c.p. In this investigation an h.c.p. phase was found in the lowest purity calcium A between 375° and 500°C, but was not found as a stable phase in calcium B or calcium C. This phase was indexed on the basis of Graf's parameters, and a check of the measured d values with a Bunn chart (18) gave $c/a = 1.63$ with $c = 6.49$Å and $a = 3.97$Å. Graf reported $c/a = 1.64$. However, even in calcium A the hexagonal phase gave way to a b.c.c. phase over 500°C. None of Graf's published patterns was taken above 500°C.

Body-centered cubic phase.—All of the samples exhibited a b.c.c. phase at high temperature. The stable range for this phase in calcium A was between 500°C and the melting point, while the range for calcium B and calcium C was between 460°C and the melting point. The measured lattice parameter for calcium C at 500°C was 4.477 ± 0.007Å. The results of this investigation are tabulated with the results of Graf in Table IV.

Electrical Resistance Measurements

Electrical resistance measurements were made to check the transition points. These were made by an alternating current potentiometric method using the apparatus described by Chiotti (19). Automatic recording and control of the temperature were employed with a slow heating and cooling speed (1°C/min). Temperature was measured with a chromel-alumel thermocouple in direct contact with the test piece between the resistivity probes. Probes were electrolytic iron wire spot-welded to the test piece.

Fig. 1 shows discontinuities in resistance vs. temperature near 300°, 375°, and 500°C for calcium A. Transitions are not sharp, but correspondence to x-ray values is satisfactory. No cooling cycle was run because of the melting of the test piece at 849°C; this value for the melting point is in excellent agreement with the value of 851 ± 1°C reported by Antropoff and Falk (20).

A graph for the corresponding heating cycle using calcium C is also shown in Fig. 1. Only a single break appears at 464°C. Repeated thermal cycling produced no additional effect except a slight smearing of the transition point. A slight surface film was noted on the specimen after the third heating and cooling cycle. The temperature dependence of the electrical resistivity for both phases of calcium C is seen to be linear.

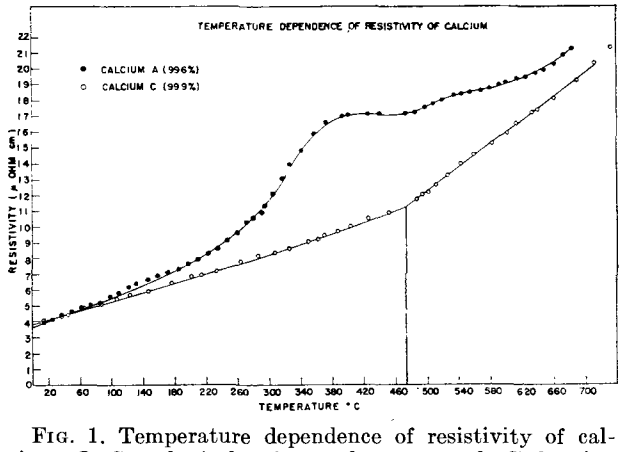

FIG. 1. Temperature dependence of resistivity of calcium. ●, Sample A, heating cycle; ○, sample C, heating cycle.

DISCUSSION

The results show that calcium is quite sensitive in its behavior to small amounts of impurities. The complex phase has been shown to be the result of contamination and must be representative of a calcium alloy system. The broad and ill-defined transition for the appearance of this phase found in this and in previous investigations fits with this interpretation. The metastability of the phases in the low purity calcium A also supports this view. In calcium A lines from all four phases could be found in the diffraction pattern immediately after rapid cooling from high temperature. The patterns stabilized to f.c.c. after approximately one hour at room temperature. Even in calcium B some metastability was noted. In contrast no metastability was observed in calcium C, patterns were of the equilibrium phase as soon as peaks could be observed from calcium C after crossing the transition temperature in either direction. Similarly, in the resistance-temperature curves, calcium A transitions were broad and sluggish, while the calcium C transition was relatively sharp.

Transformation from f.c.c. to b.c.c. with increasing temperature is consistent with Zener's theory (21) of the stability of b.c.c. phases. This theory predicts a large amplitude for the (110) [110] shear strain which gives rise to a large entropy term. Thus the free energy is lowered with increasing temperature, and the b.c.c. structure tends to be stabilized.

Supporting evidence for the importance of the entropy term in phase stabilization is Brooks' recent calculation (22) of the cohesive energy of calcium. Brooks calculated a cohesive energy of 46 kcal/mole which compares with an observed value of 48 kcal/mole. This calculation was a modification of the Wigner-Seitz (23) calculation in which structural considerations are neglected by using an approximation of spherical symmetry about an atom. The important factor in the energy evaluation is the volume per atom. The agreement between observed and calculated cohesive energy indicates the possibility that in two phases having the same volume per atom the factor controlling the relative stability may be the entropy term. In calcium Graf (4) has observed that the volume per atom in the h.c.p. and the b.c.c. phases is almost identical. Calculations based upon the observed impurity content necessary to stabilize the h.c.p. phase in this investigation show that the entropy of mixing causes a difference in entropy between the b.c.c. and h.c.p. phases of <0.1 e.u. This seems hardly sufficient to stabilize the h.c.p. phase. A second, and possibly more important, entropy term could arise from changes in the vibrational spectrum due to nonperiodic impurity atom sites. Thermodyamic studies on various purities of calcium might provide some valuable information on the problem of phase stability and transformation.

Two conclusions can be made on the basis of this in-

vestigation. First, under ambient pressure pure calcium exists in only two allotropic modifications. Second, the high temperature allotrope in pure calcium (99.9%) is b.c.c. and not h.c.p. as currently tabulated in structure compilations.

ACKNOWLEDGMENTS

The authors are indebted to Dr. V. A. Fassel and his group for the spectrographic analyses and to Dr. C. V. Banks and his group for the chemical analyses. Thanks are also extended to Dr. P. Chiotti for the use of his resistivity apparatus.

Manuscript received August 1, 1955.
Any discussion of this paper will appear in a Discussion Section to be published in the June 1957 JOURNAL.

REFERENCES

1. C. L. MANTELL AND C. HARDY, "Calcium Metallurgy and Technology," pp. 12 and 16, Reinhold Publishing Co., New York (1945).
2. P. BASTEIN, *Compt. rend.*, **198**, 831 (1934); *Rev. Met.*, **32**, 120 (1935).
3. A. SCHULZE AND H. SCHULTE-OVERBERG, "A Polymorphous Transformation in Calcium," *Metallwirtschaft*, **12**, 633 (1933).
4. L. GRAF, *Physik. Z. vereinigt mit dem Jarbuch der Radioaktivität und Elektronik*, **35**, 551 (1934).
5. L. GRAF, *Metallwirtschaft*, **12**, 649 (1933).
6. F. EBERT, H. HARTMAN, AND H. PEISKER, *Z. anorg. u. allgem. Chem.*, **213**, 126 (1933).
7. C. C. LOOMIS, *Trans. Electrochem. Soc.*, **89**, 119 (1946).
8. E. FUJITA, H. YOKOMIZO, AND Y. KUROZAKI, *J. Electrochem. Soc. Japan*, **19**, 196 (1951).
9. I. I. BETCHERMAN AND L. M. PIDGEON, *Can. Mining Met. Bull.*, **44**, 253 (1951).
10. P. E. DOUGLAS, *Proc. Phys. Soc. (London)*, **67**, No. 418B, 783, 787 (1954).
11. N. B. PILLING, *Phys. Rev.*, **18**, 362 (1921).
12. P. CHIOTTI, *Rev. Sci. Instr.*, **25**, 683 (1954).
13. A. W. HULL, *Phys. Rev.*, **17**, 42 (1921).
14. R. HESSE, *Acta Cryst.*, **1**, 200 (1948).
15. A. J. STOSICK, *ibid.*, **2**, 271 (1949).
16. H. LIPSON, *ibid.*, **2**, 43 (1949).
17. L. S. DARKEN AND R. A. ORIANI, *Acta Metallurgica*, **2**, 841 (1954).
18. C. W. BUNN, "Chemical Crystallography," p. 380, Oxford University Press, New York (1945).
19. P. CHIOTTI, *Rev. Sci. Instr.*, **25**, 876 (1954).
20. A. ANTROPOFF AND E. FALK, *Z. anorg. u. allgem. Chem.*, **187**, 405 (1930).
21. C. ZENER, "Elasticity and Anelasticity of Metals," pp. 32–37, University of Chicago Press, Chicago (1948).
22. H. BROOKS, Harvard University, Unpublished data.
23. E. WIGNER AND F. SEITZ, *Phys. Rev.*, **43**, 804 (1933); *ibid.*, **46**, 509 (1934).

Selected Physical Properties of Ternary Electrolytes Employed in Ionic Mass Transfer Studies

M. EISENBERG,[1] C. W. TOBIAS, AND C. R. WILKE

Division of Chemical Engineering, University of California, Berkeley, California

ABSTRACT

Densities and viscosities of $CuSO_4$-H_2SO_4, $AgClO_4$-$HClO_4$, and $K_3[Fe(CN)_6]$-$K_4[Fe(CN)_6]$-NaOH solutions in water have been measured over a range of compositions. Experimental values of the integral diffusion coefficients are also given for silver perchlorate in aqueous perchloric acid, and for $K_3[Fe(CN)_6]$ and $K_4[Fe(CN)_6]$ in aqueous NaOH.

INTRODUCTION

Intensive efforts have been directed toward interpretation of concentration polarization and limiting current phenomena, taking into account pertinent physical properties of the electrolytes, cell geometries, and prevailing hydrodynamic conditions (1–4). Quantitative interpretation of polarization and limiting current data requires a knowledge of densities and viscosities of the electrolyte as well as the diffusion coefficients of the reacting ionic species. The most conveniently applicable electrode reactions for purposes of mass transfer studies include the reduction of cupric ion to metal, silver ion to metal, and of ferricyanide to ferrocyanide, or vice versa. In addition to the reacting ionic species, excess "neutral" electrolyte (some strong acid or base) is frequently added to the solutions in order to render negligible the contribution of migration to the ionic mass transport. A literature survey revealed little information on the physical properties of such ternary electrolytes.

In the course of ionic mass transfer studies in this laboratory (1, 3), densities and viscosities of the electrolytes employed were determined. Diffusion coefficients were also measured, except for copper sulfate solutions, for which reliable data have already been published (1).

$CuSO_4$-H_2SO_4-H_2O SYSTEM

Materials.—All solutions were prepared with C.P. materials: copper sulfate ("Baker Analyzed") and sulfuric acid (General Chemical Co.). The compositions (molari-

[1] Present address: Stanford Research Institute, Stanford, California.

TABLE I. *Densities of aqueous* $CuSO_4$-H_2SO_4 *solutions**

Molarity of $CuSO_4$	Density, g/cc			
	15°C	20°C	25°C	30°C
0	1.0932	1.0908	1.0885	1.0856
0.05	1.0999	1.0975	1.0949	1.0922
0.10	1.1069	1.1045	1.1018	1.0988
0.20	1.1204	1.1180	1.1150	1.1120
0.30	1.1338	1.1315	1.1282	1.1252
0.40	1.1477	1.1451	1.1416	1.1386
0.50	1.1622	1.1592	1.1556	1.1522
0.60	1.1768	1.1736	1.1703	1.1671
0.70	1.1929	1.1892	1.1861	1.1830
0.80	1.2088	1.2052	1.2024	1.1994

* All solutions 1.5M in H_2SO_4.

TABLE II. *Densities and viscosities of aqueous* $CuSO_4$ + H_2SO_4 + *glycerol solutions*

Composition	20°C		25°C		30°C	
	Density	Viscosity	Density	Viscosity	Density	Viscosity
g-moles/l	*g/cc*	*cps*	*g/cc*	*cps*	*g/cc*	*cps*
0.368 $CuSO_4$ 0.751 H_2SO_4 6.38 Glycerol	1.2245	11.9	1.2210	9.14	1.2184	6.95
0.570 $CuSO_4$ 1.720 H_2SO_4 3.28 Glycerol	1.2135	4.90	1.2097	4.06	1.2068	3.40

ties) were determined analytically: Cu^{++} by the iodine-thiosulfate method and $SO_4^{=}$ gravimetrically as barium sulfate.

Densities.—Data reported in Tables I and II were obtained by means of a 50 cc pycnometer equipped with a capillary and calibrated with doubly distilled water. Solutions in the pycnometer were equilibrated in a thermostat controlled to ±0.01°C in the range 13°–35°C. The density of a given solution was determined at five or six different temperatures covering the above range. This procedure yielded for each solution a density-temperature curve that could be smoothed with an average density deviation of ±0.001 g/cc for the individual points from the line.

Viscosity.—Measurements were made by using an Ostwald viscometer with an efflux volume of approximately 1.5 cc. A working volume of 10 cc was always pipetted into the viscometer in order to maintain a constant head of solution. Efflux time was followed by visual observation and measured to 0.1 sec with an electric timer. The viscometer was calibrated with doubly distilled water at various temperatures in the range 13°–32°C. This yielded an "efflux time" vs. temperature curve that was subsequently used for calculation of viscosities of the solutions at any temperature within this range. For each of the solutions the efflux time was determined at five or six temperatures within this range. From the efflux time curves and densities of water and solution (x), the viscosity of the latter at several temperatures was determined by the familiar relation:

$$\mu_x = \mu_{H_2O} \frac{\rho_x t_x}{\rho_{H_2O} t_{H_2O}} \qquad (I)$$

where t_x and t_{H_2O} denote the efflux time at a given temperature of solution and water, respectively, and ρ_x and ρ_{H_2O} denote the respective densities.

Throughout these experiments, efflux times for water varied from 91.2 to 148.3 sec, and for the solutions from 93.0 to 235.7 sec. The experimental deviation was ±0.002 centipoise.

Data.—From a density-temperature graph containing curves for twelve solutions, all 1.5M in sulfuric acid and varying in copper sulfate molarity 0–0.760, a crossplot was prepared for 15°, 20°, 25°, and 30°C. This resulted in a four isotherm plot of density vs. copper sulfate molarity. The smoothed curves of this plot are given by the data of Table I. Average density deviation from the curves was ±0.0003 g/cc. Inasmuch as there were slight variations in sulfuric acid molarity of the solutions (1.493–1.508M H_2SO_4), the above deviation is not unexpected, and is not considered to be significant.

Similarly the viscosity temperature graph for the above mentioned solutions was crossplotted, and a smoothed plot of viscosity vs. copper sulfate composition prepared for 15°, 20°, 25°, 30°C. Although viscosity measurements could be reproduced to 0.002 centipoise, the average deviation from the smoothed curves represented by the data of Table III was ±0.02 centipoise. The magnitude of these deviations should be ascribed to the above-mentioned slight variations in the molarity of sulfuric acid.

Viscosity and density determinations were also made for two aqueous $CuSO_4$-H_2SO_4-glycerol solutions by the above methods. The results for temperatures 20°, 25°, and 30°C are reported in Table II.

Although some data on solutions of these substances are available in the literature (5, 6), they are not of a type or composition range which permit comparison with the present results. A comparison of the data of the Landolt-Börnstein Tables (7) for pure sulfuric acid solutions with the corresponding data in Table I can be made. After appropriate temperature interpolations, the two sets of data are in agreement within unity in the fourth place.

Viscosity data for aqueous $CuSO_4$-H_2SO_4 solutions could not be located in the literature.

$AgClO_4$-$HClO_4$-H_2O System

Materials.—Perchloric acid: 60% (Baker Analyzed); silver perchlorate: Reagent, (G. Frederick Smith Chemical Co.) Silver was determined as the chloride, and perchloric

TABLE III. *Viscosities of aqueous* $CuSO_4$-H_2SO_4 *solutions**

Molarity of $CuSO_4$	Viscosity, cps			
	15°C	20°C	25°C	30°C
0	1.50	1.33	1.21	1.12
0.05	1.55	1.37	1.24	1.14
0.10	1.60	1.40	1.27	1.16
0.20	1.69	1.48	1.33	1.20
0.30	1.80	1.56	1.39	1.25
0.40	1.92	1.65	1.46	1.31
0.50	2.03	1.75	1.54	1.37
0.60	2.16	1.87	1.64	1.45
0.70	2.30	2.01	1.76	1.53
0.80	2.47	2.17	1.90	1.64

* All solutions 1.5M in H_2SO_4.

TABLE IV. *Selected properties of perchloric acid*

Concentration	Temp	Density	Viscosity	Diffusion coefficient
g-moles/l	*°C*	*g/cc*	*cps*	*cm²/cc*
1.50	23	1.0823	0.955	
	25	1.0815	0.909	
	27	1.0806	0.873	
1.55	23	1.0855	0.956	At 30°C
	25	1.0843	0.910	$D = 3.88 \times 10^{-5}$
	27	1.0834	0.874	
1.60	23	1.0877	0.955	
	25	1.0867	0.909	
	27	1.0858	0.874	

TABLE V. *Densities of* $AgClO_4$ *in 1.5*M $HClO_4$

$AgClO_4$	$HClO_4$	Temp	Density
g-moles/l	*g-moles/l*	*°C*	*g/cc*
0.088	1.5	25.0	1.0976
0.195	1.5	25.0	1.1126
0.339	1.5	25.0	1.1382
0.482	1.5	25.0	1.1632
0.671	1.5	25.0	1.1913
0.931	1.5	25.0	1.2308
1.156	1.5	25.0	1.2710

acid titrated with sodium hydroxide to bromthymol blue endpoint.

Densities.—Densities were obtained by a standard method described above. The values measured between 0.088M–1.156M silver perchlorate in 1.5 perchloric acid fell on a straight line on a density vs. concentration plot, with a maximum deviation of 0.003 g/cc. Between the concentration limits 0.1–1.1M silver perchlorate in 1.5M perchloric acid this line can be represented by $\rho = 1.1005 + (M - 0.1)\ 0.1565$. The values measured are given in Tables IV and V.

Viscosities.—Viscosities were measured by an Ubbelohde type viscometer, with an estimated error less than ±0.5% (Tables IV and VI).

Diffusion coefficients.—These were measured in McBain-Northrup type (8, 9) diaphragm cells. Cell constants were based on the integral diffusion coefficient for 0.1*N* potassium chloride diffusing into initially pure water until concentrations in the two compartments were 0.075*N* and 0.025*N*, respectively, using the value of 1.870×10^{-5} cm²/sec for D_{KCl} at 25°C as determined by Harned and Nuttal (10). D_{HClO_4} was obtained by contacting approximately 1.6M perchloric acid through the diaphragm with 1.2M acid, diffusion taking place until the concentration of perchloric acid changed by about 0.1–0.15M. In the measurement of D_{AgClO_4}, silver perchlorate dissolved in 1.5M perchloric acid, was allowed to diffuse into 1.5M perchloric acid initially free of silver perchlorate. In Table VII the values of the "integral diffusion coefficients" are given for four different average concentrations. The average represents the arithmetic mean of four concentrations, i.e., the initial and final concentrations in both compartments of the cell. Concentrations of perchloric acid and Ag^+ in both compartments were established by careful analytic procedures prior to and following the mass exchange. Reproducibility of values of the diffusion coefficients was better than ±1.5%.

TABLE VI. *Viscosities of* $AgClO_4$ *in Approximately 1.5*M $HClO_4$

$HClO_4$	$AgClO_4$	Temp	μ
g-moles/l	*g-moles/l*	*°C*	*cps*
1.532		23.0	0.954
		25.0	0.910
		27.0	0.874
1.540	0.0965	22.0	0.980
		25.0	0.921
		28.0	0.859
1.516	0.4945	22.0	1.012
		25.0	0.954
		28.0	0.876
1.523	1.153	22.0	1.088
		25.0	1.027
		28.0	0.944

TABLE VII. *Diffusion coefficients of* $AgClO_4$ *in 1.5*M $HClO_4$ *at 30°C*

Avg concentration of $AgClO_4$, g-moles/l	0.05	0.1	0.3	0.8
$D \times 10^{-5}$, cm²/sec	2.30	2.26	2.1	2.07

$K_3[Fe(CN)_6]$-$K_4[Fe(CN)_6]$-NaOH-H_2O System

Materials.—All materials used were Merck's reagent grade. Ferricyanide was determined by the iodometric procedure (11) and ferrocyanide by permanganate titration (12).

Densities and viscosities.—Values for these properties were determined by methods already described for the copper sulfate and silver chlorate solutions.

Electrical conductivities.—Electrical conductivities were determined in a conventional conductivity cell, calibrated with a potassium chloride solution, using an audio oscillator as a source for 1000 cycle alternating current, a Wheatstone bridge, and an oscilloscope as a zero instrument. Estimated accuracy was ±0.5%.

Results for a number of solutions for temperatures 25° and 30° are summarized in Table VIII.

Diffusion coefficients.—A capillary technique similar to the one first described by Anderson and Saddington (13)

TABLE VIII. *Densities, viscosities, and conductivities of solutions of* $K_3[Fe(CN)_6]$ *and* $K_4[Fe(CN)_6]$ *in approximately 2N* NaOH

Composition, g-moles/l			Temp	Conductivity	Density	Viscosity
$K_3Fe(CN)_6$	$K_4Fe(CN)_6$	NaOH				
			°C	*ohm⁻¹cm⁻¹*	*g/cc*	*cps*
0.00998	0.01011	1.958	25	0.2848	1.0807	1.368
0.01224	0.01228	2.011	25	0.2863	1.0833	1.382
0.04996	0.05052	1.923	25	0.2860	1.0949	1.394
			30	0.3050	1.0929	1.257
0.0919	0.01198	1.977	25	0.2907	1.0955	1.392
0.0994	0.1008	2.007	25	0.3038	1.1174	1.494
0.3058	0.1022	2.006	25	0.3139	1.1491	1.608
0.1994	0.2030	2.004	25	0.3017	1.1535	1.642
			30	0.3264	1.1515	1.468

was chosen for this work because of its apparent simplicity and reliability. (The McBain-Northrup diaphragm cell method was not used because of the anticipated attack of the strong alkali solution on the sintered glass diaphragm.)

In the method employed here diffusion takes place from a capillary tube into an effectively infinite reservoir in which the capillary is immersed. This feature has the advantage that the width of the diffusion zone is small compared to its length, thus minimizing the effects of convection currents.

Four capillaries were simultaneously filled by means of a syringe with solutions A-2 and B-2 (see below) containing potassium ferricyanide, potassium ferrocyanide, and sodium hydroxide. The large reservoir in which they were immersed at time $t = 0$ contained solution A-1, with no ferrocyanide, or solution B-1, which contained no ferricyanide.

If the axis of the capillary is taken as x-axis then the boundary conditions for the concentration C of the diffusing species are:

$$C = C_0 \quad \text{for} \quad 0 \leq x \leq L \quad \text{at } t = 0 \tag{II}$$

$$C = 0 \quad \text{for} \quad x > L \quad \text{for all } t \tag{III}$$

where t is the time and L the length of the capillary. The solution of the diffusion equation

$$\frac{\partial C}{\partial t} = D\frac{\partial^2 C}{\partial x^2} \tag{IV}$$

under these conditions is given by:

$$\frac{C_{avg}}{C_0} = \frac{8}{\pi^2}\sum_{n=0}^{\infty}\frac{1}{(2n+1)^2}\exp\left[-\frac{(2n+1)^2\pi^2 Dt}{4L^2}\right] \tag{V}$$

where C_{avg} is the average concentration of the diffusing species in the capillary after time t. Since L and t were known, an analytic determination of C_0 and C_{avg} sufficed for the calculation of the diffusion coefficient D.

In general the times were chosen so that C_{avg}/C_0 was about 0.6–0.7. To reduce experimental error several capillaries of different lengths and volumes were used.

For the diffusion of ferricyanide ion the reproducibility was ±1.5%. In the case of the ferrocyanide, however, it was at best ±4% due to the difficult endpoint determination in permanganate titration of the small volume of solution from the capillaries.

For diffusion of ferricyanide from solution B-2 in the capillaries into solution B-1, the following average results were obtained at 25°C:

Initial concentration, g-moles/l	*B-2*	*B-1*
Sodium hydroxide	2.027	2.027
Potassium ferrocyanide	0.1919	0.1919
Potassium ferricyanide	0.1963	

$D_{avg} = 0.527 \times 10^{-5}$ cm²/sec at average viscosity $\mu = 1.419 \times 10^{-2}$ poise, hence

$$\frac{D\mu}{T} = 2.50 \times 10^{-10}\ \frac{\text{cm}^2}{\text{sec}}\frac{\text{poise}}{^\circ\text{K}} \tag{VI}$$

This value was used to calculate diffusion coefficients of the ferricyanide ion.

For diffusion of ferrocyanide ion from solution A-2 (in the capillaries) into solution A-1 the following average results were obtained at 25°C:

Initial concentration, g-moles/l	*A-2*	*A-1*
Sodium hydroxide	2.027	2.027
Potassium ferricyanide	0.1879	0.1879
Potassium ferrocyanide	0.2032	—

$D_{avg} = 0.418 \times 10^{-5}$ cm²/sec at average viscosity $\mu = 1.53 \times 10^{-2}$ poise, hence

$$\frac{D\mu}{T} = 2.15 \times 10^{-10}\ \frac{\text{cm}^2}{\text{sec}}\frac{\text{poise}}{^\circ\text{K}} \tag{VII}$$

This value was used in computing the diffusion coefficient of ferrocyanide ion.

Estimates from equivalent conductance data, corrected for viscosity, gave $D\mu/T$ values of 2.62 and 2.22 $\times 10^{-10}$ for ferri- and ferrocyanide, respectively. Since such estimates, usually satisfactory at low concentrations, were expected to be somewhat high, the results obtained in these measurements are considered reliable.

Manuscript received August 2, 1955.
Any discussion of this paper will appear in a Discussion Section to be published in the June 1957 JOURNAL.

REFERENCES

1. C. R. WILKE, M. EISENBERG, AND C. W. TOBIAS, *This Journal*, **100**, 513 (1953).
2. C. R. WILKE, M. EISENBERG, AND C. W. TOBIAS, *Chem. Eng. Progr.*, **49**, 663 (1953).
3. M. EISENBERG, C. W. TOBIAS, AND C. R. WILKE, *This Journal*, **101**, 306 (1954).
4. N. IBL, *Chimia (Switz.)*, **9**, 135 (1955).
5. H. M. GOODWIN AND W. G. HORSCH, *Chem. & Met. Eng.*, **21**, 181 (1919).
6. H. D. HOLLER AND E. PEPPER, *J. Am. Chem. Soc.*, **38**, 1021 (1916).
7. LANDOLT-BÖRNSTEIN, "Physikalisch-Chemische Tabellen", Vol. I, p. 397, Julius Springer, Berlin (1936).
8. A. R. GORDON, *Ann. N. Y. Acad. Sci.*, **46**, 285 (1945).
9. P. CHANG, "Measurement and General Correlation of Diffusion of Nonelectrolytes," Ph.D. Thesis, University of California, Berkeley (1954).
10. H. S. HARNED AND R. L. NUTTALL, *Ann. N. Y. Acad. Sci.*, **51**, 781 (1949).
11. I. M. KOLTHOFF AND N. H. FURMAN, "Volumetric Analysis," Vol. II, p. 427, John Wiley & Sons, Inc., New York (1929).
12. F. SUTTON, "Volumetric Analysis," 12th ed., p. 235, Blakiston and Co., Philadelphia (1935).
13. J. S. ANDERSON AND K. I. SADDINGTON, *J. Chem. Soc.*, **1949**, 381.

Punched-cell Batteries with Polyethylene Glycol Electrolytes

REUBEN E. WOOD

National Bureau of Standards, Washington, D. C.

ABSTRACT

For producing small, high voltage, low current batteries with long shelf lives, it has been found effective to use a waxy electrolyte whose major component is a polyethylene glycol. Results reported here deal with cells having manganese dioxide cathodes, zinc anodes, and, in most cases, a solid electrolyte composed of a polyethylene glycol containing about 5% zinc chloride. A large group of 25-cell batteries have been studied over periods of more than one year. In general, they have shown remarkably little loss of open-circuit voltage. A method of producing dense, strongly adherent, and electrically conductive layers of MnO_2 on conductive plastic films by electrodeposition from a permanganate solution is described. A modified type of cell having a gelled glycol electrolyte is described and discussed briefly.

Since the early days of electrical experimentation the pile type of battery has been appealing because of its simplicity and compact construction. Many embodiments of this kind of construction have been described (1). It is a structure particularly suitable for very small, low current, high voltage batteries. This paper is based on research on such piles, the primary objective of which was to develop a battery of this type with a long shelf life. Secondary objectives were compactness and an extended useful temperature range.

The cells reported on here are related to the Leclanché cell in that they have zinc anodes and manganese dioxide cathodes. They differ fundamentally from the ordinary dry cell as well as from related piles such as those described by Elliott (2) and Reiner (3) in having an electrolyte in which the major constituent is a polyethylene glycol.

CELL AND BATTERY CONSTRUCTION

A typical battery is made as follows. A sheet of zinc about 8 cm wide, 12 cm long, and 0.004 cm thick is degreased by dipping it briefly in 6*N* hydrochloric acid, and rinsing it immediately. Etching promotes adherence of zinc to the waxy polyethylene glycol electrolyte.

A piece of conductive vinyl film is then cut to match the zinc sheet. A piece of filter paper is cut to a slightly larger size than the zinc and plastic sheets. The zinc, conductive plastic, and filter paper sheets are incorporated into a cell as follows.

About 20 g of solid polyethylene glycol is melted and about 1 g of reagent-grade 95% $ZnCl_2$ is dissolved in it. This solution is divided into two approximately equal portions. Into one of these portions is stirred about 10 g of powdered MnO_2. The piece of filter paper is then laid on a hot plate maintained at a temperature somewhat above the melting point of the polyethylene glycol wax, and the hot MnO_2 suspension is painted on one side of it. The other side is painted with the $ZnCl_2$-polyglycol melt which does not contain MnO_2. The filter paper, so prepared, is then taken off of the hot plate and is placed between the zinc and conducting plastic sheets, the conducting plastic facing the MnO_2-coated side of the separator. This sandwich-cell is put back on the hot plate and squeezed with a roller to express excess wax. It is then cooled while being kept pressed together. Next it is put under running water and washed quickly to clean the outside zinc and plastic surfaces. Since these are quite impervious to water it is believed that very little water gets into the cell in this operation except at the edges which, after the sandwich has been wiped dry, are immediately trimmed off.

Disks, either $\frac{1}{4}$ in. (0.635 cm) or $\frac{1}{2}$ in. (1.270 cm) in diameter, are then punched from this sandwich by the use of hardened steel or tungsten carbide punch and die. Twenty-five such cells are then stacked in series in a suitable jig, and, while the battery is held pressed together, the cylindrical surface is lacquered. (A neoprene-base adhesive has also been used and the records so far give no certain indication as to whether this is superior or inferior to lacquer.) The lacquer serves both to seal the edges of the cells and to hold the cells together in the battery. When the lacquer has dried the battery is removed from the jig. Fig. 1 is a photograph of $\frac{1}{2}$ in. and $\frac{1}{4}$ in. 25-cell batteries.

MnO_2 electrodeposited from permanganate solutions.— An important modification of this method was the use of electroplated MnO_2 instead of the wax suspension of the MnO_2 powder. It was found that dense, strongly adherent, electrically conductive layers of MnO_2 could be electrodeposited on the conductive plastic films by making them the cathodes in an electrolyte containing about 20 g of $KMnO_4$ and 5 ml of concentrated HNO_3 in a liter of water. Stainless steel anodes and a current density of a few milliamperes per square centimeter were used. The heaviest deposit made was a layer of about 25 mg/cm^2; deposited layers used in batteries were usually from 2 to 5 mg/cm^2.

The surface of these layers usually had the color and texture of slate. The deposit appeared to shrink enough to cause curling when it dried. But it was dense; micrometer measurements on the conducting plastic sheets before and after plating, together with the corresponding weighings gave an apparent density for the MnO_2 of very roughly 5 g/cm^3. Considerations of the increase in resistance of the plating circuit with increase in thickness of the MnO_2 layer gave values for the specific resistance of between

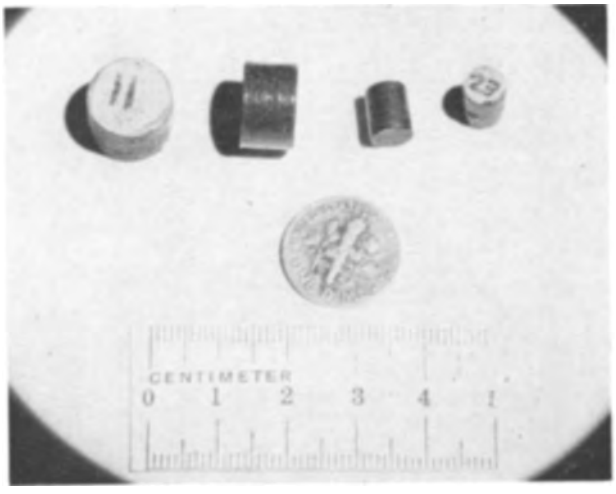

FIG. 1. ½ in. and ¼ in. 25-cell batteries

2×10^5 and 5×10^5 ohm cm. Broken edges of the layer appeared glassy under a binocular microscope; they were reminiscent of the appearance of chips of black obsidian. X-ray diffraction indicated an amorphous structure. Had time permitted it would have been interesting to study more thoroughly this electrodeposition procedure and the properties of the electrodeposited MnO_2 layers. (The symbol MnO_2 has been used broadly; it is recognized that the electrodeposited layer might have a composition departing considerably from that implied by the formula.)

Batteries with cathodes of MnO_2 electrodeposited on the conductive plastic were constructed as previously described except that the separator was impregnated with only the $ZnCl_2$—polyglycol wax mixture, no powdered MnO_2 being used. The sandwich consisted of the zinc sheet, the wax-impregnated separator, and the MnO_2-plated conductive sheet.

PHYSICAL AND ELECTRICAL CHARACTERISTICS OF BATTERIES

Table I gives characteristics of typical fresh, 25-cell batteries (of the FP separator, 4000 electrolyte type; see notes after Table II). The physical characteristics varied somewhat and the short-circuit currents varied markedly with variations in electrolyte and separator compositions.

Table II is a summary of data on 25-cell batteries. In it the batteries are divided into groups, the members of each group being rather uniform with respect to age and structure. This tabulation includes a large majority of all of the batteries that were made as already described or which involved the modifications indicated in the table. Batteries are excluded from the table for the following

TABLE I. *Physical and electrical properties of representative batteries*

Length	0.85 cm
Weight of ¼ in. battery	1.5 g
Weight of ½ in. battery	6.0 g
Electromotive force	37.5 v
Short-circuit current of ¼ in. battery	3×10^{-8} amp
Short-circuit current of ½ in. battery	3×10^{-7} amp

TABLE II. *Characteristics of polyethylene glycol punched-cell batteries after 1 year or more of shelf life*

Group No.	Number of batteries in group	Electrolyte	Separator	Age range	EMF range	S.C.C. range
Part I*a*: ½ in. (1.270 cm) batteries with powdered MnO_2						
				months	*volts*	*amp* $\times 10^9$
1	4	4000	FP	20	36–37	30–50
2	4	6000	FP	17–18	33–36	25–30
3	8	4000	FP	16	35–37	20–30
4	4	2000	FP	16	35–36	45–60
5	2	4000	Munsing paper	15	33–34	60
6	4	9000w	FP	15	32–34	5
Part I*b*: ½ in. (1.270 cm) batteries with electrodeposited MnO_2						
7	5	4000	R-25-F	13	37–38	140–190
8	5	4000	FP	13	37–38	30–45
9	5	4000	R-45-F	13	21–33	50–110
10	1	4000	Nylon cloth	12	35	80
Part II*a*: ¼ in. (0.635 cm) batteries with powdered MnO_2						
11	1	4000	FP	17	36	5
12	20	4000	FP	17–20	35–37	10–20
13	2	6000	FP	18	31–35	5
Part II*b*: ¼ in. (0.635 cm) batteries with electrodeposited MnO_2						
14	7	4000	R-25-F	13	38–39	50–60
15	13	4000	R-45-F	13	37–38	30–45
16	10	4000	FP	12–13	35–37	10
17	2	4000	Nylon cloth	12	35	25

(a) The number in the "Electrolyte" column refers to the approximate average molecular weight of the polyethylene glycol used. The 9000-w entry means that in this case polyethylene glycol of an approximate average molecular weight of 9000 was used and also that 10% by weight of water was added to the electrolyte. The 9000-w case (Group 6) was the only one in which water was added, although small amounts were doubtless present in all the batteries as an original minor constituent of the battery components and as a result of absorption from the atmosphere during construction of the battery.

(b) Under "Separator", FP means a "qualitative or rough quantitative" grade of filter paper. Actually, two slightly different grades of this type of paper were used during the course of the research but differences shown, if statistically significant at all, seemed too small to justify further subdivision of the table. R-25-F and R-45-F are nonwoven fabrics. These are tough matted sheets with much more open and less homogeneous structure than filter paper. The R means rayon, F is a soft grade and the 25 and 45 are numbers approximately proportional to thicknesses.

(c) Ages are given to the nearest month. Where only one number is given in the "Age range" column, it means that all the batteries in the corresponding group were within ½ month of the age listed.

(d) Values in the emf column represent to the nearest volt measurements made with an electrostatic voltmeter at the time when the batteries were of the ages listed. The electrostatic voltmeter was checked on the day of measurement against a precision, permanent magnet, moving-coil voltmeter.

(e) The numbers in the S.C.C. column when multiplied by 10^{-9} amp are short-circuit currents measured when the batteries were of the ages listed. They were measured with a galvanometer whose sensitivity was 6.0×10^{-9} amp/mm of deflection. Observed values are rounded to the nearest 5.

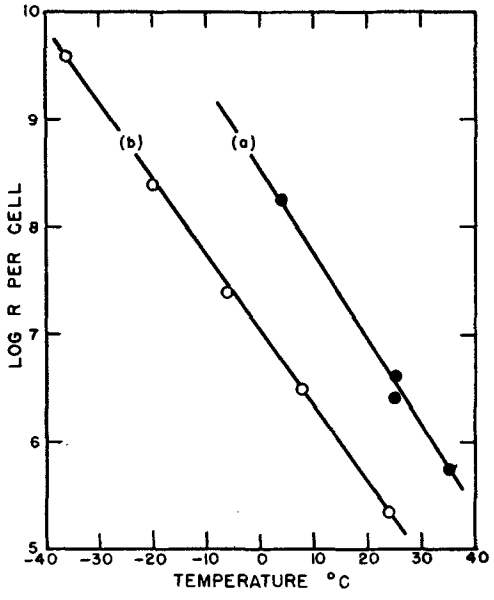

FIG. 2. Cell resistance as a function of temperature. The common logarithm of the resistance in ohms is plotted against the Centigrade temperature. Curve (*a*) is for a wax battery, Curve (*b*) is for a gel battery.

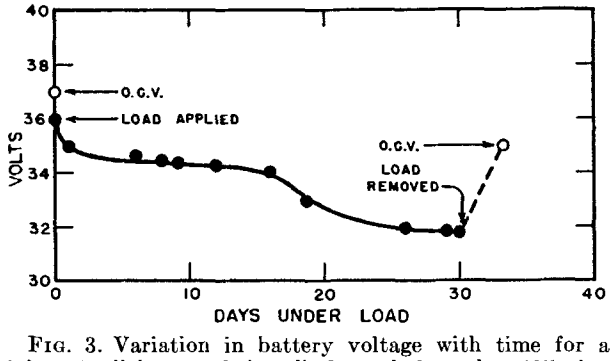

FIG. 3. Variation in battery voltage with time for a $\frac{1}{4}$ in. 25-cell battery being discharged through a 10^{11} ohm load.

reasons: (*a*) several batteries did not contain 25 cells; (*b*) five were given away for testing in another laboratory (*c*) eight were not of the punched-cell type; (*d*) seven involved more radical departure than the others from the described construction and did not seem to yield sufficiently interesting or informative results to warrant their discussion. All of the batteries in Table II are more than a year old. They have been stored during most of their lives at room temperature in desiccators containing silica gel.

Fig. 2(*a*) shows the effect of temperature on the resistance of one of these wax batteries. This battery was about one month old when the measurements were made. Resistances were calculated on the basis of the short-circuit currents at the various temperatures. Fig. 3 shows the performance of a wax battery under a constant load.

DISCUSSION

No study has been made of the electrochemistry of these batteries. A plausible guess would be that anode and cathode reactions can be represented approximately by the following equations, although it should be borne in mind that the oxides of manganese are notable for forming solid solutions or nonstoichiometric compounds:

$$Zn \rightarrow Zn^{++} + 2\,e^- \quad \text{and}$$
$$Zn^{++} + 2MnO_2 + 2\,e^- \rightarrow ZnO \cdot Mn_2O_3$$

The mechanism of conduction in the waxes and, in particular, the importance of water in these wax batteries are also unsettled questions. It is not known whether perfectly anhydrous polyethylene glycol will dissolve and ionize zinc chloride. It would not be expected to be a very good ionizing solvent for ordinary salts. The increase in internal resistance of these batteries during storage in a desiccator may be due to dehydration. Among the interesting possibilities that have suggested themselves in this connection is to try a salt such as tetramethylammonium picrate instead of zinc chloride as the solute, inasmuch as such organic salts are known to be more soluble and more largely ionized than inorganic salts in some organic solvents.

The useful temperature range for these batteries depends on shelf life and current requirements. The shelf life would probably be decreased greatly if the battery were heated above the melting point of the electrolyte, which for electrolyte 4000 (see Table II, footnote *a*) is around 45°C. And, judging from the data represented in Fig. 2(*a*), the lower temperature limit of the useful range for a battery with that electrolyte would be in the neighborhood of 0°C if one takes an arbitrary figure of 10^{-9} amp as the minimum useful current. (Since the internal resistance goes up with age, as indicated by a comparison of Tables I and II, the low temperature limit would also go up.)

The following are some of the implications of the statistics in Table II. Since a very large majority of the batteries have emf's after a year or more of storage which correspond to cell emf's between 1.3 and 1.6 v, it can be concluded that these batteries are not difficult to make and that they have good shelf-life characteristics. At present it is impossible to say whether or not there is a significant difference in shelf life between the $\frac{1}{2}$ in. and the $\frac{1}{4}$ in. batteries. The only difference between these types that has appeared so far is the difference in internal resistance indicated by short-circuit current measurements. It is interesting to note that in old batteries this difference seems to be less than the plate area difference, i.e., the ratio is less than four to one between $\frac{1}{4}$ in. and $\frac{1}{2}$ in. batteries of otherwise similar structure; in fresh batteries, however, (*see* Table I) the ratio is considerably greater than 4 to 1.

There are hardly enough data on electrolytes other than the 4000-type to permit well-founded generalizations about them. The 2000, 4000, 6000, and 9000 w batteries with filter paper separators show internal resistances increasing in that order except for the $\frac{1}{2}$ in. 6000-type batteries which fall into the same short-circuit current range as the comparable 4000-type batteries.

Likewise it seems impossible, at present, to make a relative evaluation of the shelf life and other characteristics of the batteries constructed with electrodeposited MnO_2 as compared with the other type. So far the records show about equal performance for the two types.

There is quite a clear indication with respect to separator materials. Apparently, as might be expected, the more open structured the separator, the lower the internal

resistance. The short-circuit currents from batteries with separators of the most open-structured material used, R-25-F, are greater by a factor of four or five than those of batteries with filter paper separators. A fact that could not have been predicted with assurance is that during more than one year of shelf life, no significant differences in emf have developed between these two groups of batteries. Incidentally no batteries were made which combined the use of powdered MnO_2 and an open-structured separator.

The five batteries in Group 9 have been excluded from consideration in drawing the conclusions stated in the preceding paragraph. The low emf's of that group of batteries cannot be put down to anything recorded about them. The record indicates that they were made in the same way as the ¼ in. R-45-F batteries, all of which give normal emf's. The fact that although they were all made on the same day they were not all punched from the same sandwich only deepens the mystery. However, since every battery of the 25 others with nonwoven fabric separators shows the normal emf, it seems doubtful that the anomalous behavior of Group 9 is significant with respect to the merits of this type of separator. A point of possible practical importance is that batteries in this group showed abnormally low emf's within six weeks after they were made.

Extended Temperature Range

Modifications directed toward producing piles of lower internal resistance and of extended useful temperature range were tried. The results in terms of the shelf-life statistics of a majority of these modified batteries were rather unsatisfactory. They seem, however, sufficiently interesting and, in the case of a few batteries, sufficiently encouraging to warrant a brief presentation.

The modification to be discussed involves the use of ethylene glycol or its lower, liquid polymers instead of the waxy higher polymers. A certain commercially available, synthetic, water-sensitive gum was found which will absorb ethylene glycol and its liquid polymers to form tacky gels which do not melt but retain their stickiness over extended temperature ranges. According to the limited information at present available to the author this gum is a polymeric carboxylic acid.

Punched-cell batteries similar to those described were made up using gelled glycol electrolytes. Paper separators were impregnated generously with a mucilage, a typical composition for which is: 50 ml of 1% aqueous zinc chloride, 7 ml of ethylene glycol or liquid polymer, 2 g of synthetic, water-sensitive gum. Water was evaporated from the separator by putting it on a hot plate kept at, say, 125°C. A sandwich was then made by sticking the separator between a zinc sheet and a sheet of MnO_2-plated conductive plastic, and the disk cells were punched from this sandwich.

Fig. 2(*b*) indicates the results of resistance measurements at various temperatures on one 1¼ in. 22-cell battery of this kind. In thise case, resistances were obtained not from short-circuit currents but from measurements of battery voltages under various known loads. The slope of the curve in Fig. 2(*b*) is roughly the same as that of the curve in Fig. 2(*a*), indicating that the resistance ratio of the two types of cells varies only a little with temperature over the range studied. For these two particular cases, the ½ in. wax cell has about 50 times the resistance of the ¼ in. gel cell at the same temperature. This implies that the gel cells would have a considerably lower limit to their useful temperature range than the wax cells.

The gel cells can be heated to rather high temperatures with no apparent damage. Two 25-cell batteries were heated for several minutes to temperatures above 100°C while they were being coated with de Khotinsky cement (instead of lacquer). After 11 months these two batteries still have voltages of 30 and 31 v which are, in fact, higher than the voltages of any of the other gel batteries which have stood for comparable lengths of time.

Most of the lacquered gel-type batteries which have been stored in the desiccator have become sticky, a change which has not occurred with the wax-type batteries. The gel batteries sealed with neoprene-base adhesive have not become sticky but bubbles can be seen to have formed under the surface of the coating. All of a considerable sampling of gel-type cells which were never made into batteries but have stood for periods of 10–11 months show voltages close to 1.3.

The facts stated in the two preceding paragraphs strongly suggest that the poor shelf life shown by most of the gel batteries is caused by intercell leakage and not by poor shelf-life characteristics inherent in the cells themselves. Individual cells of this kind, therefore, might be useful (as bias cells, for example) even if they cannot be successfully and simply combined into a very compact battery giving satisfactory performance. However, the comparatively good showing of the de Khotinsky-sealed batteries offers hope that the problem of intercell leakage can be solved and that the relatively low resistance and extended temperature range of the gel-type cells can be incorporated into punched-cell batteries having long and dependable shelf lives.

Acknowledgments

A number of the cells and batteries reported on in this paper were made by Mr. W. J. Vadnais. Many were made by Mr. David Gimber. For suggestions and generous assistance in various ways the author is indebted to Mr. D. W. Finger and particularly to Dr. D. N. Craig. The contribution of Mr. Cletus Bechtoldt who made the x-ray examination of the electrodeposited MnO_2 is also acknowledged with thanks.

This work was sponsored by the Diamond Ordnance Fuze Laboratories.

Manuscript received November 4, 1955.

Any discussion of this paper will appear in a Discussion Section to be published in the June 1957 Journal.

REFERENCES

1. A description of one such battery, together with a historical sketch and bibliography is given by P. L. Howard, *This Journal*, **99**, 333 (1952).
2. A. Elliott, *Electronic Eng.*, **20**, 317 (1948).
3. I. Reiner, U. S. Pat. 2,701,272, Feb. 1, 1955.

Metal-Water Reactions

III. Kinetics of the Reaction between Thorium and Water Vapor[1]

BRUCE E. DEAL AND HARRY J. SVEC

Institute for Atomic Research and Department of Chemistry, Iowa State College, Ames, Iowa

ABSTRACT

An examination of the reaction between thorium metal and water vapor has been made between 200° and 600°C and at water-vapor pressures of 25 to 100 mm Hg. Analyses of the products indicate that ThO_2 and H_2 are the main species formed during the reaction with formation of ThH_2 as a possible side reaction product. Two methods, one gravimetric and the other manometric, were used to determine rates of reaction. During these rate studies, the variables time, temperature, and pressure were examined. Reaction data were found to obey the logarithmic rate law $w = k \log(1 + 0.45t)$. The activation energy was found to have an average value of 6.44 ± 0.75 kcal/mole. From marker experiments it is postulated that inward diffusion of water molecules or a related species is the rate-determining step of the reaction. Other experiments showed that hydrogen diffused into the metal in varying amounts depending on temperature and water-vapor pressure. This hydrogen was evolved when the samples were heated under high vacuum to 1200°C.

Numerous references are available for metal-gas reaction-kinetics studies involving O_2, N_2, and H_2 (1). However, few studies have been reported on metal-water vapor reactions. Because of the increasing importance of thorium and related metals in the field of atomic energy and because of the role water vapor plays in metal corrosion, a program was initiated to study the kinetics of the reaction between thorium and water vapor.

The reaction between thorium and oxygen has been studied by Levesque and Cubicciotti (2) as well as Gerds and Mallett (3). A parabolic rate law was found to fit the data at most temperatures, which is in agreement with data for many metal-oxygen reactions. However, Brodsky and Cubicciotti (4) found that silicon-oxygen reactions obeyed a logarithmic rate law, while Alexander and Pidgeon (5) reported a similar law for the oxidation of titanium by oxygen. Deal and Svec (6) found the reaction between lithium and water vapor to proceed according to a logarithmic rate law as do the reactions of water vapor with calcium (7) and uranium (8).

EXPERIMENTAL

Thorium metal was obtained from the Metallurgical Section of the Ames Laboratory of the A.E.C. in the form of a cast billet. Spectrographic analysis indicated that the total impurities were less than 0.1% occurring principally as C, N, Fe, Be, Ca, and Si. Cylinders of the appropriate dimensions were prepared under the same conditions described in a previous paper concerning lithium-water vapor reaction kinetics (6).

The main reaction between thorium and water vapor proceeds according to the equation

$$Th + 2H_2O = ThO_2 + 2H_2$$

The reactions were followed either by a manometric method in which the amount of evolved gas was measured or a gravimetric method in which the weight gain was measured. The manometric apparatus consisted of a recording manometer (6), a reaction tube placed in a furnace, an inlet for introducing water into the system and controlling its vapor pressure, and a vacuum system consisting of a mercury diffusion pump and a mechanical pump. As hydrogen was evolved by the reaction of water vapor with thorium, its increasing pressure was recorded and converted to the weight of water vapor that had undergone reaction.

The gravimetric method made use of an electromagnetically controlled microbalance modified for simplicity and increased load but based on the design of Edwards and Baldwin (9). The balance beam was a quartz tube suspended from a quartz rod frame. A cylindrical Cunife magnet was mounted axially in this tube. The beam was placed between two coils of wire and its position could be controlled by varying the amount of current flowing in the coils. In principle the balance behaves as a tangent galvanometer. All weight measurements were made by a null method and weights were measured in terms of the amount of current flowing in the coils. The balance was enclosed in an all-glass apparatus which could be evacuated and which included a small furnace in which the thorium cylinder hung during the reaction. Both furnaces used in the manometric and gravimetric studies were controlled by a proportioning furnace-temperature controller (10). A complete description of both systems used in these studies is given in reference (11). In either system, both vapor pressure and thorium temperature could be

[1] Contribution No. 450. This work was performed in the Ames Laboratory of the Atomic Energy Commission, Iowa State College, Ames, Iowa. Other papers in this series have appeared in *J. Am. Chem. Soc.*, **75**, 6052, 6173 (1953). This paper taken from the Ph.D. dissertation of B. E. Deal.

varied independently. Vapor pressures ranged from 25 to 100 mm Hg and temperatures were varied from 200° to 600°C.

For each reaction, a freshly machined thorium cylinder was placed in the appropriate apparatus. The system was evacuated, thorium temperature was adjusted, liquid water was introduced, and water vapor pressure was adjusted to the desired value. Data obtained from either apparatus were converted to weight per unit area of water vapor undergoing reaction.

Results

Examination of the thorium-water vapor reaction products by x-ray diffraction and mass spectrometric techniques indicated that only ThO_2 and H_2 were formed. Three different-appearing oxide coatings were observed, however, depending on the temperature range. Between 200° and 275° a black oxide coating was formed; from 300° to 425° a white or gray coating was observed, and from 450° to 550° the coating was metallic in appearance. From the x-ray diffraction patterns for the three different-appearing reaction-product coatings, it appears that extremely small crystallites were formed at the lower temperatures while, as the reaction temperature became higher, larger and more perfect crystals were formed. No changes in lattice patterns were observed in any of the colored oxides.

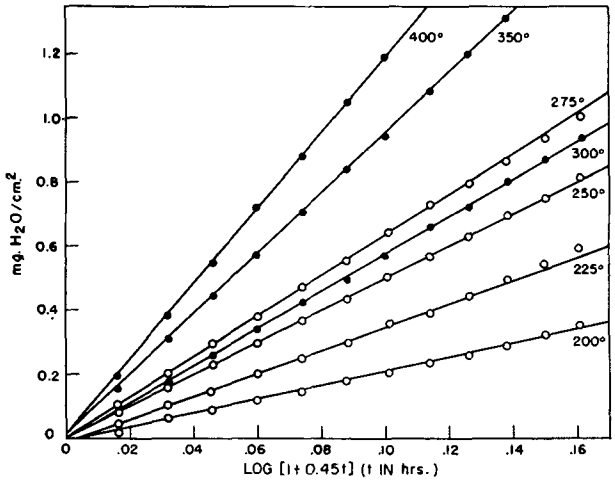

Fig. 1. Logarithmic plot of thorium-water vapor data at 70 mm Hg water-vapor pressure and varying temperatures.

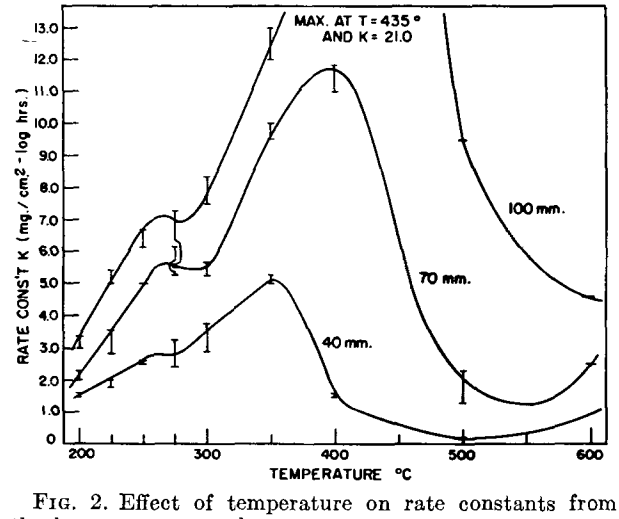

Fig. 2. Effect of temperature on rate constants from thorium-water vapor data.

Since the reaction between thorium and water vapor proceeds with the formation of a surface coating, reaction rate data were expected to fit one of the usual solid-gas rate laws. On plotting the weight of water consumed (in mg per cm^2 of thorium surface) against appropriate functions of time, a straight line was observed for the logarithmic treatment of the data, while definite curves were evident for the other laws. The value of the constant a in the logarithmic equation $w = k \log [1 + at]$ was empirically determined to be 0.45 as was the case in the Li studies and is the case in current studies with Ca and Sr. Brodsky and Cubicciotti (4) found that 0.4 was the value for this constant in the reaction of silicon with oxygen. Since the value 0.45 was obtained as the average of 0.40 and 0.50, both of which fitted the data equally well, the value found by these workers is the same as the one reported here.

Graphs were prepared for each reaction with mg H_2O/cm^2 plotted against log $[1 + 0.45t]$, where t is time in hours. Values of the logarithmic rate constants k were obtained from the slopes of the initial part of the curves. Fig. 1 shows plots of typical data for the water-vapor pressure of 70 mm Hg and indicates the temperature dependence between 200° and 400°C. The two different symbols on the graphs indicate two of the reaction-product regions mentioned above. The effect of temperature on rate constants is more clearly observed in Fig. 2, where temperatures are plotted against rate constants at three vapor pressures. These curves each have regions in the temperature ranges 200°–275°, 300°–400°, and 450°–550° which correspond to the different-colored ThO_2 coatings observed on the metal specimens used in the experiments.

The activation energy for the thorium-water vapor reaction was determined from an Arrhenius plot of the data. Fig. 3 shows this plot for two reaction products regions and for three vapor pressures using manometric data. Gravimetric data for 70 mm water-vapor pressure are plotted in Fig. 4 which also includes data for deuterium oxide reactions. A least-squares treatment of the data gives an average value of 6.44 ± 0.75 kcal/mole for the activation energy. Parallel straight lines corresponding to this value have been drawn through the points in Fig. 5 and 6 and it can be seen that all points lie near one of these lines within the experimental error.

The most important relationship showing pressure dependence of metal oxidations is based on solid-gas diffusion phenomena. The general equation

$$k = -Cp^n e^{-b/T}$$

where k is the rate constant, p the pressure, T the absolute temperature, and C, n, and b are constants has been proposed by Barrer (12). The exact mechanism of the reaction determines the value of the constant n.

A definite pressure dependence is observed in Fig. 5 for the reaction between thorium and water vapor at 300°C. In order to get a better idea of the exact order of pressure dependence, idealized rate constants were calcu-

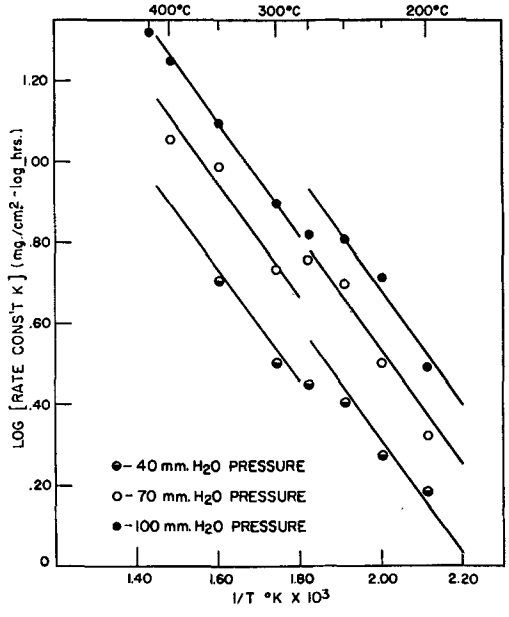

FIG. 3. Log k vs. $1/T$ at varying pressures from thorium-water vapor data.

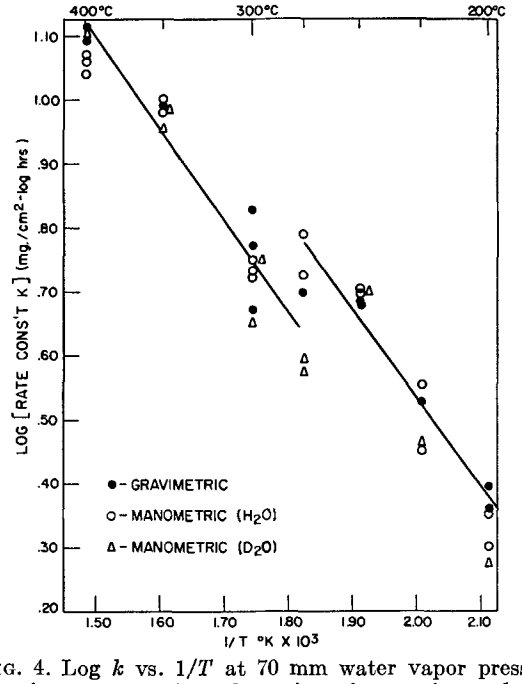

FIG. 4. Log k vs. $1/T$ at 70 mm water vapor pressure comparing manometric and gravimetric experimental procedures.

lated from the straight lines in Fig. 3 and plotted against pressure. The resulting plot showed first order dependence for all temperatures studied. Two equations,

$$k = 31.5pe^{-6440/RT}$$

and

$$k = 21.9pe^{-6440/RT}$$

were obtained for the ranges 200°–275° and 300°–400°, respectively.

Deuterium oxide was also used in a series of Th-water vapor reactions. No significant differences from the H_2O reactions were found in the observed rates. In all cases the reaction products had the same appearance as the H_2O reactions and the same discontinuities appeared in the rate data as is indicated in Fig. 4. Of considerable significance was the observation that the absolute values of rate constants obtained from gravimetric experiments were slightly, but consistently, higher than those obtained from manometric data. However, plotting gravimetric data gave the same activation energy for the reaction, indicating that the difference in absolute values for the rate constants was due to some constant effect.

Since it has been proposed that a logarithmic rate law indicates diffusion of some species in the growing reaction product coat, a pressure dependence on the reacting gas would indicate that diffusion inward of the reacting gas or some related species might be the rate-determining step. In order to determine if there were such an inward diffusion or if thorium ions were diffusing outward, an inert-marker experiment was carried out. It consisted of placing securely a 0.05-in. diameter platinum wire vertically into the side of a thorium cylinder and machining the end of the wire even with the thorium surface. After a typical reaction with water vapor the position of the thorium surface and the end of the platinum marker in relationship to each other were examined microscopically and microphotographs were made. It was observed that the

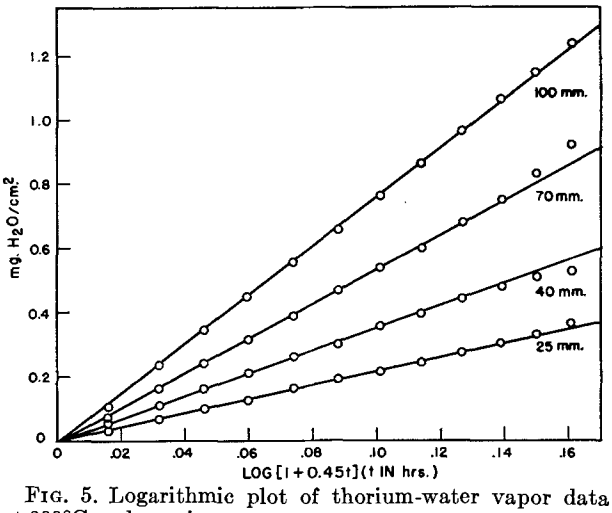

FIG. 5. Logarithmic plot of thorium-water vapor data at 300°C and varying water-vapor pressures.

end of the wire extended well above the thorium-thorium oxide interface, substantiating the possibility of an inward diffusion of some species since, for outward diffusion of thorium ions from within the metal, the end of the Pt wire and the thorium surface should have remained in the same plane.

The microphotographs showed a new phase extending into the bulk of the thorium metal from the Th-ThO_2 interface and along grain boundaries, as well as scattered throughout the bulk of the thorium within the grains. These intergranular and intragranular materials were different in appearance from known oxide inclusions and are believed to be a hydride. The presence of a hydride or dissolved hydrogen would explain the discrepancies in rate constant values obtained in the manometric and gravimetric experiments. Vacuum heating experiments

were carried out to analyze for gases in a thorium cylinder. Various specimens which had been exposed to either D_2O or H_2O vapor were heated to 1200°C and the evolved gas was collected and analyzed. This gas was found to be only hydrogen. It was found that thorium specimens in contact with water vapor contained from 33 to 111 ppm H_2 depending on the history of the specimen. Metal not previously known to be in contact with water vapor contained from 0.6 to 1.1 ppm H_2.

Metallographic examination of the thorium specimens after vacuum heating indicated that the intra- and intergranular phases mentioned above had disappeared completely. These phases then were associated with the evolved hydrogen and were assumed to be a thorium hydride which had decomposed during the heating. While no positive identification was made, from the work of Nottorf and co-workers (13) and the temperature at which the thorium-water vapor reactions were run, the new phases were assumed to be thorium dihydride. Further corroboration of this was obtained by blocking off an area on microphotographs of the interior of the metal specimens and determining the relative areas of the metal and new intragranular phase. After correcting for density differences, calculating the hydrogen content on the basis of dihydride or 3.75 hydride, and comparing with the amount of hydrogen found in a metal specimen from which the outer portion of the metal was removed, good agreement was observed assuming ThH_2 to be the new phase.

In order to determine if the presence of hydrogen gas produced during the reactions affected the values of the rate constant, a palladium diaphragm was employed to remove evolved hydrogen. The Pd diaphragm was in the form of a thimble of metal 0.001 in. thick and heated to 300°C. No differences were observed in rate-constant values. Even in the higher temperature, lower pressure range, where the vacuum heating experiments indicated that relatively large amounts of hydrogen diffuse into the thorium, the weight gain remained the same. These results indicate that a fraction of the hydrogen released during the splitting of HOH molecules diffuses into the metal without first forming molecular hydrogen and that this occurs at or near the Th-ThO_2 interface.

Discussion

Diffusion of some species in the growing reaction product coat has been assumed to control the rate of reaction between thorium and water vapor. The nature of the reaction indicates several possibilities. Water molecules may be diffusing inward, Th ions may be diffusing outward, electrons may be moving outward and hydrogen may be moving in both or either directions. It is possible that a combination of all processes are going on simultaneously.

The ratio of the molecular volumes of ThO_2 to Th is 1.32; thus as the coating thickens it is subject to severe strains and adhesion of the coating is affected. During the oxidation of the metal at constant gas pressure and temperature the various laws may apply consecutively with time depending on the extent of film thickening. These experiments were not designed to observe the linear nature of the initial association of water vapor with the metal. Indeed a parabolic law, which might have been expected when the coating film was still thin enough for the existence of a linear concentration gradient of the diffusing species, was not observed. The main observations were made after the films had apparently thickened enough to be affected by the strains due to the disparity of the molecular volumes involved. This occurred early during the reactions since most of the coatings were only about 0.01 mm thick when the observations were completed. Under these strained conditions, blistering, crazing, or even flaking should have and did occur. For long reaction times the ThO_2 coating actually flaked off irregularly causing unpredictable changes in the reaction rates after flaking began. However, the reaction during the first hour invariably proceeded with an adherent coat and reproducible data were obtained.

Fig. 3 and 4 indicate breaks in the Arrhenius plots of the data. This occurs in the temperature range where the rate also appears to be constant with temperature as indicated in Fig. 4. It is significant that for coatings formed at 250°C x-ray diffractometer tracings are extremely diffuse while those from coatings formed at 350°C are beginning to become sharp. Also the physical appearance of the coating changes from black to opaque gray-white. It is postulated that a change in the dominant rate-determining step takes place somewhere between 250° and 300°C. However, the expected change in activation energy is not evident, probably due to the insensitivity of the experimental procedure to elucidate small effects.

The marker experiments at 250° and 350°C indicate that some species are diffusing inward. However, the gas-oxide interface extended slightly beyond the end of the Pt marker indicating that outward diffusion of some species may also have been possible although this may be explained on the basis of the greater molecular volume of the oxide. This coating is highly frangible, and high power microscopic examination of its surface showed extensive crazing. It is postulated that the observed logarithmic law is due to the diffusion of water molecules through the microscopic fissures in the coating and that these diffusion paths are blocked in a random way due to the layer structure of the coating. This comes about by successive healing and re-cracking of the layers as the coating grows. Reaction takes place at or near the metal-oxide interface. This accounts for the pressure sensitivity observed which is primarily a manifestation of a mass effect. It also explains the deuterium oxide data and the high absorption of hydrogen by the metal when gaseous hydrogen is continuously removed from the reaction vessel. Hydrogen adsorption by massive metal in an atmosphere of pure H_2 is extremely slow compared to that observed in the water vapor reactions.

The decrease in reaction rate at temperatures above about 400°C is similar to a phenomenon observed in the reaction between Ca and water vapor (14). It is postulated that the rate of escape of water molecules from the oxide surface increases in this temperature range thus making fewer molecules available for diffusion through the coat.

From Fig. 4 there is a suggestion that the rate of reaction may become pressure independent beyond 600°C. X-ray patterns of the oxide formed at this temperature are very

sharp while the coating is transparent giving the metallic appearance referred to earlier in this paper. Microscopic examination indicates considerably less crazing. If the logarithmic rate still holds in this temperature region, it is probable that ionic diffusion, through statistically blocked paths, becomes rate determining. It is possible that some other rate law may apply.

Chiotti and White (15) have determined the coefficient of thermal expansion for both Th metal and ThO_2. In the temperature range 0°–1000°C the ratio of the molecular volumes of oxide to metal is 1.34–1.31. Thus, the change in rate of reaction cannot be attributed to any transformations in metal or oxide. The marked crystal growth of ThO_2 at higher temperatures is the most significant evidence that the diffusion medium changes considerably throughout the temperature range included in this study.

Manuscript received May 13, 1955.
Any discussion of this paper will appear in a Discussion Section to be published in the June 1957 JOURNAL.

REFERENCES

1. O. KUBASCHEWSKI AND B. HOPKINS, "Oxidation of Metals and Alloys," Academic Press Inc., New York (1953).
2. P. LEVESQUE AND D. CUBICCIOTTI, *J. Am. Chem. Soc.*, **73**, 2028 (1951).
3. A. GERDS AND M. MALLETT, *This Journal*, **101**, 171 (1954).
4. M. BRODSKY AND D. CUBICCIOTTI, *J. Am. Chem. Soc.*, **73**, 3497 (1951).
5. W. ALEXANDER AND L. PIDGEON, *Can. J. Research*, **28B**, 60 (1950).
6. B. DEAL AND H. SVEC, *J. Am. Chem. Soc.*, **75**, 6173 (1953).
7. Work in progress in these laboratories.
8. J. T. WABER AND J. A. O'ROURKE, "Oriented Dioxide Films on Uranium," A. E. C. Report No. ISC-585 (1955).
9. F. C. EDWARDS AND R. R. BALDWIN, *Anal. Chem.*, **23**, 357 (1951).
10. H. SVEC, A. READ, AND D. HILKER, "A Proportioning Furnace-Temperature Controller," A. E. C. Report No. ISC-585 (1955).
11. B. DEAL, "Kinetics of the Reaction between Thorium and Water Vapor," Ph.D. Thesis, Iowa State College Library, Ames, Iowa (1955).
12. R. BARRER, "Diffusion in and through Solids," p. 170, University Press, Cambridge, England (1941).
13. R. NOTTORF, A. WILSON, R. RUNDLE, A. NEWTON, AND J. POWELL, "A Physical Study of the Thorium-Hydrogen System," A. E. C. Report No. CC-2722 (1945).
14. C. A. APEL AND H. J. SVEC, Unpublished work.
15. PREMO CHIOTTI AND R. W. WHITE, Private communication of unpublished data, Ames Laboratory of A. E. C.

Effect of Aluminum Sulfate in the Sulfuric Acid Electrolyte on Anodic Polarization

RALPH B. MASON

Aluminum Research Laboratories, Aluminum Company of America, New Kensington, Pennsylvania

ABSTRACT

Anode polarization measurements have been made over a wide range of concentration of the H_2SO_4 electrolyte. For each concentration of acid, the coating ratio (weight of coating divided by weight of aluminum reacting) was also determined. Aluminum sulfate dissolved in the electrolyte decreased the polarization value, but was only about ⅕ as effective as free H_2SO_4. The presence of aluminum sulfate in the electrolyte had little effect on the coating ratio. Additions of oxalic, glycolic, and tartaric acids had only a small effect on the polarization, but increased the coating ratio and decreased the rate of solution of the oxide coating in the electrolyte in which the coating was formed.

An oxide coating is formed when aluminum is made the anode in a dilute H_2SO_4 electrolyte. Not all of the aluminum that reacts with the electrolyte remains on the surface as Al_2O_3. The electrolyte has some solvent action on the anodic coating. The amount of Al_2O_3 produced depends on the concentration of the electrolyte, temperature, current density, and various other factors (1–4). Under normal operating conditions, the amount of Al_2O_3 on the surface is only about 80% of the theoretical value (5). Either the electrolyte reacts directly with the aluminum to form aluminum sulfate (6) or some of the oxide coating dissolves chemically in the H_2SO_4 to form aluminum sulfate.

As a H_2SO_4 electrolyte is used for the anodic oxidation of aluminum, appreciable amounts of aluminum sulfate are produced and accumulate in the electrolyte. The H_2SO_4 combined with aluminum to form aluminum sulfate is usually spoken of as combined H_2SO_4. The effect of this combined H_2SO_4 on the operational characteristics of the H_2SO_4 electrolyte has been studied in various ways and the results have not been too conclusive or consistent (7).

Some investigators have suggested that aluminum sulfate should be added to H_2SO_4 electrolytes intentionally (8). This is not necessarily considered to be good practice (1) since it is known that the electrical conductivity of the H_2SO_4 electrolyte is decreased by such addition (9).

For the same current density the voltage of the 15% H_2SO_4 electrolytic cell is appreciably less when aluminum sulfate is added to the H_2SO_4 electrolyte without any dilution. In other words, the electrolyte containing aluminum sulfate acts as an electrolyte containing more than 15% H_2SO_4. It is assumed that the aluminum sulfate in the H_2SO_4 electrolyte acts as a certain amount of free H_2SO_4.

Anodic coating of aluminum in a H_2SO_4 electrolyte, in a lead tank at 21.1°C (70°F), required 16 v to give a current density of 12 amp/ft². Most of the voltage drop across the cell is from the aluminum anode to the electrolyte and usually amounts to about 13 v. To study the anode reaction it is better to consider the voltage drop from the aluminum anode to that of an auxiliary electrode since the voltage drop through the electrolyte and the lead cathode may vary considerably depending upon the size of the tank and other factors not generally controlled. In this paper, the voltage drop from the aluminum anode to the auxiliary electrode is called anodic polarization.

It has been found that the anodic polarization increases only about 1 v upon coating for 30 min, while the oxide coating increases from a very thin film to a relatively thick coating. Therefore, most of the polarization occurs across the very thin barrier layer which is about 150Å thick. In this narrow region, considerable heat is developed that must be removed rapidly. The heat developed will be greater as the polarization voltage increases. Poor agitation allows the electrode to heat up and polarization decreases. For reproducible results, it is imperative that sufficient agitation be used to give the maximum polarization values.

In the experiments to be described, polarization measurements were made over a wide range of concentration of H_2SO_4. For each concentration of acid, the coating ratio (weight of coating divided by weight of aluminum dissolved) was also determined. Aluminum sulfate, as well as other substances, was added to H_2SO_4 to determine the effect on polarization, coating ratio, and solubility of the aluminum oxide coating in the H_2SO_4 electrolyte.

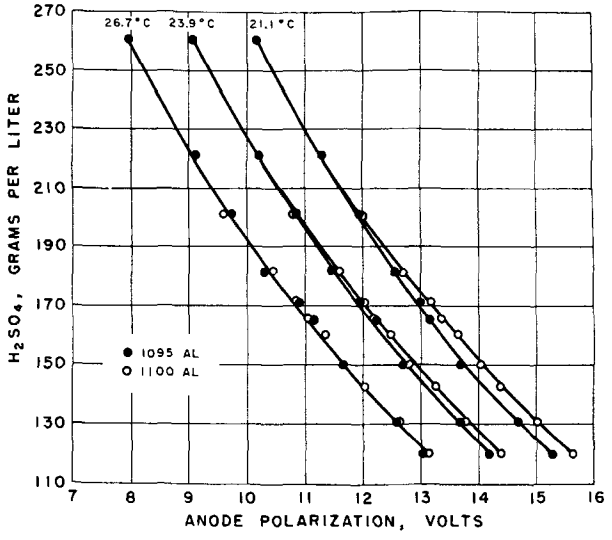

FIG. 1. Anode polarization as affected by changes in H_2SO_4 concentration.

EXPERIMENTAL PROCEDURE

Various H_2SO_4 electrolytes were prepared by weighing out the required amount of analyzed concentrated H_2SO_4 and diluting in a volumetric flask. The density of the diluted electrolyte was checked by means of a 5 cc glass thermometer-plummet and an analytical balance. Addition agents were usually added to the H_2SO_4 before diluting to the final volume and the concentration expressed as grams per liter. However, in one series of experiments, increasing amounts of aluminum sulfate with 18 molecules of water of crystallization were added to a given volume of 15% H_2SO_4. In this case, the acid was diluted by the water of crystallization. The concentration of used solutions was periodically checked by chemical analysis.

The prepared electrolyte was held in a two liter beaker containing a lead cooling coil which also served as the cathode. A motor-driven glass stirrer was used to furnish adequate agitation of the electrolyte in order to remove the heat developed at the anode surface. Aluminum anodes about 5.1 cm x 7.6 cm (exactly 12 in.² of surface) with a narrow tab coated with an acid resist were anodically coated using a current density of 1.3 amp/dm² (12 amp/ft²) at 21.1°, 23.9°, and 26.7°C (70°, 75°, and 80°F). Polarization was determined after 10-min coating time by means of a small auxiliary electrode of lead peroxide placed near the surface of the anode and a high resistance voltmeter (5000 ohms/v).

To determine the coating ratio, the aluminum anodes, 5.1 cm x 7.6 cm (2 in. x 3 in.) were cleaned, weighed, and then suspended in the electrolyte by means of tantalum clips and oxide coated for 30 min at a current density of 1.3 amp/dm² (12 amp/ft²) at the given temperature. The specimens were removed, washed, dried, and weighed. The oxide coating was then removed in a hot phosphoric-chromic acid solution and the specimen again weighed. From the weight of coating and the weight of metal dissolved, the coating ratio was determined. For the solubility determinations, specimens of aluminum sheet were anodically coated for 30 min and then suspended in the various electrolytes which were uniformly agitated. The oxide coated specimens were periodically removed, dried, and weighed to determine the rate at which the anodic coating dissolved in the electrolyte.

EXPERIMENTAL RESULTS AND DISCUSSION

Using an auxiliary electrode of lead peroxide, anode polarization measurements were made in H_2SO_4 electrolytes varying in concentration from 120 g/l to 260 g/l. The 1100 and 1095 aluminum sheet specimens having a surface area of exactly 77.4 cm² (12 in.²) were used for making the polarization measurements at 21.1°, 23.9°, and 26.7°C (70°, 75°, and 80°F) in the various concentrations of H_2SO_4, a current density of 1.3 amp/dm² (12 amp/ft²) being used for each determination. Data for these polarization values are shown graphically in Fig. 1.

The polarization value for the high purity metal is lower than that for the 1100 alloy, especially at lower temperatures and concentrations of acid. However, this difference in polarization value for the 1095 and 1100 alloy decreases as the temperature is raised or as the concentration of the acid is increased. Polarization values for aluminum of two

TABLE I. *Effect of combined H_2SO_4 on anode polarization*

Electrolyte containing	Temp.	Anode* polarization	Effective H_2SO_4	CAE†
	°F	v	g/l	%
164.5 g/l free H_2SO_4	70	12.45	183	19.7
+ 93.8 g/l combined H_2SO_4	75	11.35	184	20.8
	80	10.30	183	19.7
139.1 g/l free H_2SO_4	70	13.85	148	18.8
+ 47.3 g/l combined H_2SO_4	75	12.85	148	18.8
	80	11.85	147	16.7

* Anode polarization determined with PbO_2 auxiliary electrode. 1095 anode material.

† Per cent combined acid effective (acting as free H_2SO_4).

different purities are practically equal at higher temperatures and concentrations of acid.

Instead of plotting the polarization voltages of the anode, it is also possible to plot the total voltage of the lead-aluminum cell against the concentration of the H_2SO_4. Curves for total volts are practically identical with the curves of Fig. 1 except for the voltages. Since the total voltage is sometimes influenced by variations in cathodic polarization, only the curves for anodic polarization have been reported since they are considered to be more easily reproduced.

When aluminum sulfate is added to a H_2SO_4 electrolyte, the anode polarization decreases just the same as if a small amount of H_2SO_4 had been added. However, only a small fraction of the combined H_2SO_4 in the aluminum sulfate acts as free acid. The two electrolytes of Table I having both free and combined acid are used to illustrate this. Polarization values were used to determine from Fig. 1 the effective H_2SO_4 concentration in grams per liter. The per cent of combined acid that is effective as free acid was calculated by subtracting the free H_2SO_4 from the effective H_2SO_4 and then dividing by the combined acid. In round numbers, only about $\frac{1}{5}$ of the combined H_2SO_4 acts as free acid.

In some related experimental work, it has been noted that the voltage of the lead-aluminum cell remained constant as varying amounts of crystalline aluminum sulfate were added to a given volume of 15% H_2SO_4. This work was carefully repeated with 1095 aluminum at 21.1°, 23.9°, and 26.7°C (70°, 75°, and 80°F) using the sensitive voltmeter for the anodic polarization and the total voltage measurements. For each temperature, the voltage remained constant to within about 0.1 v even though the additions of crystalline aluminum sulfate varied from 50 g to 300 g to 1 liter of 15% H_2SO_4. The water in the crystals of aluminum sulfate was sufficient to dilute the 15% H_2SO_4 and counteract the effect of the combined acid.

After determining the densities of the various solutions, it was possible to calculate the free and combined H_2SO_4 in grams per liter as well as the per cent of combined acid which is effective. These results are recorded in Table II. Only about 18% of the combined H_2SO_4 is effective as free acid in changing the anodic polarization.

Two methods are now available for determining the active concentration of the H_2SO_4 bath. The amount of free and combined H_2SO_4 can be determined by chemical analysis. The active concentration is then obtained by adding 18% of the combined acid to the free acid. The bath may be restored to its original concentration and operating conditions by adding fresh H_2SO_4 in an amount equal to the difference between the original concentration and the active concentration as calculated above.

Another way is to determine the polarization voltage of a standard sample in a small external cell or in an immersion cell in the production bath and find the active concentration of the H_2SO_4 from the curves in Fig. 1. The amount of fresh acid required can be determined readily by subtracting the active concentration from the desired concentration.

The practice of keeping the amount of free acid constant in the H_2SO_4 bath is not recommended. About $\frac{1}{5}$ of the combined acid (as aluminum sulfate) acts as free acid and, when the actual amount of free acid is kept constant, the active concentration becomes higher as the concentration of aluminum sulfate increases. Usually the 15% H_2SO_4 bath is discarded after about 20 g of aluminum per liter have been dissolved. At this stage, a precipitate of aluminum sulfate may form at the lower temperatures.

Coating Ratios

In Fig. 2, the coating ratio values at 30 min have been plotted against the concentration in grams per liter of the H_2SO_4 electrolyte. The high purity metal (1095) gives the higher coating ratio values. The coating ratio values are straight line functions of the concentration of the acid. The curves at 21.1° and 23.9°C (70° and 75°F) are nearly parallel, but at 26.7°C (80°F) the coating ratio values fall off more rapidly as the concentration of the acid increases.

To show the effect of aluminum sulfate dissolved in the H_2SO_4 electrolyte on the coating ratio, the results of

TABLE II. *Calculation of free and combined H_2SO_4*

Electrolyte		Equivalent combined H_2SO_4	Density at 25°C	Weight	Volume	Free H_2SO_4	Combined H_2SO_4	%CAE*
1000 ml H_2SO_4 +	$Al_2(SO_4)_3 \cdot 18H_2O$							
g/l	g				ml	g/l	g/l	
164.3	—	—	1.0992	1099.2	1000.0	164.3	0	—
164.3	50	22.08	1.1216	1149.2	1024.6	160.4	21.6	18.3
164.3	100	44.15	1.1430	1199.2	1049.1	156.6	42.1	18.3
164.3	200	88.31	1.1827	1299.2	1098.5	149.6	80.4	18.3
164.3	250	110.39	1.2008	1349.2	1123.6	146.2	98.2	18.4
164.3	300	132.46	1.2181	1399.2	1148.7	143.0	115.3	18.4
164.3	350	154.54	1.2349	1449.2	1173.6	140.0	131.7	18.4

* Per cent combined acid effective (acting as free H_2SO_4).

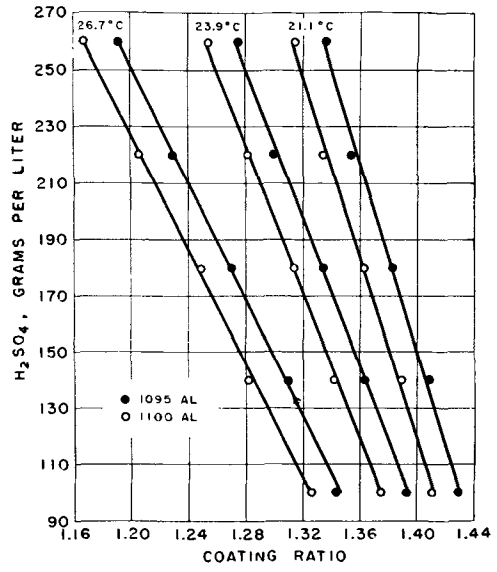

FIG. 2. Coating ratio varying with changes in H_2SO_4 concentration.

TABLE III. *Effect of aluminum, magnesium, and manganese sulfates on the coating ratio*

No.	Electrolyte	Temp °F	Temp °C	Coating ratio 1100 Al	Coating ratio 1095 Al
1	160 g/l H_2SO_4	70	21.1	—	1.391
2	160 g/l H_2SO_4	70	21.1	1.374	1.392
	50 g/l $Al_2(SO_4)_3 \cdot 18H_2O$	75	23.9	1.322	1.346
		80	26.7	1.267	1.288
3	160 g/l H_2SO_4	70	21.1	1.375	1.394
	100 g/l $Al_2(SO_4)_3 \cdot 18H_2O$	75	23.9	1.325	1.347
		80	26.7	1.265	1.286
4	160 g/l H_2SO_4	70	21.1	1.376	1.395
	200 g/l $Al_2(SO_4)_3 \cdot 18H_2O$	75	23.9	1.329	1.347
		80	26.7	1.267	1.292
5	160 g/l H_2SO_4	70	21.1	—	1.394
	100 g/l $MgSO_4 \cdot 7H_2O$	75	23.9	—	1.349
		80	26.7	—	1.289
6	160 g/l H_2SO_4	70	21.1	1.377	1.394
	40 g/l $MnSO_4 \cdot 2H_2O$	75	23.9	1.328	1.345
		80	26.7	1.265	1.286

All samples oxide coated for 30 min at 12 amp/ft² (1.3 amp/dm²).

TABLE IV. *Effect of other acids on the coating ratio*

No.	Electrolyte	Temp °F	Temp °C	Coating ratio 1100 Al	Coating ratio 1095 Al
1	160 g/l H_2SO_4	70	21.1	1.407	1.420
	40 g/l Glycolic	75	23.9	1.366	1.386
		80	26.7	1.316	1.336
2	160 g/l H_2SO_4	70	21.1	1.406	1.423
	40 g/l Oxalic	75	23.9	1.368	1.387
		80	26.7	1.324	1.347
3	160 g/l H_2SO_4	70	21.1	1.395	1.411
	40 g/l Tartaric	75	23.9	1.349	1.368
		80	26.7	1.298	1.322
4	160 g/l H_2SO_4	70	21.1	1.370	1.386
	40 g/l CrO_3	75	23.9	1.321	1.342
		80	26.7	1.260	1.280
5	160 g/l H_2SO_4	70	21.1	1.307	1.320
	40 g/l H_3PO_4	75	23.9	1.194	1.213

All samples oxide coated for 30 min at 12 amp/ft² (1.3 amp/dm²).

Table III have been recorded. It would appear that the presence of appreciable amounts of aluminum sulfate has only a very small effect on the coating ratio. Other sulfates such as magnesium or manganese behave like aluminum sulfate.

Various acids were added to the H_2SO_4 electrolyte and the coating ratio values for 30-min coatings are shown in Table IV. The greatest increase in coating ratio was ob-

TABLE V. *Rate of solution of oxide coatings*

No.	Electrolytes used for coating*	Electrolyte used for dissolving†	Time suspended	Coating dissolved
			min	*g*
A	165 g/l H_2SO_4	165 g/l H_2SO_4	20	0.0147
	100 g/l $Al_2(SO_4)_3 \cdot 18H_2O$		40	0.0321
			60	0.0514
			80	0.0754
B	174 g/l H_2SO_4	165 g/l H_2SO_4	20	0.0148
			40	0.0322
			60	0.0515
			80	0.0746
C	165 g/l H_2SO_4	165 g/l H_2SO_4	20	0.0140
			40	0.0301
			60	0.0484
			80	0.0704
D	165 g/l H_2SO_4	165 g/l H_2SO_4	20	0.0141
	100 g/l $Al_2(SO_4)_3 \cdot 18H_2O$	100 g/l $Al_2(SO_4)_3 \cdot 18H_2O$	40	0.0295
			60	0.0481
			80	0.0699

* Samples of 1095 aluminum having 12 in.² (77.4 cm²) of surface were oxide coated for 30 min at 12 amp/ft² (1.3 amp/dm²) and 70°F (21.1°C).

† Temperature 70°F (21.1°C) with good, uniform agitation.

TABLE VI. *Rate of solution of oxide coatings in mixed electrolytes*

No.	Coated* and suspended in same electrolyte	Time suspended	Coating dissolved
		min	*g*
1	160 g/l H_2SO_4	20	0.0144
		40	0.0303
		60	0.0487
		80	0.0714
2	160 g/l H_2SO_4	20	0.0148
	40 g/l CrO_3	40	0.0310
		60	0.0516
		80	0.0749
3	160 g/l H_2SO_4	20	0.0421
	40 g/l H_3PO_4	40	0.1009
		60	0.1736
		80	0.2172
4	160 g/l H_2SO_4	20	0.0071
	40 g/l Oxalic	40	0.0140
		60	0.0226
		80	0.0309
5	160 g/l H_2SO_4	20	0.0099
	40 g/l Tartaric	40	0.0214
		60	0.0327
		80	0.0481
6	160 g/l H_2SO_4	20	0.0094
	40 g/l Glycolic	40	0.0190
		60	0.0302
		80	0.0421

* Samples of 1095 aluminum having 12 in.² (77.4 cm²) of surface were oxide coated for 30 min at 12 amp/ft² (1.3 amp/dm²) and 70°F (21.1°C).

tained with oxalic acid addition. Glycolic and tartaric acid additions were nearly as good. Chromic and phosphoric acids actually decreased the coating ratio, acting as if more free H_2SO_4 had been added.

Solubility of Coatings

Thirty-minute coatings on 1095 alloy were prepared in the various electrolytes and the rate of solution determined in the electrolytes indicated in Table V.

Aluminum sulfate acts in two ways in the H_2SO_4 electrolyte. The effective acid concentration is increased and, as a consequence, a more readily soluble coating is formed. On the other hand, the presence of aluminum sulfate in the electrolyte retards the chemical solution of the coating. These two effects of aluminum sulfate apparently just counteract each other when a coating ratio determination is made.

An electrolyte containing 165 g/l H_2SO_4 and 100 g $Al_2(SO_4)_3 \cdot 18H_2O$ is equivalent to 174 g/l H_2SO_4. Coatings made in these two electrolytes dissolve at the same rate in 165 g/l H_2SO_4 (see A and B, Table V). They also dissolve at a somewhat slower rate in the H_2SO_4 electrolyte containing aluminum sulfate (see D, Table V). A coating made in a more dilute electrolyte (C, Table V) dissolves at a slower rate.

Data in Table VI have been selected to show how certain acids other than free or combined H_2SO_4 affect the rate at which the oxide coating dissolves. The samples of 1095 aluminum were oxide coated for 30 min at a current density of 1.3 amp/dm^2 (12 amp/ft^2) at 21.1°C (70°F) and tested in the electrolyte indicated. The area of each panel was 77.4 cm^2 (12 in.^{2}).

Of particular interest are the additions of oxalic, glycolic, and tartaric acids which materially decrease solution rates. These are the same substances which increased the coating ratio values.

SUMMARY

Only about 18% of the combined H_2SO_4, as $Al_2(SO_4)_3$, acts as free acid in the H_2SO_4 bath where voltage of the Pb-Al cell is concerned. A method has been suggested for controlling the active concentration of the H_2SO_4 electrolyte by anodic polarization measurements.

No marked change in coating ratio was noted as aluminum sulfate increased in concentration in the bath. The rate of solution of the anodic coating is decreased by the presence of $Al_2(SO_4)_3$. Additions of oxalic, glycolic, or tartaric acids appreciably increased the coating ratio and decreased the rate of solution of the anodic coating in the electrolyte.

Manuscript received January 20, 1956.
Any discussion of this paper will appear in a Discussion Section to be published in the June 1957 JOURNAL.

REFERENCES

1. E. BARET, *Galvano*, **14**, 107, 13 (1945).
2. B. CHANDA, *Trans. Indian Inst. Chem. Engrs.*, **1**, 67 (1947–1948).
3. J. KONUMA, *Light Metals (Japan)*, **10**, 72 (1954).
4. R. B. MASON AND C. J. SLUNDER, *Ind. Eng. Chem.*, **39**, 1602 (1947).
5. J. D. EDWARDS AND F. KELLER, *Trans. Electrochem. Soc.*, **79**, 135 (1941).
6. S. ANDERSON, *J. Appl. Phys.*, **15**, 477 (1944).
7. A. JENNY AND W. LEWIS, "The Anodic Oxidation of Aluminum and Its Alloys," pp. 177–178, Charles Griffin and Co., Ltd., London, (1940).
8. Swiss Pat. #161,851, Windsor-Bowen, Aug. 16, 1933. Swiss Pat. #171,733, Aluminum Colors Inc., Dec. 1, 1934.
9. J. GLAYMAN, *Galvano*, **16**, 122, 13 (1947).

High Temperature Scaling of Cobalt-Chromium Alloys

C. A. PHALNIKAR, E. B. EVANS, AND W. M. BALDWIN, JR.

Department of Metallurgical Engineering, Case Institute of Technology, Cleveland, Ohio

ABSTRACT

Scaling rates and scale compositions of Co-Cr alloys were determined in the temperature range 900°–1200°C. At any given temperature the scaling rate increased with low chromium additions, then dropped precipitously with further additions reaching a minimum at about 25% chromium. Thereafter the scaling rate again increased approaching the scaling rate of Cr as the upper limit. Above a critical concentration of about 25% chromium, the scale consisted exclusively of Cr_2O_3. Below this critical concentration, complex scales consisting of the oxides of both cobalt and chromium were formed. The best scaling resistance was associated with a scale consisting predominantly of Cr_2O_3, not spinel. Schematic isothermal sections of the deduced Co-Cr-O phase diagram were applied as an aid in interpreting the scaling behavior.

The scaling behavior of Co-Cr alloys has been studied only once to date, by Preece and Lucas (1). They report single values of weight increase for 50 hr exposure in a simulated gas-turbine atmosphere at 800°–1200°C for alloys containing up to 40% chromium. Their data indicate a sharp rise in weight increase for 10% additions of chromium to cobalt with a subsequent drop for 25% additions and again a rise for 40% additions. In view of the erratic weight increases vs. temperature relationship which these authors reported for pure cobalt (1), computing scaling

TABLE I. *Crystal structure and stability of* Co *and* Cr *and their oxides and nitrides*

Metal or compound	Crystal structure	Lattice constant, A		Stability range °C	Remarks
		a_0	c_0		
Pure metals (4–14)					
Cobalt	β: C. P. Hex.	2.51	4.07	Up to 430	Cubic-to-hexagonal transformation occurs at 388° on cooling.
	α: FCC	3.54		430 to at least 1100	Possible transformation to a hexagonal form at about 1120°
Chromium	BCC	2.885		Up to at least 100 below melting pont	Various structure modification when electroplated.
Oxides (1–3, 12, 14–19)					
CoO	FCC	4.260		Up to 1723	Brown or dark gray, metal-deficit.
Co_3O_4	Cubic (spinel)	8.11		Up to 920	Black
Co_2O_3	Hexagonal	4.64	5.75	Up to 367	Black-gray
CrO	Unknown				Black
Cr_2O_3	Hex. (rhombohedral)	5.38 (α = 54.83°)		Up to 1990	Can exist in several color modifications. Most common—green.
CrO_2	Tetragonal			Up to 300	Brown-black
Cr_2O_5	Unknown				
Cr_3O_8	Unknown				
CrO_3	Orthorhombic			Up to 196	Red
$CoO \cdot Cr_2O_3$	Cubic (spinel)	8.34			
Nitrides (11, 12, 14, 30–32)					
Co_3N	Hexagonal			Up to 380	
Co_2N	Hexagonal			Unstable	
Co_3N_2	Amorphous			Unstable	
CrN	NaCl-cubic			Up to 930	Black
β-Cr_2N	Hexagonal	2.76	4.45	Up to at least 1200	Gray-black

rates from their single values for the alloys is unjustifiable. Indeed, it is not possible to tell if the alloys scale in accordance with the parabolic rate law.

The lack of data on the scaling behavior of Co-Cr alloys in air makes a study of this alloy system an attractive one for a number of reasons. First, cobalt-base alloys containing chromium are of vital interest as high temperature components. Second, these alloys provide a test of Wagner's lattice defect theory (2) which predicts that the addition of a high valency solute (chromium) to a low valency solvent (cobalt) will result in an increase in the scaling rate of the solvent metal. Third, it is of interest to determine whether the other features observed in the scaling of comparable Ni-Cr alloys (3) (two parabolas at those compositions where the nature of the scale changes from solvent oxide to spinel, the formation of spinel at certain alloy compositions, etc.) are to be found.

As part of this investigation, a study of the scaling behavior of the two pure component metals was also undertaken. Since both oxygen and nitrogen may enter in the attack of air on these metals, a summary of the crystal structures of the possible oxides and nitrides is given in Table I.

Material and Procedure

One-inch diameter ingots of pure cobalt and five Co-Cr alloys (8.85, 12.25, 25.57, 38.33, and 48.50 wt % chromium) were prepared by induction melting electrolytic stock (99.9% pure) in zircon crucibles under an argon atmosphere. The top and bottom portions of each ingot were cropped and the remaining section annealed at 2200°F for ½ hr, hot forged at 2000°–1800°F to a ½ in. diameter rod, and homogenized at 2200°F for 3 hr in a helium atmosphere. The alloy with 48.5% chromium could not be worked due to its extreme brittleness, and was processed simply by annealing at 2000°F for 24 hr in a high vacuum (10^{-5} mm Hg). Slices approximately $\frac{1}{16}$ in. thick were cut from the bars, surface ground,[1] metallographically polished through 3/0 paper, and washed with methanol prior to continuous scaling runs.

Pure chromium specimens were made by electroplating chromium on one side of an oxygen-free high conductivity copper sheet. The thickness of the chromium after stripping from the copper sheet ranged from 0.025 to 0.030 in. Before polishing and subsequent scaling, 1 in. square samples were heated at 400°C for 4 hr to drive off hydrogen gas which was entrapped in the metal as a result of the electroplating operation.

Each specimen was scaled in air by suspending it in a resistance-wound vertical tube furnace from one arm of a magnetically damped chainomatic balance (sensitivity 0.1

[1] Specimens of the 48.5% Cr alloy showed grinding checks. Attempts to obtain specimens from a 63% Cr alloy were unsuccessful due to shattering in the grinding operation.

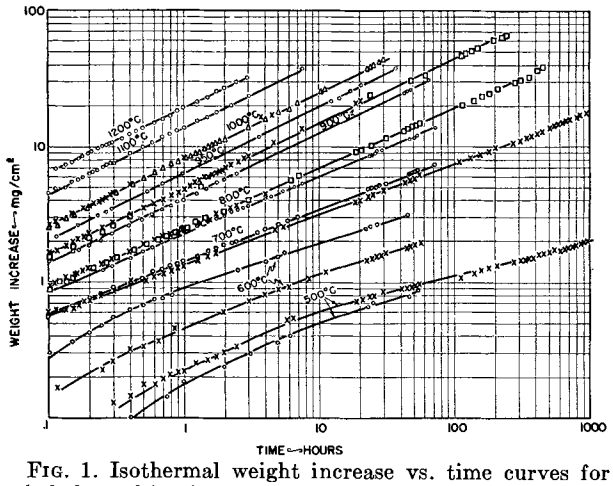

FIG. 1. Isothermal weight increase vs. time curves for cobalt heated in air.

mg). Continuous weight measurements were taken from the moment the specimen was inserted in the furnace.

Scale products formed during oxidation were identified at room temperature by x-rays. Whenever a multilayered scale was formed and wherever possible, scale layers were separated and x-rayed individually using powder samples. When the layers could not be separated cleanly, the individual layers could be identified in some instances by x-raying the scale surface before and after grinding off the outer layer; otherwise, the total scale conglomerate was x-rayed using powder samples.

Scaling Behavior of Cobalt

The weight increase vs. time data on a log-log scale are shown in Fig. 1. The parabolic law is followed between 500° and 1200°C, with the exception that from 500° to 800° the parabolic law is obeyed after an initial deviation time during which the reaction proceeds at a higher rate. Parabolic scaling constants, from slopes of weight increase squared vs. time, are plotted logarithmically as a function of the reciprocal of absolute temperature in Fig. 2, along with results from the literature. The break in the Arrhenius plot at about 700°C confirms previous investigations (21, 22).

Gulbransen and Andrew's (22) results made an interesting comparison since they studied the scaling behavior of both hexagonal (cold worked) and cubic (annealed) cobalt in oxygen (P_{O_2} = 76 mm Hg) from 200° to 700°C for 2 hr. The hexagonal form was found to oxidize more rapidly than the cubic form. They found that both forms of cobalt oxidized according to the parabolic rate law after an initial deviation, and calculated the scaling constant in the time interval of 1–2 hr. However, the present investigation indicates that from 500° to 800°C this time interval of 1–2 hr is still in the range where the oxidation rate is proceeding faster than the parabolic law would predict and that the scaling rate is somewhat higher than either form of cobalt used by Gulbransen and Andrew[2]

[2] These investigators also found that their high purity nickel oxidized at a slower rate than high purity nickel of other investigators (36). It would seem, then, that differences in experimental techniques (and possibly atmosphere) and not purity of metal cause the difference in scaling rate.

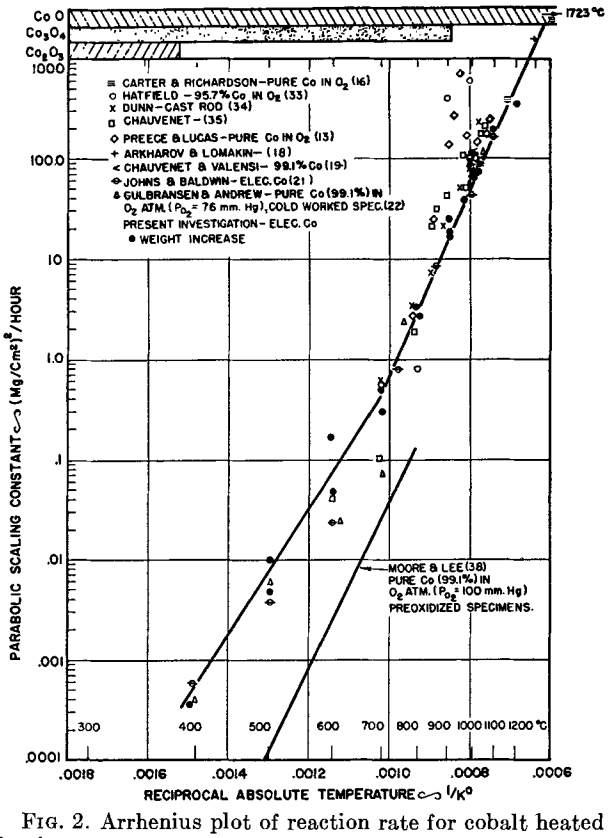

FIG. 2. Arrhenius plot of reaction rate for cobalt heated in air.

(*see* Fig. 3). It is interesting to note that rate constants calculated for 400°–1200°C for the time interval of 1–2 hr can be fitted to a single straight line in an Arrhenius plot, Fig. 3.

The precipitous changes in the oxidation rate of cobalt reported by Preece and Lucas (1) from 800° to 1075° have not been confirmed. Strangely enough, however, the high oxidation rates observed by these investigators at 900° and 950° (*see* Fig. 2) agree well with those reported by Hatfield (33) at these same temperatures, yet the latter used rather impure cobalt (95.7%) in his studies. As pointed out by Kubaschewski (11) the presence of an appreciable amount of high valency impurities in a metal which forms a metal-deficit oxide, of which CoO is an example,[3] may increase the scaling rate.

The much slower rates of oxidation observed by Moore and Lee (38) at low temperatures can again be attributed to the use of preoxidized specimens, as previously noted with nickel (36).

The scale found on cobalt was double-layered (*see* Fig. 8). At temperatures up to 900°C, the inner scale was gray and x-rayed as CoO; the outer scale was grayish black and x-rayed as Co_3O_4. Above 900°C the inner layer was

[3] Wagner (2) gives the composition as $Co_{.994}O$ at 1000°C. However, as Kubaschewski points out (37), the double-layer of CoO found by Preece and Lucas implies that the inner layer possesses vacant anion sites (metal-excess), whereas the outer layer possesses vacant cation sites (metal-deficit).

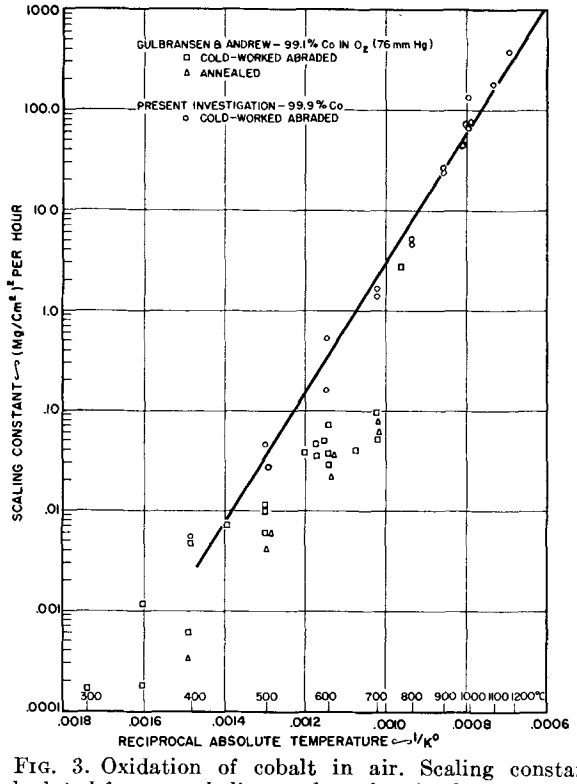

FIG. 3. Oxidation of cobalt in air. Scaling constant calculated from parabolic rate law plots in the time interval of 1–2 hr.

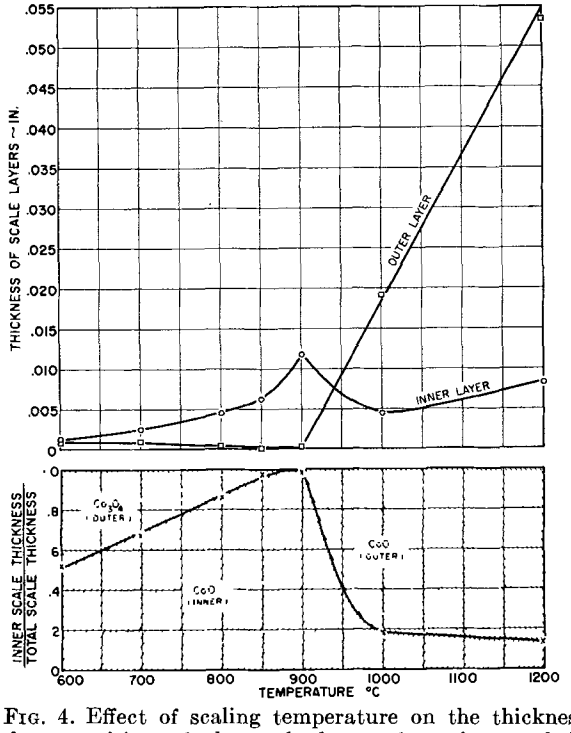

FIG. 4. Effect of scaling temperature on the thickness and composition of the scale layers formed on cobalt heated in air for 100 hr.

a thin brown; the outer layer was a crystalline grayish black, but both x-rayed as CoO.

The outer Co_3O_4 layer occupied about 50% of the total scale thickness at low temperatures (600°C) but became relatively thinner as temperature went up until, at a critical temperature of about 900°C, it disappeared. Of special note is the fact that no break is found in the Arrhenius plot at this temperature. As the temperature was further increased, the outer layer of CoO first appeared as a relatively thin layer but increased gradually until at 1200°C it occupied 90% of the total scale thickness. These relationships are shown in Fig. 4.

Bradley and Jay's method (39) was used to calculate the lattice parameter of the outer and inner CoO layers formed above 900°C. The same diffraction lines of identical intensity were obtained with powder patterns. The extrapolation of lattice parameter to $\cos^2\theta = 0$ ($\theta = 90°$) gave a value of 4.2826Å, which agrees with 4.260Å reported in the literature (16). The NaCl-type structure of CoO was confirmed by comparing theoretical and observed intensities. Good agreement was found except for the high intensity line observed from the (220) plane.

X-ray diffraction patterns of the inner brown and the outer grayish-black CoO layer were also obtained with the spectrogoniometer. This arrangement gives reflections only from those crystallographic planes that are parallel to the specimen surface. The inner brown layer when irradiated *in situ* gave all reflections for CoO, indicating a reasonable degree of randomness. The outer surface of the gray-black scale when irradiated *in situ*, however, gave only one diffraction line, that due to the (200) plane, indicating that virtually all grains had their cubic plane

FIG. 5 (a–f). Photomicrographs of the outer surface of the scale formed on cobalt and Co-Cr alloys. Unetched and unpolished. 300× before reduction for publication.

parallel to the scale surface. Further evidence of this crystallographic orientation was found in the photomicrographs of the unetched and unpolished surface of the outer scale, Fig. 5b. The scale surface is covered with growth figures having square or rectangular designs which is compatible with the orientation found by x-rays.

The growth of the oriented scale layer could occur (*a*) by nucleating pseudomorphically on an oriented substrate [examples of which are given by Pfeil (40)], (*b*) by nucleating preferentially on any arbitrary substrate [examples of this are the orientations of zinc cast against air, liquid lead, etc. (41, 42)], or (*c*) by nucleating randomly on any arbitrary substrate but growing preferentially. The first possibility seems unlikely. The lattice parameter of cubic CoO is 4.28Å, while that of cubic cobalt is 3.54Å. This combination of parameters would not produce a match between the metal and the oxide lattice for any pair of planes and directions. Moreover, it is unlikely that the method by which the cobalt was produced would yield a highly oriented structure capable of initiating an oriented substrate pseudomorphically. It should be pointed out that an inner brown layer exists between the metal and oriented scale, although it need not have existed there when the oriented scale was first formed.

The scale formed at 500°–900°, when irradiated *in situ* with the spectrogoniometer, revealed that the outer layer (Co_3O_4) had no texture, while the inner layer (CoO) had grown with the (111) and (220) planes parallel to the growth front, as evidenced by the disproportionately strong reflections from these planes. Microscopic examination of the unetched and unpolished outer surface of the scales formed between 500° and 800° showed the scale to be fine grained, see Fig. 5a.

Since the CoO was found as a double layer above 900°C the growth mechanism was studied by noting the position of the nichrome suspension wire in the scale. For a long enough scaling time and with a thick specimen (0.100 in.) the wire was buried in the scale at or close to the CoO-CoO interface, suggesting that the outer CoO layers grows by diffusion of cobalt ions outward and the inner CoO layer grows by diffusion of oxygen ions inward,[4] as previously noted by Preece and Lucas (1). The square of the thickness of each layer as a function of time at 900° and 1000°C gave a straight line, indicating that the parabolic law of growth is followed for individual layers.

To check the possibility that the scale formed at short times in the range of temperatures from 500° to 800°C differed from that at long times, the metal was oxidized at 500°C for 1 hr. Glancing x-rays of the surface revealed cobalt metal and the three strongest lines of Co_3O_4. This would indicate that at short times the reaction involving Co_3O_4 is rate-determining, whereas at long times the rate-determining reaction involves CoO or both CoO and Co_3O_4. As previously noted, the reaction at short times in the 500°–800°C temperature range proceeds at a higher rate than that at long times. Above 900°C where only CoO is formed, the reaction rate is the same at short and long times. Yet, it is interesting to note that the rate constants calculated for the temperature range from 400° to 1200°C for short times (the time interval of 1–2 hr) can be fitted to a straight line in an Arrhenius plot, Fig. 3, even though the rate-determining reaction presumably involves Co_3O_4 at low temperatures and CoO at high temperatures.

Thus, the interpretation of the break in the curve of log K vs. $1/T$ based on long time intervals, Fig. 2, cannot be explained adequately by a change in scale composition. An explanation cannot be given at the present time.

[4] The growth mechanism at low temperatures could not be determined by this method since the scale formed was too thin.

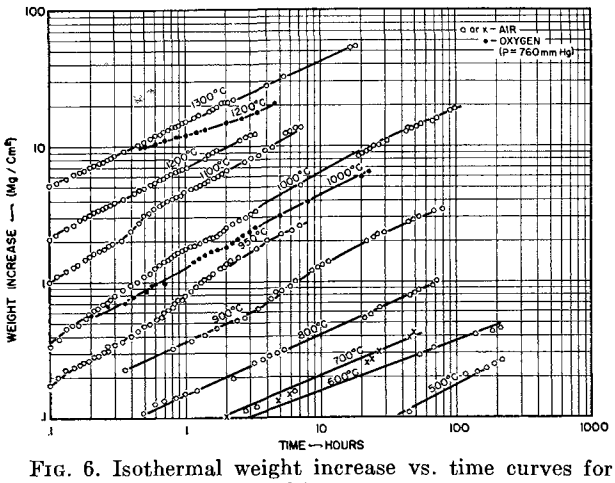

FIG. 6. Isothermal weight increase vs. time curves for chromium heated in air and in oxygen.

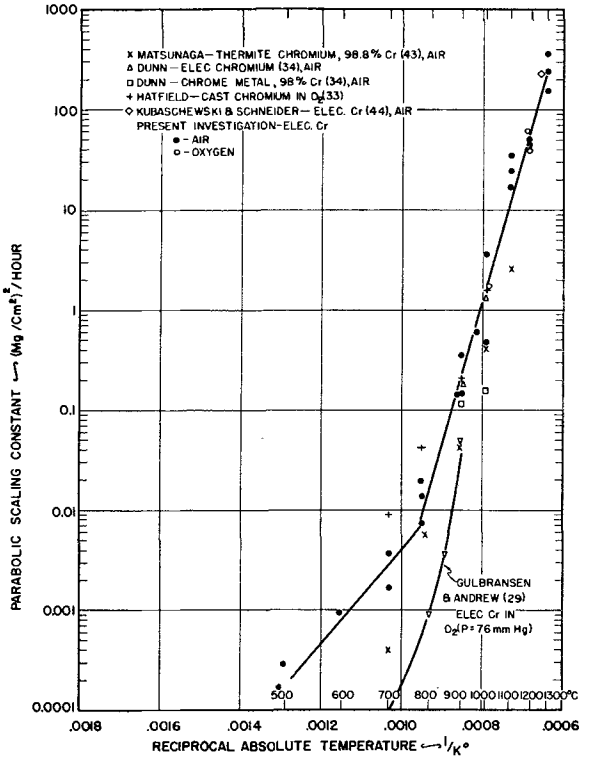

FIG. 7. Arrhenius plot of reaction rate for chromium heated in air and in oxygen.

Scaling Behavior of Chromium

Weight increase measurements as a function of time are plotted on a log-log scale in Fig. 6. The parabolic law of scaling is essentially obeyed (after an initial deviation) between 500° and 1300°C in air and at 1000° and 1200°C in oxygen (P_{O_2} = 760 mm Hg). Chromium scaled at about the same rate in oxygen as in air. The parabolic scaling constants determined from the slopes of the straight lines observed in the plots of weight increase squared against time are plotted on a log scale against the reciprocal of absolute temperature in Fig. 7. The present values are

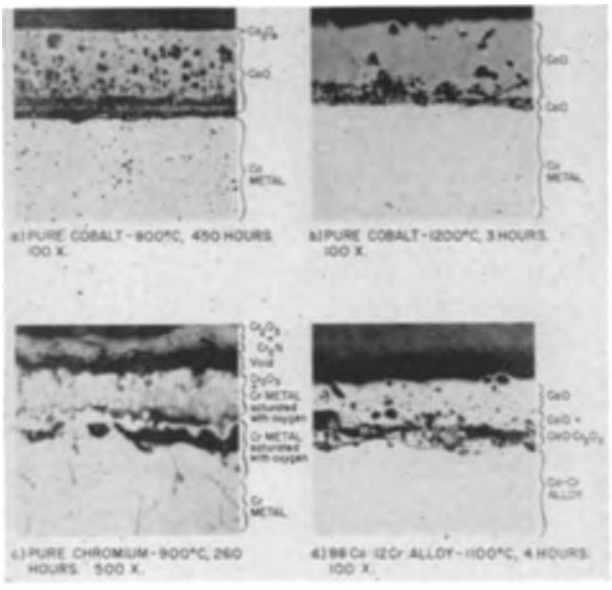

FIG. 8 (a–d). Microstructures of scale formed on cobalt, chromium, and Co-Cr alloy. Specimens air cooled after scaling at indicated temperatures and times. Unetched.

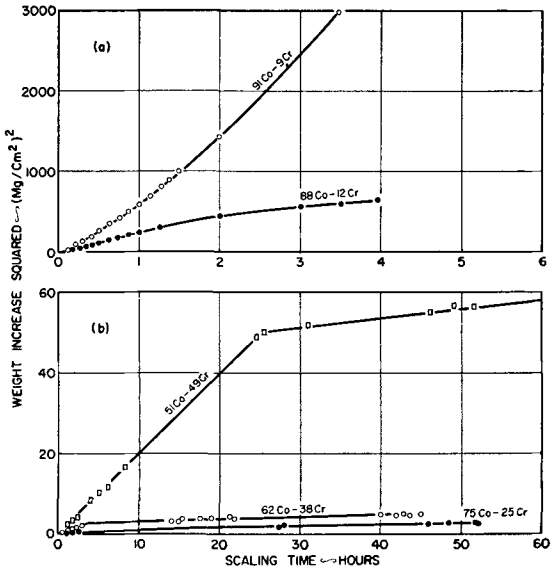

FIG. 9. Weight increase squared vs. time for Co-Cr alloys heated in air at 1100°C.

in fair agreement with those reported by Hatfield and by Dunn and are higher than those given by Matsunaga and by Gulbransen and Andrew.[5] It is apparent that as in the case of some other metals such as copper (45), iron (46), and possibly cobalt (*see* Fig. 2) there is a break in the curve. At temperatures above 800°C, the slope of the curve is three times as great as that at lower temperatures.

At low temperatures in air (500°–700°C) an adherent green scale, identified as Cr_2O_3 by x-rays, is formed. At high temperatures (800°C and up) in air or in oxygen, the outer surface of the scale is gray-black; however, after scraping the surface, the scale is noticeably green in color.

X-ray diffraction patterns of the black scale formed at 1000°C for 50 hr in air and then water-quenched revealed Cr_2O_3 only. X-ray results on the black scale formed at 900°C in 260 hr in air but then air-cooled to room temperature showed, in addition to the Cr_2O_3 lines, all the lines of β Cr_2N. Although not conclusive, these two tests indicate that the scale forms as Cr_2O_3 with nitrogen dissolved in it, and decomposes on air cooling but not on water quenching to room temperature. The scale formed at 1000° and 1200°C in oxygen consisted of Cr_2O_3 only.

Microscopic examination of specimens scaled in air revealed some interesting features. After high temperature scaling four zones were evident (*see* Fig. 8c). In order, these were: (*a*) the chromium metal matrix extensively cracked; (*b*) a darker, mottled zone indicating oxygen diffusion into the metal; (*c*) a two-phase structure consisting of Cr_2O_3 particles and chromium metal; and (*d*) an outer scale consisting of Cr_2O_3 or of Cr_2O_3 and β Cr_2N. These features indicate that chromium oxidizes largely, if not wholly, by the diffusion of oxygen ions inward. These same features were observed after low temperature scaling with the exceptions that the chromium matrix was less extensively cracked, and the presence or absence of the Cr_2O_3-Cr zone could not be determined since the specimens could not be polished without tearing away the outer zone(s).

The break in the Arrhenius curve of log K vs. $1/T$, Fig. 7, might be interpreted in the light of Valensi's theory (45) as being set by one scale product of chromium at low temperatures and another product at high temperatures. It is true that only green Cr_2O_3 is formed at low temperatures and in all probability this portion of the curve is set by the scaling rate of Cr_2O_3 only. The interpretation of the upper portion of the curve presents difficulties, however. At 900°C and up, the black scale formed in air is presumably Cr_2O_3 with (quadrivalent) nitrogen dissolved in it. This could conceivably cause defects in the anionic lattice, thereby increasing the scaling rate by increasing the rate of diffusion of oxygen. Such an explanation has been offered in the case of zirconium (47). However, since the scaling rate of chromium in oxygen was about the same as that in air, it would seem that nitrogen is not necessary for the upper portion of the curve.

Another possibility to account for the break in the Arrhenius curve could be due to the difference in crack density observed in chromium. At low temperatures, the extent of cracking is slight, resulting in a slower penetration of oxygen and a relatively low scaling rate. At high temperatures the metal is extensively cracked, resulting in a faster penetration of oxygen and a higher scaling rate than would be expected from an extrapolation of the low temperature portion of the curve.

Scaling Behavior of Co-Cr Alloys

Each of the alloys scaled at 900°–1200°C showed a deviation from a single parabolic scaling rate, as noted by

[5] Gulbransen and Andrew also reported lower scaling rates in the case of nickel (56) and cobalt (see Fig. 2). The lower scaling rates of chromium obtained by Matsunaga may be due to the rather impure metal used, since the presence of lower valency impurities would, according to Wagner, lower the oxidation rate of a metal forming a metal-deficit oxide. However, there is disagreement as to whether Cr_2O_3 is a metal-deficit (27) or a metal-excess oxide (28) when formed on chromium.

TABLE II. *Oxidation rate constants for* Co-Cr *alloys*

Weight % chromium	First parabolic rate	Second parabolic rate	End of first parabolic rate
	900°C		
	$mg^2/cm^4/hr$	$mg^2/cm^4/hr$	*hr*
8.85	22.5, 28.9	—	—
12.25	12.6	—	—
25.57	0.0040, 0.0050	0.0015, 0.0022	60
38.33	0.013, 0.022	0.0030, 0.0021	25
48.50	0.058	0.023	30
	1000°C		
8.85	294	—	
12.25	89	—	
25.57	0.017	0.0055	50
38.33	0.045, 0.073	0.013, 0.020	25
	1100°C		
8.85	445, 581	—	—
12.25	250	—	—
25.57	0.090	0.034	25
38.33	0.25	0.056	5
48.50	2.0	0.22	25
	1200°C		
8.85	860	—	—
12.25	435	—	—
25.57	0.44	0.090	3
38.33	1.2	0.40	2
48.50	3.5	1.4	15

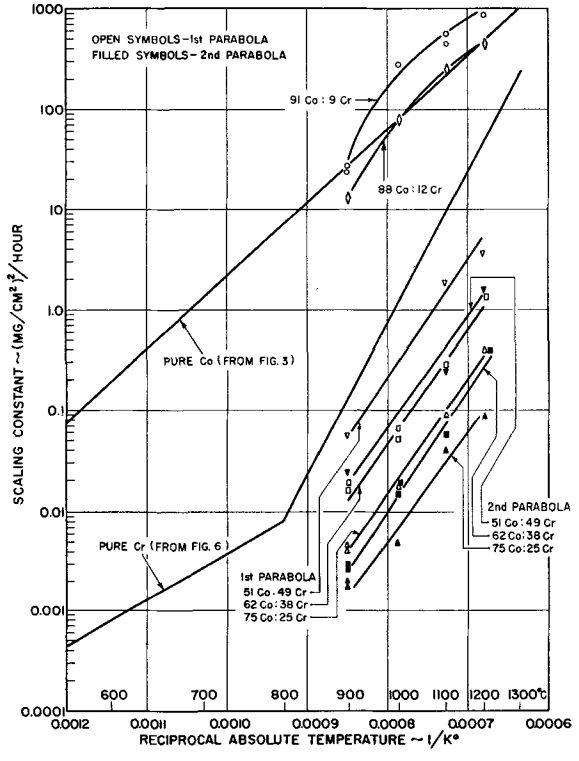

FIG. 10. Arrhenius plot of scaling rate of Co-Cr alloys heated in air.

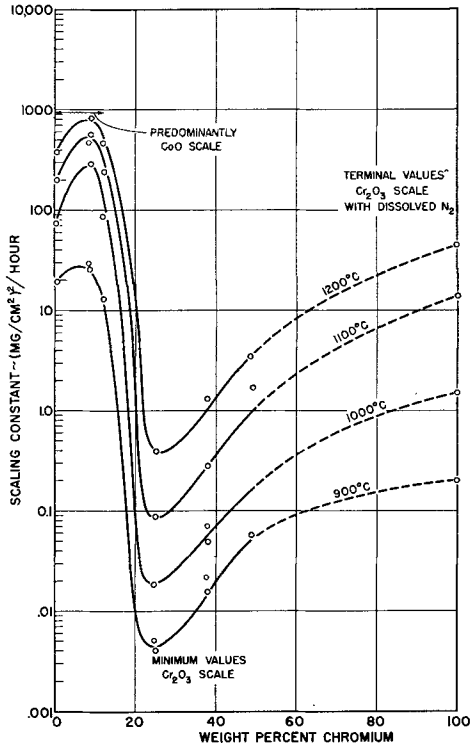

FIG. 11. First parabolic scaling constant vs. alloy composition for Co-Cr alloys heated in air.

a departure from a straight line relationship in plots of weight increased squared vs. time. Examples of these curves are shown in Fig. 9. For long scaling times, the 9 and 12% chromium alloys scaled at a higher and a lower rate, respectively, than that predicted by the parabolic rate law. Those alloys containing 25, 38, and 49% chromium, respectively, exhibited two parabolas, the first one originating from approximately zero time and the second setting in after a certain critical time with a lower slope than the first.

The first and second parabolic scaling constants, Table II, obtained from the slopes of the straight lines[6] are plotted in an Arrhenius plot of the reaction rate (log scale) against the reciprocal of absolute temperature in Fig. 10. It is seen that the data for the 9% and 12% chromium alloys appear to follow a curve, the 9% chromium curve being higher than the 12% chromium. The first and second parabolic scaling constants for 25, 38, and 49% chromium alloys adhere to a single straight line.

The first parabolic scaling rates (log scale) are also plotted as a function of the alloying element (chromium) for constant scaling temperatures in Fig. 11. It is apparent that at a constant temperature the addition of chromium up to about 9% increases the scaling rate three times over that of pure cobalt. Further additions tend to decrease the scaling rate, until at about 25% chromium a pronounced minimum is obtained. Increasing the chromium content thereafter increases the scaling rate, approaching the scaling rate of pure chromium as a limit.

Scale structures as revealed by x-rays are summarized

[6] In the case of the 91:9 and 88:12 Co-Cr alloys where a straight line was not obtained in the plots of w^2 vs. t the scaling constant was taken as the value of the weight increase square after 1 hr.

TABLE III. *Scaling patterns of* Co-Cr *alloys*

Scaling pattern	Inner layer	Outer layer
1	$CoO + CoO \cdot Cr_2O_3$	CoO*
2	(Cr_2O_3 + CoO and/or	$CoO \cdot Cr_2O_3$)†
3	—	Cr_2O_3‡

* Co_3O_4 detected along with CoO at 900°C; only CoO above 900°C.

† Whether or not a multilayered scale was present could not be determined since the scale formed was too thin.

‡ No cobalt was detected in these scales by a Feigl spot test (48).

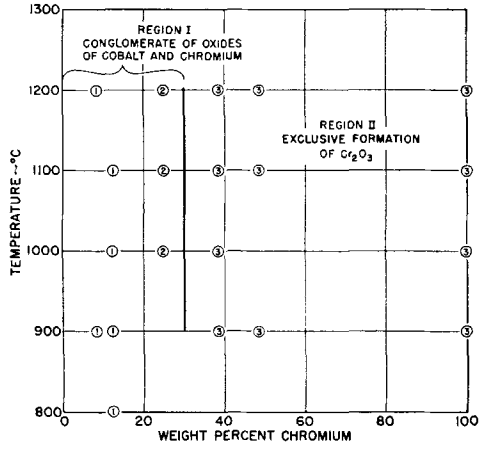

FIG. 12. Composition of scales formed on Co-Cr alloys heated in air. Scaling patterns are given by encircled numbers.

in Table III. Scales were formed on the alloys in one of three different patterns listed in Table III, depending upon alloy composition and temperature as shown in Fig. 12.[7]

A typical microstructure of the scale formed according to Pattern I is given in Fig. 8d. (Microstructures of the scales formed according to the other two patterns could not be obtained since the scales exfoliated on cooling to room temperature.) Glancing x-rays revealed that the surface scale of Pattern I (91:9 and 88:12 Co-Cr alloys) was highly oriented with the (200) plane (d = 2.13) parallel to the surface of the specimen, similar to the case of the outer scale formed on pure cobalt. Photomicrographs of the oriented outer surface are shown in Fig. 5 (c–f).

DISCUSSION

As in the case of Ni-Mn alloys (36), the scaling patterns of Co-Cr alloys can be laid out with a fair degree of certainty in schematic isothermal sections of the ternary Co-Cr-O phase diagram to aid in visualizing the progressive changes in scaling behavior wrought by alloy composition, Fig. 13(a–c).

The dotted paths shown in Fig. 13 were constructed so as to satisfy the demands of the experimentally observed

[7] In some cases the scaling pattern was also dependent upon time at the scaling temperature; however, the patterns plotted in Fig. 10 pertain to the longer scaling times where steady state is assumed to hold. A complete record of the description and x-ray identification of the scales may be obtained from the authors.

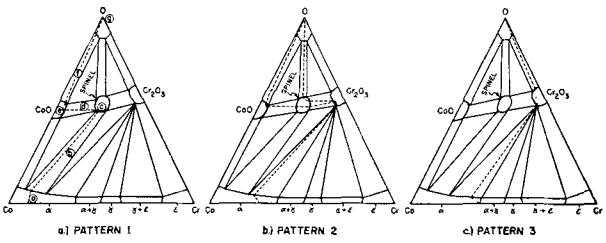

FIG. 13 (a–c). Schematic isothermal sections of the Co-Cr-O equilibrium diagram showing the scaling patterns of Co-Cr alloys.

scale structures. (The path must place the compounds found in the various layers in their proper order; it must reveal a progressive oxygen gradient and still be compatible with the topology of the phase diagram.)

Pattern I.—As Fig. 12 shows, Pattern I is found on relatively cobalt-rich alloys only (91:9 Co-Cr and 88:12 Co-Cr). The path thus starts on the Co-Cr edge of the ternary diagram near the cobalt corner (point a in Fig. 13a). The path then must be drawn such that no layer(s) would be found between the metal and the inner scale layer of CoO and spinel since no intermediate layer(s) was observed. This can be accomplished by drawing the path through the α metal-spinel zone along the tie-line b (crossing some tie lines in this zone would result in a subscale of spinel in the metal matrix), and through the one-phase spinel region c (the fact that this one-phase layer was not found may be due to the thinness of this layer). According to Table III the inner scale consists of CoO and spinel, therefore the path must cross some tie-lines in this two-phase region (point d). The outer layer of the scale according to Table III is CoO, hence the path is drawn through this one-phase region to indicate this fact (point e). The path then is carried out to the oxygen corner of the diagram (point g) along a tie-line between the CoO field and the oxygen field (point f) to indicate the sharp interface between the outer layer of CoO and the surrounding air.

Since the inner scale layer formed on the alloys which followed this scaling pattern contained only a small amount of spinel, the total scale can be considered as consisting essentially of a double layer of CoO, similar to the scales formed on pure cobalt at corresponding temperatures. And, as in the case of pure cobalt, this implies that outer scale layer is metal-deficit and grows by outward diffusion of cobalt ions, while the inner scale layer is metal-excess and grows by inward diffusion of oxygen ions. Thus, the sharp interface between the inner and outer scale layers (see Fig. 8d) may mark the original metal surface as noted by Preece and Lucas (1). This means, too, that the spinel in the inner layer was formed by the diffusion of oxygen ions inward; the fact that cobalt oxide is found exclusively in the outer layer also implies that the cobalt ion diffuses outward at a much higher rate than the chromium ion (indeed, if the chromium ion diffuses outward at all).

Pattern 2.—This pattern was followed only by the 75:25 Co-Cr alloy. The path taken by this pattern is not known exactly since the relative location of the component oxides in the scale could not be fixed, i.e., it could not be

determined if a given oxide was located in the inner scale layer or the outer layer or both, because the scale formed was very thin (this alloy had an extremely low scaling rate) and the scale exfoliated completely on cooling to room temperature. However, the path(s) may be deduced from a consideration of the following factors. First, it is known that the scale is predominately Cr_2O_3 with some CoO and/or spinel. Second, it is assumed that any CoO is to be found in the outer portions of the scale since the cobalt ion diffuses faster than the chromium ion. When all three of the oxides listed in Table III are to be found in the scale, the path may follow the lower route shown in Fig. 13b. When only Cr_2O_3 and spinel are to be found, then the path may follow the upper route shown in Fig. 13b.

It is to be noted that the 75:25 Co-Cr alloy effects a tremendous decrease in the scaling rate and that the first parabolic function corresponds to a scaling pattern which results in a scale consisting predominately of Cr_2O_3 with some spinel. Thus, it is apparent that Cr_2O_3 is responsible for the enormous drop in the scaling rate, not the spinel oxide.[8]

The second parabolic function for this alloy shows a still greater resistance to scaling, yet the scale may contain some CoO in addition to Cr_2O_3 and spinel which makes it difficult to ascribe the change in scaling rate to a change in scale composition since the formation of CoO indicates relatively poor scaling resistance. However, it is apparent that, in a scale consisting mainly of Cr_2O_3, this oxide acts as an extremely effective barrier to the diffusion of oxygen ions inward or to a diffusion of metal ions outward.

Pattern 3.—Since this scaling pattern corresponds to the formation of Cr_2O_3 exclusively,[9] the only possible path is that given in Fig. 13c. The 62:38 and the 51:49 Co-Cr alloys which scaled according to this pattern exhibited two different parabolic scaling rates during the course of oxidation at a given temperature, yet the scale x-rayed as Cr_2O_3 for either the first or second parabola even though the second parabolic rate is about ten times less than the first parabolic rate. As in the case of the 75:25 Co-Cr alloy, this change in scaling rate cannot then be ascribed to a change in scale composition.

In general, all patterns in Fig. 13 have a similar shape; instead of being straight lines from the original alloy composition to the oxygen corner of the diagram, they veer first to the chromium-rich side of a direct route and then to the cobalt-rich side. As pointed out previously, this implies that the cobalt ion diffuses outward at a much higher rate than the chromium ion. However, when the chromium content of the original alloy is high, Cr_2O_3 is formed exclusively and the change in direction of the path to the cobalt-rich side is not obtained. The minimum chromium content of the original alloy necessary for exclusive formation of Cr_2O_3 is drawn in as a solid line in Fig. 12.

The increase in the scaling rate by small additions of chromium to cobalt has also been found with small additions of chromium to nickel (50). This increase has been explained on the basis that trivalent chromium dissolves in the metal-deficit CoO (or NiO) and replaces some of the divalent cobalt (or nickel) ions (51), thus providing new cation defects for the diffusion of cobalt (or nickel) ions.[10]

Conversely, the argument that cobalt additions to chromium effect a decrease in the scaling rate on the basis of a decrease in the number of vacant cation sites may hold in the present case and account for the excellent scaling resistance at about 25% chromium. This would, however, require that Cr_2O_3 be a metal-deficit oxide, which does not seem likely since Cr_2O_3 is formed by the diffusion of oxygen ions inward, at least in the case of pure chromium.

An alternate possibility to account for the drop in scaling rate brought about by cobalt additions to chromium is analogous to the simple case of Ni-Pt alloys investigated by Kubaschewski and Goldbeck (51). They analyzed their results on the basis of diffusion and activity considerations put forth by Wagner (50) and, although their interpretation has been disputed (52), their data show clearly that oxidation rate decreases with increasing platinum content and that NiO is formed exclusively. Similarly, Cu-Pt alloys (52) show a decrease in the oxidation rate with increasing platinum, although copper oxide is formed exclusively. The Co-Cr alloys showed that in the range of chromium contents from 100 to 25% cobalt acts noble with respect to chromium, i.e., only chromium oxidizes. The attendant decrease in scaling rate as the chromium content decreases could be reconciled as due to the same effect as in the Ni-Pt and Cu-Pt alloys, dilution of the base metal (chromium) in the alloy, leading to a decrease in the scaling rate.

Last, it is to be noted that, although the Co-Cr alloys containing more than about 20% chromium exhibit high scaling resistance in continuous oxidation runs, the scales formed on these alloys spalled badly on cooling to room temperature. This would seem to preclude their use in cyclic heating and cooling service unless the spalling resistance could be improved, as in the case of Ni-Cr alloys (55), by the addition of small quantities of such elements as silicon which "peg-in" the external scale.

Conclusions

1. At a given temperature the scaling rate of Co-Cr alloys first increased with low chromium additions, then dropped precipitously with further chromium additions reaching a minimum at about 25% chromium. Higher chromium contents effected a rise in the scaling rate reaching the scaling rate of pure chromium as the upper limit.

2. The composition of the scale formed on Co-Cr alloys was dependent upon alloy composition. Above a critical

[8] Recent work at this laboratory indicates that the exclusive formation of Cr_2O_3 is responsible for the excellent scaling resistance of iron-base and nickel-base alloys containing about 25% chromium. In fact, the scaling rate at this critical concentration of chromium is independent of the base metal, be it cobalt, nickel, or iron.

[9] A number of analyses have been proposed for predicting the minimum concentration of an alloy constituent necessary for the exclusive formation of its oxide (2, 49), but none of these applies here since they are based on assumptions that are not met in the present case.

[10] The deleterious influence due to lattice defects may overshadow any beneficial effect due to the small amounts of spinel and/or Cr_2O_3 found in these alloys.

concentration of about 25% chromium (Region II), the scale consisted exclusively of chromium oxide; below this critical concentration (Region I) complex scales of the oxides of both cobalt and chromium were formed.

3. In Region I the scales were such that the cobalt ion must diffuse outward faster than the chromium ion.

4. Spinel formation observed in the complex scales had no apparent beneficial effect on the scaling resistance.

5. The poor spalling resistance of the Co-Cr alloys would seem to preclude their use as oxidation resistant components in cyclic service operation.

Acknowledgments

The authors are especially indebted to the Office of Ordnance Research whose sponsorship made this work possible. They also wish to thank Mr. C. A. Barrett who performed some of the tests.

Manuscript received January 9, 1956.

Any discussion of this paper will appear in a Discussion Section to be published in the June 1957 Journal.

REFERENCES

1. A. Preece and G. Lucas, *J. Inst. Metals*, **81**, 219 (1952).
2. C. Wagner, *This Journal*, **99**, 369 (1952).
3. L. Horn, *Z. Metallkunde*, **36**, 142 (1944).
4. A. W. Hull, *Phys. Rev.*, **17**, 571 (1921).
5. O. S. Edwards and H. Lipson, *J. Inst. Metals*, **69**, 177 (1943).
6. A. R. Troiano and J. L. Tokich, *Trans. Am. Inst. Mining Met. Engrs.*, **175**, 728 (1948).
7. J. B. Hess and C. S. Barrett, *J. Metals*, **4**, 645 (1952).
8. L. Maricq, *Phys. Rev.*, **49**, 831 (1936).
9. A. G. Metcalfe, *ASM Proc. First World Metallurgical Congress*, 717 (1951).
10. J. B. Newkirk and A. H. Geisler, *Acta Metallurgica*, **1**, 456 (1953).
11. O. Kubaschewski and B. E. Hopkins, "Oxidation of Metals and Alloys," Academic Press, Inc., New York (1953).
12. C. A. Hampel, Editor, "Rare Metals Handbook," Reinhold Publishing Corp., New York (1954).
13. K. Sasaki and S. Sekito, *Trans. Am. Electrochem. Soc.*, **59**, 437 (1931).
14. A. H. Sully, "Chromium," Academic Press, Inc., New York (1954).
15. M. Leblanc and E. Mobius, *Z. Physik. Chem.*, **142**, 151 (1929).
16. R. E. Carter and F. D. Richardson, *J. Metals*, **7**, 336 (1955).
17. V. I. Arkharov and Z. A. Voroshilova, *Zhur. Phys. Chem. (USSR)*, **A142**, 151 (1929).
18. V. I. Arkharov and G. D. Lomakin, *J. Tech. Phys. (U.S.S.R.)*, **14**, 155 (1944).
19. G. Chauvenet and G. Valensi, *Compt. rend.*, **205**, 317 (1937).
20. V. I. Arkharov and K. M. Graevski, *J. Tech. Phys. (USSR)*, **14**, 132 (1944).
21. C. S. Johns and W. M. Baldwin, Jr., *Trans. Am. Inst. Mining Met. Engrs.*, **185**, 720 (1950).
22. E. A. Gulbransen and K. F. Andrew, *This Journal*, **98**, 241 (1951).
23. R. W. G. Wyckoff, "Crystal Structures," Interscience Publishers, Inc., New York (1948).
24. R. S. Schwartz, I. Fankucher, and R. Ward, *J. Am. Chem. Soc.*, **74**, 167 (1952).
25. E. A. Gulbransen and J. W. Hickman, *Trans. Am. Inst. Mining Met. Engrs.*, **171**, 306 (1947).
26. S. Miyake, *Sci. Papers Inst. Phys. Chem. Research (Tokyo)*, **31**, 161 (1937).
27. K. Hauffe and J. Block, *Z. physik. Chem.*, **196**, 438 (1951).
28. W. J. Moore, Rept. No. 1, A. E. C., Contract No. AT(11-1)-250, Indiana University (1953).
29. E. A. Gulbransen and K. F. Andrew, *This Journal*, **99**, 402 (1952).
30. G. Tammann, *Z. anorg. u. allgem. Chem.*, **188**, 396 (1930).
31. R. Blix, *Z. Phys. Chem.*, **3**, 229 (1929).
32. A. H. Sully and T. J. Heal, *J. Inst. Metals*, **76**, 719 (1949–50).
33. W. H. Hatfield, *J. Iron Steel Inst.*, **115**, 483 (1927).
34. J. S. Dunn and F. J. Wilkins, "Review of Oxidation and Scaling of Heated Solid Metals," Department of Scientific and Industrial Research, London, His Majesty's Stationery Office (1935).
35. G. Chauvenet, *Compt. rend.*, **29**, 886 (1939).
36. E. B. Evans, C. A. Phalnikar, and W. M. Baldwin, Jr., *This Journal*, **103**, 367 (1956).
37. Discussion to Reference (1), *J. Inst. Metals*, **81**, 727 (1952–3).
38. W. J. Moore and J. K. Lee, *J. Chem. Phys.*, **19**, 255 (1951).
39. A. J. Bradley and A. H. Jay, *Phys. Soc. (London)*, **44**, 563 (1932).
40. L. B. Pfeil, *J. Iron Steel Inst.*, **119**, 501 (1929).
41. G. Edmunds, *Trans. Am. Inst. Mining Met. Engrs.*, **143**, 183 (1941).
42. G. Edmunds, *ibid.*, **161**, 114 (1945).
43. Y. Matsunaga, *Japan Nickel Rev.*, **1**, 347 (1933).
44. O. Kubaschewski and A. Schneider, *J. Inst. Metals*, **75**, 403 (1949).
45. G. Valensi, *Rev. Met.*, **45**, 208 (1948).
46. J. Bénard and O. Coquelle, *Compt. rend.*, **222**, 796 (1946).
47. C. A. Phalnikar and W. M. Baldwin, Jr., *Proc. Am. Soc. Testing Materials*, **51**, 1038 (1951).
48. F. Feigl, "Spot Tests," Elsevier Publishing Co., New York (1954).
49. L. S. Darken, *Trans. Am. Inst. Mining Met. Engrs.*, **150**, 157 (1942).
50. C. Wagner and K. E. Zimens, *Acta Chem. Scand.*, **1**, 547 (1947).
51. O. Kubaschewski and O. Goldbeck, *J. Inst. Metals*, **76**, 255 (1949–50).
52. D. E. Thomas, *J. Metals*, **3**, 926 (1951).
53. B. Lustman, *ibid.*, **188**, 995 (1950).

Hydrogen Evolution from Dissolving Titanium-Oxygen Alloys in Hydrofluoric Acid and the Constitution of Ti-O Alloys

M. E. Straumanis, C. H. Cheng, and A. W. Schlechten

Department of Metallurgy, University of Missouri School of Mines and Metallurgy, Rolla, Missouri

ABSTRACT

Titanium-oxygen alloys dissolve in HF according to the reaction $TiO_x + 3HF \Rightarrow TiF_3 + xH_2O + 0.5\ (3 - 2x)H_2$, with a maximum for $x = 1.5$, which means that Ti_2O_3 dissolves without hydrogen evolution. Higher titanium oxides do not dissolve in HF. The determination of the end point of the above reaction was affected by a secondary, but very slow reaction $TiF_3 + HF \Rightarrow TiF_4 + 0.5H_2$. Nevertheless, the experimental results agreed within ±2% for the first reaction for titanium containing oxygen up to 33 at.%. Titanium-oxygen alloys do not represent titanium oxygen solid solutions but solid solutions of titanium oxides and titanium metal.

HF dissolves titanium readily according to the equation (1, 2):

$$Ti + 3HF \Rightarrow TiF_3 + 1.5H_2 \qquad (I)$$

Also, Ti-O alloys (3) dissolve in HF with hydrogen gas evolution. However, it was not known how the oxygen in the metal would change the amount of hydrogen evolved and how it would influence the valency of the titanium ions produced. It was also thought that the study of the behavior of the alloys in HF might reveal some further clues concerning the structure of these alloys, which is still uncertain (4, 5).

Dissolution of Ti-O alloys TiO_x may occur in a manner similar to the dissolution of other soluble oxides according to the reaction:

$$TiO_x + 3HF \Rightarrow TiF_3 + xH_2O + 0.5(3 - 2x)H_2 \qquad (II)$$

By measuring the amount of hydrogen developed and knowing the composition of the Ti-O alloys, the correctness of equation (II) was checked.

Preparation and Analysis of Ti-O Alloys

The alloys were prepared by heating titanium powder (+65 mesh, 99.7% pure),[1] with a calculated amount of TiO_2 (99.9% pure);[2] the dry materials were weighed, mixed, and put into alundum or zirconia crucibles (in case of oxygen content over 25% by weight) and heated in vacuum resistance furnace for 4 hr at 1100° or 1400°C, respectively. Samples of high oxygen content were crushed and reheated at 1400°C for 2–4 hr to secure uniform composition. The charges, usually sintered in one solid piece, were crushed, ground, and stored in a desiccator. The color of the alloys No. 2 to 6 (Table I) was light gray, resembling pure titanium powder. The brittleness of the substance increased with increasing oxygen content. The color of alloy 7 and 8 was darker. Alloy 10 had a greenish tint, while alloy 11 was nearly black. Under the microscope the latter displayed crystalline grains of a dark violet color. The ten alloys prepared, varying in oxygen content from 3 to 60 at. %, were analyzed for their titanium content, and it was assumed that the balance was oxygen. No direct oxygen determinations were made.

Analyses were performed according to a method described by Rahm (6), but slightly modified. It consists in titrating the dissolved titanium alloy with ~N/10 aqueous solution of $FeNH_4(SO_4)_2$, standardized against pure TiO_2. Approximately 200–300 mg of each alloy was dissolved in 10 ml concentrated H_2SO_4 containing 5 g anhydrous sodium sulfate, and the titanium of the obtained solutions was reduced to the trivalent state by aluminum for titration under CO_2. Reagent grade chemicals were used in every instance.

Experimental Procedure

Samples of the alloys of the compositions as given in Table I were dissolved in HF in a special apparatus and the hydrogen evolved was collected. First, the finely ground charge of the alloy was weighed in a small platinum crucible, which was placed on a glass or polyethylene spoon cemented to a Pyrex glass joint. The whole was then introduced into a 200 cm^3 Erlenmeyer flask as previously described (7). The stopper of the flask was equipped with two capillaries, one of which was so arranged that the air in the flask could be displaced through it, before the dissolution procedure, by pure hydrogen, in order to prevent the oxidation of the trivalent titanium ions formed later (1). The second capillary served to lead the evolved hydrogen into the gas measuring buret. The flask, the inside of which was lined with paraffin wax, was submerged in a constant temperature water bath (25 ± .05°C). Wherever possible, glass joints were used in order to minimize loss of hydrogen by diffusion through rubber connections. After flushing the apparatus with hydrogen for some time, and after thermal equilibrium had been reached, the valves were closed, and the spoon sealed to the glass joint

[1] Supplied by the Belmont Smelting and Refining Works, Inc.

[2] Fisher Scientific Co.

TABLE I. *Hydrogen volumes (reduced to normal conditions) as developed by various* TiO_x *alloys in* HF

Concentration of HF: 3*N* (30 ml) for alloys No. 1-8, and 6*N* (60 ml) for No. 9-11

Alloy No.	Ti by chem. anal.		*x* from chem. anal. in g atoms	H_2 in ml/g alloy		Δ in	
	Wt.%	At.%		Observ.	Calc. eq(II)	ml	%
0	100.0	100.0	0	—	702	—	—
1	99.9*	99.9*	<0.001	697	700	−3	−0.43
2	98.7	96.3	0.038	677	675	+2	+0.29
3	98.3	95.1	0.052	666	666	±0	±0.00
4	97.0	91.5	0.093	646	639	+7	+1.1
5	96.7	90.7	0.103	619	632	−13	−2.0
6	94.7	85.6	0.168	580	590	−10	−1.7
7	92.7	80.9	0.236	542	548	−6	−1.1
8	86.0	67.2	0.488	410	407	+3	+0.73
9	76.4	52.0	0.925	225	206	+19	+8.4
10	74.5	49.4	1.024	185	166	+19	+10.0
11	66.1	39.4	1.538	5.6	0	+5.6	—

* Obtained by dissolving Ti produced by thermal decomposition of titanium iodide. The balance in all alloys is oxygen.

was overturned so that the crucible with the charge dropped into the acid. Usually the alloys were completely dissolved in 20 min.

Results

Although the method of working and collecting the hydrogen evolved seemed to be very simple, complications arose because the solution continued to evolve hydrogen after the titanium alloy was completely dissolved. In analogy to the reaction of divalent titanium ion with hydrogen ion (acids) (8):

$$Ti^{2+} + H^+ \Rightarrow Ti^{3+} + 0.5H_2 \qquad \text{(III)}$$

or of gaseous hydrogen fluoride with titanium fluoride (at 600°C) (9):

$$2TiF_3 + 2HF \Rightarrow 2TiF_4 + H_2 \qquad \text{(IV)}$$

it was assumed that a reaction simliar to (IV) could also occur in aqueous solutions, as HF was used in excess and TiF_3 always was formed during the dissolution processes. The presence of TiF_3 was indicated by the greenish color of the resulting acidic solutions, and by the instantaneous decoloration of large amounts of $KMnO_4$ solutions if added to them. In fact the possibility of a reaction like equation (IV) in aqueous solutions was subsequently proved by special experiments: (*a*) after the dissolution was completed, the greenish color of the solution gradually faded out; (*b*) the amounts of $KMnO_4$ solutions necessary to oxidize the solution gradually decreased; and (*c*) simultaneously the rate of hydrogen evolution dropped. However, ions of trivalent titanium were present even then, when the rate of hydrogen evolution according to equation (IV) after 20 and more hours of reaction approached zero. The slow rate of this reaction agrees with the small normal potential $E_0 = -0.05$ volts for $Ti^{3+} \rightarrow Ti^{4+} + e$ in H_2SO_4 (8). The instability of solutions of trivalent titanium is also known from the literature. For example, it was observed that $TiCl_3$ solutions slowly oxidized even in a

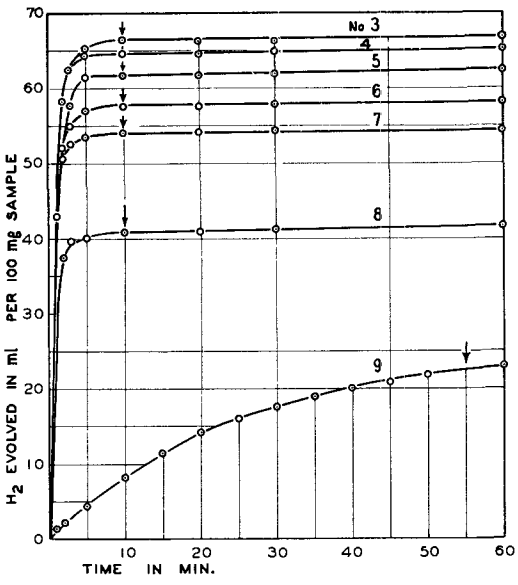

FIG. 1. Amount of hydrogen in ml developed by 100 mg of a TiO_x alloy at a time shown on the abscissa. Arrows indicate the end of reaction (II), numbers—the alloys of Table I.

hydrogen atmosphere; the rate of oxidation was much faster in presence of oxygen (10). As the presence of this gas was completely excluded in these experiments, the only possibility of explaining the oxidation of TiF_3 and hydrogen evolution after dissolution was reaction (IV) or a similar one. The reaction was catalyzed by paraffin, because glass coated with this substance and immersed into the TiF_3-HF solution quickly was covered with growing gas bubbles. Platinum was less effective. Although TiF_3 solutions are unstable, the pure and dry salt exhibits a remarkable stability (9).

Fortunately the rate of reaction (IV) was so slow that it could be completely disregarded in the case of alloys with a low oxygen content as in the beginning of the dissolution reaction (II) the TiF_3 concentration in the solution is low. It was somewhat more difficult to estimate the end of the reaction when large amounts of oxygen were present in the titanium alloy, as the concentration of TiF_3 strongly increased at the start because of rapid dissolution of Ti_2O_3 present in the alloy without any hydrogen evolution [reaction (II), $x = 1.5$]:

$$Ti_2O_3 + 6HF \Rightarrow 2TiF_3 + 3H_2O \qquad \text{(V)}$$

So in this case the decreasing rate of the hydrogen evolution reaction (II) was overlapped by an increasing rate due to reaction (IV), thus diminishing the sharpness of the bend of the volume vs. time curve (Fig. 1) and making the estimation of the end of reaction (II) more difficult. The rate of the reaction (IV) declined, as soon as the alloy was dissolved in the acid.

Powdered alloys with a low oxygen content (No. 1 to 8) dissolved completely in 3*N* HF in 10 min, while it took about 1 hr to dissolve the alloy with high oxygen content in the acid twice as strong (alloy No. 9, Fig. 1). After this hour the rate slowed down considerably, indicating that reaction (IV) alone continued. Solutions were slightly

turbid probably because of the presence of TiO_2 which does not dissolve in HF.

How good such an estimation of the end of reaction (II) was is shown in Table I, where the hydrogen volume developed is compared with the volume calculated from equation (II).

Discussion and Conclusions

The fairly good agreement between the observed and calculated hydrogen volumes (Table I) indicates that equation (II) describing the reaction of dissolution of Ti-O alloys in HF is correct. However, in such a case it should be expected that at about $x = 1.5$ (alloy Ti_2O_3) hydrogen evolution by the alloy should be zero. The observed small volume of 5.6 ml is explained by insufficient homogenization of the alloys high in oxygen content, although temperatures up to 1400°C and repeated heating up to 4 hr was used. The proof is that alloys heated at lower temperatures developed larger amounts of hydrogen, meaning that more free titanium which did not react with TiO_2 was left over. Thus the oxide which dissolves in HF without any hydrogen evolution is Ti_2O_3, and the maximum for x in equation (II) is 1.5. If x is larger, no hydrogen is evolved by such alloys.

From the behavior of TiO_x alloys toward HF one clear statement can be drawn, i.e., oxygen is bound chemically by titanium ions with formation of solid solutions of which those with highest oxygen content are represented by Ti_2O_3. Oxides with still larger oxygen content are out of this series, because they do not dissolve in HF. Evidently, at high temperatures oxygen (5) in the form of negative ions diffuses into titanium, migrating in the interstitial space from one titanium positive ion to another. However, dissolution experiments cannot determine what kind of lower oxides are formed inside the titanium metal, because the titanium ions of lower than 3 valency, as soon as they have left the lattice, react with water or with acid according to equation (III) with evolution of hydrogen. So one obtains from the total reaction the impression that all TiO_x alloys consist of a solid solution of metallic titanium which evolves hydrogen in HF and of Ti_2O_3, which does not. Although this behavior is correctly described by reaction (II), there are, on the other hand, experimental facts which contradict this statement and seem to confirm the existence of TiO as a chemical compound (11) and not as a solution $Ti(Ti_2O_3)$. For instance it was found that titanium oxide dissolving in acids produces the ions Ti^{2+} and Ti^{3+} (10); the appearance of the latter is easily explained by reaction (III) or by the dissolution of $Ti(Ti_2O_3)$. The formation of divalent titanium ions could indicate the presence of TiO in the titanium, but the ion Ti^{2+} may also result from the dissolution of the metallic part of $Ti(Ti_2O_3)$ in the acid. Because of this uncertainty it is not possible to say exactly what other oxides besides Ti_2O_3 are present in TiO_x alloys. The phase relationship of the different titanium oxides is described by Bumps, Kessler, and Hansen (12, 13).

Equation (II) can be used for an easy and fast determination of free titanium (as if unbound) or of oxygen (by difference) in titanium oxygen alloys.

Acknowledgment

The authors are grateful to the Wright Air Development Center for support of this work and for permission to publish the results obtained.

Manuscript received December 16, 1955. This paper is based on a portion of the work carried out at the Missouri School of Mines and Metallurgy for the Wright Air Development Center under Contract No. AF 33(616)-75.

Any discussion of this paper will appear in a Discussion Section to be published in the June 1957 Journal.

REFERENCES

1. M. E. Straumanis and P. C. Chen, *This Journal*, **98**, 234 (1951); *Metall*, **7**, 85 (1953).
2. M. E. Straumanis and J. I. Ballass, *Z. anorg. Chem.*, **278**, 33 (1955).
3. P. Ehrlich, *ibid.*, **247**, 53 (1941).
4. R. J. Wasilewski and G. L. Kehl, *J. Inst. Metals*, **83**, 94, 99 (1954–55).
5. M. Simnad, A. Spilners, and O. Katz, *J. Metals*, **7**, 645 (1955).
6. J. A. Rahm, *Anal. Chem.*, **24**, 1832 (1952).
7. M. E. Straumanis and J. I. Ballass, *Z. anorg. Chem.*, **278**, 33, Fig. 1 (1955).
8. G. S. Forbes and L. P. Hall, *J. Am. Chem. Soc.*, **46**, 385 (1924).
9. P. Ehrlich and G. Pietzka, *Z. anorg. Chem.*, **275**, 121, 124 (1954).
10. G. Patscheke and W. Schaller, *ibid.*, **235**, 257, 262 (1938).
11. W. O. Groves, M. Hoch, and H. L. Johnston, *J. Phys. Chem.*, **59**, 127 (1955).
12. E. S. Bumps, H. D. Kessler, and M. Hansen, *Trans. Am. Soc. Metals*, **45**, 1008 (1953).
13. T. H. Schofield and A. E. Bacon, *J. Inst. Metals*, **84**, 47 (1955).

Anodic Coprecipitation of Trace Amounts of Manganese and Silver with Lead Dioxide

J. T. Byrne[1] and L. B. Rogers

Department of Chemistry and Laboratory for Nuclear Science, Massachusetts Institute of Technology, Cambridge, Massachusetts

ABSTRACT

The applicability of anodic coprecipitation to the separation of trace amounts of ions from solution has been demonstrated by the carrying of silver and manganese on anodically formed lead dioxide. Neither of these elements could be anodically deposited under the conditions of these experiments in the absence of the lead.

Control of the anode potential is an important factor in the codeposition of an element which, like manganese, can be oxidized to higher valence states which are less readily coprecipitated than is manganese(IV). Likewise, for coprecipitation of silver, the anode potential must be positive enough for the silver(I) to silver(II) oxidation to occur.

Up to the present time, analytical applications of electrodeposition have been concerned almost entirely with the cathode. With the exception of lead and manganese which are precipitated as dioxides, little attention has been devoted to the anode despite the possibility of separating a number of elements. A disadvantage that one can anticipate arises from the fact that a compound rather than an element is formed. As a result, consideration of the solubility of the deposit becomes important, particularly when dealing with trace amounts.

Coprecipitation is frequently used to effect complete deposition at the trace level and there is no reason to expect that electrolytic coprecipitation should be any less effective. Compared to ordinary coprecipitation, the variety of compounds that can be used as a carrier in electrolytic coprecipitation is somewhat limited. However, the possibility of increasing the selectivity by control of the anode potential is a promising compensating factor. The only reported attempt to employ electrolytic coprecipitation for traces involved the carrying of plutonium dioxide with manganese dioxide and was far from successful (1). However, it appears that failure to control the anode potential undoubtedly resulted in oxidation of the plutonium beyond the tetravalent state, thereby forming the less readily coprecipitated plutonyl ion. Likewise, a high anode potential would favor oxidation of manganese beyond the tetravalent state and would mitigate against coprecipitation.

The present paper reports exploratory experiments which demonstrate that trace amounts of manganese and of silver can be quantitatively (and selectively) coprecipitated during the anodic deposition of lead dioxide. Most of the effort was devoted to manganese, silver having been studied only briefly in a qualitative manner to test the expected generality of the conclusions regarding coprecipitation.

Manganese was selected for study because of the favorable radiochemical characteristics of the nuclide, manganese-52, and because of the interesting electrochemical behavior that results from the several oxidation states of manganese in solution. The choice of silver-111 was the result of its being on hand for concurrent use in another study. The choice of lead as the carrying element was largely a matter of convenience. Its deposition behavior was well known and its concentration could be determined rapidly using the polarograph.

[1] Present address: The Dow Chemical Co., Denver, Colo.

Experimental

Reagents and solutions.—Solutions of carrier-free manganese-52 were prepared by distillation of permanganic acid from solutions of deuteron-bombarded chromic oxide (2). Experiments with similar solutions in the anodic deposition of manganese dioxide had indicated that these solutions were less than 10^{-7}M in manganese. All solutions of manganese except the carrier-free tracer were made up by dilution of a 0.0097M solution of Mallinckrodt reagent-grade manganous nitrate standardized by the bismuthate method (3). All lead solutions were made by dilution of a 0.0988M solution of Mallinckrodt reagent-grade lead nitrate standardized gravimetrically by the lead sulfate method (4). Distilled water was used throughout.

Apparatus.—The potential on the anode was controlled in every case to at least ±3 mv using potentiostats designed by Lamphere (5). The potential was adjusted at the beginning of the run and checked several times during each run using a Rubicon potentiometer reading to ±0.1 mv. Electrolyses were usually carried out in open 250 ml beakers using a volume of 160 ml and platinum gauze anodes of about 13 cm^2 or 39 cm^2 in area. Both the platinum wire cathode and the saturated calomel reference electrode (SCE) were connected to the electrolytic solution through suitable agar salt bridges. The cathode solution was 0.5*N* in potassium nitrate. The entire electrolytic set-up including a stirring motor was placed in a box-like plastic hood to protect the solutions from contamination with dust. All *p*H measurements were made with a Beckman Model G *p*H meter.

Procedures.—All solutions of manganese were preelectrolyzed for at least 12 hr prior to the addition of lead to insure that all of the manganese that could precipitate

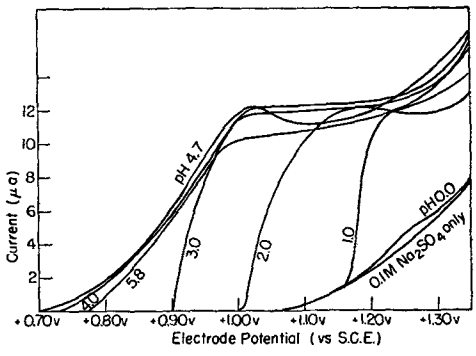

FIG. 1. Effect of *p*H on the polarographic oxidation of 10^{-3} M manganous ion to manganese dioxide at a stationary platinum microelectrode.

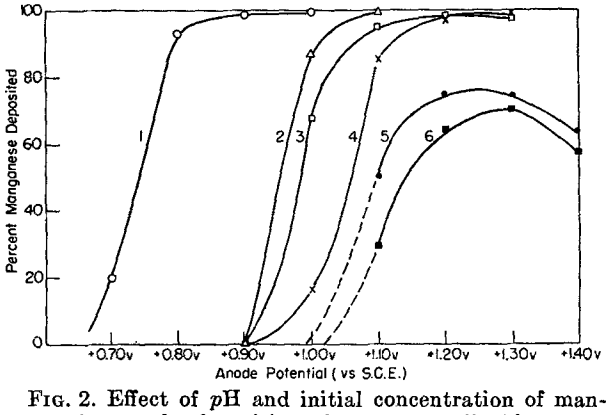

FIG. 2. Effect of *p*H and initial concentration of manganous ion on the deposition of manganese dioxide onto a 10 cm^2 platinum gauze electrode from 150 ml of 0.5M KNO_3 with an internal cathode.

	1. ○	2. △	3. □	4. ×	5. ●	6. ■
(Mn^{++})	10^{-5}M	10^{-6}M	7×10^{-6}M	3×10^{-6}M	3×10^{-7}M	2×10^{-7}M
Initial *p*H	4.69	3.04	2.53	2.82	2.89	2.89
Final *p*H	6.38	3.39	2.45	2.73	2.79	2.76

by itself would do so. An electrolysis was usually carried out at a particular potential for at least 3 hr or until a constant counting rate indicated that equilibrium had been reached. Duplicate aliquots were withdrawn using 1.00 ml pipets, transferred to lacquer-coated aluminum of copper cups, and counted according to the method or Freedman and Hume (6) using an end-window Geiger-Mueller tube. Ordinarily, 2000 to 5000 counts were obtained on each sample within 2 hr of the sampling time. The range of the duplicates was less than 5% of the total count in every case.

After analysis of the solution, the potential was changed about 0.1 v more positive and the electrolytic procedure repeated. Because of the large volume of solution that was electrolyzed, the portions taken for counting could usually be neglected during the early part of a given run. Toward the end of a run when the accumulated volume of the aliquots became appreciable, a suitable correction was made in calculating the amount deposited.

In the studies of the rates of deposition of manganese and of lead, a polarographic determination of the lead remaining in the solution was made on a 0.50 ml aliquot using the conventional dropping mercury electrode and a Sargent Model XII polarograph. All analyses were made within 3 min of sampling to minimize evaporation. Preliminary standardization of seven lead samples ranging from 10^{-4}M to 10^{-2}M showed a coefficient of variation of ±2.7%.

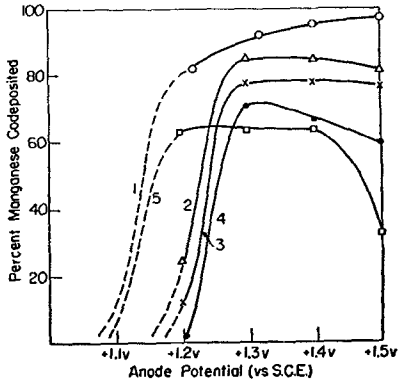

FIG. 3. Effect of anode potential on the per cent manganese coprecipitated with different amounts of lead dioxide onto a 13 cm^2 platinum gauze anode from 150 ml of 0.5M KNO_3.

	1. ○	2. △	3. ×	4. ●	5. □
mg Pb	200	80	40	20	10
Initial *p*H	2.80	2.82	2.82	2.85	2.89
Final *p*H	2.20 (internal cathode)	1.90	1.98	2.05	2.40

RESULTS

Anodic polarography of manganese.—Before starting the studies of codeposition, preliminary polarographic studies were made on solutions containing millimolar manganous nitrate in 0.1M sodium sulfate and H_2SO_4 in order to find the best conditions to use for the electrolysis. A Sargent Model XXI polarograph with a stationary platinum electrode was employed. Strictly speaking, results cannot be compared with deposition data obtained later on nitrate solutions but, since the two sets of data were consistent, it appeared unnecessary to repeat the polarograms.

Fig. 1 shows that the *p*H range from 1–3 is most suitable for an electrolytic study. Within that range the $E_{\frac{1}{4}}$'s are separated by about 120 mv/*p*H unit which is the shift with the fourth power of the hydrogen ion concentration predicted by the theoretical equation

$$Mn^{+2} + 2H_2O = MnO_2 + 4H^+ + 2e^-$$

At *p*H 2, changing the concentration of manganese to 10^{-4}M and 10^{-5}M produced successive shifts of +0.03 v also in agreement with predictions based upon the same equation. However, the formal potential was about 0.20 v more positive than the value predicted from the standard potential (7).

Effect of anode potential and pH on deposition.—As shown in Fig. 2, manganese in concentrations greater than 3×10^{-6}M could be deposited quantitatively in the absence of a carrier at a *p*H above 2.5. More important, however, is the decrease in recovery obtained at +1.40 v, presumably because of oxidation beyond the tetravalent state.

The effect of anode potential on the codeposition of manganese with different amounts of lead dioxide is shown by Fig. 3. Each of these solutions, which contained only tracer manganese of unknown concentration, had been

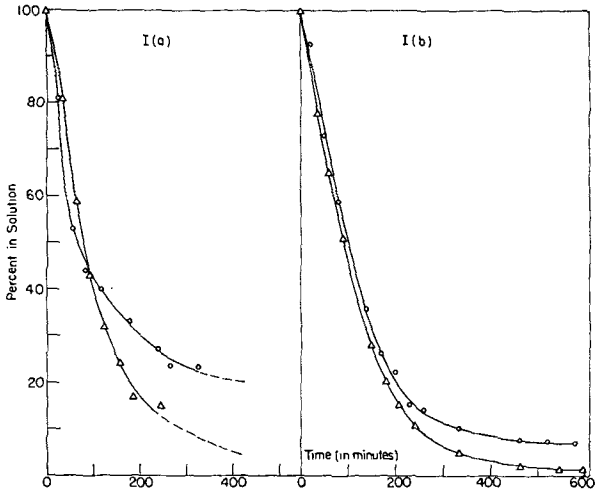

FIG. 4*a*. Rates of coprecipitation of manganese dioxide and simultaneous precipitation of lead dioxide onto a 39 cm² platinum gauze electrode from 160 ml of 0.5M KNO_3 at *p*H 1.0. Anode potential (vs. S.C.E.) 1.372 v; initial concentration, △, lead, I (a), 8.9×10^{-4}M, I (b), 2.52×10^{-3}M; ○, manganese, I (a), 4.8×10^{-8}M, I (b), 1.3×10^{-7}M.

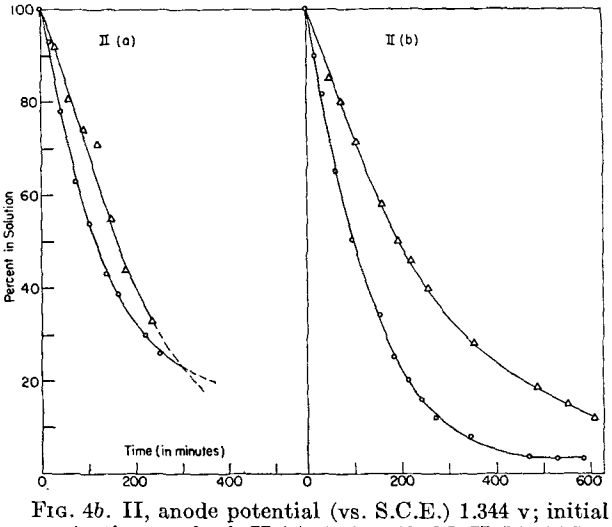

FIG. 4*b*. II, anode potential (vs. S.C.E.) 1.344 v; initial concentration, △, lead, II (a), 1.00×10^{-3}M, II (b), 2.75×10^{-3}M; ○, manganese, II (a), 3.0×10^{-7}M, II (b), 3.5×10^{-7}M.

electrolyzed for 12 hr at an anode potential of +1.20 v to insure that the manganese would not deposit on the platinum gauze anode in the absence of lead. After addition of the indicated amount of lead, electrolysis was allowed to proceed at each potential setting for 3 hr before measurement.

A decrease in *p*H during these electrolyses took place in accordance with the electrode reaction for the formation of lead dioxide.

$$Pb^{+2} + 2H_2O = PbO_2 + 4H^+ + 2e^-$$

In the only run, curve 1, where an internal platinum cathode was used, the final *p*H was out of line with the trend of a lower *p*H for a higher concentration of lead that was observed for the runs in which an external cathode was used. This anomalous behavior was probably due to cathodic evolution of hydrogen.

The downward trend of some of these curves at potentials greater than +1.4 v is again presumed to be due to oxidation of the manganese(II) to a valence higher than four. This was substantiated by the failure of manganese to coprecipitate when a potential of +1.5 v or greater was applied to an anode on which no previous precipitation had taken place. Decrease in deposition at high potentials was not so evident when the amount of lead carrier was increased, but this was probably due to burial of the manganese(IV) atoms within the lead dioxide lattice. The anomalous displacement of the 10 mg lead curve toward less positive potentials is probably due to the higher *p*H of that solution.

It is apparent from these curves that in the *p*H range from 2.7 to 3.0, the optimum anode potential for coprecipitation of manganese is between +1.3 v and +1.4 v (vs. S.C.E.). The upper limit of the anode potential should be dependent upon *p*H and concentration of manganous ion while the lower limit should be dependent not only upon these two factors but upon the concentration of lead ion as well.

Effects of initial lead and manganese concentrations.—To examine the effects of changes in lead and manganese concentrations on coprecipitation, a series of experiments was performed in which the electrolyses took place at a constant anode potential and continued until essentially all of the lead had been precipitated. Four different electrolytic cells (I–IV) were used and two runs (a, b) were made on each. During the course of each electrolysis, lead and manganese concentrations were determined frequently by polarographic and radiochemical methods, respectively. Manganese and lead concentrations were then plotted as functions of time in order to illustrate relative rates of deposition of the two components. Results are shown in Fig. 4.

Because of the high ratio of the initial lead-to-manganese concentrations used in these experiments, it appears safe to assume that the amount of manganese on the surface of the electrode deposit at any time is so small that the electrode has an activity essentially the same as an electrode of pure lead dioxide. Hence, at any given time during the electrolysis, the electrode must appear to the solution almost exactly the same as it did after the first few layers of lead dioxide had precipitated. If this assumption is true, one can select any point on the rate curve for lead, find the point on the rate curve for manganese for the same time, and use these concentrations of lead and manganese as initial values. Any one of such initial concentrations can be used to determine the fraction of manganese coprecipitated at the conclusion of the electrolysis. This procedure was used in three instances (Ib, IIa, IIIa) to evaluate the effect of different initial concentrations of lead on the fraction of manganese codeposited, starting with the same initial concentration of manganese.

For example, to compare runs Ia and Ib at the same initial manganese concentration one would select the time at which the manganese concentration in Ib equalled 4.8×10^{-8} M. This corresponds to 37% (0.48/1.3) of the

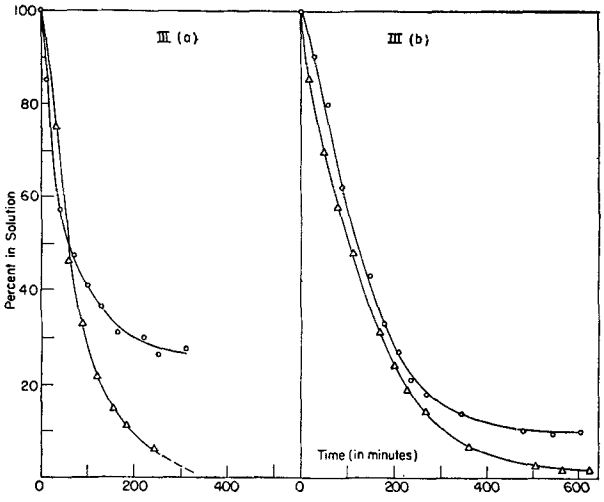

FIG. 4c. III, anode potential (vs. S.C.E.) 1.396 v; initial concentration, △, lead, III (a), 8.5×10^{-4}M, III (b), 3.10×10^{-3}M; ○, manganese, III (a), 4.5×10^{-8}M, III (b), 3.5×10^{-8}M.

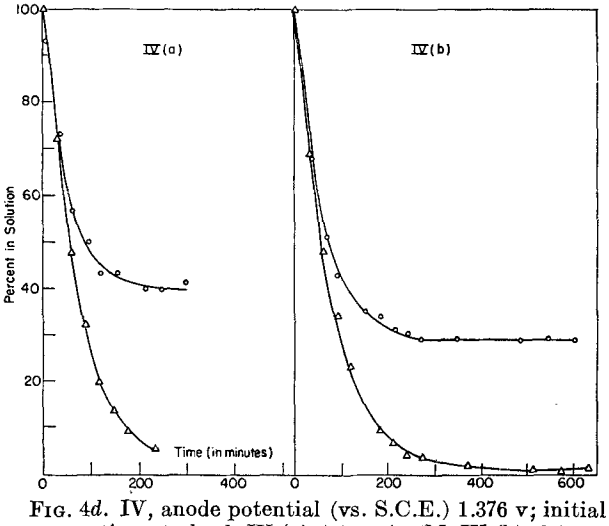

FIG. 4d. IV, anode potential (vs. S.C.E.) 1.376 v; initial concentration, △, lead, IV (a), 7.7×10^{-4}M, IV (b), 2.31×10^{-3}M; ○, manganese, IV (a), 1.4 ml tracer; IV (b), 4.3 ml tracer.

original manganese concentration of 1.3×10^{-7}M. At this same time, the lead concentration is seen to be 34% of the original 2.52×10^{-3}M and is therefore equal to 8.6×10^{-4}M. Using this time as a starting point, the fraction of manganese coprecipitated is the difference between 37% in solution at this starting point and 6.5% at the end of the electrolysis divided by 37% (37-6.5/37 = 0.82).

Table I illustrates the effect of initial concentration of lead at four different manganese concentrations and Table II illustrates the effect of initial concentration of manganese at two different lead concentrations. One can see positive correlation between the fraction of manganese coprecipitated and the initial concentration of lead. However, the effect of changes in the initial concentration of manganese is not clear from these data. In cells I, II, and III, increases of five to eightfold in initial concentration of manganese appeared to have little effect, but in cell IV,

TABLE I. *Effect of initial concentration of lead on the fraction of manganese codeposited*

Cell	Run	Initial concentration, M		Fraction of manganese codeposited
		Lead	Manganese	
IV	b	2.31×10^{-4}	1.4 ml tracer*	0.11
IV	a	7.7×10^{-4}	1.4 ml tracer*	0.60
I	b	8.6×10^{-4}	4.8×10^{-8}	0.82
I	a	8.9×10^{-4}	4.8×10^{-8}	0.77
III	a	7.2×10^{-4}	3.5×10^{-8}	0.65
III	b	3.10×10^{-3}	3.5×10^{-8}	0.91
II	a	1.00×10^{-3}	3.0×10^{-7}	0.80
II	b	2.47×10^{-3}	3.0×10^{-7}	0.97

* No inactive manganese was added to the stock solution and so its manganese concentration was unknown.

TABLE II. *Effect of initial concentration of manganese on the fraction codeposited with lead dioxide*

Cell	Run	Initial concentration, M		Fraction of manganese codeposited
		Manganese	Lead	
IV	a	1.4 ml tracer*	7.7×10^{-4}	0.60
I	a	3.7×10^{-8}	7.7×10^{-4}	0.70
III	a	3.8×10^{-8}	7.7×10^{-4}	0.68
II	a	1.9×10^{-7}	7.7×10^{-4}	0.69
IV	b	4.3 ml tracer*	2.31×10^{-3}	0.71
III	b	3.0×10^{-8}	2.31×10^{-3}	0.89
I	b	1.2×10^{-7}	2.31×10^{-3}	0.93
II	b	2.4×10^{-7}	2.31×10^{-3}	0.96

* No inactive manganese was added to the stock solution and so its manganese concentration was unknown.

where only tracer manganese was used, the fractional coprecipitation was significantly lower.

Coprecipitation of silver.—In order to examine briefly the possibility of coprecipitating other elements in a selective way, qualitative experiments were made with carrier-free silver (8). Using 180 ml portions of 0.1M $HClO_4$ containing silver-111 tracer and a 13 cm^2 platinum gauze anode, duplicate electrolyses were carried out successively for 1 hr at 0.10 v intervals from +1.50 to +2.00 v (vs. S.C.E.). At the end of each hour, the fraction of silver remaining in solution was determined by withdrawing duplicate 0.100 ml aliquots, evaporating to dryness on 1-in. watch glasses, and counting the radioactivity. The average range of the duplicates was less than 3% of the total count.

No deposition of silver was detected over the range from +1.50 to +2.00 v. However, after completion of the electrolysis at +2.00 v, 200 mg of lead was added (as 1.0 ml of lead nitrate solution) and the electrolysis continued for 3 hr at 2.00 v. At the end of that time, 96% of the silver had codeposited with lead dioxide in each cell.

Without removing the electrodes, the deposits were dissolved by allowing the electrodes to stand overnight with no potential applied. Repetition of the electrolyses at 0.1 v intervals showed that, although lead began to deposit at +1.35 v, no silver was deposited until +1.90 v. After 30 min at this potential, 25% of the silver had deposited. The potential was then changed to +2.00 v. After 30 min at this potential, 50% of the silver had deposited; after 3

TABLE III. *Effect on the manganese-lead dioxide exchange of opening the electrical circuit*

	% of Manganese deposited	
	Electrolytic coprecipitation	Coprecipitation plus exchange (open circuit)
I a	80	98
b	93	99
II a	80	97
b	97	99
III a	74	97
b	90	98
IV a	60	93
b	71	97

hr, 95%. Since potentials more positive than +2.0 v result in lower current efficiency due to concurrent oxygen evolution, the use of +2.0 v would appear to be close to optimum for making separations.

Discussion

It is clear from the results of this study, that the electrode potential was a major factor which controlled the anodic coprecipitation of manganese and of silver with lead dioxide. However, no quantitative statements can be made as yet. It appears that a relationship(s) analogous to those of Berthelot-Nernst and Doerner-Hoskins (9), which are used in chemical coprecipitation, should be applicable to electrolytic coprecipitation. However, the attainment of equilibrium conditions required by the former appears to be virtually impossible, especially when appreciable amounts of deposit are involved, because of the limited surface area of the deposit. With regard to the Doerner-Hoskins distribution, the condition that the composition of the outer layer of the deposit be proportional at all times to that of the solution would be attainable only in special cases.

In both expressions for chemical coprecipitation, the fractional coprecipitation of the trace depends on the fractional precipitation of the carrier, but is independent of the initial concentrations of both trace and carrier. The data in Table I and Fig. 4 show that the fractional electrolytic coprecipitation of a trace under the prescribed conditions was independent of the fractional precipitation of the carrier but strongly dependent on the initial concentration of the carrier. Thus, larger concentrations of lead resulted in more nearly complete precipitation of manganese. Unfortunately, the data in Table II indicate no clear-cut effect of changes in the initial concentration of manganese upon its fractional coprecipitation. In any event, it is clear that the electrolytic process of coprecipitation is affected by experimental variables in a way different from the chemical process.

It is clear from runs 4a and 4b in Fig. 4 that the exchange of manganese in solution with lead in the electrode did not take place at an appreciable rate as long as the electrical circuit was closed. It was, therefore, interesting to note that rapid exchange occurred upon opening the circuit. Table III shows the results obtained by disconnecting the anode after each of the runs in Fig. 4 and allowing it to remain in contact with the solution for 12 hr. In each case analyses showed that much of the lead dioxide had redissolved while most of the manganese had deposited. These few experiments would appear to indicate that a mechanism like the following might be operating:

$$Mn^{2+} + Pb^{4+} = Pb^{3+} + Mn^{3+} \text{ (rapid)} \quad \text{(I)}$$

$$Pb^{3+} \text{ (at electrode)} = Pb^{4+} + \text{electron (rapid)} \quad \text{(II)}$$

$$Pb^{3+} + Mn^{3+} = Pb^{++} + Mn^{4+} \text{ (slow)} \quad \text{(III)}$$

Reaction (I) could occur whether the circuit were open or closed. At open circuit, reaction (III) would be able to proceed, whereas reaction (II) could not. Trivalent manganese could disproportionate to the divalent and tetravalent states, but if this took place, it must have been at the electrode surface because most of the manganese was found in the deposit.

Further studies are now in progress to evaluate in more detail the effect of different experimental variables on the coprecipitation and to explore the possibilities of obtaining more nearly quantitative electrolytic coprecipitation of the trace.

Acknowledgment

One of the authors (J. T. B.) wishes to thank Merck and Co. for a fellowship that made this work possible. The other is indebted to the Atomic Energy Commission for partial support.

Manuscript received April 19, 1954. This paper was prepared for delivery before the Montreal Meeting, October 26 to 30, 1952.

Any discussion of this paper will appear in a Discussion Section to be published in the June 1957 Journal.

REFERENCES

1. O. A. Cook, *Nat. Nuclear Energy Ser.*, The Transuranic Elements, IV, 14-B, Part I, p. 160 (1949); see also MDDC 1657.
2. J. T. Byrne, *J. Chem. Phys.*, **19**, 504 (1951).
3. I. M. Kolthoff and E. B. Sandell, "Textbook of Quantitative Inorganic Analysis," p. 709, Revised Edition, Macmillan Co., New York (1943).
4. *Ibid.*, p. 699.
5. R. W. Lamphere, *Anal. Chem.*, **23**, 258 (1951).
6. A. J. Freedman and D. N. Hume, *Science*, **112**, 461 (1950).
7. W. M. Latimer, "Oxidation States of the Elements," 2nd ed., p. 228, Prentice-Hall, Inc., New York (1952).
8. J. C. Griess, Jr., and L. B. Rogers, *J. (and Trans.) Electrochem. Soc.*, **95**, 129 (1949).
9. N. A. Bonner and M. Kahn, "Radioactivity Applied to Chemistry," Edited by A. C. Wahl and N. A. Bonner, p. 106, John Wiley & Sons, New York (1951).

Use of Radioactive Mercury to Study the Relation of Mercury to Depreciation of Fluorescent Lamps

GEORGE BURNS AND JACOB KASTNER

Advanced Lamp Development Laboratory, General Electric Company, Nela Park, East Cleveland, Ohio

ABSTRACT

Radioactive mercury was used to determine whether there is any relationship between the depreciation of fluorescent lamps and the amount of mercury picked up on the lamp walls during lamp operation. It was found that early in lamp life there is no such relationship. However, after 1000–2000 hr, depending on the phosphor type, a relationship was established.

It has been postulated (1, 2) that mercury in one form or another is responsible for the darkening of fluorescent (F-) lamps. Some authors (3, 4) have discussed the interaction between mercury and the fluorescent powder and proposed reaction mechanisms. Attempts have even been made (5) to restrict the effect of mercury on depreciation to a specific period of the lamp life.

It was never shown, however, that there is any quantitative relationship between the mercury uptake and depreciation. This is because regular analytical methods of determining mercury uptake are difficult, are subject to many errors, and necessitate the use of a large number of samples to make the results meaningful. One must also destroy the lamp each time an analysis is made and so only one determination per lamp is possible.

With radioactive mercury (Hg 203), however, it was felt worthwhile to carry out an experiment which might provide unequivocal information about the relation of mercury to F-lamp depreciation. This isotope has a half-life of 44 days and emits beta and gamma rays of 200 and 300 electron kv, respectively. The use of this radioactive isotope enables one to follow mercury pick-up along with depreciation in a single nondestructive test. Also, possible errors in manufacturing a lamp could not influence the relationship between mercury and depreciation for that particular lamp. Therefore, this method enables one to study a variety of aspects of depreciation as related to the mercury pick-up. Effects of impurities (in the filling gas or phosphor), additives, and manufacturing processes might be successfully investigated. However, in the following experiment the authors restricted themselves to a study of the effect of phosphor type on mercury absorption.

DESCRIPTION OF EXPERIMENT

Lamp manufacture.—Standard 40 watt F-lamp bulbs were coated with suspensions of the following four phosphors: zinc silicate (activated with Mn^{+2}), calcium silicate (activated with Pb^{+2} and Mn^{+2}), magnesium arsenate (activated with Mn^{+4}), and magnesium lithium arsenate (activated with Mn^{+4}). Standard techniques for preparation of suspensions and for coating were used.

The lamps were prepared in the following way. The mercury-containing tube was sealed to the lower exhaust stem of the lamp. An oven which was vertical and short enough to allow the lower exhaust stem to protrude was put around the lamp and the lamp exhausted with no mercury dosage. Heat was applied for 5 min at 400°C. Cathodes were activated according to the standard schedule for rapid start lamps. There was, of course, no end glow. The lamp was flushed with 5 mm of argon and cooled. Mercury was then torched up from below and the bottom exhaust stem sealed about 2 in. from the lamp. Argon was introduced at about 3 mm and the lamp sealed off. The bottom stem was tipped off close to the flare and both ends based. After a number of trial runs, 9 radioactive lamps were made in this way. Eight lamps were manufactured in sets of two, with each set having a different phosphor. An additional variable was incorporated in the ninth lamp which was coated with heavily overmilled zinc silicate (24 hr of milling).

Measuring procedure.—It was assumed that mercury might deposit on the phosphors in three possible ways: (*a*) as droplets, (*b*) as a loosely adsorbed surface layer, and (*c*) as a tightly absorbed layer.

Since it has been shown that droplets cannot be related to depreciation (3), it was decided to remove them to the lower end of the lamp. This was done as soon as the lamps were finished and photometered in the standard way. The mercury was driven to the lower end by heating the upper three quarters of the lamp at about 90°C for 3 hr. Care was taken in all subsequent operations to position the upper end of the lamps above the lower in order to keep all the liquid mercury at the bottom.

To make sure no droplets were left at the top end of the lamp, x-ray, no-screen film (du Pont #508) was wrapped around the bulb and left on for 18 hr. With a rough calibration it is possible to make an estimate of the minimum size of radioactive mercury droplet which would be required to give a trace. Such an estimate has been made in Appendix I and indicates that the particles, if any, on the walls of the lamp at the upper end, must have been less than about 20 μ in diameter. Therefore, in all this work concern was only with loosely and tightly held Hg. The latter was defined as that which is held by the phosphor so strongly that it cannot evaporate into the arc even if all the vapor above it has been removed to the point where the discharge is characteristic of pure argon.

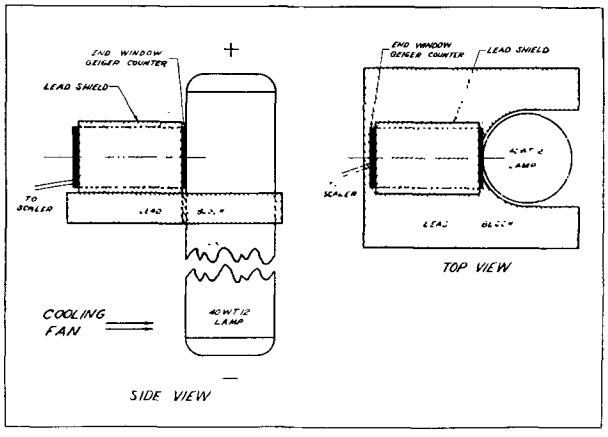

FIG. 1. Schematic diagram of apparatus

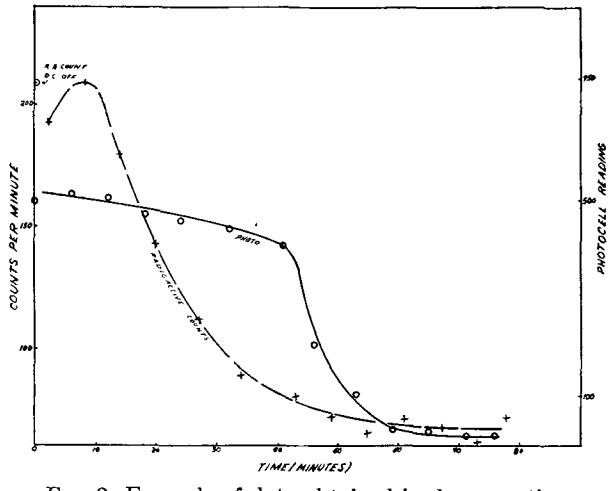

FIG. 2. Example of data obtained in d-c operation

The removal of vapor-phase Hg was achieved by operating the lamp on direct current. The bottom ends were held negative and cooled with a fan. A counting rack was supplied with 250 volts d.c. The lamp was started with a spark coil and a photocell applied periodically to the area of the lamp under investigation. The photocell current was read by means of a G.E. galvanometer. As the Hg vapor was pulled down and away from the photocell area, the light output eventually dropped quickly. No external heating of the lamp was applied during these operations. Various counting and detection methods were tried. The final set-up for counting is sketched in Fig. 1. A Nuclear Chicago Scaler Model 172 was used with a Nuclear Chicago #34 end-window beta counter. Five-minute counts were made alternately with the photocell introduced in place of the Geiger counter. This procedure of d-c counting was carried out each time after operating the lamps under a.c. for 0, 100, 500, and 1500 hr.

RESULTS AND OBSERVATIONS

Observation under d-c operation.—A typical graph obtained under d-c operation is given in Fig. 2. Although initially the counting data were somewhat erratic, at 500 and 1500 hr of a-c burning the curves were relatively smooth. The only deviation from a monotonic decrease was a slight rise in count rate immediately after a lamp was started on d-c operation and had burned for a few minutes.

In the case of two phosphors, i.e., magnesium arsenate and zinc silicate, fairly steep slopes in the count-rate curve were observed at the beginning of d-c operation. That this rapid drop in count rate was not due to a decrease in the amount of mercury in the vapor phase was shown by estimating how much the latter could contribute to the count rate. The calculations on which the estimate was based are given in Appendix II and show that the contribution due to the vapor was at the most no more than room background.

Furthermore, the mercury concentration in the vapor phase remained approximately constant, in spite of the rapid drop in count rate. This was shown by the initial steadiness of the light output as measured by the photocell.

This confirmed the preliminary hypothesis that Hg could be held loosely on the walls of the lamp. The light output remained constant as long as the vapor phase removed by d.c. was compensated by the Hg evolution from the phosphor. When this was no longer the case, the light output dropped radically (see the photocurve of Fig. 2).

The fact that a distinct point could be reached in these counting and photocell observations where insufficient Hg was available for the maintenance of light does not necessarily mean that the remainder of the mercury on the wall was tightly held. It should be emphasized, however, that the mercury remaining on the lamp wall proved to be held far more tenaciously after the light drop than before. This can be seen by comparing the initial steepness with the final slope of the count-rate curve in Fig. 2. To check on the possibility of a further change in the final slope with time, a lamp was left running under d-c operation for 18 hr. There was little change in count rate.

Relatively heavy overmilling of the zinc silicate phosphor had little effect on the Hg adsorption.

Tightly Held Mercury

The most important of the large mass of data accumulated in this experiment have been collected in Table I. It was assumed that no mercury was tightly held at zero hours.

For all phosphors, the amount of tightly held Hg increased with time of burning. Further, more of this mercury was taken up per hour in the first 100 hr than in the remainder of the time. It is also evident that different phosphors held (tightly) quite different amounts of mercury, e.g., after the lamps burned for 1500 hr, magnesium arsenate held about six times as much as calcium silicate.

There was remarkable agreement between lamps of the same phosphor. Striking exceptions, however, were the lamps with the magnesium lithium arsenate. For some reason, one of these lamps depreciated much more than the other and also picked up more mercury.

In analyzing these results, various ways of relating depreciation to mercury uptake in the phosphors were tried. Plots were made against time of burning for different functions of R, (the tightly held mercury) and L_t, (the lumen

TABLE I. *Lumens and relative mercury uptakes against hours of lamp burning*

Lamp code No.	0 Hr		100 Hr			500 Hr			1500 Hr		
	lumens	Relative "loose" Hg	lumens	Relative "loose" Hg	Relative "tight" Hg	lumens	Relative "loose" Hg	Relative "tight" Hg	lumens	Relative "loose" Hg	Relative "tight" Hg
GR13	3560	15	3154	168	47	2632	180	100	2000	128	152
GR10	3460	29	2938	196	61	2388	400	107	1892	215	155
GR2, 11	3070	2	2808	160	46	2364	128	106	1900	140	200?
CS13	2000	11	1825	10	34	1777	4	76	1670	55	140
CS14	1935	32	1793	107?	37	1746	20	82	1634	30	160
MgAs9	634	11	478	12	120	416	130	320	261	1440	860
MgAs11	600	37	485	16	111	433	196	354	268	920	900
MgLiAs5	513	12	511	48	59	478	41	155	380	15	377
MgLiAs4	568	10	476	56	60	402	175	211	270	146	556

Phosphor type:	GR	GR2	CS	MgAs	MgLiAs
	Zinc silicate	Overmilled zinc silicate	Calcium silicate	Magnesium arsenate	Magnesium lithium arsenate

Notes: 1. "Loose" Hg = DC off (t) -- Tight Hg. 2. "Tight" Hg = Final Level (t).

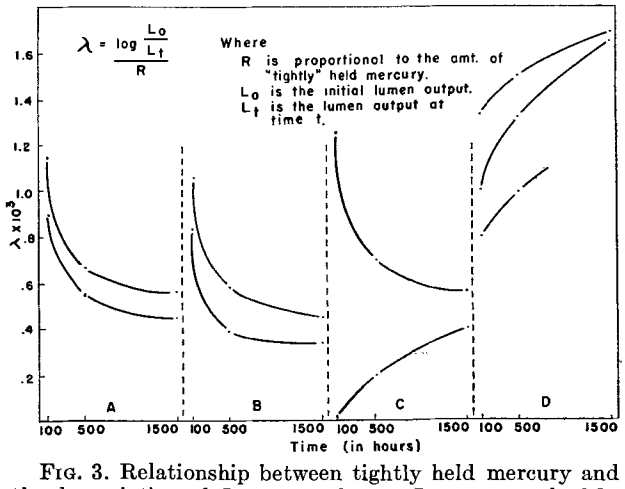

FIG. 3. Relationship between tightly held mercury and the depreciation of fluorescent lamps. Lamps coated with: A, calcium silicate; B, magnesium arsenate; C, magnesium lithium arsenate; D, zinc silicate.

output at time t). Probably the best description of the situation is given in Fig. 3 in which the ratio is plotted,

$$\lambda = \left(\frac{\log L_0/L_t}{R}\right)$$

Should λ prove to be constant with time a direct relation will have been established.

A study of Fig. 3 brings out clearly the fact that no definite relationship exists in the first 1000 hr or so between tightly held mercury and the depreciation of these lamps. Again, the fortuitous difference in behavior between the two magnesium lithium arsenate lamps is useful in that it emphasizes this point. The very poor magnesium lithium arsenate lamp has initially a very high λ which means a high depreciation per unit Hg uptake. This is true for the poor magnesium arsenate lamps as well, whereas the calcium silicate lamps have similar curves and yet depreciated very little. On the other hand, the good magnesium lithium arsenate lamp displays a curve similar to the green GR lamps which are relatively poor. Further evidence of the lack of a relationship of tightly held Hg to lumen drop in the first 1000 hr is seen, for example, in the results of the lamp # MgLiAs5 given in Table I. At 100 hr the "tight" Hg reading was as high as 59 even though there was no depreciation.

Because the lamps were manufactured as much as possible in the same way, the large difference in the λ's for the two magnesium lithium arsenate lamps is most likely due to small amounts of residual impurities as a result of improper lehring and exhaust. It seems reasonable, therefore, to conclude that in some cases the depreciation is governed in the first 1000 hr solely by impurities rather than by either Hg uptake or phosphor type.

In contrast to the preceding observations, for all phosphors λ approaches a constant after 1000 hr of burning. This point is particularly well demonstrated again by the two magnesium lithium arsenate curves. Although the lamps exhibited entirely different behavior, their λ curves approach each other asymptotically at $t > 1500$ hr. Thus, eventually, there does seem to exist a relation between the residual tightly held Hg and lumen output of the form:

$$L_t = L_0 e^{-\lambda R}$$

It should be noted that there is no experimental information about the behavior of these lamps after 1500 hr. Therefore, one is not actually justified to conclude with certainty that λ will not change at some future time in lamp operation. However, it is well known that after 1500 hr fluorescent lamp characteristics are substantially stable and change, if at all, very slowly with time. In fact, for some of these lamps, e.g., those with magnesium arsenate, λ proved to be constant within experimental error for as much as 1000 hr of burning, making it extremely unlikely for a change to occur later. Furthermore, the two magnesium lithium arsenate curves, although exhibiting ini-

TABLE II. *Comparison of lumens and tightly held* Hg *after baking and burning lamps for 100 hr*

Lamp No.	1500 Hours		Baked		100 Hours later		Remarks
	Lumens (1)	Tight Hg (2)	Lumens (3)	Tight Hg (4)	Lumens (5)	Tight Hg (6)	
GR13	2000	152	2216	336 (?)	2055	140	Baked at 300°C no fan
GR10	1895	155	2324	71	1990	125	Baked at 350°C with fan
MgAs9	261	860	470	96	343	345	Baked at 350°C with fan
MgLiAs5	380	377	475	110	446	137	Baked at 350°C with fan

Note: Lumen change $\propto$ Hg, e.g., for GR10, $\frac{(3) - (1)}{(2) - (4)} \leqq \frac{(3) - (5)}{(6) - (4)}$.

tially completely different slopes, still approach the same value, thus strongly suggesting no further change in λ.

Since λ is very small, $\sim 10^{-3}$, the relation may well be linear (i.e., $L_t = L_0 (1 - \lambda R)$. Assuming that the tightly held Hg causes depreciation by absorbing radiation, then a true linear relation would imply that this is a surface phenomenon. In other words, mercury is held tightly to the surface and acts only to screen the radiation. At 1500 hr as much as 50% of the phosphor surface might be covered by a monoatomic Hg layer (*see* Appendix III). If all this mercury were deposited on the surface of the phosphor next to the arc, the depreciation would certainly be significant and the relation linear.

However, should the mercury be taken up in the depth of the phosphor layer or within the individual particles, the relation would be logarithmic since the earliest absorption of Hg would tend to have the greatest effect.

If the mercury is indeed distributed throughout the phosphor layer, some of it could penetrate to the glass wall and be absorbed there. To check this possibility, an 8-in. section was cut from each lamp about 1 ft from the top end, using the proper precautions to avoid radiation hazard and taking care not to disturb the phosphor. A small Geiger tube was centered within the section and the radiation counted for 5 min. The section was then washed with dilute followed by concentrated nitric acid and a similar count made again. The washing was carried out a couple of times to insure complete removal of the phosphor and its mercury.

The results of this experiment showed definitely that between 10 and 20% of the mercury on the wall was retained in the glass itself, at least to the degree that it could not be removed by successive washings with nitric acid.

This information leads to the conclusion that the relation is more likely to be logarithmic, but it does not tell whether the mercury has actually penetrated the phosphor particles. To resolve this question an attempt was made to determine the order of magnitude of the activation energy for desorption of the tightly held mercury. Several lamps were heated using a vertical oven with 10 in. of the lower end of the lamp protruding and being cooled by a fan. The lamps were heated for approximately 2–3 hr at 300°–350°C. A 5-min count was carried out immediately upon cooling. The lamps were photometered in the usual way, burned vertically on a.c. for 100 hr and photometered again. They were finally counted in the usual d-c operation.

The results given in Table II show fairly well that residual mercury is held quite tightly, requiring at least 350°C to be dislodged. This activation energy is about half that necessary for the preparation of phosphors (about 1400°K). Thus, the phosphor-Hg binding energy is fairly high and therefore the Hg is more likely to be within the particle.

It should also be noted that there is a strong indication of the proportionality of tightly held mercury to lumen drop. The extra 100 hr burning effects a remarkably quick pickup or recovery of the tightly held mercury. This is, of course, associated with the characteristic rapid drop in lumens under such conditions.

The fact that a relation exists, however, does not prove that Hg is actually a primary cause of depreciation even after 1500 hr. There are three possible ways in which a relationship could arise.

(*A*) Hg may be the primary responsible agent, i.e., as indicated above, it may have a straightforward screening action. If this is the case, λ should be identical for all phosphors. In Fig. 3, however, note that $\lambda > 1500$ for the zinc silicate is at least 3 to 4 times greater than for the other lamps. This eliminates the first possible reason.

(*B*) Lumen-loss may be caused by Hg pickup which, in turn, is the result of some other primary agent (say, crystal imperfections). In this case it is reasonable to assume that λ is a function of the primary agent only. That enough Hg is present on the walls of the lamp to cause depreciation directly is shown in Appendix III.

(*C*) Hg pickup might be simply a side effect of lumen depreciation actually caused directly by another agent. The experiment of the authors cannot distinguish between case (*B*) and (*C*).

Loosely Held Mercury

It was evident as early as at 100 hr that some lamps picked up more loose mercury than did others (*see* Table I). This became much more definite as the lamps burned. Lamps which showed the greatest eventual depreciation tended to take up the largest amounts of loosely held mercury. This can be seen, for example, if one compares poor magnesium arsenate and zinc silicate coated lamps with the lamps coated with calcium silicate. In the case of magnesium lithium arsenate the lamp with abnormally high depreciation characteristics (code number MgLiAs4) also showed higher concentrations of loosely held mercury than the better lamp (code number MgLiAs5).

Thus, the amount of loose mercury seemed to be a good symptom of how poor the lamp was in terms of depreciation. It was not possible, however, to obtain any quantitative correlation.

To determine whether there was any direct effect of

loosely held mercury on depreciation, lamps were photometered immediately before and after d-c operation at 100 hr. During the d-c operation, the mercury was pulled down from the upper half of the lamp. Although the lamps had depreciated in the first 100 hr of their burning by as much as 30%, there was no significant difference in the photometric results before and after the d-c operation. Thus it is concluded that loosely held mercury cannot be responsible for depreciation.

Even though the loose mercury is an indication of the depreciation which has occurred in the lamps in the first 1000 hr or so of burning, such a relation is not quantitatively evident for the tightly held mercury. However, as noted before, the amount of tight mercury does increase also with burning. This is natural because larger amounts of loosely deposited Hg should produce, by diffusion, larger deposits of tightly held Hg.

Conclusions

A nondestructive experiment with little hazard has been designed, using Hg 203, to determine the relative amounts of mercury takeup by various phosphors. The following information was obtained.

In the first 1000 hr or so of burning there is no evident relation between tightly held Hg uptake and depreciation.

The loose Hg uptake is a strong symptom of the depreciating tendency of a lamp, but cannot be the direct cause.

After 1000 or so hours there exists a direct relation between tightly held Hg and depreciation. Whether the Hg at this time is an effect of, or a cause of, depreciation cannot be determined explicitly from this experiment.

Over 10% of the tightly held mercury is retained in the glass itself and cannot be removed by nitric acid.

Acknowledgments

The authors wish to acknowledge the interest and encouragement of their research director, D. E. Elmendorf. They are indebted, also, to their colleagues in various departments of the Lamp Division of the General Electric Company for their varied contributions and assistance.

Manuscript received February 3, 1956.

Any discussion of this paper will appear in a Discussion Section to be published in the June 1957 Journal.

APPENDIX I

Estimate of Size of Hg *Droplets Detectable by Autoradiography*

Calibration of the x-ray film showed that about 10 milliroentgens (mr) were required to give detectable density.

The output at a meter (6) from one millicurie of Hg 203 is about 0.15 mrhm.

Thus, to obtain 10 mr at 1 mm (glass wall thickness) after 18 hr exposure there is required

$$\left(\frac{10\text{ mr}}{0.15\text{ mrhm}}\right)\left(\frac{1\text{ mm}}{1\text{ meter}}\right)^2\left(\frac{1}{18}\right) \approx 3.5 \times 10^{-6}\text{ mc}$$

The specific activity of the sample was 1 mc/50 mg. $\therefore$ 3.5×10^{-6} mc corresponds to $3.5 \times 10^{-6} \times 50 = 0.2$ μg. The density of Hg is 14 g/cc.

$$\therefore 0.2\ \mu\text{g} = \frac{0.2 \times 10^{-6}}{14} \approx 10^{-8}\text{ cc}$$

The radius of a spherical droplet of this size is the order of 10^{-3} cm or 10 μ.

APPENDIX II

Estimate of Count Rate Due to Hg *Vapor*

The following calculations yield an estimate of the count rate obtained (by the apparatus of Fig. 1) as a result of the Hg initially present in the vapor phase of the lamps.

The total Hg in the form of vapor (8 μ) amounts to about 0.1 mg, volume of lamp is 1200 cc, specific activity of Hg 203 is 20 mc/g.

$$\therefore \frac{0.1 \times 10^{-3}}{1200} = 0.8 \times 10^{-7}\text{ g/cc}$$

and $0.8 \times 10^{-7} \times 20 = 16 \times 10^{-7}$ mc/cc.

The volume viewed by the GM counter is 20 cc, but not all of this volume contributes equally to the count rate. The size of the contribution due to any element of volume depends upon the solid angle it subtends at the counter, i.e., on how near it is. Dividing the volume into layers perpendicular to the counter axis and adding up the solid angles due to each layer shows that the "geometry" is about 5%. This means that the counter can receive only $0.05 \times 16 \times 10^{-7} \times 20 = 16 \times 10^{-7}$ mc.

The counter, in turn, does not respond to every gamma ray which enters. In fact, the efficiency of the beta counter is only 0.1% for rays of 0.3 mev energy (7).

Thus, the counter records only about 16×10^{-10} mc. One mc = 2.2×10^9 counts/min. The count rate due to the vapor phase is therefore estimated to be about $16 \times 10^{-10} \times 2.2 \times 10^9 = 3.5$ counts/min. This should be compared with the background count rate of 13 counts/min.

APPENDIX III

Estimate of Amount of Hg *on Walls after 1500 Hr*

There are approximately 200 counts/min from 6 cm^2. If one assumes 50% geometry and a counter efficiency of 0.1%, this corresponds to

$$\frac{200 \times 2 \times 10^3}{60} \approx 7000\text{ disintegrations/sec}$$

or about 0.16 microcuries/6 cm^2, i.e., about 0.03 μc/cm^2.

The specific activity is 20 mc/g and therefore one has $\frac{0.03 \times 10^{-3}}{20}$ or about 1.5 μg/cm^2.

Since the number of atoms in 200 g of Hg is 6×10^{23}, 1.5 μg/cm^2 corresponds to

$$\frac{1.5 \times 10^{-6}}{200} \times 6 \times 10^{23} = 5 \times 10^{15}\text{ atoms/cm}^2$$

If one takes the diameter of a Hg atom to be 3Å one can spread out $\left(\frac{10^8}{3}\right)^2$ or about 10^{15} atoms on 1 cm^2. Thus one would have about 4 to 5 atomic layers if the surface were perfectly flat. Actually, the phosphor surface has 10 to 100 times the area of the flat glass surface. This means that one could have only as much as one-half of an atomic layer present on the walls of the lamp.

REFERENCES

1. H. C. Froelich, *Trans. Electrochem. Soc.*, **87**, 429 (1945).
2. E. F. Lowry, W. S. Frolock, and G. A. Meyers, *Illum. Eng.*, **41**, 859 (1946).
3. H. C. Froelich, *J. Appl. Phys.*, **17**, 573 (1946).
4. E. F. Lowry, *J. (and Trans.) Electrochem. Soc.*, **95**, 242 (1949).
5. E. F. Lowry, *Illum. Eng.*, **43**, 141 (1948).
6. W. V. Maynebord, *Brit. J. Radiol.*, Suppl. #2 (1950).
7. H. von Bradt, P. C. Jugelot, O. Huber, H. Medicus, T. Priswerk, and P. Scherrer, *Helv. Phys. Acta*, **19**, 77 (1946).

Cathodic Reduction of 3,4,5,6-Tetrachloro-*N*-(2-Dimethylaminoethyl)-Phthalimide

M. J. Allen and J. Ocampo

Research Department, CIBA Pharmaceutical Products, Summit, New Jersey

ABSTRACT

The cathodic reduction of 3,4,5,6-tetrachloro-*N*-(2-dimethylaminoethyl)-phthalimide to its respective isoindoline has been studied using a cadmium, lead, and mercury electrode. With the aqueous CH_3COOH–H_2SO_4 medium used, the electrode overpotentials were higher than in an aqueous H_2SO_4 medium. This contributed to obtaining higher efficiencies in the reduction process. The best yield and current efficiency was obtained using a lead cathode and a current density of 0.0493 amp/cm². The current efficiency obtained under constant current density conditions was improved considerably by use of controlled potential electrolysis at −1.10 v vs. S.C.E. At a potential of −0.68 v vs. S.C.E. the partially reduced product, 4,5,6,7-tetrachloro-2(2-dimethylaminoethyl)-3-hydroxyphthalimidine, was obtained.

The reduction of 3,4,5,6-tetrachloro-*N*-(2-dimethylaminoethyl)-phthalimide to the respective isoindoline and isolation as its dimethochloride derivative has been achieved using lithium aluminum hydride as the reducing agent (1). However, because of the low solubility of this substituted phthalimide in the solvents usually used in this chemical reduction with consequent low yield of product, it was decided to investigate the use of electrolysis for the reduction of this compound.

A number of phthalimides have been studied (2) and in general are readily reduced to the respective phthalimidine and isoindoline thus

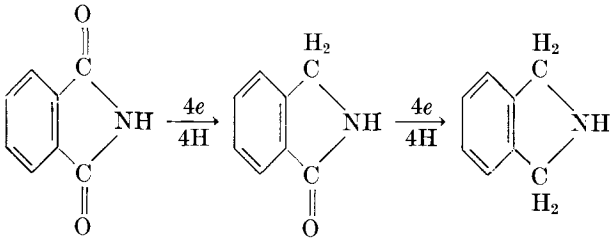

Although the reported yields of the isoindolines obtained were usually satisfactory, the current efficiency based on the yield of product was quite low. This low efficiency can be attributed to the following: in the medium commonly used, namely aqueous-H_2SO_4, the overpotential of the cathode was too low for the current densities used; as a consequence there was a large quantity of gas evolved at the cathode. Another reason for the low efficiency obtained by previous workers was that in many cases the depolarizer was not immediately soluble in the medium. As the limiting current depends on the concentration of the depolarizer, the current densities used were too high and, as a result, the excess current was utilized for the production of hydrogen gas.

The object of these experiments was, first, to develop a medium which would be both a good solvent for the 3,4,5,6-tetrachloro-*N*-(2-dimethylaminoethyl)-phthalimide and at the same time increase the overpotential of the cathode to that at which improved reduction efficiency could be obtained; second, to compare the effectiveness of various high overpotential electrodes such as cadmium, lead, and mercury for the preparation of 4,5,6,7-tetrachloro-2-(2-dimethylaminoethyl)-isoindoline; third, to compare the efficiency of the reaction at constant current density under the most ideal conditions with that obtained using controlled potential electrolysis; and, last, to determine the reaction path from the phthalimide to the isoindoline.

It has been reported (3) that the overpotential of the various cathodes studied is higher in a glacial CH_3COOH-H_2SO_4 medium than in an aqueous-H_2SO_4 medium. The tetrachlorophthalimide was quite soluble in this medium; however it could not be used as such, first, because the electrical resistance was too high, and, second, because the desired isoindoline was not obtained when the electrolysis was performed in this medium. It was found, however, that the substituted phthalimide was soluble in an aqueous solution containing CH_3COOH and H_2SO_4, for example 40% by volume of CH_3COOH and 12% by volume of H_2SO_4. The cathode potential vs. S.C.E. was determined for each of the electrodes used at the current densities which gave the optimum yields of isoindoline. These potentials were found to be higher in this medium than under comparable conditions in the aqueous H_2SO_4 medium. This was also indicated by the absence of hydrogen gas evolution at current densities at which gas evolution was obtained in an aqueous H_2SO_4 medium.

Experimental

Electrodes.—The cadmium electrode whose area was 78 cm² was prepared from pure sheet cadmium and subjected to pre-electrolysis in the aqueous-acetic-sulfuric acid prior to use. The 64.9 cm² lead electrode was purified by Tafel's method (4); the mercury was reagent grade. A platinum electrode served as the anode in all experiments.

Cells.—The cell used with the mercury cathode was

similar to that previously described (5). This gave an electrode area of 23.93 cm². The solid electrodes were used in a cell consisting essentially of two Pyrex pipe elbows held together by bolted flanges (Fig. 1). An Amberplex C-1 ion exchange membrane (Rohm and Haas Co., Philadelphia, Pa.) (E) was used to separate the anolyte from the catholyte. This membrane was chosen as a result of extensive tests to find a membrane which would give excellent conductivity with a minimum amount of diffusion. Thus it is possible to use a nonaqueous or partially aqueous working medium which, in this instance, is the catholyte and an aqueous nonworking medium The over-all result is a considerable improvement in conductivity when using the nonaqueous or partially aqueous systems so often needed to obtain solutions of organic substances. The cathode side of the cell contained a stirrer (A), thermometer (B), and the electrode (C) which was curved so as to make contact only with the glass along the electrode edge. This resulted essentially in a floating electrode whose lower surface was not shielded from current flow. Thus the current concentration was essentially the same on both surfaces. A saturated calomel reference electrode (F) was in contact with the working cathode through a salt bridge (G) in instances in which controlled potential conditions were utilized. The source of contact between the salt bridge and the working electrode consisted of a rubber policeman attached to the end of the glass bridge. The edge of the rubber policeman which makes contact with the working electrode is pierced with numerous asbestos fibers. The anode portion of the cell contained a platinum electrode (D). The whole cell was immersed in a bath for cooling or heating as dictated by the current density to maintain a temperature of 50°–55°C. This temperature gave the desired solubility to the concentration of depolarizer used.

Power supply.—The apparatus used for the controlled potential electrolysis was similar to that previously described (6). To use this instrument as a constant current device required the insertion of a 0.1 ohm resistor between the cathode lead and the cathode. The reference electrode lead is connected directly to the cathode. Current output is then controlled by the reference potential rheostat.

Electrolysis media.—In the cell used in conjunction with the cadmium or lead electrode, the catholyte consisted of 6.5 g of 3,4,5,6-tetrachloro-*N*-(2-dimethylaminoethyl)-phthalimide, 30 ml glacial CH_3COOH, 36 ml distilled water, and 9 ml concentrated H_2SO_4; the anolyte, 9 ml concentrated H_2SO_4 in 66 ml distilled water. The catholyte in the mercury cathode cell consisted of 5.2 g of the phthalimide, 24 ml glacial CH_3COOH, 28.8 ml distilled water, and 7.2 ml concentrated H_2SO_4.

Constant current density electrolysis.—The various current densities used are approximate multiples and fractions of an arbitrary limiting current (*Li*) obtained from the equation developed by Nernst (7) for electrolytic processes in which diffusion is the rate-determining step.

$$Li = 0.0223\ DCn$$

A value of 0.6 cm^{-2} day^{-1} was an arbitrary diffusion coefficient (*D*) assigned to the phthalimide on the assumption that it would be somewhat less than quinone. The concentration *C* in g moles/liter was 0.2435 and $n = 8$ based on

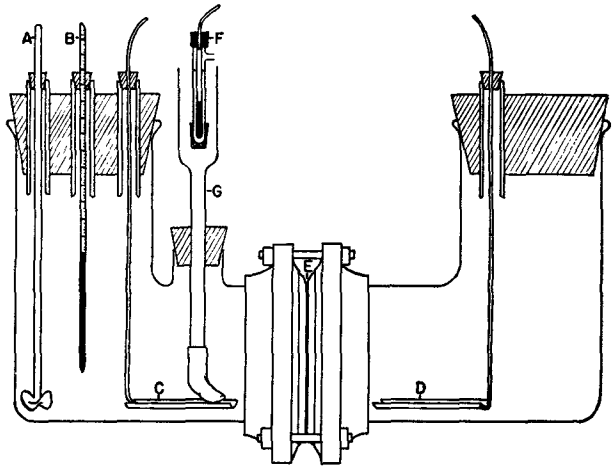

FIG. 1. Electrolysis cell

the fact that an 8-electron change occurs in going from the phthalimide to the isoindoline. Correction of the limiting current obtained for use at 55° gave a value of 0.0492 amp. No correction was made for agitation as it was thought the phthalimide was too slow a depolarizer to have this correction make any significant difference, especially as the limiting current value was merely an arbitrary focal point.

Procedure

4,5,6,7-Tetrachloro-2-(2-dimethylaminoethyl)-isoindoline and 4,5,6,7-tetrachloro-2-(2-dimethylaminoethyl)-phthalimidine.—Preliminary experiments indicated that it was necessary to pass at least twice the theoretical amount of current, calculated on the basis of an 8-electron change, to obtain the maximum yield under ideal conditions. Therefore, in all constant current density experiments in which 6.5 g of the depolarizer was used, 28,100 coulombs were passed and where 5.2 g was used, 22,530 coulombs were passed.

The products of electrolysis were isolated by making the catholyte, which had been first diluted with an equal volume of water and chopped ice, basic with aqueous NaOH. The precipitate which formed was extracted with ether, the ether extracts washed with water, dried over anhydrous Na_2SO_4, filtered, and then evaporated. The residue was triturated with warm pentane. In those experiments wherein the lower yields (less than 88%) of the completely reduced product was obtained, there was a partially reduced pentane-insoluble fraction which was 4,5,6,7-tetrachloro-2-(2-dimethylaminoethyl)-phthalimidine (III). Recrystallization of this product from ethanol gave white needles, m.p. 166°–67° (corr.); anal. found: C, 42.64; H, 3.70; N, 8.24; Cl, 41.29%. $C_{12}H_{12}ON_2Cl_4$ requires C, 42.33; H, 3.54; N, 8.19; Cl, 41.47%.

The fraction which was pentane soluble, 4,5,6,7-tetrachloro-2-(2-dimethylaminoethyl)-isoindoline (IV), was recovered by evaporation of the solvent. The oily residue on cooling formed platelets, m.p. 66–68° (corr.). Recrystallization from a small quantity of pentane gave pale yellow platelets, m.p. 69°–71° (corr.); anal. found: C, 44.22; H, 4.37; N, 8.48; Cl, 43.30%. $C_{12}H_{14}N_2Cl_4$ requires C, 43.93; H, 4.31; N, 8.54; Cl, 43.24%.

In all experiments it was possible to account for more

TABLE I. *Effect of current density on yield of isoindoline with various electrodes*

Cathode	C.D. (amp/cm²)	% Yield isoindoline	Current eff.
			%
Cd	0.0243	38.2	19.1
	0.0487	37.7	18.9
	0.0730	50.6	25.3
	0.0974	49.4	24.7
	0.1461	52.2	26.1
	0.1948	40.4	20.2
Pb	0.0243	90.5	45.2
	0.0493	91.1	45.6
	0.0770	56.4	28.2
	0.1190	53.9	27.0
	0.1540	52.0	26.0
	0.1950	39.6	19.8
Hg	0.0501	58.7	29.4
	0.1002	64.3	32.1
	0.1504	66.8	33.4
	0.2005	79.7	39.8
	0.2507	74.3	37.2
	0.3008	70.6	35.3

than 90% of the starting material based in the quantity of the phthalimidine and/or the isoindoline isolated.

Results obtained at the various current densities studied with cadmium, lead, and mercury are summarized in the Table I.

Controlled Potential Electrolysis

The potentials used in the following experiments were obtained from a voltammetric curve, the lower potential being approximately 0.1 v above that potential at which the current began to increase above the residual current. The higher potential was approximately 0.1 v below that which resulted in gas evolution at the electrode surface.

4,5,6,7-Tetrachloro-2-(2-dimethylaminoethyl)-isoindoline (IV).—The cathode used was a lead sheet whose area was 78 cm² previously treated according to Tafel's method and subjected to pre-electrolysis as a cathode in the aqueous-CH_3COOH-H_2SO_4 medium. The catholyte consisted of 6.5 g of the tetrachloro-phthalimide, dissolved in a solution of 30 ml glacial CH_3COOH, 36 ml distilled water, and 9 ml concentrated H_2SO_4; the anolyte a solution of 9 ml concentrated H_2SO_4 in 66 ml distilled water. The temperature was maintained at 50°–55°C throughout the course of the reaction. At a reference potential of −1.10 v vs. a S.C.E. the initial current density was 0.0589 amp/cm². After 80 min the current plateaued at a current density of 0.0143 amp/cm². From the area under the current vs. time curve the total number of coulombs passed was calculated as 15,280 coulombs. The catholyte was treated in the same manner as previously described. A yield of 5.05 (84.3%) of the isoindoline was obtained. The current efficiency in this instance was 77.7%.

4,5,6,7-Tetrachloro-2-(2-dimethylaminoethyl)-3-hydroxyphthalimidine (II).—The same experiment was performed at a reference potential of −0.68 v vs. S.C.E. The initial current density was 0.0189 amp/cm². After 70 min the current plateaued at 0.0107 amp/cm². The catholyte was made basic and the precipitate filtered and dried. Yield 4.31 g (66%), m.p. 158°–162°. Recrystallization from aqueous ethanol gave white crystals, m.p. 164°–165° (corr.); anal. found: C, 40.00; H, 3.45; N, 8.01; Cl, 39.15%. $C_{12}H_{12}N_2Cl_4O_2$ requires C, 40.24; H, 3.37; N, 7.82; Cl, 39.60%.

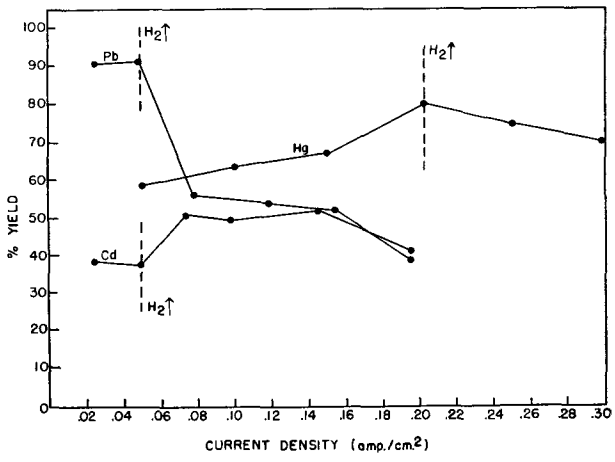

FIG. 2. Dependence of isoindoline yield on current density

DISCUSSION

From results obtained using constant current density it can be seen that with a lead cathode at a current density of 0.0493 amp/cm² the optimum yield and current efficiency is obtained. It is of interest that this is the current density obtained from the calculation of limiting current previously described. A plot of current density vs. yield of isoindoline obtained is shown in Fig. 2.

In the experiments with lead and mercury cathodes, the yield of product decreased when the current density was such that gas evolution occurred simultaneously with initiation of electrolysis. This is indicated in Fig. 2 by the current densities to the right of the vertical discontinuous lines. With cadmium the yield of product began to increase beyond the point at which gas evolution was simultaneous with onset of electrolysis and appeared to reach a plateau at 0.07 amp/cm². At this point the amount of gas evolved was moderate as compared to that at 0.048 amp/cm². Beyond the current density at 0.15 amp/cm² the product yield decreased again simultaneously with an increase in gas evolution. One explanation for this phenomena is to associate it with a catalytic effect in which the atomic hydrogen adsorbed on cadmium is a better reducing agent than atomic hydrogen adsorbed on lead or mercury. At the current densities which gave higher yields, conditions were such as to create this state at the electrode surface which enabled the depolarizer to be reduced more effectively than that prior to hydrogen evolution. Beyond the current density of 0.15 amp/cm² the amount of adsorbed hydrogen decreased, as indicated by a greater amount of gas evolution, resulting in a lower reduction efficiency.

The lead cathode may also exert such an effect as indicated by the higher yield of isoindoline obtainable with this electrode whose potential vs. S.C.E. in the aqueous CH_3COOH-H_2SO_4 medium containing the tetrachlorophthalimide appears to be lower than that of the mercury cathode at the current density which gave the maximum yield of isoindoline. Here, however, although difficult to distinguish one from the other, there may be a combination of

an overpotential effect plus a catalytic effect. As the current density is increased to the point at which the catalytic effect is brought to the foreground, the yields obtained parallel those observed at the cadmium electrode. With mercury one obtains a straightforward overpotential effect. The yield increases until the current density is reached at which the maximum effective reference potential vs. S.C.E. is obtained. Beyond that gas evolution takes place with consequent lower yields.

A comparison of the current efficiency obtained when the electrolysis was performed at a lead electrode under the optimum constant current density conditions and under controlled potential conditions shows that, with the former, the current efficiency is considerably lower (45.6%) than the 77.7% efficiency obtained using controlled potential. Thus, from these results, it is obvious that, even in instances wherein controlled potential electrolysis is not absolutely essential in directing the reaction path, providing the electrode is of proper potential to accomplish the reaction, it is important from the standpoint of the limiting current to be used which is dependent on the amount of unreacted depolarizer in the electrolysis medium.

From the products isolated the following may be considered to be the reaction path.

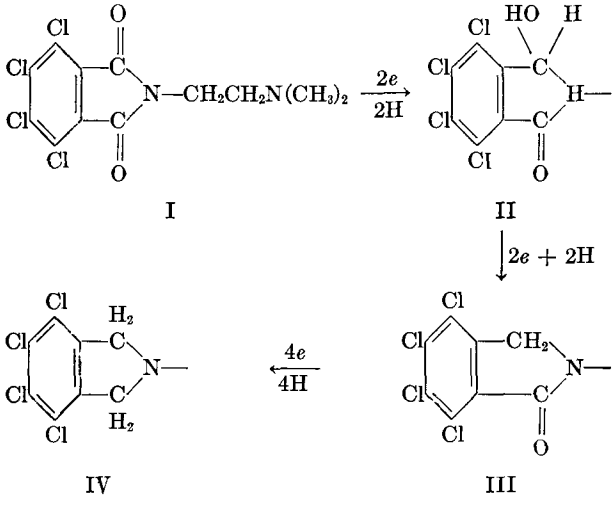

The fact that the hydroxyphthalimidine (II) was obtained at a lower potential than that required for reduction to the isoindoline is to be expected. A previous report (8) has shown that phthalimide can be reduced to hydroxyphthalimidine at a copper electrode. Use of a higher potential electrode, such as lead, resulted in reduction to phthalimidine which, in turn, could be further reduced to isoindoline (9). Reduction of both carbonyl groups does not appear to take place simultaneously for, if the reduction is allowed to proceed for approximately 45% of that required for twice theory for reduction of the tetrachlorophthalimide to the respective isoindoline, the major component isolated is the 4,5,6,7-tetrachloro-2-(2-dimethylaminoethyl)-phthalimidine (III) (78% of theory) with the balance of the isolated material being 4,5,6,7-tetrachloro-2-(2-dimethylaminoethyl)-isoindoline (IV) (10% of theory).

Conclusions

The efficiency of a high overpotential electrode for the reduction of a substituted phthalimide can be increased by utilizing a medium which will raise the overpotential of the electrode and also completely solubilize the depolarizer. This has been accomplished here by using an aqueous-CH_3COOH-H_2SO_4 medium.

It has been demonstrated that the reduction efficiency can be improved considerably by utilizing controlled potential electrolysis in preference to constant current density electrolysis. This can be attributed to the fact that essentially all the current is used for the reduction of the depolarizer, whereas under constant current density conditions, as the concentration of depolarizer diminishes, the excess current is used for the production of hydrogen gas.

The reduction of both carbonyl groups does not occur simultaneously but in a stepwise manner, with the hydroxyphthalimidine being intermediate to the formation of the phthalimidine.

Lead, although a lower potential electrode under the authors' experimental conditions than mercury, appears to exert some catalytic effect on the reduction process with resultant higher product yield and current efficiency.

Manuscript received October 21, 1955. This paper was prepared for delivery before the Pittsburgh Meeting, October 9 to 13, 1955.

Any discussion of this paper will appear in a Discussion Section to be published in the June 1957 Journal.

REFERENCES

1. C. F. Huebner, Private communication.
2. E. Späth and F. Breusch, *Monatsh.*, **50**, 349 (1928); B. Sakurai, *Bull. Chem. Soc. Japan*, **5**, 184 (1930); *ibid.*, **7**, 155 (1932); G. R. Clemo, R. Raper, and C. R. S. Tenniswood, *J. Chem. Soc.*, **1931**, 429; E. W. Cook and W. G. France, *J. Phys. Chem.*, **36**, 2383 (1932).
3. S. Swann, Jr., and E. O. Edelmann, *Trans. Am. Electrochem. Soc.*, **58**, 179 (1930).
4. J. Tafel, *Ber.*, **33**, 2209 (1900).
5. M. J. Allen, *J. Org. Chem.*, **15**, 435 (1950).
6. M. J. Allen, *Anal. Chem.*, **22**, 804 (1950).
7. E. Nernst, *Z. physik. Chem.*, **47**, 52 (1904).
8. B. Sakurai, *loc. cit.*, ref. (2).
9. E. Späth and F. Breusch, E. W. Cook and W. G. French, *loc. cit.*, ref. (2).

Polarographic Studies in Acetonitrile and Dimethylformamide

III. Behavior of Quinones and Hydroquinones

S. Wawzonek, R. Berkey, E. W. Blaha, and M. E. Runner[1]

Department of Chemistry, State University of Iowa, Iowa City, Iowa

ABSTRACT

Quinones were found to reduce stepwise to the semiquinones and hydroquinone dianions in anhydrous dimethylformamide and acetonitrile at the dropping mercury electrode. Evidence for this behavior was the shift in the second wave brought about by the presence of water and benzoic acid and the electrolytic reductive alkylation of one example, anthraquinone, by ethyl bromide to the diethyl ether of the hydroquinone. Hydroquinones are not oxidized at the dropping mercury electrode in anhydrous acetonitrile or dimethylformamide.

Work on the polarographic behavior of aromatic olefins and hydrocarbons in dimethylformamide and acetonitrile (1) has indicated that these solvents are suitable for studies of organic compounds. Studies have now been carried out with quinones and hydroquinones, examples of reversible organic systems. As in the previous work (1) the results in dimethylformamide were quite similar to those obtained in acetonitrile and will be dealt with together.

Experimental

Polarograms were obtained in a manner similar to that described previously (1). Characteristics for the various dropping mercury electrode used at 60 cm pressure for an open circuit are given in the various tables.

The solvents and supporting electrolytes were purified and prepared according to the directions mentioned earlier (1). The quinones and hydroquinones used were either obtained from stock or prepared according to directions given in the literature.

Electrolyses were carried out in a cell similar to that mentioned in the work on the reduction of hydrocarbons (1). No attempt was made to analyze the gases given off since it was assumed that the same volatile products would be obtained.

Electrolysis of anthraquinone alone.—A suspension of anthraquinone (5.0 g) in acetonitrile (250 ml), which was 0.156*M* in tetrabutylammonium bromide, was electrolyzed using a stirred mercury cathode and a platinum anode. A current starting at 0.58 amp was passed through the solution for 19 hr. The current at the end of this period was 0.10 amp. The color of the catholyte containing the suspended anthraquinone became magenta. As the electrolysis continued long finger-like yellow crystals of anthraquinone appeared on the sintered glass disk in the anode compartment; yield 3.6 g. No reduction products were identified in the solution. The hydroquinone dianion formed had apparently migrated to the anode compartment and had been oxidized either by the bromine liberated, or at the anode to anthraquinone.

[1] National Institute of Health Postdoctorate Fellow 1949–1950. Present address: Dept. of Chemistry, Illinois Institute of Technology, Chicago, Ill.

With ethyl bromide present during electrolysis.—Anthraquinone (5.0 g) and ethyl bromide (13.5 g) were electrolyzed in acetonitrile (300 ml) which was 0.175*M* in tetrabutylammonium bromide. The current starting at 0.7 amp and ending at 0.15 amp was passed through for 4 hr. The color and formation of anthraquinone needles occurred as in the previous example. The anthraquinone (3.2 g) was removed by filtration. The solution upon removal of the solvent gave a brown residue (22.3 g). Fractional crystallization from ethyl acetate gave tetrabutylammonium bromide (12.0 g) and the very soluble 9,10-diethoxyanthracene. Crystallization of the latter from ethanol gave a sample (1.3 g) melting at 143°–44° which was identified by comparison with an authentic sample (2).

With ethyl bromide added after electrolysis.—Anthraquinone (5.0 g) was electrolyzed in a solution of acetonitrile (180 ml) which was 0.26*M* in tetrabutylammonium bromide using a current of 1.3 amp. After 30 min the current was shut off and ethyl bromide (15.0 g) was added to the magenta colored catholyte and the resulting solution stirred for 2 hr. The unreacted anthraquinone (1.8 g) was filtered and the solvent removed from the resulting solution. The residue was dissolved in a small amount of ethanol and added to a large excess of water. Extraction with ether gave 9,10-diethoxyanthracene (0.3 g).

Electrolysis of benzoquinone.—Using a stirred mercury pool anode and cathode, a solution of benzoquinone (4.5 g) in acetonitrile (200 ml), which was 0.18*M* in tetrabutylammonium bromide, gave after electrolysis for 5 hr considerable tar in both compartments. Removal of the solvent gave a residue from which a trace of hydroquinone was sublimed by heating at 190° under reduced pressure (1 mm).

Reaction of potassium triiodide with 2-methyl-1,4-naphthohydroquinone.—A solution (20 ml) of 0.002*M* 2-methyl-1,4-naphthohydroquinone in acetonitrile when added to 25 ml of 0.001*M* KI_3 in acetonitrile did not decolorize the latter after a period of 8 hr. The addition of water (3 ml) to such a mixture (20 ml) caused decolorization in 6 min. Use of equal volumes of water and mixture caused immediate decolorization.

TABLE I. *Half-wave potentials, diffusion currents and diffusion current constants for various compounds in solutions containing 0.1M tetrabutylammonium bromide*

Quinone	Concn. millimoles/liter	i_d, 1st wave	i_d, 2nd wave	I_d[a] 1st wave	I_d[a] 2nd wave	E1/2(v) vs. Hg pool 1st wave	E1/2(v) vs. Hg pool 2nd wave	$0.059/n$[b] 1st wave	$0.059/n$[b] 2nd wave
Acetonitrile									
Benzoquinone[d]	1.00	4.67	3.58	3.07	2.35	−0.10[c]	−0.84	[c]	0.081
Duroquinone[d]	1.00	5.37	3.98	3.53	2.62	−0.33	−1.05	0.036	0.086
2-Methyl-1,4-naphthoquinone[d]	1.00	5.07	4.08	3.33	2.68	−0.27	−0.94	0.049	0.039
Anthraquinone[d]	1.00	4.97	3.78	3.27	2.49	−0.43	−1.05	0.050	0.048
Ethyl bromide[e]	4.86	52.7		6.35		−2.13			
Dimethylformamide									
Benzoquinone[e]	0.938	[c]	2.64	[c]	1.59	[c]	−0.92	[c]	0.107
2-Methyl-1,4-naphthoquinone[e]	1.15	4.34	3.46	2.14	1.70	−0.20	−1.02	0.085	0.093
2-Methyl-1,4-naphthoquinone[f,g]	1.12	4.07	4.05	2.12	2.10	−0.34	−1.05	0.083	0.125
Anthraquinone[e]	1.45	5.44	4.56	2.12	1.78	−0.34	−1.10	0.073	0.077
2-Methyl-1,4-naphthohydroquinone	No oxidation								
Hydroquinone	No oxidation								

[a] $I_d = \dfrac{i_d}{C m^{2/3} t^{1/6}}$.

[b] From current-voltage curve analysis.
[c] Maximum.
[d] Capillary with $m^{2/3}t^{1/6}$ of 1.52 $mg^{2/3}sec^{-1/2}$ and a droptime of 4.7 sec.
[e] Capillary with $m^{2/3}t^{1/6}$ of 1.77 $mg^{2/3}sec^{-1/2}$ and a droptime of 3.96 sec.
[f] Inert electrolyte, 0.1*M* $NaNO_3$.
[g] Capillary with $m^{2/3}t^{1/6}$ of 1.71 $mg^{2/3}sec^{-1/2}$ and a droptime of 4.28 sec.

TABLE II. *Effect of water and benzoic acid on the polarographic behavior of various quinones in solutions containing 0.1M tetrabutylammonium bromide*

Quinone	% Water by volume	i_d 1st wave	i_d 2nd wave	E1/2 (v) vs. Hg pool 1st wave	E1/2 (v) vs. Hg pool 2nd wave	$0.059/n$[a] 1st wave	$0.059/n$[a] 2nd wave
Acetonitrile							
Duroquinone[b]	0.5	5.27	3.98	−0.34	−0.76	0.115	0.075
	1.0	5.37	3.98	−0.33	−0.67	0.050	0.107
	2.44	5.57	3.78	−0.35	−0.62	0.051	0.097
	4.76	9.05	—	−0.39	—	0.115	—
2-Methyl-1,4-naphthoquinone[b]	1.0	4.97	3.78	−0.27	−0.66	0.060	0.079
	2.44	5.17	3.68	−0.29	−0.57	0.069	0.063
	4.76	4.97	3.78	−0.30	−0.50	0.049	0.071
Anthraquinone[b]	0.5	4.97	3.88	−0.45	−0.89	0.055	0.060
	1.0	4.97	3.78	−0.45	−0.83	0.035	0.063
	4.76	4.77	3.98	−0.48	−0.71	0.043	0.061
	20.0	8.05	—	−0.58	—	0.089	—
Benzoquinone[b]	1.0	4.67	3.28	−0.09[c]	−0.46	[c]	0.062
	4.76	4.27	2.78	−0.06	−0.28	0.020	0.049
Dimethylformamide							
Anthraquinone[d] and benzoic acid[e]	0	7.13	—	−0.33	—	0.069	—

[a] From current-voltage curve analysis.
[b] Concentration, 0.001*M*. Capillary with $m^{2/3}t^{1/6}$ of 1.52 $mg^{2/3}sec^{-1/2}$ and a droptime of 4.7 sec.
[c] Maximum interferes.
[d] Concentration 0.00106*M*. Capillary with $m^{2/3}t^{1/6}$ of 1.77 $mg^{2/3}sec^{-1/2}$ and a droptime of 3.96 sec.
[e] Concentration 0.0035*M*.

TABLE III. *Effect of water on the polarographic oxidation of 2-methyl-1,4-naphthohydroquinone in dimethylformamide with 0.1M $NaNO_3$ as the inert electrolyte*

Conc. millimoles/liter	% H_2O by volume	id/C[a]	E1/2 (v) vs. Hg pool	$0.059/n$[b]
2.24	0.5	5.09	+0.927	0.120
2.23	1.0	5.11	+0.889	0.103
2.22	1.48	5.00	+0.838	0.089
2.21	1.96	4.98	+0.863	0.062
3.20	1.96	4.94	+0.860	0.105
3.18	2.44	4.84	+0.886	0.110
3.10	4.76	4.71	+0.768	0.081
2.83	13.04	4.20	+0.671	0.108
2.72	16.66	3.82	+0.617	0.091
2.61	20.00	3.70	+0.543	0.103
2.17	33.33	3.24	+0.403	Max
1.86	42.86	2.96	+0.380	Max

[a] Capillary with $m^{2/3}t^{1/6}$ of 1.71 $mg^{2/3}sec^{-1/2}$ and a droptime of 4.28 sec.
[b] From current-voltage curve analysis.

Results

The polarographic data obtained for the various quinones are shown in Table I. The waves in all cases were well defined except for benzoquinone; a maximum was obtained for the first wave which could not be suppressed. To study the effect of acids on the reduction, the polarographic behavior of the quinones was studied in the presence of water and benzoic acid and is given in Table II.

The behavior of 2-methyl-1,4-naphthohydroquinone in acetonitrile and in dimethylformamide in the presence of various amounts of water is given in Tables III and IV.

TABLE IV. *Effect of water on the polarographic oxidation of 2-methyl-1,4-naphthohydroquinone in acetonitrile with 0.1M* $LiClO_4$ *as the inert electrolyte*

Conc. millimoles/liter	% H_2O by volume	*id*/C[a]	E1/2(v)[b]
1.25	0.0	No wave	No wave
1.24	0.5	No wave	No wave
1.23	1.48	8.70	+0.713
1.21	2.91	8.06	+0.623
1.19	4.76	7.53	+0.095
1.00	20.00	7.09	+0.062
0.83	33.33	6.80	+0.0620
0.71	42.86	6.39	+0.022

[a] Capillary with $m^{2/3}t^{1/6}$ of 1.62 $mg^{2/3}sec^{-1/2}$ and a drop-time of 5.13 sec.

[b] Slight maximum present.

Discussion of Results

Examination of data in Table I indicates that the reduction of quinones at the dropping mercury electrode in anhydrous acetonitrile and dimethylformamide proceeds first to the semiquinone and then to the hydroquinone dianion. The reactions involved are illustrated with benzoquinone:

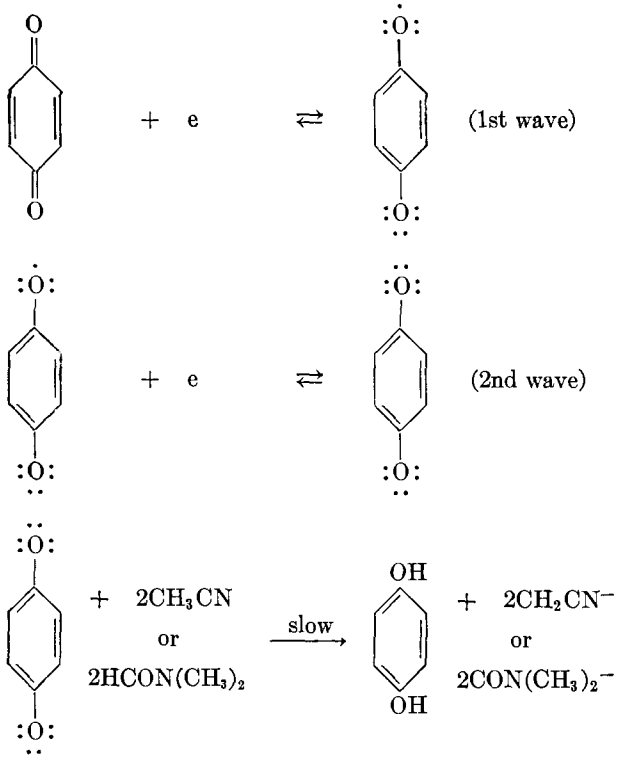

Analyses of the current-voltage curves were not consistent but approximated a one-electron change in a number of the examples and are in agreement with these steps.

Addition of water has no effect on the first wave (Table II) but causes the second wave to shift to more positive potentials. In the presence of a large amount of water the two waves merge and give a single wave approximately equal in height to the sum of the two waves obtained in anhydrous media. Benzoic acid being a stronger acid than water is effective at a much lower concentration in causing this shift to take place.

Since only the second wave is affected under these conditions, the following reactions are involved using the notation Q for quinone and S for the semiquinone or Q^-:

$$Q + e \rightleftarrows S$$
$$S + e \rightleftarrows Q^{--}$$
$$Q^{--} + 2H^+ \rightleftarrows QH_2 \text{ fast}$$

The potential of the dropping mercury at any point on the second wave should be given by

$$E_{d.e} = E^0 - \frac{RT}{n\mathbf{F}} \ln \frac{[Q^=]}{[S]}$$

Since the reaction of the quinone dianion with acid (or water) is rapid then $Q^=$ can be replaced by

$$Q^= = \frac{K[QH_2]}{[H^+]^2}$$

where K is the dissociation constant for the hydroquinone in the solvent involved. The first equation then becomes

$$E_{d.e} = E^0 - \frac{RT}{\mathbf{F}} \ln K \frac{[QH_2]}{[S]} + \frac{RT}{\mathbf{F}} \ln [H^+]^2$$

Addition of acid (or water) should shift the wave to more positive potentials and experimentally this phenomenon is observed.

This shift of the second wave with increasing acidity could also be explained by a relatively slow reaction between the

$$Q^= + H^+ \rightleftarrows QH^-$$

hydroquinone dianion and the acid since the surface concentration of $Q^=$ would decrease with increasing H^+. The first mechanism could be distinguished from this slow reaction since it predicts a quantitative shift with a change in H^+ concentration. Unfortunately not enough data were available to test this relationship.

The formation of dianions as the final products is substantiated by observations made during the polarographic reduction of anthraquinone and by the products isolated in the large-scale reduction of anthraquinone. In the former a red color has been observed surrounding the mercury drop. This phenomenon has also been reported by others (3). The coloration is similar to that observed when anthrahydroquinone is dissolved in aqueous alkali in the absence of air.

In the large-scale electrolytic reduction of anthraquinone the reduction product migrates to the anode compartment and is reoxidized to anthraquinone which crystallizes on the sintered glass disk separating the two compartments. The intermediate dianion persists even after the current is turned off since treatment of a solution, which had been electrolyzed for 30 min with a current of 1.3 amp, with ethyl bromide gave a 6% yield of 9,10-diethoxyanthracene.

Electrolysis when carried out in the presence of ethyl bromide for 4 hr with an average current of 0.5 amp, gave a 20% yield of the diether.

The reaction of the quinone dianion is very slow with

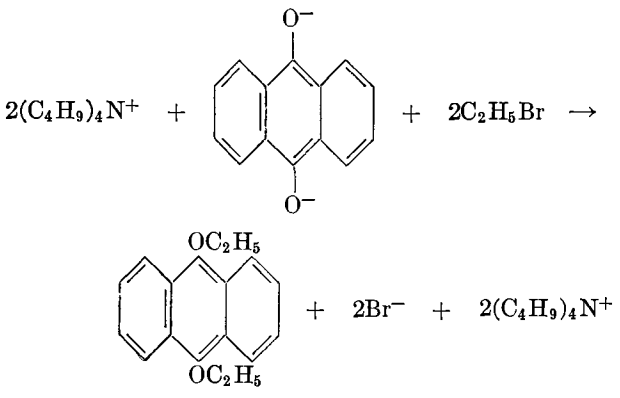

the anhydrous solvents since the yields of hydroquinone in electrolytic preparations were very low. The source of the protons is the same, however, as indicated for the reduction of unsaturated hydrocarbons (1).

The diffusion-current constants (I) for the two waves differ in each of the solvents studied; the second wave height is approximately 0.8 of that of the first wave. The reason for this difference is not known, but several explanations offer themselves.

The higher first wave may be caused by the disproportionation reaction reported to occur with semiquinones. The effective

$$2S + Q + Q^{=}$$

concentration of quinone would then become magnified by this step.

A second possibility involves the behavior of the semiquinone during the formation of the second wave. The semiquinone is negatively charged and could be repelled from the diffusion layer around the cathode into the bulk of the solution. The supporting electrolyte would not prevent this migration since only positive ions of the latter are in the vicinity of the cathode. This explanation is favored over the first since the ratio of wave heights is approximately the same for all of the quinones. If disproportionation were involved, the amount would be expected to vary with structure.

The oxidation of hydroquinone and of 2-methyl-1,4-naphthohydroquinone did not occur in anhydrous dimethylformamide or acetonitrile. Addition of water to the latter, as shown in Table III and IV, gave only one wave which shifted to more negative potentials with increasing amounts of water. The resistance of the hydroquinones to oxidation under these conditions indicates that ionization of the hydroquinones is a prerequisite for the oxidation of these compounds. Dimethylformamide and acetonitrile with dielectric constant of about 35 are poorer ionizing solvents than water and are responsible for this behavior. This property has been verified chemically by a study of the oxidation of 2-methyl-1,4-naphthohydroquinone by the triiodide ion. A solution of the two in anhydrous acetonitrile was stable for 8 hr. Addition of water accelerated the reaction; the use of a 15% water gave a reaction in 6 min.

Manuscript received January 13, 1956. This paper was prepared for delivery before the Pittsburgh Meeting, October 9 to 13, 1955, and is based in part on the theses of R. Berkey (1955) and E. W. Blaha (1954), State University of Iowa. The greater part of the research on this paper was done under A.E.C. Contract AT(11-1)-72, Project No. 6.

Any discussion of this paper will appear in a Discussion Section to be published in the June 1957 JOURNAL.

REFERENCES

1. S. WAWZONEK, E. W. BLAHA, R. BERKEY, AND M. E. RUNNER, *This Journal*, **102**, 235 (1955).
2. K. H. MEYER, *Ann.*, **379**, 72 (1911).
3. R. L. EDSBERG, D. EICHLIN, AND J. J. GAVIS, *Anal. Chem.*, **25**, 798 (1953).

Mechanism of Ozone Formation in the Silent Electric Discharge

J. C. Devins

Research Laboratory, General Electric Company, Schenectady, New York

ABSTRACT

The kinetics of ozone formation from oxygen have been studied in a Siemens ozonizer. Measurements were made at pressures from 70 to 400 mm and temperatures from −30° to −100°C. The results suggest that oxygen atoms, produced in the discharge, both form ozone by three body collisions with oxygen molecules and also destroy it, leading to a steady-state ozone concentration at sufficiently long residence times. The ratio of rate constants for these two reactions, and their activation energy difference, are similar to those found by Eucken and Patat in the photolysis of oxygen. At the higher temperatures, thermal ozone decomposition becomes an important factor in determining the steady-state ozone concentration. The variation of steady-state ozone concentration with pressure suggests that the combination of oxygen atoms and molecules to form ozone changes from termolecular to bimolecular in the pressure range investigated. The lifetime of the activated ozone complex, thus measured, is of the expected order of magnitude for the number of vibrational degrees of freedom involved. The possible role of other ozone destruction reactions is also considered.

Ozone is formed by the interaction of ionizing radiations with oxygen as well as by most types of gas discharges in oxygen (1, 2). A steady-state ozone concentration is attained, the value of which depends largely upon the system used. In general, it increases with increasing pressure and decreasing temperature, and in some cases is dependent upon the nature of the containing walls.

In a low temperature discharge plasma, the energy leading to chemical reaction is transferred to molecules by the faster electrons on the tail of an energy distribution approximating Maxwellian, to produce electronically excited states and ions. Assume as a first hypothesis that the ions, if they contribute appreciably to the over-all reaction, do so after neutralization, leading to electronically excited molecules and atoms (3). The excited molecules and atoms may then undergo reactions in a manner similar to that in which they occur in photochemical systems. It is the purpose of this work to study the kinetics of oxygen decomposition in the discharge, and to compare them with those of the photolytic reaction, in an effort to determine the validity of this hypothesis.

The limiting quantum yield, ϕ, for ozone formation at small conversions has been found to be about 2 over the wave-length range from 1295 to 2070Å (4), strongly suggesting the reactions:

$$O_2 + h\nu \xrightarrow{I_a} 2\,O \qquad (a\text{-}1)$$

$$O + O_2(+M) \xrightarrow{k_2} O_3(+M) \qquad (b)$$

Eucken and Patat (5) have studied the photolysis of oxygen in a flow system and have found the simple sequence of reactions (a-1) and (b), together with (c), to be compatible with their data over the pressure range from 13 to 40 mm.

$$O + O_3 \xrightarrow{k_3} 2\,O_2 \qquad (c)$$

Assuming the third body in reaction (b) to be an oxygen molecule, this leads to the expression:

$$\frac{d[O_3]}{dt} = \phi I_a \left\{\frac{1 - \alpha[O_3]}{1 + \alpha[O_3]}\right\} \qquad (I)$$

where

$$\alpha = \frac{k_3}{k_2[O_2]^2}$$

It is readily seen that the steady-state ozone concentration is equal to $1/\alpha$, and that, in agreement with the data of Eucken and Patat, it is proportional to the square of the pressure,[1] P_{O_2}, and is independent of the light intensity. They evaluated k_3/k_2 and measured the activation energy difference $E_3 - E_2 = 6.16$ kcal.

Experimental Method

The reaction rate was measured in a conventional Pyrex flow system. Commercial oxygen was dried by passing through a trap at −78°C, the trap containing glass wool and stainless steel helices to improve heat transfer. An aneroid-type manometer was used so that the system was free of mercury vapor. The ozonizer was of the Siemens type, with two concentric Pyrex cylinders serving as dielectrics. The outer electrode was aluminum foil 8 cm in length, with a diameter of 2 cm. The inner electrode con-

[1] Actually, the product of total pressure and oxygen pressure together with a factor defining the relative efficiencies of ozone and oxygen as third bodies for reaction (b) should appear in equation (I). Since, however, except at low temperatures, the maximum ozone concentration found in the author's investigation amounted to less than 4 volume % with a change over the complete pressure range of less than 2 volume %, the author will neglect these factors as did Eucken and Patat, and use the total measured pressure as the partial pressure of oxygen.

sisted of an aquadag coating, electrical connection being made through a small amount of mercury. The gap containing oxygen was 2 mm and the Pyrex dielectrics were each 1 mm thick. The voltage to the ozonizer was obtained from a 12,000-v ignition transformer with a Variac in the primary. The current was measured in the ground circuit with a copper oxide rectifier-type 0 to 1 ma meter, bypassed with a 0.1 μf condenser. The current below onset of the discharge was essentially zero, and rose abruptly as the discharge started.

The ozone concentration in the effluent was determined by measuring absorption of 2537Å radiation from a 4-watt G.E. germicidal lamp in a quartz cell 2.5 cm in diameter and 1 cm in depth (6). The radiation was collimated and was measured on an FJ405 photoelectric cell. The system was calibrated by passing various O_2-O_3 mixtures through the cell and a calibrated volume in series until the composition in the two was the same. The ozone in the bulb was absorbed by shaking in contact with 15 ml of 2N neutral KI, and the liberated I_2 was titrated with standard thiosulfate.

Preliminary results indicated that, at the very low flow rates used in determining steady-state ozone concentrations, a considerable error was introduced owing to ozone photolysis in the measuring cell. To obviate this difficulty, a shutter was placed between the cell and the lamp, and the photoelectric current was measured on a G.E. photoelectric potentiometer recorder. The ozone concentration could then readily be determined by extrapolation to zero time after the shutter was opened. This method was used for all the experiments reported in this paper.

Results

Comparison with the Simple Mechanism

If reaction (a-1) is replaced with the reaction corresponding to electron impact,

$$O_2 + e \xrightarrow{k_1} 2\,O + e \qquad (a\text{-}2)$$

equation (I) remains the same except that ϕI_a is replaced by k_1, where k_1 is defined for reaction (a-2) by the relation

$$\frac{d[O]}{dt} = k_1$$

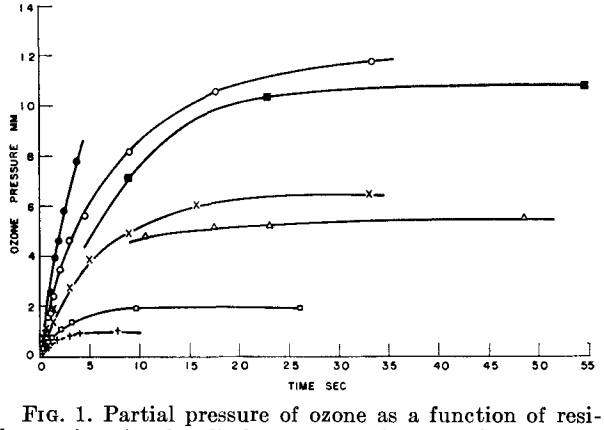

FIG. 1. Partial pressure of ozone as a function of residence time in the discharge at various total pressures. + 69 mm; □ 100 mm; △ 176 mm; × 200 mm; ■ 274 mm; ○ 301 mm; ● 500 mm.

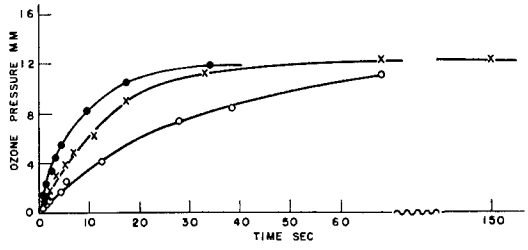

FIG. 2. Partial pressure of ozone as a function of residence time in the discharge at various currents. ○ 0.06 ma; × 0.14 ma; ● 0.30 ma.

TABLE I. *Variation of steady-state ozone pressure with total pressure at 25° and 59.2°C*

Current, 0.30 ma

Temp	P_{O_2}	P'_{O_3}	$P^2_{O_2}/P'_{O_3}$
°C	mm	mm	mm × 10^{-3}
25	69	0.92	5.16
25	100	1.92	5.21
25	176	5.26	5.91
25	200	6.41	6.24
25	274	10.5	7.18
25	301	11.9	7.63
59.2	100	0.97	10.3
59.2	150	2.12	10.6
59.2	200	3.44	11.6
59.2	301	7.02	12.9
59.2	350	8.47	14.5
59.2	399	10.7	15.0

The quantity k_1 will be a function of the current, average electron energy, pressure, and composition of the gas. The nature of k_1 needs no further consideration at this point. since, for the simple mechanism above the steady state. ozone concentration is independent of k_1 (equation I).

Variation in ozone partial pressure with residence time in the ozonizer at various total pressures is shown in Fig. 1. The current was 0.30 ma, and the ambient temperature 25°C. Values of the steady-state ozone pressure, P'_{O_3}, obtained from these and similar curves obtained at 59.2°C, together with values of $P^2_{O_2}/P'_{O_3}$, are shown in Table I. While at lower pressures $P^2_{O_2}/P'_{O_3}$ approaches a constant value [as required by equation (I)], very definite departures occur at higher pressures.

Fig. 2 shows the dependence of rate of ozone formation on discharge current. These results were obtained at 301 mm pressure with an ambient temperature of 25°C. As predicted by the simple mechanism, the steady-state ozone concentration is independent of discharge current.

Perhaps the simplest assumption one might make to account for the increase in $P^2_{O_2}/P'_{O_3}$ at higher P'_{O_3} involves decomposition of the ozone by some process in addition to that of reaction (c), as, for example, by electron impact. Thus, if $P^2_{O_2}/P'_{O_3}$ is plotted against P'_{O_3} and extrapolated to $P'_{O_3} = 0$, the value of k'_3/k'_2 [2] should be obtained. Further

[2] The quantity k_2/k_3 in equation (I) is expressed in concentration units. Since the authors, like Eucken and Patat, have expressed their results in units of pressure, the intercept in Fig. 3 gives k'_3/k'_2 mm, where $k'_3/k'_2 = (k_3/k_2)\cdot RT$. Eucken and Patat do not appear to have made this distinction, which is of importance in evaluating the activation energies. In a similar manner, k'_1 is defined in terms of pressure as $k_1\,RT$ mm.

implications of this mechanism will be considered shortly; but, assuming its validity, the value of k_2'/k_3' may be compared with that of Eucken and Patat. The data of Table I are plotted in Fig. 3, from which it is evident that a reasonable extrapolation can be made. Values of k_2'/k_3' thus obtained are 2.08×10^{-4} mm^{-1} at 25°C and 1.02×10^{-4} mm^{-1} at 59.2°C. Eucken and Patat give 5.35×10^{-4} mm^{-1} at 25°C and 1.91×10^{-4} mm^{-1} at 59.2°C. Exact comparison of these values is difficult, since the temperature of the gas in the ozonizer is probably somewhat higher than that of its surroundings. From other measurements (10) of discharge temperatures, the required temperature rise is completely reasonable, although it should be noted in Fig. 2 that no variation in P'_{O_3} occurred with changing discharge current, where a change in temperature might have been anticipated. In any event, the agreement seems fairly satisfactory and indicative of the similarity of mechanisms.

Decomposition of Ozone by Electron Impact

Including the electron decomposition reaction

$$O_3 + e \xrightarrow{k_4} O_2 + O + e \qquad (d)$$

in the simple mechanism above, one has

$$\frac{d[O_3]}{dt} = k_1 \left\{\frac{1 - \alpha[O_3]}{1 + \alpha[O_3]}\right\} - \frac{2\alpha k_4[O_3]^2}{1 + \alpha[O_3]} \qquad (II)$$

which leads to equation (I) at small ozone concentrations. Under steady-state conditions, this gives

$$\frac{[O_2]^2}{[O_3]_{ss}} = k_3/k_2(1 + 2\,k_4/k_1[O_3]_{ss}) \qquad (III)$$

Here $[O_3]_{ss}$ refers to the steady-state ozone concentration.

A comparison of equation (III) with the results in Fig. 2 and 3 indicates that, if this mechanism is correct, k_4/k_1 must be independent of pressure and discharge current. To establish these dependences, it is now necessary to examine the factors controlling these rate constants in more detail.

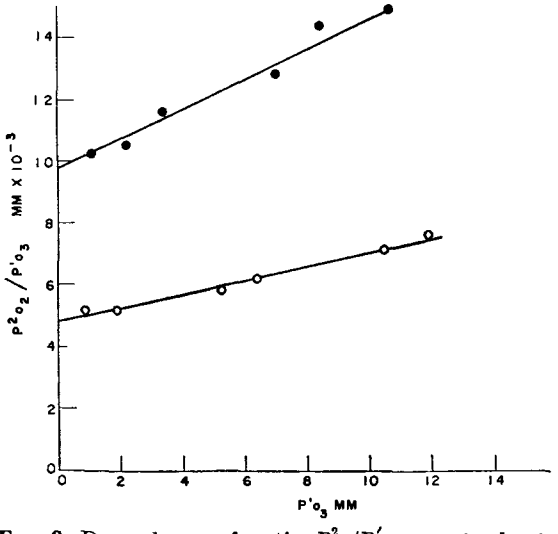

FIG. 3. Dependence of ratio $P^2_{O_2}/P'_{O_3}$ on steady-state partial pressure of ozone. ○ 25°C; ● 59.2°C.

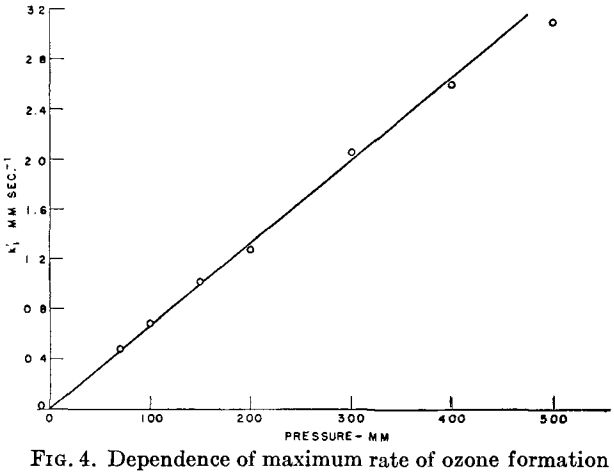

FIG. 4. Dependence of maximum rate of ozone formation on pressure.

The rate of any specified type of electron collision process in a uniform plasma is given by the expression (7)

$$R_x = k\,\frac{i[X]}{W}\int_{V_c}^{\infty} Q(V)\cdot f(V)\,dV \qquad (IV)$$

where i is the current density; $[X]$ is the concentration of the component undergoing collision; W is the electron drift velocity; $Q(V)$ is the probability cross section for the specified type of collision process; $f(V)\,d(V)$ is the probability that an electron has energy lying between V and $V + dV$; k is a constant for all such processes; and V_c is the critical potential for the specified process.

While in the silent electric discharge the plasma may not be uniform, it is to be expected that an expression similar to that above may be obtained by averaging over the discharge volume and time. The quantity W and the integral in equation (IV) are functions of E/P, where E is the field strength and P the pressure, so that one may write[3]

$$2\frac{k_4}{k_1} = \frac{1}{[O_2]}\frac{I_4}{I_1} \qquad (V)$$

where I_4 and I_1 refer to the integrals in equation (IV) for the case of electron collision with ozone and oxygen, respectively. Here we have assumed that each inelastic collision of the type given by equation (IV) leads to reactions (a-2) or (d). If more than one excited state can lead to reactions (a-2) or (d), the integrals in equation (V) must be replaced by a corresponding summation of integrals.

Since k_1' is measured directly by the initial slopes of the curves in Fig. 1, its dependence on pressure, and thus that of I_1/W, can be determined. Values of k_1' as a function of pressure are plotted in Fig. 4, where it is seen that a linear relation holds. In obtaining the initial slopes, greatly expanded scales were used, and in all cases good initial straight lines were obtained at the fast flow rates used. The discharge current was 0.30 ma and the temperature was 25°C. Comparing these results with equation (IV) indicates that with pressures from 70 to 500 mm, I_1/W and thus the electron energy distribution is relatively con-

[3] In deriving equations (II) and (III), the rates of production of oxygen atoms by reactions (a-2) and (d) have been assumed to be k_1 and k_4 $[O_3]$, respectively.

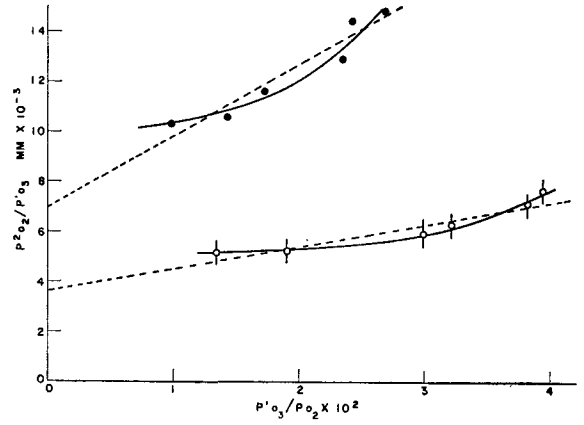

FIG. 5. $P^2_{O_2}/P'_{O_3}$ as a function of P'_{O_3}/P_{O_2}. ○ 25°C; ● 59.2°C.

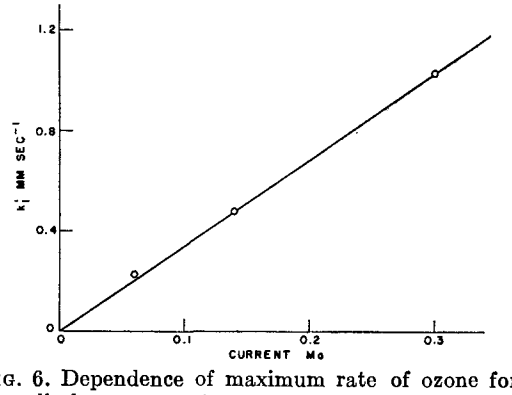

FIG. 6. Dependence of maximum rate of ozone formation on discharge current.

stant over the energy range of interest. These results are consistent with Manley's (8) observation that in the ozonizer discharge E/P is independent of pressure over the range of 1–2 atm for gaps of the order of magnitude used in this work. While some variation is to be expected, particularly at lower pressures, it is apparently insufficient to change I_1/W appreciably. It may then be expected that the ratio of I_4/I_1 appearing in equation (V) will be a constant independent of pressure.

Combining equations (V) and (III), it is apparent that the slope of the curve in Fig. 3 should not be a constant but should decrease as $1/P_{O_2}$, i.e., by a factor of about 4. For comparison with Fig. 3, $P^2_{O_2}/P'_{O_3}$ is plotted against P'_{O_3}/P_{O_2} in Fig. 5. It is evident that, while the individual points do not lie far from the dashed straight lines drawn, there is a definite trend from linearity. The data suggest, although perhaps not conclusively, that electron collision with ozone is not an important destructive step over the concentration range encountered in this work.

Equation (IV) predicts that both k_1 and k_4 should be proportional to the discharge current. Fig. 6 shows that this is indeed true for k'_1. Thus, equation (III) does predict that the steady-state ozone concentration should be independent of discharge current as was shown in Fig. 2.

Third Body Restrictions in Ozone Formation

To this point it has been assumed that reaction (*b*), the combination of oxygen atoms with oxygen molecules to form ozone, is second order in oxygen concentration, since stabilization by collision with a third body is necessary. At sufficiently high pressures all active complexes will be stabilized by collision and the reaction rate will become first order in oxygen concentration. This is similar to the order change postulated by Lindemann for unimolecular reactions, and becomes clear when reaction (*b*) is represented by the following steps.

$$O + O_2 \underset{\kappa_3}{\overset{\kappa_2}{\rightleftharpoons}} O_3^* \qquad (e)$$

$$O_3^* + O_2 \xrightarrow{\kappa_4} O_3 + O_2 \qquad (f)$$

Here O_3^* refers to the activated complex containing an amount of energy approximately equal to $D(O - O_2)$, or 25 kcal.

Solving the kinetics for this situation including reactions (*a*-2) and (*c*), and assuming a steady state in [O] and $[O_3^*]$, one finds:

$$\frac{d[O_3]}{dt} = \frac{k_1(1 - \gamma[O_3])}{1 + \gamma[O_3]} \qquad (VI)$$

an equation analogous to that obtained with the simple mechanism of equation (I), except that now

$$\gamma = \frac{k_3(\kappa_3 + \kappa_4[O_2])}{\kappa_4\kappa_2[O_2]^2} \qquad (VII)$$

Since, as before, $\gamma = 1/[O_3]_{ss}$ it is evident that at high pressures when the rate of collisional deactivation is large compared with the spontaneous decomposition of O_3^* (i.e., $\kappa_4[O_2] \gg \kappa_3$), $[O_3]_{ss} \propto [O_2]$; whereas at low pressures (when $\kappa_3 \gg \kappa_4[O_2]$), $[O_3]_{ss} \propto [O_2]^2$.

Equation (VII) may be written:

$$\frac{[O_2]^2}{[O_3]_{ss}} = \frac{k_3(\kappa_3 + \kappa_4[O_2])}{\kappa_4\kappa_2} \qquad (VIII)$$

As Fig. 7 indicates, the data taken from Table I are consistent with equation (VIII) if all of the rate constants are essentially pressure independent. While theory and experiment have indicated that for unimolecular decompositions of the type shown in (III) κ_3 will be somewhat pressure dependent, as has already been noted in the preceding section, the data shown in Fig. 7 are not sufficiently accurate to clearly show the expected variations. Thus, rate constants evaluated from Fig. 7 will be averages for the pressure range shown. From the ratios of intercepts to slopes $(\kappa_3/\kappa_4)_{298} = 2.00 \times 10^{-2}$ mole liter^{-1} and $(\kappa_3/\kappa_4)_{332} = 2.24 \times 10^{-2}$ mole liter^{-1}, where the subscripts refer to absolute temperature. If one writes $\kappa_4 = f.Z$, where Z is the collision number and f the fraction of collisions between O_2 and O_3^* leading to deactivation, one finds $(\kappa_3)_{298} = 3.31 \times 10^9 f$ sec^{-1} and $(\kappa_3)_{332} = 3.77 \times 10^9 f$ sec^{-1}. Here for the sum of the collision radii O_2 and O_3^* a value of 4Å has been used.

Comparison may be made with the mean value of κ_3 obtained using the approximate expression developed by Benson (9)

$$\kappa_3 = \nu\left[1 + \frac{\epsilon^*}{(n-1)kT}\right]^{1-n} \qquad (IX)$$

Here $\nu \sim 10^{13}$; n is the number of degrees of freedom which

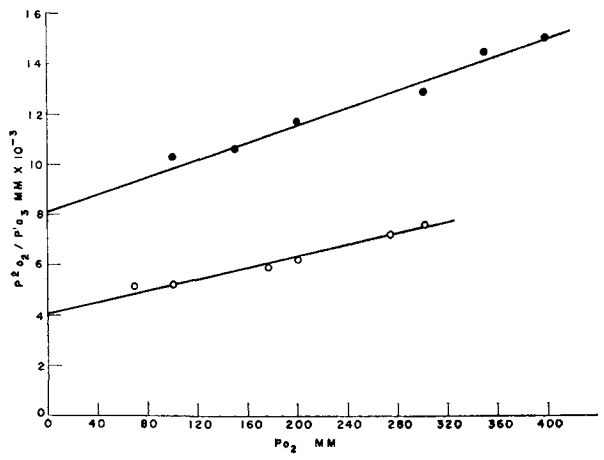

FIG. 7. $P^2_{O_2}/P'_{O_3}$ as a function of pressure. ○ 25°C; ● 59.2°C.

may contribute to reaction, in this case 3; and ϵ^* is the minimum energy for decomposition, in this case 25 kcal. With these values equation (IX) gives $(\kappa_3)_{298} = 2.34 \times 10^{10}$ sec^{-1}, which is to be compared with the measured value of 3.31×10^9 sec^{-1} if $f = 1$. In view of the approximations made in Benson's treatment, this order of magnitude agreement seems reasonable.

Fig. 7 gives somewhat different intercepts for $P^2_{O_2}/P'_{O_3}$ from those obtained using Fig. 3. For purposes of comparison with the results of Eucken and Patat these intercepts give $k_2'/k_3' = 2.44 \times 10^{-4}$ mm^{-1} at 25°C and 1.22×10^{-4} mm^{-1} at 59.2°C, values in slightly better agreement with those of Eucken and Patat than were obtained using Fig. 3.

Temperature Effects

The dependence of κ_3 on temperature is described by equation (IX). Since for this system $2kT \ll \epsilon^*$ this may be written to a close approximation as

$$\frac{(\kappa_3)_{T_1}}{(\kappa_3)_{T_2}} = \left(\frac{T_1}{T_2}\right)^2 \qquad (X)$$

From values in the preceding section $(\kappa_3)_{298}/(\kappa_3)_{332} = 0.88$. Equation (X) predicts a value of 0.81, probably fortuitous agreement considering the uncertainty of the discharge temperature and the nature of the calculation.

Assuming this temperature dependence for κ_3 [equation (X)], and that the pre-exponential factors of the remainder of the rate constants involved are proportional to $T^{1/2}$, equation (VIII) may be written

$$\frac{d \ln \phi}{d\ 1/T} = -\frac{[E_3 - E_2]}{R} \qquad (XI)$$

where

$$\phi = \frac{1}{T^{5/2}} \cdot \frac{1}{[1 + K \cdot P_{O_2} \cdot T^{-5/2}]} \cdot \frac{P^2_{O_2}}{P'_{O_3}}$$

K is temperature independent, and is evaluated from the slope and intercept of the straight line for 25°C in Fig. 7. E_3 is the activation energy for reaction (*c*), and E_2 that corresponding to κ_2 [reaction (*e*)].

Therefore, from measurements of P'_{O_3} at various temperatures, an Arrhenius plot may be constructed according to equation (XI). The results of such measurements are shown in Fig. 8, taken from the data in Table II over a temperature range from −31° to +102°C. Fig. 8 shows that, while below 60°C the curve is linear, above this temperature a large increase in apparent activation energy occurs. This change at higher temperatures is almost certainly associated with the onset of thermal ozone decomposition. The data shown in Fig. 9, where the variation in P_{O_3} with residence time at 102°C is plotted, lend support to this conclusion. Comparison of this curve with those in Fig. 1 shows that, unlike the latter, a true steady state is not reached at the higher temperatures, but rather, at longer residence times increased ozone decomposition occurs. From the linear portion in Fig. 8 one finds $E_3 - E_2 = 3.9$ kcal $mole^{-1}$ $degree^{-1}$.

Since Eucken and Patat assumed $k_3 \propto T^{1/2}$, and used pressure units instead of concentration units for k_3/k_2, a recalculation of $E_3 - E_2$ was made from their data using

TABLE II. *Variation in steady-state partial pressure of ozone with temperature*

Pressure of oxygen = 150 mm; discharge current = 0.30 ma

Temp	P'_{O_3}
°C	*mm*
−31	16.4
0	8.48
25	4.19
41	3.36
59	2.12
84	0.85
102	0.31

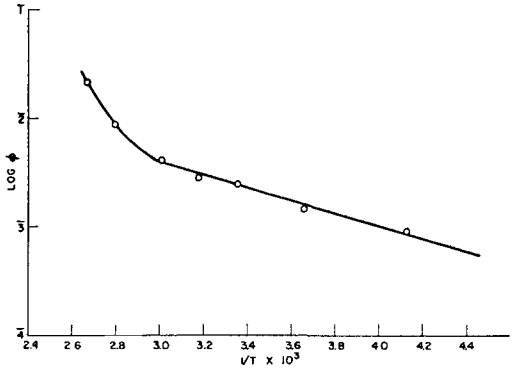

FIG. 8. Arrhenius plot determining activation energy difference $E_3 - E_2$.

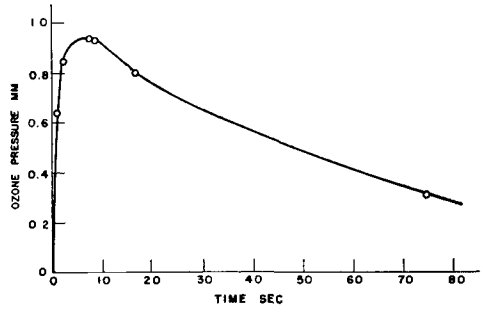

FIG. 9. Partial pressure of ozone as a function of residence time in the discharge at 102°C.

equation (XI), and assuming $K \cdot P_{O_2} \cdot T^{-5/2}$ to be essentially zero. The value of $E_3 - E_2$ obtained was 4.7 kcal mole^{-1} degree^{-1}. Whether the difference between the ΔE of Eucken and Patat and that obtained in this work is significant is not clear. The author's value would be too low if the discharge temperature were higher than ambient. The discrepancy might also be explained by assuming that in the discharge some of the oxygen atoms carry excess energy, either as kinetic energy or because they are in higher electronically excited states.

Discussion

While comparison between the photochemical and discharge data, particularly the general agreement in k_2/k_3 and $E_3 - E_2$, indicates the similarities between the mechanisms, and thus the essential importance of oxygen atoms in the discharge phenomenon, little direct information concerning the primary states leading to formation of atoms has been obtained. Of particular interest is the relative role of ions and electronically excited molecules as precursors to atom formation. It is to be noted, however, that a mechanism involving ozone formation directly from ions, such as that postulated by Brewer and Westhaver (11), is unlikely in view of our results.

The data indicate that at higher pressures than those used by Eucken and Patat the steady-state ozone concentration is lower than would be predicted by their simple mechanism. This has been explained by assuming that the lifetime of the activated ozone complex becomes comparable with the time between deactivating collisions in this higher pressure range, so that the rate of formation of ozone from oxygen atoms becomes proportional to less than the square of the pressure. Such a concept leads to a lifetime for the activated ozone complex of the expected order of magnitude for the number of degrees of freedom involved. While the results of Schumacher and Kistiakowski (12) on the photolysis of ozone fail to show the effect of order change in reaction (*b*) the experimental error claimed would be sufficient to mask the effect using the author's values for k_3 and k_4. Ritchie (13), in a study of the thermal decomposition of ozone, found evidence of a change in order of the initial step from second to first in the pressure range of 10 to 100 mm, suggesting that in this pressure range the lifetime of the thermally activated complex becomes comparable to the collision time. This would be expected to occur at a somewhat lower pressure in this case since the average energy of the activated complexes would be somewhat lower than when they are formed by combination of oxygen atoms with oxygen molecules.

The anomalously low steady-state ozone concentration at higher pressures might also be explained assuming an ozone destruction reaction in addition to reaction (*c*). The possibility that this destruction reaction involves collisions between electrons and ozone molecules according to reaction (*d*) has been discussed and while present results do not conclusively rule it out, they favor a pressure dependent process. If such a reaction were a dominant one in the mechanism I_4/I_1 can be evaluated from the best straight line through the data of Fig. 5, utilizing equations (III) and (V). The value thus obtained from the results at 25°C is 12. Electron-impact data have shown that the minimum potential for oxygen-atom formation lies between 6.3 and 9 ev (1, 14). From photochemical data, ozone is decomposed by radiation of about 1 ev. If a plasma electron temperature, T_e, of about 25,000°K is assumed, the ratio of the number of electrons capable of exciting O_3 to those capable of exciting O_2 is (assuming a Maxwellian distribution)

$$\exp(\Delta E/RT_e)$$

or about 20, which is of the order of the value found for I_4/I_1. The above argument is completely qualitative and is merely presented to show that the value of I_4/I_1 is not inconsistent with present knowledge and does not rule out reaction (*d*) in the mechanism. Any quantitative treatment must, of course, consider also the relative cross sections for the two processes as shown in equation (IV), as well as require a more precise knowledge of the distribution function.

Approximately the correct pressure dependence for the steady-state ozone concentration may be obtained by assuming that the additional destruction reaction involves collision of ozone with an active species of oxygen formed in the discharge. Such a reaction must compete with a nearly pressure independent destruction reaction of the active species. The kinetics for this mechanism lead to a relation of the form of equation (III) in which the coefficient of $[O_3]_{ss}$ is independent of discharge current.

If, in such a mechanism, the active oxygen species represents an electronically excited molecule, the most plausible state is probably $^1\Sigma_g^+$. This state is highly metastable, having a lifetime for radiation of about 7 sec (15). It would thus be expected to disappear at the walls, rather than by radiation. Its energy, 1.6 ev, is enough to cause dissociation of $O_3[D(O_2 - O) = 1.0$ ev]. Since the transition involves a change in multiplicity, O_2' would not be formed directly in photolysis, but could be formed on electron impact by the well-known resonance-exchange process. Evidence for its occurrence has been obtained in controlled-speed electron bombardment of oxygen (16). O_2' may alternatively be representations of the type O_2^+ or O_2^-. For example, the reaction

$$O_2^+ + O_3 \longrightarrow O_2 + O_3^+ \qquad (g)$$

followed by decomposition of O_3^+ on neutralization, might occur.

The possibility that ozone is destroyed in an energy chain similar to that postulated by Schumacher (17) and Heidt (18) seems remote in view of the low concentrations of ozone existing in the present experiments.

In conclusion, while the author's results cannot rule out conclusively the possibility that an ozone destruction step occurs in addition to that involving oxygen atoms, the data can be satisfactorily explained without such a step if the ozone formation step is considered in a detailed manner. From the point of view of simplicity, therefore, such a mechanism seems most plausible.

Acknowledgment

The author wishes to acknowledge the helpful discussion of this work with Dr. George Porter of Cambridge University during a visit to this laboratory.

Manuscript received November 2, 1955.

Any discussion of this paper will appear in a Discussion Section to be published in the June 1957 JOURNAL.

REFERENCES

1. G. GLOCKLER AND S. C. LIND, "The Electrochemistry of Gases and Other Dielectrics," John Wiley & Sons, Inc., New York (1939).
2. T. H. RUMMEL, "Hochspannungs-Entladungschemie," R. Oldenbourg and Hanns Reich, Munchen (1951).
3. H. EYRING, J. HIRSCHFELDER, AND H. S. TAYLOR, *J. Chem. Phys.*, **4**, 479, 570 (1936).
4. W. A. NOYES, JR., AND P. A. LEIGHTON, "The Photochemistry of Gases," Chap. 6, Reinhold Publishing Corp., New York (1941).
5. A. EUCKEN AND F. PATAT, *Z. physik. Chem.*, **33B**, 459 (1936).
6. L. R. KOLLER, *J. Appl. Phys.*, **16**, 816 (1945).
7. R. W. LUNT AND C. A. MEEK, *Proc. Roy. Soc. (London)*, **A157**, 146 (1936).
8. T. C. MANLEY, *Trans. Electrochem. Soc.*, **84**, 83 (1943).
9. S. W. BENSON, *J. Chem. Phys.*, **20**, 1064 (1952).
10. L. B. LOEB, "Fundamental Processes of Electrical Discharges in Cases," p. 596, John Wiley & Sons, Inc., New York (1939).
11. A. K. BREWER AND J. W. WESTHAVER, *J. Phys. Chem.*, **34**, 1280 (1930).
12. H. J. SCHUMACHER, *J. Am. Chem. Soc.*, **52**, 2377 (1930).
13. M. RITCHIE, *Proc. Roy. Soc. (London)*, **146A**, 848 (1934).
14. F. KRUGER AND C. ZICKERMANN, *Z. Physik.*, **99**, 428 (1936).
15. G. HERZBERG, "Spectra of Diatomic Molecules," p. 278, D. Van Nostrand Co., New York (1950).
16. G. GLOCKLER AND J. L. WILSON, *J. Am. Chem. Soc.*, **54**, 4544 (1932).
17. H. J. SCHUMACHER, *Z. physik. Chem.*, **17B**, 405 (1932).
18. L. J. HEIDT, *J. Am. Chem. Soc.*, **57**, 1710 (1935).

Technical Reviews

The Oxygen Concentration Cell as a Factor in the Localized Corrosion of Metals

WILSON LYNES

Research Department, Revere Copper and Brass Incorporated, Rome, New York

ABSTRACT

Literature on the oxygen concentration cell has been reviewed. The discovery and early history of the cell are outlined, and environmental conditions favorable to its development are classified and discussed. Theories of the mechanism of the cell are presented. The current produced by an oxygen concentration cell is considered in terms of the open-circuit potentials and polarizing characteristics of the anode and cathode, and the resistance of the metal and electrolyte. Selected quantitative data are shown in tabular and graphic form.

In the same year that Volta announced his discovery of the battery, Haldane (1) found that its action ceased in vacuum or in nitrogen, and increased in oxygen, and Davy (2) showed that, when it was exposed to the atmosphere, oxygen was absorbed.

For a long time oxygen was supposed to act on the anodes, where it produced oxidation. However, when Grove (3) demonstrated that oxygen was consumed at the cathodes of his gas battery, it became apparent that oxygen could play a part different from the one hitherto assigned to it.

DISCOVERY AND EARLY HISTORY

Around 1845, Adie (4, 5) demonstrated the cathodic function of oxygen in a more convincing manner in the following experiments: "A piece of zinc was cut into two halves, and connected in the usual manner with a long wire galvanometer, the helix containing 2000 convolutions. The two plates of zinc were immersed in water, and arranged to allow a tube containing oxygen to be placed at pleasure over the upper portion of either plate. After completing the connections, a short time was allowed for the galvanometer to reach zero; the tube filled with oxygen was then inverted over one of the plates which immediately deflected the galvanometer showing the *oxygenated plate to be the negative element of the couple.* The tube was now passed over from the negative zinc to the positive piece, when, in the course of a few minutes, the galvanometer again shewed the new oxygenated zinc to be acting the part of a negative or platinode plate. The deflections of the needles were from 15° to 20°, where they remained steadily for some time. Instead of placing a tube of oxygen over one of the plates, if the water in front of one be stirred carefully with a quill, or if the plate be attached to an elastic wire, and made to vibrate in the water, it is immediately oxygenated more rapidly than the opposite one, and becomes strongly negative. The vibrated plate forms a very beautiful experiment. Like results were obtained with two pieces of iron.

. . . . . .

"Two slips of zinc cut side by side from the same sheet were placed in a running brook, the one opposed to a rapid part of the current, the other in a still place at the edge. Connecting these in the usual manner with the galvanometer, there was a permanent deflection of 25°; and on changing the respective places of the plates in the stream without disturbing their attachments to the galvanometer, the needles immediately passed to the opposite side of the card; in both cases the piece of zinc in the current acted as a negative or platinode plate. . . . It is the greater supply of oxygen to the plate in the current which converts it into a negative or platinode. A cell containing two small silver wires and the cyanide of silver solution used for electro-plating was attached in place of the galvanometer, when, after a lapse of two hours, metallic silver was seen precipitated in a minute quantity on the silver wire connected with the piece of zinc in still water.

"Two plates of iron were placed in the stream under like conditions to the zinc; after two hours metallic silver was distinctly seen precipitated on the silver wire connected with the iron plate in still water.

. . . . . .

"A single plate of iron exposed to water and oxygen gas has local differences on its surface which act in the same way as if the iron had been in two halves and placed in a stream in the manner described. . . ."

Prior to Adie's experiments, Zamboni (6) had found that a partially immersed strip of tin, zinc, or copper was cathodic to a strip of the same metal fully immersed, and Marianini (7) had made experiments in which he obtained momentary differential aeration currents by lifting one of two electrodes of zinc or copper into the air and replacing it in the electrolyte.

Additional evidence of the cathodic influence of oxygen was obtained by Viard (8) in 1852 by means of admirably planned and executed differential aeration experiments on a number of metals in water and aqueous solutions. In all experiments analogous results were obtained without exception.

In view of the observations of Adie and Viard, there is no reason why the effect of differential oxygen concentration in producing corrosion currents should not have been taken into account by subsequent investigators of corrosion. But the significance of the experiments was not grasped at the time, and later they were forgotten. In the latter part of the nineteenth century and the early part of the present one, the opinion was expressed by those who advocated the electrochemical theory of corrosion that heterogeneity of the metal, or other factors relating to the metal, such as differential stress, were the sole causes of corrosion currents.

Conditions Favorable to Development

In 1915, Aston (9) took exception to this viewpoint, and called attention to the importance of heterogeneity of the contacting liquid. To illustrate, he cited an experiment in which an appreciable electromotive force was produced between two electrically connected bars of steel in a beaker of water through which air was bubbled, when one of the bars was wrapped with a few thicknesses of cloth. He explained the result on the basis of the differential aeration principle, and remarked that porous iron rust acts similarly to the cloth in screening oxygen, with the result that areas of iron underlying patches of porous iron rust are anodic to adjacent areas of unrusted iron, resulting in conditions favorable to pitting. As shown by Chappell (10), if iron under water is completely covered with rust, corrosion will be retarded, since the rate of diffusion of oxygen to the surface of the metal will be everywhere reduced.

Around 1923–1925, Evans (11–18) made a comprehensive and detailed study of the oxygen concentration cell,[1] and repeatedly stressed its importance as a potential cause of intense localized corrosion. In this country, the common occurrence of the cell and its destructive nature were emphasized by McKay (19).

As shown experimentally by Evans (11), the effect of restricting access of oxygen to a part of the surface of the metal is not to increase the total corrosion, but to concentrate on the nonaerated area the corrosion which would otherwise be distributed over the surface. Evans (11) also demonstrated that, at such places that are anodic owing to the absence of oxygen, the product of corrosion is generally a soluble salt. Secondary corrosion products are usually precipitated at a sensible distance from either the anode or cathode, and do not protect the metal from further attack. For these reasons, the rate of corrosion produced by an oxygen concentration cell may be dangerously high.

Conditions favorable to the development of oxygen concentration cells commonly exist in crevices, under porous deposits of corrosion products or foreign substances, in soils, at water lines, under drops of water or aqueous solutions, and in regions of unequal liquid velocities.

As early as 1840, Mallet (20) observed that clean iron immersed in water oxidized preferentially at the point of contact of a glass lens of large curvature, or at a very acute angle formed between a plate of iron and a plate of glass, or between two plates of iron. Subsequently, others made analogous observations. A rational explanation of corrosion in crevices was first given by Evans (11) on the basis of electrochemical principles. Ellis and LaQue (21), in tests on Type 430 stainless steel in flowing sea water, secured data showing that attack within a crevice increases in proportion to the increase of area of the freely exposed metal outside.

From 1819 (22) onward, the opinion was repeatedly expressed that rust accelerates subsequent rusting by virtue of the fact that iron oxide is cathodic to iron. It is not in doubt that rust can act in this manner (23, 24) but, as first demonstrated by Aston (25), a localized deposit of porous rust plays a different role. By hindering diffusion of oxygen, it renders the surface of the underlying iron anodic to the surrounding surface to which oxygen has better access.

Aside from acting as a mechanical oxygen-screen, rust can also produce chemical oxygen-screening by combining with oxygen dissolved in the liquid. By means of direct measurement of oxygen advance, Evans and Mears (26) showed that corrosion products of several kinds delayed the passage of oxygen considerably. Diffusion of oxygen through ferrous hydroxide was extremely slow, undoubtedly because the precipitate absorbed oxygen in its conversion to hydrated magnetite and ferric oxide. Other corrosion products capable of oxidation are in the same category. For example, May (27), in discussing the mechanism of the pitting of copper in water containing chlorides, said: "There is little doubt that the outward diffusion of cuprous chloride in solution from the anode is a most important factor in maintaining rapid pitting, since by reacting with the oxygen diffusing into the pit it can maintain the oxygen concentration at the anode at the lowest possible value." May also observed that the higher rates of pitting are associated with the formation of solid cuprous chloride in a highly porous state. Conversely, deposition of cuprous chloride in a compact layer with a high electrical resistance favors stifling.

Differential aeration currents are an important factor in the corrosion of metal underground. Variations in the oxygen content of soil in contact with a pipe or other metallic structure may be produced by local differences in its texture, degree of compactness, or moisture content. Denison (28) designed a laboratory soil corrosion cell in which a potential difference was developed by differential aeration between two electrodes of the same material separated by moist soil as the electrolyte. Cells constructed on this principle have been used to measure the rate of corrosion of metals and alloys for correlation with the rate of corrosion of specimens in field tests, and with the rate of corrosion of a pipe-line system (29–32). A modification of the cell has been described by Schwerdtfeger (33).

Distribution of attack on metal partly immersed in stagnant water or salt solution and partly exposed to air or oxygen is usually determined to a large extent by differential aeration. At or near the water line, where the oxygen required for the cathodic reaction is readily replenished, a cathodic zone commonly develops that is immune. The lower part of the metal, to which oxygen has less access, becomes anodic and is corroded In 1932,

[1] Known also as the differential aeration cell and the Evans cell.

Evans and Hoar (34) showed that the velocity of corrosion is quantitatively equivalent to the strength of the electric currents which flow between the cathodic region at the water line and the anodic region below it. This outstanding pioneer work gave quantitative confirmation of the electrochemical theory of corrosion.

In experiments by Evans and co-workers (34–36), it was found that practically the entire cathodic reaction was confined to the neighborhood of the meniscus. The area shown to be anodic by electrical measurements coincided with the area visibly attacked.

Conditions analogous to those existing at a water line are produced by drops of aqueous liquid on a metal surface. Corrosion develops, in most cases, below the center of the drop; below the marginal portion the metal remains unattacked.

The passage of differential aeration currents between the marginal and central parts of a drop was demonstrated by Baisch and Werner (37). It was shown by Evans (38) that, if the periphery of a drop is surrounded by nitrogen, and oxygen is blown down the center, an uncorroded center surrounded by a corroded ring develops instead of the reverse normal distribution.

The strength of an oxygen concentration cell is increased by motion of the liquid. Motion increases rate of diffusion of oxygen to the cathodic surface. Cathodic polarization is decreased, and corrosion rate is increased.

Increased rate of oxygen diffusion also increases the open-circuit potential of the cathode. Wormwell, Nurse, and Ison (39), Mansa and Szybalski (40), and Cohen (41) have found that the potential of iron in fresh water becomes increasingly more cathodic with increase in velocity up to a limiting velocity, after which further increase in velocity does not change the potential. By means of differential velocity, Cohen obtained a potential difference as high as 0.70 v.

Motion of the liquid not only increases rate of transfer of dissolved oxygen from the bulk of the solution to the surface of the cathode, but also increases rate of transfer of metal ions from the surface of the cathode to the bulk of the solution. When the anode is shielded from the motion, the effect of the latter opposes that of the former, due to increase in strength of both the oxygen concentration cell and the opposing metal ion concentration cell. Usually, the oxygen concentration cell dominates, but in the case of a noble metal, such as copper, the effect of removal of metal ions may preponderate (11, 42–44). The principal determining factors are the difference in oxygen concentration and the velocity. As the difference in oxygen concentration increases, the velocity of the liquid required to cause reversal from an oxygen concentration cell to a metal ion concentration cell also increases.

When velocity and turbulence of the liquid are sufficiently high to remove or prevent formation of a film of insoluble corrosion product on the cathode, the type of attack changes to erosion-corrosion. This is reflected by a drop in potential (44).

Cell Mechanism

In 1849, Adie (45) expressed the opinion that the electromotive force of the oxygen concentration cell is created by metal oxide produced at the aerated surface, acting as cathode, and metal at the unaerated surface, acting as anode. To test this viewpoint, a piece of zinc was cut into halves. One of the halves was oxidized by heat, and then formed into a couple with the bright half. On immersion in water, a galvanometer indicated that the oxidized half was the cathode. Similar results were obtained with iron, copper, and lead.

Much later, Adie's theory was strengthened by the observation of Lorenz and Hauser (46) that lead, silver, nickel, copper, iron, and zinc, when used as electrodes surrounded with oxygen at a pressure of one atmosphere, and in sodium hydroxide or sodium sulfate solution, show potentials almost identical with those of their oxides in the same solution.

Evans (11, 15) considered that two different mechanisms are possible, the first one that the oxygen concentration cell functions as a metal-metal oxide cell, and the second one that the cathodes of the cell consist of comparatively noble spots on the aerated area, created by impurities or lack of physical uniformity. If the second mechanism is operative "the alkali formed over the cathodic particles will spread over the iron around them, and here the principal anodic product will be a thin and invisible film of iron hydroxide; in other words, the iron in this outer portion will become passive and cease to pass into solution." Thus the second mechanism would lead to the first one. "If foreign particles were completely absent, this state of affairs would never be set up, and we should expect to get no corrosion unless the first mechanism comes into play." On the basis of special experiments, Evans concluded that both mechanisms can play a part in producing a current. Evans (18) also remarked that "since in an ordinary differential aeration cell a current is produced immediately air is bubbled into one compartment, it is clear that no oxide film of any sensible thickness is needed for the partial ennoblement of the aerated electrode. It is likely that a layer of adsorbed oxygen (such as would be formed almost instantaneously) is sufficient to cause a slight alteration in potential."

Later, Evans (47–50) said that differential aeration currents can be referred to differences in the state of repair of an oxide film on the metal surface. The potential is slightly higher at the aerated places, where the film is kept in good repair by the conjoint action of dissolved oxygen and cathodically produced hydroxyl ion.

When a metal is covered with an oxide film, it may have any potential between that of the bare metal and the solid oxide (51). If the film is highly discontinuous, the potential will be almost as low as that of the film-free metal. As the film becomes more continuous, the potential rises toward that of the solid oxide. Presumably, if the film were perfect in its ability to prevent metal ions from entering the liquid, its potential would be that of a reversible oxygen electrode (47, 51, 52).

The lower potential of an imperfect oxide film is due to polarization caused by local currents flowing between anodes located at pores, lattice defects, cracks, or other weak spots in the film, and adjacent cathodes located on sound film. In an oxygen concentration cell, the film on the area accessible to dissolved oxygen is kept in better

repair than on the area shielded from oxygen, making the former cathodic to the latter.

The ennoblement by dissolved oxygen of the potentials of chromium, stainless steels, iron, titanium, and some other metals and alloys has been attributed by Uhlig (53–55) to a chemisorbed film of oxygen.

Thermodynamic origin of the electromotive force of the oxygen concentration cell has been stressed by McKay (19, 56, 57). From this viewpoint, the source of the electrical energy of the cell is found in the tendency of the differential concentration of oxygen to equalize, the energy relationship being such that the area of metal under the higher concentration of oxygen must be cathodic. An oxide film, if present, is influential in determining the amount of current produced.

Current Determining Factors

The current produced by an oxygen concentration cell is determined by the open-circuit potentials, and polarizing characteristics of the anode and cathode, and the resistance of the electrolyte and metal. It is equal to the difference between the polarized potentials of the cathode and anode divided by the sum of the resistances of the electrolyte and metal. In most cases, the resistance of the metal is negligibly small.

It is generally not possible to determine the open-circuit and polarized potentials and current flow on a naturally corroding metal surface, since the local anodes and cathodes cannot be identified and isolated. In the case of differential aeration, this was first accomplished by Evans and Hoar (34) for iron partly immersed in dilute potassium chloride solution. The current measured accounted for the whole of the corrosion of the anodic area as measured by the estimation of iron in the corrosion product. Later, differential aeration currents on zinc in sodium chloride or sodium sulfate solution were measured by Agar (58) by an independent method.

Open-Circuit Potentials

The open-circuit electromotive force of oxygen concentration cells may be evaluated indirectly by means of electrode potential measurements made in oxygen-free and in air- or oxygen-saturated solutions, or in solutions of different oxygen content. A number of such measurements are contained in the literature. A selected list is given in Table I.

The influence of hydrogen ion concentration on the electrode potential of iron has been investigated by Reiller (65), using deaerated and aerated solutions of hydrochloric acid, 0.5*N* NaCl, and NaOH. The data (Fig. 1) show that the electromotive force of an oxygen concentration cell increases with increase in *p*H of the solution. However, above a *p*H of about 9.5, the electromotive force is unstable, since a trace of oxygen at the anode is sufficient to make its open-circuit potential much more cathodic (65).

With reference to the dependence of potential on *p*H, it should be noted that the *p*H of the solution is altered by the cell current. For example, Reiller (65), using a laboratory type of oxygen concentration cell with iron electrodes in 0.5*N* NaCl solution, found that, in course of time, the *p*H at the anode decreased to 4.5 due to formation there of ferrous chloride, whereas the *p*H at the cathode increased to 11 due to the presence of cathodically produced NaOH.

At any *p*H value, the potential of an aerated electrode may be affected to a marked degree by the nature of the

TABLE I. *Effect of dissolved oxygen on electrode potential*

Metal	Solution	Potential (normal hydrogen scale) in volts			Difference (v)	Reference
		Deaerated	Air-saturated	Oxygen-saturated		
Aluminum	1*N* H_2SO_4	−0.41	−0.19		0.21	(59)
Aluminum	1*N* KCl	−0.88		−0.53	0.35	(60)
Copper	1*N* HCl	−0.03		0.04	0.07	(61)
Copper	0.2*N* H_2SO_4	0.20		0.28	0.08	(62)
Copper	1*N* KCl	−0.03		0.05	0.08	(63)
Copper	1*N* KOH	−0.30		−0.05	0.25	(61)
70-30 Brass	Sea water	−0.04	0.01		0.05	(64)
70-30 Cupronickel	Sea water	−0.01	0.04		0.05	(64)
Iron	0.1*N* HCl	−0.18	−0.16		0.02	(65)
Iron	0.05*N* H_2SO_4	−0.28	−0.25		0.03	(66)
Iron	0.5*N* NaCl	−0.44	−0.08		0.36	(65)
Iron	0.1*N* Na_3PO_4	−0.66	0.11		0.78	(67)
Iron	0.1*N* Na_2CO_3	−0.60	0.17		0.77	(66)
Iron	0.1*N* Na_2SiO_3	−0.68	0.03		0.71	(67)
Iron	0.1*N* NaOH	−0.70	0.08		0.78	(67)
Iron	1*N* NaOH	−0.72	0.00		0.72	(68)
18-8 Stainless steel	0.25*N* H_2SO_4	−0.07	0.56		0.63	(69)
18-8 Stainless steel	0.25*N* H_2SO_4	−0.07		0.60	0.67	(69)
18-8 Stainless steel	4% NaCl	−0.11	0.35		0.46	(70)
18-8 Stainless steel	4% NaCl + 0.3*N* NaOH	−0.02	0.05		0.07	(55)
Titanium	1*N* HCl	−0.30	0.08		0.38	(71)
Titanium	5*N* HCl	−0.38	−0.30		0.08	(71)
Titanium	1*N* H_2SO_4	−0.43	0.28		0.71	(59)
Titanium	3% NaCl	0.11	0.44		0.33	(71)

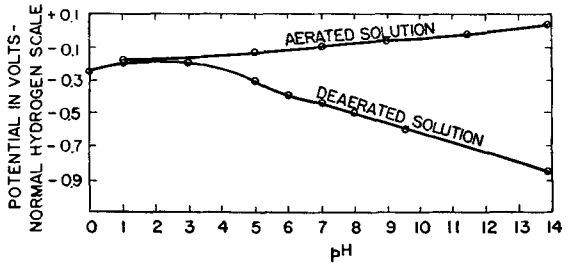

FIG. 1. Effect of *p*H on the electrode potential of iron in solutions of HCl, 0.5*N* NaCl, and NaOH. After Reiller (65).

TABLE II. *Effect of anions on electrode potential at constant pH in aerated solutions*

Metal	Solution	*p*H	Potential (normal hydrogen scale) in volts	Reference
Aluminum..	1*N* NaCl + HCl	3	−0.50	(72)
Aluminum..	1*N* Na_2SO_4 + H_2SO_4	3	−0.21	(72)
Aluminum..	1*N* NaCl	7	−0.47	(72)
Aluminum..	1*N* Na_2SO_4	7	−0.11	(72)
Copper.....	HCl	0	0.05	(73)
Copper.....	H_2SO_4	0	0.22	(73)
Copper.....	HCl	3	0.25	(73)
Copper.....	H_2SO_4	3	0.24	(73)
Copper.....	1*N* NaCl	7	−0.01	(73)
Copper.....	1*N* Na_2SO_4	7	0.23	(73)
Copper.....	0.01*N* NaCl	7	0.19	(73)
Copper.....	0.01*N* Na_2SO_4	7	0.25	(73)
Iron.....	0.1*N* NaCl	7	−0.30	(74)
Iron.....	0.1*N* CH_3COONa + CH_3COOH	7	0.14	(74)
Iron.....	0.1*N* Na_2HPO_4 + H_3PO_4	7	0.03	(74)
Iron.....	Na_2CO_3	9.5	0.13	(66)
Iron.....	Na_2CO_3 + 1% Na_2SO_4	9.5	−0.30	(66)
Iron.....	Na_2CO_3 + 1% NaCl	9.5	−0.30	(66)
Iron.....	Na_2CO_3	11	0.17	(66)
Iron.....	Na_2CO_3 + 1% Na_2SO_4	11	0.14	(66)
Iron.....	Na_2CO_3 + 1% NaCl	11	−0.30	(66)
Iron.....	NaOH	11	−0.12	(66)
Iron.....	NaOH	12	−0.02	(66)
Iron.....	NaOH + 1% Na_2SO_4	12	−0.38	(66)
Iron.....	NaOH	13	−0.02	(66)
Iron.....	NaOH + 1% Na_2SO_4	13	−0.03	(66)
Iron.....	NaOH + 1% NaCl	13	−0.04	(66)

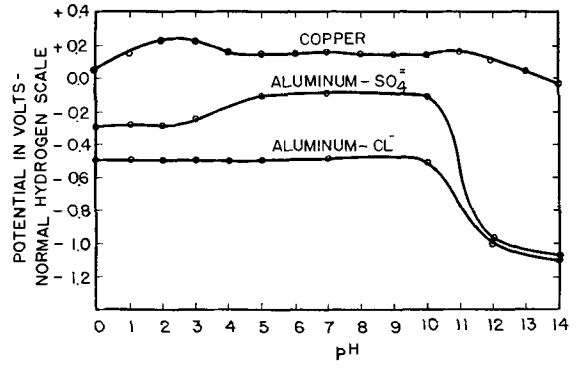

FIG. 2. Effect of *p*H on electrode potential. Aluminum in aerated 1*N* NaCl + HCl or NaOH, and 1*N* Na_2SO_4 + H_2SO_4 or NaOH. Copper in aerated 0.01*N* NaCl + HCl or NaOH. After Akimov, Glukhova, and Rosenfel'd (72, 75).

anion or anions in the electrolyte. This is illustrated in Table II.

The relationship between hydrogen ion concentration and electrode potential for aluminum in aerated 1*N* NaCl plus HCl or NaOH, and 1*N* Na_2SO_4 plus H_2SO_4 or NaOH has been determined by Akimov and Glukhova (72), and the same relationship for copper in aerated 0.01*N* NaCl plus HCl or NaOH has been determined by Akimov and Rozenfel'd (75). Data are given in Fig. 2.

Anodic Polarization

Anodic polarization is produced by development of insoluble, protective corrosion products on the surface of the anode, or by accumulation of ions released from the anode in the adjacent liquid.

Since dissolved oxygen is required for formation of most protective films, film polarization usually does not occur when dissolved oxygen is absent at the anode, or present in very small amount.

As previously mentioned, the potential of copper is appreciably increased by small increase in copper ion concentration. On the other hand, less noble metals such as iron and aluminum are relatively unaffected by changes in ionic concentration, and consequently are not subject to concentration polarization.

Cathodic Polarization

The current flowing in an oxygen concentration cell is usually controlled by polarization of the cathode. The shape of the cathodic polarization curve may be influenced by: composition, surface condition and dimensions of the cathode, composition, temperature, and movement of the solution, and difference between concentration of oxygen in the bulk of the solution and that at the cathode surface.

If oxygen is consumed at the cathode as fast as it arrives by diffusion, the rate of its arrival is the controlling factor. If oxygen reaches the cathode at a rate faster than its rate of consumption, the rate of its cathodic reduction is in control. In the second case polarization is strongly dependent upon the composition and surface state of the cathode, and the polarization curve is determined by the oxygen reduction overvoltage, which may be expressed by Tafel's equation for hydrogen overvoltage (52, 76).

The presence of film or scale on the surface of the cathode may have an important influence on the shape of the cathodic polarization curve. If the deposit possesses no electronic conductivity, and cannot itself function as cathode, it acts to hinder diffusion of oxygen to the metal surface. If it exhibits good electronic conductivity, then the course of the polarization curve in the region of oxygen ionization depends on the value of overvoltage of the deposit itself. If it exhibits poor electronic conductivity compared with the metal, then the measured potential is affected by the value of the potential drop due to the ohmic resistance of the deposit. As a result, there will be some shift in the curve for cathodic polarization toward more anodic values. The magnitude of this *IR* drop has been determined for several cathodically polarized systems by Brown, English, and Williams (77).

TABLE III. *Current density required to decrease open-circuit potential of cathode by* 0.1, 0.3, *and* 0.5 *v*

Metal	Solution	Cathodic current density (amp × 10^{-6}/cm²)									Reference
		Stagnant solution			Moving solution						
		Difference between open-circuit and polarized potential of cathode (v)									
		Air atmosphere			Air atmosphere			Oxygen atmosphere			
		0.1	0.3	0.5	0.1	0.3	0.5	0.1	0.3	0.5	
Aluminum	Buffered[a] 0.02*N* NaCl, *p*H 5	1	2	3[c]							(85)
Aluminum	0.02*N* NaCl	0.3	0.5	0.7							(85)
Aluminum	0.5*N* NaCl					4[d]	8[d]	10[d]	23[d]	32[d]	(86)
Aluminum	Buffered[b] 0.5*N* NaCl, *p*H 9							18[d]	94[d]	160[c, d]	(86)
Duralumin	0.5*N* NaCl	4	10	48[c]	24[d]	30[d]	44[c, d]				(86)
Copper	0.05*N* K_2SO_4 + 0.002*N* H_2SO_4	0.8	1	1							(87)
Copper	0.05*N* K_2SO_4 + 0.01*N* H_2SO_4	0.6	1	1							(87)
Copper	0.05*N* K_2SO_4	0.4	2	2							(87)
Copper	0.1*N* KCl	0.5	2	3							(87)
Copper	3% NaCl				10[e]	16[e]	19[e]				(83)
Copper	Sea water				10[f]	42[f]					(88)
Copper	Buffered[b] 0.5*N* NaCl, *p*H 9					10[d]	28[d]	5[d]	40[d]	150[d]	(89)
Aluminum brass	Sea water				8[f]	22[f]					(90)
90-10 Cupronickel	Sea water				7[f]	18[f]					(91)
70-30 Cupronickel	3% NaCl				1[e]	3[e]	6[e]				(83)
Iron	0.05*N* K_2SO_4 + 0.01*N* H_2SO_4	6	40	56[c]							(92)
Iron	0.05*N* K_2SO_4 + 0.001*N* H_2SO_4	2	4	20[c]							(92)
Iron	0.5*N* NaCl + 0.01*N* HCl							149[d]	250[c, d]		(93)
Iron	0.05*N* K_2SO_4	1	4	15[c]							(92)
Iron	0.1*N* KCl				13[g]	15[g]	25[c, g]				(49)
Mild steel	Sea water	0.9	7[c]		16[f]	17[f]	21[c, f]				(94)
Iron	Buffered[b] 0.5*N* NaCl, *p*H 9				18[d]	32[d]	44[d]	44[d]	150[d]	182[d]	(90)
Iron	0.05*N* K_2SO_4 + 0.01*N* NaOH	1	3	4							(92)
Iron	0.5*N* NaCl + 0.01*N* NaOH							2[d]	20[d]	120[d]	(93)
Iron	0.1*N* NaOH	0.1	0.3	2							(92)
18-8 Stainless steel	Sea water					0.5[f]	42[f]				(89)
18-8 Stainless steel	Buffered[b] 0.5*N* NaCl, *p*H 9								0.8[d]	80[d]	(93)
Titanium	0.5*N* NaCl				0.003[h]	0.006[h]	0.3[h]				(95)
Titanium	Sea water					0.3[f]	3[f]				(89)

[a] 1% CH_3COONa + CH_3COOH.
[b] 25 × 10^{-3}*N* Na_2CO_3 + 5 × 10^{-3}*N* $NaHCO_3$.
[c] Hydrogen evolution region of polarization curve.
[d] Solution stirred at 2000 rpm.
[e] Solution flowing at 0.8 ft/sec.
[f] Sea water flowing at 7.8 ft/sec.
[g] Solution stirred at 15 rpm.
[h] Electrode moving at 0.1 ft/sec.

Polarizing characteristics of oxygen concentration cells may be evaluated by means of experimentally determined polarization curves. In solutions of low electrical resistivity, the corrosion current is approximately determined by the point of intersection of the anodic and cathodic curves. As the resistivity of the solution increases, the amount of current flowing lags more and more behind the intersection point, since an increasing residual electromotive force is needed to overcome the resistance of the solution. Only a limited number (49, 78–84) of polarization curves have been determined under conditions that are relevant to those existing in an oxygen concentration cell. No study has been made of the polarizing characteristics of a metal as a function of dissolved oxygen, *p*H, cation, velocity, and temperature. If reliable data of this type were obtained, it should be possible to predict satisfactorily the behavior of an oxygen concentration cell under a wide variety of conditions.

When the anode of an oxygen concentration cell does not polarize, and the resistance of the solution is not high, which is a common case, the limiting corrosion current is reached approximately when the difference between the open-circuit and polarized potential of the aerated cathode is equal to the open-circuit electromotive force of the cell. Therefore, in this case, when the open-circuit potentials and cathodic polarization curve are known, the cell current may be determined. In Table III, values of applied cathodic current density are given for differences between the open-circuit and polarized potentials of the cathode of 0.1, 0.3, and 0.5 v.

The effect of velocity on the cathodic polarization of mild steel in sea water (90) is shown in Table IV.

TABLE IV. *Effect of velocity on the cathodic polarization of mild steel in sea water at 26°C. Reference (90)*

Velocity of sea water	Current density (amp × 10^{-5}/cm²). Difference between open-circuit and polarized potential (v)	
	0.1	0.3
ft/sec		
0.0	2	4
0.5	4	5
3.0	7	9
5.0	10	12
7.8	13	14
9.0	19	21
13.0	31	32

Cell Current Measurements

Using an oxygen concentration cell with iron electrodes in 0.5*N* NaCl solution, Reiller (65) determined the influence of temperature on current output and open-circuit potentials. The relationships are shown in Fig. 3. By means of further experiments, Reiller showed that increase in cell current with increase in temperature was due partly to decrease in resistance of the electrolyte, and partly to decrease in cathodic polarization.

The variation in the current output of an oxygen concentration cell with iron electrodes in 0.5*N* NaCl solution as a function of the relative areas of the anode and cathode was determined by Herzog (96). Results are shown in Fig. 4.

Herzog and Chaudron (97) found that the current produced by an oxygen concentration cell with iron electrodes in sea water was only 38% of that produced in 3% NaCl solution. They considered that the lower current in sea water was due to the partially protective action of cathodically deposited magnesium and calcium carbonates.

The influence of surface preparation of the cathode on cell current was shown by Wickert and Wiehr (98) for iron in 0.1*N* NaCl solution. A relatively smooth cathode surface obtained by polishing gave a significantly higher cell current than did a filed surface. When a polished iron cathode and a constant Cd/$CdSO_4$ anode were used, with oxygen aeration in the cathode vessel, variation of the *p*H of the NaCl solution gave results as follows: beyond the range of hydrogen evolution, the cell current was a maximum in the neighborhood of *p*H 7; above *p*H 8, current gradually decreased with increase in *p*H value.

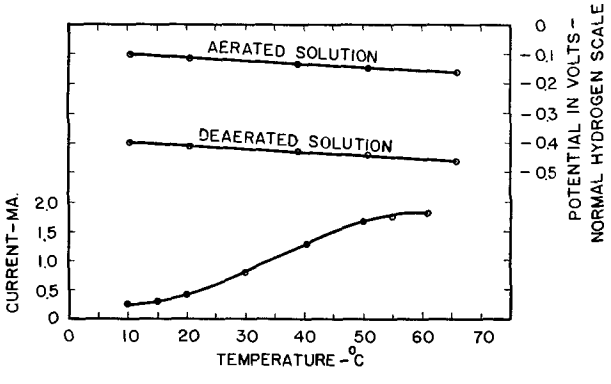

FIG. 3. Effect of temperature on the current output and open-circuit potentials of an oxygen concentration cell with iron electrodes in 0.5*N* NaCl solution. After Reiller (65).

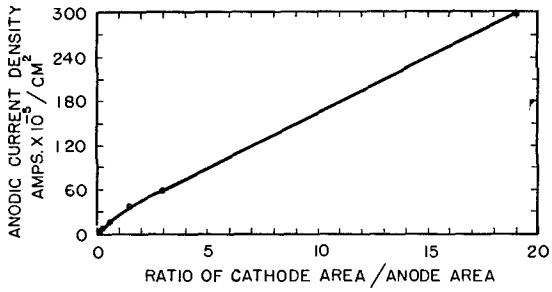

FIG. 4. Effect of relative area of the electrodes on the current produced by an oxygen concentration cell with iron electrodes in 0.5*N* NaCl solution. After Herzog (96).

Discussion

Data on the electrochemical behavior of oxygen concentration cells are scattered and limited in scope. Therefore, it is not possible to generalize to any extent on the basis of interpretation and correlation of published results. However, from the data in Tables I–IV, and Fig. 1 and 2, and from other data not included therein, certain generalizations, which may be subject to exceptions, appear to be justified. Among these are the following.

In the case of iron, open-circuit emf and cathodic polarization increase with increase in *p*H value. Activity of the cell is greatest in a *p*H range of about 5 to 9. In acid solutions, cell current is limited by lack of sufficient electromotive force, and, in alkaline solutions, by strong cathodic polarization. Movement of the liquid at the cathode results in increase in open-circuit potential and decrease in polarization.

In acid and neutral solutions, the emf of aluminum and 18-8 stainless steel is high in relation to that of copper.

In acid solutions, copper polarizes more readily than iron or aluminum. In neutral solutions, copper polarizes more readily than iron, but less readily than aluminum. Titanium polarizes with outstanding rapidity. Cathodic polarization of aluminum, copper, and 18-8 stainless steel is decreased by movement of the liquid.

Manuscript received January 3, 1956.
Any discussion of this paper will appear in a Discussion Section to be published in the June 1957 JOURNAL.

REFERENCES

1. H. HALDANE, *Nicholson's J.*, **4**, 313 (1800).
2. H. DAVY, *ibid.*, **4**, 337 (1800).
3. W. R. GROVE, *Phil. Mag.*, **21**, 417 (1842); **24**, 268, 346, and 422 (1844).
4. R. ADIE, *Edinburgh New Phil. J.*, **39**, 327 (1845).
5. R. ADIE, *Phil. Mag.*, **31**, 350 (1847).
6. G. ZAMBONI, *Wied. Ann.*, **60**, 151 (1818).
7. E. MARIANINI, *Ann. chim. et phys.*, **45**, 28 (1830).
8. VIARD, *ibid.*, **36**, 129 (1852); **42**, 5 (1854).
9. J. ASTON, *Iron Trade Rev.*, **56**, 423 (1915).
10. E. L. CHAPPELL, *Ind. Eng. Chem.*, **19**, 464 (1927).
11. U. R. EVANS, *J. Inst. Metals*, **30**, 239 (1923).
12. U. R. EVANS, *J. Oil and Colour Chemists' Assoc.*, **6**, 150 (1923).
13. U. R. EVANS, *Chemistry & Industry*, **43**, 222 (1924).
14. U. R. EVANS, *Proc. Cambridge Phil. Soc.*, **22**, 54 (1924).
15. U. R. EVANS, *Chem. Met. Eng.*, **30**, 949 (1924).

16. U. R. Evans, *J. Soc. Chem. Ind.*, **43**, 127T and 315T (1924).
17. U. R. Evans, *ibid.*, **44**, 163T (1925).
18. U. R. Evans, *Ind. Eng. Chem.*, **17**, 363 (1925).
19. R. J. McKay, *ibid.*, **17**, 23 (1925).
20. R. Mallet, *Brit. Assoc. Advance. Sci. Rept.*, **9**, 221 (1840).
21. O. B. Ellis and F. L. LaQue, *Corrosion*, **7**, 362 (1951).
22. Anon., *Ann. chim. et phys.*, **11**, 40 (1819).
23. E. Herzog, *Métaux & corrosion*, **24**, 119 (1949).
24. E. Herzog, *Bull. soc. chim. France*, **3**, 1530 (1936); **5** 187 (1938).
25. J. Aston, *Trans. Am. Electrochem. Soc.*, **29**, 449 (1916).
26. U. R. Evans and R. B. Mears, *Proc. Roy. Soc.*, **146A**, 153 (1934).
27. R. May, *J. Inst. Metals*, **82**, 65 (1953-54).
28. I. A. Denison, *J. Research Nat. Bur. Standards*, **17**, 363 (1936).
29. I. A. Denison and R. B. Darnielle, *ibid.*, **21**, 819 (1938).
30. I. A. Denison and R. B. Darnielle, *Trans. Electrochem. Soc.*, **76**, 199 (1939).
31. R. B. Darnielle, *J. Research Nat. Bur. Standards*, **25**, 421 (1940).
32. I. A. Denison, *Trans. Electrochem. Soc.*, **81**, 435 (1942).
33. W. J. Schwerdtfeger, *J. Research Nat. Bur. Standards*, **50**, 329 (1953).
34. U. R. Evans and T. P. Hoar, *Proc. Roy. Soc.*, **137A**, 343 (1932).
35. R. S. Thornhill and U. R. Evans, *J. Chem. Soc.*, **1938**, 2109.
36. U. R. Evans, *J. Iron Steel Inst.*, **141**, 219P (1940).
37. E. Baisch and M. Werner, *Korrosionstagung*, **1**, 83 (1931).
38. U. R. Evans, *Korrosion u. Metallschutz*, **6**, 74 and 173 (1930).
39. F. Wormwell, T. J. Nurse, and H. C. K. Ison, *J. Appl. Chem. (London)*, **3**, 275 (1953).
40. J. L. Mansa and W. Szybalski, *Acta Chem. Scand.*, **4**, 1275 (1950).
41. M. Cohen, *Trans. Electrochem. Soc.*, **89**, 105 (1946).
42. G. D. Bengough and O. F. Hudson, *J. Inst. Metals*, **21**, 122 (1919).
43. U. R. Evans, *J. Soc. Chem. Ind.*, **43**, 127T (1924).
44. G. D. Bengough and R. May, *J. Inst. Metals*, **32**, 82 (1924).
45. R. Adie, *J. Chem. Soc.*, **1**, 12 (1849).
46. R. Lorenz and H. Hauser, *Z. anorg. Chem.*, **51**, 81 (1906).
47. U. R. Evans, *J. Franklin Inst.*, **208**, 45 (1929).
48. U. R. Evans, *J. Chem. Soc.*, **1929**, 92.
49. U. R. Evans, L. C. Bannister, and S. C. Britton, *Proc. Roy. Soc.*, **131A**, 355 (1931).
50. U. R. Evans and D. E. Davies, *J. Chem. Soc.*, **1951**, 2607.
51. L. C. Bannister and U. R. Evans, *ibid.*, **1930**, 1361.
52. T. P. Hoar, *Proc. Roy. Soc.*, **142A**, 628 (1933).
53. H. H. Uhlig, *This Journal*, **97**, 215C (1950).
54. H. H. Uhlig and S. S. Lord, Jr., *ibid.*, **100**, 216 (1953).
55. H. H. Uhlig and A. Geary, *ibid.*, **101**, 215 (1954).
56. R. J. McKay, *Trans. Am. Electrochem. Soc.*, **41**, 201 (1922).
57. R. J. McKay and R. Worthington, "Corrosion Resistance of Metals and Alloys," p. 44, Reinhold Publishing Corp., New York (1936).
58. U. R. Evans, *J. Iron Steel Inst.*, **141**, 219P (1940).
59. D. Schlain, C. B. Kenehan, and D. V. Steele, *This Journal*, **102**, 102 (1955).
60. H. Endo and S. Kanazawa, *Science Repts. Tôhoku Imp. Univ.*, **22**, 537 (1933).
61. A. C. Krueger and L. Kahlenberg, *Trans. Am. Electrochem. Soc.*, **58**, 107 (1930).
62. A. K. Wiebe and C. A. Winkler, *Can. J. Chem.*, **31**, 1118 (1953).
63. S. J. French and L. Kahlenberg, *Trans. Am. Electrochem. Soc.*, **54**, 163 (1928).
64. J. Chapman and W. Cuthbertson, *J. Soc. Chem. Ind.*, **58**, 330 (1939).
65. R. Reiller, *Pubs. sci. et tech. secrétar. état aviation (France)*, No. 180, (1942).
66. J. Aubert, *Pubs. sci. et tech. ministère air*, No. 23, (1933).
67. M. J. Pryor and M. Cohen, *This Journal*, **100**, 203 (1953).
68. A. Travers and J. Aubert, *Compt. rend.*, **194**, 2308 (1932).
69. I. D. G. Berwick and U. R. Evans, *J. Appl. Chem.*, **2**, 576 (1952).
70. H. H. Uhlig, *Trans. Am. Inst. Mining Met. Engrs.*, **140**, 411 (1940).
71. D. Schlain and J. S. Smatko, *This Journal*, **99**, 417 (1952).
72. G. V. Akimov and A. I. Glukhova, *Compt. rend. acad. sci. U.R.S.S.*, **49**, 194 (1945).
73. G. V. Akimov and V. P. Backtrakov, *Zhur. Fiz. Khim.*, **13**, 1807 (1939).
74. H. L. Lochte and R. E. Paul, *Trans. Electrochem. Soc.*, **64**, 155 (1933).
75. G. V. Akimov and I. L. Rozenfel'd, *Zhur. Fiz. Khim.*, **14**, 1486 (1940).
76. N. D. Tomashov, *Compt. rend. acad. sci. U.R.S.S.*, **52**, 601 (1946).
77. R. H. Brown, G. C. English, and R. D. Williams, *Corrosion*, **6**, 186 (1950).
78. N. D. Tomashov, *Light Metals*, **11**, 104 (1948).
79. H. H. Uhlig, D. N. Triadis, and M. Stern, *This Journal*, **102**, 59 (1955).
80. M. Pourbaix and P. Van Rysselberghe, *Compt. rend. réunion comité thermodynam. et cinét. electrochim.*, 1950, p. 219 (Pub. 1951).
81. G. B. Hatch, *Ind. Eng. Chem.*, **44**, 1775 (1952).
82. R. Ergang, G. Masing, and M. Möhling, *Z. Elektrochem.*, **56**, 8 (1952).
83. H. B. Bomberger, F. H. Beck, and M. G. Fontana, *This Journal*, **102**, 53 (1955).
84. W. W. Kittelberger and A. C. Elm, *Corrosion*, **5**, 101 (1949).
85. G. Masing, *Metallforschung*, **1**, 97 (1946).
86. N. D. Tomashov, *Light Metals*, **11**, 155 (1948).
87. A. I. Krasil'shchikov and V. A. Andreeva, *Zhur. Fiz. Khim.*, **20**, 1199 (1946).
88. F. L. LaQue, *Proc. Am. Soc. Testing Materials*, **51**, 495 (1951).
89. N. D. Tomashov, *Light Metals*, **11**, 8 (1948).
90. T. P. May, Private communication.
91. W. C. Stewart and F. L. LaQue, *Corrosion*, **8**, 278 (1952).
92. A. I. Krasil'shchikov, *Zhur. Fiz. Khim.*, **20**, 1187 (1946).
93. N. D. Tomashov, *Light Metals*, **11**, 104 (1948).
94. H. R. Copson, *Ind. Eng. Chem.*, **44**, 1745 (1952).
95. N. Hackerman and C. D. Hall, Jr., *This Journal*, **101**, 321 (1954).
96. E. Herzog, *Chimie & industrie*, **27**, 351 (1932).
97. E. Herzog and G. Chaudron, *Pubs. sci. et tech. ministère air*, No. 19, (1933).
98. K. Wickert and H. Wiehr, *Werkstoffe u. Korrosion*, **3**, 129 (1952).

Oxidation of Copper to Cu_2O and CuO

(600°–1000°C and 0.026–20.4 atm Oxygen)

DONALD W. BRIDGES,[1] JOHN P. BAUR,[1] GRETTA S. BAUR, AND W. MARGIN FASSELL, JR.[1]

Department of Metallurgy, University of Utah, Salt Lake City, Utah

ABSTRACT

Oxygen free-high conductivity copper was oxidized to CuO and Cu_2O over the temperature range 600°–1000°C in pure oxygen (0.026–20.4 atm). Correlation of weight gained, W, and time, t, was achieved through the use of the equation: $t/W = W/K_p + 1/K_1$, where K_p is the parabolic rate constant and K_1 is a constant. Pressure variation had no effect on the magnitude of K_p, if the ratio Cu_2O/CuO was constant. Quantitative x-ray diffraction analysis of the scale disclosed approximately 96% Cu_2O at high and low pressures for temperatures above 800°C. Below 750°C high pressure coatings contained 90% Cu_2O, while subatmospheric coatings continued to assay about 96% Cu_2O. Temperature correlation was obtained by means of the equation: $K_p = A \exp(-Q/RT)$, where Q = 37,000 cal and K_p is the average value for a Cu_2O/CuO ratio of approximately 96/4 (700°–1000°C).

Recent review articles (1–3) summarize much of the work on oxidation of copper. The present survey investigates the system, $Cu/Cu_2O/CuO/O_2$, at temperatures from 600° to 1000°C in pure oxygen from 0.026 to 20.4 atm. The oxygen free-high conductivity (OFHC) copper used was the same as employed in this laboratory's study of the system, $Cu/Cu_2O/O_2$ (4). Subatmospheric experimental procedure, equipment, and sample preparation methods were described in the previous paper (4). The high pressure equipment and experimental technique are as previously reported (5). All samples were oxidized for a period of 120–150 min.

EXPERIMENTAL RESULTS

Kinetic measurements.—The correlation of weight gained and time was achieved through the use of the same equation employed in the oxidation of OFHC copper below the dissociation pressure of CuO (4):

$$t/W = W/K_p + 1/K_1 \qquad (I)$$

t is the observed elapsed time, W is the increase in weight, K_p is the parabolic rate constant, and K_1 is a thickness independent constant. Mathematically, this is the equation of a parabola that does not intersect the t-axis at $W = 0$. Its physical significance has been discussed by numerous workers (6–10). Table I presents the individual determinations here analyzed by means of equation (I), and at 600°C and 700°C the parabolic rate constant resulting from the application of the more conventional parabolic oxidation equation: $W^2 = K_p \cdot t$, which for low temperatures yielded an equally good representation of the data. At temperatures in excess of 700°C, W^2 vs. t plots resembled those published previously (4).

Composition of the oxide coating.—Quantitative x-ray diffraction analyses were performed on the oxide layers from 20 samples oxidized approximately 2 hr at various temperatures and pressures. The purpose was to ascertain if the composition changed with either temperature or oxygen concentration (pressure).

The oxide scale was mixed with an amount of high grade CaO such that the ratio of weight of oxide to weight of CaO was always 2/1. Peak intensities of the three lines (CuO, 35.45 degrees 2θ; Cu_2O, 36.43 degrees 2θ; and CaO, 37.37 degrees 2θ) were measured by means of a Geiger counter x-ray diffractometer and the ratios I_{CuO}/I_{CaO} and I_{Cu_2O}/I_{CaO} were calculated. The percentage composition was determined by comparison of these ratios to those of a "working curve" constructed by mixing known amounts of high grade CuO, Cu_2O, and CaO such that the ratios of the weight of CuO + Cu_2O to the weight of CaO were again 2/1.

Results of the analysis are shown on Table II. It is apparent that Cu_2O makes up more than 90% of the bulk oxide by weight at all temperatures and pressures with the exception of two samples: 600°C, 13.6 atm and 700°C, 20.4 atm. Below 750°C there seems to be an increase in the amount of CuO with an increase in oxygen pressure. Otherwise, there is no significant change of composition with change of pressure.

Above 750°C there is no indication of change in composition with temperature. Below 800°C there appears to be a slight increase in the amount of CuO (in high pressure oxidation) with decreasing temperature. Tylecote (11), reporting the results of x-ray analysis of the oxide coatings formed in 1 hr at 600°–900°C on copper oxidized in air, concluded that there was no "regular trend" in the oxide composition with temperature. Some of Tylecote's reported values are in agreement with the results of Table II obtained at the same temperature. The variation of composition with temperature reported by Valensi (12) is much greater than shown in Table II.

Considerable disagreement exists among earlier workers as to the effect of time of oxidation on the composition of the oxide scale. The ratio of Cu_2O to CuO for constant

[1] Present address: Central Research Lab., Howe Sound Co., Salt Lake City, Utah.

TABLE I. *A summary of rate constants resulting from application of equation (I) to experimental data*

Temp, °C	Pressure atm, O_2	K_p $mg^2 \cdot cm^{-4}$ hr^{-1}	Average K_p	K_1 $mg \cdot cm^{-2}$ hr^{-1}	K_p' determined by $W^2 = K_p^1 t$
1000	0.25	355.8	302.4	42.2	
		254.2	σ = 29.1	70.2	
	0.50	338.9	p.e. = 19.6	53.6	
		270.0		56.5	
	0.75	296.5		53.6	
		291.3		65.6	
		295.0		53.5	
	1.36	327.7		60.5	
	2.04	305.3		93.0	
	3.4	322.6		47.2	
	6.8	248.3		70.6	
		324.8		59.7	
		301.4		73.6	
	10.2	287.2		58.2	
	13.6	316.5		83.1	
900	0.026	76.6	83.1	21.5	
	0.125	78.7	σ = 13.8	19.1	
		84.6	p.e. = 9.3	25.7	
	0.250	78.7		23.6	
		75.8		25.1	
	0.500	78.8		26.8	
		84.0		30.7	
	0.750	77.4		21.4	
		83.7		33.4	
	1.00	77.0		28.1	
	2.04	120.3		35.3	
	3.4	102.6		23.3	
	6.8	71.2		30.6	
		87.7		43.3	
		89.6		47.6	
		92.9		35.6	
		87.2		50.5	
	10.2	51.5		67.5	
	13.6	82.3		39.7	
		81.7		47.6	
850	0.125	40.3	43.8	14.7	
	0.250	43.1	σ = 7.8	16.5	
	0.500	44.2	p.e. = 5.2	14.7	
	0.750	43.7		14.3	
	1.00	43.7		16.2	
	2.04	59		23.5	
		63.1		17.9	
	3.4	49.1		21.4	
	6.8	47.2		33.8	
		48.7		28.4	
		44.5		34.6	
		56.9		23.9	
	10.2	46.9		13.1	
	13.6	41.4		66.0	
	20.4	38.0		41.8	
800	0.125	19.0	19.2	9.9	
		18.8	σ = 0.5	10.4	
	0.250	19.7	p.e. = 0.3	9.5	
		19.7		11.7	
		18.8		11.3	
	0.500	19.6		10.8	
		18.5		7.4	
	0.750	19.5		9.9	
	1.00	19.9	23.2	11.9	
	2.04	24.9	σ = 1.8	12.9	
	3.4	22.8	p.e. = 1.2	24.1	
	6.8	21.9		18.1	
		23.3		37.8	
		27.7		28.6	
		22.4		37.8	
		22.4		24.8	
	10.2	24.5		20.7	
	13.6	22.8		26.5	
		22.4		55.6	
	20.4	23.4		25.1	
750	0.026	8.5	8.7	7.5	
	0.125	9.0	σ = 0.3	6.1	
	0.250	8.9	p.e. = 0.2	6.2	
		8.9		6.7	
	0.500	8.3		8.9	
	0.750	8.6		8.5	
750	1.00	8.9	11.5	10.0	
	2.04	12.4	σ = 1.8	11.4	
		12.0	p.e. = 1.2	18.4	
	3.4	7.3		887.6	
		12.5		26.2	
		12.3		18.3	
	6.8	12.6		20.9	
	10.2	12.8		12.5	
	13.6	12.6		16.9	
	20.4	11.9		20.0	
700	0.125	3.3	3.04	8.0	
		2.2	σ = 0.34	5.4	
	0.250	3.2	p.e. = 0.23	5.5	
		3.3		5.3	
		3.2		7.5	
	0.500	2.9		8.6	
		3.1		9.0	
	0.750	3.1		15.7	
	1.00	4.0	6.4	6.7	
		4.4	σ = 1.9	9.1	
		5.0	p.e. = 1.3	7.2	
		7.0		6.7	
		8.2		5.7	
		8.5		4.7	
	2.04	10.8		6.6	
	3.4	5.6		12.7	
	6.8	5.5		10.8	5.8
		7.5		8.2	
	10.2	5.8		16.4	
	13.6	5.7		−190.2	5.8
	20.4	4.7		−22.0	5.4
600	0.125	1.2	1.4	7.8	0.9
	0.250	.8	σ = 0.6	1.6	0.7
		1.4	p.e. = 0.4	3.6	1.0
	0.500	.8		12.3	0.8
		1.9		7.2	1.6
	0.750	2.3		2.3	1.2
	1.00	1.6	1.84	2.4	1.6
	2.04	1.4	σ = 0.27	75.5	1.5
		1.9	p.e. = 0.19	−32.4	1.6
		2.3		−3.7	3.0
	3.4	2.1		47.3	2.1
		1.9		−3.5	
	6.8	1.4		−53.5	1.5
		2.1		−28.5	2.1
	10.2	1.8		−9.5	1.9
	13.6	2.0		7.8	1.8
	20.4	1.7		−7.5	1.8

σ = Gaussian Distribution Standard Deviation.
p.e. = Probable Error = 0.67σ.

temperature has been reported to be both dependent on oxidation time (13–15) and to be essentially constant over a reasonable time interval (11, 12). Three samples were oxidized for longer periods of time and the coatings analyzed by the same x-ray technique described above to determine if any change occurred. Results are included in Table II. It appears that at 800°C and 6.8 atm no change

TABLE II. *Composition of the oxide coating formed on OFHC copper oxidized at various temperatures and pressures*

Temp, °C	Oxygen pressure, atm	Time of oxidation	Composition	
			% Cu_2O	% CuO
900	0.5	120 min	96.3	3.7
	13.6	120 min	97.4	2.6
850	0.25	115 min	97.0	3.0
	0.50	120 min	96.5	3.5
	6.8	100 min	95.3	4.7
	10.2	120 min	96.4	3.6
800	0.125	120 min	97.5	2.5
	0.75	120 min	96.6	3.4
	6.8	120 min	93.3	6.7
	6.8	120 min	96.2	3.8
	6.8	23 hr	96.2	3.8
750	0.125	130 min	94.7	5.3
	0.25	120 min	92.0	8.0
	3.4	120 min	93.3	6.7
	10.2	120 min	92.2	7.8
700	0.25	100 min	97.6	2.4
	20.4	115 min	88.5	11.5
600	0.25	140 min	96.6	3.4
	0.50	145 min	96.2	3.8
	2.04	120 min	91.1	8.9
	13.6	155 min	88.9	11.1
	13.6	48 hr	82.6	17.4
500	6.8	48 hr	85.3	14.7

in percentage composition occurred with time. At 600°C and 13.6 atm, however, some increase was detected in agreement with the findings of Dennison and Preece (13) who reported 22% CuO after 48 hr oxidation in air at 650°C. A sample oxidized for 48 hr at 500°C and 6.8 atm showed 15% CuO, indicating that there is no great change in the CuO present at lower temperatures.

Physical appearance of the oxide scale.—The color of the oxidized samples can be summarized as follows: 900°C, gray; 850°C, dark gray; 800°C, darker gray to soot black; 750°C, soot black; 700°C, soot black; 600°C, soot black. However, the color of all the oxides reverted to brick red on grinding.

The coatings formed at 800° and 900°C adhered to the underlying metal; there was no loss of oxide during the lowering (cooling) of the sample. At lower temperatures, 600°–700°C, some spalling occurred upon cooling the samples. In all cases the oxides formed at higher oxygen pressures were easier to remove than those formed at lower pressures, probably due to the increased thickness of the former. The high pressure coatings could be removed by flexing the samples, thereby breaking the oxide free in large slabs. This operation was not possible with the low pressure oxides; and, in the most severe cases (low temperatures and low pressures), the sample could be bent nearly 180° without cracking the film. In order to remove these films scraping was required.

Discussion of Results

Fig. 1 is the plot of the logarithm of $(K_p)_{avg}$ vs. reciprocal absolute temperature, where $(K_p)_{avg}$ is the average of K_p values of Table I, which are judged by the results of Table II to contain CuO and Cu_2O in the same proportion. A "fair" straight line can be drawn through the 700°–1000°C points of Fig. 1, which are representative of K_p values resulting from samples containing 96% Cu_2O in the oxide coating. This line yields an activation energy of 37,000 cal. Valensi (12) reports 37,700 cal from a similar type plot. Tylecote (2) published a value of 38,000 cal. Castellan and Moore (16) report 37,000 cal for the activation energy involved in the diffusion of cuprous ions in Cu_2O, and from the agreement with the oxidation activation energy it could be postulated that diffusion through the Cu_2O layer is the rate-determining step.

Oxidation data below 700°C can be correlated reasonably well by the use of the standard parabolic equation, $W^2 = K_p' \cdot t$. However, the evaluation of K_p' becomes somewhat

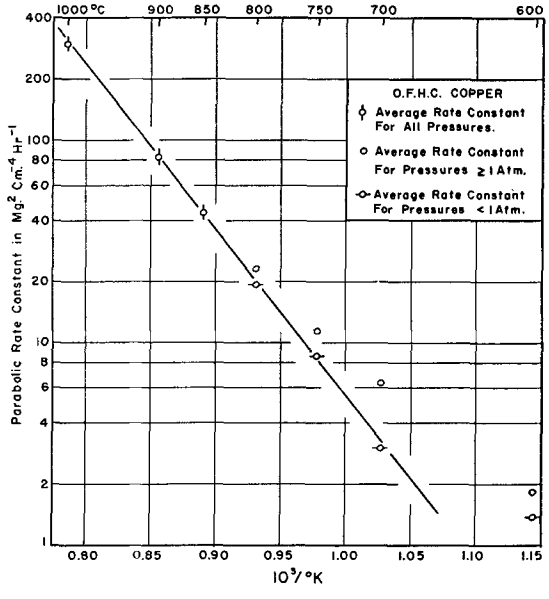

FIG. 1. Temperature dependence of average parabolic rate constants of Table I.

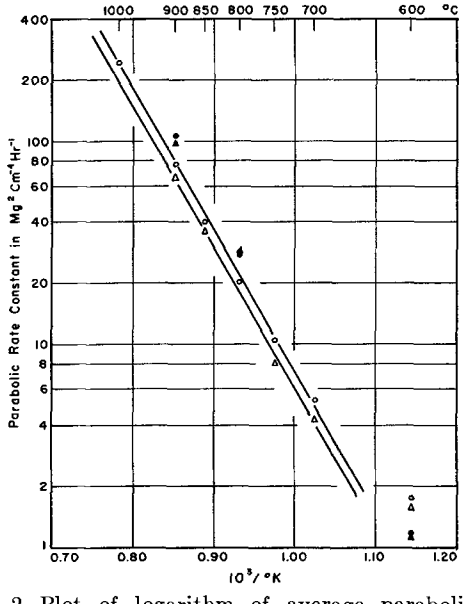

FIG. 2. Plot of logarithm of average parabolic rate constants, calculated from $W^2 = K_p't$ vs. reciprocal absolute temperature. This survey: △ = average for 1 atm; ○ = average for 6.8–20.4 atm. McKewan (3): ● = average for 1 atm; ▲ = average for 6.8–27.2 atm.

arbitrary above 700°C. For this reason equation (I) was employed. The analysis of the 600°–1000°C data above 1 atm by $W^2 = K_p' \cdot t$ is shown in Fig. 2. The average parabolic rate constants calculated from Table I (3) are also included in Fig. 2. The activation energy calculated from the slopes of Fig. 2 was 31,500 cal. In an earlier survey Tylecote (17) reported an activation energy of 31,600 cal (600°–900°C) for the oxidation in air of copper containing 0.04% phosphorus.

ACKNOWLEDGMENTS

The authors wish to thank the Office of Ordnance Research, Department of the Army, and its Watertown Arsenal Laboratory, for the funds that made this work possible. They express their thanks to Mr. Theron Odekirk who performed the bulk of the calculations involved in the preparation of Table I. Appreciation is due to Dr. John R. Lewis, Head, Dept. of Metallurgy, University of Utah, for interest shown in this project. They also acknowledge the kindness of the American Metals Co., Ltd., and its Mr. H. M. Schleicher, who graciously furnished the high purity oxygen free-high conductivity copper employed in this survey and the previous investigations (4, 18).

Manuscript received February 13, 1956.
Any discussion of this paper will appear in a Discussion Section to be published in the June 1957 JOURNAL.

REFERENCES

1. R. F. TYLECOTE, *J. Inst. Metals*, **78,** 259 (1950).
2. R. F. TYLECOTE, *ibid.*, **81,** 681 (1952).
3. W. M. MCKEWAN AND W. M. FASSELL, JR., *J. Metals*, **5,** 1127 (1953).
4. J. P. BAUR, D. W. BRIDGES, AND W. M. FASSELL, JR., *This Journal*, **103,** 266 (1956).
5. R. C. PETERSON, W. M. FASSELL, JR., AND M. E. WADSWORTH, *J. Metals*, **6,** 1038 (1954).
6. U. R. EVANS, *Trans. Am. Electrochem. Soc.*, **46,** 247 (1924).
7. U. R. EVANS, "Pittsburgh Internat. Conf. on Surface Reactions (Proc.)," p. 73, Corrosion Publishing Co., Pittsburgh (1948).
8. O. KUBASCHEWSKI AND B. E. HOPKINS, "Oxidation of Metals and Alloys," p. 43, Academic Press, Inc., New York (1953).
9. W. JOST, "Diffusion in Solids, Liquids, and Gases," p. 353, Academic Press, Inc., New York (1952).
10. C. WAGNER AND K. GRUNEWALD, *Z. physik. Chem. (B)*, **40,** 455 (1938).
11. R. F. TYLECOTE, *J. Inst. Metals*, **78,** 301 (1950).
12. G. VALENSI, "Pittsburgh Internat. Conf. on Surface Reactions (Proc.)," p. 156, Corrosion Publishing Co., Pittsburgh (1948).
13. J. P. DENNISON AND A. PREECE, *J. Inst. Metals*, **81,** 732 (1952) (Fig. A, discussion to article on p. 229, same vol.).
14. A. DRAVNIEKS, *J. Am. Chem. Soc.*, **72,** 3761 (1950).
15. P. D. DANKOV AND D. V. IGNATOV, *Izvet. Akad. Nauk S.S.S.R.*, **1949,** (Khim.), (3), 234.
16. G. W. CASTELLAN AND W. J. MOORE, *J. Chem. Phys.*, **17,** 41 (1949).
17. R. F. TYLECOTE, *J. Inst. Metals*, **78,** 327 (1950).
18. J. P. BAUR, D. W. BRIDGES, AND W. M. FASSELL, JR., *This Journal*, **102,** 490 (1955).

Effect of Prior Corrosion History on the Corrosion of Zircaloy-2 in High Temperature Water

D. E. THOMAS AND S. KASS

Bettis Atomic Power Division, Westinghouse Electric Corporation, Pittsburgh, Pennsylvania

ABSTRACT

A method is presented which permits in a relatively short time the prediction of the corrosion behavior of Zircaloy-2 after very long exposure times in high temperature water. The technique, which is of practical value, involves changing the corrosion test temperature, and yields transient effects which are of interest from a theoretical point of view.

Zircaloy-2 is a complex alloy of sponge Zr containing 1.5% Sn, 0.12% Fe, 0.10% Cr, and 0.05% Ni (60 ppm N max) which has found extensive application. The corrosion behavior of Zircaloy-2 has been studied as a function of temperature and time, and considerable data have been reported previously (1).

The corrosion behavior of Zircaloy-2 is shown by the dotted lines in Fig. 1 and 3 in which the weight gain is plotted vs. exposure time on logarithmic scales. The curve for corrosion in 750°F (400°C) degassed steam at 1500 psi shows a change in slope at a weight gain of 40 mg/dm² in the vicinity of 40 days. It will be noted in Fig. 1 that in 680°F (360°C) degassed water, an inflection in the log weight gain-log time curve normally occurs at a weight gain of approximately 35 mg/dm² after an exposure of about 115 days. No inflection or slope changes are observed in the 600°F (315°C) or 550°F (288°C) tests, evidently because very long exposures would be required to reach the weight gain at which the change in slope occurs at the lower temperature.

The term "breakaway" has been used to describe the abrupt change in slope mentioned above in the case of

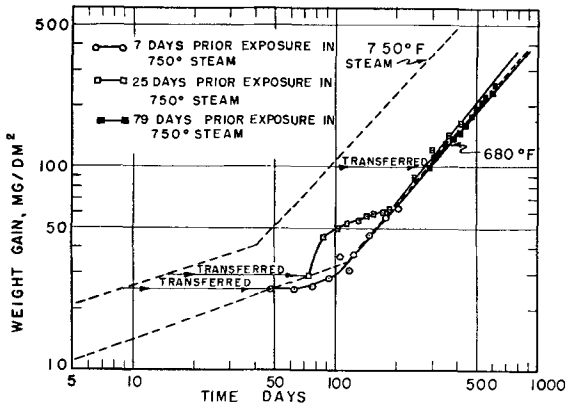

FIG. 1. Effect of transferring Zircaloy-2 corrosion specimens from higher temperatures on corrosion behavior at 680°F (360°C).

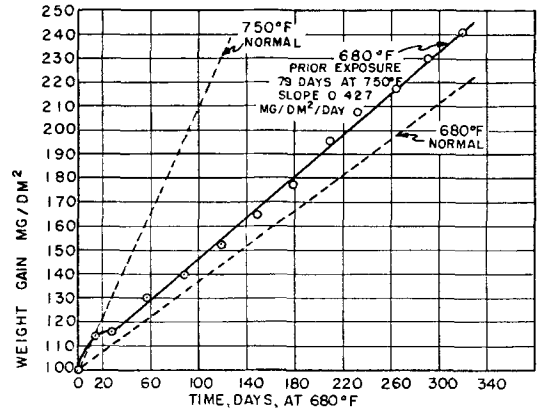

FIG. 2. Linear plot of weight gain vs. time at 680°F (360°C) subsequent to transfer from corrosion test at 400°C.

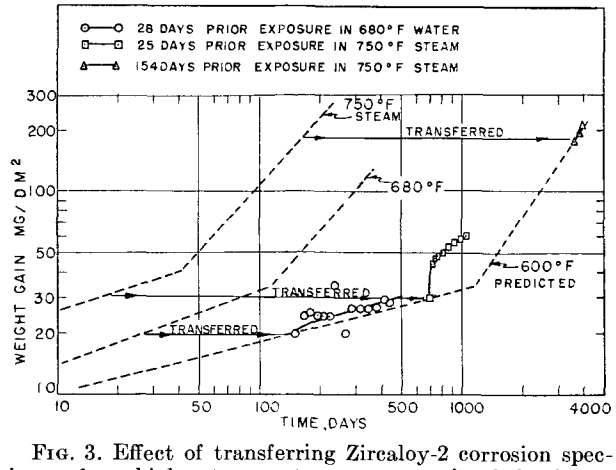

FIG. 3. Effect of transferring Zircaloy-2 corrosion specimens from higher temperatures on corrosion behavior at 600°F (315°C).

Zircaloy-2, its usage having been carried over from the behavior of unalloyed Zr. Since for unalloyed Zr "breakaway" signifies the beginning of spalling of the corrosion product, and since for Zircaloy-2 the kinetics change without spalling of the oxide, the term "transition" will be used here in connection with Zircaloy-2. The corrosion rate of Zircaloy-2 is constant after the transition and amounts to 1.1 mg/dm²/day at 750 (400°C) and 0.37 mg/dm²/day at 680°F (360°C). In view of the low value of this post-transition corrosion rate, much of the useful life of Zircaloy-2 accrues in this period. The purpose of the work described here was to determine the post-transition corrosion rate at 600°F (315°C) by a short-cut method which would avoid the long exposure times indicated in Fig. 3. It is estimated that 1150 days would be required to reach the transition at 600°F (315°C).

The short-cut method consists of exposing specimens at a high temperature for a time sufficient to pass the transition and subsequently transferring them to a lower temperature for corrosion rate measurement. The validity of such a procedure depends on the corrosion mechanism remaining unchanged in steam and water in the temperature range under consideration. The corrosion behavior of Zircaloy-2 suggests that this is the case (1).

In addition, specimens were transferred from exposures at one temperature to another before transition in the hope of obtaining transient effects which may aid in understanding the mechanism of corrosion.

Experimental Procedure

Specimens of Zircaloy-2, measuring 1 in. x 0.5 in. x 0.1 in., were vacuum annealed for 1 hr at 800°C and furnace cooled. After having been bright etched in 38% HNO_3—5% HF—57% H_2O, ten specimens were exposed according to each of the following schedules:

Initial Exposure	Final Exposure
7 days at 750°F (400°C) (1500 psi)	680°F (360°C) (2705 psi)
25 days at 750°F (400°C) (1500 psi)	680°F (360°C) (2705 psi)
79 days at 750°F (400°C) (1500 psi)	680°F (360°C) (2705 psi)
28 days at 680°F (360°C) (2705 psi)	600°F (315°C) (1553 psi)
25 days at 750°F (400°C) (1500 psi)	600°F (315°C) (1553 psi)
154 days at 750°F (400°C) (1500 psi)	600°F (315°C) (1553 psi)
154 days at 600°F (315°C) (1500 psi)	750°F (400°C) (1500 psi)
28 days at 680°F (360°C) (2705 psi)	750°F (400°C) (1500 psi)

Weight gains were determined periodically during the initial and final exposures. The corrosion product was not removed when the specimens were transferred.

Results

In general, data pertaining to all transfers to a given temperature are represented on a single log weight gain vs. log exposure time plot. In analyzing the data the accumulated weight gain was plotted against the exposure time after transfer for each experiment, e.g., Fig. 2. The results of tests which involve transfer after the transition time are presented first since these bear directly on the main purpose of the work. The results of tests which involve transfer before the transition show interesting transient effects and are presented separately.

Transfers after Transition

The group of specimens which was first exposed to 750°F (400°C) steam for 79 days then transferred to 680°F (360°C) water corrode at the latter temperature essentially as would be expected for samples having the same weight gain attained by exposure at the lower temperature (*see* Fig. 1 and 2). The post-transition corrosion rate calculated for the transferred specimens is 0.42 mg/dm²/day as compared to 0.37 mg/dm²/day for those specimens exposed only to 680°F (360°C) water. If the

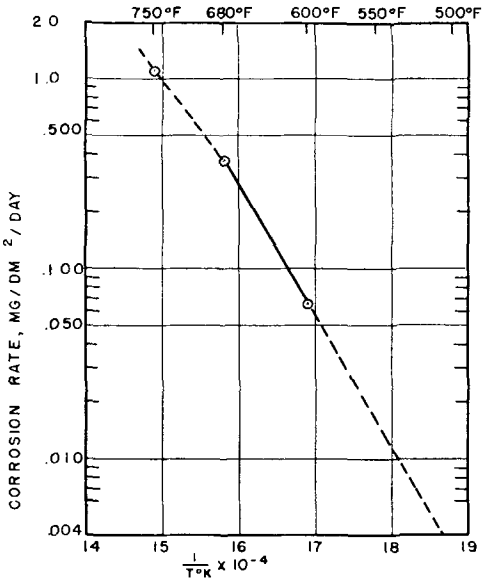

FIG. 4. Effect of temperature on the post-transition corrosion rate of Zircaloy-2 in water and steam.

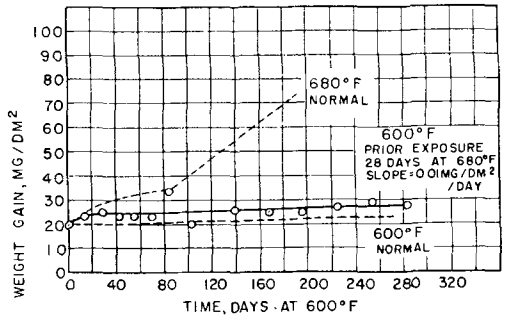

FIG. 5. Linear plot of weight gain vs. time at 600°F (315°C) subsequent to transfer from corrosion test at 680°F (360°C).

transient effect is disregarded for the moment, it is seen that the specimens initially exposed in 750°F (400°C) steam for 25 days eventually corrode at a post-transition rate of 0.46 mg/dm²/day when transferred to 680°F (360°C) water. Thus it is seen that the post-transition corrosion rate determined by the transfer method is in essential agreement with that obtained by continuous exposure.

A similar procedure was used to determine the post-transition corrosion rate at 600°F (315°C). Data for a group of specimens exposed for 154 days in 750°F (400°C) steam prior to exposure in 600°F (315°C) water are presented in Fig. 3. The linear portion of the corrosion curve so obtained has a slope of 0.065 mg/dm²/day. Using this post-transition corrosion rate it is possible to complete the corrosion curve for 600°F (315°C). In order to do this it is necessary to assume a value for the weight gain at the transition point. The corresponding weight gain values at higher temperature are 100 mg/dm² in 850°F (455°C) (1500 psi) steam, 51 mg/dm² in 750°F (400°C) (1500 psi) steam, and 34 mg/dm² in 680°F (360°C) water. Thus the weight gain at transition decreases with decreasing temperature, and the data suggest that with decreasing temperature the transition weight gain approaches a limiting value. It does not appear possible to make an accurate extrapolation to lower temperatures on the basis of existing data. A similar situation arises when an extrapolation of time to transition is attempted. It was therefore assumed that the transition weight gain is the same at 600°F (315°) and 680°F (360°C). Thus a transition point on the 600°F (315°C) curve in Fig. 3 was selected at 34 mg/dm² which corresponds to an exposure time of 1150 days. Beginning at this point a line was drawn corresponding to the experimentally determined post-transition corrosion rate of 0.065 mg/dm²/day.

The temperature dependence of the post-transition corrosion rate is illustrated in Fig. 4. Considering only the two points corresponding to corrosion in the liquid phase, an activation energy in the neighborhood of 32,000 cal/mole is suggested. This is about three times the activation energy for the rate constants applicable to corrosion prior to transition.

Transfer before Transition

Those specimens which were first exposed for a time insufficient to reach the transition and subsequently exposed at a lower temperature show a peculiar tendency for the corrosion rate characteristic of the high temperature to persist for considerable times after transfer to a lower temperature. An example of such memory behavior is seen in Fig. 3 for specimens transferred to 600°F (315°C). In Fig. 5 the actual data points may be compared with the curve which would have been followed had the exposure continued at 680°F (360°C) and the curve which would have been followed had the specimens been continuously exposed at 600°F (315°C). Data points tend to follow the former curve for a time and then to become parallel to the latter curve. Similar behavior is illustrated in Fig. 1 and 3. In Fig. 1 the memory phenomenon is seen to persist for about 100 days after transfer, and the transition weight gain appears to be shifted to a higher value for specimens transferred after 25 days at 750°F (400°C).

On the other hand, specimens transferred to 680°F (360°C) after 7 days in 750°F (400°C) steam do not show the memory phenomenon. The data points do not differ significantly from the expected curve for 680°F (360°C) exposure.

It should be noted that specimens transferred from a higher temperature to a lower temperature after transition

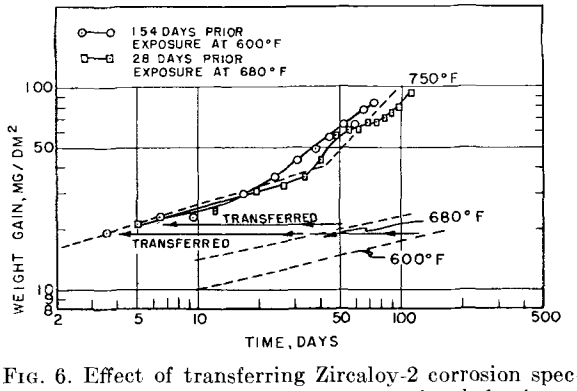

FIG. 6. Effect of transferring Zircaloy-2 corrosion specimens from lower temperatures on corrosion behavior at 750°F (400°C).

also exhibit a memory behavior as may be seen in Fig. 1 and 3.

Two experiments were performed in which the specimens were exposed first at a low temperature then at a higher temperature. Results are shown in Fig. 6. There is a slight indication that the corrosion rate after transfer is initially less than would be normally expected at the higher temperature.

Discussion

Determination of post-transition corrosion rates by the transfer technique appears to be reasonably reliable and accurate. It is believed that this technique can be applied to other alloys of the Zircaloy type, that is, alloys containing 0–2.5% tin with up to 0.5% total Fe, Ni, and Cr, since it is known that such alloys exhibit similar behavior in steam and in water.

The curious memory phenomenon should be explicable in terms of the corrosion mechanism. For the purpose of this discussion it is convenient to consider two aspects of the corrosion of Zircaloy-2, the first being the initial diffusion-controlled period, and the second the termination of the diffusion-controlled period.

The oxide film formed during the pretransition period is believed to grow by the diffusion of oxygen ions via oxygen ion vacancies from the water/oxide interface to the metal/oxide interface. It would be expected that an oxide film of a given thickness grown at a high temperature would have a greater oxygen ion vacancy gradient than that grown at a lower temperature. It is not surprising then that transfer to a lower temperature would result in an initially higher corrosion rate which persists until the excess anion vacancy gradient is removed. Referring to a particularly well defined case of the memory phenomenon shown in Fig. 5, it is seen that the increment of weight gain resulting from the memory phenomenon is about 4 mg/dm^2 for samples transferred when the weight gain was 20 mg/dm^2. At first glance it may appear that the number of vacancies which were filled is the difference between the total anion vacancy content of the film grown at the higher temperature and that of a film of the same thickness grown at the lower temperature, and to fill this number of vacancies apparently required 4 mg/dm^2 of oxygen. This implies that in excess of 20% of the oxygen ion sites in the ZrO_2 lattice are vacant, and is far greater than is to be expected. However, the more rapid corrosion rate associated with the presence of the excess vacancy gradient immediately after transfer must also result in a correspondingly continued rapid rate of generation of vacancies at the advancing metal/oxide interface. Thus, the passage of many more vacancies than suggested above would be required before the corrosion rate decays to normal.

It will be noted in Fig. 1 that no memory was observed for those samples transferred to 680°F (360°C) after having been exposed for 7 days at 750°F (400°C). This appears to be inexplicable on the basis of diffusion of excess vacancies. Since these specimens have a thinner oxide than any of the other specimens at the point of transfer, a smaller transient would be expected. However, a marked transient was observed for specimens transferred after 25 days and having only a slightly greater oxide thickness at transfer as may be seen in Fig. 5.

Alternatively, the memory phenomenon may be thought of as a premature and temporary termination of the diffusion-controlled period as a result of disturbances accompanying the temperature change. It has been suggested that the transition normally results when the pickup of hydrogen during corrosion causes hydride to form at the metal oxide interface. Since the solubility of hydrogen decreases with decreasing temperature, it is suggested that the memory phenomenon may result when the exposure at the higher temperature causes the hydrogen content at the metal/oxide interface to exceed the solubility limit characteristic of the lower temperature so that transition sets in upon transfer to the lower temperature. Upon continued exposure at the lower temperature the hydride may dissolve and the hydrogen diffuse away from the metal/oxide interface and cause the corrosion behavior to revert to normal as in Fig. 5, or, alternatively, normal transition characteristic of the lower temperature may begin as in Fig. 1 (25 day samples) before the hydride can diffuse into the bulk of the sample. The lack of the memory phenomenon shown in Fig. 1 (7 day samples) may be explained on the basis that at the higher temperature the hydrogen content at the metal/oxide interface did not exceed the solubility characteristic of the lower temperature, since the samples were held for only 7 days at 750°F (400°C) before transfer as compared to 25 days for the samples which exhibited a transient effect. Such an explanation is open to question, however, since current work indicates that the transition occurs in pure dry oxygen at the same time and weight gain as it does in steam, suggesting that hydrogen is not a factor.

The termination of the diffusion-controlled corrosion process evidently occurs when a critical oxide thickness characteristic of the exposure temperature is reached. When the critical oxide thickness is exceeded, structural faults such as cracks due to stresses developed in the film may occur. Since the critical oxide thickness increases with temperature, it seems reasonable to assume that stress in a film of a given thickness at a higher temperature is less than that in a film of the same thickness at a lower temperature. Thus, upon transfer from a high temperature to a low temperature, stress in the oxide film would be less than would be normal at the lower temperature, and it should be possible for the oxide to grow to a greater than normal thickness before transition occurs. Such a situation appears to exist in Fig. 1 (25 day samples) and Fig. 3 (25 day samples) which show corrosion rates at 80 and 420 days, respectively, which are less than post-transition rates, while the oxide thickness (weight gain) exceeds considerably the critical oxide thickness characteristic of continuous exposure of the lower temperature.

The memory phenomenon thus appears to be explicable, except in one anomolous case, on the basis of the anion diffusion process, on questionable ground with regard to the formation of hydride at the metal/oxide interface, and only partially explicable on the basis of stress in the oxide film.

In the practical sense the memory phenomenon suggests that on varying the temperature cyclically the effective

corrosion temperature is very close to the maximum temperature of the cycle.

Conclusions

The linear corrosion rate of Zircaloy-2 which occurs at very long exposure times at low temperatures can be determined in a relatively short time by measurement of the corrosion rate at the low temperature in question after sufficient previous exposure at a higher temperature to reach the linear portion of the weight gain-time curve. This technique should be applicable to other alloys of the Zircaloy type.

The transient effects which persist for a time after a change of temperature has been effected are discussed in terms of several aspects of corrosion mechanism. No completely satisfactory explanation of this behavior is offered.

Acknowledgment

This work was performed under AEC Contract AT-11-1-GEN-14.

Manuscript received October 13, 1955.
Any discussion of this paper will appear in a Discussion Section to be published in the June 1957 Journal.

REFERENCE

1. "Metallurgy of Zirconium," edited by B. Lustman and F. Kerze, Vol. 4, Div. VII, NNES, Chap 11, McGraw-Hill Book Co., New York (1955).

Natural and Thermally Formed Oxide Films on Aluminum

M. S. Hunter and P. Fowle

Aluminum Research Laboratories, Aluminum Company of America, New Kensington, Pennsylvania

ABSTRACT

Structure and rate of formation of natural and thermally formed oxide films on Al are discussed. It is shown that these films consist of a layer of barrier-type oxide, the thickness of which is primarily a function of temperature, and a porous layer, the thickness of which is determined by time and natural forces associated with the environment. Effects of temperature and environment on the formation rate and ultimate thickness of these layers are described.

One of the outstanding merits of Al is its remarkable resistance to atmospheric corrosion. This is somewhat surprising in view of its high position in the activity series. The reason for such high resistance to attack is the oxide film provided Al by nature. Although this film is extremely thin and thus easily damaged, it has such remarkable self-healing properties that, if damaged, it immediately starts to reform. The manner in which the natural oxide film forms on Al, its structure, and some of the factors affecting its rate of growth and ultimate thickness are discussed in the present paper.

Published information has revealed many interesting and valuable facts regarding the nature of natural films on Al. It has been shown that in dry oxygen at room temperature the natural film reaches an ultimate thickness of about 10Å in a matter of minutes (1). Various investigators, however, have demonstrated that the film formed in ordinary air is much thicker and takes weeks, months, and even years to reach its ultimate thickness (2–4). It has been suggested that films formed in the former case are impermeable barrier-type films; in the latter case, although the film still has a compact barrier type of film adjacent to the metal, it also has an outer layer of porous or more permeable oxide (5).

Method

The principal method of measurement used in this investigation, described in detail in a previous publication (6), is a simple electrical procedure capable of measuring the thickness of compact barrier-type oxide films with high accuracy. This method is based on the mechanism of film formation on an Al anode in an electrolyte that does not dissolve the oxide. Under these conditions, 1 v of applied potential forms oxide to a maximum thickness of 14Å on the metal surface, after which only leakage current flows. When voltage is applied gradually to a sample having a barrier oxide layer, the voltage required to produce current flow just equal to normal leakage is a measure of the thickness of the oxide barrier layer; multiplying this voltage by 14 gives the thickness in Ångstrom units. It has been found that this method measures only oxide films of the compact barrier type and that it is capable of measuring the thickness of such films with an accuracy of about 3Å.

The measuring procedure consists, briefly, of making the specimen the anode in a 3% solution of $C_4H_6O_6$ adjusted to a *p*H of 5.5 with NH_4OH. Potential is applied gradually and thickness is determined from the voltage required to produce normal leakage current.

Natural Films on Al

In the preliminary stage of the present work, the barrier measurement method was applied to a number of samples of Al and Al alloy sheet that had been stored in the laboratory at room temperature for periods of from one week to several years. It was found that on every specimen a

definite barrier could be measured, and that it was the same, approximately 10Å, on each, regardless of the storage period.

This thickness is the same as that which was observed to form on Al in dry oxygen. Thus, this value apparently represents the greatest thickness of barrier-type oxide which can be formed at room temperature, regardless of time and environment. As such, it probably represents the distance through which Al can move under the forces of thermal agitation associated with temperature, or under the influence of the potential field within the coating suggested by Mott (7). This situation is analogous to that observed in anodically formed barrier-type oxide films where the operative force is the applied potential. On this basis, it would appear that the forces controlling the formation of natural and anodically formed films on aluminum are basically the same.

As has been mentioned, a number of investigators have demonstrated that the film formed on Al at room temperature is much thicker than 10Å, the actual thickness depending on the time and the atmospheric conditions under which the film is formed. It is evident, therefore, that the natural film formed in a normal atmosphere must consist of two layers. Adjacent to the metal is a compact layer of barrier-type oxide. Covering the barrier layer is an outer layer that does not respond to the barrier measurement; therefore, it must be of a more permeable type of oxide. Since it has been shown that a film formed in a moist atmosphere contains an appreciable amount of water (8), this outer layer is probably formed from the barrier oxide by hydration.

The natural film on Al can be visualized as the net result of the competition between opposing forces—those tending to build up a compact oxide barrier layer, and those tending to break it down. The ultimate structure of the oxide depends on the relative rates of these competing forces. If the destructive forces are absent, the natural film will be of the barrier type and will form rapidly to a limiting thickness. If the destructive forces are predominant, oxide may be broken down almost as fast as it is formed, and little barrier will remain. In the intermediate range, in which the constructive and destructive forces can reach a reasonable balance, relatively thick natural films are formed.

Natural Barrier Formation in Moist Air

In the formation of natural barrier-type films in moist air, both destructive and constructive forces are at work. At any temperature, as shown in Fig. 1, barrier thickness rises gradually to a limiting thickness under the conditions of the experiment. The rate of oxide formation is probably the same as in the absence of moisture, but the destructive effect of the environment is relatively great, with the result that the net thickness of barrier oxide increases slowly. Ultimate barrier thickness increases with temperature, which gives support to the theory that thermal agitation controls barrier thickness. When the ultimate thickness has been reached, horizontal portions of Fig. 1, the barrier no longer thickens, but barrier oxide formation may still be taking place. In this case, a balance has been established between the forces of formation and breakdown, and although barrier thickness remains constant, the total thickness of the film may still be increasing.

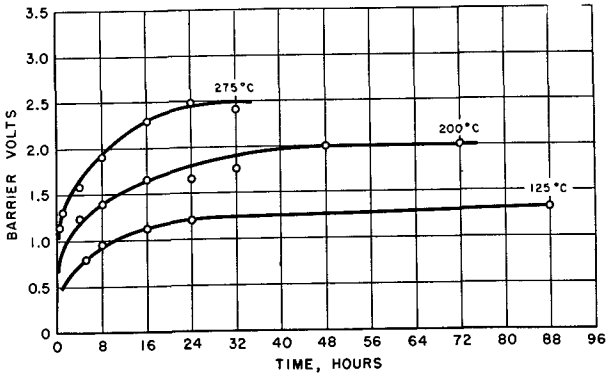

Fig. 1. Growth of oxide films on high purity aluminum in moist air.

A more direct indication of the destructive action of atmospheric moisture on the natural film was observed from the change in the barrier layer thickness of films formed at one temperature and then held at a lower temperature in humid atmospheres. A sample heated at 200°C for a sufficient time to build the barrier portion of the film to its ultimate thickness of 28Å was stored at room temperature in air saturated with water vapor. At the end of 48 hr the barrier thickness had dropped 9Å, a loss of about 30%.

Additional evidence of the destructive effect of the environment is the fact that the assorted samples stored at room temperature, which were discussed earlier, all had the same barrier thickness. Several of these specimens undoubtedly had initially high barrier layer thicknesses because they had been exposed to temperatures as high as 538°C (1000°F), but by the time they were measured the barrier layer had decreased to the thickness corresponding to that of a film formed at room temperature. From this it is apparent that, in the presence of destructive environmental forces, the thickness of the barrier portion of a natural oxide film, regardless of the temperature at which it was originally formed, tends toward a steady-state value determined by the temperature of its environment

Natural Barrier Films Formed in Dry Air and Dry Oxygen

In the formation of natural films in the absence of moisture, only the constructive forces are at work. Under such conditions, the times required to complete barrier formation are much shorter, as shown by Fig. 2. Even at low temperatures, such as those shown in Fig. 1, the ultimate thickness of barrier is reached in an hour or less in contrast to the 12–36 hr periods required in the presence of moisture. As with moist air, an ultimate barrier thickness is reached for any given temperature and, of even greater importance, the ultimate thicknesses are the same in both environments. In the present case, however, film growth has probably ceased when the ultimate barrier thickness is attained.

As the temperature of film formation is increased, unusual behavior in the time-barrier voltage curve is encountered beginning at about 475°C. At this temperature,

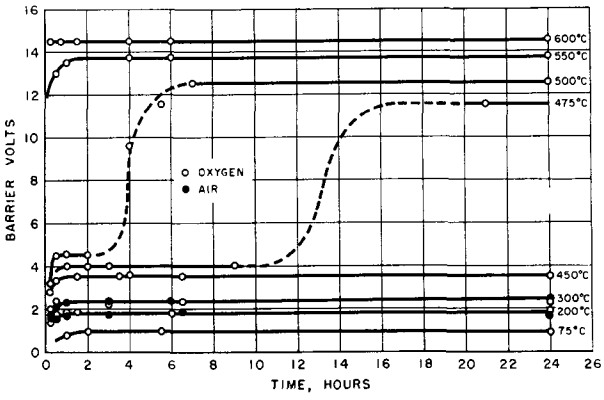

FIG. 2. Growth of oxide films on high purity aluminum in dry atmospheres.

a constant barrier thickness is reached rapidly, but, if formation time is prolonged, barrier values begin to increase for a second time. At higher temperatures, such as 500°C, two plateaus are again observed, but the time required to reach the first plateau and the time before the second rise are shorter than at the lower temperature. At still higher temperatures, the first plateau is lost and barrier values rise rapidly to high steady levels. Thus, at intermediate temperatures two different barrier thicknesses are measured; at low and at very high temperature only one barrier thickness is measured. In all cases, however, there is a constant increase in ultimate barrier thickness with increasing temperature at both the low and high levels.

From these curves, it is evident that at any given temperature the ultimate barrier thickness is the same in dry air and slightly moist air as it is in dry oxygen. It is apparent, therefore, that the maximum possible barrier thickness is a function only of temperature.

STRUCTURE OF NATURAL OXIDE FILMS

Electron microscopy and electron diffraction revealed that the unusual behavior of the curves shown in Fig. 2 was associated with the structure of the oxide. The barrier films represented by the first plateau are amorphous in nature; those represented by the upper plateau are a crystalline form of Al_2O_3, namely η-alumina. In the intermediate temperature range, the two-step curve indicates, first, the formation of an ultimate thickness of amorphous barrier and, later, the formation of an ultimate thickness of crystalline barrier. It is apparent that at intermediate temperatures the rate of amorphous barrier formation is much more rapid than the crystallization of this material to form the crystalline barrier. At higher temperatures, the rate of crystallization rises rapidly, occurring about as rapidly as oxide is formed, and the only ultimate barrier thickness observed is that of the crystalline barrier.

By following the progress of crystallization by electron microscopy and electron diffraction, the actual crystallization of amorphous oxide to crystalline oxide was observed, as shown by Fig. 3. At low temperatures, or at intermediate temperatures for short times, only amorphous oxide was found by both methods (Fig. 3A). After longer times at intermediate temperatures or very short times at high

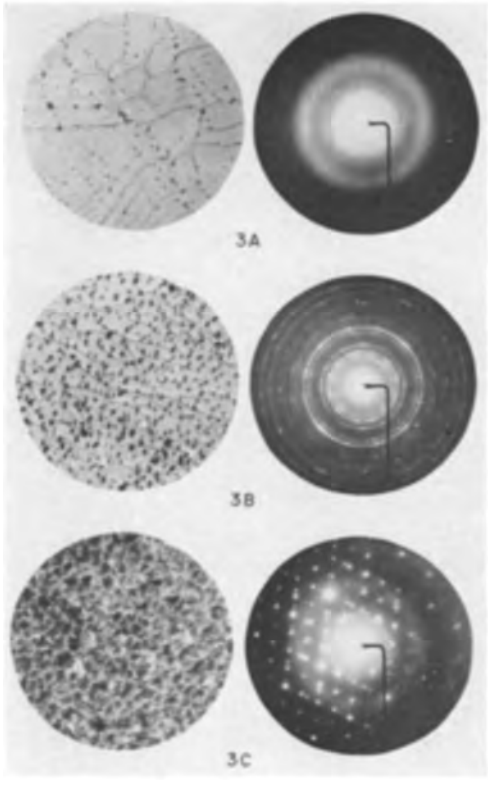

FIG. 3. Progress in crystallization of thermally formed films on aluminum as shown by electron micrographs (left) at 15,000× (before reduction for publication), and electron diffraction patterns (right).

temperatures, crystals of η-alumina were observed by the electron microscope and partial crystallinity was indicated by electron diffraction (Fig. 3B). After long periods at intermediate and high temperatures, complete crystallinity was apparent in the microstructure and diffraction patterns (Fig. 3C).

ULTIMATE THICKNESS OF NATURAL BARRIER FILMS

If the ultimate thickness of natural barrier films is considered in relation to the temperature of formation, it is found that barrier thickness is a linear function of temperature as shown by Fig. 4. In this plot, which shows a two-part curve, the lower portion represents the ultimate thickness of amorphous barrier which can be formed; the

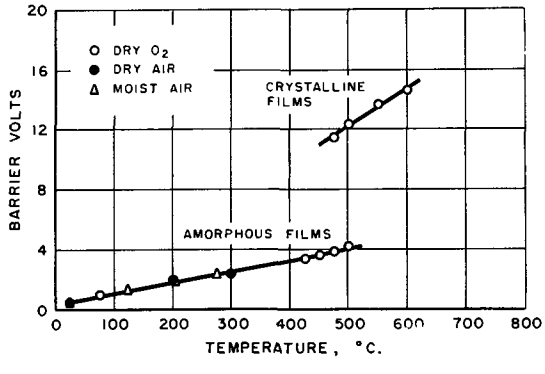

FIG. 4. Relationship between temperature and barrier thickness of natural oxide films on aluminum.

upper part represents the ultimate thickness of crystalline barrier which can be formed. Measurements made in extremely short times would probably extend the amorphous barrier curve to higher temperatures. Also, if samples were held at temperature for sufficient time, it should be possible to extend the curve representing crystalline barriers into the temperature range of 250°–450°C, which is the range in which η-alumina first forms.

From the values shown for ultimate amorphous barrier thickness, it is apparent that this ultimate thickness is a function of temperature rather than environment, since the ultimate thicknesses for moist air, dry air, and dry oxygen all fall on the same line. This would hold true in the case of moist air only if the rate of hydration was not too great. In the case of other environments which could supply sufficient oxygen to form the film but which were highly destructive to the oxide, the ultimate barrier thickness might never be reached.

In view of the linear relationship between barrier thickness and temperature, it is possible to derive a factor for natural barrier films which is analogous to the unit barrier thickness of anodically formed barrier type films. On the basis of the data presented in Fig. 4, it is apparent that about 10Å of amorphous barrier oxide is formed for each 100°C increase in temperature, whereas crystalline films appear to be formed at a rate of about 28Å for each 100°C rise in temperature.

Summary and Conclusions

Naturally and thermally formed films on Al must consist basically of two layers, a layer of compact barrier-type oxide in contact with the metal and an outer layer of more permeable oxide. The barrier layer is formed by the simple combination of Al and oxygen and exhibits rectifying characteristics similar to those of anodically formed barrier films. The maximum possible thickness of this natural barrier is controlled by temperature alone, in the same manner that the thickness of an anodic barrier film is controlled by the applied voltage. In the case of natural barrier oxide, this thickness is probably a function of thermal agitation on the atomic scale which, in turn, is a function of temperature. These natural barrier films may be either amorphous or crystalline, depending on whether they are formed below or above the temperature required to form η-alumina.

The outer portion of natural and thermally formed films is created from the barrier layer by reaction of the compact oxide with components of the environment, principally moisture. It is different from the barrier oxide in that it passes current freely in either direction, in this respect being similar to the porous portion of anodically formed oxide films. The thickness of the outer portion of natural oxide films is a function of time and the destructive effects of the environment, since the creative forces attempt to form the barrier layer to its maximum possible thickness and thus continue to furnish material for the formation of the outer layer.

Although this work has been confined solely to aluminum, it is likely that similar situations exist with films on zirconium, titanium, tantalum, and any other metal which characteristically develops a natural film of the compact barrier type.

Acknowledgment

The authors wish to express their appreciation to F. Keller under whose direction this work was conducted.

Manuscript received October 13, 1955. This paper was prepared for delivery before the Pittsburgh Meeting, October 9 to 13, 1955.

Any discussion of this paper will appear in a Discussion Section to be published in the June 1957 Journal.

REFERENCES

1. F. Keller and J. D. Edwards, *Metal Progr.*, **54,** 37 (1948).
2. G. Hass, *Optik*, **1,** 134 (1946).
3. A. Steinheil, *Ann. Physik*, **19,** 465 (1934).
4. N. Cabrera and J. Hamon, *Compt. rend.*, **225,** 59 (1947).
5. F. Keller and J. D. Edwards, *Metal Progr.*, **54,** 200 (1948).
6. M. S. Hunter and P. Fowle, *This Journal*, **101,** 481 (1954).
7. N. F. Mott, *Trans. Faraday Soc.*, **43,** 429 (1947).
8. F. Keller and J. D. Edwards, *Metal Progr.*, **54,** 196 (1948).

The Tin-Steel Couple in Air-Free Citric Acid Solution

E. L. KOEHLER

Armour Research Foundation of Illinois Institute of Technology, Chicago, Illinois

ABSTRACT

In air-free citric acid solution, specimens of uncoupled black plate were found to evolve hydrogen at rates equivalent to the dissolution rates of the steel. Additions of up to 0.3 g $SnCl_2 \cdot 2H_2O$/liter progressively decreased corrosion rates. Tin is anodic to and protects steel sacrificially in solutions containing dissolved tin. Hydrogen evolution is decreased by coupling steel to tin, not solely by inhibition but also by an apparent shift in the anodic polarization curve of the steel. All observed effects on the corrosion rates in this medium, whether traceable to the steel, dissolved tin inhibitor, or coupling to tin, appear to be the results of variations in anodic properties.

Solutions of citric acid have been used a number of times to study the corrosion of tin-steel couples with the idea that such studies are representative of corrosion in fruit-containing cans (1–3). While it is not considered here that this medium may be used directly to evaluate factors contributing to the shelf life of cans, it appears evident that the corrosion mechanisms involved will be similar in many respects to those in canned fruit. The advantage in using citric acid solution rather than food for fundamental studies are easy preparation, greater reproducibility and, presumably, a simpler corrosion mechanism. The purpose of this work is to elucidate the corrosion mechanisms of the tin-steel couple in air-free citric acid solution.

EXPERIMENTAL

The steels used in this work were in the form of full-hard, cold-rolled sheets of typical tin-plate compositions, and were electrocleaned in hot sodium orthosilicate solution. They were all annealed at 650°C. The protective atmosphere used was either dry hydrogen or wet hydrogen. It is known that wet-hydrogen annealing produces a "pickle-lag" in the steel, a condition traceable to oxidation of the grain boundaries in a surface layer of metal (4). It has been found[1] that this condition causes poor internal corrosion resistance. It was thus possible to include one factor in this work which is known to influence the shelf life of cans.

After annealing, the steel pieces were wrapped in paper and stored in a desiccator until used. The storage time in the desiccator apparently had no significant effects on test results. Steel surfaces were bright and clean. Care was taken not to touch them with the fingers, or otherwise alter them after electrocleaning. Specimens were tested with the surfaces in this condition, without abrading or any other type of preparation.

Steel specimens cut from the sheet were 6 cm x 4 cm (48 cm^2 area). For purposes of coupling these to tin, two parallel cuts, 2 mm apart, were made from the center of a 4 cm edge to the center of the specimen. The 3 cm long ribbon thus formed was bent up at right angles to the specimen.

The tin used was rolled to about 0.145 in. thickness and cut into 3.5 cm squares (24.5 cm^2). A hole, approximately 6 mm in diameter, was punched in the center. The ribbon projecting from the steel specimen was passed through this hole, and a tapered glass pin was forced through it, pressing the steel ribbon into the softer tin and giving intimate contact. The tin used was commercial Grade A Longhorn tin; the same lot was used throughout the test work. Prior to use, tin specimens were electrocleaned and treated for 5 min in cold, concentrated HCl solution.

Testing was done in Pyrex glass cells, of the type shown in Fig. 1. The test couple or steel specimen rested on the bottom of the cell, held in an almost vertical position by contact of the glass pin against the side of the cell.

The citric acid solution was 0.2M (*p*H 1.9). Solutions were prepared from redistilled water and reagent grade chemicals. Air was expelled from the solution by heating to boiling, followed by flushing with nitrogen while cooling to the filling temperature. This was done in a special flask designed for filling the cells without introducing any air. Cells were flushed with nitrogen gas prior to filling. They were filled by suction, and the height of citric acid solution in the attached buret was adjusted to zero. Cells were then put in a constant temperature water bath. Silicone stopcock grease was used in all stopcocks and in the ground glass joints. Tygon flexible tubing was used in filling the cells. A point was made of never permitting the solution to contact rubber.

The level in the water bath was about 1 in. above the top of the cells. Testing temperature was usually 60° ± 0.05°C, although some work was done at 55° and 37.78°C. During the test, hydrogen gas was evolved and collected in the top of the cell, where it was held at the temperature of the water bath. This displaced citric acid solution through the hooked tube and up the buret, where it was measured. The top of the buret was closed off by means of a rubber bulb, and the displaced nitrogen from the buret went into this bulb. Data were taken for tin and steel weight losses and for the volume of hydrogen gas evolved.

The volume of hydrogen evolved is reported in several ways. Where it was desired merely to make a comparison of relative evolution rates, it is reported as "indicated" hydrogen, which indicates a direct buret reading, or "uncorrected" hydrogen, which is corrected only for the pres-

[1] By prune pack tests at the American Can Co.

sure corresponding to the height of the liquid in the buret. Where it was desired to compare the amount of hydrogen evolved with the equivalent of the metals taken into solution, corrections are made to STP. In calculating the hydrogen equivalent of the metals taken into solution it is assumed that iron is oxidized to the ferrous state and tin is oxidized to the stannous state.

Potential Cells

For making potential measurements, another type of corrosion cell was used (Fig. 2). The potential cell was positioned in the constant temperature bath, the bridge cell and reference electrode being outside the bath. Hydrogen gas was again measured by means of a buret to correlate potential measurements with hydrogen evolution rates. Lead wires were not exposed to the solution, since the two vertical tubes shown were filled with nitrogen. Steel specimens were the same as volume cell specimens. The 2 mm ribbon was spot welded to an iron lead wire.

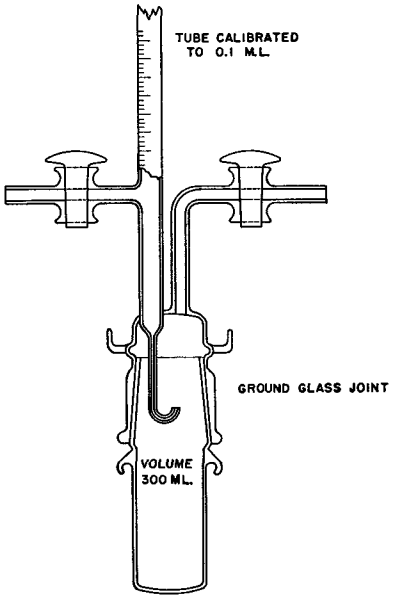

FIG. 1. Gas measuring cell

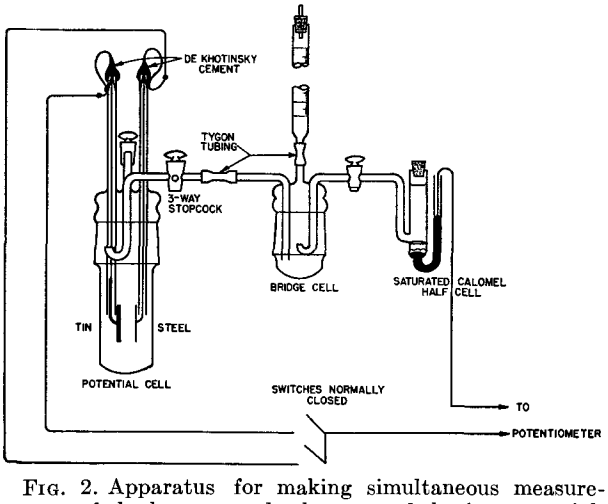

FIG. 2. Apparatus for making simultaneous measurements of hydrogen evolved, uncoupled tin potential, uncoupled steel potential, and potential of the couple.

The tin anodes used were cast disks of the same surface area as the square rolled anodes used in the volume cells. The disk was cast with a projection, bonded to an iron lead wire as indicated. The tops of the lead-in tubes were sealed with "De Khotinsky" hard cement.

The corroding potential of the couple against the reference electrode was followed throughout the period of the test. This potential was effectively at the position of a point midway between the tin and the steel. Uncoupled potentials for tin and the steel were also measured throughout the corrosion period. Such potentials naturally shift after uncoupling. Measurements indicated were made one minute after uncoupling for reasons to be given later. An indication of the magnitude of protective current was determined by the potential drop across a 10 ohm resistance or by using a zero-resistance ammeter.

TESTS ON UNCOUPLED STEEL

No difficulties were encountered in making tests on uncoupled steel in 0.2M citric acid solution at 60°C. Reproducibility of results was excellent. Typical results for a dry hydrogen annealed steel are given in Fig. 3 for seven volume-type cells. All seven tests were started at the same time; they were discontinued after varying time intervals up to five hours. After an initial period, hydrogen was evolved at the theoretical rate. The difference between the two curves represents hydrogen which goes into solution in the steel or in the citric acid solution, or possibly hy-

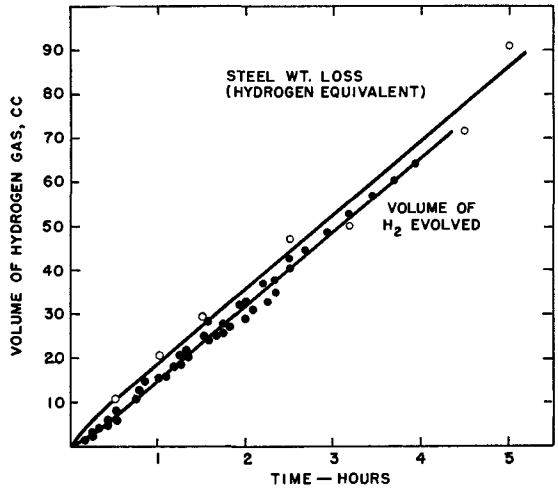

FIG. 3. Weight loss and hydrogen evolved for an uncoupled dry hydrogen annealed steel (steel J). ● = hydrogen volumes corrected to 0°C and 760 mm Hg for the seven tests; ○ = hydrogen equivalents of the steel weight losses.

TABLE I. *Results of tests on uncoupled steels*

Steel	Rate of hydrogen evolution—cc/hr	
	Dry H_2 annealed	Wet H_2 annealed
J	26.6	51.2
G	27.0	60.4
W	39.3	51.3
X	24.4	28.2
Y	27.0	30.0
Z	37.1	68.2

TABLE II. *Chemical analyses of test steels*

Steel	C	Mn	P	S	Si	Cu	Al	Ni	Mo	Cr
J	0.056	0.37	0.011	0.041	<0.002	<0.04	<0.006	<0.02	<0.01	<0.02
G	0.065	0.38	0.010	0.043	<0.002	<0.04	<0.006	<0.02	<0.01	<0.02
W	0.073	0.40	0.009	0.032	<0.002	<0.04	<0.006	<0.02	<0.01	<0.02
X	0.070	0.30	0.013	0.042	<0.002	<0.04	<0.006	<0.02	<0.01	<0.02
Y	0.056	0.35	0.013	0.047	<0.002	<0.04	<0.006	<0.02	<0.01	<0.02
Z	0.074	0.38	0.010	0.033	<0.002	<0.04	<0.006	<0.02	<0.01	<0.02

drogen which was not evolved because of equivalent reduction of some depolarizer present.

Table I shows the average rates of hydrogen evolution for six steels studied, in both the dry and wet hydrogen annealed conditions. In all cases the wet hydrogen annealed steel was attacked more rapidly than the dry hydrogen annealed steel. The steels had different corrosion rates and differed also in their response to a wet hydrogen anneal. No readily apparent correlation could be seen on comparing this behavior with the chemical analyses of the steels, which are given in Table II. Increased corrosion rates for the wet hydrogen annealed steels were found to

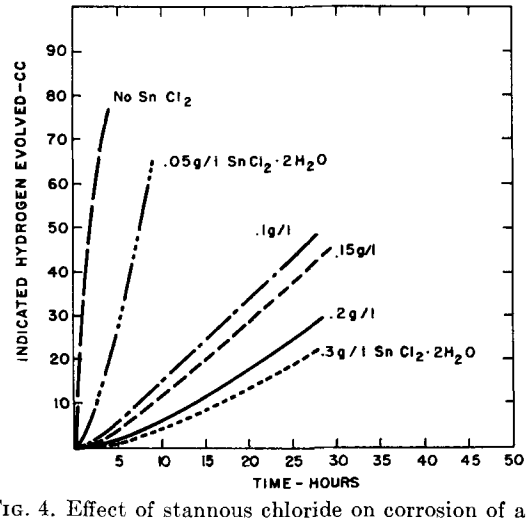

FIG. 4. Effect of stannous chloride on corrosion of a dry hydrogen annealed steel (steel Z).

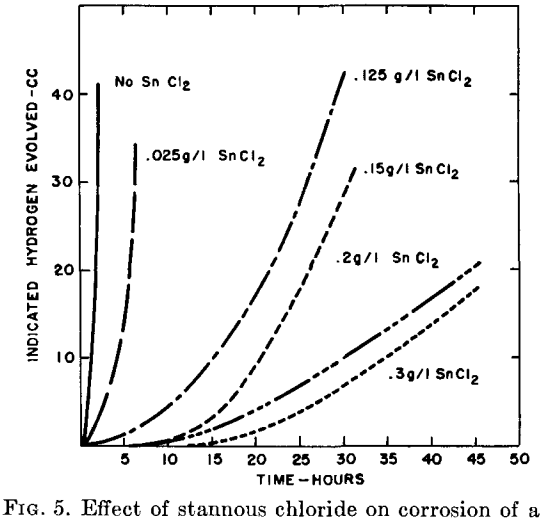

FIG. 5. Effect of stannous chloride on corrosion of a wet hydrogen annealed steel (steel Y).

persist well beyond the "pickle lag" layer, which contains the grain boundary oxides.

Dissolved Tin

Numerous tests were made on specimens of uncoupled steel with stannous chloride added as an inhibitor. As little as 0.025 g/l $SnCl_2 \cdot 2\ H_2O$ provided definite inhibition. Greater amounts produced larger effects. Results for a dry hydrogen annealed steel and a wet hydrogen annealed steel are shown in Fig. 4 and 5, respectively. Dissolved tin exhibited a greater effect on the corrosion rate of the wet hydrogen annealed steel than that of the dry hydrogen annealed steel, at least in the initial period.

Dissolved tin is known to act as an anodic inhibitor. In agreement with this, increasing amounts of dissolved tin were found to shift the corroding potential in the positive direction. The potential of wet hydrogen annealed steel "W", for example, was found to shift from −0.610 to −0.485 v on going from 0 to 0.3 g/l $SnCl_2 \cdot 2\ H_2O$.

Coupled Tests

Hydrogen evolution results of coupled tests in air-free citric acid solution are prone to be very erratic. Quite frequently corrosion rates of duplicate coupled specimens were found to vary as much as several hundred per cent. A large portion of this variation is due to the relative potentials of the steel and tin.

Tin by itself in 0.2M citric acid solution at 60°C assumed a potential of approximately −0.584 v relative to a saturated calomel electrode at 25°C. It tended to remain quite close to this value throughout the period of the tests. Specimens of uncoupled tin exposed for a week evolved no measurable hydrogen, and the amount of weight loss in this period was insignificant. This is attributable to the high hydrogen overvoltage of tin. Accordingly, any weight loss of tin in a coupled test is equivalent to the galvanic current flowing between the steel and the tin. Considerable attention has been given the fact that tin sacrificially protects steel in air-free solutions of food acids, in spite of the fact that the standard electrode potential of steel is considerably more negative (less noble) than that of tin (1, 5). This has been attributed (*a*) to the high hydrogen overvoltage of the tin, and (*b*) to the fact that tin forms stable complex ions with food anions, such as citrate, and therefore it assumes a more negative corroding potential. Both factors are probably involved; uncoupled corroding potentials of the steels studied, however, were in the range of −0.589 to −0.612 v. Accordingly, some other factor or factors are also involved in making the tin negative to the steel. As shown in Fig. 6, potential data indicate that, when tin and steel

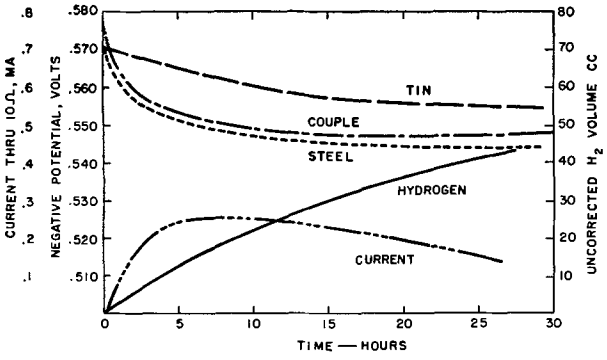

FIG. 6. Potential relationships for a coupled dry hydrogen annealed steel (steel Z).

are coupled, the potentials of both shift in the positive direction. The steel potential shifts more than the tin, and thereby becomes positive to the tin. It is interesting to note that for the particular steel illustrated in Fig. 6 the initial potential of the couple does not lie between that of the tin and that of the steel.

The potential shift of the steel in the positive direction may be attributed at least partially to the inhibiting effect of dissolved tin. With no tin initially in solution, the steel is anodic to the tin and is unprotected. At this time tin goes into solution very slowly. Until sufficient tin goes into solution to inhibit the reaction, steel corrodes rapidly. The duration of this period is dependent on minor variations in the character of the tin and steel surfaces. Accordingly, there is great variation in the results secured on coupled tests in air-free citric acid solution. This situation is overcome by adding a small amount of stannous chloride to the solution used in making the tests, enough to make the tin initially anodic to the steel. An addition of 0.025 g/l $SnCl_2 \cdot 2\ H_2O$ is sufficient for dry hydrogen annealed steels, but the wet hydrogen annealed steels require a larger amount.

This work is concerned only with tests made in the absence of air. Tests conducted in the presence of air have oxygen available as a depolarizer, by virtue of which tin dissolves at a fairly rapid rate regardless of its potential relative to steel. It is to be expected that in this case the above irregularities will not be encountered.

As in the case of uncoupled steel, hydrogen is evolved from a tin-steel couple at the theoretical rate, except during the initial period of the test. This is illustrated for a dry hydrogen annealed steel coupled to tin in Fig. 7. The major portion of the hydrogen results from oxidation of iron. On comparing only the relative corrosion rates of the tin and of the iron it would appear from customary concepts that the tin is not providing much galvanic protection for the steel even though the tin is anodic to the iron. It is evident that more is involved than simple cathodic protection. When coupled to tin, the rate of corrosion of steel is greatly reduced; in fact, the final rate of hydrogen evolution, which is equivalent to the combined solution rates of iron and tin, is only about 3% as great as for a piece of uncoupled black plate. Normally, cathodic protection involves a shift in potential in the negative direction, accompanied by an increase in the rate of the reduction processes. In the present case, there is actually a decrease in the total corrosion rate accompanied by a potential shift in the positive direction. This may be accomplished by a shift in the anodic polarization curve in the positive direction. Such an effect has been attributed to inhibition by dissolved tin. Unquestionably this is a major effect; however, another cause for such a shift appears to exist. This seems to originate in the coupling of the steel to tin.

As has been indicated in Fig. 4, the major amount of inhibition attainable with stannous chloride addition is obtained by virtue of the first 0.1 g/l added. At 0.3 g/l, the corrosion rate is less sensitive to dissolved tin. Comparative corrosion tests have been run with the addition of 0.3 g/l $SnCl_2 \cdot 2\ H_2O$ to the citric acid solution, using specimens of the same steel in both the coupled and uncoupled conditions. In such cases there is still a very great decrease in hydrogen evolution rate for the coupled specimens. This is illustrated in Fig. 8.

Perhaps even more convincing are the results shown in Fig. 9. These comparative tests on a wet hydrogen an-

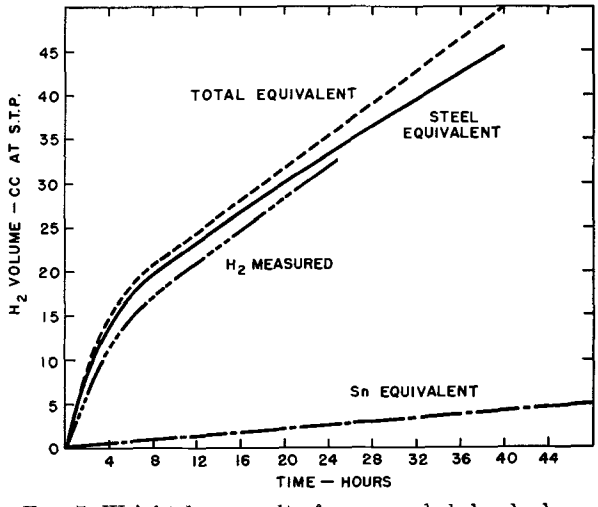

FIG. 7. Weight loss results for a coupled dry hydrogen annealed steel in citric acid solution containing 0.025 g/l $SnCl_2 \cdot 2H_2O$.

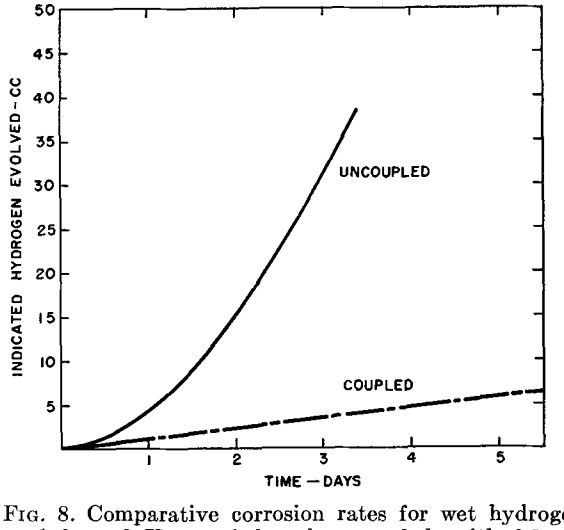

FIG. 8. Comparative corrosion rates for wet hydrogen annealed steel Y, coupled and uncoupled, with 0.3 g/l $SnCl_2 \cdot 2H_2O$.

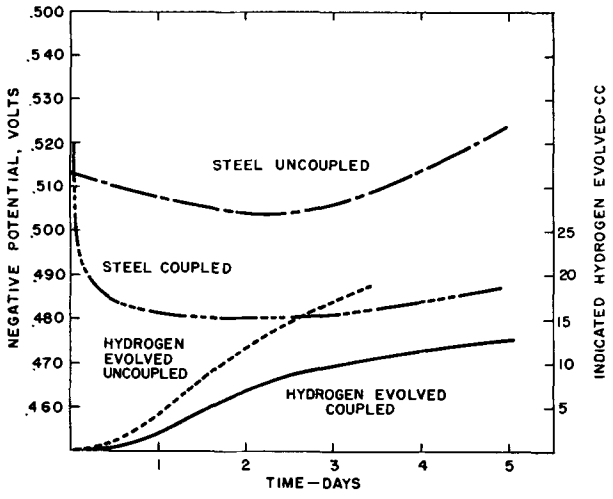

FIG. 9. Comparative relationships for uncoupled steel with 0.3 g/l $SnCl_2 \cdot 2H_2O$ and couple with 0.2 g/l $SnCl_2 \cdot 2H_2O$ (wet hydrogen annealed steel Y).

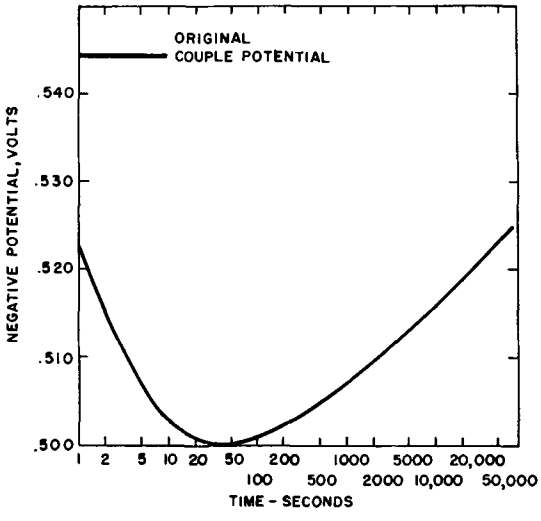

FIG. 10. Potential changes on uncoupling after first day of test—steel against saturated calomel half-cell.

nealed steel were run in potential-type cells. The uncoupled specimen was run in a solution containing 0.3 g/l $SnCl_2 \cdot 2\ H_2O$, and the coupled in a solution containing 0.2 g/l. Of course, in the coupled test, the amount of tin in solution increased by virtue of the corrosion of tin. The amount of tin in solution at any one time, however, could be calculated from the amount initially in solution and the galvanic current flowing between the steel and tin. By such a method it was found to take more than $2\frac{1}{2}$ days for the dissolved tin concentration in the coupled cell to reach the equivalent of 0.3 g/l $SnCl_2 \cdot 2\ H_2O$. Decreased hydrogen evolution rate and potential shifts in the positive direction are established well before this time, indicating that inhibition by dissolved tin cannot explain completely the decreased rate of hydrogen evolution for a tin-steel couple.

Further confirmation for the existence of such an anodic coupling shift has been found in certain food products where dissolved tin is not an effective inhibitor, yet coupling to tin produces a marked decrease in the rate of hydrogen evolution. Such data are not considered here.

An indication of anodic coupling shift is obtained by continuously recording potentials after uncoupling. A number of such tests have been run. Fig. 10 shows potentials of a steel specimen measured against a saturated calomel half-cell after uncoupling. The test was allowed to run for one day before the tin and steel were uncoupled. The corroding medium was 0.2M citric acid solution with 0.1 g/l $SnCl_2 \cdot 2\ H_2O$. On uncoupling, it would be expected that the potential of the tin would shift in the negative direction, and that of the steel in the positive direction. Potentials of tin (not shown) do shift in the negative direction about 5–10 mv. In the figure it is shown that the potential of the steel shifts in the positive direction for about 40 sec, after which it slowly shifts in the negative direction. This is direct evidence that coupling to tin somehow causes a long time shift of the anodic polarization curve for the steel in the positive direction. No completely acceptable explanation for this "anodic coupling shift" is at present known.

Data shown in Fig. 10 raise the question as to what point on this curve such "steel" potentials as indicated in Fig. 6 and 9 represent. Such potentials were measured approximately one minute after uncoupling and should correspond to the minimum in the curve.

Corrosion Rate and Potential

In tests in citric acid with air present, Hoar (3) has shown that if, for various steel specimens, the corroding potential is plotted against the corrosion rate, the points all fall along a single cathodic polarization curve. It follows that differences in corrosion rates for the steels and the inhibiting effect of dissolved tin are all reflections of anodic differences. The same has been found to hold for these tests in air-free citric acid solution at 60°C. In Fig. 11 are plotted the potential of the steel against the logarithm of the rate of hydrogen evolution. Potentials correspond to the flat portion of the steel curve in Fig. 6. Corrosion rates, likewise, are the final rates as measured in comparable volume-type cells. All results are seen to lie along a straight line, indicating that all differences in corrosion rate are

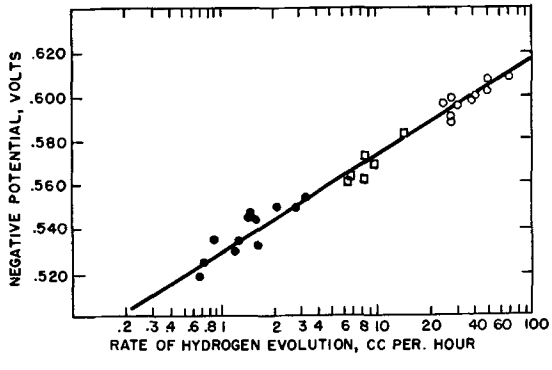

FIG. 11. Relationship between corrosion rate and corroding potential. ○ = results for uncoupled steel in citric acid solution; □ = results obtained with the addition of 0.025 g/l $SnCl_2 \cdot 2H_2O$; ● = steel potentials for tin-steel couples.

anodic effects. The corroding potential thus serves to give a direct indication of the corrosion rate. Unfortunately, it must be cautioned that this relationship cannot be generally extended to corrosion relationships in fruits or fruit juices.

ACKNOWLEDGMENT

Results presented in this paper were obtained in connection with a project on the corrosion of tin plate sponsored by the Inland Steel Co. The author wishes to thank this organization, and in particular Dr. E. D. Martin, for their support and for permitting publication of these results. He further wishes to acknowledge the help of Dr. H. T. Francis and Miss C. Jennings of the Armour Research Foundation.

Manuscript received March 21, 1955.
Any discussion of this paper will appear in a Discussion Section to be published in the June 1957 JOURNAL.

REFERENCES

1. T. P. HOAR, *Tech. Pub. Intern. Tin Research Develop. Council*, No. 5, Series A.
2. T. P. HOAR, *ibid.*, No. 30, Series A.
3. T. P. HOAR AND D. HAVENHAND, *ibid.*, No. 36, Series A.
4. E. L. KOEHLER, *Trans. Am. Soc. Metals*, **44**, 1076 (1952).
5. E. F. KOHMAN AND N. H. SANDBORN, *Ind. Eng. Chem.*, **20**, 76 (1928).

Phase Equilibria and Fluorescence in the System Zinc Oxide-Boric Oxide

D. E. HARRISON[1] AND F. A. HUMMEL

Department of Ceramic Technology, The Pennsylvania State University, University Park, Pennsylvania

ABSTRACT

Phase relationships in the system zinc oxide-boric oxide have been re-examined in detail. Two compounds exist, $5ZnO \cdot 2B_2O_3$ and $ZnO \cdot B_2O_3$, both of which exhibit low and high temperature polymorphic forms. Low temperature $(\alpha)ZnO \cdot B_2O_3$ inverts sluggishly to the cubic high temperature $(\beta)ZnO \cdot B_2O_3$ at 600°C and very rapidly at 900°C. The melting point is 982° ± 3°C. Low temperature $(\alpha)5ZnO \cdot 2B_2O_3$ is biaxial negative and inverts rapidly and reversibly to the high temperature (β) form at 964° ± 4°C. It melts incongruently at 1045°. General agreement with previous investigators has been obtained on the liquidus curve and the extent of liquid immiscibility in the system. The thermal expansion and fluorescent properties of the compounds are described. The low temperature α-$5ZnO \cdot 2B_2O_3$ phase with 0.03 moles MnO fluoresces orange, and the high temperature cubic β-$ZnO \cdot B_2O_3$ phase with 0.006 moles MnO fluoresces green, under both 2537Å and cathode ray excitation.

Six anhydrous zinc borate compounds have been reported and there has been much conjecture on the origin of the yellow and green luminescence which was characteristic of various preparations of previous investigators.

Mallard (1) reported the compound $3ZnO \cdot 2B_2O_3$ obtained by fusion of B_2O_3 and ZnO. Le Chatelier (2) isolated the same borate in the form of dodecahedrons by dissolving the matrix glass in acid. The $3ZnO \cdot 2B_2O_3$ compound was described as the only zinc borate, glassy or crystalline, insoluble in acid.

Ouvrard (3) obtained the orthoborate $3ZnO \cdot B_2O_3$ by fusing an equimolecular composition of B_2O_3 and $KF \cdot HF$ with one mole of ZnO. The orthoborate appeared as flat prisms showing high birefringence and straight extinction. It was decomposed by warm water and easily soluble in dilute acid.

Guertler (4) found that two liquids formed when zinc oxide was dissolved in fused boric acid. At greater than 53.39% ZnO a single liquid resulted. As the composition approached the $3ZnO \cdot 2B_2O_3$ molecular ratio, crystals were obtained. These were assumed to be the compound reported by Le Chatelier.

The compositions between 55 and 75% ZnO were examined by de Carli (5) by means of heating curves. Two maxima at about 900°C were observed at the $ZnO \cdot B_2O_3$ and $2ZnO \cdot B_2O_3$ compositions. Tournay (6) heated together equimolecular proportions of ZnO and B_2O_3 at temperatures up to 1000°C. After dissolving the soluble material in acid, the residue was determined to be nearly the $3ZnO \cdot 2B_2O_3$ composition.

Ingerson, Morey, and Tuttle (7) investigated the system using a quench technique (Fig. 1). Two compounds were reported: $ZnO \cdot B_2O_3$ which melted congruently at 1000°C and $5ZnO \cdot 2B_2O_3$ which melted incongruently at 1080°C. Although these authors intended to present only a brief survey of the system incidental to the study of the behavior of willemite in the ternary system ZnO-B_2O_3-SiO_2, essentially all of the principal features of the binary system

[1] Present address: Ceramics Division, Fuel Department, Leeds University, Leeds, England.

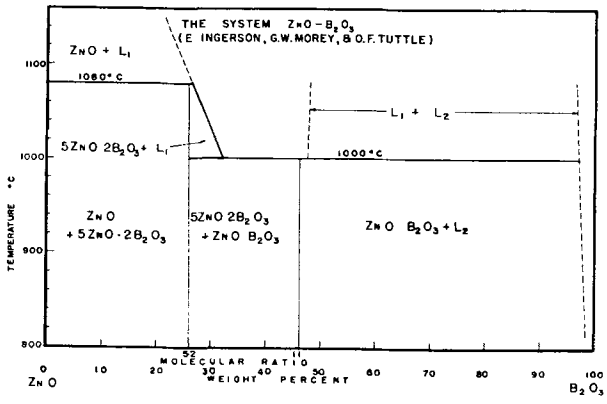

FIG. 1. The system ZnO-B_2O_3 (Ingerson, Morey, and Tuttle). (Figure courtesy of *The American Journal of Science.*)

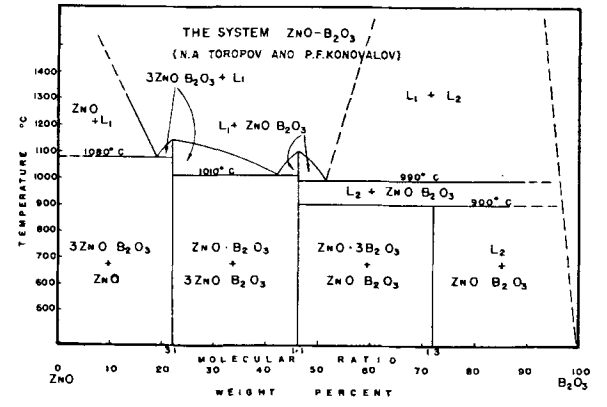

FIG. 2. The system ZnO-B_2O_3 (Toropov and Konovalov)

were determined at this time, except for the inversions of the two compounds and the composition and temperature of the eutectic. Toropov and Konovalov (8) investigated the system by means of heating curves (Fig. 2). Three compounds were reported: $3ZnO \cdot B_2O_3$ which melted congruently at 1125°C; $ZnO \cdot B_2O_3$ which melted congruently at 1050°C; and $ZnO \cdot 3B_2O_3$ which dissociated at 900°C into $ZnO \cdot B_2O_3$ and a liquid containing 2% $ZnO \cdot$ S. Terol Alonso and Gandara (9) re-examined the $ZnO \cdot B_2O_3$, $3ZnO \cdot 2B_2O_3$, $2ZnO \cdot B_2O_3$, and $3ZnO \cdot B_2O_3$ compositions. They concluded that $3ZnO \cdot 2B_2O_3$ and $2ZnO \cdot B_2O_3$ were compounds.

Phase relationships in this system were reinvestigated for the purpose of isolating the compounds which existed, studying their polymorphic forms and determining which forms were responsible for the observed fluorescence.

Experimental Procedure

Reagent grade Mallinckrodt boric acid and New Jersey Zinc Co. zinc oxide were used in preparing the various compositions. The finely divided zinc oxide was of purity sufficient for phosphor production and therefore satisfactory for phase equilibrium studies. It held 1.5% of adsorbed moisture as indicated in Table I. Repeated determinations of the B_2O_3 content of the boric acid gave 56.00% as compared to a theoretical 56.30%.

Preparation of compositions and heat treatments.—The required amounts of ZnO and H_3BO_3 were mixed in an agate mortar with reagent grade acetone until it evaporated and a dry powder resulted. Calcines were prepared in platinum crucibles at temperatures ranging from 500° to 950°C with firing times of from 10 hr to 6 weeks. For survey work in a temperature gradient, a platinum-wound furnace was used. For heat treatments at constant temperature, silicon carbide element furnaces were used.

Dry pressing was used to form bars measuring 1 cm square by 10 cm long. Calcination at 500° to 600°C for 3–5 days yielded specimens suitable for thermal expansion measurements.

TABLE I. *Composition of* $ZnO \cdot B_2O_3$ *mixtures*

No.	Molecular ratio $ZnO:B_2O_3$	Wt % composition $ZnO:B_2O_3$		ZnO (g) (98.50% ZnO)	H_3BC_3 (56.00% B_2O_3)
1	1:4	22.61	77.39	2.30	13.82
2	1:3	28.03	71.97	2.85	12.86
3	1:2	36.88	63.12	3.75	11.28
4	1:1	53.89	46.11	5.47	8.24
5		60.00	40.00	6.10	7.15
6		62.00	38.00	6.30	6.79
7	3:2	63.67	36.33	6.47	6.49
8		64.00	36.00	6.50	6.43
9		65.00	35.00	6.60	6.25
10		66.00	34.00	6.71	6.07
11		68.00	32.00	6.91	5.72
12		70.00	30.00	7.11	5.36
13	2:1	70.03	29.97	7.10	5.35
14	5:2	74.50	25.50	7.57	4.55
15	3:1	77.81	22.19	7.90	3.96
16	4:1	82.37	17.63	8.37	3.15

TABLE II. *Zinc borate compositions containing manganese*

Molecular ratio ZnO	B_2O_3	MnO	Wt % composition ZnO	B_2O_3	MnO	ZnO (g) (98.50% ZnO)	H_3BO_3 (56.00% B_2O_3)	$MnSO_4$ (57.20% MnO)
1.000	1.000	.006	53.73	45.98	0.28	27.29	41.07	0.25
5.000	2.000	.030	74.21	25.40	0.39	37.69	22.69	0.34

Apparatus and techniques.—

(*A*) X-ray Patterns: X-ray data were obtained from Norelco and General Electric recording spectrometers using $Cu_{k\alpha}$ radiation (λ = 1.537Å), filtered with nickel.

(*B*) Quench Technique: Liquidus and solidus temperatures were determined by procedures similar to those described by Shepherd, Rankin, and Wright (10), using calcines or glasses as starting material. Thermocouples were calibrated using lithium metasilicate (mp, 1201°C) and gold (mp, 1063°C).

(*C*) Refractive Index Determinations: The immersion technique was used to determine the refractive indexes of glasses and crystals to an accuracy of ±0.002, using white light and index oils which were calibrated with an Abbe refractometer.

(*D*) Differential Thermal Analysis (D.T.A.): Differential thermal analysis data were obtained with automatically recording apparatus described by Gruver (11).

(E) Thermal Expansion: Thermal expansion measurements were obtained with a calibrated fused silica dilatometer. At least two measurements were made on each sample.

(F) Fluorescent Measurements: Emission curves were obtained with an automatically recording General Electric spectroradiometer. Visual examination was made with 2537Å and cathode ray excitation.

Experimental Results and Discussion

Phase Relationships

General subsolidus study.—A detailed examination of the phase relationships below the solidus was undertaken in order to prove or disprove the existence of the compounds which have been claimed. The selection of compositions included all previously claimed compounds plus certain other possible molecular ratios (*see* Table I). All 16 compositions were heated at 800°C for 10 hr. Zinc oxide persisted in x-ray patterns of compositions containing more than 74.5% ZnO (5:2 molecular ratio) indicating that 5:2 was probably a compound and that no other compound existed between the 5:2 ratio and ZnO. Compositions richer in B_2O_3 than the 1:1 ratio gave only the cubic form of $ZnO:B_2O_3$ previously reported by Ingerson, Morey, and Tuttle (7), according to both microscopic and x-ray examination.

All lines in the x-ray patterns of compositions intermediate between a 5:2 and 1:1 ratio could be accounted for by the lines given by these two "end-member" compositions. The presence of cubic $ZnO \cdot B_2O_3$ in the mixtures was easily confirmed by microscopic examination.

Heat treatment at 850°C for 24 hr gave essentially the same results as described above.

Additional heat treatment at lower temperatures such as 650° and 750°C (10 hr) brought out the fact that the x-ray pattern of the 1:1 compound had become a much more complex one, containing many more lines than patterns obtained from the 800° and 850°C treatments.

Under the microscope, crystals of $ZnO \cdot B_2O_3$ prepared at 650°C were birefringent. At 750°C, both cubic and birefringent forms of the 1:1 compound co-existed, according to both x-ray and optical examination. Such mixtures were observed in not only the 1:1 composition, but also in compositions lying on either side of this ratio, for example in the 3:2, 1:2, and 1:3 compositions.

D.T.A. data were obtained for the 3:2, 1:1, and 1:2 compositions which had been previously heated to 800°C for 10 hr. A sharp, irreversible endothermic peak was observed at 900°C, possibly due to conversion of a low temperature form of $ZnO \cdot B_2O_3$ to the cubic high temperature form. The product in the 1:1 and 1:2 compositions after D.T.A. was shown by x-ray data to be cubic $ZnO \cdot B_2O_3$. The x-ray pattern of the 3:2 composition contained some moderately intense peaks characteristic of the 5:2 compound as well as the distinctive peaks of cubic $ZnO \cdot B_2O_3$.

These preliminary data strengthened the evidence that only the two compounds previously identified by Ingerson, Morey, and Tuttle existed, since now both optical and x-ray data supported the conclusion. The D.T.A. data also pointed toward an inversion in the $ZnO \cdot B_2O_3$ compound which had not been mentioned by previous investigators.

However, the more detailed work on the two compounds and the quench work described in the next sections provided the data on which the final conclusions were based.

Data on $ZnO \cdot B_2O_3$.—Further differential thermal analyses on the zinc metaborate composition previously heated at various temperatures in the range 600°–800°C repeatedly gave an endothermic peak at 900°C and a second peak at 980°C, the fusion temperature. The sluggish nature of the inversion complicated determination of its equilibrium temperature, and the following detailed study was necessary to understand the kinetics of the inversion process.

Seven 10-ml capacity porcelain crucibles each containing 1 g of $ZnO \cdot B_2O_3$ which had been calcined at 600°C for 5 days were placed in a fused silica container which measured 1 x 3 x 5 in. X-ray examination showed that the starting material contained no high temperature $\beta ZnO \cdot B_2O_3$. The container was placed on a refractory setter pin so as to surround it with 2 in. of air space and bring it directly under the control couple in the hottest zone of an automatically controlled Hoskins electric muffle furnace. A chromel-alumel thermocouple, accurate to ±4°C, was used to measure the temperature inside the silica container. Samples were removed periodically and air quenched. The concentration of the high temperature form of zinc metaborate in the quenched samples was determined by measuring the intensity of its most intense x-ray reflection

TABLE III. *Rate of* α-$ZnO \cdot B_2O_3 \rightarrow \beta$-$ZnO \cdot B_2O_3$ *inversion at various temperatures*

% Concentration of β-$ZnO \cdot B_2O_3$	Time (hr)	% Concentration of β-$ZnO \cdot B_2O_3$	Time (hr)
713°C		740°C	
3.4	7	11.4	2
9.3	24	16.0	4
16.1	50.5	20.7	7.4
21.2	76.2	27.0	16.7
25.5	96.2	35.7	31.8
28.3	144	43.3	63.8
34.4	207		
760°C		786°C	
16.5	2	29.8	1
23.1	4	37.8	2
26.5	8	48.9	4
34.7	17	55.2	7
42.1	32	58.4	11
48.4	67	61.9	16
51.9	144	67.5	25.2

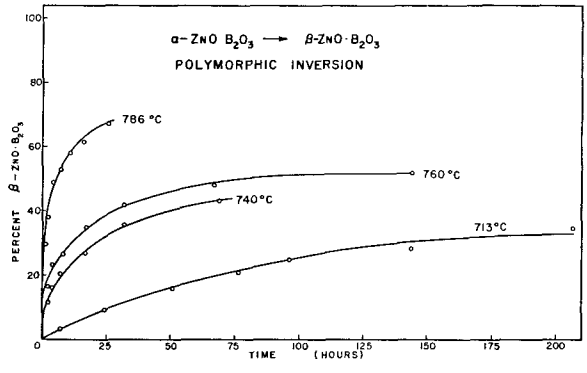

FIG. 3. Rate of inversion of α to β $ZnO \cdot B_2O_3$

TABLE IV. *X-ray patterns for zinc borate compounds*

β-$ZnO \cdot B_2O_3$						α-$ZnO \cdot B_2O_3$		α-$5ZnO \cdot 2B_2O_3$		β-$5ZnO \cdot 2B_2O_3$	
Swanson (1951)			Present work								
d	hkl	I/I_0	d	hkl	I/I_0	d	I/I_0	d	I/I_0	d	I/I_0
5.29	110	6	5.31	110	45	6.92	10	5.95	5	5.91	15
3.74	200	3	3.75	200	25	6.28	10	5.83	10	3.93	10
3.048	211	100	3.07	211	100	5.47	40	4.23	35	3.23	10
2.364	310	23	2.37	310	90	5.28	80	4.15	30	3.00	40
2.158	222	1	2.16	222	15	4.25	40	4.10	10	2.93	70
1.997	321	20	2.00	321	90	4.15	85	3.88	10	2.58	10
1.869	400	13	1.873	400	85	4.10	50	3.60	30	2.36	10
1.761	411	38	1.765	411	95	3.90	20	3.38	70	2.26	50
1.672	420	2	1.675	420	30	3.75	20	3.20	100	2.22	10
1.594	332	3	1.595	332	15	3.69	50	3.08	15	2.16	5
1.0788	444	1	1.081	444	5	3.60	35	3.05	15	2.11	5
1.0568	710	1	1.059	710	20	3.56	25	3.00	25	2.04	10
1.0365	640	1	1.038	640	10	3.51	25	2.91	55	2.00	25
1.0169	721	3	1.018	721	35	3.45	20	2.87	10	1.957	100
0.9991	642	1				3.38	55	2.80	65	1.895	10
0.9812	730	2				3.21	75	2.79	65	1.817	10
0.9490	732	1				3.15	65	2.67	15	1.778	10
0.9198	811	3				3.08	25	2.55	75	1.716	10
0.9062	820	1				3.06	20	2.49	45	1.698	10
0.8932	653	1				3.00	30	2.44	55	1.678	45
						2.94	50	2.40	30	1.626	20
a. 7.4726						2.88	75	2.34	70	1.570	10
						2.84	40	2.30	20	1.549	10
						2.79	25	2.25	20	1.532	10
						2.69	20	2.20	30	1.508	15
						2.67	21	2.15	25	1.488	20
						2.54	100	2.11	10	1.465	20
						2.50	60	2.10	10	1.437	30
						2.44	30	1.99	55	1.414	25
						2.40	20	1.98	40	1.398	50
						2.34	40	1.937	90	1.397	35
						2.30	20	1.884	10	1.339	25
						2.26	20	1.852	10	1.301	10
						2.24	40	1.794	15	1.233	15
						2.21	20	1.771	20	1.188	40
						2.17	25	1.734	60	1.176	25
						2.12	15	1.684	25	1.160	10
						2.10	10	1.664	10	1.137	10
						2.07	10	1.647	35	1.125	10
						2.03	10	1.623	20	1.114	10
						2.00	30	1.621	20	1.094	20
						1.99	20	1.610	30	1.090	60
						1.945	60	1.590	10	1.084	20
						1.906	10	1.583	10	1.066	20
						1.831	15	1.570	20	1.052	25
						1.791	15	1.540	15	1.041	30
						1.768	15	1.519	5	1.029	15
						1.752	15	1.503	15	1.016	15
						1.734	10	1.482	10		
						1.710	20	1.467	15		
						1.684	10	1.455	15		
						1.645	30	1.439	25		
						1.623	15	1.412	10		
						1.610	10	1.389	20		
						1.590	15	1.363	10		
						1.556	10	1.321	15		
						1.544	15	1.307	10		
						1.503	15				
						1.482	15				
						1.467	10				
						1.455	15				
						1.441	15				
						1.412	10				
						1.389	20				
						1.361	15				
						1.342	10				
						1.313	10				
						1.301	10				
						1.284	10				

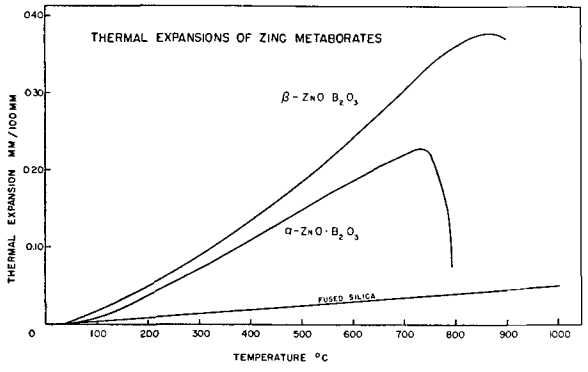

FIG. 4. Thermal expansion of zinc metaborate polymorphs.

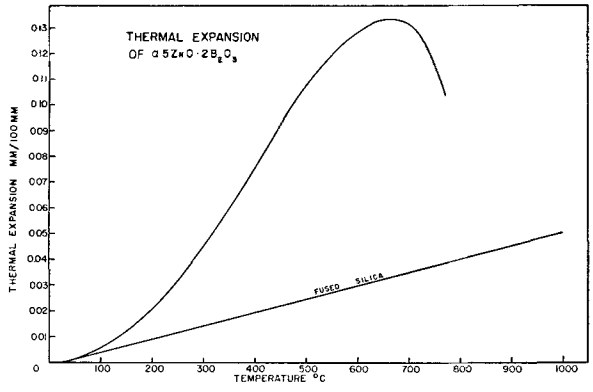

FIG. 5. Thermal expansion of α-$5ZnO \cdot 2B_2O_3$

(d = 3.07) and comparing it with the intensity observed in a sample which had completely inverted to the high temperature cubic form. Intensities were determined by a counting method using a Geiger counter spectrometer. Excellent sensitivity and accuracy could be achieved using any of the very intense peaks (d = 3.07, 2.37, 2.00, 1.765) of cubic $ZnO \cdot B_2O_3$, but the 3.07 line was most satisfactory.

Four sets of samples were treated at 713°, 740°, 760°, and 786°C. Concentrations of β-$ZnO \cdot B_2O_3$ with time are listed in Table III and they are shown graphically in Fig. 3. Calculations based on these data and long term heat treatments (6 weeks) in the neighborhood of 600°C showed this to be the equilibrium inversion temperature in air.

The high temperature form, β-$ZnO \cdot B_2O_3$, was isotropic, having a refractive index of 1.740. An x-ray pattern is given in Table IV. It is compared with the A.S.T.M. pattern of Swanson (12).

The low temperature form, α-$ZnO \cdot B_2O_3$, was birefringent, having maximum and minimum indices of 1.682 and 1.638. An x-ray pattern is given in Table IV.

The linear thermal expansions of the high and low forms are shown in Fig. 4. α-$ZnO \cdot B_2O_3$ which had been prepared by calcining a bar at 600°C for 5 days exhibited an average coefficient of thermal expansion of 35.0×10^{-7} cm/cm/°C between 50° and 600°C. Between 700° and 800°C, the sample began to contract, indicating inversion to the high temperature form. X-ray examination after the expansion run showed that most of the sample had inverted to the (β) form. β-$ZnO \cdot B_2O_3$ had an average coefficient of thermal expansion of 49.5×10^{-7} cm/cm/°C in the range 50–700°C.

Data on $5ZnO \cdot 2B_2O_3$.—Differential thermal analysis of the $5ZnO \cdot 2B_2O_3$ compound revealed a rapid reversible endothermic peak near 980°C as well as an irreversible peak at 1045°C. High temperature x-ray patterns were taken in the region from 700° to 980°C to substantiate the reversibility of the inversion indicated by D.T.A. By detailed study of many patterns, the rapid reversible inversion was found to occur at 964 ± 4°C. It was discovered that the high temperature (β) form of $5ZnO \cdot 2B_2O_3$ could be retained at room temperature due to the mechanical restraint of the sample holder. X-ray patterns taken at 980°C and on a sample quickly cooled to room temperature were identical, except for a systematic shift in the 980° pattern due to thermal expansion of the crystal. Specimens which were quickly cooled to room temperature in the sample holder gave patterns for β-$5ZnO \cdot 2B_2O_3$ as long as they remained in place, but as soon as they were removed and ground in a mortar, they inverted to well crystallized low temperature α-$5ZnO \cdot 2B_2O_3$. X-ray patterns of the α and β modifications (taken at room temperature) are given in Table IV.

Low temperature $5ZnO \cdot 2B_2O_3$ was biaxial, negative, with n_α 1.672, n_β 1.741, and n_γ ca. 1.75.

Thermal expansion was determined on a bar fired at 600°C for 3 days (Fig. 5). Low temperature $5ZnO \cdot 2B_2O_3$ had a relatively low linear coefficient of thermal expansion of 24.4×10^{-7} cm/cm/°C between 50° and 600°C. Above that temperature contraction of the bar occurred due to sintering. The effect of the polymorphic inversion on the thermal expansion was not examined.

Liquidus and solidus determinations.—It was felt that the investigation of the system might be complicated by compositional changes during the original melting of the glasses or later during the quench work. To assess this possibility, the 1:1 composition which had been prepared as a calcine and by fusion was analyzed by chemical and ignition loss methods. The 5:2 composition was analyzed by ignition loss only. Results are assembled in Table V.

Compositional changes less than 0.7 wt % were considered satisfactory for the accuracy to which the phase relationships were determined.

Compositions between 53.89% and 70.0% ZnO fused readily at 1100°C to liquids capable of being retained as transparent glasses by quenching the platinum crucible in water. The refractive indexes are shown in Fig. 6 and listed in Table VI. At greater than 70.0% ZnO, it was impossible to retain glass no matter how rapidly the sample was quenched. Between these limits, liquidus and solidus temperatures were determined by a quench technique. For most determinations the starting material was glass. Occasionally checks were made using batch material which

TABLE V. *Analyses of zinc borate compositions*

Sample	Chemical Analysis				Ignition Loss	
	Calculated		Observed		Calculated wt. % loss	Observed wt. % loss
	ZnO	B_2O_3	ZnO	B_2O_3		
$ZnO \cdot B_2O_3$						
750°/72 hr	53.89	46.11			27.07	27.54
1100°/30 min	53.89	46.11	54.54	45.46	27.07	27.64
$5ZnO \cdot 2B_2O_3$						
800°/6 hr	74.50	25.50			17.51	17.82
1100°/30 min	74.50	25.50			17.51	17.84

TABLE VI. *Liquidus and solidus determinations in the system* ZnO-B_2O_3

No.	Composition wt % ZnO	Composition wt % B_2O_3	Refractive index of glass	Temperature	Phases present
4	53.89	46.11	1.640	988	Glass
				984	Glass
				980	β-$ZnO \cdot B_2O_3$
				976	β-$ZnO \cdot B_2O_3$
5	60.00	40.00	1.652	987	Glass
				985	Glass
				979	Glass + β-$ZnO \cdot B_2O_3$
				970	Glass + β-$ZnO \cdot B_2O_3$
				965	Glass + β-$ZnO \cdot B_2O_3$
6	62.00	38.00	1.660	987	Glass
				982	Tr. β-$ZnO \cdot B_2O_3$ + Glass
8	64.00	36.00	1.665	985	Glass
				981	Tr. β-$ZnO \cdot B_2O_3$ + Glass
				966	β-$ZnO \cdot B_2O_3$ + Glass
				957	β-$ZnO \cdot B_2O_3$ + α-$5ZnO \cdot 2B_2O_3$
9	65.00	35.00	1.670	983	Glass
				980	Tr. β-$ZnO \cdot B_2O_3$ + Glass
				976	β-$ZnO \cdot B_2O_3$ + Glass
				970	β-$ZnO \cdot B_2O_3$ + Glass
				962	Tr. Glass + β-$ZnO \cdot B_2O_3$
				960	α-$5ZnO \cdot 2B_2O_3$ + β-$ZnO \cdot B_2O_3$
10	66.00	34.00	1.674	980	Glass
				979	Glass
				976	Glass
				974	β-$5ZnO \cdot 2B_2O_3$ + Glass
				969	β-$5ZnO \cdot 2B_2O_3$ + Glass
				966	β-$5ZnO \cdot 2B_2O_3$ + Glass
				962	α-$5ZnO \cdot 2B_2O_3$ + Glass
				960	β-$ZnO \cdot B_2O_3$ + α-$5ZnO \cdot 2B_2O_3$
11	68.00	32.00	1.678	1005	Glass
				999	Tr. β-$5ZnO \cdot 2B_2O_3$ + Glass

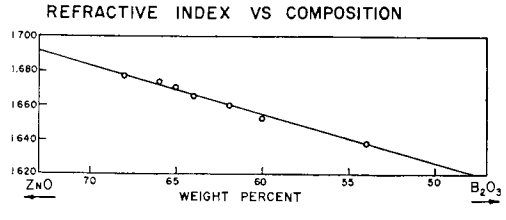

FIG. 6. Refractive index vs. composition for zinc oxide-boric oxide glasses.

had been calcined in the range 700°–900°C. The results are given in Table VI.

Zinc metaborate, $ZnO \cdot B_2O_3$, was found to melt congruently at 982° ± 3°C to a glass having an index of about 1.640. If the glass was devitrified between 650° and 850°C, a mixture of isotropic ($\beta ZnO \cdot B_2O_3$) and birefringent ($\alpha ZnO \cdot B_2O_3$) crystals resulted. At 900°C or above, the glass would yield mainly β 1:1 and at 600°C, mainly α 1:1. It should be noted that these results are similar to those obtained by subsolidus reaction of batch materials.

Glass of the metaborate composition exhibited unusual behavior during devitrification. Fragments of glass which had been heated at 650°C for 4 days acquired a very slight opalescence but they remained essentially transparent. Upon grinding the glass in a mortar, complete devitrification to α-$ZnO \cdot B_2O_3$ occurred. Large transparent fragments of glass which had been broken exhibited highly birefringent crystals along the planes of fracture.

With increasing zinc oxide content the liquidus remained flat to a concentration of 64.0% ZnO. It then dropped abruptly to a eutectic at 961° ± 3°C located at 65.5% ZnO and it rose again to 1005°C at 68.0% ZnO. Above this point the liquidus was not determined.

β-$ZnO \cdot B_2O_3$, as beautifully developed dodecahedrons, crystallized from glasses whose compositions were between 1:1 and the eutectic. β-$5ZnO \cdot 2B_2O_3$ crystallized from glass on the zinc oxide side of the eutectic, but it was never observed optically because it inverted to the low form on grinding. Below the solidus β-$ZnO \cdot B_2O_3$ and α-$5ZnO \cdot 2B_2O_3$ crystallized from glasses lying between these two composition points.

The $5ZnO \cdot 2B_2O_3$ compound was determined to melt incongruently at 1045°C by observing that the D.T.A. peak in 5:2, 3:1, and 4:1 mixtures occurred at this temperature. These data supported the previous observation of Ingerson, Morey, and Tuttle (7) that ZnO separated from the 5:2 melt at high temperatures.

The immiscible liquid region.—Five to ten gram platinum crucible melts gave a relatively clean separation of the two liquids for compositions 1, 2, and 3 at temperatures of 1000°–1100°C. Starting with batch material which had been heated at 400°–500°C, quench trials on compositions 1, 2, and 3 provided accurate measurement of the temperature of the two liquid separation.

The zinc oxide-rich liquid in equilibrium with the B_2O_3-rich liquid contained 53.5% ZnO, which is in remarkably good agreement with the 53.39% ZnO reported by Guertler (4) in 1904, and with the recent work of Ingerson, Morey, and Tuttle. The heavy liquid had a refractive index of 1.640.

Two features of the liquidus curve shown in Fig. 7 and 8 are worthy of some discussion. First, it should be recognized that the diagram is not strictly correct in a very small region to the right of the melting point of $ZnO \cdot B_2O_3$. To comply with the requirements of the Phase Rule, a slight decrease in the liquidus temperature should be experienced as B_2O_3 is added to the 1:1 composition resulting in an invariant point where two liquids and crystalline β-$ZnO \cdot B_2O_3$ are in equilibrium at a temperature slightly below the congruent melting point of the 1:1 compound.

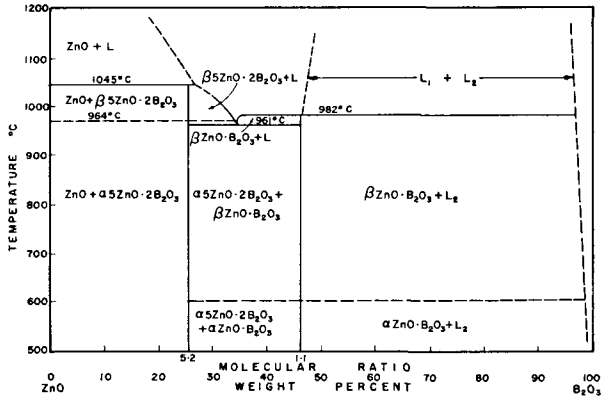

FIG. 7. The system ZnO-B_2O_3

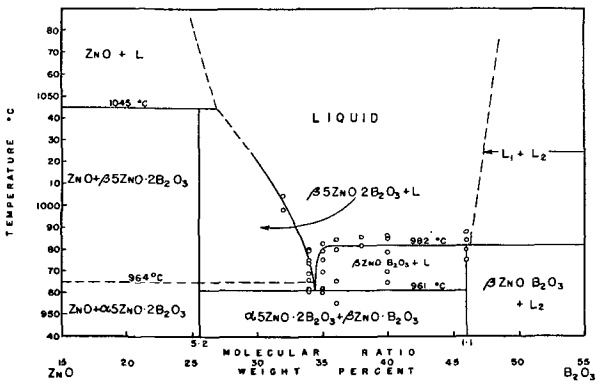

FIG. 8. Enlargement of the eutectic region in the system $ZnO-B_2O_3$.

Experimental difficulties attending the determination of the exact composition and temperature of this point lead to its elimination in the present diagrams.

The second point which should be discussed is the flatness of the liquidus curve in the range between the $ZnO \cdot B_2O_3$ composition and the eutectic. This curve resembles that shown by Morey (13) for a region of the system $Na_2O \cdot 4B_2O_3$-SiO_2 and by Greig (14) for the high silica portion of the system BaO-SiO_2.

In the case of the $ZnO-B_2O_3$ system, the flatness suggests the possible existence of a second pair of immiscible liquids or perhaps an extension of the two-liquid region which has been shown on the diagrams.

During the course of this work some evidence indicated that one of these possibilities may occur. Glass fragments of composition 9, containing 65% ZnO, were held at 1050°C for 12 hr in a platinum crucible. Tiny cigar shaped lenses developed at the edges of the fragments, which grew in size if the temperature was increased. Attempts to explore this behavior in quench envelopes at temperatures of 1000°–1125° and times of 5–60 min were unsuccessful for glass compositions containing 62 and 65% ZnO, since part or all of the liquids frequently ran out of the envelopes and no positive separations were developed. However, a number of trials using relatively large fragments of glass in platinum crucibles repeatedly yielded the lenses mentioned above and it is possible that a two-liquid field exists above 982°C for compositions between the 1:1 and 5:2 ratio.

It was evident from the preliminary trials that it would be very difficult and time-consuming to establish composition and temperature limits of such a region, if it existed, and no further work was done.

If such a region exists, it could account for the flatness of the liquidus. If it does not exist, then the curve must slope downward very slightly from the congruent melting point of the 1:1 compound toward the eutectic, as indicated in the diagram and discussion of Ingerson, Morey, and Tuttle (7).

Fluorescent Studies

Cohn (15) observed the fluorescence and thermoluminescence of zinc borate glasses containing manganese and made quantitative determinations of intensity vs. concentration of manganese for each case. From his data on the optimum concentration of manganese required for maximum fluorescence and thermoluminescence, he drew conclusions regarding the structure of the host glass and the nature of the emitting center.

Kabakjian (16) investigated the fluorescence of zinc borate compositions with and without manganese. He worked with a composition containing 57% ZnO and 43% B_2O_3 which he claimed was at the limit of glass formation and called this mixture "zinc borate compound for want of a better term". (When crystallized from a fusion this mixture should yield both compounds in the ratio 7 parts $ZnO \cdot B_2O_3$ to 1 part $5ZnO \cdot 2B_2O_3$.) He found a greater than 30 fold increase in brightness in the phosphors during the change from the "vitreous to the granular state" and speculated on the structure and mechanism of the fluorescence in the "pure" and activated "zinc borate compound".

Leverenz (17) has presented emission curves for zinc borate mole ratios of 3:1, 2:1, 3:2, and 1:1 ($ZnO:B_2O_3$). He found that the 1:1 peaked near 5420Å and the 3:1 and 2:1 near 5950Å. The 3:2 spectrum had characteristics intermediate between those of the 1:1 and 2:1 mixtures.

In this study $ZnO \cdot B_2O_3$:006MnO was prepared as a glass and in both crystalline modifications. Examination under 2537Å ultraviolet radiation showed that the glass fluoresced orange, β-$ZnO \cdot B_2O_3$ a bright green, and α-$ZnO \cdot B_2O_3$ only very faintly. The behavior under cathode ray excitation was similar, except that the α-form fluoresced with greater intensity. Under 2537Å radiation glass which had been devitrified in a gradient furnace operating between 300°–950° showed a color change at about 650°C from orange to bright green. An increase in the intensity of the green fluorescence between 650° and 900°C indicated the increase in amount of crystallization of β-

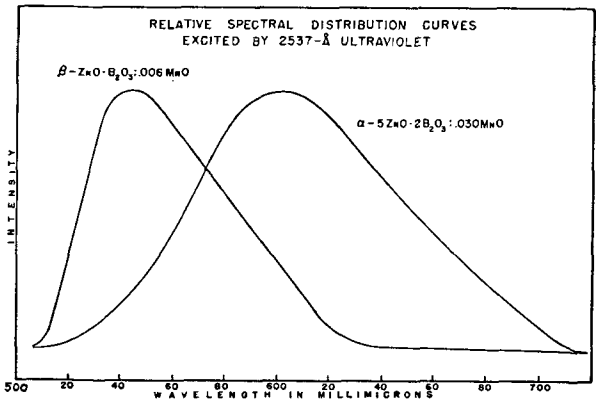

FIG. 9. Spectroradiometer curves for α-$5ZnO \cdot 2B_2O_3$ and β-$ZnO \cdot B_2O_3$.

TABLE VII. *Fluorescent color of zinc borate phosphors under 2537Å or cathode excitation*

Phosphor	2537Å	C. R.
α-$ZnO \cdot B_2O_3$:0.006MnO	Faint	Weak yellowish-green
β-$ZnO \cdot B_2O_3$:0.006MnO	Green	Green
α-$5ZnO \cdot 2B_2O_3$:0.030MnO	Orange	Orange
β-$5ZnO \cdot 2B_2O_3$:0.030MnO	Unknown	Unknown

$ZnO \cdot B_2O_3$ from the glass with rising temperature, confirming the previous observations shown in Fig. 3.

Samples of α-$5ZnO \cdot 2B_2O_3$:.030MnO were prepared at various temperatures. The compound fluoresced orange under 2537Å and cathode ray excitation. Fig. 9 shows spectroradiographs for β-$ZnO \cdot B_2O_3$:.006MnO fired at 850°C for 12 hr and α-$5ZnO \cdot 2B_2O_3$:.030MnO fired at 900°C for 12 hr. The relative intensities shown in Fig. 9 have been adjusted to 100%. Actually, β-$ZnO \cdot B_2O_3$ is considerably brighter than α-$5ZnO \cdot 2B_2O_3$ under both 2537Å and cathode ray excitation. The fluorescence data are summarized in Table VII.

Summary

1. The ZnO-B_2O_3 phase diagram of Ingerson, Morey, and Tuttle has been refined at the liquidus and new data on the polymorphic inversions of the $5ZnO \cdot 2B_2O_3$ and $ZnO \cdot B_2O_3$ compounds have been presented.

2. With manganese activation, the low temperature α-$5ZnO \cdot 2B_2O_3$ fluoresces orange and the high temperature cubic β-$ZnO \cdot B_2O_3$ fluoresces green under both 2537Å and cathode ray excitation.

Zinc borate glasses and the low temperature (α) modification of $ZnO \cdot B_2O_3$ are but weakly fluorescent.

Acknowledgment

The authors are grateful to the Chemical Products Plant of the General Electric Company for financial and technical assistance during the course of the work and to Mr. R. S. Mackie for permission to publish this paper.

Manuscript received December 12, 1955. Contribution No. 55-16 from the College of Mineral Industries, The Pennsylvania State University and abstracted from a thesis submitted by D. E. Harrison in partial fulfillment of the requirements for the Ph.D. degree.

Any discussion of this paper will appear in a Discussion Section to be published in the June 1957 JOURNAL.

REFERENCES

1. ER. MALLARD, *Compt. rend.*, **105,** 1260 (1887).
2. H. LECHATELIER, *ibid.*, **113,** 1034 (1891).
3. L. OUVRARD, *ibid.*, **130,** 335 (1900).
4. W. GUERTLER, *Z. anorg. Chem.*, **40,** 225 (1904).
5. F. DECARLI, *Atti accad. Lincei*, (**6**)**5,** 41 (1927).
6. R. TOURNAY, *Compt. rend.*, **203,** 558 (1936).
7. E. INGERSON, G. W. MOREY, AND O. F. TUTTLE, *Am. J. Sci.*, **246,** 31 (1948).
8. N. A. TOROPOV AND P. F. KONOVALOV, *Doklady Akad. Nauk S.S.S.R.*, **66,** 1105 (1949).
9. S. T. ALONSO AND M. J. OTERO DE LA GANDARA, *Anales real soc. espan. fis. y quim. (Madrid)*, **B48,** 750 (1952).
10. E. S. SHEPHERD, G. A. RANKIN, AND F. E. WRIGHT, *Am. J. Sci.*, 4th Ser., **28,** 293 (1909).
11. R. M. GRUVER, *J. Am. Ceram. Soc.*, **31,** 323 (1948).
12. H. E. SWANSON AND E. TATGE, *J. Research Nat. Bur. Standards*, **46,** 321 (1951).
13. G. W. MOREY, *J. Soc. Glass Technol.*, **35,** 270 (1951).
14. J. W. GREIG, *Am. J. Sci.*, **13,** 27 (1927).
15. B. E. COHN, *J. Am. Chem. Soc.*, **55,** 953 (1933).
16. D. H. KABAKJIAN, *Phys. Rev.*, **51,** 365 (1937).
17. H. W. LEVERENZ, "An Introduction to Luminescence of Solids," p. 234, John Wiley & Sons, Inc., New York (1950).

Cathode Ray Tube Screen Charging and Conditions Leading to Positive Ion Deterioration

A. B. LAPONSKY, M. J. OZEROFF,[1] W. A. THORNTON, AND J. R. YOUNG

Research Laboratory, General Electric Company, Schenectady, New York

ABSTRACT

Screen charging in standard cathode ray tubes is related to the effective yield of secondary electrons. This yield depends strongly on the nature and geometry of the screen surface. If the surface is smooth, a sticking potential can be defined, above which the screen potential does not rise; if the surface is rough, as with a standard powder layer, field dependence of effective secondary electron yield causes more complex charging effects. Dependence of screen charging on phosphor thickness, coverage, particle size and shape, and on gas pressure in the tube is considered.

Ion-focussing field configurations, associated with negative screen charging in tubes of different shapes, are correlated with observed patterns of phosphor deterioration by positive ions; production of these ions is considered. Effects of raster geometry, anode materials, and the magnitude of the focussing field are mentioned. Observations relevant to x-burn in commercial television tubes are summarized.

Insulating properties of phosphor screens in standard cathode ray tubes lead to dependence on secondary emission in establishing screen potential. Under certain conditions, equilibrium screen potential differs greatly from the potential of the tube anode. Effects arising from this screen-anode potential difference and from the internal electrostatic fields associated with it have long been of interest and importance. One of these effects, of potential

[1] Present address: Microwave Lab., General Electric Co., Palo Alto, Calif.

concern in commercial applications of the cathode ray tube, is a decrease in electron-induced luminescence of the phosphor screen due to bombardment of the phosphor by accelerated and focussed positive ions. An understanding of this effect involves study of (*a*) screen charging, (*b*) ion-focussing fields, (*c*) ion production, and (*d*) phosphor deterioration in the cathode ray tube.

Some of the early literature (1–7) is concerned with screen charging and first attempts to measure the potential of the insulating phosphor screen. Other papers (8–12) mention the role of ions and internal fields in producing the phosphor deterioration or "ion burn." Recently (13) screen-charging dependence on secondary emission has been considered in some detail. Some of the ideas advanced in the above references are unsupported by direct experimental evidence. It is the purpose of the present paper to present an integrated discussion of the conditions leading to positive ion deterioration of cathode ray tube phosphor screens. This discussion is based on experiments performed as well as on the existing literature. Details heretofore unpublished include: (*a*) data in the high anode voltage region by electronic measurement of screen potential; (*b*) data on dependence of screen charging on surface geometry, screen thickness and coverage, particle size and shape, and residual gas pressure; (*c*) dependence of ion-focussing field configuration on tube and raster geometry; (*d*) ion production dependence on anode material; (*e*) dependence of observed phosphor deterioration by positive ions on the strength of the internal electric field.

In the idealized case, the screen potential follows the anode potential between the first and second crossovers (the unity values of the secondary yield curve). As the anode rises above the potential corresponding to the second crossover, the screen remains at this point (the sticking potential) and a screen-anode potential difference ΔV appears. Associated with ΔV is a field throughout the tube volume which serves to accelerate secondary electrons toward the anode for collection.

Operation and associated effects in a practical tube are considerably more complex than the idealized case discussed above. A number of additional considerations, the studies of which form the body of this report, are the following. (*A*) Residual gas is present in practical tubes. Ions are formed by primary and secondary electrons and by other ions, and under certain conditions are also accelerated to the screen. (*B*) Ion production by secondary electrons striking the anode coating may also be an important effect. (*C*) The phosphor layer is rough and, as will be discussed in detail later, its secondary emission characteristics depend on the electric field at the screen, that is, on the magnitude of ΔV.

Screen Charging

The secondary electron emission process, while fundamental in the operation of unaluminized cathode ray tubes, is sufficiently complex that evaluation of actual tube performance is difficult. Studies of the effect of variation in the secondary yield on the screen potential have furthered the understanding of cathode ray tube operation and are reviewed in the following sections.

Indications of adverse charging effects.—One of the most prominent indications of adverse charging of the cathode ray tube screen has occurred in present-day television picture tubes. This is the so-called x-burn, a typical example of which is shown in Fig. 1. It occurs most prominently in rectangular tubes, although under certain conditions described later, it can occur in circular tubes also. It occurs mainly in tubes operating at second anode voltages greater than about 15 kv and is most easily observed at low voltages. In general, it appears only after many hours of tube operation, but in some cases it has been observed after only 10–15 min of operating time. A second indication of adverse screen charging has to do with reduced light output of screens at the higher voltages. If one increases the accelerating voltage of a standard unaluminized cathode ray tube, taking care to avoid current saturation, one finds that beyond a certain voltage range the light output does not continue to increase linearly, as would be expected.

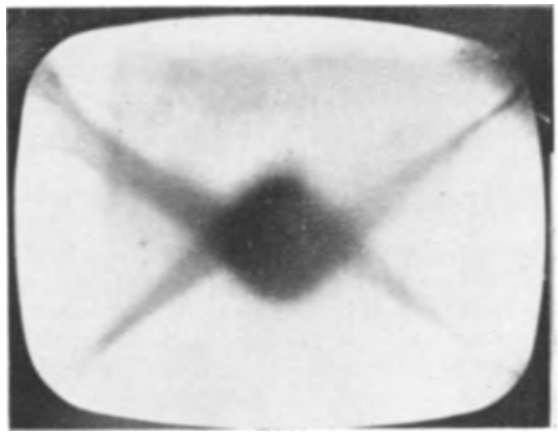

FIG. 1. Typical x-burn in rectangular tube

Surface effects.—Perhaps the simplest target surface is that of a smooth conductor. Such a surface closely approximates the condition under which the bombarding energy and angle of incidence alone control the electron yield (for a given target). The relation between the potential of a smooth conducting floating target and the anode potential of a tube may be described by plots such as curve A, Fig. 2, for a smooth silver target in which the tangent of α is unity, indicating sticking (4, 6). The importance of the surface condition to the charging process

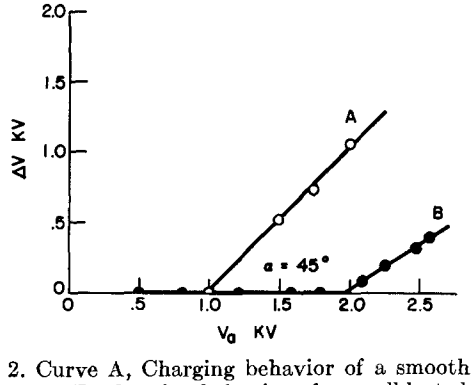

FIG. 2. Curve A, Charging behavior of a smooth silver target; curve B, charging behavior of a sandblasted nickel target.

becomes evident when a plot of ΔV vs. V_a is made for a floating conducting target having a rough surface. For a surface of this type, the secondary yield might be expected to depend markedly on the target-to-collector potential as well as on the bombarding energy. Fig. 2, curve B, indicates the charging occurring for a sandblasted nickel target. It is evident from the figure that a slope of unity does not necessarily occur when the target ceases to follow the anode. For insulating and semiconducting targets such as glass and some of the phosphors, target charging might be expected to be similar to that of the conductors; here the deviations from sticking are quite pronounced. The importance of the surface condition is seen in Fig. 3, where the effect of roughness on the charging process is observed; similar observations have been reported (4). Sticking was observed to occur for only one insulator, Fig. 4, for a smooth glass television tube face-plate target.

Evidence indicates that the charging process must be quite sensitive to conditions occurring at the target surface. Absence of sticking of the rough conductor and the rough insulator would seem to demand an explanation for the charging process in terms of electric fields external to the bombarded surface. As discussed below, occurrence of larger slopes in the ΔV vs. V_a curves for relatively smooth surfaces compared to rough surfaces suggests that effective secondary yields are controlled in part by trapping or by formation of space charges in the crevices of the rough surfaces; also, an increase in the effective secondary electron collection with increasing ΔV could then be responsible for the second crossover rising slightly as the anode-to-target potential increases.

A striking feature of this study of screen-charging phenomena in cathode ray tubes is the prevalence of a typical curve, Fig. 5, which may be represented in the region above V_o roughly by the relation

$$\Delta V = \tan \alpha (V_a - V_o)$$

where $\tan \alpha$ is often near 0.7.

The screen potential V_s continues to rise as V_a is increased above V_o, although at a slower rate. Sticking of rough screens has been observed in no case. Since the effective secondary emission yield δ_{eff} must always equal unity in the steady state, V_s must always correspond to the effective second crossover value of electron bombarding energy. Therefore, the only interpretation of Fig. 5 is that above V_o the effective second crossover moves to higher energies with the increase in ΔV that accompanies an increase in V_a. That is, the information of Fig. 5 may be presented alternatively as in Fig. 6; however, the information concerns only the second crossover points of the family of δ vs. ϵ, curves (secondary emission yield δ vs. primary electron energy ϵ).

Fig. 7, obtained by d-c measurements on a conducting

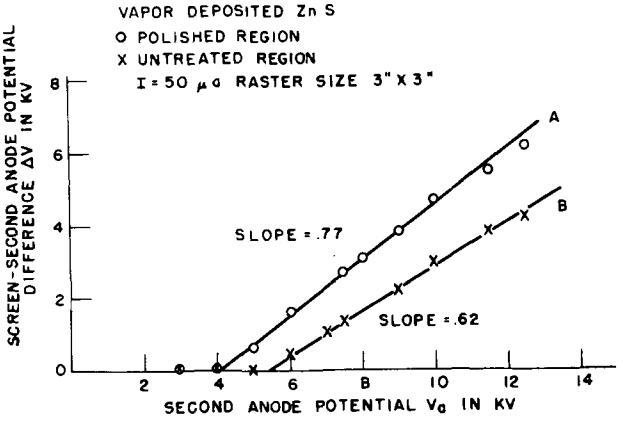

FIG. 3. Charging behavior of vapor-deposited ZnS screen.

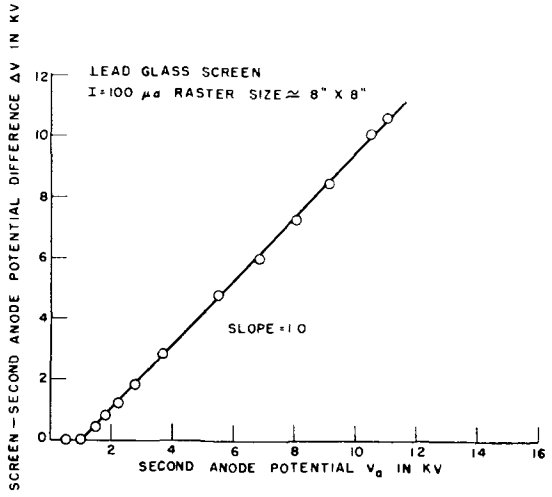

FIG. 4. Charging behavior of smooth glass

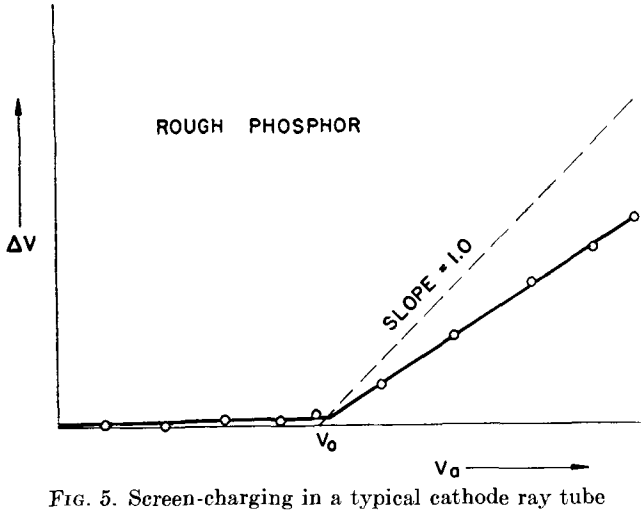

FIG. 5. Screen-charging in a typical cathode ray tube

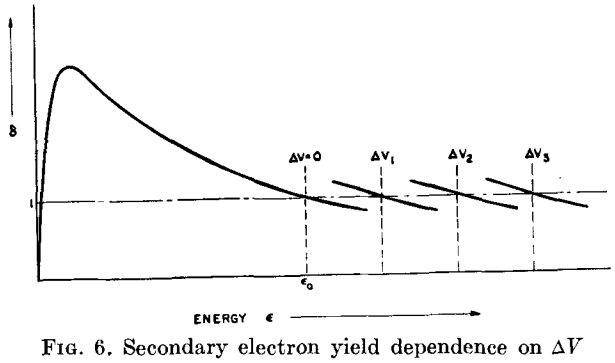

FIG. 6. Secondary electron yield dependence on ΔV

face plate tube, indicates that secondary emission ratio increases, with increase in collecting field, throughout the energy range; this is consistent with the moving of the effective crossover to higher energy with increase in field.

To arrive at an idea of how the observed field dependence of screen potential may come about, consider an ordinary cathode ray tube with a rough screen, and V_a being raised from zero. The anode at all times acts as collector; the screen at all times adjusts its potential with respect to the anode so that the latter collects one secondary electron per incident primary. At bombarding energies less than V_o, more than one secondary is produced at the screen surface per incident primary. In order that only one of these secondaries be collected in the steady state, the screen potential would be expected to rise above that of the anode by an amount that depends on the secondary electron energy distribution. One condition that may occur at the surface of the screen is suggested by considering a simple model. Assume that the screen surface is a tightly packed field of hemispheres. A constant flux of primaries produces secondaries, in this case because of increasing angle of incidence, more copiously the deeper down the primary strikes. The secondaries may escape in one free path, collide with and stick to the phosphor surface, or be degraded in energy by one or more collisions with the phosphor or other electrons until some approach thermal energies. A steady-state space charge is set up. Space charge gradient, density, and current density out of the interstice depend on the potential difference between the phosphor surface and some neighboring equipotential surface; this in turn depends on ΔV and thus on the potential V_s assumed by the screen.

One hypothesis to account for the screen-charging behavior is the following: whatever the "intrinsic" secondary emission characteristic of a phosphor may be (the δ vs. ϵ curve for a smooth sample showing no collecting field dependence) it is altered when the sample possesses a typical rough surface. The true second crossover becomes very high (above 25 kv) under the normally unrealizable condition that every secondary electron produced is collected. This high second crossover may be attributed to the increase in secondary emission with mean angle of incidence of the primaries. A moderate increase in δ should result in a large upward shift of the second crossover because here the negative slope of the δ vs. ϵ curve is small. The high true second crossover implies that at all normal operating voltages more than one secondary per primary is produced.

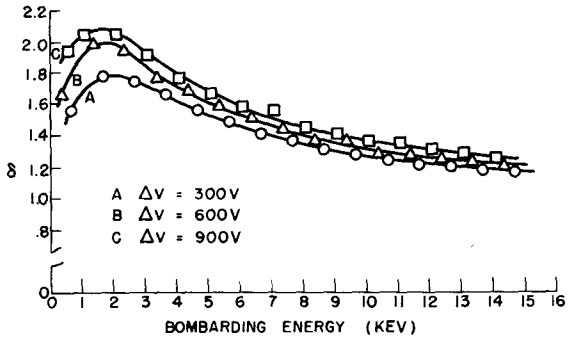

FIG. 7. Secondary electron yield dependence on collecting potential.

Since the effective secondary emission yield is always unity in the steady state, the screen potential continually adjusts itself, as the anode potential is changed, so that (*a*) field leakage into the interstice and (*b*) the electron density and energy distribution found there are such that current out is equal to current in.

Put in another way, the only externally controlled variable considered here is the anode potential. A change in this is accompanied by a change in screen potential, which may always be considered to be an equilibrium value. Once V_a is established, V_s controls two quantities: (*a*) the collecting field E at the phosphor surface, related to ΔV, and (*b*) the energy ϵ of the primary electron as it strikes the phosphor. The value of ϵ controls δ which in turn is related to electron density ρ; the effective ratio δ_{eff} remains equal to unity. Thus V_s moves to a value where E and ρ lead to $\delta_{\text{eff}} = 1$. The discussion above involves only the field collection of secondary electrons. Other processes may be important such as field enhanced secondary emission (9).

Dependence of screen charging on phosphor coating thickness and coverage.—Some early observations indicated that x-burn occurs more rapidly in television tubes whose screens are thinner than normal (14). It has also been reported that very thick screens are not as good as those of intermediate thickness with regard to maintaining anode potential (15). Therefore, it seemed worth while to investigate further the dependence of screen-anode potential difference on various screen thicknesses of a standard white sulfide phosphor.

A common coating weight employed in unaluminized television tubes is 5.5 mg/cm^2. Therefore, tubes were made using 2.75 mg/cm^2, 5.5 mg/cm^2 and 11 mg/cm^2 of standard white ZnS phosphor. Two tubes of each coating weight were made in standard 17-in. rectangular television tube bulbs. Tubes of each coating weight were placed on life test in a standard television chassis, using an auxiliary high voltage anode supply. Anode voltage was maintained at 25 kv and beam current at 150 μa. The raster size was approximately 10 x 12 in. Screen potential was measured periodically during the life testing, using the Kelvin method (16).[2] Using the electron gun as an ionization gauge, pressure was determined periodically during the life of the tubes and was found to remain almost constant, below 10^{-5} mm Hg, in all of the tubes throughout this set of experiments.

Fig. 8*a* shows a typical plot of ΔV vs. V_a at different intervals during the life of a tube with a screen coating of 2.75 mg/cm^2; Fig. 8(*b*) shows typical results obtained from a tube with a screen coating of 5.5 mg/cm^2. Differences noticed between the light-screen tubes and the standard tubes are: (*A*) the screen follows the anode in potential up to 25 kv, the limit of measurement, in standard-screen

[2] The television tube screen potential measurements in this paper were obtained using the Kelvin method. This utilizes the screen as one plate of a condenser and another vibrating plate in front of the tube face as the other condenser plate. Alternating current to the vibrating plate reduces to zero (or a minimum) when this plate is at the potential of the screen. Hence, measurement of the d-c potential of this plate when the alternating current to it is a minimum gives the value of the screen potential.

tubes before life testing, but does not for light-screen tubes; (*B*) the breakover point remains nearly constant with life in standard-screen tubes, but moves to lower anode voltages in the light-screen tubes; (*C*) the breakover point occurs at higher anode voltages for the standard-screen tubes than for the light-screen tubes; (*D*) the breakover point is sharp in the standard-screen tubes while in the light-screen tubes there is a more gradual variation. Fig. 8(*c*) shows results obtained from one of the tubes with a screen coating of 11 mg/cm^2. These results are similar to those obtained from tubes with the standard screen coating.

The increase in slope of the curves above the break point with life indicates that a larger collecting field is necessary to collect one secondary per primary. The reason for this is not certain but may involve a change in the geometry of the phosphor layer or a decrease (3) in the efficiency of secondary emission.

In an effort to determine other properties of the different screens, the tubes were cracked open and the screens observed under a microscope. Many regions of bare glass were present in the light screen, while almost complete coverage occurs in the medium and heavy screens. Since the secondary emission properties of glass are low compared with the phosphor at higher accelerating voltages, this bare glass would be expected to increase the screen-anode potential difference at high anode voltages. This is observed for the light screen-coating tubes. Therefore, it appears that screen charging does depend on the screen-coating weight or phosphor coverage of the glass, but sticking does not occur for the screen-coating

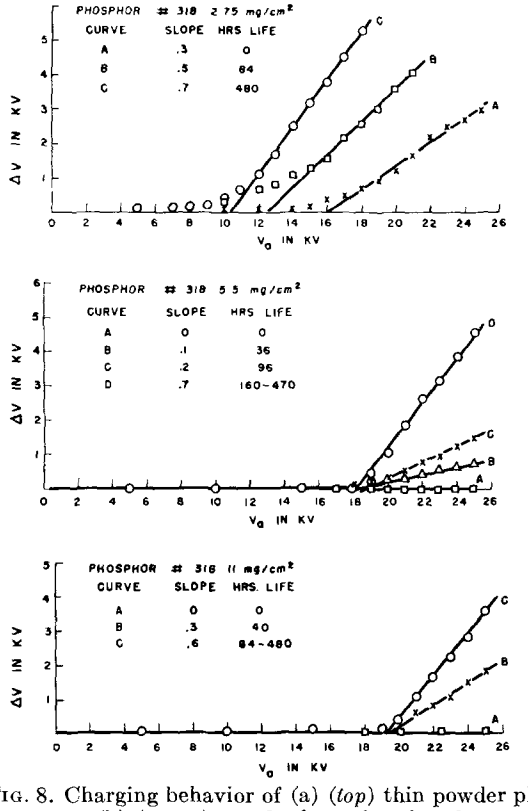

FIG. 8. Charging behavior of (a) (*top*) thin powder phosphor screen; (b) (*center*) standard powder phosphor screen; (c) (*bottom*) thick powder phosphor screen.

weights employed here. These results are different than those quoted by Zworykin and Morton (15) although those authors do not specify the screen material or coating weights used.

Dependence of screen charging on particle size and shape.—The concept of "roughness" as applied to cathode ray tube particle-layer screens needs definition. A useful one relates roughness to the mean angle of incidence of electrons in the primary beam, when the beam is traveling normal to the plane of the screen. This differs from the usual meaning of roughness, which involves size and shape of surface elements.

The mean angle of incidence of primaries approaching from a given direction depends only on the shape and not on the dimensions of the elements. In the presence of a collecting field at the phosphor layer, with its leakage between the grains, the size of the elements may well have little effect. Assuming a constant primary electron current density, the average angle of incidence of primaries on the field of hemispheres is 45°. This value of mean angle of incidence is probably about right in some practical cases, since photomicrographs of some typical phosphors show rounded spheroidal grains. Even in the case of jagged crystals, if orientation of crystal surfaces to the primary flux is integrated over the incidence angle, the mean angle again is thought to be 45°. Such reasoning leads one to expect little or no dependence of the number of secondaries emitted on either size or shape of phosphor particles making up the screen.

Experiments designed to detect a trend in screen-charging behavior with differences in particle size and shape have been made. Twelve 17-in. rectangular cathode ray tubes have been tested, two of each of six combinations, as follows:

Phosphor component	Mean particle size (μ)
Blue	<5
Blue	~10
Blue	~20
Yellow	<5
Yellow	~10
Yellow	~20

Photomicrographs of the two components show that blue-emitting phosphor crystals are relatively rough and jagged compared with the yellow particles, which are smooth and spheroidal. Differences in screen charging and ion deterioration of the phosphors were small, and no significant trend was evident, based on the limited statistics of these experiments.

Effect of gas pressure on screen charging.—A possible correlation between gassy television picture tubes and absence of x-burn was mentioned (17) some time ago. A number of tubes, peculiar in that x-burn did not occur during high voltage testing, was found to have pressure higher by a factor of 1000 than typical production tubes. Furthermore, the screens of these tubes were found to follow the anode in potential, within 200 v, up to 25 kv; that is, no screen-anode potential difference existed during test and hence no ion focusing or x-burn occurred. Subsequently, studies were begun to determine directly dependence of screen charging on ambient pressure. The first of these showed that the screen-anode potential dif-

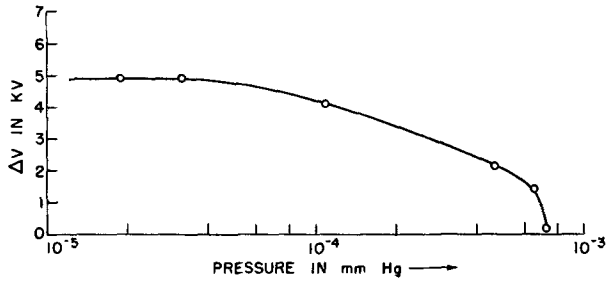

FIG. 9. Dependence of target-charging on gas pressure

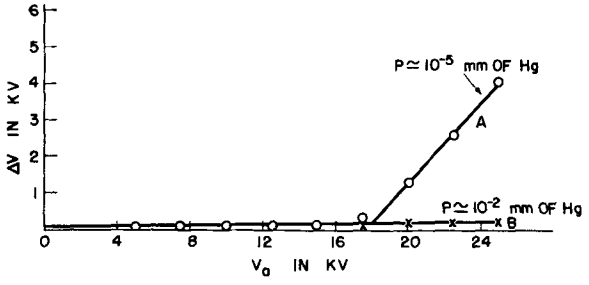

FIG. 10. Dependence of screen-charging on gas pressure in a standard tube.

ference ΔV decreased sharply toward zero at a pressure near 10^{-3} mm Hg (Fig. 9). These data were obtained by measuring the potential of a small phosphor-covered conducting slide in a demountable system, by means of an electrostatic voltmeter. A study was made of a standard television tube which had shown both ion burn and a large ΔV at higher voltages. This tube was placed on a continuously pumped system, and ΔV vs. pressure obtained by the Kelvin method. Resulting curves for nitrogen, hydrogen, and air were identical in form to that of Fig. 9. Finally, in Fig. 10 appears a routine ΔV vs. V_a curve for a standard tube (curve A). After further operation, the screen was observed to follow the anode within 300 v (curve B), and at that time the residual gas pressure was found to have risen to near 10^{-2} mm Hg. The mechanism that causes the screen to charge toward the anode potential at these higher pressures has not been established. At higher pressures, many more positive ions will be produced by the interaction of the primary and secondary electrons with the gas molecules. Therefore, one possible mechanism is that large numbers of positive ions strike the screen and thereby raise the screen potential; the same ions, striking the screen, produce "secondary" electron emission. Values of this secondary emission ratio γ up to 10 electrons per ion for 100–1000 ev light ions on metals have been reported (18).

Ion Focusing Fields; Ion Production and Deterioration Effects

Introduction

Internal electrostatic fields, produced in cathode ray tubes operated under conditions such that a screen-anode potential difference exists, are of interest in regard to the acceleration and focusing of ions present in the tube volume (8, 19). As has been seen, an insulating phosphor screen will, under bombardment by electrons of high enough energy, assume a potential considerably more negative than that of the anode or collector. Although this potential is not uniform across the screen, the effect of this nonuniformity seems to be negligible in comparison with effects due to the mean screen-anode potential difference ΔV.

The tube volume contains an electron flux consisting of high-energy (monochromatic) primaries whose distribution depends upon the method of scanning, and of lower energy secondaries whose energy depends upon their position in the field. Predominantly, positive ions are formed within the volume and at the two surfaces. The ion yield from a given volume or surface element of a material is a function of electron energy and current density. Positive ions are accelerated toward the screen; starting with near zero energy, they will follow paths roughly paralleling the field lines and will strike with energies ranging from zero to $e\Delta V$, depending on the point of origin of each. If the screen is sensitive to positive ions, it will show the effects of an integrated ion current at each point. In the absence of a gradient of field intensity, no focusing will occur.

In the practical case of the large production cathode ray tube, in which the anode is shaped somewhat like a right circular cone, some rough generalizations may be made. The primary beam is swept through most of the tube volume. The average beam current per unit volume varies as $1/r^2$; the radius r is the distance from the center of beam deflection which is near the neck-funnel intersection of the tube, measured toward the face plate. Aside from other effects, ion production per unit volume, by primary electrons interacting with the residual gas, therefore will fall off sharply with distance from the rear of the volume. If secondary electron production per unit area of screen is assumed constant, and the secondaries are liberated with only a few electron volts of energy on the average, then secondary current density in the volume will depend on focusing effects of electrostatic fields. Where a ΔV is present, the equipotential configuration appears somewhat as in Fig. 11; thus, more secondaries bombard a unit area of anode surface near the tube skirt than at the rear of the tube. While ion production by secondaries per unit volume may be somewhat greater toward the edges of the tube, that due to primaries increases by factors of 10–100 times toward the rear of the tube.

Round tube.—Fig. 11 illustrates the equipotential surfaces and field lines found in a round tube of typical geometry. Also shown is a suggested plot of positive-ion current density across the screen in the steady state. A strong maximum in positive-ion current density is expected in the center of the round tube for two reasons: (*a*) ion production is greatest at the rear of the tube, and the paths of these ions tend to remain near the axis of the tube; (*b*) focusing of ions at the center of the face plate, by the field, is present; this by itself contributes to ion-density maximum at the center. Observations on round tubes show that an intense central spot does occur, but that it has more sharply defined edges than the foregoing description might lead one to expect.

Rectangular and triangular tube.—The rectangular cathode ray tube in common use has a somewhat pyramidal shape. The four corners are blunt, as are the edges

of the pyramid. These edges become less and less well defined toward the neck region of the tube until, about two-thirds of the way to the neck, the anode loses all four-cornered symmetry and becomes nearly spherical. The four-cornered geometry of such a tube alters the electric field as compared with that in a round tube so as to cause positive-ion focusing into a definite and unique pattern. Ions traveling along field lines originating in the rear of the tube, where four-corner effects are absent, will be focused into a diffuse center spot similar to that characteristic of the round tube of Fig. 11. Ions originating in regions where corner effects are present in the equipotential configuration are concentrated at the screen into a rather sharp pattern resembling an X. This focusing action can be understood qualitatively. Coaxial cylindrical equipotentials, for instance, result in focusing at the axis of any charged particle originating with zero energy in such a field (*see* Fig. 12*a*). The family of equipotential surfaces in a rectangular tube in which a screen-anode potential difference exists will appear in cross section similar to that of Fig. 11. However, a section determined by a plane perpendicular to the tube axis and near the face plate will appear as in Fig. 12*b*. There the fine lines represent intersections with the face plate of four planes of symmetry through the corners (edges of pyramid). The sketch shown in Fig. 12*c* of equipotential surfaces in the corner region indicates the focusing action.

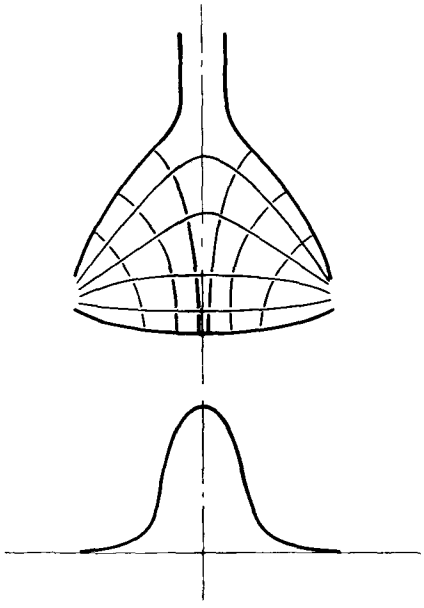

FIG. 11. Focusing fields and expected ion distribution in a round tube.

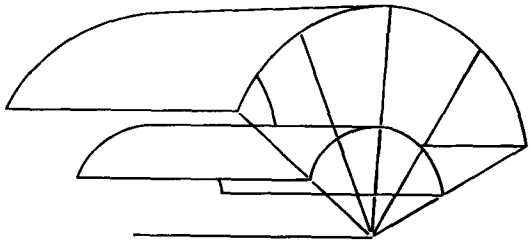

FIG. 12*a*. Focusing action of coaxial cylindrical equipotentials.

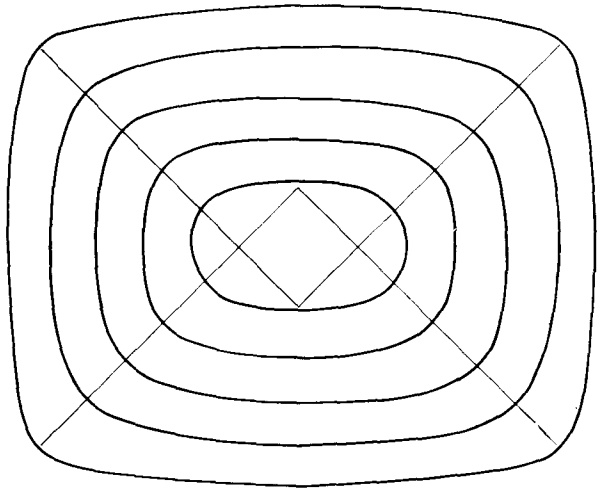

FIG. 12*b*. Axial cross section of equipotentials in a rectangular tube.

In Fig. 13 appear three photographs of positive-ion patterns on screens of different geometry. The round tube shows the ion spot of Fig. 11. The rectangular tube shows a similar diffuse area and superposed upon it the relatively sharp X of Fig. 12*b*. The tube whose screen is pictured in Fig. 13*c* is a regular tetrahedron, one face of which forms the screen. The corners and edges of this tube are sharply defined in order to maximize focusing effects. The expected Y-pattern is clearly shown. Since corner effects exert an influence throughout the tube, the diffuse center spot is less marked.

With regard to the round and rectangular tubes, x-burn should occur only in the rectangular tubes where four-corner symmetry is present, so long as the entire screen (round or rectangular) is scanned or overscanned and thus is approximately an equipotential surface.

Effect of raster geometry.—Where a rectangular raster is scanned in a round tube, an x-burn can occur, as shown in Fig. 14. While the scanned area remained at a potential far below that of the anode, adjacent unbombarded areas of the screen charged to high potentials, approaching the anode potential. When this occurs, four-corner geometry

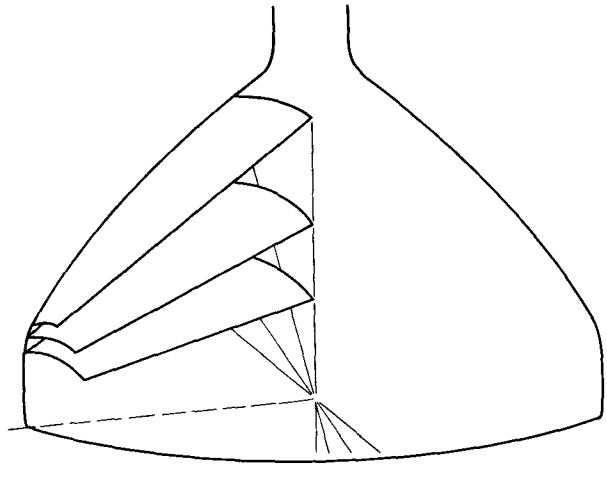

FIG. 12*c*. Corner focusing in a rectangular tube

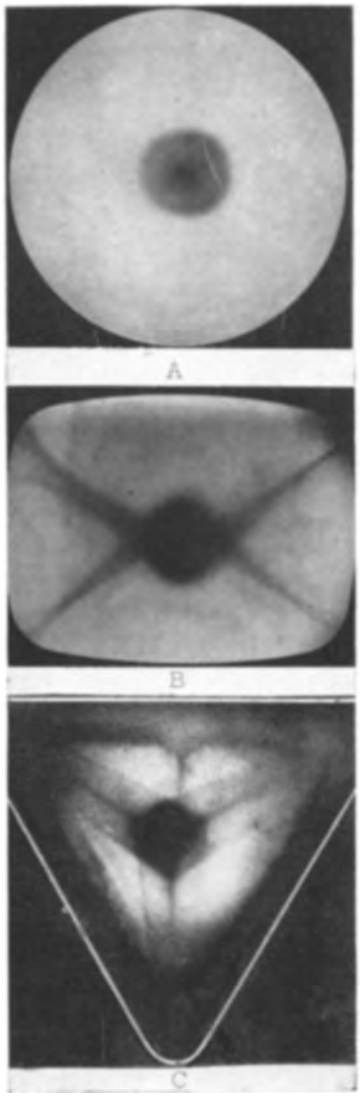

FIG. 13. Ion pattern vs. tube geometry

of the ion-focusing fields is again present, although somewhat dissimilar to that found in a rectangular tube.

Tube geometry vs. raster geometry.—In order to determine the effect of the raster on x-burn, a rectangular tube was life-tested with a small rectangular raster rotated about 30° from the horizontal. After 100 hr of life testing, a normal x-burn was found. Variation of the screen-anode potential difference over the face of this tube was measured and found to be present but small. Here it is apparent that a variation in screen-anode potential difference is present between regions inside the raster area and those outside. However, in this tube this variation was not sufficient to affect the normal orientation of the x-burn. In another tube (Fig. 15) the unbombarded areas remained near anode potential while the rotated raster area was several kilovolts below the anode in potential. In this case the x-burn was rotated with the raster, as if the focusing fields now depended on raster orientation alone. Therefore, either tube geometry or raster geometry can predominate in the orientation of x-burn, depending on how the bombarded and unbombarded portions of the screen charge.

Positive-ion production and phosphor deterioration.—Positive ions may be produced in a cathode ray tube by: (*a*) the interaction of high-energy primary electrons with the residual gas in the tubes, (*b*) the interaction of lower energy secondary electrons with the residual gas, and (*c*) the interaction of secondary electrons with the anode material of the tube. Other sources of positive ions may be present, but only the above are considered in this discussion.

Suppose a television tube operates with a residual gas pressure of 10^{-6} mm Hg and with a beam current of 100 μa. Consider the production of positive ions only in the region between the final gun anode aperture and the tube screen. Here the electron energy is usually 10 to 20 kev and the ionization probability for air is about 10^{-6} ion per electron per centimeter path at 10^{-6} *mm* Hg (20, 21). The ionization path length for the electron in a standard television tube is approximately 20 cm. Therefore, a positive-ion current of about 2×10^{-9} amp would be produced in the region between the final anode aperture and the screen. These positive ions will be accelerated toward the screen if it is negative with respect to the anode.

The effective secondary emission ratio of the screen is always unity under equilibrium conditions, so the number of secondary electrons leaving the screen is the same as the number of primaries arriving. If the screen is sufficiently negative with respect to the anode, secondary electrons will attain energies sufficient to produce ionization on their way to the anode. Since the screen-anode

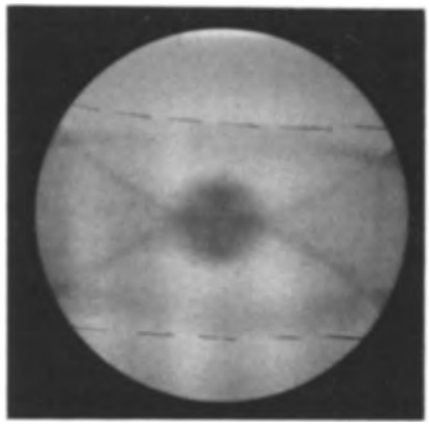

FIG. 14. X-burn in a round tube

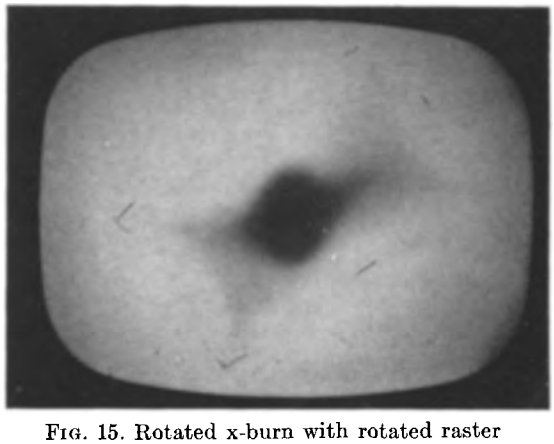

FIG. 15. Rotated x-burn with rotated raster

potential difference may be a kilovolt or more, the ionization probability for these electrons would be greater than for the higher energy primary beam. The mean ionizing path length would be somewhat less, however, and one might expect the production of positive ions by secondary electrons to be roughly equal to that by primaries.

Positive-ion production at the anode coating has been considered (22) as the cause of x-burn. Information is not available on the probability of producing positive ions by electron bombardment of the anode material. However, from indirect evidence, this process as a major source of ions seems rather unlikely.

Observations have been made (23) of the quantity of positive ions necessary to produce a detectable reduction in the luminescent efficiency of a sulfide phosphor. It was found that for H_1^+ and H_2^+ ions accelerated to energies of 2.5 kev or greater, a current of about 10^{-9} amp/mm^2 bombarding for 1 sec produces detectable deterioration, when viewed under 5-kev electron bombardment. The area of a 17-in. television screen is approximately 10^5 mm^2. If the estimate of the number of positive ions produced by the interaction of primary and secondary electrons with the residual gases in the bulb is correct, the screen will be bombarded with an ion current of about 10^{-9} amp. In order to produce detectable positive-ion deterioration over the entire screen, assuming the ions have energies as given above, it would take 10^{+5} sec or about 30 hr. Now, if the ions were focused into an X with an area one-tenth of the total screen area, deterioration could be detected in approximately 3 hr. This would indicate that x-burn could occur in a very short time by this mechanism alone, if the screen potential is suitably low.

Effect of anode coating material on x-burn.—It has been proposed (22) that the positive ions producing x-burn originate at the aquadag anode when it is bombarded by secondary electrons from the screen. Different anode materials might be expected to provide different quantities of positive ions per bombarding electron. It was therefore thought worth while to investigate the effect of different anode materials on x-burn. Tubes were made having anode coatings of platinum, silver, and aluminum. The tubes were life-tested, at an anode voltage of 25 kv, with the raster confined to the phosphor area, so that the high-energy electrons would not strike the anode material. The growth of x-burn was observed and the screen-anode potential difference measured at various intervals during the testing. The existence of a screen-anode potential difference of several kilovolts was noted in most of these tubes within the first 50 hr of life-testing, and results obtained resembled the curves shown in Fig. 8*b*. In every case when a screen-anode potential difference of 1 kv or more was observed, x-burn could also be detected. Intensity of the x-burn was greater for the tubes that had a larger screen-anode potential difference. There was little difference between the rate of occurrence of x-burn in these tubes and the aquadag anode tubes.

Several metal-cone rectangular television tubes were also life-tested, and x-burn occurred in every case in which a screen-anode potential of 1 kv or more was present. These metal-cone tubes did not have an inner aquadag coating on the cone; only the neck region was coated.

These results make it appear a little more likely that the positive ions that are believed to produce the x-burn originate in the tube volume by the interaction of primary and secondary electrons with the residual gas molecules. It is possible, however, that the materials used as anode coatings all provided a copious supply of positive ions under electron bombardment.

Dependence of x-burn on screen potential.—Early observations led to the correlation of the occurrence of x-burn with the existence of a potential difference between tube anode and screen (19). This has been amply verified during the present work. Nothing was known of the magnitude of this potential difference ΔV necessary to produce x-burn, nor of the dependence, if any, of burn intensity on ΔV; therefore, the following experiments were performed. In order to maintain the screen at any desired potential with respect to the aquadag anode, the face plates of rectangular 17-in. glass tubes were made conducting by depositing a film of tin oxide on the inner surfaces.[3] An electrical connection was made to this transparent conductive film through the skirt of the tube. A standard ZnS powder phosphor was then settled on the conductive film. Standard cathode ray tube processing techniques were employed on these tubes. Two tubes were placed on life test with the conductive screen coating connected electrically to the second anode. Anode voltage was maintained at 25 kv and beam current at 150 μa throughout the life test. The beam was scanned over the screen, providing a raster dimension of about 10–12 in. Periodically, the second-anode voltage was reduced to 2.5 kv in order to observe the growth of x-burn. No x-burn ap peared in either of the tubes during the 450 hr of life-testing. These results indicate that x-burning will not occur if the screen remains at the same potential as the anode.

Next, the electrical connection to one tube screen was disconnected from the anode and the screen allowed to float at a potential that was determined by its secondary emission properties. Life-testing was then continued for 20 hr. On reduction of the anode voltage to 2.5 kv, a pronounced x-burn was noticed. This x-burn could be detected with anode voltages up to 10 kv. It was later found that the floating potential of the screen was 2.8 kv below the anode during this final 20 hr of life-testing. Thus, x-burn will occur in a short time if the screen drops appreciably below the anode. It was of interest to determine the effect of smaller screen-anode potential differences on the growth of x-burn. Therefore, the other tube was further life-tested with the screen 1 kv below the anode. After 4 hr an x-burn was observed under 2.5 kv electrons.

It is not necessary for a variation in potential to exist across the screen in order for x-burn to occur, as shown by its occurrence in the presence of the conducting face plates.

It was observed that the intensity of the normal x-burn is greater for a larger screen-anode potential difference. This may be due to any one or more of the following processes: (*a*) higher energy positive ions striking the screen may produce a greater deterioration per ion; (*b*) the greater probable penetration depth of the ions may mean that the deterioration is more easily observed at a

[3] Obtained through the courtesy of J. L. Sheldon, Corning Glass Co.

given electron-bombarding energy; (*c*) more gas may be liberated from the anode material by the higher energy secondaries, thus enabling more positive ions to be produced; (*d*) if the positive ions originate at the anode surface, the probability of production of these ions may be increased at higher bombarding energies. Adequate information is not available at present to determine which of the above is most important or if still another mechanism is responsible for the increase in x-burn intensity with increasing screen-anode potential difference.

Summary

Screen charging behavior depends strongly on the nature of the bombarded surface. Both conducting and insulating screens, if very smooth, follow the anode up to a "sticking potential" and charge no higher regardless of anode voltage. On the other hand, a roughened surface (sand-blasted metal, vapor-deposited phosphor, settled powder-phosphor screens) continues to rise in potential above the discontinuity although at a slower rate; the slope in this region varies as the roughness of the bombarded surface. The fact that screen potential for a rough phosphor layer neither follows the anode to high potentials nor "sticks" at some intermediate value is related to the collecting action of the electric field near the phosphor grains on a steady-state secondary electron space charge in the interstices. Phosphor layer weights also govern screen charging. A standard weight of about 5 mg/cm^2 shows secondary emission sufficient initially to follow anode potentials at least as high as 25 kv; with bombardment, screen-anode potential difference ΔV appears at high voltages and increases with time, at a given anode voltage, approaching a limit. Thicker screens behave similarly. As screen weight is decreased below 5 mg/cm^2 and a larger fractional area of bare glass is exposed to the primary electrons, the screen ceases to follow initially and, for a given bombardment time, shows a larger ΔV. No dependence of screen-charging behavior on phosphor particle size and shape is observed; this is consistent with the probability that the mean angle of incidence of primary electrons on a powder phosphor layer is also independent of particle size and shape. A correlation is observed between high residual gas pressure (10^{-2} – 10^{-3} mm Hg) and the absence of potential difference ΔV.

Ion-focussing fields, due to a screen-anode potential difference, are described by the geometrical configuration of equipotential surfaces in tubes of several shapes. These configurations are shown to lead to observed patterns of ion-induced phosphor deterioration in round, rectangular, and triangular tubes. In the case of underscanning, four-cornered symmetry of focussing fields may again exist and the x-like burn pattern occur regardless of tube geometry.

Positive-ion production by bombardment of residual gas by primary and secondary electrons appears to be the major process; correlation is shown between the number of ions necessary to produce visible reduction in phosphor light output and the number of positive ions probably produced by electron bombardment of the gas. Furthermore, ion-induced screen deterioration appears to be independent of anode material.

Positive ion burn in commercial cathode ray tubes is evidently best controlled by elimination of the ion-focussing fields in the tube. In the absence of the aluminizing process or its equivalent, maintenance of secondary emission of phosphor screens appears to be the major problem, since typical screens show secondary emission properties sufficiently good initially to maintain the tube field-free. There was no observed instance when a considerable field was present in a tube that positive ion burn did not take place rapidly. This deterioration of the phosphor requires a sufficiently high screen-anode potential difference, near 1–2 kv, to be visible in the region of normal tube operating voltages. "Sticking" of the screen potential was observed in this work only with smooth surfaces, and does not occur with standard powder screens because of field dependence of the effective secondary emission ratio. The common x-pattern is not restricted to rectangular tubes, but can occur wherever four-cornered geometry of ion-focussing fields exists.

Acknowledgments

The authors are indebted to many members of the General Electric Research Laboratory, and other Departments of the General Electric Company, for their cooperative assistance during this investigation.

Manuscript received August 19, 1955. This paper was prepared for delivery before the Cincinnati Meeting, May 1 to 5, 1955.

Any discussion of this paper will appear in a Discussion Section to be published in the June 1957 JOURNAL.

REFERENCES

1. J. B. BROWN, *J. Opt. Soc. Amer.*, **27,** 186 (1937).
2. W. B. NOTTINGHAM, *J. Appl. Phys.*, **8,** 762 (1937).
3. H. NELSON, *ibid.*, **9,** 592 (1938).
4. C. HAGEN, *Physik. Z.*, **40,** 621 (1939).
5. E. R. PIORE AND G. A. MORTON, *J. Appl. Phys.*, **11,** 153 (1940).
6. H. VON SALOW, *Z. tech. Phys.*, **21,** 8 (1940).
7. V. K. ZWORYKIN AND G. A. MORTON, "Television," John Wiley & Sons, Inc., New York (1940).
8. C. H. BACHMAN AND C. W. CARNAHAN, *Proc. Inst. Radio Engrs.*, **26,** 529 (1938).
9. K. G. MCKAY, "Advances in Electronics," Vol. I, p. 66, Academic Press New York (1948).
10. G. F. J. GARLICK, "Advances in Electronics," Vol. II, p. 151, Academic Press, New York (1950).
11. H. LEVERENZ, "Luminescence of Solids," p. 388, John Wiley & Sons, Inc., New York (1950).
12. R. GRANACKI, Paper presented at Electrochemical Society Meeting, Philadelphia, May 1952.
13. J. DE GIER, A. C. KLEISMA, AND J. PEPER, *Philips Tech. Rev.*, **16,** 26 (1954).
14. C. DICHTER AND A. I. FRIEDMAN, Private communication.
15. V. K. ZWORYKIN AND G. A. MORTON, "Television," 2nd ed., p. 90, John Wiley and Sons, New York (1954).
16. J. R. YOUNG, *Rev. Sci. Inst.*, **26,** 647 (1955).
17. C. DICHTER, Private communication.
18. H. S. W. MASSEY AND E. H. S. BURHOP, "Electronic and Ionic Impact Phenomena," pp. 542 ff, Oxford Press, London (1952).
19. V. C. CAMPBELL, Unpublished material.
20. S. DUSHMAN, "Vacuum Technique," p. 351, John Wiley & Sons, Inc., New York (1949).
21. J. B. HOAG AND S. A. KORFF, "Electron and Nuclear Physics," p. 488, D. van Nostrand and Co., New York (1948).
22. L. R. KOLLER, Unpublished material.
23. J. R. YOUNG, *J. Appl. Phys.*, **26,** No. 11, 1302 (1955).

Fluorescence of Thallium-Activated Halide Phosphors

KEITH H. BUTLER

Sylvania Electric Products Inc., Salem, Massachusetts

ABSTRACT

Measurements of the emission spectra with several exciting wave lengths and of the excitation spectra with several analyzing wave lengths have been made on KCl:Tl and NH_4Br:Tl with a range of Tl concentrations. Experimental data are analyzed and discussed with relation to the energy levels of the Tl ion involved in the excitation and emission.

The absorption spectra of Tl-activated alkali halide phosphors (1, 2) have been studied extensively and their excitation and emission spectra (3, 4) have received some attention.[1] In addition an attempt has been made to calculate from first principles the absorption and emission spectrum of Tl-activated KCl (5) and to correlate this with experimental data, including data on thermoluminescence.

There appeared, however, to be some possible ambiguities in the assignment of specific excitation and emission bands to transitions between states of the thallous ion, and this prompted a study of the spectra of the alkali halides in an effort to clarify these uncertainties.

This paper reports on measurements of the spectra of NH_4Br, which is crystallographically similar to the halides of Cs, and for which no published data could be found on either absorption or fluorescence, and on measurements of the spectra of KCl, amplifying previous data (3, 4).

EXPERIMENTAL PROCEDURE

A trial of various methods of preparation showed that powder samples of the phosphors could be made by the method of Hutten and Pringsheim (6) and this was adopted. Reagent grade NH_4Br was mortar ground with C. P. thallous chloride to form a phosphor containing 10^{-2} mole fraction of Tl. This concentrated solid solution was successively diluted with additional NH_4Br to give phosphors in which the mole fractions of Tl were 10^{-3}, 10^{-4}, and 10^{-5}. Visual inspection under a u.v. source showed uniform fluorescence was obtained after a few minutes grinding. The purity of the reagent grade NH_4Br was checked by use of the excitation radiometer at a high level of sensitivity and no fluorescence could be detected at any wave length of excitation.

C. P. KCl was found to contain trace amounts of an impurity giving an excitation band at 272 mμ,[2] which resulted in very faint emission bands peaking at 335 and 485 mμ in the uncorrected emission spectra. Purification by fractional crystallization removed this impurity to the point where no fluorescence could be detected. Samples with 3.2×10^{-2}, 1.6×10^{-2}, and 8×10^{-3} mole fraction Tl were prepared by grinding the KCl with C. P. thallous chloride. Other samples were made by successive dilution of these with the pure KCl. Results were confirmed by using phosphors prepared from melts.

The excitation radiometer[3] used for the measurements will be described elsewhere. Basically, it uses radiation from a high pressure xenon arc in a quartz envelope, monochromatized by a Beckman model DU monochromator. A selected wave length from the exit beam of the excitation monochromator is focused on a phosphor coating on a small plaque. The emitted fluorescent light is focused on the entrance slit of a second Beckman monochromator (the analysis monochromator) and the intensity of a selected wave length is measured by a 1P28 photomultiplier. The magnitude of the exciting energy, with which the magnitude of the emission is compared, is measured by a second 1P28 photomultiplier tube receiving a fraction of the exciting radiation via a quartz beamsplitter. The ratio of two photomultiplier signals, after amplification and automatic attenuation of each signal, is directly plotted by a recorder at intervals of 25 Å. Either the excitation spectrum or the emission spectrum can be scanned automatically.

The attenuation circuit of the excitation monitor is adjusted to correct for the relative output of the xenon arc, the slit width of the first Beckman, and the sensitivity of the monitor photocell so that the recorded output at a fixed analysis wave length is a measure of the relative quantum efficiency of fluorescence. This adjustment of the automatic attenuator was made by using $NaC_7H_5O_3$ as a reference material of constant quantum efficiency (7). The attenuator corrections for the analysis circuit were determined by using phosphors of known emission characteristics[4] to extrapolate data into the ultraviolet.

To obtain maximum response from the analysis photomultiplier much of the data was determined with use of a constant attenuation in the analysis circuit and slit widths of 2.0 mm. In these data the emission curves obtained are not corrected for slit width or photomultiplier sensitivity. Other data giving the true emission curves were obtained with selected samples.

In the case of KCl:Tl it was necessary at times to narrow the slits on the excitation monochromator somewhat to obtain satisfactory resolution of the spectra. Slit widths

[1] Excellent bibliographies will be found in references (1), (4), and (6).

[2] This is probably due to Pb^{++} [Cf. Hilsch, *Z. Physik.*, **44**, 860 (1927)] as pointed out by one reviewer of this paper.

[3] Built by Bayside Physics Lab. of Sylvania.

[4] Phosphors emitting between 280 and 320 mμ were kindly furnished by R. Nagy.

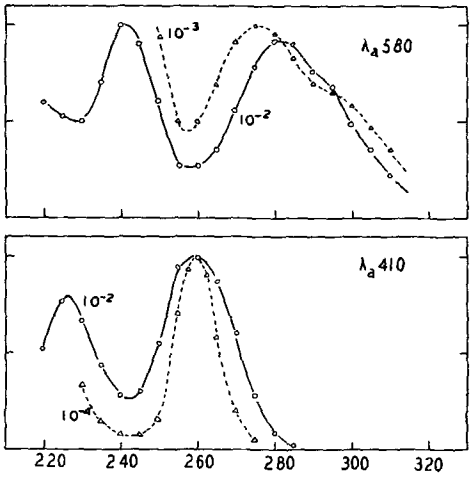

FIG. 1. Excitation spectra of NH_4Br:Tl measured at different emission wave lengths.

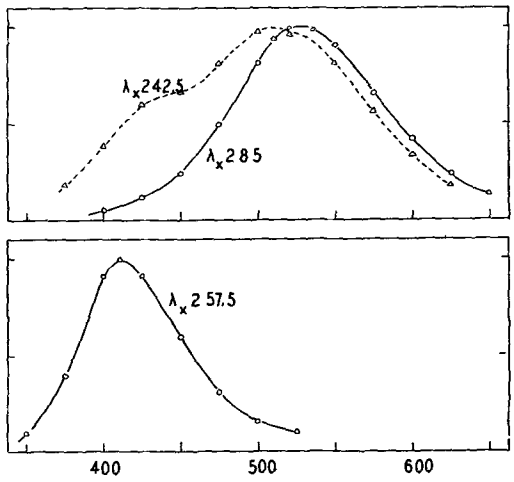

FIG. 2. Uncorrected emission spectra of NH_4Br:Tl measured with different exciting wave lengths.

of 0.50, 1.00, or 2.00 mm were used, while for the analysis monochromator a slit width of 2.00 mm was suitable.

Results with NH_4Br

The general character of the spectra of NH_4Br:Tl can be readily described. The excitation spectrum has four bands peaking at 227, 242, 258, and 280 mμ, while the emission spectrum has two bands with maxima[5] at 400 and 535 mμ. The emission band at 400 mμ is excited only by the excitation bands at 227 and 258 mμ, while the band at 535 mμ is excited by the bands at 242 and 280 mμ. The intensity of emission at 535 mμ is much lower than that of the 400 mμ band even with optimum wave length of excitation.

To determine the characteristic excitation spectrum for the short wave emission band, it was found desirable to use an analysis wave length of 410 mμ or lower, while in the case of the long wave emission an analysis wave length of 590 mμ gave the best resolution of the excitation bands. Similarly the best resolution of the emission spectrum was obtained by using wave lengths of 257.5 and 285 mμ for excitation.

Fig. 1 shows the excitation spectra of the phosphor with two different analysis wave lengths for two Tl concentrations in each case. It should be noted that increasing Tl concentration broadens the excitation spectrum for 400 mμ emission, but apparently narrows the band for 535 mμ emission. The band centered at 280 mμ has a definite hump on the long wave length side and the amount of asymmetry is variable with concentration.

Fig. 2 shows the uncorrected emission spectra of the phosphor for three different exciting wave lengths with a Tl concentration of 10^{-3} mole fraction. The important characteristic to be noted here is that excitation at 240 mμ gives substantially the same emission peak as excitation at 285 mμ. The deviation at shorter wave length will be discussed later. The effect of Tl concentration is shown in Fig. 3 using data from uncorrected spectra. The emission band at 415 mμ is appreciably less dependent on concentration than the band at 540 mμ. Over the range of concentrations shown the intensities in the uncorrected spectra can be expressed by the following equations:

$$\Delta (\log I_{415}) = 0.20\,\Delta (\log C)$$
$$\Delta (\log I_{540}) = 0.35\,\Delta (\log C)$$

There seems to be no indication of concentration quenching even at 10^{-2}Tl.

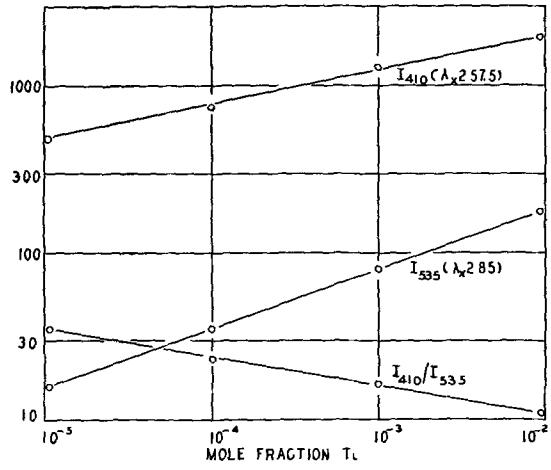

FIG. 3. Effect of Tl concentration on the peak intensity of the two emission bands of NH_4Br:Tl.

Results with KCl

The general character of the emission spectrum of KCl:Tl found in the present work is essentially that described by Hutten and Pringsheim (6) and by Johnson and Williams (4). There is a strong emission band at 302 mμ, a weaker band at 492 mμ, and a possible band at about 380 mμ. The main excitation band, which extends from 240 to 275 mμ, is found, however, to be a complex[6] formed from two closely spaced components.

Fig. 4 shows the effect of Tl concentration on the peak intensity of the 302 mμ emission band with an exciting wave length of 245 mμ and on the peak intensity of both

[5] For the uncorrected spectra the maxima are found at 415 and 540 mμ.

[6] The complex nature of the excitation band was observed by Johnson and Williams (4) but apparently they did not recognize the existence of two components.

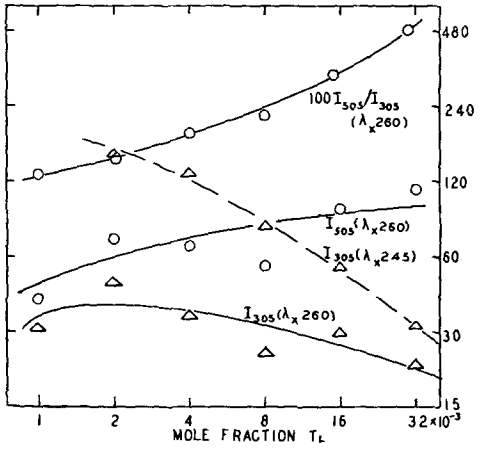

FIG. 4. Effect of Tl concentration and exciting wave length on the peak intensity of the two emission bands of KCl:Tl.

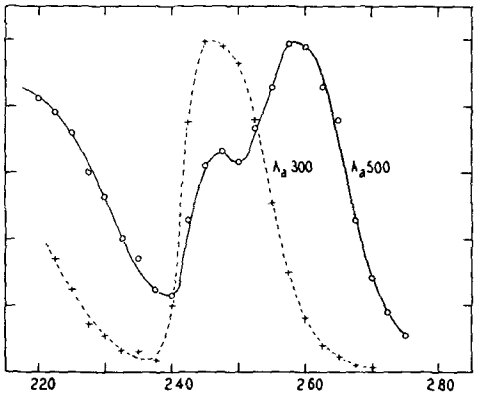

FIG. 5. Excitation spectra of KCl:Tl measured at different emission wave lengths.

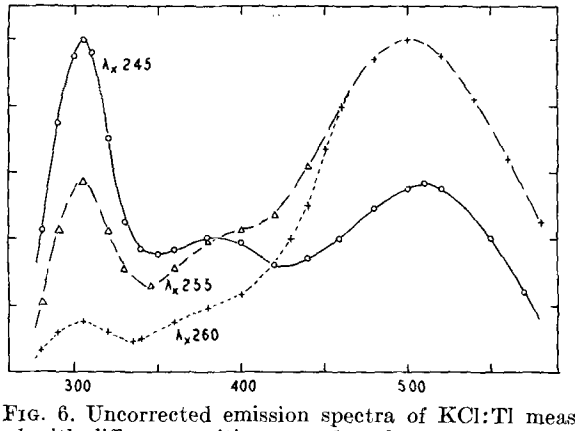

FIG. 6. Uncorrected emission spectra of KCl:Tl measured with different exciting wave lengths.

the main emission bands, when the exciting wave length is 260 mμ. In both cases data from uncorrected spectra were used, and unrelated arbitrary intensity values were used with each value of λ_x. The ratio of the visible to the ultraviolet is also shown for excitation with 260 mμ. The variation in this ratio is a sensitive indication of Tl concentration and is more reliable than measurement of intensity of emission. Fig. 5 shows the change in shape of the excitation curve as the analysis wave length is changed from 300 to

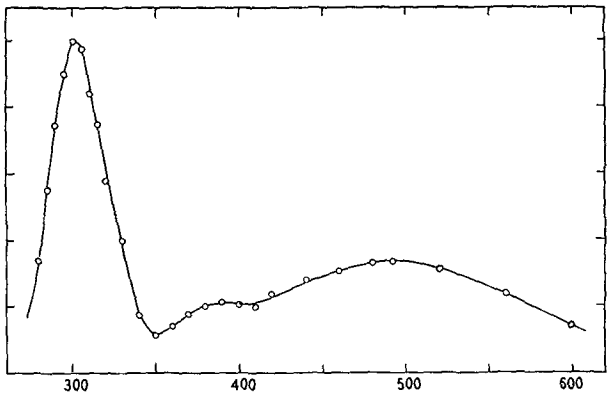

FIG. 7. Emission spectrum of KCl:Tl excited by λ 260 and corrected for photocell response.

500 mμ,[7] while Fig. 6 shows the changes in the uncorrected emission spectrum with exciting wave lengths of 245, 255, and 260 mμ. Fig. 7 shows the corrected emission curve for 260 mμ excitation. While these curves were obtained using a phosphor containing 4×10^{-3}Tl, similar variations are found with all concentrations from 1×10^{-3} up to 3×10^{-2}.

DISCUSSION

NH_4Br has a crystal structure of the CsCl type. In this structure each ion is surrounded by eight ions of the opposite charge. The packing is less close than that found in the KCl type of lattice where each ion is surrounded by only six ions of the opposite charge. The radius of the ammonium ion is about 1.43Å; this is very close to the radius of Tl of 1.44 so that substitution should occur very readily. The fact that mortar grinding gives reproducible phosphors with uniform fluorescence shows that Tl migrates into the lattices very easily, while the lack of concentration quenching and the failure to develop new emission bands at high concentration suggests that Tl ions form isolated centers.

It is probable that the Tl^+ ion in solid solution in ionic crystals has the same electron configuration and ground state as the free ion. This is $6s^2$, $^1S_0$. The first excited states, with a 6s6p configuration, are $^3P_0^\circ$, $^3P_1^\circ$, $^3P_2^\circ$ and $^1P_1^\circ$ in order of increasing energy. It is believed that the dipole radiation selection rules for angular orbital momentum $\Delta L = \pm 1$ and for total angular momentum $\Delta J = 0, \pm 1$ ($J = 0$ to $J = 0$ is forbidden) and for parity are applicable to activator ions in the crystal as well as to the free ion. While the multiplicity selection rule for LS coupling requires that $\Delta S = 0$, experimental evidence shows violation of this. However, the transition $^1S_0$ $(6s^2) \rightarrow {}^1P_1^\circ$ $(6s6p)$ would be expected to be the more probable. Therefore, the strong excitation band of NH_4Br:Tl, centered at 258 mμ, is attributed to this transition. The weaker band at 280 mμ can then be assigned to the other allowed transition $^1S_0$ $(6s^2) \rightarrow {}^3P_1^\circ$ $(6s6p)$. The corresponding emission bands, resulting from the return transitions to the ground state, are centered at 400 and 535 mμ, respectively. A summary of the experimental spectra for the two transitions is shown in Fig. 8. In this figure the corrected and normalized emission spectra are given along

[7] The curves have been normalized, thus obscuring the fact that the excitation efficiency is much higher for 300 mμ emission than for 500 mμ.

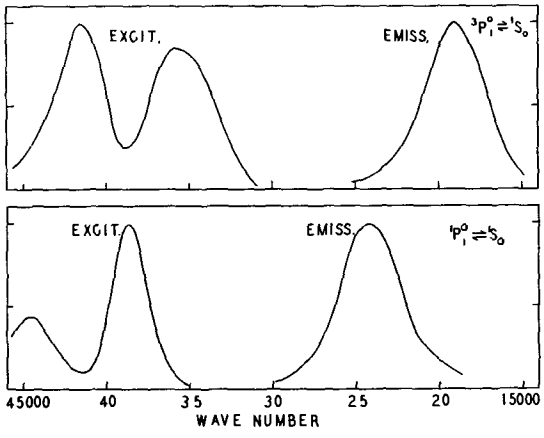

FIG. 8. Normalized excitation and emission spectra of the two excited states of Tl in NH_4Br:Tl.

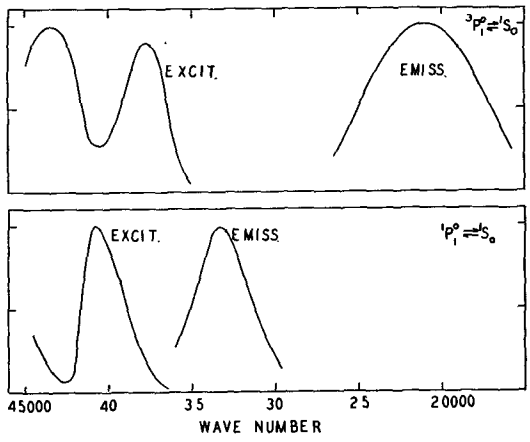

FIG. 9. Normalized excitation and emission spectra of the two excited states of Tl in KCl:Tl.

with the normalized excitation spectra on a wave number basis.

It is somewhat difficult to explain the asymmetry of the 280 mμ excitation band since the experimental evidence, showing that the asymmetry is concentration dependent, seems to point toward a separate state which does not, however, give a separate emission band. One tentative hypothesis is that this asymmetry is due to excitation to the $^3P_0^\circ$ state, normally a forbidden transition, followed by a thermal promotion to the $^3P_1^\circ$ state, possible because of crossing of the potential energy curves, at separations below the equilibrium value, with a small energy barrier. At present there is no experimental evidence either for or against this hypothesis. Another explanation is that the asymmetry is due to formation of pairs of Tl ions.

It is interesting to note that there is no experimental indication of energy transfer between the excited states $^1P_1^\circ$ and $^3P_1^\circ$ of the $6s6p$ configuration at room temperature for NH_4Br:Tl.

For KCl:Tl it is apparent from Fig. 5 that the main excitation band has at least two components located at about 245 and 260 mμ. The data reported in Fig. 6 show that excitation by 245 mμ gives predominantly 302 mμ emission while excitation by 260 mμ gives predominantly 492 mμ emission. It should be emphasized that the 302 mμ band is much stronger than the 492 mμ band, a fact obscured by the use of uncorrected photocell response curves in these figures, but readily seen by comparing Fig. 6 and 7.

If it is assumed[8] that the 245 mμ excitation band and the intense 302 mμ emission band are due to the more probable of the allowed transitions, namely $^1S_0 \rightarrow {}^1P_1^\circ$, then the 260 mμ excitation band, giving 492 mμ emission, can be assigned to the other allowed transition $^1S_0 \rightarrow {}^3P^\circ_1$. Fig. 9[9] shows normalized excitation and emission spectra on a wave number basis for the two transitions.

In the case of NH_4Br:Tl, excitation in either the 242 or the 280 mμ emission band gives identical strong emission at 530 mμ, with a weak added band at 400 for excitation at 242. With excitation at either 225 or 260 mμ the emission is almost entirely at 400 mμ. Similarly excitation of KCl:Tl by either 230 or 260 mμ gives relatively strong emission at the 492 mμ band, with the same band shape.

This virtual identity of emission indicates that the emitting transitions are the same regardless of which of two exciting transitions take place.

There are several possible explanations for the excitation bands at shorter wave lengths.

1. They may be due to splitting of the energy levels.
2. They may be due to absorption by the matrix in disturbed regions near the luminescent centers.[10]
3. They may be due to excitation to states of the $6s7p$ configuration.
4. In the case of KCl, if Williams' assignment of levels is correct, they could be $^1P_1^\circ$ states of $6s6p$.

All of these hypotheses involve difficulties and a clear-cut selection is not possible without additional experimental data. In the case of KCl, Williams' choice of levels makes it difficult to explain the marked experimental difference in emission with a slight shift in exciting wave length from 245 to 260 mμ. Splitting of energy levels would require a crossing of potential energy curves. Absorption by the matrix in the tail of the fundamental absorption band does not seem to be adequate to explain the 242 mμ excitation band in NH_4Br since the matrix absorption appears to be at a wave length below 200 mμ.

The major difficulty[11] with the hypothesis that the $6s7p$ levels are excited lies in the very marked lattice interaction perturbations involved and a very difficult quantitative calculation is needed to determine if such perturbations are possible. However, this hypothesis allows an explanation of certain experimental data more simply than the other mechanisms mentioned above.

[8] This differs from the assumption made by Williams and co-workers, that 245 mμ excitation and 302 mμ emission result from excitation to $^3P_1^\circ$, while 200 mμ excitation and 492 mμ emission result from excitation to $^1P_1^\circ$.

[9] The $^3P_1^\circ$ curve is based on measurements at 530 mμ while the curve in Fig. 5 was taken at 500 mμ. At 530 mμ there are clearly defined maxima in the excitation curves at 37,700 and 43,500 cm^{-1} which are distorted when the slightly shorter measuring wave length of 500 mμ is used.

[10] Suggested by F. Seitz in his review of the paper.

[11] While oscillator strength for the $6s \rightarrow 7p$ transition is low in the gaseous ion, placing it in a crystal matrix may greatly change transition probabilities, much as the presence of argon in a gas discharge affects the relative intensity of the 185 and 254 mμ lines of Hg.

If the 242 mμ band for NH_4Br:Tl is due to excitation to the $^3P_1^\circ$ state of $6s7p$ and if the electron drops first to $6s7s$ and then to $6s7p$, without the selection rule $\Delta S = 0$ holding rigorously, then both the $^3P_1^\circ$ and $^1P_1^\circ$ states of $6s6p$ would be excited and emission should occur in both the 400 and the 535 mμ emission bands as was found experimentally.

The effect of temperature on the emission of KCl:Tl with 254 mμ excitation can be explained by temperature broadening or by temperature shift, if the band is actually an overlapping complex of $^3P_1^\circ$ and $^1P_1^\circ$ states of $6s6p$. The assumption of thermal transfer from $^3P_1^\circ$ to $^1P_1^\circ$ would not then be required in KCl:Tl, thus increasing the resemblance of this phosphor to NH_4Br:Tl.

Preliminary Data on Other Halides

The assignment of energy levels proposed both for NH_4Br:Tl and for KCl:Tl differs considerably from that suggested by Williams (5) for KCl:Tl. The mechanism also differs in that the existence of thermal transfer between $^1P_1^\circ$ and $^3P_1^\circ$ may not be required. While it might be suggested that the difference in behavior of the two phosphors is due to difference in crystal structure, this is ruled out by data on other alkali halides for which the crystal structure difference is not found. Preliminary results on NH_4Cl, KBr, and KI, with a single Tl concentration, show that these phosphors have spectra similar to NH_4Br with well resolved emission and excitation bands. The location of the peaks in the uncorrected photocell response curves is given in Table I.

Initial results on NaCl, NaBr, and NaI also have been obtained at a single Tl concentration. These phosphors resemble KCl:Tl in having two well resolved emission bands with one main excitation band above 220 mμ, this being a complex of two components. In all of these phosphors the shape of the excitation band depends strongly on which of the emission bands is used in the measurement. Also excitation on the short wave-length side of the main band leads to predominance of the short wave emission; while excitation on the long wave-length side leads to predominance of the long wave-length emission.

TABLE I

Matrix	Emission bands in mμ	Excitation bands in mμ
NH_4Cl	385, 510	210, 222, 240, 260
KBr	360, 480	222, 230, 261, 274
KI	425, 490	242, 262, 287, 305

TABLE II

Matrix	Emission bands in mμ	Excitation band in mμ
NaCl	295, 395	255
NaBr	310, 530	270
NaI	430, 490	287

The location of the peaks in the uncorrected photocell response curves are given in Table II.

The wave-length changes in both the emission and excitation spectra show that three major factors affect the energy levels of the activator ions. These are anion size, cation size, and crystal structure. More complete data on these phosphors will be reported in later papers.

Summary

Two types of emission and excitation spectra are found in the Tl-activated alkali halides. In one type, represented by NH_4Br:Tl, both the excitation and the emission bands are well separated. In the other type, represented by KCl:Tl, the emission bands are well separated but the excitation bands overlap.

In NH_4Br:Tl the emission band at 400 mμ can be excited by bands at 227 or 258 mμ, while the emission band at 535 mμ can be excited by bands at 242 or 280 mμ. The following tentative energy level assignments are proposed for these spectra.

Wave lengths in mμ	Excited state
258 and 400	$^1P_1^\circ$ ($6s6p$)
280 and 535	$^3P_1^\circ$ ($6s6p$)
227	$^1P_1^\circ$ ($6s7p$)
242	$^3P_1^\circ$ ($6s7p$)

If there is excitation to $6s7p$ it is suggested that the electron returns via $6s7s$ to $6s7p$.

In KCl:Tl the excitation band at 240 to 270 mμ appears to be composed of two components centered at 245 and 260 mμ. Excitation at 245 gives strong emission at 302, while excitation at 260 gives strong emission at 492 mμ. An analogous assignment of energy levels is tentatively proposed for these spectra.

Wave lengths in mμ	Excited state
245 and 302	$^1P_1^\circ$ ($6s6p$)
260 and 492	$^3P_1^\circ$ ($6s6p$)
below 200	$^1P_1^\circ$ and $^3P_1^\circ$ ($6s7p$)

Manuscript received October 12, 1955. This paper was prepared for delivery before the Cincinnati Meeting, May 1 to 5, 1955.

Any discussion of this paper will appear in a Discussion Section to be published in the June 1957 Journal.

REFERENCES

1. P. H. Yuster and C. J. Delbecq, *J. Chem. Phys.*, **21**, 892 (1953).
2. M. Forro, *Z. Physik*, **58**, 613 (1930).
3. W. V. Mayern, *ibid.*, **61**, 321 (1930).
4. P. D. Johnson and F. E. Williams, *J. Chem. Phys.*, **20**, 124 (1952).
5. F. E. Williams, *J. Phys. Chem.*, **57**, 780 (1953) and earlier papers.
6. E. H. Hutten and P. Pringsheim, *J. Chem. Phys.*, **16**, 241 (1948).
7. F. S. Johnson, K. Wantanabe, and R. Tousey, *J. Opt. Soc. Amer.*, **41**, 702 (1951).

Polarographic Behavior of Organic Compounds in Methanesulfonic Acid

S. Wawzonek, R. Berkey, and D. Thomson

Department of Chemistry, State University of Iowa, Iowa City, Iowa

ABSTRACT

Aromatic nitro compounds and triarylcarbinols gave normal polarographic waves in methanesulfonic acid. Aromatic ketones and aldehydes gave waves which were complicated by maxima. Nitro compounds were reduced to the phenylhydroxylamines which were rearranged by the acid to the *p*-aminophenols. The triarylcarbinols were reduced to the triphenylmethanes under anhydrous conditions and to the free radicals in the presence of water. Ketones and aldehydes were reduced to the pinacols which, under the influence of the strong acid, underwent the pinacol rearrangement.

Most of the work on the behavior of organic compounds in strong acids has been dependent upon cryoscopic studies. The only polarographic study of organic compounds in strong acids reported to date has been in 98.65% sulfuric acid and has dealt mainly with aromatic nitro compounds (1). Carbonyl compounds which form conjugate acids and triarylcarbinols which form carbonium salts with strong acids have not been studied.

In the present work the suitability of methanesulfonic acid as a solvent for the polarographic study of organic compounds has been investigated and the behavior of aromatic nitro compounds, ketones and aldehydes, and triarylcarbinols studied.

Experimental

Polarographic data were obtained with a Sargent Model XII polarograph using an electrolytic cell similar to that described previously (2). The capillary used had a drop time of 4.19 sec and a $m^{2/3}t^{1/6}$ of 1.59 $mg^{2/3}sec^{-1/2}$ at a mercury height of 60 cm on an open circuit.

Methanesulfonic acid.—This acid was purified by filtering the technical acid obtained from Eastman Kodak Co., and then distilling at reduced pressure (1 mm) four times. The boiling point of the product used was 120°/1mm; the freezing point was 19.5°–20.1°.

The pure acid had a decomposition potential of −0.835 v. Addition of water and organic compounds shifted this value to more negative potentials.

The resistance of the pure acid in the polarographic cell was 1890 ohms. Addition of water and organic compounds lowered this resistance. Results are shown in Table I.

The resistance of the solutions in the polarographic cell was determined with a Wheatstone Bridge using a battery-powered 1000 cycle audio-oscillator as a current source and earphones to determine the null point.

Electrolyses.—Large scale electrolyses were carried out in a cell similar to that described earlier (3).

Electrolysis of benzaldehyde.—Methanesulfonic acid (350 ml) was placed in the electrolytic cell, fitted with a platinum gauze anode and a stirred mercury pool cathode, and degassed by bubbling nitrogen through it for 1 hr. Freshly distilled benzaldehyde (10 ml) was added and a current from an 85 v generator passed through for 8 hr. The initial current of 0.5 amp dropped to a value of 0.18 amp in this time. The electrolysis cell was cooled with an ice bath during this whole period. The resulting acid solution was filtered from the mercurous methanesulfonate (15 g) formed and poured into water. Extraction with ether gave an oil from which benzaldehyde (4.8 g) was recovered by distillation under reduced pressure, 90°/40 mm. The solid residue when recrystallized from ethanol gave desoxybenzoin (1.6 g) melting at 58°–9° and a tarry polymer (2.6 g).

Electrolysis of nitrobenzene.—Nitrobenzene (10 ml) was treated in methanesulfonic acid (350 ml) in a manner similar to that used for benzaldehyde. The resulting acid solution was filtered from the mercurous methanesulfonate (4.8 g) and neutralized with sodium hydroxide. Extraction with ether gave a product which was acidified with 5% HCl and steam distilled. The steam distillate gave nitrobenzene (4.3 g). The residue when made basic and steam distilled gave no aniline. Extraction with ether after neutralization followed by drying of the ether solution and then saturating with dry hydrogen chloride gas gave *p*-aminophenol hydrochloride (3.5 g) m.p. 201°–3° (4).

Electrolysis of benzophenone.—Benzophenone (5 g) was electrolyzed in methanesulfonic acid (400 ml) using a mercury anode and a mercury cathode. The resulting solution was filtered from the mercurous methanesulfonate (25 g) and poured into water. The resulting precipitate upon fractionation from ethanol gave two products. The first of these was benzophenone (2.2 g) and the second (2.5 g) benzopinacolone, m.p. 181°–182°.

Electrolysis of triphenylcarbinol.—Electrolysis of triphenylcarbinol (5 g) in methanesulfonic acid (400 ml) using a platinum anode and a mercury cathode for 8 hr was followed by filtration of the solution from the mercurous methanesulfonate (35 g) and pouring the filtrate into water. The resulting solid was separated by fractional crystallization from ethanol into triphenylcarbinol (2.5 g) and triphenylmethane (1.5 g), m.p. 90°.

Mercurous methanesulfonate.—This salt which was formed in the electrolyses was synthesized by treating mercurous oxide with methanesulfonic acid. Methanesul-

TABLE I. *Effect of various substances upon the resistance of methanesulfonic acid*

Compound	Resistance (ohms)
1% Water	358
2.91% Water	336
4.76% Water	275
9.09% Water	256
0.1*M* NH_4Cl	582
0.00526*M* $(C_6H_5)_3COH$	1170
0.00997*M* $(C_6H_5)_3COH$	880
0.00997*M* $(C_6H_5)_3COH$ + 4.76% H_2O	360
0.00997*M* $(C_6H_5)_3COH$ + 9.09% H_2O	260

fonic acid (32 g) was dissolved in water (70 ml) and neutralized with mercurous oxide. The resulting solution was decolorized twice with Nuchar (2 g), filtered, and concentrated until crystals formed. Cooling to 0° gave crystals which melted at 320°–322°.

Anal. calcd. for Hg SO_3CH_3: C, 4.10; H, 1.02. Found: C, 4.28; H, 1.06.

The compounds investigated were either obtained from stock or prepared according to directions in the literature.

Results

The present investigation indicates that methanesulfonic acid is a suitable solvent for the polarographic reduction of organic compounds in a range up to −0.9–1.0 v measured against the mercury pool. The self-ionization of the acid is large enough so that no inert electrolyte is needed. The resistance of 1900 ohms is low enough for polarographic studies. Addition of water and certain organic compounds shifted the decomposition potential to more negative values and made a slightly larger range of potentials available for study. The addition of 0.1*M* ammonium chloride, which liberated hydrogen chloride and formed ammonium methanesulfonate, did not affect the decomposition potential but lowered the resistance to 582 ohms. Addition of water and of organic compounds likewise lowered the resistance as shown in the experimental section. The amount of lowering was such that correction for *IR* drop was not necessary.

The polarographic waves obtained were well defined in most cases. Exceptions are mentioned in the discussion of the individual classes. Varying concentrations of each compound were used and are reported, since the waves close to the discharge potential of the electrolyte were only well defined at the higher concentrations of the substances being reduced.

Results for nitrobenzene and *p*-nitrotoluene are given in Table II. Reduction products of nitrobenzene such as aniline, phenylhydroxylamine, and *p*-aminophenol gave no reduction waves in methanesulfonic acid.

The first wave in each case was well defined and diffusion-controlled. At concentrations higher than 0.5 mM a round maximum appeared which did not decrease to the diffusion current at the higher concentrations. This maximum was suppressed by the addition of water.

The second wave was only well defined at the higher concentrations of nitro compounds and was kinetic in nature. This wave occurred at concentrations of nitro compound larger than 0.403 mM even though it is not listed for several concentrations in the table. Since the maximum for the first wave did not return to the diffusion current of the latter, the diffusion current constant (I_d) of the second wave decreases as that for the first wave increases. The second wave was not visible in the presence of water.

TABLE II. *Polarographic behavior of aromatic nitro compounds in methanesulfonic acid*

Conc. millimoles/liter	1st wave $E_{\frac{1}{2}}$ (v) vs. Hg pool	I_d[a]	2nd wave $E_{\frac{1}{2}}$ (v) vs. Hg pool	I_d[a]
		Nitrobenzene		
0.110	−0.26	3.30		
0.220	−0.27	3.06		
0.403	−0.30	3.12[b]	−0.97	53.3
0.462[c]	−0.25[c]	3.36[c]		
0.715	−0.27[d]	2.95		
0.824	−[d]	4.71	−0.97	40.7
1.52	−[d]	10.0	−0.95	29.1
2.18	−[d]	26.4	−1.07	20.5
3.46	−[d]	15.57		
3.26[e]	0.34	3.63	No wave visible	
		p-Nitrotoluene		
0.118	−0.29	3.59		
0.293	−0.31	3.11		
0.466	−0.30	2.87		
0.646	−0.29[d]	3.08		
0.820	−[d]	3.10	−0.99	40.7
3.54	−[d]	4.26	−0.98	11.7
3.32[e]	−0.34	2.54	No wave visible	

[a] $I_d = \dfrac{i_d}{Cm^{2/3}t^{1/6}}$

[b] Diffusion controlled. The diffusion current at 60 cm Hg was 2.00 amp and at 40 cm Hg was 1.66 amp.

[c] Temperature 35°.

[d] Maximum.

[e] The acid contained 6.10% water by volume.

Polarographic results obtained for the various triarylcarbinols in anhydrous methanesulfonic acid and methanesulfonic acid containing water are given in Table III. The behavior of triphenylmethyl chloride which dissolves in methanesulfonic acid with the liberation of hydrogen chloride is also reported in this table for comparison. The study of these compounds in the presence of water was carried out in order to obtain more information about the mechanism.

The aromatic ketones studied gave waves only at high concentrations which were similar in nature to the curves with the rounded maxima for nitrobenzene but much smaller in size. In Table IV both the height of the maximum and the height of the leveling off point are given. The latter was found to vary with the mercury height in a manner similar to that found for diffusion currents. The height of the maximum behaved differently with changes in mercury height and seems to be affected by the concentrations of the compounds used. Water, when added to the solution, eliminated the maximum only at higher concentrations, (23.07%). The diffusion current constant (I_d) under the last conditions is small and may have been lowered by the precipitation of some of the ketone.

The behavior for the aromatic aldehydes was not consistent. Benzaldehyde gave no definite wave at high

TABLE III. *Polarographic behavior of triarylcarbinols in methanesulfonic acid with varying amounts of water*

% H_2O[a] by volume	Conc. of carbinol in millimoles/liter	1st wave		2nd wave	
		$E_{\frac{1}{2}}$ (v) vs. Hg pool	I_d[b]	$E_{\frac{1}{2}}$ (v) vs. Hg pool	I_d[b]
Triphenylcarbinol					
0	0.508	−0.63	1.05(0.85)[c]	—	—
0	0.508	−0.61	(0.66)[c, d]	—	—
1.0	0.503	−0.61	0.92	—	—
2.91	0.493	−0.60	0.95	—	—
4.76	0.484	−0.56	0.84	—	—
9.09	0.461	−0.55	0.54	−0.67	0.33
0	0.918	−0.67	1.15	—	—
4.76	0.874	−0.59	0.63	−0.76	0.40
9.09	0.835	−0.52	0.49	−0.75	0.32
16.66	0.765	−0.48	0.30	−0.76	0.38
		−0.55[e]	0.19		
0	2.30	−0.70	1.02	—	—
4.76	2.19	−0.56	0.53	—	—
9.09	2.09	−0.52	0.31	—	—
		−0.60[e]	0.19		
16.66	1.92	−0.45	0.14	—	—
		−0.52[e]	0.36		
23.08	1.77	−0.42	0.12	−0.88	0.40
		−0.48[e]	0.33		
0	4.10	−0.67	0.68	—	—
4.76	3.91	−0.59	0.49	—	—
9.09	3.73	−0.54	0.23	—	—
		−0.61[e]	0.23		
16.66	3.42	−0.47	0.12	—	—
		−0.61[e]	0.30		
23.08	3.16	−0.44	0.15	−0.91	0.40
		−0.49[e]	0.24		
		−0.62[f]	0.06		
0	6.01	−0.71	0.60	—	—
4.76	5.72	−0.58	0.49	—	—
9.09	5.46	−0.53	0.22	—	—
		−0.60[e]	0.24		
		−0.72[f]	0.08		
16.67	5.01	−0.46	0.15	—	—
		−0.52[e]	0.22		
		−0.66[f]	0.05		
23.08	4.62	−0.43	0.176	−0.97	0.55
		−0.48[e]	0.175		
		−0.63[f]	(small)		
Triphenylmethyl chloride					
0	0.917	−0.67	1.22	—	—
4.76	0.874	−0.59	0.62	−0.77	0.39
9.09	0.834	−0.54	0.46	−0.77	0.34
16.66	0.765	−0.48	0.30	−0.77	0.31
		−0.56[e]	0.20		
0	0.893	−0.76	(14.1)[g]		
Tri-*p*-anisylcarbinol					
0	1.01	No wave until 16.66% H_2O added			
16.66	0.842	−0.81	0.87	—	—
23.08	0.777	−0.78	0.80	—	—
33.33	0.635	−0.72	0.88	—	—
0	5.75	No wave until 16.66% H_2O added			
16.66	4.79	−0.86	0.84	—	—
23.08	4.42	−0.86	0.81	—	—
33.33	3.83	−0.74	0.29	−1.16	0.14
		−0.94[e]	0.40		
41.18	3.38	−0.63	0.19	—	—
		−0.85[e]	0.43	—	—
Diphenyl-α-naphthylcarbinol					
0	1.12	−0.65	0.71	—	—
9.09	1.02	−0.56	0.32	—	—
16.66	0.924	−0.52	0.13	—	—
23.08	0.861	Precipitation occurred			
Diphenyl-*o*-tolylcarbinol					
0	0.972	−0.64	0.83	—	—
4.76	0.926	−0.58	0.63	−0.78	0.22
9.09	0.884	−0.53	0.64	−0.78	0.31
16.66	0.810	−0.48	0.58	−0.78	0.30
Tri-*p*-biphenylcarbinol					
0	1.16	−0.64	1.60	—	—
4.76	1.10	−0.60	1.23	−0.72	0.12
9.09	1.055	−0.57	0.86	−0.69	0.20
16.66	0.956	−0.50	0.56	−0.68	0.16
33.3	0.774	−0.33	0.30	−0.67	0.09
		−0.53[e]	0.17		

[a] Percentages represent the addition of 0.1, 0.3, 0.5, 1.0, 2.0, and 3.0 ml of water to 10 ml of acid.

[b] $I_d = \dfrac{i_d}{Cm^{2/3}t^{1.6}}$

[c] Diffusion current in microamperes.

[d] Mercury reservoir height = 40 cm.

[e] Second part of split wave.

[f] Third part of split wave.

[g] Current in microamperes. Some of the HCl gas escaped during the dissolving of the compound so that a quantitative measurement of the current was not possible.

concentrations of the compound or in the presence of water. *p*-Chlorobenzaldehyde gave signs of a wave only at high concentrations and in the presence of at least 23.00% water. *p*-Tolualdehyde gave a wave in anhydrous methanesulfonic acid. The span of the limiting current was not large enough to determine whether this curve was a maximum or not. The addition of water caused the curve to vanish. An increase in temperature had little effect on the height.

Discussion of Results

Results in Table II indicate that aromatic nitro compounds behave normally in anhydrous methanesulfonic acid. By analogy to the behavior in aqueous acid solutions the wave must correspond to a 4 electron reduction. The product, however, is *p*-aminophenol and is formed by the rearrangement of the intermediate phenylhydroxylamine. The isolation of *p*-aminophenol exclusively in a large-scale electrolytic reduction of nitrobenzene and the absence of a wave for phenylhydroxylamine in this solvent is in agreement with this mechanism. The results of the macroscale experiment closely resemble those obtained with nitrobenzene in glacial acetic acid-sulfuric acid (4).

$$C_6H_5NO_2 + 4e + 6CH_3SO_3H \rightarrow$$

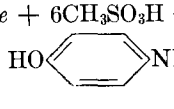

$$+ NH_3^+ + H_2O + 6CH_3SO_3^-$$

TABLE IV. *Polarographic behavior of aromatic aldehydes and ketones in methanesulfonic acid with varying amounts of water*

% H_2O[a] by volume	Conc. in millimoles/liter	$E_{\frac{1}{2}}$ vs. Hg pool	I_d[b] max	I_d[b] min	i_d max	i_d min
		Benzophenone				
0	1.41–2.71	No wave				
0	5.64	−1.03	5.61	[c]	50.3	—
0	5.64[d]	−1.02[d]	—	—	47.1[d]	—
0	11.09	−0.99	2.50	1.80	44.0	31.3
0	11.09[d]	−1.00[d]	—	—	36.4[d]	25.3[d]
4.76	10.55	−0.98	1.96	1.14	32.9	20.1
4.76[d]	10.55[d]	−0.97[d]	—	—	26.9[d]	15.64
9.09	10.08	−0.96	0.95	—	16.8	12.0
9.09[d]	10.08[d]	−0.96[d]	—	—	13.5[d]	9.6[d]
23.07	9.53	−0.95		0.28		
0	1.20[e]	No wave				
f	1.00	−0.98		1.39	—	2.31
f[d]	1.00[d]	−0.98[d]			—	1.92[d]
		p-Chlorobenzophenone				
0	1.06–2.65	No wave				
0	5.25	−0.96	4.21	3.22	35.2	26.9
0[d]	5.25[d]	−0.96[d]	—	—	31.1[d]	22.0[d]
0	6.64	−0.97	3.18	2.24		
0	8.04	−0.97	2.39	1.46		
		p-Phenylbenzophenone				
0	0.942–3.95	No wave				
0	5.29	−1.02	2.08	1.79	15.9	13.7
0	5.29[d]	−1.00[d]	—		14.8[d]	11.0
4.76	5.04	−1.01	1.06	[c]	8.47	[c]
4.76[d]	5.04	−1.02			6.93[d]	
		p-Tolualdehyde				
0	2.97	No wave				
0	5.52	−1.00	4.14	[c]		
0	7.44	−1.02	2.79	[c]		33.0
0	7.44[d]	−0.98[d]	—	[c]		22.4[d]
0	8.71	−0.98	2.20			
9.09	7.91	No wave				
0	9.18	−1.03	2.06	[c]		
0	9.18[g]	−0.98[g]	2.06[g]	[c]		
0	11.9	−1.02	1.25	[c]		
0	11.9[g]	−1.01[g]	1.25[g]	[c]		

[a] Percentages represent the addition of 0.5, 1.0, and 3.0 ml of water to 10 ml of acid.

[b] $I_d = \dfrac{i_d}{Cm^{2/3}t^{1/6}}$

[c] The limiting current span is small and combines with the discharge of the methanesulfonic acid.

[d] Mercury reservoir at 40 cm.

[e] In the presence of 0.1*M* $NH_4O_3SCH_3$.

[f] In 0.1*N* HCl—50% ethanol.

[g] Temperature 35°.

The second wave, which is very much larger, is practically completely kinetic in nature and must be a catalytic hydrogen wave brought on by the *p*-aminophenol formed in the reduction.

The half-wave potentials for nitrobenzene and *p*-nitrotoluene differ very little from each other. This similarity was also found by James (1) in 98.65% sulfuric acid. The data obtained in methanesulfonic acid for these compounds are surprisingly similar to those obtained by James (1).

Examination of the results in Table III indicates that the various triphenylcarbinols form triphenylcarbonium ions which are reducible polarographically at the dropping mercury electrode in methanesulfonic acid. The diffusion current constant (I_d) when compared with that obtained for nitrobenzene at concentrations below 0.5 mM (Table II), which takes up four electrons, points to a two-electron change or a reduction to the triphenylmethane. The waves were diffusion controlled and had a slope of approximately 0.059. These data suggest the following steps for the electrode reactions:

$$(C_6H_5)_3C^+ + e \rightarrow (C_6H_5)_3C\cdot$$

$$(C_6H_5)_3C\cdot + e + CH_3SO_3H \rightarrow (C_6H_5)_3CH + CH_3SO_3^-$$

The free radical is reduced rapidly and directly to the triphenylmethane. The possibility also exists that the lability of the free radical in this solvent is caused by the following reaction:

$$2(C_6H_5)_3C\cdot + CH_3SO_3H \rightarrow (C_6H_5)_3CH + (C_6H_5)_3C^+ + CH_3SO_3^-$$

This reaction would be similar to that reported for the triphenylmethyl radical in glacial acetic acid (5).

An electrolytic reduction of triphenylcarbinol on a large scale gave triphenylmethane and is in agreement with the over-all mechanism. The attempt to verify this mechanism further by studying the reduction of the intermediate compound, triphenylmethyl or hexaphenylethane, was prevented by the insolubility of the latter in methanesulfonic acid.

In such electrolyses in this solvent copious amounts of the insoluble mercurous methanesulfonate are formed. The formation of this salt in electrolyses using a platinum anode probably resulted from the mercury transported from the cathode compartment into the anode portion by entrainment during the electro-osmosis of the solvent. Stirring the mercury cathode forms mercury droplets fine enough to pass through the sintered glass diaphragm and to allow amalgamation of the platinum anode.

Further evidence for the reduction of the triphenylcarbonium ion is the identical polarographic behavior of triphenylmethyl chloride. This compound dissolves in methanesulfonic acid with the liberation of hydrogen chloride and the formation of triphenylmethyl methanesulfonate. The hydrogen chloride is removed by degassing with nitrogen since it gives a wave at −0.76 v.

The ease of reduction was approximately the same for all the carbonium ions with the exception of the tri-*p*-anisylcarbonium ion. The similar behavior for triphenylcarbonium ion and α-naphthyldiphenylcarbonium ion is in agreement with the observation made by Conant (6) using the classical method, that these two compounds have single electrode potentials differing only by 20–40 mv.

The greater stability of the tri-*p*-anisylcarbonium ion toward reduction is in agreement with its stability toward hydrolysis.

The diffusion current for the triphenylcarbonium ion is proportional to concentration in the region 0.508–2.30 mM. Beyond this region the diffusion current constant becomes smaller.

Addition of water to the methanesulfonic acid solutions of the triarylcarbinols in limited amounts caused the formation of two polarographic waves. The sum of these two waves was approximately equal to the wave observed under anhydrous conditions. Since the second wave occurs at more negative potentials and close to the decomposition potential of the acid, it was not observed for all the examples or concentrations studied. Both waves are diffusion controlled and had slopes of approximately 0.058 for the examples analyzed.

The first wave under these conditions corresponds to the reduction of the carbonium ion to the free radical which, because of the change in solvent brought about by the addition of water, becomes more stable and therefore can dimerize to the hexaphenylethane,

$$(C_6H_5)_3C^+ + e \rightarrow (C_6H_5)_3C\cdot$$
$$2(C_6H_5)_3C\cdot \rightarrow (C_6H_5)_3C{-}C(C_6H_5)_3$$

which is not reducible at this potential and must dissociate very slowly to triphenylmethyl, since no kinetic current is observed for the first wave. That solvents have an effect on the stability of triarylmethyl free radicals is shown by the large variation in the equilibrium constant for the dissociation of hexaphenylethane in various solvents (7, 8) and by the different behavior of such free radicals in concentrated hydrochloric acid from that in glacial acetic acid (5). In the former the free radical forms a dimer known as the Chichibabin compound.

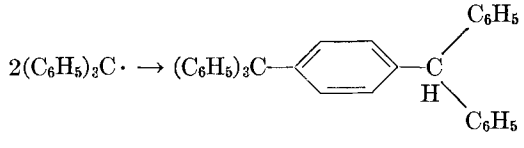

The second wave in the presence of water would represent a reduction of the carbonium ion directly to the triarylmethane.

$$(C_6H_5)_3C^+ + 2e + H^+ \rightarrow (C_6H_5)_3CH$$

The smaller wave height obtained may be caused simply by a loss of some of the free radical during the reduction through the dimerization to the Chichibabin compound.

The half-wave potential of the first wave shifted to more positive potentials with the addition of water. This shift may be caused simply by a change in the anode potential with the addition of water. The second wave shows the opposite behavior and shifts to more negative potentials. This behavior would be in agreement with the decrease in acidity brought about by the dilution since hydrogen ions are involved in the second reduction process.

The first wave at higher concentrations of water was found to split into two and three waves. The second wave, when apparent, was not affected by these conditions. The second part of the split wave increased with an increase in the amount of water at the expense of the first part and probably represents the reduction of the hydrated carbonium ion to the free radical. In the presence of large concentrations of water the carbonium ion would form the hydrated ion or the conjugate acid of the carbinol,

$$(C_6H_5)_3C^+ + H_2O \rightleftarrows (C_6H_5)_3COH_2^+$$

The shift of this equilibrium is very slow since the waves were diffusion controlled. The half-wave potential for the hydrated carbonium ion is more negative than that for the carbonium ion. This behavior is in agreement with the results obtained by Conant and Chow (9) by the classical method in glacial acetic acid solutions.

The second part of the split wave was not observed for diphenyl-α-naphthylcarbinol even though the first part decreased with the addition of water. This carbinol was the least soluble of the examples studied and may precipitate partially in these solutions even though this phenomenon was not observed visually.

The third part of the split wave which occasionally occurred was very small and may be simply a desorption wave.

The interpretation of the polarographic behavior of the aromatic ketones and aldehydes is made difficult by the proximity of the curve to the discharge of methanesulfonic acid. The high diffusion current constant (I_d) max obtained for benzophenone and the high concentrations necessary to bring out the curve indicate that maxima are involved in these waves. The leveling off current for benzophenone and *p*-chlorobenzophenone was diffusion controlled, however, and implied that the formation of the conjugate acid, which is being reduced, in the following equilibrium is rapid:

$$(C_6H_5)_2C{=}O + CH_3SO_3H \rightleftarrows (C_6H_5)_2C{=}OH^+ + CH_3SO_3^-$$

A similar diffusion-controlled current was found for benzophenone in a 0.1*N* hydrochloric acid-50% ethanol solution.

The electrode reaction is the following and is substantiated by the formation of benzopinacolone in the large-scale electrolytic reduction of benzophenone. These results closely resemble the macroscale reduction of benzophenone in glacial acetic acid-sulfuric acid mixtures (10).

$$2(C_6H_5)_2C{=}OH^+ + 2e \rightarrow \begin{matrix}(C_6H_5)_2C{-}OH\\ |\\ (C_6H_5)_2C{-}OH\end{matrix}$$

$$\begin{matrix}(C_6H_5)_2C{-}OH\\ |\\ (C_6H_5)_2C{-}OH\end{matrix} \xrightarrow{H^+} (C_6H_5)_3C{-}COC_6H_5$$

Benzaldehyde which did not give a visible polarographic wave gave desoxybenzoin in a large-scale reduction. This behavior implies that the reduction of benzaldehyde occurs simultaneously with that for the supporting electrolyte.

Manuscript received February 2, 1956. Part of this paper was prepared for delivery before the New York Meeting, April 12 to 16, 1953, and was abstracted from the Ph.D. Thesis of R. Berkey (1955) and the M.S. Thesis of D. Thomson (1953), State University of Iowa, Iowa City, Iowa. The greater part of the research was supported by the A.E.C. under Contract AT (11-1)-72 Project #6.

Any discussion of this paper will appear in a Discussion Section to be published in the June 1957 JOURNAL.

REFERENCES

1. J. C. JAMES, *Trans. Faraday Soc.*, **47**, 1240 (1951).
2. S. WAWZONEK AND M. E. RUNNER, *This Journal*, **99**, 457 (1952).
3. S. WAWZONEK, E. W. BLAHA, R. BERKEY, AND M. E. RUNNER, *ibid.*, **102**, 235 (1955).
4. K. ELBS, *Z. Elektrochem.*, **2**, 472 (1896).
5. J. B. CONANT AND N. M. BIGELOW, *J. Am. Chem. Soc.*, **53**, 676 (1931).
6. J. B. CONANT, L. F. SMALL, AND B. S. TAYLOR, *ibid.*, **47**, 1959 (1925).
7. J. E. LEFFLER AND R. A. HUBBARD, *J. Org. Chem.*, **19**, 1089 (1954).
8. K. ZIEGLER AND L. EWALD, *Ann.*, **473**, 163 (1929).
9. J. B. CONANT AND B. F. CHOW, *J. Am. Chem. Soc.*, **55**, 3752 (1933).
10. S. SWANN, JR., *Trans. Electrochem. Soc.*, **64**, 313 (1933).

Preparation of High Purity Rhenium

D. M. ROSENBAUM, R. J. RUNCK, AND I. E. CAMPBELL

Battelle Memorial Institute, Columbus, Ohio

ABSTRACT

Rhenium powder containing a maximum of 0.05% impurities has been prepared by hydrolysis of rhenium pentachloride and subsequent hydrogen reduction of the resultant hydrated rhenium dioxide. Particle size of the rhenium powder is such as to lead to easy densification by methods standard to powder metallurgy. Advantages of this method of preparation over previously employed methods are given.

Despite the fact that rhenium is quite rare, being only one-tenth as abundant as iridium, its potential usefulness in specialized applications has prompted an extensive investigation of its properties.

Rhenium was discovered in 1925 and concentrated and separated shortly afterward. Because of the importance of the discovery in further confirmation of the periodic theory of the elements and the controversial nature of the claims surrounding its discovery, rhenium received considerable attention for a few years. However, the limited availability of ores and the potentially high cost of the metal soon relegated it to the role of a laboratory curiosity. As additional deposits of rhenium have been discovered, it has found limited commercial use, and the recent prospect of a continuing commercial source in modest quantities has stimulated interest in this potentially useful metal.

In 1952, Battelle Memorial Institute undertook an investigation of the properties of rhenium for the Aeronautical Research Laboratory of the Wright Air Development Center.

Of particular interest were potential high temperature applications of the metal itself. Of the metals, only tungsten, which rhenium resembles in many of its properties, has a higher melting point.

At the outset of the investigation, little was known about fabrication of the metal. However, it was concluded that the techniques used in the fabrication of tungsten should be followed in fabricating rhenium. Although there was no specific information on the effect of impurities in the metal on its fabrication and properties, experience with other metals had led to the conclusion that certain nonmetallic impurities might have a decidedly adverse effect on the properties of the metal. In any event it was desirable to prepare high purity powder to provide uniform metal of high quality for fundamental studies of its properties. Therefore, preparation of high purity rhenium powder was undertaken.

Experimental Work

Three methods of preparation were investigated, all using potassium perrhenate, the anticipated principal commercial source of rhenium, as the starting material. These methods have been referred to as the potassium perrhenate method, the ammonium perrhenate method, and the halide method. In the first, potassium perrhenate is reduced with hydrogen, potassium hydroxide is removed by leaching, and the crude rhenium powder reduced again to give fairly pure rhenium powder. In the second, potassium perrhenate is converted to ammonium perrhenate which is then reduced to metal with hydrogen. The chief advantage of the ammonium perrhenate method is the production of metal of lower potassium and oxygen content. In the halide method, rhenium pentachloride is prepared from crude rhenium powder, and converted by hydrolysis to rhenium oxide, which is then reduced with hydrogen to give a high purity rhenium powder. The halide method has given consistently purer metal than the first two and has the added advantage of involving substantially fewer operations than the ammonium perrhenate method.

Potassium Perrhenate Method

The potassium perrhenate method which involves steps common to all three of the preparative schemes is discussed first.

Commercial potassium perrhenate was converted to crude rhenium metal by reaction with hydrogen at 500°C in a vertical stainless steel reactor 4 in. in diameter by 24 in. high. The reactor, charged with 3 lb of potassium perrhenate, was first heated to 200°C and held at that tempera-

ture for 1 hr. It was then heated to 500°C and the reduction was carried out by passing purified dried hydrogen through the reactor at 18 cc/sec (STP). About ½ lb of potassium perrhenate was reduced per hour under these conditions. Reduction was considered complete when condensation of moisture from the exit gas could no longer be detected.

On completion of the reduction reaction, the charge was cooled to room temperature in an inert or reducing atmosphere. The reaction products, consisting of rhenium metal and small amounts of rhenium dioxide, potassium perrhenate, and potassium hydroxide, were then washed with hot distilled water until essentially free of alkali.

The leached rhenium-rhenium dioxide mixture was placed in a molybdenum boat and further reduced in hydrogen for 2 hr at 1000°C. The metal product was leached with dilute HCl to remove residual KOH, and then washed by decantation with hot distilled water until neutral. The powder was then again treated with hydrogen at 1000°C. Approximately 93% of the rhenium was recovered as rhenium powder. An additional 5% of the available rhenium was recovered from the wash water as unreacted potassium perrhenate, finely divided rhenium dioxide, and rhenium metal.

A typical analysis of the powder, given in Table I, indicates that traces of potassium remained in the powder. Additional leachings failed to reduce the amount of potassium in the powder.

In consolidating rhenium metal powder (1), it was necessary to reduce the particle size to less than 325 mesh in order to obtain pressed bars of sufficient green strength to permit handling. The sintered bars of rhenium metal powder made by direct reduction of potassium perrhenate had a density only 60% of the theoretical density and could not be fabricated. Many of these bars melted at temperatures far below the known melting point of rhenium.

TABLE I. *Table of analysis*

Element	Weight Per Cent		
	Rhenium metal prepared from potassium perrhenate	Rhenium metal prepared from ammonium perrhenate	Rhenium metal prepared by the halide method
Aluminum	0.009	0.094	0.008
Calcium	0.008	0.017	0.002
Chromium	0.004	N.F.*	N.F.
Copper	0.0012	0.0021	0.0002
Iron	0.05	0.024	0.012
Lead	N.F.	N.F.	N.F.
Magnesium	0.002	0.038	0.005
Manganese	0.007	0.002	0.007
Molybdenum	0.15	N.F.	N.F.
Nickel	0.003	N.F.	N.F.
Potassium	0.41	N.F.†	N.F.
Rhenium	Major	Major	Major
Silicon	0.005	0.028	0.015
Sodium	0.15	N.F.	N.F.
Tungsten	N.F.	N.F.‡	N.F.
Total	0.799	0.205	0.049

* N.F. = Not found.

† Not found in the first batches of rhenium prepared by this method, but found in increasingly greater amounts, up to 0.40%, in later batches.

‡ When tungsten carbide rods were used in the ball milling operation, the amount of tungsten present was 0.25.

Elements checked for but not found: Sb, As, Ba, Be, Bi, B, Cd, Co, Cb, Ga, Ge, Au, Pt, Ag, Sr, Te, Sn, Ti, V, Zn, Zr.

In consolidating and fabricating rhenium, procedures similar to those employed in the fabrication of tungsten were followed. Rhenium powder was pressed into bars at pressures up to 30 tons/in.^{2}. The bars were presintered at 1200°C in hydrogen for 2 hr in an externally heated furnace and then heated resistively in hydrogen at temperatures of approximately 2700°C for 1 hr.

Powder prepared by the ammonium perrhenate or chloride methods could be converted into bars which could be worked into sheet or wire, but the bars obtained from powders prepared by the potassium perrhenate method were of low density and could not be fabricated. The poor densification and low melting points of bars obtained from powder prepared directly from potassium perrhenate may be attributed to the effect of residual potassium oxide.

Ammonium Perrhenate Method

Of the 0.8% impurities present in the powder obtained from potassium perrhenate, over one-half was potassium. Since further treatment of the powder did not reduce the potassium content, it was decided that potassium perrhenate should be converted to ammonium perrhenate which could then be reduced to produce a metal low in potassium.

In the preparation of ammonium perrhenate, potassium perrhenate was first reduced to a rhenium-rhenium dioxide mixture by the method previously described. This mixture was then converted to rhenium heptoxide by reaction with oxygen at 800°C in a Vycor tube furnace, the volatilized heptoxide condensing in the cooler portions of the tube (*see* Fig. 1).

The rhenium heptoxide was leached from the Vycor tube with as small a quantity of distilled water as possible, giving a perrhenic acid solution which was filtered to remove any acid insoluble materials. The filtrate was then neutralized with concentrated ammonium hydroxide to precipitate ammonium perrhenate. The ammonium perrhenate was filtered off and the filtrate was concentrated by evaporation to recover the small amount of ammonium perrhenate which remained in solution. The precipitated ammonium perrhenate contained some ferric hydroxide, which probably was obtained as a result of contamination of the powder with iron from the initial reactor. The ferric hydroxide was removed in a Soxhlet extractor using dilute ammonium hydroxide as a solvent for the ammonium perrhenate.

Approximately 85% of the rhenium present in the potassium perrhenate is recovered as ammonium perrhenate. Rhenium values in leach waters and filtrates were, however, recovered by further processing.

The ammonium perrhenate was obtained principally in the form of large crystals, about ¼ in. in diameter. In order to obtain the rhenium powder in as finely divided form as possible, the crystalline ammonium perrhenate was comminuted in a Canadian rubber-lined ball mill using Burundum balls. The initial impurity pickup in ball

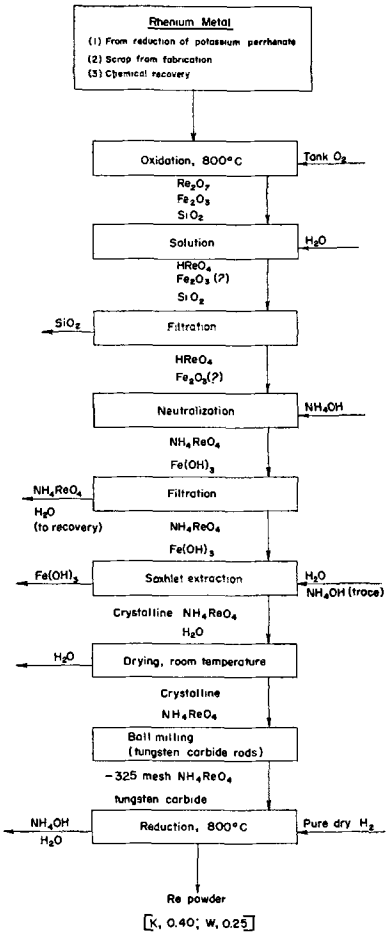

FIG. 1. Flow sheet for preparation of rhenium by the ammonium perrhenate method.

milling amounted to about 0.15% but as the balls became slightly worn, the impurity level went up rapidly to a point where the mill could no longer be used. Therefore, tungsten carbide rods were substituted for Burundum balls. The carbide rods gave a tungsten pickup of about 0.25% but this had neglegible effect on the fabrication, because tungsten is soluble in rhenium without noticeable solution hardening.

After reduction to minus-325 mesh the ammonium perrhenate was placed in a molybdenum boat in a $\frac{1}{4}$-in. layer and reduced with hydrogen. It was first reduced at 300°C for 1 hr and then at 800°C for 1 hr, following which it was cooled to room temperature in a hydrogen atmosphere. The reduced powder which was loosely sintered was broken up in an agate mortar, and again reduced for 1 hr at 800°C. A metal powder of minus-325 mesh particle size was obtained.

This powder could be sintered to 90% of theoretical density and the bars obtained in initial work could be rolled readily into sheet or drawn into wire. However, as the reprocessing of rhenium scrap and other rhenium residues continued, difficulties were encountered in fabrication and a gradual increase in potassium content was noted. The potassium impurity level finally reached 0.4% at which point the densities of the sintered bars decreased to 70% of the theoretical density and metal could not be fabricated. A typical analysis of rhenium powder prepared by the ammonium perrhenate method is given in Table I.

The cause of the increase in potassium in later batches of rhenium prepared from ammonium perrhenate is not known. However, it appears that hot spots developed in the charge during the oxidation reactions, and the temperature of these areas often exceeded the boiling point of potassium hydroxide. Potassium hydroxide was therefore probably carried over with the rhenium heptoxide during the oxidation reaction. The potassium transfer could undoubtedly have been avoided by careful control of the oxidation.

HALIDE METHOD

However, since the ammonium perrhenate method is complicated and tedious and a shorter method was desired, the chloride method was investigated. This appeared attractive in that (*a*) it eliminated, or at least minimized, the potassium problem by utilizing a vaporization step in which the potassium could be left in the residue, and (*b*) it gave a much simpler procedure.

In the chloride process, crude rhenium metal was treated in hydrogen for 1 hr at 1000°C to reduce any oxides present and then chlorinated at 750°C to give the pentachloride. Chloride was hydrolyzed by adding it cautiously to distilled water cooled to about 10°C in an ice bath. The main product of hydrolysis was hydrated rhenium dioxide. Perrhenic acid and chlororhenic acid were present in smaller amounts. If the hydrolysis is not carried out in cold water, the yield of rhenium dioxide is somewhat lower. Under the conditions specified, about 75% of the available rhenium was recovered as hydrated rhenium

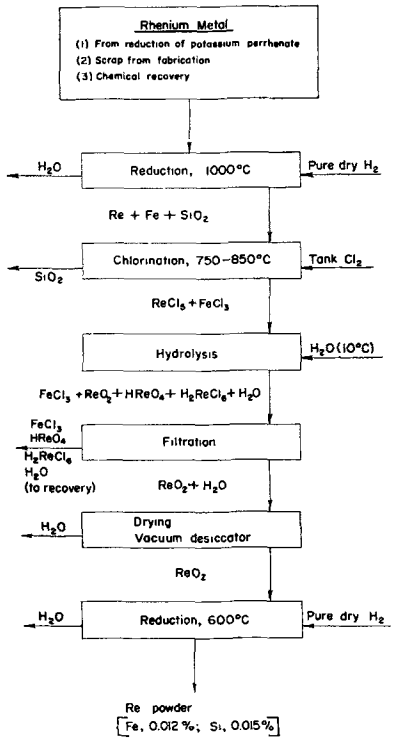

FIG. 2. Flow sheet for preparation of rhenium by the halide method.

dioxide. The hydrated oxide has the consistency of a gel and is difficult to filter. However, the filtration time can be reduced (2) substantially by bubbling carbon dioxide through the hydrolysis product for about 30 min before filtering.

The finely divided rhenium dioxide was filtered off or separated from the liquor by centrifuging, washed several times with distilled water, and dried in a vacuum desiccator.

To recover rhenium from the filtrate, a small amount of 30% H_2O_2 was added to convert all rhenium present to perrhenic acid. The perrhenic acid solution was then neutralized with concentrated NH_4OH and the resultant ammonium perrhenate crystals filtered off and set aside for recycling.

The major reaction product, rhenium dioxide, was hydrogen reduced in a $\frac{1}{2}$-in. layer in molybdenum boat for 1 hr at 400°C and for a second hour at 600°C. The resultant rhenium powder, which was loosely sintered, was broken up in an agate mortar, and treated with hydrogen at 800°C for 2 hr, following which it was cooled to room temperature in an inert or reducing atmosphere.

A typical analysis of rhenium powder prepared by the halide method is given in Table I.

The powder produced by the halide process could be pressed to a density of almost 60% of the theoretical density (3), i.e., almost equal to the sintered density of metal made by the hydrogen reduction of potassium perrhenate. Despite the fact that the metal prepared from the halide had a higher as-pressed density than metal prepared by the other methods, its sintered density of 80% of theoretical was lower than the sintered density of metal produced from ammonium perrhenate. Nevertheless, metal produced from the chloride could be fabricated without difficulty.

The over-all rhenium recovery efficiency in the chloride process is about 95%, comparing favorably with the efficiency of recovery by the other methods.

Because the chloride process involves fewer steps than the ammonium perrhenate process and because it gives a purer product than either the ammonium perrhenate process or the potassium perrhenate process and, especially one free of potassium, the chloride process is now used in preparing rhenium for powder metallurgy studies at Battelle.

ACKNOWLEDGMENT

The powder metallurgy work was conducted by C. T. Sims of Battelle Memorial Institute, Division of Nonferrous Physical Metallurgy. The authors wish to express their appreciation of E. J. Hassell and the Air Research and Development Command, United States Air Force, Wright-Patterson Air Force Base, for permission to publish the results of work obtained at Battelle Memorial Institute under Contract No. AF 33(616)-232. They also are indebted to the Kennecott Copper Corporation for supplying the potassium perrhenate used in the preparation of rhenium powder.

Manuscript received November 4, 1955. This paper was prepared for delivery before the Pittsburgh Meeting, October 9 to 13, 1955.

Any discussion of this paper will appear in a Discussion Section to be published in the June 1957 JOURNAL.

REFERENCES

1. C. T. SIMS, C. M. CRAIGHEAD, AND R. I. JAFFEE, *J. Metals*, **7**, 168 (1955).
2. J. G. F. DRUCE, "Rhenium", p. 51, Cambridge University Press, Cambridge, England (1948).
3. C. T. SIMS, Unpublished data.

Uranium Purification by Electrorefining

LEONARD W. NIEDRACH AND ARTHUR C. GLAMM

Knolls Atomic Power Laboratory, General Electric Company, Schenectady, New York

ABSTRACT

The feasibility of a high temperature electrorefining process for decontamination of U from associated fission products was demonstrated. Low-melting alloys of U with Ni were used to obtain molten products at temperatures below the melting point of pure U. Effects of temperature, current, and salt-bath composition on cell efficiency and cell operation are discussed.

Periodically the fuel from nuclear reactors must be removed and reprocessed to repair radiation damage, to restore reactivity, and to remove fission products. In some applications a high degree of decontamination from the fission products is not essential, and the possibility of employing an electrorefining process to accomplish the required decontamination is feasible. A process employing a fused-salt electrolyte was chosen for investigation because the chemical activity of U precludes the use of aqueous electrolytes, and danger from radiation damage makes the use of organic solvents undesirable. A general description of the over-all process has been given elsewhere (1). Background investigations performed in connection with the demonstration of the electrolysis step of such a process for U are detailed in this paper.

In this work, U-rich alloys with Ni were used to obtain

molten products at temperatures considerably below the melting point of pure U. In this way, continuous cell operation was facilitated because a molten, salt-free product can be removed readily from an electrolysis cell. Probably the information gained from this work will result in a process that can be operated at temperatures at which the electrolysis product is molten U. Until then, if unalloyed U is desired as the ultimate product, it should be possible to choose an alloying agent that behaves like Ni during electrolysis, but which can later be removed from the product alloy. Details of this step have not yet been investigated intensively. However, in some exploratory experiments it was found that the Mn content could be reduced to a few ppm by distillation from a U-Mn eutectic alloy (6.0 wt% Mn) (2) by heating in a vacuum to about 1300°C. Because of the low Mn content in the eutectic alloy, use of reasonably pure metal should prevent serious recontamination of the U.

Only limited electrolysis work has been done on U. Driggs and Lilliendahl (3) used a salt bath containing NaCl, $CaCl_2$, and KUF_5 for electrowinning U. The electrolysis operation was performed at 775°C and produced powdered or dendritic deposits. Rosen (4) described a similar procedure in which powdered U was obtained by electrolysis of UF_4 in a mixture of alkali and alkaline earth halides at 800–850°C. A quantitative study of the effects of current density and temperature on the deposition characteristics of U obtained from mixed fluoride-chloride baths has been reported (5). The temperature range was 725–900°C, and finely divided metal was again obtained as the product.

An electrorefining process gave U of exceptional purity when fairly pure U was used as the starting material (6). Electrorefining has also been examined as a processing method for spent reactor fuels (7). In both cases, electrolyses were performed at temperatures below the melting point of U, and dendritic deposits were obtained.

In all of the work mentioned above, the metal produced at the cathode required thorough washing to remove adhering salts before the metal had been compacted. Because of the nature of the products a batch-type operation was dictated in order to remove bulky deposits from the electrolysis cells. This is an awkward procedure, but the literature contains no description of a process for U purification in which a readily handled, molten product is formed.

Experimental

Equipment and Operating Procedure

In most of the present work aimed at demonstrating the principles of an electrorefining process for U decontamination, alloys of U with Ni were formed as the electrolysis product by employing a Ni rod as the cathode in the electrolysis cell. The deposited U and the Ni interdiffuse and form a molten layer of alloy on the electrode surface. When molten material accumulates, it eventually drips from the cathode rod and collects as a pool in the bottom of the crucible. While this procedure has not been used before for the production of U alloys, electrolyses in which eutectic alloys are formed in other systems have been described. For example, Fischer and Dorsch (8) prepared Ti alloys by employing cathodes of Cu, Ni, Fe, Co, and Al. Andrieux (9) used a similar method to form boron alloys, and Steinberg and co-workers (10) reported the formation of Zr-Ni alloys by electrodepositing Zr on Ni cathodes.

Ni has been used as the alloying agent in most of the work because of its availability in the form of rods suitable for use as cathodes, and because phase data on the U-Ni system are available (11). Runs of a similar nature have also been made with Fe, steel, and a Mn-10 wt% Cu alloy as cathodes.

The diluent salt used in an electrorefining bath must be less readily reduced than that of the metal to be deposited. In the case of U, this requirement is satisfied by alkali or alkaline earth halides, and a brief consideration of vapor pressures narrows the choice to chlorides or fluorides or a mixture of the two. It is possible to start with a tetravalent U salt in the bath, but rapid reduction to the trivalent state occurs either electrolytically or by reaction with the anode material. Chlorides or mixtures of chlorides and fluorides were used for most of the work because they are easier to handle than pure fluorides. For example, it is easy to dissolve away any chlorides coating the deposited metal to obtain a clean piece of metal. In addition, samples of chloride baths are also readily dissolved to provide samples for analyses.

The literature contains very little information regarding the resistance of refractories to both U metal and alloys and to fused salts in the temperature range of interest. Therefore, tests were made on a number of materials. Included were magnesia, thoria-lined alumina, cerium sulfide, and various grades of graphite. National Carbon's AUC grade graphite was considered to be the most satisfactory material, and was used in all of the runs reported.

Several types of cell have been used. The simplest type employs a 3 in. high, $1\frac{1}{2}$ in. OD graphite crucible to hold the salt melt and to retain the cathode alloy drippings. In this type of cell a U rod anode having a nominal diameter of $\frac{3}{8}$ in. was used. Cathode rods $\frac{1}{4}$ in. in diameter were used. Salt depths of 1–2 in. were employed.

This type of crucible can be used only for relatively short batch-type runs because of the limited capacity for holding the cathode product. Therefore, electrolyses for extended periods of time were carried out in the graphite crucible shown in Fig. 1 which is referred to as the weir-type crucible. This type of crucible allows the product alloy to overflow to a collecting vessel as the electrolysis proceeds. Because the overflowing product drops to a collecting vessel, product alloy from short intervals of an extended run can be separated and analyzed. In this way, any variation in the alloy composition may be followed. Also, since anode and cathode weight losses can be taken without disturbing the crucible and its contents, the electrolysis can be resumed under a different set of electrolysis conditions while maintaining the same fused-salt and cell variables. In this manner, U alloys weighing up to 300 g have been produced.

A third type of cell is illustrated in Fig. 2. It employs a graphite anode basket and can be operated with a feed consisting of U pellets. For runs of short duration the product metal has been collected in a well of small diam-

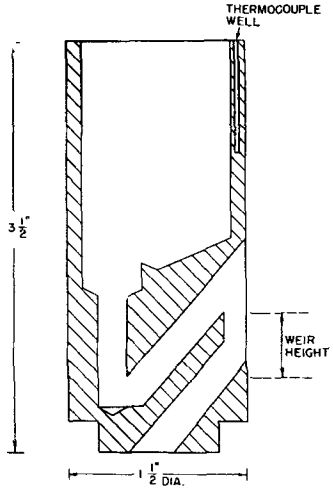

FIG. 1. Weir-type graphite crucible (cross section)

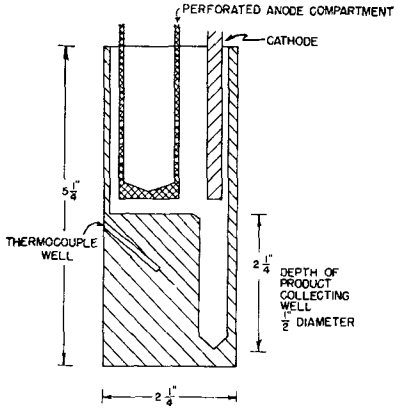

FIG. 2. Cross section of electrolysis cell with product collecting well.

eter as shown in the diagram; however, the weir arrangement for removing product alloy, as described above, can also be used with such a cell arrangement.

The general arrangement of the electrolysis cell when the weir-type crucible was used is shown in Fig. 3. A similar arrangement was used in the other cases. The crucible was supported by Mo rods inside a chamber which consisted of a lower quartz cylinder and an upper Pyrex cylinder. The latter was closed on the top by a brass plate. The seal between the brass plate and the Pyrex section was made with de Khotinsky cement, while the seal between the upper Pyrex glass section and the lower quartz section was made with Apiezon wax. The glass surfaces were ground for better seals. The entry of movable stainless steel electrode-supporting rods through vacuum seals attached to the brass plate permitted adjustment of the depth of immersion of the electrodes in the fused-salt bath and allowed continuous electrolysis to be maintained. The electrodes were insulated from each other by mounting the vacuum seals in Bakelite plugs, which in turn were attached to the brass plate.

A chromel-alumel thermocouple and the Mo supporting rods for the crucible entered the chamber through ball and socket joints on the Pyrex top section. The thermocouple was placed in the graphite crucible wall about 2 in. below

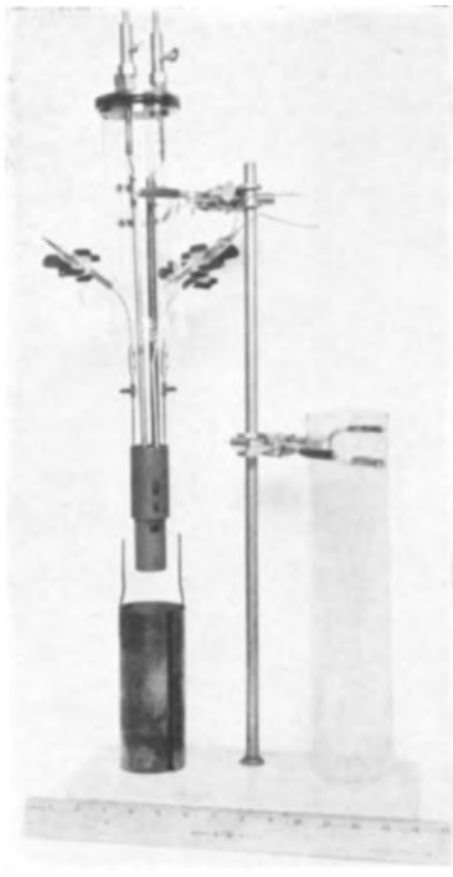

FIG. 3. Electrolysis cell assembly

the crucible top and definitely below the fused-salt bath surface. A Ta shield, which was lowered for the photograph, served as a heat reflector and allowed temperatures in excess of 1200°C to be obtained with a 6 kw Ajax-Northrup Spark-Gap Converter under usual electrolysis cell conditions.

In all cases the assembled electrolysis apparatus was connected to a vacuum system employing a mercury diffusion pump capable of producing and maintaining a vacuum of 1 μ. Provision was made to add purified gases to the system. Electrolyses were run under a pressure of about 1 atm He to prevent excessive volatilization of the salt during operation. Air cooling was provided for the Apiezon wax seal and for the quartz vessel at the induction coil region.

A continuous record was kept of temperature, cell voltage, and cathode-crucible voltage during an electrolysis run. The cathode-crucible voltage indicated which of the working electrodes required adjustment as its area decreased.

The source of electrolysis current was a 110-volt d-c line which had about 4% ripple. Desired cell current was obtained by the use of suitable resistances in series with the electrodes.

The general operating procedure used during an electrolysis was as follows. The graphite crucible was degassed by heating to 1200°C under vacuum, then cooled in a He atmosphere. This procedure was used to minimize surface contamination of the charged U as well as the alloy

TABLE I. *Summary of conditions and data for electrolysis runs with Ni cathodes*[1]

Run no.	Crucible type[2]	Temp,[3] °C	Salt phase wt %	*I*, amp	Length of run amp-hr	% Anode[4] efficiency	Wt % of U in product[5]
31	W	1050	66% $BaCl_2$—34% UF_4	5	15	53	(83)
34(A)	W	1025	As in Run 31	5	11.7	34	(84)
34(B)	W	1025	Reuse from A	1	9	82	(77)
34(C)	W	1035	Reuse from B	0.4	8.2	89	(73)
					28.9		
35	W	975	As in Run 31	2.5	7.9	59	(56)
36	W	975	Reuse from 35	2.5	5	55	(87)
37	W	1025	Reuse from 36	2.55	5.1	69	(85)
38	W	1075	Reuse from 37	2.55	5.1	60	(93)
					23.1		
41	W	1025	As in Run 31	2.6	25.6	59	(84)
46	S	850	62% $CaCl_2$—38% UCl_3	0.35	10.5	81	80 (83)
44	S	850	As in Run 46	2	16	56	86 (95)
47	S	850	As in Run 46	5	20	36	79 (81)
49A	W	950	As in Run 46	3	17.5	71	85.7
B	W	950	Reuse from A	3	19.5	46	87.6
C	W	950	Reuse from B	3	19.5	49	88.8
D	W	950	Reuse from C	3	19.5	71	87.5
E	W	950	Reuse from D	3	31.5	62	85
F	W	950	Reuse from E	3	36	55	84.5
G	W	950	Reuse from F	3	36	55	83.8
					180	Avg 58	
50	S	950	24% $CaCl_2$—76% UCl_3	3	18	66	86 (94)
51	S	950	75% $CaCl_2$—25% UCl_3	3	15	80	91
52	S	950	90% $CaCl_2$—10% UCl_3	3	13.5	70	95
65A	B-W	990	As in Run 46	3	18		84
B	B-W	1000	Reuse from A	3	15	79	77
C	B-W	1000	Reuse from B	3	15		70
D	B-W	1000	Reuse from C	3	18	79	68
66	B	900	As in Run 46	3	31	90	84
67	B	900	As in Run 46	10	50	70	(91)
69[6]	B	900	As in Run 46	10	49	58	(91)
70[7]	B	900	As in Run 46	10	55	78	(92)

[1] ¼ in.-diameter Ni rods used in all runs.
[2] S—simple; W—weired; B—basket anode.
[3] Temperature in °C ± 10°C.
[4] Based on theoretical reaction of $U^0 \rightarrow U^{+3}$ at anode.
[5] The weight per cent of U in the product was obtained by analysis. Values in parenthesis were calculated from electrode weight losses.
[6] Alloy anode run.
[7] Radioactive run.

product. When a weir-type crucible was used, sufficient Ni-U eutectic alloy (melting point 740°C) was added to the degassed crucible to fill the weir passages and to overflow a small quantity of alloy. The alloy was melted at low pressure, preferably less than 10 μ. The salt phase, which had been premelted under a He atmosphere, was then added to the cell. Heating of the electrolysis cell to about 500°C was carried out at 25 μ or less. Approximately 1 atm He was introduced into the system before the cell was heated to the operating temperature. The electrodes were then lowered into the salt, and when the temperature became stabilized, electrolysis was started. During a run the electrodes were lowered into the fused-salt bath as the voltage record indicated the need.

When the electrolysis run was completed and the circuit was opened, the electrodes were removed from the salt bath and heating was stopped. The system was not opened until the temperature of the cell had fallen to 50°C. Opening of the system at higher temperatures would have resulted in oxidation of the alloy product, preventing free flow of the product from the weir opening.

Results and Discussion

Detailed experimental conditions and data relating to electrolyses with a dripping alloy cathode are summarized in Table I. In all of the runs listed, a ¼ in. Ni rod cathode was used. A U rod was used for the anode in most of the runs. In the last few runs employing a basket-type anode, U was added in the form of pellets, chips, or short bars.

The total electrolysis current rather than current density is listed in the table because the continual change in electrode size during a run caused variations in the current density. However, it is estimated that the initial current densities when rod electrodes were employed varied from 0.1 to 1 amp/cm^2 as the electrolysis current was changed from 0.4 to 5 amp. Current densities for the material in the basket anode could not be readily estimated, but they were believed to be considerably lower than with the rod

anodes. Cell voltages during essentially all the runs were found to fall in the range 0.3–0.7 v.

Anode efficiencies shown in the table were calculated from the loss in weight of the anode and an assumed ideal reaction involving a three-electron oxidation to form trivalent U. This was done whether the initial charge to the salt bath consisted of trivalent or tetravalent U, because a consideration of existing thermal data for U halides indicated that the lower valence state is the stable one under the conditions employed (12). Preliminary experiments to determine the valence states in the bath at the end of an electrolysis indicated that the above assumption was correct.

Cathode efficiencies are not listed because complete recovery of the product was not attempted in most cases. Generally the product alloys wet the crucible, and complete recovery would have been difficult. The material that was recovered generally accounted for 70% or more of the metals that had been lost from the two electrodes proper. In the case of Run 49, a complete material balance was performed, and the product alloy was found to account for 98% of the charged materials.

Composition of the product alloy was often calculated from the weight losses of the two electrodes. This was generally necessary when a weired crucible was employed because of mixing of the product with the original metal. Because of the uncertainty of the calculated alloy compositions the alloys were analyzed directly whenever possible. A few comparative values are included in the table. Generally, calculated values indicated slightly low Ni contents. No attempt was made to determine the exact cause of the discrepancy. It was evident, however, that U held up on the cathode surface decreased the apparent weight loss of the cathode and could thereby be the cause. It is also possible that formation of some U^{+4} in the bath could contribute to the deviation.

In addition to the runs listed in the table a few were made using Fe, steel, and a Mn-10 wt % Cu alloy as the cathode. Actually, Mn would have been preferred over the alloy, but it was too brittle for fabrication into an electrode. The high C content of the steel resulted in formation of a solid on the cathode, presumably caused by carbide formation. Both the Fe and the Mn-Cu alloy produced molten U alloys that behaved like the Ni alloys. It was also found that Mn can be removed from such an alloy by heating at 1300°C.

Of primary concern in the investigation were the effects of temperature, current, and bath composition on cell efficiency and operation. The data for Runs 35–41 in particular indicated that the effect of temperature on anode efficiency was small relative to that of current. In addition, data for efficiency vs. cell current as plotted in Fig. 4 showed no marked trends attributable to temperature. However, the temperature range was limited by salt volatilization at high temperatures and by dendrite formation at low temperatures. An operating temperature as high as 1100°C was possible with baths containing chloride, and dendrites have been observed at 850°C.

The marked effect of cell current on efficiency is shown clearly in Fig. 4. This effect of current transcends the effects of temperature and of bath composition as illustrated by the mixed data. The scatter among the data was caused in large part by the ever changing current densities at the consumable electrodes. It is these variations which also prevent a correlation of the effects with current density.

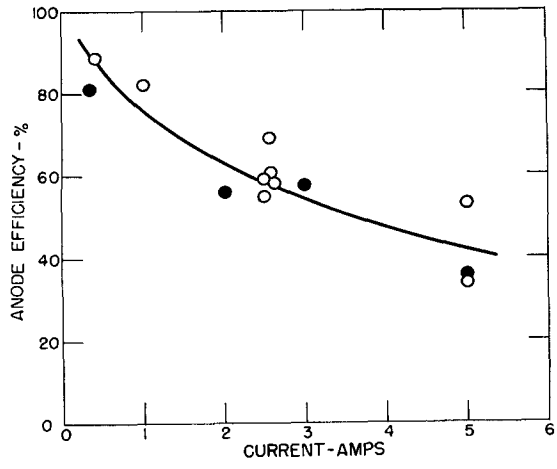

FIG. 4. Effect of current on anode efficiency. ○ = 66 wt % $BaCl_2$—34 wt % UF_4 at 975°–1075°. ● = 62 wt % $CaCl_2$—38 wt % UCl_3 at 850°–950°C.

While the effect of current density for the individual electrodes was not examined, it is still possible on the basis of the chemistry of U to arrive at a mechanism which explains the decrease in efficiency with increasing current. Thermal data indicate that trivalent U is the stable state in the bath at the operating temperatures (12). At low currents, then, U should enter the bath as U^{+3}, and diffusion away from the electrode should occur rapidly enough to prevent polarization to the extent that U^{+4} is formed. Since there are no stable oxidation states between U^{+3} and U^0, the only reaction possible at the cathode is reduction to the metal; and since the nickel alloying agent is present, difficulties from fog formation should be minimized. Therefore, high cell efficiencies are in order at low current densities. As the current is increased it seems probable that a point is eventually reached when diffusion of the oxidized species away from the electrode is not rapid enough to prevent formation of significant amounts of U^{+4}. When such a state is reached, current could be carried in part by a cyclic oxidation and reduction involving U^{+3} and U^{+4}, and the current efficiency would decrease.

In Runs 65–67 and 70, pellets or chips of U were used with the basket anode; therefore, a much larger than normal surface area of U was available, and the anode efficiencies were higher than previously observed. In Run 60 a $\frac{3}{8}$ in. diameter bar was charged to the basket. The surface area was, therefore, similar to the earlier runs and the efficiency was again lower.

The composition of the salt bath seemed to have a minor effect on the cell efficiency (Fig. 4). In addition, no effect on general operability of the cell was observed with the baths listed in Table I. However, U concentration in the salt bath was an important variable as far as product contamination by the bath diluent is concerned (Table II). These data show that the bath should contain a

TABLE II. *Effect of U concentration in bath on product alloy composition*
$CaCl_2$—UCl_3 bath; Ni cathode; T = 950°C; I = 3 amp

Wt % UCl_3 in salt bath	Wt % Ni in alloy	Wt % Ca in alloy
10	2.6	2.7
25	7.7	1.3
38	14.4	0.1–0.3
76	13.8	0.06

definite minimum amount of the U salt if the deposition of significant amounts of the diluent cation is to be avoided.

A few additional tests of the effect of salt composition were made with salt mixtures of BaF_2 containing 38–66 wt % UCl_3 and with an all-fluoride system of NaF with 50–91 wt % UF_4. All of the former mixtures performed satisfactorily but offered no advantages over the $BaCl_2$-UF_4 mixture which replaces the hygroscopic UCl_3 with the readily handled UF_4.

When the NaF-containing baths were used, distillation of Na metal was observed except when the highest concentration of UF_4 was employed. However, the metal produced in this run was encased in a black salt-like envelope about 1 mm thick which had apparently solidified from the bath while it was at operating temperature (1035°C). The envelope was found by x-ray diffraction analysis to be largely UF_3, which has a melting point higher than the operating temperature of the bath. Apparently the billet of product alloy reacted chemically with some unreduced UF_4 in the bottom of the bath and formed the solid-salt phase. Although this behavior was not observed with the $BaCl_2$-UF_4 baths, it was decided to use all chloride baths in later runs in order to preclude such a problem. In the $CaCl_2$-UCl_3 system no high melting salt phases are likely to form. These baths, however, do suffer from higher volatility if attempts are made to use them above 1000°C.

Both the current and the operating temperature have significant effects on the Ni content in the product alloy. This is shown roughly by the data in Fig. 5. The points correspond to actual alloy compositions obtained at the temperatures indicated. The alloys from Runs 51 and 52 are not plotted because they contained a large amount of Ca. Only one point is shown for Run 65 because of the gradual shift in composition during successive stages of this run. The alloy obtained in Run 65 contained that which was initially charged to the weir, and it was only after several throughputs that the composition of the overflowing product would be expected to correspond to that dripping from the cathode. Because of the variations in current density and probably other more subtle factors, the scatter in the data is too great to distinguish the effect of minor changes in current. For this reason the data were grouped; alloys obtained at 0.4 and 1 amp are in one group, those obtained at 2, 2.5, 3, and 5 amp are in a second group, and those obtained at 10 amp are in the third. In this way it becomes evident that at low currents the alloy composition tends toward that at equilibrium on the Ni-rich side of the eutectic. At higher current densities the composition moves toward the U-rich side of the eutectic This is expected since a greater rate of deposition of U at the cathode should result in less chance for the Ni to diffuse into the deposit before the drop grows heavy enough to fall. These results indicate that higher cathode current densities than have been employed would be desirable in order to increase the U content of the alloy. Care must be taken, however, to avoid excessive cathode current densities, or the rate of U deposition will so exceed the rate of diffusion of Ni into the deposit that a solid deposit will result and dendrites will grow.

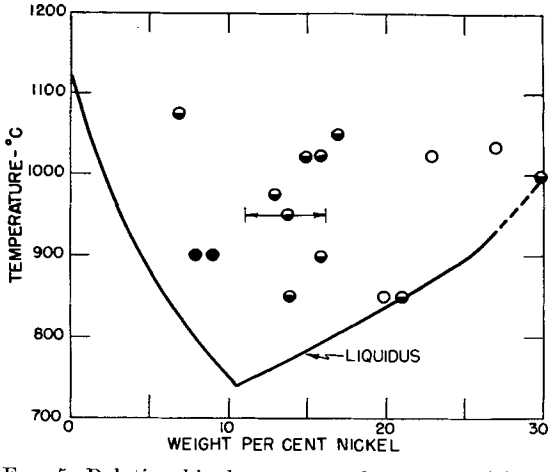

FIG. 5. Relationship between product composition and U-Ni phase diagram. ○—Electrolysis current, 0.4, 1.0 amp; ◒—electrolysis current 2, 2.5, 3, 5 amp; ●—Electrolysis current 10 amp. Liquidus from reference (11).

Continuous Operation and Decontamination Runs

The feasibility of continuous electrolysis for an extended period of time was demonstrated by Run 69 which was carried out for a duration of 60 hr or 180 amp-hr. During this time approximately 30 changes of uranium, or throughputs, occurred in the salt phase. Because of a larger holdup of uranium in the weir reservoir, this was equivalent to only ten throughputs in this reservoir. Electrodes and product from this run are shown in Fig. 6,

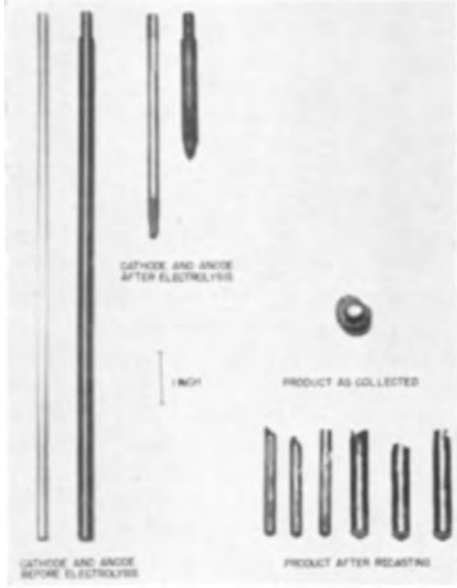

FIG. 6. Electrodes and products from extended electrolysis

TABLE III. *Summary of data for Run 49*
Temp: 950°C; *I*: 3 amp; Bath: 41.7 g of 62 wt % $CaCl_2$, 38 wt % UCl_3; anode: U; cathode: Ni; initial weir reservoir: 35 g of U-Ni (13 wt %) alloy

Increment	ΔT, hr	ΔA-hr, amp-hr	ΔW anode, g	ΔW, cathode, g	ΔW billet, g	Anode eff., %	Wt % Ni in product
A	5.8	17.5	36.8	3.4	36.6	71	14.3
B	6.5	19.5	26.6	3.2	19.3	46	12.1
C	6.5	19.5	28.1	4.7	31.6	49	11.2
D	6.5	19.5	41.4	7.5	38.5	72	12.5
E	10.5	31.5	57.3	9.2	65.9	62	15.0
F	12	36	58.3	9.7	53.2	55	15.5
G	12	36	58.9	12.9	61.6	55	16.2
	60	180	307.4	50.6	306.7	58*	14.4*
Alloy Residue in crucible					78.9		
Total weight of alloy recovered					385.6		

* Weighted average.

and a summary of the data for the run is given in Table III. From Fig. 6 it is seen that a rather uniform consumption of each electrode occurred, and no signs of undercutting are evident. The condition of these electrodes is also typical of those from runs of shorter duration. The product is shown both as the button that forms in the collecting crucible suspended under the weir and in the form of recast billets.

An average anode efficiency of 58% based on a three electron valence change was obtained. Although some of the fluctuations are undesirably high, it is encouraging that the efficiency does not decrease with increasing time of electrolysis. Composition of the alloy produced is also satisfactory. Greater control to maintain uniform cathode current density should result in less variation in this composition.

Although the cathode efficiency for U production could not be determined accurately during the course of the run, it is evident from the good over-all material balance of 98% that the cathode efficiency must be essentially identical with that of the anode for the greater part of the run. However, this high material balance does not preclude the possibility of side reactions that would result in an initial or a gradual change in the bath composition during the run. In this connection no volatile products of side reactions were ever found. However, analyses for Ca in the product samples indicated that a very gradual reduction of Ca content in the bath occurred. A small change in U concentration resulted. In addition the possibility of an alteration due to changes in the U valence state in the bath must be considered. While analytical evidence was not obtained on this point, the lack of evidence in the literature for U halides with valence states below three would seem to eliminate such from serious consideration. An observation that the salt bath had not assumed the green color associated with U^{+4} coupled with the fact that the salt was reducing in nature at the end of the run and liberated H from water would indicate that extensive oxidation to a higher valence state also did not occur.

Fluctuations in material balances during the run were caused by inevitable variations in the amount of metal holdup in the weir reservoir. It was observed also that wetting of the crucible occurred; therefore, there was a greater hold-up of the alloy at the end of the run than was initially charged. These errors were eliminated from the final material balance by dissolving and analyzing the metal that was left in the crucible.

TABLE IV. *Analysis of products for minor constituents in Run 49*

Increment	C, ppm	O, ppm	Ca, ppm
A	—	—	600
B	—	—	500
C	—	—	700
D	—	—	600
E	450	8	900
F	240	12	1100
G	240	26	900

Typical analyses for minor constituents obtained on the recast billets are summarized in Table IV. Both C and O contents are satisfactory for the conditions employed. A considerable reduction in C content of the product should result on perfection of a satisfactory nongraphite container.

The Ca content too is satisfactorily low, indicating that the U content of the bath is high enough to be the principal current carrier at the electrodes.

While the feasibility of electrolysis over extended periods of time has been demonstrated for one set of conditions, it would appear from earlier data that a wide range of conditions should give equally satisfactory results.

Two runs were made to determine the magnitude of the decontamination from fission products that can be achieved with this method of processing. In one the anode charge consisted of a mixture of unirradiated U with about $\frac{1}{10}$ its weight of irradiated metal that had been cooled 2–3 yr. This gave enough activity so that decontamination through the cell could be followed through radioactivity. The second run used a U alloy containing 1 wt % each of Ru, Mo, and Zr. Data are summarized in Table V. An appreciable decontamination was achieved from both the active and noble metal fission products.

The two runs that are reported were made for a duration of only two bath throughputs, and the need for runs of greater throughput is evident. The data, however, do give an indication of the magnitude of decontamination that is possible with the method.

The information obtained to date on Pu decontamination are inconclusive; however, there is an indication that the Pu tends to concentrate in the salt phase when the chloride bath is used.

TABLE V. *Decontamination factors* obtained by electrorefining*

	Hot run	Alloy run
Cs	260	—
Sr-Y	80	—
Total Rare Earths	170	—
Zr-Nb	80	200
Mo	—	500
Ru	250	400

* Decontamination Factor = $\frac{\text{amount/g U at start}}{\text{amount/g U in product}}$

Summary and Conclusions

This study of U purification by electrorefining has shown that decontamination of U from fission products can be achieved by electrolysis through fused salts. The work has also demonstrated the feasibility of employing cathodes of transition metals in order to obtain U-rich alloy products that are molten at temperatures considerably below the melting point of pure U. The formation of such molten products should facilitate continuous cell operation without introducing the problems associated with operation at temperatures above the melting point of U.

The effects of temperature, current, and bath composition on cell efficiency and operation were investigated. Temperatures in the range 900°–1050°C are satisfactory, and changes in this range have little effect on cell efficiency. The lower temperatures are most satisfactory from the point of view of attack on container materials and salt volatilization. For high cell efficiency low current densities are indicated, especially at the anode. Bath composition has little effect on cell operation, but a minimum concentration of the U salt is required to prevent excessive contamination of the product with the cation of the salt diluent. In the case of $CaCl_2$-UCl_3 baths a minimum UCl_3 concentration of 38 wt % is desirable.

Acknowledgments

The authors express their appreciation to Burton E. Dearing for his work in fabricating most of the graphite crucibles and to the members of the Metallurgical and Chemical Analysis Activity at the Knolls Atomic Power Laboratory for the analytical work.

Manuscript received July 20, 1955.

Any discussion of this paper will appear in a Discussion Section to be published in the June 1957 Journal.

REFERENCES

1. L. W. Niedrach and A. C. Glamm, *Ind. Eng. Chem.*, **48,** 977 (1956).
2. H. A. Wilhelm and O. N. Carlson, *Trans. Am. Soc. Metals*, **42,** 1311 (1950).
3. F. H. Driggs and W. C. Lilliendahl, *Ind. Eng. Chem.*, **22,** 516 (1930); U S. Pat. 1,861,625, June 7, 1932.
4. R. Rosen, U. S. Pat. 2,519,792, Aug. 22, 1950.
5. S. K. Kantan, N. Shreenivasan, and G. S. Tendolkar, *Chem. Eng. Prog. Symposium Ser. No. 12,* **50,** 63 (1954).
6. C. Marzano and R. A. Noland, ANL-5102 (1953).
7. A. Glassner, N. R. Chellew, and R. C. Vogel, ANL-4872, 147 (1952); ANL-4922, 154 (1952).
8. H. Fischer and K. Dorsch, German Pat. 615,951, (1935).
9. J. L. Andrieux, French Pat. 753,394, (1933); U. S. Pat. 2,033,172, (1936). *Rev. met.*, **32,** 487 (1935).
10. M. A. Steinberg, M. E. Sibert, and E. Wainer, Chapter on "The Extractive Metallurgy of Zirconium by the Electrolysis of Fused Salts" in "Zirconium and Zirconium Alloys," pp. 58–60, American Society of Metals, Cleveland (1953).
11. J. D. Grogan and R. J. Pleasance, *J. Inst. Metals*, **82,** 141 (1953).
12. L. Brewer, L. Bromley, P. W. Gilles, and N. L. Lofgren, MDDC-1543, 9 (1945).

Report of the Chlor-Alkali Committee of the Industrial Electrolytic Division for the Year 1955

WILLIAM C. GARDINER,[1] MORTON S. KIRCHER,[2] AND WARREN D. SHERROW[3]

PRODUCTION IN 1955

There is little doubt that 1955 was the greatest year in the history of the chlor-alkali industry. Production of chlorine set a new record of 3,407,842 tons,[4] exceeding 1954 by 18%. The industry was running full for the last three months of 1955 and averaged 10,240 tons per day. The lowest month was April with an average of 7,600 tons per day of chlorine.

Caustic soda production was 3,907,149 tons,[4] an increase of 15% over 1954. Lime-soda caustic was 12% of the total and showed no decline during the year, indicating that the demand for caustic soda and chlorine were in balance. However, there were periods during the year when rayon grade liquid caustic and dry caustic were on the scarce side.

Caustic potash production was 90,000 tons. Solvay announced production of potash in mercury cells and several others have indicated their intention of entering the field with production by mercury cells.

Chlorine is estimated to have been produced in the following manner: 78% in 45 plants with diaphragm cells, 16% in 15 plants using mercury cells, 5% in 4 plants producing metallic sodium, and 1% by two chemical processes. Production at two electrolytic magnesium plants is not included because they consume more than they produce.

Canadian production capacity for chlorine is now 447 tons per day in ten plants, six of which use mercury cells.

DEVELOPMENTS DURING 1955

Diamond Alkali brought their plant at Muscle Shoals, Ala., into production during the summer.

Dow Chemical started shipping soda ash made by carbonating caustic soda at Freeport, Texas.

Hercules Powder Co. ran into more trouble than they expected in their plant to oxidize by-product hydrogen chloride to chlorine at Brunswick, Ga. The plant is operating intermittently at 44 tons per day. They hope to be in regular production by the middle of 1956.

The price of mercury continued to be of considerable concern to mercury cell users. The average annual quotation in 1955 established a new peak at 10% above the previous high in 1954. Quotations ranged from $322 to $324 a flask through February, increased slightly in March and then declined gradually to $253–$255 a flask in August. The price then rose to $280–$284 a flask in November and remained there.

EXPANSION NEWS IN 1955

Columbia-Southern is adding 50 tons per day at each of their plants at Lake Charles, La., and Barberton, Ohio.

E. I. du Pont de Nemours and Co. is planning a sodium and chlorine plant at Antioch, Calif., for tetraethyl lead, ethyl chloride, trichlorethylene, and perchlorethylene.

Pennsylvania Salt Manufacturing Co. is adding more deNora mercury cells at Calvert City, Ky., to produce caustic potash early in 1956.

Solvay Process Division of Allied Chemical and Dye Corp. announced a new mercury cell plant at Brunswick, Ga., for late 1956.

Union Chemical and Materials (Frontier Chemical) is doubling capacity at Wichita, Kans. The chlorine is for production of chlorinated solvents.

Westvaco Chlor-Alkali Division of Food Machinery and Chemical Corp. will modernize its Charleston, W. Va., plant by replacing Vorce and Nelson cells with Hooker S3B cells. Production is 370 tons of chlorine per day.

The Weyerhauser Timber Co. is constructing a plant to make 75 tons of chlorine per day at Longview, Wash., using deNora mercury cells.

ANNOUNCEMENTS TO DATE IN 1956

Canadian Industries, Ltd., will triple its capacity to produce chlorine, hydrochloric acid, and caustic soda at Cornwall, Ont., by mid 1956.

Dow Chemical Co. will build a $20 million plant to produce chlorine, caustic, and organics in the Baton Rouge, La., area.

General Aniline and Film Corp. started its 50 ton per day chlorine plant using Mathieson mercury cells at Linden, N. J.

Hooker Electrochemical Co. has merged with Niagara Alkali Co. at Niagara Falls. The Tacoma, Wash., plant is to be expanded 30%. A Canadian subsidiary, Hooker Chemicals, Ltd., is building a plant to cost $11 million at Vancouver, B. C. Hooker has joined Pennsylvania Salt to form the Chemical Salt Production Co. to produce solar salt from Great Salt Lake, Utah. This will assure a source of salt for the western operations of both companies.

Kaiser Aluminum Corp. will spend $8 million for a chlor-alkali plant at Gramercy, La. Hooker cells will probably be used. The caustic soda will be used for purifying bauxite.

Mathieson Alabama Chemical Corp., a subsidiary of Olin Mathieson Chemical Corp., is doubling capacity at McIntosh, Ala.

[1] Olin Mathieson Chemical Corp., Niagara Falls, N. Y.
[2] Hooker Electrochemical Co., Niagara Falls, N. Y.
[3] Great Lakes Carbon Corp., Niagara Falls, N. Y.
[4] U. S. Department of Commerce, "Facts for Industry."

Shawinigan Chemicals, Ltd., will probably install mercury cells at Shawinigan Falls, Que.

Wyandotte Chemical Corp. has purchased land for a 100 tons per day chlor-alkali plant in Louisiana.

Technical Developments

Ion permeable membranes are being investigated for use in chlor-alkali cells.

The search for a practical vertical mercury cell continues. Dr. deNora discussed his developments on a fluent amalgam cell at our Symposium last May in Cincinnati. French Patent 1,062,041 discloses a development of the Hooker Electrochemical Co. in which mercury flows down the outside of a multiplicity of steel cathode tubes surrounded by graphite anodes. At the San Francisco Meeting Dr. Shiro Yoshizawa discussed work with the rotating mercury cathode in Japan.

Germanium rectifiers for high currents are being used on hydrogen-oxygen cells but have not yet been applied to chlor-alkali cell circuits. Their development is being watched with interest.

The graphite industry is producing new grades of graphite for mercury cell anodes with particular emphasis on vanadium content. A standard grade contains 150 ppm vanadium maximum. Premium grades contain less than 50, 20, and 2 ppm vanadium, respectively. Several operators are willing to pay the extra cost to obtain better cell efficiencies, particularly at high current densities.

Diamond Alkali is offering to license their process for recovery of waste chlorine from "sniff gas" using a carbon tetrachloride absorption-desorption system.

Markets

The end use patterns of chlorine and caustic soda have shown no material change in 1955. The big uses of chlorine are in pulp and paper, organic chemicals, and insecticides. Caustic soda goes to rayon and film, petroleum, inorganic chemicals, and soap. Pulp bleaching with chlorine dioxide is increasing and replacing some chlorine. This has contributed to an expansion of sodium chlorate production.

It has been predicted by the Business and Defense Services Administration that chlor-alkali output and sales will hold at or may top 1955 for the first half of 1956. The new capacity coming in later in 1956 assures an easier supply for next year. The international caustic market will remain tight until 1957 when new foreign plants start up.

Some Studies on the Fused Salt Cell

$Mg/LiNO_3$, KCl/Ag

CHARLES W. JENNINGS

Department of Chemistry, North Carolina State College, Raleigh, North Carolina

ABSTRACT

The fused salt cell, $Mg/LiNO_3$, KCl/Ag, was studied at temperatures from 300° to 500°C. Cell characteristics varied with the KCl content. With greater than 20 mole % KCl open-circuit voltages of 1.4–1.6 v were obtained. Cells were discharged at 4–100 ma/cm². Both Ag and Mg reacted directly with the electrolyte. The extent of reaction of Mg varied with the KCl content. Substitution of Pt, Ni, or graphite for Ag increased the open-circuit voltage. A mechanism is proposed in which Ag is involved in the cell reaction.

The literature on fused salt cells relates principally to reversible cells, usually of the type M/MCl_y, XCl/Cl_2, where X is an alkali metal and M a metal like Pb, Bi, Ag, Zn, Co, Cu, Ni, or Fe (1–3). Similar cells with bromide salts and bromine have also been reported (4). The cells were studied mainly to obtain thermodynamic values; discharge characteristics were not given. Fused salt cells that have been used to furnish electric current have been reported by Hamer and Schrodt (5) and Goodrich and Evans (6), and the general subject of fuel cells in which fused salts have been used has been discussed by Kortum and Bockris (7), Vinal (8), and others.

This investigation was initiated to study fused salt cells that could deliver electrical energy under load at temperatures under 500°C. One such cell, $Mg/LiNO_3$, KCl/Ag, was studied in detail. The work on this cell is largely qualitative in nature, but at the present time it cannot be extended. Because of the scarcity of published data on electrochemical discharges in fused salt systems, it is believed that the results will be of interest to workers in this field.

EXPERIMENTAL

Negative electrodes were of $\frac{1}{8}$ or $\frac{3}{32}$ in. commercially pure Mg rod. Typical analyses of the rod, obtained from the Dow Chemical Co., gave Al, 0.003; Cu, 0.003; Fe, 0.03; Mn, 0.08; Ni, 0.001; Si, 0.005; and Mg, 99.878% (by difference). The positive electrodes were of rolled silver sheet. Both electrodes were cleaned with HNO_3, washed, and dried at 110°C prior to use in the cells. The salts were Merck's or Baker and Adamson's Reagent Grade. For most of the experiments about 50 g of salt mixture was weighed out on a balance (accurate to ±0.02 g) and placed in a Pyrex test tube. The mixture was dried at 110°C for several days and heated in a Hoskins type FD 101 electric furnace. The lower half of the Pyrex tube was in the furnace. An inert gas, helium, was passed through the melt for ½–3 hr. The electrode assembly, shown in Fig. 1, was inserted and the emf of the cell was read with a Heathkit vacuum tube voltmeter. The meter could be read to ±0.01 v and had an input impedance of 11 megohms. The temperature was read to ±2°C with an iron-constantan thermocouple. Unless noted otherwise, an atmosphere of He was maintained above the melt at all times.

Moisture content was controlled by maintaining uniform conditions of operation. Salts were weighed, dried, and heated in the same manner in all experiments. No attempt was made to determine the exact moisture content of the mixtures in the fused state, although it is realized that small amounts of moisture could affect cell behavior. Moisture contents of cells in He atmosphere were not sufficient to account for the large currents obtained during discharge at the temperatures studied.

Distance between electrodes was about 1.5 cm. Discharge characteristics of the cells were obtained by applying external loads of 1, 2, 5, 10, 25, 50, or 100 ohms. Values of current density were obtained by dividing the current obtained after 1 min of cell discharge at a given load by the original surface area of the Mg electrode. This area was from 3 to 4 cm². The Ag electrode had approximately the same surface area as the Mg. Voltage-time characteristics of a number of cells were recorded by inserting a Brush Amplifier, Model BL 932 and Recorder, Model 202/931 in parallel with the vacuum-tube voltmeter. The input impedance of the amplifier was 9 megohms. No measurements were made for cell capacity. Cells were usually discharged for 3 min under each set of conditions.

Open-circuit voltage (OCV) and closed-circuit voltage (CCV) measurements were made on cells with electrolyte compositions of 0–70 mole % KCl in $LiNO_3$. Table I gives the OCV's for five cells, each with a different mole per cent KCl in $LiNO_3$. The cells, contained in small test tubes, were heated simultaneously. He was bubbled alternately through the tubes for 2–3 hr before the Mg and Ag electrodes were added. The temperature was read from a thermocouple outside of, but next to, the tubes. The discharge characteristics of these cells with 100 ohms load at 360°C are given in Table II. The lower values in the table give the recovery of OCV after 1-min discharge. Values in Tables I and II are similar to those obtained from cells heated individually in large test tubes.

The best discharge characteristics with heavy current drains were obtained when an electrolyte of 50 mole % KCl in $LiNO_3$ was used. Table III gives the CCV's for

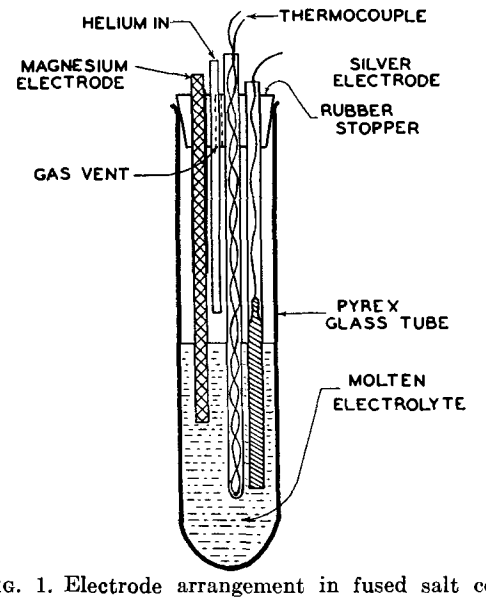

FIG. 1. Electrode arrangement in fused salt cell

TABLE I. *OCV for* Mg/$LiNO_3$, KCl/Ag

Time (min)	Mole % KCl					Temp* (°C)
	0	10	20	30	50	
0	1.14	1.06	1.60	1.55	1.55	366
10	1.14	0.94	1.56	1.59	1.52	325
20	1.14	0.92	1.50	1.58	1.51	308
35	1.09	0.80	1.53	1.56	1.51	323
50	1.06	0.75	1.57	1.57	1.52	324
60	1.04	0.70	1.56	1.56	1.55	345
130	0.88	0.56	1.59	1.56	1.57	
160	0.55	0.51	1.60	1.58	1.57	
180	0.45	0.45	1.59	1.58	1.57	360
200	0.35	0.42	1.59	1.58	1.57	
240	0.26	0.45	1.56	1.56	1.57	380
420	0.02	0.30	†	†	1.57	384

* Outside of tubes.
† Magnesium electrode broke.

this cell at the end of the 3-min discharge period at 475°C. CCV's were averaged at each load from 6 cells, each heated separately. A few cells were discharged at 25 ma/cm^2 for 15 min or longer at 1.2 v. The voltage changed less than 10% during the discharges. Under loads of 5–100 ohms the magnitude of polarization at the Mg electrode was of the same order as at the Ag electrode. Polarization was measured by comparing an operating electrode with an idle electrode in the same electrolyte.

The electrical output from cells containing less than 20% KCl was poor. The reason for the poor performance of cells with low chloride contents is not known, but appears to be related to film formation on the Mg electrode. Analysis of the system was complicated by side reactions, the principal ones being the direct or corrosion reactions of the Mg and Ag electrodes with the electrolyte.

The characteristics of the cells varied with the proportion of KCl to $LiNO_3$. Cells with only $LiNO_3$ had initial OCV's of 1.0–1.4 v at 300°–370°C. OCV's decreased appreciably with time at any temperature (*see* Table I). In cells with 10% KCl and 90% $LiNO_3$, OCV decreased

TABLE II. *Discharge of* Mg/$LiNO_3$, KCl/Ag *at 100 ohms load at 360°C*

Time (sec)	Mole % KCl									
	0		10		20		30		50	
	V (v)	I (ma)	V (v)	I (ma)	V (v)	I (ma)	V (v)	I (ma)	V (v)	I (ma)
0	0.28		0.54		1.57		1.57		1.58	
5	0.24	2.0	0.43	3.8	1.42	12.5	1.50	13.2	1.49	13.2
15	0.23	2.0	0.41	3.5	1.42	12.6	1.48	13.1	1.48	13.2
30	0.22	1.9	0.41	3.3	1.42	12.6	1.48	13.1	1.48	13.2
45	0.22	1.9	0.41	3.2	1.41	12.6	1.47	13.1	1.48	13.2
60	0.22	1.9	0.41	3.2	1.41	12.6	1.47	13.1	1.48	13.2
3	0.26		0.40		1.50		1.54		1.55	
15	0.30		0.50		1.52		1.55		1.56	
30	0.31		0.50		1.53		1.56		1.57	
60	0.34		0.48		1.54		1.56		1.57	

TABLE III. *Discharge characteristics for the cell* Mg/50$LiNO_3$-50KCl/Ag *at 475°C*

OCV (v)	CCV (v)	Current density (ma/cm^2)
1.45	1.40	4
	1.34	12
	1.25	25
	1.15	50
	0.9	100

with time at all temperatures up to 450°C. Mg corroded rapidly in the electrolyte. With electrolytes of 15% KCl the OCV was stable with time, its value being 1.5 v above 360°C and 0.5 v below 300°C. Somewhere between 300° and 360°C, the OCV changed abruptly, about 1 v, within a few degrees. A fresh Mg electrode inserted in the melt at 300°C region had an initial OCV of 1.4–1.5 v, but decreased with time to 0.5 v. The OCV did not decrease with time above 360°C. With electrolytes containing more than 20 mole % KCl (and less than 80 mole % $LiNO_3$) the OCV did not change abruptly with temperature or KCl content and was from 1.5 to 1.6 v between 300° and 400°C. As the KCl content of the electrolyte was increased, cells could be operated at higher temperatures without excessive electrolyte decomposition or Mg corrosion. Minimum temperature of operation, the melting point of the mixture, also increased with KCl content. The difference between OCV and CCV for a given load decreased as temperature was increased.

The corrosion reaction of Mg with the electrolyte, in which gas was evolved, was greatest between 10 and 30 mole % KCl. Mg reacted much less in $LiNO_3$ than in $LiNO_3$-KCl mixtures. At KCl concentrations of greater than 30 mole %, the corrosion reaction decreased with increasing KCl content. Rate of corrosion reaction increased in an exponential-like manner with temperature; at any given chloride concentration the extent of corrosion increased slowly with temperature up to a certain temperature region and then accelerated. Gas samples analyzed with the mass spectrometer contained N_2O, N_2, NO, and NO_2. Alkali oxide and nitrite were found in the solidified residues. Ag was oxidized in all electrolytes in which $LiNO_3$

TABLE IV. Mg/50$LiNO_3$–50KCl/M

	Ni	Ag	Pt	C	°C
Initial OCV	1.70	1.55	2.14	1.86	366
After 10 min	1.82	1.55	2.14	1.85	364
After 2 hr	1.85	1.54	2.12	1.80	362
After 4 hr	1.75	1.52	1.85	1.66	372
CCV (30 sec after load applied*)	1.50	1.41	1.32	1.36	372
OCV (30 sec after load removed)	1.57	1.55	1.55	1.51	372
OCV (30 min after load removed)	1.65	1.55	1.70	1.65	368

* Load of 100 ohms was applied for 1 min.

was present. In the absence of Mg [1] about 12 % of the Ag electrode reacted in 1 hr at 400°C in an electrolyte containing 50% $LiNO_3$ and 50% KCl. About the same amount of Ag reacted in a 70$LiNO_3$–30KCl mixture. Less reaction occurred with 100% $LiNO_3$.

Analysis of the reactions in which Ag and Mg were oxidized was complicated by subsequent reactions that could occur between products, for example, a reaction between Li_2O and NO_2 to form $LiNO_2$ and $LiNO_3$ (9). Decomposition of $LiNO_3$ offered a further complication, although the cells were usually operated at temperatures well below the region at which gas evolution could be observed.

In cells with electrolytes containing no $LiNO_3$, but only LiCl and KCl, OCV's of 1.45–1.65 v were obtained at 360°–500°C. The cells polarized badly in comparison with cells containing $LiNO_3$. Gas was evolved at both the Ag and Mg under load but only at the Mg when no load was applied. As there was no apparent oxidizing agent, the discharge reactions that were obtained are attributed to the presence of moisture, or other impurity like NH_4Cl, in the salts. Salts taken directly from the reagent bottles showed better discharge characteristics than those given the usual drying treatment. A cell made up to contain 1% NH_4Cl, a better acid than H_2O in the LiCl-KCl electrolyte, had good discharge characteristics. There was evidence for NH_3 in the evolved gases in this cell. In cells with a LiCl-KCl electrolyte, that is, no $LiNO_3$ present, AgCl was not found.

Positive Electrodes Other Than Ag

The OCV's for different positive electrodes were compared in the cell, Mg/50$LiNO_3$–50KCl/*M*, where *M* was Ni, Ag, Pt, or graphite (Table IV). The OCV was highest for the Pt and lowest for the Ag electrode. The Ag and Ni electrodes were etched in the electrolyte. The cell Mg/85 $LiNO_3$-15 KCl/Pt gave an OCV of 2.19 v at 340°C. Under load this cell polarized badly, and there was a very long recovery period. When a Ni electrode was used in place of Ag, with an electrolyte of 90$LiNO_3$–10KCl, the OCV was 0.3–0.4 v higher, but as with the Ag electrode, the initial OCV decreased with time to around 0.5 v. In cells with an electrolyte containing only LiCl and KCl, that is, no $LiNO_3$ present, Pt positives were similar to Ag positives.

[1] Mg reacts with $LiNO_3$ producing reduction products of $LiNO_3$, such as $LiNO_2$, NO_2, and NO. In addition to the Ag-$LiNO_3$ reaction, a reaction could occur between Ag and the reduction products of $LiNO_3$.

Discussion

In cells with a Mg electrode and $LiNO_3$-KCl electrolyte, lower OCV's were obtained with Ag or Ni positive electrodes than with Pt. This indicated that Ag and Ni were not inert, but took some part in the cell reaction. This is further confirmation of the results obtained by Selis (10) and Rubin (11) on the behavior of different metal positives in fused salt cells.

One explanation that can be offered for the behavior of the Ag positive is based upon the continuous oxidation of the Ag by nitrate. The Ag compound formed in the oxidation covered the metal, preventing direct access of the nitrate. The film never became thick, as the Ag compound was soluble in the electrolyte. When current was drawn from the cell, the Ag compound was reduced in preference to the nitrate. The oxidizing action of nitrate on Ag could account for the Ag compound always found in the electrolyte of cells containing nitrate. Such a film was not formed on Pt and the nitrate had direct access to the Pt metal. Pt acted as an inert electrode. The large amount of polarization observed in the cells with Pt indicated a slow electrode reduction of nitrate at an inert electrode. The electrochemical reduction of the Ag compound is considered to be much faster than the electrochemical reduction of the nitrate at an inert electrode.

An electrochemical reaction for this postulated mechanism is: $Li_2O + Mg + 2AgCl = MgO + 2Ag + 2LiCl$. LiO_2 would be produced in the reduction of nitrate. Solubility of MgO was not appreciable and it accumulated at the bottom of the melts during cell activation.

Acknowledgments

This research was supported by the Diamond Ordnance Fuze Laboratories, Dept. of the Army, formerly a part of the National Bureau of Standards.

Manuscript received May 9, 1955. This paper was prepared for delivery before the Cleveland Meeting, September 30 to October 4, 1956.

Any discussion of this paper will appear in a Discussion Section to be published in the June 1957 Journal.

REFERENCES

1. J. H. Hildebrand and G. C. Ruhle, *J. Am. Chem. Soc.*, **49**, 722 (1927).
2. E. J. Salstrom, *ibid.*, **55**, 2426 (1933).
3. S. I. Rempel and I. N. Ozeryanya, *Zhur. Fiz. Khim.*, **25**, 1181 (1951).
4. J. H. Hildebrand and E. J. Salstrom, *J. Am. Chem. Soc.*, **54**, 4257 (1932).
5. W. J. Hamer and J. P. Schrodt, *ibid.*, **71**, 2347 (1949).
6. R. B. Goodrich and R. C. Evans, *This Journal*, **99**, 207 (1952).
7. G. Kortüm and J. O'M. Bockris, "Electrochemistry," Vol. II, p. 479, Elsevier Co., Amsterdam (1951).
8. G. W. Vinal, "Primary Batteries," p. 324, John Wiley & Sons, Inc., New York (1950).
9. T. Oza, *J. Indian Chem. Soc.*, **22**, 180 (1945).
10. S. M. Selis, Private communication.
11. B. Rubin, Private communication.

Association of Co^{60} Ions with Metal Surfaces

R. T. Foley, B. T. Stark, and C. J. Guare

General Engineering Laboratory, General Electric Company, Schenectady, New York

ABSTRACT

The radiochemical technique for the study of surface reactions has been investigated. This technique readily demarks on the metal surface areas that are cathodic to adjacent areas. The steel-copper and aluminum-copper couples were observed and the strong attraction of radiocobalt to the cathode member of the couple was measured. The sorption of radiocobalt ions on surface films is a complicating effect in the employment of this technique if not considered and understood. The extent of this effect varies with the surface film under consideration, being considerable for oxide and sulfide films on copper and small for oxide films on alloy steels and anodized films on aluminum.

The sorption of ions from solution has a great significance in so far as corrosion mechanism is concerned as it would appear that ion concentration cells are common occurrences when part of a metal surface is covered with an oxide film and part is bare.

The fact that atoms on a metal surface may exchange with ions of the same metal in solution has been known for a number of years and has been of particular interest to those working on the theoretical aspects of corrosion, catalysis, and other applications of surface chemistry. Recently pickup of radioactive ions from solution by metals has been used to study electrode reactions (1), adsorption processes (2), and corrosion mechanisms (3, 4).

In this laboratory there has been a critical appraisal of the radiochemical technique with respect to its usefulness in studying corrosion mechanisms. There are several possible mechanisms by which tracers, as radiocobalt ions, may be transferred from solution to a metal surface: (*a*) exchange between metal ions on surface and in solution; (*b*) sorption; (*c*) electrolytic action.

The more recent publications on this technique have contained experiments interpreted in terms of the electrolytic action mechanism. However, some of the authors' earliest experiments demonstrated that the cobalt ion tracer was rather loosely held on the surface, suggestive of a sorption mechanism.

If this technique is to be of value for the study of corrosion processes there should be no ambiguity in the interpretation of the results obtained. The objective of this work was to contribute to the understanding of the mechanism and interpretation of the technique.

Experimental

All the radiochemical studies were carried out using solutions containing tracer concentrations of the radioactive isotope, cobalt-60. This isotope has a half-life of 5.27 years and emits β-radiation of 0.306 mev energy as well as 1.33 mev and 1.17 mev γ-rays. The original solution was obtained from Oak Ridge National Laboratory and was in the form of $CoCl_2$ (7.1 mg Co/ml) in 0.34*N* HCl solution. Separate dilutions of this solution were used for each of the metals investigated. Concentrations of cobalt ion and H^+ after dilution are shown in Table I. This table also records the activity of each solution. In all cases the metal samples in strip form were immersed in the tracer solution for 10 min at a constant temperature of 30°C. Usually a volume of 500 ml was taken. The size of the samples varied, 1.2 cm x 1.2 cm squares being used most frequently. In some of the experiments with aluminum 5.1 cm x 5.1 cm samples were used. In a typical experiment a large number of samples would be prepared in an identical manner and 10 from the group would be carried through the experiment and given similar treatment. The use of a large number of samples compensated for the small size of each sample. All activity figures were normalized to unit area.

Autoradiographs were made by placing the samples directly in contact with Kodak No-Screen x-ray film. Exposure time varied with the activity of the samples, but in most cases it was possible to obtain sufficient contrast in 3–4 hr. During preliminary experiments the samples were dipped in a 2% solution of VYNS (vinylite) in acetone to prevent fogging of the film by the bare metal (5, 6), but this was subsequently discontinued since no fogging was observed from dry, untreated control samples.

Radioactivity measurements were made using a thallium activated sodium iodide scintillation crystal coupled to a photomultiplier tube as a detector. The observed data were corrected for physical geometry and detector efficiency by direct comparison with a standard cobalt-60 source.

Influence of Surface Films on Pickup of Radiocobalt

In the study of a corrosion process the influence of surface films on the pickup of radiocobalt from solution would be an important factor. The influence of surface films would also be suggestive of the mechanism by which Co became attached to the surface. If only the potential differences existing on the surface account for the pickup of activity, then the pickup would be expected to remain constant or decrease with increase in film thickness. It would seem reasonable to assume that as the film increased in thickness anode sites would be covered up. On the other hand, if adsorption accounted for the pickup, one would expect an increase in pickup of radiocobalt ions with increased weight of sorbent. The location of Co on

TABLE I. Co *solutions*

Solution	Calculated total conc. of Co	Calculated conc. of H^+	Measured activity (Co)
	μg/ml	*N*	d/min/ml*
*1-Used with Al samples	0.8	4×10^{-5}	3.4×10^6
*2-Used with Cu samples	0.5	2.5×10^{-5}	2.0×10^6
*3-Used with steel samples	0.7	3.5×10^{-5}	2.6×10^6

* Disintegrations per minute per milliliter of solution.

TABLE II. *Activity pickup as related to oxide film thickness on* Cu

Surface treatment—Oxidized at 400°C for:	Weight of oxide† (mg/cm²)	Co pickup—(d/min/cm²)	
		Prior immersion in H_2O	Prior immersion in NaCl solution
Experiment 1			
min			
0	0.00	278	642
5	0.010	529	1,840
10	0.062	10,200	4,170
20	0.194	8,450	6,710
Experiment 2			
0	0.00	210	
5	*	178	
10	0.128	4,420	
20	0.190	5,530	
30	0.401	6,620	

* Less than experimental error.
† Found by stripping after oxidation.

the metal surface, whether it was attached to the basis metal or the surface film, would be of interest. Association with the surface film would not argue entirely for adsorption as opposed to electrochemical action as the surface film may be the cathode in the electrolytic cell. The influence of surface film thickness on Co pickup was studied with oxide and sulfide films on Cu, oxide films on Al, and oxide films on alloy steels.

Oxide Films on Copper

The oxide films were developed on strips of copper[1] by oxidizing in air at 400°C for various lengths of time. Samples (1.25 cm x 1.25 cm x 0.064 cm thick) were used for the radiochemical experiments, ten samples being taken for each variation. To characterize the film layer, samples (3.8 cm x 3.8 cm x 0.064 cm thick) were oxidized along with the squares that would be later exposed to radiocobalt. The oxide strips were immersed in distilled water for 10 min, in radiocobalt solution for 10 min, and rinsed for 30 min. After drying, the samples were counted to determine the radioactive pickup and autoradiographs were made. Variation in this procedure included substituting a 10-min immersion in NaCl solution (5 g/l) for the prior immersion in distilled water. Following the completion of these operations, the samples were immersed for a short time in H_2SO_4 solution (5 ml of concentrated H_2SO_4 diluted to 100 ml) and again counted. This H_2SO_4 reagent is known to strip oxide films from Cu without attacking the Cu itself. Results of two experiments with oxide films are summarized in Table II. Another set of experiments confirmed these results in a qualitative manner. These experiments demonstrate that with increased thickness (or amount) of oxide on the surface the pickup of Co increases. Treatment with the oxide stripping reagent removes all of the activity. This indicates that the activity is associated with the oxide film rather than firmly attached to the basis metal.

[1] Analysis 99.90% copper, 0.04% oxygen.

TABLE III. *Activity pickup related to copper sulfide film thickness*

Surface treatment—Exposure time to polysulfide solution	Weight gain (mg/cm²)	Co pickup (d/min/cm²)
hr		
3.5	0.023	1,160
8	0.051	5,680
15	0.113	11,500
27.5	0.186	16,200

Sulfide Films on Copper

Films of copper sulfide were developed on copper by holding Cu strips over a polysulfide solution (1 ml of Baker's dark ammonium polysulfide solution diluted to one liter) in a closed desiccator-type jar. Subsequent treatment was similar to that given the oxidized copper strips and described above. Results of a typical experiment are summarized in Table III. The Co pickup relative to the increase in film thickness is pronounced.

The autoradiographs of this series of filmed samples demonstrated that the variation of activity along the surface of the individual sample was similar to the distribution of the surface film itself. This comprised qualitative confirmation of the influence of surface film.

Aluminum Oxide Films

Oxide films of varying thickness were developed on aluminum[2] by means of an anodic treatment in H_2SO_4 solution (15% by weight). A current density of 1.3 amp/dm² and 16 v were used at 25°C. Strips of aluminum 5.1 cm x 5.1 cm x 0.064 cm thick were treated for various lengths of time. The anodic film thicknesses for the individual panels were characterized by the weight loss through stripping in chromic-phosphoric acid reagent. In one series of experiments the strips were immersed in NaCl solution for 30 min before immersion in the Co tracer. In another series the prior immersion was in distilled water. Experimental results are given in Tables IV and V. From these results it may be concluded that the thicker anodic films show very little tendency to pick up the Co tracer. Co was picked up by strips which were not anodized or which were anodized to produce thin films to produce a strong activity. This pickup is interpreted as electrodeposited. Even in distilled water, sites of different potential are set up over the surface accounting for the electrochemical action. Autoradiographs confirmed the results set down in Tables IV and V.

[2] Analysis 99.0% Al; Fe and Si 1.0%.

TABLE IV. *Activity pickup as related to aluminum oxide film thickness*
(After activation in NaCl solution)

Thickness of oxide (by stripping) (mg/cm²)	Activity (d/min/cm²)
0.0	5,633
0.0	9,546
0.14	7,353
0.26	3,557
0.84	601
0.84	988
0.91	2,842
1.28	968
1.28	556
1.38	558
2.34	432
2.47	427

TABLE V. *Activity pickup and aluminum oxide film thickness*
(After activation in distilled water)

Thickness of oxide (by stripping) (mg/cm²)	Activity (d/min/cm²)
0.00*	11,414
0.00*	13,860
0.00*	15,089
0.00†	8,514
0.88	116
0.93	885
0.98	679
1.11	183
4.87	198

* Annealed strip.
† As rolled strip.

TABLE VI. *Activity pickup and oxide film thickness on stainless steel*

Weight gain on oxidation (mg/cm²)	Activity (d/min/cm²)
0.00	9
0.00	12
0.008	84
0.008	33
0.012	34
0.012	65
0.016	33
0.020	33
0.031	33

Oxide Films on Alloy Steel

Stainless steel strips[3] were oxidized at 1000°C to develop oxide films of varying thickness. These oxidized samples were allowed to stand in NaCl solution for 30 min along with unoxidized controls. Results are given in Table VI.

The cleaned surface of the stainless steel picks up a negligible amount of Co during the immersion period. There is a slight increase in pickup of activity with increase in oxide film thickness as would be suggested by the adsorption mechanism. However, stainless steel surfaces appear to be passivated and equipotential surfaces appear to have been developed even with air-formed oxide films. In some experiments, oxidized stainless steel panels were scribed before immersion in the tracer solution. Considerable Co was attracted to the scratch. Results obtained with this alloy steel were different from those obtained during experiments with an Fe-Ni alloy containing 42% Ni and 58% Fe. In the latter case a great deal of activity was attracted to the alloy surface possessing only the room temperature air-formed film.

[3] Type 302, 18% Cr, 9% Ni.

Study of Worked Surfaces

One method of introducing cold work into the surface is by abrasion. Cleaned strips of Cu (1.25 cm x 1.25 cm x 0.064 cm thick) were abraded in air, under acetone and under benzene. Strips were stored under benzene before and after the abrasion. They were rinsed in acetone and activated for 30 min in NaCl solution before immersion in the tracer solution. After rinsing for 30 min in running water the samples were counted.

Surface treatment	Activity—(d/min/cm²)
Abraded in air	5,542
Abraded under acetone	1,185
Abraded under benzene	2,429

A further experiment checked this effect and also the retention of the activity after rinsing.

Surface treatment	Activity—(d/min/cm²)	
	After 30 min rinsing	After 18 hr rinsing
Abraded in air	3,996	2,014
Abraded under benzene	996	440

Autoradiographs from this last experiment reveal increased activity when abrasion is carried out in air as well as the fact that much of the activity is confined to the edges of the sample. In both cases some of the activity is loosely held and is lost on prolonged rinsing. Increase in activity through abrasion in air is attributed to adsorption on the oxide film that must be formed. When only a portion of the strip is abraded, radioactivity is restricted to the abraded area.

Further experiments were performed to estimate the competitive influence of the presence of an abraded area and a filmed area on the same sample. Strips of Cu (3.8 cm x 3.8 cm x 0.064 cm) were treated in the following ways:

(*A*) The entire side of the sample was coated with a sulfide layer by exposure over an ammonium sulfide solution.

(*B*) One half of the area was abraded with 2/0 emery under benzene. This abraded area was masked by painting with a paraffin wax solution in benzene, then the whole strip was exposed above the sulfide solution. Thus, one-half the face was abraded, the other half filmed.

(*C*) One-half the area was abraded.

(*D*) No treatment was given the sample, and it was carried through as a control.

Duplicate samples with these treatments were allowed to stand for 30 min in NaCl solution, then immersed in the Co tracer solution.

Autoradiographs of this series of samples demonstrated how the activity is drawn to the sulfide covered area when

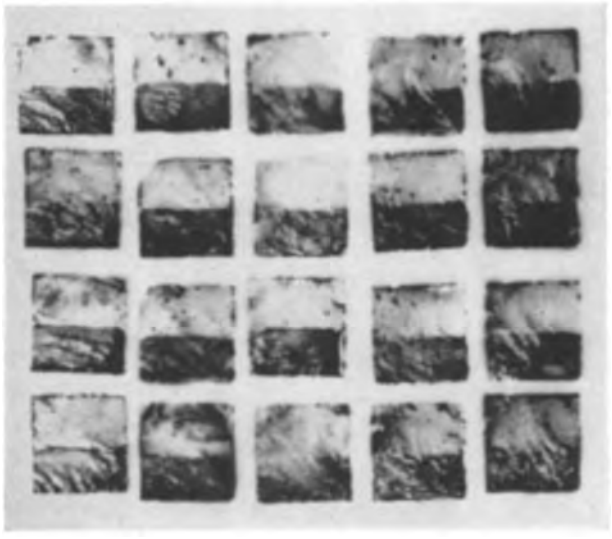

FIG. 1. Co activity pickup on the copper-steel couple. These samples were rinsed in running tap water for varying lengths of time. Starting with right column and proceeding to the left, rinsing times of 30 min, 2.5 hr, 4 hr, 5.5 hr, and 22.5 hr, respectively.

it is adjacent to an area which represents an acknowledged worked area. The activity associated with the filmed area would obscure the effects of the worked surfaces. When abrasion is carried out in air the pickup of the tracer is enhanced. While the greater amount of activity is associated with the filmed area the worked area is also quite distinct.

EXAMINATION OF GALVANIC COUPLES

Several cases were considered that would represent obvious galvanic couples. The object was to compare the behavior of galvanic couples with the behavior of those systems characterized by adsorption on surface films.

A Cu-Fe couple was prepared by the displacement plating of Cu from copper chloride solution. The steel[4] panel (2.5 cm x 2.5 cm x 0.050 cm) after being annealed and pickled was painted with a solution of paraffin in benzene so that only one half of one side was left exposed. This exposed area was covered with a few drops of a solution of copper chloride (5 g of $CuCl_2 \cdot 2H_2O$ dissolved in 100 ml of concentrated HCl) and allowed to stand for a few minutes. After rinsing the strip in water the wax was removed by standing first in benzene and then in acetone. The sample was allowed to stand in NaCl solution (1 g NaCl/100 ml), rinsed, and immersed in the cobalt tracer solution. Autoradiographs in Fig. 1 illustrate the cathode-anode relationship of this couple. In this particular experiment four samples were taken for each of five different rinsing periods. Retention of activity during rinsing is described below. This couple is characterized by the deposition of a high activity which is associated with the Cu member of the cell.

In a similar manner a Cu-Al cell was prepared. The

[4] This was AISI Type 1020 Analysis; Carbon = 0.12%; Mn—0.30–0.60%.

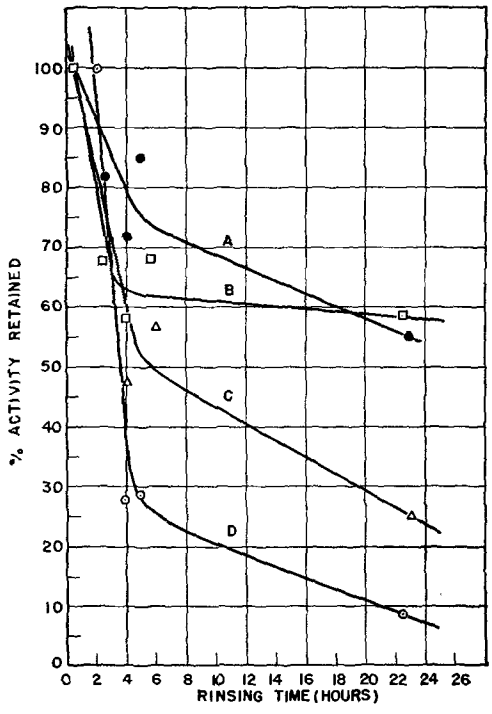

FIG. 2. Effect of continual rinsing on retention of activity. A = Cu plated on Al; B = Cu plated on steel; C = thin copper sulfide film; D = thick copper sulfide film.

autoradiograph showed that while most of the activity was concentrated on the cathode copper area there was some distributed over the rest of the surface. Distribution was not as clear cut as in the Fe-Cu case. The experiments did, however, demonstrate the ability of the technique to outline the areas of different potential as has been described by other investigators.

It is well known that inert matter, as silica residing on a surface, sets up a concentration cell which leads to corrosion. An attempt was made to simulate this sort of cell. A colloidal sol was prepared by suspending very finely divided silica in water, spreading the colloidal material of Fe, Cu, and Al and allowing to dry over night. The strips were allowed to stand in NaCl solution for 1 hr and then transferred to the Co tracer.

From autoradiographs prepared it was evident that metal surfaces acted differently. It was noticed that the silica on Cu and steel attracts the Co and thus would be termed the cathode area. On Al the Co was attached to the Al surface not covered by the silica. The area covered was relatively free of activity. If the period of activation in NaCl solution is reduced from 60 to 15 min slightly different results are obtained. With Al the activity is still associated with the metal proper rather than the silica. However, upon examining the steel and copper samples subjected to a shorter exposure to chloride solution it was observed that the activity resided with the metal surface rather than the silica.

The effect of silica on influencing the direction in which the Co goes is difficult to interpret, but it is apparent that the technique can outline areas of different potential on the metal surface.

Retention of Activity as Influenced by Method of Deposition

During the preliminary work with this technique it was observed that the time of rinsing following the Co immersion step required control if reproducible results were to be obtained. Previous workers on exchange reactions indicated that there was no appreciable drop in activity if the rinsing was longer than a few minutes. The degree of retention of Co would suggest the mechanism by which Co was attached to the surface. If Co ions were adsorbed, one would expect desorption with continued rinsing. On the other hand, electrodeposited Co would be tightly bound and moreover should be electrochemically protected from dissolution by the anodic elements immediately adjacent.

In the present work, the activity associated with the copper sulfide film has been termed "adsorbed." The greater part of that associated with systems like the Cu-Al couple has been termed "electrolytically deposited." Loss of activity with continual rinsing is depicted in Fig. 2. In these experiments a large number of samples were taken and groups of six rinsed for various times. Thus, the points on the curve represent the behavior of separate groups of samples rather than the same group carried through the whole experiment. This explains why apparently the activity does not always drop continually with continued rinsing. The copper-steel couple and the Al-Cu couple lose about 30–40% of their activity within the first few hours. After 24-hr rinsing time 40–50% has been lost.

About 60–70% of the activity associated with the copper sulfide film is lost in the first few hours. After 24-hr rinsing, as much as 92% may be removed by running water. In cases wherein the activity was slight at the start the retained activity may be 25% after the 24-hr rinsing time. Retention of active Co is apparently a means of differentiating between the two mechanisms involved in the collection of the activity on the surface.

Discussion and Conclusions

These experiments have demonstrated that the tracer Co may be picked up from solution by two processes: (*a*) adsorption, and (*b*) electrolytic deposition.

Both mechanisms probably are involved to some degree as discussed by King (2). When porous films lacking in density are studied, the major contribution is from adsorbed Co. With galvanic couples, as for example, the Fe-Cu couple, the electrolytic effect predominates. It appears that the adsorption may be either on the metal or on the oxide film. The two types of deposition are distinguished by the higher intensity and the greater retention associated with electrolytically deposited Co. Most of the adsorbed Co may be removed from the metal by prolonged rinsing.

It has been demonstrated that when a surface film exists along side of a worked area on a given sample the greater portion of the activity may be attracted to the filmed area. This may not be entirely a competitive effect as the activity associated with the worked area may not be great. It had been pointed out by previous investigators that polished or abraded surfaces picked up the radioactive tracer much more readily than annealed or unworked surfaces. Some of this pickup is contributed by the oxide film developed by polishing in air.

Various oxide films act in a different manner insofar as the collection of the Co tracer is concerned. Films of the nature of copper oxide and copper sulfide adsorb a great deal of cobalt whereas films like the oxide on aluminum produced by anodizing or the oxide of stainless steel adsorb only a negligible amount.

When a particular mechanism is under investigation consideration must be given to this adsorption by oxide films. For example, in the pitting of Al one of the products situated near the cathode products is the hydrated oxide of Al. It seems likely that Co is attracted to the site not only because of the cathode nature of the site but also because of the adsorptive ability of the hydrated oxide.

The attraction of ions from solution to the oxide films covering a surface would appear to have a broader significance from the standpoint of corrosion mechanisms. If the oxide films represent sites whereon clusters of cations may be accumulated, it is logical to conclude that oxide films of varying thickness represent in themselves the sites for concentration cells on metal surface.

Acknowledgment

The authors wish to express their appreciation to Dr. A. H. Bushey, Dr. H. R. Schmidt, and Mr. M. B. Leboeuf for their suggestions and stimulating discussion of this radiochemical technique.

Manuscript received December 22, 1955.
Any discussion of this paper will appear in a Discussion Section to be published in the June 1957 Journal.

REFERENCES

1. M. Haissinsky, *Z. Elektrochem.*, **59**, 750 (1955).
2. C. V. King, *Ann. N. Y. Acad. Sci.*, **58**, 910 (1954).
3. M. T. Simnad, "Properties of Metallic Surfaces," p. 23, Institute of Metals, London (1953).
4. P. M. Aziz, *This Journal*, **101**, 120 (1954).
5. H. Yagoda, "Radioactive Measurements with Nuclear Emulsions," John Wiley & Sons, Inc., New York (1949).
6. G. C. Towe, H. J. Gomberg, and J. W. Freeman, *Nucleonics*, **13**, 54 (1955).

A Mechanism for the Anodic Dissolution of Magnesium

J. H. GREENBLATT

Naval Research Establishment, Dartmouth, Nova Scotia

ABSTRACT

Magnesium anodes were electrolyzed in 3% NaCl solution in a simple electrolysis cell. Mg in the anolyte, Mg in the corrosion product, total hydrogen evolved, and weight loss were determined. It was found that the quantities soluble Mg, insoluble Mg, Mg calculated from the current passed were in approximate one to one relationship with each other and all of these quantities are roughly half of the total weight loss. Hydrogen evolved was always slightly less than the soluble and insoluble Mg. These facts are explained and integrated into existing knowledge of the behavior of Mg anodes by postulating that Mg dissolves in the solution investigated mainly as a univalent ion followed by reaction of this univalent ion with water.

The problem of hydrogen evolution at a magnesium anode during electrolysis is an old one with literature references dating back to the work of Beetz (1) and Elsoesser (2). Recently, the problem has been reconsidered by Petty, Davidson, and Kleinberg (3), who measured the apparent valence of Mg anodes in a variety of aqueous electrolytes and found that their results could be explained by postulating the presence of both uni- and divalent Mg during electrolysis at a Mg anode. Hydrogen evolution was explained as being a reduction product of the reaction between univalent Mg ions and water. Other substances, such as $KMnO_4$, ClO_3^-, introduced into the anolyte compartment of their apparatus were also reduced, and in a recent paper by Kleinberg and co-workers (4), where measurements of apparent valence in organic liquids are described, reductions of such test liquids that were electron acceptors were obtained.

The existence of univalent Mg has been postulated at various times, and in the earlier work (1, 2, 5) the continued evolution of hydrogen after current shut-off, and the ability of the grayish-black corrosion product that had accumulated on the Mg to evolve hydrogen from water were ascribed to the existence of a suboxide in the corrosion product. However, all efforts to isolate and identify such a compound failed. More recently, Faivre and Michel (6) have shown by x-ray analysis that the grayish product formed on oxidation of Mg in humid air is $Mg(OH)_2$ with Mg atoms inserted in the lattice. Brouchere (7) and Huber (8) claim that x-ray and electron diffraction of corrosion films on Mg indicate that the films are mainly MgO with Mg atoms in the lattice.

Insofar as none of the work to date has given a clear picture of the mechanism of solution of Mg at an anode, the work described was undertaken with the purpose of attempting to obtain the necessary information to accomplish this.

EXPERIMENTAL

Mg of 99.92% purity with an iron content of 0.0001–0.0005% was used as the anode material. Anodes were of varying lengths and were 16.5 mm in diameter, except for a short portion that was machined slightly smaller to fit inside the untapered portion of a 19/38 ground joint. Before use, the anodes were cleaned by immersion in 5% HNO_3 and then inserted in the apparatus shown in Fig. 1.

All experiments were conducted in 3% reagent grade NaCl solutions. A silver-silver chloride cathode was used, and the driving voltages, in all except the high current density experiments, was that of the magnesium, silver-silver chloride couple. For the high current density experiments, an impressed d-c source was used. The procedure followed was to electrolyze at constant current, collecting the gas during electrolysis. At the end of the electrolysis, current was shut off, the cathode removed, and the electrolyte quickly run out. After a quick rinse, the electrolysis vessel was filled with hot 5% chromic acid containing 0.5% silver chromate. This cleaning solution was left in contact with the Mg cylinder for 10 min, after which it was run out, the electrolysis vessel was rinsed, and the rinsings were added to the chromic acid. All gas evolved during cleaning of the Mg cylinder was also collected. After cleaning, the Mg cylinder was removed from the apparatus, washed in distilled water, dried, and weighed.

The electrolysis solution was filtered to remove any solid particles of corrosion product that had spalled off the cylinder during electrolysis, and Mg was determined in the filtrate by the standard oxime method. The solid particles of corrosion product on the filter were dissolved by washing with a portion of the hot chromic acid cleaning solution. The washings were then combined with the main portion of the chromic acid cleaning solution and the Mg was separated from chromium by precipitation in excess NaOH after first oxidizing with bromine water. The precipitated $Mg(OH)_2$ was then redissolved in acid, and titrated with versene after buffering. The collected gases were analyzed for hydrogen by absorption by hot cupric oxide after first analyzing for oxygen by absorption in alkaline pyrogallate. Blanks run by immersing uncorroded Mg cylinders in chromic acid cleaning solution gave average weight losses of 3 mg.

The effect of surface area, current density, and temperature on the anodic dissolution of Mg were studied. The effect of varying anode area was studied only at room temperature and anodes of 16.5 mm diameter and

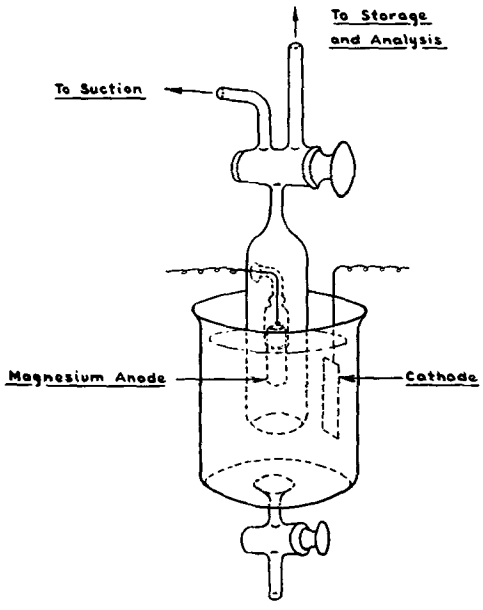

FIG. 1. Sketch of electrolysis cell

exposed lengths of 51, 38, and 25 mm were used. At all other temperatures, anodes 51 mm long were used, and, in the set of experiments with varying current densities, anodes 25 mm long were used. The volume of solution in the electrolysis vessel was the same in all cases, approximately 500 ml. In the usual experiments, the current density was 0.0035 amp/cm^2, except for those shown in Fig. 3, where the area was varied, and for some of the experiments in Fig. 2 at 75°C where current densities of 0.0017, 0.0023, and 0.0026 amp/cm^2 were also used. In the experiments with varying current density, this variable was varied over the range 0.0196–0.369 amp/cm^2, the total number of coulombs during each experiment being kept constant.

RESULTS

The data obtained are shown graphically in Fig. 2 and in Table I. Examination of the data obtained at room temperature shows that the quantities: Mg soluble in the electrolyte, insoluble Mg retained on the surface of the test cylinder as corrosion product, and the magnesium calculated from the current passed (coulombs $\times$ 12)/F bear an approximate 1:1 ratio to each other. Moreover, all these quantities are approximately half the total weight loss. These relationships persist over the

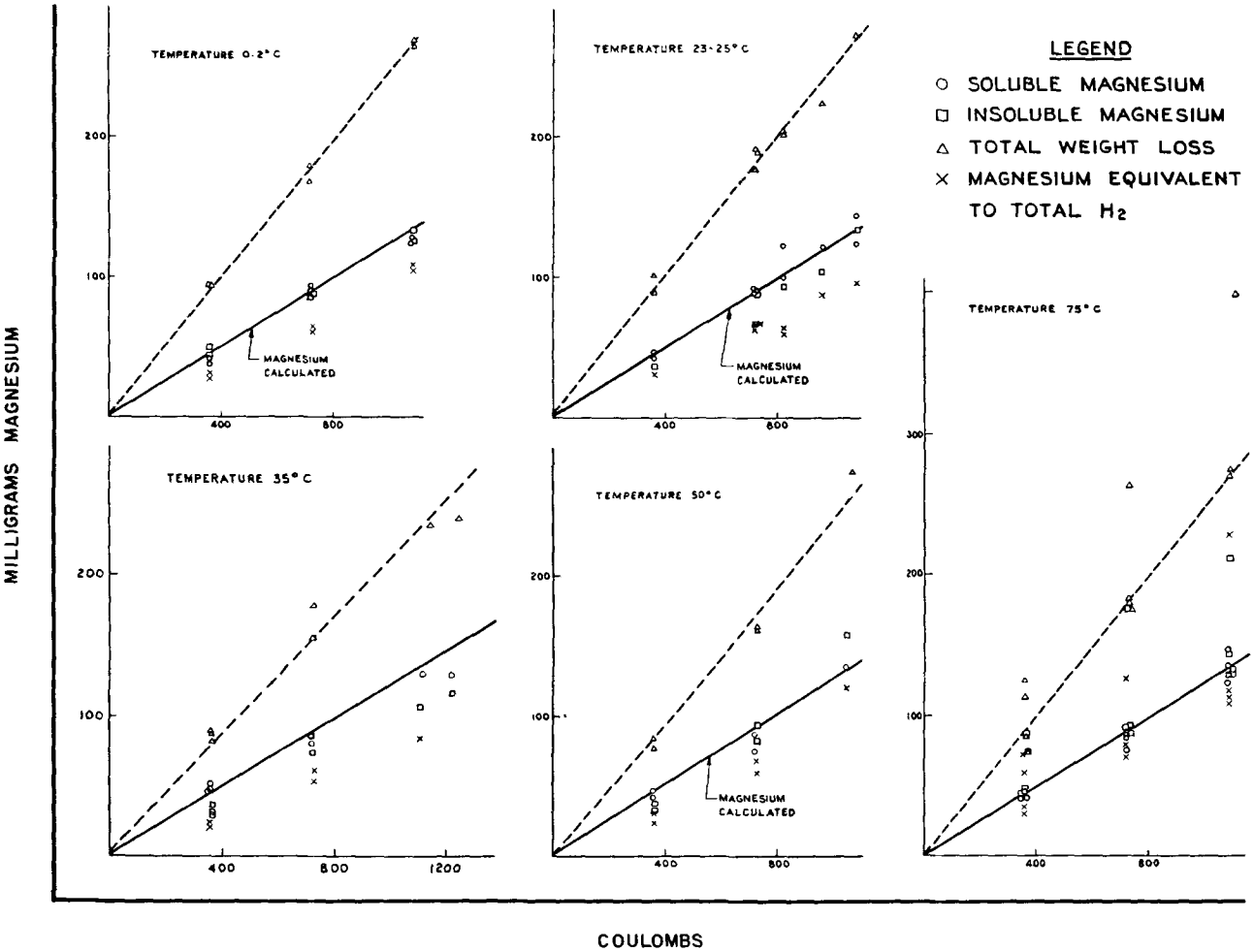

FIG. 2. Electrolysis data obtained over the temperature range 0°–75°C

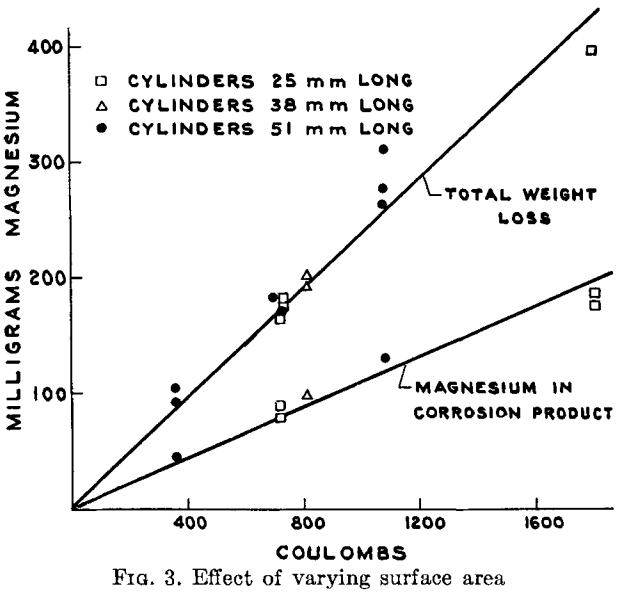

FIG. 3. Effect of varying surface area

TABLE I. *Effect of varying current density*

Current density (amp/cm²)	Soluble Mg (mg)	Insoluble Mg (mg)	Magnesium equivalent to H_2 (Evolved mg)	Total weight loss (mg)
0.0196	553	413	365	978
0.0196	542	419	358	976
0.0922	506	309	276	831
0.0922	475	354	278	825
0.102	—	—	314	891
0.102	—	—	311	846
0.115	529	365	299	892
0.148	520	324	292	849
0.184	—	—	321	897
0.184	—	—	314	906
0.278	—	—	318	902
0.278	—	—	321	910
0.369	—	—	320	901
0.369	—	—	312	895

Total quantity of electricity = 4500 coulombs in all experiments.

range of temperatures 0°–75°C as seen from the data. At 75°C, however, it can be seen that there are scattered experiments in which the insoluble Mg is considerably greater than both the soluble and calculated Mg. Where this occurs, it can also be seen that the total weight loss and hydrogen evolved are correspondingly greater than in so-called normal experiments. The total hydrogen evolved expressed in milligrams of equivalent Mg is also plotted. This is somewhat lower than the quantities soluble Mg, insoluble Mg, and calculated Mg, except for the instance already mentioned at 75°C where amounts of hydrogen greater than one-half the total weight loss were obtained.

It can also be seen from the graphs under consideration that the quantities soluble Mg, insoluble Mg, total hydrogen evolved, and total weight loss give reasonable linear relationship with the number of coulombs passed. This relationship persisted in spite of variations in surface area, as can be seen from Fig. 3; also, the data of Fig. 2 at 75°C includes variations in current density at constant surface area and quantity of electricity. These

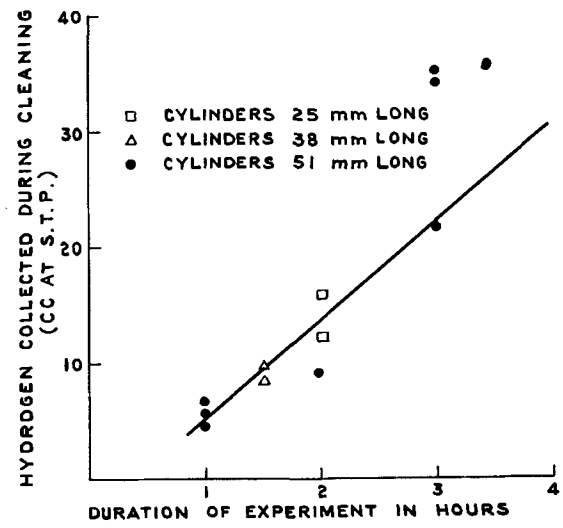

FIG. 4. Relation between hydrogen evolved during cleaning and time of experiment.

variations were made when scattered unusual weight losses and quantities of hydrogen evolved were obtained. None of these experiments with slight changes in current density ($\frac{1}{2}$, $\frac{2}{3}$, $\frac{3}{4}$ normal) showed abnormal behavior, and they are all included in the graph for 75°C. This linearity could be evidence that soluble Mg, insoluble Mg, total hydrogen evolved depend on a primary current carrying reaction.

The effect of varying current density is shown in Table I. There is an indication of a small decrease in weight loss, insoluble Mg, and total hydrogen evolved, but decreases are small and do not indicate any great change of mechanism. Petty, Davidson, and Kleinberg (3) report similar results in their study of the variation of apparent valance with current density in dilute solutions.

Total hydrogen was obtained by adding the quantities collected during cleaning and during electrolysis. At 0° and at room temperatures, the amount of hydrogen evolved during cleaning was about $\frac{1}{3}$ the amount obtained during electrolysis. As the temperature increased, the amount obtained decreased, and at high temperatures practically none was obtained. Also, in experiments with varying current densities, where a large number of coulombs (4500) were passed, practically no hydrogen was obtained during cleaning. At room temperatures, the hydrogen obtained during cleaning was found to be linearly dependent on the time during which current had been passing, as can be seen from Fig. 4. Deviation from linearity at the longer times occurred due to spalling off of the corrosion product as it thickens with the fragments lost falling outside the gas collecting bell. This explanation also accounts for the small amounts of hydrogen obtained on cleaning in the experiments with varying current densities, since in these cases the experiments were of long duration and most of the insoluble Mg spalled off the cylinders and fell outside the gas collecting bell.

A few blank experiments were made in which Mg cylinders were allowed to remain in the electrolyte without any current being passed. The amount of hydrogen

evolved at 75° was equivalent to 3 mg of Mg during a 2-hr period. At room temperature, less than this amount was recovered in a 24-hr period.

Discussion of Results

The significant fact from the data given is that the quantities soluble Mg, insoluble Mg, and calculated Mg all bear an approximate 1:1 relationship to each other and are all approximately equal to half the total weight loss. This relationship persists over a range of temperature, current density, and surface area. To ascribe the 50% efficiencies of Mg anodes to self-corrosion requires acceptance of the fact that the self-corrosion reaction, which does not occur when the anode remains uncoupled in the electrolyte, is by fortuitous circumstances proceeding at the same rate as the current carrying reaction, and is linked to the latter in such a way that this constancy is maintained through all conditions studied. A more satisfactory explanation from the kinetic point of view would be to postulate a series of consecutive reactions all dependent on the current carrying reaction as the primary step. The following series of reactions are proposed to explain the data obtained.

$$Mg \rightarrow Mg^{+} + e \qquad \text{(I)}$$

$$2Mg^{+} + H_2O \rightarrow [Mg^{+}O_{H_2}^{Mg^{+}}] \rightarrow MgO + Mg^{++} + H_2 \qquad \text{(II)}$$

$$2Mg^{+} \rightarrow Mg^{++} + Mg \qquad \text{(III)}$$

$$Mg \rightarrow Mg^{++} + 2e \qquad \text{(IV)}$$

$$Mg + H_2O \rightarrow MgO\ H_2 \qquad \text{(V)}$$

The above reaction scheme is in accord with all the data obtained. Reaction (I), followed by reaction (II), would lead to the one to one ratio of soluble to insoluble Mg and would also give values of soluble, insoluble, and calculated Mg that are half the weight loss. Reaction (III) would account for the accumulation of Mg in the MgO lattice with time, and this Mg when dissolved in the chromic acid cleaning bath would account for the hydrogen evolved there. Reaction (II) also predicts one mole of hydrogen for each mole of soluble or insoluble Mg. Examination of the data shows that the amount of hydrogen evolved is considerably less than that predicted. There are several reasons for this discrepancy. The occurrence of (IV) to any extent would decrease the amount of hydrogen produced. The occurrence of (III) should not do so, as the removal of Mg^{+} from the system would be compensated for by the production of hydrogen from the dissolution during cleaning of the Mg trapped in the corrosion product. Loss of hydrogen could occur during the changing of solutions in the electrolysis vessel, since hydrogen is evolved continuously from the wet Mg surface during this operation.

Reaction (I) is favored over reaction (IV) on energy consideration (9, 10), as the heat of hydration of Mg is 33 kcal less than the ionization potential of Mg^{++} (g). However, the relative occurrence of (I) and (IV) can be changed by factors which influence this energy difference, such as electrolyte and concentration, as shown by the variation of apparent valence with electrolyte and concentration reported by Kleinberg and co-workers (3) and by the earlier work of Beetz (1) and Turrentine (5). Beetz found that the sum of the quantities: Mg equivalent to hydrogen evolved and the Mg calculated from the current passed were sometimes less than the total weight loss, indicating that (IV) was occurring to some extent. With sodium sulfate solutions, Turrentine found that the ratio of Mg equivalent to hydrogen evolved at the anode to Mg calculated from the current passed varied from ½ to 1, indicating that (IV) could occur to an appreciable extent. Robinson (11) has reported similar variations of Mg anode efficiencies while Bodforss (12), on the basis of potential measurements over a range of *p*H's, postulates (I) and (IV) co-existing over the range he investigated, with (IV) existing almost exclusively at high *p*H's.

Self-corrosion, which does not appear to any great extent at low temperatures, appeared significantly in scattered cases at 75°C. The self-corrosion reaction (V) is written as shown because, where self-corrosion occurred, the excess Mg appeared as insoluble Mg and such a reaction is analogous to that postulated by Lepin, Tetere, and Schmitt (13) for the reaction between colloidal aluminum and water. Where self-corrosion occurred, the amount of hydrogen evolved was always large and both the hydrogen evolved and the insoluble Mg were greater than the calculated weight loss, when (V) occurred to a significant extent.

The occurrence of (IV) to any extent should lead to values of soluble Mg greater than insoluble. Examination of the data shows many cases where this is so, but no unequivocal conclusions can be drawn from the data. In experiments of long duration, there is more definite evidence that the amount of soluble Mg obtained is greater than the insoluble Mg. Also, the ratio of calculated weight loss to total weight loss, i.e., the efficiency, is greater than half. Both these factors indicate occurrence of (IV) to some extent and this occurrence of (IV) may be due to the fact that the solution close to the anode surface in these experiments is separated from the bulk of the electrolyte by a reasonably thick layer of corrosion product on the anode, and thus the anode surface may be in contact with an electrolyte differing from that in the bulk of the solution for a longer time than in the shorter experiments. As electrolyte composition and concentration influences the ratio of (I) to (IV), it is possible that a change in the relative amount of reactions (I) and (IV) can occur under the conditions described.

The occurrence of (III) also explains the linear dependence of the hydrogen evolved during the cleaning on duration of current passage. One would expect that the number of Mg atoms trapped in the corrosion product lattice would increase with duration of the experiment.

There is room for considerable speculation as to the nature of the reaction complex in (II). Since the zone from which gas bubbles come was extremely narrow, it is

likely that (II) occurs at the surface between an adsorbed water molecule and univalent Mg ions.

Conclusions

Study of the electrolysis of magnesium in 3% NaCl solutions shows that the data obtained can be explained and integrated into existing knowledge of the behavior of Mg as an anode by postulating that Mg dissolves predominately as a univalent ion and then the univalent ion reduces water forming an insoluble oxide film, divalent Mg, and hydrogen.

Acknowledgment

The author wishes to acknowledge permission of the Defence Research Board to publish. The work described was carried out as part of Defence Research Board Project D-12-75-10-21.

Manuscript received November 7, 1955.
Any discussion of this paper will appear in a Discussion Section to be published in the June 1957 Journal.

References

1. W. Beetz, *Pogg Ann*, **27**, 115 (1866); *Phil. Mag.*, **4**, C32, 269 (1866); *Ber.*, **10**, 118 (1877).
2. E. Elsoesser, *Ber.*, **9**, 1818 (1876).
3. R. L. Petty, A. W. Davidson, and J. Kleinberg, *J. Am. Chem. Soc.*, **76**, 363 (1954).
4. M. D. Rausch, W. E. McEwen, and J. Kleinberg, *ibid.*, **77**, 2093 (1955).
5. J. W. Turrentine, *J. Phys. Chem.*, **12**, 448 (1908).
6. R. Faivre and A. Michel, *Compt. rend.*, **208**, 1008 (1939).
7. C. Brouchere, *J. Inst. Metals*, **71**, 131 (1943).
8. K. Huber and H. Fluckiger, Comte International de Thermodynamique and de Cinetique Electro Chemiques Comptes Rendus, p. 123 (1951).
9. H. J. Emeleus and J. S. Anderson, "Modern Aspects of Inorganic Chemistry," pp. 43 and 46, Routledge & Kegan Paul, London (1952).
10. J. O'M. Bockris, "Modern Aspects of Electro Chemistry," p. 52, Butterworths, London (1954).
11. H. A. Robinson, *Trans. Electrochem. Soc.*, **90**, 49 (1946).
12. S. Bodforss, *Z. physik. Chem.*, **A153**, 101 (1931); *ibid.*, **124**, 81 (1926).
13. L. Lepin, A. Tetere, and A. Schmitt, *Doklady Akad. Nauk SSSR*, **88**, 871 (1953).

Properties of Paper Made from Glass Flakes

T. D. Callinan and R. T. Lucas

U. S. Naval Research Laboratory, Washington, D. C.

ABSTRACT

The preparation and properties of paper made from glass flakes are described. The electrical properties of a capacitor made from this paper are presented. Glass flake paper was impregnated with varnishes and became mechanically strong and water resistant.

Glass is now available commercially in the form of transparent colorless flakes. The flakes vary in size and shape but average 0.25 in. x 0.25 in. x 0.0003 in. A number of patents have described the process for manufacturing such flakes (1–3). Each entails the formation of a thin film of molten glass which, on cooling rapidly, shatters into fine pellicles.

The glass flakes employed in this work are described by the manufacturer as being a borosilicate glass, Type "E" (10% boron oxide, 54% silicon dioxide, 16% calcium oxide, 16% aluminum oxide, and 4% sodium and potassium oxide), which softens at 840°C. The density of such glass is 2.56 g/cm^3; refractive index, 1.549; tensile strength, 200,000 psi, and modulus of elasticity 11 $\times$ 10^6 psi. The material has been suggested as a filler for inorganic plastics and molding compounds. The electrical properties of such glass have been reported (4).

The preparation and properties of a paper-like product made from these flakes is described. As a class, such paper-like products have been made from flakes other than glass; thus, mica flake has been successfully made into paper and is now commercially available from several sources. The process by which this valuable item is manufactured (5) entails separating the thin leaves of naturally occurring books of mica either mechanically or chemically and depositing the pulp on the rapidly moving wire of a Fourdrinier paper machine.

At present, such a paper can be used in transformers and motors as slot armor, segment insulators, and spacers. By incorporating varnishes and impregnants, these papers can be strengthened enormously to yield laminates and plates. Again, by backing the paper with fabrics, yarns, or cellulose papers, tapes have been produced that have sufficient mechanical strength to permit use as wire and cable insulation.

As part of the continuing interest of this laboratory in inorganic papers (6), laboratory handsheets have been prepared from glass flakes. While machine runs yielding continuous sheets have not been possible because no such facilities are available here, it is thought that data summarized in this article suggest the value of industrial trials.

Laboratory Handsheet Preparation

Handsheets were prepared by dispersing 3 g of glass flakes in 500 ml of water (*p*H 3.5), with vigorous agitation in a Waring blendor for 30 sec. H_2SO_4 was used to adjust the *p*H. The flakes dispersed readily and remained sus-

TABLE I. *Properties of 100% glass-flake paper*

Physical		Electrical	
Appearance: Transparent sheet		Dielectric constant	
Glass content %	100	(a) 60 cps	1.45
Binder, %	0	(b) 1000 cps	1.36
Thickness, in.	0.010	(c) 10,000 cps	1.35
Tensile strength, psi	86	Power factor (%)	
Density, g/cc	0.75	(a) 60 cps	0.68
Mullen burst number	1	(b) 1000 cps	0.66
Elmendorf tear, lb	20	(c) 10,000 cps	0.66
Voids, %	61	Dielectric loss factor	
Uniformity	Very high	(a) 60 cps	0.0098
Dirt count	0	(b) 1000 cps	0.0090
Basis weight (25 × 40–500)	150	(c) 10,000 cps	0.0089
		Volume resistivity 2×10^{11} ohm-cm	
		Dielectric strength 90 v/mil	
		Conducting particles	0

TABLE II. *Properties of varnish impregnated glass-flake paper*

Characteristics	Alkyd (GE 1202)	Phenolic (DuPont 8995)	Polysiloxane (D-C 993)
Physical			
Color	Tan	Brown	Colorless
Transparency, %	85	80	95
Thickness, mils	10.1	9.0	9.4
Build, mils	1.0	1.0	0.9
Tensile strength, psi	900	1800	700
Density, g/cc	1.14	1.16	1.74
Resin content, %	39	40	55
Fold strength, psi	0	0	0
H_2O absorption, %	0.4	1.5	0.0
Electrical			
Dielectric constant			
(a) 60 cps	2.45	1.93	1.91
(b) 1000 cps	2.32	1.70	1.82
(c) 10,000 cps	2.30	1.69	1.80
Power factor, %			
(a) 60 cps	1.99	1.26	0.96
(b) 1000 cps	1.70	0.36	0.24
(c) 10,000 cps	1.69	0.24	0.20
Volume resistivity, ohm-cm	10^{13}	10^{13}	10^{13}
Dielectric strength, v/mil	100	120	105

pended under gentle agitation. Depending on the time and degree of beating, a finer and more dispersed pulp was secured; the number of larger sized flakes was necessarily reduced.

The slurry was then added to a standard sheet mold and the wet web couched from the 200-mesh screen. Drainage time was 42 sec. The white water was clear enough to show the filtering action of the web. A uniform transparent sheet approximately 10 mils thick was obtained. Reflected light gave the sheet a silvery sheen.

The properties found are listed in Table I. The sheet was uniform, porous, brittle, and transparent. In thinner sheets it was more flexible, albeit weaker mechanically. Without a binder it would be difficult to handle in common production techniques, although the product was self-supporting. It possessed a finite although extremely low tear strength. It is thought that this might be associated with the thickness of the presently available flakes.

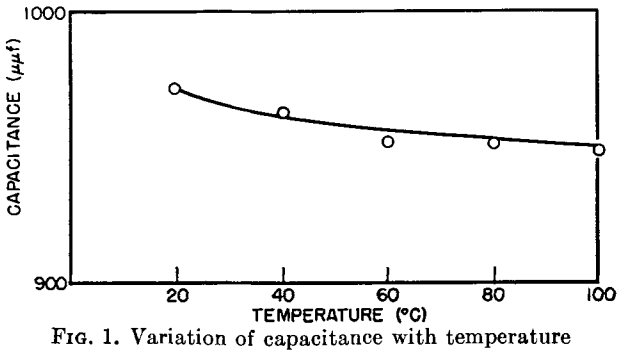

FIG. 1. Variation of capacitance with temperature

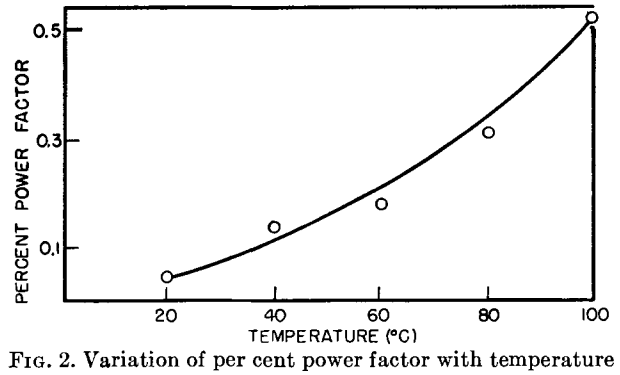

FIG. 2. Variation of per cent power factor with temperature

Thus, thin flakes (less than 4μ) might be expected to yield both stronger and more flexible glass-flake papers.

IMPREGNATED GLASS-FLAKE PAPER

Three varnishes were studied as impregnants for glass-flake paper and the properties obtained are listed in Table II. In all cases the paper was found to saturate readily and to yield, on drying, mechanically strong, water resistant, transparent dielectric sheets. No effort was made to produce either the most highly saturated item or the highest in strength. Requirements vary so widely that each problem would require its discrete solution. From the data collected, the practicing engineer may judge the degree of saturation to satisfy his own need.

In these studies an alkyd varnish (GE 1202), an enamel used in motor insulation (Du Pont 8995 Formvar), and a silicone (Dow-Corning 993) were employed. A handsheet of glass-flake paper was dipped into a varnish and allowed to remain there (1 min) until no air bubbles or discontinuities were visible. Each impregnated sample was then permitted to air dry for 16 hr, after which it was subjected to a temperature of 125°C for 8 hr. At this point the alkyd-impregnated paper and the formvar-impregnated paper were tested. The silicone was heated 16 hr longer at 200°C to effect cure before it was tested.

All samples were found to have increased substantially in tensile strength, density, dielectric constant, and water resistance. Differences in the degree of impregnation are attributable to the viscosity of the impregnating varnishes and the techniques employed, rather than to any specific absorptivity characteristic of the glass-flake paper. The dielectric constants and the dielectric loss factors of the impregnated papers are seen to be low; greater resin content might be expected to result in higher values of both.

Glass-Flake Paper Capacitor

A capacitor was prepared by sandwiching a piece of glass-flake paper (4 in. x 6 in. x 0.010 in.) between two aluminum electrodes (3 in. x 3 in.) held together by sheet glass clamped securely. After drying at 210°C for 24 hr, the specimen was evacuated and impregnated with silicone oil (GE SF 81/40). The capacitor was found to have the characteristics shown in Fig. 1 and 2. While glass-flake paper is not now of sufficient quality to permit it being made into tissues (0.0003 in.), the characteristics obtained on the relatively thick specimens suggest the value of studies on developing such items.

Conclusions

From the foregoing tests, it would appear that a useful paper product can be prepared experimentally from glass flakes and that the characteristics of the items justify pilot and mill trials.

Preparation of thinner sheets containing binders deposited *in situ* seems likely from what is common knowledge of this art. It has been proved that mechanically strong and electrically good impregnated structures can be prepared in laboratory equipment; this is probably also true of continuous mill made glass-flake paper.

Tissue paper made from glass flakes, 8 μ in thickness, does not seem feasible; a sheet 0.003 in. thick would consist of flakes stacked only six high. It would appear, however, that when thinner flakes are made available, thinner as well as stronger paper will be practicable.

Manuscript received August 29, 1955. This paper was prepared for delivery before the Cincinnati Meeting, May 1 to 5, 1955.

Any discussion of this paper will appear in a Discussion Section to be published in the June 1957 Journal.

References

1. (To Corning Glass Works) British Pat. 503,369, April 5, 1939.
2. E. H. Wellech and W. C. Weber (to Corning Glass Works), U. S. Pat. 2,251,726, Aug. 5, 1941.
3. E. H. Wellech and W. C. Weber (to Corning Glass Works) U. S. Pat. 2,251,727, Aug. 5, 1941.
4. T. D. Callinan, *This Journal*, **100**, 141 (1952).
5. H. George and L. Metzger, *Rev. gen. elec.*, **59**, 514 (1950).
6. T. D. Callinan, R. T. Lucas, and R. C. Bowers, *Elec. Mfg.*, **48**, 94 (1951).

Permeation of Gases Through Nickel Deposits

I. Determination of the Intrinsic Permeability of Nickel Deposits to Gases

D. T. Ewing[1] and J. Martin Tobin[2]

Michigan State College, East Lansing, Michigan

and

D. Gardner Foulke

Hanson-Van Winkle-Munning Company, Matawan, New Jersey

ABSTRACT

Values have been obtained for permeability constants of Ni electrodeposits to hydrogen and helium with a good degree of reproducibility, the values for 0.0001 in. deposits being of the order of 9 and 6 $\times$ 10^{-8}, respectively. Electrodeposited Ni has a porosity, in contrast to rolled Ni for which no permeability could be measured. Data show that the pores present in sound Ni electrodeposits are extremely small and that flow occurs by molecular streaming, probably at grain boundaries.

Ni electrodeposits subject to corrosive conditions may become perforated to the base metal at certain discrete points. The failure of Ni from the standpoint of protective coating is not wholly understood. A number of theories have been postulated to explain such failures (1) and a number of tests have been devised to measure either the tendency to fail or the porosity of Ni deposits.

Thon and associates discovered a structural porosity or gas permeability characteristic of Ni deposits based on the fact that, when a difference in pressure is established across a detached deposit, gas atoms or molecules flow through these "pores" or "capillaries" which extend through the deposit. Difficulty in obtaining reproducible results by this method (2) led to attempts to develop other methods, such as the passage of light rays or low energy particles, to measure the porosity of Ni deposits.

The procedure used by the authors to study this characteristic of Ni electrodeposits is similar in most respects to that used by Thon with certain modifications which have resulted in highly reproducible gas permeability data.

[1] Deceased.

[2] Present address: General Electric Co., Richland, Wash.

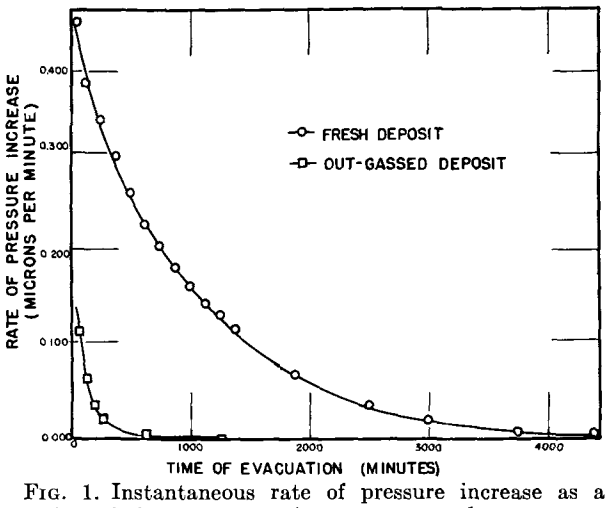

FIG. 1. Instantaneous rate of pressure increase as a function of time of evacuation at constant low pressure.

The modifications fall into two categories. Certain correctable errors were reduced to small reproducible values by improvements in technique such as the use of gases with constant moisture content, controlled out-gassing of the apparatus, and vacuum out-gassing of the foils. Second, a greater degree of reproducibility from sample to sample was attained by careful selection of samples, even though all were prepared and plated with great care.

METHOD

The apparatus and method used were in principle the same as those already described by Thon (3). For most of the permeation measurements, Ni deposits were produced on a passive, buffed Ni base metal from which they were readily detached.

Ni deposits were prepared under controlled conditions of bath composition, temperature, current density, etc. They were then cut through to the base metal and detached. The foil was tested for "photographable" pores according to the procedure described by Ogburn (2). Deposits which were carefully prepared showed no photographable pores. When an occasional photographable pore was detected, however, that part of the deposit was not used for the permeability test.

The mean thickness of the deposit was estimated from the area of the deposit sample (a circle of $\frac{5}{8}$ in. diameter) and the weight of the sample as determined on a semimicro balance. The density of the deposit was assumed to be 8.90 g/cm^3.

Six circular disk samples were cut from each deposit panel and numbered according to a definite pattern. Deposit samples were then examined under a low power microscope, using transmitted light, as a further precaution against using a sample with a gross defect.

Ni deposits studied were found to be relatively impervious to the flow of gas through the deposit. Consequently, the increase in pressure in the evacuated system on the one side of the deposit which was caused by gas flowing through the deposit was of the same order of magnitude as the increase of pressure in the system caused by other effects. Correction must be made for these other effects in order to obtain the rate of permeation of gas through the deposit.

One effect is the desorption of gases from the walls of the system. This effect was controlled to a large extent by the use of compressed gases, which had a more constant composition than the dry air prepared in the laboratory.

The other effect of importance is the removal of dissolved or occluded gases and vapors from the Ni deposit itself. This effect can be very large for a freshly deposited sample. The amount of gas and vapor in a freshly deposited sample of Ni from a Watts' bath at a *p*H of 2.2 was determined in the following manner. The rate of dissolution of gas was followed as the instantaneous rate of pressure increase per unit of time and recorded as a function of time of evacuation at 25°C under a constant pressure of 1μ. Correction for pressure increase caused by desorption was made by testing a sample treated in the same manner, except that it was previously out-gassed in a vacuum (Fig. 1).

A graph of the instantaneous rate of pressure increase as a function of the time of evacuation at a constant, low pressure is shown in Fig. 2. The area between the two curves was obtained by graphical integration, and is approximately 3.4×10^{-5} atm. From the known volume of the high vacuum side and the temperature, the number of moles of gas can be calculated.

$$n = \frac{PV}{RT}$$

$$= \frac{3.40 \times 10^{-5} \text{ atm} \times 1.45 \text{ liters}}{8.20 \dfrac{\text{liter-atm}}{\text{mole-degree}} \times 298^\circ}$$

$$= 2.02 \times 10^{-8} \text{ moles}$$

A very simple qualitative test to determine the proportion of the pressure indicated by a McLeod gauge which was due to vapor was to cool the capillary tip of the gauge. In the McLeod gauge, the absolute pressure of the gas in the tip of the capillary was approximately equal to the difference in height of the two mercury

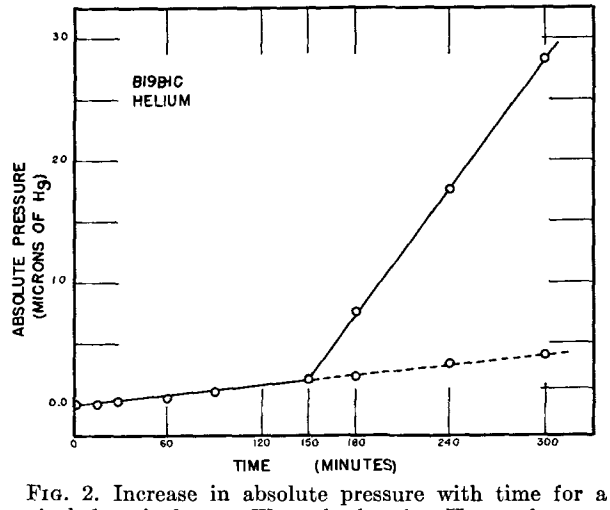

FIG. 2. Increase in absolute pressure with time for a typical deposit from a Watts bath using He as the permeating gas.

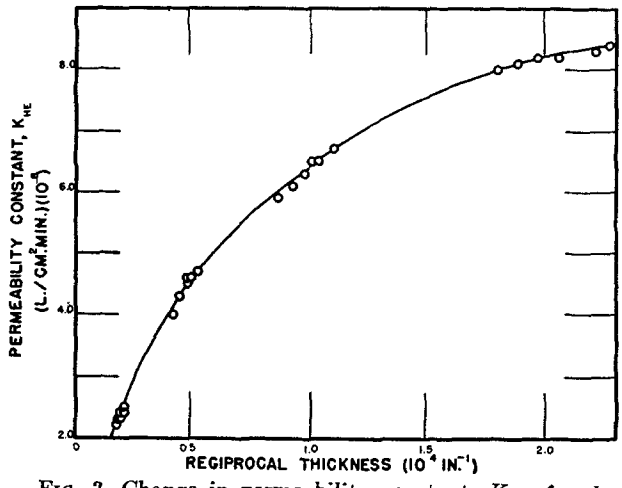

FIG. 3. Change in permeability constant, K_{He}, for deposits from a Watts' bath of varying thicknesses.

columns, and was easily measured in millimeters of mercury of pressure. When the tip was cooled, vapors in the tip condensed and the pressure indicated by the gauge was that caused by the permanent gases. When the tip was cooled after out-gassing a fresh deposit into the vacuum, most of the gas given off by the deposit was found to be a vapor, presumably water vapor.

Assuming the gas to be all water vapor, the per cent of water in the deposit was calculated to be as follows:

$$\% H_2O = \frac{\text{Wt } H_2O}{\text{Wt Ni}} \times 100 = \frac{2.02 \times 10^{-8} \times 18.0 \times 10^2}{4.5 \times 10^{-3}}$$

$$= 0.00809\%$$

Rise in absolute pressure as a function of time was measured by a triple scale McLeod gauge. Adjustments were made for the increase in pressure caused by the two effects previously mentioned in order to obtain the increase in pressure caused by permeation of the gas through the deposit.

Typical data with He as the permeating gas are plotted in Fig. 3. The curve of pressure as a function of time was established over a long period with a vacuum on both sides of the deposit; it was essentially linear in the range which was studied.

When a gas was admitted to the system on one side of the deposit to provide an overpressure, 1 atm in this work, a sharp inflection occurred. The increase in rate, the difference between the slopes of the two curves, was caused by gas permeating through the deposit.

The permeability constant, a measure of the flow rate at a constant overpressure, as defined by Thon, is calculated from the following equation:

$$K = V/F \times 1/P \times \Delta P/\Delta t$$

where K = permeability constant, liter/cm²-min, V = volume of vacuum system on the low pressure side of the deposit (1.45 l), F = area of deposit being measured (0.375 cm²), P = overpressure in mm Hg, ΔP = change in pressure in the evacuated system in mm Hg, and Δt = time interval in minutes.

Thus, if the overpressure is kept constant for a series of foils, the ratio of the permeability constants is the same as the ratio of the rates of diffusion.

RESULTS

Using a Watts' bath at 60°C, a current density of 40 asf at a *p*H of 2.2, four series of six samples of electrodeposits were prepared varying in thickness from 0.00005 in. to 0.0005 in.

Rates of flow of helium and nitrogen through these deposits with 1 atm overpressure were measured. Values of the permeability constant K_{He} were calculated from the rates of flow as shown in Fig. 3. K values for nitrogen were not plotted because the increase in rate of flow for this gas is smaller than the error involved in reading the McLeod gauge.

TABLE I. *Effect of deposit thickness on permeability*

Deposit sample	Mean thickness (in.)	Inverse mean thickness (10^4 in.$^{-1}$)	$K_{H_2} \times 10^8$ (l/cm²min)	$K_{He} \times 10^8$ l/cm²min.
B16A-1A	0.00055	0.18	—	2.2
B16A-1B	0.00051	0.20	—	2.4
B16A-1C	0.00047	0.21	—	2.4
B16A-2A	0.00057	0.18	—	2.3
B16A-2B	0.00053	0.19	—	2.3
B16A-2C	0.00048	0.21	—	2.5
B16B-1A	0.00022	0.45	—	4.3
B16B-1B	0.00021	0.48	—	4.5
B16B-1C	0.00020	0.50	—	4.6
B16B-2A	0.00024	0.42	—	4.0
B16B-2B	0.00021	0.48	—	4.6
B16B-2C	0.00019	0.53	—	4.7
B19A-1A	0.000107	0.93	8.7	6.1
B19A-1B	0.000102	0.98	9.0	6.3
B19A-1C	0.000096	1.04	9.2	6.5
B19A-2A	0.000115	0.87	8.5	5.9
B19A-2B	0.000099	1.01	8.9	6.5
B19A-2C	0.000093	1.08	9.4	6.7
B19B-1A	0.000053	1.88	—	8.1
B19B-1B	0.000049	2.06	—	8.2
B19B-1C	0.000045	2.22	—	8.3
B19B-2A	0.000055	1.80	—	8.0
B19B-2B	0.000051	1.97	—	8.2

TABLE II. *Conformity with Graham's law*

$$\frac{K_{H_2}}{K_{He}} = \sqrt{M_{He}/M_{H_2}}$$

Sample	Ratio K_{He}/K_{H_2}
B30-1A	1.43
B30-1B	1.41
B30-1C	1.43
B30-2A	1.41
B30-2B	1.41
B30-2C	1.50
B19-1A	1.43
B19-1B	1.43
B19-1C	1.41
B19-2A	1.44
B19-2B	1.37
B19-2C	1.40
Mean Value	1.42

It should not be assumed that the foils were impermeable to nitrogen. Instead, the permeability of the foils to nitrogen was consistently less than the sensitivity of the measurement. The correction applied to the data (Fig. 2) depends on the permeating gas. He gas was adsorbed on the walls of the system to a lesser extent than nitrogen and the correction for out-gassing was smaller. As a result, the lower limit for measurement of the permeability constant for both hydrogen and helium was about 8×10^{-9}, while the lower limit for nitrogen was 5×10^{-8}.

The permeability of a substance which is uniform throughout its thickness is inversely proportional to its thickness. Many substances follow this relationship linearly, including metallurgically prepared Ni sheet at high temperature. However, when values for the permeability constant, K_{He}, of electrolytically prepared Ni deposits from the Watts' bath were plotted against the reciprocal thickness, this simple relationship was not obtained (Fig. 3). Apparently, the microstructure of the Ni deposit changed with increasing thickness in such a way that the thicker deposits were less permeable to gases than would be expected.

The rate of flow of hydrogen through the series of deposits approximately 0.0001 in. thick was determined and compared with the rate of flow for helium (Table I).

Comparison of the flow rates for hydrogen and helium with this series shows that the mean value of the ratio of the hydrogen flow rate to the helium flow rate is 1.42 as predicted from Graham's law of diffusion when both permeability constants are obtained at the same temperature and overpressure (Table II).

Agreement of the experimentally measured ratio of flows with that predicted from Graham's law is an indication that the pores are so small that the flow through any one pore occurs by molecular streaming and not by turbulent flow. According to Barrer (4), this type of diffusion takes place when the size of the capillary is less than the mean free path of the gas molecule at that pressure. Since the pore or capillary must also be larger than the diameter of the gas atom or molecule, the pores through which the gas flows in the electrolytic Ni deposit must be of the order of 1–1000 Å (size of atom or molecule and mean free path at entrance of pore at 1 atm pressure) and the flow must occur along grain boundaries, crystal defects, etc. They must also extend through the deposit. The same reasoning would hold for a large number of such pores in parallel.

Effect of the Base Metal

Much of the early work on gas permeability of Ni deposits was done using buffed stainless steel as the base metal. In order to eliminate the possibility that the substitution of Ni for stainless steel would yield deposits of different permeabilities a series of measurements were made on electrodeposits prepared from a 2.2 *p*H Watts' bath with stainless steel as the base metal. Resultant values were nearly identical with values obtained for electrodeposits from the same bath with a buffed Ni base.

Rolled Ni of about the same thickness as the electrodeposits studied were reported impermeable when air was used. This was confirmed on an 0.0001 in. thick rolled Ni sample kindly supplied by August Mendizza of the Bell Telephone Laboratories. No measurable gas flow could be noted for nitrogen, hydrogen, or helium.

Manuscript received December 5, 1955. This paper was prepared for delivery before the Boston Meeting, October 3 to 7, 1954.

Any discussion of this paper will appear in a Discussion Section to be published in the June 1957 JOURNAL.

REFERENCES

1. N. Thon and E. T. Addison, *Monthly Rev. Am. Electroplaters' Soc.*, **34**, 831 (1947).
2. F. Ogburn and A. Benderly, *Plating*, **41**, 61, 169 (1954).
3. N. Thon, *et al.*, *ibid.*, **36**, 362 (1949).
4. R. M. Barrer, "Diffusion In and Through Solids," p. 53–5, Cambridge Press at the University, Cambridge (1951).

New Design of an Electrolytic Cell for the Study of Electroplating Phenomena

ROGER GILMONT

Manostat Corporation, New York, N. Y., and Polytechnic Institute of Brooklyn, Brooklyn, New York

AND

ROBERT F. WALTON

Tube Department, RCA Laboratories, Radio Corporation of America, Harrison, New Jersey

ABSTRACT

By means of the theory of the electropotential, the geometrical shape of a new electroplating cell was deduced in which the current density along the cathode is linear and can be calculated directly from the total current and voltage of the cell.

The new cell consists of a container with two straight sides intersecting at 45° and two curved sides consisting of rectangular hyperbolic cylinders orthogonal to each other, and each in turn orthogonal to one of the straight sides. One of the straight sides and its opposite curved surface are insulators, the other straight side is the cathode while the remaining curved surface is the anode.

The new cell may not only be used for current density studies, but may also be used to determine the total polarization directly from simple measurements on the cell combined with the electrical conductivity of the solution.

The use of the Hull cell (1) for making plating tests is well known. It consists of a small trapezoidal cell in which the two parallel sides are insulators, the third side perpendicular to the parallel sides is the anode, and the fourth side inclined to the parallel sides is the cathode. Because the cathode is inclined, the current density varies along its length. Thus, the cell permits studies to be made of the interrelation between plating characteristics and current density in a single plating experiment.

As simple as the construction of the Hull cell is, the theoretical analysis of the variation of current density along its cathode leads one to an almost insurmountable barrier of higher mathematics. Thus, Kasper (2) pointed out that, although a mathematical solution does exist for the Hull cell, it is of such complexity that it is of no practical use to the electroplater, although to the theoretical mathematician it is a brilliant advance in the theory of the potential. Hull was able to surmount the mathematical difficulties by the simple expedient of empirically determining the current density along the inclined cathode. By a series of ingenious experiments, he measured the current density variation for a number of important electroplating solutions.[1]

Kasper maintained that the proper choice of electrode geometry would yield sufficiently simple mathematical solutions so as to eliminate the need for empirical methods. This paper attempts to show that by proper choice of geometry, it was possible to construct a simple electrolytic cell in which the current density function along the cathode could be predicted by simple mathematics and what is more, this function could be made proportional to distance, that is, linear.

THEORY

The correct geometry was obtained by utilizing one of the fundamental principles of the theory of potential, namely, that the current density lines must be orthogonal to the equipotential surfaces. Many geometrical arrangements were considered until the desired result was obtained. But, for purposes of clarity, it will be shown how the theory of the potential may be used to derive the proper geometrical shapes to give the desired linear relationship of current density along the cathode.

In the following derivation, use is made of the four basic conditions as defined by Kasper (2):

1. The electrolyte obeys Ohm's law, namely, that the rate of dissipation of potential energy (current) is proportional to the potential energy gradient (voltage change).
2. The electrolyte is homogeneous, that is, electrically isotropic.
3. Voltage change along an electrode is negligible, so that it may be considered as an equipotential surface.

[1] The senior author of this paper had the good fortune to make the acquaintance of Kasper at the National Bureau of Standards in Washington, D. C., where both were employed in the Chemistry Division. At that time Kasper was engaged in his studies of the theory of the potential in relation to electroplating. His main thesis was that electroplaters were seriously neglecting the application of this theory to their problems. He believed that simple application of the theory would lead to the solution of the most baffling problems in electroplating and warned against the continued use of intuition and so-called "common sense" in dealing with these problems. His classic example was the Hull cell, because in all its apparent simplicity was hidden a complexity of mathematics that would frighten away the most stout-hearted.

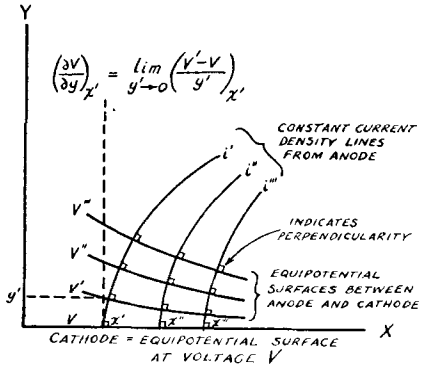

FIG. 1. Equipotential surfaces are cylinders with axes perpendicular to the x-y plane, that is, parallel to the z-axis. The cathode lies in the x-z plane. Thus, current density does not vary with the z-coordinate, which is perpendicular to the plane of the paper.

4. A discontinuity in potential between the electrode and the solution (polarization) may exist, but it must be uniform over the electrode surface.

Since Ohm's law generally holds for electrolytes, condition 1 is a good assumption. But, condition 2 normally does not hold for electrolytes since the flow of current sets up inhomogeneities in the electrolyte. However, by vigorous stirring of the electrolyte and avoiding extremely high current densities, these inhomogeneities can be made negligible. The specific resistance of the electrode is usually negligible compared to that of the electrolyte so that condition 3 is also a good assumption. Condition 4 cannot be readily shown to hold. In fact, since the current density usually varies along the electrode surface, polarization would vary accordingly. However, experiments with the new cell have verified the fact that polarization is uniform along an equipotential surface, such as an electrode.

Thus, for a fixed geometry the polarization may be expressed as a function of the total voltage, which is constant over the electrode. In order to compare this polarization with that produced on electrodes of uniform current density and voltage, the average current density on the variable electrode is used. Although the polarization is fundamentally a function of current density, for a fixed geometry, the current density is a function of the total voltage. Since the former varies over the electrode surface in question, it is more convenient to utilize the latter as the independent variable. This procedure is equivalent to expressing the polarization as a function of the average current density on the electrode. [See equations (XIV) and (XVIII)].

Condition 1 may be expressed mathematically as follows:

$$i = -\kappa\left(\frac{\partial V}{\partial y}\right)_x \qquad \text{(I)}$$

where i = current density along the cathode, κ = conductivity in consistent units, V = potential, and $(\partial V/\partial y)_x$ = potential gradient along the cathode. The minus sign indicates that the flow of current is in the direction of decreasing potential. In equation (I) the positive x-axis is considered to be the cathode. Since the constant current density lines are normal to an equipotential surface, the potential gradient along the cathode is given by the rate of change of voltage with respect to the y-coordinate at constant x. This condition is shown in Fig. 1.

It is desired to select the anode in such manner that the current density along the cathode is proportional to the distance from the origin. Mathematically stated:

$$i = -bx]_{y=0} \qquad \text{(II)}$$

where b = proportionality constant. Again the minus sign indicates that the current flows opposite to increasing potential gradients. Combining equations (I) and (II) gives:

$$\left(\frac{\partial V}{\partial y}\right)_x = \frac{b}{\kappa}x$$

or

$$dV = \frac{b}{\kappa}x\,dy\Big]_{\text{constant } x} \qquad \text{(III)}$$

Condition 2 implies that κ is constant so that equation (III) may be integrated at constant x, from the limits of $V = 0$ at $y = 0$, to give,

$$V = \frac{b}{\kappa}xy \quad \text{or} \quad xy = \frac{\kappa V}{b} \qquad \text{(IV)}$$

Equation (IV) proves that the equipotential surfaces are rectangular hyperbolic cylinders. These appear as rectangular hyperbolas in the x-y plane with the x- and y-axes as asymptotes.

Similarly for the cathode as negative x-axis:

$$xy = -\frac{\kappa V}{b} \qquad \text{(V)}$$

From equations (IV) and (V), the potential of the y-axis (both positive and negative parts) is also at zero potential.

The equation of the current lines may now be derived from the fact that these lines must be orthogonal with the equipotential surfaces, that is, the tangents to the line and surface at their point of intersection are perpendicular. In the x-y plane, this means that the slopes of the current lines are the negative reciprocals of the slopes of the constant voltage lines. Differentiating equation (IV) gives the slope of the constant voltage lines,

$$\frac{dy}{dx} = -\frac{y}{x}\Big]_{V=\text{constant}} \qquad \text{(VI)}$$

Thus, the slopes of the current lines become,

$$\frac{dy}{dx} = \frac{x}{y}\Big]_{i=\text{constant}}$$

or

$$x\,dx - y\,dy = 0]_{i=\text{constant}} \qquad \text{(VII)}$$

Integrating differential equation (VII), from the limits of equation (II), gives,

$$x^2 - y^2 = \frac{i^2}{b^2} \qquad \text{(VIII)}$$

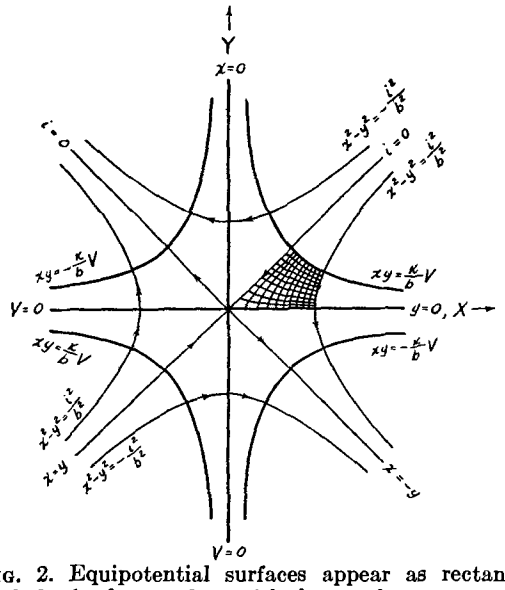

FIG. 2. Equipotential surfaces appear as rectangular hyperbolas in the x-y plane with the x and y axes as asymptotes. The current lines are also rectangular hyperbolas in the x-y plane, but with the lines $x = \pm y$ as asymptotes. Both sets of hyperbolas are mutually orthogonal in accordance with the theory of the potential.

For no current flow, i.e., $i = 0$,

$$x^2 = y^2 \quad \text{or} \quad x = \pm y \tag{IX}$$

The constant current lines are, thus, rectangular hyperbolas, but with asymptotes $x = \pm y$ (the 45° lines through the origin).

The desired result is then obtained by choosing a cell in which the equipotential surfaces are rectangular hyperbolic cylinders and the current lines are the corresponding orthogonal rectangular hyperbolas. In Fig. 2, the plating cell is a portion of the first quadrant shown by cross-hatching which simulates the current and voltage lines. Two such cells may be selected from each of the four quadrants; in the first cell, the cathode lies in the x-axis, in the second, the cathode lies in the y-axis (they are mirror images). All of the eight cells are geometrically equivalent. Those in the first and third quadrant have the cathodes in the x- and y-axes, while those in the second and fourth quadrant have the anodes in the x- and y-axes.

CELL DESIGN

The cell was designed with two straight sides of equal length intersecting each other at 45°. The other two sides are rectangular hyperbolas orthogonal to each other and to the straight sides which each intersects (Fig. 3). The anode is placed on one of the hyperbolic sides and made to conform to its shape. The cathode is placed on the straight side opposite the anode. The remaining sides are insulators. The electrodes may be reversed in those cases where the anode is the electrode of interest such as in anodizing or electropolishing.

If the length of the cathode is made equal to L and a potential difference equal to V is placed across the electrodes causing a current equal to I to flow between them, then it is possible to calculate the current density distribution along the cathode and evaluate the conductivity factor, κ, as follows.

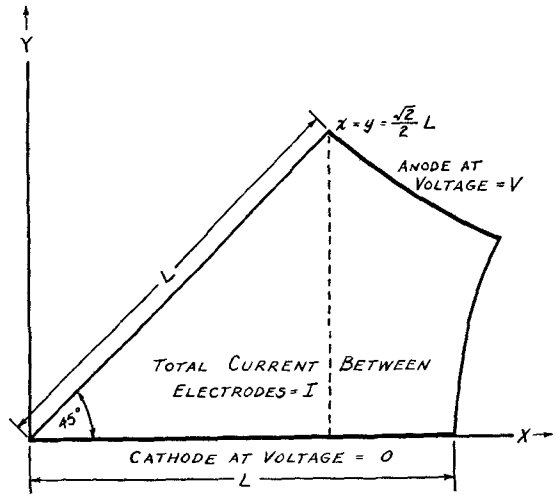

FIG. 3. Anode is placed on one of the hyperbolic sides and the cathode is placed on the opposite straight side of the cell. The length of the cathode is L, the voltage drop across the electrodes is V, and the total current flowing between them is I.

From equation (II),

$$b = -\frac{i}{x} = \frac{2I}{LA} \tag{X}$$

where A = area of cathode receiving current. This follows from the fact that the average current density, $(-I/A)$, occurs at the midpoint of the cathode, $(x = L/2)$, which in turn is true because the current density is proportional to distance along the cathode. Substituting equation (X) in (II) gives,

$$i = -\frac{2I}{LA}x \tag{XI}$$

Taking the cathode along the positive x-axis, the coordinates of the point of intersection between the anode and the straight insulating side are,

$$x = y = \frac{\sqrt{2}}{2}L \tag{XII}$$

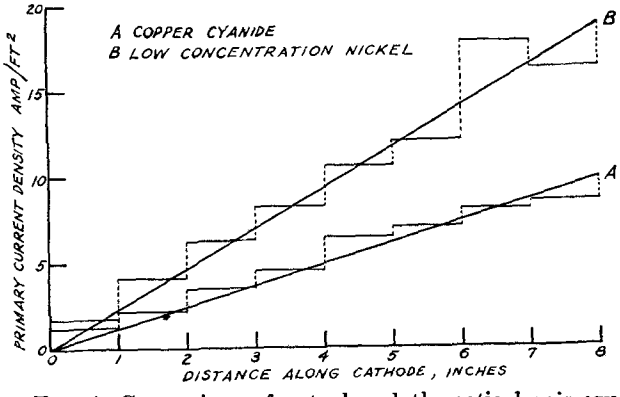

FIG. 4. Comparison of actual and theoretical primary current density curves for two typical plating solutions. Actual data are plotted as horizontal segments, while the theoretical curve is plotted as a straight line through origin.

Substituting in equation (IV) gives,

$$\frac{L^2}{2} = \frac{\kappa V}{b} \quad \text{or} \quad \kappa = \frac{b}{V}\left(\frac{L^2}{2}\right) \tag{XIII}$$

Substituting (X) in (XIII),

$$\kappa = \frac{IL}{VA} \tag{XIV}$$

If there is no polarization at the electrodes, this value of κ should correspond to the specific conductivity of the electrolyte used in the cell, represented by κ_c.

Polarization

If polarization does occur, condition 4 (above) may be applied. Thus, the total voltage drop, V, may be considered as the sum of a uniform polarization voltage, V_p, and the voltage drop due to resistance of the electrolyte, V_c, giving for the fixed geometry:

$$V = V_p + V_c \tag{XV}$$

In the absence of polarization, equation (XIV) may be written as

$$\kappa_c = \frac{IL}{V_c A} \quad \text{or} \quad V_c = \frac{IL}{\kappa_c A} \tag{XVI}$$

In the presence of polarization, equation (XVI) is a measure of the voltage drop due to electrolytic resistance only. Combining equations (XV) and (XVI) yields

$$V_p = V - \frac{IL}{\kappa_c A} \tag{XVII}$$

Adding equation (XIV) gives

$$V_p = V\frac{\kappa_c - \kappa}{\kappa_c} \tag{XVIII}$$

Equation (XVII) permits evaluation of the total polarization voltage (anode plus cathode) from simple measurements taken on the cell combined with the specific conductivity of the electrolyte. Equation (XVIII) shows that the ratio of polarization voltage to total voltage is given by the fractional loss in conductivity due to the polarization. Thus, the new cell affords a simple, rapid means of determining polarization voltage at the same time that it is used for current density studies of electroplated films.

Cell Construction

Full details of the construction of the new cell for experimental purposes will be published elsewhere. In order to verify the theoretical basis for the cell, provisions were made to divide the cathode into vertical segments. The segments were then individually wired so that the average current to each segment could be measured and compared against the theoretical values. In addition the weight of metal deposited on each segment could also be checked against the theoretical secondary current densities. Since it is the purpose of this paper merely to develop the theoretical basis of the design of the new cell, only representative data are given here.

Representative Data

Experimental data taken on the new cell for several key electrolytes amply verify the linear variation of current density along the cathode. In Fig. 4 are shown two typical curves of experimental data compared against theory for plating solutions with relatively high polarization. The small apparent intercept can be explained by a slight plating behind the electrode segments. Experimental error also appeared to be larger at higher current densities, although most of this error could be correlated with appearance of the plate. These examples were selected to illustrate the average extent of agreement; some were better, others were worse. On the whole, maximum deviation from theory did not exceed 10% of the maximum current density.

Total polarization voltages calculated from the data check with literature values well within the experimental error. For example, the calculated value for copper sulfate was 0.3 v compared to the literature value of 0.2 v. For copper cyanide the calculated values varied from 2.0 to 2.5 v compared to the literature value of 2.1 v. The best agreement was found with silver cyanide where both calculated and literature value were approximately equal at 0.4 v. The worst agreement was with the nickel sulfate baths, both regular and low concentration, where calculated values of 1.4 to 1.6 v compared against literature values of 0.9 to 1.1 v. This agreement must be considered excellent in light of the fact that literature values themselves were found to differ by several tenths of a volt in some cases.

Acknowledgment

The authors wish to express their thanks to Miss Anne Michalko of the Manostat Corp. for her assistance in preparing the manuscript and drawings.

Manuscript received December 2, 1955. This paper was prepared for delivery before the Cleveland Meeting, September 30 to October 4, 1956, and was submitted to the Polytechnic Institute of Brooklyn in partial fulfillment of the degree of Master of Chemical Engineering by R. F Walton.

Any discussion of this paper will appear in a Discussion Section to be published in the June 1957 Journal.

REFERENCES

1. R. O. Hull, *Proc. Am. Electroplaters' Soc.*, 52 (1939).
2. C. Kasper, *Trans. Am. Electrochem. Soc.*, **77**, 353 (1940).

Electron Microscope Studies of Copper Anodes Obtained in Sulfate and Cyanide Baths

SHINZŌ OKADA, SABURŌ MAGARI, AND KENTARŌ KATSUI

Engineering Research Institute, Kyoto University, Kyoto, Japan

ABSTRACT

Copper anodes in sulfate and cyanide plating baths, at low current densities, were studied by the use of the electron microscope and it was found that the appearance of the microstructure of the surface formed during electrolysis varied with the electrolytes, but the same crystal planes were developed in both baths and in a number of etching solutions. The microstructure was characteristic for a given crystal face at the surface. {210} planes were developed.

Much work has been done on the etch structure developed on single-crystal and polycrystalline copper, and it is believed that, with a single crystal of copper, the {111} and {100} planes, and sometimes the {210}, {311}, {310}, and {511} planes, are developed by etching (1, 2).

In this study, the microstructure of the surface of the copper anode formed during electrolysis in sulfate and cyanide plating baths, at low current densities, was examined by the electron microscope. In addition, the orientation of the microstructure of the anode was determined.

EXPERIMENTAL

The sulfate bath contained 150 g/l copper sulfate pentahydrate and 40 g/l sulfuric acid. The cyanide bath contained 22.5 g/l copper cyanide, 30.0 g/l sodium cyanide, and 10.0 g/l sodium carbonate. Electrolysis was carried out, without agitation, at 30°C in all experiments. Cathodes were 2 x 2 cm^2 rolled copper plates, while the anodes were copper plates, the characteristics of which varied for different experiments. One side of each anode and cathode was coated with polyvinyl formal.

The two-step replica method was used for electron microscopy. A benzol solution of polymethyl methacrylate was poured on the anode before electrolysis and allowed to dry. The resin was then carefully removed from the anode, placed in a vacuum evaporator, coated with aluminum, and shadowed with chromium. After electrolysis the anode was rinsed with distilled water, dried, and again treated with polymethyl methacrylate as outlined above. The technique outlined previously was used to locate the identical spot on the anode under the electron microscope before and after electrolysis (3).

Orientation of facets developed on the surface during electrolytic etching was determined by combined x-ray transmission analysis and light reflections.

RESULTS

Dissolution in copper sulfate electrolyte.—The electropolished surface of a rolled copper anode, 2 x 2 cm^2 in area and 0.5 mm thick, was electrolyzed at between 1.6 and 20 ma/cm^2. Plate I shows the surface after electrolysis for 12 min at 3 ma/cm^2.

Electrolysis was also carried out between 1.6 and 20 ma/cm^2 on a rolled copper anode etched with 10% ammonium persulfate solution. Electrolysis for 24 min at 1.6 ma/cm^2 gave the surface shown in Plate II.

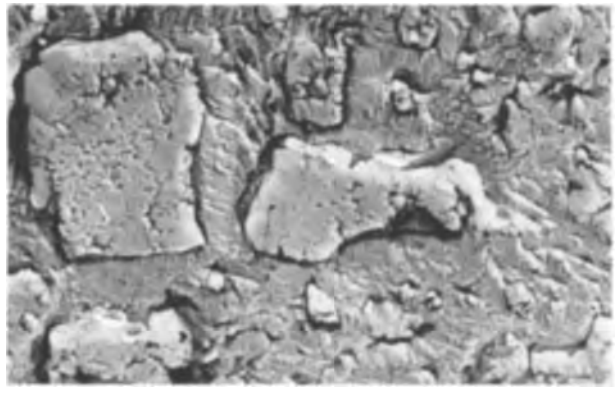

PLATE I. Electropolished rolled copper anode in sulfate bath. 3000×.

PLATE II. Chemically etched rolled copper anode in sulfate bath. 3000×.

In order to determine whether or not the facets that developed on the polycrystalline anode were related to a crystallographic plane in the crystals on which they formed, an electropolished anode composed of two single crystals of known orientation was electrolyzed at 1 ma/

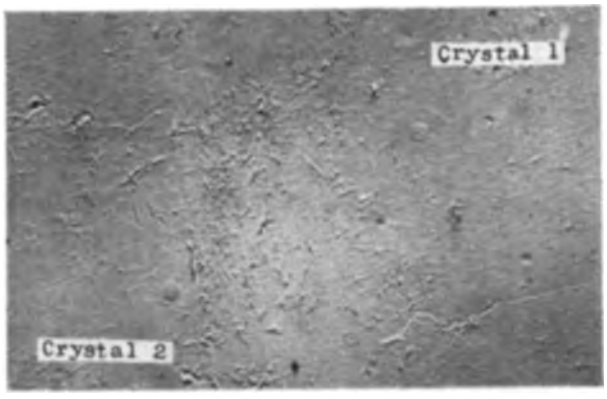

PLATE III(a). Single-crystal copper anode in sulfate bath, initial surface. 3000×.

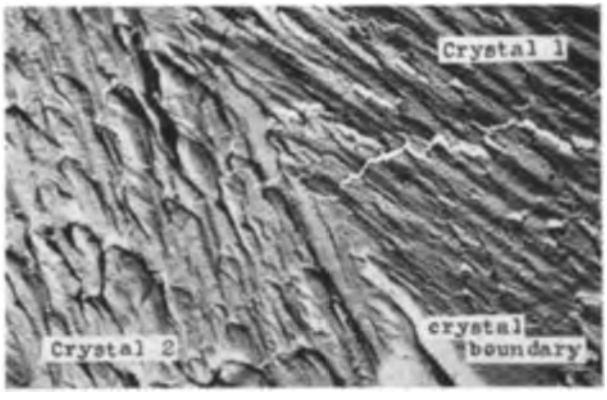

PLATE III(b). Single-crystal copper anode in sulfate bath after electrolysis for 20 min. 3000×.

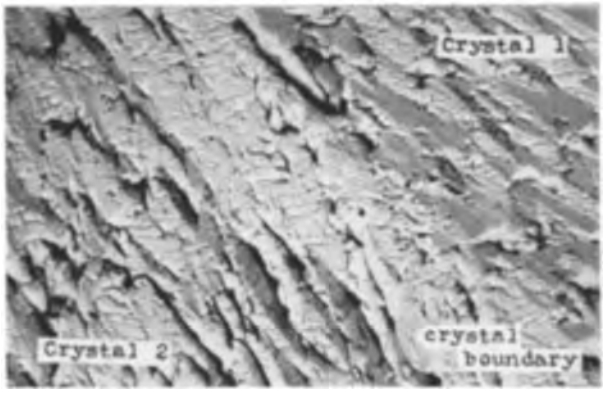

PLATE III(c). Single-crystal copper anode in sulfate bath after 40 min additional electrolysis. 3000×.

cm². Plate III(a) shows the initial surface, preparing for electrolysis. After 20 min the surface shown in Plate III(a) became rougher as shown in Plate III(b). An additional 40 min gave the surface shown in Plate III(c). Plate V shows the surface corresponding to Plate III(c) under greater magnification.

Optical reflecting data are recorded in Table I.

Dissolution in copper cyanide electrolyte.—Rolled copper

TABLE I

	Crystal 1		Crystal 2	
	$\delta°$	$\theta°$	$\delta°$	$\theta°$
Optical	−135	76	−122	75
	(a_1)		(b_1)	
X-ray	−142	76	−130	76
	(021)		(120)	
Optical	25	70	78	68
	(a_2)		(b_2)	
X-ray	28	68	80	65
	($\bar{1}20$)		($02\bar{1}$)	

δ: angle between a reference plane including the normal to the surface of the specimen and the plane including this normal and the normal to the crystallographic plane or facets in question.

θ: angle between the normal to the crystallographic plane or facets and the normal to the surface of the specimen.

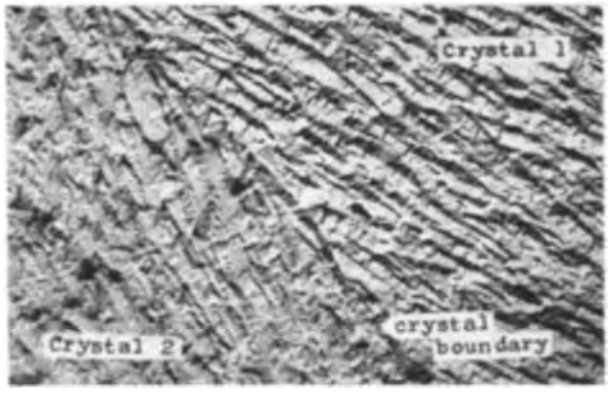

PLATE IV(a). Single copper anode in cyanide bath after electrolysis for 60 min. 3000×.

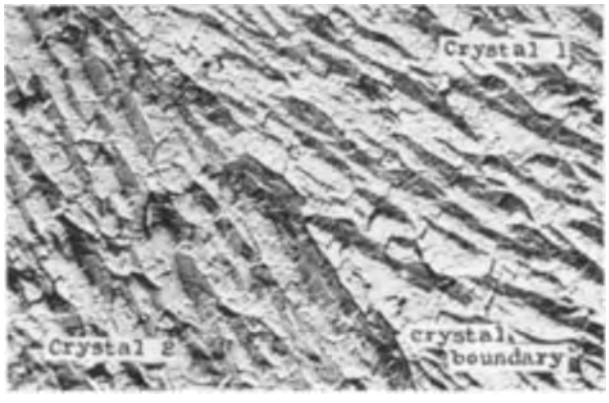

PLATE IV(b). Single copper anode in cyanide bath after 60 min additional electrolysis. 3000×.

anodes were electrolyzed at current densities between 10 ma/cm² and 1.6 ma/cm².

To determine whether dissolution in a cyanide electrolyte would show a characteristic plane on a single-crystal anode, the electropolished bi-crystal anode was electrolyzed at 1 ma/cm². Plate IV(a) shows the surface

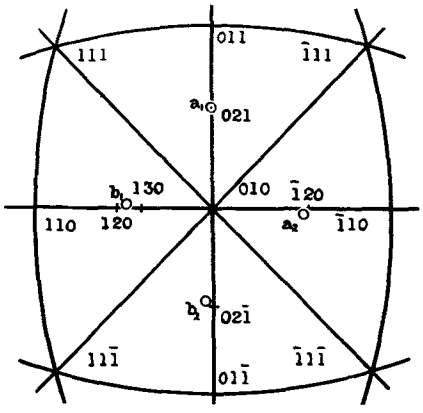

FIG. 1. a_1 and a_2 represent the normals to the optical reflecting facets for electrolyzed crystal 1, and b_1 and b_2 represent the corresponding facets for crystal 2.

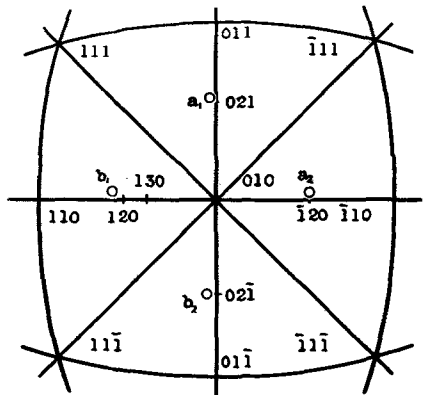

FIG. 2. a_1 and a_2 represent the normals to the optical reflecting facets for electrolyzed crystal 1, and b_1 and b_2 represent those for crystal 2.

after electrolysis for 60 min and further electrolysis for another 60 min gave the surface shown in Plate IV(b).

Optical analysis was carried out on the surface.

Dissolution in etching solutions.—To learn the relation between the dissolution in copper plating baths and that in etching solutions for metallography, the bi-crystal copper plate was etched in the following manner: (*a*) immersed in aqua regia for 2 min, then in 10% ammonium persulfate solution for 15 min; (*b*) anodically etched with 1 part nitric acid (d = 1.38) to 5 parts water at 20 ma/cm² for 5 min; (*c*) anodically etched with 10% ammonium persulfate solution at 20 ma/cm² for 5 min.

DISCUSSION

Dissolution in copper sulfate electrolyte.—Dissolution of electropolished rolled copper anodes was almost uniform over the surface at higher current densities. The lower the current density, the more uneven the surface was left. Nonuniform dissolution is seen in Plate I, and further electrolysis accentuated the unevenness. Unevenness of the surface at lower current densities is believed to be due to the difference of the solutional potential of each crystal in the anode.

In the case of chemically etched rolled copper anode, nonuniformity of dissolution was not observed at any current density and indeed the surface became smoother than the initial one. No characteristic dissolution was revealed as shown in Plate II. It is possible that the orientation formed by chemical etching of the facets on the anode might be the same as that formed by electrolysis.

In the case of the electropolished bi-crystal anodes, the crystal boundary is discernible after electrolysis as shown in Plate III(b), while on the initial surface the boundary was not evident [Plate III(a)]. The boundary became accentuated after further electrolysis as shown in Plate III(c). The ability to distinguish the boundary after electrolysis shows that the orientation of the microstructure of the surface on the two crystals was different.

The data of Table I are summarized stereographically in Fig. 1. It is considered that a_1, a_2, b_1, and b_2 correspond to the (021), ($\bar{1}20$), (120), and ($02\bar{1}$) planes of the base crystal, respectively.

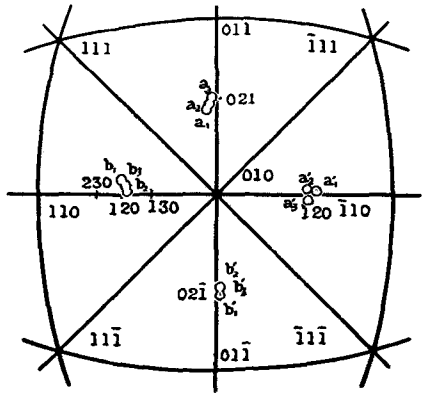

FIG. 3. a_1, a_2, a_3, a_1', a_2', and a_3' represent the normals to the optical reflecting facets for electrolyzed crystal 1, respectively, and b_1, b_2, b_3, b_1', b_2', and b_3' represent the corresponding facets for crystal 2.

It is concluded that the dissolution of a single copper crystal in a sulfate bath occurs with the development of {210} planes of the base crystal.

Dissolution in copper cyanide electrolyte.—Regardless of whether the rolled anode had been electropolished or chemically etched, no characteristics of the microstructure of the surface was observed at any current density.

The initial surface of electropolished bi-crystal anode again did not reveal the crystal boundary. After electrolysis, however, the boundary became evident and additional electrolysis made it much more pronounced. This is shown more clearly by the greater magnification of Plate VI. It is clear from the evidence presented that the orientation of the base crystal has an influence on that of the microstructure of the surface.

Optical data are summarized stereographically in Fig. 2. As before, the reflecting facets are {210} planes of the base crystal.

It is concluded that the dissolution of a single copper crystal in a cyanide bath also shows {210} planes of the base crystal.

Dissolution in etching solutions.—Optical data are summarized stereographically in Fig. 3. The normals to the optical reflecting facets are near the normals to {210} planes of the base crystal.

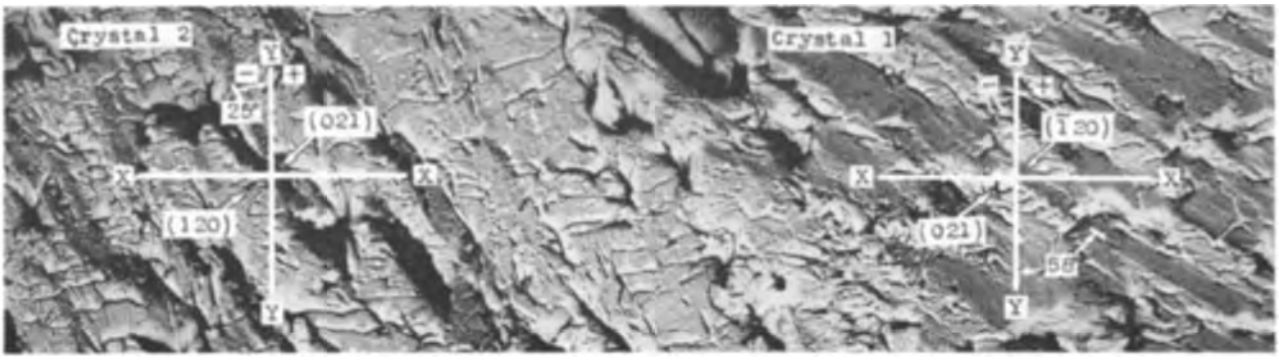

PLATE V. Enlargement of Plate III(c). 5500×.

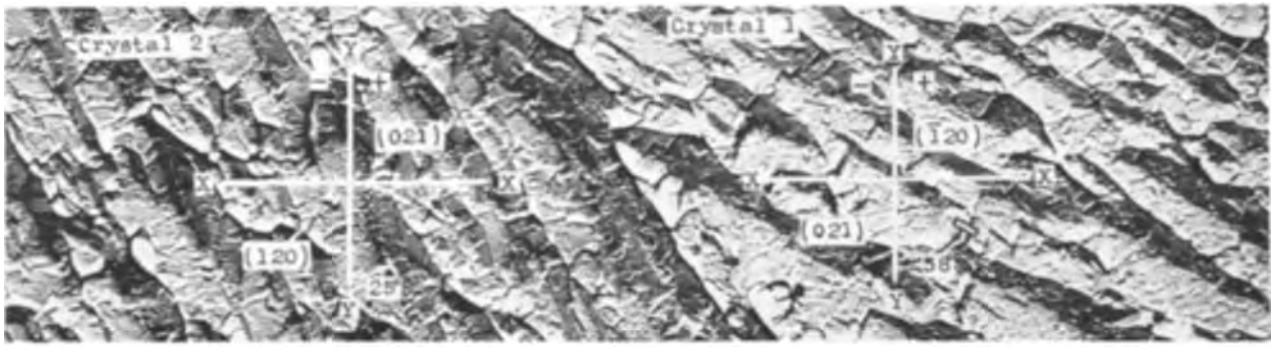

PLATE VI. Enlargement of Plate IV(b). 5500×.

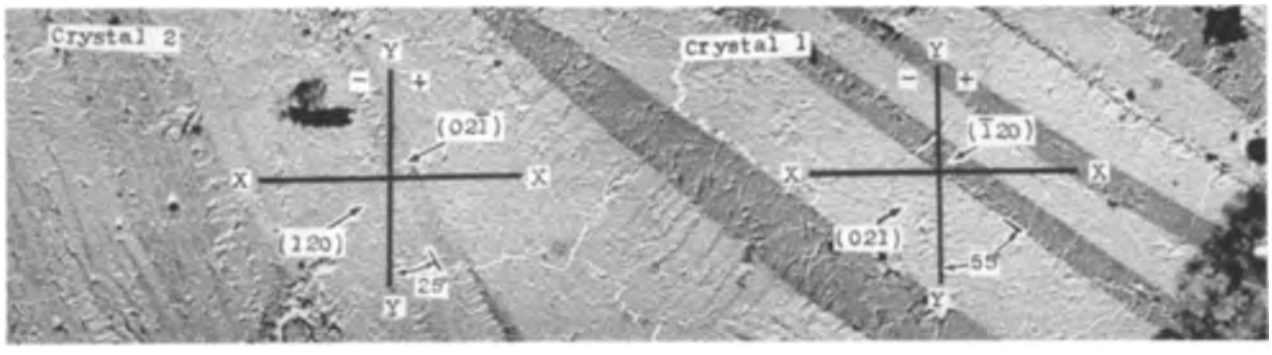

PLATE VII. Etched with 10% ammonium persulfate solution for 15 min. 5500×.

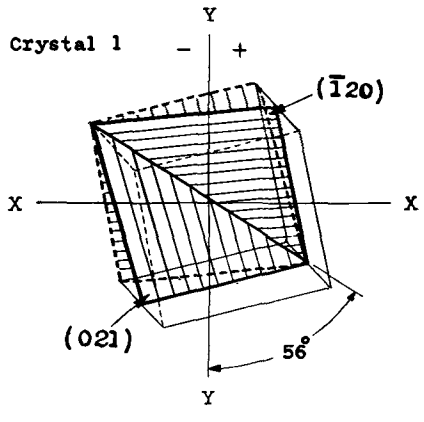

FIG. 4(a). Unit cell of the base crystal

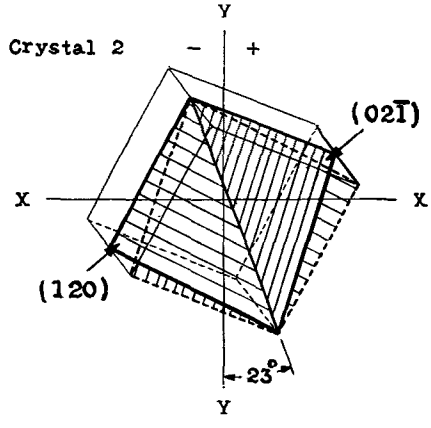

FIG. 4(b). Unit cell of the base crystal

It is concluded that the dissolution of a single crystal in etching solution also shows {210} planes of the base crystal.

Fig. 4(a) and (b) show a unit cell of base crystals 1 and 2, as determined from x-ray examinations, corresponding to Plate V, Plate VI, and Plate VII. The lightly shadowed planes in the electron micrographs are (021) planes of base crystal 1 and (120) planes of crystal 2, while the heavily shadowed planes are ($\bar{1}20$) planes of crystal 1 and (02$\bar{1}$) planes of crystal 2, respectively.

Analysis of the data of x-ray and optical reflection and electron micrographs showed that the facets in the surface were parallel to {210} planes and that the ridges were nearly parallel to the line of intersection on the {210} planes that were parallel to the facets. This was a [212] direction.

ACKNOWLEDGMENT

The authors are deeply indebted to Dr. J. Takamura, Faculty of Engineering, Kyoto University, for supplying copper single crystals and for his valuable advice.

Manuscript received June 3, 1955.
Any discussion of this paper will appear in a Discussion Section to be published in the June 1957 JOURNAL.

REFERENCES

1. S. TAKEYAMA, *Mem. Coll. Sci. Univ. Kyoto*, **13**, 353 (1930).
2. H. LEIDHEISER AND A. T. GWATHMEY, *Trans. Electrochem. Soc.*, **91**, 95 (1947).
3. S. OKADA AND S. MAGARI, *Bull. Eng. Research Inst. Kyoto Univ.*, **3**, 59 (1953).

Electron Microscope Studies on Copper Electrodes in Sulfate Bath Containing Addition Agent

SHINZŌ OKADA, SABURŌ MAGARI, AND KENTARŌ KATSUI

Engineering Research Institute, Kyoto University, Kyoto, Japan

ABSTRACT

Thiourea, gelatin, or glue in a copper sulfate bath at low current densities prevent development of facets in the surface parallel to the {111} planes of a single-crystal cathode but have no influence on the facets of the deposit parallel to the {010} planes. Thiourea gave the smoothest deposits, in which the facets of the deposit were parallel to the {120} planes of the base crystal. At a single-crystal anode, planes developed parallel to the {010} planes of the crystal when gelatin or glue was present, but thiourea did not cause development of a characteristic plane. Aging the electrolyte did not influence the orientation of facets on the anodes, but did increase the smoothness of its surface.

In the absence of addition agents, facets in the surface parallel to the {111}, {010}, and {120} planes of a single-crystal cathode are developed during electrodeposition from a copper sulfate bath at low current densities (1). At the anode, facets in the surface parallel to the {120} planes of the base crystal were developed. The present study was made to determine the influence of addition agents on the orientation of the facets on the electrode surfaces, if the addition of thiourea, gelatin, and glue to the electrolyte influences the character of the new surface developed on large copper crystals during electrolysis.

EXPERIMENTAL

The electrolytic bath contained 150 g/l copper sulfate pentahydrate, 40 g/l sulfuric acid (d = 1.84) and the desired amount of addition agent (gelatin, glue, or thiourea). In all experiments, the current density was 1 ma/cm^2, the electrolyte was unstirred. Gelatin or glue were dissolved in the bath at 35°C after which the temperature was reduced to 30°C, at which temperature electrolysis occurred in all experiments.

Electrodes to be examined with the electron microscope were 1 cm x 2 cm bi-crystal (denoted as crystals 1 and 2) copper plates of known orientation. (Orientation was determined by transmitted x-ray analysis.) Other electrodes were 2 cm x 2 cm rolled copper sheet. One side of each anode and cathode was coated with polyvinyl formal.

The 2-step replica method was used for electron microscopy. A benzol solution of polymethyl methacrylate was poured on the surface of each electrode before electrolysis and allowed to dry. The resin film was then carefully removed and placed in a vacuum evaporator, where it was coated with aluminum and shadowed with chromium in the usual way. The procedure was repeated after electrolysis. The technique outlined previously (2) was used to locate the identical spot on the electrode under the microscope before and after electrolysis.

Orientation of the facets on the electrode surface was determined by reflection of light from the surface passed through a 0.5 mm slit to establish the position of the facets relative to an arbitrary set of axes. Then, with the crystal in the same position, orientation of the original

single crystal was determined with transmitted x-rays. By comparison of the two sets of data, it was possible to determine which planes of the base crystal were parallel to the facets on the electrode surface.

TABLE I. *Optical and x-ray data for deposits and for anodes after electrolysis for 120 min in the presence of gelatin*

Gelatin, %	0.1				0.3				1.0			
Cathode crystal	1		2		1		2		1		2	
	δ°	θ°	δ°	θ°	δ°	θ°	δ°	θ°	δ°	θ°	δ°	θ°
Optical	−41	70	142	66	−40	68	143	66	−43	68	147	69
X-ray	−40	68	145	65	−40	68	145	65	−40	68	145	65
	(010)		(010)		(010)		(010)		(010)		(010)	
Optical	−140	78	−128	76								
X-ray	−140	76	−130	78								
	(021)		(120)									
Anode crystal	1		2		1		2		1		2	
Optical	−145	74	−130	75	30	67	76	65	−42	70	140	68
X-ray	−142	76	−130	76	28	68	80	63	−40	68	145	65
	(021)		(120)		(1̄20)		(021)		(010)		(010)	
Optical					−140	74	−128	74				
					−142	76	−130	76				
					(021)		(120)					

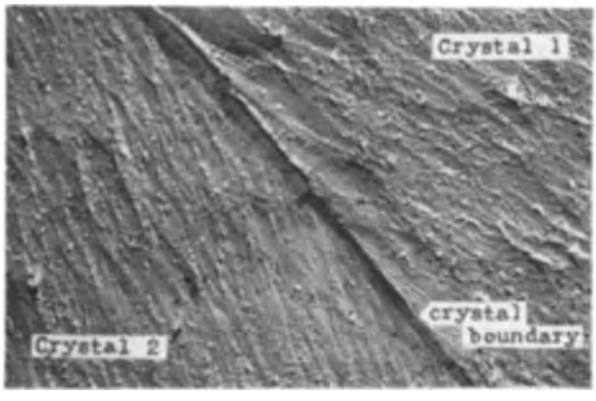

Plate I(a). Deposit from fresh bath containing 1% gelatin after 120-min electrolysis. 3000×.

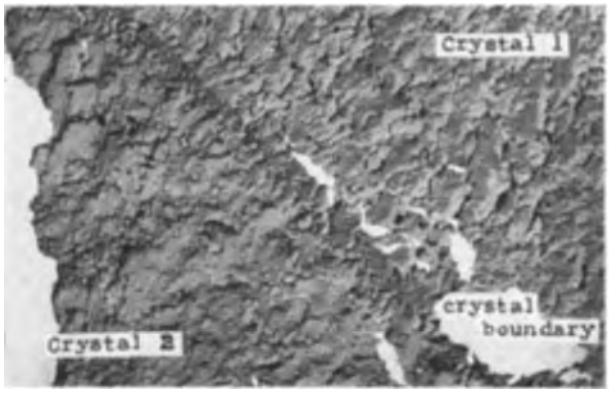

Plate I(b). Anode in fresh bath containing 1% gelatin after 120-min electrolysis. 3000×.

Results

Gelatin as addition agent.—In Table I are recorded the average angular coordinates of the normals to facets in the new surfaces of electrodes and the angular coordinates of the normals to crystallographic planes of low indices in the electrodes that are nearly parallel to the facets. X-ray data give only the index of the plane of the facets on the electrode determined by back reflection of light. θ is the angle between normal to surface and normal to facet and is also used as the angle between normal to surface and normal to crystallographic plane. δ is the angle between a reference line in the surface examined and the plane including the surface and facet normals, measured in clockwise and counter clockwise relations. It is used in a similar way for the crystallographic planes.

Prior to the experiments with 1% gelatin, no boundary was evident between cathode crystals 1 and 2, but the boundary was discernible after electrolysis [Plate I (a)], which indicates that the deposits on the two crystals were different. The surface of the anode after electrolysis in the presence of 1% gelatin is shown in Plate I (b).

Aging the electrolyte containing 1% gelatin gave results shown in Table II. The data of treatment C in the table were obtained with copper crystals which had been electropolished and showed no boundaries prior to electrolysis. However, after 20 min of electrolysis the boundaries on both cathode and anode were revealed. The cathode surface resembled that in Plate I (a). After the electrolyte had aged for 8 days, and electrolysis resumed for 100 min, the surface of the cathode [Plate II (a)] became quite different from that of Plate I (a), although the total time of electrolysis was the same. Similarly, the surface of the anode was smoother [Plate II (b)] than that shown in Plate I (b).

Glue as addition agent.—Electrolysis for 120 min in fresh electrolyte containing 0.5% glue gave a cathode surface [Plate III (a)] rougher than that obtained with gelatin. The corresponding anode surface [Plate III (b)] had a blocky mosaic structure.

Electropolished crystals, which again showed no boundaries, developed boundaries at both cathode and anode after 20 min electrodeposition in fresh electrolyte containing 0.5% glue. This boundary became accentuated after 40-min electrolysis when the electrolyte had been allowed to age for 4 days. With 60 min additional electrolysis after the electrolyte had aged for 8 days, the cathode surface of Plate IV(a) and the anode surface of Plate IV(b) were obtained; the cathode was smoother than that with gelatin in similar circumstances [Plate II (a)], while the anode surface was rougher than that in a new bath [Plate II(b)]. The optical and x-ray data are shown in Table III.

Thiourea as addition agent.—Electrodeposition for 120 min in fresh electrolyte containing 0.04 g/l thiourea revealed the boundaries between the crystals [Plate V(a) and V(b)] although the reflected light was weak from the cathode and insufficient from the anode to permit characterization of the surface. Optical and x-ray data for the cathode were recorded in Table IV.

TABLE II. *Effect of aging the electrolyte on cathode deposits and on anodes in the presence of 1.0% gelatin*

Treatment		Cathode crystal 1		Cathode crystal 2		Anode crystal 1		Anode crystal 2	
		$\delta°$	$\theta°$	$\delta°$	$\theta°$	$\delta°$	$\theta°$	$\delta°$	$\theta°$
A. Aged 2 days, electrolyzed 120 min	Optical	−41	70	145	69				
	X-ray	−40	68	145	65				
		(010)		(010)					
	Optical	−141	77						
	X-ray	−142	76						
		(021)							
B. Aged 3 days, electrolyzed 120 min	Optical	−41	68	142	68				
	X-ray	−40	68	145	65				
		(010)		(010)					
	Optical	−140	76	−128	77				
	X-ray	−142	76	−130	78				
		(021)		(120)					
C. Electrolyzed 20 min, aged 8 days, electrolyzed further for 100 min	Optical	−40	68	142	65	25	66*		
	X-ray	−40	68	145	65	28	65		
		(010)		(010)		($\bar{1}$20)			
	Optical	−143	77	−130	78	−40	72	144	69
	X-ray	−142	76	−130	78	−40	69	145	65
		(021)		(120)		(010)		(010)	

* Weak.

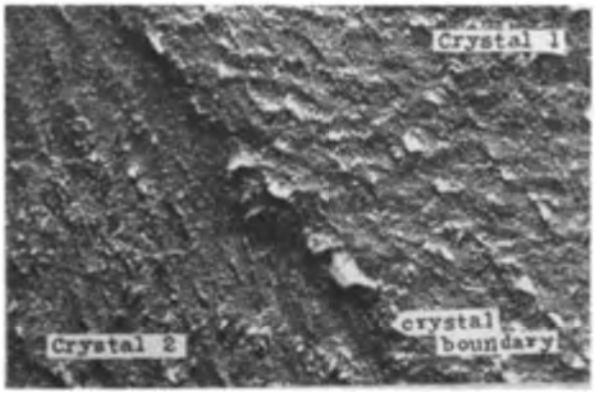

Plate II(a). Deposit from aged bath containing 1% gelatin after 120-min electrolysis. 3000×.

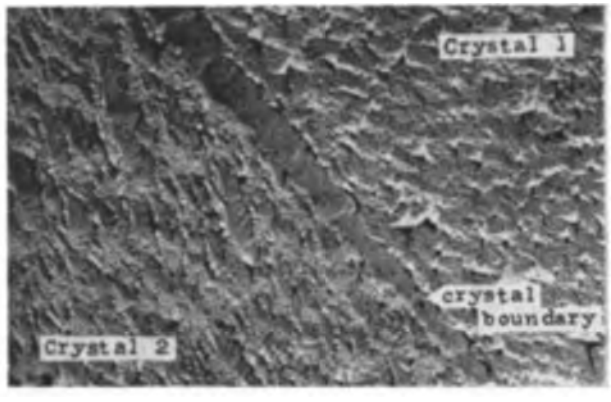

Plate III(a). Deposit from fresh bath containing 0.5% glue after 120-min electrolysis. 3000×.

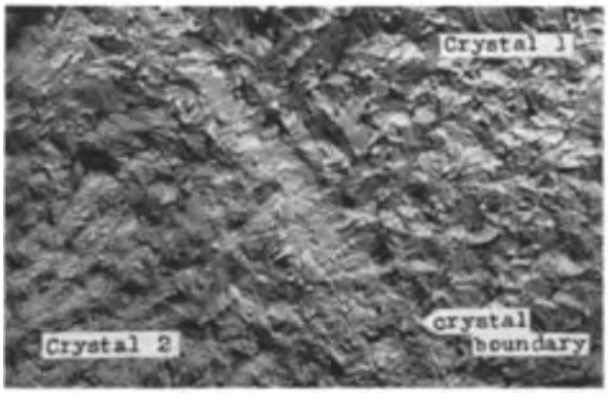

Plate II(b). Anode in aged bath containing 1% gelatin after 120-min electrolysis. 3000×.

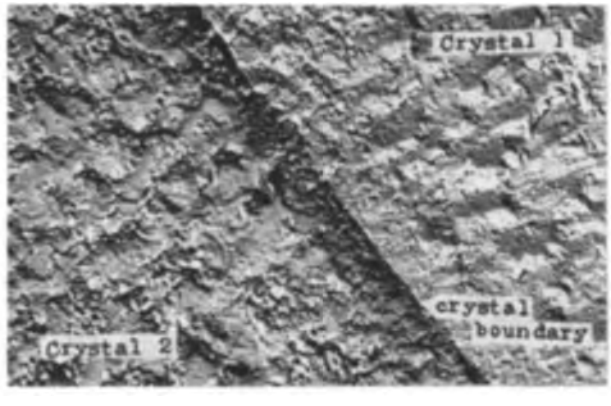

Plate III(b). Anode in fresh bath containing 0.5% glue after 120-min electrolysis. 3000×.

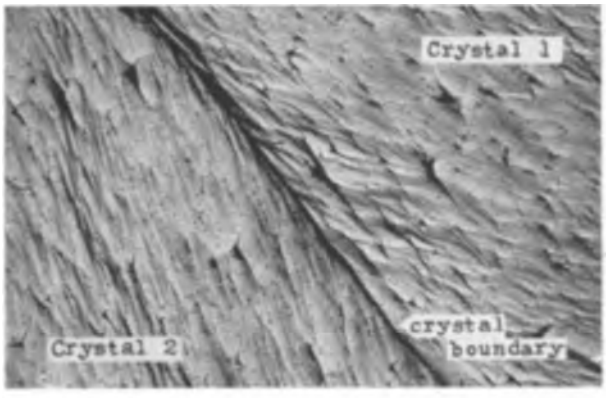

Plate IV(a). Deposit from aged bath containing 0.5% glue after 120-min electrolysis. 3000×.

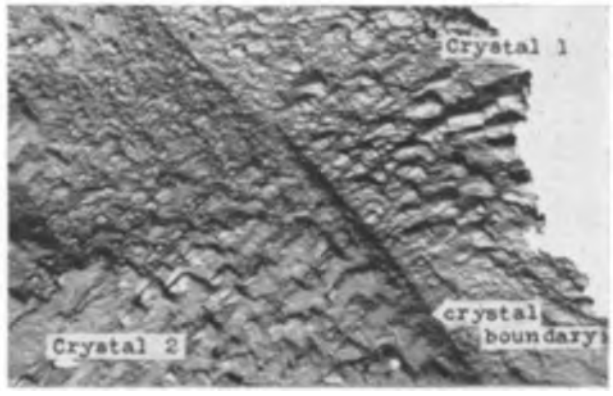

Plate IV(b). Anode in aged bath containing 0.5% glue after 120-min electrolysis. 3000×.

TABLE III. *Effect of glue on fresh and aged electrolyte on cathode deposit and on anode*

Treatment		Cathode crystal 1 δ°	Cathode crystal 1 θ°	Cathode crystal 2 δ°	Cathode crystal 2 θ°	Anode crystal 1 δ°	Anode crystal 1 θ°	Anode crystal 2 δ°	Anode crystal 2 θ°
Electrolysis for 120 min in fresh electrolyte	Optical	−38	72	144	69	−42	68	140	69
	X-ray	−40	68	145	65	−40	69	145	65
		(010)		(010)		(010)		(010)	
	Optical	−140	76*	−132	78*				
	X-ray	−142	76	−130	78				
		(021)		(120)					
Electrolysis for 20 min in fresh electrolyte, 40 min after 4 days aging, and 60 min after 8 days aging	Optical	−37	68	145	69	−40	70	141	68
	X-ray	−40	68	145	65	−40	69	145	65
		(010)		(010)		(010)		(010)	
	Optical	−144	75*	−129	78*				
	X-ray	−142	76	−130	78				
		(021)		(120)					

* Weak.

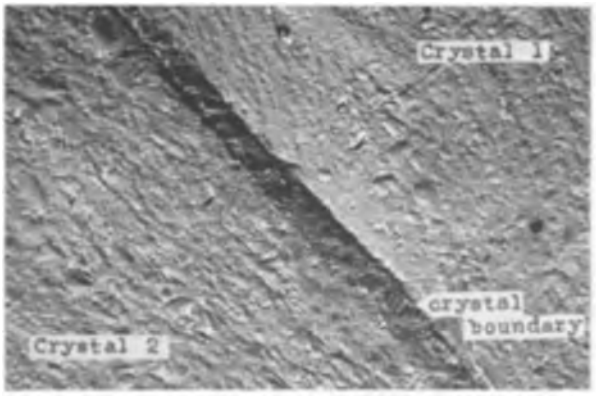

Plate V(a). Deposit from fresh bath containing 0.04 g/l thiourea after 120-min electrolysis. 3000×.

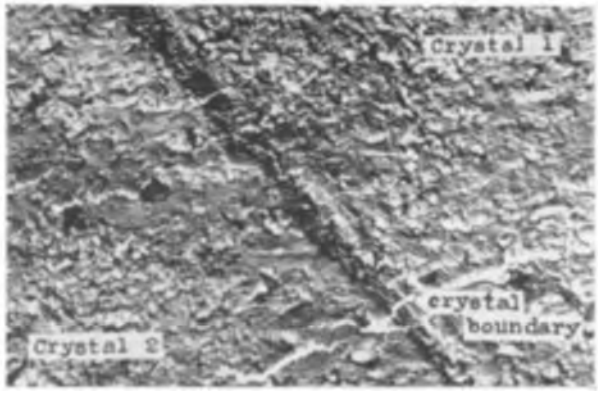

Plate V(b). Anode in fresh bath containing 0.04 g/l thiourea after 120-min electrolysis. 3000×.

Discussion

The effect of gelatin on orientation of the facets in the cathode deposit changed with concentration; with 0.1% gelatin, facets corresponded to the {120} and {010} planes of the base crystal, but with 0.3% and 1% gelatin the orientation changed to that of the {010} planes. A strong spot in the center indicates that a large portion of the new surface remained parallel to the initial surface, that is, the deposition or dissolution did not completely cover the surface with facets parallel to crystallographic planes. Aging the electrolyte affects the orientation of the facets on the cathode corresponding to {120} planes of the base

TABLE IV. *Optical and x-ray data for deposits after electrolysis for 120 min in the presence of thiourea*

	Cathode crystal			
	1		2	
	$\delta°$	$\theta°$	$\delta°$	$\theta°$
Optical	25	68	78	68
X-ray	28	65	80	65
	($\bar{1}20$)		($02\bar{1}$)	
Optical	−142	75	−133	78
X-ray	−142	76	−130	78
	(021)		(120)	

crystal, probably because the life of gelatin as an addition agent is very short. At the anode, the presence of 0.1% and 0.3% gelatin had no influence on the orientation of the facets, and the {120} planes of the base crystal developed in the bath without addition agent, while in the 1% bath those corresponding to the {120} planes disappeared. Aging the electrolyte appeared to have no influence on the orientation of the facets, but seemed to affect the evenness of the anode surface.

With glue as the addition agent in fresh electrolyte, the behavior was different from that observed with gelatin. Strong development corresponding to the {010} planes of the base crystal occurred in the cathode, together with weaker development corresponding to the {120} planes. The reverse occurred in aged electrolyte, which yields a smoother deposit than fresh electrolyte. At the anode, glue promoted development of the {010} planes in both fresh and aged electrolyte, although the anode was smoother in the aged than in the fresh.

Thiourea gave a very smooth cathode, with weak development of facets corresponding to the {120} planes of the base crystal, and a strong center spot. At the anode, uniform solution of each crystal would account for the optical data and electron micrographs, but the existence of a boundary between the crystals suggests that they dissolved at different rates.

Manuscript received October 13, 1955. This paper was prepared for delivery before the Pittsburgh Meeting, Oct. 9 to 13, 1955. Any discussion of this paper will appear in the June 1957 Discussion Section.

REFERENCES

1. S. Okada and S. Magari, *This Journal*, **102**, 580 (1955).
2. S. Okada and S. Magari, *Bull. Eng. Research Inst. Kyoto Univ.*, **3**, 59 (1953).

Effect of Impurities on the Hardness of Titanium

T. D. McKinley

Research Division, Pigments Department, E. I. du Pont de Nemours & Company, Wilmington, Delaware

ABSTRACT

The individual effects of 15 impurities on the as-cast hardness of Ti buttons prepared under reproducible conditions have been determined. The data presented allow the estimation of oxygen in unalloyed Ti from a hardness measurement and a few conventional chemical analyses with an error of less than 10% from the value as determined by vacuum fusion analysis.

Numerous experimenters (1–15, 17, 18) have studied the effect of impurities on the hardness of Ti. In general, correlations were obtained using Ti that had been mechanically worked. Since the hardness of a metal is a function of thermal and mechanical history as well as of impurity level, it is not surprising that reported values have considerable variance.

Determination of the as-cast hardness of arc melted Ti has been and continues to be a primary measure of Ti quality for both sponge producers and fabricators. The primary object of the present work is to correlate the individual effects of varying amounts of some 15 impurities on the as-cast hardness of Ti buttons prepared under reproducible conditions. These correlations show the relative hardening effect of the impurities and allow estimation of variation of hardness with impurity level. Above and beyond the obvious applications of such correlations, the data presented also allow the estimation of oxygen in unalloyed Ti from a hardness measurement and a few conventional chemical analyses, that is, without recourse to an actual oxygen determination. Estimation of oxygen can be made in this manner with an expected error of less than 10% from the value as determined by vacuum fusion analysis. A further result of this work, and one having a direct bearing on the accuracy of the data, is the development of a simple, reproducible procedure for preparing homogeneous Ti buttons.

Preparation of Samples

Ti buttons were prepared in a furnace with water-cooled copper crucible and water-cooled tungsten electrode (Fig. 1). Direct current was supplied by either a motor-generator or a rectifier. For melting 100-gram buttons, the standard weight used throughout this study, the maximum power requirement is 200 amp at 25 v. Melting was performed under pure helium at 650–800 mm absolute pressure.

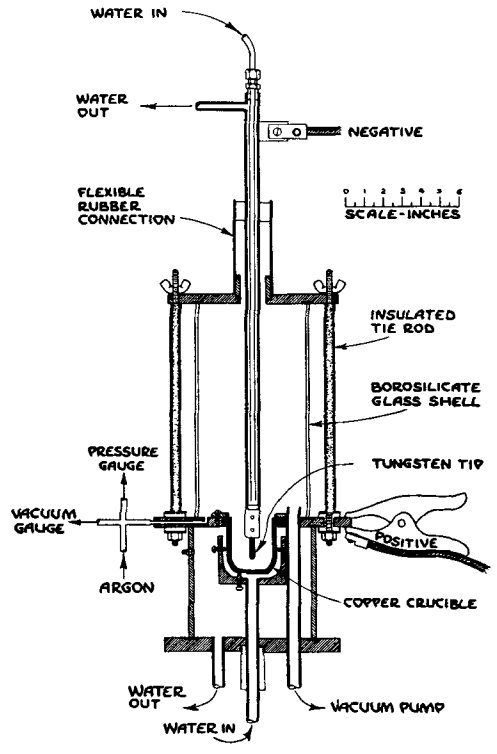

FIG. 1. Button melting furnace

For the work on all impurities, except oxygen, buttons were prepared by a triple melting process:

1. The base sponge and measured quality of impurity were thoroughly mixed and formed into a cylindrical compress. This compress was then melted in the furnace.
2. The button so formed was placed on edge in the crucible and remelted.
3. The button was turned over and melted a third time.

Approximately 80% of the button was fully molten in each step.

Contamination by tungsten from the electrode is negligible. Analyses of several buttons showed an average tungsten content of 0.005% with none over 0.01%.

Contamination by atmospheric oxygen and nitrogen is also negligible. Buttons remelted 10 to 12 times showed no measurable increase in Brinell hardness.

Most of the contaminants were prepared as master alloys and homogenized by this triple melting process. The master alloy buttons were then broken up and added to the base sponge in measured quantities and buttons were prepared from this mixture. In a few cases it was found expedient to add metallic impurities directly and in one case (vanadium) the impurity was added both directly and as a master alloy.

Buttons were prepared for hardness measurement by grinding parallel flat surfaces, about 1 in. in diameter, on both top and bottom by means of a belt grinder. Since the buttons had a shallow elliptical cross section, only a small amount of metal needed to be removed to provide these flat surfaces. Water cooling between short grinding periods precluded contamination by atmospheric oxygen or nitrogen. For hardness measurement the surface was given a smooth finish by application of successively finer abrasive papers. The finished buttons were approximately 50 mm in diameter and 12 mm in thickness between parallel faces. Hardness measurements were made on a standard Brinell machine using a 1500 kg load on a 10 mm steel ball for 20 sec. The hardness of each button was determined as the average reading of two impressions.

Oxygen and Nitrogen

The effect of oxygen and nitrogen was first established by treating the two impurities as a single impurity. Data in Fig. 2 were collected from routine analyses of early sponge products; each point represents a different sponge. Buttons were prepared by single melting and Brinell hard-

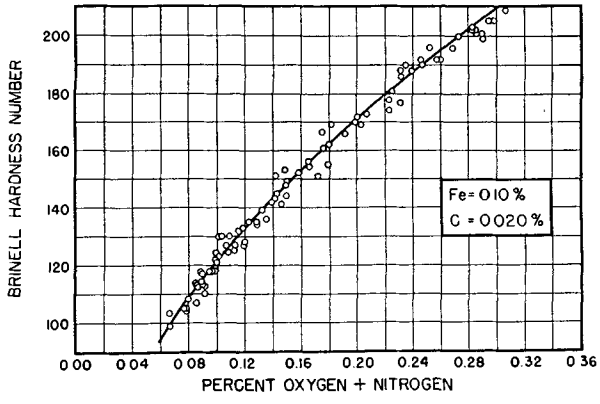

FIG. 2. BHN vs. oxygen + nitrogen content

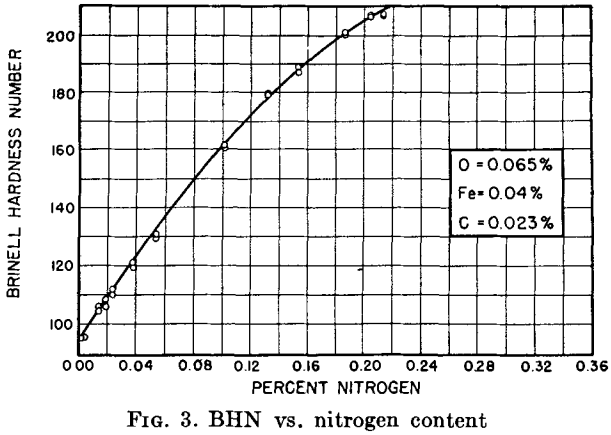

FIG. 3. BHN vs. nitrogen content

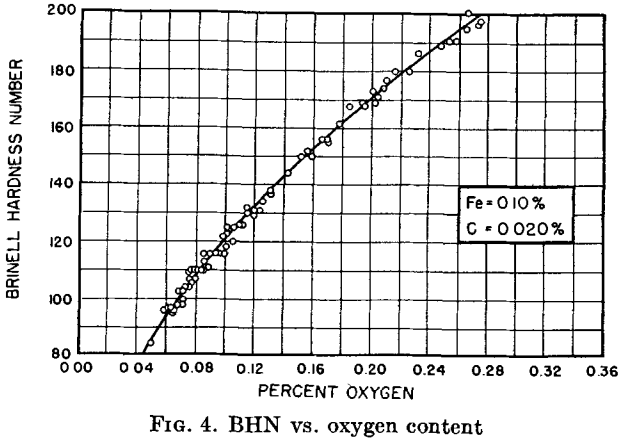

FIG. 4. BHN vs. oxygen content

ness was determined. These buttons were then analyzed for oxygen by the vacuum fusion method using the Walter technique (16). Drillings of the buttons were analyzed for nitrogen, iron, and carbon by conventional methods. Commercial sponge contains, beside oxygen and nitrogen, variable amounts of iron and carbon. To obtain a single curve on a two-dimensional plot, it was necessary to adjust the data to some arbitrary levels of iron and carbon. Levels of 0.10% iron and 0.02% carbon were selected for this purpose. The hardness of the sample was translated to the value it would have if it contained 0.10% iron and 0.02% carbon. Correction factors for this adjustment were taken from iron and carbon curves to be discussed later. In the range 100–200 BHN the oxygen + nitrogen curve is parabolic with the formula:

$$\text{Weight-per cent (O + N)} = 6.85 \times 10^{-6} (\text{BHN})^2 \quad \text{(I)}$$

Fig. 3 shows the nitrogen curve. A master alloy containing 5% nitrogen was prepared by directly nitriding sponge at 1000°C. This was homogenized by triple melting, crushed to 8–10 mesh, and added to the base sponge to yield the compositions shown. All buttons were prepared by the triple melting procedure.

With the effect of nitrogen established, it is a simple matter to convert the oxygen + nitrogen data to oxygen alone. The oxygen curve is shown in Fig. 4. The conversion is not drastic since oxygen and nitrogen have similar hardening capacities and the oxygen content is normally close to a magnitude higher than the nitrogen content. It is readily seen that nitrogen is a slightly more potent hardener on a weight basis but that up to a few hundredths of a per cent, nitrogen and oxygen can be treated as equivalent in hardening effect for all practical purposes.

Carbon and Iron

Fig. 5 shows the curve for carbon. A master alloy containing 10% spectroscopically pure graphite was prepared and homogenized by triple melting. This alloy was crushed and added to sponge to yield the compositions shown; buttons were prepared by triple melting.

Fig. 6 shows the curve for iron. Specimens were prepared in the same way except that a 50–50 master alloy was used.

Data from these curves were used in making the corrections to arbitrary levels of carbon and iron in the oxygen + nitrogen curve.

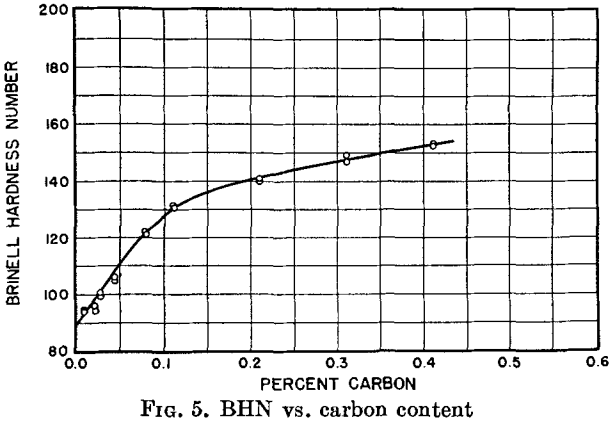

FIG. 5. BHN vs. carbon content

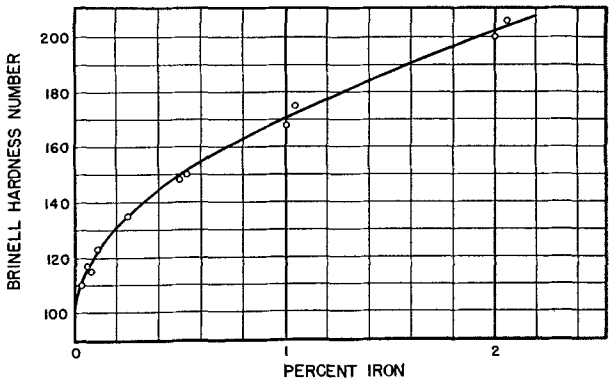

FIG. 6. BHN vs. iron content

Other Impurities

The effects of silicon and of ten metallic impurities were also determined. All metals used were of the highest purity obtainable and in all cases where impurities were suspected they were checked by analysis to assure the absence of spurious results. All buttons were prepared by the triple melting technique. The sponge used in all tests was from a single lot of good quality sponge of high uniformity. The weight-per cent composition is shown in Table I. This sponge was also used in establishing the nitrogen curve. The iron and carbon curves had been determined earlier using different sponges of approximately the same composition. Data are shown in Fig. 7, 8, and and 9.

TABLE I. *Composition of sponge*

Oxygen	0.069
Nitrogen	0.004
Iron	0.045
Carbon	0.025
Silicon	0.007
Chromium	<0.005
Hydrogen	0.0014
BHN	96

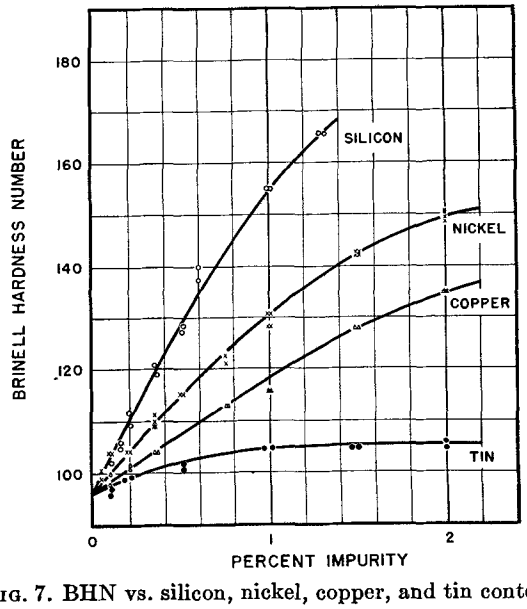

FIG. 7. BHN vs. silicon, nickel, copper, and tin content

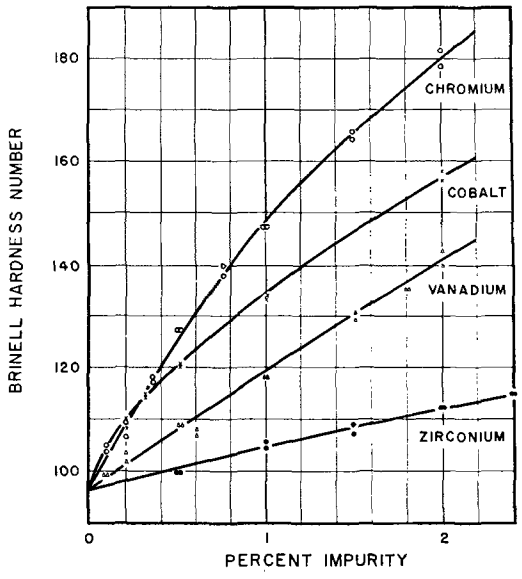

FIG. 8. BHN vs. chromium, cobalt, vanadium, and zirconium content.

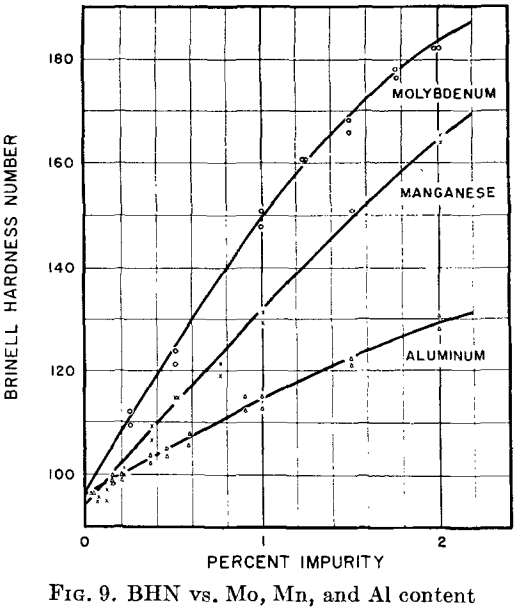

FIG. 9. BHN vs. Mo, Mn, and Al content

Methods of addition of impurities to the titanium are summarized in Table II.

TABLE II

Element	50-50 Master alloy, crushed	50-50 Master alloy, drillings	Added directly
Si	X		
Mo			X [1]
Cr	X		
Mn	X		
Co			X [2]
Ni	X		
V		X	
Cu	X		
Al	X		
Zr			X [1]
Sn			X [3]

[1] Turnings of pure metal.
[2] Drillings of pure metal.
[3] Small pieces of pure metal.

Composite Results

Fig. 10 shows results plotted on one chart for comparative purposes. This shows the incremental hardening effect of the various impurities when added to Ti of 100 Brinell base hardness. Oxygen is shown as a dotted line since it has been transposed to the common origin. Note that in most cases the impurities maintain their relative positions over the entire range. Relationships at low concentrations are shown in Fig. 11.

Relative hardening effects of the various impurities at low levels, assuming a linear relationship, are shown in Table III. Oxygen in each case is taken as unity for reference. It should be noted that on a weight basis values vary over a range of almost two magnitudes. On an atomic basis there are some interesting twists. For example, atom for atom, iron is a more potent hardening agent than even oxygen or nitrogen.

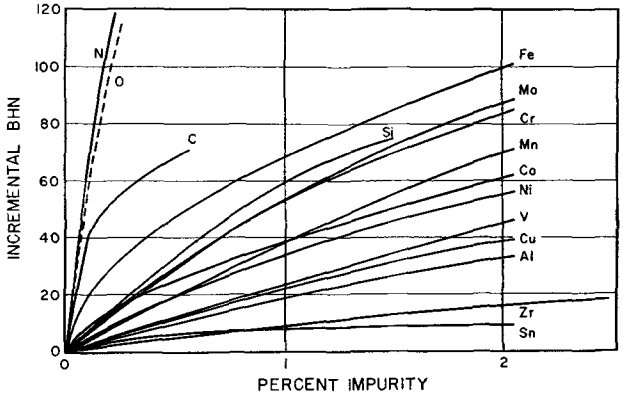

FIG. 10. BHN vs. impurity level

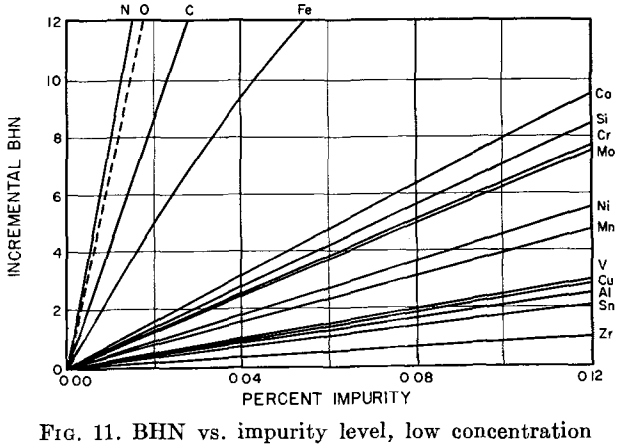

FIG. 11. BHN vs. impurity level, low concentration

TABLE III. *Relative hardening effects of small amounts of impurities added to 100 BHN* Ti

Impurity	Weight basis	Atomic basis
N	1.33	0.99
O	1.00 (Standard of reference)	1.00
C	0.63	0.47
Fe	0.35	1.23
Co	0.11	0.41
Si	0.10	0.18
Cr	0.090	0.29
Mo	0.089	0.53
Ni	0.065	0.24
Mn	0.056	0.19
V	0.037	0.12
Cu	0.034	0.10
Al	0.030	0.05
Sn	0.025	0.17
Zr	0.013	0.08

Discussion

Hardness data are shown for some 230 buttons ranging roughly from 90 to 200 BHN. The mean deviation from the best curve is less than 2 points BHN, indicating thorough homogenization. Moreover, chemical analyses of buttons invariably checked theoretical compositions within the usual limits of analytical error. On the basis of these facts, together with precautions taken to avoid extraneous contamination during preparation, it is concluded that the data presented are truly representative for conditions prescribed. The triple melting procedure is recommended for the preparation of uniform specimens of titanium containing nonvolatile impurities or alloying agents.

In attempting to duplicate these data, the most critical point perhaps would be reasonable duplication of the rate of cooling of the buttons following the melting step. In this work, buttons were prepared in a water-cooled crucible. After the power was turned off, the buttons cooled to 650°C in about 35 sec. Small deviations from such a cooling rate would not be expected to affect hardness materially. One bit of evidence substantiating this view is the fact that triple melted buttons, after removal of the small amount of metal necessary to prepare them for measurement, exhibited substantially the same hardness on top and bottom. However, greater differences might be expected to arise in the case of large ingots because of the poor heat conductivity of Ti. As mentioned earlier, mechanical working of specimens will in itself be a factor in determining the hardness of the metal.

It should be mentioned that trouble was experienced in attempting to prepare homogeneous buttons containing tungsten. Tungsten crushed to 8–10 mesh, added to the Ti sponge, and triple melted using 150% of normal power was not dispersed in the Ti. Radiographs indicated that the 8–10 mesh tungsten had been reduced to about 10–12 mesh by this treatment. Apparently the high density of tungsten forces it into the pasty region near the bottom of the molten button where solution is very slow. It would seem that tungsten must be fairly finely divided to allow uniform solution without recourse to an excessively long melting procedure. Investigations along this line were not pursued. On the other hand, radiographs of Mo alloy buttons did not show segregation.

Estimation of Oxygen in Ti

One application of these data is the estimation of oxygen in unalloyed Ti without the actual performance of an oxygen analysis. As applied to Ti sponge, the sponge is melted to form a 100-g button. The Brinell hardness of the button is determined. Drillings of the button are analyzed for nitrogen, iron, and carbon by conventional methods. The Brinell hardness is adjusted to correspond to arbitrary levels of 0.10% iron and 0.02% carbon. A chart such as shown in Table IV is convenient to use in making these adjustments. Actually, this chart extends much farther than the usual range. For most commercial sponge products, the adjustment is of the order of 10 points Brinell or less. Of course, if other impurities are present in significant amounts, adjustments can be made in a similar manner. Referring again to the oxygen + nitrogen curve (Fig. 2), the oxygen + nitrogen content is found corresponding to the adjusted Brinell hardness. Subtracting the nitrogen gives the estimated figure for oxygen content. From the data on 87 specimens shown in Fig 2, the expected accuracy of a single estimation is within about 6% of the value as determined by vacuum fusion analysis.

While the accuracy of an estimation of this method is, on the average, slightly poorer than a vacuum fusion analysis by a competent analyst, it is of sufficient accuracy for most work at the present time. This method is used here in upward of 90% of the determinations of oxygen content of sponge products, reserving vacuum fusion analyses for critical or unusual samples only.

The question may reasonably be asked whether this method involves less work than an actual oxygen analysis. If oxygen content is considered as an isolated property,

TABLE IV. *Chart for BHN adjustment for iron and carbon contents*

% Fe	BHN adjust.	% Fe	BHN adjust.	% Fe	BHN adjust.	%C	BHN adjust.	%C	BHN adjust.	%C	BHN adjust.
0.00	+19	0.20	−10	0.40	−23	0.000	+9	0.020	0	0.040	−8
0.01	+16	0.21	−10	0.41	−23	0.001	+8	0.021	0	0.041	−9
0.02	+14	0.22	−11	0.42	−24	0.002	+8	0.022	−1	0.042	−9
0.03	+12	0.23	−12	0.43	−25	0.003	+7	0.023	−1	0.043	−10
0.04	+10	0.24	−13	0.44	−25	0.004	+7	0.024	−2	0.044	−10
0.05	+8	0.25	−14	0.45	−26	0.005	+7	0.025	−2	0.045	−10
0.06	+6	0.26	−14	0.46	−26	0.006	+6	0.026	−3	0.046	−11
0.07	+4	0.27	−15	0.47	−27	0.007	+6	0.027	−3	0.047	−11
0.08	+3	0.28	−16	0.48	−27	0.008	+5	0.028	−3	0.048	−11
0.09	+1	0.29	−16	0.49	−28	0.009	+5	0.029	−4	0.049	−12
0.10	0	0.30	−17	0.50	−28	0.010	+4	0.030	−4	0.050	−12
0.11	−1	0.31	−18	0.55	−31	0.011	+4	0.031	−5	0.055	−14
0.12	−2	0.32	−18	0.60	−33	0.012	+4	0.032	−5	0.060	−16
0.13	−3	0.33	−19	0.65	−35	0.013	+3	0.033	−5	0.065	−18
0.14	−4	0.34	−19	0.70	−37	0.014	+3	0.034	−6	0.070	−20
0.15	−5	0.35	−20	0.75	−39	0.015	+2	0.035	−6	0.075	−22
0.16	−6	0.36	−21	0.80	−42	0.016	+2	0.036	−7	0.080	−24
0.17	−7	0.37	−21	0.85	−44	0.017	+1	0.037	−7	0.085	−26
0.18	−8	0.38	−22	0.90	−45	0.018	+1	0.038	−8	0.090	−28
0.19	−9	0.39	−22	0.95	−47	0.019	+1	0.039	−8	0.095	−29
				1.00	−49					0.100	−31

the answer must be negative. However, under normal circumstances, when oxygen content is of interest, hardness of the metal, nitrogen content, iron content, and possibly even the carbon content are also of interest. These determinations are commonly made on a routine basis so that the necessary data for making an oxygen estimation are normally at hand. Therefore, an estimate of oxygen content may be made in less than a minute, whereas an actual determination of oxygen would take up to a few hours.

Limitations

There are certain limitations to the use of these data that should be pointed out. In the first place the data apply only to 100-g buttons melted as prescribed. Second, the effect of impurities on hardness is not strictly additive and attempts to apply the data to grossly impure samples or samples containing a large number of impurities at significant levels may lead to serious error. However, the method was found to be reliable when applied to normal sponge products.

It should be remembered that the incremental hardening effects of the various impurities are based on Ti of 100 BHN, e.g., Ti containing 0.067% oxygen + nitrogen, 0.10% iron, 0.02% carbon. Addition of impurities at a higher base level will have a somewhat lesser effect on the numerical hardness increment. However, within the normal commercial range of hardness, the error introduced is usually insignificant.

Examples of Use of Data

The usefulness of the data is illustrated by the following examples.

I. A sample of sponge has a 100-g button hardness of 120 BHN. Nitrogen content is 0.012%, iron 0.15%, carbon 0.026%. Other impurities are negligible. Estimate the oxygen content.

From Table IV the iron and carbon adjustments are −5 and −3, respectively. The adjusted BHN is then 120 − 5 − 3 = 112 (this is the hardness this specimen would have if it contained 0.10% iron and 0.02% carbon rather than the actual levels). From Fig. 2 it is found that 112 BHN corresponds to 0.086% oxygen + nitrogen. Estimated oxygen content is then 0.086 − 0.012 = 0.074%.

II. Estimate the BHN of Ti containing 0.104% oxygen, 0.008% nitrogen, 0.14% iron, and 0.015% carbon.

Oxygen + nitrogen = 0.104 + 0.008 = 0.112%. This corresponds (Fig. 2) to 128 BHN. Adjustments for iron and carbon (Table IV) are +4 and −2, respectively. (Note that the signs are reversed since the translation is away from rather than toward the arbitrary levels.) BHN = 128 + 4 − 2 = 130.

III. A sponge product containing 0.20% iron has a hardness of 130 BHN. Estimate the hardness if iron were reduced to 0.05%, other impurities remaining constant.

Table IV shows that the BHN decrease would be 18 points. 130 − 18 = 112 BHN.

IV. An impure Ti product contains 0.08% Si, 0.05% Cr, and 0.10% Mn. BHN is 115. Estimate the BHN if these impurities were eliminated. From Fig. 11 the hardness would be 115 − 6 − 3 −4 = 102 BHN.

V. A mixture of sponge of 100 BHN and 0.40% TiO_2 is melted to form an ingot. Estimate the BHN of the resultant ingot.

Oxygen content of TiO_2 is 40%. Therefore 0.16% oxygen is added to the Ti. From Fig. 2 the resultant BHN would be 183.

VI. Equal parts of sponge products A & B are mixed. Estimate the resultant BHN.

Sponge A	*Sponge B*
100 BHN	200 BHN
0.08% Iron	0.16% Iron
0.016% Carbon	0.028% Carbon

Adjusted BHN for sponge A is 100 + 3 + 2 = 105 BHN. Oxygen + nitrogen = 0.076%. Adjusted BHN for sponge B is 200 − 6 − 3 = 191 BHN. Oxygen + nitrogen = 0.250%.

Resultant mixture would then contain 0.163% oxygen + nitrogen, 0.12% iron, and 0.022% carbon.

Oxygen + nitrogen = 0.163% corresponds to 154 BHN.

Adjustments for iron and carbon are +2 and +1 respectively. BHN = 154 + 2 + 1 = 157.

Acknowledgments

The author acknowledges with thanks the contributions of research personnel of the Pigments Department in various phases of the work. Among these are Andrew K. Palese who prepared the buttons and made hardness determinations, John M. Thompson who made the chemical analyses, Frederick Walls and Cortland Warrington who performed vacuum fusion analyses for oxygen content, and William Miller who prepared the line drawings.

Manuscript received December 20, 1955. This paper was prepared for delivery before the Pittsburgh Meeting, October 9 to 13, 1955.

Any discussion of this paper will appear in a Discussion Section to be published in the June 1957 JOURNAL.

REFERENCES

1. W. J. BARTH AND A. L. FEILD, JR., *Metal Prog.*, **64**, 74 (1953).
2. C. I. BRADFORD, J. P. CATLIN, AND E. M. WEMPLE, *ibid.*, **55**, 348 (1949).
3. I. E. CAMPBELL, R. I. JAFFEE, J. M. BLOCHER, JR., J. GURLAND, AND B. W. GONSER, *J. (and Trans.) Electrochem. Soc.*, **96**, 271 (1948).
4. C. M. CRAIGHEAD, O. W. SIMMONS, AND L. W. EASTWOOD, *Trans. Am. Inst. Mining Met. Engrs.*, **188**, 485 (1950).
5. C. M. CRAIGHEAD, O. W. SIMMONS, AND L. W. EASTWOOD, *ibid.*, **188**, 514 (1950).
6. W. L. FINLAY AND J. A. SNYDER, *ibid.*, **188**, 277 (1950).
7. R. I. JAFFEE AND I. E. CAMPBELL, *ibid.*, **185**, 646 (1949).
8. R. I. JAFFEE, H. R. OGDEN, AND D. J. MAYKUTH, *ibid.*, **188**, 1261 (1950).
9. R. I. JAFFEE, *Iron Age*, **171**, 162 (1953).
10. R. I. JAFFEE, F. C. HOLDEN, AND H. R. OGDEN, *J. Metals*, **6**, 1282 (1954).
11. A. E. JENKINS AND H. W. WORNER, *J. Inst. Metals*, **80**, 157 (1951–52).

12. D. J. Maykuth, *et al.*, Summary report AF 33 (038)-8344, (1953).
13. D. A. Sutcliffe, *Metal Treatment*, **21**, 191 (1954).
14. D. A. Sutcliffe and A. C. Spickett, Royal Aircraft Est. (Gt. Brit.) R.A.E. Met. 73 (N-23-199).
15. F. S. Wartman, D. H. Baker, J. R. Nettle, and V. E. Homme, *This Journal*, **101**, 507 (1954).
16. D. I. Walter, *Ind. Eng. Chem.*, **42**, 297 (1950).
17. H. W. Worner, *J. Inst. Metals*, **80**, 213 (1951-52).
18. H. W. Worner, *ibid.*, **81**, 521 (1953).

Mathematical Studies of Galvanic Corrosion

VI. Limiting Case of Very Thin Films

J. T. Waber

University of California, Los Alamos Scientific Laboratory, Los Alamos, New Mexico

ABSTRACT

The limiting case of a very thin electrolyte layer which covers a coplanar electrode arrangement has been analyzed by making the electrode dimensions infinitely larger than the corrodent depth. A Fourier integral expression for the potential throughout the corrosive medium has been derived from the Fourier series treatment of the potential pertinent to finite electrode widths. The electrolyte depth becomes the critical cell dimension. The variation of the potential along the inner and outer boundaries of the liquid are presented in two graphs with a separate curve for each value of the ratio of the liquid depth to the Wagner polarization parameter. The distribution of the corrosion current over the anode is also presented graphically as a function of this ratio.

Although the effect of thin films on minimizing the corrosion rate and concentrating the attack into the vicinity of the anode-cathode junction has been discussed (1), the case of an electrolyte film much thinner (in depth) than the electrode dimensions was not discussed. Such a film might be an adsorbed multimolecular film on a piece of commercially pure metal or a stagnant layer on a large welded structure containing gross inhomogeneities. As has been pointed out previously in this series, the actual physical dimensions of a galvanic system do not dictate the behavior of the system, but their relation to the magnitude of the polarization parameter $\mathfrak{P}$ does dictate it. It is clear from the earlier discussion of the effect of electrolyte thickness b that this dimension is the critical one which most strongly affects the distribution of current density on the electrodes. Thus the systems under consideration can be characterized by the one dimensionless ratio $(b/\mathfrak{P})$.

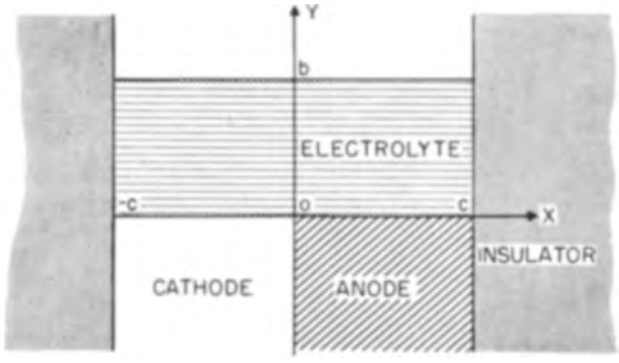

Fig. 1*a*. Geometric relation of the electrodes and the thin electrolyte. Insulating walls at $x = c$.

In previous papers, Fourier series and Fourier integrals have been used independently. One may start from the geometric arrangement of electrodes and liquid depicted in Fig. 1*a*, for which a Fourier series is appropirate, and, by increasing the distance between insulating walls to infinity, lead to the arrangement of Fig. 1*b* and to a Fourier integral. Use of this limiting process, although it is not new, may be helpful in solving similar heat transfer and diffusion problems. An independent derivation of the Fourier integral used here has been presented elsewhere (2) and will not be discussed.

Boundary Conditions

One may assume a periodic arrangement of long narrow electrodes to determine the effects of juxtaposing an anode and a cathode in a common surface and analyze the potential distribution in terms of a Fourier series. It is sufficient, however, to examine the behavior within only one period. With the arrangement depicted in Fig. 1*a* it can be shown that only sine terms remain in the Fourier serie

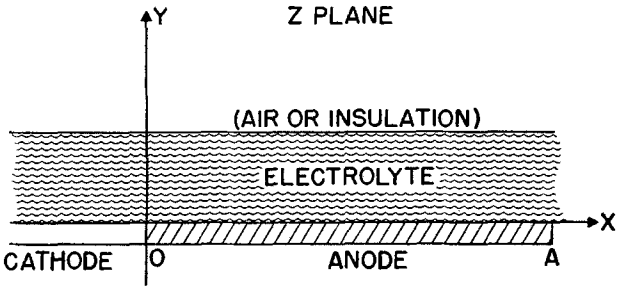

Fig. 1*b*. Effect of moving insulating walls to infinity.

since an odd symmetry about point (0, ½) has been assumed. One can ignore edge effects and concentrate on the anode-cathode junction if

$$\left.\frac{\partial P^*}{\partial x}\right|_{x=-c} = \left.\frac{\partial P^*}{\partial x}\right|_{x=c} = 0 \qquad \text{(I)}$$

Using the definition of the effective potential difference E_a discussed elsewhere (3), the potential of the polarized electrode at the electrode interface, namely $P^*(x, 0)$, is

$$P^*(x, 0) - \mathfrak{L}\left.\frac{\partial P^*}{\partial y}\right|_{y=0} = E_a \qquad \text{(II)}$$

in the "anodic" region $0 < x \leq c$ and is

$$P^*(x, 0) - \mathfrak{L}\left.\frac{\partial P^*}{\partial y}\right|_{y=0} = 0 \qquad \text{(III)}$$

in the cathodic region $-c \leq x < 0$. The unpolarized interfacial potential $P(x, 0)$ takes on the values E_a and 0. The relation between the two potentials is illustrated in Fig. 2.

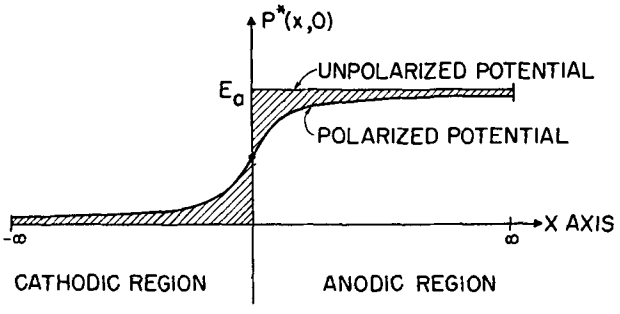

FIG. 2. Distribution of interfacial potential over the electrodes.

Since the line $y = b$ represents the upper surface of the electrolyte, an insulator type of boundary condition

$$\left.\frac{\partial P^*}{\partial y}\right|_{y=b} = 0 \qquad \text{(IV)}$$

applies. Although $P^*(x, 0)$ is a periodic function, it is not necessary to specify its behavior beyond this range $-c \leq x \leq c$.

Potential Function

It can be established that the potential at any point is given by

$$P^*(x, y) = \frac{E_a}{2} + \frac{2E_a}{\pi}\sum_{m=0}^{\infty} \left\{ \frac{\cosh\left[\frac{(2m+1)(b-y)\pi}{2c}\right]\sin\left[\frac{(2m+1)\pi x}{2c}\right]}{(2m+1)\left\{\cosh\left[\frac{(2m+1)b\pi}{2c}\right] + \frac{(2m+1)\mathfrak{L}\pi}{2c}\sinh\left[\frac{(2m+1)b\pi}{2c}\right]\right\}} \right\} \qquad \text{(V)}$$

and that this function satisfies boundary conditions (I), (II), (III), and (IV).

It is demonstrated in the Appendix that, as c becomes larger and larger, the value of the terms in (V) changes very slowly with respect to m and a very large number of terms are required for even a poor approximation to the function. In the limit as c approaches infinity, the summation can be replaced by integration and (V) becomes

$$P^*(x, y) = \frac{E_a}{2} + \frac{E_a}{\pi}\int_0^{\infty} \frac{\cosh\left[\frac{\omega(b-y)}{\mathfrak{L}}\right]\sin\left(\frac{\omega x}{\mathfrak{L}}\right)d\omega}{\omega\left[\cosh\left(\frac{\omega b}{\mathfrak{L}}\right) + \omega\sinh\left(\frac{\omega b}{\mathfrak{L}}\right)\right]} \qquad \text{(VI)}$$

The details of transforming the series to this aperiodic solutions are indicated in the Appendix.

The integrand becomes simpler if only the interfacial potentials are computed. The two simplified integrands are listed below.

Interface	Integrand
Metal-solution $y = 0$ (inner)	$\dfrac{\sin\left(\frac{\omega x}{\mathfrak{L}}\right)}{\omega\left[1 + \omega\tanh\left(\frac{\omega b}{\mathfrak{L}}\right)\right]}$
Solution-insulator $y = b$ (outer)	$\dfrac{\sin\left(\frac{\omega x}{\mathfrak{L}}\right)}{\omega\left[\cosh\left(\frac{\omega b}{\mathfrak{L}}\right) + \omega\sinh\left(\frac{\omega b}{\mathfrak{L}}\right)\right]}$

An expression different from (V) is used when b is infinite, the hyperbolic cosine is replaced by a similar exponential term. Proceeding as above, the integral is

$$P^*(x, y) = \frac{E_a}{2} + \frac{E_a}{\pi}\int_0^{\infty} \frac{\exp\left(-\frac{\omega y}{\mathfrak{L}}\right)\sin\left(\frac{\omega x}{\mathfrak{L}}\right)d\omega}{\omega(1+\omega)} \qquad \text{(VII)}$$

A simplified expression can be obtained when y is set equal to zero. It is

$$P^*(x, 0) = E_a - \frac{E_a}{\pi}\left[\mathrm{Ci}\left(\frac{x}{\mathfrak{L}}\right)\sin\left(\frac{x}{\mathfrak{L}}\right) - \mathrm{si}\left(\frac{x}{\mathfrak{L}}\right)\cos\left(\frac{x}{\mathfrak{L}}\right)\right] \qquad \text{(VIII)}$$

where si and Ci stand for sine and cosine integrals, namely

$$\mathrm{si}(z) = -\int_z^{\infty} \frac{\sin t\, dt}{t} \qquad \text{(IX)}$$

$$\mathrm{Ci}(z) = \int_z^{\infty} \frac{\cos t\, dt}{t} \qquad \text{(X)}$$

These functions have been tabulated, for example, by Jahnke and Emde (5). The potential at $y = \infty$ is equal to $E_a/2$ since the integral vanishes at this limit. This quantity has been referred to in earlier reports (3, 4) as the potential of the composite electrode.

Corrosion Current Parameter

A slightly different expression must be used since both the anode and the cathode widths are infinite. The new

dimensionless quantity which represents the local variation in the corrosion attack is

$$C_b^*(x) = -\left(\frac{2b}{E_a}\right)\left.\frac{\partial P^*}{\partial y}\right|_{y=0} \qquad \text{(XI)}$$

Boundary conditions (III) and (IV) permit calculation of the normal gradient from the interfacial potential at $y = 0$. The expression is given as equation (XV) of Reference (2).

Discussion

One practical way of minimizing the number of parameters in a problem is to discuss limiting cases, for the mathematical answers are independent of that variable or parameter taken to the limit. Specifically, it is assumed that widths of both electrodes are infinitely larger than the depth b of the electrolyte. Analysis of this case would apply to adsorbed films of moisture and multiphase alloys where the film thickness is smaller than the smallest dimension of the individual grains of the microconstituent. Although there are well-known examples of precipitates forming from solid solutions, which cannot be resolved by the optical microscope, the average constituent of commercial alloys has dimensions larger than a few microns.

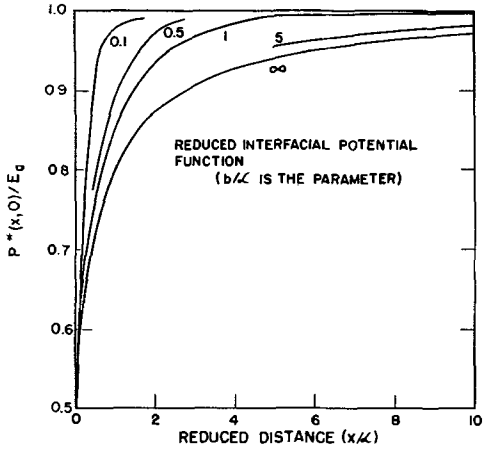

Fig. 3. Distribution of the reduced potential over the anode surface. Curves are for different values of ($b/\mathfrak{L}$).

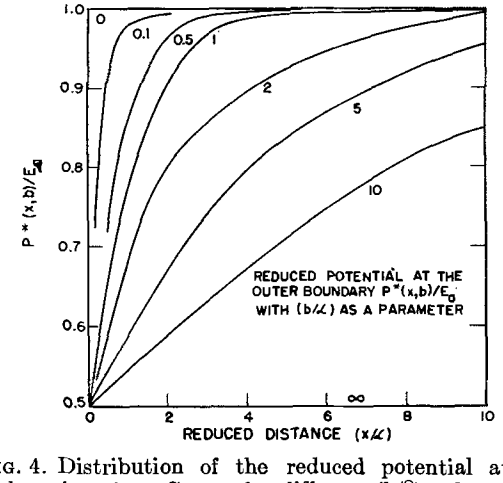

Fig. 4. Distribution of the reduced potential at the liquid-gas interface. Curves for different ($b/\mathfrak{L}$) values apply to the anodic region ($x/\mathfrak{L} > 0$).

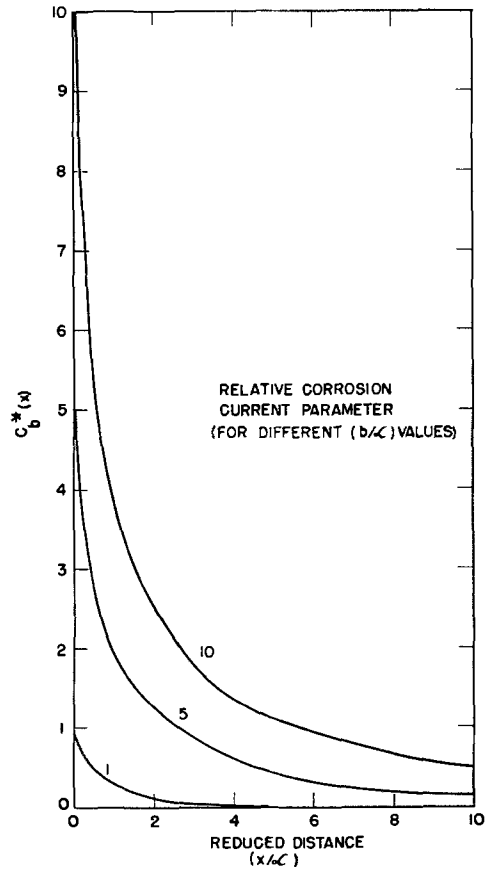

Fig. 5. Variation of the modified corrosion current parameter near the anode-cathode junction.

Values of the polarization parameter employed in previous papers (1, 3) were all larger than 0.01 cm, so for most practical cases, $\mathfrak{L}$ is much larger than the thickness of an adsorbed film.

The potentials at the interface $y = 0$ and at the outer boundary $y = b$ are shown in Fig. 3 and 4, respectively. At a given $x/\mathfrak{L}$ value, the difference between the potential at the two boundaries increases as $b/\mathfrak{L}$ increases. The potential at the outer boundary varies more rapidly with $b/\mathfrak{L}$ than it does at the other boundary.

Distribution of current over the anode is shown in Fig. 5. The corrosion current is concentrated into the immediate vicinity of the anode-cathode junction and the maximum value is reduced as $b/\mathfrak{L}$ decreases. It is evident that b is the critical dimension λ of this galvanic couple. When $b/\mathfrak{L}$ is as small as one, only small portions of the anode suffer appreciable corrosion attack. It is suggested that greatest part of the attack takes place within a distance $x/\mathfrak{L} = 2(b/\mathfrak{L})$ of the junction.

Equations (VIII) and (XI) apply as well to the potential and current distribution near the anode-cathode junction when the polarization parameter is very much smaller than any of the physical dimensions. Even though $\mathfrak{L}$ becomes very small, $y/\mathfrak{L}$ need not approach infinity simultaneously with $b/\mathfrak{L}$, since $0 \leq y \leq b$. Fig. 3 and 5 describe the situation very near the anode-cathode junction when $\mathfrak{L}$ is almost negligible. Thus, the foregoing analysis, with $b/\mathfrak{L}$ very large, can be regarded as a bridging link between

Part I in which polarization was neglected (3) and Parts II and III in which it was considered (4). Note that the relation

$$C^*(x) = a/b\ C_b^*(x) \qquad \text{(XII)}$$

must be used to correct the corrosion parameter found herein to the values previously tabulated (1, 3, 4).

Acknowledgment

The author is deeply indebted to Professor Carl Wagner for having pointed out the merit of the mathematical method used herein. The services of Donald Prys and Marguerite Coleman in preparing this manuscript are gratefully acknowledged.

Manuscript received December 7, 1955. Work on this paper was done under the auspices of the Atomic Energy Commission.

Any discussion of this paper will appear in a Discussion Section to be published in the June 1957 JOURNAL.

REFERENCES

1. J. T. WABER AND BERTHA FAGAN, *This Journal*, **103**, 64 (1956).
2. J. T. WABER, "Mathematical Analysis of Galvanic Corrosion, IX. Solution for Ultra Thin Liquid Films and Very Small Polarization Parameters" (in preparation).
3. J. T. WABER, *This Journal*, **101**, 271 (1954).
4. J. T. WABER AND M. ROSENBLUTH, *ibid.*, **102**, 344, 420 (1955).
5. E. JAHNKE AND F. EMDE, "Tables of Functions with Formulae and Curves," Table I, p. 8, 4th ed., Dover Publications, New York (1945).

APPENDIX

Equation (V) may be written with the coefficient of the m-th term indicated as an integral. This is a useful form when applying the limiting process of making c infinite and generating the potential function for this aperiodic case. In this form

$$P^*(x, y) = \frac{E_a}{2} + \sum_{m=0}^{\infty} \cdot\left\{\frac{2}{2c}\int_{-c}^{c} P^*(x', 0)\sin\left[\frac{(2m+1)\pi x'}{2c}\right]dx'\right\} \times \sin\left[\frac{(2m+1)\pi x}{2c}\right]\cosh\left[\frac{(2m+1)(b-y)\pi}{2c}\right] \qquad \text{(XIII)}$$

Define a dimensionless frequency ω_m as an auxiliary variable

$$\omega_m \equiv (2m+1)\pi\mathfrak{L}/2c$$

The change $\Delta\omega$ between two successive terms is $(\pi\mathfrak{L}/c)$. One may rewrite (XIII) as

$$P^*(x, y) = \frac{E_a}{2} + \sum_{m=0}^{\infty} \cdot\left\{\frac{\Delta\omega}{\pi\mathfrak{L}}\int_{-c}^{c} P^*(x', 0)\sin\left(\frac{\omega_m x'}{\mathfrak{L}}\right)dx'\right\} \times \sin\left(\frac{\omega_m x}{\mathfrak{L}}\right)\cosh\left[\frac{\omega_m(b-y)}{\mathfrak{L}}\right] \qquad \text{(XIV)}$$

One may substitute the values of $P^*(x, 0)$ from equations (II) and (III) and after differentiating termwise show that

$$P^*(x, y) = \frac{E_a}{2} + E_a\sum_{m=0}^{\infty}\left\{\frac{\Delta\omega}{\pi\mathfrak{L}D(\omega_m)}\int_0^c \sin\left(\frac{\omega_m x'}{\mathfrak{L}}\right)dx'\right\} \times \sin\left(\frac{\omega_m x}{\mathfrak{L}}\right)\cosh\left[\frac{\omega_m(b-y)}{\mathfrak{L}}\right] \qquad \text{(XV)}$$

since the unpolarized potential $P(x, 0)$ takes on the values of 0 and E_a. In this equation, the denominator

$$D(\omega_m) \equiv \cosh\left(\frac{\omega_m b}{\mathfrak{L}}\right) + \omega_m \sinh\left(\frac{\omega_m b}{\mathfrak{L}}\right) \qquad \text{(XVI)}$$

is independent of x'. One may integrate then with respect to x' and obtain

$$P^*(x, y) = \frac{E_a}{2} + \frac{E_a}{\pi}\sum_{m=0}^{\infty} \sin\left(\frac{\omega_m x}{\mathfrak{L}}\right)\cosh\left[\frac{\omega_m(b-y)}{\mathfrak{L}}\right]\frac{1}{D(\omega_m)}\left(\frac{\Delta\omega}{\omega_m}\right) \qquad \text{(XVII)}$$

If c becomes large, the frequency ω_m becomes small for any finite values of m and $\mathfrak{L}$. Thus, the potential function $P^*(x, y)$ can be regarded as the sum of products of the infinitesmal $\Delta\omega$ times a function of ω_m. As c approaches infinity, the dense denumerable set ω_m can be replaced by a continuous variable ω and the limit of the sum of products is a definite integral.

Thus it can be shown that

$$P^*(x, y) = \frac{E_a}{2} + \frac{E_a}{\pi}\int_0^{\infty} \frac{\sin\left(\frac{\omega x}{\mathfrak{L}}\right)\cosh\left[\frac{\omega(b-y)}{\mathfrak{L}}\right]d\omega}{\omega\left[\cosh\left(\frac{\omega b}{\mathfrak{L}}\right) + \omega\sinh\left(\frac{\omega b}{\mathfrak{L}}\right)\right]} \qquad \text{(XVIII)}$$

which is identical to the expression derived (2) directly by assuming a Fourier integral with an undefined coefficient function subsequently "chosen" to satisfy the boundary conditions.

Oxidation of Alloys Involving Noble Metals

CARL WAGNER

Department of Metallurgy, Massachusetts Institute of Technology, Cambridge, Massachusetts

ABSTRACT

Diffusion processes during the oxidation of alloys involving noble metals are analyzed theoretically. An oxide film of uniform thickness is stable only if diffusion in the alloy is relatively rapid compared with diffusion in the oxide of the less noble metal. Otherwise, there is the tendency to form a rugged alloy-oxide interface. The oxidation rate is calculated for the limiting case of a scale consisting of protruding sections of the oxide of the less noble metal interspersed with slender trunks of alloy rich in the more noble metal. Under these conditions, the oxidation rate of alloys containing up to 50% of noble metal is supposed to be of the same order of magnitude as the oxidation rate of the less noble metal in its pure state.

In a previous paper (1), the oxidation of alloys involving noble metals was discussed. In particular, oxidation of Ni-Pt alloys was considered in conjunction with experimental results obtained by Kubaschewski and von Goldbeck (2). At 1000°C, only nickel oxide is formed. Thus Pt is enriched in the alloy which is a substitutional solid solution without miscibility gap. Accordingly, Ni diffuses from the bulk alloy toward the alloy-oxide interface, and Pt diffuses in the opposite direction. The oxidation rate is, therefore, determined by the interplay of diffusion of Ni ions and electrons in nickel oxide, and interdiffusion of Ni and Pt in the alloy. In this analysis it has been assumed that the thickness of the nickel oxide film is uniform and the interface between the oxide and the alloy is plane. This situation, however, is not always found. It is also possible that oxidation of an alloy involving a noble metal yields a two-phase scale with the alloy consisting mostly of the more noble metal embedded in a matrix of the oxide of the less noble metal, as shown schematically in Fig. 1. Such a structure of the scale was observed in several cases discussed below.

In what follows it is shown that an oxide film of uniform thickness is stable only under certain conditions and unstable under other conditions. In the latter case, a two-phase scale is formed. In order to understand the decisive factors which determine diffusion in a two-phase scale, calculations have been made for idealized conditions. In particular, exclusive diffusion control is assumed and effects due to space charge layers are disregarded.

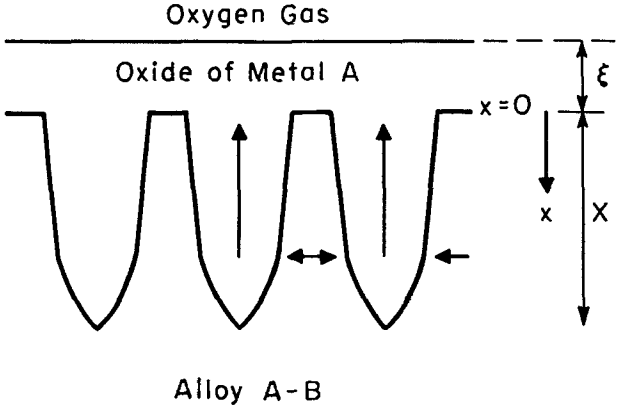

FIG. 1. Schematic cross section of the scale at the surface of an alloy A-B with an outer layer of oxide of metal A and an inner two-phase layer of oxide of metal A and B-rich alloy. The main diffusion path of A in the alloy and in the oxide is indicated by arrows.

STABILITY OF A PLANE ALLOY-OXIDE INTERFACE

Consider an alloy A-B in which only metal A forms one oxide. To examine the stability of a plane oxide-alloy interface, inquire into the changes of a nearly plane interface involving slight perturbations. In particular, consider a sine wave profile shown in Fig. 2.

In the metallic phase, the transport rate of metal A per unit area in the x-direction due to diffusion is given by

$$j_A'^{(x)} = -D'(\partial c_A'/\partial x) \qquad [1]$$

where D' is the interdiffusion coefficient of the alloy, c_A' is the concentration of A in mole/cm^3, and x is the distance from the original surface of the alloy.

For an ideal metallic solution,

$$a_A = N_A' = c_A'V' \qquad [2]$$

where a_A is the activity of A referred to pure metal A as the reference state, N_A' is the mole fraction of A in the alloy, and V' is its molar volume, which is supposed to be independent composition.

Substitution of Eq. [2] in Eq. [1] yields

$$j_A'^{(x)} = -(D'/V')(\partial a_A/\partial x) \qquad [3]$$

Analogous equations hold for transport in the y-direction. Fick's second law may, therefore, be formulated as

$$\partial c_A'/\partial t = (\partial a_A/\partial t)/V' = -\partial j_a'^{(x)}/\partial x - \partial j_A'^{(y)}/\partial y$$
$$= (D'/V')(\partial^2 a_A/\partial x^2 + \partial^2 a_A/\partial y^2) \qquad [4]$$

if the interdiffusion coefficient D' is independent of composition.

In the oxide, diffusion is supposed to be accomplished by metal ions and electrons, whereas the oxygen ions are supposed to be virtually immobile. If the oxide exhibits

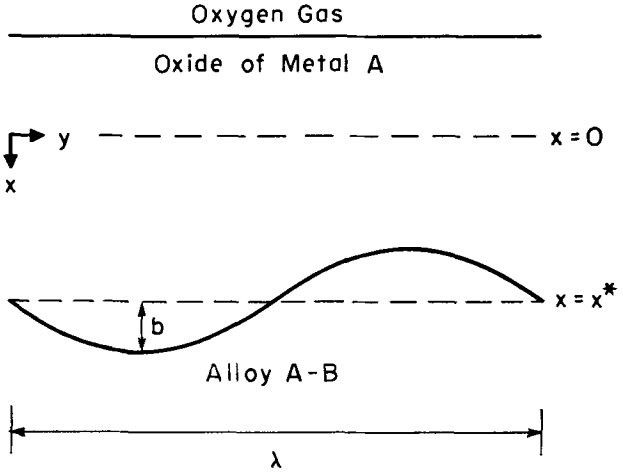

FIG. 2. Cross section of the scale at the surface of an alloy A-B with a sine-wave profile of the interface between alloy and oxide of metal A.

predominant electronic conduction, the rate of transport of A per unit area in the x-direction with respect to the original surface $x = 0$ is given by (3)

$$j''_A{}^{(x)} = -D''c''_A(\partial \ln a_A/\partial x) + u_x c''_A \quad [5]$$

where D'' is the self-diffusion coefficient of A in the oxide, c''_A is the concentration of A in the oxide in mole/cm^3, and u_x is the drift velocity of the oxide toward the bulk alloy due to the recession of the alloy-oxide interface.

The dependence of the self-diffusion coefficient D'' is assumed to be given by

$$D'' = D''^{(o)}a_A^m \quad [6]$$

where $D''^{(o)}$ is the self-diffusion coefficient of A in the oxide at unit activity of A, and m is a constant, which is positive for an oxide with metal excess, e.g., equal to about $\frac{1}{2}$ for zinc oxide (4), and negative for an oxide with metal deficit, e.g., equal to $-\frac{1}{3}$ for nickel oxide if there are equivalent concentrations of cation vacancies and electron holes (5).

The concentration c''_A is equal to the reciprocal of the volume V'' of the oxide involving one mole of metal A,

$$c''_A = 1/V'' \quad [7]$$

Substitution of Eqs. [6] and [7] in Eq. [5] yields

$$j''_A{}^{(x)} = -(D''^{(o)}/mV'')(\partial a_A^m/\partial x) + u_x/V'' \quad [8]$$

An analogous equation holds for transport of A in the y-direction.

If the oxide deforms plastically and its molar volume is constant, the divergence of the flow rate of the oxide must vanish,

$$\partial u_x/\partial x + \partial u_y/\partial y = 0 \quad [9]$$

The oxide is supposed to involve only slight deviations from the ideal metal-to-oxygen ratio and, therefore, the change in the concentration of A in the oxide with time virtually vanishes. Thus it follows from Eqs. [8] and [9] that

$$\partial c''_A/\partial t = -\partial j''_A{}^{(x)}/\partial x - \partial j''_A{}^{(y)}/\partial y = (D''^{(o)}/mV'')(\partial^2 a_A^m/\partial x^2 + \partial^2 a_A^m/\partial y^2) \cong 0 \quad [10]$$

As shown in Fig. 2, the locus of the oxide-alloy interface is supposed to be given by

$$x = x^* + b \sin (2\pi y/\lambda) \quad [11]$$

where x^* is the distance of the average interface from the original surface of the alloy, λ is the wave length, and b is the amplitude of the sine wave profile.

The following restrictions for the values of b and λ are assumed

$$b \ll \lambda \quad [12]$$

$$\lambda \ll x^* \quad [13]$$

At the interface moving in the x-direction at rate u, the concentration of A changes discontinuously from c''_A to c'_A. From the principle of the conservation of mass, it follows that

$$u_x(c''_A - c'_A) = j''_A{}^{(x)} - j'_A{}^{(x)}$$

at

$$x = x^* + b \sin (2\pi y/\lambda) \quad [14]$$

At the interface, also the concentration of B changes discontinuously from 0 to c'_B. Since the transport rate of B in the oxide is zero,

$$-u_x c'_B = -j'_B{}^{(x)} \text{ at } x = x^* + b \sin (2\pi y/\lambda) \quad [15]$$

where $j'_B{}^{(x)}$ is the transport rate of B per unit area in the x-direction in the alloy.

Since the molar volume of the alloy is assumed to be independent of composition,

$$j'_B{}^{(x)} = -j'_A{}^{(x)} \quad [16]$$

and in view of Eq. [2]

$$c'_B = N'_B/V' = (1 - N'_A)/V' = (1 - a_A)/V' \quad [17]$$

Upon substitution of Eqs. [2], [3], [7], [8], [16], and [17] in Eqs. [14] and [15], it follows that

$$-u_x a_A/V' = -(D''^{(o)}/mV'')(\partial a_A^m/\partial x)_{\text{oxide}} + (D'/V')(\partial a_A/\partial x)_{\text{alloy}}$$

at

$$x = x^* + b \sin (2\pi y/\lambda) \quad [18]$$

$$u_x(1 - a_A) = D'(\partial a_A/\partial x)_{\text{alloy}}$$

at

$$x = x^* + b \sin (2\pi y/\lambda) \quad [19]$$

Combining Eqs. [18] and [19] and eliminating u_x, one obtains the boundary condition

$$(D'/V')(\partial a_A/\partial x)_{\text{alloy}} = (1 - a_A)(D''^{(o)}/mV'')(\partial a_A^m/\partial x)_{\text{oxide}}$$

at

$$x = x^* + b \sin (2\pi y/\lambda) \quad [20]$$

The solution of differential Eq. [4] for diffusion in the alloy may be written as the sum of two terms,

$$a_A = F(x, t) + f(x, y, t) \text{ if } x > x^* + b \sin (2\pi y/\lambda) \quad [21]$$

where $F(x, t)$ represents the known solution of Eq. [4] with $a_A = N'_A$ for a plane oxide-alloy interface, and $f(x, y, t)$ is a perturbation function, which is the difference of the solution for a sine wave profile interface and that for a plane interface.

Since $a_A = F(x, t)$ is supposed to satisfy Eq. [4],

$$\partial f/\partial t = D'(\partial^2 f/\partial x^2 + \partial^2 f/\partial y^2) \quad [22]$$

As an approximation one may use a solution f_o independent of time,

$$f_o = \gamma' C' b \exp[-2\pi(x - x^*)/\lambda] \sin(2\pi y/\lambda) \quad [23]$$

where x^* denotes the location of the average interface plane at time $t = t^*$, γ' is a constant calculated below, and

$$C' = \partial F/\partial x \text{ at } x = x^*, \quad t = t^* \quad [24]$$

Thus the right-hand member of Eq. [22] is found to be

$$D'(\partial^2 f_o/\partial x^2 + \partial^2 f_o/\partial y^2) = 4\pi^2 f_o/\lambda^2 - 4\pi^2 f_o/\lambda^2 = 0 \quad [25]$$

Since f_o is assumed to be independent of time and, therefore, $\partial f_o/\partial t = 0$, the function f_o suggested in Eq. [23] satisfies Eq. [22].

Actually, however, the perturbation function f cannot be independent of time since the interface moves at a rate u_x in the x-direction. In order to obtain the order of magnitude of $\partial f/\partial t$, assume that the perturbation function is essentially stationary with respect to the interface and its magnitude changes only slowly. Thus the change of the perturbation function at a given distance from the interface with time is supposed to be nearly equal to zero, i.e.,

$$(\partial f/\partial t) + u_x(\partial f/\partial x) \cong 0 \quad [26]$$

Substituting the approximate solution suggested in Eq. [23] in [26], one obtains for the right-hand member in Eq. [22]

$$\partial f/\partial t \cong 2\pi u_x f_o/\lambda \quad [27]$$

The value of $\partial f/\partial t$ calculated in Eq. [27] may be compared to the individual terms in [25]. If $\partial f/\partial t$ is much less than each of the individual terms of the right-hand member of Eq. [25], i.e., if

$$u_x \ll 2\pi D'/\lambda \quad [28]$$

a relatively slight modification of the function f_o will result in sufficient changes in the individual terms in Eq. [25] so that the difference of these terms becomes equal to $\partial f/\partial t$ as is required by Eq. [22]. Therefore, Eq. [28] represents a necessary condition for using the function f_o in Eq. [23] as an approximation for f.

Transformation of Eq. [28] yields

$$\lambda \ll 2\pi D'/u_x \quad [29]$$

Use of Eq. [23] as a convenient approximation, therefore, confines the following conclusions to sufficiently small values of the wave length λ in order to satisfy Eq. [29].

From Eq. [15] of a previous calculation (1) for a plane interface, it follows that

$$u_x \sim D'/x^* \text{ if } D' \sim (D'')_{avg} \quad [30]$$

where $(D'')_{avg}$ is the self-diffusion coefficient of the cations in the oxide averaged over the activity range occurring in the oxide layer. Under these conditions, Eq. [29] is automatically satisfied if [13] is satisfied.

The perturbation function in Eq. [23] vanishes if $(x - x^*) \gg \lambda$, i.e., is significant only in the vicinity of the interface. Therefore, as an approximation, use the first two terms of a Taylor series expansion for $F(x, t)$ as a function of x and obtain for $t = t^*$ in view of Eqs. [23] and [24]

$$a_A \cong a_A^* + C' \{(x - x^*) + \gamma' b \exp[-2\pi(x - x^*)/\lambda] \sin(2\pi y/\lambda)\} \quad [31]$$

where a_A^* is the average activity of A at the average interface plane $x = x^*$.

Similarly, a particular solution of differential Eq. [10] is

$$a_A^m = (a_A^*)^m + C'' \{(x - x^*) - \gamma'' b \exp[2\pi(x - x^*)/\lambda] \sin(2\pi y/\lambda)\} \quad [32]$$

if $x < x^* + b \sin(2\pi y/\lambda)$

where γ'' is a constant calculated below and

$$C'' = \partial a_A^m/\partial x \text{ at } x = x^*, \quad t = t^* \text{ if } b = 0 \quad [33]$$

The last term in Eq. [32] vanishes if the distance from the interface in the negative x-direction is much greater than the wave length λ. In view of Eq. [13], the activity a_A is, therefore, virtually independent of y at the outer surface in accordance with the assumption that a_A at the outer surface is determined by the oxygen partial pressure of the surrounding gas.

Next, calculate the activity of A at the oxide-alloy interface from Eqs. [11] and [31]. Using a Taylor series expansion for the exponential function in Eq. [31] and disregarding terms involving higher powers of b,

$$a_{A(\text{interface})} = a_A^* + C'(1 + \gamma')b \sin(2\pi y/\lambda) \quad [34]$$

Likewise, it follows from Eqs. [11] and [32] that

$$[a_{A(\text{interface})}]^m = (a_A^*)^m + C''(1 - \gamma'')b \sin(2\pi y/\lambda) \quad [35]$$

Since only small deviations from a plane interface are considered, and therefore, $|a_{A(\text{interface})} - a^*| \ll a^*$, one may calculate a_A at the interface approximately from Eq. [35] by using the first two terms of a series expansion for the mth root of the right-hand member of Eq. [35]. Thus

$$a_{A(\text{interface})} = a_A^*\{1 + [C''(1 - \gamma'')/m(a_A^*)^m]b \sin(2\pi y/\lambda)\} \quad [36]$$

Equating the right-hand members of Eqs. [34] and [36],

$$(1 + \gamma')C' = (1 - \gamma'')a_A^* C''/m(a_A^*)^m \quad [37]$$

Substituting Eqs. [31], [32], and [34] in Eq. [20], using a Taylor series expansion for the exponential function and disregarding terms involving higher powers of b,

$$(D'/V')C'[1 - (2\pi\gamma' b/\lambda) \sin(2\pi y/\lambda)] = (D''^{(o)}/mV'')C''\{(1 - a_A^*) - [(1 - a_A^*)(2\pi\gamma'' b/\lambda) + (1 + \gamma')bC'] \sin(2\pi y/\lambda)\} \quad [38]$$

Eq. [38] can be satisfied only if both the sum of the constant terms and the sum of the terms involving the factor $\sin(2\pi y/\lambda)$ are equal to zero. Thus

$$C'D'/V' = (1 - a_A^*)C''D''^{(o)}/mV'' \quad [39]$$

$$2\pi\gamma'C'D'/\lambda V' = [2\pi(1 - a_A^*)\gamma''/\lambda + (1 + \gamma')C']C''D''^{(o)}/mV'' \quad [40]$$

If, in accordance with Eqs. [13] and [29], the wave length λ is sufficiently small, the first term in brackets on the right-hand side of Eq. [40] predominates and the second term may be ignored. Thus

$$\gamma'C'D'/V' \cong (1 - a_A^*)\gamma''C''D''^{(o)}/mV'' \quad [41]$$

On dividing corresponding sides of Eqs. [41] and [39], it follows that

$$\gamma' = \gamma'' \quad [42]$$

Substituting Eq. [42] in [37] and solving for $\gamma' = \gamma''$,

$$\gamma' = \gamma'' = (q - 1)/(q + 1) \quad [43]$$

where

$$q = C''a_A^*/mC'(a_A^*)^m \quad [44]$$

Eliminating the ratio C''/C' with the help of Eq. [39], substituting [6] with D''^* as self-diffusion coefficient of A in the oxide for the activity a_A^* prevailing at the average interface plane, and setting a_A^* equal to the average mole fraction N_A^* in the alloy at the average interface plane,

$$q = \frac{N_A^*}{1 - N_A^*}\frac{D'/V'}{D''^*/V''} \quad [45]$$

The rate of change in the position of the interface with time is equal to the drift velocity u_x of the oxide. From Eqs. [3] and [15], [16], and [17] it follows that

$$u_x = D'(\partial a_A/\partial x)_{\text{alloy}}/(1 - a_A) \quad [46]$$

at

$$x = x^* + b\sin(2\pi y/\lambda)$$

Substituting Eqs. [31] and [34] in [46], using Taylor series expansions, and disregarding terms involving higher powers of b,

$$u_x = D'C'\frac{1 - (2\pi\gamma'b/\lambda)\sin(2\pi y/\lambda)}{(1 - a_A^*) - (1 + \gamma')bC'\sin(2\pi y/\lambda)} \cong [D'C'/(1 - a_A^*)]\{1 - [(2\pi\gamma'/\lambda) - (1 + \gamma')C'/(1 - a_A^*)]b\sin(2\pi y/\lambda)\} \quad [47]$$

If, in accordance with Eq. [13] and [29], the wave length λ is sufficiently small, the term $2\pi\gamma'/\lambda$ prevails and the following term can be ignored. Thus the difference between the local value of u_x and the average value u_x^* is found to be

$$u_x - u_x^* = -u_x^*(2\pi b\gamma'/\lambda)\sin(2\pi y/\lambda) \quad [48]$$

If q defined by Eq. [45] is greater than unity, γ' calculated from [43] is positive. Then it follows from Eq. [48] that at points where the local thickness of the oxide film exceeds the average value, the local rate of change in the position of the interface is smaller than the average value. Thus, if $q > 1$, there is a tendency that deviations from a plane interface will disappear in the course of time. In other words, a plane interface is stable if $q > 1$, or if

$$\frac{N_A^*}{1 - N_A^*}\frac{D'/V'}{D''^*/V''} > 1 \quad [49]$$

Conversely, if $q < 1$, a plane interface is not stable since any irregularities tend to increase in the course of time.

A value of q less than unity, however, is only a necessary but not a sufficient condition for the formation of a rugged interface since there are some factors which counteract the tendency to form a rugged interface.

First, it must be recalled that the activities of A in adjacent phases are equal only in the case of a plane interface. In principle, Eq. [37] is to be supplemented by a term involving interface tension and the local radius of curvature of the interface. According to calculations omitted in this paper, such an additional term does not affect the validity of the stability criterion in Eq. [49] if the thickness of the oxide film exceeds $4 \cdot 10^{-6}$ cm. This is not a serious limitation since, in the case of thinner oxide films, the diffusion equations also must be modified in view of electrical double layers in the oxide film (6).

Second, local differences in the oxidation rate correspond to local differences in the drift velocity of the oxide lattice toward the alloy. Thus, slip of lattice planes in the oxide is required. From oxidation experiments involving cylindrical and spherical samples of pure metals (7) and observations on stressed oxide samples (8), it is known that oxides deform plastically at elevated temperatures. Certain stresses, however, may remain under quasi-steady-state conditions. Consequently, there will be additional terms in the condition for equilibrium between adjacent phases, and these terms also counteract the tendency of the formation of a rugged oxide-alloy interface.

Even if a plane alloy-oxide interface is not stable, local differences in the thickness of the oxide film may evolve rather slowly and, therefore, the over-all oxidation rate may not differ widely from that calculated for an oxide film of uniform thickness. It seems possible that irregularities in the alloy-oxide interface can be triggered by different grain orientations in the alloy. An alloy involving a small grain size may, therefore, have a greater tendency to form a rugged alloy-oxide interface and finally a structure of the scale as shown in Fig. 1 than an alloy involving coarse grains.

Eqs. [45] and [49] involve values of N_A and D'' prevailing at the alloy-oxide interface. These values are determined by Eqs. [11] and [19] of the previous paper (1). In this paper, it has been pointed out that there are two limiting cases. First, diffusion in the oxide layer may be the rate-determining step and the concentration of A at the alloy-oxide interface does not differ widely from the bulk concentration of the alloy. In this case, D'' at $x = x^*$ is much less than D', the value of q defined by Eq. [45] is much greater than unity, and accordingly a plane alloy-oxide interface is stable. Second, diffusion in the alloy may be the rate-determining step and the oxygen activity at the alloy-oxide interface is only slightly lower than the oxygen activity in the surrounding atmosphere. In the latter case, the

value of q defined by Eq. [45] is much less than unity, the mole fraction of A at the interface, N_A^*, is very low, and accordingly a plane alloy-oxide interface is not stable.

By and large, if the rate of the displacement of the boundary between two phases is controlled by diffusion or electrolytic migration of a reactant from the "forward direction," i.e., from the phase whose volume decreases, there is the tendency that deviations from a plane interface become enlarged in the course of time. This is especially true for cathodic electrodeposition of a metal from a liquid or solid electrolyte (9). But it is known that, under most conditions, the resulting roughness of the moving interface is not very distinct. Treelike growth of an electrodeposit is an exception rather than a rule.

On the other hand, if the rate of displacement of the boundary between the two phases is controlled by diffusion of a reactant from the "backward direction," i.e., from the phase whose volume increases, there is the tendency to even out irregularities of the interface as in electropolishing (10, 11) and in the high temperature oxidation of pure metals.

The inequality $q < 1$ is, therefore, only a necessary but not a sufficient condition for lack of stability of a plane alloy-oxide interface. Even if a plane alloy-oxide interface is not stable, local differences in the thickness of the oxide film may evolve rather slowly and, therefore, the over-all oxidation rate may not differ widely from that calculated for an oxide film of uniform thickness (1).

The quotient q defined in Eq. (45) becomes definitely smaller than unity if the concentration of A in the bulk alloy and likewise the concentration of A in the alloy at the interface is small. Therefore, an oxide film of nonuniform thickness may be expected especially on alloys involving low concentrations of metal A which forms an oxide. Actually, however, the oxidation rate of Pt-rich Pt-Ni alloys ($N_{Ni} = 0.15$ and 0.20) observed by Kubaschewski and von Goldbeck (2) agrees fairly well with the oxidation rate calculated under the assumption of a NiO film of uniform thickness, although q is less than unity.

According to Raub and Engel (12, 13) oxidation of a Cu-Au alloy containing 5 wt % Cu ($N_{Cu} = 0.14$) yields a CuO film whose thickness is essentially uniform, whereas the oxidation of Cu-Au alloys involving higher copper concentrations ($N_{Cu} = 0.50$, 0.69, and 0.87) yields oxide layers with large local variations of the thickness as discussed below.

These observations show that alloys involving low concentrations of an oxide-forming metal may yield an oxide film of nearly uniform thickness, although the parameter q is less than unity.

Formation of a Two-Phase Scale Consisting of the Oxide of the Less Noble Metal and Alloy Rich in the More Noble Metal

The foregoing considerations have been confined to small perturbations of a plane alloy-oxide interface. Now consider the opposite case illustrated in Fig. 1. Protruding sections of the oxide of metal A are supposed to alternate with slender trunks of the alloy depleted with respect to the less noble metal A. In addition, a compact layer of oxide is assumed on top of the original surface of the alloy because the volume of the oxide is supposed to be greater than that of the metal.

In the oxide, cations of metal A and electrons are supposed to move. When atoms of metal A are transferred to the oxide, voids at the alloy-oxide interface would originate if the oxygen ion lattice were at rest with respect to a reference plane inside the alloy. In the following analysis, however, it is assumed that the space initially occupied by atoms A is filled concurrently by oxide which moves inward by virtue of plastic flow. No voids are supposed to occur.

If the diffusivity of the alloy is very low, atoms of component B can move only over small distances. As a limiting case, it may be assumed that atoms of component B move only in directions parallel to the original surface and accumulate in slender trunks of the alloy depleted with respect to A. Plastic flow of the alloy is assumed to be negligible.

A rigorous analysis deals with diffusion and plastic flow normal and parallel to the original surface of the alloy. In view of the geometry shown in Fig. 1, the distance to be overcome by diffusion or plastic flow is supposed to be much greater in the x-direction normal to the original surface than in the y-direction parallel to the surface. As an approximation, equations are formulated only for transport normal to the surface and thus have a one-dimensional problem. This is possible only if the trunks of the remaining alloy are so slender that diffusion equilibrium within the alloy in the y-direction is virtually established. Deviations from these highly idealized conditions are discussed below.

In the two-phase region of the scale, the rate of transport is determined not only by the gradient of the activity a_A of metal A but also by the available cross section of the oxide, i.e., by the volume fraction ϕ of the oxide, which is a function of distance x from the original surface of the alloy and is not given but has to be calculated.

Consider a volume element Sdx of the scale at distance x from the original surface of area S. Because of oxidation of metal A, the mole fraction of the alloy at distance x and a given time t has decreased from the initial value N_A^o to N_A. The molar volume V' of the alloy is supposed to be independent of composition. The initial amount of B in the volume element Sdx is $(1 - N_A^o)Sdx/V'$ and must be equal to the amount in the same volume element in the scale, $(1 - N_A)(1 - \phi)Sdx/V'$ since metal B is not supposed to move in the x-direction. Thus

$$(1 - N_A^o) = (1 - N_A)(1 - \phi) \qquad [50]$$

whence

$$\phi = (N_A^o - N_A)/(1 - N_A) \qquad [51]$$

valid for any value of x in the two-phase region, with the special value $\phi = 0$ at the inside boundary of the two-phase region where $N_A = N_A^o$.

The rate of transport $j_A''^{(x)}$ of A per unit total area in the x-direction is given by the product of the right-hand member of Eq. [5] and the fraction of the cross section of the oxide, which is equal to the volume fraction ϕ in view of the geometry assumed in Fig. 1. Thus, using Eq. [7],

$$j_A''^{(x)} = -\phi(D''/V'')(\partial \ln a_A/\partial x) + \phi u_x/V'' \qquad [52]$$

The rate of change in the oxide volume per unit total area in the space beyond a given value of x with time is ϕu_x and must be equal to the product of the molar volume V' of the alloy and the amount of metal A oxidized per unit area per unit time beyond the given value of x. This value in turn is equal to the number of moles of A diffusing with respect to the oxygen ion sublattice in the oxide in the negative x-direction at distance x per unit total area per unit time. The latter value is given by the first term on the right-hand side of Eq. [52]. Thus

$$\phi u_x = V'\phi(D''/V'')(\partial \ln a_A/\partial x) \quad [53]$$

Substitution of Eq. [53] in Eq. [52] yields

$$j_A''^{(x)} = -\phi \frac{V'' - V'}{V''} \frac{D''}{V''} \frac{\partial \ln a_A}{\partial x} \quad [54]$$

Since the activity a_A increases in the direction toward the bulk alloy, i.e., $\partial \ln a_A/\partial x$ is positive and the molar volume of the oxide is supposed to exceed that of the alloy, i.e., $V'' - V' > 0$, $j_A''^{(x)}$ is negative, i.e., metal A is transported outward with respect to the original surface as the reference plane.

Next, consider the movement of oxygen due to plastic flow of oxide. The average number of gram-atoms of oxygen per unit volume of the heterogeneous scale is $\nu\phi/V''$ where ν is the number of oxygen atoms per atom A in the oxide. The transport rate in gram-atoms of oxygen per unit total area in the x-direction is $\nu\phi u_x/V''$. From the principle of the conservation of mass, it follows that the rate of change of the number of gram-atoms of oxygen per unit volume with time must be equal to the negative value of the divergence of the transport rate. Thus, omitting common factors, for the two-phase region of the scale

$$\partial\phi/\partial t = -\partial(\phi u_x)/\partial x \text{ at } 0 \leqq x \leqq X \quad [55]$$

where X is the maximum distance at which oxide is found at a given time.

Substitution of Eq. [53] in Eq. [55] yields

$$\frac{\partial\phi}{\partial t} = -\frac{V'}{V''}\frac{\partial}{\partial x}\left(\phi D'' \frac{\partial \ln a_A}{\partial x}\right) \text{ at } 0 \leqq x \leqq X \quad [56]$$

Solutions of problems involving diffusion in a semi-infinite space are known to be functions of $x/t^{1/2}$. Thus, one introduces

$$z = x/2(D''^{(o)}t)^{1/2} \quad [57]$$

as independent variable where $D''^{(o)}$ is the value of D'' for $a_A = 1$. Hence Eq. [56] becomes

$$\frac{V'}{V''}\frac{d}{dz}\left[\phi \frac{D''}{D''^{(o)}} \frac{d \ln a_A}{dz}\right] - 2z\frac{d\phi}{dz} = 0 \text{ at } 0 \leqq z \leqq Z \quad [58]$$

where, in view of Eq. [57],

$$Z = X/2(D''^{(o)}t)^{1/2} \quad [59]$$

Likewise, introduce

$$\zeta = \xi/2(D''^{(o)}t)^{1/2} \quad [60]$$

where ξ is the thickness of the compact oxide film on top of the original surface of the alloy (*see* Fig. 1).

To obtain the solution of the ordinary differential Eq. [58] of second order, two independent boundary conditions are needed. In addition, it is necessary to calculate the parameters Z and ζ defined in Equations [59] and [60]. Therefore, as a whole, four conditions are to be formulated.

1. At $x = X$ or $z = Z$, the volume fraction ϕ of the oxide tends to zero. Thus, in view of Eq. [50],

$$a_A = a_A^o \text{ at } z = Z \quad [61]$$

where a_A^o is the activity of A in the original alloy of mole fraction N_A^o.

2. For the front of the inward penetrating oxide, there is the relation

$$dX/dt = u_x(x = X) \quad [62]$$

Substitution of Eqs. [53], [57], and [59] in Eq. [62] yields

$$\frac{V'}{V''}\frac{D''(z = Z)}{D''^{(o)}}\left(\frac{d \ln a_A}{dz}\right)_{z=Z} = 2Z \quad [63]$$

3. In the compact oxide layer where $\phi = 1$, the transport rate of A is independent of x. Thus, substituting Eq. [57] in Eq. [54] and letting $\phi = 1$,

$$j_A''^{(x)} = -\frac{V'' - V'}{V''}\frac{D''}{V''}\frac{1}{2(D''^{(o)}t)^{1/2}}\frac{d \ln a_A}{dz} \quad [64]$$

$$\text{at } -\zeta \leqq z \leqq 0$$

where $j_A''^{(x)}$ is independent of x. Integrating Eq. [64] with respect to z from $z = -\zeta$ to $z = 0$ and dividing through by ζ,

$$j_A''^{(x)} = -\frac{(D''^{(o)})^{1/2}}{2\zeta V''t^{1/2}}\frac{V'' - V'}{V''}\int_{a_A^{(s)}}^{a_A(z=0)} \frac{D''}{D''^{(o)}}\frac{da_A}{a_A} \quad [65]$$

at

$$-\xi \leqq x \leqq 0$$

where $a_A^{(s)}$ is the activity of A in the oxide coexisting with the surrounding oxidizing atmosphere.

The transport rate calculated in Eq. [65] must be equal to the transport rate at $x = 0$ calculated in Eq. [54]. Substituting Eq. [57] in Eq. [54] and omitting common factors,

$$\frac{1}{\zeta}\int_{a_A^{(s)}}^{a_A(z=0)} \frac{D''}{D''^{(o)}}\frac{da_A}{a_A} = \left[\phi \frac{D''}{D''^{(o)}}\frac{d \ln a_A}{dz}\right]_{z=0} \quad [66]$$

where the differential quotient $(\partial \ln a_A/\partial z)_{z=0}$ is to be taken as the limiting value for the region $z > 0$.

4. Next, consider the movement at the outer surface of the oxide ($x = -\xi$). The rate of change of ξ with time is equal to the product of the molar volume V'' and the rate of formation of oxide per unit area minus the drift velocity u_x. The rate of formation in turn is given by the number of moles of A diffusing in the oxide per unit area per unit time in the negative x-direction at $x = -\xi$. Thus

$$\frac{d\xi}{dt} = \left[D''\frac{\partial \ln a_A}{\partial x} - u_x\right]_{x=-\xi} \quad [67]$$

Substituting Eqs. [53], [57], and [60] in Eq. [67]

$$\zeta = \frac{1}{2}\frac{V'' - V'}{V''}\left(\frac{D''}{D''^{(o)}}\frac{d \ln a_A}{dz}\right)_{z=-\zeta} \quad [68]$$

From Equations [64] and [65], it follows that

$$\left(\frac{D''}{D''^{(o)}}\frac{d\ln a_A}{dz}\right)_{z=-\zeta} = \frac{1}{\zeta}\int_{a_A^{(s)}}^{a_A(z=0)} \frac{D''}{D''^{(o)}}\frac{da_A}{a_A} \qquad [69]$$

Substitution of Eq. [69] in Eq. [68] yields

$$\zeta^2 = \frac{1}{2}\frac{V''-V'}{V''}\int_{a_A^{(s)}}^{a_A(z=0)} \frac{D''}{D''^{(o)}}\frac{da_A}{a_A} \qquad [70]$$

If the relation between activity a_A and mole fraction N_A is given, the differential Eq. [58], the boundary conditions in Equations [61], [63], [66], and [70], and the auxiliary Eq. [51] determine the activity a_A and the volume fraction ϕ of the oxide as functions of z between $z = 0$ and $z = Z$, and the parameters Z and ζ. Substitution of the values of Z and ζ in Equations [59] and [60] yields the depth X of the two-phase scale and the thickness ξ of the compact oxide film at time t.

Finally, the oxidation rate $\dot{n}_A/S$ in gram-atom of metal A oxidized per unit area per unit time may be calculated as the amount of A diffusing with respect to the oxygen ion sublattice in the negative x-direction at $x = 0$ per unit area per unit time. Taking the first term on the right-hand side of Eq. [52] for $x = 0$ and substituting Eq. [57],

$$\frac{\dot{n}_A}{S} = \frac{1}{2V''}\left(\frac{D_A''^{(o)}}{t}\right)^{1/2}\left(\phi\frac{D''}{D''^{(o)}}\frac{d\ln a}{dz}\right)_{z=0} \qquad [71]$$

Thus a consistent set of equations has been obtained to account for diffusion processes when a two-phase scale, as shown in Fig. 1, is formed. The evaluation of the foregoing equations is the next problem to be solved.

If the relation between mole fraction and activity of A in the alloy is given, the volume fraction ϕ of the oxide may be expressed in terms of the local activity of a_A with the aid of Eq. [51]. Substitution of the relation between ϕ and a_A in Eq. [58] gives a second-order differential equation for a_A, which is to be solved in accordance with Eqs. [61], [63], [66], and [70]. Even for an ideal metallic solution, the transformed Eq. [58] and the boundary conditions with two unknown parameters Z and ζ are rather involved. Therefore, numerical integration is required.

Calculations are simplified by assuming equal molar volumes of alloy and oxide,

$$V' = V'' \qquad [72]$$

Thus the outer surface of the oxide coincides with the original surface of the alloy at any time, i.e., $\zeta = 0$.

Furthermore, an ideal metallic solution is assumed, i.e.,

$$a_A = N_A \qquad [73]$$

and a value of D'' independent of a_A, i.e.,

$$D'' = D''^{(o)} \qquad [74]$$

In what follows it is shown that a_A and ϕ as functions of z may be obtained by means of consecutive approximations. To this end, it is expedient to introduce the auxiliary variable

$$\eta = (z - Z)/Z \qquad [75]$$

whereupon Eqs. [58] and [63] in view of Eqs. [72] and [74] become

$$\frac{d}{d\eta}\left[\phi\frac{d\ln a_A}{d\eta}\right] + 2Z^2(1-\eta)\frac{d\phi}{d\eta} = 0 \qquad [76]$$

$$\text{at} \quad 0 \leqq \eta \leqq 1$$

and

$$(d\ln a_A/d\eta)_{\eta=0} = -2Z^2 \qquad [77]$$

Integrating Eq. [76] once with respect to η with $\phi = 0$ at $\eta = 0$ as the lower limit according to Eq. [51],

$$\begin{aligned}\phi(d\ln a_A/d\eta) &= -2Z^2\int_0^\eta (1-\eta)(d\phi/d\eta)\,d\eta \\ &= -2Z^2\left[(1-\eta)\phi(\eta) + \int_0^\eta \phi\,d\eta\right]\end{aligned} \qquad [78]$$

which also satisfies Eq. [77].

Dividing through Eq. [78] by ϕ and integrating with $a_A = N_A^o$ at $\eta = 0$ as the lower limit,

$$\ln(a_A/N_A^o) = -2Z^2\int_0^\eta\left[1-\eta+\phi^{-1}\int_0^\eta \phi\,d\eta\right]d\eta \qquad [79]$$

For $\eta = 1$ as the upper limit, Eq. [79] becomes

$$\ln(a_A^{(s)}/N_A^{(o)}) = -2Z^2\int_0^1\left[1-\eta+\phi^{-1}\int_0^\eta \phi\,d\eta\right]d\eta \qquad [80]$$

Dividing corresponding sides of Eqs. [79] and [80],

$$\frac{\ln(a_A/N_A^o)}{\ln(a_A^{(s)}/N_A^{(o)})} = \frac{\int_0^\eta\left[1-\eta+\phi^{-1}\int_0^\eta \phi\,d\eta\right]d\eta}{\int_0^1\left[1-\eta+\phi^{-1}\int_0^\eta \phi\,d\eta\right]d\eta} \qquad [81]$$

If the absolute value of the standard free energy of formation of the oxide of metal A is much greater than RT, the trunks of the alloy in two-phase region consist mostly of metal B and, accordingly, the volume fraction of ϕ is close to N_A^o except for the vicinity of the front of the two-phase region where ϕ tends to zero. Therefore, in order to obtain a first approximation, $a_A^{(1)}$, for the activity of A as a function of η, substitute $\phi = N_A^o$ as a constant value in Eq. [81] and obtain

$$\ln a_1^{(1)} = \ln N_A^{(o)} - \eta\ln(N_A^o/a_A^{(s)}) \qquad [82]$$

Substituting $\phi = N_A^{(o)}$ in Eq. [80],

$$Z^{(1)} = [\tfrac{1}{2}\ln(N_A^o/a_A^{(s)})]^{1/2} \qquad [83]$$

as a first-order approximation for Z.

In view of Eq. [73], $a_A^{(1)}$ calculated from Eq. [82] is also a first-order approximation of the mole fraction $N_A^{(1)}$, which may be substituted in Eq. [51] in order to obtain a first-order approximation of the volume fraction, $\phi^{(1)}$. Substituting the latter value in Eqs. [80] and [81], one may calculate second-order approximations for Z and a_A. This procedure may be repeated until differences between consecutive approximations are sufficiently small.

Numerical calculations have been made for $N_A^o = 0.5$, $a_A^{(s)} = 0.01$. The second-order approximations, $N_A^{(2)}$ and $\phi^{(2)}$, deviate from the first-order approximations by less

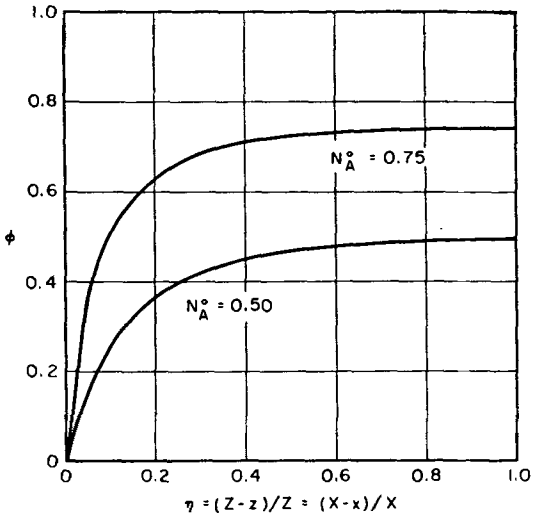

FIG. 3. Volume fraction φ of oxide of metal A as a function of the distance from the inner boundary of the two-phase scale for $a_A^{(s)} = 0.01$.

than 0.015 at any value of η, and $Z^{(2)}$ is only 6% greater than $Z^{(1)}$.

The satisfactory convergence of this iteration procedure is due to the fact that the actual value of ϕ does not differ widely from the value N_A° used for the start except for the vicinity of the inner boundary of the two-phase region ($\eta = 0$). This is illustrated in Fig. 3 for two different compositions of the bulk alloy.

Upon substituting $Z^{(2)}$ in Eq. [59], the depth of the scale at any time is obtained and may be compared with the value for pure metal A. It follows that the depth of the scale for the alloy $N_A^\circ = 0.5$ is only 2% less than the depth of the scale on pure metal A.

This special result may be generalized. By and large, the depth of the scale on an alloy A-B containing not more than 50% of a noble metal B is expected to be nearly the same as on pure metal A even if the special conditions formulated in Eqs. [72] to [74] do not hold.

From Eqs. [71] and [75] and the numerical values for $a_A = N_A$ and Z one may also calculate the rate of oxidation of metal A in moles per unit area per unit time and find that the rate for the alloy $N_A^\circ = 0.5$ is equal to 0.4 times the rate for pure metal A at the same time. This decrease in rate is due essentially to the smaller fraction of the cross section available for diffusion of A in the oxide corresponding to the factor ϕ in Eq. [71].

In the foregoing calculations, it has been assumed that diffusion equilibrium within the slender trunks of the alloy in directions parallel to the surface is established. According to Einstein (14), the time τ for a given value b^2 of the average square of the displacement of a particle in a given direction is

$$\tau = b^2/2D \qquad [84]$$

Diffusion equilibrium within the alloy in directions parallel to the surface will be virtually established if the time t is much greater than the time τ calculated from Eq. [84] with a value of b equal to the diameter of the trunks of the alloy, i.e., if

$$t \gg b^2/2D \qquad [85]$$

or

$$b \ll (2Dt)^{1/2} \qquad [86]$$

From Eq. [86] it follows that very small diameters of the trunks of the alloy are required if the diffusion coefficient for the alloy is small.

As an example, apply Eq. [86] to the oxidation of Cu-Au alloys at 750°C (10, 11). The diffusion coefficient of gold in copper is 2 to $4 \cdot 10^{-11}$ cm^{2}sec^{-1} (15). For an oxidation time of 10 hr, it follows from Eq. [86] that the diameter of the trunks must be considerably smaller than $1.5 \cdot 10^{-3}$ cm, whereas the depth of the scale is about ten times greater under the same conditions. This shows that the mechanism suggested in Fig. 1 requires very slender trunks of the remaining alloy corresponding to a small diameter-to-length ratio. Further investigations are needed in order to check under which experimental conditions the irregularities of an alloy-oxide interface have a sufficiently short wave length in order to form the slender trunks presupposed in the foregoing theoretical analysis.

Among the various deviations from the presuppositions of the foregoing theoretical analysis, the occurrence of plastic flow of the alloy deserves special attention. It has been assumed that there is diffusion of atoms B parallel to the original surface of the alloy but no transport of B normal to the original surface. Consequently, atoms of type B are supposed to stay at this location, i.e., the outer boundary of the two-phase region is supposed to be at the location of the initial surface at any time. This presupposition can be checked readily by microscopical examination of sectioned oxidized samples. Under most conditions, smaller or greater deviations may occur because diffusion in the alloy in the x-direction is appreciable and the alloy is not completely rigid, i.e., the alloy may deform plastically and move inward in order to fill the space left by atoms of A which are transferred from the alloy to the oxide at the inner boundary of the two-phase region. Under these conditions, the volume fraction of the oxide will be greater near the surface but smaller near the front of the protruding oxide than has been assumed in the foregoing analysis, especially Eq. [51]. It can be shown, however, that in general the transport rate of A in the oxide is affected only slightly by variations in the local distribution of the alloy enriched with respect to the noble metal.

The following situation is amenable to an analytical evaluation. Consider oxidation of a heterogeneous alloy A-B so that the metal left over after oxidation is virtually pure B.

As case 1, assume that there is no transport of B normal to the original surface from the alloy. Then it follows from Eq. [51] that the volume fraction of the oxide has a constant value in the two-phase region,

$$\phi = N_A^\circ \quad \text{if} \quad 0 \leqq x \leqq X \qquad [87]$$

As case 2, assume that metal B has retreated from the outer region up to $x = x_0$ and is evenly distributed be-

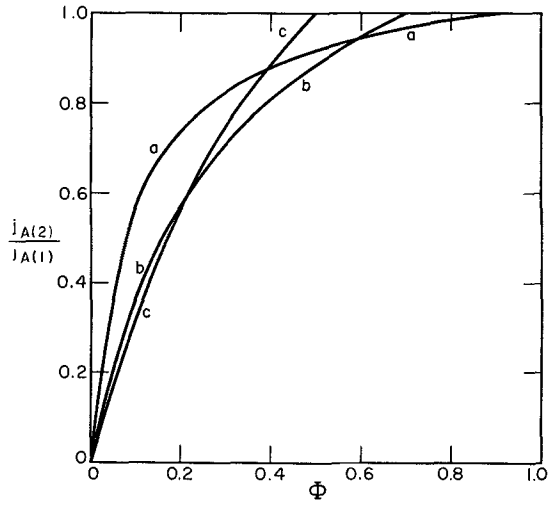

FIG. 4. Ratio of transport rates according to Eq. [90] for $N_A^0 = 0.9$ (curve a), 0.7 (curve b), and 0.5 (curve c).

tween $x = x_0$ and $x = X$,

$$\phi = 1 \quad \text{if} \quad 0 < x < x_0$$
$$\phi = \Phi \quad \text{if} \quad x_0 < x < X \qquad [88]$$

If $V' = V''$, the volume of the oxide of metal A per unit area of the sample is $N_A^0 X$ in the first case, and $x_0 + \Phi(X - x_0)$ in the second case. Hence,

$$N_A^0 X = x_0 + \Phi(X - x_0) \qquad [89]$$

whereby x_0 is determined if the value of Φ is given.

The ratio of the transport rates of A for case 1 and case 2 per unit area, $j_{A(1)}$ and $j_{A(2)}$, respectively, is given by the reciprocal of the respective diffusion resistances, R_1 and R_2, which in turn are given by the integrals $\int \phi^{-1}\, dx$. From Eqs. [87] to [89] it follows that

$$\frac{j_{A(2)}}{j_{A(1)}} = \frac{\Phi}{N_A^0(1 + \Phi - N_A^0)} \qquad [90]$$

where Φ is necessarily smaller than N_A^0.

The ratio of the transport rates for the two cases is plotted as a function of Φ for various alloy compositions in Fig. 4. For A-rich alloys, the transport rate for case 2 differs from that for case 1 markedly only if the value of Φ approaches zero, i.e., if the available cross section for diffusion of A in the oxide is very narrow between $x = x_0$ and $x = X$. Consequently, even if recession of the alloy takes place, the depth of the scale on alloys containing only 10 or 20 at. % of a noble metal is expected to be of the same order of magnitude as on a pure metal.

Discussion

In the literature, there are the following observations which support the assumption of a composite scale as shown in Fig. 1. Raub and Engel (12, 13) have presented microphotographs of sections of the scale on Cu-Au alloys oxidized at 750°C ($N_{Cu} = 0.50, 0.69, 0.87$) which resemble the structure shown in Fig. 1. A similar structure of the scale is found on Cu-Ag alloys oxidized at 750°C (16), but in this case, diffusion of oxygen in nonoxidized Ag plays an important part. Oxygen diffusing in a Ag-rich alloy may lead to formation of Cu_2O or CuO in the interior of the alloy as a "subscale" consisting of separate oxide particles without connection with the surrounding atmosphere. This process is known as internal oxidation (17). Internal oxidation may also be significant in Cu-Pd alloys (9, 19) but seems to be negligible in Au-Cu alloys in view of the very low solubility of oxygen in gold (18).

Oxidation rates of Cu-Au alloys observed by Raub and Engel (12) are listed in Table I. In accord with the foregoing analysis, the oxidation rate varies only to a minor extent between $N_{Cu}^0 = 1.00$ and 0.42 and falls off at lower Cu concentrations. Rate constants k_{PB} have been calculated according to the parabolic rate law in the form suggested by Pilling and Bedworth (28),

$$k_{PB} = (\Delta m/A)^2/t \qquad [91]$$

where $\Delta m/A$ is the weight increase per unit area and t is time.

Moreover, a composite scale similar to that shown in Fig. 1 has been found on a Ag-Au alloy containing 10 at. % Au after exposure to sulfur vapor at 800°C (20). In view of the size of the sulfur atom, no significant diffusion of sulfur in the alloy can be expected. The observed pattern of the scale is explainable only if the mechanism assumed in Fig. 1 is operative.

The structure of the scale shown in Fig. 1 may also occur on alloys involving two nonnoble metals both of which oxidize in their pure states. When Fe-Ni alloys (e.g., $N_{Ni} = 0.30$) are oxidized, a heterogeneous scale consisting of wüstite and Ni-rich alloy is found underneath an outer layer of iron oxides (21–25). It may be assumed that initially both iron oxide and nickel oxide nucleate at the surface of an Fe-Ni alloy. When the oxidation is continued, the faster growing iron oxide buries nickel oxide in the same manner as inert material, e.g., Cr_2O_3 placed on the surface of pure Fe heated in oxygen is buried (22). Buried nickel oxide, however, is not stable. Since the absolute value of the standard free energy of formation of nickel oxide is considerably less than that of wüstite, the oxygen activity at the alloy-wüstite interface is so low that nickel rather than oxidized nickel is found at this location. Thus, Ni in Fe-Ni alloys behaves in the same manner as a noble metal.

Also in the case of Fe-Ni alloys, the oxidation rate has

TABLE I. *Oxidation rate of* Cu-Au *alloys in oxygen of atmospheric pressure at 750°C according to Raub and Engel (12)*

N_{Cu}^0	N_{Au}^0	Weight increase after 30 hr mg/cm²	Rate constant $k_{PB} \cdot 10^9$ (g/cm²)²/sec
1.00	0.00	18.3	3.1
0.67	0.33	18.1	3.0
0.42	0.58	16.1	2.6
0.25	0.75	10.4	1.0
0.10	0.90	3.8	0.15
0.05	0.95	1.2	0.014

been found to vary only slightly with the Ni content up to 30 at. % Ni (22, 23, 27).

Likewise, oxidation of Fe-Cu alloys yields an outer scale consisting of iron oxides and an inner scale consisting of wüstite and nearly pure Cu as separate phases (23, 25).

To summarize, alloys involving noble metals may exhibit two distinct modes of oxidation, viz., (*a*) formation of an oxide layer of the less noble metal of essentially uniform thickness with a plane alloy-oxide interface, and (*b*) formation of a composite scale with an outer homogeneous oxide layer, and an inner heterogeneous layer consisting of oxide and alloy enriched with respect to noble metal. The second mode may also occur when each of the pure components of an alloy oxidizes, but the oxidation rate of the less noble component exceeds considerably that of the more noble component, and the interdiffusion coefficient of the alloy has a relatively low value.

Experimental investigations are in preparation in order to check more thoroughly the hypotheses suggested in this paper and in order to determine under which particular conditions the different modes of oxidation occur.

ACKNOWLEDGMENT

This investigation was sponsored by the Office of Ordnance Research under Contract DA-19-020-ORD-2244, Project TB2-0001 (779).

Manuscript received October 17, 1955.
Any discussion of this paper will appear in a Discussion Section to be published in the June 1957 JOURNAL.

REFERENCES

1. C. WAGNER, *This Journal*, **99**, 369 (1952).
2. O. KUBASCHEWSKI AND O. VON GOLDBECK, *J. Inst. Metals*, **76**, 255, 740 (1949).
3. C. WAGNER, "Diffusion and High Temperature Oxidation of Metals" in "Atom Movements," p. 153, American Society for Metals, Cleveland, Ohio (1951).
4. E. A. SECCO AND W. J. MOORE, *J. Chem. Phys.*, **23**, 1170 (1955).
5. H. H. VON BAUMBACH AND C. WAGNER, *Z. physik. Chem.*, **B24**, 59 (1934).
6. N. F. MOTT, *Trans. Faraday Soc.*, **43**, 429 (1947); *J. chim. phys.*, **44**, 172 (1947); *Bull. Soc. chim. France*, **1949**, D84; N. CABRERA AND N. F. MOTT, *Repts. Prog. Phys.*, **12**, 163 (1949); K. HAUFFE AND H. J. ENGELL, *Z. Elektrochem.*, **56**, 366 (1952); K. HAUFFE AND B. ILSCHNER, *ibid.*, **58**, 467 (1954).
7. W. J. MOORE, *J. Chem. Phys.*, **21**, 1116 (1953); U. R. EVANS, *Research*, **6**, 130 (1953); B. ILSCHNER AND H. PFEIFFER, *Naturwissenschaften*, **40**, 603 (1953).
8. R. F. TYLECOTE, *J. Inst. Metals*, **78**, 301 (1950).
9. H. FISCHER, "Elektrolytische Abscheidung und Elektrokristallisation von Metallen," pp. 487 ff., Springer, Berlin (1954).
10. J. EDWARDS, *J. Electrodepositors' Tech. Soc.*, **28**, 137 (1952); *This Journal*, **100**, 189*C*, 223*C* (1953).
11. C. WAGNER, *This Journal*, **101**, 225 (1954).
12. E. RAUB AND M. ENGEL, "Vorträge der Hauptversammlung der Deutschen Gesellschaft für Metallkunde 1938," p. 83, VDI Verlag, Berlin (1938).
13. E. RAUB, "Die Edelmetalle und ihre Legierungen," pp. 195–196, Springer, Berlin (1940).
14. A. EINSTEIN, *Ann. Physik*, (4) **17**, 549 (1905).
15. A. B. MARTIN, A. B. JOHNSON, AND F. ASARO, *J. Appl. Phys.*, **25**, 364 (1954).
16. J. A. A. LEROUX AND E. RAUB, *Z. anorg. u. allgem. Chem.*, **188**, 205 (1930).
17. F. N. RHINES, *Trans. Am. Inst. Mining Met. Engrs.*, **137**, 246 (1940); F. N. RHINES, W. A. JOHNSON, AND W. A. ANDERSON, *ibid.*, **147**, 205, (1942); F. N. RHINES AND H. GROBE, *ibid.*, **147**, 318 (1942); F. N. RHINES, *Corrosion and Material Protect.*, **4**, No. 2, 15 (1947).
18. F. J. TOOLE AND F. M. G. JOHNSON, *J. Phys. Chem.*, **37**, 331 (1933).
19. D. E. THOMAS, *Trans. Am. Inst. Mining Met. Engrs.*, **191**, 926 (1951).
20. J. B. WAGNER AND C. WAGNER, Unpublished results.
21. J. E. STEAD, *J. Iron Steel Inst.*, **94**, 243 (1916).
22. L. B. PFEIL, *ibid.*, **119**, 501 (1929).
23. E. SCHEIL AND K. KIWIT, *Archiv Eisenhüttenwesen*, **9**, 405 (1936).
24. J. BÉNARD AND J. MOREAU, *Rev. Métall.*, **47**, 317 (1950).
25. A. TAYLOR, Private communication.
26. F. NEHL, *Stahl und Eisen*, **53**, 773 (1933).
27. W. HATFIELD, *J. Iron Steel Inst.*, **115**, 483 (1927).
28. N. B. PILLING AND R. E. BEDWORTH, *J. Inst. Metals* **29**, 529 (1923).

Alternating Current Bridge for Measurement of Electrolytic Conductance

F. S. FEATES, D. J. G. IVES, AND J. H. PRYOR

George Senter Laboratory, Birkbeck College, University of London, London, England

ABSTRACT

Various theoretical and practical aspects of the problem of attaining high accuracy in conductance measurements are discussed. A number of refinements are reported, including the use of a double conductance cell.

Jones and Josephs (1) and Shedlovsky (2) established the main conditions for minimizing errors in the a-c bridge method for measuring electrolytic conductance. A fundamental criterion of accuracy in such measurements is their complete independence of the frequency, within the audible range, of the alternating emf supplied to the bridge. This criterion has seldom, if ever, been fully satisfied (3). It is true that frequency dependence has

been reduced to limits which are negligible for many purposes, but there are certain applications of conductance measurements in which high accuracy is of critical importance and which call for further development of the a-c bridge method. No discussion of very accurate conductance measurements has appeared recently, and it is the purpose of the present paper to give consideration to various theoretical and practical aspects of this problem, and to report the development of further refinements.

The case for improving upon existing procedures may be made in two ways. The first is to indicate two applications of conductance measurements of a kind requiring the best attainable accuracy. The explicit solution of the complete conductance equation, to derive dissociation constant and equivalent conductance at zero concentration, is based on an extrapolation which must always be extremely sensitive to systematic experimental errors. This may readily be seen by reference to methods of solution of this equation (4–11). These same methods lend themselves to the second application, namely, the evaluation of the enthalpy, entropy, and heat capacity changes accompanying the ionization of weak electrolytes. Apart from the classical work of Schaller (12), no determinations of these thermodynamic functions have been based on conductance measurements until recently, when it was shown (13) that this can be done with advantage. It is clear, however, that great accuracy is needed in determining the dependence of conductance on both concentration and temperature.

The Conductance Bridge

The second way of supporting the case that the normal bridge method has deficiencies is to direct attention to the electrodes of the conductance cell. These are commonly made of platinum and, when in contact with solutions containing no dissolved hydrogen, they must approximate the behavior of polarized electrodes (14) in which no charge is transferred across the metal-solution interface (15). The alternating current is therefore carried through the conductance cell less by reversible ion-discharge processes occurring at the electrodes than by the very large capacitance of the electrical double layers which reside there. On this view, the conductance bridge approximates a Wien bridge of the type shown in Fig. 1, where R_3 and R_4 are identical, purely ohmic ratio arms, R_1 is the resistance of the electrolyte in the conductance cell, C_1 the double-layer capacitance at the electrodes, R_2 the standard, noninductive resistance box, and C_2 the variable parallel capacitance invariably required to produce a sharp bridge balance. Thus, with $R_3 = R_4$, conditions for balance may be expressed by the relations,

$$f = 1/2\pi\sqrt{R_1R_2C_1C_2} \qquad \text{(I)}$$

where f is frequency

and

$$C_2/C_1 = 1 - R_1/R_2 \qquad \text{(II)}$$

which is true at any frequency.

It is clear that the assumption that $R_2 = R_1$ when the bridge is balanced requires C_2/C_1 to be zero, and this can never be the case in practice. The use of black-platinized electrodes greatly increases the value of C_1 and, for a given cell and solution, increase of frequency reduces C_2. By these devices the error is reduced to a magnitude normally regarded as insignificant, but the approximation remains. That this approaches a correct electrical model of the conductance bridge is supported by the usual experience that an increase of frequency requires a decrease in C_2 to restore bridge balance, and this simultaneously proves that the measurements cannot be independent of frequency. It is perhaps more serious that C_1 is a function of ionic concentration (16), so that the effect of frequency dependence varies along the concentration scale, thus producing the kind of systematic error particularly to be avoided in extrapolation methods. On this simple bridge model, which is not new (17), the true value of R_1 may be obtained by an extrapolation to infinite frequency. For values of the measured resistance, R_2^A and R_2^B, determined at the two frequencies f^A and f_2^B, the true value of the cell resistance is given by

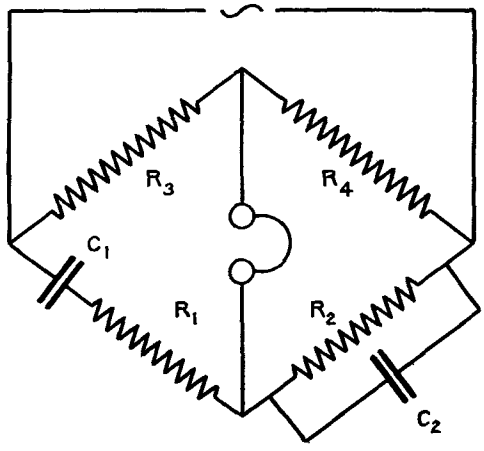

Fig. 1. Wien bridge

$$R_1 = \frac{(f^A)^2R_2^A - (f^B)^2R_2^B}{(f^A)^2 - (f^B)^2} \qquad \text{(III)}$$

There is, however, an important respect in which the conductance bridge differs from the simple Wien model and which invalidates this extrapolation. This has been shown by a study of frequency dependence, using a bridge capable of measuring purely ohmic resistance with an accuracy of better than 0.001% over the full frequency range and a conductance cell, entirely free from Parker effect, with gray-platinized electrodes. In this study it has been found that impossible values of C_2/C_1 are required to express the observed frequency dependence in terms of equations (I) and (II). Further, values of C_1, the double-layer capacitance at the electrodes, on this basis have been found to be less by orders of magnitude than those reasonably to be expected in the light of existing knowledge of the double layer and the superficial area of the electrodes. This leaves no doubt that the Wien bridge of Fig. 1 is not a satisfactory approximation to the conductance bridge.

In seeking a closer approximation, consideration was given to the fact that the conductance cell electrodes are unlikely to be ideally polarized, for the methods of conductance measurement preclude rigorous deoxygenation.

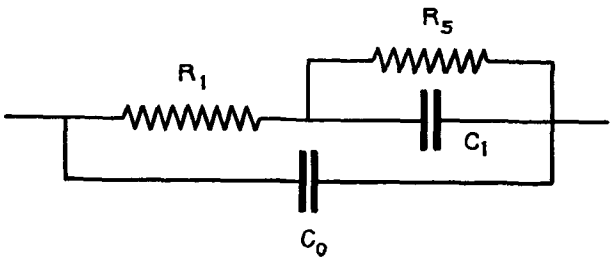

FIG. 2. Cell arm of the conductance bridge

Reference to the literature on hydrogen overpotential shows the stringency of the requirements to avoid depolarization and the practical impossibility of meeting them in conductance work. Even if depolarization is not significant, which is regarded as very unlikely, the occurrence of a faradaic process, involving charge transfer across the electrode-solution interface, cannot be excluded, and will provide an additional admittance in parallel with that due to the double-layer capacitance.

On this basis, a closer approximation to the cell arm of the conductance bridge is represented in Fig. 2, which is identical with the model proposed by Grahame (18) for a metal-solution system, except that the Warburg impedance has been set at zero, and an additional capacitance, C_0, has been added to represent "stray capacitance" due to the dielectric properties of the cell solution, capacitance between cell connections and the like. R_5 represents the faradaic "leakage" of the double-layer capacitance, and is assumed, to all intents and purposes, to be purely resistive.

This assumption can be justified in two ways. First, R_1 is overwhelmingly large in conductance measurements, and the total frequency dependence of R_2 is small; attempts to analyze this frequency dependence beyond conceivable limits of experimental error would lead to fruitless complexities. The present task is to find a sufficiently close approximation for the particular purpose. Second, in the extremely dilute solutions which are of interest, it is more than probable that the small portion of the current which is faradaic is concerned with the reversible electrodeposition of hydrogen from water molecules. Whether this is depolarized by traces of dissolved oxygen or not, the reactants belong to Grahame's Class I (18), and there will be no Warburg impedance. Further, the voltage swing across the cell in conductance measurements will not normally exceed 100 mv, so that current will remain proportional to voltage. In the present work, linearity between observed resistance and the reciprocal of the square root of frequency, as recorded by Jones and Christian (19), has not been observed. It may be suggested that perhaps this relation appears under conditions where the frequency dependence is relatively high and where the Warburg impedance is considerable. It may be noted that Wien (17) suggested this model, although his physical ideas on how it arose are not now acceptable.

Conditions for balance of this bridge model are

$$4\pi^2 f^2 (C_2 - C_0) C_1 R_1 R_2 R_5 = R_1 + R_5 - R_2 \qquad \text{(IV)}$$

and

$$C_1 R_5 (R_2 - R_1) = (C_2 - C_0)(R_1 R_2 + R_2 R_5) \qquad \text{(V)}$$

An approximation, based on the likely assumptions that $C_0 \ll C_2$ and $R_5 \ll R_1$, allows some check to be made of this bridge model. Although separate quantities cannot be evaluated, substitution of known or reasonably assessed data in the equation

$$C_1 R_5 = \frac{C_2 R_1 R_2}{R_2 - R_1} \qquad \text{(VI)}$$

indicates values of C_1 in the range 200–2000 μF for corresponding values of R_5 from 1 to 10^{-1} ohm. These are physically reasonable for a very dilute solution in a cell with gray-platinized electrodes. No more quantitative data in support of this model can be advanced, but it can be said with confidence that the kind of frequency dependence of R_2 which is observed in practice is inconsistent with the simple Wien model (Fig. 1), but is in agreement with the suggested model (Fig. 2).

Equations (IV) and (V) show that, as the frequency is increased to very high values, both $(C_2 - C_0)$ and $(R_2 - R_1)$ tend to zero; but the form of these equations is such that no simple extrapolation method can be devised. If, by black platinization of the electrodes, frequency dependence has been largely reduced, use of equation (III) may be a justifiable approximation. Black platinization, however, is open to objection for a number of reasons[1] and, although it makes the extrapolation shorter by increasing C_1, it also makes equation (III) less applicable by reducing R_5. Where gray-platinized or bright electrodes are used, there is little doubt that significant error arises from the use of this formula.

Double Cell Procedure

Ives and Pryor (13) used a double-cell method in an attempt to achieve increased accuracy in conductance measurements, a device similar in principle to that suggested by Shedlovsky (20). Two conductance cells were made as closely similar as possible except for the distances between the electrodes, which stood in the ratio 4:1. With both cells filled with the same solution, it was hoped that the difference between their apparent resistances (R_2 values) would be free, by cancellation, of any errors due to electrode effects, whether these were due to "transfer resistance," specific ion adsorption, or any other cause. It can be seen from equation (IV) that as frequency tends to zero (excluding the onset of finite electrolysis) R_2 tends to $(R_1 + R_5)$. If R_5 can be assumed to be the same for each cell, then it is clearly cancelled out in the difference method. It is also clear that the method involves no error when frequency tends to infinity. Between these frequency limits, however, it can be shown from equations (IV) and (V) that the difference method is not strictly valid; furthermore, it is impossible in practice to construct absolutely identical electrodes. For these reasons, it was found that the resistance differences, ΔR_2, were dependent on frequency, though to an order of mag-

[1] Instability, adsorbent properties, catalytic action, facilitation of undesired electrode reactions.

TABLE I. *Cell constant determinations*

Concentration (g mole/liter × 10⁴)	Ω	Constants from R_2 at 1150 cps		Constant from ΔR_1
106.299	141.08	0.46502	0.11802	0.34749
74.5656	142.34	0.46496	0.11799	0.34745
49.1596	143.64	0.46475	0.11754	0.34748
36.6060	144.44	0.46470	0.11740	0.34750
14.9472	146.32	0.46449	0.11705	0.34744
13.0958	146.54	0.46449	0.11703	0.34747
5.85475	147.62	0.46444	0.11696	0.34745
4.31205	147.94	0.46448	0.11695	0.34748
		Mean:		0.34747 ± 0.00002

nitude less than the separate R_2 values. This residual effect was eliminated by extrapolating the resistance differences to infinite frequency, involving an adjustment of the order of 0.01% in the case of solutions not exceeding 0.005 g equiv/liter in concentration. The extrapolation was carried out by means of the empirical equation

$$\Delta R_1 = \frac{f^A \Delta R_2^A - f^B \Delta R_2^B}{f^A - f^B} \qquad \text{(VII)}$$

two standard frequencies, 3880 and 1150 cps (f^A and f^B), being used. This equation, which is supported by the work of Wien (17) on this type of bridge, may be justified by Table I which relates to a set of determinations of cell constant. Potassium chloride solutions at 25°C were used for these calibrations, the extended Onsager equation (21), with values of coefficients due to Gunning and Gordon (22), being used to interpolate conductance values appropriate to the concentrations used. Table I shows the constants for each cell, based on the values of R_2 determined at 1150 cps, and the constant for the double cell based on the corresponding values of ΔR_1 calculated from equation (VII).

The mean deviation of the values of the constant derived from ΔR_1 is only 0.005% and it is entirely random over the concentration range. It is well within the limits of error associated with the primary data and the preparation of the solutions. Since they are referred to conductance standards obtained by a high-precision d-c method (22), these results may be taken to give strong support to the validity of the double-cell method, which may therefore be advocated as a means of attaining the highest accuracy.

Experimental Procedures

It is apparent that these considerations, concerned as they are with extending accuracy to a further significant figure, are supererogatory unless all sources of error are reduced to appropriate limits. It is for this reason that some reference must be made to certain practical aspects of conductance technique in which there is some improvement to be reported.

Leads resistance.—The usual method of making electrical contact to the conductance cell involves the use of mercury cups and copper wires of large cross section. This is open to many objections, apart from its clumsiness and inconvenience, especially when elevated temperatures are to be used. These difficulties may be absolutely avoided, and all uncertainties about the "leads correction" to be applied to measured resistances may be removed, by adoption of the "four-leads" system which is invariably used in modern platinum resistance thermometry. The advantages to be gained are so great that it would appear desirable to outline the principle involved. Two connecting leads are attached to each electrode of the conductance cell, and these are led to a switch box arranged in such a way that, by means of a mercury-contact switch of negligible resistance, reversals of connections may be made as shown in Fig. 3. The resistances a, b, c, and d represent the four contact leads, X is the resistance between the cell electrodes, and R_3 and R_4 have the same significance as in Fig. 1; R_2' and R_2'' are the values of R_2 in the alternative bridge arrangements. When the bridge is balanced with equal ratio arms ($R_3 = R_4$) the connections represented in Fig. 3 require that

$$a + X = d + R_2' \qquad \text{(VIII)}$$

and

$$d + X = a + R_2'' \qquad \text{(IX)}$$

so that the mean of the two values R_2' and R_2'' gives the true value of X, all extraneous resistances being cancelled out. This device at once allows greater flexibility of cell design, and the elimination of thermal disturbance of the cells by the use of thin leads of any length; it also removes all objection to the inclusion of selector switches of the normal radio type in the cell circuit. The same circuitry may be used to include a platinum resistance thermometer in the equipment of the bridge, thus facilitating precise temperature control of the cells and investigation over a temperature range. This arrangement is, in fact, regarded

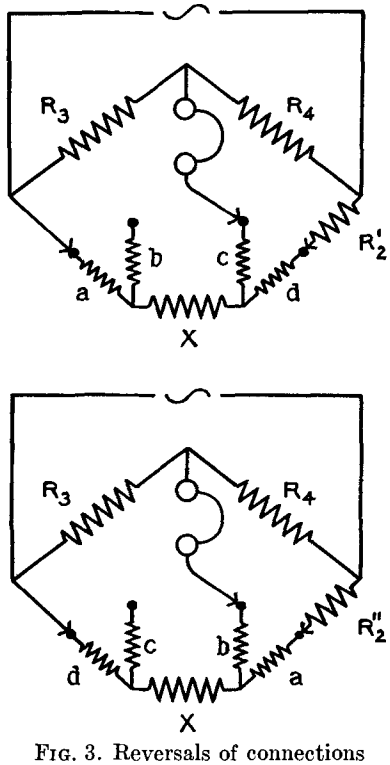

Fig. 3. Reversals of connections

as practically essential for use in conjunction with the double-cell method.

Cell design and use.—The first requirements in the design of a completely satisfactory cell are absolute rigidity of the electrodes and the absence from the cell of any dead space containing enclaves which do not readily mix with the bulk of solution in washing and filling operations. These conditions are difficult to satisfy because of the properties of platinum and borosilicate glasses; leakage of solution past imperfect seals is likely to be troublesome unless the functions of electrode support and electrical connection are separated. "Graded seals" and electrodes fused bodily to the glass cell envelope have their peculiar difficulties and disadvantages. These problems have been satisfactorily solved in the design used to construct the double cell, which is shown in Fig. 4. The electrodes were formed from platinum hemispheres, a shape offering maximum rigidity with minimum weight, and these were drilled in the center to allow free flow of solution and near the edges to permit the insertion of Pyrex anchoring "rivets," which were subsequently fused to the inside of the Pyrex envelope. Two fine tags of platinum foil, 0.001 cm thick, were welded to each electrode at opposite edges of the central drilling. These were taken through the envelope by means of thin-walled Pyrex pinch seals, which are known to be vacuum-tight (23, 24). The contact tags, which are destructively amalgamated if mercury is used, were welded to platinum contact wires which were in turn connected to coned brass terminals sealing the upper ends of the contact tubes. It may be noted that the leads resistance arising from this method of construction, from flexible connections and from the selector switch-gear amounted to some 2–3 ohms, but that measurements reproducible to 10^{-4} ohm could be made with certainty on account of the properties of the "four-leads" system.

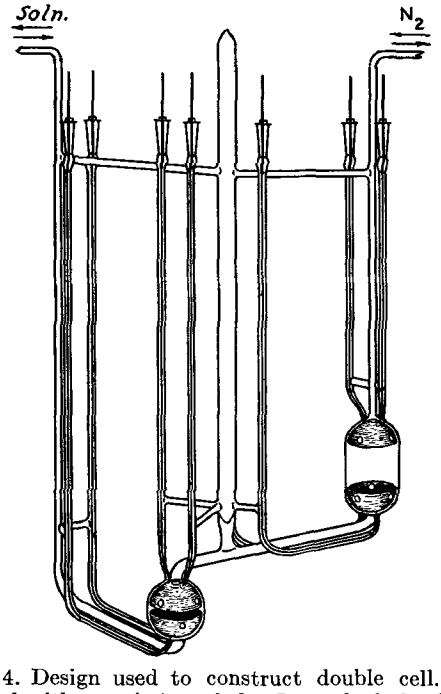

FIG. 4. Design used to construct double cell. (Figure published with permission of the Journal of the Chemical Society, London.)

The double cell was permanently mounted in an oil-filled thermostat and was filled, emptied, rinsed, and washed by the manipulation of solutions under pressure of highly purified nitrogen in a totally enclosed, all-glass apparatus. After the initial cleaning of the cell, following gray platinization of the electrodes *in situ*, it was not again subjected to drastic chemical cleaning agents. Scrupulous care was taken to be certain that only solutions for measurement or water of ultimate purity were ever admitted to the cell; this procedure proved to be entirely satisfactory. The opinion is held that the repeated use of cleaning mixture and steam is deleterious to conductance cells.

Bridge design and use.—It is well known that the oscillator supplying the bridge must provide a sinusoidal wave symmetrical about earth potential. This is not the case in many otherwise suitable commercial oscillators, one side of the output often containing an actual or "reflected" earth connection. This difficulty may be obviated by inserting a phase-splitting valve, with symmetrical anode and cathode loads, between the oscillator and the bridge input.

It has been found advantageous to feed the oscillator output first into a simple network consisting of two potentiometers of 1000 ohms each arranged in parallel. From this feeder circuit a signal of any desired amplitude and degree of asymmetry about earth potential may be supplied to the bridge. Sufficient stability of adjustment over the time interval required for a bridge measurement is provided by ordinary radio potentiometers and no complications have been found to occur as a result of using wire-wound types. In principle, this unit is capable of performing, if somewhat crudely, the functions of a Wagner earth; a conventional Wagner earth circuit was, however, used in the present work. In any case, tests of symmetry of input signal to the bridge can be made in the usual way by adjusting the bridge output to zero when taken alternatively from opposite bridge points, or from one bridge point and earth.

Finally, two points concerning standard resistance boxes call for comment. The authors have found that their resistance box (by Cambridge Instrument Co.), which has negligible temperature coefficient and frequency dependence, undergoes a slow change in resistance and requires recalibration at intervals of six to twelve months. It is also found that contact resistance develops over the course of a day or two, and is only countered by frequent routine cleaning of all contacts. For this operation, polishing alumina suspended in benzene has been found to be the ideal medium. So-called "contact lubricants" have been found to be deleterious.

ACKNOWLEDGMENTS

The authors are indebted to the Chemical Society for permission to reproduce Fig. 4. One of the authors (F. S. F.) thanks Birkbeck College for a research studentship, during the tenure of which part of this work was carried out.

Manuscript received November 17, 1955.
Any discussion of this paper will appear in a Discussion Section to be published in the June 1957 JOURNAL.

REFERENCES

1. G. Jones and R. C. Josephs, *J. Am. Chem. Soc.*, **50,** 1049 (1928).
2. T. Shedlovsky, *ibid.*, **52,** 1793 (1930).
3. G. Jones and G. M. Bollinger, *ibid.*, **53,** 411 (1931).
4. R. M. Fuoss and C. A. Kraus, *ibid.*, **55,** 476 (1933).
5. D. J. G. Ives, *J. Chem. Soc.*, **1933,** 731.
6. T. Shedlovsky and H. H. Uhlig, *J. Gen. Physiol.*, **17,** 594 (1934).
7. R. M. Fuoss, *J. Am. Chem. Soc.*, **57,** 488 (1935).
8. T. Shedlovsky, *J. Franklin Inst.*, **225,** 739 (1938).
9. D. Belcher, *J. Am. Chem. Soc.*, **60,** 2744 (1938).
10. M. L. Kilpatrick, *J. Chem. Phys.*, **8,** 306 (1940).
11. D. J. G. Ives and K. Sames, *J. Chem. Soc.*, **1943,** 511.
12. R. Schaller, *Z. Physik. Chem.*, **25,** 497 (1898).
13. D. J. G. Ives and J. H. Pryor, *J. Chem. Soc.*, **1955,** 2104.
14. A. Slygin and A. Frumkin, *Acta Physicochim.*, **3,** 791 (1935).
15. D. C. Grahame, *Chem. Rev.*, **41,** 441 (1947).
16. J. D. Ferry, *J. Chem. Phys.*, **16,** 737 (1948).
17. M. Wien, *Ann. Phys., Lpz.*, **58,** 37 (1896).
18. D. C. Grahame, *This Journal*, **99,** 370C (1952).
19. G. Jones and S. M. Christian, *J. Am. Chem. Soc.*, **57,** 272 (1935).
20. T. Shedlovsky, *ibid.*, **52,** 1806 (1930).
21. T. Shedlovsky, A. S. Brown, and D. A. MacInnes, *Trans. Electrochem. Soc.*, **66,** 165 (1934).
22. H. E. Gunning and A. R. Gordon, *J. Chem. Phys.*, **10,** 126 (1942).
23. W. B. Campbell, *J. Amer. Chem. Soc.*, **51,** 2419 (1929).
24. G. J. Hills and D. J. G. Ives, *J. Chem. Soc.*, **1951,** 305.

Technical Feature

Alaska's Power Resources in Relation to Mineral Development[1]

IVAN BLOCH

Ivan Bloch and Associates of North Pacific Consultants, Portland, Oregon

ABSTRACT

A large number of potential Alaskan hydropower sites appear feasible of development. Some of them are favorably situated to facilitate the utilization of the Territory's mineral resources such as Fe, Cu, Ni, chromites, and possibly others. With decreasing availability of abundant, low-cost supplies of hydroelectricity in the 48 States, Alaska's power potential warrants immediate consideration, especially in the southeastern and central portion accessible to tidewater for electroprocess industry establishment.

The enormous expansion of electroprocess industries in the United States combined with equally enormous consumption of electric power for other industrial, residential, and commercial purposes, has resulted in a rapid exhaustion of large, low-cost hydroelectric power supplies. Although the utilization of large coal properties for mine-mouth electric steam-generating plants in various parts of the United States will provide large blocks of comparatively low-priced electricity for electroprocess industries, it will not be adequate for the electric furnace and electrolytic cell treatment of many mineral substances located long distances from consuming markets.

In the North Pacific region of America there are enormous hydroelectric potentials, largely unexplored and of great logistic importance for the processing of mineral ores known to exist in those areas. The tremendous development of hydroelectric power in the Kitimat-Nechako, Kemano area of northern British Columbia is clear evidence of the interest of industry in the North Pacific region.

This paper deals in summary with Alaska and its various hydro potentials. In exemplary manner, it points to the potential utilization of some mineral ores as well as to the positive establishment of electroprocess industries in the Territory.

GENERAL DESCRIPTION OF ALASKA BASINS

The hydroelectric potential of Alaska, now believed to be in excess of 16 million kw, is examined in terms of major regions and subareas. These are:

Southeastern Alaska Region: (potential—over 2¼ million kw) (*a*) Ketchikan area, (*b*) Wrangell area, (*c*) Sitka area, (*d*) Angoon area, (*e*) Juneau area.

Southwestern Alaska Region: (potential—over 4¼ million kw) (*f*) Gulf of Alaska area, (*g*) Matanuska Valley area, (*h*) Susitna Basin area, (*i*) Kenai Peninsula area, (*j*) Bristol Bay, Alaska Peninsula, Aleutian and Kodiak Island area.

Central Alaska Region: (potential—over 10 million kw) (*k*) Kuskokwim Basin area, (*l*) Upper Yukon Basin area, (*m*) Middle and Lower Yukon Basin area, (*n*) Tanana Basin area.

Northern Alaska Region: (potential—over ¼ million kw) (*o*) Seward Peninsula area, (*p*) Arctic Region area.

In each of these areas will be found physiographic and climatic characteristics which generally will control the type of eventual hydroelectric development (*see* Fig. 1).

Both the Southeastern Alaska and Kenai Peninsula areas have a substantial number of lakes emptying into short, rapid streams providing considerable hydraulic head. The major portion of potential hydroelectric sites in these two regions, therefore, entail the tapping of lakes by means of tunnels, pipelines, and penstocks to high-head turbine installations. A few streams in those regions are susceptible of development by means of low-head dam installations and transmountain diversion.

On the other hand, the Yukon, Kuskokwim, Susitna, Tanana, and Copper rivers—each with very large drainage basins and consequent large stream flows—will be developed by means of substantial reservoirs, created by large dams, and providing very large individual generating capacity potentials.

Most of the proposed installations at Southeastern Alaska and Kenai Peninsula power sites involve lakes containing little or no sediment. Contrariwise, most of the large rivers are heavily laden with the products of erosion and glacial action and contain substantial sedimentary materials carried as bed load.

The Southeastern Alaska region is one of very heavy rainfall at lower elevations and substantial snowfall in the mountains. Temperatures are moderate and not unlike those which occur in the Puget Sound area, increasing in severity with distance from the coastal areas and altitude of the land masses. The Southwestern Alaska region contains a number of different climatic regions. The Kenai

[1] Paper delivered before the San Francisco Meeting, April 29 to May 3, 1956.

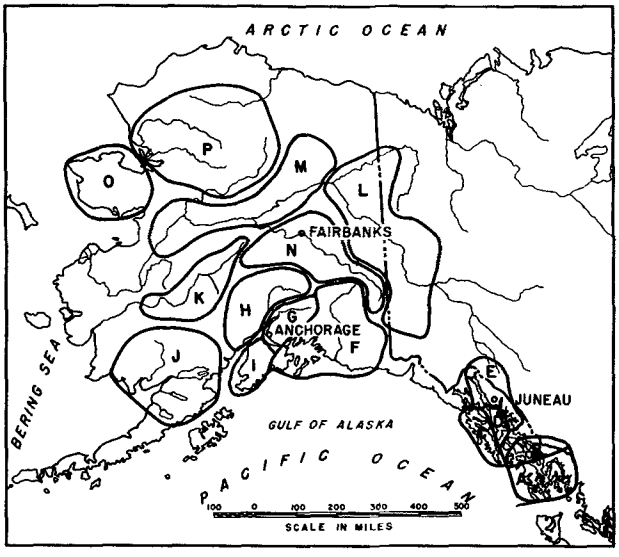

FIG. 1. Hydro power regions of Alaska

Peninsula, Coastal Gulf of Alaska and Bristol Bay areas which adjoin ocean and tidal waters are characterized by somewhat more rigorous but still moderate climate. Rainfall and snowfall are heavy along coastal areas, but decline in interior areas, with much lower winter temperatures. The regions which contain the Yukon, Kuskokwim, Tanana, Seward Peninsula, and Arctic drainages are subject to extremely low and long-duration winter temperatures, sometimes surprisingly high summer temperatures, with moderate annual precipitation.

Although long visualized as a region of forbidding physical and climatic aspects, remote from civilization, even the farthest reaches no longer are considered beyond the possibility of development. Recent experience gained in Arctic operations of both the military and civilians tempers the awe naturally stimulated by past account of long periods of subzero temperatures, and boundless areas of mountainous or tundra terrain. The very physiographic and climatic characteristics which have presented barriers to general development in the past may well be turned to advantage in large-scale development of hydroelectric resources.

Alaska's population, estimated at some 225,000, is largely concentrated in the Southeastern, Kenai Peninsula, and Fairbanks areas. Anchorage, at the head of Kenai Peninsula, at the upper end of Cook Inlet, is the largest city and modern in every sense. The Greater Anchorage area which includes Anchorage and its immediate environs stretching into the famed Matanuska Valley, now has a population well in excess of 100,000. Fairbanks, to the north, is also a completely modern city, serving an area with a population of close to 50,000. It is served by the Alaska Railroad from the ports of Seward, Whittier, and Anchorage. Southeastern Alaska contains a number of communities. The capital of the Territory, Juneau, has an area population of 16,000. Other communities include Ketchikan, Wrangell, Sitka, and Petersburg.

Transportation is well developed for all of the Territory. The airplane is possibly the most important means of transportation and it serves every area of Alaska with modern equipment operating both on regular schedules or by charter. Four major scheduled airlines operate in the inter-Alaska service, and a European airline is scheduled for Trans-Polar service between Europe, the Orient, and West Coast cities. Ocean vessel as well as ocean-going barge services are well established to major ports of the Territory. Sea-train service is projected from Puget Sound points to Gulf of Alaska terminals. The Alaska Railroad serves an area from the Gulf of Alaska, via Anchorage to Fairbanks. An excellent network of good, surfaced highways serves major points. These highways interconnect with the Alaska Highway, and traffic of all kinds, including modern trucking, is continuous the year around. A new type of transportation in the areas north of the Arctic Circle is now established. This consists of "Cat-trains" and the specially built "snow-trains."

Alaska's economy is undergoing a transition of considerable importance. The tremendous increase in population during the past ten years, especially in the Greater Anchorage and the Fairbanks areas, in very large measure has been due to construction activities required in the establishment of large military bases. However, a noticeable stabilization of population and of the related economy is taking place. The pattern seems to parallel that observable in the historical development of the West, which centered about the establishment of military outposts and garrisons. That is to say, people drawn to Alaska in the main by construction activity are putting down their roots in the Territory, building and purchasing modern homes, engaging in commercial and service establishments, and gradually building a sizeable agricultural economy in the Matanuska and Tanana River valleys.

Although it is common to view Alaska as an area of very high labor costs, this is not the case in enterprises with steady all-year employment activity. The most striking example is in the well-established contract between the U. S. Smelting, Refining and Mining Co. in Fairbanks, and the local A.F.L. Union, which sets forth rates comparable with those prevailing in the Puget Sound area.

In an area of about one-fifth that of the 48 states, which until recent years has been considered remote and inaccessible, it follows that much of the area is unexplored. There is a dearth, for example, of reliable, long-term information on stream-flows, hydrologic data, and on the geology of potential water power sites. Although the geologic literature on mineral discovery and development is substantial, it remains sketchy for many large areas. Further, it reflects traditional interest in precious metals such as gold. The analysis, therefore, of mineral potential in relation to hydroelectric power development must be of most preliminary nature.

In the following sections, an attempt is made to sketch some principal possibilities of development. It is believed that, with the passage of time, the importance of many developments will be much greater than can be anticipated.

SOUTHEASTERN ALASKA

Total Potential Installed Kilowatts: Over 2¼ Million

This region comprises the large archipelago and the land strip which is the southern Panhandle of Alaska. It is bordered on the east by British Columbia, and on the west

by the Pacific Ocean. The region is very mountainous, with long inland fjords. One of the greatest rain forests of the world cloaks the area which, as a consequence, is now well on the way to becoming a principal producer of pulp and other forest products. Major communities include Ketchikan, Wrangell, Petersburg, Sitka, Juneau, Haines, and Skagway.

The hydroelectric potential (for units in excess of 5,000 kw installed capacity) is estimated at a total of over 2 million kw.[2] As previously noted, most sites involve relatively small individual units, from 10,000 to 70,000 kw, usually involving the tapping of lakes at moderate altitudes. Power costs from these plants are conservatively estimated as 5 to 12 mills/kwhr averaging 6 to 7 mills/kwhr.

One outstanding potential project is the Yukon-Taiya project located near Skagway. It involves utilization of seven Canadian (Yukon Territory) lakes on the Yukon river above Whitehorse, Y. T., by diverting these flows across the Alaska-Canadian border near Skagway and dropping them to sea level at the head of deep-water Lynn Canal. The project's main features involve tapping Sloko Lake into Atlin Lake, thence into Taku Arm Lake, Marsh, and Tagish Lakes, into Bennett Lake, reversing the flow of Lindeman Lake, and dropping 2,800 ft³/sec of water through the Coast Mountains by means of a 14-mile tunnel to the power house. An ultimate power capacity ranging from 900,000 to as high as 2 million kw has been indicated. Estimates of possible power costs from this huge project have varied, but are all in the general range of 2 mills/kwhr. The Taiya project's projected power plant is at the head of Lynn Canal near Skagway and Haines, with industrial plant site areas within less than 25 miles.

Because of the international character of the project, its construction poses substantial problems. On the one hand, diversion of the Canadian water of the upper Yukon drainage basin would affect navigation and power potentials of the Yukon river further downstream in Alaska, a matter of grave concern to the United States. On the other hand, diversion by means of this project would, in effect, utilize Canadian waters for power production in Alaska, a matter which the Canadians look upon with some disfavor.

As a consequence, other schemes have been recently investigated by Canadian industrial interests. One scheme in particular would involve utilization of approximately the same watershed of the upper Yukon as for the Taiya project, but diverting the flows to the head of Taku Inlet (in Canada), a tidal body to the east of Juneau. Power capabilities for this scheme would be substantially less than for Taiya. Power production would be all-Canadian, but access to deep-draft navigation would necessitate crossing the American Panhandle of Alaska. In addition, there are sizeable physiographic limitations regarding plant sites and access thereto.

Therefore, development of either project must await resolution of some rather difficult international problems between the United States and Canada. It appears, however, that the Taiya project is far superior in every respect to alternative suggestions so far made for the use of this section of the Yukon watershed.

[2] This total includes the Taiya project with a potential listing of 1,600,000 kw.

The possibilities of interconnecting the potential hydroelectric sites of Southeastern Alaska by high-voltage transmission networks are limited because of the rugged topography and the relative isolation of individual sites. Some grouping by a combination of overland transmission lines and submarine cables is indicated as warranting further consideration. Suggested groupings are the following: (*a*) Ketchikan area—Grace, Mirror, Ella, Manzanita, and Swan Lakes; (*b*) Wrangell area—Cascade and Scenery Creeks; (*c*) Sitka area—Green, Blue, and Takatz Lakes; (*d*) Juneau area—Long, Crater, and Dorothy Lakes, Speel River.

Thus, development of most of these sites will be for utilization in generally close proximity to power plants. Suitable areas for industrial or processing plant location are limited or will require very careful consideration because of the sharply rising nature of the terrain from tidewater.

There are at least three possibilities of interest regarding the utilization of Southeastern Alaska's power potential for mineral beneficiation and processing. These include the utilization of the very large quantities of magnetites in the Klukwan area near Haines in the Chilkat Mountain range. There are also apparently extensive nickel-bearing ores in the Takobi-Chichagof-Baranof Island area, and copper-bearing areas in various parts of the Archipelago, especially on Prince of Wales Island and in the Ketchikan area. Considerable exploration of these principal minerals has taken place within the last few years. Tonnages are great, with grades quite variable. Should the Yukon-Taiya hydroelectric project be built, a sizeable portion of its output would be consumed by electric furnace treatment of the Klukwan magnetites. Similarly, processing of the relatively low-grade nickel-bearing ores by electric furnace means (possibly by the low density carbon or dry-top method developed by the U. S. Bureau of Mines at Albany, Oreg.) appears worthy of considerable attention. Regarding the copper-bearing materials of the area, electric-matte smelting might provide a satisfactory economic answer to their exploitation. These possibilities are within the foreseeable future, and promising hydroelectric sites (in addition to Taiya) are favorably situated with respect to major ore bodies. Companies most prominent in evincing interest in the location of electroprocess industries in this area are the Aluminum Co. of America, Reynolds Metals Co., and the Frobisher interests of Canada.

Southwestern Alaska Region

Total Potential Installed Kilowatts: Over 4¼ Million

This enormous region contains some of the most interesting power potentials for mineral and electroprocess industry development. The hydroelectric possibilities of the Gulf of Alaska, the Matanuska Valley, Susitna and Kenai Peninsula area are susceptible of eventual interconnection by means of a high-voltage and high-capacity electric transmission system. It is in this general area that the major portion of Alaska's population resides, and therefore it is the principal center of economic activity in the Territory. Physiographic conditions are such that major land communication routes are well developed, and there exist numerous areas accessible to tidewater which offer facilities for industrial plant establishment.

The largest individual hydroelectric potential is that of the Copper River. The principal project is at Wood Canyon, a few miles below the confluence of the Copper and Chitina rivers, at which point the combined run-off of two valleys, draining an area of 24,000 square miles, flows through a deep rock-walled canyon. About 35 miles below Wood Canyon is a site which appears favorable for the construction of another large dam. Conservative estimates place the potential installed capacity of these two dams in excess of 1,500,000 kw and prime power capabilities of over 1,100,000 kw. A preliminary appraisal of power costs at the two plants is around 3 mills/kwhr, although this figure is very conservative.

Of particular importance with regard to the Wood Canyon and Peninsula site projects is that the upper dam would create a reservoir about 100 miles long. This reservoir would extend into the Chitina Valley to the abandoned site of the famous Kennecott operations (Kennecott Copper Co.), and up the Copper river into the Copper Center-Gulkana area. This reservoir would provide an excellent possibility for the establishment of barge transportation to highly mineralized areas now inaccessible except by air or very arduous surface trails. Industrial plant site areas in the vicinity of Chitina or the upper end of the proposed reservoir near Copper Center would have access to the Edgerton Cut-off Highway and the Richardson Highway into Valdez, with its all-year ocean port. Considerable headway is being made toward the building of a highway along the right-of-way of the abandoned Copper River and Northwestern Railway, built by Kennecott in the early 1900's, from the Cordova area, with its all-year port, up the Copper river past the Peninsula dam and the Wood Canyon sites to Chitina. A highway has been built from Cordova to the Copper river; the route from this area up-river will require some modification, depending on the possible construction of the Copper river dams.

There are many other power sites on various tributaries of the Copper in its head waters such the Nizina, Kennecott, and Tebay in the Chitina drainage; The Tonsina, Klutina, and Tazlina in the upper Copper drainage; and the Bremner and Tiekel rivers below the Wood Canyon site. Preliminary estimates show power costs in ranges between 9 and 15 mills/kwhr. However, as will be the case with most Alaska power sites, investigations have been meager and on a bare reconnaissance basis. It would appear that additional investigations will lead to the development of construction plans for much lower power rates than now estimated.

The Matanuska Valley area has interesting hydroelectric potentials. The largest of those involves a most unusual scheme of development proposed by Reuben Hack, an engineer with the U. S. Corps of Engineers in Alaska. Considerable reconnaissance work carried out by Mr. Hack on his own responsibility shows remarkable possibilities for a power scheme having an installed potential capacity of between 120,000 and 190,000 kw with high prime power capabilities.

The Hack scheme for the Lake George project contemplates using the Knik Glacier as a permanent dam to make possible the full use of waters impounded intermittently in back of the glacier. Under present conditions, Lake George represents the annual accumulation of run-off from an area of approximately 870 square miles, of which 40% comprises glaciers and perennial ice fields Each year, in July or August, the lake overflows the ice barricade across the valley, cutting a channel which widens as it undercuts the glacier front, and empties into the Knik river below the glacier in a torrential flow which lasts only 8–10 days. After the lake empties, the glacier continues its advance and again blocks the channel to repeat the annual cycle. The estimated annual run-off is in excess of 3½ million acre-feet.

In the Hack scheme, one or two large tunnels would be driven through the valley wall (ahead of the glacier front) from the lake to a power plant below the glacier. The tunnels would act both as spillways to pass excess waters below the glacier and as penstocks to the power plant. As a consequence, the Knik glacier would advance against the valley wall, permanently closing the gap or channel which is now cut each year by the overtopping waters of Lake George. Although several questions come to mind, sufficient reliable information is available to indicate that the Hack scheme merits careful consideration.

Power costs from the Hack scheme would range from slightly over 3 mills to slightly under 4 mills for various load factors at the power plant, and between 3½ and slightly over 4 mills transmitted to the Anchorage area, approximately 50 miles distant.

Other power potentials of the Matanuska Valley include the Matanuska river itself, Caribou Creek, and others. The Eklutna project, constructed by the U. S. Bureau of Reclamation, began operations in 1955. This project involves the tapping of a high mountain lake by means of a long tunnel driven through a mountain massif, dropping the waters to the power plant at near tidewater elevation on Knik Arm. The output of this 30,000 installed kilowatt project is transmitted to the Matanuska Valley communities and to the Anchorage area by means of a 115-kv transmission line.

Until the Eklutna project began operations, the Anchorage and Matanuska Valley area depended entirely on thermal power generation. A substantial portion of this generation is obtained by means of modern steam-electric plants in Anchorage and immediate environs utilizing coal from the fields in the lower Matanuska Valley.

The Kenai Peninsula contains a number of relatively small hydro sites. Their development is of considerable importance, not only for the rapidly growing population of the Anchorage area, as well as of the Matanuska Valley and Peninsula area, but also in terms of potential mineral development. It is significant that active planning is under way for the construction of a regional high-voltage, high-capacity transmission network by the Central Alaska Power Association, Inc. (*see* Fig. 2).[3] This network would interconnect the various sites of the Kenai Peninsula, starting with the extremely interesting Bradley Lake at the southwestern extremity of the Peninsula, picking up Kasilof and Kenai river development sites, and then the sites involving the tapping of mountain lakes including Cooper, Crescent, Juneau, Ptarmigan, and Grant. Under preliminary design also is a single-span transmission line crossing of Turnagain Arm to interconnect into the present

[3] A local power agency at present composed of a number of aggressive rural electric cooperative corporations.

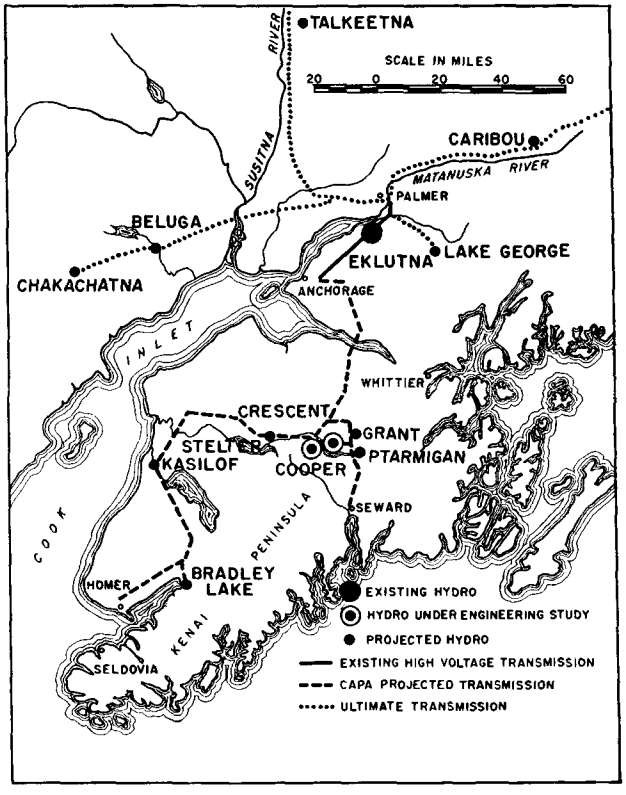

FIG. 2. Hydroelectric system of Kenai Peninsula-Anchorage-Matanuska valley.

Anchorage-Matanuska Valley power systems; this single span, if determined feasible of construction, will be the world's largest, or approximately 12,500 ft long.

At present, a detailed engineering report has been completed on Cooper Lake,[4] and engineering studies are under way on Crescent Lake.[5] It is possible that construction will start on Cooper Lake in the summer of 1956. This project would have an installed capacity of 15,000 kw and will tap Cooper Lake by means of a short tunnel, pipeline, and penstock dropping some 740 ft to a power house on Kenai Lake.

With the exception of Bradley Lake, most of the Kenai Peninsula power projects involve estimated power costs ranging from slightly over 5 mills (for Cooper Lake) to around 11 mills/kwhr.

In terms of potential mineral development, Bradley Lake appears to offer the most significant opportunities, especially when considered as a part of the regional transmission network proposed by the Central Alaska Power Association. Present reconnaissance investigations by the U. S. Corps of Engineers and U. S. Geological Survey show that power installations of 30,000 kw may provide costs of between 3 and 4 mills/kwhr depending on load factor. Capacity available on better than 90% load factor would be in the neighborhood of 40,000 to 50,000 kw.

The Susitna Basin, almost directly north of Anchorage, contains some sizeable potential hydroelectric sites. Reconnaissance surveys indicate at least three of them with prime power capabilities of around 200,000 kw. Cost estimates for these are somewhat high, probably about 9 mills/kwhr, but such estimates undoubtedly err on the "high side." These sites lie along the general route thought feasible for interconnection by means of the transmission network discussed later.

Draining into Cook Inlet from the northwest are two important rivers, the Beluga and the Chakachatna. Three possible sites have been reconnoitered for a prime power total of around 150,000 kw. These might have some future importance, with reference particularly to the development of the Beluga coal fields.

Along the base of the Alaska Peninsula and into the Bristol Bay area are a number of streams and lakes. These are generally of small individual hydro potential, and costs are roughly estimated at 8–15 mills/kwhr, and upward. The same situation prevails generally along the Aleutian Peninsula.

Attention has been given to the desirability of constructing a large-capacity and high-voltage transmission system to interconnect the Copper and Chitina, Matanuska, Anchorage, and Kenai Peninsula projects, thence northward up the Susitna Basin to the drainages in which

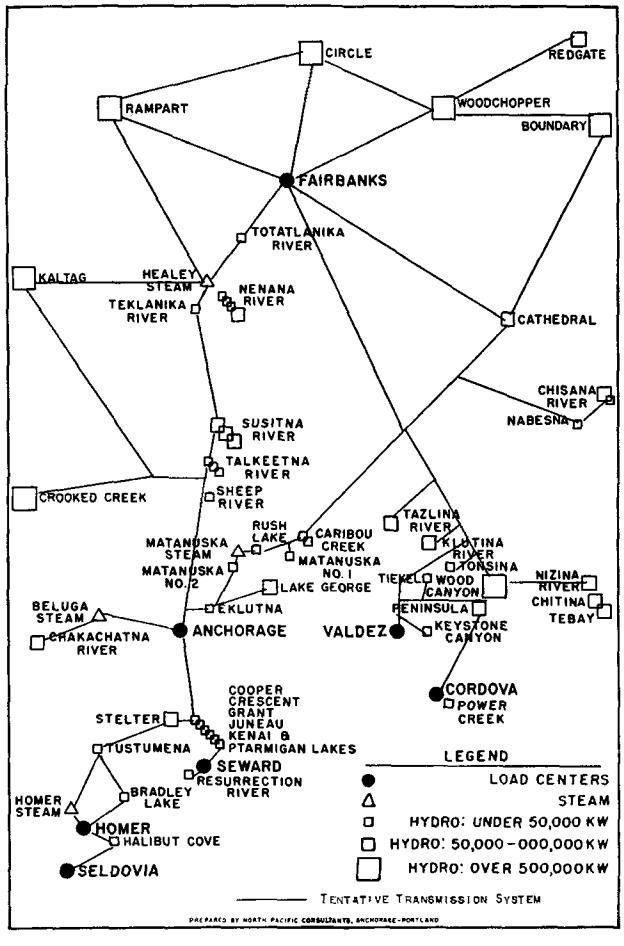

FIG. 3. Generalized scheme showing ultimate high capacity, high voltage electric power transmission network for the Central Alaska region. No attempt has been made to show transmission line routes nor to indicate potential operating voltages. Engineering and economic feasibility of several generating plants is yet to be determined.

[4] Under the auspices of the Central Alaska Power Association.

[5] Under the auspices of the City of Seward.

Fairbanks may be considered centrally located. Preliminary studies have been made by various governmental agencies, by the Central Alaska Power Association, Inc., and by North Pacific Consultants of what would be one of the nation's largest power grid systems (*see* Fig. 3). There appears to be sufficient hydrologic diversity between the various drainage basins to provide definite advantages for large-scale interconnection. Such a power network would make possible the large-scale utilization of the coal resources of the Matanuska, Beluga, and Healy fields by means of steam-electric plants located at mine-mouth. At this juncture, the economics of such a system are not sufficiently clear to warrant an opinion as to ultimate feasibility, but the national power situation urges immediate study and consideration for the portions interconnecting the Copper river areas with those centering about Anchorage and the Kenai Peninsula.

The area described above is immense, and portions are known to be highly mineralized. There is not much question, for example, that the Copper and Chitina drainages contain very large reserves of copper-bearing ores. The abandonment of the Copper River and Northwestern Railroad in the 1930's withdrew the Chitina river area from access; most of the rest of the area is incredibly rugged. The combination of a reservoir such as would result from the construction of the Wood Canyon Dam together with large blocks of low-cost power would not fail to open up a territory rich in mining possibilities. The extent to which electric copper-matte smelting could be conducted near the Wood Canyon site, with ores or concentrates being barged to a plant site in that area, is of course subject to considerable study. However, it would appear to be a logical way to provide high-value matte which could then be trucked down to Valdez or Cordova for transhipment to ocean-going vessels.

The possibility of opening up the area to barge transportation over the reservoir would no doubt stimulate exploration and development so far frustrated by access difficulties. Occurrences of nickel, lead, zinc, and other ores have been reported over the years, but relatively little has been done to explore the area with modern means.

The possibilities of establishing large units of electroprocess industries based on water-borne imports from Pacific Basin countries in the Valdez-Cordova areas, served by means of an appropriate transmission system from the various large hydroelectric sites in the Copper and Chitina basins, are also worthy of attention. To date, Harvey Aluminum, Inc., has obtained a preliminary permit to investigate the Wood Canyon site for precisely that type of power utilization.

As mentioned before, the Bradley Lake potential hydro site also has much merit for investigation with relation to mineral development. The proposed power plant is at the head of Kachemak Bay. At the mouth of the bay, in the Seldovia area, are the well-known chromites of the Kenai Peninsula. Mining operations, which have been under way on portions of the deposits, have been for the purpose of shipping metallurgical, lump chromite. Reserves of other chromites suitable for simple concentration are known to be substantial. The possibilities of an electric furnace operation for the production of various grades of ferrochrome should be considered as good, especially with low-cost power from Bradley Lake and its interconnection with the proposed transmission grid system of the Central Alaska Power Association. Plant sites which might be suitable for the establishment of concentrating and furnace operations would have access to all-year ocean-going transportation.

Of some interest also are possibilities of calcium carbide furnace operations in the same general area, possibly centering at Homer on Kachemak Bay. In this respect, limestones of varying quality are available on Kachemak Bay, and it appears worth investigation to utilize some of the better seams of the Homer area coals for the production of a metallurgical char. Some investigations of this possibility as well as of the ferrochrome operation are under way in a preliminary manner. There is also much discussion of the feasibility of establishment in that area of an ammonium nitrate plant similar to that now operating in Iceland.

The eventual development of power resources in this entire area would have beneficial effects on the expansion of mining activities for gold, platinum, and possibly for other materials such as molybdenum. As pointed out previously, the area is vast and relatively unexplored, so that appraisal of mineral utilization potential cannot be more than sketchy beyond the examples cited.

Central Alaska Region

Total Potential Installed Kilowatts: Over 10 Million

The principal rivers of this tremendous land mass are the Yukon, the Kuskokwim, and the Tanana. Remote and enormous, these rivers until recent years were not considered as having much hydroelectric potential. For the most part, they flow sluggishly with great volume, meandering across great areas of uninhabited country. However, reconnaissance, particularly by the U. S. Corps of Engineers, is changing the former appraisal greatly. It now appears that their hydroelectric potential may be among the world's largest. Three sites have potentials ranging from 1½ to over 3 million kw each of installed capacity, and estimates of the prime power capabilities of these are on the order of 75% of installed capacity. Information so far available does not permit indicating possible power costs, but they may be surprisingly low and suitable for industrial utilization.

Obviously, the development of industrial interest in these sites must be related to accessibility. In that regard, the Kaltag site on the lower Yukon is about 275 miles up the river from Norton Sound on the Bering Sea. Past experience with river boat and barge commerce along the Yukon for almost its entire length would lead one to conclude that this method of transportation is worthy of consideration when open-water navigation is possible during the summer. The same observation regarding water transportation might be applied for the Rampart Circle and Woodchopper sites. Obviously, these are items necessitating careful analysis.

Interconnection of the hydro sites of this area by an extension of the power system described in the previous sections may be desirable and feasible ultimately.

It is not possible to sketch any specific examples in which the development of the water power resources of this area would be advantageous to mineral development. Substantial placer mining for gold is continuing, and possibly the availability of system electric power would assist in its expansion. The immensity of the area and its isolation still place it in the general category, mineral-wise, of "terra incognita." However, there are a number of operations in the area for a variety of minerals. Among those known to exist in variable quantity are silver, zinc, lead, antimony, barite, tungsten, tin, bismuth, mercury, and others. In addition, the Healy coal fields near Fairbanks have been operated for many years. The availability of high-quality limestones in the Windy area on the Alaska Railroad about ⅔ rds of the way from Anchorage to Fairbanks has also stimulated some interest in the establishment of a cement plant to meet the substantial needs for that material in Alaska.

Northern Alaska Region

Total Potential Installed Kilowatts: Over ¼ Million

Most of this area adjoins and is above the Arctic Circle. Several of the large rivers possess substantial summer flows. Surveys have been limited to reconnaissance with interest developing to the point where previous examinations are in the process of revision. The potential susceptible of development may exceed 400,000 kw of prime power. The Noatak river, for example, which empties north of Kotzebue, may possess well in excess of 250,000 kw of prime power. The Colville, which empties into the Arctic Ocean east of Barrow, is by far the largest river of the entire area, but its potential is unevaluated.

Mining operations at present are centered in the Seward Peninsula in the vicinity of Nome. Minerals of interest include gold, silver, lead, zinc, antimony, bismuth, graphite, platinum, mercury, and tin. Most operations depend on captive diesel-generated electric power at high costs. Eventual development of the hydro potential of the area might facilitate expansion of mining activity.

General Notes

As noted above, there are at least two areas of immediately promising hydroelectric development: Southeastern Alaska with the Taiya-Yukon project, and Southwestern Alaska with the Cooper river (Wood Canyon and Peninsula sites), and the Matanuska-Anchorage, Kenai Peninsula, Susitna areas (Lake George, the Central Alaska Power Association developments and Bradley Lake). These areas combine potentially large blocks of power at costs competitive with those projects remaining in the Pacific Northwest, with access to deep-draft ocean transportation and available population with a substantial labor force. Although mineralization is known to be extensive, the outstanding possibilities are in the electroprocess utilization of iron, nickel, copper, and chromites of the two areas.

In the development of some of the enormous hydro potential of such rivers as the Yukon and Kuskokwim, much work of an investigatory nature must be performed. In this, new engineering approaches must be devised to make feasible lowest cost design and construction of dam and control structures. That is, it is within reason that climatic and soil conditions which appear at first to provide obstacles may well be turned to advantage. For example, considerable thought is being given to permanently frozen earthen structures.

High-voltage, high-capacity networks to transmit huge blocks of hydroelectric power are not unusual in the modern world. Their construction and operation under conditions prevailing in Alaska, however, will require adept use of engineering principles. A promising start is being made in the plans of the Central Alaska Power Association for interconnecting the power potentials of the Matanuska-Anchorage-Kenai Peninsula area.

It is also quite probable that the hydro potential of Alaska, especially southwestern, central, and northern regions, will be developed in concert with the establishment of large coal mine-mouth steam-electric plants, as well as of nuclear reactor power plants. Regarding the latter, preliminary discussions are now under way for two reactors of approximately 10,000 kw capacity.

Depth of Surface Damage Due to Abrasion on Germanium

T. M. Buck and F. S. McKim

Bell Telephone Laboratories, Inc., Murray Hill, New Jersey

ABSTRACT

The approximate depth of surface damage on Ge as it influences surface recombination velocity has been measured for a variety of abrasive treatments by etching, weighing, and making two types of photomagnetoelectric measurements. Values range from 1μ or less for fine polishes to 35μ for heavy sandblasting. Close correlation is found with changes in reverse characteristics of grown junction p-n diodes treated in the same manner.

The drastic effect of mechanical surface damage, produced by sawing and abrasive shaping, was one of the earliest surface effects recognized in Ge transistor research. Various chemical etchants, CP-4 for example (1), were developed for removing damaged material.

The aim of the present work was to measure the depth of damage, as shown by surface recombination velocity, when Ge was subjected to a variety of abrasive treatments including very fine polishes. Such information may be useful in device fabrication, as smaller and more critical physical dimensions become necessary. It should also contribute to a more complete description and definition of surface effects on semiconductors.

The principal technique employed was one involving measurement of open-circuit photomagnetoelectric (PME) voltage, simply to determine qualitatively whether recombination velocity was increased or decreased by a given treatment. In addition to this, a method based on the recently developed theory of the PME effect by van Roosbroeck (2) was used to test a few of the same abrasive treatments and to follow the values of recombination velocity quantitatively. Abrasive treatments were further investigated in regard to their effect on the reverse characteristics of grown junction p-n diodes.

Some work on abrasion damage has been published recently. Clarke and Hopkins (3) found that sand-blasting a thin rod of Ge produced a high-conductivity surface layer which they estimated to be about 0.7×10^{-4} cm ($0.7\ \mu$) thick. In etching-rate experiments Camp (4) found the depth of the disturbed layer for several abrasive treatments to be in the range 2–10 μ. McKelvey and Longini (5) found that a Ge surface lapped with 800 grit Alundum required removal of about 5 μ to bring S (surface recombination velocity) down to the order of magnitude associated with etched surfaces. Uhlir (6) has found greater depths than these, 20–50 μ even for fine polishes, in studies of voltage-current curves of electrolyte-Ge barriers.

Qualitative PME Method

A method for determining surface recombination velocity from a simple measurement of open-circuit PME voltage was proposed by Moss, Pincherle, and Woodward (7). This method has been used to test a variety of surface treatments on Ge (8, 9) and gave a convenient qualitative indication of recombination velocity. Most of the data in the present work was obtained by a similar method, but with treatments applied to the illuminated surface rather than to the dark surface. The principle is illustrated in Fig. 1. A thin slab of Ge is illuminated on one large surface by water-filtered light which is highly absorbed at the surface. A magnetic field is applied perpendicular to the direction of illumination and to the long edge of the specimen. The dark surface of the slab is sand-blasted, and remains in that condition, to provide a high-recombination sink for carriers diffusing from the illuminated surface. Electrons and holes in the photodiffusion current are deflected in opposite directions by the magnetic field and this sets up the PME open-circuit voltage normal to both the magnetic field and the diffusion current across the slab. After an abrasive treatment on the front surface PME voltage is very low, perhaps a few tenths of a millivolt, since in this situation most of the carriers created by the nonpenetrating light recombine at the illuminated surface so that concentration gradient and diffusion current are small. As the front surface is given a series of etching treatments, PME voltage increases, since S at the illuminated surface decreases, causing larger concentration gradient and diffusion current. With continued etching V_x eventually levels off, at 200 mv for example, and in this region it is assumed that the disturbed material has been removed, at least insofar as recombination velocity is concerned. The height of the plateau is not of particular interest here; in general it depends on resistivity, volume lifetime, recombination at both surfaces, light intensity, and specimen thickness. All of these are taken into account directly or indirectly when actual values of S are determined (2) and quantitative measurements of this sort are mentioned later. In the simple open-circuit voltage measurements, however, S is not determined, but rather the depth at which PME voltage ceases to change, which is taken as the depth of damage.

The specimen mounting for the open-circuit PME voltage studies is pictured in Fig. 2. The Ge specimens used were p-type, 5.5 ohm-cm slabs 3.17 cm long, 0.635 cm wide, and about 0.127 cm thick initially. The large surfaces were (100) crystal faces. The dark surface was sandblasted, leads were soldered about 1.9 cm apart, and the whole assembly was cast in Araldite resin with a glass backing so that only the front surface and the ends of the

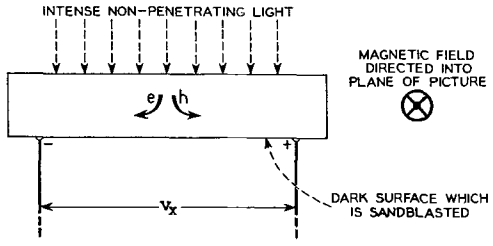

FIG. 1. Photomagnetoelectric method of investigating surface recombination velocity; open-circuit voltage measurements; treatments on illuminated surface.

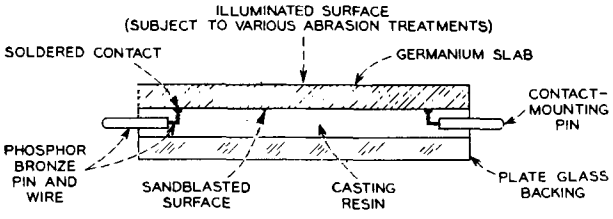

FIG. 2. Specimen mounting for abrasion treatments and PME measurements.

leads were exposed, as shown in Fig. 2. The specimen could then be cemented to a holder for lapping or polishing.

After an abrasive treatment the progressive etching was performed by dipping the front surface into diluted CP-4.[1] The slab was moved about gently to obtain uniform etching. Etching was followed by rinsing in a stream of distilled water and blotting on filter paper. PME measurements were made with the specimen in an atmosphere of dry nitrogen. The specimen was exposed to light for only brief intervals to avoid heating; balance on the type K-2 potentiometer was reached by trial and error which can be accomplished with good precision.

The magnetic field, supplied by a permanent magnet, was 6400 gauss. Light from a 300-watt projection lamp was filtered through a 1.7 cm water filter. Intensity was fairly high, about 10^{18} quanta/cm^2 sec.

The depth of material removed by etching was determined from weight loss. Uniform etching over the surface was assumed. For the specimens used, 1 mg corresponded to about 1-μ change in thickness. Checks with a micrometer at various convenient times during the series agreed fairly well with the weight loss values, within about 10–15%. Weight loss values are inherently more precise and it is felt that if there is an error it is caused by a slight tendency to etch more toward the edges so that the apparent values from weight loss may be too high by a few per cent.

Results of Open-Circuit PME Voltage Measurements

Fig. 3 shows that all the abrasive treatments tested caused high surface recombination velocity (low V_x) but that the amount of etching required for recovery varied widely and in a reproducible manner with the type of abrasive treatment. Thus, a surface which was sandblasted with 180 mesh SiC required removal of 32–34 μ, compared with 1–2 μ for a fine diamond polish. Some details on these

[1] 15 ml glacial CH_3COOH, 15 ml conc. HF, 25 ml conc. HNO_3, 2 drops Br_2, 15 ml H_2O.

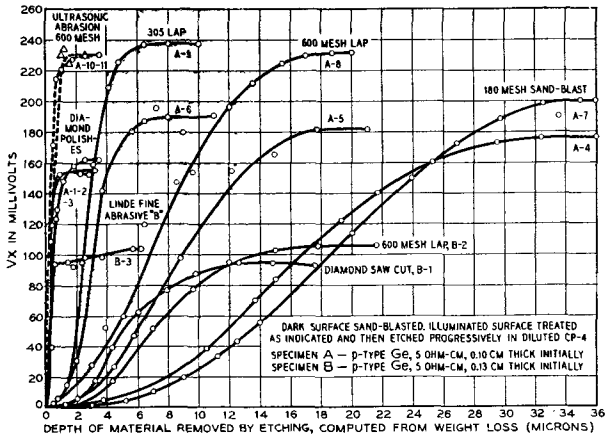

FIG. 3. Change of open-circuit PME voltage with etching, after various abrasive treatments.

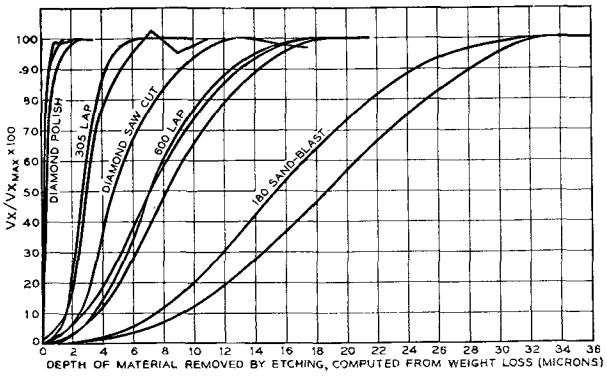

FIG. 4. Change of PME voltage with etching; normalized curves.

TABLE I. *Approximate depth of damage for various treatments on* Ge

Treatment	Depth of damage (μ)	Nominal particle size of abrasive (μ)
Linde fine abrasive "B" polish	1	0.1
Ultrasonic abrasion (600 mesh SiC in water ultrasonically agitated)	1–2	25
Diamond polish	1–2	0.5
No. 305 lap	6–7	5
Diamond saw cut	12–13	
600 Mesh SiC lap	17–18	25
180 Mesh sandblast	32–34	125

treatments are given below. Differences in height of curves for a given treatment are due to gross differences in thickness of the specimen at these particular points in the complete series. In Fig. 4 the curves have been normalized. These results together with those for several other treatments are shown in Table I. As this table shows, an interesting correlation of depth of damage with particle size of abrasive in the lapping treatments was observed.

Five separate applications of the 600 mesh lap, three of which are shown in the curves, yielded approximately the same depth of damage although the total amount of material removed varied from 0.7 to 5 mils. Several times the freshly lapped or polished surfaces were carefully

washed in alcohol, toluene, water, etc., to determine whether any cleaning action short of actual removal of material would raise V_x. None of these attempts was successful; it appeared that the high recombination velocities were indeed due to mechanical damage even with the very finest abrasive treatment.

Remarks on Abrasive Treatments

180 Mesh sandblast.—180 mesh silicon carbide was blown through a 5/16 in. tube under 25 lb/in.^{2} air pressure.

600 Mesh lap.—The 600 mesh SiC was slurried in water and the lapping done by hand on a glass plate with moderate pressure.

Diamond saw cut.—Cutting was done with a new Norton diamond wheel D220-N100 M1/8. It was surprising to find that sawing caused slightly less damage than the 600 mesh lap. Only one test was made, but there seemed to be no reason to believe it was misleading

#305 Lap.—Lapping was done by hand on glass with a water slurry of American Optical Co. #305 abrasive after preliminary laps with 600 mesh SiC and #303½. The depth of damage is in good agreement with the value of 6 μ obtained by Camp (4) from etching rates for the same abrasive on the same crystal face (100).

Diamond polish and Linde fine abrasive B.—Buehler diamond dust or Linde fine abrasive B (Alumina) was held in Buehler microcloth on a power driven wheel. Fine polishes usually involve several steps in which progressively finer abrasive materials are used. The coarsest material (600 mesh SiC) is used first in order to arrive quickly at a fairly true surface. The last step with the fine abrasive must of course go far enough to remove disturbed material left by preceding steps. The same depth of damage was obtained, however, by using the fine abrasive directly on an etched surface.

Ultrasonic abrasion (600 mesh).—The specimen which had been thoroughly etched in CP-4 was immersed for 5–10 min in a suspension of 600 mesh SiC in water which was ultrasonically agitated in a Brush hypersonic generator. Surface recombination velocity was increased drastically even though there was no visible appearance of any change on the etched surface under a low-powered microscope.

Quantitative PME Measurements

As a check on the qualitative open-circuit PME voltage measurements, two representative treatments were tested by a PME method which permits quantitative determination of recombination velocity (2). Results for fine polishes and the 600 mesh lap are shown in Fig. 5. In this method values of S on the dark surface of the specimen are determined from measurement of short-circuit PME current and of relative conductance increase, $\Delta G/Go$, at the same light intensity but with no magnetic field. The ratio of these quantities multiplied by a factor containing constants for the material is used to compute S (2). Introduction of relative conductance increase makes it unnecessary to know either light intensity or S at the illuminated surface explicitly. Specimens were mounted as in Fig. 2 except that two additional current leads were attached at the ends and the dark surface received abrasive treatments and etching while the other large surface with

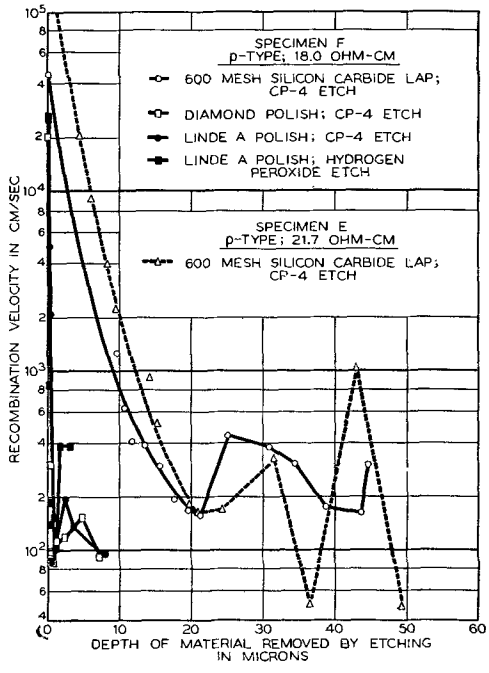

FIG. 5. Surface recombination velocity as a function of depth of material removed by etching. S determined from short-circuit PME current and relative conductance increase.

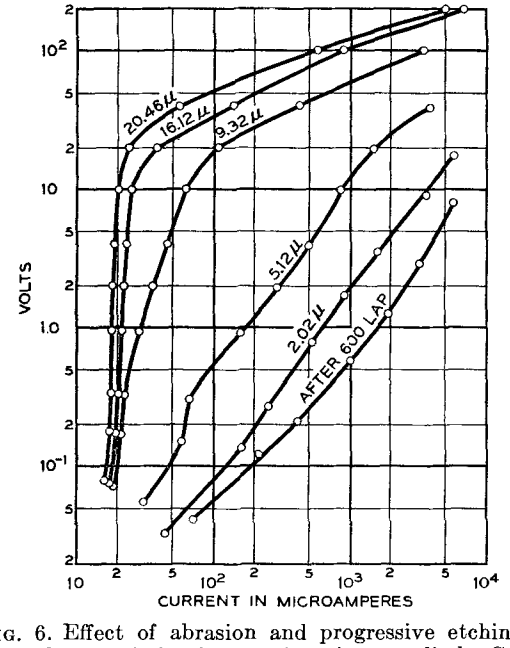

FIG. 6. Effect of abrasion and progressive etching on reverse characteristic of grown-junction p-n diode. Ge p-n diode; n-side 3.5 ohm-cm, p-side 0.2 ohm-cm; volume lifetime 100–300 μsec; dimensions = 0.238 cm x 0.238 cm x 1.25 cm; 600 mesh lap.

leads attached was etched and was exposed to the illumination through the glass and Araldite resin.

It is seen in Fig. 5 that the measurements by the new method show recombination velocities of 30,000 cm/sec and larger for polished or lapped surfaces. The damage appears to be removed at about 20 μ for the 600-mesh lap and at a micron or less for the fine polishes. After that,

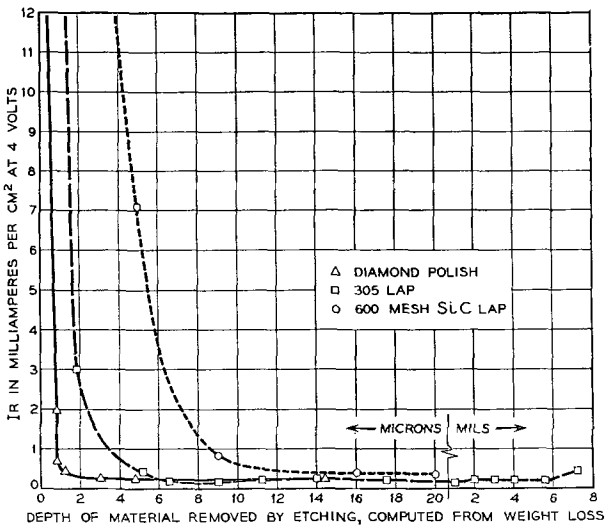

FIG. 7. Change of reverse dark current (at 4 v) with etching, after abrasion by three different methods. Ge grown-junction p-n diode.

random fluctuations appear with further etching. Presumably these are due to subtle differences in etching and atmosphere. Random fluctuations do not appear in the open-circuit voltage measurements presumably because that method is not so sensitive to small changes at low levels of S.

The physical picture of the abrasion damage seems to be one of a thin layer of very low lifetime material which excess carriers diffuse into as if encountering a surface of very high recombination velocity. Lifetime in this layer is probably lower toward the true outer surface. A considerable amount of the damaged layer must be removed before chemical effects on the true outer surface begin to influence S very strongly.

Diode Studies

Three of the abrasive treatments were given to two large grown junction p-n diodes in order to determine whether differences shown by the PME measurements would appear also in treatment of a junction device. Diodes were lapped or polished on all four sides and then put through the etching and weighing procedure. After etching and washing, a diode was allowed to stand over silica gel in a bottle for 24 hr before measurement of the reverse characteristic.

Results are shown in Fig. 6 and 7. Correlation of the recovery points with the PME data is quite close. [Data on the diodes, however, pertain to the (110) crystal face while PME results were obtained on (100) faces.]

However, the behavior of reverse characteristic, after abrasion, cannot be explained on the basis of surface recombination alone by existing theoretical treatments of p-n junctions. From the equation (10)

$$I_s = A \frac{kTb\sigma_i^2}{q(1+b)^2}\left(\frac{1}{\sigma_n L_p} + \frac{1}{\sigma_p L_n}\right) \qquad \text{(I)}$$

I_s = reverse saturation current, A = area of junction, b = ratio of electron mobility to hole mobility, q = electron charge, σ_i = intrinsic conductivity, σ_n = conductivity on n-side, L_p = diffusion length of holes on the n-side = $\sqrt{D_p\tau_p}$; D_p is diffusion constant for holes and τ_p is the effective or filament lifetime, which depends on volume lifetime and S (11). For the case shown in Fig. 6, one obtains I_s = 7.32 μamp for ρ_n = 3.5; ρ_p = 0.2; A = 0.0558 cm²; body lifetime = 100 μsec; S = 100 cm/sec.

Allowing S to approach infinity would lower the filament ("effective") lifetime (11) from 100 μsec to 40 μsec on the n-side and to 24 μsec on the p-side, not a very large decrease since the cross section is so large. This would then increase I_s to only 11.7 μamp and would not, of course, account for the slopes of the curves.

However, as Shockley (10) has pointed out, equation (I) is not expected to hold for very large values of S, in which case the junction may be expected to become substantially ohmic.

Two alternative explanations of the diode behavior are: (*A*) the effect of abrasion is due entirely to surface recombination in a manner not yet quantitatively explained (10); (*B*) the effect may be due to a conductive layer across the junction of the type found by Clarke and Hopkins (3) on a sandblasted filament.

In any event, the PME measurements are evidently revealing surface "damage" of some sort which is detrimental to junctions, and the depth of this damage appears to be the same in both types of measurement.

Greater depths of damage for fine polishes have been found by Uhlir (6) in studies of the reverse characteristics of electrolyte-Ge barriers. He suggests that the discrepancy between PME measurements of S and the Ge-electrolyte studies may be due to the fact that the latter method is more sensitive to local spots of damage whereas the PME method determines an average over a relatively large surface. Undoubtedly in device work it would be safer generally to remove an excess of material, say 2–3 mils, but in situations where dimensions are critical and only very slight etching can be tolerated the fine polishes appear to offer a possible advantage.

Acknowledgment

The authors gratefully acknowledge the help of J. Andrus, E. Berry, and W. L. Bond who developed and administered the fine polishing treatments; the availability of these polishes was responsible for initiation of this work. D. R. Mason performed the ultrasonic abrasion treatment. Thanks are also due to W. van Roosbroeck and W. H. Brattain for helpful discussions.

Manuscript received May 12, 1956. This paper was prepared for delivery before the Cincinnati Meeting, May 1 to 5, 1955.

Any discussion of this paper will appear in a Discussion Section to be published in the June 1957 JOURNAL.

REFERENCES

1. R. D. HEIDENREICH, U.S. Pat. 2,619,414, Nov. 25, 1952.
2. W. VAN ROOSBROECK, *Phys. Rev.*, **101**, 1713 (1956). Additional experimental details of the method to be published by T. M. Buck and F. S. McKim.

3. E. N. Clarke and R. L. Hopkins, *Phys. Rev.*, **91**, 1566 (1953).
4. P. R. Camp, *This Journal*, **102**, 586 (1955).
5. J. P. McKelvey and R. L. Longini, *J. Appl. Phys.*, **25**, 634 (1954).
6. A. Uhlir, *Bell System Tech. J.*, **35**, 333 (1956).
7. T. S. Moss, L. Pincherle, and A. M. Woodward, *Proc. Phys. Soc. (London)*, **66B**, 743 (1953).
8. T. S. Moss, *ibid.*, **66B**, 993 (1953); *Physica*, **20**, 989 (1954).
9. T. M. Buck and W. H. Brattain, *This Journal*, **102**, 636 (1955).
10. W. Shockley, *Bell System Tech. J.*, **28**, 435 (1949).
11. W. Shockley, "Electrons and Holes in Semiconductors," pp. 322-323, D. Van Nostrand and Co., New York (1950).

Solid Solubilities and Electrical Properties of Tin in Germanium Single Crystals

F. A. Trumbore

Bell Telephone Laboratories, Inc., Murray Hill, New Jersey

ABSTRACT

The solid solubility of Sn in Ge has been determined in the range from 400°C to the melting point of Ge using conventional crystal pulling techniques and crystal growth from melts in a thermal gradient. The distribution coefficient changes from 0.020 ± 0.003 at the melting point of Ge to 0.012 ± 0.002 at the lower temperatures, corresponding to solid solubilities of up to about 5×10^{20} at./cc. X-ray measurements substantiate the conclusion that these relatively large amounts of Sn are in solid solution. In spite of the presence of between 10^{19} and 10^{20} at./cc of Sn in the pulled crystals, resistivities as high as 40-50 ohm-cm and minority carrier lifetimes as high as 100-200 μsec were obtained. These results confirm the electrical neutrality of Sn in Ge.

Although Sn is assumed generally to have neither donor nor acceptor properties in Ge, no systematic study appears in the literature. In the present work Ge single crystals were grown from melts containing relatively large amounts of very pure Sn. The results of resistivity, lifetime, x-ray, and solid solubility measurements on these crystals provide a conclusive answer to the question of the electrical neutrality of Sn in Ge.

Experimental

Crystal pulling experiments.—A conventional crystal pulling machine (1) was used to grow Ge single crystals from 100-g melts initially containing from 1 to 5 at. % Sn. The crystals were grown under a hydrogen atmosphere in the <100> direction at pull rates of 3 and 0.5 cm/hr and a rotation rate of 60 rpm. Ge[1] was zone-refined material from which single crystals of resistivities greater than 40 ohm-cm could be grown. Analyses of three different samples of high purity Sn[2] are shown in Table I. Two of these samples were taken from zone-refined lots and, as is evident from the table, were of exceptional purity.

Thermal gradient crystal growth.—With melts containing more than a few atom per cent Sn the crystal pulling method was found to be unsatisfactory. For these melts, which contained up to about 90% Sn, a technique was employed which made use of the fact that the solubility of Ge in Sn increases with temperature. In this method Ge was dissolved in Sn at a given temperature and then precipitated or grown on a seed crystal at a lower temperature.

As shown in Fig. 1 a vertical, doubly wound furnace was used in these experiments. By regulating the current independently in the two windings a controlled thermal gradient could be established. The furnace was mounted on a swivel support so that it could be inverted with the sample tube in place. A number of different seed and melt arrangements were used in these experiments. The most successful design is shown schematically in Fig. 1. A Ge single-crystal seed is held by a constriction in one end of a sealed evacuated vitreous silica tube. The Sn, together with Ge in excess of that needed for saturation, is placed in the other end. The Sn used in these experiments was the "super-pure" material (*see* Table I).

After mounting in the furnace as shown in Fig. 1, Sn and excess Ge were heated out of contact with the seed crystal in order to saturate the Sn with Ge. This was done to minimize solution of the seed crystal when the furnace was inverted. The molten metal was saturated at a temperature slightly lower than that of the seed crystal to prevent spurious crystals from forming on the seed crystal when the furnace was inverted into the growing position. After inversion into the growing position the thermal gradient was adjusted to that the hottest part of the solution was at the top in order that any spurious crystals not grown on the seed would float to the top of the melt. As measured with the thermocouple outside the silica tube, essentially linear

[1] Obtained from the Western Electric Co.
[2] Obtained from the Vulcan Detinning Co.

TABLE I. *Analyses of* Sn *samples*

Sample designation	Impurities
[1] Vulcan "super-pure".....	<0.001% Ag, Al, Ca, Cu, Fe, Mg, Na, Pb
[2] Vulcan #1466.....	<0.00003% Fe; <0.00002% Pb; <0.0005% Sb[a]
[3] Vulcan #VS27SP.....	<0.00001% Fe, Pb; <0.0005% Sb[a]

[a] Actually no Sb was detected. The figure 0.0005% represents the upper limit of detection for the analytical method

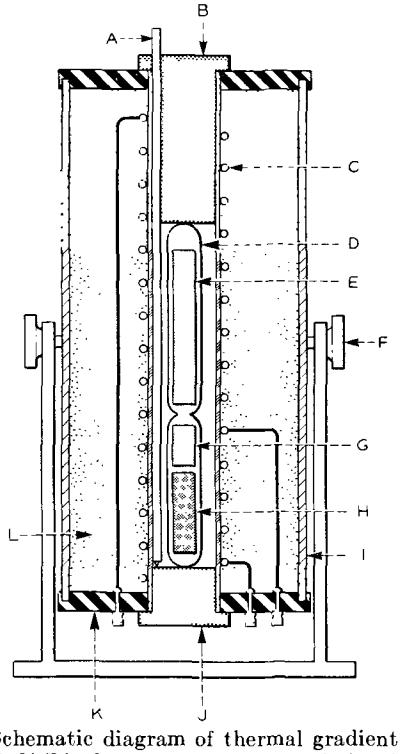

FIG. 1. Schematic diagram of thermal gradient furnace: (A) Pt-Pt 10% Rh thermocouple in ceramic insulator; (B) alundum plug; (C) nichrome heating element; (D) vitreous silica tube; (E) Ge seed crystal; (F) swivel support; (G) excess Ge; (H) Sn; (I) steel furnace shell; (J) alundum plug; (K) transite; (L) silocel insulation.

thermal gradients averaging about 5°C/cm were maintained during growth of the crystals. The total gradient varied with the lengths of the seed crystals which ranged up to 10 cm. The periods of growth varied from about 2 to 4 weeks. At the end of this time the furnace was again inverted to drain off most of the molten alloy, following which the tube was removed from the furnace and quenched in water to minimize further growth on the Ge crystals. Excess Sn then was removed by digesting the sample in hot concentrated HCl. A sketch of the type of growth, typical of this particular geometry, found in these experiments is shown in Fig. 2. In most cases the dimensions of the grown crystals were on the order of 1–3 mm. Growth temperatures were determined by comparison of the positions of the crystals in the tube and the temperature profile in the furnace.

Chemical analyses.—The crystals were analyzed for Sn using spectrochemical techniques. In the case of crystals grown by the thermal gradient method it was found necessary to crush and digest the crystals in HCl in order to remove any occluded Sn. The analyses are believed to be accurate to about ±10% of the total concentration of Sn in the crystals.

Electrical measurements.—Almost all of the electrical measurements reported in this paper were performed on the crystals grown by the pulling technique since the samples grown in a thermal gradient were in general either polycrystalline, too small, and (or) irregular in shape for accurate measurements to be made. Resistivities were determined using the conventional four-point probe technique (2) and are accurate to better than ±10%. Minority carrier lifetimes were determined by observing the decay in photoconductivity as described by Hornbeck and Haynes (3) and are believed to be accurate to better than ±25%. In addition to the photoconductivity decay measurements, a few diffusion length measurements were made using the Goucher technique (4). Results of the two methods were generally in good agreement.

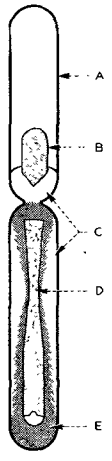

FIG. 2. Schematic diagram of crystal growth: (A) vitreous silica tube; (B) excess Ge; (C) Sn-Ge melt; (D) original seed crystal; (E) grown crystals.

X-ray measurements.—The lattice constants of pure Ge, one pulled crystal, and two crystals grown in a thermal gradient were determined by x-ray diffraction measurements with a precision cell camera.

RESULTS AND DISCUSSION

Solid Solubility of Sn *in* Ge

Results of the crystal pulling experiments are discussed first. Because of the relatively high concentrations of Sn in the melts difficulty was encountered in obtaining equilibrium between the bulk of the melt and the growing crystal. For example, the effect of constitutional supercooling (5) is of more importance where the solute element is present in larger concentrations. In addition, polycrystalline growth and the presence of occluded Sn presented problems. A crystal pulled at the rate of 3 cm/hr contained numerous patches of occluded Sn about 0.05 mm in diameter. With a pull rate of 0.5 cm/hr little or no microscopic evidence of occlusions was observed in the crystals In order to determine whether the observed distribution

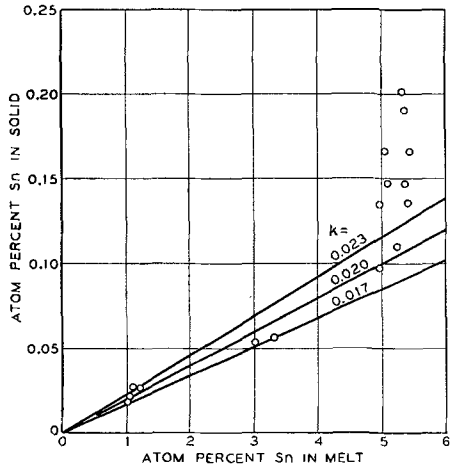

FIG. 3. Solid solubility of Sn in Ge as a function of melt concentration in the crystal pulling experiments.

TABLE II. *Analyses of thermal gradient crystals*

T (°C)	N^S_{Sn}	k
401	0.0111	0.011_5
619	0.0088	0.011_5
637	0.0093	0.012_6
759	0.0056	0.011_9

coefficients corresponded to equilibrium values, a study of the effect of melt concentration on the observed distribution coefficient at a pull rate of 0.5 cm/hr was carried out. Results of these experiments are shown in Fig. 3 where the observed solid solubility is plotted against the concentration of Sn in the melt. The points correspond to individual analyses on sections of eight different crystals. Straight lines, corresponding to three values of the distribution coefficient, k, are also plotted. The best fit to the data is seen to be the line corresponding to a value of k equal to 0.020 with an estimated error of ± 0.003. An obvious scatter or upward trend in the data is observed in the region of 5–6 at. % Sn. It is in this region that difficulty was encountered with polycrystalline growth, occlusions, and undoubtedly with constitutional supercooling. It should be noted that all sources of error (other than the analytical error) lead to high values of the solid solubility. The limiting value of 0.020 is in agreement with a value of 0.02 near the melting point of Ge determined by Struthers (6) using radiotracers and growing crystals from melts much more dilute with respect to Sn.

Results of chemical analyses for Sn in the thermal gradient crystals are summarized in Table II where N^S_{Sn} and k are the atom fraction of Sn in the crystal and the distribution coefficient of Sn in Ge, respectively. In calculating k, the liquidus compositions of Thurmond, Hassion, and Kowalchik (7) were used. Temperatures quoted in Table II must be regarded as being uncertain to perhaps ± 10°C since, due to the relatively high thermal conductivity of the melt, the thermal gradient in the melt probably differed from the gradient measured by the thermocouple outside the sample tube. In addition to any inherent errors, the values for k and N^S_{Sn} are subject to an error

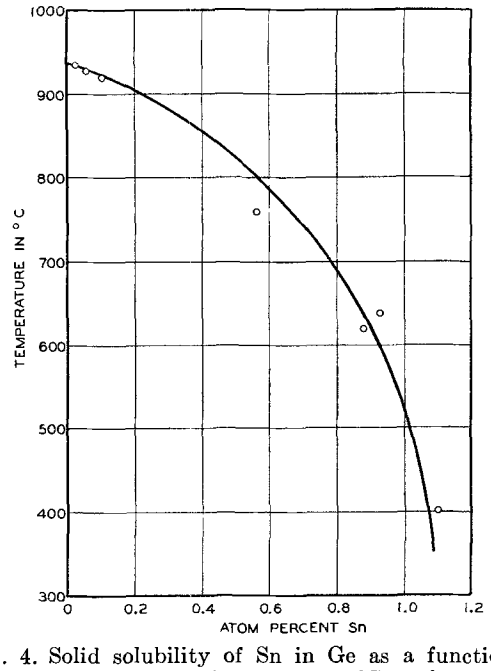

FIG. 4. Solid solubility of Sn in Ge as a function of temperature. The three points above 900°C are from analyses on pulled crystals, while the points at lower temperatures are from thermal gradient experiments.

TABLE III. *Lattice parameters*

N^S_{Sn}	d (observed)	d (calculated)
0 (Ge)	5.6574 ± 0.0003	5.6576[a]
0.0012	5.6576 ± 0.0004	5.6586
0.0066	5.6639 ± 0.0003	5.6631
0.0105	5.6667 ± 0.0014	5.6663
1.00 (Sn)		6.489[a]

[a] ASTM values. The value for Sn is that corresponding to the diamond structure of gray Sn.

TABLE IV. *Electrical properties*

Crystal[a]	Resistivity[b] (ohm-cm)	Lifetime (μsec)	C_{Sn} (atoms/cc)
1[5]	11–12(n)	15	7×10^{19}
2[5]	9–17(n)	10	7.5×10^{19}
3[5]Ga	30–34(n)	45	6×10^{19}
3[5]Sb	0.5–0.6(n)	5	6×10^{19}
3[3]	35–46(n)	>140	3×10^{19}
3[1]	42 (p)–46(n)	185(p)	2×10^{19}

[a] The number outside the brackets refers to the source of Sn (corresponding to the numbers in Table I) used in the growth of the crystal. The number inside the bracket refers to the initial concentration (in atom per cent) of Sn in the melt. Two crystals, 3[5]Ga and 3[5]Sb, were deliberately doped with Ga and Sb, respectively. The amount of Ga added was insufficient to convert crystal 3[5]Ga to p-type.

[b] The resistivities quoted here are the values found near the top and the bottom of the crystal.

of about $\pm 10\%$ because of uncertainties in the chemical analyses.

The solidus curve based on both the crystal pulling and thermal gradient data is plotted in Fig. 4. Near the melting point of Ge the curve is drawn with a slope corresponding to $k = 0.020$ assuming a freezing point lowering constant

of 3.6°C/at. % Sn obtained from a value for the heat of fusion of Ge of 8.1 kcal/g-atom (8).

X-ray Measurements

Results of lattice constant determinations are summarized in Table III. In this table N^S_{Sn} is the atom fraction of Sn in the crystal, d(observed) is the measured lattice parameter in Angstroms at 25°C, and d(calculated) is the value of the lattice parameter assuming a linear variation of the lattice constant over the entire composition range from 0 to 100% Sn. Within the rather wide limits of experimental error, the expansion of the Ge lattice by Sn is in agreement with the assumption that Vegard's law holds over the entire composition range. While the measurements are not sufficiently precise to determine whether this assumption is strictly true, the results do show that Sn is truly in solid solution and is not present as occluded material.

Electrical Properties

Results of electrical measurements on the pulled crystals are summarized in Table IV. As expected, the crystals grown from melts containing the purer Sn samples (and no added impurities) had the higher resistivities. Resistivities of these crystals correspond to differences on the order of 10^{13}–10^{14} at./cc in donor-acceptor concentrations (9) even though Sn concentrations were between 10^{19} and 10^{20} at./cc. Furthermore, qualitative spectrochemical analyses excluded the presence of other detectable impurities at concentrations higher than about 10^{17}–10^{18} at./cc. In addition, low temperature resistivity measurements on one sample gave a resistivity vs. temperature curve typical of ordinary donors and acceptors. These observations indicate that impurities other than Sn are responsible for the observed resistivities.

Minority carrier lifetimes in certain crystals are seen to be relatively high and comparable in magnitude with lifetimes obtained in undoped crystals. There does appear to be a rough correlation between the resistivity and the lifetime which does not depend on the concentration of Sn in the crystal. An explanation of the lower lifetimes found for crystals with low resistivities may be found in the effect of the Fermi level on lifetime as discussed by Hall (10) and by Shockley and Read (11). In addition, there are probably more impurity recombination centers in the lower resistivity samples where the more impure Sn was used. However, a knowledge of both the identity and concentration of the impurity or impurities acting as recombination centers is lacking so that no quantitative calculations will be attempted here.

Rough resistivity measurements were made on some of the thermal gradient crystals containing as much as 1 at. % Sn. Values ranging from 1 to 20 ohm-cm, n-type, were found. However, since the samples were either polycrystalline or too small for accurate measurement, it is possible that these values could be too high by a factor of about ten. Even allowing for an error of a factor of 100 the resistivities obtained correspond to N_D-N_A values of only about 10^{18} at./cc compared to Sn concentrations of more than 10^{20} at./cc.

Conclusions

The presence of near-intrinsic resistivities in conjunction with such large solid solubilities of Sn in Ge is taken as conclusive proof that at concentrations of Sn as high as 10^{20} at./cc Sn is truly neutral insofar as its effect on the conductivity of Ge is concerned. The high lifetimes also show that at these concentration levels Sn is definitely not an effective recombination center for holes and electrons in Ge. These results confirm the conclusions of Woodbury and Tyler (12) who, assuming Struther's value for k at the melting point of Ge, deduced that they had grown crystals containing more than 10^{18} at./cc of Sn without affecting resistivity or lifetime.

Acknowledgments

The author gratefully acknowledges the contributions of many members of the Bell Telephone Laboratories to this work. He especially wishes to thank W. H. Richards for the growth of the pulled crystals, Mrs. M. H. Read for the x-ray measurements, C. R. Isenberg for technical assistance and the Analytical Chemistry Department for the spectrochemical analyses. Helpful discussions with C. D. Thurmond and C. R. Landgren are also acknowledged.

Manuscript received April 18, 1956. This paper was prepared, in part, for delivery before the Pittsburgh Meeting, October 9 to 13, 1955.

Any discussion of this paper will appear in a Discussion Section to be published in the June 1957 JOURNAL.

REFERENCES

1. J. A. Burton, G. W. Hull, F. J. Morin, and J. C. Severiens, *J. Phys. Chem.*, **57**, 853 (1953).
2. L. Valdes, *Proc. I.R.E.*, **42**, 420 (1954).
3. J. A. Hornbeck and J. R. Haynes, *Phys. Rev.*, **97**, 311 (1955).
4. F. S. Goucher, *ibid.*, **81**, 475 (1951).
5. J. W. Rutter and B. Chalmers, *Can. J. Phys.*, **31**, 15 (1953).
6. J. D. Struthers, quoted by J. A. Burton, *Physica*, **20**, 845 (1954).
7. C. D. Thurmond, F. X. Hassion, and M. Kowalchik, to be published.
8. E. S. Greiner, *J. Metals*, **4**, 1044 (1952).
9. M. B. Prince, *Phys. Rev.*, **92**, 681 (1953).
10. R. N. Hall, *ibid.*, **83**, 228 (1951); **87**, 387 (1952).
11. W. Shockley and W. T. Read, *ibid.*, **87**, 835 (1952).
12. H. H. Woodbury and W. W. Tyler, *ibid.*, **100**, 659 (1955).

A Shot Tower for Producing Germanium Doping Pellets of Uniform Composition

I. A. Lesk

General Electric Company, Syracuse, New York

ABSTRACT

A shot tower may be used as a convenient and accurate way to obtain uniform mixtures of Ge and an impurity in a finely divided form. This shot may be used as master alloys for controlled impurity addition during growth of Ge crystals. This method gives convenient small pellets with the impurity fraction in each pellet (in a given batch) the same. The impurity fraction in a given batch of shot is easily controlled. The size range can be controlled, facilitating subsequent weighing procedures. Insoluble materials in the melt, e.g., carbon dust, are left behind, and there is no need to etch the shot.

Present day techniques for producing Ge crystals include zone refining to a high level of purity and doping during crystal pulling with selected impurities to the desired resistivity range. Since resistivity of Ge is dependent on the impurity content, and since, for many practical cases, very small amounts of impurity are required, accurate weighings of elements in amounts of the order of milligrams are necessary. The difficulties associated with such weight determinations have led to the use of master doping alloys, consisting of Ge and an impurity. By using these alloys, only larger doping samples need be weighed, greatly facilitating this procedure. Doping alloys are usually prepared by melting the two elements together, and then rapidly quenching in order to produce a uniform solid solution. However, due to segregation and grain boundary effects, large samples prepared in this way tend to be nonhomogeneous Also, since they must be broken into small pieces for use, the possibility of contamination is introduced

The production and use of Ge shot (for making point contact rectifiers) was first described by Dunlap (1). If a master doping alloy is blown into shot instead of being cooled as one piece, each drop should contain constituents in exactly the same ratio as in the total melt, although the ratio may vary from point to point in the drop. If the shot are made small enough and cover a range of sizes, an integral number of them may be used for any doping application. (Broken shot should not be used because of the impurity variation from point to point in the sphere.) In this way, successive doping samples chosen from a master doping alloy in shot form should be uniform in content of doping element.

The production and use of Ge master doping alloys in the form of shot are described in this paper.

Germanium Shot Tower

The tower for producing Ge master doping alloys in shot form was designed to be versatile, easily disassembled, permit easy viewing of the molten Ge and solid shot, and to consist of few specially made parts. Fig. 1 shows a sectional view.

The tower, of 150 ml capacity, was made gas-tight by means of ground butt joints, under slight pressure vertically by means of a rod pressing down on the rubber stopper at the top. Components were held in position by means of clamps fastened to a large vertical stand. Argon was used as an inert atmosphere, the relative amounts of flow to top and bottom of the tower being controlled by the needle valve. With the needle valve closed, the entire gas flow was into the upper chamber. A pressure of 15 cm Hg could easily be obtained in the upper chamber in this way. With the needle valve fully open, most of the argon flow was into the lower chamber. This produced an agitation of the silicone oil which continued even with the needle valve almost closed. Small grooves were cut in the bottom of the carbon crucible to permit easy access of the argon in the lower chamber to the atmosphere. Hence, the lower chamber always remained at essentially room pressure.

The Ge and impurity were melted in the carbon boat under an argon pressure $\lesssim 1$ cm Hg by means of energy coupled from the r.f. heater coil. A pressure difference of about 2 cm Hg between top and bottom of the carbon crucible was sufficient to overcome surface tension and force the molten constituents through the 0.010 in. hole in the form of droplets.

Care had to be taken in construction and assembly of the tower to make sure that the components were vertical and lined up with each other. Otherwise, during descent, the shot would strike the sides of the tower and splatter.

After a fall of 4 ft, the shot were still mostly molten. Hence, a cooling liquid was required to prevent the shot from sticking together. Allowing the shot to fall into a silicone oil bath worked very well. Shot towers with larger drop distances might be used, where practicable, so that no cooling liquid would be required.

Because of the height of the tower and its support from only one stand it swayed easily. This caused small pressure fluctuations, which resulted in a range of shot sizes being produced during a single run, since the particle size depends on the pressure with which it is blown.

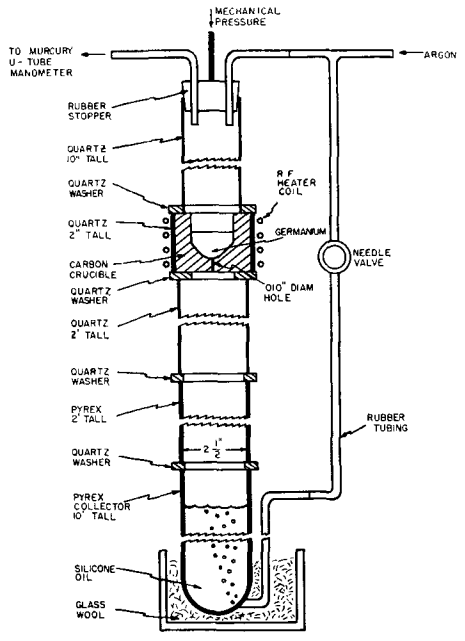

FIG. 1. Germanium shot tower, sectional view

TABLE I

Impurity	Mass % of impurity in alloy		
As	1	0.1	0.02
Sb	10	1.0	0.1
Ga	1	0.1	0.02

Operation

The amount of each element used in a master doping alloy depends on the amount of shot and the ratio of impurity to Ge in the shot that are desired. Some useful alloy compositions that have been made using common doping elements are shown in Table I.

A mass of impurity element of approximately the desired size was weighed accurately. Then, the amount of Ge required to form the correct ratio was weighed. In cases involving impurity elements that are not very volatile at high temperatures, i.e., Ga, Sb, the constituents were simply melted together in the carbon crucible in the shot tower. The short melting time, about 4 min for a 100 g charge, insured little loss of these materials (or the Ge) by vaporization during the melting period. In cases involving impurities that are volatile at high temperatures, i.e., As, it is desirable to melt the constituents together before putting them in the tower. This was done with little loss due to vaporization by plunging the impurity into molten Ge in a quartz tube, such that any vapor from the doping element bubbled into the molten Ge and hence had a good chance of dissolving. It was also necessary to use this apparatus to mix Ge and doping element in cases of heavy doping where the impurity has a lower melting point and surface tension than Ge. In such cases, i.e., 10% Sb, 90% Ge, the doping element melts first and may be blown through the crucible opening by the (low) pressure before the Ge has a chance to melt and dissolve it.

It should be emphasized that since relatively large amounts of doping elements are involved in the production

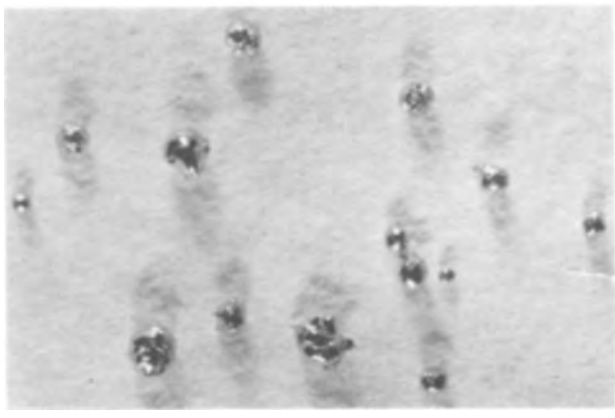

FIG. 2 (*a*). 99% Ge: 1% Sb shot. 6× before reduction for publication.

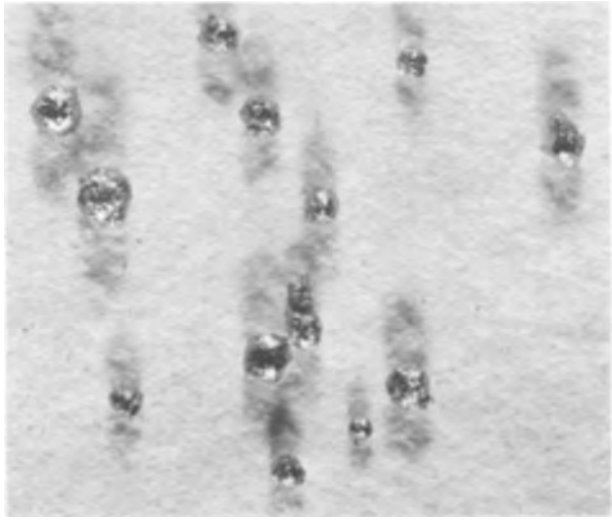

FIG. 2 (*b*). 90% Ge: 10% Sb shot. 6× before reduction for publication.

of shot, adequate ventilation facilities should be present when toxic materials are used. If they are dissolved in Ge first, as for volatile impurities, they are less dangerous.

Before melting alloys in the tower crucible, the needle valve was opened sufficiently so that the pressure in the upper chamber was less than that required to force molten material through the hole ($\lesssim$1 cm Hg).

The mixture should be kept in the molten state in the shot tower carbon crucible long enough to insure complete mixing, but not so long that appreciable evaporation of the impurity or Ge takes place; a few minutes is a reasonable time. The temperature of the molten alloy should not be much above the melting point when the shot are blown; otherwise, the shot will be difficult to cool quickly, and agglomeration in the collector may result.

To blow the shot the needle valve was closed until the upper chamber pressure was sufficient to force the liquid through the hole in the carbon crucible ($\gtrsim$2 cm Hg). It emerged as a fine stream of droplets, which fell into the oil bath and settled to the bottom in a pile. There was no sign of smoke or fumes arising from the silicone oil bath when the red hot droplets entered.

After each run, a small amount of slag composed partially of carbon dust and Ge remained in the carbon crucible. Hence, a further advantage of this method is that the slag is separated from the doping material.

After the run was completed, the shot were removed from the collector, given several washes in CCl_4, and allowed to dry. No stickiness of pellets was observed if the CCl_4 washings were thorough. The shot were not etched, since this would change the impurity concentration.

Results

Fig. 2(*a*) shows a photomicrograph of some typical shot, in this case 1% Sb, 99% Ge. Fig. 2(*b*) shows some 10% Sb, 90% Ge shot, the wrinkled appearance being due to the large Sb content. In each case, the sizes of the particles range from a few tenths of a milligram to about 10 mg.

Doping pellets produced in the shot tower have been used to dope several dozen Ge crystals, grouped according to amount of shot added and crystal growth conditions. Reproducibility of resistivity among crystals pulled under the same conditions with the same amount of doping shot was in all cases about ±10%. However, largely because of limitations of experimental accuracy, distributions with distance down the crystals varied in most cases with that predicted from theory (2) by factors of this order. Hence, shot consistency could be much better than 10%. In any case, this accuracy of crystal resistivity is well within that required for fabrication of most transistors and other Ge devices. The shot composition for doping to a particular resistivity was chosen so that neither very small nor very large quantities of shot are required. A suggested amount of shot is between 10 and 100 mg.

A possible source of contamination is from decomposition products or impurities in the silicone oil bath. Trouble from this source, however, has not been observed. The pure silicone oil used[1] has no known third of fifth group contaminants.

The shot tower should also be useful for producing conveniently sized doping alloys of other materials. The number of constituents need not be limited to two.

Acknowledgment

This work has been supported by the U.S.A.F. Air Research and Development Command, U.S.A.F. Air Material Command, Army Signal Corps, and Navy Bureau of Ships, under Contract AF 33(600)17793.

The help of A. C. Sheckler, W. E. Engeler, and R. E. Shepp is greatly appreciated.

Manuscript received April 20, 1956. This paper was prepared for delivery before the Cleveland Meeting, September 30 to October 4, 1956.

Any discussion of this paper will appear in a Discussion Section to be published in the June 1957 Journal.

References

1. W. C. Dunlap, Jr., *J. Appl. Phys.*, **24**, 448 (1954).
2. W. G. Pfann, *J. Metals*, **4**, 747 (1952).

[1] G.E. SF-81(4D).

Hydrogen and Oxygen in Single-Crystal Germanium as Determined by Vacuum Fusion Gas Analysis

C. D. Thurmond, W. G. Guldner, and A. L. Beach

Bell Telephone Laboratories, Inc., Murray Hill, New Jersey

ABSTRACT

Concentrations of hydrogen from 3 to 4 × 10^{18} at./cc have been found by vacuum fusion gas analysis in specially prepared single crystals of Ge. In these same crystals oxygen concentrations of 1 to 2 × 10^{18} at./cc were also found.

Three special preparations of Ge were made by the hydrogen reduction of GeO_2 in graphite. In the first, Ge was melted once under hydrogen, in the second, 12 times, and in the third, 42 times. Single crystals were grown from portions of these ingots in graphite crucibles under an atmosphere of hydrogen. Resistivities of the *n*-type crystals were in the range 1–10 ohm cm, and lifetimes of several hundred microseconds were observed. There was no significant variation in hydrogen and oxygen concentration from one crystal to the other. Since the ratio of hydrogen to oxygen is around two, the possibility exists that these elements may be present in the crystal as H_2O.

Vacuum crystal growing lowered the hydrogen and oxygen content 20–30 fold.

It has been reported (1) that hydrogen dissolves in Ge to the extent of 0.186 ml (room temperature and atmospheric pressure) per gram of Ge. This was determined by collecting and analyzing the gas evolved when a sample of Ge was melted under vacuum after it had been melted and solidified under an atmosphere of hydrogen. This amount of hydrogen corresponds to about 5 × 10^{19} at./cc of Ge.

Present day, high purity single crystals of Ge are grown frequently under an atmosphere of hydrogen. The presence

of such high concentrations of hydrogen could be expected to influence the electrical properties of the crystals although such evidence has not been reported in the literature. Recently, however, Reiss (2) has suggested that interstitial hydrogen would not be expected to ionize in Ge since the volume of the interstice is large compared to the volume of a hydrogen atom, and consequently the hydrogen atom would be in a medium having a dielectric constant which is essentially unity rather than the bulk dielectric constant of germanium which is 16.

Kaiser, Keck, and Lange (3) concluded that oxygen may be present in Ge crystals and at concentrations as high as an estimated 10^{16} at./cc when grown from silica crucibles. They concluded that less than 10^{15} at./cc were present when Ge crystals were grown from graphite crucibles.

The following work is presented as evidence that both hydrogen and oxygen can be present at concentrations as high as several times 10^{18} at./cc in single crystals of Ge, although the presence of these impurities is not reflected in the electrical properties of the crystals in any known way.

Experimental

Three 300–400 g lots of Ge were prepared by hydrogen reduction of GeO_2 in a graphite crucible. Portions of each polycrystalline preparation were analyzed for hydrogen and oxygen by vacuum fusion gas analysis. Single crystals of Ge were then grown under an atmosphere of hydrogen and portions of the crystals again subjected to vacuum fusion gas analysis. The resistivity and minority carrier lifetime were determined for each of the single crystals.

Materials.—Eagle-Picher Company GeO_2 was used. Reductions were carried out in standard equipment frequently used for such reductions. Tank hydrogen was used without further purification both for the reduction and crystal growth.

Multifusions.—Each of the three lots of Ge obtained from the oxide reduction was treated differently. After the initial reduction to sponge Ge (3 hr at 675°C) the first lot was fused by raising the temperature to 1020°C for 1½ hr, and then removed from the furnace. The second lot was heated to 1020°C for 1½ hr, cooled to 800°C for ½ hr, then reheated to 1020°C. This cycle was repeated twelve times before the Ge was removed from the furnace. The third lot was cycled 42 times before removal from the furnace.

Single crystal preparation.—A single crystal of Ge weighing about 100 g was grown from each of the three lots of Ge by the crystal pulling technique (4). Growth rates of approximately 2 mils/sec were used, and the seed was rotated at 60 rpm. The melt was contained in a graphite crucible and the hydrogen stream at atmospheric pressure was taken directly from the tank.

After cutting samples for vacuum fusion gas analysis from the single crystal grown from the 12-cycle lot of Ge, the remainder of this crystal was regrown under vacuum. Growing conditions were essentially the same as before except that the melt was held for 30 min about 50° above the melting point of Ge under a pressure of about 10^{-4} mm Hg, prior to growth at this pressure.

Resistivity and lifetime measurements.—Resistivities were measured by the standard 4-point probe technique (5). Lifetimes were measured by the photodecay technique described by Valdes (6).

Vacuum fusion gas analysis.—The principle of this method is based on the fusion of Ge in a graphite crucible resulting in the evolution of oxygen as CO and hydrogen and nitrogen in elementary form. The high temperature furnace designed for this work has been described (7). The graphite crucible is outgassed in vacuum for 2 hr at 2500°C. After this treatment, the temperature of the crucible is lowered to the fusion temperature, 1650°C, and the gas evolved in 30 min from the furnace assembly is collected in a capillary pipet. This is accomplished by means of a high-speed two-stage mercury diffusion pump working in combination with an automatic Toepler pump. This gas can be analyzed and constitutes the correction made on the gases evolved from the sample subsequently dropped into the furnace. For this work, 3–11 g samples of Ge were loaded in the glass side-arms and were injected at will into the crucible by a magnetic pusher. During a 30-min fusion period the gases evolved were collected in a capillary pipet to determine the quantity of gas evolved. Composition of the gas mixture was determined by circulating the gas mixture over a selective reagent or group

TABLE I

Polycrystalline Ge	1 cycle	12 cycles	42 cycles
Wt. of sample, g	4.577	2.851	10.954
Total gases, blank, cc mm	13	13	7
Total gases, sample, cc mm	114	124	256
Residual gases, cc mm	8	8	1
Hydrogen, at./cc	$2.8 \pm 0.1 \times 10^{18}$	$7.8 \pm 0.1 \times 10^{18}$	$5.2 \pm 0.1 \times 10^{18}$
Oxygen, at./cc	$2.6 \pm 0.1 \times 10^{18}$	$2.9 \pm 0.1 \times 10^{18}$	$1.1 \pm 0.1 \times 10^{18}$
Single-crystal Ge			
Resistivity, ohm cm	2–7	1–4	2–10
Lifetime, microsec	65	230	350–500
Wt. of samples, g	5.593	5.711	5.124
Total gases, blank, cc mm	8	8	8
Total gases, sample, cc mm	100	106	93
Residual gases, cc mm	0	0	0
Hydrogen, at./cc	$3.3 \pm 0.1 \times 10^{18}$	$3.7 \pm 0.1 \times 10^{18}$	$3.8 \pm 0.1 \times 10^{18}$
Oxygen, at./cc	$1.3 \pm 0.1 \times 10^{18}$	$1.8 \pm 0.1 \times 10^{18}$	$0.9 \pm 0.1 \times 10^{18}$

TABLE II

Single-crystal, vacuum-grown Ge (*12 cycle*)

	A	B
Resistivity, ohm cm	4	4
Lifetime, microsec	65	65
Wt. of sample, g	7.637	6.967
Total gases, blank, cc mm	0	0
Total gases, sample, cc mm	4	5
Residual gases, cc mm	2	1
Hydrogen, at./cc	$1 \pm 1 \times 10^{17}$	$1 \pm 1 \times 10^{17}$
Oxygen, at./cc	$6 \pm 6 \times 10^{16}$	$6 \pm 6 \times 10^{16}$

of reagents to remove a specific gas. The gas is collected again in the pipet to measure the pressure-volume drop. In this work, the gas is circulated over copper oxide which converts the hydrogen to water and then over magnesium perchlorate which removes the water. The pressure-volume drop is a quantitative measure of the hydrogen. Likewise, during this operation CO has been converted to CO_2 with no pressure-volume change. Then, the gas is recirculated over copper oxide to ensure oxidation of the CO, and circulated over Ascarite to remove CO_2. From this pressure-volume drop the quantity of CO present is obtained. The residual gas which did not react with the reagents is a measure of nitrogen and noble gases. This scheme of analysis is similar to standard Orsat procedures except that micro low-pressure techniques have been applied.

Results

The three polycrystalline preparations of Ge were *n*-type and exhibited resistivities in the range 1–10 ohm cm. Cubes, approximately $\frac{1}{4}$ in. on an edge, were cut from each ingot for vacuum fusion gas analysis and etched in a mixture of HNO_3, HF, and $C_2H_4O_2$ containing Br. Voids could be seen in these cubes. Four or five cubes were analyzed at a time. Results of analyses are given in Table I.

Three single crystals of Ge, grown under an atmosphere of hydrogen, were also *n*-type. Vacuum fusion gas analyses, resistivities, and lifetimes are included in Table I.

The 12-cycle crystal, regrown under vacuum, was *n*-type and two portions were reanalyzed for hydrogen and oxygen. These results are given in Table II.

Discussion

Multifusions of Ge under hydrogen were carried out in an effort to study several effects. It had been reported that the melting point of Ge could be changed by repeated fusions under hydrogen (8, 9) and a recent paper (10) reports that the melting point of the 42-cycle Ge, which is included in Table I, was not detectably different from the starting material. The possibility existed, however, that the hydrogen content of the crystals was sufficiently high (1) to be measured by vacuum fusion gas analysis techniques. In addition, multifusions would indicate if the rate of solution of hydrogen was slow and also might give information as to how effectively oxygen could be removed by such hydrogen treatment.

The constancy of the hydrogen concentration in the three Ge single crystals shows that the multifusions under hydrogen did not add additional hydrogen. Hydrogen concentrations in the polycrystalline samples were not as reproducible as in the single-crystal samples which is consistent with the observation that voids were present in the polycrystalline ingots.

Oxygen analyses have given surprisingly constant results in view of the treatment given the Ge. It is believed that this oxygen is dissolved in the crystal and cannot be accounted for as surface oxygen.

Analyses of the vacuum-grown Ge provide proof that oxygen and hydrogen are both present in the body of the single crystals of Ge. Since the surfaces of the samples from the vacuum-grown crystal received the same treatment as the other crystal samples, it is concluded that the amount of GeO_2 and adsorbed H_2O on the surfaces should be about the same. The vacuum fusion gas analysis of the vacuum-grown crystal puts an upper limit on the amount of oxygen and hydrogen coming from the sample surfaces.

The variation in lifetime shown in Table I is apparently unrelated to the hydrogen and oxygen in the crystals. It is possible that a recombination center such as Cu was removed during repeated fusions under H_2.

Conclusions

It is concluded that hydrogen and oxygen can be present in single crystals of Ge at concentrations around 10^{18} at./cc. The molecular state of these impurities is such that ionization does not occur to give conduction electrons or holes in significant concentrations. This is in agreement with the conclusion of Reiss (2) pertaining to hydrogen, although it has not yet been established that hydrogen is present as an interstitial proton. The fact that the ratio of hydrogen to oxygen is around two in these crystals suggests that either the molecular state of these elements in the crystal may be principally molecular H_2O, or that the source of the hydrogen and oxygen is principally water vapor.

Acknowledgments

The authors wish to thank K. M. Olsen for the special GeO_2 reductions and M. Kowalchik for technical assistance.

Manuscript received May 1, 1956. This paper was prepared for delivery before the San Francisco Meeting, April 29 to May 3, 1956.

Any discussion of this paper will appear in a Discussion Section to be published in the June 1957 Journal.

REFERENCES

1. J. A. Müller, E. F. Pike, and A. K. Graham, *Proc. Am. Phil. Soc.*, **65**, 15 (1926).
2. H. Reiss, *Bull. Am. Phys. Soc.*, Dec. 1955, Los Angeles Meeting.
3. W. Kaiser, P. H. Keck, and C. F. Lange, *Phys. Rev.*, **101**, 1264 (1956).
4. J. A. Burton, E. D. Kolb, W. P. Slichter, and J. D. Struthers, *J. Chem. Phys.*, **21**, 1991 (1953).
5. L. B. Valdes, *Proc. I.R.E.*, **42**, 420 (1954).
6. L. B. Valdes, *ibid.*, **40**, 1420 (1952).
7. W. G. Guldner and A. L. Beach, *Anal. Chem.*, **22**, 366 (1950).
8. T. R. Briggs, R. O. McDuffie, and L. H. Willisford, *J. Phys. Chem.*, **33**, 1080 (1929).
9. F. H. Roninger, *ibid.*, **33**, 1086 (1929).
10. F. X. Hassion, C. D. Thurmond, and F. A. Trumbore, *ibid.*, **59**, 1076 (1955).

Adsorption of Sodium Ions by Germanium Surfaces

SUMNER P. WOLSKY AND PATRIA M. RODRIGUEZ

Research Division, Raytheon Manufacturing Company, Waltham, Massachusetts

AND

WORDEN WARING

Semiconductor Division, Raytheon Manufacturing Company, Newton, Massachusetts

ABSTRACT

Sodium ions are adsorbed from a NaOH solution by Ge surfaces during an electrolytic etching process. Techniques for determining approximate quantities and location of the adsorbed ions using radioactive tracers have been developed. Alloyed junction *p-n-p* transistors, grown junction diodes, and *p*-type and *n*-type Ge bars were studied. Results show approximately 10^{15} Na ions/cm^2 to be adsorbed with some concentration at the junction region and at surface cracks.

The effect of surface characteristics on the behavior of Ge devices has been well recognized. Consequently, the behavior of Ge surfaces has been widely studied. For the most part the experiments have been designed to observe the electrical properties of the semiconductor surface. More recently, the physical behavior of Ge surfaces in various gaseous ambients has been studied. Experiments dealing with the adsorption and kinetic behavior of Ge in various ambients have yielded interesting information. This paper deals with the physical behavior of Ge surfaces in an etch solution, more specifically, with adsorption of Na ions from NaOH solution during electrolytic etching.

The only previous attempt to determine the type and number of impurity ions present on a Ge surface was that reported by Law (1). In that instance the mass spectrograph was used to analyze the materials produced by passing a spark between two Ge electrodes. Approximately 10^{14} ions/cm^2 were present, consisting mainly of Ca, Na, and K. No detailed description was given of the etching and washing procedure used on the Ge studied.

EXPERIMENTAL PROCEDURE

The experimental method used in this research involved the use of radioactive tracers and a scintillation counter. The process of following the adsorption of ions from a solution in which many ions are present was simplified by making only one ion radioactive and by choosing an etch solution in which the ion being observed was one of the major constituents. Radioactive Na (Na^{24}, with a half life of 14.8 hr) in the form of $Na_2{}^{24}CO_3$ was used in a 1% NaOH etch solution. Two counting standards of different dilutions, prepared from the $Na_2{}^{24}CO_3$ for each experiment, were checked against each other. Na residues on the various samples were calculated on the basis of the standards. A Co^{60} standard was used to check the scaler for instrumental fluctuations at frequent intervals during each experiment. The background count was also closely observed.

The experimental procedure was as follows. The Ge unit (transistor, diode, or bar) was electrolytically etched in a solution usually consisting of 0.1 cc of 7% by weight $Na_2{}^{24}CO_3$ and 0.4 cc of 1% by weight NaOH. Total volume of the etch solution was 0.5 cc. Etching conditions for the various units are described below. After etching, the unit was given a controlled wash consisting of the following steps: (*a*) three rinses in deionized water at room temperature (requiring only a few seconds total time), (*b*) a 10-min dip in deionized water maintained at 65°C, (*c*) a rinse with C.P. acetone, and (*d*) drying in a stream of dry nitrogen. In general, these steps were followed in all experiments. After etching, washing, and drying, the activity on the units was counted. In several cases autoradiographs were prepared. These were made by placing the Ge unit on a film plate for several days.

RESULTS AND DISCUSSION

A large number of alloyed type *p-n-p* transistors were studied. In was used as the alloying material. All transistors were etched in the same manner: the emitter, base, and collector leads were tied together and a current of 250 ma was passed for 10 sec. After etching, the unit was washed and counted as described above. The transistor is a rather complicated device containing other adsorbing materials in addition to Ge. The glass stem, for example, would be expected to show a high Na count caused by adsorption and exchange. Therefore, an adsorption figure obtained for the transistor as a whole has little significance. In order to determine the quantity of Na adsorbed by the various sections of the unit, the transistor was carefully dissected into three or four parts. These parts, shown in Fig. 1, were the Ge chip and dot section, the tab, the leads, and the stem. Because of the construction of the transistor, the leads usually retained some In and solder, and the tab usually held a small piece of the Ge chip. Care was taken in the sectioning process to prevent contamination of one unit or section by the prior unit or section. The sum of the parts was checked against the original count of the undissected unit; in general the agreement was quite good. The dissection technique made it possible to obtain quantitative data on the amount of Na actually present on the

chip and dot section. Some typical results are shown in Table I. The numbers in parentheses are values from later readings on the same samples; they give some indication of the precision of the counting process.

The techniques of autoradiography were used to locate the Na adsorbed by the Ge chip and dot section. After cutting the emitter and collector dots flat and parallel to the base of the chip, the section was placed on photographic film. Fig. 2 is an example of an autoradiograph obtained from a transistor. The dark areas in the center represent the In dots. No activity is shown there since, as mentioned above, the major portions of the emitter and collector dots above the surface of the chip were removed. Because the radiation emitted by Na is highly penetrating, the autoradiographs are really composites of the radiation emitted from both sides of the chip. Information was obtained from the autoradiographs by superimposing the negative on the actual chip and dot section. From Fig. 2 it can be seen that Na was present at the junction region and on the chip itself. The electrolytic etching process outlines the junction region quite sharply, forming a well-defined Ge-In interface. Greater adsorption or trapping at this region is consistent with the results of other experiments described below.

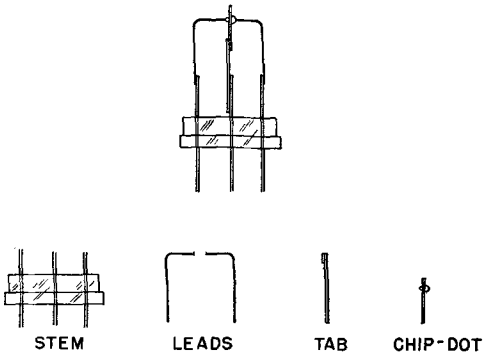

FIG. 1. Transistor assembly and parts after dissection

TABLE I. *Distribution of retained* Na

Unit No.	Parts	Na (μg)	
307	Entire	0.10	
	Total of parts	0.10	
	Chip-dot and tab sections		0.01
	Leads		0.06
	Stem		0.03
406	Entire	1.60	
	Total of parts	1.58	
	Chip-dot section		0.07
	Tab		0.02
	Leads		0.19
	Stem		1.30
408	Entire	0.84	
	Total of parts	0.73	
	Chip-dot section		0.05
	Tab		0.02
	Leads		0.04 (0.02)
	Stem		0.62 (0.58)
409	Entire	0.50	
	Total of parts	0.41	
	Chip-dot section		0.09 (0.06)
	Tab		0.04
	Leads		0.05
	Stem		0.23 (0.23)

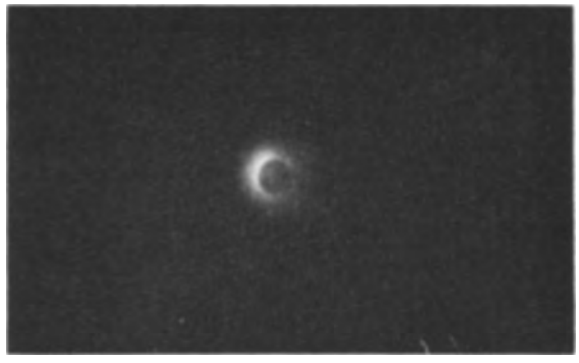

FIG. 2. Autoradiograph of transistor chip and dot section.

The results in Table I show 0.01–0.1 μg Na is adsorbed by the chip and dot section. Assuming that Na is held only by the Ge surface, there are approximately 10^{15} to 10^{16} ions/cm^2 present. Some Na is held on the In dot and this must be considered as a maximum value. However, on the basis of some preliminary experiments on the adsorption of Na by In dots, it is believed that most of the Na on the chip and dot section was on the Ge surface.

Similar experiments were performed using *p-n* grown junction diodes and *p*-type and *n*-type Ge bars. The bars, all having very nearly the same dimensions, were cut quite small so as to fit into the small volume of etch solution. Only one lead was attached to a bar. The diode bars were prepared with leads on either the *n* or the *p* side; the junction was usually near the other end of the bar. Solder was used for attaching the leads to the end of the Ge bar. The solder was not dipped into the etch solution; because of splashing during the etching and washing processes, the solder usually picked up Na, but not always. The unit as a whole was biased anodic and etched under the same conditions as were the transistors. Each unit was counted after the standard washing procedure. Results obtained are shown in Table II. Except for unit number 415, there is excellent agreement in the amount of Na retained. Also, there does not appear to be any appreciable difference in the adsorption of Na by *p-n* grown junction diodes, *n*-type bars, and *p*-type bars.

The amount of Na retained by the Ge bars generally was about 0.15–0.25 μg. This is equivalent to approximately 10^{15}–10^{16} ions/cm^2. For example, bars 416, 417, and 418 showed approximately 1×10^{16}, 1×10^{16}, and 2.5×10^{15} ions/cm^2, respectively. Again, these amounts must be considered as maximum values, for there is usually some Na held by the solder used to join the lead to the end of the bar. However, in those instances in which the autoradiographs showed little, if any, Na on the solder, there were approximately 10^{15} ions/cm^2 present on the Ge surface.

Autoradiographs were made of a number of the Ge bars in an effort to determine the distribution of Na on the bar. A typical autoradiograph of a Ge *p-n* grown junction diode is shown in Fig. 3. The bright areas indicate the loca-

TABLE II. *Retention of* Na *on bars*

Unit No.	Type	Lead on	Na (μg)
414	*n-p*	*n*	0.22
415	*n-p*	*p*	4.40
416	*n-p*	*p*	0.23
417	*n-p*	*p*	0.25
418	*n*		0.13
420	*p*		0.16
421	*p*		0.21
1	*n-p*	*p*	0.16
2	*n-p*	*n*	0.39
3	*n-p*	*p*	0.13
4	*n-p*	*n*	0.06

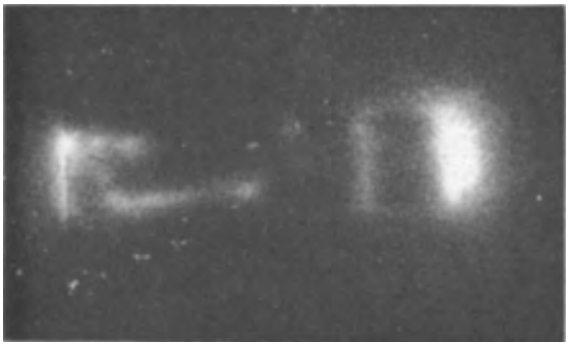

FIG. 3. Autoradiograph of *p-n* grown junction diode bar

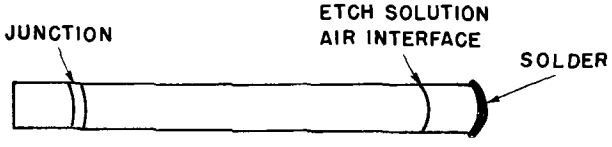

FIG. 4. Schematic drawing of bar shown in Fig. 3

tion of the radioactive material. By superimposing the autoradiograph on the bar, by microscopic examination of the bar, and by hot probe measurements, the active areas were found to be at (*a*) the solder connection to the bar, (*b*) the position of the interface between etch solution and air when the bar is in the process of being etched, and (*c*) the junction of the bar. The autoradiograph of Fig. 3 is shown schematically in Fig. 4. Other bright regions shown in Fig. 3 have been correlated with surface cracks and scratches One bar which had been cracked so as to expose a very rough and jagged surface showed considerable adsorption at the broken areas. Adsorption at such surface irregularities accounts for the excessive amount of sodium retained by units such as No. 415. Microscopic examination of all the bars revealed considerable erosion at the solution-air interface. Also, the electrolytic etch outlined the junction on all diodes. The *p*-type and *n*-type bars showed activity only at the solution-air interface and occasionally at the solder connection.

The results, therefore, indicate that: (*a*) adsorbed Na is not distributed homogeneously on the germanium surface; certain areas have a greater tendency to retain more of the impurity ions; (*b*) with any differential etch that outlines the junction, there is a probability of adsorption and concentration of the ions at the junction region; (*c*) eroded, cracked, or scratched surfaces tend to hold Na ions; and (*d*) although the result obviously depends somewhat on the treatment of the surface prior to the etching process, as well as on the etching and washing procedure, there appear to be about 10^{15} ions/cm^2 adsorbed on the Ge surfaces.

Data obtained from the alloy-type transistors and Ge bars are generally in good agreement. Considering the assumptions that have been made, the value of approximately 10^{15} ions/cm^2 can also be considered to be in general agreement with the figure of 10^{14} ions/cm^2 found by Law to be present on Ge surfaces after a CP-4 etch. Neither Law's experiments nor these could detect the presence of anions.

No detailed study has been made yet of the effect of adsorbed Na ions on device properties The only experiment performed in this direction consisted of taking some electrical data on a group of transistors that had been etched, washed, and counted in the usual manner and then were placed in a desiccant box. Collector to base amplification factors of the several units were from 30 to 80, and collector currents on reverse bias were around 10 μamp at low voltages, which are normal for such units treated as these were. From this experiment it appears that in a dry atmosphere electrical properties are not affected by the presence of impurity ions on the surface. Experiments are planned to study the impurity ion effect on device properties in various humidities and ambients. However, changes caused by impurity ions may be of such small magnitude or occur so rapidly as not to be easily observable.

Although these experiments were carried out using Na, it is probable that the results can be extrapolated to other ions. Since there is a substantial number of foreign ions present on the Ge surface at or near the junction region, one must consider their effect on the surface properties. It has been recognized that a sizable portion of the surface conduction observed for Ge, especially in the presence of water vapor, is "ionic." However, the simple "ionic" conduction in an adsorbed water film proposed by Law (1, 2) seems unlikely. It requires either many more ions than can be present, or else some unspecified ionic regeneration process. Other interpretations of the "ionic" process are possible (3, 4), one of them having been proposed since Kingston's review of the surface phenomena on Ge (5).

In considering the effect of impurity ions one must consider their location with respect to the oxide film, which is probably always present on the Ge surface. If the ions are located at the oxide-air interface, they probably influence the adsorption of such materials as water. For example, Law (1) found indications that more adsorption occurred at lower humidities on units previously exposed to NaCl solution or HCl gas than on cleaner units. On the other hand, if the ions are located at the germanium-germanium oxide interface, they may act as trapping centers thereby influencing the surface recombination rate. No experiments has been carried out yet to test these alternatives. It is possible that impurity ions are present both at the oxide-air and at the germanium-germanium oxide interfaces, so their contributions to the observed surface properties may be quite complex.

ACKNOWLEDGMENT

The authors thank Professor John W. Irvine, Jr., of M. I. T., for the radioactive Na and for discussions with them during the course of this work.

Manuscript received February 3, 1956. This paper was prepared for delivery before the Pittsburgh Meeting, October 9 to 13, 1956.

Any discussion of this paper will appear in a Discussion Section to be published in the June 1957 JOURNAL.

REFERENCES

1. J. T. LAW, *Proc. Inst. Radio Engrs.*, **42**, 1367 (1954).
2. J. T. LAW AND P. S. MEIGS, *J. Appl. Phys.*, **26**, 1265 (1955).
3. E. N. CLARKE, *Phys. Rev.*, **99**, 1899 (1955).
4. H. STATZ, W. ERIKSEN, AND G. DEMARS, paper presented at the Institute of Radio Engineers' Semiconductor Device Conference, Purdue University, June 25-27, 1956.
5. R. H. KINGSTON, *J. Appl. Phys.*, **27**, 101 (1956).

New Semiconductors with the Chalcopyrite Structure

I. G. AUSTIN, C. H. L. GOODMAN, AND A. E. PENGELLY

Research Laboratories, The General Electric Company, Ltd., Wembley, England

ABSTRACT

Compounds of the chalcopyrite group are related to well-known semiconductors such as Ge and the zinc blende compounds. This relationship is discussed briefly and some new data are presented regarding the preparation and properties of five chalcopyrite compounds $AgInS_2$, $AgInSe_2$, $CuInSe_2$, $AgInTe_2$, and $CuInTe_2$.

Compounds of the chalcopyrite type are of considerable interest as they are closely related to the well-known semiconductors with diamond and zinc blende structures.

The general formula for chalcopyrite type compounds is ABX_2, where A is Cu or Ag, B is Al, Ga, In, or, in some cases, Fe or Tl, and X is S, Se, or Te (1). They can be considered as being derived from II–VI zinc blende type compounds by replacing a pair of Group II atoms by one from each of Groups I and III (tervalent Fe belongs formally to Group III). Thus silver indium telluride, $AgInTe_2$, is, in this sense, derived from cadmium telluride, CdTe. It is found that, like the related zinc blende-type compounds, chalcopyrite type compounds are semiconductors with a wide range of energy gap (2). The present communication gives limited information on five such compounds with energy gaps close to 1 ev; these are $CuInS_2$, $AgInSe_2$, $CuInSe_2$, $AgInTe_2$, and $CuInTe_2$; some information on chalcopyrite itself, $CuFeS_2$, is also given.

It may be noted that an analogous group of semiconducting compounds derived from III–V zinc blende compounds, may also exist, e.g., InSb would give $CdSnSb_2$. Sufficient work has not been done to establish this definitely.

EXPERIMENTAL PROCEDURES AND RESULTS

All compounds except $CuFeS_2$ were prepared directly from the elements. Starting materials of high purity were used (Cu and Ag, Johnson Matthey spectroscopically pure; S, recrystallized, with traces of Mn, Fe, Si at the 1–10 ppm level; Te, zone melted, with no spectroscopically detectable impurities; Se, 99.995%; In, 99.95%). Synthesis was carried out in sealed evacuated silica tubes, usually heated in an argon-filled furnace. Large ingots (50–100 g) were prepared of all except $CuInS_2$, usually by directional freezing. Zone melting was also used, particularly for $CuInSe_2$.[1] All ingots as prepared were polycrystalline and showed numerous cracks. Attempts to grow large crack-free crystals by directional freezing, zone-melting, or pulling techniques were quite unsuccessful, in marked contrast to experiments with related zinc blende compounds. This difficulty is probably connected with the slight distortion of the diamond-type lattice present in all chalcopyrite compounds, which gives rise to a small degree of anisotropy and with it a differential thermal expansion. For example a differential thermal expansion of 3×10^{-6}/deg (for a and c directions) was found for $CuInSe_2$.

The information obtained for the compounds investigated is summarized in Table I. Energy gaps E_g were calculated from infrared measurements and are values for minimum detectable transmission in polycrystalline specimens. Except for $CuInSe_2$, which was studied in greatest detail, temperature coefficients of the energy gaps dE_g/dT are mean values based on only a few readings between 90° and 300°K. Mobilities are given in cases where it proved possible to obtain crack-free specimens for measurement of Hall effect. Results for chalcopyrite itself were obtained with mineral specimens.

Over 50 ingots of $CuInSe_2$ were prepared. The best n-type samples had a carrier concentration rather less than 10^{16}/cm^3 and showed good point contact rectification (3). The specimens used showed twinning and, although crack-free, were probably appreciably strained since they were cut from ingots which showed many cracks. X-ray examination of crystal structure gave some evidence of thermal disordering above 700°C, an effect similar to that observed in $CuFeS_2$ (4). Zone melting or directional freezing of $CuInSe_2$ appeared to bring about slight changes in the lattice constants along the length of the ingot, as

[1] Zone-melting was carried out using a sealed tube in a high temperature ambient.

TABLE I

Material	Optical gap E_g (ev)	$\frac{dE_g}{dT} \times 10^4$ ev/deg C	μ_e (cm²/v sec)	μ_h (cm²/v sec)	Melting point (°C)
$CuInS_2$	1.2				
$AgInSe_2$	1.18	−1.2			~1000
$CuInSe_2$	0.92	−1.5	300	26	990
$AgInTe_2$	0.96	−2.3			675
$CuInTe_2$	0.95	−3.2			~700
$CuFeS_2$	0.53	−2.2		32	

did additions of Se and Cu. This behavior suggests that an appreciable range of composition is possible; however, infrared transmissions of samples of differing lattice constant were very similar. Transmission beyond the absorption edge was high and at least comparable with that of Ge. Variation of absorption edge with temperature was -1.5×10^{-4} ev/deg at low temperatures, gradually changing to -5×10^{-4} ev/deg above room temperature.

It was found that the vapor pressure of $CuInSe_2$ is high near the melting point. It was not possible to compensate for the loss of a volatile component by the method of van den Boomgaard and co-workers (5) as the vapor appeared to be of complex composition. X-ray analysis of condensed deposits usually indicated the presence of a well-defined but unidentified phase. Comparisons with known structures showed that this was not a known binary compound between In, Cu, Se, or oxygen.

$AgInTe_2$ showed less cracking than $CuInSe_2$ even though it has a much greater differential thermal expansion, more than 9×10^{-6}/°C. This may be connected with the fact that the crystal size in the ingots investigated, zone melted at about 1 in./hr, did not exceed 0.1 mm compared with several centimeters for $CuInSe_2$ grown under similar conditions. $AgInTe_2$, like $CuInSe_2$, had an appreciable vapor pressure at the melting point. X-ray analysis of deposits condensed from the vapor revealed the presence of a complex mixture of phases including In_2Te_3. Some variation in lattice constants could be observed along a zone-melted bar. There was also evidence of thermal disordering above about 400°C. Some material of high resistivity was obtained, but the difficulty of making good contacts prevented electrical measurements being made.

Only a brief study was made of the other compounds. Both $AgInSe_2$ and $CuInTe_2$ have high vapor pressures above their melting points. *n*-type specimens having resistivity of the order of 1 ohm cm gave good point contact rectification. As with $CuInSe_2$, crystal size tended to be large, of the order of 1 cm or more. However, all ingots were badly flawed by cracks.

Only small specimens of $CuInS_2$ were prepared. No attempt was made to zone melt this material because of its high vapor pressure. Photoconductive effects were observed with high resistivity material, with response maxima near 1 μ.

It may be noted that for synthetic chalcopyrite Boltaks and Tarnovskii (6) recently made resistivity measurements and deduced values of thermal activation energy ranging from 0.18 to 0.58 ev for different samples. However, it is not clear from their paper how these values are to be interpreted for comparison with the present value of 0.53 ev for the optical gap for natural chalcopyrite.

The melting point of $CuFeS_2$ was not determined here, but Schlegel and Schüller (7) obtained a value of 950°C.

Summary

1. The pairs $CuInS_2$-$CuInSe_2$ and $AgInSe_2$-$AgInTe_2$ show differences in energy gap in much the same way as do the related zinc blende compounds CdS-CdSe and CdSe-CdTe, but no such difference is found for the pair $CuInSe_2$-$CuInTe_2$. There is no simple explanation of this behavior.

2. The energy gap and melting point of a chalcopyrite-type compound appear to be lower than those for the related II-VI compound.

3. The mobility values measured were low, as shown in the Table I. This may be due in part to crystalline imperfection. Arguing from general views about bonding in diamond-type crystal lattices (8), a "neutral bond" is less likely to be found with ternary compounds of this type than with the related II-VI zinc blende structures. The possible relationship between high mobility and near-neutral bonding would then indicate that very large mobilities are unlikely in compounds of the chalcopyrite type.

Acknowledgments

Thanks are due to Dr. E. A. D. White and Mr. M. H. Francombe for x-ray measurements, and to Dr. L. Ainsworth and Mr. A. West for preparing some of the compounds.

Manuscript received April 2, 1956. This paper was prepared for delivery before the San Francisco Meeting, April 29 to May 3, 1956.

Any discussion of this paper will appear in a Discussion Section to be published in the June 1957 JOURNAL.

REFERENCES

1. H. Hahn, *et al.*, *Z. anorg. u. allgem. Chem.*, **271**, 153 (1953).
2. C. H. L. Goodman and R. W. Douglas, *Physica*, **20**, 1107 (1954).
3. R. W. Douglas and C. H. L. Goodman, *G.E.C. Journal*, **21**, No. 4, 3 (1954).
4. A. J. Frueh, *J. Am. Mineralogist*, **35**, 282 (1950).
5. J. van den Boomgaard, *et al.*, *J. Electronics*, **1**, 212 (1955).
6. B. I. Boltaks and N. N. Tarnovskii, *Zhur. Tekh. Fiz.*, **25**, 402 (1955).
7. H. Schlegel and A. Schüller, *Z. Metallkunde*, **43**, 421 (1952).
8. C. H. L. Goodman, *J. Electronics*, **1**, 115 (1955).

A Metal-Semiconductor Capacitor

R. L. Taylor and H. E. Haring

Bell Telephone Laboratories, Inc., Murray Hill, New Jersey

ABSTRACT

A porous $Ta/Ta_2O_5/MnO_2$ capacitor is described. This capacitor, which might be termed a solid electrolytic capacitor, provides a higher capacitance per unit of volume than can be obtained with any other capacitor heretofore available. Its small size makes it extremely attractive for use in transistor circuits and in other low voltage circuits requiring the ultimate in miniaturization. Construction, characteristics, and advantages of the new electronic device are discussed.

Invention of the transistor and related semiconductor devices has served to emphasize the rapidly growing need for miniaturization of all varieties of electrical circuit components.

The electrolytic capacitor is known for its extremely high capacitance per unit of volume, and for this reason it has become increasingly popular with circuit designers (1, 2). Nevertheless it has several disadvantages, most of which result from the use of an aqueous electrolyte. For example, the tendency of the electrolyte to dry out is always a problem, and the use of a tight seal to prevent this also prevents the necessary venting of gas that may be generated. Also, aqueous electrolytes impose severe limitations because of the relatively narrow operating range between freezing and boiling points. Furthermore, the large temperature coefficients of capacitance and power factor associated with the electrolytic capacitor, particularly in the low temperature region, are largely properties of the aqueous electrolyte. Shelf life, too, is dependent principally on the stability of the oxide film in the liquid electrolyte.

Recognition of the limitation imposed on the electrolytic capacitor by the use of a liquid electrolyte led to the conclusion that a solid "electrolyte" might be substituted for the liquid electrolyte, thus eliminating the disadvantages of the conventional form of electrolytic capacitor without sacrificing its advantages. The purpose of this paper is to describe the "all-solid" electrolytic capacitor developed in three laboratories.

General Description

This solid electrolytic capacitor consists essentially of a porous Ta electrolytic capacitor in which the conventional liquid electrolyte has been replaced by MnO_2, an electronically conductings emiconductor. A schematic cross-sectional view of the device is shown in Fig. 1.

Ta powder sintered to form a porous slug is coated anodically with a current-blocking film of Ta_2O_5 over the entire surface of its porous body. Over the oxide film, and in intimate contact with it, is deposited a layer of an electronically conducting semiconductor, such as MnO_2. Improved electrical contact to the semiconductor is obtained with a coating of graphite followed by a layer of lead-alloy or copper which may be applied by spraying.

The new capacitor retains most characteristics common to electrolytic capacitors. Its capacitance is proportional to the dielectric constant of the oxide film and inversely proportional to film thickness. The film thickness is proportional to and controlled by the forming voltage. The unit has rectifying properties, blocking current when the filmed electrode is made anode and passing current when it is made cathode. The power factor is comparable in magnitude to that of conventional electrolytic capacitors, but superior in respect to temperature and frequency variation. Except for the absence of an initial current surge, the leakage current in the all-solid electrolytic capacitor follows the pattern for electrolytic capacitors with regard to temperature and voltage variation.

Although any of the film-forming metals may be used as anode, Ta was selected because of the excellent quality of its oxide film, its outstanding resistance to corrosion, and because the metal is available in the porous, sintered form. The porous type of electrode represents the most efficient use of Ta metal, yielding a large usable area within a small compact space, approximately 1000 cm^2 of area/cm^3 of porous Ta. Fig. 2 shows some experimental porous Ta electrodes illustrating the variety of shapes and sizes in which porous Ta can be supplied.

Dielectric Film

The heart of any electrolytic capacitor is the electrolytically formed film which serves as the dielectric. The Ta_2O_5 film is formed by the outward movement of Ta ions, under the influence of a high field, through the oxide film already present to combine with oxygen which is held on its outer surface as a further consequence of this same high field. Under the circumstances it is generally assumed that the resulting Ta_2O_5 film cannot be stoichiometric Ta_2O_5 but must be Ta_2O_5 containing a slight excess of Ta ions decreasing in concentration toward stoichiometric as the outer surface of the film is approached. This slight excess of Ta ions agrees with the fact that the Ta_2O_5 film is an n-type semiconductor. A concentration gradient of the kind which has been described may be regarded as a "frozen electrolytic polarization" which, it has been suggested (3), is part of the rectification barrier in the electrolytically formed film.[1]

The electrolytically formed film which constitutes the dielectric of the electrolytic capacitor is not pore free.

[1] For a more detailed discussion of film formation and rectification see reference (3). In this connection, a recent theoretical consideration of the kinetics of formation of anode films by Dewald also may be of interest (4).

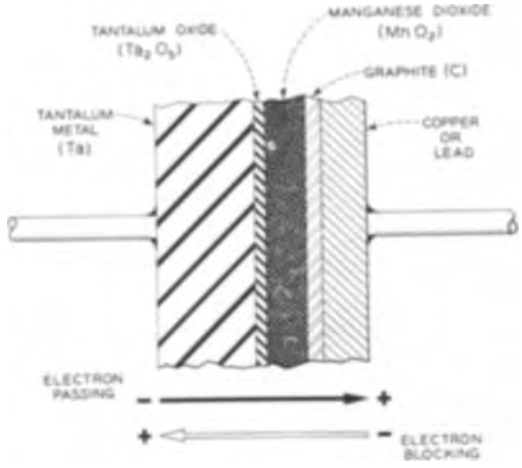

FIG. 1. Enlarged cross section of metal-semiconductor capacitor.

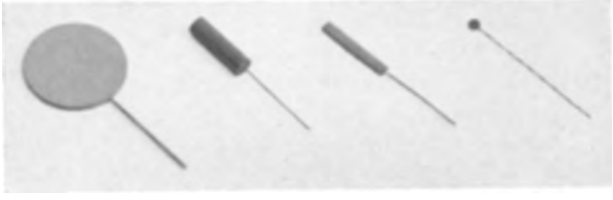

FIG. 2. Experimental porous Ta anodes. Ta metal occupies 60% of volume.

The pores which are present usually result from the inclusion of traces of impurities in the Ta surface and imperfection in the oxide lattice, and are a major cause of leakage current Pores in the oxide film can be detected visually by electroplating Cu on a filmed Ta sheet. Cu plates out at the numerous points of imperfection. Obviously these pores must be effectively blocked or "healed" if the capacitor is to operate successfully. In the liquid electrolytic capacitor, minute oxygen bubbles form within the pores of the film on the anodically charged Ta electrode as a result of the passage of leakage current, and these minute bubbles act as "corks" which make the film sufficiently impervious to be practicable.

In the all-solid electrolytic capacitor there are strong indications that healing of the pores is effected by an irreversible oxidation-reduction reaction which takes place between the Ta or impurity metal which constitutes the pore base and the MnO_2 semiconductor. This reaction, made possible by the extremely high field within the MnO_2 filled pore, must oxidize simultaneously the exposed metal at the base of the pore and reduce the MnO_2 in contact with it, thus forming a permanently nonconducting plug which effectively blocks the leakage current that otherwise would pass through the pores. This permanent healing in the all-solid capacitor eliminates the initial surge of current characteristic of the conventional capacitor with liquid electrolyte.

The fact that a semiconductor, such as MnO_2, can function electronically throughout its bulk, and yet be capable of reacting chemically at the interface with the film-forming metal, may seem incongruous until it is realized that in the healing process only minute localized areas are involved and, in consequence, the field available is tremendous.

As indicated previously, formation of the dielectric film is accomplished ordinarily by the conventional method, viz., by making the film-forming metal anode in aqueous salt solution at temperatures within the boiling range of the electrolyte. However, it is of interest to note that formation also may be accomplished in fused salt electrolytes at comparatively high temperatures. Molten salt formation is of interest because it produces a high quality film in a short time at relatively low voltages. An excellent fused salt electrolyte developed in these laboratories is a eutectic mixture of $NaNO_3$ and $NaNO_2$ operated at a temperature of 250°C, which is slightly above its melting point. A temperature of 300°C is considered maximum for molten salt formation of Ta, because at temperatures above this heat oxidation begins to take place rapidly and a crystalline gray oxide begins to form. Film formation is carried out until the desired oxide film thickness and leakage currents are obtained.

The Semiconductor "Electrolyte"

Preparation of the electrolytically oxidized Ta anode has followed established practice. At this point, however, construction of the all-solid capacitor deviates from the conventional. Use of a semiconductor such as a higher oxide of Pb, Ni, or Mn as an "electrolyte" in combination with a porous type of anode presents many practical problems.

The most obvious problem involves obtaining a uniform coating of the semiconductor over the oxide film throughout the interior of the porous anode. This was solved by dipping the porous electrode into an aqueous solution of manganous nitrate and then heating the wet electrode to evaporate the water and pyrolytically convert the manganous nitrate to MnO_2.

The pyrolytic decomposition of manganous nitrate is accompanied by evolution of steam and other gaseous decomposition products (oxides of nitrogen) which tend to produce minute openings in the MnO_2. In consequence several successive coatings of MnO_2 are applied. The temperature should be higher than that required to convert manganous nitrate to MnO_2, but not high enough to decompose the MnO_2.

Defects in the Ta_2O_5 film which may develop during the pyrolytic process may be repaired by re-anodizing after the first few coatings of MnO_2 have been applied. Re-anodizing involves returning the coated electrode to the forming bath and anodizing as before. Following re-anodizing the final applications of MnO_2 can be made.

Principle of Operation

The metal-semiconductor capacitor utilizes the current blocking properties and high capacitance of a thin electrolytically formed film of high resistivity Ta_2O_5 in contact with Ta on one side and MnO_2 on the other. The resistivity of the Ta_2O_5 film in an operating capacitor is extremely high, e.g., 10^{14} ohm-cm; the resistivity of the MnO_2 is relatively low, e.g., 10–100 ohm-cm, depending on its porosity. Both of these materials are *n*-type semiconductors.

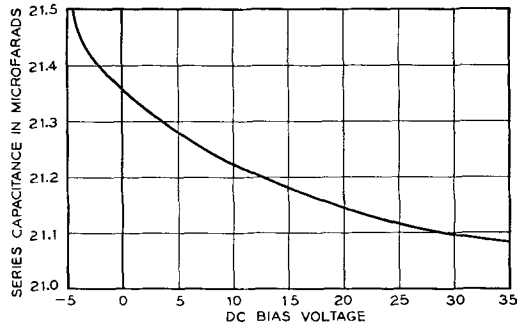

FIG. 3. Effect of d.c. bias on capacitance. (Capacitance measured at 1000 cps and 0.05 v a.c.)

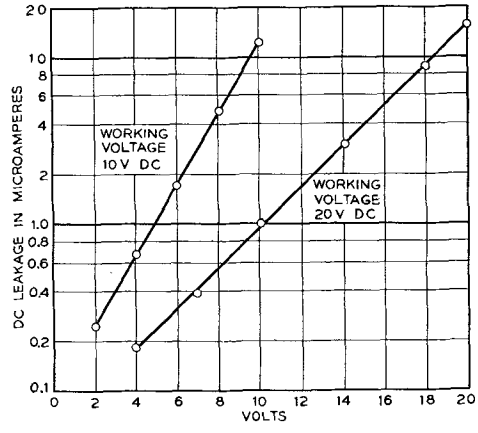

FIG. 4. Leakage current characteristics of 25 μf metal-semiconductor capacitors.

MnO_2 serves not only as an electronically conducting connection with the Ta_2O_5 dielectric but also as an oxidizing "electrolyte" which heals any pores or other defects in the Ta_2O_5 film and thus maintains it in operating condition. In addition to these functions, MnO_2 serves in another extremely important way. MnO_2 must share some of its oxygen with the entire outer surface of the Ta_2O_5 film thus establishing a p/n junction between the n-type Ta_2O_5 and a thin p-type inversion layer induced in the surface region of the Ta_2O_5 by the film of negatively charged oxygen adsorbed on it.

In summary, the rectifying and current blocking barrier which constitutes the dielectric of the solid electrolytic capacitor consists of (*a*) Ta_2O_5 film (containing a decreasing concentration of excess tantalum ions), (*b*) a thin p-type inversion layer at the surface of the Ta_2O_5, and (*c*) the extremely thin film of oxygen (and reduced MnO_2) on the outer surface of this inversion layer. Note that this current blocking system is similar to that previously described (3) as the rectifying and current blocking barrier in the wet electrolytic rectifier and capacitor. In one case the oxygen layer is provided by the incipient decomposition of water (H_2O) in contact with Ta_2O_5; in the other case the oxygen

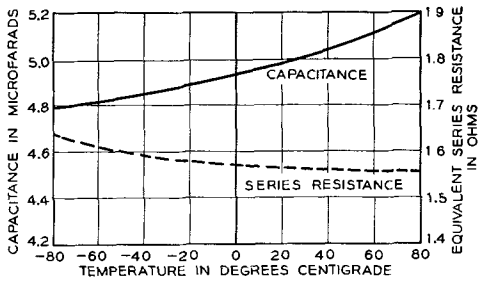

FIG. 5. Effect of temperature on 1000 cps capacitance and series resistance of metal-semiconductor capacitor.

layer is provided by the incipient decomposition (reduction) of MnO_2.

The slight decrease in capacitance with increased bias voltage, shown in Fig. 3, is probably the result of widening of the barrier layer at the p-n junction located at the interface between Ta_2O_5 and MnO_2. This change is experienced not only with the solid electrolytic capacitor but also with the liquid electrolytic capacitor, which is further indication of the close similarity between the current blocking systems in the two cases.

Operating Characteristics

The breakdown voltage in the solid electrolytic capacitor is related to the oxide film thickness The maximum voltage that it may be expected to withstand will not be greater than the formation voltage under comparable temperature conditions. A practical working voltage is roughly one-third the forming voltage.

Typical leakage-current data for capacitors of two voltage ratings are shown in Fig. 4. These curves follow the leakage vs. voltage pattern common to liquid electrolytic capacitors. Steps in the processing for the two ratings differed somewhat.

The effect of temperature on capacitance and series resistance is given in Fig. 5. The temperature range shown, −80° to +80°C, represents considerable improvement over the paste and other liquid-type electrolytic capacitors.

Detailed operating characteristics of the solid electrolytic capacitor are given elsewhere (5).

Manuscript received April 11, 1956. This paper was prepared for delivery before the San Francisco Meeting, April 29 to May 3, 1956.

Any discussion of this paper will appear in a Discussion Section to be published in the June 1957 JOURNAL.

REFERENCES

1. M. WHITEHEAD, *Bell Labs. Record*, **28**, 448 (1950).
2. J. H. HALL AND F. H. BERGHORN, *Elec. Mfg.*, **46**, 82 (1950).
3. H. E. HARING, *This Journal*, **99**, 30 (1952).
4. J. F. DEWALD, *ibid.*, **102**, 1 (1955).
5. D. A. MCLEAN AND F. S. POWER, *Proc. I. R. E.*, **44**, 872 (1956).

Effect of Oxygen Pressure on the Oxidation Rate of Cobalt

DONALD W. BRIDGES,[1] JOHN P. BAUR,[1] AND W. MARTIN FASSELL, JR.[1]

Department of Metallurgy, University of Utah, Salt Lake City, Utah

ABSTRACT

Co was oxidized from 800° to 1200°C in 0.013–27.2 atm O_2. It oxidized in accordance with the parabolic rate law above 950°C and formed the single oxide, CoO, above 900°C. Pressure increase accelerated the rate of oxidation. However, the oxidation rate eventually ceased to increase with increase of oxygen pressure at temperatures below 1150°C. Theoretical considerations employing a vacancy saturation mechanism correlated the data. Photomicrographs of the oxide layer are included. Activation energy for the diffusion process is 58,000 cal.

A review of the oxidation literature for the metal Co is available elsewhere (1). Oxidation of Co above 900°C and 150 mm Hg oxygen pressure involves the single oxide, cobaltous oxide, CoO. CoO is a semiconductor of the metal deficit type (NiO and Cu_2O type) (2). Below 900°C the surface oxide is a thin layer of Co_3O_4, although most of the oxide layer is CoO. The CoO vacancy concentration has been estimated to be 25 times that of NiO (3) The present survey investigates the oxidation behavior of cobalt from 800° to 1200°C over the oxygen pressure range 0.013–27.2 atm; however, theoretical evaluation of the data is limited to temperatures above 900°C where the only oxide present is CoO.

Experimental Procedure

Details of the high-pressure equipment and general procedure have been described (4) as has the low-pressure equipment (5). All rate data were obtained using the quartz spring technique. Two types of Co were employed: (*a*) spectrographically pure Co,[2] and (*b*) high-purity electrolytic Co.[3] Each was rolled to desired thickness, and vacuum annealed prior to oxidation. The sample size was: (*a*) 1.3 in. x .37 in. x .01 in.; (*b*) 1.1 in. x .5 in. x .01 in. Spectrographic analysis of sample (*a*) metal is as follows: Si <0.0002%; Fe <0.0005%; Mg <0.0001%; Ag <0.0001%; and a slight trace of Na and Ca. Comparison of the spectrograms of both metals showed sample (*b*) Co to be of comparable purity, with a trace of Ni and Si. Oxidation time varied from 2 hr to 45 min depending on the rate of reaction.

Experimental Results

Above 950°C and at all oxygen pressures investigated the metal rigorously obeyed the parabolic oxidation rate equation, $\Delta W^2 = K_p \cdot t$. At lower temperatures irregularities sometimes occurred as others have noted (1). Table I summarizes the parabolic rate constants for corresponding temperatures and oxygen pressures.

The parabolic constants of Carter and Richardson (2) compare favorably with those obtained in this survey. As no determinations were made at one atmosphere in this study, direct comparison is impossible. However, if the parabolic constants are plotted vs. oxygen pressure, interpolation yields remarkably close agreement. Values thus obtained and those of Carter are as follows: 1000°C, 1 atm, CR, 87.6; BBF, 83; 1148°C, 1 atm, CR, 334.5; BBF, 320; 1148°C, 0.15 atm, CR, 180.1, BBF (0.125 atm), 134.5. The units are those of Table I; the authors' initials are used to designate the investigators.

Due to the proximity of the sample to the furnace winding in the high-pressure furnace, together with the increased current required to maintain the elevated temperature at higher oxygen pressures, 1200°C data are not available above 1 atm. The sample was seized as it entered the magnetic field of the winding and fused to the furnace tube wall. Fusion occurred at the lower guard winding where the temperature is just below the Curie temperature of 1130°C. At high-oxygen pressures the current must be higher in the guard windings than in the center winding in order to maintain a uniform temperature zone adjacent to the sample thermocouple. Seizure did not occur in the low-pressure furnace because the furnace winding is approximately twice the distance from the sample, and the current requirement is not as great. In determinations at lower temperatures in both furnaces, current requirements are less, resulting in a smaller magnetic field and less chance of arrestment during the raising of the sample.

Experimental conditions above 950°C were such as to suppress the decomposition of CoO to Co_3O_4 or the formation of Co_3O_4 as a layer over the CoO substrate when the sample is lowered at the completion of a determination. X-ray diffraction showed the oxide formed at 800°C and 6.8 atm to be a mixture of CoO and Co_3O_4 spinel, but mainly CoO. At 1000°C and 6.8 atm the oxide was predominantly CoO with a slight trace of the spinel possibly due to quenching in an excess of oxygen. The oxide formed at 1200°C and 0.125 atm was entirely CoO. Oxidized samples resembled silvered mirrors in physical appearance. The same type of grain structure and triangular grain boundary shape exist on high-pressure samples as have been observed on copper oxidized to Cu_2O (5). Fig. 1 shows CoO grains formed on Co at 1100°C at various oxygen pressures for a period of 45 min. Photographs are of the *in situ* oxide layer unetched. Grain growth phe-

[1] Present address: Howe Sound Co., Salt Lake City, Utah.

[2] Obtained from Jarrell-Ash Co., manufactured by Johnson-Matthey Co., Ltd.

[3] Prepared by Howe Sound Co Research Lab.

TABLE I. *Compilation of observed parabolic rate constants*

P, atm	K_p, $mg^2cm^{-4}hr^{-1}$								
	800°C	850°C	900°C	950°C	1000°C	1050°C	1100°C	1150°C	1200°C
0.013				8.0*	15.9*	27.7*	46.1*	91.7*	121.0*
0.033				13.0*			56.4*	98.3*	144.3*
0.066				18.1*	18.0*	46.4*	71.3*	116.7*	191.5*
0.092				13.8*					
0.125				19.2*	37.7*	66.3*	107.0*	134.5*	237.8*
0.250				24.7*			129.8*		
0.500				35.1*	63.1*	116.3*	160.4*	229.1*	
1.36	1.5†	4.4*	12.7*	59.4†	96.8*	171.7†	302.3†	531.7†	
		5.3†	14.1†		96.6†				
6.81	2.0†	5.0*	13.0*	56.3†	156.1†	326.5†	536.5*	951.9†	
		5.2†	19.3†		167.9*	323.9†	507.0†		
13.61	2.7†	5.1*	15.5*	55.5†	144.5†	365.6†	822.8*	1049.8†	
		7.4†	21.1†		144.8*		717.8†		
20.41	1.7†	6.0*	16.0*	50.2†	143.8†	306.3†	835.0*	1066.7†	
		8.5†	19.8†		144.1*		809.1†		
27.2							738.2*	1376.1†	
							742.1†		

* Johnson-Matthey cobalt.
† Howe Sound Co. cobalt.

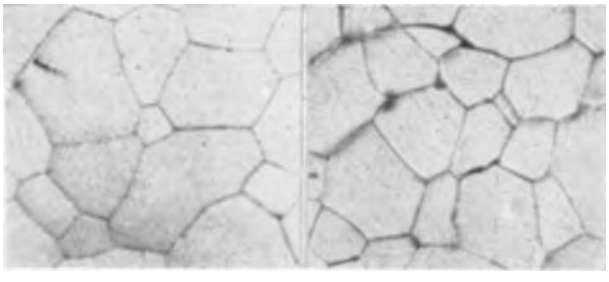

FIG. 1. Photomicrographs of CoO layers formed in 45 min at 1100°C and (*left*) 6.81 atm and (*right*) 20.4 atm. 250× before reduction for publication.

nomena are quite apparent. Grain size is larger as the temperature of oxidation is increased.

Discussion of Results

No attempt is made to explain the mechanism of oxidation below 900°C where the oxidation process involves two oxides.

According to Mott and Gurney (6), the parabolic constant for oxidation involving a metal deficit type of oxide whose migrating cations are divalent is:

$$K_p = 3\Omega D_o(n_g - n_m) \qquad (I)$$

where K_p is the parabolic constant as defined by $\Delta W^2 = K_p \cdot t$; Ω is the volume of metal oxide containing 1 mole of the cation, and D_o is the temperature dependent part of the diffusion coefficient. n_g is the number of vacancies per unit volume near the oxide-oxygen interface, and n_m is the corresponding quantity for the region near the metal-oxide interface. If the concentration of vacancies at the oxygen interface, n_g, is much greater than the vacancy concentration at the metal-oxide boundary, n_m (i.e., $n_g \gg n_m$), one obtains the expression:

$$K_p = n_g \cdot K_p' \qquad (II)$$

where n_g is a function of the external oxygen concentration and

$$K_p' = 3\Omega D_o = A \cdot \exp(-\Delta H^*/RT) \qquad (III)$$

ΔH^* is the activation energy for the diffusion process. The assumption of temperature invariance of the parabolic constant other than the variation in the exponential term, $\exp(-\Delta H^*/RT)$, is universal but never rigorously correct. The success of this assumption depends on the parameter A containing only factors involving powers of T near unity. For small temperature changes the variation of A will then be negligible compared to that of the exponential term. The explicit form for the factor A depends on the theory of diffusion preferred (7).

For all isotherms except those at 1150° and 1200°C, the parabolic constant reaches a maximum value. This suggests two possible saturation effects: (*A*) The surface sites become saturated with oxygen. This effect is discussed in detail elsewhere (5). (*B*) Alternatively, the vacancy density has obtained a limiting condition. Co oxidation data are correlated through the assumptions of sufficiently low oxygen surface coverage to allow the bulk oxygen gas pressure to be used as the surface oxygen activity, and of equilibrium between the gas phase and the near surface vacancy concentration. Cessation of increase in the parabolic rate constant with increased oxygen pressure is attributed to saturation of the cation vacancies.

The Schottky-Wagner (8) theory of defects, which is the basis of the Wagner (9) theory of parabolic oxidation, assumes that the number of vacancies is much smaller than the number of lattice sites and that interaction between the vacancies (defects) is negligible. Anderson (10) expanded the theory to encompass large defect concentrations with interaction between the pairs of like defects. This theory yields, for oxides of the form MeO, the expression (10–12)

$$\lambda = [p(\theta)]^{1/2} = \frac{\theta}{1-\theta} P^o \cdot \exp(2\theta w/kT) \qquad (IV)$$

where θ the fraction of unoccupied sites is defined by $\theta = n_g/N$, n_g is the number of vacant sites per unit volume,

TABLE II. *Summary of the calculations necessary in the application of Eq. (IX)*

950°C $K_p'' = 55$ $p(1/2) = 0.225$

$p(\theta)$	θ	K_p	$\frac{p(\theta)}{p(1/2)}$	$1/2 \ln \frac{p(\theta)}{p(1/2)}$
0.500	0.637	35.07	2.222	0.399
0.250	0.448	24.65	1.111	0.0525
0.125	0.350	19.22	0.556	−0.294
0.092	0.250	13.77	0.409	−0.446
0.0658	0.329	18.09	0.292	−0.615
0.0329	0.236	12.95	0.146	−0.961
0.0132	0.146	8.04	0.0587	−1.481

1000°C $K_p'' = 144$ $p(1/2) = 0.54$

$p(\theta)$	θ	K_p	$\frac{p(\theta)}{p(1/2)}$	$1/2 \ln \frac{p(\theta)}{p(1/2)}$
1.361	0.672	96.71	2.520	4.606
0.5000	0.438	63.05	0.926	−0.0384
0.1250	0.262	37.70	0.232	−0.731
0.0658	0.125	17.95	0.122	−1.052
0.0132	0.110	15.88	0.0244	−1.858

1050°C $K_p'' = 340$ $p(1/2) = 1.20$

$p(\theta)$	θ	K_p	$\frac{p(\theta)}{p(1/2)}$	$1/2 \ln \frac{p(\theta)}{p(1/2)}$
1.361	0.505	171.67	1.134	0.0629
0.500	0.342	116.25	0.4167	−0.438
0.125	0.195	66.29	0.1042	−1.131
0.0658	0.136	46.36	0.0548	−1.451
0.0132	0.081	27.71	0.0110	−2.255

1100°C $K_p'' = 760$ $p(1/2) = 2.50$

$p(\theta)$	θ	K_p	$\frac{p(\theta)}{p(1/2)}$	$1/2 \ln \frac{p(\theta)}{p(1/2)}$
6.805	0.687	521.75	2.722	0.500
1.361	0.398	302.31	0.544	−0.304
0.500	0.221	160.40	0.200	−0.805
0.250	0.171	129.76	0.100	−1.151
0.125	0.141	107.01	0.050	−1.499
0.0658	0.094	71.26	0.02632	−1.819
0.0329	0.074	56.37	0.01316	−2.165
0.0132	0.061	46.13	0.00528	−2.618

1150°C $K_p'' = 1550$ $p(1/2) = 5.00$

$p(\theta)$	θ	K_p	$\frac{p(\theta)}{p(1/2)}$	$1/2 \ln \frac{p(\theta)}{p(1/2)}$
27.218	0.888	1376.0	5.444	0.8475
20.414	0.688	1066.7	4.083	0.704
13.609	0.676	1049.0	2.722	0.501
6.805	0.614	951.0	1.361	0.154
1.361	0.343	531.0	0.2722	−0.651
0.500	0.148	229.1	0.1000	−1.151
0.125	0.087	134.5	0.0250	−1.841
0.0658	0.075	116.3	0.01316	−2.165
0.0329	0.063	98.3	0.00658	−2.515
0.0132	0.059	91.7	0.00264	−2.965

1200°C $K_p'' = 3200$ $p(1/2) = 9.5$

$p(\theta)$	θ	K_p	$\frac{p(\theta)}{p(1/2)}$	$1/2 \ln \frac{p(\theta)}{p(1/2)}$
0.125	0.0740	237.82	0.01316	−2.165
0.0658	0.0599	191.46	0.00693	−2.485
0.0329	0.0452	144.29	0.00346	−2.818
0.0132	0.0378	120.97	0.00139	−3.285

and N is the total number of sites per unit volume; λ is the absolute activity of the surface oxygen and is assumed to be equal to $[p(\theta)]^{\frac{1}{2}}$, the square root of the oxygen pressure for a particular value of θ; w is the vacancy interaction energy; P^o is determined by the temperature dependent portion of the partition function for the oxygen gas and may be approximated for the purpose of expansion in this paper as,

$$P^o = B \cdot \exp[(E^v + \tfrac{1}{2}E^d)/kT] \qquad (V)$$

B is a function containing the absolute temperature to powers of the order of unity; E^v is the energy required to form a vacancy; and E^d is the dissociation energy for an oxygen molecule.

In applying the theory underlying Eq. (IV) to the oxidation of Co to CoO one must introduce two generalities of the theory as applied to equilibrium monolayers by Fowler (12). It is felt that these modifications are necessary to form a three-dimensional analogy of the two-dimensional monolayer in the immediate neighborhood of the oxide-oxygen interface: (*a*) gross deviations from stoichiometric proportions must be capable of existence near the oxide-oxygen interface so that θ may approach unity while the bulk of the oxide remains of near stoichiometric proportions, and (*b*) concentration of vacancies near the interface must increase sharply over that in the bulk oxide phase.

Multiplication of Eq. (II) by N/N yields the following forms:

$$K_p = \theta \cdot N \cdot K_p' = \theta \cdot K_p'' \qquad (VI)$$

where $K_p'' = N \cdot K_p'$. Eq. (IV) cannot be solved explicitly for θ in terms of p, the oxygen pressure. It is necessary to resort to an indirect method in order to illustrate the closeness of fit between the experimentally observed parabolic rate constants and the theory underlying Eq. (IV). The steps of the method are enumerated below.

Step 1. Approximate values of K_p'' for all temperatures below 1150°C are selected easily from the data of Table I. Compatible K_p'' values for 1150° and 1200°C are found by plotting the logarithm of K_p'' vs. 1/°K and extrapolating to the desired temperature. This extrapolation requires that ΔH^* is constant over the investigated temperature range. Table II lists K_p'' values for all temperatures.

Step 2. Experimental θ values are calculated from division of the observed parabolic rate constant by the compatible K_p''. θ is tabulated in Table II.

Step 3. Substitution of $\theta = \frac{1}{2}$ in Eq. (IV) results in the particular solution,

$$[p(\tfrac{1}{2})]^{\frac{1}{2}} = P^o \cdot \exp(w/kT) = B \cdot \exp[(E^v + \tfrac{1}{2}E^d + w)/kT] \qquad (VII)$$

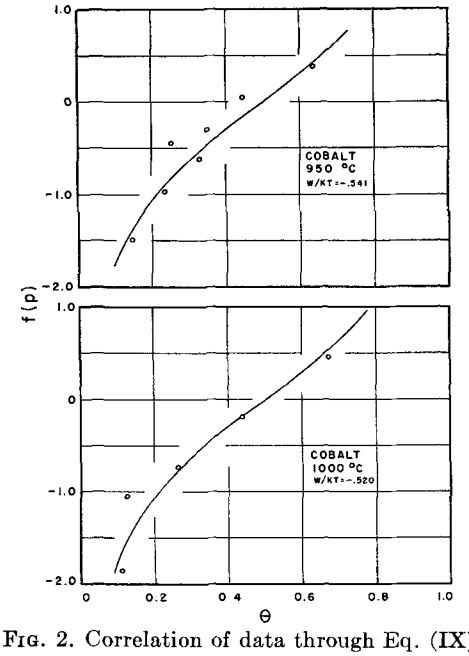

FIG. 2. Correlation of data through Eq. (IX)

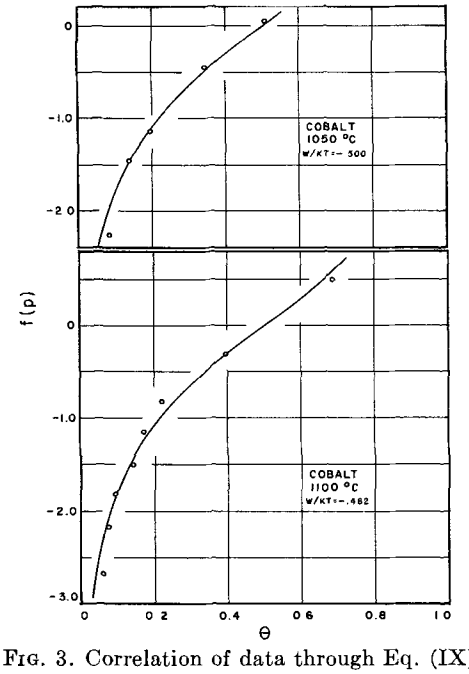

FIG. 3. Correlation of data through Eq. (IX)

Division of Eq. (IV) by Eq. (VII) eliminates the variable P^o and gives the forms:

$$\left[\frac{p(\theta)}{p(\tfrac{1}{2})}\right]^{\frac{1}{2}} = \frac{\theta}{1-\theta}\exp\left[(2\theta-1)w/kT\right] \qquad \text{(VIII)}$$

or

$$f(p) = \tfrac{1}{2}\ln\frac{p(\theta)}{p(\tfrac{1}{2})} = (2\theta-1)w/kT + \ln\frac{\theta}{1-\theta} \qquad \text{(IX)}$$

The left-hand member of Eq. (IX) is a function of oxygen pressure suitable for use in plotting the experimental data of Table I. Table II shows the calculated values of this function for θ values found in Step 2 and $p(\frac{1}{2})$ values (also tabled in Table II) estimated by plotting K_p vs. p and determining the pressure corresponding to $\frac{1}{2}K''_p$.

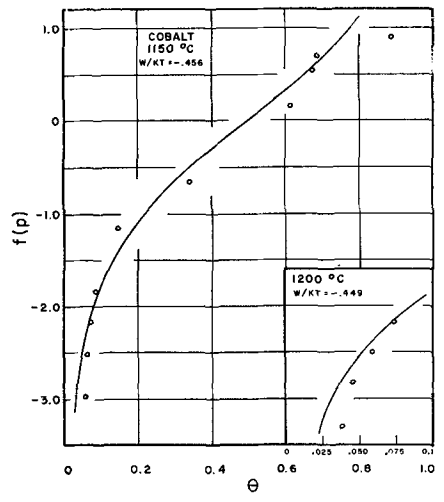

FIG. 4. Correlation of data through Eq. (IX)

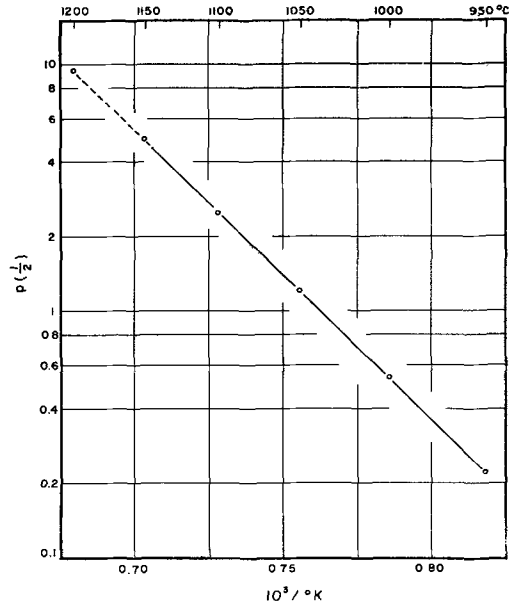

FIG. 5. Plot of the logarithm of Eq. (VII)

Step 4. Theoretical plots of Eq. (IX) vs. θ can be formulated by selection of a value of w and computation of the right-hand side of Eq. (IX) for selected values of θ.

Fig. 2 through 4 are the plots of $f(p)$ of Eq. (IX) vs. θ. The solid theoretical curves were calculated by the method described under Step 4. The assumed values of w/kT used to fit the data vary from -0.541 to -0.449. These values correspond to an interaction energy w of -1324 cal/mole.[4]

Differentiation, with respect to the reciprocal absolute temperature, of the logarithms of both sides of Eq. (VII) yields:

$$\frac{d\ln[p(\tfrac{1}{2})]}{d(1/T)} = 2(E^v + \tfrac{1}{2}E^d + w)/K \qquad \text{(X)}$$

[4] Molar energy quantities can be found from the cited equations by substituting R (2 cal/mole·°K) in place of the Boltzmann constant, k, or alternatively by multiplying the molecular energies of the equations by Avogadro number.

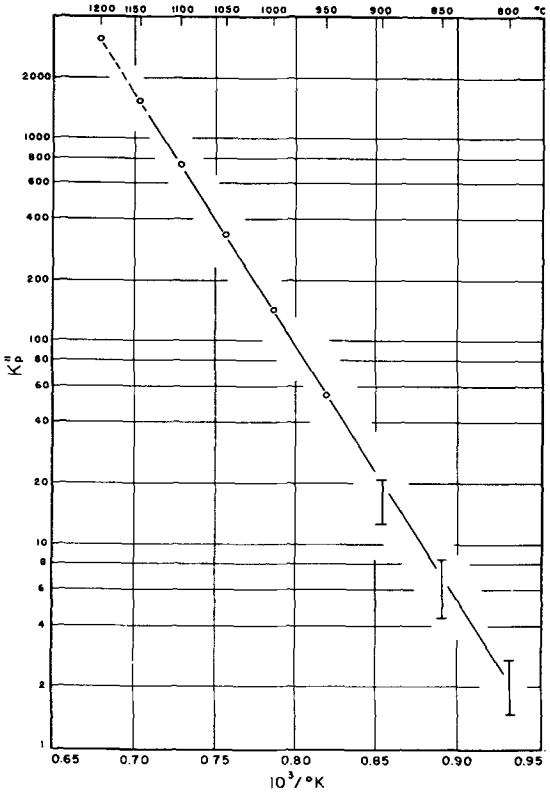

FIG. 6. Plot of the logarithm of Eq. (III)

If each of the energies is reasonably insensitive to temperature in the range of experimental determination, a plot of the logarithm of $p(\frac{1}{2})$ vs. the reciprocal absolute temperature would yield a straight line. Fig. 5 is the curve obtained from the estimates of $p(\frac{1}{2})$ in Table II. From the slope of Fig. 5 the summation of the molar energies of Eq. (X) was found to be $-28{,}300$ cal/mole. The dissociation of oxygen molecules requires an E^d of 117,200 cal/mole (13). Use of the above values of the energies results in an energy of vacancy formation, E^v, of $-85{,}576$ cal/mole or 3.71 ev.[5] No reference could be found for the energy of vacancy formation in an oxide. However, energies are reported for hole formation in silver and alkali metal halides. Halide crystals, as well as oxides, have ionic crystal lattices. E^v for AgCl is 25,000 cal/mole and for AgBr, 20,200 cal/mole (15). For the alkali metal halides the following values are available: NaCl, 1.86 ev; KCl, 2.08 ev; and KBr, 1.92 ev (16).

[5] Literature estimates of involved energies are sometimes reported in electron volts (ev); 1 ev equals 23,052 cal/mole (14).

Fig. 6 is a plot of the limiting parabolic rate constant, K_p'', vs. the reciprocal absolute temperature. The vertical lines at 900°C and lower temperatures are the spread of the parabolic rate constants at these temperatures, which were not analyzed as the oxidation process involved two oxides. The slope of this graph yields an activation energy for the diffusion process, i.e., the diffusion of Co^{++} through CoO of 58 kcal.

ACKNOWLEDGMENTS

The authors are indebted to the Office of Ordnance Research, U. S. Army, and the Watertown Arsenal Laboratory, for the funds necessary for this work. Thanks are due to J. R. Lewis, Head, Department of Metallurgy, for his interest in this work and Mr. Theron Odekirk for his assistance in the numerous calculations involved.

Manuscript received January 23, 1956.
Any discussion of this paper will appear in a Discussion Section to be published in the June 1957 JOURNAL.

REFERENCES

1. O. KUBASCHEWSKI AND B. E. HOPKINS, "Oxidation of Metals and Alloys," p. 176, Academic Press, Inc., New York (1953).
2. R. E. CARTER AND F. D. RICHARDSON, *J. Metals*, **7**, 336 (1955).
3. W. J. MOORE AND J. K. LEE, *J. Chem. Phys.*, **19**, 255 (1951).
4. R. C. PETERSON, W. M. FASSELL, JR., AND M. E. WADSWORTH, *J. Metals*, **6**, 1038 (1954).
5. J. P. BAUR, D. W. BRIDGES, AND W. M. FASSELL, JR., *This Journal*, **103**, 273, (1956).
6. N. F. MOTT AND R. W. GURNEY, "Electronic Processes in Ionic Crystals," 2nd ed., p. 256, Oxford Press, New York (1948).
7. B. CHALMERS, Editor, "Progress in Metal Physics," vol. 4, chap. 6, pp. 265–332, Interscience Publishers, Inc., New York (1953).
8. W. SCHOTTKY AND C. WAGNER, *Z. phys. Chem.*, **B11**, 163 (1930).
9. C. WAGNER, "Atom Movements," p. 153, American Society of Metals, Cleveland (1951).
10. J. S. ANDERSON, *Proc. Roy. Soc.*, **A185**, 69 (1946).
11. A. L. G. REES, "Chemistry of the Defect Solid State," p. 41, Methuen & Co., Ltd., London (1954).
12. R. H. FOWLER AND E. A. GUGGENHEIM, "Statistical Thermodynamics," p. 431, Cambridge (1949).
13. A. G. GAYDON, "Dissociation Energies and Spectra of Diatomic Molecules," p. 212, Dover Publications, Inc., New York (1950).
14. "Handbook of Chemistry and Physics," 30th ed., p. 2634 (1948).
15. W. JOST, "Diffusion in Solids, Liquids, Gases," p. 95, Academic Press, Inc., New York (1952).
16. *Ibid.*, p. 113.

Kinetics of Formation of Porous or Partially Detached Scales

C. Ernest Birchenall

Forrestal Research Center, Princeton University, Princeton, New Jersey

ABSTRACT

Growth of oxide scales on metals is often accompanied by the development of porosity in the oxide or at the metal-oxide interface. These irregularities should affect the kinetics of the reaction and, if ignored, may lead to incorrect conclusions about the mechanism of the reaction. A number of simple models in which pores are assumed to grow in the oxide or at the interface are investigated, and it is shown that a sequence of ranges governed by different kinetics might be found in several cases. Recent experiments which seem to contradict Wagner's theory of scale growth are discussed and an explanation in terms of pore growth is offered.

For the formation of thin oxide films on metals Mott and coworkers (1) have shown how a number of rate laws may arise out of the physical requirements of the metal-oxide composite. These rate equations may be linear, parabolic, cubic, or logarithmic in form. During the oxidation of a single material at constant oxygen pressure and temperature the various rate laws may apply in time sequence due to the thickening of the film. However, when the oxide product is a thick scale without porosity and firmly attached to the metal base the number of possibilities seems to be rather severely limited. Reaction at one of the phase interfaces in the system may be rate controlling, in which case the rate of growth will be constant. Alternatively, diffusion through the oxide layer may be controlling, leading to the familiar parabolic dependence of thickness on time. Although there may be an initial period of linear growth, once the parabolic law is established it should persist indefinitely in the absence of other physical changes in the system. These observations are embodied in the equation

$$\frac{x}{l} + \frac{x^2}{k} = t \qquad \text{(I)}$$

frequently employed in the past (2). The squared term is small at short times and large at long times as required if the rate constants l and k are chosen properly.

A metal or alloy seldom oxidizes precisely according to the parabolic law or a sequence of linear followed by parabolic rates. Sometimes the behavior belongs properly to the thin film range, but often it is simply an indication of the difficulty of providing the ideal conditions postulated above: nonporous and closely adherent oxide. In fact, Dravnieks and MacDonald (3) have given a rather detailed picture of a possible mechanism by which vacancies, halted in their flow by the metal-oxide interface, condense to destroy the metal-oxide contact. They suggest the need for an appreciable oxide ion diffusion contribution. This suggestion is not adopted here because recent experiments in this laboratory seem to rule out this contribution for the growth of wüstite on iron and to show that, when it can, the oxide follows the retreating metal interface by a plastic flow mechanism (4).

It is instructive to examine the variety of rate equations which may be obtained for simple assumptions which are reasonable for oxidizing metals. Consider a metal on which an oxide grows by the diffusion of metallic ions by a cationic vacancy mechanism. The oxide will usually find some coherency relationship with the underlying metal in which a common plane of metallic ions is shared. A continuous barrier of oxide prevents direct access of oxygen gas to the metal surface.

Actual cases will not be as simple as this, since plastic deformation processes can be taken into account in only incomplete fashion and cracking, blistering, and spalling (5) have been disregarded. The nucleation step and the possible irregular shape of the initial oxide are less serious omissions, since this stage is over very quickly in the cases of greatest interest here.

In order for the oxide to form a new layer at the oxide-oxygen interface the appropriate number of metal ions must be removed from the metal and carried across the oxide, and an equal number of vacancies must be carried in the reverse direction. Therefore, the number of vacancies transported across the scale will be proportional to the thickness of the scale if the area remains constant. This means that somewhere in the system, by some mechanism, vacancies must be removed. The two likely mechanisms are plastic deformation, which might prevent porosity growth and interfacial detachment, and condensation and precipitation to form pores within a phase or at an interface. It is recognized that for cations to condense to form pores anions must somehow be removed. In some systems where the anion mobilities are not too much smaller than those of the cations a creep process, like that suggested by Nabarro and Herring for metals, in which anion vacancies arrive by relatively short diffusion paths from grain boundaries may be possible. If anion diffusion is too slow the high concentration of negative charge in the region of cation vacancy supersaturation may promote slip in the anion lattice. This should lead to a preference for nucleation at dislocation lines if more serious disturbances like inclusions are absent. In some oxides anion vacancies may form at the metal-oxide interface and be unable to diffuse far. If porosity develops in this region, as is often observed, the supply of anion vacancies may be no problem.

A number of cases will be examined consisting of simple assumptions about the location at which porosity forms and the form and rate at which it accumulates. Condensation of vacancies to form pores in the underlying metal has been sought several times (4, 6, 7), but has not been observed unequivocally. For this reason the case of pores in the metal phase will be excluded. Copious porosity has been found in the metal during the oxidation of alloys, but this is presumably a consequence of unequal metal atom diffusion rates in the alloy (8).

It should be emphasized that, even though the mechanism assumed for the growth of porosity may not be correct, the effects on the over-all rates of reaction should still apply as long as the growth rates of the pores are approximated adequately. If the pores develop at rates different than those deduced here, the fact of the existence of porosity insures deviations from the simple parabolic rate law.

Calculations

Confine attention to unit area and represent the specific rate constant for interface transport by l_o and that for diffusion transport by k_o where the latter contains as factors $D\ \Delta c$. D is the average diffusion coefficient and Δc the change in concentration of the diffusing species across the thickness of the oxide. In order to show the properties of some of the equations derived below in graphical form the rate constants measured by Wagner and Grünewald (9) for the oxidation of Cu at 1000°C have been substituted (*see* appendix A).

Case 1. If the porosity forms entirely at the metal-oxide interface, as suggested by Dravnieks and MacDonald (3), it will act to decrease the rate of interface transport by an amount corresponding to the decrease in contact area (if transport of ions by vaporization is neglected). For a thick specimen on which a film may grow indefinitely interface control must eventually overcome diffusion control, for there are interfacial sites available only in limited number. Whether this will happen in a reasonable time will depend on the constants of the system.

If all vacancies condense as pancake pores at the metal-oxide interface the loss in area is proportional to Δx. Diffusion remains in control until interface transport is reduced to a comparable rate. That is until

$$l_o A \approx k' D \frac{dc}{dx} A_d \approx k' D \frac{\Delta c}{\Delta x} A_d \approx \frac{k_o}{x} A_d \qquad \text{(II)}$$

where x is distance in the growth direction, A_i is the area for the interfacial reaction, and A_d is the area for diffusive flow. If the effective diffusive area is unchanged and ϕ represents the fraction of the contact area remaining,

$$\frac{k_o}{x_a} = l_o \phi_a \qquad \text{(III)}$$

where the subscripts a indicate that interface control is replacing diffusion control. But $(1 - \phi)$ is proportional to x; or $\phi = 1 - cx$, hence

$$\frac{k_o}{l_o} = x_a(1 - cx_a) \qquad \text{(IV)}$$

If a constant fraction of the vacancies passing through the scale are effective in reducing the area, the remainder being removed by plastic flow, the value of c can be determined from equation (IV). If all vacancies are removed by plastic flow until the scale reaches a critical thickness[1] x_c and then all or some constant fraction become effective, the equation should be modified to the following form:

$$\{1 - c(x_a - x_c)\}x_a = \frac{k_o}{l_o} \qquad \text{(V)}$$

Since enough vacancies to detach the interface should be provided by the growth of a few layers of scale, if all vacancies are effective, loss of contact may be precipitous when the scale becomes thick enough to resist further plastic deformation It is apparent from general experience that c is seldom large, so condensation of vacancies in this fashion must be inefficient or repair processes must be rapid.

Quadratic equations (IV) and (V) yield two roots, the smaller value of x_a indicating approximately the thickness at which the initial linear rate passes to the diffusion-controlled parabolic rate, the larger value of x_a indicating return of interface control. However, if the interface reaction at the oxide-oxygen interface is slower than that at the metal-oxide interface, the former will control the initial stage.

Once the interface is in control with contact area ϕ_a remaining at time t_a the further course of the reaction should be determined there. The appropriate relation is

$$\frac{dx}{dt} = l_o \phi = l_o[1 - c(x - x_c)] \qquad \text{(VI)}$$

which, upon integration, gives

$$\ln \frac{[1 - c(x - x_a)]}{[1 - c(x - x_c)]} = c l_o (t - t_a) \qquad \text{(VII)}$$

where $t > t_a$ and x_a is the thickness of the scale when interface control again becomes effective. For the conditions corresponding to equation (IV), $x_c = o$.

If the metal-oxide interfacial porosity does not form as a very thin layer but condenses as a series of hemispherical voids the contact area will decrease at a rate proportional to $x^{2/3}$ rather than x. Also, inert inclusions accumulating at the interface from the reacted metal volume should correspond to this case. Such effects have been noted in the sulfidation of iron (10), although the rates were not determined precisely enough nor over long enough times to test the equations. Then

$$1 - \phi = c(x - x_c)^{2/3} \qquad \text{(VIII)}$$

Interface control reappears when

$$\frac{k_o}{l_o} = \{1 - c(x_a - x_c)^{2/3}\}x_a \qquad \text{(IX)}$$

The appropriate rate equation is

$$\frac{d_x}{dt} = l_o\{1 - c(x - x_c)^{2/3}\} \qquad \text{(X)}$$

[1] Alternatively, growth to a thickness x_c may be required to produce the vacancy supersaturation required for nucleation of pores.

This integrates to

$$\ln\left[\frac{1 + a(x - x_c)^{1/3}}{1 - a(x - x_c)^{1/3}}\right] - a(x - x_c)^{1/3} = \tfrac{2}{3}a^3 l_o t + \text{const} \quad \text{(XI)}$$

where $a = \sqrt{c}$ and the constant may be determined from the condition $x = x_a$ at $t = t_a$. Letting $z = (x_a - x_c)^{1/3}$, which is fixed for a given set of experimental conditions, and $y = (x - x_c)^{1/3}$

$$\ln\left[\frac{(1 + ay)(1 - az)}{(1 - ay)(1 + az)}\right] + 2az - 2ay = \tfrac{2}{3}a^3 l_o (t - t_a) \quad \text{(XII)}$$

For these conditions of porosity developing at the interface the sequence of rate laws is expected to be linear, parabolic, logarithmic. The growth by solid diffusion primarily must cease when the interface is destroyed, but some other process such as evaporation or dissociation and evaporation may make it possible for the reaction to continue (10). Also the metal must rest against the oxide at some places for support. These regions of contact may become preferred sites for continued reaction (4).

If the metal and oxide are unable to yield plastically and the specimen geometry tends to promote shrinkage of the metal away from the oxide, the formation of porosity at the metal-oxide interface may assist in the start of a crack between the two phases. Thus, the growth rate might diminish faster than predicted by equations (VII) and (XII).

Case 2. If the porosity forms entirely within the oxide it is important to determine how it is distributed, whether generally dispersed in such a way as to reduce the area nearly equally in all cross sections or whether restricted to a narrow region. In either case the pseudosteady-state condition ordinarily assumed for diffusion-controlled scaling will be retained. That is, it will be required that the rate of flow be constant through any cross section in the scale parallel to the interface. The initial period of interface control will be neglected in this section.

If the vacancies condense to form pores uniformly distributed throughout the thickness of scale (the same as oxide forming with uniform porosity) the effective cross-sectional area will be the same in all cross sections at all times; hence a simple parabolic law will be observed, but the diffusion coefficient will be somewhat greater than estimates based on the growth of dense oxides would give.

An induction time prior to the formation of any porosity, that is $\phi = 1$ until $t = t_c$, followed by random distribution of porosity so that $\phi = 1 - c\Delta x$ for $t > t_c$ would yield a parabolic relation until t_c followed by an exponential relationship.

$$\frac{dx}{dt} = \frac{k}{x}\phi \quad \text{(XIII)}$$

integrates to

$$c^2 k_o (t - t_c) = c(x_c - x) - (1 + cx_c)\ln\{1 + c(x_c - x)\} \quad \text{(XIV)}$$

For times large compared with t_c the porosity may become essentially uniform again and the parabolic growth re-established with a smaller rate constant. Thus the sequence—parabolic, logarithmic, parabolic—is conceivable.

For porosity concentrated in the region of width δ, which is considerably smaller than x, the requirement of constant flow rate means that through the region δ the concentration gradient will be steeper than in the remainder of the oxide. Hence the remaining gradient will be less steep than normal, for the concentration extremes at the ends of the scale are determined by equilibria with metal and oxygen, respectively.

In the thickness δ if ϕ_2 is the average nonporous area, assuming that D varies little over the thickness, and since Δc is constant, Δc will be given by

$$\left(\frac{dc}{dx}\right)_1 (x - \delta) + \left(\frac{dc}{dx}\right)_2 \delta = \Delta c \quad \text{(XV)}$$

and the steady-state condition requires that

$$D\left(\frac{dc}{dx}\right)_1 = D\left(\frac{dc}{dx}\right)_2 \phi_2 \quad \text{(XVI)}$$

where $(dc/dx)_1$ and $(dc/dx)_2$ are the concentration gradients outside of and within region δ, respectively.

If, on the other hand, D varies with position in the scale, the usual case, let D_1 be the average value in the sound layer and D_2 the average value in the porous region and m be their ratio defined by

$$m = \frac{D_1}{D_2} \quad \text{(XVII)}$$

Then the steady-state condition becomes

$$mD_1\left(\frac{dc}{dx}\right)_1 = D_1\left(\frac{dc}{dx}\right)_2 \phi_2 \quad \text{(XVIII)}$$

Substituting in the equation for the concentration range yields

$$\left(\frac{dc}{dx}\right)_1 (x - \delta) + m\left(\frac{dc}{dx}\right)_1 \frac{\delta}{\phi_2} = \Delta c \quad \text{(XIX)}$$

The growth rate is proportional to the flow through any cross section, hence to $D_1 (dc/dx)_1$ or

$$\frac{dx}{dt} = \frac{k'\Delta c}{x + \left(\dfrac{m - \phi_2}{\phi_2}\right)\delta} \quad \text{(XX)}$$

For a constant number, n, of roughly spherical pores per unit area, $(1 - \phi_2)$ is proportional to $x^{2/3}$, while δ is approximately proportional to $x^{1/3}$.

$$\begin{aligned} (1 - \phi_2) &= nax^{2/3} \\ \delta &= bx^{1/3} \end{aligned} \quad \text{(XXI)}$$

where $\sqrt{a} = b$ for true spheres. Substituting these expressions in the rate equation yields

$$\frac{dx}{dt} = \frac{k''}{x + \left(\dfrac{nax^{1/3} + m - 1}{1 - nax^{2/3}}\right) bx^{1/3}} \quad \text{(XXII)}$$

which, integrated for $x = o$ at $t = o$, yields

$$x^2 - \tfrac{3}{2}bx^{4/3} - \frac{3mb}{na}x^{2/3} - \frac{3mb}{n^2a^2}\ln(1 - nax^{2/3}) = kt \quad \text{(XXIII)}$$

TABLE I. *Growth rate of cobalt oxide from Eq. (XXIII)*

x (cm)	t (sec)
10^{-6}	14
10^{-5}	67
10^{-4}	580
10^{-3}	1450
10^{-2}	8000
10^{-1}	10^5

This expression would be simplified for spherical pores or for a diffusion coefficient independent of distance through the scale.

It seems likely in the last case that the formation of porosity would be delayed either by plastic deformation or by the difficulty of nucleation. Thus a parabolic law should be established initially, then the rate should drop off as the other terms grow.

These relationships break down when the pores begin to impinge seriously. At this point the reaction should go slightly more rapidly than the equations predict, and complete cessation due to separation of the scale should occur at a later time than predicted. Before this occurs the rate may be determined principally by the rate of the dissociation of oxide on the side of the pores nearest the oxide-oxygen interface, or by vaporization of metal or oxide.

Discussion

It is evident that porosity forming in the locations in the oxide scale in which the rate of growth is controlled can affect the kinetics of growth strongly. The simple cases treated here do not exhaust the possible modes of pore development, but they do give some idea of the sequences of rate laws which might be anticipated, if concurrent cracking and spalling are absent. The idealized cases are not likely to be found without some complication.

No very systematic attempts have been made to investigate the sites at which porosity develops nor the factors controlling its development However, metallographic evidence of its presence is abundant Unfortunately it is impossible to correlate the amount and distribution with measured growth rates for lack of sufficient data on any one case.

Another serious difficulty in studying a rate curve which follows a sequence of rate laws is that the number of points and the precision with which they must be determined far exceeds the current practices and standards. The procedure of fitting the oxide growth rate curve after some arbitrary initial period of deviation with a simple parabola will succeed quite well in almost any case since the procedure has two disposable constants built into it. The need for careful correlation of microstructure with growth rate measurements is obvious.

There is one kind of recent observation which may find its explanation in considerations of this type. Moore (11), in studying the oxidation of Cu and diffusion of Cu ions in cuprous oxide, and Carter and Richardson (12), in similar studies on Co and its oxide, found that they could calculate the growth rate constants reasonably well from diffusion coefficients determined on isolated oxides and the Wagner theory of oxide growth on metals. Himmel, Mehl, and Birchenall also succeeded in this for the iron oxides (13). However, Moore and Carter and Richardson found that they obtained anomalous distributions of radioactive tracers in growing oxides when they performed the experiment first done by Bardeen, Brattain, and Shockley (14)—oxidizing a specimen initially covered with a thin layer of radioisotope of the same element, followed by sectioning of the oxide product to determine the resulting distribution of the tracer. In both cases, instead of finding a distribution corresponding to a steady but gradual decrease of the cation diffusion coefficient from oxide-oxygen to metal-oxide interface, the distribution suggested that the diffusion coefficient was high over most of the thickness then dropped rather abruptly near the metal-oxide interface. An explanation is suggested by a photomicrograph [Fig. 1 in reference (12)] which shows a layer of pores with diameters about 15–20% of the thickness of the cobalt oxide scale near the metal-oxide interface. Taking into account the magnification of the photograph, a rough estimate indicates that δ is about one sixth of the total thickness when the thickness is $\frac{3}{4}$ mm. If the area is reduced to one half in this thickness about 4000 spherical pores are required per cm^2. (A rough count on the photomicrograph suggested an even larger number than this.) The ratio of diffusion coefficients m would be about 4, and the concentration gradient would be about 8 times as steep in the porous region as in the balance of the scale. Then the concentration gradient in the sound part of the scale would be less than half as steep as the ideal and in the porous region would be almost four times as steep as the ideal (*see* Appendix B). This is illustrated in Fig. 1. Concentration gradients of this type would produce the kind of deviation from the Bardeen, Brattain, and Shockley distribution that has been observed, although a quantitative check would require better data on the pore distribution and kinetics of growth.

Calculations based on equation (XXIII) (*see* Appendix B) indicate that porosity growth such as Carter and Richardson's sample shows should markedly affect the

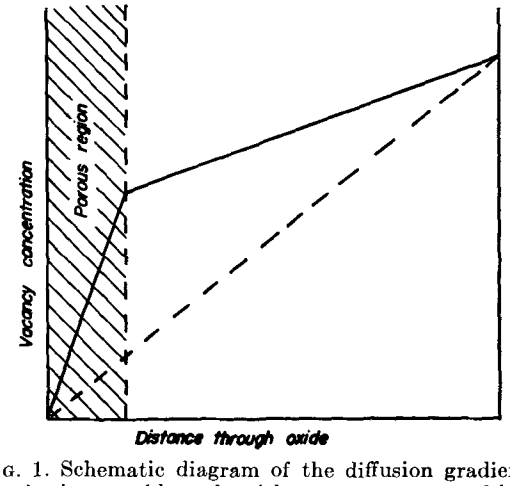

Fig. 1. Schematic diagram of the diffusion gradient of vacancies in an oxide scale with pores concentrated in one region. The gradient in the absence of pores is given by the dashed line. For more detailed discussion, *see* Appendix B.

kinetics of scale growth. Yet strong deviations from the parabolic law are not reported for cobalt. This is probably due to the model chosen here.

Summary

It has been shown by a series of simple models that growth rates of oxide scales on metals may be strongly affected by the development of porosity. The ability of porosity to form must be related to the plastic properties of oxide and metal to some extent. A suggestion is made concerning a recent discrepancy in relating oxide growth rates to cation diffusion processes in cuprous and cobaltous oxides.

Acknowledgment

This research was supported by the United States Air Force, through the Office of Scientific Research of the Air Research and Development Command.

Manuscript received December 12, 1955. This paper was prepared for delivery before the Pittsburgh Meeting, October 9 to 13, 1955.

Any discussion of this paper will appear in a Discussion Section to be published in the June 1957 JOURNAL.

REFERENCES

1. N. CABRERA AND N. F. MOTT, *Repts. Progr. Phys.*, **12**, 163 (1948–49).
2. U. R. EVANS, *Trans. Electrochem. Soc.*, **46**, 247 (1924).
3. A. DRAVNIEKS AND H. J. MCDONALD, *J. (and Trans.) Electrochem. Soc.*, **94**, 139 (1948).
4. D. W. JUENKER, R. A. MEUSSNER, AND C. E. BIRCHENALL, To be published.
5. U. R. EVANS, *Trans. Electrochem. Soc.*, **91**, 547 (1947).
6. C. E. BIRCHENALL AND M. WEINBAUM, Unpublished research.
7. W. J. MOORE, *J. Chem. Phys.*, **21**, 1117 (1953).
8. F. N. RHINES AND B. J. NELSON, *Trans. Am. Inst. Mining Met. Engrs.*, **156**, 171 (1944).
9. C. WAGNER AND K. GRÜNEWALD, *Z. physik. Chem.*, **B40**, 455 (1938).
10. R. A. MEUSSNER AND C. E. BIRCHENALL, To be published.
11. G. W. CASTELLAN AND W. J. MOORE, *J. Chem. Phys.*, **17**, 41 (1949); W. J. MOORE AND B. SELIKSON, *ibid.*, **19**, 1539 (1951).
12. R. E. CARTER AND F. D. RICHARDSON, *Trans. Am. Inst. Mining Met. Engrs.*, **203**, 336 (1955).
13. L. HIMMEL, R. F. MEHL, AND C. E. BIRCHENALL, *ibid.*, **197**, 827 (1953).
14. J. BARDEEN, W. N. BRATTAIN, AND W. SHOCKLEY, *J. Chem. Phys.*, **14**, 714 (1946).

APPENDIX A

Numerical Evaluation of Rate Curves for Interfacial Porosity

For 1000°C and 63 mm Hg pressure of oxygen Wagner and Grünewald (9) found these rate constants for the growth of cuprous oxide on copper: $k_o = 7.37 \times 10^{-8}$ cm²/sec and $l_o = 4.06 \times 10^{-5}$ cm/sec. In Fig. 2 on a log-log plot of thickness against time, which exaggerates the early part of the rate curve and compresses the later part, a number of equations are compared using these values of k_o and l_o and compatibly chosen constants. Reference slopes for simple linear and parabolic growth may be inferred from curve 1 corresponding to Eq. (I), which has a slope appropriate to linear growth at short times and to parabolic growth at long times.

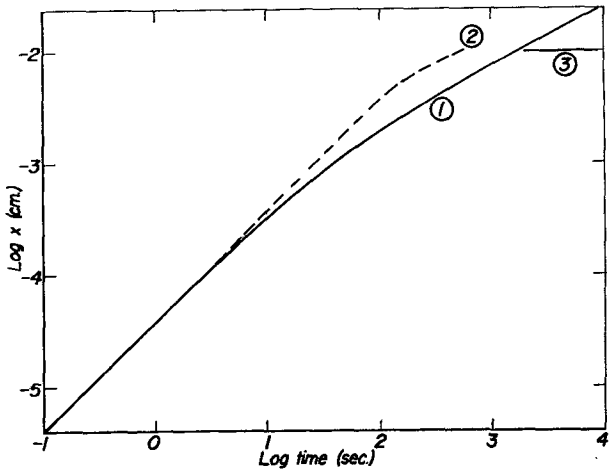

FIG. 2. Rate curves based on Wagner and Grünewald's constants for copper at 1000°C and 63 mm oxygen pressure. Curve 1 is for Eq. (I), curve 2 for Eq. (VII) with x_c equal to zero, and curve 3 for Eq. (VII) with x_c equal to 5×10^{-3} cm.

Eq. (VII) with x_c equal to zero can be solved with these rate constants only for c less than 125. Curve 2 is plotted for c equal to 25. Higher values of c lead to interface control with larger residual areas of contact. The curve terminates at x equal to $1/c$ for very long times. When a critical thickness x_c is postulated, the permissible values of c depend on x_c when x_c is below 3.6×10^{-3} but not above. To avoid the range of restricted c, the value of x_c is taken as 5×10^{-3} cm. Then ϕ_a increases as c increases and x_a approaches x_c asymptotically. For c equal to 125 the thickness increase is only 10^{-3} cm between 400 sec and the end of the reaction at very long times as shown by curve 3. At 1.25×10^{-2} cm $d \log x/d \log t$ is about 1/320.

For Eq. (XII), for $a = 11$ corresponding to $c = 121$ and other constants chosen as before, x increases only from 5.41×10^{-3} to 5.73×10^{-3} as the time goes from 400 sec to very long times. At a thickness of 5.51×10^{-3} and t of 444, $d \log x/d \log t$ is about 1/3, so the rate drops off rapidly once porosity returns interface control.

In all cases it has been assumed that no other transport mechanism capable of moving metal or oxygen across the pore volume intervenes to increase the rate of reaction.

APPENDIX B

Rough Estimate of Concentration Gradients in Porous Scale Layers for Carter and Richardson's Cobalt Oxide Specimen

If the pores are spherical, Eq. (XXI) becomes

$$1 - \phi = n\delta^2$$

For x about 0.067 cm, δ about 0.011 cm, m about 4, ϕ about one half, it is found that

$$n \backsim 4.2 \times 10^3$$
$$a \backsim 7.6 \times 10^{-4}$$

From Eq. (XVIII)

$$\left(\frac{dc}{dx}\right)_2 \Big/ \left(\frac{dc}{dx}\right)_1 = \frac{m}{\phi} \backsim 8$$

And from Eq. (XIX)

$$\frac{\Delta c}{\Delta x} = \frac{13}{6}\left(\frac{dc}{dx}\right)_1 = \frac{13}{48}\left(\frac{dc}{dx}\right)_2$$

Fig. 1 is plotted on this basis to show the large deviation from ideal conditions for these conservatively estimated conditions.

Since the reaction layer does not know the thickness of the underlying metal, the equation need not terminate at the experimental thickness. However, ϕ may approach zero before the metal is consumed. If k is chosen to make the theoretical and experimental values agree at a thickness of 10^{-2} cm, k becomes 4.83×10^{-7} and the growth rate predicted by Eq. (XXIII) is given in the Table I. The last three values correspond to the usual range of experimental measurement of from 1/3 to 36 hr. Since this does not approximate the parabolic slope, it is probable that Carter and Richardson's porosity has a different rate of formation than that postulated, and perhaps a different origin. However, the effect of the porosity on the concentration gradient should be qualitatively as described.

Mass Spectrometric Examination of Hydrogen in Chromium-Plated Steel

CHARLES LEVY AND GEORGE A. CONSOLAZIO[1]

Watertown Arsenal Laboratory, Watertown, Massachusetts

ABSTRACT

Specimens of chromium-plated SAE 1015 steel were examined for hydrogen in the mass spectrometer. The peak heights obtained in arbitrary units were plotted as a function of time. Evolution of hydrogen was studied in the temperature range 100°–800°C. At any given temperature, the amount of hydrogen liberated approached a limit asymptotically over a long period of time. No specimen could be run to complete exhaustion of hydrogen.

Evolution of hydrogen from steel and chromium-plated steel was measured for a constant temperature rise of 2°C/min. In the chromium-plated specimens, it was shown that below 350°C hydrogen was evolved almost exclusively from the chromium plate, while above 490°C evolution occurred primarily from the steel.

Hydrogen evolution at 350°C from a chromium-plated specimen and from a steel specimen was also compared, with time as a parameter. The major portion of the hydrogen available for release in both specimens was liberated after approximately 80 min of heating.

The problem of the concurrent electrodeposition of hydrogen and chromium on various basis metals has been studied by numerous investigators. Most attempted to correlate deposition of hydrogen with hardness, crystal structure of the chromium plate, or the embrittlement of steel basis metal. It has been shown (1–3) that virtually all of the hydrogen is removed from chromium plate at 400°C without any appreciable loss in hardness. A rapid decrease in hardness occurs on heating above 500°C, indicating that there is no direct correlation between the high hardness of the chromium electrodeposit and the hydrogen content. It has been postulated, however, that during deposition, hydrogen enters the chromium lattice and then escapes, leaving the lattice in a state of strain which results in increased hardness.

Snavely (4) states that chromium is normally deposited from the chromic acid bath as unstable hydrides. Being unstable, the hydrides decompose rapidly after deposition into atomic hydrogen and body-centered cubic chromium. The hardness of chromium plate is related to the volume change of 15.6% which accompanies this decomposition. Gaydon (5) and Muro (6) observed evidence for the existence of chromium hydrides by use of the optical spectrograph and x-ray methods, respectively. Brenner (7) believes that oxygen content and fine grain size are the two most important factors which determine the hardness of electrolytic chromium. An excellent summary of work done on gases in chromium is given by Sully (8).

Embrittlement of steels resulting from chromium plating is much more severe than that produced by cathodic pickling under the same conditions of temperature and current density (9). Heating to temperatures above 400°C was necessary to regain completely the original bend value of the unplated steel. In the discussion of reference (9), Snavely states that when the hydrides decompose, the released hydrogen is sparingly soluble in body-centered cubic chromium and tends to diffuse in both directions out of the plate. The diffusion path into the basis metal is greatly favored because of the high concentration of atomic hydrogen in the surface layer of the plate. By contrast, when plating 100% hydrogen on steel (cathodic pickling) the atomic hydrogen available for diffusion into the metal is at the metal-solution interface. It seems likely that a large portion of the hydrogen escapes in molecular form and that this proportion is larger than in the case of chromium plating.

Conventional vacuum methods used for studying gas-metal systems fall into two categories: vacuum fusion and

[1] Present address: Atlantic Gelatin Div., General Foods Corp., Woburn, Mass.

warm vacuum extraction. In both procedures, gases are collected and the pressures are subsequently measured by a McLeod gauge or other pressure measuring device. An inherent disadvantage of these methods is that the total pressure of the system is measured, rather than the partial pressure of the individual gases. Furthermore, it is necessary to analyze for a gas such as hydrogen by combustion or oxidation methods.

The mass spectrometer comprises a sensitive measuring device which is highly selective with regard to ion species. Thus, it is possible to measure a peak height which is proportional to the partial pressure of hydrogen, to the exclusion of the partial pressures of any other gases present. In a similar manner, this technique can also be applied to oxygen, nitrogen, water vapor, or other gases for the chromium-plated steel system being studied.

In this study, absolute hydrogen gas pressures were not measured. This could have been done, however, by incorporating a micromanometer into the modified inlet system. Use of a micromanometer is necessary in order to measure absolute pressures in the micron range. A McLeod gauge or ionization gauge might be used, but difficulty would be encountered in regard to sensitivity of these gauges to gases other than hydrogen, particularly water vapor.

Experimental

The steel specimens used were annealed at 871°–882°C (1600°–1620°F), hardness 59 Rockwell B, and had the following analysis, which corresponds approximately to that of SAE 1015:

C	Mn	S	P
0.17	0.40	0.022	0.008

Specimens were 1.27 cm (½ in.) in diameter and 0.64 cm (¼ in.) in height, and surface ground on all sides. Specimens were cleaned prior to plating by a cycle involving electrolytic alkali treatment for 20 sec anodically, 5 sec cathodically, and a 30 sec 50% HCl dip, with water rinses following each step. Specimens were reverse etched in the plating bath at 15.5 amp/dm² (1 amp/in.²) for 1 min immediately prior to plating. The plating bath consisted of an aqueous solution containing 250 g/l of chromic acid and 2.5 g/l of H_2SO_4. The temperature of the bath was maintained at 55°C and a current density of 31 amp/dm² (2 amp/in.²) was applied, using lead anodes.

After plating over the entire surface, the specimen was rinsed and air-blast dried. In the early experiments, drying was accomplished by immersing in acetone prior to the air blast, and then in liquid nitrogen after the air blast, but subsequently this was found not to be necessary to prevent the escape of hydrogen. The weight of chromium deposited was found to be the major factor controlling the amount of hydrogen produced in the specimen. A weight of 180 ± 9 mg of deposited chromium was chosen since it could be produced in approximately 30 min and the specimen did not evolve more hydrogen than could be handled conveniently in the mass spectrometric analysis. The thickness of chromium deposited was approximately 0.0076 mm.

The mass spectrometer used was a commercially available dual purpose instrument capable of operation in both the isotope ratio and analytical mixture analysis mode. The sample inlet system was somewhat modified from conventional usage. The expansion chamber was replaced by a specimen-containing Vycor tube which was heated to the required temperature by a Nichrome-wound furnace. Temperature measurements were made by means of an external chromel-alumel thermocouple.

Initially, the mass spectrometer was adjusted to "sit" on the hydrogen molecule ion (H_2^+) peak. Before heat was applied to the Vycor tube and specimen, the entire inlet system was evacuated to approximately 10^{-5} mm Hg. The molecules of gas, including hydrogen, which were released from the specimen upon heating were allowed to flow into the ionization chamber where they were bombarded by electrons emitted from a tungsten filament. The beam of positive ions so produced was then accelerated by a controlled potential into the analyzer tube where the moving ions were deflected 180° by a magnetic field according to the equation:

$$m/e = B^2r^2/2E$$

where B = magnetic field strength, e = charge on the particle, m = mass of the ion, r = radius of deflection, and E = accelerating potential.

Only ions having an m/e value which satisfied the equation would travel the semicircle of the analyzer tube and emerge through a slit at the far end, where they would be focussed.

Therefore, if B, r, and E were fixed, only one species of ion came to a focus. In this instrument, the radius of the tube r and the accelerating potential E are fixed. The magnetic field was varied until mass position 2, or the hydrogen molecule ion, was located, as noted above.

To obtain each peak on the mass spectrometer recorder chart, gases evolved from the specimen were collected for a period of 5 min, at the end of which time the gases were allowed to flow through a stopcock into the ionization chamber. The signal which resulted exclusively from the ionized hydrogen molecules was amplified and recorded as a peak which is directly proportional to the number of hydrogen molecule ions and also to the partial pressure of hydrogen in the gas system. After the peak was recorded, the entire inlet system was again evacuated. The stopcock leading to the ionization chamber, which was open for 30 sec during recording and evacuation, was then closed and the pressure in the Vycor tube was allowed to build up for another 4.5-min period. The peak height value was adjusted to correct for the 30 sec during which gases were not collected. This procedure was continued until the required data were obtained.

Evolution of hydrogen from chromium-plated steel was studied at 100°, 200°, 300°, 400°, 500°, 600°, 700°, and 800°C. Ten to fifteen minutes were required to reach temperature once the heat was applied. Peak heights obtained were plotted as a function of time in the following manner. For each constant temperature run, the first peak value in arbitrary units was plotted as the first point. The next peak value was added to the first and plotted as the second point. The third peak value was added to the second and plotted as the third point, and so on until all the points were plotted. Thus, the final point in each curve for each tem-

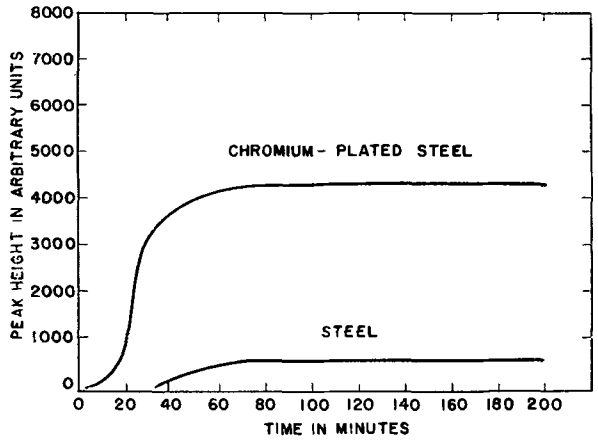

FIG. 1. Comparison of hydrogen evolution from steel and from chromium-plated steel at 350°C.

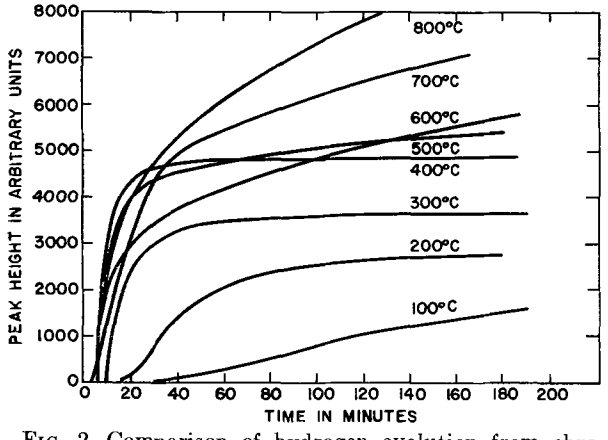

FIG. 2. Comparison of hydrogen evolution from chromium plated steel at various constant temperatures.

perature shows the total hydrogen evolved from the specimen in arbitrary units for the total time of the run.

In another set of experiments, evolution of hydrogen was measured for a constant rise of 2°C/min. Specimens included steel and chromium-plated steel. Peak height data were plotted as a function of time, which is directly related to temperature in this case. Graphical representation of the peak values was achieved in the same manner as above.

Hydrogen evolution at 350°C from a chromium-plated steel specimen and from a steel specimen was also compared, with time as a parameter.

Some hydrogen evolution runs at 350°C were also made after aging chromium-plated steel specimens at room temperature in a desiccator for periods from 1 day to 3 weeks.

RESULTS AND DISCUSSION

The comparison of hydrogen evolution from steel and chromium-plated steel at 350°C is shown in Fig. 1. At this temperature the chromium-plated specimen evolved many times more hydrogen than did the steel specimen. The major portion of the hydrogen available for release at this temperature in both specimens was liberated after 80 min of heating.

Fig. 2 gives the constant temperature evolution of hydrogen vs. time. After a heating period of 180 min at the

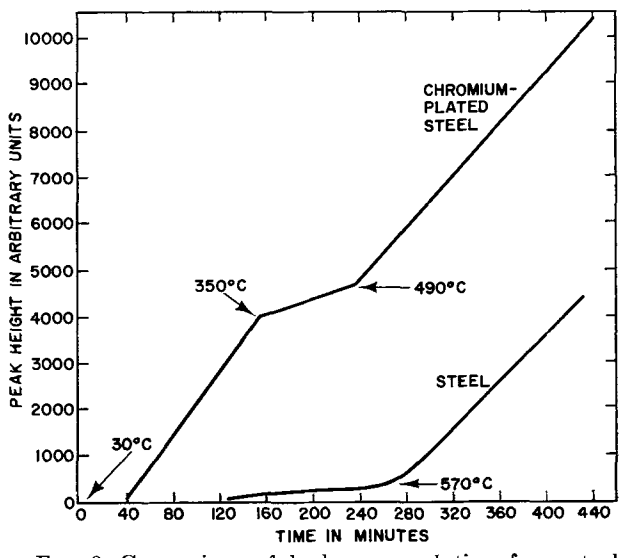

FIG. 3. Comparison of hydrogen evolution from steel and from chromium-plated steel measured at a constant temperature rise of 2°C/min.

given constant temperature, the curves for the 100°, 200°, 300°, 400°, and 500°C runs leveled out, indicating that small amounts of hydrogen were being evolved. Further heating did not release appreciable amounts of hydrogen from these specimens. Above 600°C, extrapolation of the curves in Fig. 2 to a time of 180 min would show no leveling out such as occurs at the lower temperatures.

Since only very small amounts of hydrogen would be liberated on further heating at a given constant temperature, it is apparent that the temperature must be raised in order to release the residual hydrogen in the specimen in a reasonable length of time. For example, at 300°C, after 180 min, 3680 arbitrary units of hydrogen were evolved. At this time, the rate of evolution had decreased to approximately ½ unit/min. In order to increase appreciably the amount of hydrogen liberated, a higher temperature must be used, such as 400°C, where 4890 arbitrary units of hydrogen were evolved after 180 min. As can be seen from Fig. 2, at each higher temperature the amount of hydrogen evolved is considerably increased.

Hydrogen evolution from steel and from chromium plated steel measured at a constant rise of 2°C/min is shown in Fig. 3. The steel began to evolve appreciable amounts of hydrogen at 570°C and continued at a constant rate. Hydrogen evolved rapidly from the chromium plated steel specimen at an approximately constant rate from 130°C to 350°C, leveled off, and then broke upward at 490°C and continued at a slightly lower constant rate of evolution than at below 350°C.

It appears that hydrogen is virtually exhausted from the chromium plate at 350°C, at which point the curve in Fig. 3 levels out. The curve does not attain a zero slope because slight amounts of hydrogen are still being evolved from the chromium plate and, in addition, the steel is beginning to evolve hydrogen at an appreciable rate. Above 490°C, the hydrogen is apparently being evolved entirely from the steel basis metal. Comparing the slopes of the curves for steel and chromium plated steel at temperatures above approximately 550°C, it may be con-

cluded that chromium plate has little or no effect on the rate of diffusion of hydrogen from steel.

Hydrogen evolution did not vary appreciably in chromium-plated steel specimens which had been aged for periods from 1 day to 3 weeks before heating at 350°C. These data, if plotted, would closely approximate the curve shown for chromium plated steel in Fig. 1. Experimentation in this vein was therefore abandoned since other investigators (1, 7) have found similar results over longer periods of aging time.

It should be noted that no specimen, either steel or chromium plated steel, was completely exhausted of hydrogen in any of the above experiments. An attempt was made to completely exhaust the hydrogen from a chromium-plated steel specimen by heating in the mass spectrometer inlet system at 800°C. After approximately 20 hr appreciable quantities of hydrogen were still being evolved.

Conclusions

1. The mass spectrometer, by virtue of its selectivity, provides a useful technique for the investigation of metal-gas systems.

2. Hydrogen is evolved from both plated and unplated specimens at virtually the same rate at temperatures above approximately 550°C. Apparently chromium plate 0.0076 mm (0.0003 in.) in thickness has no effect on the rate of diffusion of hydrogen from steel in this temperature range.

3. Below 350°C, hydrogen is evolved almost exclusively from the chromium plate, while above 490°C, the evolution occurs primarily from the steel basis metal, with a transition region in the 350°–490°C temperature range.

4. At any given temperature, the amount of hydrogen which can be liberated approaches a limit asymptotically. No specimen could be run to the complete exhaustion of hydrogen, although an attempt was made by heating at 800°C for approximately 20 hr. At the end of this time, appreciable quantities of hydrogen were still being evolved.

5. The major portion of the hydrogen available for release at 350°C in both steel and chromium-plated steel is liberated after approximately 80 min of heating.

Manuscript received April 11, 1955. This paper was prepared for delivery before the Boston Meeting, October 3 to 7, 1954.

Any discussion of this paper will appear in a Discussion Section to be published in the June 1957 Journal.

References

1. S. P. Makariewa and N. D. Birukoff, *Z. Elektrochem.*, **41**, 623, 838 (1935).
2. Guichard, Clausmann, Billon, and Lanthony, *Bull. Soc. chim.*, [5], **1**, 679 (1934).
3. C. A. Snavely and C. L. Faust, *This Journal*, **97**, 466 (1950).
4. C. A. Snavely, *Trans. Electrochem. Soc.*, **92**, 537 (1947).
5. A. G. Gaydon and R. W. B. Pearse, *Nature*, **140**, 110 (1937).
6. Z. Muro, *Oyo Butsuru (Japan)*, **21**, 321 (1952).
7. A. Brenner, P. Burkhead, and C. Jennings, *J. Research Nat. Bur. Standards*, **40**, 31 (1948).
8. A. H. Sully, "Chromium," Metallurgy of the Rarer Metals Series, Vol. I, Academic Press, New York (1954).
9. C. A. Zapffe and M. E. Haslem. *Trans. Am. Soc. Metals*, **39**, 241 (1947).

Formation of Composite Scales Consisting of Oxides of Different Metals

Carl Wagner

Department of Metallurgy, Massachusetts Institute of Technology, Cambridge, Massachusetts

Abstract

This paper presents a theoretical analysis of diffusion processes during the oxidation of an alloy when oxides of different alloying elements are formed concurrently. For idealized conditions it is possible to calculate the decrease in the oxidation rate which results from alloying a base metal, having a relatively high oxidation rate such as Cu or Fe, with less noble metals such as Al, Cr, or Be whose oxides form relatively slowly.

In a previous paper (1) it was shown that high temperature oxidation of an alloy consisting of metals A and B may result in the formation of only one oxide. In particular, on A-rich alloys only oxide AO may be formed, and on B-rich alloys only oxide BO may be formed. At intermediate compositions of the alloy, however, formation of only one oxide does not correspond to a stable state and, therefore, two oxides of different metals are formed simultaneously. Under these conditions, diffusion rates depend decisively on the spatial distribution of the two oxides in the scale. This distribution is not given *a priori* but is the result of simultaneous diffusion processes. In spite of this rather involved situation, a mathematical analysis is possible as is shown below.

Both oxides AO and BO are supposed to have a greater volume per gram-atom of metal than the alloy and to grow by outward migration of cations and electrons. It may be assumed that both oxides are nucleated initially at

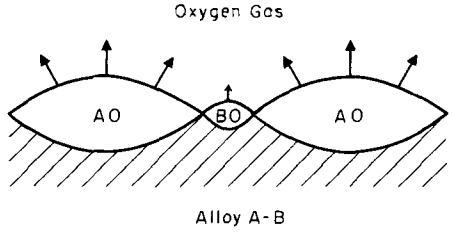

FIG. 1. Initial stage of oxidation of an alloy A-B

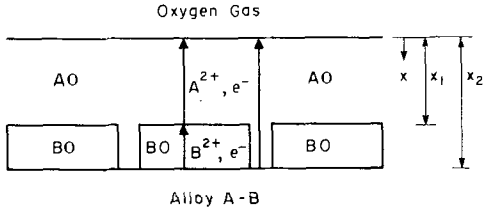

FIG. 2. Schematic cross section of the scale of an alloy A-B with an outer layer of oxide AO and an inner two-phase layer of oxides AO and BO. At the interface of oxides AO and BO, the displacement reaction

$$B^{2+} + 2e^- + AO = A^{2+} + 2e^- + BO$$

is supposed to take place so that oxide BO can grow, although it is not in contact with the oxidizing atmosphere.

different points of the surface of the alloy. Each oxide nucleus grows inward because it fills the space of the metal being oxidized; and grows outward because the volume of the oxide is supposed to be greater than the volume of the metal. If oxide AO grows faster than oxide BO as is shown schematically in Fig. 1, oxide AO will bury oxide BO after some time in the same way as markers of inert material are buried by oxide growing on a pure metal due to outward migration of cations and electrons (2, 3). The final pattern is shown schematically in Fig. 2. Rhines and Nelson (4) have shown that this pattern of a scale is found on Cu-Zn alloys and have discussed qualitatively the various diffusion processes involved. Such a configuration is essentially stable if metal B whose oxide has the lower growth rate has a higher affinity for oxygen than metal A. Although oxide BO is not in direct contact with atmospheric oxygen, oxide BO can continue to grow as is shown in Fig. 2. However, if metal B has a considerably lower affinity for oxygen than metal A, oxide BO is not stable when it is buried near the oxide-alloy interface where the oxygen activity is very low and the displacement reaction

$$BO + A \text{ (alloy)} = AO + B \text{ (alloy)}$$

may take place unless the concentration of A in the alloy is very low. Diffusion in a scale involving B-rich alloy as a second phase has been considered in another paper (5). Therefore, calculations in the present paper are confined to conditions shown in Fig. 2 where the buried oxide BO is stable. Exclusive diffusion control is assumed. Effects due to space charge layers are disregarded.

Mathematical Analysis

In view of the rather complex situation, it is advisable to introduce simplifying presuppositions.

First, if the molar volumes V_{AO} and V_{BO} of oxides AO and BO, respectively, are equal, the reaction at the BO-AO interface shown in Fig. 2 does not result in a volume change. Under these conditions, oxidation of a plane sample can proceed by virtue of diffusion and phase boundary reactions but without plastic flow of the alloy or the oxide. Therefore, assume that $V_{AO} = V_{BO}$ and plastic flow of each of the phases involved is negligible.

Second, although a protective oxide film is to be expected only if the volume of each of the oxides per gram-atom metal is greater than the molar volume V of the metal (6), in the following equations the limiting case that the volume ratio is equal to unity is assumed. Thus each volume element of the oxides and the alloy contains the same number of metal atoms and there is no expansion of a sample during oxidation.

The first condition, $V_{AO} = V_{BO}$ is essential for neglect of plastic flow. If $V_{AO} \neq V_{BO}$, additional equations accounting for plastic flow are needed. The second condition, $V = V_{AO} = V_{BO}$, however, is chosen only for the sake of mathematical simplification. If $V \neq V_{AO} = V_{BO}$, the following equations would not change basically but become only somewhat more involved.

Under the conditions assumed in Fig. 2, it is necessary to consider diffusion normal and parallel to the surface of the sample. To simplify calculations, it is assumed that the thickness of the two-phase layer is large in comparison to the dimensions of the particles of oxide BO and the width of the channels of oxide AO parallel to the surface of the sample. Hence, diffusion equations are formulated only in the direction normal to the surface and, therefore, correspond to a one-dimensional problem.

The diffusion rate in an individual phase may be expressed in terms of either a concentration or an activity gradient. In the region involving two oxides, it is convenient to use the activity of atomic oxygen, a, as the characteristic variable and to let $a = 1$ at the outer surface, $x = 0$, where the oxygen activity is determined by the oxidizing atmosphere.

x denotes the distance from the outer surface toward the interior of the sample, and x_1 and x_2, respectively, denote the locations of the outer and the inner boundary of the two-oxide region at a given time t (*see* Fig. 2).

Diffusion of cations in oxides may take place either by migration of interstitial ions or via vacancies. The concentration of such lattice defects has been found to be proportional to a fractional power of the oxygen partial pressure of a coexisting atmosphere (7). Consequently, it is assumed that the self-diffusion coefficients D_A and D_B of the metal ions in oxides AO and BO, respectively, as functions of the oxygen activity are given by

$$D_A = D_A{}^0 a^\alpha \quad [1]$$

$$D_B = D_B{}^0 a^\beta \quad [2]$$

where α and β are constants, which are positive for oxides involving a metal deficit and negative for oxides with metal excess, e.g., equal to about $-\frac{1}{2}$ for ZnO (8).

Moreover, predominant electronic conduction in the oxides AO and BO is assumed. Thus, transport rates of metals A and B in oxides AO and BO in the x-direction, j_A and j_B, respectively, in moles per unit total area per unit time are (9)

$$j_A = (1 - \psi)(D_A^0/V)a^\alpha \ (\partial \ln a/\partial x) + u(1 - \psi)/V \quad [3]$$

$$j_B = \psi(D_B^0/V)a^\beta \ (\partial \ln a/\partial x) + u\psi/V \quad [4]$$

where $u = dx_2/dt$ is the drift velocity of the oxides toward the bulk alloy due to the recession of the oxide-alloy interface and ψ is the volume fraction of oxide BO at distance x from the surface, which is supposed to be equal to the fraction of the cross section of oxide BO for transport in the x-direction.

Since the molar volumes of the oxides are assumed to be equal to the molar volume of the alloy and, therefore, the outer oxide surface remains at the position of the original surface of the alloy, there is no net transport of metal, i.e., the sum of the transport rates of A and B vanishes,

$$j_A + j_B = 0 \quad [5]$$

Substituting Eqs. [3] and [4] in Eq. [5], one obtains

$$u = dx_2/dt = -[(1 - \psi)D_A^0 a^\alpha + \psi D_B^0 a^\beta] \ (\partial \ln a/\partial x) \quad [6]$$

Since no special assumptions have been made, Eqs. [3] to [6] hold for the outer scale involving only oxide AO with $\psi = 0$, and for the inner scale involving oxides AO and BO with $\psi > 0$.

Substitution of Eq. [6] in Eq. [4] yields

$$j_B = -\psi(1 - \psi)[(D_A^0/V)a^\alpha - (D_B^0/V)a^\beta] \ (\partial \ln a/\partial x) \quad [7]$$

Solving Eq. [6] for $(\partial \ln a/\partial x)$ and substituting in Eq. [7]

$$j_B = \frac{\psi(1 - \psi)[D_A^0 a^\alpha - D_B^0 a^\beta]}{V[(1 - \psi)D_A^0 a^\alpha + \psi D_B^0 a^\beta]} \frac{dx_2}{dt} \quad [(8)]$$

The over-all concentration of B in the two-phase region II is equal to ψ/V. From the principle of the conservation of mass, it follows that the rate of change in the concentration of B is equal to the divergence of the transport rate. Thus

$$\partial(\psi/V)/\partial t = -\partial j_B/\partial x \quad [9]$$

Substitution of Eq. [8] in Eq. [9] yields

$$\frac{\partial \psi}{\partial t} = -\frac{dx_2}{dt}\frac{\partial}{\partial x}\left\{\frac{\psi(1 - \psi)[D_A^0 a^\alpha - D_B^0 a^\beta]}{(1 - \psi)D_A^0 a^\alpha + \psi D_B^0 a^\beta}\right\} \quad [10]$$

The rate of transport of B per unit area in the alloy is

$$j_B = -D\partial(N_B/V)/\partial x \quad [11]$$

where N_B is the local mole fraction of B in the alloy, and D is the interdiffusion coefficient in the alloy, which is supposed to be independent of concentration. Then Fick's second law reads

$$\partial N_B/\partial t = D(\partial^2 N_B/\partial x^2) \quad [12]$$

At the oxide-alloy interface, $x = x_2$, equilibrium between the two oxides AO and BO and the alloy is assumed and, therefore, the oxygen activity has a definite value a_2. Likewise, the mole fraction of B in the alloy has a definite value N_{B2}. Thus there are the boundary conditions

$$a = a_2 \text{ at } x = x_2 \quad [13]$$

$$N_B = N_{B2} \text{ at } x = x_2 \quad [14]$$

Integrating Eq. [6] with respect to x at constant time t between the limits $x = 0$, $a = 1$ and $x = x_1$, $a = a_1$ where only phase AO is present, i.e., $\psi = 0$,

$$D_A^0(1 - a_1^\alpha) = \alpha x_1(dx_2/dt) \quad [15]$$

At $x = x_1$, the over-all concentration of B changes discontinuously from 0 to ψ_1/V where ψ_1 is the volume fraction of oxide BO at the outer boundary of the two-oxide region. Since no oxide BO is present at $x < x_1$, only transport of B at $x > x_1$ is to be taken into account. From the principle of the conservation of mass, it follows that

$$-(\psi_1/V)(dx_1/dt) = -j_B(x = x_1 + \epsilon) \quad [16]$$

where ϵ denotes an infinitesimal positive value.

Substitution of Eq. [8] in Eq. [16] yields

$$\frac{dx_1}{dt} = \frac{(1 - \psi_1)(D_A^0 a_1^\alpha - D_B^0 a_1^\beta)}{(1 - \psi_1)D_A^0 a_1^\alpha + \psi_1 D_B^0 a_1^\beta}\frac{dx_2}{dt} \quad [17]$$

The over-all concentration of B also changes quasi-discontinuously at $x = x_2$. From the principle of the conservation of mass it follows that

$$\left[\frac{\psi(x = x_2 - \epsilon)}{V} - \frac{N_B(x = x_2 + \epsilon)}{V}\right]\frac{dx_2}{dt} = j_B(x = x_2 - \epsilon) - j_B(x = x_2 + \epsilon) \quad [18]$$

Substitution of Eqs. [8], [11], and [14] in Eq. [18] yields

$$[\psi_2 - N_{B2}](dx_2/dt) = \frac{\psi_2(1 - \psi_2)(D_A^0 a_2^\alpha - D_B^0 a_2^\beta)}{(1 - \psi_2)D_A^0 a_2^\alpha + \psi_2 D_B^0 a_2^\beta}\frac{dx_2}{dt} + D(\partial N_B/\partial x)_{x=x_2+\epsilon} \quad [19]$$

where ψ_2 is the volume fraction of oxide BO at the end of the two-oxide region II ($x = x_2$).

The alloy is supposed to have initially a uniform composition corresponding to the mole fraction N_B^0. Since diffusion into a semi-infinite space with time-independent conditions at the outer surface is considered, it may be assumed that solutions of the foregoing partial differential Eqs. [10] and [12] involve only the combination $x/t^{\frac{1}{2}}$ of the independent variables x and t. Consequently, the dimensionless variable is introduced

$$z = x/2(D_A^0 t)^{\frac{1}{2}} \quad [20]$$

and the constant parameters

$$z_1 = x_1/2(D_A^0 t)^{\frac{1}{2}} \quad [21]$$

$$z_2 = x_2/2(D_A^0 t)^{\frac{1}{2}} \quad [22]$$

In addition,

$$\gamma = \beta - \alpha \quad [23]$$

and introduce the symbols q and r for the ratio of the diffusion coefficients,

$$q = D_B^0/D_A^0 \quad [24]$$

$$r = D/D_A^0 \quad [25]$$

For the mole fraction of B in the alloy, use is made of the particular solution

$$N_B = N_B^0 + C \operatorname{erfc}[x/2(Dt)^{\frac{1}{2}}] \quad [26]$$

which involves the constant C eliminated below and satisfies Eq. [12] and the initial condition $N_B = N_B^0$. Upon substitution of Eqs. [20] and [25], Eq. [26] becomes

$$N_B = N_B^0 + C \operatorname{erfc}(z/r^{\frac{1}{2}}) \quad [27]$$

In view of Eqs. [14] and [22], Eq. [27] may be rewritten as

$$N_B = N_B^0 + (N_{B2} - N_B^0) \operatorname{erfc}(z/r^{\frac{1}{2}})/\operatorname{erfc}(z_2/r^{\frac{1}{2}}) \quad [28]$$

Upon substitution of Eqs. [20] to [25] and [28] in Eqs. [6], [10], [13], [15], [17], and [19] it follows that

$$2z_2 = -[(1 - \psi) + \psi q a^\gamma] a^\alpha (d\ln a/dz) \text{ at } z_1 \leqq z \leqq z_2 \quad [29]$$

$$z_2 \frac{d}{dz}\left[\frac{\psi(1-\psi)(1-qa^\gamma)}{(1-\psi)+\psi q a^\gamma}\right] - z(d\psi/dz) = 0 \quad \text{at } z_1 \leqq z \leqq z_2 \quad [30]$$

$$a = a_2 \text{ at } z = z_2 \quad [31]$$

$$1 - a_1^\alpha = 2\alpha z_1 z_2 \quad [32]$$

$$\frac{z_1}{z_2} = \frac{(1-\psi_1)(1-qa_1^\gamma)}{(1-\psi_1)+\psi_1 q a_1^\gamma} \quad [33]$$

$$z_2(\psi_2 - N_{B2}) = z_2 \frac{\psi_2(1-\psi_2)(1-qa_2^\gamma)}{(1-\psi_2)+\psi_2 q a_2^\gamma} - (N_{B2} - N_B^0)\frac{r^{1/2}}{\pi^{1/2}} \frac{\exp(-z_2^2/r)}{\operatorname{erfc}(z_2/r^{1/2})} \quad [34]$$

For the following discussion it is profitable to transform the two latter equations. Subtracting corresponding sides of Eq. [33] from unity, one obtains

$$\frac{z_2 - z_1}{z_2} = \frac{q a_1^\gamma}{1 - \psi_1 + \psi_1 q a_1^\gamma} \quad [35]$$

Eq. [34] may be rewritten as

$$\frac{(1 - \psi_2 + \psi_2 q a_2^\gamma)(N_B^0 - N_{B2})}{\psi_2 q a_2^\gamma (1 - N_{B2}) - N_{B2}(1 - \psi_2)} = F(z_2/r^{1/2}) \quad [36]$$

where $F(w)$ for w as general argument is defined as

$$F(w) = \pi^{\frac{1}{2}}\, w(1 - \operatorname{erf} w) \exp w^2 \quad [37]$$

For small and large arguments, respectively, the following approximations hold

$$F(w) \cong \pi^{\frac{1}{2}}\, w \text{ if } w \ll 1 \quad [38a]$$

$$F(w) \cong 1 - \tfrac{1}{2} w^{-2} \text{ if } w \gg 1 \quad [38b]$$

Eqs. [28] to [32], [35], and [36] are sufficient in order to calculate the constants z_1 and z_2, and both the oxygen activity a and the volume fraction ψ in the two-phase region as functions of z if the values of the parameters α, β, q, r, a_2, N_{B2}, and N_B^0 are given. The relatively large number of the parameters makes the discussion somewhat difficult but some general conclusions may be drawn.

Discussion

In view of practical situations, it is assumed that the absolute values of the standard free energies of formation of the oxides are much greater than RT and, therefore, the oxygen activity a_2 for coexistence of alloy, oxide AO, and oxide BO, is much smaller than the oxygen activity at the surface, i.e.,

$$a_2 \ll 1 \quad [39]$$

In addition, it is assumed that the difference of the absolute values of the standard free energies of formation of oxides BO and AO is much greater than RT and, therefore,

$$N_{B2} \ll 1 \quad [40]$$

In view of the latter condition, the oxidation rate of the alloy changes gradually from a high value characteristic of pure metal A to a low value characteristic of pure metal B at fairly low concentrations of B in the alloy as is shown below.

Throughout the following discussion, it is assumed that oxide AO involves a metal deficit and, therefore, α is positive. This is true, e.g., for Fe, Ni, and Cu.

If $r \gg 1$, i.e., $D \gg D_A^0$, concentration differences in the alloy are very small as has been discussed previously (1). Thus the composition of the alloy at the alloy-oxide interface is virtually equal to the bulk composition. In essence, only oxide AO is formed if $N_B^0 < N_{B2}$, and, conversely, only oxide BO is formed if $N_B^0 > N_{B2}$.

On the other hand, if $r \ll 1$, a two-oxide scale is expected in a certain range of alloy composition. For the following discussion one assumes, therefore, $r \ll 1$.

A particularly simple case occurs if both oxide AO and oxide BO have a metal deficit and $\alpha = \beta$, i.e.,

$$\gamma = 0 \quad [41]$$

Since it has been assumed above that oxide AO grows much faster than oxide BO, D_A^0 must be much greater than D_B^0 if $\alpha = \beta$, i.e., in view of Eq. [24],

$$q \ll 1 \quad [42]$$

Upon substitution of Eq. [41] in Eq. [30], it follows that the volume fraction of oxide BO in the two-phase region is independent of x,

$$\psi = \psi_1 = \psi_2 \text{ at } z_1 < z < z_2 \quad [43]$$

In view of Eqs. [41] and [43], integration of Eq. [29] between $z = z_1$ and $z = z_2$ yields

$$2\alpha z_2(z_2 - z_1) = (1 - \psi_1 + q\psi_1)(a_1^\alpha - a_2\alpha) \quad [44]$$

If $\gamma = 0$, Eq. [35] becomes

$$(z_2 - z_1)/z_2 = q/(1 - \psi_1 + q\psi_1) \quad [45]$$

Multiplying corresponding sides of Eq. [44] and Eq. [45], one obtains

$$2\alpha(z_2 - z_1)^2 = q(a_1^\alpha - a_2^\alpha) \quad [46]$$

Substituting Eqs. [41] and [43] in Eq. [36] and solving for ψ_1, one obtains

$$\psi_1 = \frac{N_B^0 - N_{B2}[1 - F(z_2/r^{1/2})]}{(N_B^0 - N_{B2})(1-q) + [q + N_{B2}(1-q)]F(z_2/r^{1/2})} \quad [47]$$

Thus for $\alpha = \beta$, the problem has been reduced to a calculation of the four unknowns ψ_1, a_1, z_1, and z_2 from Eqs. [32], [44], [46], and [47].

The general characteristics of the problem may be obtained from a discussion of the behavior of alloys with gradually increasing concentrations of B.

1. For pure metal A, there is only formation of AO and,

therefore, $z_1 = z_2$, $a_1 = a_2$. For $\alpha > 0$ it follows from Eqs. [32] and [39] that

$$z_1 = z_2 \cong (2\alpha)^{-\frac{1}{2}} \quad [48]$$

2. A-B alloys involving small concentrations of B below a certain limit N_B' also yield only oxide AO according to previous calculations (1). Component B is enriched at the alloy-AO interface and diffuses backward at a sufficient rate so that the concentration of B at the alloy-AO interface does not reach the concentration N_{B2} at which alloy, oxide AO, and oxide BO coexist. The maximum concentration N_B' of the alloy at which only oxide AO is formed is obtained from Eq. [47] with $\psi_1 = 0$ and $N_B^0 = N_B'$. In view of Eqs. [48] and [38b] it follows from Eq. [47] that

$$N_B' = N_{B2}\{1 - F[(2\alpha r)^{-1/2}]\} \cong \alpha r N_{B2} \quad [49]$$

3. If the concentration of B in the alloy exceeds the concentration N_B', both oxides AO and BO are formed simultaneously, but a small excess of B will change conditions for diffusion of A only slightly. Therefore, if $N_B^0 \gtrsim N_B'$, one may still use the approximation

$$z_1 \cong z_2 \cong (2\alpha)^{-\frac{1}{2}} \quad [50]$$

Substituting Eqs. [38b] and [50] in Eq. [47],

$$\psi_1 = \frac{N_B^0 - \alpha r N_{B2}}{N_B^0 + q - N_B^0 q - \alpha r(N_{B2} + q - N_{B2}\, q)} \quad [51]$$

If $N_B^0 \ll 1$, $q \ll 1$, and $r \ll 1$, the terms $N_B^0 q$ and $N_{B2} q$ in the denominator of Eq. [51] can be neglected and, therefore, Eq. [51] becomes

$$\psi_1 \cong \frac{N_B^0 - \alpha r N_{B2}}{N_B^0 + q - \alpha r(N_{B2} + q)} \cong \frac{N_B^0 - \alpha r N_{B2}}{N_B^0 + q - \alpha r N_{B2}} \quad [52]$$

4. If the concentration of B in the alloy is further increased, the volume fraction of BO will increase. Accordingly, the available cross section for diffusion of A in AO within the two-phase region will decrease, and thereby the growth rate of the AO layer will decrease.

If $N_B^0 < N_{B2}$, i.e., if the concentration of B at the alloy-oxide interface is higher than in the bulk alloy, only a certain fraction of B present in the original alloy is oxidized, whereas another fraction of B diffuses backward from the alloy-oxide interface toward the bulk alloy.

On the other hand, if $N_B^0 > N_{B2}$, conditions are reversed, i.e., B diffuses from the bulk alloy toward the alloy-oxide interface and, therefore, the relative amount of B in the scale is greater than in the original alloy. The excess of B in the scale, however, is small if the over-all oxidation rate of the alloy is of the same order of magnitude as that of pure metal A since diffusion in the alloy is assumed to be slow in comparison to diffusion of A in AO, i.e., $D \ll D_A^0$ or $r \ll 1$.

If the concentration of B remains below a certain limit calculated below in Eq. [62], there results the inequality

$$(2\alpha)^{\frac{1}{2}} > z_2 \gg r^{\frac{1}{2}} \quad [53]$$

where α is supposed to be of the order of unity, and r is much smaller than unity. Under these conditions, the argument of the function F in Eq. [47] is much greater than unity. Therefore, one may use the approximation $F(z_2/r^{\frac{1}{2}}) \cong 1$ according to Eq. [38b] in order to calculate ψ_1 from Eq. [47] if $N_B^0 \gtrsim N_{B2}$. Hence

$$\psi_1 \cong \frac{N_B^0}{q + N_B^0 - N_B^0 q} \quad [54]$$

As a further approximation,

$$\psi_1 \cong \frac{N_B^0}{q + N_B^0} \quad [55]$$

5. If $N_B^0 \gg q$, ψ_1 is close to unity, i.e., the two-phase region contains mostly BO and only a small amount of AO.

Upon substitution of Eq. [54] in Eq. [45], it follows that

$$z_2 - z_1 = (q + N_B^0 - N_B^0 q)\, z_2 \cong N_B^0 z_2 \text{ if } N_B^0 \gg q \quad [56]$$

Substitution of Eq. [56] in Eq. [46] yields

$$2\alpha(N_B^0 z_2)^2/q \cong a_1^{\alpha} - a_2^{\alpha} \text{ if } N_B^0 \gg q \quad [57]$$

For $N_B^0 \ll 1$, $q \ll 1$, and $z_2 - z_1 \ll z_2$ according to Eq. [56], Eq. [32] may be rewritten as

$$2\alpha z_2^2 \cong 1 - a_1^{\alpha} \quad [58]$$

Adding corresponding sides of Eq. [57] and [58], letting $1 - a_2^{\alpha} \cong 1$ in view of Eq. [39], and solving for z_2, one obtains

$$z_2 \cong \left[\frac{1}{2\alpha}\frac{q}{q + (N_B^0)^2}\right]^{1/2} \text{ if } N_B^0 \gg q \quad [59]$$

Substitution of Eq. [59] in Eq. [56] yields

$$z_2 - z_1 \cong \left[\frac{1}{2\alpha} \cdot \frac{q(N_B^0)^2}{q + (N_B^0)^2}\right]^{1/2} \text{ if } N_B^0 \gg q \quad [60]$$

The foregoing equations, in particular Eqs. [59] and [60], are only valid if the inequality in Eq. [53] holds.

Substituting Eq. [59] in Eq. [53], one obtains the limiting condition

$$N_B^0 \ll \{q[(2\alpha r)^{-1} - 1]\}^{\frac{1}{2}} \quad [61]$$

Since $\alpha \sim 1$ and $r \ll 1$, Eq. [61] may be rewritten as

$$N_B^0 \ll (q/2\alpha r)^{\frac{1}{2}} \quad [62]$$

The following special relations are noteworthy. If N_B^0 is much greater than $q^{\frac{1}{2}}$ but much smaller than $(q/2\alpha r)^{\frac{1}{2}}$, it follows from Eqs. [59] and [60] that

$$z_2 \cong (q/2\alpha)^{\frac{1}{2}}/N_B^0 \quad [63]$$

$$z_2 - z_1 \cong (q/2\alpha)^{\frac{1}{2}} \quad [64]$$

Thus the thickness $(x_2 - x_1)$ of the two-phase region, which is proportional to $(z_2 - z_1)$ according to Eqs. [21] and [22], tends to a limiting value corresponding to an oxygen activity of a_1 nearly equal to unity at the outer boundary of the two-phase region as follows by a comparison of Eqs. [46] and [64].

6. If the alloy concentration approaches the right-hand member in Eq. [62], N_B^0 is necessarily much greater than q, $\psi_1 \cong 1$ in view of Eq. [55], $a_1 \cong 1$, and Eq. [64] holds. Multiplying corresponding sides of Eqs. [44] and [47], letting $\psi_1 = 1$, $a_1 \cong 1$, and $a_2 \cong 0$, $1 - N_{B2} \cong 1$ and substituting Eq. [64], one obtains

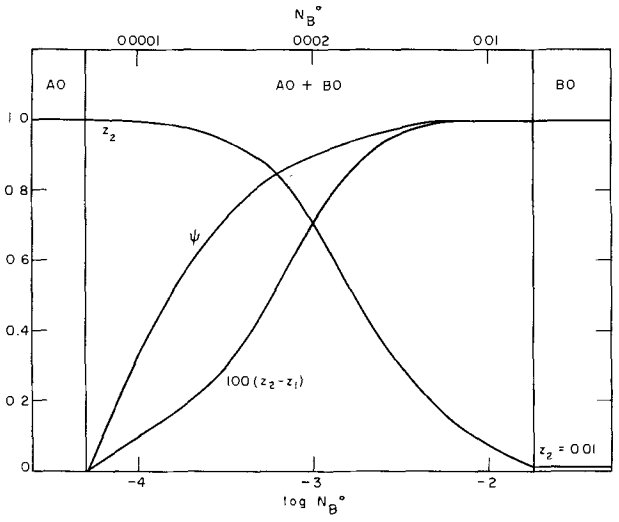

FIG. 3. Oxidation of an alloy A-B as a function of mole fraction N_B^0 for $N_{B2} = 10^{-3}$, $q = D/D_B^0 = 10^{-4}$, $r = D/D_A^0 = 10^{-2}$.

$z_2 = x_2/2(D_A^0 t)^{\frac{1}{2}}$, relative thickness of the entire scale;

$z_2 - z_1 = (x_2 - x_1)/2(D_A^0 t)^{\frac{1}{2}}$, relative thickness of the two-oxide region;

ψ: volume fraction of BO in the two-oxide region.

$$z_2(2\alpha/q)^{\frac{1}{2}}(N_B^0 - N_{B2}) = F(z_2/r^{\frac{1}{2}}) \quad [65]$$

Eq. [65] gives a relation between z_2 and alloy composition N_B^0, which may be evaluated by computing values of N_B^0 for appropriately chosen values of z_2. A limiting value N_B'' is reached if the thickness of the homogeneous AO layer approaches zero, i.e., if $z_1 = 0$, or $z_2 - z_1 = z_2$. Substituting Eq. [64] for $z_2 = z_2 - z_1$ in Eq. [65],

$$N_B'' = N_{B2} + F[(q/2\alpha r)^{\frac{1}{2}}] \text{ if } z_1 = 0 \quad [66]$$

In view of Eq. [38a], Eq. [66] may be rewritten as

$$N_B'' = N_{B2} + (\pi q/2\alpha r)^{\frac{1}{2}} \text{ if } z_1 = 0 \text{ and } (q/2\alpha r)^{\frac{1}{2}} \ll 1 \quad [67]$$

From Eq. [67] it follows that the minimum concentration for exclusive formation of BO is relatively low if $q \ll r$, i.e., in view of Eqs. [24] and [25], if

$$D \gg D_B^0 \quad [68]$$

7. If the alloy contains more B than the limiting concentration calculated in Eq. [67], only BO is formed.

Fig. 3 illustrates the dependence of the thickness of the scale, the thickness of the two-oxide region, and the volume fraction ψ on alloy composition for selected values of N_{B2}, q, and r.

CONCLUSIONS

In the literature, there are numerous investigations on the oxidation of alloys consisting of a base metal which oxidizes rather rapidly and alloying metals which are less noble and whose oxides form more slowly. In accordance with the foregoing analysis, it has been found that the oxide of the base metals appears preferably in the outer scale, and the oxide of the alloying element in the inner scale (10–17). Moreover, it has been found that the oxidation rate of base metals such as Fe and Cu is considerably decreased by the presence of small amounts of less noble elements such as Al, Cr, Si, and Be (10–21). So far, however, no observations are available to check quantitatively the theoretical calculations for the dependence of the oxidation rates on alloy composition.

Deviations are to be expected since, according to Pilling and Bedworth (22) and Dunn (23), alloys do not always follow the parabolic rate law even under conditions where the pure components obey the parabolic rate law. Observations on Cu-Al alloys by Dennison and Preece (15) are of particular interest. At 850°C, the initial oxidation rate of copper containing from 2–4 wt % Al is relatively high, although much lower than that of pure Cu. After 20 hr the oxidation rate decreases to virtually zero. During the initial stage, both Cu and Al are oxidized, as has also been found by Price and Thomas (19). Calculations based on Eq. [67] indicate that the aforementioned Al concentrations are much higher than the limiting value N_B'' for exclusive formation of Al_2O_3 (1). At present, details of the formation of a two-phase scale under these conditions are not understood. Formation of a two-phase scale on these alloys, however, seems to represent only a transient state. Finally, steady-state conditions presupposed in the foregoing analysis are presumably approached, i.e., a coherent layer of Al_2O_3 is formed. Slow attainment of steady-state conditions confines the applicability of the foregoing theoretical analysis but does not make it worthless. Oxidation rates calculated above may be considered as lower limiting values which are attainable either after long times or after appropriate pretreatment in order to shorten an induction period of rapid oxidation (19).

To obtain results which can be applied directly to practical situations, a more sophisticated approach seems to be needed with due regard to finite lateral dimensions of the grains of the constituent phases, diffusion normal and parallel to the surface of a sample, internal oxidation, and the occurrence of plastic deformation. The latter must definitely be taken into account if the condition $V_{AO} = V_{BO}$ is not satisfied as has been pointed out above.

If oxides of different metals have a noticeable mutual solubility, cations of metal A may also diffuse in oxide BO, and conversely. Moreover, mutual solubility of oxides of metals having different valences may change the number of lattice defects and thereby diffusion coefficients (24). On some alloys, ternary oxide phases such as $NiCr_2O_4$ are formed. Theoretical and experimental work on diffusion and lattice defects in ternary oxides is still almost completely missing but is prerequisite for a better understanding of the oxidation of such alloys.

It would be rather impractical to deal with all these problems in a "unified theory." Instead, it seems appropriate to consider relatively simple limiting cases. The choice of the special presuppositions introduced above is somewhat arbitrary. Its usefulness can be shown only by future experimental investigations on a variety of systems. None of these may satisfy all presuppositions, but deviations may be minor for some systems so that the foregoing considerations apply at least semiquantitatively.

ACKNOWLEDGMENT

This investigation was sponsored by Office of Ordnance Research under Contract DA-19-020-ORD-2244, Project TB2-0001 (779).

Manuscript received October 17, 1955.
Any discussion of this paper will appear in a Discussion Section to be published in the June 1947 JOURNAL.

REFERENCES

1. C. WAGNER, *This Journal*, **99**, 369 (1952).
2. L. B. PFEIL, *J. Iron Steel Inst.*, **119**, 501 (1929).
3. M. H. DAVIES, M. T. SIMNAD, AND C. E. BIRCHENALL, *Trans. Am. Inst. Mining Met. Engrs.*, **191**, 889 (1951).
4. F. N. RHINES AND B. J. NELSON, *ibid.*, **156**, 171 (1944).
5. C. WAGNER, *This Journal*, **103**, 571 (1956).
6. N. B. PILLING AND R. E. BEDWORTH, *J. Inst. Metals*, **29**, 529 (1923).
7. H. DÜNWALD AND C. WAGNER, *Z. physik. Chem.*, **B22**, 212 (1933); J. GUNDERMANN AND C. WAGNER, *ibid.*, **B37**, 155 (1937); C. WAGNER AND K. GRÜNEWALD, *ibid.*, **B40**, 455 (1938).
8. E. A. SECCO AND W. J. MOORE, *J. Chem. Phys.*, **23**, 1170 (1955).
9. C. WAGNER, "Diffusion and High Temperature Oxidation of Alloys" in "Atom Movements", p. 153, American Society for Metals, Cleveland (1951).
10. A. PORTEVIN, E. PRÉTET, AND H. JOLIVET, *Rev. mét.*, **31**, 101, 186, 219 (1934); *J. Iron Steel Inst.*, **130**, 219 (1934).
11. E. SCHEIL AND E. KIWIT, *Arch. Eisenhüttenw.*, **9**, 405 (1935/36).
12. E. SCHEIL, *Z. Metallkunde*, **29**, 209 (1937).
13. K. W. FROEHLICH, *ibid.*, **28**, 368 (1936).
14. A. PREECE AND G. LUCAS, *J. Inst. Metals*, **81**, 219 (1952/53).
15. J. P. DENNISON AND A. PREECE, *ibid.*, **81**, 229 (1952/53).
16. J. MOREAU, *Compt. rend.*, **236**, 85 (1952); *Publs. inst. recherches siderurg.*, **A49**, 7 (1953); J. MOREAU AND J. BÉNARD, *Compt. rend.*, **237**, 1417 (1953).
17. H. J. YEARIAN, "Investigations of the Oxidation of Chromium and Chromium-nickel Steels," Report Contract N7onr-39419 (1954).
18. E. SCHEIL AND E. H. SCHULZ, *Arch. Eisenhüttenw.*, **6**, 155 (1932/33).
19. L. E. PRICE AND G. J. THOMAS, *J. Inst. Metals*, **63**, 21, 29 (1938).
20. A. DES. BRASUNAS, J. T. GOW, AND O. E. HARDER, *Proc. Am. Soc. Testing Materials*, **46**, 870 (1946).
21. L. DE BROUCKÈRE AND L. HUBRECHT, *Bull. soc. chim. Belges*, **61**, 101 (1952); L. HUBRECHT, *ibid.*, **61**, 205 (1952).
22. N. B. PILLING AND R. E. BEDWORTH, *Ind. Eng. Chem.*, **17**, 372 (1925).
23. J. S. DUNN, *J. Inst. Metals*, **46**, 25 (1931).
24. C. WAGNER AND K. E. ZIMEN, *Acta Chem. Scand.*, **1**, 547 (1947); W. HIMMLER, *Z. physik. Chem.*, **195**, 129 (1950); K. HAUFFE AND C. GENSCH, *Z. physik. Chem.*, **195**, 116 (1950); C. GENSCH AND K. HAUFFE, *ibid.*, **195**, 386 (1950); **196**, 427 (1951); K. HAUFFE AND H. PFEIFFER, *Z. Elektrochem.*, **56**, 390 (1952); H. PFEIFFER AND K. HAUFFE, *Z. Metallkunde*, **43**, 364 (1952); K. HAUFFE, *Werkstoffe u. Korrosion*, **1**, 131, 221, 243 (1951); "The Mechanism of Oxidation of Metals and Alloys at High Temperatures" in "Progress in Metal Physics", edited by B. Chalmers, Vol. 4, p. 71 (1953)

Conductances of Some Acids, Bromides, and Picrates in Dimethylformamide at 25°C

PAUL G. SEARS, RICHARD K. WOLFORD, AND LYLE R. DAWSON

Department of Chemistry, University of Kentucky, Lexington, Kentucky

ABSTRACT

Conductances of five acids, three partially substituted ammonium salts, and three alkali metal and quaternary ammonium picrates in dimethylformamide have been investigated at 25° for solute concentrations in the range 1–50 × 10^{-4} N. Results indicate that dimethylformamide exhibits differentiating properties toward the acids and the partially substituted ammonium salts and also that the picrates are completely dissociated.

Previous studies which have been reported from this laboratory (1–3) indicate that dimethylformamide (DMF) is a potentially useful electrolytic solvent. Na, K, and quaternary ammonium salts have been found to be appreciably soluble and also apparently completely dissociated in dilute DMF solutions. The purpose of this study has been to examine the leveling or differentiating properties of DMF toward acids and some partially substituted ammonium salts and also to investigate the conductance behavior of several picrates.

EXPERIMENTAL

Commercial grade DMF which had been dried for several days over KOH pellets was fractionated at atmospheric pressure and then redistilled at 5 mm pressure. The middle fractions which were retained had conductivities of 2 × 10^{-7} ohm^{-1} cm^{-1} or less.

Picric acid ('Baker Analyzed' Reagent) was recrystallized three times from ethanol. From this acid, K, Na, triethylammonium and tetramethylammonium picrates were synthesized by reacting with the proper base. Each product was recrystallized several times from water-ethanol mixtures.

HBr was prepared by dropping Br_2 into tetrahydronaphthalene. The evolved gas was passed through three towers containing tetrahydronaphthalene in order to remove any gaseous Br which may have been carried from the reaction flask into the gas stream.

Reagent grade glacial acetic acid was distilled at atmospheric pressure and a small middle fraction was retained.

TABLE I. *Equivalent conductances of some electrolytes in dimethylformamide at 25°C*

$C \times 10^4$	Λ	$C \times 10^4$	Λ	$C \times 10^4$	Λ
(*a*) Picric acid		(*e*) Acetic acid		(*i*) Monoethylammonium bromide	
2.326	69.39	1.751	24.73	2.593	87.00
3.852	68.56	3.744	19.20	4.380	85.16
6.111	67.65	5.871	16.39	7.411	82.28
8.978	66.79	9.544	13.67	13.63	77.55
16.65	65.05	14.91	11.48	18.92	74.05
18.29	64.76	20.35	10.08	37.07	66.56
		41.56	7.34		
(*b*) Hydrobromic acid		(*f*) Potassium picrate		(*j*) Triethylammonium bromide	
0.7748	86.69	1.468	66.81	0.8966	85.68
1.133	86.18	3.104	66.11	2.245	82.32
3.048	84.02	6.689	65.02	4.163	78.50
6.300	82.13	9.910	64.27	6.741	74.54
10.08	80.51	13.94	63.54	10.43	70.06
14.76	78.12	19.00	62.74	16.29	64.76
		34.61	60.91		
(*c*) Trichloroacetic acid		(*g*) Sodium picrate		(*k*) Triethylammonium picrate	
0.8852	33.33	1.172	65.84	0.8069	71.59
2.753	23.65	2.373	65.11	2.085	70.89
6.167	20.46	4.762	64.15	3.609	70.32
10.06	19.96	6.967	63.53	5.920	69.59
14.21	19.74	12.18	62.36	14.35	67.73
22.99	19.28	23.81	60.60	22.58	66.87
(*d*) Hydrochloric acid		(*h*) Tetramethylammonium picrate			
1.568	72.07	0.6171	75.29		
2.979	59.01	1.920	74.48		
4.829	49.93	3.308	73.82		
7.240	42.94	5.468	72.91		
12.78	34.35	9.118	72.15		
20.98	28.16	14.59	71.05		
44.17	20.74				

Trichloroacetic acid (Eastman White Label) was fractionated also at atmospheric pressure. The middle fraction which boiled at 194°–195° was retained.

Triethylammonium and monoethylammonium bromides (Fisher Reagent) were recrystallized three times from ethanol.

Prior to using, all salts were dried to constant weight in a vacuum oven. Approximately 0.01*N* stock solutions were prepared on a weight basis and all other solutions were prepared from these by a weight-addition technique. Transfers were made in a dry box under a positive pressure of nitrogen. All weights were corrected to vacuum. In converting concentrations from a weight basis to a volume basis, it was assumed that densities of the solutions were equal to that of DMF at 25°C. Conductivity of an electrolyte was obtained by subtracting the conductivity of the solvent from that of the solution.

The bridge assembly, conductance cells, constant temperature bath, and other aspects of the experimental procedure have been described previously (1, 2).

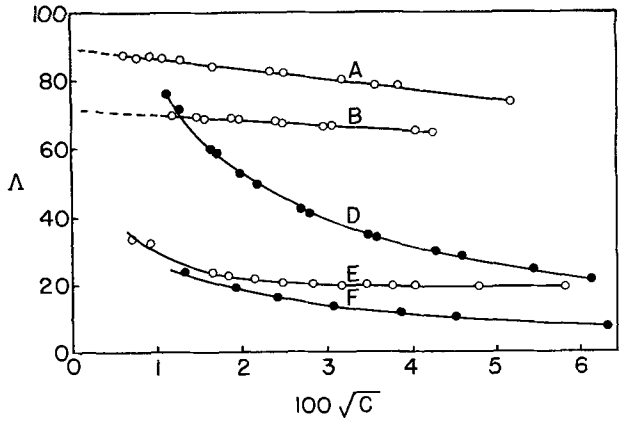

FIG. 1. Kohlrausch plots for some acids in dimethylformamide. A—HBr; B—HPi; D—HCl; E—CCl_3COOH; F—CH_3COOH.

TABLE II. *Data pertinent to experimental and theoretical slopes of Kohlrausch plots for some electrolytes in DMF*

Electrolyte	Experimental slope (S_E)	Theoretical slope (S_T)	$\frac{S_E - S_T}{S_T\ 100}$
HBr	−313	−163	91
HPi*	−169	−151	12
Et_3NHBr	−672	−165	308
Et_3NHPi	−128	−151	−16
$EtNH_3Br$	−478	−167	186
Me_4NPi	−138	−154	−10
NaPi	−133	−145	−9
KPi	−130	−148	−12

* Pi is symbol used for picrate.

The following data for DMF at 25°C were used in the calculations: density, 0.9443 g/ml; viscosity, 0.00796 poise; dielectric constant, 36.71 (4). Values of the fundamental constants which were used in the evaluation of the Onsager constants were taken from a recent report of the Subcommittee on Fundamental Constants (5).

RESULTS

Corresponding values of the equivalent conductance, Λ, and the concentration in gram equivalents of solute per liter of solution, *C*, for each salt are presented in Table I. Confirmatory data for another series of solutions for each electrolyte have been omitted from Table I for conciseness. In each case, however, results for the two series of solutions agreed within an estimated error of 0.2%.

DISCUSSION

Plots of the equivalent conductances of several acids in DMF as a function of the square root of the concentration are shown in Fig. 1. Those for acetic and trichloroacetic acids in DMF are similar to plots which are characteristic of weak electrolytes in water. Nevertheless, the nature of the two plots indicates that the greater electronegativity or electron-attracting property of the chlorine atoms enhances the dissociation of trichloroacetic acid at comparable concentrations. The plot for HCl, which is shown as curve *D* in Fig. 1, is characteristic of an incompletely dissociated electrolyte. Owing to the impossibility of establishing accurate values of the limiting equivalent conduct-

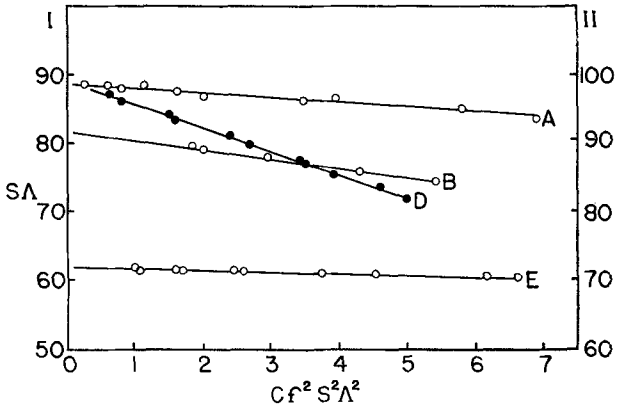

FIG. 2. Fuoss-Shedlovsky plots for some electrolytes in dimethylformamide. Ordinate I: A, HBr; D, Et_3NHBr; ordinate II: B, $EtNH_3Br$; E, HPi.

TABLE III. *Limiting equivalent conductances and dissociation constants for some electrolytes in DMF obtained by the Fuoss-Shedlovsky method*

Electrolyte	Λ_0	$K \times 10^3$
HBr	88.7	17
HPi	71.7	63
Et_3NHBr	89.1	3
$EtNH_3Br$	91.8	8

ances of acetic, trichloroacetic, and hydrochloric acids, no further treatment of the data was attempted.

In contrast to the behavior of the three acids which have been mentioned above, HBr and $C_6H_3O_7N_3$ (2,4,6-trinitrophenol) in DMF are characterized by linear Kohlrausch plots and are more completely dissociated. The weakening of the bond due to the increased size of the nonmetal atom more than compensates for the decrease in ionic character and gives corresponding greater acidity in DMF to HBr than to HCl. Hantzsch and Caldwell (6) and Kolthoff and Willman (7) have observed the same relative behavior for these acids in pyridine and acetic acid, respectively.

Data pertinent to the comparison of the experimental and the theoretical slopes of the plots of Λ vs. $\sqrt{C}$ for HBr and $C_6H_3O_7N_3$ and some other electrolytes are presented in Table II. The experimental slopes of the plots for the acids and the partially substituted ammonium bromides are numerically greater than the corresponding slopes calculated using the Onsager equation (8). Inasmuch as this behavior is usually typical of incomplete dissociation, data for these electrolytes were analyzed by the Fuoss-Shedlovsky method (9) (*see* Fig. 2). The resulting values of the dissociation constants and the limiting equivalent conductances are given in Table III.

It is interesting to note that the results provide evidence that $C_6H_3O_7N_3$ is stronger than HBr in DMF. The reversal of the dissociation constants for these two acids in water and in DMF probably can be attributed primarily to the bromide ion being relatively less solvated in DMF than in water whereas the picrate ion can be assumed to be a large unsolvated ion in both solvents. If this were the case, the bromide ions with their relatively smaller size and greater charge density may be sufficiently more susceptible

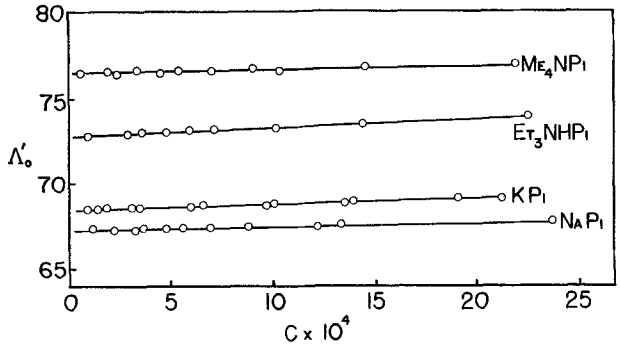

FIG. 3. Plots of Shedlovsky equation for some picrates in dimethylformamide.

TABLE IV. *Data obtained from plots of the Shedlovsky equation for some electrolytes in DMF*

Electrolyte	Λ_0	$B \times 10^2$
NaPi	67.3	1.5
KPi	68.5	3.0
Me_4NPi	76.4	1.9
Et_3NHPi	72.8	4.5

than picrate ions to ion-pair formation with solvated protons in DMF to reduce the degree of dissociation of HBr below that of $C_6H_3O_7N_3$. Although the results indicate that it is less dissociated, HBr may be more ionized than $C_6H_3O_7N_3$ in DMF.

Like other strictly electron-donor solvents such as acetone, methyl ethyl ketone, acetonitrile, nitrobenzene, and nitromethane (10–13), DMF exhibits differentiating properties toward partially substituted ammonium salts. Wynne-Jones (12) has made a reasonable postulation that these substances are partially covalent in nature and that in solution there exists an equilibrium between ions and un-ionized molecules formed through hydrogen bonding. Data in the literature concerning the conductances of partially substituted ammonium salts in electron-donor solvents show that picrates generally are more dissociated than bromides which, in turn, are much more dissociated than chlorides. The authors' results agree with this generalization inasmuch as monoethylammonium and triethylammonium bromides have dissociation constants of 8×10^{-3} and 3×10^{-3}, respectively, and triethylammonium picrate is dissociated completely in DMF. In most electron-donor solvents the partially substituted ammonium picrates are incompletely dissociated also; however, triethylammonium picrate is dissociated completely in acetonitrile as it is in DMF.

Slopes of the Kohlrausch plots for some of the electrolytes were found to be numerically less than the calculated Onsager slopes (*see* Table II). Data for these completely dissociated electrolytes were analyzed using the Shedlovsky equation (14) which may be written as follows:

$$\Lambda_0' \equiv \frac{\Lambda + \beta\sqrt{C}}{1 - \alpha\sqrt{C}}\Lambda_0 + BC$$

The results are presented in Fig. 3 and in Table IV. The behavior of the picrates is very similar to that of the perchlorates and iodides in DMF (1, 2).

Utilizing data in this and earlier papers (1–3), the following series of decreasing relative cationic conductances in DMF may be established:

$$Me_4N^+ > EtNH_3^+ > Et_4N^+ > Et_3NH^+ > DMF \cdot H^+ > Me_3PhN^+ > K^+ > Na^+ > Pr_4N^+ > Bu_4N^+$$

Inasmuch as the cationic conductance is related inversely to the effective cationic size, this series suggests that several of the cations are solvated probably through hydrogen bonding or ion-dipole attraction or both.

Manuscript received January 25, 1956. The paper was taken from a thesis submitted by R. K. Wolford in partial fulfilment of the requirements for the M.S. degree. University of Kentucky, Lexington, Ky. The work was supported in part by a contract with the U. S. Army Signal Corps.

Any discussion of this paper will appear in a Discussion Section to be published in the June 1957 JOURNAL.

REFERENCES

1. D. P. AMES AND P. G. SEARS, *J. Phys. Chem.*, **59,** 16 (1955).
2. P. G. SEARS, E. D. WILHOIT, AND L. R. DAWSON, *ibid.*, **59,** 373 (1955).
3. P. G. SEARS, E. D. WILHOIT, AND L. R. DAWSON, *J. Chem. Phys.*, **23,** 1274 (1955).
4. G. R. LEADER AND J. F. GORMLEY, *J. Am. Chem. Soc.*, **73,** 5731 (1951).
5. F. D. ROSSINI, F. T. GUCKER, JR., H. L. JOHNSTON, L. PAULING, AND G. W. VINAL, *ibid.*, **74,** 2699 (1952).
6. A. HANTZSCH AND K. S. CALDWELL, *Z. physik. Chem.*, **61,** 227 (1908).
7. I. M. KOLTHOFF AND A. WILLMAN, *J. Am. Chem. Soc.*, **56,** 1007 (1934).
8. L. ONSAGER, *Physik. Z.*, **28,** 277 (1927).
9. R. M. FUOSS AND T. SHEDLOVSKY, *J. Am. Chem. Soc.*, **71,** 1496 (1949).
10. P. WALDEN AND E. J. BIRR, *Z. physik. Chem.*, **144,** 269 (1929); **153,** 1 (1931); **163,** 263, 281 (1933).
11. D. M. MURRAY-RUST, O. GATTY, W. A. MACFARLANE, AND H. HARTLEY, *Ann. Repts. Progr. Chem. (Chem. Soc. London)*, **27,** 342 (1930).
12. W. F. K. WYNNE-JONES, *J. Chem. Soc.*, **1931,** 795.
13. S. GLASSTONE, "The Electrochemistry of Solutions," pp. 172–177, D. Van Nostrand Co., Inc., New York (1937).
14. T. SHEDLOVSKY, *J. Am. Chem. Soc.*, **54,** 1405 (1932).

JUNE 1957 DISCUSSION SECTION

A Discussion Section, covering papers published in the July–December 1956 JOURNALS, is scheduled for publication in the June 1957 issue. Any discussion which did not reach the Editor in time for inclusion in the December 1956 Discussion Section will be included in the June 1957 issue. Those who plan to contribute remarks for this Discussion Section should submit their comments or questions in triplicate to the Managing Editor of the JOURNAL, 216 W. 102nd St., New York 25, N. Y., *not later than March 1, 1957.* All discussions will be forwarded to the author, or authors, for reply before being printed in the JOURNAL.

Technical Review

Rectifying Semiconductor Contacts

H. K. Henisch[1]

Research Laboratories, Sylvania Electric Products Inc., Bayside, New York

The behavior of rectifying contacts between metals and semiconductors constitutes a topic of major interest in the semiconductor field from theoretical as well as practical points of view. The literature of the subject contains well over a thousand publications, and it is now desirable to review the extent of knowledge and to discriminate between contributions which add to operational understanding and those which add only ingenious algebra. The present review is intended for readers who have not made the study of contacts their special field, but who would like to be acquainted with the present state of the art.

Barrier Concepts

The aim of this paper is the understanding of the behavior of single contacts as such, whereas practical systems nearly always include two contacts and some bulk material as well. There is a well-known method of separating these components, as illustrated on Fig. 1. By means of potential probe measurements, it is possible to determine the voltage distribution across the system for various currents. Accordingly, one can also distinguish (semi-quantitatively) between high resistance and low resistance contacts. Very little is known about the latter and the present review is therefore restricted to high resistance contacts. The probe measurements generally indicate a voltage step at the contact and it was soon realized that this voltage must exist across some definite layer of material, however thin. This is called the barrier layer. Its identification and characterization occupied many years of research. It was not found possible to identify the layer as a distinct new phase and this gave rise to the concept of a potential barrier, i.e., a region of high electrical potential for the charge carriers concerned. The high energy required for transmission of carriers across the region accounts for the high contact resistance, and the asymmetrical deformation of the barrier under the influence of an externally applied voltage is responsible for rectification. These simple concepts have survived numerous changes in the theoretical outlook on contacts and may thus be regarded as reassuringly stable. Geometrical features, e.g., the point-contact configuration, were at one time regarded as essential requirements of rectification, but are now known to play only a secondary role. They can enhance the effective rectification ratio, but are not themselves responsible for asymmetric conduction. Similarly, heating effects at contacts can be responsible for symmetrical nonlinearities of the voltage-current relation, but not for rectification as such. Fig. 1 shows that the achievement of pronounced rectification depends on eliminating as much bulk material as possible and on emphasizing electrical and structural differences between the two end contacts. This is the aim of the sophisticated manufacturing processes now in use, most of which have been developed by empirical methods.

Conditions encountered in practice are more complicated than Fig. 1 suggests. When a voltage is applied to a rectifier assembly, the current is not constant, but is generally a function of time. This is referred to as current creep and distinction is made between positive creep (corresponding to an increase of current with time) and negative creep (corresponding to a decrease of current). It follows that the voltage-current relation is not uniquely defined, except in operational terms. By using short voltage pulses instead of constant applied voltages, the processes which involve longer time constants can be rendered inoperative. On the other hand, electronic quasi-equilibrium is not necessarily established during short pulses; this may lead to a new difficulty in the interpretation of experimental results.

Contacts on Transistor Materials

Since potential probes always occupy some space, the experiment illustrated on Fig. 1 involves an extrapolation. To determine the voltage across the contact itself, one assumes that the bulk material is electrically homogeneous to within the immediate neighborhood of the barrier layer itself. This extrapolation is permissible as long as the bulk material remains unaffected by the current flowing. However, many types of contacts on transistor materials support the well-known process of carrier injection which is responsible for the appearance of additional charge carriers in the neighborhood of a contact passing a forward current. These additional carriers alter the electrical properties of the material and the above extrapolation is then no longer meaningful. Under these conditions, it is no longer helpful to regard the contact as being in any important sense "in series connection" with the bulk material. Instead, the system must be studied as a whole, the contact being regarded as the location in which the additional carriers originate, and the bulk material as the location in which they decay. One may thus distinguish between theoretical approaches to contacts on transistor specimens and on other (nontransistor) specimens. The distinction is above all a matter of degree and must be handled with care. Methods of detecting injection (and, indeed, various other effects, like exclusion, extraction, and accumulation) are of limited sensitivity, and it is

[1] On leave of absence from the University of Reading, Berks, England.

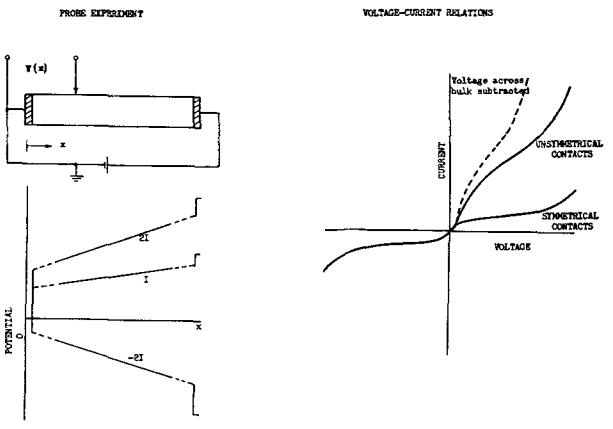

FIG. 1. Principle of contact rectification

therefore impossible to assert with complete confidence that any particular contact is definitely noninjecting.

NATURE OF THE BARRIER LAYER

Potential barriers of the kind referred to above can be envisaged as arising in many different heights and shapes, and it is plausible that the most important single parameter in this context is the barrier height. Many detailed theories are available which concern themselves with the effect of various barrier shapes on the voltage-current relation of the contact, but the models on which such theories are based can seldom be established by independent means. One learns about contact structure through experiments on contact behavior and alters the models to reach agreement with experimental results. Quite generally, modifications of the barrier height provide more sensitive corrections than almost any other modification of the theoretical model. The barrier height and its changes under the influence of the applied voltage are therefore our principal concern.

A barrier of the kind envisaged here can in principle arise from one of three causes: (*a*) because the semiconductor and the metal have different thermionic work-functions, (*b*) because the semiconductor surface is characterized by so-called surface states, and (*c*) because there is a thin foreign layer between the metal and the semiconductor which, in turn, involves contacts with barriers by way of mechanisms (*a*) or (*b*). Such a layer is called an artificial barrier layer. Thermionic work functions were given great prominence in theoretical treatments before the formulation of Bardeen's theory of surface states in 1947. There are few well-authenticated cases (although there appear to be some) in which thermionic work functions have been demonstrated definitely to play an important role, whereas there are many in which they have been shown to be irrelevant in practice. In view of this, most present-day theoretical accounts are based on models involving barriers arising from surface states. There is little systematic knowledge of the behavior of thin foreign layers at the interface, and models for barriers arising in this way have too many arbitrary features to make discussion desirable here. In any case, it is firmly established that distinct macroscopic foreign layers are not an essential requirement for rectification.

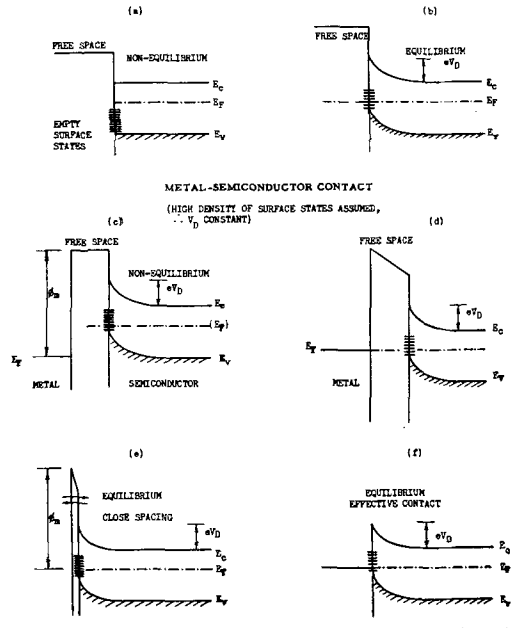

FIG. 2. Formation of surface and contact barriers in the presence of surface states.

The manner in which surface states, even in the absence of a metallic contact, can lead to the formation of a potential barrier is shown on Fig. 2 (*a*) and Fig. 2 (*b*). Use is made of the band structure model, subject to the additional and somewhat arbitrary hypothesis that the band structure which is characteristic of the material in bulk also applies in the immediate vicinity of the surface. Surface states are localized electronic states which are permitted within the otherwise forbidden band, and at least some of which are empty when the surface is neutral. When equilibrium is established these states become filled or partially filled; this gives the surface a negative charge. The corresponding positive charge of the double layer produced in this way resides primarily in the impurity centers of the semiconductor within a narrow region which, in fact, constitutes the barrier layer. The surface states thus act as one electrode of a capacitor and the adjoining semiconductor region acts partly as the other electrode and partly as the dielectric. A pictorial way to express the action of surface states is to consider that the semiconductor is covered by a two-dimensional metallic shield. If the density of surface states is large enough, the barrier layer is screened by this shield from all external electrostatic influences and thus is independent of the external contact material and its thermionic work function. Diagrams (*c*) to (*f*) of Fig. 2 illustrate the energetic conditions at and near the interface when a contact is established. The closest spacing between metal and semiconductor considered here is of the order of an interatomic spacing, as in (*e*). The thin part of the potential barrier which arises under these conditions can be neglected, since it can be shown to be transparent to electrons. It is therefore omitted on (*f*) which represents the essential features of the barrier when in equilibrium.

The barrier profiles of Fig. 2 are known as Schottky barriers and are based on an important simplification, already recognized by Schottky. These energy profiles

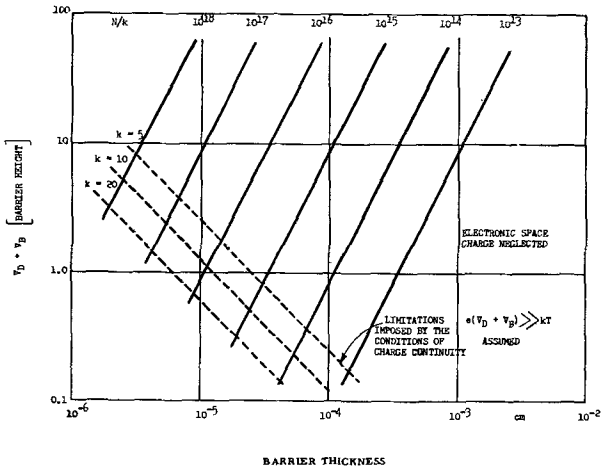

FIG. 3. Properties of a Schottky barrier

imply a continuous space charge, whereas any charge residing in discrete impurity centers must be discontinuous. The assumption of continuity is permissible as an approximation as long as the impurity centers are relatively closely spaced. It is not permissible when the thickness of the barrier layer extends over only a few inter-center distances. This limits the validity of theories based on the traditional profile of the Schottky barrier. Fig. 3 illustrates this limitation for various barrier heights, impurity contents, and dielectric constants. In this case the limitation has been based on the somewhat arbitrary but perhaps still plausible assumption that the barrier layer must be at least five times as thick as the inter-center distance, if the assumption of continuity is to be at all applicable. Some cases of considerable practical importance must be excluded from the simplified treatment under this heading. Satisfactory theories of discontinuous space-charge layers are difficult to formulate in view of the random distribution of impurity centers.

Charge Transport across a Barrier

The most general rectification theory would deal with the transport of both types of charge carriers (electrons and holes) through a contact on near-intrinsic semiconducting material of high carrier lifetime. The corresponding equations are those for the electron and hole flow, Poisson's equation, and the corresponding boundary conditions. They can be formulated without difficulty, but explicit solutions are not available. Simplifying assumptions must always be introduced and these may or may not be applicable to particular cases encountered in practice. The coarsest simplification is to assume that the current is carried either wholly by majority or wholly by minority carriers. The practical case in which holes and electrons participate in an arbitrary ratio has not yet been satisfactorily solved. In the remainder of this section only unipolar rectification is considered and the assumption is made that charge carriers are electrons in extrinsic n-type material.

There are two ways in which electrons can, in principle, move from one side of a potential barrier to the other: they can tunnel through the barrier (wave-mechanical tunnel effect) even though their energy may be small, or

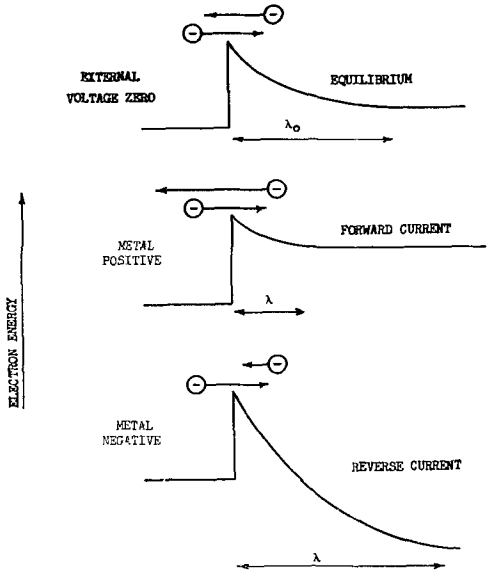

FIG. 4. Principle of diode rectification by a metallic contact of an n-type semiconductor.

they can pass over it, if their energy is sufficiently high. The first mechanism is known to play only a subsidiary role, since rectification theories based primarily on the tunnel effect predict rectification in the wrong direction. In any case, barriers which are of practical importance are known to be too thick for the tunnel effect to operate. The tunnel effect can, however, be operative near the thin top of a barrier and thus can modify rectification characteristics which depend essentially on the other mechanism. The concept of rectification by charge transport over a barrier lends itself to a simple pictorial representation (Fig. 4). The length of the horizontal arrows is intended to be a measure of the charge flow. The arrows pointing toward the right remain constant in (*a*), (*b*), and (*c*), since the barrier height as seen from the metal is assumed to remain constant. Those pointing to the left change in response to the applied voltage which alters the barrier height as seen from the semiconductor side. This process is in agreement with the observed direction of rectification.

In this context one may distinguish between two limiting cases: that in which the charge carriers make normal collisions while passing over the barrier, and that in which they make no collisions at all. The last case applies if the mean free path is greater than the barrier thickness. The current can then be calculated on the basis of streamline flow, using only classical kinetic gas theory. This is known as the diode theory of rectification. If, on the other hand, normal collisions are envisaged, diffusion terms must be taken into account in the usual way. This leads to the diffusion theory of contact rectification. It will be clear that the diode theory is, in a sense, contained in the diffusion theory, of which it represents a special case. If collisions within the barrier are postulated as being absent, the barrier shape cannot influence the rectification process. Accordingly, the diode theory is concerned only with the barrier height, whereas the diffusion theory is concerned with height and shape.

A straightforward comparison between the currents cal-

TABLE I. *Comparison of unipolar rectification theories* (Equations apply to n-type material before correction for image force and tunnel effect.) Based on $V_D + V_B >> kT/e$

Diode theory:
Independent of barrier profile
$j = ne(kT/2\pi m)^{1/2} \exp(-eV_D/kT)[\exp(-eV_B/kT)-1]$
Diffusion theory: (uncorrected for high field effects)
Schottky barrier
$j = ne\mu[(V_D + V_B)8\pi Ne/K]^{1/2} \exp(-eV_D/kT[\exp(-eV_B/kT)-1]$
Mott barrier
$j = ne\mu[(V_D + V_B)/\lambda_0] \exp(-eV_D/kT)[\exp(-eV_B/kT)-1]$
Diffusion theory: (with simplest correction for high field effects)
Independent of barrier profile
$j = nev_m \exp(-eV_D/kT)[\exp(-eV_B/kT)-1]$

V_D = diffusion potential; V_B = barrier voltage; v_m = maximum drift velocity of electrons in high fields; λ_0 = thickness of the Mott barrier; j = current density.

culated on the basis of the diode and the simplest diffusion theories, respectively, leads to an apparent paradox. For a given applied voltage, the current predicted by diffusion theory is greater than that predicted by the diode theory, whereas, by virtue of the collisions, it should be smaller. The reason for this discrepancy has been recognized only recently. The electric fields which prevail within a barrier may be (and usually are) very strong. Electrons in such a field can be accelerated to velocities which are comparable with thermal velocities, whereas the usual drift equation assumes that the energy gained from the field is negligibly small. Again, the usual diffusion equations postulate small concentration gradients, whereas the gradients applying within a barrier layer may be very large. For these reasons, the conventional formulation of drift and diffusion problems cannot be accepted as satisfactory when applied to rectifying barriers, and corrections must be introduced which take account at least of the strong electric fields. The simplest correction of this kind postulates that the electrons move throughout the barrier with a limiting drift velocity which remains constant and independent of the field as long as the field is high enough. The corresponding equations can be explicitly integrated. Results of various theoretical approaches are compared in Table I. It will be seen that the differences between them are not great on the whole, and that, in particular, the diode theory and the diffusion theory with the correction for strong fields lead to similar equations.

All rectification theories make some explicit or implicit assumption concerning the space charge density within the barrier layer and its dependence (or lack of it) on the current flowing. To simplify the mathematical treatments, it is usually postulated that the space charge due to majority carriers passing the barrier can be neglected, but this cannot be a good approximation for high forward currents and may also break down in the extreme reverse direction. Moreover, theoretical treatments of the voltage-current relation concern themselves nearly always with isothermal conditions, whereas Joule heating of the contact by the current flowing is known to be an important factor. At high reverse voltages, especially on point contacts, a voltage-turnover phenomenon is often observed, i.e., a maximum voltage which cannot be exceeded. For currents higher than the turnover current, the differential resistance becomes negative. It can be shown, e.g., by comparison with experiments under pulse conditions, that this turnover phenomenon is primarily thermal in character. However, as far as is known, no satisfactory theory has been developed yet which gives an adequate description of turnover in terms of thermal processes alone. It is now considered that electronic processes must play a secondary but not unimportant part.

Variations in Barrier Height

In the above discussion, the barrier height, at any rate as seen from the metal side, has been treated as a constant. In view of the great importance attached to this parameter, this particular assumption calls for special comment. An effective lowering of the barrier by the tunnel effect has already been envisaged. Most theoretical treatments also include some reference to the image force which acts on charges just outside a conductor and distorts the electric field in which the charges move. This image force would also lead to a smaller effective barrier height than otherwise expected. A more general reservation can be formulated as follows: if a barrier arises from a difference of thermionic work functions, it is plausible to assume that it should be of constant height and (except for the operation of tunnel effect and image force lowering) independent of the current flowing. Likewise, it should be practically independent of temperature. On the other hand, if the barrier arises from charges in surface states, there is no particular reason to believe that either of these conclusions necessarily applies. The charge in surface states may be temperature-dependent and it may increase and decrease in response to the density of charge flow across the barrier. As far as is known, no theoretical treatment is available at present which takes account of these very real possibilities. Uncertainties arising in this connection have an important bearing on the interpretation of experimental results, since most information on barrier heights is derived from procedures which assume this height to be firmly constant. These procedures indicate that most barrier heights (eV_D) encountered in practice are in the neighborhood of 0.3 ev. Results quoted to a large number of significant figures may safely be distrusted when encountered in the literature.

Inversion Layer and Injection

Fig. 2 gives profiles of barriers which are wholly characterized by a pronounced diminution in the concentration of majority carriers, in this case of electrons. However, it is possible to envisage barrier profiles which enable minority carriers (in this case positive holes) to play an important and even predominating role. Fig. 5(a) shows such a barrier. The hole concentration in the immediate vicinity of the metal interface is high by virtue of the fact that the barrier is high or that the forbidden band is narrow. Indeed, there is a region in which the hole concentration exceeds the electron concentration and this is called the inversion layer. This system has some of the features of a p-n junction, although some important differences remain. Fig. 5(a) shows the positive hole population in the full

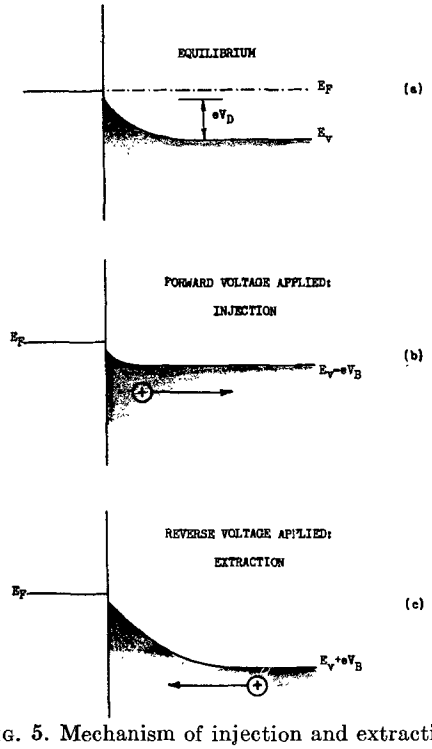

FIG. 5. Mechanism of injection and extraction

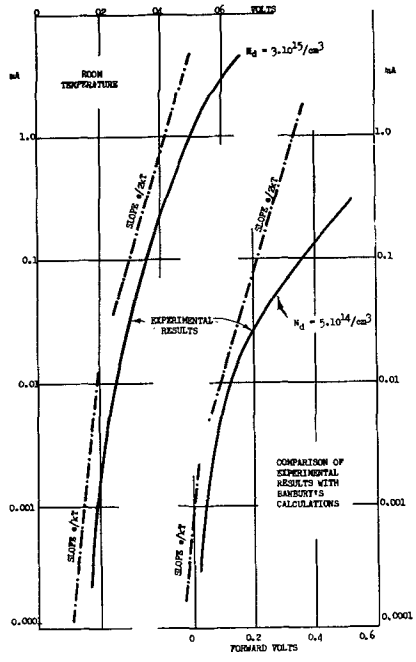

FIG. 6. Forward characteristics of point contacts on n-germanium.

band of the semiconductor within the barrier region. It can be shown that the presence of these minority carriers increases the effective field in the immediate vicinity of the metal and also makes it less dependent on the external voltage. When the barrier is distorted by the application of an external forward voltage, as in Fig. 5(*b*), the equilibrium evidently is disturbed and positive holes pass into the interior of the semiconductor. This is the process on minority carrier injection mentioned above. As long as the applied fields are small, the current is carried mainly by a diffusion process. With increasing field strength, drift effects tend to predominate over diffusion effects. The carriers that pass into the semiconductor decay in accordance with an approximately exponential law, the time constant of which is called the carrier lifetime. If the lifetime is high, these carriers may move through considerable distances before decaying. By so doing they modulate the resistivity of the bulk material adjoining the injecting barrier. If the adjoining material embodies a spreading resistance, as it does in the case of point contacts, this modulation may be very pronounced indeed. In general, the forward current is carried by both majority and minority carriers in a ratio which depends on the barrier height and probably on other factors. A quantity known as the current composition ratio which can be used to characterize the mechanism of current flow is defined. It denotes the fraction of the total current which is carried by minority carriers. In a near-intrinsic material, some of the current even within the bulk (far away from contacts) is carried by minority carriers. Thus, a further quantity that characterizes the injection properties of a contact is needed: the *injection "ratio"*. This is the difference between the current composition ratios at the contact interface and within the bulk material, respectively. A noninjecting contact is thus not one which is free from the participation of minority carriers, but one in which minority carriers contribute to the current flowing to the same degree as they do within the bulk material. It is then at once plausible that completely noninjecting contacts would represent a very special case which is not encountered often in practice. Experimental methods have been developed for the measurement of the injection ratio under a variety of conditions. Special interest attaches to the measurement of very low injection ratios, e.g., of base contacts on diodes, and to the measurement of high injection ratios for very small currents, since this is the condition best suited for a comparison between calculated and observed results.

On the basis of the injection mechanism illustrated above, it is possible to calculate the forward characteristic of the rectifier. Fig. 6 shows this for point contacts of two different specimens of germanium, at any rate as far as slopes are concerned. Slopes are calculated and the full lines represent experimental results. The agreement must be regarded as satisfactory, considering that certain special assumptions had to be introduced into the calculations, e.g., that recombination could be neglected because of the high fields present, and that the injection ratio is unity. Three general methods are available for the detection of injected charge carriers. They are illustrated on Fig. 7, which is largely self-explanatory. Each of these idealized experiments is also the basis of practical applications.

Fig. 5(*c*) shows the conditions that apply in the presence of an inversion layer when a reverse voltage is applied. The minority carriers then tend to move toward the metal, and to contribute to the reverse current. It is clear that this will result in a deficit of minority carriers just inside the semiconductor. This is the effect known as carrier extraction. The extraction current can be calculated on the basis of simple and well-known equations, and again on the assumption that minority carrier flow alone is of

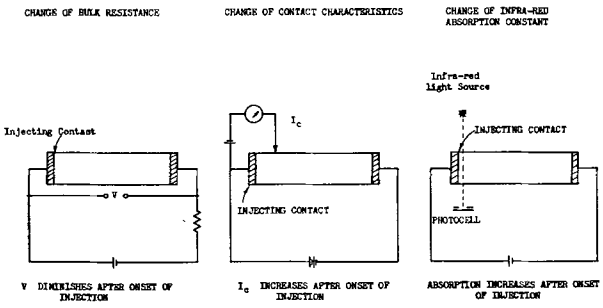

FIG. 7. Three methods of detecting carrier injection

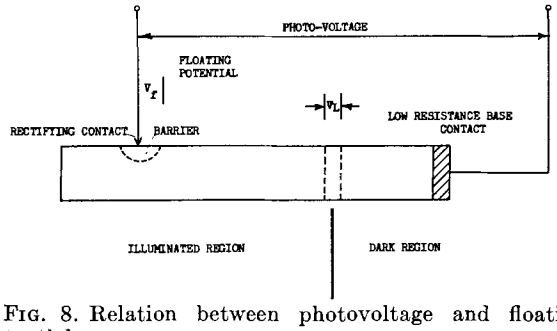

FIG. 8. Relation between photovoltage and floating potential.

concern; but when the calculated results are compared with actual observations, they tend to be too low. The precise origin of the higher currents observed is not yet certain, although one may well suppose that additional minority carriers are generated at the surface of the semiconductor in the immediate vicinity of the contact. Once generated, they would augment the reverse extraction current. Calculations of the extraction current are handicapped by lack of precise understanding of the phenomenon of current gain. It is known that a certain amount of current multiplication takes place when minority carriers pass through a contact in the reverse direction. The extent of this current multiplication must be intimately related to the mechanism whereby the space charge within the barrier tends to be neutralized by charge carriers of opposite sign.

Corresponding to the two phenomena of injection and extraction already discussed, two other processes can be envisaged and have been observed in practice. They are: (*a*) carrier exclusion, corresponding to a negative "injection ratio" (in this case a misnomer, of course), and forward current, and (*b*) carrier accumulation, corresponding to a negative "extraction ratio" (again a misnomer when applied to this case) and reverse current. These four phenomena can be analyzed by a single set of equations, subject to various changes in signs. They can be detected by the methods illustrated on Fig. 7, except of course, that extraction and exclusion lead to a diminution in the concentration of charge carriers near the contact. Experimental methods have recently been developed whereby the extraction ratio can be estimated. As discussed above, the phenomenon of injection is governed by (among other things) the carrier lifetime; in a similar way, exclusion and extraction are governed by carrier generation time. For infinitesimal displacements from equilibrium these times must be identical, but for large displacements the situation may be much more complicated. All current composition ratios are somewhat dependent on the current itself, and their behavior in this respect is generally in accordance with theoretical expectations.

Effect of Additional Charge Carriers

The foregoing discussions concern contact systems that are in equilibrium in the absence of any current flowing. It is of interest to consider how the various contact properties are changed when the semiconductor is permanently in a nonequilibrium state, e.g., if it is continuously illuminated. The illumination produces electron and hole pairs, and these pairs affect the conduction processes through contacts. This problem can be dealt with as if the illumination produces only minority carriers, as long as the native majority carriers predominate sufficiently over the native minority carriers and as long as the displacement from equilibrium is quite small. These are then the minority carriers which are described as being "additional". Fig. 8 shows such a system. The field in the barrier at the rectifying contact draws positive holes into the contact where they eventually decay. Since their decay requires a certain amount of time, these carriers constitute a net positive charge and the metal point thus becomes positive with respect to the semiconductor. When a metal is positive with respect to an *n*-type specimen of transistor material, injection of minority carriers occurs and this clearly counteracts the original drift of additional minority carriers into the barrier. A steady state arises when this drift and the injection just balance. The metal contact is then somewhat positive and the voltage which exists across the barrier under these conditions is called the floating potential. It is not the voltage measured (even for zero current) in the external circuit; this is the photovoltage. The two voltages differ by the amount V_L, as indicated in Fig. 8; V_L is a diffusion voltage which, in principle, must always arise between illuminated and nonilluminated portions of a semiconductor. This diffusion voltage can be negligibly small if the contact under test is highly rectifying and has a high floating potential, but it need not be so. If it is negligibly small the external photovoltage can be regarded as equal to the floating potential. Fortunately, V_L can be calculated with confidence from existing equations. The floating potential itself exists whenever there are additional charge carriers in the neighborhood of a contact, independent of how these carriers are produced, whether by illumination or by injection from another contact. The voltage V_L cannot be eliminated or even modified by illuminating the specimen as a whole. It has been found possible to calculate the floating potential explicitly, but only for contacts of unit injection ratio. In other cases a semi-empirical treatment must be used.

The change in contact properties in the presence of additional charge carriers, e.g., change of conductance near the origin or change of saturation current in the reverse direction, can be used as a measure of the additional minority carrier concentration. Care must be taken when these methods are used in the context of other investigations. Simple tests show that point contacts are nonlinear

detectors of additional carriers. They are in fact more sensitive to low than to high concentrations. When this method is used in the course of certain forms of lifetime determinations, it tends to produce fictitiously high lifetimes which arise from this nonlinearity.

Fig. 8 shows a situation in which there is no external voltage applied to the system. However, in other contexts, the conditions are of special interest when the rectifying contact carries a reverse voltage. In this case the migration of minority carriers is enhanced, and this is the phenomenon known as carrier collection. It is concerned primarily with additional carriers, as compared with extraction which concerns resident minority carriers. Again, theoretical calculations of the collection current depend on the assumptions made with regard to the mechanism of current gain and the extent to which space charge compensation can be achieved by having carriers of opposite sign within the barrier region.

Outstanding Problems

Many important contact problems are still in need of theoretical clarification, such as the detailed relation between contact structure and the current composition ratio, the relation between surface generation of charge carriers and contact characteristics, the nature of transient phenomena observed during measurements on contacts, the dependence of contact characteristics on the surrounding gas atmosphere, the mechanism of various relaxation effects observed at ultra-high frequencies, and so on. Most of these problems are complicated, and it seems likely that their solution will occupy semiconductor physicists for a long time to come.

Manuscript received April 21, 1956. This paper was prepared for delivery before the San Francisco Meeting, April 29 to May 3, 1956.

Any discussion of this paper will appear in a Discussion Section to be published in the June 1957 Journal.

New Method of Studying Corrosion Inhibition of Iron with Sodium Silicate

E. F. Duffek and D. S. McKinney

Department of Chemistry, Carnegie Institute of Technology, Pittsburgh, Pennsylvania

ABSTRACT

A rapid laboratory method is presented for testing the effectiveness of sodium silicate as an anodic inhibitor. Passivity curves taken on polished steel electrodes, pretreated for 24, or better, 48 hr in aerated solutions of sodium silicate (3–500 ppm silica) and compared with sodium hydroxide solutions of the same *p*H, indicate that silica, and not merely an increase in *p*H, caused inhibition. No corrosion products were observed in the short pretreatment time for electrodes treated with 15 and more ppm silica, whereas all sodium hydroxide treated electrodes corroded. The method can be made the basis of a practical test by pretreating the electrodes, in the actual environment being treated, with sodium silicate. The procedure also appears to be applicable in the testing of other anodic inhibitors.

Sodium silicate and sodium hydroxide are nonoxidizing anodic inhibitors. As such, since the corrosion of Fe is under cathodic control, a certain minimum concentration is required to promote passivity and corrosion inhibition. In insufficient amounts, these inhibitors may merely contract the anodic areas, localizing the corrosion and causing pitting. Minimum concentration required for inhibition depends on the impurities in the water, some of which may aid formation of a protective film; others may peptize or dissolve the protective film; still others, by reacting with the silica, may make it unavailable for the production of a film.

Very thin films have been found to give effective protection against corrosion. Thresh (1) was the first to observe this effect in the case of silica; using a silicate of a high silica-to-alkali ratio at 8 ppm silica, he was able to minimize the concentration of lead in water carried in lead pipes.

Weston (2) controlled the corrosion of iron pipe carrying water by maintaining a protective coating by the addition of a small amount of sodium silicate once a week.

The anticorrosive action of silicate was not thought of at first as a deposit of an inhibiting film. Texter's work (3) showed that, when silicate is added to the water, the maximum effect, measured as a specific rate of corrosion by the removal of dissolved oxygen from water, was not obtained for a matter of 22 days.

These films do not build up to heavy obstructive layers and are self-healing if the water is continuously treated. Stericker (4) summarized the known facts of inhibition with sodium silicate.

Lehrman and Shuldener (5, 6) also controlled rust in water pipes with soluble silicates. Their results show that the films deposited from dilute solutions of silicate (12–1400 ppm silica) depend on the presence of small quantities of corrosion products on the metal surfaces.

Above *p*H 9.5, the corrosion rate of steel is dependent on the alkalinity of the surrounding medium, with an increase of *p*H causing a decrease in the rate (7). In order to study the full effect of sodium silicate, it is therefore necessary to conduct another experiment with sodium hydroxide solutions of the same *p*H. Any effect noticed above that due merely to raising the *p*H of the solution must be attributed to the silicate present.

Passivity and weight loss determinations are two ways in which the factors affecting corrosion may be studied.

Passivity may be visualized in the following way. At low applied current densities, the major reaction for steel as anode is the solution of Fe. An anodic inhibitor should cover these anodic areas of the steel and cause the effective area to decrease. Local current density at the exposed portions of the electrode is very large and hence the potential rises rapidly until another process, the evolution of oxygen, takes place. Silicates, if they are better inhibitors than sodium hydroxide, should cause the steel anode to become passive at a lower average current density.

Weight loss experiments are of great value when corrosion is uniform, but, when studying anodic inhibitors, it is more important to note visually whether the inhibitor is preventing pitting. A procedure for evaluating anodic inhibitors in a relatively short time seems to be desirable.

A testing procedure has been devised which combines exposure in the environment being treated with passivity measurements. In the experiments reported, steel specimens are exposed for 24 or 48 hr in a treated distilled water solution of the inhibitor, after which passivity curves are taken in comparably treated sodium sulfate solutions to study the anodic polarization effects. Of course it is possible to expose the specimens in the actual water being treated prior to making the polarization measurements. In this case, it appears feasible to correlate the passivity measurements with corrosion observed in the actual situation being treated.

Experimental

Passivity Measurements

Potentials were measured with a L&N student potentiometer vs. a saturated calomel reference cell. The current

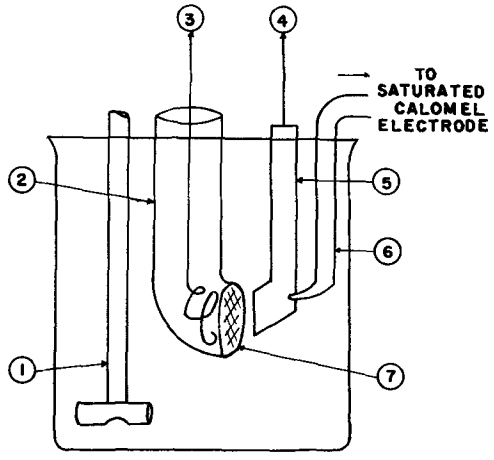

FIG. 1. Passivity cell assembly. 1-glass stirrer; 2-cathode compartment; 3-cathode; 4-anode; 5-specimen; 6-probe; 7-sintered glass disc.

TABLE I. *Composition of silicate*

	%
Na_2O	8.76
SiO_2	28.38
Fe_2O_3	0.0057
TiO_2	0.0031
Al_2O_3	0.069
CaO	0.042
MgO	0.034
CuO	0.00036
NiO	0.00013
Cl	0.052
SO_3	0.065
CO_2	0.02

to the passivity cell was supplied by a 32-v Edison battery and was measured with two milliammeters having ranges of 100 and 500 ma. The passivity cell, Fig. 1, consisted of a tall, 1-l beaker with a separate compartment for the Pt cathode. This was made by attaching a 30-mm sintered glass disk vertically to a section of 20-mm glass tubing. Junction to the calomel cell was made by means of a salt bridge of saturated KCl in agar-agar. The salt bridge was constructed so that it ended in a capillary brought very close to the back, or enameled, face of the anode. The solution in the passivity cell was 0.1*N* sodium sulfate containing the same amount of silicate as the water being treated. The sodium sulfate serves to conduct the current as well as to minimize concentration changes in the solution due to electrolysis. The potential measured is that between the steel anode and the calomel electrode. The potential drop through the solution is negligible, with this arrangement. Stirring reduced concentration gradients at the anode interface. Sodium silicate containing SiO_2: Na_2O in the ratio of 3.24 to 1 was used for the silica solutions. The composition of this material, furnished by the maker, is given in Table I.

Electrodes were cut from the same piece of mild steel (0.13% C, 0.3% Mn, 0.04% P, 0.05% S) 1.5 mm thick. A square area, 15 x 15 mm, was used as anode and a tang of the same metal, left attached, 20 cm x 7 mm, served as a lead. After pickling in concentrated HCl, specimens were polished with 600 emery, No. 2 metallographic paper,

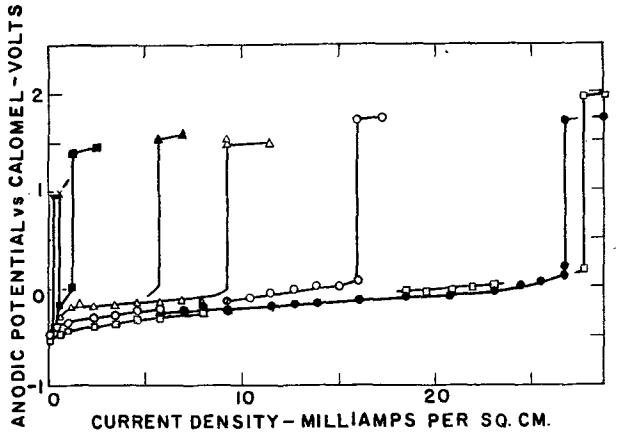

FIG. 2. Passivity curves of mild steel in treated 0.1*N* Na_2SO_4 after 24 hr presoaking in a correspondingly treated distilled water solution. ▼-500 ppm silica equivalent; ×-200 ppm silica equivalent; ■-100 ppm silica equivalent; ▲-40 ppm silica equivalent; △-15 ppm silica equivalent; ○-7 ppm silica equivalent; ●-3 ppm silica equivalent; □-0 ppm silica equivalent.

and lightly buffed. Buffing was carried out to inspect the surface for pits and scratches. To obtain the best results possible, specimens were polished and buffed in this manner until no imperfections were noted. With the exception of one face of the 15 x 15 mm area, the entire electrode was coated with G. E. enamel No. 6844 and baked at 135°C for 1 hr. Before immersion in the soak solution, the uncoated face was refinished with No. 2 metallographic paper and exposed to 20% HF for 30 sec. With such small specimens, great care must be exercised in the preparation of the surface. Defects or pits due to imperfect preparation may not receive sufficient inhibitor during the soaking period and will not become passive when electrolyzed.

Procedure.—Two of the prepared electrodes were immersed in approximately 3.5 l of distilled water containing the desired concentration of silicate. This solution was contained in 4-l beakers. They were stirred mechanically and saturated with CO_2-free air. At the end of 24 hr, one of the electrodes was removed, rinsed in distilled water, and placed in the passivity cell. The silicate solution was renewed and the second electrode removed at the end of 48 hr, after which it was treated in the same manner as the first. The passivity cell contained a comparably treated 0.1*N* sodium sulfate solution. Definite current values were impressed between the anode and cathode and the resulting potential of the anode relative to the calomel electrode was measured. Starting with the "open circuit" or zero current value, the current was increased in steps from about 0.25 ma/cm² to passivity of the metal. The resulting potential for each particular current density was measured, allowing 10 min for attainment of steady potential values. Passivity was recognized by a sudden, sharp rise in potential and was obtained just after the electrodes' polarity reversed, that is, the calomel cell became negative with respect to the steel. Typical curves are shown in Fig. 2. Steady values of the potential were not obtained with current densities greater than the critical value, the potentials dropping slowly to less positive values.

TABLE II. *Critical current densities of mild steel in treated 0.1N Na_2SO_4 solutions presoaked for 24 and 48 hr in treated distilled water solution*

Treating solution	pH	Surface just prior to readings	Critical current densities, ma/cm²	
			24 hr	48 hr
500 ppm silica*	9.3	No visible corrosion	0.231	0.231
500 ppm silica*	9.3	No visible corrosion	4.62	6.93
NaOH	9.3	Well-corroded	25.33	33.33
200 ppm silica	9.15	No visible corrosion	0.462	0.693
100 ppm silica	9.0	No visible corrosion	1.16	4.62
100 ppm silica	9.0	No visible corrosion	—	0.495
NaOH	9.0	Even coating of corrosion	38.89	38.89
40 ppm silica	8.95	No visible corrosion	5.78	4.62
40 ppm silica	8.95	No visible corrosion	6.93	—
15 ppm silica	8.9	No visible corrosion†	9.24	6.93
15 ppm silica	8.9	No visible corrosion	—	13.87
NaOH	8.9	Even coating of corrosion	36.67	30.00
7 ppm silica	8.5	Several small stains	9.24	5.08
7 ppm silica	8.5	Very mild corrosion	15.02	10.39
7 ppm silica	8.5	Very mild corrosion	16.18	—
7 ppm silica	8.5	Very mild corrosion	18.49	—
3 ppm silica	7.9	Moderate corrosion	26.71	10.39
NaOH	7.9	Spotted corrosion	24.44	26.71
Distilled water	7.0	Even coating of corrosion	27.78	25.55

* Lower critical current densities were always obtained with well-polished electrodes.
† The 48-hr treated electrode had two small spots of corrosion.

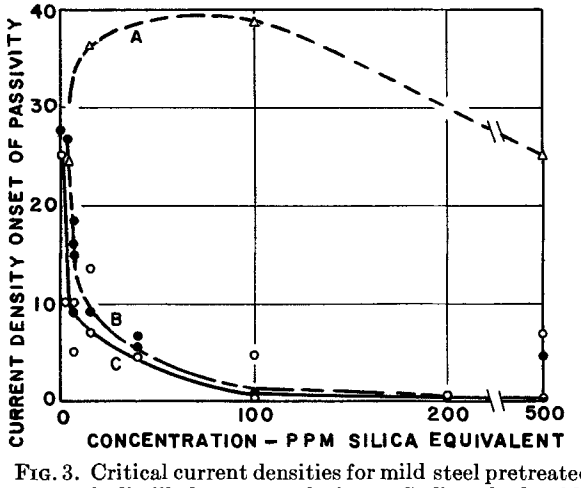

FIG. 3. Critical current densities for mild steel pretreated in aerated distilled water solutions. Sodium hydroxide plotted at the same pH as the silicate solutions. A-sodium hydroxide, presoaked 24 hr; B-sodium silicate, presoaked 24 hr; C-sodium silicate, presoaked 48 hr.

Results.—Results of these experiments are summarized in Table II.

Four out of the seven concentrations of silicate were paralleled by a test containing no silicate but sufficient sodium hydroxide to produce the same pH as the silicate solutions. These experiments show that current densities required for passivity of electrodes treated with sodium hydroxide are considerably higher than for those containing silicate, the values of the critical current density ranging from 25 to 39 ma/cm² (Fig. 3).

As previously mentioned, care must be exercised in the preparation of specimens. Inspection of Table II shows the critical current densities for the 48-hr experiments with the more concentrated silicate solutions are frequently higher than for 24 hr. For a greater concentration of silicate the steel electrode becomes passive at a lower current density than for the dilute solutions and it is in this region that the surface condition becomes more critical, any surface defect or pit causing a considerably higher current density.

The passivity curves for the various silica concentrations after 24-hr immersion are illustrated in Fig. 2. These experiments indicate the sodium silicate solutions bring about a large anodic inhibition on mild steel during the pretreating period. The protective action appears to be in the form of an invisible film which causes passivity to take place at a much lower current density than in the matching sodium hydroxide solution (Fig. 3). Fig. 3 also suggests that lower concentrations of silica require a longer time to become effective.

Other measurements.—Some passivity measurements were carried out without presoaking. That is, the only silicate available was that contained in the sodium sulfate solution in the passivity cell. In these tests, the silicate was effective only at rather large concentrations. Under these circumstances, it is apparent that insufficient silicate was available to inhibit the anodic areas in the short time required for the passivity tests.

The same situation was observed when the anodes were presoaked in solutions of 0.1N sodium sulfate containing the inhibitor. That is, the lower inhibitor concentrations are not effective in forming a passivating film in competition with the rather corrosive sodium sulfate solution, whereas they are effective in distilled water.

Conclusions and Summary

The present experiments show that at 3 ppm silica the electrodes were well spotted with corrosion products, whereas at 7 ppm there was very slight corrosion on the steel surface [cf. with 8 ppm by Thresh (1)]. No corrosion products were observed on the specimens treated with 15 ppm silica. These facts indicate that a 3 ppm silica solution contained an insufficient amount of inhibitor and the

7 ppm silica solution was enough to exhibit some corrosion inhibition. In addition, 15 ppm silica is enough to cause passivity of the steel and it is probable that in practice, after an initial treatment at 15 ppm, the concentration could be reduced to 7 ppm and still hinder corrosion effectively.

It has been found that if the steel samples are allowed to soak in silicate-treated water for 24 hr before the polarization curves are taken, rather small concentrations of silicate have a pronounced effect on polarization. Measurements of critical current density vs. silica and sodium hydroxide concentrations are closely related to the corrosion rate, with a lower critical current density indicating corrosion inhibition.

It seems fairly obvious that specimens can be exposed in an actual system being treated and then transferred at intervals to the passivity apparatus to follow the effectiveness of any treatment. Also, it appears that the method is applicable for the testing of other inhibitors.

ACKNOWLEDGMENT

This research was supported by the Sodium Silicate Manufacturers Institute to whom the authors express their appreciation.

Manuscript received March 15, 1956.
Any discussion of this paper will appear in a Discussion Section to be published in the June 1957 JOURNAL.

REFERENCES

1. J. C. THRESH, *Analyst*, **47**, 459, 500 (1922).
2. R. S. WESTON, *Water & Sewage Works*, **98**, (4), R79 (1951).
3. C. R. TEXTER, *J. Am. Water Works Assoc.*, **10**, 765 (1923); *Sanit. Heating Eng.*, **102**, 329 (1924).
4. W. STERICKER, *Ind. Eng. Chem.*, **37**, 716 (1945); **30**, 348 (1938).
5. L. LEHRMAN AND H. L. SHULDENER, *J. Am. Water Works Assoc.*, **43**, 179 (1951).
6. H. L. SHULDENER, *Proc. Water Conf. Eng. Soc., West Penna.*, **2**, 71 (1941); U. S. Pat. 1,796,407 (1931).
7. F. N. SPELLER, "Corrosion, Causes and Prevention," p. 35, 3rd ed., McGraw-Hill Book Co., New York (1951).

Permeation of Gases through Electrolytic Nickel Deposits

II. Determination of the Effect of Several Variables on the Intrinsic Permeability of Nickel Deposits to Gases

D. T. EWING[1] AND J. MARTIN TOBIN[2]

Michigan State College, East Lansing, Michigan

AND

D. GARDNER FOULKE

Hanson-Van Winkle-Munning Company, Matawan, New Jersey

ABSTRACT

Conditions of temperature, current density, and *p*H used when plating from a Watts' bath were each varied independently to determine the effect on the intrinsic permeability of the deposit. Total Ni, chloride, and H_3BO_3 concentration of a Watts' bath were studied similarly, and the effect of various addition agents which tend to produce bright deposits from Watts' baths was also determined. Several bath impurities were found to increase the intrinsic permeability of the Ni deposit.

A method has been described (1) for determining the permeability of detached Ni deposits to gases with a good degree of reproducibility. The method used is intended to be a measure of the "porosity" of a Ni deposit which is characteristic of the particular bath composition and plating conditions used, in the absence of accidental effects such as gas pores, particle inclusions in the deposit, and pores caused by base metal defects.

The present paper is concerned with the measurement of the effect of changing the bath composition, and varying the *p*H, temperature, and cathodic current density on the so-called intrinsic permeability of Ni deposits to gases.

[1] Deceased.

[2] Present address: General Electric Co., Richland, Wash.

The effect of adding small amounts of colloidal graphite, gelatin, anode sludge, Fe(III), Cu(II), and Zn as impurities in a Watts' bath was also measured.

EXPERIMENTAL RESULTS

Bath Composition

Effect of varying Ni *concentration.*—The effect of varying Ni concentration on the permeability of electrodeposits obtained in what were substantially Watts' Ni baths was carried out by plating foils from baths in which the amount of Ni salts was decreased[3] stepwise by 10%.

[3] Standard bath contained 240 g/l $NiSO_4 \cdot 6H_2O$ and 45 g/l $NiCl_2 \cdot 6H_2O$.

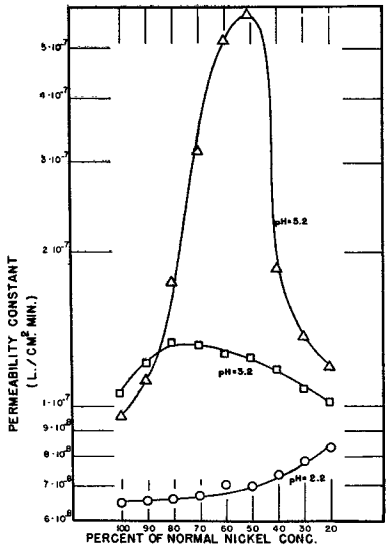

FIG. 1. Effect of Ni concentration on permeability constants of Ni electrodeposits at various *p*H values.

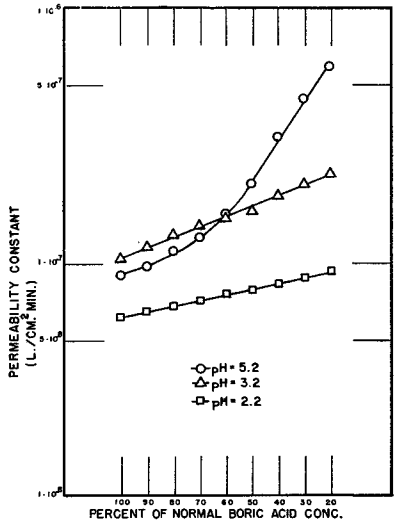

FIG. 2. Effect of varying the H_3BO_3 concentration on Ni electrodeposits at several *p*H values.

H_3BO_3 was held at 4 oz/gal. The temperature was 140°F (55°C) and the current density 40 asf.

In order to prepare deposits 0.0001 in. thick at the various *p*H values studied, 2.2, 3.2, and 5.2 electrometric, the deposition rate was determined and the deposition time for the samples was determined by these data. Some of the deposits from baths low in Ni at *p*H 5.2 were fairly bright. This was most evident in the bath operated at about 50% of normal Ni concentration which was shown by the Tyndall effect to contain a colloid even in the case of a carefully purified and filtered bath.

The permeability of these deposits was measured in triplicate. Values for log permeability constant as defined by Thon (2) plotted (Fig. 1) as a function of the per cent normal Ni concentration in baths of *p*H 2.2 show only a slight increase in permeability with decrease of Ni content in spite of considerable gassing at the cathode. At higher *p*H values, a maximum is apparent at about 50% of normal Ni concentration. At *p*H 5.2, the maximum appeared to be associated with the presence of a colloid, probably hydrous nickel oxide, observed in the bath. At *p*H 3.2, it is possible that a similar colloid was present in the cathode film, although shown to be absent in the bulk of the solution by the Tyndall effect.

Effect of varying H_3BO_3 *concentration.*—A series of baths, deviating from a H_3BO_3 content of 30 g/l (4 oz/gal), were carefully purified. Deposits were prepared in these baths at three different *p*H values at 140°F (55°C) and 40 asf and the permeability determined (Fig. 2).

In general, the appearance of the deposit did not change materially with decrease in H_3BO_3 concentration, although it was noted that the brittleness increased with decrease in H_3BO_3 content. The effect of decreased H_3BO_3 concentration was most marked at the higher *p*H (5.2), undoubtedly due to the development of unusually high *p*H values in the cathode film in the absence of sufficient buffer capacity.

Effect of chloride.—In order to determine the effect of the chloride concentration of the bath on the initial permeability of Ni deposits, two baths were prepared and purified.

Nickel chloride ($NiCl_2 \cdot 6H_2O$)	300 g/l	(40 oz/gal)
Boric acid (H_3BO_3)	30 g/l	(4 oz/gal)
and		
Nickel chloride ($NiCl_2 \cdot 6H_2O$)	132 g/l	(17.6 oz/gal)
Nickel sulfate ($NiSO_4 \cdot 7H_2O$)	162 g/l	(21.6 oz/gal)
Boric acid (H_3BO_3)	30 g/l	(4 oz/gal)

Panels were plated in these baths at 55°C and *p*H 3.2 at 40 asf. Results obtained by making six permeability determinations are compared with previous results obtained for a Watts' bath under similar conditions. They show a small increase in permeability with increase in chloride concentration (Table I).

Effect of brighteners.—Deposits from various proprietary bright Ni baths and several sulfamate baths were compared with deposits obtained from the Watts' solution with results shown in Table II. No significant differences in the "intrinsic" porosity of these deposits was apparent, although the bright Ni deposits were in general less permeable to gases than deposits from the Watts' bath.

Plating Conditions

Effect of varying the *p*H.—The *p*H of the Watts' nickel bath, operated at 55°C and 40 asf, was varied with all other variables held constant. Six samples were taken from each deposit and the permeability to H, He, and N determined. Deposits prepared at *p*H 3.2 had a greater permeability than deposits prepared at *p*H 2.2 or 5.2 (Table III).

Effect of varying temperature.—Five series of samples were prepared at five different temperatures using a Watts' bath at *p*H 2.2 and a current density of 40 asf. The permeability of three samples from each series was then determined using He gas. As can be seen from Fig. 3 the permeability constant increased exponentially with temperature.

Effect of varying current density.—The current density at the cathode was varied from 30 to 80 asf by 10 asf intervals for the 2.3 *p*H Watts' bath. Three samples at

TABLE I. *Effect of chloride concentration on permeability*

Deposit thickness	Permeability constant, 1/cm² min	
	K_{H_2}	K_{He}
All chloride		
0.000115	8.9×10^{-7}	6.2×10^{-7}
0.000110	9.3	6.5
0.000102	9.7	6.8
0.000119	8.7	6.1
0.000116	8.9	6.2
0.000114	9.2	6.4
0.000113	Avg. 9.1	6.4
1:1 Chloride to sulfate		
0.000121	3.2×10^{-7}	2.2×10^{-7}
0.000117	3.5	2.4
0.000110	3.9	2.7
0.000123	3.5	2.4
0.000118	3.7	2.6
0.000115	4.0	2.8
0.000115	Avg. 3.6×10^{-7}	2.5×10^{-7}
Watts		
0.000107	8.7×10^{-8}	6.1×10^{-8}
0.000102	9.0	6.3
0.000096	9.2	6.5
0.000115	8.5	5.9
0.000099	8.9	6.5
0.000093	9.4	6.7
0.000102	Avg. 9.0×10^{-8}	6.3×10^{-8}

TABLE II. *Permeability constants for various bright* Ni *baths*

C.D. = 40 asf, thickness 0.0001 in.

Bath	Permeability constants, (1/cm² min)		
	$K_{H_2} \times 10^8$	K_{N_2}	$K_{He} \times 10^8$
°C			
Watts, 3.2 at 55°	14.5	(0)	10.5
Watts, 5.2 at 55°	13.8	(0)	9.65
Organic[1], 3.2 at 55°	4.65	(0)	3.30
Organic[2], 3.5 at 50°	3.63	(0)	2.60
Watts, 2.2 at 55°	9.15	(0)	6.40
Organic[3], 3.5 at 50°	4.85	(0)	3.35
Co-Ni, 3.7 at 55°	9.20	(0)	6.45
Organic[4], 3.2 at 55°	3.40	(0)	2.35
Organic[5], 3.5 at 60°	4.35	(0)	2.95
Organic[5], 3.7 at 50°	3.80	(0)	2.60
Sulfamate, 3.5 at 50°	9.95	(0)	7.15
Sulfamate[6], 3.5 at 50°	7.65	(0)	5.40

[1] AES Project No. 5 bath; [2] Polysulfonic acid + Class II brightener + wetting agent; [3] No. 2 without wetting agent; [4] Sulfonamide + Class II brightener; [5] Polysulfonic acid + Class II brightener, each different and not same as No. 1; [6] With naphthalene sulfonic acid.

each current density were measured for permeability to He with results shown in Fig. 4. The permeability constant increases with increase in current density but tends to level off at about 45 asf.

Effect of impurities.—Impurities of a colloidal nature were introduced into the 2.2 *p*H Watts' bath. Gelatin, colloidal graphite, and black anode slime at a concentration of 1.0 ppm were found to increase greatly the porosity

TABLE III. *Effect of* p*H of the plating bath on permeability*

Deposit sample	Mean thickness	$K_{H_2} \times 10^8$ (1/cm² min)	K_{N_2}	$K_{He} \times 10^8$ (1/cm² min)
pH = 2.2				
G31A-1A	0.000126	8.60	(0)	6.05
G31A-1B	0.000122	8.70	(0)	6.15
G31A-1C	0.000104	8.95	(0)	6.40
G31A-2A	0.000142	8.65	(0)	6.00
G31A-2B	0.000125	8.85	(0)	6.25
G31A-2C	0.000113	9.00	(0)	6.30
pH = 3.2				
C21A-1A	0.000110	14.2	(0)	10.2
C21A-1B	0.000103	14.5	(0)	10.5
C21A-1C	0.000097	—	(0)	—
C21A-2A	0.000120	14.0	(0)	10.0
C21A-2B	0.000104	14.5	(0)	10.5
C21A-2C	0.000099	15.5	(0)	11.0
pH = 5.2				
D21B-1A	0.000107	13.0	(0)	9.05
D21B-1B	0.000103	13.8	(0)	9.50
D21B-1C	0.000098	14.0	(0)	9.75
D21B-2A	0.000114	13.0	(0)	9.00
D21B-2B	0.000102	13.5	(0)	9.20
D21B-2C	0.000095	14.2	(0)	9.85

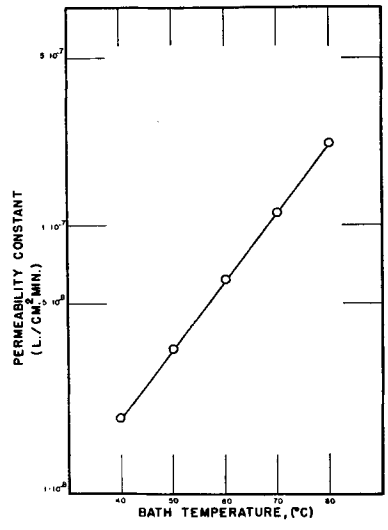

FIG. 3. Effect of bath temperature on the gas permeability constant of Ni deposits.

of Ni deposits as shown in Table IV. It should be noted that these foils were free of photographable pores.

The study of the effect of inorganic impurities was not extensive, but the order of magnitude of the effect was determined for Fe, Cu, and Zn (as sulfates) present to the extent of 5 and 10 ppm 2.2 bath (55°C and 40 asf). As shown in Fig. 5, the intrinsic permeability was greater for deposits made in the baths containing metallic impurities.

SUMMARY AND DISCUSSION

A decrease in the Ni salt concentration of baths at lower *p*H values did not exert a marked increase in the permeability of deposits plated therein, even though considerable

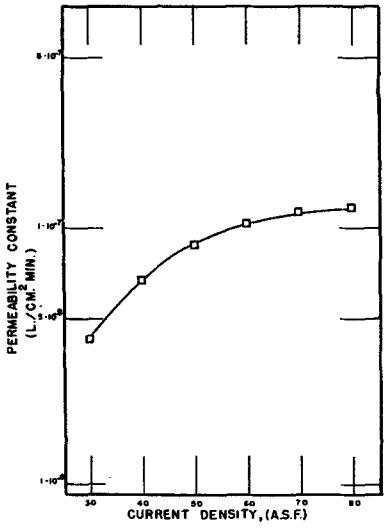

FIG. 4. Effect of current density on the gas permeability of Ni deposits.

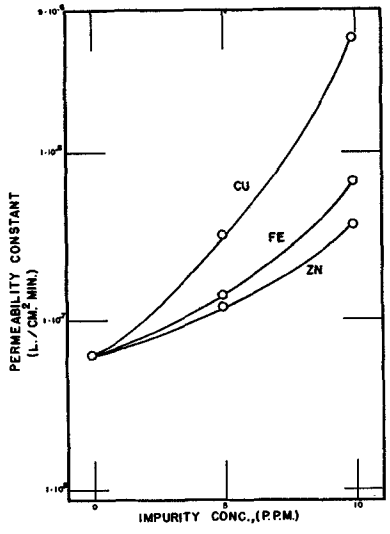

FIG. 5. Effect of metal ion impurities on the gas permeability of Ni deposits.

TABLE IV. *Effect of colloidal impurities on permeability*

Impurity	Amount	K_{He} 1/cm^{-2} × 10^{-6} min		
0	0	6.1	6.3	6.5
Gelatin	1.0 ppm	6,000	7,000	7,000
Colloidal graphite	1.0 ppm	9,000	10,000	30,000
Anode slime	1.0 ppm	20,000	40,000	20,000

gassing took place at the cathode. There is a tendency for more permeable deposits to be formed in Ni baths at higher *p*H values. This may be caused by colloidal basic Ni compounds formed in the bath.

The effect of a decrease in H_3BO_3 concentration was greatest in the case of the 5.2 *p*H bath. This may have been due to the decrease in buffering action in the cathode layer where the *p*H tends to rise.

In general, there was a very little difference in the intrinsic permeability of various purified proprietary Ni baths. However, deposits from the purified Watts' type of bath are slightly more permeable to gases than the bright deposits, in spite of the finer grain structure of bright baths. This may be related to the laminar structure of bright baths as opposed to the columnar structure of Ni deposited from the Watts' bath. Furthermore, it would appear that there is no evidence so far of a direct correlation between permeability and corrosion resistance. It is probable that the accidental defects in the deposit such as gas pores, etc., and codeposited materials such as brighteners are more important controlling factors in the corrosion resistance of plated articles than the initial permeability of deposits.

On the other hand, bath impurities have been recognized as a factor causing a decrease in corrosion resistance of Ni deposits. From the data given in Table IV and Fig. 5 it can be seen that colloidal and metallic impurities can cause an increase in permeability of the deposit to gases which may be of a very large order of magnitude; as much as a hundred to ten thousand times the value of permeability of such Ni deposits is at least one of the factors related to the low corrosion resistance observed in practice for deposits from impure baths.

ACKNOWLEDGMENT

The sponsorship by the Hanson-Van Winkle-Munning Company of a Fellowship at Michigan State University, under which the work reported in this paper was done, is gratefully acknowledged.

Manuscript received December 5, 1955. This paper was prepared for delivery before the Boston Meeting, October 3 to 7, 1954.

Any discussion of this paper will appear in a Discussion Section to be published in the June 1957 JOURNAL.

REFERENCES

1. D. T. EWING, J. M. TOBIN, AND G. D. FOULKE, *This Journal*, **103**, 545 (1956).
2. N. THON, *et al.*, *Plating*, **36**, 369 (1949).

Electrodeposition of Metals from Organic Solutions

I. General Survey

ABNER BRENNER

National Bureau of Standards, Washington, D. C.

ABSTRACT

General principles, methods, solutes, and solvents used for depositing metals from organic solvents are surveyed.

This paper covers general principles and methods for electrodepositing metals from nonaqueous media that are common to four subsequent papers in this series concerned with deposition of Al, Be, Mg, and alloys of Al with Ti and Zr.

Of 70 known metallic elements, only about 30 have been electrodeposited from aqueous solution. Many of the metals which have not been deposited would have useful applications if they could be obtained in the form of coatings or electroformed into objects. Several of these metals are of considerable current interest, namely, Ti, Zr, Mo, Ta, and W. Since a majority of the metals could not be deposited from aqueous solution, electrochemists turned their attention to nonaqueous media. These are of two types: fused salts, and compounds which are liquid at ordinary temperatures.

Practically all metals can be deposited from fused electrolytes. However, electrodeposition from fused electrolytes has not solved the problem of obtaining coherent coatings of these metals, because, with the few exceptions noted below, the deposits are obtained in the form of powders, crystals, sponges, or dendrites which are of no value as coatings. Metals in this form may, however, be of value for electrowinning purposes. From fused salt baths operated on a laboratory scale, coatings of Mo about 0.25 mm thick and coatings of Ti and Al about 0.025 mm thick have been obtained, but thus far no commercially successful process has been developed. Fused electrolytes are not discussed further in this paper.

Those metals which can be deposited from aqueous solutions can also be deposited from nonaqueous media, but such plating solutions are at present of no practical importance. In the following discussions, to distinguish between those metals which can and those which cannot be deposited from aqueous solutions, the latter group is referred to as the nonaqueous or "NQ" metals. The following discussions apply only to the NQ metals, unless otherwise noted.

Researches reported here deal with the use of organic solvents in plating baths. A nonaqueous plating bath which is liquid at room temperature has obvious advantages over a fused salt bath which must be operated at elevated temperatures. Some inorganic liquids, such as liquid NH_3, liquid SO_2, and hydrazine, have been studied as media for depositing metals, but none of the NQ metals has been deposited from them; therefore, they are not considered further in this paper. Organic compounds which melt at a sufficiently low temperature, e.g., 100°C, so that they can be handled with about the same ease as ordinary organic solvents may be considered as intermediate between fused salt baths and organic liquids. In contrast with the universality with which metals have been deposited from fused salt baths, few of the NQ metals have been deposited from organic solvents. Until recent years no satisfactory plating bath had been developed for depositing an NQ metal as a sound coating with good mechanical properties.

Although the literature contains a number of publications on the electrodeposition of metals from organic baths, the coverage of the field has been rather desultory. Work reported in the literature covers a wide miscellany of electrodepositions ranging from the alkali metals to some of the more noble metals which are not in the NQ group, e.g., Cu. In addition to the alkali metals, the literature touches on electrodeposition of Mg, Be, Ge, and Al, the last metal probably receiving the largest amount of attention. The practical accomplishments reported in the literature are disappointing. Mg was deposited from Grignard reagents (1), but in a mossy form which probably was heavily contaminated with organic matter. The reported electrodeposition of Be (2) from NH_3 and other solvents has not been substantiated here. Deposition of Ge (3) from a glycol type of bath occurs with very low cathode current efficiency. Deposition of Al from organo-metallic compounds of the alkyl type or from Friedel-Crafts reagents (4) did not yield deposits having good mechanical properties. The *n*-ethylpyridinium bromide-$AlCl_3$ bath of Hurley and Wier (5) was probably the first organic bath for satisfactorily depositing an NQ metal. It yielded the best deposits of Al obtained from an organic bath up to that time. However, this bath is more like a fused salt bath than the organic solvent type of bath of interest here. The recent development of an organic Al plating bath (6) based on the utilization of hydrides encouraged further studies of baths containing organic solvents.

General Principles

The failure of early workers in electrodeposition to obtain active metals like Al from water solutions was clearly understood. It is known that electrodeposition of a metal usually requires a potential which is less noble than its standard electrode potential. Potentials which can be reached at the cathode in aqueous solution are

limited by the discharge of H which, fortunately, usually discharges at a potential less noble than its equilibrium value, sometimes by as much as 1 v. This overvoltage makes possible the electrodeposition of a metal like Zn which is less noble than H, because H is discharged on a Zn cathode less readily than is Zn itself.

In view of the important role of H in determining which metals can or cannot be deposited from aqueous solution, it was assumed that the NQ metals could be obtained by simply electrolyzing solutions of their salts dissolved in solvents which have no active H or in which the H is more firmly bound than in water. This hypothesis is supported by the fact that alkali metals are obtained by electrolysis of solutions of certain salts in organic solvents. However, the failure of some of the NQ metals to deposit from aqueous media is not explained satisfactorily by the limitation imposed by the preferential discharge of H. For example, W, Mo, and Ge cannot be deposited in the pure state from aqueous solutions, yet their theoretical electrode potentials for reduction from acid solutions, calculated from thermodynamic data, are close to zero, e.g. (7):

(*a*) $WO_3 + 6H^+ + 6e \rightarrow W + 3H_2O$ $\quad E^0 = -0.09$ v

(*b*) $H_2GeO_3(aq) + 4H^+ + 4e \rightarrow Ge + 3H_2O$ $\quad E^0 = -0.131$

(*c*) $Ge^{++} + 2e \rightarrow Ge$ $\quad E^0 = 0$

(*d*) $H_2MoO_4(aq) + 6H^+ + 6e \rightarrow Mo + 4H_2O$ $\quad E^0 = 0$

The negative sign of the electrode potential indicates that the electrode of the metal in question is less noble than the standard H electrode. The potentials are approximate values and are calculated rather than measured, since no reversible electrodes for these metals have been prepared. A further uncertainty in these values exists because the state of the ion in solution is not fully known.

If the electrode potentials were the only criterion of deposition, these metals could be electrodeposited from aqueous solutions, since in acid solutions their potentials appear to be more noble than those of easily deposited metals like Ni or Co. The fact that alloys containing appreciable contents of W, Mo, or Ge can be obtained from aqueous solutions supports the view that the theoretical deposition potentials of these metals are not very negative. Moreover, the deposition potentials of Ni-W and Co-W alloys are more noble than those for the Fe-group metal alone (8), and this fact is additional evidence that the potential of W is more noble than that of the Fe-group metals.

The reason that some of the NQ metals do not deposit from aqueous media may lie in some kind of nonreactivity of their lower valent ions with electrons at the cathode, and not on the difficulty of attaining the equilibrium electrode potential. If this view is correct, the NQ metals can be divided into two groups: class 1, those which cannot be deposited from water solutions because their deposition potentials are too negative, and class 2, those which have a deposition potential theoretically attainable in water solution but whose ions do not react at the cathode. Attempts to deposit NQ metals of these two classes require different approaches. Metals of class 1, e.g., the alkali metals, can be deposited by utilizing solvents in which the H is more tightly bound. This type of deposition is fairly easily achieved, but a considerable difficulty has been encountered in establishing conditions for depositing NQ metals of class 2 because no knowledge exists for predicting the types of ions most likely to react at the cathode.

The question now arises as to whether or not organic solvents have any advantage over water in bringing about the deposition of the NQ metals of class 2, since with these the preferential discharge of H is not the controlling factor. There are two possible advantages of the organic solvents. First, a larger variety of complex ions can exist in organic solvents. Water is such a reactive solvent that many complex ions are immediately hydrolyzed. Second, if the electrolytic decomposition of the organic solvent requires a higher potential than that of water, perhaps a sufficiently high voltage can be attained to bring about reaction of the ions of the NQ metals of class 2.

At the present time sufficient data are not available to divide into classes 1 and 2 the NQ metals of particular interest here. However, it is believed that Al and Be are probably of class 1. These two metals are relatively easily deposited from organic solvents. The lack of success in depositing pure Ti, Zr, or Mo from organic solvents indicates that these metals may belong to class 2. The fact that Ti and Zr can be codeposited with Al lends support to the view that they belong in class 2. Probably the best way to classify the metals would be to calculate the theoretical reversible electrode potential in the solvent of interest.

The literature on electrodeposition of NQ metals from organic solvents is rather sparse and is of little help in devising means to electrodeposit a particular member of the NQ group. For such a study several thousand organic solvents and several hundred compounds of each element might be utilized. For a completely empirical approach this would present an almost unlimited number of combinations.

There are some loose concepts that (*a*) solvents having a high dielectric constant are the best for producing ionization of solutes (9–15), and (*b*) solid substances having ionic bonds in the crystal tend to ionize readily in solution (16, 17). These ideas have led to the tacit assumption that metals are most likely to be deposited from solutions composed of substances (*a*) and (*b*). Consequently, most of the nonaqueous solutions investigated consist of ordinary salts that yield conducting solutions in water, dissolved in polar solvents.

In contradiction to (*a*) it was found that ordinary ethyl ether, which has the very low dielectric constant of 4.3 as compared with 80 for water, was the best solvent for depositing the particular NQ metals studied. While some relation may exist between the conductivity of a solution of a given solute and the dielectric constant of the medium, conductivity is not a sufficient criterion of a satisfactory medium for electrodeposition. In the course of the researches to be described, many conductive solutions were obtained with a variety of organic solvents, but few yielded a metal on electrolysis.

The following observations concerning (*b*) show that the ionic nature of chemical bonds does not alone determine conductivity, as the role of the solvent is equally important. In the course of the investigations many examples were found in which a compound yielded a conducting solution in one solvent but not in another. For example, silver perfluorobutyrate, which is a salt and forms a conducting solution in water, does not form a conducting solution in benzene, although it is highly soluble. Another example is $MoCl_5$ which forms a conducting solution in water, a poorly conducting solution in ether, and a nonconducting solution in toluene. Thus, the property of two substances to yield a conducting solution is about as specific as chemical reactivity. Discussion of points (*a*) and (*b*) shows that, at present, data on the physical properties of solvents and solutes are inadequate for predicting whether a given solution will conduct and is still less useful for predicting whether the solution will yield a metallic deposit on electrolysis. However, experience here with NQ plating has resulted in some loose generalizations which make the search for plating baths somewhat more systematic.

It is concluded that the chemical nature of the solvents and solutes, not the dielectric constant of the solvent or the crystal structure of the compound, is the prime factor that determines whether a solution will conduct or whether a metal can be deposited from it. Only certain classes of solutes and solvents form plating baths, and for this to be possible, a loose ionic complex must form between solute and solvent. In the absence of the complex, no conductivity occurs. If the complex between solute and solvent is too stable, conductivity may occur, but not metal deposition. The complexes that ionize to give a conducting solution often exist only in solution. The aluminum hydride plating bath illustrates the specificity involved in forming plating baths from organic compounds. Both $AlCl_3$ and lithium aluminum hydride in diethyl ether form poorly conducting solutions, which do not yield a satisfactory deposit. If the two solutions are mixed, the resulting solution is a good conductor and on electrolysis yields a smooth, coherent deposit of Al.

Types of Solutes and Solvents Used for Electrodeposition of Al, Be, Mg, Ti, and Zr

The following discussion contains generalizations concerning types of solutes and solvents which in this research were found most satisfactory for depositing the following metals or their alloys: Al, Be, Mg, Ti, and Zr. The last two metals were not obtained in the pure state, but as Al alloys.

Solutes.—Only a few types of metallic compounds were satisfactory as solutes for plating baths. In general these were simple compounds of low molecular weight, and any organic radicals present were rather small. Only the following four classes gave any promise of success: halides, hydrides, borohydrides, and organo-metallic compounds. Of these compounds the halides and organo-metallic compounds had been used before. The use of hydrides and borohydrides constitutes an advance in the field. No single solute yielded the optimum plating bath. Usually two of these four types of compounds had to be present. For example, the hydride aluminum plating bath required both $AlCl_3$ and aluminum hydride.

These solutes contain no oxygen or N. From solutes in which the metal atom is directly bonded to oxygen or N, none of the five metals mentioned above could be deposited. Apparently, the bond between the metal and oxygen or N is too strong. For example, magnesium perchlorate or aluminum perchlorate are soluble in organic solvents, but do not yield metallic deposits on electrolysis, whereas the halides yield a metallic deposit, although powdery and of poor quality.

The number of compounds in any class of solute that is satisfactory in plating baths is limited. For example, the organo-metallics, dimethylberyllium and diethylberyllium in ethyl ether, yield a metallic deposit on electrolysis, but the phenyl derivative does not even form a conducting solution in ether. Similarly, the borohydrides of Be, Al, and Mg in ether yield metallic deposits, whereas the borohydrides of Ti and Zr in ether are not even conductive. As another example, the chloride-hydride type of plating bath yields good electrodeposits of Al but very poor deposits of Be or Mg. These examples show that the solutes which must be used for depositing each of the five elements discussed here are rather specific and limited in application.

Solvents.—As a result of numerous experiments with a variety of solvents, the following generalizations were reached. The solvent must have sufficient chemical reactivity to form, with the solute, a coordination compound that is not too stable. This requirement at once eliminates nonreactive liquids, such as paraffin hydrocarbons and some of their halogen derivatives, which do not readily coordinate. A large variety of organic liquids form coordination compounds with the four types of solutes mentioned above. Among these are oxygen-containing compounds such as alcohols, ethers, ketones, acids, and acid anhydrides; N-containing compounds, such as amines, amides, and nitriles; and unsaturated hydrocarbons, such as benzene and toluene. The molecules of these solvents have an active center consisting of an atom of either N, oxygen, or C, that is capable of coordinating with other compounds. From all these types of solvents, electrodeposits were obtained only from baths of ethers and aromatic hydrocarbons. It would appear that all the other solvents formed too stable a complex with the solute. Apparently the ethers are the best solvents because the oxygen atom coordinates sufficiently, but not too strongly, with the four types of metallic solutes which were investigated. Of the ethers investigated, ordinary ethyl ether yielded the best plating baths for the five metals with which this research was concerned.

The foregoing discussion applies only to the five NQ metals, Mg, Al, Be, Ti, and Zr, with which this research dealt, and the conclusions do not necessarily apply to other NQ metals. It is believed, however, that with the exception of the alkali metals and a few others, e.g., Ge, the conclusions are valid for the NQ metals. Some of the alkali metals can be deposited from solutions of their salts in alcohols and ketones, whereas the NQ metals discussed in this report cannot be deposited from these solvents. In particular, Li can be deposited so readily from

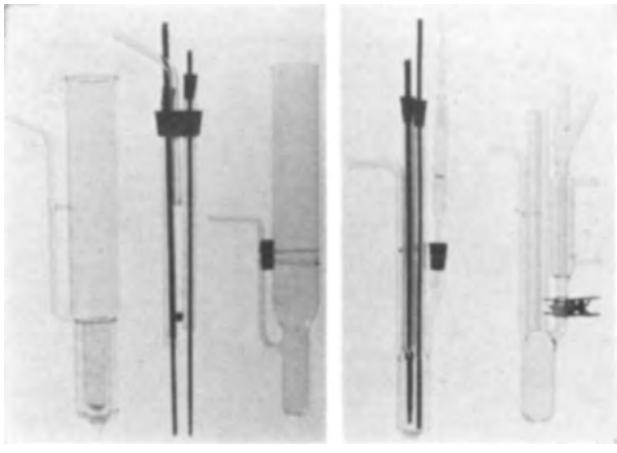

FIG. 1. Cells for electrolysis of nonaqueous solutions in absence of air. A slow current of A is passed through each cell during operation; a fast current when electrodes are removed or introduced. Cells are numbered from left to right 1–4. Cell 1 is of the Dewar type for use with low boiling liquids such as NH_3. Cell 2 is a simpler type. Between these two cells are shown the electrodes enclosed in glass chimneys. Cells 3 and 4 are of all glass construction. Cell 3 has a Hg seal valve for escape of excess pressure. Cell 4 has a condenser for volatile liquids.

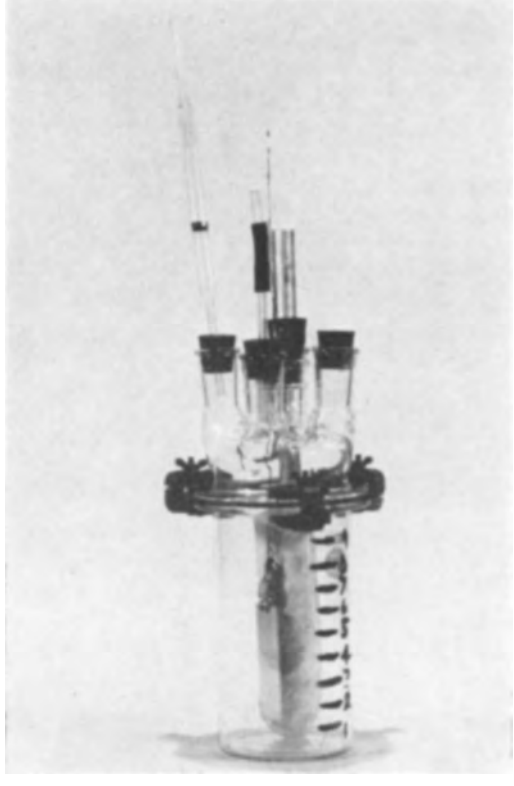

FIG. 2. Resin reaction vessel used as electrolytic cell for larger volumes of solution than can be handled by cells in Fig. 1.

a variety of organic solvents that it often constitutes a nuisance, if Li complexes of the NQ metals are used for solutes. The deposition of Li prevents the potential from rising high enough to deposit the NQ metal. Apparently, the lower coordinating power of the alkali metal salts

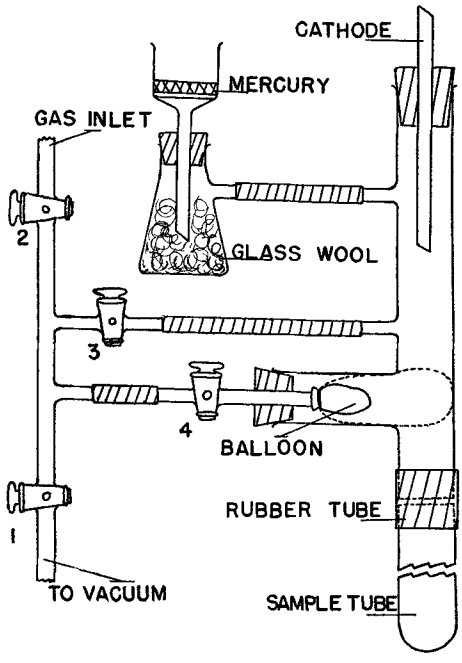

FIG. 3. Atmosphere lock for removing or introducing cathodes without ingress of air. (a) To flush the system after connecting the sample tube, previously loaded in an inert atmosphere chamber: Stopcock 2 is closed and stopcocks 1, 3, and 4 are opened while the system is evacuated. Stopcock 1 is closed, and the system is returned to atmospheric pressure by opening stopcock 2 to admit A. (b) To remove cathode: cathode is pulled up beyond the balloon which is then inflated to the desired size by closing stopcock 3 and opening 2 and 4. (c) To replace cathode: stopcocks 2 and 3 are opened and the chimney flushed while the balloon is inflated. Stopcock 2 is then closed and 4 is opened so that the balloon reduces to original size. Cathode can then be lowered into sample bath.

compensates for the higher coordinating power of the more active organic solvent. It seems paradoxical that a very active metal like Li is readily electrodeposited from organic solvents, whereas inert metals like Mo and W have not yet been deposited.

The results which were obtained in the present studies of electrodeposition from nonaqueous media may be summarized as: (*A*) The following metals and alloys were deposited: Be, Be-B alloy, Mg-B alloy, Mg-Al alloy, Ti-Al and Zr-Al alloys. (*B*) Borohydrides and hydride complexes were introduced as solutes for plating the NQ metals. (*C*) The evaluation of a variety of solvents has shown that ethers in general, and ethyl ether in particular, are the best media for the electrodeposition of the NQ metals.

APPARATUS

To complete this general survey, a brief description is given of the apparatus used for the nonaqueous electrolytes with which the other four papers of this series are concerned.

Electrodeposition of metals from nonaqueous media involves the use of solutes which are very sensitive to moisture and/or to oxygen. This situation necessitates the use of special equipment for conducting both the preparation of the compounds and the electrolysis of their solutions in a moisture-free and/or oxygen-free atmosphere.

For example, $AlCl_3$ absorbs moisture very rapidly from the atmosphere and may become useless for an Al plating bath if weighed in the open. Be and Al borohydrides are spontaneously inflammable and may explode when air is introduced into the apparatus. Dimethylberyllium is also spontaneously inflammable, and its ether solution absorbs traces of oxygen, the cumulative effect of which eventually ruins the bath.

The classical way of handling these sensitive compounds is in all-glass apparatus. This necessitates using special valves, breaking internal glass seals with an iron ball and magnet, scaling off parts of the apparatus with a flame, etc. Such methods proved far too cumbersome for this work which required compounds in larger quantities than the gram lots which are normally handled in sealed glass apparatus. In order to carry on the program expeditiously inert atmosphere chambers were constructed because at that time they were not available commercially with all the required features. These chambers were described in a recent publication (18).

Although the inert chamber was indispensable for making preparations and for handling sensitive materials, electrolysis of solutions inside the chamber proved to be rather cumbersome. Difficulties encountered in removing, observing, testing, cleaning, and replacing electrodes led to development of special electrolytic cells such as those shown in Fig. 1. An atmosphere of A was maintained in or passed through the cell. When a cathode was removed for inspection, it passed upward through a long glass chimney through which a rapid stream of A was issuing, to prevent ingress of air. The replacement of electrodes was done similarly. These cells operated quite satisfactorily for baths of 25–50 ml. For larger baths, resin-reaction flasks, shown in Fig. 2, with tubulated glass covers were used. In some experiments a more positive exclusion of air was required during removal and replacement of electrodes. This was accomplished by an air lock consisting of small rubber balloons, dime-store variety, which were inflated so as to close off the chimney when the electrode was removed. This is shown diagrammatically in Fig. 3.

The cathodes most convenient for exploratory work were Cu or Au rods about 6 mm in diameter. An Al rod was frequently used as anode because it dissolved readily, and the amounts of Al introduced into the bath were not sufficient to affect the cathode deposits in the short time that a solution was investigated.

Manuscript received October 12, 1955. This paper was prepared for delivery before the Boston Meeting, October 3–7, 1954.

Any discussion of this paper will appear in a Discussion Section to be published in the June 1957 JOURNAL.

REFERENCES

1. P. JOLISBOIS, *Compt. Rend.*, **155,** 353 (1912); **156,** 712 (1913); D. M. OVERCASH AND F. C. MATHERS, *Trans. Electrochem. Soc.*, **64,** 305 (1933); N. W. KONDYREW, *Ber.*, **58,** 459, 464 (1925); L. W. GADDUM AND H. E. FRENCH, *J. Am. Chem. Soc.*, **49,** 1295 (1927).
2. H. S. BOOTH AND G. G. TORREY, *J. Phys. Chem.*, **35,** 2464 (1931).
3. G. SZEKELY, *This Journal*, **98,** 318 (1951).
4. R. D. BLUE AND F. C. MATHERS, *Trans. Electrochem. Soc.*, **65,** 339 (1934); **69,** 519, 529 (1936).
5. F. H. HURLEY, U. S. Pat. 2,446,331, Aug. 3, 1948; F. H. HURLEY AND T. P. WIER, U. S. Pat. 2,446,349, Aug. 3, 1948; T. P. WIER, U. S. Pat. 2,446,350, Aug. 3, 1948. W. H. SAFRANEK, W. C. SCHICKNER, AND C. L. FAUST, *This Journal*, **99,** 53 (1952).
6. D. E. COUCH AND A. BRENNER, *This Journal*, **99,** 234 (1952).
7. W. M. LATIMER, "The Oxidation States of the Elements and Their Potentials in Aqueous Solutions," 2nd ed., pp. 146, 147, 252, 255, Prentice-Hall, New York (1952).
8. H. OFFERMANS AND M. V. STACKELBERG, *Metalloberfläche*, **1,** 142 (1947); M. L. NIELSON, *Trans. Electrochem. Soc.*, **29,** 226 (1942); A. BRENNER AND E. SEEGMILLER, Unpublished work.
9. S. GLASSTONE, "Introduction to Electrochemistry," p. 13, D. Van Nostrand Co., Inc., New York (1942).
10. H. J. CREIGHTON, "Electrochemistry," p. 51, John Wiley and Sons, Inc., New York (1943).
11. K. FREDENHAGEN, *Trans. Electrochem. Soc.*, **60,** 153 (1931).
12. P. WALDEN, *Z. physik. Chem.*, **46,** 169 (1903); **54,** 129 (1905).
13. L. W. GADDUM AND H. E. FRENCH, *J. Am. Chem. Soc.*, **49,** 1295 (1927).
14. H. ROHLER, *Z. Elektrochem.*, **16,** 420 (1910).
15. L. F. YNTEMA AND L. F. AUDRIETH, *J. Am. Chem. Soc.*, **52,** 2694 (1930).
16. S. GLASSTONE, *op. cit.*, p. 12.
17. H. J. CREIGHTON, *op. cit.*, p. 40.
18. J. M. SHERFEY, *Ind. Eng. Chem.*, **46,** 435 (1954).

Electrodeposition of Metals from Organic Solutions

II. Further Studies on the Electrodeposition of Aluminum from a Hydride Bath

JEAN H. CONNOR AND ABNER BRENNER

National Bureau of Standards, Washington, D. C.

ABSTRACT

Stability and operating life of the hydride aluminum plating bath were improved, and addition agents were found which permit thick deposits suitable for electroforming work. Adhesion of Al to other metals was studied. A model continuous-strip Al plating unit is described.

A process for the deposition of smooth, ductile, and coherent Al was described by Couch and Brenner (1). The metal was deposited from an ethereal hydride bath, operated at room temperature, which showed promise for commercial Al plating. It differed from other nonaqueous baths in that a hydride was used as a primary constituent of the bath, and that ordinary ethyl ether was the solvent. The plating solution consisted of an ethereal solution of 2-3M $AlCl_3$ and 0.5–1.0 M lithium hydride. Lithium aluminum hydride could be used in place of lithium hydride, but sodium and calcium hydrides were insufficiently soluble.

The appearance of the deposits depended on conditions of plating and on the amount of hydride present. With a low hydride concentration (0.25–0.4M), deposits were stressed, brittle, and dark in color, and at a still lower concentration of hydride, no deposition occurred at all. The hydride as well as the $AlCl_3$ in the bath was decomposed by moisture of the air; therefore plating was conducted in closed containers. It was possible to add lithium hydride 2 or 3 times to rejuvenate the bath, but eventually this was not effective.

The present paper describes improvements in composition and operation of the bath (1).

STABILITY OF THE BATH

Preliminary Studies

When attempts were made to electroplate on a larger scale, for example with baths of 15-l volume, it was evident that improvement was necessary because the baths could not be operated for more than a few weeks despite efforts to rejuvenate with additional lithium hydride. This was surprising because samples of the bath that had been sealed for 6 months still plated satisfactorily. A study of the stability of the solution and of the operating life was therefore made.

It was first thought that even a trace of moisture was detrimental to bath life, but it was found that a solution 3.3M in $AlCl_3$ tolerated up to 3.7 g water/l and still produced a good deposit. The water was added in the form of wet ether.

Some attempts were made to improve the stability of the solution by adding other hydrides, vacuum distilling, etc. Since these attempts were not successful, they are not discussed here, but a summary of the experiments is given in Table I.

Al deposits were also obtained on electrolysis of various other nonaqueous solutions (Table II); however, none of the baths was as satisfactory as the hydride bath with regard to appearance of the Al and stability of the solution.

The effect of the atmosphere on the bath was studied to determine the extent of decomposition by oxygen, CO_2, and moisture. Baths of 300-ml capacity were subjected to streams of dry CO_2-free air, pure CO_2, and air saturated with water. The decomposition rate of the solution was followed by observing the change in hydride concentration. These baths were compared with 3 controls: one bath which was electrolyzed continuously and two "standing" baths, not electrolyzed, one of which was opened to the atmosphere daily for analysis and the other opened weekly. This experiment showed that bubbling oxygen, CO_2, or moisture-laden air through the solution had a deleterious effect and could destroy the bath within a few hours. In the case of the "standing" control baths where the solution was not exposed to this extent, the one opened to the atmosphere for a few minutes a day lasted two weeks, while the one opened weekly lasted four weeks. The bath electrolyzed continuously lasted nearly four days. Since there appeared to be both an electrolytic decomposition and a spontaneous decomposition, the effect of each was studied under more refined conditions.

Spontaneous decomposition was observed by measuring the amount of gas evolved by a sealed sample of the plating solution. A 20-ml portion of the solution was sealed in a glass tube, and the gas given off was measured in a buret over Hg (*see* Fig. 1). Fig. 2 shows the relative decomposition rates of two solutions containing lithium hydride, one at a concentration of 10 g/l, and the other, 5 g/l. The solution higher in hydride gave off more gas during the run. It appeared that spontaneous decomposition was not rapid enough to be entirely responsible for the short life of the baths. The faster rate of decomposition at the onset of the experiment was probably due to a reaction of the solution with the air that was admitted to the tube at the same time as the solution.

Effect of Electrolysis

Electrolysis caused a much more rapid rate of decomposition as seen by the sudden increase in the volume of gas

TABLE I. *Summary of experiments to improve stability of the $AlCl_3$-lithium hydride bath*

Experiment	Purpose	Result
1. Vacuum distillation of deteriorated bath	Remove impurities. Recover plating solution.	Much residue containing Al left in distilling flask. Distillate consisting of $AlCl_3$ in ether yielded good deposits on electrolysis when hydride was added.
2. Addition of Grignard reagents	—	Too reactive with the bath. No improvement in deposit.
3. Addition of dry liquid NH_3	Precipitate impurities	Insoluble precipitate formed. No deposit obtained.
4. Addition of BCl_3	Improve conductivity	Precipitate formed with $LiAlH_4$. No deposit obtained.

TABLE II. *Variations on bath composition*

Solution	Result
1. $AlCl_3$ + butyllithium in ether	Fair deposit of Al, but Licodeposits at high concentrations of butyllithium
2. $AlCl_3$ + lithium borohydride in ether	Yielded only black deposits on electrolysis
3. Al alkyls:	
(*a*) Ethylaluminum bromide	Deposits Al on long electrolysis
(*b*) Ethylaluminum bromide + ethylsodium	Deposit and conductivity improved with addition of ethylsodium
4. $AlCl_3$ or $AlBr_3$ in toluene or benzene, Hg_2Cl_2 as catalyst	Deposited only Hg
5. Aluminum borohydride in ether	Deposit of Al obtained. Improved with addition of $AlCl_3$ and/or LiH
6. Ethers: (containing $AlCl_3$ + hydride or added to working bath)	$AlCl_3$ not sufficiently soluble or ether reacted with the bath
(*a*) Benzyl ethyl ether	
(*b*) Bis(2-ethylhexyl) ether	
(*c*) Benzyl ether	
(*d*) Ethylene glycol dibenzyl ether	
(*e*) Methyl benzyl ether	
(*f*) *p*-Diethoxybenzene	
(*g*) *n*-Methylmorpholine	
(*h*) Morpholine	
(*i*) Ethylene glycol dimethyl ether	
(*j*) Diethylene glycol dimethyl ether	
(*k*) Triethylene glycol dimethyl ether	
(*l*) Tetraethylene glycol dimethyl ether	

given off when the solution was electrolyzed by means of the electrodes in Fig. 1. The volume of gas evolved during continuous electrolysis for 1.5 days was greater than the volume of gas given off by the solution on standing for the preceding 40 days (Fig. 2). The gas evolved during electrolysis was found by mass spectrochemical analysis to be H_2.

To study further the effect of electrolysis, the solution was electrolyzed in a U-tube (Fig. 3), and the volume of gas given off at each electrode was measured. The volume from the anode was $2\frac{1}{2}$ times that from the cathode, indicating greater decomposition at the anode. This observation suggested the use of a diaphragm around the anode to confine deterioration of the bath to a small volume. The following materials were found to be insufficiently porous for diaphragms as evidenced by the high voltage required for deposition: neoprene, butyl, silicone, and natural rubbers, a self-vulcanizing rubber, polyethylene, and glass cloth. Alundum thimbles were unsatisfactory as anode compartments because electroosmosis occurred. The anolyte passed slowly into the cathode compartment during electrolysis, leaving the anode almost uncovered and thus raising the voltage of the bath. The increase in volume of catholyte raised the level of the solution and caused it to overflow back into the anode section. Thimbles made of ordinary cellulose pulp were satisfactory inasmuch as they were sufficiently porous as well as unattacked by the solution. They must be thoroughly dried before use. Experiments with baths of 500-ml volume showed that after about one week of continuous electrolysis the hydride in the anolyte was almost depleted, while the catholyte had only about a 10% loss in hydride. Without a diaphragm, a bath operated under the same conditions had about a 30% loss in hydride after one week of electrolysis. Small amounts of hydride were then added to the anode compartment to maintain the electrode efficiencies of the bath. When the anolyte became tarry and viscous (after about three weeks of continuous electrolysis) it was

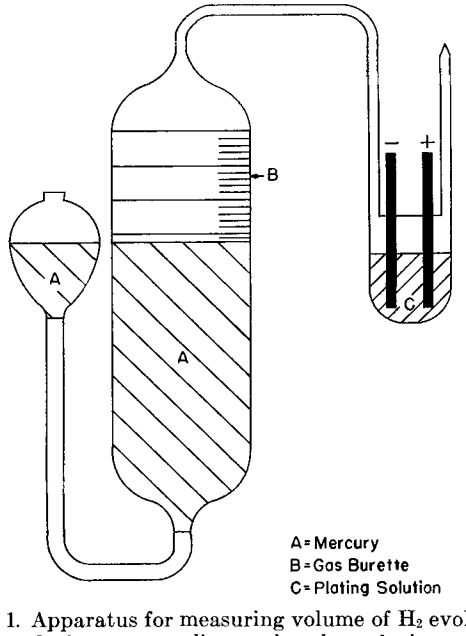

FIG. 1. Apparatus for measuring volume of H_2 evolved by plating solution on standing or by electrolysis.

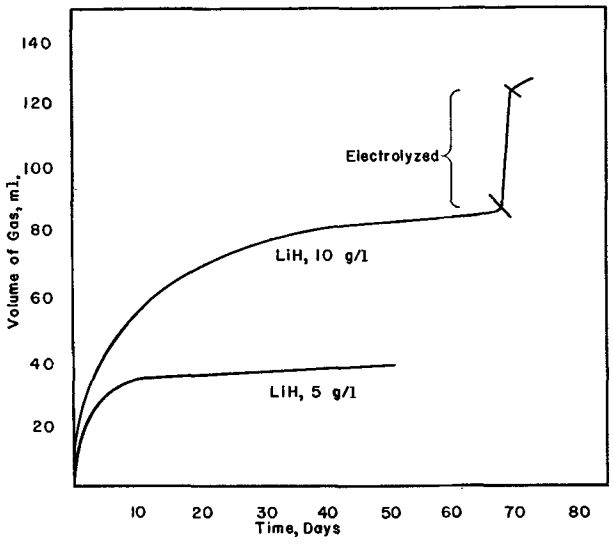

FIG. 2. Rate of H_2 evolution from 20 ml samples as measured by apparatus in Fig. 1.

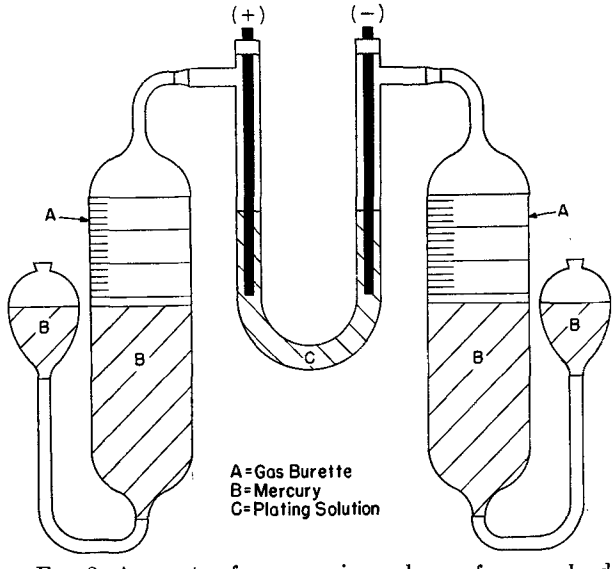

FIG. 3. Apparatus for measuring volume of gas evolved at each electrode.

siphoned out and replaced by fresh plating solution. This procedure extended the bath life considerably.

Major Factors Affecting Bath Life

The term "bath life" is used here as a measure of the quantity of good Al that can be deposited from the plating solution. It is expressed in terms of F/l of solution. Attempts were made to keep the baths operating at optimum efficiency during life tests. A newly prepared solution operated at 100% efficiency, but use of anode diaphragms decreased the cathode efficiency to 93–94%. The normal rate of deposition of 100% efficiency is 1 mil (0.025 mm)/hr at a current density of 2 amp/dm^2.

In further experiments on bath life, the detrimental effect of the atmosphere was largely obviated by using tightly sealed plating vessels that were flushed with an inert gas when the vessels were opened. Spontaneous decomposition may be considered to be a minor factor affecting bath life. Important factors are (*a*) bath composition and (*b*) operating conditions.

Bath composition.—Bath life depended on its composition. The main variables of composition were: type of hydride, type of solvent, and concentration of $AlCl_3$. Addition of lithium aluminum hydride rather than lithium hydride more than doubled the bath life. Ethyl ether was proved superior to several other solvents regarding bath life, even though some mixed ether baths gave satisfactory deposits (*see* Table III).

The bath life was approximately proportional to the concentration of $AlCl_3$ in solution, e.g., the life of a 3M bath was about three times that of a 1M bath. Baths 1, 2, and 3 of Table III show a direct relationship between the concentration of $AlCl_3$ and the bath life. Experiments indicated that the amount of Al obtainable as good deposits was equal to the amount of Al originally present in solution as $AlCl_3$. This amounts to about 80 g of Al for a 1-l bath, 3 M in $AlCl_3$, which is equivalent to the passage of 9 F. When approximately 9 F had passed through the bath, the deposits became inferior, even though the hydride concentration was normal. It was found that more $AlCl_3$ could be added at this point to prolong the bath life. The dependency of bath life on the initial $AlCl_3$ content of the baths is rather odd, because the anodes maintained the initial concentration of Al in solution. It is apparent that the Al dissolved at the anode to form a new ionic species that did not deposit at the cathode. Further evidence of a change in bath structure is the fact that the solution at the anode became viscous and was not completely soluble in ether.

Operating conditions.—The bath life under actual operating conditions was determined in terms of F/l by electrolyzing small baths continuously, changing one variable at a time. Table III shows the results of representative electrolytic life tests. The criterion for the end of the life tests was the appearance of the deposits. If they were dark, stressed, or if on standing they absorbed moisture and corroded, the bath was considered no longer serviceable. As deterioration of the quality of the deposits occurred gradually, the endpoint of the test was not definite, but involved a personal equation. For this reason reproducibility of the short life-tests was of the order of 50%. These baths were run at a current density of 0.5 amp/dm^2 because the 1M $AlCl_3$ bath had low conductivity and could not be operated at a higher current density. The 1M and 2M baths also showed an undesirable tendency to form two immiscible layers after a few days of operation or when more hydride was added. For these reasons the $AlCl_3$ concentration was chosen as 3M for the rest of the life tests and for plating in general. At higher concentrations the solution became more viscous and the hydride solubility decreased. Comparison of experiments 3 and 4 (Table III) shows that with a higher amperage effected by using larger electrodes, there was an increase in bath life, probably because there was less time for spontaneous decompcsition to occur. Lithium aluminum hydride dissolved in worked baths even after lithium hydride failed to dissolve. Lithium aluminum hydride was added

TABLE III. *Life tests on hydride* Al *plating baths*

No.	Conc. of $AlCl_3$ M	C.D. amp/dm²	Total bath life Days	Total bath life Faradays/l	Remarks
Baths with no diaphragms					
1	1	0.5	6	0.7	LiH used
2	2	0.5	11	1.1	LiH used
3	3	0.5	18	2.3	LiH used‡
4	3	0.5	10	4.1	Amperage three times that of No. 3, by using larger electrodes
4A	—	—	22	7.7	$LiAlH_4$ added to Bath No. 4
Baths with diaphragms					
5	3	0.7–1.0	67	12.2	$LiAlH_4$ to rejuvenate. Alundum diaphragm. Electroosmosis occurred.
6	3	1–2	59	17.0	$LiAlH_4$ throughout. Addition of solid $AlCl_3$. Alundum diaphragm. Electroosmosis occurred.
7	3	2–3	60	30.0	Paper diaphragm, $LiAlH_4$ and $AlCl_3$ additions.
Mixed-solvent baths*					
	Solvent†	% by Vol			
8	Phenyl ether*	50	18	3.1	Cathode effic.: 60–70%
9	Anisole	50	10	2.2	
10	Toluene	25	1	0.2	

* Diaphragm and $LiAlH_4$ used.
† Ethyl ether was used for remainder.
‡ This is the life of the plating solution described in previous publication (1).

to the bath of experiment 4 and the bath life was thereby extended to 22 days, or 7.7 F/l of solution.

The next series of life tests (Table III) show the effect of anode diaphragm on the bath life. Experiment 7 represented a culmination of preceding improvements and developed the longest bath life. This bath accommodated 30 F/l, lasting 60 days. The number of days is not too significant, e.g., bath 5 lasted a week longer, but only 12 F/l were passed through it. In experiment 7, lithium aluminum hydride was used throughout the life of the bath, and $AlCl_3$ was added by replacing the anolyte with fresh plating solution or by adding solid $AlCl_3$ to the bulk of the solution. The total weight of the deposits from this bath was 250 g/l of plating solution, indicating an over-all cathode current efficiency of 93.5%. It should be possible to extend the bath life even longer than 30 F/l of solution, because a filtered portion of bath 7 continued to yield satisfactory deposits.

A 12-l plating bath was kept in operation for intermittent plating for over 18 months. Paper anode diaphragms were used, and lithium aluminum hydride in ether solution was added to maintain the hydride concentration.

Good deposits have been reported (1) using anisole, phenetole, or phenyl ether, respectively, mixed with ethyl ether as the solvent in the bath. In the present study, life tests were performed on these baths. Table III shows that none of the baths containing mixed solvents had a life comparable to that of the bath made up with ethyl ether alone. For example, the phenyl ether bath (50% volume, experiment 8) produced good deposits, but had a bath life of only 3.1 F/l. The current efficiency of this bath was also very low. Several other ethers were evaluated for the purpose of producing a less volatile and less flammable solution, but none yielded as satisfactory deposits as the ethyl ether bath. The majority of the ethers listed in Table II were too reactive when added to the bath.

Adhesion

Al plated on cleaned and dried base metals was satisfactory but nonadherent, and the deposits could be peeled off readily. Procedures for obtaining adhesion are described below. In all cases, the degree of adhesion was judged by severe mechanical tests on deposits about 0.15 mm thick.

Al adhered excellently to Ti, to 2S and 24S Al, and to electrodeposited Al. These metals were etched anodically in the bath to give a clean, bright surface and were then made cathodic. Al plated in this way had a high degree of adhesion. Interrupting the current during Al plating sometimes resulted in formation of nonadherent layers. Therefore, as a precautionary measure, when the current was interrupted the specimen was treated anodically in the bath before plating was resumed.

If other metals were anodically etched in the bath, it decomposed, and the metals were soon covered with a heavy smut of organic matter which prevented subsequent adherent plating.

Good adhesion has been obtained to Cu, brass, steel, Ag, Cr, and Zn. (*See* Appendix for plating procedure.) Schickner (2) reported good adhesion to steel by immersing the specimen, after cleaning, in an ethereal solution of a fatty acid such as oleic acid prior to plating. Several other organic acids (not necessarily fatty acids) have been found which can be used to obtain adhesion to the above metals. Salicylic, benzoic, pyrogallic, phenylacetic, and heptafluorobutyric acids have been satisfactory, with salicylic acid giving the most consistent results. In transferring the specimen to the bath from the acid-ethereal solution, the ether evaporated, leaving a coating of acid crystals which in turn reacted with the plating solution. Whether the resulting foaming action in the bath further cleaned the metal surface is not known. The results with steel, using salicylic acid, have not been very consistent. However, treating the steel with Quilon, a chromium complex in 2-propanol, has produced very good adhesion.

Plating on Mg was not satisfactory. Mg displaced Al from the solution without current, and deposits obtained by electrolysis were thin and blistered.

Addition Agents

An addition agent that would reduce the crystallinity of deposits and allow thicker deposits to be built up was almost a necessity in electroforming objects of Al. Without an addition agent, deposits over 0.3 mm became nodular. Several articles were electroformed from baths containing no addition agents by a process involving a series of alternate plating and machining steps until the desired thickness was reached.

The smoothing effect of a number of representative compounds having various functional groups was evaluated by adding them to baths of 50-ml volume and comparing thick deposits obtained on rods 0.5 cm in diameter with deposits from an ordinary bath. The majority of compounds reacted violently with the bath, shortened the bath life considerably, or had no beneficial effect on the deposit. The most promising compounds were amines, S compounds, and B compounds. If the additions were satisfactory on a small scale, larger baths were prepared to determine the effect on bath life and to check more critically the thickness and appearance of the deposits. Methyl borate was chosen for most of the electroforming work because the concentration of 5–10 ml/l was not critical, and it yielded the thickest smooth deposits. Deposits 1.5–2 mm thick were obtained. A large amount of gelatinous precipitate, which did not interfere with plating, formed when methyl borate was added to the bath.

Applications

A model strip plater was constructed for demonstration purposes to show that with proper engineering the Al bath could be adapted for practical purposes. The plating vessel was fitted with 3 anodes and the strip metal passed lengthwise around the center anode. The top of the vessel had 2 rubber-edged slits for the entrance and exit of the strip metal. There was no appreciable loss of ether by evaporation or drag-out through the slits. The sequence of plating was: acid etch, water rinse, air-dry, plate, rinse, and dry.

Properties of Electrodeposited Al

Details on the microstructure, ductility, and hardness of the deposit have already been given (1). The deposit, as plated, is white, matte, and ductile. Thicker deposits (about 0.25 mm) and deposits plated at current densities higher than 2 amp/dm^2 have a more crystalline appearance. No quantitative tests on purity of the Al deposits were carried out, but spectrochemical analyses showed traces of Mn, Cr, Ag, Sn (0.001–0.01%) and Ti, Si, Mg, and Cu (0.01–0.1%) which probably were due to the anode material (2S Al) and impurities in the $AlCl_3$, which was a commerical grade. Li was absent. Traces of B (0.01–0.1%) were found in a deposit from a bath containing methyl borate. However, the purity of the deposits appeared to be better than that of 2S Al because the deposits withstand the action of boiling concentrated HNO_3 longer than does the 2S Al.

Electrodeposited Al may be anodized and dyed. Other processes applicable to commercial Al could be applied to electrodeposited Al.

Summary

Electrolytic decomposition at the anode was the principal cause of bath deterioration. The bath tolerated traces of moisture and CO_2; it decomposed very slowly on standing. The following factors increased the life of the Al plating bath from about 2.3 to about 30 **F**/l of plating solution: (*a*) use of lithium aluminum hydride rather than lithium hydride; (*b*) use of coarse paper anode diaphragms; (*c*) addition of $AlCl_3$ by replacing the anolyte with fresh plating solution when the bath voltage began to increase and by adding solid $AlCl_3$ to the bulk of the bath when lithium aluminum hydride failed to rejuvenate the bath. The maximum amount of Al that was deposited from a bath, rejuvenated as required, was equivalent to the amount of Al present as $AlCl_3$, even though the anode erosion maintained the Al concentration at 3M. This amounted to about 250 g/l of bath. The cathode current efficiency was about 90%; the anode current efficiency was close to 100%.

The addition of methyl borate, 5–10 ml/l of plating solution, is recommended for plating thick deposits.

Procedures are given for obtaining adhesion of the Al deposit to Cu, brass, Ag, Cr, steel, Al, and Ti.

Acknowledgments

This work was sponsored by the Department of the Army, Office of the Chief of Ordnance, ORDTA. Paul A. Krasley of NBS assisted in the designing of the model strip plater.

Manuscript received October 2, 1955. This paper was prepared for delivery before the Boston Meeting, October 3 to 7, 1954.

Any discussion of this paper will appear in a Discussion Section to be published in the June 1957 Journal.

REFERENCES

1. D. E. Couch and A. Brenner, *This Journal*, **99**, 234 (1952).
2. W. C. Schickner, *Steel*, **133**, 125 (1953).
3. J. M. Sherfey, *Ind. Eng. Chem.*, **46**, 435 (1954).
4. M. D. Banus, *Chem. Eng. News*, **32**, 2424 (1954).

APPENDIX

Preparation and Operation of the Bath

The plating solution (3M $AlCl_3$, 0.4M lithium aluminum hydride) was made up directly in the plating vessel from stock solutions of 5M $AlCl_3$ in ether and lithium aluminum hydride in ether, both of which were quite stable on standing when protected from the atmosphere. The concentration range of hydride ($LiAlH_4$) that yielded good deposits was approximately 0.13–0.4M. The upper limit was set arbitrarily, since more hydride could be added as needed. The hydride solution was added slowly to the $AlCl_3$ solution which had been diluted with ether. The $AlCl_3$ solution was cooled to permit more rapid addition of the hydride, but cooling was not necessary. A separate layer sometimes formed when the hydride solution was added, but this reacted slowly with the bulk of the solution and disappeared. In preparing the stock solutions and the

bath, the liquids were pipetted or siphoned to prevent contact with the atmosphere.

The baths were kept under an inert atmosphere to avoid exposure to the atmosphere for any length of time, e.g., when changing the anolyte.

Large quantities of $AlCl_3$ in ether were prepared in the following way: enough ether (or preferably aluminum chloride etherate) was added to the $AlCl_3$ to wet it. The remainder of the ether could then be added quickly. The mixture was stirred occasionally, and solution occurred over a 2-3 day period. If the solution was stirred too vigorously, the heat evolved caused a foaming action and the solution overflowed very quickly. $AlCl_3$ was transferred in an inert gas chamber because of its hygroscopic nature. The inert gas chamber used in this laboratory has already been described (3).

The vapor pressure of the plating solution was considerably lower than that of pure ether. Therefore, the flammability of the solution was less than expected. Electrical connections were made at a distance from the bath to avoid sparks, and Hg traps were used so that a pressure of ether or inert gas would not build up.

The plating solution was disposed of by pouring slowly into running water. This operation was carried out in a hood because of fuming. A buret arrangement whereby the solution dripped into a sink was convenient. This did not apply to the hydrides or solutions of hydrides in ether which could ignite spontaneously with water. Special care was needed in handling lithium aluminum hydride (4). It was decomposed by reaction with dioxane before adding to water.

The rate of deposition at a current density of 2 amp/dm^2 was 0.025 mm/hr.

Procedures for Obtaining Adhesion

Adhesion to Al and Ti.—(*A*) Pretreatment: 2S Al—dip in HNO_3—HF—H_2O, 10:8:82 (vol). 24S Al—dip in HNO_3—HF—H_2O, 10:8:82 (vol); rinse; dip in HNO_3, 1:1 (vol). Ti—dip in HNO_3—HF—H_2O, 1:20:80 (HNO_3, conc.; HF, 48%). (*B*) Rinse and dry. Anodic etch in bath, C.D. 10–13 amp/dm^2, 2 min. (*D*) Reverse current to make specimen cathodic. (*E*) Strike, C.D. 5 amp/dm^2, 1 min; plate, C.D. 2 amp/dm^2.

The anodic etching of Ti can be done in a separate bath to reduce the time of etching and hence the extent of decomposition in the plating bath.

Adhesion to Cu and brass.—(*A*) Bright dip, HCl—HNO_3—H_2SO_4—H_2O, 1:38:78:10 (vol). (*B*) Dip in 5% H_2SO_4 containing 2% H_2O_2. (*C*) Rinse, dry. (*D*) Immerse in ethereal solution of salicylic acid (10% wt) 10 min. (*E*) Transfer quickly to bath, plate.

Adhesion to Cr.—(*A*) Dip in warm 6*N* HCl until piece turns gray. Rinse. (*B*) Cobalt strike, C.D. 5 amp/dm^2, approximately 2 min. (*C, D, E*) Same as for Cu.

Adhesion to Ag.—(*A*) 2–3 min in hot NaOH solution (12 g NaOH + 12 g Na_2CO_3/500 cc water), rinse. (*B*) Approximately 20 sec dip in dilute HCl. (*C, D, E*) Same as for Cu. (*Note:* More drastic cleaning procedure may be necessary, depending on the specimen.)

Adhesion to steel.—(*A*) Anodic etch in H_2SO_4 (about 74% by vol), C.D. 20 amp/dm^2, 2 min. (*B*) Rinse, dry. (*C*) 10–15 min in Quilon (diluted 50% with ethyl ether). (*D*) Transfer quickly to bath and plate. No strike is necessary.

Theory of Dynamic Quenching of Photoconductivity and Luminescence

FRANK MATOSSI

U. S. Naval Ordnance Laboratory, White Oak, Maryland

ABSTRACT

The influence of infrared radiation or electric fields on photoconductivity and luminescence can be described by the following simplified model. Electrons are excited to empty centers and/or filled traps are emptied. Furthermore, radiationless transitions from conduction band to centers may be induced. The "dynamic quenching" curves (dependence of quenching effects on time) of photoconductors continuously excited to equilibrium conduction or luminescence are obtained from the particle balance between the energy levels of the model. Good qualitative agreement with experimental results of conductivity quenching of CdS is obtained by adjusting the parameters of the theory, viz., transition probabilities, efficiencies of center-filling and trap-emptying, and equilibrium densities of conduction electrons and empty centers. In some cases, it is necessary to assume the existence of two kinds of centers or traps with different values of the parameters. Simple approximate formulas for computing the numerical values of the parameters from characteristic features of the dynamic quenching curves are derived.

The modification of photoconductivity or luminescence in CdS and ZnS semiconductors by infrared radiation or by electric fields has recently been investigated in some detail (1–6). The aspect of this phenomenon with which this paper is concerned is "dynamic quenching" (3), that is, the change of photoconductivity or luminescence with time while the quenching agent (infrared radiation or electric field) is applied, or after its removal. Usually, the

"quenching" is a superposition of stimulation effects and quenching proper.

This paper deals with a mathematical description of the dynamic quenching in terms of a simplified model of the energy levels and transitions in a semiconductor by considering the particle balance among the energy levels in a similar manner as was utilized for the description of electrophotoluminescence effects in a-c fields (7). The present approach is more general, although it is restricted to d-c effects.

It may be mentioned now that dynamic quenching is satisfactorily described by the simplified model. But this very fact precludes the use of such observations alone for the determination of the properties of more refined models such as that of Rose (8). On the other hand, the same fact permits one to characterize the behavior of the phosphor by a few phenomenological parameters, whose numerical values can be evaluated independent of any mechanism. The variation of these values with varying experimental conditions may, however, provide clues with respect to the underlying mechanisms.

The Model

Three single energy levels, the conduction band, traps, and luminescence centers, are assumed. Empty centers are not explicitly distinguished from holes in the valence band, although this distinction is implicitly contained in the mechanisms that may be used to interpret the formulas. The quenching agent may excite electrons from traps to the conduction band, resulting in stimulation of conductivity and luminescence, or it may fill centers by exciting electrons from the valence band to the centers. This filling of centers impedes radiative transitions from conduction band to the centers, thus producing luminescence quenching. In addition, another trap emptying may occur by radiationless transitions from traps to centers. Whether conductivity is quenched or stimulated by this effect depends on whether the increased opportunity of trapping overcompensates loss of transitions to centers or not. Furthermore, there may be radiationless transitions from the conduction band to the centers or to holes in the valence band, induced by the quenching agent (7).

This model can be thought of as a much simplified form of Rose's model (8) used by Bube (3). There is also some relation to the model employed by Kallmann and Kramer (1) except for a different treatment of the radiative transitions, which here are assumed to be "bimolecular." In any case, these and other models (9) were not worked out to determine the time dependence of the quenching effect.

The mathematical formulation of the model is given by the following equations for the particle balance:

$$\begin{aligned} dN/dt &= \eta - A_1Nm - A_2N(n - m + N) + \epsilon' - \beta \\ dm/dt &= \eta - A_1Nm - \zeta' - \beta \end{aligned} \qquad \text{(I)}$$

N is the number of free electrons in the conduction band; m is the number of empty centers; n, the total number of traps; $n - m + N$, the number of empty traps; η, the number of electrons excited per unit time, by ultraviolet for instance, from centers to the conduction band. ϵ', ζ', β describe the possible actions of the quenching agent per unit time; ϵ' gives the number of electrons emptied from traps to the conduction band; ζ', the number of electrons raised to the centers; β, radiationless transitions induced by the quenching agent (7). All these numbers refer to unit volume. A_1 and A_2 are appropriate transition probabilities, A_1 referring to the radiative transitions that produce a luminescence intensity $L = A_1Nm$, and A_2, to the trapping of conduction electrons. Thermally excited transitions, which are assumed to be in equilibrium, are not considered explicitly. Their influence would be implicitly contained in the values of A_i, which may be temperature-dependent. It will be assumed that $\epsilon' = \epsilon(m - N)$, $\zeta' = \zeta m$, but the specific dependence of ϵ' and ζ' on N and m is not very important.

In addition to the β-transitions, Eq. (I) contains radiationless transitions between the trap and center levels since

$$d(m - N)/dt = A_2N(n - m + N) - \epsilon' - \zeta' \qquad \text{(II)}$$

so that an equal number ζ' of traps is emptied as are centers filled.

Eqs. (I) and (II) do not tell anything about mechanisms. They describe a phenomenological model. Therefore, it is immaterial whether, for instance, the β-process refers to direct transitions between the pertinent levels or to any other process that results indirectly in an equal loss of conduction electrons and empty centers, such as the one envisaged for the interpretation of electrophotoluminescence effects (6). There it is assumed that some electrons may be trapped at the surface, where they attract holes, thus impeding the capture of these holes by centers. Similarly, the ζ'-transitions in Eq. (II) may be direct transitions from traps to centers or transitions from traps to holes in the valence band created by the ζ'-process of Eq. (I). The last possibility is the more probable one.

The simplification of the model lies in the assumption of single trap and center levels and treating empty centers and holes in the valence band as mathematically identical. The parameters of the theory, i.e., A_i, m, N, ϵ, ζ, β, have, therefore, the character of "effective" properties of aggregates of levels. The impact of the simplifications on the results are considered later. Suffice to say that the simplified model proves well suitable for the description of the observations.

Furthermore, it is assumed that the phosphor is excited to equilibrium photoconductivity or luminescence, for instance by ultraviolet radiation, and that this excitation is maintained throughout.

As long as ϵ' and ζ' can be considered as constants, the three parameters ϵ', ζ', β reduce to only two, viz., $\epsilon' - \beta$ and $\zeta' + \beta$. β will, therefore, be deleted as mathematically superfluous. The question, whether it is necessary to retain β explicitly for the interpretation of the experiments, is discussed later.

The assumption $m_0 = n$ implies that the total number of centers is larger than the number of traps (10). It must be kept in mind that m_0 is the number of empty centers, not that of excited centers. This last number determines the equilibrium density. For the justification of other approximations *see* Ref. (10), which is the basis of the present theory.

Results

The solution of Eqs. (I) and (II) will be given for small deviations from equilibrium by putting $N = N_0 + \Delta$, $m = m_0 + \delta$ with $m_0 = n$ and retaining only linear terms in Δ and δ. For N_0 and m_0, Eqs. (I) and (II) with $\epsilon = \zeta = \beta = 0$ are assumed to be valid. Calculations are further simplified by the approximations $N \ll m$; $\epsilon, \zeta \ll A_i m$. A_1 shall be of the same order of magnitude as A_2. N and m are used again as notation for the equilibrium values N_0 and m_0 unless otherwise stated.

Then the relative change of conductivity

$$s = (\sigma - \sigma_0)/\sigma_0 = \Delta/N,$$

and the relative change of luminescence intensity, $l = (L - L_0)/L_0 = (N\delta + m\Delta)/Nm$ is given by

$$s = [\mu_0 + \mu_1 \exp(\rho_1 t) + \mu_2 \exp(\rho_2 t)]\epsilon/N + [\nu_0 + \nu_1 \exp(\rho_1 t) + \nu_2 \exp(\rho_2 t)]\zeta/N \quad \text{(III)}$$

$$l = [\kappa_0 + \kappa_1 \exp(\rho_1 t) + \kappa_2 \exp(\rho_2 t)]\epsilon/N + [\lambda_0 + \lambda_1 \exp(\rho_1 t) + \lambda_2 \exp(\rho_2 t)]\zeta/N \quad \text{(IV)}$$

with

$$\rho_1 = -A_2 N - \epsilon - \zeta, \qquad \rho_2 = -A_1 m$$

$$\begin{aligned} \mu_0 &= 1/A_2, & \mu_1 &= (A_2 - A_1)/A_1 A_2, & \mu_2 &= -1/A_1 \\ \nu_0 &= -\mu_1, & \nu_1 &= \mu_1, & \nu_2 &= 0 \\ \kappa_0 &= N/A_1 m \cong 0, & \kappa_1 &= 1/A_1, & \kappa_2 &= -1/A_1 \\ \lambda_0 &= \kappa_2, & \lambda_1 &= \kappa_1, & \lambda_2 &= 0 \end{aligned} \quad \text{(V)}$$

κ_0 should be zero in the approximation used, but a second approximation is included for reference later.

As mentioned earlier, the quenching effect caused by the β-process can be obtained by substituting $\epsilon' - \beta$ and $\zeta' + \beta$ for ϵ' and ζ', respectively, or by substituting $\epsilon - \beta/m$ and $\zeta + \beta/m$ for ϵ and ζ. The coefficients of the exponentials in Eq. (III), (IV), and (V) then have the form $\nu_i - \mu_i$ and $\lambda_i - \kappa_i$. For $\zeta = 0$, the formulas derived previously (7) for electrophotoluminescence are obtained.

The method of obtaining these equations is standard and need not be described in detail. The Appendix gives the rigorous formulas from which the approximate Eqs. (III), (IV), and (V) are derived.

When the quenching agent is removed after a long time ($t = \infty$) so that constant values s_∞ or l_∞ have been reached, s and l follow the equations

$$s_r = s_\infty - s, \qquad l_r = l_\infty - l \quad \text{(VI)}$$

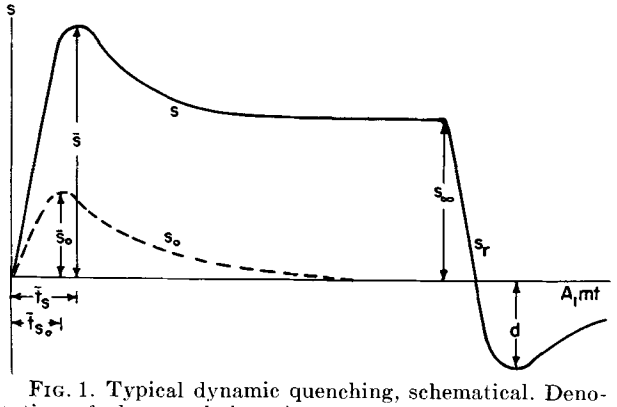

Fig. 1. Typical dynamic quenching, schematical. Denotation of characteristic points.

where the subscript r indicates the return to original equilibrium and where the zero of the time scale is shifted to the beginning of this decay. s and l in Eq. (VI) are again given by Eq. (III), (IV), and (V) with, however, a slight change of the coefficients insofar as the expressions for a, b, d in the Appendix must be replaced by $a + \epsilon$, $b - \epsilon$, $d + \zeta$. This substitution changes ρ_1 to $\rho_{1r} = \rho_1 + \epsilon + \zeta = -A_2 N$, apart from minor changes in the coefficients μ_i, etc. This is a consequence of the assumptions $\epsilon' = \epsilon(m - N)$ and $\zeta' = \zeta m$ if N and m in these correction terms assume their actual values and not the constant equilibrium values N_0 and m_0. Then ϵ and ζ appear in the coefficients of the differential equations for Δ and δ (Appendix). The specific form of $\rho_{ir} - \rho_i$ depends, of course, on the particular assumptions made about $\epsilon' = \epsilon'(m, N)$, $\zeta' = \zeta'(m, N)$ and on the approximations applied. This specific form is not of interest at the present time, and it will only be noted that $|\rho_1| > |\rho_{1r}|$. In general, the difference between ρ_1 and ρ_{1r} is disregarded in first approximation, and $\rho_1 = -A_2 N$ is used.

Fig. 1 shows a typical curve as given by Eqs. (III) to (V) and (VI) with the denotation of characteristic points. Except for the difference of the coefficients a to d during "infrared on" and "infrared off," the curve for s_r is the mirror image of s reflected at the abscissa axis and shifted to another point of origin, viz., s_∞.

One of the characteristic features of the dynamic quenching curves given by Eqs. (III) to (V) is a "stimulation" maximum at $\bar{t}_s$ or $\bar{t}_l$, given, respectively, by the formulas

$$\begin{aligned} A_1 m \bar{t}_s &\cong \ln[(m/N)(\epsilon/(\epsilon + \zeta))A_1/(A_2 - A_1)] \\ A_1 m \bar{t}_l &\cong \ln[(m/N)(\epsilon/(\epsilon + \zeta))A_1/A_2] \end{aligned} \quad \text{(VII)}$$

The maximum values themselves are given by

$$\bar{s} \cong \epsilon/A_1 N, \qquad \bar{l} \cong \epsilon/A_1 N \quad \text{(VIII)}$$

The maximum may disappear or may even become a minimum, depending on the signs of $A_2 - A_1$ and ϵ.

Equilibrium values reached at large times are

$$s_\infty \cong \epsilon/A_2 N + (A_1 - A_2)\zeta/A_1 A_2 N, \qquad l_\infty \cong \epsilon/A_1 m - \underline{\zeta/A_1 N} \quad \text{(IX)}$$

If $\zeta = \zeta_0 = A_1\epsilon_0/(A_2 - A_1)$, one writes $s = s_0$, $l = l_0$ with $s_{0\infty} = 0$ and $l_{0\infty} = \epsilon_0/(A_1 - A_2)N$.

The slopes at $t = 0$ are

$$s' \cong \underline{m\epsilon/N} - (A_2 - A_1)\zeta/A_1, \qquad l' \cong \underline{(m/N} - A_2/A_1)\epsilon \quad \text{(X)}$$

Some terms of a second order approximation have been retained in Eqs. (IX) and (X). The principal terms are underlined.

With these approximations for the characteristic points of dynamic quenching curves, the simple and useful expression

$$\begin{aligned} s &= (\bar{s} - s_\infty)\exp(\rho_1 t) - \bar{s}\exp(\rho_2 t) + s_\infty \\ &= \bar{s}[\exp(\rho_1 t) - \exp(\rho_2 t)] + s_\infty[1 - \exp(\rho_2 t)] \end{aligned} \quad \text{(XI)}$$

and a similar one for l can easily be derived.

In principle, the foregoing formulas can be used to determine values of the parameters from the observa-

tions. But not all of them are practicable for this purpose since they involve magnitudes difficult to measure exactly, for instance, s' for large values of ϵ. This is particularly so if only conductivity or luminescence data are available, where the first approximation does not provide for sufficient independent equations. If both kinds of data exist, especially such including s_0 and l_0, some simple relations for the ratios of some parameters can be deduced, viz.,

$$\begin{aligned} A_1 m &= s_0'/\bar{s}_0 , \\ A_2/A_1 &= 1 - (l_0'/l_{0\infty})(\bar{s}_0/s_0') = \\ &\qquad 1/[1 - \exp A_1 m(\bar{t}_{l_0} - \bar{t}_{s_0})], \\ m/N &= (A_2/A_1) \exp A_1 m \bar{t}_{s_0} \end{aligned} \qquad \text{(XII)}$$

The second relation offers the opportunity of checking the internal consistency of the theory or of the approximations used. These relations contain only ratios of measured magnitudes.

Discussion

Fig. 2 and 3 give some examples of dynamic conductivity quenching for a particular choice of the parameters ($\rho_2 = 10\rho_1$; $A_1/A_2 = \frac{3}{4}$ or 2; different values of ϵ, ζ). These parameters were chosen so that Bube's experimental results (3) with CdS could be fitted. The results are not very sensitive to changes in either ρ_2/ρ_1 or A_1/A_2. The experimental points indicated are read from Bube's published figures after an appropriate adjustment of the time scale.

As is obvious from Fig. 2 and 3, the simplified model used in deriving the theoretical curves is in very good qualitative and also in good quantitative agreement with the observations, even in some details:

1. According to Fig. 2, increasing ζ is equivalent to increased quenching if $A_1 < A_2$. This is to be expected from the model, since filling of the centers empties an equal number of traps, and this creates a loss of conduction electrons because of increased trapping opportunities. However, if $A_1 > A_2$ (Fig. 3), the decrease of opportunities for transitions from conduction band to centers with its correlated increase of conduction electrons is the more important contribution so that a net increase of conductivity results. Thus, the difference between curves like those in Fig. 2 and those in Fig. 3 is not so much the consequence of different time constants, as was suggested previously (2, 3), but is primarily controlled by different ratios A_1/A_2.

2. The difference $\bar{s} - s_\infty$ is observed to be nearly the same for different curves that show maxima at all. This difference is given, in the author's approximation, by $\bar{s} - s_\infty = (A_2 - A_1)(\epsilon + \zeta)/A_1A_2N$. Therefore, it is constant if $\epsilon + \zeta = \text{const}$ and if all curves refer to the same kind of traps and centers (A_1, A_2 constant). The experimental curves were obtained by applying radiation of different wave length, keeping the number of photons constant. Since the total number of trap emptyings and center fillings is determined by the number of incident photons, it is reasonable to consider $\epsilon' + \zeta'$ or $\epsilon + \zeta \cong (\epsilon' + \zeta')/m$ as a measure of the photon density, which is kept constant. However, the relative contributions of the two processes may change, for instance be-

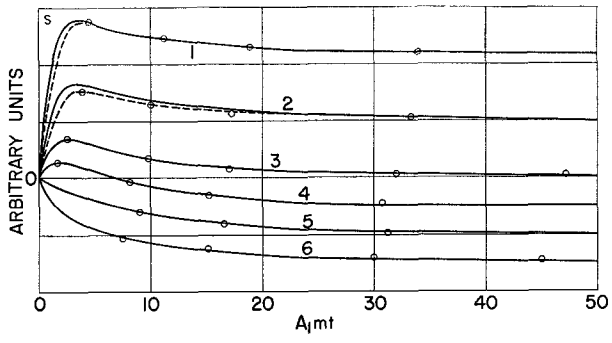

Fig. 2. Conductivity quenching. $A_1/A_2 = \frac{3}{4}$; $\rho_2/\rho_1 = 10$; ———— theory, · · · O · · ·—O— observation (3); ϵ and ζ in arbitrary units ($\epsilon + \zeta = \text{const}$). Curve 1: $\epsilon = 3.1$, $\zeta = 0.9$; curve 2: $\epsilon = 2$, $\zeta = 2$; curve 3: $\epsilon = 1$, $\zeta = 3$; curve 4: $\epsilon = 0.5$, $\zeta = 3.5$; curve 5: $\epsilon = 0$, $\zeta = 4$; curve 6: $\epsilon = -0.5$, $\zeta = 4.5$.

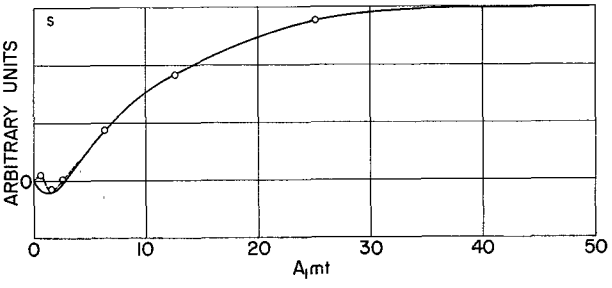

Fig. 3. Conductivity quenching. $A_1/A_2 = 2$; $\rho_2/\rho_1 = 10$; ———— theory, · · · O · · · —O— observation (3); $\epsilon = -0.5$, $\zeta = 2.5$ in arbitrary units.

cause different sublevels of the composite "single" trap level of the model are affected. Any contribution of β-processes is irrelevant in this respect, since the influence of β cancels out in $\epsilon + \zeta$.

3. The position of the maxima shifts to longer times with increasing ϵ/ζ, but the observed shift seems to be larger than the computed one. However, experimental data for the position of the peaks are not as accurate as the other measurements. The same is true for the initial slopes, which do not grow as fast as Eq. (X) indicates.

4. In order to obtain complete coverage of the observations described in Fig. 2, it is necessary to use negative values of ϵ. This means that it is necessary to introduce explicitly radiationless transitions from the conduction band to the centers or to the valence band since only $\epsilon - \beta/m$ may assume negative values. This point will be discussed later in more general terms.

5. Bube finds that radiation with wave lengths smaller than 6500Å does not produce curves like those in Fig. 1 or 2 but only a general increase of s to an equilibrium value. Such curves cannot be obtained by merely adjusting ϵ and ζ but only by another choice for A_1/A_2, for instance $A_1 = A_2$. This forces the conclusion that another kind of centers or traps with different transition probabilities becomes involved and not only different sublevels of one kind of traps or centers.

6. A superposition of two different kinds of centers is also necessary to describe the small peak observed in Fig. 3. Here not only the ratio A_1/A_2 would have to be changed

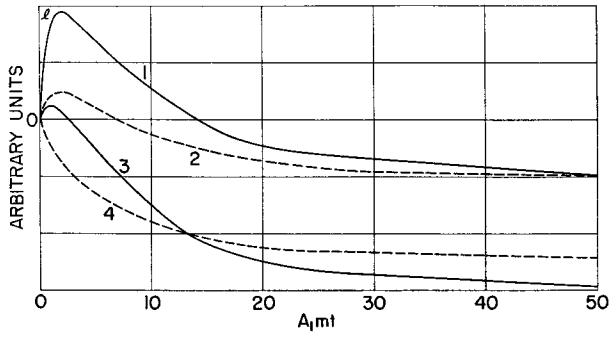

FIG. 4. Luminescence quenching, theoretical $\rho_2/\rho_1 = 10$. Curve 1: $\epsilon = 3$, $\zeta = 1$; curve 2: $\epsilon = 1$, $\zeta = 1$; curve 3: $\epsilon = 1$, $\zeta = 3$; curve 4: $\epsilon = -0.5$, $\zeta = 2.5$.

but also the absolute value of A_1m, which determines the time scale.

7. After removal of the quenching radiation, the photoconductivity follows curves that are nearly the mirror images of s, as required by Eq. (VI). Because of $\bar{s} - s_\infty =$ const, the minima corresponding to the peaks of s should all have the same depth $d = \bar{s} - s_\infty$ below the abscissa axis. Actually, this is not rigorously so [*see* Fig. 1 of Bube (3)], but the difference of the observed minima is much smaller than that of the peak heights. However, complete agreement with the curves obtained during irradiation need not be expected because of the difference of the coefficients a to d during "infrared on" and "infrared off." In particular, the increase of the time constants because of $|\rho_{1r}| < |\rho_1|$ is clearly indicated in the observations. Furthermore, it can be shown, by extending the calculations to second-order approximations, that the difference between the absolute value of the depth of the return curves and $\bar{s} - s_\infty$ is proportional to $(A_2 - A_1)\zeta^2 - A_1\epsilon^2 + (A_2 - 2A_1)\epsilon\zeta$. This expression is negative for curves 1 and 2 of Fig. 2, zero for curve 3, and positive for $\zeta/\epsilon > \zeta_0/\epsilon_0$. The observations confirm this qualitative result quite well, but the calculation is not sufficiently accurate for a quantitative comparison. It must be mentioned that the expectation of constant $\bar{s} - s_\infty$ is based on an approximation where ϵ and ζ are supposed to be zero in the coefficients a to d. Therefore, it should be valid for the "off" period, while it is actually observed for the "on" period. This means that $A_1/A_2 =$ const cannot be rigorously true for the curves of Fig. 2.

8. Fig. 4 shows theoretical curves for luminescence quenching. Published data on infrared luminescence quenching (4) are not sufficient for a detailed comparison of theory and experiment, but there is general qualitative agreement. It should, however, be mentioned that curves of the type shown in curves 1 and 2 of Fig. 2, with $l_\infty > 0$, have actually been observed in a few cases of luminescence quenching by electric fields (5), although from Eq. (IX) only negative values would be expected as long as $N \ll m$ and ϵ/ζ are not extremely large. But without these restrictions, it seems possible to account also for positive values of l_∞. The specific form of the Eqs. (III) to (XI) would then become much more complicated.

The foregoing discussion shows that a very simplified model of the quenching mechanism is indeed sufficient to account for the general and many of the detailed observations. At the same time, this means that an unequivocal decision between different more complicated and detailed mechanisms cannot be obtained from dynamic quenching alone, although in special cases conclusions of this kind seem possible, such as the inference of β-processes from the necessity of using negative ϵ-values. The necessity of ζ-processes cannot be established in this way since it is always possible to replace ζ entirely by β. However, the model may be refined to provide for three independent constants ϵ, ζ, β by separating the centers explicitly from the valence band, assigning ζ-processes to transitions from valence band to centers and β-processes to transitions from conduction band to valence band. If this is done, a cubic equation for ρ is obtained of which two roots are very close together and practically identical with ρ_2. The third root is about equal to ρ_1. Therefore, this refined model would give similar results as Eqs. (III) to (V) only with more complicated expressions for the coefficients μ_i, etc. These will not be presented here. There is one significant result of the refined model. Luminescence quenching is obtained only for $\zeta \neq 0$ or if again an equivalent β-process of the kind introduced in the simplified model is used, i.e., one involving transitions from conduction band to centers, not to the valence band. Still more general equations (9) lead to similar conclusions.

There is one essential difference in ζ-processes and β-processes of the simplified model. The ζ-process has a time constant $1/\rho_2$ because of $\nu_2 = 0$ and $\lambda_2 = 0$ [*see* Eq. (III to V)]. The β-process has a time constant $1/\rho_1$ because of $\nu_1 - \mu_1 = 0$ and $\lambda_1 - \kappa_1 = 0$ [*see* Eqs. (III) to (V) and the paragraph following them], but different time constants of the basic processes are not necessarily reflected in different time constants of the quenching curves because the ϵ-processes interfere. However, electrophotoluminescence quenching curves show evidence (6) for the occurrence of both the ζ-process and the β-process. In this case, the two processes can be separated because the β-process stops at a certain time while the other remains active. It may be mentioned again that the β-process is considered to be not a direct transition between conduction band and centers but an indirect process involving holes in the valence band with the same net result: equal loss of empty centers and conduction electrons.

CONCLUSIONS

The considerations presented here afford a simple formalism, which provides at least a qualitative description of the observations in terms of different electron transitions induced by the quenching agent. Furthermore, it is possible to evaluate the parameters of the theory quantitatively. Although the parameters describe average properties of aggregates of energy levels, they can be used for characterization of the behavior of the material within a certain range of experimental conditions. The set: $A_1/A_2 = \frac{3}{4}$; $m/N = 40/3$; $A_1m = \frac{4}{3}$; $\epsilon + \zeta =$ const; only ϵ/ζ variable, describes, for instance, observations on conductivity quenching obtained with radiation of a wide range of wave lengths (Fig. 2). The formalism as such is independent of any specific mechanism and may be considered a simplified model of several more elaborate mechanisms. It permits one to ascribe quantitative sig-

nificance to the parameters of any appropriate mechanism within the limits imposed by the simplification and approximation inherent in the model.

Manuscript received February 17, 1956.
Any discussion of this paper will appear in a Discussion Section to be published in the June 1957 JOURNAL.

REFERENCES

1. H. KALLMANN AND B. KRAMER, *Phys. Rev.*, **87**, 91 (1952).
2. E. A. TAFT AND M. H. HEBB, *J. Opt. Soc. Amer.*, **42**, 249 (1952).
3. R. H. BUBE, *Phys. Rev.*, **99**, 1105 (1955).
4. K. NAKAMURA, *J. Phys. Soc. Japan*, **10**, 715 (1955).
5. G. DESTRIAU, J. MATTLER, M. DESTRIAU, AND H. E. GUMLICH, *This Journal*, **102**, 682 (1955); M. DESTRIAU, *Compt. rend.*, **238**, 2298 (1954).
6. F. MATOSSI AND S. NUDELMAN, *This Journal*, **103**, 122 (1956).
7. F. MATOSSI, *Phys. Rev.*, **98**, 434 (1955). For correction of errors in this paper, *see Phys. Rev.*, **101**, 1835 (1956).
8. A ROSE, *ibid.*, **97**, 322 (1955).
9. I. BROSER AND R. WARMINSKY, *Ann. Physik*, **7**, 289 (1950).
10. J. T. RANDALL AND M. H. F. WILKINS, *Proc. Roy. Soc. (London)*, **A 184**, 390 (1945).

APPENDIX

From Eq. (I) with $\beta = 0$ are obtained, according to the method outlined in the text before Eqs. (III) to (V), the differential equations

$$d\Delta/dt = a\Delta + b\delta + \epsilon_0', \qquad d\delta/dt = c\Delta + d\delta - \zeta_0' \qquad \text{(XIII)}$$

where

$$a = -A_1m_0 - 2A_2N_0 - \epsilon, \qquad b = (A_2 - A_1)N_0 + \epsilon,$$
$$c = -A_1m_0, \quad d = -A_1N_0 - \zeta;$$
$$\epsilon_0' = \epsilon(m_0 - N_0) \cong \epsilon m_0, \qquad \zeta_0' = \zeta m_0.$$

The solutions are given by

$$\begin{aligned} \Delta &= B_1\exp(\rho_1 t) + B_2\exp(\rho_2 t) + E \\ \delta &= B_1'\exp(\rho_1 t) + B_2'\exp(\rho_2 t) + E' \end{aligned} \qquad \text{(XIV)}$$

with

$$\begin{aligned} E &= -(d\epsilon_0' + b\zeta_0')/(ad - bc) \\ E' &= \zeta_0'/d - cE/d \\ B_1 &= \rho_2(\rho_1 - d)E/(\rho_2 - \rho_1)d - (\rho_1 - d)(\rho_2 - d)\zeta_0'/(\rho_2 - \rho_1)cd \\ B_1' &= cB_1/(\rho_1 - d) \\ B_2 &= \rho_1(d - \rho_2)E/(\rho_2 - \rho_1)d + (\rho_1 - d)(\rho_2 - d)\zeta_0'/(\rho_2 - \rho_1)cd \\ B_2' &= cB_2/(\rho_2 - d) \end{aligned} \qquad \text{(XV)}$$

$$B_1 + B_2 + E = 0 = B_1' + B_2' + E'$$

and where ρ_1 and ρ_2 are solutions of $(a - \rho)(d - \rho) - bc = 0$

The coefficients μ_i to λ_i in Eqs. (III) to (V) are obtained from Eq. (XV) by neglecting ϵ and ζ in the coefficients a to d. This approximation is equivalent to putting $\epsilon' = \epsilon_0'$, $\zeta' = \zeta_0'$ already in Eq. (I). This procedure is sufficient for the purpose of obtaining a description of the dynamic quenching during "infrared on." But the difference of the quenching curves during "infrared on" and "infrared off" (3) indicates that a more refined treatment may be valuable [*see* item 7 under Discussion and the text after Eq. (VI)].

Voltage Dependence of Electroluminescence of Powdered Phosphors

WILLI LEHMANN

Lamp Division, Westinghouse Electric Corporation, Bloomfield, New Jersey

ABSTRACT

The time-average electroluminescent emission intensity, L, of powdered phosphors has been measured over wide ranges of the applied sinusoidal voltage, V. The best fit for moderate and high voltages has been obtained with $L = A\exp[-B/(V + V_0)]$. The emission intensity of all phosphors goes to a finite saturation value if the applied voltage becomes very large. The approach to this saturation is given by $L = A\exp(-B/V)$. The saturation brightness, A, is in almost all cases proportional to the applied frequency. Since the emission of the particles of a powdered electroluminescent phosphor is in general very nonuniform, the over-all emission intensity, L, must be the integral over all volume elements, dv, of the local brightness β. This integral fits the experimental results if $\beta = a\exp(-b/cF)$ and $cF = V$. It is believed that normally a and b are essentially constant in this integral but that the constant of proportionality, c, between the electric field strength, F, and the voltage, V, obeys a certain statistical distribution throughout the phosphor due to the complex geometrical structure of the phosphor.

The electroluminescent brightness of a powdered phosphor is dependent on many parameters, such as amplitude and frequency of exciting voltage, shape of the voltage curve, temperature, thickness of the phosphor layer, and kind of phosphor (1–15). Since a clear interpretation of an experiment requires the variation of only one parameter at a time, the dependence of the time-average of the electroluminescent emission intensity, L, on the exciting sinusoidal voltage, V, has been examined for several types of phosphor. The powdered phosphors were mixed with a little castor oil and this mixture was placed in a cell consisting of an Al back electrode and a front electrode of

conducting glass with an electrode spacing of about 60–80 μ. The cell and its typical effect of "phosphor bridges" between the electrodes, as well as the other apparatus used, have been described already (1). The phosphor in the cell was excited by sinusoidal voltages up to 600 v rms and with frequencies between about 20 and more than 50,000 cps. Additionally, some measurements have been carried out with 60 cps only, but up to 3,000 v rms. The average electric field strength across the phosphor particles in the cell was always very nearly proportional to the applied voltage, due to the "bridges" of the phosphor particles (1). Special attempts were made to cover a voltage range as large as possible.

Experimental Results and Comparison with Some Equations

Most of the phosphors examined show no noticeable color change when the voltage is varied (only observed exception: ZnS-Mn, Cu with two independent emission bands) and qualitatively all these phosphors have the same dependence of the emitted light intensity on the exciting voltage. A typical example is shown in Fig. 1 for a green emitting ZnS-Cu (0.6%), Cl[1] phosphor. Some special points of significance are: (*a*) the light intensity increases rapidly for low, and more slowly for high voltages; (*b*) rate of increase is greater for higher frequencies, and vice versa; and (*c*) the dependence of L on V cannot be expressed by a simple power law, otherwise the curves in Fig. 1 would be straight lines. These three points (except for some double activated ZnS-Cu, Mn phosphors) were observed on all phosphors examined (over 500 samples of different composition) and at all temperatures between $-150°$ and $+150°$C. Also, occurrence of a strong thermal quenching of the electroluminescent emission, e.g., at higher temperatures, does not affect the character of the $L(V)$ curves and the conclusions outlined in this paper.

Several workers have attempted to find a mathematical expression for the experimental dependence of $L(V)$. The first, by Destriau (2), was

$$L = A \exp(-B/V) \qquad \text{(I)}$$

with A and B as constants. Later (3), Destriau changed this to

$$L = AV^n \exp(-B/V) \qquad \text{(II)}$$

with n being a constant of the order of two. Since then, many other more or less empirical equations have been discussed (4–13). Many equations fit the experimental data over several decades of brightness but none fits in any case over the whole range of 6 or 8 or more decades of brightness which actually can be measured. In view of this confusing situation it may be useful to describe here the voltage behavior of the brightness by a simple empirical equation without any claim to a theoretical background. Two such empirical equations, describing two essentially different possibilities for the law $L(V)$ in the region of very high voltages, are discussed here in detail.

[1] 0.6 mole % Cu added before firing. The amount of Cu retained in the finished phosphor may be of the order of 0.1 mole %.

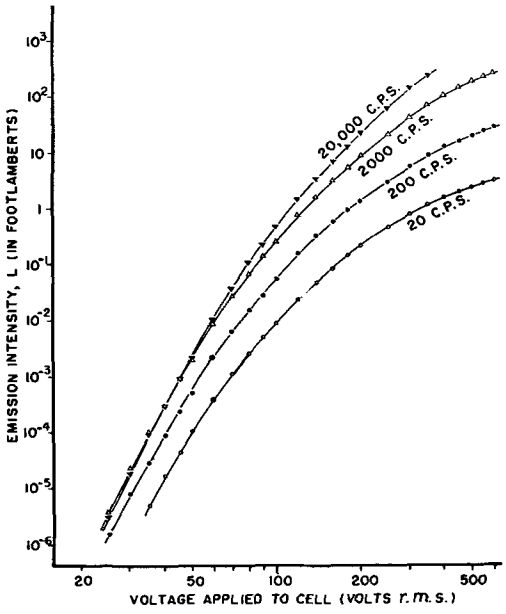

FIG. 1. Dependence of electroluminescent brightness, L, on voltage, V, for several frequencies. Phosphor: ZnS—Cu(0.6%), Cl, (950°C; 1 hr), green emission for all frequencies.

(*A*) The brightness L may go to a finite saturation value if the voltage V becomes (theoretically) infinite. An equation expressing such saturation has been given by Ivey (13)

$$L = A \exp[-B/(V + V_0)] \qquad \text{(III)}$$

with A, B, and V_0 as constants. The brightness approaches $L = A$ if the voltage V goes to infinity

(*B*) The brightness L may become infinite for infinite voltage V as far as the mechanism valid for finite V is also valid for infinite V (theoretically). An equation expressing such nonsaturation has been proposed by Howard and published by Howard, Ivey, and Lehmann (9)

$$L = AV \exp[-B/(V + V_0)] \qquad \text{(IV)}$$

with A, B, and V_0 again as constants. These two equations are used here to decide whether there is a saturation of brightness with increasing voltage, or whether there is no saturation. For experimental proof of this question, measurements at highest voltages are most important. Therefore, some measurements were carried out, at a frequency of 60 cps, up to 3,000 v rms, corresponding to an average field strength across the phosphor of about 5×10^5 v/cm. Results of a typical series of measurements are plotted in Fig. 2 with log L as a function of $1/(V + V_0)$ and in Fig. 3 with log (L/V) as a function of $1/(V + V_0)$. In both diagrams, the parameter V_0 has been so chosen that the best possible fit is reached. It is seen that Eq. (III) gives a good fit for moderate and high voltages, while Eq. (IV) fits well for low and moderate voltages, but shows a strong deviation just in the region of highest voltages of most interest here. Fig. 2 shows distinctly the approach of L to a limiting value for V approaching infinity.

Of course, there is uncertainty in extrapolating an experimental curve such as that of Fig. 2 down to $1/V = 0$, a value which can never be reached by experiment. But, as far as can be stated from these experiments,

two important conclusions may be drawn: (*a*) the electroluminescent brightness goes to a saturation value $L = A$ if the applied voltage goes to infinity; and (*b*) the approach to $L = A$ is given by Eq. (I). [Eq. (I) and (III) are identical for $V_0 \ll V$]. These two conclusions have been checked by examining all other known, more or less empirical, equations for $L(V)$ (1–13) and on many other series of measurements. All equations which predict an infinite L for infinite V predict values of L which are too high compared with experimental data in the high voltage region. The reason for the relatively good fit of Eq. (III) with experiment in the high voltage region is probably due to the fact that this equation gives not only the correct value of $L = A$ for $1/V = 0$, but also of the slope

$$d(\log L)/d(1/V) = -B$$

and the second derivative

$$d^2(\log L)/d(1/V)^2 = 2BV_0$$

at the point $1/V = 0$ if the constant V_0 has been properly chosen. It is believed that the constant V_0 has no other significance.

This result of a voltage saturation of the electroluminescent brightness seems to be important for the theory of electroluminescence since it indicates that only a very limited number of carriers can be excited during each cycle of the applied alternating voltage even if this voltage becomes infinite. It seems to be important also from a technical standpoint, since it predicts that, for a given phosphor and for other given conditions, a brightness exceeding the saturation value cannot be obtained by an increase in voltage. The saturation brightness can be determined graphically for each phosphor and under given conditions, e.g., frequency, temperature, amount of phosphor in the cell. It should be emphasized, however, that the saturation value A probably is real, but that the constants B and V_0 of Eq (III) have no simple physical significance at all.

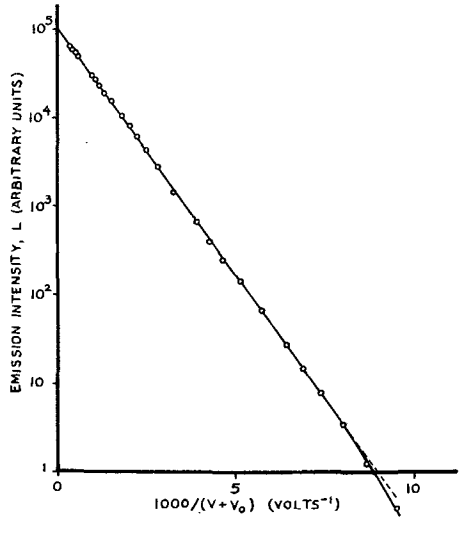

FIG. 2. Dependence of log L as a function of $1/(V + V_0)$. Phosphor: green emitting ZnS—Cu, Cl; frequency: 60 cps; $V_0 = 55$ v.

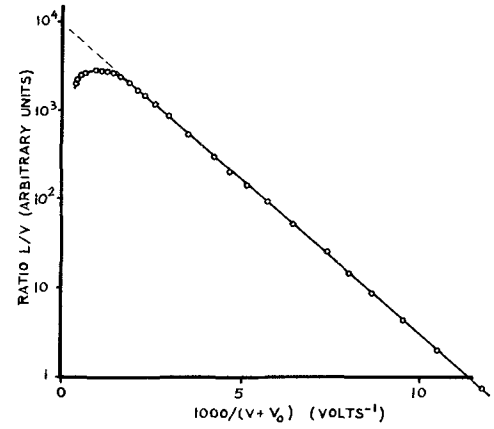

FIG. 3. Dependence of log (L/V) as a function of $1/(V + V_0)$. Phosphor: green emitting ZnS—Cu, Cl; frequency: 60 cps; $V_0 = 35$ v.

The dependence of the emission intensity L on the applied frequency has also been studied but, unfortunately, the situation here is rather complex even from the experimental standpoint. It is easy to vary the frequency and to hold constant the voltage applied to the cell. Furthermore, any process of electroluminescence in the phosphor occurs with exactly the same frequency as that applied to the cell. But field strength at any point in the phosphor particles is not known, nor is its dependence on frequency, even when the voltage to the cell remains constant, because of the complicated and nonhomogenous structure of the particles. This may be one reason for the complicated behavior of the electroluminescent brightness during frequency variations as long as finite voltages are applied. The frequency behavior of the brightness at such voltages where voltage variations no longer play a role, i.e., the

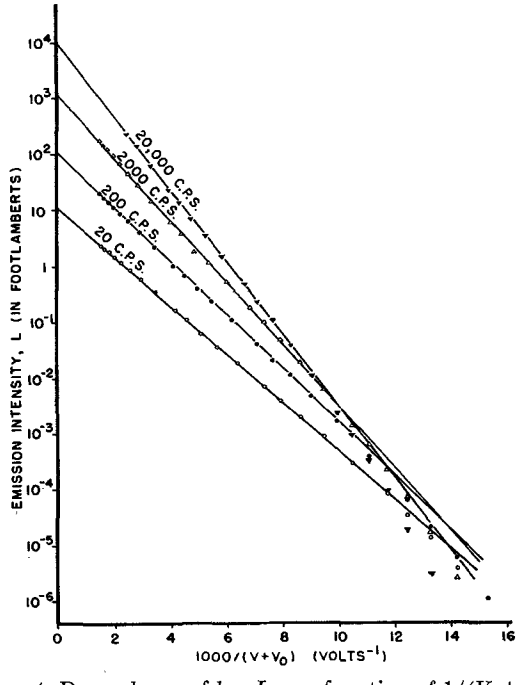

FIG. 4. Dependence of log L as a function of $1/(V + V_0)$ for various frequencies. Phosphor: ZnS—Cu(0.6%), Cl, (950°C; 1 hr).

behavior of the voltage-saturated brightness, is somewhat simpler, however.

Fig. 1 has been replotted in Fig. 4 with log L as a function of $1/(V + V_0)$. The value of V_0 for each frequency was so chosen that the best possible approximation to a straight line occurs. It may be observed that the saturation brightness, A, is proportional to the applied frequency, f. In Eq. (III), therefore,

$$A = A_0 f \qquad \text{(V)}$$

where A_0 is a constant independent of frequency. This proportionality of the saturation brightness, A, to the frequency, f, is found in almost all cases where this dependence has been examined and where the emission color of the phosphor remains constant when the frequency is varied. There are exceptions to this rule, however, but these are relatively rare.

Influences of the Nonuniformity of the Phosphor

The time-averaged emission intensity, L, of a layer of a powdered electroluminescent phosphor is dependent in a complicated way on the alternating voltage applied to this phosphor layer due to the nonuniformity of the emission throughout the phosphor volume. Even the emission of a single phosphor particle normally is very nonuniform, as can be seen microscopically and as was shown by Zalm, Diemer, and Klasens (4) and by Waymouth and Bitter (10). This nonuniformity of the electroluminescent emission throughout the phosphor particles is well known and is quite in contradiction to the uniform emission for excitation with ultraviolet radiation. Because of this nonuniform emission distribution, the measured over-all emission intensity, L, must be expressed by an integral of the strongly position-dependent local brightness, β, over the entire phosphor volume v in the cell:

$$L = \int_0^v \beta \, dv \qquad \text{(VI)}$$

The over-all emission intensity L and its dependence on the voltage V can be measured directly, but it is the local brightness β and its dependence on the local field strength F, neither directly measurable, which are basically correlated to the excitation mechanism of electroluminescence. It is evident that the two dependences $L(V)$ and $\beta(F)$, or (since the local field F is also dependent on the applied voltage V) $L(V)$ and $\beta(V)$ must be quite different. However, it is known that $\beta(V)$ must also have a saturation if V increases to infinity; otherwise the integral (VI) would not describe the observed saturation of L with increasing V.

The considerations thus far do not apply to any specific mechanism of electroluminescence or to any special law of $\beta(V)$. Their basis is only the well-known fact of the nonuniform distribution of the local emission intensity throughout the phosphor crystals and they are, therefore, rigorously valid. The situation shall now be illustrated in two special cases.

Case A.—Let the local emission intensity β be dependent on the voltage V according to

$$\beta = a \exp(-b/V^{1/2}) \qquad \text{(VII)}$$

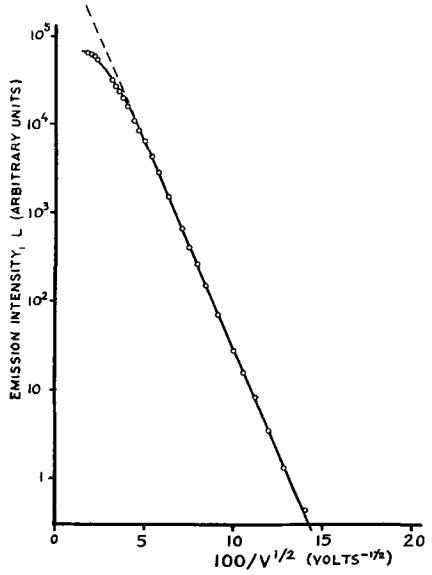

Fig. 5. Dependence of log L as a function of $V^{-\frac{1}{2}}$. Phosphor: green emitting ZnS—Cu, Cl; frequency: 60 cps.

with a and b as constants. This equation has some significance in the exhaustion-barrier theory of electroluminescence where a square root dependence of the local field strength, F, on the applied voltage, V, is predicted for those parts of the phosphor where excitation occurs, i.e., the exhaustion barriers, (5, 8, 12, 15). Inserting (VII) into (VI) one obtains

$$L = \int_0^v a \exp(-b/V^{\frac{1}{2}}) \, dv \qquad \text{(VIII)}$$

where generally a and b may be dependent on the location dv in the phosphor. Since these dependencies are unknown, the integral (VIII) cannot be solved analytically. But the integral can be replaced approximately by a series

$$L = \sum_i a_i \exp(-b_i/V^{\frac{1}{2}}) \Delta v_i$$

or, after substitution:

$$a_i \, \Delta v_i = A_i \text{ and } b_i = B_i:$$
$$L = \sum_i A_i \exp(-B_i/V^{\frac{1}{2}}) \qquad \text{(IX)}$$

Each term of this series represents a finite fraction of the phosphor with approximately equal values of A_i and B_i. Evidently all terms of the series must be positive since they represent light intensities. Each term of the series (IX) can be presented as a straight line in a diagram where log L is plotted as a function of $V^{-1/2}$. Therefore, if Eq. (VII) describes the real dependence of the local emission intensity β on the voltage V, it should be possible to approach the experimentally obtained values of $L(V)$ graphically by a summation of the ordinates L_i of several suitably chosen straight lines in a diagram showing log L as a function of $V^{-1/2}$. The actual situation is shown in Fig. 5. The fit is remarkably good, except for the region of the highest voltages, if only one term of the series (IX) is used, i.e.,

$$L = A \exp(-B/V^{1/2}) \qquad \text{(X)}$$

This equation has been mentioned frequently (5, 11, 15), but there are several reasons why it may be assumed that (X) is only an approximation, although a good one:

(*A*) Even if the deviation in the high voltage region is neglected, the fit with only one term of the series (IX) is too simple to be real, since it means, according to the integral (VIII), that at least b is constant throughout the phosphor volume. But a constant value of b means a uniform electric field inside the phosphor crystals and this is in strong contradiction to all observations (4, 10, 14).

(*B*) The deviation in the high voltage region cannot be covered by any choice of positive values of A_i in (IX).

Therefore, the conclusion must be drawn that Eq. (VIII) is not able to describe the true dependence of the local emission intensity β on the applied voltage V.

Case B.—Let the local emission intensity β be dependent on the voltage V according to

$$\beta = a \exp(-b/V) \qquad \text{(XI)}$$

with a and b again as constants. This equation may find its theoretical basis also in a collision excitation mechanism but, in contrast to the case A, with an internal local field strength F proportional to the applied voltage V. Then the integral (VI) in this case becomes

$$L = \int_0^V a \exp(-b/V)\, dv \qquad \text{(XII)}$$

The values of a and b are generally dependent on the location in the phosphor and, since this dependence is largely unknown, an analytical treatment of (XII) is impossible. Therefore the integral must be replaced by a series,

$$L = \sum_i L_i = \sum_i A_i \exp(-B_i/V) \qquad \text{(XIII)}$$

where only positive values of A_i (and B_i) have meaning. In a diagram, each term $L_i(V)$ gives a straight line if log L is plotted as a function of $1/V$. Therefore, if Eq. (XI) should represent the true dependence of β on V, the experimental dependence of $L(V)$ should be approached by a sum of straight lines in this diagram. This is indeed possible as is shown in Fig. 6 where, within the accuracy of the measurements, three terms of the series (XIII) are sufficient to cover the experimental values completely over the whole range. More exact measurements would probably require more terms of the series in order to get a good fit, quite in agreement with the fact that the series (XIII) is only an approximation to the integral (XII).

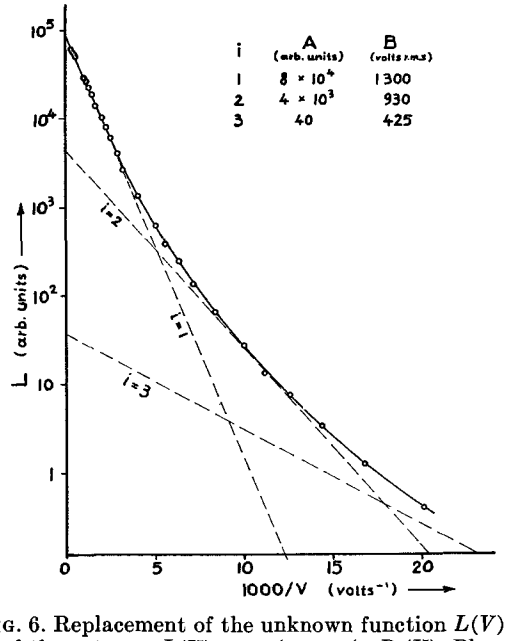

FIG. 6. Replacement of the unknown function $L(V)$ by a sum of three terms $L(V) = \Sigma_i A_i \exp(-B_i/V)$. Phosphor: green emitting ZnS—Cu, Cl; frequency: 60 cps.

DISCUSSION AND CONCLUSIONS

The considerations given above have been extended also to other more or less empirical equations for the unknown function $\beta(V)$, e.g., to the functions

$$\beta(V) = a(V - b)^n$$
$$\beta(V) = aV^n \exp(-b/V)$$
$$\beta(V) = aV \exp(-b/V^{1/2})$$

but none of these equations, inserted into a series like (IX) and (XIII), fits the experimental data over the whole range. Thus, simple Eq. (XI) seems to have some validity in describing the real dependence of $\beta(V)$, at least approximately. If so, then the conclusion must be drawn that the local field strength F is proportional to the applied voltage V

$$V = cF$$

(c = const.) also for those limited parts of the phosphor where electroluminescent excitation and emission occurs. The local excitation and emission density then is given by

$$\beta = a \exp(-b/cF) \qquad \text{(XIV)}$$

an equation which can easily and quantitatively be explained by the common collision excitation mechanism.

In general, nothing can be said about the dependence of the three constants a, b, and c in (XIV) on the volume position within the phosphor, but the writer tends to the assumption that in a normal good electroluminescent phosphor the two constants a and b are essentially independent of the position within the phosphor and only dependent on the bulk material of the phosphor. In this case, only the constant c of proportionality between field F and voltage V would obey a certain distribution throughout the phosphor volume. This distribution may be determined by statistical reasons related to the complex geometrical structure of a powdered electroluminescent phosphor.

The question remains open as to how far the really observed dependence of $L(V)$ is due not to one, but to several mechanisms differently dependent on the voltage. Such addition of the influences of several mechanisms is possible, at least in principle; but this assumption is not necessary since the collision excitation mechanism in connection with Eq. (XIV) is easily able to cover the whole range of $L(V)$, if the nonuniformity of the emission distribution is considered.

ACKNOWLEDGMENTS

The author is indebted to H. F. Ivey, C. H. Haake, and B. T. Howard for discussions.

Manuscript received February 24, 1956. Some of the material in this paper was presented at the Symposium on Electroluminescence and Photoconduction commemorating the Centennial of the Polytechnic Institute of Brooklyn, Sept. 9, 1955.

Any discussion of this paper will appear in a Discussion Section to be published in the June 1957 JOURNAL.

REFERENCES

1. W. LEHMANN, *This Journal*, **103**, 24 (1956).
2. G. DESTRIAU, *J. Chim. Phys.*, **34**, 117 (1937).
3. G. DESTRIAU, *Compt. rend.*, **209**, 36 (1939).
4. P. ZALM, G. DIEMER, AND H. A. KLASENS, *Philips Res. Repts.*, **9**, 81 (1954).
5. G. F. ALFREY, *Brit. J. Appl. Phys.*, Suppl. No. 4, p. 44 (1955).
6. J. B. TAYLOR, *ibid.*, p. 45 (1955).
7. P. ZALM, *ibid.*, p. 48 (1954).
8. W. W. PIPER AND F. E. WILLIAMS, *ibid.*, p. 39 (1954).
9. B. T. HOWARD, H. F. IVEY, AND W. LEHMANN, *Phys. Rev.*, **96**, 799 (1954).
10. J. F. WAYMOUTH AND F. BITTER, *ibid.*, **95**, 941 (1954).
11. F. A. SCHWERTZ, J. J. MAZENKO, AND E. R. MICHALIK, *ibid.*, **98**, 1133 (1955).
12. B. T. HOWARD, *ibid.*, **98**, 1544 (1955).
13. G. DESTRIAU AND H. F. IVEY, *Proc. I.R.E.*, **43**, 1911 (1955).
14. E. E. LOEBNER, *Phys. Rev.*, **98**, 1545 (1955).
15. P. ZALM, G. DIEMER, AND H. A. KLASENS, *Philips Res. Repts.*, **10**, 205 (1955).

Anodic Reactions

I. Kolbe Electrosynthesis of Ethane Using Alternating Current

CHRISTOPHER L. WILSON[1] AND WILLIAM T. LIPPINCOTT[2]

McPherson Chemical Laboratories, The Ohio State University, Columbus, Ohio

ABSTRACT

Kolbe electrosynthesis with acetate has been studied in a variety of solvents using 60-cycle AC. Results were qualitatively similar to those obtained with DC. With AC, however, yields of ethane were 30–40% lower and the critical current density was considerably higher. Ethylene glycol, H_2O, and glacial HOAc were the best of those solvents studied. H_2SO_4 in glacial HOAc provides an excellent medium for ethane production. Quantitative data on the effect of current density, temperature, and added reagents is presented.

The Kolbe electrosynthesis has been extensively studied using DC (1). Shipley and Rogers (2) published some quantitative data on the a-c electrolysis of KOAc in H_2O and in glacial HOAc. This work has now been extended to cover a wider range of conditions in these and other solvents. In addition, a new system for ethane production, H_2SO_4 in anhydrous HOAc, has been found to offer interesting possibilities.

EXPERIMENTAL

Reagents.—All reagents used in this work were A.C.S. grade.

Electrolysis cells.—These were large Pyrex test tubes varying in volume from 150 to 500 ml, fitted with rubber stoppers. Twenty gauge platinum wire served as electrodes. The electrode area was either 1.0 or 1.52 cm^2. Collodion was used to seal the rubber stoppers to the cells.

Sixty cycle AC was controlled by a Superior Electric Co. Powerstat and the current measured by a Weston Model 528 ammeter which had been calibrated. This instrument reads rms current.

Cells were immersed in 2 l Dewar flasks filled with ice and water or ice, salt, and water. At high current densities temperature control was difficult and at all current densities with AC there was a large conversion of electrical power to heat.

Preparation of electrodes.—Electrodes were placed in aqua regia for 5 min. Then, after washing thoroughly with water, they were rinsed with the solution to be electrolyzed and placed in the cell.

Gas analysis.—Analyses for CO_2 and C_2H_6 were made by infrared absorption spectrometry. Checks on the spectrophotometric method for CO_2 were made by absorption in aqueous KOH. Oxygen was determined by absorption in alkaline pyrogallol and hydrogen by reduction of hot copper oxide.

Gas samples were collected in a Baird Model 1028–6 gas analysis cell of approximately 100-ml capacity having NaCl windows and twin brass needle valves for entrance and exit of gases. Gases leaving the electrolysis cell were first passed through a dry ice trap to remove water vapor and collected in the gas cell by displacement of air. The required sample was collected only after about 20 times the volume of the gas cell had been allowed to pass through. After each analysis the gas cell was flushed with nitrogen before being used again.

A Baird Infrared Spectrophotometer Model B was used for analysis. Calibration curves using samples of pure CO_2

[1] Present address: Hudson Foam Plastics Corp., Yonkers, N. Y.

[2] Present address: Kedzie Chemical Lab., Michigan State University, East Lansing, Mich.

and C_2H_6 were obtained by regulating the pressure of the pure components in the cell using a gas handling system and measuring the height of chosen bands. These data gave curves relating height and gas pressure. In all analyses two wave lengths were used for each compound. For CO_2 the bands at 4.4 and 14.8 μ were used, for C_2H_6 the 3.2 and 6.8 μ bands were used.

The base line density technique was employed in all cases to determine peak heights.

The amount (per cent) of each component in the gaseous mixture was obtained by dividing the pressure of that component by the atmospheric pressure and multiplying by 100.

Electrolysis with AC.—Solutions to be electrolyzed were placed in the electrolysis cells and the circuit closed. Electrolysis was allowed to proceed for an hour while current density and temperature were adjusted. Samples were then removed at regular time intervals and analyzed. Values reported are averages of many analyses made during at least two separate runs with each solution.

Current efficiencies and current densities were calculated using the average current, i.e., the ammeter reading multiplied by 0.90.

Results and Discussion

Current density.—In the Kolbe reaction the products of electrolysis usually consist of O_2, H_2, CO_2, and hydrocarbon. As current density is raised, hydrocarbon increases rapidly, becomes the predominant anodic product along with CO_2, and thereafter changes but little with increasing current density. The approximate position where this independence begins is known as the "critical current density." At this point oxygen formation is usually very small.

For 1M aqueous acetate solution the critical current density with DC at smooth platinum electrodes is well defined at 0.25 amp/cm² (Fig. 1). With AC (Fig. 1), although small amounts of ethane are obtained at 0.6 amp/cm², appreciable quantities are not liberated until the critical current density is reached at about 4 amp/cm². Even then, the current efficiency for ethane formation is less than half that for the DC process. At 4.0 amp/cm²

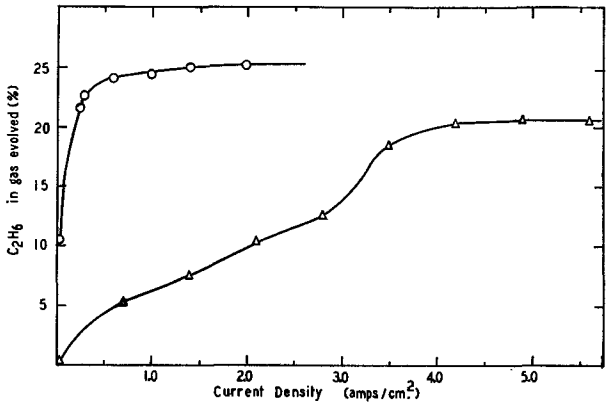

Fig. 1. Effect of current density on ethane formation from aqueous KOAc using AC and DC. Temp, 25°C; KOAc, 0.75M, HOAc, 0.25M. ○ = DC; △ = 60 cycles AC.

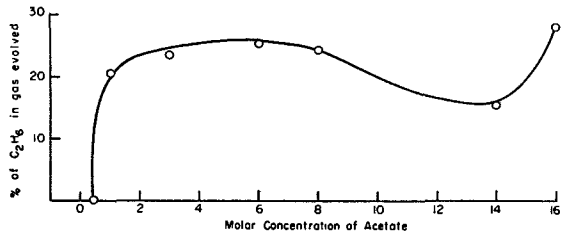

Fig. 2. Relationship between ethane formation and acetate concentration using AC. Temp, 25°C; current density, 5.5 amp/cm²; frequency, 60 cycles; medium, 0.25M HOAc containing KOAc.

using 1M acetate solution the current efficiency is approximately 65% with DC and less than 25% with AC.

The lower current efficiencies with AC may be explained by the operation possibly of three factors. First, there can be considerable power loss due to the charging and discharging of a condenser formed by gas films on the electrodes; second, there are undoubtedly stored on the electrode products either stable molecules such as oxygen and hydrogen or intermediates of a radical character, which revert to their original state or are otherwise degraded when the polarity changes; third, there will be power dissipation due to the building up and subsequent dissolution of concentration layers adjacent to the electrode. Reference to Fig. 1 shows the presence of two inflection points in the AC curve relating products and current density. It could be that between these points all three factors are operative, but at the second inflection point the formation and reversion of intermediate compounds attains a limit since the electrode surface is only capable of handling a limited amount of surface process. In principle there is no limit to the magnitude of the other two factors.

Influence of added ions.—As with DC, electrolysis with AC produces Kolbe product best when the solution is free from all anions other than acetate. Addition of carbonate, which happens if the solution turns alkaline, sulfate, nitrate or iodide in molar concentration leads to the formation of methanol or esters by the so-called Hofer-Moest reaction, and the yield of ethane is cut in half.

On the other hand, increase in acetate concentration itself leads to a slight over-all increase in ethane formation as illustrated in Fig. 2.

The curve goes through a minimum at about 14M acetate concentration and then increases rapidly. There is no obvious explanation of the minimum which has no parallel in d-c electrolysis.

Certain cations such as Cu^{++}, Co^{++}, and Fe^{+++} at 0.03M inhibit the d-c formation of ethane. These cations, however, have no appreciable effect in the a-c experiments. There has never been a really satisfactory explanation of the effect of these cations in d-c electrolysis except, perhaps, that of Glasstone and Hickling (1) who pointed out that these cations catalyze the decomposition of H_2O_2 and the effect is, therefore, support for the H_2O_2 theory of the Kolbe reaction. The absence of any similar effect in a-c electrolysis must, however, either introduce some scepticism regarding the H_2O_2 theory or require some other special explanation. It may be that under conditions of

TABLE I. *Effect of temperature on a-c electrolysis of aqueous* KOAc
(Current density, 5.5 amp/cm². Frequency 60 cycles) KOAc, 0.75M; HOAc 0.25M

Temp, °C	Gaseous products (%)		Efficiencies (%)	
	C_2H_2	CO_2	Oxidation	Current
0	21.6	51.0	84.8	19.7
25	20.5	50.3	81.6	18.4
50	25.3	58.2	87.0	23.3
75	15.4	55.4	55.6	14.1
95	5.4	64.2	16.8	4.9

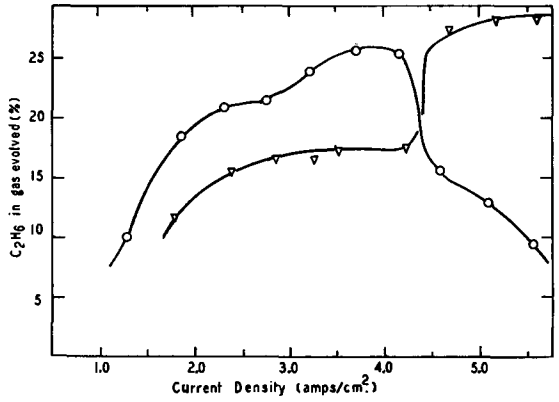

FIG. 3. Effect of current density on ethane formation from HOAc containing KOAc or H_2SO_4 using AC. Temp, 25°C; frequency, 60 cycles. △ = KOAc 1.0M; ○ = H_2SO_4 10%.

a-c electrolysis the ions spend most of their time at a lower state of valence in which they have much less catalytic effect on the decomposition of H_2O_2.

It could be pointed out here that in d-c electrolysis in nonaqueous as contrasted with aqueous media, the cations mentioned above do not affect the Kolbe synthesis. This is further evidence for H_2O_2 as intermediate in aqueous media since it is unlikely to form in organic media.

Temperature.—Change of temperature has the same effect with AC as with DC. Table I shows that a slight rise in yield occurs up to about 50° after which there is a sharp decline.

Organic media.—The effect of changing from aqueous to organic media is essentially the same with both AC and DC. In organic media, temperature, current density, and the nature of the anode are no longer as critical as in aqueous solution. In the present experiments the yield of ethane (Fig. 3) is slightly higher in glacial HOAc as solvent and the critical current density is about the same. Above current densities of 5.5 amp/cm², yields drop because of excessive local heating.

H_2SO_4 dissolved in glacial HOAc appears to be an excellent medium for ethane production. The critical current density appears (Fig. 3) to be considerably lowered and an appreciable quantity of ethane is produced at a current density of 1.8 amp/cm². Above 4.0 amp/cm² local heating, charring, and electrode deterioration occur and the yield drops off sharply. Increasing the concentration of H_2SO_4 has an adverse effect on yield of ethane, the best (25.6%) is obtained at low (5%) concentration (Table II).

The mechanism of the electrode process with acetate and H_2SO_4 should be very different, but yet the results (Fig. 3) are not greatly dissimilar. If peroxide intermediates (H_2O_2, Ac_2O_2, persulfate) were involved greater differences might be expected. On the whole the data speak for a single electrode process easily adaptable to all conditions. Such a process could be the discharge of acetate ion or acetic acid molecule, a conclusion reached by Shipley and Rogers (2) in their studies on a-c electrolysis.

Other organic solvents show essentially similar behavior. Methanol (Fig. 4) and ethanol are about as good as water except conductivity is lower. $CHCl_3$ and $C_6H_{11}OH$ were less desirable, the latter giving some adipic acid. Ethylene glycol (Fig. 4) is one of the best organic media studied.

TABLE II. *Effect of concentration on electrolysis of* H_2SO_4 *in anhydrous* HOAc *using AC*
(Temp, 25°C; current density 3.5 amp/cm²; frequency 60 cycles)

H_2SO_4 (%)	Gaseous products (%)		Efficiency (%) oxidation
	C_2H_6	CO_2	
5	25.6	52.1	98.2
10	23.8	48.9	97.4
15	20.4	50.3	81.2
20	14.3	53.4	53.6

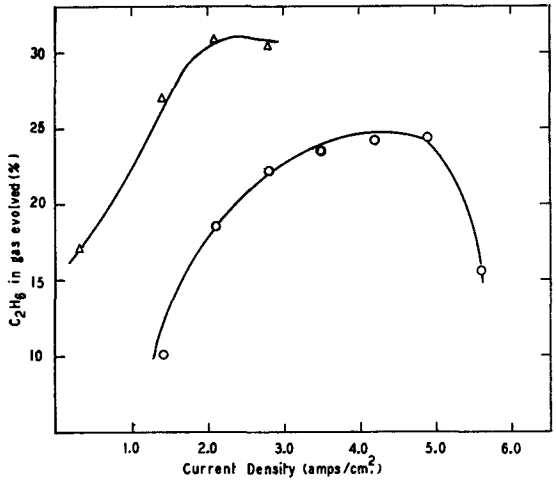

FIG. 4. Effect of current density on formation of ethane from acetate in organic media using AC. Temp, 25°C; frequency, 60 cycles. △ = KOAc 1.0M, HOAc 1.0M in ethylene glycol; ○ = KOAc 0.75M, HOAc 0.25M in methanol.

TABLE III. *Effect of added furan on electrolysis of* KOAc *in* HOAc *using AC*
(Temp, 25°C; current density, 3.5 amp/cm²; frequency 60 cycles) KOAc, 1.0M in HOAc

Furan added (M)	Gaseous products (%)		Efficiency (%) oxidation
	C_2H_6	CO_2	
0.0	17.0	36.8	97.4
0.5	19.2	39.0	98.4
3.0	23.4	42.1	111.2
6.0	24.8	43.4	114.2

having the lowest critical current density. It is of interest to point out that the addition of 10% glycol to a glacial HOAc solution of KOAc did not affect the yield of ethane whereas 10% of water instead caused an appreciable drop.

Effect of added furan, benzene, and anisole.—In glacial HOAc solution the addition of furan has the unexpected result of increasing current efficiency of ethane formation. Table III shows that the addition of furan to make the solution 6M raises the ethane content of the gaseous products from 17 to almost 25%. Even more startling is the increase in oxidation efficiency from 97 to 114%. Oxidation efficiency is defined as twice the ratio of ethane to CO_2 and is a measure of the efficiency of the coupling process. This is used in preference to hydrogen efficiency since the behavior of the cathode and anode are not the same with AC (3). If hydrogen efficiency were used, misleadingly high values of yield would be obtained since hydrogen evolution with AC is much lower than Faraday's law would suppose.

Oxidation efficiencies of 85% or below suggest that either ethane, or acetoxyl, or methyl radicals are being oxidized (Hofer-Moest reaction). On the other hand, efficiencies of over 100% suggest some abnormal reaction involving CO_2. Table III illustrates this. The effect of furan is even more surprising than is apparent from the figures since the electrolyte after the experiment contains appreciable amounts of 2,5-diacetoxy-2,5-dihydrofuran, a compound produced by addition of two acetoxyl groups to the furan molecule. It would appear that furan is able to capture acetoxyl radicals before they have time to either lose CO_2 and give ethane or be reduced to HOAc when the polarity reverses. The increased yield of ethane must result from furan molecules displacing acetoxyl radicals which would otherwise revert to HOAc. Still other adsorbed acetoxyl groups react with the furan to give the product mentioned above.

These considerations indicate that the furan molecule and the acetoxyl radical are closely associated with the anode in a geometrical sense. On the other hand, absence of methylated furan suggests that loss of CO_2 by the acetoxyl radical occurs only when a bimolecular reaction between two such radicals gives ethane. If the furan molecule does have the effect of changing the proportion of acetoxyl radicals which revert to HOAc it means that the life of such a radical on the anode is comparable with the frequency of the alternations. One sixtieth of a second quite a long lifetime for such a radical.

It is further significant that with DC the effect of added furan is even more pronounced than with AC.

In contrast to the effect of furan, addition of benzene had no effect on ethane formation, but anisole, although it did not change the current and oxidation efficiencies, was converted into *o*-hydroxy- and *o*-acetoxy-anisole. This behavior parallels that with DC. At the moment there appears to be no satisfactory way of explaining the high oxidation efficiencies in the presence of furan.

Ester formation.—The formation of ester, which occasionally accompanies the Kolbe reaction, is usually associated with specific compounds such as CCl_3CO_2H rather than special conditions. When AC is used, corrosion of electrodes is greatly enhanced and it was frequently observed that ester formation became appreciable when the electrode was thus visibly changed. In aqueous solution, methyl acetate was sometimes formed with as high as 6% current efficiency. Although x-ray diffraction did not show the presence of foreign compounds on the electrode, immersion in aqua regia was sufficient to restore it to the status of a clean anode giving no ester. It may be that a layer of platinum oxide is the cause of ester formation.

Under no circumstances was methane identified in the gaseous reaction products.

ACKNOWLEDGMENTS

The authors wish to thank the du Pont Company for a teaching fellowship granted to one of them (W. T. L.) and Dr. S. E. Lippincott for her help and advice during the course of the investigation.

Manuscript received February 6, 1956. This paper was prepared for delivery before the Pittsburgh Meeting, October 9 to 13, 1955, and is part of a thesis presented by W. T. Lippincott in partial fulfillment of the requirements for the Ph.D. degree, to Ohio State University.

Any discussion of this paper will appear in a Discussion Section to be published in the June 1957 JOURNAL.

REFERENCES

1. For Reviews *see*: C. J. BROCKMAN, "Electro-Organic Chemistry," John Wiley & Sons, Inc., New York, pp. 11–101 (1926): S. GLASSTONE AND A. HICKLING, "Electrolytic Oxidation and Reduction," pp. 312–31, Chapman and Hall, Ltd., London (1935); F. FICHTER, "Organische Elektrochemie," pp. 39–71, Steinkopff, Leipzig (1942); B. C. L. WEEDON, *Quart. Rev.*, **6**, 380 (1952); G. W. THIESSEN, *Trans. Illinois State Acad. Sci.*, **43**, 77 (1950).
2. J. W. SHIPLEY AND M. ROGERS, *Can. J. Res.*, **17B**, 167 (1939).
3. J. W. SHIPLEY, *ibid.*, **1**, 305 (1929).

Electrochemical Behavior of 2-Chlorocyclohexanone and Derived Imines

PHILIP J. ELVING[1] AND ROBERT E. VAN ATTA[2]

The Pennsylvania State University, University Park, Pennsylvania

ABSTRACT

Polarographic reduction of 2-chlorocyclohexanone results in a single *p*H-independent, diffusion-controlled, irreversible wave, which is due to carbon-halogen bond fission. The mechanism probably involves formation of a carbanion which reacts rapidly with the solvent to form cyclohexanone. In ammonia buffer of high *p*H (high NH_3 concentration) a second kinetic-controlled wave appears which is apparently largely due to reduction of the imine present in equilibrium with the 2-ketocyclohexanol formed by hydrolysis of the chloroketone; as the first wave due to the chloroketone decreases with time, the second wave increases.

Under the conditions of macroscale electrolysis in solution of high ammonia concentration, as in a coulometric experiment, the reduction product of 2-chlorocyclohexanone, cyclohexanone, reacts with ammonia to give cyclohexanonimine, which is in turn reduced to cyclohexylamine. The hydrolysis product of 2-chlorocyclohexanone, 2-ketocyclohexanol, reacts similarly to form 2-iminocyclohexanol, which is presumably reduced to 2-aminocyclohexanol.

In connection with the systematic investigation of the electrochemical behavior of halogenated organic compounds (1), 2-chlorocyclohexanone was studied as a typical cyclic haloketone. Its polarographic behavior was investigated from the viewpoints of (*a*) the relation of half-wave potential, $E_{1/2}$, and diffusion current, i_d, to *p*H, ionic strength, buffer component nature and concentration, and ketone concentration, (*b*) the probable reduction mechanism, and (*c*) the role of hydrolysis. Particular attention was given to the effect on the observed behavior of the imines formed by reaction of ammonia with the haloketone and its reduction and hydrolysis products. Coulometric and similar macroscale electrolyses at controlled potential were performed to determine the number of Faradays per mole electrolyzed and to obtain sufficient product for isolation and identification.

Little work has been reported on the polarography of α-halogenated alicyclic ketones. In 1954, several years after the studies described in the present paper had been completed, Pariaud and Perruche (2), who claimed to be unable to obtain waves in buffered solution, reported $E_{1/2}$ and diffusion current constant, I, values of −1.35 v and 2.93 for 2-chlorocyclopentanone in 0.1*N* KCl, and of −1.45 v and 1.86 for 2-chlorocyclohexanone in 0.01*N* KCl; $E_{1/2}$ became less negative with decreasing concentration, especially below 2 m*M* chlorocyclohexanone. Brezina (3) studied polarographically the reaction of ammonia and amines with several cyclanones; emphasis was on the 2-electron reduction of the ketimine formed when ammonia or an amine reacts with the carbonyl group.

[1] Present address: Dept. of Chemistry, University of Michigan, Ann Arbor, Mich.

[2] Present address: Dept. of Chemistry, Southern Illinois University, Carbondale, Ill.

EXPERIMENTAL

A Sargent Model XXI Polarograph and a Leeds & Northrup Type E Electro-Chemograph were used; potential measurements with the former were checked potentiometrically. Beckman Model G and H-2 *p*H meters were used for *p*H measurement; a Type E electrode was used above *p*H 10. The dropping mercury electrodes (prepared from Corning marine barometer tubing) had m and t values, respectively, (open circuit in distilled water) at 25°C of 1.02 mg/sec and 5.6 sec at 60 cm Hg and 1.58 and 3.7 at 90 cm, and at 0° of 1.09 and 5.7 at 55 cm; m and t for the capillary used in the hydrolysis study was 1.39 mg/sec and 4.3 sec at 45 cm. Water at 25 ± 0.1° or 0 ±0.1°C was circulated through the jackets of the H-type polarographic cells (4) which contained reference saturated calomel electrodes. Resistance of cell-solution systems was measured with a General Radio Type 650A impedance bridge; all potentials are reported vs. the S.C.E. and are corrected for iR drops.

The apparatus and procedure used in coulometric and macroscale electrolyses were essentially as described by Lingane (5). In electrolyses in ammonia buffer, potentials selected were on the limiting current portion of each wave, i.e., −1.45 v for wave I and −1.75 v for II. For wave I, the electrolysis was continued until no indication of this wave was obtained on recording a polarogram for a portion of the cell solution. The solution remaining after macroelectrolysis to remove wave I completely (at *p*H 9.5) was then electrolyzed at −1.75 v in order to determine n for wave II.

Materials.—2-Chlorocyclohexanone (Farchan Laboratories), purified by vacuum distillation, had b.p. 79°–80° at 8 mm, and d_4^{28} 1.1575 [literature (6): b.p. 79° at 7 mm, d_{15}^{20} 1.161]. Stock aqueous solutions (11 to 18 m*M* in ketone) were relatively stable to hydrolysis over periods of 1–2 hr,

TABLE I. *Composition of buffer solutions*

No.	pH	Components
1	1.5	0.45 *M* KCl + HCl
2	4.6	0.50 *M* NaOAc + HOAc
2a	4.6	0.10 *M* NaOAc + HOAc
3	7.0	0.27 *M* KH_2PO_4 + NaOH
4	8.2	0.18 *M* KH_2PO_4 + NaOH
5	8.2	0.50 *M* NH_4Cl + NH_3
5a	8.2	0.10 *M* NH_4Cl + NH_3
6	8.8	0.50 *M* NH_4Cl + NH_3
7	9.5	0.50 *M* NH_4Cl + NH_3
8	10.5	0.16 *M* Na_2HPO_4 + NaOH
9	11.5	0.14 *M* Na_2HPO_4 + NaOH
10	12.5	0.10 *M* Na_2HPO_4 + NaOH
11	12.6	0.45 *M* KCl + NaOH

although a drop of about 10% in i_d was observed at *p*H 4.6 during the first few minutes after preparation of the test solution.

Buffer solutions (Table I) were prepared by initial dilution to within a few ml of the final volume of calculated amounts of the buffer components (analytical reagent grade), plus sufficient KCl, where necessary, to give the desired ionic strength. The *p*H was then adjusted to the desired value by careful addition of the required buffer component, followed by dilution to the final volume. Ionic strength values were calculated in the usual manner, using the customary ionization constants.

Nitrogen used for deoxygenation was purified and equilibrated by bubbling it through concentrated H_2SO_4, alkaline pyrogallol, distilled H_2O and, finally, a portion of the specific test solution being investigated.

Experimental procedure.—The test solution, prepared by mixing accurately measured volumes of stock and background solutions, was deoxygenated in the H-cell for 5 min and then electrolyzed; a nitrogen atmosphere was maintained above the solution throughout the electrolysis. Values for *t*, the drop-life, were determined for the limiting current, i_l, portions of each polaragram; *i* values were corrected for the electrocapillary curve effect where necessary.

In the hydrolysis study at *p*H 9.5, the test solution was prepared by diluting 5 ml of 32.0 m*M* stock ketone solution to 50 ml with Buffer 7. After 5 min deoxygenation, the test solution was electrolyzed; successive curves were then recorded for the same solution at 10-min intervals without additional deoxygenation, but with a nitrogen atmosphere being maintained over the test solution in the polarographic cell.

Observed Behavior[3] and Discussion

One cathodic wave was observed in *p*H range 4.6 to 10.5 with a second appearing only at *p*H 9.5; the latter will be separately discussed (Fig. 1). No wave was found at *p*H 1.5 (Buffer 1) due to the presence of a water wave (7) followed by hydrogen discharge; rapid hydrolysis of the compound in the more alkaline region prevented investigation at *p*H greater than 10.5 (Buffers 9–11). The first wave is unusually long and drawn out, spanning nearly 0.5 v at a concentration of 0.5 m*M*; α, determined from the slope of the wave, remains essentially constant at 0.3 in the *p*H range investigated; such geometrical characteristics are an obvious indication of the irreversible nature of the polarographic reduction.

Variation of i_l with drop time, i.e., mercury head, and with temperature indicate the wave to be diffusion-controlled (Tables I and II). $E_{1/2}$ values at 0° are approximately 0.1 v more negative than at 25°C.

An *n* value of 2 ± 0.2 was obtained by coulometric analysis at *p*H 4.6 and 8.2. Calculation of *n* from the Ilkovic equation and a diffusion coefficient computed on basis of the Stokes-Einstein diffusion equation gave values of approximately one; however, since the molecular weight of the haloketone is below 180 and the molecule does not conform to the specification of being spherical, the Stokes-Einstein diffusion equation cannot be legitimately applied.

$E_{1/2}$ for the first wave is constant from *p*H 4.6 to 10.5 for each buffer system at about 0.98 ± 0.03 v. Apparent slight *p*H-dependence indicated with ammonia buffers is probably due to mutual interference between the crest of wave I and the start of wave II.

The diffusion current constant, *I*, increases slightly from *p*H 4.6 to a maximum at *p*H 7.0, then decreases at about the same rate to *p*H 9.5, and finally falls off rapidly due to hydrolysis to nearly 0 at *p*H 10.5 (Fig. 2).

Effects of ketone concentration and of ionic strength.—*I* is relatively constant in all buffers used except Nos. 3 and 4 for ketone concentrations of 1.8 to 0.6 m*M*, but decreases

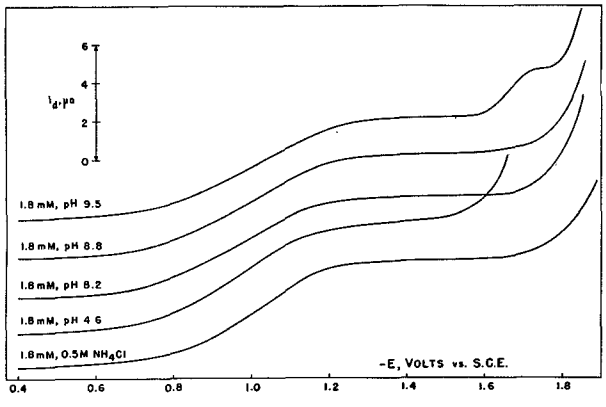

FIG. 1. Typical polarograms for 2-chlorocyclohexanone in various media.

TABLE II. *Ratio of i at two drop times (heads of mercury) for 2-chlorocyclohexanone*

Mercury heads corrected for back pressure. With capillary and heads used, theoretical value for diffusion-controlled process is 1.23; for kinetic control, 1.00, and for adsorption control, 1.52

Buffer No.	pH	Ratio	
		1st Wave	2nd Wave
2	4.6	1.25	
3	7.0	1.19	
4	8.2	1.29	
5	8.2	1.27	
6	8.8	1.32	
7	9.5	1.35	1.04
7	9.5	1.35	0.98

[3] Detailed tables of the polarographic data are available from the authors.

appreciably at smaller concentrations (Fig. 3). This decrease is apparently due largely to the drawn-out wave geometry which results in increased measurement error at lower wave heights. It must be emphasized that probably neither the present nor past workers (2) have ever actually measured true i_d values for 2-chlorocyclohexanone due to more or less conversion of this compound to the nonreducible ketoalcohol by hydrolysis. Consequently, I values given are low by an indeterminate amount although apparently reproducible enough under standardized conditions for analytical purposes.

$E_{1/2}$ tends to become very slightly more negative with increasing concentration at pH 4.6; there is some indication of the reverse effect in the alkaline region. Such behavior may be attributed to the wave geometry as well as to the presence of different reducible species. Although cyclohexanone enolizes very little (8), the haloketone

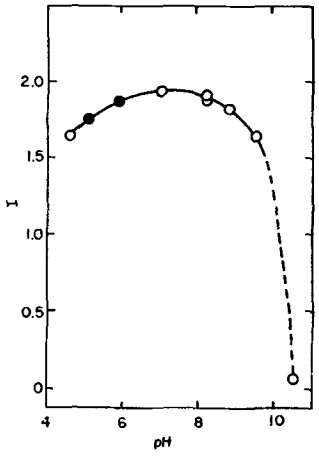

FIG. 2. Variation with pH of the diffusion current constant for 2-chlorocyclohexanone. Shaded points refer to nonbuffered solutions (0.5M NH_4Cl at pH 5.1 and 0.5M LiCl at pH 5.9).

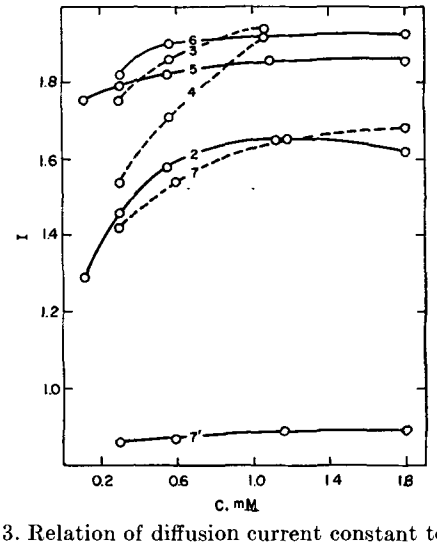

FIG. 3. Relation of diffusion current constant to concentration of 2-chlorocyclohexanone in various buffered solutions. The numbers refer to the buffer solutions as designated in Table I; curve labeled 7′ represents data for the second wave at pH 9.5.

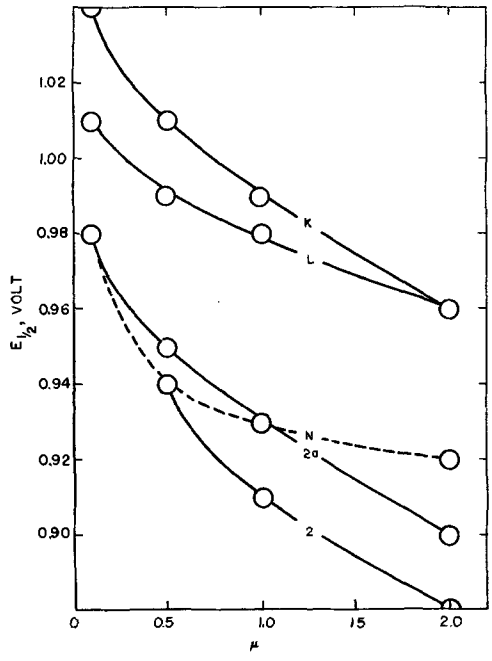

FIG. 4. Effect of ionic strength and buffer concentration on $E_{1/2}$ of 2-chlorocyclohexanone in the acidic region. Numbers refer to buffer solutions as designated in Table I; N, L, and K refer to nonbuffered solutions in which the background electrolytes are NH_4Cl, LiCl, and KCl, respectively.

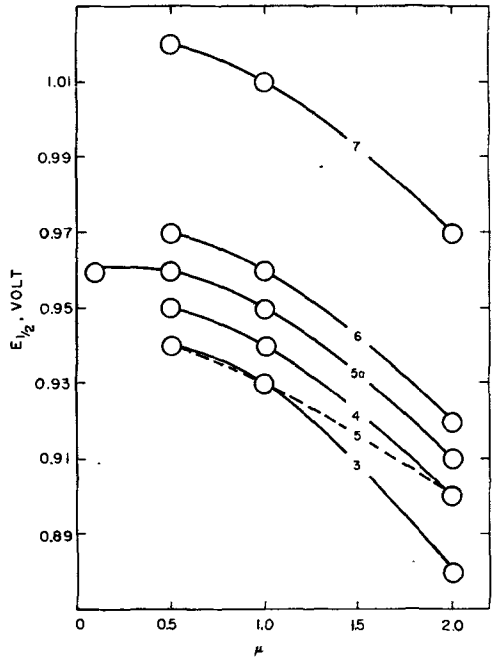

FIG. 5. Effect of ionic strength and buffer concentration on $E_{1/2}$ of 2-chlorocyclohexanone in the alkaline region. Numbers refer to buffer solutions as designated in Table I.

might be presumed to enolize to a somewhat greater extent; consequently, in alkaline solution, the observed polarographic behavior should reflect any conversion to enolate. Ionic strength effects do seem to indicate some such behavior. In buffered and nonbuffered solution below

*p*H 7 (Fig. 4), reduction becomes less difficult as ionic strength is increased, giving a concave shaped relationship; the same effect is observed at *p*H 7 and above with, however, a convex inflection (Fig. 5).

I is little affected by change in ionic strength except for a slight increase up to ionic strength 0.5. α generally tends toward slightly lower values at the higher ionic strengths.

Reduced buffer component concentration (Buffers 2a and 5a vs. 2 and 5) results in $E_{1/2}$ values about 0.02 v more negative and in *I* values approximately 10% greater.

Second wave in ammonia solution.—In NH_4Cl—NH_3 Buffer 7 at *p*H 9.5, as previously mentioned, a second polarographic wave ($E_{1/2} = -1.66$ v) occurs, whose characteristics are markedly different from those of the first wave. This second wave is much more clearly defined and more symmetrical geometrically; α is about 1, tending to become slightly smaller with decreasing ketone concentration and with increasing ionic strength; *n*, determined by coulometry, is 2 ± 0.1. Variation of *i* with drop time and temperature indicates the wave to be kinetic-controlled. On examination immediately after deoxygenation, *i* for the second wave is proportional to ketone concentration, even at the lower concentrations (Fig. 3); $E_{1/2}$ becomes very slightly less negative as concentration is increased, similar to the first wave. The increase in height of the second wave with time as the height of the first wave decreases is shown in Fig. 6.

TABLE III. *Temperature coefficient of i for 2-chlorocyclohexanone*
Based on I values since different capillaries were used at 0° and 25°; calculated from compound interest formula

Buffer No.	*p*H	Temp. coeff. %/deg.	
		1st Wave	2nd Wave
2	4.6	2.54	
5	8.2	2.23	
7	9.5	2.06	8.04

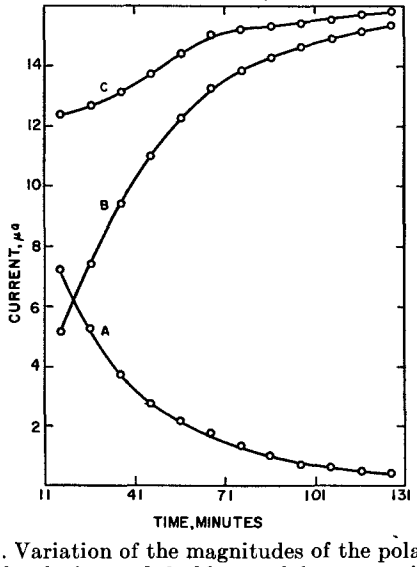

FIG. 6. Variation of the magnitudes of the polarographic waves of solutions of 2-chlorocyclohexanone in *p*H 9.5 ammonia buffer with time as the result of hydrolysis. A: first wave; B: second wave; C: total current for both waves. Original concentration of haloketone: 3.20 m*M*; calculated current for such a concentration: 16 μa; $E_{1/2}$ values: −1.02 and −1.66 v.

Nature of the Reactions Involved

Based on the observed polarographic behavior of 2-chlorocyclohexanone, the reduction giving rise to wave I is an irreversible, diffusion-controlled, *p*H-independent process, whose probable mechanism is

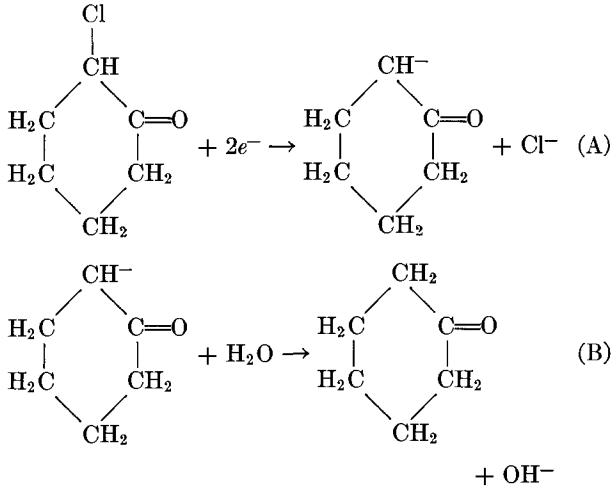

As in the case of other halogenated organic compounds (1, 9), reaction A would be the potential-controlling step with electrons acting as displacement agent (whether the electrons are added simultaneously or in rapid succession does not alter the basic picture); B involves rapid reaction of the carbanion with the solvent (or H^+) to form cyclohexanone. The principal energy steps involve the rearward approach of the electrons to the carbon center and the simultaneous fission of the carbon-chlorine bond; formation of the carbon-hydrogen bond is not involved in the controlling electrode reaction, i.e., the reduction is *p*H-independent (any variation due to keto-enol equilibrium affects the nature of the electroactive species, not the electrode process *per se*).

Reactions in ammonia solution.—The situation in a solution containing an appreciable concentration of ammonia is complicated by two factors: hydrolysis resulting in replacement of the chlorine by hydroxyl and production of an equilibrium concentration of imine by condensation between the carbonyl group and ammonia.

The second wave in *p*H 9.5 ammonia buffer is due to reduction of the imine or imines corresponding to the reaction products of ammonia with one or more of the series: 2-chlorocyclohexanone, its reduction product (cyclohexanone) and its hydrolysis product (2-ketocyclohexanol). An imine group is more readily reduced than the carbonyl group from which it is derived. The kinetic character of the wave results from the equilibrium between imine and ketone; as the imine is reduced, more is generated from the ketone. The over-all polarographic reduction process itself where *X* represents Cl, OH, or H, is probably

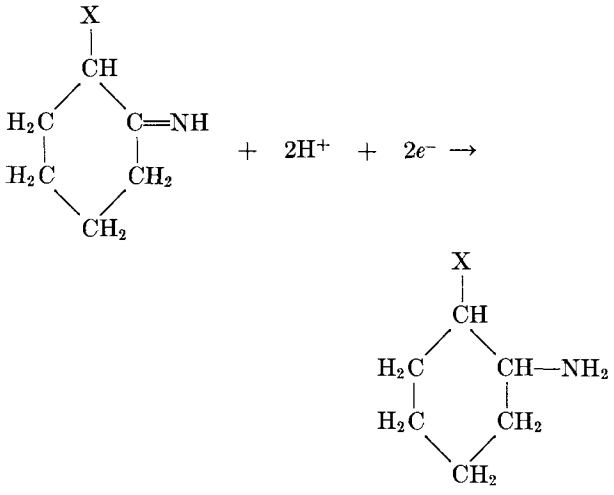

Reductions of this type, occurring as the result of similar amine-carbonyl reactions, have been studied polarographically and found to be 2-electron processes (3).

A more definite statement as to the imine involved may be secured by considering the possible reaction paths for 2-chlorocyclohexanone in ammonia solution via electrolysis, hydrolysis, and imine formation. Fission of the carbon-halogen bond in ketone or imine is a 2-electron process as is reduction of the carbon-nitrogen double bond in an imine; consequently, the following possible compounds and situations would give the waves indicated: (*a*) haloketone is reduced to ketone (wave I) which may form imine which can in turn be reduced (wave II); (*b*) haloketone is converted to haloimine which is reduced first to imine (wave I) and then further to cyclohexylamine (wave II); and (*c*) haloketone is hydrolyzed to ketoalcohol which may form a reducible imine (wave II):

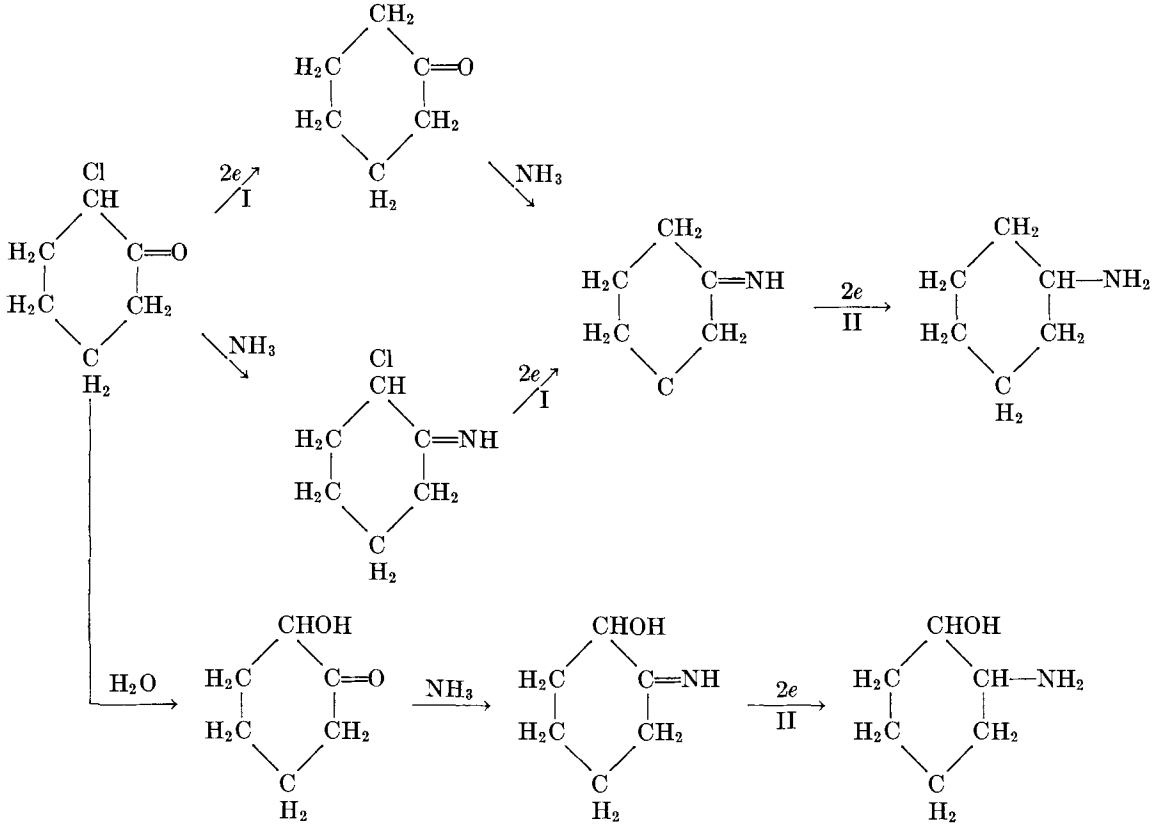

I refers to a process contributing to the first wave and II to one contributing to the second wave.

Effect of hydrolysis in ammonia solution.—In alkaline media hydrolysis of 2-chlorocyclohexanone to 2-ketocyclohexanol is greatly increased through neutralization of the HCl formed. The reaction with NH_3 to form an imine is known to occur with cyclohexanone (3); in the case of a solution of the chloroketone on standing, the reaction occurs with 2-ketocyclohexanol to a much greater extent than with 2-chlorocyclohexanone itself. Evidence for such a conclusion is given by Fig. 6. Data indicate that an appreciable concentration of ketoalcohol was formed rapidly in the test solution. Decrease of the first wave with time, which reflects disappearance of the carbon-halogen bond due to hydrolysis of the haloketone, is accompanied by a correspondingly sharp increase in the imine wave. If the ammonia condensation reaction occurred rapidly with 2-chlorocyclohexanone, the imine wave should be of approximately maximum current height initially and would not show the increase observed as hydrolysis of the haloketone proceeds.

The initial variation of the total current reflects a difference in rates of the two reactions involved, i.e., the ammonia condensation reaction is somewhat slower than the haloketone hydrolysis. Consequently, the total current is initially somewhat less than expected and remains so until the ammonia reaction begins to "catch up" with the hydrolysis, when it increases to a relatively constant value. In a plot of log (i for wave I) vs. time, the first four points (corresponding to 80% or more hydrolysis) lie on a straight line whose slope corresponds to a value of 0.0320 sec^{-1}; the latter is probably the sum of two pseudo first order rates, i.e., the solvolysis rate and the ammonolysis rate. Points beyond these show increasing deviation from the

straight line. The time given in Fig. 6 is the estimated time at which i_l for wave I was measured. Since it took about 10 min to prepare the test solution and remove oxygen, and 10 min to record the polarogram (0 to -2 v with $E_{1/2}$ for wave I at -1.0 v), the time at which i_l for the first point of wave I was recorded was about 16 min after start of the hydrolysis. Extrapolating the data to 0 min gives approximately 16 μa for C_0 of the haloketone, which is in agreement with the experimental total final current.

Due to the nature of the recording polarograph used, i_l of wave II was recorded 3 min after i_l of wave I; if curve B of Fig. 6 were shifted accordingly, the additive curve C would not change significantly.

The second wave was not observed in Buffer 6, *p*H 8.8, except after the solution had stood for several hours and, even then, was very small. The NH_3 concentration in Buffer 6 is approximately 0.07 *M* or about one-tenth that of Buffer 7.

It must be emphasized that the foregoing discussion applies to solutions under conditions of polarographic electrolysis, which would be expected to contain appreciable amounts of only haloketone and hydroxyketone which can react more or less slowly with ammonia to form imines. Under conditions of macroscale electrolysis where comparable amounts of the reduction product of the haloketone, the ketone itself, would be present, a third imine could be produced; this situation is considered in the following section.

Product produced in macroscale electrolysis.—In order to isolate and identify the principal reduction product or products produced in *p*H 9.5 ammonia solution, a solution of 2-chlorocyclohexanone in Buffer 7 was electrolyzed coulometrically using a large stirred mercury cathode, until no first wave was obtained on polarographing a portion of the cell solution. The resulting yellowish solution was then extracted several times with small portions of ether. The ether was removed from the combined extracts by aspiration; a small residue of oily yellow material remained. The latter was identified as cyclohexylamine when a phenylthiourea derivative of melting point 146°–149°C was prepared from it [literature (10): 148°]; the yield was apparently quantitative although the small amount of product (ca. 0.15 g) prevents an actual percentage figure being given.

Cyclohexylamine is evidently the reduction product of the imine formed in the reaction of NH_3 with cyclohexanone. Under the experimental conditions of macroscale electrolysis, the electrolytic reduction of 2-chlorocyclohexanone to cyclohexanone apparently occurs initially more rapidly than its hydrolysis.

The apparently more rapid reaction of ammonia with cyclohexanone than with the corresponding α haloketone or ketoalcohol may be due to steric factors. Although the electron-withdrawing properties of the chlorine might be considered to have so modified the reactivity of the carbonyl group as to make 2-chlorocyclohexanone more reactive to ammonia than the ketone itself, the existence of the haloketone in the chair form with the halogen in a polar, i.e., axial, position (11) would indicate that the haloketone is less reactive than the ketone.

Due to the solubilizing properties of the hydroxyl group, the other reduction product, 2-aminocyclohexanol, present in the final solution would be appreciably more soluble in basic aqueous solution than the amine; because of the foregoing and of the probably relatively smaller amount formed, the 2-aminocyclohexanol may not be extracted with ether, as was the cyclohexylamine.

Effect of cyclic structure.—2-Chlorocyclohexanone is somewhat more easily reducible than monochloroacetone (9). However, an entirely valid generalization cannot be drawn, since comparative polarographic data are not yet available for a C_6 aliphatic or a C_3 alicyclic haloketone. Several cyclic homologs of 2-chlorocyclohexanone must be similarly investigated before conclusions can be drawn as to any steric effect of the cyclic structure on the ease of electrochemical fission of carbon-halogen bonds in such compounds.

The reduction mechanism of the cyclic ketone appears to be generally similar to that for chloroacetone, although the current magnitudes are considerably smaller. The latter is probably due to the relatively large difference in diffusion coefficients for the two compounds expected on comparison of their respective structures, and to hydrolysis in the cyclic ketone, although satisfactorily reproducible current values are obtained.

ACKNOWLEDGMENT

The authors wish to thank the Atomic Energy Commission for support of the work described.

Manuscript received August 1, 1955. This paper was abstracted from the Ph.D. thesis of R. E. Van Atta (1952).

Any discussion of this paper will appear in a Discussion Section to be published in the June 1957 JOURNAL.

REFERENCES

1. P. J. ELVING, *Record Chem. Progr.*, **14,** 99 (1953).
2. J. C. PARIAUD AND C. PERRUCHE, *Compt. rend.*, **238,** 1514 (1954).
3. M. BREZINA, Congress of Practical Polarography, Bratislave (1952); *Anal. Chem.*, **24,** 916 (1952).
4. J. C. KOMYATHY, F. MALLOY, AND P. J. ELVING, *Anal. Chem.*, **24,** 431 (1952).
5. J. J. LINGANE, *J. Am. Chem. Soc.*, **67,** 1916 (1945).
6. R. E. MEYER, *Helv. Chim. Acta*, **16,** 1291 (1933).
7. E. ORLEMANN AND I. M. KOLTHOFF, *J. Am. Chem. Soc.*, **64,** 1970 (1942).
8. G. SCHWARTZENBACH AND C. WITTWER, *Helv. Chim. Acta*, **30,** 669 (1947).
9. P. J. ELVING AND R. E. VAN ATTA, *Anal. Chem.*, **27,** 1908 (1955).
10. R. L. SHRINER AND R. C. FUSON, "The Systematic Identification of Organic Compounds," 3rd ed., John Wiley & Sons, Inc., New York (1948).
11. E. J. COREY, *J. Am. Chem. Soc.*, **75,** 2301 (1953).

Cathodic Reduction of 3,4,5,6-Tetrachloro-*N*-(2-Dimethylaminoethyl)-Phthalimide in an Aqueous Medium at a Lead Cathode

M. J. Allen and J. Ocampo

Research Department, CIBA Pharmaceutical Products Inc., Summit, New Jersey

ABSTRACT

It has been shown that electrolytic reduction of 3,4,5,6-tetrachloro-*N*-(2-dimethylaminoethyl)-phthalimide in an aqueous H_2SO_4 medium at high current densities yields a compound which is probably the 4,6,7-trichloro-2-(2-dimethylaminoethyl)-isoindoline. The side reaction which resulted in dehalogenation can be attributed possibly to the general inefficiency of the system for reduction of the carbonyl groups which permitted a relatively stable *p*-quinoid intermediate with resultant nucleophilic substitution on carbon-5.

In a previous paper (1) the cathodic reduction of 3,4,5,6-tetrachloro-*N*-(2-dimethylaminoethyl)-phthalimide in an aqueous CH_3OOH—H_2SO_4 medium was shown to yield the respective isoindoline in varying yields and current efficiencies depending on the experimental conditions. Cook and France (2) demonstrated that phthalimides such as *N*-methyl phthalimide could be reduced to *N*-methyl isoindoline at a lead electrode using an aqueous H_2SO_4 medium. However, because of the relatively lower overpotential of Pb in this medium as compared to that in an aqueous CH_3COOH—H_2SO_4 medium, the current densities used were too high with resultant excessive hydrogen evolution and low current efficiencies.

It was thought that, although a low current efficiency would be anticipated, it might be of interest to determine if the tetrachlorophthalimide could be reduced to 4,5,6,7-tetrachloro-2-(2-dimethylaminoethyl)-isoindoline in the aqueous H_2SO_4 medium.

Experimental

The Pb cathode used in these experiments was 78 cm^2 in area. Prior to use it was purified according to Tafel's method (3). The cell and apparatus used were described in the prior publication (1). The medium, molar concentration of depolarizer, current density, and electrolysis time were essentially the same as used by Cook and France in their experiments.

Electrolysis

The catholyte consisted of a suspension of 7.66 g of the imide in 75 ml 5.7% aqueous H_2SO_4. The same background electrolyte was used for the anolyte. The electrolysis was performed at a temperature of 50°C and a current density of 0.0448 amp/cm^2. The total electrolysis time was 381 min at 3.5 amp. After 302 min the last traces of suspended material had gone into solution. Gas evolution was considerable throughout the course of the reaction.

The catholyte was mixed with chopped ice and made basic with dilute sodium hydroxide. The precipitate which formed was extracted a number of times with ether, the ether extracts combined, washed with water, dried over anhydrous Na_2SO_4, and evaporated to yield 5.99 g of dark yellow oil. Attempted crystallization of this oil gave negative results. The free base was converted to the dihydrochloride by dissolving in methanol and treating with methanolic-hydrogen chloride. The precipitate was collected and washed lightly with cold methanol. Yield 5.96 g, mp 281°–282° (dec.). Recrystallization from methanol gave white prisms, mp 285°–286° (dec.).

Anal. Found: C, 39.98; H, 4.77; N, 7.90; Cl, 46.92%. $C_{12}H_{17}N_2Cl_5$ requires C, 39.82; H, 4.68; Cl, 48.35%.

Titration for ionic halogen showed the compound to contain 96% of that required for a dihydrochloride. A sample subjected to a permanganate oxidation gave 13.8% of an acidic material which, on sublimation, yielded a compound mp 146°–149°.

Anal. Found: C, 38.34; H, 0.60; Cl, 42.76%. $C_8HCl_3O_3$ requires C, 38.21; H, 0.39; Cl, 42.30%.

As the melting point corresponds to that of 3,4,6-trichlorophthalic anhydride (mp 148°), the isoindoline obtained is probably the 3,4,6-trichloro isomer. The 3,4,5-trichlorophthalic anhydride has a mp of 157° (4).

In order to determine the effect of a shorter period of electrolysis, the experiment was repeated but discontinued after a period of 106 min. From the catholyte was isolated 2.46 g of the starting material, 1.27 g of 4,5,6,7-tetrachloro-2-(2-dimethylaminoethyl)-3-hydroxyphthalimidine (1) and 2.16 g of the trichloroisolindoline identified by its dihydrochloride.

The susceptibility of the imide molecule to further dehalogenation was determined by repeating the electrolysis for a period of 762 min. From the catholyte was isolated 4.23 g of oily material identified as the trichloroisoindoline by conversion to the dihydrochloride salt.

Discussion

Based on the results obtained the following mechanism is proposed:

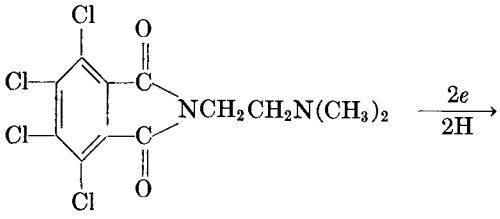

I.

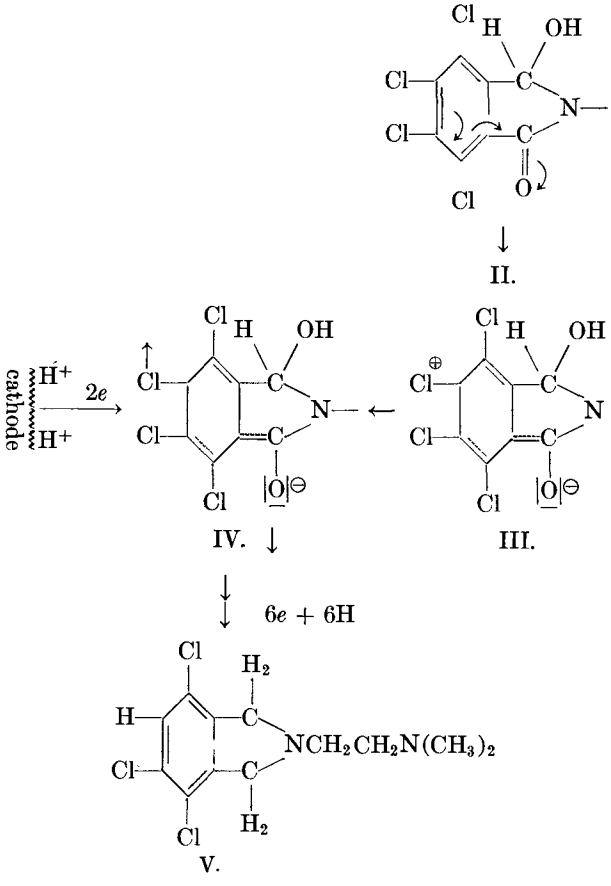

The low efficiency obtained in this reduction was anticipated for reasons given earlier. However, the elimination of one halogen was considered rather unusual in that aromatic halogens are quite resistant to removal by electrochemical means. That it was removed in this instance can be attributed possibly to the low reductive efficiency as a consequence of the lower potential of a Pb electrode in an aqueous H_2SO_4 medium as compared to that in an aqueous CH_3COOH—H_2SO_4 medium. As a result of these experimental conditions, the subsequent reduction of the hydroxyphthalimidine (II) to the isoindoline is relatively slow, thus making possible the isolation of this intermediate from the reaction. This is to be anticipated for it was found in previous investigations (1) that 3,4,5,6-tetrachloro-*N*-(2-dimethylaminoethyl)-phthalimide (I) can be reduced to the hydroxyphthalimidine (II) at a lower electrode potential than that required for complete reduction to 4,5,6,7-tetrachloro-2-(2-dimethylaminoethyl)-isoindoline. If the electrode potential were higher, as is the case when using the aqueous CH_3COOH—H_2SO_4 medium, the reduction of the carbonyl groups would be quite rapid. Thus, the intermediate suggested by (III), which is possibly stabilized in this form by adsorption on the cathode surface at the lower electrode potential, would not exist as such for a sufficient period to enable nucleophilic substitution to occur on carbon-5. However, in the medium used the chlorine on carbon-5 is reduced cathodically due to the experimental conditions, which very possibly results in stabilization of the *p*-quinoid intermediate. The remaining carbonyl is reduced eventually to the 4,6,7-trichloro-2-(2-dimethylaminoethyl)-isoindoline. It is possible that prior to dehalogenation the hydroxyphthalimidine (II) is reduced to the phthalimidine. However, as none of this compound could be isolated from the catholyte of the short period experiment, it was not included in the schematic. One cannot overlook the possibility of the 4,5,6-trichloro-isomer which could be formed via the following mechanism yielding the *o*-quinoid type intermediate.

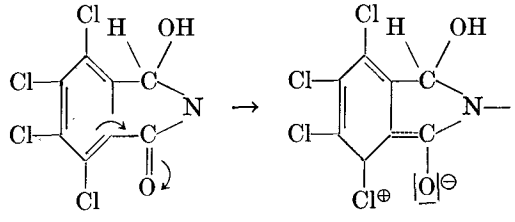

However, as aromatic compounds are reluctant to assume an *o*-quinoid structure, the probability of any amount of the 4,5,6-trichloro-2-(2-dimethylaminoethyl)-isoindoline being formed is quite unlikely. The proposed mechanism also accounts for the fact that only one chlorine was removed from the ring for, as soon as the carbonyl is reduced, resonance with the benzene ring is impossible. Were this not so, the expected product would be the 4,7-dichloroisoindoline.

Conclusions

Electrolytic reduction of 3,4,5,6-tetrachloro-*N*-(2-dimethylaminoethyl)-phthalimide, using the experimental conditions described, yields the 4,6,7-trichloroisoindoline and not the 4,5,6,7-tetrachloroisoindoline obtained using the CH_3COOH—H_2SO_4 medium.

The unexpected results obtained can be attributed possibly to the general inefficiency of the electrolytic process due to the use of a lower overpotential electrode system and also to the fact that the medium used was a poor solvent for the tetrachlorophthalimide. As a result it was possible for the intermediate, hydroxyphthalimidine, to assume a relatively stable *p*-quinoid resonant form which permitted nucleophilic substitution on carbon-5.

Manuscript received February 16, 1956.
Any discussion of this paper will appear in a Discussion Section to be published in the June 1957 Journal.

References

1. M. J. Allen and J. Ocampo, *This Journal*, **103**, 452 (1956).
2. E. W. Cook and W. G. France, *J. Phys. Chem.*, **36**, 2383 (1932).
3. J. Tafel, *Ber.*, **33**, 2209 (1900).
4. C. Graebe and S. Rostowzew, *ibid.*, **34**, 2107 (1901).

Floating Zone Purification of Zirconium

G. D. Kneip, Jr., and J. O. Betterton, Jr.

Metallurgy Division, Oak Ridge National Laboratory, Oak Ridge, Tennessee

ABSTRACT

The Fe and Ni contents of iodide Zr have been reduced to less than 2 ppm by the floating zone refining technique. The α/β transformation takes place over a temperature interval of 865°–873°C in the purified material instead of the 16°–70°C intervals found in grade 1 crystal bar. Fe and Ni distributions after multiple pass refining have been established by neutron activation analyses and the values agree with those calculated by the theory.

Zr made by the iodide decomposition process contains sufficient impurities to cause the α/β transformation to take place over a considerable temperature range. For this reason it is unsuitable as the base material for the study of the effects of solutes on the α/β transformation. Trace amounts of impurities such as Fe and Ni present in iodide material have a pronounced effect on the temperature width of the transition region and, hence, are particularly injurious. Floating zone refining (1) was chosen as a likely means of attaining the desired purification since the chemical affinity of Zr for other elements dictates the use of a purification process which can be carried out in an inert atmosphere and which introduces no crucible contamination. The theory of zone refining has been extended to this case of the finite length bar and to consideration of the limits imposed on the calculations by the physical nature of the systems involved. Purification efficiency for eutectoid forming impurities has been assayed qualitatively by annealing the refined ingots slightly below the pure Zr transition temperature and observing the distribution of the high temperature β-phase. Redistribution of Fe and Ni has also been established by activation analyses.

Zone Refining Theory for Finite Length Passes

The zone refining process (2) is based on the difference in solubility of an impurity in the liquid and solid phases. For impurities which lower the melting point and thus are more soluble in the liquid phase, the first material to freeze as the liquid zone is put into motion contains less impurities than the liquid, and hence is purer than the original solid. As the movement of the liquid zone is continued, concentration of impurities in the liquid zone increases and the composition of the material freezing behind the zone gradually returns toward its initial value. When the motion is stopped and the liquid allowed to freeze, a region of higher impurity content than the original material is developed. Impurities which raise the melting point of the solute and thus are more soluble in the solid phase migrate in the opposite direction since the material freezing behind the liquid zone has a higher impurity concentration than the liquid. In this case, the purified region is found in the last zone to solidify. Further purification can be attained by making successive passes over the same ingot. Analytical expressions for the impurity distribution in a semi-infinite bar after a single pass have been presented by Pfann (2) and for multiple passes by Reiss (3) and Lord (4). Of these, the expression developed by Lord (Eq. I) is perhaps the most useful since it is exact and utilizes ordinary numerical computation procedures. The expression

$$C_n(a) = \left[\int_0^a C_{n-1}(a+1)e^{ka}\,da + \int_0^1 C_{n-1}(a)\,da\right] ke^{-ka} \qquad O \le a \le N-1 \tag{I}$$

is based on the assumptions that there is no diffusion in the solid phase, the impurity concentration is uniform throughout the liquid region, the ratio of solid to liquid solubilities is constant for the concentrations involved, and the zone length does not vary. In this expression, $C_n(a)$ is the concentration of the impurity in the solid after n passes at a distance, a, measured in zone lengths from the starting point of the passes, and k is the distribution coefficient or the ratio of solid to liquid solubilities. It is valid for the region $O \le a \le N-1$ where N is the total length of the pass measured in zone lengths, since the final zone is excluded because of the changing zone length during its solidification.

The equation can be integrated pass by pass, starting with a uniform concentration prior to the first pass. In this case the integrated expressions are only valid over the region $O \le a \le N-n$, since with successive passes the effects of the excluded final zone region are reflected back one zone length for each pass due to the $C_{n-1}(a+1)$ term in the equation.

For the region $N-n \le a \le N-1$ this expression can be written

$$C_n(a) = C_n(N-n)e^{-k[a-(N-n)]} + ke^{-ka}\int_{N-n}^{a} C_{n-1}(a+1)e^{ka}\,da \qquad N-n \le a \le N-1 \tag{II}$$

where $C_{n-1}(a+1)$ is a complicated expression dependent on the solidification of the final zone and its back reflection into the bar.

For floating zone refining the final zone is assumed to solidify from both ends, according to the normal solidification process described by Pfann (2) and others (5–7). The expressions for the impurity concentration in the final zone then are

$$C_n(a) = C_n(N-1)\{2[(N-\tfrac{1}{2}) - a]\}^{k-1} \quad N-1 \leq a \leq (N-\tfrac{1}{2}) - A \quad \text{(III)}$$

$$C_n(a) = C_n(N-1)\{2[a - (N-\tfrac{1}{2})]\}^{k-1} \quad (N-\tfrac{1}{2}) + A \leq a \leq N \quad \text{(IV)}$$

and the impurity distribution is seen to be symmetrical about $a = N - \frac{1}{2}$. For values of k less than one, the concentration rises rapidly from both ends of the zone toward infinity. This is plainly inconsistent with the densities of physical materials or more frequently with the solid solubility limits. The applicability of Eq. (III) and (IV) then must be limited to that part of the range where k is constant and where the solubility limit is not exceeded in the solid phase as indicated by the parameter A in the limits for expressions (III) and (IV). In many systems in which a eutectic reaction takes place, k is approximately constant from the melting point to the eutectic temperature, and the value of the solid solubility at the eutectic temperature then determines the parameter A.

When the distribution coefficient is greater than one, similar limitations on the maximum concentration apply to the region at the beginning of the bar. In the final zone in this case the parameter A has a value of zero and expressions (III) and (IV) are valid over the whole region.

As will be shown later, iron is one of the elements which has a dominant effect on the temperature interval over which the allotropic transformation takes place in Zr. For this reason the ability of the zone refining process to redistribute Fe is of particular interest.

Fig. 1 shows Fe distribution for a zone refined ingot computed from Eq. (I) to (IV), and the distribution coefficient taken from the Zr-Fe phase diagram (8). Concentration in the final zone rises rapidly from both ends of the zone until the composition of the solid reaches the maximum solid solubility, at which time the liquid has attained the eutectic composition and the center section of the zone freezes as material of the eutectic composition. This rapid rise in concentration in the final zone is then reflected back one zone length in the succeeding pass. In the third pass both the peak in the final zone and the step in the next to the last zone of the second pass are reflected back into the purified region one zone length farther. In the initial region the shape of the curve is established by two parameters, the zone length and the distribution coefficient. The zone length establishes the rapidity with which the impurity concentration returns to its initial value. Hence, a long zone length is more effective in transporting impurities than a short one for purification processes which are limited by experimental conditions to a small number of passes and, thus, where the back reflection effect in a finite length pass does not affect the initial region. The distribution coefficient establishes the purification which is attained at the starting point for distribution coefficients less than one, or the increase of impurity for $k > 1$.

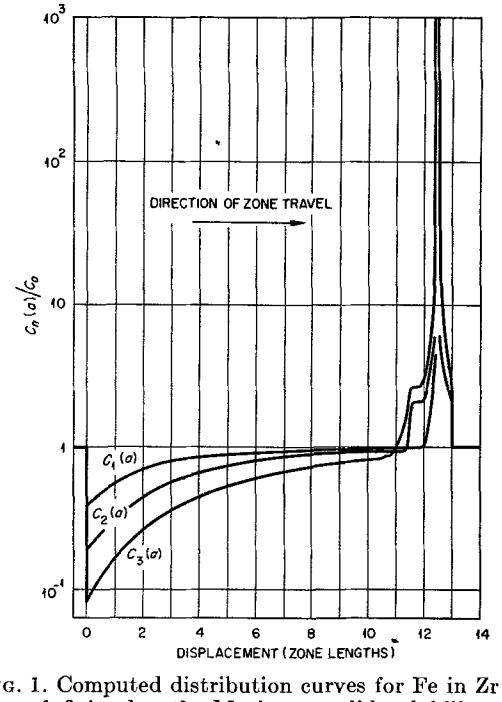

FIG. 1. Computed distribution curves for Fe in Zr after passes of finite length. Maximum solid solubility 5.5%, Co = 45 ppm, k = 0.35, N = 13.

EXPERIMENTAL METHODS

The experimental apparatus in which the zone refining experiments were carried out is shown in Fig. 2. In order to prevent buckling of the rod due to thermal expansion during the initial heating, it is necessary to make the bottom support free to move vertically under small stresses and at the same time to constrain the ends of the rod in firm axial alignment. This is accomplished by making the bottom support a spring loaded piston and cylinder device. The Cu supports for the rod are sealed with neoprene "O" rings to the quartz tube, and the apparatus evacuated through the side tube to approximately 10^{-6} mm Hg. For most of the experiments the apparatus was evacuated and flushed with argon several times prior to filling to approxi-

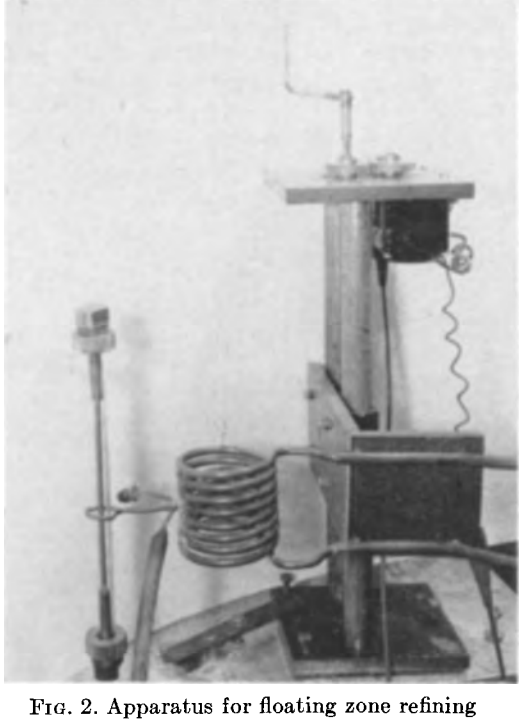

FIG. 2. Apparatus for floating zone refining

mately atmospheric pressure with argon. The argon atmosphere retards the evaporation of Zr and its deposition on the walls of the quartz tube, which interferes with visual observation of the liquid zone and which in some cases absorbs considerable radiant and high-frequency energy. When argon was used there also appeared to be a small advantage in improved zone stability which the authors attribute to convective cooling of the rod by the gas. The mechanism for moving the high-frequency work coil and the impedance matching transformer, necessary to match the coil to the generator, are shown on the right side of the figure. The source of power is a 20-kw output electronic generator with a nominal frequency of 220 kc. The generator is equipped with an induction regulator in the primary of the high voltage supply transformer to provide continuous control of the output power.

Zr rod diameters for these experiments were chosen empirically because of the disagreements in the current theoretical treatments of the stability of floating zones (9, 10). By analogy with other types of free surfaces, however, the ratio of the density and surface tension should be inversely related to the maximum size of the stable molten zone. For Zr this ratio was estimated from the curvatures of free liquid surfaces and it was found to be appreciably greater than that for the other metals which have been zone refined. On the above basis, the Zr liquid zone would be expected to be stable only for relatively small rod diameters and short zone lengths.

Experimentally, no appreciable difference was found in the zone stability for 3–6.5 mm diameter rods; however, with rods 5 mm in diameter the stability of the liquid zone was found to be critically dependent on the zone length. The length of the liquid zone was made as short as possible by the single turn heating coil and by adjusting the radio frequency input power to the coil to be just sufficient to melt the bar. Even then it was found necessary to readjust the power continuously in order to keep the liquid zone from collapsing. Zone lengths on the order of 8 mm were observed for the 5 mm diameter rods. The molten zone was assumed to extend throughout the bar when the two ends

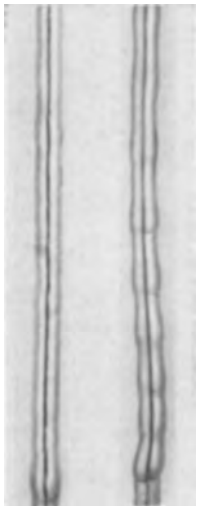

FIG. 3. Zone refined Zr rods. The liquid zone has traversed the rod on the left three times and the rod on the right six times.

TABLE I. *Impurity content of grade 1 iodide Zr*

Impurity	Spectrographic analysis	Activation analysis
Ti	80 ± 50 ppm	—
Hf	120 ± 40 ppm	132 ppm
Cr	2 ± 2	7
Fe	15 ± 15	45 ± 8
Ni	11 ± 7	4.0 ± 1.0
Si	38 ± 37	6 ± 4
All others	<5	<5
	Chemical analysis	Vacuum fusion analysis
C	20–175 ppm	—
O_2	105–340	50–250 ppm
N_2	4–50	4–50
H_2	—	30–45

of the bar vibrated independently upon gentle tapping of the apparatus. This assumption is supported by metallographic examination in which the gradation of the impurity containing β-phase was shown to be in planes normal to the axis of the rod.

The maximum number of passes which could be made on a given rod is limited by the irregularities in the diameter of the rod which increase as the number of passes is increased. Fig. 3 shows the typical shapes of the rods after 3 and 6 passes. As many as 10 passes have been made in some cases. In all of the experiments reported in this paper the refining was started at the bottom of the bar and the liquid zone moved upward at a rate of 2.5 mm/min for a total pass length of 10 cm.

All of the Zr used for these experiments was prepared from a grade 1 iodide crystal bar by swaging. This material contained 99.95 wt % Zr; analytical values for the various impurities are given in Table I. The rods were annealed at various stages in the reduction. Steps taken to prevent contamination during annealing included: chemical cleaning, protective Zr foil wrappings, and outgassing at 1000°C in quartz tubes and vacuums of 10^{-6} mm Hg. No change in Vickers hardness was found between the crystal bar and the annealed rods, indicating little contamination by oxygen, nitrogen, or carbon. In addition, the outgassing was sufficient to reduce the hydrogen content to less than 5 ppm.

METALLOGRAPHIC EVIDENCE OF PURIFICATION

Experiments with a number of lots of grade 1 iodide Zr have indicated that the α- and β-phases coexist over temperature intervals of 16°C in the best lot to 70°C in the worst. The upper limit of this two-phase region is approximately constant at 873°C, while the lower limit varies from 800° to 857°C, suggesting the presence of eutectoid forming impurities of limited solubility in α-Zr. If a zone refined ingot is isothermally annealed slightly below the transformation temperature of the pure material and rapidly cooled to room temperature, regions which are high in eutectoid forming impurities will show the α- and β-phases[1] to be distributed in proportion to the impurities. Accord-

[1] The β-phase, of course, transforms martensitically to α-prime during cooling, but the isothermal boundaries of the β-phase are recognized easily.

ingly, a zone refined ingot was segmented and isothermally annealed for 100 hr at two temperatures in quartz capsules. The same precautions were taken to avoid contamination as described previously. A Pt-Pt 10% Rh thermocouple which had been calibrated at the melting points of Al, Ag, and Au was used to measure the furnace temperature frequently during the annealing period. The temperature gradient over the specimens amounted to about ± 0.3°C and the variation in furnace temperature from time to time ± 0.2°C so that the annealing temperatures reported are believed to be well within ± 1°C. At the finish of the anneal the specimens were quenched by breaking the quartz capsules under water.

Fig. 4 shows the β-phase distribution in a refined rod after isothermal annealing and indicates the concentration of the eutectoid forming impurities in the final zone. The proportions of the α- and β-phases were determined by the method of lineal analysis. If the impurity causing the broadening of the transition range is Fe, examination of the Zr-Fe phase diagram (8) will show that the absence of the β-phase in the purified part of the rod after isothermal annealing at 860°C indicates that the Fe content is less than 30 ppm. The higher annealing temperature of 865°C provides increased sensitivity. In this case the homogeneous α region presumably contains less than 15 and the maximum beta region approximately 380 ppm Fe. The hardness at various positions along the bar after annealing at 865°C is also shown in Fig. 4. The peak at the beginning of the pass is attributed to a concentration of oxygen and nitrogen which are more soluble in the solid than liquid phase, and thus would be expected to move in opposition to the direction of zone travel. The peak at the other end of the pass is assumed to be the result of the other impurities. Hardness measurements on two other rods show the same general trend but with increased scatter, and, because

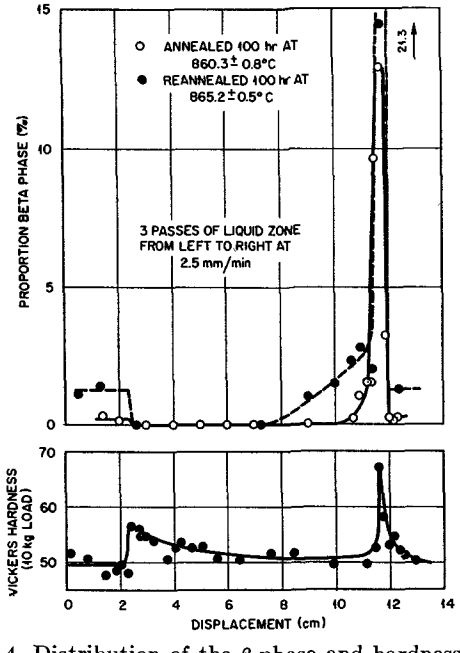

Fig. 4. Distribution of the β-phase and hardness variation for a zone refined Zr ingot after isothermal annealing treatments near the transition temperature.

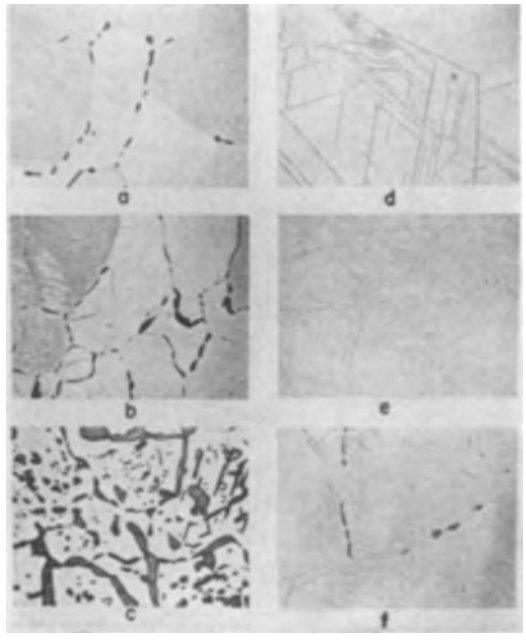

Fig. 5. Microstructures of zone refined Zr after isothermal annealing 100 hr at 865.2° ± 0.5°C. Etchant 57% $C_3H_6O_3$, 40% HNO_3, 3% HF. 50× before reduction for publication.

of the uncertainty of hardness measurements on polycrystalline and two-phase metals, results should be considered with caution. Since small amounts of oxygen and nitrogen markedly increase the hardness of Zr these data also indicate that very little contamination occurred during the 2 hr that a portion of the bar was molten.

The original material for these bars has a two-phase region extending from approximately 855°–873°C so that the purification for three passes of the molten zone has reduced the transformation range to less than one-half of its original value, or from 865° to 873°C. This temperature interval for the transformation provides supporting evidence for other experiments at ORNL which indicate that the allotropic transformation of Zr takes place at 870° ± 3°C instead of the lower value reported in the literature.

The actual microstructures observed after the 865°C anneal are shown in Fig. 5, where it will be appreciated that the Fe content is essentially indicated by the amount of the β-phase. The unrefined ends of the bar contain about 1.2% by volume of the β-phase in the boundaries of the α grains as shown in Fig. 5*a* and 5*f*. The interface between the upper end of the bar and the final zone is shown in Fig. 5*b*, and the center of the final zone with a greatly increased amount of the high temperature β-phase is shown in Fig. 5*c*. Microphotographs of Fig. 5*d* and 5*e* are at points approximately 2 cm apart in the purified region and show no traces of the high temperature β-phase.

Activation Analyses of Purified Rods

The Fe and Ni distribution in several zone refined rods was determined by neutron activation analyses in order to show that the above interpretation of the metallography is reasonable and also to provide an experimental test of the theory. Fig. 6 shows Fe distribution after three passes of the molten zone. The analytical sample for each of these

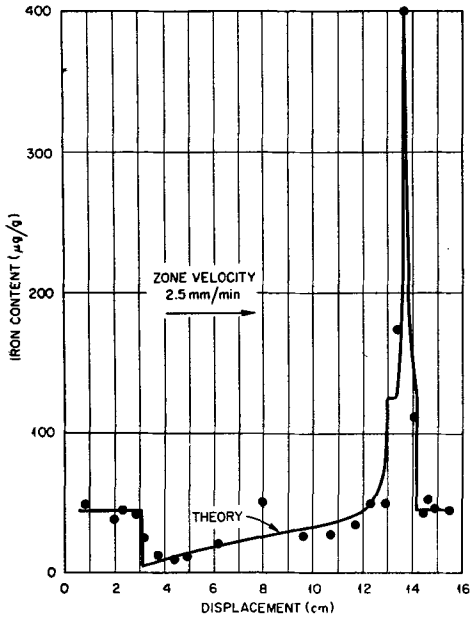

FIG. 6. Iron distribution after 3 passes of the liquid zone

points was a segment of the refined ingot approximately 3 mm in length. To remove tool contamination each specimen was chemically cleaned. After irradiation each specimen was put into solution and at least duplicate aliquots taken for the analyses. Duplicate samples for Fe analyses all agreed to within ±3 ppm except for the high values in the final zone for which the agreement was about ±13 ppm. The experimental points are in substantial agreement with the prediction of the theory of zone refining and thus, in this system at least, the assumptions of the theory are experimentally realized. For the computation of the theoretical curve a distribution coefficient of 0.35 as obtained from the Zr-Fe phase diagram (8), and a zone length of 8 mm as observed experimentally were used. The experimental zone length is difficult to estimate since there is no color distinction between the liquid and solid metals. Furthermore, for stable zones the liquid region is very nearly cylindrical in shape and hence its boundaries are not clearly defined. The agreement of the experimental points with the theoretical curve, however, indicates that the 8-mm length is approximately correct.

Maximum and minimum Fe contents, as determined by the activation analyses, agree remarkably well with estimates from isothermal annealing experiments. This quantitative agreement indicates the marked effect of Fe on the allotropic transformation of Zr. In this Zr other impurities, such as carbon, for example, are undoubtedly redistributed during the zone refining process. However, they are present either in small quantities or their effects on the allotropic transformation are small compared to Fe. The particular case of Ni will be discussed below.

Fe distribution after six passes of the molten zone, Fig. 7, shows a lower minimum value as predicted by the theory. In other respects the curve is similar in shape to the previous one. In each of the Fe distribution curves one of the experimental points does not agree with the rest of the data. These two values are higher than would be expected so that they may have been caused by a momentary solidification of the liquid zone. It is also possible that these points represent tool contamination of the analysis sample which was not removed by the chemical cleaning treatment. The latter point of view is favored by the fact that no scatter of this nature was observed for Ni.

Ni is another example of a eutectoid forming impurity similar to Fe in its limited solubility in α-Zr (11). Since it is a relatively common impurity in Zr, the ability of the zone refining process to redistribute Ni is of interest. As shown in Fig. 8, Ni is distributed in much the same way as Fe. After six passes of the molten zone, the minimum value of Ni was about $\frac{3}{4}$ of a part per million, with an appreciable portion of the ingot containing less than 2 ppm. A three-pass rod was also analyzed for Ni. The shape of the distribution curve was the same as that of the six pass curve; the minimum value in this case was 2 ppm. Ni analyses

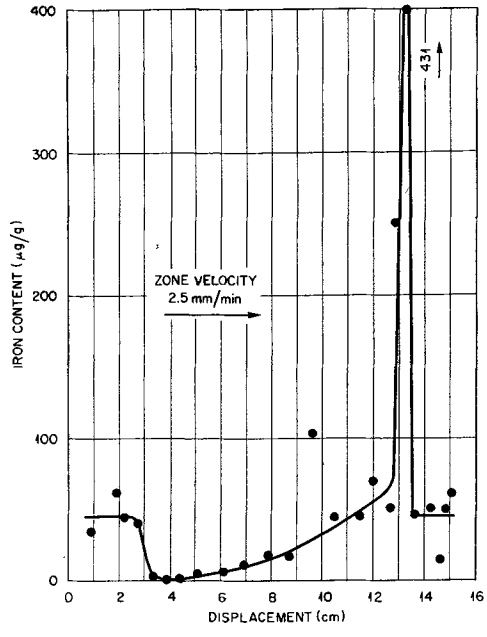

FIG. 7. Fe distribution after 6 passes of the liquid zone

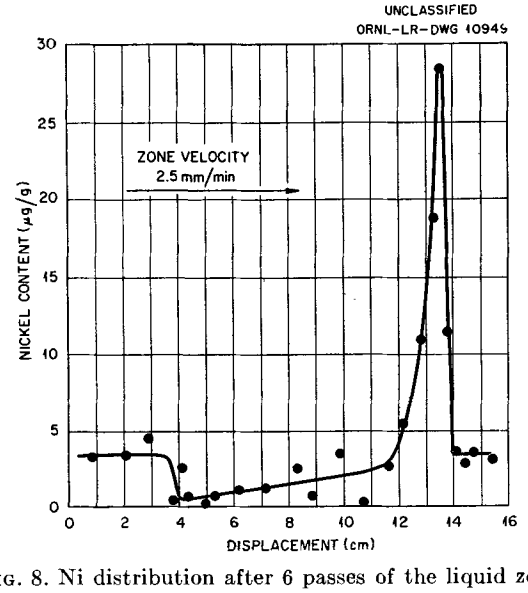

FIG. 8. Ni distribution after 6 passes of the liquid zone

were carried out in the same fashion as the Fe analyses, the scatter in the duplicate analyses for the lower regions of the curve lying between ±0.1 and ±0.5 ppm while at the peak the scatter was ±2.5 ppm. According to these curves, Ni is transported with an effective distribution coefficient of 0.3 to 0.4. This value of the distribution coefficient is only in qualitative agreement with the solubilities of Ni in liquid and solid Zr, but this is not surprising because of the uncertain nature of this portion of the Zr-Ni phase diagram. It is apparent that the redistribution of Ni in this particular lot of Zr would not interfere significantly with the correlation between the metallography and the Fe analyses because of its very low original concentration.

While the general shape of the experimental impurity distribution curves is in agreement with theory, the distribution curves show a rounded instead of a sharp change in concentration at the beginning of the pass. This may be due either to diffusion of the impurities from the unmelted portion or to slight changes in the starting point of the successive passes.

Summary

It has been shown that the Fe and Ni contents of iodide Zr can be reduced to less than 2 ppm by the technique of floating zone refining. The importance of these impurities on the temperature interval over which the α/β transformation takes place is indicated by the excellent quantitative agreement between the purification curves determined metallographically, assuming Fe is the major impurity, and the analytical Fe distribution curves. The purified metal has a transition range no greater than 865°–873°C. This is in good agreement with other experiments which indicate that the α/β transformation temperature in pure Zr is 870° ±3°C.

The absence of hardness changes during refining shows that oxygen, carbon, and nitrogen contamination were substantially prevented. These measurements, however, are not sufficiently sensitive to permit conclusions to be drawn about the effect of zone refining on these impurities. The theory of zone refining was extended to include the effects of back reflection from the solidification of the final zone. In this case restrictions imposed by the physical nature of the system must be considered. The agreement of the experimental and theoretical Fe distributions provides for this impurity an experimental verification of the assumptions of the theory. The purified material, although produced in relatively small amounts, will permit establishment of the effects of a number of solutes on the Zr α/β transformation to a much greater degree of accuracy than was possible heretofore.

Acknowledgment

The authors wish to acknowledge the assistance of G. W. Leddicotte, who established the analytical procedures and performed the activation analyses, and also the assistance of R. J. Bohnhoff in the performance of the zone refining experiments.

Manuscript received February 1, 1956. This paper was prepared for delivery before the Pittsburgh Meeting, October 9 to 13, 1955.

Any discussion of this paper will appear in a Discussion Section to be published in the June 1957 JOURNAL.

REFERENCES

1. P. H. KECK AND M. J. E. GOLAY, *Phys. Rev.*, **89**, 1297 (1953).
2. W. G. PFANN, *Trans. Am. Inst. Mining Met. Engrs.*, **194**, 747 (1952).
3. H. REISS, *ibid.*, **200**, 1053 (1954).
4. N. W. LORD, *ibid.*, **197**, 1531 (1953).
5. G. H. GULLIVER, "Metallic Alloys" (Appendix), Charles Griffin and Co., London (1922).
6. E. SCHEUER, *Z. Metallkunde*, **23**, 237 (1931).
7. A. HAYES AND J. CHIPMAN, *Trans. Am. Inst. Mining Met. Engrs.*, **135**, 85 (1939).
8. E. T. HAYES, A. H. ROBERSON, AND W. O'BRIEN, *Trans. Am. Soc. Metals*, **43**, 888 (1951).
9. P. H. KECK, M. GREEN, AND M. L. POLK, *J. Appl. Phys.*, **24**, 1479 (1953).
10. W. HEYWANG AND G. ZIEGLER, *Z. Naturforsch.*, **9a**, 561 (1954).
11. E. T. HAYES, A. H. ROBERSON, AND O. G. PAASCHE, *Trans. Am. Soc. Metals*, **45**, 893 (1953).

Technical Note

Rate-Determining Step for Anodic Oxidation of Tantalum

D. A. VERMILYEA

Research Laboratory, General Electric Company, Schenectady, New York

This note summarizes evidence, some previously published and some new, that the energy barriers which impede the flow of ionic current through anodic Ta_2O_5 films are not located at the interfaces of the film but within the film itself. There are two pieces of information which indicate that the metal-oxide interface does not play a controlling part. In the first place, there is no dependence of the field required to produce a given ionic current on the orientation of the metal crystal on which the film is formed. The evidence for this statement is as follows. A large-grained arc-melted button of Ta was anodized at constant current to about 300 v. No variation of the thickness (as measured by interference colors) could be detected either on different crystals or on differently oriented regions of the same crystal at any time during the period of growth. If a different field-current relationship existed for different crystal orientations, it would be expected that the current density would not be uniform, and hence that differences in thickness would be observed after anodization for a given period of time. The absence of such variations in thickness means that the orientation of the metal has no influence on the rate of growth at a given field.

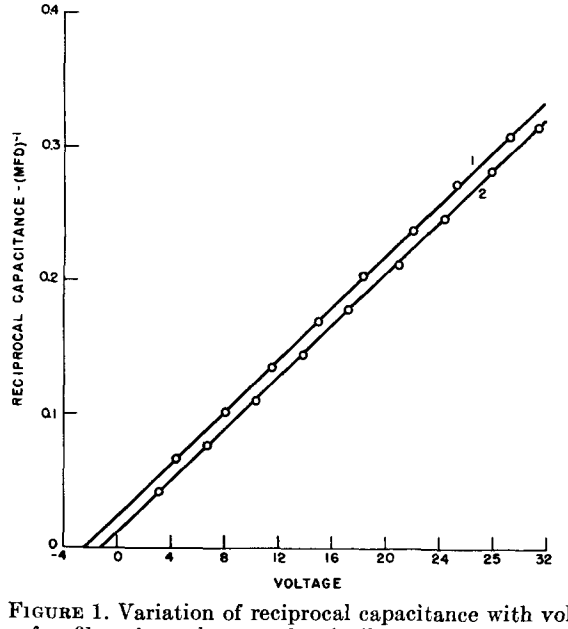

FIGURE 1. Variation of reciprocal capacitance with voltage for films formed on a chemically polished specimen (Curve 1) and on the same specimen after removing with HF the film left by chemical polishing (Curve 2).

The second indication that the metal-oxide interface is not involved in the rate-determining step is that the presence of a film of different composition left by the chemical polishing solution does not affect the current-field relationship. The presence of the polishing film is readily detected by measurements of the capacitance of the entire oxide film, for when the polishing film is present the plot of reciprocal capacitance vs. voltage is shifted toward higher reciprocal capacitances but remains parallel to the plot obtained by first removing the polishing film with HF, as shown in Fig. 1. That the polishing film remains at the metal-oxide interface is shown by the fact that if a film of 5000Å is formed and then all but about 100Å is dissolved in HF, reformation still results in a shifted plot of C^{-1} vs. V. If all of the film is removed, the C^{-1} vs. V plot coincides with one formed on a clean specimen containing no polishing film. Although the presence of the polishing film affects the value of capacitance at a given voltage, it does not affect either the slope of the C^{-1} vs. V plot or a plot of optical thickness vs. voltage. The field in the oxide film required for a given ionic current flow is therefore the same whether the polishing film is present or not. It would be expected that, if the interface played an important role in determining the passage of current, such changes as that of the orientation of the base metal or the interposition of another film would cause a change in the field-current relationship.

That the oxide-solution interface does not play a major role is shown by the fact that the presence of a different type of film between the Ta_2O_5 and the solution does not change the field-current relationship. A film of composition different from Ta_2O_5 is produced between the Ta_2O_5 and the solution by many solutions based on ethylene glycol rather than water, and yet the field required for a given current flow is the same whether such a film is present or not. (1).

It appears, therefore, that neither interface of the film controls the ionic current, and that the controlling step is within the film itself.

Manuscript received April 23, 1956.

Any discussion of this paper will appear in a Discussion Section to be published in the June 1957 JOURNAL.

REFERENCE

1. D. A. VERMILYEA, *This Journal*, **101**, 389 (1954).

Technical Feature

Use of Electric Furnaces in Ferroalloy Research

NORWOOD B. MELCHER

Division of Mineral Industries, U. S. Bureau of Mines, Pittsburgh, Pa.

The Bureau of Mines has a wide variety of electric furnaces for ferroalloy research; these have been installed at stations in areas that, insofar as possible, are contiguous to mining or metallurgical centers. The important facilities for this work are at Albany, Oreg.; Salt Lake City, Utah; Boulder City, Nev.; Rolla, Mo.; and Pittsburgh, Pa., although smaller auxiliary equipment, used to support nonsmelting research, is available at several other stations.

The Bureau's research work on ferroalloys is normally of a type in which private industry would not engage. Such work includes utilization of offgrade ores to produce ferroalloys for which these ores are suited, production of new ferroalloys, and consumption of ferroalloys. Frequently the Bureau of Mines conducts experiments in cooperation with private companies when its facilities can be utilized with advantage to both industry and Government. Such arrangements seem extremely desirable because they give the research maximum practical value.

This paper presents a brief review of the Bureau's equipment and typical examples of completed research projects that may be helpful in suggesting further cooperative work. Such agreements can be reached under a wide variety of arrangements. They can vary from simply having observers from either organization on hand during a research project, through utilization of Bureau facilities by private companies, to situations where both parties have engineers working together.

The Bureau of Mines in conducting research is, of course, expending public funds, and is obliged by law to publish reports disseminating information for public use as a product of its work. Anyone wishing to enter into cooperative work with the Bureau may make preliminary arrangements with the appropriate field station or the Washington office. However, the Bureau of Mines is not a consulting organization in the sense that it would conduct research for the exclusive benefit of any individual or company, nor is it the function of the Bureau, as an agency of Government, to compete with private consulting firms. The Bureau welcomes cooperative work of broad national interest and in certain instances will base cooperative projects on the availability of unique or specialized equipment that would prevent a private firm from undertaking the work.

In the Bureau's work, electric furnaces have played an important role in developing new methods that were later studied on a larger pilot-plant scale with other types of equipment. Processes are first tried in electric furnaces because other types of melting or smelting furnaces must be much larger and more expensive to operate and usually cannot be operated for short periods. For example, with an experimental blast furnace, a test requires a minimum of 1 week, during which the furnace consumes 1 car each of ore and coke; in contrast, an electric smelting furnace can be quite small and inexpensive, and a satisfactory test may be obtained with as little as several thousand pounds of raw materials. Similarly, a fuel-fired melting furnace, such as an open hearth, has a minimum efficient melting capacity of about 2 tons and after a shutdown requires several days of heating to attain the desired operating temperature. On the other hand, an electric furnace can be operated only a few hours at a time with small charges. Therefore, where conditions in other furnaces can be simulated in electric furnaces, they are very desirable for initial investigations.

Albany, Oreg.—The five ferroalloy furnaces at Albany, Oreg., range in size from a W Lectromelt, single-phase furnace of 50-kw power rating to a Bureau of Mines designed, 3-phase, round, open-top smelting furnace with a maximum power rating of 1000 kw. The furnaces at Albany are described in Table I.

All continuous electric-smelting-furnace research has been conducted in Bureau-designed furnaces. Most of the smelting research has been done in the ESA furnace, with test runs of not less than 80-hr duration. Both open-top furnaces have flat bottoms using standard brick shapes for the refractory lining and can be easily relined. The ESA furnace can be used either as an open-top or roofed furnace. Fig. 1 shows this furnace being used as a roofed furnace in smelting a siliceous nickel ore (2). Fig. 2 shows a view of the same furnace being used as an open-top furnace in smelting lateritic Philippine Ni ore to produce a low-carbon ferronickel product containing about 50% Ni.

The large ESB furnace has been used mostly in complete reduction tests where low voltage is required, and no slag is tapped from the furnace. Fig. 3 illustrates this operation when producing ferrochrome-silicon alloy. The power input to the furnace was approximately 420 kw. The ferrochrome-silicon product analyzed 47% Si, 17% Fe, 30.9% Cr, and 0.035% C and was produced at the rate of approximately 165 lb/hr (1).

The Pittsburgh Lectromelt ST furnace is used mostly in refining metals and alloys. One particularly interesting job conducted in this furnace was the melting and refining of approximately 52 tons of Co powder. Refined Co was poured into a 9-ft-deep water tank to form granules. Fig. 4 illustrates the appearance of the Co granules as they were removed from the tank. Co powder was produced

TABLE I. *Electric furnaces at the Bureau of Mines' Laboratories, Albany, Oreg.*

Bureau of Mines Designation	Type	Manufacturer	Power rating kw	Capacity (lb)	Electrodes	Shell, in.
ESA	3-phase, round open-top, smelting furnace	Bureau of Mines*	100 350		3 in. or 4 in. graphite	50 55 60 (ID) 60 (h.)
ESB	3-phase, round open-top, smelting furnace	Bureau of Mines*	500 1000		8 in. or 6 in. graphite	96 (ID) 78 (h.)
ST Lectromelt	Heroult, steel-melting arc furnace, 3-phase	Pittsburgh Lectromelt Furnace Corp.	500	2000	4 in. graphite	57 (ID) 45 (h.)
W Lectromelt	Single phase	Pittsburgh Lectromelt Furnace Corp.	50	50	1½ in. graphite	17 (ID) 12 (h.)
Swindell	Single-phase arc-melting furnace	Swindell Dressler	100	500	3 in. graphite	36 (ID) 38 (h.)

* Water-cooled electrode clamp-arm assemblies built by Pittsburgh Lectromelt Furnace Corp.

FIG. 1. Smelting siliceous Ni ore in roofed ESA furnace

FIG. 3. Production of low-carbon ferrochrome silicon in ESB furnace.

FIG. 2. Smelting nickeliferous Philippine laterite with bagasse in ESA furnace.

FIG. 4. Removing Co granules from quench tank

by the Calera Mining Co. at its plant in Garfield, Utah, and was experimentally refined and granulated under a cooperative agreement.

The single-phase Swindell Dressler furnace and size W Lectromelt furnace are used mostly for batch-smelting tests. These tests are valuable for determining metal recoveries and slag characteristics, electrical energy consumption, and electrode consumption of a continuous smelting operation. Fig. 5 shows slag and metal being poured from the Swindell Dressler furnace.

Salt Lake City, Utah.—A Lectromelt size U furnace is installed in the Salt Lake Experiment Station. The steel-melting capacity of this furnace is approximately 500 lb. Power is supplied to the furnace by a 200 kva, 3-phase Pennsylvania transformer. Four secondary voltages are

available at the switchboard. Electrode arms are provided with both manual and automatic control. The 2½ in. graphite electrodes are threaded on the ends to permit continuous feeding.

This furnace has been used to smelt nickel-bearing iron ores (4) from Cle Elum, Wash., Blewett Pass, Wash., and Riddle, Oreg., for Ni recovery as ferronickel. These tests not only involved partial reduction of the ores but also oxidation of the ferronickel to improve its grade and resmelting of the high-iron slags obtained. It was concluded from this work that partial reduction of the ores in an electric arc furnace would yield over 90% of the Ni in an alloy containing up to 30% Ni. These tests were preliminary to larger-scale tests at Albany. The Salt Lake Station also has 2 Lectromelt size W furnaces, which are used primarily in small-scale experiments to determine proper smelting methods to guide subsequent larger-scale tests in the size U furnace.

An experimental deep-shaft, single-phase furnace (Fig. 6) for continuous smelting was designed and constructed at Salt Lake City for smelting sintered Artillery Peak manganese flotation concentrates and sintered blends of concentrate and dithionate plant precipitate to produce standard ferromanganese. This furnace has been moved to Boulder City, Nev., where adequate transformer capacity is available and where a number of continuous smelting tests have been made on sintered concentrates assaying 44.4% Mn, 15.8% SiO_2, 2.5% Al_2O_3, 4.6% CaO, and 9.5% BaO, using coke as fuel and limestone as flux. No difficulties were encountered in smelting campaigns of 100 hr duration. Dust and volatilization losses were low, and recovery of 85% of the manganese was experienced in making standard 80% ferromanganese. Using a sintered blend of flotation concentrate and hydroxide precipitates assaying 50.8% Mn, 11.2% SiO_2, and 2.2% Al_2O_3, standard ferromanganese was made with a 90% recovery. The power input was about 2,000 amp at 22 v, and the power consumption ranged from 2.0 to 2.5 kwhr/lb of metal produced.

This furnace consists of a 29-in. square steel shell, 31 in. deep, and the single 3-in. electrode is hand-operated. The furnace is lined with 5 in. of insulation brick on the sides and bottom. Above the bottom is a 6-in. double layer of 3 × 6 in. graphite blocks. The smelting shaft is 12 in. square; the furnace is mounted on trunnions and can be tilted for tapping slag and metal. The Salt Lake Station also has a 17- and 30-lb Ajax-Northrup, high-frequency induction melting furnace which has been used for melting ferrous and nonferrous metals and alloys, making synthetic-slag composition studies, and other miscellaneous purposes.

Boulder City, Nev.—In addition to the small single-phase furnace described, the Boulder City Station also has a 3-phase, 500-kw furnace with a 3 × 5 ft hearth, using 6- or 8-in. graphite electrodes. The single-phase transformer is a Westinghouse 396-kva transformer with secondary taps for 18, 22, 26, 32, 38, 46, 55, and 66 v and a current capacity of 6,000 amp on all taps. The 3-phase transformer is a 658 kva Pennsylvania transformer with secondary voltages available at full power from 57.5 v to 330 v and voltages from 34.5 to 57 available at 5590 amp.

FIG. 5. Pouring test products from Swindell Dressler furnace.

FIG. 6. Deep-shaft, single-phase electric furnace designed and constructed by the Bureau of Mines, used in studies on production of ferromanganese from domestic Mn ores.

Current work at the Boulder City Station concerns the production of standard ferromanganese from offgrade domestic ores and concentrate; induction and crucible resistance furnaces are used in some of the work on abrasives and hard materials. These furnaces have been used for smelting offgrade chrome ores and concentrates, matte smelting of Chamberlain manganese nodules, electric smelting of Bunkerville Cu-Ni concentrates to produce matte for subsequent refining, and in numerous problems in connection with other work being done at the station, for instance, the production of a rutile-titanium carbide sinter from rutile concentrates for chlorinator feed. In cooperation with private industry, the furnaces have been used in investigations of the smelting of ilmenite to produce a titanium slag and a usable iron product, and the

FIG. 7. With this vacuum melting induction furnace installation, 60-lb heats can be melted and cast at pressures below 10 μ. Mn-Cu alloys are degassed at these low pressures and then melted and cast under a positive pressure of He to minimize Mn vaporization.

smelting of a Zn-Pb-Mn ore for recovery of Zn and Pb as fume and the Mn as spiegeleisen.

Rolla, Mo.—The electric furnace facilities at the Rolla station are particularly adapted to basic research in extractive and physical metallurgy of ferroalloy metals, and research has included work on Cb, Co, Ni, Mn, and Ti.

Induction furnaces and arc furnaces (direct and indirect) with capacities up to 300 lb of iron, and smaller nonmetallic elemented furnaces, are available for melting and smelting-refining investigations. Vacuum melting furnaces and wire-wound heat-treating furnaces also supplement its hot- and cold-working facilities, which include casting, forging, rolling, swaging, drawing, and extrusion equipment.

Rolla also has one type-V laboratory Lectromelt arc furnace which has been used in recent years on two principal projects: first, the production of titanium sulfide by matte smelting with coke, rutile, and pyrite, and second, for tuyère and lance blowing of Pb, Cu, Zn, Fe, Co, and Ni matte to fume off the Pb and Zn while oxidizing Fe into a slag and retaining the Cu, Ni, and most of the Co in an upgraded matte.

Recently, this type-V furnace was prepared for smelting experiments on the low-grade iron ores of East Texas. Fig. 7 shows one phase of the research work at the Rolla laboratories.

Pittsburgh, Pa.—The Bureau's Pyrometallurgical Laboratory at Pittsburgh is concerned mainly with the use of new or substandard raw materials by the steel industry and the improvement of processes for manufacturing steel and ferroalloys.

The Pittsburgh staff has used extensively an Arsem-type furnace with a carbon spiral heating element of 2½ in. ID. High-quality graphite tubes, when cut into the form of a spiral, have considerable flexibility, and little difficulty has been experienced with breakage. A Mo-wound furnace has been employed for similar work. These furnaces have the advantage that dense crucibles which resist slag attack can be used to retain the melts with virtually no breakage due to thermal shock. This is a serious problem with induction heating.

In such equilibrium tests with resistance heated furnaces, the weight of the melt usually ranges from 50 to 300 g. When larger melts up to 15 lb are desired, a 20-kw high-frequency mercury gap-type Ajax furnace is used. A large, high-frequency, vacuum-tube oscillator is also available for making melts of this size.

A 500-lb, 3-phase arc furnace has been employed for many unusual applications. Power is supplied to this furnace from two 200-kw single-phase transformers connected in open delta. Each has four secondary windings, with knife switches arranged to provide voltages of 50, 100, 150, and 200. The open delta connection limits the power to about 325 kw, but owing to the secondary switching, full power is realized at 50, 100, and 200 v. The primaries are connected to induction regulators so that a continuous variation in voltage can be obtained from 25 to 270 v. External reactances are used, one of which is larger than the others and of such value that approximately balanced 3-phase voltages and currents are secured over a wide range. The furnace is run at power inputs between 125 and 200 kw.

This arc furnace has often been used as a converter. For example, high-phosphorus spiegeleisen was melted in this furnace and the Mn oxidized from the metal by blowing air through a lance consisting of a graphite tube, an iron pipe, or a water-cooled copper tube. A special method of blowing spiegeleisen to obtain a high-Mn slag, low in Fe and P, was developed by use of this furnace. Melts of 200–300 lb could be blown readily and required the services of only 2 or 3 men for a few hours to obtain valuable data.

The furnace shell can be removed easily and a smelting unit of 3-ft shell diameter substituted for the tilting furnace. This equipment was used in studying the smelting of manganiferous iron ores and open-hearth slags which were later run in the experimental blast furnace. Considerable preliminary information was gained on anticipated metal composition and the quantity of flux required to obtain slag of satisfactory fluidity. This small smelting furnace is normally operated with the standard arc-furnace roof as a cover, and is charged through a small door in the side of the shell. With this construction it is easy to melt the entire contents of a charge at the end of a test so a clean furnace will be available for the next test. Small tilting and smelting arc furnaces therefore played an important role in development of a process for recovering Mn from open-hearth slag, even though the process does not envision the use of arc furnaces.

The Bureau of Mines station at Redding, Calif., utilized extensively a size ST Lectromelt furnace of 2,000 lb holding capacity for an investigation of the effect of Mn and S on the hot-working properties of steel. The work of this station and the associated equipment have since been transferred to a new metallurgical laboratory at the Bureau of Mines station at Bruceton, Pa., near Pittsburgh.

A top-charge 5-ton Heroult arc furnace also installed at the Redding station was transferred to the new laboratory.

Acknowledgments

The author wishes to acknowledge the assistance of the following Bureau of Mines personnel who furnished data concerning the facilities of their respective laboratories: L. H. Banning, Northwest Electrodevelopment Experiment Station, Region I, Albany, Oreg.; R. S. Lang, Electrometallurgical Experiment Station, Region II, Boulder City, Nev.; J. Bruce Clemmer, Intermountain Experiment Station, Region III, Salt Lake City, Utah; R. G. Knickerbocker, Mississippi Valley Experiment Station, Region IV, Rolla, Mo.; and R. C. Buehl, Pyrometallurgical Laboratory, Region V, Pittsburgh, Pa.

Manuscript received April 15, 1955. This paper was prepared for delivery before the Cincinnati Meeting, May 1 to 5, 1955.

Any discussion of this paper will appear in a Discussion Section to be published in the June 1957 JOURNAL.

REFERENCES

1. L. H. BANNING, *This Journal*, **101**, 619 (1954).
2. H. CREMER, Bureau of Mines, R.I. 5021, January 1954.
3. R. T. C. RASMUSSEN, *J. Metals*, **4**, 1273 (1952).
4. S. F. RAVITZ, Bureau of Mines R. I. 4122, September 1947.

Technical Review

Latest Developments in Electric Pig Iron Smelting

K. SANDVOLD

Metallurgical Department, Engineering Division, Elektrokemisk A/S, Oslo, Norway

In April 1955, A/S Norsk Jernverk, the Norwegian Government's Iron and Steel Works, was put into operation at Mo i Rana, a small town in Northern Norway not far from the Arctic Circle. The basis for the steel production in Mo i Rana is at present three 20,000 kw electric pig iron furnaces of the Tysland-Hole type. These are the largest electric pig iron furnaces ever built and have about double the capacity of the largest furnaces previously in operation. The daily production of the Mo i Rana furnaces was planned for about 200 metric tons of pig iron per unit.

Previous Developments

Electric smelting of pig iron is well established in many countries and general interest in this process is increasing. The dominating furnace design is the Tysland-Hole type, a covered, low shaft furnace, originating from the cooperation established in Norway in 1922–23 between the Government, Christiania Spigerverk A/S, and Elektrokemisk A/S. The intention was to develop an electric pig iron furnace using coke as reducing agent, based on the newly developed Söderberg electrode. The furnace derives its name from the two Norwegian engineers, G. Tysland and I. Hole, who conducted the tests. The first successful commercial furnace was started up at Christiania Spigerverk, Oslo, in 1928.

The exploitation of the Tysland-Hole furnace was carried out by Elektrokemisk A/S; by January 1956 37 furnaces had been put into operation or are under erection in Norway, Sweden, Finland, Switzerland, Italy, Spain, Yugoslavia, India, Japan, and Peru. With the exception of the three new 20,000 kw furnaces in Norway, furnace loads range from about 5,000 to 10–11,000 kw; annual production capacity reaches 30–33,000 metric tons.

The success of the Tysland-Hole furnaces is due to several factors, the most important of which are the following.

The furnace possesses an extraordinary flexibility with regard to the most varied ore and fuel conditions. For example, iron ores with iron contents down to 30%, or with high contents of Al_2O_3 or TiO_2, are smelted regularly. With regard to the reducing agents, coke breeze and coke fines are normally used, but in several cases, charcoal, lignite, and anthracite have proved suitable reductants.

The electric power consumption of the furnace is low. Normally about 2,300–2,500 kwh/metric ton of pig iron (about 2,090–2,270 kwh/short ton) is required but, under favorable conditions, yearly averages of 2,000–2,100 kwh/metric ton (1,815–1,905 kwh/short ton) are experienced.

Electrode consumption is favorable. Figures of 12–17 kg/metric ton (24–34 lb/short ton), with an average of about 15 kg (30 lb), are obtained normally. Electrode breakages are rare.

The rigid, simple design allows reliable operation, and operating time factors of 95–99% are normal. The operation is smooth with a regular load curve, causing negligible variations in the external electric circuit. At the same time, the furnace load may be varied within wide limits, in general, below 50% of maximum load, without appreciably affecting operation figures. Composition of the pig iron can be varied within an extensive range, the silicon content, for instance, from about 0.2% up to 3–4% or more. Electric pig iron is known to be of excellent quality.

Development of the 20,000 kw Electric Pig Iron Furnace

Since the beginning of this century, plans have been in existence for the development of a modern iron and steel industry in Norway based on domestic raw materials. The country's old, traditional iron production based on charcoal smelters had an international reputation, but the industry declined a hundred years ago, unable to face competition from coke blast furnaces. Since Norway has no domestic coking coals suitable for the blast furnace process, cheap hydroelectric power was considered the natural basis for the solution of the problem.

Among the first attempts to smelt iron ores electrically was the production of foundry pig iron at Tinfos Jernverk from 1910–1922 in small single-phase furnaces. The electric furnace process, however, came to stay in 1928 with the first Tysland-Hole furnace at Christiania Spigerverk, which thereby became the first modern integrated iron and steel works in Norway. A substantial quantity of the country's increased requirements of miscellaneous steel products—today about half a million tons—had, nevertheless, to be provided by imports. After World War II the Government developed plans for erecting a new large integrated iron and steel plant in a district where hydroelectric power was available. In 1946 A/S Norsk Jernverk was formed, and started the planning and erection work at Mo i Rana, with government capital. The production was to be based on electric smelting of Norwegian iron ore concentrates, the limited quantities of coke required for the reduction to be imported.

The elaborate project included a sintering plant for ore, electric pig iron furnaces, Bessemer and electric steel plant, and rolling mills. In the initial stage, the works were scheduled to produce about 180,000 tons of rolled steel

per year with a proposed gradual increase up to 500,000 tons.

The most important question was the type and size of the electric pig iron furnaces to be adopted. For this purpose, close cooperation between A/S Norsk Jernverk and Elektrokemisk A/S was established. As the Tysland-Hole furnace had given excellent results, the new design was based on the same principles. The largest units previously installed were considered too small for the production at Mo i Rana, and a new and larger furnace had to be designed. The 10,000 kw furnaces previously installed in many plants by Elektrokemisk A/S were all designed for 50-cycle power. When planning the Mo i Rana plant, electric power of 25 cycles was expected to be delivered from an existing power station. This low frequency considerably reduced the problems of designing an increased furnace size and, taking advantage of this feature, a unit of 20,000 kw was chosen.

In the initial stage of erection the installation of three of these units was assumed. According to the original plan the second and the third erection stage would comprise a total of six, and then eight furnaces.

When preparation of plans was far advanced, a serious problem arose. The Government decided to reserve the available power of 25 cycles for other purposes and to erect a new hydroelectric power plant 40 km from the anticipated plant site. For civilian consumption, the frequency had to be 50 cycles. Used at the furnaces, this would give twice the reactance in the furnace system, and consequently a very low power factor. After thorough studies, whereby an installation including two different systems of generators and transmission lines was also considered (for 25- and 50-cycle power), A/S Norsk Jernverk decided to adhere to the 20,000 kw furnaces with the use of 50-cycle power by installing condenser batteries of sufficiently large capacity for correction of the external power factor.

Originally the equipment for power factor correction was supposed to be shunt-connected capacitors, since this seemed to be the cheapest and simplest solution. After further studies it was decided to connect static capacitors directly in series in the high-tension circuit of the furnace transformers. This arrangement was found preferable, as the tension over the capacitors will increase with the current, whereby the effect of the capacitors is automatically adjusted, and the character of the furnace system will be very similar to that of a 25-cycle system.

This was a radical solution and, for electric smelting furnaces of this size, it would be a new experience. Even after the most careful preparation by experts, such an arrangement undoubtedly involved a certain risk of unexpected complications and operating difficulties in the electric system and at the furnace. The experiment has in practical operation proved successful, and A/S Norsk Jernverk's management and experts deserve credit for their decision.

The condenser batteries with their safety devices, as well as electric equipment for the furnace regulation, are supplied by ASEA, Sweden.

FIG. 1. Electric pig iron plant and sintering department at A/S Norsk Jernverk.

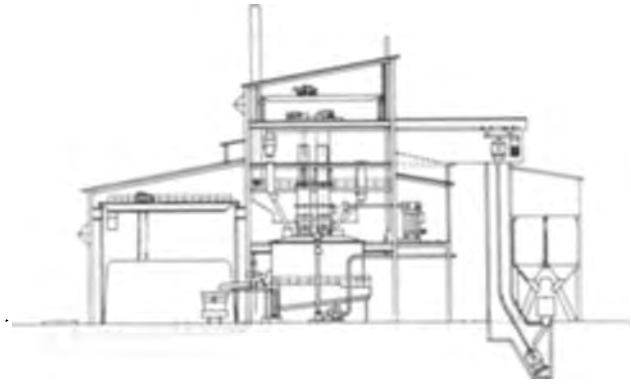

FIG. 2. Cross section of an electric pig iron plant with 33,000 kva Tysland-Hole furnaces.

LAYOUT AND FURNACE DESIGN

The iron and steel works' first stage of erection with a scheduled annual production of about 180,000 metric tons rolled steel comprises three electric pig iron furnaces, each with a planned annual production of 60,000 metric tons pig iron based on a furnace load of 18–20,000 kw. This stage is now completed.

Each furnace is equipped with three single-phase, 11,000 kva transformers, in total 33,000 kva/furnace. This is somewhat on the high side for an assumed furnace load of 20,000 kw, but it was decided not to limit maximum furnace capacity by the electrical system. The total yield of the capacitors is approximately 14,000 kvar per furnace. Primary voltage is 22,000 v; secondary voltage can be varied from 120 to 245 v.

The furnace shell is circular with three Söderberg electrodes arranged in triangular formation. The electrode diameter is 1,500 mm (approx. 59 in.). The furnace has a fixed roof of fire-bricks supported by water-cooled beams. Six charging shafts are placed on the roof, symmetrically arranged at a certain distance from the electrodes. During operation, the shafts are always filled with the mixed burden which is fed by gravity from chutes connected to the furnace bins suspended from the upper floor. From the small gaps between the chutes and the shafts, the downward flow of the charge can be watched closely, giving an excellent control of the operating conditions in the furnace interior.

The roof is equipped with a number of inspection holes and openings through which correction materials can be

FIG. 3. A/S Norsk Jernverk's 20,000 kw Tysland-Hole furnace No. 1.

FIG. 4. View from the furnace platform showing three completed 20,000 kw Tysland-Hole furnaces at A/S Norsk Jernverk.

added. Such additions can also be made at the top of the furnace shafts.

Gases are drawn from the furnace through two water-sprayed outlets in the cover. Suction is controlled automatically. The gas is cleaned in a wet scrubber system and is used for heating purposes in the steel shop, rolling mills, and other departments. The pressure inside the furnace is slightly positive, allowing a small amount of gas to escape through the shafts where it burns on the top. This ensures that no air is sucked into the furnace and, at the same time, the gas flames give a good indication of the operating conditions of the furnace.

The electrode holders with their clamps are suspended from electrical hoists placed under the roof of the furnace building. According to the consumption, the electrodes

FIG. 5. Charging floor showing top of furnace bins and telpher for charging raw materials.

have to be slipped occasionally a small distance downward through the holders. This is done at full load and without loosening the clamps. A brake system regulates electrode slipping. On the upper floor, welding of new electrode casings and filling of electrode paste is performed, without disturbing furnace operation.

An automatic weighing system is arranged at a lower level in the raw material department adjacent to the furnace building. Separate scales under each raw material bin automatically and simultaneously weigh out the different charge components, which afterwards are sandwiched on a rubber conveyor. Via an intermediate hopper and a telpher hoist, the charge is transported to the upper floor in the furnace building and distributed to the furnace bins. During full operation, one desk operator and two telpher drivers per shift with two telphers are able to weigh out and feed four furnaces with the required amount of raw materials of 1,800–2,000 metric tons per day, or 470–500 tons per furnace.

One control room per two furnaces contains instrument and control panels for each furnace, instruments for safety devices, and control desk and instruments for the gas cleaning system.

The furnace regulation is similar to that at other electric smelting furnaces. The load is controlled by regulation of the secondary voltage and by raising or lowering the electrodes. The secondary voltage can be changed in steps by a button-operated on-load tap changer. A constant furnace load is maintained by means of automatic electrode regulators, which govern the electrode hoists. The furnace load can also be controlled by hand operation.

Iron and slag are tapped through one single tap-hole which is opened by electric arcing. The tap-hole is closed by means of a clay gun. Slag is skimmed off in the launder, granulated with water, and pumped away through a rubber pipeline. Iron is tapped into 60-ton ladles on ladle

carriages, by which it is transported to the nearby pig casting machine or to the hot metal mixer in the steel shop.

Operation

The iron and steel works started operation in April 1955 when the hydroelectric power plant was ready to deliver energy. The works were erected in a district which was very little industrialized, most of the laborers being former fishermen and farmers.

The start of the pig iron plant was awaited with special interest. After a period for baking the electrodes, furnace No. 1 was first tapped in the middle of May 1955. The furnace load was gradually increased to 14–15,000 kw, where it was maintained for some time in order to watch the operation and to give the crew sufficient training. The next furnace was started in July.

During August and September, the load was slowly raised, and at the end of September it reached 20,000 kw. At the time of writing, a load of 19–20,000 kw has been applied for a period of about three months. During this time, furnace operation has been smooth and regular, and only minor adjustments have been made. Iron and slag are tapped regularly and at good temperatures. The burden feeds evenly, and the tendency to "bridge-building" and "hanging" in the smelting zone seems to be less than normal. Poking the furnaces has not been necessary. On the whole, furnace operation must be characterized as being at least as good as that of smaller types of well-operated Tysland-Hole furnaces, which is also indicated by the operating figures.

Tappings are performed at about 5-hr intervals, giving about 40 metric tons of pig iron and 12–14 tons of slag.

The iron ore used consists of high quality sintered magnetite concentrates which, before sintering, are mixed with crushed limestone. The iron content in the sintered product is 62–63%. Slag volume is low; a quantity of 0.26–0.30 tons of slag per ton iron has been maintained. The daily production from one furnace unit has reached 200 metric tons, in some periods even higher.

Consumption of electric power has averaged about 2,200 kwh per metric ton pig iron (2,000 kwh per short ton). Even if the raw material conditions are favorable, this low power consumption is remarkable and considerably lower than anticipated.

Silicon content of the pig iron has been maintained at 1.7–2.0%. Power consumption figures generally given from other plants often refer to 1% Si. Taking this into consideration, the power consumption at the Mo i Rana furnaces is even more favorable. An increase in the silicon content of 1% requires some 120–130 kwh.

Consumption of electrode paste also shows favorable figures. Compared with 15 kg/metric ton pig iron (30 lb/short ton), which is a normal average, the monthly average at A/S Norsk Jernverk has been maintained between 8 and 10 kg/metric ton (16–22 lb/short ton).

The electrical installation with the capacitors has been working to the best of expectations. The external power factor is 0.93–0.95.

Raw material consumption is about 1,500 kg of sintered ore per metric ton of pig iron, and 400–430 kg of coke. A large quantity of coke fines below 10 mm size is used. Consumption of fuel is dependent on the content of silicon in the pig iron.

On the basis of results obtained up to the present, it is expected that each furnace will give an annual output of 65–70,000 metric tons of pig iron (72–77,000 short tons). Whether it will be possible to increase the load and output is a matter which will have to be judged from experience in future operation.

The increasing problems of supplying sufficient quantities of metallurgical coke and the rising prices of this material are factors in favor of extended employment of the electric smelting process. Development of the process has not yet reached its limits. A further evolution toward larger units and more power-saving methods must be expected. With the 20,000 kw Tysland-Hole furnaces of A/S Norsk Jernverk at Mo i Rana, an important step in this direction has been taken.

Acknowledgment

The author wishes to acknowledge the kind permission of A/S Norsk Jernverk to refer to figures and data from the operation of their plant.

Manuscript received April 16, 1956.
Any discussion of this paper will appear in a Discussion Section to be published in the June 1957 Journal.

BIBLIOGRAPHY

H. Cowes, *Iron Age*, **150,** 41, 50 (1942).
R. Durrer, *J. Iron Steel Inst. (London)*, **156,** 257 (1947).
W. M. Bonham, *Can. Mining J.*, **69,** 55 (1948).
P. E. Cavanagh, *Trans. Can. Inst. Mining Met.*, **51,** 398 (1948).
H. Christiansen, Jr., *J. Iron Steel Inst. (London)*, **162,** 11 (1949).
H. U. Ross, *Can. Mining J.*, **70,** 66 (1949).
B. M. Müller, *Chemistry in Can.*, **2,** 24 (1950); Watkins Cyclopedia of the Steel Industry, 1951.
M. Sem, *J. four élec.*, **61,** 39, 77 (1952).
M. Sem, *Iron Age*, **170,** 95 (1952).
F. C. Collin, III° Congrés International D'Electrothermie, Paris, May 1953, Section 1-No. 109, 57; *Metal Bullet.*, The Metal Bulletin is published by: Metal Information Bureau Ltd., London, No. 3975, 11 (1955).
U. Styren, *Iron & Coal Trades Rev.*, **171,** 1007 (1955).

Discussion Section

ELECTROKINETIC POTENTIALS OF BULK METALS BY STREAMING CURRENT MEASUREMENTS

I. Method

Ray M. Hurd and Norman Hackerman
(pp. 594–597, Vol. 102)

D. A. VERMILYEA[1]: The authors draw the conclusion, based on data shown in Fig. 3 of their paper, that the current (I_1) flowing through the measuring circuit is much greater than the current (I_2) flowing through the capillary. This deduction is based on equation (VII) and the fact that the external resistance R can be varied over quite a range without significantly affecting the current flowing in the measuring circuit. According to equation (VII), however, the ratio I_1/I_2 (and, hence, I_1, the measured current) will remain constant provided only that R remains very much smaller than $(k_A + k_B)/a_{AB}$. Hence, the fact that I_1 does remain constant as R varies from 10^4 to 10^6 ohms merely means that $(k_A + k_B)/a_{AB} \gg 10^6$ ohms. Nothing can be deduced from these data regarding the value of the ratio I_1/I_2; it could easily be less than unity, and the same type of variation of I_1 with R would still be observed.

In order to be certain that I_1/I_2 is actually very large, it is necessary to know that the ratio $\left[\frac{k_C + k_D}{k_A + k_B}\right]\frac{a_{AB}}{a_{CD}}$ is very large. I would like to ask the authors whether they have other evidence which shows that this latter ratio is actually very large.

NORMAN HACKERMAN AND RAY M. HURD: The point regarding our interpretation of the current ratio I_1/I_2 is well taken, as it is certainly true that curves of the type shown in Fig. 3 may be obtained with almost any initial ratio. It was not made clear that in equation (VIII) of the paper the quantity $(k_C + k_D)/a_{CD}$ is much larger than the quantity $(k_A + k_B)/k_{AB}$. Since $k_A + k_B$ is approximately equal to $k_C + k_D$, the relative magnitude of the above ratios is determined by the relative values of a_{CD} and a_{AB}. The area a_{CD} was *made* much smaller than a_{AB} by at least a factor of 10^3 to 10^4, so $(k_C + k_D)/a_{CD} \gg (k_A + k_B)/a_{AB}$. From this point there follows:

If, initially, (*a*) $R \ll (k_A + k_B)/a_{AB}$, it has essentially no influence on I_1/I_2, but I_1/I_2 must be greater than 10^3; (*b*) R is approximately equal to $(k_A + k_B)/a_{AB}$, I_1/I_2 is about 10^3, and a decrease in I_1 would be noted where R is increased about two orders of magnitude; (*c*) $R \gg (k_A + k_B)/a_{AB}$, the ratio of I_1/I_2 may have any value but it would be impossible to obtain curves like those in Fig. 3.

It is virtually certain that condition (*b*) obtains when R is initially 10^4 ohms, as it was in this work. We appreciate Dr. Vermilyea's interest and the opportunity thus afforded to make this important point clear.

This Discussion Section includes discussion of papers appearing in the JOURNAL of The Electrochemical Society, **102,** No. 10 and 11 (October and November 1955), and **103,** No. 1–6 (January–June 1956). Discussion not available for this issue will appear in the Discussion Section of the June 1957 JOURNAL.

[1] Metallurgy and Ceramics Research Dept., General Electric Co., Schenectady, N. Y.

SURFACE CONTAMINATION OF COPPER BY PHOSPHATE ION DURING ELECTROPOLISHING—USE OF P^{32}

N. H. Simpson and Norman Hackerman
(pp. 660–661, Vol. 102)

P. A. JACQUET[2]: I am rather surprised that the authors did not mention any of the papers in which I have since 1935 described in detail the electropolishing technique of copper in orthophosphoric acid.[3]

I do not agree with the need of first dissolving a certain amount of metal to obtain correct polishing. This is altogether unnecessary. A new solution gives as good results as an old one, provided that the requested operation conditions are satisfied (density of the PO_4H_3 solution: 1.34 to 1.44; electrical circuit with potentiometer resistance, horizontal electrodes, voltage: 1.80 v).

In 1950, Dr. M. Jean and I published two papers concerning the quantitative estimation of phosphorous compounds retained on copper, zinc, or magnesium surfaces electropolished in aqueous or alcoholic PO_4H_3 solutions.[4] The method is sufficiently sensitive ($\geqslant 5 \times 10^{-8}$ g/cm^2) to allow determination of the most favorable washing conditions to reduce to the minimum the quantity of superficial impurity containing the phosphorus.

It is regrettable that the authors did not mention this work performed without the help of radioactive phosphorus.

N. H. SIMPSON AND NORMAN HACKERMAN: We thought that Dr. Jacquet's influence in this general field was so well known that it was not necessary to refer in this short note to the long list of papers he has to his credit. He is entirely correct, however, in stating that reference should have been made to the paper cited in footnote 4, and we appreciate having the opportunity to correct this oversight.

THEORETICAL ELECTROMOTIVE FORCES FOR CELLS CONTAINING A SINGLE SOLID OR MOLTEN CHLORIDE ELECTROLYTE

Walter J. Hamer, Marjorie S. Malmberg, and Bernard Rubin (pp. 8–16, Vol. 103)

PAUL DROSSBACH[5]: The authors discuss the difference between the thermodynamic and experimental values of the emf of the cell $Pb/PbCl_2/Cl_2$.

New Russian measurements from Lantratov and Alaby-

[2] 75, Rue Jeanne-D'Arc, Saint-Mandé (Seine), France.

[3] P. A. JACQUET, *Nature*, **195,** 1076 (1935); *Trans. Electrochem. Soc.*, **69,** 629 (1936); *Rev. mét.*, **37,** 210, 244 (1940); *ibid.*, **42,** 133 (1945).

[4] P. A. JACQUET AND M. JEAN, *Compt. rend.*, **230,** 1862 (1950); *Rev. mét.*, **48,** 537 (1951).

[5] Nibelungenstrasse 50, München 19, Germany.

tev[6] are also available that provide the following comparisons:

Temp, °C	500	600	700	800
Thermodynamic value	1.271	1.215	1.162	1.112
Lantratov	1.275	1.221	1.168	1.115

The present existing deviations may well be within the tolerance of the thermodynamic values. Deviations of considerable magnitude between thermodynamic and direct emf values of other cells lie mostly outside the error of measurement. We have made complete investigations of the behavior of the chlorine electrode in molten chlorides wherein the porosity of the carbon anode was varied from 20% to 3%. In addition, common carbon of technical quality, spectrum clean carbon, and atomic graphite were studied for anodic material. In accordance with my measurements of approximately 20 years ago, an overvoltage of chlorine was determined in the electrolysis of molten (fused) salts. In addition, there exist impedance measurements that point to a slow heterogeneous reaction upon the evolution of the chlorine (probably $Cl + Cl = Cl_2$).

If the emf of the cells is measured when a capsulated carbon electrode is used as a chlorine electrode by washing it only with chlorine, then the measured emf values are mostly too low. However, if one electrolyzes for only a few minutes with, for example, 1 amp, then one obtains very constant values of the emf, always, of course, by further introduction of Cl_2 into the anodic chamber, which are somewhat higher than if one proceeds without this current impulse. Evidently, by only washing the electrode with chlorine one does not obtain anywhere near sufficient saturation of the electrode, as is obtained by a brief electrolization. The various kinds of carbon behave in a manner so that, for example, with spectrum-clean carbon as well as with carbon of 3% porosity, one obtains constant values considerably faster. The overvoltage of chlorine is higher with carbon of higher porosity than with lower porosity. The same result also was determined in aqueous solutions during the evolution of hydrogen or oxygen or chlorine on carbon electrodes.

On the basis of our experiments we feel that we can state that one should not make cell measurements in molten (fused) salts (but also in aqueous solutions) without a thorough study of the kinetics of the electrode processes. In thermodynamics one should never overlook the fact that cells, which on charging show an overvoltage, with current drain (as well as with cell measurements in presumed equilibrium), must give values that lie under the equilibrium values.

W. J. Hamer: It is gratifying that the recent experimental work of Lantratov and Alabytev on the cell $Pb/PbCl_2/Cl_2$ agrees so well with the theoretical thermodynamic values given in our paper. The Russian literature is so difficult to keep up with, and I regret the oversight. Mr. Drossbach's remarks on deviations that might be expected from the theoretical values are concordant with those we mentioned. I believe his remarks on the behavior of carbon electrodes, especially prior to the passage of current, are novel and interesting.

[6] M. F. Lantratov and A. F. Alabytev, *J. Appl. Chem. (U.S.S.R.)*, **26**, 353 (1953).

REACTIONS OF REFRACTORY SILICIDES WITH CARBON AND NITROGEN

Leo Brewer and Oscar Krikorian (pp. 38–51, Vol. 103)

Leo Brewer and Oscar Krikorian: Since publication of our data, new calorimetric and vapor pressure data have become available. Robins and Jenkins[7] have taken advantage of the rapid rate of reaction of metals with silicon to determine the heats of formation of a number of silicides. They initiated each reaction by a thermite charge which evolved a known amount of heat. Thus the difference between the calorimetrically determined heat evolution and the heat due to the thermite charge gave them the heat of reaction. Searcy and Davis[8] have determined the vapor pressures of silicon over pure silicon and over mixtures of metal silicide phases.[9]

The heats of formation of the silicides listed by Robins and Jenkins fall in or close to the ranges given by us except for the zirconium silicides. The excess of silicon observed in the final samples of Robins and Jenkins indicates that their zirconium silicide heats should be somewhat more negative due to incomplete reaction. On the other hand, the zirconium silicide heats given by us are much too negative due to a misinterpretation of our results for the Zr-O-Si phase diagram. From the observation that silicon reacted with ZrO to form $ZrSi_2$, we concluded that silicon and ZrO_2 could not coexist and thus we drew joins between $ZrSi_2$ and SiO_2. However, calculation of the SiO partial pressure under our conditions shows that a partial pressure of over 10^{-3} atm SiO can be expected. This is large enough to cause loss of SiO even with an inert atmosphere blanket. Thus the reaction observed between ZrO_2 and Si must be $\frac{1}{2}ZrO_2(s) + 2Si(l) = SiO(g) + \frac{1}{2}ZrSi_2$, and Si and the ZrO_2 phase can remain in equilibrium with one another without reaction if loss of gas can be prevented. Thus the phase diagram given in Fig. 1 of our paper must be modified as indicated in Fig. 1 given here.

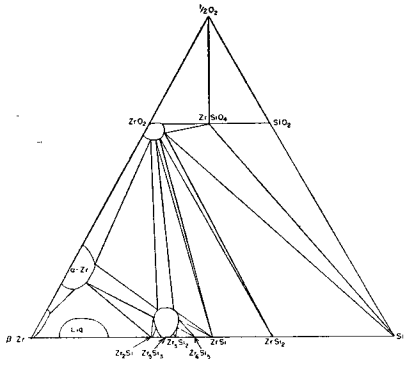

Fig. 1. Provisional diagram of the Zr-Si-O system at 1950°K and 1 atm.

By combination of our phase diagram data with the calorimetric determinations of Robins and Jenkins and the vapor pressure data of Searcy, it is possible to present

[7] D. A. Robins and I. Jenkins, *Acta Met.*, **3**, 598 (1955).

[8] A. W. Searcy and S. G. Davis, Private communication.

[9] A. W. Searcy and A. G. Tharp, Mo-Si System, Private communication; A. W. Searcy and C. E. Myers, Ta-Si System, Private communication.

TABLE I. ΔH°_{298} *of formation in kcal/gram atom* Si

$\frac{1}{2}$ $TiSi_2$ (orthorhombic $TiSi_2$ type)	−16.1	$\frac{1}{2}$ $TaSi_2$ (hex. $CrSi_2$ type)	−11.6 ± 3
TiSi	−31.0	$\frac{5}{3}$ Ta_5Si_3 (tet. Cr_5Si_3 type)	−26.7 ± 3
$\frac{1}{3}$ Ti_5Si_3 (hex. Mn_5Si_3 type)	−46.2	Ta_2Si (tet. $CuAl_2$ type)	−29.3 ± 3
$\frac{1}{2}$ $ZrSi_2$ (orthorhombic $ZrSi_2$ type)	−19	5 $TaSi_{0.2}$	−34.4 ± 3
ZrSi (orthorhombic FeB type)	−37	$\frac{1}{3}$ $Ta_{4.8}Si_3C_{0.5}$ (hex. Mn_5Si_3 type)	−25 to −38
$\frac{1}{5}$ Zr_6Si_5	−41	$\frac{1}{2}$ $MoSi_2$ (tet. $MoSi_2$ type)	−15 ± 5
$\frac{1}{2}$ Zr_3Si_2 (tet. U_3Si_2 type)	−46	$\frac{1}{3}$ Mo_5Si_3 (tet. Cr_5Si_3 type)	−20.5 ± 5
$\frac{1}{3}$ Zr_5Si_3 (hex. Mn_5Si_3 type)	−46	Mo_3Si (cubic Cr_3Si type)	−21 ± 5
Zr_2Si (tet. $CuAl_2$ type)	−50	$\frac{1}{3}$ Mo_4CSi_3 (hex. Mn_5Si_3 type)	−21 ± 5
Zr_4Si (several types)	−52	$\frac{1}{2}$ WSi_2 (tet. $MoSi_2$ type)	−11.2
$\frac{1}{2}$ $CeSi_2$ (tet. $\alpha ThSi_2$ type)	−16.6 to −34.4	$\frac{1}{3}$ W_5Si_3 (tet. Cr_5Si_3 type)	−11 to −20
$1/x$ $CeSi_x$	<-16.6	$\frac{1}{2}$ $ReSi_2$ (tet. $MoSi_2$ type)	−8.3
$\frac{1}{2}$ $NbSi_2$ (hex. $CrSi_2$ type)	−8.5 to −21	ReSi (FeSi type)	−10.2
$\frac{1}{3}$ Nb_5Si_3 (hex. Mn_5Si_3 type)	−21 ± 10	2 $ReSi_{0.5}$	−12.6
$\frac{1}{3}$ Nb_5Si_3 (tet. Cr_5Si_3 type)	−21 ± 10		

a rather complete table of heats of formation of the refractory silicides. These are presented in Table I; the x-ray structure type is indicated when known. The x-ray designations were obtained from Templeton and Dauben[10] and Parthé.[11] All known binary silicide phases of the Ti, Zr, Nb, Ta, Mo, W, and Re systems are listed except for $NbSi_{0.2}$, which is isomorphous with $TaSi_{0.2}$ but not with $Ta_{4.5}Si$ (hex. Ni_3Sn type), and for Nb_5Si_3 and Ta_5Si_3 of the tet. Cr_5B_3 type which should have heats close to those given for Nb_5Si_3 and Ta_5Si_3 of the tet. Cr_5Si_3 type.

These new values allow a more precise examination of the variation of bonding energy. In the discussion of bonding energy, the energy required to form 2 g atoms of atomic vapor is used as the bonding energy for all the compounds as well as the elements. Brewer and Krikorian[12] have plotted vs. position in the periodic table the bonding energies of the elements as well as those for many of the refractory compounds.

The similarities between the curves suggest that the bonding must be similar in the metals and in the refractory borides, silicides, carbides, and nitrides. A striking indication of the similarities of the bonds in the elemental phases and in the silicide phases is shown by the virtually constant values for the heats of formation of the MSi_2 phases ranging from the third to the seventh group of the periodic table. The ratio of the bonding energies of nitrides, carbides, and silicides to those of the corresponding metal also shows regularities that are useful for prediction of unknown heats.

Perhaps an even better way of predicting trends in the bonding energies is to compare bonding energies for compounds of a group in the periodic table. Thus the ratio of the bonding energies of MoN to WN is 1.090. The same ratio for the silicides Mo_5Si_3 and $WSi_{0.7}$ is 1.087. For the carbides MoC and WC the ratio is 1.091.

There are now enough data and sufficient indication of trends across the periodic table to allow rather good predictions of the heats of formation of refractory compounds.

D. A. Robins[13]: It is interesting to compare the estimated heats of formation data for the transition metal silicides, given in the discussed paper, with the experimentally determined values of Robins and Jenkins[14] (*see* Table I). Except for the zirconium silicides the experimental values do, in fact, lie within the wide limits estimated from their reactions with carbon and nitrogen, although the mean estimated value is usually higher than the experimental value. For the zirconium silicides the measured heats of formation lie outside the lower limits given in this paper. From plots of the bonding energy against atomic number, Brewer and Krikorian have estimated narrower limits for a number of silicides and again the experimental values all lie outside the lower limits given. Although estimated values can only be approximate, can the authors suggest why the methods they have employed should yield results nearly all of which are rather high?

TABLE I. *A comparison of estimated and experimental heats of formation data*

Compound	Heat of Formation (kcal/g atom Si $x(-1)$)		
	Brewer & Krikorian Table III	Brewer & Krikorian, from ref. (1) p. 50	
$\frac{1}{2}TiSi_2$	15.4 to 34.9	28 ± 5	16.1
TiSi	15.4 to 65.8	48 ± 10	31.0
$\frac{1}{3}Ti_5Si_3$	20 to 86.1	75 ± 20	46.2
% $ZrSi_2$	30.5 ± 5		17.9
ZrSi	58 ± 10		35.3
$\frac{1}{5}Zr_6Si_5$	66 ± 10		40.7
$\frac{1}{3}Zr_5Si_3$	72 ± 10		48.8
$\frac{1}{2}TaSi_2$	12.8 to 32.3	25 ± 8	13.9
$\frac{1}{5}Ta_5Si_3$	20 to 77.2	53 ± 20	25.3
$\frac{1}{2}MoSi_2$	5.8 to 15.5		15.7
$\frac{1}{2}WSi_2$	1.6 to 17.2	13 ± 5	11.2

It is a well-known characteristic of the transition metals that the bond strengths of the elements in a given group of the periodic table increases with increasing atomic number.[15] As pointed out by the authors, similarities between the transition metal and their silicides in this respect indicate that the types of bonding present in the two cases are similar; other properties of the silicides, such as their electrical conductivity, confirm that the bonding is essentially metallic in character. For the disilicides the metal-

[10] D. H. Templeton and C. Dauben, In preparation.

[11] E. Parthé, Private communication.

[12] L. Brewer and O. H. Krikorian, University of California Radiation Lab. Report UCRL-3352, March 1956; *see* also, O. H. Krikorian, University of California Radiation Lab. Report UCRL-2888, April 1955.

[13] Research Labs., General Electric Co., Ltd., Wembley, Middlesex, England.

[14] D. A. Robins and I. Jenkins, *Acta Met.*, **3**, 598 (1955).

[15] W. Hume-Rothery and B. R. Coles, *Advances in Physics*, **3**, 149 (1954).

metal bonding present in the uncombined metal is completely destroyed on combination with silicon, it being replaced by strong metal-silicon bonding.[14] In these compounds the metal-silicon bonding must, therefore, be metallic in character. It seems likely that, in the lower silicides also, the silicon atoms can best be described as sharing in the metallic bonding rather than simply contributing electrons to it; the presence of the silicon atoms alters the character of the spd hybrid bond orbitals of the metal atoms, although some electron transfer may take place in addition.[16]

It is undoubtedly true that the most stable silicides are to be found farther to the left in the periodic table than are the metals of highest bonding energy. Hume-Rothery, Irving, and Williams have shown that, when an atom of valency n has N neighbors, a maximum in the stabilization due to resonance might be expected when $n = N/2$ suggesting a bonding energy maximum for the Group VIa metals.[17] In spite of the different crystal structures of the Group IVa, Va, and VIa disilicides, in each case the metal atoms are surrounded by ten silicon atoms.[14] This lower coordination number coupled with the relationship for maximum resonance stabilization is in agreement with the most stable silicides occurring farther to the left in the periodic table than do the metals of highest bonding energy. As more crystallographic data become available for the lower silicides, it would be of interest to see if, for these compounds also, the coordination number of the metal atoms is lowered by combination with silicon.

Leo Brewer: I believe our note above answers Dr. Robins' question as to why the zirconium silicide heats were high. As the estimated heats for the other elements depended upon the zirconium silicide values, they were also high. The estimates based on the present values should be reliable.

In regard to the trend of stability in the periodic table, the correlation with coordination number does not seem to be a useful one. We have examined the data for silicides, carbides, borides, and nitrides and it is difficult to find such a correlation. For one thing, it is difficult to define a coordination number for the more complex structures, but even an attempt to use approximate coordination numbers does not seem fruitful. Dr. Robins has suggested that the lower silicides would have low coordination numbers. Crystallographic data are now available for many of the lower silicides and many of them show quite high coordination numbers for the metal atoms. For example, the Mo_3Si has the β-W structure for the metal atoms, which has a coordination number of 13.

ELECTROCHEMICAL CORROSION IN NEARLY NEUTRAL LIQUIDS

U. R. Evans (pp. 73–85, Vol. 103)

G. T. Paul[18]: I would like to inquire how well an electrochemical mechanism has been established in nonaqueous organic corrosive media. There are, of course, anhydrous media containing conductive components other than water, such as ammonia, sulfur dioxide, or ethylene diamine. (*Ed. Note*: Dr. Evans replied to this initial question that he was not aware that an electrochemical mechanism had been established at all in such media, and asked if the discussor had some indication to offer. The rest of this discussion was substantially Dr. Paul's reply.)

In a previous position I was concerned with a case of corrosion (aggravated by erosion) of austenitic stainless steel (Types 304 and 316) autoclave parts in such a medium. A chemical process exposed lining and heating coils to an anhydrous solution of methanol, dicyandiamide, and ammonia, containing suspended matter. Inspection showed "low" surfaces with the smooth appearance of actively corroding anodes. Some of these areas of coils were found, by caliper measurement, to have lost thickness. Some also collapsed and perforated. There were also "high" surfaces with a rougher appearance, apparently cathodes in more nearly original condition. The medium was known to be electrically conductive, and the probably electrochemical nature of this corrosion occurred to several corrosion engineers.

Detection of the passage of currents within an autoclave is not simple, and none was proven. The investigation was discontinued after wear plates had been installed to protect the liners, and a relaxation in the production schedule had made it possible to reduce the heat load on the coils, thus reducing their exposure temperature.

FUSION ELECTROLYSIS OF BISMUTH TRICHLORIDE

Paul M. Gruzensky (pp. 171–173, Vol. 103)

A. C. Loonam[19]: The advantage of high current density for the fused bath mentioned by Dr. F. A. Lowenheim is offset by the high energy consumption. I imagine that deposition from an aqueous bath would not require more than 0.5 kwhr/lb.

The evidence seems to be that metallic bismuth is in true solution in the molten trichloride. If I remember correctly, bismuth and its triiodide are miscible in all proportions in the liquid state and the system has a eutectic.

Paul M. Gruzensky: Subhalide formation and colloidal dispersion or "fog" have been postulated in the past as possible explanations for the solubility of metals in their molten halide salts. However, recent evidence apparently indicates that a true solution is formed. In this connection the outstanding work of D. Cubicciotti is noted.

Two of the primary objections to aqueous electrolytes are (*a*) bismuth compounds hydrolyze readily in aqueous solutions so that a high acidity is required, and (*b*) deposits are often dendritic in nature and must be scraped from the cathode periodically to prevent short-circuiting. We carried out a few experiments with deposition from an aqueous $BiCl_3$-HCl electrolyte and found the power requirements to be approximately 0.4 kwhr/lb. At the present price of bismuth, energy consumption would represent only a small fraction of total cost and, in cases of increased demand as could be visualized in a national emergency, a high current density process might offer many advantages.

[16] L. Pauling, *Proc. Roy. Soc.*, **196(a)**, 343 (1949).

[17] W. Hume-Rothery, H. M. Irving, and R. J. P. Williams, *Proc. Roy. Soc.*, **208(A)**, 431 (1951).

[18] Corrosion Engineering Section, International Nickel Co., Inc., New York 5, N. Y.

[19] 70 E. 45th St., New York 17, N. Y.

F. C. MATHERS[20]: There is no trouble with a crystallined cathode deposit from an aqueous electrolyte of bismuth perchlorate. So far as our work went, all other salts of bismuth gave very crystalline deposits. Another unexplained property of all perchlorates compared to other salts is that hydrolysis is much less, hence less free acid is required in the solution. It perhaps can be assumed that there are complexes in solutions of perchlorates.

PAUL M. GRUZENSKY: Several complexes have been reported in which bismuth has a coordination number of 6; however, little is known concerning the chemical nature of bismuth in perchlorate solutions. Perhaps higher reagent costs and the instability of perchlorates in general have aided in discouraging work with bismuth perchlorate electrolytes.

POLARIZATION IN AN ALUMINUM REDUCTION CELL

Warren E. Haupin (pp. 174–178, Vol. 103)

ROBERTO PIONTELLI AND GIULIO MONTANELLI[21]: The objection of the author to the use of corundum containers for reference electrodes seems to us rather excessive. Making use of corundum of the sintered compact type (available on the market), we[22] obtained tolerably good results.

In a bath having an initial content of 4% Al_2O_3 the rate of the attack on corundum, at 1000°C, is in the range of 0.06 to 0.17 g/cm² of exposed surface and per hour. The resulting change in composition of the bath is thus by no means severe, especially at the polarized electrode.

The local addition of Al_2O_3 at the polarized electrode causes a potential change of 15 to 20 mv, in absence of current, indicating that the bath actually is not saturated with Al_2O_3. Al_2O_3 is as important at the cathode as a bath constituent as at the anode where it supplies oxygen. On the other hand, aluminum fluoride appears to have its major effect at the cathode by increasing the activity of the Al ion in the bath. Both Al_2O_3 and aluminum fluoride cause the Al reference electrodes to become more noble, but the potential shift is smaller for Al_2O_3.

Concentration polarization accompanying the flow of current is increased by increasing the concentration of Al_2O_3. Therefore, the main effect of the solution of Al_2O_3 from the container of the reference electrode is to produce a small increase in the concentration overvoltage. It therefore appears that the use of a reference electrode, with the aim of giving conclusive evidence on the processes at a single electrode, is still a justified practice, especially for studying the cathode processes. This also holds true in spite of the fact that the problem of finding a very stable reference electrode for cryolite baths is still unsolved. Our last results with aluminated graphite are encouraging, however, while Russian authors[23] claim the advantages of oxygen-graphite reference electrode.

To compare, as Haupin attempts, our cathode overvoltage data with the one oscillographic record given by Rempel and Khodak,[24] a more accurate analysis seems necessary.

The data of Rempel and Khodak on cathode processes were reported at an anodic current density of 0.25 amp/cm². The cathodic current density was not specified, but must have been much less than this figure. The overvoltages given in our preliminary paper[25] correspond to an actual cathode current density of 1 amp/cm². With our present improved technique, we have investigated both anodic and cathodic polarization at 1 amp/cm² and lower current densities by use of the Al reference electrode. Although the data of Rempel and Khodak are not sufficiently complete for accurate interpretation, their data still do not seem to agree with our data. Their cathodic overvoltage seems to be constant. According to our results, the cathode overvoltage is almost entirely of the "concentration type," the "exchange" (or transfer) overvoltage being negligible in practice. The cathode overvoltage is thus governed by the initial value of the Al/Na ratio, by the c.d., and by the circumstances deciding the diffusion rate.

This overvoltage increases not only with c.d. but, at any given c.d., with time, as the Al/Na ratio at the electrode surface decreases till a steady state is eventually attained.

The influence of the ratio AlF_3/NaF, we found in our overvoltage measurements, has been confirmed by measuring (*a*) "static voltages" of some concentration cells, (*b*) "polarization voltages" in cells in which both the anode and the cathode were formed by Al.

This influence lies in the opposite direction to that found by Haupin in determining the whole cell polarization by his method. We are unable at present to advance any statement on this method.

Perhaps the influence of the ratio AlF_3/NaF at the carbon anode is opposite in direction and greater than that found by us at the Al cathode. It is in fact probable that the anode polarization predominates over cathode polarization. This is especially true in the Haupin cell and the cell of Rempel and Khodak because the dissymmetry of current distribution will increase considerably the anodic polarization in respect to the cathodic polarization. We hope to be able to give in the near future more conclusive evidence also on the overvoltage phenomena at the anode of Al cells.

MECHANISMS OF HYDROGEN PRODUCING REACTIONS ON PALLADIUM

II. Diffusion of Electrolytic Hydrogen through Palladium

Sigmund Schuldiner and James P. Hoare (pp. 178–181, Vol. 103)

GEORGE DUBPERNELL[26]: The authors are to be congratulated for their painstaking work in a field which can be very fruitful from a theoretical point of view. It was particularly good to see the effort which was expended to

[20] Indiana University, Bloomington, Ind.

[21] Lab. of Electrochemistry, Physical Chemistry, and Metallurgy, Polytechnic Institute of Milan, Milan, Italy.

[22] R. PIONTELLI AND G. MONTANELLI, *Alluminio*, **25**, 79 (1956).

[23] S. I. REMPEL, N. A. ANISHEVA, AND L. P. KHODAK, *Doklady Akad. Nauk S.S.S.R.*, **97**, 859 (1954).

[24] S. I. REMPEL AND L. P. KHODAK, *Zhur. Priklad. Khim.*, **26**, 931 (1953).

[25] R. PIONTELLI AND G. MONTANELLI, *Alluminio*, **22**, 672 (1953).

[26] Metal and Thermit Corp., Detroit 20, Mich.

check the diaphragms for holes or porosity. Attention is called to a simple method for doing this which was suggested some years ago.[27] Briefly, this consisted of reversing the polarity, and, if anode polarization diffused as well as cathode polarization, it seemed a safe assumption that a hole was present. Other tests confirmed the presence of such holes.

S. SCHULDINER AND J. P. HOARE: We thank Dr. Dubpernell for his comments. However, we must point out that the reversing of polarity test which he mentions would not conclusively prove the presence of holes if there was some diffusion of oxygen atoms or ions through the metal. Evidence that, under electrolytic polarization, oxygen can diffuse through a metal was given by Smith,[28] De Boer and Fast,[29] and Kalish and Burshtein.[30]

ELECTROCHEMICAL TECHNIQUES IN THE THERMODYNAMICS OF METALLIC SYSTEMS

R. A. Oriani (pp. 194–201, Vol. 103)

F. A. TRUMBORE[31]: In his review article, the author proposes a new application of the emf method to the determination of surface free energies. Another thermodynamic application of the emf technique is suggested by relatively recent work on the supercooling of metals. For example, Turnbull and Cech[32] found that small samples of certain metals could be supercooled hundreds of degrees below their melting points. Hence, an emf cell of the type

$$\text{M (supercooled liquid)} \mid \text{M}^{n+} \mid \text{M (solid)}$$

might well be stable and reversible for appreciable lengths of time. The free energy change associated with this cell would be the free energy of fusion, $\Delta \mathbf{F}_f$, of the metal M at the temperature of operation of the cell, i.e.,

$$\Delta \mathbf{F}_f = nE\mathfrak{F}$$

Assuming the heat of fusion to be independent of temperature, a good assumption near the melting point, T^{M}, the equation

$$\Delta H_f = nE\mathfrak{F}\frac{(T^{\text{M}})}{(T^{\text{M}} - T)}$$

is valid and the heat of fusion, ΔH_f, of the metal could be obtained from the emf of such a cell. If the temperature dependence of the emf is known accurately, the value of $\Delta C_p = C_p{}^L - C_p{}^S$ could also be determined along with the variation of ΔH_f with temperature. An attempt to determine the heat of fusion of germanium by this method is at present under way at this laboratory.

A further comment may be of interest to workers in the emf field. I have found that, by playing a jet of air on the quartz cells on removal from the furnace, the solidification of the fused electrolyte can be controlled in such a way that breakage of the cell, mentioned by the author, can be prevented in most cases.

[27] A. L. FERGUSON AND G. DUBPERNELL, *Trans. Electrochem. Soc.*, **64**, 221 (1933).

[28] D. P. SMITH, *Z. Physik*, **78**, 815 (1932).

[29] J. H. DE BOER AND J. D. FAST, *Rec. trav. chim.*, **59**, 161 (1940).

[30] T. V. KALISH AND R. K. BURSHTEIN, *Doklady Akad. Nauk. S.S.S.R.*, **88**, 863 (1953).

[31] Bell Telephone Labs., Inc., Murray Hill, N. J.

[32] D. TURNBULL AND R. E. CECH, *J. Appl. Phys.*, **21**, 804 (1950).

SODIUM-ALUMINUM EQUILIBRIA IN CRYOLITE-ALUMINA MELTS

Morris Feinleib and Bernard Porter (pp. 231–236, Vol. 103)

ROBERTO PIONTELLI[33]: The authors present as the "primary aluminum school" a group also including Belyaev and Pearson. As a matter of fact the point of view of Belyaev,[34] shared again by Pearson in his recent presentation of the matter,[35] is different in principle from ours,[36] in spite of the apparent coincidence of conclusions. Belyaev tries to obtain conclusive evidence on the mechanism of the electrode processes from measurements of decomposition voltages for the cell. The apparent uncertainty of the Belyaev data is now explicitly admitted by Pearson himself, but, in our opinion, the principle of this method is also untenable, and therefore we cannot accept the presentation Pearson gives of the problem.

Considering the kinetic aspects of the cathode processes and the evidence furnished by our experimental results, we think that the distinction we made between the different contributions, from which the measured overvoltage results, is essential.

These contributions are: (*a*) the "concentration overvoltage"; (*b*) the "exchange (or transfer) overvoltage"; (*c*) any ohmic contribution which may not have been taken into account in the correction of the systematic errors; (*d*) the contribution deriving from the instability of the reference electrode.

Taking into account the last two terms, it appears that, at 1000°C, with usual bath conditions, in the c.d. range from 0 to 1 amp/cm², both at the cathodic and the anodic side, the contribution (*b*) is negligible for the Al electrode.

Neither thermodynamic nor kinetic reasons seem to subsist therefore at present for not considering the primary aluminum separation as the preferred and actual cathode process. This conclusion is true, however, provided that, in the layer at the electrode surface, the Al/Na ratio is high enough for avoiding the inversion of the relative nobility of the two metals.

The decrease of the Al/Na ratio at the cathode surface results in a concentration overvoltage, corresponding, in practice, to the total true overvoltage. This concentration overvoltage increases with the current density.

At any given c.d. it increases moreover with time, tending to an eventual steady value which, at 1 amp/cm², under the conditions of our experiments, amounts to 0.20 v or more, according to the initial bath composition.

When the values of the Al/Na ratio, at the electrode

[33] Lab. of Electrochemistry, Physical Chemistry, and Metallurgy, Polytechnic Institute of Milan, Milan, Italy.

[34] A. I. BELYAEV, *Tsvetnaya Met.*, **13** (7), 87 (1938).

[35] T. G. PEARSON, "The Chemical Background of the Aluminum Industry," Royal Institute of Chemistry, London (1955).

[36] R. PIONTELLI, *Chimica e industria (Milan)*, **22**, 501 (1940); *J. Chim. Phys.*, **49**, 29 (1952); *Alluminio*, **22**, 731 (1953); R. PIONTELLI AND G. MONTANELLI, *ibid.*, **22**, 672 (1953); *ibid.*, **25**, 79 (1956).

surface, become low enough, the parasitic side reaction of sodium separation intervenes. In the absence of any kinetic hindrance opposing not only the aluminum ionic exchange but also the sodium one, the results would then be governed by the bath composition in quite the same manner as this composition decides the heterogeneous equilibrium in the absence of current.

We have at present no arguments for checking the hypothesis of the authors which admits an overvoltage governing the evolution of sodium on a liquid aluminum cathode. This overvoltage would constitute in practice a further defense against the sodium evolution, even as a parasitic process. The experimental evidence accumulated in the last years[37] shows the tendentious absence of any overvoltage of the exchange type at high enough temperatures in melted electrolytes.

However, since sodium is a gas at 1000°C and 1 atm, one could admit the existence of some kinetic hindrance in this case. The displacement reactions, in which sodium is evolved, are however so fast in practice that no conclusive evidence seems to exist at present in favor of this hypothesis.

Among the possible sources of current inefficiency in industrial aluminum cells, the authors seem to neglect the metallic fog, which here is considered by many industrial experts to be an important one.

MORRIS FEINLEIB AND BERNARD PORTER: The authors welcome Dr. Piontelli's comments and find little quarrel with most of them.

We have not neglected the so-called "metallic fog" or "metal fog." We are simply reluctant to use this term, since it merely covers up our ignorance of what really constitutes this fog. As we see it, the "metal fog" may consist of one or more of the following: (*A*) Monovalent aluminum compounds; (*B*) Finely dispersed aluminum present in the melt and arising (*a*) mechanically, (*b*) by disproportionation of monovalent aluminum species, (*c*) by sodium vapor reduction; (*C*) Sodium vapor bubbles.

All of these have been mentioned in our paper. We hope one day to be able to carry out experiments which will shed some light on the nature of the "metal fog" in aluminum cells.

ACCELERATION OF THE DISSOLUTION OF IRON IN SULFURIC ACID BY FERRIC IONS

Harry C. Gatos (pp. 286-391, Vol. 103)

A. C. MAKRIDES[38]: Dr. Gatos has made a worthwhile experimental contribution to the study of dissolution of steel in the presence of depolarizers. Interpretations of measurements of total dissolution rate usually assume that the contribution of the hydrogen evolution reaction is negligible. Dr. Gatos' determination of a material balance for the whole reaction helps, therefore, to clear up this point. Further, his discovery that at large concentrations of ferric ion (>0.5 M) the reaction rate decreases with concentration of ferric ion is interesting and a promising subject for further investigation. Unfortunately, some of the conclusions presented in the paper are open to question.

TABLE I

Ferric ion concentration (m/l)	k (cm/sec)	Ferric ion concentration (m/l)	k (cm/sec)
0.010	1.7×10^{-4}	0.270	1.8×10^{-4}
0.021	1.4	0.274	1.8
0.077	2.1	0.311	1.7
0.113	1.2	0.342	2.0
0.180	1.6	0.383	1.9
0.221	1.7	0.467	2.0

Note: The value $k = 0.03$ cm/sec given by the author for 0.416 and 0.042 m/l $FeCl_3$ does not agree with the values calculated from Table II and given above. Results show considerable scatter at small concentrations. This may be due to our assumption that in all cases the area was 19.4 cm².

While transport of matter under free convection, particularly with the added complication of stirring by evolved gas, is not entirely understood, it can be treated empirically and to a certain extent even in theory. Previous investigations of this phenomenon[39, 40] have been ignored by the author with the result that some of the presumed difficulties of diffusion-control theory to account for the author's observations do not in reality exist.

In Fig. 2 of his paper the author has drawn two straight lines through the experimental points and then in his discussion has attached significance to their difference in slope. This figure presents *total* weight loss as a function of concentration of ferric ions whereas the appropriate quantity is weight loss due to ferric ion reduction (or ferric ion consumption) which he does plot in Fig. 6. Diffusion-control theory certainly does not apply to hydrogen evolution which is known to proceed at a considerably slower rate than the rate of transport of hydrogen ions to the interface.

Even Fig. 6 is not entirely satisfactory as a basis of the author's discussion since it makes no allowance for solution depletion which is about 10% in his experiments. First order rate constants, calculated from the data given by the author in Table II of his paper, show a slight increase with concentration (*see* Table 1). However, the increase of k with concentration is much smaller than implied by the author in his discussion and, furthermore, is in at least qualitative accord with the predictions of diffusion-control theory. Under conditions of free convection k should increase with concentration as shown by Wagner.[39] Specifically, if it is assumed that the solution depletion is negligible, we have

$$\text{Consumption of } Fe^{+++} \text{ (moles/cm}^2\text{)} \propto (C_{Fe^{+++}})^{5/4} \quad \text{(I)}$$

[37] R. PIONTELLI, B. RIVOLTA, AND G. MONTANELLI, *Z. Elektrochem.*, **59**, 64 (1955); R. PIONTELLI AND G. MONTANELLI, *J. Chem. Phys.*, **22**, 1781 (1954); R. PIONTELLI AND G. STERNHEIM, *ibid.*, **23**, 1358. 1971 (1955); R. PIONTELLI, G. MONTANELLI, AND G. STERNHEIM, *Rev. Mét.*, In print (1956); *J. Chem. Phys.*, In print, **24** (1956); R. PIONTELLI, G. STERNHEIM, M. FRANCINI, AND R. MANOCHA, *Rend. ist. lombardo sci.*, **90**, 3 (1956).

[38] Dept. of Chemistry, University of Texas, Austin 12, Texas.

[39] C. WAGNER, *J. (and Trans.) Electrochem. Soc.*, **95**, 161 (1949).

[40] C. R. WILKE, M. EISENBERG, AND C. W. TOBIAS, *This Journal*, **100**, 513 (1953).

instead of the linear relation assumed by the author. The constant of proportionality depends on solution density and viscosity, on diffusion coefficient of ferric ion, and on the geometrical arrangement used. The Discussion on pp. 290 and 291 of the author's paper, and the presumed inability of diffusion-control theory to account for the results quoted, are therefore incorrect.

The arguments advanced by the author in support of his statement that "acceleration by Fe^{+++} is due to direct reduction of Fe^{+++}" are not convincing. There is no firm basis for assuming that indirect reduction of ferric ions by adsorbed hydrogen should proceed "with 100% efficiency while no hydrogen was being evolved." On the contrary, there is evidence suggesting that discharge of hydrogen ions to adsorbed atomic hydrogen is fast compared to the over-all rate of hydrogen evolution,[41] in which case one would expect that hydrogen evolution would not be completely suppressed except at high ferric ion concentrations.

The kinetic behavior before the establishment of a steady state is apparently quite complex. While it is perhaps not easily explainable in terms of indirect reduction, neither is it easily accounted for on the basis of direct reduction of ferric ions.

The effect of H_2SO_4 concentration on the over-all dissolution rate does not necessarily support the hypothesis that "direct Fe^{+++} reduction is suppressed by the hydrogen evolution reaction." The thesis developed by the author completely ignores the effect of changing ionic strength on diffusion coefficient of ferric ion, and of changes of solution viscosity and density. The expected change in these quantities should lead to a decrease of transport rate of ferric ions and may account for the observed decrease of ferric ion consumption. Fig. 4 actually shows that the weight loss corresponding to hydrogen evolution is a small fraction (less than five %) of the total weight loss and that the change of this quantity with increasing acid concentration is also a small fraction (ten %) of the change in total weight loss. Further, the relation demonstrated between these two quantities is of the most general kind. Indeed, the only secure inference to be drawn from Fig. 4, in the absence of additional information, is that the rate of hydrogen evolution increases as the rate of ferric ion reduction decreases. This observation is not surprising if ferric ion is indirectly reduced.

Finally, at the University of Texas we have studied the dissolution of mild steel in the presence of ferric ions using the rotating cylinder technique. We found that in 2*N* HCl and for ferric ion concentrations 0.01 to 0.3 m/l, the system exhibits behavior characteristic of diffusion-controlled reactions: the temperature coefficient gives 6000 cal for the energy of activation, and there is a very pronounced dependence on stirring speed up through the highest speeds used (60,000 cm/min). These results are in agreement with those obtained several years ago by Abramson and King[42] in dilute acid. In view of these results we must conclude that up to ferric ion concentrations of about 0.3 m/l the diffusion-control theory seems to be in agreement with experiment. We also note that, if this is the case, the postulate of "adsorption" of ferric ions is not a useful one. In this concentration range no meaningful distinction can be made between an ion reacting and an ion "adsorbed" at the interface, the act of "adsorption" being the same as the act of reaction.

HARRY C. GATOS: The comments of Dr. Makrides regarding Fig. 2, 4, and 6, although obviously valid in principle, have little or no bearing on the over-all thesis presented in the paper.

Dr. Makrides has overlooked the statement in the paper that diffusion control theory *can* account for total dissolution of iron within a certain range of Fe^{+++} (0.15–0.47 g ions/l). In view of experimental results, however, (Fig. 2) it is inconceivable that, under any treatment of these results, diffusion of Fe^{+++} ions controls dissolution of iron above 0.47 Fe^{+++} g ions/l. It is also inconceivable that diffusion control can account for the subject dissolution process at very low Fe^{+++} concentrations where hydrogen evolution contributes appreciably to the dissolution process.

No distinction, direct or implied, is made in the paper between "an ion reacting and an ion adsorbed." Clearly, adsorption sites on the metal are treated as reaction sites.

Regarding the results of Dr. Makrides in HCl solutions, the diffusion control theory could, of course, be in agreement with experiment up to 0.3 Fe^{+++} g ions/l if the hydrogen evolution did not interfere with the diffusion control process in these solutions at very low concentrations of Fe^{+++} ions.

PREPARATION OF PURE NICKEL BY ELECTROLYSIS OF A CHLORIDE SOLUTION

W. A. Wesley (pp. 296–300, Vol. 103)

JOHN MCCALLUM[43]: What is the boron content of your pure nickel?

W. A. WESLEY: The boron content was so low that the only statement the spectrographer could make was that it was less than 1 ppm.

HAROLD J. READ[44]: Was the density of the nickel measured on "as plated" or on wrought material? It might well be that working of the "as plated" nickel would increase the density through reduction of the slight porosity often encountered in electrodeposited metals.

W. A. WESLEY: The density of the nickel was calculated from lattice constant measurements by Jette and Foote[45] which were made on annealed cathode nickel. Less precise measurements were made here by gravimetric procedures. These showed that cold rolling the as-plated cathode nickel tended to decrease its density slightly instead of increasing it.

[41] *See*, for example, O. GATTY AND E. C. R. SPOONER, "The Electrode Potential Behaviour of Corroding Metals in Aqueous Solutions," Oxford University Press, Oxford (1938).

[42] M. B. ABRAMSON AND C. V. KING, *J. Am. Chem. Soc.*, **61**, 2290 (1939).

[43] Battelle Memorial Institute, Columbus 1, Ohio.

[44] Pennsylvania State University, University Park, Pa.

[45] E. R. JETTE AND F. J. FOOTE, *J. Chem. Phys.*, **3**, 605 (1935).

INHIBITION OF IRON DISSOLUTION IN ACID SOLUTIONS

Cecil V. King and Eric Rau (pp. 331-337, Vol. 103)

MORRIS EISENBERG[46]: It is commendable that the authors employed a well-defined hydrodynamic condition offered by rotating cylinders. This assures a fixed and reproducible mode of mass transfer to the metal.

However, one wonders why the authors did not make this a steady-state problem by use of acid flow or employment of large containers to assure constant bulk concentration of the acid. By failure to do so an additional variable, that of time, is introduced in all cases in which the corrosion rate is not negligible.

[46] 307 Diablo Court, Palo Alto, Calif.

C. V. KING: It is true, as Dr. Eisenberg says, that a method of maintaining constant acid concentration would be helpful in some of the experiments, for example, those with carbon monoxide. Also, in solutions without inhibitor, the weight loss in 5 min would be considerably higher at constant 0.02M acid than the values in Table I. However, the work did not include large weight losses as a quantitative feature. In measuring potentials it was desired to allow the *p*H to rise and the ferrous ion concentration to increase until precipitation occurred.

JUNE 1957 DISCUSSION SECTION

A Discussion Section, covering papers published in the July–December 1956 JOURNALS, is scheduled for publication in the June 1957 issue. Any discussion which did not reach the Editor in time for inclusion in the December 1956 Discussion Section will be included in the June 1957 issue. Those who plan to contribute remarks for this Discussion Section should submit their comments or questions in triplicate to the Managing Editor of the JOURNAL, 216 W. 102nd St., New York 25, N. Y., *not later than March 1, 1957*. All discussions will be forwarded to the author, or authors, for reply before being printed in the JOURNAL.